SOUNDINGS SECTION

CONTENTS—*Continued from preceding page*

CONTENTS—*Continued from preceding page*

CONTENTS—*Continued from preceding page*

SOUNDINGS

This front section of the *Journal* includes acoustical news, views, reviews, and general tutorial or selected research articles chosen for wide acoustical interest and written for broad acoustical readership.

ACOUSTICAL NEWS—USA

Elaine Moran
Acoustical Society of America, 500 Sunnyside Boulevard, Woodbury, New York 11797

Editor's Note: Deadline dates for news items and notices are 2 months prior to publication.

Announcement of the 1998 Election

In accordance with the provisions of the bylaws, the following Nominating Committee was appointed to prepare a slate for the election to take place on 10 June 1998:

Robert E. Apfel, *Chair* — Murray Strasberg
Ilene J. Busch-Vishniac — Sally G. Revoile
David I. Havelock — Diana F. McCammon

The bylaws of the Society require that the Executive Director publish in the *Journal* at least 90 days prior to the election date an announcement of the election and the Nominating Committee's nominations for the offices to be filled. Additional candidates for these offices may be provided by any Member or Fellow in good standing by letter received by the Executive Director not less than 60 days prior to the election date and the name of any eligible candidate so proposed by 20 Members or Fellows shall be entered on the ballot.

Biographical information about the candidates and statements of objectives of the candidates for President-Elect and Vice President-Elect will be mailed with the ballots.

CHARLES E. SCHMID
Executive Director

The Nominating Committee has submitted the following slate:

─────────── **FOR PRESIDENT-ELECT** ───────────

Patricia K. Kuhl
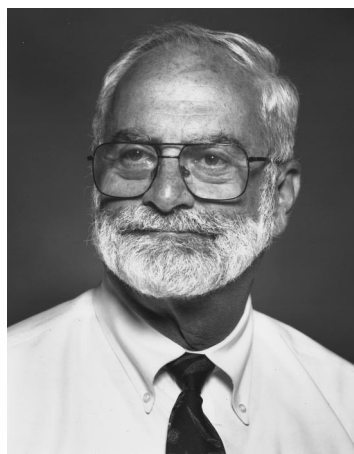
Richard Stern

─────────── **FOR VICE PRESIDENT-ELECT** ───────────

Sabih I. Hayek
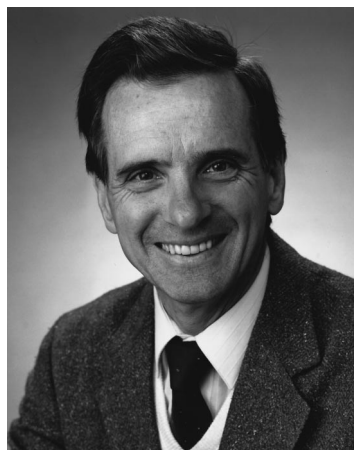
Mauro Pierucci
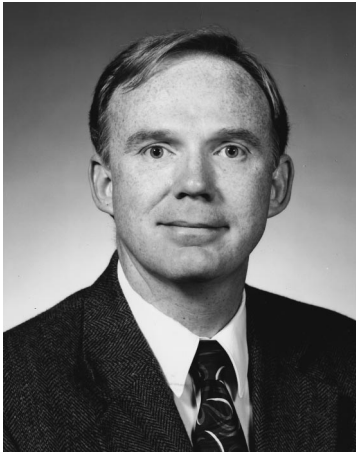
Anthony A. Atchley

Fredericka Bell-Berti

J. Stuart Bolton
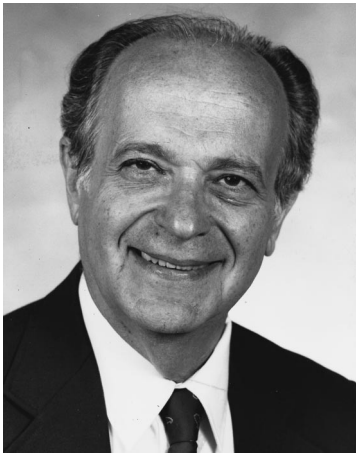
David Feit
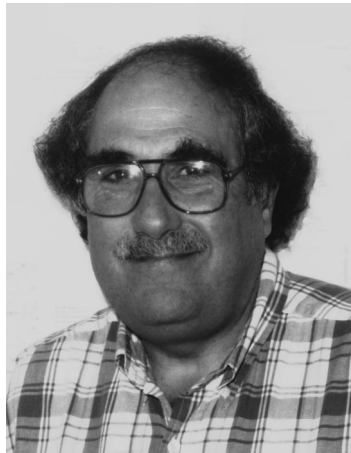
Ervin R. Hafter
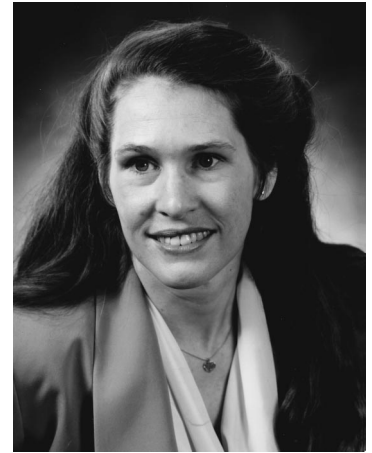
Dana S. Hougland

Michael R. Stinson becomes New Associate Editor of the *Journal*
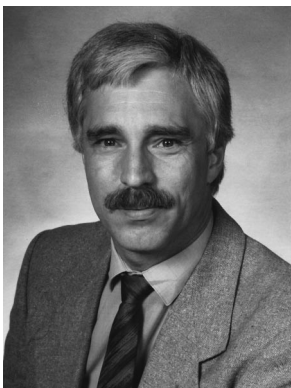
Michael R. Stinson

Gilles A. Daigle

In July 1997 Dr. Michael R. Stinson of the Acoustics and Signal Processing Group at the Institute for Microstructural Sciences, National Research Council, Ottawa, Canada, became a new Associate Editor of the *Journal* for papers in Noise, Its Effects and Control (PACS 43.50). At the invitation of the Editor-in-Chief Dr. Stinson succeeded Dr. Gilles A. Daigle of the same institution, who requested replacement after four years of faithful and effective service. The Editor-in-Chief is happy to express his deep appreciation to Dr. Daigle and to his institution for support services.

Michael Stinson received his B.S. in physics in 1971, and an M.Sc. in physics in 1973 from Simon Fraser University in British Columbia, Canada. He received a Ph.D. in physics in 1979 from Queen's University in Kingston, Ontario.

From 1979 to 1984 he was an Assistant Research Officer in the Physics Division, then Associate Officer, becoming Senior Research Officer in 1992. He is also an Adjunct Professor at University of Waterloo. He was elected a Fellow of ASA in 1990, and was Technical Program Chairman for the 1993 meeting of the Society in Ottawa. He is a member of the Technical Committee on Noise, and has also served on the Technical Committees on Physical Acoustics and on Psychological and Physiological Acoustics.

Stinson's principal research areas have been in modeling the acoustical behavior of the middle ear and ear canal, sound propagation in porous media, and study of meteorological factors affecting outdoor sound propaga-

tion. He has authored or co-authored 23 research publications, primarily in our *Journal.*

The Editor-in-Chief and his colleagues welcome Michael Stinson to membership on the Editorial Board.

DANIEL W. MARTIN
Editor-in-Chief

Position open

Acoustics Technologist: W. L. Gore & Associates, Inc., manufactures a diverse range of products—from GORE-TEX® fabric to printed circuit board materials, from Glide® dental floss to Elixir guitar strings. Our Music Products Team is seeking a hands-on technologist to develop and expand our understanding of the physics of sound and music.

Qualifications: Ph.D. in Physics, or another technical discipline if coupled with a very strong background in physics and acoustics; two years or more of experience in technology and/or process development; background in metallurgy desirable.

Qualified candidates should mail or fax their resume to: W. L. Gore & Associates, Inc., P.O. Box 9206, Newark, DE 19714-9206, Attn: 2729, Fax: 302/292-4156. (An Equal Opportunity Employer.)

USA Meetings Calendar

Listed below is a summary of meetings related to acoustics to be held in the U.S. in the near future. The month/year notation refers to the issue in which a complete meeting announcement appeared.

1998

9–13 Feb.	1998 Ocean Sciences Meeting, San Diego, CA [American Geophysical Union, 2000 Florida Ave., N.W., Washington, DC 20009, Tel.: 202-462-6900; Fax: 202-328-0566; WWW: http://www.agu.org].
19–21 Feb.	23rd Annual National Hearing Conservation Association Conference, Albuquerque, NM [NHCA, 611 E. Wells St., Milwaukee, WI 53202; Tel.: 414-276-6045; Fax: 414-276-3349; E-mail:nhca@globaldialog.com].
5–8 April	NOISE-CON 98, Ypsilanti, MI [Noise Control Foundation, P.O. Box 2469, Arlington Branch, Poughkeepsie, NY 12603; Tel.: 914-462-4006; Fax: 914-463-0201; E-mail: noisecon98@aol.com; WWW: users.aol.com/noisecon98/nc98_cfp.html].
4–7 June	7th Symposium on Cochlear Implants in Children, Iowa City, IA [Center for Conferences and Institutes, The University of Iowa, 249 Iowa Memorial Union, Iowa City, IA 52242-1317; Tel.: 800-551-9029; Fax: 319-335-3533]. Deadline for receipt of abstracts: 1 March.
20–26 June	135th meeting of the Acoustical Society of America/16th International Congress on Acoustics, Seattle, WA [ASA, 500 Sunnyside Blvd., Woodbury, NY 11797, Tel.: 516-576-2360; Fax: 516-576-2377; E-mail: asa@aip.org, WWW: http://asa.aip.org].
26 June–1 July	International Symposium on Musical Acoustics, ISMA 98, Leavenworth, WA [Maurits Hudig, Catgut Acoustical Society, 112 Essex Ave., Montclair, NJ 07042, Fax: 201-744-9197; E-mail: catgutas@msn.com, WWW: www.boystown.org/isma98].
7–12 July	Vienna and the Clarinet, Ohio State Univ., Columbus, OH [Keith Koons, Music Dept., Univ. of Central Florida, P.O. Box 161354, Orlando, FL 32816-1354, Tel.: 407-823-5116; E-mail: kkons@pegasus.cc.ucf.edu].
9–14 Aug.	International Acoustic Emission Conference, Hawaii, HI [Karyn S. Downs, Lockheed Martin Astronautics, P.O. Box 179, M.S. DC3005, Denver, CO 80201; Tel.: 303-977-1769; Fax: 303-971-7698; E-mail: karyn.s.downs.@lmco.com].
13–17 Sept.	American Academy of Ontolaryngology—Head and Neck Surgery, San Francisco, CA [American Academy of Otolaryngology—Head and Neck Surgery, One Prince St., Alexandria, VA 22314; Tel.: 703-836-4444; Fax: 703-683-5100].
12–16 Oct.	136th meeting of the Acoustical Society of America, Norfolk, VA [ASA, 500 Sunnyside Blvd., Woodbury, NY 11797, Tel.: 516-576-2360; Fax: 516-576-2377; E-mail: asa@aip.org, WWW: http://asa.aip.org].

1999

27–30 June	ASME Mechanics and Materials Conference, Blacksburg, VA [Mrs. Norma Guynn, Dept. of Engineering Science and Mechanics, Virginia Tech, Blacksburg, VA 24061-0219; Fax: 540-231-4574; E-mail: nguynn@vt.edu; WWW: http://www.esm.vt.edu/mmconf/]. Deadline for receipt of abstracts: 15 January 1999.

REPORTS OF RELATED MEETINGS

Fiftieth Anniversary Celebration of the Audio Engineering Society

The opening ceremony of the 103rd Convention of the Audio Engineering Society, held 26–29 September 1997 at the Jacob K. Javits Convention Center in New York City, was a special celebration of the fiftieth anniversary of AES. The first meeting had been held in March 1948 in the New York recording studios of RCA Victor by a committee of audio engineers with about 150 interested people attending. C. J. LeBel was the first president and Norman C. Pickering was the first secretary.

The opening ceremony events, planned by a team headed by AES pioneer Irv Joel, included a video documentary of the 70 years from Edison to the founding of AES, followed by a tour through ''The AES Years,'' which included the arrival of the vinyl LP record, stereophonic tape, compact cassettes, compact disc, and surround sound. Thirty ''living legends'' from those years stood for introduction and recognition including some past AES presidents and other key contributors to the world of audio engineering. A Distinguished Service Medal was presented to Donald Plunkett, in recognition of extraordinary service to AES since 1948, much of that time as Executive Director.

There were 16 sessions of technical papers on auditory modeling, microphones, loudspeakers, signal processing, multichannel sound, room acoustics simulation, binaural audio, sound reinforcement, audio perception, measurements, and electronic music synthesis. Some of the sessions began with invited tutorial papers intended to set the scene for more specific coverage, and to ensure that coverage was broad as well as deep.

Sixteen workshops on subjects of current audio interest were held, including one on Implications of the New DVD-Audio Format, and another on Internet Audio Server Setup and Operation. A full program of audio standards meetings occurred both before and during the convention.

A major feature of each AES Convention is the Exhibition. The Exhibition Guide listed approximately 330 exhibitors, many of them with audible demonstrations heard on headsets or in rooms designed and erected for the purpose. Many new audio products and services were introduced. Total attendance at the Convention and Exhibition was reported to be over 20 000 people, the largest in AES history.

DANIEL W. MARTIN

REVIEWS OF ACOUSTICAL PATENTS

Daniel W. Martin

7349 Clough Pike, Cincinnati, Ohio 45244

The purpose of these acoustical patent reviews is to provide enough information for a Journal reader to decide whether to seek more information from the patent itself. Any opinions expressed here are those of reviewers as individuals and are not legal opinions. Printed copies of United States Patents may be ordered at $3.00 each from the Commissioner of Patents and Trademarks, Washington, DC 20231.

Reviewers for this issue:

GEORGE L. AUGSPURGER, *Perception Incorporated, Box 39536, Los Angeles, California 90039*

SAMUEL F. LYBARGER, *101 Oakwood Road, McMurray, Pennsylvania 15317*

D. LLOYD RICE, *11222 Flatiron Drive, Lafayette, Colorado 80026*

CARL J. ROSENBERG, *Acentech Incorporated, 33 Moulton Street, Cambridge, Massachusetts 02138*

5,659,173

43.25.Yw CONVERTING ACOUSTIC ENERGY INTO USEFUL OTHER ENERGY FORMS

Seth J. Putterman *et al.*, assignors to The Regents of the University of California

19 August 1997 (Class 250/361); filed 23 February 1994

This patent describes means for sustaining sonoluminescence light emission, and for converting the acoustic energy into other energy forms. ''The initial stage of the energy focusing is effected by the nonlinear oscillations of a gas bubble trapped in the liquid. For sufficiently high drive pressures an imploding shock wave is launched into the gas by the collapsing bubble. The reflection of the shock from its focal point results in high temperatures and pressures. The sonoluminescence light emission can be sustained by sensing a characteristic of the emission and feeding back
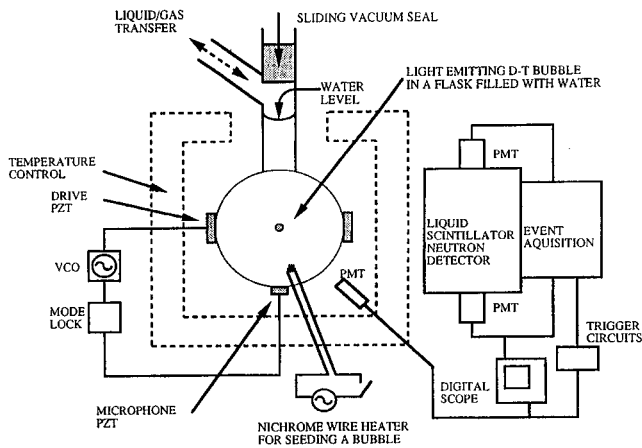
changes into the driving mechanism. The liquid is in a sealed container and the seeding of the gas bubble is effected by locally heating the liquid after sealing the container.'' The concept is broadened by showing that ''different energy forms than light can be obtained from the converted acoustic energy. When the gas contains deuterium and tritium there is the feasibility of the other energy form being fusion, namely including the generation of neutrons.'' The diagram shown here is a block diagram of the system for creating fusion energy.—DWM

5,616,826

43.35.Ud PHOTOACOUSTIC ANALYZER AND METHOD

Jean-Paul Pellaux *et al.*, assignors to Orbisphere Laboratories Neuchatel SA

1 April 1997 (Class 73/24.02); filed in European Patent Office 4 June 1994

This is a ''photoacoustic device for analysis of fluids. The device is made up of (A) a source of a pulsating beam of light, preferably of the chopper type, and (B) an enclosure, preferably an elongated structure having a generally cylindrical, e.g., essentially tubular shape; and containing and holding—in sonic insulation—at least one reference chamber and at least one measuring chamber in an essentially linear or serial arrangement in a
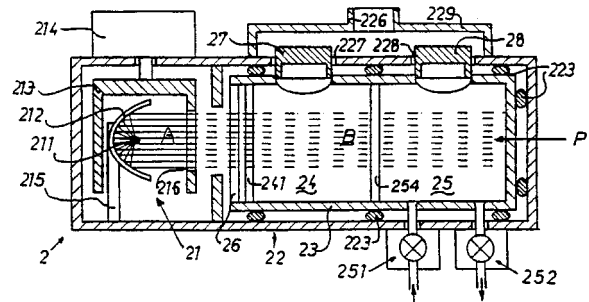
common cell within the enclosure, preferably in an essentially coaxial arrangement; the enclosure and the common cell provide a path P for the pulsating beam of light through the reference chamber and through the measuring chamber. For most purposes, it is preferred that the light beam pass first through the reference chamber and subsequently into the measuring chamber.''—DWM

5,650,572

43.35.Ze DEVICE FOR ULTRASONIC FLOW MEASUREMENT

Thomas Vontz, assignor to SiemensAktiengesellschaft

22 July 1997 (Class 73/861.28); filed in Germany 25 October 1993

This ultrasound flow measuring tube arranges the transmitter **USW1**, receiving transducer **USW2**, and reflectors **R1** and **R2** to reflect the ultrasound wave multiply off the inner wall of the tube along a spiral path, in
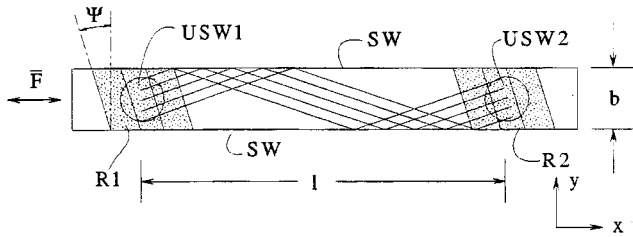
contrast to previous methods in which the ultrasound wave passes through the axis of the flow pattern, in order to avoid the turbulent flow at the center of the tube.—DWM

5,602,367

43.38.Ja MULTIPLE TUNED HIGH POWER BASS REFLEX SPEAKER SYSTEM

John D. Meyer, assignor to Meyer Sound Laboratories, Incorporated
11 February 1997 (Class 181/156); filed 19 December 1994

If you decide to build a dual-woofer box containing two vented chambers, each tuned to a different frequency, this patent appears to anticipate the project. In musical program material waveform crests occasionally synchronize, resulting in a peak-to-average ratio of 10 dB or more. Power amplifiers and loudspeakers must somehow cope with these momentary peaks. However, if the signal is divided into several bands of frequencies, it seems possible that relative peak levels in individual bands will be reduced. This forms the basis for the patent, even though it is a point of argument among audio engineers. By using three powered loudspeakers in three vented chambers to cover the range from about 30 to 150 Hz the system is said to produce high sound levels with, ''...minimum driver cone excursion and distortion.''—GLA

5,629,502

43.38.Ja SPEAKER APPARATUS

Yasuhide Nakano, assignor to Sony Corporation
13 May 1997 (Class 181/156); filed in Japan 2 March 1994

This series-type bandpass loudspeaker system has a passive radiator 18 coupling front and back chambers 3 and 4. Sound emerges from vent 6. What has thus far been described would seem to be anticipated by patents
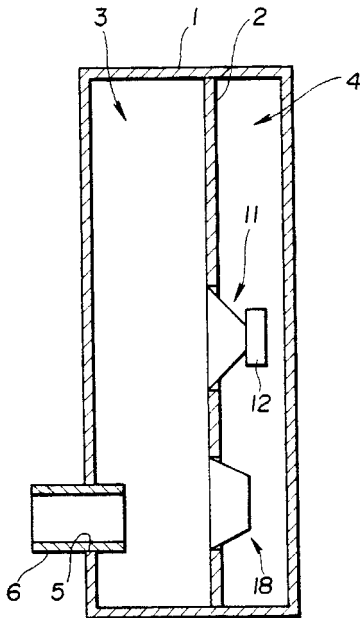
4,875,546 and 5,010,977, both of which are cited. The difference, however, is to locate passive radiator 18 so that it directly faces the exit vent. The patent document includes test results showing that this particular arrangement gives improved performance, believe it or not.—GLA

5,629,987

43.38.Ja LOUDSPEAKER SYSTEM WITH CLOSED HOUSING FOR IMPROVED BASS REPRODUCTION

Maximillian H. Hobelsberger, Wurenlingen, Switzerland
3 May 1997 (Class 381/96); filed in Switzerland 15 February 1992

The invertor's earlier active-isobaric loudspeaker enclosure has been improved by mounting its feedback pressure sensor 11 directly on cone 10
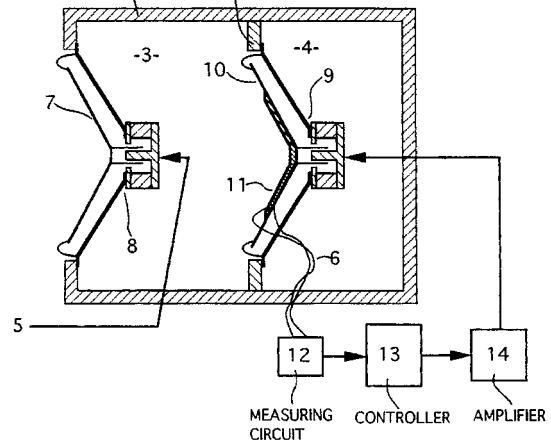
of pressure compensating transducer 9.—GLA

5,647,012

43.38.Ja TRI-CHAMBER SPEAKER BOX

Sang Wu Han, Rowland Heights, CA
8 July 1997 (Class 381/188); filed 10 June 1996

The loudspeaker box has a tuned chamber in front and two more vented chambers in series behind the loudspeaker. What is described may have been anticipated by patent 5,092,424 (assigned to Bose Corporation) which does not appear among the 20 citations.—GLA

5,659,620

43.38.Kb EAR MICROPHONE FOR INSERTION IN THE EAR IN CONNECTION WITH PORTABLE TELEPHONE OR RADIOS

Peer Kuhlman, Hvidovre, Denmark
19 August 1997 (Class 361/68); filed in Denmark 10 September 1992

The patent shows a microphone that fits into the ear outside the ear canal. It is designed to operate from speech sounds transmitted through the wearer's tissue from the mouth and throat. A rubber cover is stated to make the microphone insensitive to airborne sounds.—SFL

5,633,938

43.38.Lc AUDIO TRACK MIXING PROCESSOR

Frederick E. Porter III, Tucson, AZ
27 May 1997 (Class 381/98); filed 22 September 1994

If it works, this is a clever idea. In sound reinforcement or recording mixdown it can be difficult to maintain the right subjective balance between a vocalist or lead instrument and everything else. The patent describes rela-

tively simple circuitry for continuously analyzing octave-band levels of the main channel, and simultaneously equalizing the combined signals of everything else accordingly.—GLA

5,631,968

43.38.Lc SIGNAL CONDITIONING CIRCUIT FOR COMPRESSING AUDIO SIGNALS

Douglas R. Frey and Patrick Copley, assignors to Analog Devices, Incorporated
20 May 1997 (Class 381/106); filed 6 June 1995

A simplified, single-chip audio compressor is described that has a programmable compression ratio within a desired range, and amplitude limiting and expansion capabilities outside that range.—GLA

5,633,940

43.38.Lc AUDIO AMPLIFIER ARRANGEMENT

Derk J. C. Wassink, assignor to U.S. Philips Corporation
27 May 1997 (Class 381/107); filed in European Patent Office 19 March 1993

Audio-frequency power amplifiers often have overload indicators that flash when the output stage is driven into clipping. Some amplifiers include more elaborate circuitry to provide limiting action or reduce gain in discrete steps when clipping is detected. Now, suppose that an unusually high input signal drives the circuitry into full limiting when the volume control is only halfway up. The innocent listener turns the knob another notch *and nothing happens!* This intolerable situation has at last been addressed by Philips.—GLA

5,649,015

43.38.Lc SPEAKER SIMULATOR

Thomas L. Paddock and Robert H. Weir, assignors to Midnite Kitty, Incorporated
15 July 1997 (Class 381/61); filed 15 September 1995

A popular music recording session rarely has the luxury of simulating a concert environment. To maintain reasonable separation between tracks the instrument amplifiers must be turned down or, better yet, a direct electronic feed is taken from each instrument. Yet, when an electric guitar is played very loud at a concert its sound quality is quite different. The patent shows an interesting electronic circuit that includes the impedance of its cooling fan to accurately mimic the characteristics of an amplifier-loud speaker combination.—GLA

5,648,778

43.38.Md STEREO AUDIO CODEC

Alfredo R. Linz *et al.*, assignors to Advanced Micro Devices, Incorporated
15 July 1997 (Class 341/110); filed 17 July 1996

If you know what a CODEC is, this patent offers a wealth of information including 61 pages of charts and illustrations. An improved stereo audio CODEC is described that includes some interesting tricks with filters and means for reducing digitally induced noise.—GLA

5,659,317

43.38.Md APPARATUS FOR REPRODUCING DIGITAL AUDIO WAVEFORM DATA

Akira Toyama and Kazuyuki Fujiwara, assignors to Nippon Precision Circuits, Incorporated
19 August 1997 (Class 341/144); filed in Japan 9 March 1994

Pre-emphasis and post-equalization processes have long been techniques used in analog recording and reproduction for improving the ratio of signal to noise. Now in digital audio systems (e.g., compact disk, digital audio tape) pre-emphasis and de-emphasis processing is done. Sometimes digital audio data are transmitted with emphasis, and at other times there is no emphasis. The present patent provides a switching choice ahead of the digital-to-analog converter, which provides digital pre-emphasis for nonemphasized digital signals, with analog de-emphasis after conversion.—DWM

5,659,156

43.38.Si EARMOLDS FOR TWO-WAY COMMUNICATIONS DEVICES

Daniel W. Mauney and Robert W. MacKay, assignors to JABRA Corporation
19 August 1997 (Class 181/130); filed 3 February 1995

The patent shows a microphone and receiver mounted in a rather loose fitting earmold that can be easily inserted or removed. The earmold is designed to minimize protrusion into the ear canal.—SFL

5,610,986

43.38.Vk LINEAR-MATRIX AUDIO-IMAGING SYSTEM AND IMAGE ANALYZER

Michael T. Miles, Niles, MI
11 March 1997 (Class 381/27); filed 7 March 1994

The patent document provides a good discussion of pan pots and two-into-three matrix schemes. The system provides a fully variable matrix that allows the user to control the width of the apparent sound stage.—GLA

5,625,696

43.38.Vk SIX-AXIS SURROUND SOUND PROCESSOR WITH IMPROVED MATRIX AND CANCELLATION CONTROL

James W. Fosgate, assignor to Harman International Industries
29 April 1997 (Class 381/18); filed 2 April 1996

This is a continuation-in-part of seven earlier patents. These describe various versions of sophisticated circuitry intended to decompose two-channel stereophonic signals into three or more channels for surround-sound reproduction.—GLA

5,631,964

43.38.Vk AUDIO APPARATUS

Takeshi Harada and Eiki Nasu, assignors to Kabushiki Kaisha Kenwood
20 May 1997 (Class 381/74); filed in Japan 7 May 1993

The patent describes an adjustable, compact apparatus, ''... capable of playing music programs with desired surrounding sounds.'' Left and right loudspeaker enclosures each contain two loudspeaker systems, one relatively directional and the other (surround) nondirectional. The relative levels of the two pairs can be set manually by the user or automatically by a sound field control unit.—GLA

5,633,981

43.38.Vk METHOD AND APPARATUS FOR ADJUSTING DYNAMIC RANGE AND GAIN IN AN ENCODER/DECODER FOR MULTIDIMENSIONAL SOUND FIELDS

Mark F. Davis, assignor to Dolby Laboratories Licensing Corporation
27 May 1997 (Class 395/2.39); filed 8 January 1991

This multichannel sound encoder is intended primarily for recording film soundtracks. The playback gain and dynamic range in each of several subbands is controlled by a block floating point representation of the origi-

nal subband energies. The patent text includes extensive discussion of the control and encoding of sound field directionality, although the claims deal mainly with the scaling issues involved in the floating point format.—DLR
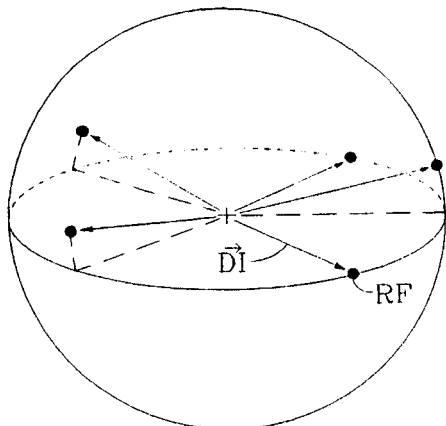
5,638,343

43.38.Vk METHOD AND APPARATUS FOR RE-RECORDING MULTI-TRACK SOUND RECORDINGS FOR DUAL-CHANNEL PLAYBACK

Steven R. Ticknor, assignor to Sony Corporation and Sony Electronics, Incorporated
10 June 1997 (Class 369/4); filed 13 July 1995

Multi-channel sound tracks can be electronically mixed down to two tracks for release as stereo albums. But for a listener using earphones, why not make a true binaural recording of the full, multi-channel theatre experience using a top-quality sound system in a real theatre?—GLA

5,644,640

43.38.Vk SURROUND SOUND PROCESSOR WITH IMPROVED CONTROL VOLTAGE GENERATOR

James W. Fosgate, assignor to Harman International Industries, Incorporated
1 July 1997 (Class 381/18); filed 27 March 1996

This is yet another in this inventor's long series of patent continuations of earlier patents. All of these describe circuitry for deriving multi-channel audio reproduction from a two-channel stereophonic source. Readers interested in surround-sound reproduction will want to maintain a library of Fosgate patents.—GLA

5,652,415

43.55.Ev MOLDED ARTICLE DESIGNED TO ABSORB AIRBORNE SOUND

Helmut Pelzer *et al.*, assignors to Helmut Pelzer, Germany
29 July 1997 (Class 181/286); filed 2 May 1995

This patent presents a liner to absorb airborne sound in the engine compartment of motor vehicles inside partial and complete motor encapsulations, using features of a Helmholtz resonator, injection molding, and porous absorption.—CJR

5,651,405

43.55.Fw PORTABLE ACOUSTIC SHELL

David Boeddeker *et al.*, assignors to Wenger Corporation
29 July 1997 (Class 160/135); filed 16 February 1995

The proposed acoustic shell is an improved version of other Wenger panels for a collapsible stage panel assembly. The system includes a pivoted
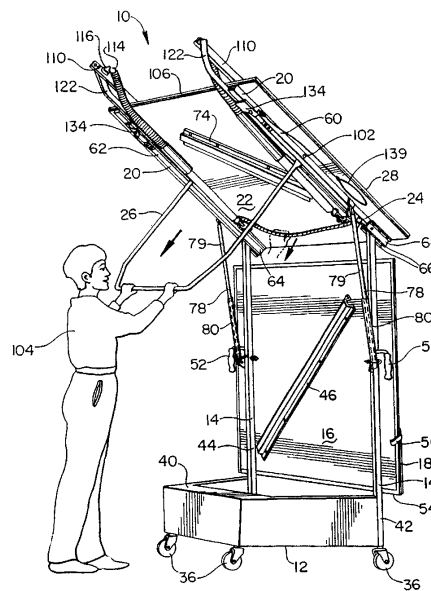
third panel unfolding from the top, and has springs that help rapid assembly.—CJR

5,644,877

43.55.Ti DEMOUNTABLE CEILING CLOSURE

Richard J. Wood, Bloomfield, CT
8 July 1997 (Class 52/241); filed 25 July 1995

This closure system provides a way to install a filler panel between a partial height office furniture partition and the ceiling, so the open plan furniture system can be made into a closed office arrangement. The filler
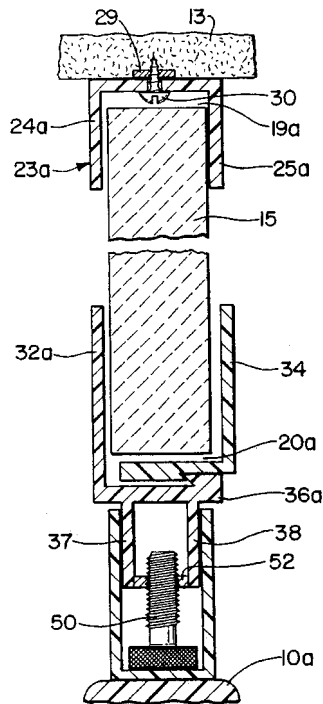
panels of gypsum board are set in elongated channels top and bottom; the weight of the panels themselves keeps an L-shaped member in place, forming the locking mechanism for the channel to hold the panel.—CJR

5,647,183

43.55.Vj RESILIENT FLOORING

James C. Counihan, Piedmont, SC
15 July 1997 (Class 52/403.1); filed 9 August 1996

The patent is an extension on an earlier system for developing a resilient flooring system (as for a gymnasium), which can be easily and quickly installed, and which comprises a substantially continuous subfloor surface, and which adjusts for the high and low spots from the base floor, and which minimizes the dead spots on the finished floor.—CJR

5,659,621

43.66.Ts MAGNETICALLY CONTROLLABLE HEARING AID

James R. Newton, assignor to Argosy Electronics, Incorporated
19 August 1997 (Class 381/68); filed 27 April 1995

The patent shows a completely in-the-ear hearing aid having characteristics, such as gain and other parameters, that can be controlled by means of a small permanent magnet held near the aid, but outside the ear canal. The permanent magnet operates a reed switch in the aid to activate process-

ing circuitry which cycles a chosen parameter, such as volume, through its range of available settings when the reed switch is closed. The magnet is removed when the desired condition is reached. The control circuitry may include a memory circuit to allow a desired setting of an adjustable parameter to be saved when the hearing aid is turned off.—SFL
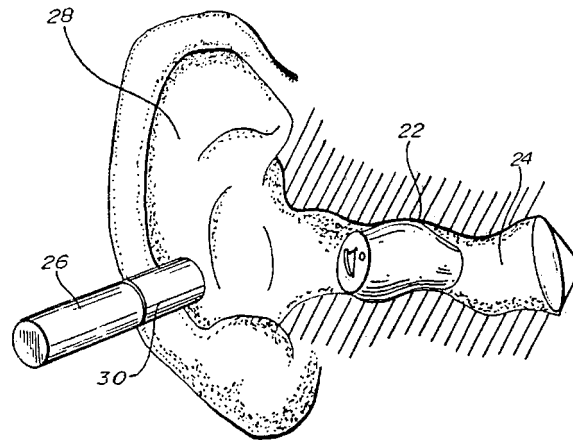
5,420,581

43.66.Vt MATERNAL SOUND LEVEL DEVICE AND METHOD FOR PROTECTING FETAL HEARING

Aemil J. M. Peters *et al.*, assignors to BodySonics, Incorporated
30 May 1995 (Class 340/573); filed 26 May 1993

Recent medical studies have shown that the children of women involved in employment or recreational noise during pregnancy have hearing loss which may be attributed to a high level of noise exposure before birth. This patent describes a small sound pressure level monitoring system that can be attached to the belt of a pregnant woman for monitoring sound at the abdomen in the range of 80–100 dB. An alarm alerts the mother to an excessive level. Low-frequency sound is emphasized, and high-frequency sound is de-emphasized, since the studies report that hearing loss was greatest when low frequencies were present. ''Preliminary data suggest that intense sound pressures result in disruption of fetal sleep state and altered fetal hearing sensitivity.''—DWM

5,636,325

43.71.Hw SPEECH SYNTHESIS AND ANALYSIS OF DIALECTS

Peter W. Farrett, assignor to International Business Machines Corporation
3 June 1997 (Class 395/2.67); filed 13 November 1992

This is a system for recognizing or synthesizing the dialect of a speech signal based on a system of musical intervals observed in pitch-frequency estimates. The hypothesis is that speakers of a language or dialect use a distinctive pattern of musical intervals in the prosodic structure of speech in that language or dialect. A few example rules are given stating relationships between pitch frequency changes and certain phoneme sequences.—DLR

5,638,487

43.72.Bs AUTOMATIC SPEECH RECOGNITION

Benjamin Chigier, assignor to PureSpeech, Incorporated
10 June 1997 (Class 395/2.62); filed 30 December 1994

This is a method of assigning frames of acoustic speech analysis vectors to phonetic segments using a boundary probability assessment. A neural network is trained to assign phonetic segment boundary probabilities to acoustic feature vectors based on the spectral shape and other characteristics of the current vector and at least one vector preceding and following the

current one. After recognition processing by any of several means has been completed, the boundary probability assignments are used to modify the resulting scores.—DLR

5,633,941

43.72.Gy CENTRALLY CONTROLLED VOICE SYNTHESIZER

Chi-mao Huang, assignor to United Microelectronics Corporation
27 May 1997 (Class 381/118); filed 26 August 1994

This compressed-audio sound playback system integrates sound data, silence codes, control, and address information into a central read-only memory chip. The primary novelty seems to be that a table of control codes
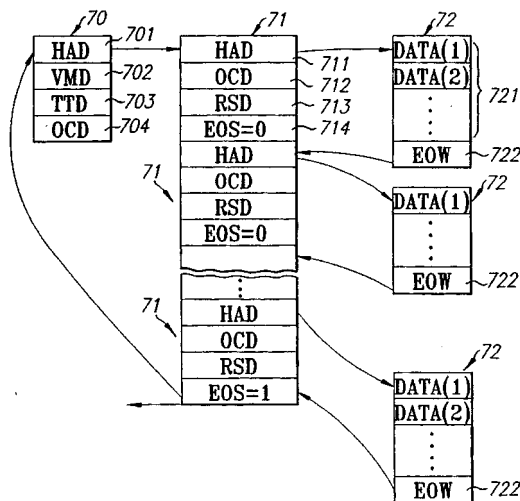
resides in a separate memory area from the speech data, allowing for a more uniform ROM memory structure. It is said that the arrangement simplifies the wiring.—DLR

5,633,980

43.72.Gy VOICE CODER AND A METHOD FOR SEARCHING CODEBOOKS

Kazunori Ozawa, assignor to NEC Corporation
27 May 1997 (Class 395/2.31); filed in Japan 10 December 1993

The coding method involves computing a set of auditory perceptual masking weights for each 5-ms speech subframe. The masking coefficients are used in the calculation of synthetic waveforms during a codebook search. A variety of codebook arrangements makes use of the various masking techniques.—DLR

5,633,982

43.72.Gy REMOVAL OF SWIRL ARTIFACTS FROM CELP-BASED SPEECH CODERS

Kalyan Ganesan *et al.*, assignors to Hughes Electronics
27 May 1997 (Class 395/2.42); filed 20 December 1993

The patent discloses an improvement in code-excited linear predictive (CELP) vocoding. Linear prediction typically provides good coding quality only in clean, low-noise conditions. CELP coders in the presence of noise are subject to a low-frequency artifact known as ''swirl.'' In this patent various speech characteristics computed during the normal operation of the transmitter are used to make speech/nonspeech and periodicity decisions. When no speech is present, low-frequency components are removed. Also, the pitch detector is disabled when no periodicity is detected.—DLR

5,633,984

43.72.Gy METHOD AND APPARATUS FOR SPEECH PROCESSING

Takashi Aso *et al.*, assignors to Canon Kabushiki Kaisha
27 May 1997 (Class 395/2.69); filed in Japan 11 September 1991

This apparatus appears to be primarily a speech vocoder based on vector quantization (VQ) of spectral feature vectors. In addition to the storage of codebook indices for transmission or reproduction, the system also contains a correspondence between VQ codes and speech phonemes. These phonemes can be accessed from a text parser, providing a text-to-speech capability. Very little technical information is included and the descriptions of speech-related aspects of the system are somewhat muddled.—DLR

5,634,085

43.72.Gy SIGNAL REPRODUCING DEVICE FOR REPRODUCING VOICE SIGNALS WITH STORAGE OF INITIAL VALUES FOR PATTERN GENERATION

Shuichi Yoshikawa *et al.*, assignors to Sharp Kabushiki Kaisha
27 May 1997 (Class 395/2.75); filed in Japan 28 November 1990

In this patent 8-bit data words are transmitted as coded values for particular excitation sequences. At the receiver, a feedback shift register random number generator is seeded with the 8-bit value and generates a longer bit stream, which serves as the excitation sequence.—DLR

43.72.Gy APPARATUS AND METHOD FOR STEREO AUDIO ENCODING OF DIGITAL AUDIO SIGNAL DATA

Do-Hui Teh and Ah-Peng Tan, assignors to Matsushita Electric Industrial Company
3 June 1997 (Class 315/2.35); filed in Japan 30 March 1992

This is a method for encoding stereo channel data such that correlations between left and right channel signals are not redundantly transmitted. If the left and right signals are found to be more or less in phase, a channel scale factor is computed based on a power equalization model. If the channels are found to be out of phase, an error minimization model is used.—DLR

5,633,983

43.72.Ja SYSTEMS AND METHODS FOR PERFORMING PHONEMIC SYNTHESIS

Cecil H. Coker, assignor to Lucent Technologies, Incorporated
27 May 1997 (Class 395/2.69); filed 13 September 1994

This patent presents a text-to-speech synthesis system which accepts English text and produces acoustic parameters such as formant frequencies and bandwidths and speech amplitude information. The first stage generates a phonetic segment sequence having units labelled with stress and duration
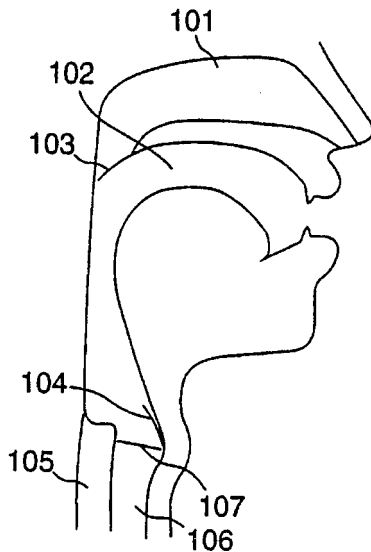
values. One or more acoustic descriptors are assigned to each segment. The acoustic parameter generator is based on models of the transition characteristics with frequent reference to physiological constraints.—DLR

5,636,323

43.72.Kb SPEECH COMMUNICATION APPARATUS HAVING AN ECHO CANCELER

Yuji Umemoto and Koki Otsuka, assignors to Kabushiki Kaisha Toshiba
3 June 1997 (Class 395/2.35); filed in Japan 20 January 1993

This echo cancellation system is designed for use in a speakerphone such as in an automobile or desktop device. It includes a volume limiting system in the loudspeaker pathway so that the loudspeaker signal will not become so loud as to distort, which would disrupt the adapted state of the cancellation system.—DLR

43.72.Kb METHOD AND APPARATUS FOR DETECTING A NEAR-END SPEECH SIGNAL

Stephen S. Oh, assignor to Texas Instruments, Incorporated
27 May 1997 (Class 381/66); filed 9 January 1995

This acoustic echo canceller is designed for hands-free speakerphone applications. The circuit is said to provide improved detection of the near-end speech signal and rejection of the far-end signal so that only the near-end signal will be transmitted to the receiver. Both microphone and line
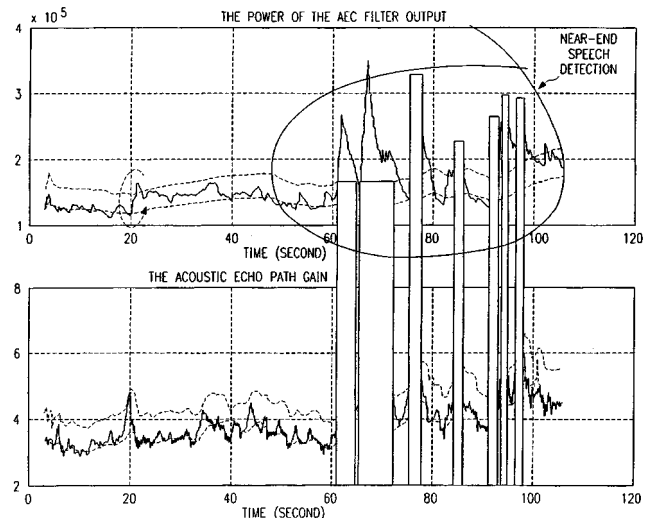
signals are filtered and the average power is measured. The echo path gain/loss and its long-term average are compared to detect near-end speech.—DLR

5,638,436

43.72.Kb VOICE DETECTION

Chris Hamilton and Nicholas Zwick, assignors to Dialogic Corporation
10 June 1997 (Class 379/351); filed 12 January 1994

The system described here is a combination DTMF and voice signal presence detector. It adjusts its sensitivity levels depending on the current signal state. Voicelike signal characteristics such as the spectral envelope or higher harmonic content are examined to determine whether a speech signal is present. Depending on that outcome, the thresholds for DTMF detection may be altered.—DLR

5,632,002

43.72.Ne SPEECH RECOGNITION INTERFACE SYSTEM SUITABLE FOR WINDOW SYSTEMS AND SPEECH MAIL SYSTEMS

Hideki Hashimoto *et al.*, assignors to Kabushiki Kaisha Toshiba
20 May 1997 (Class 395/2.4); filed in Japan 28 December 1992

This speech recognition control system includes a number of interface facilities making it suitable for operation in the Microsoft Windows operating system. A program management table contains current information on each application which has been set up for speech capability, including state information which is used to activate the appropriate syntax corresponding to the current state of the application. All necessary Windows message handling functions are available to exert control over the applications depending on text strings returned by the speech recognition system.—DLR

5,634,083

43.72.Ne METHOD OF AND DEVICE FOR DETERMINING WORDS IN A SPEECH SIGNAL

Martin Oerder, assignor to U.S. Philips Corporation
27 May 1997 (Class 395/2.62); filed in Germany 3 March 1993

The patent discloses a method for searching the space of possible word sequences in a phonetic space such as acoustic analysis feature vectors. Further details of the phonetic feature space are not considered. Dynamic programming is used to hypothesize the occurrences of all possible vocabulary items in the feature space. A graph tracing process then scores the many possible word sequences to find the most likely decoded result. A weighting system reduces the tendency for short words to fit in ubiquitously.—DLR

5,638,486

43.72.Ne METHOD AND SYSTEM FOR CONTINUOUS SPEECH RECOGNITION USING VOTING TECHNIQUES

Shay-Ping T. Wang and Michael K. Lindsey, assignors to Motorola, Incorporated
10 June 1997 (Class 395/2.45); filed 26 October 1994

A voting strategy is presented for selecting the best choice of speech recognizer outputs among multiple recognition systems. The approach described here would seem to be applicable primarily to phrase or discrete word recognizers. It is described in the context of a continuous speech recognition system. However, the matching scores of each recognition system are presented as simple distance measures from the acoustic features, with no mention of phonetic structure or other such speech units.—DLR

5,627,335

43.75.Wx REAL-TIME MUSIC CREATION SYSTEM

Alexander P. Rigopulos and Eran B. Egozy, assignors to Harmonix Music Systems, Incorporated
6 May 1997 (Class 84/635); filed 16 October 1995

The ambitious main object of the patented electronic music system is to let non-musicians ''generate melodic, creative music in real-time without knowledge of music theory and without the ability to play an instrument or keep time.'' The system includes a computer, storage media, a rhythm generator, a pitch selector, and input mechanisms to which the computer is responsive. In addition to the computer keyboard and mouse, an input
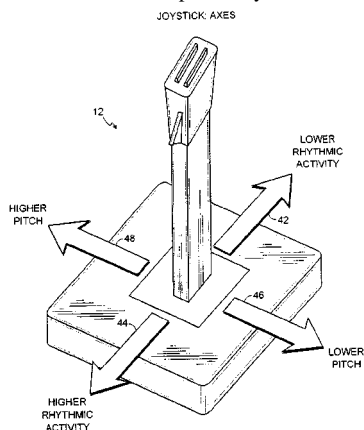
mechanism in the form of a joystick **12** is provided. The nonmusician operates the joystick along two axes, one for pitch control and the other for the tempo of the rhythmic pattern chosen. Buttons and other controls at the manual end of the joystick are used to select rhythm and chordal patterns to accompany the melody or solo controlled by the joystick.—DWM

5,521,328

43.75.Tv ELECTRONIC MUSICAL INSTRUMENT FOR SIMULATING WIND INSTRUMENT MUSICAL TONES

Masahiro Kakishita, assignor to Yamaha Corporation
28 May 1996 (Class 84/661); filed in Japan 21 August 1992

This patent describes a circuit for simulating organ pipe tone using a loop circuit containing a linear portion and a nonlinear portion. ''The linear portion simulates a pipe portion of the wind instrument, while the nonlinear portion simulates a breath-blowing portion of the wind instrument so as to produce an excitation signal, which is supplied to the linear portion. By an interaction between the linear portion and the nonlinear portion which is carried out while a signal circulates through the loop circuit, a sounding characteristic of the wind instrument is simulated. In order to accurately simulate a jet reed instrument (e.g., organ pipe), there are further provided a delay circuit and an edge tone generator. The delay circuit imparts a delay time to the output signal of the linear portion, and then, a delayed signal is supplied to the nonlinear portion. The delay time corresponds to a time which is required when an air flow passing through a slit reaches an edge in the jet reed instrument. The edge tone generator generates a noise signal representing an edge tone (or an aeolian tone) which is unique to the jet reed instrument. The noise signal is mixed with the output signal of the nonlinear portion, and then, a mixed signal is supplied to the linear portion.''—DWM

5,523,526

43.75.Tv SUSTAINING DEVICES FOR STRINGED MUSICAL INSTRUMENTS

Steve Shattil, assignor to Genesis Magnetics Corporation
4 June 1996 (Class 84/728); filed 23 July 1993

Magnetic drivers and pickups in proximity to the magnetic strings of a musical stringed instrument have been connected previously in a feedback relationship to sustain the duration of the string vibration. In this patent a ''cancellation circuit is provided for reducing electromagnetic feedback between the pickup and driver by adjusting the relative phase and amplitude between a first and second pickup signal and combining the signals so that the responses to electromagnetic interference cancel.'' One version ''of the cancellation circuit includes a second electromagnetic driver that generates an amplitude-adjusted and phase-adjusted electromagnetic field to cancel electromagnetic interference.''—DWM

5,536,902

43.75.Tv METHOD OF AND APPARATUS FOR ANALYZING AND SYNTHESIZING A SOUND BY EXTRACTING AND CONTROLLING A SOUND PARAMETER

Xavier Serra *et al.*, assignors to Yamaha Corporation
16 July 1996 (Class 84/623); filed 14 April 1993

This electronic computer musical system analyzes an original sound, then extracts from the analysis data the data indicative of a selected tonal characteristic, then removes from the analysis data the selected characteristic, and synthesizes a sound waveform based upon the analysis data minus the original selected characteristic to which a processed version of the selected characteristic has been added. ''In such a sound synthesis technique of the analysis type, it is allowed to apply free controls to various sound elements such as a formant and a vibrato.''—DWM

5,578,781

43.75.Tv TONE SIGNAL SYNTHESIS DEVICE BASED ON COMBINATION ANALYZING AND SYNTHESIZATION

Hideo Suzuki, assignor to Yamaha Corporation
26 November 1996 (Class 84/661); filed in Japan 4 October 1993

This is another electronic computer musical system (see review above of patent 5,536,902) based upon a combination of analysis and synthesis of an original sound signal. In this patent both the analysis and synthesis circuits include a signal circulation loop having a delay element and a filter element for processing the signal input from the analyzer. The fundamental processing characteristics of the synthesizer signal circulation loop are in opposite functional relation to the fundamental processing characteristics of the analyzer signal circulation loop. Controls are provided for controlling the parameters of the processing characteristics of both the analyzer and the synthesizer independently. Output is provided from the synthesizer circuit.—DWM

Phase conjugation in the ocean: Experimental demonstration of an acoustic time-reversal mirror[a)]

W. A. Kuperman, William S. Hodgkiss, and Hee Chun Song
Marine Physical Laboratory, Scripps Institution of Oceanography, University of California, San Diego, La Jolla, California 92093-0701

T. Akal and C. Ferla
SACLANT Undersea Research Centre, La Spezia, Italy

Darrell R. Jackson
Applied Physics Laboratory, University of Washington, Seattle, Washington 98105

An experiment conducted in the Mediterranean Sea in April 1996 demonstrated that a time-reversal mirror (or phase conjugate array) can be implemented to spatially and temporally refocus an incident acoustic field back to its origin. The experiment utilized a vertical source–receiver array (SRA) spanning 77 m of a 125-m water column with 20 sources and receivers and a single source/receiver transponder (SRT) colocated in range with another vertical receive array (VRA) of 46 elements spanning 90 m of a 145-m water column located 6.3 km from the SRA. Phase conjugation was implemented by transmitting a 50-ms pulse from the SRT to the SRA, digitizing the received signal and retransmitting the time reversed signals from all the sources of the SRA. The retransmitted signal then was received at the VRA. An assortment of runs was made to examine the structure of the focal point region and the temporal stability of the process. The phase conjugation process was extremely robust and stable, and the experimental results were consistent with theory. © *1998 Acoustical Society of America.* [S0001-4966(97)00212-9]

PACS numbers: 43.10.Ln, 43.30.Vh, 43.30.Bp, 43.30.Hw, 43.30.Re [DLB]

INTRODUCTION

Phase conjugation is a process that has been first demonstrated in nonlinear optics[1] and more recently in ultrasonic laboratory acoustic experiments.[2,3] Aspects of phase conjugation as applied to underwater acoustics also have been explored recently.[4–7] The Fourier conjugate of phase conjugation is time reversal; implementation of such a process over a finite spatial aperture results in a ''time-reversal mirror.[2,3]'' In this paper we describe an ocean acoustics experiment in which a time-reversal mirror was demonstrated.

In nonlinear optics, phase conjugation is realized using high intensity radiation propagating in a nonlinear medium. Essentially, the incident radiation imparts its own time dependence on the dielectric properties of the medium. The incident radiation is then scattered from this time-varying dielectric medium. The resulting scattered field is a time reversed replica of this incident field propagating in the opposite direction of the incident field. For example, the scattered field that results from an outgoing spherical wave is a spherical wave converging to the original source point; when it passes through the origin it has the time reversed signature of the signal which was transmitted from that point at the originating time. Clearly, this phenomenon can be thought of as a self-adaptive process, i.e., the process constructs a wavefront of the exact required curvature. (An alternative would be to use a concave spherical mirror with the precise radius of curvature of the incident wavefront.) There is an assortment of nonlinear optical processes which can result in phase conjugation.[1] In acoustics, however, we need not use the propagation medium nonlinearities to produce a phase conjugate field.

Because the frequencies of interest in acoustics are orders of magnitude lower than in optics, phase conjugation can be accomplished using signal processing. As in the optical case, phase conjugation takes advantage of reciprocity which is a property of wave propagation in a static medium and is a consequence of the invariance of the linear lossless wave equation to time reversal. In the frequency domain, time reversal corresponds to conjugation invariance of the Helmholtz equation. The property of reciprocity allows one to retransmit a time reversed version of a multipath dispersed probe pulse back to its origin, arriving there time reversed, with the multipath structure having been undone.[8,9] This process is equivalent to using the ocean as a matched filter since the probe pulse arrival has embedded in it the transfer function of the medium. This process can be extended further by receiving and retransmitting the probe signal with a source–receiver array. Depending on the spatial extent of the array, the above process results in some degree of spatial focusing of the signal at the origin of the probe signal.

A time-reversal mirror (TRM) can therefore be realized with a source–receiver array. The incident signal is received, time reversed, and transmitted from sources contiguous with the receiving hydrophones. The time reversal can be accomplished in a straightforward way, for example, by using the rewind output of an analog tape recorder or by a simple

---

[a]''Selected research articles'' are ones chosen occasionally by the Editor-in-Chief that are judged (a) to have a subject of wide acoustical interest, and (b) to be written for understanding by broad acoustical readership.

program that reverses a digitized segment of a received signal.

An acoustic TRM has already been demonstrated in an ultrasonic laboratory using an array of source/receiver transducers (SRA).[3] The array length was 10 cm and a single 4-MHz source was placed at a transverse distance of 5 cm together with another receive array. The single source transmitted a probe pulse which was received at the SRA; the received pulse was time reversed and retransmitted from the SRA and subsequently received at an array (with the same orientation as the SRA) near the single source. The results showed a 15-dB peak at the location of the source relative to sidelobes away from the probe source location. Note that this focal point was at a range one-half the size of the aperture.

Phase conjugation (PC) or the implementation of a TRM in the ocean is relevant to recent trends in acoustic signal processing which have emphasized utilizing knowledge of the environment, e.g., matched feld processing (MFP).[10] However, MFP requires accurate knowledge of the environment throughout the propagation path, which of course is difficult or impossible to obtain. Phase conjugation is an environmentally self-adaptive process which may therefore have significant applications to localization and communications in complicated ocean environments. Although the ''effective'' ocean environment must remain static over the turn around time of the PC process, ocean variability on timescales shorter than the turn around time might be compensated for with feedback algorithms. However, an understanding of relevant ocean time scales *vis a vis* the stability of the PC process will be required.

In this paper we describe an April 1996 experiment in which an acoustic TRM was demonstrated in the ocean. In this initial experiment, a focal range of about 100 times the SRA aperture was accomplished easily with a 445-Hz probe source, a water depth of the order of 100 m, and a focal range of about 6.3 km. Large focal distances are obtainable in the ocean because in a waveguide geometry, a SRA has images which increase its effective aperture. Hence, there is an advantage to having a waveguide geometry over a free-field environment as was used first in the ultrasonic laboratory experiment. Measurements in this first low-frequency ocean experiment also suggest a temporal stability of the PC process which is longer than what was expected intuitively. Some quantitative results on this stability are presented.

In the next section we review the relevant theoretical issues including some simulation results leaving the details to an Appendix and appropriate references. Section II describes the experiment in which the TRM was demonstrated and Sec. III presents the results.

I. BACKGROUND THEORY AND SIMULATION FOR THE TRM EXPERIMENT

The theory of phase conjugation *vis a vis* ocean acoustics already has been presented.[4–7] Here we briefly review salient issues using the basic geometry of the TRM experiment (shown schematically in Fig. 2). More detail on theory is given in Appendix A and some additional details concerning experimental equipment are given in Appendix B.
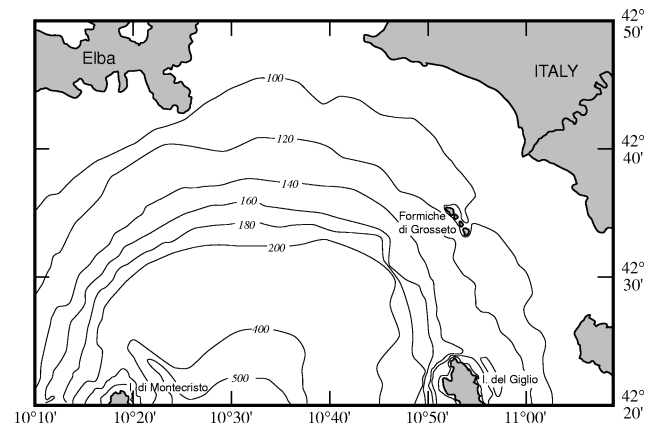
FIG. 1. Location of phase conjugation experiment. A source/receiver array (SRA) was deployed in 125-m-deep water and cabled approximately 1 km back to a small island, Formica Grande, the northernmost island of Formiche di Grosseto (42° 34.6′ N, 10° 52.9′ E). A rf telemetered vertical receive array (VRA) was deployed in 145-m-deep water approximately 6.3 km west of Formica.

A. Experimental geometry

The TRM experiment was performed off the west coast of Italy in April 1996 as indicated in Fig. 1. Figure 2 is a schematic of the experiment and indicates the types of environmental measurements that were made. The TRM was implemented by a 77-m source–receiver array (SRA) in 125-m-deep water which was hardwired to the Isola di Formica di Grosseto. The SRA consisted of 20 hydrophones with 20 contiguously located slotted cylinder sources with a nominal resonance frequency of 445 Hz. The sources were operated at a mean nominal 165-dB source level. The received signals were digitized, time reversed, and after being converted back to analog form, retransmitted. A probe source (PS) of the same type used in the SRA was deployed from the NATO research vessel ALLIANCE. The probe source together with a hydrophone was also used in parts of the experiment as a transponder. The ALLIANCE also deployed a vertical 46 element receive array (VRA) spanning 90 m located 6.3 km from the SRA which radio telemetered all individual element data back to the ALLIANCE. Ideally, the PS should be in the vertical SRA-VRA plane to correspond perfectly to the simulations in the following section; for practical reasons the PS was placed a few tenths of a km out of this plane. This did not introduce a significant error because the bathymetry
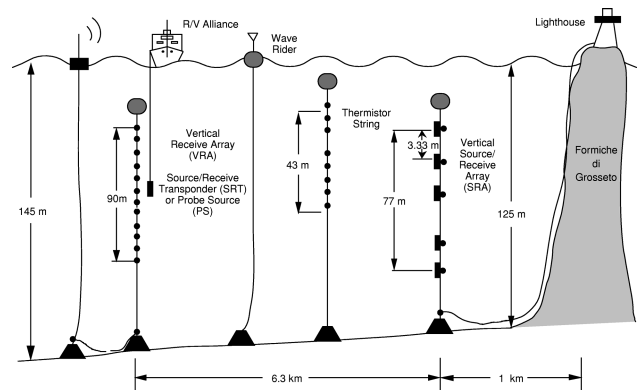
FIG. 2. Experimental setup of the phase conjugation experiment.

Kuperman *et al.*: Phase conjugation in the ocean
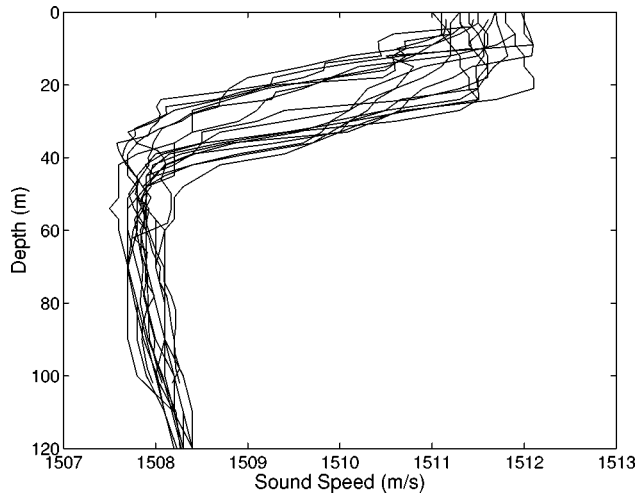
FIG. 3. Collection of sound-speed profiles from CTDs taken during the experiment.

was flat in the vicinity of the VRA. Figure 3 is a collection of the sound speed profiles (SSP's) obtained from the conductivity–temperature–depth probe (CTD) as an indication of the variability over the duration of the experiment. The bottom sound-speed structure as determined from earlier experiments[11] is shown in Fig. 4(a). More details on the instrumentation and processing are given in Appendix B.

B. Overview of theory

For simplicity in this subsection, we analytically summarize the basics of phase conjugation in a range-independent waveguide. The simulations and comparisons with experimental data presented later on in the paper will include range-dependent modeling. The source, PS, is located a horizontal distance R from the source/receive phase conjugate array, SRA.

1. Harmonic excitation

The acoustic field, $G_\omega(R;z_j,z_{ps})$, at the jth receiver element of the SRA from the point source PS in Fig. 2 is determined from the Helmholtz equation[12] [assuming a harmonic time dependence of $\exp(-i\omega t)$]

$$\nabla^2 G_\omega(\mathbf{r};z,z_{ps}) + k^2(z) G_\omega(\mathbf{r};,z,z_{ps})$$

$$= -\delta(\mathbf{r}-\mathbf{r}_{ps})\delta(z-z_{ps}), \quad k^2(z) = \frac{\omega^2}{c^2(z)}, \quad (1)$$

where z is taken positive downward and $\mathbf{r} = (x,y)$. Letting r be the horizontal distance from the probe source, Eq. (1) has the far field, azimuthally symmetric normal mode solution for pressure given by

$$G_\omega(r;z,z_{ps}) = \frac{i}{\rho(z_{ps})(8\pi r)^{1/2}} \exp(-i\pi/4)$$

$$\times \sum_n \frac{u_n(z_{ps})u_n(z)}{k_n^{1/2}} \exp(ik_n r), \quad (2)$$

where u_n, k_n are the normal mode eigenfunctions and modal wave numbers obtained by solving the following eigenvalue problem with well-known boundary conditions:[12]

(a)

(b)

(c)
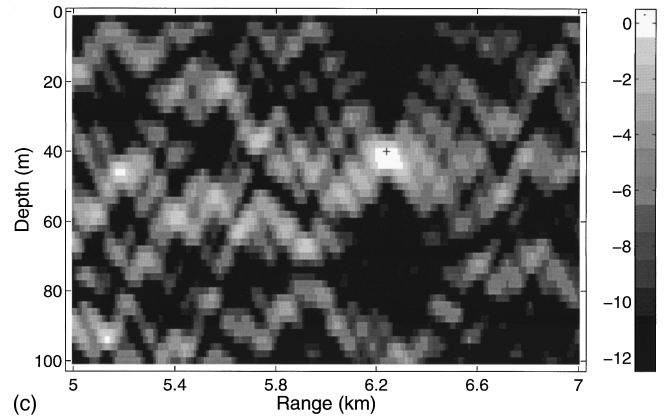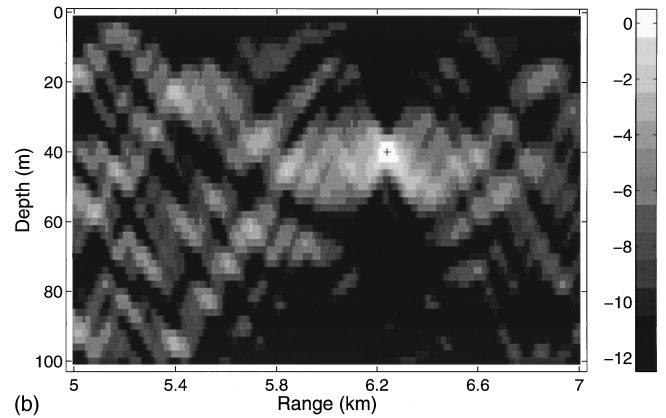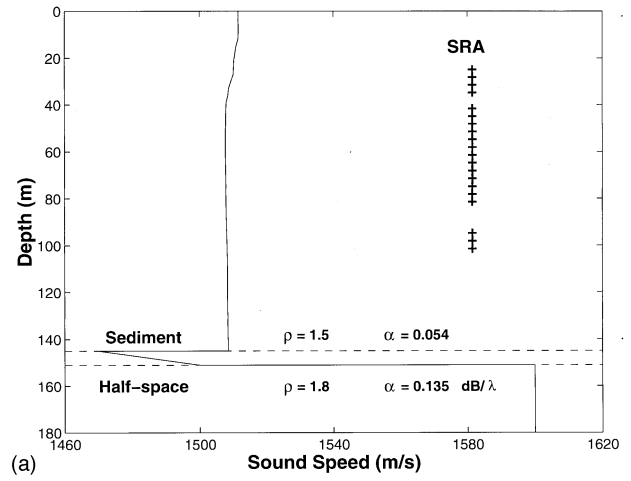
FIG. 4. Single frequency simulation of phase conjugation for the geometry of Fig. 2 for a probe source located at a depth of 40 m and a range of 6.3 km. (a) Sound-speed profile. The density, ρ and attenuation, α (in dB/wavelength) of the bottom two layers are also given. (b) Simulation for a 20-element SRA. Note the sharp focus in depth. (c) Simulation for only the bottom 10 elements of the SRA.

$$\frac{d^2 u_n}{dz^2} + [k^2(z) - k_n^2]u_n(z) = 0. \quad (3)$$

The mode functions form a complete set (for simplicity we omit discussion of the continuous spectrum though a good approximation is to use a set of discrete mode functions obtained from a waveguide extended in depth and terminated by a pressure release or rigid boundary)

$$\sum_{\text{all modes}} \frac{u_n(z)u_n(z_s)}{\rho(z_s)} = \delta(z - z_s), \qquad (4)$$

and satisfy the orthonormality condition

$$\int_0^\infty \frac{u_m(z)u_n(z)}{\rho(z)} \, dz = \delta_{nm}, \qquad (5)$$

where δ_{nm} is the Kronecker delta symbol.

The received field at the source/receiver array (SRA) at range R from PS with source/receive elements at depths z_j, is $G_\omega(R;z_j,z_{ps})$. The phase conjugation process consists of exciting the SRA sources by the complex conjugate of the received field, $G_\omega^*(R;z_j)$. The resulting acoustic field transmitted from the J sources satisfies the wave equation,

$$\nabla^2 P_{pc}(r,z) + k^2(z)P_{pc}(r,z) = \sum_{j=1}^J \delta(z-z_j)G_\omega^*(R;z_j,z_{ps}), \qquad (6)$$

where the range r is with respect to the SRA. Using Green's function theory, the solution of Eq. (6) is the volume integral of the product of the Green's function as specified by Eq. (1) and the source term of Eq. (6). For a vertical line of discrete sources, the integral reduces to a sum over the source positions,

$$P_{pc}(r,z;\omega) = \sum_{j=1}^J G_\omega(r;z,z_j)G_\omega^*(R;z_j,z_{ps}), \qquad (7)$$

where R is the horizontal distance of the SRA from PS and r is the horizontal distance from the SRA to a field point.

Note that the magnitude squared of the right-hand side (rhs) of Eq. (7) is the ambiguity function of the Bartlett matched-field processor[10] (with an appropriate normalization factor) where the data are given by $G_\omega(R;z_j,z_{ps})$ and the replica field by $G_\omega(r;z,z_j)$. In effect, the process of phase conjugation is an implementation of matched-field processing where the ocean itself is used to construct the replica field. Or, alternatively, matched-field processing simulates the experimental implementation of phase conjugation in which a source/receive array is used. To demonstrate that $P_{pc}(r,z)$ focuses at the position of the probe source, (R,z_{ps}), we simply substitute Eq. (2) into Eq. (7) which specifies that we sum over all modes and array sources

$$P_{pc}(r,z;\omega) \approx \sum_m \sum_n \sum_j \frac{u_m(z)u_m(z_j)u_n(z_j)u_n(z_{ps})}{\rho(z_j)\rho(z_{ps})\sqrt{k_m k_n rR}}$$

$$\times \exp i(k_m r - k_n R). \qquad (8)$$

For an array which substantially spans the water column and adequately samples most of the modes, we may approximate the sum of sources as an integral and invoke orthonormality as specified by Eq. (5). Then the sum over j selects out modes $m = n$ and Eq. (8) becomes

$$P_{pc}(r,z;\omega) \approx \sum_m \frac{u_m(z)u_m(z_{ps})}{\rho(z_{ps})k_m\sqrt{rR}} \exp ik_m(r-R). \qquad (9)$$

The individual terms change sign rapidly with mode number. However, for the field at PS, $r=R$, the closure relation of Eq. (4) can be applied approximately (we assume that the

k_n's are nearly constant over the interval of the contributing modes) with the result that $P_{pc}(r,z) \approx \delta(z - z_{ps})$. Figure 4 is a simulation of the phase conjugation process using Eq. (7) for a probe source at 40-m depth and at a range of 6.3 km from a 20 element SRA as specified in Fig. 2 verifying the above discussion. Range-dependent bathymetry was used as the input to an adiabatic mode model[13] for the specific sound-speed profile taken from the ensemble of profiles in Fig. 3 and a bottom sound-speed structure shown in Fig. 4(a) which includes a low speed layer as has been ascertained experimentally.[11] Notice that the focusing in the vertical is indicative of the closure property of the modes. As a matter of fact, for an SRA with substantially fewer elements, we see that the focusing still is relatively good. For example, Fig. 4(c) also shows a result for the bottom 10 elements of the SRA which are below the thermocline.

2. Pulse excitation

In this experiment a 50-ms pure-tone pulse with center frequency 445 Hz was used for the probe transmission. We can Fourier synthesize the above results to examine phase conjugation for pulse excitation. Here, in the context of this experiment, we remind the reader that phase conjugation in the frequency domain is equivalent to time reversal in the time domain. The jth element of the SRA receives the following time-domain signal, given by Fourier synthesis of the solution of Eq. (1):

$$P(R,z_j;t) = \int G_\omega(R;z_j,z_{ps})S(\omega)e^{-i\omega t} \, d\omega, \qquad (10)$$

where $S(\omega)$ is the Fourier transform of the probe source pulse. This expression incorporates all waveguide effects, including time elongation due to multipath propagation. For convenience, take the time origin such that $P(R,z_j;t)=0$ outside the time interval $(0,\tau)$. Then the time reversed signal that will be used to excite the jth transmitting element of the SRA is $P(R,z_j;T-t)$ such that $T>2\tau$. This condition is imposed by causality; the signal has to be completely received before it can be time reversed. Then

$$P(R,z_j;T-t) = \int G_\omega(R;z_j,z_{ps})S(\omega)e^{-i\omega(T-t)} \, d\omega$$

$$= \int [G_\omega^*(R;z_j,z_{ps})e^{i\omega T}S^*(\omega)]e^{-i\omega t} \, d\omega, \qquad (11)$$

where the sign of the integration variable, ω, has been reversed and the conjugate symmetry of the frequency-domain Green's function and probe pulse has been used. The quantity in brackets in Eq. (11) is the Fourier transform of the signal received by the jth SRA receiver element after time reversal and time delay. Hence there is an equivalence of time reversal and phase conjugation in their respective time and frequency domains.

Noting that the bracketed quantity in Eq. (11) is the frequency-domain representation of the signal retransmitted by the jth element of the SRA, Fourier synthesis can be used to obtain the time-domain representation of the field produced by the TRM. Using Eq. (7),

28   J. Acoust. Soc. Am., Vol. 103, No. 1, January 1998

Kuperman *et al.*: Phase conjugation in the ocean   28

$$P_{pc}(r,z;t) = \sum_{j=1}^{J} \int G_\omega(r,z,z_j) G_\omega^*(R,z_j;z_{ps}) e^{i\omega T}$$

$$\times S^*(\omega) e^{-i\omega t} \, d\omega. \tag{12}$$

This expression can be used to show that the TRM produces focusing in time as well as in space. Focusing in time occurs because a form of matched filtering occurs. To understand this, examine the TRM field at the focus point [that is, take $r=R$, $z=z_{ps}$ in Eq. (12)]. Neglecting density gradients, reciprocity allows the interchange $G_\omega(R,z_{ps},z_j) = G_\omega(R,z_j,z_{ps})$. Then the time-domain equivalent of Eq. (12) is

$$P_{pc}(r,z;t) = \frac{1}{(2\pi)^2} \int \sum_{j=1}^{J} \left[\int G_{t'+t''}(R,z_j,z_{ps}) \right.$$

$$\left. \times G_{t'}(R,z_j,z_{ps}) dt' \right] S(t''-t+T) dt'', \tag{13}$$

where the time-domain representations of the Green's function and probe pulse are used. Note that the Green's function is correlated with itself. This operation is matched filtering, with the filter matched to the impulse response for propagation from the probe source to the jth SRA element. This operation gives focusing in the time domain, that is, it reduces the time elongation due to multipath propagation.[8] The sum over array elements is a form of spatial matched filtering, analogous to that employed in the Bartlett matched-field processor.[10] In addition, this sum further improves temporal focusing as the temporal sidelobes of the matched filters for each channel tend to average to zero which also is analogous to broadband matched-field processing results.[14] Finally, note that the integral over t'' in Eq. (13) is a convolution of each matched-filtered channel impulse response with the time-reversed and delayed probe pulse. As a consequence, this pulse is *not* matched filtered, for example, a linear FM up-sweep will appear as a down-sweep at the focus and will not be compressed.

Figure 5(a) shows a simulation for a 50-ms rectangular pulse with center frequency 445 Hz for the same geometry used in Fig. 4(a) as received at the SRA and Fig. 5(b) shows the pulse as transmitted to a plane at a range of 6.3 km, the range of PS. Four sources were excluded from the simulation because these phones were not used in the experiment. Note the temporal focusing; that is, the 50-ms pulse disperses to about 75 ms at the SRA but the time reversed pulse received at the VRA is compressed (focused) to 50 ms as opposed to exhibiting even further time dispersion. On the other hand, Fig. 5(c) shows a pulse 500 m outbound of PS (i.e., the VRA is at the same location but PS is 500 m closer to the SRA). The pulse is not spatially focused and it is temporally more diffuse than the result for the focal spot.

3. Properties of the focal region

A detailed discussion of the spatial and temporal factors affecting the focus is given in Appendix A. The primary result is that the TRM focus is robust, provided the SRA adequately samples the field in the water column. First, the focus tends to depend primarily on the properties of the

a)

b)

c)
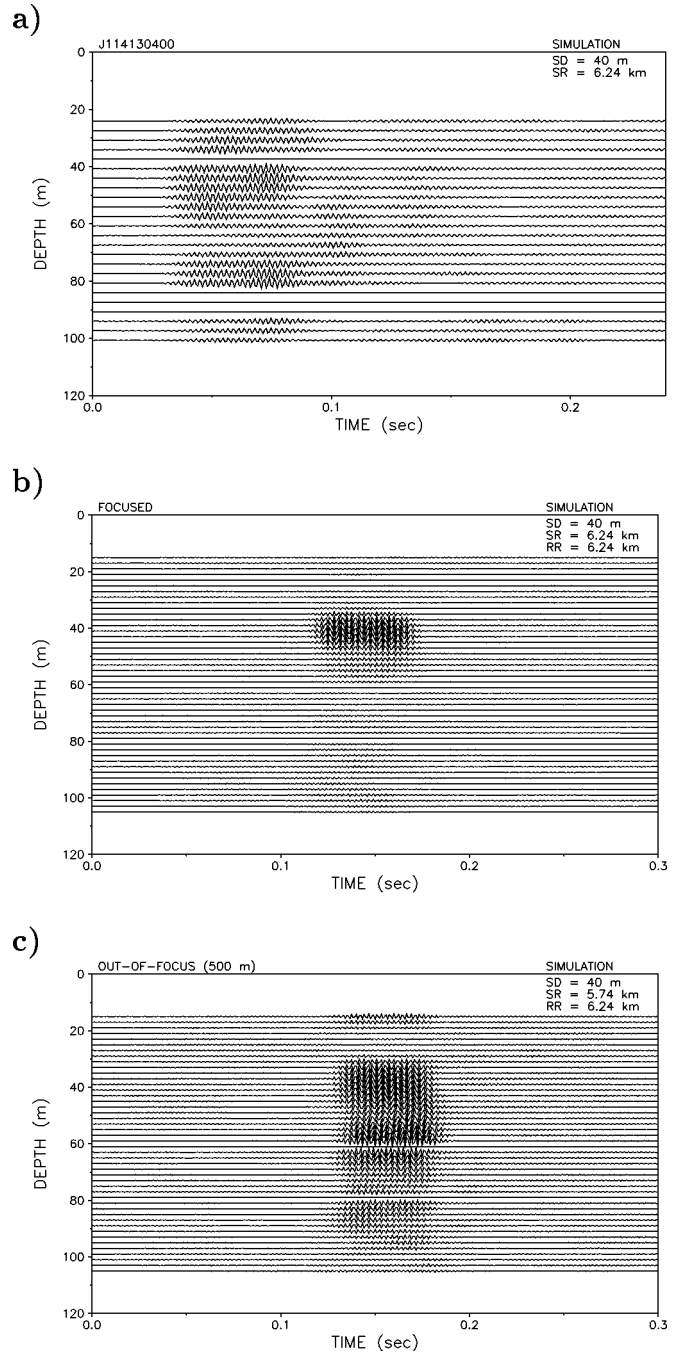
FIG. 5. Simulation of a 445-Hz, 50-ms transmitted pulse for the geometry in Fig. 2 for a probe source located at a depth of 40 m. (a) Pulse received on the SRA at range of 6.3 km from PS. There is a temporal dispersion of about 75 ms and significant energy throughout the water column. (b) The focus of the time reversed pulse at the VRA. There is pulse compression back to the original transmitted 50-ms duration as well as spatial focusing in depth. (c) Vertical and temporal distibution for a pulse 500 m outbound of PS (the VRA is at the same location but PS is 500 m closer to the SRA).

ocean near the focus and tends to be independent of (the possibly range-dependent) properties of the medium between the SRA and the focus. Temporal changes in the medium due to, for example, surface waves and internal waves degrade the focus, but this degradation will be tolerable if the average (or coherent) Green's function is not severely reduced by these time variations. Generally, the shape of the focus is approximated by the field that a point source placed at the
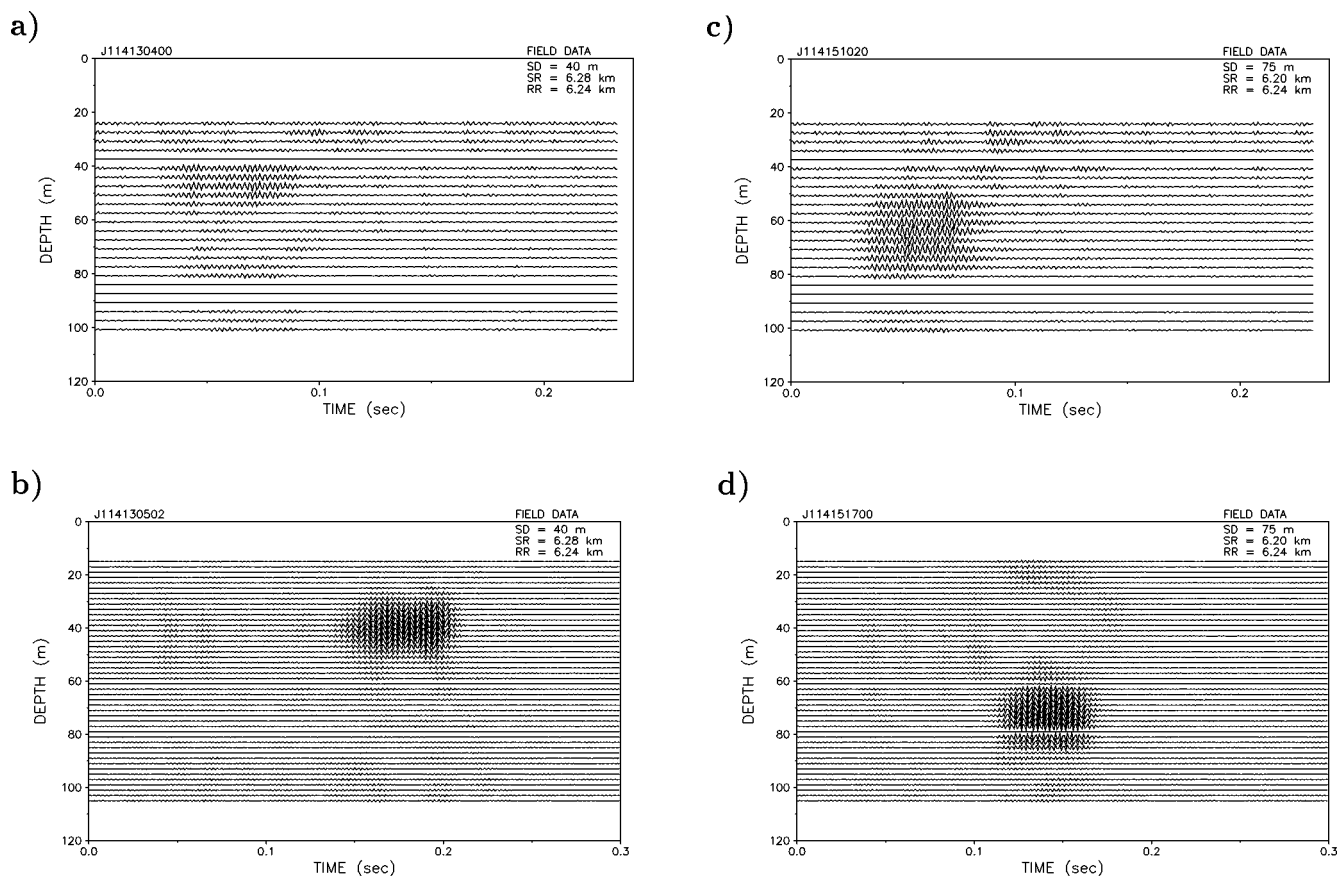
FIG. 6. Experimental results for probe source PS and VRA at same range. (a) The pulse data received on the SRA for PS at depth of 40 m. (b) The data received on the VRA from the time reversed transmission of pulses shown in (a). The VRA is 40 m inbound from the focus as determined by DGPS. (c) The pulse data received on the SRA for PS at depth of 75 m. (d) The data received on the VRA from the time-reversed transmission of pulse shown in (c). The VRA is 40 m outbound from the focus as determined by DGPS.

focus generates after nonpropagating modes are subtracted. Thus if absorption or scattering tends to eliminate high-order modes, the focus will be comprised of the remaining lower order modes and will be relatively broader. Very roughly, the vertical width of the focus will be equal to the water depth (or depth of the duct) divided by the number of contributing modes if the sound speed (in the duct) is not strongly dependent on depth.

The TRM focus is also robust with respect to array shape[4] provided the shape does not change between the probe reception and time reversed transmission. This property makes it unnecessary to know the exact shape of the TRM array and offers a considerable advantage over conventional beamforming.

II. EXPERIMENTAL DEMONSTRATION OF A TRM IN THE OCEAN

An assortment of runs was made to examine the structure of the focal point region and the temporal stability of the process. Here we will be reporting on three types of experiments (note that range refers to the distance from the SRA):

(1) Demonstration of the time-reversal mirror (TRM) in the ocean. The probe source (PS) is moved from shorter range to a longer range past the VRA. At each PS range, it sends out a 445-Hz, 50-ms pulse on the even minute. The pulse is received at the SRA, time reversed and retransmitted

five times (once every 10 s) starting at the odd minute. This signal is received at the VRA and data from all channels are recorded. Note that when PS is at the same range of the VRA, the data recorded at the VRA are a vertical slice of the focal range as indicated in the simulation for a harmonic source in Fig. 4. Figure 5(b) is a simulation of the expected results at that range. When PS is closer than the VRA, the VRA data correspond to a measurement beyond the focal range and vice versa when PS is beyond the VRA.

(2) Stability of TRM. PS is at the VRA range which means that we are measuring the vertical profile of the focal region. A 50-ms, 445-Hz pulse is sent out once and the SRA retransmits the same time reversed signal every 10 s for an extended period. Here the goal is to determine how long a single probe signal remains a valid phase conjugate probe for the specific ocean environment and source location. These results are constrained by the limitations of the actual experiment.

(3) Acoustic ping pong. The probe source with colocated receiver now acts as a tranponder. The SRA transmits a 50-ms water column filling signal to the transponder which is at a depth of 75 m. The transponder retransmits the received signal (no time reversal) to the SRA which then transmits the time-reversed signals from the full array. This commences an acoustic ping pong iteration between SRA and PS with PS acting as a transponder (SRT).
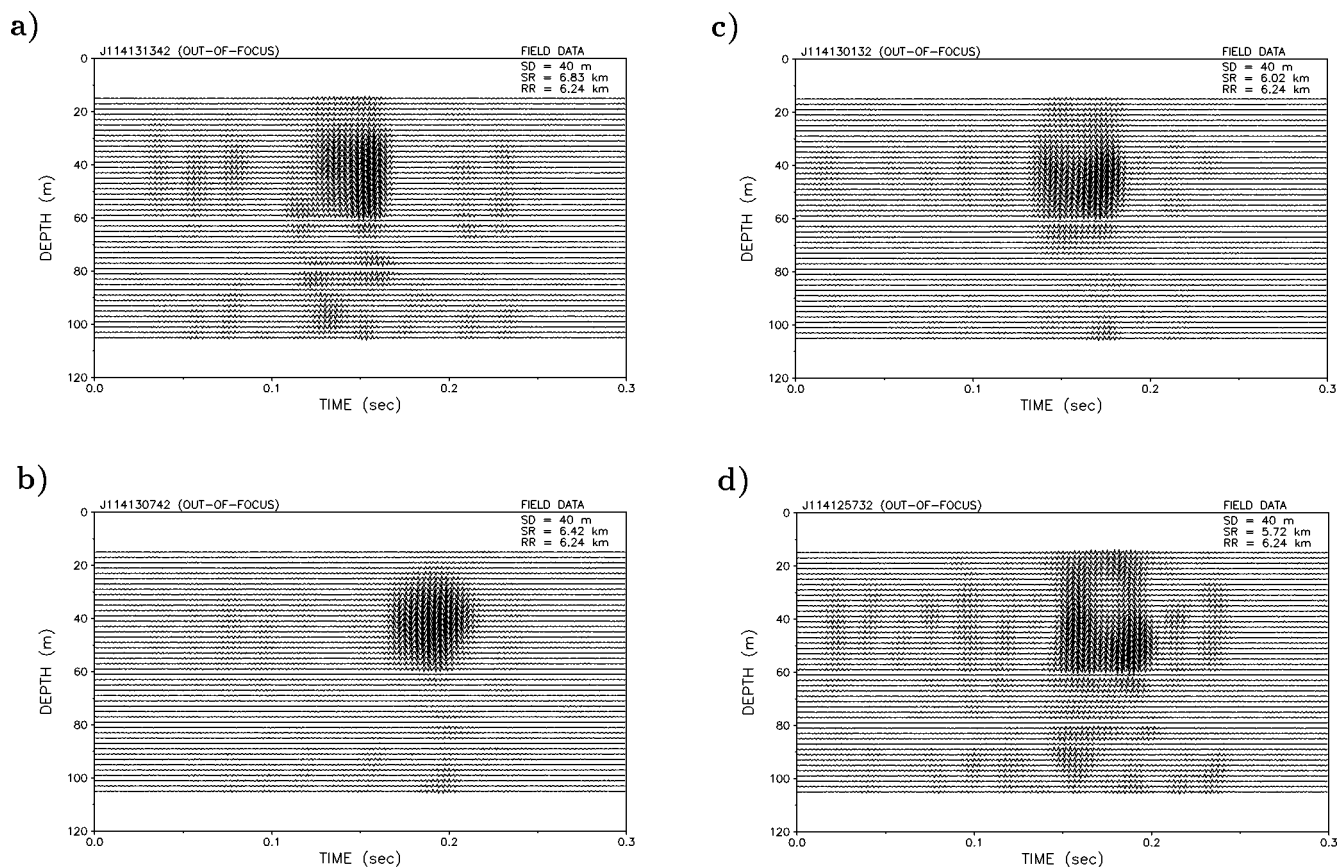
FIG. 7. Out of focus data received on the VRA from the time-reversed transmission of pulses with PS at a depth of 40 m. (a) PS is outbound 600 m. (b) PS is outbound 200 m. (c) PS is inbound 200 m. (d) PS is inbound 500 m.

A. Demonstration of TRM in the ocean

The vertical receive array VRA was deployed at a range, determined by DGPS, of 6.24 km from the SRA and the probe source PS was deployed at two different depths, 40 m and 75 m. Figure 6 shows the pulse as received on the SRA and VRA for both source depths. The data at the SRA are a combination of signal and noise. A 233-ms window was digitized and time reversed for transmission to the VRA. When the VRA and PS have the same range (experimentally within 40 m by a DGPS measurement) to the SRA, we see the focusing as predicted in Sec. I for a probe source at 40 m depth and similar results for a probe source at 75-m depth. Clearly, we have implemented a time-reversal mirror focusing at the range and depth of the probe source.

Figure 7 shows the result as we sweep through the focal point. Note that because of the way the experiment had to be performed, we are actually keeping the VRA fixed and changing the range of PS An alternative way to present the focusing effect which displays the sidelobes off the main peak is shown in Fig. 8. The solid line with circles is the nearest to the focal region. Here we see the sidelobes in the vertical becoming large as we move away from the focal region.

B. Stability of TRM

The variability of the sound-speed structure in the water column is indicated in Fig. 3 which contains a collection of

sound speeds derived from CTD's at different positions and times throughout the experiment. A thermistor chain placed at the position indicated in Fig. 2 reveals the varying temperature structure as shown in Fig. 9. In addition, there is information concerning wave heights from the waverider shown in Fig. 2. The time series of the rms waveheight is
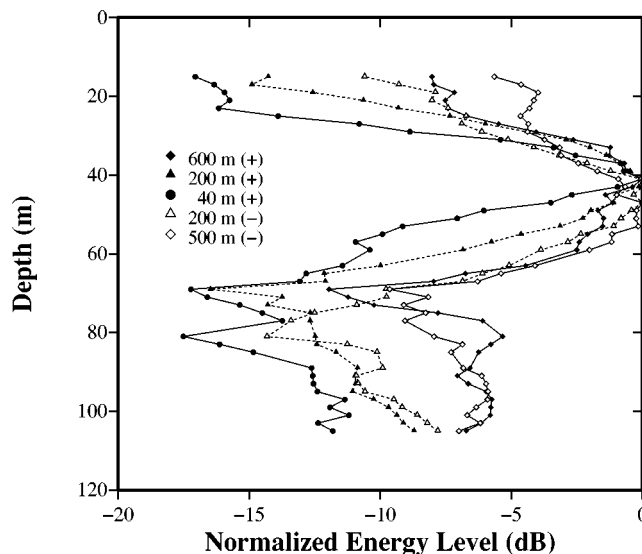
FIG. 8. The energy over a 0.3-s window as a function of depth for various ranges from the focal region. The depth of the probe source was 40 m. + means VRA is outbound from the focus (PS).
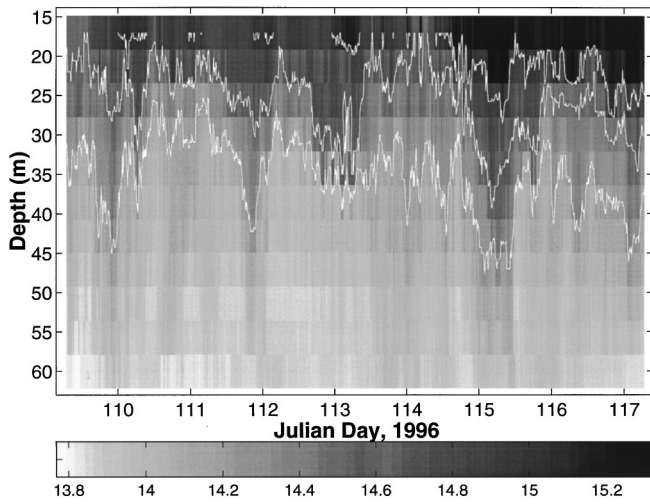
FIG. 9. Thermistor chain data. The contours from the top down are 15, 14.6, and 14.2 °C.
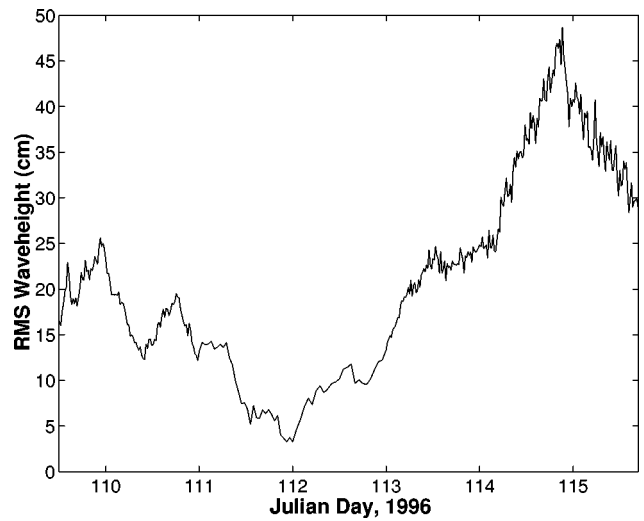
FIG. 10. Surface waveheight measurements from the waverider.

a)
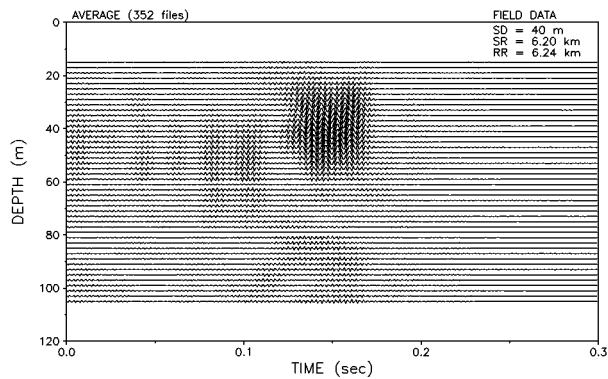
b)
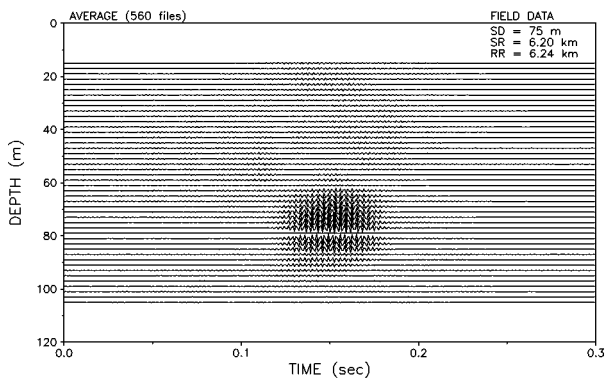
c)
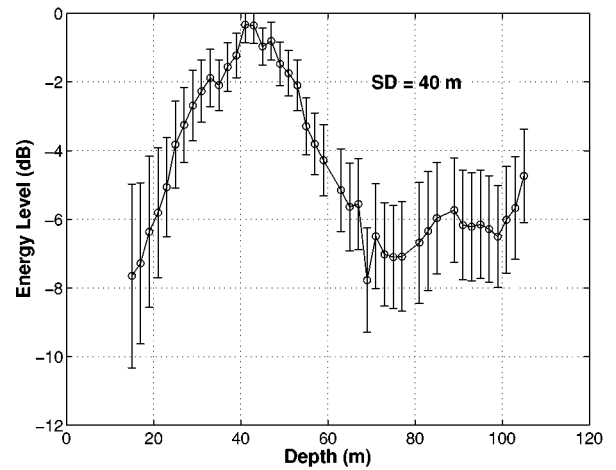
d)
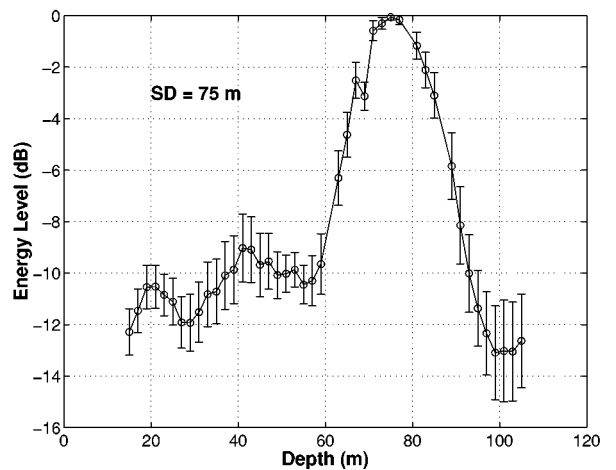
FIG. 11. Results on stability of the focal region. (a) Pulse arrival structure at VRA for probe source at 40 m depth averaged over 1 h. (b) Pulse arrival structure at VRA for probe source at 75 m depth averaged over 2 h. (c) Mean and standard deviation of energy in a 0.3-s window for 40-m probe source. (d) Mean and standard deviation of energy in a 0.3-s window for 75-m probe source.

a)

Mean Conjugate Field Strength Simulation, Rough Ocean Surface

Source Depth = 40 m

Source–Array Range = 6.25 km

Frequency = 445 Hz

RMS = 0.0 m
RMS = 0.3 m
RMS = 0.5 m

b)

Mean Conjugate Field Strength Simulation, Rough Ocean Surface

Source Depth = 74.4 m

Source–Array Range = 6.25 km

Frequency = 445 Hz

RMS = 0.0 m
RMS = 0.3 m
RMS = 0.5 m
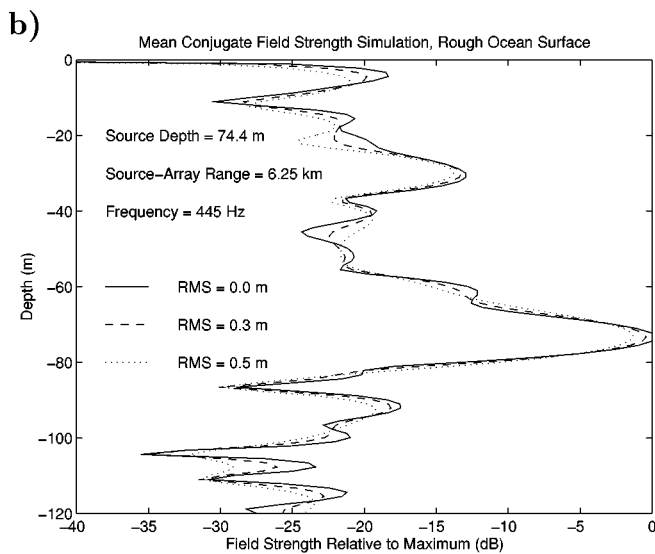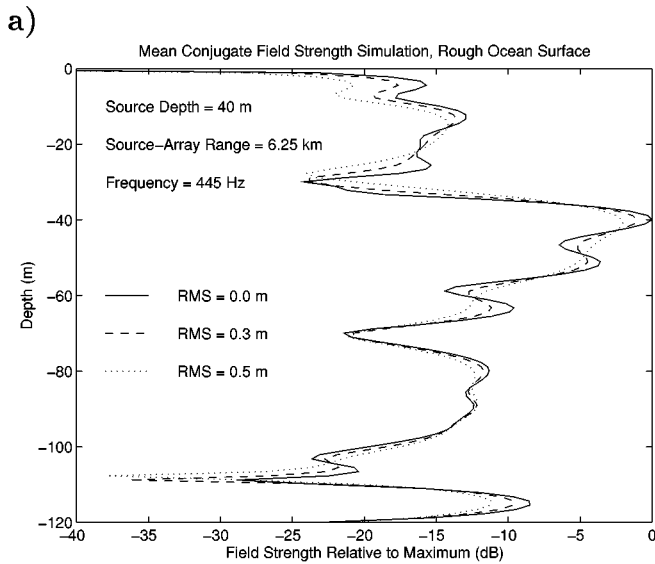
FIG. 12. Simulation of vertical profile of the mean field at the focal range for different values of surface roughness. (a) Probe source at 40 m. (b) Probe source at 75 m.

FIG. 13. Acoustic ping pong between a transponder at 75 m depth and a range of 6.24 km from the SRA. The waterfall plot shows the energy in a 0.3-s window at the VRA (which is at the same range as the transponder) as a function of depth for each of the 15 round trips. There were two minutes between each round trip.

17:07 and J114 18:47–19:47, respectively. Figure 11 shows the results of these runs. These plots indicate that the focus was considerably more stable for the deep probe source versus the shallower probe source and that the focus is broader for the shallower probe source.

Simulations using representative rms wave heights from Fig. 10 and the environment of the experiment with a normal mode rough surface mean field scattering theory[15] are shown in Fig. 12. The results indicate that surface scattering does not have a significant impact on the focal region for this particular environment. On the other hand, examination of the environmental data indicates that the probe source at the shallower depth was at the bottom of the thermocline where the water column variability was the greatest. As derived in Appendix A, we expect the focusing phenomenon to be most sensitive to the environment at the endpoints of the experimental geometry. The tentative conclusion is that the fluctuations in this case were caused by sound-speed fluctuations in the water column, but more analysis and finer sampled volume data are required.

shown in Fig. 10. Although the time series of the environmental data does not have the temporal and spatial resolution for an exhaustive comparison of theory and data, the two stability data collection periods show qualitative agreement with a first order analysis of the nature of the fluctuations.

Basically, as shown in Appendix A, theory predicts that the mean field dominates the focal region with fluctuations, being a diffuse phenomenon, becoming more apparent away from the focus. That is, if one considers the total field to be composed of a mean field and a fluctuating field, it is the mean field which has the coherence properties which produce the focusing whereas the fluctuating field is a form of signal-generated noise.

Two stability data collection periods for the probe source depths of 40 m and 75 m were made for 1 h and 2 h, respectively (the lengths of the runs were dictated by experimental circumstance). The Julian day and times of the stability runs for SD=75 m and SD=40 m were J114 15:11–

FIG. 14. Sound-speed profiles. The solid line was the optimum profile from the inversion process. The dashed line is thermistor chain derived sound-speed closest in time to the data shown in Fig. 6(a),(b).

a)

b)
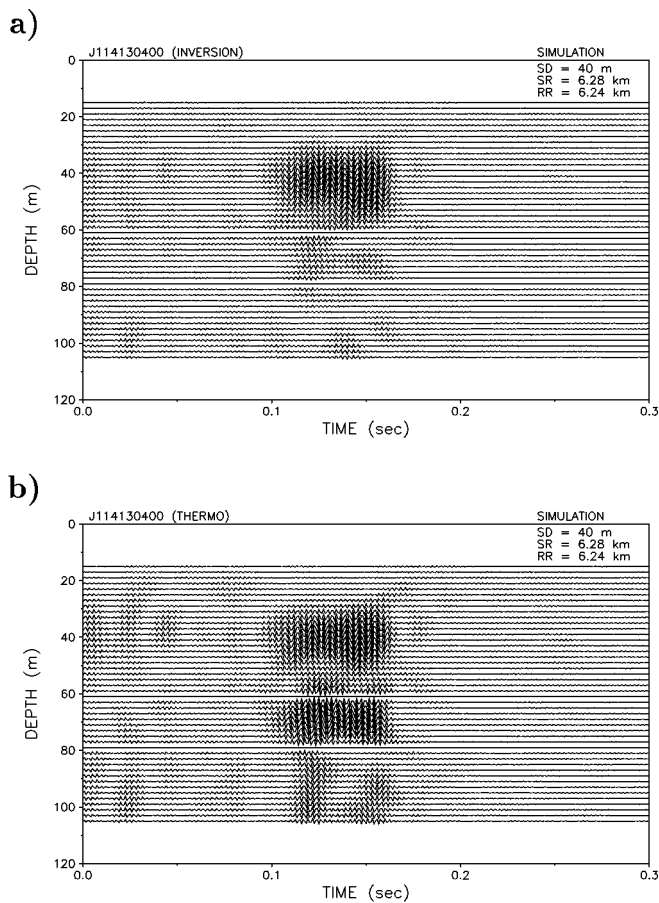
FIG. 15. Backpropagation using data from the SRA for the probe source at a depth of 40 m. (a) From the inversion process. (b) From the profile measured at the time of the experiment.

a)

b)

FIG. 16. Backpropagation using data from every other element of the SRA: 10-element TRM. (a) Probe source at a depth of 40 m. (b) Probe source at a depth of 75 m.

C. Acoustic ping pong: iterative focusing

The purpose of the acoustic ping pong experiment is to demonstrate that focusing can be iteratively improved. This has already been demonstrated and explained in earlier free-field multiscatterer, ultrasonic experiments.[16–18] Basically, since a TRM returns signals to their origin in proportion to their original relative strengths, repeating the process a second time will reduce the level of the focused field for the weaker signals versus the stronger signals, and so on. The theoretical explanation is in terms of eigenvalues and eigenvectors of the time-reversal operator. Eventually, only the strongest signal (or that part of the field corresponding to the largest eigenvalue) is focused.

In this experiment, ping pong was initiated and kept going for 15 round trips. Figure 13 is a waterfall plot of the energy in a 0.3-s window of the pulses received on the VRA which was at the same range as the transponder. There are 2 min between each round trip.

These results show the increased focusing brought about by the iteration process. However, this single source result is not completely analogous to the free-space multiscatterer results in Refs. 16–18. Rather, it depends on the particular TRM array-data eigenvector structure in the specific waveguide environment. A paper with a detailed explanation of this process is in preparation.

III. EXTRAPOLATING THE EXPERIMENTAL RESULTS

We have demonstrated that a time reversal mirror (TRM) can be implemented in the ocean and that its performance is consistent with theory. In this section we use a combination of data and theory to gain some additional insight into the potential usefulness of this process. In particular, we examine:

(1) its potential as a tool for inversion;
(2) whether a smaller aperture or few source/receiver elements would still be effective for producing a TRM.

Further, we use item 1 to help estimate the TRM performance of a smaller SRA.

A. TRM applied to sound speed inversion

Empirical orthogonal functions[19] (EOFs) about the mean of the profiles shown in Fig. 3 were constructed. It was then found through trial and error that the mean profile was sufficient to provide the optimum focusing using simulated back propagation from the SRA data. That is, the coefficient of the first term of an EOF expansion was negligible with respect to the expected accuracy of the sound-speed profiles. A plot of this result compared to ''CTD 11'' which was used in the simulations in Sec. I is shown in Fig. 14. This procedure is akin to matched field tomography[10,20,21] except that more information is available because of the vertical array at the
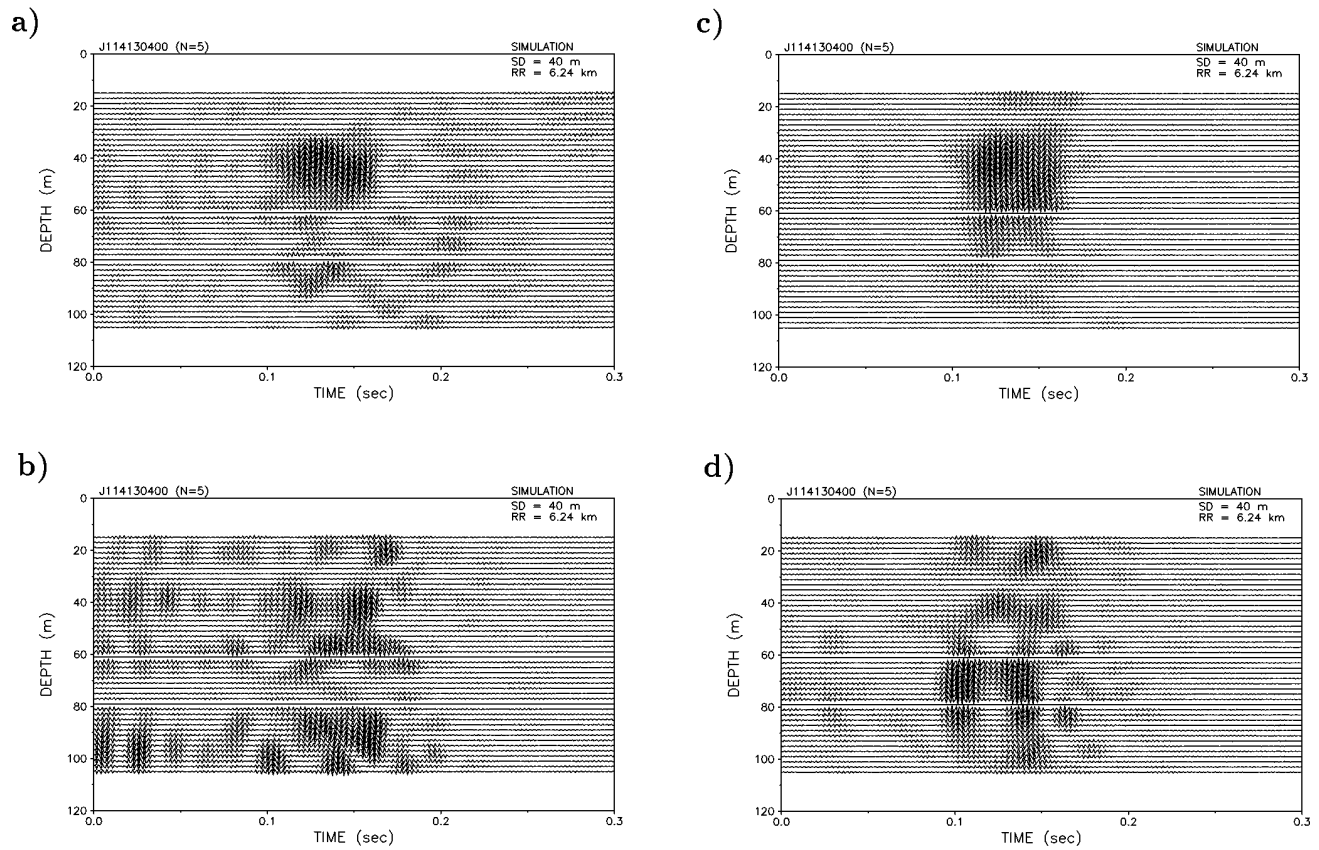
FIG. 17. Backpropagation produced TRM from a five-element SRA for the probe source at 40 m. (a) Elements 1, 5, 9, 13, 17 as numbered from the top. (b) First quarter of SRA. (c) Second quarter of SRA. (d) Third quarter of SRA.
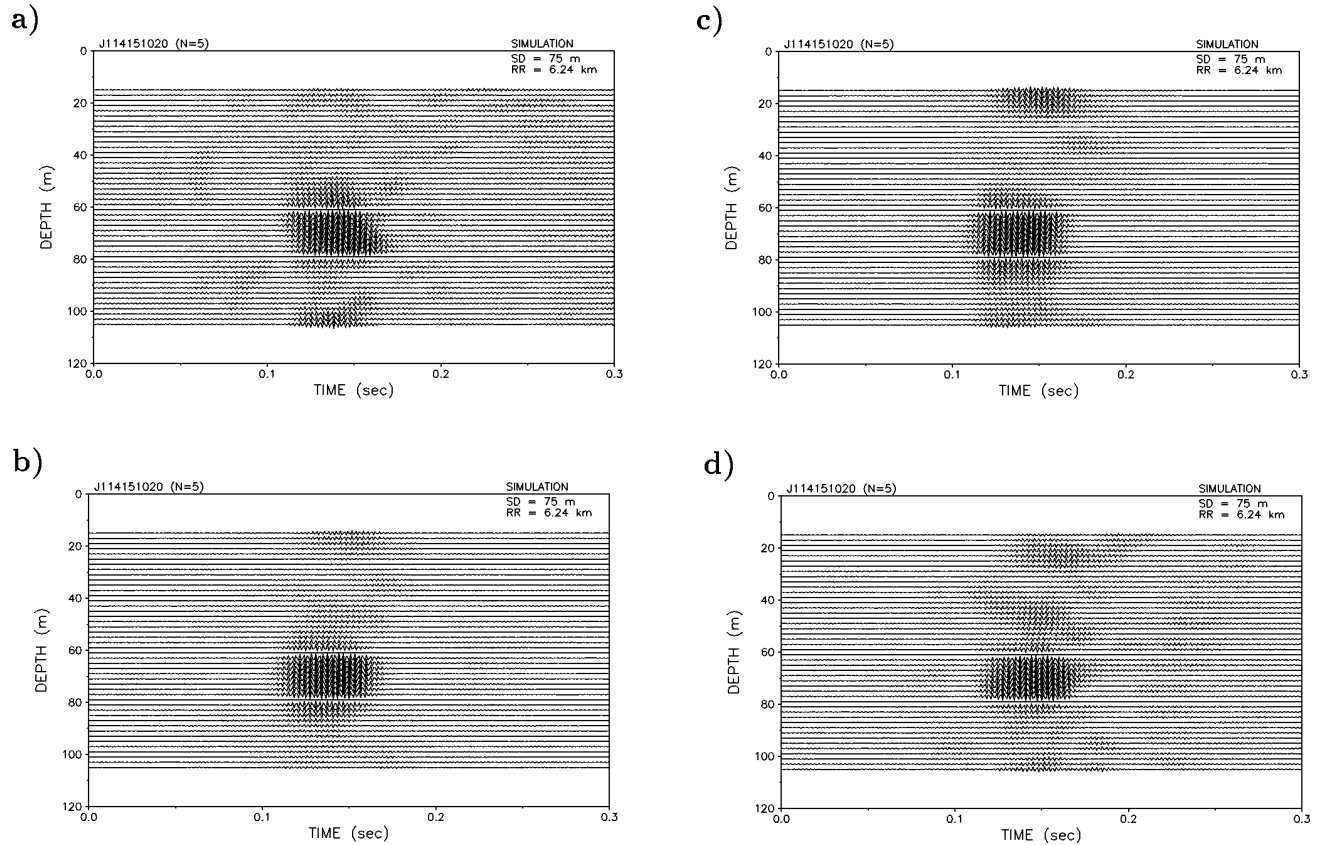
FIG. 18. Backpropagation produced TRM from a five-element SRA for the probe source at 75 m. (a) Elements 1, 5, 9, 13, 17 as numbered from the top. (b) Elements 12, 14, 16, 18, 20. (c) Third quarter of SRA. (d) Lowest quarter of SRA.

a)

b)
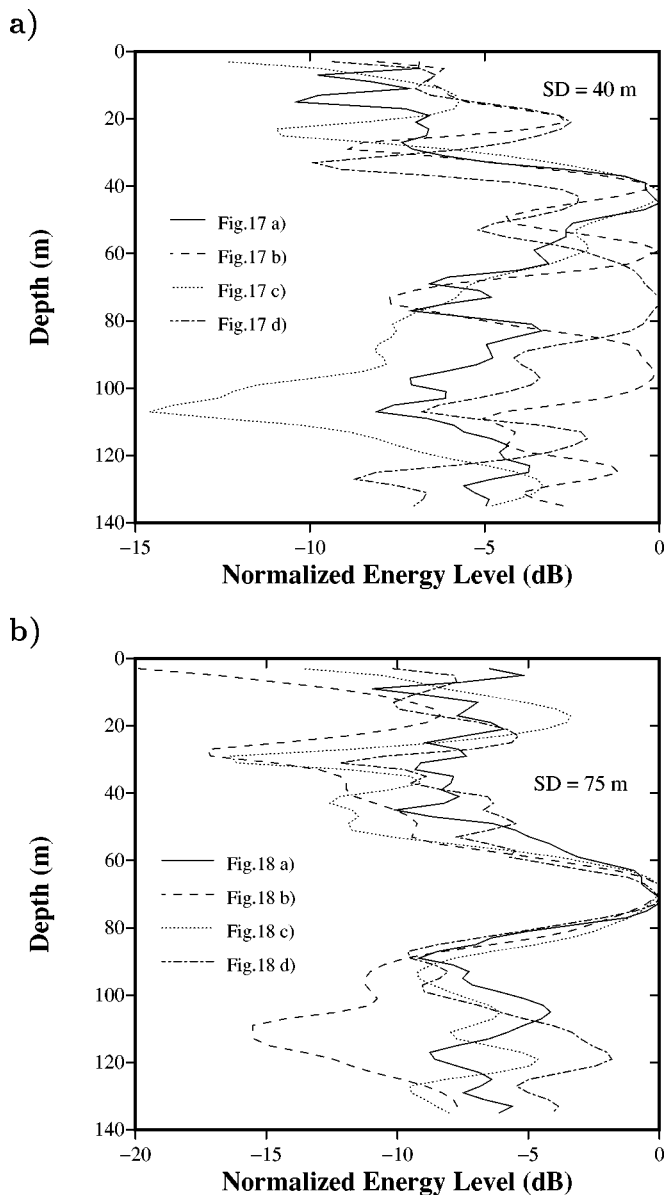
FIG. 19. Energy strength of five-element SRA backpropagation to the VRA. (a) Probe source at 40 m. (b) Probe source at 75 m.

focal distance. Also shown in Fig. 14 is the sound-speed profile taken closest in time to the experimental runs under discussion.

Figure 15 shows backpropagation results initiated from SRA data using (a) the profile obtained from the inversion and (b) the profile taken at the time of the TRM experiment. Clearly, the single experimental profile does not represent a range-independent profile descriptive of the experimental acoustic results, whereas the profile derived from the inversion represents an adequate range-independent approximation to the structure of the water column. These results are also meaningful in the context of mismatch in matched-field processing. The experimental results indicate that a matched field processor using the measured profile would not localize the source.

B. Reduced and sparse aperture TRM

A reduced aperture SRA would enhance the practicality of an ocean TRM. We have already shown through simula-

tion of a harmonic source in Fig. 4(c) that we can expect the phase conjugation process to remain effective as a focusing procedure as aperture is reduced. We should be able to reliably estimate the focal properties of a TRM using data from a subset of source/receiver elements and simulations of the backpropagation using the effective soundspeed profile shown in Fig. 14 found from the inversion. Of course, direct measurement for the sparse arrays would best study this aspect of the TRM, but such data were not taken in this experiment.

Figure 16 shows the results of an adiabatic mode model backpropagation of time-reversed pulse data from every other element of the SRA. We see that for both PS depths the focal region remains prominent for the ten-element SRA. We also present some results for an assortment of five element arrays in Figs. 17 and 18. Figure 19 shows a prediction of the vertical profile of the energy strength of these results which use five element subsets of SRA elements. The results are extended in depth to show the fields near the boundaries. The key thing to notice is that there are some very small arrays which still produce significant concentration of sound in the desired focal region. This probe source depth-dependent result has practical ramifications for active sonar system concepts in which one desires to minimize boundary reverberation at the range of the target. These results are not conclusive for the 40-m probe source depth because that was the depth of more or less maximum variation of the sound-speed profile. Hence, the sound-speed inversion result used in the backpropagation calculation might be the cause of the poorer focusing of the shallow source.

IV. CONCLUSIONS

We have constructed a time-reversal mirror (TRM) in the ocean and hence demonstrated that phase conjugation (PC) is realizable in the ocean using a source–receive array and rather simple signal processing. The waveguide nature of the ocean enhances the focusing properties over a free-space environment because the boundaries in effect enlarge the TRM aperture through its images. The degree of focusing is in excellent agreement with theory. Furthermore, an effective TRM need not be a full water column array. We also have investigated the stability of the PC process *vis a vis* ocean fluctuations and measurements suggest a relatively long stability of the PC process. Future studies will be aimed at the detailed relationship between ocean variability and the PC process and an investigation into the possibility of using PC for inverting for the ocean environment. In addition, it should be straightforward to experimentally confirm predictions of the focal size versus SRA aperture.

ACKNOWLEDGMENT

APPENDIX A: FACTORS AFFECTING THE FOCUS

In interpreting the results of the 1996 phase conjugation experiment, a primary issue is degradation of phase-conjugate focusing. Such degrading influences can be di-

vided into static and dynamic categories, the former including propagation and array structure effects and the latter including effects due to the time-varying ocean surface and volume. The object of study is the field produced by a phase conjugate source–receiver array (SRA), which can be written in the general form

$$P_{pc}(r,z;\omega) = \sum_{j=1}^{J} G_2(\mathbf{r},\mathbf{r}_j)G_1^*(\mathbf{r}_j,\mathbf{r}_s). \tag{A1}$$

In Eq. (A1), $P_{pc}(r,z;\omega)$ is the field produced at the field point, $\mathbf{r}=(r,z)$, by the phase-conjugate array with probe source placed at $\mathbf{r}_{ps}=(R,z_{ps})$. The sum is over the J elements of the SRA whose position vectors are denoted $\mathbf{r}_j = (0,z_j)$. Following the convention used in the main text, horizontal ranges are measured from the SRA. Propagation from the probe source to the array is described by the Green's function $G_1(\mathbf{r}_n,\mathbf{r}_{ps})$, while propagation from the array to the field point is described by $G_2(\mathbf{r},\mathbf{r}_n)$. The subscripts 1 and 2 allow for the possibility that time variation of the ocean might cause changes in the Green's function between the probe and phase-conjugate transmission cycles. During either propagation cycle, the ocean is assumed to be ''frozen'' in the sense that it behaves as a time-invariant linear system. In this view, the Green's function is the frequency-dependent system transfer function for acoustic propagation between any two points in the ocean. The frequency argument of the Green's function used in the main text is suppressed here for convenience, but it becomes important in treating pulsed transmissions.

1. Phase conjugation in static environments

The factors that control phase-conjugate focusing in static environments will be examined by considering a general nonuniform, nonadiabatic waveguide. The conditions for ''ideal'' phase-conjugate focusing in such a waveguide will be derived and this will implicitly identify the factors that degrade focusing. To simplify the discussion, only vertical phase-conjugate arrays will be considered. The main objective is to generalize Eq. (9) of the main text to the range-dependent case, using the approach given by Siderius et al.[22] in connection with the ''guide source'' concept. In this approach, small regions near the probe source and SRA are assumed to be range independent, but the larger region between is allowed to have arbitrary range dependence in bathymetry and sound speed. Losses are neglected and will be discussed later in qualitative terms.

The Green's function for the probe field near the probe source is approximated using range-independent normal modes.

$$G_{\omega}(r,z;R,z_{ps}) = \sum_{n} \frac{a_n(z_{ps})u_n(R,z)}{\sqrt{k_n(R)|r-R|}} e^{ik_n(R)|r-R|}. \tag{A2}$$

Similarly, the Green's function for the probe field at the SRA is written in the form

$$G_{\omega}(0,z_j;R,z_{ps}) = \sum_{n} \frac{b_n(z_{ps})u_n(0,z_j)}{\sqrt{k_n(0)R}} e^{ik_n(0)R}. \tag{A3}$$

The modal eigenfunctions in the vicinity of the probe source and SRA are denoted $u_n(R,z)$ and $u_n(0,z)$, respectively. The corresponding eigenvalues are $k_n(R)$ and $k_n(0)$. These Green's functions do not bear the subscripts 1 and 2 introduced earlier because a time-invariant environment is under consideration. The subscript ω is used here in the same sense as in the main text. The mode amplitudes for the near-source Green's function are

$$a_n(z_{ps}) = \frac{ie^{-i\pi/4}}{\sqrt{8\pi\rho(z_{ps})}} u_n(R,z_{ps}), \tag{A4}$$

and the mode amplitudes for the Green's function near the SRA are given by the linear transformation

$$b_m(z) = \sum_{n} U_{mn}a_n(z). \tag{A5}$$

For convenience, it is assumed that there are the same number of modes near the source and near the array, so that U_{mn} is a square matrix. Cases for which these numbers are similar but not equal can be treated by discarding high-order modes. The matrix U_{mn} includes any mode coupling that is due to the range dependence of the ocean and is defined in such a way as to be independent of source depth. Furthermore, to the extent that absorption loss in the water column and seafloor can be neglected, U_{mn} is unitary.

The field produced by the SRA is

$$P_{pc}(r,z;\omega) = \sum_{j=1}^{J} G_{\omega}(r,z;0,z_j)G_{\omega}^*(0,z_j;R,z_{ps}). \tag{A6}$$

The Green's function for propagation from the jth array element to the field point (r,z) can be expressed in terms of the Green's function for propagation in the opposite direction by using reciprocity:

$$G_{\omega}(r,z;0,z_j) = \frac{\rho(z)}{\rho(z_j)} G_{\omega}(0,z_j;r,z). \tag{A7}$$

In terms of mode amplitudes,

$$G_{\omega}(r,z;0,z_j) = \frac{\rho(z)}{\rho(z_j)} \sum_{n} \frac{c_n(z)u_n(0,z_j)}{\sqrt{k_n(0)r}} e^{ik_n(0)R}, \tag{A8}$$

where the mode amplitudes, $c_n(z)$, are

$$c_m(z) = \sum_{n} U_{mn}a_n(z)e^{ik_n(R)(r-R)}. \tag{A9}$$

Note that the mode amplitudes, $c_n(z)$, are essentially the same as the $b_n(z)$, but with the source range coordinate shifted by $r-R$.

Equations (A3) and (A8) can be inserted in Eq. (A6) to obtain an expression for the phase-conjugate field in a range-dependent waveguide:

$$P_{pc}(r,z;\omega) = \frac{\rho(z)}{\sqrt{Rr}} \sum_{m,n} \frac{c_m(z)\Delta_{mn}b_n^*(z_{ps})}{\sqrt{k_m(0)k_n^*(0)}} e^{i[k_m(0)-k_n^*(0)]R},$$

$$\tag{A10}$$

where

$$\Delta_{mn} = \sum_{j=1}^{J} \frac{u_m(0,z_j)u_n(0,z_j)}{\rho(z_j)}. \tag{A11}$$

In the ideal case, the array spans the entire water column with elements having uniform spacing, d_a, and the modal eigenfunctions have negligible amplitude in the bottom. In this case, the sum over array elements in Eq. (A11) approximates the orthogonality integral for modal eigenfunctions [Eq. (5)], and $\Delta_{mn}d_a$ can be taken equal to δ_{mn}. This ideal can be approached quite closely in the environment of the 1996 experiment. Using the environmental parameters defined in Fig. 4(a), and considering only the first 12 modes, an array with 36 elements with spacing $d_a = 3.33$ m and with the shallowest element 4.44 m below the surface gives diagonal elements in $\Delta_{mn}d_a$ that are within 3% of unity and off-diagonal elements that are of order 0.03 or less. The first mode is an exception; it has a small diagonal element as it is trapped in the first sediment layer and not adequately sampled by the array. This is of no consequence, as this mode is very lossy and does not contribute to propagation. The element placement of the actual array gives smallest diagonal elements of about 0.5 with a few off-diagonal elements as large as 0.3.

Returning to the derivation of the conditions for ideal phase-conjugate focusing, take $\Delta_{mn} = \delta_{mn}/d_a$ in Eq. (A10) to obtain

$$P_{pc}(r,z;\omega) = \frac{\rho(z)}{d_a\sqrt{Rr}} \sum_{m,n} Q_{mn}a_m(z)a_n^*(z_{ps})e^{ik_m(R)(r-R)}, \tag{A12}$$

where

$$Q_{mn} = \sum_l \frac{U_{lm}U_{ln}^*}{k_l(0)} e^{-2\Im[k_m(0)]R}. \tag{A13}$$

Losses due to absorption and scattering are detrimental to phase-conjugate focusing, as they cause attenuation of higher-order modes, yielding a blurrier focus than would be possible with lower loss. Furthermore, this blurring will increase as the range between the source and the array increases owing to the strong range and mode number dependence of attenuation. Thus in defining the ideal case, losses are set to zero and the mode coupling matrix, U_{mn}, is taken to be unitary. If the mode dependence of $k_l(0)$ in Eq. (A13) is neglected,

$$Q_{mn} = \frac{\delta_{mn}}{k_m(0)}, \tag{A14}$$

and the phase-conjugate field for an ideal array in a lossless environment can be approximated as

$$P_{pc}(r,z;\omega) = \sum_n \frac{u_n(R,z)u_n(R,z_{ps})e^{ik_n(R)(r-R)}}{8\pi\rho(z_{ps})k_n(0)d_a\sqrt{Rr}}. \tag{A15}$$

Apart from inessential factors, this expression is the same as Eq. (9) of the main text which was derived for the range-independent case. Even though Eq. (A15) represents the ideal case, it illustrates properties that actual phase-conjugate arrays may possess, provided they are not too far from ideal.

One such property is independence of the focus pattern on the distance between the probe source and the array (when absorption can be neglected and apart from the cylindrical spreading factor $1/\sqrt{Rr}$). Even more strikingly, the focus field is independent of the (possibly range-dependent) environment between the focus and the array (see examples presented by Siderius et al.[22]). That is, the focus depends only on the local properties of the water column and sea floor and is not affected by bathymetry or range-dependent water column properties in the region between the array and the focus, provided the latter do not change apprcciably during the two propagation cycles. This means that, in the ideal case, phase conjugation is not affected by time-invariant forward scattering due to bathymetry, fronts, etc. It also implies that, in simulations of phase-conjugate focusing, it is important to accurately model the ocean in the vicinity of the focus, but less accuracy is required for the more distant parts of the propagation path. One important reservation must be added at this point. The derivation above is essentially two dimensional in that cross-range spatial variation of the ocean is neglected. Static out-of-plane scattering *will* degrade phase-conjugate focusing if one-dimensional vertical arrays are used. Planar or volumetric arrays of sufficient aperture, on the other hand, will not suffer due to static out-of-plane scattering.

The invariance seen in the ideal case is similar to that predicted for an ideal, closed phase-conjugate surface array[4] which produces a strictly invariant focal field that resembles the original field of the probe source, except that the phase-conjugate field is a standing wave. In the present case, the probe source field (including only propagating modes) is given by Eq. (A2) which can be put in the form

$$G(r,z;R,z_{ps}) = \frac{ie^{-i\pi/4}}{\rho(z_{ps})\sqrt{8\pi|r-R|}}$$
$$\times \sum_n \frac{u_n(R,z)u_n(R,z_{ps})e^{ik_n(R)|r-R|}}{\sqrt{k_n(R)}}. \tag{A16}$$

Apart from a difference in spreading loss and an overall phase difference, Eqs. (A15) and (A16) are quite similar. There is a slight term-by-term difference owing to differing factors involving modal eigenvalues, but the primary difference is in the propagation phase factor. The source field propagates *away* from the source location while the phase-conjugate field propagates *past* the source location in the direction away from the array.

2. Phase conjugation in time varying environments

Time-dependent forward scattering due to surface and internal waves causes change in the propagation characteristics of the medium in the time interval between the probe and phase-conjugate transmission cycles with attendant degradation of phase-conjugate focusing.[5] In discussing scattering from a general point of view, it is convenient to decompose the Green's function into coherent and incoherent parts:

$$G_\alpha(\mathbf{r},\mathbf{r}') = \bar{G}(\mathbf{r},\mathbf{r}') + \delta G_\alpha(\mathbf{r},\mathbf{r}'). \tag{A17}$$

The subscript α takes on the values 1 and 2 for the probe and conjugate transmission cycles, respectively. The coherent, or mean, Green's function, $\bar{G}(\mathbf{r},\mathbf{r}')$ is not assigned a subscript because the random time variations are assumed to be stationary in the statistical sense. It will be assumed that sufficient time has elapsed between the probe and conjugate transmission cycles that variations in the two Green's functions are uncorrelated.

$$\langle \delta G_2(\mathbf{r}_d,\mathbf{r}_c) \delta G_1^*(\mathbf{r}_b,\mathbf{r}_a) \rangle = \langle \delta G_2(\mathbf{r}_d,\mathbf{r}_c) \delta G_1(\mathbf{r}_b,\mathbf{r}_a) \rangle$$

$$= 0. \qquad (A18)$$

This condition was very likely satisfied in the 1996 experiment with respect to scattering by surface waves, which have correlation timescales on the order of seconds, while the time between transmission cycles was measured in minutes and hours. Internal waves have relatively long correlation time scales, but the longer transmission intervals (several minutes to a few hours) of the experiment were most likely sufficient to produce decorrelation of fluctuations in volume scattering.

Combining Eqs. (A1), (A17) and (A18), the mean phase-conjugate field is

$$\bar{P}_{pc}(r,z;\omega) = \sum_{j=1}^{J} \bar{G}(\mathbf{r},\mathbf{r}_j)\bar{G}^*(\mathbf{r}_j,\mathbf{r}_{ps}), \qquad (A19)$$

and the variance of the field is

$$\overline{|P_{pc}(r,z;\omega)|^2} - |\bar{P}_{pc}(r,z;\omega)|^2$$

$$= \sum_{j=1}^{J} \sum_{j'=1}^{J} [\bar{G}(\mathbf{r},\mathbf{r}_j)\bar{G}^*(\mathbf{r},\mathbf{r}_{j'})K_{jj'}(\mathbf{r}_{ps})$$

$$+ \bar{G}(\mathbf{r}_{ps},\mathbf{r}_j)\bar{G}^*(\mathbf{r}_{ps},\mathbf{r}_{j'})K_{jj'}(\mathbf{r}) + K_{jj'}(\mathbf{r})K_{jj'}(\mathbf{r}_{ps})],$$

$$(A20)$$

where

$$K_{jj'}(\mathbf{r}) = \langle \delta G_\alpha(\mathbf{r}_j,\mathbf{r}) \delta G_\alpha^*(\mathbf{r}_{j'},\mathbf{r}) \rangle. \qquad (A21)$$

The covariance, $K_{jj'}(\mathbf{r})$, is proportional to the correlation between the incoherent field at elements j and j' of the array with a unit point source situated at $\mathbf{r}$. In deriving Eq. (A20), free use was made of reciprocity (which allows interchange of the two arguments of the Green's function) and stationarity (which means that δG_1 and δG_2 have identical statistics).

Equations (A19) and (A20) are general and include three-dimensional scattering (i.e., in-plane and out-of-plane scattering). They lead to two general conclusions regarding focusing in the 1996 experiment for those cases in which sufficient time elapsed between the two transmission cycles. First, the mean focus field, that is, the focus field averaged over many independent probe-conjugate-transmission cycles, is obtained by using the coherent Green's function in place of the actual (random) Green's function. Second, and most important, the field near the focus does not fluctuate appreciably, that is, it is well approximated by the mean focus field. This conclusion is supported by careful inspection of Eq. (A20), which shows that the variance of the phase-conjugate field is not localized near the focus, but is spread diffusely in range and depth. Thus near the focus, the mean

field dominates, unless scattering is strong enough to diminish the mean Green's function to such a degree that focusing is essentially destroyed.

To see that the field variance is unfocused, it is necessary to discuss each term in Eq. (A20) The first term can be viewed as being proportional to the intensity of a phase reversed retransmission of the incoherent field produced by scattering of the probe transmission. This retransmission will be directed back toward the the scatterers responsible for the incoherent component of the probe field, and these are spread over the entire volume and surface of the ocean. Similarly, the second term is proportional to the intensity produced at the source location by a coherent retransmission of the phase-reversed incoherent field produced from a fictitious source placed at the field point (reciprocity is being used in this interpretation). Again, this retransmission will be diffuse and will not peak as the field point approaches the source location. The last term in Eq. (A20) is more difficult to assess. It is a double sum over all array elements of the product of covariances due to sources placed at both the field point and probe source location. If scattering and propagation are very complicated in a spatial sense, these covariances will not be strongly dependent upon the source locations. That is, the incoherent field produced by these sources does not contain information on the source location. If this is the case, the covariances will be largely independent of $\mathbf{r}$ and $\mathbf{r}_{ps}$, and the last term of Eq. (A20) will not peak as $\mathbf{r}$ approaches $\mathbf{r}_{ps}$.

APPENDIX B: HARDWARE DESCRIPTION

The phase conjugation (time reversal mirror) experiment was carried out in April 1996 off the northwest coast of Italy. As shown in Fig. 2, a source–receiver array (SRA) was deployed in 125-m-deep water and cabled approximately 1 km back to a small island, Formica di Grosseto (42° 34.6′ N, 10° 52.9′ E). A rf telemetered vertical receive array (VRA) was deployed in 145-m-deep water approximately 6.3 km west of Formica and used to measure the structure of the acoustic field across the water column. The R/V ALLIANCE received this rf telemetered data stream and also deployed a source–receive transponder (SRT) (echo repeater) which also was used as a probe source (PS).

The vertical source array portion of the SRA consisted of 24 slotted cylinder sources spaced 3.33 m apart (total aperture 76.6 m). The sources have a resonance at approximately 445 Hz and a 3 dB bandwidth of approximately 35 Hz as shown in Fig. B1. Thus the SRA sources were separated by approximately one wavelength at their center frequency. Each source was hardwired individually back to the transmit control system on Formiche di Grosseto via a multiple twisted pair umbilical cable. The transmit control system synthesized the low-level analog signals for each source and these then were amplified prior to coupling onto the umbilical cable. Based on a nominal driving level of 100 VRMS, the nominal source level of the transducers was 165 dB re: μPa.

In addition to the vertical source array, the SRA included a colocated (i.e., physically strapped together) vertical receive array consisting of 48 hydrophones spaced half the separation of the source array transducers. The time se-

Slotted Cylinder Transducer 22A - Voltage Source Level
Driving Voltage 100 V rms
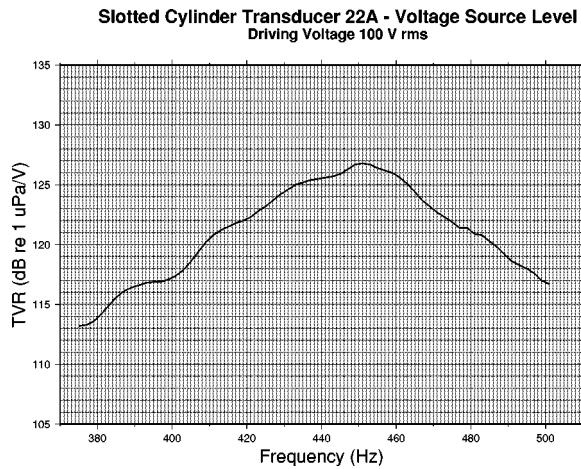
FIG. B1. Transmitting voltage response (TVR) versus frequency for one of the slotted cylinder source array transducers.

ries from each array element was sampled at $f_s = 1.5$ kHz using 24 bit A/D converters, multiplexed onto a single digital data stream, and cabled back to Formiche di Grosseto via a separate coaxial umbilical cable.[23] The shore-based digital data acquisition system archived the data stream and enabled capturing short segments of the array time series (from the 24 hydrophones colocated with the source array transducers) for time reversal and retransmission by the transmit control system. Due to high-level contaminants observed in four of the time series, these channels were set to zero during the retransmission process.

The rf telemetered vertical receive array (VRA) consisted of 64 hydrophones in a nested configuration over a 90-m aperture.[24] A 46 element subset of these hydrophones with 2-m spacing was used to generate the results discussed in the main text. The time series from each array element was sampled at $f_s = 1.2$ kHz, multiplexed onto a single digital data stream, and sent via rf telemetry to the R/V ALLIANCE for both quick-look analysis and archival purposes.

Last, the source–receive transponder (SRT) (echo repeater) and probe source (PS) consisted of a slotted cylinder transducer identical to those used in the source array, and it was operated at the same nominal source level of 165 dB re: 1 μPa. When used as an echo repeater, the SRT included a separate receiving hydrophone to sample the acoustic field at the depth of the source. In this case, a short segment of the received time series containing a SRA transmission was captured, amplified, and retransmitted (without time reversal). When used simply as a source, the SRT transmitted a 50-ms, 445-Hz pulse which probed the multipath structure of the channel. In this case, the SRA received the temporally and spatially spread transmission, time reversed and amplified the 24 time series, and retransmitted them from the source

array transducers. By allowing the R/V ALLIANCE to tow the PS slowly through the range between the SRA and VRA, the focal region of the phase conjugation process could be studied and these results are discussed in the main text.

[1] B. Y. Zel'dovich, N. F. Pilipetsky, and V. V. Shkunov, *Principles of Phase Conjugation* (Springer-Verlag, Berlin, 1985).
[2] M. Fink, C. Prada, F. Wu, and D. Cassereau, ''Self-focusing with time reversal mirror in inhomogeneous media,'' Proc. IEEE Ultrason. Symp. 1989 Montreal **2**, 681–686 (1989).
[3] M. Fink, ''Time Reversal Mirrors,'' in *Acoustical Imaging*, Vol. 21, edited by J. P. Jones (Plenum, New York, 1995), pp. 1–15.
[4] D. R. Jackson and D. R. Dowling, ''Phase conjugation in underwater acoustics,'' J. Acoust. Soc. Am. **89**, 171–181 (1991).
[5] D. R. Jackson and D. R. Dowling, ''Narrow-band performance of phase-conjugate arrays in dynamic random media,'' J. Acoust. Soc. Am. **91**, 3257–3277 (1992).
[6] D. R. Dowling, ''Phase-conjugate array focusing in a moving medium,'' J. Acoust. Soc. Am. **94**, 1716–1718 (1993).
[7] D. R. Dowling, ''Acoustic pulse compression using passive phase-conjugate processing,'' J. Acoust. Soc. Am. **95**, 1450–1458 (1994).
[8] A. Parvulescu and C. S. Clay, ''Reproducibility of signal transmissions in the ocean,'' Radio Electron Eng. **29**, 223–228 (1965).
[9] A. Parvulescu, ''Matched-signal (''Mess'') processing by the ocean,'' J. Acoust. Soc. Am. **98**, 943–960 (1995).
[10] A. B. Baggeroer, W. A. Kuperman, and P. N. Mikhalevsky, ''An overview of matched field methods in ocean acoustics,'' IEEE J. Ocean Eng. **18**, 401–424 (1993).
[11] F. B. Jensen, ''Sound propagation in shallow water: A detailed description of the acoustic field close to the surface and bottom,'' J. Acoust. Soc. Am. **70**, 1397–1406 (1981).
[12] F. B. Jensen, W. A. Kuperman, M. B. Porter, and H. Schmidt, *Computational Ocean Acoustics* (American Institute of Physics, New York, 1994).
[13] M. B. Porter, ''The KRAKEN normal mode program,'' SACLANTCEN Memorandum, **SM-245**, La Spezia, Italy (1991).
[14] R. K. Brienzo and W. S. Hodgkiss, ''Broadband matched-field processing,'' J. Acoust. Soc. Am. **94**, 2821–2831 (1993).
[15] W. A. Kuperman and F. Ingenito, ''Attenuation of the coherent component of sound propagating in shallow water with rough boundaries,'' J. Acoust. Soc. Am. **61**, 1178–1187 (1977).
[16] C. Prada, F. Wu, and M. Fink, ''The iterative time reversal mirror: A solution to self-focusing in the pulse echo mode,'' J. Acoust. Soc. Am. **90**, 1119–1129 (1991).
[17] C. Prada, J. L. Thomas, and M. Fink, ''The iterative time reversal process: Analysis of the convergence,'' J. Acoust. Soc. Am. **97**, 62–71 (1995).
[18] C. Prada, S. Manneville, D. Spoliansky, and M. Fink, ''Decomposition of the time reversal operator: Detection and selective focusing on two scatterers,'' J. Acoust. Soc. Am. **99**, 2067–2076 (1996).
[19] A. Tolstoy, ''Linearization of the matched field processing approach to acoustic tomography,'' J. Acoust. Soc. Am. **91**, 781–787 (1992).
[20] M. D. Collins and W. A. Kuperman, ''Focalization: Environmental focusing and source localization,'' J. Acoust. Soc. Am. **90**, 1410–1422 (1991).
[21] A. Tolstoy, *Matched Field Processing for Underwater Acoustics* (World Scientific, Singapore, 1993).
[22] M. Siderius, D. R. Jackson, D. Rouseff, and R. P. Porter, ''Multipath compensation in range dependent shallow water environments using a virtual receiver,'' J. Acoust. Soc. Am. (submitted).
[23] W. S. Hodgkiss, J. C. Nickles, G. L. Edmonds, R. A. Harriss, and G. L. D'Spain, ''A large dynamic range vertical array of acoustic sensors,'' in *Full Field Inversion Methods in Ocean and Seismic Acoustics*, edited by O. Diachok, A. Caiti, P. Gerstoft, and H. Schmidt (Kluwer Academic, Dordrecht, The Netherlands, 1995), pp. 205–210.
[24] L. Troiano, P. Guerrini, and A. Barbagelata, ''SACLANTCEN towed and vertical array system characteristics'' (1995).

The acoustics of the snapping shrimp *Synalpheus parneomeris* in Kaneohe Bay[a)]

Whitlow W. L. Au[b)]

Hawaii Institute of Marine Biology, P.O. Box 1106, Kailua, Hawaii 96734

Kiara Banks

Florida Institute of Technology, Melbourne, Florida 32901

Snapping shrimp are among the major sources of biological noise in shallow bays, harbors, and inlets, in temperate and tropical waters. Snapping shrimp sounds can severely limit the use of underwater acoustics by humans and may also interfere with the transmission and reception of sounds by other animals such as dolphins, whales, and pinnipeds. The shrimp produce sounds by rapidly closing one of their frontal chela (claws), snapping the ends together to generate a loud click. The acoustics of the species *Synalpheus paraneomeris* was studied by measuring the sound produced by individual shrimp housed in a small cage located 1 m from an H-52 broadband hydrophone. Ten clicks from 40 specimens were digitized at a 1-MHz sample rate and the data stored on computer disk. A low-frequency precursor signature was observed; this previously unreported signature may be associated with a ''plunger'' structure which directs a jet of water forward of the claw during a snap. The peak-to-peak sound pressure level and energy flux density at 1 m (source level and source energy flux density) varied linearly with claw size and body length. Peak-to-peak source levels varied from 183 to 189 dB *re*: 1 μPa. The acoustic power produced by a typical snap was calculated to be about 3 W. A typical spectrum of a click had a low-frequency peak between 2 and 5 kHz and energy extending out to 200 kHz. The spectrum of a click is very broad with only a 20-dB difference between the peak and minimum amplitudes across 200 kHz. A physical model of the snapping mechanism is used to estimate the velocity, acceleration, and force produced by a shrimp closing its claws. [S0001-4966(97)00312-3]

PACS numbers: 43.10.Ln, 43.80.Lb, 43.80.Nd [FD]

INTRODUCTION

One of the most pervasive sources of biological noise in shallow waters (less than about 60 m depth) at latitudes less than 40° is the snapping shrimp (Knudsen *et al.*, 1948; Everest *et al.*, 1948; Albers, 1965; Cato, 1993). Snapping shrimp noise is extremely pervasive and exhibit only a small (2–5 dB higher at night) diurnal variation (Albers, 1965); the noise is constantly present. Snapping shrimp noise in Kaneohe Bay, O'ahu in the Hawaiian Islands, has been reported to be among the loudest anywhere (Albers, 1965), although snapping shrimp noise recently reported near Gladstone, Australia (Readhead, 1996) may even exceed that of Kaneohe Bay.

The snapping shrimp responsible for producing the high ambient noise levels in Kaneohe Bay belongs to a family of crustaceans, Alpheidae, in the genus *Synalpheus*. Each shrimp has one enlarged claw (see Fig. 1) which produces a sharp transient acoustic signal when snapped closed. The claw of this genus has two important characteristics. First, each enlarged claw has a chitonous plunger on the dactlylus and a socket on the propodius. As the claw closes the plunger slides into the socket and causes a water jet to shoot out through a groove producing a jet stream of water in the forward direction. Second, each claw has hard chitonous edges on the propodus and dactylus. As the claw closes rapidly, the chitonous edges forcefully hit each other, and a loud audible snap is produced. The closing of the claw produces a short transient acoustic signal that is extremely broadband with components up to 200 kHz (Au, 1981; Cato, 1993). An example of the spectrum of snapping shrimp noise in Kaneohe Bay and San Diego Bay is shown in Fig. 2. Both the jet stream of water and loud snap have been shown to be important weapons in the territorial behavior of alpheidae shrimp (Hazlett and Winn, 1962; Schein, 1975, 1977; Conover and Miller, 1978). Snapping shrimp occur in large populations, burrowing into various marine habitats including coral beds (Banner, 1953), the cavities of sponges (Banner, 1953; Hazlett and Winn, 1962), shell-filled mudflats (Schein, 1975), coral rubble and rocks (Hazlett and Winn, 1962; Conover and Miller, 1978).

Measurements of snapping shrimp noise have usually been performed over large beds of snapping shrimp. The snapping shrimp noise over these beds has the quality of sizzling fat in a frying pan. During World War II extensive measurements were performed over areas along the Southeast coast of the United States, central Pacific and the southwest Pacific (Albers, 1965; Urick, 1984). Knowlton and Mouton (1963) performed extensive measurements of snapping shrimp noise in the waters of Bermuda at 56 stations covering an area of about 225 square miles. Readhead (1996)
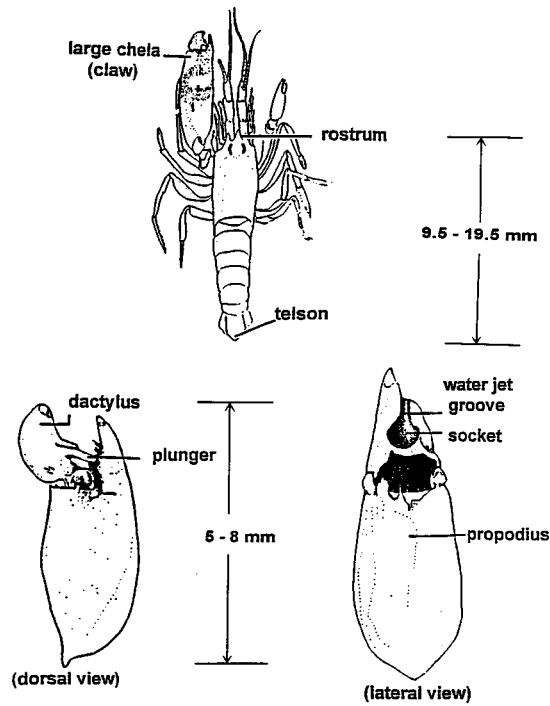
FIG. 1. Drawing of a snapping shrimp showing the top view of the whole shrimp and the dorsal and lateral views of the large claw. The lateral view is with the dactylus removed to show the water jet groove. The dimensions are for the specimens used in this study (after Knowlton and Moulton, 1963).

has performed measurements of snapping shrimp noise near Gladstone, Australia, with stations between the Auckland Wharf to over 82 km from the mainland. However, all these measurements were confined to frequencies below 20 kHz. Widener (1967) extended measurements to 50 kHz, showing substantial noise levels out to that frequency. Au *et al.* (1974, 1981) were one of the first to show that the noise spectrum of snapping shrimp sounds could extend to frequencies beyond 150 kHz and out to 200 kHz. Cato and Bell
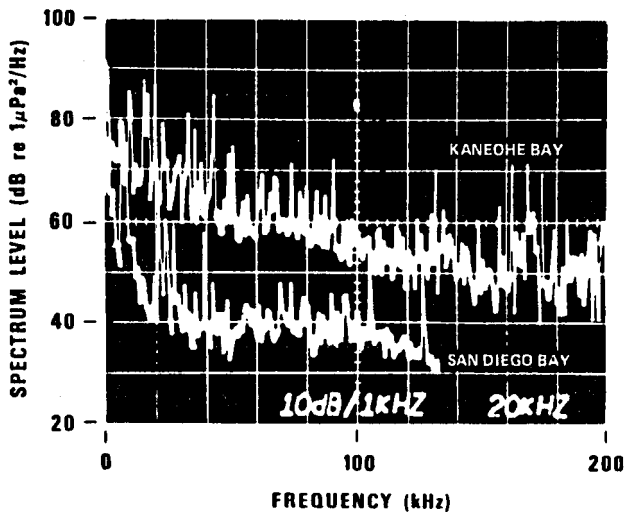
FIG. 2. Ambient noise in Kaneohe Bay and San Diego Bay. The biological noises in both bays are dominated by snapping shrimp noise (from Au, 1993).

(1992) conducted an extensive study of ultrasonic (to 200 kHz) ambient noise produced by snapping shrimp in Australian waters. Ahn *et al.* (1993a, 1993b) also measured snapping shrimp sounds up to frequencies of 200 kHz in Tateyama Bay and Sagami Bay in Japan.

In measuring the acoustic signals of a population of snapping shrimps, individual snaps can be isolated, however the effects of reflections from near by objects (rocks, coral heads, pier pilings etc.) and the sea surface usually cannot be separated out. Therefore, it is difficult to state unequivocally that an interference free click has been isolated and what species produced the snap. It is also difficult to obtain an estimate of the range to the individual responsible for the snap, so that source level cannot be easily and accurately estimated. Hazlett and Winn (1962) and Schein (1975) have performed measurements on individual shrimp in a controlled environment; however, their equipment was bandlimited to sonic frequencies and neither study measured absolute acoustic levels.

In this study, the acoustic signature of the snapping shrimp *Synalpheus paraneomeris* from Kaneohe Bay was measured individually in a controlled environment with broadband recording instrumentation. The snaps were characterized by source level, source energy flux density, and frequency spectrum. The relationship between source levels and both claw and body lengths, and the effects of sexual dimorphism were considered.

I. EXPERIMENTAL CONFIGURATION AND PROCEDURE

Snapping shrimp specimens from Kaneohe Bay were collected by removing sponges found on the wire mesh and floats of the dolphin pen facility at the Marine Mammal Research Program of the Hawaii Institute of Marine Biology. The sponges were torn open and snapping shrimp were removed from the cavities of the sponges. The shrimp were usually found in pairs but occasionally they were found individually or in groups of three. Sponges larger than about 10 cm in diameter usually housed at least one shrimp. The specimens were stored individually in round plastic containers (7.5×10.5 cm) filled with seawater and containing a small piece of coral for the shrimp to hide in. The water was changed twice a week with freshly collected seawater. The shrimps were fed defrosted pieces of frozen baby shrimp. Acoustic measurements were usually done within two days of collection.

The acoustic measurements were made in a 2.4-m-diam tank that was 1.8 m in depth. Each shrimp specimen was placed in a cage (3.8×3.8×3.8 cm) with a top door that could be swiveled open. The frame of the cage was made of 3-mm-diam wooden dowels and covered with a net made of 0.25-mm treads having a mesh size of 3 mm. The cage was placed in the tank at a depth of 0.8 m and a Naval Underwater Sound Reference Division H-52 hydrophone was located 1 m from the center of the cage at the same depth, as shown in Fig. 3. The response of the H-52 hydrophone was flat to about 180 kHz and was down 4 dB at 200 kHz. The output of the H-52 was connected to a low-pass filter and fed into an RC-Electronics Inc. 12-bit analog-to-digital converter
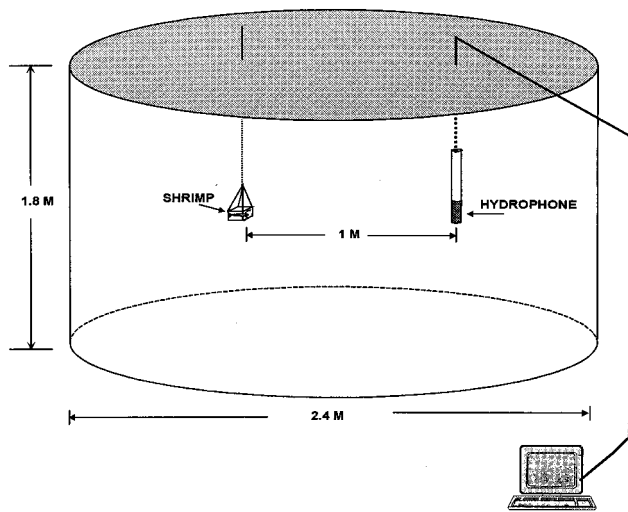
FIG. 3. Diagram of the measurement setup with a snapping shrimp cage located approximately 1 m from an H-52 hydrophone.

FIG. 4. An example of the waveform and frequency spectrum of a typical snap from *Synalpheus parneometris*.

board housed in an IBM compatible personal computer. The analog-to-digital converter was operated at a sample rate of 1 Mhz in a pretriggered mode and 512 points of data were collected per trigger.

The snaps of 42 individual shrimp were digitized and stored on disk files, 10 snaps per shrimp. The shrimp were stimulated to snap by prodding the claw with a long metal wire that was inserted into the cage. The data were analyzed after all of the shrimp were measured.

After the acoustic data collection, the specimens were identified using Banner's (1994) key, using the appropriate name changes given by Banner (1974) and Titgen (1991). Forty of the 42 specimens used were identified as *Synalpheus paraneomeris*. The other specimens were *Metalpheus paragracilis* and *Alpheus crassimanus* and data obtained with these were not included in our analysis. The body length of each shrimp was measured along the mid-dorsal line of the body from the tip of the rostrum to the end of the telson (Banner, 1953). The claw size of the large claw was measured from the tip of the dactylus to the base of the palm where it meets the carpus.

Two female specimens were oviparous with eggs attached to their swimmerettes under their bodies. Other specimens were sexed by dimorphic features of the first pleopod, following the method of Dardeau (1984) to sex *Synalpheus* specimens. By examining the biramous feature of the first pleopod, females were identified as having equal length branches while the males had unequal smaller branches.

II. RESULTS

An example of the waveform and frequency spectrum of a typical snap is shown in Fig. 4. The source level is the peak-to-peak sound pressure level measured at 1 m from the animal. The signal has a low intensity positive excursion (precursor) that preceded the high intensity oscillations by approximately 290 μs. This precursor pulse may be associated with the plunger on the large claw entering into the socket of the opposite appendage to produce the jet water
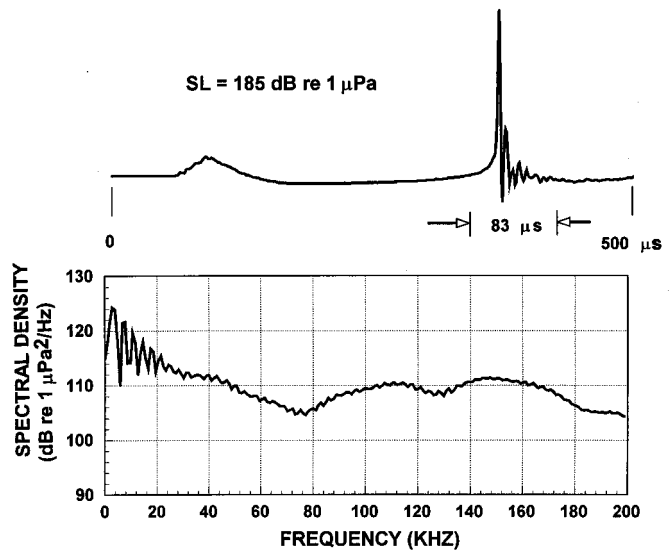
stream that is directed forward of the claw. It has not been previously reported, although this is not surprising since most measurements in the past have been done with the hydrophone relatively far from a shrimp bed so that precursor signature may have been buried in noise. The main part of the signal is extremely short and has a slow rise time for about 15 μs before accelerating to a peak followed by a number of oscillations. The peak-to-peak source level of this snap is relatively high with a value of 185 dB *re*: 1 μPa. When a subject was in the test tank, its snaps could be heard audibly by observers standing about 3 m from the tank as the sound traveled through the water and fiberglass tank wall.

The frequency spectrum of the snap is extremely broad with energy beyond 200 kHz. The difference in the peak and minimum of the spectral density is only 20 dB, indicating an extremely broad spectrum. The snaps of the *Synalpheus* are broader than the echolocation signals of bats (Pye, 1980; Fenton, 1995) and dolphins (Au, 1993) and may have the broadest spectrum of any signal produced by animals. The peak frequency is at a relatively low frequency of 2 kHz and is due to the energy in the precursor and the slow rise time portion of the main click. The energy between 80 and 200 kHz is associated with the fast rising and oscillatory portions of the main signal. The ripples in the spectrum are caused by the interaction of the low-frequency precursor with the slow rise time portion of the main snap that occurs about 290 μs later. If we let τ equals the time between the precursor and the beginning of the main snap, the ripples should have a frequency of $1/\tau$ or 3.4 kHz. When the precursor is zeroed out, the ripples disappear and the spectrum of a click becomes relatively smooth.

Ten consecutive snaps from a single specimen are shown in Fig. 5. The time between the onset of the precursor and the main part of the signal was approximately the same from click to click. The shape and amplitude of each snap was also similar from click to click, indicating a consistency in the sound producing mechanism.

The mean and standard deviation of the center (centroid)
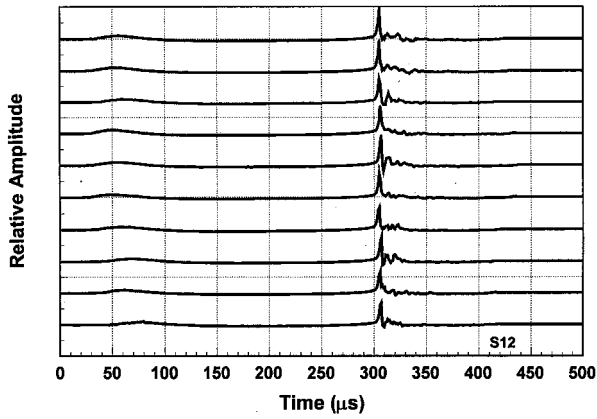
FIG. 5. The waveform of ten consecutive snap from a specimen.

FIG. 7. The average and standard deviation of the peak-to-peak source level in dB *re*: 1 μPa and the corresponding source energy flux density in dB *re*: 1 μPa^2 s.

and peak frequency of the 10 snaps collected for each of the 40 specimens are shown in Fig. 6. The center frequency is defined as

$$f_0 = \langle f \rangle = \frac{\int_{-\infty}^{\infty} f |S(f)|^2 \, df}{\int_{-\infty}^{\infty} |S(f)|^2 \, df}, \tag{1}$$

where $S(f)$ is the Fourier transform of the signal. The center frequencies were very consistent from specimen to specimen, varying between 32 and 45 kHz. The peak frequencies were also consistent between specimens with most of the means between 3 and 5 kHz. Only three shrimps had a mean peak frequency outside the 3–5 kHz range. These values are consistent with reported peak frequencies (Albers, 1965; Cato and Bell, 1992).

The mean and standard deviation of the peak-to-peak source level and source energy flux density level (SE) of the 40 specimens are shown in Fig. 7. SE is defined as

$$\mathrm{SE} = 10 \log \left(\int_0^T p^2(t) dt \right), \tag{2}$$

where $p(t)$ is the instantaneous acoustic pressure referenced to a distance of 1 m from the source and T is the duration of the signal. The units of SE is dB *re*: 1 μPa^2 s. The averaged

peak-to-peak source levels varied from 183 to 190 dB while the source energy flux density varied from 127 to 135 dB. The source level and source energy flux density did not vary much from snap to snap. The standard deviations were typically about ± 2 dB. The variations from subject to subject of the mean source level and energy flux density were also not very high, only about 6 dB.

The relationship between claw and body lengths of the 40 test specimens are shown in Fig. 8. There is almost a linear relationship between claw length and body length. The males had larger claws relative to body length than the females. These data are consistent with the findings of Schein (1975). The solid lines are the least square error linear fit of the data. The correlation coefficients between the fitted lines and the data are 0.90 for the females and 0.94 for the males. If we let l_B be the body length and l_C be the claw length of a shrimp, the equations for the fitted lines are

$$l_C = 2.80 + 0.25 l_B \quad \text{(female)},$$

$$l_C = 0.93 + 0.47 l_B \quad \text{(male)}.$$

The relationship between source level and claw length is shown in Fig. 9. Each symbol in the figure represents the average peak-to-peak source level from the ten consecutive

FIG. 6. The average and standard deviation of the center (median) and peak frequencies of 40 specimens.
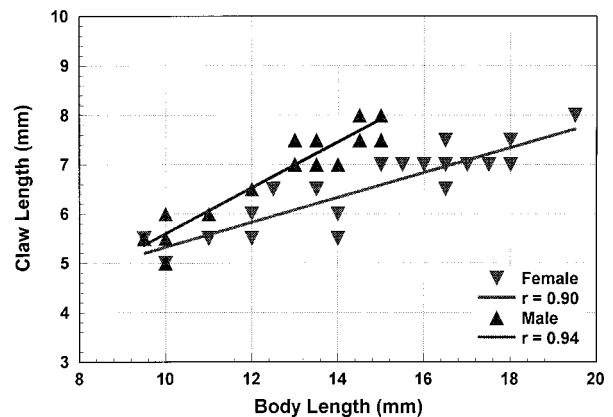
FIG. 8. Relationship between the claw length and body length of the 40 test specimens.
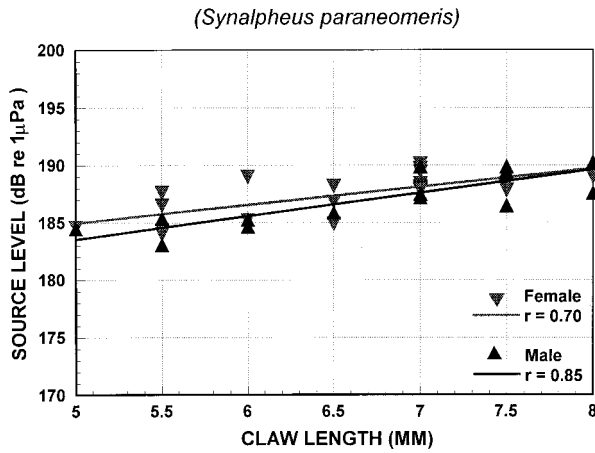
FIG. 9. Relationship between peak-to-peak source level and claw length.

FIG. 10. Schematic of the snapping shrimp claw on the left and a model representing the snapping mechanism of the shrimp.

snaps collected for each specimen. The linear least-square error curve fit of the data pertaining to male and female shrimps are also shown in the figure. The data indicate a strong correlation between claw length and source level, with the source level in dB varying almost linearly with claw length. The correlation coefficient between the fitted lines and the data were 0.85 for the male and 0.70 for the female shrimps. The equation for the fitted lines can be expressed as

$$Sl_{pp} = 177.0 + 1.6l_C \quad \text{(females)},$$

$$Sl_{pp} = 173.0 + 2.0l_C \quad \text{(males)}.$$

Therefore, the major factor affecting the strength of a snap is claw length, although body length is also related to claw length. Similar results would be obtained if the variation of source level with body length was considered. Schein (1975) also found that the relative source level varied linearly with claw length. However, Schein (1975) did not measure the absolute levels of the signals. For our specimens, the average source level varied about 6–7 dB for claws 5–8 mm long.

III. DISCUSSION AND CONCLUSIONS

The intensity of the clicks produced by the snapping shrimp *Synbalpheus parneomeris* is extremely high. By comparison, bottlenose dolphins in tanks typically produce echolocation clicks that have peak-to-peak intensity levels on the order of 170–180 dB and energy flux densities between 120 and 130 dB. The snaps produced by *S. parneomeris* have higher intensity and energy than a bottlenose dolphin clicks in a tank. However, the dolphin can emit many hundreds of clicks at rates up to several hundreds clicks per second. Snapping shrimp, on the other hand, snap their claws at much lower rates although no specific data were collected on snap rates and there seems to be no data available on this topic. Nevertheless, when you consider the disparity in size between a dolphin and a snapping shrimp, the high intensity of the snap seems remarkable.

The acoustic power averaged over duration T of the signal of the snapping shrimp can be calculated using the equation (Urick, 1983)
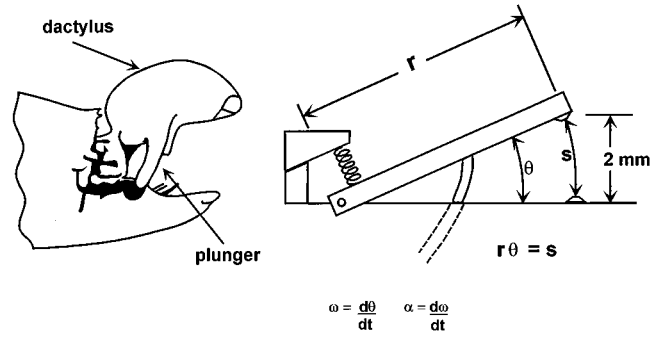
$$P_a = 4\pi r^2 I_a, \tag{3}$$

where I_a is the average intensity over duration T, at a distance r, which in our case is 1 m. This equation assumes an ominidirectional transmitter which would be applicable to the snapping shrimp since the cross section area of the tip of the claws is much smaller than a wavelength at 200 kHz. I_a is given by the equation (Urick, 1983)

$$I_a = \frac{1}{T} \int_0^T \frac{P^2}{\rho c}\, dt, \tag{4}$$

where ρ is the density of water (1060 kg/m^3) and c is the velocity of sound in sea water (1500 m/s). The rms acoustic pressure is defined as

$$p_{\text{rms}} = \sqrt{\frac{1}{T} \int_0^T p^2\, dt}. \tag{5}$$

Considering the snap shown in Fig. 4, and calculating the rms acoustic pressure of the main snap that is approximately 83 μs in duration, we obtain an acoustic pressure of 176 dB *re*: 1 μPa or 6.3×10^8 μPa. Inserting this result into Eqs. (3) and (4), the acoustic power in the snap of Fig. 4 is approximately 3 W.

Another way to appreciate the intensity of a snapping shrimp snap is to compare a snap with an underwater acoustic tone pulse. Assume that we are considering a tone pulse of duration T, the relationship between rms source level and energy flux density from Eqs. (2) and (5) is

$$SE = 10 \log(p_{\text{rms}}^2 T), \tag{6}$$

where p_{rms} is given by Eq. (5). Then

$$SL = SE - 10 \log T. \tag{7}$$

If we assume the SE of a shrimp to be equal to 134 dB (from Fig. 6), then a 1-ms tone pulse must have an intensity of 164 dB *re*: 1 μPa in order to have the same amount of energy as a snapping shrimp snap. For a 10-ms tone pulse, the corresponding intensity would be 154 dB.

The snapping mechanism can be analyzyed by modeling the dactylus as a spring-loaded lever as shown in Fig. 10. The shrimp typically cocks the dactylus back and locks it in place, analogous to a trigger on a hand gun being cocked against a spring. When producing a snap, the ''spring-loaded'' dactylus is unlatched and is driven against the opposite stationary claw. There is a time delay (Δt) of 290–300 μs between the start of the precursor signature and the

main snap. If we assume that the precursor signature is cause by the plunger on the dactylus entering the socket of the opposite claw we can estimate the velocity, acceleration and force involved with a snap. The average claw length of our 40 specimens was 6.7±0.8 mm. When the dactylus is cocked in the open position, the separation between both claws is about 2 mm so that $\theta_0 = 0.303$ radians and the arc length, s, separating the tip of the dactylus and the opposite jaw is 2.03 mm. The angular velocity and acceleration of the tip of the dactylus can be expressed by the equations

$$\omega = \frac{d\theta}{dt}, \quad \alpha = \frac{d\omega}{dt}, \tag{8}$$

where ω is the angular velocity and α is the angular acceleration. If we assume that the acceleration of the tip of the dactylus is constant, then we have from Eqs. (8)

$$\theta = 1/2\alpha t^2 + C, \tag{9}$$

where C is a constant of integration. At time $t=0$, $\theta=\theta_0 = 0.303$ rad so that $C=\theta_0$. At time $t=290$ μs, $\theta=0$, so that

$$\alpha = \frac{-2\theta_0}{(290\ \mu s)^2} = -7.2 \times 10^6\ \text{rad/s}^2. \tag{10}$$

Each radian of angular travel corresponds to arc length of $s/\theta_0 = 6.7$ mm/rad so that the acceleration of the tip of the dactylus is approximately

$$\alpha = -48 \times 10^6\ \text{mm/s}^2 = -48 \times 10^3\ \text{m/s}^2. \tag{11}$$

The minus sign indicates a downward direction of the acceleration. The acceleration of the dactylus is 4800 times the acceleration due to gravity. We can also estimate the force of the dactylus by using the acceleration and the mass of a claw. We collected the dactylus of 16 specimens, weighed them together and obtained an average mass of 1.6 mg or 1.6×10^{-6} kg. Therefore the force of dactylus striking the opposite claw is about 0.08 n. The average velocity of the dactylus will be $s/\Delta t$ which is 7 m/s. It would be interesting to use simultaneous high speed cinematography and acoustics to verify the origin of the precursor signature and to analyze the mechanisms involved with the dactylus motion in producing snaps.

This experiment has revealed four general features associated with the sounds produced by the *Synalpheus paraneomeris*. First, claw length was linearly related to body length although the relationship varied by sex with the increase in claw length with body length being greater in males than females. Second, source level was proportional to claw length. Third, all clicks had a low-frequency precursor that occurred 290–300 μs before the main snap. Finally, the spectrum of the snapping shrimp signal is very broad and may well be the broadest sound produced by any animal. The intensities in the frequency domain varied less than 20 dB over a 200-kHz range.

ACKNOWLEDGMENTS

Ahn, J. Y., Hamada, H., and Saito, K. (**1993a**). ''On the components of high frequency of the snapping shrimp sounds,'' J. Tokyo Univ. Fishes **80**, 69–73.

Ahn, J. Y., Hamada, H., and Saito, K. (**1993b**). ''Study of positioning of snapping shrimps and the source levels of their sounds,'' J. Tokyo Univ. Fishes **80**, 75–81.

Au, W. W. L. (**1993**). *The Sonar of Dolphins* (Springer-Verlag, New York).

Au, W. W. L., and Penner, R. H. (**1981**). ''Target detection in noise by echolocating Atlantic bottlenose dolphins,'' J. Acoust. Soc. Am. **70**, 687–693.

Au, W. W. L., Floyd, R. W., Penner, R. H., and Murchison, A. E. (**1974**). ''Measurement of echolocation signals of the Atlantic bottlenose dolphin, *Tursiops truncatus* Montagu, in open waters,'' J. Acoust. Soc. Am. **56**, 1280–1290.

Albers, V. M. (**1965**). *Underwater Acoustics Handbook-II* (The Pennsylvania State University Press, University Park, PA).

Banner, A. H. (**1953**). ''The crangonidae, or snapping shrimp of Hawaii,'' Pacific Sci. **7**, 3–144.

Banner, A. H. (**1974**). ''Contributions to the knowledge of the alpheid shrimp of the Pacific Ocean Part XVII. Additional notes on the Hawaiian alpheids: New Species, Subspecies, and Some Nomenclaturial Changes,'' Pacific Sci. **28**, 423–437.

Cato, D. (**1993**). ''The biological contribution to the ambient noise in waters near Australia,'' Acoust. Australia **20**, 76–80.

Cato, D. H., and Bell, M. J. (**1992**). ''Ultrasonic ambient noise in Australian shallow waters at frequencies up to 200 kHz,'' Material Research Laboratory Technical Report MRL-TR-91–23, Ascot Vale, Victoria.

Conover, M. R., and Miller, D. E. (**1978**). ''The importance of the large chela in the Territorial and Pairing behavior of the snapping shrimp, *Alpheus heterochaelis*,'' Mar. Behav. Physiol. **5**, 185–192.

Dardeau, M. R. (**1984**). ''*Synalpheus* shrimp (crustacea: decapoda: alpheidae). I. The Gambarelliodes group, with a description of a new species,'' Mem. Hourglass Cruises **7**.

Everest, F. A., Yound, R. W., and Johnson, M. W. (**1948**). ''Acoustical characteristics of noise produced by snapping shrimp,'' J. Acoust. Soc. Am. **20**, 137–142.

Fenton, M. B. (**1995**). ''Natural history and biosonar signals,'' in *Hearing by Bats*, edited by A. N. Popper and R. R. Fay (Springer-Verlag, New York), pp. 37–86.

Hazlett, B. A., and Winn, H. E. (**1962**). ''Sound production and associated behavior of Bermuda crustaceans (*Panulirus, Gonodactylus, Alpheus* and *Synalpheus*),'' Crustaceana **4**, 25–38.

Knowlton, R. E., and Moulton, J. M. (**1963**). ''Sound production in the snapping shrimp Alpheus (Crangon) and Synalpheus,'' Biol. Bull. **125**, 311–331.

Knudsen, V. O., Alford, R. S., and Emling, J. W. (**1948**). ''Underwater ambient noise,'' J. Mar. Res. **7**, 410–429.

Pye, J. D. (**1980**). ''Echolocation signals and echoes in air,'' in *Animal Sonar Systems*, edited by R.-G. Busnel and J. F. Fish (Plenum, New York), pp. 309–353.

Readhead, M. L. (**1996**). ''Snapping shrimp noise near Gladstone, Queensland,'' J. Acoust. Soc. Am. **101**, 1718–1722.

Schien, H. (**1975**). ''Aspects of the aggressive and sexual behavior of *Alpheus heterochaelis* Say,'' Mar Behav. Physiol. **3**, 83–96.

Schien, H. (**1977**). ''The role of snapping in *Alpheus heterochaelis* Say, 1818, the big clawed snapping shrimp,'' Crustaceana **33**, 182–188.

Titgen, R. H. (**1991**). ''Summary of Albert H. and Dora M. Banner's contribution to the knowledge of the family Alpheidae (*Decapodia Caridea*),'' Pacific Sci. **45**, 232–245.

Urick, R. J. (**1983**). *Principles of Underwater Sound* (McGraw-Hill, New York).

Urick, R. J. (**1984**). *Ambient Noise in the Sea* (Naval Sea Systems Command, Washington, DC).

Widener, M.W. (**1967**). ''Ambient noise levels in selected shallow waters off Miami, Florida,'' J. Acoust. Soc. Am. **42**, 137–142.

Three-dimensional wave-envelope elements of variable order for acoustic radiation and scattering. Part I. Formulation in the frequency domain

R. J. Astley and G. J. Macaulay[a]
Department of Mechanical Engineering, University of Canterbury, Private bag 4800, Christchurch, New Zealand

J-P. Coyette and L. Cremers
LMS Numerical Technologies, Researchpark Haasrode, Zone 1, Interleuvenlaan 70, 3001, Leuven, Belgium

Mapped wave-envelope elements of variable radial order are presented for the computation of time-harmonic, unbounded, three-dimensional acoustical fields. Their application to transient problems is described in a companion article (Part II). Accuracy is assessed by a comparison of computed and analytic solutions for multi-pole fields generated by a vibrating sphere. Solutions are also presented for plane wave scattering. Elements of radial order $m+l$ are shown to be capable of modeling multi-pole components of order m, although the provision of adequate transverse resolution is shown to be a stringent requirement, particularly at high frequencies. Ill-conditioning of the coefficient matrix limits the practical implementation of the method to elements of radial order eleven or less. The utility of the method for more general geometries is demonstrated by the presentation of computed solutions for the sound field generated by the vibration of a cylindrical piston in a plane baffle and of an idealised engine casing under anechoic conditions. The computed results are shown to be in close agreement with the analytic solution in the case of the cylindrical piston, and with a boundary element solution in the case of the engine casing. © *1998 Acoustical Society of America.* [S0001-4966(97)06512-0]

PACS numbers: 43.20.Fn, 43.20.Rz, 43.30.Jx, 43.40.Rj [ANN]

INTRODUCTION

The solutions of exterior wave problems involve the representation of many spatial cycles of a wavelike solution over a large or infinite domain. This poses particular difficulties for computation both in the frequency and in the time domains. Only the steady or "time-harmonic" problem will be considered here, the solution of the transient problem being treated in part II of this article. In part I, solutions are sought for the steady acoustical field generated by prescribed time-harmonic motion of a closed surface in an unbounded region. Alternatively, solutions are sought for the acoustical field scattered by a rigid body for a known incident sound field. In both cases, acoustic energy must be radiated rather than absorbed in the "far field." Numerical methods developed for such problems are listed by Burnett.[1] More extensive reviews which touch also on the transient case can be found in Givoli's monograph[2] and in Bettess' text on infinite elements.[3] To summarize, solution methods for the steady problem can be divided into two broad categories; those based on *boundary* representations of the field variable and those based on *domain* representations. The former are dominated by a variety of boundary element (BE) formulations[4] which pose the problem as the solution of an integral equation on the surface of the radiating or scattering body and solve it in discrete form. The unknown quantities in such a scheme are surface values of the acoustic pressure or its gradient at discrete nodes. Methods of this type use source solutions which satisfy the field equation identically and which radiate rather than absorb acoustical energy so that the troublesome radiation condition is inherently satisfied. The most straightforward BE formulations give nonunique solutions at discrete eigenfrequencies of an associated interior problem but can be modified to produce unique solutions by the addition of auxiliary points in the interior region[5] or by the use of more complex integral formulations which involve higher-order derivatives of the kernel functions.[6] It is a characteristic of all BE methods that they reduce the dimension of the problem by one by using a surface rather than a volume discretisation, but in doing so generate a *full* coefficient matrix. Also, since the solution is obtained in the first instance only on the surface, the calculation of field variables at points within the exterior domain involves subsequent computation. This can be substantial, given that the evaluation of the field variable at any exterior point requires the computation of a frequency-dependent integral over the entire radiating surface.

Domain-based methods do not attempt an *exact* solution of the field equations but approximate their solution within a finite region close to the radiating or scattering body. This is generally achieved by means of a conventional volume discretization, most commonly the finite element (FE) method, in which case the unknowns become nodal values of the acoustic pressure. The anechoic termination is then represented by an approximate local or nonlocal operator at a finite boundary. The "*plane wave damper*" or "*ρc bound-*

---
[a]Presently at: The National Institute of Water & Atmospheric Research Ltd., PO Box 14-901 Kilbimie, Wellington, New Zealand.

ary'' is the simplest local condition of this type but is valid only if the boundary is sufficiently distant from the scattering body or radiating source. This requirement can be relaxed by the use of higher-order local boundary operators,[7-9] but these introduce higher derivatives which must be approximated numerically on the boundary. Nonlocal operators can also be used. Models of this type include hybrid BE/FE models[10-12] and more recently nonlocal FE-DtN models[2,13,14] based on a truncated version of an *exact* ''Dirichlet to Neumann'' (DtN) map. These are equivalent in the context of discrete solutions of the Helmholtz equation to mode matching at the intermediate surface.[15] The coefficient matrix generated by domain-based methods is generally sparse or banded within the inner domain. Connectivity on the boundary of the region depends upon the local or nonlocal nature of the boundary treatment.

A more radical approach to domain-based computation is embodied in the ''infinite element'' concept.[3] This method does not attempt to truncate the unbounded domain but models it in its entirety by using elements of *infinite* extent. These incorporate oscillatory shape functions whose amplitude decays with radial distance to model the behavior of a spherical or cylindrical wave. The earliest such elements[16] incorporated an exponential decay in the radial direction which did not correctly model the required asymptotic behavior but could be ''tuned'' to give reliable results for a given inner domain. Subsequent formulations[17,18] incorporate the correct cylindrical or spherical decay via a local element mapping. More recently Burnett[1] has proposed elements which use prolate spheroidal coordinates. This permits the required extent of the conventional mesh to be reduced in the case of slender objects which otherwise would need to be enclosed in a circumscribing sphere or cylinder.

The wave-envelope (WE) method,[19-22] and more recently the mapped WE approach[23-26] are variants of the infinite element concept. They are characterized by the use of the complex conjugates of the element shape functions as weighting functions in a Petrov–Galerkin procedure. This removes by cancellation all wavelike terms from the element integrals and simplifies the frequency dependence of the resulting coefficient matrix. Gerdes and Demkowicz[27] have obtained the same equations by using an equivalent variational formulation of the problem and have demonstrated stability and convergence, the first in a rigorous context and the second inferred from numerical experiment. In the remainder of this article, a family of variable-order three-dimensional elements of this type is described and results are presented to demonstrate their effectiveness for frequency-domain calculations of radiated and scattered fields. The accuracy of the scheme is demonstrated by comparisons of computed solutions with known test solutions and with solutions obtained from BE computation.

The formulation presented here follows closely that proposed for lower-order two- and three-dimensional elements.[24] It also can be regarded as an extension of current variable-order, two-dimensional and axi-symmetric formulations.[25] It is presented here in some detail as a definitive account of the WE method in its most general, three-dimensional form, and as a necessary preliminary to the
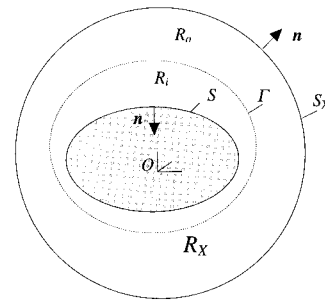
FIG. 1. Problem geometry.

analogous treatment of transient problems to be presented in part II of this article.

I. THE PROBLEM STATEMENT

Figure 1 shows the geometry of the problem. A closed surface S is surrounded by an unbounded region R. A bounded subregion, R_X, is contained within a far-field spherical boundary S_X at $r=X$, where r is a spherical polar radius measured from a global origin O in the vicinity of the radiating surface. During the course of the analysis, R_X is subdivided into a ''near-field'' region R_i and a ''far-field'' region R_O. These are separated by an interface Γ. The shape of the interface is arbitrary except that no radial ray from the origin O should intersect it more than once. The surface S experiences a prescribed normal acceleration $a_n(\mathbf{x},t)$. No other sources of sound are present. The acoustical pressure $p(\mathbf{x},t)$ in the exterior region is governed by the linearized wave equation

$$\nabla^2 p = \frac{1}{c^2}\frac{\partial^2 p}{\partial t^2}, \text{ in } R, \tag{1}$$

where ∇^2 is the Laplacian operator and c is the sound speed. A time-harmonic solution is sought of the form

$$p(\mathbf{x},t)=\mathrm{Re}\{\bar{p}(\mathbf{x},\omega)e^{i\omega t}\}, \tag{2}$$

where $\bar{p}(\mathbf{x},\omega)$ is the complex pressure amplitude for a radian frequency ω. Equation (1) then becomes

$$\nabla^2\bar{p}+k^2\bar{p}=0 \text{ in } R, \tag{3}$$

where $k=\omega/c$. If it is assumed also that the surface acceleration $a_n(\mathbf{x},t)$ in the direction of a unit normal $\mathbf{n}$ on S (see Fig. 1) is of time-harmonic form with an amplitude $\bar{a}_n(\mathbf{x},\omega)$, continuity of normal displacement requires that

$$\nabla\bar{p}\cdot\mathbf{n}+\rho\bar{a}_n=0 \text{ on } S, \tag{4}$$

where ρ is the mean fluid density. A further constraint is required on the ''infinite'' boundary to ensure that energy propagates in an outward direction. The Sommerfeld radiation condition ensures that this is the case provided that

$$r\{\partial\bar{p}/\partial r+(ik)\bar{p}\}\to 0, \text{ as } r\to\infty. \tag{5}$$

Condition (5) will also be applied as an approximate impedance condition on Γ_X. This gives the ''*plane wave damper*'' or ''*ρc impedance*'' boundary condition

$$\nabla\bar{p}\cdot\mathbf{n}+(ik)\bar{p}=0, \text{ on } \Gamma_X. \tag{5a}$$

A discrete numerical solution is first developed on the bounded domain R_X subject to boundary conditions (4) and (5a). The limiting case as $X \to \infty$ is then considered.

The problem statement is easily modified to accommodate scattered rather than radiated fields. This is done by redefining the radiated acoustic pressure to as the scattered component. That is to say, if a known sound field $p_i(\mathbf{x},t) = \bar{p}_i(\mathbf{x},\omega)\exp(i\omega t)$ is incident of the surface S, and if $\bar{p}(\mathbf{x},\omega)$ is defined as the scattered component of the resulting total field, Eq. (3) and boundary condition (5) are unaltered, and boundary condition (4) becomes

$$\boldsymbol{\nabla}\bar{p}\cdot\mathbf{n} = -\rho\bar{a}_n - \boldsymbol{\nabla}\bar{p}_i\cdot\mathbf{n} \quad \text{on} \quad S. \tag{6}$$

Scattering is therefore modelled by imposing an "effective" boundary acceleration, $\bar{a}'_n$, on the surface S, where $\bar{a}'_n = \bar{a}_n + (1/\rho)\boldsymbol{\nabla}\bar{p}_i\cdot\mathbf{n}$. In all that follows, the analysis is presented for the radiation problem only.

II. THE WAVE-ENVELOPE FORMULATION

A. Formulation of the residual equations

The wave-envelope formulation is based on a weighted residual solution for Eq. (3) over the bounded region R_X subject to boundary conditions (4) and (5a). First a discrete trial function, $p'(\mathbf{x},\omega)$, is chosen for the acoustic pressure amplitude $\bar{p}(\mathbf{x},\omega)$. This takes the general form

$$p'(\mathbf{x},\omega) = \sum_{j=1}^{n} \bar{q}_j(\omega)\varphi_j(\mathbf{x},\omega), \tag{7}$$

where $\varphi_j(\mathbf{x},\omega)$ $(j=1,...,n)$ are known basis functions, continuous on R_X, and $\bar{q}_j(\omega)$ $(j=1,...,n)$ are unknown coefficients. The selection of appropriate basis functions will be dealt with subsequently. The Galerkin procedure is then applied to Eqs. (2), (4), and (5a). That is to say, the field and surface residuals are multiplied by weighting functions $W_j(\mathbf{x},\omega)$ $(j=1,2...,n)$—yet to be determined—and integrated over R_X, S, and S_X, respectively. This poses an over-specified problem in which $3n$ equations are formulated for n unknown quantities [the coefficients $\bar{q}_j(\omega)$]. A linear combination of these equations then yields a set of n composite equations which can be written;

$$-\int_{R_X} W_i(\nabla^2 p' + k^2 p')dR + \int_{S_X} W_i(\boldsymbol{\nabla} p'\cdot\mathbf{n} + ikp')dS$$

$$+ \int_S W_i(\boldsymbol{\nabla} p'\cdot\mathbf{n} + \rho\bar{a}_n)dS = 0. \tag{8}$$

Finally, the application of Green's theorem to he first integral and cancellation of the resulting surface terms gives

$$\int_{R_X} (\boldsymbol{\nabla} W_i\cdot\boldsymbol{\nabla} p' - k^2 W_i p')dR + \int_{S_X} ikW_i p' dS$$

$$+ \int_S W_i\rho\bar{a}_n \, dS = 0. \tag{9}$$

A similar set of integral relationships is derived by Gerdes[27] from a variational statement of the problem. Substitution of the trial solution (7) into Eq. (9) now yields a set of linear equations

$$[\mathbf{A}(\omega)]\bar{\mathbf{q}} = \bar{\mathbf{f}}, \tag{10}$$

where $\bar{\mathbf{q}}$ is the vector whose components are the trial coefficients $q_i(\omega)$ $(i=1,...,n)$, $\mathbf{A}$ is an $n \times n$ coefficient matrix, and $\bar{\mathbf{f}}$ an $n \times l$ forcing vector, given by

$$A_{ij} = \int_{R_X} \{\boldsymbol{\nabla} W_i\cdot\boldsymbol{\nabla}\varphi_j - k^2 W_i\varphi_j\}dR + \int_{S_X} ikW_i\varphi_j \, dS, \tag{11}$$

and

$$\bar{f}_i = -\int_S \rho W_i\bar{a}_n dS. \tag{12}$$

The basis functions will subsequently be chosen so that

$$\varphi_j(\mathbf{x},\omega) \sim f(\theta,\phi)\frac{e^{-ikr}}{r} \quad \text{as} \quad r \to \infty, \tag{13}$$

where r, θ, and ϕ are spherical polar coordinates in the usual notation. At this stage, Eq. (10) yields a discrete Helmholtz solution over the bounded region R_X. A number of options now present themselves. These include the following:

(1) The problem can be solved as it stands for a large but *finite* values of X. If the weighting functions are taken as simple complex conjugates of the basis functions—which renders the volume integrals in expression (11) particularly simple to evaluate—this gives the wave-envelope formulation proposed by Astley, Eversman, and others[19–21] and used extensively since the early 1980's to model inlet and outlet noise in the vicinity of turbofan engines. In such applications, the boundary S_X is taken typically at 10–50 inlet diameters from an engine nacelle. Each wave-envelope element then contains many radial wavelengths of the resulting solution. In such formulations, the residual integral over S_X is explicitly included in expression (11). Mean flow and thermal gradients can be included in such models.[20–22]

(2) A regular (Bubnov) Galerkin scheme can be implemented and the limit is taken as $X \to \infty$. This gives the mapped infinite element formulation of Zienkiewicz and Bettess[17,18] and the spheroidal formulation of Burnett[1] when a spheroidal rather than spherical radius is used. In both instances, the weighting and basis functions are assumed to be identical. This yields undefined terms in both the volume and surface integrals of expression (11). These are of the form "$\exp(-2ikX)$." In the initial formulation of such elements[17] the offending surface integral was overlooked and the undefined term in the volume integral was simply omitted in the calculation of A_{ij}. The two offending terms have subsequently been shown to cancel identically leaving a well-defined residue as $X \to \infty$.[28] This fortuitous cancellation is also discussed by Burnett[1] and Gerdes.[27]

(3) A conjugated (Petrov) Galerkin scheme can be implemented and the limit taken as $X \to \infty$. This gives the mapped wave-envelope formulation of Bettess,[23] Astley,[24] and others.[25,26] Here weighting functions are chosen which behave asymptotically as

$$W_j(\mathbf{x},\omega) \sim f(\theta,\phi)\frac{e^{+ikr}}{r^m} \quad \text{as} \quad r \to \infty, \tag{14}$$
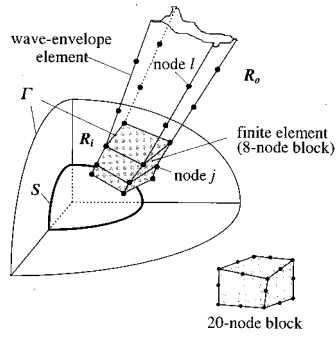
FIG. 2. The inner (FE) and outer (WE) meshes.

FIG. 3. Topology of the wave envelope element, (a) physical element, (b) parent element.

where $m \geq 1$. Improper integrals proportional to ''X''and ''$\log X$'' as $X \to \infty$ are generated independently within the surface and boundary terms of Eq. (11) for the cases $m = 1$ and $m = 2$. These cancel identically when carefully segregated from the remaining contributions and the formulation yields a valid solution as $X \to \infty$ when this is done.[24] Alternatively, and more conveniently from a computational standpoint, improper terms are avoided altogether when m is chosen equal to (or greater than) 3. When this is done, the integral over S_X vanishes identically as $X \to \infty$ and expression (11) can be rewritten more simply as

$$A_{ij} = \int_R \{ \boldsymbol{\nabla} W_i \cdot \boldsymbol{\nabla} \varphi_j - k^2 W_i \varphi_j \} dR. \tag{15}$$

It is this in this form that the wave-envelope formulation is developed in the remainder of this article. The stability and convergence of essentially the same formulation has been discussed by Gerdes and Demkowicz.[27] They observe that in removing the boundary integral on S_x from the integral equations (9) it appears that the Sommerfeld condition has been removed from the formulation. They show that this can be remedied by requiring the trial and weight functions to be taken from appropriate weighted Sobelev spaces. Functions which have the asymptotic behavior noted in expressions (13) and (14) with $m \geq 3$ certainly satisfy this requirement. Alternatively, using a more heuristic approach, it can be argued that in this particular case any trial basis function of type (13) satisfies the Somerfeld condition *explicitly* and hence that no integral statement of the Sommerfeld condition is needed.

B. The spatial discretization in the inner region

Within the inner region R_i, the basis functions φ_j are chosen as conventional finite element shape functions. For a typical node j within this region (see Fig. 2) or on its boundary, $\varphi_j(\mathbf{x}, \omega)$ is therefore defined as

$$\varphi_j(\mathbf{x}, \omega) = N_j(\mathbf{x}). \tag{16}$$

Elsewhere $\varphi_j(\mathbf{x}, \omega)$ is defined to be zero. Here $N_j(\mathbf{x})$ is a finite element shape function defined explicitly within each element of the mesh. The coefficients $\bar{q}_j(\omega)$ then become nodal values of the pressure amplitude $\bar{p}(\mathbf{x}, \omega)$.

Linear or quadratic isoparametric serendipity blocks with 8 or 20 nodes, respectively, are used in the current analysis. A linear block is indicated in Fig. 2; the topology of the quadratic block is also shown in the same figure. The formulation of the shape functions for these elements is documented elsewhere.[29]
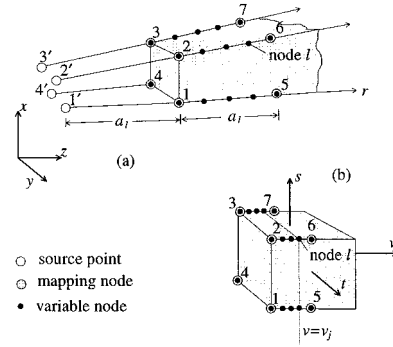
C. The spatial discretization in the outer region

The topologies of the WE elements used in the outer region depend upon whether linear or quadratic elements are used for the inner mesh. If linear elements are used, as shown in Fig. 2, the corresponding wave envelope element has a ''base'' defined by four nodes. If a quadratic mesh is used, the base of the element is defined by eight nodes to ensure a compatible common topology at the interface Γ. In either event, the base topology is repeated m times in a radial direction to give an element of radial order m with $4m$ or $8m$ nodes. The basis function $\varphi_l(\mathbf{x}, \omega)$ associated with a typical node l (see Fig. 2) is then defined as

$$\varphi_l(\mathbf{x}, \omega) = P_l(\mathbf{x}) e^{-ik\mu}(\mathbf{x}), \tag{17}$$

where $P_l(\mathbf{x})$ is an interpolation function and $\mu(\mathbf{x})$ is a phase function. Both are defined locally within each element. For conciseness, the formulation of the interpolation and phase functions $P_l(\mathbf{x})$ and $\mu(\mathbf{x})$ is presented here for the linear case only. An element of this type is shown in somewhat greater detail in Fig. 3(a). The shape functions for such an element are defined as follows: First, a radial direction is established for each of the base nodes, labeled 1, 2, 3, and 4 [see Fig. 3(a)] by specifying *source* points at locations $1'$, $2'$, $3'$, and $4'$. These define radial directions $1'-1$, $2'-2$, etc., along the infinite edges of the element. Parameters a_i $(i = 1, ..., 4)$ denote radial distances from the source point i' to the base node i. In many instances it is convenient and desirable to define all source points in a single location for the entire mesh, but this is not strictly necessary. Mapping points, 5, 6, 7, and 8 are also defined at radial distances a_i $(i = 1, ..., 4)$ from the base points but in an outward radial direction, as shown in Fig. 3(a). The infinite element defined by this nodal topology is then transformed onto a square *parent* block of side 2 in the s-t-v coordinate system [see Fig. 3(b)] by a mapping of the form

$$\mathbf{x} = \sum_{i=1,8} M_i(s, t, v) \mathbf{x}_j, \tag{18}$$

where $\mathbf{x}_j$ ($j=1,...,8$) denote the coordinates of the *mapping nodes* 1,2,...,8 and where $M_j(s,t,v)$ ($j=1,...,8$) are mapping functions. Details are given elsewhere.[30] The resulting transformation from the physical element to the parent element has the property that faces of the infinite element map to constant planes in the s,t,v coordinate system. Also, along any infinite edge which contains the base node i ($i=1,...,4$), the relationship between the mapped coordinate v and the radial distance r measured from the source point i' takes the form

$$v = 1 - 2a_i/r, \tag{19a}$$

or

$$r - a_i = a_i(1+v)/(1-v). \tag{19b}$$

Note that as $r \to \infty$ points in the physical element map to the plane $v = +1$ in the parent element. The interpolation and phase functions, $P_l(\mathbf{x})$ and $\mu(\mathbf{x})$, are now defined in terms of the parent coordinates s, t and v. First, however, the geometric parameter a_i is interpolated over the base of the element to give

$$a(s,t) = \sum_{i=1,4} S_i(s,t)a_j, \tag{20}$$

where $S_i(s,t)$ ($i=1,...,4$) are two-dimensional shape functions defined over the base of the parent element. This ensures that $a(s_i,t_i) \equiv a_i$ at each of the base nodes. The phase component $\mu(\mathbf{x})$ of Eq. (17) is then defined to be

$$\mu(\mathbf{x}) = a(s,t) \frac{(1+v)}{(1-v)}. \tag{21}$$

Along each infinite edge of the element this is equivalent to a statement that, $\mu = r - a_i$, by virtue of expression (19b), and Eq. (21) can be regarded as an interpolated form of this relationship. The exponential term $e^{-ik\mu(\mathbf{x})}$ in expression (17) therefore represents a radial wavelike factor, $e^{-ik(r-a)}$, within each element.

The remaining portion of the basis function, $P_1(\mathbf{x})$, is defined in the following way. First, m nodes are placed along each edge of the element where m defines the radial order of the element. The nodes are placed at points which correspond to m discrete values of v, say $v_1,v_2,...,v_m$, where $v_1 = -1$, so that the first point lies on the base face of the element. In the current model the remaining points are equally spaced between $v=-1$ and $v=0$. The corresponding locations of the nodes in the physical element are given by Eq. (18). The interpolation function $P_l(\mathbf{x})$ for node l on a radial edge which emanates from the base point i ($i=1,...,4$) and is located at the jth radial point (i.e., at $v=v_j$) is then given by

$$P_l(\mathbf{x}) = \tfrac{1}{2}S_i(s,t)(1-v)L_j^m(v), \tag{22}$$

where $L_j^m(v)$ is the Lagrange polynomial

$$L_j^m(v) = \prod_{\substack{k=1,m \\ (k \neq j)}} (v - v_k) \Big/ \prod_{\substack{k=1,m \\ (k \neq j)}} (v_j - v_k). \tag{23}$$

The resulting basis function $\varphi_l(\mathbf{x},\omega)$ defined by expressions (17), (21), and (22) has the following properties;

(i) $\varphi_l(\mathbf{x},\omega) \equiv 0$ at all nodes of the element except for node l;

(ii) $\varphi_l(\mathbf{x},\omega) \equiv S_i(s,t)$ on the base of the element; and

(iii) $\varphi_l(\mathbf{x},\omega) = (polynomial \ of \ order \ ``m" \ in \ v) \times (e^{-ik(r-a)})$, on an infinite edge.

Properties (i) and (ii) ensure that compatible matching occurs along the base face when the element is attached to a finite element with the same face topology. Given that polynomial terms in v are equivalent to ascending powers in (a/r)—by virtue of mapping Eq. (19b)—property (iii) tells us that the radial behaviour of $\varphi_l(\mathbf{x},\omega)$ when s and t are held constant is given by

$$\varphi_l \sim \left\{ \frac{\alpha_1}{r} + \frac{\alpha_2}{r^2} + \frac{\alpha_3}{r^3} + \cdots \frac{\alpha_m}{r^m} \right\} e^{-ik(r-a)}$$

$$(\alpha_1,\alpha_2,...,\alpha_m \ \text{constants}). \tag{24}$$

The absence of a constant "α_0" term in the above series is guaranteed by the inclusion of the factor $(1-v)$ in expression (22). This ensures that $\varphi_l(\mathbf{x},\omega) \to 0$ as $r \to \infty$, i.e., as $v \to +1$. Clearly expression (24) also satisfies the Sommerfeld radiation condition for any integer value of $m \geq 1$. Moreover, an expansion of this type with m terms contains a radial basis for spherical Bessel functions up to and including those of order $m-1$. We would therefore expect a first-order element ($m=1$) to model accurately the radial behavior of an acoustic monopole, a second-order element to model that of a dipole, a third-order element that of a quadrupole, and so on. This will indeed be shown to be the case.

D. The selection of weighting functions

The weighting functions are chosen in the following way:

(i) In the inner region;

$$W_j(\mathbf{x},\omega) = \varphi_j(\mathbf{x},\omega) = N_j(\mathbf{x}), \tag{25}$$

where $N_j(\mathbf{x})$ is the finite element shape function associated with node j (see Fig. 2). The contribution to the coefficient matrix $\mathbf{A}$ which is received from an element in the inner region is then

$$\Delta A_{ij} = \int_{\Delta R} \{ \boldsymbol{\nabla} N_i \cdot \boldsymbol{\nabla} N_j - k^2 N_i N_j \} dR, \tag{26}$$

where ΔR is the subregion of R_i occupied by the element. Similarly, the contribution to $\bar{\mathbf{f}}$ is given by

$$\Delta \bar{f}_i = \int_{\Delta S} \rho N_i \bar{a}_n dS, \tag{27}$$

where ΔS is any portion of the boundary S which lies on the boundary of the element.

(ii) In the outer region;

$$W_l(\mathbf{x},\omega) = D(\mathbf{x})P_l(\mathbf{x})e^{+ik\mu(\mathbf{x})}. \tag{28}$$

Here $D(\mathbf{x})$ is a geometric factor $[=((1-v)/2)^2]$ which behaves locally as the inverse square of the radius and takes the value of unity at the inner edge of the element. Substitution of Eqs. (17) and (28) into (15) gives an element contribution to $\mathbf{A}$ of the form

$$\Delta A_{ij} = \int_{\Delta R} \{(P_i \boldsymbol{\nabla} D + D \boldsymbol{\nabla} P_i + ikDP_i \boldsymbol{\nabla} \mu)$$

$$\cdot (\boldsymbol{\nabla} P_j - ikP_j \boldsymbol{\nabla} \mu) - k^2 DP_i P_j\} dR, \tag{29}$$

where ΔR is the portion of the outer region occupied by the element.

There are several points to note here:

(a) Integral (29) is finite—for the reasons already discussed in Sec. III A—and receives no contribution in the limiting case from the integral over S_X.

(b) The presence of complex conjugates $e^{\pm ik\mu}$ in the basis and weight functions ensures the cancellation of all spatially harmonic terms in the integrand of expression (29).

E. The form of the discrete equations

Property (b) above has two important consequences. First, the cancellation of all oscillatory terms in the integrand means that standard Gauss–Legendre integration can be used to evaluate expression (29). Second, the dependence of the coefficient matrix $\mathbf{A}$ on frequency is of simple quadratic polynomial form. That is to say, if the terms within the integrands of expressions (26) and (29) are written in powers of ω ($= ck$) the element contributions to $\mathbf{A}$ in both the inner and outer domains can be written in the form

$$\Delta[\mathbf{A}(\omega)] = \Delta\mathbf{K} + i\omega\Delta\mathbf{C} + (i\omega)^2 \Delta\mathbf{M}, \tag{30}$$

where $\Delta\mathbf{K}$, $\Delta\mathbf{C}$, and $\Delta\mathbf{M}$ are independent of frequency. In the inner (conventional) mesh they are given by

$$\Delta\mathbf{K}_{ij} = \int_{\Delta R} \{\boldsymbol{\nabla} N_i \cdot \boldsymbol{\nabla} N_j\} dR, \tag{31a}$$

$$\Delta\mathbf{C}_{ij} = 0, \tag{31b}$$

and

$$\Delta\mathbf{M}_{ij} = (1/c^2) \int_{\Delta R} \{N_i N_j\} dR. \tag{31c}$$

In the wave-envelope region the corresponding expressions are

$$\Delta\mathbf{K}_{ij} = \int_{\Delta R} \{(P_i \boldsymbol{\nabla} D + D \boldsymbol{\nabla} P_i) \cdot \boldsymbol{\nabla} P_j\} dR, \tag{32a}$$

$$\Delta\mathbf{C}_{ij} = (1/c) \int_{\Delta R} \{DP_i \boldsymbol{\nabla} \mu \cdot \boldsymbol{\nabla} P_j - P_i P_j \boldsymbol{\nabla} D \cdot \boldsymbol{\nabla} \mu$$

$$- DP_j \boldsymbol{\nabla} P_i \cdot \boldsymbol{\nabla} \mu\} dR, \tag{32b}$$

and

$$\Delta\mathbf{M}_{ij} = (1/c^2) \int_{\Delta R} \{DP_i P_j (1 - \boldsymbol{\nabla} \mu \cdot \boldsymbol{\nabla} \mu)\} dR. \tag{32c}$$

These can be assembled to give frequency-independent acoustic *mass*, *stiffness*, and *damping* matrices, $\mathbf{M}$, $\mathbf{K}$, and $\mathbf{C}$, for the system as a whole. Calculation of the acoustic response for a particular frequency therefore requires assembly only of the load vector $\bar{\mathbf{f}}(\omega)$ followed by the solution of the matrix equation

$$[\mathbf{K} + i\omega\mathbf{C} - \omega^2\mathbf{M}]\bar{\mathbf{q}} = \bar{\mathbf{f}}(\omega), \tag{33}$$

where $\mathbf{M}$, $\mathbf{K}$, and $\mathbf{C}$ are assembled once for *all* frequencies. This contrasts with the procedure required for an equivalent infinite element or BE solution, in which the frequency dependence of the coefficient matrix $\mathbf{A}$ is much more complex, requiring assembly at each frequency increment. Burnett's infinite element formulation[1] goes some way to ameliorate this requirement by isolating the frequency-dependent portion of $\mathbf{A}$ in a separable radial integral common to all outer elements. Element contributions must still be assembled at each frequency step however. Note that in the current formulation both the stiffness *and* damping contributions from the WE elements [expressions (32a) and (32b)] are nonsymmetric. Note also that the contribution to the mass matrix $\mathbf{M}$ assembled from expression (32c) is identically zero when a spherical interface exists between the inner and outer regions and a common location is taken for the virtual sources [the phase function $\mu(\mathbf{x})$ is then equal to $(r\text{-}a)$, where r is a spherical polar radius and a constant, so that $(1 - \boldsymbol{\nabla}\mu \cdot \boldsymbol{\nabla}\mu)$, is identically zero]. This tells us that there is no "added mass" effect from the outer region for such meshes and hence that any trapped or standing wave effects are confined to the inner mesh.

III. RESULTS

Computed results presented in this section were obtained from three-dimensional codes developed at the University of Canterbury and at LMS Numerical Technologies. Both incorporate wave envelope elements of variable radial order and permit linear or quadratic transverse interpolation. Studies of the effects of using linear versus quadratic meshes in the transverse direction for two-dimensional and axisymmetric cases[25] have demonstrated that greater accuracy is obtained for a given dimensionality when quadratic elements are used. Studies conducted with the current codes[31]—but not reported here—support this conclusion. Unless stated otherwise, the results that follow have been calculated by using meshes with quadratic interpolation in the transverse direction.

A. Multi-pole spherical radiation

The effect of radial element order on the accuracy of the computed solution is demonstrated by a comparison of computed and analytic solutions for spherical multi-pole sound fields. These are generated by motion of a spherical surface of radius R which experiences a normal surface acceleration

$$\bar{a}_n = a_0 P_N(\cos \theta). \tag{34}$$

Here $P_N(\ )$ denotes the Legendre polynomial of order N and θ is a spherical polar angle in the usual notation. The analytic solution for the acoustic pressure amplitude at points external to the sphere is then

$$\bar{p}(\mathbf{x}) = \left(\frac{\rho a_0}{k}\right) P_N(\cos \theta) \frac{h_N^{(2)}(kr)}{h_N^{(2)'}(kR)}, \tag{35}$$

where $h_N^{(2)}(\ )$ denotes the spherical Bessel function of the second kind and r is a spherical polar radius. Solutions for
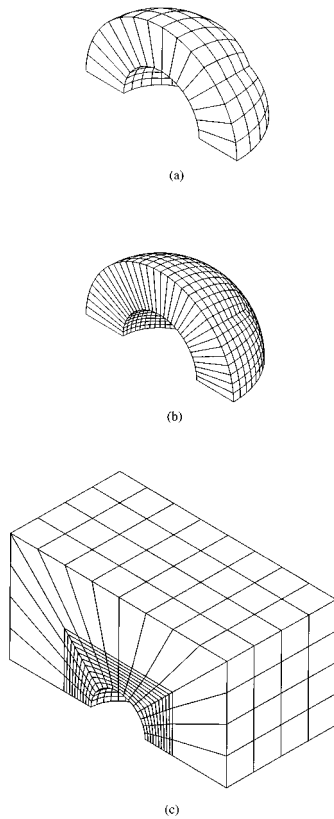
FIG. 4. WE and FE meshes surrounding a sphere. (a) WE mesh, 96 elements; (b) WE mesh, 384 elements; (c) FE+WE mesh (960 blocks, 96 WE elements).

FIG. 6. Acoustic pressure amplitude; multi-pole order 2; element order 3; computed values for mesh (a).

the exterior field have been computed for various multi-pole and element orders using the three meshes shown in Fig. 4. The first two—meshes (a) and (b)—are formed by attaching WE elements directly to the spherical surface. For display purposes, the elements are truncated in Fig. 4 at $r=2R$. Meshes (a) and (b) contain 96 and 384 elements, respectively, and model one quadrant of the exterior region. Symmetry constraints are used to represent the remaining quadrants. The third mesh—mesh (c)—contains an inner finite element mesh of 960 block elements which surround the

sphere. These extend to a block-shaped interface where they attach to a compatible wave envelope mesh of 96 elements.

1. Results for a multi-pole of order 2

Figure 5 shows the absolute value of the nondimensional pressure amplitude, $|\bar{p}\omega/\rho c a_0|$, for a multi-pole solution of order 2 (a quadrupole). The solution is sampled at points A and B located as shown (see inset). The response is plotted for frequencies in the range $0 < kR < 30.0$. Computed results are shown for elements of order 2 and 3. Both solutions are calculated using mesh (a). The analytic solution is also shown. The elements of radial order 2 show some error in the mid-frequency range. Those of order 3 are indistinguishable from the analytic data to the scale shown. This supports the observation made in Sec. III B that in terms of radial interpolation, elements of order m are capable of representing exactly multi-pole fields of order $m-1$. A similar correspondence exists at all points in the exterior field. This is illustrated in Fig. 6 which shows computed and analytic contours of sound pressure for ''low'' and ''high'' frequency cases ($kR=1.0$ and $kR=30.0$).

FIG. 5. Pressure amplitude response, multi-pole of order 2: — analytic; — WE order 2; —○— WE order 3.
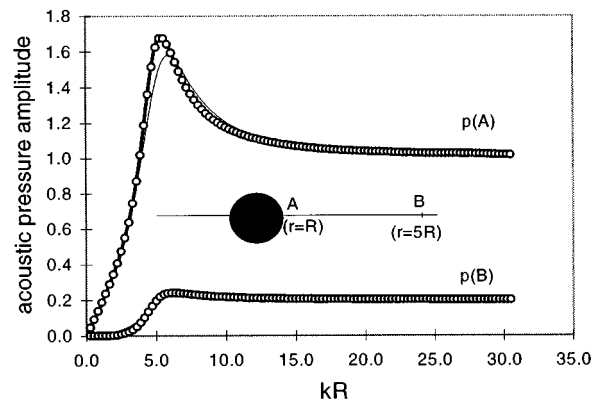
FIG. 7. Pressure amplitude response, multi-pole of order 5; — analytic; — WE order 3; —○— WE order 6.

55   J. Acoust. Soc. Am., Vol. 103, No. 1, January 1998

Astley *et al.*: 3-D wave-envelope elements. I   55
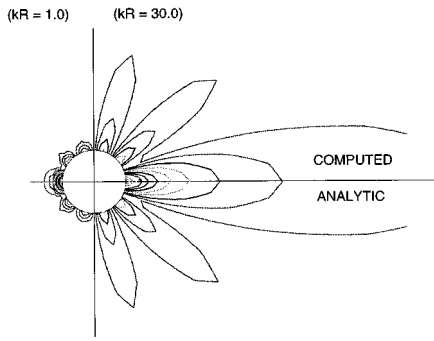
FIG. 8. Acoustic pressure amplitude; multi-pole order 5; element order 6; computed values for mesh (a).

2. Results for a multi-pole of order 5

Figures 7 and 8 show solutions for a multi-pole of order 5. Mesh (a) is again used and results are presented for elements of radial orders 3 and 6 (the latter being one greater than the multi-pole order). Once again the higher order case gives close correspondence between the computed and analytic solutions over the entire frequency range (Fig. 7) and over the entire exterior field (Fig. 8).

Results for the same problem obtained by using mesh (c) are presented in Figs. 9 and 10. The inclusion of a conventional FE mesh in the inner region reduces solution accuracy at higher frequencies since resolution is limited by the spacing of the conventional nodes. A minimum node spacing of, say, five nodes per wavelength for satisfactory resolution of wavelike disturbances would imply an upper frequency limit of approximately $kR = 5.0$ for this particular mesh. In reality, the solution remains accurate for somewhat larger values but then deteriorates rapidly. Contours of the analytic and computed solutions both in the FE and WE portions of the mesh are shown in Fig. 10 for the case $kR = 5.0$. Their close correspondence and the absence of detectable reflections at the interface between the inner and outer regions—indicated in Fig. 10 by a rectangular box—is confirmation that the WE mesh acts as an effective anechoic termination notwithstand-
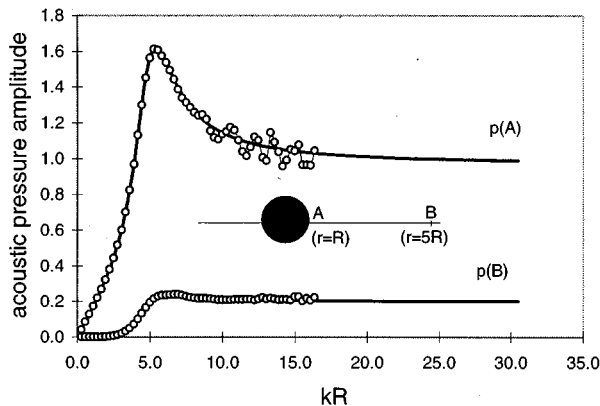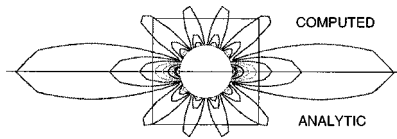
FIG. 10. Acoustic pressure amplitude; multi-pole order 5; element order 6; $kR = 5.0$, computed values for mesh (c).

ing the rectangular geometry of the interface. The somewhat ''spikey'' appearance of both sets of contours is an artefact of the contour plotting procedure which interpolates from nodal values.

3. Results for a multi-pole of order 10

Computed and analytic solutions for a multi-pole of order 10 are presented in Figs. 11 and 12. WE solutions are computed for elements of radial order 11. Meshes (a) and (b) are used. The results obtained from mesh (a) lie close to the analytic solution over most of the frequency range but show some error as kR approaches 30.0. Given that the elements used are of radial order 11, this appears to contradict the assertion that elements of radial order m should resolve multi-pole fields of order $m - 1$. That this is not the case in the current instance at higher frequencies can be attributed *not* to any inadequacy in the radial representation of the numerical solution but to the transverse resolution of the mesh. This is demonstrated by the presentation—also in Fig. 11—of results obtained from mesh (b) which has greater higher transverse resolution. These data, for elements of the same radial order, are in close agreement with the analytic solution over the entire frequency range. This extends to the entire field as illustrated by a comparison of computed and analytic pressure contours for $kR = 30$, shown as Fig. 12. Although the radiated field is quite complex, it is nonetheless surprising that mesh (a) which is able to resolve this transverse radiation pattern at lower frequencies is unable to do so as kR increases. This is symptomatic of a more general interaction between the radial and transverse resolution. A brief discussion of this behavior follows.

FIG. 9. Pressure amplitude response, multi-pole of order 5; — analytic; —○— WE order 6 [mesh (c)].
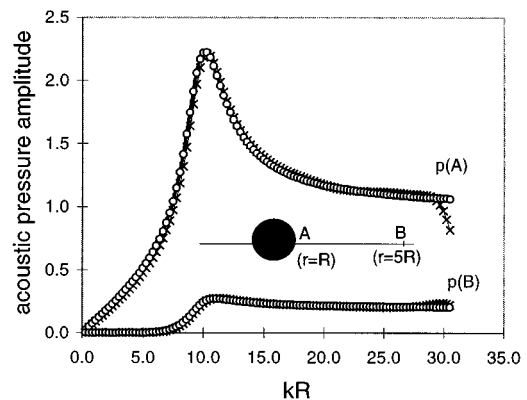
FIG. 11. Pressure amplitude response, multi-pole of order 10; — analytic, × WE order 11 [mesh (a)]; ○ WE order 11 [mesh (b)].
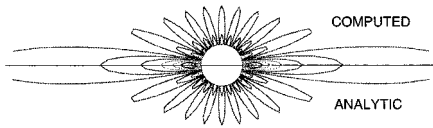
FIG. 12. Acoustic pressure amplitude; multi-pole order 10; element order 11; $kR = 30.0$ computed values for mesh (b).

4. The interaction between transverse and radial resolution at high frequencies

A tendency of the WE solution to deteriorate at high frequencies, even when adequate radial interpolation is present in the model, can be detected in *all* multi-pole solutions if the frequency is increased to a sufficiently high value. The quadrupole response of Fig. 5, for example, shows the same behavior when it is plotted over an extended frequency range. Such results are shown in Fig. 13 for the range; $0 < kR < 1000$. Solutions are plotted for meshes (a) and (b) but also for a coarser mesh (a*) which is obtained by doubling the node spacing of mesh (a) in each direction. WE elements of radial order 3 are used in all cases. These give an exact representation for the radial variation of the exact solution. Notwithstanding the relatively simple form of the radiation pattern (see Fig. 6) for this problem, mesh (a*) although accurate at low frequencies looses resolution when the nondimensional wave number kR exceeds approximately 10.0. Mesh (a) can just be seen to do so as kR approaches 1000, while mesh (b) resolves the solution over the whole frequency range. Given that the exact solution exhibits the same transverse behavior [i.e., $\sim P_2(\cos \theta)$] at *all* frequencies, it is perplexing that the transverse resolution of the mesh must be increased in this way as the wave number increases. An explanation of this behavior is to be found in the phase term, $\exp[-ik\mu(\mathbf{x})]$ which is incorporated into the numerical trial solution via expression (9). This radial behavior derives from the analytic solution and is therefore identically ''correct'' in the limit as the transverse resolution increases indefinitely. It is not correct however for a finite level of transverse resolution. In such cases, the remaining portion
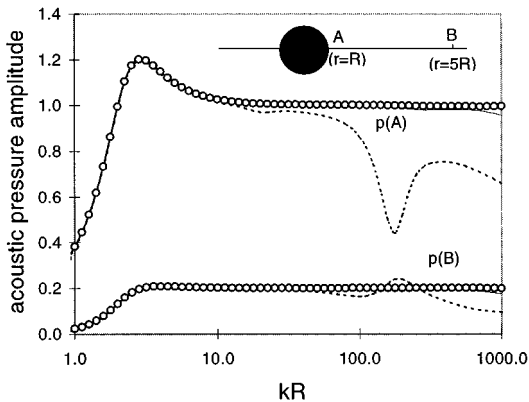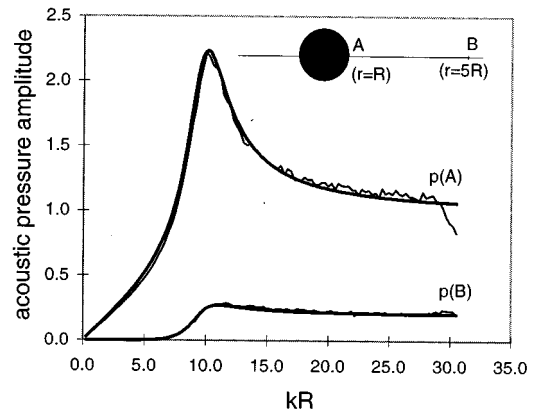
FIG. 14. Pressure amplitude response, multi-pole of order 10; — analytic; — WE order 12.

of the numerical trial function, $P_l(\mathbf{x})$, which is used primarily to model the transverse amplitude modulation of the solution, must also (implicitly) *accommodate any radial amplitude modulation which arises from the discrepancy between the assumed (analytic) radial phase component and the approximate discrete value of this quantity associated with a particular transverse mesh.* $P_l(\mathbf{x})$ must therefore accommodate a residual phase variation of the form, $\exp[-ik\Delta\mu(\mathbf{x})]$, where $\Delta\mu(\mathbf{x})$ approaches zero as the transverse mesh is refined. This requirement clearly becomes more demanding as the frequency increases as demonstrated in Figs. 11 and 13.

5. Ill-conditioning at high radial orders

An absolute upper limit is imposed on the radial order which can be used in the current elements by ill-conditioning of the coefficient matrix which occurs for radial orders greater than or equal to 12. The onset of ill-conditioning is illustrated in Fig. 14 which shows the solution obtained for a tenth-order spherical multi-pole by using WE elements of order 12. It manifests itself in rapid fluctuations of the frequency response. The onset of this behavior is quite abrupt, as demonstrated by a comparison of Figs. 11 and 14, the only difference between these solutions being that the radial order of the elements has been increased from 11 to 12. Similar behavior has been reported in two-dimensional elements at radial orders of 11 or greater and has been correlated with condition number.[31] In practice, a restriction of the current scheme to elements of radial order 11 or less does not constitute a significant limitation to its use. Radiation from higher order sources *can* still be modeled provided that a sufficiently extensive inner mesh is used. That is to say, if the highest radial order components of a sound field involve inverse powers of r greater than 11, these terms will attenuate more rapidly with distance than the lower order terms which are also present. When WE elements are attached directly to the radiating body, *all* of these terms must be represented within the WE interpolation. When a conventional FE inner mesh is present, however, the highest-order near-field attenuation can readily be accommodated within the FE mesh, so that the WE elements need only represent the lower

FIG. 13. Pressure amplitude response, multi-pole of order 2; — analytic; ---- WE order 3; mesh (a*); — WE order 3, mesh (a); ○ WE order 3, mesh (b).
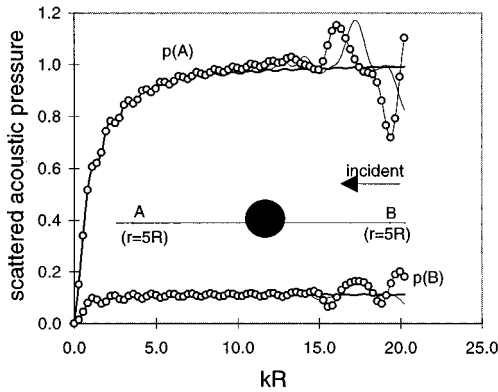
FIG. 15. Scattered acoustic pressure amplitude, plane wave incident on a sphere; — analytic; — WE order 5; —○— WE order 10 [mesh (a)].

FIG. 17. Computed and analytic total pressure amplitude (scattered +incident) for a plane wave incident on a sphere, $kR=10.0$.

order and more persistent contributions in the intermediate and far fields. The more extensive the FE mesh and the more distant the FE/WE interface, the lower the order of WE elements which are required in the outer region. It is for this reason, that the complex multi-lobed fields in the vicinity of turbofan inlets and exhausts are modeled very effectively[21,26] by WE elements of relatively low radial order—of order 1 or 2 in the current notation—when these are attached to extensive conventional meshes which enclose the near field.

B. Scattering by a rigid sphere

Computed and exact solutions for the scattered field due to a plane wave incident on a rigid sphere are shown in Figs. 15–17. Meshes (a) and (b) are used with WE elements of orders 5 and 10. The scattered acoustical pressure amplitude—made dimensionless with respect to the incident wave amplitude—is shown in Figs. 15 and 16 plotted at points A and B five radii in front of and behind the sphere. Also shown is the analytic solution.[32] The discrepancy, particularly at higher frequencies, between the computed and analytic solutions which is apparent in Fig. 15 is associated again with transverse rather than radial resolution. This is demonstrated by the results shown in Fig. 16 obtained from

FIG. 16. Scattered acoustic pressure amplitude, plane wave incident on a sphere; — analytic; — WE order 5; —○— WE order 10 [mesh (b)].

mesh (b). That is to say, little improvement is evident when the radial order of the elements is increased from 5 to 10, but a significant improvement occurs as the transverse resolution is increased from mesh (a) to mesh (b) (cf. Figs. 15 and 16). Computed and analytic pressure contours for the total sound field (scattered+incident) are plotted in Fig. 17 in the upper and lower half planes, respectively, for the case $kR=10$. The same field point mesh and the same contour levels are used for both solutions. The correspondence is clearly excellent (the wiggles which are present are artefacts of the common display mesh used for both solutions).

C. Application to nonspherical geometries

The numerical solutions presented to date, although fully three dimensional in terms of modeling, involve spherical radiating or scattering geometries. With the exception of the results presented in Figs. 9 and 10 they consist entirely of models in which the WE elements attached directly to the body. Such test cases are useful in assessing the accuracy and limitations of the method but do not demonstrate convincingly its utility for more realistic three-dimensional problems involving bodies of irregular shape where an inner mesh of finite elements is generally present and where the interface between the FE and WE regions is not necessarily spherical in shape. Two additional test problems are included to demonstrate the effectiveness of the method for such problems. In the first of these test problems, an analytic solution is available for comparison. In the second, comparison is made with results obtained from a boundary element computation.

1. Radiation from a cylindrical piston in a plane baffle

The geometry of the test problem is shown in Fig. 18(a). A circular rigid piston of diameter D ($=2a$) oscillates at a steady frequency ω perpendicular to the plane of a piston. The piston surrounded by a plane baffle. The amplitude of the piston acceleration is a_0. The sound field is modeled by a combination of finite elements and WE elements. Two models are considered. In each, the FE mesh occupies an inner cylindrical region indicated in Fig. 18(a). It is bounded by symmetry planes at $x=0$ and $y=0$, by a cylindrical sur-
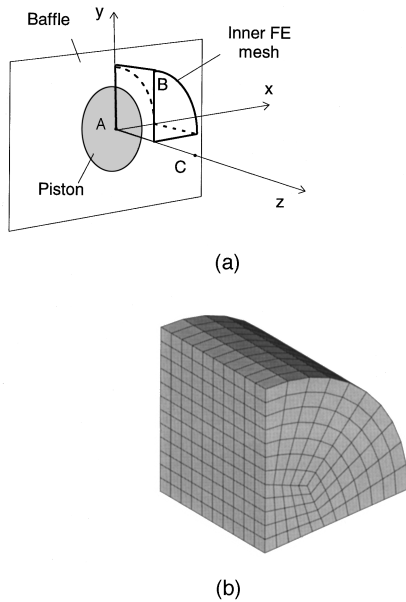
FIG. 18. Vibrating piston in a plane baffle. (a) Geometry and location of response points. (b) FE mesh (a).

FIG. 19. Cylindrical piston in a plane baffle. (a); pressure amplitude response at point A. (b); pressure amplitude response at points B and C. — exact; — computed mesh (a) order 2; -------- computed mesh (a) order 3; —◇— computed mesh (a) order 4; ○ computed mesh (b) order 4.

face at a distance of $1.2a$ from the z axis of symmetry and by the planes $z=0$ and $z=a$. The coarser of the two meshes which will be termed mesh (a) is shown in Fig. 18(b). It comprises 950 8-noded isoparametric block elements. The finer of the two meshes—mesh (b)—models the same region by using 7600 elements (this represents a halving of the internode spacing). In each case, WE elements of variable radial order 1–5 are matched compatibly to the finite element on the outer cylindrical surface of this region and on the plane $z=a$. Results are presented for nondimensional wave numbers kD in the range $0-6\pi$, corresponding to a node spacing along the z axis of 7.5 nodes per wavelength for the coarser of the two meshes at the upper end of the frequency range. Computed and exact values of the nondimensional pressure amplitude $|\bar{p}/\rho a_0 D|$ are plotted against wave number in Fig. 19. Figure 19(a) shows the response at point A, and Fig. 19(b) at points B and C. These have coordinates $(0,0,0)$, $(0,1.2a,a)$, and $(0,0,2a)$, respectively; A lies on the piston surface, B at the outer edge of the FE mesh, and C on the z axis of symmetry within the WE region. Computed solutions are presented for mesh (a) for elements of radial order 2, 3, and 4, and for meshes (b) for elements of radial order 4. Computed solutions have also been obtained for higher-order elements but are indistinguishable from the order 4 results to the scale shown. The computed solutions clearly converge as the radial order of the elements increases, and converge to the analytic solution as the mesh is refined. This latter effect is difficult to spot since even the coarse mesh gives a solution which is virtually indistinguishable from the exact solution over most of the frequency range. A small error is detectable in the coarse mesh solutions however at higher frequencies which reduces when mesh (b) is used. Note that the WE envelope elements in meshes are highly ''mapped'' due to the cylindrical geometry of the interface between the FE and WE regions.
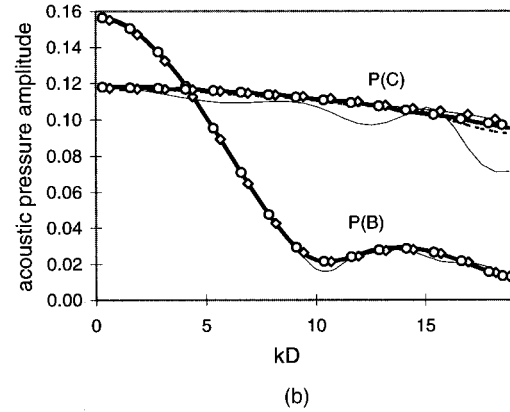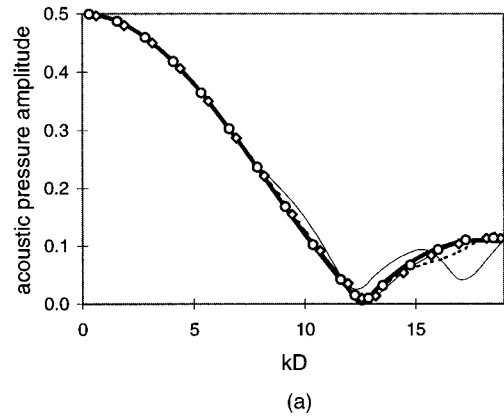
2. Radiation from an idealized engine casing, comparison with BE computation

To conclude, computed solutions are presented for the sound field generated by the vibration of an idealized engine casing which is harmonically and symmetrically excited. The geometry and dimensions of the casing—which is formed from 5-mm steel plate—are shown in Fig. 20. It is free-standing within an anechoic environment. Clearly no ana-
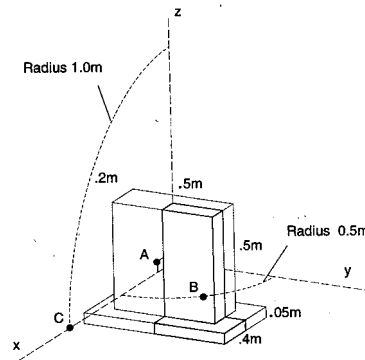
FIG. 20. Idealized engine casing, geometry, and dimensions.
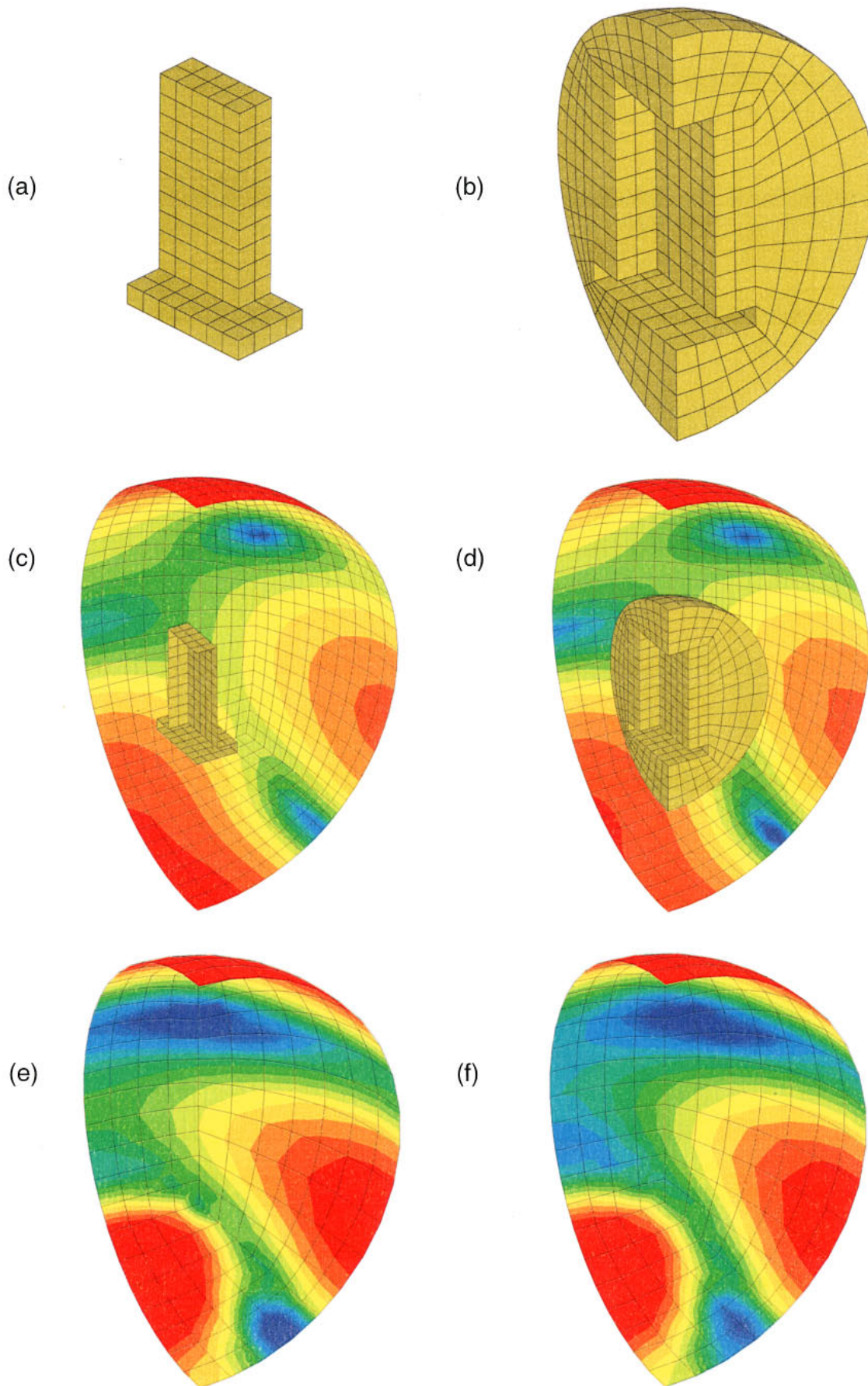
FIG. 21. Acoustic radiation from an idealized engine casing. (a) BE model; (b) WE model; (c) SPL contours, $r = 1$ m, BE model; (d) SPL contours, $r = 1$ m, WE model; (e) SPL contours, $r = 0.5$ m, BE model; (f) SPL contours, $r = 0.5$ m, WE model.
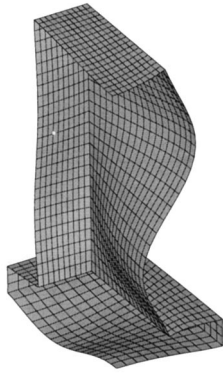
FIG. 22. Engine casing, surface displacement at 350 Hz.

FIG. 23. Engine casing, acoustic response; (a) at point A; (b) at point B; (c) at point C; — BE; — WE order 1; ---- WE order 2; ○ WE order 3.

lytic solutions are available to validate the WE solution. A BE solution is therefore used for this purpose. The BE and WE models for one quadrant of the problem are shown as Fig. 21(a) and (b). Symmetry constraints are used to model the effect of the remaining quadrants. The BE model is formed from 137 four-noded surface elements. The WE model has an inner FE mesh of 888 8-noded, isoparametric block elements which are matched to a mesh of 177 WE elements of variable radial order. The interface is a spherical boundary of radius 0.5 m. The transverse resolution of the BE and WE models is equivalent in the sense that the distribution of element faces on the inner surface of the FE model coincides with the BE discretization of the same surface. An FE plate model is used to determine the surface displacement of the casing for a given, symmetric force excitation. The resulting surface acceleration is then applied to the BE and WE models.

The BE and WE solutions predict the acoustical pressure amplitude at the nodes of each model. In the case of the BE model, these lie on the surface of the casing. The acoustic pressure can however be obtained at exterior points by further computation. This involves a numerical integration over the surface of the casing for each exterior field point. In the case of the WE model, the acoustic pressure can be obtained at all exterior points by interpolation, a less demanding computational exercise.

Sound pressure levels (SPL) predicted by the BE and WE solutions for an excitation frequency of 350 Hz, have been determined at the nodal points of each model and at 200 points on two spherical display surfaces. The inner surface lies at the interface between the FE and WE regions. The outer surface is concentric with this at a radius of 1.0 m. The predicted SPL contours for the outer surface are shown in Fig. 21(c)–(d). Similar contours for the inner surface are plotted in Fig. 21(e)–(f). The contours are plotted at equal increments on the interval 40–75 dB in the case of Fig. 21(c) and (d), and on the interval 60–80 dB in the case of Fig. 21(e) and (f). The displaced shape of the casing is shown in Fig. 22. The structural FE mesh is also indicated. The correspondence between BE and WE predictions is close on both surfaces, although a small some discrepancy is apparent on the far field directly below the casing.

The acoustic response is also plotted at three specific points—A, B, and C—over a frequency range 50 Hz–750
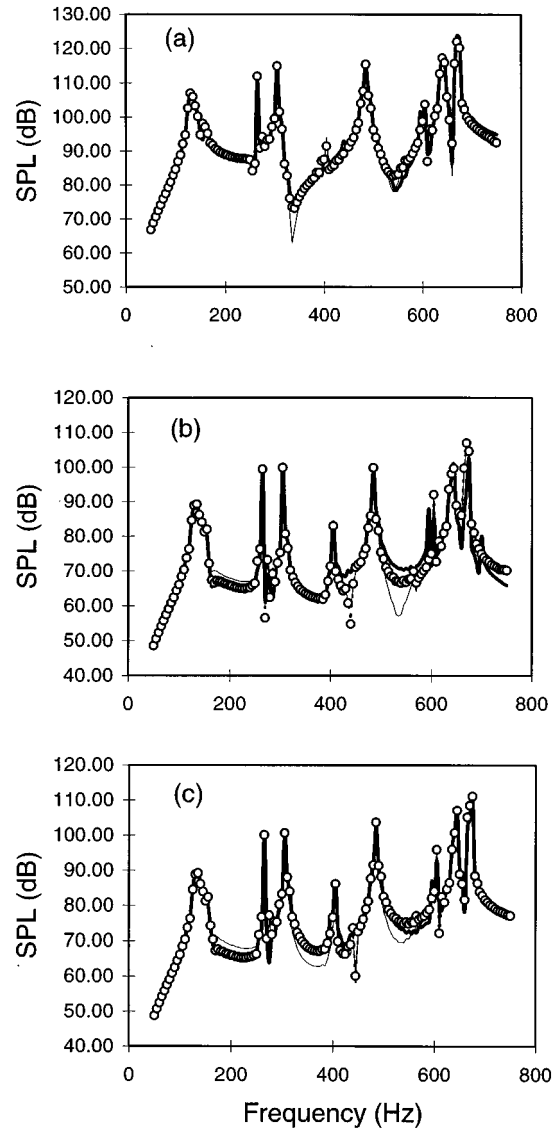
Hz. These data are shown in Fig. 23. The points lie adjacent to he surface (point A), on the FE/WE interface (point B), and at a radius of 1.0 m (point C). Predicted values of SPL are shown for the BE model and for the WE model. In the latter case, solutions are presented for elements of radial order 1, 2, and 3. The BE and WE solutions are in excellent agreement and it is noticeable that the WE results converge to the BE solution as the radial order of the elements increases. Some resolution is lost as the frequency increases, but even at 750 Hz, which corresponds to a coarse FE node spacing in the inner region of less than 5 nodes per wavelength; the agreement between WE and BE results remains close for elements of order 3.

The BE and WE computations presented in Fig. 23 were performed on the same computer (an IBM RS 6000 PW2). A direct comparison of computational effort can therefore be made. This is presented in Table I, which shows the CPU usage for each scheme. The figures are averaged over 140

TABLE I. CPU times for solution and post-processing.

	WE Order 1	WE Order 2	WE Order 3	BE
Solution, CPU secs per frequency[a]	1.15	1.45	1.80	4.4
Post-processing CPU secs—first frequency[b] (200 field points)	1.41	1.41	1.41	3.0
Post-processing CPU secs—subsequent frequencies (200 field points)	0.01	0.01	0.01	3.0

[a]The solution time per frequency is averaged for 140 frequency steps.
[b]The WE post-processing for the first frequency includes computation of an inverse mapping to define the location of the field points within the WE mesh.

frequency steps (required to produce the response curves of Fig. 23). Surprisingly, the WE solution is computationally less demanding not only during the post-processing phase, where this might be anticipated, but also during the solution phase where such an outcome is less predictable. The WE model benefits—as do all WE solutions in response calculations over a range of frequencies—from the relatively low computational overhead associated with assembly of the coefficient matrix. Assembly of the coefficient matrix is required only *once* in the WE response calculation since the acoustic mass, damping and stiffness matrices are frequency independent, whereas it must be performed at every frequency step in the BE solution. This particular WE model also has an unusually favourable bandwidth, somewhat smaller than the dimension of the full BE coefficient matrix. These two factors more than compensate for the obvious advantage which the BE scheme holds in terms of the overall dimension of the system of equations which must be solved (160 degrees of freedom in this instance versus 1200 or more for the WE schemes depending on element order).

In terms of post-processing, the WE scheme enjoys a significant but predictable advantage for reasons already discussed (i.e., the calculation of the solution at exterior field points involves interpolation rather than the evaluation of a surface integral). There is a small overhead associated with the WE formulation at the first frequency step, where an inverse mapping must be established to define the location of the field points in reference to the WE mesh; but this is negligible compared to the computational effort which is required at every frequency step in the BE computation.

In comparing process times for very large problems modeled by infinite elements and by BE methods, Burnett has noted the increasing margin of computational advantage which accrues to the infinite element scheme as the problem size increases.[1] The current elements are at least as effective as those of Burnett in reducing assembly and integration times, so that in extrapolating the figures of Table I to larger problems, the relative advantage of the WE computation can be expected to increase in a similar fashion.

IV. CONCLUSIONS

(1) A three-dimensional wave-envelope scheme has been demonstrated for general unbounded acoustical problems.

(2) The formulation has been shown to give accurate solutions for mth order spherical multi-pole sound fields when elements of radial order $m+1$ are used.

(3) A complex interaction exists between transverse and radial resolution at high frequencies, accuracy being limited by the transverse mesh rather than the radial order of the elements.

(4) The accuracy of the scheme improves with radial order to order 11. Ill-conditioning of the coefficient matrix limits further improvement beyond this point.

(5) Ritz vector condensation can be used in conjunction with the current model to reduce computational effort in cases where the shape of the surface excitation is independent of frequency.

(6) In application to a realistic three-dimensional problem, the current scheme has been shown to give solutions which agree well with those given by an equivalent BE model

(7) In application to a realistic three-dimensional problem, the WE scheme has been shown to offer significant computational efficiencies when compared to an equivalent BE model.

[1] D. S. Burnett, ''A three dimensional acoustic infinite element based on a prolate spheroidal multipole expansion,'' J. Acoust. Soc. Am. **96**, 2798–2816 (1994).
[2] D. Givoli, *Numerical Methods for Problems in Infinite Domains* (Elsevier Science, Amsterdam, 1992).
[3] P. Bettess, *Infinite Elements* (Penshaw, Sunderland, 1992).
[4] R. D. Ciscowski and C. A. Brebbia (Eds.), *Boundary Element Methods in Acoustics* (Computational Mechanics Publications & Elsevier Applied Science, Southampton, 1991).
[5] H. A. Schenk, ''Improved integral formulation for acoustic radiation problems,'' J. Acoust. Soc. Am. **44**, 41–58 (1968).
[6] A. J. Burton and G. F. Miller, ''The application of the integral equation method to the numerical solution of some exterior boundary value problems,'' Proc. R. Soc. London, Ser. A **323**, 201–210 (1971).
[7] B. Engquist and A. Madja, ''Radiation boundary conditions for acoustic and elastic waves,'' Commun. Pure Appl. Math. **32**, 313–357 (1979).
[8] A. Bayliss and E. Turkel, ''Radiation boundary conditions for wave-like equations,'' Commun. Pure Appl. Math. **33**, 707–725 (1980).
[9] A. Bayliss, M. Gunzberger, and E. Turkel, ''Boundary conditions for the numerical solution of elliptic equations in exterior regions,'' SIAM (Soc. Ind. Appl. Math.) J. Appl. Math. **42**, 430–450 (1982).
[10] Y. Kagawa, T. Yamabuchi, K. Sugihara, and T. Shindou, ''A finite element approach to a coupled structural acoustic radiation system with application to loudspeaker design,'' J. Sound Vib. **69**, 229–243 (1980).
[11] R. K. Sigman, S. J. Horowitz, and B. T. Zinn, ''Optimisation of acoustic liners by the hybrid finite element integral approach,'' *American Institute of Aeronautics and Astronautics, paper 83-0670* (1983).
[12] G. C. Everstine and F. M. Henderson, ''Coupled finite element/boundary element approach for fluid-structure interaction,'' J. Acoust. Soc. Am. **87**, 1938–1947 (1990).
[13] M. J. Grote and J. B. Keller, ''On nonreflecting boundary conditions,'' J. Comput. Phys. **122**, 231–243 (1995).
[14] D. Givoli, I. Patlashenko, and J. B. Keller, ''High-order boundary conditions and finite elements for infinite domains,'' Comput. Methods Appl. Mech. Eng. **143**, 13–39 (1997).
[15] R. J. Astley, ''FE mode-matching schemes for the exterior Helmholtz problem and their relationship to the FE-DtN approach,'' Commun. Numer. Methods Eng. **12**, 257–267 (1996).
[16] P. Bettess and O. C. Zienkiewicz, ''Diffraction and refraction of surface waves using finite and infinite elements,'' Int. J. Numer. Methods Eng. **11**, 1271–1290 (1977).
[17] O. C. Zienkiewicz, K. Bando, P. Bettess, C. Emson, and T. C. Chiam, ''Mapped infinite elements for exterior wave problems,'' Int. J. Numer. Methods Eng. **21**, 1229–1252 (1985).
[18] J. P. E. Gorranson and C. F. Davidsson, ''Three dimensional infinite ele-

ment for wave propagation,'' J. Sound Vib. **115**, 556–559 (1987).

[19] R. J. Astley, ''Wave envelope and infinite elements for acoustic radiation,'' Int. Numer. Methods Fluids **3**, 507–526 (1983).

[20] R. J. Astley and W. Eversman, ''Wave envelope elements for acoustical radiation in inhomogeneous media,'' Comput. Struct. **30**, 801–810 (1988).

[21] W. Eversman, ''Radiated Noise of ducted fans,'' *DGLR/AIAA 92-02-139, 14'th Aeroacoustics Conference, Aachen, Germany* (1992).

[22] W. Eversman, ''Aft fan duct acoustic radiation,'' *CEAS/AIAA 95-155, 16'th AIAA Aeroacoustics Conference, Munich, Germany* (1995).

[23] P. Bettess, ''A simple wave envelope example,'' Commun. Appl. Numeri. Methods **3**, 77–80 (1987).

[24] R. J. Astley, G. J. Macaulay, and J. P. Coyette, ''Mapped wave envelope elements for acoustic radiation and scattering,'' J. Sound Vib. **170**, 97–118 (1994).

[25] L. Cremers, K. R. Fyfe, and J. P. Coyette, ''A variable order infinite acoustic wave envelope element,'' J. Sound Vib. **171**, 483–508 (1994).

[26] B. A. Regan and J. A. Eaton, ''Application of an Efficient Iterative 3D Finite element Scheme to the Fan Noise radiation Problem,'' *paper CEAS/AIAA–95–012, 1'st Joint CEAS/AIAA Aeroacoustics Conference, Munich* (1995).

[27] K. Gerdes and L. Demkowicz, ''Solution of 3D Laplace and Helmholtz equations in exterior domains using p-infinite elements,'' Comput. Methods Appl. Mech. Eng. **137**, 239–273 (1996).

[28] R. J. Astley, P. Bettess, and P. J. Clark, ''On 'Mapped infinite elements for exterior wave problems' by O. C. Zienciewicz *et al.*,'' Int. J. Numer. Methods Eng. **32**, 207–209 (1991).

[29] O. C. Zienkiewicz and R. L. Taylor, *The Finite Element Method* (McGraw-Hill, London, 1989), 4th ed., Vol. 1, Chaps. 7 and 8.

[30] J. M. M. C. Marques and D. R. J. Owen, ''Infinite elements in quasi-static materially nonlinear problems,'' Comput. Struct. **18**, 739–751 (1984).

[31] G. J. Macaulay, ''Wave Envelope Elements for Acoustics,'' Ph.D. thesis, University of Canterbury (1995).

[32] M. C. Junger and D. Feit, *Sound, Structure and Their Interactions* (MIT, Cambridge, 1972).

Three-dimensional wave-envelope elements of variable order for acoustic radiation and scattering. Part II. Formulation in the time domain

R. J. Astley

Department of Mechanical Engineering, University of Canterbury, Private bag 4800, Christchurch, New Zealand

J.-P. Coyette and L. Cremers

LMS Numerical Technologies, Researchpark Haasrode, Zone 1, Interleuvenlaan 70, 3001, Leuven, Belgium

A variable-order, infinite ''wave-envelope'' element scheme is formulated for transient, unbounded acoustical problems. The transient formulation which is local in space and time is obtained by applying an inverse Fourier transformation to a time-harmonic wave-envelope model whose formulation is described in a companion article. This procedure yields a coupled system of second-order differential equations which can be integrated in time to yield transient pressure histories at discrete nodal points. Far-field transient pressures can also be obtained at adjusted times. The method can be applied quite generally to two-dimensional and three-dimensional problems and is compatible with a conventional finite element model in the near field. The utility of the method is confirmed by the presentation of transient solutions for axisymmetric and fully three-dimensional test problems. An implicit time integration scheme is used and computed results are compared to analytic solutions and to solutions obtained from alternative numerical schemes. Close correspondence is demonstrated and the scheme is shown to be stable for the problems which are presented. CPU times for a large three-dimensional problem are shown to compare favorably with those required for an equivalent transient boundary element computation. © *1998 Acoustical Society of America.* [S0001-4966(97)06612-5]

INTRODUCTION

The prediction of time-harmonic and transient wave fields in unbounded domains poses particular difficulties for computation. The time-harmonic problem is discussed in a companion article[1] in which a three-dimensional wave-envelope (WE) approach is proposed for its solution. The same formulation is modified in the current article to deal with transient acoustics. Numerical solutions are sought for the sound field generated by the prescribed transient motion of a closed surface in an unbounded homogeneous domain. The equivalent time-harmonic problem arises when the excitation is time-harmonic and sufficient time has elapsed so that the acoustical field throughout the exterior region has the same time-harmonic dependence. The transient problem is governed by the homogeneous wave equation. The steady problem is governed by Helmholtz' equation.

A review of numerical techniques which exist for the solution of the steady problem is given in part I and will not be repeated here. Review treatments which touch also on the transient case are found in Givoli's monograph[2] and in Bettess' text on infinite elements.[3] In theory, any method which predicts the acoustic response in the frequency domain over a full range of frequencies can be used to obtain a transient solution. That is to say, the transient solution can be evaluated numerically as a Fourier integral of the time-harmonic response. In practice, such an approach is often impracticable, particularly when broadband excitation is present. Various boundary or domain-based options then exist.

The transient boundary element (BE) concept[4] is widely used. It is based on a discrete implementation of Kirchhoff's retarded potential formulation.[5,6] This gives a system of integral or differential equations which are nonlocal in time and space and hence computationally intensive. A boundary-related approach which is less demanding in terms of computation, but still well-suited to impulsive or broadband problems, is the ''doubly asymptotic approximation'' (DAA).[7,8] Here a discrete surface formulation is constructed which is local in time and which converges asymptotically to the full retarded potential formulation in the limits of high and low frequency. A family of such approximations of increasing accuracy has been proposed of which the first two (DAA$_1$ and DAA$_2$) have been implemented and evaluated.[9]

Domain-based strategies for transient computation take as their starting point a conventional numerical representation—usually a finite element model—over a finite inner domain which surrounds the radiating or scattering object. Transient nonreflecting boundary conditions are applied at the outer boundary of the inner domain. A variety of *local* nonreflecting boundary conditions have been proposed[10–12] and implemented.[13] *Nonlocal* integral forms of the anechoic condition can also be used. Examples are two-dimensional dampers based on a local approximation of a transient ''DtN type'' map,[14] and the DtN method itself which has been implemented in the time domain in a semi-discrete form for two-dimensional problems.[2,15,16] The effectiveness of the
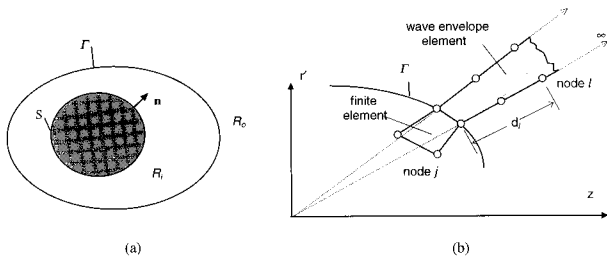
FIG. 1. (a) Problem geometry. (b) Matching of FE and WE meshes at Γ.

semi-discrete DtN approach for three-dimensional problems has yet to be demonstrated.

The ''infinite'' element concept represents a more radical approach to domain-based computation. It is well developed in the frequency domain[3] but does not lend itself to direct application in the time domain, although a transient infinite element formulation has been proposed by Olson.[17] This is consistent with the DAA$_1$ approximation, being strictly valid only in the asymptotic limit of high or low frequency. Transient infinite elements based on Burnett's spheroidal frequency-domain formulation[18] have also been proposed[19] but their implementation has yet to be demonstrated.

In this article, a family of variable-order transient infinite elements is proposed. The formulation is based on an inverse Fourier transform of a discrete wave-envelope (WE) model for the time-harmonic problem.[1] The resulting transient scheme can accommodate elements of variable radial order and can be applied to three-dimensional geometries without restriction. An implicit time integration scheme is used and its accuracy and stability are assessed with respect to axisymmetric test problems for which analytic solutions exist. Computed solutions for a fully three-dimensional problem are also presented to demonstrate the effectiveness of the method in treating bodies of irregular shape. In this case, computed WE solutions are compared to solutions obtained from a transient BE computation. Good agreement is demonstrated and a comparison is made of relative computational efficiencies.

I. THE PROBLEM STATEMENT

A. The transient equations

Figure 1(a) shows the geometry of the problem to be solved. It is identical to that of the time-harmonic problem treated in part I.[1] A closed surface S is enclosed by an unbounded region R which is subdivided into a finite inner region R_i and an unbounded outer region R_0. These are separated by an interface Γ. Initially (at time $t=0$) the surface S is at rest and the acoustical pressure $p(\mathbf{x},t)$ is zero throughout the exterior region. The normal component of acceleration $a_n(\mathbf{x},t)$ is prescribed on the surface S. No other sources of sound are present. The sound field is then governed by the linearized wave equation

$$\nabla^2 p = \frac{1}{c^2}\frac{\partial^2 p}{\partial t^2}, \quad \text{in } R, \tag{1}$$

where ∇^2 is the Laplacian operator and c is the sound speed. On the surface S, continuity of normal velocity requires that

$$\boldsymbol{\nabla} p \cdot \mathbf{n} = -\rho a_n \quad \text{on } S, \tag{2}$$

where $\mathbf{n}$ is a unit normal vector and ρ is the mean fluid density. Equations (1) and (2), supplemented by homogeneous initial conditions, pose an initial value problem for $p(\mathbf{x},t)$. The analysis and results which follow are restricted to the case of homogeneous initial conditions $[p(\mathbf{x},t)\equiv 0$ for $t\leq 0]$. However, preliminary studies have indicated that the method can also be applied without significant modification to problems which are defined by nonhomogeneous initial conditions. These will not be discussed further at present but reported more fully at a later date. Whether the initial conditions are homogeneous or nonhomogeneous, energy propagates in an outward direction into the infinite domain. That is to say, all solutions should satisfy the Sommerfeld radiation condition

$$r\{\partial p/\partial r + (1/c)\partial p/\partial t\}\rightarrow 0, \quad \text{as } r\rightarrow\infty, \tag{3}$$

where r is a spherical polar radial coordinate. This forms a necessary asymptotic boundary condition for the time-harmonic problem treated in part I, and indeed for the transient initial value problem if the infinite domain is truncated in any way. In the current instance however where the transient solution is sought on an unbounded domain, this condition will be satisfied implicitly *by* the solution rather requiring imposition as part of the problem statement.

The problem defined by Eq. (1) and boundary condition (2) is one of ''radiation'' rather than ''scattering.'' The latter can however be accommodate by assuming a known incident sound field $p_i(\mathbf{x},t)$ which identically satisfies Eq. (1). If $p(\mathbf{x},t)$ is then taken to be the scattered field, Eq. (1) and condition (3) still hold, and boundary condition (2) becomes

$$\boldsymbol{\nabla} p \cdot \mathbf{n} = -\rho a_n - \boldsymbol{\nabla} p_i \cdot \mathbf{n} \quad \text{on } S.$$

The scattering of an incident sound field is therefore modelled by an effective boundary acceleration, a_n' say, where $a_n' = a_n + (1/\rho)\boldsymbol{\nabla} p_i \cdot \mathbf{n}$. Without loss of generality, the analysis which follows is presented for the radiation problem only.

B. The transformed equations

The acoustic pressure $p(\mathbf{x},t)$ and surface acceleration $a_n(\mathbf{x},t)$ can be written in terms of their complex Fourier transforms $\bar{p}(\mathbf{x},\omega)$ and $\bar{a}_n(\mathbf{x},\omega)$ by using relationships of the form

$$\bar{f}(\mathbf{x},\omega) = \mathscr{F}\{f(\mathbf{x},t)\} = \int_{-\infty}^{+\infty} f(\mathbf{x},t)e^{-\omega t}\,dt, \tag{4a}$$

and

$$f(\mathbf{x},t) = \mathscr{F}^{-1}\{\bar{f}(x,\omega)\} = \frac{1}{2\pi}\int_{-\infty}^{+\infty}\bar{f}(\mathbf{x},\omega)e^{i\omega t}\,d\omega. \tag{4b}$$

By taking a Fourier transform of Eqs. (1)–(3), it is simple to show that $\bar{p}(\mathbf{x},\omega)$ and $\bar{a}_n(\mathbf{x},\omega)$ satisfy the boundary value problem:

$$\nabla^2\bar{p} + k^2\bar{p} = 0 \quad \text{in } R, \tag{5}$$

$$\nabla \overline{p} \cdot \mathbf{n} = -\rho \overline{a}_n \quad \text{on} \quad S, \tag{6}$$

and

$$r\{\partial \overline{p}/\partial r + (ik)\overline{p}\} \rightarrow 0, \quad \text{as} \quad r \rightarrow \infty, \tag{7}$$

where $k = \omega/c$. These are also the equations and boundary conditions which govern the steady time-harmonic problem treated in part I.[1]

II. THE DISCRETE MODEL

A. Formulation in the frequency domain

The transient WE formulation is obtained by discretising the steady problem posed by Eqs. (5)–(7) and taking an inverse Fourier transform of the resulting discrete equations. The formulation of the discrete model in the frequency domain is described in part I.[1] It is based on a subdivision of the exterior region R into a near-field mesh of conventional finite elements (in R_i) matched to infinite ''wave-envelope'' elements in R_0. A typical discretization of this type is illustrated in Fig. 1(b) for an axisymmetric geometry (z denotes the axis of symmetry and r' is a cylindrical polar radial coordinate). A four-noded quadrilateral finite element is shown joined to a compatible six-noded wave-envelope element of radial order 3. Details of the mapping and shape functions used to define such elements in two and three dimensions are to be found elsewhere[1,20,21] and will not be repeated here, except to note that the shape functions for the unbounded WE elements include a complex wavelike factor appropriate to an outwardly propagating solution.

A Petrov–Galerkin procedure is used to formulate the discrete equations. It is an essential element of the procedure that complex conjugates of the shape functions are used as weighting functions. This yields a set of discrete equations of the form

$$[\mathbf{A}(\omega)]\overline{\mathbf{q}} = \overline{\mathbf{f}}, \tag{8}$$

where $\mathbf{A}$ is an $n \times n$ coefficient matrix, $\overline{\mathbf{q}}$ is a solution vector containing nodal parameters, $\overline{q}_j(\omega)$ ($j=1,...,n$), and $\overline{\mathbf{f}}$ is an $n \times l$ forcing vector. The coefficient matrix $[\mathbf{A}(\omega)]$ can be written in terms of frequency-independent, acoustic ''stiffness,'' ''damping,'' and ''mass'' matrices $\mathbf{K}$, $\mathbf{C}$, and $\mathbf{M}$. This follows directly from the use of conjugated weighting functions. The components of $\overline{\mathbf{f}}$ are given by[1]

$$\overline{f}_i(\omega) = \int_S \rho N_i(\mathbf{x}) \overline{a}_n(\mathbf{x}, \omega) dS, \tag{9}$$

where $N_i(\mathbf{x})$ is the finite element shape function associated with node i. Equation (8) can therefore be written in the form

$$[\mathbf{K} + i\omega\mathbf{C} - \omega^2\mathbf{M}]\overline{\mathbf{q}} = \overline{\mathbf{f}}. \tag{10}$$

The physical interpretation of the components of the solution vector $\overline{\mathbf{q}}$ is different in the inner and outer regions. For an index j, where node j lies in the *inner* region, the component $\overline{q}_j(\omega)$ is the complex pressure amplitude at that node. For an index l, where node l lies in the *outer* region, the component, $\overline{q}_l(\omega)$, is given in terms of the nodal pressure amplitude, $\overline{p}_l(\omega)$, by the relationship

$$\overline{q}_l(\omega) = \overline{p}_l(\omega) e^{ikd_l}, \tag{11}$$

where d_l is the radial distance along the infinite edge of the wave-envelope element measured from the FE/WE interface [see Fig. 1(b)]. Both of these statements follow directly from the trial expansion which is used in the WE model, details of which are given in part I.[1]

B. Transformation of the discrete equations to the time domain

The discrete problem is transformed from the frequency domain to the time domain by taking an inverse Fourier transform of Eqs. (10). This gives a system of second order, ordinary differential equations;

$$\mathbf{Kq} + \mathbf{C\dot{q}} + \mathbf{M\ddot{q}} = \mathbf{f}(t), \tag{12}$$

where

$$q_i(t) = \mathscr{F}^{-1}\{\overline{q}_i(\omega)\}, \tag{13a}$$

and

$$f_i(t) = \mathscr{F}^{-1}\{\overline{f}_i(\omega)\}. \tag{13b}$$

Also, since $\overline{a}_n(\mathbf{x}, \omega)$ is the Fourier transform of the surface acceleration $a_n(\mathbf{x}, t)$ [see Eqs. (4a), (4b)], Eq. (13b) is equivalent to the statement

$$f_i = \int_S \rho N_i(\mathbf{x}) a_n(\mathbf{x}, t) dS. \tag{14}$$

In practical terms this means that the components $f_i(t)$ can be obtained *directly* in the time domain by assembling element contributions of the above form which involve surface integrals of the transient acceleration.

C. Solution of the equations

Equations (12) are identical in form to the discrete equations encountered in the analysis of linear structures. Many efficient single and multi-step methods have been developed for treating such problems. In the absence of any clear strategy for lumping the mass and damping matrices—which would make an explicit scheme attractive—an implicit scheme has been implemented to solve Eqs. (12). Specifically, the Newmark method[22] (with parameters $\beta = 1/4$ and $\gamma = 1/2$) is used. The algorithm at each time step is given by

$$\mathbf{E}_0\ddot{\mathbf{q}}_{t+\delta t} = \frac{1}{\beta \delta t^2} \mathbf{f}_{t+\delta t} + \mathbf{E}_1\mathbf{q}_t + \mathbf{E}_2\dot{\mathbf{q}}_t + \mathbf{E}_3\ddot{\mathbf{q}}_t, \tag{14a}$$

$$\dot{\mathbf{q}}_{t+\delta t} = \dot{\mathbf{q}}_t + ((1-\gamma)\ddot{\mathbf{q}}_t + \gamma\ddot{\mathbf{q}}_{t+\delta t})\delta t, \tag{14b}$$

$$\mathbf{q}_{t+\delta t} = \mathbf{q}_t + \dot{\mathbf{q}}_t \delta t + ((1/2 - \beta)\ddot{\mathbf{q}}_t + \beta\ddot{\mathbf{q}}_{t+\delta t})\delta t^2, \tag{14c}$$

where the subscripts ''t'' and ''$t+\delta t$'' denote values of $\mathbf{q}$ at successive time steps. The matrices $\mathbf{E}_0$, $\mathbf{E}_1$, $\mathbf{E}_2$, and $\mathbf{E}_3$ are given by

$$\mathbf{E}_0 = \mathbf{K} + \frac{\gamma}{\beta \delta t} \mathbf{C} + \frac{1}{\beta \delta t^2} \mathbf{M}, \quad \mathbf{E}_1 = -\frac{1}{\beta \delta t^2} \mathbf{K},$$

$$\mathbf{E}_2 = -\frac{1}{\beta \delta t^2} \mathbf{C} - \frac{1}{\beta \delta t} \mathbf{K}, \tag{14d}$$

and

$$\mathbf{E}_3 = \left(\frac{\gamma-1}{\beta\delta t}\right)\mathbf{C} + \left(\frac{\beta-1/2}{\beta}\right)\mathbf{K}.$$

An L-U solver is used to solve Eq. (14a), the decomposition being performed once only at the first time step. This scheme is known to be unconditionally stable for symmetric systems of equations. There is no assurance that this is the case in the current instance given that the matrices $\mathbf{K}$ and $\mathbf{C}$ are not symmetric. However, the numerical results which are presented in Sec. III along with computed values of the spectral radius for the associated amplification matrix indicate that this is the case, certainly for the specific problems which have been solved to date.

D. Interpretation of the transient solution vector

The physical interpretation of the components of the transient solution vector $\mathbf{q}(t)$ is as follows: At node j within the inner region, the component $q_j(t)$ is simply the transient pressure $p(\mathbf{x},t)$ evaluated at that node; i.e., the inverse Fourier transform of $\bar{q}_j(\omega)$ the complex pressure amplitude. This is not the case within the WE region. Here the physical interpretation of $q_l(t)$ is obtained by taking an inverse Fourier transform of Eq. (11). Application of the ''shift'' property of the Fourier transform then gives

$$q_1(t) = \mathscr{F}^{-1}\{\bar{q}_1(\omega)\}$$
$$= \mathscr{F}^{-1}\{\bar{p}_t(\omega)e^{i(\omega/c)d_1}\} = p_l(t+d_l/c). \qquad (15)$$

That is to say, $q_l(t)$ is the transient acoustic pressure at node l but at a time, ''$t+d_l/c$,'' the time shift, ''d_l/c,'' being the time which elapses as a disturbance travels to node l from the outer edge of the conventional mesh.

To summarize, the solution of Eq. (12) with the initial conditions $\mathbf{q} = \mathbf{f} = \mathbf{0}$ at $t=0$, yields; (i) transient instantaneous acoustical pressures at all nodes in the inner mesh; and (ii) transient pressures in the outer mesh which are advanced by the time taken for the disturbance to reach them.

III. IMPLEMENTATION

The transient WE formulation has been implemented in axisymmetric and fully three-dimensional codes. In the axisymmetric code, four-noded isoparametric quadrilateral finite elements are used as indicated in Fig. 1(b). The outer WE elements are linear in the transverse direction and of variable radial order. In the three-dimensional code, eight-noded block elements are used for the FE mesh. Compatible WE elements of variable radial order are used for the outer mesh. The results which follow have been obtained by using WE elements of radial orders 1–3.

IV. RESULTS

A. Test case 1. The sound field generated by unsteady axial motion of a rigid sphere

Solutions are presented first for the transient dipole sound field generated by the motion of a rigid sphere which is subject to a prescribed acceleration along the z axis of
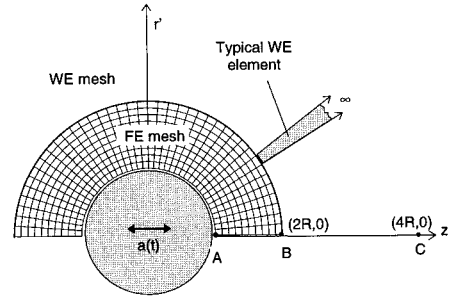
FIG. 2. Test problem 1. Unsteady axial motion of a rigid sphere, FE and WE meshes.

symmetry. The axial acceleration is denoted by $a(t)$. An exact solution for the transient acoustic pressure field is given by

$$p(\mathbf{x},t) = p(r,\theta,t) = \mathscr{L}^{-1}\left\{\frac{\rho R^3 A(s)e^{-s(r-R)/c}}{[2+2(sR/c)+(sR/c)^2]}\right.$$
$$\left. \times\left\{\frac{1}{r^2}+\frac{s}{cr}\right\}\cos\theta\right\}, \qquad (16)$$

where $\mathscr{L}\{\ \}$ denotes a Laplace transform, $A(s) = \mathscr{L}\{a(t)\}$, r and θ are spherical polar coordinates, and R is the radius of the sphere. Results are presented for the case, $a(t) = a_0 \sin \omega t$, commencing from rest at time $t=0$. The mesh used is shown in Fig. 2. It comprises a conventional inner mesh of 400 elements and a compatible WE mesh of 40 infinite elements. The inner mesh and a typical WE element are shown in Fig. 2.

A comparison of computed and analytic solutions for the case $\omega R/c = 2\pi$ is presented in Figs. 3 and 4. These show nondimensional acoustic pressure $(=p(t)\omega/\rho ca_0)$ plotted against dimensionless time $(=ct/D)$ calculated at points A, B, and C whose location is indicated in Fig. 2. The first two points lie within the FE mesh, on the surface of the sphere and at the FE/WE interface, respectively, while the third lies within the WE region. Computed solutions are shown for WE elements of radial orders 1 and 2 in Figs. 3 and 4, respectively. The elements of order 1 have nodes only on the FE/WE interface, and do not therefore yield a nodal result at point C. The second-order elements do so, but the response at C is subject to a time delay of 1.0 dimensionless units,
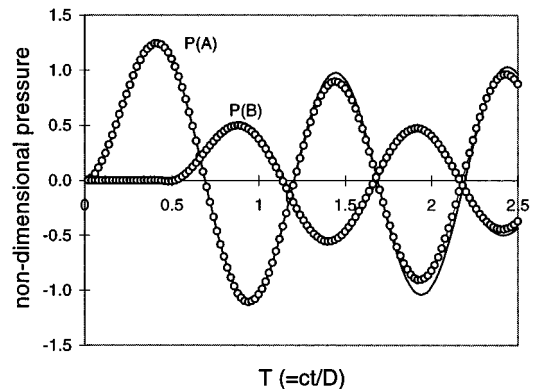
FIG. 3. Test case 1. Pressure histories at A and B; — exact; –O– computed; WE elements of order 1.
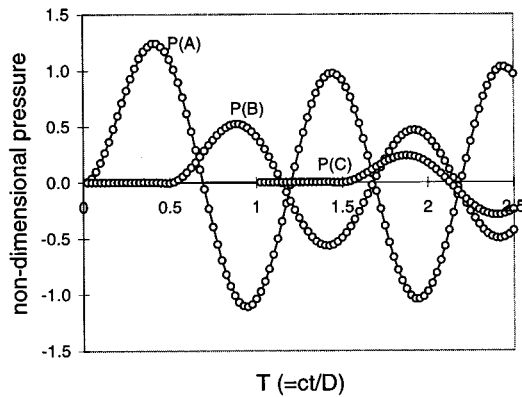
FIG. 4. Test case 1. Pressure histories at A and B; — exact; –O– computed; WE elements of order 2.

given by Eq. (15), so that the computed numerical pressure history at this point commences at $T=1.0$. The time step has been chosen in this instance to be sufficiently small that further reduction of the time step does not affect either solution to the scale shown. The comparison between the analytic computed transient solutions can therefore be made without considering the additional discretisation error associated with the temporal integration scheme (the time increments used in Figs. 3 and 4 are $\Delta T=0.02$ *and* $\Delta T=0.025$ for the first- and second-order solutions, respectively; these are approximately one-half of the dimensionless time required for a disturbance to traverse the smallest element in the inner mesh).

In comparing the computed and analytic solutions, a small discrepancy is apparent when first-order WE elements are used (Fig. 3). The second-order solution is indistinguishable from the analytic result to the scale shown (Fig. 4). This is true both within the inner mesh (at points A and B) and in the WE region (at point C). This is predictable given the performance of the same elements in the frequency domain. That is to say, elements of radial order $m+l$ have been shown to model exactly the radial variation of multi-pole components of order m for all frequencies.[1] Second-order elements therefore resolve dipole fields without approximation in the radial direction. The degree of correspondence between analytic and computed solutions demonstrated in Figs. 3 and 4 at points A, B, and C is characteristic of the entire solution domain.

B. Test case 2. The sound field generated by impulsive motion of a circular piston

A solution for the transient sound field generated by a circular piston of diameter D ($=2R$) mounted in an infinite rigid plane baffle and subject to a normal acceleration $a(t)$, is given by

$$\bar{p}(\mathbf{x},\omega) = -\frac{\rho}{2\pi} \int_{S_Q} \frac{a(t-(1/c)|\mathbf{x}-\mathbf{x}_Q|)}{|\mathbf{x}-\mathbf{x}_Q|}\, dS, \qquad (17)$$

where $\mathbf{x}$ and $\mathbf{x}_Q$ are position vectors of the field point and of a point on the surface of the piston S_Q, as indicated in Fig. 5(a).

Computed solutions for this problem are presented in Figs. 6–8. The FE/WE model used is shown in Fig. 5(b). It comprises an inner FE mesh of 270 quadrilateral elements which extends to a diameter 1.2D, and an outer mesh of 30 WE elements of variable radial order. The extent of the inner mesh is constrained by the requirement that the FE/WE interface enclose a spherical surface which contains the piston surface S_Q. Provided that this condition is satisfied, the wave field in the outer region consists entirely of outwardly propagating components[23] and the WE trial solution is therefore complete in the limit as the radial order of the elements and transverse resolution are increased.

Computed results are presented in Figs. 6 and 7 for elements of radial order 1, 2, and 3. Nondimensional pressures are plotted against dimensionless time T ($=ct/D$). The impulsive acceleration of the piston has the shape and duration indicated in Fig. 6(a). Comparisons of computed and analytic nondimensional pressure histories at the points A, B, and C [see Fig. 5(b)] are plotted in Fig. 6(a)–(c). Once again the time step is chosen to be sufficiently small—in the range 0.03–0.032 dimensionless units—that further reduction does not affect the computed solution to the scale shown (the minimum time for a disturbance to propagate between adjacent nodes in this case is 0.033 dimensionless units). Solutions are plotted in Figs. 6 and 7 at every second time step. It is clear from Fig. 6 that the computed solution improves with the radial order. This is particularly apparent in the time history at point B [Fig. 6(b)] which lies on the FE/WE interface. To the scale shown, the numerical solution has converged to the analytic result at all points for elements of radial order 3 or greater. Note also that at point C, which lies

(a)

(b)
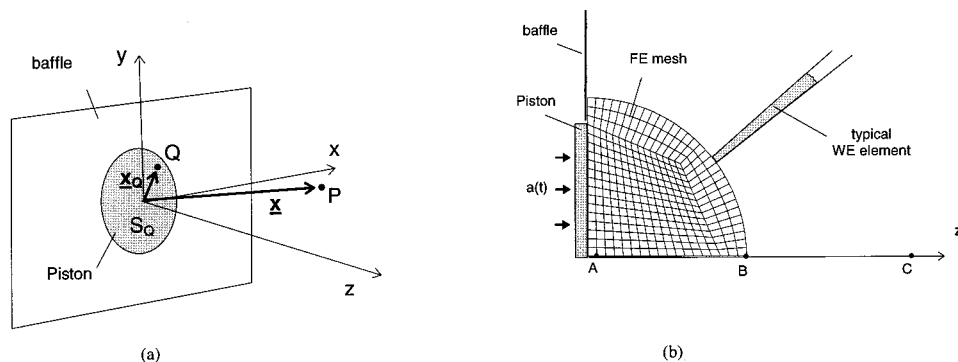
FIG. 5. Test case 2. (a) Geometry; (b) FE and WE meshes.

(a)

(b)

T (=ct/D)

(c)
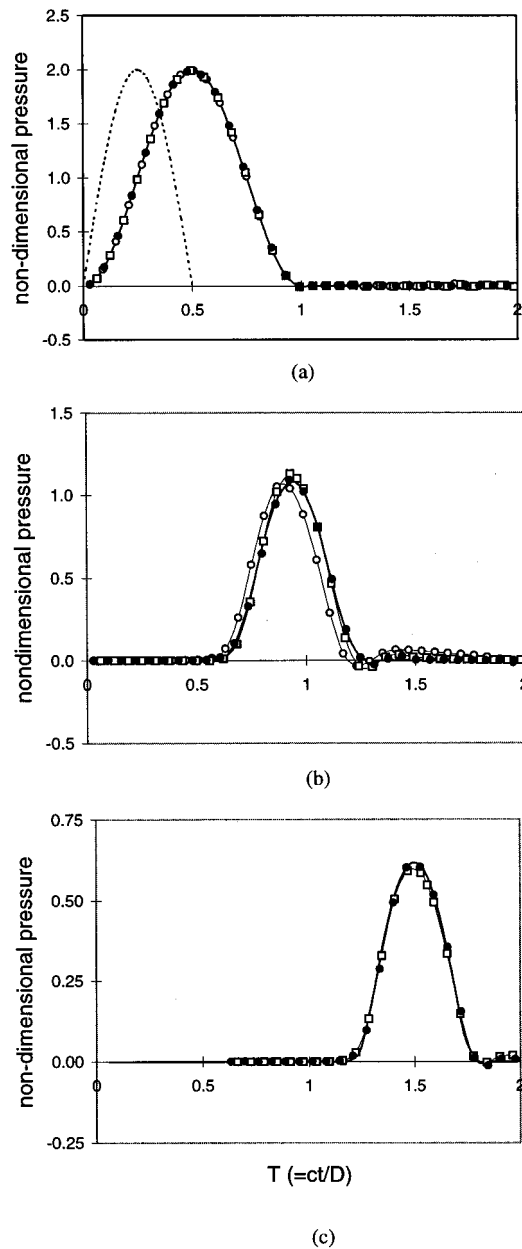
FIG. 6. Test case 2. Pressure histories at *A* (a); *B* (b); and *C* (c); — exact; −○− WE order 1; −□− WE order 2; ● WE order 3; ------- piston acceleration (shape and duration of pulse).

FIG. 7. Test case 2. Computed acoustic pressure contours at $T = 0.5$ (a); $T = 0.75$ (b); and $T = 1.0$ (c).

C. Test case 3. Transient vibration of an engine casing

To conclude, transient solutions are presented for the sound field generated by the vibration of a three-dimensional engine casing whose geometry and dimensions are shown in Fig. 8. Symmetry constraints are used so that one quadrant only need be modeled (see the portion of casing indicated by the heavy outline in Fig. 8). A fully three-dimensional FE/WE model is used. It is formed by an inner mesh of 888 isoparametric block elements which is joined to an outer mesh of 177 WE elements of variable radial order. The FE and WE meshes are matched at a spherical interface of diameter 1.0m (this contains the points *B*, *C*, and *D* of Fig. 8). The FE mesh itself is shown in Fig. 21(b) of the companion article (part I).[1]

No analytical solution is possible for this configuration but comparison is made with numerical results obtained from a transient ''retarded potential'' BE scheme implemented in the acoustical code SYSNOISE.[24] The BE model has the same surface discretisation as the FE/WE model. The form of the surface acceleration which is used to drive the acoustic field is shown in Fig. 9, which also shows the BE surface model for the casing. The casing is initially at rest (at $t = 0$) and is then driven at a frequency of 200 Hz for two- and one-half cycles before being brought again to rest. The sound speed in the surrounding medium is 340 m/s.

Computed pressure histories at points *A*, *B*, *C*, and *D* (see Fig. 8) are shown in Fig. 10(a)–(d). Solutions are presented for the BE model and for WE meshes of radial orders 1, 2, and 3. The WE solutions converge with radial order,

at a distance 0.6*D* beyond the FE/WE interface, the numerical solution commences at $T = 0.6$ by virtue of expression (15).

Confirmation of the effectiveness of the WE scheme in representing the sound field as a whole is illustrated in Figs. 7(a)–(c). These show contours of the computed sound pressure amplitude for the WE model of order 3 plotted at times $T = 0.5$, $T = 0.75$, and $T = 1.0$ as the disturbance propagates through the inner FE region. Contours are plotted at equally spaced intervals labelled 1,2,...,7 in ascending order. Clearly the numerical scheme permits the sound pulse generated on the piston to pass through the FE/WE interface without reflection. Corresponding exact contours of the same parameter (not shown here) are indistinguishable from the computed contours when displayed on the same mesh.

FIG. 8. Engine casing. Geometry and dimensions.

FIG. 9. Engine casing. Boundary element mesh and surface acceleration.

FIG. 11. Engine casing. CPU usage; — BE; ---- WE radial order 3; --- WE radial order 2; --- WE radial order 1.

being fully converged to the scale shown for the mesh of order 3. The agreement between the WE and BE solutions is generally good, although some small discrepancies are apparent particularly at the innermost field point A.

The same computer system and configuration—a DEC Alphaserver 2100A—was used to calculate the WE and BE solutions shown in Fig. 10. A direct comparison of computational effort associated with each calculation is therefore possible. This is presented in Fig. 11 which shows cumulative CPU times for the BE and WE schemes for the first 100 time steps. The CPU time required for each time increment remains constant with elapsed time in the case of the WE solution, but increases in the case of the BE scheme until a maximum is reached after 17 time steps, at which point the

elapsed time is equal to the time taken for a disturbance to traverse the casing. It is clear from Fig. 11 that the WE scheme is computationally more efficient than the BE scheme almost by an order of magnitude in spite of the much larger number of equations which must be integrated (the current WE model has 1200 or more degrees of freedom, depending on radial order, compared to 160 degrees of freedom for the BE scheme). The critical factor in favor of the WE scheme is that the resulting discrete equations are local both in the spatial and temporal domains. A direct solver is currently used to solve Eq. (12). Preliminary studies (not reported here) have indicated that significant further im-

(a)

(b)

(c)
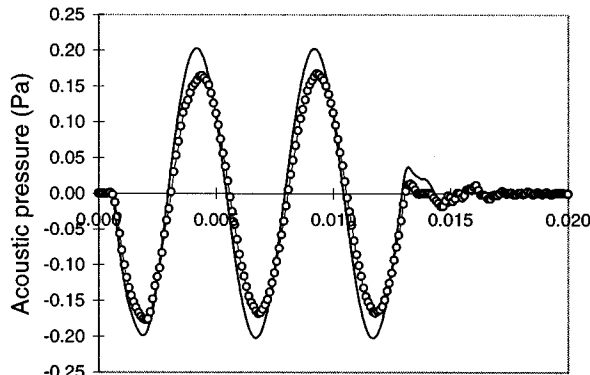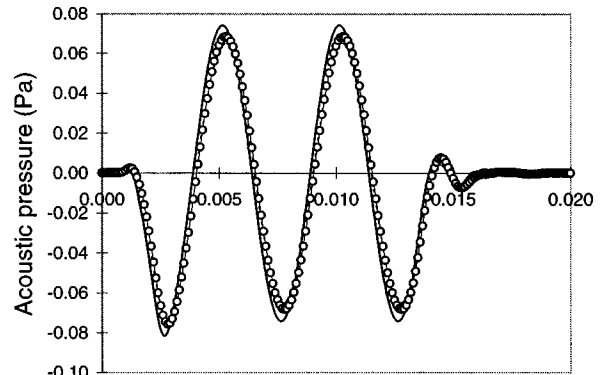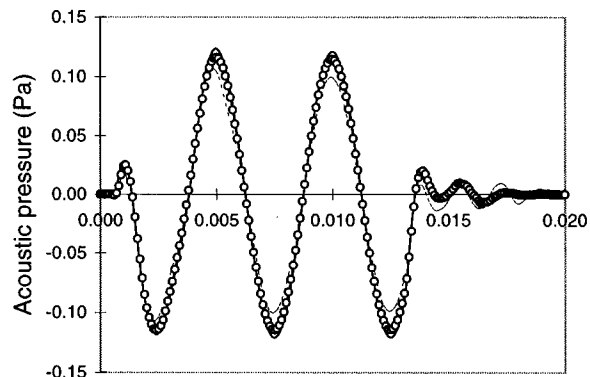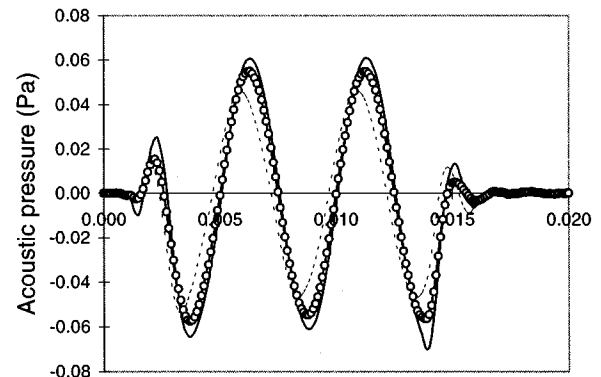
(d)

FIG. 10. Engine casing. Pressure histories at points A (a); B (b), C (c); and D (d); — BE; --- WE order 1; — WE order 2; ○ WE order 3.

provements in computational efficiency can be achieved from the use of an iterative solver at each time step. This removes the necessity for a matrix inversion of the coefficient matrix at the first time step and avoids the requirement to store ''fill'' terms in the coefficient matrices. This concept has been applied with success to two-dimensional and axisymmetric problems. It will be reported more fully at a later date.

D. Accuracy and stability; The effect of step size

The computed solutions presented in Figs. 4–7 and 10 are obtained by using relatively small time steps, comparable to the time taken for a disturbance to traverse an element of the inner mesh. Such step sizes are characteristic of those required in an explicit rather than an implicit scheme. They have the advantage however that the transient computed solution can be compared to analytic or alternative solutions in a manner which is effectively independent of step size. The performance of time-stepping scheme is however of interest and will determine to a large degree the practical utility of the method. In Fig. 12, computed solutions are presented for the first test case (the oscillating sphere accelerating from rest) for time steps of 0.1 and 0.2 dimensionless units respectively. These are four and eight times greater than the time step used for Fig. 4 (second-order elements are used) and many times greater than the time required for a wave to traverse an element of the inner mesh. Clearly the accuracy of the average acceleration scheme deteriorates with increasing time step, as one would expect, but does so in what appears to be a stable and predictable way (''predictable'' in the sense that it reflects the performance of the same algorithm for symmetric problems). Similar results not shown here have been obtained for the second and third test problems. In none of the test problems to date has instability been
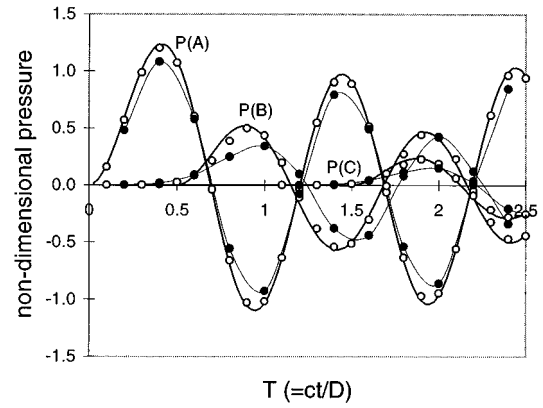
FIG. 12. Test case 1. Pressure histories at A and B; — exact; $\bigcirc$ computed; WE order 2; $DT=0.1$; $-\bullet-$ computed; WE order 2, $DT=.2$.

observed as the time step is increased. This does not of course constitute proof that the implicit scheme used here is always stable but does provide a strong indication that this may be the case.

The stability of any time integration scheme applied to the system of simultaneous second-order, ordinary differential Eq. (12) can also be studied by calculating the spectral radius of a suitable ''amplification matrix.'' This follows a general approach applied to conventional structural dynamic problems.[25] Stability is assured provided that the spectral radius is less than or equal to unity. In the current instance the method must be recast to accommodate an unsymmetric system of equations. This is done by rewriting Eqs. (14a)–(14c) in the form

$$\begin{pmatrix} \ddot{\mathbf{q}}_{t+\delta t} \\ \dot{\mathbf{q}}_{t+\delta t} \\ \mathbf{q}_{t+\delta t} \end{pmatrix} = \begin{bmatrix} & \mathbf{A} & \end{bmatrix} \begin{pmatrix} \ddot{\mathbf{q}}_t \\ \dot{\mathbf{q}}_t \\ \mathbf{q}_t \end{pmatrix} + (g), \qquad (18)$$

where

$$\mathbf{A} = \begin{bmatrix} \mathbf{E}_0^{-1}\mathbf{E}_3 & \mathbf{E}_0^{-1}\mathbf{E}_2 & \mathbf{E}_0^{-1}\mathbf{E}_1 \\ (1-\gamma)\delta t\mathbf{I}+\beta\delta t\mathbf{E}_0^{-1}\mathbf{E}_3 & \mathbf{I}+\gamma\delta t\mathbf{E}_0^{-1}\mathbf{E}_2 & \gamma\delta t\mathbf{E}_0^{-1}\mathbf{E}_1 \\ (1/2-\beta)\delta t^2\mathbf{I}+\beta\delta t^2\mathbf{E}_0^{-1}\mathbf{E}_3 & \delta t\mathbf{I}+\beta\delta t^2\mathbf{E}_0^{-1}\mathbf{E}_2 & \mathbf{I}+\beta\delta t^2\mathbf{E}_0^{-1}\mathbf{E}_1 \end{bmatrix}, \qquad (19)$$

$$\mathbf{g} = \begin{pmatrix} \mathbf{E}_0^{-1}\mathbf{f}_{t+\delta t}/\beta\delta t^2 \\ 0 \\ 0 \end{pmatrix}, \qquad (20)$$

and $\mathbf{I}$ denotes a unit diagonal matrix.

The stability analysis is performed for the homogeneous problem ($\mathbf{f}$ is assumed to be zero) and relies on the evaluation of the spectral radius (largest eigenvalue) of the ''amplification'' matrix $\mathbf{A}$.[22,25] Since a modal reduction procedure is not available for the current problem, the stability analysis could not be performed in the usual way [i.e., by the derivation of a formal expression for the spectral radius of operator $\mathbf{A}$ related to a scalar version of Eq. (12) resulting from its projection into the modal basis]. Instead the spectral radius of $\mathbf{A}$ has been evaluated numerically for each particular

problem. An eigenvalue solver for unsymmetric real matrices (subroutine DGEEV) from LAPACK[26] was used.

These calculations have confirmed that for all of the numerical examples reported in the present paper, the spectral radius of the discrete operator $\mathbf{A}$ is less or equal to 1 for Newmark parameters, $\beta=0.25$, and $\gamma=0.5$, irrespective of the time step δt, indicating once again that the time integration scheme is unconditionally stable for these particular examples.

V. CONCLUSIONS

(1) A wave-envelope scheme has been formulated for unbounded transient acoustical problems.
(2) The method is local in time requiring the solution of a

system of coupled, linear, second-order, time-dependent equations for nodal values of acoustical pressure.

(3) Accurate results have been obtained for axisymmetric and three-dimensional problems by the use of the Newmark time integration scheme with $\beta = 0.25$ and $\gamma = 0.5$.

(4) The scheme has been shown to be stable irrespective of step size for all problems attempted to date.

(5) In application to a realistic three-dimensional problem, the method has been shown to give solutions which agree well with those given by an equivalent BE transient model.

(6) In application to a realistic three-dimensional problem, the method has been shown to offer significant computational efficiencies when compared to an equivalent BE scheme.

[1] R. J. Astley, G. J. Macaulay, J. P. Coyette, and L. Cremers, ''Three-dimensional wave-envelope elements of variable order for acoustic radiation and scattering. Part I. Formulation in the frequency domain,'' J. Acoust. Soc. Am. **103**, 49–63 (1998).

[2] D. Givoli, *Numerical Methods for Problems in Infinite Domains* (Elsevier Science, Amsterdam, 1992).

[3] P. Bettess, *Infinite Elements* (Penshaw, Sunderland, 1992).

[4] R. D. Ciscowski and C. A. Brebbia (Eds.), *Boundary Element Methods in Acoustics* (Computational Mechanics Publications & Elsevier Applied Science, Southampton, 1991).

[5] J. L. Dohner, R. Shoureski, and R. J. Bernhard, ''Transient analysis of three dimensional wave propagation using the boundary element method,'' Int. J. Numer. Methods Eng. **24**, 621–634 (1987).

[6] A. S. M. Israil and P. K. Banerjee, ''Advanced development of time-domain BEM for two-dimensional scalar wave propagation,'' Int. J. Numer. Methods Eng. **29**, 1003–1020 (1990).

[7] T. L. Geers, ''Doubly asymptotic approximations for transient motions of submerged structures,'' J. Acoust. Soc. Am. **64**, 1500–1508 (1978).

[8] T. L. Geers and C. A. Felippa, ''Doubly asymptotic approximations for vibration analysis of submerged structures,'' J. Acoust. Soc. Am. **73**, 1152–1159 (1983).

[9] T. L. Geers and P. Zhang, ''Doubly asymptotic approximations for submerged structures with internal fluid volumes: Formulation and evaluation,'' J. Appl. Mech. **61**, 893–906 (1994).

[10] B. Engquist and A. Madja, ''Radiation boundary conditions for acoustic and elastic waves,'' Commun. Pure Appl. Math. **32**, 313–357 (1979).

[11] A. Bayliss and E. Turkel, ''Radiation boundary conditions for wavelike equations,'' Commun. Pure Appl. Math. **33**, 707–725 (1980).

[12] A. Bayliss, M. Gunzberger, and E. Turkel, ''Boundary conditions for the numerical solution of elliptic equations in exterior regions,'' SIAM (Soc. Ind. Appl. Math.) J. Appl. Math. **42**, 430–450 (1982).

[13] P. M. Pinsky, L. L. Thompson, and N. N. Abboud, ''Local high-order radiation boundary conditions for the two-dimensional time-dependent structural acoustics problem,'' J. Acoust. Soc. Am. **91**, 1320–1335 (1992).

[14] L. F. Kallivokas, J. Bielak, and R. C. Macamy, ''Symmetric local absorbing boundaries in time and space,'' J. Eng. Mech. **117**, 2027–2048 (1991).

[15] L. L. Thompson and P. M. Pinsky, ''A space-time finite element method for the exterior structural acoustics problem: time dependent radiation boundary conditions in two dimensions,'' Int. J. Numer. Methods Eng. **39**, 1635–1657 (1996).

[16] D. Givoli, ''A spatially exact nonreflecting boundary condition for time dependent problems,'' Comput. Methods Appl. Mech. Eng. **95**, 97–113 (1992).

[17] L. G. Olson and K. J. Bathe, ''An infinite element for the analysis of fluid-structure interaction,'' Eng. Comput. **2**, 319–329 (1985).

[18] D. S. Burnett, ''A three dimensional acoustic infinite element based on a prolate spheroidal multipole expansion,'' J. Acoust. Soc. Am. **96**, 2798–2816 (1994).

[19] J. L. Cipolla, ''Transient infinite elements for acoustics and shock,'' in DE-Vol 84-2, 1995 Design Engineering Technical Conferences, Volume 3-part B, 113-127, ASME (1995).

[20] R. J. Astley, G. J. Macaulay, and J. P. Coyette, ''Mapped wave envelope elements for acoustic radiation and scattering,'' J. Sound Vib. **170**, 97–118 (1994).

[21] L. Cremers and K. R. Fyfe, ''On the use of a variable order infinite wave envelope element for acoustic radiation and scattering,'' J. Acoust. Soc. Am. **97**, 2028–2040 (1995).

[22] R. D. Cook, *Concepts and Applications of Finite Element Analysis* (Wiley, New York, 1981), Chap. 11.

[23] C. H. Wilcox, ''An expansion theorem for electromagnetic fields,'' Commun. Pure Appl. Math. **9**, 115–134 (1956).

[24] SYSNOISE *REFERENCE MANUAL*, version 5.3 (LMS Numerical Technologies, Leuven, 1996).

[25] K. J. Bathe and E. L. Wilson, *Numerical Methods in Finite Element Analysis* (Prentice-Hall, Englewood Cliffs, 1976), Chap. 9.

[26] E. Anderson *et al.*, LAPACK *User's Guide* (SIAM, Philadelphia, 1995), 2nd ed.

Correlation length of ultrasonic speckle in anisotropic random media: Application to coherent echo detection

Arnaud Derode and Mathias Fink

Laboratoire Ondes et Acoustique, Université Paris 7-ESPCI, URA CNRS 1503, 10 rue Vauquelin, 75005 Paris, France

In a recent paper [Derode and Fink, J. Acoust. Soc. Am. **101**, 690–704 (1997)], a technique for studying spatial coherence properties of backscattered speckle noise by means of a transducers array was described. In this paper another approach is presented. Here, a single transducer, focusing inside a scattering medium, is moved in a plane; correlation is studied between signals acquired in two different positions. A study investigates how the correlation function of the medium determines that of the speckle noise. This is applied to fully or partially incoherent media, and media with anisotropic scatterer distribution such as unidirectional and cross-ply composites; we show that it is possible to extract information about the medium from a measurement of the backscattered field correlation length. The influence of correlation length on defect detection is discussed. Experimental as well as theoretical results are presented, they are found in good agreement. © *1998 Acoustical Society of America.* [S0001-4966(98)04501-9]

LIST OF SYMBOLS

ω	angular frequency
λ	wavelength
$\mathbf{r}(x,y)$	coordinates in the plane of the transducer
$\mathbf{R}(X,Y)$	coordinates in the z plane
z	axial coordinate
F	focal length
δ	transducer displacement
$O(\mathbf{r})$	aperture function
$\widetilde{O}(\mathbf{r})$	modified aperture function $\widetilde{O}(\mathbf{r}) = O(\mathbf{r})\exp(j\pi r^2(1/z - 1/F)/\lambda)$
$\mathrm{FT}\{f(x)\}_{X/\lambda x}$	Fourier transform $= \int_{-\infty}^{+\infty} f(x) e^{-2\pi x X/\lambda z} dx$
$\Omega(\mathbf{R})$	$\mathrm{FT}_{\mathrm{2D}}\{\widetilde{O}(\mathbf{r})\}_{(X/\lambda z, Y/\lambda z)}$
$\chi(\mathbf{R})$	random reflectivity function

INTRODUCTION

The idea underlying all correlation techniques is to compare two sets of data recorded from the same sample under different conditions, in order to extract some information about the sample. ''Under different conditions'' means that one of the relevant variables has to be changed. Generally, the ultrasonic signal scattered from a sample depends on space, time, and frequency variables. So one can, for instance, compare the response of a medium at two different frequencies, and see by how much the frequency has to be varied before the response shows significant changes.[1] One can also study time correlations, in order to follow the evolution of the speckle pattern with time, and, e.g., to deduce information on the elasticity of a scattering medium.[2] The subject of this paper is *spatial* correlation, i.e., comparing data received from the same medium insonified by the same signal, but at two different places; the aim is to deduce information about the second-order statistics of the scatterers and improve defect detection.

Spatial correlation can be studied in two ways. The first one requires an N-elements array of transducers. A pulse is sent into a medium, the N channels receive the scattered signals, and the correlation degree between signals #n and #p (n and p ranging from 1 to N) is studied as a function of the distance $|n-p|$. Two neighboring elements are likely to receive almost the same information, and the question is how far apart must they be to receive uncorrelated signals? It was shown in a recent paper[3] that the key parameter in this technique is the transmitting aperture size, regardless of the wavelength and focal distance; this was applied to composite media, in which the scatterers are highly anisotropic, and the influence of spatial correlation of the speckle noise on defect detection was also discussed. We will refer to this technique as the ''Zernike method,''[4,5] since it is an extension of Frederik Zernike's works on coherence of random optical sources.[6]

The second method[7–10] is simpler; it uses a single transducer which is moved step by step in front of a scattering medium. At each step the backscattered signal is recorded, and correlation between two signals is studied as a function of distance.

This paper deals with the second technique, particularly its application to anisotropic materials such as the composites studied in Ref. 3. A comparison with the results of the Zernike method is drawn, and consequences on defect detection are discussed.

Understanding how the scattered signals can be more or less correlated is essential in adaptive speckle reduction techniques, and can also provide information about the medium. Indeed, as we will see, the scatterer distribution (particularly its anisotropy) determines the correlation function of the
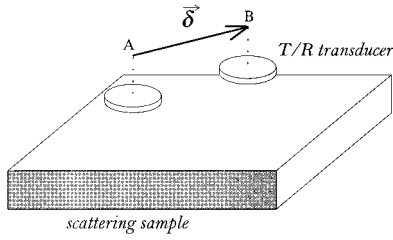
FIG. 1. Experimental setup. A single T/R transducer is moved in a plane; we measure the correlation coefficient between signals recorded at two positions A and B as a function of $\boldsymbol{\delta}$.

backscattered signals measured from B scans.

The paper is divided into four parts. Section I presents a theoretical analysis. In the second part, the results of Sec. I are applied to particular examples (composite media scanned in a plane with a circular focused probe). Section III presents experimental results obtained on three types of composite materials. Finally, the consequences of all this in terms of defect detection are discussed in Sec. IV.

I. THEORETICAL ANALYSIS

We recall as a preliminary the definition of the autocorrelation function $R_{AA}(x_1,x_2)$ of a random process $A(x)$:

$$R_{AA}(x_1,x_2) = E\{A(x_1)A^*(x_2)\}. \tag{1}$$

In this expression, E denotes an ensemble average. If $A(x)$ is a stationary process, then $R_{AA}(x_1,x_2)$ only depends on one variable $\Delta x = x_1 - x_2$, and we will call *coherence length* the effective width of $R_{AA}(\Delta x)$. In the same way, a random process will be called coherent or incoherent according to whether its autocorrelation function is wide or narrow.

Generally speaking, the setup we consider consists in a single transducer with any shape, that transmits a short pulse into a scattering medium (Fig. 1). The same transducer records a backscattered signal (speckle) that results from the summation of all echoes coming from the scatterers. The transducer is moved along an axis by a distance δ, and the experiment is repeated. Thus a set of signals is recorded that constitutes a B scan of the medium. Selecting a time window inside each of these signals, we can isolate the contribution coming from the depth of interest. Then we measure the correlation between two signals, as a function of the distance δ between the observing points.

Since we consider a short time window corresponding to the depth of interest inside the medium, everything happens as if we were studying the reflection of the incident pulse on a random mirror located at this very depth; the mirror's reflectivity is a random process $\chi(\mathbf{R})$. To be valid, this approach implies that no multiple scattering takes place; it is also restricted to cases where the isochronous volume, i.e., the region that is insonified by the incoming pulse at a given time, can be reduced to a thin slice.

We also assume that the lateral dimension of the region of interest is small compared to the transducer size, which is true within the depth of focus of a focused transducer. It has been shown[3] that under these assumptions the ω component in the backscattered field could write:

$$\psi^\omega(\mathbf{r}) = \frac{1}{\lambda^2 z^2} \, \widetilde{O}(\mathbf{r}) \mathrm{FT}_{2\mathrm{D}}\{\chi(\mathbf{R})\Omega(\mathbf{R})\}_{(\mathbf{r}/\lambda z)}. \tag{2}$$

Here $\mathbf{r}(x,y)$ represents the position of a point at the transducer surface. Within Fresnel's approximation, this expression reduces to a simple two-way Fourier transform (FT) in the case of a focused transducer: the field in the focal plane $\Omega(\mathbf{R})$ is the FT of the aperture function $O(\mathbf{R})$, and the backscattered field is the FT of $\Omega(\mathbf{R})$ multiplied by $\chi(\mathbf{R})$, the random reflectivity function.

If the transducer position is laterally shifted by $\mathbf{d}$, the backscattered field at frequency ω writes:

$$\psi^\omega(\mathbf{r};\mathbf{d}) = \frac{1}{\lambda^2 z^2} \, \widetilde{O}(\mathbf{r}) \mathrm{FT}_{2\mathrm{D}}\{\chi(\mathbf{R}+\mathbf{d})\Omega(\mathbf{R})\}_{(\mathbf{r}/\lambda z)}. \tag{3}$$

The echographic signal $s(\mathbf{d};t)$ recorded in $\mathbf{d}$ results from the summation of the acoustic field over the receiving surface; the amplitude of its ω component, which will be denoted by $S^\omega(\mathbf{d})$, can be written as

$$S^\omega(\mathbf{d}) = \frac{1}{\Sigma} \int \int \psi^\omega(\mathbf{r};\mathbf{d})d\mathbf{r}, \tag{4}$$

where Σ is the transducer surface.

In the following, we will use three functions Γ, Λ, and H defined as

$$\Gamma(\mathbf{r}) = \widetilde{O} * \widetilde{O} = \int \int \widetilde{O}(\tilde{\xi})\widetilde{O}(\mathbf{r}+\xi)d\xi$$

$$(\widetilde{O} \text{ is assumed to be even}),$$

$$\Lambda(\mathbf{R}) = \mathrm{FT}_{2\mathrm{D}}\{\Gamma(\mathbf{r})\}_{(\mathbf{R}/\lambda z)}, \tag{5}$$

$$H(\mathbf{r}) = \mathrm{FT}_{2\mathrm{D}}\{|\Gamma(\mathbf{R})|^2\}_{(\mathbf{r}/\lambda z)}.$$

Then the expression of the echographic signal $S^\omega(\mathbf{d})$ reduces straightforwardly to

$$S^\omega(\mathbf{d}) = \frac{1}{\Sigma} \frac{1}{\lambda^2 z^2} \int \Lambda(\mathbf{R})\chi(\mathbf{R}+\mathbf{d})d\mathbf{R} \tag{6}$$

and the correlation function we are interested in is

$$R_{SS}^\omega(\mathbf{d}_1,\mathbf{d}_2) = E\{S^\omega(\mathbf{d}_1)S^{\omega*}(\mathbf{d}_2)\}. \tag{7}$$

Consider the case of a random medium with a stationary reflectivity function $\chi(\mathbf{R})$; then its autocorrelation function $R_{\chi\chi}(\mathbf{R}_1,\mathbf{R}_2)$ only depends on $\Delta\mathbf{R} = \mathbf{R}_1 - \mathbf{R}_2$. As it is shown in the Appendix, the correlation function of the echographic signal eventually writes as a convolution:

$$R_{SS}^\omega(\boldsymbol{\delta}) = \frac{1}{\lambda^2 z^2} H(\boldsymbol{\delta}) * R_{\chi\chi}(\boldsymbol{\delta}) \tag{8}$$

with $\boldsymbol{\delta} = \mathbf{d}_1 - \mathbf{d}_2$ being the distance by which the transducer has been moved. The backscattered correlation coefficient then writes

$$\rho_{SS}(\boldsymbol{\delta}) = R_{SS}(\boldsymbol{\delta})/R_{SS}(\mathbf{0}). \tag{9}$$

R_{SS}^ω depends only on $\boldsymbol{\delta} = \mathbf{d}_2 - \mathbf{d}_1$, which means that $S^\omega(\mathbf{d})$ is also a stationary random process. Equation (8) gives the degree of correlation between the echographic signals received at two points $\mathbf{d}_1$ and $\mathbf{d}_2$ apart by the distance $\delta = \sqrt{\delta_x^2 + \delta_y^2}$ in the plane of the scan. In this expression, H characterizes the

controllable parameters (shape and size of the transducer, focal distance, depth of interest, frequency), whereas $R_{\chi\chi}$ carries the statistical information about the medium.

This result calls for several comments. First, unlike the Zernike method, the field $S^\omega(\mathbf{d})$ we consider here remains stationary as long as the medium reflectivity χ is itself stationary, that is to say as long as the scanned region has the same statistical properties. In addition, its correlation function R_{SS}^ω is directly related to $R_{\chi\chi}$, and no longer by means of a Fourier transform, as was the case with the Zernike method; hence a more direct access to the coherence length of the medium.

Indeed, R_{SS}^ω contains two terms related by a convolution product: the first one, H, depends on the beam pattern at the depth of interest, the second one, $R_{\chi\chi}$, on the statistics of the scatterers. So the coherence length of the echographic signal (i.e., the effective width of R_{SS}^ω) is roughly equal to the sum of the effective width of H, plus the coherence length of the medium. So one can hopefully deduce quantitative information on the medium structure from the second-order statistics of the speckle patterns.

II. EXAMPLES

So far, apart from the Fresnel approximation, the theoretical analysis made no assumption regarding the aperture shape, its focal distance F, and the depth of interest z. In the following examples, we will consider the case of a circular transducer with diameter a and focal distance F; the region of interest is located around the focal plane at depth $z=F$. Under these conditions, we have

$$\widetilde{O}(\mathbf{r}) = \begin{cases} 1 & \text{if } r < a/2 \\ 0 & \text{if } r > a/2 \end{cases} \quad \text{with } r = \sqrt{x^2 + y^2},$$

$$\Gamma(\mathbf{r}) = \begin{cases} \arccos\left(\dfrac{r}{a}\right) - \dfrac{r}{a}\sqrt{1 - \dfrac{r^2}{a^2}} & \text{if } r < a \\ 0 \quad \text{if } r > a \end{cases}. \tag{10}$$

Given the circular symmetry, H only depends on $\delta = \sqrt{\delta_x^2 + \delta_y^2}$ and can be written as a Hankel transform:

$$H(\delta) = \int_0^\infty R|\Gamma(R)|^2 J_0\left(2\pi \frac{\delta R}{\lambda z}\right) dR. \tag{11}$$

This function can be evaluated by numerical calculation, the result is plotted in Fig. 2(a). Note that H may be written as a function of a dimensionless variable $a\delta/\lambda F$ which represents the distance in ''number of focal spots,'' since $\lambda F/a$ is the typical width of the beam pattern in the focal plane.

A. Fully incoherent medium

For a fully incoherent medium, each scatterer is completely uncorrelated even from its closest neighbor. Then the reflectivity function χ is a ''white noise'' such that $R_{\chi\chi}(\Delta R) \propto \delta(\Delta R)$ so Eq. (8) simply yields

$$R_{SS}^\omega(\delta_x, \delta_y) \propto H(\delta_x, \delta_y) = H(\delta), \tag{12}$$

where $\delta = \sqrt{\delta_x^2 + \delta_y^2}$ is the distance by which the transducer has been shifted.
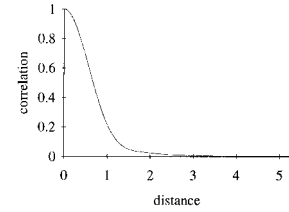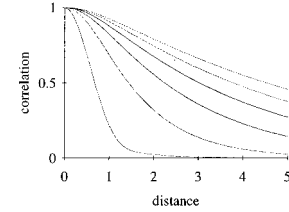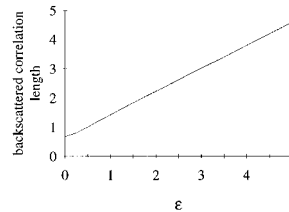
FIG. 2. (a) $H(\delta)$. δ is expressed in $\lambda F/a$ units, i.e., in ''number of focal spots.'' (b) Backscattered correlation coefficient ρ versus distance δ for an isotropic medium with coherence length ϵ ($\epsilon = 0$, 1, 2, 3, 4, and 5 $\lambda F/a$). (c) -6 dB width of $\rho(\delta)$ as a function of the medium coherence length ϵ. Abscissa and ordinate are expressed in $\lambda F/a$ units.

Figure 2(a) shows that in that case R_{SS}^ω decreases almost to 0 for distances larger than $\delta = 2\lambda F/a$, which can be easily accounted for as $2\lambda F/a$ is the effective diameter of the beam pattern in the focal plane. Since the medium is fully incoherent, if the transducer is moved by a distance larger than $2\lambda F/a$, there is no reason why the two signals should be correlated. This result is consistent with that obtained by Wagner et al.,[7,9] and later by Cancre[11] with a different formalism.

Note that the relevant parameter when measuring the correlation of the backscattered field with a single transducer is the beamwidth $\lambda F/a$, whereas with the Zernike method, it was the transducer size a.

B. Partially coherent medium

When the medium is partially coherent, the scatterers are correlated up to a certain distance ϵ. The correlation length ϵ is the characteristic width of $R_{\chi\chi}$. Then convolving $R_{\chi\chi}$ by H gives a correlation curve $R_{SS}^\omega(\delta)$ that is wider than $H(\delta)$ alone. Measuring this spreading permits to estimate ϵ. In the extreme case where the medium is perfectly coherent ($\epsilon \to \infty$), then it behaves as a perfect mirror and R_{SS}^ω becomes infinitely wide, since whatever the distance δ, the reflected signals are identical.

In the intermediate case where ϵ is neither 0 nor ∞, the medium exhibits a partial coherence. Figure 2(b) presents as

an example the backscattered correlation function R_{SS}^{ω} that would be obtained for a partially coherent isotropic medium. The autocorrelation function of the medium reflectivity was chosen to be $R_{\chi\chi}(\Delta R) \propto e^{-\Delta R/\epsilon}$. The detailed calculations are given in the Appendix. Since the relevant characteristic scale is $\lambda F/a$, the curves are plotted for $\epsilon = 0, 1, 2, 3, 4, 5 \, \lambda F/a$.

Knowing the transmission parameters (frequency, aperture size, and focal distance) and the depth of interest permits us to calculate H in any configuration, and thereby to know the minimum amount of correlation that can be expected. Then the coherence length ϵ of a medium could be estimated from experimental measurements of R_{SS}^{ω}. Precisely, Fig. 2(c) shows the -6 dB width of R_{SS}^{ω} for an isotropic medium with coherence length ϵ as a function of ϵ. We see that it varies almost linearly with ϵ, in $\lambda F/a$ units:

$$l_{-6 \text{ dB}} \approx 0.8\epsilon + 0.6. \tag{13}$$

Hence a possible estimation of ϵ from the measurement of $l_{-6\text{ dB}}$ by an empiric formula:

$$\hat{\epsilon} \approx 1.25 l_{-6 \text{ dB}} - 0.75. \tag{14}$$

C. Slightly outside the focal plane

If the depth of interest z is different from the focal distance F, then the modified aperture function $\widetilde{O}$ is no longer real-valued:

$$\widetilde{O}(x,y) = O(x,y) e^{-j(\pi/\lambda)(1/F - 1/z)r^2}. \tag{15}$$

Its effective width is smaller, and as a consequence, H is wider. So the spatial correlation function R_{SS}^{ω} must also be wider when the region of interest is out of the focus. This makes sense, since the beam is wider out of the focus, and the transducer must be moved by a larger distance to obtain uncorrelated data. This result is the contrary of that obtained by the Zernike method,[3] where the correlation length was at its largest when the region of interest was in the focal zone.

D. The unidirectional composite

A unidirectional composite is made of a regular stacking of long and thin fibers drowned in a matrix. All the fibers are aligned along the same direction. To model the reflectivity of such a sample, the fibers are supposed to be infinitely long, infinitely thin, perfectly lined up along the same axis Y, and randomly distributed along the perpendicular direction X. Then the autocorrelation function of the reflectivity may be written as

$$R_{\chi\chi}(\Delta X, \Delta Y) \propto \delta(\Delta X) 1_{\Delta Y}. \tag{16}$$

So from (8) we derive the expression of the spatial correlation function for the backscattered signal:

$$R_{SS}^{\omega}(\delta_x, \delta_y) \propto H(\delta_x, \delta_y) ** \delta(\delta_x) 1_{\delta_y}. \tag{17}$$

Using (5) and applying the convolution theorem yields

$$R_{SS}^{\omega}(\delta_x, \delta_y) \propto \text{FT}_{2D}\{|\Gamma^2|(x,y)\delta(y)\}_{(\delta_x/\lambda z, \delta_y/\lambda z)}$$

$$= \text{FT}_{1D}\{|\Gamma^2(x,0)|\}_{(\delta_x/\lambda z)}. \tag{18}$$
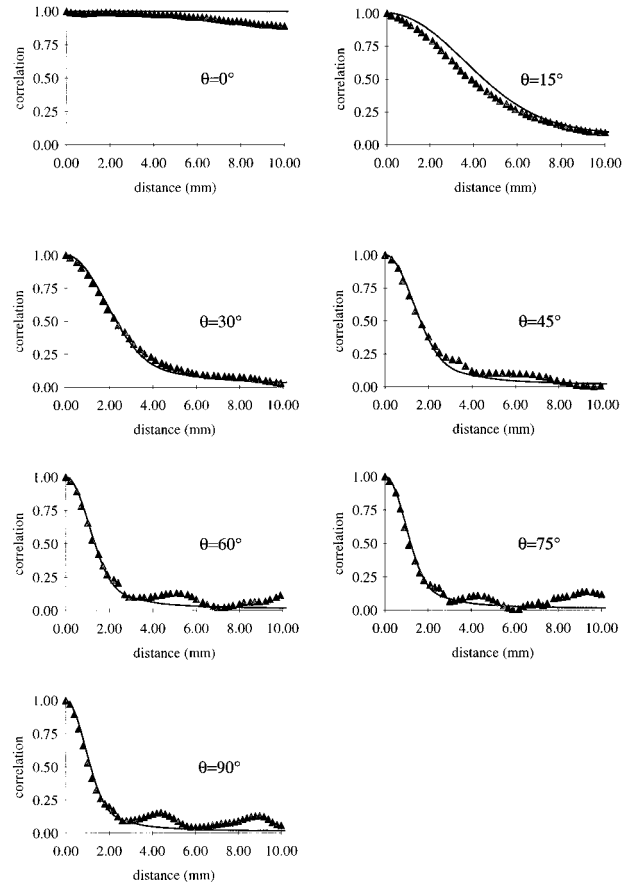
FIG. 3. Unidirectional composite. Theoretical (line) and experimental (triangles) results for seven orientations: $\theta = 0°$, 15°, 30°, 45°, 60°, 75°, and 90°. Focal spot: $\lambda F/a = 1.6$ mm.

In order to calculate this expression, since $|\Gamma^2(x,y)|$ is a two-dimensional function with circular symmetry, one simply has to consider it as a function of one variable $r = \sqrt{x^2 + y^2}$ and to take its one-dimensional Fourier transform at spatial frequency $\delta_x/\lambda z$. Then we can remark that the result only depends on δ_x, which is logical since the fibers are supposed to be perfectly lined up along the Y axis: The spatial correlation function of the backscattered field is invariant under any translation along this direction.

Let G be defined as

$$G(x) = \text{TF}_{1D}\{|\Gamma(r)|^2\}_{(x/\lambda z)}. \tag{19}$$

If the scanning direction makes an angle θ with the fiber direction Y, then in polar coordinates, the correlation function writes

$$R_{SS}^{\omega}(\delta_x, \delta_y) = R_{SS}^{\omega}(\delta \sin \theta, \delta \cos \theta) = G(\delta \sin \theta), \tag{20}$$

where $\delta = \sqrt{\delta_x^2 + \delta_y^2}$ denotes the distance between two points on the scan axis.

From R_{SS}^{ω}, we deduce the dimensionless correlation coefficient

$$\rho_{SS}(\delta, \theta) = G(\delta \sin \theta)/G(0). \tag{21}$$

Figure 3 shows how this coefficient varies with the distance δ for fixed values of θ. The curves were plotted with $\lambda F/a = 1.6$ mm, as in the experiments presented in Sec. III. We
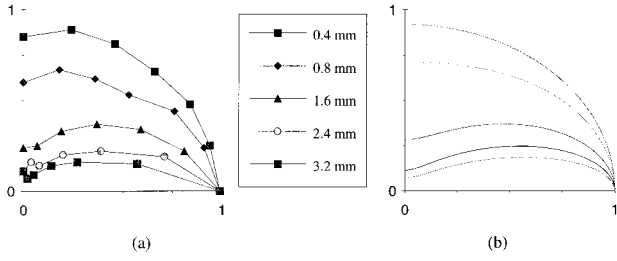
FIG. 4. Unidirectional composite. Experimental (a) and theoretical (b) polar diagrams. Each curve corresponds to a given value of distance δ ranging from 0.4 to 3.2 mm; for each orientation θ, we lay down a length proportional to $\rho_{SS}(\delta)$.

FIG. 5. Thin line: transducer bandwidth $B(\omega)$. Dashed line: spectrum of the incoming signal $E(\omega)$. Thick line: ponderation coefficient $P(\omega)$.

observe that when the direction of scan is perpendicular to the fibers ($\theta = 90°$), the correlation decreases almost as if the medium was fully incoherent. Then, as the angle θ decreases, the effective width of R_{SS}^ω progressively increases (Fig. 6), proportionally to $1/\sin\theta$, until the limiting value $\theta = 0°$ for which the correlation coefficient is constantly equal to 1, since the alignment between the fibers and the scan direction is perfect.

These results are also presented in a polar diagram in Fig. 4. Each curve corresponds to a given value of δ ranging from 0.4 to 3.2 mm, and for each angle θ, we lay down a length proportional to $R_{SS}(\delta, \theta)$. The curves are plotted for $0° < \theta < 90°$. One can see that at large distances, the anisotropy of the scattering structure becomes more and more obvious.

E. Frequency averaging effect

So far, we only considered the propagation of one frequency component ω in the transmitted signal. In a real experiment, the backscattered signal is a combination of all frequencies that exist in the transmitted signal spectrum, each component having its own coherence function R_{SS}^ω.

Experimentally, correlation between signals recorded in $\mathbf{d}_1$ and $\mathbf{d}_2$ is measured by an integral:

$$C(\mathbf{d}_1, \mathbf{d}_2) = \int s(t; \mathbf{d}_1) s(t; \mathbf{d}_2) dt. \quad (22)$$

This is normalized to a dimensionless correlation coefficient:

$$\rho(\mathbf{d}_1, \mathbf{d}_2) = \frac{C(\mathbf{d}_1, \mathbf{d}_2)}{\sqrt{C(\mathbf{d}_1, \mathbf{d}_1) C(\mathbf{d}_2, \mathbf{d}_2)}}. \quad (23)$$

There is a simple relation between this coefficient estimated from time signals, and the coherence function defined for each frequency; indeed, the signals $s(t; \mathbf{d})$ can be written as a continuous summation of complex exponentials:

$$s(t; \mathbf{d}) = \int S^\omega(\mathbf{d}) e^{j\omega t} d\omega \quad (24)$$

which yields straightforwardly:

$$E\{C(\mathbf{d}_1, \mathbf{d}_2)\} = \int_{\text{spectrum}} R_{SS}(\mathbf{d}_1, \mathbf{d}_2) d\omega. \quad (25)$$

So, in average, the degree of resemblance between time signals measured at two points apart by $\boldsymbol{\delta} = \mathbf{d}_2 - \mathbf{d}_1$ equals the

sum of all coherence functions for all frequencies that existed in the transmitted pulse. In this summation, one has to take into account the spectrum $E(\omega)$ of the incoming electrical signal, as well as the transducer acousto-electric frequency response $B(\omega)$, which yields:

$$E\{C(\boldsymbol{\delta})\} = \int |E(\omega)|^2 |B(\omega)|^4 R_{SS}(\boldsymbol{\delta}) d\omega$$

$$\propto \int \omega^4 |E(\omega)|^2 |B(\omega)|^4 (H(\boldsymbol{\delta}) ** R_{\chi\chi}(\boldsymbol{\delta})) d\omega. \quad (26)$$

Thus appears an averaging effect over all the spatial coherence functions, for all frequencies of the spectrum. Such an effect was also pointed out with the Zernike method,[3] but it was shown that in most cases of interest, all spectral components had the same coherence function. With this technique, this can never be true.

Indeed, apart from $\omega^4 |E(\omega)|^2 |B(\omega)|^4$, the frequency dependence in (26) is due to H. As we have seen, H can be written as a function of one dimensionless variable $a\delta/\lambda F = (a\delta/2\pi cF)\omega$. So for two different frequencies ω_1 and ω_2, H has the same shape, except for a similarity with ratio ω_2/ω_1. Hence ω_1 and ω_2 can *never* have the same spatial correlation function, even for a fully incoherent medium.

The physical interpretation is quite simple: indeed, we noted that the characteristic scale with this technique was the size of the focal spot. But to each angular frequency $\omega = 2\pi c/\lambda$ corresponds a different focal spot size $\lambda F/a$. Hence higher frequencies exhibit a narrower correlation function. Also note that the weighting coefficient is far from negligible, since it varies as the fourth power of the transducer response (the ω^4 coefficient due to diffraction is in reality compensated by frequency-dependent attenuation), so the transducer center frequency is highly emphasized by the averaging effect.

The weighting coefficient $P(\omega) = |E(\omega)|^2 |B(\omega)|^4$ is plotted in Fig. 5 for the following example: the incoming signal is a short sine burst (two periods, center frequency $f_0 = \omega_0/2\pi = 3$ MHz), its spectrum is

$$E(\omega) \propto \text{sinc}\left(2\pi \frac{\omega - \omega_0}{\omega_0}\right) \quad (27)$$

and the transducer center frequency is also 3 MHz, with a 80% bandwidth at -6 dB, its frequency response is modeled as a Gaussian function:

A. Derode and M. Fink: Coherent echo detection

$$B(\omega) = \exp\left(-\frac{(\omega - \omega_0)^2}{2\Delta\omega^2}\right) \tag{28}$$

with $\Delta\omega/2\pi = 1$ MHz.

These values for $E(\omega)$ and $B(\omega)$ correspond to the experimental situation presented in Sec. III.

III. EXPERIMENTAL RESULTS

A. Unidirectional composite

The sample we studied is a $20 \times 14.5 \times 2.1$-cm piece of unidirectional carbon-epoxy composite. The fiber diameter is 7 μm. The sample is immersed in water. The transducer is a circular probe with a diameter of 60 mm, a focal distance of 196 mm, and its center frequency is 3 MHz ($\lambda F/a \approx 1.6$ mm). The transducer is moved in a plane parallel to the plane of the fibers; the motion of the transducer is controlled by step motors and a PC.

The transducer is located roughly 180 mm off the water–composite interface, in order to focus inside the medium. The incoming signal is a short sine burst (two periods, 3 MHz). The scanned area is a 2×2-cm square, with 0.2-mm steps. Seven scanning directions were explored: $\theta = 0°$, 15°, 30°, 45°, 60°, 75°, and 90°. For each direction, the transducer is moved with a regular step p; at each step, the backscattered signal $s_i(t)$, where the index i denotes the step number, is sampled at a 40-MHz rate and stored in the computer. Then a time window $[T_1, T_2]$, centered around the focal time, is extracted from all signals; its typical duration $T_2 - T_1$ ranges from 3 to 5 μs. The correlation coefficient $C(i,j)$ is calculated for all pairs of signals:

$$C(i,j) = \sum_{t=T_1}^{t=T_2} (s_i(t) - \overline{s_i})(s_j(t) - \overline{s_j})$$

$$\text{with } \overline{s_i} = \frac{1}{T_2 - T_1} \sum_{t=T_1}^{t=T_2} s_i(t). \tag{29}$$

Then this coefficient is averaged for all pairs (i,j) apart by the same distance $\delta = p|i-j|$, and normalized in order to obtain a dimensionless correlation coefficient ρ as a function of distance δ:

$$\rho(\delta) = \rho(kp) = \frac{N}{N-k} \frac{\sum_{i=1}^{i=N-k} C(i, i+k)}{\sum_{i=1}^{i=N} C(i,i)}, \tag{30}$$

where N is the total number of steps.

As it is difficult to ensure a perfect parallelism between the plane of the fibers and that of the transducer, we make a slight correction in order to compensate the lack of parallelism before calculating the correlation coefficient. This correction is based on the time of arrival of the front face echo: the signals are time shifted in such a way that this echo always arrives at the same time. The maximum shift we had to take into account was eight samples (0.2 μs) for a maximum distance of 28 mm. Once this correction is made, the correlation coefficient is calculated as described above; experimental results are displayed in Figs. 3 and 4.

We observe a good agreement between theoretical and experimental results, with a progressive transition from coherence to incoherence as θ increases. The effective width of
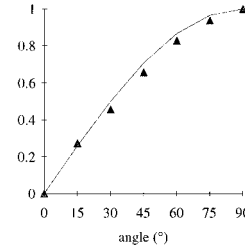
FIG. 6. Let $l(\theta)$ be the effective width of the correlation coefficient $\rho(\delta, \theta)$ for a given orientation θ. Experimental values of $l(90°)/l(\theta)$ are plotted versus the angle θ. The theoretical curve is $\sin\theta$.

the experimental correlation curves corresponds to what was expected; in particular, when $\theta = 90°$, the correlation becomes negligible beyond a distance $\delta = 2\lambda F/a$. Figure 6 represents the width of the spatial correlation coefficient as a function of θ, which does vary proportionally to $1/\sin\theta$ as expected.

Figure 4 shows the same results on polar diagrams. As we expected from theoretical predictions, the anisotropy of the medium in terms of spatial correlation becomes more apparent at larger distances.

B. Cross-ply composites

The same approach, theoretically as well as experimentally, has been applied to the case of cross-ply bidirectional and quadridirectional composites.

The bidirectional composite is made of a regular stacking of elementary unidirectional layers, with an angular step of 90° around the vertical axis. Thus the fibers are aligned along two perpendicular directions. So the reflectivity function can be modeled as

$$R_{\chi\chi}(\Delta X, \Delta Y) = \delta(\Delta X)1_{\Delta Y} + \delta(\Delta Y)1_{\Delta X}. \tag{31}$$

Hence from (20) the spatial correlation function of the back-scattered field is written as

$$R_{SS}^\omega(\delta, \theta) = G(\delta \sin\theta) + G(\delta \cos\theta). \tag{32}$$

When the scanning direction corresponds to one of the two fiber directions ($\theta = 0°$ or 90°), the correlation coefficient reduces to

$$\rho_{SS}(\delta, 0°) = \rho_{SS}(\delta, 90°) = R_{SS}^\omega(\delta, 0°)/R_{SS}^\omega(0, 0°)$$

$$= 0.5 + G(\delta)/G(0). \tag{33}$$

The correlation coefficient shows a constant coherent component (due to the fiber layer that is oriented along the direction of scan) and an incoherent component (due to the perpendicular layer) that decreases as δ increases. For intermediate angles, $R_{SS}^\omega(\delta, \theta)$ results from the summation of two partially coherent components. Figure 7 shows the curves $\rho_{SS}(\delta)$ for fixed values of θ. The results are symmetrical with respect to $\theta = 45°$, due to the symmetry of the layer stacking.

The polar diagram in Fig. 8(b) shows that it is still possible to see the anisotropy of the composite and the directions of the fibers, this anisotropy being more and more ob-
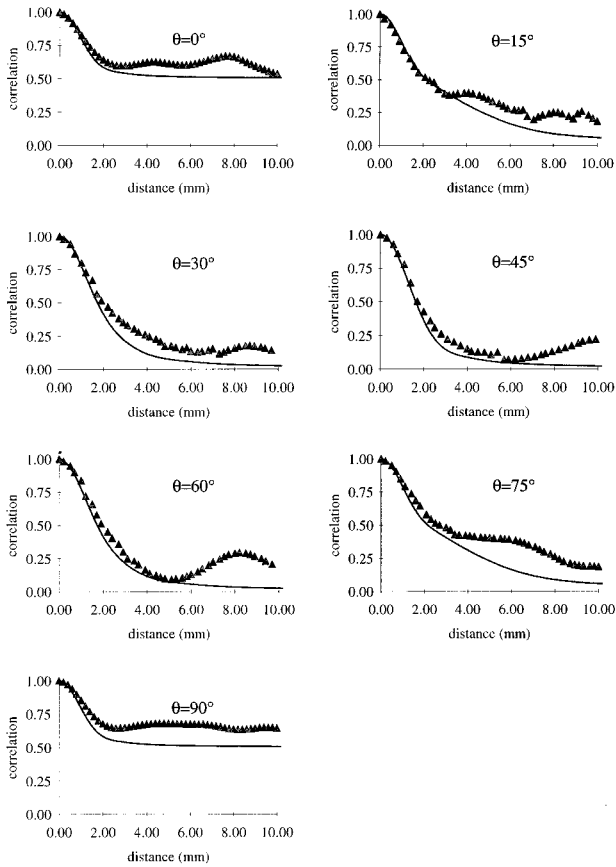
FIG. 7. Bidirectional composite. Theoretical (line) and experimental (tri-angles) results for seven orientations: $\theta = 0°$, 15°, 30°, 45°, 60°, 75°, and 90°. Focal spot: $\lambda F/a = 1.6$ mm.

vious as distance δ increases. This explains some results obtained in 1990[12] that were misinterpreted at that time.

The experimental procedure is the same as that described above, and the same transducer was used. The sample dimensions are $18 \times 15 \times 1.5$ cm, the distance between two ''superlayers'' is 2×130 μs. Experimental results are presented in Fig. 7 (correlation coefficient versus distance δ for a given direction of scan θ) and Fig. 8(a) (corresponding polar diagrams). As expected theoretically, we observe that even when the scanning direction is perpendicular to one of the fiber directions, there is still a remaining coherent background due to the other direction of alignment, which explains the plateau observed for $\theta = 90°$ and θ
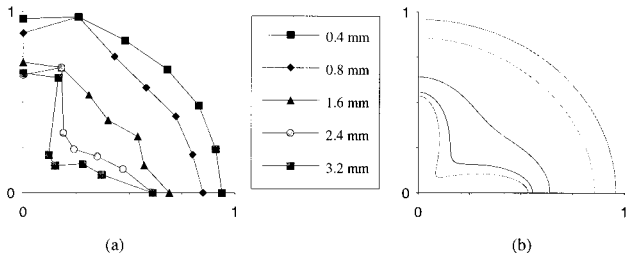
FIG. 8. Bidirectional composite. Experimental (a) and theoretical (b) polar diagrams. Each curve corresponds to a given value of distance δ ranging from 0.4 to 3.2 mm; for each orientation θ, we lay down a length proportional to $\rho_{SS}(\delta)$.
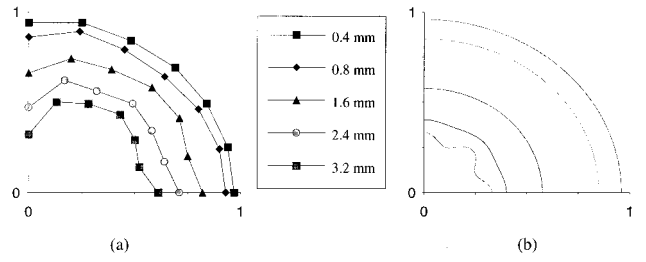
FIG. 9. Quadridirectional composite. Experimental (a) and theoretical (b) polar diagrams. Each curve corresponds to a given value of distance δ ranging from 0.4 to 3.2 mm; for each orientation θ, we lay down a length proportional to $\rho_{SS}(\delta)$.

$= 0°$; in addition, it is still possible to point out the anisotropy and the two directions of alignment, especially at larger distances.

The quadridirectional composite is built according to the same pattern as the bidirectional composite, except that each ''superlayer'' results from the stacking of four elementary unidirectional layers with respective orientation 0°, 90°, 45°, and $-45°$. Each superlayer is 4×130-μs thick, a distance that is still unresolved at 3 MHz. Following the same principles, the autocorrelation function of the reflectivity of the quadridirectional composite writes as a combination of four terms:

$$R_{\chi\chi}(\Delta X, \Delta Y) = \delta(\Delta X) 1_{\Delta Y} + \delta(\Delta Y) 1_{\Delta X}$$
$$+ \delta(\Delta X - \Delta Y) + \delta(\Delta X + \Delta Y). \quad (34)$$

Hence the spatial correlation function of the echographic signal:

$$R_{SS}^{\omega}(\delta, \theta) = G(\delta \sin \theta) + G(\delta \cos \theta)$$
$$+ G\left(\frac{\delta}{\sqrt{2}} \sin \theta + \frac{\delta}{\sqrt{2}} \cos \theta \right)$$
$$+ G\left(\frac{\delta}{\sqrt{2}} \sin \theta - \frac{\delta}{\sqrt{2}} \cos \theta \right). \quad (35)$$

The corresponding polar diagrams are presented in Fig. 9(b). One can see that stacking more and more layers with different orientations tends to make the spatial correlation function more and more isotropic, it results in a blurring between coherent, incoherent, and partially coherent contributions. Yet it is still possible, in theory, to determine the directions of alignment from the correlation curves; indeed, if the scan direction is parallel to one of the four fiber directions, we should observe a plateau of height 0.25 in the correlation function due to the remaining coherent component.

Experimental results [Fig. 9(a)] can only give a partial confirmation of these predictions. Indeed, the quadridirectional composite seems to behave as an isotropic medium. Even at large distances it becomes more difficult to point out the anisotropy as clearly as for the unidirectional and bidirectional composites. It would require a scan of the medium over large areas (much larger that the focal spot), and to assume that the fibers stay perfectly lined up over such distances, which can only be a local approximation.
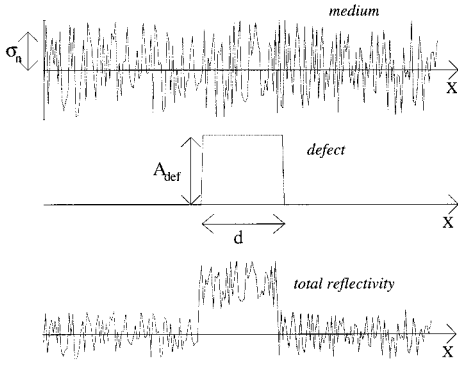
FIG. 10. (a) Sample of a random reflectivity function (zero mean, rms σ_n). (b) Defect reflectivity function. (c) Total reflectivity function.

Nevertheless, higher frequencies could be used in order to reduce the beam width in the focal plane; then it should be possible to reveal the anisotropy with a reasonable scan area. From experimental results, with an aperture $F/a = 3.3$ and center frequency 3 MHz, the quadridirectional composite behaves as a quasi-isotropic medium as far as spatial correlation is concerned, since the polar diagrams are almost circular. It shows a coherence length ($l_{-6\,\mathrm{dB}} \approx 4$ mm $= 2.5\,\lambda F/a$) which is quite larger than the coherence length of the field that would be observed with a fully incoherent medium inspected under the same conditions ($l_{-6\,\mathrm{dB}} = 0.65\,\lambda F/a$); so under these experimental conditions, the quadridirectional composite, despite its anisotropy, seems to behave as an isotropic partially coherent medium with a coherence length that can be estimated to $\hat{\epsilon} \approx 3.8$ mm from (14).

IV. DETECTION OF A COHERENT REFLECTOR

The spatial correlation method we presented so far is by nature an averaging technique that requires a scan of the medium over a large area in order to extract statistical information. It is thereby inadequate to detect a small defect. Yet, some of the results derived here can help study the detection of a small coherent reflector drowned in speckle noise.

Consider an ideal flat defect with size d inside a scattering medium with coherence length ϵ. The transducer is at a given position, for convenience the origin 0. The scattering medium reflectivity is modeled as a random noise $\chi(X)$ with zero mean and variance σ_n^2; the defect has a constant reflectivity A_{def} (Fig. 10).

The backscattered signal contains a contribution due to the defect plus a contribution (speckle) due to the medium. The transducer delivers a signal that results from the summation of the acoustic pressure all over its surface Σ.

If the defect is small compared to the focal spot ($d < \lambda F / \sqrt{\Sigma}$), we see from Eq. (D3) in Ref. 3 that the contribution due to the defect in the backscattered signal at frequency ω simply writes:

$$S^{\omega}(0) = \frac{1}{\Sigma} \int O(\mathbf{r})\psi_{\omega}(\mathbf{r})d\mathbf{r} \approx \frac{d^2\Sigma}{\lambda^2 F^2} A_{\mathrm{def}}. \qquad (36)$$

The average intensity of the defect contribution is

$$I_{\mathrm{def}} = E\{S_{\omega}^2(0)\} = \frac{d^4\Sigma^2}{\lambda^4 F^4} A_{\mathrm{def}}^2. \qquad (37)$$

Now, from Eq. (8) the average intensity of the speckle contribution is

$$\sigma_{\mathrm{sp}}^2 = R_{SS}^{\omega}(0) = \frac{1}{\Sigma^2} \frac{1}{\lambda^2 F^2} \int \int H(x,y)R_{\chi\chi}(x,y)dx\,dy. \qquad (38)$$

Consider that the medium coherence length is smaller than the focal spot (i.e., $\epsilon < \lambda F / \sqrt{\Sigma}$), then the integral in (38) can be approximated by $\epsilon^2 \sigma_n^2 H(0,0)$, and from the definition of H, it can be shown that $H(0,0)$ is of the order of Σ^3. Hence the intensity of the speckle contribution:

$$\sigma_{\mathrm{sp}}^2 \approx \frac{\Sigma \epsilon^2}{\lambda^2 F^2} \sigma_n^2. \qquad (39)$$

The defect can be detected if its contribution is strong enough relative to the speckle contribution, which depends on the ratio:

$$\frac{\sqrt{I_{\mathrm{def}}}}{\sigma_{\mathrm{sp}}} = \frac{A_{\mathrm{def}}}{A_{\mathrm{sp}}} \frac{d^2 \sqrt{\Sigma}}{\lambda F \epsilon}. \qquad (40)$$

Let us comment on this result. First, the ratio is proportional to d^2, which means that a large defect is more detectible than a small one; moreover, a defect is more likely to be detected if its strength A_{def} is larger than that of the medium σ_n. Also notice that the smaller ϵ, the easier the detection of a defect. This is also logical. Indeed, if the coherence length of the medium is small, then the coherence length of the backscattered field ψ^{ω} will be small too,[3] which means that the transducer surface will integrate (partially) uncorrelated data, which will tend to average out the speckle contribution.

So the best situation to detect a defect would be to have a fully incoherent medium ($\epsilon \rightarrow 0$). However, a fully incoherent medium can only be an idealization of reality. Even if such a medium existed, we know from the scalar theory of diffraction[13–15] that spatial frequencies superior to $1/\lambda$ do not propagate and generate evanescent waves. A fully incoherent medium is supposed to contain infinitely high spatial frequencies, but as they are low-pass filtered by propagation, the receiver cannot feel them. So the minimum realistic value for ϵ would be roughly λ.

Finally, the ratio (40) is inversely proportional to the focal spot size $\lambda F / \sqrt{\Sigma}$, so using a very sharply focused transducer should increase defect detection. But if the focal spot size becomes too small, then the assumption $\epsilon < \lambda F / \sqrt{\Sigma}$ cannot be true and (40) does not hold any longer. Indeed, with a very sharply focused transducer, the medium might become coherent at the scale of a wavelength, which means that the backscattered speckle field will be coherent too, and the transducer surface will integrate correlated data, which therefore will not average out the speckle contribution.

This result shows how important the *information grains* are. By information grains, we mean the number of uncorrelated data available on the receiving surface. Generally, when one wants to eliminate an unwanted noise, one tries to average several uncorrelated realizations of that noise. But the Van Cittert–Zernike theorem[3] states that the larger the
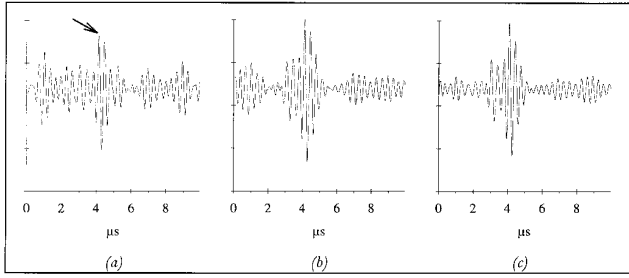
FIG. 11. Addition of backscattered signals received on the array, for three receiving aperture sizes: (a) $\Sigma_{rec} = \Sigma_{tr} = 16$ elements (b) $\Sigma_{rec} = 4\Sigma_{tr} = 64$ elements (c) $\Sigma_{rec} = 8\Sigma_{tr} = 128$ elements. The echo of the metallic wire is pointed at by the arrow in (a).

transmitting aperture, the larger the backscattered speckle coherence length. Which means that as long as we use the same single T/R transducer, we do not get more uncorrelated data by increasing the aperture size. However, if we use a small transmitting aperture Σ_t and a large receiving aperture Σ_r, then we increase the number of information grains by a factor of Σ_r/Σ_t.

To demonstrate this, let us consider a simple defect detection experiment. A thin metallic wire (diameter $= 0.11$ mm) is put inside a piece of foam, in the focal region of a 128-elements array. The experiment was carried out with a 16-elements transmitting aperture size. Foam alone behaves as an incoherent medium.[3] If the receiving aperture is the same as the transmitting aperture, the echo of the wire cannot be detected (Fig. 11). However, since we use an array, we can easily increase the receiving aperture to 64 then 128 elements and we observe that the echo of the wire that was hardly detectible becomes more and more apparent amongst the ambient noise.

This is due to the fact that we have a small defect in the focal region of the transducer: therefore, it generates a reflected coherent spherical wavefront that arrives at the same time on all elements of the array, whatever the transmitting aperture size. Whereas the coherence length of the speckle noise is determined by the transmitting aperture size. When increasing the receiving aperture size, we add more and more uncorrelated speckle grains which tend to be averaged out, whereas the contributions from the small defect add constructively.

V. CONCLUSION

Spatial correlation of the ultrasonic backscatter with a single T/R aperture was studied. We applied theoretical results to the case of composite materials. Experimental results were presented on three types of composites. The backscattered correlation length is clearly influenced by the anisotropy of the composites. In the case of quadridirectional composites, the stacking of four layers with different orientations tends to make the medium seem isotropic and partially coherent. Finally, the importance of coherence length of the backscattered speckle noise in defect detection was shown for the case of a small wire hidden in foam.

The notion of spatial coherence, which was first introduced in monochromatic optics, is crucial in the quality of echographic images. In particular, speckle reduction techniques use successive averaging of presumably uncorrelated data: one needs to know what parameter must be changed, and by how much, to obtain uncorrelated data and therefore to reduce the speckle noise level adaptively. Moreover, if speckle is considered as a signal, and not as a noise, it has been shown that a measurement of the coherence length of the backscattered signal can provide statistical information about the medium structure.

APPENDIX

1. Spatial correlation function

Consider the case of a random medium with a stationary reflectivity function $\chi(\mathbf{R})$; then its autocorrelation function $R_{\chi\chi}(\mathbf{R}_1,\mathbf{R}_2)$ only depends on $\Delta\mathbf{R} = \mathbf{R}_1 - \mathbf{R}_2$ and (6) yields:

$$R_{SS}^{\omega}(\mathbf{d}_1,\mathbf{d}_2) = \frac{1}{\Sigma^2} \frac{1}{\lambda^4 z^4} \int \int \Lambda(\mathbf{R})\Lambda^*(\mathbf{R}+\Delta\mathbf{R})$$

$$\times R_{\chi\chi}(\Delta\mathbf{R} + \mathbf{d}_2 - \mathbf{d}_1)d\mathbf{R}\, d\Delta\,\mathbf{R}. \quad (A1)$$

Then R_{SS}^{ω} can be written as a convolution product:

$$R_{SS}^{\omega}(\boldsymbol{\delta}) = \frac{1}{\lambda^4 z^4} \Lambda(\boldsymbol{\delta})*\Lambda^*(-\boldsymbol{\delta})*R_{\chi\chi}(\boldsymbol{\delta})$$

$$= \frac{1}{\lambda^2 z^2} H(\boldsymbol{\delta})*R_{\chi\chi}(\boldsymbol{\delta}). \quad (A2)$$

2. Calculation of R_{ss}^{ω} for an isotropic medium with coherence length ϵ

Given a function $f(X,Y)$ with circular symmetry, its 2-D Fourier transform can be written as a Hankel transform:

$$FT\{f(X,Y)\}_{x/\lambda F, y/\lambda F}$$

$$= \phi(x,y) = \int \int e^{-j(2\pi/\lambda F)(xX+yY)}f(X,Y)dX\,dY. \quad (A3)$$

With the change of variables:

$$x = r\cos\theta, \quad X = R\cos\varphi,$$
$$y = r\sin\theta, \quad Y = R\sin\varphi, \quad (A4)$$

the Jacobian is R, and ϕ also has circular symmetry:

$$\phi(r) = \int_{-\pi}^{\pi} d\varphi \int_0^{\infty} dR\, f(R)e^{j(\pi/\lambda F)rR[\cos(\theta-\varphi)]}$$

$$= \int_0^{\infty} Rf(R)J_0\left(2\pi\frac{rR}{\lambda F}\right)dR, \quad (A5)$$

where J_0 is the zero-order Bessel function.

From (8), R_{SS} is equal to a convolution product, and the convolution theorem yields:

$$R_{SS}^{\omega} = \frac{1}{\lambda^2 F^2} FT_{2D}\{|\Gamma|^2 FT\{R_{\chi\chi}\}\}. \quad (A6)$$

$|\Gamma|^2$, $R_{\chi\chi}$, and its Fourier transform have circular symmetry, so the 2-D-FT reduce to 1-D Hankel transforms. If the medium reflectivity correlation function is

$$R_{\chi\chi}(\Delta X, \Delta Y) = e^{-(\sqrt{\Delta X^2 + \Delta Y^2}/\epsilon)} \qquad \text{(A7)}$$

then its Hankel transform is

$$K(r) = \epsilon^2 \left/ \left[1 + \left(2\pi \frac{\epsilon r}{\lambda F} \right)^2 \right]^{3/2} \right. . \qquad \text{(A8)}$$

Hence

$$R_{SS}^{\omega}(\delta) = \frac{1}{\lambda^2 F^2} \int K(r) \Gamma^2(r) J_0 \left(2\pi \frac{r\delta}{\lambda F} \right) dr. \qquad \text{(A9)}$$

Since the characteristic scale is the focal spot size $\lambda F/a$, it is interesting to use the dimensionless variables

$$\bar{r} = r/a \quad \text{and} \quad \bar{\delta} = Ra/\lambda F, \qquad \text{(A10)}$$

δ expresses the distance along the scan axis in ''$\lambda F/a$ units,'' the final expression is

$$R_{SS}^{\omega}(\bar{\delta}) \propto \int_0^l K(\bar{r}) \Gamma^2(\bar{r}) J_0(2\pi \bar{r} \bar{\delta}) d\bar{r} \qquad \text{(A11)}$$

which is computed numerically and plotted in Fig. 2.

[1] K. D. Donohue, J. M. Bressler, T. Varghese, and N. M. Bilgutay, ''Spectral correlation in ultrasonic pulse echo signal processing,'' IEEE Trans. Ultrason. Ferroelectr. Freq. Control **40**, 4, 330–337 (1993).

[2] J. Ophir, I. Cespedes, H. Ponnekanti, Y. Yazdi, and X. Li, ''Elastography: a quantitative method for measuring the elasticity of biological tissues,'' Ultrason. Imaging **13**, 111–134 (1991).

[3] A. Derode and M. Fink, ''Partial coherence of transient ultrasonic fields in anisotropic random media: Application to coherent echo detection,'' J. Acoust. Soc. Am. **101**, 690–704 (1997).

[4] R. Mallart and M. Fink, ''The van Cittert–Zernike theorem in pulse echo measurements,'' J. Acoust. Soc. Am. **90**, 2718–2727 (1991).

[5] W. F. Walker and G. Trahey, ''Speckle coherence and implications for adaptive imaging,'' J. Acoust. Soc. Am. **101**, 1847–1858 (1997).

[6] F. Zernike, ''The concept of degree of coherence and its application to optical problems,'' Physica (Amsterdam) **V**, 785–795 (1938).

[7] C. B. Burckhardt, ''Speckle in ultrasound B-mode scans,'' IEEE Trans. Sonics Ultrason. **25**, 1–6 (1978).

[8] R. F. Wagner, S. W. Smith, J. M. Sandrik, and H. Lopez, ''Statistics of speckle in ultrasound B-scans,'' IEEE Trans. Sonics Ultrason. **30,3**, 156–163 (1983).

[9] G. E. Trahey, S. W. Smith, and O. T. von Ramm, ''Speckle pattern correlation with lateral aperture translation: experimental results and implication for spatial compounding,'' IEEE Trans. Ultrason. Ferroelectr. Freq. Control **UFFC-33,3**, 257–264 (1986).

[10] R. F. Wagner, M. F. Insana, and S. W. Smith, ''Fundamental correlation lengths of coherent speckle in medical ultrasonic images,'' IEEE Trans. Ultrason. Ferroelectr. Freq. Control **35,1**, 34–43 (1988).

[11] F. Cancre, ''Speckle acoustique: étude et méthode de réduction,'' Thèse de doctorat, Université Paris 7, 1988.

[12] T. Lhermitte and M. Fink, *1990 IEEE Ultrasonics Symposium Proceedings* (IEEE, New York, 1991), pp. 1075–1080.

[13] J. W. Goodman, *Introduction to Fourier Optics* (McGraw-Hill, New York, 1968).

[14] J. W. Goodman, *Statistical Optics* (Wiley, New York, 1985).

[15] A. Maréchal and M. Françon, *Diffraction, structure des images, influence de la cohérence de la lumière* (Masson & Cie, Paris, 1970).

Interaction of a slender vortex with a rigid sphere: Dynamics and far-field sound

Omar M. Knio
Department of Mechanical Engineering, The Johns Hopkins University, Baltimore, Maryland 21218

Lu Ting
Courant Institute of Mathematical Sciences, New York University, New York, New York 10012

Rupert Klein
Fachbereich Sicherheitstechnik, Bergische Universität Wuppertal, D-42097 Wuppertal, Germany

Interactions between a slender vortex filament and a stationary rigid sphere are analyzed using a vortex element scheme which tracks the motion of the filament centerline. The filament velocity is expressed as the sum of a self-induced velocity and potential velocity due to the presence of the sphere. The self-induced velocity is estimated numerically using a line Biot–Savart integral which is carefully desingularized so as to reflect the correct asymptotic behavior of the core vorticity distribution under the influence of stretching and viscous diffusion. Meanwhile, the potential velocity is evaluated from a recently derived formula, which expresses it as a line integral along the image of the filament centerline in the sphere with regular weight functions. From the far-field behavior of an unsteady vortical flow outside a stationary sphere, formulas for the acoustic far field are obtained. It is shown that the interaction between the slender vortex filament and the sphere generates dipoles and quadrupoles in addition to the quadrupoles generated by the filament alone in space. The strengths and orientations of the dipoles and quadrupoles are completely determined by the time evolution of the weighted first and second moments of vorticity. The formulas are applied to compute the far-field sound generated by the passage of a slender vortex ring over the sphere. Both coaxial and noncoaxial passage events are analyzed in the computations, as well as the effects of initial core size and asymmetric perturbations. © *1998 Acoustical Society of America.* [S0001-4966(98)02101-8]

INTRODUCTION

Interactions between slender vortices with moving and/or stationary solid bodies play a major role in a large number of applications, including pumps, turbines, propellers, and helicopter blades. In most of these examples, detailed computation of the flow and acoustic fields is, unfortunately, not possible due to extreme complexity of the flow—which is characterized by a multitude of length scales—and of the boundaries. Due to these difficulties, it is generally necessary, if not desirable, to consider simplified models which enable us to isolate essential dynamics of the flow and of the acoustic field, and thus render the analysis tractable.

Some of the simplest, yet highly nontrivial, models of sound generation by slender vortices consist of either the unsteady motion at low Mach number of one or more vortices in free space, or the interaction of a slender vortex structure with a compact simple body at low Mach number. Even in these idealized situations, analysis of the flow field and sound generation is complicated, in particular, by two distinct difficulties. The first is due to the disparity between the acoustic wavelength, $\tilde{\mathscr{l}}_a$, and the characteristic length scale of the low-Mach-number flow, $\tilde{L}$. The second is due to the large disparity between $\tilde{L}$, and the physical core size of the slender vortex filament, $\tilde{\delta}$. Due to this stiff scale complexity,

direct simulation (e.g., Ref. 1) of the flow and acoustic fields is generally not possible.

To overcome these difficulties, most previous studies have relied on a combination of a well-established aeroacoustic theory (e.g., Refs. 2–11) together with simplifying assumptions of the flow field. Thus, numerous computational studies have focused on 2-D (e.g., Refs. 12–14) or axisymmetric vortices (e.g., Refs. 15, 16). Meanwhile, studies of slender vortex sound in three dimensions have been scarce, and have for the most part relied on highly simplified flow models, including frozen passive vortical structures (e.g., Refs. 17, 18), simplified evolution equations (e.g., Ref. 19), or thin filaments with frozen core structure (e.g., Ref. 20). While all of these approaches efficiently overcome the scale disparity of the ''inner'' flow, this advantage is typically achieved at the expense of oversimplification of the filament dynamics. For instance, it has long been known that models based on the local induction approximation[21–23] do not capture filament self-stretching[24] and altogether ignore the role of vortex core dynamics. These simplifications often lead to large predictive errors;[25,26] large errors may also arise when a frozen core structure is assumed, or when its variations are described using *ad hoc* approximate relationships.[27] The occurrence of large flow modeling errors may severely restrict the applicability of the corresponding acoustic prediction or cast some doubts regarding its relevance.

To address these issues, we focus in the present study on a simplified setting which enables us to *simultaneously* tackle the complexity of the slender vortex flow and the resulting sound generation. Specifically, we focus on inviscid interaction of a single, slender vortex filament with a stationary rigid sphere at low Mach number and high Reynolds number. As discussed in Section I, our approach to the problem relies on several key ''results'' which have been recently obtained: (1) asymptotic analyses of the vorticity structure of slender vortex filaments[26,28] which have led to the construction of numerical scheme which: (a) accounts for the effects of stretching and diffusion for arbitrary leading-order axisymmetric core structure, and (b) reflects the *correct* asymptotic behavior of the core dynamics in the limit of small core size to radius of curvature ratio; and (2) analytical results on the evolution of a vortical flow outside a rigid sphere and of the far-field behavior of the corresponding velocity potential.[30] These analyses are combined with the asymptotic aeroacoustic theory of Ting and Miksis[9] into a computational model which enables accurate and efficient simulation of the slender filament dynamics and its interaction with a rigid sphere and incorporates simple means for predicting the resulting noise emission. Specifically, it is shown in Section I that the interaction of a slender vortex filament with a rigid sphere generates an acoustic far field that is dominated by dipoles and quadrupoles. The strengths of these dipoles and quadrupoles are respectively expressed in terms of the *weighted* first and second moments of vorticity using new, simple, explicit formulas, which also relate the evolution of the acoustic source terms to the motion of the filament centerline.

In Section II, the model is applied to analyze the evolution of the flow and the acoustic far field during the passage of slender vortex rings over a rigid stationary sphere. Several scenarios are considered, and used to investigate the relationships between three-dimensional slender filament dynamics and radiated noise. In particular, the numerical examples illustrate the effect of the core structure variation on the dynamics of the slender vortex, and show that moderate changes in the filament motion can have significant impact on the acoustic far field.

I. FORMULATION AND NUMERICAL SCHEMES

As mentioned in the Introduction, attention is focused on the interaction of a slender vortex filament with a rigid sphere at high Reynolds number. The study is restricted to interaction events in which the filament remains at all times well separated from the surface of the sphere, by a distance of at least a few core radii. In addition, the characteristic Mach number is assumed to be so small that the motion surrounding the vortex and the sphere can be treated as essentially incompressible. Furthermore, the Reynolds number is assumed to be large enough so that the thickness of the boundary layer on the surface of the sphere is much smaller than the sphere radius. Consequently, viscous effects near the surface of the sphere,[31] and their potential contribution to sound emission,[32] are ignored. The impact of the sphere on the motion of the filament is thus approximated by the po-

tential velocity field needed to satisfy zero normal velocity at the rigid boundary. This leads to a simplified flow model whose construction is summarized below.

A. Filament motion

For a slender vortex filament, the vorticity distribution is localized in the neighborhood of a time-dependent curve $\mathscr{L}(t)$, which describes the evolution of its center line. Thus, the core size of the filament $\widetilde{\delta}$ is much smaller than the characteristic radius of curvature of the center line or of the outer flow, $\widetilde{L}$. (Here and in the following, tildes are used to denote dimensional quantities.) A large number of practical applications—including trailing vortices, propeller wakes, and tip vortices[33–35]—are characterized by a large disparity between $\widetilde{\delta}$ and $\widetilde{L}$, with ratios $\delta \equiv \widetilde{\delta}/\widetilde{L}$ of the order of 0.01 or even smaller. In these situations, detailed resolution of the vorticity distribution is prohibitively expensive, and one must instead rely on a flow description which accurately and efficiently overcomes its scale complexity.

To this end, we rely on recent analysis from Refs. 26 and 27 which shows that when the filament evolves in an infinite domain with no internal boundaries, an equation of motion for its center line can be derived from the vorticity transport equation,

$$\frac{\partial \boldsymbol{\omega}}{\partial t} + \boldsymbol{u} \cdot \nabla \boldsymbol{\omega} = \boldsymbol{\omega} \cdot \nabla \boldsymbol{u} + \frac{1}{\text{Re}} \nabla^2 \boldsymbol{\omega}, \tag{1}$$

and the three-dimensional Biot-Savart integral,[36]

$$\boldsymbol{u}(\boldsymbol{x},t;\boldsymbol{\omega}) = \frac{1}{4\pi} \int \frac{\boldsymbol{x}' - \boldsymbol{x}}{|\boldsymbol{x}' - \boldsymbol{x}|^3} \times \boldsymbol{\omega}(\boldsymbol{x}',t) d^3 \boldsymbol{x}'. \tag{2}$$

Here, $\boldsymbol{\omega}$ denotes the vorticity, $\boldsymbol{u}$ the velocity, $\boldsymbol{x}$ the coordinate vector, and $\text{Re} \equiv \widetilde{U}_{\text{ref}} \widetilde{L}_{\text{ref}} / \widetilde{\nu}$ is the Reynolds number. $\widetilde{U}_{\text{ref}}$ and $\widetilde{L}_{\text{ref}}$ are reference velocity and length scales, respectively, whose precise definitions will be provided later. The analysis is based on applying (2) to a localized vorticity field of the form:

$$\boldsymbol{\omega}(\boldsymbol{x},t;\delta) = \frac{1}{\delta^2} \left[\eta^{(0)}\left(\frac{r}{\delta},s,t\right) \boldsymbol{e}_\theta + \zeta^{(0)}\left(\frac{r}{\delta},s,t\right) \boldsymbol{t} \right]$$

$$+ \frac{1}{\delta} \left[\xi^{(1)}\left(\frac{r}{\delta},\theta,s,t\right) \boldsymbol{e}_r + \eta^{(1)}\left(\frac{r}{\delta},\theta,s,t\right) \boldsymbol{e}_\theta \right.$$

$$+ \left. \zeta^{(1)}\left(\frac{r}{\delta},\theta,s,t\right) \boldsymbol{t} \right] + O(1) \tag{3}$$

where (r,θ,s) and $(\boldsymbol{e}_r,\boldsymbol{e}_\theta,\boldsymbol{t})$ are the filament attached coordinates and their associated basis vectors, as defined by Callegari and Ting.[37] Within the filament core, the local velocity field corresponding to (3) is given by

$$\boldsymbol{V}(\boldsymbol{x},t;\boldsymbol{\omega}) = \frac{1}{\delta} [v^{(0)} \boldsymbol{e}_\theta + w^{(0)} \boldsymbol{t}] + u^{(1)} \boldsymbol{e}_r + v^{(1)} \boldsymbol{e}_\theta + w^{(1)} \boldsymbol{t}$$

$$+ O(\delta), \tag{4}$$

where $\boldsymbol{V}$ is the fluid velocity in the filament attached coordinate system, i.e., it represents the core velocity distribution relative to the local filament velocity $\dot{\boldsymbol{X}}(s,t)$. Following (3),

the leading order core structure is taken to be axisymmetric, i.e. the leading vorticities, $\eta^{(0)}$ and $\zeta^{(0)}$, and velocities, $v^{(0)}$ and $w^{(0)}$ are independent of θ. Since the vorticity field is localized around the filament centerline $\mathscr{L}$, the flow field outside the vortex core is irrotational and is described by the line Biot–Savart integral:

$$v(\boldsymbol{x},t;\mathscr{L},\Gamma)=\frac{\Gamma}{4\pi}\int_{\mathscr{L}}\mathbf{F}(\boldsymbol{x},\boldsymbol{x}')\times d\boldsymbol{x}',\qquad(5)$$

where

$$\mathbf{F}(\boldsymbol{x};\boldsymbol{x}')\equiv\frac{\boldsymbol{x}'-\boldsymbol{x}}{|\boldsymbol{x}'-\boldsymbol{x}|^3}\qquad(6)$$

and Γ is the circulation of the filament.

The velocity of the filament centerline is obtained by matching the "outer" potential flow to the "inner" vortical core structure. The result is expressed as:[37,26]

$$\dot{\boldsymbol{X}}(s)=v^{\mathrm{si}}(s)\equiv\frac{\Gamma}{4\pi}\left[\ln\left(\frac{2}{\delta}\right)+C\right]\kappa(s)\boldsymbol{b}(s)+\boldsymbol{Q}^f(\boldsymbol{X}(s)),\qquad(7)$$

where v^{si} is the self-induced velocity, s is the arc length parameter along $\mathscr{L}$, κ and $\boldsymbol{b}$ are the curvature and unit binormal at $\boldsymbol{X}$, respectively, $C(t)$ is the time-dependent core structure coefficient, and $\boldsymbol{Q}^f$ is the so-called finite part of the line Biot–Savart integral. The core structure coefficient represents the contributions of the local swirling and axial velocities to the leading order velocity of the filament; it is expressed as[28]

$$C(t)=C_v(t)+C_w(t),\qquad(8)$$

where

$$C_v(t)=\lim_{\bar{r}\to\infty}\left\{\frac{4\pi^2}{\Gamma^2}\int_0^{\bar{r}}\bar{r}v^{(0)2}d\bar{r}-\ln\bar{r}\right\}-\frac{1}{2},\qquad(9)$$

$$C_w(t)=-\frac{1}{2}\left(\frac{4\pi}{\Gamma}\right)^2\int_0^{\infty}\bar{r}w^{(0)2}d\bar{r},\qquad(10)$$

and $\bar{r}\equiv r/\delta$. Meanwhile, $\boldsymbol{Q}^f$ is given by

$$\boldsymbol{Q}^f(\boldsymbol{X})=\int_{\mathscr{L}}\hat{\mathbf{F}}(\boldsymbol{X}(s);\boldsymbol{X})-H(1-|\tilde{s}-\tilde{s}_1|)\hat{\mathbf{F}}_1(\tilde{s})d\tilde{s},\qquad(11)$$

where $\hat{\mathbf{F}}_1$ represents the first two terms of the Taylor expansion of $\mathbf{F}$ around $\boldsymbol{X}$.[37,24]

The core structure coefficients evolve in time according to the evolution of the leading-order axial vorticity and axial velocity distributions. As shown by Callegari and Ting,[37] the leading-order axial vorticity and velocity within the core obey inhomogeneous heat equations with a source term that depends on the stretching of the filament center line. In the inviscid limit, simple closed-form expressions for the evolution of C_v and C_w have been obtained by Klein and Ting:[28]

$$C_v(t)=C_v(0)+\ln\sqrt{\frac{S(t)}{S(0)}},\qquad(12)$$

$$C_w(t)=\left[\frac{S(0)}{S(t)}\right]^3 C_w(0),\qquad(13)$$

where $S(t)$ is the total arc length of the filament. When viscous effects are present, the expressions describing the evolution of the core structure coefficient are more involved. Their derivation has been discussed in detailed in Refs. 27 and 28 and only the results of these analyses are provided here. Briefly, the approach for determining $C(t)$ is based on expressing the initial distributions of the axial vorticity and axial velocity as truncated Laguerre function expansions,[28,27]

$$\zeta(\bar{r},t=0)\approx\frac{\exp(-\beta^2)}{\mathsf{s}_v}\left\{c_0+\sum_{n=1}^{L}c_n L_n(\beta^2)\right\}\qquad(14)$$

and

$$w(\bar{r},t=0)\approx\frac{\exp(-\gamma^2)}{\mathsf{s}_w}\left\{d_0+\sum_{n=1}^{L}d_n L_n(\gamma^2)\right\},\qquad(15)$$

where $\beta\equiv\bar{r}/2K\sqrt{\mathsf{s}_v}$, $\gamma\equiv\bar{r}/2K\sqrt{\mathsf{s}_w}$,

$$K\equiv\delta^{-2}\frac{\tilde{\nu}}{\tilde{\Gamma}}\qquad(16)$$

is a normalized viscosity, while s_v and s_w are arbitrary time shifts whose values are selected so as to eliminate the coefficients c_1 and d_1 from the expansions in (14) and (15), respectively.[38] The coefficients c_n and d_n are determined from the initial data using the orthogonality of the Laguerre polynomials; we have:[28,27]

$$c_n=\mathsf{s}_v\int_0^{\infty}\zeta^{(0)}(2K\sqrt{\lambda\mathsf{s}_v},t=0)L_n(\lambda)d\lambda\qquad(17)$$

and

$$d_n=\mathsf{s}_w\int_0^{\infty}w^{(0)}(2K\sqrt{\lambda\mathsf{s}_w},t=0)L_n(\lambda)d\lambda.\qquad(18)$$

Once the coefficients c_n and d_n are found, the evolution of the core structure coefficients can be directly evaluated using the solutions obtained in Ref. 27. The contribution of the swirl velocity distribution is obtained from

$$C_v(\mathsf{s})-C_v(0)=-\alpha I(\mathsf{s})+\ln\sqrt{\frac{S(\mathsf{s})}{S(0)}},\qquad(19)$$

where s is a stretched time variable defined by

$$\mathsf{s}=\frac{1}{S(0)}\int_0^t S(t')dt',\qquad(20)$$

$$\alpha\equiv\frac{8\pi^2 K^2}{\Gamma^2},\qquad(21)$$

while $I(\mathsf{s})$ is a quadratic functional given by:

$$I(\mathsf{s})=2K^2\sum_{m=0}^{L}\sum_{n=0}^{L}A_{mn}F_{mn}(\mathsf{s}),\qquad(22)$$

with

$$F_{mn}(\mathsf{s}) = \begin{cases} \ln\left(\dfrac{\mathsf{s}+\mathsf{s}_v}{\mathsf{s}_v}\right), & \text{if} \quad m=n=0; \\[2ex] \dfrac{1}{m+n}\left[1-\left(\dfrac{\mathsf{s}_v}{\mathsf{s}+\mathsf{s}_v}\right)^{m+n}\right], & \text{otherwise} \end{cases} \quad (23)$$

and

$$A_{mn} = \frac{(m+n+1)!}{m!\,n!\,2^{m+n+1}} c_m c_n. \quad (24)$$

Meanwhile, the contribution of the axial velocity is found from

$$C_w(\mathsf{s}) = -2\alpha(\mathsf{s}+\mathsf{s}_w)\sum_{m=0}^{L}\sum_{n=0}^{L} B_{mn}\left(\frac{\mathsf{s}_w}{\mathsf{s}+\mathsf{s}_w}\right)^{m+n}, \quad (25)$$

where

$$B_{mn} = \frac{(m+n+1)!}{m!\,n!\,2^{m+n+1}} d_m d_n. \quad (26)$$

In an unbounded domain with no internal boundaries, the motion of the filament is simulated using a recently constructed slender filament model[27] that is consistent with equation (7) and the definitions of C and Q^f in (8) and (11), respectively. The scheme is based on a Lagrangian discretization of the filament geometry into a finite number of regularized vortex elements with spherical overlapping cores. The vortex elements are described in terms of their Lagrangian position vectors, $\chi_i(t)$, $i,\ldots,N$, which are indexed consecutively such that the collection $\{\chi_i(t)\}_{i=1}^{N}$ approximates the filament centerline $\mathscr{L}(t)$.[39,26] Based on the Lagrangian variables, a smooth representation of the *regularized* filament vorticity is obtained using the expression[40]

$$\boldsymbol{\omega}(\boldsymbol{x},t) = \sum_{i=1}^{N} \Gamma \,\delta\chi_i(t) f_\sigma(\boldsymbol{x}-\chi_i(t)), \quad (27)$$

where f_σ is a rapidly decaying spherical core function of unit mass, $\delta\chi_i(t)$ is the arc length increment associated with the ith element, and σ is a *numerical* core radius. When inserted into the three-dimensional Biot-Savart integral (2), the above representation yields the following desingularized velocity field:

$$v^{\mathrm{ttm}}(\boldsymbol{x},t) = -\frac{\Gamma}{4\pi}\sum_{i=1}^{N} \frac{(\boldsymbol{x}-\chi_i(t))\times\delta\chi_i(t)}{|\boldsymbol{x}-\chi_i(t)|^3}\kappa_\sigma(\boldsymbol{x}-\chi_i(t)), \quad (28)$$

where $\kappa_\sigma(\boldsymbol{x})$ is the velocity smoothing kernel corresponding to f_δ.[40] In the computations, the arc length increments $\delta\chi_i(t)$ are related to the distribution of particle positions using the procedure described by Klein and Knio.[26] It is based on a Lagrangian spectral collocation interpolation of the filament geometry onto the particle positions, and approximating the arc length based on spectral collocation derivatives of the interpolated filament centerline.

As described in Ref. 27, the numerical core radius σ is related to the physical core structure so that the regularized velocity field coincides with the theoretical prediction in (7) at the particle positions. The relationship is expressed as:

$$\sigma = \delta \exp(C^{\mathrm{ttm}}-C), \quad (29)$$

where C^{ttm} is the numerical core constant which corresponds to the choice of core smoothing function f_σ.[26]

Application of the slender filament scheme in free space is summarized as follows: (a) In a preprocessing step, the coefficient matrices A_{mn} and B_{mn} are computed from (24) and (26) based on the Laguerre function expansion of the axial vorticity and axial velocity distributions, respectively. (b) The corrected slender filament scheme is used to evaluate the velocity of the Lagrangian particles which represent the filament center line.[26,27] (c) The second-order Adams-Bashforth scheme is used to update the Lagrangian position vector of the vortex elements, namely by integrating:

$$\frac{\partial\chi_i}{\partial t} = v^{\mathrm{ttm}}(\chi_i(t),t) \quad (30)$$

with v^{ttm} from (28). (d) Based on the new particle positions, the new value of the filament arclength is computed. (e) The Crank–Nicolson scheme is used to advance the stretched variable s, and thus update the core structure coefficients C_v and C_w. As indicated above, Eqs. (12) and (13) are used in inviscid calculations, while expressions (19) and (25) are used for viscous computations. (f) Using the new values of C_v and C_w, equation (29) is used to update the numerical core radius σ. Steps (b)–(f) are repeated in order to advance the solution in time.

In the presence of the rigid sphere, the filament velocity is altered by the potential velocity field induced by the sphere. In this case the filament equation of motion is modified from its previous form in (7) in order to account for the potential or ''image'' velocity field; it is expressed as:[30]

$$\dot{\boldsymbol{X}}(s) = v^{\mathrm{si}}(s) + v^{\mathrm{im}}(s), \quad (31)$$

where v^{si} denotes the velocity induced by the filament alone, and v^{im} is the potential velocity induced by the sphere. The latter has been analyzed by Knio and Ting[30] who provide analytical formulas for the ''image'' potential field and the associated velocity distribution. These formulas are based on a detailed analysis which extends the classical results of Weiss[41] and Lighthill.[42] In particular, the analysis in Ref. 30 shows that when the vortical flow outside sphere is induced by a slender filament, the image velocity v^{im} can be expressed as a line integral along the image of the filament center line in the sphere with regular weight functions. For a sphere of radius a that is centered at the origin of a Cartesian coordinate system, the result in component form is:[30]

$$v_j^{\mathrm{im}}(\boldsymbol{x}) = -\frac{\Gamma}{4\pi a}\int_{\mathscr{L}}\left\{ G\frac{\partial\hat{\boldsymbol{r}}}{\partial x_j} + \left[\frac{\partial G}{\partial\lambda}\frac{\partial\lambda}{\partial x_j} + \frac{\partial G}{\partial\mu}\frac{\partial\mu}{\partial x_j}\right]\hat{\boldsymbol{r}}\right\}$$
$$\cdot[\hat{\boldsymbol{\tau}}(s)\times\hat{\boldsymbol{X}}(s)]ds, \quad (32)$$

where $\hat{\boldsymbol{\tau}}$ is the unit tangent vector to $\mathscr{L}$ at $\boldsymbol{X}(s)$, $r\equiv|\boldsymbol{x}|$, $R\equiv|\boldsymbol{X}|$, $\hat{\boldsymbol{r}}\equiv\boldsymbol{x}/r$, $\hat{\boldsymbol{X}}\equiv\boldsymbol{X}/R$, $\mu\equiv\hat{\boldsymbol{r}}\cdot\hat{\boldsymbol{X}}$, $\lambda\equiv a^2/rR$,

$$G(\lambda,\mu) \equiv \frac{\lambda^2}{Z[Z+1-\lambda\mu]} \quad (33)$$

and

$$Z(\lambda,\mu) \equiv \sqrt{1-2\lambda\mu+\lambda^2}. \qquad (34)$$

The partial derivatives in the integrand are defined by:

$$\frac{\partial G}{\partial \lambda} = \frac{\lambda}{Z^3(\lambda,\mu)}; \quad \frac{\partial G}{\partial \mu} = \frac{\lambda^3[Z^2+2Z+1-\lambda\mu]}{Z[Z^2+Z(1-\lambda\mu)]^2} \qquad (35)$$

and

$$\frac{\partial \lambda}{\partial x_j} = -\frac{a^2 x_j}{R r^3}; \quad \frac{\partial \hat{\boldsymbol{r}}}{\partial x_j} = \frac{\hat{\boldsymbol{j}}}{r} - \frac{x_j \boldsymbol{x}}{r^3}; \quad \frac{\partial \mu}{\partial x_j} = \hat{\boldsymbol{X}} \cdot \frac{\partial \hat{\boldsymbol{r}}}{\partial x_j}, \qquad (36)$$

where $\hat{\boldsymbol{j}}$ is the unit vector along the jth coordinate direction.

In order to extend the computations to account for the presence of the sphere, the integral in (32) is numerically evaluated in the same fashion used in computing the self-induced component. With the image velocity known, the free-space filament scheme is adapted by replacing the equation of motion of the particles in (30) with:

$$\frac{\partial \chi_i}{\partial t} = v^{\text{ttm}}(\chi_i(t),t) + v^{\text{im}}(\chi_i(t),t). \qquad (37)$$

All other aspects of the algorithm remain unchanged.

B. Far-field sound

In order to predict the far-field sound due to the interaction of the slender filament with the rigid sphere, we follow the asymptotic matching procedure devised by Ting and Miksis[9] (see also Ting and Klein[43]). One of the key features of the analysis in Ref. 9, which assumes a small Mach number and a compact source region, is that the acoustic pressure field is obtained directly from the far-field behavior of the potential flow field which surrounds the compact vortical region. The procedure is based on matching the far-field potential induced by the localized vortical flow to the acoustic potential in the stretched variable $\tilde{\boldsymbol{x}} \equiv M\boldsymbol{x}$, where M is the Mach number.[8] The advantage of the approach is that it provides insightful relationships between the behavior of the vorticity of the ''inner'' flow and ''outer'' acoustic field, and avoids the need for constructing complicated Green's functions for the solution of the inhomogeneous wave equation.[7,8] In performing the matching described in detail in Ref. 9, we take advantage of the analyses of Klein and Ting[29] and Knio and Ting[30] who provide expressions for the far-field potential induced by a rapidly decaying vorticity field and by the image potential due to sphere, respectively. Using these expressions, the far-field acoustic pressure due to the filament sphere interaction is expressed as[30]

$$p_a(\boldsymbol{x},t) = \frac{1}{4\pi r^2}\dot{D}_i(t_r)\hat{x}_i + \frac{M}{4\pi r}\ddot{D}_i(t_r)\hat{x}_i$$

$$+ \frac{1}{4\pi r^3}\dot{Q}_{il}(t_r)\hat{x}_i\hat{x}_l + \frac{M}{4\pi r^2}\ddot{Q}_{il}(t_r)\hat{x}_i\hat{x}_l$$

$$+ \frac{M^2}{12\pi r}\dddot{Q}_{il}(t_r)\hat{x}_i\hat{x}_l, \qquad (38)$$

where $\boldsymbol{x}$ is the observer location, $r=|\boldsymbol{x}|$, $\hat{\boldsymbol{x}}=\boldsymbol{x}/r$, and $t_r = t - Mr$ is the retarded time. The first two terms in (38)

represent dipoles with strengths, D_i, while the remaining three represents quadrupoles with strengths, Q_{il}. The dipole strengths D_i are related to the first moments of the filament vorticity and to the weighted first moments of its ''image'' within the sphere. We identify these two contributions by expressing D_i as[30]

$$D_i(t) = d_i(t) - d_i^{\text{im}}(t), \qquad (39)$$

where

$$d_i(t) = \frac{\Gamma}{2}\int_{\mathscr{L}(t)}[X_j\tau_k - X_k\tau_j]ds, \qquad (40)$$

$$d_i^{\text{im}}(t) = \frac{\Gamma}{2}\int_{\mathscr{L}(t)}[X_j\tau_k - X_k\tau_j]\left(\frac{a}{|\boldsymbol{x}|}\right)^3 ds \qquad (41)$$

for $i=1,2,3$ and i, j, k in cyclic order. Note that the contribution of the filament alone $d_i(t)$ represents the instantaneous impulse associated with the slender vortex filament, and that d_i^{im} is a first moment of vorticity weighted by $(a/|\boldsymbol{X}|)^3$. Similarly, the quadrupole strengths are expressed as:[30]

$$Q_{il}(t) = q_{il}(t) - q_{il}^{\text{im}}(t), \qquad (42)$$

where

$$q_{il}(t) = \Gamma\int_{\mathscr{L}(t)}[X_j\tau_k - X_k\tau_j]X_l ds, \qquad (43)$$

$$q_{il}^{\text{im}} = \Gamma\int_{\mathscr{L}(t)}[X_j\tau_k - X_k\tau_j]X_l\left(\frac{a}{|\boldsymbol{X}|}\right)^5 ds \qquad (44)$$

for $i,l=1,2,3$ and i, j, k in cyclic order. Note that the second moment q_{il} represents the contribution of the filament alone, and that the contribution of the image vorticity q_{il}^{im} is a second moment of vorticity that is weighted by $(a/|\boldsymbol{X}|)^5$. It is interesting to note how the present 3D expressions generalize the axisymmetric results of Miyazaki and Kambe.[44]

In the acoustic far field, $Mr \gg 1$, only the second and last terms on the right-hand side of equation (38) survive, and one obtains the following far-field acoustic pressure expression:

$$p_a^F(\boldsymbol{x},t) = \frac{M}{4\pi r}\ddot{D}_i(t_r)\hat{x}_i + \frac{M^2}{12\pi r}\dddot{Q}_{il}(t_r)\hat{x}_i\hat{x}_l. \qquad (45)$$

Thus, the far-field acoustic pressure is governed by $O(M)$ dipoles and $O(M^2)$ quadrupoles. This behavior will be exploited in the following section in the analysis of the computations.

It is interesting to indicate how the present representations of the acoustic pressure in (38) and (45) relate to classical results of the aerodynamic theory of sound. We first note that the leading-order dipole term, expressed in terms of the first moments of vorticity, reflect the changes in the impulse of the slender filament and of its image within the sphere, i.e. in the total impulse of the flow.[45] Thus, the result coincides with the classical results for sound generation in the presence of a compact rigid body.[46–48] It is also interesting to point out that the leading dipole term in (45) has exactly the same form as that predicted by Obermeier[8] for vortical flow outside a rigid sphere. The contributions of the
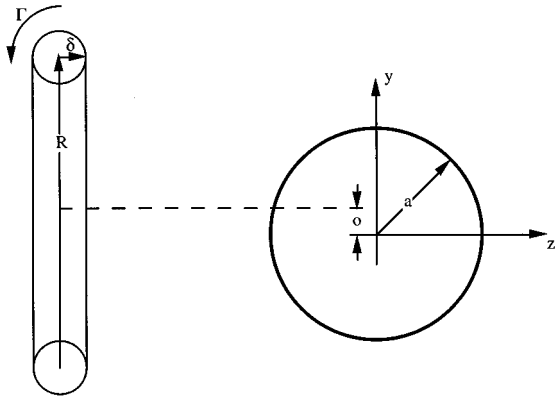
FIG. 1. Schematic illustration of the initial flow configuration.

present analysis are that, for the case of a slender vortex interacting with a rigid sphere, it: (1) provides simple explicit formulas for the acoustic source terms, and (2) relates the evolution of the acoustic source terms to the *correct* leading-order behavior of the slender filament motion. The present expressions of the far-field pressure account for dipole and quadrupole emission and may be easily extended, if so desired, to account for octopoles and higher-order contributions as well. We also point out that the above explicit representation of the acoustic dipole in terms of the first moments of vorticity is computationally more attractive than the well-known expressions of Powell[3,4] and Curle,[48] since they do not involve integrals of velocity derivatives over the solid surface.

We also note that in the absence of the sphere the contributions of the image of the filament, d_i^{im} and q_{il}^{im}, drop out, and the first and second moments of vorticity reduce to $D_i = d_i$ and $Q_{il} = q_{il}$, respectively. In this situation, Moreau's theorem[49] applies and is used to conclude that the first vorticity moment d_i is time invariant. Consequently, the dipole contribution to the acoustic field vanishes identically, and the acoustic pressure is dominated by the effect of the quadrupoles. In particular, in the absence of the sphere, equation (45) simplifies to:

$$p_a^F(\boldsymbol{x},t) = \frac{M^2}{12\pi r} \dddot{Q}_{il}(t_r)\hat{x}_i\hat{x}_l \qquad (46)$$

and one exactly recovers Möhring's formula[7] (see also Refs.

50, 51) for the far-field acoustic pressure due to vortex sound at low Mach number.

In the implementation of (38) and (45), the first moments d_i and d_i^{im} and the second moments q_{il} and q_{il}^{im} are determined by numerically evaluating the integrals in (40)–(41) and (43)–(44) using the same spectral collocation approximation that is employed for computing the line Biot–Savart integral. The first and second moments are stored during the computations; second-order centered differences are then used in order to estimate the first and second time derivatives of the first moments and the first, second and third time derivatives of the second moments of vorticity.

II. RESULTS AND DISCUSSION

The numerical scheme summarized in the previous section is applied to analyze the far-field sound emitted during various interactions between a slender vortex filament with a rigid sphere. Different test cases are chosen in order to observe and analyze the effects of initial configuration and core structure variation on the dynamics of the flow and the associated far-field sound. Consistent with the approximation used in the formulation of the model, we restrict our attention to low-Mach-number and high-Reynolds-number conditions. For brevity, we focus exclusively on initial filament configurations that correspond to slender vortex rings. In Section II B, we consider symmetric arrangements with the axis of the ring passing through the center of the sphere.[52,27] In this situation, the ring remains axisymmetric as it passes over the sphere. We restrict the analysis of axisymmetric passage events to the high-Reynolds-number limit, but use this setting to analyze the effect of initial core radius. In Section II C, the computations are extended to vortex rings whose centerlines are initially perturbed using helical waves, and the computations are used to analyze the effect of perturbation amplitude and wavenumber on the dynamics of the filament and the radiated noise. Finally, we consider asymmetric initial configurations corresponding to circular vortex rings whose axis does not pass through the center of the sphere; these computations are contrasted with earlier cases and used to illustrate the effect of diffusion within the core of the filament on the motion and far-field sound. However,
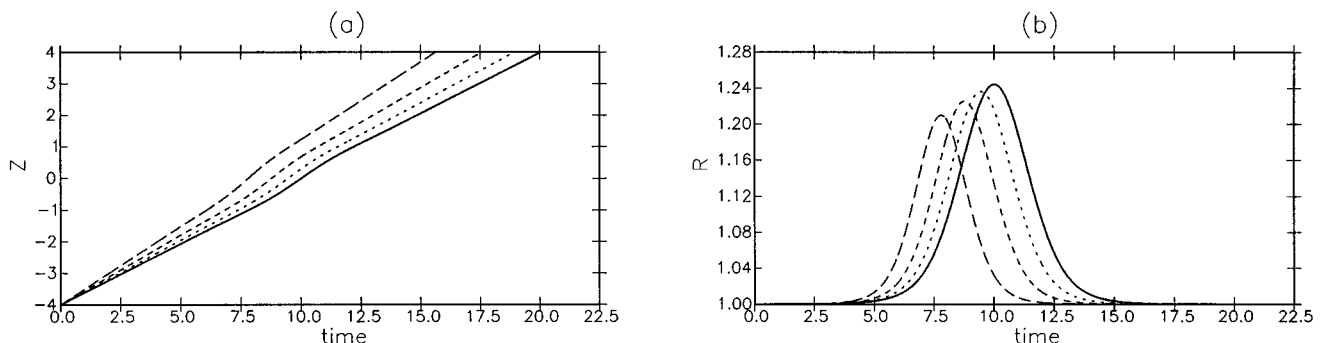
FIG. 2. Evolution of (a) the ring posistion and (b) the ring radius. The initial core radius $\sigma = 0.04$ (——), 0.03 (- - - -), 0.02 (– – –) and 0.01 (— —), and the initial ring radius $R = 1$.

Knio *et al.*: Interaction of vortex with sphere
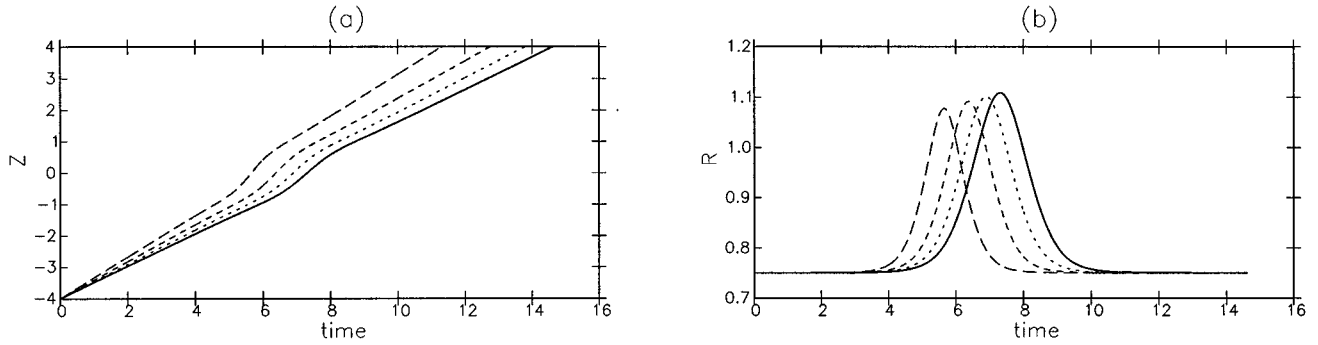
FIG. 3. Evolution of (a) the ring posistion and (b) the ring radius. The initial core radius $\sigma = 0.04$ (———), 0.03 (- - - -), 0.02 (– – –) and 0.01 (—— —), and the initial ring radius $R = 0.75$.

before discussing the simulations, we first provide a precise definition of reference quantities and of the corresponding dimensionless parameters.

A. Setup, scalings and parameters

As stated in the Introduction, the physical setup presently considered consists of a vortex ring of radius $\tilde{R}$, circulation $\tilde{\Gamma}$ and core size $\tilde{\delta}$ initially located ''upstream'' of sphere of radius $\tilde{a}$ (Fig. 1). A Cartesian (x,y,z) coordinate system is used whose origin coincides with the center of the sphere. The axis of the vortex ring is assumed to point along the z direction, and to intersect the y-axis at an offset distance o from the origin. We choose the sphere radius $\tilde{a}$ as reference lengthscale, i.e. $\tilde{L}_{ref} = \tilde{a}$, and use the circulation of the filament in defining the following reference velocity $\tilde{U}_{ref} = \tilde{\Gamma}/\tilde{a}$. With these definitions, the normalized circulation of the filament $\Gamma = 1$, and the Reynolds number $Re = \tilde{\Gamma}/\tilde{\nu}$. Following the same conventions, the normalized acoustic pressures defined in Section I B are related to their dimensional counterparts using

$$ p = \frac{\tilde{p}}{\tilde{\rho}_0 \tilde{\Gamma}^2/\tilde{a}^2} \tag{47} $$

and the Mach number $M = \tilde{\Gamma}/\tilde{a}\tilde{c}_0$. Here, $\tilde{\rho}_0$ and $\tilde{c}_0$ are the dimensional density and speed of sound of the undisturbed medium, respectively. Meanwhile, the normalized viscosity parameter used in the description of the core structure evolution is given by $K = \delta^{-2}\tilde{\nu}/\tilde{\Gamma} = 1/Re\ \delta^2$, where $\delta = \tilde{\delta}/\tilde{a}$ is the normalized physical core radius.

In all of the computations presented below, the core function used to regularize the vorticity field is $f(r) = \mathrm{sech}^2(r^3)$, with corresponding velocity kernel $\kappa(r) = \tanh(r^3)$ (Ref. 40) [see Eqs. (27) and (28)]. For this choice of core smoothing function, the numerical core structure coefficient $C^{ttm} = -0.4202$.[26] As discussed in Ref. 26, the effect core dynamics can be completely represented in terms of the parameter ε defined by:

$$ \varepsilon^2(t) - \ln(\varepsilon(t)) = \ln\left(\frac{2}{\sigma(t)}\right) + C^{ttm}. \tag{48} $$

Thus, having specified the core smoothing function and the corresponding value of C^{ttm}, the initial core structure of the

filament shall be described in terms of the initial value of σ only.

B. Axisymmetric interactions

When the axis of the circular vortex ring goes through the center of the sphere, the flow and the ring maintain their symmetry with respect to the ring axis. This physical setting has been used by Wang[52] to analyze the effect of diffusion on nonswirling vortex rings, and by Klein et al.[27] to study the evolution of the core structure of both swirling and non-swirling rings due to stretching and diffusion. Here, we exploit these well-known solutions to analyze the sound emitted during such interactions. As mentioned earlier, we focus here on nonswirling rings at high Reynolds number. Accordingly, the leading-order axial flow within the filament core is assumed to vanish identically, and the normalized viscosity parameter $K = 0$. Thus, the present axisymmetric problem essentially coincides with that of Miyazaki and Kambe,[44] who used this set up to briefly examine the effect of the initial ring radius on the behavior of the dipole and quadrupole strengths.

Simulations of axisymmetric passage events are performed for rings with initial radii $R_0 = 0.75$, 1, and 1.5, and initial core radii $\sigma_0 = 0.04$, 0.03, 0.02 and 0.01. For all four values of σ, the trajectories of the vortex rings are plotted in Fig. 2 for $R_0 = 1$, and in Fig. 3 for $R_0 = 0.75$. Results obtained for $R_0 = 1.5$ exhibit similar trends and are omitted.

Figures 2 and 3 show that in the initial stages the slender ring propagates under its self-induced velocity towards the sphere ($z = 0$). As the ring approaches the sphere, its radius stretches and its core size decreases. During the interaction of the sphere, the propagation speed of the ring increases due
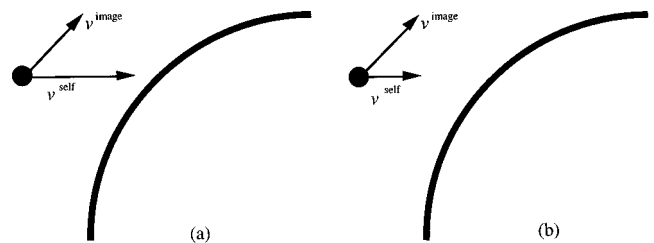
FIG. 4. Schematic illustration of the effect of the core size on the propagation velocity of an axisymmetric vortex ring in the neighborhood of a rigid sphere: (a) thin ring, (b) fat ring.
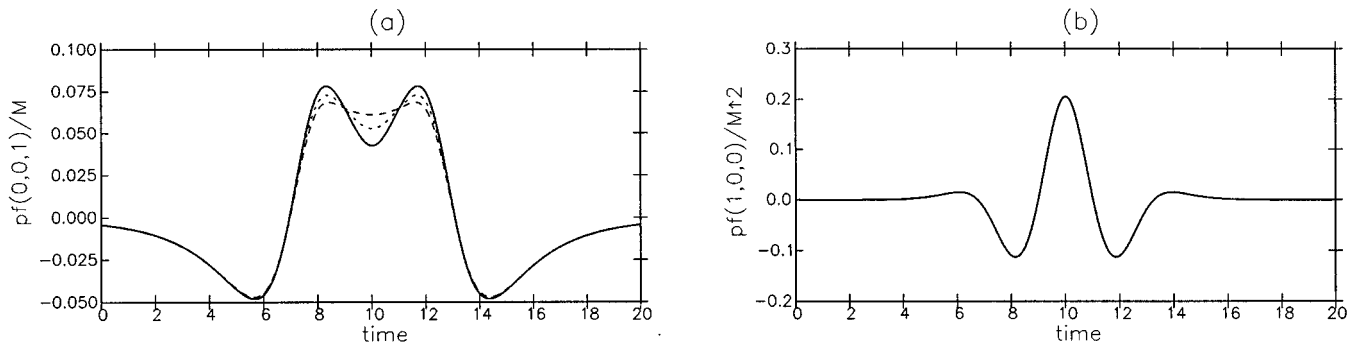
FIG. 5. Far-field noise emission along (a) the z axis and (b) the x axis for the axisymmetric passage of a vortex ring over a sphere: ——, $M = 0.05$; - - - -, $M = 0.025$; – – –, $M = 0.005$. Note that the far-field pressure p^R is scaled by M in (a) and by M^2 in (b). The initial ring radius $R = 1$ and the initial core size $\sigma = 0.04$.

to the combined effect of core thinning and of the velocity induced by its "image" within the sphere.[52,27] For the present range of parameters, the initial ring radius is comparable to that of the sphere, so that the overall stretching of the radius is modest. As a result, since viscous effects are ignored in the simulations of Figs. 2 and 3, variations in the core size are also modest. Consequently, these variations have a small effect on the ring propagation speed which depends on the core size in a logarithmic fashion. Thus, the acceleration that the ring experiences as it passes over the sphere is dominated by its interaction with its image, and the differences between the various cases are in large part due to the different initial conditions.

The dominant role of the image velocity during the interaction of the ring with the sphere enables us to provide a simple interpretation of the results which show that thinner rings tend to come closer to the surface of the sphere than thicker rings. Briefly, let us consider two rings having the same circulation and position but different core sizes. As mentioned earlier, the total velocity of the ring consists of the sum of the self-induced velocity and the velocity induced by the image of the ring within the sphere. The image velocity is independent of the core size of the filament, while the self-induced velocity increases as the core size decreases. Thus, the total velocity also depends on the core size, as schematically illustrated in Fig. 4. The sketch provides a clear explanation of the observed effects of the initial core size on the ring trajectory.

It is interesting to note that in the 2-D analogue of the present setup, which would consist of a pair of concentated point vortices passing symmetrically over a circular cylinder, the effect of the vortex core size would vanish identically. This observation underscores the role of the filament curvature and the need for accurate treatment of the core structure and its evolution. We also note that in the selected parameter range, the vortex rings remain well separated from the sphere surface, by a distance of at least several core radii. This justifies the present simplifying assumptions that viscous boundary layer effects can be ignored, and that the slender filament core vorticity structure remains, to leading order, axisymmetric.[27] It is also interesting to point out that, for the present inviscid computations, the slender vortex ring should "recover" its initial radius after it has completed its passage over the sphere. Since in the absence of diffusion the core

radius σ depends on the ring radius only (Section I A), σ should also return to its initial value. Thus, the ring is expected to return to its initial "state." One can easily observe from Figs. 2 and 3 that this is in fact the case for the present computations. This observation reflects the absence of numerical diffusion, which generally tends to produce an "irreversible" flow.[27]

The relative simplicity of the motion associated with the axisymmetric passage leads us to expect several trends in the acoustic far field. Specifically, since the impulse vector (D_i) is always aligned with the axis of the ring, one would expect that the acoustic dipoles have a fixed directivity along the z axis. Furthermore, since the strength of the dipoles scales as $O(M)$ while the contribution of the quadrupoles is $O(M^2)$, one would expect that the dipole emission is dominant, at least for emission directions that are closely aligned with the ring axis. In planes normal to this axis, however, the contribution of the dipoles vanishes identically, and one would thus expect a purely quadrupolar sound emission with acoustic pressure amplitudes scaling as $O(M^2)$. In addition, one
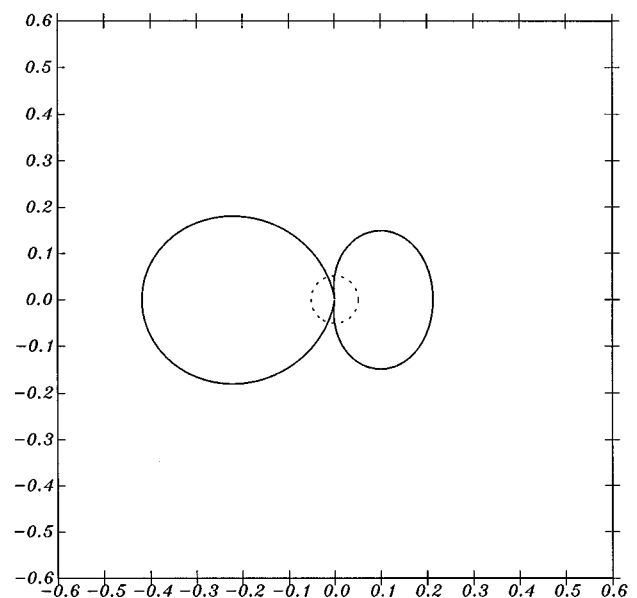
FIG. 6. Directivity of the acoustic far field for the axisymmetric passage of a vortex ring over a sphere: ——, z-y plane; - - - -, x-y plane. The magnitude of p^R is scaled by a factor of 100 in order to enhance the illustration.
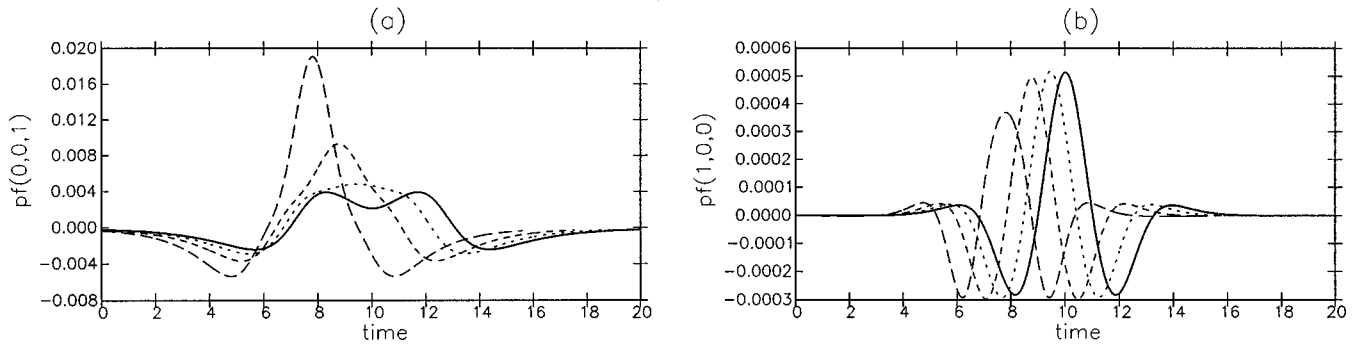
FIG. 7. Far-field noise emission along (a) the z axis and (b) the x axis for the axisymmetric passage events of Figure 2: ——, $\sigma = 0.04$; - - - -, $\sigma = 0.03$; – – –, $\sigma = 0.02$; —— ——, $\sigma = 0.01$. The Mach number $M = 0.05$.

would also expect that the quadupolar sound generation has characteristics that resemble those associated with the motion of vortex rings in free space (e.g. Refs. 17, 20, and 53), namely that the directivity of the quadrupoles is time-independent, with major axis along the z direction and uniform emission in the x-y plane. Moreover, since thinner rings complete the passage over the sphere faster than thicker rings (Figs. 2 and 3), one would expect that the far-field acoustic pressure amplitudes increase as the core size decreases.

For clarity of the presentation, we shall absorb the dependence of the far-field acoustic pressure on the distance of the observer by defining a reduced acoustic pressure $p^R \equiv 4\pi r p_a^F$. Using this definition, all the computed results on the far-field sound are presented by plotting p^R in lieu of p_a^F. However, we shall not distinguish between the two quantities in the discussion and refer to both simply as far-field pressure.

In order to examine these expected trends, we plot in Fig. 5 the evolution of the far-field acoustic pressure along the z and x directions for three values of the Mach number, $M = 0.005$, 0.025, and 0.05. Figure 5(b) shows that when scaled by M^2, the far-field acoustic signals along the x axis collapse onto a single curve. This confirms our earlier expectation that emission along the x axis consists of quadrupoles only. Meanwhile, Fig. 5(a) shows that when scaled by the Mach number M, the acoustic pressure signals along the z axis are close to each other, but noticeable differences exist during the passage of the ring over the sphere. The differences between the curves are small, and occur so that the

humps of the pressure signal are amplified as the Mach number increases. These observations are consistent with our earlier expectation that along the z axis the dipole contribution is dominant, and that quadrupoles have a weak modulating effect on the sound emission for this direction. These trends are further examined in Fig. 6 which depicts the directivity of the acoustic far field for $M = 0.05$. This figure illustrates the dominant role of the dipole emission along the axis of the slender vortex ring, and the uniform quadrupole emission in the x-y plane.

The effects of the core size are analyzed in Figs. 7 and 8, which depict the evolution of p^R for slender axisymmetric rings with initial radii $R_0 = 1$ and $R_0 = 0.75$, respectively. Consistent with our earlier expectation, Figs. 7(a) and 8(a) show that as the core radius decreases the acoustic emission along the z axis increases substantially. However, the results reveal a number of curious trends that are rather counterintuitive. Specifically, as the core radius decreases, the acoustic pressure signal along the z axis [Figs. 7(a) and 8(a)] changes from a pulse with two humps to a narrow single-peak spike. Detailed examination of the data indicates that this change is due to the previously discussed dependence of the trajectory of the slender ring on the initial value of σ. Thus, as can be appreciated from Figs. 7(a) and 8(a), small changes in the core size and filament trajectory can have a significant impact on the details of the acoustic far field.

Figures 7(b) and 8(b) show that as σ decreases the acoustic pressure signals along the x direction maintain a similar shape, but that the pressure amplitudes decrease. This result is in disagreement with our earlier expectation that
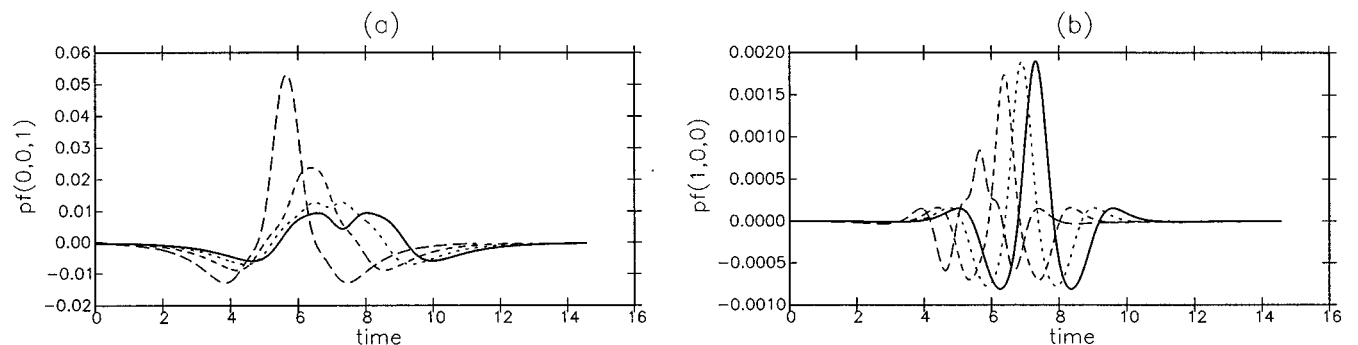
FIG. 8. Far-field noise emission along (a) the z axis and (b) the x axis for the axisymmetric passage events of Figure 3: ——, $\sigma = 0.04$; - - - -, $\sigma = 0.03$; – – –, $\sigma = 0.02$; —— ——, $\sigma = 0.01$. The Mach number $M = 0.05$.
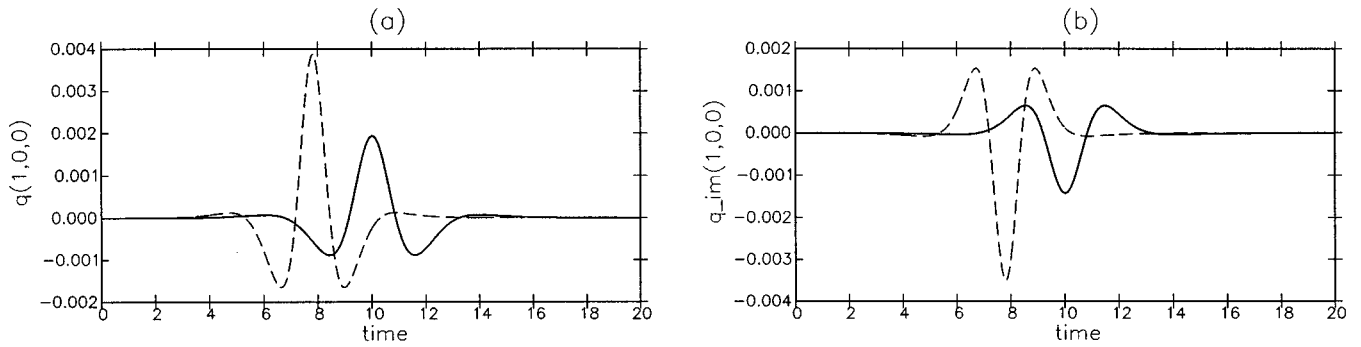
FIG. 9. Contributions to the quadupole noise from (a) the filament vorticity, q_{11}, and (b) the ''image'' vorticity, q_{11}^{im}, for the axisymmetric passage of a vortex ring whose initial radius $R=1$: ——, $\sigma=0.04$; — —, $\sigma=0.01$. The Mach number $M=0.05$.

more rapid interactions tend to produce stronger acoustic signals. In order to examine the origin of this phenomenon, we examine in Fig. 9 the contributions of the filament vorticity and of its ''image'' to the total quadrupole emission along the x axis. Specifically, Fig. 9(a) and (b) shows the evolution of the components q_{11} and q_{11}^{im} for two values of the initial core size, $\sigma=0.04$ and 0.01. Note that the sum of these components yields the total quadrupole strength which governs for emission along the x axis. Figure 9 shows that as the core radius decreases, the magnitudes of q_{11} and q_{11}^{im} increase. However, as σ decreases, the tendency of the two signals is to assume equal and opposite values. Consequently, the trend observed in Figs. 7(b) and 8(b) can be traced to opposing contributions from the filament vorticity and its image, and to a more effective cancellation between them. The occurrence of this phenomenon is consistent with the above discussion of the dynamics of the slender filament, which shows that thinner vortices tend to come closer to the surface of the sphere and consequently to their image. The present results also underscore the important role that the core structure can play, both regarding the dynamics of the filament and the associated sound generation.

C. Three-dimensional interactions

We now turn our attention to 3-D filament/sphere interactions, and focus in this section on the passage of non-axisymmetric rings over the rigid sphere. Specifically, we generalize the setup of the previous section by imposing at the start of the computations a single-mode helical perturbation to the filament center line.[20] The perturbation is specified in terms of its wave number k and (dimensionless) ''amplitude'' ϵ', and is applied in such a way that the filament centerline is initially described by

$$\chi_1(\theta') = R(1+\epsilon')\sin(k\theta')\cos(\theta'),$$

$$\chi_2(\theta') = R(1+\epsilon')\sin(k\theta')\sin(\theta'), \qquad (49)$$

$$\chi_3(\theta') = \epsilon' R \cos(k\theta') + z_i,$$

where θ' is the azimuthal angle, $0 \leq \theta' \leq 2\pi$, and z_i is the original undisturbed position of the center of the ring. In the computations, we consider perturbations with three different wavenumbers $k=1$, 2 and 8, and two different amplitudes $\epsilon'=0.01$ and 0.1, and restrict the analysis to slender rings

with initial core radius $\sigma_0=0.06$, and unperturbed mean radius $R_0=1.5$.

As the ring propagates under its own self-induced velocity, the helical perturbations travel around its circumference. Since the perturbations have small (but finite) amplitudes, their evolution does not significantly alter the broad features of the propagation of the slender ring nor its passage over the sphere. Thus, the objective of the present computations is to determine whether the evolution of the helical waves affects the sound emission, and if so, to quantify the associated effects as a function of the properties of the waves. In particular, due to the moderate amplitudes, the spinning of the waves occurs at a frequency that is in large part determined by the wave number (e.g. Ref. 25). Thus, an interesting issue is the investigation of waves whose frequencies are higher than or comparable to the ''frequency'' of the passage event itself. This motivates our selection of the different wave numbers specified above, as will be evident shortly.

Figure 10 shows the evolution of the far-field pressure p^R for a vortex ring perturbed using a helical wave with $k=8$ and $\epsilon'=0.01$. The figure shows that the present perturbation has a weak effect on the far-field pressure amplitude. The effect of the helical wave is more pronounced in Fig. 10(b) and (d), which depict the evolution of the far-field pressure along the x axis for $M=0.05$ and $M=0.005$, respectively. These plots clearly reflect the spinning of the wave, whose characteristic period is substantially smaller than the interaction time between the ring and the sphere. Furthermore, comparison of Fig. 10(b) and (d) indicates the effect of the waves on the acoustic pressure along the x axis is proportional to the square of the Mach number, thus suggesting that the present perturbation affects the evolution of the quadrupoles only. Further examination of the results (not shown) indicates that this is in fact the case. Specifically, the computations show that the dipole vector remains aligned with the ring axis and that its amplitude does not appear to be affected by the evolution of the perturbation. Thus, one would expect that for the present small-amplitude perturbation, the far-field emission along the z axis remains dominated by the contribution of the dipoles. Not surprisingly, the pressure signals of Fig. 10(a) and (c) show only small departures from the axisymmetric prediction, which consist of weak ondulations at the same frequency of the helical wave. The ondulations are easier to detect prior to and following
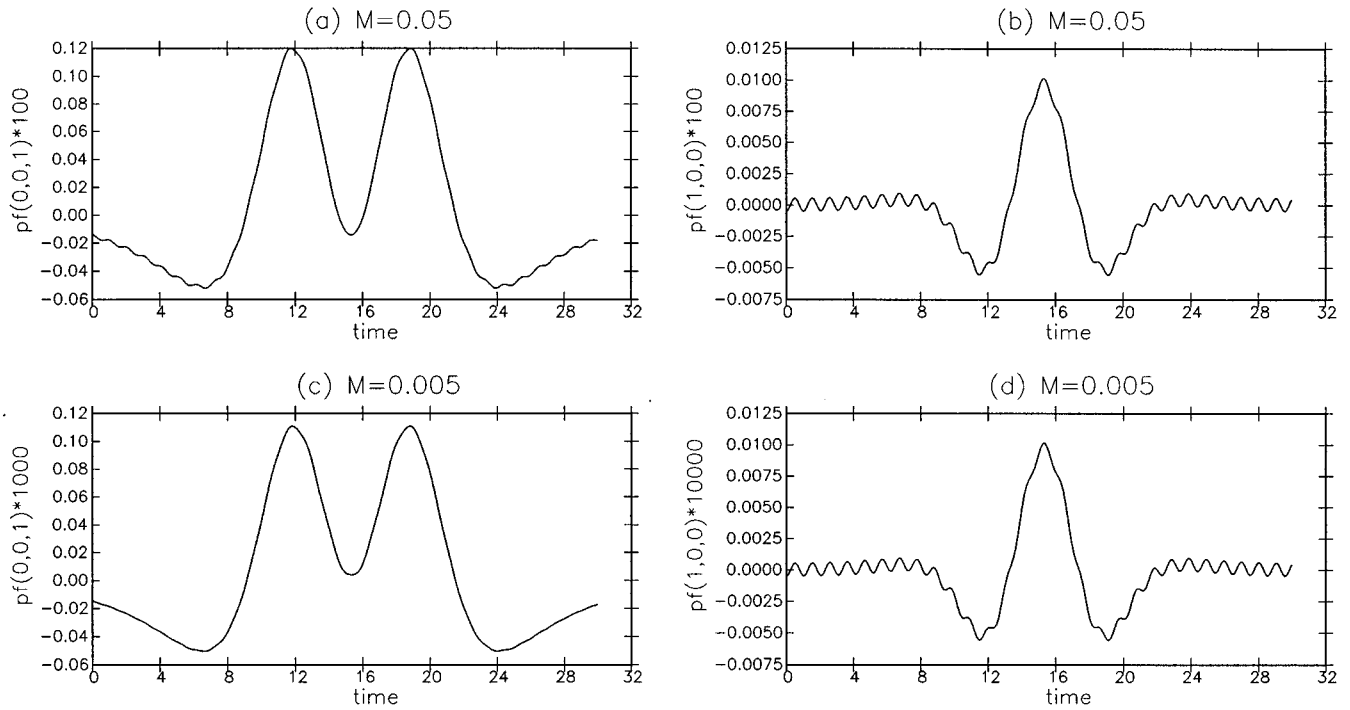
FIG. 10. Evolution of the far-field pressure p^R during the passage of a 3-D vortex ring over a rigid sphere. The initial ring radius $R = 1.5$, and core radius $\sigma = 0.06$. The center line of the ring is initially perturbed with a helical mode with $k = 8$ and $\epsilon' = 0.01$. The plots show the far-field emission along the z axis (a,c) and the x axis (b,d). The value of the Mach number M is indicated.

the passage of the ring over the sphere and, as expected, become more pronounced as M increases.

The situation described above is dramatically altered as the amplitude of the perturbation is increased, as illustrated in Fig. 11. The latter shows that for a helical perturbation with $k = 8$ and $\epsilon' = 0.1$, the *quadrupolar* emission associated with the helical wave can dominate the sound emission. Specifically, the pressure signal along the x axis is overwhelmed by the effect of the perturbation [Fig. 11(b) and (d)]. In addition, for the present wave amplitude, the amplitude of the
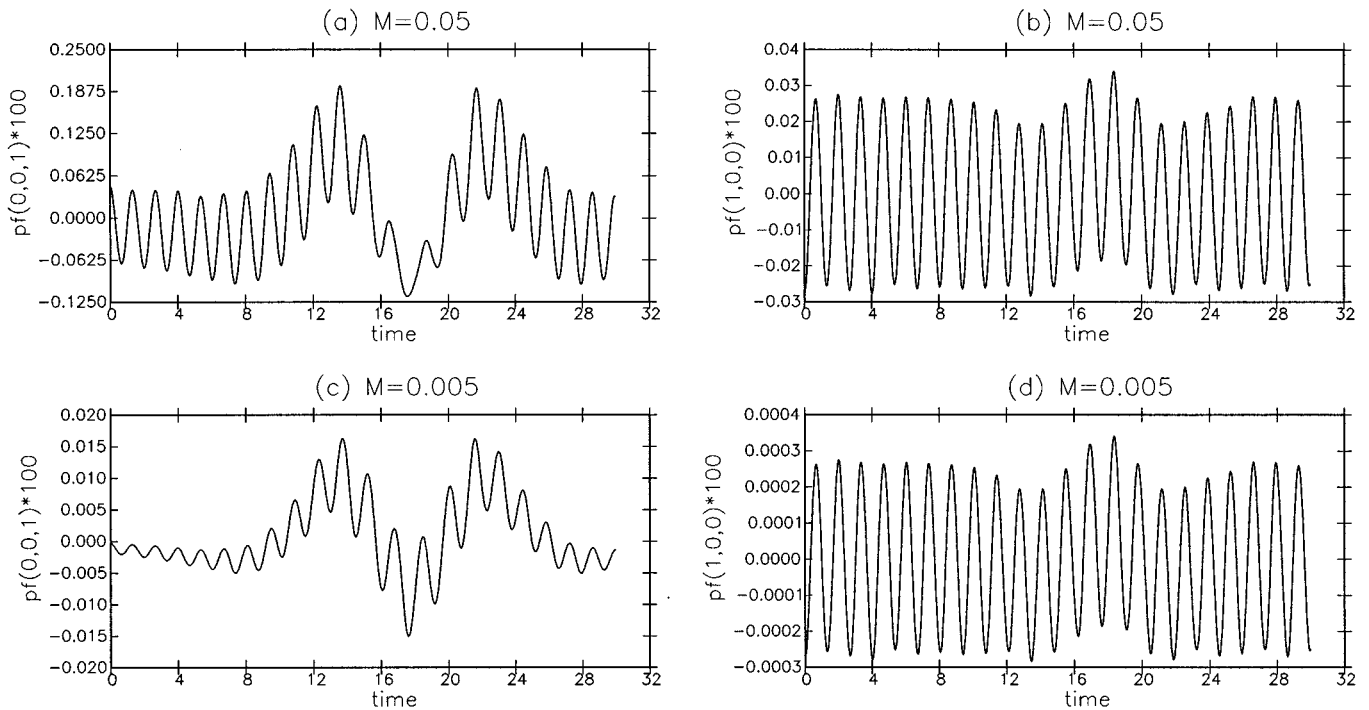
FIG. 11. Evolution of the far-field pressure p^R during the passage of a 3-D vortex ring over a rigid sphere. The initial ring radius $R = 1.5$, and core radius $\sigma = 0.06$. The center line of the ring is initially perturbed with a helical mode with $k = 8$ and $\epsilon' = 0.1$. The plots show the far-field emission along the z axis (a,c) and the x axis (b,d). The value of the Mach number M is indicated.
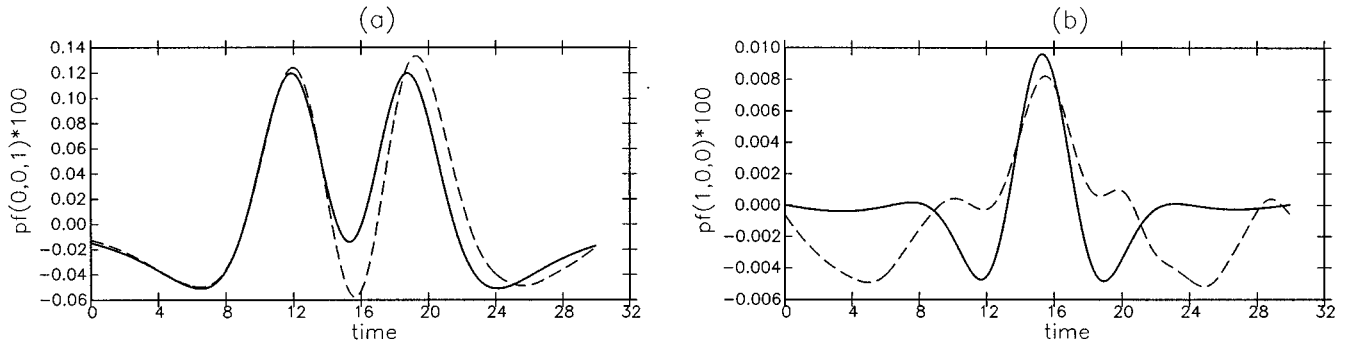
FIG. 12. Evolution of the far-field pressure p^R during the passage of a 3-D vortex ring over a rigid sphere. The initial ring radius $R = 1.5$, and core radius $\sigma = 0.06$. The plots show the far-field emission along (a) the z axis and (b) the x axis. The center line of the ring is initially perturbed with a helical mode with $k = 2$: ——, $\epsilon' = 0.01$; — —, $\epsilon' = 0.1$. The Mach number $M = 0.05$.

quadrupole sound becomes comparable to that of the dipole sound. As shown in Fig. 11(a) and (c), the "underlying" dipole emission due to the interaction of the filament with the sphere can be hidden by the effect of the perturbation. Naturally, the observed "competition" between dipole and quadrupole sound is dependent on the Mach number. The role of the quadrupoles becomes relatively more important as M increases but nonetheless may not be ignored even at low Mach numbers.

We now consider a helical perturbation with larger pitch, starting with waves having $k = 2$ and amplitudes $\epsilon' = 0.01$ and 0.1. Results of the computations are plotted in Fig. 12 which shows, for both wave amplitudes, the evolution of p^R along (a) the z axis and (b) the x axis. The results show that for the present wave number, the characteristic period of the perturbation is comparable to that of the passage event. In these situations, we find that for observer lo-

cations that are significantly affected by the dipole emission, the role of the perturbation is restricted to a moderate modulation of the acoustic pressure signal [Fig. 12(a)]. On the other hand, for emission directions for which quadrupole sound is dominant [Fig. 12(b)], the perturbation can still significantly affect the acoustic far field.

Results obtained using mode-1 helical perturbations reveal many similarities to those obtained with $k = 2$, and also some unexpected differences. The evolution of the far-field acoustic pressure p^R is shown in Fig. 13 for a perturbation having $k = 1$ and $\epsilon' = 0.1$. The pressure signals show that, similar to the effect of mode-2 perturbations, the evolution of the helical wave leads to a modulation of sound emission along both the z and x axes. However, unlike the mode-2 case, it is now observed that the acoustic pressure along the x axis is comparable amplitude to the emission along the z axis. Furthermore, examination of the results in Fig. 13(c)
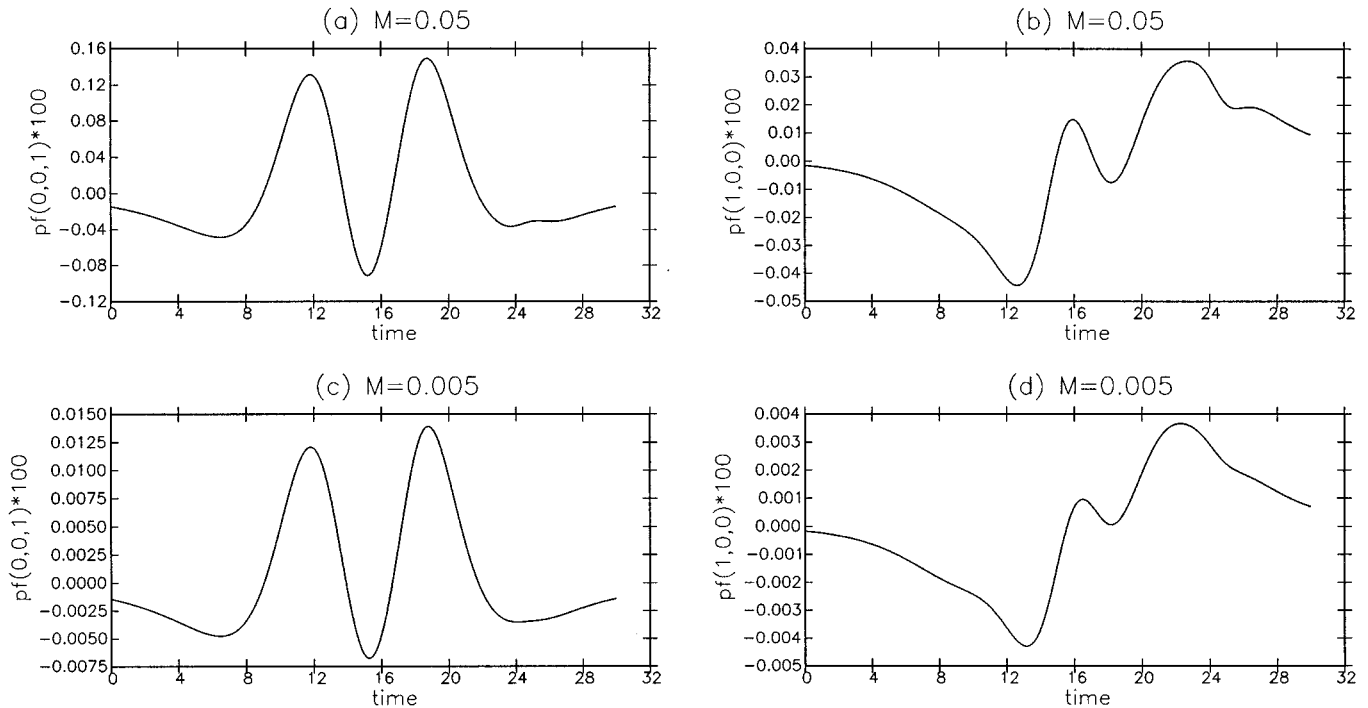
FIG. 13. Evolution of the far-field pressure p^R during the passage of a 3-D vortex ring over a rigid sphere. The initial ring radius $R = 1.5$, and core radius $\sigma = 0.06$. The center line of the ring is initially perturbed with a helical mode with $k = 1$ and $\epsilon' = 0.1$. The plots show the far-field emission along the z axis (a,c) and the x axis (b,d). The value of the Mach number M is indicated.
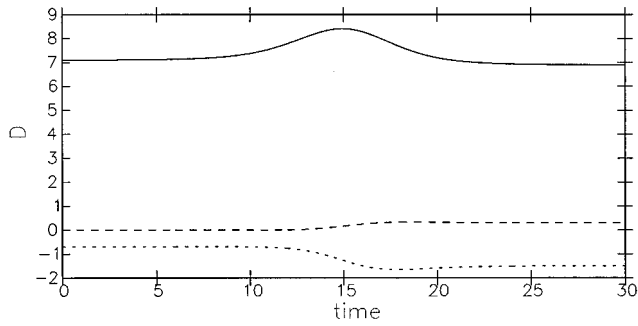
FIG. 14. Evolution of the dipole vector for the ring of Fig. 13: - - - -, D_1; – – –, D_2; ——, D_3.

and (d) indicates that the acoustic pressure along the x axis no longer follows the $O(M^2)$ dependence that characterizes quadrupole emission. Detailed examination of the results reveals that the origin of this phenomenon is due to asymmetry of the perturbation. As a result of this asymmetry, the ring is initially slightly tilted towards the x direction, and its interaction with the sphere occurs in such a way the dipole vector is gradually displaced from its initial position. As shown in Fig. 14, the dipole vector initially has a major component along the z direction and admits a small but finite component along the x direction. During the passage, all the components of the dipole vector change in a time-dependent fashion and, unlike the axisymmetric case, the ring does not return to its initial state. In particular, the results in Fig. 14 clearly show that during the interaction a net (finite) momentum is transferred to the fluid. These observations enable us to relate the behavior of the acoustic pressure signals in Fig. 13(b) and (d) to the time-dependent directivity of the dipole emission.

D. Asymmetric interactions and effect of viscosity

In order to isolate and further analyze the properties and effects of asymmetric filament/sphere interactions, we consider in this section the noncoaxial passage of an initially circular slender ring. Specifically, we focus on a single initial condition consisting of a vortex ring of radius $R_0 = 1.5$ that is initially centered at $(0, 0.4, -4)$. With respect to Figure 1, the axis of the ring is displaced in the y direction by an offset $o = 0.4$. We assume that the ring has a self-similar Gaussian core structure,[28,27] with numerical core size $\sigma = 0.06$. Following the discussion in Sections I A and II A, the initial physical core size $\delta = \sigma(0)/\exp(C^{\text{ttm}} - C(0)) = 0.05228$ [see Eq. (29)]. We compare results of an inviscid computation to predictions obtained using the same initial conditions but with diffusivity $K = 0.1$ and $K = 0.3$ which, based on the normalization convention in Section II A, correspond to Reynolds numbers $\text{Re} \equiv \widetilde{\Gamma}/\widetilde{\nu} = 3659$ and 1220, respectively.

In the computation of filaments with viscous cores, we still rely on expressions (38) and (45) for the prediction of sound emission. Thus, the formulation is not altered in order to account for the effects of monopole radiation.[9,17] This simplification facilitates the analysis of the acoustic far-field and enables straightforward comparison of the different cases. For the present setup, it also constitutes a reasonable
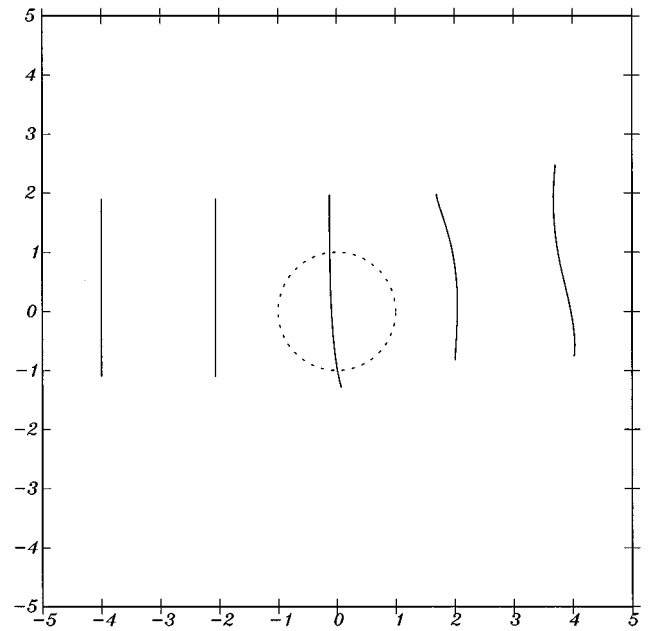
FIG. 15. Projections of the vortex ring on the y-z plane at different instances of time. The surface of the sphere is indicated using a dashed line. The results are obtained using an inviscid computation of a slender ring initially having $R = 1.5$, $\sigma = 0.06$, and located at $(-4, 0, 0.4)$.

approximation since the vortices are mildly stretched and the Reynolds number is high.[54]

Figure 15 shows the projection of the ring center line on the y-z plane for a simulation with $K = 0$. The figure shows that as the ring passes over the sphere its centerline is deformed, such that elements that come closer to the sphere surface acquire a larger velocity than those further away. As a result, the centerline of the vortex ring is no longer axisymmetric, but symmetry with respect to the y-z plane is maintained. The results also indicate that the trajectory of the center of the ring is deflected during the interaction. Initially, the ring propagates along the z axis and, once the passage over the sphere is completed, the self-induced velocity is tilted towards the y axis. The deflection of the trajectory of the center of the ring is examined further in Fig. 16 for all three cases considered. The results show that for $K = 0$, the deflection of the trajectory is roughly 15°. As the normalized viscosity is increased to $K = 0.3$ the deflection angle increases to approximately 17°, i.e., it changes by more than 10%. Thus, the effect of viscosity is noticeable, but moderate.

The symmetry of the flow with respect to the y-z enables us to easily interpret the evolution of dipole vector, whose component along the x axis vanishes identically. The evolutions of the z and y components of the dipole vector are shown in Fig. 17(a) and (b), respectively, for $K = 0, 0.1$ and 0.3. Figure 17(a) shows that the z component of the dipole vector increases as the filament is stretched during the passage over the sphere, and then decreases as the arc length shrinks and the trajectory of the center of the ring is deflected. Note that D_3 does not return to its initial value once the passage is completed; instead it assumes a slightly smaller value, with the magnitude of the difference increasing as the Reynolds number decreases. Meanwhile, the over-
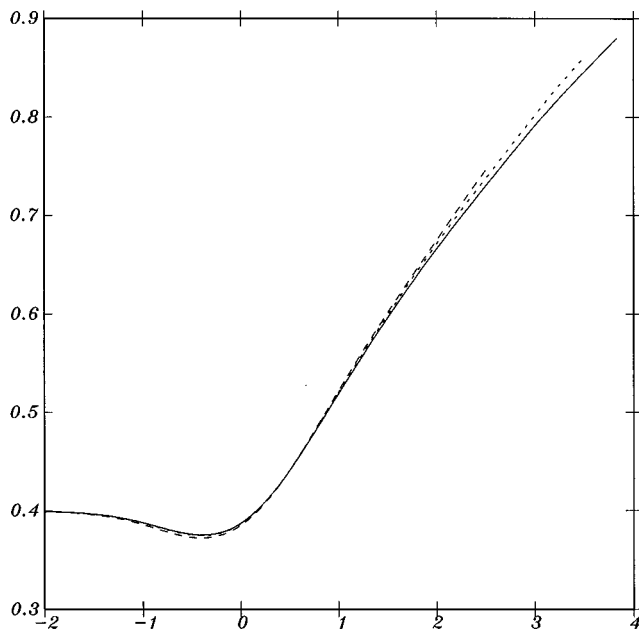
FIG. 16. Trajectories of the center of the vortex ring for an asymmetric passage with $o=0.4$: ——, $K=0$ (inviscid); - - - -, $K=0.1$; – – –, $K=0.3$.

all trend in the evolution of D_2 is generally increasing with time. The evolution curves of D_2 exhibit a slight dip at the start of the passage and a more pronounced overshoot towards the end of the interaction, the magnitude of which increases as Re decreases. These observations suggest that the evolution of the dipole is governed by two, at times competing, effects: the stretching of the ring centerline and the deflection of its trajectory. It is interesting to note the similarity between the evolution of the dipole vector and earlier observations of the motion of the ring, and that, consistent with these observations, the amplitude of the changes in the dipole vector are noticeably more pronounced as viscosity increases.

Following the discussion of the previous section, computed results on the dynamics of the filament lead us to expect a number of trends in the far-field sound. In particular, due to the tilting of the dipole vector towards the y-axis, one would expect that emission along this direction would now be dominated by dipole sound. However, the effects of the (small) viscosity are hard to guess. On one hand, as discussed above, viscous effects tend to increase the variations

of the vorticity moments. On the other hand, viscous effect tend to slow down the time scales over which these variations occur. This dual role makes it difficult to predict what the net effect on sound generation is.

To examine this issue, we plot in Fig. 18 the evolution of the far-field acoustic pressure along the x, y, and z directions, for all values of K considered and Mach numbers $M=0.05$ and 0.005. The results show that, as expected, the acoustic pressure signals along the y and z directions are dominated by dipole sound, while emission along the x axis is due to quadrupoles only. The pressure curves in Fig. 18(a)–(d) indicate that viscous effects lead to a slight increase in the amplitude of the dipole sound, and result in more significant variations than one would anticipate based on the ring dynamics. Meanwhile, the acoustic pressure amplitudes associated with the quadrupoles [Fig. 18(e) and (f)] are less affected by viscosity. The pressure curves in Fig. 18(e) and (f) have similar shapes and assume very close values, and the major effect of viscosity is an increase in the characteristic time of the pressure variations. The present observations also underscore the effect of the core structure evolution on the filament motion, and its potentially large impact on sound generation.

III. CONCLUSIONS

Sound generation by the interaction of slender vortex filament with a rigid sphere are analyzed using a vortex element scheme that tracks the motion of the filament centerline. The scheme is based on the discretization of the filament center line into Lagrangian particles, and transport of these particles according to the self-induced velocity and the potential velocity field due to the sphere. The self-induced velocity is estimated using a desingularized Biot–Savart law which reflects the correct asymptotic behavior of the core structure and its evolution due to stretching and diffusion. Meanwhile, the contribution of the sphere to the motion of filament is evaluated using an analytical formula which expresses the potential velocity as a line integral along the image of the filament center line with regular weight functions. Based on the far-field behavior of the velocities induced by the filament and its image, expressions for the acoustic far field are obtained. In particular, the interaction of the filament with the sphere generates an acoustic pressure field that
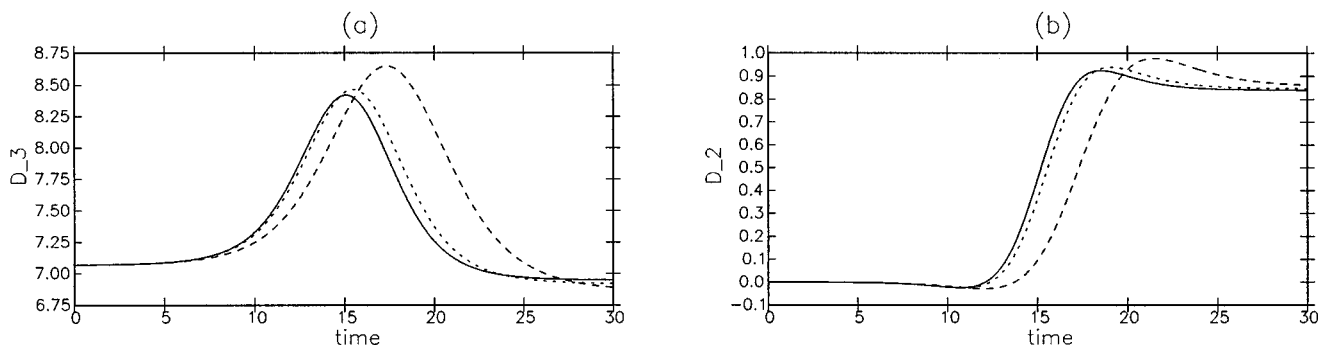
FIG. 17. Evolution of (a) D_3 and (b) D_2 for asymmetric passage with $o=0.4$: ——, $K=0$ (inviscid); - - - -, $K=0.1$; – – –, $K=0.3$.
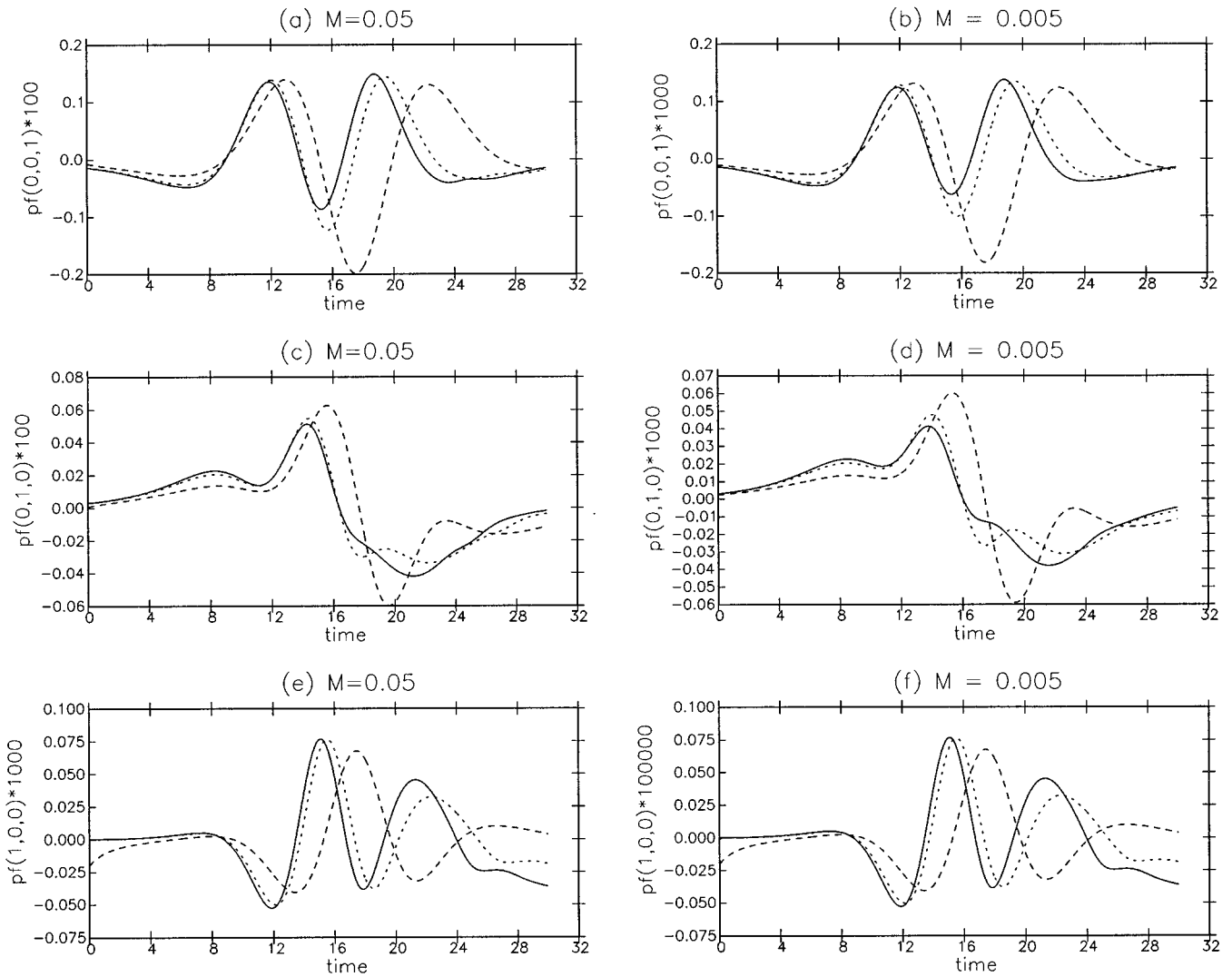
FIG. 18. Evolution of the far-field pressure p^R along the x, y, and z axes for asymmetric passage with $o = 0.4$: ———, $K = 0$ (inviscid); - - - -, $K = 0.1$; – – –, $K = 0.3$. The value of the Mach number is indicated.

is dominated by dipoles and quadrupoles, whose strengths correspond to the weighted first and second moments of vorticity, respectively.

The computational model is first applied to study sound generation during the axisymmetric passage of a slender vortex ring over the sphere. Computed results show that for axisymmetric passage events the directivity of the far-field pressure is independent of time, and reflects a dipole emission along the axis of the ring and quadrupole emission with major axis along the propagation direction and minor axis along the primary normal of the ring. The dipole emission is found to be dominant and both the shape and amplitude of the corresponding pressure signal depend strongly on the initial vortex core size.

Three-dimensional passage events are next considered, and simulations of slender rings whose center line is initially perturbed with a helical wave are performed. For moderate amplitude and high wave number, the motion of the wave around the center line generates strong quadrupole sound whose amplitude is comparable to the dipole noise. At small

amplitude or smaller wave number, the dipole sound is once again dominant, but the quadrupole emission due to the spinning of the helical wave still has a noticeable effect on the acoustic signal. It is also shown that for a mode-1 wave, the perturbation results in tilting of the dipole vector. Consequently, the trajectory of the ring is deflected during the interaction of the sphere and the directivity of the dipole emission becomes time dependent. This phenomenon is also observed during simulations of noncoaxial rings. The latter also show that viscous diffusion within the slender vortex core significantly affects the dynamics of the filament and has a substantial impact on the resulting sound generation.

Consistent with the approximations used in the construction of the model, the applications are restricted to a flow regime where boundary layer effects, axial core structure variations and nonaxisymmetric core deformation can be ignored. Extensions of the present approach to capture these phenomena and analyze their effect on sound generation are currently being contemplated.

[1] B. E. Mitchell, S. K. Lele, and P. Moin, J. Fluid Mech. **285**, 181–202 (1995).

[2] M. J. Lighthill, Proc. R. Soc. London, Ser. A **222**, 1–32 (1954).

[3] A. Powell, J. Acoust. Soc. Am. **36**, 177–195 (1964).

[4] A. Powell, J. Acoust. Soc. Am. **32**, 982–990 (1960).

[5] J. E. Ffowcs Williams and D. C. Hawkings, Philos. Trans. R. Soc. London, Ser. A **264**, 321–342 (1969).

[6] M. S. Howe, J. Fluid Mech. **67**, 596–610 (1975).

[7] W. Möhring, J. Fluid Mech. **85**, 685–691 (1977).

[8] F. Obermeier, J. Sound Vib. **72**, 39–49 (1980).

[9] L. Ting and M. J. Miksis, SIAM (Soc. Ind. Appl. Math.) J. Appl. Math. **50**, 521–536 (1990).

[10] M. S. Howe, Proc. R. Soc. London, Ser. A **420**, 157–182 (1988).

[11] M. S. Howe, J. Acoust. Soc. Am. **94**, 2353–2364 (1993).

[12] Y. Kimura, I. Zawadki, and A. Aref, Phys. Fluids A **2**, 214–220 (1990).

[13] O. M. Knio, L. Collorec, and D. Juvé, J. Comput. Phys. **116**, 226–246 (1995).

[14] M. S. Howe, J. Sound Vib. **156**, 303–325 (1992).

[15] K. Shariff, A. Leonard, N. Zabusky, and J. Ferziger, Fluid Dyn. Res. **3**, 337–343 (1988).

[16] S. K. Tang and N. W. M. Ko, J. Acoust. Soc. Am. **98**, 3418–3427 (1995).

[17] T. Kambe, J. Fluid Mech. **173**, 643–666 (1986).

[18] C. C. Chang and T. L. Chen, Proc. R. Soc. London, Ser. A **445**, 141–155 (1994).

[19] W. Möhring, J. Sound Vib. **140**, 155–162 (1990).

[20] O. M. Knio and D. Juvé, C. R. Acad. Sci. Paris Ser. II **322**, 591–600 (1996).

[21] R. J. Arms and F. R. Hama, Phys. Fluids **8**, 533–559 (1965).

[22] L. S. Da Rios, Rend. Circ. Mater. Palermo **22**, 117–135 (1906).

[23] H. Hasimoto, J. Fluid Mech. **51**, 477–485 (1972).

[24] R. Klein and A. J. Majda, Physica D **49**, 323–352 (1991).

[25] R. Klein and A. J. Majda, Physica D **53**, 267–294 (1991).

[26] R. Klein and O. M. Knio, J. Fluid Mech. **284**, 275–321 (1995).

[27] R. Klein, O. M. Knio, and L. Ting, Phys. Fluids **8**, 2415–2425 (1996).

[28] R. Klein and L. Ting, Appl. Math. Lett. **8**, 45–50 (1995).

[29] R. Klein and L. Ting, J. Appl. Math. Phys. (ZAMP) **41**, 395–418 (1990).

[30] O. M. Knio and L. Ting, SIAM J. Appl. Math. **57**, 972–981 (1997).

[31] G. Pedrizetti, J. Fluid Mech. **245**, 701–722 (1992).

[32] M. S. Howe, J. Fluid Mech. **329**, 89–101 (1996).

[33] T. Vitting, *Struktur von Randwirbeln und Maßnahmen zur Wirbelabschwächung* (VDI Verlag, Düsseldorf, Germany, 1991).

[34] M. Van Dyke, *An Album of Fluid Motion* (Parabolic, Standford, CA, 1982).

[35] H. J. Lugt, *Vortex Flow in Nature and Technology* (Wiley, New York, 1983).

[36] G. K. Batchelor, *An Introduction to Fluid Dynamics* (Cambridge U. P., Cambridge, UK, 1967).

[37] A. Callegari and L. Ting, SIAM J. Appl. Math. **15**, 148–175 (1978).

[38] G. Kleinstein and L. Ting, J. Appl. Math. Mech. (ZAMM) **51**, 1–16 (1971).

[39] O. M. Knio and A. F. Ghoniem, J. Comput. Phys. **86**, 75–106 (1990).

[40] J. T. Beale and A. Majda, J. Comput. Phys. **58**, 188–208 (1985).

[41] P. Weiss, Proc. Cambridge Philos. Soc. **40**, 259–261 (1944).

[42] M. J. Lighthill, Proc. Cambridge Philos. Soc. **452**, 317–321 (1956).

[43] L. Ting and R. Klein, *Viscous Vortical Flows* (Springer-Verlag, Berlin, 1991).

[44] T. Miyazaki and T. Kambe, Phys. Fluids **29**, 4006–4015 (1986).

[45] J. Wells, Phys. Fluids **8**, 442–450 (1996).

[46] M. J. Lighthill, *Waves in Fluids* (Cambridge U. P., Cambridge, UK, 1978).

[47] M. S. Howe, J. Fluid Mech. **71**, 625–673 (1975).

[48] N. Curle, Proc. R. Soc. London, Ser. A **231**, 505–514 (1955).

[49] J. J. Moreau, C. R. Acad. Sci. Paris **229**, 1420–1422 (1948).

[50] A. Powell, J. Acoust. Soc. Am. **97**, 1534–1537 (1995).

[51] A. Powell, J. Acoust. Soc. Am. **97**, 684–686 (1995).

[52] H.-C. Wang, ''The Motion of a Vortex Ring in the Presence of a Rigid Sphere,'' Annual Report of the Institute of Physics, Academia Sinica, Taiwan, 85–93 (1970).

[53] K. Pothou, S. G. Huberson, S. G. Voutsinas, and O. M. Knio, ESAIM Proceedings **1**, 349–362 (1996).

[54] A. Iafrati and G. Riccardi, J. Sound Vib. **196**, 129–146 (1996).

Waves in elastic and anelastic stratified microstructure: A numerical comparison

Lawrence H. Le
Division of Imaging Sciences, Department of Radiology and Diagnostic Imaging, 2A2.42 Walter C. Mackenzie Health Sciences Centre, The University of Alberta, Edmonton, Alberta T6G 2B7, Canada

Robert Burridge
Schlumberger-Doll Research, Old Quarry Road, Ridgefield, Connecticut 06877

Burridge *et al.* [J. Acoust. Soc. Am. **94**, 2884–2894 (1993)] presented a fast algorithm to compute wave propagation through a stack of finely layered elastic or anelastic microstructure. The method goes beyond previous work in two aspects: (a) the sample autocorrelation is used so that the coda of the computed response is preserved; and (b) the anelastic effect due to intrinsic attenuation is incorporated and by *order-of-magnitude* argument, the terms governing the scattering and anelastic effects enter separately but in a similar way. The present work is a numerical justification of the perturbation theory. Using a standard linear solid model with a single Debye relaxation mechanism, a finely layered microstructure was made anelastic. Using the *SH* case as an example, impulse responses were computed using two methods: the approximate method and an exact method for both elastic and anelastic media at normal and oblique angles of incidence. The impulse responses obtained by the two methods agree well for both elastic and anelastic cases. The results of the investigation can be summarized in several points: (a) accuracy is best for the head of the pulse; (b) the presence of anelasticity increases the time delay and dispersion of the broad pulse; and (c) the perturbation code is 30–54 times faster than the exact code. © *1998 Acoustical Society of America.* [S0001-4966(98)04301-X]

PACS numbers: 43.20.Bi, 43.40.Ph [ANN]

INTRODUCTION

The Earth's crust is intrinsically dissipative and varies greatly in spatial scales. For plane-stratified subsurface models, it has been shown by many authors[1–4] that small scale variation gives rise to the apparent attenuation of the transmitted wavefield. The short-path intrabed multiples can cause pulse-broadening and time delay due to loss of coherence of energy. The phenomena are widely observed in field data[5,6] and known, in the geophysical literature, as stratigraphic filtering and seismic drift leading to the travel time discrepancy between sonic logs and seismic surveys. Similar attenuative and dispersive effects are also caused by the intrinsic absorption and the associated velocity dispersion of the Earth's material. However, the relative contribution of intrinsic absorption and multiple elastic scattering to the character of seismograms remains uncertain since it is difficult to separate the two effects in the analysis.[7]

In their previous work, Burridge and Chang[8] studied the dispersive wave propagation for an impulsive pulse propagating normally or obliquely through a one-dimensional microstructure consisting of a large number of elastic homogeneous and isotropic layers. Immediately following the directly transmitted arrival is a broad pulse. The dispersive effect, in this case, is due to multiple scattering. The coda of the pulse was lost because the averaged autocorrelation function was used in the computation. As well, the dispersive effect due to intrinsic attenuation is not considered. Recently, Burridge *et al.*[9] proposed a method to use the sample autocorrelation function to retain the local details of the reflection series. By this means, the coda of the computed transmitted response is preserved. Anelastic effects can also be incorporated into the same approximate theory. By assuming that the reflection coefficients are small, a small parameter $\epsilon (0 < \epsilon \ll 1)$ is introduced to systematize the retention of the relevant terms in the governing equations. It is found that if the reflection coefficients are of order ϵ and the relaxation effect of order ϵ^2, their effects on the pulse shape can be calculated separately and have similar magnitude. The separation of these two terms allows one to gain a deeper understanding of the similarities and dissimilarities between the effects of anelasticity and of multiple scattering. The proposed method provides a faster way to compute seismic wave propagation through layered microstructure than conventional methods while retaining accuracy within tolerance. Besides, the computation can be done either using the Fourier transform or by convolution. The latter is preferred since aliasing associated with the FFT is avoided.

The work is a sequel to that presented in Ref. 9 in which only numerical seismograms for perfectly elastic structures and at normal incidence were given. In the following, we derive the approximate solution for a downgoing *SH* shear wave using a standard linear solid (SLS) model with a single Debye relaxation mechanism to simulate anelasticity. Finally, numerical results for elastic and anelastic microstructures at several angles of incidence are presented that demonstrate the accuracy of the approximate method. Even though the assumption of small reflection coefficient variation is necessary to derive the final equations in Ref. 9, our
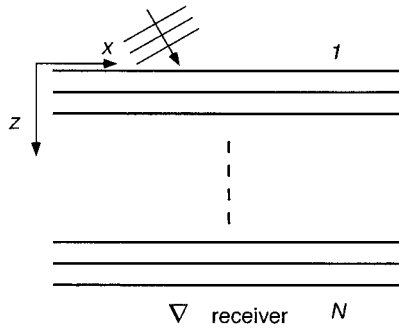
FIG. 1. A piecewise homogeneous medium consisting of N homogeneous and isotropic layers including two half-spaces.

numerical results, using a sequence of reflection coefficients, which are not small, agree well with the exact results.

I. THE APPROXIMATE *SH* SOLUTION

The problem we want to address is depicted in Fig. 1 where x and z are spatial Cartesian coordinates. The figure shows an inhomogeneous medium consisting of a stack of $(N-2)$ homogeneous and isotropic layers, which can be elastic or anelastic, bounded by two half-spaces. An impulse acts on the first interface at different angles of incidence. Reference feature of the pulse, for instance its first motion, sweeps over the origin at time equal to zero. We would like to find the *SH* response of the receiver located at the bottom interface on the z axis, directly below the point of impact on the first interface ($z=0$). As we want the plane waves to go through the whole layered structure, the ray parameter p is restricted to be less than the slowness in any layer. The directly transmitted arrival is not of interest to us but close to this arrival is a broad pulse made up of multiple scattering energy. For ease of investigating the evolution of the broad pulse, we use, instead of the evolved time t, a retarded time θ by means of the following transformation $(z,t) \rightarrow (z,\theta)$ where

$$\theta = t - px - T \tag{1}$$

and T is the vertical travel time of the downgoing directly transmitted arrival through the stack of layers. Equation (1) describes basically a co-moving frame with respect to the directly transmitted arrival.[10] The mathematical steps leading to the approximate solution for the amplitude of a general downgoing mode $W(z,\theta)$ were discussed in detail in Ref. 9. Without repeating the derivation, we quote the final expression

$$W(z,\theta) = \exp[a(z,\theta) \otimes + b(z,\theta) \otimes] W(z=0,\theta), \tag{2}$$

where the $\otimes$ is a convolution operator. In (2), $a(z,\theta)$ accounts for the effect of multiple scattering upon the pulse shape and $b(z,\theta)$ for the effect of anelasticity.

We adopt the following notation for the *SH* reflection and transmission coefficients. R^{DU} is the reflection coefficient for a downgoing incident wave and an upgoing scattered wave, R^{UD} is the reflection coefficient for an upgoing incident wave and a downgoing scattered wave, T^D is the transmission coefficient for downgoing incident and trans-
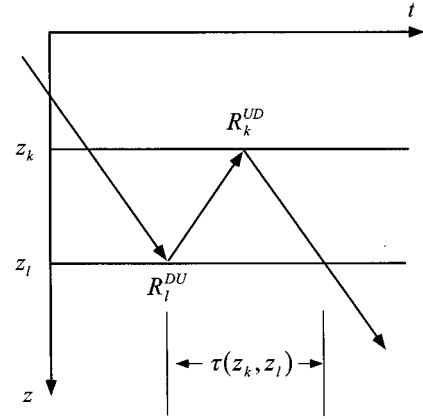
FIG. 2. A time–space diagram showing a double scattering made up of a backscattering and then a forward scattering.

mitted waves and T^U is the transmission coefficient for upgoing incident and transmitted waves. The coefficients are normalized by the energy flux. A subscript l is used to denote the coefficients $R_l^{DU}[=-R_l^{UD}]$ and $T_l^D(=T_l^U)$ for the lth interface.

A. The elastic scattering component

In a piecewise homogeneous medium, we write explicitly

$$a(z,\theta) = \sum_{k \leqslant l} \sum_{l=k}^{N-1} c_{kl} R_l^{DU} R_k^{UD} \delta[\theta - \tau(z_k,z_l)], \tag{3}$$

where

$$c_{kl} = \begin{cases} 1/2, & \text{if } k=l, \\ 1, & \text{otherwise}, \end{cases} \tag{4}$$

δ is the Kronecker delta function and $\tau(z_k,z_l)$ is the travel time of a double scattering (Fig. 2) within the thickness interval bounded above by the kth interface and below by the lth interface. The *SH* reflection coefficient of the lth interface is given by

$$R_l^{DU} = -R_l^{UD} = \frac{\mu_l \gamma_l - \mu_{l+1} \gamma_{l+1}}{\mu_l \gamma_l + \mu_{l+1} \gamma_{l+1}}$$

and $\tag{5}$

$$\gamma_l = \sqrt{\frac{\rho_l}{\mu_l} - p^2},$$

with μ_l and ρ_l the modulus and density.

Figure 2 shows a double scattering between z_k and z_l with characteristic travel time:

$$\tau(z_k,z_l) = 2 \sum_{j=k+1}^{l} \gamma_j \Delta z_j, \tag{6}$$

and Δz_j the thickness of the jth layer. Burridge *et al.*[9] suggested the use of the characteristic travel time of an equivalent effective homogeneous medium to emphasize the timing of the centroid of the pulse. Hence, $\hat{\tau}$ replaces τ in (3) by

$$\hat{\tau}(z_k,z_l)=2\hat{\gamma}\sum_{j=k+1}^{l}\Delta z_j \quad \text{and} \quad \hat{\gamma}=\sqrt{\langle\rho\rangle\left\langle\frac{1}{\mu}\right\rangle-p^2}, \tag{7}$$

where $\langle\cdot\rangle$ denotes the thickness-weighted average.

In (3), $a(z,\theta)$ accumulates the forward transmission effect of the pulse through the medium. For $k=l$, we approximate the normalized SH transmission coefficient T_l^D of the lth interface by

$$\text{Ln}(T_l^D)=\text{Ln}[1-(R_l^{DU})^2]^{1/2}=\tfrac{1}{2}\text{Ln}[1-(R_l^{DU})^2]$$
$$\approx-\tfrac{1}{2}(R_l^{DU})^2, \tag{8}$$

or

$$T_l^D\approx\exp[-\tfrac{1}{2}(R_l^{DU})^2]. \tag{9}$$

Considering the forward transmission through all interfaces yields

$$\prod_{l=1}^{N-1}T_l^D\approx\exp\left[-\frac{1}{2}\sum_{l=1}^{N-1}(R_l^{DU})^2\right]. \tag{10}$$

Hence $c_{kl}=1/2$ in (4). For $k\neq l$, the transmission effect due to backward scattering and then forward scattering (Fig. 2) is neglected, i.e., $T_l^D\approx1$. The assumption deteriorates with the increase of the characteristic travel time between z_k and z_l. This might also happen when $|z_k-z_l|$ increases and the wavefield penetrates a deeper part of the structure. In this case, the ignored accumulated transmission effect becomes significant. Finally, $a(z,\theta)$ may be discretized in θ for fixed z by $\theta=mh$, where h is the retarded time step and m is an integer. Then,

$$a(z,m)=\sum_{k\leq l}\sum_{l=k}^{N-1}c_{kl}R_l^{DU}R_k^{UD}\delta[mh-\hat{\tau}(z_k,z_l)]. \tag{11}$$

B. The *SH* system of a standard linear solid

A standard linear solid (SLS) can be represented mechanically by the springs and Newtonian dashpots. The dashpot consists of a piston moving in an ideally viscous liquid. The velocity of the piston is proportional to the applied force, thus providing internal friction to dissipate work done on it as heat.[11] We consider a SLS consisting of a single Debye relaxation mechanism to simulate anelasticity. The relaxation mechanism is governed by the stress-strain relation[12]

$$\sigma+\tau_\sigma\dot{\sigma}=\mu_r[e+\tau_e\dot{e}], \tag{12}$$

where σ and e are stress and strain, μ_r is the relaxed modulus, τ_σ is the characteristic relaxation time due to constant strain, τ_e is the characteristic relaxation time due to constant stress and the dot denotes the time derivative.

For a unit step load $\sigma=\sigma_0 H(t)$, the creep function $J(t)$ of a SLS for a single mechanism is

$$J(t)=\frac{\epsilon(t)}{\sigma_0}=J_r\left\{1-\left(1-\frac{\tau_\sigma}{\tau_e}\right)\exp\left(-\frac{t}{\tau_e}\right)\right\}H(t), \tag{13}$$

where $J_r=1/\mu_r$ is the relaxed compliance. Note that the instantaneous strain response is unrelaxed and elastic,

$$J(t=+0)=J_u=\frac{1}{\mu_u}=\frac{J_r\tau_\sigma}{\tau_e}=\frac{\tau_\sigma}{\mu_r\tau_e}, \tag{14}$$

where J_u and μ_u are the unrelaxed compliance and modulus, and the long-time strain response is relaxed and anelastic:

$$J(t\to\infty)=J_r=\frac{1}{\mu_r}. \tag{15}$$

For an impulsive load $\sigma=\sigma_o\delta(t)$, the impulse creep function is obtained by differentiating (13) with respect to t:

$$J(t)=\underbrace{J_u\delta(t)}_{\substack{\text{instantaneous}\\\text{and elastic}\\\text{compliance}}}+\underbrace{J_u\left(\frac{1}{\tau_\sigma}-\frac{1}{\tau_e}\right)\exp\left(-\frac{t}{\tau_e}\right)H(t)}_{\text{relaxed and anelastic compliance}}, \tag{16}$$

with J_u replacing J_r by (14). Similarly for a unit step strain $e=e_0 H(t)$, the stress relaxation function is

$$\mu(t)=\frac{\sigma(t)}{e_0}=\mu_r\left\{1-\left(1-\frac{\tau_e}{\tau_\sigma}\right)\exp\left(-\frac{t}{\tau_\sigma}\right)\right\}H(t) \tag{17}$$

and for an impulsive strain $e=e_0\delta(t)$, the impulse stress relaxation response is

$$\mu(t)=\underbrace{\mu_u\delta(t)}_{\substack{\text{instantaneous and}\\\text{elastic modulus}}}-\underbrace{\mu_u\left(\frac{1}{\tau_\sigma}-\frac{1}{\tau_e}\right)\exp\left(-\frac{t}{\tau_\sigma}\right)H(t)}_{\text{relaxed and anelastic modulus}}, \tag{18}$$

where (14) is used to replace μ_r by μ_u. The right-hand sides of Eqs. (16) and (18) express the total compliance and modulus of a SLS with a single relaxation mechanism. The total compliance or modulus contains two parts. One part describes the perfectly elastic and instantaneous response of the solid and the other part describes the relaxation effect of the solid due to anelasticity.

Fourier transforming (16), we get the dynamic response of the complex compliance $\hat{J}(\omega)$ of a SLS with a Debye relaxation mechanism:

$$\hat{J}(\omega)=J_u\frac{\tau_e}{\tau_\sigma}\left(\frac{1-i\omega\tau_\sigma}{1-i\omega\tau_e}\right). \tag{19}$$

We note the following:

$$\hat{J}(\omega\to0)=J_r=\frac{1}{\mu_r} \tag{20}$$

and

$$\hat{J}(\omega\to\infty)=J_u=\frac{1}{\mu_u}. \tag{21}$$

By comparing (14) and (15) with (20) and (21), we find the low frequency behavior corresponds to the long-time anelastic response and the high frequency behavior to the instantaneous perfectly elastic response. This can be predicted from (12) describing a SLS with a single Debye relaxation mechanism. Since the differentiation in time goes into multiplication by frequency via Fourier transform, at low frequency the contribution from the differentiated terms is negligible and the relaxed modulus governs the behavior. At high fre-

quency, the opposite is true. The undifferentiated terms drop out and the unrelaxed modulus takes control of the system.

For the lth SLS layer with a single relaxation mechanism, consider the 2×2 stiffness coefficient matrix $A_l(\theta)$ of a SH system,

$$A_l(\theta)=\begin{bmatrix} 0 & J_l(\theta) \\ \rho_l-p^2\mu_l(\theta) & 0 \end{bmatrix},\qquad(22)$$

where μ_l and J_l, which are functions of the retarded time θ, are the total modulus and compliance given by (16) and (18)

with the retarded time θ replacing the absolute time t. Using Eqs. (16) and (18), we separate the matrix $A_l(\theta)$ explicitly into two components

$$A_l(\theta)=A_l^e(\theta)+A_l^a(\theta),\qquad(23)$$

where

$$A_l^{(e)}(\theta)=\begin{bmatrix} 0 & (J_u)_l\delta(\theta) \\ \rho_l-p^2(\mu_u)_l\delta(\theta) & 0 \end{bmatrix}\qquad(24)$$

and

$$A_l^a(\theta)=\begin{bmatrix} 0 & (J_u)_l\left[\dfrac{1}{(\tau_\sigma)_l}-\dfrac{1}{(\tau_e)_l}\right]\exp[-\theta/(\tau_e)_l]H(\theta) \\ p^2(\mu_u)_l\left[\dfrac{1}{(\tau_\sigma)_l}-\dfrac{1}{(\tau_e)_l}\right]\exp[-\theta/(\tau_\sigma)_l]H(\theta) & 0 \end{bmatrix}.\qquad(25)$$

In Eqs. (23)–(25), $A_l^e(\theta)$ represents the instantaneous elastic response and $A_l^a(\theta)$ represents the long-time relaxation and anelastic response.

C. The intrinsically absorptive component

The anelastic argument $b(z,\theta)$ of the exponential convolution operator in (2) is defined by

$$b(z,\theta)=\sum_{i=l}^{N-1} e_l^T J \frac{\partial A_l^a(\theta)}{\partial\theta} e_l\Delta_{z_l},\qquad(26)$$

where the subscript T denotes the transpose,

$$J=\begin{bmatrix} 0 & 1 \\ 1 & 0 \end{bmatrix},\qquad(27)$$

and e is a normalized eigenvector of $A_l^e(\theta=0)$ representing a downgoing wave

$$e_l=\frac{1}{\sqrt{2}}\begin{bmatrix} 1/\sqrt{(\mu_u)_l\gamma_l} \\ \sqrt{(\mu_u)_l\gamma_l} \end{bmatrix},\qquad(28)$$

with the unrelaxed modulus $(\mu_u)_l$ being used to evaluate γ_l in (5). Differentiating (25) with respect to θ, substituting the result into (26) and performing the matrix multiplication yield

$$\begin{aligned} b(z,\theta)=\frac{1}{2}\sum_{l=1}^{N-1}\ \Delta z_l&\left[\frac{1}{(\tau_\sigma)_l}-\frac{1}{(\tau_e)_l}\right]\left\{\frac{p^2}{\gamma_l}\,\delta(\theta)+\gamma_l\delta(\theta)\right. \\ &-\frac{p^2}{\gamma_l}\frac{1}{(\tau_\sigma)_l}\exp\left[-\frac{\theta}{(\tau_\sigma)_l}\right]H(\theta) \\ &\left.-\gamma_l\frac{1}{(\tau_e)_l}\exp\left[-\frac{\theta}{(\tau_e)_l}\right]H(\theta)\right\}, \end{aligned}\qquad(29)$$

where the relation $J_u=1/\mu_u$ is used.

To discretize $b(z,\theta)$ in θ for fixed z by $\theta=mh$, we need to represent the expression $(1/\tau_e)\exp(-\theta/\tau_e)H(\theta)$ or

FIG. 3. Plots of the velocity and thickness sequence for the structure used in the computation. The structure consists of three distinct sections that are statistically stationary. The density was assumed constant.
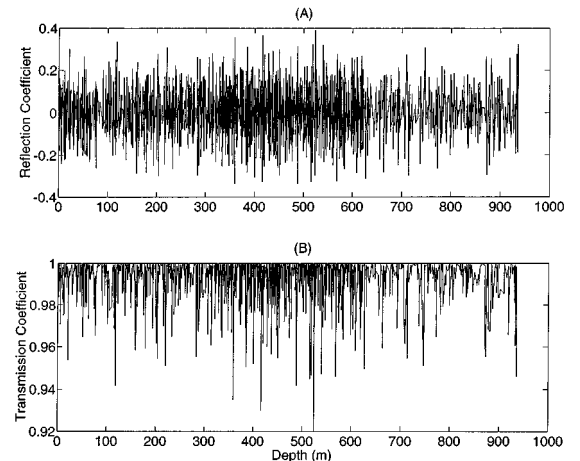
FIG. 4. Plots of the transmission and reflection coefficient sequence for the structure shown in Fig. 3.
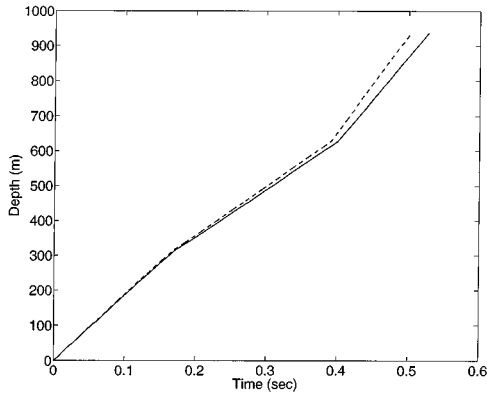
FIG. 5. The accumulated one-way travel time at normal incidence through the finely layered structure shown in Fig. 3 (dashed) and through the equivalent homogeneous effective medium (solid).

$(1/\tau_\sigma)\exp(-\theta/\tau_\sigma)H(\theta)$ in discrete form. To achieve this, we make use of the following identity to express the integral in terms of a discrete summation in m:

$$\frac{1}{\tau_e}\int_0^\infty \exp\left(-\frac{\theta}{\tau_e}\right)d\theta$$

$$=\frac{1}{\tau_e}\int_0^{h/2}\exp\left(-\frac{\theta}{\tau_e}\right)d\theta$$

$$+\sum_{m=1}^\infty \frac{1}{\tau_e}\int_{(m-1/2)h}^{(m+1/2)h}\exp\left(-\frac{\theta}{\tau_e}\right)d\theta$$

$$=1-\exp\left(-\frac{h}{2\tau_e}\right)+\sum_{m=1}^\infty 2\exp\left(-\frac{mh}{\tau_e}\right)\sinh\left(\frac{h}{2\tau_e}\right). \quad (30)$$

Similarly,

$$\frac{1}{\tau_\sigma}\int_0^\infty \exp-(\theta/\tau_\sigma)d\theta$$

yields the same result with τ_σ replacing τ_e in (30). The first two terms in (30) are the zero-terms, i.e., $m=0$. Using (30),
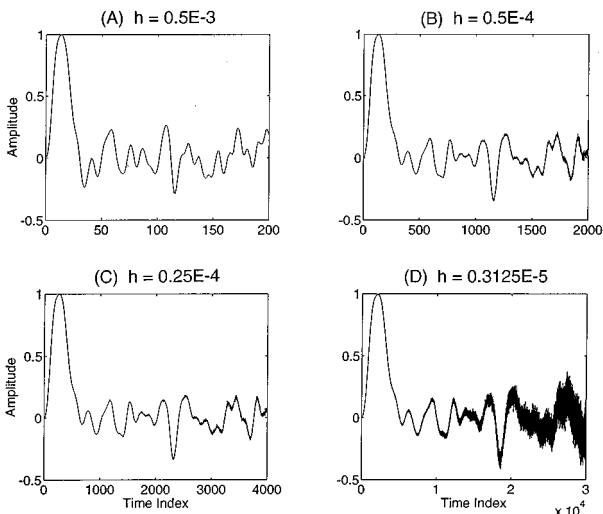
FIG. 6. Comparison of the elastic impulse responses calculated by the approximate method using different time steps.
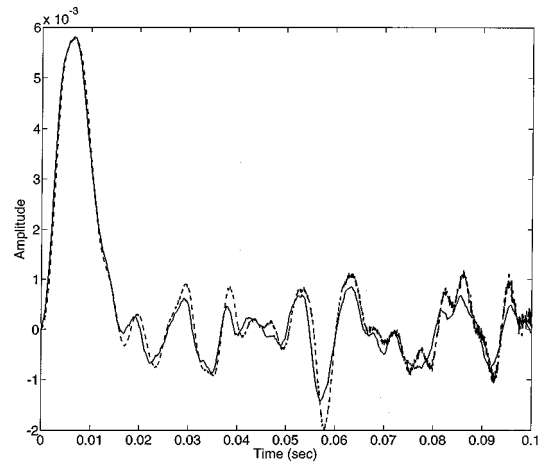
FIG. 7. Comparison of the elastic impulse responses at 0° angle of incidence (solid: exact solution; dashed: approximate solution).

Eq. (29) is discretized in θ as follows. For $m=0$,

$$b(z,m=0)=\frac{1}{2}\sum_{l=1}^{N-1}\Delta z_l\left[\frac{1}{(\tau_\sigma)_l}-\frac{1}{(\tau_e)_l}\right]$$

$$\times\left\{\frac{p^2}{\gamma_l}\exp\left[-\frac{h}{2(\tau_\sigma)_l}\right]\right.$$

$$\left.+\gamma_l\exp\left[-\frac{h}{2(\tau_e)_l}\right]\right\}. \quad (31)$$

Otherwise,

$$b(z,m\neq0)=-\sum_{l=1}^{N-1}\Delta z_l\left[\frac{1}{(\tau_\sigma)_l}-\frac{1}{(\tau_e)_l}\right]$$

$$\times\left\{\frac{p^2}{\gamma_l}\exp\left[-\frac{mh}{(\tau_\sigma)_l}\right]\sinh\left[\frac{h}{2(\tau_\sigma)_l}\right]\right.$$

$$\left.+\gamma_l\exp\left[-\frac{mh}{(\tau_e)_l}\right]\sinh\left[\frac{h}{2(\tau_e)_l}\right]\right\}. \quad (32)$$
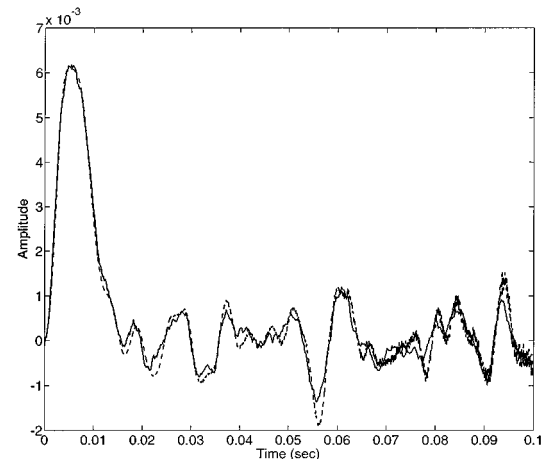
FIG. 8. Comparison of the elastic impulse responses at 10° angle of incidence (solid: exact solution; dashed: approximate solution).
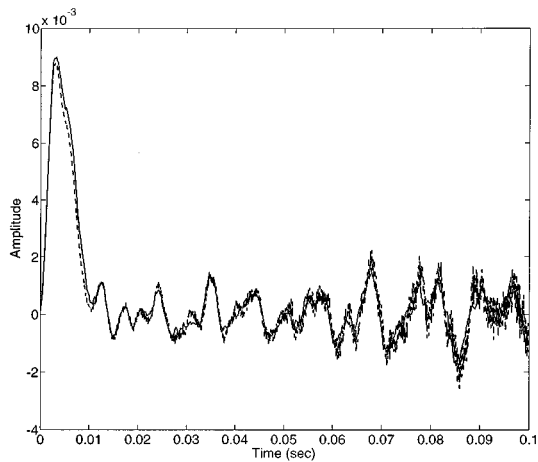
FIG. 9. Comparison of the elastic impulse responses at 20° angle of incidence (solid: exact solution; dashed: approximate solution).

The computation of the convolutional exponential (2) in terms of the generating functions has been described in Ref. 9.

II. DISCUSSION OF THE NUMERICAL RESULTS

The synthetic model consists of 1750 inhomogeneous isotropic layers bounded between two half-spaces. Figure 3 shows the model in metric scale. Velocities were randomly generated and uniformly distributed with means 2, 1.4, and 2.9 km/s and standard deviations 0.3, 0.25, and 0.5 km/s, respectively, to make up three distinct zones. Constant density of 2.5 g/cc is used for all layers. The thicknesses are statistically independent and exponentially distributed with means 0.6, 0.3, and 1.2 m. The reflection and transmission coefficients against depth are displayed in Figure 4. The coefficients are normalized by the energy flux so that the sum of the squared transmission coefficient and squared reflection coefficient of any interface is unity. As seen from Figure 4, the model has a wide range of reflection coefficient values.
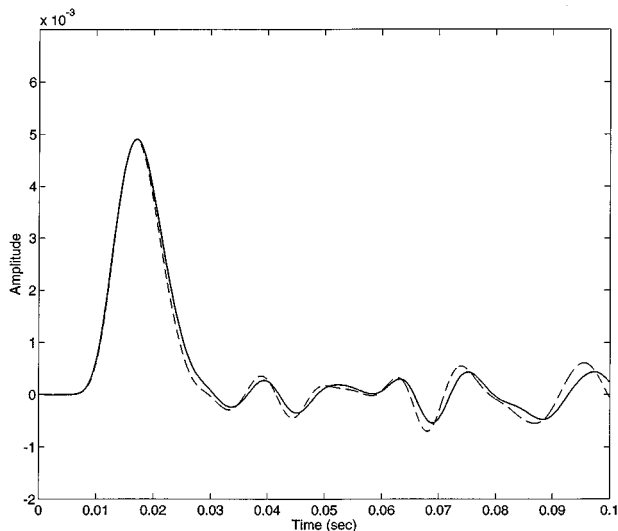
FIG. 10. Comparison of the anelastic impulse responses at 0° angle of incidence (solid: exact solution; dashed: approximate solution).
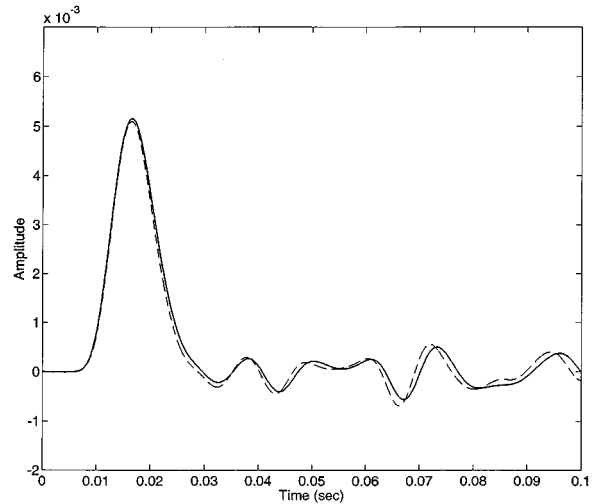
FIG. 11. Comparison of the anelastic impulse responses at 10° angle of incidence (solid: exact solution; dashed: approximate solution).

Figure 5 shows the one-way travel time for normal incidence through the equivalent homogeneous effective medium in solid curve. For comparison, the one-way travel time through the original finely layered homogeneous isotropic structure is also shown in dashed curve. The maximum discrepancy between the two characteristic travel times is found to be approximately 25 ms.

Figure 6 shows the sensitivity of the computed approximate elastic results to different time steps used. A larger time step increases the smoothing effect since more values are added to the same bin [Fig. 6(a)]. Using a very small time step, on the other hand, conveys more details than necessary [Fig. 6(d)]. Bearing these two limitations in mind, we chose to calculate the approximate results using a time step 0.5E-4. Figure 6(c) used half the time step of Figure 6(b) but the overall shape of both results looks similar. The exact results were calculated by a method similar to the Thomson–Haskell algorithm[13] using 8192 frequency points up to a maximum frequency of 2.5 kHz.
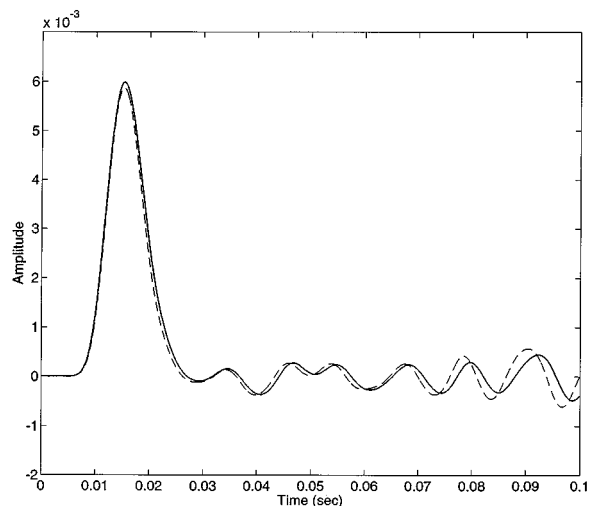
FIG. 12. Comparison of the anelastic impulse responses at 20° angle of incidence (solid: exact solution; dashed: approximate solution).
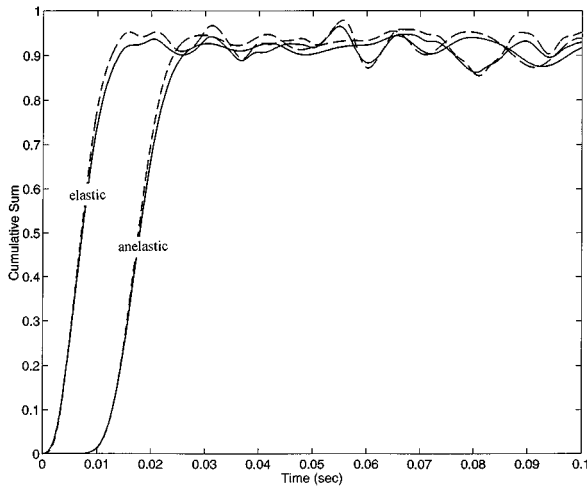
FIG. 13. The cumulative sums of the elastic and anelastic impulse responses at normal incidence (solid: exact solution; dashed: approximate solution).

Figures 7–9 show the comparison between the approximate and exact elastic impulse responses at three different angles of incidence (0°, 10°, 20°). The exact solutions are solid curves and the approximate solutions are dashed. Accuracy is best for the head of the pulse and deteriorates as time increases. This is predictable from the theory as discussed in Section I A. For larger angles of incidence, the transmitted wavefield will reach the receiver sooner, larger amplitude results, and the discrepancy between the approximate and the exact results becomes smaller. The computation was performed on the IBM RS/6000 model 580 and took 4.0 s for the approximate results and 3.6 min for the exact results.

For anelastic results, we adopted a SLS model with a single relaxation mechanism. The relaxation parameters used were $\tau_\sigma = 2.4 \times 10^{-4}$ s and $\tau_e = 2.5 \times 10^{-4}$ s for all layers. The model yields an internal friction $(=1/Q)$ curve peaking at 0.02 for normalized frequency $\omega \sqrt{\tau_\sigma \tau_e} = 1$.[12] The anelastic comparison is shown in Figs. 10–12. Time delay and dispersion are obvious. Anelasticity attenuates the high frequencies and, thus, smoothes the roughness of the signal. The computing time for the anelastic case was 30 s for the approximate results and 15 min for the exact results.

The cumulative sums of the elastic and anelastic responses for normal incidence are given in Figure 13, providing another means of comparison. It is easier to think of it in the frequency domain. The cumulative sum is the time integral, which is the same as the dc (zero frequency) component. The anelastic form to the O'Doherty/Anstey formula gives $\hat{W}(\omega) = \exp[\hat{a}(\omega) + \hat{b}(\omega)]z$, where $\hat{a}(\omega)$ is the Fourier transform of the positive lag of the autocorrelation function of the reflection coefficients and $\hat{b}(\omega)$ is the Fourier transform of $b(z, \theta)$ given in (29). Because the reflection coeffi-

cient series is effectively the derivative of the impedance function, the autocorrelation of the reflection coefficients is effectively minus the second derivative of the autocorrelation of the impedance function, which is constant, usually zero at infinity. Thus for most cases the integral of the autocorrelation function of the reflection coefficients will be zero. Hence $\hat{a}(0) = 0$. Also, $\hat{b}(0) = 0$ since the integral of (29) with respect to θ is 0. So, at zero frequency, $\hat{W}(\omega = 0) = 1$, i.e., in the time domain the cumulative sum is 1.

III. CONCLUSION

We have numerically justified the accuracy of the approximate method by using the *SH* case as an example. The accuracy is best for the broad pulse immediately after the directly transmitted arrival. The approximate code is significantly faster than the exact code. The gain factor in computation speed is 54 for the elastic case and 30 for the anelastic case. Since the current algorithm is limited to pre-critical reflection study, inhomogeneous wave or tunneling effect is not included. However, the approximate theory proposed has succeeded in separating the scattering and anelastic terms in forward modeling, thus providing a powerful means of understanding the effects of multiple scattering and anelasticity on seismic wave.

[1] R. F. O'Doherty and N. A. Anstey, ''Reflections on amplitudes,'' Geophys. Prosp. **19**, 430–458 (1971).
[2] M. Schoenberger and F. K. Levin, ''Seismic attenuation due to intrabed multiples,'' Geophysics **39**, 278–291 (1974).
[3] P. G. Richards and W. Menke, ''The apparent attenuation of a scattering medium,'' Bull. Seismol. Soc. Am. **73**, 1005–1021 (1983).
[4] I. Lerche, ''Stratigraphic filtering of *SH* waves in a spherical layered earth,'' PAGEOPH **124**, 1021–1037 (1987).
[5] R. R. Stewart, P. D. Huddleston, and T. K. Kan, ''Seismic versus sonic velocities: a vertical seismic profiling,'' Geophysics **49**, 1153–1168 (1984).
[6] K. Hsu, R. Burridge, and J. Walsh, ''*P*-wave and *S*-wave drift in a slow formation,'' Extended Abstracts, Sixty-Second Annual International Meeting, Society of Exploration Geophysicists, New Orleans, 1992.
[7] L. Wennerberg and A. Frankel, ''On the similarity of theories of anelastic and scattering attenuation,'' Bull. Seismol. Soc. Am. **79**, 1287–1293 (1989).
[8] R. Burridge and H. W. Chang, ''Multimode, one-dimensional wave propagation in a highly discontinuous medium,'' Wave Motion **11**, 231–249 (1989).
[9] R. Burridge, M. V. de Hoop, K. Hsu, L. Le, and A. Norris, ''Waves in stratified viscoelastic media with microstructure,'' J. Acoust. Soc. Am. **94**, 2884–2894 (1993).
[10] M. V. de Hoop, R. Burridge, and H. W. Chang, ''Wave propagation with tunneling in a highly discontinuous layered medium,'' Wave Motion **13**, 307–327 (1991).
[11] A. S. Nowick and B. S. Berry, *Anelastic Relaxation in Crystalline Solids* (Academic, New York, 1972), Chap. 3.
[12] H. P. Liu, D. L. Anderson, and H. Kanamori, ''Velocity dispersion due to anelasticity; implications for seismology and mantle composition,'' Geophys. J. R. Astron. Soc. **47**, 41–58 (1976).
[13] H. W. Chang, ''3-D reflection/transmission coefficients from cylindrical layered elastic media,'' IEEE Ultrasonics Symposium (1987), pp. 455–459.

A new formalism for wave scattering from a bounded obstacle

Luciano Misici
Dipartimento di Matematica e Fisica, Università di Camerino, 62032 Camerino (MC), Italy

Graziella Pacelli
Istituto di Matematica e Statistica, Università di Ancona, 60100 Ancona, Italy

Francesco Zirilli
Dipartimento di Matematica "G. Castelnuovo," Università di Roma "La Sapienza," 00185 Roma, Italy

Let $\Omega \subset \mathbf{R}^3$ be an obstacle that is a simply connected bounded domain. The exterior Dirichlet problem for the Helmholtz equation in $\mathbf{R}^3\backslash\Omega$ with the Sommerfeld radiation condition at infinity is considered. Based on an integral representation formula, a new method to compute the solution of the exterior boundary value problem mentioned above is proposed. This method generalizes the formalism introduced for an unbounded obstacle by Milder [J. Acoust. Soc. Am. **89**, 529–541 (1991)] and consists in computing a perturbation series whose coefficients are integrals. These integrals are independent one from the other so that the computation of the series is fully parallelizable. Finally, some numerical results obtained on test problems are shown. In particular, numerical experiments for obstacles with nonsmooth boundaries such as polyhedra and obstacles with multiscale corrugations are shown. © *1998 Acoustical Society of America.*
[S0001-4966(98)01301-0]

PACS numbers: 43.20.Bi, 43.20.Fn [JEG]

INTRODUCTION

Let $\mathbf{R}^3$ be the three-dimensional real Euclidean space, $\underline{x} = (x,y,z)^T \in \mathbf{R}^3$ be a generic vector. The superscript "T" denotes the transposition operation. Let us denote with $(\cdot,\cdot)$ the Euclidean scalar product and with $\|\cdot\|$ the induced euclidean vector norm. Let $\Omega \subset \mathbf{R}^3$ be a bounded simply connected domain that contains the origin, and let $\partial\Omega$ be the boundary of Ω. Let $a > 0$, $B_a = \{\underline{x} \in \mathbf{R}^3 | \|\underline{x}\| < a\}$ be the sphere of radius a and let ∂B_a be its boundary. In the following B_1 and ∂B_1 will be denoted also with B and ∂B. Without loss of generality we assume that Ω contains the sphere B_a.

Given a complex valued function $f(\underline{x})$, $\underline{x} \in \partial\Omega$, we consider the following Dirichlet boundary value problem for the Helmholtz equation

$$\Delta u + k^2 u = 0 \quad \underline{x} \in \mathbf{R}^3\backslash\Omega, \tag{1}$$

$$u(\underline{x}) = f(\underline{x}) \quad \underline{x} \in \partial\Omega, \tag{2}$$

$$\lim_{r \to +\infty} r\left(\frac{\partial u}{\partial r} - iku\right) = 0, \tag{3}$$

where $r = \|\underline{x}\|$, $\Delta = (\partial^2/\partial x^2) + (\partial^2/\partial y^2) + (\partial^2/\partial z^2)$ is the Laplace operator and $k > 0$ is the wave number. Problems (1), (2), (3) has been widely studied; see, for example, Refs. 1 and 2. Let $\Phi(\underline{x},\underline{y})$ be the fundamental solution of the Helmholtz equation in $\mathbf{R}^3$ with the Sommerfeld radiation condition at infinity, that is,

$$\Phi(\underline{x},\underline{y}) = \frac{1}{4\pi} \frac{e^{ik\|\underline{x}-\underline{y}\|}}{\|\underline{x}-\underline{y}\|} \quad \underline{x},\underline{y} \in \mathbf{R}^3, \quad \underline{x} \neq \underline{y}. \tag{4}$$

Under some regularity assumptions on $\partial\Omega$ for a regular function $u(\underline{x})$ satisfying Eqs. (1), and (3), we have

$$u(\underline{x}) = \int_{\partial\Omega} \left\{ \frac{\partial \Phi(\underline{x},\underline{y})}{\partial \underline{n}(\underline{y})} u(\underline{y}) - \Phi(\underline{x},\underline{y}) \frac{\partial u(\underline{y})}{\partial \underline{n}(\underline{y})} \right\} dS(\underline{y}),$$
$$\underline{x} \in \mathbf{R}^3\backslash\Omega, \tag{5}$$

where $\underline{n}(\underline{y})$ is the outward unit normal vector to $\partial\Omega$ in $\underline{y} \in \partial\Omega$ and dS is the surface measure on $\partial\Omega$.

Moreover for $\underline{x} \neq \underline{0}$, let $\hat{\underline{x}} = \underline{x}/\|\underline{x}\|$; then $u(\underline{x})$ has the following expansion:[1]

$$u(\underline{x}) = \frac{e^{ik\|\underline{x}\|}}{\|\underline{x}\|} F_0(\hat{\underline{x}}) + O\left(\frac{1}{\|\underline{x}\|^2}\right), \quad \|\underline{x}\| \to \infty, \tag{6}$$

where $F_0(\hat{\underline{x}})$ is the far-field pattern and is a piece of the leading order term of a series in inverse powers of $\|\underline{x}\|$. The function $F_0(\hat{\underline{x}})$ contains information about the shape $\partial\Omega$, so that the computation of the far-field pattern is of special interest. If we consider the scattering of a given incoming acoustic wave $u^i(\underline{x})$ solution of Eq. (1) in $\mathbf{R}^3$, by an acoustically soft obstacle Ω, then the acoustic scattered field $u(\underline{x})$ satisfies the boundary value problems (1), (2), and (3) with $f(\underline{x}) = -u^i(\underline{x})$.

In this paper we describe a new method to compute the solution $u(\underline{x})$ of problems (1), (2), and (3) or the far-field pattern $F_0(\hat{\underline{x}})$ associated to it. This method is based on formula (5) and a formalism that generalizes the formalism introduced in Ref. 3 by Milder in the case of an unbounded obstacle.

From Eq. (5) it follows that the knowledge of $u(\underline{x})$ and $\partial u(\underline{x})/\partial n$ on $\partial\Omega$ determines $u(\underline{x})$ everywhere. We define a nonlocal operator $\hat{N}$ that acting on the values of $u(\underline{x})$ on $\partial\Omega$ from the fact that u satisfies Eqs. (1) and (3), and gives $\partial u(\underline{x})/\partial\underline{n}$ on $\partial\Omega$, that is,

$$\frac{\partial u(\underline{x})}{\partial \underline{n}} = [\hat{N}u](\underline{x}), \quad \underline{x} \in \partial \Omega. \tag{7}$$

We obtain a ''power series'' expansion for $\hat{N}$. The substitution of the boundary condition (2) and of the ''power series'' expansion of $\hat{N}$ into Eq. (5) gives a ''power series'' expansion for $u(\underline{x})$. In a similar way we obtain a ''power series'' expansion of $F_0(\hat{\underline{x}})$. The computation of this expansion is the method proposed here to approximate $u(\underline{x})$ and $F_0(\hat{\underline{x}})$. The coefficients of this series are integrals independent one from the other so that the computation of the series is fully parallelizable. Our method presents some advantages with respect to the standard numerical methods used to solve exterior boundary value problems, such as finite differences, finite elements methods, boundary integral equations, or methods particularly suited to solve scattering problems such as the T-matrix method. In particular, finite difference methods and finite elements methods restrict the computation to a bounded domain containing Ω, employing absorbing boundary conditions on the artificial boundaries.[4] Moreover, with finite differences and finite elements, the computation involves the solution of linear systems of equations. The direct numerical solution of boundary integral equations also involves the solution of linear systems. In Refs. 5 and 6, the T-matrix method to solve acoustic and electromagnetic scattering problems is described. The T-matrix method solves the scattering problem associated to the obstacle Ω, for different incoming fields applying the T-matrix to the incoming field considered. However, construction of the T-matrix involves the solution of a linear system. The solution of linear systems is not fully parallelizable. The formalism proposed here involves only quadratures and is fully parallelizable.

In this paper we compare the numerical results obtained using the generalized Milder formalism presented here and the T-matrix method when Ω is a bounded domain with smooth boundary. In this case, the two methods give the same results for the scattered field. However, the formalism presented here is able to compute the solution of the boundary value problems (1), (2), and (3) when Ω is a bounded domain with nonsmooth boundary such as a polyhedron or with a smooth boundary with multiscale corrugations for a wide range of values of the wave number k. These are acoustic problems of great interest and are not easily solvable with the T-matrix approach.

In Sec. I we obtain the operator $\hat{N}$. In Sec. II we give the ''power series'' expansion of the operator $\hat{N}$ and we give a formula to approximate the solution of the boundary value problems (1), (2), and (3). Finally in Sec. III the method developed in the previous sections is applied to the acoustic scattering problem considered above, and some numerical results are shown and compared with the results obtained with the T-matrix approach.

I. THE OPERATOR $\hat{N}$

Let (r, θ, ϕ) be the canonical spherical coordinate of $\underline{x} \in \mathbf{R}^3$; for $\underline{x} \neq 0$, we have

$$\hat{\underline{x}}(\theta, \phi) = \frac{\underline{x}}{\|\underline{x}\|} = (\sin \theta \cos \phi, \sin \theta \sin \phi, \cos \theta)^T, \tag{8}$$

where $0 \leq \theta \leq \pi$, $0 \leq \phi < 2\pi$. Note that $\|\hat{\underline{x}}\| = 1$. In order to fix the ideas in developing our formalism, we assume that the boundary of the obstacle $\partial \Omega$ can be represented by a single valued function in spherical coordinates. That is $\partial \Omega$ is a starlike surface with respect to the origin. We have

$$\partial \Omega = \{ \underline{x} = r\hat{\underline{x}} \in \mathbf{R}^3 \, | \, r = \zeta(\hat{\underline{x}}), \quad \hat{\underline{x}} \in \partial B \},$$

so that, from Eq. (2), we can define

$$f_1(\hat{\underline{x}}) = f(\zeta(\hat{\underline{x}})\hat{\underline{x}}), \quad \hat{\underline{x}} \in \partial B. \tag{9}$$

Formulas similar to the ones derived in the following can be obtained if the spherical coordinate system is substituted with some other coordinate system.

We build now the operator $\hat{N}$ of (7). Let $H(\underline{x})$, $x \in \mathbf{R}^3 \backslash \Omega$ be a function, we define

$$h(\hat{\underline{x}}) = H(\zeta(\hat{\underline{x}})\hat{\underline{x}}), \quad \hat{\underline{x}} \in \partial B; \tag{10}$$

that is, $h(\hat{\underline{x}})$ is the restriction of $H(\underline{x})$ to $\partial \Omega$ as a function of $\hat{\underline{x}}$. We have

$$\frac{\partial H(\underline{x})}{\partial \underline{n}} = (\underline{n}(\underline{x}), \boldsymbol{\nabla} H(\underline{x})), \quad \underline{x} \in \partial \Omega, \tag{11}$$

where $\boldsymbol{\nabla} = (\partial/\partial x, \partial/\partial y, \partial/\partial z)^T$ is the gradient operator.

We define the operator $\hat{D}$ as follows:

$$[\hat{D}H](\hat{\underline{x}}) = \left. \frac{\partial H(r\hat{\underline{x}})}{\partial r} \right|_{r = \zeta(\hat{x})}, \quad \hat{\underline{x}} \in \partial B, \tag{12}$$

and we denote with $\overline{\boldsymbol{\nabla}}$ the operator:

$$\overline{\boldsymbol{\nabla}} = \frac{1}{\zeta(\hat{\underline{x}})} \left(\frac{\partial}{\partial \theta}, \frac{1}{\sin \theta} \frac{\partial}{\partial \phi} \right)^T. \tag{13}$$

We have

$$g(\hat{\underline{x}}) = \frac{\partial H}{\partial \underline{n}} (\zeta(\hat{\underline{x}})\hat{\underline{x}})$$

$$= \frac{1}{(1 + \|(\overline{\boldsymbol{\nabla}}\zeta)\|^2)^{1/2}} \{ (1 + \|(\overline{\boldsymbol{\nabla}}\zeta)\|^2) \hat{D}H - (\overline{\boldsymbol{\nabla}}\zeta, \overline{\boldsymbol{\nabla}}h) \},$$

$$\hat{\underline{x}} \in \partial B, \tag{14}$$

where $(\cdot, \cdot)$, $\|\cdot\|$ denote Euclidean scalar product and induced norm in $\mathbf{R}^2$. Let $v(\overline{x})$ be a function defined on ∂B and $F(x)$ be the unique solution of the boundary value problem:

$$\Delta F + k^2 F = v(\hat{\underline{x}}) \delta(\|\underline{x}\| - a), \quad \underline{x} \in \mathbf{R}^3, \tag{15}$$

$$\lim_{r \to +\infty} r \left(\frac{\partial F}{\partial r} - ikF \right) = 0, \tag{16}$$

where $\delta(\|x\| - a)$ is a ''Dirac's delta'' concentrated on ∂B_a. From the convolution theorem we have

$$F(\underline{x}) = \int_{\mathbf{R}^3} \Phi(\underline{x}, \underline{y}) v(\hat{\underline{y}}) \delta(\|\underline{y}\| - a) d\underline{y}, \quad \underline{x} \in \mathbf{R}^3. \tag{17}$$

We note that $F(\underline{x})$ satisfies the homogeneous Helmholtz equation in $\mathbf{R}^3 \backslash \partial B_a$. Let $f(\underline{x})$ be a function defined on $\partial \Omega$ and let $v(\hat{\underline{x}})$, defined on ∂B, be the solution of the integral equation

$$a^2 \int_{\partial B} \Phi(\underline{x}, a\hat{\underline{y}}) v(\hat{\underline{y}}) ds(\hat{\underline{y}}) = f(\underline{x}), \quad \underline{x} \in \partial\Omega, \qquad (18)$$

where ds is the surface measure on ∂B. We assume that Eq. (18) has a unique solution. Given a function $f(\underline{x})$ defined on $\partial\Omega$ let $F(\underline{x})$ be the solution of the boundary value problems (15) and (16), when $v(\hat{x})$ is chosen to be the unique solution of the integral equation (18). We note that since $v(\hat{x})$ is the solution of Eq. (18), we have

$$F(\underline{x}) = f(\underline{x}), \quad \underline{x} \in \partial\Omega; \qquad (19)$$

that is, $F(\underline{x})$ for $\underline{x} \in \mathbf{R}^3 \backslash \Omega$ is the unique solution of Eqs. (1), (2), and (3), so that, from (14) we have

$$[\hat{N}f](\zeta(\hat{\underline{x}})\hat{\underline{x}}) = \frac{1}{(1 + \|\overline{\nabla}\zeta\|^2)^{1/2}} \{(1 + \|\overline{\nabla}\zeta\|^2)\hat{D}F$$

$$- (\overline{\nabla}\zeta, \overline{\nabla}f)\}, \quad \hat{\underline{x}} \in \partial B. \qquad (20)$$

II. THE SOLUTION OF THE BOUNDARY VALUE PROBLEMS (1), (2), AND (3)

In Sec. I we have shown that given a function $f(\underline{x})$, $\underline{x} \in \partial\Omega$ if $v(\hat{x})$, $\hat{\underline{x}} \in \partial B$ is the solution of Eq. (18) and $F(\underline{x})$, $\underline{x} \in \mathbf{R}^3$ is the solution of Eqs. (15) and (16) given by (17), then $F(\underline{x})$ for $\underline{x} \in \mathbf{R}^3 \backslash \Omega$ is the unique solution of Eqs. (1), (2), and (3) and $\partial F/\partial n$, $\underline{x} \in \partial\Omega$ is given by Eq. (20). So that the ability to obtain $\partial F/\partial n$, $\underline{x} \in \partial\Omega$ depends on the ability to obtain $v(\hat{x})$, $\underline{x} \in \partial B$ solution of Eq. (18). The numerical solution of Eq. (18) as an integral equation involves the solution of a linear system and will made the method proposed here to solve Eqs. (1), (2), and (3) equivalent to a boundary integral method. To avoid this difficulty, in Lemma 3.1, we solve Eq. (18) perturbatively using ∂B as base point of the perturbation expansion. Finally, in Sec. III the integral equations on ∂B are solved expanding data and unknown in spherical harmonics. This corresponds to the solution of a diagonal linear system.

Let $G(\underline{x})$ be a function defined on ∂B. For $a < 1$ and $\|\underline{x}\| > a$, we consider the operators q_m, $m = 0,1,2,...$, defined as follows:

$$[q_m G](\underline{x}) = a^2 \int_{\partial B} \frac{\partial^m \Phi(\underline{x}, a\hat{\underline{y}})}{\partial \|\underline{x}\|^m} G(\hat{\underline{y}}) ds(\hat{\underline{y}}),$$

$$\|\underline{x}\| > a, \quad m = 0,1,2,... . \qquad (21)$$

For later convenience we define $\hat{q}_m$, $m = 0,1,2,...$ to be

$$[\hat{q}_m G](\hat{\underline{x}}) = [q_m G](\hat{\underline{x}}), \quad \hat{\underline{x}} \in \partial B. \qquad (22)$$

Since $B_a \subset \Omega$, we have $\zeta(\hat{\underline{x}}) > a$, $\hat{\underline{x}} \in \partial B$, then from Eqs. (21) and (17), we have the following (formal) series expansions

$$F(\zeta(\hat{\underline{x}})\hat{\underline{x}}) = \sum_{m=0}^{+\infty} \frac{(\zeta(\hat{\underline{x}}) - 1)^m}{m!} [\hat{q}_m v](\hat{\underline{x}}), \quad \hat{\underline{x}} \in \partial B \qquad (23)$$

and

$$\frac{\partial F(r\hat{\underline{x}})}{\partial r}\bigg|_{r=\zeta(\hat{x})} = [\hat{D}F](\hat{\underline{x}}) = \sum_{m=0}^{+\infty} \frac{(\zeta(\hat{\underline{x}}) - 1)^m}{m!}$$

$$\times [\hat{q}_{m+1} v](\hat{\underline{x}}), \quad \hat{\underline{x}} \in \partial B. \qquad (24)$$

Lemma 3.1: Let $v(\hat{\underline{x}})$, $\hat{\underline{x}} \in \partial B$ be such that $F(\underline{x})$ given by Eq. (17) is the solution of problems (1), (2), and (3). Then:

$$v(\hat{\underline{y}}) = \sum_{m=0}^{+\infty} \frac{(\zeta(\hat{y}) - 1)^m}{m!} v^{\langle m \rangle}(\hat{\underline{y}}), \quad \hat{y} \in \partial B, \qquad (25)$$

where

$$v^{\langle 0 \rangle}(\hat{\underline{y}}) = [\hat{q}_0^{-1} f_1](\hat{\underline{y}}), \quad \hat{y} \in \partial B \qquad (26)$$

and for $m = 1,2,...$,

$$\frac{(\zeta - 1)^m}{m!} v^{\langle m \rangle}(\hat{\underline{y}}) = -\left[\hat{q}_0^{-1}\left(\sum_{k=0}^{m-1} \frac{(\zeta - 1)^{m-k}}{(m-k)!}\right)\right.$$

$$\left.\times \hat{q}_{m-k}\left[\frac{(\zeta - 1)^k}{k!} v^{\langle k \rangle}\right]\right)\right](\hat{\underline{y}}),$$

$$\hat{\underline{y}} \in \partial B. \qquad (27)$$

Proof: From Eqs. (18), (23), and (25), we have

$$\sum_{m=0}^{+\infty} \frac{(\zeta(\hat{\underline{x}}) - 1)^m}{m!}\left[\hat{q}_m \sum_{k=0}^{+\infty} \frac{(\zeta - 1)^k}{k!} v^{\langle k \rangle}\right](\hat{\underline{x}})$$

$$= f_1(\hat{\underline{x}}), \quad \hat{\underline{x}} \in \partial B. \qquad (28)$$

That is, Eqs. (26) and (27).

Lemma 3.2: Let $f(\underline{x})$, $\underline{x} \in \partial\Omega$ and $F(\underline{x})$, $\underline{x} \in \mathbf{R}^3$ be as above then we have the following (formal) expansion:

$$\frac{\partial F(r\hat{\underline{x}})}{\partial r}\bigg|_{r=\zeta(\hat{x})} = \sum_{m=0}^{+\infty} [\hat{D}_m f_1](\hat{\underline{x}}), \quad \hat{\underline{x}} \in \partial B, \qquad (29)$$

where $\hat{D}_m = O((\zeta - 1)^m)$ when $\zeta \to 1$, $m = 0,1,2,...$. In particular we have

$$\hat{D}_0 = \hat{q}_1 \hat{q}_0^{-1}, \qquad (30)$$

$$\hat{D}_1 = (\zeta - 1)\hat{q}_2 \hat{q}_0^{-1} - \hat{q}_1 \hat{q}_0^{-1}(\zeta - 1)\hat{q}_1 \hat{q}_0^{-1}, \qquad (31)$$

$$\hat{D}_2 = \frac{(\zeta - 1)^2}{2!} \hat{q}_3 \hat{q}_0^{-1} - (\zeta - 1)\hat{q}_2 \hat{q}_0^{-1}(\zeta - 1)\hat{q}_1 \hat{q}_0^{-1}$$

$$+ \hat{q}_1 \hat{q}_0^{-1}(\zeta - 1)\hat{q}_1 \hat{q}_0^{-1}(\zeta - 1)\hat{q}_1 \hat{q}_0^{-1}$$

$$- \hat{q}_1 \hat{q}_0^{-1} \frac{(\zeta - 1)^2}{2} \hat{q}_2 \hat{q}_0^{-1}. \qquad (32)$$

Proof: From Eqs. (24) and (29) we have:

$$\sum_{m=0}^{+\infty} [\hat{D}_m f_1](\hat{\underline{x}}) = \sum_{m=0}^{+\infty} \frac{(\zeta - 1)^m}{m!} [\hat{q}_{m+1} v](\hat{\underline{x}}), \quad \hat{\underline{x}} \in \partial B. \qquad (33)$$

Using Eqs. (25), (26), and (27) we obtain

$$\sum_{m=0}^{+\infty} [\hat{D}_m f_1](\hat{\underline{x}})$$

$$= \sum_{m=0}^{+\infty} \frac{(\zeta - 1)^m}{m!}\left\{\hat{q}_{m+1}\left[\hat{q}_0^{-1} - \hat{q}_0^{-1}(\zeta - 1)\hat{q}_1 \hat{q}_0^{-1}\right.\right.$$

$$+ \hat{q}_0^{-1}(\zeta - 1)\hat{q}_1 \hat{q}_0^{-1}(\zeta - 1)\hat{q}_1 \hat{q}_0^{-1}$$

$$\left.\left.- \hat{q}_0^{-1} \frac{(\zeta - 1)^2}{2} \hat{q}_2 \hat{q}_0^{-1} + \cdots\right]f_1\right\}(\hat{\underline{x}}), \quad \hat{\underline{x}} \in \partial B. \qquad (34)$$
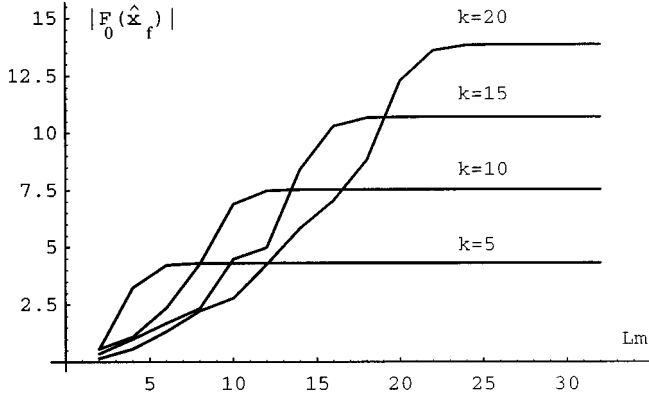
FIG. 1. $|F_{0,L_m}(\hat{\underline{x}}_f)|$ as a function of L_m and k relative to the sphere of radius $R = 1.1$.

From Eq. (34) we obtain Eqs. (30), (31), and (32). We note that some algebraic manipulations give a general formula for $\hat{D}_m$, $m = 3,4,...$.

Lemma 3.3: Let $f(\underline{x})$, $\underline{x} \in \partial\Omega$ and $F(\underline{x})$, $\underline{x} \in \mathbf{R}^3$ be as above then we have the following (formal) expansion:

$$\frac{\partial F(\zeta\hat{\underline{x}})}{\partial \underline{n}} = [\hat{N}f](\underline{x}) = \sum_{m=0}^{+\infty} [\hat{N}_m f_1](\zeta\hat{\underline{x}}), \quad \underline{x} = \zeta\hat{\underline{x}} \in \partial\Omega, \tag{35}$$

where $\hat{N}_m = O((\zeta - 1)^m)$ when $\zeta \to 1$ $m = 0,1,2,...$, and

$$\hat{N}_0 = \frac{1}{(1 + \|\overline{\mathbf{\nabla}}\zeta\|^2)^{1/2}} \hat{D}_0, \tag{36}$$

$$\hat{N}_1 = \frac{1}{(1 + \|\overline{\mathbf{\nabla}}\zeta\|^2)^{1/2}} [\hat{D}_1 - (\overline{\mathbf{\nabla}}\zeta, \overline{\mathbf{\nabla}})], \tag{37}$$

and

$$\hat{N}_m = \frac{1}{(1 + \|\overline{\mathbf{\nabla}}\zeta\|^2)^{1/2}} [\hat{D}_{m+2} + \|(\overline{\mathbf{\nabla}}\zeta)\|^2 \hat{D}_m],$$

$$m = 2,3,4,... . \tag{38}$$

Proof: From Eq. (20) using Eqs. (30), (31), and (32), we obtain formulas (36), (37), and (38).

We give now the desired formula to solve boundary value problems (1), (2), and (3). Let $u(\underline{x})$ be the solution of the boundary value problems (1), (2), and (3) from Eqs. (5) and (7), we have

$$u(\underline{x}) = \int_{\partial\Omega} \left\{ \frac{\partial\Phi(\underline{x},\underline{y})}{\partial\underline{n}(\underline{y})} f(\underline{y}) - \Phi(\underline{x},\underline{y})[\hat{N}f](\underline{y}) \right\} dS(\underline{y}),$$

$$\underline{x} \in \mathbf{R}^3 \backslash \Omega, \tag{39}$$

so that we have (formally)

$$u(\underline{x}) = \int_{\partial\Omega} \left\{ \frac{\partial\Phi(\underline{x},\underline{y})}{\partial\underline{n}(\underline{y})} f(\underline{y}) - \Phi(\underline{x},\underline{y}) \sum_{m=0}^{+\infty} [\hat{N}_m f_1](\underline{y}) \right\}$$

$$\times dS(\underline{y}), \quad \underline{x} \in \mathbf{R}^3 \backslash \Omega. \tag{40}$$

Let us consider now the acoustic scattering problem of the Introduction, that is, let $f(\underline{x}) = -u^i(\underline{x})$, $\underline{x} \in \partial\Omega$, where the

TABLE I. The computational cost.

	"T-matrix"	OE_1	OE_2
Number of integrals	$(L_m+1)^4$	$(L_m+1)^2$	$2(L_m+1)^2$

incident wave $u^i(\underline{x})$ verify the Helmholtz equation for $\underline{x} \in \mathbf{R}^3$ we have

$$\int_{\partial\Omega} \left(u^i(\underline{y}) \frac{\partial\Phi(\underline{x},\underline{y})}{\partial n(\underline{y})} - \frac{\partial u^i(\underline{y})}{\partial n(\underline{y})} \Phi(\underline{x},\underline{y}) \right) dS(\underline{y}) = 0,$$

$$\underline{x} \in \mathbf{R}^3 \backslash \Omega, \tag{41}$$

so that integral representation (40) for the scattered field becomes

$$u(\underline{x}) = -\int_{\partial\Omega} \Phi(\underline{x},\underline{y}) \left(\frac{\partial u^i(\underline{y})}{\partial\underline{n}(\underline{y})} - \sum_{m=0}^{\infty} [\hat{N}_m u^i](\underline{y}) \right) dS(\underline{y}),$$

$$\underline{x} \in \mathbf{R}^3 \backslash \Omega. \tag{42}$$

Moreover, we have

$$\Phi(\underline{x},\underline{y}) = \frac{e^{ik\|\underline{x}\|}}{4\pi\|\underline{x}\|} e^{-ik(\hat{x},\underline{y})} + O\left(\frac{1}{\|\underline{x}\|^2}\right), \quad \|\underline{x}\| \to \infty \tag{43}$$

from Eqs. (6) and (42) we obtain the following expression for the far field:

$$F_0(\hat{x}) = -\frac{1}{4\pi} \int_{\partial\Omega} e^{-ik(\hat{x},\underline{y})} \left(\frac{\partial u^i(\underline{y})}{\partial\underline{n}(\underline{y})} - \sum_{m=0}^{\infty} [\hat{N}_m u^i](\underline{y}) \right)$$

$$\times dS(\underline{y}), \hat{\underline{x}} \in \partial B. \tag{44}$$

III. AN ACOUSTIC SCATTERING PROBLEM: SOME NUMERICAL RESULTS

We consider the acoustic scattering problem of the Introduction for an acoustic plane wave that hits the obstacle Ω.[1] Let $u^i(\underline{x})$ be an incoming acoustic plane wave, that is,

$$u^i(\underline{x}) = e^{ik(\hat{\alpha},x)}, \tag{45}$$

where $k > 0$ is the wave number and $\hat{\underline{\alpha}} \in \mathbf{R}^3$ is a unit vector (i.e., $\|\hat{\underline{\alpha}}\| = 1$) that gives the direction of propagation of the incoming wave. Let us denote with $u(\underline{x})$ the acoustic field scattered by the obstacle Ω when hit by $u^i(\underline{x})$. When Ω is an acoustically soft obstacle, the scattered field $u(\underline{x})$ satisfies Eqs. (1), (2), and (3) with

$$f(\underline{x}) = -u^i(\underline{x}), \quad \underline{x} \in \partial\Omega, \tag{46}$$

TABLE II. Accuracy of the far field computed with the perturbative series.

	$E_L^{|F_0|}$		
k	Sphere	Ellipsoid	Modified pipe
2	5.15(−4)	2.02(−4)	1.95(−2)
4	2.74(−3)	7.61(−3)	2.83(−2)
6	7.60(−3)	2.85(−2)	2.06(−2)
8	1.56(−2)	6.85(−2)	2.39(−2)
10	2.73(−2)	1.27(−1)	4.00(−2)
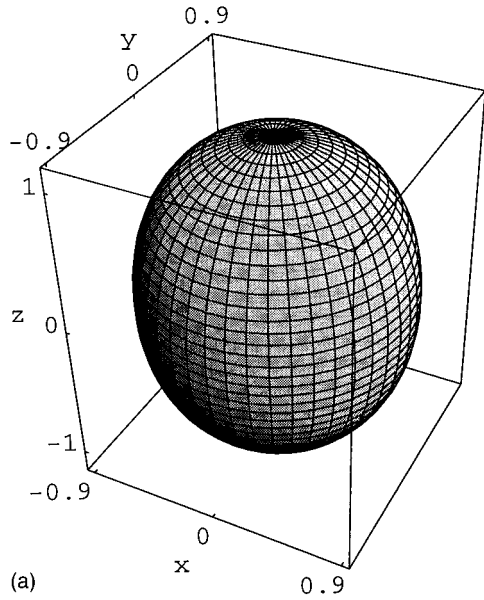
(a)
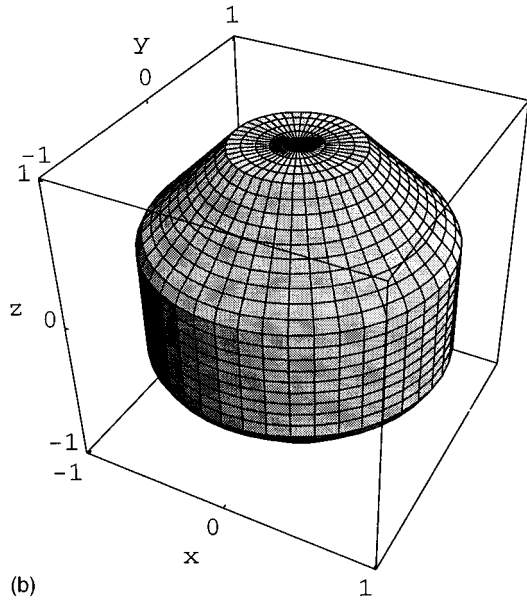
(b)

FIG. 2. (a) Ellipsoid $a=1.1$, $b=0.9$. (b) Modified pipe $r_0=0.965$.

and from Eq. (44) using Eqs. (36)–(38), we obtain

$$F_0(\hat{\underline{x}})=-\frac{1}{4\pi}\int_{\partial B}e^{-ik\zeta(\hat{\underline{y}})(\hat{\underline{x}},\hat{\underline{y}})}(\zeta(\hat{\underline{y}}))^2(1+\|\overline{\boldsymbol{\nabla}}\zeta\|^2(\hat{\underline{y}}))$$

$$\times\left(ik(\hat{\underline{\alpha}},\hat{\underline{y}})-\sum_{m=0}^{\infty}\hat{D}_m\right)e^{ik\zeta(\hat{\underline{y}})(\hat{\underline{\alpha}},\hat{\underline{y}})}\,ds(\hat{\underline{y}}),\quad\hat{\underline{x}}\in\partial B.$$

(47)

We expand $F_0(\hat{\underline{x}})$ in a (formal) power series in $(\zeta-1)$. That is,

$$F_0(\hat{\underline{x}})=F_0^{\langle 0\rangle}(\hat{\underline{x}})+F_0^{\langle 1\rangle}(\hat{\underline{x}})+F_0^{\langle 2\rangle}(\hat{\underline{x}})+O((\zeta-1)^3),$$

$$\zeta\to 1,$$

(48)

where $F_0^{\langle i\rangle}(\hat{\underline{x}})=O((\zeta-1)^i)$, $\zeta\to 1$, $i=0,1,2$. Let $\hat{\beta}$ is a unit vector in $\mathbf{R}^3$ from the expansions:
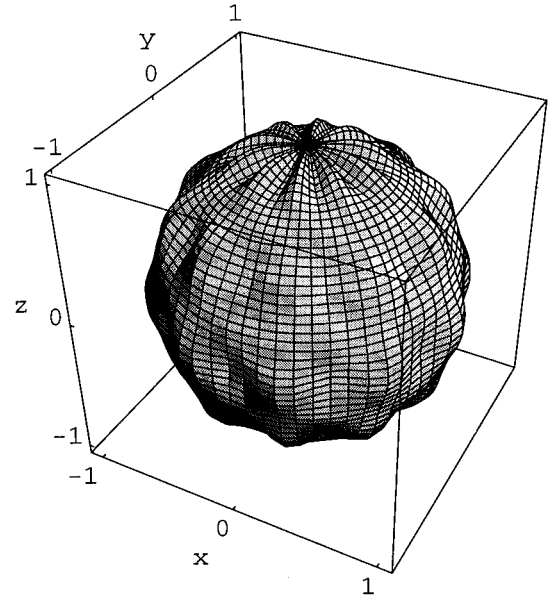
FIG. 3. Corrugated sphere $r_0=1$, $h=0.05$, $m=5$, $n=10$.

$$e^{\pm ik(\hat{\beta},\hat{\underline{y}})\zeta}=e^{ik(\hat{\beta},\hat{\underline{y}})}\sum_{n=0}^{\infty}\,(\pm 1)^n\,\frac{[ik(\hat{\beta},\hat{\underline{y}})]^n}{n!}\,(\zeta-1)^n,$$

it is easy to see that

$$F_0^{\langle 0\rangle}(\hat{\underline{x}})=-\frac{1}{4\pi}\int_{\partial B}e^{-ik(\hat{\underline{x}},\hat{\underline{y}})}[ik(\hat{\underline{\alpha}},\hat{\underline{y}})-\hat{D}_0]e^{ik(\hat{\underline{\alpha}},\hat{\underline{y}})}\,ds(\hat{\underline{y}})$$

(49)

and

$$F_0^{\langle 1\rangle}(\hat{\underline{x}})=-\frac{1}{4\pi}\int_{\partial B}e^{-ik(\hat{\underline{x}},\hat{\underline{y}})}\{(2-ik(\hat{\underline{x}},\hat{\underline{y}}))(\zeta-1)$$

$$\times[ik(\hat{\underline{\alpha}},\hat{\underline{y}})-\hat{D}_0]+[ik(\hat{\underline{\alpha}},\hat{\underline{y}})-\hat{D}_0]ik(\hat{\underline{\alpha}},\hat{\underline{y}})$$

$$\times(\zeta-1)-\hat{D}_1\}e^{ik(\hat{\underline{\alpha}},\hat{\underline{y}})}\,ds(\hat{\underline{y}}).$$

(50)

FIG. 4. Cutted octahedron.

110   J. Acoust. Soc. Am., Vol. 103, No. 1, January 1998

Misici *et al.*: Formalism for wave scattering   110
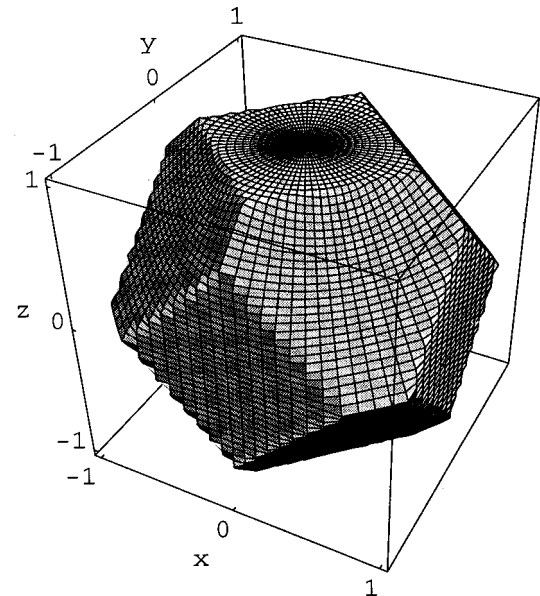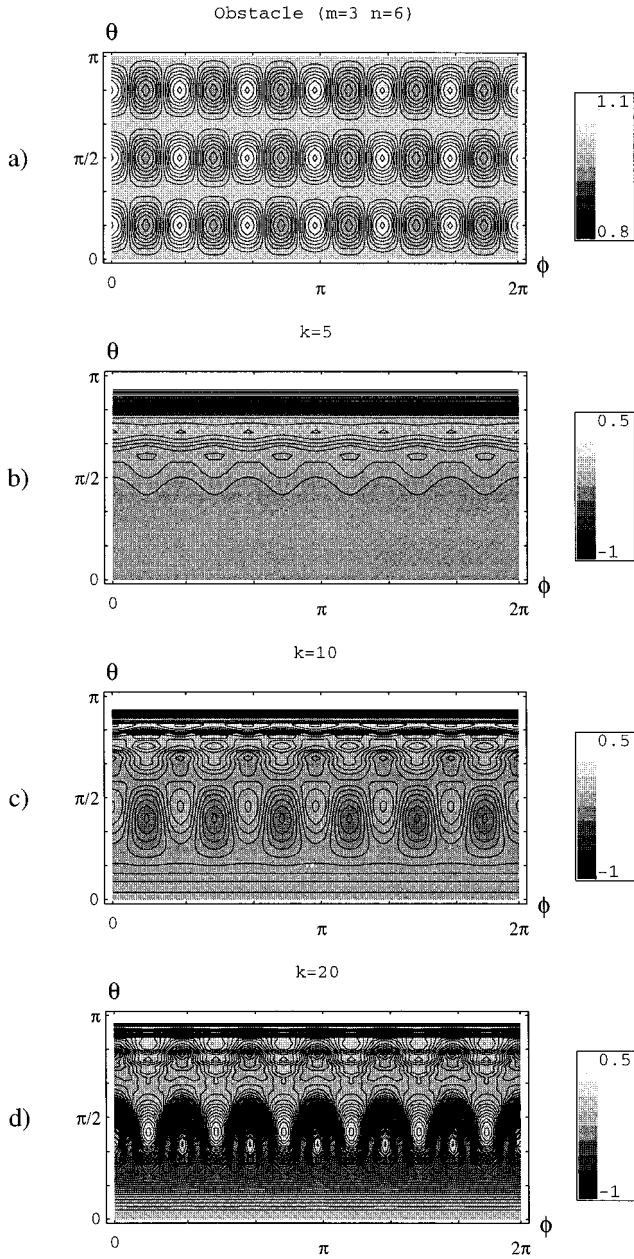
FIG. 5. (a) Contour plot of the corrugated sphere for $m=3$, $n=6$; (b), (c), (d) contour plots of $\log_{10}|OE_2(\hat{x})|$ relative to the geometry for different values of k.
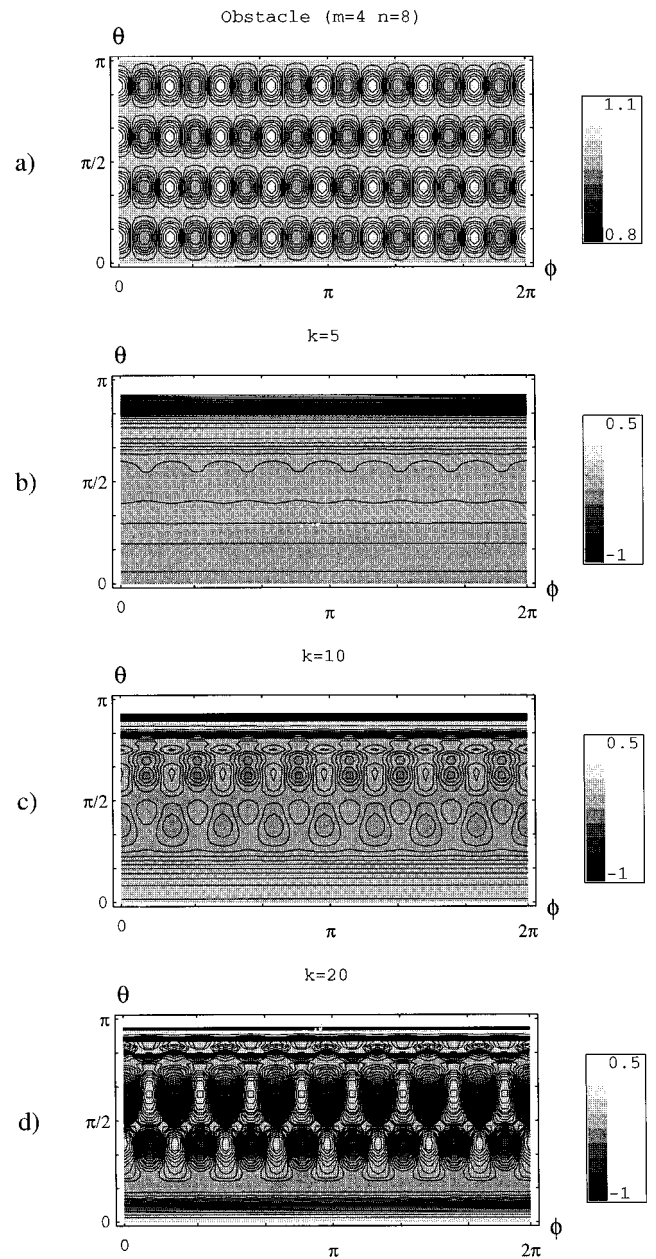
FIG. 6. (a) Contour plot of the corrugated sphere for $m=4$, $n=8$; (b), (c), (d) contour plots of $\log_{10}|OE_2(\hat{x})|$ relative to the geometry for different values of k.

A similar but more involved formula can be obtained for $F_0^{\langle 2 \rangle}(\hat{\underline{x}})$.

Let us denote with $Y_{lm}^{\tau}(\hat{\underline{x}})$ the real spherical harmonics:

$$Y_{lm}^{\tau}(\hat{\underline{x}}) = \begin{cases} \gamma_{lm} P_l^m(\cos\theta)\cos m\phi, & \tau=0 \\ \gamma_{lm} P_l^m(\cos\theta)\sin m\phi, & \tau=1 \end{cases}$$

with $\tau=0,1$, $l=\tau,\ldots,\infty$; $m=\tau,\ldots,l$, where $P_l^m(\cos\theta)$ are the Legendre polynomials and γ_{lm} are normalization factors, that is,

$$\gamma_{lm} = \left[\epsilon_m \frac{2l+1}{4\pi} \frac{(l-m)!}{(l+m)!} \right]^{1/2},$$

$$l=\tau,\ldots,\infty; \quad m=\tau,\ldots,l,$$

with $\epsilon_m=2$ if $m=0$ and $\epsilon_m=1$ if $m\neq 0$, and $0!=1$. In the following we denote with $\Sigma_{\tau lm}(\cdot)$ the sum $\Sigma_{\tau=0}^{1}\Sigma_{l=\tau}^{\infty}\Sigma_{m=\tau}^{l}(\cdot)$. The expressions for $F_0^{\langle 0 \rangle}$ and $F_0^{\langle 1 \rangle}$ involve the computation of the action of the operators defined in Sec. II.

From the Jacobi–Anger expansion[7] of $e^{ik(\hat{\alpha},\hat{y})}$ and $e^{-ik(\hat{x},\hat{y})}$ it is easy to compute $F_0^{\langle 0 \rangle}$, $F_0^{\langle 1 \rangle}$, and $F_0^{\langle 2 \rangle}$. In particular, using the property of the Bessel functions j_l and Hankel functions h_l, it is easy to see that the zero order term $F_0^{\langle 0 \rangle}$ is the far-field pattern generated by the obstacle B, when hit by the same incoming wave, that is,

$$F_0^{\langle 0 \rangle}(\hat{\underline{x}}) = \frac{4\pi i}{k} \sum_{\tau lm} \frac{j_l(k)}{h_l(k)} Y_{lm}^{\tau}(\hat{\underline{\alpha}}) Y_{lm}^{\tau}(\hat{\underline{x}}), \quad \hat{\underline{x}} \in \partial B. \tag{51}$$
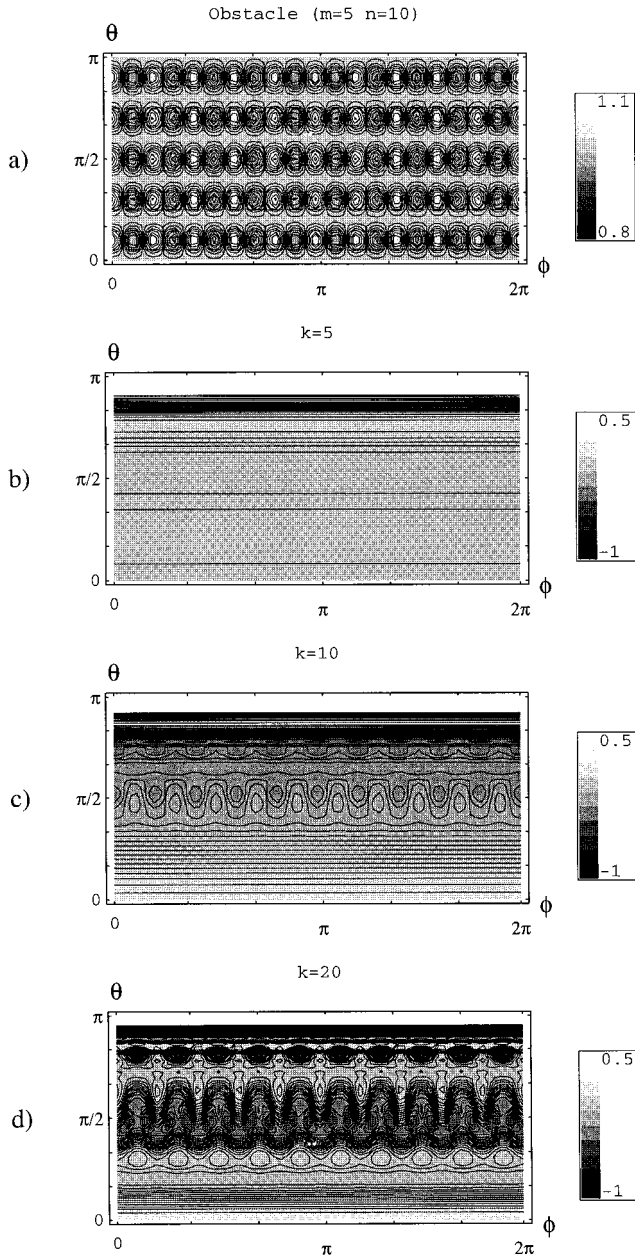
FIG. 7. (a) Contour plot of the corrugated sphere for $m=5$, $n=10$; (b), (c), (d) contour plots of $\log_{10}|OE_2(\hat{x})|$ relative to the geometry for different values of k.

FIG. 8. (a) Contour plot of the octahedron; (b), (c), (d) contour plots of $\log_{10}|OE_2(\hat{x})|$ relative to the geometry for different values of k.

We consider the simplest possible obstacle that is the sphere B_R; we have $\partial B_R = \{r = \zeta(\theta,\phi) = R = \text{const.}\}$. First of all, we consider the problem of where to truncate the series expansion $\Sigma_{\tau l m}$ to obtain satisfactory numerical results. Let us consider the series representing the far field generated by the sphere $\{r=R\}$ when hit by the plane wave (45) truncated at $L_m > 0$, that is,

$$F_{0,L_m}(\hat{\underline{x}}) = \frac{4\pi i}{k} \sum_{\tau=0}^{1} \sum_{l=\tau}^{L_m} \sum_{m=\tau}^{l} \frac{j_l(kR)}{h_l(kR)} Y_{lm}^{\tau}(\hat{\underline{\alpha}}) Y_{lm}^{\tau}(\hat{\underline{x}}). \tag{52}$$

Given R the number of spherical harmonics (i.e., the value of L_m) that must be considered to guarantee that Eq. (52) is a satisfactory approximation of the far field $F_0(\hat{x})$ depends on the wave number k, and increases with k.

In Fig. 1 we indicate with $\hat{x}_f$ the forward scatter direction $\hat{\underline{\alpha}}$. Figure 1 shows that, for $R=1.1$, numerical convergence is reached at values of L_m that increase linearly with k. We observe that if the geometry of the obstacle is more complicated than the geometry of the sphere and the far field pattern is expressed in a truncated series of spherical harmonics the value of L_m that ensures numerical convergence for a given k must be expected to be greater or equal than the value of L_m that ensures numerical convergence of the similar expansion for the sphere.

Let us make a comparison of the computational work needed to solve a given problem with the ''T-matrix'' method or with the truncated perturbative series (48).

For a fixed L_m and a fixed incident direction $\hat{\underline{\alpha}}$ Table I gives the number of double integrals that must be computed. With OE_M we indicate

$$OE_M(\hat{\underline{x}}) = \sum_{i=0}^{M} F_0^{\langle i \rangle}(\hat{\underline{x}}), \quad M = 0,1,2,..., \quad \hat{\underline{x}} \in \partial B. \qquad (53)$$

When k increases L_m increases and the ''T-matrix'' method becomes very expansive computationally. In fact, in the ''T-matrix'' method after computing the integrals considered in Table I we must solve a real linear system of order $2(L_m + 1)^2$. An advantage of the ''T-matrix'' method is that after computing the integrals the far field corresponding to any incident wave can be obtained solving the linear system mentioned above.

Table II shows a comparison between the results obtained with the perturbative series (48) and results obtained with the ''T-matrix'' method for a set of axially symmetric obstacles.

The obstacles considered in Table II are the following:

(1) Sphere $\quad \zeta(\theta, \phi) = 1.05$

(2) Ellipsoid $\quad \zeta(\theta, \phi) = \left[\left(\dfrac{\sin \theta}{a} \right)^2 + \left(\dfrac{\cos \theta}{b} \right)^2 \right]^{1/2}$

(3) Modified pipe

$$\zeta(\theta, \phi) = \begin{cases} r_0 / \cos \theta & \text{if } 0 \leq \theta < \theta_1 \\ r_0 \sqrt{2} / (\sin \theta + \cos \theta) & \text{if } \theta_1 \leq \theta < \theta_2 \\ r_0 / \sin \theta & \text{if } \theta_2 \leq \theta < \theta_3 \\ r_0 \sqrt{2} / (\sin \theta - \cos \theta) & \text{if } \theta_3 \leq \theta < \theta_4 \\ -r_0 / \cos \theta & \text{if } \theta_4 \leq \theta \leq \pi, \end{cases}$$

where $0 \leq \theta \leq \pi$, $0 \leq \phi < 2\pi$ and with r_0, a, $b \in \mathbf{R}^+$, $\theta_1 = \arccos(2 + \sqrt{2}/4)^{1/2}$, $\theta_2 = \pi/2 - \theta_1$, $\theta_3 = \pi/2 + \theta_1$, $\theta_4 = \pi - \theta_1$. Figure 2 shows the graphics of the obstacles 2 and 3.

Let $\hat{\alpha} = (0,0,1)$ be the incident direction of the incoming wave and let $F_0^T(\hat{\underline{x}})$ be the far field obtained with the ''T-matrix'' method corresponding to that incoming wave. In Table II we indicate with $E_{\mathbf{L}_2}^{|F_0|}$ the quantity

$$E_{\mathbf{L}_2}^{|F_0|} = \frac{\left[\sum_{j=0}^{20} |F_0^T(\hat{\underline{x}}_j) - OE_2(\hat{\underline{x}}_j)|^2 \right]^{1/2}}{\left[\sum_{j=0}^{20} |F_0^T(\hat{\underline{x}}_j)|^2 \right]^{1/2}},$$

where $\hat{\underline{x}}_j = (\sin \theta_j, 0, \cos \theta_j)$ with $\theta_j = j\pi/20$, $j = 0,1,2,...,20$. The notation $Y(-n)$ means $Y \times 10^{-n}$.

The geometries considered in Table II are axially symmetric, and the far field F_0^T is obtained exploiting, in the computation, the symmetry of the obstacles. The relative errors $E_{\mathbf{L}_2}^{|F_0|}$, shown in Table II, increases for increasing values of k, this is due to the fact that the two methods used to compute the far-field loose accuracy for increasing values of k.

We can see that $E_{\mathbf{L}_2}^{|F_0|}$ is always small and depends on $k(\zeta - 1)$. For $k \leq 10$ and $\max|\zeta(\theta,\phi) - 1| \leq 0.05$ we have $E_{\mathbf{L}_2}^{|F_0|}$ less than 3%. Higher order terms of the perturbative series (48) can be used to maintain the accuracy of the results when studying obstacles such that $k|\zeta - 1| > 0.5$.

We now consider more complicated geometries and for these geometries the computational work needed to approximate the far field using the ''T-matrix'' method becomes substantially greater than the work needed with the method presented here when k increases.

We have considered two special classes of geometries:

(i) obstacles with multiscale corrugations;
(ii) obstacles with Lipschitz continuous boundaries such as polyhedra.

The obstacles with multiscale corrugations are represented by

(4) Corrugated sphere $\quad \zeta(\theta, \phi) = r_0 + h \sin^2 m\theta \cos n\phi$,

where $r_0 \in \mathbf{R}^+$, $h \in \mathbf{R}$, $|h| < r_0$, m, n are integers (see Fig. 3).

The obstacles with Lipschitz continuous boundary are represented by

(5) Cutted octahedron (see Fig. 4).

The analytical expression of $\zeta(\theta, \phi)$ for the cutted octahedron is complicated and will be omitted. We mention that the smallest sphere containing the cutted octahedron has radius $r = 1.0455$ and the largest sphere contained in the cutted octahedron has radius $r = 0.965$

Figures 5, 6, 7, and 8 show the contours plots of the geometry [i.e., Figs. 5(a), 6(a), 7(a), 8(a)] and the contours plots of $\log_{10}|OE_2(\hat{x})|$ for three different values of k [i.e., Figs. 5(b), (c), (d), 6(b), (c), (d), 7(b), (c), (d), 8(b), (c), (d)]. In Figs. 5, 6, and 7, relative to the corrugated sphere, for different corrugations, we observe that, as expected, expansion (48) shows the higher frequency corrugations for higher values of k. For example, Fig. 7(b) shows a far-field pattern independent of ϕ, that is the far field of an axially symmetric object. This means that the corrugation shown in Fig. 7(a) is not seen by the incoming wave when $k = 5$ [Fig. 7(b)]. Figure 8 relative to the cutted octahedron shows as for increasing values of k we can see first the facets then the corners and finally the vertices of the cutted octahedron.

[1] D. Colton and R. Kress, *Integral Equation Methods in Scattering Theory* (Wiley, New York, 1983).
[2] A. G. Ramm, *Scattering by Obstacles* (Reidel, Dordrecht, The Netherlands, 1986).
[3] D. M. Milder, ''An improved formalism for wave scattering from rough surface,'' J. Acoust. Soc. Am. **89**, 529–541 (1991).
[4] J. B. Keller and D. Givoli, ''Exact nonreflecting boundary conditions,'' J. Comput. Phys. **82**, 172–192 (1989).
[5] P. C. Waterman, ''New formulation of acoustic scattering,'' J. Acoust. Soc. Am. **45**, 1417–1429 (1969).
[6] G. Kristensson and P. C. Waterman, ''The T-matrix for acoustic and electromagnetic scattering by circular disk,'' J. Acoust. Soc. Am. **72**, 1612–1625 (1982).
[7] D. Colton and R. Kress, *Inverse Acoustic and Electromagnetic Scattering Theory* (Springer-Verlag, Berlin, 1992).

Dynamical surface response of a semi-infinite anisotropic elastic medium to an impulsive force

C. Bescond and M. Deschamps

Laboratoire de Mécanique Physique, Université de Bordeaux I, URA C.N.R.S. No. 867,
351, Cours de la Libération, 33405-Talence Cedex, France

The dynamical surface response to an impulsive point source or line source at any location on the free surface of an anisotropic half-space is solved. The calculation of the Green's functions of the elastic homogeneous medium is based on the Cagniard–de Hoop method. This theoretical study models the generation–detection of transient surface acoustic waves with a point source–point receiver or with a line source–point receiver. An inspection of singular points in the complex plane of the phase slownesses points out the striking phenomena due to anisotropy of surface wave propagation. As a result, the propagation of the Rayleigh wave, of the surface skimming waves, and of the pseudosurface wave are studied as well as the wavefronts focusing. In addition, the diffraction effects by the cusps are emphasized. © *1998 Acoustical Society of America.*
[S0001-4966(97)05412-X]

INTRODUCTION

The study of the elastodynamic response of an elastic half-space to a pulsed concentrated force is of fundamental importance in many areas. Diverse investigations have been presented for this so-called Lamb's problem to calculate the displacement field inside isotropic or anisotropic half-spaces submitted to either a line or a point source.[1–7]

For anisotropic solids, the bulk wavefront generated from such concentrated sources may be folded to form cuspidal structures. This point has attracted considerable attention in the literature dealing with either the ray surface calculation or the Green's function calculation or the analysis of bulk phonon focusing.[8–11] Recently, interest for this Lamb's problem has been revitalized due to the applications of laser impact generation of ultrasonic waves as reviewed by Castagnède and Berthelot[12] and Monchalin,[13] see also V. Gusev *et al.*[14] who present theoretical backgrounds for both frequency and time domains laser-induced interface waves and references for laser applications.

Numerous authors have studied similar effects dealing with surface acoustic waves. In the literature, the existence of surface waves was first discussed in terms of medium anisotropy and surface orientation.[15–17] More recently, numerous theoretical and experimental analyses concerning the surface phonon focusing effects[18–20] have been done for piezoelectricity and acoustics. The analyses of surface acoustic waves generated by a point source is significant since numerous new developments use this wave generation technique as applied in microscopy,[21] photoacoustic spectroscopy,[22] flaw detection,[23] and the investigation of elastically anisotropic solids. For instance, the stiffness coefficients of anisotropic materials can be obtained from the measurement of bulk group velocities[24–26] or from the measurement of Rayleigh wave velocities.[27]

Consequently, the fundamental phenomena occurring in surface acoustic wave propagation have caused a revival of interest for anisotropic half-spaces. In several papers, the analyses of these remarkable phenomena due to anisotropy are performed by means of asymptotic expressions of the surface waves generated with a harmonic[28,29] or a pulsed point source.[19] In other papers, the behavior of surface waves is studied by analyzing the surface elastodynamic response. Pekeris,[30] 40 years ago, obtained closed-form solutions for transversely isotropic half-spaces submitted to a point source buried within the medium. Using the Cagniard–de Hoop method, Burridge obtained the displacement field for a general anisotropic half-space submitted to an impulsive surface line load[31] without explicitly calculating residues. Others authors have presented similar problems[32] and more recently Maznev and Every[33] have presented a Fourier transform technique to solve the problem of a line impacting the free surface of an anisotropic elastic medium. Maznev *et al.*[34] also reported recently experimental observations of the cusp of the Rayleigh wavefront propagating from a point source. In a recent paper, using the Radon transform, Wang and Achenbach have presented a new formulation of the two-dimensional (2-D) and three-dimensional (3-D) Lamb's problem for anisotropic half-spaces.[35] In this theoretical work, the cusp for both the Rayleigh and the surface skimming waves are not observable, neither is the pseudosurface wave.

In the present paper, the surface displacement response in any location on the free surface of a general anisotropic half-space to an impulsive point source is treated. Particular attention is paid to the focusing phenomena for the Rayleigh wave and for the surface skimming waves as well as the diffraction caused by the cusps. For this purpose, an original procedure is developed which makes use of the Cagniard–de Hoop method, residue calculations, and integration of distributions. Moreover, to gain a better understanding of the complexity of the physical phenomena, the plane problem of an impacting line source on the surface is also considered.

Our work is organized into three main steps. First, the Cauchy problem is formulated. Second, the solution is pre-
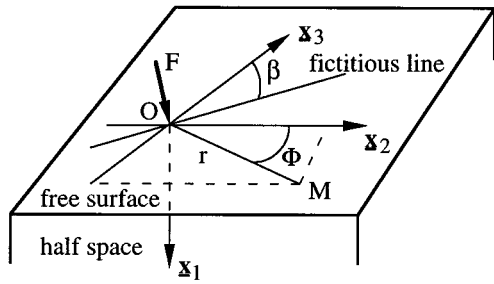
FIG. 1. Geometry of the problem.

sented in the time–space domain where the physical phenomena appear distinctly from different mathematical terms referring to singular points in the complex plane. Third, a numerical implementation illustrates different physical phenomena for a half-space belonging to the cubic class of symmetry. The focusing of the surface skimming waves and the diffraction effects by the cusp of the Rayleigh wave and by the cusp of the surface skimming waves are discussed. In addition, the generation of the pseudosurface wave by a point source is clearly discussed.

I. FORMULATION OF THE PROBLEM

A semi-infinite anisotropic elastic medium which occupies the region $x_1 \geq 0$ with a plane surface located at $x_1 = 0$ is impacted on its top by a pointlike source. The transient source acts at the origin on the surface ($x_2 = 0$, $x_3 = 0$). A pointlike receiver is situated on the surface, its coordinates are $M = (x_1 = 0, x_2, x_3)$ or $M = (x_1 = 0, r, \Phi)$, as shown in Fig. 1. The components $u_i(M,t)$ ($i = 1 \cdots 3$) of the displacement field, in the fixed reference ($\mathbf{x}_1, \mathbf{x}_2, \mathbf{x}_3$), due to acoustic disturbances propagating outwards from the source will be calculated.

The solutions of this classical Lamb's problem satisfy the Sommerfeld assumption, the causality principle, and the following system of partial differential equations:

$$C_{ijkl} \frac{\partial^2 u_k}{\partial x_l \, \partial x_j} = \rho \frac{\partial^2 u_i}{\partial t^2}, \tag{1}$$

$$C_{i1kl} \frac{\partial u_k}{\partial x_1} = -F_i \delta(x_2, x_3) H(t) \quad \text{for } x_1 = 0, \tag{2}$$

which are the wave equation, the boundary and initial conditions on the free surface. Note that, throughout this paper, the summation convention over repeated indices is employed with $i,j,k,l = (1 \cdots 3)$. In these equations C_{ijkl} expresses the stiffness tensor, ρ stands for the density, F_i ($i = 1 \cdots 3$) are the components of the loading, $\delta(x_2, x_3)$ represents the 2-D Dirac delta function, which models the spatial behavior of the source on the surface, and $H(t)$ is the Heaviside unit step function in time, which expresses the transient time function of the source. The choice of this time dependence is made since in such a case the calculations are more directly obtained. However, the response to a delta function could be obtained if necessary by a simple calculation of the derivative with respect to t.

The problem considered will be restricted to the calculation of the normal displacement $u_1(M,t)$ due to a point

loading normal to the surface, such that $F_1 \neq 0$ and $F_i = 0$ for $i = 2,3$. Taking such a spatial source into consideration, the dynamic Green's function is in agreement with the generation of acoustic waves in the ablation regime when using a pulsed laser beam as a source. However, from a temporal point of view, to correctly model the ablation range, a time derivative will be required. In addition, only the normal displacement is calculated, because it is the easiest to determine experimentally, using a laser interferometer probe which detects the acoustic events. The generalization to the other components of the Green's tensor G_{ij} can be obtained quite easily by considering a point force acting in the x_j direction and by calculating the Green's function related to the displacement in the x_i direction $u_i(M,t)$.

The above theoretical problem is solved according to the Cagniard–de Hoop method. The solutions of the analytical system with inhomogeneous boundary and initial conditions are found by using mixed Laplace–Fourier transforms as presented by Van der Hijden.[4,7] A Laplace transform over time t (denoted by a caret on a capital letter) for which the associated Laplace parameter is s and a double Fourier transform over the spatial variables x_2 and x_3 for which the associated Fourier parameters are, respectively, p_2 and p_3, are performed. The Laplace transform of the normal displacement $\hat{U}_1(M,s)$ is then in the form:

$$\hat{U}_1(M,s) = \frac{1}{(2i\pi)^2} \int_{-\pi/2}^{+\pi/2} \left(\int_0^{+i\infty} + \int_0^{-i\infty} \right) f(p,\beta)$$
$$\times e^{-spr\cos(\beta - \Phi)} p \, dp \, d\beta, \tag{3}$$

where the changes of variable $p_2 = p \cos(\beta)$ and $p_3 = p \sin(\beta)$ have been introduced for convenience. Physically, when assuming the plane problem of a line source, which makes an angle β with the x_3 axis, the introduced parameter p is a slowness vector component on the free surface following the direction normal to the fictitious line source (see Fig. 1). In other words, this parameter is the phase slowness component on the surface and following the direction β with respect to the x_2 axis, of an homogeneous or inhomogeneous plane wave. In the remainder, the propagation directions will be systematically referred to the x_2 axis. The three-dimensional feature of the spatial distribution of the source is taken into account by the integration over β.

The function $f(p,\beta)$ introduced in the integrand of Eq. (3) is the solution of the system of partial differential equations in the Laplace–Fourier transform space, such that:

$$f(p,\beta) = s^2 A_n \nu_1(\eta_n). \tag{4}$$

The functions $\eta_n = \eta_n(p,\beta)$ and $\nu_1(\eta_n)$ are, respectively, the slowness and the polarization vector components, perpendicular to the surface for each mode n ($n = 1 \cdots 3$). These two quantities are related to the slowness vector component on the surface p, by the Christoffel's equation.[36] The functions $\eta_n = \eta_n(p,\beta)$ are the eigenvalues of the Christoffel's equation and accordingly they are the roots of the Christoffel's characteristic equation. The function $\nu_1(\eta_n)$ is the component along the x_1 axis of the eigenvector associated to the eigenvalue η_n. The weighting factors, $A_n = A_n(\eta_1, \eta_2, \eta_3)$,

fixed β

branch cut
○ branch point
● Rayleigh pole
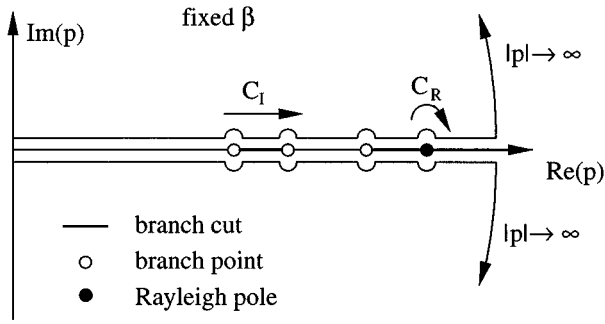
FIG. 2. Cagniard–de Hoop's contours associated to the surface response.

are the solutions of the linear system associating the boundary and the initial conditions, see Eq. (2):

$$[M]\begin{bmatrix} A_1 \\ A_2 \\ A_3 \end{bmatrix} = [S], \tag{5}$$

where M is a 3×3 matrix for which each component is given by $M_{in} = C_{i1kl}\,\partial_l \nu_k(\eta_n)$, where $\nu_k(\eta_n)$ is the polarization vector component following the x_k axis of the mode for which the slowness components on the surface and on the normal to the surface are, respectively, p and η_n. The expressions ∂_i $(i=1\cdots3)$ are such that: $\partial_1 = -s\,\eta_n$, $\partial_2 = -sp_2$ and $\partial_3 = sp_3$. The vector $[S]$ represents the source. Assuming a loading normal to the free surface and taking into account the temporal and the spatial expressions of the source, Eq. (2), it is found that:

$$[S]=\begin{bmatrix} -F_1/s \\ 0 \\ 0 \end{bmatrix}. \tag{6}$$

The weighting factor is given by

$$A_n(\eta_1,\eta_2,\eta_3) = \frac{N_n}{R}, \tag{7}$$

where R is the determinant of the matrix M and represents the Rayleigh function which ensures the free-surface condition. The functions N_n, which are the determinant of the matrix $[M]$ when its nth column is replaced by the vector $[S]$, ensures that the inhomogeneous boundary condition, due to the transient loading, is satisfied. In these boundary and initial conditions, the function $f(p,\beta)$ does not depend on the Laplace parameter s, as is required to apply the Cagniard–de Hoop method.

In the p-variable complex plane, the function $f(p,\beta)$ exhibits branch points associated to the functions η_n and poles for which the Rayleigh function is zero. The complex p-plane possesses branch cuts to keep the η_n single valued, as illustrated in Fig. 2. The condition for downward propagating waves is satisfied by restricting the choice of the real pair (p,η_n) to those for which the associated ray vector is directed towards the elastic medium. In addition, the Cauchy–Riemann differential equations ensures analytic continuity of the vertical slownesses η_n.

Classically, the Cagniard–de Hoop method consists in closing the original paths of the integrals (3) along the imaginary axes by a large circular path ($|p|\rightarrow\infty$) and by a path

along the positive real axis where the branch cuts and a pole are located. The inversion of the Laplace transform is then immediate. From Eq. (3), according to the Cauchy's principle, to the Jordan's lemma, and to the Schwarz's reflection principle, i.e., $f(p^*)=f^*(p)$ where the asterisk denotes the complex conjugate, the Laplace transform of the normal displacement field is given by

$$\hat{U}_1(M,s) = \hat{U}_I(M,s) + \hat{U}_R(M,s), \tag{8}$$

with

$$\hat{U}_i(M,s)$$

$$= -\frac{1}{2\pi^2}\,\text{Re}\int_{-\pi/2}^{+\pi/2}\int_{C_i} f(p,\beta)e^{-\text{spr}\cos(\beta-\Phi)}p\;dp\;d\beta, \tag{9}$$

where $i=R,I$ and where Re stands for the real part, C_I is the path which skims the positive real axis of the complex p plane, and C_R is the semicircular path of integration around the Rayleigh pole. The deformation of the original paths, initially along the imaginary axes has been suggested by Cagniard.[37]

The path C_I is above the edges of the branch cuts situated on the real axis. Consequently and according to the Cauchy–Riemann differential equations, the imaginary part of the solutions η_n is systematically negative. Let us denote the Rayleigh pole p_R, such that the dispersion equation of the associated surface wave is given by $R(p_R,\beta)=0$. As it is well known, the solution of this equation in terms of p is real.[15] With our notations, as already pointed out, the quantity p_R represents the slowness of the Rayleigh wave in the β direction with respect to the x_2 axis. Due to anisotropy, this Rayleigh wave slowness depends, of course, on the β angle.[38]

For anisotropic crystals, a so-called pseudosurface wave can exist for certain directions of propagation β.[39] As a matter of fact, it can be shown that, in addition to the Rayleigh pole, there exists another particular point for which the Rayleigh function $R(p,\beta)$ tends to zero for a real value of the variable p. The Rayleigh function is effectively zero for a complex value of p. Moreover, in this case, the Cauchy–Riemann conditions are not simultaneously satisfied by the three η_n solutions.[40] In other words, this pole lies on other Riemann sheets which are different from the principal sheet of integration. Accordingly, this is not a pole to take into consideration for our problem. However, a pseudosurface wave can be associated to this particular solution. This wave is similar to the Rayleigh wave in the sense that its energy flow is essentially parallel to the surface. However, the imaginary component of p leads to a radiation into the solid. As this wave propagates along the interface, some of its energy leaks into the solid. It is similar to the generalized Rayleigh wave present at the solid–liquid interface which leaks its energy into the liquid. To conclude this part and to come back to the integration problem under consideration, no particular attention is required to avoid this "pseudopole" in contrast with the Rayleigh pole.

II. LAPLACE INVERSION OF THE SOLUTION

It is the purpose of this section to calculate the inverse Laplace transform of the normal displacement field $\hat{U}_I(M,s)$ as given by Eq. (3). To this end, owing to the different features of the two functions introduced in Eq. (8), a different process will be applied on each term. The first integral over p of the function $\hat{U}_I(M,s)$ will be calculated by means of the Cagniard–de Hoop method[41] while the second integral over β will be obtained numerically. Finally, the inversion of the Laplace transform $\hat{U}_R(M,s)$ will provide an exact analytical calculation.

A. Integral in the sense of Cauchy principal values

Let us calculate first the inverse Laplace transform of the integral $\hat{U}_I$ along the path C_I. The inversion of $\hat{U}_I$ follows immediately by inspection, if the right-hand side can be re-arranged into the standard expression for a Laplace transform. This is accomplished by means of the Cagniard–de Hoop change of variable given by

$$p = \frac{t}{r \, \cos(\beta - \phi)}, \tag{10}$$

which defines the Cagniard–de Hoop t-parametric C_I path of integration for a fixed integration parameter β. The solution can be then written as

$$u_I(M,t) = -\frac{1}{2\pi^2} \, \text{Re} \int_{-\pi/2}^{+\pi/2} f(p,\beta) p \, \frac{dp}{dt} \, d\beta. \tag{11}$$

It should be noted that, by applying this technique to evaluate the integral over p, a singular point is introduced for $\beta - \Phi = \pm \pi/2$ in agreement with the Cagniard–de Hoop change of variable, as seen in Eq. (10). This singular point, artificially introduced, is a simple pole of the integrand of Eq. (11). A residue calculation is therefore required. The result of this residue calculation represents the residual elevation of the surface when all the transient divergent waves have propagated outwards from the point source to the point receiver. This contribution appears when both the emitter and the receiver are located on the same free surface while it is not present when the point receiver is inside the half-space, i.e., for example, on the rear interface of the layer. From Eq. (11), a residue evaluation and a numerical integral calculation over β leads to:

$$u_I(M,t) = u_{pv}(M,t) + u_s(M), \tag{12}$$

where the new functions are defined by

$$u_{pv}(M,t) = -\frac{1}{2\pi} \, P.V \int_{-\pi/2}^{+\pi/2} \text{Re}\left\{ f(p,\beta) p \, \frac{dp}{dt} \right\} d\beta, \tag{13}$$

$$u_s(M) = -\frac{1}{2\pi} \, \text{Im}\left\{ \text{Res}\left[f(p,\beta) p \, \frac{dp}{dt} \right]\bigg|_{\beta = \pm \pi/2 + \phi} \right\}, \tag{14}$$

where Im stands for the imaginary part. The integral over β, noted $u_{pv}(M,t)$, is the Cauchy principal values (symbolized by $P.V$) of the integral (11) to avoid on the one hand the Rayleigh poles situated on the real axis and on the other hand the singular point encountered when $\beta - \Phi = \pm \pi/2$. For this last singular point, a residue calculation (symbolized by Res) is necessary and yields to the waveform contribution $u_s(M)$, which represents the above-mentioned static solution. In the calculation performed by Kolomenskii and Maznev that use Fourier transforms to solve the surface response in the laser irradiation of an isotropic medium, this contribution is associated with the residue at the zero frequency pole.[42] Note that for anisotropic solids this contribution depends on the distance from the source to the receiver as well as on the observation direction.

B. Rayleigh pole contributions

To complete this study, it remains to determine the Rayleigh pole contribution by the inversion of the integral around the Rayleigh pole $\hat{U}_R$, introduced in Eq. (9). Classically, the integration along the semicircle of infinitesimal radius around a pole is performed by a residue calculation. The solution $\hat{U}_R$ being the Laplace transform of the Dirac delta function with translation of the t variable, its inverse Laplace transform is immediate and leads to:

$$u_R(M,t) = -\frac{1}{2\pi} \, \text{Im} \int_{-\pi/2}^{+\pi/2} \frac{N(p_R,\beta)}{R'(p_R,\beta)}$$

$$\times \delta(t - p_R r \, \cos(\beta - \Phi)) p_R d\beta, \tag{15}$$

where $N(p_R,\beta)$ is the numerator of the function $f(p,\beta)$ evaluated at the pole p_R and $R'(p_R,\beta)$ is the derivative of the Rayleigh function with respect to p, evaluated at the pole p_R. This integral of Dirac delta functions corresponds to the Rayleigh wave contributions to the normal displacement. At a fixed time t, let β_R be the particular angle of integration such that the integrand of Eq. (15) is not null and then such that the following system of equation is satisfied:
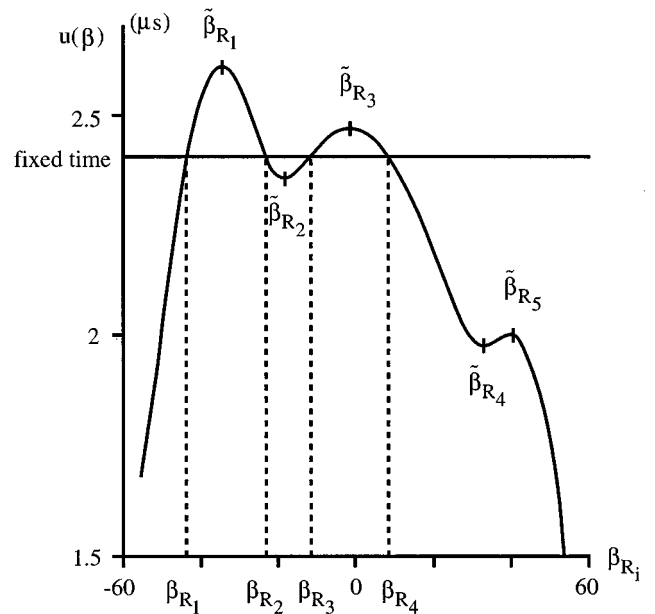
FIG. 3. Location of the Rayleigh poles in the range of integration as a function of time $t = u(\beta)$ for the wave form presented in Fig. 10(a): Rayleigh poles β_{R_i} ($i = 1$ to 4) for the fixed time (horizontal solid line) and $\tilde{\beta}_{R_j}$ ($j = 1$ to 5) extrema of the function $t = u(\beta)$.

$$t - p_R(\beta_R) r \cos(\beta_R - \Phi) = 0,$$
$$R(p_R(\beta_R), \beta_R) = 0 \qquad \beta_R \in \left] -\frac{\pi}{2}, \frac{\pi}{2} \right[. \qquad (16)$$

If this particular angle exists, it is not necessarily unique. Let n be the number of such particular angles, indexed i, such that $\beta_{R_i} < \beta_{R_{i+1}}$ ($i = 1 \cdots n$). In order to evaluate the integral of distributions (15), the following change of variable is needed:

$$u(\beta) = p_R(\beta) r \cos(\beta - \Phi). \qquad (17)$$

In the β range of integration this change of variable is not single valued. Consequently, to calculate the time response, the integral over β is split into subintervals as follows:

$$u_R(M,t) = -\frac{1}{2\pi} \, \mathrm{Im} \left(\int_{-\pi/2}^{\widetilde{\beta}_{R_j}} + \sum_{j=1}^{m-1} \int_{\widetilde{\beta}_{R_j}}^{\widetilde{\beta}_{R_{j+1}}} + \int_{\widetilde{\beta}_{R_m}}^{+\pi/2} \right)$$

$$\times \left\{ \frac{N(p_R, \beta)}{R'(p_R, \beta)} \, \delta(t - u(\beta)) p_R d\beta \right\}, \qquad (18)$$

where the parameters $\widetilde{\beta}_{R_j}$ ($j = 1 \cdots m$) are the extrema of the function $u(\beta)$ (cf. Fig. 3). These points, in addition to Eq. (16), satisfy the following equation:

$$\frac{\partial p_R(\widetilde{\beta}_{R_j})}{\partial \widetilde{\beta}} \, r \cos(\widetilde{\beta}_{R_j} - \Phi) - p_R(\widetilde{\beta}_{R_j}) r \sin(\widetilde{\beta}_{R_j} - \Phi) = 0. \qquad (19)$$

These particular angles $\widetilde{\beta}_{R_j}$, of prime importance in the waveform, define the Rayleigh wave slownesses $p_R(\widetilde{\beta}_{R_j})$ for which the normal to the slowness curve of the Rayleigh wave is oriented following the observation direction Φ. It is easy to show that the Rayleigh pole contributions to the normal displacement can be expressed, at time $t = u(\beta_{R_i})$, by an explicit function such that (cf. Appendix):

$$u_R(M,t) = -\frac{1}{2\pi} \sum_{i=1}^{n} \left[\left| \left| \frac{\partial u}{\partial \beta} \right|_{\beta_{R_i}} \right|^{-1} \right.$$

$$\left. \times \mathrm{Im} \left\{ \frac{N(p_R(\beta_{R_i}), \beta_{R_i})}{R'(p_R(\beta_{R_i}), \beta_{R_i})} \, p_R(\beta_{R_i}) \right\} \right], \qquad (20)$$

with

$$\frac{\partial u}{\partial \beta} = \frac{\partial p_R}{\partial \beta} \, r \cos(\beta - \Phi) - p_R r \sin(\beta - \Phi), \qquad (21)$$

where the symbol $\|$ indicates the absolute value. This absolute value appears because the derivative function, defined by Eq. (21), is only negative when the lower limit of the subinterval is greater than the higher limit (cf. Appendix).

To fix ideas, a concrete example, for which the waveform will be presented later on in Fig. 10(a), is illustrated in Fig. 3. The solutions β_{R_i} of Eq. (16) are plotted as a function of time expressed by $u(\beta)$ as well as the particular points $\widetilde{\beta}_{R_j}$. For this example $m = 5$ and at a fixed time, schematized by the straight horizontal line, four different Rayleigh poles (β_{R_i}, $i = 1 \cdots 4$) contribute to the solution (20), i.e., $n = 4$. Moreover, it should be noted that for an isotropic half-space

(or transversely isotropic material with the axis of transversal isotropy normal to the free surface), the two relations $n \leq 2$ and $m = 1$ hold true. By contrast, for anisotropic media, in particular for cubic symmetry, n and m can be, respectively, greater than 2 and 1. This feature reveals the presence of a folded Rayleigh wavefront. As a matter of fact, as the time increases, the straight horizontal line goes up and the Rayleigh poles meet together two by two at the particular points $\widetilde{\beta}_{R_j}$ and subsequently vanish. At these points the derivative $\partial u / \partial \beta$ is zero by definition and consequently the displacement tends to infinity, as it can be seen in Eq. (21). At this time, in the waveform, a sharp discontinuity appears[34] that corresponds to the Rayleigh wavefront, propagating outwards from the source to the pointlike receiver. Similar comments may be drawn concerning the wavefronts of the surface skimming waves (or the pseudosurface waves) by analyzing the plot of the branch points (or the ''pseudopole'') versus angle β. One difference is that these two contributions take place directly in the Cauchy principal values of the integral $u_{pv}(M,t)$. In fact, the contributions to the displacement due to the arrival of the surface skimming waves are connected to the branch points associated to the functions $\eta_n(p,\beta)$ ($n = 1 \cdots 3$). In this way, as the time increases, two branch points associated to the same function $\eta_n(p,\beta)$ meet together and subsequently vanish. At this time of disappearance, a discontinuity in the calculation of the Cauchy principal values $u_{pv}(M,t)$ reveals the arrival of a surface skimming wavefront.

These phenomena are typical of the point source case on a free surface and they do not exist with a line source excitation. In the next section, our interest is focused on this restrictive problem of the line source excitation.

C. Line source

This section is, in terms of notation, completely analogous to the preceding sections. For a better understanding of the different behaviors of the surface waves for the above 3-D problem, the line source excitation is briefly presented. From an experimental point of view, there are differences that arise from the employment of either a spherical lens or a cylindrical lens. The 2-D problem is illustrated in Fig. 1 by considering, as a real source, the so-called fictitious line which makes an angle β with the x_3 axis. The wavefronts are then supposed infinite in the direction of the line source and they propagate along the direction normal to this line.

The excitation differing from that given in Eq. (2), the boundary and the initial conditions become

$$C_{i1kl} \frac{\partial u_k}{\partial x_1} = -F_i \delta(x_3 \sin(\beta) - x_2 \cos(\beta)) \delta(t), \qquad (22)$$

for $x_1 = 0$, where F_i is, in this case, a positive magnitude constant force multiplied by unit time per unit length, $\delta(x_3 \sin(\beta) - x_2 \cos(\beta))$ is a spatial Dirac delta function to model a line load position, $\delta(t)$ is the temporal Dirac delta function. As previously, a normal load is assumed $F_i = 0$, for $i = 2,3$, and the normal displacement calculation is presented.

This calculation can, of course, be considered more restrictive in comparison with the point source, since the solu-

tion, in terms of Laplace transform, is reduced to a single Fourier transform. The Fourier parameter is p and represents the slowness vector component on the free surface in the direction normal to the line source. By skipping the detailed calculations, the solution by means of the Cagniard–de Hoop method is

$$u_1(M,t) = \frac{1}{\pi} \, \mathrm{Im} \left\{ f(p,\beta) \, \frac{dp}{dt} \right\}$$

$$- \mathrm{Re} \left\{ \frac{N(p_R,\beta)}{R'(p_R,\beta)} \, \delta(t - u(\beta)) \right\}, \qquad (23)$$

where the Cauchy principal value and the Rayleigh pole contribution are expressed by the first and the second terms, respectively. The variable p is, of course, related to time t by the Cagniard–de Hoop equation (10). In the present calculation, discontinuities associated to the Rayleigh wave or to the pseudosurface wave or to the surface skimming wave appear when the Cagniard–de Hoop t-parametric path reaches, respectively, the Rayleigh pole or the pseudopole or a branch point. It is of interest to remark that the residue calculation associated to the normal displacement is zero. Thus the Rayleigh wave disturbance appears only in the Cauchy principal value of the integral. A different behavior would be observed on the tangent displacement for which the Rayleigh pole contribution is nonzero. In this case, the Rayleigh disturbance appears as a delta function singularity at $t = p_R r \cos(\beta - \Phi)$.

In the next section, typical examples of surface waves, concerning both point and line spatial distributions of source, are illustrated.

III. NUMERICAL RESULTS

The theory described in the previous sections is used to compute the acoustic field for various source–receiver configurations. For the purpose of illustration, the [1, 0, 0] surface of a Copper crystal is selected. The nonzero stiffness constants of the Copper crystal are as follows: $C_{11} = C_{22} = C_{33} = 170$, $C_{12} = C_{13} = C_{23} = 123$, $C_{44} = C_{55} = C_{66} = 75.5$ (in GPa). The mass density is 8932 kg/m^3. For the line source, the magnitude of the load is 1 N μs m^{-1} and for the point source a force of 1 N is considered. The distance r between the observation point and the excitation is assumed to be constant and equal to 5 mm.

The numerical integration over β, Eq. (13), is carried out by an adaptive Gauss method which ensures an accurate value of the integral. The temporal step used for the waveform calculations is 5 ns. The impulse response is undersampled, being thus similar to applying low-pass filter with 200-MHz cut-off frequencies. This in turn explains some differences about the amplitudes of the various waves arrivals, which are sometimes very small, and nonobservable in a few cases. Rigorously, if one gains access to the continuous slope of the impulse response, some infinite discontinuities should be expected at the arrival of any Rayleigh wave. Since very large displacements appear, the numerical waveforms are truncated with the aim of emphasizing all the singularities. However, the waveform presented results from an exact calculation.
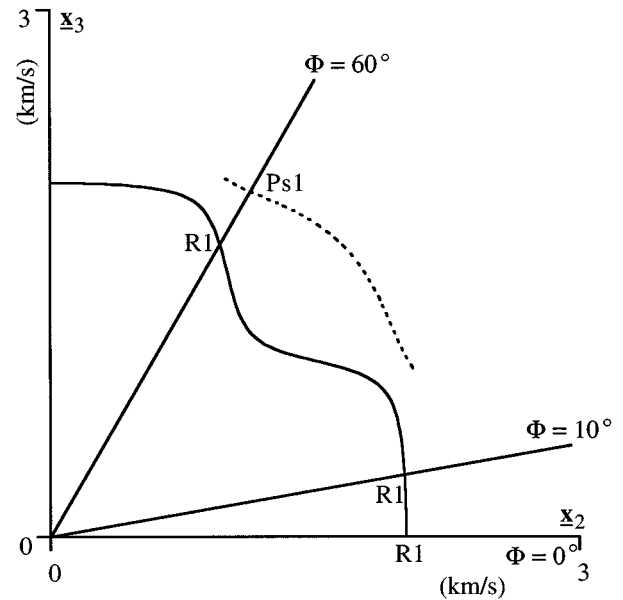
FIG. 4. Phase velocity curves of the Rayleigh wave (———) and of the pseudosurface wave (-----) for the [1,0,0] surface of a Copper crystal.

In the previous calculations, the line source has delta function dependence on time, whereas for the point source, this dependence is expressed by a unit step function. These two different kinds of temporal excitation are related since the response to the delta function may be considered as the derivative of the response to the step function. Accordingly, in order to compare the 2-D and the 3-D results, the derivative with respect to time will be performed on the Green's function obtained for the point source given by Eqs. (13), (14), and (20). Furthermore, referring to experiment, when a pulsed laser is used to produce ablation, a temporal Dirac delta function should approximately be applicable. For the point-source response with delta function dependence on time, the magnitude of the load F_1 is taken equal to 1 N μs.

First of all, for inspection purposes, the angular dependence of the surface wave velocities on the crystal surface under consideration are analyzed to predict the numerous arrivals in the wavefront calculation. Figures 4 and 6 present the phase velocity curves and the associated group velocity curves of both the Rayleigh wave and the pseudosurface wave. The angular dependence of the skimming surface waves velocities is plotted, in Fig. 5, as a function of the line-source orientation and, in Fig. 7, as a function of the observation direction, for the point source. The axes x_2 and x_3 refer to the crystallographic axes [0, 1, 0] and [0, 0, 1], respectively. The three source–receiver orientations, for which the calculation has been performed, i.e., $\Phi = 0°$, $\Phi = 10°$, and $\Phi = 60°$, are represented by the straight lines. In Figs. 4 and 6, the velocities of the different wavefronts, in these directions, are given by the intersections of these straight lines with either the ray curve or the phase velocity curve for the point source and the line source, respectively. Obviously, for the line source, the velocity of a wavefront in a direction Φ corresponds to the configuration of a line source orthogonal to this direction ($\beta = \Phi$). In Figs. 5 and 7, the intersections of these straight lines with the ray curves
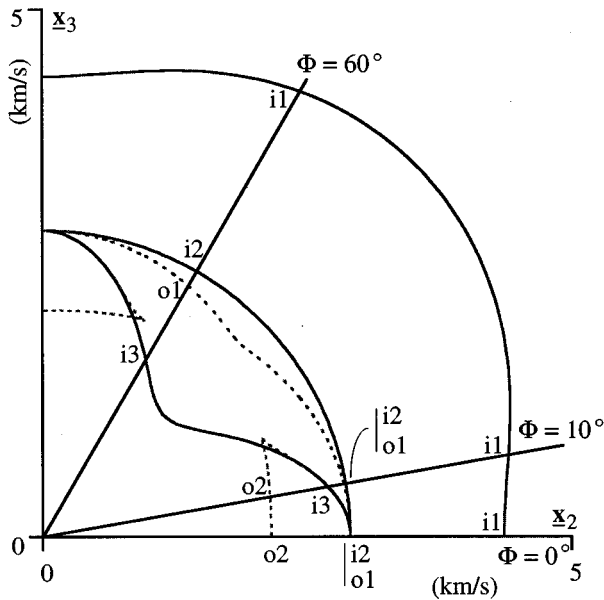
FIG. 5. Ray curves for the surface skimming waves generated with a line source: wave vectors in the plane of the interface (————), wave vectors out of the plane of the interface (-----).

FIG. 7. Ray curves for the surface skimming waves generated with a point source: wave vectors in the plane of the interface (————), wave vectors out of the plane of the interface (-----).

give the velocities of the surface skimming wavefronts, in these directions, for the line source and the point source, respectively. These different points are reported in the figures with the following rules: (R) for the Rayleigh wave, (Ps) for the pseudosurface wave, (i) for the surface skimming waves which have wave vectors in the plane of the interface, (o) for the surface skimming waves which have wave vectors out of the plane of the interface. These two latter wave types are distinguished since, although both have surface skimming rays, the wave vector associated to the first belongs to the free surface whereas the wave vector associated to the second is not contained in the plane of the free surface. It should be noted that, for the surface skimming wave gener-

FIG. 6. Group velocity curves of the Rayleigh wave (————) and of the pseudosurface wave (-----) for the [1,0,0] surface of a Copper crystal.

ated by a line source, the ray vector is the projection of the phase velocity vector on the surface. Consequently, for the restrictive case of the waves denoted (i), which exists when the free surface is a symmetry plane, the energy velocity vectors and the phase velocity vectors are identical. The additional indexes give number, by increasing time of flight, to the waves of the same type that exist for a fixed observation angle. In addition, two particular points (Rc) in Fig. 6 and (Sc) in Fig. 7, corresponding to the proximity of the cups, are marked.

Before focusing our interest on the waveforms, let us discuss the relative contributions of the Cauchy principal value $u_{pv}(M,t)$, of the Rayleigh poles $u_R(M,t)$ and of the static solution $u_s(M)$, to the impulse response in the case of a point source, as outlined in Eqs. (13), (14), and (20). As expected, the summation leads to a causal waveform, as shown in Fig. 8 in the case of a point source and of an Heaviside temporal excitation for the observation angle $\Phi = 0°$. Clearly, the displacement field is zero before the arrival time of the faster surface skimming wavefront, denoted (i1). Let us remark that the physical phenomena appear distinctly from different mathematical evaluations. The Cauchy principal value has rough discontinuities at the surface skimming waves arrivals and additionally becomes zero at the arrival time of the slowest surface skimming wave. As previously specified, the contributions of the Rayleigh wavefront to the normal displacement occur, in the present calculations, exclusively in the Rayleigh pole contributions $u_R(M,t)$. Moreover, as shown in Fig. 8(a), the residue calculation $u_s(M)$ yields the solution of equilibrium for an infinite time. It is of interest to note that when calculating the tangential displacement, these two observations do not hold true. In this case, all the physical phenomena appear in the Cauchy principal value and consequently some numerical difficulties are encountered.
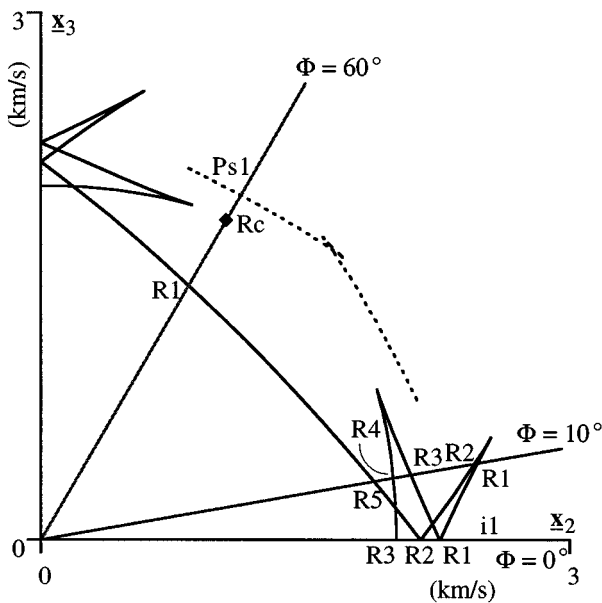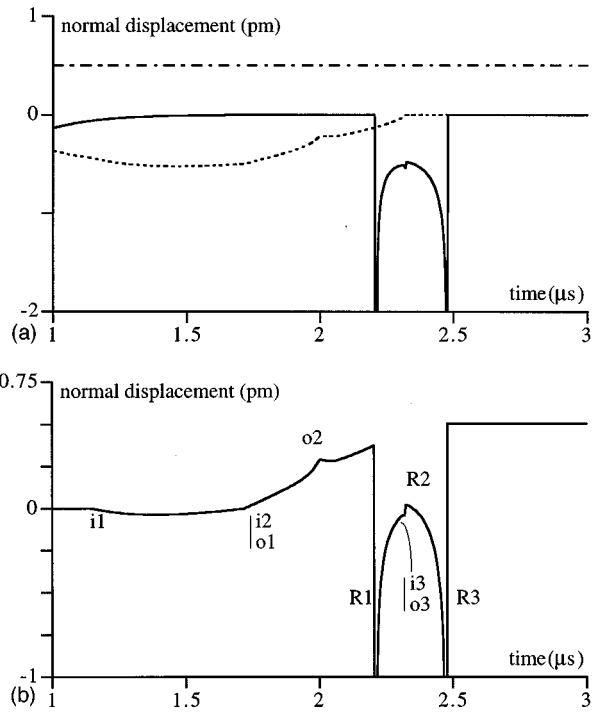
FIG. 8. Waveform calculation for a point source and a Heaviside temporal excitation at the observation point ($r=5$ mm, $\Phi=0°$). (a) The three contributions to the wave form: ----- $u_{pv}(M,t)$, ——— $u_R(M,t)$, and ––– $u_s(M)$. (b) Waveform. Summation of the three contributions: $u_{pv}(M,t)$, $u_R(M,t)$, and $u_s(M)$.
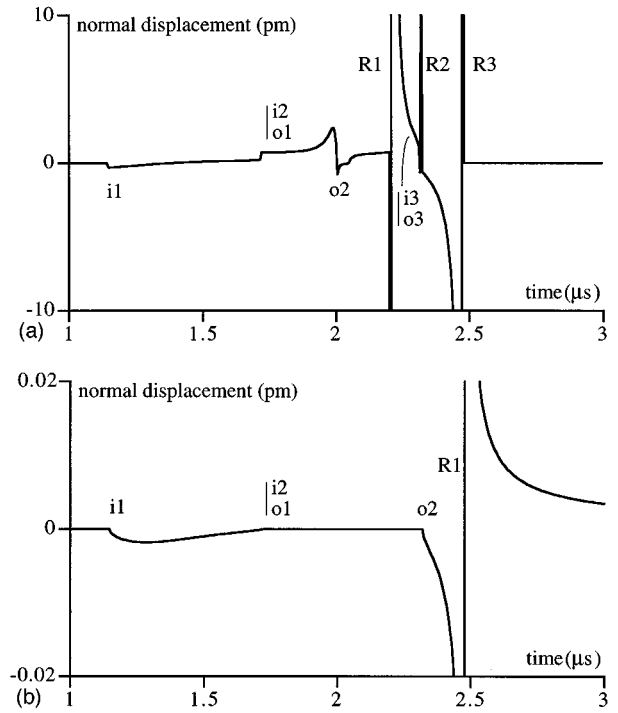
FIG. 9. Waveform calculated for a Dirac temporal excitation at the observation point ($r=5$ mm, $\Phi=0°$). (a) Point source. Arrival time: "in plane" (i1,i2,i3) and "out of plane" (o1, o2, o3) skimming surface waves, Rayleigh waves (R1,R2,R3). (b) Line source. Arrival time: "in plane" (i1,i2) and "out of plane" (o1,o2) skimming surface waves, Rayleigh wave (R1).

From the result given in Fig. 8(b), it is now a simple matter to calculate the response of the temporal Dirac delta function by a simple numerical time derivative, as illustrated in Fig. 9. For the three angles of observation which are analyzed, both the 2-D and the 3-D responses are systematically presented, see Figs. 9–11. For the 2-D problem, the line sources are orthogonal to the observation directions ($\beta=\Phi$). In agreement with the rules used in Figs. 4–7, the surface wavefronts arrivals are located in the waveforms.

Let us now analyze in detail these three situations.

First for $\Phi=0°$, Fig. 9(a) shows the complexity of the waveform due to numerous wavefront arrivals. The associated discontinuities in the temporal shape are in agreement with the arrival times of the wavefronts that propagate at the group velocity, as pointed out in Refs. 16 and 34. The folding wavefronts for both the Rayleigh wave and the surface skimming wave is made clear by this calculation. For instance, three Rayleigh wave arrivals and four surface skimming wave arrivals are visible. Of course different behaviors are observed for the line source. In fact, the Rayleigh wavefront generated by a line impact is known to propagate at phase velocity.[31] In contrast, focusing phenomena occur for the skimming surface wavefronts generated by a line source. Consequently, one Rayleigh wave arrival and three surface skimming wave arrivals among which the contribution (o2) resulting from the focusing, are observed. Of course, there are many more contributions for the point source considering the dimension of the problem, see Figs. 5 and 7. Comparing these results with those obtained for a point receiver located inside the solid and close to the surface (see Ref. 7 for an
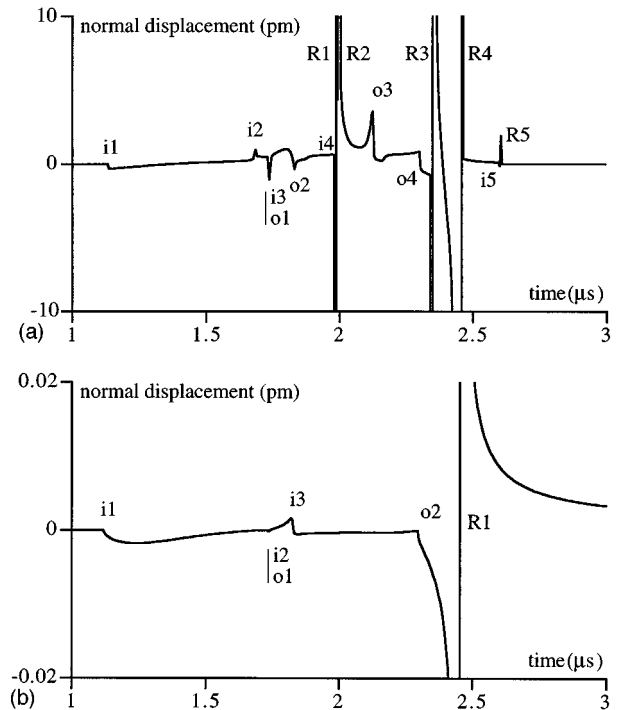
FIG. 10. Waveform calculated for a Dirac temporal excitation at the observation point ($r=5$ mm, $\Phi=10°$). (a) Point source. Arrival time: "in plane" (i1,i2,i3,i4,i5) and "out of plane" (o1,o2,o3,o4) skimming surface waves, Rayleigh waves (R1,R2,R3,R4,R5). (b) Line source. Arrival time: "in plane" (i1,i2,i3) and "out of plane" (o1,o2) skimming surface waves, Rayleigh wave (R1), diffraction by the Rayleigh wave cusp (Rc) and the skimming surface wave cusp (Sc).
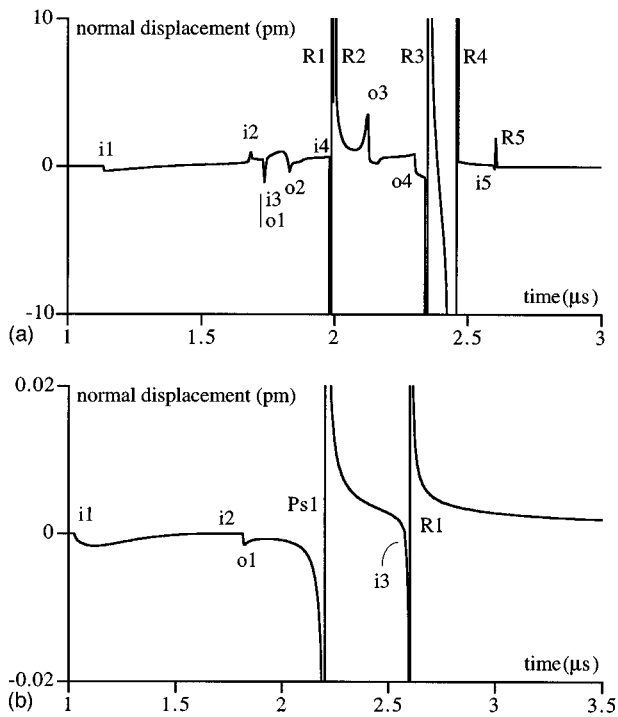
FIG. 11. Waveform calculated for a Dirac temporal excitation at the observation point $\Phi = 60°$. (a) Point source. Arrival time: ''in plane'' (i1,i2,i3) and ''out of plane'' (o1,o2) skimming surface waves, Rayleigh wave (R1), Pseudosurface wave (Ps1). (b) Line source. Arrival time: ''in plane'' (i1,i2,i3) and ''out of plane'' (o1) skimming surface waves, Rayleigh wave (R1), Pseudosurface wave (Ps1).

angle of observation of 80°), it should be remarked that the Rayleigh pulse shapes are very different. Below the free surface the Rayleigh pulse shape is broadened and rounded since the integration path does not skim the Rayleigh pole and only its contribution is observed. On the contrary, when the pointlike receiver is on the free surface, a sharp discontinuity can be really associated to a wavefront.

Although they are not presented here, different comparisons with results issued from the literature have been successfully made. For the line source, our calculations are in agreement with those shown in Refs. 31, 33, and 35. Nevertheless, in the literature, no significant numeral results for the dynamic surface response to a transient point force on an anisotropic half-space can be compared to the results presented here, except in a parallel study.[43] In addition, our calculations have been successfully compared with the results of Pekeris and Lipson[30] for the vertical point force with a Heaviside time dependence in the case of an isotropic media.

For the direction of observation $\Phi = 10°$, Fig. 10, which does not correspond to a crystallographic axis, the phenomena become intricate. In fact, there are 13 singularities, among which most are related to the focusing effect of surface phonons. On that particular graph, five Rayleigh waves corresponding to the different branches of the cuspidal structure in Fig. 6 are clearly discernible. The analysis of the discontinuities is greatly facilitated by using angle versus time diagrams. Such a diagram was presented in Fig. 3 for the Rayleigh waves and for the example under consideration. The times of flight of the five Rayleigh waves Ri (i

$= 1 \cdots 5$) correspond then to the ordinates $t = u(\widetilde{\beta}_{R_j})$ with $j = 1 \cdots 5$ where i and j are not necessarily equal. For instance, the different behaviors of the singularities R4 and R5 are noteworthy. Typically, depending on the branch of the cuspidal structure, the acoustic energy is either focused (R4) or defocused (R5). The same comment is available concerning the surface skimming waves. Obviously, the difference between the responses at $\Phi = 10°$ and at $\Phi = 0°$ is important. In contrast, for the line source, no important difference appears by comparing Figs. 10(b) and 9(b).

As a final example, the observation angle $\Phi = 60°$ is inspected in Fig. 11. In addition to the effects already mentioned, first the presence of the pseudosurface wave (Ps1) is significant. Its temporal shape is very similar to the temporal shape of a real pole which behaves as the derivative of a Dirac function. Second, in the calculated signal, it is important to observe the discontinuities (Sc) and (Rc) caused by the so-called effect of diffraction by the cusp. Such phenomena are not predicted by the ray calculation. Nevertheless, the particular velocity associated to (Rc) [or (Sc)] is approximately the intersection between the straight line $\Phi = 60°$ and the prolongation of the cusp of the Rayleigh wave around the axis x_3 [or the surface skimming wave], see Figs. 6 and 7. These discontinuities reveal diffraction effects by their rough shape as previously described theoretically[7] and experimentally[25] in the case of bulk waves. Due to its distance, the Rayleigh wavefront cusp, situated around the axis x_2, does not affect the waveform at the angle of observation $\Phi = 60°$. However, although the cusp of the pseudosurface wave, located around the crystallographic axis [0,1,1], is weakly spread out, it causes the pulse to broaden and become round, which is observable between the arrival times (o1) and (o2). This singularity has disappeared for $\Phi = 10°$, see Fig. 10(a).

For the line source, Fig. 11(b) the pseudosurface wavefront is clearly visible. Let us remark that for this angle of line orientation, the wave denoted (i2) could be observed since its velocity is not close to the velocity of the wave (o1). However, no discontinuity is discernible in the waveform at the time of flight of the wave (i2). At this time, this surface wave becomes a bulk wave and the waveform becomes zero.

IV. CONCLUSION

The transient surface wavefronts generated by either a point source or a line source on an anisotropic solid have been studied by means of a Green's function calculation based on the Cagniard–de Hoop method. The normal displacement at a pointlike receiver in any location on a free surface subjected to a normal transient loading has been investigated.

In addition to the well-known Rayleigh wavefront focusing, some other striking phenomena are made clear. The behavior of the pseudosurface wave and the focusing of the surface skimming wavefront as well as the effects of diffraction by the cusps are pointed out from this elastodynamic surface response. The phenomena are much more intricate for a point source than for a line source. For instance, in the case of a medium belonging to the cubic class of symmetry,

numerous surface wave arrivals are observed in certain directions of propagation.

The point generation and point detection of surface acoustic waves is a very attractive experimental configuration for applications such as the measurement of stiffness coefficients of anisotropic solids. In this case, when acoustic wave focusing induced by anisotropy is critically sensitive, the waveforms become very complex, implying difficulties in their interpretation. The present work is then of prime importance as it provides an accurate interpretation of the observed acoustic disturbances. From this point of view, the perfect agreement between these calculations and experimental results using a focused pulsed laser beam as a point source and a laser interferometer as a pointlike receiver[44] should be noted.

APPENDIX

The integral function $g(t)$ defined by the following integral over β:

$$g(t) = \mathrm{Im} \int_{\widetilde{\beta}_{R_j}}^{\widetilde{\beta}_{R_{j+1}}} f(u(\beta)) \delta(t - u(\beta)) d\beta,$$

is calculated with the change of variable $\beta \rightarrow u(\beta)$ which is single valued in the interval $[\widetilde{\beta}_{R_j}, \widetilde{\beta}_{R_{j+1}}]$. It is then obtained:

$$g(t) = \mathrm{Im} \int_{u(\widetilde{\beta}_{R_j})}^{u(\widetilde{\beta}_{R_{j+1}})} f(u(\beta)) \delta(t - u(\beta)) \left(\frac{\partial u}{\partial \beta} \right)^{-1} du.$$

Let β_{R_i} be such as $t = u(\beta_{R_i})$. According to the definition of the Dirac function, the calculation of $g(t)$ is reduced to an algebraic evaluation:

$$g(t) = \mathrm{sgn}(u(\widetilde{\beta}_{R_j}) - u(\widetilde{\beta}_{R_{j+1}}))$$

$$\times \left(\frac{\partial u}{\partial \beta} \bigg|_{\beta_{R_i}} \right)^{-1} \mathrm{Im}\{f(u(\beta_{R_i}))\},$$

if $\beta_{R_i} \in [\widetilde{\beta}_{R_j}, \widetilde{\beta}_{R_{j+1}}]$ else $g(t) = 0$. It is then clear that

$$g(t) = \left| \frac{\partial u}{\partial \beta} \bigg|_{\beta_{R_i}} \right|^{-1} \mathrm{Im}\{f(u(\beta_{R_i}))\}.$$

[1] H. Lamb, ''On the propagation of tremors over the surface of an elastic solid,'' Philos. Trans. R. Soc. London, Ser. A **203**, 1–42 (1904).

[2] K. Aki and P. G. Richards, *Quantitative Seismology* (Freeman, San Francisco, 1980), Vol. 1.

[3] J. D. Achenbach, *Wave Propagation in Elastic Solids* (North-Holland, Amsterdam, 1973).

[4] J. H. M. T. Van Der Hijden, *Propagation of Transient Elastic Waves in Stratified Anisotropic Media* (North-Holland, Amsterdam, 1987).

[5] A. G. Every and K. Y. Kim, ''Time domain dynamic response functions of elastically anisotropic solids,'' J. Acoust. Soc. Am. **95**, 2505–2516 (1994).

[6] A. Mourad and M. Deschamps, ''Lamb's problem for an anisotropic half space studied by the Cagniard de Hoop method,'' J. Acoust. Soc. Am. **97**, 3194–3197 (1995).

[7] A. Mourad, M. Deschamps, and B. Castagnède, ''Acoustic waves generated by a transient line source in an anisotropic half space,'' Acta Acust. (China) **52**, 839–851 (1996).

[8] H. J. Maris, ''Enhancement of heat pulses in crystals due to elastic anisotropy,'' J. Acoust. Soc. Am. **50**, 812–818 (1970).

[9] R. L. Weaver, M. R. Hausser, and J. P. Wolfe, ''Acoustic flux imaging in anisotropic media,'' Z. Phys. B **90**, 27–46 (1993).

[10] A. G. Every, W. Sachse, K. Y. Kim, and M. O. Thompson, ''Phonon focusing in silicon at ultrasonic frequencies,'' Phys. Rev. Lett. **65**, 1446–1449 (1990).

[11] B. Taylor, H. J. Maris, and C. Elbaum, ''Focusing of phonon in crystalline solids due to elastic anisotropy,'' Phys. Rev. B **3**, 1462–1472 (1971).

[12] B. Castagnède and Y. Berthelot, ''Photoacoustic interactions by modulation and laser impact: Applications in mechanics and physics of anisotropic solids,'' J. Acoust. **5**, 417–453 (1992).

[13] J. P. Monchalin, ''Progress towards the application of laser-ultrasonics,'' Rev. Prog. Quant. Nondestruct. Eval. **12**, 495–506 (1993).

[14] V. Gusev, C. Desmet, W. Lauriks, C. Glorieux, and J. Thoen, ''Theory of Scholte, leaky Rayleigh and lateral wave excitation via laser-induced thermoelastic effect,'' J. Acoust. Soc. Am. **100**, 1514–1528 (1996).

[15] T. C. Lim and G. W. Farnell, ''Search for forbidden directions of elastic surface-wave propagation in anisotropic crystals,'' J. Appl. Phys. **39**, 4319–4325 (1968).

[16] V. T. Buchwald and A. Davis, ''Surface waves in elastic media with cubic symmetry,'' Q. J. Mech. Appl. Math. **16**, 283–293 (1963).

[17] J. Lothe and D. M. Barnett, ''On the existence of surface-wave solutions for anisotropic elastic half-spaces with free surface,'' J. Appl. Phys. **47**, 428–433 (1976).

[18] H. Shirasaki and T. Makimoto, ''Energy propagation properties of piezoelectric surface waves on cubic crystals,'' J. Appl. Phys. **49**, 658–660 (1977).

[19] Al. A. Kolomenskii and A. A. Maznev, ''Phonon-focusing effect with laser-generated ultrasonic surface waves,'' Phys. Rev. B **48**, 14502–14508 (1993).

[20] A. A. Maznev and A. G. Every, ''Ray surface and focusing of surface acoustic waves on the basal plane of cubic crystals,'' Acta Acust. (China) **1**, 137–143 (1994).

[21] G. Veith, ''High resolution photoacoustic microscopy on a surface acoustic wave device,'' Appl. Phys. Lett. **41**, 1045 (1982).

[22] A. A. Karabutov, ''Laser excitation of surface acoustic waves: a new direction in optoacoustic spectroscopy of a solid,'' Sov. Phys. Usp. **28**, 1042–1051 (1985).

[23] C. B. Scruby and L. E. Drain, *Laser Ultrasonics Techniques and Applications* (Hilger, Bristol, 1990).

[24] M. Deschamps and C. Bescond, ''Numerical method to recover the elastic constants from ultrasound group velocities,'' Ultrasonics **33**, 205–211 (1995).

[25] B. Audoin, C. Bescond, and M. Deschamps, ''Measurement of stiffness coefficients of anisotropic materials from point-like generation and detection of acoustic waves,'' J. Appl. Phys. **80**, 3760–3771 (1996).

[26] A. G. Every and W. Sachse, ''Determination of the elastic constants of anisotropic solids from acoustic-wave group-velocity measurements,'' Phys. Rev. B **42**, 8196–8205 (1990).

[27] J.-F. Chai and T.-T. Wu, ''Determination of anisotropic elastic constants using laser generated surface waves,'' J. Acoust. Soc. Am. **95**, 3232–3241 (1994).

[28] S. Tamura and K. Honjo, ''Focusing effects of surface acoustic waves in crystalline solids,'' Jpn. J. Appl. Phys. **20** (Suppl. 20-3), 17–19 (1981).

[29] R. E. Camley and A. A. Maradudin, ''Phonon focusing at surfaces,'' Phys. Rev. B **27**, 1959–1964 (1983).

[30] C. L. Pekeris and H. Lipson, ''Motion of the surface of a uniform elastic half-space produced by a buried pulse,'' J. Acoust. Soc. Am. **29**, 1233–1238 (1957).

[31] R. Burridge, ''Lamb's problem for an anisotropic half-space,'' Q. J. Mech. Appl. Math. **24**, 81–98 (1971).

[32] R. L. Ryan, ''Pulse propagation in a transversely isotropic half-space,'' J. Sound Vib. **14**, 511–524 (1971).

[33] A. A. Maznev and A. G. Every, ''Time-domain dynamic surface response of an anisotropic elastic solid to an impulsive line force,'' Int. J. Eng. Sci. **35**, 321–330 (1997).

[34] A. A. Maznev, Al. A. Kolomenskii, and P. Hess, ''Time-resolved cuspidal structure in the wave front of surface acoustic pulses on (111) Gallium Arsenide,'' Phys. Rev. Lett. **75**, 3332–3335 (1995).

[35] C.-Y. Wang and J. D. Achenbach, ''Lamb's problem for solids of general anisotropy,'' Wave Motion **24**, 227–242 (1996).

[36] B. A. Auld, *Acoustic Fields and Waves in Solids* (Wiley-Interscience, New York, 1973), Vol. 1.

[37] L. Cagniard, *Réflexion et réfraction des ondes séismiques progressives* (Gauthiers-Villars, Paris, 1939).

[38] V. T. Buchwald, ''Rayleigh waves in anisotropic media,'' Q. J. Mech. Appl. Math. **14**, 461–468 (1960).

[39] T. C. Lim and G. W. Farnell, ''Character of pseudo surface waves on anisotropic crystals,'' J. Acoust. Soc. Am. **45**, 845–851 (1968).

[40] R. Burridge, ''The direction in which Rayleigh waves may be propagated on crystal,'' Q. J. Mech. Appl. Math. **23**, 217–224 (1970).

[41] A. T. De Hoop, ''A modification of Cagniard's method for solving seismic pulse problem,'' Appl. Sci. Res., Sect. B **8**, 349–356 (1960).

[42] Al. A. Kolomenskii and A. A. Maznev, ''Surface responses in the laser irradiation of a solid: Rayleigh waves and precursors,'' Sov. Phys. Acoust. **36**, 258–261 (1990).

[43] A. G. Every, K. Y. Kim, and A. A. Maznev, ''The elastodynamic response of a semi-infinite anisotropic solid to sudden surface loading,'' J. Acoust. Soc. Am. (to be published).

[44] C. Bescond, M. Deschamps, B. Audoin, and M. Qian, ''Bulk and surface waves in anisotropic solids generated with pulsed laser beam: comparison between theory and experiment,'' in *International Conference on Photoacoustic and Photothermal Phenomena*, Nanjing, People's Republic of China, 1996 [Prog. Nat. Sci. **6** (Suppl. A), 374–377 (1996)].

Study of energy distribution of guided waves in multilayered media

Bixing Zhang
Institute of Applied Geophysics, Central South University of Technology, Changsha, 410083, People's Republic of China

Wei Xiong, M. Yu, C. Q. Lan, and Long Li
Wuhan Institute of Physics, The Chinese Academy of Sciences, Wuhan, 430071, People's Republic of China

The energy distributions of guided waves in multilayered elastic solid media are investigated in three dimensions. A guided wave is the result of the interaction of the acoustic source and the interfaces in the material structure, and does not lose energy in the course of propagation along the horizontal direction. It should be pointed out that the guided wave cannot be excited alone by a practical acoustic source in this paper. The mean energy flux density of the guided waves (excited by a nonaxisymmetric acoustic source) has the tangential component except the radial component, but the effective part of the mean energy flux density has only the radial component. Only in the case that the propagation distance is greater than the wavelength, is the propagation velocity of the mean value of the total energy equal to the group velocity of the guided wave. It is found that the propagation velocity of the mean energy density is equal to the phase velocity of the guided wave in the lowest layer medium in the multilayered media, but in other layers, the propagation velocity of the mean energy density is related to the distance from the free surface to the receiving point. Two categories of guided waves, Rayleigh and trapped waves, are also numerically investigated in this paper in the multilayered media in which a low-velocity area is comprised. It is also found that one category of the guided waves decays rapidly with the distance from the free surface while the another category of guided waves concentrates its energy within the low-velocity area and decays with the distance from the low-velocity area. These two categories of guided waves have different energy distributions and propagation characteristics. However, since they are closely related, it is not always easy to distinguish them from each other. The excitation and propagation mechanism of the guided waves are useful for exploring the structures of the interfaces and the low-velocity area under the free surface. © *1998 Acoustical Society of America.* [S0001-4966(98)02501-6]

PACS numbers: 43.20.Gp, 43.20.Fn, 43.35.Cg, 43.40.Ph [JEG]

INTRODUCTION

Waves propagating through multilayered media are of great interest due to their vital applications in many branches of physical sciences and engineering, and considerable effort has been expended by researchers on this research topic.[1–10] The studies on the guided waves in stratified media seem to be more characteristic.[11–27] A guided wave, which is a cylindrical wave, is the result of the interaction of the elastic wave fields (compressional and shear fields) to the material interfaces. It is a complicated and important elastic wave field. Not only is much information about the material structure carried in guided waves, but also it is easy to excite and receive the guided waves (especially for the surface waves) in the laboratory domain. Harkrider[11] studied the surface waves in multilayered elastic media. Mal[12] considered the guided waves in a stratified isotropic solid containing imperfectly welder interfaces. Zhang *et al.*[13] investigated waves in multilayered media and presented two physical quantities about the Rayleigh wave that are sensitive to the material property of the medium and the layered geometry. Most of the works in this facet focused on the phase and group velocities, the dispersion characteristic, and the propagation mechanism.

In general, the guided waves in multilayered media can be separated into two categories: surface waves and trapped waves. The surface waves are fundamentally related to the existence of the free surface. These waves at high frequencies correspond to the waves that are concentrated below the free surface and decay with the distance from the free surface. The trapped waves are fundamentally related to the interfaces under the free surface. These waves concentrate their energy within an area under the free surface and decay with the distance from this area. Both surface waves and trapped waves do not lose energy as they propagate radially. Guided waves are very important for extracting the information of the multilayered structure in geophysical research and other application branches. Parra *et al.*[14] studied the dispersion and attenuation of acoustic guided waves trapped in a low-velocity porous layer. Johnson *et al.*[15] discovered the evidence for mode conversion of borehole Stoneley waves (tube waves) to stratigraphically guided waves in data from cross-hole acoustic experiments conducted by the Department of Energy in Colorado. This shows that the guided waves trapped in multilayered media (for example, trapped in layered low-velocity formations) are very likely to confirm the continuity of heterogeneous formations.

Energy is an important physical quantity for the guided

waves in multilayered media. The excitation mechanism and propagation characteristic of the guided waves can be understood thoroughly by investigating the energy distribution in three dimensions. A trapped wave, which is trapped in an area under the free surface, concentrates most of its energy into the layer between the interfaces. Therefore the information about the trapped waves received in the receiving borehole at some depth means the possibility of existence of the interfaces in stratified formations at that depth. The energy distribution of the guided waves is more accurate for reflecting the existence and the structure of the medium layer than the displacement and stress components. Zhang *et al.*[16] studied the Love wave in stratified media and found that the energy distribution of the Love wave is more convenient to describe the structure of the medium layer than the displacement-stress vector. Guzhev[17] investigated the energy distribution of the Stoneley wave propagating along the solid–liquid interface in two dimensions. His results show the energy distribution of a Stoneley wave can be conveniently used to demonstrate the material structure. Unfortunately, the investigations about the energy distributions of the guided waves in three dimensions in multilayered media have seldom been seen in previous works.

In this paper, the energy distributions of the guided waves in multilayered elastic solid media are studied in three dimensions based on the boundary value problem given by Zhang *et al.*[13] This paper can be divided into two parts. In the first part, the guided waves are theoretically investigated, the distribution characteristics of the mean energy of the guided waves excited by the symmetric and nonsymmetric acoustic sources are analyzed. The propagation mechanisms of the guided waves are analyzed from the energy sense. In the second part, the mean energy fluxes of the Rayleigh wave and the guided waves trapped in low-velocity formation in multilayered media are numerically investigated in two models of the system. Many results are obtained, and it will be told how extract the Rayleigh and trapped waves are from each other. This article provides the foundation for further investigating the guided wave propagation in multilayered poroelastic media and complicated media.

I. THEORY

It is considered a half-space system that is composed by N homogeneous and isotropic elastic solid layers. A cylindrical coordinate system (r, θ, z) is introduced. The interfaces of N heterogeneous media are all parallel. $z=0$ is the free surface, at which the system has free boundary conditions, of the first medium. The ith layer is bounded by the planes $z=z_{i-1}$ and $z=z_i$. The Nth medium extends to infinity along the z axis. The displacement and stress field satisfy the boundary conditions of continuity of displacements and tractions across each interface, and the radiation condition at infinity. In this paper, Only the guided wave of the $P-SV$ field is considered and the guided wave of the SH field is omitted. This is mainly because the SH field is decoupled from the $P-SV$ field and the SH field is relatively simple.[23,24,13]

A. Displacement-stress and energy flux density vectors

It is convenient to introduce B, P, C coordinate system[4]

$$\mathbf{B} = \mathbf{e}_r \frac{\partial}{\partial(kr)} + \mathbf{e}_\theta \frac{\partial}{kr \, \partial\theta},$$

$$\mathbf{C} = \mathbf{e}_r \frac{\partial}{kr \, \partial\theta} - \mathbf{e}_\theta \frac{\partial}{\partial(kr)}, \quad \mathbf{P} = \mathbf{e}_z, \tag{1}$$

and the vectors of the displacement stress and the potential[13,23,24]

$$S = (U_B/k, U_P/k, \tau_P/\omega^2, \tau_B/\omega^2)^T,$$

$$\phi = (\alpha_1 e^{iaz}, \alpha_2 e^{-iaz}, \alpha_3 e^{ibz}, \alpha_4 e^{-ibz})^T, \tag{2}$$

for the field of the P-SV wave. The following relationships can be then obtained:[13,23,24]

$$S = M\phi, \quad \phi(z_i) = \lambda \phi(z_{i-1}),$$

$$\lambda = \operatorname{diag}(P, P^{-1}, Q, Q^{-1}),$$

$$M = \begin{pmatrix} 1 & 1 & \gamma_s & -\gamma_s \\ \gamma_p & -\gamma_p & 1 & 1 \\ \rho(\gamma-1) & \rho(\gamma-1) & \rho\gamma\gamma_s & -\rho\gamma\gamma_s \\ \rho\gamma\gamma_p & -\rho\gamma\gamma_p & \rho(\gamma-1) & \rho(\gamma-1) \end{pmatrix}, \tag{3}$$

where k is the horizontal wave number, ω the angular frequency, and U and τ represent the displacement and stress, respectively. The definition of the other physical quantities can all be seen in the related references.

Menke[24] introduced the following vector as the up-going method to simplify the elastic wave field in multilayered media:

$$E = (E_1, E_2, E_3, E_4, E_5, E_6)^T. \tag{4}$$

If the wave field is excited by a source $(P-SV)$ in the first layer medium $(z=z_s, r=0)$, then the components of the displacement-stress vector on the free surface $(z=0)$ are of forms[13]

$$S_1 = \left(T_{11} - \frac{E_3^{(1)}}{E_6^{(1)}} T_{31} + \frac{E_2^{(1)}}{E_6^{(1)}} T_{41} \right) A_{sn}$$

$$+ \left(T_{12} - \frac{E_3^{(1)}}{E_6^{(1)}} T_{32} + \frac{E_2^{(1)}}{E_6^{(1)}} T_{42} \right) B_{sn},$$

$$S_2 = \left(T_{21} - \frac{E_5^{(1)}}{E_6^{(1)}} T_{31} + \frac{E_4^{(1)}}{E_6^{(1)}} T_{41} \right) A_{sn} \tag{5}$$

$$+ \left(T_{22} - \frac{E_5^{(1)}}{E_6^{(1)}} T_{32} + \frac{E_4^{(1)}}{E_6^{(1)}} T_{42} \right) B_{sn},$$

where T_{ij}, A_{sn}, and B_{sn} are related to the source. The solutions of the guided waves are obtained by the dispersion equation $E_6^{(1)} = 0$, and its intensities of the displacement-stress vectors are given by the residues of the poles. So the components $(S_i, i=1,2,3,4)$ of the displacement-stress vector of the guided wave at an arbitrary depth z can be derived by Eq. (5) and the propagator matrix $p(=M\lambda M^{-1})$.[13]

With the relation of the B, P, C coordinate system to the spatial coordinate system, the displacement components of the $P-SV$ field in the spatial domain can be written as

$$U_r = \frac{\partial U_B}{k\,\partial r}, \quad U_\theta = \frac{\partial U_B}{kr\,\partial\theta}, \quad U_z = U_P. \tag{6}$$

Then the spatial components of the displacement and stress of a guided wave can be obtained by above relations, and they are of forms

$$
\begin{aligned}
U_r &= i\pi k^2 S_1 [nH_n^{(1)}(kr)/kr - H_{n+1}^{(1)}(kr)]\cos(n\theta),\\
U_\theta &= -i\pi kn S_1 H_n^{(1)}(kr)\sin(n\theta)/r,\\
U_z &= i\pi k^2 S_2 H_n^{(1)}(kr)\cos(n\theta),\\
\tau_{zr} &= i\pi k^3 V^2 S_4 [nH_n^{(1)}(kr)/kr - H_{n+1}^{(1)}(kr)]\cos(n\theta),\\
\tau_{z\theta} &= -i\pi k^2 V^2 n S_4 H_n^{(1)}(kr)\sin(n\theta)/r,\\
\tau_{zz} &= i\pi k^3 V^2 S_3 H_n^{(1)}(kr)\cos(n\theta).
\end{aligned} \tag{7}
$$

Here, the nth Hankel function $[H_n^{(1)}(kr)]$ of the first kind is used because of the time dependence $e^{-i\omega t}$, and the value of n is given by the source. V is the phase velocity of the Rayleigh wave and S_1, S_2, S_3, and S_4 are components of the displacement-stress vector of the guided wave and can be obtained by the propagator matrix and Eq. (5).

About the time-harmonic wave whose angular frequency is ω, the energy flux density is[17,28]

$$\mathbf{P} = -\boldsymbol{\tau}\cdot\frac{\partial\mathbf{U}}{\partial t} = i\omega\boldsymbol{\tau}\cdot\mathbf{U}, \tag{8}$$

and its spatial components are of forms

$$
\begin{aligned}
P_r &= i\omega(\tau_{rr}U_r + \tau_{r\theta}U_\theta + \tau_{rz}U_z),\\
P_\theta &= i\omega(\tau_{\theta r}U_r + \tau_{\theta\theta}U_\theta + \tau_{\theta z}U_z),\\
P_z &= i\omega(\tau_{zr}U_r + \tau_{z\theta}U_\theta + \tau_{zz}U_z).
\end{aligned} \tag{9}
$$

So the energy flux densities of the guided waves can be obtained by Eqs. (7) and (9).

B. Mean value of the energy flux densities of the guided waves to the time

Consider the mean value of the energy flux density to the time

$$\langle P_i\rangle = \frac{1}{T}\int_0^T P_i\,dt \quad (i=r,\theta,z), \tag{10}$$

in which each item is the quadratic factor of the time. Suppose A and B are the linear functions of the time-harmonic waves, then, the following equation,

$$\langle AB\rangle = \tfrac{1}{2}A^*B, \tag{11}$$

is utilized for determining the mean value of the energy flux density to the time in an arbitrary point in multilayered media. Here the asterisk represents the complex conjugate. If the horizontal wave number k of the wave is a real number, it could be then verified that the mean value of the energy flux density is also real. So the guided waves, whose horizontal wave number is real, do not lose their energy in the

course of propagation along the horizontal direction in multilayered media. It is easy to derive by Eqs. (7), (9), (10), and (11) that the mean value of energy flux density $\langle P\rangle$ of the guided wave, and their components are

$$\langle P_r\rangle = \frac{\pi\omega^5}{rV^2}[H\cos^2(n\theta) - \rho\gamma n^2 S_1^2\cos(2n\theta)/k^2 r^2],$$

$$\langle P_\theta\rangle = -\frac{\pi n\rho\gamma\omega^3}{r^3}S_1^2\sin(2n\theta), \tag{12}$$

$$\langle P_z\rangle = 0,$$

where $H = [\gamma(1-\gamma_\rho^2)-1]S_1 S_3 + S_2 S_4 + \rho\gamma[2-\gamma(1-\gamma_\rho^2)] \times S_1^2$ is related to the layered structure of the stratified media.

The third equation of Eqs. (12) shows that the components of mean energy flux density propagated along the z axis are equal to zero, so the energy of the guided waves propagates along the horizontal direction which is parallel to the interfaces of the media. This is the familiar result. In fact, it is known that the wavefront of the guided wave is a cylindrical surface whose symmetric axis coincides with the z axis, and the phase and group velocities of the guided wave are both parallel to the horizontal surface. This conclusion is consistent with the third equation of Eqs. (12). The second equation of Eqs. (12) indicates that $\langle P_\theta\rangle$ is not equal to zero when $n\neq 0$, it is also shown that the mean energy of the guided waves can propagate along the tangential direction ($\mathbf{e}_\theta$). This is significantly different from that in two dimensions. In the case of the axisymmetric (z axis) system ($n=0$), the mean energy of the guided wave does propagate along the radial direction ($\mathbf{e}_r$). But for the nonaxisymmetric system, the mean energy flux density has not only the tangential component but also the radial component.

The mean energy flux density can be also written as

$$\langle\mathbf{P}\rangle = \langle\mathbf{P}_1\rangle + \langle\mathbf{P}_2\rangle,$$

$$\langle\mathbf{P}_1\rangle = \frac{\pi\omega^5}{rV^2}H\cos^2(n\theta)\mathbf{e}_r, \tag{13}$$

$$\langle\mathbf{P}_2\rangle = -\frac{\pi n\rho\gamma\omega^3}{r^3}S_1^2[n\cos(2n\theta)\mathbf{e}_r + \sin(2n\theta)\mathbf{e}_\theta].$$

Here, $\langle P_1\rangle$ is in direct proportion to $1/r$ while $\langle P_2\rangle$ is in direct proportion to $1/r^3$. So $\langle P_1\rangle$ is the dominant in the far field but $\langle P_2\rangle$ is the dominant in the near field. As a typical example, Eqs. (13) are explained further by the horizontal dipole source. The horizontal dipole source ($n=1$) can be constructed from two point sources of opposite sign placed close together in the same horizontal plane.[29] The distance between the two point sources of opposite sign is represented by $2l$ (Fig. 1). According to Eqs. (13), two mean energy flux densities generated by two symmetric point sources can be written as

$$\langle\mathbf{P}_1'\rangle = \frac{\alpha}{r}\mathbf{e}_{r1}, \quad \langle\mathbf{P}_2'\rangle = \frac{\alpha}{r}\mathbf{e}_{r2}. \tag{14}$$

Then, the mean energy flux density generated by the horizontal dipole source is the sum of $\langle\mathbf{P}_1'\rangle$ and $\langle\mathbf{P}_2'\rangle$.

127   J. Acoust. Soc. Am., Vol. 103, No. 1, January 1998

Zhang *et al.*: Multilayered media   127
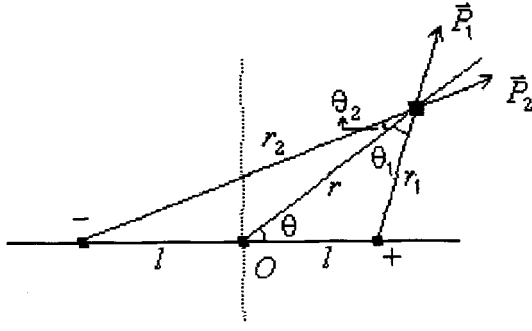
FIG. 1. Schematic diagram of the horizontal dipole source.

$$\langle P'_\theta \rangle = \langle P'_1 \rangle \sin\theta_1 - \langle P'_2 \rangle \sin\theta_2$$

$$= \frac{(r_2+r_1)(r_2-r_1)}{r_2^2 r_1^2}\, \alpha l\, \sin\theta \approx \frac{2\alpha l^2}{r^3}\, \sin(2\theta),$$

$$\langle P'_r \rangle = \langle P'_1 \rangle \cos\theta_1 + \langle P'_2 \rangle \cos\theta_2$$

$$= \alpha \left(\frac{r-l\cos\theta}{r_1^2} + \frac{r+l\cos\theta}{r_2^2} \right)$$

$$\approx \frac{2\alpha}{r} + \frac{2\alpha l^2}{r^3}\cos(2\theta). \tag{15}$$

This is consistent with Eqs. (13).

It follows from Eqs. (13) that

$$\boldsymbol{\nabla}\cdot\langle \mathbf{P}_1 \rangle = \frac{\pi\omega^5}{V^2}\, H\, \cos^2(n\theta)\boldsymbol{\nabla}\cdot(\mathbf{e}_r/r)$$

$$= \frac{\pi\omega^5\delta(r)}{rV^2}\, H\, \cos^2(n\theta), \tag{16a}$$

$$\boldsymbol{\nabla}\cdot\langle \mathbf{P}_2 \rangle = 0. \tag{16b}$$

This shows that there is a source at $r=0$ in $\langle P_1 \rangle$ while there is no source at an arbitrary point in $\langle P_2 \rangle$. Equation (16a) also indicates that the mean energy flux $\langle P_1 \rangle$ propagates to infinity along the radial direction ($\mathbf{e}_r$) without loss (as the form of $1/r$). The acoustic field is excited by the acoustic source at the point $z=z_s$, $r=0$, so the source of $\langle P_1 \rangle$ does not come directly from the acoustic source but comes from that which is provided at $r=0$ by the conversion of the waveforms owing to the existence of the interfaces. Therefore it is not possible that the practical acoustic source only generates the guided waves. The guided waves (which are created by the acoustic source and the interfaces in the material structure) and the body waves are excited simultaneously by the acoustic source. However, the guided waves have different characteristics and velocities from that of the body waves in the practical case. They are separated from and the interaction is less when the far field is considered. In this situation, the guided waves can be considered alone.

It can be seen from Eq. (16b) that the flux of $\langle P_2 \rangle$ is equal to zero through an arbitrary closed surface, even if the origin is comprised. This shows that the mean energy of the guided wave cannot be propagated to infinity by $\langle P_2 \rangle$, but a part of energy of the guided wave is cyclically flowed as a

fixed fashion, and the fashion of mean energy of the guided wave propagated to infinity could not be changed by $\langle P_2 \rangle$. Therefore $\langle P_1 \rangle$ is the effective part of the mean energy flux density of the guided waves. $\langle P_2 \rangle$ is omitted in the following analyses of the mean energy propagation to infinity, and simply look upon $\langle P_1 \rangle$ as the mean energy flux density of the guided wave. This is reasonable and convenient. That is to say, the total mean energy flux density of the guided wave can be considered as

$$\langle \mathbf{P} \rangle = \frac{\pi\omega^5}{rV^2}\, H\, \cos^2(n\theta)\mathbf{e}_r. \tag{17}$$

C. Mean energy density and propagation of energy

The density of the kinetic energy (K) and strain potential energy (V) are of forms

$$K = \frac{1}{2}\,\rho\,\frac{\partial \mathbf{U}}{\partial t}\cdot\frac{\partial \mathbf{U}}{\partial t}, \quad V = \frac{1}{2}\tau_{ij}e_{ij}. \tag{18}$$

Then the mean density of the total energy is

$$\langle W \rangle = \langle K \rangle + \langle V \rangle = \tfrac{1}{2}\rho\omega^2\langle U_r^2 + U_\theta^2 + U_z^2 \rangle$$

$$+ \tfrac{1}{2}\langle\lambda e^2 + 2\mu e_{ij}e_{ij}\rangle, \tag{19}$$

where λ and μ are Lamé elastic constants, $e_{ij}=\tfrac{1}{2}(U_{i,j}+U_{j,i})$, $e=e_{kk}$.

The displacement of the guided waves is related to the Hankel function $H_n^{(1)}(kr)$. However, it can be seen that the mean energy flux density given by Eqs. (13) is not a related Hankel function, and it has a simple relation to the radial distance r. But the mean density of the total energy given by Eq. (19) is related to the Hankel function, and it has a complicated relation to the radial distance r.

The vector of the energy flux density describes the energy propagation of the wave. The propagating velocity of the energy should be the group velocity of the wave. Then, the mean density of the total energy and the mean energy flux density satisfy

$$\int_S \langle P \rangle ds = V_g \int_S \langle W \rangle ds. \tag{20}$$

Where the integration is to the whole wavefront of the guided wave, and V_g is the group velocity. This is the familiar result in the cases of the plane and spherical waves. But for the cylindrical wave (guided wave is a cylindrical wave), the mean energy density is related to the Hankel function while the mean energy flux density is not. So the velocity (denoted by V_g) obtained by Eq. (20) is related to the Hankel function and is not equal to the group velocity ($d\omega/dk$) given by the dispersion equation.

A guided wave is a cylindrical wave whose wavefront is a semi-infinite cylindrical surface. The Hankel function is comprised in the representation of the guided waves, and $H_n^{(1)}(kr) \approx \sqrt{2/\pi kr}\, e^{i[kr-(2n+1)\pi/4]}$ when the variant $kr\to\infty$. The phase velocity should be the propagation velocity of the isophase surface. So it is easy to see that ω/k is equal to the real phase velocity of the wave only in the case of the variant $kr\to\infty$. To analyze this in detail, let

$$H_n^{(1)}(kr) = Ae^{i\phi} = Ae^{ik_1 r}, \tag{21}$$

where A is the amplitude and k_1 is the function of r. Then the real phase velocity V, which is given by k_1, satisfies

$$\frac{V}{V_p} = k \bigg/ \frac{d\phi}{dr} = 2\pi \bigg/ \frac{d\phi}{d(r/\lambda)}, \tag{22}$$

where $V_p = \omega/k$ and $\lambda = 2\pi/k$ are the phase velocity and the wavelength in the far field.

It can be found by analyzing the Hankel function that the phase angle of $H_0^{(1)}(kr)$ is greater than $kr - \pi/4$, and the real phase velocity V is greater than V_p. It can also be found that the phase angles of $H_1^{(1)}(kr)$ and $H_2^{(1)}(kr)$ are less than $kr - 3\pi/4$ and $kr - 5\pi/4$, respectively, and their real phase velocities are less than V_p. However, when $r = 0.5\lambda$, the real phase velocities of the Hankel functions of the orders of 0, 1, 2 can be obtained by numerical simulation that are equal to $1.011 V_p$, $0.966 V_p$, and $0.825 V_p$, respectively. This shows that the approximate representation of the Hanker–function of the large argument can be used when the far field ($r > \lambda$) is investigated. Then, it follows from Eq. (19) and the approximate representation of the Hankel function that

$$\langle W \rangle = \frac{\pi \rho \omega^5}{2 r V^3} H_1 \cos^2(n\theta), \tag{23}$$

where

$$H_1 = [1 + 2\gamma - \gamma^2(1 - \gamma_p^2)] S_1^2 + S_2^2$$
$$+ \frac{1 - \gamma_p^2}{\rho^2} S_3^2 + \frac{2}{\rho^2 \gamma} S_4^2,$$

Hence both the mean energy flux density $\langle P \rangle$ and mean energy density $\langle W \rangle$ have the same factor $1/r$. It is then not difficult to get

$$H_1 - 2H/\rho = S_1' S_4 + S_2' S_3 - S_3' S_2 - S_4' S_1, \tag{24}$$

where the superscripts represent the derivation to the variant z. It can be obtained by the compressional potential (φ) and the vertical polarized potential (ψ) that

$$H_1 - 2H/\rho = \frac{\rho}{k} [(\varphi' + k\gamma_p \varphi)(\varphi' - k\gamma_p \varphi)$$
$$+ (\psi' + k\gamma_s \psi)(\psi' - k\gamma_s \psi)]. \tag{25}$$

When the receiving point (z) is in the lowest layer medium of the multilayered media (in the Nth medium), $\varphi' = k\gamma_p \varphi$, $\psi' = k\gamma_s \psi$, then $H_1 - 2H/\rho = 0$, so it is obtained from Eqs. (17) and (23) that

$$\langle P \rangle = V \langle W \rangle \quad (z \geq z_{N-1}). \tag{26}$$

In general, the propagation velocity of the energy density is related to r and z. When $r \gg \lambda$, the propagating velocity of the mean energy density of the guided waves in the lowest layer medium is equal to the phase velocity of the wave which is not related to z [Eq. (26)], but in the other layers, the propagation velocity of the mean energy density is related to z.

For the total energy flux and the total energy of the guided waves, it could be verified From Eqs. (17) and (23) that

$$V_g = \frac{\int_s \langle P \rangle ds}{\int_s \langle W \rangle ds} \xrightarrow{r \to \infty} 2 V_p \frac{\int_0^\infty H \, dz}{\int_0^\infty \rho H_1 \, dz} = \frac{d\omega}{dk}. \tag{27}$$

II. NUMERICAL RESULTS

In this section, the numerical results about the mean energy flux densities and the mean energy densities of the guided waves in multilayered media are presented and analyzed in detail by two models of the system.

At first, the problem of the numerical calculation of mean energy flux densities of guided waves in an arbitrary point is considered. Because the original propagator matrix has the problem of precision loss, the resultant values would lose some or maybe all of the significant digits at the large value of z and the high-frequency range. Some methods were introduced to avoid loss of the precision problem[23,24] at high-frequency range for a small value of z. If the value of z is large, the problem of precision loss is also existent. Now we adopt another representation to overcome this shortage.

Menke[24] defined the following antisymmetric matrix for every layer medium

$$D_{ij} = W_i^p W_j^s - W_i^s W_j^p. \tag{28}$$

It is easy to find that

$$D = \begin{pmatrix} 0 & E_1 & E_2 & E_3 \\ -E_1 & 0 & E_4 & E_5 \\ -E_2 & -E_4 & 0 & E_6 \\ -E_3 & -E_5 & -E_6 & 0 \end{pmatrix},$$
$$D^{(1)} = p^{-1}(z,z_0) D^{(2)} p^{-1^T}(z,z_0), \tag{29}$$

where p is the propagator matrix and z is an arbitrary point in multilayered media. Here, $E_6^{(1)}$ is equal to zero for the guided waves. So the displacement-stress vector at z is

$$S = pS(z_0) = \frac{S_2(z_0)}{E_3^{(1)}} p(-E_2^{(1)}, E_3^{(1)}, 0, E_6^{(1)})^T$$
$$= \frac{S_2(z_0)}{E_3^{(1)}} p D^{(1)}(0,0,-1,0)^T$$
$$= \frac{S_2(z_0)}{E_3^{(1)}} D^{(2)} p^{-1^T}(0,0,-1,0)^T$$
$$= \frac{S_2(z_0)}{E_3^{(1)}} \begin{pmatrix} p_{32}E_1 - p_{33}E_2 + p_{34}E_3 \\ p_{31}E_1 - p_{33}E_4 + p_{34}E_5 \\ p_{31}E_2 - p_{32}E_4 + p_{34}E_6 \\ p_{31}E_1 - p_{32}E_5 + p_{33}E_6 \end{pmatrix}_{(z)}, \tag{30}$$

where the right-hand side of Eq. (30) is related to values at point z, and it can be obtained from $E_i^{(N)}$ ($i=1,...,6$) of the lowest medium according to the up-going fashion.[24] The propagation fashion, that propagates from the lowest medium to the free surface by vector E and then propagates from the free surface to the receiving point z by the propa-

TABLE I. Three groups of the parameters of the layered media.

Note	Velocities of compressional wave (m/s)	Velocities of shear wave (m/s)	Densities (kg/m³)	Thicknesses (m)
1	4000	2500	2600	∞
2	4000	2500	2600	5
	4500	3000	2800	∞
	4000	2500	2600	5
3	4500	3000	2800	3
	5000	3500	3000	∞

gator matrix p, is complicated and may not be used. On the basis of Eq. (30), not only the problem of precision loss at a large value of z can be avoided, but also the calculation course is simplified.

Having obtained the displacement-stress vector of the guided wave by Eq. (30), we can calculate the value of H in Eqs. (12), (13), and (17). Then, the effect part of the mean energy flux density of the guided wave can be given by Eq. (17).

A. Energy characteristics of the Rayleigh wave

We consider the first model of the multilayered media in which the speeds of the compressional and shear waves increase as the ordinal number of the medium increases. Three groups of the parameters of the multilayered media are selected, see Table I. In this case, the energy characteristics of the Rayleigh wave are numerically analyzed.

Figure 2 displays the relation of the mean energy flux density of the Rayleigh wave to the frequency in the parameter group 2. The parameters of the medium are given in Table I. It can be seen that the mean energy flux density of the Rayleigh wave is related to the source frequency. The mean energy flux density approaches zero when the frequency tends toward zero and infinity, and there is a maximum value, at which the frequency is greater than the frequency that is corresponding to the lowest group velocity (the dispersion curves can be seen in previous works), in its spectrum. The detailed numerical results show that the differences of the mean energy flux densities and displacement-stress vectors of the Rayleigh waves among the parameter groups 1, 2, and 3 are not significant. So it is not convenient
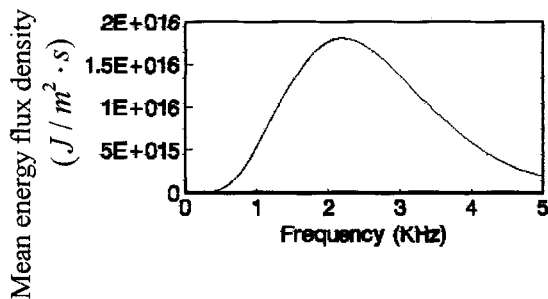
FIG. 2. Mean energy flux density of the Rayleigh waves, $z_s = 0.5$ m, $z = 0$, $r = 10$ m.
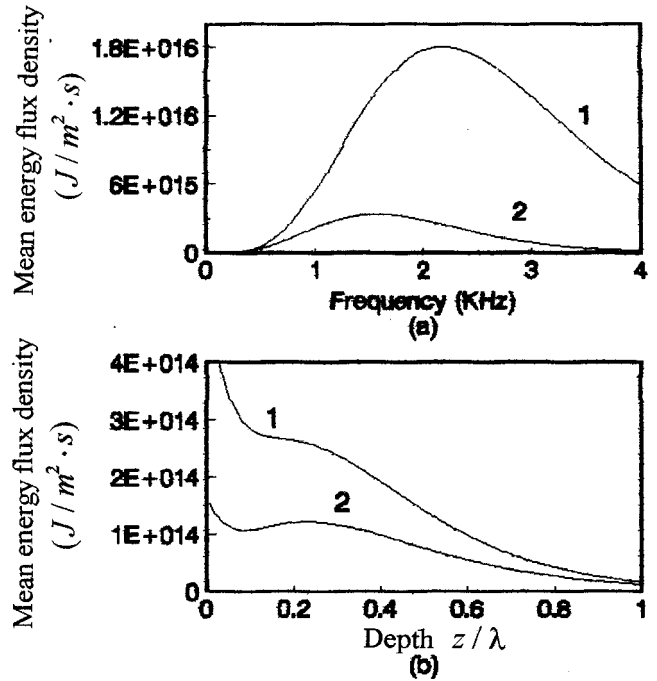
FIG. 3. (a) The relation of the mean energy flux density of Rayleigh wave in parameter group 1 to the acoustic frequency. $r = 10$ m, $z = 0$, 1. $z_s = 0.5$ m, 2. $z_s = 0.7$ m. (b) The relation of the mean energy flux density of Rayleigh wave to the depth z/λ. $r = 10$ m, $z_s = 0.5$ m, $f = 0.5$ kHz. 1. parameter group 1, 2. Speeds of the compressional and shear wave (half-space) are $V_p = 4500$ m/s, $V_s = 2000$ m/s, respectively.

to extract directly the differences among the different parameter groups by the intensity of the Rayleigh wave received at the free surface. Further works and methods should be conducted for investigating the structures of the media. Zhang et al.[13] introduced two physical quantities for the Rayleigh wave, which are sensitive to the material property of the medium and the layered geometry, for exploring the structures of the interfaces and the velocity distributions of layers under the free surface.

The mean energy flux density of the Rayleigh wave is also related to the distance from the acoustic source to the origin (z_s) and distance from the receiving point (z) to the plane $z = 0$ (see Fig. 3). As the value of z_s increases the mean energy flux density of the Rayleigh wave decreases, and the position of the maximum value of the mean energy flux density shifts to the low-frequency range [Fig. 3(a)]. Figure 3(b) gives the relation of the mean energy flux density to the depth z/λ (λ is the wavelength of the Rayleigh wave). It can be seen from Fig. 3(b) that most of the energy of the Rayleigh wave concentrates the region about the free surface of the multilayered media. This is mainly why the Rayleigh wave is named the surface wave.

It can also be seen from Fig. 3(b) that there is a maximum and a minimum value in the curves. This case can be illustrated by a half-space medium, for example. For the half-space medium, the relation of the quantity H in Eqs. (12), (13), and (17) to the variant z is of the form

$$H \sim A e^{2\gamma_p kz} + B e^{2\gamma_s kz} - C e^{(\gamma_p + \gamma_s)kz}, \tag{31}$$

where $A = \gamma(1 + 2\gamma\gamma_p^2)$, $B = (\gamma - 1)(\gamma\gamma_s + \gamma\gamma_p - \gamma_s)/\gamma_s$, and $C = \gamma^2 - 1 + 2\gamma^2\gamma_p^2 - \gamma\gamma_p^2 + (\gamma - 1)\gamma\gamma_p/\gamma_s$.
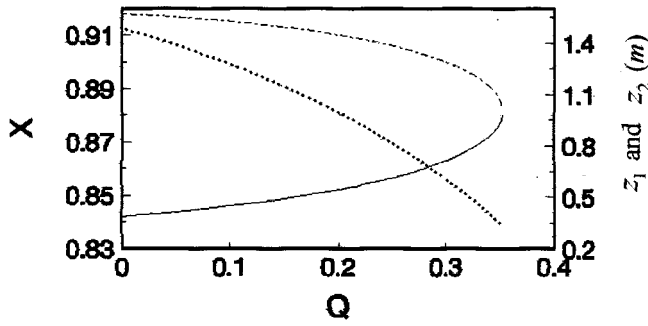
FIG. 4. Relation of phase velocity X $(=V^2/V_s^2$, left vertical axis, dotted line), z_1 (right vertical axis, real line), and z_2 (right vertical axis, dotted-dashed line) of Rayleigh wave in half-space medium to the Q $(=V_s^2/V_p^2)$ value of the medium, $f=0.3$ kHz.

TABLE II. Three groups of the parameters of three-layered media.

Note	Velocities of compressional wave (m/s)	Velocities of shear wave (m/s)	Densities (kg/m³)	Thicknesses (m)
4	4000	2500	2600	5
	3000	2400	2000	3
	4000	2500	2600	∞
5	4000	2500	2600	5
	3000	2000	2000	3
	4000	2500	2600	∞
6	4000	2500	2600	5
	3000	1600	2000	3
	4000	2500	2600	∞

Therefore the maximum and minimum values of z (z_1 and z_2) are obtained by letting $\partial H/\partial z$ equal to zero

$$z_{1,2} = \frac{1}{k(\gamma_p - \gamma_s)}$$
$$\times \ln\left[\frac{(\gamma_p - \gamma_s)C \pm \sqrt{(\gamma_p - \gamma_s)^2 C^2 - 16\gamma_p\gamma_s AB}}{4\gamma_p A}\right]. \quad (32)$$

Equation (32) demands that $(\gamma_p - \gamma_s)^2 C^2 \geq 16\gamma_p\gamma_s AB$, and it is also demanded that $Q = V_s^2/V_p^2 \leq 0.3525...$, where V_p and V_s are the speeds of the compressional and shear waves, respectively. Figure 4 gives the relations of the phase velocity (V^2/V_s^2) of the Rayleigh wave, z_1, and z_2 to the Q value of the medium, and it is easy to see from Fig. 4 that there is really a maximum and a minimum point in the energy flux density of the Rayleigh wave when $Q < 0.3523...$.

As seen in the above section, only in the case that the distance r is greater than the wavelength of the Rayleigh wave, the velocity given by the left-hand side of Eq. (27) is equal to the group velocity $d\omega/dk$. Figure 5 displays this relation. It can be seen that the bigger the radial distance r and the frequency f are, the smaller the differences between V_g and $d\omega/dk$ are.
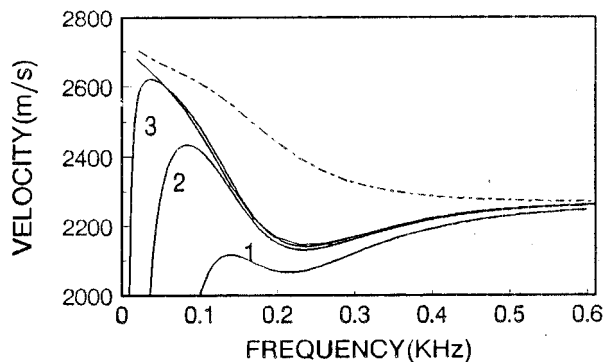
FIG. 5. Relation of velocity V_g given by the left-hand side of Eq. (27) to the frequency in parameter group 2, 1. $r=4$ m, 2. $r=10$ m, 3. $r=40$ m, $-\cdot-\cdot-\cdot$ phase. ——— group.

B. Guide waves and mean energy characteristics

We now consider the second model of three layered media in which an area of low velocity is encompassed. Three groups of parameters of each layer medium are given in Table II. The guided waves trapped in multilayered media are studied, and their dispersions and propagation characteristics and the energy fluxes are analyzed. The guided modes can be separated into two categories: surface modes and trapped modes. The surface modes are fundamentally related to the existence of the free surface $z=0$. The trapped modes are fundamentally related to the interfaces under the free surface. These modes also do not lose energy as they propagate radially.

When the frequency approaches infinity, the phase and group velocities of the Rayleigh wave in multilayered media should tend toward that in the case where there is only the first medium (half-space), and we represent this velocity with V_∞. It can be calculated that $V_\infty = 2269$ m/s in three groups of parameters in Table II. So the following discussions are separated into two parts.

1. $V_s(2) > V_\infty$

In this case the velocity, which is denoted by $V_s(2)$, of the shear wave in the second layer medium is greater than $V_\infty (= 2269$ m/s). The parameter group 4 is just this situation. Figure 6(a) and (b) give the dispersion and energy flux of the Rayleigh wave in this case. The group velocity (dotted-dashed line) is smaller than the phase velocity (real line) in the low-frequency range but greater that that in the high-frequency range [Fig. 6(a)]. The mean energy flux density is very similar in which there is only the first layer medium (half-space) [Fig. 6(b)]. It also has the property that the Rayleigh wave decays rapidly with the distance from the free surface and does not have sensitivity to the structures under the free surface. So it is difficult to distinguish the different structures directly by the information about the Rayleigh wave.

Figure 7 illustrates the dispersion characteristic and the energy flux density of a guided wave. The phase and group velocities of this guided wave tend toward the shear wave velocity $V_s(2)(=2400$ m/s) of the second layer medium when the frequency approaches infinity [Fig. 7(a)]. The guided wave has a cut-off frequency at which the phase and group velocities equal to the shear wave velocity $V_s(1)$
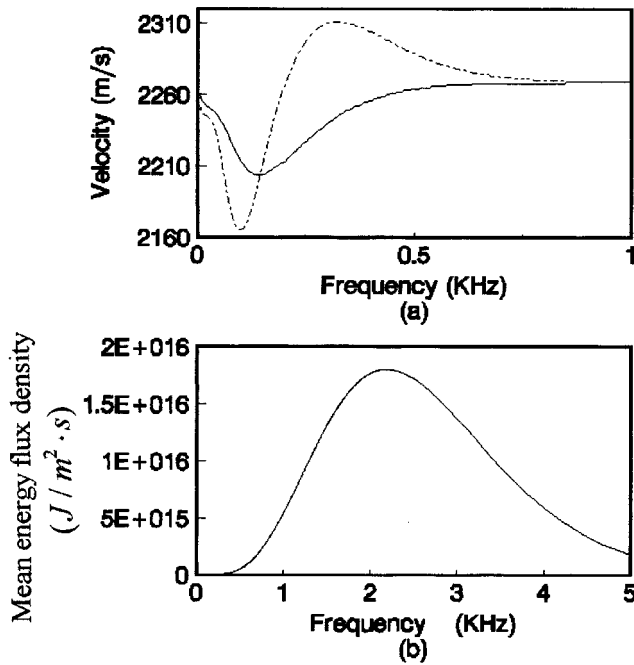
FIG. 6. Dispersion curves (a) and mean energy flux density (b) of the Rayleigh wave in the parameter group 4.

(=2500 m/s) of the first layer medium. The mean energy flux density of the guided wave is equal to zero when the frequency tends toward zero and infinity, and the significant values appear in a narrow range behind the cut-off frequency [Fig. 7(b)]. The position of the maximum value is significantly lower than that in the case of the Rayleigh waves.

The relations of the mean energy flux densities of the trapped wave and the Rayleigh wave to the depth z are dis-
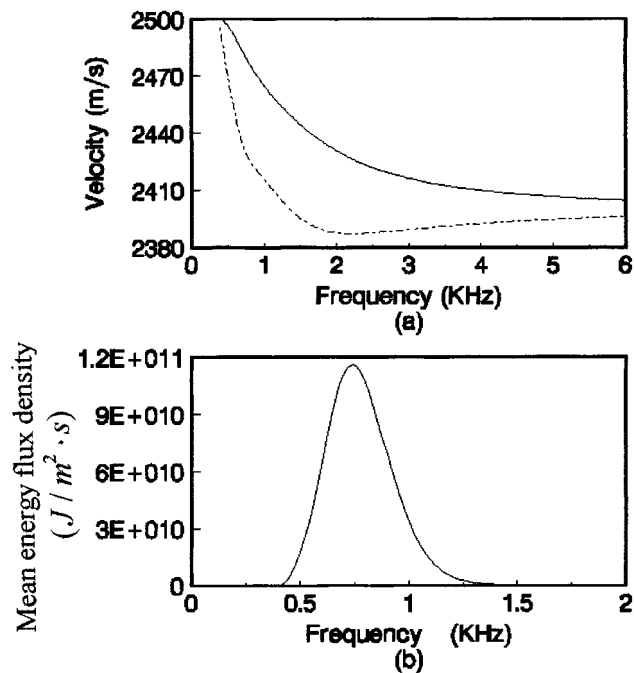
FIG. 7. Dispersion curves (a) and mean energy flux density (b) of the trapped wave in the parameter group 4.
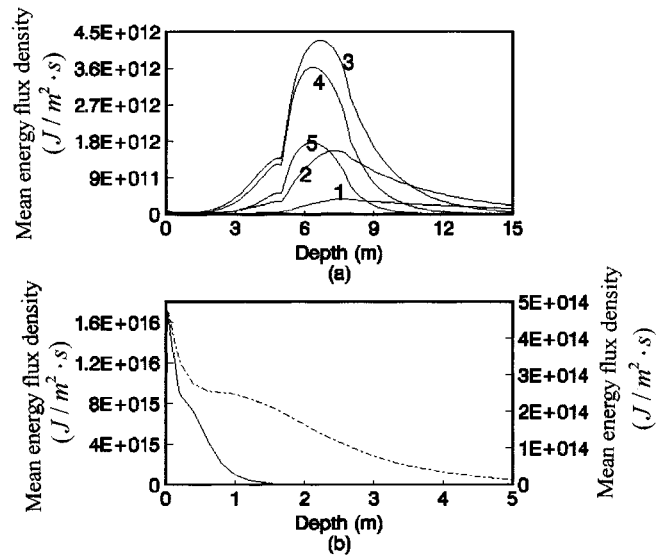
FIG. 8. Relation of mean energy flux densities of guided waves to the depth. (a) Trapped wave, 1. $f=0.5$ kHz, 2. $f=0.6$ kHz, 3. $f=0.8$ kHz, 4. $f=1.0$ kHz, 5. $f=1.2$ kHz. (b) Rayleigh wave, ——— left vertical axis, $f=2.0$ kHz, $-\cdot-\cdot-\cdot$ right vertical axis, $f=0.5$ kHz.

played in Fig. 8(a) and (b), respectively. In the case of the trapped wave [Fig. 8(a)], most of the energy is trapped in the second layer medium ($z=5\sim8$ m). The trapped wave decays rapidly with the distances from the interfaces $z=z_1$ (receiving point is up the plane $z=z_1$) and $z=z_2$ (receiving point is down the plane $z=z_2$). The values of the mean energy flux densities are greatest in the middle of the second layer medium. It can also be seen that the curve of the greatest intensity is corresponding to the frequency 0.8 kHz, this is consistent with Fig. 7(b).

So in this case, the mean energy distribution of the trapped wave shows that the trapped wave propagation along the second layer (low-velocity layer) is wholly trapped in this layer. When the guided waves are extracted from the logs of the receiving borehole, the position and extent of the low-velocity zones corresponding to the guided waves can be obtained from the energy distribution of the guided waves.

However, in Fig. 8(b), there is no such situation. Most of energy of the Rayleigh wave concentrates on a little range beneath the free surface. So it follows from Fig. 8(a) and (b) that the trapped wave propagates within the second layer medium (low-velocity area) while the Rayleigh wave, which is a surface wave, propagates in a little range beneath the free surface.

In addition to Fig. 8(a) and (b), the mean energy flux density of the Rayleigh wave is significantly greater than that of the trapped wave. This situation is related to the value of z_s. If z_s increases (the acoustic source approaches the low-velocity area), the intensity of the trapped wave should increase and exceed that of the Rayleigh wave.

The propagation velocity of the mean energy density of the guided wave is related to the depth z. Figure 9 gives this relation in parameter group 4. The real line is for the Rayleigh wave and the imaginary line for the trapped wave in
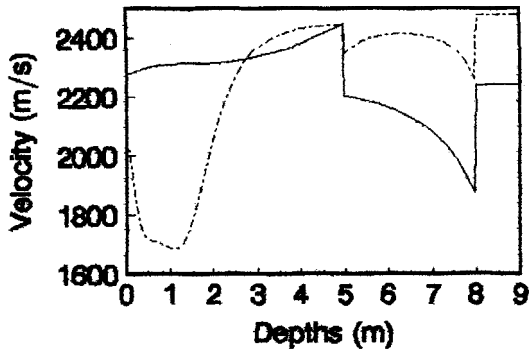
FIG. 9. Distributions of the propagation velocities of energy densities of guided waves in multilayered media (parameter group 4). ———— Rayleigh wave, $f = 0.3$ kHz, $-\cdot-\cdot-\cdot-$ trapped wave, $f = 0.8$ kHz.

Fig. 9. In the case of the Rayleigh wave (real line), the frequency $f = 0.3$ kHz, and the phase and group velocities can be obtained by the dispersion equations which are equal to 2240 and 2312 m/s. But for the trapped wave (imaginary line), the frequency $f = 0.8$ kHz, the phase and group velocities are 2477 and 2425 m/s, respectively. It can be seen that the propagating velocity of the mean energy flux density is not continuous at the interfaces under the free surface.

In fact, a number of the trapped waves may be excited, depending upon the acoustic frequency. In above analyses, it is the first trapped wave, which is in the lowest frequency range, that is analyzed. This is because the others are similar and the first trapped wave is the most important in theoretical study and practical applications.

2. $V_s(2) < V_\infty$

In this case, the shear wave velocity $[V_s(2)]$ of the second layer medium is smaller than V_∞. The parameter groups 5 and 6 are in this situation.

The Rayleigh wave in this case is different from that in the above analyses. It has a cut-off frequency in the low-frequency range. The group velocity is smaller than the phase velocity, and has a minimum value [Fig. 10(a)]. This is somewhat like the trapped wave in the case $V_s(2) > V_\infty$ [Fig. 7(a)]. However, the energy flux density of the Rayleigh wave is also very similar to the case where there is only the first layer medium (half-space) [Fig. 10(b)]. From Figs. 10 and 6, it could be seen that the Rayleigh waves in the two cases have significant different dispersion features although the energy fluxes are similar.

The dispersion characteristic of the trapped wave is also significantly different from that in the case $V_s(2) > V_\infty$ [Fig. 11(a)]. The phase and group velocities tend toward $V_s(2)$ in the high-frequency range, and the trapped wave has no cut-off frequency. It can be seen similarly that the group velocity is smaller than the phase velocity in the low-frequency range but greater than that in the high-frequency range.

Figure 11(b) displays the mean energy flux density of the trapped wave. Its significant values appear in a little range. The position of the maximum mean energy flux density is near that of the smallest group velocity. As $V_s(2)$ decreases, the mean energy flux density of the trapped wave decreases.
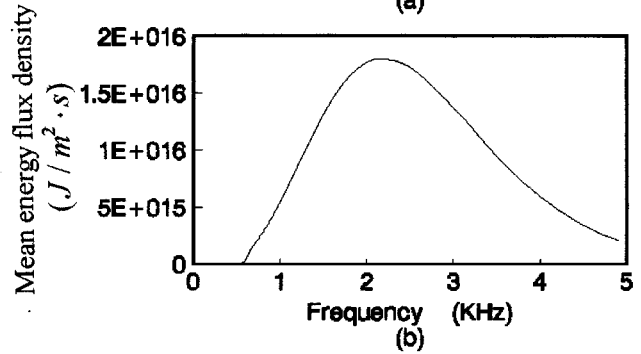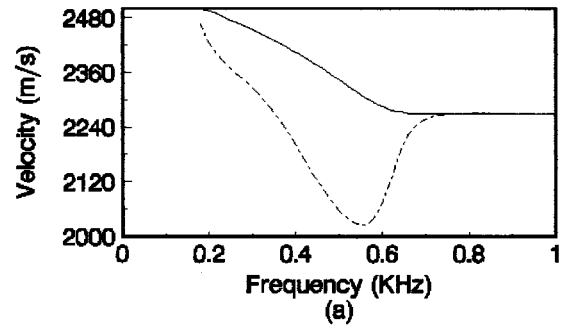
FIG. 10. Dispersion curves (a) and energy flux density (b) of Rayleigh wave in the parameter group 5.

The relations of the mean energy flux density of two categories of guided waves to the depth z are illustrated in Fig. 12(a) and (b). Figure 12(a) is for the trapped wave while Fig. 12(b) is for the Rayleigh wave. It is easy to find that the energy of trapped wave decays with depth z when the acoustic frequency is less (about $f < 0.6$ kHz). As frequency increases, the energy of the trapped wave concentrates signifi-
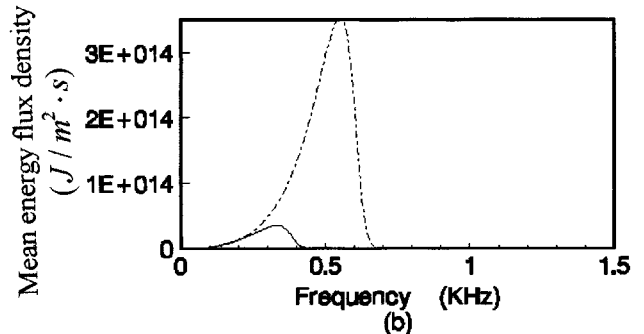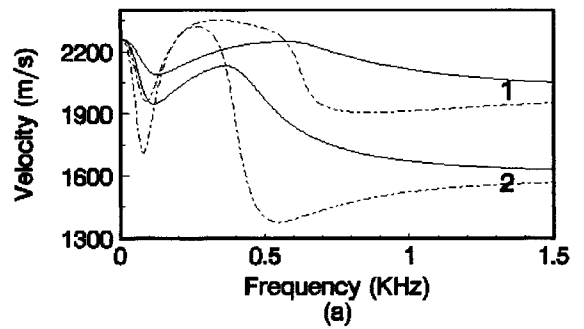
FIG. 11. Dispersion curves (a) and energy flux density (b) of the trapped wave. (a) 1. parameter group 5, 2. parameter group 6, (b) $-\cdot-\cdot-\cdot-$ parameter group 5, ———— parameter group 6.
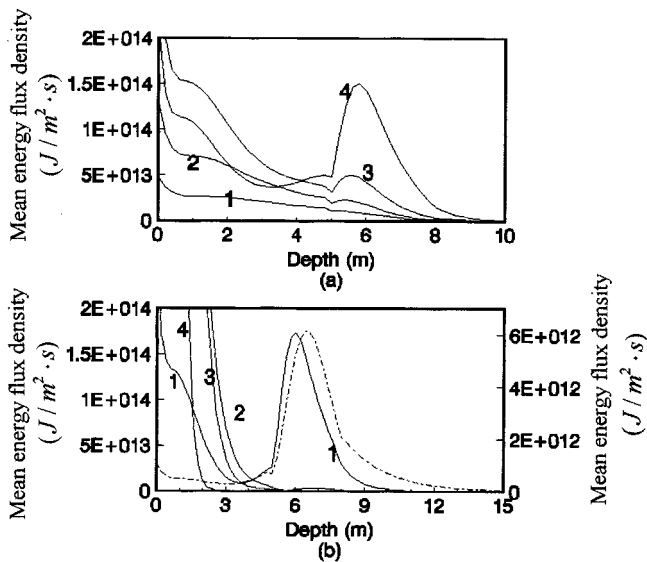
FIG. 12. Relation of energy flux densities of guided waves to depth. (a) Trapped wave, 1. $f = 0.3$ kHz, 2. $f = 0.4$ kHz, 3. $f = 0.5$ kHz, 4. $f = 0.6$ kHz, (b) Rayleigh wave, ——— left vertical axis, 1. $f = 0.6$ kHz, 2. $f = 0.8$ kHz, 3. $f = 1.0$ kHz, 4. $f = 2.0$ kHz, $-\cdot-\cdot-\cdot$ right vertical axis, $f = 0.4$ kHz.

cantly within the second layer medium ($z = 5 \sim 8$ m). However, the situation is inversed in Fig. 12(b). The mean energy flux density of the Rayleigh wave concentrates within the second layer medium in the low-frequency range (also about $f < 0.6$ kHz), while the mean energy flux density of the Rayleigh wave decays significantly with the depth z in the high-frequency range.

In the high-frequency range, the phase and group velocities and the mean energy flux densities of the guided waves (Rayleigh and trapped waves) are familiar to that in the case $V_s(2) > V_\infty$. This is the main reason that we separate the guided waves into Rayleigh and trapped waves. However, as seen in the preceding paragraph, this division is not reasonable in the low-frequency range because the Rayleigh wave will not be a surface wave in this case according to the division method. So there is no good simple method in the whole frequency range to distinguish the Rayleigh wave from the trapped wave. The characteristics of the dispersion and energy distribution should be considered together.

III. CONCLUSIONS AND DISCUSSIONS

The mean energy flux density and mean energy density of the guided wave propagating along the multilayered media are theoretically and numerically studied. Two categories of the guided waves, Rayleigh and trapped waves trapped in an area, are investigated via numerical simulation in some groups of parameters. The dispersion characteristics and the energy distributions of the guided waves are also studied.

Energy is an important quantity of the guided waves. The propagation fashion of the guided waves can be illustrated further by the energy concept. It can be clearly explained that the guided waves cannot be excited by a practical acoustic source alone. The energy distribution of the

guided waves can more accurately reflect the structures and extents of the multilayered media than the displacement-stress vector and other physical quantities.

Only in the case that the propagation distance r is greater than the wavelength, is the mean velocity of the total energy of the guided waves equal to the group velocity of the guided waves. The propagation velocity of the mean energy flux density is related to the depth, but equal to the phase velocity of the guided waves in the lowest layer of the multilayered media.

Two categories of the guided waves, Rayleigh and trapped waves, can be excited in the three-layered media in which a low-velocity area is comprised. When the shear velocity of the second layer medium is greater than the velocity limitation of the Rayleigh wave at the high-frequency range $[V_s(2) > V_\infty]$, most of energy of the Rayleigh wave concentrates on a little range beneath the free surface (known as the surface wave), while the trapped wave concentrates its energy in the second layer medium (low velocity). However, when the shear velocity of the second layer medium is smaller than the velocity limitation of the Rayleigh wave at the high-frequency range $[V_s(2) < V_\infty]$, the energy distributions of the Rayleigh and trapped waves are related to the frequency range. Most of energy of the Rayleigh wave is in the nearby range beneath the free surface and most of the energy of the trapped wave is in the second layer medium in the high-frequency range, the situation is the inverse in the low-frequency range. That is to say, the trapped wave displays a kind of surface wave while the Rayleigh wave concentrates its energy in the second layer medium in the low-frequency range. So it is not easy to distinguish the Rayleigh wave from the trapped wave in the whole frequency range in this case. It also shows that it is important for the problem to extract the Rayleigh and trapped waves from each other.

Although the model of this paper is based on the multilayered elastic solid and isotropic media, the results lay the foundation for investigating the guided waves in multilayered poroelastic and anisotropic formations.

ACKNOWLEDGMENTS

[1] W. T. Thomson, "Transmission of elastic waves through a stratified solid," J. Appl. Phys. **21**, 89–93 (1950).
[2] F. Gilbert and G. Backus, "Propagation matrices in elastic wave and vibration problems," Geophysics **31**, 326–332 (1966).
[3] M. Saito, "Excitation of free oscillations and surface waves by a point source in a vertical heterogeneous," J. Geophys. Res. **72**, 3689–3899 (1967).
[4] A. Ben-Menahem and S. J. Singh, "Multiploar elastic field in a layered half-space," Bull. Seismol. Soc. Am. **58**, 1519–1572 (1968).
[5] Y. Zhen-Xing, "Generalized reflection coefficients for a layered medium and asymmetrical source," Acta Geophys. Sinica **22**, 181–194 (1979).
[6] T. Kundu and A. K. Mal, "Elastic wave in a multilayered solid due to a dislocation source," Wave Motion **7**, 459–571 (1985).
[7] H. Schmidt and G. Tango, "Efficient global matrix approach to the computation of synthetic seismograms," Geophys. J. R. Astron. Soc. **84**, 331–359 (1986).
[8] C. Boutin, G. Bonnet, and P. Y. Bard, "Green functions and associated

sources in infinite and stratified poroelastic media,'' Geophys. J. R. Astron. Soc. **90**, 521–550 (1987).

[9] M. Tajuddin and S. Ahmed, ''Dynamic interaction of a poroelastic layer and half-space,'' J. Acoust. Soc. Am. **89**, 1169–1175 (1991).

[10] J. O. Parra, ''Analysis of elastic wave propagation in stratified fluid-filled porous media for interwell seismic applications,'' J. Acoust. Soc. Am. **90**, 2557–2575 (1991).

[11] D. G. Harkrider, ''Surface waves in multilayered elastic media. I. Rayleigh–Love waves from buried sources in a multilayered elastic half-space,'' Bull. Seismol. Soc. Am. **54**, 627–679 (1964).

[12] A. K. Mal, ''Guided waves in layered solids with interface zones,'' Int. J. Eng. Sci. **26**, 873–881 (1988).

[13] B. Zhang, M. Yu, C. Q. Lan, and W. Xiong, ''Elastic wave and excitation mechanism of surface waves in multilayered media,'' J. Acoust. Soc. Am. **100**, 3527–3538 (1996).

[14] J. O. Parra and P. C. Xu, ''Dispersion and attenuation for acoustic guided waves in layered fluid-filled porous media,'' J. Acoust. Soc. Am. **95**, 91–98 (1994).

[15] P. A. Johnson and J. N. Albright, ''Conversion of borehole Stoneley waves to channel waves in coal,'' Proceedings of SEG 57th Annual International Meeting (1987), pp. 22–27.

[16] Bixing Zhang, C. Q. Lan, M. Yu, Wei Xiong, and Long Li, ''Energy distribution of surface waves in stratified media,'' Acta Acustica (to be published).

[17] S. N. Guzhev, ''Study of phase velocity and energy distribution of Stoneley waves at a solid–liquid interface,'' J. Acoust. Soc. Am. **95**, 661–667 (1994).

[18] N. A. Haskell, ''The dispersion of surface waves on multilayered media,'' Bull. Seismol. Soc. Am. **43**, 17–34 (1953).

[19] E. N. Thrower, ''The computation of the dispersion of elastic eaves in layered media,'' J. Sound Vib. **2**, 210–226 (1965).

[20] F. Schwab and L. Knoff, ''Surface waves on multilayered inelastic media,'' Bull. Seismol. Soc. Am. **61**, 893–912 (1971).

[21] M. Tajuddin, ''Rayleigh waves in a poroelastic half-space,'' J. Acoust. Soc. Am. **75**, 682–684 (1984).

[22] M. Tajuddin, ''Rayleigh waves on a convex cylindrical poroelastic surface,'' J. Acoust. Soc. Am. **76**, 1252–1254 (1984).

[23] A. Abo-zena, ''Dispersion function computations for unlimited frequency values,'' Geophys. J. R. Astron. Soc. **58**, 91–105 (1979).

[24] W. Menke, ''Comment on 'Dispersion function computations for unlimited frequency values' by A. Abo-zena,'' Geophys. J. R. Astron. Soc. **59**, 315–323 (1979).

[25] H. F. Tiersten and B. K. Sinha, ''A perturbation analysis of the attenuation and dispersion of surface waves,'' J. Appl. Phys. **49**, 87–95 (1978).

[26] G. Xiao-Ping, H. Jia-Zheng, and Z. Hong-Qin, ''Probe the interpretation theory of steady-state Rayleigh wave method in engineering exploration,'' Acta Geophys. Sinica **36**, 96–105 (1993).

[27] L. You-Ming and S. Pei-Yi, ''On surface wave dispersion and body wave generalized reflection coefficient computations for layered media,'' Acta Geophys. Sinica **25**, 130–139 (1982).

[28] B. A. Auld, *Acoustic Field and Waves in Solids* (Wiley, New York, 1973).

[29] A. L. Kurkjian and S. K. Chang, ''Acoustic multipole sources in fluid-filled boreholes,'' Geophysics **51**, 148–163 (1986).

Implementation of transparent sources embedded in acoustic finite-difference time-domain grids

John B. Schneider,[a] Christopher L. Wagner, and Shira L. Broschat
School of Electrical Engineering and Computer Science, Washington State University, Pullman, Washington 99164-2752

The finite-difference time-domain (FDTD) method is a simple but powerful numerical method which has been used to perform a wide variety of complex simulations. One of the considerations in using this method is modeling the source of the incident field. When the physical source of acoustic energy is located within the FDTD grid it has typically been modeled as a ''hard'' source for which a source function determines the field at a source node. One drawback of a hard source is that it acts itself as a scatterer. Moreover, its scattering cross section is dictated by the spatial step size within the grid; thus, scattering is independent of the underlying physical size of the source. In this paper a scheme is presented that permits the creation of completely transparent sources. These sources, although more expensive to implement than traditional hard sources, radiate the same field as a hard source, but do not scatter energy. © *1998 Acoustical Society of America.* [S0001-4966(98)04101-0]

PACS numbers: 43.20.Px, 43.55.Ka [JEG]

INTRODUCTION

The finite-difference time-domain (FDTD) method was first introduced by Yee in 1966[1] for the study of electromagnetic scattering problems. A counterpart was later developed in acoustics which has been used to study a wide variety of problems, including acoustic propagation in shallow water and in large rooms. The FDTD method permits the use of several different types of insonification. The source can be within the computational grid so that the near-field interaction of the source and its surroundings can be modeled. Alternatively, the source can be located outside the grid (the insonifying field is then introduced using one of the techniques briefly described below). This readily permits the study of the interaction of the source far-field with any scattering object or with the local ''environment'' (such as a rough surface).

When a source is external to the FDTD grid, the field radiated by that source, i.e., the incident field, is coupled into the grid typically by means of a total-field/scattered-field formulation or a scattered-field formulation. In the total-field/scattered-field formulation (e.g., section 6.5 of Ref. 2) the grid is divided into a total-field region and a scattered-field region and the incident field is introduced over the boundary between the two. In the scattered-field formulation (e.g., section 6.6 of Ref. 2 or 3.4 of Ref. 3), the scattered field radiates directly from any material that differs from the background medium. This latter approach requires calculation of the incident field over all such materials. Both approaches are ''mature'' and have well-understood advantages and disadvantages.

For many simulations, however, the source of energy must be embedded within the FDTD grid, e.g., for resonators or radiating structures. Most commonly sources are embedded as ''hard'' sources (e.g., section 6.4 of Ref. 2 or the velocity membrane described in Ref. 4). A hard source is implemented simply by specifying the field at a given node with a source, or ''driving,'' function. Since the update equation does not apply to this source node, its value is fixed solely by the driving function so that it effectively scatters any field incident upon it. In most instances scattering from the source node is a spurious artifact of the source implementation which degrades the quality of the simulation. One approach to eliminating source scattering requires the use of a pulsed driving function that vanishes after a finite duration. Once the driving function is zero, the value of the source node is set by the update equation. For this approach to succeed, the duration of the driving function must be shorter than the time it takes for energy to travel from the source node to any material discontinuity and back again to the source. Unfortunately, in many circumstances this requirement is overly restrictive. In this paper the implementation of a source that radiates the same field as a hard source, but that does not scatter, is presented. We call such a source ''transparent.''

A node in a FDTD grid that has the same material properties as its neighbors and that is governed by the standard update equation does not, *per se*, scatter energy. It therefore appears that one may simply implement a transparent source by setting the value of the source node equal to the sum of the value returned by the update equation and the value of the driving function. Indeed, this approach yields a node that does not act as a scatterer, but the field that radiates from it may bear little resemblance to the actual driving function. In fact the field that radiates from the node, as compared to that from a hard source, is a filtered version of the driving function. The filter transfer function is dictated by the difference between a hard (boundary value) source and the additive (volume) source. (For a discussion of these different sources the reader is directed to section 7.3 of Ref. 5.) Unfortunately,

---
[a]Electronic mail: schneidj@eecs.wsu.edu

it does not appear possible to obtain a simple closed-form expression for this transfer function. Thus, there is no way to obtain analytically a function that can be used to drive a simple additive source so that it will radiate the same field as a hard source. However, it is possible to measure, directly from the finite-difference grid, the filter impulse response at the source node and then use it to construct a transparent source that radiates the same field as a hard source. The impulse response is measured at the source node and is fundamentally different from the time-domain Green's function (which is itself an impulse response, but one for which the source and observation points are not collocated). In one dimension, the impulse response is of finite duration when the Courant limit is used. In two and three dimensions, and in one dimension for Courant numbers other than the limit, the impulse response is infinite in duration. For the remainder of the paper, unless stated otherwise, ''transparent source'' implies a source that radiates the same field as a hard source (thus this source is distinct from a simple additive source).

Perhaps the simplest way to implement a transparent source, and the one used in this study, is first to run a simulation that records the impulse response of the grid. This simulation must use the number of dimensions and the Courant number that pertain in the problem of interest (symmetry can be exploited to reduce the size of the simulation as discussed later). The transparent source is then realized, in part, by convolving the impulse response with the driving function. Once found, the impulse response can be used for all subsequent simulations that have the same number of dimensions and the same Courant number, i.e., it is independent of any other aspect of the problem under consideration. This approach is only appropriate for a single-node source or a collection of noninteracting source nodes (as would be used in a ''classic'' phased array). Nevertheless, it can be extended to permit the construction of multiple, interacting source nodes. Thus, it is possible to construct transparent source ''screens'' that excite a system exactly as would a hard boundary-valued source. These transparent screens can be used, for example, to excite waveguides and, unlike hard screens, a transparent screen can be placed immediately adjacent to any waveguide discontinuity. (A full discussion of transparent screens is presented in Ref. 6.)

In Sec. I implementation of transparent sources in one dimension is described, and in Sec. II implementation in two and three dimensions is described.

I. ONE-DIMENSIONAL TRANSPARENT SOURCES

Although a transparent source in one dimension is of little practical use, it is helpful first to consider implementation in one dimension (the extension to two and three dimensions is trivial). The differential equations governing acoustic propagation are

$$\frac{\partial \mathbf{v}}{\partial t} = -\frac{1}{\rho} \boldsymbol{\nabla} p, \tag{1}$$

$$\frac{\partial p}{\partial t} = -c^2 \rho \boldsymbol{\nabla} \cdot \mathbf{v}, \tag{2}$$

where c is the speed of sound, ρ is the density, p is the pressure, and $\mathbf{v}$ is the velocity. We reduce the problem to one dimension so there is no variation in the y and z directions. By employing finite differences to approximate the derivatives and offsetting the pressure and velocity evaluation points, both temporally and spatially, one can solve for future field values in terms of current and past field values (see, for example, Ref. 4 or 7). This leads to the standard update equations for the FDTD method in one dimension:

$$v_x^{n+1/2}(i) = v_x^{n-1/2}(i) - \frac{1}{c\rho} \frac{c\Delta t}{\Delta x} [p^n(i+1) - p^n(i)], \tag{3}$$

$$p^{n+1}(i) = p^n(i) - c\rho \frac{c\Delta t}{\Delta x} [v_x^{n+1/2}(i) - v_x^{n+1/2}(i-1)], \tag{4}$$

where Δx and Δt are the spatial and temporal step sizes, respectively, the superscript indicates the time step, and the argument indicates the spatial location so that $p^n(i) = p(i\Delta x, n\Delta t)$ and $v_x^{n+1/2}(i) = v_x([i+1/2]\Delta x, [n+1/2]\Delta t)$. For brevity, the spatial offset between the p and v_x nodes is suppressed in the arguments of the discrete forms. The term $c\Delta t/\Delta x$, hereafter identified as s, is the Courant number which must be chosen to satisfy the stability requirements: $s \leq 1/\sqrt{N}$, where N is the number of spatial dimensions. The maximum value of s yields the minimum amount of numerical dispersion and the longest simulation duration for a given number of time steps. Although the maximum value of s should be used whenever possible, the Courant limit cannot be used throughout the computational domain for simulations of inhomogeneous regions since, for stability, the limit must hold in the fastest medium as discussed below. Thus it is important to consider source implementations that do not restrict the Courant number. Note that in one dimension with an s of unity the FDTD algorithm yields an exact solution for propagation in a homogeneous medium.

Consider a one-dimensional (1-D) computational domain in which the source is a pressure node at i_{src}. A hard source is realized by setting the source node equal to a given driving function $f(n\Delta t) = f^n$. The pressure at the source node is then $p^n(i_{\text{src}}) = f^n$, but all other nodes are governed by the update equations (3) and (4). Assuming that the driving function is zero prior to $n = 0$, Fig. 1 shows the values of p and v_x in the vicinity of the source for the first two time steps. At the Courant limit, a 1-D FDTD simulation of propagation in a homogeneous medium is equivalent to a series of shift operations. Hence, the pressure at node i and time step n is given by

$$p^n(i) = f^{n-|i-i_{\text{src}}|}. \tag{5}$$

Since a hard source only depends on the driving function and is independent of other propagating fields, it is effectively perfectly reflecting. Therefore, if a space is inhomogeneous and a reflected field propagates back to the source, the source will, in turn, reflect that field. Although we explicitly consider only pressure sources here, the transparent-source implementation presented applies equally to pressure and velocity sources.

$p(i_{src}-2)$	$v_x(i_{src}-2)$	$p(i_{src}-1)$	$v_x(i_{src}-1)$	$p(i_{src})$	$v_x(i_{src})$	$p(i_{src}+1)$	$v_x(i_{src}+1)$	$p(i_{src}+2)$
$n=0$				f^0				
$n=\frac{1}{2}$			$-\frac{1}{c\rho}f^0$		$\frac{1}{c\rho}f^0$			
$n=1$		f^0		f^1		f^0		
$n=\frac{3}{2}$	$-\frac{1}{c\rho}f^0$		$-\frac{1}{c\rho}f^1$		$\frac{1}{c\rho}f^1$		$\frac{1}{c\rho}f^0$	
$n=2$	f^0		f^1		f^2		f^1		f^0

FIG. 1. Values of p and v_x in a one-dimensional grid when the node $p(i_{src})$ is implemented as a hard source. The values assume the Courant number s is unity. Node location is given along the top and the time step is indicated along the left. A blank indicates the field is zero.

With the goal of creating a transparent source, let us implement the source as the sum of the driving function and the update equation that pertains at that node. The value of the source node is then given by

$$p^{n+1}(i_{src}) = p^n(i_{src}) - c\rho s[v_x^{n+1/2}(i_{src}) - v_x^{n+1/2}(i_{src}-1)] + f^{n+1}. \qquad (6)$$

Figure 2 shows the values of p and v_x in the vicinity of the source for the first two time steps for this source implementation. Significantly, the field throughout the grid cannot be obtained simply by a shifted (or delayed) value of the driving function. Instead, the pressure at an arbitrary node is given by

$$p^n(i) = \sum_{m=0}^{n-|i-i_{src}|} (-1)^{m+n-|i-i_{src}|} f^m. \qquad (7)$$

In contrast to the hard source, any field that is reflected back to the source node will pass through it. In this sense the source node is "transparent." Unfortunately, the field that is radiated by the source node may not resemble the driving function as desired. To illustrate this, consider the case $f^n = \delta[n]$ (the Kronecker delta function) for which f^0 is unity and all other values of f^n are zero. In this case the field that propagates away from the source node is a series of ones with alternating signs. Since, at the Courant limit, the field propagates without error, this result is directly attributable to the source implementation and is not indicative of any error inherent in the FDTD simulation.

Inspection of Fig. 2 shows that the radiated field can be made identical to that of the hard source with the addition of a delayed sample of the driving function. This delayed term,

which is added to the update equation and the undelayed driving function as given by (6), cancels the "echo" of the previous source term (i.e., f^n) caused by using the update equation at the source node. Thus, a truly transparent source that radiates the same field as the hard source can be achieved using

$$p^{n+1}(i_{src}) = p^n(i_{src}) - c\rho s[v_x^{n+1/2}(i_{src}) - v_x^{n+1/2}(i_{src}-1)] + f^{n+1} + f^n. \qquad (8)$$

This source implementation produces the fields shown in Fig. 1, but the source node does not scatter (or reflect) any field incident upon it as it does with the hard source implementation.

One-dimensional FDTD simulations performed using Courant numbers other than the limit do not permit such a simple implementation of a transparent source. At the Courant limit, the term that is echoed by the update equation back onto the source node depends only on the value of the driving function at the previous time step. When the Courant number is less than unity, the FDTD algorithm is not equivalent to a set of simple shift operations nor can it provide an exact solution. This is a consequence of the inherent numerical dispersion.

Numerical dispersion is a function of the number of points per wavelength for a given spectral component of the signal. Thus, the spatial step size, Δx, typically is determined by the amount of dispersion that can be tolerated and then, assuming one dimension, the Courant number is dictated by the stability requirement $\Delta t \leq \Delta x / c_{fastest}$, where $c_{fastest}$ is the speed of sound in the fastest material within the grid. For the source implementation considered here, numeri-

$p(i_{src}-2)$	$v_x(i_{src}-2)$	$p(i_{src}-1)$	$v_x(i_{src}-1)$	$p(i_{src})$	$v_x(i_{src})$	$p(i_{src}+1)$	$v_x(i_{src}+1)$	$p(i_{src}+2)$
$n=0$				f^0				
$n=\frac{1}{2}$			$-\frac{1}{c\rho}f^0$		$\frac{1}{c\rho}f^0$			
$n=1$		f^0		f^1-f^0		f^0		
$n=\frac{3}{2}$	$-\frac{1}{c\rho}f^0$		$-\frac{1}{c\rho}(f^1-f^0)$		$\frac{1}{c\rho}(f^1-f^0)$		$\frac{1}{c\rho}f^0$	
$n=2$	f^0		f^1-f^0		$f^2-f^1+f^0$		f^1-f^0		f^0

FIG. 2. Values of p and v_x in a one-dimensional grid when the node $p(i_{src})$ is given by the sum of the usual update equation and the driving function f^n. The values assume the Courant number s is unity.

cal dispersion is not an issue. What is significant, as shown shortly, is that a Courant number less than unity results in echoed terms that depend on the entire history of the driving function.

To facilitate the construction of transparent sources that will work for any Courant number, we define a grid impulse response. First, consider a grid in which the source node is implemented as a hard source and the driving function is a Kronecker delta function. We define the grid impulse response as the values that are obtained using the update equation at the source node. (The update equation is used at the source node and the value returned is recorded as part of the impulse response. However, the value of the source node is not set to this value.) Thus, the impulse response is calculated from the previous value of the source node and its surrounding velocity nodes, but the impulse response does not couple back to the source node because the node is ''hard'' and its value is fixed by the Kronecker delta function. Therefore, the source node is given by $p^n(i_{\mathrm{src}}) = \delta[n]$ while the impulse response is

$$I^n = p^{n-1}(i_{\mathrm{src}}) - c\rho s[v_x^{n-1/2}(i_{\mathrm{src}}) - v_x^{n-1/2}(i_{\mathrm{src}} - 1)]. \quad (9)$$

Using the Courant limit, $s=1$, the impulse response is $I^n = -\delta[n-1]$. For Courant numbers less than unity, the impulse response is infinite in duration. One can obtain the impulse response analytically—it is simply a polynomial whose order increases with each time step—but it quickly becomes unwieldy. For example, the first few terms of I^n are

$$I^0 = 0,$$

$$I^1 = 1 - 2s^2,$$

$$I^2 = -2s^2 + 2s^4,$$

$$I^3 = -2s^2 + 6s^4 - 4s^6,$$

$$I^4 = -2s^2 + 12s^4 - 20s^6 + 10s^8,$$

$$I^5 = -2s^2 + 20s^4 - 60s^6 + 70s^8 - 28s^{10}.$$

Fortunately, it is not necessary, nor even desirable, to obtain the polynomial form of the impulse response. Instead, the impulse response can be obtained numerically via a simple FDTD simulation using a homogeneous grid that has the same material properties as those found at the source node in the problem of interest. In the simulation, a hard source is driven impulsively and the impulse response is recorded using (9). Alternatively, symmetry can be exploited, since the velocity $v_x^{n-1/2}(i_{\mathrm{src}} - 1)$ is the negative of $v_x^{n-1/2}(i_{\mathrm{src}})$, so that only half the 1-D space is needed. The impulse response can then be found using

$$I^n = p^{n-1}(i_{\mathrm{src}}) - 2c\rho s v_x^{n-1/2}(i_{\mathrm{src}}), \quad (10)$$

where $I^n = 0$ for $n \leq 0$.

The impulse response can be used to give the field that will echo back to the source node if the source node is equal to the sum of the update equation and the driving function as given by (6). Assuming such a source and that the first nonzero value of the driving function is $p^0 = f^0$, the source node at the next time step is $p^1 = f^1 + I^1 p^0$; at the next it is $p^2 = f^2 + I^1 p^1 + I^2 p^0$; and so on. Clearly, if a transparent source

is to couple the same field into the grid as a hard source, the source node must, in the absence of any reflected field, take on the same values as those of a hard source, i.e., the source node must take on the values of the driving function and the echoed values must all be canceled so that $p^0 = f^0$, $p^1 = f^1$, $p^2 = f^2$, etc. The cancellation is realized by subtracting $I^1 f^0$ from the source node at the first update, subtracting $I^1 f^1 + I^2 f^0$ at the next update, subtracting $I^1 f^2 + I^2 f^1 + I^3 f^0$ at the next, and so on. Stated another way, to implement a transparent field source, one must subtract the convolution of the impulse response and the driving function from the source node. Specifically, a transparent field source for an arbitrary Courant number is obtained using

$$p^{n+1}(i_{\mathrm{src}}) = p^n(i_{\mathrm{src}}) - c\rho s[v_x^{n+1/2}(i_{\mathrm{src}}) - v_x^{n+1/2}(i_{\mathrm{src}} - 1)]$$

$$+ f^{n+1} - \sum_{m=0}^{n} I^{n-m+1} f^m. \quad (11)$$

Although the discussion has been for the implementation of a single pressure source, the same approach can be used when the source is a velocity node, and multiple (noninteracting) sources can exist in the same computational domain. In one dimension, the impulse response for a velocity node is the same as for a pressure node. In two and three dimensions, the impulse responses for pressure and velocity nodes differ, but the basic source implementation, which is described in the next section, is the same.

II. TRANSPARENT SOURCES IN TWO AND THREE DIMENSIONS

A more general form of (11) that also holds in two and three dimensions is

$$p^{n+1}(\mathbf{r}_{\mathrm{src}}) = (N\text{-D update equation}) + f^{n+1}$$

$$- \sum_{m=0}^{n} I_N^{n-m+1} f^m, \quad (12)$$

where N is the number of dimensions, $\mathbf{r}_{\mathrm{src}}$ is the source location, ''N-D update equation'' is the update equation for a pressure node for the given number of dimensions, and I_N is the grid impulse response. With a change in dimension, the update equation changes and the values of the impulse response change, but the underlying approach does not change. The definition of the impulse response also remains unchanged: A hard source is driven impulsively and the impulse response is obtained using the update equation at the source node. (Note that the goal is to obtain transparent sources that radiate the same fields as a hard source in an unbounded medium. It is also possible to obtain the impulse response that would correspond to a hard source in a bounded medium or with a scatterer present. In these cases the impulse response must be measured with any scatterers present. This distinction is important, for example, when using a transparent screen to excite a waveguide.[6])

As was the case for one dimension, symmetry can be exploited when measuring the impulse response in two and three dimensions. For a pressure source located at the origin, the horizontal and vertical components of velocity satisfy

$$v_x(x,y) = -v_x(-x,y), \tag{13}$$

$$v_y(x,y) = -v_y(x,-y), \tag{14}$$

$$v_x(x,y) = v_y(y,x). \tag{15}$$

With (13) the computational domain can be divided in half and only the ''right'' half retained; with (14) the remaining computational domain can be divided in half and only the ''top'' half retained; and, finally, with (15) the remaining computational domain can be cut in half along a diagonal and only the lower right half retained. In this way the impulse response can be found using a computational space that is only one-eighth the size of a full two-dimensional space. This is important when the impulse response must be determined over a long duration. In addition, the reduction of the grid size is of practical importance since the impulse response should be calculated in an ''unbounded'' homogeneous grid. Because the driving function is an impulse, termination of the grid with artificial absorbing boundary conditions (ABC's) cannot provide an adequate model of an unbounded medium. Instead, the computational domain should be large enough so that reflections from the termination of the computational domain are insignificant over the duration of interest. This obviates the need for ABC's and the edge of the computational domain can be left perfectly reflecting.

In three dimensions, for a pressure node at the origin, the following hold:

$$v_x(x,y,z) = -v_x(-x,y,z), \tag{16}$$

$$v_y(x,y,z) = -v_y(x,-y,z), \tag{17}$$

$$v_z(x,y,z) = -v_z(x,y,-z), \tag{18}$$

$$v_x(x,y,z) = v_y(y,x,z), \tag{19}$$

$$v_y(x,y,z) = v_z(x,z,y), \tag{20}$$

$$v_z(x,y,z) = v_x(z,y,x). \tag{21}$$

These symmetry relations can be exploited to reduce the size of the computational domain needed to obtain the impulse response to $\frac{1}{64}$ the size of a full three-dimensional computational domain.

To illustrate how the impulse response is obtained in two dimensions, consider a problem which must be run for 16 000 time steps and for which the Courant number ''seen'' by the source is the Courant limit. To obtain an impulse response that is completely free of any boundary artifacts over 16 000 time steps, a simulation could be done using an 8000 by 8000 cell grid with the source at the center. Since there are three fields per cell, a pressure node and two velocity nodes, this requires a simulation with 192 million unknowns. By exploiting symmetry, however, this number is reduced to 24 million which, unlike the original number of unknowns, is handled easily on inexpensive workstations. In practice, 24 million unknowns, which guarantees the absence of boundary artifacts in the impulse response, is excessive. In two dimensions, the magnitude of the leading edge of the impulse is reduced by the square of the Courant number as it travels to successive neighbors. Thus, after the leading edge

of the impulse has traveled from the source to the edge of the computational domain and back it is reduced by $s^{32\,000}$. (This reduction is, however, purely theoretical. In practice, for both two and three dimensions, this theoretical reduction is smaller than the smallest number that can be represented using double-precision numbers. Thus, it is not meaningful to consider reductions of the leading edge below that of the numeric noise floor for double precision numbers.) In two dimensions the maximum value of s, i.e., the Courant limit, is $1/\sqrt{2}$. In three dimensions, the Courant limit is $1/\sqrt{3}$ and the leading edge of the impulse dies out even more quickly. Therefore, the simulation domain may be reduced further in size without incurring significant errors in the impulse response.

Since an impulse response only needs to be calculated once and then can be recalled for use in any simulation that has the same dimensions and the same Courant number, it is anticipated that, by exploiting symmetry and using a powerful workstation, impulse responses of sufficient duration can be obtained to satisfy the requirements of the vast majority of problems. Thus, for example, if an impulse response of 16 000 time steps has been obtained, it subsequently can be used for any problem that uses 16 000, or fewer, times steps. However, some problems may require an exceedingly large number of time steps for which a completely ''clean'' impulse response does not exist. For these cases is there a way to obtain the impulse response in a reasonable fashion? There appear to be simple solutions in one and three dimensions, but not in two dimensions. In one dimension, the impulse response will decay to zero and the rate at which it approaches zero is a function of the Courant number. The closer the Courant number is to the stability limit, the more rapidly the response approaches zero. Therefore, after a sufficient number of time steps, the impulse response can be approximated by zero. The actual number of steps beyond which this approximation can be employed is determined by inspection of the impulse response for a given Courant number.

In three dimensions, the impulse response approaches a nonzero constant that depends on the Courant number. The ''envelope'' of the deviation from this constant is inversely proportional to the time step. Hence, the longer the simulation, the closer the impulse response is bound to this constant. Figure 3 shows the 3-D impulse responses over 280 time steps that correspond to Courant numbers of $1/\sqrt{3}$ (i.e., the limit), 0.40, 0.25, and 0.10. The inset shows the case for the Courant number $1/\sqrt{3}$ with the vertical scale expanded by a factor of approximately 2500. Clearly the fluctuations are small and decreasing. Though not shown, expanded views for the other Courant numbers exhibit similar behavior. Thus, after a sufficient number of time steps the impulse response can be approximated by this constant.

Figure 4 shows the 2-D impulse response over 750 time steps for four different Courant numbers. Unlike in one and three dimensions, the response does not quickly converge to a constant value, but rather decays very slowly to zero. This type of response can be problematic for simulations requiring a large number of time steps. There are ways, however, to work around this. For example, the decay rate is so slow
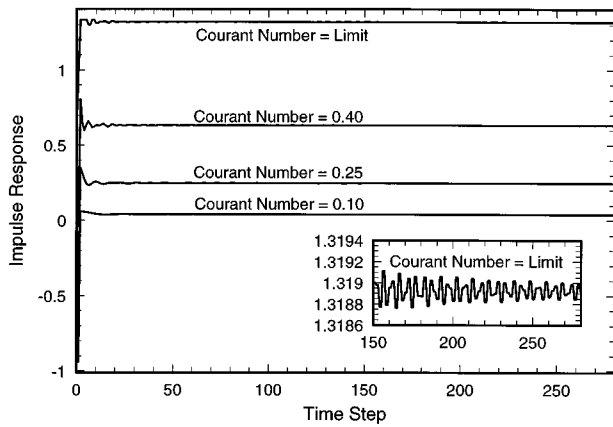
FIG. 3. Three-dimensional impulse response for Courant numbers of $1/\sqrt{3}$, 0.40, 0.25, and 0.10. The inset box shows an expanded view of the case where the Courant number is $1/\sqrt{3}$.

that the convolution of the driving function and the impulse response eventually can be approximated by zero for a finite-duration driving function with no dc component. (The convolution of a constant with a signal that has no dc component is zero. The impulse response decay is slow enough that for signals of sufficiently short duration, the convolution may be well approximated by zero.)

Finally, to demonstrate the different behavior of hard and transparent sources, consider a two-dimensional point source (i.e., a line source in three dimensions) near a planar pressure-release surface as shown in Fig. 5(a). The source is a pressure node and the driving function is a Ricker wavelet. The spatial step is such that there are 32 points per wavelength at the peak frequency of the wavelet and the temporal step is set to yield the Courant limit. Figure 5(b) and (c) shows the pressure in the vicinity of a hard and a transparent source, respectively, after 220 time steps. In these grayscale field maps, black corresponds to zero and the brightness of a pixel is indicative of the absolute value of the pressure found at the corresponding node. The hard source, Fig. 5(b), while radiating the same primary field as the transparent source, scatters the reflected field as evidenced by the nonblack region between the reflected wave and the pressure-release sur-

FIG. 5. Pressure about a source node in the vicinity of a pressure-release surface after 220 time steps. (a) Sketch of problem geometry. (b) Hard source. (c) Transparent source.

face. For the transparent source, Fig. 5(c), the primary wave is identical to that of the hard source, but the source does not interfere with the field reflected by the pressure-release surface.

III. CONCLUSIONS

By convolving the driving function and the grid impulse response, 1-D, 2-D, and 3-D transparent sources can be created that radiate the same fields as hard sources but that do not scatter energy themselves. Multiple transparent sources can be used in the same simulation and, if necessary, used in adjacent nodes. This permits the creation of a wide variety of insonifications that would be difficult or impossible to achieve otherwise. Transparent sources also can be used to finely control the excitation of resonant structures without affecting the resonances. Though more expensive to implement than hard sources, the impulse response required to implement a transparent source must be calculated only once and can be saved for subsequent simulations. The cost of the convolution is typically small compared to other computations for realistic two- and three-dimensional simulations.

FIG. 4. Two-dimensional impulse response for Courant numbers of $1/\sqrt{2}$, 0.50, 0.30, and 0.10.

[1] K. S. Yee, ''Numerical solution of initial boundary value problems involving Maxwell's equations in isotropic media,'' IEEE Trans. Antennas Propag. **14**, 302–307 (1966).

[2] A. Taflove, *Computational Electrodynamics: The Finite-Difference Time-Domain Method* (Artech House, Boston, MA, 1995).

[3] K. S. Kunz and R. J. Luebbers, *The Finite Difference Time Domain Method for Electromagnetics* (CRC, Boca Raton, FL, 1993).

[4] D. Botteldooren, ''Finite-difference time-domain simulation of low-frequency room acoustic problems,'' J. Acoust. Soc. Am. **98**, 3302–3308 (1995).

[5] P. M. Morse and H. Feshbach, *Methods of Theoretical Physics* (McGraw–Hill, New York, 1953).

[6] J. B. Schneider, C. L. Wagner, and O. M. Ramahi, ''Implementation of transparent sources in FDTD simulations,'' submitted to IEEE Trans. Antennas Propag.; preprints available as http://www.eecs.wsu.edu/~schneidj/journal-papers/trans-array.ps.

[7] D. Botteldooren, ''Acoustical finite-difference time-domain simulation in a quasi-Cartesian grid,'' J. Acoust. Soc. Am. **95**, 2313–2319 (1994).

Acoustic radiation force on a bubble: Viscous and thermal effects

Alexander A. Doinikov

Institute of Nuclear Problems, Byelorussian State University, 11 Bobruiskaya St., Minsk 220050, Belarus

The acoustic radiation forces on a gas bubble in a plane standing wave and a plane traveling wave are calculated, taking account of viscous and thermal effects. The dissipative effects are introduced into calculations in a natural way, by applying the viscous heat-conducting equations of fluid motion to both the surrounding liquid and the gas inside the bubble. The limits of low and high energy dissipation are examined. © *1998 Acoustical Society of America.* [S0001-4966(97)04312-9]

PACS numbers: 43.25.Qp, 43.25.Yw [MAB]

INTRODUCTION

Part I of this study[1] provides a general expression for the acoustic radiation force on an arbitrary spherical particle in a viscous heat-conducting fluid. Part II[2] and Part III[3] apply this expression to a rigid sphere and a liquid drop, respectively. The purpose of this paper is to examine the case of a gas bubble.

The acoustic radiation force on a bubble in an ideal liquid was first calculated by Yosioka and Kawasima.[4] [Note that there is a misprint of fundamental importance in Eq. (75) of their paper, which was noticed by Lee and Wang:[5] The numerator of Eq. (75) must have $(k*a)^3$ instead of $(k*a)$.] For bubbles much smaller than the wavelength of sound, Yosioka and Kawasima's results were repeated by many authors[5–12] in different contexts and approaches. Worthy of special mention in the context of this study is the work of Crum and coauthors[8,10] who refined Yosioka and Kawasima's result for a plane standing wave by allowing for the thermal and viscous damping of volume pulsations of bubbles. Experiments, however, show (see, for example, Refs. 7, 8, 10, and 13–15) that the dissipative effects, when they are weak, are not of fundamental importance in standing waves. This is not the case for traveling waves. A significant discrepancy between theory and experiment for waves of this sort was observed by Yosioka and Kawasima themselves,[4] although in their experiments the viscous and thermal wavelengths were small compared with bubble radii and therefore dissipative effects on the radiation force were expected to be insignificant. Only when Yosioka and Kawasima incorporated the thermal damping of volume pulsations of bubbles into their calculations was a satisfactory agreement with experiments attained.[13] An essential role of the damping due to the bulk viscosity of a bubble in determining the traveling wave radiation force is also noted in a theoretical work by Löfstedt and Putterman.[12]

The present paper first examines consistently and rigorously dissipative effects on the radiation force on a bubble, naturally deducing these effects from the viscous heat-conducting equations of fluid motion, which are taken for both the surrounding liquid and the gas inside the bubble. This approach enables one to calculate the radiation force for any values of viscosity and heat conduction and thus to study

the behavior of the force under strong as well as weak dissipative effects.

I. RADIATION FORCE ON A BUBBLE IN THE LIMITS OF WEAK AND STRONG DISSIPATIVE EFFECTS

The general expression for the radiation force on a spherical particle, given by Eqs. (65) and (66) of Part I, is determined by three quantities: $F_n^{(jk)}$, A_n, and α_{jn}. F_n^{jk} are known functions of the parameters x_j ($j = 1,2,3$), where $x_j = k_j R_0$, R_0 is the equilibrium radius of the particle, and k_1, k_2, k_3 are, respectively, the sound, thermal, and viscous wave numbers in the surrounding fluid. The functions $F_n^{(jk)}$ are given in the Appendix of Part I. The quantities A_n specify the type of incident sound field. Finally, α_{jn} ($j = 1,2,3$), referred to as linear scattering coefficients, define the type of particle. So, to apply the general expression derived in Part I to a gas bubble, one must find α_{jn} for a bubble. Part III, which deals with the radiation force on a liquid drop, contains a set of three algebraic equations in α_{1n}, α_{2n}, and α_{3n}, derived on the assumption that both external and internal media are viscous heat-conducting fluids [see Eqs. (28) of Part III]. Clearly these equations can also be applied to a gas bubble. In the general case, however, they give very complicated expressions for α_{jn}, which does not allow us to see clearly how dissipative mechanisms influence the radiation force. Therefore we make some simplifications. First of all, we go to the limit of long sound wavelength: $|x_1|, |\widetilde{x_1}| \ll 1, |x_2|, |\widetilde{x_2}|, |x_3|, |\widetilde{x_3}|$, where the tilde denotes quantities that concern the gas inside the bubble. Note also that in this limit $x_1 \approx \omega R_0 / c_0$, and $x_2 \approx (1+i) R_0 / \delta_t$, where ω is the angular frequency of the incident field, and c_0 and δ_t are, respectively, the sound speed and the thermal penetration depth in the surrounding liquid. Similar equations hold for the gas.

In the limit of long sound wavelength the main contribution to the radiation force on a bubble comes from the zero term of Eq. (65) of Part I, so that this equation reduces to

$$F_r = \pi \rho_0 \, \mathrm{Re}(Z_0 A_0 A_1^*), \tag{1}$$

where F_r is the radiation force, ρ_0 is the equilibrium density of the surrounding liquid, Re means ''the real part of,'' the asterisk indicates the complex conjugate, and Z_0 is given by Eq. (66) of Part I to be

$$Z_0 = \sum_{j=1}^{3} \left(F_0^{(0j)} \alpha_{j1}^* + F_0^{(j0)} \alpha_{j0} + \alpha_{j0} \sum_{k=1}^{3} F_0^{(jk)} \alpha_{k1}^* \right). \quad (2)$$

Expressions for $F_0^{(jk)}$ in the limit of long sound wavelength are given in Appendix B of Part II. Expressions for α_{j0} and α_{j1}, which are obtained from Eqs. (28) of Part III by applying those equations to a gas bubble, are presented in Appendix A of this paper. Inspection of these expressions shows that F_r has to be of the first order in the small parameter x_1. Keeping in Eq. (2) only terms of this order, one obtains

$$Z_0 = \alpha_{10}(F_0^{(10)} + \alpha_{11}^* F_0^{(11)} + \alpha_{31}^* F_0^{(13)})$$
$$+ \alpha_{20}(F_0^{(20)} + \alpha_{11}^* F_0^{(21)} + \alpha_{31}^* F_0^{(23)}) + O(x_1^2). \quad (3)$$

In general, the total radiation force, in addition to F_r, involves the drag F_d given by Eq. (67) of Part I. For a gas bubble, however, F_d is of higher order in x_1 than F_r and can thus be neglected.

An expression for F_r in the limit of long sound wavelength still is too complicated to analyze and therefore we make further simplifications, considering two opposite limiting cases. In the first of these, dissipative effects are assumed to be weak, so that the bubble radius is large compared with the viscous and thermal wavelengths both outside and inside the bubble, which results in the following inequality: $|x_1|, |\tilde{x}_1| \ll 1 \ll |x_2|, |\tilde{x}_2|, |x_3|, |\tilde{x}_3|$. In the second case, dissipative effects are assumed to be strong, so that the bubble radius is much smaller than the above wavelengths, which is expressed as follows: $|x_1|, |\tilde{x}_1| \ll |x_2|, |\tilde{x}_2|, |x_3|, |\tilde{x}_3| \ll 1$.

As regards the incident field we shall consider two cases: (i) a plane standing wave with the velocity potential given by

$$\varphi_I^{(\text{st})} = A \, \cos(\mathbf{k}_1 \cdot \mathbf{r} + k_1 d) \exp(-i\omega t), \quad (4)$$

and (ii) a plane traveling wave for which

$$\varphi_I^{(\text{tr})} = A \, \exp(i\mathbf{k}_1 \cdot \mathbf{r} - i\omega t), \quad (5)$$

where $\mathbf{k}_1$ is the wave vector, $\mathbf{r}$ is the position vector with the origin at the equilibrium center of the bubble, and d is the distance between the equilibrium center of the bubble and the nearest plane of the velocity nodes.

For a standing wave, the radiation force is obtained from Eq. (74) of Part I to be

$$F_r^{(\text{st})} = -\tfrac{3}{2} \, \pi \rho_0 |A|^2 \, \sin(2\omega d/c_0) \mathrm{Re}(Z_0). \quad (6)$$

For a traveling wave, the radiation force is given by Eq. (70) of Part I as

$$F_r^{(\text{tr})} = 3 \pi \rho_0 |A|^2 \, \mathrm{Im}(Z_0), \quad (7)$$

where Im denotes "the imaginary part of."

A. Weak dissipative effects: $|x_1|, |\tilde{x}_1| \ll 1$ $\ll |x_2|, |\tilde{x}_2|, |x_3|, |\tilde{x}_3|$

Expressions for $F_0^{(jk)}$ for this limit are given in Appendix C of Part III, and expressions for α_{j0} and α_{j1} are given in Appendix B of the present paper. Substituting them into Eq. (3) and retaining only the leading terms, one obtains

$$Z_0 = \frac{2}{3} \, k_0 R_0 \left[\left(\frac{\omega_0^2}{\omega^2} - 1 \right)^2 + \Delta^2 \right]^{-1} \left\{ \frac{\omega_0^2}{\omega^2} - 1 + i k_0 R_0 \right.$$
$$\left. + \frac{7i}{2} \left(\frac{\delta_v}{R_0} \right)^2 + \frac{3i}{2} \left(\frac{\omega_0}{\omega} \right)^2 \left[(\tilde{\gamma}_0 - 1) \frac{\delta_t}{R_0} - \left(\frac{\delta_v}{R_0} \right)^2 \right] \right\}, \quad (8)$$

where

$$\Delta = k_0 R_0 + 2 \left(\frac{\delta_v}{R_0} \right)^2 + \frac{9 \tilde{\rho}_0 \tilde{c}_0^2 (\tilde{\gamma}_0 - 1) \tilde{\delta}_t}{2 \rho_0 R_0^3 \omega^2}, \quad (9)$$

ω_0 is the monopole resonance frequency of the bubble, defined as

$$\omega_0 = \left(\frac{3 \tilde{\rho}_0 \tilde{c}_0^2}{\rho_0 R_0^2} - \frac{2\sigma}{\rho_0 R_0^3} \right)^{1/2}, \quad (10)$$

$k_0 = \omega/c_0$, δ_v is the viscous penetration depth in the surrounding liquid, $\tilde{\gamma}_0$ is the specific heat ratio of the gas, and σ is the surface tension.

Let us now consider the above-mentioned types of incident field.

1. Plane standing wave

Substitution of Eq. (8) into Eq. (6) yields

$$F_r^{(\text{st})} = \frac{\pi \rho_0 |A|^2 k_0 R_0 (1 - \omega_0^2/\omega^2) \sin(2k_0 d)}{(\omega_0^2/\omega^2 - 1)^2 + \Delta^2}. \quad (11)$$

This equation coincides with Crum and coauthors' result[8,10] provided the latter is taken in the limit of low dissipation. Thus the "ideal" theory, which only takes account of the damping of volume pulsations of bubbles, and our theory, which deduces dissipative effects consistently and rigorously from the viscous heat-conducting equations of fluid motion, give for standing waves the same result. This explains why Eq. (11) is in good agreement with experiments.

2. Plane traveling wave

Upon substitution of Eq. (8) into Eq. (7), one has

$$F_r^{(\text{tr})} = \frac{2 \pi \rho_0 |A|^2 k_0 R_0}{(\omega_0^2/\omega^2 - 1)^2 + \Delta^2} \left[k_0 R_0 + \frac{3(\tilde{\gamma}_0 - 1) \omega_0^2}{2\omega^2} \frac{\tilde{\delta}_t}{R_0} \right.$$
$$\left. + \frac{1}{2} \left(7 - \frac{3\omega_0^2}{\omega^2} \right) \left(\frac{\delta_v}{R_0} \right)^2 \right]. \quad (12)$$

The first term between square brackets in Eq. (12), $k_0 R_0$, gives the result derived by Yosioka and Kawasima in their first paper, Ref. 4 (provided we also omit the thermal and viscous damping in Δ). We shall name this term the "ideal" term as it gives the radiation force in an ideal liquid. Yosioka and Kawasima found that the "ideal" term did not provide agreement with experiments and they had to incorporate the thermal damping into their calculations. The refined result is given by Eq. (18) of their next paper, Ref. 13; in the limit $|\tilde{x}_2| \gg 1$ this result coincides with the second term between square brackets in Eq. (12). [Note that there is a misprint in Eq. (18): The denominator of Eq. (18) should contain $aG/(aF)^2$ instead of aG/aF.]

It is seen from Eq. (12) that viscous effects also contribute to the radiation force (see the third term between square brackets). This term was first calculated in a previous work by the present author [see Eq. (6.2) of Ref. 16] in which, however, heat conduction was neglected. Thus, Eq. (12) first provides, for the case considered, a complete expression allowing for both dissipative mechanisms.

To compare contributions from the ''ideal'' and dissipative terms, let us consider a specific example, say, an air bubble in water. Let $R_0 = 50$ μm and $f = 100$ kHz, where f is the frequency of the incident sound wave. Then $|x_1| \approx 0.021$, $|\tilde{x}_1| \approx 0.095$, $|x_2| \approx 109$, $|\tilde{x}_2| \approx 8$, $|x_3| \approx 39$, and $|\tilde{x}_3| \approx 11$. It is seen that the required limiting conditions are satisfied. The magnitudes of the ''ideal,'' thermal, and viscous terms between square brackets in Eq. (12) are, respectively, 0.021, 0.048, and 0.004, intimating that the contribution from the dissipative terms is dominant.

B. Strong dissipative effects: $|x_1|, |\tilde{x}_1| \ll |x_2|, |\tilde{x}_2|, |x_3|, |\tilde{x}_3| \ll 1$

Expressions for $F_0^{(jk)}$ for this limit are given in Appendix D of Part III, and expressions for α_{j0} and α_{j1} are given in Appendix C of the present paper. Substituting them into Eq. (3) and retaining only the leading terms, one has

$$\dot{Z}_0 = \frac{2k_0 R_0 [(\Omega/\omega)^2 + (\delta_v/R_0)^4 - (i/2) (\delta_v/R_0)^2(\Omega/\omega)^2]}{3[(\Omega/\omega)^4 + 4(\delta_v/R_0)^4]}, \tag{13}$$

where

$$\Omega^2 = \omega_0^2 - \frac{3\tilde{\rho}_0 \tilde{c}_0^2 (\tilde{\gamma}_0 - 1)}{\rho_0 \tilde{\gamma}_0 R_0^2}. \tag{14}$$

1. Plane standing wave

Substitution of Eq. (13) into Eq. (6) results in

$$F_r^{(st)} = -\pi\rho_0 |A|^2 k_0 R_0 \sin(2k_0 d) \frac{(\Omega/\omega)^2 + (\delta_v/R_0)^4}{(\Omega/\omega)^4 + 4(\delta_v/R_0)^4}. \tag{15}$$

Let us first compare Eq. (15) with Eq. (11) to feel distinctions between the two limiting cases. Since at high dissipation, as a rule, $\omega_0 \gg \omega$, the equations have the same sign, i.e., both of them predict that bubbles should agglomerate at the velocity nodes. There is, however, a great difference in magnitude between the forces given by these equations. To have an idea of the difference, let us consider a specific example. To satisfy the conditions of high dissipation, we take an air bubble in glycerin setting $R_0 = 1$ μm and $f = 1$ kHz. This gives the ratio of Eq. (15) to Eq. (11) to be equal to about 1.5×10^4.

Let us now compare Eq. (15) with an expression that has been obtained by the present author previously without considering heat conduction [see Eq. (7.26) of Ref. 16]:

$$F_R = -\pi\rho_0 |A|^2 k_0 R_0 \sin(2k_0 d) \frac{(\omega_0/\omega)^2 + (\delta_v/R_0)^4}{(\omega_0/\omega)^4 + 4(\delta_v/R_0)^4}. \tag{16}$$

[Equation (16) differs slightly from Eq. (7.26) as we have taken into account here that $\omega_0^2/\omega^2 \gg 1$ in the limit considered.] Comparison of Eqs. (15) and (16) shows that thermal effects lead to replacing ω_0 with the smaller quantity Ω. As a result, the radiation force can be substantially increased. For an air bubble in glycerin at $R_0 = 1$ μm and $f = 1$ kHz, one has $F_r^{(st)}/F_R \approx 2.8$.

2. Plane traveling wave

Substituting Eq. (13) into Eq. (7), one obtains

$$F_r^{(tr)} = -\pi\rho_0 |A|^2 k_0 R_0 \frac{(\Omega/\omega)^2(\delta_v/R_0)^2}{(\Omega/\omega)^4 + 4(\delta_v/R_0)^4}. \tag{17}$$

Comparison of Eqs. (17) and (12) shows that for a plane traveling wave, the limits of low and high dissipation differ both quantitatively and qualitatively. It is seen from these equations that whereas at low dissipation bubbles are urged away from the sound transducer, at high dissipation they are drawn toward the sound transducer.

It is also interesting to compare Eq. (17) with the result derived in Ref. 16, Eq. (7.23), for zero heat conduction:

$$F_R = -\pi\rho_0 |A|^2 k_0 R_0 \frac{(\omega_0/\omega)^2(\delta_v/R_0)^2}{(\omega_0/\omega)^4 + 4(\delta_v/R_0)^4}. \tag{18}$$

[In reproducing here Eq. (7.23) we again took into account that $\omega_0^2/\omega^2 \gg 1$.] It is seen that thermal effects again result in replacing ω_0 by Ω and so increase the magnitude of the force. For the same example, an air bubble in glycerin at $R_0 = 1$ μm and $f = 1$ kHz, we have $F_r^{(tr)}/F_R \approx 1.7$.

II. CONCLUSIONS

In this paper, expressions have been deduced for the acoustic radiation forces exerted on a gas bubble in the limit of high energy dissipation. Account of both viscous and thermal effects has been taken. Two sound fields, a plane standing wave and a plane traveling wave, have been considered. The expressions obtained have been compared with the known results for the limit of low dissipation. Fundamental differences between the two limits have been shown. Comparison has also been conducted between results derived in the limit of high dissipation with and without heat conduction, which has disclosed that thermal effects increase substantially the magnitude of the radiation force in both sound fields considered.

ACKNOWLEDGMENT

APPENDIX A: EXPRESSIONS FOR α_{j0} AND α_{j1} IN THE LIMIT OF LONG SOUND WAVELENTH

Expressions presented here are found from Eqs. (28) of Ref. 3 by solving them for a gas bubble. Expressions for α_{j0} are given by

$$\alpha_{10} = -\frac{ix_1}{D_0}, \quad \alpha_{20} = \frac{1}{d_1 D_0}, \quad \alpha_{30} \equiv 0.$$

Here

$$D_0 = 1 + ix_1 + \frac{2\sigma}{\rho_0\omega^2R_0^3} - \frac{4}{x_3^2} + \frac{(\gamma_0-1)\lambda_\kappa j_0(\widetilde{x}_2)\widetilde{\rho}_0\widetilde{c}_0^2}{(\widetilde{\gamma}_0-1)\lambda_\alpha\widetilde{x}_2 j_1(\widetilde{x}_2)\rho_0c_0^2}$$

$$- \frac{d_2}{d_1},$$

$$d_1 = \frac{x_2^2 h_0^{(1)}(x_2)}{3\lambda_\alpha(\widetilde{\gamma}_0-1)} + x_2 h_1^{(1)}(x_2)$$

$$\times \left[1 - \frac{x_2^2\lambda_\kappa[\widetilde{x}_2 j_0(\widetilde{x}_2) + 3(\widetilde{\gamma}_0-1)j_1(\widetilde{x}_2)]}{3\lambda_\alpha(\widetilde{\gamma}_0-1)\widetilde{x}_2^2 j_1(\widetilde{x}_2)} \right],$$

$$d_2 = h_0^{(1)}(x_2)\left(1 + \frac{x_2^2\widetilde{\rho}_0\widetilde{c}_0^2}{x_1^2(\widetilde{\gamma}_0-1)\lambda_\alpha\rho_0c_0^2} \right) + x_2 h_1^{(1)}(x_2)$$

$$\times \left(\frac{2\sigma}{\rho_0\omega^2R_0^3} - \frac{4}{x_3^2} - \frac{x_2^2\lambda_\kappa j_0(\widetilde{x}_2)\widetilde{\rho}_0\widetilde{c}_0^2}{x_1^2(\widetilde{\gamma}_0-1)\lambda_\alpha\widetilde{x}_2 j_1(\widetilde{x}_2)\rho_0c_0^2} \right),$$

$$\lambda_\kappa = \kappa_0/\widetilde{\kappa}_0, \quad \lambda_\alpha = \alpha_0/\widetilde{\alpha}_0,$$

κ_0 and α_0 are, respectively, the thermal conductivity and the volume thermal expansion coefficient of the surrounding liquid at equilibrium, the tilde denotes quantities concerning the gas, j_n is the spherical Bessel function, and $h_n^{(1)}$ is the spherical Hankel function of the first kind.

Expressions for α_{j1} are found to be

$$\alpha_{11} = \frac{ix_1^3}{3D_1}\left[x_3 h_2^{(1)}(x_3) + \frac{\rho_0\widetilde{x}_3 j_2(\widetilde{x}_3)}{\widetilde{\rho}_0 x_3 j_1(\widetilde{x}_3)}(2h_2^{(1)}(x_3) \right.$$

$$\left. - x_3 h_1^{(1)}(x_3)) \right],$$

$$\alpha_{21} = \frac{(\gamma_0-1)x_1^3}{x_2^2 D_1[(a-b)h_1^{(1)}(x_2) - ax_2 h_2^{(1)}(x_2)]}$$

$$\times \left\{ 2(b-a)h_1^{(1)}(x_3) + \left(1 - a + \frac{b\widetilde{\rho}_0}{\rho_0}\right)x_3 h_2^{(1)}(x_3) \right.$$

$$+ \frac{\rho_0\widetilde{x}_3 j_2(\widetilde{x}_3)}{\widetilde{\rho}_0 x_3^2 j_1(\widetilde{x}_3)}\left[\left(1 - a + \frac{b\widetilde{\rho}_0}{\rho_0}\right)(2x_3 h_2^{(1)}(x_3) \right.$$

$$\left.\left. - x_3^2 h_1^{(1)}(x_3)) + 4(b-a)h_1^{(1)}(x_3) \right] \right\},$$

$$\alpha_{31} = \frac{x_1}{D_1}\left(1 + \frac{2\rho_0\widetilde{x}_3 j_2(\widetilde{x}_3)}{\widetilde{\rho}_0 x_3^2 j_1(\widetilde{x}_3)} \right).$$

Here

$$D_1 = \frac{\rho_0\widetilde{x}_3 j_2(\widetilde{x}_3)}{\widetilde{\rho}_0 x_3^2 j_1(\widetilde{x}_3)}[(x_3^2-12)h_1^{(1)}(x_3) - 2x_3 h_2^{(1)}(x_3)]$$

$$- 6h_1^{(1)}(x_3) - x_3 h_2^{(1)}(x_3),$$

$$a = \frac{(\gamma_0-1)\widetilde{c}_0^2\lambda_\kappa j_1(\widetilde{x}_2)}{(\widetilde{\gamma}_0-1)c_0^2\lambda_\alpha\widetilde{x}_2 j_2(\widetilde{x}_2)},$$

$$b = \frac{(\gamma_0-1)\widetilde{c}_0^2}{(\widetilde{\gamma}_0-1)c_0^2\lambda_\alpha}\left(\frac{j_1(\widetilde{x}_2)}{\widetilde{x}_2 j_2(\widetilde{x}_2)} - 1 \right).$$

APPENDIX B: EXPRESSIONS FOR α_{j0} AND α_{j1} IN THE LIMIT $|x_1|, |\widetilde{x}_1| \ll 1 \ll |x_2|, |\widetilde{x}_2|, |x_3|, |\widetilde{x}_3|$

The expressions presented below for α_{j0} and α_{j1} are obtained from the expressions of Appendix A by going to the above limit. The coefficients α_{j0} are given by

$$\alpha_{10} = \frac{ix_1}{\omega_0^2/\omega^2 - 1 - i\Delta},$$

$$\alpha_{20} = \frac{3i(\widetilde{\gamma}_0-1)\lambda_\alpha\widetilde{x}_2\exp(-ix_2)[1 - i(3\widetilde{\gamma}_0-2)/\widetilde{x}_2]}{x_2^2\lambda_\kappa(1 - \omega_0^2/\omega^2 + i\Delta)}.$$

In deriving these expressions, it has also been taken into account that for bubbles

$$\frac{x_2^2\lambda_\kappa}{\widetilde{x}_2^2\lambda_\alpha} \gg 1, \quad \frac{\lambda_\kappa x_2}{\widetilde{x}_2} \gg 1, \quad \frac{x_2}{\widetilde{x}_2} \gg 1, \quad \frac{2\sigma(\widetilde{\gamma}_0-1)\lambda_\alpha\widetilde{x}_2^2}{R_0\widetilde{\rho}_0\widetilde{c}_0^2\lambda_\kappa x_2^2} \ll 1.$$

The coefficients α_{j1} take the form:

$$\alpha_{11} = -\frac{ix_1^3}{3}\left(1 - \frac{6i\widetilde{\rho}_0}{\rho_0\widetilde{x}_3} + \frac{12}{x_3^2} \right),$$

$$\alpha_{31} = ix_1\exp(-ix_3)\left(\frac{2i}{x_3} + \frac{x_3\widetilde{\rho}_0}{\widetilde{x}_3\rho_0} \right).$$

APPENDIX C: EXPRESSIONS FOR α_{j0} AND α_{j1} IN THE LIMIT $|x_1|, |\widetilde{x}_1| \ll |x_2|, |\widetilde{x}_2|, |x_3|, |\widetilde{x}_3| \ll 1$

The expressions presented below are found from Appendix A by going to the limit indicated in the heading:

$$\alpha_{10} = \frac{ix_1}{\Omega^2/\omega^2 - 1 + 4/x_3^2},$$

$$\alpha_{20} = \frac{i(\widetilde{\gamma}_0-1)\lambda_\alpha\widetilde{x}_2^2(1 - x_2^2/2)}{\lambda_\kappa\widetilde{\gamma}_0 x_2(\Omega^2/\omega^2 + 4/x_3^2)},$$

$$\alpha_{11} = -ix_1^3(3 - x_3^2)/27, \quad \alpha_{31} = -ix_1 x_3^2(3 - x_3^2)/27.$$

Here

$$\Omega^2 = \omega_0^2 - 3\widetilde{\rho}_0\widetilde{c}_0^2(\widetilde{\gamma}_0-1)/(\rho_0 R_0^2\widetilde{\gamma}_0).$$

[1] A. A. Doinikov, ''Acoustic radiation force on a spherical particle in a viscous heat-conducting fluid. Part I. General formula,'' J. Acoust. Soc. Am. **101**, 713–721 (1997).

[2] A. A. Doinikov, ''Acoustic radiation force on a spherical particle in a viscous heat-conducting fluid. Part II. Force on a rigid sphere,'' J. Acoust. Soc. Am. **101**, 722–730 (1997).

[3] A. A. Doinikov, ''Acoustic radiation force on a spherical particle in a viscous heat-conducting fluid. Part III. Force on a liquid drop,'' J. Acoust. Soc. Am. **101**, 731–740 (1997).

[4] K. Yosioka and Y. Kawasima, ''Acoustic radiation pressure on a compressible sphere,'' Acustica **5**, 167–173 (1955).

[5] C. P. Lee and T. G. Wang, ''Acoustic radiation force on a bubble,'' J. Acoust. Soc. Am. **93**, 1637–1640 (1993).

[6] L. P. Gor'kov, ''On the forces acting on a small particle in an acoustic field in an ideal fluid,'' Sov. Phys. Dokl. **6**, 773–775 (1962).

[7] A. I. Eller, ''Force on a bubble in a standing acoustic wave,'' J. Acoust. Soc. Am. **43**, 170–171 (1968).

[8] L. A. Crum and A. I. Eller, ''Motion of bubbles in a stationary sound field,'' J. Acoust. Soc. Am. **48**, 181–189 (1970).

[9] L. A. Crum and D. A. Nordling, ''Velocity of transient cavities in an acoustic stationary wave,'' J. Acoust. Soc. Am. **52**, 294–301 (1972).

[10] L. A. Crum and A. Prosperetti, ''Nonlinear oscillations of gas bubbles in liquids: An interpretation of some experimental results,'' J. Acoust. Soc. Am. **73**, 121–127 (1983).

146   J. Acoust. Soc. Am., Vol. 103, No. 1, January 1998

Alexander A. Doinikov: Radiation force on a bubble   146

[11] J. Wu and G. Du, ''Acoustic radiation force on a small compressible sphere in a focused beam,'' J. Acoust. Soc. Am. **87**, 997–1003 (1990).

[12] R. Löfstedt and S. Putterman, ''Theory of long wavelength acoustic radiation pressure,'' J. Acoust. Soc. Am. **90**, 2027–2033 (1991).

[13] K. Yosioka, Y. Kawasima, and H. Hirano, ''Acoustic radiation pressure on bubbles and their logarithmic decrement,'' Acustica **5**, 173–178 (1955).

[14] T. J. Asaki, P. L. Marston, and E. H. Trinh, ''Shape oscillations of bubbles in water driven by modulated ultrasonic radiation pressure: Observations and detection with scattered laser light,'' J. Acoust. Soc. Am. **93**, 706–712 (1993).

[15] T. J. Asaki and P. L. Marston, ''Acoustic radiation force on a bubble driven above resonance,'' J. Acoust. Soc. Am. **96**, 3096–3099 (1994).

[16] A. A. Doinikov, ''Acoustic radiation pressure on a compressible sphere in a viscous fluid,'' J. Fluid Mech. **267**, 1–21 (1994).

Model experiment to study sonic boom propagation through turbulence. Part I: General results

Bart Lipkens[a)] and David T. Blackstock

Applied Research Laboratories and Mechanical Engineering Department, The University of Texas at Austin, P.O. Box 8029, Austin, Texas 78713-8029

A model experiment to study the effect of atmospheric turbulence on sonic booms is reported. The model sonic booms are N waves produced by electric sparks, and the model turbulence is created by a plane jet. Of particular interest are the changes in waveform, peak pressure, and rise time of the model N waves after they have passed through the model turbulence. A review is first given of previous experiments on the effect of turbulence on both sonic booms and model N waves. This experiment was designed so that the scale factor (approximately 10^{-4}) relating the characteristic length scales of the model turbulence to those of atmospheric turbulence is the same as that relating the model N waves to sonic booms. Most of the results reported are for plane waves. Sets of 100 or 200 pressure waveforms were recorded, for both quiet and turbulent air, and analyzed. Sample waveforms, scatter plots of peak pressure and rise time, histograms, and cumulative probability distributions are given. Results are as follows: (1) The model experiment successfully simulates sonic boom propagation through the atmosphere. The waveform distortion of actual sonic booms is reproduced, both in scale and in character, in the laboratory study. (2) Passage through turbulence almost always causes rise time to increase; decreases are rare. (3) Average rise time is always increased by turbulence, threefold for the particular data reported here. (4) Average peak pressure is always decreased by turbulence, but the change is not as striking as that for average rise time. © *1998 Acoustical Society of America.* [S0001-4966(97)06511-9]

PACS numbers: 43.28.Mw, 43.28.Py, 43.25.Cb, 43.20.Px [LCS]

INTRODUCTION

Supersonic passage of an aircraft through the atmosphere creates a sonic boom. The sonic boom wavefront spreads out conically from the aircraft at an angle $\sin^{-1} M^{-1}$, where M is the aircraft Mach number. Propagation through the atmosphere is affected by weak acoustic nonlinearity, absorption, and stratification. At ground level the sonic boom has the general shape of an N wave, as shown in Fig. 1. The waveform in this figure is taken from the Lee–Downing database,[1] which is also known as the Boomfile 2 data. Defined in the figure are certain important characteristics of the waveform: peak pressure Δp, duration T, and rise time τ, which in this paper is defined as the time required for the pressure to increase from 10% of Δp to 90% of Δp. Typical values are $\Delta p = 100$ Pa, $T = 150$ ms, and $\tau = 5$ ms. These are the main factors that determine the annoyance caused by sonic booms when heard outdoors.[2–5] The annoyance question provided the underlying motivation for our investigation.

The aspect of the sonic boom noise problem addressed in this paper is the effect of atmospheric turbulence on sonic boom waveform, rise time, and peak pressure. Particular attention is paid to rise time. Molecular relaxation, namely that of oxygen and nitrogen, has been put forward as a chief factor determining rise time; see, for example, the recent results of Pierce and Kang.[6] Turbulence, which is known to

cause a substantial distortion of the waveform,[7,8] has often been proposed as another candidate for this change in rise time.[9,10]

Field measurements of sonic booms are expensive and are conducted in an environment very difficult to control. Laboratory studies with small-scale N waves produced by electrical sparks, and with a downscaled atmosphere, offer an attractive alternative. The experiments are much cheaper and simpler than flight tests, and the physical parameters that affect the propagation are much easier to control. Model experiments are also attractive as a means of testing various theoretical predictions. Finally, laboratory experiments can play an important role in the planning for full-scale studies.

This paper is the first in a series of three, called Parts I, II, and III, on the use of model experiments to study the effect of turbulence on sonic boom propagation. The purpose of Part I (the present paper) is first to show that model N waves and model turbulence can be used to simulate sonic boom propagation through the atmospheric turbulent boundary layer, and second to demonstrate the very substantial effect turbulence can have on waveform, rise time, and peak pressure. The next paper, Part II, will describe a parametric study of the effect of (1) turbulence intensity and (2) propagation distance (through the turbulent medium) on N wave characteristics. In the final paper, Part III, data from the model experiments will be used to test predictions from various theories that have been proposed to explain waveform distortion and rise time of sonic booms. For related theoretical work, see Ref. 11.

Section I of the present paper contains a review of past

[a)]Current address: MacroSonix, 1570 East Parham Road, Richmond, VA 23228.
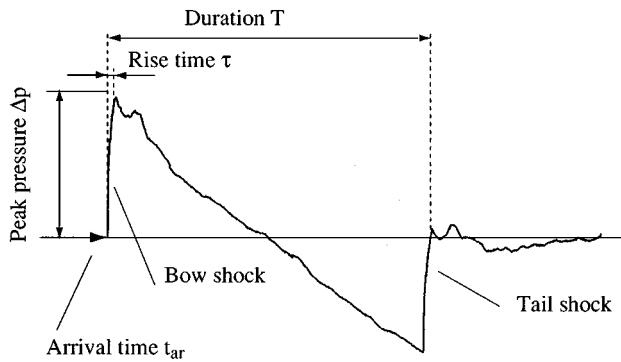
FIG. 1. Sonic boom terminology. Ordinate is acoustic pressure (positive upward), abscissa is time. Waveform from Lee and Downing database (Ref. 1).

measurements, both field and laboratory, showing the effect of turbulence on sonic boom waveform and rise time. In Sec. II the design and apparatus of the model experiment are described; measurements and results appear in Sec. III. The final section contains the conclusions.

I. PRIOR RELEVANT WORK

In this section, sonic boom measurements that bear on waveform and rise time are reported first. Although we could have relied on 1960's data for illustrations, we have chosen to draw mainly on the more recent Boomfile 2 database.[1] Next, relevant model experiments are described. Finally, we review a recent theoretical study of the effect of molecular relaxation on sonic boom rise time. Molecular relaxation and turbulence are currently the chief contenders in the competition to explain the measurements of sonic boom rise time.

A. Sonic boom measurements

Extensive sonic boom measurements were made in several countries during the 1960's. Of particular interest here are the studies of waveform variability attributed to random inhomogeneity of the atmosphere; see, for example, the studies reported by Maglieri and others.[12–15] The 1972 paper by Pierce and Maglieri[16] contains a good review of work done up to that time. More recent measurements include those of Lee and Downing (1991)[1] and Willshire and DeVilbiss (1992).[17]

The nearly ideal N wave shape shown in Fig. 1 is not observed very often in sonic boom field measurements. Instead a wide variety of distorted N waves is encountered. Selected waveforms from the field data of the Boomfile 2 database[1] are shown in Fig. 2 to illustrate the classification often used to specify the distortion of sonic booms. In the 1960's, NASA investigators distinguished 10 categories of waveform distortion,[12,18] while more recently Gionfriddo[19] devised a scheme of 7 categories. Reported here is Gionfriddo's scheme. Sonic booms that are called normal (a) show little deviation in their shape from the classical N wave signature; these waves usually occur only when the atmosphere is quiet. Peaked (or spiked) booms (b) exhibit a distinctive, narrow spike, almost always at the tail shock as well as at the bow shock. Rounded booms (c) are those for which the pres-
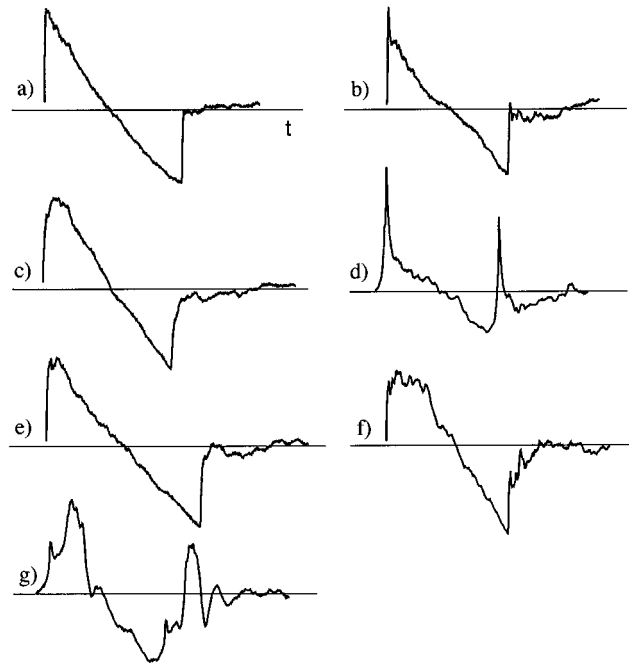
FIG. 2. Classification of sonic boom waveforms: (a) normal; (b) peaked; (c) rounded; (d) U-shaped; (e) double-peaked; (f) multi-peaked; and (g) messy. Selected waveforms from Lee and Downing database (Ref. 1).

sure rises more slowly to its peak, that is, the bow and tail shocks are smooth, not abrupt. A U-shaped waveform (d) implies that the sonic boom has passed through a caustic. The waveform resembles the derivative of an N wave, i.e., each frequency component has experienced a 90° phase shift. The double-peaked wave (e) still resembles an N wave with few irregularities in the expansion part, but two peaks of similar magnitude occur at the bow shock location and usually also at the tail shock. Multi-peaked waveforms (f) are similar but have three or more distinctive spikes at the bow and tail shock. The presence of many spikes of nearly equal amplitude gives the bow shock a flat-top appearance. Finally, sonic boom signatures that do not fit in any of the previous classes are classified messy (g). Notice that all classes have the common property that the distortion at the tail shock is very similar to that at the bow shock. The implication is that the bow and tail shocks pass through the same pattern of random inhomogeneity. In other words, over time T the pattern may be considered frozen.

The inhomogeneity is not, however, invariable (1) when different propagation paths, even neighboring ones, are considered, or (2) when two sonic booms traverse the same path but are separated by a short time interval. An example of the effect of different propagation paths is given by Fig. 3, which shows three sonic boom signatures due to the same aircraft in steady horizontal flight at an altitude of 4.3 km. The microphone positions were on a line perpendicular to the flight path. The plane's ground track intercepted the microphone array at a distance of 0.6 km from the middle microphone; the two flanking microphones were 1.28 km and 1.92 km, respectively, on either side of the middle. The slight difference in travel paths taken by the three waves is seen to produce a large variation in waveform. Similar data are re-
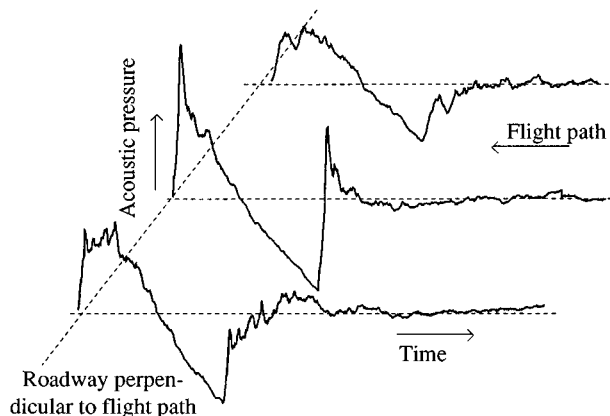
FIG. 3. Sonic boom pressure waveforms measured at three positions perpendicular to the flight path of an F-16 aircraft in steady horizontal flight, Mach number 1.13 and altitude 4.3 km (from Lee and Downing, Ref. 1).

ported in Ref. 13. Next consider two (presumably) identical sonic booms generated at different times but at the same point in the atmosphere and received by the same microphone on the ground. In an experiment reported by Maglieri,[13] the time interval between two aircraft of the same type which were flown at the same altitude and Mach number was only 5 s; yet the two sonic booms received were grossly different. The first sonic boom waveform was strongly peaked while the second one was rounded. One concludes, therefore, that the random inhomogeneity of the atmosphere has little correlation over time intervals as short as, say, $50T$.

It is now generally accepted that atmospheric turbulence causes the inhomogeneity responsible for the wide variability of sonic boom waveforms. Indeed, the role played by turbulence was made clear by several experiments performed in the 1960's. For example, Garrick and Maglieri[14] report an experiment done at Wallops Station, Virginia, in which sonic boom waveforms were recorded at the ground and at the top of a 250-ft tower. Waveforms measured at two points on the same ray path (tower and ground) were similar, whereas waveforms on neighboring rays (incident and reflected waves, both measured on the tower) varied significantly. In another experiment, performed at Edwards Air Force Base,[12,13] a blimp at an altitude of 2000 ft was used to measure incident and ground-reflected sonic booms. The incident booms had the normal N wave shape, while the ground-reflected booms exhibited considerable distortion, similar to that of sonic booms measured at the ground. The conclusion is that propagation through the lower portion of the atmosphere, i.e., the turbulent boundary layer, gave rise to the distortion of the sonic boom signature.

Next we review some quantitative measures of waveform variability, focusing on peak pressure and rise time data from recent experiments. The cumulative distribution function of peak pressure of a large number of waveforms taken during tests at Edwards Air Force Base[1] is presented in Fig. 4. The random variable is the ratio $\Delta p_{meas}/\Delta p_{calc}$, where Δp_{meas} is the measured value of the peak pressure and Δp_{calc} is the value of the peak pressure calculated for a nonturbulent steady atmosphere. The cumulative distribution function is
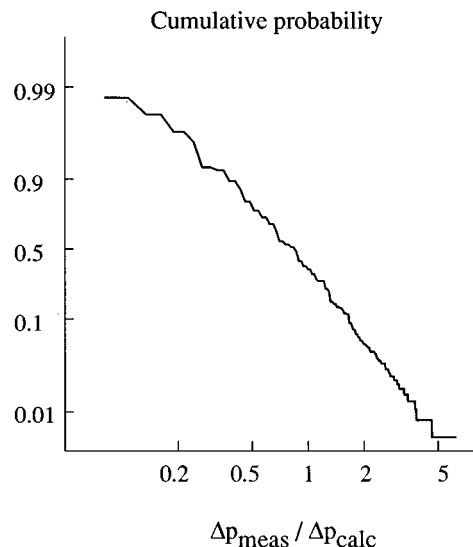
FIG. 4. Cumulative probability curve of peak pressure for a large number of sonic boom waveforms, measured during tests at Edwards Air Force Base (from Lee and Downing, Ref. 1).

plotted on a log-normal scale. If the curve defined by the measurements were a straight line, the probability would be described as log normal. It is seen that the log-normal distribution fits the large majority of the measurements very well. This result is representative of most sonic boom data sets.[16]

The histograms in Fig. 5 show relative probabilities for rise time (upper graphs) and peak pressure (lower graphs) at low and moderate turbulence levels in the atmosphere. The data were obtained from the sonic boom propagation experiment conducted at White Sands Missile Range during August 1991 as a part of the NATO Joint Acoustic Propagation Experiment (Willshire and DeVilbiss[17]). The histograms in-
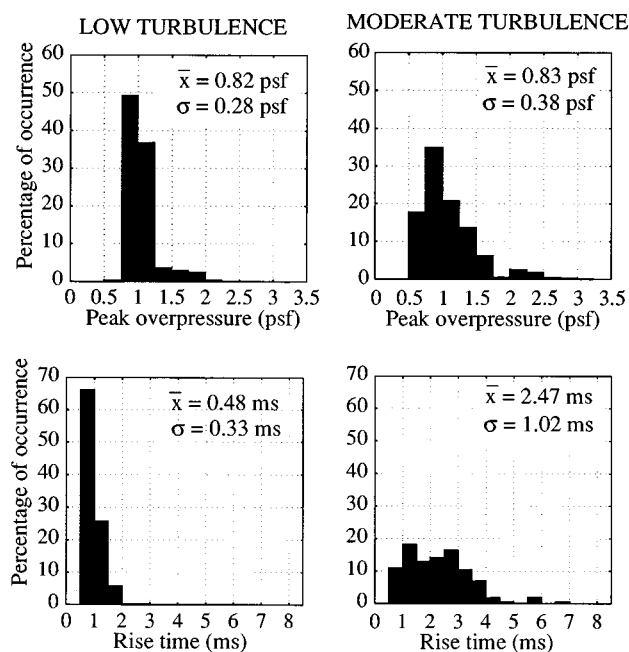
FIG. 5. Rise time and peak pressure distributions for sonic booms from a T-38 aircraft, low and moderate turbulence in the atmosphere (from Willshire and DeVilbiss, Ref. 17).

dicate that when turbulence is present some people will be subjected to overpressures much larger than the nominal value. However, the occurrence of large overpressures is partially compensated for by an increase in rise time. Although mean peak pressure is nearly the same for the two levels of turbulence, mean rise time is four times larger for moderate turbulence than for low turbulence. The distributions are more peaked for low turbulence, dramatically so in the case of rise time. Moderate turbulence produces a larger standard deviation for both measures. Since both distributions are positively skewed, i.e., the median is less than the average, positive deviations tend to be larger than negative deviations.

B. Model experiments

Several model experiments have been used to investigate the effect of turbulence on sonic boom waveform distortion and rise time. Bauer and Bagley[20] performed a series of ballistic experiments. Supersonic bullets, which produce short N waves, were fired into an open chamber. A turbulent flow was established over one wall of the chamber. The authors gathered a large data set for several combinations of bullet Mach number and turbulent flow velocity. They also studied effects of topography and atmospheric variation. They found that the turbulence caused large distortions of the shock fronts and an increase in rise time.

Motivated by a desire to test Pierce's explanation[18] that spiked and rounded sonic booms are due to atmospheric inhomogeneities that act as converging and diverging lenses, respectively, Davy and Blackstock[21] used a gas-filled soap bubble to refract and diffract short N waves produced by an electrical spark. In support of Pierce's theory they found that an argon-filled bubble (converging lens) produced a spiked N wave whereas a helium-filled bubble caused the waveform to be rounded.

Ribner et al.[22] used a jet to study spiking and rounding of an N wave generated in a conical shock tube. The N waves traveling upstream were found to be spiked, those traveling downstream rounded. Refraction due to the mean flow pattern of the jet caused the wave to be focused when it traveled upstream, defocused when it traveled downstream. Ribner concluded that jets in the atmosphere are a viable mechanism for the spiking and rounding of sonic booms.

Tubb[23] measured the effect of grid-generated turbulence on the rise time of a weak shock produced in a shock tube. He found that, on a statistical average, passage through the turbulence doubled the rise time. However, because he was trying to explain why sonic boom shock thickness is 1000 times larger than the Taylor shock thickness,[24] he concluded that his experiment was not successful in showing thickening of shocks by turbulence.

Bass et al.[25,26] measured rise time and overpressure of N waves produced by supersonic projectiles. In contrast to sonic boom data, no correlation between rise time and atmospheric turbulence was observed. However, because projectile N waves and sonic booms have vastly different shock thickness and total signature length scales relative to the scale of atmospheric turbulence, atmospheric turbulence would not be expected to have much effect on the propagation of projectile N waves.
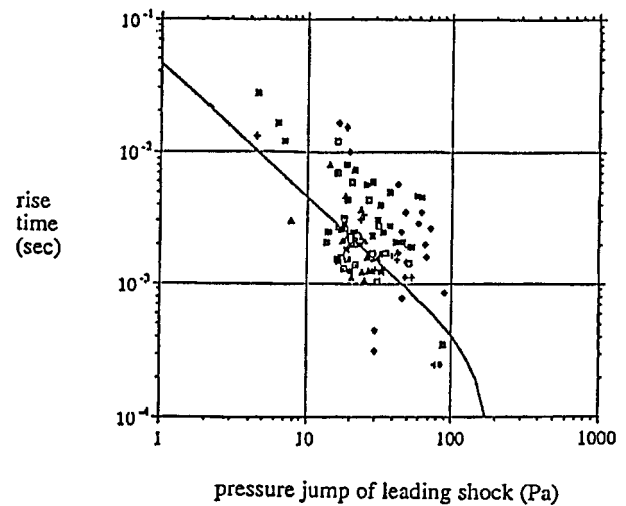
FIG. 6. Kang–Pierce prediction for the rise time of a steady step shock (solid curve) compared with sonic boom measurements made in Mohave Desert for various airplanes, flight altitudes, and Mach numbers. Relative humidity 24%, temperature 33 °C (from Pierce, Ref. 29).

C. Theoretical rise time model based on molecular relaxation

A consensus exists that when a sonic boom propagates through a quiet atmosphere, the large rise time (once thought to be anomalously large[24]) is due to molecular relaxation. The most recent theoretical analysis is that of Pierce and Kang.[6] Their model was Burgers' equation, augmented to include the effect of multiple relaxation processes.[27] Taking account of nitrogen as well as oxygen vibrational relaxation, they obtained the steady shock solution (steady flow both ahead of and behind the shock) of the augmented equation.[28] This solution was assumed to be applicable to the bow shock of the sonic boom because for a sonic boom the pressure decrease behind the shock is very gradual.

To test his results, Kang compared the measured rise times of a large number of sonic boom signatures[1] with the theoretical curve of τ vs Δp. In early reports of the compari-
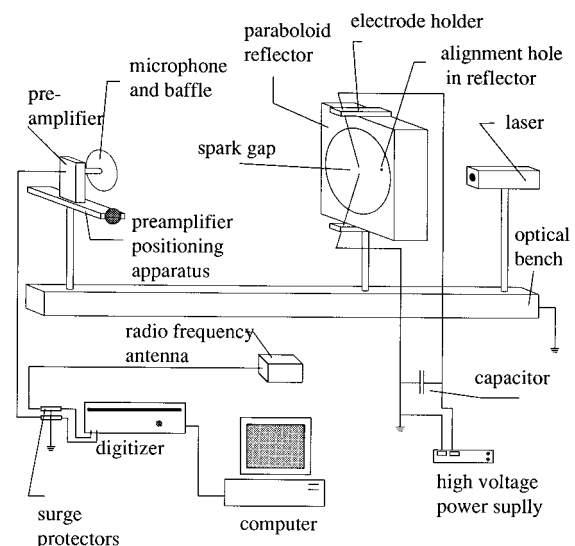
FIG. 7. Model experiment: spark source and receiving system.

Rise Time = 0.82 μs
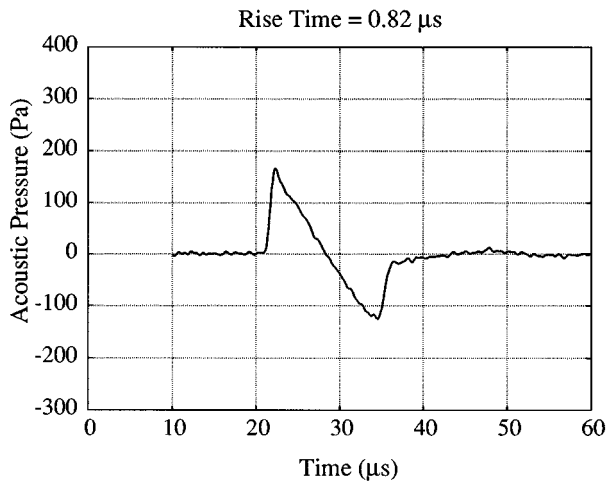
FIG. 8. Example of the signature of a spherical N wave measured 400 mm from the spark source.

son the theoretical curve appeared to be only a lower bound for the measured data, which have a substantial scatter. The trend of the data was parallel to the predicted curve, but on average the measured rise times were 2–5 times the predicted values. The discrepancy was attributed to atmospheric turbulence. Later, however, they made a correction for the pressure doubling at the ground. When replotted,[29] data and prediction seemed to be in much better agreement; see Fig. 6. Note, however, that Fig. 6 shows many measured rise times substantially less than the theoretical prediction. The fact that molecular relaxation does not seem to provide a lower bound to the measurements is somewhat surprising.

II. EXPERIMENT DESIGN AND APPARATUS

In our model experiment the N waves were produced by electrical sparks and the turbulence was generated by a plane jet. Care was taken to make the downscaling for the model turbulence the same as that for the model N waves. The N waves were measured by a wide-band condenser microphone and preamplifier.

Figure 7 shows all the components of the experiment except the apparatus to produce the plane jet, which is shown later. The energy for the spark was provided by a Glassman series EH high voltage power supply, which charged a 0.01-μF capacitor. Spontaneous discharge of the capacitor across tungsten electrodes, at the natural breakdown potential of the air, produced a spark. The gap between the electrodes, usually 1–5 mm, was set to control the amplitude and duration of the N wave produced. The natural breakdown potential was in the range 2–5 kV. The spark source ran free, not trigger controlled, at a repetition rate of about 5 sparks/

TABLE I. Typical values of rise time τ, peak pressure Δp, and duration T for sonic booms and spark-produced N waves.

	Sonic boom	Spark-produced N wave
Δp	30–200 Pa	100–500 Pa
T	100–300 ms	10–30 μs
τ	2–10 ms	0.4–2 μs

TABLE II. Turbulence parameters: typical atmosphere and design and achieved values for the model experiment.

	Atmospheric turbulence	Model exp. turb. scaled down	Model exp. turb. measured
Turb. boundary layer thickness	1000 m	0.1–0.2 m	0.05–0.3 m
Outer length scale	100–200 m	0.01–0.02 m	0.01–0.08 m
Inner length scale	10 mm	0.001 mm	0.1–0.01 mm

second. Because the electrode gap was small, the N waves generated had good reproducibility. Figure 8 shows a typical pressure signature measured 400 mm from the spark. It is almost perfectly N-shaped except that the tail shock is not as well formed as the head shock.

Although data were taken with spherical as well as plane N waves, most of the results reported in this paper are for plane waves. To generate a plane N wave, we placed the spark gap at the focus of a heavy aluminum paraboloidal reflector, which is shown in Fig. 7. Also shown is the laser used to align the spark source, reflector, and microphone. The reflected field established by the paraboloid was found by Hester[30] to be planar enough over the measurement range to satisfy the needs of the model experiment.

Because our spark-produced N waves had short duration ($\sim$15 μs) and very short rise time ($\sim$0.5 μs), demands on the receiving system were severe. Design and construction of the very wide-band condenser microphones fabricated in our laboratory for measuring N waves from sparks are described elsewhere.[31–33] The inherent rise time of the particular microphone used in this study was about 0.4 μs. The combined sensitivity of the microphone and its preamplifier, measured by a method based on nonlinear propagation effects (which cause lengthening and extra decay of an N wave),[21,32–34] was found to be 0.0521 mV/Pa. The frequency response of the preamplifier itself was flat from 10 Hz to 2.25 MHz. The microphone was mounted flush in a rigid baffle of radius 64 mm. The baffle was used to postpone the arrival of the edge wave, which would otherwise have come from the rim of the microphone case, long enough not to interfere with measurement of the direct wave.
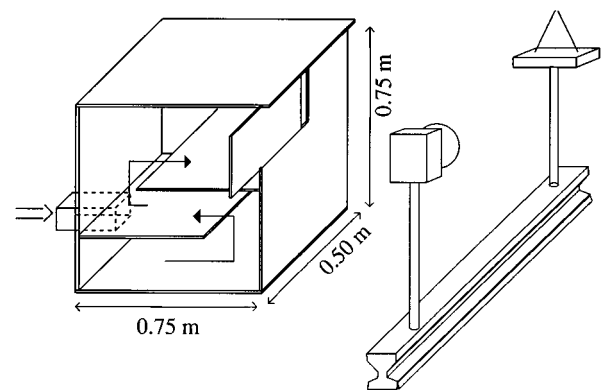
FIG. 9. Arrangement of the experiment: plane jet source, spark source (without the parabolic reflector), and receiver. The dimensions shown are in meters.
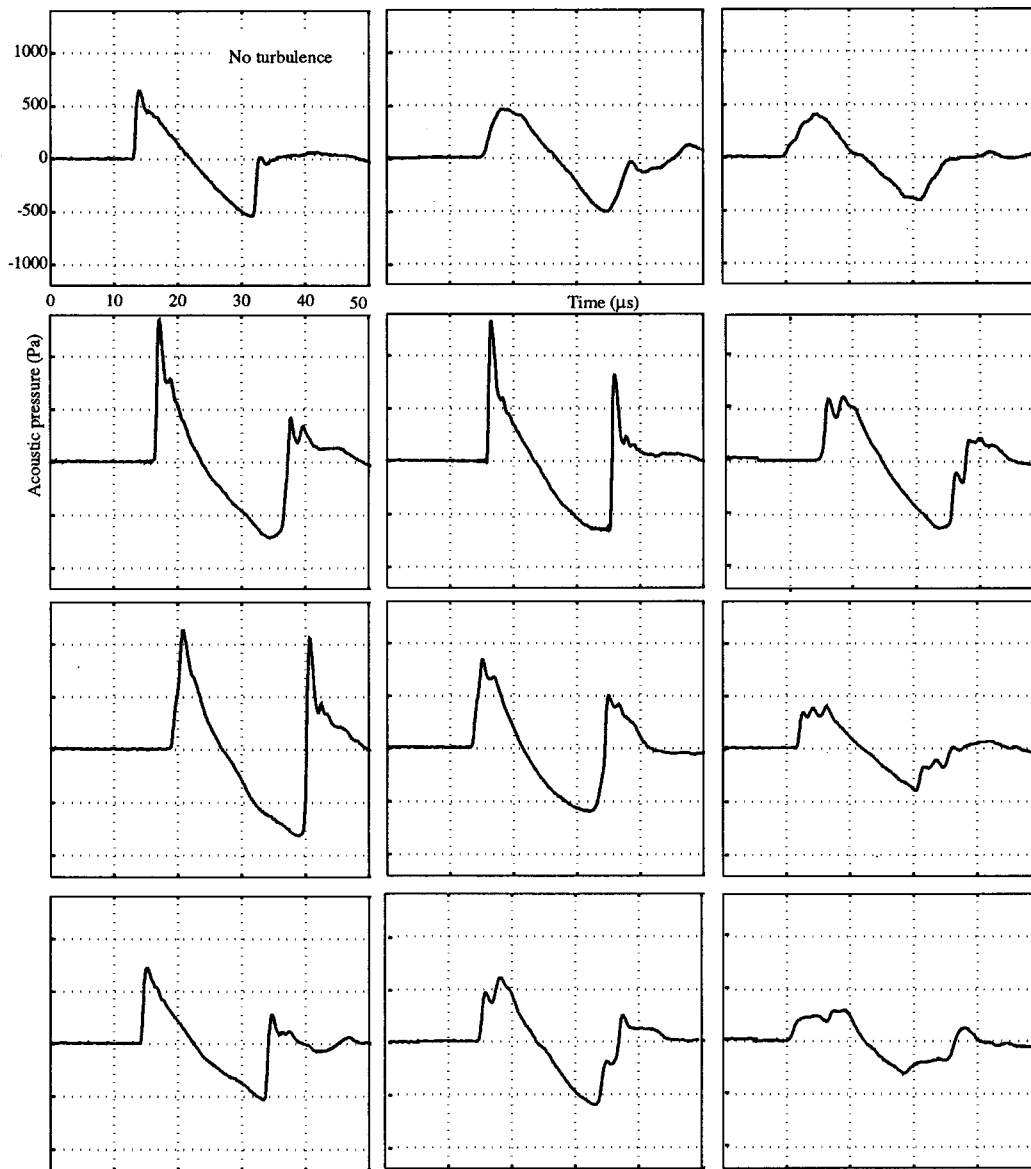
FIG. 10. Waveforms of plane N waves: the upper left trace is a reference N wave recorded in the absence of turbulence; all others recorded after propagation through turbulence.

Crucial to the experiment design was selection of the model turbulence to imitate the turbulence that exists in the atmosphere. The most important requirement was that the model turbulence be scaled down from atmospheric turbulence by the same factor that the model N waves were scaled down from sonic booms. Only then could the model experiment be expected to duplicate the conditions of actual field tests. Table I presents typical values of Δp, T, and τ for sonic booms and spark-produced N waves. It is seen that for both duration and rise time the ratio between full scale and experiment is of order 5000–10 000. (The fact that the ratio is about the same for both T and τ is a fortunate coincidence.) The first column of Table II gives three characteristic lengths for atmospheric turbulence: thickness H of the atmospheric turbulent boundary layer, outer length scale L_0 (a measure of the size of large eddies of permanent character), and inner, or Kolmogorov, length scale l_0 (a measure of the smallest eddies present). Although l_0 may not be significant

for sonic booms (since it is about two orders of magnitude less than a typical shock thickness of sonic booms), it is included here for completeness. The ratio derived from Table I was used to design the model turbulence. The design values, which appear in the middle column of Table II, turned out to be very convenient for the laboratory experiment.

To realize the model turbulent velocity field, we used a plane jet, which was generated by a fan, settling chamber, and rectangular nozzle. The settling chamber was made of 9.53-mm-thick plexiglas. Its dimensions are given in Fig. 9, which also shows the position of the nozzle relative to the N wave propagation path between the spark source (for simplicity the paraboloidal reflector is not shown) and the microphone. The air input to the settling chamber came from a 1-hp centrifugal fan, which was controlled by a Variac. The height of the nozzle was 0.25 m; the width was controlled by a sliding door. For example, in a typical experiment the nozzle width was 25.4 mm and the N wave propagation path
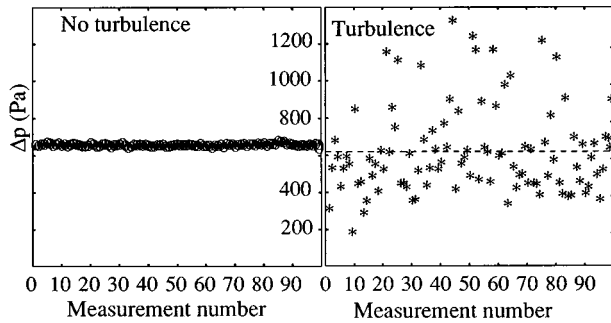
FIG. 11. Values of peak pressure for 100 plane N waves measured with and without turbulence. The dashed line shows the average for the measurements with turbulence.

FIG. 12. Values of rise time for 100 plane N waves measured with and without turbulence. The dashed line shows the average for the measurements with turbulence.

was 0.7 m downstream. At this distance the jet had a width of about 0.2 m (distance between points at which the velocity drops to half its axial value). The combination of adjustable fan flow rate and variable nozzle width permitted us to obtain a wide variety of jet configurations and Reynolds numbers. For example, a nozzle Reynolds number of about 53 000 could be achieved when the nozzle width was 25.4 mm.

The third column of Table II shows how well the turbulence developed by the plane jet, measured by hot wire anemometry, satisfied the design goals listed in the second column. Except for the Kolmogorov length scale (which, as noted above, is not important for our experiment), the measured values agree very well with the design values. We conclude that the turbulence of the plane jet has about the right scale to mimic the role of the atmosphere when our model N waves are substituted for sonic booms. For a detailed description of the characteristics of the turbulent flow field and the hot-wire measurements, see Ref. 11.

Although in this study the use of spark-produced N waves as miniature sonic booms has been successful, the modeling is not without limits. Despite the similarity of their waveforms, the two waves have important inherent differences. Most obvious is the fact that the sonic boom is a cylindrical wave while our model N wave is either spherical or plane. Normally, however, the difference in geometry is easily taken into account, even for finite-amplitude waves. More subtle is the difference in physical mechanisms that are responsible for shock rise time. The bow shock of a typical 50–150 Pa sonic boom is so weak that the dominant mechanism (for a homogeneous atmosphere) is molecular relaxation; thermoviscous effects are not very important. Moreover, the (temporal) pressure gradient behind the bow shock is so small (of order 1 Pa/ms) that it has no effect on the shock profile. In other words, in the absence of turbulence
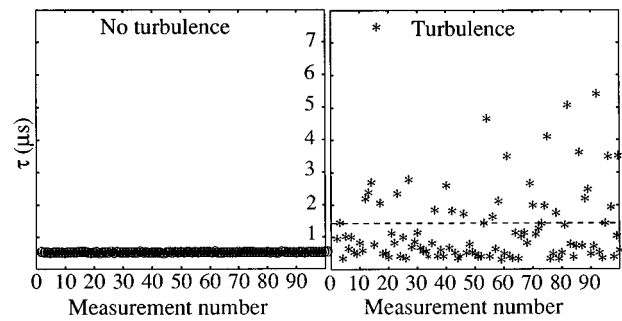
sonic boom rise time is due almost entirely to a single mechanism: molecular relaxation. By contrast, two mechanisms are at work in determining the rise time of the small scale spark-produced N waves employed in this study, and neither is molecular relaxation. First, the amplitude of a typical spark-produced N wave is high enough that the shock profile is affected much more by thermoviscous effects than by molecular relaxation. Second, the pressure gradient behind the head shock is so large (of order 10^4 Pa/ms) that it too affects the profile.[35] In summary, while rise time of sonic booms is due mainly to molecular relaxation, the important mechanisms for spark-produced N waves are thermoviscous effects and the rapid decrease of pressure behind the head shock. We believe, however, that our experiment was not affected by the differences discussed in this paragraph. Properly scaled, turbulence agitates N waves with little or no regard for either geometry or rise time physics.

III. EXPERIMENTAL RESULTS

The results presented here demonstrate the similarity between propagation of the spark-produced N waves through the plane jet and propagation of sonic booms through the turbulent atmosphere. Properties of particular interest are waveform, rise time, peak pressure, half duration, and arrival time t_{ar} of each N wave. For the plane wave measurements, special emphasis is placed on statistical representation of the results.

The data were taken as follows. First, 100 N waves were fired and measured with the air quiet. The jet was then turned on and a second set of N wave signatures, this time 200, was captured. This procedure was followed for both plane N waves (the paraboloidal reflector installed) and spherical N waves (the reflector removed). Although jet nozzle width, jet nozzle velocity, and propagation path placement were varied

TABLE III. Statistical results, plane N waves.

	τ (μs)		Δp (Pa)		T (μs)		t_{ar} (μs)	
	mean	σ	mean	σ	mean	σ	mean	σ
no turb.	0.506	0.010	651.4	6.0	10.642	0.191	13.692	0.389
turb.	1.450	1.450	620.7	228.4	11.317	1.286	12.786	2.471
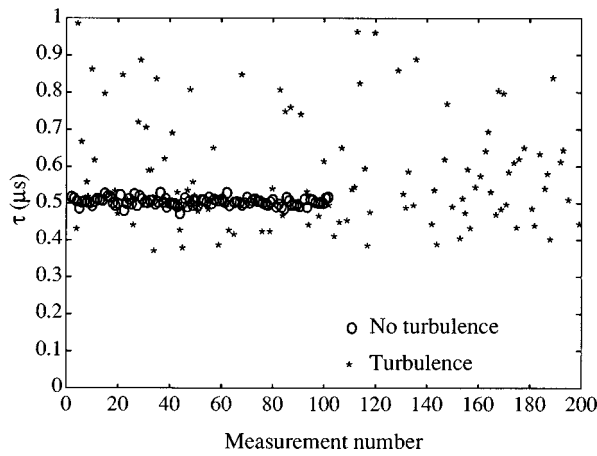
FIG. 13. Close-up of the rise time values of plane N waves measured with and without turbulence.

FIG. 15. Histogram of rise time values for plane N waves measured with and without turbulence. The bin size is 0.25 μs.

in order to obtain a range of conditions,[11] detailed results for two experiments are shown below, one for plane waves and one for spherical waves. For these experiments the width of the jet nozzle was 25.4 mm, and the jet velocity was 31.3 m/s, which resulted in a lateral (i.e., the propagation direction) rms velocity fluctuation of 2.27 m/s. The distance between the spark source and microphone was 0.45 m, and the propagation path was 0.7 m downstream from the jet nozzle. Deductions from other runs done under other conditions (different nozzle width, different nozzle velocity, different distance from the nozzle to the propagation path, and so on) are also mentioned.

A. Plane N waves

Some raw data from an experiment done with the paraboloidal reflector in place are shown in Fig. 10. The results presented here are for the specific conditions cited at the beginning of this section. The upper left signature is a reference waveform recorded in the absence of turbulence. The rest are typical waveforms recorded when the propagation path was through turbulence. An immediate conclusion is that they possess the same distortion that is observed for sonic boom signatures such as shown in Figs. 2 and 3. The distortion is most pronounced near the bow and tail shocks. The fact that the tail shock usually has the same pattern of distortion as the bow shock is an indication that the turbu-

lence is frozen during passage of the N wave. Variations in waveform from peaked to rounded and U-shaped are present. Double-peaked and multi-peaked waveforms and messy wave shapes are also evident.

Figures 11 and 12 show the data in the form of scatter diagrams; that is, values of peak pressure and rise time, respectively, are registered as a function of measurement number in the run. Average values are indicated by a dashed horizontal line. Without turbulence, the N waves received were quite uniform. (The small amount of variability that can be seen is due to source jitter. The breakdown potential and the spark channel vary a little from spark to spark.) The variability of peak pressure and rise time became very large, however, when the turbulent jet was turned on. The mean and standard deviation of the data are given in Table III. The presence of turbulence caused the mean peak pressure to decrease by about 5% and the standard deviation to grow more than tenfold. Twelve runs with plane N waves were done under other conditions. The average peak pressure with the jet turned on was always found to be smaller than that

FIG. 14. Histogram of peak pressure values for plane N waves measured with and without turbulence. The bin size is 40 Pa.
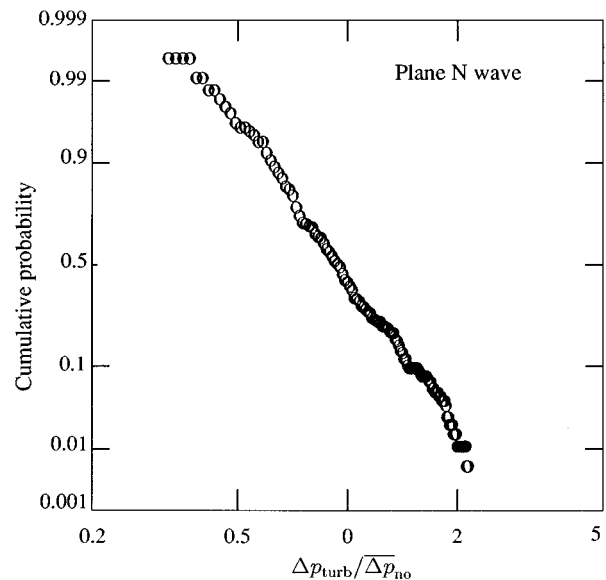
FIG. 16. Cumulative probability curve of peak pressure of plane N waves after propagation through turbulence. The curve is plotted on a log-normal scale, and $\overline{\Delta p}_{no}$ is the average peak pressure measured in the absence of turbulence.
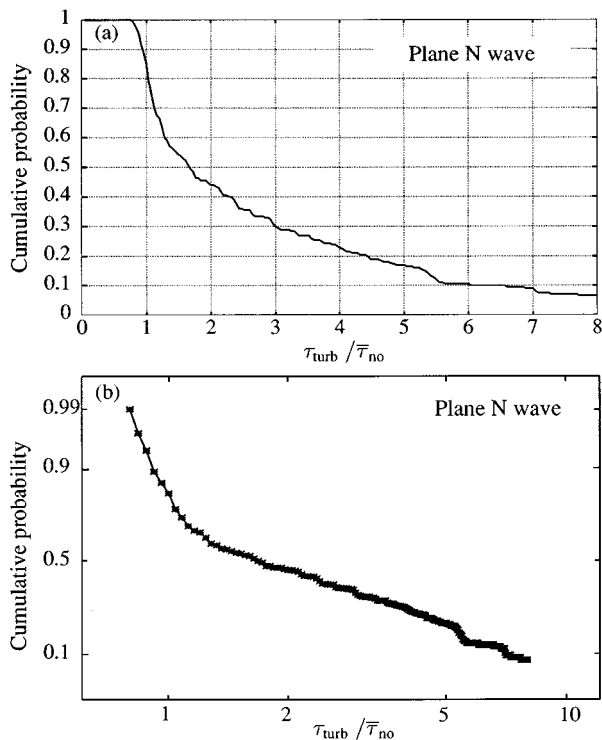
FIG. 17. Cumulative probability curve of rise time of plane N waves after propagation through turbulence; $\bar{\tau}_{no}$ is the average rise time measured in the absence of turbulence.

FIG. 18. The peak pressure values for 100 spherical N waves measured with and without turbulence. The dashed line shows the average for the measurements with turbulence.

with the jet turned off. The maximum decrease that occurred was 18%. A related observation is that the number of spiked waveforms ($\Delta p > \overline{\Delta p}_{turb}$, where $\overline{\Delta p}_{turb}$ is the average peak pressure with turbulence present) is about half the number of rounded waveforms ($\Delta p < \overline{\Delta p}_{turb}$). The effect of turbulence on rise time was more spectacular: mean rise time nearly tripled and only a few N waves had a significantly lower rise time. The implication for sonic booms is important, since an increase in rise time causes a decrease in loudness associated with the boom when heard outdoors. Finally, Table III shows that mean half duration increased 6% while the mean arrival time decreased slightly. In other words, on average turbulence caused the N waves to be longer and to arrive earlier.

In order to demonstrate that the rarity of decreased rise time was not simply due to limitations of our receiving system, we show in Fig. 13 a close-up of the data for τ <1 μs. The no-turbulence data points are those clustered around $\tau = 0.5$ μs in the first half of the figure. Although the rise time dropped for some N waves that passed through turbulence, the large majority sustained an increase. The data may be somewhat microphone limited, but the strong tendency of turbulence to increase rise time is clear. In other words a roughly unbiased scatter above and below the no-turbulence value, like that shown in Fig. 6, was not observed in our model experiment. Another observation is that N waves having a decreased rise time were usually of the spiked type and had increased peak pressure.

Histograms of peak pressure and rise time are shown in Figs. 14 and 15, respectively. The bin size is 40 Pa for the peak pressure and 0.25 μs for the rise time. The peak pressure distribution is positively skewed because of the occur-

rence of some very large peak pressures. The cumulative probability curve of the peak pressure data fits a straight line when plotted on a log-normal scale (Fig. 16). This fact further illustrates the similarity of our data to that for sonic booms. The rise time cumulative probability function (Fig. 17) is plotted on a linear (a) and a log-normal scale (b). The linear curve confirms that for plane N waves turbulence almost always (i.e., in 85% of the cases) increases the rise time. Some extremely high values of rise time were observed. More than 10% of the N waves have rise times more than seven times larger than that of the average no-turbulence rise time. The log-normal curve displays a bimodal behavior, i.e., one straight line for rise time values greater than the no-turbulence average value and a second straight line for values smaller than the average.
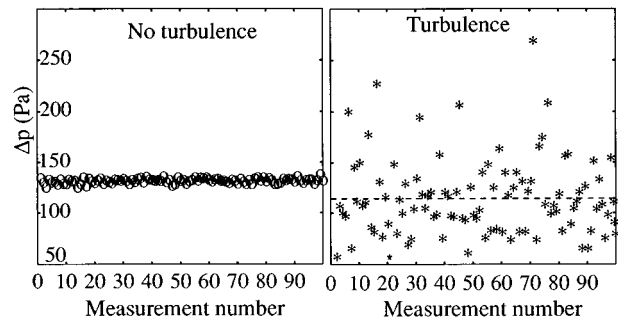
B. Spherical N waves

Scatter diagrams for the spherical wave measurements are shown in Figs. 18 and 19. The effects observed are qualitatively the same as those seen in the plane N wave experiments. Some differences do exist, however. Because of spherical spreading, peak pressure is less than for the plane waves and nonlinear effects are correspondingly weaker. Consequently the rise times are larger. Nevertheless, once the jet is turned on, an enormous increase in variability of the peak pressure and rise time is noticed. The mean and standard deviation of the N wave parameters are given in Table IV. After turbulence was introduced, the average peak pres-
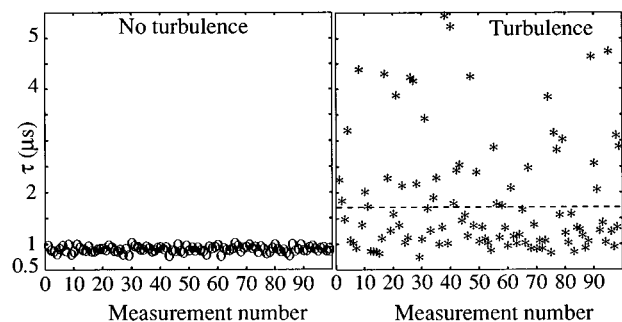
FIG. 19. The rise time values for 100 spherical N waves measured with and without turbulence. The dashed line shows the average for the measurements with turbulence.

TABLE IV. Statistical results, spherical N waves.

	τ (μs)		Δp (Pa)		T (μs)		t_{ar} (μs)	
	mean	σ	mean	σ	mean	σ	mean	σ
no turb.	0.877	0.056	130.5	2.4	7.867	0.170	19.614	0.325
turbulence	1.743	1.030	114.8	38.0	8.509	0.877	16.477	5.052

sure decreased by about 10%, while the standard deviation increased more than tenfold. Of the 38 runs done with spherical N waves, in 34 the average peak pressure with turbulence present was lower than the average no-turbulence peak pressure. The largest decrease was 16%. The number of spiked signatures was 87 and the number of rounded signatures 113, an indication that the median value is less than the mean. On average, the rise time with turbulence was double that without turbulence. The standard deviation of the rise time also increased enormously. Just as for plane waves, turbulence produced a decrease in rise time for only a few of the N waves.

IV. SUMMARY AND CONCLUSIONS

A model experiment is reported in which spark-produced N waves, both plane and spherical, propagate through a turbulent velocity field established by a plane jet. It is shown that the effect of the model turbulence on waveform and rise time of the N waves is similar to that produced by the atmospheric turbulent boundary layer on sonic booms. The waveform distortion suffered by sonic booms is reproduced, both in scale and in character, in the model experiment. Passage through the turbulence causes an enormous variability in rise time and peak pressure. Turbulence almost always increases the rise time. On average, the rise time increases up to a factor of 3, while the peak pressure decreases by as much as 20%. It is shown that turbulence causes a decrease in rise time for only a small percentage of N waves. A slightly larger fraction attain a higher peak pressure.

If the results of this model experiment were to be extrapolated to sonic booms, on average, a decrease in peak pressure combined with an increase in rise time would lower the loudness level associated with the booms when heard outdoors. However, up to 10% of the waves have smaller rise times and higher peak pressures than the no-turbulence wave. The effect of these waves on the overall loudness needs further study.

ACKNOWLEDGMENTS

[1] R. A. Lee and J. M. Downing, ''Sonic boom produced by United States Air Force and United States Navy aircraft: measured data,'' AL-TR-1991-0099, Biodynamic Environment Branch, Biodynamics and Bioengineering Division, Armstrong Laboratory, Wright-Patterson Air Force Base, Ohio (1991). This report contains a valuable database and is available to the general public. The database is known in the sonic boom community as the Boomfile 2 data. All the data are in digital format. At the time of the measurements aircraft tracking data and local weather data were gathered.

[2] A. Niedzwiecki and H. S. Ribner, ''Subjective loudness of N-wave sonic booms,'' J. Acoust. Soc. Am. **64**, 1622–1626 (1978).

[3] A. Niedzwiecki and H. S. Ribner, ''Subjective loudness of minimized sonic boom waveforms,'' J. Acoust. Soc. Am. **64**, 1617–1621 (1978).

[4] J. D. Leatherwood and B. M. Sullivan, ''Subjective loudness response to simulated sonic booms,'' *Proceedings, High-Speed Research Workshop on Sonic Boom*, edited by C. M. Darden (NASA Langley Research Center, Hampton, VA, 1992), Vol. 1, pp. 151–170.

[5] B. M. Sullivan and J. D. Leatherwood, ''Experimental studies of loudness and annoyance response to sonic booms,'' *Proceedings, High-Speed Research Workshop on Sonic Boom*, edited by T. A. Edwards (NASA Ames Research Center, Moffet Field, CA, 1992), Vol. I, pp. 153–175.

[6] A. D. Pierce and J. Kang, ''Molecular relaxation effects on sonic boom waveforms,'' in *Frontiers of nonlinear acoustics: Proceedings of the 12th ISNA*, edited by M. F. Hamilton and D. T. Blackstock (Elsevier Applied Science, London, 1990), pp. 165–170.

[7] S. C. Crow, ''Distortion of sonic bangs by atmospheric turbulence,'' J. Fluid Mech. **37**, 529–563 (1969).

[8] G. Kamali and A. D. Pierce, ''Time dependence of variances of sonic boom waveforms,'' Nature (London) **234**(5323), 30–31 (5 November 1971).

[9] A. D. Pierce, ''Statistical theory of atmospheric turbulence on sonic boom rise times,'' J. Acoust. Soc. Am. **49**, 906–924 (1971).

[10] K. J. Plotkin and A. R. George, ''Propagation of weak shock waves through turbulence,'' J. Fluid Mech. **54**, 449–467 (1972).

[11] B. Lipkens, ''Experimental and theoretical study of the propagation of N waves through a turbulent medium,'' Ph.D. dissertation, Department of Mechanical Engineering, University of Texas at Austin (1993).

[12] Anon., ''Sonic boom experiments at Edwards Air Force Base'' prepared by Stanford Res. Inst. for the National Sonic Boom Evaluation Office, Rep. NSBEO-1-67 (1967).

[13] D. J. Maglieri, ''Sonic boom flight research—some effects of airplane operations and the atmosphere on sonic boom signatures,'' Sonic Boom Research, NASA SP-147 (1967).

[14] I. E. Garrick and D. J. Maglieri, ''A summary of results on sonic boom pressure-signature variations associated with atmospheric conditions,'' NASA TN D-4588 (1968).

[15] D. J. Maglieri, V. Huckel, H. R. Henderson, and N. J. McLeod, ''Variability in sonic-boom signatures measured along an 8000-foot linear array,'' NASA TN D-5040 (1969).

[16] A. D. Pierce and D. J. Maglieri, ''Effects of atmospheric irregularities on sonic boom propagation,'' J. Acoust. Soc. Am. **51**, 702–721 (1972).

[17] W. L. Willshire and D. W. DeVilbiss, ''Preliminary results from the White Sands Missile Range sonic boom propagation experiment,'' *Proceedings, High-Speed Research Workshop on Sonic Boom*, edited by C. M. Darden (NASA Langley Research Center, Hampton, VA, 1992), Vol. I, pp. 137–149.

[18] A. D. Pierce, ''Spikes on sonic boom pressure waveforms,'' J. Acoust. Soc. Am. **44**, 1052–1061 (1968).

[19] T. A. Gionfriddo, ''Analysis of sonic boom data to quantify distortions of shock profiles,'' *Proceedings, High-Speed Research Workshop on Sonic Boom*, edited by C. M. Darden (NASA Langley Research Center, Hampton, VA, 1992), Vol. 1, pp. 63–76.

[20] A. B. Bauer and C. J. Bagley, ''Sonic boom modeling investigation of topographical and atmospheric effects,'' McDonnell-Douglas Corp., Long Beach, Calif., Rep. No. FAA-NO-70-10 (1970).

[21] B. A. Davy and D. T. Blackstock, ''Measurements of the refraction and diffraction of a short N-wave by a gas-filled soap bubble,'' J. Acoust. Soc. Am. **49**, 732–737 (1971).

[22] H. S. Ribner, P. J. Morris, and W. H. Chu, ''Laboratory simulation of development of superbooms by atmospheric turbulence,'' J. Acoust. Soc. Am. **53**, 926–928 (1973).

[23] P. E. Tubb, ''Measured effects of turbulence on the rise time of a weak shock,'' AIAA paper 75-543 (1975).

[24] G. M. Lilley, ''The structure of shock waves at large distances from bodies traveling at high speeds,'' in 5th Congres Internationale d'Acoustique, edited by Daniel E. Commins (Liege, Belgium, 1965), Vol. II, pp. 109–162.

[25] H. E. Bass, J. Ezell, and R. Raspet, ''Effect of vibrational relaxation on rise times of shock waves in the atmosphere,'' J. Acoust. Soc. Am. **74**, 1514–1517 (1983).

[26] H. E. Bass, B. A. Layton, L. N. Bolen, and R. Raspet, ''Propagation of medium strength shock waves through the atmosphere,'' J. Acoust. Soc. Am. **82**, 306–310 (1987).

[27] A. D. Pierce, *Acoustics: An Introduction to its Physical Principles and Applications* (McGraw-Hill, New York, 1981), pp. 547–562, 587–593.

[28] J. Kang, ''Nonlinear acoustic propagation of shock waves through the atmosphere with molecular relaxation,'' Ph.D. thesis, Department of Mechanical Engineering, Pennsylvania State University, 1991.

[29] A. D. Pierce, ''Molecular relaxation effects on sonic boom waveforms: A tutorial survey,'' J. Acoust. Soc. Am. **92**, 2329A (1992).

[30] D. M. Hester, ''N wave field produced by a paraboloidal reflector and application to microphone calibration,'' M. S. Report, Mechanical Engineering Department, The University of Texas at Austin (1992).

[31] W. M. Wright, ''Studies of N waves from weak sparks in air, Final Report,'' ONR Report NR-384-321, Physics Department, Kalamazoo College, Kalamazoo, Michigan (1971) (AD 725 865).

[32] E. P. Cornet, ''Focusing of an N wave by a spherical mirror,'' Technical Rep. ARL-TR-72-40, Applied Research Laboratories, The University of Texas at Austin (1972) (AD 157 035).

[33] M. O. Anderson, ''The propagation of a spherical N-wave in an absorbing medium and its diffraction by a circular aperture,'' Technical Rep. ARL-TR-74-25, Applied Research Laboratories, The University of Texas at Austin (1974) (AD 787 878).

[34] R. D. Essert, ''Axisymmetric propagation of a spherical N wave in a cylindrical tube,'' Technical Rep. ARL-TR-81-22, Applied Research Laboratories, The University of Texas at Austin (1981) (ADA 099 990).

[35] L. B. Orenstein, ''The rise time of N waves produced by sparks,'' Technical Rep. ARL-TR-82-51, Applied Research Laboratories, The University of Texas at Austin (ADA 120 817) (1982).

A note on differential equations of coupled-mode propagation in fluids

Oleg A. Godin[a)]

School of Earth and Ocean Sciences, University of Victoria, Victoria, British Columbia V8W 2Y2, Canada

There is a significant discrepancy between bathymetric contributions to ocean acoustic mode coupling matrix elements derived by various authors. In this paper, the discrepancy is shown to be due to incorrectness of the traditional approach to mode coupling theory, originated by A. D. Pierce [J. Acoust. Soc. Am. **37**, 19–27 (1965)] and D. M. Milder [J. Acoust. Soc. Am. **46**, 1259–1263 (1969)], in the presence of a sloping interface or a range-dependent rigid boundary. Physically, their approach is consistent with neither energy conservation nor reciprocity. Mathematically, the problem with the traditional approach consists of formal, unjustified, term-by-term differentiation of a series representing the acoustic pressure in terms of local normal modes. The series is poorly convergent when a nonhorizontal interface of fluids with distinct densities is present. A rigorous derivation of the acoustic mode coupling equations in media with piecewise continuous density and sound speed is given here on the basis of the reciprocity principle. Necessary corrections to the results presented recently by B. E. McDonald [J. Acoust. Soc. Am. **100**, 219–224 (1996)] are discussed. © *1998 Acoustical Society of America.* [S0001-4966(98)01701-9]

PACS numbers: 43.30.Bp, 43.30.Qd [JHM]

INTRODUCTION

This article, motivated by a recent paper,[1] addresses some misconceptions which unfortunately became rather wide spread in the literature on coupled-mode theory of underwater sound propagation. In the very interesting paper[1] McDonald considers, among other issues, acoustic normal mode coupling resulting from varying bathymetry and volumetric changes in sound speed and density in a three-dimensional (3-D) fluid waveguide. The importance of mode coupling, and particularly of bathymetric interaction near New Zealand, for proper interpretation of the Heard Island Feasibility Test[2] (HIFT) data has been cited as a motivation for the study. Besides global scale acoustics, important applications of mode coupling equations with significant contributions from irregular interfaces include reverberation, sound propagation in coastal zones, and low-frequency scattering from the ocean bottom. In the context of underwater acoustics, mode coupling at irregular interfaces and boundaries has been considered previously by many authors.[3–7] Additional references, including those to related work in other branches of acoustics, in optics, and in radio wave propagation, may be found in Refs. 6 and 8. Mode coupling equations were systematically derived by Fawcett[7] for a two-dimensional problem with a single interface between fluids of different but constant density. The general case of piecewise continuous variations in both sound velocity $c(x,y,z)$ and density $\rho(x,y,z)$ has been discussed by Brekhovskikh and Godin (Ref. 6, Sec. 7.1). Whereas presence of an interface has been accounted for[1,7] by different means than that of volumetric inhomogeneities, bathymetric contributions to

mode coupling have been determined[6] by considering the interface as a limiting case of smooth but rapid variations in c and ρ.

In Refs. 1, 9, 10 acoustic pressure in an irregular fluid waveguide is represented as an expansion

$$p(x,y,z) = \sum_m F_m(x,y) f_m(z;x,y) \tag{1}$$

in local vertical eigenmodes f_m. The mode amplitudes F_m satisfy the simultaneous coupling equations

$$\nabla_\perp^2 F_n + \xi_n^2 F_n = \sum_m (\alpha_{nm} F_m + \beta_{nm} \cdot \nabla_\perp F_m), \tag{2}$$

where $\nabla_\perp = (\partial/\partial x, \partial/\partial y, 0)$, $\xi_n(x,y)$ is the propagation constant of the corresponding local mode. An emphasis has been made in Ref. 1 on expressing the coupling coefficients β_{nm} in terms of environmental gradients, whereas the coefficients α_{nm} were not discussed in detail. To derive Eq. (2), McDonald followed Pierce[9] and Milder[10] in term-by-term differentiating series (1) and substituting the result into the wave equation. However, as clearly explained by Fawcett[7] and as has been known for a long time,[11,12] in the presence of a nonhorizontal interface or a range-dependent rigid boundary, poor convergence of series (1) makes term-by-term differentiation with respect to z an illegitimate mathematical procedure. The poor convergence arises from the fact that, in general, the acoustic field in a range-dependent waveguide obeys different boundary conditions than the local modes. [Obviously, if the term-by-term differentiation of Eq. (1) were admissible, the *vertical* component of the oscillatory velocity would be continuous at the interface instead of the *normal* component.] Whether formal differentiation of series (1) leads to physically meaningful results for mode coupling must be verified using a more rigorous approach.
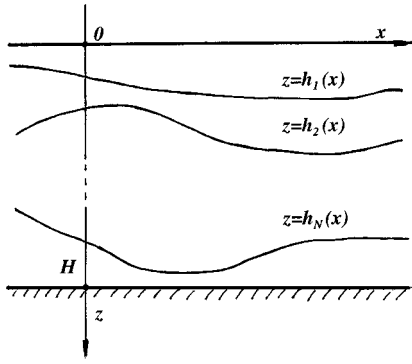
FIG. 1. Geometry of the problem.

According to McDonald, a bathymetric contribution to the matrix β_{nm}, contrary to the volumetric one, is not antisymmetric. This is counterintuitive and suggests there is an error since the interaction of any two modes of given orders should be indifferent to substitution of an interface by a smooth transition in a very thin layer. That is, if β_{nm} is always antisymmetric for a volumetric variation it should also be antisymmetric for a bathymetric one. Indeed, comparison of the expression for coupling coefficients derived by McDonald[1] with respective results of Brekhovskikh and Godin[6] and Fawcett[7] reveals a contradiction. It is the intent of this paper to demonstrate that McDonald's results for the bathymetric contribution to mode coupling coefficients are not correct, to indicate the origin of the error, and to derive the correct expressions for both matrices α_{nm} and β_{nm} in terms of environmental gradients under quite general assumptions about the sound velocity and density variations. The remainder of the note is organized as follows. A new derivation of the mode coupling equations is presented in Sec. I. To avoid the dubious operation on series (1) of differentiation with respect to z, the new derivation relies on the reciprocity principle rather than the wave equation. A means of calculating the mode coupling coefficients in terms of environmental gradients is established in Sec. II. Results of different authors are compared in Sec. III. Section IV summarizes our conclusions. Some of the conclusions are illustrated in Appendices A and B by considering specific problems admitting explicit exact or asymptotic solution.

I. DERIVATION OF THE DIFFERENTIAL EQUATIONS OF MODE COUPLING

For notational convenience we assume the waveguide to be bounded by pressure release or rigid horizontal boundaries at $z=0$ and at $z=H$ (Fig. 1). [In a waveguide with infinite or semi-infinite extent in z, summation over discrete modes in Eq. (1) has to be complemented by integration over the continuous spectrum.] There can be an arbitrary number N of interfaces $z=h_1(x,y)$, $l=1,2,...,N$ $0<h_1<h_2<\cdots<h_N<H$ in the waveguide. Apart from discontinuities at these interfaces, the density and sound speed are smooth functions of the coordinates; h_l are smooth functions of x, y. Under these assumptions the mode amplitudes F_m in Eq. (1) are smooth functions of the horizontal coordinates. The ver-

tical eigenmodes $f_m(z;x,y)$ form a complete set of functions at each cross section of the waveguide. They satisfy the equation

$$\frac{\partial}{\partial z}\frac{\partial f_m(z;x,y)/\partial z}{\rho(x,y,z)} + \frac{k^2(x,y,z)-\xi_m^2(x,y)}{\rho(x,y,z)}f_m(z;x,y)=0,$$
(3)

at $0<z<h_1$, $h_1<z<h_2,...,$ $h_N<z<H$, the continuity conditions

$$f_m(z;x,y)\Big|_{z=h_l^-(x,y)}^{z=h_l^+(x,y)}=0,$$
(4a)

$$\rho^{-1}(x,y,z)\partial f_m(z;x,y)/\partial z\Big|_{z=h_l^-(x,y)}^{z=h_l^+(x,y)}=0,$$
(4b)

at the interfaces, the respective boundary conditions at the perfect boundaries $z=0, H$, and the orthogonality relationship

$$(f_n,f_m)=\delta_{nm}.$$
(5)

In Eq. (4) the superscript $+$ $(-)$ denotes values of z which are just greater (less) than h_l, $k=\omega/c$ is the wave number, and ω is the sound frequency. The inner product used in Eq. (5) is defined for arbitrary piecewise continuous functions ψ and χ as follows:

$$(\psi,\chi)=\left(\int_0^{h_1}+\int_{h_1}^{h_2}+\cdots+\int_{h_N}^{H}\right)\frac{dz}{\rho(x,y,z)}$$
$$\times \psi(x,y,z)\chi(x,y,z).$$
(6)

Consider first a 2-D problem. We assume that neither the waveguide parameters nor the acoustic field depend on the Cartesian coordinate y. (Analysis of a cylindrically symmetric problem is quite similar.) Following Ref. 6, Sec. 7.1.3, we write acoustic pressure and x-component of particle velocity in terms of new variables F_m^+ and F_m^-:

$$p(x,z)=\sum_m [F_m^+(x)+F_m^-(x)]f_m(z;x);$$
(7)

$$v_x(x,z)=\frac{1}{\omega\rho}\sum_m [F_m^+(x)-F_m^-(x)]\xi_m(x)f_m(z;x).$$
(8)

In a range-independent segment of the waveguide, where an unambiguous decomposition of the sound field into waves traveling in opposite directions is possible, $F_m^+(F_m^-)$ has meaning as the amplitude of the mth normal mode traveling to the right (to the left). The acoustic field in a source-free region of the waveguide is uniquely determined by prescribing p and v_x profiles at a vertical cross section. Hence, derivatives of the mode amplitudes at arbitrary x must be a function of the amplitudes themselves. Because of the superposition principle, the function is linear. We choose to write this linear relationship in the following way:

$$\frac{dF_n^+}{dx}-i\xi_n F_n^+=\sum_m (b_{nm}^+ F_m^+ + b_{nm}^- F_m^-).$$
(9)

As defined in Eq. (9), the matrices b_{mn}^+ and b_{mn}^- vanish in a range-independent segment of the waveguide. In general, these matrices equal some integrals over z of horizontal de-

rivatives of c, ρ, and h_l and, hence, change their sign when direction of the x axis is inverted. Then F_m^+ becomes F_m^- and vice versa, while $\partial/\partial x$ becomes $-\partial/\partial x$. Since the mode coupling equations should not depend on choice of the reference frame, we obtain from Eq. (9)

$$\frac{dF_n^-}{dx}+i\xi_n F_n^- = \sum_m (b_{nm}^- F_m^+ + b_{nm}^+ F_m^-). \tag{10}$$

Let us determine the coupling coefficients b_{mn}^+ and b_{mn}^-. As $\nu_x = (i\omega\rho)^{-1}\ \partial p/\partial x$, it follows from Eqs. (7) and (8) that

$$\sum_m \left[f_m \partial(F_m^+ + F_m^-)/\partial x - i\xi_m(F_m^+ - F_m^-)f_m \right.$$

$$\left. + (F_m^+ + F_m^-)\frac{\partial f_m}{\partial x}\right]=0. \tag{11}$$

Note, that according to completeness of the vertical eigen-functions and the orthogonality relation (5)

$$\frac{\partial f_m(z;x)}{\partial x} = \sum_n B_{nm}(x)f_n(z;x), \tag{12}$$

where B_{nm} is the x component of the vector

$$\mathbf{B}_{nm} = (f_n, \boldsymbol{\nabla}_\perp f_m). \tag{13}$$

Expressing derivatives of f_m, F_m^+, and F_m^- in Eq. (11) through Eqs. (9), (10), and (12), one obtains

$$b_{nm}^+ + b_{nm}^- + B_{nm} = 0. \tag{14}$$

To derive additional equations for the coupling coefficients, consider the reciprocity principle. For an arbitrary surface surrounding a source-free fluid volume the reciprocity principle reduces to the statement (Ref. 6, Sec. 4.2) that surface integral of the vector $\mathbf{j} = \rho^{-1}(p_1 \boldsymbol{\nabla} p_2 - p_2 \boldsymbol{\nabla} p_1)$ is zero for any two acoustic fields p_1 and p_2. For the 2-D waveguide considered, the reciprocity principle takes the form

$$\frac{dJ}{dx} = 0; \quad J(x) \equiv -0.5i\left[\left(p_1, \frac{\partial p_2}{\partial x}\right) - \left(p_2, \frac{\partial p_1}{\partial x}\right)\right]. \tag{15}$$

Let fields p_1 and p_2 be represented, respectively, by sets of modal amplitudes F_m^+, F_m^- and E_m^+, E_m^-. Using Eqs. (5)–(8) to calculate the inner products in (15) as well as Eqs. (9) and (10), one finds

$$\frac{dJ}{dx} = \sum_{m,n}\left[(F_n^+ E_m^+ + F_m^- E_n^-)(\xi_m b_{mn}^- - \xi_n b_{nm}^-) + (F_n^- E_m^+ \right.$$

$$\left. - F_n^+ E_m^-)\left(\xi_m b_{mn}^+ + \xi_n b_{nm}^+ + \delta_{nm}\frac{\partial\xi_m}{\partial x}\right)\right]. \tag{16}$$

As the rhs in Eq. (16) should equal zero for *arbitrary* F_m^+, F_m^- and E_m^+, E_m^-, the mode coupling coefficients must satisfy the following equations:

$$\xi_m b_{mn}^- - \xi_n b_{nm}^- = 0; \tag{17}$$

$$\xi_m b_{mn}^+ + \xi_n b_{nm}^+ + \delta_{nm}\frac{\partial\xi_m}{\partial x} = 0. \tag{18}$$

The simultaneous algebraic equations (14), (17), and (18) can be easily solved for the mode coupling coefficients, giving

$$b_{nm}^\pm = \mp \delta_{nm}\frac{\partial\xi_n/\partial x}{2\xi_n} \pm \frac{\xi_m}{2\xi_n}B_{mn} - \frac{1}{2}B_{nm}. \tag{19}$$

Note that Eq. (19) holds for bathymetric as well as volumetric mode coupling. In the absence of interfaces in the waveguide, such equations were derived earlier from other considerations by Brekhovskikh and Godin[6] and, for $\rho=\rho(z)$, by Boyles.[5]

It should be emphasized, that the mode coupling equations (9) and (10) with coefficients (19) are an *exact* reformulation of the original 2-D boundary-value problem. The equations hold regardless of the presence of irregular interfaces. It is clear from the very derivation of the coupling equations that their solutions obey the reciprocity principle. Acoustic energy conservation in a lossless medium is also guarantied by the coupling equations. Indeed, with p_2 chosen as the complex conjugate of p_1 the reciprocity equation (15) expresses energy conservation. A close relationship between energy conservation and symmetry of coupling coefficients with respect to interchange of their indexes is considered in some detail in Appendix A.

Having derived Eq. (19), it is not difficult to reformulate the mode coupling equations in terms of $F_m = F_m^+ + F_m^-$. The equations for F_m are of second order in x. Differentiating the sum of Eqs. (9) and (10) with respect to x, after algebraic manipulation leads to the two-dimensional version of Eq. (2) with $\partial/\partial y = 0$ and

$$\alpha_{nm} = \sum_s B_{sn}B_{sm} - \frac{\partial B_{nm}}{\partial x}; \tag{20a}$$

$$\beta_{nm} = B_{mn} - B_{nm}. \tag{20b}$$

In the 2-D problem β_{nm} has only an x component. It is this component that is given by Eq. (20b).

According to Ref. 6, Sec. 7.1.1, in the 3-D problem, the mode coupling coefficients in Eq. (2) can be expressed in terms of those for the 2-D problem as follows:

$$\alpha_{nm} = \sum_s \mathbf{B}_{sn}\cdot\mathbf{B}_{sm} - \boldsymbol{\nabla}_\perp\cdot\mathbf{B}_{nm}; \tag{21a}$$

$$\beta_{nm} = \mathbf{B}_{mn} - \mathbf{B}_{nm}, \tag{21b}$$

where the matrix $\mathbf{B}_{nm}$ is given by Eq. (13).

Of course, one can directly apply reciprocity considerations to the mode coupling equations (2) for the 3-D case without a preliminary analysis of the 2-D case. Then, repeating the reasoning outlined above and with account of acoustic pressure and oscillatory velocity normal component continuity at interfaces, one has instead of Eqs. (15) and (16), respectively,

$$\boldsymbol{\nabla}_\perp\cdot\mathbf{J}=0; \quad \mathbf{J}=(p_1,\boldsymbol{\nabla}_\perp p_2)-(p_2,\boldsymbol{\nabla}_\perp p_1); \tag{22}$$

$$\sum_{m,n} [C_{nm}F_nE_m + \mathbf{D}_{nm}\cdot(F_n\nabla_\perp E_m - E_n\nabla_\perp F_m)] = 0;$$

$$C_{nm} = \nabla_\perp\cdot\mathbf{B}_{nm} - \nabla_\perp\cdot\mathbf{B}_{mn} + \alpha_{nm} - \alpha_{mn}, \qquad (23)$$

$$\mathbf{D}_{nm} = \mathbf{B}_{nm} - \mathbf{B}_{mn} + \beta_{nm}.$$

These equations must hold for any acoustic fields p_1 and p_2 in the waveguide. As mode amplitudes F_n, E_m and their horizontal gradients $\nabla_\perp F_n$, $\nabla_\perp E_m$ can be chosen arbitrarily, it follows from Eq. (23) that $C_{nm} = 0$, $\mathbf{D}_{nm} = 0$. Indeed, let $F_n = \delta_{nN}$, $E_m = \delta_{mM}$, and $\nabla_\perp F_n = \nabla_\perp E_m = 0$ at a given cross section of the waveguide. Then Eq. (23) reduces to $C_{NM} = 0$. As N,M, and the cross section have been chosen arbitrary, $C_{nm} = 0$ identically. One can prove validity of equation $\mathbf{D}_{nm} = 0$ in a similar way. It leads to Eq. (20b) for the coupling matrix β_{nm}. Representing the other coupling matrix, α_{nm}, as a sum of symmetric and antisymmetric matrices, one obtains from $C_{nm} = 0$ that $\alpha_{nm} = \gamma_{nm} - \nabla_\perp\cdot\mathbf{B}_{nm}$, where γ_{nm} is an undefined symmetric matrix, $\gamma_{nm} = \gamma_{mn}$. Hence, direct application of the reciprocity considerations to the simultaneous coupling equations (2) allows one to determine α_{nm} only up to an arbitrary symmetric matrix.

II. MODE COUPLING COEFFICIENTS

Because of the simple relation between the coupling coefficients in the 2-D and 3-D problems, it is sufficient to analyze the coefficients in the 2-D case. We first rearrange expressions (20) to better compare with results reported in the literature. Integrating by parts in the rhs of Eq. (13), one can cast Eq. (20b) as

$$\beta_{nm} = -2B_{nm} + \left(\frac{1}{\rho}\frac{\partial\rho}{\partial x}f_n, f_m\right) + \sum_{j=1}^{N}\left.\frac{\partial h_j}{\partial x}\frac{f_n f_m}{\rho}\right|_{z=h_j^-}^{z=h_j^+}. \tag{24}$$

Using the completeness relationship

$$\sum_n f_n(z;x,y)f_n(z_1;x,y) = \rho(x,y,z)\delta(z - z_1) \tag{25}$$

for the vertical eigenfunctions, the mode coupling coefficient α_{nm} Eq. (20a) can be expressed in terms of quantities pertaining to modes of orders n and m only. Substituting B_{nm} from Eq. (13) and changing order of summation and integration, one obtains from Eqs. (20a) and (25)

$$\alpha_{nm} = -\left(\rho f_n, \frac{\partial}{\partial x}\left(\frac{1}{\rho}\frac{\partial f_n}{\partial x}\right)\right)$$

$$+ \sum_{j=1}^{N}\left.\frac{\partial h_j}{\partial x}\left(\frac{f_n}{\rho}\frac{\partial f_m}{\partial x}\right)\right|_{z=h_j^-}^{z=h_j^+}. \tag{26}$$

Now, let us express the mode coupling coefficients in terms of environmental gradients. Consider the so-called generalized orthogonality relationship (Ref. 6, Sec. 4.5.1), which relates fields of eigenmodes in two different waveguides, or, in the case under consideration, in two different cross sections of the irregular waveguide:

$$0 = \left(\int_0^{h_1} + \cdots + \int_{h_N}^{H}\right)\left[\frac{\partial f_n(z;x,y)}{\partial z}\frac{\partial f_m(z;x_1,y)}{\partial z}\right.$$

$$\times\left(\frac{1}{\rho(x_1,y,z)} - \frac{1}{\rho(x,y,z)}\right) + f_n(z;x,y)f_m(z;x_1,y)$$

$$\times\left(\frac{k^2(x,y,z) - \xi_n^2(x,y)}{\rho(x,y,z)}\right.$$

$$\left.\left. - \frac{k^2(x_1,y,z) - \xi_m^2(x_1,y)}{\rho(x_1,y,z)}\right)\right]dz. \tag{27}$$

[This identity can be easily derived from Eqs. (3) and (4).] Differentiating Eq. (27) with respect to x_1 and putting $x_1 = x$, one finds

$$(\xi_m^2 - \xi_n^2)B_{nm} + \frac{\partial\xi_m^2}{\partial x}\delta_{nm} + \sum_{j=1}^{N}\left.\frac{\partial h_j}{\partial x}\left[\frac{1}{\rho}\frac{\partial f_n}{\partial z}\frac{\partial f_m}{\partial z}\right.\right.$$

$$\left.\left. + \frac{k^2 - \xi_m^2}{\rho}f_n f_m\right]\right|_{z=h_j^-}^{z=h_j^+}$$

$$= \left(\frac{1}{\rho}\frac{\partial\rho}{\partial x}\frac{\partial f_n}{\partial z}, \frac{\partial f_m}{\partial z}\right)$$

$$+ \left(\left[\frac{\partial k^2}{\partial x} + \frac{\xi_m^2 - k^2}{\rho}\frac{\partial\rho}{\partial x}\right]f_n, f_m\right). \tag{28}$$

With $n = m$, Eq. (28) gives the derivative of the mode propagation constant:

$$\frac{\partial\xi_n}{\partial x} = -\frac{1}{2\xi_n}\sum_{j=1}^{N}\left.\frac{\partial h_j}{\partial x}\left[\frac{1}{\rho}\left(\frac{\partial f_n}{\partial z}\right)^2 + \frac{k^2 - \xi_n^2}{\rho}f_n^2\right]\right|_{z=h_j^-}^{z=h_j^+}$$

$$+ \left(\frac{1}{\rho}\frac{\partial\rho}{\partial x}\frac{\partial f_n}{\partial z}, \frac{\partial f_n}{\partial z}\right)$$

$$+ \left(\left[\frac{\partial k^2}{\partial x} + \frac{\xi_n^2 - k^2}{\rho}\frac{\partial\rho}{\partial x}\right]f_n, f_n\right), \tag{29}$$

while at $n \neq m$ it gives off-diagonal terms of the matrix B_{nm}:

$$B_{nm} = (\xi_n^2 - \xi_m^2)^{-1}\left[\sum_{j=1}^{N}\left.\frac{\partial h_j}{\partial x}\left(\frac{1}{\rho}\frac{\partial f_n}{\partial z}\frac{\partial f_m}{\partial z}\right.\right.\right.$$

$$\left.\left.\left. + \frac{k^2 - \xi_m^2}{\rho}f_n f_m\right)\right|_{z=h_j^-}^{z=h_j^+} - \left(\frac{1}{\rho}\frac{\partial\rho}{\partial x}\frac{\partial f_n}{\partial z}, \frac{\partial f_m}{\partial z}\right)\right.$$

$$\left. - \left(\left(\frac{\partial k^2}{\partial x} + \frac{\xi_m^2 - k^2}{\rho}\frac{\partial\rho}{\partial x}\right)f_n, f_m\right)\right]. \tag{30}$$

To determine the diagonal terms, it is sufficient to integrate the definition (13) of B_{nm} by parts:

$$B_{nn} = \left(\frac{f_n}{2\rho}\frac{\partial\rho}{\partial x}, f_n\right) + \sum_{j=1}^{N}\left.\frac{\partial h_j}{\partial x}\frac{f_n^2}{2\rho}\right|_{z=h_j^-}^{z=h_j^+}. \tag{31}$$

Of some interest is the case when the waveguide has a range-variable boundary, either pressure release or rigid, say,

$z = h_N$. Such problems do not require a separate treatment but may be considered as special cases of the problem at hand by transition to the limit $\rho \to 0$ or $\rho \to \infty$ at $h_N < z < H$. It results in two modifications of the above results: (i) integrals over $h_N < z < H$ contribute zero to the inner products in Eqs. (29)–(31); and (ii) under the summation signs in Eqs. (29)–(31), summands should be prescribed zero value at $z = h_N^+$.

Equations (24), (26), and (29)–(31) hold in the 3-D case as well, provided $\nabla_\perp$ is substituted for $\partial/\partial x$ everywhere.

III. DISCUSSION

Let us compare the coupled mode equations of Secs. I and II with the results reported in the literature. With $N = 1$ Eq. (24) for β_{nm} reduces to the earlier result by Brekhovskikh and Godin[13] [see Eqs. (7.1.7, 9, 10, 23, and 24) in Ref. 6]. Equations (19) for $b_{mn}^\pm$ and (20a) for α_{mn} are identical with Eqs. (7.1.34) and (7.1.15) in Ref. 6, respectively. Finally, within the assumptions made in their derivation, Eqs. (7.1.17, 24 and 36) of Ref. 6 for B_{mn} and $\partial \xi_n / \partial x$ agree with the more general Eqs. (29)–(31) of this paper. Hence, treatment of interfaces within a waveguide as a limiting case of smooth but rapid volumetric changes in medium parameters leads to exactly the same results as the strict analysis outlined above. Note, that account of mode coupling due to horizontal gradients of medium density in Ref. 6 is a prerequisite to consider range-dependent interfaces as a limiting case of volumetric inhomogeneities.

In Ref. 7, coupled-mode equations were cast in the form (2) for a 2-D problem. With $N = 1$ and $\partial \rho / \partial x = 0$, our Eqs. (24) and (26) reduce to Fawcett's results[14] [see his Eqs. (11) and (12)]. There are no expressions for the coupling coefficients in Ref. 7 in terms of environmental gradients to compare with our Eqs. (29) and (30). Note the explicit interface contributions to the coupling coefficients as sums over j in Eqs. (24) and (26). The importance of these contributions for a consistent description of bathymetric mode coupling was demonstrated by Fawcett[7] using numerical simulations. It is these contributions which are missing in Eqs. (16) and (17) of Ref. 1. [McDonald's expressions (28) and (29) for B_{mn} and $\partial \xi_n / \partial x$ in terms of environmental gradients agree with our Eqs. (29)–(31) under the unnecessarily restrictive assumptions about the medium density variation made in Ref. 1.] The same deficiency is shared by a number of earlier works on mode coupling, including Refs. 3, 4, 15, and 16.

The procedure of the coupled-mode equations derivation originated by Pierce[9] and Milder[10] and adopted by McDonald[1] and numerous other authors consists of formal term-by-term differentiation of series (1) and substitution of the result into the wave equation. Term-by-term differentiation of an infinite series requires that it converges rapidly enough, a condition which is not met in many acoustic problems of interest. As it is demonstrated in Appendix B by considering two elementary problems admitting explicit closed-form solutions, the formal term-by-term differentiation leads to contradictions and erroneous coupling equations. In the general case, the Pierce–Milder procedure results[1,9,10] in the expressions for the coupling coefficients

(24) and (26), but without explicit interface contributions (sums over j). The formal term-by-term differentiation of series (1) does not lead to incorrect results only when the abovementioned interface contributions are zero or negligible. According to Eqs. (4), (24), and (26), the interface contributions vanish at a pressure-release boundary, at horizontal interfaces and boundaries, and at interfaces without a jump in density. (In all these cases the acoustic field in the waveguide and the local modes obey the same boundary conditions.) It is also important to note that the interface contributions have no effect on the field within the adiabatic approximation. Hence, Pierce's original derivation of the adiabatic approximation[9] in a 3-D waveguide from the coupled-mode equations (2), repeated later in many textbooks, is not compromised by the limited applicability of the term-by-term differentiation of series (1).

One can say that, when mode coupling coefficients are expressed in terms of environmental gradients, bathymetric coupling originates from two sources: first, from the sums over j in Eqs. (24) and (26) and, second, from the sum over j in Eq. (30). Only the latter contribution was accounted for in Ref. 1. According to Eqs. (24) and (30), both contributions are *of the same order* with respect to density contrast at an interface and slope of the latter. (The issue is discussed in more detail for two specific cases in Appendix B.) Hence, it is not consistent to omit the first contribution. It should be emphasized, according to Eqs. (20) and (21), the matrix β_{nm} is always antisymmetric, $\beta_{nm} = -\beta_{mn}$, in a fluid waveguide regardless of range-dependent interfaces or the presence of rigid boundaries. As it was demonstrated in Sec. I above, the antisymmetry is a necessary condition for acoustic reciprocity and energy conservation to be preserved in coupled mode formulation. By omitting the first source of bathymetric coupling this important symmetry property of the matrix β_{nm} was violated in Ref. 1. Relation between energy conservation and β_{nm} antisymmetry is further illustrated in Appendix A through an analysis of explicit solutions of mode coupling equations in the important special case of a waveguide with gradual, slow variation of its parameters in range.

IV. CONCLUSION

The coefficients in the mode coupling equations (9) and (10) are expressed in terms of environmental gradients by Eqs. (19), (29)–(31). For the alternative form of the coupling equations, (2), the coupling coefficients are given by Eqs. (30), (31), and (20) [or (29)] for the 2-D (respectively, 3-D) problem. With these coefficients, the mode coupling equations are an exact reformulation of the wave equation and boundary conditions in terms of modal amplitudes. In particular, these insure, as long as sufficient number of terms is retained in the modal expansion (1), acoustic reciprocity and energy conservation in lossless media.

Bathymetric coupling is not properly accounted for in McDonald's theory.[1] The error occurred at an early stage of analysis, namely, in the derivation of the mode coupling equation (2). The error can be easily corrected by taking into account the true relation (21) between mode coupling coefficients and the matrix $\mathbf{B}_{nm}$ (13) which was properly calculated in Ref. 1.

In Ref. 16 the mode coupling theory[1] was applied to interpret acoustic pulse structure of Heard to Christmas Island transmission. It would be of interest to determine how the indicated corrections to McDonald's theory effect the correspondence between numerical simulations[16] and the HIFT experimental data.

APPENDIX A: ENERGY CONSERVATION AND SYMMETRY OF MODE COUPLING COEFFICIENTS

As mentioned in the Introduction, perhaps the most apparent difference between mode coupling coefficients due to McDonald[1] and those due to Brekhovskikh and Godin (Ref. 6, Sec. 7.1) is their different symmetry properties. It is shown in the main body of the present paper that consistent theory leads to an antisymmetric coupling matrix β_{nm} in the mode coupling equations (2), whereas within the conventional approach[1,9,10] β_{nm} is generally not antisymmetric when a sloping interface or a range-dependent rigid boundary is present. Below, to further clarify its relation to energy conservation, antisymmetry of β_{nm} is derived for a specific problem from physical considerations.

Consider a 2-D problem of sound propagation in a lossless waveguide composed of a range-dependent segment $0 < x < D$ and two semi-infinite range-independent segments $x < 0$ and $x > D$. Then mode amplitudes $F_n(x)$ satisfy the coupling equations

$$\frac{d^2 F_n}{dx^2} + \xi_n^2 F_n = \sum_m \left(\alpha_{nm} F_m + \beta_{nm} \frac{dF_m}{dx} \right). \quad (A1)$$

The coupling matrices α_{nm} and β_{nm} are real. These are nonzero for $0 < x < D$. Assuming a horizontal linear scale L of the waveguide variation that is large compared with the acoustic wavelength, one then has $\alpha_{nm} = O(\epsilon^2)$ and $\beta_{nm} = O(\epsilon)$, where $\epsilon = (kL)^{-1} \ll 1$. Let $F_n^{(0)}$ represent the acoustic field in the limit of no range dependence ($\epsilon = 0$). For gradual range dependence, solving the mode coupling equations (A1) within the Born approximation and using the WKB approximation for the Green's function, we have (Ref. 6, Sec. 7.1.3):

$$F_n(x) = F_n^{(0)}(x) - \frac{i}{2} \int_0^D dx_1 [\xi_n(x_1)\xi_n(x)]^{-1/2}$$

$$\times \exp\left(i \int_{x_<}^{x_>} \xi_n(x_2) dx_2 \right) \sum_m \beta_{nm} \frac{dF_m^{(0)}}{dx} + O(\epsilon^2),$$

$$x_< = \min(x, x_1), \quad x_> = \max(x, x_1). \quad (A2)$$

Now, analyze two particular cases.

(1) A single normal mode with propagation constant $\xi_N(x) > 0$ and unit amplitude is incident on the range-dependent segment of the waveguide from the left. Us-

ing the WKB approximation, one has

$$F_n^{(0)}(x) = \delta_{nN} \left[\frac{\xi_n(0)}{\xi_n(x)} \right]^{1/2} \exp\left(i \int_0^x \xi_n(x_2) dx_2 \right).$$

According to Eq. (A2), the amplitudes of the normal modes scattered by the range-dependent segment into region $x < 0$ are $O(\epsilon)$. For $x > D$, the amplitudes of modes with $n \neq N$ are $O(\epsilon)$ as well. Note that energy flux integrated over waveguide's cross section $x = \text{const}$ is additive for normal modes of different index n and also of the same index but propagating in opposite directions (Ref. 6, Sec. 7.1.1). The abovementioned scattered modes carry energy fluxes $O(\epsilon^2)$. Hence, energy conservation law can be written as

$$\xi_N(0) = \xi_N(D)|F_N(D)|^2 + O(\epsilon^2). \quad (A3)$$

Using Eq. (A2) and equating terms $O(\epsilon)$ in Eq. (A3), one obtains

$$\int_0^D dx_1 \cos\left(\int_0^{x_1} \xi_N(x_2) dx_2 \right) \beta_{NN}(x_1) = 0. \quad (A4)$$

Since D is arbitrary and β_{nm} for $x_1 < D$ does not depend on D, it follows that $\beta_{NN} \equiv 0$.

(2) Two normal modes are incident on the range-dependent segment from the left;

$$F_n^{(0)}(x) = a_N \delta_{nN} \left[\frac{\xi_N(0)}{\xi_N(x)} \right]^{1/2} \exp\left(i \int_0^x \xi_N(x_2) dx_2 \right)$$

$$+ a_M \delta_{nM} \left[\frac{\xi_M(0)}{\xi_M(x)} \right]^{1/2} \exp\left(i \int_0^x \xi_M(x_2) dx_2 \right). \quad (A5)$$

Here a_N and a_M are constant, ξ_N and ξ_M are assumed positive.

In this case, the first-order contributions to the energy flux coming to and from the range-dependent segment arise from perturbation of amplitudes of modes N and M for $x > D$. The energy conservation law takes the form

$$\xi_N(0)|a_N|^2 + \xi_M(0)|a_M|^2$$

$$= \xi_N(D)|F_N(D)|^2 + \xi_M(D)|F_M(D)|^2 + O(\epsilon^2). \quad (A6)$$

The first-order perturbations in mode's N amplitude are solely due to mode's M scattering because of $\beta_{NN} = 0$. Using Eq. (A2) and equating terms $O(\epsilon)$ in Eq. (A6), one obtains

$$\text{Re}\left[a_M a_N^* \int_0^D dx_1 \cos\left(\int_0^{x_1} (\xi_N - \xi_M) dx_2 \right) \right.$$

$$\left. \times [\beta_{NM}(x_1) + \beta_{MN}(x_1)] \right] = 0. \quad (A7)$$

As a_M and a_N are arbitrary, the integral over x_1 in Eq. (A7) should be zero. Again using the arbitrariness of D, we have

$$\beta_{NM}(x) = -\beta_{MN}(x). \quad (A8)$$

Consequently, antisymmetry of the coupling matrix β_{nm} is a necessary condition for energy conservation. Although demonstrated here for a waveguide with weak mode coupling, the conclusion holds in the general case as shown by different means and without any approximations in Sec. I above.

APPENDIX B: CONVERGENCE OF NORMAL MODE EXPANSIONS AND ITS IMPLICATIONS ON MODE COUPLING EQUATIONS: TWO EXAMPLES

Within the conventional approach to mode coupling,[1,9,10] acoustic pressure is represented as expansion (1) in local vertical eigenmodes and substituted into the wave equation assuming that

$$\frac{\partial^2 p}{\partial z^2} + k^2 p = \sum_m F_m(x,y) \xi_m^2(x,y) f_m(z;x,y). \quad (B1)$$

(For simplicity, it is here assumed that medium's density is piecewise constant.) When term-by-term differentiation of the infinite series (1) is valid, Eq. (B1) is certainly true—it follows directly from the 1-D wave equation (3) for local eigenmodes. To demonstrate limited applicability of the term-by-term differentiation of the modal expansion (1), below we present elementary examples when Eq. (B1) does not hold.

It has been argued by Rutherford and Hawker[17] and others (see, for instance, Refs. 1 and 4) that decomposition (1) is inconsistent with boundary conditions at sloping interfaces of fluids of distinct density. The reasoning[1,4] goes as follows. The modal decomposition (1) is differentiated term-by-term with respect to z,

$$\frac{\partial p}{\partial z} = \sum_m F_m \frac{\partial f_m}{\partial z}, \quad (B2)$$

then it follows from the boundary conditions (4b) satisfied by local eigenmodes that $\rho^{-1} \partial p/\partial z$ is continuous at an interface, whereas the true boundary condition requires continuity of $\rho^{-1} \partial p/\partial n$, with $\partial p/\partial n$ being the normal derivative. Obviously, $\partial p/\partial z$ and $\partial p/\partial n$ are generally different at a sloping interface.

On the other hand, the acoustic field is represented *exactly* by expansion (1) at any point away from boundary because eigenmodes comprise a complete set of functions. The mode expansion should therefore ensure fulfilment of the correct boundary conditions.

This apparent contradiction is resolved by noting that Rutherford–Hawker reasoning *implicitly assumes* that the series in the rhs of Eq. (B2) converges to $\partial p/\partial z$ at the point on the boundary. It is the latter assumption, not boundary conditions, that is violated at a sloping rigid boundary and an interface.

To illustrate, consider the 2-D acoustic field in a wedge (Fig. B1) in which the homogeneous fluid occupies the domain $x > 0$, $0 < z < h(x) = x \tan \alpha$, bounded above by a
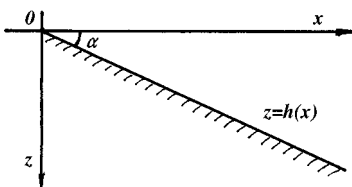
FIG. B1. Wedge-shaped waveguide.

pressure-release surface $z = 0$ and below by a rigid boundary $z = h(x)$. Consider a wedge mode propagating down slope:

$$p(x,z) = \sin\left(\nu \arctan \frac{z}{x} \right) H_\nu^{(11)}(k(x^2+z^2)^{1/2}),$$

$$\nu = (N+1/2)/\alpha. \quad (B3)$$

Here $N \geq 0$ is an integer and $H_\nu^{(1)}$ is the Hankel function. The field (B3) is an exact solution of the 2D boundary-value problem. Note that $\partial p/\partial n = 0$ but $\partial p/\partial z = \tan \alpha \, \partial p/\partial x \neq 0$ at $z = h(x)$. For the wedge, the normalized local eigenmodes are

$$f_n(z;x) = (2\rho/h)^{1/2} \sin[(2n+1)\pi z/h], \quad h = h(x), \quad (B4)$$

whereas range-dependent mode amplitudes in Eq. (1) are given by the integrals

$$F_n(x) = \left(\frac{2}{\rho h} \right)^{1/2} \int_0^h dz \, \sin[(2n+1)\pi z/h] p(x,z). \quad (B5)$$

Note that for an arbitrary smooth function ϕ

$$\int_0^h da \, \phi(a) \sin \mu a = -\left[\frac{\cos \mu a}{\mu} (\phi - \mu^{-2}\phi'') \right.$$
$$\left. - \frac{\sin \mu a}{\mu^2} (\phi' - \mu^{-2}\phi''') \right]\Bigg|_{a=0}^{a=h}$$
$$+ O(\mu^{-5}). \quad (B6)$$

This identity is easily obtained by integrating by parts. Another mathematical formula we will need in what follows is

$$\frac{1}{2} - |1-a| = -\frac{4}{\pi} \sum_{m=1}^{+\infty} \frac{\cos[\pi(2m-1)a]}{(2m-1)^2}$$
$$= \frac{4}{\pi} \sum_{m=1}^{+\infty} (-1)^m \frac{\sin[\pi(2m-1)(a-1/2)]}{(2m-1)^2},$$
$$0 \leq a \leq 2. \quad (B7)$$

It is simply the Fourier expansion of the leftmost side of Eq. (B7) into functions $\sin \pi n a$ and $\cos \pi n a$.

Applying Eq. (B6) to the integral (B5), one can represent p as a sum of fields $p^{(1)} + p^{(2)}$ with mode amplitudes $F_m^{(1)}$ and $F_m^{(2)}$, respectively, equal to

$$F_m^{(1)}(x) = \frac{4h}{\pi^2} \sqrt{\frac{2h}{\rho}} p_z(x,h) \frac{(-1)^m}{(2m+1)^2},$$
$$F_m^{(2)}(x) = O(m^{-4}). \quad (B8)$$

Because of rapid decrease of its coefficients with m increasing, the series (1) for $p^{(2)}$ can be differentiated twice with respect to z term-by-term.[18] (Indeed, the twice differentiated series can be majorized by a convergent series const$\cdot\Sigma m^{-2}$ and, hence, converges absolutely.[18]) Equation (B2) is therefore correct with $p = p^{(2)}$ and $F_m = F_m^{(2)}$, and $\partial p^{(2)}(x,h(x))/\partial z = 0$ for $\partial f_m/\partial z = 0$ on the boundary.

For the same reason, $\Sigma F_m^{(1)} \partial f_m/\partial z = 0$ at $z = h(x)$. However, it would be *wrong* to conclude that
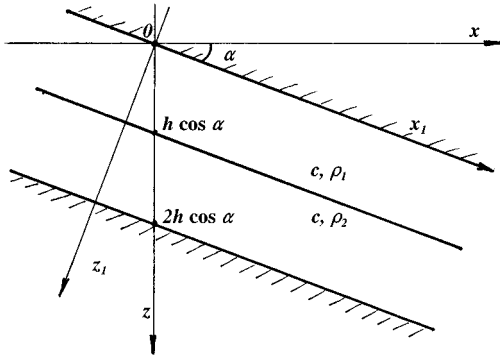
FIG. B2. ''Rotated'' waveguide.

$\partial p^{(1)}(x,h(x))/\partial z=0$ because the latter series does not converge to $\partial p^{(1)}/\partial z$ at $z=h$. Indeed, it follows from Eqs. (B7) and (B8) that

$$p^{(1)}(x,z)=z\,\frac{\partial p(x,h)}{\partial z}=z\,\tan\,\alpha\,\frac{\partial p(x,h)}{\partial x}. \tag{B9}$$

For a given range x, $p^{(1)}$ is a linear function of depth. It is now evident that the mode expansion (1) obeys the same boundary conditions as Eq. (B3), not the boundary condition $\partial p/\partial z=0$, in direct contradiction to Hawker–Rutherford argument. Moreover, as $\partial^2 p^{(1)}/\partial z^2\equiv0$ at $0<z<h(x)$, we have

$$\frac{\partial^2 p}{\partial z^2}=\sum_m\,(\xi_m^2-k^2)F_m^{(2)}(x)f_m(z;x). \tag{B10}$$

If the Pierce–Milder equation (B1) were correct for the wedge, there would be $F_m^{(1)}+F_m^{(2)}$ instead of $F_m^{(2)}$ in Eq. (B10). Furthermore, according to Eqs. (B4) and (B8), the resulting infinite series would be *divergent* in the problem at hand.

As a second example, consider sound propagation in a two layered isovelocity waveguide $-\infty<x_1<+\infty$ with pressure-release boundaries $z_1=0$ and $z_1=2h$ (Fig. B2). Fluid's density ρ takes value ρ_1 at $0<z_1<h$ and ρ_2 at $h<z_1<2h$. Let the waveguide boundaries make an acute angle α with the x-axis, that is, two Cartesian coordinate systems are related by the equations: $x_1=x\cos\,\alpha-z\sin\,\alpha$, $z_1=x\sin\,\alpha+z\cos\,\alpha$, $y_1=y$. In (x,y,z) coordinates one has a ''rotated'' waveguide. It is a range-dependent waveguide with local vertical eigenfunctions

$$f_n=Q_n\,\sin[\mu_n(z-h_1)],\quad h_1=-x\,\tan\,\alpha,$$

$$\mu_n=\pi n\,\cos\,\alpha/2h,$$

$$Q_n=\left[\frac{2\rho_1\rho_2\,\cos\,\alpha}{h(\rho_1+\rho_2)}\right]^{1/2},\quad n=2m-1; \tag{B11}$$

$$Q_n=\left[\frac{2\,\cos\,\alpha}{h(\rho_1+\rho_2)}\right]^{1/2}\rho,\quad n=2m;\quad m=1,2,...$$

corresponding to a two layered waveguide of thickness $2h/\cos\,\alpha$. The local propagation constants $\xi_n=(k^2-\mu_n^2)^{1/2}$ are range independent. Note that ρ and Q_{2m} are discontinuous at the layers' common interface $z=H(x)$, $H(x)=h_1$

$+h/\cos\,\alpha$, but f_n in Eq. (B11) and $\rho^{-1}\partial f_n/\partial z$ are, of course, continuous.

The acoustic field

$$p=\exp(i\gamma x_1)\sin\,\nu z_1$$

$$=\exp[i\gamma(x/\cos\,\alpha-(z-h_1)\sin\,\alpha)]$$

$$\times\sin[\nu\,\cos\,\alpha(z-h_1)] \tag{B12}$$

with $\gamma=(k^2-\nu^2)^{1/2}$, $\nu=\pi(N+1/2)/h$, and integer N is a normal mode of the rotated waveguide. It is an exact solution of the 2-D boundary-value problem. Using Eq. (B11), for the mode amplitudes in expansion (1) of the acoustic field p Eq. (B12), one obtains

$$F_n(x)=\int_{h_1}^{h_1+2h/\cos\,\alpha}\frac{dz}{\rho}\,p(x,z)f_n(z;x)$$

$$=e^{i\gamma x/\cos\,\alpha}\int_0^{h/\cos\,\alpha}\sin(\mu_n a)\phi_n(a)da, \tag{B13}$$

$$\phi_{2m}=2i[2\,\cos\,\alpha/h(\rho_1+\rho_2)]^{1/2}$$

$$\times\exp(-i\gamma h\,\tan\,\alpha)\sin(\nu a\,\cos\,\alpha)$$

$$\times\sin[\gamma\,\sin\,\alpha(h/\cos\,\alpha-a)],$$

$$\phi_{2m-1}=\left[\frac{2\rho_1\rho_2\,\cos\,\alpha}{h(\rho_1+\rho_2)}\right]^{1/2}e^{-i\gamma h\,\tan\,\alpha}\,\sin(\nu a\,\cos\,\alpha)$$

$$\times\left[\frac{1}{\rho_1}e^{i\gamma\,\sin\,\alpha(h/\cos\,\alpha-a)}\right.$$

$$\left.+\frac{1}{\rho_2}e^{-i\gamma\,\sin\,\alpha(h/\cos\,\alpha-a)}\right]. \tag{B14}$$

Integrals over a in Eq. (B13) can be easily evaluated in the closed form. Instead of writing down cumbersome exact expressions, we use Eq. (B6) to obtain $F_m=F_m^{(1)}+F_m^{(2)}$,

$$F_{2m-1}^{(1)}=(-1)^{N+m}\frac{4i\gamma h\,\tan\,\alpha}{\pi^2(2m-1)^2}\,[2h/\rho_1\rho_2(\rho_1$$

$$+\rho_2)\cos\,\alpha]^{1/2}(\rho_1-\rho_2)\exp(i\gamma x/\cos\,\alpha$$

$$-i\gamma h\,\tan\,\alpha), \tag{B15}$$

$$F_{2m}^{(1)}=0;\quad F_n^{(2)}=O(n^{-3}).$$

Much as in the previous example, designate $p^{(1)}$ and $p^{(2)}$ sums of mode expansions (1) with coefficients $F_m^{(1)}$ and $F_m^{(2)}$, respectively. And here again $p^{(2)}$ can be differentiated term-by-term twice with respect to z because of $F_m^{(2)}$ rapid decrease with m increasing; the series in the rhs of Eq. (B2) with $F_m^{(2)}$ substituted for F_m converges absolutely to $\partial p^{(2)}/\partial z$ at $0\leq z-h_1<h/\cos\,\alpha$ and $h/\cos\,\alpha<z-h_1\leq2h/\cos\,\alpha$ making $\rho^{-1}\,\partial p^{(2)}/\partial z$ continuous at the interface $z=H(x)$.

Now, consider $p^{(1)}$. The mode expansion (1) for $p^{(1)}$ can be summed using Eqs. (B7), (B11), and (B15) giving

$$p^{(1)}(x,z) = (-1)^N i\gamma h \sin \alpha \frac{\rho_1 - \rho_2}{\rho_1 + \rho_2} e^{i\gamma(x \cos \alpha - h \tan \alpha)}$$

$$\times \left(1 - \frac{|z \cos \alpha + x \sin \alpha - h|}{h} \right). \quad (B16)$$

Amplitude of $p^{(1)}$ is zero at waveguide's boundaries and reaches its maximum at the interface. Contrary to the assumption implicit in the Rutherford–Hawker argument, series (B2) with $F_m^{(1)}$ substituted for F_m *does not converge* to $\partial p^{(1)}/\partial z$ at a vicinity of the interface. Indeed, $\rho^{-1} \partial f_n/\partial z$ are continuous at the interface, whereas $\rho^{-1} \partial p^{(1)}/\partial z$ is discontinuous:

$$\frac{1}{\rho} \frac{\partial p^{(1)}}{\partial z}\bigg|_{z=H^-(x)}^{z=H^+(x)} = (-1)^N i\gamma(\rho_1^{-1} - \rho_2^{-1})\exp[i\gamma(x \cos \alpha$$

$$- h \tan \alpha)]. \quad (B17)$$

By using Eq. (B17) and differentiating (B12), it is easy to check that the mode expansion, $p^{(1)} + p^{(2)}$, and the original field obey the same boundary conditions at the interface, as it is to be expected.

If the Pierce–Milder equation (B1) were correct, then

$$\int_{h_1}^{h_1 + h/\cos \alpha} \frac{dz}{\rho_1} f_n \frac{\partial^2 p}{\partial z^2} + \int_{h_1 + h/\cos \alpha}^{h_1 + 2h/\cos \alpha} \frac{dz}{\rho_2} f_n \frac{\partial^2 p}{\partial z^2}$$

$$= (\xi_n^2 - k^2)(F_n^{(1)} + F_n^{(2)}) \quad (B18)$$

because of local mode orthogonality (5). Noting that $\partial^2 p^{(1)}/\partial z^2 \equiv 0$ in both fluid layers, one has instead an expression which differs from Eq. (B18) by substitution of $F_m^{(2)}$ for $F_m^{(1)} + F_m^{(2)}$ in the rhs. [The latter expression can be also obtained by first integrating the lhs of Eq. (B18) by parts and then substituting convergent series (1) for p in the integrand.] The contradiction demonstrates again that term-by-term differentiation of the mode expansion (1) leads to erroneous results when a sloping interface of fluids of distinct densities is present. An extra term in the rhs of Eq. (B18) is directly related to the difference between mode coupling coefficients derived in the main body of the paper and those of Refs. 1, 9, and 10.

To quantify the difference, for the two particular waveguides considered compare values of coupling coefficients β_{nm} in Eq. (2) in the rigorous theory and in Ref. 1. [Coupling coefficients α_{nm}, which are also present in Eq. (2), were not calculated in Ref. 1.] In the McDonald's theory,[1] $-2B_{nm}$ enters Eq. (2) instead of β_{nm}. The first difference between the two expressions for the coupling coefficients is that at $n = m$ $\beta_{nm} = 0$ but, according to Eqs. (31) and (B4), $B_{nm} \neq 0$ for the wedge-shaped waveguide. For the rotated waveguide, according to Eq. (B11), $B_{nn} \neq 0$ when n is an odd number. As discussed in Appendix A and in the main body of the paper, nonzero diagonal elements of the coupling matrix β_{nm} lead to violations of energy conservation and reciprocity.

At $n \neq m$ designate the ratio of coupling coefficients between the same modes in the two theories as

$$q_{nm} = -2B_{nm}/\beta_{nm}. \quad (B19)$$

For the wedge-shaped waveguide, from Eqs. (24), (30), and (B4) one has

$$q_{nm} = 2(2m+1)^2/[(2m+1)^2 + (2n+1)^2]. \quad (B20)$$

The ratio q_{nm} is an increasing function of m and decreasing function of n, $0 < q_{nm} < 2$, $q_{nm} > 1$ at $n < m$ and $q_{nm} < 1$ at $n > m$. With one of the indices tending to infinity, q_{nm} tends to 0 or 2. So, McDonald's theory[1] exaggerates excitation of low-order modes by high-order ones while underestimating scattering of low-order modes into high-order ones. With orders of the interacting modes sufficiently different, the quantitative error in the rate of coupling can be arbitrarily close to 100%.

For the rotated waveguide, the difference between the expressions for the coupling coefficients occur when n and m are odd numbers, $n = 2n_1 + 1$ and $m = 2m_1 + 1$. Then it follows from Eqs. (24), (30), and (B11) that q_{nm} is given again by Eq. (B20) but with n_1 instead of n and m_1 instead of m. For instance, for coupling between the first and seventh modes one has from Eq. (B20) $q_{1,7} = 1.96$ and $q_{7,1} = 0.04$. Note that q_{nm} depends on neither the interface slope nor density contrast. Consequently, however small or large the contrast and the slope are, the conventional approach[1,9,10] leads to up to 100% errors in the bathymetric contributions to mode coupling coefficients.

[1] B. E. McDonald, ''Bathymetric and volumetric contributions to ocean acoustic mode coupling,'' J. Acoust. Soc. Am. **100**, 219–224 (1996).

[2] A. Baggeroer and W. Munk, ''The Heard Island feasibility test,'' Phys. Today **45**, 22–30 (1992).

[3] R. D. Graves, A. Nagl, H. Überall, and G. L. Zarur, ''Range-dependent normal modes in underwater sound propagation: Application to the wedge-shaped ocean,'' J. Acoust. Soc. Am. **58**, 1171–1177 (1975).

[4] S. T. McDaniel, ''Mode coupling due to interaction with the seabed,'' J. Acoust. Soc. Am. **72**, 916–923 (1982).

[5] C. A. Boyles, ''Coupled mode solution for a cylindrically symmetric oceanic waveguide with range and depth dependent refractive index and a time varying rough sea surface,'' J. Acoust. Soc. Am. **73**, 800–805 (1983).

[6] L. M. Brekhovskikh and O. A. Godin, *Acoustics of Layered Media. 2: Point Sources and Bounded Beams*, Springer Series on Wave Phenomena, Vol. 10 (Springer-Verlag, Berlin, 1992).

[7] J. A. Fawcett, ''A derivation of the differential equations of coupled mode propagation,'' J. Acoust. Soc. Am. **92**, 290–295 (1992).

[8] A. W. Snyder and J. D. Love, *Optical Waveguide Theory* (Chapman and Hall, London, 1983).

[9] A. D. Pierce, ''Extension of the method of normal modes to sound propagation in an almost-stratified medium,'' J. Acoust. Soc. Am. **37**, 19–27 (1965).

[10] D. M. Milder, ''Ray and wave invariants for SOFAR channel propagation,'' J. Acoust. Soc. Am. **46**, 1259–1263 (1969).

[11] A. F. Stevenson, ''Exact and approximate equations for waves propagating in acoustic horns,'' J. Appl. Phys. **22**, 1461–1463 (1951).

[12] B. Z. Katsenelenbaum, ''On the theory of irregular acoustic waveguides,'' Sov. Phys. Acoust. **7**, 159–164 (1961).

[13] Regrettably, a number of misprints have slipped into Sec. 7.1 of our book (Ref. 6). In particular, the right hand sides of Eqs. (7.18, 23) and $d\eta/dx$ in (7.1.22) should be taken with the opposite sign; in the second line of Eq. (7.1.24) $(1/\rho_1 - 1/\rho_2)$ is to be substituted by $(\rho_1 - \rho_2)$. In comparing the results of the present paper to those of Ref. 6, we assume the misprints have been corrected.

[14] There are some misprints and notational differences in Ref. 7. In particular, the right hand sides of Eqs. (9), (10), (12c), and (12d) should be taken with the opposite sign to correspond to positive $H(x)$ in the positive z direction. Equations (12a) and (12b) have to be interchanged. Numerical simulations reported in Ref. 7 have been carried out with correct values of the coupling coefficients (J. A. Fawcett, private communication). In com-

paring the results of the present paper to those of Ref. 7, we assume the misprints have been corrected.

[15] J. F. Miller, A. Nagl, and H. Überall, ''Sound propagation in a range-dependent shallow ocean with a bottom containing vertical sound speed gradients,'' in *Progress in Underwater Acoustics*, edited by H. M. Merklinger (Plenum, New York, 1987), pp. 533–540.

[16] B. E. McDonald, M. D. Collins, W. A. Kuperman, and K. D. Heaney, ''Comparison of data and model predictions for Heard Island acoustic transmissions,'' J. Acoust. Soc. Am. **96**, 2357–2370 (1994).

[17] S. R. Rutherford and K. E. Hawker, ''Consistent coupled mode theory of sound propagation for a class of nonseparable problems,'' J. Acoust. Soc. Am. **70**, 554–564 (1981).

[18] G. A. Korn and T. M. Korn, *Mathematical Handbook for Scientists and Engineers* (McGraw-Hill, New York, 1968).

Bistatic bottom scattering: Model, experiments, and model/data comparison

Kevin L. Williams and Darrell R. Jackson
Applied Physics Laboratory, College of Ocean and Fishery Sciences, University of Washington,
1013 NE 40th Street, Seattle, Washington 98105

A model is presented for bistatic scattering from ocean sediments. It treats scattering due to both roughness of the seabed and volume inhomogeneities within the sediment. Accordingly, the scattered intensity is assumed to be a sum of two terms, one proportional to the roughness-scattering cross section and the other proportional to the volume-scattering cross section. The model is tested against data acquired as part of the Coastal Benthic Boundary Layer (CBBL) research program. As part of that program, an autonomous, circularly scanning sonar system was deployed in well-characterized regions. This sonar operated at 40 kHz, had a 5° horizontal beam, and acquired backscattering data over a 50-m radius. During part of the deployment, it operated in conjunction with a mobile receiving array so as to acquire bistatic data. The experimental apparatus and procedures are presented, and results are compared with model predictions. © *1998 Acoustical Society of America.* [S0001-4966(98)02201-2]

PACS numbers: 43.30.Bp, 43.30.Dr, 43.30.Gv, 43.30.Ma [JHM]

INTRODUCTION

The model for bistatic scattering from the seabed discussed here is an extension of the model for high-frequency backscatter strength presented by Jackson *et al.*[1] in 1986, improved by Mourad and Jackson,[2] and employed by Jackson and Briggs.[3] The model is intended for use at high frequencies (10–100 kHz). A brief discussion of the bistatic model has been given by Jackson,[4] and references to prior work by other investigators can be found in Refs. 1–3.

Backscattering of high-frequency (10–100 kHz) acoustic energy from the seabed has been the subject of investigation for many years.[1] Recent interest in scattering geometries where the transmitter and receiver are not colocated has led to the development of a bistatic scattering model that incorporates much of the same physics as the backscattering model of Ref. 2. In particular, it includes contributions to scattering from both the rough sediment interface and inhomogeneities within the sediment. Both the model and its incorporation into an integral expression for bistatic scattered intensity are given in Sec. I.

Tests of the bistatic model require both acoustic experiments in which specified geometries can be accurately realized and concurrent determination of the environmental parameters needed as inputs to the model. Such was the case in the experiments described in Sec. II. Both backscattering and bistatic scattering experiments are described, since the bistatic model includes backscattering as a special case.

The fundamental quantity predicted by the model is the bistatic scattering strength. Section III compares model predictions and experimental results for two different sediments. The expression for the scattered intensity given in Sec. I plays a fundamental role in this comparison.

I. BISTATIC MODEL AND SCATTERED INTENSITY CALCULATIONS

The bistatic scattering strength model is presented in Sec. I A and its incorporation into expressions for calculating scattered intensity is discussed in Sec. I B. The expressions for scattered intensity are the direct link between the model and the experiments, from which values for bistatic scattering strength are obtained using a method defined in Secs. I B and III.

The bistatic scattering model is a generalization of a backscattering model that has been tested against data with good results.[1–3] The model treats scattering due to both roughness of the seabed and inhomogeneities in the sediment volume. Accordingly, the intensity is assumed to be a sum of two terms, one proportional to the roughness-scattering cross section and the other to the volume-scattering cross section. It is assumed that the acoustic penetration of the seabed is slight, so sediment volume scattering can be described as a surface process and quantified by an effective interface scattering cross section.

A major assumption in the model is that the sediment can be treated as a lossy fluid; any effects due to elasticity or porosity are neglected. It is further assumed that there are no gradients in sediment properties, apart from the random fluctuations responsible for volume scattering. Thus the sediment can be characterized by three parameters: mass density, sound speed, and acoustic absorption coefficient. The seabed relief is assumed to be an isotropic, two-dimensional Gaussian random process completely determined by a spectral density that follows a simple power law in wave number. This adds two more parameters to the model: the exponent of the power law and a parameter that sets the overall spectral level. The spectrum of volume inhomogeneities is also assumed to follow a power-law form, which adds the final three parameters to the model: the exponent of the power law, a parameter that sets the overall spectral level, and a parameter that relates density and compressibility fluctuations. Volume scattering is assumed to be weak in the sense that the scattered field is much smaller in magnitude than the incident field (defined as the field that would exist in the sediment in the absence of volume scattering).
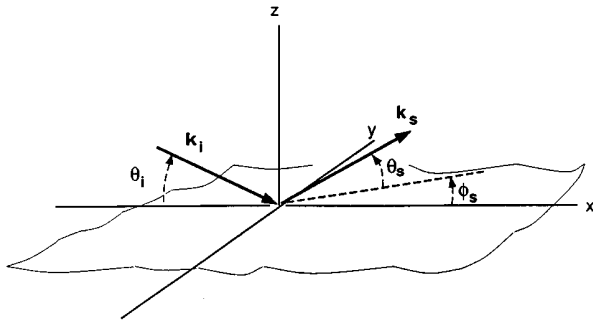
FIG. 1. Definition of bistatic angles.

The link between the bistatic scattering model and the experiments is the model for the intensity of scattering from the seabed as a function of time. The experiments used transmitters and receivers with known beam patterns and measured their separation, orientation, and height above the bottom. The transmitted pulses were short (2 ms). In the experiments, the energy received at any point in time thus depends not only on the bistatic scattering cross section of the seabed, but also on the geometrical parameters and the type of pulse used. The intensity model accounts for all these factors via an integration over the area of the seabed that is scattering energy into the receiver at any point in time. The results of this integration were directly compared with the experimental results, and, where appropriate (see Sec. III), experimental values for bistatic scattering strength and the associated bistatic angles were extracted.

A. Bistatic model

1. Definitions

The equation for bistatic scattering strength is of the form

$$S_b(\theta_s, \phi_s, \theta_i) = 10 \log[\sigma_{br}(\theta_s, \phi_s, \theta_i)$$
$$+ \sigma_{bv}(\theta_s, \phi_s, \theta_i)], \qquad (1)$$

where log is base 10 and $\sigma_{br}(\theta_s, \phi_s, \theta_i)$ and $\sigma_{bv}(\theta_s, \phi_s, \theta_i)$ are, respectively, the roughness and volume contributions to the scattering cross section per unit area. The angles θ_s, ϕ_s, and θ_i are defined in Fig. 1. The incident grazing angle is denoted θ_i, the scattered grazing angle is denoted θ_s, and the bistatic angle, defined as the difference in azimuth between the incident and scattered directions, is denoted ϕ_s. In general, one needs four angles to describe bistatic scattering, two grazing angles and two azimuths; however, only the azimuthal difference is needed here because bottom statistics are assumed to be transversely isotropic. Later expressions for the scattering cross section will employ the following geometric parameters:

$$\Delta_t = \tfrac{1}{2}[(\cos \theta_i)^2 - 2 \cos \theta_i \cos \theta_s \cos \phi_s + (\cos \theta_s)^2]^{1/2} \qquad (2)$$

and

$$\Delta_z = \tfrac{1}{2}(\sin \theta_i + \sin \theta_s). \qquad (3)$$

These dimensionless parameters are proportional, respectively, to the transverse and vertical components of the

change in the acoustic wave vector upon scattering. A parameter proportional to the magnitude of the change is also used:

$$\Delta = \sqrt{\Delta_t^2 + \Delta_z^2}. \qquad (4)$$

The bistatic model treats the sediment as a fluid, homogeneous except for fluctuations responsible for volume scattering. The mean values of fluid properties are defined by three dimensionless mean ratios, ρ, ν, and δ. These are, respectively, the sediment/water density ratio, the sediment/water sound-speed ratio, and the ratio of imaginary to real wave number in the sediment. The statistics of the sediment properties are assumed to be spatially stationary; thus the ratios defined above are independent of position, that is, there are no gradients in the mean parameters.

The surface roughness part of the bistatic model uses the Kirchhoff approximation near the specular direction. In other directions, it employs the small-roughness perturbation approximation. Bottom roughness is assumed to be a random process described by a two-parameter, isotropic, two-dimensional roughness spectral density:

$$W(K) = \frac{w_2}{(h_0 K)^{\gamma_2}}, \qquad (5)$$

where K is the magnitude of the two-dimensional wave vector and the spectrum is normalized so that the integration over a finite region in K space gives the mean-square vertical deviation of the seabed from the mean plane due to those Fourier components included in the integration (the spectrum includes both positive and negative wave vector components). The exponent is restricted to the range

$$2 \leq \gamma_2 \leq 4. \qquad (6)$$

The parameter w_2 in Eq. (5) gives the strength of the spectrum and has dimensions (length).[4] The parameter h_0 is simply a reference length needed to balance dimensions in the equation. It is assigned the numerical value 1 and hence does not appear in calculations.

The volume-scattering portion of the bistatic model is an improvement on the backscattering phenomenological approach.[1-3] The bistatic model uses perturbation theory for volume scattering along the lines developed by Ivakin and Lysanov,[5] Hines,[6] Tang,[7] Lyons et al.,[8] and Yamamoto.[9] Where the older backscatter model employed a single parameter to quantify sediment volume scattering strength, the bistatic model requires three parameters to characterize spectra for inhomogeneities in density and compressibility. The spectrum for density fluctuations is taken to be of the same power-law form as the roughness spectrum:

$$W_{\rho\rho}(k) = \frac{w_3}{(h_0 k)^{\gamma_3}}. \qquad (7)$$

This spectrum is isotropic and normalized such that an integral over a finite volume of k space yields the mean-square density fluctuation divided by the square of the mean density. Compressibility fluctuations are treated analogously and are assumed to be proportional to the density fluctuations. This is equivalent to assumptions used by other authors.[5,8] Thus the spectrum of compressibility fluctuations is

TABLE I. Bottom parameters used as model inputs.

Symbol	Definition	Short name	Eckernförde	Panama City
ρ	Ratio of sediment mass density to water mass density	Density ratio	1.18	1.97
ν	Ratio of sediment sound speed to water sound speed	Sound speed ratio	0.991	1.126
δ	Ratio of imaginary wave number to real wave number for the sediment	Loss parameter	0.001 86	0.0166
γ_3	Exponent of sediment inhomogeneity spectrum	Inhomogeneity exponent	4	4
w_3	Strength of sediment inhomogeneity spectrum (cm^3) at wave number $(2\pi)/\lambda = 1\ cm^{-1}$	Inhomogeneity strength	0.000 13	0.000 016 1
μ	Ratio of compressibility to density fluctuations in the sediment	Fluctuation ratio	-0.69	-2.44
γ_2	Exponent of the bottom relief spectrum	Spectral exponent	3.42	3.12
w_2	Strength of bottom relief spectrum (cm^4) at wave number $(2\pi)/\lambda = 1\ cm^{-1}$	Spectral strength	0.002 31	0.008 49

$$W_{KK} = \mu^2 W_{\rho\rho}, \qquad (8)$$

and the cross spectrum is

$$W_{\rho K} = \mu W_{\rho\rho}, \qquad (9)$$

where μ is a dimensionless parameter and is one of the eight environment parameters needed to calculate bistatic scattering under the assumptions of the present model. These eight parameters are defined in Table I and were described in the third paragraph of Sec. I. Also given in Table I are the numerical values used for these parameters for the two sites examined experimentally. With these definitions in hand, we are now ready to discuss the roughness and volume cross sections of Eq. (1).

2. Bistatic roughness scattering

In this section, expressions are presented for the bistatic cross sections in the Kirchhoff and perturbation approximations. The net roughness-scattering cross section, $\sigma_{br}(\theta_s, \phi_s, \theta_i)$, appearing in Eq. (1) is formed by smooth interpolation between the Kirchhoff cross section near the specular direction and the perturbation-theory cross section elsewhere. The interpolation between these two approximations is defined so that the smaller cross section takes precedence. This procedure is based on the fact that, for power-law spectra, the perturbation approximation overpredicts scattering near the specular direction owing to the singularity in the relief spectrum at zero wave number. In contrast, the Kirchhoff approximation tends to overpredict in other directions.[10] The interpolation scheme used here is

$$\sigma_{br}(\theta_s, \phi_s, \theta_i) = [\sigma^\eta_{kr}(\theta_s, \phi_s, \theta_i)$$
$$+ \sigma^\eta_{pr}(\theta_s, \phi_s, \theta_i)]^{1/\eta}, \qquad (10)$$

with $\eta = -2$. The σ_{kr} and σ_{pr} cross-section expressions are defined next and are standard results, expressed here in notation convenient to the bistatic application.

a. Kirchhoff approximation. Analogous to the monostatic expression used by Jackson *et al.*,[1] the bistatic Kirchhoff cross section[11,12] can be expressed in the following form:

$$\sigma_{kr}(\theta_s, \phi_s, \theta_i) = \frac{|R(\theta_{is})|^2}{8\pi} \left(\frac{\Delta^2}{\Delta_z \Delta_t} \right)^2$$
$$\times \int_0^\infty e^{-qu^{2\alpha}} J_0(u) u\ du, \qquad (11)$$

where

$$q = 2k^2 \Delta_z^2 C_h^2 (2k\Delta_t)^{-2\alpha}. \qquad (12)$$

In Eqs. (11) and (12), $J_0(u)$ is the zeroth-order Bessel function of the first kind and k is the acoustic wave number in water. The parameters α and C_h are roughness structure function parameters related to γ_2 and w_2 as follows:

$$\alpha = \frac{\gamma_2}{2} - 1 \qquad (13)$$

and

$$C_h^2 = \frac{2\pi w_2 \Gamma(2-\alpha) 2^{-2\alpha}}{h_0^{\gamma_2} \alpha (1-\alpha) \Gamma(1+\alpha)}. \qquad (14)$$

The function $R(\theta_{is})$ is the complex plane-wave reflection coefficient (the so-called Rayleigh or Fresnel reflection coefficient) for a flat interface separating water and sediment. It can be expressed in terms of the parameters ρ, ν, and δ^2 and is evaluated at the grazing angle

$$\theta_{is} = \arcsin(\Delta). \qquad (15)$$

This angle is not the actual incident or scattered grazing angle relative to the horizontal; rather, it is the grazing angle that would result if the seabed were tipped in such a way as to provide specular reflection between the transmitter and receiver. Thorsos (private communication) finds that this value gives improved accuracy compared to other choices, as reflection from suitably oriented facets tends to dominate the scattering process near the specular direction.

b. Perturbation approximation. The bistatic back-scattering cross section computed in the perturbation approximation[13–15] can be put in the following form:[15]

$$\sigma_{pr}(\theta_s,\phi_s,\theta_i)=\tfrac{1}{4}k^4|1+R(\theta_i)|^2$$
$$|1+R(\theta_s)|^2|G|^2W(2k\Delta_t).\qquad(16)$$

Equation (16) involves the reflection coefficient and roughness spectral density discussed earlier. The argument of the roughness spectral density is the ''Bragg wave number.'' The complex function G is

$$G=\left(\frac{1}{\rho}-1\right)\left[\cos\theta_i\cos\theta_s\cos\phi_s-\frac{P(\theta_i)P(\theta_s)}{\rho}\right]$$
$$+1-\frac{\kappa^2}{\rho}.\qquad(17)$$

In Eq. (17),

$$\kappa=\frac{1+i\delta}{\nu}\qquad(18)$$

is the complex wave number in the sediment divided by the real wave number in water and

$$P(\theta)=\sqrt{\kappa^2-(\cos\theta)^2}.\qquad(19)$$

3. Sediment bistatic volume scattering

Mourad and Jackson[2] used a volume scattering expression similar to that of Stockhausen[16] in their backscatter model. The bistatic equivalent is readily obtained. It relates the sediment volume-scattering cross section, σ_v, to the effective interface bistatic scattering cross section, $\sigma_{bv}(\theta_s,\phi_s,\theta_i)$, appearing in Eq. (1):

$$\sigma_{bv}(\theta_s,\phi_s,\theta_i)=\frac{|1+R(\theta_i)|^2|1+R(\theta_s)|^2\sigma_v}{2k\rho^2\ \mathrm{Im}[P(\theta_i)+P(\theta_s)]}.\qquad(20)$$

Perturbation theory is used to obtain the volume-scattering cross section, σ_v. Adapting a result given by Ishimaru[17] to the present situation and using Eqs. (7)–(9) yields

$$\sigma_v=\frac{\pi}{2}k^4|\mu\kappa^2+\cos\theta_i\cos\theta_s\cos\phi_s$$
$$-P(\theta_i)P(\theta_s)|^2W_{\rho\rho}(\Delta k).\qquad(21)$$

Acoustic loss in the sediment has been included by allowing the wave number in the sediment to be complex. The spectrum $W_{\rho\rho}$ is evaluated at the Bragg wave number for volume scattering, which is the magnitude of the difference between the real parts of the incident and scattered three-dimensional wave vectors (defined in the sediment).
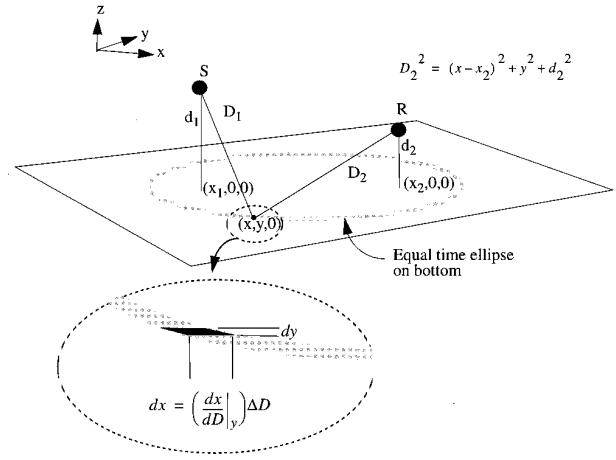
FIG. 2. Bistatic geometry and definitions of variables.

$$\Delta k=k|4\Delta_t^2+\{\mathrm{Re}[P(\theta_i)+P(\theta_s)]\}^2|^{1/2}.\qquad(22)$$

B. Scattered intensity

The experiments described in Sec. II use a directional receiver and a directional source that emits a short FM slide. To determine values for the bistatic scattering strength from these experiments, an expression for the bistatic scattered intensity as a function of time was derived in terms of the bistatic cross sections given in Eq. (1). The expression given below is for the scattered intensity $I(t)$ of a short-duration, or ''impulse,'' pulse. This expression must be convolved with the transmitted signal (intensity versus time) to obtain predictions of the absolute levels and temporal structure of scattered intensity for any experiment.

The impulse response is

$$I(t)=I_0\int\int\left[\frac{(\sigma b_x b_r)}{(D_1 D_2)^2}10^{-\alpha_w(D_1+D_2)/10}\right]dx\ dy\qquad(23)$$

(see definitions in Fig. 2). Here, σ is the sum of the surface- and volume-scattering cross sections appearing in Eq. (1), α_w is the attenuation of sound in water for the frequency of interest in decibels per unit length, b_x and b_r are the beam patterns of the transmitter and receiver, respectively, and D_1 and D_2 are the distances shown in Fig. 2. The source is assumed to emit a rectangular pulse of infinitesimal length dt that has intensity I_0 at a range of 1 m.

The integrations in Eq. (23) are over the infinitesimal area lying between the two ellipses, which have associated travel times from transmitter to seabed to receiver of t and $(t+dt)$. Therefore the limits on the x and y integrations in Fig. 2 are actually functions of time. Furthermore, at any time t the position x can be written as a function of y. Thus as shown next, the integral in Eq. (23) can be rewritten as a pair of one-dimensional integrals over y.

Using the variable

$$D=D_1+D_2=ct,\qquad(24)$$

where c is the speed of sound in water, the relation between x and y for a given t (or equivalently D) can be put in the form of an equation for an ellipse:

$$\frac{(x-x_0)^2}{a^2} + \frac{y^2}{b^2} = 1, \qquad (25)$$

with

$$a = \frac{Q}{\epsilon}, \qquad (26a)$$

$$b = \frac{Q}{2D}, \qquad (26b)$$

$$x_0 = -\frac{\beta}{2\epsilon^2}, \qquad (26c)$$

$$\epsilon = 2\sqrt{D^2 - (x_1 - x_2)^2}, \qquad (26d)$$

$$\beta = 4(x_2 - x_1)(x_2^2 - x_1^2 + d_2^2 - d_1^2 - D^2) - 8x_1 D^2, \qquad (26e)$$

$$Q = D \sqrt{\frac{[D^2 - (x_1 - x_2)^2 - d_1^2 - d_2^2]^2 - 4d_1^2 d_2^2}{D^2 - (x_1 - x_2)^2}}. \qquad (26f)$$

Using the enlargement of the $(x,y,0)$ region shown in Fig. 2 and Eqs. (24) and (25) allows Eq. (23) to be rewritten as

$$I(t) = I_0(\Delta D) \int_{-b}^{b} \left[\frac{|dx/dD|(\sigma b_x b_r)}{(D_1 D_2)^2} 10^{-\alpha_w D/10} \right] dy, \qquad (27)$$

where dx/dD can be calculated using Eq. (25). Equation (27) was numerically implemented using the measured beam patterns of the source and receiver and was used as described in Sec. III to obtain experimental values of the bistatic scattering strength. It is important to note that in practice two integrals are calculated and summed using Eq. (27), since x is double valued in y; i.e., from Eq. (25),

$$x = x_0 \pm a \sqrt{1 - \frac{y^2}{b^2}}. \qquad (28)$$

II. BISTATIC EXPERIMENTS

Sections II A and II B describe the transmitter and receivers used in obtaining the backscattering and bistatic scattering results presented in Sec. III. Section II C describes a typical data-acquisition cycle. Section II D describes the sites where the experiments were conducted.

A. The Benthic acoustic measurement system

The Benthic acoustic measurement system (BAMS) [Fig. 3(a)] operates at 40 kHz and acquires data on acoustic backscattering from a circular region whose radius is set by surface reverberation. The system employs a planar transmitter/receiver array mounted on a rotator mechanism at the top of a 5-m-high tripod. All system operations are under control of an on-board computer with a data storage capacity of approximately 120 Mbyte. Storage batteries provide sufficient energy to operate the computer, electronics, and rotator for the time required to reach the limit of the data storage capacity. This time may be days or months, depending on the rate at which data are acquired. In the experiments reported here, the interval between sonar scans was variously set at 20 min, 30 min, and 1 h, and each scan covered a full 360° in 72 steps of 5°. The 5° step increment was chosen on the basis of
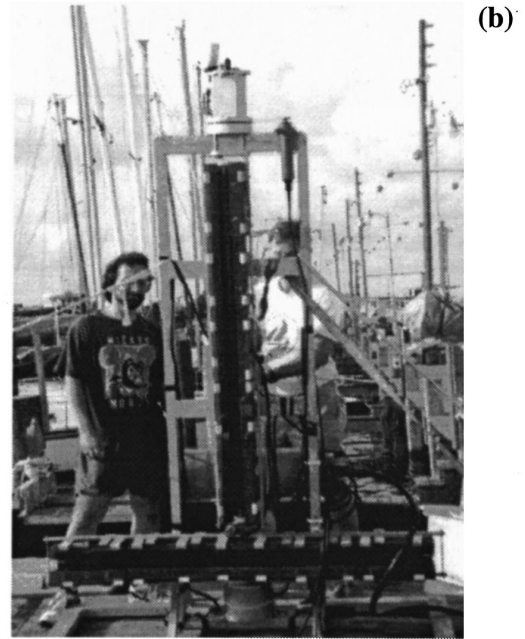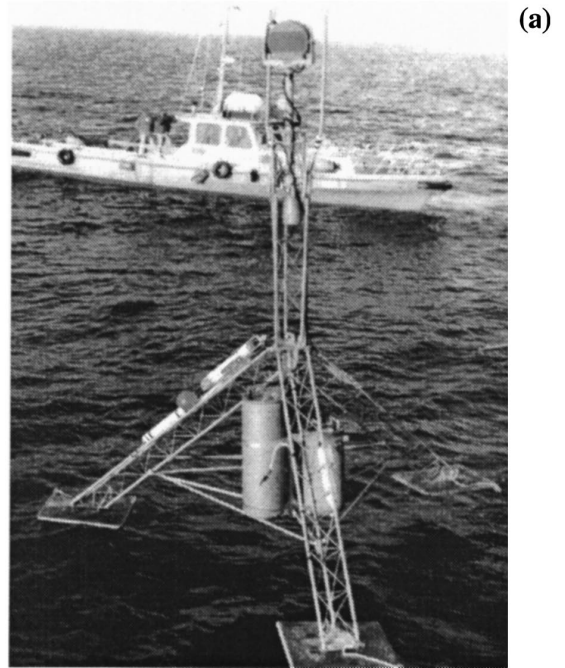
FIG. 3. Bistatic acoustic measurement system (BAMS) (a) and mobile receiving arrays (b).

the horizontal directivity patterns of the transmitter and receivers, which were essentially identical in the horizontal plane with a full width of 6.5° at one-half maximum power. The full array aperture was used for transmission, giving a vertical directivity pattern with a full width of 14° at one-half maximum power. For reception, the aperture was divided into upper and lower halves, yielding vertical directivity patterns of 27° for the receivers. The levels of the first sidelobes were down 13–15 dB relative to the main lobe for the various directivity patterns. The maximum response axis of the array was depressed approximately 12.5° below the horizontal. Because the tower was not perfectly vertical, the depres-
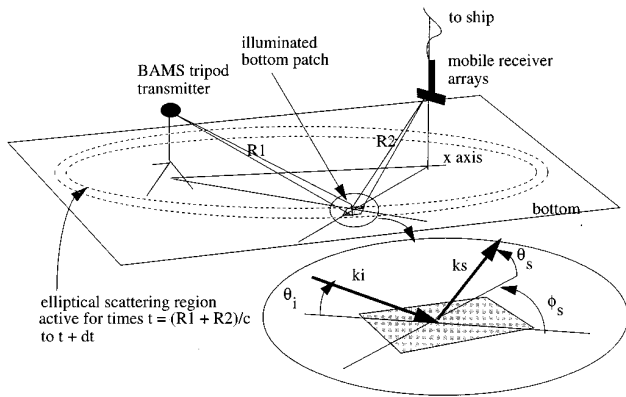
FIG. 4. Design of bistatic scattering experiment.

sion angle varied slightly as the transducer was rotated. A pendulum potentiometer measured the depression angle at each step in each scan. The azimuthal orientation of the apparatus was measured by an on-board fluxgate compass and by a magnetic compass mounted on the array which was read visually by divers assisting in the deployment. The time interval between rotational steps was 5 s, of which about 2 s were required to achieve the change in direction. The remaining time allowed the transmitter/receiver array to come to complete rest before each transmission.

The transmitted signal was a 2-ms-long, FM wave form with a constant amplitude over its duration. During this 2-ms interval, the frequency was swept from 39 to 41 kHz. The transmitter provided a source level of 217 dB *re*: 1 μPa@1 m. The transmitted wave form was digitized and stored for each transmission. These data show that the transmitter voltage remained constant to within a small fraction of 1 dB during each experiment. Each of the two receiver chan-

nels was digitized with an interval between samples equal to one quarter of a cycle at 40 kHz. Pairs of adjacent samples were saved every 0.5 ms to provide a baseband complex signal.[18] This sampling rate is very close to the limit imposed by the sampling theorem for bandlimited signals, and some aliasing occurred as a result. Sampling was started 10 ms prior to signal transmission; these early samples were used to estimate the noise level. The sampling window extended to 81 ms after transmission, which allowed digitization of approximately 1400 scans before the data storage capacity of the system was exceeded. Digitization and signal generation are controlled by a single clock. This makes it possible to make sensitive comparisons between echoes acquired in separate scans, even when the scans are weeks apart. Such processing has been used to obtain remote temperature measurements[19] and to observe changes in the seabed.[20] The backscattering results to be presented in Sec. III are derived from this data set.

B. Mobile bistatic receiving arrays

During the bistatic measurements, the ship-mounted mobile, steerable arrays shown in Fig. 3(b) were also deployed. The array on the BAMS tripod served as the transmitter and the ship-deployed arrays served as receivers. The receiving arrays were steered by means of a hydraulically controlled rotator, which can be seen at the top of the arrays in Fig. 3(b). The hydraulic controls were available during data acquisition, so different geometries could be obtained within a data-acquisition cycle (see next section).

The mobile arrays were divided in quadrants, each 32 cm long. The narrow and wide beamwidths of the quadrants were 8° and 37°. The bistatic data were acquired with the horizontal array, with each quadrant being recorded sepa-
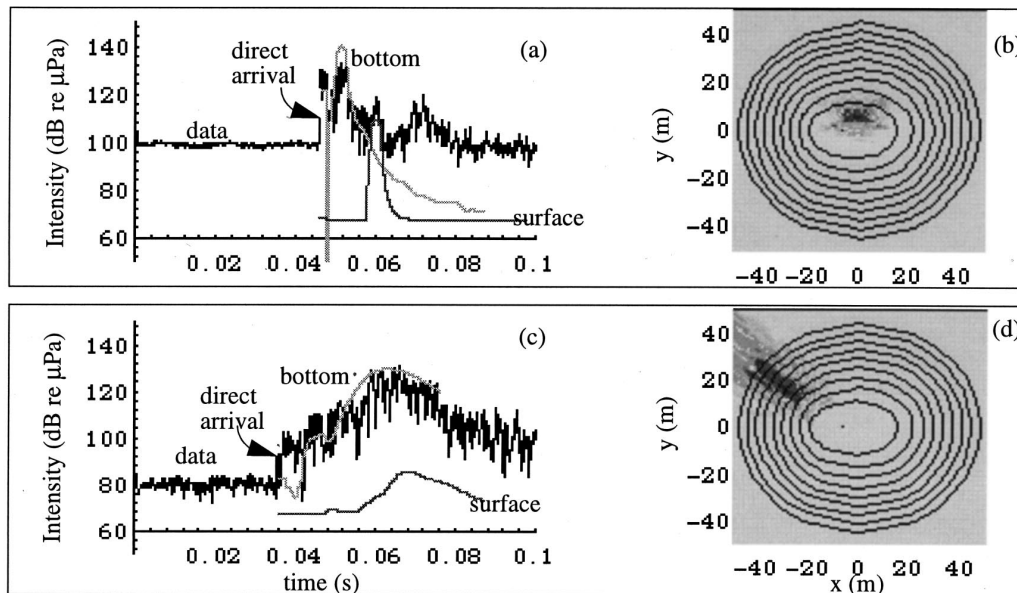
FIG. 5. Model/data comparisons from the Panama City sand site and corresponding integrands of Eq. (23). (a) and (c) show experimental wave forms along with simulations of the bottom- and surface-scattered signals based on Eq. (27) (see text for details). The vertical axis is the absolute level at the face of the receiver. (b) and (d) show the integrand of Eq. (23) for the geometries of (a) and (c), respectively. The transmitter and receiver are along the $y=0$ axis symmetrically placed around $x=0$. The dark gray regions indicate integrand values at least 30 dB higher than the light gray regions. The ellipses indicate regions of the surface that contribute 4, 8, 12 ms, etc., after the initial bottom-scattered arrival.
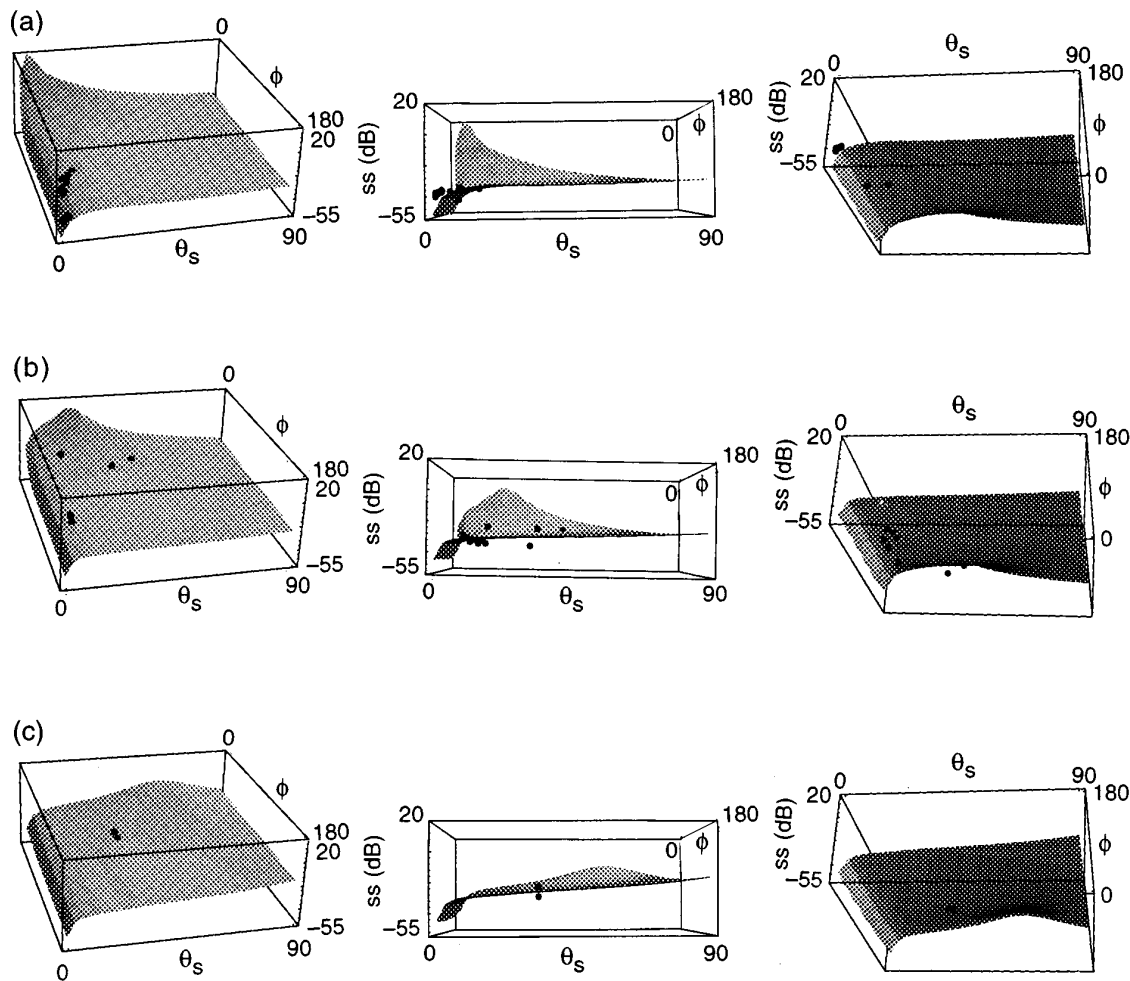
FIG. 6. Model predictions of scattering strength [Eq. (1)] for incident angles of (a) 5°, (b) 20°, and (c) 60°, shown as surfaces, and the experimental data from the Panama City site, shown as points. Three views are given for each plot so that the locations of all data point can be seen. See text for further discussion.

rately at two different gains to increase the dynamic range. The analog signals were conditioned using the APL MAME system;[21] the conditioned data were recorded using Lab-VIEW software controlling National Instruments data-acquisition boards.[22]

C. Data acquisition cycle

A simplified diagram of the bistatic experiment is shown in Fig. 4. The three independent bistatic angles $(\theta_i, \theta_s, \phi_s)$ are also shown in the figure. The mobile array was suspended from the tending vessel, which was placed in a one-point moor near the BAMS tripod. It is necessary to use a mobile receiving array to obtain a statistically significant number of bistatic-scattering cross-section measurements in any region of bistatic scattering angle space. The horizontal distance between the source and receivers ranged from 20 to 100 m. In the data presented here, the horizontal distance was always less than 60 m.

A data cycle consisted of taking data with the mobile array during a 360° rotation of the tripod array. This rotation comprises 72 positions (5° increments) at each of which the 40-kHz signal was emitted. As shown in Fig. 4, the mobile array was steered so that the centers of the transmit and receive beams intersected each other on the seabed.

One primary data-analysis effort was determining the bistatic angles from the data set. Measuring all the geometrical parameters needed to determine the bistatic angles obtained during each data run requires the use of the split-beam phase from the receiver-array quadrants (time resolved to $\pm 5\ \mu$s) as well as several supplemental devices, including compasses (accurate to within $\pm 2°$), ranging transducers (± 1 m), an altimeter (± 30 cm), a pressure gauge (± 30 cm), and inclinometers ($\pm 0.1°$). The largest uncertainty in the experiment is in the ranging since it could not be performed on a ping-by-ping basis. The range was acquired an average of once every 5–10 pings. Because of this, data taken when the receiving array moved significantly (>3 m) between range measurements were not processed. The uncertainty in range is felt to be on the order of 2 m for the data set having the greatest receiver movement. The uncertainties quoted for the altimeter and pressure gauge come from side-by-side measurements at 10 depths throughout the water column in which the difference between the two results had a standard deviation of 26 cm. The uncertainty quoted for the compass is greater than that claimed by the manufacturer but is felt to be realistic given the calibration of the compass while embedded in the receiver apparatus shown in Fig. 3. The inclinometers were also calibrated while on the receiver
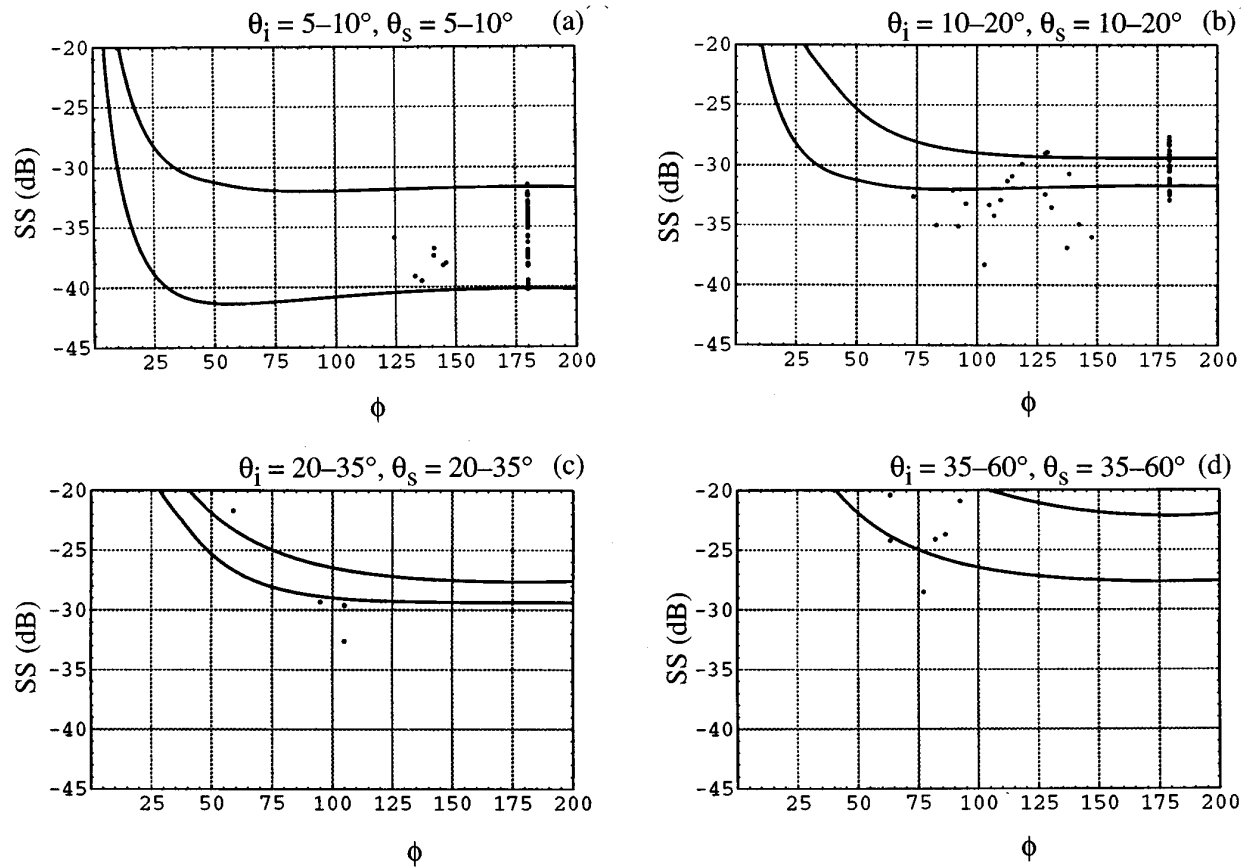
FIG. 7. Model predictions of scattering strength compared with experimental data from Panama City site. Model predictions, shown as curves, are for the upper and lower values of the grazing angles given at the top of the figure (see Table I for site parameter values).

array by use of a digital inclinometer with $\pm 0.01°$ accuracy.

The bistatic scattering strengths given in Sec. III were derived by comparing the pressures received at the face of the mobile arrays with those predicted by simulations of the experiment using Eq. (27), the experimental geometry, the transmitted pulse length, and the beam patterns of the receiving and transmitting arrays.

D. Experimental sites

1. Eckernförde Bay

The properties of the sediment at this site are documented in Ref. 23. The sediment had a very high water content, with a porosity of approximately 85%, and rather low acoustic attenuation (0.18 dB/kHz/m).[24] The most striking acoustic feature at this site was a layer of free methane bubbles with an upper boundary 0.5–2.0 m below the sediment/water interface.[25,26] The size distribution of these bubbles was measured using computer tomography,[27] and estimates made from these data indicate that volume scattering strengths should be very high, between -10 and -20 dB/m.[28] Tang *et al.*[29] have shown that these gas bubbles are the principal cause of backscattering at 40 kHz. This is due to the combination of low acoustic attenuation in the overlying sediment and high volume-scattering strength. The model parameters for this site (Table I) were determined as part of the CBBL program and, with one exception (discussed below), are those given in Ref. 30. *In situ* acoustic

probes were used to determine the values for the compressional-wave velocity and attenuation in the sediment. Diver cores were used to determine sediment density, and underwater photography was used to determine the surface-roughness parameters. From comparisons of the backscattering data with the backscatter model of Ref. 2, it was determined that surface-roughness effects played only a small role in backscattering from this sediment (a result consistent with Ref. 29). The volume scattering approximation used in the present model (characterized by γ_3, w_3, and μ) comes from a perturbation analysis, and bubble scattering does not fit this assumption. However these volume parameters can be regarded as phenomenological rather than physical and can be used to obtain an initial estimate of the bistatic scattering. In this regard, the w_3 parameter quoted in Table I is not the one found in Ref. 30. It was adjusted to give good initial estimates of the intensity time series from which bistatic scattering strengths are derived (see Sec. III B).

2. Panama City

This was a coarse sand site. The parameters shown in Table I are those given in Ref. 30. The techniques used to determine the environmental parameters were similar to those used at the Eckernförde Bay site. Note that the model predictions are dominated by the measured parameters ρ, ν, δ, γ_2, and w_2 for this site.
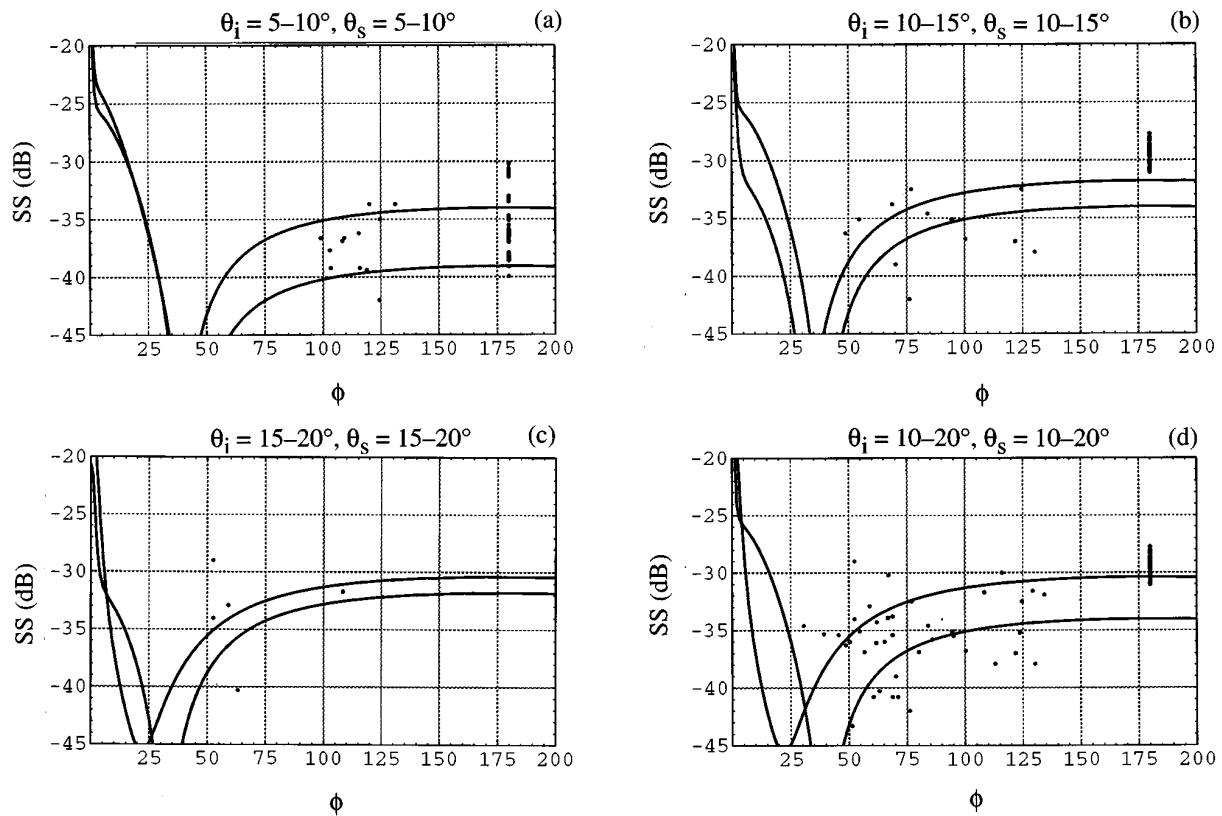
FIG. 8. Same as Fig. 7, but for Eckernförde Bay.

III. MODEL/DATA COMPARISONS

The objective of the model/data comparisons was to obtain experimental values for the bistatic scattering strength and compare them with the model predictions. For each transmission, the geometry information recorded at the time of transmission, the attenuation in the water, the beam patterns of the source and receiver, and the values for the bistatic cross section predicted using Table I were used in Eq. (27) to obtain an impulse response by numerical integration. This result was convolved with the rectangular transmitted wave form to predict the amplitude and temporal structure of the intensity scattered from the seabed into the receiver. This prediction was then compared with its experimental counterpart. Two typical examples from the Panama City sand site are shown in Fig. 5(a) (near forward scattering) and (c) (near backscattering). Calculations of the time and amplitude of the direct arrival and the signal scattered from the air/water interface are also shown.

The air/water signal was calculated with Eq. (27) using only the surface-roughness-scattering component of the bistatic model and roughness, sound speed, and density parameters typical of the ocean/air surface. This calculation was intended to give the signal's time of arrival relative to that of the bottom signal and to be quantitative only to the extent that an assessment could be made of its possible contamination of the bottom signal. Near forward scattering [Fig. 5(a)], the air/water signal arrives well after the bottom signal; near backscattering [Fig. 5(c)], the air/water signal is of much lower amplitude than the bottom signal. Thus contamination of the bottom signal is mitigated both by time separation and by beam-pattern effects. Similar checks of other geometries demonstrated that the data examined here were insignificantly affected by air/water interface scattering.

Figure 5(b) and (f) are plots, in decibels, of the integrand in Eq. (23) for the curves shown in Fig. 5(a) and (c), respectively. Superimposed are ellipses showing the region of the seabed contributing to the signal received 4, 8, 12 ms, etc., after arrival of the initial bottom-scattered signal. This type of figure allowed a quick determination of whether the scattering was sufficiently localized that a definite set of bistatic angles (Fig. 4) could be associated with the time of the peak bottom-scattered intensity. When this was possible, the bistatic angles were determined, and the difference between the theoretical prediction and the data was used to derive an experimental value for the bistatic scattering strength. This method has the advantage of being straightforward, but it is not applicable at some geometries. In particular, there are many cases where the scattering includes significant contributions from two regions: (1) from the main lobes of the two beams, and (2) from the sidelobes of the beams in combination with the peak in bistatic cross section in the forward direction. Near backscattering, the region making a significant contribution can be quite large; however, the times at which various regions contribute vary significantly, so time was used to help determine specific bistatic angles and associated scattering strengths. The bistatic angles for which data were obtained allow an assessment of the model's predictive capability for the experimental sites.

This method has an inherent advantage over sonar-equation-type analyses used to obtain scattering strength. In a sonar-equation calculation, one must make some estimate of surface area that is contributing to the signal. Furthermore, if the bistatic scattering strength is varying over the ensonified area, it is a challenge to account for this effect. In carrying out the integral to predict the intensity time series, this is all implicitly taken into account.

Backscattering is a special case of bistatic scattering. Experimental backscattering values were obtained using the tower as both a transmitter and a receiver. In the following sections, both the backscattered data and the bistatic data are shown for each site. The Panama City site is examined first, since the sediment was more in keeping with the model assumptions. Tables of the experimental results are given in the appendix.

A. Panama City site

In Fig. 6, model predictions of bistatic scattering strength are plotted as a function of ϕ and θ_S for incident angles of 5°, 20°, and 60°. All experimental values for incident angles within $\pm 2.5°$ of these angles are plotted as points for comparison with the model. Three views are shown for each incident angle so that data above and below the predictions can be seen. The data points are about 4 dB in diameter. The agreement between the data and the model predictions is sufficient to confirm much of the overall angular dependence predicted by the model. The 5° data show that the angular dependence and scattering level are well predicted for small incident and scattered grazing angles. The 20° data suggest that the increase in scattering predicted near forward scattering is also being observed. All three data sets suggest that the plateau predicted by the model for combinations of incident and scattered angles that are not near forward scattering and that are not too small is correct. However, the 20° data indicate that the plateau predicted by the model may be too high. All of these conclusions are retained when the full data set is examined.

An alternative method of examining the data is shown in Fig. 7, in which all data for incident and scattered angles within specified ranges have been grouped and plotted as a function of ϕ. Model predictions were then calculated using $\theta_i = \theta_s$ for the lower and upper ends of each range. In Fig. 7(a), for example, the upper curve is for $\theta_i = \theta_s = 10°$ and the lower curve is for $\theta_i = \theta_s = 5°$. This technique eliminates data where the incident and scattering angles are not similar but does allow a simpler view of the data/model comparison. This view of the data again indicates an overall agreement between the model and the data, but Fig. 7(b) still implies that the model predictions for the plateau level may be slightly high.

B. Eckernförde Bay site

The bubbles contained in the Eckernförde Bay mud have been identified as the major contributors to the backscattering,[29] and it is physically reasonable to assume the same is true for bistatic scattering. The model described in Sec. I was not developed to address strong scatterers within the sediment volume, so its applicability for this site is questionable. It is still valid to use Eq. (27) as a starting point in determining experimental values for the bistatic scattering strength. In this case, the model and the parameters given in Table I for this site can be viewed simply as a complicated means of obtaining an initial estimate.

Even though the model does not explicitly handle bubbles, it does allow for volume scatterers that have both monopole and dipole components.[31] The model developed explicitly for this type of sediment structure by Chu and Tang and documented by Chu et al.[32] indicates that, for the frequency being used, the monopole and dipole components of the bubble scattering amplitude are the primary contributors to the scattering. This fact motivated the plots of experimental data and model predictions shown in Fig. 8, using the method employed in constructing Fig. 7. The model curves use the parameters given in Table I for Eckernförde Bay. Although it is not useful to dwell long on the model/data comparison, examination of the figure demonstrates that, at least, the model is not in obvious conflict with the overall behavior of the data.

IV. CONCLUSIONS

A model has been presented for describing bistatic scattering from ocean sediments. The model has its genesis in the backscattering model of Ref. 2. The bistatic model has been tested using data from two different sites visited as part of the Coastal Benthic boundary layer program. One of the sites had a bottom composed of coarse-grained sand; the other was a gassy mud. Of the two sites, the one with coarse sand better follows the assumptions of the model. For this site, the overall agreement between the model and the experimental data is good, with some indication that the model overpredicts the bistatic scattering by a few decibels at some angles (see Sec. III A). A comprehensive list of the bistatic experimental results is included in the Appendix for both the sand and mud sites for use in testing alternative bistatic models.

In the case of the gassy-mud site, gas bubbles within the sediment contribute most of the scattering.[29] The agreement between the model and the data (shown in Fig. 8) is sufficient for the model to be of practical use for this site, even though in this case it should be considered an empirical, rather than a physical, model. The more physically correct model of Chu et al.[32] was compared with our experimental intensity time series to determine bistatic cross sections referenced back to the bubble layer (i.e., refraction and attenuation within the sediment are taken into account). One conclusion from this comparison is that inclusion of multiple scattering may be needed to fully model the Eckernförde site.

ACKNOWLEDGMENTS

APPENDIX: TABLES SUMMARIZING BACKSCATTERING AND BISTATIC-SCATTERING RESULTS

TABLE AI. Summary of Eckernförde backscattering and bistatic scattering results.

θ_i	θ_s	ϕ	σ	θ_i	θ_s	ϕ	σ	θ_i	θ_s	ϕ	σ	θ_i	θ_s	ϕ	σ	θ_i	σ_s	ϕ	σ	θ_i	θ_s	ϕ	σ	θ_i	θ_s	ϕ	σ
5	5	180.0	−38.21	6	6	180.0	−36.55	7	7	180.0	−35.01	8	8	180.0	−33.37	9	9	180.0	−31.32	10	10	180.0	−30.86	11	11	180.0	−30.39
12	12	180.0	−29.74	13	13	180.0	−28.82	14	14	180.0	−29.64	5	5	180.0	−38.12	6	6	180.0	−36.44	7	7	180.0	−34.83	8	8	180.0	−33.32
9	9	180.0	−31.22	10	10	180.0	−30.60	11	11	180.0	−30.28	12	12	180.0	−29.55	13	13	180.0	−29.01	14	14	180.0	−29.64	5	5	180.0	−38.43
6	6	180.0	−36.27	7	7	180.0	−34.83	8	8	180.0	−33.33	9	9	180.0	−31.27	10	10	180.0	−30.76	11	11	180.0	−30.33	12	12	180.0	−29.56
13	13	180.0	−28.79	14	14	180.0	−29.57	5	5	180.0	−37.87	6	6	180.0	−36.00	7	7	180.0	−34.82	8	8	180.0	−33.18	9	9	180.0	−31.11
10	10	180.0	−31.05	11	11	180.0	−30.21	12	12	180.0	−29.14	13	13	180.0	−28.62	14	14	180.0	−29.26	5	5	180.0	−38.33	6	6	180.0	−35.86
7	7	180.0	−34.70	8	8	180.0	−33.00	9	9	180.0	−31.08	10	10	180.0	−30.65	11	11	180.0	−30.21	12	12	180.0	−29.36	13	13	180.0	−28.95
14	14	180.0	−29.42	5	5	180.0	−39.09	6	6	180.0	−36.79	7	7	180.0	−35.07	8	8	180.0	−33.03	9	9	180.0	−31.04	10	10	180.0	−30.13
11	11	180.0	−29.46	12	12	180.0	−29.00	13	13	180.0	−28.56	14	14	180.0	−28.37	5	5	180.0	−39.93	6	6	180.0	−36.99	7	7	180.0	−35.52
8	8	180.0	−33.47	9	9	180.0	−31.02	10	10	180.0	−30.22	11	11	180.0	−29.52	12	12	180.0	−28.56	13	13	180.0	−27.72	14	14	180.0	−28.05
5	5	180.0	−38.59	6	6	180.0	−36.51	7	7	180.0	−34.92	8	8	180.0	−33.20	9	9	180.0	−30.83	10	10	180.0	−30.24	11	11	180.0	−29.73
12	12	180.0	−28.86	13	13	180.0	−28.12	14	14	180.0	−28.63	5	5	180.0	−38.43	6	6	180.0	−36.13	7	7	180.0	−34.83	8	8	180.0	−32.26
9	9	180.0	−31.17	10	10	180.0	−30.77	11	11	180.0	−30.29	12	12	180.0	−29.57	13	13	180.0	−28.68	14	14	180.0	−29.48	5	5	180.0	−38.52
6	6	180.0	−36.40	7	7	180.0	−34.95	8	8	180.0	−33.36	9	9	180.0	−31.22	10	10	180.0	−30.79	11	11	180.0	−30.33	12	12	180.0	−29.67
13	13	180.0	−28.81	14	14	180.0	−29.58	19.9	9.0	111.2	−32.4	19.3	9.2	106.9	−32.4	19.2	9.5	102.8	−34.4	17.6	9.6	101.3	−30.4	18.4	10.0	95.0	−35.5
15.7	11.6	80.1	−36.9	14.6	12.3	76.2	−42	14.5	12.9	70.2	−39	15.1	13.8	65.3	−36	17.9	13.2	50.4	−36	12.3	12.9	130.3	−37.9	13.2	14.3	124.5	−32.5
13.4	15.0	121.8	−37	14.4	16.2	116.0	−30	14.4	17.3	113.1	−37.9	15.1	18.4	108.4	−31.7	15.3	20.2	103.1	−29	16.1	20.3	100.4	−38.4	14.6	24.8	96.8	−33.4
15.8	24.4	92.0	−33.4	16.1	26.8	85.7	−32.2	15.9	28.5	83.0	−37.2	15.6	32.8	78.0	−29.1	17.7	28.7	72.7	−32.1	6.7	6.8	124.4	−42	7.0	7.5	119.1	−39.4
7.1	8.1	116.0	−39.2	7.7	8.8	109.2	−36.6	7.9	9.7	103.4	−39.2	9.9	9.2	99.0	−36.6	9.4	10.5	92.0	−37.6	8.6	11.6	91.1	−37.6	8.8	13.5	80.5	−34.3
8.5	15.1	77.9	−36.3	18.1	12.2	30.5	−34.6	10.1	5.6	171.1	−38.7	13.1	6.2	171.5	−37.3	14.3	6.5	167.8	−35.9	18.5	7.1	162.5	−37.9	11.2	5.9	167.6	−32.1
13.6	6.3	163.6	−36.1	13.9	6.5	160.4	−38.0	12.2	6.3	157.1	−37.6	13.8	6.7	151.8	−36.0	14.3	6.9	146.1	−35.8	16.4	7.2	141.9	−39.3	16.9	7.3	138.8	−41.1
19.5	7.7	132.5	−39.6	20.2	7.9	128.3	−37.6	20.2	7.9	128.3	−34.6	18.5	11.5	39.2	−35.3	15.0	12.2	48.8	−36.3	14.4	11.9	54.7	−35.1	17.1	10.6	60.6	−40.8
15.7	6.4	168.2	−35.1	15.5	6.5	165.6	−38.1	19.1	6.9	160.7	−37.7	14.4	6.8	149.7	−33.1	18.4	7.3	145	−33.2	18.3	7.5	140.1	−37.3	34.6	8.6	131.5	−30.2
37.1	8.8	123	−27.6	33.1	8.9	120.8	−28.8	34.5	9.2	112.3	−32.4	34.7	9.2	112.3	−34.1	35.3	10.4	85.2	−31.4	34.1	10.8	77.1	−32.2	34.3	10.9	77.1	−33.9
32.7	11.4	70	−32.1	22.1	12.3	72.1	−36.5	21.2	12.8	68.9	−36.7	20.3	13.3	66.1	−42.2	15.2	15.7	63.1	−40.3	13.5	17.9	56.7	−36.9	13.1	19.1	51.4	−43.3
12.2	21.5	46.7	−33.3	12.3	22	40.7	−35.5	10.7	31.5	48.4	−39	12.2	23.3	53.4	−38.9	12.4	21	58	−32.4	13.2	19	62.1	−34.3	13.4	17.7	66.8	−33.9
13.9	17	67	−30.2	14	15	77	−32.5	12.2	15	84.1	−34.6	15.4	12	86	−35.8	14.4	12	94.5	−35.1	13.1	11	100.4	−36.8	10.9	6.1	164.4	−39.6
11.9	6.4	159.8	35.5	15.8	7.2	151.2	−37.9	12.8	20.7	40.0	−36.5	13.9	18.4	45.6	−35.4	15.8	15.9	52.5	−29.0	15.9	16.0	52.5	−34.0	16.4	15.2	58.9	−32.9
18.2	14.2	61.8	−36.1	18.4	13.5	68.8	−35.4	18.5	13.6	68.8	−40.8	19.5	13.3	71.1	−40.8	20.4	12.9	73.8	−41.5	22.3	12.2	80.3	−37.8	16.7	7.4	148.8	−36
18.3	7.7	143.3	−34.7	17.3	7.7	141.9	−34.9	18.6	7.9	135.4	−32.6	19.2	8.1	131.7	−33.5	18.4	8.2	127.5	−30.6	18.8	8.4	123.6	−30.5	19.1	8.6	119.6	−32.4
14.6	10.8	68.8	−33.8	16.7	9.7	76.8	−33.5	16.3	9.3	84.4	−29.5	14.2	9.0	91.6	−39.7	11.7	8.8	98.3	−36.2	9.7	8.8	103.1	−37.7	9.6	8.2	108.4	−36.9
9.5	7.5	115.4	−36.2	8.7	7.1	120.2	−33.7	8.4	6.7	124.7	−35.0	7.7	6.2	131.2	−33.7	15.9	47	96.1	−30.1	16.1	36.1	100.5	−33.3	16.3	29	105.6	−35.5
16.2	25	112	−38.7	14.5	28.5	117.3	−35.8	14.8	20.0	123.6	−35.2	13.6	19	129.3	−31.6	13.5	16	134.3	−31.9								

TABLE AII. Summary of Panama City backscattering and bistatic scattering results.

θ_i	θ_s	ϕ	σ	θ_i	θ_s	ϕ	σ	θ_i	θ_s	ϕ	σ	θ_i	θ_s	ϕ	σ	θ_i	θ_s	ϕ	σ	θ_i	θ_s	ϕ	σ	θ_i	θ_s	ϕ	σ
5	5	180.0	−37.53	6	6	180.0	−37.04	7	7	180.0	−35.77	8	8	180.0	−34.80	9	9	180.0	−33.65	10	10	180.0	−32.11	11	11	180.0	−31.53
12	12	180.0	−30.47	13	13	180.0	−29.97	14	14	180.0	−27.95	15	15	180.0	−28.76	5	5	180.0	−39.46	6	6	180.0	−37.58	7	7	180.0	−36.2
8	8	180.0	−34.60	9	9	180.0	−33.33	10	10	180.0	−32.36	11	11	180.0	−31.29	12	12	180.0	−30.23	13	13	180.0	−29.52	14	14	180.0	−28.02
15	15	180.0	−28.06	5	5	180.0	−38.27	6	6	180.0	−37.30	7	7	180.0	−35.75	8	8	180.0	−34.38	9	9	180.0	−33.	10	10	180.0	−32.20
11	11	180.0	−31.21	12	12	180.0	−30.05	13	13	180.0	−27.88	14	14	180.0	−28.01	15	15	180.0	−28.07	5	5	180.0	−40.00	6	6	180.0	−37.28
7	7	180.0	−35.80	8	8	180.0	−34.24	9	9	180.0	−33.72	10	10	180.0	−32.39	11	11	180.0	−31.61	12	12	180.0	−29.59	13	13	180.0	−28.31
14	14	180.0	−27.90	15	15	180.0	−27.64	5	5	180.0	−40.21	6	6	180.0	−36.95	7	7	180.0	−35.85	8	8	180.0	−34.13	9	9	180.0	−33.12
10	10	180.0	−31.45	11	11	180.0	−31.43	12	12	180.0	−30.14	13	13	180.0	−29.07	14	14	180.0	−28.28	15	15	180.0	−28.01	5	5	180.0	−39.74
6	6	180.0	−38.09	7	7	180.0	−36.97	8	8	180.0	−35.11	9	9	180.0	−33.93	10	10	180.0	−32.87	11	11	180.0	−32.45	12	12	180.0	−31.11
13	13	180.0	−29.25	14	14	180.0	−29.06	15	15	180.0	−29.50	10.0	10.0	180.0	−32.11	15.0	15.0	180.0	−28.0	13.8	13.7	147.6	−36.0	15.2	14.6	142.3	−34.9
16.8	15.3	138.3	−30.7	18.9	16.3	130.9	−33.5	18.9	16.7	128.2	−32.4	21.5	17.6	121.7	−31.2	21.5	18.6	115.3	−34.1	25.0	19.6	108.8	−33.7	25.0	20.2	105.0	−32.6
25.0	20.2	105.0	−29.6	25.0	21.5	95.0	−29.3	17.7	33.4	45.7	−35.2	16.8	35.1	45.6	−32.2	16.8	37.2	39.7	−35.0	9.9	16.7	14.3	−36.3	11.7	18.6	137.5	−36.9
13.2	20.8	131.5	−37.6	16.0	22.2	125.7	−36.2	33.4	12.5	91.1	−35.0	17.8	12.7	93.1	−32.0	37.7	12.9	74.5	−30.2	37.7	13.2	63.7	−29.8	37.7	13.2	63.7	−29.8
20.1	14.3	65.2	−34.0	13.8	22.2	58.0	−31.4	13.2	23.0	57.3	−33.4	12.7	24.7	51.4	−32.7	12.2	25.6	45.6	−34.8	11.3	28.9	40.1	−29.9	5.5	8.7	146.0	−38.0
5.5	8.8	144.7	−38.2	5.9	9.4	141.0	−37.4	6.8	10.7	133.3	−34.4	7.5	12.0	125.3	−38.7	6.5	7.9	141.1	−36.8	6.5	8.3	136.0	−39.5	5.7	8.6	133.3	−39.1
6.6	9.8	124.6	−35.9	6.7	10.1	122.0	−42.7	7.5	10.9	115.9	−38.0	23.3	33.1	58.9	−21.7	22.1	36.3	51.8	−21.8	20.9	40.0	45.5	−27.7	18.8	45.9	40.7	−22.7
57.6	35.6	63.3	−20.4	58.2	36.2	63.3	−24.2	61.0	35.9	71.2	−22.7	57.5	36.0	77.1	−28.5	54.2	36.0	82.0	−24.1	51.1	36.0	86.2	−23.7	52.2	35.3	92.4	−20.9
49.6	34.5	101.2	−22.6	19.8	11.5	129.1	−28.9	18.3	11.5	128.3	−29.0	19.5	12.2	118.8	−29.9	18.2	12.5	114.5	−30.9	18.5	12.9	109.8	−32.9	15.9	12.7	112.6	−31.3
15.8	13.4	105.0	−33.3	14.8	13.3	107.1	−34.2	13.7	14.0	103.1	−38.3	13.0	15.2	95.4	−33.2	13.8	15.5	92.2	−35.1	13.5	16.0	89.9	−32.1	11.9	18.1	83.1	−35.0
11.2	20.5	76.4	−29.8	12.6	19.7	73.6	−32.6	20.5	16.8	26.0	−20.5	13.7	20.6	21.0	−20.7	6.1	11.4	126.3	−35.6	6.6	11.4	125.1	−35.0	6.5	12.6	121.0	−35.1
6.4	14.9	114.9	−34.8	6.8	16.6	108.7	−35.4																				

[1] D. R. Jackson, D. P. Winebrenner, and A. Ishimaru, ''Application of the composite roughness model to high-frequency bottom backscattering,'' J. Acoust. Soc. Am. **79**, 1410–1422 (1986).

[2] P. D. Mourad and D. R. Jackson, ''High frequency sonar equation models for bottom backscatter and forward loss,'' *Proceedings of OCEANS'89*, 1168–1175 (1989). [There is a typographical error in Eq. (39) which is corrected in Ref. 3.]

[3] D. R. Jackson and K. B. Briggs, ''High-frequency bottom backscattering: Roughness versus sediment volume scattering,'' J. Acoust. Soc. Am. **92**, 962–977 (1992).

[4] D. R. Jackson, ''Models for scattering from the sea bed,'' Proc. Inst. Acoust. **16**, 161–169 (1994).

[5] A. N. Ivakin and Y. P. Lysanov, ''Underwater sound scattering by volume inhomogeneities of a bottom medium bounded by a rough surface,'' Sov. Phys. Acoust. **27**, 212–215 (1981).

[6] P. C. Hines, ''Theoretical model of acoustic backscatter from a smooth seabed,'' J. Acoust. Soc. Am. **88**, 324–334 (1990).

[7] D. Tang, ''Acoustic wave scattering from a random ocean bottom,'' Ph.D. thesis, Massachusetts Institute of Technology and Woods Hole Oceanographic Institution, June 1991.

[8] A. P. Lyons, A. L. Anderson, and F. S. Dwan, ''Acoustic scattering from the seafloor: Modeling and data comparison,'' J. Acoust. Soc. Am. **95**, 2441–2451 (1994).

[9] T. Yamamoto, ''Acoustic scattering in the ocean from velocity and density fluctuations in the sediments,'' J. Acoust. Soc. Am. **99**, 866–879 (1996).

[10] E. I. Thorsos, ''Acoustic scattering from a 'Pierson–Moskowitz' sea surface,'' J. Acoust. Soc. Am. **88**, 335–349 (1990).

[11] A. Ishimaru, *Wave Propagation and Scattering in Random Media* (Academic, New York, 1978), Vol. 2.

[12] E. I. Thorsos, ''The validity of the Kirchhoff approximation for rough surface scattering using a Gaussian roughness spectrum,'' J. Acoust. Soc. Am. **83**, 78–92 (1988).

[13] E. Y. T. Kuo, ''Wave scattering and transmission at irregular surfaces,'' J. Acoust. Soc. Am. **36**, 2135–2142 (1964).

[14] A. N. Ivakin and Yu. P. Lysanov, ''Theory of underwater sound scattering by random inhomogeneities of the bottom,'' Sov. Phys. Acoust. **27**, 61–64 (1981).

[15] J. E. Moe and D. R. Jackson, ''First-order perturbation solution for rough surface scattering cross section including the effects of gradients,'' J. Acoust. Soc. Am. **96**, 1748–1754 (1994).

[16] J. H. Stockhausen, Scattering From the Volume of an Inhomogeneous Half-Space, Report No. 63/9, Naval Research Establishment, Canada, 1963.

[17] A. Ishimaru, *Wave Propagation and Scattering in Random Media* (Academic, New York, 1978), Vol. 1.

[18] O. D. Grace and S. P. Pitt, ''Sampling and interpolation of bandlimited signals by quadrature methods,'' J. Acoust. Soc. Am. **48**, 1311–1318 (1970).

[19] D. R. Jackson and J. G. Dworski, ''An acoustic backscatter thermometer for remotely mapping seafloor water temperature,'' J. Geophys. Res. **97**, 761–767 (1992).

[20] D. R. Jackson, K. L. Williams, and K. B. Briggs, ''High-frequency acoustic observations of benthic spatial and temporal variability,'' Geo-Marine Lett. **16**, 212–218 (1996).

[21] R. Stein, ''A modular acoustic measurement equipment system,'' *Proceedings of Oceans'83*, 176–181 (1983).

[22] National Instruments Corporation, Austin, Texas.

[23] *Proceedings of the Gassy Mud Workshop*, edited by T. F. Wever, FWG Report 14 (Federal Armed Forces Underwater Acoustics and Marine Geophysics Research Institute, Germany, 1994).

[24] K. B. Briggs and M. D. Richardson, ''*In situ* and laboratory measurements in Eckernfoerde Bay,'' in *Proceedings of the Gassy Mud Workshop*, edited by T. F. Wever, FWG Report 14 (Federal Armed Forces Underwater Acoustics and Marine Geophysics Research Institute, Germany, 1994), pp. 39–46.

[25] H. M. Fielder and I. H. Stender, ''The absorption layer in Eckernfoerde Bay sediments,'' in *Proceedings of the Gassy Mud Workshop*, edited by T. F. Wever, FWG Report 14 (Federal Armed Forces Underwater Acoustics and Marine Geophysics Research Institute, Germany, 1994), pp. 19–23.

[26] J. A. Hawkins, D. N. Lambert, D. J. Walter, and J. C. Cranford, ''Acoustic imaging of near-surface bubbly sediments,'' in *Proceedings of the Gassy Mud Workshop*, edited by T. F. Wever, FWG Report 14 (Federal Armed Forces Underwater Acoustics and Marine Geophysics Research Institute, Germany, 1994), pp. 54–58.

[27] F. Abegg, A. Anderson, L. Buzi, A. P. Lyons, and T. H. Orsi, ''Free methane concentration and bubble characteristics in Eckernfoerde Bay, Germany,'' in *Proceedings of the Gassy Mud Workshop*, edited by T. F. Wever, FWG Report 14 (Federal Armed Forces Underwater Acoustics and Marine Geophysics Research Institute, Germany, 1994), pp. 84–89.

[28] A. L. Anderson, A. P. Lyons, L. Buzi, F. Abegg, and T. Orsi, ''Modeling acoustic interaction with a gassy seafloor including examples from Eckernfoerde Bay,'' in *Proceedings of the Gassy Mud Workshop*, edited by T. F. Wever, FWG Report 14 (Federal Armed Forces Underwater Acoustics and Marine Geophysics Research Institute, Germany, 1994), pp. 90–94.

[29] D. Tang, G. Jin, D. R. Jackson, and K. L. Williams, ''Analyses of high-frequency bottom and subbottom backscattering for two distinct shallow water environments,'' J. Acoust. Soc. Am. **96**, 2930–2936 (1994).

[30] D. R. Jackson, K. B. Briggs, K. L. Williams, and M. D. Richardson, ''Tests of models for high-frequency sea-floor backscatter,'' IEEE J. Ocean Eng. **21**, 458–470 (1996).

[31] D. R. Jackson, ''A Model for Bistatic Bottom Scattering in the Frequency Range 10–100 kHz,'' APL-UW TR 9305, Applied Physics Laboratory, University of Washington, August 1993.

[32] D. Chu, K. L. Williams, D. Tang, and D. R. Jackson, ''High-frequency bistatic scattering by subbottom gas bubbles,'' J. Acoust. Soc. Am. **102**, 806–814 (1997).

Comparison of basin-scale acoustic transmissions with rays and further evidence for a structured thermal field in the northeast Pacific

David E. Norris
Graduate Program in Acoustics, Pennsylvania State University, University Park, Pennsylvania 16802

John L. Spiesberger
Department of Meteorology and the Applied Research Laboratory, Pennsylvania State University, University Park, Pennsylvania 16802

Daniel W. Merdes
Applied Research Laboratory, Pennsylvania State University, University Park, Pennsylvania 16802

From May to September of 1987, 250-Hz, 16-ms resolution acoustic signals were transmitted between four sources and nine receivers in the northeast Pacific. This paper examines the acoustic transmissions across nine of the sections within this group, with path lengths ranging from approximately 1700 to 3300 km. Acoustic multipaths are tracked in the data, and ray theory is successfully used to identify the multipaths, where the spring and summer Levitus' climatological databases are used to determine the sound speeds. The observed multipaths arrive on the order of 1 s later than the predicted rays. Travel time differences greater than 0.15 s are due to temperature errors in Levitus' climatology within the ocean's upper 1 km. The resulting corrections to Levitus' spring and summer oceans are -0.2 and $-0.3\,°C$, respectively. The upper turning depths for all rays are found to vary by less than 50 m from spring to summer. Variations in the measured travel times over the four month period are about 0.5 s. Some sections warm between the spring and summer seasons, while other sections cool. This variability is inconsistent with a temperature field dominated by seasonal effects. The spatial and temporal scales of the heat content are qualitatively similar to those found from other basin-scale acoustic sections in the northeast Pacific [J. L. Spiesberger *et al.*, J. Acoust. Soc. Am. **92**, 384–396 (1992)]. © *1998 Acoustical Society of America.* [S0001-4966(98)02401-1]

INTRODUCTION

In order to study climatic temperature changes in the ocean with sound, it is useful to be able to interpret the pattern of acoustic multipaths with some quantitative theory. To date, two basin-scale sections have bene successfully interpreted with ray theory, the simplest solution to the wave equation.[1,2] It is of interest to find out how general this result is; that is, can basin-scale transmissions usually be successfully interpreted with rays or not. To this end, eight more basin-scale transmissions are interpreted with rays here. We find that ray theory is able to account for almost all of the multipaths among these sections.

Evidence has been presented that basin-scale changes in acoustic travel time are due to changes in temperature.[2–4] Transmissions from the Kaneohe source exhibit changes in travel time of about ± 0.2 s, with rates of change of about 0.1 s/month.[2] Sections separated by about 500 km exhibit quite different changes in travel time.[3] This suggests that the temperature field which affects travel time is structured with scales less than 500 km. It is of interest to investigate whether these results apply in other regions and at other times. The nine sections investigated here exhibit changes in travel time that are qualitatively similar to those found from the Kaneohe source. That is, travel changes are about

± 0.2 s, rates of these changes are of order 0.1 s/month, and sections separated by about 500 km exhibit quite different variations in temperature.

The experiment is described in Sec. I. Section II summarizes the data analysis. In Sec. III, the ray modeling is described. Section IV presents the comparisons between the data and model. A discussion of the travel time changes and ocean structure is given in Sec. V.

I. THE EXPERIMENT

In 1987, acoustic transmissions from four sources[5–7] were recorded at nine bottom mounted receivers. In this work, we examine nine sections between three of these sources[7] and three of these receivers (Fig. 1). One of these sections, source 3, receiver 3, has previously been analyzed with rays.[1] The sections extend from approximately 1700 to 3300 km. The sources were deployed on taut moorings[7] with reference depths of 676.5 m for source 1, 909.5 m for source 2, and 857.0 m for source 3. Source 1 was positioned at 40.444 618 °N, 202.858 544 °E, source 2 at 31.473 664 °N, 202.888 173 °E, and source 3 at 40.467 537 °N, 194.070 267 °E, all in the World Geodetic System 1984. The sources transmitted pulselike signals 12 times per day at 2-h intervals on every fourth day. The acoustic frequency was centered at
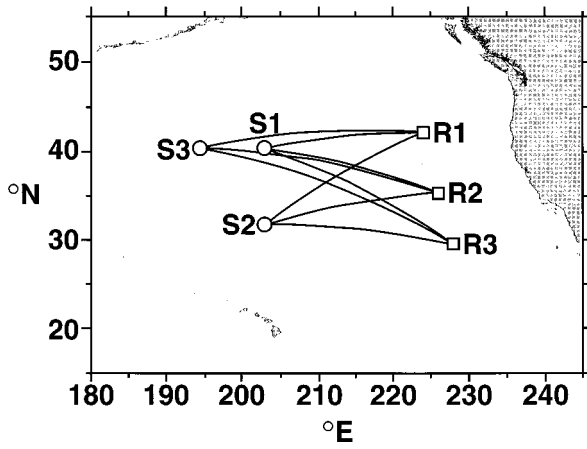
FIG. 1. Positions of acoustic sources, S1–S3, and approximate positions of receivers, R1–R3, for 1987 tomography experiment.
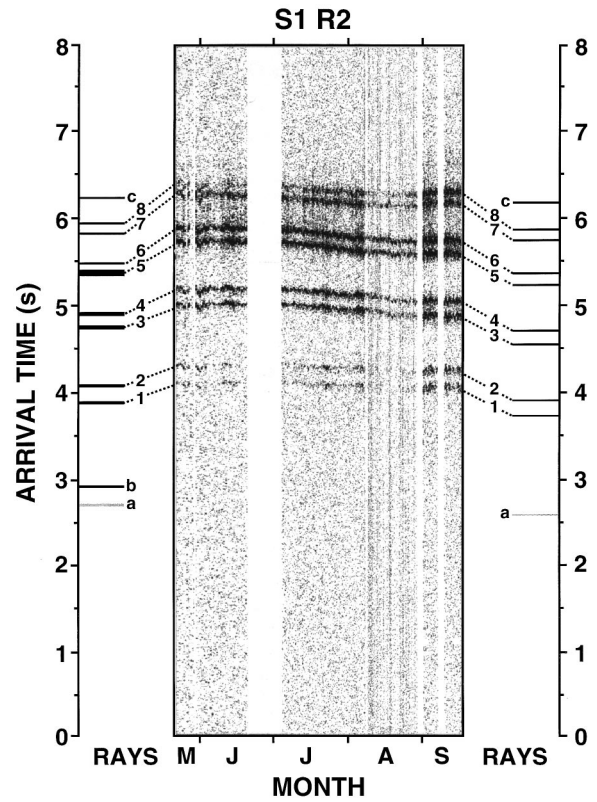
FIG. 3. Same as Fig. 2, except for source 1, receiver 2 (S1R2).
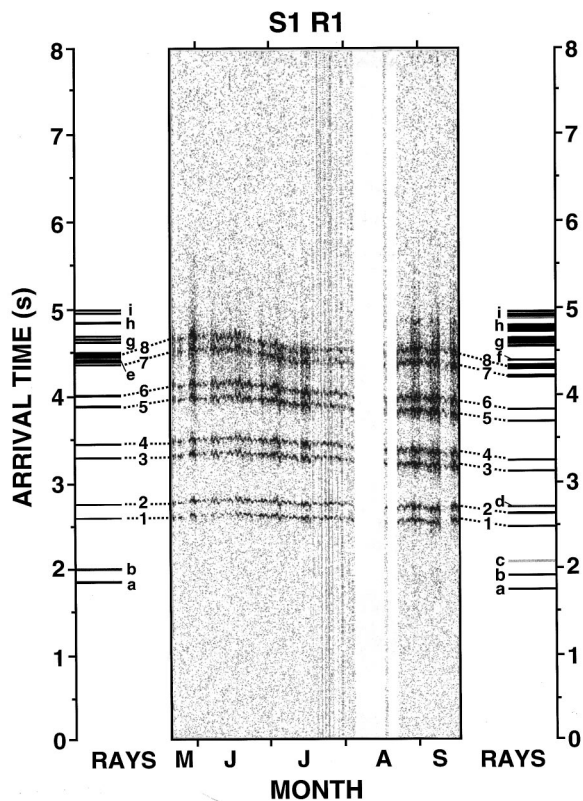
FIG. 2. Observed acoustic pulses for source 1, receiver 1 (S1R1). The horizontal axis specifies the five month period, May to September. Note that the three day gaps in the data are not shown. The vertical axis specifies the arrival time of the predicted rays and observed multipaths, relative to the same absolute travel time. The predicted rays for spring and summer are shown to the extreme left and right, respectively. The identified multipaths are marked with numbers and are matched to predicted rays with dashed lines. The predicted rays that are not matched to multipaths are marked with letters.
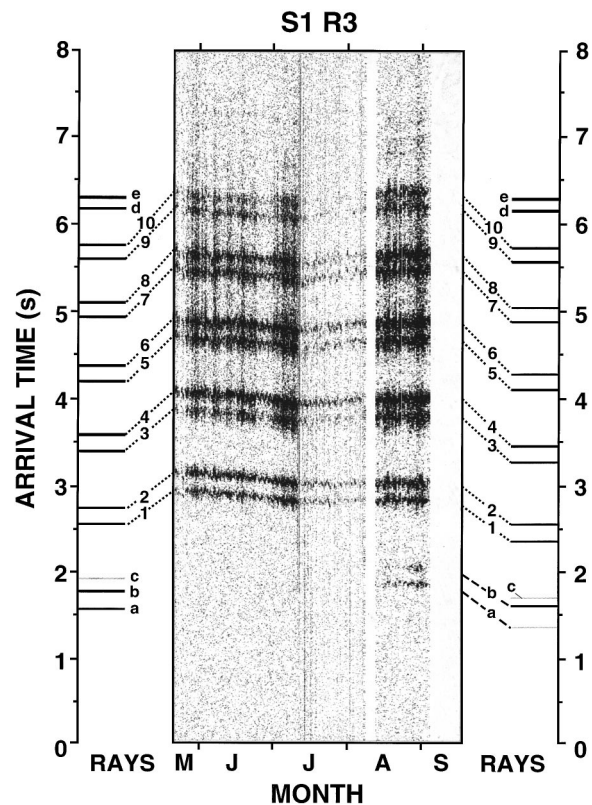
FIG. 4. Same as Fig. 2, except for source 1, receiver 3 (S1R3).
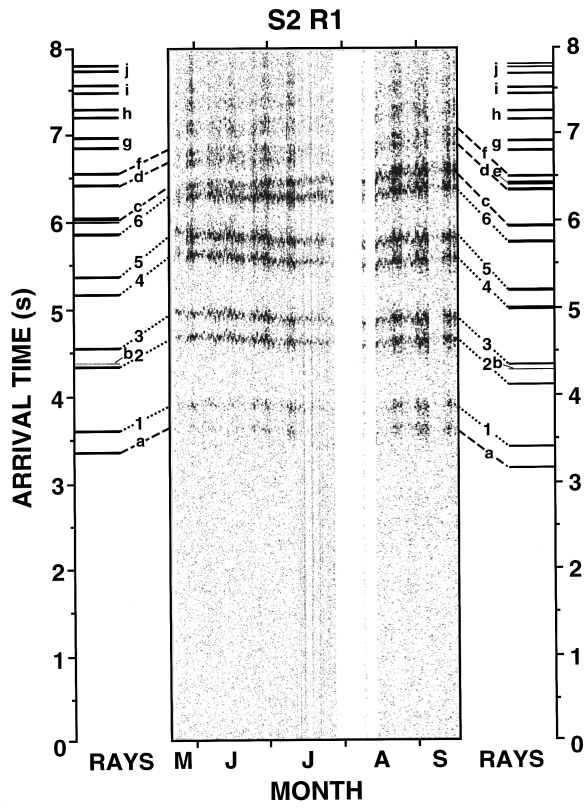
FIG. 5. Same as Fig. 2, except for source 2, receiver 1 (S2R1).
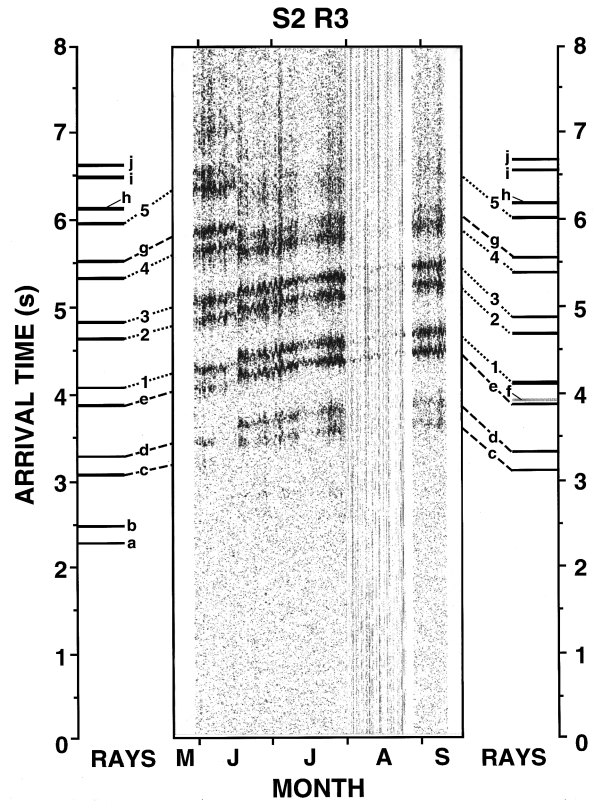
FIG. 7. Same as Fig. 2, except for source 2, receiver 3 (S2R3).
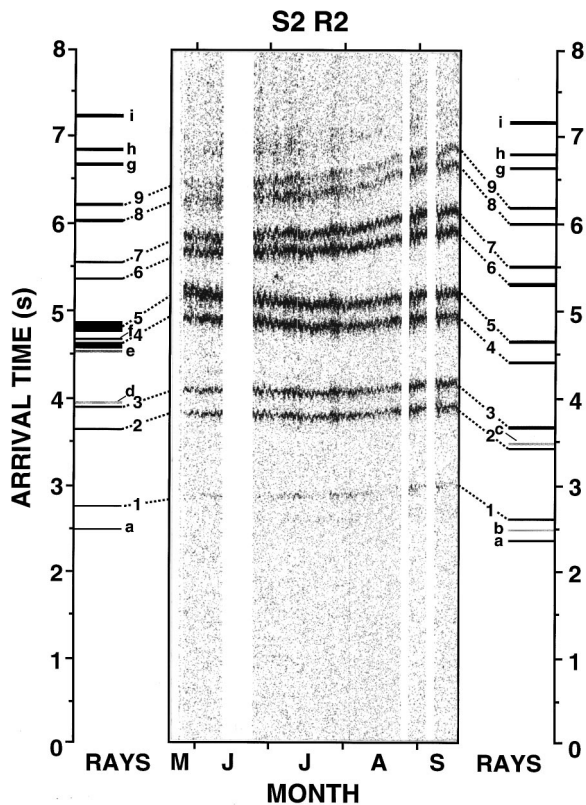
FIG. 6. Same as Fig. 2, except for source 2, receiver 2 (S2R2).
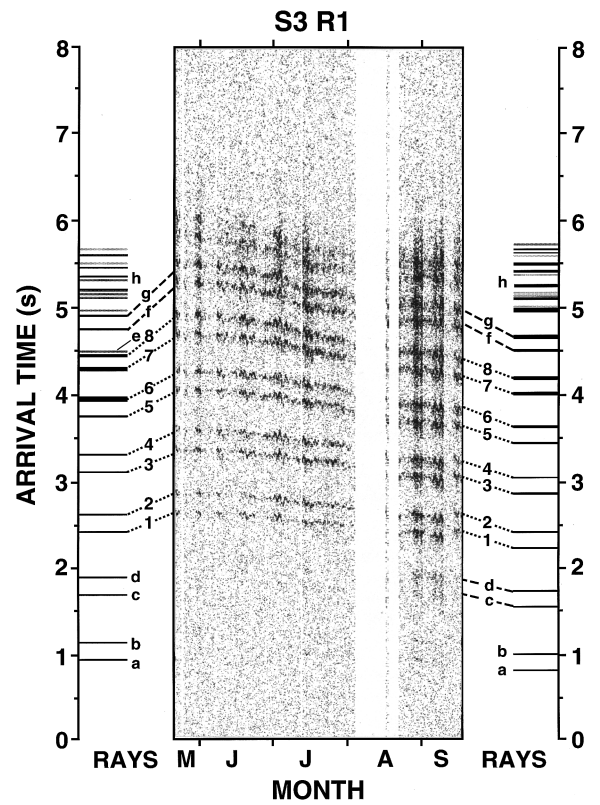
FIG. 8. Same as Fig. 2, except for source 3, receiver 1 (S3R1).
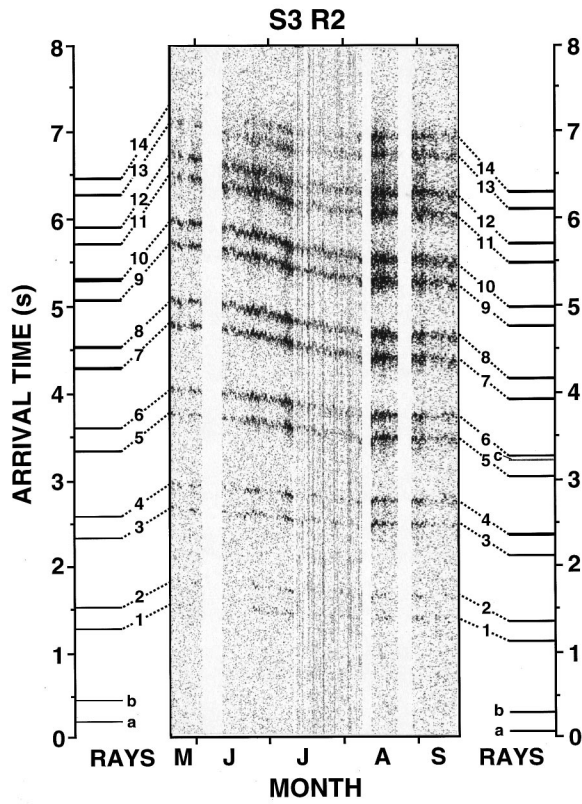
FIG. 9. Same as Fig. 2, except for source 3, receiver 2 (S3R2).
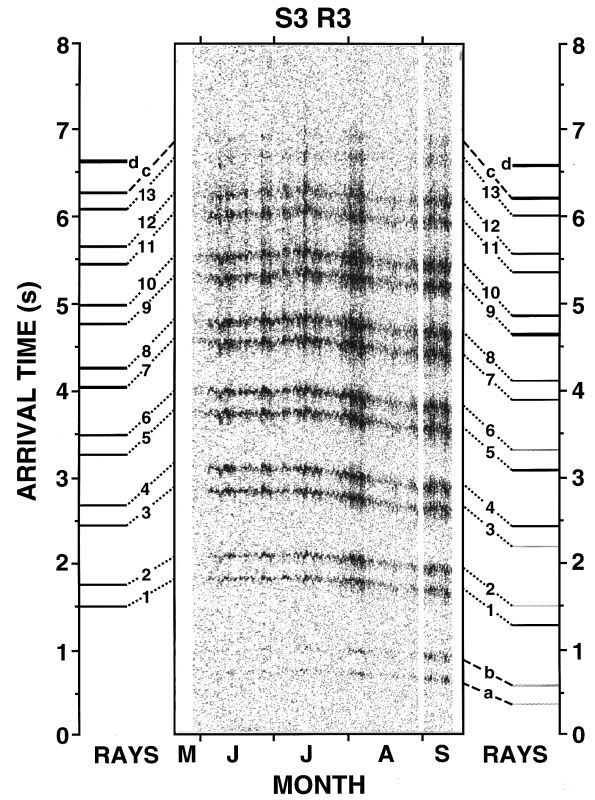
FIG. 10. Same as Fig. 2, except for source 3, receiver 3 (S3R3).

TABLE I. Ray parameters for source 1, receiver 1 (S1R1). The labeling of the ray group follows that of Fig. 2. Refer to Sec. IV A for an explanation of the parameters and notation.

Ray group	Upper turning depth (m)	Individual rays in ray group	Launch angle (°)	Type	Number of bottom bounces	Unmatched ray classification
i	300	1	6 , 6	D , D	0 , 0	weak diffracting
		2↔3	−6 , 6	D , D	0 , 0	weak diffracting
		4↔6	- , −6	- , D	- , 0	weak diffracting
h	250	1	6 , 7	D , D	0 , 0	weak diffracting
		2↔4	- , 7	- , D	- , 0	weak diffracting
		5	- , −7	- , D	- , 0	weak diffracting
g	150	1	7 , −9	D , D	0 , 0	weak diffracting
		2	7 , 7	D , D	0 , 0	weak diffracting
		3↔4	−7 , 7	D , D	0 , 0	weak diffracting
		5	- , −8	- , D	- , 0	weak diffracting
		6	- , −7	- , D	- , 0	weak diffracting
f	100	1	- , 8	- , D	- , 0	weak diffracting
8	100	1	8 , 10	D , D	0 , 0	
		2	8 , 4	D , D	0 , 0	
		3	9 , 4	D , D	0 , 0	
		4	7 , 4	D , D	0 , 0	
		5↔7	- , 3↔4	- , D	- , 0	
e	100	1↔5	−8 , -	D , -	0 , -	weak diffracting
7	50	1	−10 , −10	D , G	0 , 0	
6	50	1	10 , 11	G , G	0 , 0	
5	50	1	−11 , −11	G , G	0 , 0	
4	50	1	12 , 12	G , G	0 , 0	
3	50	1	−12 , −12	G , G	0 , 0	
d	50	1	- , 12	- , D	- , 1	bottom interacting
		2↔3	- , 12	- , D	- , 0	weak diffracting
2	50	1	13 , 13	G , G	0 , 0	
1	50	1	−13 , -13	G , G	0 , 0	
c	50	1↔4	- , 13↔14	- , D	- , 1	bottom interacting
b	50	1	−14 , 14	D , G	1 , 0	bottom interacting
		2	15 , -	G , -	7 , -	bottom interacting
		3	14 , -	G , -	0 , -	bottom interacting
a	50	1	−14 , −14	G , G	0 , 0	bottom interacting

TABLE II. Same as Table I, except for source 1, receiver 2 (S1R2) (Fig. 3).

Ray group	Upper turning depth (m)	Individual rays in ray group	Launch angle (°)		Type		Number of bottom bounces		Unmatched ray classification
c	100	1	−9 ,	−10	D ,	D	0 ,	0	weak diffracting
8	100	1	10 ,	11	D ,	D	0 ,	0	
7	100	1	−11 ,	−11	D ,	D	0 ,	0	
6	50	1	11 ,	12	D ,	D	0 ,	0	
5	50	1	−12 ,	−12	D ,	D	0 ,	0	
		2↔7	−11 ,	-	D ,	-	0 ,	-	
4	50	1	13 ,	13	G ,	G	0 ,	0	
		2	13 ,	-	G ,	-	0 ,	-	
3	50	1	−13 ,	−13	G ,	G	0 ,	0	
		2	−13 ,	-	G ,	-	0 ,	-	
2	50	1	14 ,	14	G ,	G	0 ,	0	
1	50	1	−14 ,	−14	G ,	G	0 ,	0	
b	50	1↔2	15 ,	-	G ,	-	1 ,	-	bottom interacting
a	50	1↔2	−15 ,	−15	G ,	G	1 ,	1	bottom interacting

250 Hz with an rms bandwidth of 63 Hz. The source level was 191 dB *re*: 1 μPa@1 m.[7] To increase the detectability of the source, coded waveforms were transmitted and then averaged and correlated with a replica waveform at the receivers. This resulted in a signal-to-noise ratio increase of about 36 dB.[8] Travel time corrections were made to remove the effects of mooring motion.[9] Mooring motion was tracked by measuring two-way travel times between an interrogator mounted near the source and four bottom-mounted transponders.[10] See Ref. 4 for a complete description of the experiment.

II. DATA ANALYSIS

For a given section, the received signal is processed over the period from 20 May to 17 September of 1987. In this time period, there are 31 days of data, spaced every four days, with each day consisting of 12 recorded time series, one every 2 h, for a total of 312 records. Each record has a different noise level which is dependent on the local oceanic conditions. The signal-to-noise ratios for each record are calculated. Each record consists of 16.368 s of data, and the noise level is estimated by taking the variance of the data over a four second period in which no source signal is received. Referring to Fig. 2(a) of Ref. 1, the first second is typical of data used to calculate the noise level. The resulting signal-to-noise ratios range from low values up to approximately 40 dB. To clearly exhibit the multipaths, the large dynamic range is compressed through the use of threshold filters. Both a lower and upper threshold are specified, and if the signal-to-noise ratio exceeds either bound, it is clipped to that threshold limit. We use lower and upper thresholds of −5 and 10 dB. The records are plotted by mapping the signal-to-noise ratios to a gray scale. A value of 10 dB or more is assigned a black pixel, and a value of −5 dB or less

TABLE III. Same as Table I, except for source 1, receiver 3 (S1R3) (Fig. 4). Ray groups *a* and *b* for spring contain unmatched rays classified as bottom interacting. Ray groups *a* and *b* for summer contained matched rays.

Ray group	Upper turning depth (m)	Individual rays in ray group	Launch angle (°)		Type		Number of bottom bounces		Unmatched ray classification
e	200	1	10 ,	1	D ,	D	0 ,	0	weak diffracting
		2	- ,	9	- ,	D	- ,	0	weak diffracting
d	200	1	−10 ,	−10	D ,	D	0 ,	0	weak diffracting
10	150	1	11 ,	11	D ,	D	0 ,	0	
9	150	1	−11 ,	−11	D ,	D	0 ,	0	
8	100	1	12 ,	12	D ,	D	0 ,	0	
7	100	1	−12 ,	−12	D ,	D	0 ,	0	
6	100	1	12 ,	12	D ,	G	0 ,	0	
		2	12 ,	13	D ,	G	0 ,	0	
		3	12 ,	-	D ,	-	0 ,	-	
5	100	1↔2	−12 ,	−13	G ,	G	0 ,	0	
4	50	1	13 ,	13	G ,	G	0 ,	0	
		2	13 ,	-	G ,	-	0 ,	-	
3	50	1	−13 ,	−13	G ,	G	0 ,	0	
		2	−13 ,	-	G ,	-	0 ,	-	
2	50	1	13 ,	14	G ,	G	0 ,	0	
1	50	1	−14 ,	−14	G ,	G	0 ,	0	
c	50	1	14 ,	14	D ,	D	0 ,	0	weak diffracting
b	50	1	15 ,	15	G ,	G	0 ,	0	see caption
		2	- ,	15	- ,	G	- ,	0	see caption
a	50	1	−15 ,	−14	G ,	D	0 ,	0	see caption

TABLE IV. Same as Table I, except for source 2, receiver 1 (S2R1) (Fig. 5).

Ray group	Upper turning depth (m)	Individual rays in ray group	Launch angle (°)	Type	Number of bottom bounces	Unmatched ray classification
j	300	1	7 , 7	D , D	0 , 0	weak diffracting
		2	−7 , 7	D , D	0 , 0	weak diffracting
		3	- , −7	- , D	- , 0	weak diffracting
i	300	1	8 , 8	D , D	0 , 0	weak diffracting
		2	−8 , −8	D , D	0 , 0	weak diffracting
h	250	1	8 , 8	D , D	0 , 0	weak diffracting
		2	−8 , −8	D , D	0 , 0	weak diffracting
g	200	1	9 , 9	D , D	0 , 0	weak diffracting
		2	−9 , −9	D , D	0 , 0	weak diffracting
f	150	1	10 , 10	D , D	0 , 0	
e	150	1↔3	- , −1	- , D	- , 0	weak diffracting
d	150	1	−10 , −10	D , G	0 , 0	
		2	- , −10	- , G	- , 0	
c	100	1	10 , 11	G , G	0 , 0	
		2	6 , -	D , -	0 , -	
6	100	1	−11 , −11	G , G	0 , 0	
5	50	1	12 , 12	G , G	0 , 0	
4	50	1	−12 , −10	G , G	0 , 0	
		2↔4	- , −12	- , G	- , 0	
3	50	1	13 , 13	G , G	0 , 0	
b	50	1	−6 , 5	D , D	0 , 0	weak diffracting
2	50	1	−13 , −13	G , G	0 , 0	
		2	- , −13	- , D	- , 0	
1	50	1	14 , 14	G , G	0 , 0	
a	50	1	−14 , −14	G , G	0 , 0	

TABLE V. Same as Table I, except for source 2, receiver 2 (S2R2) (Fig. 6).

Ray group	Upper turning depth (m)	Individual rays in ray group	Launch angle (°)	Type	Number of bottom bounces	Unmatched ray classification
i	200	1	−10 , −9	D , D	0 , 0	weak diffracting
h	150	1	11 , 10	D , D	0 , 0	weak diffracting
g	150	1	−11 , −11	D , D	0 , 0	weak diffracting
9	150	1	11 , 11	D , D	0 , 0	
8	150	1	−11 , −11	D , D	0 , 0	
7	100	1	12 , 12	D , D	0 , 0	
6	100	1	−12 , −12	D , D	0 , 0	
		2↔4	- , −12	- , D	- , 0	
5	50	1	12 , 14	D , G	0 , 0	
		2	13 , -	D , -	0 , -	
		3↔4	13 , -	G , -	0 , -	
f	50	1↔2	4 , -	D , -	0 , -	weak diffracting
		3	−4 , -	D , -	0 , -	weak diffracting
4	50	1	−10 , −14	D , G	0 , 0	
		2↔6	−13 , -	D , -	0 , -	
		7	−13 , -	D , -	1 , -	
		8↔9	−13 , -	D , -	0 , -	
		10	−13 , -	D , -	1 , -	
		11↔12	−13 , -	G , -	0 , -	
		13↔16	−13↔−12 , -	D , -	0 , -	
e	50	1↔2	−13 , -	D , -	1 , -	bottom interacting
d	50	1↔3	14 , -	D , -	0 , -	weak diffracting
3	50	1	−15 , 15	G , D	0 , 0	
		2↔4	- , 14	- , D	- , 0	
		5	- , 14	- , G	- , 0	
		6	- , 14	- , D	- , 1	
		7	- , 10	- , D	- , 0	
c	50	1	- , −15	- , D	- , 0	weak diffracting
2	50	1	−15 , −15	G , D	0 , 0	
		2↔3	- , −15	- , D	- , 0	
		4	- , −13	- , D	- , 0	
1	50	1	16 , 16	G , G	0 , 0	
b	50	1	- , −15	- , D	- , 1	weak diffracting
a	50	1	−16 , −16	G , G	0 , 0	bottom interacting

TABLE VI. Same as Table I, except for source 2, receiver 3 (S2R3) (Fig. 7).

Ray group	Upper turning depth (m)	Individual rays in ray group	Launch angle (°)		Type		Number of bottom bounces		Unmatched ray classification
j	300	1	9 ,	9	D ,	D	0 ,	0	weak diffracting
i	300	1	−10 ,	−10	D ,	D	0 ,	0	weak diffracting
h	250	1	10 ,	11	D ,	D	0 ,	0	weak diffracting
5	200	1	−11 ,	−11	D ,	D	0 ,	0	
g	200	1	11 ,	11	D ,	D	0 ,	0	
4	200	1	−12 ,	−12	D ,	D	0 ,	0	
3	150	1	12 ,	12	D ,	D	0 ,	0	
2	150	1↔2	−12 ,	−12	D ,	D	0 ,	0	
		3	- ,	−12	- ,	D	- ,	0	
1	100	1	13 ,	13	G ,	G	1 ,	2	
		2	13 ,	13	G ,	G	1 ,	1	
		3	13 ,	12	G ,	D	2 ,	1	
		4	13 ,	12	G ,	D	1 ,	2	
		5	13 ,	14	G ,	G	2 ,	2	
		6↔7	13 ,	14	G ,	G	1 ,	1	
		8	- ,	14	- ,	G	- ,	2	
f	100	1	- ,	−13	- ,	G	- ,	1	bottom interacting
		2	- ,	−13	- ,	D	- ,	1	bottom interacting
e	100	1	−13 ,	−14	G ,	G	1 ,	1	
		2	−13 ,	−14	G ,	G	2 ,	1	
		3↔10	−13 ,	-	G ,	-	1↔2 ,	-	
d	100	1	13 ,	14	G ,	G	0 ,	2	
		2	- ,	14	- ,	G	- ,	0	
c	100	1	−13 ,	−14	G ,	G	1 ,	2	
		2	- ,	−14	- ,	G	- ,	2	
		3	- ,	−14	- ,	D	- ,	1	
		4	- ,	−14	- ,	G	- ,	1	
b	50	1↔4	14 ,	-	G ,	-	1↔2 ,	-	bottom interacting
		5	11 ,	-	D ,	-	0 ,	-	weak diffracting
a	50	1↔3	−14 ,	-	G ,	-	1 ,	-	bottom interacting
		4	−14 ,	-	G ,	-	0 ,	-	bottom interacting

TABLE VII. Same as Table I , =except for source 3, receiver 1 (S3R1) (Fig. 8). Ray groups *c* and *d* for spring contain unmatched rays classified as bottom interacting. Ray groups *c* and *d* for summer contain matched rays. Ray group *h* is not tabulated due to the large number of rays.

Ray group	Upper turning depth (m)	Individual rays in ray group	Launch angle (°)		Type		Number of bottom bounces		Unmatched ray classification
g	50	1	9 ,	6	D ,	D	0 ,	0	
		2↔5	- ,	6	- ,	D	- ,	0	
f	50	1	−9 ,	−10	D ,	G	0 ,	0	
		2	- ,	−10	- ,	G	- ,	0	
e	50	1↔3	10 ,	-	D ,	-	0 ,	-	weak diffracting
8	50	1	10 ,	10	D ,	G	0 ,	1	
		2	- ,	10	- ,	G	- ,	0	
		3	- ,	11	- ,	G	- ,	0	
7	50	1	−10 ,	−11	G ,	G	0 ,	0	
		2↔3	−10 ,	−11	G ,	G	0 ,	1	
		4	−8 ,	−11	D ,	G	0 ,	0	
6	50	1	11 ,	11	G ,	G	1 ,	0	
		2	11 ,	-	G ,	-	0 ,	-	
5	50	1	−11 ,	−11	G ,	G	0 ,	0	
4	50	1	12 ,	12	G ,	G	0 ,	0	
3	50	1	−12 ,	−12	G ,	G	0 ,	0	
		2↔3	- ,	−12	- ,	G	- ,	0	
2	50	1	13 ,	13	G ,	G	0 ,	0	
		2	- ,	10	- ,	D	- ,	0	
1	50	1	−13 ,	−13	G ,	G	0 ,	0	
		2↔3	- ,	−13	- ,	G	- ,	0	
d	50	1	14 ,	13	G ,	G	0 ,	0	see caption
c	50	1	−14 ,	−13	G ,	G	0 ,	0	see caption
b	50	1	14 ,	14	G ,	G	0 ,	0	bottom interacting
a	50	1	−14 ,	−14	G ,	G	0 ,	0	bottom interacting

TABLE VIII. Same as Table I, except for source 3, receiver 2 (S3R2) (Fig. 9).

Ray group	Upper turning depth (m)	Individual rays in ray group	Launch angle (°)		Type	Number of bottom bounces	Unmatched ray classification
14	100	1	10 ,	10	D , D	0 , 0	
13	100	1	−10 ,	−11	D , D	0 , 0	
12	50	1	11 ,	11	D , D	0 , 0	
11	50	1	−11 ,	−11	D , D	0 , 0	
10	50	1	12 ,	12	D , D	0 , 0	
		2↔6	11↔12 ,	-	D , -	0 , -	
9	50	1	−12 ,	−12	D , D	0 , 0	
		2↔7	−12↔−11 ,	-	D , -	0 , -	
8	50	1	12 ,	13	G , G	0 , 0	
		2	13 ,	-	G , -	0 , -	
		3	13 ,	-	D , -	0 , -	
		4	13 ,	-	G , -	0 , -	
7	50	1	−13 ,	−13	G , G	0 , 0	
6	50	1	14 ,	14	G , D	0 , 0	
		2	- ,	14	- , G	- , 0	
c	50	1	- ,	7	- , D	- , 0	weak diffracting
5	50	1	−14 ,	−14	G , G	0 , 0	
4	50	1	15 ,	14	G , G	0 , 0	
		2	- ,	14	- , G	- , 0	
3	50	1	−15 ,	−15	G , G	0 , 0	
2	50	1	15 ,	15	G , G	0 , 0	
1	50	1	−16 ,	−15	G , G	0 , 0	
b	50	1	16 ,	16	G , G	0 , 0	bottom interacting
a	50	1	−16 ,	−16	G , G	0 , 0	bottom interacting

TABLE IX. Same as Table I, except for source 3, receiver 3 (S3R3) (Fig. 10).

Ray group	Upper turning depth (m)	Individual rays in ray group	Launch angle (°)		Type	Number of bottom bounces	Unmatched ray classification
d	200	1	−10 ,	−10	D , D	0 , 0	weak diffracting
		2	−9 ,	−9	D , D	0 , 0	weak diffracting
c	150	1	11 ,	11	D , D	0 , 0	
13	150	1	−11 ,	−11	D , D	0 , 0	
12	100	1	11 ,	12	D , D	0 , 0	
11	100	1	−11 ,	−12	D , D	0 , 0	
10	100	1	12 ,	12	D , D	0 , 0	
		2↔4	- ,	12	- , D	- , 0	
9	100	1	−12 ,	−12	D , G	0 , 0	
		2	- ,	−12	- , G	- , 0	
8	50	1	12 ,	13	G , G	0 , 0	
		2	12 ,	-	G , -	0 , -	
7	50	1	−12 ,	−13	G , G	0 , 0	
		2	−13 ,	-	G , -	0 , -	
		3	−13 ,	-	G , -	1 , -	
6	50	1	13 ,	13	G , D	0 , 1	
		2	- ,	13	- , G	- , 0	
		3↔4	- ,	13	- , D	- , 0	
5	50	1	−13 ,	−14	G , G	0 , 0	
4	50	1	14 ,	14	G , G	0 , 0	
3	50	1	−14 ,	−14	G , D	0 , 0	
2	50	1	15 ,	15	G , D	0 , 0	
		2	- ,	15	- , D	- , 0	
		3	- ,	15	- , G	- , 0	
1	50	1	−15 ,	−15	G , G	0 , 0	
		2	- ,	−15	- , G	- , 0	
b	50	1	- ,	16	- , G	- , 0	
		2	- ,	16	- , G	- , 1	
a	50	1	- ,	−15	- , G	- , 0	
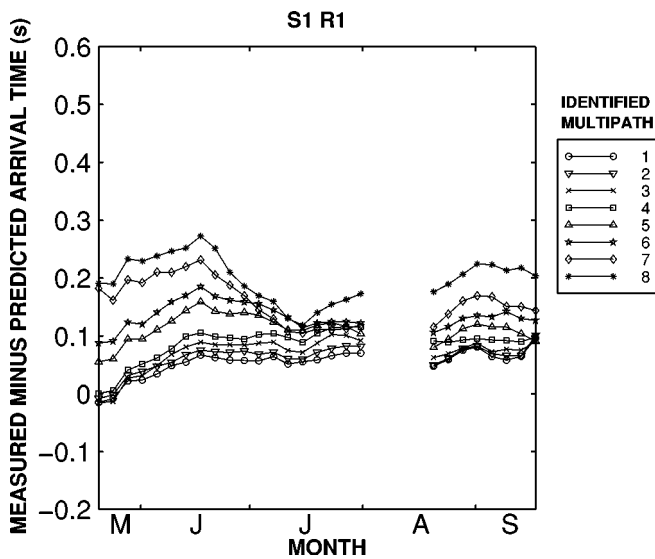
FIG. 11. Measured minus predicted arrival times of the identified multipaths for source 1, receiver 1 (S1R1) from May to September. The labeling of the identified multipaths follows that of Fig. 2.

FIG. 12. Same as Fig. 11, except for source 1, receiver 2 (S1R2).

is assigned a white pixel. The gray scale mapping in this range can be linear or nonlinear. We find that defining the mapping to be linear in the signal intensity , resulting in an exponential mapping in signal-to-noise ratio, provides a good way to visualize the multipaths (Figs. 2–10). Note that in some plots there are gaps in the data due to incomplete or missing records.

III. RAY MODELING

Levitus' climatological database contains seasonally averaged values of temperature and salinity.[11] The horizontal resolution is one degree in both latitude and longitude, and the data are given at 33 reference depths. For this analysis, temperature and salinity data are extracted over the sections of interest at 100-km intervals. Del Grosso's algorithm is used to calculate the sound speed.[12] The Del Grosso algorithm is chosen because it is found to provide better agreement between predicted and measured acoustic travel times than Chen and Millero's algorithm.[9,13–16]

Ray calculations are carried out using the program ZRAY.[17] By specifying source–receiver locations, bathymetry, and sound speed profiles at specified depths and ranges along the section, ZRAY and its associated eigenray finder[1] calculate all pertinent ray parameters including travel time, received level, and number of turning points. The sound speed between data points is found by using linear interpolation in the horizontal direction and quadratic spline interpolation in the vertical direction (see Fig. 1 of Ref. 1). The bathymetry is defined using ETOPO5.[18] If a ray hits the ocean bottom, it is reflected specularly and attenuated by 3 dB. For additional details, see Refs. 1 and 17.

To include the effects of source and receiver directivity, matched filter gain, and background noise, the sonar equation is used and the received signal-to-noise ratios are estimated for all rays. The ray impulses are convolved with a Gaussian function having an rms bandwidth of 63 Hz. All the rays, with their respective travel times, are then superim-

posed to construct a predicted time series record at the receiver. These predictions are now in a form where they can be directly compared to the data (Figs. 2–10). To the left of the data are the predicted rays for Levitus' spring season, and to the right of the data are the predicted rays for Levitus' summer season. The predictions are processed for plotting in the exact same way as the data, as described in Sec. II.
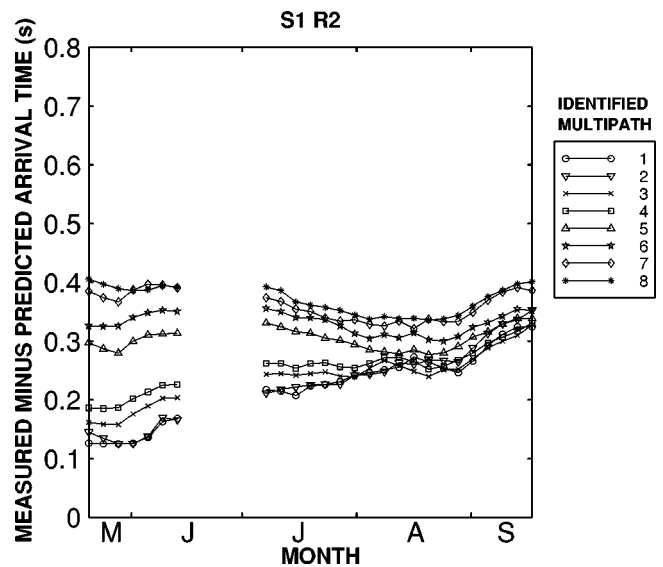
IV. COMPARISONS

A. Ray identification

A peak picking routine is used to track the multipaths in the data. The tracked multipaths are connected to spring and summer rays with dotted lines (Figs. 2–10). Some multipaths are observed in the data but not tracked by the peak picking routine. These observed multipaths are connected to rays with dashed lines. Rays matched to tracked multipaths are labeled with numbers. All other rays, either matched to observed multipaths or unmatched, are labeled with letters. All tracked and observed multipaths can be accounted for with rays. There do exist weaker multipaths in the data whose boundaries are too fuzzy to be clearly identified. It is plausible that these multipaths could be matched to rays if the signal-to-noise ratio was greater. For example, see source 2, receiver 1 (Fig. 5) at arrival times greater that 7.0 s.

Detailed ray parameters for each section are tabulated (Tables I–IX). Referring to the table header, *Ray Group* uses the same labeling as found in the corresponding data plots (Figs. 2–10). *Upper turning depth* is an average value over each ray group. A value of 50 m indicates an upper turning depth in the range from 0 to 50 m, a value of 100 m corresponds to the range from 50 to 100 m, etc. *Individual Rays in Ray Group* specifies the rays that make up a ray group. Rays with similar parameters are listed together. The next three columns have paired entries. The left entry refers to spring rays, and the right entry refers to summer rays. *Launch Angle* gives the grazing angle of the ray at the source defined as positive upwards. *Type* classifies the rays as either geometric (G) or diffracted (D). Geometric rays pass through the re-

FIG. 13. Same as Fig. 11, except for source 1, receiver 3 (S1R3).
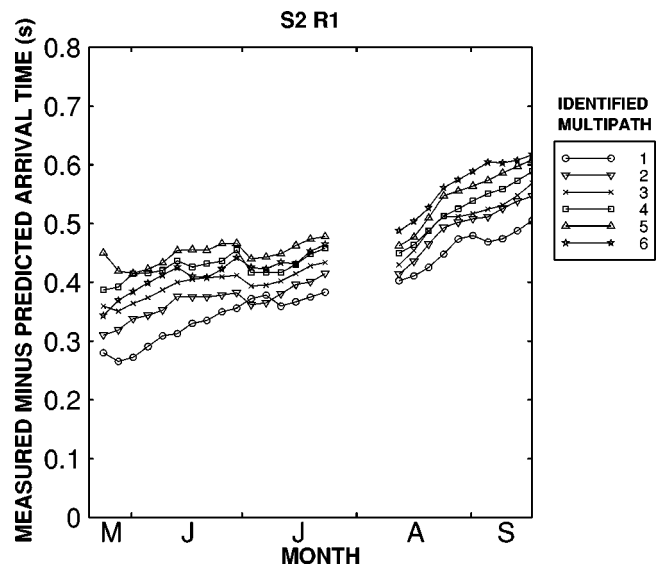
FIG. 14. Same as Fig. 11, except for source 2, receiver 1 (S2R1).

ceiver, while diffracted rays refer to energy which reaches the receiver in the shadow zone of a caustic. *Number of Bottom Bounces* is self-explanatory. Finally, *Unmatched Ray Classification* describes the unmatched rays as either ''weak diffracting'' or ''bottom interacting,'' as describe in the next paragraph.

There are two reasons reason why the unmatched rays from ZRAY have no corresponding multipaths in the data. First, it is currently difficult to make an accurate estimate of received sound levels at these acoustic frequencies because of the effects of scattering from meso and fine scales. The levels are particularly difficult to estimate when the receiver is in the shadow zone of a caustic. The surface of caustics is estimated from a set of sound-speed profiles that have been smoothed to suppress the meso and fine scale structure. Experimental and numerical evidence suggests that this structure scatters sound deep into the shadow zones of caustics.[2,19] It is beyond the scope of this paper to predict the amplitude of this scattered energy. Instead, the received level in a shadow zone is estimated using a standard formula which relates intensity to the radius of curvature of the caustic and the distance between the receiver and the caustic [Eq. (2.5.6) of Ref. 20]. The unmatched rays which correspond to energy leaking deep into the shadow zones of caustics are classified as ''weak diffracting.'' Second, rays may strike the bottom and have unrealistic received levels due to ZRAY's use of a simple bottom interaction model.[17] In some cases, rays may approach the bottom quite closely but in actuality will strike it due to small errors in the ray path or bathymetry. The unmatched rays which either strike the bottom or closely approach it are classified as ''bottom interacting.''

B. Travel times: Measured minus predicted

Differences are calculated between the measured and predicted travel times for the identified multipaths of each section (Figs. 11–19). The predicted travel times are based on the rays traced through the spring and summer seasons, where the predictions between the seasons are synthesized with linear interpolation.

With the exception of the early May arrivals of the first four multipaths of source 1, receiver 1 (Fig. 11), all of the identified multipaths arrive later than predicted. Table X summarizes all of the nonthermal effects that contribute to this difference. The estimate of total error from these effects is 0.15 s. Differences greater than 0.15 s correspond to differences between the actual ocean temperatures and those specified in Levitus' climatology. Since the observed differences between the measured and predicted travel times are of order 1 s, we conclude that the ocean's actual temperature field is significantly different than that given by Levitus.

C. Upper turning depths

Average upper turning depths are calculated for all ray groups within a section (Tables I–IX). In general, the early arriving rays, having steep launch angles, travel into the upper 50 m of the ocean. The late arriving rays, having small launch angles, travel up to within 200–300 m of the surface. For source 3, the first eight matched rays for all receivers travel into the upper 50 m of the ocean. All of the matched rays for all sections travel to within 200 m of the surface, where a majority travel into the upper 50 m. Between spring and summer, the upper turning depths for all rays differ by less than 50 m.

A majority of the matched rays travels within the seasonal thermocline, as observed previously,[4] and is therefore sensitive to seasonal variability. An area of future research is the reconstruction of the temperature field using tomography.[21]

V. DISCUSSION

Measured travel times 0.15 s different than predictions are due to discrepancies between the ocean and Levitus' climatological temperatures (Sec. IV). Temperature errors in the climatology might be reflected in the data by a correla-
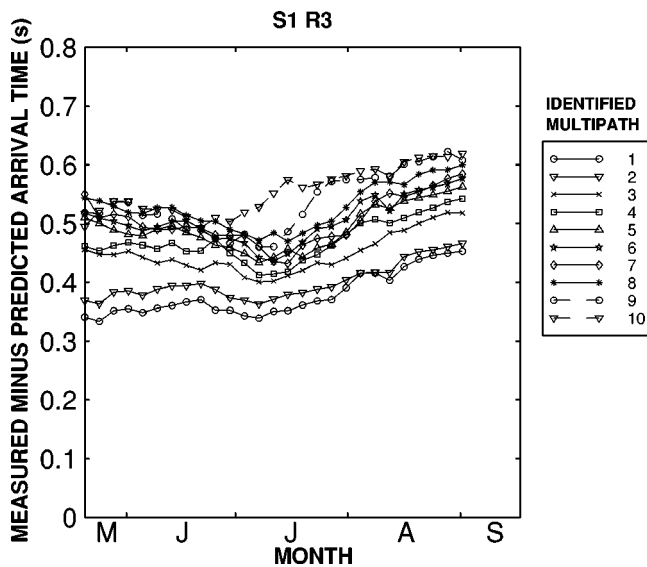
FIG. 15. Same as Fig. 11, except for source 2, receiver 2 (S2R2).
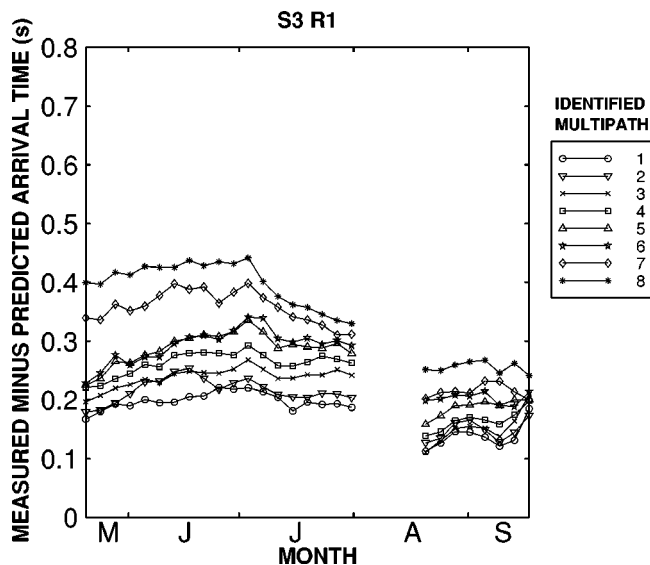
FIG. 17. Same as Fig. 11, except for source 3, receiver 1 (S3R1).

tion between range and the measured-predicted travel times difference. Average travel time differences are calculated for each section and plotted versus range (Figs. 20 and 21). The correlation for spring is high. The correlation for summer is less, but there is a trend exhibiting larger differences with increasing range. Most of the temperature variability occurs within the upper 1 km in the northeast Pacific.[22–31] About 25% of a typical ray path samples this region. To relate the difference in temperature between the real ocean and Levitus' ocean, $\delta\theta$, to the differences between the measured and predicted travel times, δt, we use the approximation,

$$\delta\theta \cong -\frac{c\,\delta t}{3.19\times10^{-3}R}\ (°C),\qquad(1)$$

where R is the ray distance traveled in the upper 1 km and c is the sound speed reference.[6] δt is calculated as an average over all of the identified rays within a section. Under our

assumptions, we estimate that the ocean within the upper 1 km is colder than Levitus' spring ocean by about 0.2 °C and colder than Levitus' summer ocean by about 0.3 °C.

If seasonal changes in temperature dominate the travel times over the test period of May to September, we would expect a decrease in the travel times, since the warming ocean yields higher sound speeds. Although there are periods where some travel times exhibit these seasonal trends, in general the travel times exhibit nonseasonal variability. For example, consider multipath 6 of source 1, receiver 3 (Fig. 4). The travel time *decreases* from June to early July by about 0.1 s/month. From early July to August it *increases* by about the same amount. The opposite trend exists for multipath 8 of source 3, receiver 3 (Fig. 10). Here the travel time *increases* by about 0.05 s/month from June to early July, and *decreases* by about 0.14 s/month from early July to August. The travel times vary from changing very little (multipaths 1–2, source 1, receiver 1, Fig. 2) to changing by about 0.25
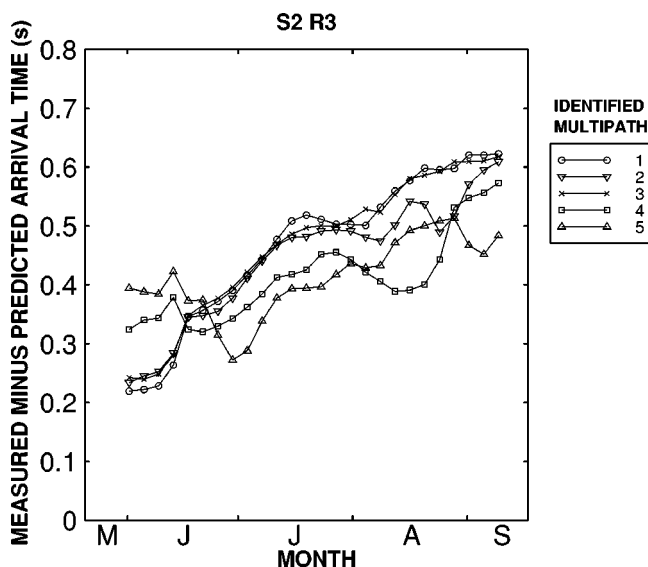
FIG. 16. Same as Fig. 11, except for source 2, receiver 3 (S2R3).

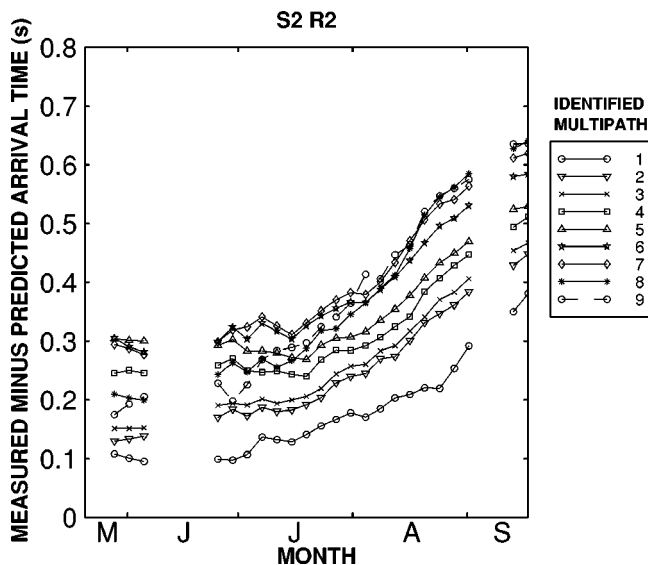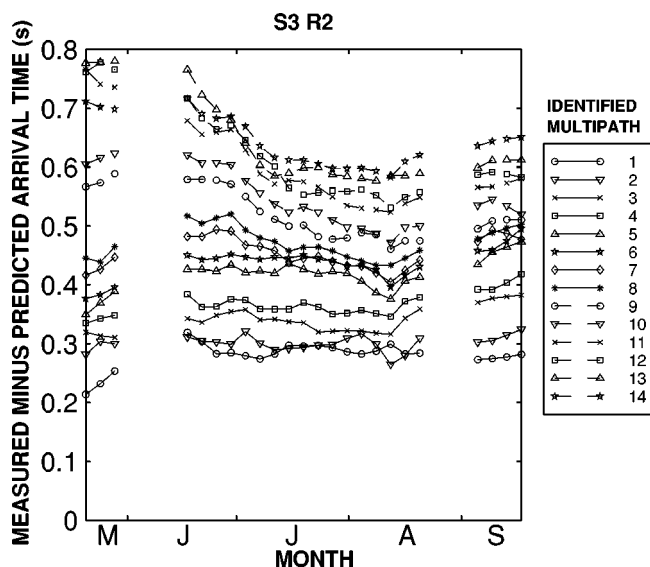

FIG. 18. Same as Fig. 11, except for source 3, receiver 2 (S3R2).

FIG. 19. Same as Fig. 11, except for source 3, receiver 3 (S3R3).

FIG. 20. Measured minus predicted arrival times as a function of range for the spring season. Each data point represents the average value over all of the rays within a section. The solid line is a least squares fit of the data. The correlation coefficient is 0.94.

s/month (multipaths 8–9, source 2, receiver 2, Fig. 6). In addition, travel time changes greater than 0.1 s/month are observed to continue for over a month. For example, see multipaths 7–12, source 3, receiver 2 (Fig. 9). During August and September, the travel times for source 2, receiver 1 (Fig. 5) tend to increase, while for source 3, receiver 1 (Fig. 8), they tend to decrease. The distance between these paths at the midpoint is about 500 km.

Variations in travel times over sections of about 1000 km have been attributed to the seasonal temperature cycle.[32] For the sections considered in this paper, with ranges of about 1700–3300 km, the observed variability in travel times implies that the temperature has spatial and temporal structure beyond that due solely to seasonal variability. The data have record lengths of four months and path separations around 500 km. Based on the travel time variability within this domain, we estimate temperature time scales to be greater than one month and temperature length scales to be 500 km or less.

It has been suggested that Rossby waves should be considered when studying basin-scale propagation.[33] Basin-scale transmissions from the Kaneohe source at Oahu have been compared with models of the ocean's circulation and it was found that Rossby waves linked to El Nino/Southern Oscillation are the only modal features which yield travel time changes large enough to be consistent with observations of ± 0.2 s.[33]

Our work supports the conclusions that (1) ray theory is successful in identifying multipath transmissions over ranges up to about 3300 km (2) the travel times have variations that, for the most part, can not be explained by seasonal variability, and (3) the thermal field is structured, with length scales of 500 km or less. Thus our findings are qualitatively consistent with those found previously and give further evidence that the Kaneohe experiment results may be generic for the northeast Pacific.[33]

TABLE X. Possible causes for differences between measured and predicted travel times. The estimate of total error is the square root of the sum of the squares of the tabulated values. (Compiled from the applicable items in Table III of Ref. 2 and Table AI of Ref. 14.)

Type of error	rms travel time (s)
Uncertainty in distance between source and receiver	0.08
Interpolating sound speed in vertical	0.07
Interpolating sound speed in horizontal	0.05
Internal wave bias	0.05
Eddy bias	0.05
Uncertainty in sound speed algorithm	0.05
Ray theory	0.01
Horizontal refraction	0.01
Currents	0.01
Clocks	0.001
Acoustic noise	0.0004
Estimate of total error	0.15

FIG. 21. Same as Fig. 20, except for the summer season. The correlation coefficient is 0.49.

[1] J. L. Spiesberger, E. Terray, and K. Prada, ''Successful ray modeling of acoustic multipaths over a 3000-km section in the Pacific,'' J. Acoust. Soc. Am. **95**, 3654–3657 (1994).

[2] J. L. Spiesberger and F. D. Tappert, ''Kaneohe acoustic thermometer further validated with rays over 3700 km and the demise of the idea of axially trapped energy,'' J. Acoust. Soc. Am. **99**, 173–184 (1996).

[3] J. L. Spiesberger, K. Metzger, and J. A. Furgerson, ''Listening for climatic temperature change in the northeast Pacific: 1983–1989,'' J. Acoust. Soc. Am. **92**, 384–396 (1992).

[4] J. L. Spiesberger and K. Metzger, ''Basin-scale tomography: A new tool for studying weather and climate,'' J. Geophys. Res. **96**, 4869–4889 (1991).

[5] J. L. Spiesberger, P. J. Bushong, K. Metzger, and T. G. Birdsall, ''Ocean acoustic tomography: Estimating the acoustic travel time with phase,'' IEEE J. Ocean Eng. **14**, 108–119 (1989).

[6] J. L. Spiesberger, P. J. Bushong, K. Metzger, and T. G. Birdsall, ''Basin-scale tomography: Synoptic measurements of a 4000-km length section in the Pacific,'' J. Phys. Oceanogr. **19**, 1073–1090 (1989).

[7] P. F. Worcester, B. D. Dushaw, and B. M. Howe, ''Gyre-scale current measurements using reciprocal acoustic transmissions,'' in *Proceedings of the IEEE Fourth Working Conference on Current Measurement* (Clinton, MD, 1990), pp. 65–70.

[8] K. Metzger, ''Signal processing equipment and techniques for use in measuring ocean acoustic multipath structures,'' Ph.D. thesis, University of Michigan, Ann Arbor, 1983.

[9] B. D. Dushaw, P. F. Worcester, B. D. Cornuelle, and B. M. Howe, ''On equations for the speed of sound in seawater,'' J. Acoust. Soc. Am. **93**, 255–275 (1993).

[10] S. P. Liberatore, ''Modified Quad-M Interrogator,'' Internal report, Department of Applied Ocean Physics and Engineering, Woods Hole Oceanograpy Institute, Woods Hole, MA (1985).

[11] S. Levitus, ''Climatological atlas of the world ocean,'' NOAA prof. paper No. 13, US Government Printing Office, Washington, DC (1982).

[12] V. A. Del Grosso, ''New equation for the speed of sound in natural waters,'' J. Acoust. Soc. Am. **56**, 1084–1091 (1974).

[13] J. L. Spiesberger and K. Metzger, ''A basin-scale (3000 km) tomographic section of temperature and sound speed in the northeast Pacific,'' Trans. Am. Geophys. Union **71**, 157 (1990).

[14] J. L. Spiesberger and K. Metzger, ''New estimates of sound speed in water,'' J. Acoust. Soc. Am. **89**, 1697–1700 (1991).

[15] J. L. Spiesberger and K. Metzger, ''A new algorithm for sound speed in seawater,'' J. Acoust. Soc. Am. **89**, 2677–2688 (1991).

[16] J. L. Spiesberger, ''Is Del Grosso's sound-speed algorithm correct?'' J. Acoust. Soc. Am. **93**, 2235–2237 (1993).

[17] J. B. Bowlin, J. L. Spiesberger, T. F. Duda, and L. F. Freitag, ''Ocean acoustical raytracing software RAY,'' Technical Report WHOI-93-10, Woods Hole Oceanography Institute, Woods Hole, MA (1992).

[18] National Geophysical Data Center, ETOPO5, ''5 minute gridded world elevations and bathymetry—A digital database,'' Boulder, CO (1987).

[19] T. F. Duda, S. M. Flatté, J. A. Colosi, B. D. Cornuelle, J. A. Hildebrand, W. S. Hodgkiss Jr., P. F. Worcester, B. M. Howe, J. A. Mercer, and R. C. Spindel, ''Measured wave-front fluctuations in 1000-km pulse propagation in the Pacific Ocean,'' J. Acoust. Soc. Am. **92**, 939–955 (1992).

[20] L. M. Brekhovskikh and Y. P. Lysanov, *Fundamentals of Ocean Acoustics* (Springer-Verlag, New York, 1991), pp. 40–42.

[21] W. Munk and C. Wunsch, ''Ocean acoustic tomography: A scheme for large-scale monitoring,'' Deep-Sea Res. **26**, 123–161 (1979).

[22] R. L. Bernstein and W. B. White, ''Time and length scales of baroclinic eddies in the central North Pacific ocean,'' J. Phys. Oceanogr. **4**, 613–624 (1974).

[23] W. B. White and A. E. Walker, ''Time and depth scales of anomalous subsurface temperature at ocean weather stations P, N, and V in the North Pacific,'' J. Geophys. Res. **79**, 4517–4522 (1974).

[24] W. B. White and R. L. Bernstein, ''Design of an oceanographic network in the midlatitude North Pacific,'' J. Phys. Oceanogr. **9**, 592–606 (1979).

[25] Y. Q. Kang, ''Low frequency temperature fluctuations in the upper 400 meters of the central north Pacific,'' Ph.D. thesis, University of Hawaii, Honolulu, 1980.

[26] W. B. White and J. F. T. Saur, ''A source of annual baroclinic waves in the eastern subtropical north Pacific,'' J. Phys. Oceanogr. **11**, 1452–1462 (1981).

[27] W. B. White and J. F. T. Saur, ''Sources of interannual baroclinic waves in the eastern subtropical north Pacific,'' J. Phys. Oceanogr. **13**, 531–544 (1983).

[28] W. B. White, ''Traveling wavelike mesoscale perturbations in the North Pacific current,'' J. Phys. Oceanogr. **12**, 231–243 (1982).

[29] C. N. K. Mooers and A. R. Robinson, ''Turbulent jets and eddies in the California current and inferred cross-shore transports,'' Science **223**, 51–53 (1984).

[30] M. M. Reinecker, C. N. K. Mooers, D. E. Hagan, and A. R. Robinson, ''A cool anomaly off northern California: An investigation using IR imagery and *in situ* data,'' J. Geophys. Res. **90**, 4807–4818 (1985).

[31] P. P. Niiler and M. M. Hall, ''Low-frequency eddy variability at 28°N, 152°W in the eastern north Pacific subtropical gyre,'' J. Geophys. Res. **18**, 1670–1685 (1988).

[32] B. D. Dushaw, P. F. Worcester, B. D. Cornuelle, and B. M. Howe, ''Variability of heat content in the central North Pacific in summer 1987 determined from long-range acoustic transmissions,'' J. Phys. Oceanogr. **23**, 2650–2666 (1993).

[33] J. L. Spiesberger, H. E. Hurlburt, M. Johnson, M. Keller, S. Meyers, and J. O'Brien, ''Acoustic thermometry data compared with two ocean models: The importance of Rossby waves and ENSO in modifying the ocean interior,'' Dyn. Atmos. Oceans **26** (4) (1998).

Single mode excitation, attenuation, and backscatter in shallow water

Donald F. Gingras

Naval Command, Control and Ocean Surveillance Center San Diego, California 92152

In shallow water, bottom interaction may have a negative effect on the performance of active sonars. In this paper it is shown that a vertical array of weighted sources driven in an appropriate frequency band can be used to minimize the deleterious effects of bottom interaction, i.e., attenuation and backscatter. Simulation results (based on two-dimensional cw field calculations) are presented for three canonical geoacoustic models using both a winter and summer sound speed profile. It is shown through selective excitation of only mode one there exists a favorable frequency band providing both minimum attenuation and bottom generated backscatter. [S0001-4966(98)06001-9]

PACS numbers: 43.30.Es, 43.30.Gv, 43.30.Vh [SAC-B]

INTRODUCTION

It has long been known that the ocean bottom can exert a strong influence on acoustic propagation in shallow water; see for example Refs. 1–5 and the references therein. Two important effects of the bottom influence are attenuation due to bottom interaction and backscatter generated by reflection from the water sediment interface. For shallow water active sonar applications, it may be useful to consider spatial focusing of the signal energy away from the water–sediment interface in order to reduce the effects of bottom interaction and reflection. By exploiting the geometric and geoacoustic characteristics of the shallow water channel, it is possible to accomplish this focusing by proper design of the signal transmitter.

The minimization of attenuation and backscatter can be accomplished through the exploitation of two well-known shallow water phenomena. First, individual modes can be excited, and second, each mode has a frequency band of minimum attenuation. Using the fact that the first mode often experiences the least attenuation and propagates with the smallest grazing angle leads to a transmitter design that excites only the first mode. Excitation of only the first mode, in the frequency band of minimum attenuation, will provide a favorable shallow water propagation situation. The determination of the frequency band that provides minimum attenuation and minimum bottom generated backscatter was an important aspect of this analysis. Surface scattering effects were not considered in the analysis, but since mode one propagates with a small grazing angle the surface scattering effects due to surface interaction will also be reduced.

There has been a significant amount of work conducted on the use of a vertical array of receivers and/or sources to isolate individual modes in an underwater channel. Ingenito[6] showed that mode separation could be achieved experimentally in shallow water for both range-independent and range-dependent environments. King[7] reported on experimental results aimed toward individual mode enhancement. Gazanhes *et al.* reported on successful experimental mode identification work in a reduced scale model waveguide.[8] Clay and Huang[9] also reported on experimental work in a scale model

waveguide where the first mode was excited by shading a vertical array in amplitude to match the mode one eigenfunction. Finally, Gazanhes *et al.*[10] reported on a comprehensive set of mode excitation and filtering experiments in a scale model waveguide where mode interference and mode conversion was also examined. Some initial work directed toward the demonstration that individual modes could be excited to reduce backscatter appeared in Refs. 11–13.

A commonly observed effect in shallow water is that the ocean bottom acts as a low-loss acoustic reflector confining the acoustic energy to a duct, bounded below by the ocean bottom and above by the pressure release surface. Such a waveguide has the property that each of the propagating modes has a low-frequency cutoff. High frequencies are attenuated both by sea water absorption and bottom interaction leaving a band capable of propagating acoustic signals with relatively low loss. The presence of an optimal propagation band for shallow water was investigated by Jensen and Kuperman by comparing theory with experimental results.[14] More recently Eller and Gershfeld investigated the optimum frequency of propagation issue analytically using canonical bottom models.[15]

The approach followed herein employed a transmitter consisting of a vertical array of sources (with 12 and 24 sources) weighted in amplitude and polarity to excite only mode one. The number of sources was selected to coincide with an experimental system currently under development. The performance as a function of frequency issue was addressed by evaluating the mode one attenuation as a function of frequency to determine a frequency band of minimum attenuation. The bottom generated backscatter was evaluated using random realizations of bathymetry profiles generated using a linear stochastic model. Average backscatter was computed over multiple realizations of the random bathymetry profile. The two-way parabolic equation (PE) model developed by Collins and Evans was used for backscatter computations.[16]

The issue of reverberation modeling in shallow water has been addressed often; for example see Refs. 17–21, and the references therein. In most cases the reverberation mod-

els use an empirical scattering function such as Lambert's law. For example, Refs. 17, 18, 20, and 21 combine a Lambert's law scattering function with a normal mode approach for propagating the field for a range-independent environment, whereas Schneider[19] used the same scattering method but with a range-dependent PE model to propagate the field. In Ref. 20 Lambert's law calculations are provided illustrating the effects of bottom loss, bistatic geometry, water depth and array beam patterns for a range-independent case. Ideally, one would like to have a three-dimensional range-dependent time domain calculation based on a realistic physical scattering method, but such a model does not yet exist.

In this paper the calculation of bottom reflected energy is made with a range-dependent PE backscatter model which instead of a Lambert's law scattering approach introduces a rough bottom to directly generate the forward scatter and backscatter; see Ref. 16. This backscatter approach should be superior to a Lambert's law calculation because it solves a deterministic problem that includes all of the physics. The use of the two-way PE backscatter model falls short of the ideal model by the fact that it is limited to two-dimensional calculations and by the fact that a single frequency calculation was used. In spite of these shortcomings, it appears that the two-way PE model provides important realism, i.e., complicated range dependence and many scattering events.

The objective of this work was the evaluation of single mode excitation in a shallow water waveguide. The motivation being that excitation of a single mode may lead to a performance benefit for some active sonars through two mechanisms: (i) reduced bottom interaction (and thus reduced bottom attenuation loss) for the propagating signal; and (ii) reduced backscatter from the water–sediment interface. It is implicity assumed that by reducing bottom attenuation loss the signal energy in the water column will be increased and thus the target echo as seen by the receiver should be greater, furthermore that by reducing the energy reflected from the bottom the reverberation seen by the receiver should be decreased.

I. MODE EXCITATION AND FILTERING

The introduction of a directional source into the calculation of the acoustic field using normal modes was first discussed by Bucker and Morris in 1965.[22] In that paper the authors indicated that the introduction of directional sources into the normal-mode calculations was quite straightforward and provided a solution based on superposition. In 1966 Clay[23] provided the theoretical framework for understanding the use of vertical arrays as mode filters. In 1974 Williams and Novak[24] discussed the issue of using a vertical array of discrete sources to excite or receive a single mode and provided a directivity pattern for excitation of the first mode in shallow water. The only at-sea experimental results involving a vertical source array in shallow water were reported by King in 1974, he showed results obtained at a sight in the Block Island Sound.[7] Through the use of amplitude and phase shading of the source array he successfully enhanced the signal level at desired locations in the water column, but did not report on individual mode excitation. At the same

time Ingenito[6] reported on experimental results in shallow water where mode separation was achieved using a weighted vertical receive array. In 1978 Gazanhes *et al.*[8] reported on the identification of individual modes using a weighted receive array in an acoustic tank.

References 9 and 10 conducted mode excitation experiments in acoustic tanks. Clay and Huang[9] conducted experiments at 220 kHz and demonstrated excitation and propagation of the first mode. Gazanhes and Garnier[10] working at 124 kHz used a vertical source array containing 15 sources, whose gain and polarity depended on the mode to be excited, to demonstrate the individual excitation and propagation of modes 1 through 5.

In this section, in order to simplify the discussion, it is assumed that the ocean waveguide is horizontally stratified, i.e., the sound speed varies only with depth. In the subsequent sections this assumption is eliminated. For long range propagation it is well established that under the stratified assumption the solution of the wave equation and boundary conditions can be expressed as a sum of normal modes.[25] Assuming azimuthal symmetry and using cylindrical coordinates the horizontal distance from the origin to some point in the channel is r, and the depth with respect to the ocean surface is z with the depth axis pointing downward. For a harmonic point source at the origin at depth z_0 the pressure field in the far field at the point r,z can be expressed as

$$p(r,z;z_0) = \sum_{m=1}^{\infty} \phi_m(z)\phi_m(z_0)H_0^{(1)}(\kappa_m r), \qquad (1)$$

where the mode eigenfunctions $\{\phi_m\}$ and the mode eigenvalues $\{\kappa_m\}$ satisfy the equation

$$\frac{d^2\phi_m(z)}{dz^2} + \left[\left(\frac{\omega}{c(z)}\right)^2 - \kappa_m^2\right]\phi_m(z) = 0 \qquad (2)$$

together with boundary conditions; $H_0^{(1)}$ is the zeroth-order Hankel function of the first kind. The normal-mode eigenfunctions $\{\phi_m\}$ form a complete orthonormal set satisfying the orthonormality relation

$$\int_0^{\infty} \rho(z)\phi_n(z)\phi_m(z)dz = \delta_{n,m}, \qquad (3)$$

where the density $\rho(z)$ takes an appropriate value in each layer and $\delta_{n,m}$ is the Kronecker delta function.

The mode orthonormality condition of Eq. (3) provides the basis for single mode excitation. Assume there is a vertical array of sources at the origin located at depths $z_1, z_2, \ldots, z_L$. Furthermore assume that only a finite number of modes M propagate to the point r,z in the field. In this case by applying Eq. (1) the pressure field at the point r,z to the array of sources is written as

$$p(r,z;z_1,z_2,\ldots,z_L) = \sum_{j=1}^{L} a_j \sum_{m=1}^{M} \phi_m(z_j)\phi_m(z)H_0^{(1)}(\kappa_m r),$$

$$(4)$$

where the set of coefficients $\{a_j\}$ $j = 1,2,\ldots,L$ are the shading or weighting coefficients for each of the L sources in the array. Let the weighting coefficients be defined by the eigen-

Model	Sediment type	Relative density ρ_s/ρ_w	Relative speed c_s/c_w	Compressional speed c_s (m/s)	Compressional attenuation $\alpha(\mathrm{dB}/\lambda)$	Critical angle θ_c (deg.)
A	Coarse sand	2.03	1.20	1800	0.70	32
B	Silt	1.77	1.06	1593	1.02	17
C	Clayey silt	1.47	1.01	1516	0.12	7

function of the nth mode sampled at the source depths, that is

$$a_j \equiv \phi_n(z_j) \quad j=1,2,...,L. \qquad (5)$$

In this case the pressure field at the point r,z due to the weighted source array is given by

$$p(r,z;z_1,z_2,...,z_L) = \phi_n(z)H_0^{(1)}(\kappa_n r)\sum_{j=1}^{L} \phi_n^2(z_j)$$
$$+ \sum_{\substack{m=1 \\ m \neq n}}^{M} \gamma_{mn}\phi_m(z)H_0^{(1)}(\kappa_m r), \qquad (6)$$

where $\gamma_{mn} \equiv \Sigma_{j=1}^{L}\phi_m(z_j)\phi_n(z_j)$; note that γ_{mn} is a discrete approximation of the integral of Eq. (3). The first term of Eq. (6) represents the field contribution at the point r,z due to mode n, the second term represents the cross-mode contributions. For L sufficiently large, by the mode orthonormality condition of Eq. (3), it would be expected that the cross-mode contributions would be small. The magnitude of these contributions are governed by two factors: (1) the spatial sampling scheme used in the source array and (2) that the discrete approximation is carried out over the depth range of 0 to z_L rather than the full range of 0 to ∞.

II. MODE ATTENUATION

Since both attenuation and backscatter are affected by the geoacoustic parameters of the sediment, the analysis was carried using three different canonical geoacoustic models. All models contained a homogeneous sediment layer 450 m thick with a highly attenuating infinite half-space below the sediment, $\alpha_c = 10$ dB/λ. The first model, model A (coarse sand), represented a situation where the compressional speed in the sediment was high the density was high and the acoustic energy was returned primarily by reflection at the water sediment interface. Model B (silt) represented a "softer" sediment situation. Both the compressional speed and density were closer to the water values at the interface. Model C (clayey silt) represented a situation where the sediment density was lower than models A and B and the compressional speed was close to the water value at the interface. These three models represent a wide variation of sediment types. The sediment parameters are from Ref. 15. Table I summarizes the geoacoustic parameters for the three canonical models.

The plane-wave reflection loss at the water sediment interface as a function of grazing angle was evaluated for each of the canonical geoacoustic models, using the relationships from Ref. 15. The magnitude of the plane-wave reflection coefficient was evaluated for each of the three canonical

models over a range of grazing angles from 0 to 35 degrees. The results are illustrated by Fig. 1, an estimate of the critical angle was included in Table I. As expected for model A with the coarse sand sediment the critical angle is quite large, on the order of 32 degrees, and the reflection loss coefficient is small. Models B and C represent intermediate cases with critical angles of around 17 and 7 degrees, respectively. As indicated by Fig. 1 the range of critical angles and bottom reflection loss coefficients is fairly large, thus these three canonical geoacoustic models represent a wide variety of propagation conditions.

For evaluation of attenuation versus frequency both a winter and summer sound speed profile was included; see Fig. 2. The attenuation coefficient associated with the first mode for each of the canonical models was evaluated as a function of frequency using the SACLANTCEN normal-
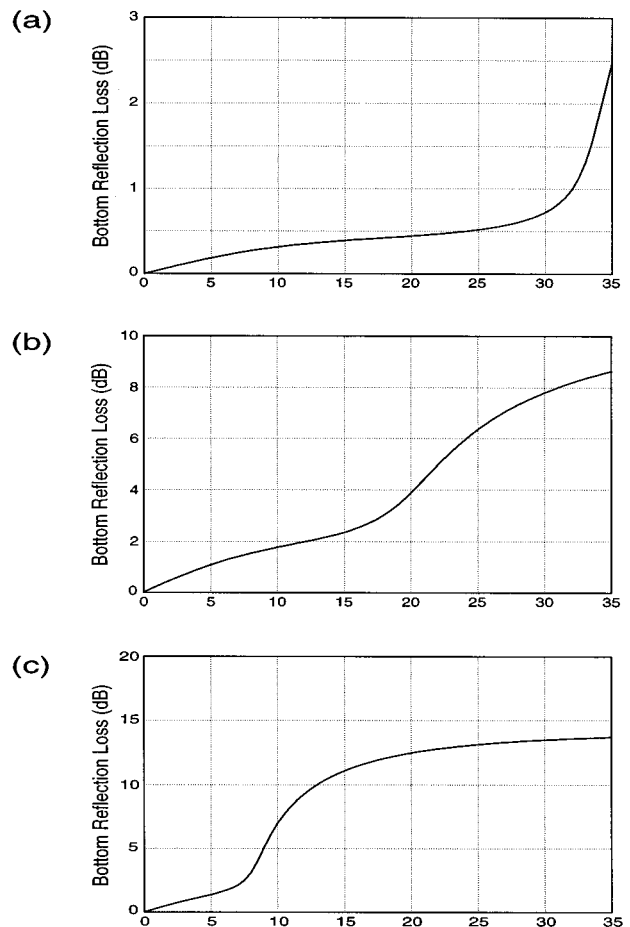
FIG. 1. Bottom reflection loss at the water–sediment interface as a function of grazing angle, (a) Model A—coarse sand; (b) model B—silt; (c) model C—clayey silt.
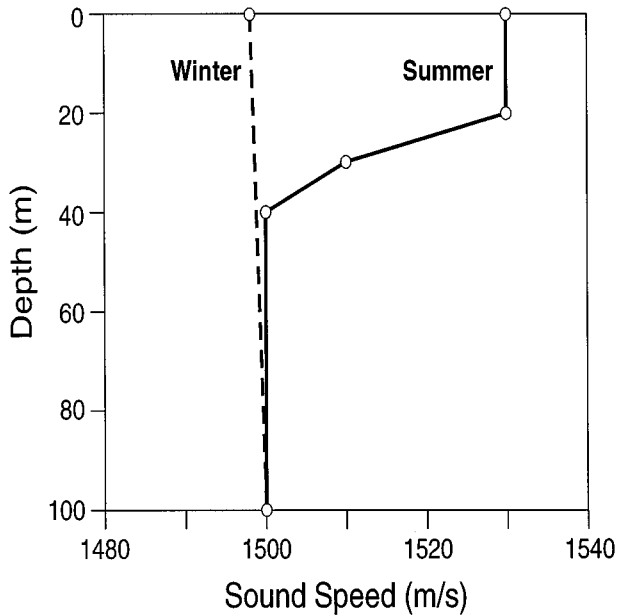
FIG. 2. The canonical sound-speed profiles for winter and summer.

FIG. 3. Mode one attenuation as a function of frequency; (a) winter and (b) summer. The dashed portion indicates the frequency region where the attenuation in the sediment is greater than the attenuation in the water.

mode model, SNAP.[26] The SNAP attenuation coefficients are computed for each mode as a sum of individual loss terms with each term corresponding to a particular loss mechanism. The loss mechanisms considered herein were compressional-wave attenuation in the water and compressional-wave attenuation in the sediment. Due to the thickness of the sediment layer the attenuation in the subbottom was not a factor. These results are illustrated in Fig. 3. Figure 3(a) illustrates the attenuation of mode one for the three canonical models using the winter profile. The results are quite interesting. Note the strong dependence on frequency for all models. For each model the transition frequency where the attenuation in the sediment is a minimum and the attenuation in the water is a minimum is clearly indicated. For model A the minimum is in the 200–300 Hz region, while for models B and C the minimum has moved up in frequency to about 250–500 Hz. Figure 3(b) illustrates the situation using the summer sound speed profile. Overall the attenuation is higher for the summer case and the minimum as a function of frequency is not as pronounced as it was for the winter case. For the summer case the minimum for model A occurs at about the same frequency as for the winter case. But for models B and C the minimum has moved up in frequency to about 600 Hz. From the results of Fig. 3(a) and (b), it is clear that a frequency band of minimum attenuation can be selected for the propagation of mode one for each of the geoacoustic models.

III. BACKSCATTER SIMULATION RESULTS

In this section the results obtained using the two-way PE method to evaluate backscatter as a function of frequency are presented. Results are presented for the three canonical geoacoustic models using both the winter and summer sound speed profiles. The effect of shear was not included in the backscatter simulations. The backscatter results presented are the result of averaging over backscatter calculations computed using multiple realizations of random bathymetry profiles.
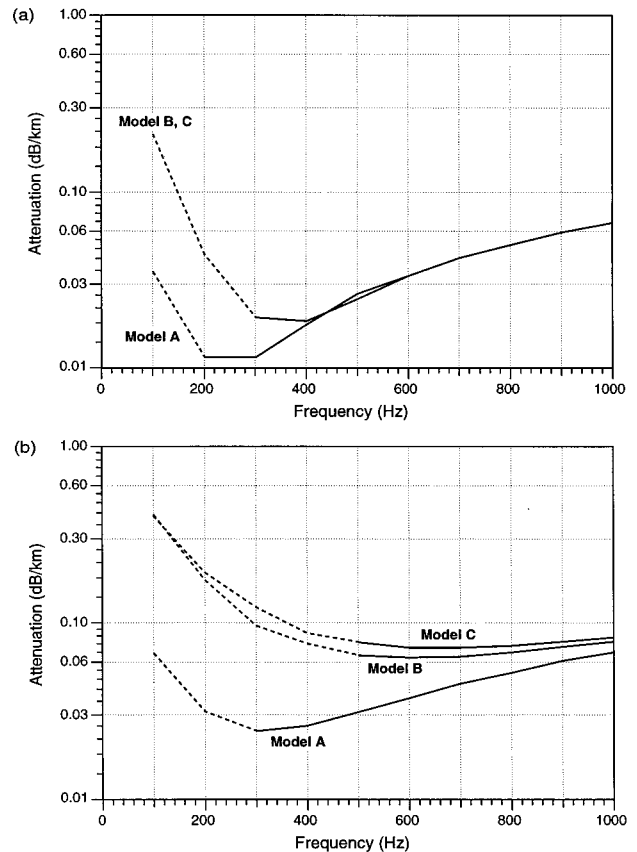
A. Bathymetry model

The bathymetry profile or two-dimensional surface height function, h_n, where the index n represents the range variable, is treated as a discrete random process. That is, for any value of n h_n is a random variable whose properties are determined by some underlying probability distribution function. As discussed by Ogilvy[27] the numerical generation of the surface height function often involves the application of linear stochastic models such as autoregressive (AR) and moving average (MA) models; see also Ref. 28. The correct choice of the linear model parameters allows for careful control of the statistics of the surface realizations, such as height probability distribution and autocorrelation function properties.

The random variable h_n represents the surface height at some range $r_n = n\Delta r$, where Δr represents the discretization interval on the range axis. For the analysis presented herein an autoregressive process model was used. In this case the surface height random process is defined by

$$h_n = \sum_{l=1}^{N} \phi_l h_{n-l} + u_n, \tag{7}$$
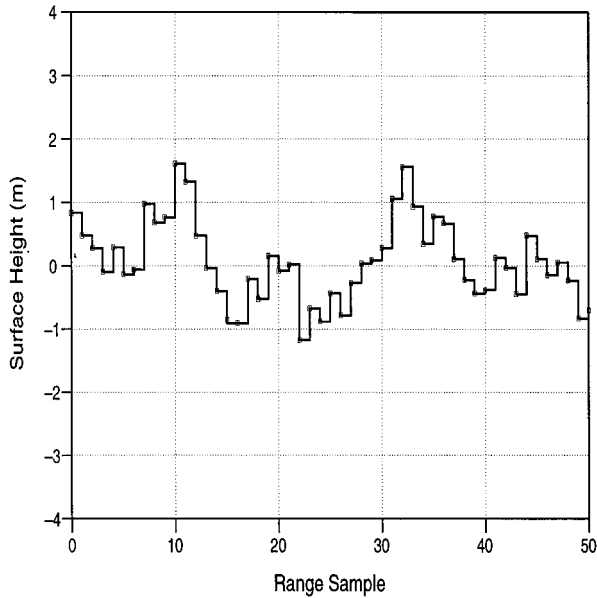
FIG. 4. Single realization of AR(1) random surface height generated with $\sigma_u^2 = 0.25$ m and $\phi = 0.8$.

where u_n is an uncorrelated random process with variance σ_u^2, N is the order of the process and the set of coefficients $\{\phi_l\}$ are the constants which control the statistical properties. A first-order autoregressive process AR(1) was used, in this case we have

$$h_n = \phi h_{n-1} + u_n. \tag{8}$$

Under the assumption that $|\phi| < 1$ the process is considered to be asymptotically stationary (up to order 2) with the surface autocorrelation function given by

$$C_n = \phi^{|n|}, \tag{9}$$

which, for $\phi > 0$, is an exponentially decaying function.

For the analysis conducted herein large-scale slow variations of bathymetry as a function of range were desired. Thus, the surface realizations were generated using a highly correlated first-order autoregressive process driven by an uncorrelated Gaussian process with variance $\sigma_u^2 = 0.25$ m. The AR coefficient ϕ was set equal to 0.8 which provides a high degree of correlation. From Eq. (9) the autocorrelation is seen to be on the order of 0.5 at $n = 3$ for the above described AR(1) process. The variance of the surface height process is given by

$$\sigma_h^2 = \frac{\sigma_u^2}{(1-\phi^2)}. \tag{10}$$

By Eq. (10) with the variance of the Gaussian process u_n set at 0.25 m and the AR coefficient ϕ, set to 0.8 the resulting standard deviation for the surface height process h_n was 0.83 m. Figure 4 illustrates an example realization of a random surface height function generated using the AR(1) model. Examining Fig. 4 it is seen that this AR(1) model, with $\Delta r = 100$ m, provides the type of large-scale slowly varying bathymetry versus range profile that was desired, that is on the order of ± 1 m of surface height variation over 1 km.

For each realization of the surface height random process a realization of a bathymetry versus range profile was constructed for input to the two-way PE propagation model. The bathymetry vs range profile contained a deterministic component, constant as a function of range, and a zero-mean Gaussian component generated by the random surface height function; see Eq. (8).

B. PE based backscatter

It is well known that the PE method is efficient for solving acoustic propagation problems with range-dependent environments. Recently the PE method was extended to handle backscatter from deterministic deformations in the boundaries, this version is referred to as the two-way PE.[16] The two-way PE is based on a single-scattering approximation and the approach of two-way coupled modes in which range-dependent environments are approximated by a sequence of range-independent regions. At the vertical boundaries between regions the solution of the two-way PE is required to satisfy continuity conditions. Note, as discussed in Ref. 16, in order to avoid the unrealistic focusing and multiple scattering that occurs for a point source in cylindrical geometry the two-way PE was implemented as a line source in plane geometry, the spreading factor $1/\sqrt{r}$ is not included in the field computation.

As with all PE based propagation codes the forward propagation was initiated with a ''starting field.'' For this application a mode-based starting field which was a function of the source depth was used. This application required a vertical array of sources to be used rather than a single omnidirectional source, thus the PE starting field was modified to incorporate multiple sources as follows. Let $\mathbf{w}_j(z)$ be the starting-field pressure vector for a source at depth z_j, i.e., pressure vs depth sampled on some grid as generated by the mode-based field starter. Then by Eq. (4) it follows that the total starting-field vector $\mathbf{u}(z)$ for a source array with sources at depths $z_1, z_2, \ldots, z_L$ is given by

$$\mathbf{u}(z) = a_1 \mathbf{w}_1(z) + a_2 \mathbf{w}_2(z) + \cdots + a_L \mathbf{w}_L(z), \tag{11}$$

where the set $\{a_j\}$ $j = 1, 2, \ldots, L$ are weighting coefficients used to effect single mode excitation. To facilitate comparing backscattered fields for various source array configurations, the weighting coefficients were normalized for constant power, i.e., $\Sigma_{j=1}^{L} a_j^2 = 1$.

Given the starting-field $\mathbf{u}(z)$ the PE solution proceeds in two steps. Starting at the source array, $r = 0$, the outgoing PE is used to propagate the forward field across the range-independent regions. In regions in which backscattering is expected to be important, transmitted (forward scattered) and reflected (backscattered) fields are computed at the vertical interfaces between range-independent regions. The reflected fields are stored for later use. After this process has reached the maximum range, the incoming PE is used to propagate the incoming reflected fields. See Ref. 16 for further details on the PE based scattering method.

Throughout the following section, in order to display the results as a function of frequency, an average of the backscattered field $B_{avg}(z)$ is used. Let $u(\alpha, r, z)$ be the reflected (backscattered) field [u_r of Eq. (15) of Ref. 16] where α
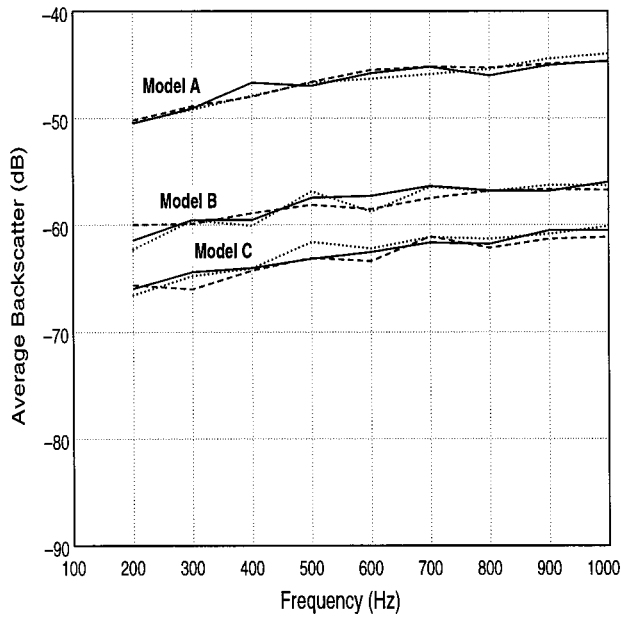
FIG. 5. Average backscatter as a function of frequency for one source at 50 m at three receiver depths, 40 m (dotted), 50 m (solid), and 60 m (dashed) for winter profile.

FIG. 6. Average backscatter as a function of frequency for one source at 50 m at three receiver depths, 40 m (dotted), 50 m (solid), and 60 m (dashed) for summer profile.

represents the bathymetry realization, r the range in meters and z the depth in meters. The average backscatter is computed as follows:

$$B_{avg}(z) = 20 \log \sum_\alpha \sum_r |u(\alpha,r,z)/u(\alpha,1,z)| \qquad (12)$$

for $\alpha = 1,..., 20$, and for the range interval $r = 0$ to 5 km.

C. Monte Carlo simulation results

The objective of the Monte Carlo simulations was to evaluate bottom generated backscatter, $B_{avg}(z)$, as a function of frequency, season, and sediment properties. The average backscatter as a function of frequency was computed for each of the three geoacoustic models (see Table I) using the winter and summer sound speed profiles of Fig. 2. The random bathymetry versus range realizations were calculated using a range step interval of 100 m. The deterministic component of the bathymetry was set to 100 m.

Figure 5 illustrates the average backscatter as a function

of frequency for a single source at 50 m for the winter profile. The backscatter at three receiver depths, 40, 50, and 60 m, is presented for the three geoacoustic models. There is almost no variation of the average backscatter as a function of receiver depth. For this case, a single source at 50 m, it is seen that there is only a fairly small variation of the average backscatter as a function of frequency, the backscatter increases with increasing frequency. The dependence of the average backscatter on geoacoustic parameters is seen to be significant. For model A, the highly reflecting case (largest critical angle), the average backscatter is the largest of the three models. There is a substantial difference, 15 dB, for the average backscatter between that obtained with model A versus model C. The results of Fig. 5 clearly indicate that the average backscatter level is reduced as the critical angle decreases. Figure 6 illustrates the average backscatter as a function of frequency for a single source at 50 m for the summer profile. Overall the backscatter versus frequency as a func-

TABLE II. Source array configurations as a function of frequency for the winter profile.

	12 sources			24 sources		
Frequency (Hz)	First source (m)	Last source (m)	Source spacing (m)	First source (m)	Last source (m)	Source spacing (m)
200	2.0	94.4	8.4	2.0	98.6	4.2
300	2.0	94.4	8.4	2.0	98.6	4.2
400	2.0	94.4	8.4	2.0	98.6	4.2
500	2.0	90.0	8.0	2.0	94.0	4.0
600	2.0	90.0	8.0	2.0	94.0	4.0
700	2.0	76.8	6.8	2.0	80.2	3.4
800	2.0	72.4	6.4	2.0	75.6	3.2
900	2.0	68.0	6.0	2.0	71.0	3.0
1000	2.0	63.6	5.6	2.0	66.4	2.8
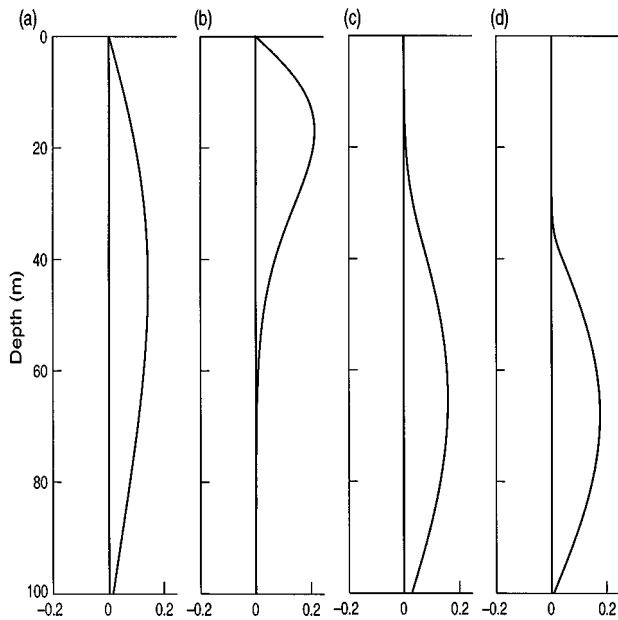
FIG. 7. Mode one eigenfunction as a function of depth, model A; (a) winter 200 Hz, (b) winter 1000 Hz, (c) summer 200 Hz, and (d) summer 1000 Hz.

FIG. 8. Average backscatter at 50 m as a function of frequency for model A using three source arrays, winter profile.

tion of geoacoustic model are about the same for the winter and summer profiles.

Table II illustrates the source array configurations used for the winter profile. The source-to-source spacing varied with frequency to account for the fact that the shape of the mode one eigenfunction varies with frequency; see Fig. 7. For example, at 200 Hz the winter mode one eigenfunction is nonzero over the entire water column, but at 1000 Hz the eigenfunction is only nonzero over the interval from 0 to 60 m. Thus the source-to-source spacing was adjusted with frequency in an attempt to keep most of the sources in the nonzero portion of the eigenfunction. The selection of the array source positions in the water column could be optimized to provide a configuration that is ''optimum'' with respect to backscatter reduction. This optimization could not feasibly be carried out over all frequencies and all geoacoustic models, thus the configurations of Table II may not provide the best results (minimum backscatter) obtainable. These configurations do provide a good indication of the performance that could be expected. Some of the variability

of the average backscatter as a function of frequency observed in the results presented below may be due to a non-optimum array configuration at a particular frequency. Table III provides the source array configurations used for summer profile.

Figure 8 illustrates average backscatter for geoacoustic model A with the winter profile. The average backscatter was calculated for three source array configurations (one source at 50 m, 12 sources, and 24 sources as in Table II) as a function of frequency. As shown by Fig. 5 there was little variation of the backscatter as a function of frequency when there was only one source. The average backscatter for the source array with 12 sources was substantially below that for a single source in the lower part the frequency band, that is below 400 Hz. Above 400 Hz there was no advantage (less backscatter than single source) when the source array with 12 sources was used. The reduction at 200 Hz was on the order of 12 dB. At the higher frequencies, above 400 Hz, 12 sources were not sufficient to eliminate the higher-order

TABLE III. Source array configurations as a function of frequency for the summer profile.

	12 sources			24 sources		
Frequency (Hz)	First source (m)	Last source (m)	Source spacing (m)	First source (m)	Last source (m)	Source spacing (m)
200	18.0	97.2	7.2	15.0	97.8	3.6
300	23.0	97.8	6.8	20.0	98.2	3.4
400	27.0	97.4	6.4	25.0	98.6	3.2
500	30.0	96.0	6.0	28.0	97.0	3.0
600	33.0	96.8	5.8	31.0	97.7	2.9
700	33.0	96.8	5.8	31.0	97.7	2.9
800	35.0	96.6	5.6	33.0	97.4	2.8
900	35.0	96.6	5.6	33.0	97.4	2.8
1000	35.0	96.6	5.6	33.0	97.4	2.8

FIG. 9. Average backscatter at 50 m as a function of frequency for model A using three source arrays, summer profile.

FIG. 10. Average backscatter at 50 m as a function of frequency for model B using three source arrays, winter profile.

mode excitation and thus were not as effective at reducing the backscatter. Alternatively, for the source array with 24 sources, there was a substantial reduction of the bottom generated backscatter across the entire frequency band. The reduction was most significant, 18–24 dB with respect to the single source case, in the band from 300 to 450 Hz. Overall, for geoacoustic model A, the use of a source array with 24 sources weighted to excite mode one significantly reduced the bottom generated backscatter over the band from 200 to 1000 Hz with the band from 300 to 450 providing the minimum backscatter.

Figure 9 illustrates average backscatter for geoacoustic model A as a function of frequency with the summer profile. The summer results were quite similar to those obtained using the winter profile except that there was not a null in backscatter in the 300–450 Hz band. For the summer profile the backscatter reduction due to using source arrays was fairly uniform as a function of frequency across the band from 300 to 700 Hz. The average reduction was on the order of 12 dB across the band. As with the winter profile a source array with 24 sources was required to obtain significant reduction of backscatter over a large band. For the summer profile there is an anomaly from 200 to 300 Hz, the average backscatter is greater for the 24 source array than for the 12 source array. This is due to the shape of the summer mode one eigenfunctions (see Fig. 7) the summer mode function is nonzero at the bottom interface. The array configuration is such that the 24 source array has a source closer to the bottom than the 12 source array, thus this nonzero mode function at the bottom is excited more efficiently and there is more backscatter. Above 300 Hz the mode function is zero at the bottom interface and the anomaly disappears. This anomaly will also be apparent for the other models for the summer profile.

Figure 10 illustrates average backscatter for geoacoustic model B with the winter profile. For this model the average
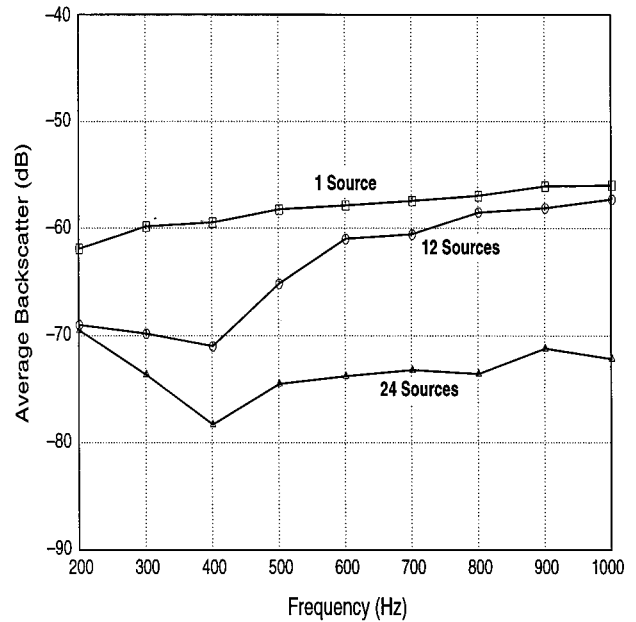
backscatter for all three source array configurations was less than those for model A. The source array with 12 sources provided a reduction, with respect to that obtained with one source, across the entire frequency band varying from 2 to 10 dB. Above 600 Hz the source array with 12 sources did not provide a significant reduction of the backscatter. The source array with 24 sources provided a substantial reduction (about 16 dB) for the average backscatter across the band from 350 to 1000 Hz, the minimum backscatter level was at 400 Hz.

Figure 11 illustrates the average backscatter for model B with the summer profile. It is seen that with the summer
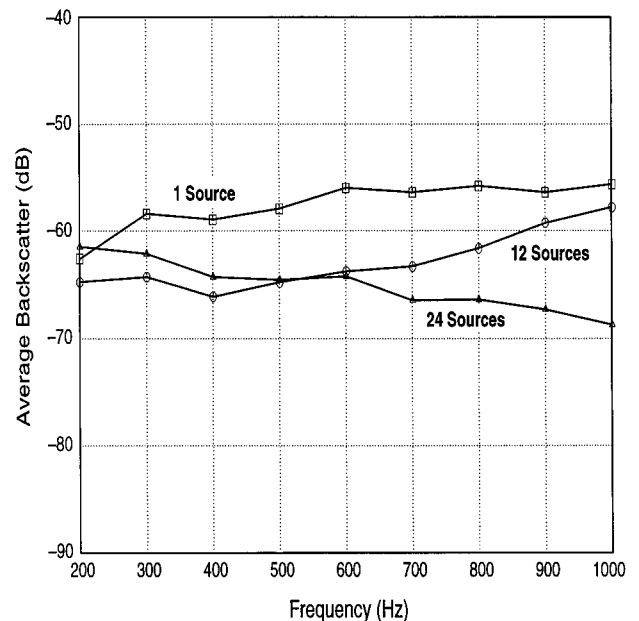
FIG. 11. Average backscatter at 50 m as a function of frequency for model B using three source arrays, summer profile.

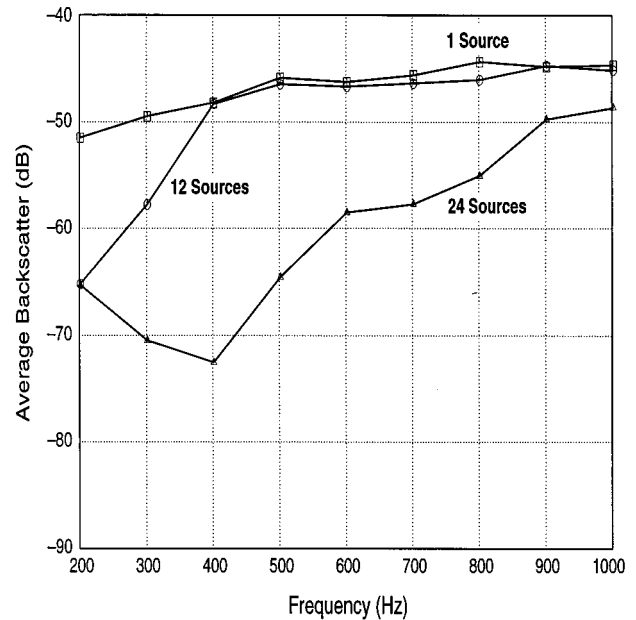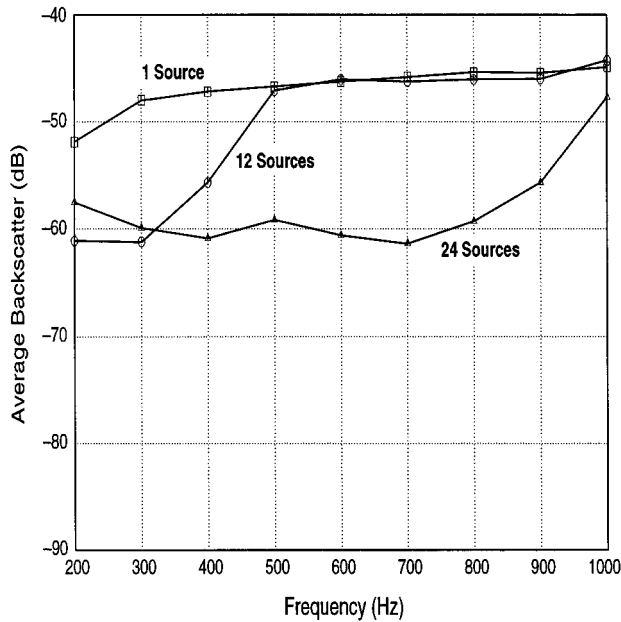FIG. 12. Average backscatter at 50 m as a function of frequency for model C using three source arrays, winter profile.
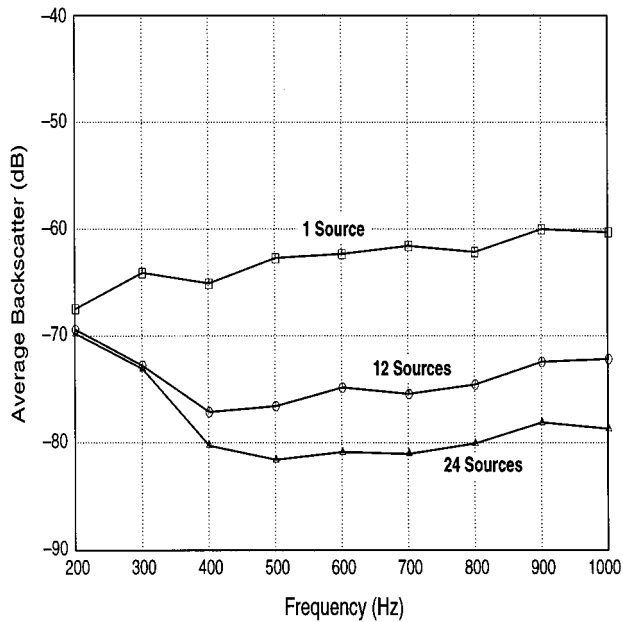
FIG. 13. Average backscatter at 50 m as a function of frequency for model C using three source arrays, summer profile.

profile the effectiveness of the multiple source arrays for backscatter reduction is less than for the winter profile. The reduction is greatest across the band from 700 to 1000 Hz for the 24 source array. For frequencies below 600 Hz, the 12 source array is slightly more effective, again because of the shape of the summer mode one eigenfunction at the sediment interface.

Figure 12 illustrates the average backscatter for geoacoustic model C with the winter profile. For this geoacoustic model the average backscatter for all three source array configurations is less than that for models A and B. The source array with 12 sources provided a reduction, with respect to that obtained with one source, of 13 dB in the band from 400 to 800 Hz. The result obtained using 24 sources is on average about 4 dB better than that obtained with 12 sources. The result for the source array with 24 sources is quite impressive, the reduction is on the order of 16 dB across the band from 400 to 1000 Hz.

For geoacoustic model C with the summer profile the average backscatter results are presented on Fig. 13. For this case the backscatter reduction is only on the order of 2 dB below 400 Hz. Above 400 Hz the reduction varies from 4 dB to 8 dB. The band from 700 to 1000 provides the greatest reduction. As previously discussed, due to the shape of the summer mode one eigenfunction, the source array with 12 sources outperforms the 24 source array over most of the frequency band.

For all three geoacoustic models with the summer profile there was a frequency where the amplitude of the mode one eigenfunction becomes small at the water sediment interface and the source array with 24 sources begins to outperform the source array with 12 sources. For model A this occurred at 300 Hz, for model B at 600 Hz, and for model C at 900 Hz.
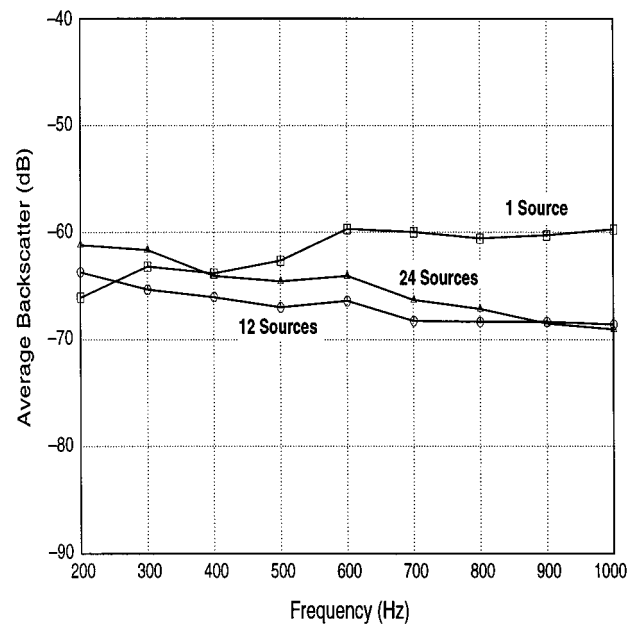
IV. SUMMARY

In this section the combined results for minimum attenuation and minimum backscatter are discussed. We first consider the winter profile. Examining Fig. 3(a) it is apparent that there is a well-defined minimum for attenuation as a function of frequency for each of the geoacoustic models. Comparing Figs. 8, 10, and 12, a frequency band of minimum backscatter can also be identified. Overall, the backscatter reduction obtained using a source array with 24 sources was significant over a large band for all three geoacoustic models. A band containing both minimum attenuation and minimum backscatter can be identified. These results are compiled in Table IV. The last column of Table IV contains the limits for the frequency band of minimum attenuation and minimum backscatter for the winter profile. For this profile the width of the band for both minimum attenuation and backscatter is fairly narrow, i.e., 100–150 Hz, because there is only a fairly limited region of overlap for the two bands. The center frequency of the favorable band increases as a function of the geoacoustic model from A to C, clearly indicating that the properties of the sediment are an important factor in the selection of an operating band. Note also that the amount of backscatter reduction is also dependent on the sediment properties.

Similar results were compiled using Figs. 3(b), 9, 11,

TABLE IV. Frequency bands of minimum attenuation and backscatter for the winter sound speed profile.

Geoacoustic model	Minimum attenuation band (Hz)	Minimum backscatter band (Hz)	Maximum backscatter reduction (dB)	Combined best band (Hz)
A	150–400	300–450	24	300–400
B	250–500	350–800	18	350–500
C	250–500	400–800	18	400–500

TABLE V. Frequency bands of minimum attenuation and backscatter for the summer sound speed profile.

Geoacoustic model	Minimum attenuation band (Hz)	Minimum backscatter band (Hz)	Maximum backscatter reduction (dB)	Combined best band (Hz)
A	200–600	300–700	16	300–600
B	400–1000	700–1000	12	700–1000
C	400–1000	700–1000	8	700–1000

and 13 for the summer profile; see Table V. For this case, since the mode one attenuation is fairly flat as a function of frequency, it is seen that the favorable bands are wider, i.e., 300 Hz. Overall for the summer profile the backscatter reduction is less than that obtained for the winter profile.

From Figs. 5 and 6 it was seen that the seasonal (winter versus summer) effect was small when one source was used. But when mode one excitation was used the seasonal effect was seen to be important. This of course follows directly from the shape of the mode one eigenfunctions. The mode one eigenfunction for the summer profile ''peaks'' closer to the water sediment interface than that for the winter profile; see Fig. 7. It should be noted, even though the backscatter reduction for the summer profile is not as significant as that for the winter profile there remains a significant reduction for all three models with respect to a single source.

In summary, it appears that the use of source arrays with multiple sources weighted in amplitude and polarity to excite the mode one eigenfunction provides a significant improvement in terms of minimizing both attenuation and backscatter for a wide variety of geoacoustic models and for a wide range of frequencies. While the simulations were limited to the 200–1000 Hz band the results of the backscatter computations indicate that backscatter reduction via mode one excitation may well be effective at frequencies above 1000 Hz.

ACKNOWLEDGMENTS

[1] D. E. Weston, ''Propagation of sound in shallow water,'' J. Br. IRE **26**, 329–337 (1963).

[2] D. E. Weston, ''Intensity-range relations in oceanographic acoustics,'' J. Sound Vib. **18**, 271–287 (1971).

[3] F. Ingenito and S. N. Wolf, ''Acoustic propagation in shallow water overlying a consolidated bottom,'' J. Acoust. Soc. Am. **60**, 611–617 (1976).

[4] L. A. Rubano, ''Acoustic propagation in shallow water over a low-velocity bottom,'' J. Acoust. Soc. Am. **67**, 1608–1613 (1980).

[5] F. B. Jensen, ''Sound propagation in shallow water: A detailed description of the acoustic field close to surface and bottom,'' J. Acoust. Soc. Am. **70**, 1397–1406 (1981).

[6] F. Ingenito, ''Excitation, propagation, and attenuation of acoustic normal modes in shallow water,'' in *Sound Propagation in Shallow Water*, edited by O. F. Hastrup and O. V. Olesen, Rep. CP-14, SACLANT Undersea Research Centre (La Spezia, Italy, 1974).

[7] L. A. King, ''Enhancement techniques in transmitting and receiving underwater acoustic modes,'' in *Sound Propagation in Shallow Water*, edited by O. F. Hastrup and O. V. Olesen, Rep. CP-14, SACLANT Undersea Research Centre (La Spezia, Italy, 1974).

[8] C. Gazanhes, J. P. Sessarego, and J. L. Garnier, ''Identification of modes in some conditions of sound propagation in shallow water,'' J. Sound Vib. **56**, 251–259 (1978).

[9] C. S. Clay and K. Huang ''Single mode transmission and acoustic backscattering measurements in a laboratory waveguide,'' J. Acoust. Soc. Am. **67**, 792–794 (1980).

[10] C. Gazanhes and J. L. Garnier, ''Experiments on single mode excitation in shallow water propagation,'' J. Acoust. Soc. Am. **69**, 963–969 (1981).

[11] R. B. Williams, ''A modal interference method for shallow water reverberation suppression,'' J. Acoust. Soc. Am. **92**, 2468 (1992).

[12] R. B. Williams, ''A shallow water system for maximizing echo to reverberation,'' in *Low Frequency Active Sonar*, edited by R. Weatherburn and G. Murdock, Rep. CP-42, SACLANT Undersea Research Centre (La Spezia, Italy, 1993).

[13] D. F. Gingras, ''Channel-adapted source for shallow water,'' in *Low Frequency Active Sonar*, edited by R. Weatherburn and G. Murdock, Rep. CP-42, SACLANT Undersea Research Centre (La Spezia, Italy, 1993).

[14] F. B. Jensen and W. A. Kuperman, ''Optimum frequency of propagation in shallow water environments,'' J. Acoust. Soc. Am. **73**, 813–819 (1983).

[15] A. I. Eller and D. A. Gershfeld, ''Low frequency acoustic response of shallow water ducts,'' J. Acoust. Soc. Am. **78**, 622–631 (1985).

[16] M. D. Collins and R. B. Evans, ''A two-way parabolic equation for acoustic backscattering in the ocean,'' J. Acoust. Soc. Am. **91**, 1357–1368 (1992).

[17] H. P. Bucker and H. E. Morris, ''Normal-mode reverberation in channels or ducts,'' J. Acoust. Soc. Am. **44**, 827–828 (1968).

[18] R. Zhang and G. Jin, ''Normal mode theory of the average reverberation intensity in shallow water,'' J. Sound Vib. **119**, 215–223 (1984).

[19] H. Schneider, ''Surface loss, scattering, and reverberation with the split step parabolic wave equation model,'' J. Acoust. Soc. Am. **93**, 770–781 (1993).

[20] D. D. Ellis, ''Shallow water reverberation: Normal mode model predictions compared with bistatic towed-array measurements,'' IEEE J. Ocean. Eng. **18**, 474–482 (1993).

[21] D. D. Ellis, ''A shallow water normal mode reverberation model,'' J. Acoust. Soc. Am. **97**, 2804–2814 (1995).

[22] H. P. Bucker and H. E. Morris, ''Normal-mode intensity calculations for a constant-depth shallow water channel,'' J. Acoust. Soc. Am. **38**, 1010–1017 (1965).

[23] C. S. Clay, ''Use of arrays for acoustic transmission in a noisy ocean,'' Rev. Geophys. **4**, 475–507 (1966).

[24] A. O. Williams and B. M. Novak, ''Normal-mode analysis of underwater-sound propagation with directional sources and receivers,'' J. Acoust. Soc. Am. **55**, 80–83 (1974).

[25] F. B. Jensen, W. A. Kuperman, M. B. Porter, and H. Schmidt, *Computational Ocean Acoustics* (American Institute of Physics, New York, 1994).

[26] F. B. Jensen and M. C. Ferla, ''SNAP-The SACLANTCEN normal mode propagation model,'' SACLANT Undersea Research Centre, SM-121 (La Spezia, Italy, 1979).

[27] J. A. Ogilvy, *Theory of Wave Scattering from Random Rough Surfaces* (Hilger, Bristol, 1991).

[28] G. E. P. Box and G. M. Jenkins, *Time Series Analysis: Forecasting and Control* (Holden-Day, San Francisco, 1976).

The effect of temperature, pressure, and salinity on sound attenuation in turbid seawater

Simon D. Richards

Defence Evaluation & Research Agency, DERA Winfrith, Winfrith Technology Centre, Dorset DT2 8XJ, United Kingdom

The acoustic attenuation coefficient in shallow coastal waters is of interest to designers and operators of devices such as naval mine-hunting sonars, sidescan surveying sonars, and acoustic Doppler current profilers, typically employing frequencies ranging from tens of kHz to several hundred kHz, possibly up to 1 MHz. At these frequencies attenuation due to suspended particulate matter which characterizes turbid coastal waters is an important contribution to the total attenuation coefficient. In this paper the effect of temperature, pressure, and salinity on the total attenuation coefficient for seawater containing a suspension of solid particles is investigated by employing suitable expressions for the sound speed, density, and viscosity of seawater as functions of temperature, salinity, and pressure. Results presented demonstrate that while there is little variation in the attenuation with pressure in up to a few hundred meters of water, there is significant variation with temperature and salinity over the ranges found globally in the sea. [S0001-4966(98)00301-4]

PACS numbers: 43.30.Es, 43.30.Ft [DLB]

INTRODUCTION

Sonar performance modeling has traditionally focused on the low-frequency, long-range deep ocean problem, well away from coastal influences. More recently, attention has turned to the study of the performance of acoustic devices operating in shallow, coastal environments, characterized by high levels of suspended mineral particles relative to the open ocean. Devices operating in these environments, such as naval minehunting sonars, sidescan surveying sonars, and acoustic Doppler current profilers, typically employ frequencies from tens of kHz to hundreds of kHz, possibly up to 1 MHz, with propagation paths of up to several hundred meters. At these frequencies and ranges the additional sound attenuation arising from viscous absorption and scattering by particles suspended in the water has been shown[1,2] to be an important contribution to the total volume attenuation coefficient, and should therefore be taken into account in high-frequency sonar performance models in shallow water environments.

Shallow coastal environments are highly variable, with temperature varying both seasonally and as a result of diurnal heating locally, as well as exhibiting large variations with geographic location. Salinity also varies greatly, from nearly fresh water in river estuaries to highly saline water in very warm, shallow seas such as the Persian Gulf. The variation in the attenuation of sound in clear seawater with temperature, pressure (or depth), and salinity is well established, and is accounted for in the various empirically derived formulas for the attenuation coefficient of seawater. The attenuation by suspended particles will also depend on temperature, pressure, and salinity, since it depends on the compression wave speed, density, and viscosity of the seawater, which all depend on temperature, pressure, and salinity. In this paper suitable expressions are employed for density, viscosity, and sound speed in seawater as a function of temperature, salinity, and pressure in order to investigate the variation in the attenuation coefficient of seawater containing suspended particles over the ranges of these parameters found in the environment.

It is recognized that microbubbles which are prevalent in shallow water environments may also contribute to the total attenuation, and that it is likely that this effect will also depend on temperature, pressure, and salinity. It is also possible that the bubble population itself may be influenced by these parameters. These effects are not discussed in the present paper.

I. THEORY

The intensity attenuation coefficient of seawater containing suspended particles may be written

$$\alpha = \alpha_w + \alpha_v + \alpha_s, \tag{1}$$

where α_w is the attenuation coefficient in clear seawater, α_v is the attenuation due to viscous absorption by suspended particles, and α_s is the attenuation due to scattering by suspended particles. Expressions for these terms are given in the following sections.

A. Attenuation in clear seawater

The absorption of sound in clear seawater is considered as the sum of the contributions from pure water, and two ionic relaxation processes involving magnesium sulphate $(MgSO_4)$ and boric acid $[B(OH)_3]$. Contributions from other ionic reactions are small and are neglected. Several expressions exist for calculating the absorption in seawater (e.g., Refs. 3–5), but the one that appears to be the most complete is that due to Francois and Garrison.[6] Their expression yields the total attenuation due to the three contributions as a function of frequency, pressure, temperature, salinity, and pH, and may be written as

$$\alpha_w = 10^{-3}\left[\frac{A_1 P_1 f_1 f^2}{f^2 + f_1^2} + \frac{A_2 P_2 f_2 f^2}{f^2 + f_2^2} + A_3 P_3 f^2\right] \text{ dB m}^{-1}, \tag{2}$$

where the A_i represent the temperature and salinity dependencies, the P_i are the pressure dependencies, the f_i are the relaxation frequencies, and the subscripts 1,2,3, refer to the boric acid, magnesium sulphate, and pure water contributions, respectively. These terms are given below.[6]

1. Boric acid contribution

$$A_1 = \frac{8.86}{c} \times 10^{(0.78pH - S)} \text{ dB km}^{-1} \text{ kHz}^{-1}, \tag{3}$$

$$P_1 = 1, \tag{4}$$

$$f_1 = 2.8(S/35)^{0.5} \times 10^{(4 - 1245/(t + 273))} \text{ kHz}, \tag{5}$$

where c is the sound speed (m s^{-1}), t is the temperature (°C), and S is the salinity (ppt).

2. Magnesium sulphate contribution

$$A_2 = 21.44(S/c)(1 + 0.025t) \text{ dB km}^{-1} \text{ kHz}^{-1}, \tag{6}$$

$$P_2 = 1 - 1.37 \times 10^{-4}d + 6.2 \times 10^{-9}d^2, \tag{7}$$

$$f_2 = \frac{8.17 \times 10^{(8 - 1990/(t + 273))}}{1 + 0.0018(S - 35)} \text{ kHz}, \tag{8}$$

where d is the depth (m).

3. Pure water contribution

$$P_3 = 1 - 3.83 \times 10^{-5}d + 4.9 \times 10^{-10}d^2. \tag{9}$$

For $t \leq 20$ °C,

$$A_3 = 4.937 \times 10^{-4} - 2.59 \times 10^{-5}t + 9.11 \times 10^{-7}t^2$$
$$- 1.50 \times 10^{-8}t^3 \text{ dB km}^{-1} \text{ kHz}^{-1}. \tag{10}$$

For $t > 20$ °C,

$$A_3 = 3.964 \times 10^{-4} - 1.146 \times 10^{-5}t + 1.45 \times 10^{-7}t^2$$
$$- 6.5 \times 10^{-10}t^3 \text{ dB km}^{-1} \text{ kHz}^{-1}. \tag{11}$$

B. Attenuation by suspended particles

The presence of solid particles in suspension leads to two additional attenuation mechanisms; viscous absorption and scattering. Viscous absorption arises from the phase lag between the particles and the ambient fluid, due to the particles having higher inertia than an equivalent volume of fluid. This leads to a velocity gradient in a boundary layer on the surface of the particles which leads to frictional heat generation and hence absorption in a viscous fluid. The particles also scatter sound in all directions, representing a loss of energy from the primary wave.

1. Viscous absorption

Urick[7] derived an expression for the viscous absorption attenuation coefficient based on consideration of the expression for viscous drag developed by Stokes.[8] Urick's expression can be written

$$\alpha_v = (10 \log e^2)\left(\frac{\epsilon k(\sigma - 1)^2}{2}\left[\frac{\tau}{\tau^2 + (\sigma + \delta)^2}\right]\right) \text{ dB m}^{-1} \tag{12}$$

with

$$\delta = \frac{1}{2}\left[1 + \frac{9}{2\beta a}\right], \quad \tau = \frac{9}{4\beta a}\left[1 + \frac{1}{\beta a}\right], \tag{13}$$

where ϵ is the volume fraction of suspended material, $k = \omega/c$ is the wave number of the incident compression waves with c the compression wave speed, $\sigma = \rho'/\rho$ is the ratio of the solid density to the fluid density, a is the particle radius, and $\beta = \sqrt{\omega/2\nu}$ is the reciprocal of the skin depth for viscous shear waves, with ω the angular frequency and ν the kinematic viscosity of the fluid.

2. Scattering

Many workers have investigated sound scattering from suspended spheres, and expressions may easily be found in the literature (e.g., Ref. 9) for the far-field scattering form function, f_∞. Such approaches generally treat the particle as a homogeneous sphere which may be rigid and movable, rigid and immovable, or elastic. The elastic models in particular lead to complicated scattering form functions due to resonant excitation and are in agreement with laboratory measurements of scattering from single scatterers.[9] However, when dealing with naturally occurring sediment populations the particles will be irregular in shape and size and well-defined resonances will not occur.[10] In addition, each particle will have differences in the detailed structure of the scattering form functions. Therefore, when considering the combined effect of a large number of such irregular particles, details of any resonant structure become smeared out, and it is appropriate to use a simpler form for the scattering form function. Such an approach was used by Johnson[11] in developing the so-called high-pass model for backscattered intensity from a fluid sphere. Here, a simple second-order polynomial in $x = ka$ is used to represent the amplitude scattering form function approximately by requiring that it fits the form of f_∞ exactly in the Rayleigh (small x) and geometric (large x) regimes. The exact amplitude scattering form function for a sphere varies as x^2 in the Rayleigh regime and becomes constant in the geometric regime, so a polynomial fit to this resembles the response curve of a high-pass filter, hence the nomenclature. When discussing intensity, a fourth-order polynomial is required since intensity varies as the square of the amplitude.

Sheng and Hay[12] constructed a high-pass model for the attenuation coefficient for scattering by a suspension of spheres, and their expression may be written

$$\alpha_s = (10 \log e^2) \frac{\epsilon K_\alpha x^4}{a(1 + \xi x^2 + \frac{4}{3}K_\alpha x^4)} \text{ dB m}^{-1}, \tag{14}$$

where

$$K_\alpha = \frac{1}{6}\left(\gamma_\kappa^2 + \frac{\gamma_\rho^2}{3}\right) \tag{15}$$

TABLE I. Coefficients for calculation of viscosity.

	$j=0$	$j=1$	$j=2$	$j=3$
Q_{0j}	1.79×10^{-2}	-6.1299×10^{-4}	1.4467×10^{-5}	-1.6826×10^{-7}
Q_{1j}	-1.8266×10^{-7}	1.3817×10^{-8}	-2.6363×10^{-10}	0
Q_{2j}	9.8972×10^{-12}	-6.3255×10^{-13}	1.2116×10^{-14}	0
R_j	2.4727×10^{-5}	4.8429×10^{-7}	-4.7172×10^{-8}	7.5986×10^{-10}

and ξ is an adjustable constant $\geqslant1$. The ξ term allows the form of the polynomial to be adjusted to improve the fit to experimental data for intermediate x values. Here γ_κ and γ_ρ are the compressibility and density contrasts given by

$$\gamma_\kappa=\frac{\kappa'-\kappa}{\kappa}, \tag{16}$$

$$\gamma_\rho=\frac{3(\rho'-\rho)}{2\rho'+\rho}, \tag{17}$$

where κ and κ' are the bulk compressibilities of the fluid and solid, respectively.

C. Temperature, pressure, and salinity dependencies

The empirically based Francois and Garrison equation for sound attenuation in clear seawater explicitly includes temperature, pressure, and salinity dependencies. The expressions for absorption and scattering by suspended particles do not, however, include these quantities explicitly. Nevertheless the absorption will depend on temperature, pressure, and salinity since the density, compressibility, and viscosity of seawater all depend on these quantities. Therefore, by employing suitable expressions for density, compressibility, and viscosity as functions of temperature, pressure, and salinity, the effect of these quantities on the total attenuation may be investigated.

1. Viscosity

Matthäus[13] gives a formula for calculating the molecular viscosity, η (Pa s), of seawater as a function of temperature t ($^\circ$C), salinity S (ppt), and pressure p (dbar), which is valid for $0\,^\circ$C$\leqslant t\leqslant30\,^\circ$C, $0\leqslant S\leqslant36$, and 1 dbar$\leqslant p\leqslant1000$ dbar. By employing summation notation his formula may be expressed in the following form:

$$\eta(S,t,p)=0.1\left[\sum_i p^i\sum_j Q_{ij}t^j+S\sum_k R_k t^k\right], \tag{18}$$

where Q_{ij} and R_k are coefficients obtained by fitting to experimental data. These coefficients are given in Table I.

The kinematic viscosity used in Eq. (12) is given by $\nu=\eta/\rho$.

2. Sound speed

The UNESCO standard formula[14] for computing sound speed in seawater as a function of temperature, pressure, and salinity is that due to Chen and Millero.[15] More recent measurements[16] of acoustic pulse propagation time in the ocean have suggested that this formula predicts a sound speed that is too high at high hydrostatic pressures, and that

the formulism due to Del Grosso[17] is more accurate. However, the difference between the predictions of the Del Grosso equation and the international standard are only significant at depths of greater than about 1000 m,[16] and since this paper is concerned with shallow water applications in water which is much shallower than 1000 m, the standard formula has been used.

Using summation notation as for viscosity, the Chen and Millero formula may be written

$$c(S,t,p)=C_w(t,p)+A(t,p)S+B(t,p)S^{3/2}+D(p)S^2 \tag{19}$$

with

$$C_w(t,p)=\sum_i p^i\sum_j C_{ij}t^j, \tag{20}$$

$$A(t,p)=\sum_i p^i\sum_j A_{ij}t^j, \tag{21}$$

$$B(t,p)=\sum_i p^i\sum_j B_{ij}t^j, \tag{22}$$

$$D(p)=\sum_i D_i p^i. \tag{23}$$

The coefficients C_{ij}, A_{ij}, B_{ij}, and D_i are given in Table II. This expression is valid for $0\,^\circ$C$\leqslant t\leqslant40$ C, $0\leqslant S\leqslant40$, and 0 dbar$\leqslant p\leqslant10\,000$ dbar.

3. Density

The expressions for the density of seawater as a function of temperature, pressure, and salinity used here are taken from Ref. 14. These are based on the international equation of state for seawater diluted with pure water or concentrated by evaporation,[18,19] which is valid for $-2\,^\circ$C$\leqslant t\leqslant40\,^\circ$C, $0\leqslant S\leqslant42$, and 0 dbar$\leqslant p\leqslant10\,000$ dbar.

The density of seawater may be written

$$\rho(S,t,p)=\frac{\rho(S,t,0)}{1-p/K(S,t,p)}, \tag{24}$$

where $K(S,t,p)$ is the secant bulk modulus.

Using summation notation as before, the density at $p=0$ may be expressed

$$\rho(S,t,0)=\rho_w+S\sum_i b_i t^i+S^{3/2}\sum_j c_j t^j+d_0 S^2, \tag{25}$$

where

$$\rho_w=\sum_i a_i t^i \tag{26}$$

TABLE II. Coefficients for the calculation of sound speed.

	$j=0$	$j=1$	$j=2$	$j=3$	$j=4$	$j=5$
A_{0j}	1.389	-1.262×10^{-2}	7.164×10^{-5}	2.006×10^{-6}	-3.21×10^{-8}	0
A_{1j}	9.4742×10^{-5}	-1.2580×10^{-5}	-6.4885×10^{-8}	1.0507×10^{-8}	-2.0122×10^{-10}	0
A_{2j}	-3.9064×10^{-7}	9.1041×10^{-9}	-1.6002×10^{-10}	7.988×10^{-12}	0	0
A_{3j}	1.100×10^{-10}	6.649×10^{-12}	-3.389×10^{-13}	0	0	0
B_{0j}	-1.922×10^{-2}	-4.42×10^{-5}	0	0	0	0
B_{1j}	7.3637×10^{-5}	1.7945×10^{-7}	0	0	0	0
C_{0j}	1402.388	5.03 711	$-5.80\,852\times10^{-2}$	3.3420×10^{-4}	-1.478×10^{-6}	3.1464×10^{-9}
C_{1j}	0.153563	6.8982×10^{-4}	-8.1788×10^{-6}	1.3621×10^{-7}	-6.1185×10^{-10}	0
C_{2j}	3.1260×10^{-5}	-1.7107×10^{-6}	2.5974×10^{-8}	-2.5335×10^{-10}	1.0405×10^{-12}	0
C_{3j}	-9.7729×10^{-9}	3.8504×10^{-10}	-2.3643×10^{-12}	0	0	0
D_0	1.727×10^{-3}	...	...	...	...	...
D_1	-7.9836×10^{-6}	...	...	...	...	...

and coefficients a_i, b_i, c_i, and d_i are given in Table III.

The secant bulk modulus is given by

$$K(S,t,p)=K(S,t,0)+Ap+Bp^2, \qquad (27)$$

where

$$K(S,t,0)=K_w+S\sum_i f_it^i+S^{3/2}\sum_j g_jt^j, \qquad (28)$$

$$A=A_w+S\sum_i i_it^i+j_0S^{3/2}, \qquad (29)$$

$$B=B_w+S\sum_i m_it^i, \qquad (30)$$

$$K_w=\sum_i e_it^i, \qquad (31)$$

$$A_w=\sum_i h_it^i, \qquad (32)$$

and

$$B_w=\sum_i k_it^i. \qquad (33)$$

Again, the coefficients are listed in Table III.

II. RESULTS

The attenuation in turbid seawater has been calculated using the Francois and Garrison expression [Eq. (2)] for absorption in clear seawater together with the expressions for attenuation due to absorption and scattering by a suspension of spherical particles [Eqs. (12) and (14)]. The sound speed, density, and viscosity of seawater used in these equations were calculated using the expressions in the previous section as functions of temperature, salinity, and pressure. Results are thus presented for attenuation in turbid seawater as a function of temperature, salinity, and pressure, over the ranges

$$0\,°\text{C}\leqslant t\leqslant 30\,°\text{C},$$

$$0\ \text{ppt}\leqslant S\leqslant 35\ \text{ppt},$$

$$1\ \text{dbar}\leqslant p\leqslant 900\ \text{dbar}.$$

It has been assumed that the variation in the bulk compressibility and density of solid mineral particles can be considered to be negligible compared with the variation of the physical properties of the seawater over these parameter ranges.

It may be seen from Sec. I A that only the boric acid relaxation is dependent on pH. Since we are interested in frequencies well above the boric acid relaxation frequency, this is not an important attenuation mechanism and the effect of pH on the attenuation may be neglected. All results pre-

TABLE III. Coefficients for the calculation of density.

	$j=0$	$j=1$	$j=2$	$j=3$	$j=4$	$j=5$
a_i	999.842 594	$6.793\,952\times10^{-2}$	$-9.095\,290\times10^{-3}$	$1.001\,685\times10^{-4}$	$-1.120\,083\times10^{-6}$	$6.536\,332\times10^{-9}$
b_i	$8.24\,493\times10^{-1}$	-4.0899×10^{-3}	7.6438×10^{-5}	-8.2467×10^{-7}	5.3875×10^{-9}	0
c_i	$-5.72\,466\times10^{-3}$	1.0227×10^{-4}	-1.6546×10^{-6}	0	0	0
d_i	4.8314×10^{-4}	0	0	0	0	0
e_i	19 652.21	148.4206	$-2.327\,105$	$1.360\,477\times10^{-2}$	$-5.155\,288\times10^{-5}$	0
f_i	54.6746	$-0.603\,459$	$1.09\,987\times10^{-2}$	-6.1670×10^{-5}	0	0
g_i	7.944×10^{-2}	1.6483×10^{-2}	-5.3009×10^{-4}	0	0	0
h_i	3.239 908	$1.43\,713\times10^{-3}$	$1.16\,092\times10^{-4}$	$-5.77\,905\times10^{-7}$	0	0
i_i	2.2838×10^{-3}	-1.0981×10^{-5}	-1.6078×10^{-6}	0	0	0
j_i	$1.91\,075\times10^{-4}$	0	0	0	0	0
k_i	$8.50\,935\times10^{-5}$	$-6.12\,293\times10^{-6}$	5.2787×10^{-8}	0	0	0

FIG. 1. Attenuation as a function of temperature and salinity for $p = 1$ dbar, $f = 1$ MHz, $a = 1$ μm, and $M = 1$ kg m^{-3}.

FIG. 3. Attenuation as a function of pressure and salinity for $t = 0$ °C, $f = 1$ MHz, $a = 1$ μm, and $M = 1$ kg m^{-3}.

sented in this paper were calculated using a pH of 8.0. It is evident from Eqs. (12) and (14) that the attenuation due to suspended particles is assumed to be linearly dependent on ϵ, the volume fraction of solid in suspension. This assumption is valid for dilute suspensions where particle interaction effects such as multiple scattering may be ignored. It has been shown experimentally[7] that this is the case for quartz (sand) grains in water at frequencies of order MHz for volume fractions of up to 8%–9%. In this paper a mass concentration of $M = 1$ kg m^{-3} has been assumed, which for quartz-like particles [$\rho' = 2600$ kg m^{-3} (Ref. 20)], corresponds to a volume fraction of $\epsilon = M/\rho' \sim 0.04\%$. This is therefore well within the dilute regime. This concentration is relatively high, and has been chosen to demonstrate the effects under investigation. However, concentrations of this order and greater have been observed in shallow, turbid environments e.g., Ref. 21.

Figure 1 shows the attenuation as a function of tempera-

ture and salinity for $p = 1$ dbar, $f = 1$ MHz, $a = 1$ μm, and $M = 1$ kg m^{-3}. This figure shows that, for the given parameters, the attenuation decreases significantly as the temperature is increased. Over the range 0 °C$\leq t \leq$30 °C the attenuation in dB m^{-1} changes by a factor of approximately 1.24 for a salinity of 35 ppt, while in fresh water ($S = 0$) the factor is approximately 1.4. The variation with salinity is less significant, but it is notable that there is a positive variation with salinity at the upper end of the temperature range, while the opposite is true at the lower end of the temperature range. Figure 2 is similar to Fig. 1, but with a pressure of 900 dbar. The similarity between these figures indicates that pressure does not have a very significant impact on attenuation over the range of parameters studied here.

Figure 3 and 4 show the attenuation as a function of salinity and pressure for $t = 0$ °C and $t = 30$ °C, respectively, with $f = 1$ MHz, $a = 1$ μm, and $M = 1$ kg m^{-3}. Temperature clearly has a significant effect on the attenuation as noted in

FIG. 2. Attenuation as a function of temperature and salinity for $p = 900$ dbar, $f = 1$ MHz, $a = 1$ μm, and $M = 1$ kg m^{-3}.
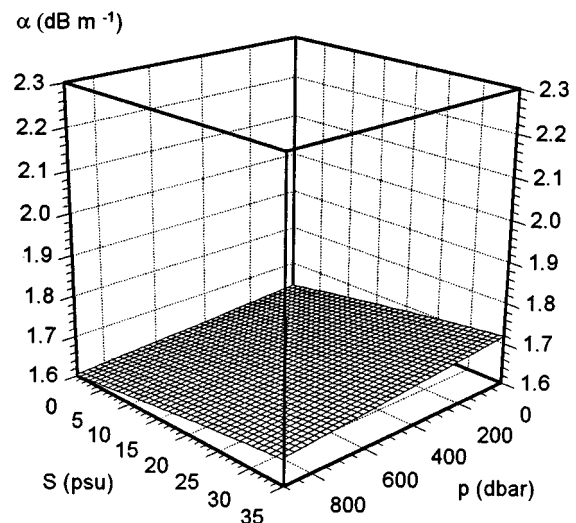
FIG. 4. Attenuation as a function of pressure and salinity for $t = 30$ °C, $f = 1$ MHz, $a = 1$ μm, and $M = 1$ kg m^{-3}.

FIG. 5. Attenuation as a function of pressure and temperature for $S = 35$ ppt, $f = 1$ MHz, $a = 1$ μm, and $M = 1$ kg m^{-3}.

FIG. 7. Attenuation as a function of frequency and particle radius for $t = 30$ °C, $S = 35$ ppt, $p = 1$ dbar, and $M = 1$ kg m^{-3}.

Figs. 1 and 2. These figures demonstrate that the effect of pressure on the attenuation over the range 0–900 dbar is small and, since for shallow water applications we are generally only interested in water depths of order 100 m or less (p up to about 100 dbar), the effect on the attenuation of pressure variation with depth may be neglected. This is supported by Figs. 5 and 6, which show that there is little variation in attenuation with pressure over the entire temperature range considered, for salinities of 35 and 0 ppt, respectively.

Figures 7 and 8 show the variation in attenuation with frequency and particle radius, for temperatures of 30 °C and 0 °C, respectively, and Fig. 9 shows the difference between these two cases. The peak occurring in the small a region of Figs. 7 and 8 is due to viscous absorption, which peaks when the skin depth (e-folding length) of the viscous shear waves in the fluid is of the order of the particle size. The increase in absorption at large a is due to scattering, which becomes

important as the frequency and particle size become large, i.e., with increasing ka. There is clearly a significant difference between Figs. 7 and 8 in terms of both the overall magnitude of the absorption, with a maximum difference of over 0.5 dB m^{-1}, and also in the position of the viscous absorption peak along the particle radius axis at a given frequency. It is this shift in the absorption peak which leads to the negative regions of Fig. 9. From Figs. 7 and 8 it can be seen that the absorption peak moves towards smaller particles as the temperature is increased. This may be understood in terms of the viscosity, ν, and the skin depth of the viscous shear waves, $\delta = \sqrt{2\nu/\omega}$. As the temperature increases, the viscosity decreases, and hence δ decreases. Since the absorption peak occurs when $\delta \sim a$, we would expect the peak to shift to smaller a as δ decreases. Therefore the peak should shift to smaller a as the temperature increases, as observed.
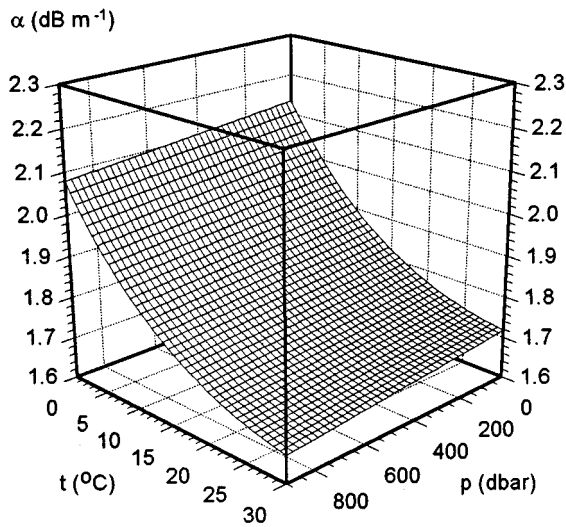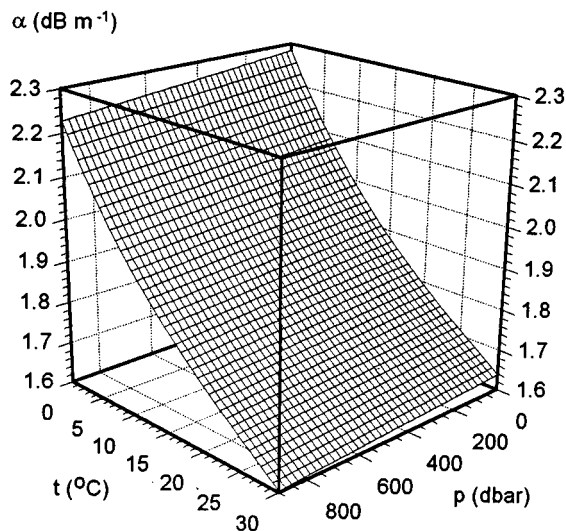

FIG. 6. Attenuation as a function of pressure and temperature for $S = 0$ ppt, $f = 1$ MHz, $a = 1$ μm, and $M = 1$ kg m^{-3}.

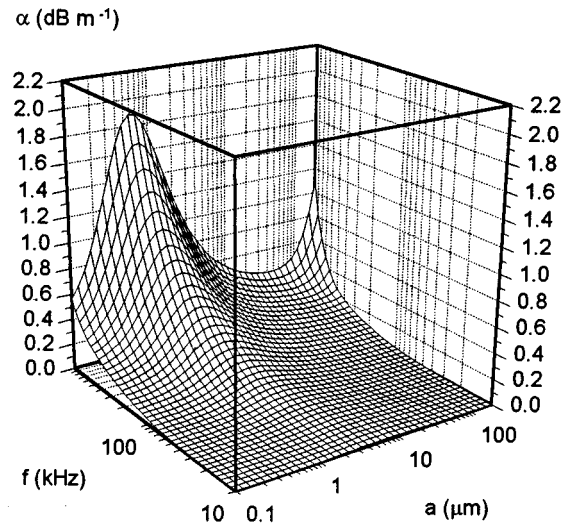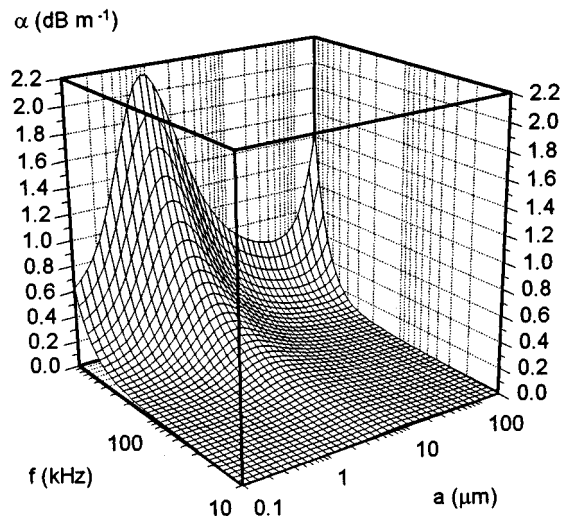FIG. 8. Attenuation as a function of frequency and particle radius for $t = 0$ °C, $S = 35$ ppt, $p = 1$ dbar, and $M = 1$ kg m^{-3}.
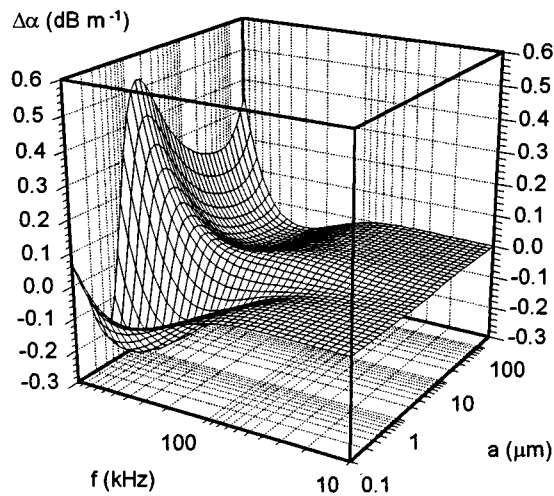
FIG. 9. Difference between attenuation at $t = 0\,°C$ and $t = 30\,°C$, for $S = 35$ ppt, $p = 1$ dbar, and $M = 1$ kg m^{-3}.

III. CONCLUSIONS

A method has been described for including the effects of temperature, pressure, and salinity into the formula [Eq. (1)] for calculating total attenuation by seawater containing dilute suspensions of solid mineral particles. This involves the substitution of suitable expressions for sound speed, density, and viscosity as functions of temperature, pressure, and salinity into the formulas for the attenuation contributions due to scattering and viscous absorption by suspended particles. Combined with the Francois and Garrison expression for the absorption coefficient of clear seawater, this gives the capability for calculating the total absorption coefficient of seawater containing solid particles as a function of temperature, salinity, pressure, frequency, particle size, particle concentration, and the density and bulk compressibility of the solid particles.

Results presented have shown that over the range of values found in the environment, temperature has the most significant impact on the attenuation coefficient of turbid water, while the effect of salinity is less significant and the effect of pressure may normally be neglected in the shallow water environments where the presence of solid mineral particles is of interest.

Future sonar models applied to high-frequency acoustic devices operating in shallow, coastal waters should include the effects of suspended particulate matter on the attenuation coefficient and these results suggest that the local salinity and particularly temperature should be taken into account in such calculations. The method presented in this paper can be used to carry out these calculations.

While experimental validation of the dependencies predicted by these calculations is highly desirable, it should be recognized that the expressions for density, viscosity, sound speed, and clear-water absorption are all empirically derived. Laboratory measurements of viscous absorption by aqueous suspensions of mineral particles are currently underway, and investigations of the temperature and salinity dependencies predicted in this paper are planned. Results of these investigations will be presented in a future article.

Finally, it is important to note that microbubbles, which have not been considered in this paper, may lead to a significant contribution to the attenuation in coastal waters, and that this contribution will also be influenced by temperature, pressure, and salinity. This subject is beyond the scope of the present paper.

[1] A. D. Heathershaw, S. D. Richards, and P. D. Thorne, J. Defence Sci. **1**, 200–206 (1996).

[2] S. D. Richards, A. D. Heathershaw, and P. D. Thorne, J. Acoust. Soc. Am. **100**, 1447–1450 (1996).

[3] F. H. Fisher and V. P. Simmons, J. Acoust. Soc. Am. **62**, 558–564 (1977).

[4] W. H. Thorpe, J. Acoust. Soc. Am. **42**, 648–654 (1965).

[5] M. Schulkin and H. W. Marsh, J. Acoust. Soc. Am. **34**, 864–865 (1962).

[6] R. E. Francois and G. R. Garrison, J. Acoust. Soc. Am. **72**, 896–907 (1982).

[7] R. J. Urick, J. Acoust. Soc. Am. **20**, 283–289 (1948).

[8] G. G. Stokes, Math. Phys. Papers **3**, 1–122 (1922).

[9] J. J. Faran, Jr., J. Acoust. Soc. Am. **23**, 405–418 (1951).

[10] A. E. Hay and D. G. Mercer, J. Acoust. Soc. Am. **78**, 1761–1771 (1985).

[11] R. K. Johnson, J. Acoust. Soc. Am. **61**, 375–377 (1977).

[12] J. Sheng and A. E. Hay, J. Acoust. Soc. Am. **83**, 598–610 (1988).

[13] W. Matthäus, Beiträde zur Meereskunde **29**, 93–107 (1972).

[14] N. P. Fofonoff and R. C. Millard, Jr., Unesco Technical Papers in Marine Science, Vol. 44 (1983).

[15] C. Chen and F. J. Millero, J. Acoust. Soc. Am. **92**, 1129–1135 (1977).

[16] J. L. Spiesberger and K. Metzger, J. Acoust. Soc. Am. **89**, 1697–1700 (1991).

[17] V. A. Del Grosso, J. Acoust. Soc. Am. **56**, 1084–1091 (1974).

[18] F. J. Millero, C. Chen, A. Bradshaw, and K. Schleicher, Deep Sea Res. A **27**, 255–264 (1980).

[19] F. J. Millero and A. Poisson, Deep Sea Res. A **28**, 625–629 (1981).

[20] G. W. C. Kaye and T. H. Laby, *Tables of Physical and Chemical Constants* (Longman, London 1982), 15th ed.

[21] P. D. Thorne and P. J. Hardcastle, J. Acoust. Soc. Am. **101**, 2603–2614 (1997).

Pilot experiment for the acquisition of marine sediment properties via small scale tomography system

Brian Rapids,[a] Tom Nye, and Tokuo Yamamoto

Geoacoustics Laboratory, Rosenstiel School for Marine and Atmospheric Science (RSMAS), University of Miami, 4600 Rickenbacker Causeway, Miami, Florida 33149

A 3-D high resolution crosswell acoustic tomography system was designed and tested in a shallow water environment. This system makes use of a damped least-squared inversion technique and is used to construct compressional wave velocity images from measured travel time data. Use of singular value decomposition allowed checks of the linear inversion confirming the validity of the modeled environment. It is shown that when the ratio of width to depth of the cross section is about unity or smaller and the domain has not been overparametrized the inverted image model has sufficiently good figures of merit in resolution and variance to visualize small variations in the magnitude compressional velocity field. © *1998 Acoustical Society of America.*
[S0001-4966(98)01601-4]

INTRODUCTION

The broad term of tomography refers to the process by which a single plane of a subject is reconstructed by modeling its internal structure. This was first applied to medical imaging using x rays to penetrate the human body, but within the past 15 years has received much attention from the geologic/geophysics community. The notion of tomography is supported as a tool for exploration of the earth's surface and impacts a wide range of fields from volcanology and petroleum geology to civil engineering and groundwater geology.[1–3] However, its application extends to any field which has the need of knowing the ground structure with minimal disturbance to the site.

Marine environments are a particular area where sediment structure on large and small scales is of interest to many communities. It has been suggested that the fluctuation of physical properties, such as compressional wave velocity and density within a marine sediment, are major contributors to the acoustic scattering by sediment volumes.[4–6] Many models describing this type of acoustic backscatter incorporate this variability into their analytical equations requiring an investigation into its measurement. Empirical studies of the physical properties generally base themselves on discrete measurements from individual sediment cores manually extracted from the seabed. The extraction of these cores from the ocean floor is difficult and the process inevitably disturbs the sample to some extent. This limited source of data forces assumptions to be made about the continuity of the measurements vertically within a core and horizontally between coring locations. The coring method generally provides a description of property variability in one dimension and requires that the sediment be disturbed prior to the examination. Tomography is revealing itself to be capable of estimating the *in situ* structure and variations of sediment properties

in at least two dimensions by transforming the compressional velocity models into complement descriptions of porosity, density, shear wave velocity, and shear strength using the methods outlined by Yamamoto *et al.*[3,7,8]

Since ray theory is implemented in the general travel time tomography method, the methodology is equally applicable to both large and small inversion domains containing both large and small scales of velocity variability. This is due to the high-frequency approximation inherent in ray theory and that the analytical ray tracing through the medium involves gradients of the local velocity field and not its magnitude. Care must be taken when interpreting the estimate given by the inversion because tomography is greatly affected by the source and receiver geometry. The solution is not necessarily unique for the inversion domain and becomes an estimate based on the limited data set.

In order to estimate these small scale fluctuations in the uppermost marine sediment a large number of source–receiver pairs must be sampled at shallow and steep angles or the tomographic experiment must itself be conducted on a small scale. While constructing the system of travel time equations, the ray paths are traced through discrete sections of the sediment which themselves must be small in order to resolve variability on small spatial scales. One must take the bad with the good because when the region is divided into smaller sections during the ray tracing a proportionate number of unknowns are introduced into the system of equations. However there are only as many equations as there are ray paths being traced through the medium, i.e., as many source–receiver pairs sampled for first arrival times in the experiment. If too fine of a grid is created, the system of equations can become underdetermined and care must be taken when interpreting the results. Therefore it is more suitable to reduce the scale of the experiment itself.

This preliminary effort is intended to achieve three goals, the first of which is to demonstrate the feasibility of constructing and deploying a small scale tomography system

---

[a] Currently at: Sanders, A Lockheed Martin Company, 955 Perimeter Road, Manchester, NH 03108.

Forward Model
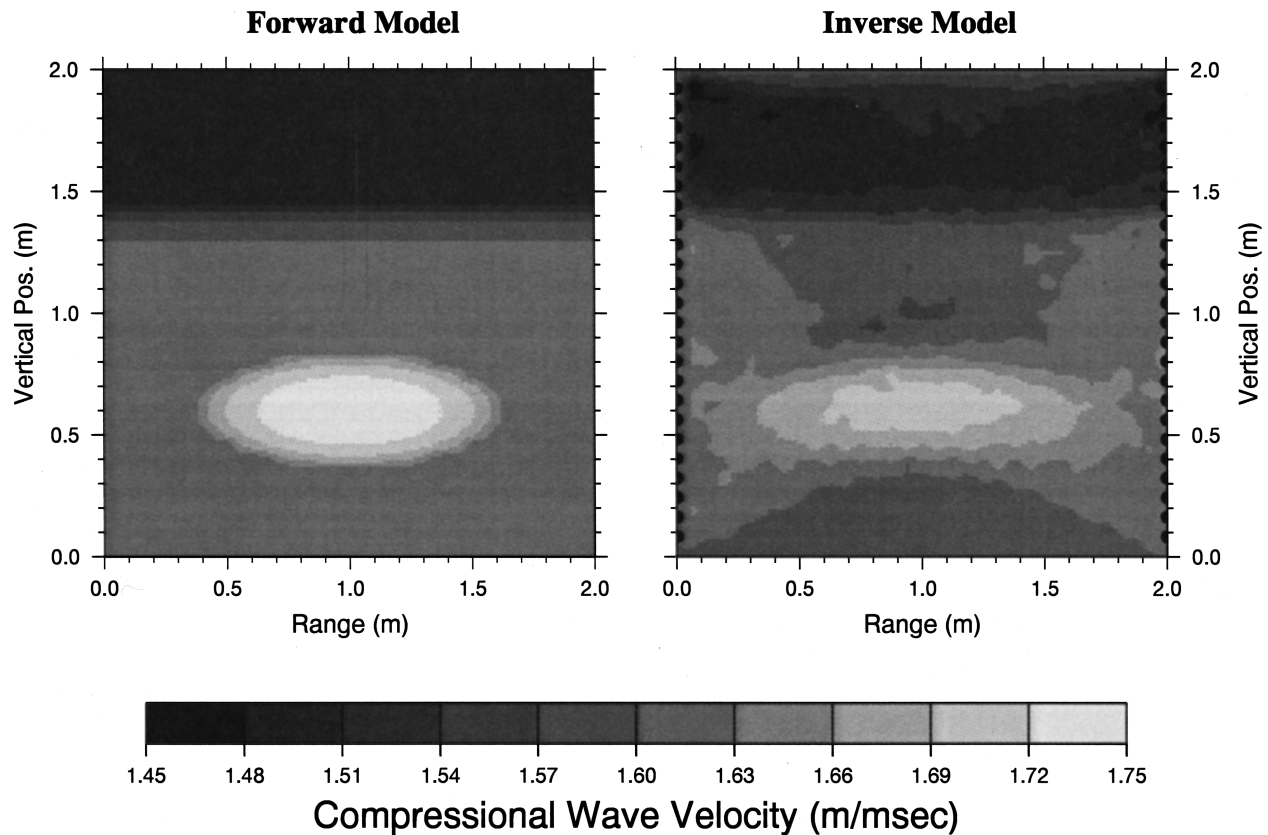
Inverse Model

FIG. 1. Two layer velocity model used to create synthetic data for input to the inverse model. Source and receiver locations are depicted in the inverted velocity field.

in the marine environment. Sinking the well casing manually while on SCUBA such that the geometry is exactly known and the source and receiver planes are parallel is quite difficult. No-decompression limits, primitive communication methods, and environmental conditions (rough seas and currents) compound to make the task of installing an underwater experiment site difficult. Determining methods to most accurately relate the positions of the source and receiver elements to the seafloor while under these conditions is instrumental to a successful deployment.

The first arrival times along various source–receiver paths will be inverted to reconstruct the compressional velocity structure. Particular attention will be paid to the caveats of linear inverse theory concerning the resolution of the parameterized environment and the variance of the model velocities at each environment node. These analyses are intended to be a sanity check on the inversion process verifying that the environment is not being overparametrized and provide figures of merit for the linear inversion. As a pilot experiment it is hoped that this work will aid future system design and data analysis during more extensive surveys. This quite possibly might result in an autonomous or semi-autonomous system capable of modeling a variety of sediments in a variety of sea depths.

I. TOMOGRAPHIC INVERSION

The University of Miami GeoAcoustic Laboratory (UM-GAL) tomographic inversion method is based on the work of

Bregman et al.[9–11] which is an iterative process to calculate a velocity field $v(\mathbf{r})$ based on travel times $\mathbf{T}$ of rays propagating through a given domain. The inversion domain is represented as a grid of node points. Each node on the grid is assigned an appropriate velocity value depending on the current iteration and a constant gradient is imposed within a triangular element created by three nodes to simulate a continuous environment. The continuous gradient method has the advantage that it simplifies the ray tracing, making each section dl of the ray path in the grid sections an arc of a circle. A brute force shooting method is employed that sends out a fan of rays at different launching angles from the source, and traces each one through the environment to find the two rays that are just above and just below the receiver position. Fans of rays are launched between these two bounding angles until a raypath is found which connects to the receiver position within allowable error. Experimentally determined first arrival times can be subtracted from those along hypothesized raypaths to create a vector of residual traveltimes $\delta\mathbf{T}$.

The first variation of Fermat's principle is the basis of a given iteration,

$$\delta\mathbf{T} = -\int_{\Gamma} \frac{\delta v(\mathbf{r})}{v^2(\mathbf{r})}\, dl. \qquad (1)$$

This corresponds a set of simultaneous linear equations denoted by the matrix equation:

$$\delta\mathbf{T} = \mathbf{A}\,\delta\mathbf{v}, \qquad (2)$$
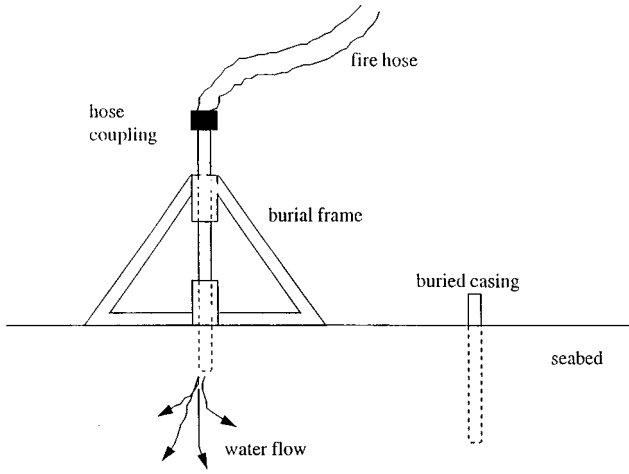
FIG. 2. Cartoon depicting the use of a burial frame and high-pressure fire hose to sink a PVC well casing in sandy sediments.

FIG. 3. Top: Depiction of a 2-ms chirp sampled at 60.0 kHz. Middle: Depiction of the autocorrelation demonstrating the pulse compression effect. Bottom: Power spectral density of the chirp signal.

in which $\delta \mathbf{T}$ is the difference in travel time between measured data and the model travel times along the model ray paths (Γ). The problem can be posed once the length of each ray element in each environment cell dl has been determined. The matrix equation that must be solved in order to perturb the estimated velocity field has many different methods of solution. The matrix equation is nonsymmetric, having M equations each composed of N linear contributions. The magnitude of M is determined by the number of source–receiver pairs that could be connected during ray tracing. The second dimension of $\mathbf{A}$, N, is the number of grid point the environment has been parametrized into. For every execution of the inversion, a forward problem is solved by taking an initial velocity structure and determining the travel time along hypothesized ray paths. These are compared with measured travel times to compute $\delta \mathbf{T}$ and the inverse problem is solved by adjusting the velocity field with $\delta \mathbf{v}$ accordingly. The forward problem is then solved again with this new velocity field finding new ray paths and travel times to compare with the data. This iterative process is continued until $\delta \mathbf{T}$ approaches zero or has arrived at acceptable values. A demonstration of the inversion is shown in Fig. 1 with a two layer field containing a region of high velocity to create a synthetic set of arrival times. The sources and receivers span the two layer field, as seen on the left and right axes of the inverted field, allowing for reconstruction of the interface. This demonstrates that the forward and inverse models are self-consistent.

The inversion can be solved by employing the singular value decomposition (SVD) of the environment matrix $\mathbf{A}$ and its inverse $\mathbf{A}^{-1}$ given by

$$\mathbf{A} = \mathbf{U}\mathbf{S}\mathbf{V}^T, \tag{3}$$

$$\mathbf{A}^{-1} = \mathbf{V}\mathbf{S}^{-1}\mathbf{U}^T. \tag{4}$$

The SVD creates the matrices $\mathbf{U}$ and $\mathbf{V}$ containing the data and the eigenvectors of the problem in their respective columns as well the diagonal matrix of eigenvalues $\mathbf{S}$. This method directly provides the components necessary to interpret the estimated parameter fields. The SVD inverse opera-

tor is applied to the original matrix equation obtaining a solution to Eq. (2),
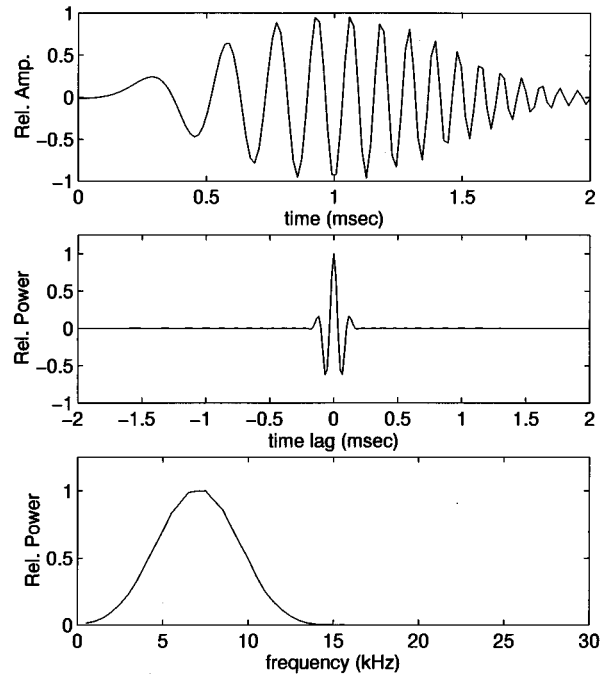
$$\delta \mathbf{v} = \mathbf{A}^{-1}\delta \mathbf{T} = (\mathbf{V}\mathbf{S}^{-1}\mathbf{U}^T)\delta \mathbf{T}. \tag{5}$$

Since small eigenvalues could amplify noise in the data sets, a tapered cutoff is used to condition the eigenvalues prior to formulation of the SVD solution. A parameter k is introduced to the SVD formulation to curtail the magnitude of the singular values (eigenvalues) allowed to contribute to the solution.[12] With this included the SVD solution is transformed into

$$\delta \mathbf{v} = (\mathbf{V}\mathbf{S}^2\mathbf{V}^T + k^2\mathbf{I})^{-1}\mathbf{V}\mathbf{S}\mathbf{U}^T\delta \mathbf{T}$$

$$= (\mathbf{A}^T\mathbf{A} + k^2\mathbf{I})^{-1}\mathbf{A}^T\delta \mathbf{T}. \tag{6}$$

The inverse operator, which originally was represented by $\mathbf{A}^{-1}$, is now represented by the entire quantity $(\mathbf{A}^T\mathbf{A} + k^2\mathbf{I})^{-1}\mathbf{A}^T$. This new inverse operator will be denoted by $\mathbf{L}^{-1}$ and can be represented in terms of its eigenvectors solution using the SVD components of A:

$$\mathbf{L}^{-1} = (\mathbf{A}^T\mathbf{A} + k^2\mathbf{I})^{-1}\mathbf{A}^T = \mathbf{V}\left(\frac{\mathbf{S}}{\mathbf{S}^2 + k^2\mathbf{I}}\right)\mathbf{U}^T. \tag{7}$$

Bregman[8] felt that the damped least-square algorithm developed by Paige and Saunders[13] was convenient and well suited to dealing with large and sparsely populated sets of equations that are typical in this application. This method prevents small oscillations from corrupting the solution to $\delta T = \mathbf{A}\delta v$ and creates the set of normal equations

$$(\mathbf{A}^T\mathbf{A} + k^2\mathbf{I})\delta \mathbf{v} = \mathbf{A}^T\delta \mathbf{T}, \tag{8}$$

where $\mathbf{I}$ is the identity matrix and k^2 is the damping parameter. The solutions to these equations are identical to that

214   J. Acoust. Soc. Am., Vol. 103, No. 1, January 1998

Rapids *et al.*: Sediment tomography   214

obtained using a tapered cutoff in the SVD shown in Eq. (6).

Two items should be addressed concerning the velocity perturbation estimate δv_i specifically its spatial resolution and variance. Denoting the variance for each element δv_i by its covariance matrix $\langle \Delta b \Delta b^T \rangle$. The error Δb in the solution of $\mathbf{A}x = b$ due to error Δx in the data shall be expressed as

$$\Delta b = \mathbf{L}^{-1} \Delta x, \tag{9}$$

$$\langle \Delta b \Delta b^T \rangle = \mathbf{L}^{-1} \langle \Delta x \Delta x^T \rangle (\mathbf{L}^{-1})^T. \tag{10}$$

It is now assumed that all elements of the data vector are independent and have the same variance σ_0^2 that depends on the ability to pick first arrival times or the sampling rate used to acquire the data. This then replaces the covariance matrix of the data resulting in

$$\langle \Delta b \Delta b^T \rangle = \sigma_0^2 \mathbf{L}^{-1} (\mathbf{L}^{-1})^T$$
$$= \sigma_0^2 \mathbf{V} \left(\frac{\mathbf{S}^2}{(\mathbf{S}^2 + k^2 \mathbf{I})^2} \right) \mathbf{V}^T. \tag{11}$$

This covariance can then be used as an estimate of the variance for each environment node σ_i and computed as

$$\sigma_i = \sigma_0 \sum_j \left[\frac{s_j}{(s_j^2 + k^2)} v_{ij} \right]^2, \tag{12}$$

where v_{ij} are elements of the eigenvector matrix $\mathbf{V}$ obtained from the SVD.

A second uncertainty complements the variance associated with the δv_i magnitudes. The velocity perturbations themselves represent an estimate of a spatial average of the true δv_i. The extent of the spatial average can be represented in a resolution matrix $\mathbf{R}$ which gives a flavor for the resolution of the δv_i parameter in its general vicinity and can be found for a particular solution of a general equation. For a general equation $\mathbf{A}x = b$ there can be a particular solution for it based on experimental data $x_p = \mathbf{A}_p^{-1} b$. This solution can then be expressed as

$$x_p = \mathbf{A}_p^{-1} \mathbf{A} x, \tag{13}$$

which relates the particular solution suited to the experimental data x_p to the "true solution" x by the matrix product $\mathbf{A}_p^{-1} \mathbf{A}$. This product can also be represented by their SVD components as

$$x_p = \mathbf{V}_p \mathbf{V}_p^T x. \tag{14}$$

There exists a way to determine if the inversion process is capable of distinguishing one vector element δv_i from another. A resolution matrix is generally defined as the product[14]

$$\mathbf{R} = \mathbf{V} \mathbf{V}^T. \tag{15}$$

However, introduction of the inverse operator $\mathbf{L}^{-1}$ from the tapered cutoff solution in place of $\mathbf{A}^{-1}$ results in

$$\mathbf{R} = \sum_j \left(\frac{s_j^2}{s_j^2 + k^2} \right) V_j V_j^T = \mathbf{V} \mathbf{S}^{\text{cond}} \mathbf{V}^T, \tag{16}$$

where the notation has been compacted to reference the conditioned eigenvalue matrix $\mathbf{S}^{\text{cond}}$
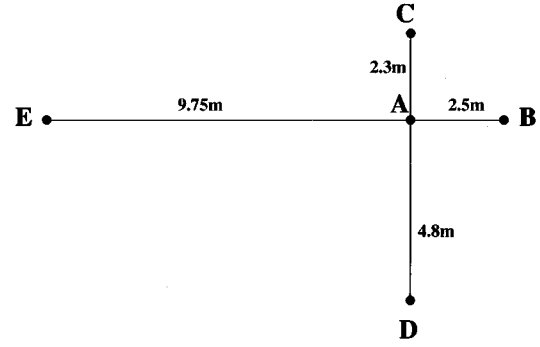
FIG. 4. Overhead geometry of the experiment domain.

$$\mathbf{S}^{\text{cond}} = \text{diag} \left(\frac{s_j^2}{s_j^2 + k^2} \right). \tag{17}$$

If an element of δv_i is spatially unique and independent then the respective element of the resolution matrix $R_{ij} = \delta_{ij}$. As the velocity perturbation represents an average of the velocity perturbations in adjacent grid nodes, the delta function will be smeared out but retains significant values in the immediate area. This condition is referred to a compact resolution. If however information has leaked into other nodes far away the delta function might have a relatively high value in the immediate area but there will be other R_{ij} elements far away with significant values as well constituting a noncompact resolution due to the "crosstalk" of the node values or leakage during the mathematical operation on the matrices. When the condition of compact resolution is satisfied the meaning of the resolution matrix becomes apparent since $\delta \mathbf{v}_{\text{est}} = \mathbf{R} \delta \mathbf{v}_{\text{true}}$ and the degree to which spatial averaging is present in the perturbation can be estimated. The diagonal elements of the $\mathbf{R}$ matrix provide quick indication to the spatial averaging effect. The closer the elements are to unity the more unique the perturbation at that node is, lower values can be interpreted as being averages about the surrounding X nodes where X is the integer needed to bring the R_{ii} element close to unity ($R_{ii} X \approx 1$).

The concept of spatial resolution is affected by the choice of spacing between node points when imposing a grid on the domain during ray tracing. Small R_{ii} values indicate that the grid spacing chosen for the domain is too fine and should be made coarser. This will increase the individuality of each node during the inversion, but will also increase the variance of the velocity value at each node. Similar effects can be observed in the choice of the damping parameter k. A high damping parameter will cut off small eigenvalue solutions in order to stabilize the solution and reduce the variance of the velocity estimation but will decrease the spatial resolution at the same time. Thus there is a trade-off between the two effects and a compromise should be made or acknowledgment of the two quantities. One may reduce the variance in the estimations and force a match to the measured travel times exactly, but the spatial resolution matrix will indicate that the node values are not distinct. Individual features would be smeared or blurred over several nodes of

215   J. Acoust. Soc. Am., Vol. 103, No. 1, January 1998

Rapids *et al.*: Sediment tomography   215
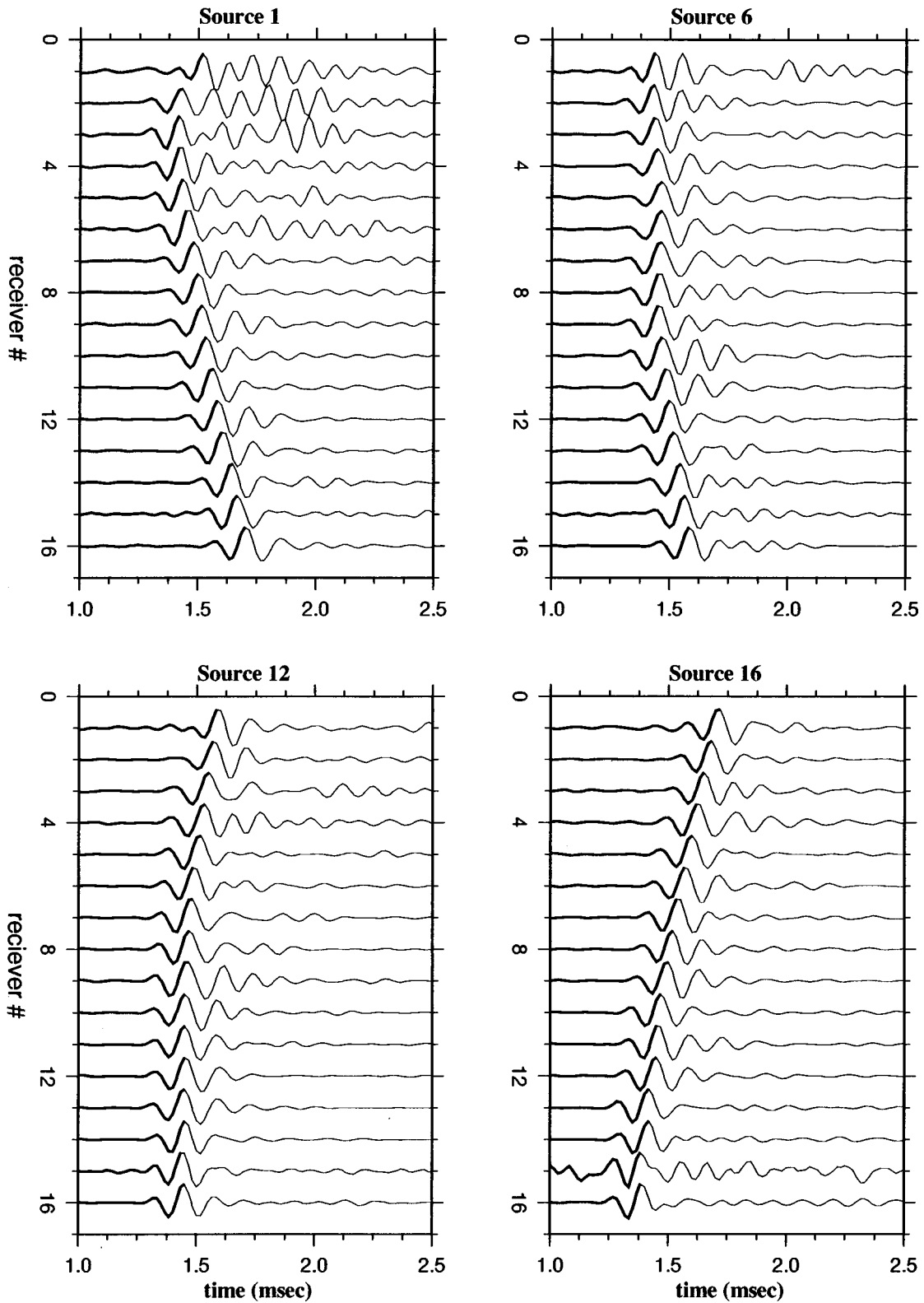
FIG. 5. Samples of cross-correlated data from cross section AC. Source and receiver are numbered such that element #1 is shallow in the PVC well, while #16 is near the bottom.

the image. On the other hand, if the resolution is satisfied by setting the damping parameter to allow for small grid sizes, the variance in the estimations will be very large making node values of velocity indistinguishable from one another in a statistical sense.

II. SYSTEM DESIGN

The goal of this pilot experiment is to reconstruct small variations of the acoustic velocity in the sediment structure, requiring both a high-frequency signal and small sensor size
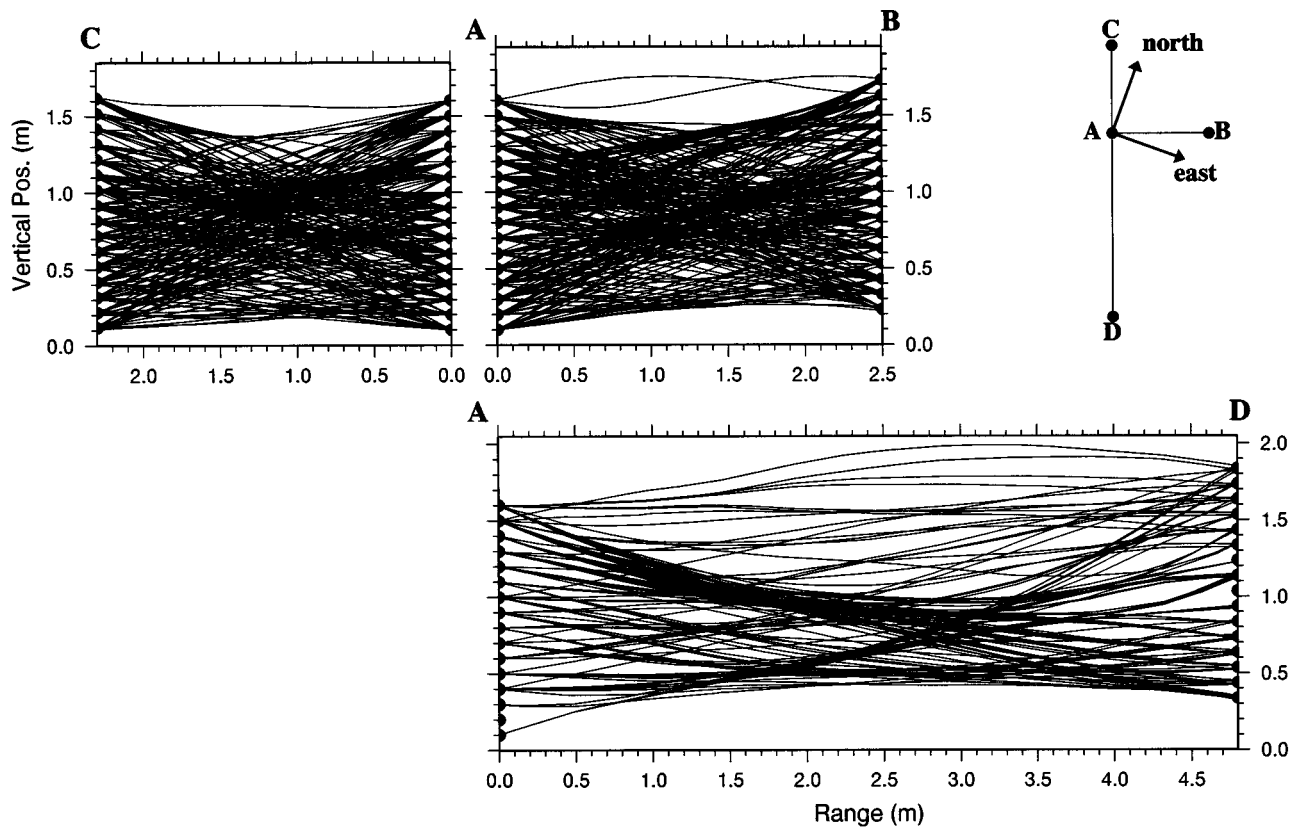
FIG. 6. Side view of the geometry of the experiment. Ray paths traced through the parameterized environment are depicted originating and ending at the known source–receiver locations.

to be used in the experiment. This demand on sensor size and the required deployment geometry led to the construction of two acoustic receiver arrays and one source array at that the University of Miami GeoAcoustic Laboratory (UMGAL). All three linear arrays contained 16 elements at 10-cm intervals for a total length of 1.5 m. Benthos AQ-4 underwater hydrophone cartridges were chosen to be the receiver elements for their small size (1.3 cm diam/3.3 cm length), high sensitivity (−201 dB V), and wide advertised frequency range (1 Hz–15 kHz). The AQ-4 was combined with molded UMGAL preamplifier circuits having a 50× gain over the frequency range of the hydrophone. Due to budgetary and spatial constraints, it was decided to drive the AQ-4 hydrophones and use them as acoustic sources as well. Benthos had no information concerning this application of their product, but in-house bench tests at UMGAL demonstrated that the hydrophones were capable of sustaining driving voltages as high as 20 V at frequencies up to 15 kHz. At this voltage the elements qualitatively appeared to emit a sufficiently high sound level in air to perform the tomographic experiments and it was agreed that this would be the maximum voltage applied to satisfy concerns of sensor survivability. A test was later performed in a large ballast tank (3.05 m×1.22 m×2.44 m) to perform a quick and dirty calibration of the source array. Each source element had a 7.5-kHz sine wave applied to it by a source function generator. A Benthos AQ-17 hydrophone was suspended approximately 1 m across from each source element. The received sine wave did not have an amplitude that was constant in time, but had

an average value of 25 mV±5 mV for all 16 elements. The AQ-17 is a general purpose, broadband hydrophone with a built-in preamplifier and an overall sensitivity of −174.5 dB V. This resulted in measured sound pressure levels of 142.5 dB±1.5 dB for each source array element.

The 16-channel arrays were strung tautly along 3.175 mm (1/8 th-in.) galvanized wire in a 37.9 mm i.d./ 42.5 mm o.d. (1 1/4-in. 160-psi working pressure) PVC pipe such that the elements could not shift their positions. The pipes were filled with Exxon Isopar-M oil and sealed. Isopar-M and the PVC were chosen since they both have acoustic impedances similar to that of water, additionally Isopar-M is relatively inert and will not chemically react with any of the array components.

Previous deployments of a tomography system in the seabed by the UMGAL have not been completely successful due to complications inserting the arrays vertically into the seabed and due to the absence of a source array. In past experiments a source array was synthesized by moving a ''large'' commercial source vertically in the well. The complications created uncertainty in the element locations leading to uncertainties in the inverted velocity image. It is most desirable to know each sensor position accurately and have the source–receiver arrays define a planar domain or cross section. The domain must then be referenced absolutely to the water–sediment interface for interpretation of the inversion image. In order to facilitate the burial of the arrays, a frame was constructed in a pyramidal shape with guide tubes
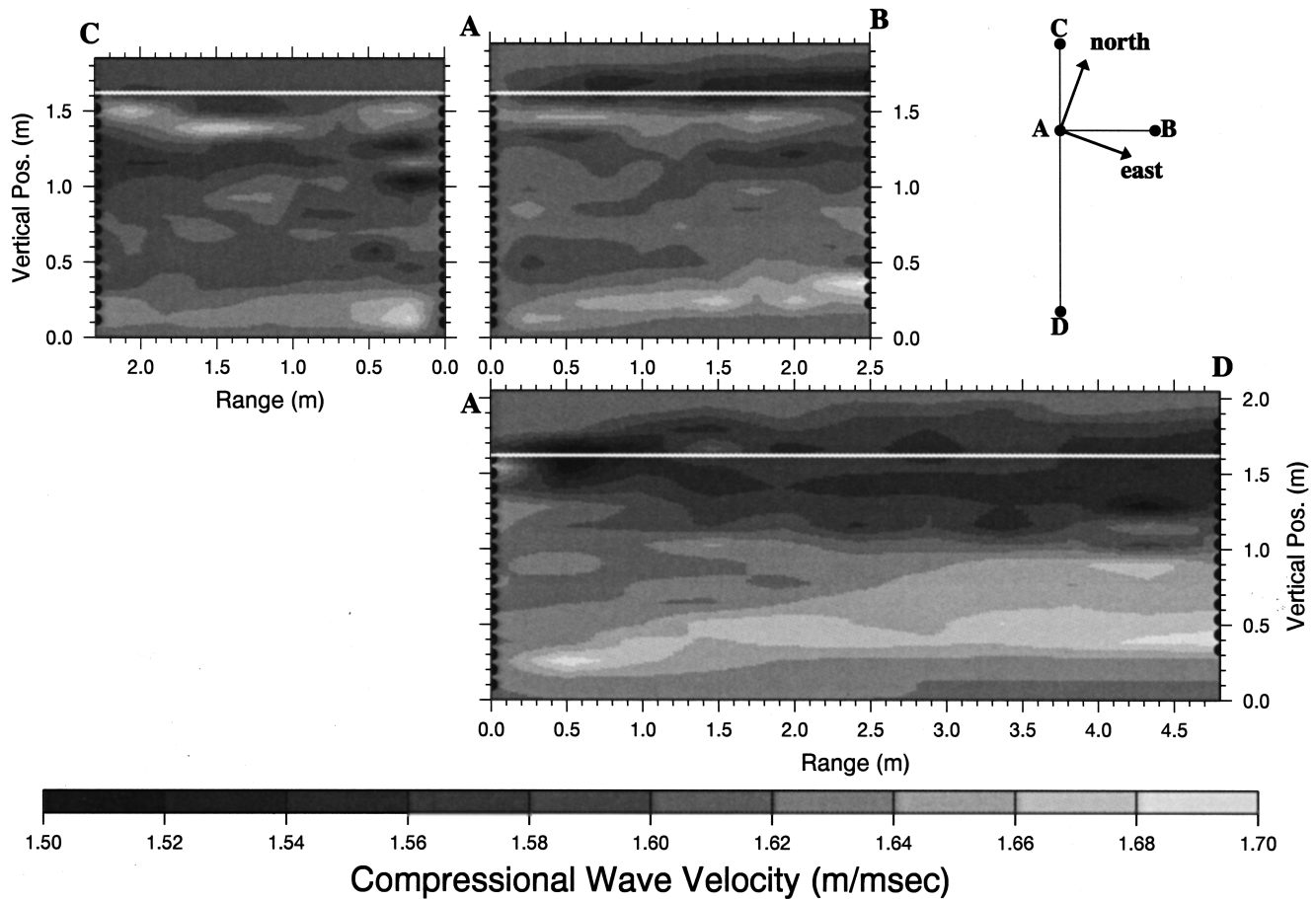
FIG. 7. Inverted compressional wave velocity fields. The horizontal white lines mark the measured location of the seabed.

arranged along its vertical axes. With the frame on the ocean floor, the guide tubes would restrict the side to side motion of 3.05-m-long sections of 51.7 mm i.d./60.3 mm o.d. (2-in. SCH40) PVC pipe used as well casing, thereby keeping the pipes in the same orientation during the burial. High pressure water would be forced through the casings with a fire pump and hoses to liquefy the sediment structure immediately below. The cartoon in Fig. 2 depicts such a deployment and well casing burial. By combining liquefaction with supporting effort from divers on SCUBA, the casing could be sunk or pile driven if necessary. Disassembly and removal of the frame would reveal an evacuated PVC casing sunk vertically into the seabed with approximately 20–30 cm of well casing remaining visible in the water column.

The ability to pick the first arrival times on the seismic traces is dependent on the sampling frequency and the signal-to-noise ratio (SNR). Pulse compression techniques were employed to maximize the SNR in the received signal. The received signals are passed through a matched filter ''compressing'' the energy into a pulse τ_c which can be approximated by the reciprocal of the transmitted signal bandwidth B_t:

$$\tau_c = 1/B_t. \tag{18}$$

The compressed pulse contains sidelobes whose size depends on the characteristics of the modulation used in the transmission.

A FM sweep centered at 7.5 kHz was decided on as a source function for its simplicity. The signal $s(t)$ is composed of a cosine function whose frequency varies linearly with time over the bandwidth B_t during a pulse duration T as in the manner

$$s(t) = \cos\left[\omega_0 t + \frac{1}{2}\left(\frac{2\pi B_t}{T}\right)t^2\right]. \tag{19}$$

To reduce the sidelobes associated with this type of modulation, thus increasing the SNR in the cross-correlated traces, the amplitude of the signal was weighted in the time domain with a Hamming weighting scheme:

$$w(t) = 0.54 + 0.46\cos\left(\frac{2\pi t}{T}\right). \tag{20}$$

The implementation of the weighting function in producing the transmitted signal $S(t)$ then becomes

$$S(t) = w(t)\cdot s(t), \tag{21}$$

whose autocorrelation is depicted in Fig. 3. The hydrophones used in the experiments had bandwidths up to 15 kHz and were spaced at 10 cm. For these reasons the source function depicted in Fig. 3 has a bandwidth of 100 Hz–15 kHz and a transmission time of 2.0 ms. This indicates that the compressed pulse would have a width on the order of 0.07 ms as shown in its autocorrelation. The received signal would be

(a)

(b)

(c)
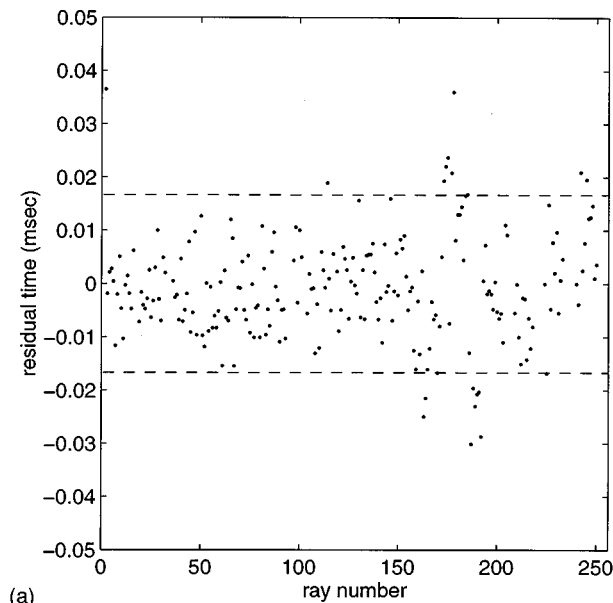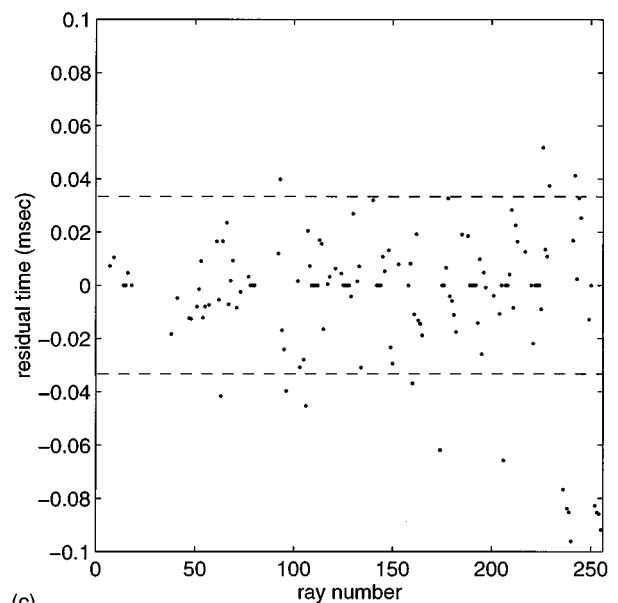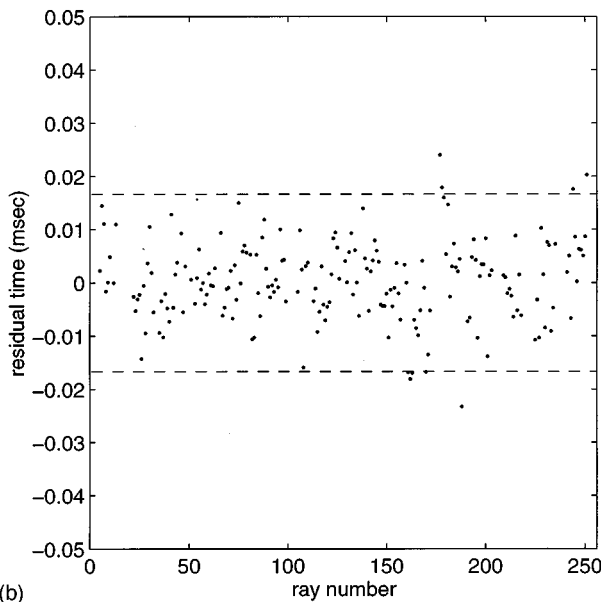
FIG. 8. Residual arrival times, vectors $\delta\mathbf{T}$, for cross sections (a) AB, (b) AC, (c) AD. The dotted lines represent ± 1 sampling point and only those rays which were found to connect the source–receiver pair are shown.

sampled at 60 kHz indicating that the peak of the compressed pulse will be represented by several samples and that its peak should be readily visible and capable of representing the time of first arrival.

Since the marine sediment is a stationary medium during the short time scales the experiment was conducted, the signal SNR could be increased if needed by performing coherent averaging. After the cross correlation with the matched filter, each trace is referenced to the same time zero, and therefore traces between the same source/receiver locations can be summed. The noise which is random will destructively interfere and tend to go toward zero while the compressed pulse will constructively interfere and increase in size.

III. DEPLOYMENT AND DATA ACQUISITION

In July 1995 the UMGAL deployed the high resolution seabed tomography system from the Harbor Branch Oceano-

graphic Institute (HBOI) R/V Seward Johnson. The experiment was conducted in 11.6 m of water off of Ft. Pierce, FL, in a sediment whose surface consisted primarily of a medium sand and small shell fragments. The sediment was dense at the surface as was evident by minimal penetrations of a gravity core and manual coring attempts. A central 76.6 mm i.d./59.02 mm o.d. (3-in. SCH40) PVC pipe was buried first as a source well. The larger size made it difficult and several resistive layers with intermediary soft layers were encountered ultimately allowing only about 2–2.5 m of the 3.05-m casing to be buried. Four 50.7 mm i.d./60.3 mm o.d. (2-in. SCH40) PVC receiver wells were sunk with similar encounters of hard layers but a more successful burial intentionally leaving about 20–30 cm of casing visible in the water column. Careful measurements were made of well depth, height of exposed well casing from the surrounding sand, compass bearing to the source well, northward and eastward tilts from vertical, and distances from the
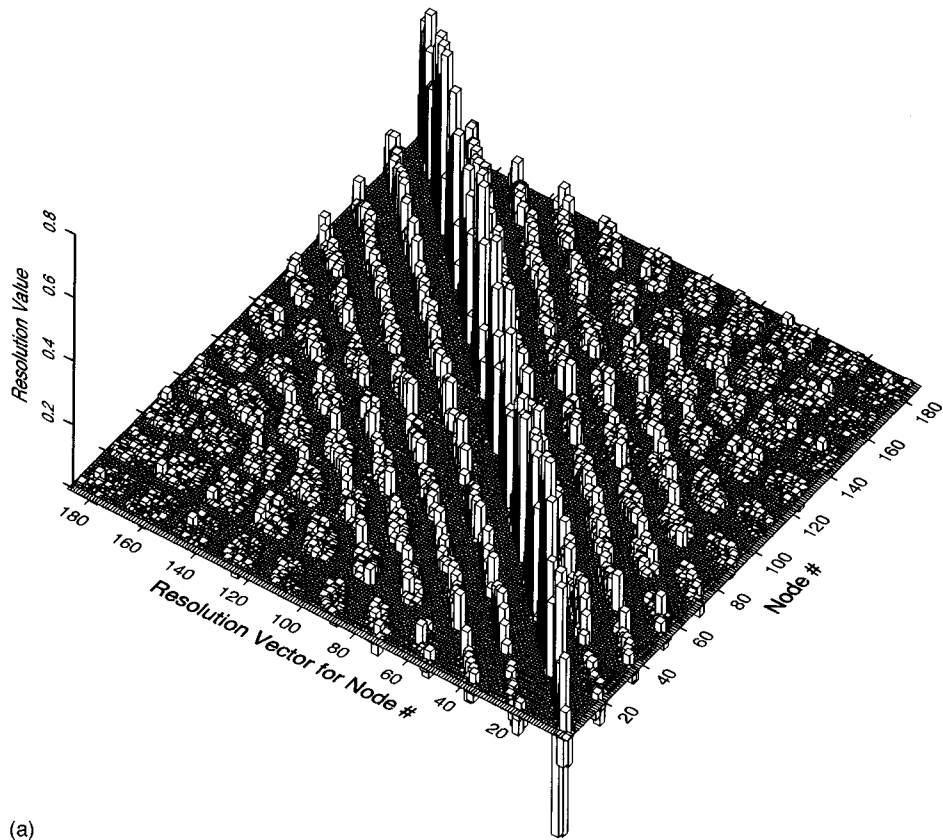
(a)
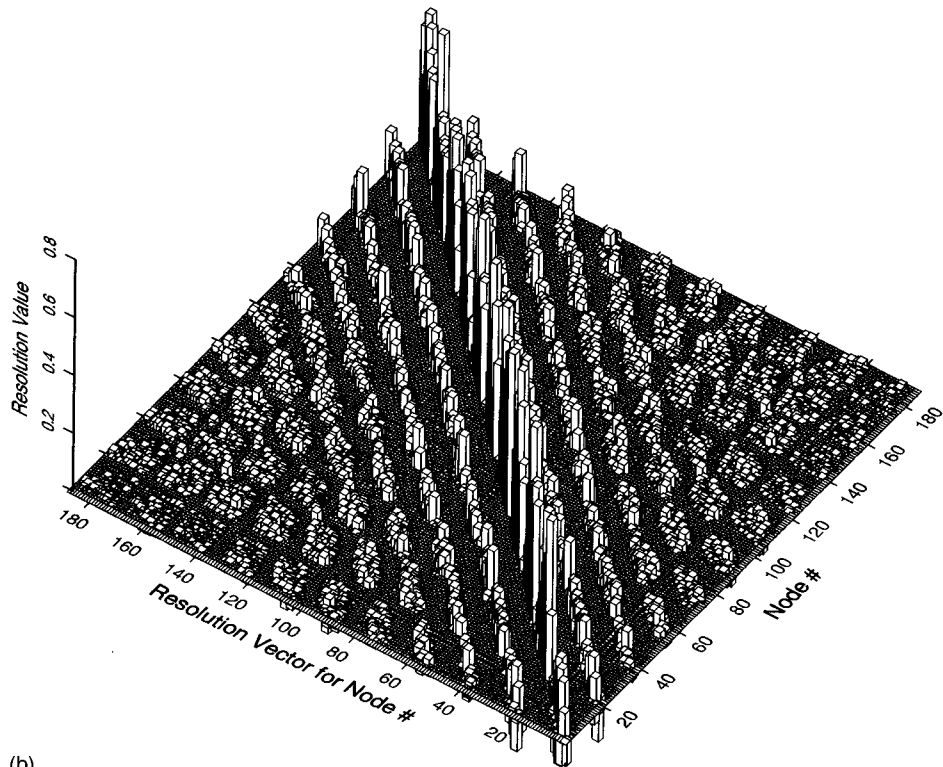
(b)

FIG. 9. Resolution matrices R for the three independent inversions (a) AB, (b) AC, (c) AD. The footprint of these matrices is a square—187×187 in size (the number of node points in the parameterized environment). Each of the 187 nodes has a resolution vector associated to it that can be remapped into the parametrized environment. This would result in 187 individual images showing the spatial resolution and independence associated with each model node.
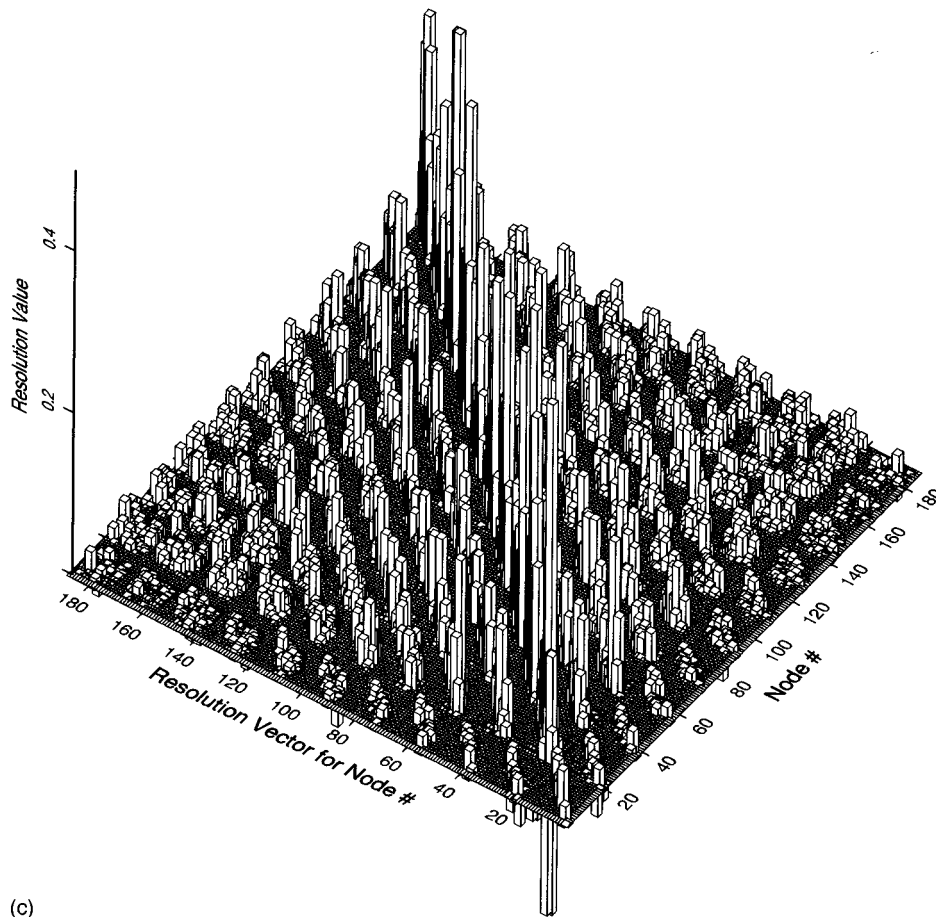
(c)

FIG. 9. (*Continued.*)

source well. Repeated measurements with inclination levels determined that the wells were $\pm 1°$ from vertical and orthogonal to one another within the precision of compass measurements. The seabed was assumed to be horizontal over the small scales and casing height were referenced to the sand so that relative height of the well casings to one another could be determined. This approximation was verified by running mason strings between the wells and using a level to determine the relative elevations of the wells while underwater. These measurements define a well understood deployment of the seabed tomography system because they allow for precise determination of source/receiver array locations in each well referenced to an absolute coordinate system. The wells were labeled as source well A and receiver wells B, C, D, and E with respective horizontal distances from the source well of 2.5, 2.28, 4.82, and 9.75 m as depicted in Fig. 4.

The collected data represent the sum of approximately 7–10 traces sampled at 60.0 kHz between source well A and receiver wells B and C while the data along the segment AD is an ensemble of 25 traces. For this longer cross section the chirp was modified to be 4 ms in period and the sampling rate was accordingly adjusted to 30 kHz but otherwise had no property change. During the transmission to well E the signal was too corrupted due to the long distance and therefore was not sampled as a data set.

IV. INVERSION RESULTS

The selection of first arrival times is a very tedious process and is performed by hand on the digitized cross correlations. From the properties of the pulse compression technique, the autocorrelation has a maximum value at zero lag time. Therefore upon the assumption of little or no multipath phase interference, the first arrival times along each source–receiver trace should occur at the maxima of the first signal packet above ambient noise levels. These first wave packets are very sharp and clear in the 2-m tomography cross sections and is represented by the gather from the bottommost source in cross section ac in Fig. 5. The first arrival times are noted on the source gathers by the end of the bold trace plotted overtop the lighter one representing the entire time signal.

The first arrival times are then tallied and arranged for use in the inversion process. For the 16 sources and 16 receivers there are 256 possible raypaths or equations to be solved during the inversion. These raypaths will be referenced by order in the matrix equation whereby ray #1 is that connecting the bottommost source (array element #16) and bottommost receiver (array element #16), ray #2 connects the bottommost source (array element #16) and the receiver second to the bottom (array element #15), ray #16 connects the bottom source again (array element #16) and the uppermost hydrophone (array element #1), and so on until ray
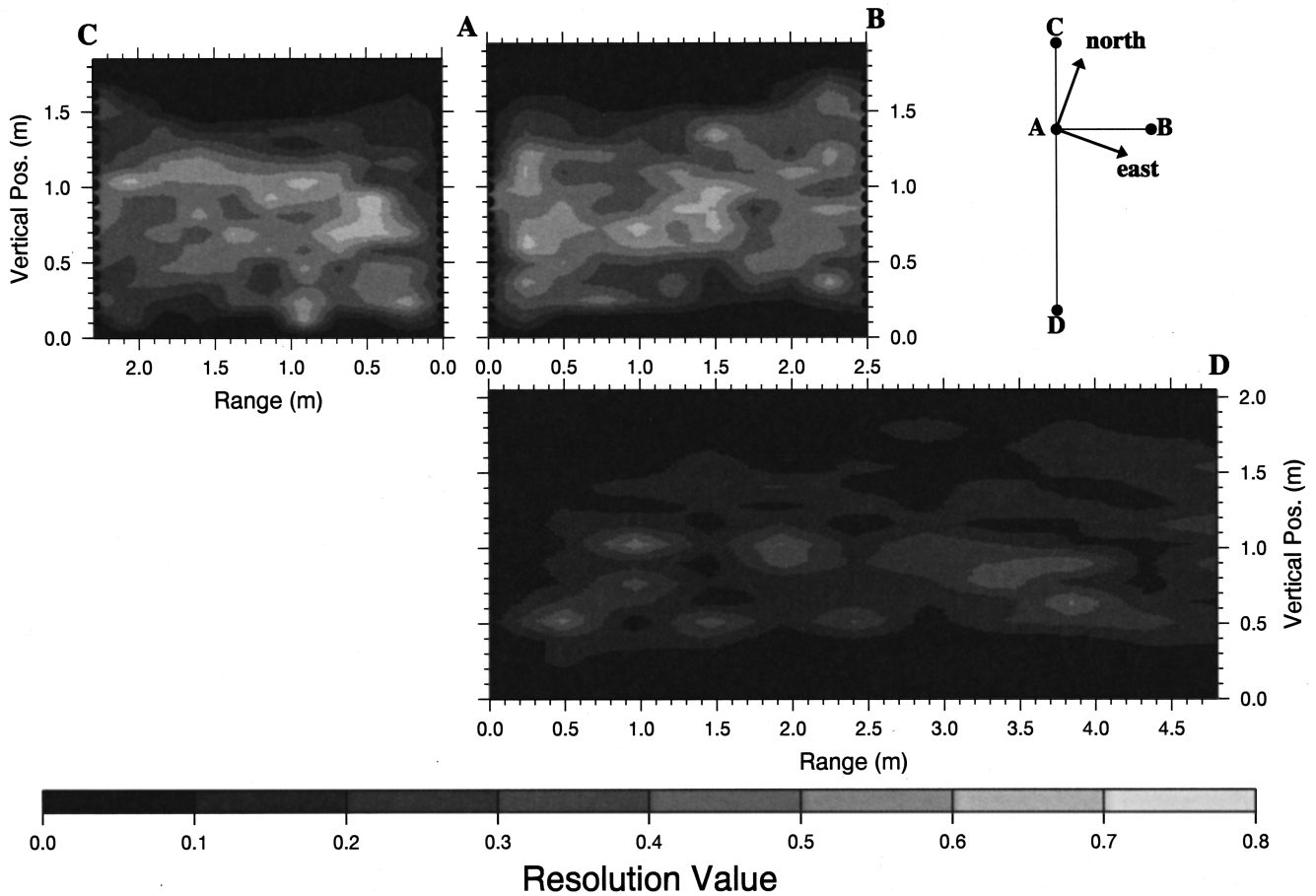
FIG. 10. The main diagonal of each matrix **R** is remapped into the environment model to give a relative feeling for the locations of good spatial resolution. Values closer to 1.0 indicate little bleeding into surrounding nodes took place during the inversion.

#256 connecting the uppermost source (array element #1) and the uppermost receiver (array element #1).

A reasonable horizontal resolution from an imaging point of view that could be observed would be a single wavelength. Since the source function had the bulk of its spectral power centered about 7.5 kHz which corresponds to an acoustic wavelength of 20 cm in water, the inversion domain was divided into 10 horizontal sections for the 2-m cross sections (the same was done for the 5-m tomography due to the particularly poor geometry of the sources and receivers). The domain was then divided into 16 sections vertically corresponding to the receiver spacing, yielding 187 node points (17×11 points when including the axes). These 187 node points are arranged in a particular fashion and will also be noted by their corresponding position. The bottommost node on the source well of the domain (referenced as the origin of the coordinate system in the inversion) is node #1. The numbers proceed upward until the top of the domain is reached which herecorresponds to node #16. The bottom of the next vertical column is #17 and the top is #23. This continues across the domain horizontally to the bottom of the receiver well which is node #181 while the top is the farthest point in the domain and has node #187 representing it.

The inversion was limited to only a couple iterations allowing for minor refraction of the ray paths shown in Fig. 6. The areas of the images which contain the highest density

of ray paths are cells which have many constraints to satisfy in the inversion while cells with many ray paths passing through at various angles are bounded on many different sides yielding good spatial resolution in a mathematical sense.

The inversion was initialized with a homogeneous velocity field based on the average compressional velocity observed in the seismic traces. In all three cases the images in Fig. 7 reveal distinct vertical layers of fast sediment and slow sediment (fast and slow being relative over the scale of 1.5–1.7 m/ms). The white horizontal line at 1.62 m depicts the location of the seabed surface and was successfully recreated in cross sections AC and AB. The ray paths can be seen to refract at the faster upper surface, causing it to be depicted as a curved surface concave to the water column but corrects itself at the sides of the domain to connect with the receiver. These layers of a hard and soft material correspond to the upper surface of medium sand and broken shell fragments seen during system deployment, occasional layers of ''hard'' material encountered during well casing burial presumed to be sand and shell, and a dark gray silt or clay expelled during the burial and water intrusion. Individual layers match well between the two independent and orthogonal cross section implying a relatively horizontally homogeneous but vertically layered environment. The fast (hard) layer seen at the bottom of the images is difficult to interpret since it occurs
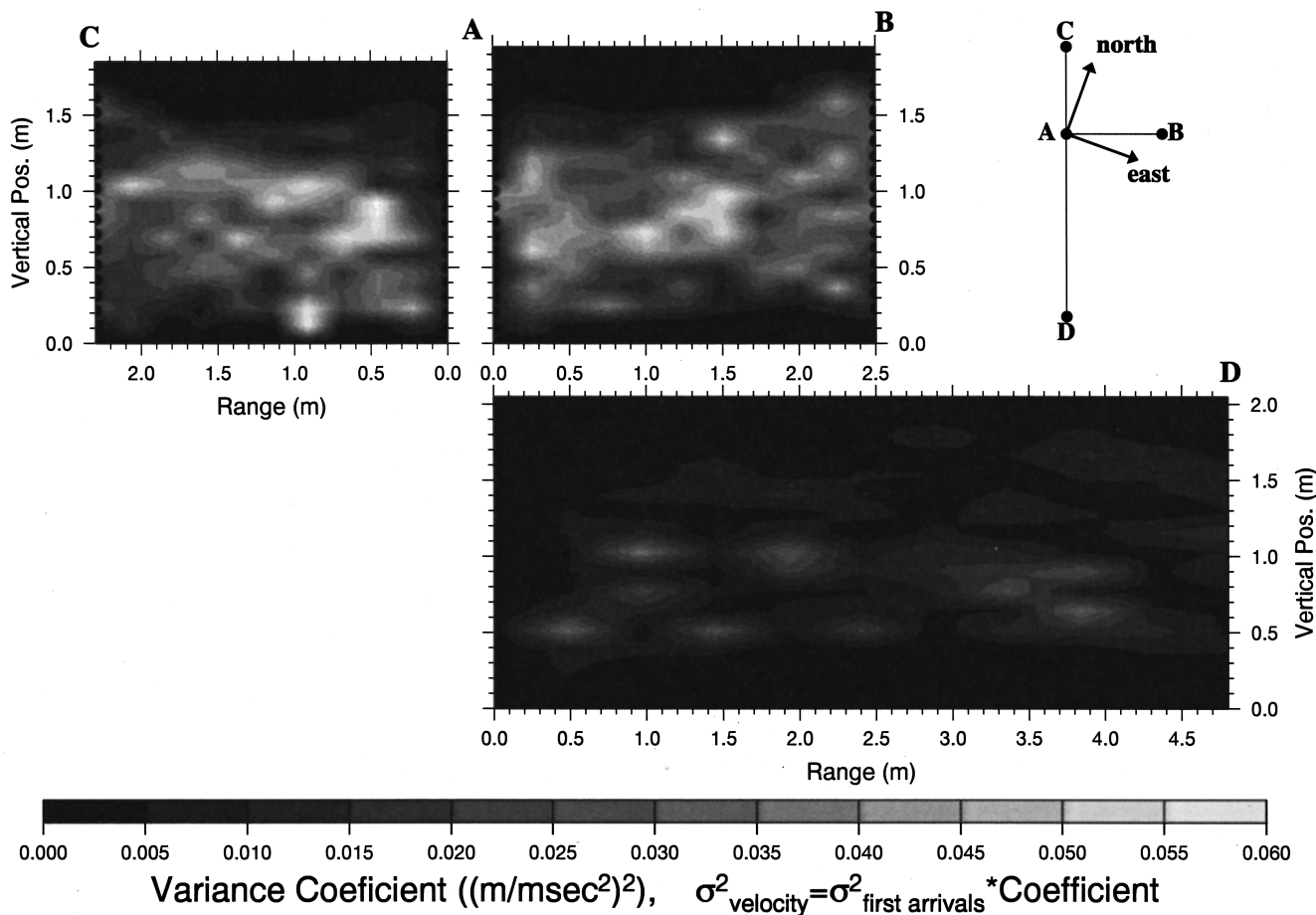
FIG. 11. The variance of the compressional model is depicted. One should take note of the similarity of the image with Fig. 10. Areas that have a high degree of spatial independence also have a larger variance associated with their velocity estimate.

where the available data ends. However during the burial two of the 3.05-m sections of PVC out of the five wells buried two had to be cut short by approximately 0.5 m since they could not break through a hard layer. This depth roughly corresponds to the location of that in the tomograms.

The travel time data measured for each source–receiver pair was subtracted from that along the ray paths through the model environment and plotted in Fig. 8 to examine the residual travel time error in each cross section. It is seen that the model environment and ray paths match the experimental data within the error associated to picking the first arrival time on the data traces. This numerical accuracy and qualitative field comparisons lend plausibility and some groundtruth to the images.

General linear inverse theory extends a concept of spatial resolution and resolution in data space (variance). These ideas represent the mathematical resolution which are not necessarily representative of the limits incurred by use of ray tomography or imaging theory.[15,16] The resolution matrices for each of the cross sections has been plotted in Fig. 9. Each node of the environment has a resolution vector associated with it which represents that node's spatial independence from the other nodes in the environment. The maximum values should lie along the main diagonal of **R**—the location of that node in it's resolution vector. Therefore the main diagonal of the resolution matrix **R** can coarsely represent the

independence of each environmental node from one another spatially. The closer these values are to unity, the more Independent the node is. Off-diagonal elements represent the dependence of surrounding nodes. This resolution vector can be mapped into "domain space" by matching the correct vector element with domain node. Upon doing so, the image resembles a two-dimensional delta function centered on the node in the modeled domain. Since the diagonal corresponds to the grid nodes, it should have high values while elements in its general vicinity should fall off quickly. Due to the high values along the main diagonal in cross sections AC and AB, they are said to be in states of compact resolution and the off diagonal elements decay quickly. Cross section AD, on the other hand, does not fall off as quick and does not possess good values over its diagonal, an example of noncompact resolution.

The diagonal of these matrices when mapped into the domain are more understandable but are only of use when off-diagonal elements are relatively of low value and the inversion is in a state of compact resolution. This has been done and forms the image in Fig. 10. As can be seen the areas of high resolution correspond to areas of high ray density. For AC and AD, these dense areas yield node values that are virtually distinct from the rest of the image. If one were able to take a photograph of the sediment cross section, the picture would be fuzzy at low resolution values and sharp

at high values. This indicates that for section AD the result-ant grid values are actually blurred and each grid value approximately represents an average of the surrounding three or four cells.

The variance or resolution in data space can similarly be represented as an image in Fig. 11. The inverse relationship between the two quantities discussed previously, in which the resolution is good where the variance is high, is apparent after comparison of the two figures. Again these can also be related to the ray density distribution through the domain, if the density is large there are a lot of constraints to solve resulting in high variance for that cell. On the other hand, the cell is bounded by the different rays resolving that particular cell particularly well. The picture depicts the velocity variance as a function of the input variance. Assuming that the first arrival times were picked correctly with one standard deviation being a single sampling point (0.0167 ms), then the scale should be multiplied by an input variance of 278 μs^2.

V. CONCLUSIONS

This effort has successfully demonstrated the feasibility of deploying a small scale tomography system suitable for a high resolution survey of the marine seabed. The model compressional wave velocity environment matches the traveltimes attained experimentally extremely well for the two cross sections AB and AC of interest and possess well behaved ray paths. The mathematical resolution reveals the base gridding for the images is adequate for the data and represent unique points in space while possessing reasonable variance coefficients for the velocity values. The results of the linear inversion analysis demonstrated the effect of source–receiver geometry on the resolution an variance of the model. When the ratio of the cross-section width to depth was approximately unity (AB and AC), the inverted model possessed good figures of merit while with a ratio greater than one (AD) the figures of merit were unacceptable. This observation falls back to the choice of how to parameterize the environment and how the ray paths trace through the environment. Many ray paths passing through an environment cell constrain the spatial resolution but increase the variance of the value associated with that cell.

The deployment and data processing of a small scale tomography system is therefore deemed a feasible project with much potential. The data obtained in the pilot experiment are of good quality and its inversion is mathematically stable yielding plausible results. Unfortunately, a firm groundtruth was not available to confirm the modeled structure and determine the viability of the system. Future sys-

tems should attempt this in various sediments. Improvements to the system could include the use of higher frequencies and narrower bandwidths along with a calibration of the sources and receivers at the operating frequencies. This will allow the interpretation of the amplitude of the data as well as the first arrival times.

[1] J. W. Rector III, Ed., ''Crosswell methods: Where are we, where are we going?,'' Geophysics **60**(6), 629–630 (1995).

[2] J. M. Harris *et al.*, ''High resolution crosswell imaging of a west Texas carbonate reservoir: Part I—Projects summary and interpretation,'' Geophysics **60**(3), 667–681 (1995).

[3] T. Yamamoto Th. Nye, and M. Kuru, ''Imaging the permeability structure of a limestone aquifer by crosswell acoustic tomography,'' Geophysics **60**(6), 1634–1645 (1995).

[4] D. R. Jackson and K. B. Briggs, ''High frequency bottom backscattering: roughness versus sediment volume scattering,'' J. Acoust. Soc. Am. **92**, 962–977 (1992).

[5] K. Aki and P. Richards, *Quantitative Seismology: Theory and Methods* (Freeman, San Francisco, 1980), Vol. II.

[6] T. Yamamoto, ''Acoustic scattering in the ocean from velocity and density fluctuation in the sediments,'' J. Acoust. Soc. Am. **99**, 866–879 (1996).

[7] T. Yamamoto, T. Nye, and M. Kuru, ''Porosity, permeability, shear strength: Crosswell tomography below and iron foundry,'' Geophysics **59**(10), 1530–1541 (1994).

[8] T. Yamamoto, ''Velocity variabilities and other physical properties of marine sediments measured by crosswell acoustic tomography,'' J. Acoust. Soc. Am. **98**, 2235–2248 (1995).

[9] N. D. Bregman, R. C. Bailey, and C. H. Chapman, ''Crosshole seismic tomography,'' Geophysics **54**(2), 200–215 (1989).

[10] N. D. Bregman, C. H. Chapman, and R. C. Bailey, ''Travel time and amplitude analysis in seismic tomography,'' J. Geophys. Res. **94**(6), 7577–7587 (1989b).

[11] N. D. Bregman, R. C. Bailey, and C. H. Chapman, ''Ghosts in tomography: The effects of poor angular coverage in 2D seismic traveltime inversion,'' Can. J. Explor. Geophys. **25**(1), 7–27 (1989).

[12] L. R. Lines and S. Tritel, ''Tutorial: A review of least-squares inversion and its application to geophysical problems,'' Geophys. Prospect. **32**, 159–186 (1984).

[13] C. C. Paige and M. A. Saunders, ''LSQR: An Algorithm for Sparse Linear Equation and Sparse Least Squares,'' ACM Trans. Math. Softw. **8**(1), 43–71 (1982); **8**, 195–209 (1982).

[14] R. A. Wiggins, ''The general linear inverse problem: Implication of surface waves and free oscillations for earth structure,'' Rev. Geophys. Space Phys. **10**(1), 251–285 (1972).

[15] P. R. Williamson, ''A guide to the limits of resolution imposed by scattering in ray tomography,'' Geophysics **56**(2), 202–207 (1991).

[16] P. R. Williamson and M. H. Worthington, ''Resolution limits in ray tomography due to wave behavior: Numerical experiments,'' Geophysics **58**(5), 727–735 (1993).

224   J. Acoust. Soc. Am., Vol. 103, No. 1, January 1998

Rapids *et al.*: Sediment tomography   224

Sound scattering by several zooplankton groups. I. Experimental determination of dominant scattering mechanisms[a),b)]

Timothy K. Stanton and Dezhang Chu
Department of Applied Ocean Physics and Engineering, Woods Hole Oceanographic Institution, Woods Hole, Massachusetts 02543-1053

Peter H. Wiebe and Linda V. Martin
Department of Biology, Woods Hole Oceanographic Institution, Woods Hole, Massachusetts 02543-1049

Robert L. Eastwood
Department of Applied Ocean Physics and Engineering, Woods Hole Oceanographic Institution, Woods Hole, Massachusetts 02543-1053

The acoustic scattering properties of live individual zooplankton from several gross anatomical groups have been investigated. The groups involve (1) euphausiids (*Meganyctiphanes norvegica*) whose bodies behave acoustically as a fluid material, (2) gastropods (*Limacina retroversa*) whose bodies include a hard elastic shell, and (3) siphonophores (*Agalma okeni* or *elegans* and *Nanomia cara*) whose bodies contain a gas inclusion (pneumatophore). The animals were collected from ocean waters off New England (Slope Water, Georges Bank, and the Gulf of Maine). The scattering properties were measured over parts or all of the frequency range 50 kHz to 1 MHz in a laboratory-style pulse-echo setup in a large tank at sea using live fresh specimens. Individual echoes as well as averages and ping-to-ping fluctuations of repeated echoes were studied. The material type of each group is shown to strongly affect both the overall echo level and pattern of the target strength versus frequency plots. In this first article of a two-part series, the dominant scattering mechanisms of the three animal types are determined principally by examining the structure of both the frequency spectra of individual broadband echoes and the compressed pulse (time series) output. Other information is also used involving the effect on overall levels due to (1) animal orientation and (2) tissue in animals having a gas inclusion (siphonophores). The results of this first paper show that (1) the euphausiids behave as weakly scattering fluid bodies and there are major contributions from at least two parts of the body to the echo (the number of contributions depends upon angle of orientation and shape), (2) the gastropods produce echoes from the front interface and possibly from a slow-traveling circumferential (Lamb) wave, and (3) the gas inclusion of the siphonophore dominates the echoes, but the tissue plays a role in the scattering and is especially important when analyzing echoes from individual animals on a ping-by-ping basis. The results of this paper serve as the basis for the development of acoustic scattering models in the companion paper [Stanton *et al.*, J. Acoust. Soc. Am. **103**, 236–253 (1998)]. © *1998 Acoustical Society of America.* [S0001-4966(97)01010-2]

PACS numbers: 43.30.Ft, 43.30.Sf, 43.20.Fn, 43.30.Xm [JHM]

LIST OF SYMBOLS

α absorption coefficient

β_r pressure-to-voltage conversion factor for receive transducer

β_t voltage-to-pressure conversion factor for transmit transducer

c sound speed in water

CP compressed pulse output

f scattering amplitude

f_{bs} scattering amplitude in backscattering direction

γ_g amount by which the amplifier gain is reduced during calibration [$=v_t^{(s)}(\omega)/v_t^{(c)}(\omega)$]

i $\sqrt{-1}$

H system response of backscattering setup (not including scatterer response)

k acoustic wave number ($=2\pi/\lambda$)

k_{CP} normalization coefficient for compressed pulse output

λ acoustic wavelength

p_{scat} scattered pressure

P_{inc} incident pressure at the object

r_c distance between transducers during calibration measurement

r_{ref} reference distance for β_t

r_s distance between source/receiver transducer pair and animal during scattering measurement

$\mathscr{R}_{vcal}$ autocorrelation function of the modified calibration signal

σ_{bs} differential backscattering cross section

σ	backscattering cross section $(=4\pi\sigma_{bs})$
t	time
TS	target strength
$v_r^{(s)}$	receiver voltage in scattering measurement
$v_r^{(c)}$	receiver voltage in calibration measurement
$v_t^{(s)}$	transmitter voltage in scattering measurement

$v_t^{(c)}$	transmitter voltage in calibration measurement
ω	angular frequency
$\langle...\rangle$	average over ensemble of statistically independent samples
*	convolution
$\otimes$	correlation

INTRODUCTION

Because of the great distances sound can travel in the water, echosounders have long been used in the remote detection and classification of marine organisms. Schools of fish quite often involve animals of similar size and the same species which makes the conversion of echo levels to abundance of animals a relatively reliable procedure (Foote and Stefánsson, 1993; MacLennan, 1990; Simmonds *et al.*, 1992). However, characterizing assemblages of zooplankton using sound generally poses a greater challenge as the assemblages quite often contain a diverse collection of animals. As the morphological properties of the zooplankton may vary from species to species (and sometimes even from animal to animal within the same species), so do the acoustic scattering properties. For example, recent laboratory studies quantitatively illustrate how the relative backscattered acoustic energy per unit animal biomass varies dramatically between the gastropods (hard elastic shell), decapod shrimp (fluidlike), siphonophores (gas bearing), and salps (fluidlike) (Stanton *et al.*, 1994a). Knowledge of this variability in scattering properties across the groups was necessary in interpreting volume reverberation levels recently observed in oceanic regions containing a mixture of species (Wiebe *et al.*, 1996).

While the study by Stanton *et al.* (1994a) confirms predictions that the overall echo levels from the zooplankters will depend strongly upon the material properties of the animals, it did not address details of the scattering signature of the animals. Much progress has been made toward describing the scattering of sound by decapod shrimp (Chu *et al.*, 1992; Stanton *et al.*, 1993a, 1993b) and euphausiids (Foote *et al.*, 1990; Chu *et al.*, 1993; Stanton *et al.*, 1993b). However, until now, little data have existed regarding other animal types, such as gastropods and siphonophores, to permit adequate acoustic characterization of those animals.

A major practical issue in modeling the scattering of sound by zooplankton is that there are thousands of species of zooplankton and a continuum of sizes present within each species. Furthermore, the scattering by the various animals depends upon the acoustic frequency and animal size, shape, orientation, and material properties. Rather than developing a different model for each size of each species (an effort that is impractical), models are being developed for animals systematically grouped according to their gross anatomical features. Such scattering models can then be developed to describe the scattering over a wide range of sizes of animals (or equivalently, a wide range of acoustic frequencies) that fit into each particular group.

In this two-paper series, the scattering properties of animals from three distinct groups are studied in depth: fluidlike (euphausiid), hard elastic shell (gastropod), and gas bearing

(siphonophore) (Fig. 1). The fluidlike group is named as such because the boundary of the animal behaves acoustically as a fluid–fluid interface and does not support a shear wave (the animal actually has a thin exoskeleton surrounding the body which is being considered acoustically transparent for these applications). In this first paper, broadband measurements of acoustic backscatter by the animals are presented. The frequency spectra, compressed pulse output, and ping-to-ping variability of the echoes are analyzed. The dominant acoustic scattering properties of the animals are identified and the acoustic boundary conditions are inferred in the analysis. In the second paper, mathematical scattering models are developed based on the boundary conditions and compared with data (Stanton *et al.*, 1998). Scattering models such as these can be used to infer animal size and possibly group, as discussed in various previous studies involving inversions. See, for example, reviews on inversions of single frequency echo envelope data in Stanton and Clay (1986) and inversions of multifrequency data in Holliday and Pieper (1995), as well as recent papers on spectral classification of broadband data in Martin *et al.* (1996) and temporal classification through pulse-compression of broadband data in Chu and Stanton (submitted).

I. BASIC EQUATIONS

The scattered pressure p_{scat} is expressed in terms of the pressure P_{inc} of the incident sound field as

$$p_{scat} = P_{inc} \frac{e^{ikr}}{r} f, \qquad (1)$$
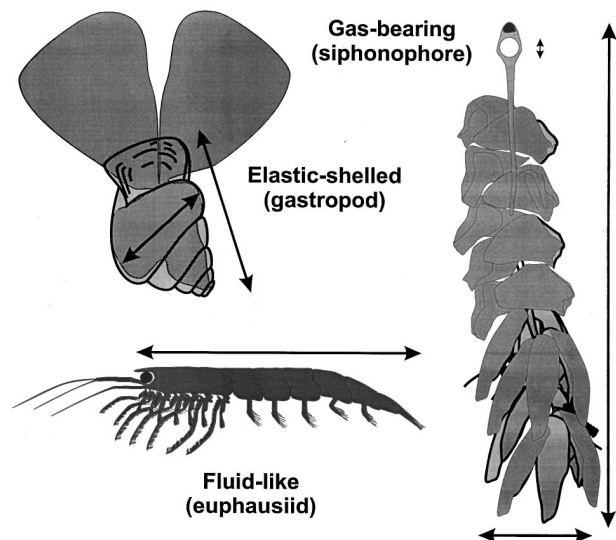
FIG. 1. Sketches of zooplankton from several major anatomical groups. The arrows indicate parts of bodies over which various dimensions were measured.

where f is the scattering amplitude of the scattered field and r is the distance between the object and the receiver. This quantity f indicates the efficiency to which an object scatters sound and depends upon the acoustic frequency and object size, shape, orientation, and material properties. The target strength TS is a logarithmic measure of the backscattered field (i.e., the part of the field scattered back toward the sound source) and can be expressed in terms of the scattering amplitude as

$$\text{TS} = 10 \log |f_{\text{bs}}|^2 = 10 \log \sigma_{\text{bs}}. \tag{2}$$

Using the definition $\sigma_{\text{bs}} = |f_{\text{bs}}|^2$, the target strength was also expressed above in terms of the *differential* backscattering cross section σ_{bs} (this differential cross section should not be confused with the commonly used backscattering cross section σ where $\sigma = 4\pi\sigma_{\text{bs}}$). The dimensions in the above cross sections have been suppressed. The units of target strength are in decibels relative to 1 m^2.

The above equations pertain to single echoes. Quite often, many pings from one animal or the pings from many animals are recorded and averaged. The echoes from the individual animals at the high frequencies used to detect them tend to have random phases. As a result, the energy of the echoes from an aggregation of moving animals averaged over a number of pings is equal to the sum of the average energies of the echoes from the individual animals. Hence, it is convenient to describe the "average" target strength in terms of the average value of the backscattering cross section since the cross section is proportional to echo energy:

$$\langle \text{TS} \rangle = 10 \log \langle \sigma_{\text{bs}} \rangle. \tag{3}$$

Here, the averaging process was performed on a linear scale before the logarithm was taken. The brackets $\langle \cdots \rangle$ denote the average over an ensemble of independent realizations. The average is typically over a range of animal sizes and/or orientations.

II. EXPERIMENTAL SETUP, PROCEDURES, AND DESCRIPTIONS OF ANIMALS

We conducted a series of acoustic backscatter measurements at sea in a laboratory-style acoustic measurement tank filled with filtered seawater. The work involved catching animals from the Slope Water, Georges Bank, and the Gulf of Maine areas offshore of Cape Cod, Massachusetts, USA, and performing the scattering measurements in our 2.4-m-diam by 1.5-m-tall tank on the deck of the RV OCEANUS (1993) and RV ENDEAVOR (1994). The acoustic measurements for each animal involved a portion or all of the frequency range 50 kHz to 1 MHz. Simultaneous with the acoustic measurements in 1994, high magnification video footage of the animals was recorded. All animals were live and fresh during the measurements and were tethered so they would remain in the main beam of the transducers. In the experiments described below, data from a single euphausiid species (*Meganyctiphanes norvegica*) and gastropod species (*Limacina retroversa*) and two siphonophore species (*Agalma okeni* or *elegans* and *Nanomia cara*) were analyzed.

A. Animals

The animals were collected with a 1-m-diam plankton net (335-μm mesh) hauled slowly and vertically from depths of 50 to 500 m. They were carefully transferred to maintenance vessels and kept alive throughout the experimental period. After acoustic data were collected, individuals were frozen for later measurements of length, wet weight, and dry weight. Other planktonic groups were also collected and used in the acoustic measurements (e.g., salps, ctenophores, and fish), but additional data are needed to accurately develop scattering models for them.

Great care was taken with the animals so that they were not exposed to air throughout the entire process of catching, sorting, examining through a microscope, tying, and deploying in and removing from the tank. This precaution was taken to prevent the possibility of bubbles attaching themselves to the animals and contaminating the measurements. Even the glue that was used in one of the tethering arrangements was applied and cured underwater. As an additional precaution the animals were gently shaken underwater to help release any bubbles that may have become attached to the animals in the process. The animals also were kept underwater in the experiment tank for a period prior to the measurements so that in case there was trapped air, it would be released from the animal or absorbed into the seawater.

Physical dimensions and weights of the animals were measured before the experiments and also sometimes after, when appropriate. Measurements of the euphausiids were straightforward. Because of the light weight of the gastropods and possible inaccuracy of direct measurement of the small millimeter-sized animals, the weights were estimated by use of the direct measurements of length and width and a published size–weight regression equation (Davis and Wiebe, 1985). The weight was sometimes used to calculate the equivalent spherical radius of the animals as a guide for scattering predictions.

The morphology of the siphonophores presented the greatest challenge in characterizing and that information presented should be considered at best approximate. When the animals were first brought onto the deck and then examined under the microscope (before the acoustic measurements took place), in several cases there were many (between two and nine) gas inclusions within the inner longitudinal tract of each animal. This is considered to be atypical and not representative of the actual morphology of the animals. These siphonophores contain only a single bubble in their natural environment (Mackie *et al.*, 1987) and the act of bringing them to the sea surface apparently caused the bubble to expand and fragment.

Once the animal was tethered in the acoustic tank, the back-and-forth sloshing of the water tended to (slightly) jerk the animal once the tether became tight at the end of each half cycle of water motion. By the end of the experiment, each animal had undergone hundreds of jerks. Upon removing each animal from the tank, it was discovered through inspection under the microscope that the gas inclusions within the animals containing multiple inclusions had not only changed position, but also quite often coalesced forming fewer or a single larger inclusion(s).

Naturally, the phenomenon of coalescing most likely had a strong effect on the measured scattering properties and definitely affected the predicted scattering properties. The

degree to which the sloshing affected the animal morphology varied from animal to animal. In some cases, the differences seemed minimal, while in several cases in 1993 only a single large gas inclusion remained. One of these latter cases, as well as animals that had a single inclusion from the initial time of capture, are studied here in detail because a single gas bubble is considered to be more typical of the animal in its natural environment. The acoustic scattering properties of a siphonophore with multiple inclusions are illustrated in Appendix A of Stanton *et al.* (1998) to illustrate the possible effects of these artifacts on the properties.

B. Pulse-echo system

1. Setup

The experimental apparatus and certain critical aspects of the data acquisition have been discussed in detail in Stanton (1990) and Chu *et al.* (1992), and summarized in Stanton *et al.* (1994a), and will only be briefly summarized here. The system involved a set of high-power single-frequency transducers: 50, 75, 120, 165, 200, 305, and 470 kHz, and 1 MHz, and a set of broadband transducers with less sensitivity, but an octave band of usable frequencies centered about the frequencies 250 kHz, 500 kHz, and 1 MHz. The transmit signals for all data in these experiments were 200 μs long. The transducers were mounted on the bottom of a 2.4-m-diam $\times$1.5-m-high tank, looking up at the animals that were tethered approximately 50 cm above the transducers. A pair of closely spaced identical transducers was used for each frequency or band of frequencies in the backscatter measurements. One transducer was the transmitter while the other was the receiver.

The animals were typically tethered with a combination of thin monofilament lines: a "main" line (59- or 158-μm diameter, depending on the experiment) and a secondary 59-μm-diam line. The tethers needed to be thin so that the echoes from them would be negligibly small. The euphausiids and siphonophores were tied to the main line with the secondary line, while the gastropods were glued directly to either the main or secondary line as they were too small to be tied.

The main tether was strung vertically between the midpoint of each transducer pair (even with the transducer faces) and a point out of water directly over the transducer pair. Since the tether was strung essentially parallel to the direction of acoustic transmission and backscattering, backscattering from this tether was minimized. A small loop was formed from this tether at 50-cm range from the transducers so the secondary tether could attach the animal to this main tether. The top and bottom points of the main tether were allowed to move where desired (a sliding monofilament system for the base and a moveable clip at the top) so that the animal could be easily moved horizontally over the desired transducer pair.

The two-transducer arrangement eliminated the need for a network used to isolate the transmitter signal from the receiver preamps (a circuit required in single transducer systems) and also eliminated the problem where the ringing of the transmitting transducer would interfere with the received echo at these short ranges. Furthermore, system calibration

for target strength measurements is very straightforward, as discussed later, and does not require additional hardware or a reflecting surface (this system can be calibrated at sea). A computer-based pulse-echo system was used to generate bursts of sound (tone bursts for the single frequency transducers and chirp signals for the broadband transducers) and to digitize and store each individual echo onto the computer for display and further processing.

A high-magnification underwater video camera system was also deployed in 1994 to facilitate viewing of the animal while the acoustic measurements were made. The camera was located at 50 cm above the transducers and aimed horizontally so that it was "looking" in a direction perpendicular to the direction of transmitted/backscattered acoustic waves. The directions needed to be perpendicular to enable accurate monitoring of the angle of orientation of the elongated animals relative to the direction of propagation of the acoustic signal for near broadside incidence angles where the scattered signals tend to be strongest. The video data were also stored onto tape so that the animal orientation could later be correlated with the acoustic data. The trigger signal for the acoustic ping was recorded onto the audio channel of the tape so that the correlation could be made on a ping-by-ping basis. A computer-based frame grabber, activated by the trigger signal, was used to automatically digitize video frames corresponding to acoustic pings. The digitizing was done during play back of the free running tape. For this study, the angle of orientation of one elongated animal was determined from each image by measuring the angle between the axis of the body and the main tether. With the exception of camera angle and automatic grabbing process, this method is similar to an arbitrary camera angle method described in detail in McGehee *et al.* (accepted).

The tank was filled with seawater to within 10–20 cm from the top of the tank. The at-sea measurements used water that was pumped from the ocean at the measurement site through the fire hose system of the ship and filtered with a 64-μm mesh net.

2. System response, calibration, and scattering amplitude

The voltage due to the received echo in the backscattering experiment can be expressed in terms of the voltage applied to the transmit transducer, voltage-to-pressure conversion factor of the transmit transducer $\beta_t(\omega)$, pressure-to-voltage conversion factor of the receive transducer $\beta_r(\omega)$, reference distance r_{ref}, distance to target, phase shifts, absorption in the water, and scattering amplitude of the target as

$$v_r^{(s)}(\omega) = \underbrace{v_t^{(s)}(\omega)}_{\substack{\text{applied} \\ \text{voltage}}} \underbrace{\beta_t(\omega)\beta_r(\omega) \frac{r_{ref} \, e^{(i2\omega/c)r_s}}{r_s^2} e^{-2\alpha(\omega)r_s}}_{\substack{\text{system response} \\ H(\omega)}}$$

$$\times \underbrace{f_{bs}(\omega)}_{\substack{\text{scatterer} \\ \text{response}}} \quad \text{(backscattering)}, \tag{4}$$

where the left term $v_r^{(s)}(\omega)$ is the receiver voltage.

where the expression is given in the frequency domain. Although this equation is used in the context of scattering by targets that lie on the center axis (maximum response axis) of the transmit and receive transducers, β_t and β_r can be used to account for beampattern diffraction effects if the target is not on one or either of the center axes. Equation (4) can also be written in the time domain in terms of the convolution of the inverse Fourier transforms of the various terms on the right-hand side:

$$v_r^{(s)}(t) = v_t^{(s)}(t) * H(t) * f_{bs}(t), \tag{5}$$

where $H(t)$ is the system *impulse* response which is the inverse Fourier transform of the system *frequency* response $H(\omega)$ (Oppenheim and Willsky, 1983). Note that the conventional notation in the signal processing literature involves upper case variables in the frequency domain and lower case variables in the time domain. Given the number of lower case terms (e.g., f_{bs}) in the scattering literature that are in the frequency domain, the domain here is indicated strictly by the arguments (t) and (ω). For example, $v_r^{(s)}(t)$ is the inverse Fourier transform of $v_r^{(s)}(\omega)$, etc.

In order to determine transducer efficiencies in the system response term H, the system is calibrated by separating the transducers, aiming them toward each other, and measuring signals as a result of the acoustic pulse traveling along the direct path between the two. With the target removed from the scattering region, the measurement is performed in a manner similar to that of the scattering experiment, but with the transmitter voltage greatly reduced to prevent saturation of the receiver preamps. During calibration, it was obvious that the response of the broadband transducers was not uniform across the band. The normalization process in the calibration procedure removed any nonuniformity. The system was calibrated at the beginning and end of each cruise. The spectrum of the receiver voltage in this calibration setup is

$$v_r^{(c)}(\omega) = v_t^{(c)}(\omega) \beta_t(\omega) \beta_r(\omega) \frac{r_{\text{ref}}}{r_c}$$
$$\times e^{(i\omega/c)r_c} e^{-\alpha(\omega)r_c} \quad \text{(calibration)}, \tag{6}$$

where the superscript (c) denotes calibration voltages.

Equation (4) shows that only the product of the transmit and receive transducer factors is required to relate the receiver voltage to the scattering amplitude rather than those quantities separately. Rearranging the terms in Eq. (6), the product can be written as

$$\beta_t(\omega)\beta_r(\omega) = \frac{v_r^{(c)}(\omega)}{v_t^{(c)}(\omega)} \frac{r_c}{r_{\text{ref}}} e^{-(i\omega/c)r_c} e^{\alpha(\omega)r_c}. \tag{7}$$

Inserting this expression for the product directly into Eq. (4) gives the following equation for the spectrum of the receiver voltage:

$$v_r^{(s)}(\omega) = \frac{v_t^{(s)}(\omega)}{v_t^{(c)}(\omega)} \frac{r_c}{r_s^2} e^{(i\omega/c)(2r_s - r_c)} e^{-\alpha(\omega)(2r_s - r_c)}$$
$$\times v_r^{(c)}(\omega) f_{bs}(\omega) \tag{8}$$
$$= \gamma_g(\omega) \frac{r_c}{r_s^2} e^{(i\omega/c)(2r_s - r_c)} e^{-\alpha(\omega)(2r_s - r_c)}$$
$$\times v_r^{(c)}(\omega) f_{bs}(\omega), \tag{9}$$

where now the receiver voltage in the scattering experiment is expressed in terms of voltage spectra from both the scattering and calibration measurements. For convenience, the term $\gamma_g(\omega) \equiv v_t^{(s)}(\omega)/v_t^{(c)}(\omega)$ is defined as the ratio of the transmitter voltage spectra in the two types of measurements. In the cases where the reduction in transmitter voltage for the calibration experiment is uniform across the frequency band, then γ_g is a constant.

As with Eq. (5) the convolution operator can be used to write the above equation in the time domain:

$$v_r^{(s)}(t) = s(t) * v_r^{(c)}(t) * f_{bs}(t), \tag{10}$$

where $s(t)$ is the inverse Fourier transform of

$$s(\omega) \equiv \gamma_g(\omega) \frac{r_c}{r_s^2} e^{(i\omega/c)(2r_s - r_c)} e^{-\alpha(\omega)(2r_s - r_c)}. \tag{11}$$

In Eq. (10) the receiver voltage time series in the scattering experiment is expressed in terms of the convolution of the system term, $s(t)$, with the received voltage time series in the calibration experiment and inverse Fourier transform of the scattering amplitude. Rearranging Eq. (9) and using the definition of $s(\omega)$ results in the following expression for the scattering amplitude of the target in terms of the various terms from the scattering and calibration experiments:

$$f_{bs}(\omega) = \frac{v_r^{(s)}(\omega)}{s(\omega) v_r^{(c)}(\omega)}. \tag{12}$$

Aside from the system term $s(\omega)$, the scattering amplitude is shown to be related to the receiver voltage from the scattering experiment normalized by the receiver voltage from the calibration measurement. It is the above expression that is used to calculate target strength versus frequency according to Eq. (2). While Eq. (12) is written in general form, it simplifies in the following cases: (1) When $\gamma_g(\omega)$ is constant in the band of interest (see above discussion) and the frequencies are low enough or $2r_s = r_c$, then $|s(\omega)|$ is independent of frequency. (2) For narrowband transducers, the various terms are quite often evaluated in terms of the envelope levels of their signals.

For both cases, it is advantageous to set up the experiment so that $2r_s = r_c$. With $2r_s - r_c = 0$ in the exponent of the attenuation term in $s(\omega)$, it is not required to know the attenuation coefficient of the water and

$$s = \gamma_g r_c / r_s^2, \tag{13}$$

where now the frequency dependence of γ_g has been removed. Here, r_s and r_c are still both given explicitly to account for cases in which $r_c \neq 2r_s$ and effects due to attenuation and phase shifts are not important.

3. Pulse compression processing

Pulse compression techniques are applied to the time series of the receiver voltage in the scattering experiment in order to both enhance the signal-to-noise ratio as well as to help determine some of the underlying physical mechanisms of the scattering processes. Pulse compression processing, which involves cross-correlating the received voltage with the transmit signal waveform, is generally very useful for detection of a broadband signal in the presence of noise as it

will tend to compress the signal to a short, higher level signal with a duration comparable to the inverse bandwidth of the signal (Skudrzyk, 1971; Turin, 1960; Winder and Loda, 1981). Uncorrelated noise in this case is not enhanced from the process and the signal-to-noise ratio is subsequently increased as a result of the filtering. In fact, it has been proven that when the signal component of the received voltage is identical (or proportional) to the transmitted wave form, then the pulse compression process maximizes the signal-to-noise ratio (this special case is referred to as a *matched* filter). For traditional detection of a signal in the presence of noise, the noisy signal is cross correlated with the original (noiseless) signal, which produces a signal resembling the autocorrelation function of the original signal (in the absence of noise, the result is exactly equal to the autocorrelation function).

In the scattering experiment, the (noiseless) ''signal'' (or ''replicate'') ideally would be the convolution of the applied signal with the known response of the system and the scattering amplitude of the target which is typically unknown. With an unknown scattering amplitude, it is not possible then to form the true signal or replicate. Hence, the filter cannot truly match the signal. In order to perform pulse compression processing of the signals in this scattering experiment, the replicate is constructed from the case resembling ideal scattering—that is, the scattering amplitude used in the convolution in Eq. (10) is uniform over all frequencies (e.g., such as with a perfectly reflecting wall). In practice, this replicate is the received voltage in the bistatic calibration when the transducers are facing each other. Applying this replicate when processing echoes from a real target will result in deviations from the matched filter output from the idealized ''expected'' case, due to deviations of the scatterer from the idealized target. These deviations contain useful information on the boundary conditions of the animals as will be shown in later sections.

The expression for the compressed pulse output is determined by using all components of Eq. (10) except for the scattering amplitude for the replicate:

$$CP(t) = k_{CP} \, v_r^{(s)}(t) \otimes v_r^{(c)'}(t), \tag{14}$$

where $v_r^{(s)}(t)$ is the measured noisy signal and the replicate $v_r^{(c)'}(t)$ is a filtered and scaled version of the receiver voltage in the calibration experiment:

$$v_r^{(c)'}(t) = s(t) * v_r^{(c)}(t) \tag{15}$$

(see above discussions for simplification of s). Equation (14) is a true matched filter only for the case of an ideal reflector where $f(\omega) = 1$ [i.e., $f(t) = \delta(t)$ where $\delta(t)$ is the delta function]. In that ideal case, beginning with Eq. (10): $v_r^{(s)}(t) = s(t) * v_r^{(c)}(t) * f_{bs}(t) = s(t) * v_r^{(c)}(t) * \delta(t) = s(t) * v_r^{(c)}(t) \equiv v_r^{(c)'}(t)$, hence making $v_r^{(c)'}(t)$ a true replicate. When real scatterers are involved, deviations in the compressed pulse output from the idealized (matched filter) case provide information on the target scattering amplitude $f(t)$. Note also that the cross correlation process in Eq. (14) is equivalent to (1) the convolution between one of the time series and the time-reversed time series of the other and (2) the inverse Fourier transform of the product of the spectrum of one signal and the complex conjugate (corresponding to time-reversal) of the spectrum of the other signal (Skudrzyk, 1971).

The normalization coefficient is equal to the inverse of the autocorrelation function of the modified calibration receiver voltage evaluated at the maximum point ($t=0$):

$$k_{CP} = R_{vcal}^{-1}(0), \tag{16}$$

where the autocorrelation function of $v_r^{(c)'}(t)$ is defined as

$$R_{vcal}(t) \equiv v_r^{(c)'}(t) \otimes v_r^{(c)'}(t). \tag{17}$$

Substituting expressions for k_{CP} from Eq. (16) and $v_r^{(s)}(t)$ from Eq. (10) into Eq. (14) and using Eq. (15) and the relations $s_1 * s_2 = s_2 * s_1$ and $(s_1 * s_2) \otimes s_3 = s_1 \otimes (s_2 \otimes s_3)$ gives

$$CP(t) = f_{bs}(t) \otimes \frac{R_{vcal}(t)}{R_{vcal}(0)} \tag{18}$$

[see, for example, Appendix B of Chu and Stanton (submitted) for a derivation of the latter above identities involving s_1, s_2, and s_3].

This expression shows the compressed pulse output to be equal to the scattering amplitude of the target cross correlated with the normalized autocorrelation function of the modified calibration signal. This output is very useful in analyzing the scattering by targets. For a target with only one dominant scattering feature, the compressed pulse output due to an incident chirp signal will resemble a sinc function time series. For a target with multiple scattering features, the output will resemble a series of sinc functions with different time delays and amplitudes according to the relative location and scattering amplitudes of the individual features, respectively. The above equation will be used to extract fundamental scattering information from the time series of the echoes from the animals. A much more extensive treatment of pulse compression techniques and application to the zooplankton scattering problem is presented in Chu and Stanton (submitted).

III. RESULTS

A. Data quality

A great challenge in the experiments involved the contaminants in the data. With most target strengths below about -70 dB, there were several sources of contamination in the data with comparable equivalent target strength levels. As with any system, self noise (electrical in this case) was one limiting factor. The (self-) noise floor of the broadband transducers was roughly -90 to -85 dB in a given spectral bin. The floor of the narrowband transducers was usually well below -90 dB. In addition to electrical self-noise, there were several sources of unwanted echoes: 1) Echoes from the surrounding walls of the tank and mounts. These echoes were stable in time and were generally not a problem as they were digitally removed in real-time with the oscilloscope. 2) Echoes from the tether of the animal. The target strength of too large of a tether can sometimes be comparable to or greater than the target strength of the animal. Great effort was made to ensure that the tether had a target strength much lower than that of the animal. Since the thinnest tethers (thinner than human hair) were so difficult to handle, they were

usually used only with the animals with the lowest target strength. Thicker tethers were used with animals that had higher target strengths. 3) Echoes from the glue that was sometimes used to attach the tether to the animal. When the animal was so small that a tether could not be tied around it, the tether needed to be glued to the animal. Sometimes the echoes from the glue dominated the overall echoes and those data were discarded. Great effort was made to minimize the use of glue as well as to minimize the amount of glue applied when it was used. 4) Echoes from other parts of the water volume. Reverberation from the water from near the animal degraded many sets of data. This reverberation was associated with the turbulent motion of the water due to ship motion. It was present when the water was sloshing back and forth and tended to disappear when the tank was still (for example, on calm nights when the ship was moving slowly downwind). The reverberation tended to be stronger at the lower frequencies.

Tether target strengths as low as −95 dB at 200 kHz were achieved during calm sea conditions. Tether plus glue target strengths lower than about −85 dB with the 500-kHz broadband transducers could be achieved with the right combination of tether and small application of glue. The reverberation associated with the motion of the tank easily reached levels of about −70 dB for certain sea conditions.

Because of the above sources of contamination, the data were examined with great scrutiny both during the time of experimentation as well as afterward. Generally, the single ping analysis was affected the most by the contamination as any source of unwanted signal would tend to alter the structure of the target strength versus frequency curves (see the Appendix). Hence, only a minority of data is usable for the single ping analysis where the precise structure of the TS curves is examined. However, for examination of echoes averaged over many pings, the criteria for selection were not as strict and far more data are usable. As long as the target echo was at least about 6 dB greater than the level of the unwanted echo, averages could be calculated with reasonable accuracy.

B. Single ping echoes

Because of the relatively high quality of data (a combination of signal-to-noise ratio and bandwidth) coming from the broadband 500-kHz transducers, the spectral nature of the scattering as measured from those transducers is analyzed on an individual ping basis. The scattering measurements over the ~400 to 650-kHz band showed significant structure in most target strength versus frequency plots for the euphausiids and a significant fraction of the pings for the gastropods and siphonophores (Fig. 2). In the case of the gastropods and siphonophores, there are also many pings where the variability in the spectra was small and random. A small fraction of data from the euphausiids also exhibited low variability in the spectra. Each of the echoes recorded from the 500-kHz broadband transducers from the euphausiid typically showed a series of peaks and dips (or nulls), some mostly regularly spaced and others mostly irregularly spaced. Since some of the nulls dip below the noise/unwanted reverberation level of the system, it is expected that the lowest part of the nulls are affected accordingly. The
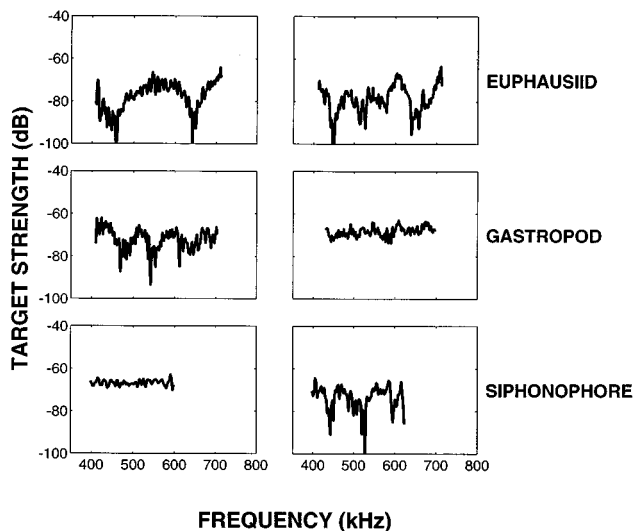
FIG. 2. Target strength versus frequency for two individual pings (left/right panel), each from single zooplankters. Since the euphausiid and siphonophore were allowed to change orientation throughout the ping sequence, two (nonconsecutive) pings from the same case were selected in each case to illustrate ping-to-ping variability. The gastropods remained nearly fixed at a random orientation and one ping each from two same-size animals were selected to illustrate variability. Species and lengths of the animals are, euphausiid: *Meganyctiphanes norvegica*, 34 mm; gastropod: *Limacina retroversa*, 2 mm; siphonophore: *Agalma okeni* or *elegans*, 48 mm (gas inclusion is 1.3 mm long by 0.5 mm wide).

Fourier component of the noise that is at or near the null will tend to shift the position of the null. The target strength pattern, even when regular and with a high signal-to-noise ratio, tended to shift randomly from ping-to-ping—a phenomenon also observed with broadband echoes from decapod shrimp (Chu *et al.*, 1992). The euphausiid was tethered in such a way (around its mid-section) that it was free to change orientation over the entire range of angles (Fig. 3) and significant variability in the type of pattern is expected.
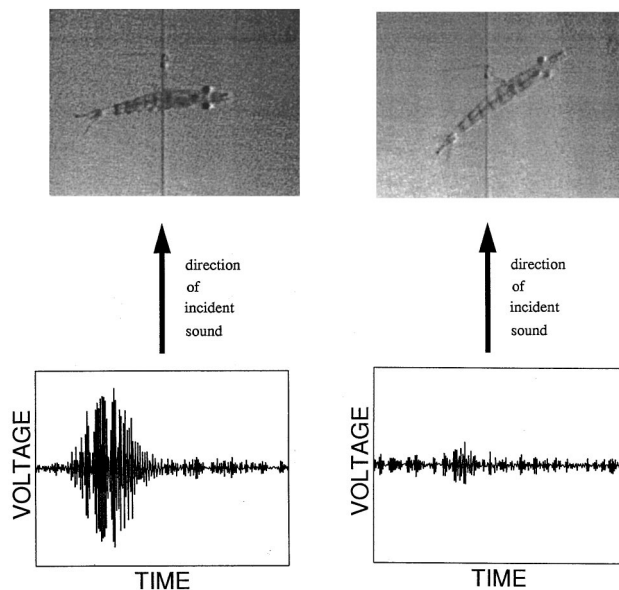
FIG. 3. Illustration of orientation effects of the backscattering by a 36-mm-long euphausiid (*Meganyctiphanes norvegica*). The video image was captured to within one frame (~33 ms) of the time the 500-kHz broadband signal was transmitted.
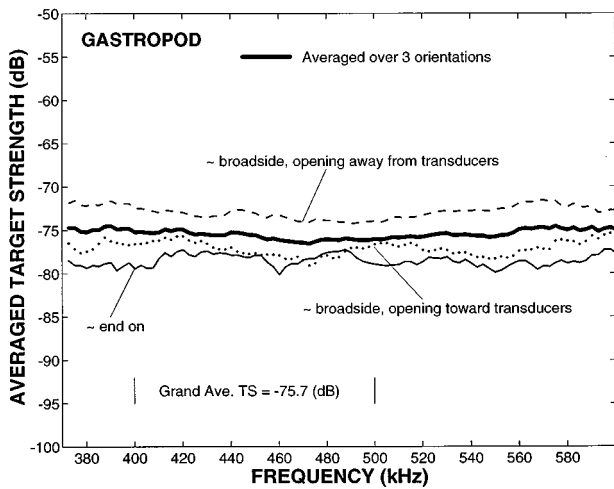
FIG. 4. Target strength versus frequency from averages over hundreds of pings for a single gastropod in each of three different orientations. The thick line corresponds to an unweighted average of the average levels from each orientation. All averages performed on a linear scale before the logarithm is taken. The gastropod (*Limacina retroversa*) was 1.5 mm long.

Similarly, the siphonophore was tethered in such a way (near its pneumatophore) which allowed much freedom of movement and, in turn, much ping-to-ping variability in the pattern. Because of the small size of the gastropods and the fact that they were not trying to swim during the experiments, they did not move much, if at all, and demonstrated relatively consistent patterns from ping to ping for a given animal.

C. Orientation effects

The effects of orientation (as determined by high-magnification video footage) on the scattering by the euphausiids were quite noticeable (Fig. 3). While the animal was near broadside incidence, the echo levels were, on the average, relatively high, although there was significant variability in the level from ping to ping. Off broadside incidence, the echo levels were generally much lower. The scattering by the siphonophores tended to remain relatively high regardless of orientation and there tended to be variability in the level from ping to ping. The gastropod data also demonstrated an orientation dependence. Since the orientation of the animals tended to be relatively fixed throughout a ping sequence, a large number of pings could be collected and averaged for a given orientation angle.

In one series of gastropod experiments, three orientation angles were studied for a single animal: one in which the opercular opening of the animal was facing away from the transducers (with body axis near broadside incidence), one in which the opening was facing toward the transducers (with body axis about 30° off broadside incidence), and one in which the opening was facing perpendicular to the propagation of the incident sound waves with the apex of the animal aimed toward the transducers (i.e., "end-on"). The average target strength values varied over a range of about 5 dB over the range of orientation angles (Fig. 4). The broadside orientation in which the opercular opening was facing away from

the transducers resulted in the highest values of target strength.

D. Removal of gas inclusion from siphonophore

In order to further investigate the dominant scattering mechanisms of the siphonophores, the target strength was measured for one animal for a series of pings first as a whole (undissected) animal, and then with the pneumatophore removed (the animal remained alive after the pneumatophore was removed) (Fig. 5). The target strengths, averaged over the various 200-ping series, showed a significant drop in level of roughly 5 dB once the pneumatophore was removed. The statistics of the echo envelopes of the animal with and without the gas also showed a change in shape and average level (Fig. 6). The shape of the PDF (at 560 kHz) associated

FIG. 5. Target strength versus frequency from averages over hundreds of pings for a siphonophore with and without its pneumatophore. Average performed on a linear scale before logarithm was taken. Same animal as in Fig. 2.
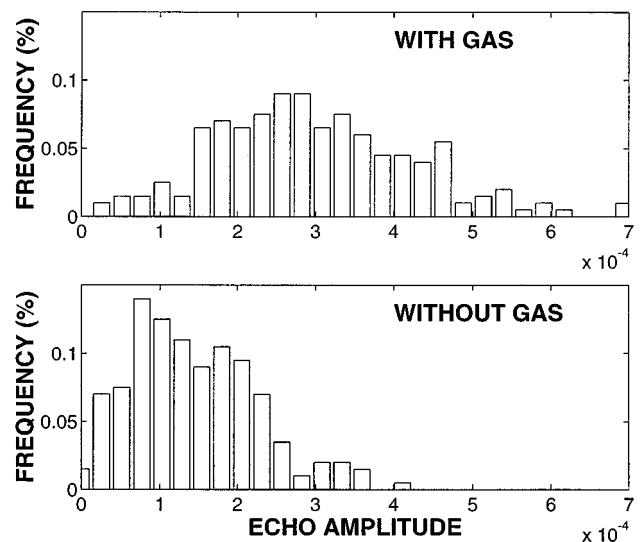
FIG. 6. Echo envelope histograms of siphonophore from Fig. 5 with and without its pneumatophore. Echo amplitude is $|f_{bs}|$ expressed in units of meters. Data from 560-kHz Fourier bin of 500-kHz broadband echo. Here, 200 echoes per plot are used to form the histograms.
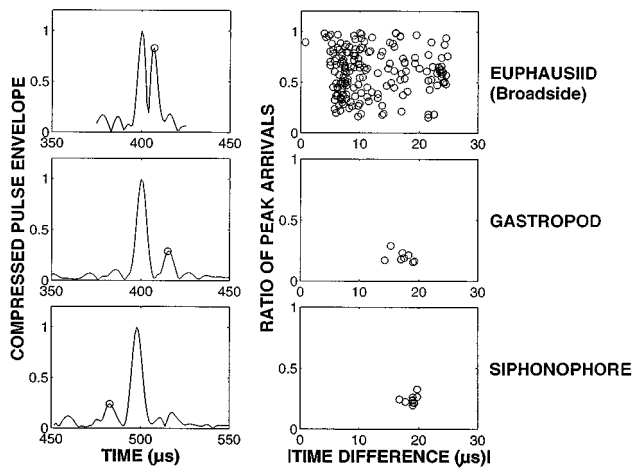
FIG. 7. Envelope of compressed pulse output of a single ping (left column) and statistics (right column) of secondary arrival from each of the three animal types. The 200-μs-long echoes were compressed to about 10-μs-long through cross correlation with the calibration waveform. This process allows certain features of the animals to be resolved acoustically. Examples of secondary arrivals are indicated by circled peaks in left column. The ratio of the amplitude of the secondary arrival to the amplitude of the principal arrival for various pings is given in the right column. The secondary return arrived after the principal arrival for the euphausiid and gastropod and before for the siphonophore. The euphausiid was very near broadside (dorsal) incidence for the example ping in the left plot. For the entire ping series shown in the plot on the right, the euphausiid was generally near broadside (dorsal) incidence with occasional exceptions. The main body of the siphonophore is closer to the transducer than the gas for the selected ping series. Species and lengths of animals are, euphausiid: same animal as in Fig. 3; gastropod, same animal as in Fig. 4; siphonophore: *Nanomia cara*, 26 mm (gas inclusion was 1.5 mm long by 1 mm wide). Absolute value of time difference given on right side because siphonophore values are all negative for this particular ping sequence.

with the whole animal tends to be Gaussian-like while the shape of the PDF of the body-only animal appears Rayleigh-like.

E. Statistics of secondary arrivals

In addition to examining the spectral content of individual pings, the envelope of the compressed pulse output of
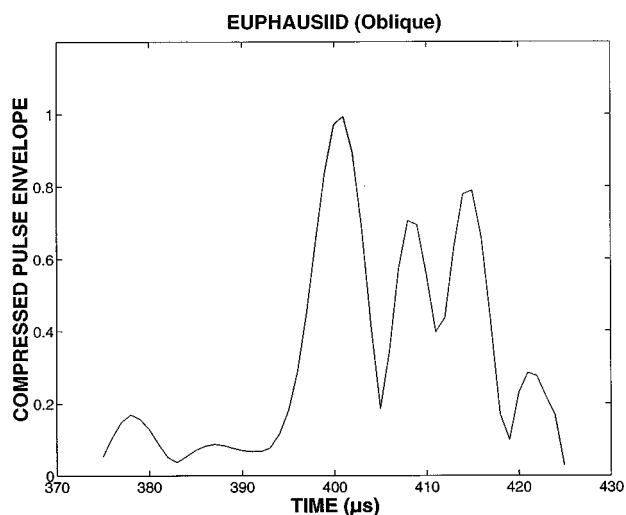
FIG. 8. Envelope of compressed pulse output of a single echo from a euphausiid near head-on incidence. Same animal as in Fig. 7.

the time series of the individual pings was also studied (Figs. 7 and 8). The compressed pulse output showed typically more than one main lobe. The level of each "secondary" main lobe was usually lower than that of the "principal" main lobe but higher than the sidelobes of the principal main lobe that would be artifacts of the signal processing. The statistics of the relative amplitude and time of arrival of the secondary main lobes were also studied using the highest quality echoes (i.e., least contamination due to noise and reverberation) for each animal (right column of Fig. 7). In the euphausiid data, there were typically two main peaks when the animal was oriented near broadside (Fig. 7) and quite often more than two peaks once the animal was well away from broadside (Fig. 8). The statistical analysis for euphausiids in Fig. 7 involved just the near-broadside echoes.

IV. DISCUSSION

Most data indicate that there are scattering returns coming in from more than one part of the body: (1) Frequency domain: the pattern of the target strength versus frequency curves quite often had a series of peaks and nulls. This type of pattern is similar to that of an optical interferometer in which light waves experience multiple bounces and interfere upon exiting the device. The position of the peaks and nulls depends upon a combination of optical wavelength and separation between the mirrors. For the animals, a similar argument may hold as the interference patterns imply that there are echoes (at least two) coming from different parts of the body and are interfering according to the acoustic wavelength and separation between the scatterers (or more generally, the total path length experienced by each echo). (2) Time domain: the compressed pulse output shows that the echoes from the animals typically possessed more than one highlight, indicating that more than one part of the animal is contributing to the echo. Sometimes the secondary arrivals were not large enough to cause an oscillatory pattern in the target strength versus frequency curve (not shown). (3) In addition to the spectral and temporal studies of all animals, examination of the siphonophore data before and after the gas inclusion was removed indicated clearly that, although the gas contributes significantly to the echo, the tissue cannot be ignored under some conditions.

The broadest separation between nulls in the target strength versus frequency curve for the euphausiid was consistent with receiving echoes from the front and back body walls of the animal at broadside incidence. This observation is consistent with the data collected involving decapod shrimp by Chu *et al.* (1992). The closer separations between the nulls are consistent with distances greater than the (cylindrical) diameter of the animal, which is consistent with the animal being off broadside (in the extreme case of end-on, it is possible that echoes could be separated by a distance equal to the length of the animal). The compressed pulse output was not able to resolve individual echoes when the separation between the nulls was the largest (i.e., a single main lobe in the output was observed). When the separation between the nulls was slightly smaller, two main lobes were

resolved with temporal spacing consistent with distances slightly larger than the diameter of the animal.

While some patterns of target strength versus frequency were regular (implying that there were only two major sources of scattering per euphausiid), other patterns for the same animal were quite irregular. As shown in Stanton *et al.* (1994b) with decapod shrimp, there can be at least six major sources of scattering in that case. It is hypothesized that once the animal is away from broadside incidence and/or possibly configured in an irregular shape, then other parts of the body will also contribute significantly to the scattering. Hence, at least two sources of scattering must be modeled for the euphausiid and possibly more.

The data analyzed for the siphonophore indicate that the scattering is due to a combination of the gas and surrounding tissue. The separation between the main lobes of the compressed pulse output for the siphonophore data is consistent with distances comparable to the length of the siphonophore. While the gas is shown to dominate the average target strength levels, the tissue apparently plays a role in the pattern of target strength versus frequency for single ping data. If the tissue contributed a negligible amount, then the pattern would be flat. For a fraction of the pings, the pattern was flat, indicating that the variable echo from the tissue did not contribute during those pings. However, when the patterns were irregular, the echo from the tissue in these realizations may have been large enough (i.e., on the tail of the echo envelope PDF) to interfere with the echo from the gas.

While the various patterns of data for the euphausiids and siphonophores are consistent with two-way paths due to scattering from different parts of the animal bodies, the patterns for the gastropods are not consistent with separations of any dimension of the body. In fact, the oscillatory pattern of target strength versus frequency for the gastropod contains a null separation consistent with a fluidlike animal diameter of approximately 10 mm. Because the gastropods were about 1 mm×2 mm in size, it is apparent that another scattering mechanism must be contributing to the echo: A thin but hard elastic shell may not allow waves to significantly penetrate into the body and reflect back to interfere with the echo from the front interface. However, it is possible that the elastic shell is supporting a circumferential wave. One strong candidate is the zeroth-order antisymmetric Lamb wave (i.e., a_0 or flexural wave). It is quite strong and travels at subsonic speeds in this range of ka (near unity). If one were to use one-half the circumference of the shell as its travel path, then the 75-kHz null spacing would be consistent with the interference between the echo from the front interface of the shell and a Lamb wave traveling at about $\frac{1}{8}$ that of the speed of sound in water. This subsonic speed is within a reasonable range of expected values for thin shells and near unity values of ka (see, for example, Kargl and Marston, 1989; Kaduchak *et al.*, 1995). The hypothesis of the animal shell supporting a Lamb wave is consistent with the appearance and disappearance of the interference pattern in the target strength versus frequency curve for single pings. It is possible that the animal can be oriented in such a way that the opercular opening can stop the propagation of the Lamb waves, hence only the echo from the front interface would remain with no interference.

V. CONCLUSIONS

In conclusion, through a series of controlled laboratory studies, key scattering mechanisms of several types of zooplankton have been inferred acoustically. The data indicate that scattering is typically due to more than one part of the body. The euphausiid (a fluidlike animal) gives rise to at least two echoes. When broadside, the echoes are due to arrivals from the front and back interfaces (body walls) of the animal. The gas inclusion of the siphonophore (a gas-bearing, fluidlike body) dominates the overall levels of the scattering, but the tissue can play a role, especially when analyzing data on a ping-by-ping basis. The gastropod (elastic-shelled animal) gives rise to echoes from the front interface and possibly a slow-traveling circumferential (Lamb) wave. These scattering mechanisms will be taken into account in the companion paper (Stanton *et al.*, 1998) in the formulation of mathematical scattering models.

APPENDIX: CONTAMINATION OF ECHO DATA DUE TO TURBULENT WATER VOLUME

There was scattering from the water volume associated with the water motion. The greater the motion, the greater the level of scattering. Although no controlled study was performed to determine the source of the reverberation, one possible source could be salinity and temperature microstructure (Stanton *et al.*, 1994b; Seim *et al.*, 1995). If that were the case, the salinity and temperature microstructure would give rise to a sound velocity microstructure which, in turn, would diffusely scatter the incident acoustic field. Regardless of the source of reverberation, it occurred frequently enough that it had to be taken into account in the identification of valid data.

The scattering from the turbulent water volume surrounding the animal quite often dramatically affected the pattern of curves of the target strength versus frequency from individual pings. As a result of this observation, single pings
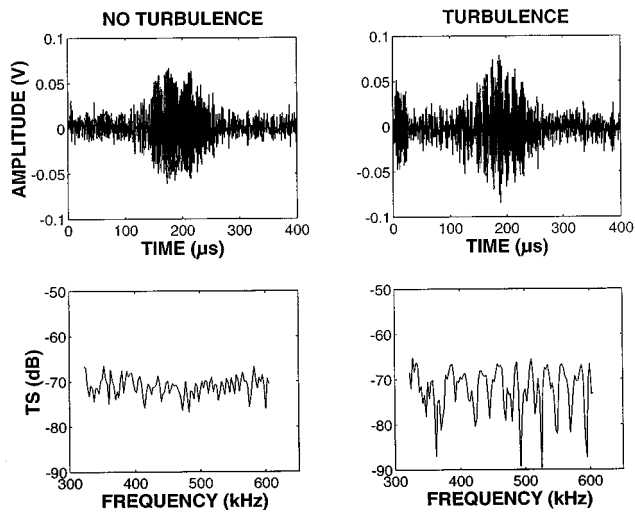
FIG. A1. Time series and target strength versus frequency for single echoes from a siphonophore with and without the presence of local volume reverberation associated with turbulence. Same animal as in Fig. 7. Left column shows echo due to animal with apparently no turbulence. Right column shows echo due to animal with turbulence echo explicitly appearing at left-most part of time series. Deep rapid oscillations in TS pattern occurred (lower right) even with the (visible) turbulence echo gated out, indicating presence of another turbulence echo occurring during time of animal echo. The leading and trailing edges of the 200-μs-long waveforms are below the noise level in the time series.

that were selected for detailed analysis were chosen with great scrutiny. Those that were selected for single ping analysis must have been part of a series of pings where there was no apparent background reverberation activity for several pings before and after (both raw time series and compressed pulse output were used in the examinations). Only then was there confidence that there was little or no contamination of the animal echo due to volume reverberation from turbulence.

The turbulence effects could be seen in the time series as an irregular short-lived echo appearing at times not corresponding to the location of the animal (left-most echo in turbulence time series in top right-hand plot in Fig. A1). In the sampling window of the data acquisition system, the background echoes could be observed before, during, and/or after the echo from the animal. The resultant pattern of target strength versus frequency curve sometimes contained deep rapid oscillations, departing from the slower oscillations or even relatively flat curves observed when reverberation was apparently not present (Fig. A1). The target strength pattern was sometimes oscillatory even when a turbulence echo apparent in the time series was gated out. Evidently, there was another turbulence echo arriving at nearly the same time as that from the animal. In that case, this other echo could not be gated out.

Chu, D., and Stanton, T. K. (**submitted**). ''Application of pulse compression techniques to broadband acoustic scattering by individual marine organisms,'' submitted to J. Acoust. Soc. Am.

Chu, D., Foote, K. G., and Stanton, T. K. (**1993**). ''Further analysis of target strength measurements of Antarctic krill at 38 and 120 kHz: Comparison with deformed cylinder model and inference of orientation distribution,'' J. Acoust. Soc. Am. **93**, 2985–2988.

Chu, D., Stanton, T. K., and Wiebe, P. H. (**1992**). ''Frequency Dependence of Sound Backscattering from Live Individual Zooplankton,'' ICES J. Mar. Sci. **49**, 97–106.

Davis, C., and Wiebe, P. (**1985**). ''Macrozooplankton Biomass in a Warm-Core Gulf Stream Ring: Time Series Changes in Size, Structure, and Taxonomic Composition and Vertical Distribution,'' J. Geophys. Res. **90**, 8871–8884.

Foote, K. G., and Stefánsson, G. (**1993**). ''Definition of the Problem of Estimating Fish Abundance Over an Area from Acoustic Line-Transect Measurements of Density,'' ICES J. Mar. Sci. **50**, 369–381.

Foote, K. G., Everson, I., Watkins, J. L., and Bone, D. G. (**1990**). ''Target strengths of Antarctic krill (*Euphausia superba*) at 38 and 120 kHz,'' J. Acoust. Soc. Am. **87**, 16–24.

Holliday, D. V., and Pieper, R. E. (**1995**). ''Bioacoustical Oceanography at High Frequencies,'' ICES J. Mar. Sci. **52**, 279–296.

Kaduchak, G., Kwiatkowski, C. S., and Marston, P. L. (**1995**). ''Measurement and interpretation of the impulse response for backscattering by a thin spherical shell using a broad-bandwidth source that is nearly acoustically transparent,'' J. Acoust. Soc. Am. **97**, 2699–2708.

Kargl, S. G., and Marston, P. L. (**1989**). ''Observations and modeling of the backscattering of short tone bursts from a spherical shell: Lamb wave echoes, glory, and axial reverberations,'' J. Acoust. Soc. Am. **85**, 1014–1028.

Mackie, G. O., Pugh, P. R., and Purcell, J. E. (**1987**). ''Siphonophore Biology,'' Adv. Mar. Sci. **24**, 97–111.

MacLennan, D. N. (**1990**). ''Acoustic measurement of fish abundance,'' J. Acoust. Soc. Am. **87**, 1–15.

Martin, L. V., Stanton, T. K., Wiebe, P. H., and Lynch, J. F. (**1996**). ''Acoustic Classification of Zooplankton,'' ICES J. Mar. Sci. **53**, 217–224.

McGehee, D. E., O'Driscoll, R. L., and Martin Traykovskii, L. V., ''Effects of orientation on acoustic scattering for Antarctic krill at 120 kHz,'' Deep Sea Research (accepted).

Oppenheim, A. V., and Willsky, A. S. (**1983**). *Signals and Systems* (Prentice–Hall, London).

Seim, H. E., Gregg, M. C., and Miyamoto, R. T. (**1995**). ''Acoustic Backscatter from Turbulent Microstructure,'' J. Atmos. Ocean. Tech. **12**, 367–380.

Simmonds, E. J., Williamson, N. J., Gerlotto, G., and Aglen, S. (**1992**). ''Acoustic Survey Design and Analysis Procedure: A Comprehensive Review of Current Practice,'' ICES Cooperative Research Report No. 187. International Council for the Exploration of the Sea. Palaegrade 2-4, DK-1261, Copenhagen K, Denmark.

Skudrzyk, E. (**1971**). *The Foundations of Acoustics* (Springer-Verlag, New York).

Stanton, T. K. (**1990**). ''Sound scattering by spherical and elongated shelled bodies,'' J. Acoust. Soc. Am. **88**, 1619–1633.

Stanton, T. K., and Clay, C. S. (**1986**). ''Sonar Echo Statistics as a Remote-Sensing Tool: Volume and Seafloor,'' IEEE J. Ocean Eng. **OE-11**, 79–96.

Stanton, T. K., Chu, D., and Wiebe, P. H. (**1998**). ''Sound scattering by several zooplankton groups. II. Scattering models,'' J. Acoust. Soc. Am. **103**, 236–253.

Stanton, T. K., Clay, C. S., and Chu, D. (**1993a**). ''Ray representation of sound scattering by weakly scattering deformed fluid cylinders: Simple physics and application to zooplankton,'' J. Acoust. Soc. Am. **94**, 3454–3462.

Stanton, T. K., Chu, D., Wiebe, P. H., and Clay, C. S. (**1993b**). ''Average echoes from randomly oriented random-length finite cylinders: Zooplankton models,'' J. Acoust. Soc. Am. **94**, 3463–3472.

Stanton, T. K., Wiebe, P. H., Chu, D., and Goodman, L. (**1994b**). ''Acoustic Characterization and Discrimination of Marine Zooplankton and Turbulence,'' ICES J. Mar. Sci. **51** 469–479.

Stanton, T. K., Wiebe, P. H., Chu, D., Benfield, M., Scanlon, L., Martin, L., and Eastwood, R. L. (**1994a**). ''On Acoustic Estimates of Zooplankton Biomass,'' ICES J. Mar. Sci. **51**, 505–512.

Turin, G. L. (**1960**). ''An Introduction to Matched Filters,'' IRE Trans. Inf. Theory **IT-6(3)**, 311–329.

Wiebe, P. H., Mountain, D., Stanton, T. K., Greene, C., Lough, G., Kaartvedt, S., Manning, J., Dawson, J., and Copley, N. (**1996**). ''Acoustical Study of the Spatial Distribution of Plankton on Georges Bank and the Relationship Between Volume Backscattering Strength and the Taxonomic Composition of the Plankton,'' Deep-Sea Res. II **43**, 1971–2001.

Winder, A., and Loda, C. J. (**1981**). *Space-time Information Processing* (Peninsula, Los Altos, CA), pp. 153–156.

Sound scattering by several zooplankton groups.
II. Scattering models

Timothy K. Stanton and Dezhang Chu
Department of Applied Ocean Physics and Engineering, Woods Hole Oceanographic Institution,
Woods Hole, Massachusetts 02543-1053

Peter H. Wiebe
Department of Biology, Woods Hole Oceanographic Institution, Woods Hole, Massachusetts 02543-1049

Mathematical scattering models are derived and compared with data from zooplankton from several gross anatomical groups—fluidlike, elastic shelled, and gas bearing. The models are based upon the acoustically inferred boundary conditions determined from laboratory backscattering data presented in part I of this series [Stanton *et al.*, J. Acoust. Soc. Am. **103**, 225–235 (1998)]. The models use a combination of ray theory, modal-series solution, and distorted wave Born approximation (DWBA). The formulations, which are inherently approximate, are designed to include only the dominant scattering mechanisms as determined from the experiments. The models for the fluidlike animals (euphausiids in this case) ranged from the simplest case involving two rays, which could qualitatively describe the structure of target strength versus frequency for single pings, to the most complex case involving a rough inhomogeneous asymmetrically tapered bent cylinder using the DWBA-based formulation which could predict echo levels over all angles of incidence (including the difficult region of end-on incidence). The model for the elastic shelled body (gastropods in this case) involved development of an analytical model which takes into account irregularities and discontinuities of the shell. The model for gas-bearing animals (siphonophores) is a hybrid model which is composed of the summation of the exact solution to the gas sphere and the approximate DWBA-based formulation for arbitrarily shaped fluidlike bodies. There is also a simplified ray-based model for the siphonophore. The models are applied to data involving single pings, ping-to-ping variability, and echoes averaged over many pings. There is reasonable qualitative agreement between the predictions and single ping data, and reasonable quantitative agreement between the predictions and variability and averages of echo data. © *1998 Acoustical Society of America.* [S0001-4966(97)01110-7]

PACS numbers: 43.30.Ft, 43.30.Sf, 43.20.Fn [JHM]

LIST OF SYMBOLS

a	radius of sphere or cylinder
$\bar{a}$	average radius
α_B, T_B, C_B	numerically determined coefficients in ray-based bent fluid cylinder model
α_L	real part of ν_L
b_j	scattering amplitude of local facet that is broadside to incident beam
$b_m^{(f)}$	modal series coefficient for homogeneous fluid sphere
β	L/a
β_{tilt}	tilt angle of infinitesimally thin disk or cross section of body at an arbitrary point $\mathbf{r}_{\text{pos}}$. This is the angle between the direction of the incident wave $\hat{k}_i$ and the plane containing the disk. Specifically, $\beta_{\text{tilt}} = 90° - \cos^{-1}(\hat{k}_i \cdot \hat{r}_{\text{tan}})$ where $\hat{r}_{\text{tan}}$ is the tangent to the body axis at point $\mathbf{r}_{\text{pos}}$ ($\beta_{\text{tilt}} = 0$ corresponds to broadside incidence to the disk axis at the arbitrary point on the body axis). β_{tilt} is not to be confused with the orientation angle, θ, of the body, although the two are the same when the body axis is straight.
β_L	imaginary part of ν_L; attenuation coefficient of Lamb wave on elastic shelled sphere
$\beta_L'(\infty)$	attenuation coefficient of Lamb wave on flat plate ($a = \infty$)
c	sound speed
c_L	sound speed of Lamb wave
D	center-to-center distance between bubbles
Δ_a	deviation in effective radius from mean radius of rough sphere
η_L	phase shift due to partial circumnavigation (i.e., path between $\pm\theta_L$ points) of Lamb waves
ϵ_j	distance between the point of scatter and the zero phase reference plane (ϵ_j is negative for points on the source/receiver side of zero phase reference plane)
f	scattering amplitude
f_{bs}	scattering amplitude in backscattering direction
F_L	factor, ranging in value from 0 to 1, to account for loss of Lamb wave due to discontinuity in shell
g	ρ_2/ρ_1
$\gamma_\kappa, \gamma_\rho$	material property parameters in DWBA formulation
G_L	coupling coefficient for combination of landing and launching of Lamb waves on shell

h	c_2/c_1
i	$\sqrt{-1}$ unless used as a summation index or subscript to $\mathbf{k}$
k	acoustic wave number ($=2\pi/\lambda$)
κ	compressibility
$\mathbf{k}_i$	wave number vector of incident field
$\mathbf{k}_s$	wave number vector of scattered field
L	length of body
$\overline{L}$	average length of body
λ	acoustic wavelength
μ	semi-empirical phase shift term for ray model
ν_L	complex root of denominator of modal series coefficient for fluid-filled elastic spherical shell
Φ_L	phase shift of Lamb wave heuristically added for nonideal body
ϕ_M	meridional angle
ρ_c	radius of curvature of longitudinal axis of uniformly bent cylinder
ρ	mass density
$\mathbf{r}_{pos}$	position vector of axis of deformed cylinder
$\mathbf{r}_v$	position vector of volume
$\mathscr{R}_{12}$	plane wave/plane interface reflection coefficient (reflection off of medium ''2'' due to incident beam in medium ''1'') $[=(\rho_2 c_2/\rho_1 c_1 -1)/(\rho_2 c_2/\rho_1 c_1 +1)]$
s_θ, s_L	standard deviation of angle of orientation and length, respectively
s	$s_L/\overline{L}$
σ	$\langle \Delta_a^2 \rangle^{1/2}$
$(\sigma_{bs})_1$	backscattering cross section of one bubble
$(\sigma_{bs})_N$	backscattering cross section of N-bubble array
TS	target strength ($=10\log|f_{bs}|^2$)
T_{12}, T_{21}	transmission coefficients for transmission from medium ''1'' to ''2'' or ''2'' to ''1,'' respectively $[T_{ij}=2(\rho_j c_j/\rho_i c_i)/(1+(\rho_j c_j/\rho_i c_i))]$
θ	angle of orientation of body relative to the direction of the incident wave ($\theta=0$ corresponds to broadside incidence)
θ_L	launch/land angle for Lamb wave
v	volume of body
ζ	deviation of radius from mean radius of irregular sphere at a given point on sphere
1,2	subscripts indicating medium ''1'' (surrounding fluid) and medium ''2'' (body medium)
$\langle \cdots \rangle$	average over ensemble of statistically independent samples

INTRODUCTION

In the first part of this series of papers, laboratory data showed that the scattering properties of zooplankton from different gross anatomical groups varied between the groups (Stanton *et al.*, 1997). In this paper, the acoustic boundary conditions inferred from that study are used to derive approximate scattering models of single echoes from an individual animal, the ping-to-ping variability of the echoes as the animal changes shape and orientation, as well as the average echo value. The models are compared with the laboratory data.

The single ping data and variability analyses in this two-part study are most revealing of the fundamental physics of the scattering processes and serve at least as a guide toward development of the models. In addition, those analyses are useful when examining resolved echoes in the field. The analysis involving average echoes is less revealing of the fundamental scattering process, but is useful in modeling of volume reverberation in field surveys.

I. SCATTERING MODELS

A. Euphausiids (deformed fluid cylinder)

In Stanton *et al.* (1998), our analysis of data acquired in at-sea laboratory studies indicated that there were typically at least two arrivals from the body of the animal. We hypothesized that, near broadside incidence, there are two major arrivals, one from the front interface of the body and the other from the back interface (after the incident wave has traveled into the body) (Fig. 1). For a weakly scattering body (i.e., one in which the density and sound speed of the body are close to that of the surrounding medium), the wave that travels into the body suffers little transmission loss at the front boundary. As a result, once reflected off the back interface, it can be of comparable strength to that of the echo from the front interface. The strong regular interference patterns of target strength versus frequency imply that the two waves are indeed of comparable strength and that the animal can be considered as a weakly scattering body. It was also hypothesized that for other orientations (or even irregular shapes at broadside), other parts of the body may also contribute significantly to the scattering, giving rise to six or more echoes from the body. As a result, many of the target strength versus frequency curves had an irregular structure.

The scattering by this type of animal is quite complex as its shape resembles that of a deformed finite length cylinder, a shape for which there is no exact analytical solution. The choice of which approach to use in modeling the scattering depends upon the application. If the emphasis is on the structure of the target strength versus frequency curves for individual ping data, then enough detail of the boundaries must be included so that the interference patterns can be predicted (at least qualitatively). However, if only averages over many pings and animals are of interest, then the structure of the interference pattern is reduced as a result of the average and a simpler model can be considered.

There has been much development to date on description of scattering by weakly scattering finite-length fluid cylinders which involves a modal-series-based line integral (deformed cylinder formulation), a ray summation (derivable from surface integrals or Sommerfeld–Watson transformation imbedded in deformed cylinder formulation), and a distorted wave Born approximation (DWBA, a volume integral which can be reduced to a line integral in this case) (Stanton, 1988, 1989a, 1989b; Stanton *et al.*, 1993a, 1993b, 1994a, 1994b; Chu *et al.*, 1992, 1993). The DWBA approach has been very useful in calculating (through numerical integra-

237   J. Acoust. Soc. Am., Vol. 103, No. 1, January 1998

Stanton *et al.*: Several zooplankton scattering. II   237

tion) average echoes from animals of arbitrary distributions of sizes and orientation angles. The ray formulation has been especially useful in both qualitatively illustrating the structure of target strength versus frequency curves as well as being easy to manipulate in deriving simple (yet accurate) closed-form expressions for echoes averaged over a constrained set of distributions of size and orientation angle.

The DWBA formulation is given in a general volume integral form for backscattering in the farfield due to a finite-length body as (Morse and Ingard, 1968)

$$ f_{bs} = \frac{k_1^2}{4\pi} \int \int \int_v (\gamma_\kappa - \gamma_\rho) e^{2i(\mathbf{k}_i)_2 \cdot \mathbf{r}_v} \, dv, \tag{1} $$

where the material property parameters are expressed in terms of compressibility (κ) and density (ρ) as

$$ \gamma_\kappa = (\kappa_2 - \kappa_1)/\kappa_1, \tag{2} $$

$$ \gamma_\rho = (\rho_2 - \rho_1)/\rho_2, \tag{3} $$

where medium "1" (indicated by a subscript) is the surrounding water and medium "2" (also indicated by a subscript) is the body of the animal. Also, the subscript "2" to ρ in the denominator in Eq. (3) represents a correction to the subscript "1" given in Chu *et al.* (1993) and Stanton *et al.* (1993b). Given that these are weakly scattering bodies and $\rho_2 \simeq \rho_1$, the difference is negligible. The compressibility is written in terms of density and sound speed as

$$ \kappa = (\rho c^2)^{-1}. \tag{4} $$

In this formulation, the material property terms are allowed to vary inside the volume. Note that this formula is the complex conjugate of the one presented in Morse and Ingard and is consistent with the phase shift convention of e^{+ikr} for an outgoing scattered wave. Also, in this "distorted wave" formulation, the incident wave number in the exponent is evaluated *inside* the medium $[(\mathbf{k}_i)_2]$. That is, the wave number of the wave traveling inside the body has a magnitude k_2. There will be phase errors associated with this distorted wave formulation for conditions under which the incident ray will pass through part of the body, into the surrounding medium, and back into the body again (such as in the case of end-on incidence for a bent cylinder). Correction for the phase shift for the path in the water can, in principle, be taken into account through piecewise integration. For an object whose cross section is circular at every point along the lengthwise axis (i.e., a deformed circular cylinder), two dimensions of the integration (within a cross section at an arbitrary point along the cylinder) can be performed analytically, which reduces the formulation to a line integral:

$$ f_{bs} = \frac{k_1}{4} \int_{\mathbf{r}_{pos}} (\gamma_\kappa - \gamma_\rho) e^{2i(\mathbf{k}_i)_2 \cdot \mathbf{r}_{pos}} $$
$$ \times a \frac{J_1(2k_2 a \cos \beta_{tilt})}{\cos \beta_{tilt}} |d\mathbf{r}_{pos}|, \tag{5} $$

where now the material properties are allowed to vary with respect to position along the lengthwise axis, but restricted to remaining constant within each infinitesimally thin cross section at any given point along that axis. In this equation, γ_κ,
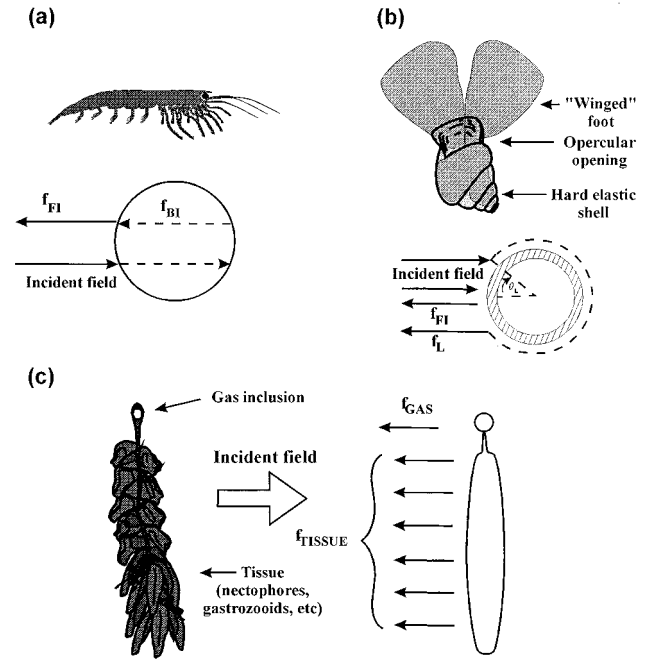
FIG. 1. Zooplankton and corresponding illustrations of certain important scattering components.

γ_ρ, a, and β_{tilt} can be functions of $\mathbf{r}_{pos}$. The term J_1 is the Bessel function of the first kind of order 1.

This DWBA-based deformed cylinder formulation is similar in form to the modal-series-based deformed cylinder formulation presented in Stanton (1989a). The differences lie in the fact that the DWBA is only accurate for weakly scattering bodies while the modal-series-based solution can describe a wide range of (axisymmetric) material profiles (elastic shelled body, etc.). However, the DWBA formulation, by the nature of its volume integration, is accurate for all angles of orientation, while the modal-series-based solution is only accurate near broadside incidence because it uses modal-series coefficients from an infinitely long cylinder.

For a uniformly bent cylinder, the term in the exponent $(\mathbf{k}_i)_2 \cdot \mathbf{r}_{pos} = k_2 \rho_c (1 - \cos \beta_{tilt})$. Using $|d\mathbf{r}_{pos}| = \rho_c d\beta_{tilt}$ gives the integral expression

$$ f_{bs} = \frac{k_1 \rho_c}{4} e^{i2k_2 \rho_c} \int (\gamma_\kappa - \gamma_\rho) e^{-i2k_2 \rho_c \cos \beta_{tilt}} $$
$$ \times \frac{a J_1(2k_2 a \cos \beta_{tilt})}{\cos \beta_{tilt}} d\beta_{tilt}. \tag{6} $$

This expression is accurate for all angles of orientation and arbitrary variability of the cross-sectional radius along the length of the body (such as a tapered cylinder). The cylinder is bent in the plane containing $\mathbf{k}_i$. For broadside incidence (i.e., the body is bent symmetrically away from the echo sounder), the integral is symmetrical about $\beta_{tilt} = 0$. For end-on incidence, the integral is symmetrical about $\beta_{tilt} = \pi/2$.

For broadside incidence, the integral can be performed using the method of stationary phase,

$$f_{bs} \simeq \frac{k_1 a}{4\sqrt{2}} (\gamma_\kappa - \gamma_\rho) \sqrt{\rho_c \lambda_1} J_1(2k_2 a) e^{i\pi/4}, \tag{7}$$

where the condition $2k_2 \rho_c (1 - \cos(\beta_{\text{tilt}})_{\text{max}}) \gg 1$ was required in order to use the method of stationary phase. This condition requires the body to be bent enough so that many Fresnel zones are present on it (this corresponds to having deflection of the end points much greater than an acoustic wavelength).

Limiting expressions (with respect to wavelength) of the scattering can be determined from both Eqs. (1) and (7). At very low values of ka and wavelengths long enough so that the bend does not affect the scattering, Eq. (1) can be evaluated in the long wavelength limit. For shorter wavelengths, there are two other regions of scattering: (i) $ka \ll 1$ with the condition that the wavelength is short enough so that the bend *does* affect the scattering and (ii) $ka \gg 1$. For these latter two cases, Eq. (7) can be evaluated by inserting the appropriate limiting expression for the Bessel function. Using Eqs. (1) and (7) as indicated above, the scattering limits for broadside incidence are given by

$$f_{bs} = \frac{(k_1 a)^2}{4} L(\gamma_\kappa - \gamma_\rho),$$

$$ka \ll 1 \quad \text{and} \quad 2k\rho_c(1 - \cos(\beta_{\text{tilt}})_{\text{max}}) \ll 1, \tag{8}$$

$$f_{bs} = \frac{(k_1 a)^2}{4\sqrt{2}} \sqrt{\rho_c \lambda_1}(\gamma_\kappa - \gamma_\rho) e^{i\pi/4},$$

$$ka \ll 1 \quad \text{and} \quad 2k\rho_c(1 - \cos(\beta_{\text{tilt}})_{\text{max}}) \gg 1, \tag{9}$$

$$f_{bs} = \frac{\sqrt{\rho_c a}}{4} (\gamma_\kappa - \gamma_\rho) \cos\left(2k_2 a - \frac{3}{4}\pi\right) e^{i\pi/4},$$

$$ka \gg 1 \quad \text{and} \quad 2k\rho_c(1 - \cos(\beta_{\text{tilt}})_{\text{max}}) \gg 1, \tag{10}$$

$$= -\frac{\sqrt{\rho_c a}}{8} (\gamma_\kappa - \gamma_\rho) e^{-i2k_1 a}(1 + i e^{i4k_2 a})$$

(ray form). $\tag{11}$

The approximation $k_2 \simeq k_1 \simeq k$ was used, where appropriate, in the above equations. Typically, it is important to distinguish between k_1 and k_2 in phase shift terms but not in amplitude terms. Phase terms such as the exponent in $e^{i4k_2 a}$ greatly influence the position of the nulls in the target strength versus frequency curves. Equation (11) is equivalent to Eq. (10) and is written to illustrate arrivals from the front and back interface of the body (first and second term within the parentheses, respectively). For $ka \ll 1$ and $kL \ll 1$, Eq. (8) applies for all angles of orientation.

While these limiting expressions at broadside incidence are very useful, the orientation dependence of the scattering (for all ka) generally must be determined through numerical integration of Eq. (6). Predicting volume scattering strengths due to aggregations of animals in the ocean involves numerically calculating averages over angle of orientation and size. In this case, structure in the target strength versus frequency curves for single echoes from individuals will be greatly reduced. The structure is quite sensitive to the precise size, shape, orientation, and material properties of the animal.

Since this structure is greatly reduced or washed out in an average, these parameters do not need to be known as accurately for the predictions. However, when the structure of the curves of single resolved echoes is required for analysis, the boundary must be made more realistic, which tends to make the problem more complex. It can be taken into account either by directly incorporating a complex, realistic boundary into the integral in Eq. (1) or by direct summation of echoes from various parts of the body. Use of Eq. (1) is far more precise (providing that the actual boundary is known precisely); however, summation of echoes in an approximate manner has utility as it can provide the statistical properties of the echoes quite readily. Analytical manipulation of the sum can also be done more readily than with the general integral formula.

A general high-frequency (geometric scattering region) ray formula which adds an arbitrary number of (N) ''glint'' rays together to produce the total echo of the animal can be written as

$$f_{bs} \simeq \sum_{j=1}^{N} b_j e^{i2k_1 \epsilon_j}, \tag{12}$$

where the (complex) amplitude coefficient b_j is given for two common cases of spherical curvature as follows:

$$b_j \simeq \tfrac{1}{2} \mathscr{R}_{12} a \quad \text{(facing interface, convex}$$

$$\text{from viewpoint of source/receiver)}, \tag{13}$$

$$b_j \simeq -\tfrac{1}{2} T_{12} T_{21} \mathscr{R}_{21} a$$

$$\text{(back interface, concave from viewpoint}$$

$$\text{of source/receiver)}. \tag{14}$$

The phase shift of each ray due to the relative location of the interface from which it scatters is taken into account in the exponent where ϵ_j is the deviation of the point of scatter from a (zero phase) reference plane that is normal to the direction of the incident acoustic wave. The term ϵ_j is negative for points on the source/receiver side of the reference plane. For a sphere whose center is on the zero phase plane, $\epsilon_j = -a$ and $+a$ for the front interface [Eq. (13)] and back interface [Eq. (14)] cases, respectively. The reflection coefficients of the front and back interfaces have been taken into account in b_j (note that $\mathscr{R}_{21} = -\mathscr{R}_{12}$). The plane tangent to the middle of each curved section is perpendicular to the direction of incidence giving rise to the glint (i.e., the sections are broadside to the transducers). For surfaces with more complex curvature such as the side of a bent cylinder, then b_j is more complex. For example, for a convex interface described in planes ''(1)'' and ''(2)'' by two local radii of curvature $(\rho_j^{(1)}, \rho_j^{(2)})$, a is replaced by $(\rho_j^{(1)} \rho_j^{(2)})^{1/2}$ (Gaunaurd, 1985). The phase of b_j depends specifically upon the curvature (convex, concave, cylindrical, spherical, compound, etc.). For example, the phase for the concave spherical surface is π as indicated by the minus sign in Eq. (14). The wave number is held fixed at k_1 in this formulation for simplicity. As a result, the position of the nulls in any TS versus frequency curve would be slightly in error. The simplification does not significantly affect the results, especially

when averages or statistics of random phase $(2k_1\epsilon_j)$ ensembles are analyzed.

This formula is written down heuristically based upon various other formulations. Great success has been achieved with a two-ray formulation (Stanton *et al.*, 1993a, 1993b) in which the rays only from the front and back interfaces at broadside incidence are taken into account. In the two-ray formulation, the local reflection and transmission coefficients were taken into account as well as the phase shifts, radius of curvature of the bent axis, and cylindrical radius of the cross section. A six-ray model in which each local scatterer had associated a random phase and unity amplitude was used in Stanton *et al.* (1994b) to describe the statistical properties of the scattering by a decapod shrimp off broadside incidence (more than six rays gave the same statistical behavior of the echo envelope, so the summation was truncated to include only six rays).

The two-ray version of Eq. (12) has experienced much development and use. In Stanton *et al.* (1993a, 1993b), an approximate two-ray model was derived for all angles of incidence:

$$f_{\mathrm{bs}} \simeq \tfrac{1}{2}\sqrt{\rho_c a}.\mathscr{R}_{12}e^{-i2k_1a}I_0 e^{-\alpha_B(2\theta\rho_c/L)^2}, \tag{15}$$

where

$$I_0 = 1 - T_{12}T_{21}e^{i4k_2a}e^{i\mu(k_1a)}. \tag{16}$$

This expression for scattering amplitude was shown to depend upon the radius of curvature ρ_c of the longitudinal axis of the body, radius a of the cross section of the body, reflection coefficient $\mathscr{R}_{12}$ of the front interface, length L, and angle of orientation θ. The width of the main lobe of the scatter versus angle pattern based on this formula best fit more precise DWBA-based calculations when the parameter $\alpha_B = 0.8$. In order for this ray solution to be valid for values of k_1a less than unity, the following phase shift term was used (Stanton *et al.*, 1993a):

$$\mu(k_1a) \simeq \frac{-(\pi/2)k_1a}{k_1a + 0.4}. \tag{17}$$

As a result, the scattering amplitude is valid for values of k_1a as low as 0.1. For orientations far away from broadside incidence, more sophisticated models, such as the DWBA, must be used and evaluated numerically. However, the above equation for the scattering amplitude works well for single echoes near broadside or can be used in accurately averaging over angle of orientation over a wide range of angles (the inaccuracies far from broadside incidence are not significant provided the average includes contributions from near broadside incidence where the scattering is the strongest).

The above expression for backscattering amplitude can be used to average the backscattering cross section over an arbitrary range of length and angle of orientation provided the average includes broadside incidence. A convenient formula was derived in Stanton *et al.* (1993b) for an average over a narrow range of animal sizes:

$$\langle \sigma_{\mathrm{bs}} \rangle_{\theta,L} / \bar{L}^2 = A_{ij} \mathscr{R}_{12}^2 \langle |I_0|^2 \rangle_L \beta^{-1}, \tag{18}$$

where $\bar{L}$ is the mean of the narrow length distribution (and narrow in this case means the width of the distribution is much less than the mean length). For a narrow distribution, $\langle |I_0|^2 \rangle_L = 2\{1 - \exp[-8(k\bar{a}s)^2]\cos(4k\bar{a} + \mu)\}$, where s is the standard deviation of length, normalized by the mean length. The term A_{ij} was determined in that paper for all four combinations of straight and bent cylinders, and Gaussian and uniform $(0 - 2\pi)$ distributions of angle of orientation. For a bent cylinder whose angle of orientation is Gaussian distributed, A_{ij} is given as

$$A_{ij} = T_B^2 C_B^2 / (16\sqrt{\alpha_B}s_\theta), \tag{19}$$

where s_θ is the standard deviation of orientation distribution (in radians), and T_B and C_B are empirically determined parameters from simulations using the DWBA ($T_B = 1$, $C_B = 1.2$).

B. Gastropods (deformed elastic-shelled sphere)

The backscatter data from gastropods presented in Stanton *et al.* (1998) showed overall (high) echo levels consistent with that of a dense and/or hard scatterer. Furthermore, the data indicate the possibility of an echo from part of the body traveling at a subsonic speed and then interfering with the echo from the front interface (Fig. 1). These properties of the echoes are consistent with the fact that the outer boundary of the animal is a dense, hard elastic shell made of aragonite. The subsonic wave is possibly a flexural Lamb wave that circumnavigates the body at a subsonic speed before returning to the transducer (see, for example, Kargl and Marston, 1989; Kaduchak *et al.*, 1995).

Modelling the scattering of sound by gastropods is a great challenge because of the complexity of the boundary. The shell is irregular and contains a major discontinuity (the opercular opening). Our attempts (not shown) to model it as an idealized spherical shell using the exact formulation of Goodman and Stern (1962) (and taking into account differences between the interior tissue and surrounding fluid) were unsuccessful, even as a first approximation. The idealized sphere model produced resonances not seen in the data (some of the broader resonances remained even after averaging over a distribution of sizes). Therefore, a more realistic model must be used. Rigorous treatment of this problem would include numerical evaluation of the wave equation (Jansson, 1993) or a sophisticated generalized ray theory (Felsen and Lu, 1989; Ho and Felsen, 1990; Norris and Rebinsky, 1994; Ho, 1994; Yang *et al.*, 1995; Rebinsky and Norris, 1995, and Yang *et al.*, 1996).

In order to describe the scattering by such an irregular body, we chose a (analytical) ray approach over a numerical one because certain ray models can not only provide greater insight into the physics of the scattering process, but can also be manipulated algebraically for other calculations. The ray formulation in the case of the weakly scattering body described above [Eqs. (12)–(19)] involved rays scattering from the front and back interfaces of the body. However, with the hard elastic shell of the gastropod, the incident ray cannot penetrate the shell with much energy. In contrast, (circumferential) shell waves are excited by the incident field and travel around the shell, continuously shedding off energy. Some of this energy sheds or "leaks" back toward the sound

source/receiver and will interfere with the ray that is reflected off the front portion of the shell. As a result, the scattering amplitude versus frequency plots have peaks and dips corresponding to the constructive and destructive interference, respectively.

Given the complexity of the problem of scattering by an irregular shell, we have found it convenient to begin with the ray formulation for an idealized spherical shell, and then heuristically modify the formulation to take into account roughness and discontinuities. The result is an approximate formula that illustrates effects due to those features. We begin with a ray formulation from Kargl and Marston (1989) and summarized in Marston *et al.* (1990) and Marston (1992). It gives the usual decomposition of the scattered wave into various components:

$$f_{bs} \simeq f_{spec} + f_{tw} + f_{Lamb} + f_{Franz}, \qquad (20)$$

where the f_{spec} or specular term contains specularly "reflected" echoes from the front interface, and f_{tw} corresponds to all internal refractions and reflections within the shell and interior fluid. The term f_{Lamb} contains the summation of the different classes of Lamb waves, antisymmetric and symmetric of all order, each of which involves the superposition of all singly and multiply circumnavigated waves. The last term is due to the Franz wave. The Lamb and Franz waves are both circumferential waves—the Lamb or "plate" waves represent various classes of plate deformations that circumnavigate the body in a wavelike manner while continuously leaking energy into the surrounding fluid. The Franz or "creeping" waves travel along the boundary but within the surrounding fluid.

Evaluation of each term in Eq. (20) is quite involved. The backscattering data involving gastropods indicate the presence of two major echoes coming from each animal. We assume that one of the echoes is from the front interface of the animal. The other echo has the strength and (subsonic) speed consistent with that of Lamb waves under certain conditions. In order to model the scattering by those animals and for simplicity in the analysis, we retain only the (hypothesized) dominant terms for the case of hard, dense spherical elastic shells, f_{spec} and f_{Lamb}:

$$f_{bs} \simeq \underbrace{\frac{a}{2} \mathscr{R}_{12} e^{-i2k_1 a}}_{\substack{\text{scattering} \\ \text{from front} \\ \text{interface}}} - \underbrace{\frac{1}{2} G_L a e^{-2(\pi - \theta_L)\beta_L} e^{i\eta_L} \sum_{m=0}^{\infty} (-1)^m e^{-2\pi m \beta_L} e^{i2\pi m k_1 a c_1/c_L}}_{\text{Lamb wave (flexural) leakage}}, \qquad (21)$$

where

$$\eta_L = 2k_1 a[(c_1/c_L)(\pi - \theta_L) - \cos \theta_L] - \pi/2, \qquad (22)$$

$$\theta_L = \sin^{-1}(c_1/c_L), \qquad (23)$$

$$G_L \simeq 8\pi\beta_L c_1/c_L, \qquad (24)$$

and

$$c_L/c_1 \simeq k_1 a/(\alpha_L + 1/2). \qquad (25)$$

The two terms in the expression for the scattering amplitude correspond to the scattering from the front portion of the shell and the lowest-order antisymmetric Lamb wave (flexural wave) that circumnavigates the shell m times, respectively [$m=0$ corresponds to traveling around the shell an amount $2(\pi - \theta_L)$ radians, $m=1$ corresponds to traveling around the shell an amount $2(\pi - \theta_L) + 2\pi$, etc.] where θ_L is the angle at which the Lamb wave lands onto and launches from the shell (for subsonic waves, $\theta_L = \pi/2$). The term η_L is a phase shift term corresponding to the phase shift incurred on the shell by the $m=0$ Lamb wave (this travel-path and caustic-related phase is relative to the zero-phase reference plane that contains the center of the sphere and is perpendicular to the direction of the incident wave), G_L is the combined coupling coefficient for the conversion of the fluid-borne sound into the Lamb wave and back into fluid-borne sound, c_L is the speed of the Lamb wave, and α_L and β_L are the real and imaginary parts of the complex root ν_L of the denominator of the modal series coefficient (not shown) for a fluid-filled spherical elastic shell (β_L is the attenuation coefficient of the Lamb wave due to its continuous shedding or leaking of energy into the surrounding fluid) (Marston, 1992). Here, c_L, α_L, and β_L are generally complicated functions of ka.

The above expression describing the scattering by a shell is approximate as it only takes into account one class of Lamb wave (other Lamb waves could quite readily be taken into account by simply summing over other "L"-type indices, however the zeroth-order antisymmetric Lamb wave tends to dominate the scattering for the low-to-moderate values of ka in our data sets and is the only wave being included in this analysis (Kargl and Marston, 1989). Furthermore, the thickness resonance is ignored. This resonance is due to the front ray penetrating the outer boundary of the shell and experiencing multiple internal reflections within the shell material (for the hard shell of the gastropod, it is assumed that little energy penetrates the outer boundary). For similar reasons, internal refractions and reflections within the body interior are ignored. Exact values of the terms G_L, c_L, β_L, and α_L must be obtained through numerical evaluation of the Sommerfeld–Watson transformation of the modal series solution and is beyond the scope of this present analysis (Kargl and Marston, 1989).

As previously discussed, one major complication of the modeling for the gastropod involves the fact that the body is not perfectly spherical but irregular. In order to estimate effects of roughness on the scattering, the above approximate

ray-based formulation is heuristically modified. The radius of the body at a given point on the body is written as a stochastic parameter,

$$a = \bar{a} + \zeta,$$ (26)

where $\bar{a}$ is the mean radius and ζ is the random deviation of the radius from the mean at a given point on the shell. The Lamb wave will travel many different paths resembling meridional lines (not shown in the two-dimensional plot in Fig. 1). Because of the boundary deformations, the paths will randomly deviate from pure meridional lines. Each path will experience variations in local radii of curvature resulting in a slightly different effective radius $\bar{a} + \Delta_a$ for that path [where the effective radius is the circumference (along a rough path) divided by 2π]. The phase shift of the differential portion of the Lamb wave that travels along a given path will vary depending upon the particular path taken.

In order to estimate the effects of roughness on the total Lamb wave, we use Eq. (21) to heuristically write an approximate expression for the differential Lamb wave that travels within a differential meridional angle:

$$df_{\text{Lamb}} \simeq -\frac{1}{2} G_L a e^{-2(\pi-\theta_L)\beta_L} e^{i\eta_L} \sum_{m=0}^{\infty} (-1)^m$$

$$\times e^{-2\pi m \beta_L} e^{i2\pi m k_1 a c_1 / c_L} \frac{d\phi_M}{2\pi},$$ (27)

where ϕ_M is the meridional angle. The total Lamb wave is calculated by integrating the above expression over all meridional angles:

$$f_{\text{Lamb}} = -\frac{1}{2} \int_0^{2\pi} G_L a e^{-2(\pi-\theta_L)\beta_L} e^{i\eta_L}$$

$$\times \sum_{m=0}^{\infty} (-1)^m e^{-2\pi m \beta_L} e^{i2\pi m k_1 a c_1 / c_L} \frac{d\phi_M}{2\pi},$$ (28)

where now a is the effective radius, as defined above ($a = \bar{a} + \Delta_a$), for a given meridional angle. Note that, given the symmetry of the scattering geometry, only half of the range of angles contains a unique set of effective radii. For a perfectly smooth ideal sphere, the integrand is constant with respect to the meridional angle and the integral reduces to the Lamb wave component of Eq. (21). If a is randomly distributed over the $0-2\pi$ range of meridional angles, then this integral is roughly equivalent to the ensemble average over the distribution of Δ_a:

$$f_{\text{Lamb}} \simeq \left\langle -\frac{1}{2} G_L a e^{-2(\pi-\theta_L)\beta_L} e^{i\eta_L} \right.$$

$$\left. \times \sum_{m=0}^{\infty} (-1)^m e^{-2\pi m \beta_L} e^{i2\pi m k_1 a c_1 / c_L} \right\rangle.$$ (29)

This equivalency is analogous to the ergodic theorem where a temporal average of a quantity is equal (under certain conditions) to the ensemble spatial average of that quantity (Skudrzyk, 1971). In this analysis, ϕ_M replaces time. The analogy to the ergodic theorem is not perfect as the temporal average in the theorem is taken over the limit of all time

whereas the integral over ϕ_M involves a finite range of ϕ_M.

Using the fact that the complex phase shift terms in this average are more important in this average than the random (real) amplitude terms, only the random complex exponential terms will be treated in this average (Stanton, 1992). For mathematical convenience and given the fact that many random natural processes tend to follow Gaussian statistics, Δ_a is assumed to be Gaussian distributed and the formula

$$\langle e^{i\gamma\Delta_a} \rangle = e^{-(1/2)\gamma^2\sigma^2}$$ (30)

is used to obtain the following approximate expression:

$$f_{\text{bs}} \simeq \frac{a}{2} \mathcal{R}_{12} F_{\text{spec}} e^{-i2k_1 a} - \frac{1}{2} G_L e^{i\Phi_L} \bar{a} e^{-2(\pi-\theta_L)\beta_L}$$

$$\times e^{i2k_1\bar{a}[(c_1/\bar{c}_L)(\pi-\theta_L)-\cos\theta_L]-i\pi/2} F_L$$

$$\times \sum_{m=0}^{\infty} (-1)^m e^{-2\pi m \beta_L} e^{i2\pi m k_1 \bar{a} c_1 / \bar{c}_L} e^{-(1/2)\gamma^2\sigma^2},$$ (31)

where

$$\gamma = k_1 \{ 2[(c_1/\bar{c}_L)(\pi-\theta_L) - \cos\theta_L] + 2\pi m c_1 / \bar{c}_L$$

$$+ B k_1 \bar{a} [2(\pi-\theta_L) + 2\pi m] \}.$$ (32)

This formula takes into account dispersion of the Lamb wave by linearizing the dependence of c_1/c_L upon $k_1 a$ over the narrow range of values of ka as $k\bar{a}$ is fixed and Δ_a is varied. Here $c_1/c_L = c_1/\bar{c}_L + B k_1 \Delta_a$, where $\bar{c}_L$ is the value of c_L evaluated at $k\bar{a}$. Dispersion of the flexural wave is much stronger for lower values of ka (e.g., $ka < 20$) than for higher values (Kargl and Marston, 1989). The angle θ_L stays fixed at $\pi/2$ during the averaging provided c_L remains subsonic.

While the derivation of Eq. (31) was far from rigorous, these results show that the Lamb wave term in the scattering amplitude becomes attenuated due to the randomness of the phase of the various Lamb wavelets traveling around the irregular body. In addition to taking into account the randomness of the irregularities, three other terms were incorporated heuristically: (1) the term F_{spec} to take into account a reduction of echo level from the front interface for orientations in which part or all of the opercular opening is facing the echosounder ($F_{\text{spec}} = 1$ when the opening is facing away from the sounder, $0 \leq F_{\text{spec}} < 1$ when part or all of the opening is facing the sounder). (2) The term F_L takes into account the fact that part of the Lamb wave does not travel beyond the opening that it may encounter ($F_L = 0$ when the opening faces away from the echosounder and no Lamb waves can propagate beyond the opening, $0 < F_L \leq 1$ for other angles of orientation). This term must be determined strictly from geometrical arguments. Reflections of the Lamb wave off the discontinuity are ignored. (3) Because of irregularities and uncertainties in material properties, the term $e^{i\Phi_L}$ was inserted to account for any deviation in phase shift from that predicted from an idealized theory. The a in the first term represents the local radius of curvature of the shell surface seen by the acoustic source/receiver.

C. Siphonophore (bubble plus tissue)

The backscatter data from siphonophores presented in Stanton *et al.* (1998) indicated that the gas inclusion in the pneumatophore dominated the overall average levels of the echoes. However, the tissue surrounding the gas sometimes significantly contributed to the pattern of the target strength versus frequency curves. The scattering amplitude can be written in terms of the separate contributions of the scattering from the two parts of the body (Fig. 1):

$$f_{bs} = f_{bubble} + f_{tissue}. \tag{33}$$

This formulation assumes that shadowing from each component does not significantly affect the scattering by the other. This is a reasonable assumption since the tissue is most likely a weakly scattering material and the incident acoustic wave travels through it essentially unperturbed. Since the gas inclusion is so small, the shadow region behind it is much smaller than the total volume of the tissue and hence little of the scattering by the tissue will be affected.

Prediction of the total echo from the siphonophore requires evaluation of each of the above components of the scattered field. The following exact formula is used to calculate the scattering by the pneumatophore:

$$f_{bubble} = \frac{-i}{k_1} \sum_{m=0}^{\infty} (2m+1)$$

$$\times (-1)^m b_m^{(f)} \quad \text{exact,} \quad \text{all } k_1 a. \tag{34}$$

This formula was taken directly from Anderson (1950). It is an exact expression for the scattering of sound by a fluid sphere (gas behaves acoustically as a fluid as it does not support shear waves). The gas inclusion in siphonophores may depart from being a perfect sphere, hence this equation should be considered to be an approximation to the scattering by the bubble. The term $b_m^{(f)}$ is the modal series coefficient for a fluid sphere.

Evaluation of the scattering by the tissue is a great challenge. If one were to choose a simple boundary like a smooth bent cylinder, the statistical nature of the structure of the target strength versus frequency curve may not be accurately predicted. However, the boundary of the siphonophore is sometimes quite complex, and it may not be possible to produce a reasonable mathematical construction of the outer boundary. A general approach in estimating the scattering by the tissue would be to use the general volume integral of the DWBA. Adding that contribution to the one from the gas gives the backscattering amplitude from the entire animal:

$$f_{bs} \approx \underbrace{-\frac{i}{k_1} \sum_{m=0}^{\infty} (2m+1)(-1)^m b_m^{(f)}}_{\text{gas inclusion}}$$

$$+ \underbrace{\frac{k_1^2}{4\pi} \int \int \int_v (\gamma_\kappa - \gamma_\rho) e^{2i(\mathbf{k}_i)_2 \cdot \mathbf{r}_v} dv}_{\text{tissue}}, \tag{35}$$

where the terms of the integral are defined earlier in this paper. This approach allows one to construct a complex

mathematical boundary describing the body of the siphonophore and perform the integration directly. In order for the statistics of the target strength versus frequency curve to be determined, the boundary must be randomly perturbed (changing shape and orientation, etc.) over an ensemble of pings. Such a procedure, while rigorous, would be quite tedious.

Another approach to obtain echo statistics can involve the heuristic ray formulation described earlier in this paper. With that approach, only the contributions from various major scattering features of the body are included in a ray summation. A major feature in this context is defined as a facet or facetlike part of the body that is broadside to the incident beam (giving rise to ''glint''). This feature would scatter the sound back toward the receiver with a level much greater than that of a feature that is not broadside. With this ray approach, the echo from the whole animal is

$$f_{bs} \approx -\frac{i}{k_1} \sum_{m=0}^{\infty} (2m+1)(-1)^m b_m^{(f)} + \sum_{j=1}^{N} b_j e^{i2k_1 \epsilon_j}. \tag{36}$$

There is great utility to this approach. *Modal-series component*: This exact solution to a spherical bubble will predict echo levels that are accurate for all values of ka. For the siphonophores in which the gas dominates the average echo level at all frequencies, use of the expression can produce reasonable estimates of the average target strength of the siphonophores. *Ray component*: (1) It is simple in form and can be readily manipulated and evaluated. (2) For six or more random-phase rays, the statistical nature or probability density function (PDF) of this ray component will be Rayleigh–PDF-like. Once the ray component is added to the modal series component, the statistics of the envelope of the total echo will be Ricean. As a practical matter, it may be difficult to directly determine the values of b_j. If data are available on a particular siphonophore, it is reasonable to adjust the values of b_j according to the observed contribution from the tissue.

Analytical averaging of the predicted backscattering cross section from the siphonophore over a range of orientation angles, in general, involves many cross terms, and it would be more practical to perform the average numerically. However, at high enough frequencies where the length of the body is much greater than a wavelength, the energies from the gas and tissue will add independently:

$$\langle \sigma_{bs} \rangle = (\sigma_{bs})_{bubble} + \langle \sigma_{bs} \rangle_{tissue}, \quad k_1 L \gg 1. \tag{37}$$

There are no brackets around $(\sigma_{bs})_{bubble}$ since the scattering by the bubble is independent of orientation.

II. COMPARISON BETWEEN MODELS AND DATA

The above theoretical models are now compared with laboratory scattering data from Stanton *et al.* (1997) involving single pings, ping-to-ping variability of the echoes from individual animals, and averages of the echoes.

A. Single ping data

There was reasonable success in using the models to qualitatively predict the various classes of patterns of measured target strength versus frequency (Fig. 2).
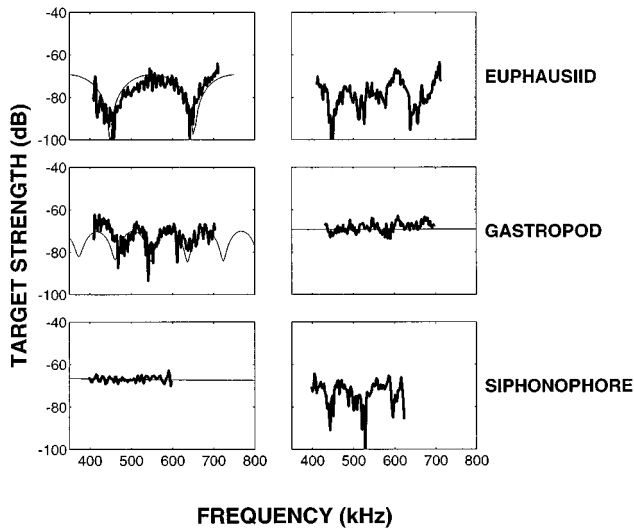
FIG. 2. Target strength versus frequency for individual echoes from a euphausiid, two different gastropods, and a siphonophore. Two-ray models are given in the (left) euphausiid and gastropod plots where the structure of the data is regular. A one-ray model is used for the nearly flat gastropod curve while the exact gas sphere model is used for the flat siphonophore curve. Thin curves are model predictions, thick curves are data. Description of the animals is given in Fig. 2 of Stanton *et al.* (1998). Simulation parameters are a combination of measured values, values published for similar animals or materials, semi-empirical model-based values, and values inferred from the data: euphausiid, left panel only: Eq. (15) used with $\theta=0$, (g,h) $=(1.0357,1.0279)$ based on properties measured for *Euphausia superba* (Foote, 1990 and Foote *et al.*, 1990), $a=1.9$ mm (within range of measured values, used for best fit to structure of plot), $\rho_c/L=2.2$ (consistent with visual observations, used for best fit to overall levels of data), $L=29$ mm (length, based on measurement, is ''reduced'' acoustic length since tail contributes so little to the scattering); gastropod, left panel: Eq. (31) used with $\mathscr{R}_{12}=0.84$, $a=\bar{a}=0.63$ mm (this is the radius of a sphere whose volume is the same as the gastropod modeled as a 2-mm-long by 1-mm-wide prolate spheroid), $\sigma=.025\bar{a}$ (inferred from data), $\beta_L=0.002k_1a$ (the ka functional dependence is based on the analytical Lamb-wave model and the coefficient 0.002 is based upon a fit to the data), $\alpha_L=8k_1a$ (based on model), $\Phi_L=$ $-\pi/2$ (inferred from data) for the subsonic wave, $\theta_L=\pi/2$ (based on model), $c_L/c_1=k_1\bar{a}/(\alpha_L+0.5)\approx1/8$ (this value was predicted theoretically and observed), $F_L=1$ (inferred), $F_{spec}=0.71$ (the $\mathscr{R}_{12}=0.84$ is calculated for the coefficient expected for a semi-infinite planar half-space of calcite where the published values for calcite $g=2.646$ and $h=4.345$ (longitudinal waves), the inferred value of $F_{spec}=0.71$ in essence ''corrects'' that value down to 0.6), also, the series was truncated to include only the $m=0$ term in the Lamb wave series; gastropod, right panel: same as left panel except a $=0.81$ mm, $F_{spec}=1$ and $F_L=0$ (the inferred value $F_L=0$ corresponds to total loss of Lamb wave due to change in orientation, change in a from left panel corresponds to the incident wave ''seeing'' a different radius of curvature at front of gastropod due to change in orientation); siphonophore, left panel only: Eq. (34) using $a=0.35$ mm (this is the radius of a sphere whose volume is the same as the elongated gas bubble modeled as a 1.3-mm-long by 0.5-mm-wide prolate spheroid), $(g,h)=(0.0012,0.22)$ which are published values for air at one atmosphere pressure.

Euphausiids. The regular pattern of TS versus frequency for the euphausiid can be described by the two-ray model (Fig. 2, left plot). The positions of the peaks and dips (or nulls) for this particular plot were satisfactorily described by the model indicating that the pattern was most likely due to constructive and destructive interference between rays from the front and back interfaces of the animal near broadside. It was not possible to make objective comparisons between the overall predicted echo levels and those observed as the pre-

cise orientation and shape of the animal was not known. Here, the radius of curvature of the bent cylinder model was fixed at a reasonable value ($\rho_c=2.2L$) that also resulted in a best fit to the data and the orientation was assumed to be broadside for the modeling of the individual ping. Other echo data (not shown) from this animal showed the nulls changing position and spacing (typically smaller spacing) which indicates that changes in the orientation and shape will change the pattern. Adjustment of the relative phases of the rays in the two-ray model can account for this effect provided the pattern is periodic. For slight changes in phase, the adjustment corresponds to the (tapered) animal changing orientation so that a different part of its cross section with a different thickness is in the first Fresnel zone of the acoustic beam which dominates the scattering. Larger changes may correspond to the possibility of rays from other parts of the body contributing to the echo.

This work with a freshly caught euphausiid is consistent with the modeling performed on the decapod shrimp (Stanton *et al.*, 1993a) where the two-ray model was first developed. In that work, the animals were oriented so that they were nearly broadside to the incident field. The regular patterns observed with the euphausiids reported in this more recent work also correspond to nearly broadside incidence. Visual observation of the orientation of the animal used in Fig. 2 was made periodically with a viewing window and indicated that the animal was generally near broadside throughout the experiment.

The irregular patterns in the euphausiid data observed in this study (Fig. 2, right plot) are similar to the ones observed in Stanton *et al.* (1994b) involving broadband insonification of an obliquely oriented decapod shrimp. It was determined in that analysis that the echo could be approximated from a statistical standpoint by as few as six randomized rays. The six rays were formulated with random phases and added together to form a random signal whose spectral characteristics are irregular. This type of signal is expected when the animal is either not at broadside incidence or near broadside but with an irregular shape. With this random set of rays, comparison of a single realization of the predicted echo with data is not particularly useful, hence a prediction is not shown. The statistical properties of the predictions and data are compared below.

Gastropods. The gastropod that exhibited a consistent periodic pattern of TS versus frequency was best modeled by a two-ray model where one ray was from the front interface of the body and the other ray was due to a single ($m=0$) Lamb wave that traveled around the body once while experiencing roughness-induced attenuation (Fig. 2, left plot). The periodicity exhibited by the data is characteristic of the dominant subsonic zeroth order antisymmetric Lamb wave. Initial application of the model with no roughness resulted in a pattern (not shown) that had the same periodicity as the one measured, but with sharp peaks and nulls that did not resemble the data. Once roughness was incorporated, the m >0 Lamb waves were attenuated to the point that they did not significantly contribute to the scattering. The result was two terms dominating the expression, the echo from the front interface and a (roughness-induced) attenuated Lamb wave.

With roughness incorporated, the resultant pattern is more smoothly varying like the data and exhibits the same periodicity as that of the data. In the computations, the infinite Lamb wave series must be truncated at some point. We chose to truncate at the $m=0$ point (i.e., to include only the $m=0$ wave) which further improved the fit to the data.

In contrast to the above gastropod whose particular orientation was apparently conducive to the Lamb wave traveling readily around the body, another gastropod was oriented in such a way so that the Lamb waves were apparently blocked (Fig. 2, right plot). The resultant pattern is relatively flat and was modeled simply by eliminating the Lamb wave term in the model (i.e., by setting $F_L=0$). It is hypothesized in this case that the opening of the shell was facing in a direction that prevented the traveling of Lamb waves in paths along the body that would have eventually shed toward the receiving transducer.

A major challenge in modeling the scattering by the gastropods involved choice of material properties and associated Lamb wave coupling coefficients and speed. The animal bodies consist of aragonite. Since all critical material parameters (density, longitudinal sound speed, and shear sound speed) were not available for aragonite, we used published parameters associated with calcite, a very similar substance. The density and longitudinal speed were used directly for predicting the Rayleigh reflection coefficient. Given the difficulty of determining the Lamb wave parameters for a body of this complexity, we used certain values inferred from the data. We also compared numerical calculations of Lamb wave parameters based on backscattering by an idealized spherical shell with the inferred values to test the validity of the hypothesis that the observed subsonic waves are indeed the zeroth-order antisymmetric Lamb wave.

The shell of the gastropods used was approximately 5 μm thick according to our measurements of shell thickness of other similar-sized animals. We are uncertain as to the thickness of the shell within all parts of the body and assume that layering of the spiral shell will cause the thickness to vary within a given shell. Because of the variation in thickness, it is expected that there would be deviation between predictions of Lamb wave parameters based upon an idealized sphere and comparisons with the data.

Using the calcite material parameters, predictions of acoustic backscattering were made for individual water-filled spherical shells and for individual tissue-filled shells, each for a variety of shell thickness (the thickness was held fixed for a given simulation) (Kaduchak, 1997). The predictions were based upon the Sommerfeld–Watson transformation of the modal series solution. This transformation converts the modal series into a series of ray terms (specular ray, Lamb-wave ray, etc.). The tissue material properties were chosen to be the similar to those of weakly scattering fluidlike animals (density and sound speed were set equal to 1.1 times that of the surrounding water) for lack of available information.

The idealized shell calculations show that for a 5-μm thick shell and ka in the range of 1–4, the speed of the zeroth-order antisymmetric Lamb wave was roughly $\frac{1}{8}$ that of the surrounding water. This value is the same as that which we observed in the measurements. For shells of 20-μm

thickness, the predicted value was about $\frac{1}{3}$ that of the surrounding water, which is much greater than what we observed. However, the predictions of β_L produce values of about 0.005 for the 20-μm-thick shell for $ka=1$ and values very close to zero for higher ka and/or thinner shells. The inferred value of β_L (from the data) was about 0.002 once roughness was taken into account (if roughness was not taken into account, that inferred value would be smaller but not small enough to be consistent with a value predicted for 5-μm-thick idealized shells). Thus one inferred value (β_L) is consistent with predictions from a shell thicker than that associated with the predictions that were consistent with the other inferred value (c_L). Nonetheless, both inferred values involving data from the rough irregular animal shell of variable thickness were consistent with the range of predictions involving a range of (idealized) shell thickness close to that of the animal, which is perhaps the best one could expect given the differences between the animal shell and the idealized spherical shell. These inferred values therefore appear to be reasonably consistent with the hypothesis that the subsonic wave is the zeroth-order antisymmetric Lamb wave.

Given the facts that the shell thickness is nonuniform and that the observed subsonic wave had significant energy for values of ka greater than unity (which implies a nonzero value of β_L), we used the values of the Lamb wave speed and coupling coefficient that were inferred from the data rather predicted from the idealized predictions.

Siphonophores. The nearly flat pattern exhibited in some echoes by the siphonophore could be modelled by the single bubble model (Fig. 2, left plot). The single bubble alone will give a flat spectrum in this frequency range regardless of angle of orientation. Alternatively, the flat pattern could be modeled by the more general bubble-plus-tissue model for realizations in which the tissue does not contribute significantly to the scattering. The irregular pattern (Fig. 2, right plot) must be predicted by the model which includes both the gas and tissue. Because of the stochastic nature of the scattering by the tissue, it is not useful to make direct comparisons between single realizations of the predicted and measured patterns. The statistics of the predicted and measured echoes can be compared and are done so in the next section.

B. Orientation dependence of echoes

Orientation of one of the euphausiids was digitized from the video camera data and compared with the echo levels that correspond to each video frame (Fig. 3). Scattering predictions based upon the DWBA model using observed orientation data were also compared with the observed scattering levels (Fig. 3).

The data illustrate that the echoes are generally higher for broadside incidence than for end-on. There was also significant variability from ping-to-ping in the echo level. Because of the variability and for direct comparisons, the scattering data, scattering predictions, and orientation data were averaged over a running seven-ping interval (before the averaging was performed the scattering predictions for a given ping were based on the observed instantaneous (i.e., not averaged) orientation angle). Also, the data and simulations represent an average over the 350–600-kHz spectrum,
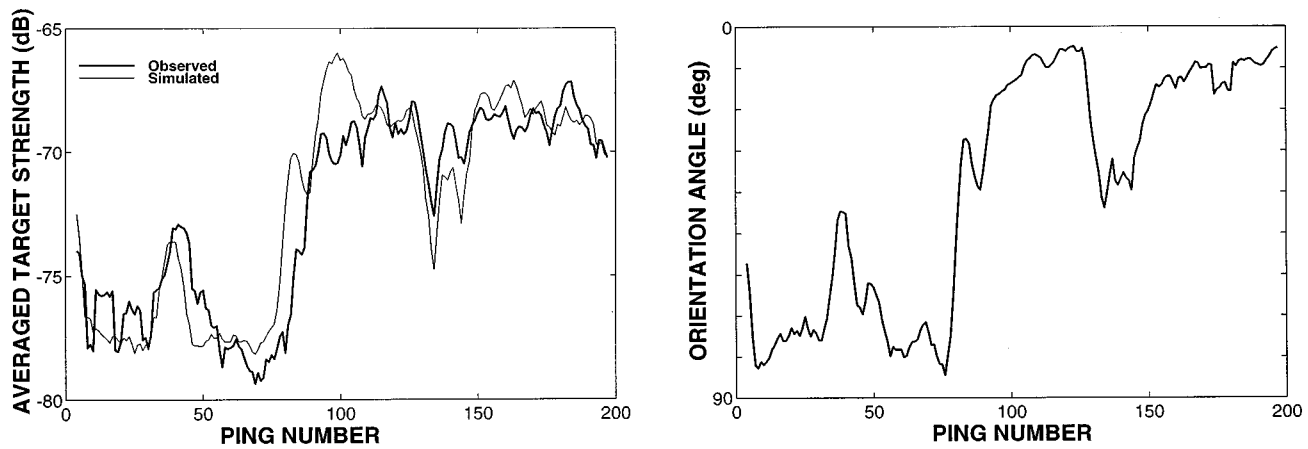
FIG. 3. Average target strength data from an individual 36-mm-long euphausiid and predictions from 200 consecutive acoustic pings as animal changes orientation [same animal as in Fig. 3 of Stanton *et al.* (1998)]. Left plot: Measured and simulated acoustic backscattering. The measured scattering has had the measured noise (equivalent TS$=-81.5$ dB) removed from it (removed on a linear scale first before logarithm is taken). The simulations use a rough tapered inhomogeneous cylinder model, based on the DWBA line integral given in Eq. (5). Right plot: measured orientation angle of euphausiid averaged over seven-ping running average for smoothing purposes. Scattering and orientation data collected simultaneously for each ping. Predictions use same (instantaneous, not averaged) orientation angle as measured for each corresponding ping although head-tail reversals are not distinguished for the near-broadside-incidence data. Pings 10–30 and 60–70 involved near head-on incidence and pings 100–120 and 150–200 involved near broadside incidence (where the head of the body was observed to be, on average, slightly farther from the transducers than the telson or ''tail''). The measured and simulated backscattering levels were averaged over a seven-ping window (a simple uniformly weighted seven-ping average for the data and a 30-realization Gaussian-distributed average based on the mean and standard deviation of angles over the seven pings used for the simulations). The backscatter data and simulations were averaged over the 350–600-kHz band of frequencies (all averaging, over pings and frequencies, involved averages of backscattering cross-section before the logarithm was taken). The measured noise and unwanted reverberation was reduced through first time-gating the compressed pulse output (Chu and Stanton, submitted) and had (after processing) an equivalent average target strength of -81.5 dB resulting in the worst case SNR of about 2.5 dB near ping number 70 (near end-on incidence), but typically about 4 dB and better for other near end-on incidence values and better than about 11 dB for near broadside incidence. Simulation parameters: $L=30.5$ mm (this measured quantity is the reduced or acoustic length that corresponds to the fact that the telson or ''tail'' of the euphausiid does not contribute substantially to the scattering), mean cylindrical radius $\bar{a}=1.9$ mm (inferred from measurement of length), $\rho_c/L=0.8$ (this is an intermediate value within the range of values of the ratio as measured from the video images), and the mean values $\bar{g}=\bar{h}=1.054$. These values of $\bar{g}$ and $\bar{h}$ were adjusted for a better fit to the data and are higher than the values in other simulations in this paper. The value of ρ_c/L, which is based on measurements, is lower than that used in other simulations in this paper. The higher values of g and h, in essence, offset the decrease in scattering levels due to the decrease in ρ_c/L, making this combination of g, h, and ρ_c/L somewhat compatible with the combinations used in other simulations. The values of g and h varied independently and randomly (Gaussian distributed) along the length of the body with a standard deviation of 0.005 over six segments of equal length. The value of radius varied independently and randomly (i.e., uncorrelated adjacent values, each following a Gaussian distribution with a standard deviation of 10% of the expected value) over 200 segments of equal length.

which corresponds to the spectrum of useful energy of the transducers. Because of the low signal-to-noise ratio of some of the echoes, the average measured noise level was subtracted from the measured (noisy) echo levels which resulted in a better representation of actual measured target strength.

The scattering modeling for angles of orientation near broadside was relatively straightforward as the levels were predictable using smooth homogeneous bent tapered cylinders. However, for angles near end-on, it was a significant challenge to predict the echo levels. This fact, coupled with the facts that (a) there was variability from ping to ping in the echoes as the animal changed orientation slowly and (b) the statistics of end-on echoes were consistent with echoes due to many parts of the bodies (Stanton *et al.*, 1994b; Fig. 4 of this paper), required a more complex shape and material profile to be used. As shown in Stanton (1992) and Stanton and Chu (1992), roughness of bounded bodies can cause significant variability in echoes and has been used to explain ping-to-ping variability of tethered animals (Wiebe *et al.*, 1990). Roughness elements of a target can be treated as individual scatterers. Once the target is at an oblique angle to the sonar transceiver and the main returns are not coming from the front and back interface, then these individual elements play a significant role in the scattering. It is quite

possible that the roughness elements are the source of the multiple ray echoes observed near end-on. Adding to the complexity of the problem is the possibility that the material property of the animals is not uniform throughout the body. The inhomogeneities of the material properties could also give rise to scattering levels near end-on.

Predictions using a smooth homogeneous cylinder model underestimated the scattering levels near end-on incidence. For the reasons given above, we used a more complex description of the animal morphology in order to describe the near end-on scattering levels. We used an elongated teardrop tapering function much like that illustrated in Fig. 1 of Stanton (1992) and incorporated both roughness and inhomogeneities of material properties of the body. Given the lack of knowledge of the precise roughness and material profile, we arbitrarily assigned 10% random variability to the cross-sectional radius along the length of the body and 0.5% random variability to the mass density and sound speed along the length of the body [the 0.5% variability corresponds to about 10% of the *difference* between the (weakly scattering) body material properties and that of the surrounding water].

The actual roughness profile of the animals has both a small smoothly varying component (dorsal side) and large

rapidly varying component (ventral side which contains legs). For simplicity, an intermediate (10% of radius) rapidly varying profile was used which involved statistically independent rapidly varying values of cross-sectional radius. The material property profile consisted of six statistically independent sections to represent the fact that there are a small number of sections of the body of a euphausiid.

With these added complexities, we made predictions of acoustic scattering over the entire range of orientation angles (Fig. 3). The predictions of backscattering with the rough inhomogeneous bent tapered cylinder generally follow the pattern of the measured levels over the full range of orientation angles. Most importantly, the near-end-on levels could be predicted by taking into account the added complexities of the model (the predictions near broadside were not significantly affected by taking into account the added complexities). Although the modeling of the complexities was far from ideal in this particular study, it is clear that the fine-scale complexities of the animal body must be included in order to predict near-end-on backscattering.

C. Statistics of echoes

The statistics of some sets of echoes are analyzed for one euphausiid and one siphonophore. The animals were free to change orientation throughout the measurements and many orientations and shapes were realized. However, because of the small size of the gastropods and nature of the tethering process, their movement was highly constrained and a statistical analysis is less meaningful and not included.

1. Euphausiids

The statistical behavior of the echo envelopes of the scattered signal from the euphausiid was analyzed with both the ray approach (Fig. 4) as well as with the DWBA approach (Fig. 5). The ray approach helps provide physical insight into the scattering process, although the results for this type of approach tend to be qualitative. The DWBA-based method, while more complex than the ray approach, is also potentially more predictive. Given the significant difference in the variability of the echoes between the cases involving broadside and end-on incidence, the analysis treats each of those cases. We perform this statistical analysis on the data set presented in Fig. 3 in which the video data of the animal were used to measure animal orientation for each of the echoes measured. Only the 560-kHz components of the broadband echoes were examined in this statistical study (data and simulations).

Ray approach. Depending upon the orientation information as well as pattern of target strength versus frequency, either the two-ray model or the six-ray model was used in the ray description (Fig. 4). The two-ray model is used in the case when the animal was generally near broadside during the measurements, which resulted in a regular pattern for about 40% of the echoes. The six-ray model is used in the case when the animal was generally near end-on (head-on in this case), which resulted in an irregular pattern for about 90% of the echoes. In the two-ray model, variations in orientation angle and shape are taken into account by randomly and uniformly varying the cylindrical radius of the animal
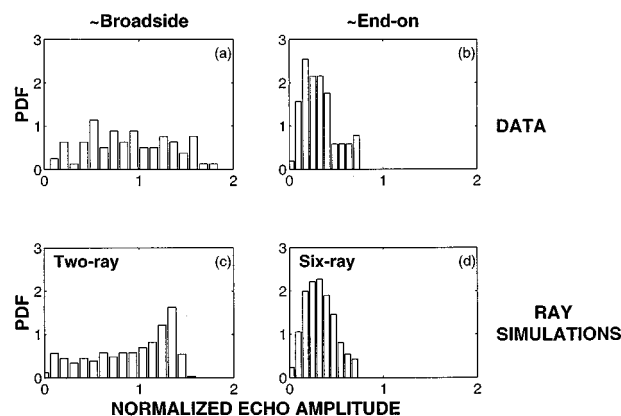
FIG. 4. Echo envelope histograms of echoes from an individual 36-mm-long euphausiid from sets of pings in which the animal is either generally broadside or end-on to the incident acoustic wave (same animal as in Fig. 3 of Stanton *et al.* (1998) and using subset of data presented in Fig. 3 of this paper). Acoustic frequency is the 560-kHz component of the broadband echo. Two-ray ($N=2$) and six-ray ($N=6$) models are used in those cases, respectively, using Eq. (12). All b_j for a given simulation [plots (c) and (d)] are of the same value. The horizontal scale of each of the four plots is normalized by the rms amplitude of the values plotted in plot (a). The end-on and broadside pings were selected from a fraction of pings within the range of ping numbers 5–70 and 100–200, respectively. The mean (near) end-on angle is measured to be 14.1° off head-on incidence (s.d.=9.9°) and the mean (near) broadside angle is measured to be 10.1° off broadside incidence (dorsal aspect) (s.d.=5.1°) with the head of the body observed to be slightly farther, on average, by about 10° from the transducers than the telson or "tail." Certain pings within those ranges were excluded; for example, pings near pings 40 and 140 were excluded where intermediate angles were observed.

over a range of values within ±30% of the average cylindrical radius (this distribution coincidentally corresponds to a uniform distribution in phase difference between the two rays over the 0–2π range at 560 kHz). This randomization
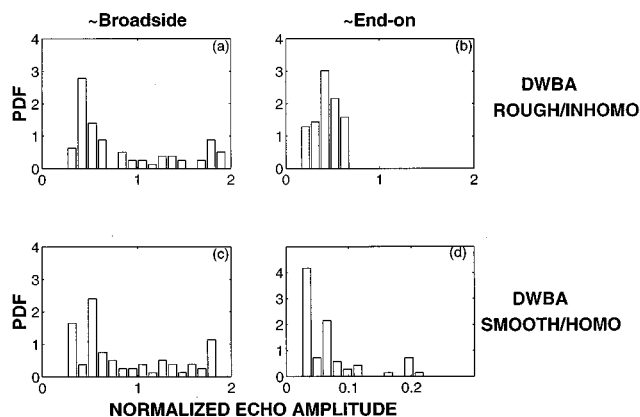
FIG. 5. Echo envelope histograms of simulated echoes from an individual 36-mm-long euphausiid using two DWBA-based models. The predictions were based on the simulations performed in Fig. 3 using selected pings for broadside and end-on incidence. The rough and inhomogeneous model used the 560-kHz component of the Fig. 3 simulations directly using the same broadside and end-on pings that were used in the data plots as in Fig. 4. The smooth and homogeneous model used the 560-kHz component of simulations that were similar to those performed for Fig. 3, using the same broadside and end-on pings that were used in the data plots in Fig. 4, but with no variability in radius (except for the taper) or in material properties. The simulations for these four plots excluded noise.

takes into account the fact that the animal has a cross-sectional radius that varies along the length of the body. When it changes orientation, a different part of the body (with a different radius) will make up the first Fresnel zone of the scattering and dominate the scattering.

Both measured and predicted echo amplitude histograms show marked differences between the two cases of animal orientation. The histograms for the data involving near broadside incidence show a more-or-less featureless pattern. Those histograms can be explained, in part, by first examining the model shown in the left plot of target strength versus frequency in Fig. 2. For a two-ray model, one expects there to be echo levels spanning the full range of values from 0 (total destructive interference) to twice the level of one ray (constructive interference) with more values occurring near the maximum value. The corresponding histogram of echo envelope values based on the two-ray simulations takes on a set of nearly uniformly distributed values up to the maximum echo value which has a peaked histogram value. The data histogram is similar to the simulated pattern with differences at the high echo levels—the data do not show a peak in the histogram near the maximum echo value.

In contrast, the histograms for the case of end-on incidence show a Rayleigh-like PDF with a distinct peak. The data for end-on incidence here have a lower SNR than in the broadside case which adds a Rayleigh-distributed component to the echo. However, the (Rayleigh-like) variability of these end-on incidence echoes are consistent with the variability at end-on incidence observed in an earlier experiment with a similar elongated animal (decapod shrimp), but with a higher SNR (Stanton *et al.*, 1994b). In order for the envelope of the scattered signal to be Rayleigh distributed, the scattering must be random and diffuse, which implies that there are echoes coming from many parts of the body that contribute significantly to the total echo.

With both classes of animal orientation, the ray simulations predicted the general nature of the histograms involving the euphausiids. In addition to the six-ray model also being consistent with the end-on decapod shrimp data and associated ray modeling presented in Stanton *et al.* (1994b), the two-ray model is also consistent with the broadside decapod shrimp data and ray modeling presented in Stanton *et al.* (1993a, 1994b) confirming the earlier results for animals of this body form.

DWBA approach. In addition to the more qualitative ray-based approach, we also investigated the statistical nature of the echo with the more predictive DWBA method (Fig. 5). Both a smooth homogeneous asymmetrically tapered bent cylinder as well as a rough inhomogeneous asymmetrically tapered bent cylinder were used. The simulation parameters for the latter case are identical to those used in the study of backscatter versus angle described in Fig. 3 while using the orientations used in Fig. 4 for direct comparison. The parameters for the smooth-homogeneous-model simulations were identical to those of the rough-inhomogeneous-model case in every respect except for the fact that the mean values of the cylindrical radii and mass density and sound speed contrasts from the rough inhomogeneous case were used rather than the stochastic values (the

radius still varied according to the same taper function).

The DWBA-based simulations show that the variability of the echoes for angles of incidence near broadside for the rough inhomogeneous case is broadly similar to that of the smooth homogeneous case (left plots in Fig. 5). The echo envelope PDFs based on both sets of DWBA simulations for broadside incidence span a relatively wide range of echo values like the echo data PDF presented in the top left plot of Fig. 4. However, the data PDF has much less structure than either of the sets of DWBA-based simulations.

The greatest differences between the DWBA-based approaches involved end-on incidence. The mean value of the predictions for the smooth, homogeneous case was significantly lower than the corresponding value for the rough, inhomogeneous case (right plots in Fig. 5). The difference in mean level is consistent with the differences observed between the two different models averaged over the band of frequencies that were discussed above. Furthermore, the shapes of the two histograms in the end-on case are also different from each other. The shape of the PDF of the echo envelope data (top right plot in Fig. 4) is closer to the shape predicted by the rough inhomogeneous model than that predicted using the smooth homogeneous model, although there are some distinct differences.

In conclusion, predictions of the echo envelope statistics appear to be relatively insensitive to the complexity of the DWBA model (rough inhomogeneous versus smooth homogeneous) for the distribution of angles of incidence near broadside. The greatest sensitivity involved the case where the distribution of angles was near end-on incidence. Here, the rough inhomogeneous model explained the overall (mean) levels of the data much better than for the predictions involving the smooth homogeneous model and it explained the shape of the PDF data somewhat better. The improvements are due to the fact that there are elements both within the body interior and on the surface that can contribute to the scattering. These elements are insignificant near broadside incidence as the echoes from the front and back interface tend to dominate the scattering. However, off normal incidence, the two rays do not contribute significantly to the scattering and effects due to these other sources of scattering dominate. The fact that these multiple elements dominate near end-on is consistent with the fact that a six-ray model is required to describe the scattering in that region (Fig. 4).

2. Siphonophores

In the case where the siphonophore was studied both whole and without its pneumatophore, the measured echo envelope PDFs were markedly different (Stanton *et al.*, 1997, and Fig. 6 of this paper). When comparing the predictions with the data, a model including both the gas contribution (one ray of constant phase) and tissue contribution (six randomized rays) was used to describe the whole animal while the six-ray model alone was used to describe the scattering by the animal without its pneumatophore. The phase of the gas ray was held constant while the phase of each tissue ray was randomized uniformly over the range 0 to 2π. The use of six rays was chosen to describe the scattering by the tissue because of the generally random shape and ori-
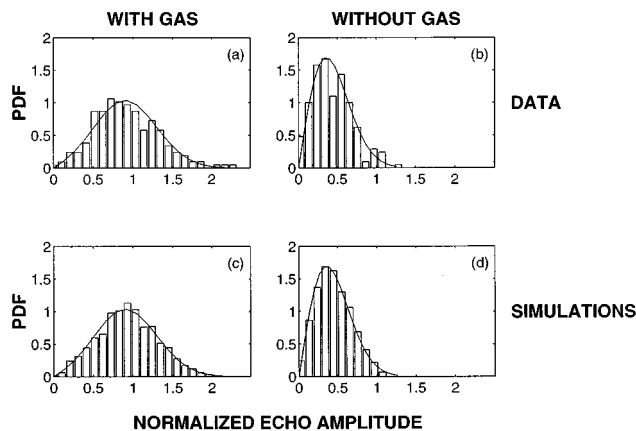
FIG. 6. Statistical study of echoes from an individual siphonophore both whole and with pneumatophore removed. Measured data (histograms in upper plots) are compared with simulation histograms (lower plots). Rice PDF curves are superimposed upon all histograms. Data taken directly from Fig. 6 of Stanton *et al.* (1998). Acoustic frequency is the 560-kHz component of the broadband echo. The horizontal scale from each plot is normalized by the rms value of the values plotted in (a). Rice PDF shape parameter: using a (γ_{RICE}) notation similar to that (γ) of Stanton and Chu (1992), $\gamma_{RICE}=2$ for both plots in left column and $\gamma_{RICE}=0$ for both plots in right column where γ_{RICE} is the ratio of coherent to incoherent energy of the signal [this γ_{RICE} and the γ in Stanton and Chu (1992) are not to be confused with the other γ given explicitly in the text of this paper]. For $\gamma_{RICE}=0$, the Rice PDF reduces to the Rayleigh PDF. The simulations in the left plot used Eq. (12) inserted into each of the two terms on the right-hand side of Eq. (33). For the bubble, $N=1$ and $\epsilon_j=0$, while for the tissue $2k_1\epsilon_j$ was randomized in the range $0–2\pi$ and $N=6$ (six random rays from the tissue). The energy of each tissue ray was set equal to 0.083 of the energy from the gas ray to be consistent with the observed $\gamma_{RICE}=2$. The simulations in the right plot use the same ray summation as in the left plot, but now excluding the gas term.

entation of the body which would tend to produce diffuse scattering at these high frequencies. As described above, six rays is a reasonable approximation for describing the statistics of a diffuse scatterer.

In order to further understand the statistics of the echoes and to determine the relative value of the rays, the Rice PDF is used in this analysis. The Rice PDF was originally derived in electrical signal theory to describe the envelope of a sine wave with added noise (Rice, 1954). The PDF has since been applied to various scattering problems where there may exist a consistent echo with a highly variable one superimposed (Clay and Heist, 1984; Stanton, 1984; Stanton and Chu, 1992). In the case of the siphonophore, the consistent echo would correspond to the scattering by the gas and the variable echo would correspond to the scattering by the tissue. Fits of the Rice PDF to the siphonophore data result in values of the shape parameter γ_{RICE} to be equal to 2 and 0 for the whole animal and animal-less-gas data, respectively (Fig. 6). In this context γ_{RICE} is defined as the ratio of coherent scattered energy to incoherent scattered energy. The value of $\gamma_{RICE}=2$ for the whole animal indicates that the incoherent energy is $\frac{1}{3}$ of the total energy. The observed decrease of about 5 dB in echo energy when the gas inclusion was cut off is consistent with this fraction $(10 \log(1/3) \simeq -4.8 \text{ dB})$. The value of $\gamma_{RICE}=0$ for the tissue-only case corresponds to the limiting case of the Rice PDF when it becomes a Rayleigh PDF (i.e., diffuse random-phase scattering with no coherent component), while the $\gamma_{Rice}=2$ case corresponds to

a more Gaussian-like PDF. For this latter, whole animal, case the relative strengths of the rays in the ray modeling can be estimated. The value $\gamma_{RICE}=2$ implies that the sum of the energies of the six (tissue) rays is 0.5 times that of the simulated gas echo. By arbitrarily assigning equal strength to each tissue ray, then the energy of each tissue ray would be 0.083 times that of the energy of the gas ray.

Using the relative values for the ray strengths as estimated above, there is reasonable qualitative agreement between the ray simulations of echo envelope histograms and data (Fig. 6). Data involving the whole animal and corresponding simulations show the distribution of the echo envelope to be Gaussian-like. Data and simulations involving the animal without the pneumatophore show the distributions to be Rayleigh-like. All histograms are consistent with the Ricean PDF for different γ_{RICE}. As discussed in Stanton *et al.* (1997), this variability in shape of echo histogram for the animal with and without the gas is consistent with the hypothesis that the gas produces a strong consistent return. The tissue at these high acoustic frequencies produces a highly variable return, indicating that there are interfering echoes coming from various parts of the tissue.

D. Averaged echoes

The backscattering cross sections from individual animals were averaged over a large number of pings and compared with the appropriate models on a decibel scale (Fig. 7). Data used are from a larger range of acoustic frequencies than with the single ping analyses.

The averaging has the general effect of smoothing out most of the structure of the scattering. Some structure remains in the euphausiid data where there is a dip and peak at 500 and 600 kHz, respectively. The structure in the siphonophore data quite expectedly disappeared as the echo from the gas should be relatively strong, featureless, and stable while the structure from the echo due to the tissue should be random with no consistent structure. The structure in the gastropod data mostly disappeared, possibly due to the variability in path length of the Lamb wave (and hence variability in structure) as the animal changed orientation.

Two models for the euphausiids were used in the predictions—both the more precise DWBA model numerically averaged over orientation and size and the two-ray-based model analytically averaged over orientation and size. The size averages correspond to the fact that the animal is tapered and the part of the cross section that dominates the scattering depends upon orientation angle. Consequently, the section dominating the scattering for a given ping varies in diameter from ping to ping which results in an effective change in animal size. The average over a small range of length is equivalent to an average over a small range of radius in this case. The rough elastic shell ray model, numerically averaged over size, was used for the gastropods. The sum of the backscattering cross section using the exact modal series solution for a gas bubble and the cross section based on the analytically averaged bent fluid cylinder (ray) model for the tissue was used to model the scattering by the

FIG. 7. Target strength versus frequency averaged over many echoes from euphausiid, gastropod, and siphonophore (cross section averaged before logarithm was taken). Both two-ray (dashed) and DWBA (solid) fluid cylinder models given in euphausiid plot, two-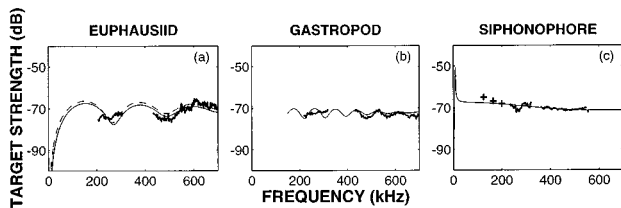ray rough elastic shell model used for gastropod plot, and hybrid model of fluid bent cylinder containing gas sphere used for siphonophore plot. Thin smoothly varying curves (dashed and solid) are predictions, thick irregular curves are data from broadband transducers, and ''+'' are data from single frequency transducers. Predictions using the euphausiid curves with similar parameters that successfully predicted scattering levels down into the Rayleigh scattering region at 50 kHz with decapod shrimp (Stanton $et\ al.$, 1993b). Predictions similar to the siphonophore curve (but with two gas spheres to model split gas inclusions) follow the increase in levels near the resonance region as far down as 50 kHz (Fig. A4 of this paper). Plot parameters: (a) euphausiid: same (individual) animal as in Fig. 2 of this paper, data averaged over first 50 pings of data from each transducer; Eq. (18) used for (analytically averaged) ray model using the same (g, h) simulation parameters as in Fig. 2 and $L=29$ (measured reduced length), $a=1.75$ mm (average value of measured radius at mid point in body, averaged between widthwise and depthwise directions), $s=0.08$ (estimated), $s_\theta=10°$ (inferred), and the parameters $(C_B, T_B, \alpha_B)=(1.2, 1, 0.8)$ were previously determined through comparisons with DWBA predictions (Stanton $et\ al.$, 1993b); an equation equivalent to Eq. (6) (but written in Cartesian coordinates) is used in (smooth, homogeneous) DWBA modeling [$|f_{bs}|^2$ in Eq. (6) was numerically averaged using above parameters (where appropriate) plus $\rho_c/L=3$ and a tapering function $a=a_0\sqrt{1-(z/(L/2))^{10}}$ is used where a_0 is the radius in the middle of the body and z is the position along the axis of the body relative to the ($z=0$) mid-point of the body]. (b) Gastropod: averaged data from 50 pings each from eight individual (one at a time) Limacina retroversa. All animals were in the range 1.8–2.0 mm long. Numerical average of square of magnitude of Eq. (31) with the same parameters as given in Fig. 2 caption except for the inferred values $\Phi_L=\pi$, $F_L=1$, and $\sigma=0.06\bar{a}$. The average spanned $\bar{a}\pm3$ s.d. where s.d.$=0.1\bar{a}$ (it is expected in this case for certain parameters with the average echo model to be different than those of the single echo model because for one realization, the ping will only ''see'' the front interface from one angle which has a fixed radius of curvature and related Lamb waves will only experience a certain range of radii whereas averaging over orientation involves the full range of values. (c) Siphonophore: one individual $Nanomia\ Cara$ 26 mm long with only one gas inclusion 1.5 mm long by 1 mm wide [same siphonophore as used in Fig. 7 of Stanton $et\ al.$ (1997)]. Here, 200 pings per frequency were averaged except for the 120-kHz measurements where only 10 pings were averaged. Equation (37) was used with modal series solution [Eq. (34)] used for bubble component and averaged two-ray model [Eq. (18)] for tissue component. Model parameters are, gas: $a_{sphere}=0.425$ mm based on measurement of bulbus side of gas inclusion facing the transducers, $(g, h)=(0.0012, 0.22)$ based on published values for air at one atmosphere pressure. Tissue: $a_{cyl}=0.6$ mm and $L=22$ mm (both based on direct measurements of tissue section of body), $g=h=1.02$ (chosen to be consistent with those parameters of other weakly scattering bodies), $(C_B, T_B, \alpha_B)=(1.2, 1, 0.8)$ which were previously determined through comparisons with DWBA predictions (Stanton $et\ al.$, 1993b), $s_\theta=0.15$ rad (inferred), and $s=1.0$ (this high length variability corresponds equivalently to the high variability in effective cross-sectional radius of the body, a_{cyl} is considered to be an effective radius because of the complex structure of the tissue section). The inclusion of the tissue scattering term adjusted the predictions at the highest frequencies upward by about 1.5 dB, making the predictions more in line with the data.

(whole) siphonophore. The data and model for the siphonophore both indicate a rise in the levels for lower frequencies as the gas approaches resonance. The model predicts a resonance for this animal at about 4.6 kHz.

III. SUMMARY AND CONCLUSIONS

The scattering properties of zooplankton from various gross anatomical groups have been shown to be strongly dependent upon the material properties of the animals. The fluidlike euphausiids, hard-shelled gastropods, and gas-bearing siphonophores all have distinctly different acoustic signatures. Mathematical models were used to relate the signatures to the basic physics of the scattering process.

The plots of (single ping) target strength versus frequency for individual euphausiids showed significant structure, regardless of orientation of the animals. The structure is sometimes regular for angles of orientation near broadside incidence, while it is random for all other angles. The type of structure for the gastropods varied dramatically with angle of orientation. For some angles, the structure was quite regular with pronounced peaks and nulls, while at others the pattern was more random. For some sets of angles, the pattern was nearly flat with random fluctuations of minimal amplitude. The siphonophores produced patterns that were sometimes nearly flat and sometimes irregular. Once the data were averaged over a set of pings, the structure of the target strength patterns tended to wash away. In some cases, there was some structure that would remain. For example, there is structure in the upper frequency range of the data for both the euphausiid and gastropod data in Fig. 7. However, the pattern of the residual structure varies with ping set. Other euphausiid data (not shown) have a different pattern of residual structure while other averaged gastropod data (Fig. 4 of Stanton $et\ al.$, 1998) show no structure. No doubt, the orientation distribution of the animals for each ping set greatly affects the structure of the averaged data.

The greatest challenge in the modeling involved identifying the dominant scattering mechanisms and formulating reliable approximate formulas. Up to several models per animal were derived, depending upon the application and approximation used. The structure of both the target strength versus frequency data as well as compressed pulse output for single echoes provided most of the basis for the model development. The two-ray model (one ray from the front interface and one from the back) for the euphausiid seems to work well for orientations near broadside incidence and for averages over angle of orientation while more rays (corresponding to other parts of the body) are required for single ping data far off broadside. A predictive model incorporating roughness and material property inhomogeneities was also shown to describe scattering off broadside. A two-ray model is also required to model the gastropod in the geometric scattering region where one of the rays is from the front interface and the other is due to excitation of a Lamb wave on the shell. The siphonophore was characterized by the sum of an exact single bubble solution which was used to describe the scattering by its gas inclusion plus a model (DWBA or ray) for the tissue.

In conclusion, as a result of conducting controlled laboratory measurements, the fundamental scattering properties of zooplankton from several gross anatomical groups have been determined. This served as the basis for developing approximate acoustic scattering models which are predictive in nature. That is, they are written in a general enough form

so that they can make predictions beyond the existing set of data and be used to describe scattering by other species within those groups. The models are limited, in part, by the amount of available scattering data. For example, direct measurements of the material properties of the animals need to be made to reduce the number of empirical parameters in the modeling. Certainly, more controlled experiments and sophisticated models will help improve the accuracy and range of usefulness of the existing models.

ACKNOWLEDGMENTS

APPENDIX. EFFECTS OF FRAGMENTATION OF GAS INCLUSION OF SIPHONOPHORE ON ACOUSTIC PROPERTIES

One challenge in the experiment involved maintaining the physical integrity of the siphonophores so that their morphology during the acoustic experiment represented its morphology in its natural environment. Some of the siphonophores were observed to have contained several gas inclusions. It is believed that during the netting procedure in which the animals were caught by the net at deep depths and raised to the surface, the gas inclusion of the siphonophore split into an array of smaller bubbles. The resultant scattering properties were dramatically different than that of an animal with a single inclusion. In this Appendix, the array of smaller inclusions is modeled to a first approximation as a linear array of N equally spaced bubbles (Fig. A1). Scattering predictions based on this model are compared with data involving a siphonophore whose gas remained fragmented during the acoustic experiment.

The backscattering from a linear array of N equally spaced bubbles at an arbitrary angle of orientation θ is written in terms of the backscattering amplitude f_1 of a single bubble as

$$f_N = f_1 \sum_{j=1}^{N} e^{-i2(j-1)k_1 D \sin \theta},\tag{A1}$$

where D is the center-to-center separation between the bubbles. This equation was adapted from Eq. (12) by setting $b_j = f_1$ and $\epsilon_j = -(j-1)D \sin \theta$. The relative phase of each scatterer due to its respective position in the array is indicated in the summand. This equation is approximate as it assumes first-order scattering only. That is, any multiple scattering between the bubbles is ignored, as are any shadowing effects.

The average scattering cross section can be derived by first calculating the square of the magnitude of the above expression, then averaging over all angles of orientation assuming that the angles are uniformly distributed over the range $0-2\pi$. The resultant expression can be written in compact form as

$$\langle (\sigma_{bs})_N \rangle = (\sigma_{bs})_1 A,\tag{A2}$$

where

$$A = \sum_{j=1}^{N} \sum_{j'=1}^{N} J_0(2(j'-j)k_1 D)\tag{A3}$$

$$= N + \sum_{j=1}^{N} \sum_{j'=1}^{N} J_0(2(j'-j)k_1 D), \quad j \neq j'.\tag{A4}$$

Here, $(\sigma_{bs})_1 = |f_1|^2$ and J_0 is the zeroth-order Bessel function. The latter expression for A is given as it helps show its limiting values:

$$A \rightarrow \begin{cases} N^2, & 2(N-1)k_1 D \ll 1, & \text{(A5)} \\ N, & 2k_1 D \gg 1. & \text{(A6)} \end{cases}$$

For very high frequencies where $2k_1 D \gg 1$, the echoes from the individual bubbles add incoherently (i.e., the phases of the echoes from the individual bubbles are randomly distributed over the range $0-2\pi$) and the average backscattering cross section is equal to N times the cross section $(\sigma_{bs})_1$ of an individual bubble. For very low frequencies where $2(N-1)k_1 D \ll 1$, the echoes from the individual bubbles add coherently (i.e., the phases of these echoes are essentially the same) and the average cross section is equal to N^2 times the cross section of an individual bubble. For intermediate values of frequencies, A will take on a much more complicated dependence upon the parameters of the array as given in the general equation above.

For one or two bubbles, A reduces to simple forms:

$$A = 1, \quad N = 1,\tag{A7}$$

$$A = 2(1 + J_0(2k_1 D)), \quad N = 2,\tag{A8}$$

where for one bubble, A is simply equal to unity (i.e., the average cross section is equal to the cross section of a single bubble, as expected), and for two bubbles, A is equal to the sum of two terms. For low frequencies, the Bessel function term in the two-bubble expression becomes equal to unity making $A = 4$ (i.e., coherent addition), while at high frequencies, the Bessel function approaches zero and $A = 2$ (i.e., incoherent addition).

The scattering by the siphonophores whose gas inclusion remained fragmented was characterized by a target strength versus frequency pattern that contains significant structure (Fig. A2). The pattern was irregular and consisted of one or more peaks and dips (or nulls) that varied in position and level from ping to ping. Occasionally, the animals that produced this type of pattern would produce a flat pattern. It is hypothesized that the irregular pattern is due, in part, to interference between the echoes from the different gas inclu-
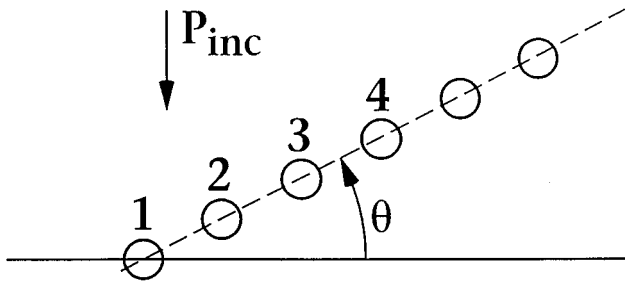
FIG. A1. Simplified scattering geometry for array of gas inclusions in siphonophore.

FIG. A3. Comparison between two-bubble model (thin curve) and single ping data (thick curve) from siphonophore whose gas inclusion remained fragmented throughout the experiment (animal described in Fig. A2 caption). Equation (A1) was used using Eq. (34) for f_1 and $N=2$, $a=0.7$ mm (slightly above measured value, adjusted for best fit), $g=0.0012$, and $h=0.22$. Here $D \sin \theta$ was adjusted arbitrarily to fit the location of the null (orientation is not known).

sions from each animal. Tissue, of course, plays a role in the interference pattern as well. The pattern, when dominated by multiple bubbles, would vary as the animal changed orientation and would be flat or nearly so when the axis of the array of inclusions is perpendicular or nearly so to the direction of incidence of the incoming signal.

While there were two to nine inclusions in any given siphonophore with a fragmented gas bubble, some were larger than others. After modeling the scattered signals, the best fits were obtained by assuming that two of the bubbles dominated the scattering (i.e., setting $N=2$). This approach was successful both modeling the single ping data (Fig. A3) and average echo data (Fig. A4). Since the orientation of the animal was not known for any given ping, the angle of orientation in the modeling of the single ping data was arbitrarily varied to move the position of the null and obtain a good fit to the data. Of course, for the average echo modeling, averages were calculated over all angles of orientation.

The average echo is shown to increase with decreasing frequency, an effect that is due to a combination of effects from both scattering by each individual bubble and the coherent addition of the scattering by the two bubbles within the animals at the lower frequencies (Fig. A4). Furthermore,

the deep nulls exhibited by those animals on a ping-by-ping basis were generally washed out during the averaging process, although some structure remained in this case.

To summarize, as a result of the net sampling process, the gas inclusions of some siphonophores apparently fragmented into multiple smaller inclusions (ranging from two to nine). The resultant scattering behavior of these animals was characterized by a very irregular pattern in single ping data, which is in sharp contrast to a much smoother one observed

FIG. A2. Frequency spectrum (TS versus frequency) for four sequential echoes from a 24-mm-long siphonophore whose gas inclusion remained fragmented during the acoustics experiment. Throughout the experiment, it had two main bubbles each measuring about 1 mm in diameter with several smaller bubbles 0.5 mm in diameter and smaller. The pattern contained at least one null or dip for a significant fraction of the pings.

FIG. A4. Comparison between two-bubble model and 50-ping average of data from siphonophore whose gas inclusion remained fragmented throughout the experiment. Animal described in Fig. A2 caption. Equation (A2) used with the same (inclusion) radius of 0.7 mm used in this two-bubble simulation as in Fig. A3. In addition, a center-to-center separation, D, of 1.40 mm was required for a good fit. This should be compared with the 2.65 mm (before experiment) to 0.95 mm (after experiment) range of separations the animal experienced during the experiment. Thin curve is from predictions, thick irregular curve from broadband transducers, and "+" data from single frequency transducers.

with some data with animals that contained only a single inclusion during the measurements. While the pattern is smoothed out once averaged over many pings, the resultant average level should be generally higher than that from a single gas inclusion of the same volume. For example, for a split of a single 1-mm-diam bubble into two bubbles, the increase in level averages about 1 dB at 200 kHz over a range of separations.

Anderson, V. C. (**1950**). ''Sound scattering from a fluid sphere,'' J. Acoust. Soc. Am. **22**, 426–431.

Chu, D., and Stanton, T. K. (**submitted**). ''Application of pulse-compression techniques to broadband acoustic scattering by live individual zooplankton,'' submitted to J. Acoust. Soc. Am.

Chu, D., Foote, K. G., and Stanton, T. K. (**1993**). ''Further analysis of target strength measurements of Antarctic krill at 38 and 120 kHz: Comparison with deformed cylinder model and inference of orientation distribution,'' J. Acoust. Soc. Am. **93**, 2985–2988.

Chu, D., Stanton, T. K., and Wiebe, P. H. (**1992**). ''Frequency Dependence of Sound Backscattering from Live Individual Zooplankton,'' ICES J. Mar. Sci. **49**, 97–106.

Clay, C. S., and Heist, B. G. (**1984**). ''Acoustic scattering by fish-acoustic models and a two parameter fit,'' J. Acoust. Soc. Am. **75**, 1077–1083.

Felsen, L. B., and Lu, I. T. (**1989**). ''Ray treatment of wave propagation on thin-walled curved elastic plates with truncations,'' J. Acoust. Soc. Am. **86**, 360–374.

Foote, K. G. (**1990**). ''Speed of sound in *Euphausia superba*,'' J. Acoust. Soc. Am. **87**, 1405–1408.

Foote, K. G., Everson, I., Watkins, J. L., and Bone, D. G. (**1990**). ''Target strengths of Antarctic krill (*Euphausia superba*) at 38 and 120 kHz,'' J. Acoust. Soc. Am. **87**, 16–24.

Gaunaurd, G. C. (**1985**). ''Sonar Cross Sections Partially Insonified by Finite Sound Beams,'' IEEE J. Ocean Eng. **OE-10**(3), 213–230.

Goodman, R. R., and Stern, R. (**1962**). ''Reflection and transmission of sound by elastic spherical shells,'' J. Acoust. Soc. Am. **34**, 338–344. For modal series coefficients involving spherical shells with an interior fluid different than that of the exterior fluid see, for example, Stanton (1990).

Ho, J. M. (**1994**). ''Geometrical theory of acoustic scattering by thin elastic shells,'' J. Acoust. Soc. Am. **96**, 3115–3125.

Ho, J. M., and Felsen, L. B. (**1990**). ''Nonconventional traveling wave formulations and ray-acoustic reductions for source-excited fluid-loaded thin elastic spherical shells,'' J. Acoust. Soc. Am. **88**, 2389–2414.

Jansson, P.-Å. (**1993**). ''Acoustic scattering from a rough sphere,'' J. Acoust. Soc. Am. **93**, 3032–3042.

Kaduchak, G. (**1997**). Personal communication.

Kaduchak, G., Kwiatkowski, C. S., and Marston, P. L. (**1995**). ''Measurement and interpretation of the impulse response for backscattering by a thin spherical shell using a broad-bandwidth source that is nearly acoustically transparent,'' J. Acoust. Soc. Am. **97**, 2699–2708.

Kargl, S. G., and Marston, P. L. (**1989**). ''Observations and modeling of the backscattering of short tone bursts from a spherical shell: Lamb wave echoes, glory, and axial reverberations,'' J. Acoust. Soc. Am. **85**, 1014–1028.

Marston, P. L. (**1992**). ''Geometrical and Catastrophe Optics Methods in Scattering,'' in *Physical Acoustics*, edited by A. D. Pierce and R. N. Thurston (Academic, New York), Vol. 21.

Marston, P. L., Kargl, S. G., and Williams, K. L. (**1990**). ''Rayleigh, Lamb, and Whispering Gallery Wave Contributions to Backscaterring from Smooth Elastic Objects in Water Described by a Generalization of GTD,'' in *Elastic Wave Propagation and Ultrasonic Nondestructive Evaluation*, edited by S. K. Datta, J. D. Achenback, and Y. S. Rajapakse (Elsevier, Amsterdam), pp. 211–216.

Morse, P. M., and Ingard, K. U. (**1968**). *Theoretical Acoustics* (Princeton U. P., Princeton, NJ).

Norris, A. N., and Rebinsky, D. A. (**1994**). ''Acoustic coupling to membrane waves on elastic shells,'' J. Acoust. Soc. Am. **95**, 1809–1829.

Rebinsky, D. A., and Norris, A. N. (**1995**). ''Benchmarking an acoustic coupling theory for elastic shells of arbitrary shape,'' J. Acoust. Soc. Am. **98**, 2368–2371.

Rice, S. O. (**1954**). ''Mathematical Analysis of Random Noise,'' in *Selected Papers on Noise and Stochastic Processes*, edited by N. Wax (Dover, New York), pp. 133–294.

Skudrzyk, E. (**1971**). *The Foundation of Acoustics* (Springer-Verlag, New York).

Stanton, T. K. (**1984**). ''Sonar estimates of sea floor microroughness,'' J. Acoust. Soc. Am. **75**, 809–818.

Stanton, T. K. (**1988**). ''Sound scattering by cylinders of finite length. I. Fluid cylinders,'' J. Acoust. Soc. Am. **83**, 55–63.

Stanton, T. K. (**1989a**). ''Sound scattering by cylinders of finite length. III. Deformed cylinders,'' J. Acoust. Soc. Am. **86**, 691–705.

Stanton, T. K. (**1989b**). ''Simple approximate formulas for backscattering of sound by spherical and elongated objects,'' J. Acoust. Soc. Am. **86**, 1499–1510.

Stanton, T. K. (**1990**). ''Sound scattering by spherical and elongated shelled bodies,'' J. Acoust. Soc. Am. **88**, 1619–1633.

Stanton, T. K. (**1992**). ''Sound scattering by rough elongated elastic objects. I. Means of scattered field,'' J. Acoust. Soc. Am. **92**, 1641–1664.

Stanton, T. K., and Chu, D. (**1992**). ''Sound scattering by rough elongated elastic objects. II: Fluctuations of scattered field,'' J. Acoust. Soc. Am. **92**, 1665–1678.

Stanton, T. K., Clay, C. S., and Chu, D. (**1993a**). ''Ray representation of sound scattering by weakly scattering deformed fluid cylinders: Simple physics and application to zooplankton,'' J. Acoust. Soc. Am. **94**, 3454–3462.

Stanton, T. K., Chu, D., Wiebe, P. H., and Clay, C. S. (**1993b**). ''Average echoes from randomly oriented random-length finite cylinders: Zooplankton models,'' J. Acoust. Soc. Am. **94**, 4363–4472.

Stanton, T. K., Chu, D., Wiebe, P. H., Martin, L. V., and Eastwood, R. L. (**1998**). ''Sound scattering by several zooplankton groups. I. Experimental determination of dominant scattering mechanisms,'' J. Acoust. Soc. Am. **103**, 225–235.

Stanton, T. K., Wiebe, P. H., Chu, D., Benfield, M., Scanlon, L., Martin, L., and Eastwood, R. L. (**1994a**). ''On Acoustic Estimates of Zooplankton Biomass,'' ICES J. Mar. Sci. **51**, 505–512.

Stanton, T. K., Wiebe, P. H., Chu, D., and Goodman, L. (**1994b**). ''Acoustic Characterization and Discrimination of Marine Zooplankton and Turbulence,'' ICES J. Mar. Sci. **51**, 469–479.

Wiebe, P. H., Greene, C. H., Stanton, T. K., and Burczynski, J. (**1990**). ''Sound scattering by live zooplankton and micronekton: Empirical studies with a dual-beam acoustical system,'' J. Acoust. Soc. Am. **88**, 2346–2360.

Yang, Y., Norris, A. N., and Couchman, L. S. (**1995**). ''Acoustic scattering from fluid-loaded elastic shells: A Gaussian beam approach,'' J. Acoust. Soc. Am. **98**, 611–622.

Yang, Y., Norris, A. N., and Couchman, L. S. (**1996**). ''Ray tracing over smooth elastic shells of arbitrary shape,'' J. Acoust. Soc. Am. **99**, 55–65.

Differences between sound scattering by weakly scattering spheres and finite-length cylinders with applications to sound scattering by zooplankton

Timothy K. Stanton
Department of Applied Ocean Physics and Engineering, Woods Hole Oceanographic Institution, Woods Hole, Massachusetts 02543-1053

Peter H. Wiebe
Department of Biology, Woods Hole, Oceanographic Institution, Woods Hole, Massachusetts 02543-1049

Dezhang Chu
Department of Applied Ocean Physics and Engineering, Woods Hole Oceanographic Institution, Woods Hole, Massachusetts 02543-1053

A modeling study was conducted to determine the conditions under which fluidlike zooplankton of the same volume but different shapes (spherical/cylindrical) have similar or dramatically different scattering properties. Models of sound scattering by weakly scattering spheres and cylinders of finite length used in this analysis were either taken from other papers or derived and herein adapted for direct comparison over a range of conditions. The models were examined in the very low- ($ka \ll 1$, $kL \ll 1$), moderately low- ($ka \ll 1$, $kL \gtrsim 1$), and high-frequency regions ($ka \gg 1$, $kL \gg 1$), where k is the acoustic wave number, a is the radius (spherical or cylindrical) of the body, and L is the length of the cylinders (for an elongated body with $L/a = 10$, ''moderately low'' corresponds to the range $0.1 \lesssim ka \lesssim 0.5$). Straight and bent cylinder models were evaluated for broadside incidence, end-on incidence, and averages over various distributions of angle of orientation. The results show that for very low frequencies and for certain distributions of orientation angles at high frequencies, the averaged scattering by cylinders will be similar, if not identical, to the scattering by spheres of the same volume. Other orientation distributions of the cylinders at high frequencies produce markedly different results. Furthermore, over a wide range of orientation distributions the scattering by spheres is dramatically different from that of the cylinders in the moderately low-frequency region and in the Rayleigh/geometric transition region: (1) the Rayleigh to geometric scattering turning point occurs at different points for the two cases when the bodies are constrained to have the same volume and (2) the functional dependence of the scattering levels upon the volume of the bodies in the moderately low-frequency region is quite often different between the spheres and cylinders because of the fact that the scattering by the cylinders is still directional in this region. The study demonstrates that there are indeed conditions under which different shaped zooplankton of the same volume will yield similar (ensemble average) scattering levels, but generally the shape and orientation distribution of the elongated bodies must be taken into account for accurate predictions. © *1998 Acoustical Society of America.* [S0001-4966(97)01210-1]

PACS numbers: 43.30.Ft, 43.30.Sf, 43.20.Fn [JHM]

LIST OF SYMBOLS

A	area
a	radius of sphere or cylinder
$\bar{a}$	average radius
$b_m^{(s)}$	modal series coefficient for homogeneous fluid sphere
β_{tilt}	tilt angle of infinitessimally thin disk or cross section of body at a particular point on the body axis relative to the incident wave ($\beta_{\text{tilt}} = 0$ corresponds to broadside incidence to the disk axis at a particular point on the axis)
β	L/a
c	sound speed
Δ	distance that the end of the bent cylinder is bent
f	scattering amplitude
f_{bs}	scattering amplitude in backscattering direction
$f^{(\infty)}$	form function for an infinitely long cylinder

$\gamma_\kappa, \gamma_\rho$	material property parameters in DWBA formulation
g	ρ_2/ρ_1
h	c_2/c_1
i	$\sqrt{-1}$ unless used as a summation index or subscript to $\vec{k}$
k	acoustic wave number ($= 2\pi/\lambda$)
$\mathbf{k}_i$	wave number vector of incident field
K	$k \cos \theta$
κ	compressibility
L	length of body
$\bar{L}$	average length of body
λ	acoustic wavelength
$\mu_{p=2}$	phase advance associated with crossing of caustics [$\simeq -(\pi/2)k_1 a/(k_1 a + 0.4)$]
p_{scat}	scattered pressure

P_0	incident pressure
r	distance between scatterer and receiver
ρ_c	radius of curvature of longitudinal axis of uniformly bent cylinder
ρ	mass density
$\mathbf{r}_{pos}$	position vector of axis of deformed cylinder
$\mathbf{r}_v$	position vector of volume
$\mathbf{r}_A$	position vector of area
$\mathscr{R}_{12}$	plane wave/plane interface reflection coefficient (reflection off medium ''2'' due to incident beam in medium ''1'') $[=(\rho_2 c_2/\rho_1 c_1 - 1)/(\rho_2 c_2/\rho_1 c_1 + 1)]$
RTS	reduced target strength
s	$s_L/\bar{L}$
s_θ, s_L	standard deviation of angle of orientation or length, respectively

σ_{bs}	differential backscattering cross section
σ	backscattering cross section
TS	target strength
T_{12}, T_{21}	transmission coefficients for transmission from medium ''1'' to ''2'' or ''2'' to ''1,'' respectively $[T_{ij}=2(\rho_j c_j/\rho_i c_i)/(1+(\rho_j c_j/\rho_i c_i))]$
θ	angle of orientation relative to the direction of the incident acoustic wave ($\theta=0$ corresponds to broadside incidence)
V	total volume of body
v	volume of integration
1,2	subscripts indicating medium ''1'' (surrounding fluid) and medium ''2'' (body medium)
$\langle...\rangle$	average over ensemble of statistically independent samples

(all quantities in mks units)

INTRODUCTION

There has been an evolution of modeling of the scattering of sound by zooplankton in recent years. Up until the mid-1980s, zooplankton had been modeled mathematically almost exclusively as spheres (Greenlaw, 1977, 1979; Johnson, 1977; Holliday and Pieper, 1989; Stanton et al., 1987; and summarized in Holliday and Pieper, 1995). The approaches involving sphere models have seen success as (1) some animals are nearly spherical and (2) the sphere model can be considered to be a ''first-order approximation'' under some conditions for the very complicated scattering process of animals with more complex shape. However, the shape of some animals deviates significantly from that of a sphere and can possess dramatically different scattering properties under certain conditions. For example, euphausiids and shrimp are quite elongated with length-to-width ratios of order 5 or higher. These animals have recently been modeled as finite length cylinders and it has been shown that the scattering properties are dependent upon shape and distribution of orientation angles (Stanton, 1989; Stanton et al., 1993b; Chu et al., 1993; Demer and Martin, 1995) in addition to material properties, size, and acoustic frequency.

Certain important aspects of our understanding of the scattering of sound by finite cylinders are relatively mature. It is therefore timely to perform a systematic comparison between the scattering by cylinders and spheres under a wide range of conditions. Biomass is an important quantity in zooplankton abundance estimation and acoustic scattering levels are quite often expressed in terms of animal biomass. Thus, for zooplankton acoustics applications and for these comparisons, it is important to formulate the scattering in terms of bodies of the same biomass.

In this paper, various sphere and cylinder models from previous publications are reviewed and others are derived herein. All are written in a form so that direct comparisons can be made analytically under certain limiting conditions. Numerical simulations are performed to provide comparison over a broader range of conditions. Dependence of the scattering upon size, shape, orientation distribution, and acoustic frequency are investigated for the various bodies. Given the focus on geometrical factors, the dependence upon bulk material properties of the bodies will receive only minor attention. The work is limited to homogeneous weakly scattering bodies that have smooth boundaries. Direct comparisons are made between bodies of the same volume. (Since the animals have mass densities close to that of water, comparisons based on bodies of the same volume are approximately equivalent to comparisons based on bodies of the same biovolume.) The models are presented in terms of both single realizations of size and orientation as well as averages over angles of orientation (in the case of cylinders) and narrow distributions of size. The average over size is performed to relate to either ''single-sized'' aggregations of zooplankton whose size distribution has a narrow, yet finite width, or a particular size bin of an aggregation with a broader size distribution.

I. MODELS

A. Basic quantities

A fundamental quantity common to all scattering models is the scattering amplitude f which can be defined in terms of the incident and scattered pressures as

$$p_{scat} = P_0 \frac{e^{ik_1 r}}{r} f, \tag{1}$$

where k_1 is the wave number in the surrounding water (medium ''1'').

From this definition, the target strength can be defined as

$$TS = 10 \log|f_{bs}|^2 = 10 \log \sigma_{bs} = 10 \log(\sigma/4\pi), \tag{2}$$

where the target strength is also expressed in terms of the two backscattering cross sections that appear in the literature (Urick, 1983; Clay and Medwin, 1977). Here the scattering amplitude is evaluated for the backscatter direction. The units of target strength are dB relative to 1 m^2. The ''mean target strength'' is based upon the ensemble average of the square of the magnitude of the scattering amplitude:

$$\langle TS \rangle = 10 \log \langle |f_{bs}|^2 \rangle. \tag{3}$$

Sometimes it is convenient to examine the target strength on a dimensionless scale. The "reduced" target strength RTS normalizes the target strength by the square of some outer dimension of the body:

$$\text{RTS}^{(s)} = \text{TS} - 10 \log(\pi a^2) \quad \text{(sphere of radius } a \text{)}, \quad (4)$$

$$\text{RTS}^{(eb)} = \text{TS} - 10 \log(L^2)$$

$$\text{(elongated body of length } L \text{)}. \quad (5)$$

B. General models

There are many approaches to modeling the scattering of sound by objects. The particular approach depends upon the shape and material properties of the body as well as conditions such as frequency range (or more precisely, range of size-to-wavelength ratio). Ideally, one would wish to use an exact model. However, exact solutions to the acoustic wave equation exist only for a small number of shapes, the sphere being one of them. For shapes such as a finite cylinder, an approximate approach is required.

The exact solution for the scattering by a fluid sphere was derived by Anderson (1950) and can be written for the (farfield) backscattering direction as

$$f_{\text{bs}} = \frac{i}{k_1} \sum_{m=0}^{\infty} b_m^{(s)} (-1)^m, \quad (6)$$

where $b_m^{(s)}$ is the modal series coefficient for the fluid sphere and k_1 is the acoustic wave number in the surrounding fluid medium. This equation is exact for all homogeneous materials that do not support a shear wave (gas or liquid). (The above equation is also written in a general enough form to apply to solid elastic spheres and spherical shells, provided the appropriate modal series coefficients are used.)

For more complex shapes for which there is no exact solution to the wave equation, approximate solutions are required to describe the scattering. The distorted wave Born approximation (DWBA) is a useful formulation as it can predict scattering over the entire range of ka and for arbitrarily shaped bodies at any angle of orientation. It is restricted to weakly scattering materials in that the density and speed of sound of the body must be very close (within about 10%) to that of the surrounding medium. Animals like euphausiids fit that requirement as their density and sound speeds are to within several percent of those of the surrounding water. The DWBA is given in general form as (Morse and Ingard, 1968)

$$f_{\text{bs}} = \frac{k_1^2}{4\pi} \int \int \int_v (\gamma_\kappa - \gamma_\rho) e^{i2(\vec{k}_i)_2 \cdot \vec{r}_v} \, dv, \quad (7)$$

where the integration is within the entire body whose volume is described by the position vector $\vec{r}_v$. This formula is the complex conjugate of the one presented in Morse and Ingard and is consistent with the phase shift convention e^{+ikr} for an outgoing scattered wave. Also, in this "distorted wave" formulation, the incident wave number vector in the exponent is evaluated *inside* the body or medium "2" $[(\vec{k}_i)_2]$. This equation is very convenient to perform numerical integrations to check other formulations as well as to be used to

derive analytical expressions for scattering (Chu *et al.*, 1993; Stanton *et al.*, 1993b, 1998). The material properties are described by the terms γ_κ and γ_ρ and are allowed to vary within the body in this formulation. Those parameters can be expressed in terms of the compressibility κ, mass density ρ, density contrast g, and sound speed contrast h as

$$\gamma_\kappa \equiv \frac{\kappa_2 - \kappa_1}{\kappa_1} = \frac{1 - gh^2}{gh^2}, \quad (8)$$

$$\gamma_\rho \equiv \frac{\rho_2 - \rho_1}{\rho_2} = \frac{g-1}{g}, \quad (9)$$

where the relation

$$\kappa = (\rho c^2)^{-1} \quad (10)$$

and the definitions

$$h = \frac{c_2}{c_1}, \quad g = \frac{\rho_2}{\rho_1}, \quad (11)$$

were used (the "1" subscripts refer to the surrounding water and the "2" subscripts refer to the body). For weakly scattering zooplankton where g and h are each approximately several percent above unity (e.g., ~ 1.04), γ_κ and γ_ρ are approximately -0.1 and 0.04, respectively.

For elongated bodies of circular cross section and uniform material properties within any given cross-sectional slice, two of the integrations can be performed analytically, leaving a one-dimensional integral:

$$f_{\text{bs}} = \frac{k_1}{4} \int_{\mathbf{r}_{\text{pos}}} a(\gamma_\kappa - \gamma_\rho)$$

$$\times e^{2i(\mathbf{k}_i)_2 \cdot \mathbf{r}_{\text{pos}}} \frac{J_1(2k_2 a \cos \beta_{\text{tilt}})}{\cos \beta_{\text{tilt}}} |d\mathbf{r}_{\text{pos}}|, \quad (12)$$

where J_1 is the Bessel function of the first kind of order one and the integral is along the axis of the body whose position is described by $\mathbf{r}_{\text{pos}}$ (Stanton *et al.*, 1998). This formulation describes the scattering by deformed finite length cylinders in which the radius of each circular cross section as well as the material properties are allowed to vary with position along the lengthwise axis. The axis of the body is allowed to bend. This formulation is valid for all ka and all angles of orientation, but restricted to weakly scattering materials.

A formulation that is very convenient to use in the geometric scattering region is the Kirchhoff or geometric optics integral (Born and Wolf, 1991; Gaunaurd, 1985). This surface integral is given by

$$f_{\text{bs}} = \frac{ik_1}{2\pi} \mathscr{R}_{12} \int \int_A (\hat{k}_i)_1 \cdot \hat{n}_A e^{i2(\mathbf{k}_i)_1 \cdot \mathbf{r}_A} \, dA, \quad (13)$$

where the integral is over the surface described by $\mathbf{r}_A$. $(\mathbf{k}_i)_1$ is the incident wave number vector evaluated in medium 1. The "^" indicates a unit vector and $\hat{n}_A$ is the outward normal unit vector to the surface. The plane wave/plane interface reflection coefficient $\mathscr{R}_{12}$ is used in the Kirchhoff approximation that led to this formula and takes into account the penetrability of the material by the following (Clay and Medwin, 1977; Ogilvy, 1991):

$$\mathscr{R}_{12} = \frac{gh-1}{gh+1}. \tag{14}$$

Holding the reflection coefficient fixed during the integration is an approximation as it will, in general, vary with angle of incidence.

Finally, another formulation describing the scattering of sound by deformed cylinders is given by the following line integral (Stanton, 1989, 1992):

$$f_{bs} = \frac{-i}{2\sqrt{\pi}} e^{i\pi/4} \int_{\mathbf{r}_{pos}} f_{bs}^{(\infty)}$$

$$\times (k_1 a \cos \beta_{tilt})^{1/2} e^{i2(\mathbf{k}_i)_1 \cdot \mathbf{r}_{pos}} |d\mathbf{r}_{pos}|, \tag{15}$$

where the form function $f^{(\infty)}$ for an infinitely long cylinder is used in the integrand. The term $\vec{r}_{pos}$ is the position vector for the axis. This approximate formulation is valid for all ka and for any material property profile (e.g., fluid, solid elastic, fluid-filled shell, etc.) that is symmetrical about the axis in any given cross-sectional slice. The formulation is only valid for angles near broadside incidence (within about 15° of broadside for straight cylinders and a wider range for bent cylinders) and for high ratios of length to width (length/width$\gtrsim$5). For a study on the range of accuracies of this model, see Partridge and Smith (1995). Hence two deformed cylinder formulations are provided above. One based on the DWBA weak scattering theory [Eq. (12)] that is valid for all angles of orientation, but is only useful for weakly scattering materials. The other is based upon infinite cylinder form functions [Eq. (15)] and is applicable to a wide range of material properties, but is limited in its usefulness with respect to angle of orientation.

C. Arbitrarily shaped bodies—$kd \ll 1$

For weakly scattering bodies of any shape and with all dimensions of the body much smaller than the acoustic wavelength (or more precisely, $kd \ll 1$, where d is the greatest outer dimension of the body such as length), the scattering can quite readily be calculated with the DWBA approach:

$$f_{bs} = \frac{k_1^2}{4\pi} (\gamma_\kappa - \gamma_\rho) V. \tag{16}$$

In this Rayleigh scattering limit, the scattering amplitude is shown to depend upon the product of the square of the wave number and volume, V, of the body. The integral in the general DWBA integral [Eq. (7)] was performed quite readily as the exponent in the integrand was negligibly small and the integral reduced to integrating a constant value (assuming that the material properties were constant inside the body) over the volume. The scattering does not depend upon angle of orientation which is what one would expect in this long wavelength limit. An average of the square of the magnitude of the scattering amplitude over angle of orientation and a distribution of sizes gives, quite trivially,

$$\langle |f_{bs}|^2 \rangle = \frac{k_1^4}{16\pi^2} (\gamma_\kappa - \gamma_\rho)^2 \langle V^2 \rangle. \tag{17}$$

These formulas are convenient for making calculations of the scattering by complex weakly scattering bodies in the long wavelength limit, especially when there is no exact solution for the body of interest. Because of the long wavelength restriction, the usefulness is limited. For objects resembling spheres, the equations are valid for $ka \lesssim 0.5$, where a is the equivalent spherical radius. While the scattering levels for spheres are small in this region, they might be detectable. However, for objects that are very elongated such as euphausiids, the usefulness of the equations is more limited than for spheres because of the condition $kL \lesssim 1.0$. For elongated bodies with ratios of L/a of the order 5 or greater, this (kL) condition results in the equations being valid only for $ka \lesssim 0.2$, where a is the cylindrical radius. In the $ka < 0.2$ region, the scattered levels might not be detectable by an echosounder (especially when individuals rather than dense aggregations are involved), hence a more complex approach with fewer approximations needs to be used in calculating the scattering by elongated bodies in the detectable region.

D. Sphere-single realizations

For spheres in the $ka \ll 1$ or Rayleigh scattering region, the exact modal series solution can easily be used to predict scattering levels by taking the low ka limit in the modal series terms. In the low ka limit, the first two modes of vibration ($m=0$ monopole term and $m=1$ dipolelike term) are of the same order of ka and dominate the remaining terms of the series. Keeping only those terms gives the following commonly used expression:

$$f_{bs} = a(k_1 a)^2 \alpha_{\pi s}, \quad k_1 a \ll 1, \tag{18}$$

where

$$\alpha_{\pi s} \equiv \frac{1 - gh^2}{3gh^2} + \frac{1-g}{1+2g}. \tag{19}$$

This equation shows that the scattering is a function of a product of the square of the wave number and the cube of the radius (Anderson, 1950). This limiting expression can be compared directly with the DWBA result given in Eq. (16) by writing a in terms of the volume of the body and substituting equivalent expressions for γ_κ and γ_ρ given in Eqs. (8) and (9) into the DWBA result. The comparison shows that the two approaches produce nearly identical results with the only difference being in the material property term: the denominator $1+2g$ in the modal-series-based solution is replaced by the term $3g$ in the DWBA expression (this comparison is made with a factor of $\frac{1}{3}$ moved from outside to inside the parentheses in the DWBA expression for direct comparison). For weakly scattering bodies, g is to within several percent of unity making $1+2g \approx 3g \approx 3$.

In the region in which ka is of the order unity or greater, the modal series solution requires more terms to converge and it becomes cumbersome to deal with analytically. Certainly, the solution can be programmed into a computer for numerical results. However, making use of the modal series for analytical means is tedious. One approach to circumvent this problem involves applying the (approximate) Kirchhoff integral in which the scattered field is estimated by summing contributions from the front and back interface of the body in

the $ka \gg 1$ region. Using the Kirchhoff integral given above, the backscattering by a weakly scattering sphere is approximately

$$f_{bs} = \tfrac{1}{2} a \mathscr{R}_{12} e^{-i2k_1 a} (1 + T_{12} T_{21} e^{i4k_2 a}), \tag{20}$$

where the transmission coefficients due to the passing of the wave through the front interface (first into the body, then back out of the body) are given as

$$T_{12} = \frac{2gh}{1+gh} \simeq 1, \quad T_{21} = \frac{2}{1+gh} \simeq 1. \tag{21}$$

The reflection coefficient from the back interface is simply equal to the negative of the one from the front interface and a simple substitution for it in terms of $\mathscr{R}_{12}$ was made.

Here the integral was performed by dividing the integral into two parts, one over the front interface where the Kirchhoff expression was used directly and the other over the back interface where the expression was multiplied by the product $T_{12} T_{21}$ to account for the fact that the wave experiences a slight loss of signal when traveling through an interface. The normal to the surface in each integral is aimed in the general direction of the sound source (i.e., it is the outward normal for the front interface and inward normal for the back interface). The resultant equation [Eq. (20)] shows contributions from both interfaces where the first term (''1'') in the parentheses corresponds to the contribution from the front interface and the second term is due to the back interface. The phase shift difference between the echoes from the front and back interfaces is clear in the second term. This phase difference will give rise to interferences between the echoes from the two interfaces. The interference will be constructive or destructive, depending upon the value of ka.

E. Sphere—Average echoes

Since the scattering by spheres does not depend upon the angle of orientation of the sphere, the average over angle of orientation is trivial. Averaging the square of the magnitude of the backscattering amplitude in the $ka \ll 1$ region [Eq. (18)] over a range of sizes is quite simply

$$\langle |f_{bs}|^2 \rangle_a \simeq k_1^4 \langle a^6 \rangle_a \alpha_{\pi s}^2, \quad k_1 a \ll 1. \tag{22}$$

The bracket $\langle \cdots \rangle_a$ denotes the average over a distribution of a. For the $ka \gg 1$ region, the average over a narrow Gaussian distribution of sizes using Eq. (20) is

$$\langle |f_{bs}|^2 \rangle_a \simeq \tfrac{1}{2} \bar{a}^2 \mathscr{R}_{12}^2 [1 + e^{-8(k_2 \bar{a} s)^2} \cos(4k_2 \bar{a})], \quad k_1 a \gg 1 \tag{23}$$

$$\simeq \tfrac{1}{2} \bar{a}^2 \mathscr{R}_{12}^2, \tag{24}$$

where $T_{12} \simeq T_{21} \simeq 1$ was used.

This average shows that the oscillatory effect due to the interference between the two interfaces becomes exponentially small for high ka. In the high ka limit, the average backscattering energy is simply equal to the sum of the energy from each interface (the square of the magnitude of the backscattering amplitude from each interface is equal to $\tfrac{1}{4} \bar{a}^2 \mathscr{R}_{12}^2$).

F. Cylinders—Single realizations

For the backscattering by straight cylinders in the $ka \ll 1$ region, the deformed cylinder formulation has been used to produce the following equation (Stanton, 1988, 1989):

$$f_{bs} \simeq \tfrac{1}{2} (K_1 a)^2 L \alpha_{\pi c} D_{SC}(\theta), \quad \text{straight cylinder}, \ k_1 a \ll 1, \tag{25}$$

where the directivity function is given as

$$D_{SC}(\theta) = \frac{\sin(k_1 L \sin \theta)}{k_1 L \sin \theta} \tag{26}$$

and the material property term is

$$\alpha_{\pi c} = \frac{1 - gh^2}{2gh^2} + \frac{1 - g}{1 + g}. \tag{27}$$

Here, the modal-series-based form function of the infinitely long fluid cylinder was used in the calculations. By the nature of this approximation, the result is only valid for near broadside incidence. Calculations for near end-on incidence would depend strongly upon the particular shape of end (flat, pointed, rounded, etc.). It has been convenient to approximate the directivity function in Eq. (26) in terms of a Gaussian function as (Stanton et al., 1993b)

$$D_{SC} \simeq e^{-\alpha_{SC}(k_1 L)^2 \theta^2}, \quad \alpha_{SC} \simeq 0.2. \tag{28}$$

The empirical directivity parameter α_{SC} should not be confused with the material property parameters $\alpha_{\pi s}$ and $\alpha_{\pi c}$. With this expression, averages over orientation can easily be made as shown in a later section (Stanton et al., 1993b).

The same modal-series-based deformed cylinder formulation has also been used to estimate the scattering by bent cylinders. The resultant formula for low ka is derived from Stanton (1989) and Stanton et al. (1993b) as

$$f_{bs} \simeq \frac{1}{2\sqrt{2}} (\rho_c \lambda)^{1/2} (k_1 a)^2 \alpha_{\pi c} D_{BC}(\theta) e^{i\pi/4},$$

$$\text{bent cylinder}, \ k_1 a \ll 1, \ 2k_1 \Delta \gg 1, \tag{29}$$

where the directivity function,

$$D_{BC}(\theta) \simeq e^{-\alpha_{BC}(2\theta \rho_c / L)^2}, \quad \alpha_{BC} \simeq 0.8, \tag{30}$$

has been added heuristically to include effects due to orientation (Stanton et al., 1993b) ($\theta = 0$ corresponds to the case of ''broadside'' incidence where the cylinder is bent symmetrically away from the transducer). The empirical directivity parameter α_{BC} should not be confused with the material property parameters $\alpha_{\pi s}$ and $\alpha_{\pi c}$. Here Δ is the distance that the end of the cylinder is bent ($\Delta = 0$ for a straight cylinder). This directivity function is based upon a reasonable estimate of the angle beyond which the scattering decreases dramatically with angle. However, it does not provide accurate estimates of the scattering for near end-on incidence, which, as discussed in the above straight cylinder case, depends strongly upon the particular shape of the end. The function is convenient for averages over orientation as discussed in a later section.

In the $ka \gg 1$ case, the modal-series-based approach becomes difficult to manipulate algebraically because of the

fact that it takes many terms for the series to converge. Several approaches can be used in this case—the DWBA, Kirchhoff, or form-function-based deformed cylinder solution. In a recent study, a ray-based (form function) deformed cylinder formulation was used to produce the following equation for the straight cylinder and $ka \gtrsim 0.1$ (Stanton et $al.$, 1993a, 1993b):

$$f_{bs} = \frac{-i}{2\sqrt{\pi}} e^{i\pi/4} e^{-i2k_1 a} L \sqrt{k_1 a} . \mathcal{R}_{12} D_{SC}(\theta) I_0,$$

$$k_1 a \gtrsim 0.1, \qquad (31)$$

where

$$I_0 = 1 - T_{12} T_{21} e^{i4k_2 a} e^{i\mu_{p=2}(k_1 a)} \qquad (32)$$

and

$$\mu_{p=2}(k_1 a) = -(\pi/2) k_1 a / (k_1 a + 0.4). \qquad (33)$$

The term $\mu_{p=2}(k_1 a)$ was added heuristically to remove certain phase effects so that the formula, normally valid only for $ka \gg 1$, could be applied to values of ka down to about 0.1. In this formulation, a ray-based form function for the infinitely long fluid cylinder as presented in Marston (1992) was incorporated into the deformed cylinder formulation. Equation (31) is broadly similar to that of the sphere for $ka \gg 1$ in that two terms appear, one corresponding to the echo from the front interface of the body and the other due to the back interface. They differ greatly due to the dependence of the scattering by the cylinder upon ka and orientation.

For the uniformly bent cylinder, the same ray-based deformed cylinder formulation as described above is applied to the bent cylinder geometry (Stanton et $al.$, 1993a, 1993b). The result of that analysis is

$$f_{bs} = \tfrac{1}{2} (\rho_c a)^{1/2} \mathcal{R}_{12} e^{-i2k_1 a} D_{BC}(\theta) I_0, \qquad (34)$$

where the directivity term has the same limitations as in the $ka \ll 1$ case.

G. Cylinders—average echoes

Averaging the square of the magnitude of the backscattering amplitude over angle of orientation takes advantage of the Gaussian form of the above-mentioned directivity functions. Averaging over both angle of orientation and a narrow Gaussian distribution of size results in the following set of expressions:

$$\langle |f_{bs}|^2 \rangle_{L,\theta} = A_{ij} \pi (k_1 \bar{a})^3 \bar{a} \bar{L} \alpha_{\pi c}^2, \quad k_1 a \ll 1, \ k_1 L \gtrsim 1, \qquad (35)$$

$$\langle |f_{bs}|^2 \rangle_{L,\theta} = 2 A_{ij} \mathcal{R}_{12}^2 \bar{a} \bar{L} [1 - e^{-8(k_2 \bar{a} s)^2}$$

$$\times \cos(4k_2 \bar{a} + \mu_{p=2})], \quad k_1 a \gtrsim 0.1, \qquad (36)$$

$$\langle |f_{bs}|^2 \rangle_{L,\theta} \simeq 2 A_{ij} \mathcal{R}_{12}^2 \bar{a} \bar{L}, \quad k_1 a \gg 1, \qquad (37)$$

where the term A_{ij} takes on different values for different combinations of shapes and orientation conditions (straight/bent cylinder, Gaussian/uniformly distributed orientation angle). Because Eq. (36) involves an extension into the $ka < 1$ region, there is overlap in the frequency regions in which Eqs. (35) and (36) can be used. Equation (36) is from

Stanton et $al.$ (1993b). Equation (35) was derived here in the same manner as Eq. (36). Since A_{ij} was verified numerically down to about $ka = 0.1$ in Stanton et $al.$ (1993b), the same A_{ij} are used in both Eqs. (35) and (36). For the case of bent cylinders with a Gaussian distributed orientation angle, $A_{ij} = T_B^2 C_B^2 \mathbf{S}_\theta / (16 \sqrt{\alpha_B} s_\theta)$. A_{ij} for other cases are given in Table I of Stanton (1993b). C_B is an empirical parameter and is approximately equal to 1.2 while T_B in this case is equal to unity. $\mathbf{S}_\theta$ is a complex function of the width of the main lobe of the scatter pattern and orientation distribution parameters (Stanton et $al.$, 1993b). For orientation distributions that are wide enough so that the entire main lobe is ''seen'' by the receiver over the course of the averaging, then $\mathbf{S}_\theta \sim 1$. The approximation $T_{12} \simeq T_{21} \simeq 1$ was used in Eq. (36).

Each formula involving a Gaussian distribution of orientation angles assumes that the bell part of the Gaussian distribution contains the broadside angle. It is this assumption that allows use of the Gaussian form of the directivity function. If the broadside angle is part of the averages, then the resultant levels near broadside will dominate the small near-end-on levels. Hence, errors in the end-on levels are not significant in this case. Various numerical simulations involving the more precise DWBA approach support this assumption (Stanton et $al.$, 1993b).

H. Average scattering by targets of equal volume

Some of the above formulas for averaged echoes are now reformulated so that they can be compared with each other. As discussed above, an important quantity in zooplankton studies is biomass, which is directly proportional to the volume of the animal. The scattering formulas are therefore reformulated in terms of the volume of the body.

For arbitrarily shaped objects in the low-frequency region, Eq. (17), which describes the average square of the magnitude of the backscattering amplitude (or average backscattering cross section), can be used directly from the above analysis without modification. The formula is valid for weakly scattering bodies where the wavelength is much longer than any dimension of the body (or more precisely, $kd \ll 1$).

At moderately low frequencies where $ka \ll 1$ but $kL \gtrsim 1$ for cylinders, Eq. (17) does not apply (although it is still valid for spheres). In the moderately low-frequency case for cylinders [Eq. (35)], the relationship for volume $V = \pi a^2 L$ is used along with $\beta = L/a$ to obtain the following formula:

$$\langle |f_{bs}|^2 \rangle = \left(\frac{A_{ij} \alpha_{\pi c}^2}{(\pi \beta)^{2/3}} \right) k_1^3 V^{5/3},$$

$$\text{all cylinders,} \quad k_1 a \ll 1, \ k_1 L \gtrsim 1, \qquad (38)$$

where now the average backscattering levels from cylinders depend upon the product of $k^3 V^{5/3}$. For an object with $L/a = 10$, these moderately low frequencies are in the range $0.1 \lesssim ka \lesssim 0.5$. As with Eq. (35), this equation is restricted to the cases in which the main lobe of the scattering pattern faces the receiver during part of the averaging.

		Cylinders straight and bent $\langle |f_{bs}|^2 \rangle_{L,\theta}$ $(0 \le \theta \le 2\pi)$	Sphere $\langle |f_{bs}|^2 \rangle_a$
$ka \ll 1$	$kL \ll 1$	$k^4 V^2$	$k^4 V^2$
	$kL \gtrsim 1$	$k^3 V^{5/3}$	
$ka \gg 1$	$kL \gg 1$	$V^{2/3}$	$V^{2/3}$

In the high-frequency region where $ka \gg 1$ (kL is, of course, much greater than unity in this region also), the corresponding average echo formulas are reformulated in terms of the volume of the body to obtain

$$\langle |f_{bs}|^2 \rangle_a \simeq \frac{1}{2} \left(\frac{3}{4\pi} \right)^{2/3} \mathscr{R}_{12}^2 V^{2/3}, \quad \text{sphere,} \quad k_1 a \gg 1, \quad (39)$$

$$\simeq 0.19 \mathscr{R}_{12}^2 V^{2/3} \quad (40)$$

and

$$\langle |f_{bs}|^2 \rangle_{a,\theta} \simeq \frac{2}{\pi^{2/3}} A_{ij} \beta^{1/3} \mathscr{R}_{12}^2 V^{2/3},$$

all cylinders, $ka \gg l$, (41a)

$$\simeq \frac{T_B^2 C_B^2 S_\theta}{8\sqrt{\alpha_B} \pi^{2/3}} \frac{\beta^{1/3}}{s_\theta} \mathscr{R}_{12}^2 V^{2/3},$$

bent cylinder, Gaussian distributed $\theta, ka \gg 1$, (41b)

$$\simeq 0.094 \frac{\beta^{1/3}}{s_\theta} \mathscr{R}_{12}^2 V^{2/3}, \quad (41c)$$

where the same orientation restrictions apply to Eqs. (41a)–(41c) as for Eqs. (35)–(37). Equations (39) and (40) were based on an average of Eq. (24); Eq. (41a) was based on an average of Eq. (37); Eq. (41b) used an A_{ij} element from Table I of Stanton et al. (1993b); and $T_B = 1$, $\alpha_B = 0.8$, $C_B = 1.2$, and $S_\theta \sim 1$ were used for Eq. (41c) and were taken from Stanton et al. (1993b).

For the case of euphausiids where $\beta \approx 16$ and $s_\theta = 0.349$ rad (20°), Eq. (41c) can be further reduced to

$$\langle |f_{bs}|^2 \rangle_{a,\theta} \simeq 0.68 \mathscr{R}_{12}^2 V^{2/3},$$

euphausiid, $\pm 20°$ motion, $ka \gg 1$. (42)

The motion is distributed about an arbitrary mean angle provided that the main lobe of the scatter pattern is "seen" by the transceiver within the range of motion. As can be seen in the above equations in Secs. IC–H, while the formulas for single-realization broadside echoes from the various cylinders and spheres depart from each other (except at very low frequency where shape is not a factor), the averaged echoes are functionally very similar under certain conditions (Table
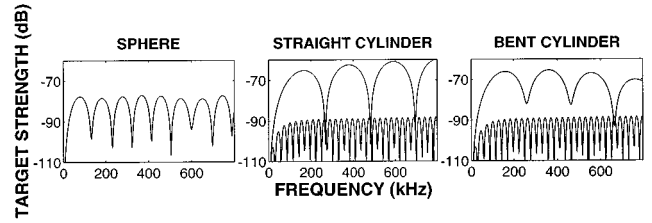
FIG. 1. Theoretical target strength versus frequency for one ping each off of an individual sphere, straight cylinder, and bent cylinder. All bodies have the same volume of 0.30 cm³, which corresponds to a 34-mm-long euphausiid. The upper curves in the cylinder plots are for broadside incidence and the lower plots are for end-on incidence. The acoustic or "reduced" length of the animal is 29 mm, the cylindrical radius is 1.82 mm for the cylinder model, and the equivalent spherical radius is 4.16 mm for the sphere model. The length is reduced to account for the fact that the 5-mm telson or "tail-section" of the animal is thin and probably does not scatter much sound. The exact modal-series solution was used for the sphere case [Eq. (6)] and the DWBA method was used for both cylinders [Eq. (12)]. For all plots, $g = 1.0357$ and $h = 1.0279$ [these values were taken from Foote et al. (1990) and Foote (1990), respectively, as they were measured directly from live euphausiids]. For the bent cylinder $\rho_c/L = 3.0$ (this value for curvature is chosen as it is a reasonable representation of the degree of bend for a fully extended euphausiid). All objects have a smooth boundary and homogeneous material properties.

I). There are significant deviations in scattering levels in the moderately low-frequency case and high-frequency case for certain ranges of orientation distribution.

II. NUMERICAL EXAMPLES

A. Bodies of fixed volume and material properties

Numerical evaluation of some of the general solutions allows examination of the scattering properties over a wide range of conditions. The exact modal series solution for the fluid sphere and the DWBA integral are used in numerical calculations of backscattering by fluid spheres and straight and uniformly bent cylinders, respectively (Figs. 1–3). All bodies have smooth boundaries and homogeneous material properties. Calculations involving the cylinders were done for fixed angle of orientation (Fig. 1) and distributions of orientation angle (Figs. 2 and 3). The mean angles of 20° and 45° and standard deviations of 20° in Fig. 2 were chosen to represent swimming krill insonified by a downward looking echo sounder (Kils, 1981; Endo, 1993; Miyashita et al., 1996). The mean angle of 90° was chosen to represent certain elongated animals that would be swimming toward or away from a downward looking sounder such as during diurnal migration. The uniform distribution of angles represents the case in which the sounder is looking sideways and there is no preferred swimming direction in the horizontal plane. Since volume (or biomass) of zooplankton is of particular interest, the volume of each object (spheres and cylinders) is held fixed at 0.30 cm³ as other parameters such as frequency are varied. This volume corresponds to a 34-mm-long euphausiid (a shrimplike animal) whose length-to-width ratio is about 8. The material properties, density and sound speed contrast, were also chosen to resemble those of a euphausiid. The radius of the sphere is considered the "equivalent spherical radius" of the animal.
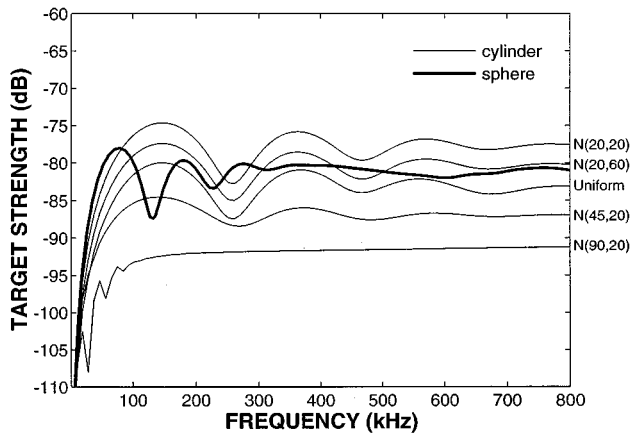
FIG. 2. Average theoretical target strength versus frequency for scattering by statistical ensemble of spheres and bent cylinders. The target strength was averaged on a linear scale as described in Eq. (3) for the models used in Fig. 1. The scattering by all bodies is averaged over a narrow Gaussian distribution of sizes (s.d. of Gaussian is 10% of mean body length or diameter, averaging is done over the range, mean size ± 2 s.d.). In addition, the cylinders are also averaged over various normal distributions $[N(\bar{\theta}, \text{ s.d. of } \theta)]$ of angle of orientation and over a uniform $[0, 2\pi]$ distribution in one case. $\theta = 0°$ corresponds to broadside incidence and N(90°, 20°) is a distribution centered about end-on incidence. The models, body dimensions, and values of g, h, and ρ_c /L are the same as in Fig. 1. Units of all angles in figure are in degrees.

In general, the overall levels of the scattering by the cylinders depend upon the distribution of orientation angle, especially at the higher frequencies (Fig. 2). Some distributions will produce scattering levels close to that of the sphere, while others will cause it to deviate significantly (of the order 3–10 dB). At the very low frequencies, all models converge to the same levels.

The scattering properties of all objects under investigation are characterized by a Rayleigh scattering region ($ka \ll 1$, where a is either the spherical or cylindrical radius of the body). Also, each object possesses a geometric scattering
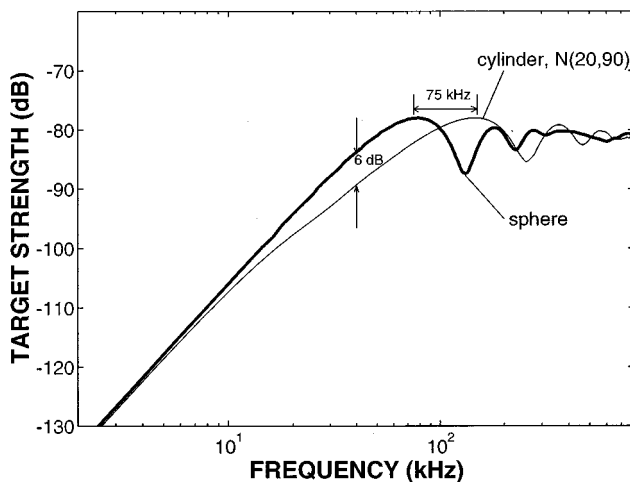
FIG. 3. Comparison between average theoretical target strength of sphere and bent cylinder under conditions where the predictions were close to each other at high frequencies. Averaging performed over narrow Gaussian distribution of sizes for both the sphere and cylinder (as described in Fig. 2) and angle of orientation (cylinder only). The models, body dimensions, and values of g, h, and ρ_c /L are the same as in Fig. 1.

region ($ka \gg 1$). Although the transition or "turning" point at which the scattering changes from Rayleigh to geometric occurs at $ka \approx 1$ for both spheres and cylinders at broadside incidence, the point occurs at different frequencies for those bodies once the volume is held constant (the "a" is different for the sphere and cylinders). For example, for bodies of the same volume of 0.30 cm^3, the point occurs at about 75 kHz for the sphere and at about 150 kHz for the cylinders whose orientation is at broadside incidence or includes broadside in the averages (Fig. 3). The turning point for end-on cylinders is at a lower frequency than for the cylinders at broadside incidence.

In addition, the target strength versus frequency pattern for each object possesses an oscillatory pattern in the geometric scattering region. These oscillations are especially pronounced when only single echoes are examined (Fig. 1). An interesting trend occurs in the geometric region of the straight cylinder at broadside incidence where the trend of scattering increases with frequency.

The levels of the backscattering for end-on incidence are markedly lower for these elongated bodies than for the broadside cases (Fig. 1). The level of the scattering in this case is strongly dependent upon the shape of the end of the body [rounded in this case according to the equation $a(z) = a_0 \sqrt{(1 - (2z/L)^{10})}$, where z is the position along the axis ($z = 0$ is the center of the body and $z = \pm L/2$ at the ends) and $a_0 = a(0)$ is the (maximum) radius at the middle of the tapered body.] Note also that boundary roughness and material heterogeneities also strongly influence backscattering for end-on incidence (Stanton *et al.*, 1998).

Once the echoes are averaged over a range of orientations and sizes, some of the differences between the scattering by the sphere and cylinders tend to diminish (Figs. 2 and 3). For example, for distributions of orientation that include broadside incidence in the bell part of the distribution, the average backscattering by all bodies at high frequencies ($ka \gg 1$ or frequencies much greater than 150 kHz in this example) tends to be nearly constant with respect to frequency and within about a 10-dB range of values [Fig. 2 and other calculations, such as N(0°,20°), not shown]. Average scattering levels for straight cylinders have been shown to be quite similar to those of bent cylinders over a wide range of conditions (due to conservation of energy) and are not shown in this paper (Stanton *et al.*, 1993b).

B. Bodies with other volumes and/or material properties

For bodies with different volumes and/or material properties, predictions (not shown) are broadly similar in form (but with different magnitudes) to those given in Figs. 1–3. For example, for an animal $\frac{1}{10}$ the length of the 34-mm-long one simulated in the figures (and $\frac{1}{10}$ the width, correspondingly), all curves would shift down uniformly by 20 dB and to the right by one decade of frequency. This uniform shift comes about by the fact that the square of the diameter (sphere) or square of the length (cylinder) can be factored out of each prediction of backscattering cross section. Furthermore, the predictions can be expressed in terms of the dimensionless product ka. As a result, predictions are quite often presented in terms of *reduced* target strength (i.e., nor-

malized by the square of a dimension) versus ka (Stanton, 1988, 1989). The RTS plots are valid only when the absorption of sound within the bodies is negligible (absorption does not scale according to wavelength and body size). It is also particularly useful when the ratios of length-to-width and length-to-radius-of-curvature of the lengthwise axis of the elongated bodies remain fixed for a given RTS plot. The last set of conditions is a restriction of self-similarity of the object shape which is reasonable for marine organisms.

For weakly scattering bodies of different material properties, the changes are related to differences between the material properties (or their products) and unity [e.g., Eqs. (7)–(9) of this paper; Anderson, 1950; Greenlaw, 1977]. Repeating scattering calculations in this paper for different density and sound speed contrasts (g and h, respectively), the levels increase by about 10 dB when $(g,h)=(1.1,1.1)$ and decrease by about 10 dB for $(g,h)=(1.01,1.01)$ when compared with calculations in this paper which used $(g,h)=(1.0357,1.0279)$. The locations of the peaks and dips in the TS versus frequency plots shifted horizontally (somewhat) as the material properties were varied.

III. DISCUSSION

The similarities and differences between the various scattering predictions can be explained in terms of basic scattering principles.

In the very-low-frequency case in which all dimensions of the bodies are much smaller than a wavelength, the models show that the scattering levels for the sphere, straight cylinder, and bent cylinder are the same. This is due to the fact that in this very-low-frequency region, the phase of the echo from each part of the body is the same, regardless of position within the body. The scattered levels then depend only upon the volume of the body, regardless of the shape.

In the case of moderately low frequencies (i.e., $ka \ll 1$ and $kL \gtrsim 1$), the length of the cylinders plays a role. Because of phase variabilities of the echoes along the length of the elongated bodies, the scattering becomes dependent upon shape and orientation of the cylinders. This dependence occurs in spite of the fact that $ka \ll 1$ where the scattering is in the Rayleigh region with respect to the radius of the body. Here, the phase variabilities are small across any given cross-sectional slice of the bodies. However, for the bent cylinder, the phase will vary along the length of the body, regardless of orientation. Furthermore, for orientations of the straight cylinder away from broadside incidence, the phase will vary along the length of that body as well.

The transition or ''turning point'' from Rayleigh to geometric scattering is different for spheres versus cylinders having the same volume. For broadside incidence or averages over a wide range of angles of orientation, it depends upon the cross-sectional radius of the body. For bodies of constant volume, the radius of the spherical body is about two times bigger than the (cylindrical) radius of the cylinder whose length to (cylindrical) radius is 16 (i.e., for euphausiids). For end-on incidence, the turning point of the cylinders depends upon the length which, in this case, is much greater than the radius of the sphere of the same volume.

In the geometric scattering region, the phase varies within each cross-sectional slice of each body (sphere and cylinders) as well as along the length of the elongated bodies (except for the straight cylinder at broadside incidence). The complex phase variabilities give rise to both an oscillatory pattern in the target strength versus frequency plots as well as a trend in that pattern that depends upon shape. The oscillatory pattern is due to the fact that there is more than one echo coming from the body. A small fraction of the energy of the incident acoustic signal will reflect off an interface facing the acoustic source. However, since this is a weakly scattering body, most of the incident acoustic signal passes into the body relatively unaffected. The internal acoustic signal will then reflect off of an interface that is facing away from the sound source and reflect back toward the source. These two echoes will interfere constructively or destructively according to the value of the separation of the faces with respect to the wavelength of the sound. For a sphere, the two faces are simply the front and back interface of the body, regardless of orientation. For each type of cylinder at broadside incidence, the interferences correspond to echoes from the front and back portions of the body cross section, while for end-on incidence the echoes from these extended bodies come from the front and back ends of the bodies. The period of oscillation of the target strength versus frequency curves is related to the radius of the sphere and cylindrical radius of the cylinders at broadside incidence, while it is related to the length of the cylinders at end-on incidence.

The trend of the oscillations depends upon whether or not the object is curved in one or two dimensions. For spheres and bent cylinders at broadside incidence, the trend is constant with respect to frequency. This is related to the fact that both are curved in two dimensions. However, for the straight cylinder at broadside incidence, the trend increases with frequency (actually ka) because of the fact that this cylinder is curved only in one dimension. This effect is related to the fact that the size of the cylinder remains much smaller than the first Fresnel zone in these (finite cylinder) calculations (Stanton, 1988). Once the frequencies are high enough or the range to the target small enough, then many Fresnel zones occupy the cylinder and the cylinder appears acoustically like an infinitely long cylinder (DiPerna and Stanton, 1991). The trend in this latter case levels off as with the other bodies (not shown). For end-on incidence, the scattering is due to the rounded ends of the cylinders and the trend is constant, but at a lower level since the cross section of the ends is relatively small.

Once the scattering is averaged over angle of orientation, some of the differences between the scattering by the sphere and cylinders tend to diminish. This is due to the directional nature of the scattering by the cylinders: for a single orientation, a substantial portion of the scattered signals from a cylinder may or may not be in the direction back toward the receiver. However, once averaged over all angles of orientation, the orientations where substantial backscattered energy occurs become part of the average, hence reducing the differences between the average scattering by the different bodies. For example, at broadside incidence, the scattering by a straight cylinder may be stronger than that of

the bent cylinder at broadside incidence. For orientations away from broadside incidence, the scattered signal from the straight cylinder will diminish much more rapidly than that from the bent cylinder because the width of the main lobe of the scatter pattern of the straight cylinder is narrower than that of the bent cylinder of the same length. Hence, the straight cylinder has a stronger but narrower main lobe compared with that of the bent cylinder. The average over all angles gives nearly the same value for each type of cylinder, indicating that the change in shape of the main lobes offsets the differences in overall levels within the main lobes. This phenomenon, in essence, is related to the principle of conservation of energy (Stanton et al., 1993b). [Of course, averaging over narrower distributions can sometimes result in differences as well, as illustrated, for example, in Figs. 2 and 3 of this paper, Stanton et al. (1993b), and Demer and Martin (1995).]

Another effect in the averaging over size and angle of orientation involves the smoothing out of the oscillatory pattern of target strength versus frequency. For the sphere, this effect of smoothing out is due solely to the fact that the positions of the nulls and peaks of the pattern are related to the radius of the body. The pattern is slightly different from realization to realization in the averaging over sizes, and hence the null value of one realization will be averaged with higher values from other realizations, which will tend to fill in the nulls. The nulls become increasingly affected for high frequencies as a given change in size will be larger with respect to wavelength at the higher frequencies.

For the cylinders, the pattern of target strength versus frequency is dependent upon both size (as with the sphere) as well as orientation. Consequently, averages over both size and orientation cause reduced structure in the pattern. However, because of the fact that the backscattering values at broadside incidence are much greater than those at end-on, the pattern near broadside incidence will tend to dominate the scattering. Still, the average over sizes affects the pattern as much as with the sphere.

While the averaging reduces differences between the scattering by the bodies of various shapes, the scattering still depends upon the particular distribution of orientation of the bodies. For averages over the distribution of angles of orientation $N(20°,90°)$ for the cylinders, the scattering levels were similar for the cylinders and spheres in the geometric region (Fig. 3). For other distributions, the averages were sometimes quite different, especially when the mean angle of orientation of the cylinders was well away from broadside incidence (Fig. 2). For distributions of $N(20°,20°)$, $N(20°,60°)$, and uniform $(0–2\pi)$, the scattering is within several dB of that of the sphere at high frequencies (Fig. 2).

IV. FIELD IMPLICATIONS

The results show that for high enough acoustic frequencies and certain distributions of angle of orientation, interpretation of surveys of elongated animals is relatively insensitive to the choice of model shape (i.e., sphere versus cylinder). However, for lower frequencies or other behavioral conditions, the animal shape and orientation distribution need to be taken into account. For example, interpreta-

TABLE II. Number of objects per cubic meter it would require to produce a volume scattering strength of -70 dB. The volume of each object is fixed at 0.30 cm³. The angular distributions of the bent cylinders are varied as indicated at the top of the columns. The models, body dimensions, average over size, and values of g, h, and ρ_c/L (cylinders only) are the same as in Fig. 2. The frequencies chosen correspond to those of commercially available echosounders.

Freq. (kHz)	Sphere	Cylinder				
		N (20°, 20°)	N (30°, 20°)	N (40°, 20°)	N (50°, 20°)	Uniform [0, 360°]
38	27	50	76	140	280	160
120	31	3.3	5.6	14	55	11
200	12	4.9	8.2	20	60	16
420	11	5.9	9.9	24	74	19

tion of the echoes from a 38- or 120-kHz single frequency system could be affected by about 5 dB when surveying 34-mm-long euphausiids with a $N(20°,90°)$ distribution while the work at 200 or 420 kHz would be relatively unaffected for that length of animals (Fig. 3). For a distribution of $N(45°, 20°)$ the interpretation for 34-mm-long euphausiids is affected by about 6–7 dB for most frequencies at or above 38 kHz, except for frequencies near 120 kHz where the differences are much less (Fig. 2). These types of (decibel) errors can translate into errors in estimates of the numbers of animals causing the scattering (Table II).

Success of a two- or multi-frequency system is also affected by the shape and behavioral conditions. Each approach not only depends upon the value of the scattering levels, but the ''transition point'' between the Rayleigh and geometric scattering region (Greenlaw, 1979; Holliday and Pieper, 1995). A crucial phenomenon illustrated in these calculations is the fact that the transition point for the sphere is different from that of a cylinder (Fig. 3). For example, for a 29-mm-long cylinder, the point is at about 150 kHz. For a sphere with the same volume as that of a 29-mm-long cylinder, the point is at about 75 kHz. Hence the transition points are different by a factor of 2. This difference would have a profound effect on an analysis or algorithm that relies on knowing where the transition point is.

V. SUMMARY AND CONCLUSIONS

Comparisons between the scattering by weakly scattering spheres and cylinders of the same volume have shown similar or identical levels under certain limiting conditions and dramatic differences under other conditions. The levels are identical in the limit of very low frequencies when the product of the wave number and all outer dimensions of the body is much less than unity. However, that region is not particularly useful because the echo levels tend to be negligibly small in practical survey systems. For moderately low frequencies ($ka \lesssim 1, kL \gtrsim 1$) and higher, there are distinct differences between the scattering levels of the different bodies due to the elongated nature of the cylinders and orientation effects. For certain orientation distributions, the averaged scattering levels of all bodies are very close to each other in the geometric scattering region. Other distributions produce substantially different average levels between the sphere and

cylinders. Regardless of orientation distribution, the turning point between Rayleigh and geometric scattering occurs at different frequencies for the bodies.

These results show that for surveys of elongated animals in the ocean, the averaged echo energies (say, from an echo integrator) could be relatively insensitive to shape at high enough acoustic frequencies (for example, greater than 300 kHz for a 34-mm-long euphausiid) and for certain distributions of angles of orientation. However, for surveys involving other distributions of angles of orientations at high frequencies or lower frequencies (the ''moderately low frequency range'' which would be, for example, 20–200 kHz for 34-mm-long euphausiids), the results become strongly dependent upon shape and the modeling must distinguish between spherical and cylindrical animals.

Also, while the focus of this work involved shape dependencies of acoustic scattering for bodies with the same material properties, variations in material properties also significantly affect the scattering levels as briefly discussed herein [see, for example, Stanton *et al.* (1994) for data and modeling of animals with various material properties as well as references in that paper to other works on the subject].

In conclusion, as observed in this study and the many studies referenced herein, the scattering of sound is a complex function of size, shape, orientation, and material properties of the body as well as acoustic wavelength. Ideally, one should take each factor into account in scattering predictions as accurately as possible. However, some of these factors may be more important than others, depending upon conditions such as which scattering region the object is in (Rayleigh/geometric) or whether or not the echoes are being averaged over a particular distribution of angles of orientation. Analysis of the scattering therefore requires determination of the conditions and which factors (such as shape and orientation distribution) need to be taken into account in the modeling.

ACKNOWLEDGMENTS

Anderson, V. C. (**1950**). ''Sound scattering from a fluid sphere,'' J. Acoust. Soc. Am. **22**, 426–431.

Born, M., and Wolf, E. (**1991**). *Principles of Optics* (Pergamon, New York).

Chu, D., Foote, K. G., and Stanton, T. K. (**1993**). ''Further analysis of target strength measurements of Antarctic krill at 38 kHz and 120 kHz: Comparison with deformed cylinder model and inference of orientation distribution,'' J. Acoust. Soc. Am. **93**, 2985–2988.

Clay, C. S., and Medwin, H. (**1977**). *Acoustical Oceanography: Principles and Applications* (Wiley–Interscience, New York).

Demer, D. A., and Martin, L. V. (**1995**). ''Zooplankton target strength: Volumetric or areal dependence?'' J. Acoust. Soc. Am. **98**, 1111–1118.

DiPerna, D. T., and Stanton, T. K. (**1991**). ''Fresnel zone effects in the scattering of sound by cylinders of various lengths,'' J. Acoust. Soc. Am. **90**, 3348–3355.

Endo, Y. (**1993**). ''Orientation of Antarctic Krill in an aquarium,'' Nippon Suisan Gakkaishi **59**, 465–468.

Foote, K. G. (**1990**). ''Speed of sound in *Euphausia superba*,'' J. Acoust. Soc. Am. **87**, 1405–1408.

Foote, K. G., Everson, I., Watkins, J. L., and Bone, D. G. (**1990**). ''Target strengths of Antarctic krill (*Euphausia superba*) at 38 and 120 kHz,'' J. Acoust. Soc. Am. **87**, 16–24.

Gaunaurd, G. C. (**1985**). ''Sonar cross sections of bodies partially insonified by finite sound beams,'' IEEE J. Ocean Eng. **OE-10**, 213–230.

Greenlaw, C. F. (**1977**). ''Backscattering spectra of preserved zooplankton,'' J. Acoust. Soc. Am. **62**, 44–52.

Greenlaw, C. F. (**1979**). ''Acoustical estimation of zooplankton populations,'' Limnol. Oceanogr. **24**, 226–242.

Holliday, D. V., and Pieper, R. E. (**1995**). ''Bioacoustical oceanography at high frequencies,'' ICES J. Mar. Sci. **52**, 279–296.

Holliday, D. V., Pieper, R. E., and Kleppel, G. S. (**1989**). ''Determination of zooplankton size and distribution with multi-frequency acoustic technology,'' J. Conseil Int. L'Explor. Mer. **46**, 52–61.

Johnson, R. K. (**1977**). ''Sound scattering from a fluid sphere revisited,'' J. Acoust. Soc. Am. **61**, 375–377; ''Erratum: 'Sound scattering from a fluid sphere revisited','' J. Acoust. Soc. Am. **63**, 626 (1978).

Kils, U. (**1981**). ''The swimming behavior, swimming performance and energy balance of Antarctic krill, *Euphausia superba*,'' BIOMASS Science Series Vol. 3.

Marston, P. L. (**1992**). ''Geometrical and catastrophe optics methods in scattering,'' in *Physical Acoustics*, edited by A. D. Pierce and R. N. Thurston (Academic, New York), Vol. 21.

Miyashita, K., Aoki, I., and Inagaki, T. (**1996**). ''Swimming behavior and target strength of isada krill (*Euphausia pacifica*),'' ICES J. Mar. Sci. **53**, 303–308.

Morse, P. M., and Ingard, K. U. (**1968**). *Theoretical Acoustics* (Princeton U. P., Princeton, NJ), Chap. 8.

Ogilvy, J. A. (**1991**). *Theory of Wave Scattering from Random Rough Surfaces* (Adam Hilger, New York).

Partridge, C., and Smith, E. R. (**1995**). ''Acoustic scattering from bodies: Range of validity of the deformed cylinder method,'' J. Acoust. Soc. Am. **97**, 784–795.

Stanton, T. K. (**1988**). ''Sound scattering by cylinders of finite length. I. Fluid cylinder,'' J. Acoust. Soc. Am. **83**, 55–63.

Stanton, T. K. (**1989**). ''Sound scattering by cylinders of finite length. III. Deformed cylinders,'' J. Acoust. Soc. Am. **86**, 691–705.

Stanton, T. K. (**1992**). ''Sound scattering by rough elongated elastic objects: I. Means of scattered field,'' J. Acoust. Soc. Am. **92**, 1641–1664.

Stanton, T. K., Chu, D., and Wiebe, P. H. (**1998**). ''Sound scattering by several zooplankton groups. II. Scattering models,'' J. Acoust. Soc. Am. **103**, 236–253.

Stanton, T. K., Clay, C. S., and Chu, D. (**1993a**). ''Ray representation of sound scattering by weakly scattering deformed fluid cylinders: Simple physics and application to zooplankton,'' J. Acoust. Soc. Am. **94**, 3454–3462.

Stanton, T. K., Chu, D., Wiebe, P. H., and Clay, C. S. (**1993b**). ''Average echoes from randomly oriented random-length finite cylinders: Zooplankton models,'' J. Acoust. Soc. Am. **94**, 3463–3472.

Stanton, T. K., Nash, R. D. M., Eastwood, R. L., and Nero, R. W. (**1987**). ''A field examination of acoustical scattering from marine organisms at 70 kHz,'' IEEE J. Ocean. Eng. **OE-12**(2), 339–348.

Stanton, T. K., Wiebe, P. H., Chu, D., Benfield, M. C., Scanlon, L., Martin, L., and Eastwood, R. L. (**1994**). ''On acoustic estimates of zooplankton biomass,'' ICES J. Mar. Sci. **51**, 505–512.

Urick, R. J. (**1983**). *Principles of Underwater Sound* (McGraw–Hill, New York).

Double monopole resonance of a gas-filled, spherical cavity in a sediment

Steven G. Kargl and Kevin L. Williams
Applied Physics Laboratory, University of Washington, 1013 N. E. 40th Street, Seattle, Washington 98105

Raymond Lim
Coastal Systems Station, Code 130B, 6703 West Highway 98, Panama City, Florida 32407-7001

The monopole response of a gas-filled, spherical cavity in a sediment is investigated. The sediment is either a fluid, elastic solid, or saturated poroelastic medium. The present method entails the scattering of an incident displacement field that preferentially excites the monopole resonance of the cavity. The main result demonstrates that a gas-filled, spherical cavity in a saturated poroelastic medium can exhibit two distinct monopole resonances. These resonances arise from the two distinct longitudinal modes of propagation in saturated poroelastic medium as described by Biot's theory. © *1998 Acoustical Society of America.* [S0001-4966(98)00401-9]

INTRODUCTION

In 1980, Anderson and Hampton summarized existing experimental measurements and theoretical analyses of bubble resonance behavior in gas-bearing sediments.[1] In a companion article, Anderson and Hampton examined resonance frequency data from single-bubble and multiple-bubble events that they obtained from careful laboratory experiments and compared their results with available models.[2] Their technique involved the use of an impedance tube and cylindrical air sacs with polyethylene walls. They measured the resonance frequency for these sacs in water, agar gel, and kaolinite clay where the volume of the sacs range from 0.26–9.3 cm^3. The results of the kaolinite clay experiment agreed with a theoretical result [see Eq. (18) below] when they used shear moduli found in the literature. Based on this success they used the same formula to give theoretical expressions for $f_0 a$ for several sediment types where f_0 is the resonance frequency and a is the equilibrium radius of the bubble. Their expression for an ocean sediment composed of fine-grain sand at approximately 10 m below the water surface is

$$f_0 a \approx 15.3 \text{ kHz·cm}, \tag{1}$$

where the density and shear modulus needed for (1) predict a shear wave speed of approximately 480 m/s. This value, surmised from the material parameters given by Anderson and Hampton, falls within the upper range of values reported by Hamilton.[3] The measured shear wave speeds tabulated by Hamilton suggest that 100–200 m/s is a typical shear wave speed for a fine-grain sand sediment. This then implies that $f_0 a \approx 4.79$ kHz·cm. A corresponding expression for an air bubble in water is $f_0 a \approx 0.464$ kHz·cm. Thus, a 0.3-cm-radius bubble in fine sand would presumably have a resonance frequency in the range of 16–51 kHz. The prediction of (1), and even our lower estimate for $f_0 a$, is at extreme odds with the results of Hawkins and Bedford who treat the sediment as a porous medium.[4] They use Biot's theory to calculate sound speed curves for a porous medium with a monodispersed population of bubbles where $a = 0.3$ cm.

Their results imply a resonance frequency of the order of 1 kHz. This is consistent with what one would find for a bubble in an ''effective fluid'' sediment. No conclusive experiments have been carried out to test which, if either, of these predictions is correct. There is no *a priori* reason to believe that the assumptions implicit in either of these theories are valid.

Recently, Kargl and Lim developed an exact transition matrix (T-matrix) scattering formalism for objects embedded in a saturated poroelastic medium characterized by Biot's theory.[5] Kargl has considered the scattering from a bubble with $a = 0.1$ cm embedded in a typical water-saturated sand sediment. His computations suggest that the bubble can support two distinct monopole resonance frequencies. In a subsequent effort, Kargl *et al.* have analyzed the scattering from a bubble where the incident wave field is the lowest-order, fast-longitudinal, regular vector wave function appropriate for a saturated poroelastic medium.[6] This chosen field will preferentially excite the monopole behavior of the bubble, and, in fact, calculations manifest two resonance peaks in the scattered field amplitude. It is our contention that these two resonances are related to the two distinct longitudinal modes of propagation in a Biot medium (i.e., the slow and fast waves). Thus, the apparent paradox between Anderson and Hampton and Hawkins and Bedford may now be resolved.

It is our hypothesis that the degrees of freedom implicit in a saturated poroelastic medium can result in the existence of both the low-frequency resonance of Hawkins and Bedford and the high-frequency resonance of Anderson and Hampton. It is this possibility that is to be explored via the incident monochromatic wave method described here. The use of a simple incoming wave (along with other simplifications we anticipate) leads to analytical results where the sensitivity to various material parameters can be examined, physical insight sought, and experimental tests defined.

The remainder of this article is organized as follows. Section I develops a scattering method that preferentially

excites the monopole resonance behavior of a spherical bubble in a fluid medium. It is then demonstrated that the scattering coefficient yields the well-known Minnaert resonance frequency under the appropriate conditions. In Sec. II, the scattering method is generalized to an elastic medium containing either an evacuated spherical cavity or a gas-filled spherical cavity. Again, simple expressions for the monopole resonance frequency are obtained. The adaptation of the scattering method to a gas-filled spherical cavity in a saturated poroelastic medium is discussed in Sec. III. Although appropriate coefficients for the scattered fast and slow longitudinal waves are obtained, deduction of simple resonance frequency expressions are hampered by the complicated frequency dependence of Biot's theory. Section IV gives numerical comparisons between the scattering coefficients derived in Secs. I–III for realistic (sand) sediment parameters. Concluding remarks follow in Sec. V. Finally, this article contains two appendices. Appendix A contains a Lagrangian formulation for the monopole resonance behavior of a gas-filled bubble in a fluid medium. This Appendix provides a simple physical model of the resonance phenomenon. Appendix B provides a mathematical formulation for Biot's theory as applied throughout the article.

I. FLUID MEDIUM

Although the Lagrangian formulation outlined in Appendix A provides an estimate of the monopole resonance frequency for a spherical bubble in an incompressible fluid, Lagrangian methods may become cumbersome for other materials (e.g., a saturated poroelastic medium). This section develops an alternative method for estimating the resonance frequency of a spherical bubble based on the steady-state scattering of an incident, spherically symmetric, displacement. The fluid supports propagating waves, so many of the assumptions imposed in Appendix A are relaxed or inapplicable. The only requirement is the existence of a bubble insofar as a gas-filled, spherical cavity is assumed to exist without regards to its mechanical stability. Our purpose here is to develop a method that can be easily extended to elastic and saturated poroelastic media.

Figure 1(a) depicts a gas-filled, spherical bubble in a compressible fluid. The density and speed of sound in the gas are ρ_g and c_g. Likewise, the density and speed of sound in the fluid are ρ_f and c_f, respectively. The origin of our spherical coordinate geometry (r, θ, ϕ) coincides with the center of the bubble. A spherically, symmetric displacement $\mathbf{u}_{fi} = \psi_f j_0'(k_f r)\hat{r}$ is incident upon the bubble (the $e^{-i\omega t}$ time convention is suppressed). The spherical Bessel function of zeroth order is j_0 and the prime denotes differentiation with respect to its argument. The wave number k_f and angular frequency ω satisfy $\omega = c_f k_f$, and $\psi_f = (4\pi)^{-1/2}$ is a normalization constant. The unit vector in the radial direction is $\hat{r}$. Boström describes a complete set of regular basis functions appropriate for a fluid.[7] A comparison of $\mathbf{u}_{fi}$ with this set of basis functions indicates that $\mathbf{u}_{fi}$ is the lowest-order member of the set (with a slight modification to the normalization imposed by Boström). Typically, the scattered displacement is expanded in a complete set of irregular basis functions that
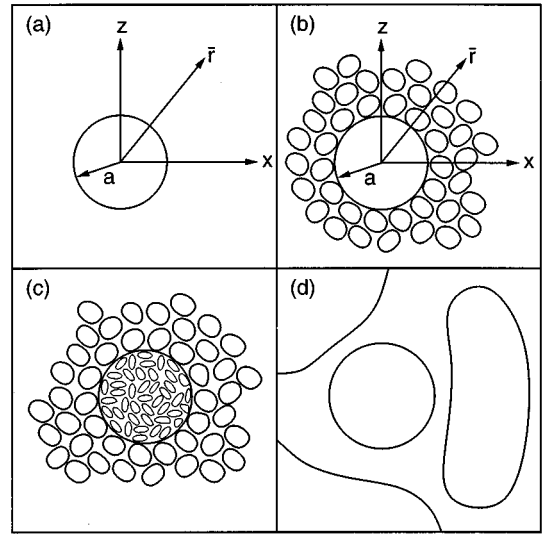
FIG. 1. Spherical coordinate system for the scattering geometry. The center of the spherical bubble (or cavity) of equilibrium radius $r = a$ coincides with the coordinate origin. (a) Homogenous fluid or elastic solid. (b) Bubble in fluid-saturated poroelastic medium. (c) Gas-saturated poroelastic sphere in a fluid-saturated poroelastic medium. (d) Bubble residing within the pore space between grains of the a sediment.

satisfy the Helmholtz wave equation, but the symmetry of the incident displacement indicates that only a single basis function is required. Superposition of the incident and scattered displacements gives

$$\mathbf{u}_f = \psi_f j_0'(k_f r)\hat{r} + B_f \psi_f h_0'(k_f r)\hat{r}, \tag{2}$$

where the second term is the scattered displacement. h_0 is the zeroth-order spherical Hankel function of the first kind, and B_f is an unknown coefficient to be determined from boundary conditions at the surface of the bubble. As in the exterior fluid, the gas within the bubble supports wave propagation and the interior displacement is expandable in a complete set of regular basis functions. Furthermore, symmetry again indicates that the basis function expansion collapses to a single term,

$$\mathbf{u}_g = B_g \psi_g j_0'(k_g r)\hat{r}. \tag{3}$$

The wave number in the gas is $k_g = \omega/c_g$; B_g is a second coefficient to be determined; and, $\psi_g = (4\pi)^{-1/2}$ is again a normalization constant.

As stated above, B_g and B_f are determined from boundary conditions at the surface of the bubble; i.e., $r = a$. These conditions are continuity of the radial component of the displacement and continuity of the pressure. For small perturbations from equilibrium, the equation of continuity and a Taylor's series expansion of an isentropic equation of state for a fluid yield a relationship between the displacement and the pressure fluctuation, $p_q = -\rho_q c_q^2 \nabla \cdot \mathbf{u}_q$ where $q = f, g$. These conditions with (2) and (3) lead to a linear system of equations for the unknown coefficients:

$$\begin{bmatrix} j_0'(x_g) & -h_0'(x_f) \\ \zeta_{gf} j_0(x_g) & -h_0(x_f) \end{bmatrix} \begin{bmatrix} B_g \\ B_f \end{bmatrix} = \begin{bmatrix} j_0'(x_f) \\ j_0(x_f) \end{bmatrix}. \tag{4}$$

We introduce $x_f = k_f a$ and $x_g = k_g a$ and the ratio of characteristic impedances of the gas and fluid, $\zeta_{gf} = \rho_g c_g / \rho_f c_f$. A

necessary and sufficient condition for a unique solution to (4) is a nonzero determinant of the coefficient matrix. Hence, by Cramer's rule, we find

$$B_f = -\frac{\zeta_{gf} j_0(x_g) j_0'(x_f) - j_0'(x_g) j_0(x_f)}{\zeta_{gf} j_0(x_g) h_0'(x_f) - j_0'(x_g) h_0(x_f)}. \qquad (5)$$

The bubble experiences resonances for those values of x_f that cause the imaginary part of the denominator in (5) to vanish. Trigonometric representations for the spherical Bessel and Hankel functions and simple algebraic manipulations lead to a transcendental equation for the resonance condition,

$$\xi_{fg} \zeta_{gf} - 1 + \xi_{fg} x_f \cot(\xi_{fg} x_f) = 0, \qquad (6)$$

where $\xi_{fg} = c_f/c_g$ and $x_g = \xi_{fg} x_f$. The monopole resonance frequency (or equivalently x_{f0}) corresponds to the smallest, positive value of x_f that satisfies (6). For an air bubble in water with typical material parameters, the Minnaert resonance frequency corresponds to $x_{M0} \approx 0.014$ (see Appendix A). This implies that $\cot(\xi_{fg} x_f)$ in (6) can be approximated by the first two terms of its power series. That is, ξ_{fg} is of order 5 for typical fluids and gases and x_{f0} should not deviate substantially from x_{M0}. Algebraic manipulations lead to

$$x_{f0} = \left(\frac{3\zeta_{gf}}{\xi_{fg}}\right)^{1/2} = \left(\frac{3\rho_g c_g^2}{\rho_f c_f^2}\right)^{1/2} = \left(\frac{3\gamma p_e}{\rho_f c_f^2}\right)^{1/2}. \qquad (7)$$

The final equality in (7) uses $\rho_g c_g^2 = \gamma p_e$, and p_e is an adiabatic, equilibrium pressure.[8] Comparison of (7) and (A1) is possible, once ω_{M0} is converted to a dimensionless spatial variable by $x_{M0} = \omega_{M0} a/c_f$. Finally, it becomes evident that $x_{f0} \equiv x_{M0}$ because p_e is simply the ambient pressure P_0.

Surface tension becomes important for small bubbles, so we conclude Sec. I with a brief discussion of the modifications necessary to account for surface tension. From Appendix A, the Laplace pressure is $2\sigma/r_b$. The surface tension σ is essentially constant for small deviations from the equilibrium radius $r_b(t) = a + \delta(t)$. The pressure fluctuation within the bubble is

$$p_g(r) = B_g \psi_g \rho_g \omega^2 j_0(k_g r)/k_g + \frac{2\sigma}{a+\delta}$$

$$\approx B_g \psi_g \rho_g \omega^2 j_0(k_g r)/k_g + \frac{2\sigma}{a}\left(1 - \frac{\delta}{a}\right), \qquad (8)$$

where the approximate equality in (8) results from a binomial expansion of the denominator and higher-order terms are neglected. Inspection of (8) shows an increase in the bubble radius ($\delta > 0$) causes the expected decrease in internal pressure. The displacement remains unchanged because the linearized Euler's equation implies that contributions from σ are at most second-order effects for displacement. Finally, the radial variation is $\delta = -\hat{r} \cdot \mathbf{u}_g$ and it is evaluated at $r = a$.

We now use (8) with the boundary conditions on continuity of pressure and radial component of displacement at $r = a$ to obtain

$$\begin{bmatrix} j_0'(x_g) & -h_0'(x_f) \\ \dfrac{\rho_g}{k_g} j_0(x_g) + \left(\dfrac{2\sigma}{a}\right)\dfrac{1}{a\omega^2} j_0'(x_g) & -\dfrac{\rho_f}{k_f} h_0(x_f) \end{bmatrix} \begin{bmatrix} B_g \\ B_f \end{bmatrix}$$

$$= \begin{bmatrix} j_0'(x_f) \\ \dfrac{\rho_f}{k_f} j_0(x_f) - \left(\dfrac{2\sigma}{a}\right)\dfrac{(4\pi)^{1/2}}{a\omega^2} \end{bmatrix}. \qquad (9)$$

We note that any shift in the resonance frequency caused by surface tension is completely contained in the coefficient matrix on the left-hand side of (9), while the term on the right-hand side will simply alter the amplitude of the scattered pressure fluctuation. The procedure for determining the monopole resonance frequency follows our previous discussion above and it leads to

$$x_{f0} = \left[\frac{1}{\rho_f c_f^2}\left(3\rho_g c_g^2 - \frac{2\sigma}{a}\right)\right]^{1/2}. \qquad (10)$$

Here, we note that the equilibrium pressure $p_e = \rho_g c_g^2/\gamma$ is equivalent to $p_0 = P_0 + 2\sigma/a$ from Appendix A. Finally, (10) and (A6) can be compared after ω_{m0} is converted to a dimensionless spatial variable with $x_{m0} = \omega_{m0} a/c_f$.

II. ELASTIC MEDIUM

The method developed in Sec. I can be adapted to the scattering from a spherical cavity embedded in an elastic medium. Figure 1(a) again depicts the geometry, but the exterior medium is now elastic. The monopole resonance of such a cavity can be preferentially excited by scattering the following incident longitudinal displacement,

$$\mathbf{u}_{ei} = \psi_e j_0'(k_l r)\hat{r}, \qquad (11)$$

where $\psi_e = (c_s^3/4\pi c_l^3)^{1/2}$ is a normalization constant. The longitudinal and shear sound speeds for the elastic medium are c_l and c_s, respectively. The longitudinal wave number is $k_l = \omega/c_l$ and ρ_e denotes the density of the elastic medium. Equation (11) is simply the lowest-order, regular basis function that appears in a T-matrix formulation of elastic wave scattering.[9] The resulting scattered displacement is

$$\mathbf{u}_{es} = B_e \psi_e h_0'(k_l r)\hat{r}, \qquad (12)$$

where B_e is a unknown coefficient determined from boundary conditions. A comparison of (12) with (15) from Lim and Hackman shows that $\mathbf{u}_{es}$ is the lowest-order, irregular basis function. Finally, the total displacement within the elastic medium takes the usual form $\mathbf{u}_e = \mathbf{u}_{ei} + \mathbf{u}_{es}$.

The traction at the surface of an elastic medium is the tensorial contraction of the elastic stress tensor and the outward unit normal vector at that surface. The radial components of traction on a spherical surface for the displacements given in (11) and (12) are

$$t_{rr}(\mathbf{u}_{ei}) = -\rho_e k_l \psi_e [c_l^2 j_0(k_l r) + 4c_s^2 j_0'(k_l r)/k_l r] \qquad (13)$$

and

$$t_{rr}(\mathbf{u}_{es}) = -\rho_e k_l \psi_e B_e [c_l^2 h_0(k_l r) + 4c_s^2 h_0'(k_l r)/k_l r], \qquad (14)$$

respectively. Finally, the radial component of the total traction is $t_{rr}(\mathbf{u}_e) = t_{rr}(\mathbf{u}_{ei}) + t_{rr}(\mathbf{u}_{es})$.

When the spherical cavity is evacuated, B_e can be determined from the boundary condition $t_{rr}(\mathbf{u}_e) = 0$ at $r = a$. Simple algebraic manipulation involving (13) and (14) leads to

$$B_e^v = -\frac{c_l^2 j_0(x_l) + 4c_s^2 j_0'(x_l)/x_l}{c_l^2 h_0(x_l) + 4c_s^2 h_0'(x_l)/x_l},\tag{15}$$

where $x_l = k_l a$. The superscript "v" denotes an evacuated cavity. Monopole oscillation of the evacuated cavity occurs for x_l such that the imaginary part of the denominator in (15) vanishes. This gives

$$x_{l0}^v = 2\left(\frac{c_s}{c_l}\right),\tag{16}$$

in agreement with the results of Meyer *et al.*, who consider an alternate scattering methodology where the incident and scattered displacement potential fields are spherically converging and diverging waves.[10]

Extension of the scattering formulation to a gas-filled, spherical cavity in a homogeneous elastic medium is straightforward. The required boundary conditions are continuity of the radial component of displacement and continuity of the radial component of traction at the surface of the cavity. The scattering coefficient becomes

$$B_e = -\frac{\zeta_{ge} j_0(x_g) j_0'(x_l) - j_0'(x_g)[j_0(x_l) + 4(c_s/c_l)^2 j_0'(x_l)/x_l]}{\zeta_{ge} j_0(x_g) h_0'(x_l) - j_0'(x_g)[h_0(x_l) + 4(c_s/c_l)^2 h_0'(x_l)/x_l]},\tag{17}$$

where $\zeta_{ge} = \rho_g c_g / \rho_e c_l$. Again, the monopole resonance frequency corresponds to the smallest positive value of x_l such that the imaginary part of the denominator in (17) vanishes. The analysis leads to a transcendental equation that yields

$$x_{l0} = \left(\frac{3\rho_g c_g^2 + 4\mu_s}{\rho_e c_l^2}\right)^{1/2} = \left(\frac{3\gamma p_e + 4\mu_s}{\rho_e c_l^2}\right)^{1/2}.\tag{18}$$

as the resonance frequency. The shear Lamé coefficient for the elastic material, μ_s, satisfies the usual relationship $\mu_s = \rho_e c_s^2$. Equation (18) agrees with an expression given by Andreeva (without derivation or citation) for a gas-filled cavity in an elastic medium.[11] Neither Andreeva nor Anderson and Hampton[1,2] discuss the validity of (18). To arrive at (18), the assumption $(c_l/c_g)x_l < 1$ is required in the reduction of the transcendental equation to a simple quadratic form. Substitution of x_{l0} into this assumption shows that (18) is valid when $c_s < c_g/2$.

We conclude Sec. II with the following observation. The monopole resonance frequency for a spherical cavity within an isotropic, homogeneous elastic medium has been investigated by Blake.[12] He estimates a monopole resonance frequency through a steady-state specific radiation impedance and a spectral analysis of an exponentially decaying impulsive pressure within an initially evacuated cavity. He gives a resonance frequency that corresponds to $x_{l0}^B = 2(c_s/c_l)[1 - (c_s/c_l)^2]^{1/2}$ in our notation. The impulsive loading appears to affect the evacuated cavity result of (16) above, but x_{l0}^B does not contain any dependence on the medium that supports the impulsive pressure.

III. SATURATED POROELASTIC MEDIUM

Sections I and II have established the scattering method for determining the resonance frequency of a spherical cavity within a fluid or an elastic medium. This method will now be extended to the scattering from a spherical cavity embedded within a saturated poroelastic medium. Figure 1(b) illustrates an implicit assumption about the cavity size in comparison to either a typical sediment grain size or a pore dimension. That is, Fig. 1(b) is appropriate for the boundary conditions discussed below [see (26)–(28)]. Figure 1(c) and (d) depict other possible gas-filled cavities embedded within a sediment. Kargl and Lim discuss the scattering from a cavity as shown in Fig. 1(c) where the exterior medium is an infinite saturated poroelastic medium.[5] Lim has recently extended those results to the scattering from an object embedded in a plane-stratified poroelastic environment.[13] Figure 1(d) shows a bubble contained entirely within the saturating fluid. This situation falls outside the scope of the present article and the previous work of Kargl and Lim. Finally, the variational method used by Hawkins and Bedford assumes the bubble radius is smaller than the average grain size, so Fig. 1(d) applies to their analysis.

The dynamic behavior of the medium is assumed to comply with Biot's theory[14] as summarized in Appendix B. One important aspect of Biot's theory is the existence of two distinct longitudinal degrees of freedom with differing propagation velocities. A wave propagating with the lower velocity is commonly referred to as a *slow wave* while the *fast wave* obviously propagates at the higher velocity. In the absence of neighboring boundaries, the monopole resonance of a spherical bubble in either a fluid or elastic medium produces a spherically symmetric, out-going, compressional wave. An extension of this behavior to a saturated poroelastic medium suggests that if Biot's theory is a proper characterization of the medium, then a spherical cavity will have two distinct monopole resonance frequencies. The possibility of the simultaneous propagation of slow and fast longitudinal waves introduces sufficient complication that simple expressions for estimating the monopole resonance frequencies are not attainable. Nontrivial dispersion relationships for the slow and fast waves further complicate the deduction of simple resonance frequency expressions.

Biot's theory describes the motion of the individual constituents within a saturated poroelastic medium through an average lattice displacement and an average fluid displace-

ment. We will consider the problem of scattering an incident, fast, longitudinal wave from a spherical cavity such that the displacements of the lattice and saturating fluid are

$$\mathbf{u}_{bi} = \psi_1 j_0'(k_1 r)\hat{r}, \quad \mathbf{U}_{bi} = A_1 \psi_1 j_0'(k_1 r)\hat{r}, \quad (19)$$

respectively. The coefficient A_1 accounts for the coupling of the lattice displacement with the displacement of the saturating fluid. This coupling coefficient is typically a frequency-dependent quantity. Here k_1 denotes the wave number of the fast wave. As in Secs. I and II, $\psi_1 = (4\pi\Gamma_1^2)^{-1/2}$ is an appropriate normalization constant, and Γ_1 is defined in (B18). A comparison of (19) with (27a) in Kargl and Lim[5] illustrates that $\mathbf{u}_{bi}$ is the lowest-order regular vector eigenfunction for a Biot medium. The resulting scattered displacements are a simple superposition of the lowest-order irregular vector eigenfunctions for fast and slow longitudinal waves,

$$\mathbf{u}_{bs} = [B_1 \psi_1 h_0'(k_1 r) + B_2 \psi_2 h_0'(k_2 r)]\hat{r}, \quad (20)$$

$$\mathbf{U}_{bs} = [B_1 A_1 \psi_1 h_0'(k_1 r) + B_2 A_2 \psi_2 h_0'(k_2 r)]\hat{r}, \quad (21)$$

where B_1 and B_2 are unknown coefficients determined from boundary conditions. Throughout the remainder of this section, quantities carrying the subscript ''1'' correspond to the fast wave while the subscript ''2'' will denote slow wave quantities. Hence, k_2, A_2, and ψ_2 are the wave number, fluid-lattice coupling coefficient, and normalization constant for the slow wave, respectively. Although the saturated poroelastic medium can support coupled and uncoupled shear waves, these are not present in the scattered displacements because of our choice for $(\mathbf{u}_{bi}, \mathbf{U}_{bi})$. That is, there are no zeroth-order regular or irregular vector eigenfunctions for the coupled and uncoupled shear degrees of freedom.

The radial component of the traction on a spherical surface for the lattice due to the incident field $(\mathbf{u}_{bi}, \mathbf{U}_{bi})$ is

$$t_{rr}(\mathbf{u}_{bi}, \mathbf{U}_{bi}) = -k_1\psi_1[(P+QA_1)j_0(k_1 r) + 4Nj_0'(k_1 r)/k_1 r], \quad (22)$$

where P, Q, and N are Biot material parameters that are defined in Appendix B. Equation (22) may be verified by substitution of (19) into (B6) and performing the double contraction of the lattice stress tensor T with the radial unit vector $\hat{r}$. Likewise, the contribution to the radial component of the traction for the lattice due to $(\mathbf{u}_{bs}, \mathbf{U}_{bs})$ is

$$t_{rr}(\mathbf{u}_{bs}, \mathbf{U}_{bs}) = -k_1 B_1 \psi_1[(P+QA_1)h_0(k_1 r) + 4Nh_0'(k_1 r)/k_1 r] - k_2 B_2 \psi_2[(P + QA_2)h_0(k_2 r) + 4Nh_0'(k_2 r)/k_2 r]. \quad (23)$$

Equations (22) and (23) only apply to the lattice constituent of the saturated poroelastic medium. A similar reduction for the fluid traction is necessary. The radial components of traction on a spherical surface for the fluid part of the Biot medium are

$$s_{rr}(\mathbf{u}_{bi}, \mathbf{U}_{bi}) = -k_1\psi_1(Q+RA_1)j_0(k_1 r), \quad (24)$$

$$s_{rr}(\mathbf{u}_{bs}, \mathbf{U}_{bs}) = -k_1 B_1 \psi_1(Q+RA_1)h_0(k_1 r) - k_2 B_2 \psi_2(Q+RA_2)h_0(k_2 r), \quad (25)$$

where R represents another material parameter for a Biot medium. The displacements and radial components of traction given in (19)–(25) will be used with appropriate boundary conditions to determine the unknown coefficients B_1 and B_2.

We are primarily interested in the resonance response of a gas-filled cavity embedded within a saturated poroelastic medium. Deresiewicz and Skalak provide the necessary and sufficient conditions for the boundary conditions at a surface separating a homogeneous fluid and saturated poroelastic medium.[15] Under the assumption that the pores are open at the surface of the bubble (i.e., the gas and saturating fluid are in contact), the boundary conditions can be manipulated into the following forms:

$$t_{rr}(\mathbf{u}_{bi}, \mathbf{U}_{bi}) + t_{rr}(\mathbf{u}_{bs}, \mathbf{U}_{bs}) = -(1-\beta)p_g, \quad (26)$$

$$(1-\beta)\hat{r}\cdot(\mathbf{u}_{bi}+\mathbf{u}_{bs}) + \beta\hat{r}\cdot(\mathbf{U}_{bi}+\mathbf{U}_{bs}) = \hat{r}\cdot\mathbf{u}_g, \quad (27)$$

$$s_{rr}(\mathbf{u}_{bi}, \mathbf{U}_{bi}) + s_{rr}(\mathbf{u}_{bs}, \cdot\mathbf{U}_{bs}) = -\beta p_g, \quad (28)$$

where β is the porosity. Equations (26) and (28) are conditions on the continuity of the radial component of traction for the lattice and fluid such that the Biot medium and gas in the cavity remain in contact. The second condition, (27), is essentially the continuity of the normal component of displacement. Finally, these conditions are applied to (19)–(25) at the surface of the cavity $r=a$. The displacement within the gas is given by (3), and the gas pressure comes from the linearized Euler's equation. The result is a matrix equation, $m_{ij}B_j = y_i$, for the unknown coefficients where

$$m_{11} = (P+QA_1)h_0(x_1) + 4Nh_0'(x_1)/x_1,$$

$$m_{12} = (x_2\Gamma_1/x_1\Gamma_2)[(P+QA_2)/h_0(x_2) + 4Nh_0'(x_2)/x_2],$$

$$m_{13} = -(1-\beta)\Gamma_1\rho_g c_g^2 x_g j_0(x_g)/x_1,$$

$$m_{21} = (Q+RA_1)h_0(x_1),$$

$$m_{22} = (x_2\Gamma_1/x_1\Gamma_2)(Q+RA_2)h_0(x_2),$$

$$m_{23} = -\beta\Gamma_1\rho_g c_g^2 x_g j_0(x_g)/x_1,$$

$$m_{31} = (1-\beta+\beta A_1)h_0'(x_1),$$

$$m_{32} = (1-\beta+\beta A_2)(\Gamma_1/\Gamma_2)h_0'(x_2),$$

$$m_{33} = -\Gamma_1 j_0'(x_g),$$

$$y_1 = -[(P+QA_1)j_0(x_1) + 4Nj_0'(x_1)/x_1],$$

$$y_2 = -(Q+RA_1)j_0(x_1),$$

$$y_3 = -(1-\beta+\beta A_1)j_0'(x_1).$$

$$(29)$$

Here, we use $B_3 \equiv B_g$ and $x_j = k_j a$ $(j=1,2)$. The scattering coefficients are now determined via Cramer's rule as in Secs. I and II. Unfortunately, the deduction of resonance frequencies from the imaginary part of the determinant of m_{ij} is not feasible. One of the complications preventing a simple reduction is the frequency dependence of A_j and Γ_j $(j=1,2)$ [see (B14)–(B18)].
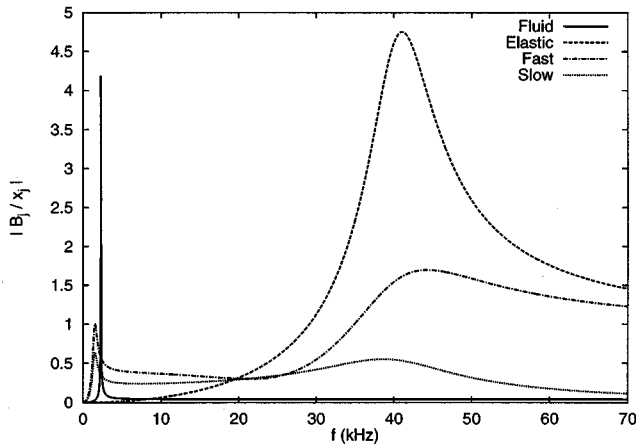
FIG. 2. Normalized scattering coefficients. The fluid curve is computed from (5) while the line marked as elastic is calculated from (17). The fast and slow curves are obtained from (29).

IV. NUMERICAL RESULTS

A universal set of material constants for a fine-grain, sand sediment does not exist. For computational purposes, we adopt the parameters from Stern *et al.*[16] These parameters are attributed to Stoll and Kan,[17] however, a slight but obvious discrepancy occurs in the value of K_b. Water saturates the sand sediment such that $\rho_f = 1000 \text{ kg/m}^3$, $K_f = 2.25$ GPa, and $\eta = 0.001$ kg/m·s. An individual grain of the sediment consists of a single homogeneous material with $\rho_e = 2650 \text{ kg/m}^3$ and $K_s = 36$ GPa. The bulk modulus and shear coefficient for the lattice are $K_b = 4.36 - \iota 0.208$ GPa and $N = 26.1 - \iota 1.25$ MPa, respectively. These complex quantities provide absorption within the lattice. The porosity, tortuosity, and hydrostatic permeability are $\beta = 0.47$, $\alpha = 1.654$, and $K_d = 10^{-10} \text{ m}^2$. The density and speed of sound of the gas are $\rho_g = 1.2 \text{ kg/m}^3$ and $c_g = 331$ m/s. The gas properties correspond to dry air, however values appropriate for 100% humidity did not appreciably affect the computations. Finally, the radius of the spherical cavity is $a = 0.001$ m.

The fluid model, elastic model, and saturated poroelastic model for a fine-grain, sand sediment are compared where the necessary parameters for the fluid and elastic models are consistent with the saturated, poroelastic sediment parameters given above. An effective density for either a fluid or elastic model is $\rho_m = (1 - \beta) \rho_e + \beta \rho_f = 1875 \text{ kg/m}^3$. The sound speeds, c_f, c_l, and c_s, from Secs. I and II are determined from Biot's theory. That is, Biot's theory is used as an effective medium theory to obtain estimates for c_f, c_l, and c_s. These estimates are $c_f = c_l = c_1$ and $c_s = c_3$ where c_3 is the Biot shear wave speed. It is noted that c_1 and c_3 are frequency-dependent, complex quantities, and, thus, the fluid and elastic model computations include attenuation.

The resonance behavior of a scatterer is normally isolated in the scattering coefficient. Figure 2 shows $|B_j / x_j|$, ($j = f, e, 1, 2$), for the three sediment models. Each scattering coefficient is normalized by its corresponding wave number, and $|B_f / x_f|$ is reduced by a factor of 25 to accommodate the figure. Clearly, the large peak in $|B_f / x_f|$ (solid line) is the enormous monopole resonance of a spherical bubble in a

fluid. Equation (7) predicts a Minnaert resonance frequency of 2.30 kHz while the peak in Fig. 2 occurs nears 2.31 kHz. For an elastic sediment, the peak in the scattering coefficient, $|B_e / x_l|$ (dashed line), occurs near 41.1 kHz. An estimate from (18) for this resonance frequency can be accomplished in two different manners. Equation (18) contains the shear Lamé coefficient for an elastic material which is unavailable from Stern *et al.* One possibility is to set $\mu_s = \Re(N)$ which predicts 37.6 kHz. Alternatively, $\mu_s = \rho_m c_s^2 \approx \rho_m \Re(c_3)^2$, and the Biot shear wave sound speed is approximately 125 m/s over the entire frequency range of Fig. 2. This gives 39.8 kHz, which is in close agreement with 41.1 kHz given the level of approximation of μ_s. Finally, the frequency resolution of Fig. 2 is 0.029 kHz.

The magnitudes of the normalized scattering coefficients for the fast and slow waves are represented by the dot-dashed line and the dotted line in Fig. 2, respectively. Two important features are immediately evident. First, a sharp peak occurs near 1.55 kHz in both $|B_1 / x_1|$ and $|B_2 / x_2|$. The presences of this peak provides support for the low-frequency resonance of Hawkins and Bedford. A second broad feature appears near 44.3 kHz in $|B_1 / x_1|$ and approximately at 38.6 kHz in $|B_2 / x_2|$. We speculate that these peaks are in fact a manifestation of the same resonance dynamics. However, the much higher attenuation of the slow wave, particularly at high frequencies, introduces an apparent shift in the resonance frequency. Nevertheless, the appearance of a high-frequency peak suggests a second monopole resonance of a gas-filled cavity, and thus, the high-frequency resonance of Anderson and Hampton is supported. Thus, a saturated poroelastic model resolves the paradox as discussed in the Introduction, and it implies that a gas-filled cavity will support two monopole resonances.

Equations (7) and (18) yield resonance frequencies of 2.30 and 39.8 kHz for the fluid and the elastic sediment models. These values compare favorably to 1.55 kHz and 38.6 and 44.3 kHz of the saturated poroelastic model. A simple, intuitive explanation would assign the low-frequency resonance to the dynamics of the saturating fluid and the high-frequency resonance would be associated with the motion of the lattice. This is incorrect because two resonance peaks appear in the scattering coefficients B_1 and B_2, and, hence, both resonances would contribute to the scattered displacements $\mathbf{u}_{bs}$ and $\mathbf{U}_{bs}$ [see (20) and (21)]. An alternate physical description of the resonance behavior would ascribe the low-frequency resonance to either the slow or fast wave and the high-frequency resonance to the remaining wave. An out-of-phase motion of the saturating fluid with respect to the lattice characterizes the slow wave while the fast wave is an in-phase motion. This, again, is incorrect because the normalized scattering coefficients for the fast and slow waves contain two peaks, and in the presence of a boundary, the slow and fast waves are not decoupled. Therefore, the manifestation of two monopole resonances appears to be a unique, intrinsic property of a saturated poroelastic medium as described by Biot's theory.

The scattering coefficients are independent of the distance to an observation point, and ψ_j and A_j ($j = 1, 2$) are frequency-dependent normalization and Biot coupling coef-

270   J. Acoust. Soc. Am., Vol. 103, No. 1, January 1998

Kargl *et al.*: Double monopole resonance   270
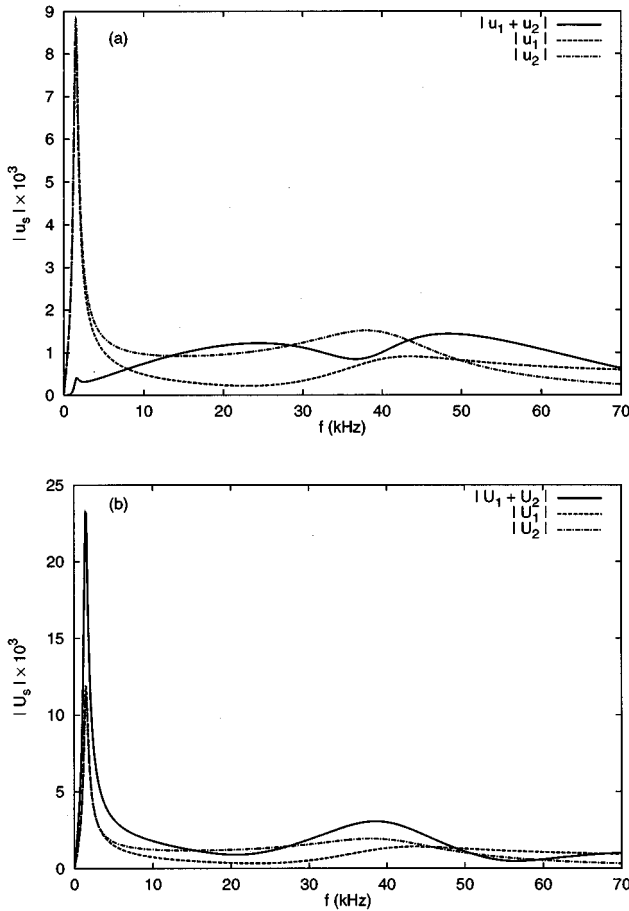
FIG. 3. Magnitudes of displacements at a distance of ten bubble radii. The upper figure shows the displacements for the elastic constituent of Biot's theory. The lower figure corresponds to the displacements for the saturating fluid.

FIG. 4. Magnitudes of displacements at a distance of 100 bubble radii. The upper figure shows the displacements for the elastic constituent of Biot's theory. The lower figure corresponds to the displacements for the saturating fluid.

ficients. Inspection of (20) and (21) and the intrinsic absorption within Biot's theory suggest $|\mathbf{u}_{bs}|$ and $|\mathbf{U}_{bs}|$ merit consideration. Figure 3(a) illustrates $|\mathbf{u}_{bs}|=|\mathbf{u}_1+\mathbf{u}_2|$ (solid line) at a distance of 0.01 m from the coordinate origin ($r=10a$) as well as the magnitudes of the fast and slow waves, $|\mathbf{u}_1|$ (dashed line) and $|\mathbf{u}_2|$ (dot-dashed line). The low-frequency resonance is clearly evident in $|\mathbf{u}_{bs}|$, $|\mathbf{u}_1|$, and $|\mathbf{u}_2|$ (although it is diminished in $|\mathbf{u}_{bs}|$). The high-frequency resonance appears to be completely absent from $|\mathbf{u}_{bs}|$ while $|\mathbf{u}_1|$ and $|\mathbf{u}_2|$ contain broad features near 40 kHz. Interference due to the superposition of the slow and fast wave displacements renders a measurement of $|\mathbf{u}_{bs}|$ as inconclusive with respect to the two monopole resonances. Figure 3(b) is similar to Fig. 3(a), but now Fig. 3(b) depicts the relevant displacements for the fluid constituent. It is clear that $|\mathbf{U}_{bs}|$ contains features related to the low- and high-frequency resonances.

Figure 4 shows the magnitudes of the displacements at $r=100a=0.1$ m from the coordinate origin. The interference between $\mathbf{u}_1$ and $\mathbf{u}_2$ in Fig. 4(a) is more pronounced than in Fig. 3(a). However, both resonance peaks are present in $|\mathbf{u}_{bs}|$. The low-frequency resonance occurs near 1.55 kHz, but an accurate identification of the high-frequency resonance (in the neighborhood of 40 kHz) is obfuscated by the interference. Figure 4 suggests that a measurement of $|\mathbf{u}_{bs}|$ or $|\mathbf{U}_{bs}|$ at $r \gg a$ will reveal two resonance features. The dis-

placements associated with the saturating fluid are shown in Fig. 4(b) for completeness.

Figures 3 and 4 demonstrate an important consequence of the highly attenuated slow wave. A comparison of $|\mathbf{u}_2|$ (or $|\mathbf{U}_2|$) in these figures shows the high-frequency resonance peak will be suppressed due to the attenuation of the slow wave. The scattering from an isolated bubble in a sediment will have a negligible effect on a bottom penetrating sonar. Figures 3 and 4 indicate that if the sediment contains a sparse population of bubbles, then the slow wave scattered displacement can be ignored in the context of a multiple scattering theory. For dense bubble populations, the scattered slow wave must be retained. Although the slow wave contribution can be neglected for a sparse bubble population, the full machinery of Biot's theory is still required because two resonance peaks occur in the fast wave displacement.

V. CONCLUSIONS

The research of Anderson and Hampton and Hawkins and Bedford indicate bubbles embedded in a saturated sediment have two distinct monopole resonances. The fluid and elastic scattering models developed in Secs. I and II cannot predict both of these monopole resonances. If Biot's theory is a correct characterization of the saturated sediment, then

two monopole resonances appear to be intrinsic properties of the model. An experimental effort is currently underway to definitely identify these resonances, and to explore the sensitivity of the resonance dynamics to changes in the material parameters.

We conclude this article with a cautionary note on performing sensitivity studies of the monopole resonances. By introducing variations in one of the material parameters in Biot's theory, one can observe shifts in the resonance peak locations and changes in the amplitudes. Equation (18) suggests that the Biot shear coefficient, N, is a good candidate for such an analysis because μ_s dominates the other parameters in (18). Another candidate parameter is the hydrostatic permeability, K_d; because it is often difficult to measure and reported values in the literature show a large variation. Extreme caution is warranted in any such sensitivity analysis because a change in N or K_d implies an implicit change in other material parameters. It is fairly well established that N and K_d as well as the tortuosity, α, and lattice bulk modulus, K_b, have complicated dependencies on the porosity.[5,18,19]

ACKNOWLEDGMENTS

APPENDIX A: MINNAERT BUBBLE

The resonance response of a gas-filled, spherical bubble in an infinite, incompressible fluid was first reported by Minnaert.[20] His classical result for the resonance, angular frequency is

$$\omega_{M0} = (3\gamma P_0/\rho_f a^2)^{1/2}. \tag{A1}$$

The equilibrium radius of the bubble is a, ρ_f is the constant density of the fluid, and P_0 is the ambient fluid pressure at infinity. The gas occupying the interior of the bubble satisfies an adiabatic, polytropic equation of state where γ is the polytropic gas constant.

Since Minnaert's initial work, others have developed complex (nonlinear) theories for the dynamics of a bubble in a realistic fluid (e.g., Rayleigh-Plesset[21,22] and Gilmore[22]). If standard linearization procedures are applied to these theories, ''corrections'' to ω_{M0} are obtained. These corrections typically involve such physical quantities as surface tension and the fluid's viscosity.[21–23] At this point, we could provide the Rayleigh–Plesset equation (or Gilmore equation), outline a linearization process, and then cite an expression for the resonance frequency of a spherical bubble in an incompressible fluid. A pedantic presentation often obfuscates the simple underlying physical mechanisms. Thus, our intention here is presentation of a simple physical, but intuitive, method to establish the resonance behavior of a Minnaert bubble.

Figure A1 shows volume element dv at the surface of a spherical bubble in an incompressible fluid. Under spherical volume pulsations, the mass $\rho_f dv$ exhibits harmonic motion about the equilibrium radius. Hence, a Lagrangian formula-
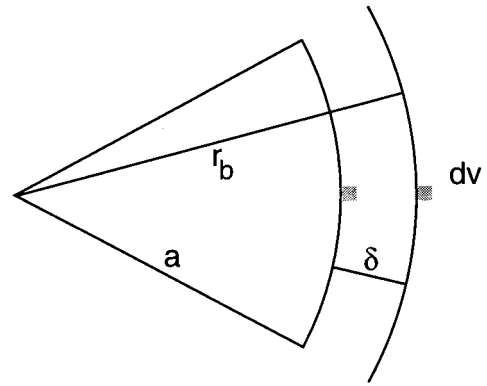
FIG. A1. Schematic for Minnaert bubble derivation. The volume dv undergoes harmonic oscillation about equilibrium radius $r_b = a$. The elemental area dA for dv at the surface of the bubble is essentially constant throughout the entire motion of dv. The dynamic radius is $r_b(t) = a + \delta(t)$.

tion is suitable for our purpose.[24] The Lagrangian density for dv is $\mathscr{L} = \mathscr{T} - \mathscr{U}$, where $\mathscr{T}$ and $\mathscr{U}$ are kinetic and potential energy densities, respectively. The incompressibility of the fluid, constant density, and the constraint that dv must remain at the bubble's surface imply $\mathscr{T} = \rho_f \dot{r}_b^2/2$. This is simply the kinetic energy of a mass $\rho_f dv$ moving with velocity $\dot{r}_b = \partial r_b/\partial t$. The Lagrangian formulation is completed by specifying the potential energy density. The incremental force required to move $\rho_f dv$ from a to r_b is $dF = \Delta p\, dA$, where dA is the elemental, cross-sectional area of $\rho_f dv$ at a, and dA remains essentially constant in going from a to r_b. The corresponding force density is approximately $\mathscr{F} = dF/(a\,dA) = a^{-1}\Delta p$ for small displacements from equilibrium. At the level of our heuristic argument, $\mathscr{F}$ is a conservative force density, so the potential energy density is

$$\mathscr{U} = -\int_a^{r_b} \mathscr{F}\, dr' = -a^{-1}\int_a^{r_b} \Delta p\, dr'. \tag{A2}$$

The change in pressure, Δp, is the difference between the pressure in the fluid, $p_f(r)$, and the ambient pressure, P_0. For mechanical stability (to first order), the force exerted by the interior gas balances the forces exerted by the exterior fluid and surface tension.[21,25] This implies that $p_g(r_b) = p_f(r_b) + 2\sigma/r_b$, where $p_g(r_b)$ is the pressure within the bubble and σ is the surface tension. The surface tension contribution is known as the Laplace pressure. We, here, ignore the distinction between vapor and gas and assume that mass transfer by condensation and evaporation is negligible. Additionally, σ is essentially constant to first order for small deviations of the radius from its equilibrium value. With the adiabatic polytropic equation of state, $pV^\gamma = $ const, the fluid pressure becomes

$$p_f(r_b) = p_0(a/r_b)^{3\gamma} - 2\sigma/r_b. \tag{A3}$$

Here p_0 is determined from a quiescent bubble and the equilibrium condition $p_g(r_b = a) = P_0$. This yields $p_0 = P_0 + 2\sigma/a$. Substitution of (A3) into (A2) and performing the integration leads to

$$\mathscr{U} = \frac{p_0}{3\,\gamma-1}\left[\left(\frac{a}{r_b}\right)^{3\gamma-1}-1\right]+\frac{2\sigma}{a}\ln\left(\frac{r_b}{a}\right)+P_0\left(\frac{r_b-a}{a}\right).\tag{A4}$$

The monopole resonance frequency is determined from a bubble experiencing linear oscillations where the instantaneous radius deviates from equilibrium by a small amount; i.e., $r_b(t)=a+\delta(t)$ such that $\delta(t)\ll a$. The linearized Lagrangian density satisfies

$$2\mathscr{L}=\rho_f\dot{\delta}^2-\left(\frac{3\gamma p_0}{a^2}-\frac{2\sigma}{a^3}\right)\delta^2.\tag{A5}$$

Clearly, δ is a generalized coordinate and $\dot{\delta}$ is the corresponding generalized velocity. Equation (A5) corresponds to a simple harmonic oscillator where straightforward manipulations involving Lagrange's equation yield

$$\omega_{m0}=\left(\frac{3\gamma p_0}{\rho_f a^2}-\frac{2\sigma}{\rho_f a^3}\right)^{1/2}\tag{A6}$$

as the monopole resonance frequency for a spherical bubble.[21,22,26] Inspection of (A1) and (A6) shows surface tension effects become important for small bubbles (typically $a<10\ \mu$m).

APPENDIX B: MATHEMATICAL FORMULATION OF BIOT THEORY

Since the seminal work of Biot,[14] literally hundreds of articles have addressed wave propagation in a saturated porous medium (e.g., see the references in Kargl and Lim[5] and Bourbié *et al.*[27]) Unfortunately, two mathematical formulations for this phenomenon have gained acceptance. The Biot representation[28,29] is written in terms of the average lattice displacement **u** and the average fluid displacement **U**. The Biot–Stoll representation,[17,30] develops the wave propagation model in terms of **u** and the relative fluid displacement $\mathbf{w}=\beta(\mathbf{u}-\mathbf{U})$. Although these formulations can be shown to be entirely equivalent, each has certain advantages and disadvantages in the interpretation of the fundamental physics. The intent of this Appendix is to provide sufficient details of the Biot representation used as the basis of Sec. III.

The time-harmonic, coupled equations governing wave propagation in a saturated poroelastic medium are

$$\rho_{11}\omega^2\mathbf{u}+\rho_{12}\omega^2\mathbf{U}+\mathbf{D}(\omega)=-\nabla\cdot\mathsf{T},\tag{B1}$$

$$\rho_{12}\omega^2\mathbf{u}+\rho_{22}\omega^2\mathbf{U}-\mathbf{D}(\omega)=-\nabla\cdot\mathsf{S},\tag{B2}$$

where (B1) describes the motion of the viscoelastic lattice and (B2) corresponds to the fluid's motion. The effective densities ρ_{11}, ρ_{12}, and ρ_{22} are related to the fluid's density ρ_f and the density of the viscoelastic material ρ_e through

$$\rho_{11}+\rho_{12}=(1-\beta)_{\rho_e},\tag{B3}$$

$$\rho_{12}+\rho_{22}=\beta\rho_f,\tag{B4}$$

$$\rho_{22}=-\beta^2 F_i(\omega)/\omega.\tag{B5}$$

The porosity of the medium (ratio of pore volume to total volume) is β and $F_i(\omega)$ accounts for viscous inertial effects (see below). The effective stress tensors for the viscoelastic lattice T and saturating fluid S are

$$\mathsf{T}=N\mathsf{I}\times\nabla\times\mathbf{u}+2N\nabla\mathbf{u}+\mathsf{I}(P-2N)\nabla\cdot\mathbf{u}+\mathsf{I}Q\nabla\cdot\mathbf{U},\tag{B6}$$

$$\mathsf{S}=\mathsf{I}Q\nabla\cdot\mathbf{u}+\mathsf{I}R\nabla\cdot\mathbf{U}=-\mathsf{I}\beta p_f,\tag{B7}$$

where I is the identity tensor, p_f is the pressure in the saturating fluid, and P, Q, R, and N are material parameters. Here N is a shear Lamé constant for the lattice while the other parameters are defined in terms of the bulk moduli of the lattice, K_b, the viscoelastic solid, K_s, and the fluid, K_f. Expressions for P, Q, and R are

$$P=\frac{(1-\beta)(1-\beta-K_b/K_s)K_s+\beta K_s K_b/K_f}{1-\beta-K_b/K_s+\beta K_s/K_f}+\frac{4N}{3},\tag{B8}$$

$$Q=\frac{(1-\beta-K_b/K_s)\beta K_s}{1-\beta-K_b/K_s+\beta K_s/K_f},\tag{B9}$$

$$R=\frac{\beta^2 K_s}{1-\beta-K_b/K_s+\beta K_s/K_f}.\tag{B10}$$

Energy absorption by the lattice is included in Biot's theory by permitting K_b and N to be complex-valued constants.

In (B1) and (B2), the frequency-dependent dissipation function $\mathbf{D}(\omega)$ contains the viscous drag force associated with fluid motion relative to the lattice. For the time convention specified in Sec. I, we have

$$\mathbf{D}(\omega)=-i\omega\beta^2 F_r(\omega)(\mathbf{U}-\mathbf{u}).\tag{B11}$$

According to homogenization theory, $F_r(\omega)$ and the inertial factor $F_i(\omega)$ in (B5) are specified as the real and imaginary components of the fluid viscosity divided by a generalized dynamic permeability. The dynamic permeability is available for several pore geometries in the low-frequency limit; however, exact analytic results valid over an extended frequency range are only available for pore geometries composed of cylindrical slits or circular cylinders.[31] Others have argued that the dynamic permeability of a medium consisting of circular cylindrical pores is nearly universal provided its amplitude and frequency dependence are properly scaled.[18,32,33] For our purposes in Secs. III and IV, this universality is assumed valid. Lim gives[13]

$$F_r(\omega)+iF_i(\omega)=\frac{\eta}{K_d}\left(\frac{i\omega J_0(\sqrt{i8\omega/\omega_c})}{\omega_c J_2(\sqrt{i8\omega/\omega_c})}\right),\tag{B12}$$

$$\omega_c=\beta\eta/\alpha K_d\rho_f,\tag{B13}$$

where η is the fluid viscosity, K_d is the intrinsic permeability (Darcy's constant), and α is the tortuosity parameter characterizing the microstructure of the porous medium. The critical angular frequency ω_c defines the transition from the low-frequency regime to the high-frequency regime. It can be interpreted as the angular frequency where viscous boundary layer effects become important.

One consequence of (B11) and (B12) with respect to (B1) and (B2) is the introduction of complex-valued, frequency-dependent effective densities

$$\widetilde{\rho}_{jj'}\equiv\rho_{jj'}+i(-1)^{j+j'}\beta^2 F_r(\omega)/\omega,\quad j\leq j'=1,2.\tag{B14}$$

Additionally, the assumed time harmonic dependence of the wave fields (i.e., $e^{-i\omega t}$) and the decomposition of (B1) and (B2) along with (B6) and (B7) into longitudinal and transverse vector components yields the characteristic equations

$$(PR - Q^2)k^4 - (\tilde{\rho}_{11}R + \tilde{\rho}_{22}P - 2\tilde{\rho}_{12}Q)\omega^2 k^2$$
$$+ (\tilde{\rho}_{11}\tilde{\rho}_{22} - \tilde{\rho}_{12}^2)\omega^4 = 0 \qquad (B15)$$

and

$$k_3 = \omega[(\tilde{\rho}_{11}\tilde{\rho}_{22} - \tilde{\rho}_{12}^2)/\tilde{\rho}_{22}N]^{1/2}. \qquad (B16)$$

Equation (B15) has two roots corresponding to the fast and slow longitudinal wave numbers. (The remaining two roots are discarded from consideration of causality.) The dispersion relation in (B16) gives the shear wave number. The vector decomposition also allows one to eliminate $\mathbf{U}$ in terms of $\mathbf{u}$ from (B1) and (B2). This procedure gives the simple relationship $\mathbf{U}_j = A_j\mathbf{u}_j$ where

$$A_j = -\frac{\tilde{\rho}_{11}\omega^2 - Pk_j^2}{\tilde{\rho}_{12}\omega^2 - Qk_j^2} = -\frac{\tilde{\rho}_{12}\omega^2 - Qk_j^2}{\tilde{\rho}_{22}\omega^2 - Rk_j^2}, \quad j = 1,2, \quad (B17)$$

for longitudinal waves and $A_3 = -\tilde{\rho}_{12}/\tilde{\rho}_{22}$ for the shear wave. Finally, the constant

$$\Gamma_j = [k_3(P + 2QA_j + RA_j^2)/k_jN]^{1/2}, \quad j = 1,2, \qquad (B18)$$

is a result of the normalization imposed by Kargl and Lim on the vector eigenfunctions.[5]

[1] A. L. Anderson and L. D. Hampton, ''Acoustics of gas-bearing sediments I. Background,'' J. Acoust. Soc. Am. **67**, 1865–1889 (1980).

[2] A. L. Anderson and L. D. Hampton, ''Acoustics of gas-bearing sediments. II. Measurements and models,'' J. Acoust. Soc. Am. **67**, 1890–1903 (1980).

[3] E. L. Hamilton, ''Shear-wave velocity versus depth in marine sediments: A review,'' Geophysics **41**, 985–996 (1976).

[4] J. A. Hawkins and A. Bedford, ''Variational theory of bubble media with a distribution of bubble sizes—II. Porous solids,'' Int. J. Eng. Sci. **30**, 1177–1186 (1992).

[5] S. G. Kargl and R. Lim, ''A transition-matrix formulation of the scattering in homogeneous, saturated, porous media,'' J. Acoust. Soc. Am. **94**, 1527–1550 (1993).

[6] S. G. Kargl, K. L. Williams, and R. Lim, ''Double monopole resonance of a gas-filled cavity in a sediment,'' J. Acoust. Soc. Am. **96**, 3218(A) (1994).

[7] A. Boström, ''Scattering of stationary acoustic waves by an elastic obstacle immersed in a fluid,'' J. Acoust. Soc. Am. **67**, 390–398 (1980).

[8] A. D. Pierce, *Acoustics — An Introduction to Its Physical Principles and Applications* (Acoustical Society of America, Woodbury, NY, 1989), p. 28, Eq. 1-9.1.

[9] R. Lim and R. H. Hackman, ''Comments on the calculation of cross sections for elastic-wave scattering using the T matrix,'' J. Acoust. Soc. Am. **87**, 1070–1075 (1990).

[10] E. Meyer, K. Brendel, and K. Tamm, ''Pulsation oscillations of cavities in rubber,'' J. Acoust. Soc. Am. **30**, 1116–1124 (1958).

[11] I. B. Andreeva, ''Scattering of sound by air bladders of fish in deep sound-scattering ocean layers,'' Sov. Phys. Acoust. **10**, 17–20 (1964).

[12] F. G. Blake, Jr., ''Spherical wave propagation in solid media,'' J. Acoust. Soc. Am. **24**, 211–215 (1952).

[13] R. Lim, ''Scattering by an obstacle in a plane-stratified poroelastic medium: Application to an obstacle in ocean sediments,'' J. Acoust. Soc. Am. **95**, 1223–1244 (1994).

[14] M. A. Biot, in *Acoustics, Elasticity, and Thermodynamics of Porous Media: Twenty-one papers by M. A. Biot*, edited by I. Tolstoy (Acoustical Society of America, New York, 1992).

[15] H. Deresiewicz and R. Skalak, ''On uniqueness in dynamic poroelasticity,'' Bull. Seismol. Soc. Am. **53**, 783–788 (1963).

[16] M. Stern, A. Bedford, and H. R. Millwater, ''Wave reflection from a sediment layer with depth-dependent properties,'' J. Acoust. Soc. Am. **77**, 1781–1788 (1985).

[17] R. D. Stoll and T. K. Kan, ''Reflection of acoustic waves at a water-sediment interface,'' J. Acoust. Soc. Am. **70**, 149–156 (1981).

[18] D. L. Johnson, J. Koplik, and R. Dashen, ''Theory of dynamic permeability and tortuosity in fluid-saturated porous media,'' J. Fluid Mech. **176**, 379–402 (1987).

[19] J. Bear, *Dynamics of Fluids in Porous Media* (Dover, New York, 1988), p. 43ff.

[20] M. Minnaert, ''On musical air-bubbles and the sounds of running water,'' Philos. Mag. **16**, 235–248 (1933).

[21] A. A. Atchley and L. A. Crum, in *Ultrasound: Its Chemical, Physical, and Biological Effects*, edited by K. S. Suslick (VCH, New York, 1988), pp. 1–64.

[22] T. G. Leighton, *The Acoustic Bubble* (Academic, New York, 1994), Chap. 4.

[23] A. Shima, ''The natural frequency of a bubble oscillating in a viscous compressible liquid,'' Trans. Am. Soc. Mech. Eng. Ser. D **92**, 555–562 (1970) (formerly J. Basic Eng.).

[24] C. Devin, Jr., ''Survey of thermal, radiation, and viscous damping of pulsating air bubbles in water,'' J. Acoust. Soc. Am. **31**, 1654–1667 (1959).

[25] A. A. Atchley, ''The Blake threshold of a cavitation nucleus having a radius-dependent surface tension,'' J. Acoust. Soc. Am. **85**, 152–157 (1989).

[26] R. B. Robinson and R. H. Buchanan, ''Undamped free pulsation of an ideal bubble,'' Proc. Phys. Soc. London, Sect. B **69**, 893–900 (1956).

[27] T. Bourbié, O. Coussy, and B. Zinszner, *Acoustics of Porous Media* (Gulf, Houston, TX, 1987).

[28] D. L. Johnson and T. J. Plona, ''Acoustic slow waves and the consolidation transition,'' J. Acoust. Soc. Am. **72**, 556–565 (1982).

[29] S. Feng and D. L. Johnson, ''High-frequency acoustic properties of a fluid/porous solid interface. I. New surface mode,'' J. Acoust. Soc. Am. **74**, 906–914 (1983).

[30] R. D. Stoll, ''Acoustic wave in ocean sediments,'' Geophysics **42**, 715–725 (1977).

[31] A. N. Norris, ''On the viscodynamic operator in Biot's equations of poroelasticity,'' J. Wave-Mater. Interaction **1**, 365–380 (1986).

[32] P. Sheng and M. Y. Zhou, ''Dynamic permeability in porous media,'' Phys. Rev. Lett. **61**, 1591–1594 (1988).

[33] E. Charlaix, A. P. Kushnick, and J. P. Stokes, ''Experimental study of dynamic permeability in porous media,'' Phys. Rev. Lett. **61**, 1595–1598 (1988).

Near-field scattering through and from a two-dimensional fluid–fluid rough interface

John E. Moe[a)] and Darrell R. Jackson

Applied Physics Laboratory, College of Ocean and Fishery Sciences, Department of Electrical Engineering, University of Washington, Seattle, Washington 98105

A general analytical expression for the *time-dependent* mean-square incoherent field scattered *from* or *through* (penetrating) a 2-D fluid–fluid rough interface for a narrow-band incident plane-wave source is derived and expressed in terms of the second moment of the rough interface T-matrix. This analytical expression is independent of the scattering solution technique, and for distances greater than only a few wavelengths from the interface, is equivalently expressed in terms of the bistatic scattering cross section per unit area per unit solid angle (differential cross section) of the rough interface. Using this rigorously derived result, the scattered field for a narrow-band point source is heuristically derived. This derivation leads to the usual sonar equation in the limit as the narrow-band signal approaches the cw (continuous wave) case. First-order perturbation calculations for the case of a baseband Gaussian shaped source pulse illustrate narrow-band pulse dispersion effects of the incoherent field for forward scattering into a lossy sediment. For the case of incidence below the critical grazing angle, first-order perturbation computations also show that the incoherent field scattered through a rough interface can be much greater than the zeroth-order field (coherent) transmitted below the corresponding flat-surface depending on loss and receiver depth. These computations for the first-order mean square incoherent field penetrating the rough interface are compared to the results for the flat-surface case, for both plane-wave and point sources. © *1998 Acoustical Society of America.* [S0001-4966(98)01501-X]

INTRODUCTION

The time-dependent mean-square incoherent scattered field can be expressed in terms of a two-dimensional integral over the two-frequency mutual coherence function, $\Gamma(\omega_1, \omega_2)$, (see Ishimaru, 1978a, or Ishimaru *et al.*, 1994a). Scattering of a pulse from the ocean surface is addressed in Ziomek (1982a, b), where $\Gamma(\omega_1, \omega_2)$ is presented in terms of a Kirchhoff representation. Ishimaru *et al.* (1994a) derive an analytical expression for $\Gamma(\omega_1, \omega_2)$ for scattering from rough surfaces based on the Kirchhoff approximation, and Ishimaru *et al.* (1994b) use a second-order Kirchhoff approximation with shadowing corrections (Ishimaru and Chen, 1990, 1991) to obtain an analytical expression for $\Gamma(\omega_1, \omega_2)$ that includes backscattering enhancement effects. In this paper, we obtain a general expression for $\Gamma(\omega_1, \omega_2)$ appropriate for rough interface scattering for a narrow-band incident plane wave that does not depend on a particular scattering approximation, and is valid for scattering through the interface into a lossy fluid, in addition to scattering from the interface.

In order to obtain simple analytic expressions for the time-dependent scattered field, Ishimaru *et al.* (1994a, b) assume the scattering channel is WSSUS (wide-sense stationary uncorrelated scattering channel) (Ishimaru, 1978a)—the two-frequency mutual coherence function, $\Gamma(\omega_1, \omega_2)$ is only dependent on the frequency difference, $\omega_d = \omega_2 - \omega_1$, and

not on $(\omega_1 + \omega_2)/2$. Because of frequency-dependent attenuation in ocean sediment, we do not assume that $\Gamma(\omega_1, \omega_2)$ is only dependent on ω_d. However, we assume that the incoherent T-matrix correlation function varies slowly over the source frequency range, and dispersion effects due to frequency-dependent phase speed are treated by expanding phase terms in a power series about the center frequency. Both the incoherent T-matrix correlation function approximation, and the power series expansion require that the source signal be narrowband. Using this approach, a general analytical expression for the time-dependent mean-square incoherent field scattered *from* and *through* a 2-D fluid–fluid rough interface for a narrow-band incident plane wave is derived and expressed in terms of the second moment of the T-matrix. When sufficiently far from the rough interface to neglect evanescent waves, this expression can be expressed in terms of the scattering cross section per unit area per unit solid angle (differential cross section) of the rough interface. This example [also presented by Moe (1996)] shows that the differential cross section, a far-field quantity, can be useful at very short ranges. Jackson *et al.* (1997) generalizes this result to arbitrary cw esonification. First-order perturbation results illustrate the contribution of the evanescent component to the incoherent scattered field for a cw plane-wave source for the field scattered through the interface. The resulting profile of mean-square incoherent field versus depth is compared with the profile for the flat-surface case (coherent), also illustrating the effect of roughness on the field penetrating a fluid–fluid interface.

Using the expression for the scattered time-dependent

[a)]Present address: Acuson Corporation, 1220 Charleston Rd., P.O. Box 7393, Mountain View, CA 94039.
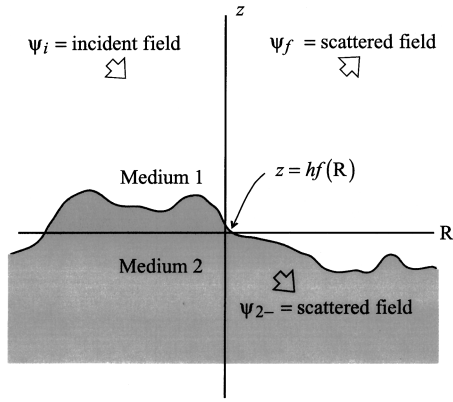
FIG. 1. Scattering problem geometry for rough interface separating a lossless fluid in medium 1 ($z > hf(\mathbf{R})$), from a lossy fluid in medium 2 ($z < hf(\mathbf{R})$). This diagram can be viewed as a slice through a 2-D surface.

mean-square incoherent field due to an incident plane wave, the expression for the scattered field resulting from a narrow-band point source is heuristically obtained. This result leads to the usual sonar equation in the limit as the narrow-band signal approaches the cw (continuous wave) case. A simple analytical expression is obtained for the case of a baseband Gaussian shaped source pulse, also in terms of the differential cross section. First-order perturbation calculations for this case illustrate narrow-band pulse dispersion effects of the incoherent field for forward scattering into a lossy sediment. When incidence is below the critical grazing angle, first-order perturbation computations also show that the incoherent field scattered through a rough interface can be much greater than the zeroth-order (flat-surface) field transmitted below the corresponding flat-surface depending on loss and receiver depth.

I. FORMULATION OF THE SCATTERING EQUATIONS

Figure 1 shows a 2-D slice of the 3-D ocean model. A time-dependent field in a homogenous fluid (water) above a 2-D rough water–sediment interface results in energy scattered from the interface back into the water, and through the rough interface into the sediment. The sediment is represented by a homogenous lossy fluid. The zero-mean rough interface is defined by

$$z = hf(\mathbf{R}), \tag{1}$$

where $\mathbf{R}$ is the transverse component of the three-dimensional position vector $\mathbf{r}$, and h is the root-mean-square (rms) height of the rough interface. The total field, $\psi_1(\mathbf{r})$, above the rough interface is a sum of the incident field, $\psi_i(\mathbf{r})$, and the resulting scattered pressure field, $\psi_f(\mathbf{r})$:

$$\psi_1(\mathbf{r}) = \psi_i(\mathbf{r}) + \psi_f(\mathbf{r}). \tag{2}$$

The boundary conditions on the interface consist of the continuity of pressure:

$$\psi_1(\mathbf{r})|_{z=hf(\mathbf{R})} = \psi_2(\mathbf{r})|_{z=hf(\mathbf{R})}, \tag{3}$$

and the continuity of normal velocity:

$$\frac{1}{\rho_1} \hat{n} \cdot \nabla \psi_1(\mathbf{r}) \bigg|_{z=hf(\mathbf{R})} = \frac{1}{\rho_2} \hat{n} \cdot \nabla \psi_2(\mathbf{r}) \bigg|_{z=hf(\mathbf{R})}, \tag{4}$$

where ψ_2 is the pressure field in the sediment, $\hat{n}$ is the unit vector normal to the interface, ρ_1 is the density of the water, and ρ_2 is the density of the sediment. The scattered field in the region above the highest point on the interface, $\psi_f(\mathbf{r})$, and the incident field, are expressed in terms of the following (Weyl) plane-wave expansions (Devaney and Sherman, 1973):

$$\psi_f(\mathbf{r}) = \int d^2K \ \Psi_f(\mathbf{K}) e^{ik_1 \beta_1(\mathbf{K})z} e^{i\mathbf{K}\cdot\mathbf{R}} \tag{5}$$

and

$$\psi_i(\mathbf{r}) = \int d^2K \ \Psi_i(\mathbf{K}) e^{-ik_1 \beta_1(\mathbf{K})z} e^{i\mathbf{K}\cdot\mathbf{R}}, \tag{6}$$

where $\mathbf{K}$ is the two-dimensional transverse wave vector with magnitude K, k_1 is the wave number in the medium above the interface, and

$$\beta_1(\mathbf{K}) = \sqrt{1 - K^2/k_1^2}. \tag{7}$$

The square root in Eq. (7) is chosen so that β_1 is either positive or positive imaginary. For the cw (continuous wave) case, a factor of $e^{-i\omega t}$ is suppressed, but in general, Eqs. (5) and (6) are the Fourier transforms of the time domain field,

$$\psi_1(\mathbf{r}) \equiv \psi_1(\mathbf{r},\omega) = \int dt \ \psi_1(\mathbf{r},t) e^{i\omega t}. \tag{8}$$

The field below the rough interface is expressed as a plane-wave expansion of waves traveling in the negative z direction,

$$\psi_{2-}(\mathbf{r}) \equiv \int d^2K \ \Psi_{2-}(\mathbf{K}) e^{-ik_2 \beta_2(\mathbf{K})z} e^{i\mathbf{K}\cdot\mathbf{R}}, \quad z < 0, \tag{9}$$

where

$$\beta_2(\mathbf{K}) = \sqrt{1 - K^2/k_2^2} \tag{10}$$

and

$$k_2 = \frac{(1+i\delta)\omega}{\nu c_1} \tag{11}$$

is the complex wave number in the lossy medium below the interface with frequency independent loss parameter, δ. The speed ratio, ν, is the ratio of the sound speed in the sediment, c_2, to the sound speed in the water, c_1. Although the definition of k_2 in Eq. (11) violates causality (Aki and Richards, 1980; Wingham, 1985), these noncausal effects are seen to be negligible and consistent with the approximations made in deriving the analytical result. The square root in Eq. (10) is chosen such that β_2 is in the first quadrant of the complex plane. The field scattered back into medium 1 can be expressed in terms of the incident field and the T-matrix, T_{11}:

$$\Psi_f(\mathbf{K}) = \int d^2K' \ T_{11}(\mathbf{K},\mathbf{K}') \Psi_i(\mathbf{K}'). \tag{12}$$

Likewise, the downward component of the scattered field penetrating below the interface is expressed in terms of the T-matrix, T_{12}:

$$\Psi_{2-}(\mathbf{K}) = \int d^2K' \ T_{12}(\mathbf{K},\mathbf{K}') \Psi_i(\mathbf{K}'). \tag{13}$$

The scattered field for the case of an incident plane wave is found by substituting,

$$\Psi_i(\mathbf{K}) = \delta(\mathbf{K} - \mathbf{K}_i), \tag{14}$$

into Eq. (12), and the result into Eq. (5), yielding

$$\psi_f(\mathbf{r}) = \int d^2K \ T_{11}(\mathbf{K}, \mathbf{K}_i) e^{ik_1\beta_1(\mathbf{K})z} e^{i\mathbf{K}\cdot\mathbf{R}}. \tag{15}$$

The scattered field penetrating the interface for the incident plane wave case is found in the same way from Eqs. (9), (13), and (14),

$$\psi_{2-}(\mathbf{r}) = \int d^2K \ T_{12}(\mathbf{K}, \mathbf{K}_i) e^{-ik_2\beta_2(\mathbf{K})z} e^{i\mathbf{K}\cdot\mathbf{R}}. \tag{16}$$

For convenience, let $\psi(\mathbf{r})$ represent both $\psi_f(\mathbf{r})$ and $\psi_{2-}(\mathbf{r})$. Define

$$\widetilde{\psi}(\mathbf{r}) \equiv \psi(\mathbf{r}) - \langle \psi(\mathbf{r}) \rangle, \tag{17}$$

where $\langle \psi(\mathbf{r}) \rangle$ is the mean of the field averaged over the ensemble of rough interfaces. Similarly, define

$$\widetilde{T}(\mathbf{K}, \mathbf{K}_i) = T(\mathbf{K}, \mathbf{K}_i) - \langle T(\mathbf{K}, \mathbf{K}_i) \rangle \tag{18}$$

to be the incoherent T-matrix. Using the definitions above, $\widetilde{\psi}(\mathbf{r})$, is expressed as

$$\widetilde{\psi}(\mathbf{r}) = \int d^2K \ \widetilde{T}(\mathbf{K}, \mathbf{K}_i) e^{-ik_2\beta_2(\mathbf{K})z} e^{i\mathbf{K}\cdot\mathbf{R}}. \tag{19}$$

II. GENERAL RESULT FOR INCIDENT PLANE WAVE

The purpose of this section is to derive an expression for the time-dependent mean-square incoherent field at the receiver position, $\mathbf{r}$, due to a narrow-band plane-wave source. Although the following derivation considers the more general case of scattering *through* a rough interface, the solution also applies to scattering *from* a rough interface.

A. Time domain received signal

A narrow-band source signal $s(t)$, with units of pressure, and with Fourier transform:

$$S(\omega) = \int_{-\infty}^{\infty} dt \ s(t) e^{i\omega t}, \tag{20}$$

can be represented as

$$s(t) = \mathrm{Re}\{u(t) e^{-i\omega_c t}\}, \tag{21}$$

where $u(t)$ is the corresponding complex baseband input signal, with Fourier transform, $U(\omega)$, and ω_c is the carrier frequency, or center frequency of the pulse (see for example Ishimaru, 1978a; Proakis, 1989). An incident plane-wave pulse with direction denoted by the transverse unit vector, $\hat{\alpha}_i$, and incident grazing angle θ_i, is expressed in terms of its 2-D Fourier transform as

$$\Psi_i(\mathbf{K}, \omega) = S(\omega) \delta(\mathbf{K} - \mathbf{K}_i) e^{i\omega z_s \sin \theta_i / c_1}, \tag{22}$$

where

$$\mathbf{K}_i = \frac{\omega}{c_1} \cos \theta_i \hat{\alpha}_i, \tag{23}$$

is the incident transverse wave vector, and z_s is taken to be an arbitrary source height. Using Eqs. (9), (13), (17), (18), (20), (21), (22), and chapter 5 of Ishimaru (1978a), the incoherent field $\widetilde{\psi}_{bb}(\mathbf{r},t)$ at a position $\mathbf{r} = (\mathbf{R}, z)$ below the interface is expressed as

$$\widetilde{\psi}_{bb}(\mathbf{r}, t) = \frac{1}{2\pi} \int d\omega' \ U(\omega') \mathscr{H}_{12}(\omega' + \omega_c) e^{-i\omega' t}, \tag{24}$$

where

$$\mathscr{H}_{12}(\omega' + \omega_c) = \int d^2K \{ \widetilde{T}_{12}(\mathbf{K}, \mathbf{K}_i, \omega'$$
$$+ \omega_c) e^{i \sin \theta_i z_s (\omega' + \omega_c)/c_1}$$
$$\times e^{-i\kappa\beta_2(\mathbf{K}, \omega' + \omega_c)z(\omega' + \omega_c)/c_1} e^{i\mathbf{K}\cdot\mathbf{R}} \} \tag{25}$$

is the Fourier transfer of the impulse response of the incoherent field, generally known as the transfer function. The complex wave number ratio is given by

$$\kappa \equiv \frac{k_2}{k_1} = \frac{(1 + i\delta)}{\nu}, \tag{26}$$

and

$$\mathbf{K}_i = \frac{\omega' + \omega_c}{c_1} \cos \theta_i \hat{\alpha}_i \tag{27}$$

is the transverse wave vector of the incident field. The dependence of β_2 on frequency and $\mathbf{K}$ is explicitly shown.

B. Time-dependent mean square incoherent field

The time-dependent mean-square incoherent field at position $\mathbf{r}$ can be expressed as (Ishimaru, 1978a, Chap. 4):

$$I_2(\mathbf{r}, t) = \langle |\widetilde{\psi}_{bb}(\mathbf{r}, t)|^2 \rangle. \tag{28}$$

Combining Eqs. (24) and (28) yields Eq. (5–17) (Ishimaru, 1978a):

$$I_2(\mathbf{r}, t) = \left(\frac{1}{2\pi}\right)^2 \int d\omega' \int d\omega'' \{ U(\omega') U^*(\omega'')$$
$$\times e^{-i\omega' t} e^{i\omega'' t} \Gamma(\omega' + \omega_c, \omega'' + \omega_c) \}, \tag{29}$$

where

$$\Gamma(\omega' + \omega_c, \omega'' + \omega_c) = \langle \mathscr{H}_{12}(\omega' + \omega_c) \mathscr{H}_{12}^*(\omega'' + \omega_c) \rangle, \tag{30}$$

is defined by Ishimaru (1978a) as the two-frequency mutual coherence function. Using the expression for $\mathscr{H}_{12}$ in Eq. (25), Eq. (30) is equivalent to

277   J. Acoust. Soc. Am., Vol. 103, No. 1, January 1998

J. E. Moe and D. R. Jackson: Near-field scattering   277

$$\Gamma(\omega'+\omega_c,\omega''+\omega_c)$$

$$=\int d^2K''\int d^2K'\langle\widetilde{T}_{12}(\mathbf{K}',\mathbf{K}'_i,\omega'+\omega_c)\widetilde{T}^*_{12}(\mathbf{K}'',\mathbf{K}''_i,\omega''$$

$$+\omega_c)\rangle e^{i\mathbf{K}'\cdot\mathbf{R}}e^{-i\mathbf{K}''\cdot\mathbf{R}}e^{i\sin\theta_i z_s\omega'/c_1}e^{-i\sin\theta_i z_s\omega''/c_1}$$

$$\times e^{-i\kappa\beta_2(\mathbf{K}',\omega'+\omega_c)z(\omega'+\omega_c)/c_1}$$

$$\times e^{i(\kappa\beta_2(\mathbf{K}'',\omega''+\omega_c))^*z(\omega''+\omega_c)/c_1}\},\tag{31}$$

where the transverse wave vectors for the incident field at the angular frequencies ω'', and ω' are

$$\mathbf{K}''_i=\frac{\omega_c+\omega''}{c_1}\cos\theta_i\hat{\alpha}_i,\quad\mathbf{K}'_i=\frac{\omega_c+\omega'}{c_1}\cos\theta_i\hat{\alpha}_i.\tag{32}$$

Define $\mathscr{C}_{12}(\mathbf{K}',\mathbf{K}'',\mathbf{K}'_i,\mathbf{K}''_i,\omega_c+\omega',\omega_c+\omega'')$ (see for example Voronovich, 1994) such that

$$\langle\widetilde{T}_{12}(\mathbf{K}',\mathbf{K}'_i,\omega'+\omega_c)\widetilde{T}^*_{12}(\mathbf{K}'',\mathbf{K}''_i,\omega''+\omega_c)\rangle$$

$$\equiv\mathscr{C}_{12}(\mathbf{K}',\mathbf{K}'',\mathbf{K}'_i,\mathbf{K}''_i,\omega_c+\omega',\omega_c+\omega'')$$

$$\times\delta(\mathbf{K}''-\mathbf{K}'+\mathbf{K}'_i-\mathbf{K}''_i).\tag{33}$$

We refer to $\mathscr{C}_{12}$ as the incoherent T-matrix correlation function. In the expression above, the subscript is used to represent scattering into the sediment and the dependence of $\widetilde{T}_{12}$ on ω is included in the argument. Substituting Eq. (33) and

$$\mathbf{K}''_i-\mathbf{K}'_i=\frac{\omega''-\omega'}{c_1}\cos\theta_i\hat{\alpha}_i\equiv\mathbf{K}_d\tag{34}$$

into Eq. (31), and changing the integration variable $\mathbf{K}'$ to

$$\mathbf{K}=\mathbf{K}'+\mathbf{K}_d/2,\tag{35}$$

yields

$$\Gamma(\omega'+\omega_c,\omega''+\omega_c)$$

$$=\int d^2K\{\mathscr{C}_{12}(\mathbf{K}-\mathbf{K}_d/2,\mathbf{K}+\mathbf{K}_d/2,\mathbf{K}'_i,\mathbf{K}''_i,\omega_c+\omega',\omega_c$$

$$+\omega'')e^{-i\mathbf{K}_d\cdot\mathbf{R}}e^{i\sin\theta_i z_s\omega'/c_1}e^{-i\sin\theta_i z_s\omega''/c_1}$$

$$\times e^{-i\kappa\beta_2(\mathbf{K}-\mathbf{K}_d/2,\omega_c+\omega')z(\omega_c+\omega')/c_1}$$

$$\times e^{i(\kappa\beta_2(\mathbf{K}+\mathbf{K}_d/2,\omega_c+\omega''))^*z(\omega_c+\omega'')/c_1}\}.\tag{36}$$

Equation (36) is now evaluated by making a few approximations. When $\mathscr{C}_{12}$ is a slowly varying function of frequency, and the source signal is narrow band—the source signal center frequency is much greater than its bandwidth—

$$\mathscr{C}_{12}(\mathbf{K}-\mathbf{K}_d/2,\mathbf{K}+\mathbf{K}_d/2,\mathbf{K}'_i,\mathbf{K}''_i,\omega_c+\omega'',\omega_c+\omega')$$

$$\cong\mathscr{C}_{12}(\mathbf{K},\mathbf{K},\mathbf{K}_i,\mathbf{K}_i,\omega_c,\omega_c)\equiv\mathscr{C}_{12}(\mathbf{K},\mathbf{K}_i,\omega_c),\tag{37}$$

where the relation (Thorsos and Jackson, 1989; Berman, 1992),

$$\mathscr{C}_{12}(\mathbf{K},\mathbf{K}_i,\omega_c)\delta(\mathbf{K}-\mathbf{K}'')$$

$$\equiv\langle\widetilde{T}_{12}(\mathbf{K},\mathbf{K}_i,\omega_c)\widetilde{T}^*_{12}(\mathbf{K}'',\mathbf{K}_i,\omega_c)\rangle\tag{38}$$

is a special case of Eq. (33), and $\mathbf{K}_i$ is evaluated at the center frequency:

$$\mathbf{K}_i=\frac{\omega_c}{c_1}\cos\theta_i\hat{\alpha}_i.\tag{39}$$

Using perturbation theory (Sec. III and Appendix A), the approximation in Eq. (37) is valid for $K+|\mathbf{K}_d|/2<k_1$ (Appendix C), and is therefore valid if

$$K<k_1-\pi f_{\mathrm{BW}}\cos\theta_i/c_1,\tag{40}$$

where

$$|\omega''-\omega'|\leqslant2\pi f_{\mathrm{BW}},\tag{41}$$

and K is the magnitude of the transverse wave vector for the scattered field, and f_{BW} is the bandwidth of the source signal. The first-order T-matrix representing scattering from the water into the sediment, $T^{(1)}_{12}$, is derived in Appendix A. Note that when $k_2<k_1$, then the inequality in Eq. (40) will be true for all scattering directions if the source signal bandwidth is sufficiently narrow, and for scattered directions that do not correspond to small grazing angles.

Define the vertical component of the wave vector in medium 2,

$$B_2(K,\omega_c+\omega',\omega_c+\omega'')\equiv((\omega_c+\omega')/c_1)\kappa$$

$$\times\beta_2(\mathbf{K}-\mathbf{K}_d/2,\omega_c+\omega').\tag{42}$$

Analytical expressions for dispersion in a waveguide can be found by expanding the propagation constant of the time-dependent field in a power series (for example, see Ishimaru, 1991, Chap. 4). Similarly, B_2 is expanded in a power series in ω' and ω''; for the case of a narrow-band signal:

$$B_2(K,\omega_c+\omega',\omega_c+\omega'')$$

$$\cong B_{2c}(K)+\frac{\partial B_2}{\partial\omega'}\omega'+\frac{\partial B_2}{\partial\omega''}\omega''+\frac{1}{2}\left[\frac{\partial^2 B_2}{\partial\omega'^2}\omega'^2\right.$$

$$\left.+2\frac{\partial^2 B_2}{\partial\omega'\partial\omega''}\omega'\omega''+\frac{\partial^2 B_2}{\partial\omega''^2}\omega''^2\right],\tag{43}$$

where the derivatives are evaluated at $\omega'=\omega''=0$, and

$$B_{2c}(K)\equiv\kappa k_1\beta_2(\mathbf{K},\omega_c).\tag{44}$$

In the equation above and in all following equations, the wave number k_1 is evaluated at the center frequency ($k_1=\omega_c/c_1$). Although B_2 begins to vanish close to the critical angle, contributions to the scattered field are insignificant close to this angle due to propagation loss, and attenuation due to spherical spreading. Solving the derivatives in Eq. (43) by using Eqs. (10) and (42), combining like powers of ω' and ω'' in Eq. (36), and substituting the result into Eq. (29) yields

$$I_2(\mathbf{r},t)\cong\int d^2K\Big\{\mathscr{C}_{12}(\mathbf{K},\mathbf{K}_i,\omega_c)e^{2k_{1c}\mathrm{Im}(\kappa\beta_2(\mathbf{K},\omega_c))z}$$

$$\times\frac{1}{2\pi}\int d\omega''\ U^*(\omega'')e^{i\omega''(t-t_1-t_2)^*}$$

$$\times e^{i\omega''^2P^*/4}\frac{1}{2\pi}\int d\omega'\ U(\omega')e^{-i\omega'(t-t_1-t_2)}$$

$$\times e^{-\omega'\omega''P}e^{-i\omega'^2P/4}\Big\},\tag{45}$$

where (see Appendix B)

$$t_1 = \frac{\mathbf{R} \cdot \hat{\alpha}_i}{c_1} \cos \theta_i + \frac{z_s}{c_1} \sin \theta_i$$

$$+ z \frac{\hat{\alpha}_i \cdot \mathbf{K} \cos \theta_i}{c_1 k_1} \operatorname{Re}\left(\frac{1}{\kappa \beta_2(\mathbf{K}, \omega_c)} \right), \qquad (46)$$

and

$$t_2 = \frac{-z \kappa / c_1}{\beta_2(\mathbf{K}, \omega_c)}. \qquad (47)$$

The physical significance of these parameters is mentioned later. Note that t_1 is real and t_2 is complex. The complex coefficient

$$P = \{(2\kappa^2/B_{2c}^3)(\hat{\alpha}_i \cdot \mathbf{K} \omega_c \cos \theta_i / c_1^3 - (K/c_1)^2)$$

$$- i \operatorname{Im}(1/B_{2c})(\cos \theta_i / c_1)^2$$

$$- i \operatorname{Im}(1/B_{2c}^3)(\hat{\alpha}_i \cdot \mathbf{K} \cos \theta_i / c_1)^2\} z \qquad (48)$$

and the real coefficient

$$P = \operatorname{Im}\{(\hat{\alpha}_i \cdot \mathbf{K} \cos \theta_i / B_{2c}^3)(\kappa^2 \omega_c / c_1^3 - \hat{\alpha}_i$$

$$\cdot \mathbf{K} \cos \theta_i / (2c_1^2)) - \cos^2 \theta_i / (2c_1^2 B_{2c})\} z \qquad (49)$$

can represent the contribution to pulse dispersion of the frequency-dependent phase term. This result is simplified by setting

$$g^2(t) \equiv \frac{1}{2\pi} \int d\omega'' U^*(\omega'') e^{i\omega'' t^*} e^{i\omega''^2 P^*/4}$$

$$\times \frac{1}{2\pi} \int d\omega' \, U(\omega') e^{-i\omega' t} e^{-\omega' \omega'' P} e^{-i\omega'^2 P/4}. \qquad (50)$$

The definition above leads to a simple expression for the time-dependent mean-square incoherent field in medium 2:

$$I_2(\mathbf{r}, t) \cong \int d^2 K \, \mathscr{C}_{12}(\mathbf{K}, \mathbf{K}_i, \omega_c) e^{2k_1 \operatorname{Im}(\kappa \beta_2(\mathbf{K}, \omega_c)) z} g^2(t - t_d). \qquad (51)$$

In addition to being a function of the complex argument t, $g(t)$ is a function of K, the incident field direction, and fluid–sediment parameters. Note that

$$t_d \equiv t_1 + t_2. \qquad (52)$$

is also a complex function of K. For an arbitrarily small pulse bandwidth (cw), P, P, $\operatorname{Im}(t_2)$ are arbitrarily small, and $g(t) \rightarrow u(t)$. Equation (51) is the main result of this paper.

The definition of κ in Eq. (26) violates causality (see Aki and Richards, 1980; Chap. 5; Wingham, 1985). Using a corrected version of Eq. (8) in Wingham (1985), causality will not be violated if $\kappa - 2\delta \ln|(\omega_c + \omega')/\omega_c|/(\pi\nu)$ is substituted for κ beginning with Eq. (25). Using this substitution results in causal versions of the parameters P, P, t_1, and t_2. Since $\delta \ll 1$ for ocean sediment, causal representations of P, P, t_1, and t_2, and Eqs. (46)–(49) are equivalent.
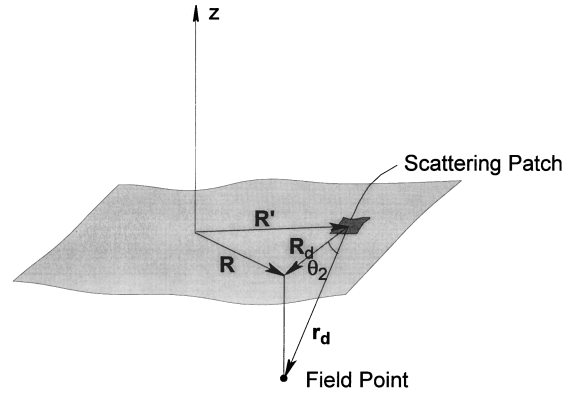
FIG. 2. Diagram describing geometry of variables.

While Eq. (51) involves an integral over the transverse wave vector, it can be converted to an integral over the scattering interface by neglecting evanescent waves and making the change of variable,

$$\mathbf{R}' = \mathbf{R} - \nu r_d \mathbf{K}/k_1. \qquad (53)$$

As shown in Fig. 2, $\mathbf{R}'$ is the location of a small scattering patch on the interface, and $r_d = |\mathbf{r}_d|$ is the distance from this patch to the field point $\mathbf{r}$,

$$r_d = \sqrt{|\mathbf{R} - \mathbf{R}'|^2 + z^2}. \qquad (54)$$

Evanescent waves are neglected by constraining K to $K < k_1/\nu$ in Eq. (53). This constraint is justified later when the contribution of evanescent waves on the mean-square scattered incoherent field is illustrated using first-order perturbation computations for an incident plane wave. This constraint is also consistent with the frequency independence assumption of the T-matrix correlation function [see Eq. (37)]. The Jacobian follows from Eq. (53),

$$\left(\frac{\partial K}{\partial R'} \right) = \frac{k_1^2}{\nu^2 r_d^6} \begin{vmatrix} y_d^2 + z^2 & x_d y_d \\ x_d y_d & x_d^2 + z^2 \end{vmatrix} = \frac{k_1^2}{\nu^2 r_d^4} z^2, \qquad (55)$$

where x_d, and y_d are the transverse coordinates of $\mathbf{r}_d$. The geometric significance of these definitions is apparent when one assumes that the loss parameter is small ($\delta \ll 1$). Then

$$k_1 \kappa \beta_2(\mathbf{K}, \omega_c) = \sqrt{(\kappa k_1)^2 - K^2}$$

$$\cong (k_1 \sin \theta_2 / \nu)(1 + i\delta/\sin^2 \theta_2), \qquad (56)$$

where

$$\sin \theta_2 = \sqrt{1 - K^2 \nu^2 / k_1^2} = |z|/r_d \qquad (57)$$

is the sine of the scattered grazing angle defined in Fig. 2. Equation (46) is equivalently written as

$$t_1 = \mathbf{R}' \cdot \hat{\alpha}_i \cos \theta_i / c_1 + z_s \sin \theta_i / c_1 \qquad (58)$$

and is seen to be the time required for the incident plane-wave front with direction $(\hat{\alpha}_i \cos \theta_i, \sin \theta_i)$ to travel from the source reference point, $(0,0,z_s)$ to the scattering patch, $(\mathbf{R}',0)$, and

$$\operatorname{Re}(t_2) = r_d / c_2 \qquad (59)$$

is the time required for a spherical wave scattered from the patch at $(\mathbf{R}',0)$ to travel through the sediment to the field

point $(\mathbf{R}, z)$, $z < 0$. According to Eq. (56), the absorption exponent in medium 2 is given by

$$\text{Im}(k_1 \kappa \beta_2(K, \omega_c))|z| = \frac{k_1 \delta}{\nu} |z|/\sin \theta_2 = \text{Im}(k_2) r_d. \quad (60)$$

Substituting Eqs. (55) and (60) into Eq. (51) results in:

$$I_2(\mathbf{r}, t) = \int d^2 R' \frac{k_1^2 \sin^2(\theta_2)}{\nu^2 r_d^2} \mathscr{C}_{12}(\mathbf{K}, \mathbf{K}_i, \omega_c)$$
$$\times e^{-2 \text{Im}(k_2) r_d} g^2(t - t_d). \quad (61)$$

Substituting the following quantities:

$$\sigma_{12}(\hat{\alpha}, \hat{\alpha}_i) \equiv \frac{k_1^2 \sin^2(\theta_2)}{\nu^2} \mathscr{C}_{12}(\mathbf{K}, \mathbf{K}_i, \omega_c), \quad (62)$$

where

$$\hat{\alpha} = \mathbf{K}/K, \quad \text{and} \quad \hat{\alpha}_i = \mathbf{K}_i/K_i \quad (63)$$

into Eq. (61) yields

$$I_2(\mathbf{r}, t) \cong \int d^2 R' \frac{\sigma_{12}(\hat{\alpha}, \hat{\alpha}_i)}{|\mathbf{r} - \mathbf{r}'|^2} e^{-2 \text{Im}(k_2)|\mathbf{r} - \mathbf{r}'|} g^2(t - t_d). \quad (64)$$

The interpretation of σ_{12} as a differential cross section will be justified later in this section. Since $\mathbf{K} = k_1 (\mathbf{R} - \mathbf{R}')/(\nu r_d)$, t_1, t_2, g, and therefore P and P are functions of $|\mathbf{R} - \mathbf{R}'|$. Note that the cw result follows from Eq. (64) when $g(t - t_d) = 1$. For this case, the result in Eq. (51) for the mean-square incoherent field is exact. We show later that Eq. (64) approaches the exact result at distances a few wavelengths from the interface, where the evanescent waves contribute very little to the mean-square incoherent field.

The mean square incoherent field scattered back into the water, $I_1(\mathbf{r}, t)$ also follows from Eq. (64) by substituting medium 1 parameters for medium 2 parameters. For example, 1 is substituted for κ, β_1 for β_2, etc. For this case, Eq. (64) simplifies to

$$I_1(\mathbf{r}, t) \cong \int d^2 R' \frac{\sigma_{11}(\hat{\alpha}, \hat{\alpha}_i)}{|\mathbf{r} - \mathbf{r}'|^2} g_{11}^2(t - t_d), \quad (65)$$

where from Eq. (62)

$$\sigma_{11}(\hat{\alpha}, \hat{\alpha}_i) = k_1^2 \sin^2(\theta_2) \mathscr{C}_{11}(\mathbf{K}, \mathbf{K}_i, \omega_c). \quad (66)$$

Here, θ_2 is also the scattered field grazing angle measured from the mean horizontal plane, $|z|/r_d = \sin(\theta_2)$. Again, the quantity $\mathscr{C}_{11}$ is found from the relation [Eq. (38)]

$$\mathscr{C}_{11}(\mathbf{K}, \mathbf{K}_i, \omega_c) \delta(\mathbf{K} - \mathbf{K}'')$$
$$\equiv \langle \widetilde{T}_{11}(\mathbf{K}, \mathbf{K}_i, \omega_c) \widetilde{T}_{11}^*(\mathbf{K}'', \mathbf{K}_i, \omega_c) \rangle. \quad (67)$$

There is no loss for this case—$P = 0$, and therefore,

$$g_{11}^2(t) \equiv \left| \frac{1}{2\pi} \int d\omega' U(\omega') e^{-i\omega' t} e^{-i\omega'^2 P_{11}/4} \right|^2, \quad (68)$$

$$P_{11} \equiv (2/B_{11c}^3)(\omega_c \hat{\alpha}_i \cdot \mathbf{K} \cos \theta_i / c_1^3 - (K/c_1)^2), \quad (69)$$

and

$$B_{1c}(K) \equiv k_1 \beta_1(K, \omega_c). \quad (70)$$

Note that t_d is still given by Eq. (52), but it is a real quantity for this case, representing the propagation time from the surface patch to the receiver observation point above the interface:

$$t_2 = \frac{z/c_1}{\beta_1(K, \omega_c)}. \quad (71)$$

As given by Voronovich (1994), the quantity $\sigma_{11}(\hat{\alpha}, \hat{\alpha}_i)$ in Eq. (66) is actually the differential cross section defined by Ishimaru (1978b):

$$\sigma_{11}(\hat{\alpha}, \hat{\alpha}_i) = \frac{|\mathbf{r} - \mathbf{r}'|^2}{\Delta A} \frac{\langle |\widetilde{\psi}_f|^2 \rangle}{|\psi_i|^2}, \quad (72)$$

where ψ_i is a plane-wave field incident on a surface patch of area ΔA, and $\hat{\alpha}_i$ is the unit vector in the direction of propagation of the incident field; $\widetilde{\psi}_f$ is the scattered coherent field at a long distance $|\mathbf{r} - \mathbf{r}'|^2$ from the interface, in the direction denoted by the unit vector, $\hat{\alpha}$. Similarly, σ_{12}, is the differential cross section relating the mean square incident field to the mean-square scattered incoherent field in medium 2 (the sediment), defined by

$$\sigma_{12}(\hat{\alpha}, \hat{\alpha}_i) = \frac{|\mathbf{r} - \mathbf{r}'|^2}{\Delta A} \frac{\langle |\widetilde{\psi}_{2-}|^2 \rangle}{|\psi_i|^2} e^{2 \text{Im}(k_2)|\mathbf{r} - \mathbf{r}'|}, \quad (73)$$

where $\widetilde{\psi}_{2-}$ is the incoherent field in the sediment at the receiver, a distance $|\mathbf{r} - \mathbf{r}'|$ from the surface patch, and the unit vector $\hat{\alpha}$ represents the transverse direction of the scattered field in the lower medium. When $u(t)$ is substituted for $g(t)$, Eq. (64) becomes the sonar equation, in which the mean-square incoherent field is obtained by integrating the differential cross section over the interface with appropriate attenuation due to spreading and sediment loss. Equations (38) and (62) are a convenient way to find σ_{12} in theoretical developments; Eqs. (66) and (67) are a convenient way to find σ_{11}.

C. Dispersion of a Gaussian input pulse

Dispersion due to scattering contributions over the scattering surface is treated by the integral in Eq. (64); dispersion due to the frequency dependence of the propagation constant is embodied in Eq. (50). This subsection focuses on the latter form of dispersion. Consider the case of a pulse with a peak pressure, p_{peak}, and Gaussian envelope,

$$u(t) = p_{\text{peak}} e^{-t^2/t_s^2}. \quad (74)$$

Its Fourier transform is given by

$$U(\omega) = p_{\text{peak}} t_s \sqrt{\pi} e^{-t_s^2 \omega^2/4}. \quad (75)$$

The parameter t_s is chosen to vary the width of this input pulse, and therefore the pulse bandwidth, and energy. Substituting Eq. (75) into Eq. (50) and integrating over ω' and ω'' yields

$$g^2(t) = p_{\text{peak}}^2 \frac{t_s^2}{q' q''} e^{-t^2/q'^2} e^{-(t^* + 2tP/q'^2)^2/q''^2}, \quad (76)$$

where
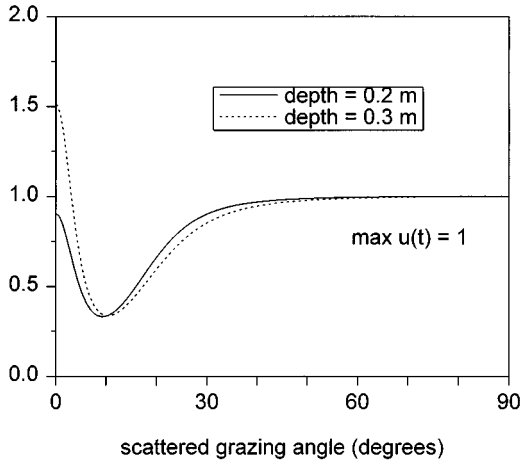
FIG. 3. Illustration of effect of dispersion on peak intensity. Peak of $g^2(t)$, normalized with respect to $\max(u^2(t))$ as a function of grazing angle.

$$q' \equiv \sqrt{t_s^2 + iP}, \tag{77}$$

$$q'' \equiv \sqrt{t_s^2 - iP''}, \tag{78}$$

and

$$P'' \equiv P^* - i(2P/q')^2, \tag{79}$$

Substituting Eqs. (77) and (78) into Eq. (76), and simplifying, yields an expression equivalent to Eq. (76)

$$g^2(t) = p_{\text{peak}}^2 \frac{t_s^2}{\sqrt{|t_s^2 - iP^*|^2 - (2P)^2}}$$

$$\times \exp\left(\frac{-2\,\text{Re}\{(t_s^2 - iP^*)t^2\}}{|t_s^2 - iP^*|^2 - (2P)^2}\right). \tag{80}$$

As mentioned previously, $\text{Re}(t_d) = \text{Re}(t_2) + t_1$ represents the propagation delay of the pulse. The imaginary part of t_2 results from modeling the sediment as lossy. Since higher-frequency signals are attenuated more than lower-frequency signals, the lower-frequency components of a narrow-band signal will be less attenuated than the center frequency. The imaginary component of t_2, along with P, and the imaginary component of P compensate for typically excessive loss in the cw loss term—the exponential term in Eq. (51) or Eq. (64). Note that for the zero loss case, the parameter $P = 0$. The effect of loss and the parameters P and P is shown in Fig. 3 for $g^2(t - t_d)$ from Eq. (80) [or Eq. (76)] evaluated at

$$g^2(t - t_d)|_{t = \text{Re}(t_d)} = g^2(-t_{2i}), \quad t_{2i} = \text{Im}(t_d) = \text{Im}(t_2), \tag{81}$$

and plotted as a function of scattered grazing angle. In Fig. 3, the pulse length parameter, t_s, is equal to two periods of the center, or carrier frequency for both cases shown. When the loss and dispersion are small, $|g(-t_{2i})|$ approaches $u(0) = 1$. The smaller the scattered grazing angle, the greater the dispersion, and the smaller one would expect the pulse peak amplitude. However, the loss of the cw signal represented by the term, $e^{-2\,\text{Im}(k_2)|r - r'|}$, is greater than the loss of the narrow-band signal, and the propagation distance becomes large for small scattered grazing angles (z is fixed). Even though there is dispersion, the loss for the narrow-band case is signifi-

cantly less than for the cw case, and $|g(-t_{2i})| > 1$. In the case of Fig. 3, with depth of 0.3 m, $|g(-t_{2i})| > 1$ for very small grazing angles since the propagation distance becomes very large. An example with zero loss always has $P'' = P^*$, $t_{2i} = 0$, and $|g(0)| \leqslant p_{\text{peak}}$.

III. ANALYTICAL SCATTERING MODEL (PERTURBATION THEORY)

In the examples in this section, the incoherent intensity in medium 2 is treated using first-order perturbation theory, and the coherent intensity is treated using the exact zeroth-order solution—the exact flat-surface solution is used. There is a slight inconsistency in this approach, in that the incoherent intensity is proportional to the second power of $k_1 h$, while the coherent intensity is only computed to an accuracy of zeroth order. However, as Rice (1951) has shown, the coherent intensity to second order in $k_1 h$ is obtained by subtracting the power carried by the incoherent intensity. For small $k_1 h$, this correction is slight.

A. Incoherent intensity using the first-order perturbation approximation

In this section, the first-order perturbation results are given for $\mathscr{C}_{12}$ and σ_{12}. The first-order T-matrix is proportional to the 2-D Fourier transform of the surface, $F(\mathbf{K})$, [see Appendix A or Moe (1996)] and is given by

$$T_{12}(\mathbf{K}, \mathbf{K}_i) \cong (k_1 h) T_{12}^{(1)}(\mathbf{K}, \mathbf{K}_i)$$

$$= (k_1 h) H_{12}(\mathbf{K}, \mathbf{K}_i) F(\mathbf{K} - \mathbf{K}_i), \tag{82}$$

where

$$H_{12}(\mathbf{K}'', \mathbf{K}) = \frac{\mathscr{T}(\mathbf{K}'')}{2i\beta_1(\mathbf{K}'')} \left[a(\mathbf{K}'', \mathbf{K})(1 + \Gamma(\mathbf{K})) \right.$$

$$\left. - b(\mathbf{K}'', \mathbf{K})(1 - \Gamma(\mathbf{K})) \right] \tag{83}$$

is a function of the flat-surface reflection coefficient, Γ, the flat-surface transmission coefficient,

$$\mathscr{T}(\mathbf{K}) = 1 + \Gamma(\mathbf{K}) \tag{84}$$

and the factors $a(\mathbf{K}'', \mathbf{K})$ and $b(\mathbf{K}'', \mathbf{K})$ defined in Appendix A. Using

$$h^2 \langle F(\mathbf{K}'' - \mathbf{K}_i) F(\mathbf{K}' - \mathbf{K}_i) \rangle = W(\mathbf{K}' - \mathbf{K}_i) \delta(\mathbf{K}'' - \mathbf{K}') \tag{85}$$

together with Eq. (38) and Eq. (82) yields

$$\mathscr{C}_{12}(\mathbf{K}, \mathbf{K}_i, \omega_c) = |k_1 H_{12}(\mathbf{K}, \mathbf{K}_i)|^2 W(\mathbf{K} - \mathbf{K}_i) \tag{86}$$

where $W(\mathbf{K})$ is the two-dimensional roughness spectrum. An expression for the mean-square first-order incoherent field results from substituting Eq. (86) into Eq. (51). The mean-square first-order incoherent field is found from Eq. (64), where the differential cross section from first-order perturbation theory, is found from substituting Eq. (86) into Eq. (62),

$$\sigma_{12}^{(1)}(\hat{\alpha}_f, \hat{\alpha}_i) = \frac{k_1^2 \sin^2(\theta_2)}{\nu^2} |k_1 H_{12}(\mathbf{K}_f, \mathbf{K}_i)|^2 W(\mathbf{K}_f - \mathbf{K}_i). \tag{87}$$

Although the differential cross section in this approximation is actually second order in $k_1 h$, (Thoros and Jackson, 1989),

we will refer to it as the first-order differential cross section (differential cross section obtained from first-order perturbation theory).

B. Zeroth-order coherent field

The magnitude squared zeroth-order, or flat-surface transmitted coherent field for an incident plane wave, is given by the magnitude squared of Eq. (16), with $T_{12}^{(0)}(\mathbf{K},\mathbf{K}_i)$ given by Eq. (A7):

$$|\psi_{2-}^{(0)}(\mathbf{r})|^2 = |\mathcal{T}(\mathbf{K}_i)|^2 e^{\mathrm{Im}(k_2\beta_2(\mathbf{K}_i))z}. \tag{88}$$

C. Roughness spectrum

The two-dimensional Gaussian random process $f(\mathbf{R})$ describing the seafloor surface is assumed to be isotropic, with a roughness spectrum, $W(\mathbf{K})$, in the form of a filtered power law (Moe and Jackson, 1994b; Moe, 1996)

$$W(\mathbf{K}) = \frac{w_2}{K^\gamma}(1-e^{-(Ka)^2/2})^2, \tag{89}$$

with rms height,

$$
\begin{aligned}
h &= \sqrt{2\pi \int_0^\infty W(\mathbf{K})K\,dK} \\
&= \sqrt{\frac{2\pi w_2 a^{\gamma-2}}{\gamma-2}\,\Gamma(2-\gamma/2)[2^{2-\gamma/2}-1]}. \tag{90}
\end{aligned}
$$

Here Γ refers to the gamma function—not the reflection coefficient. The factor $(1-e^{-(Ka)^2/2})^2$ is obtained by subtracting a Gaussian weighted moving average (see for example, Papoulis, 1984) of the surface from itself.

IV. APPLICATIONS AND CALCULATIONS

Although the theoretical results in this paper are general and include the scattered field on both sides of the interfaces, these examples examine the field scattered through a rough fluid–fluid interface ($z<0$). Both plane-wave and point sources are considered, and the mean square scattered incoherent field is computed for both the flat surface case, and the rough surface case.

A. Continuous plane-wave source

The contribution of the evanescent waves to the field scattering through a rough interface is shown in the following cw incident plane wave examples. In Fig. 4(a), the first-order field penetrating through a rough interface, with roughness spectrum given in Eq. (89), and $k_1h=0.2545$, is calculated using Eq. (86) in Eq. (51), and setting $g(t-t_d)=1$ Pa. The solid line in the plot represents the first-order result including evanescent waves, and the dashed line is the first-order result excluding evanescent waves—Eq. (64). Since the grazing angle in this example is below critical, the zeroth-order field (dotted line) is evanescent. Near the interface, the mean square incoherent field decays with increasing depth at rate comparable to the square of the magnitude of the zeroth-order field, but further from the interface decays at
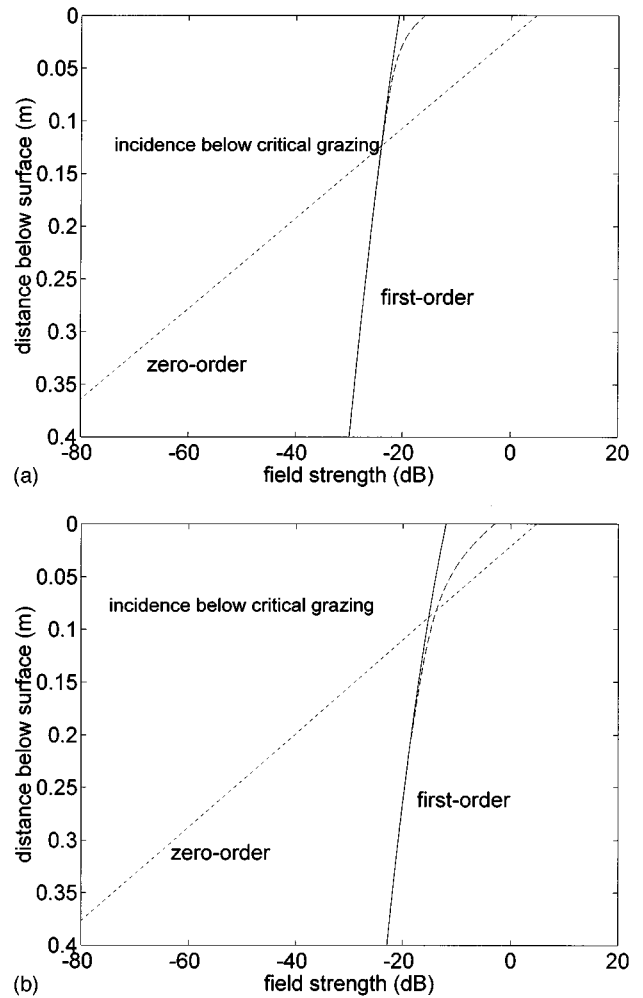
FIG. 4. First-order and zeroth-order field strength as a function of depth. Field strength given in dB with respect to incident pressure. Critical angle is 27.75°, $f=20$ kHz, $a=0.1$ m, $\gamma=3$, $w_2=2\times10^{-5}$ m, $\rho=2$, $\delta=0.019$, $c_1=1500$ m/s, $\nu=1.13$, incident angle is 20°.

a rate dictated by the sediment loss. Including the evanescent waves ($K>k_1/\nu$) does not make a significant difference at a distance greater than about a wavelength (7.5 cm) below the interface for this example. The sediment parameters used in the plot in Fig. 4(b) are the same as Fig. 4(a), except the roughness parameters are chosen such that $k_1h=1.0$. Perturbation theory is shown valid for $k_1h=1$ by Thorsos (1996); Thorsos et al. (1997) for scattering through a rough interface with truncated power-law roughness spectrum. For this case, including the evanescent waves of the integral ($K>k_1/\nu$) does not make a significant difference at a distance greater than about two wavelengths below the interface.

These examples show that including the evanescent waves in the calculation of the mean-square incoherent first-order field is only necessary close to the interface, and the contribution of evanescent waves to the mean-square incoherent field is dependent on the interface roughness. It is important to note that, in the region below the interface where the incoherent evanescent contribution is significant, the zeroth-order coherent contribution to the mean square field is typically much greater.

B. Mean-square incoherent field due to a point source

A heuristic derivation of the scattered field due to a point source is given here. Starting with the incident plane-wave result in Eq. (64), and expressing the 2-D integral in terms of a summation over the interface yields

$$I_2(\mathbf{r},t) \cong \Delta A \sum_n \frac{\sigma_n(\hat{\alpha}_{fn}, \hat{\alpha}_i)}{r_{2n}^2} g^2(t - t_{1n} - t_{2n}) e^{-2\,\mathrm{Im}(k_2)r_{2n}}, \tag{91}$$

where

$$r_{2n} = |\mathbf{r} - \mathbf{r}'_n| \tag{92}$$

is the distance from surface patch n, of size ΔA at position $\mathbf{r}'_n$ to the observed field point, $\mathbf{r}$, and

$$\hat{\alpha}_{fn} = \frac{\mathbf{R} - \mathbf{R}'}{|\mathbf{R} - \mathbf{R}'|}. \tag{93}$$

The propagation time from this surface patch to the receiver, $\mathrm{Re}(t_{2n})$, is also given by

$$\mathrm{Re}(t_{2n}) = r_{2n}/c_2. \tag{94}$$

As the area of each surface patch, ΔA, approaches zero, the summation in Eq. (91) approaches the exact integral in Eq. (64).

An expression for the first-order mean-square field below the interface due to a point source follows heuristically from Eq. (91):

$$I_2(\mathbf{r},t) \cong \Delta A \sum_n \frac{\sigma_n(\hat{\alpha}_{fn}, \hat{\alpha}_{in})}{r_{1n}^2 r_{2n}^2} r_0^2 g^2(t - t_{dn}) e^{-2\,\mathrm{Im}(k_2)r_{2n}}, \tag{95}$$

where

$$\hat{\alpha}_{in} = \frac{\mathbf{R}'_n - \mathbf{R}_s}{|\mathbf{R}'_n - \mathbf{R}_s|}, \tag{96}$$

$\mathbf{R}_s$ is the transverse coordinate vector of the source, $g(t)$ is the pressure at 1 m from the source, and $r_0 = 1$ m. The total propagation time is given by the real part of

$$t_{dn} = \frac{r_{1n}}{c_1} + t_{2n}, \tag{97}$$

with

$$r_{1n} = \sqrt{|\mathbf{R}'_n - \mathbf{R}_s|^2 + z_s^2}. \tag{98}$$

Here, the surface patch must be small in relation to the distance r_{1n} from the point source to surface patch n, to insure that the field incident on the interface is approximately a plane wave. The size of ΔA cannot be chosen arbitrarily small (Winebrenner and Ishimaru, 1986), and the distance between the source and interface is therefore constrained to be greater than some minimum value ($z_s > d_{\min}$). The validity of this solution for the cw case is demonstrated by Jackson *et al.* (1997) by comparisons with exact integral calculations.

The effect of $g(t)$ in Eq. (95) is shown in the following example. Using the expression for the first-order differential cross section given in Eq. (87), the approximate mean square incoherent field pulse is lossy sediment below a rough inter-
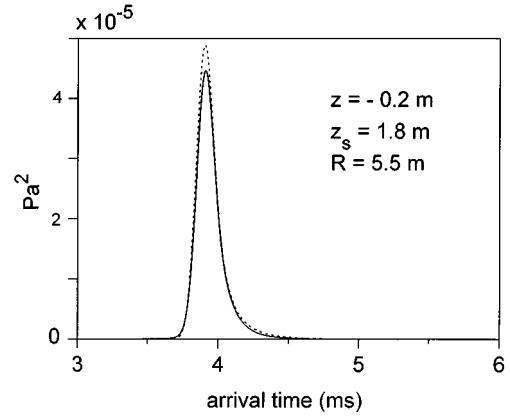
FIG. 5. Time-dependent intensity at depth 0.2 m below the mean surface. Source frequency = 20 kHz, $t_s = 100\ \mu$s. Solid line: dispersion terms included; dotted line: dispersion terms set to zero, $g(t) = u(t)$. Same sediment parameters and incident angle as Fig. 4.

face due to a Gaussian narrow-band point source above the interface is found for two cases. In Fig. 5, the time-dependent mean-square incoherent field at a position below a rough interface in a lossy medium due to a point source is found using Eq. (76) [or Eq. (80)] for $g^2(t)$ in Eq. (95), and is compared to the result obtained setting P and $\mathcal{P}$ to zero— $g(t) = u(t)$. Note that when the approximation $g(t) = u(t)$ is made, Eq. (95) is in the form of a convolution with reduced computation time. Although the resulting pulse shapes are close in magnitude, as well as peak arrival time, using $g(t)$ does result in an incoherent pulse that has a smaller peak magnitude. In this example, the parameter t_s in Eq. (74) is equal to two cycles of the center frequency of $f_c = 20$ kHz. This frequency results in $k_1 h = 0.25$, which is within the region of accuracy for first-order perturbation theory (Thorsos and Jackson, 1989; Thorsos, 1990, 1996). The incident grazing angle is defined here to be the angle between the mean surface and the line containing the source and receiver points.

C. Zeroth-order calculations

Setting

$$\Psi_{2-}^{(0)}(\mathbf{K}) = \mathcal{T}(\mathbf{K})\Psi_i(\mathbf{K}) \tag{99}$$

and

$$\Psi_i(\mathbf{K}) = \frac{i r_0 U}{2\pi k_1 \beta_1(\mathbf{K})} e^{-i\mathbf{K}\cdot\mathbf{R}_s} e^{i k_1 \beta_1(\mathbf{K})z_s} \tag{100}$$

in Eq. (9) results in an expression for the field penetrating a flat fluid–fluid interface due to a point source at $(\mathbf{R}_s, z_s)$ with unit pressure magnitude at m from the source. The quantity U has unit magnitude and dimensions of pressure×time. The resulting exact expression for the square of the time-dependent zeroth-order, or flat-surface coherent field magnitude

$$I(\mathbf{r},t) = \left| \int_{-\infty}^{\infty} d\omega\, U(\omega) e^{-i\omega t} \int_0^{\infty} dK\, \frac{r_0 K \mathcal{T}(\mathbf{K})}{k_1 \beta_1(\mathbf{K})} \right.$$

$$\left. \times e^{i(z_s k_1 \beta_1(\mathbf{K}) - z k_2 \beta_2(\mathbf{K}))} J_0(K R_d) \right|^2, \tag{101}$$
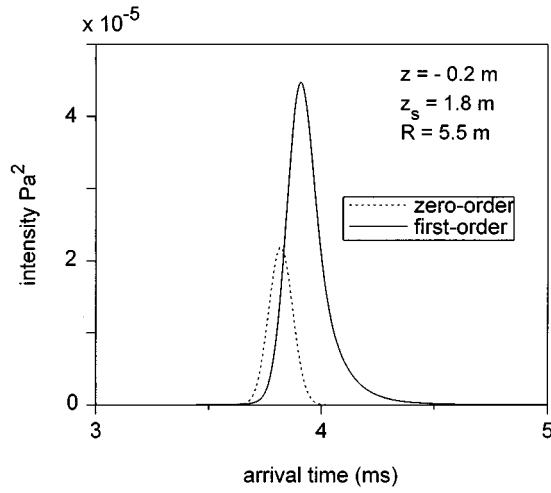
FIG. 6. Zeroth-order coherent time-dependent intensity shown with dotted line, first-order incoherent intensity shown with solid line. All parameters identical to Fig. 5.

where R_d is the transverse distance between source and receiver, and J_0 is the Bessel function of order zero. For comparison purposes, the square of the time-dependent zeroth-order, or flat-surface coherent field magnitude, is plotted in Fig. 6 along with the time-dependent mean-square incoherent first-order field using the same parameters as in Fig. 5. In this example, the incident angle is below the critical angle. Although the zeroth-order component can be approximated from Eq. (101) using the method of stationary phase to solve the resulting integral (see for example Brekhovskikh, 1980; Ishimaru, 1991) when the incident angle is above the critical angle, a numerical method is more suitable when the incident grazing angle is close to critical (Westwood, 1989). Figure 6 shows an ''exact'' solution of the square of the flat-surface transmitted coherent field magnitude, along with the mean-square incoherent first-order field from Fig. 5(a). For this example, the zeroth-order coherent pulse arrives earlier and with less magnitude than the first-order incoherent pulse.

Note that Eq. (101) generalizes to an exact expression for the coherent field due to a point source if the transmission coefficient is replaced with the intensity transmission coefficient (Moe, 1996).

V. CONCLUSION

A general analytical expression for the time-dependent narrowband mean square incoherent field scattered from and through a fluid–fluid rough interface for a narrow-band incident plane-wave source is expressed in terms of the second moment of the rough interface T-matrix, and is therefore independent of the scattering solution technique. This result is valid for narrow-band source signals when the T-matrix correlation function is a slowly varying function of frequency over the source signal frequencies. Using the exact cw incident plane-wave result, along with first-order perturbation theory, and sediment parameters characteristic of a sandy seafloor, we show that the evanescent component of the scattered incoherent field in the sediment can be insignificant about a wavelength from the interface—depending on the interface roughness. Neglecting the evanescent com-

ponent of the field, an general expression for the mean-square incoherent field is obtained in terms of the differential cross section.

The formalism above applied to the scattering through a rough interface shows the effect of roughness on penetration through an interface. When the grazing angle of a plane wave incident field is below the critical angle in relation to the mean surface, the zeroth-order component of the transmitted field is evanescent, and does not penetrate deeply into the seafloor. Higher-order components contain downward traveling waves, which can increase the depth of penetration of sound relative to the flat-surface case.

APPENDIX A: PERTURBATION THEORY RESULTS

The fields and T-matrices are expanded in their zeroth-order and first-order components, with the factor $k_1 h$ displayed explicitly:

$$\Psi(\mathbf{K}) = \Psi^{(0)}(\mathbf{K}) + k_1 h \Psi^{(1)}(\mathbf{K}), \tag{A1}$$

$$T(\mathbf{K}, \mathbf{K}_i) = T^{(0)}(\mathbf{K}, \mathbf{K}_i) + k_1 h T^{(1)}(\mathbf{K}, \mathbf{K}_i). \tag{A2}$$

1. Zeroth-order

The zeroth-order scattered field, or reflected field is

$$\Psi_f^{(0)}(\mathbf{K}) = \Gamma(\mathbf{K}) \Psi_i(\mathbf{K}), \tag{A3}$$

where $\Gamma(\mathbf{K})$ is the flat-surface reflection coefficient,

$$\Gamma(\mathbf{K}) = \frac{\rho \beta_1(\mathbf{K}) - \kappa \beta_2(\mathbf{K})}{\rho \beta_1(\mathbf{K}) + \kappa \beta_2(\mathbf{K})}. \tag{A4}$$

Comparing Eq. (12) to (A3), the reflection coefficient is related to the zeroth-order T-matrix $T_{11}^{(0)}$ by

$$T_{11}^{(0)}(\mathbf{K}, \mathbf{K}_i) = \Gamma(\mathbf{K}) \delta(\mathbf{K} - \mathbf{K}_i). \tag{A5}$$

The transmitted field is given in terms of the incident field and transmission coefficient,

$$\Psi_{2-}^{(0)}(\mathbf{K}) = \mathcal{T}(\mathbf{K}) \Psi_i(\mathbf{K}). \tag{A6}$$

Comparing Eq. (13) with (A6), the transmission coefficient is related to the zeroth-order T-matrix $T_{12}^{(0)}$ by

$$T_{12}^{(0)}(\mathbf{K}, \mathbf{K}_i) = \mathcal{T}(\mathbf{K}) \delta(\mathbf{K} - \mathbf{K}_i). \tag{A7}$$

2. First-order

The first-order T-matrices are proportional to the 2-D Fourier transform of the surface, $F(\mathbf{K})$, and can be written as

$$T_{11}^{(1)}(\mathbf{K}, \mathbf{K}_i) = H_{11}(\mathbf{K}, \mathbf{K}_i) F(\mathbf{K} - \mathbf{K}_i), \tag{A8}$$

$$T_{12}^{(1)}(\mathbf{K}, \mathbf{K}_i) = H_{12}(\mathbf{K}, \mathbf{K}_i) F(\mathbf{K} - \mathbf{K}_i), \tag{A9}$$

where

284   J. Acoust. Soc. Am., Vol. 103, No. 1, January 1998

J. E. Moe and D. R. Jackson: Near-field scattering   284

$$F(\mathbf{K}) = \frac{1}{(2\pi)^2} \int d^2R\, f(\mathbf{R}) e^{-i\mathbf{K}\cdot\mathbf{R}}. \qquad (A10)$$

From Moe and Jackson (1994a) Eqs. (26) and (29)

$$H_{11}(\mathbf{K}'',\mathbf{K}) = \frac{(1+\Gamma(\mathbf{K}''))(1+\Gamma(\mathbf{K}))}{2i\beta_1(\mathbf{K}'')}\left[1 - \frac{\kappa^2}{\rho} + \left(\frac{1}{\rho}-1\right)\right.$$

$$\times\left(\frac{\mathbf{K}''\cdot\mathbf{K}}{k_1^2} - \rho\beta_1(\mathbf{K}'')\beta_1(\mathbf{K})\right.$$

$$\left.\left.\times\frac{(1-\Gamma(\mathbf{K})'')(1-\Gamma(\mathbf{K}))}{(1+\Gamma(\mathbf{K}''))(1+\Gamma(\mathbf{K}))}\right)\right]. \qquad (A11)$$

Since in the perturbation expansion (A1) the factor k_1 is displayed explicitly, Eq. (A11) is actually Eq. (29) of Moe and Jackson (1994a) divided by a factor of k_1. The following expression is equivalent to Eq. (A11):

$$H_{11}(\mathbf{K}'',\mathbf{K}) = \frac{1}{2i\beta_1(\mathbf{K}'')}\{a(1+\Gamma(\mathbf{K}''))(1+\Gamma(\mathbf{K}))$$

$$+ b(1-\Gamma(\mathbf{K}''))(1-\Gamma(\mathbf{K}))\}, \qquad (A12)$$

where

$$a(\mathbf{K}'',\mathbf{K}) = \left(\frac{1}{\rho}-1\right)\frac{\mathbf{K}''\cdot\mathbf{K}}{k_1^2} + 1 - \frac{\kappa^2}{\rho}, \qquad (A13)$$

$$b(\mathbf{K}'',\mathbf{K}) = \beta_1(\mathbf{K}'')\beta_1(\mathbf{K})(\rho-1). \qquad (A14)$$

From Eq. (24) of Moe and Jackson (noting the difference in scalar field definitions, and no stratified media; that is, $\Gamma_{23} = 0$), the continuity of pressure boundary condition for first-order fields yields:

$$\Psi_{2-}^{(1)}(\mathbf{K}'') = -i\int d^2K\ \Psi_1(\mathbf{K})F(\mathbf{K}''-\mathbf{K})\{iH_{11}(\mathbf{K}'',\mathbf{K})$$

$$+ (1-\Gamma(\mathbf{K}))\beta_1(\mathbf{K}) - \kappa\beta_2(\mathbf{K})(1+\Gamma(\mathbf{K}))\}. \qquad (A15)$$

A second expression for $\Psi_{2-}^{(1)}(\mathbf{K}'')$ follows from Eqs. (13) and (A9):

$$\Psi_{2-}^{(1)}(\mathbf{K}'') = \int d^2K\ \Psi_i(\mathbf{K})H_{12}(\mathbf{K}'',\mathbf{K})F(\mathbf{K}''-\mathbf{K}). \qquad (A16)$$

Equating Eqs. (A15) and (A16) yields

$$H_{12}(\mathbf{K}'',\mathbf{K}) = H_{11}(\mathbf{K}'',\mathbf{K}) + (1-\Gamma(\mathbf{K}))\beta_1(\mathbf{K})$$

$$+ i\kappa\beta_2(\mathbf{K})(1+\Gamma(\mathbf{K})). \qquad (A17)$$

Noting

$$\frac{\rho\beta_1}{\kappa\beta_2} = \frac{1+\Gamma}{1-\Gamma}, \qquad (A18)$$

Eq. (A17) simplifies to

$$H_{12}(\mathbf{K}'',\mathbf{K}) = \frac{1}{i\sqrt{\rho}}\{iH_{11}(\mathbf{K}'',\mathbf{K}) + (1-\rho)$$

$$\times\beta_1(\mathbf{K})(1-\Gamma(\mathbf{K}))\}. \qquad (A19)$$

Substituting Eq. (A12) into (A19) results in a convenient expression for $H_{12}(\mathbf{K}'',\mathbf{K})$, given as Eq. (83).

For another derivation of these results, see Moe (1996).

APPENDIX B: DERIVATION OF NARROW-BAND COEFFICIENTS

Equations (46)–(49) (expressions for t_1, t_2, P, and P) are derived here. For convenience, define

$$\omega_t' = \omega_c + \omega', \quad \omega_t'' = \omega_c + \omega''. \qquad (B1)$$

From Eqs. (10), (34), and (42), and (B1),

$$B_2(K,\omega_t',\omega_t'') = \sqrt{\kappa^2\left(\frac{\omega_t'}{c_1}\right)^2 - K^2 + \left(\frac{\omega_t''-\omega_t'}{c_1}\right)\cos\theta_i\hat{\alpha}_i\cdot\mathbf{K} - \left(\frac{\omega_t''-\omega_t'}{c_1}\right)^2\left(\frac{\cos\theta_i}{2}\right)^2}. \qquad (B2)$$

The derivatives in Eq. (43) are found using (B2),

$$\frac{\partial B_2}{\partial\omega_t'} = \frac{1}{2B_2}\left[\frac{2\kappa^2\omega_t'}{c_1^2} - \frac{\hat{\alpha}_i\cdot\mathbf{K}}{c_1}\cos\theta_i + 2\left(\frac{\omega''-\omega'}{c_1^2}\right)\left(\frac{\cos\theta_i}{2}\right)^2\right], \qquad (B3)$$

and

$$\frac{\partial B_2}{\partial\omega_t''} = \frac{1}{2B_2}\left[\frac{\hat{\alpha}_i\cdot\mathbf{K}}{c_1}\cos\theta_i - 2\left(\frac{\omega''-\omega'}{c_1^2}\right)\left(\frac{\cos\theta_i}{2}\right)^2\right]. \qquad (B4)$$

Taking partial derivative of Eq. (B3) with respect to ω_t' yields

$$\frac{\partial^2 B_2}{\partial\omega_t'^2} = -\frac{1}{4B_2^3}\left[\frac{2\kappa^2\omega_t'}{c_1^2} - \frac{\hat{\alpha}_i\cdot\mathbf{K}}{c_1}\cos\theta_i + 2\left(\frac{\omega''-\omega'}{c_1^2}\right)\left(\frac{\cos\theta_i}{2}\right)^2\right]^2 + \frac{1}{2B_2}\left[\frac{2\kappa^2}{c_1^2} - \frac{2}{c_1^2}\left(\frac{\cos\theta_i}{2}\right)^2\right]. \qquad (B5)$$

Taking partial derivative of Eq. (B4) with respect to ω_t'' yields

$$\frac{\partial^2 B_2}{\partial \omega_t''^2} = -\frac{1}{4B_2^3}\left[\frac{\hat{\alpha}_i\cdot\mathbf{K}}{c_1}\cos\theta_i - 2\left(\frac{\omega''-\omega'}{c_1^2}\right)\left(\frac{\cos\theta_i}{2}\right)^2\right]^2 - \frac{1}{c_1^2 B_2}\left(\frac{\cos\theta_i}{2}\right)^2. \tag{B6}$$

Also,

$$\frac{\partial^2 B_2}{\partial \omega_t'\,\partial \omega_t''} = -\frac{1}{4B_2^3}\left[\frac{2\kappa^2\omega_t'}{c_1^2} - \frac{\hat{\alpha}_i\cdot\mathbf{K}}{c_1}\cos\theta_i + 2\left(\frac{\omega''-\omega'}{c_1^2}\right)\left(\frac{\cos\theta_i}{2}\right)^2\right]$$

$$\times\left[\frac{\hat{\alpha}_i\cdot\mathbf{K}}{c_1}\cos\theta_i - 2\left(\frac{\omega''-\omega'}{c_1^2}\right)\left(\frac{\cos\theta_i}{2}\right)^2\right] + \frac{1}{c_1^2 B_2}\left(\frac{\cos\theta_i}{2}\right)^2. \tag{B7}$$

Evaluating the derivatives at $\omega'=\omega''=0$, or $\omega_t'=\omega_t''=\omega_c$ and substituting into Eq. (43) yields an approximate expression for

$$B_2(K,\omega_c+\omega',\omega_c+\omega'')\cong B_{2c}(K)+\omega'\,\frac{1}{2B_{2c}}\left(\frac{2\kappa^2\omega_c}{c_1^2}-\frac{\hat{\alpha}_i\cdot\mathbf{K}}{c_1}\cos\theta_i\right)+\omega''\,\frac{\hat{\alpha}_i\cdot\mathbf{K}}{2c_1 B_{2c}}\cos\theta_i - \frac{1}{2}\,\omega'^2\left[\frac{1}{4B_{2c}^3}\left(\frac{2\kappa^2\omega_c}{c_1^2}\right.\right.$$

$$\left.-\frac{\hat{\alpha}_i\cdot\mathbf{K}}{c_1}\cos\theta_i\right)^2 - \frac{1}{2B_{2c}}\left(\frac{2\kappa^2}{c_1^2}-\frac{2}{c_1^2}\left(\frac{\cos\theta_i}{2}\right)^2\right)\right] - \omega'\omega''\left[\frac{\hat{\alpha}_i\cdot\mathbf{K}}{4c_1 B_{2c}^3}\cos\theta_i\left(\frac{2\kappa^2\omega_c}{c_1^2}\right.\right.$$

$$\left.\left.-\frac{\hat{\alpha}_i\cdot\mathbf{K}}{c_1}\cos\theta_i\right) - \frac{1}{c_1^2 B_{2c}}\left(\frac{\cos\theta_i}{2}\right)^2\right] - \frac{1}{2}\,\omega''^2\left[\frac{1}{4B_{2c}^3}\left(\frac{\hat{\alpha}_i\cdot\mathbf{K}}{c_1}\cos\theta_i\right)^2 + \frac{1}{c_1^2 B_{2c}}\left(\frac{\cos\theta_i}{2}\right)^2\right]. \tag{B8}$$

Subtracting $B_2(K,\omega_c+\omega',\omega_c+\omega'')$ from $B_2^*(K,\omega_c+\omega'',\omega_c+\omega')$, combining the ω' terms leads to Eqs. (46) and (47).

Starting with the ω'^2 terms in Eq. (B8), define

$$P=2\left\{\frac{1}{4B_{2c}^3}\left(\frac{2\kappa^2\omega_c}{c_1^2}-\frac{\hat{\alpha}_1\cdot\mathbf{K}}{c_1}\cos\theta_i\right)^2 - \frac{1}{2B_{2c}}\right.$$

$$\times\left(\frac{2\kappa^2}{c_1^2}-\frac{2}{c_1^2}\left(\frac{\cos\theta_i}{2}\right)^2\right) - \frac{1}{4B_{2c}^{3*}}\left(\frac{\hat{\alpha}_i\cdot\mathbf{K}}{c_1}\cos\theta_i\right)^2$$

$$\left. -\frac{1}{c_1^2 B_{2c}^*}\left(\frac{\cos\theta_i}{2}\right)^2\right\}z. \tag{B9}$$

Equation (48) is obtained by rearranging terms in Eq. (B9), and Eq. (49) is obtained from the cross term, $\omega''\omega'$.

APPENDIX C: INCOHERENT *T*-MATRIX CORRELATION FUNCTION APPROXIMATION IN EQ. (37), AND POWER SERIES EXPANSION APPROXIMATION IN EQ. (43)

1. Equation (37)

In order to evaluate the approximation in Eq. (37) for the incoherent field using first-order perturbation theory, $\mathbf{K}-\mathbf{K}_d/2$ is substituted for $\mathbf{K}'$, and $\mathbf{K}+\mathbf{K}_d/2$ is substituted for $\mathbf{K}''$ in Eqs. (37), (82), and (85):

$$\mathscr{C}_{12}(\mathbf{K}-\mathbf{K}_d/2,\mathbf{K}+\mathbf{K}_d/2,\mathbf{K}_i',\mathbf{K}_i'',\omega_c+\omega',\omega_c+\omega'')$$

$$\cong k_1^2 H_{12}(\mathbf{K}-\mathbf{K}_d/2,\mathbf{K}_i',\omega_c+\omega')H_{12}^*(\mathbf{K}+\mathbf{K}_d/2,\mathbf{K}_i'',\omega_c$$

$$+\omega'')\times W(\mathbf{K}-(\mathbf{K}_i'+\mathbf{K}_i'')/2) \tag{C1}$$

is the first-order solution, where $\mathbf{K}_d$ is given in Eq. (34). From Eq. (37), $\mathscr{C}_{12}$ is approximated by

$$\mathscr{C}_{12}(\mathbf{K}-\mathbf{K}_d/2,\mathbf{K}+\mathbf{K}_d/2,\mathbf{K}_i',\mathbf{K}_i'',\omega_c+\omega',\omega_c+\omega'')$$

$$\cong \mathscr{C}_{12}(\mathbf{K},\mathbf{K}_i,\omega_c) \quad \cong k_1^2|H_{12}(\mathbf{K},\mathbf{K}_i,\omega_c)|^2 W(\mathbf{K}-\mathbf{K}_i), \tag{C2}$$

where $\mathbf{K}_i$ is given in Eq. (23). The roughness spectrum, $W(\mathbf{K}-(\mathbf{K}_i'+\mathbf{K}_i'')/2)$, is not a function of

$$\omega_d=\omega''-\omega'. \tag{C3}$$

(see Ishimaru *et al.*, 1994a). For a narrow-band signal, it is a slowly varying function of

$$\omega_a=\omega_c+\frac{\omega'+\omega''}{2}. \tag{C4}$$

Note that for the roughness spectrum used in the examples [Eq. (89)]

$$\frac{\partial W}{\partial K}\left/\,W(\mathbf{K})\ll\frac{c_1}{f_{\text{BW}}}\right. \tag{C5}$$

is true everywhere except where W and its contribution to Eq. (36) is negligible. Equations (A13), (A14), and (82) show that the dependence of the term $H_{12}(\mathbf{K}-\mathbf{K}_d/2,\mathbf{K}_i',\omega_c+\omega')H_{12}^*(\mathbf{K}+\mathbf{K}_d/2,\mathbf{K}_i'',\omega_c+\omega'')$ on ω_a is insignificant. In addition, the dependency on ω_d is primarily in the factor T/β outside the square brackets in Eq. (83):

$$\frac{T(\mathbf{K}+\mathbf{K}_d/2)}{\beta_1(\mathbf{K}+\mathbf{K}_d/2)}=\frac{2\rho}{\kappa\beta_2(\mathbf{K}+\mathbf{K}_d/2)+\rho\beta_1(\mathbf{K}+\mathbf{K}_d/2)}. \tag{C6}$$

Equation (37) is therefor valid if (C5) and the following equation are true:

$$f_{\text{BW}}\frac{\partial}{\partial K}(T/\beta_1)\ll c_1 T/\beta_1. \tag{C7}$$

Although the magnitude of Eq. (C1) varies slowly with frequency, the phase becomes very dependent on ω_d when $|\mathbf{K}$

$+\mathbf{K}_d/2|$ approaches either κk_1 or k_1. When $k_1 > k_2$ and the signal narrow band, this situation occurs only for evanescent scattered waves and scattering at shallow grazing angles. However, as shown in Fig. 4, including the evanescent scattered field is only necessary within a wavelength or two of the interface, depending on the roughness.

For frequency and sediment parameters used in the examples, the magnitude of Eq. (C1) becomes slightly dependent on $f_d = (\omega'' - \omega')/(2\pi)$ only for shallow grazing angles and the phase of Eq. (C1) becomes dependent on large f_d only for the evanescent scattered field, and for scattering at shallow grazing angles—even for a relatively wideband signal. The simplifying approximation for $\mathscr{C}$ in Eq. (37) is valid for all values of K, except those values corresponding to evanescent waves, and those corresponding to scattering at small grazing angles. Because of loss in the sediment, energy scattered at these small grazing angles is insignificant compared to energy scattered at larger grazing angles. Therefore, Eq. (C1) can be considered to be independent of f_d and the approximation in Eq. (37) is valid for the examples everywhere, except near the surface.

2. Equation (43)

The validity of the power-series is found by examining the higher-order terms. From Eq. (50),

$$|P/4| \leq D \frac{k_1}{8} \frac{f_{BW}^2}{\omega_c^2} \frac{1}{\sin^2 \theta}, \tag{C8}$$

where D is the maximum dimension of the surface that contributes to the scattered field. The next higher-order term is on the order of Eq. (C8) multiplied by $f_{BW}/(\omega_c \sin^2 \theta)$. The contribution of this next term is negligible for a narrow-band source. As mentioned above, the contribution due to scattering at very small grazing angles is negligible.

Aki, K., and Richards, P. G. (**1980**). *Quantitative Seismology, Theory and Methods* (Freeman, New York).

Berman, D. H. (**1992**). ''Renormalization of propagation in a waveguide with rough boundaries,'' J. Acoust. Soc. Am. **92**, 309–314.

Brekhovskikh, L. M. (**1980**). *Waves in Layered Media* (Academic, San Diego), Chap. 4.

Devaney, A. J., and Sherman, G. C. (**1973**). ''Plane-wave representations for scalar wave fields,'' SIAM (Soc. Ind. Appl. Math.) Rev. **15**, 765–786.

Ishimaru, A. (**1978a**). *Wave Propagation and Scattering in Random Media I* (Academic, San Diego).

Ishimaru, A. (**1978b**). *Wave Propagation and Scattering in Random Media II* (Academic, San Diego).

Ishimaru, A. (**1991**). *Electromagnetic Wave Propagation, Radiation, and Scattering* (Prentice-Hall, Englewood Cliffs, NJ), Chaps. 4, 15.

Ishimaru, A., Ailes-Sengers, L., Phu, P., and Winebrenner, D. (**1994a**). ''Pulse broadening and two-frequency mutual coherence function of the scattered wave from rough surfaces,'' Waves Random Media **4**, 139–148.

Ishimaru, A., Ailes-Sengers, L., Phu, P., and Winebrenner, D. (**1994b**). ''Pulse broadening of enhanced backscattering from rough surfaces,'' Waves Random Media **4**, 453–465.

Ishimaru, A., and Chen, J. S. (**1990**). ''Scattering from very rough surfaces based on the modified second-order Kirchhoff approximation with angular and propagation shadowing,'' J. Acoust. Soc. Am. **88**, 1877–1883.

Ishimaru, A. and Chen, J. S. (**1991**). ''Scattering from very rough metallic and dielectric surfaces: A theory based on the modified Kirchhoff approximation,'' Waves Random Media **1**, 21–34.

Jackson, D. R., Thorsos, E. I., and Moe, J. E. (**1997**). ''Far-field considerations in boundary scattering,'' International Conference on Shallow Water Acoustics, Beijing, China.

Moe, J. E. (**1996**). ''Near and Far-Field Acoustic Scattering through and from Two Dimensional Fluid–Fluid Rough Interfaces,'' Ph.D. dissertation, Univ. of Washington, Seattle, available as Applied Physics Laboratory report APL-UW TR 9606.

Moe, J. E., and Jackson, D. R. (**1994a**). ''First order perturbation solution for rough surface scattering cross section including the effects of gradients,'' J. Acoust. Soc. Am. **96**, 1748–1754.

Moe, J. E., and Jackson, D. R. (**1994b**). ''The effect of roughness on acoustic penetration of the ocean bottom,'' J. Acoust. Soc. Am. **96**, 3265.

Papoulis, Athanasios (**1984**). *Probability, Random Variables, and Stochastic Processes* (McGraw-Hill, New York), pp. 273–274.

Proakis, J. G. (**1989**). *Digital Communications* (McGraw-Hill, New York), Chap. 3.

Rice, S. O. (**1951**). ''Reflection of electromagnetic waves from slightly rough surfaces,'' Commun. Pure Appl. Math. **4**, 351–378.

Thorsos, E. I. (**1990**). ''Acoustic scattering from a 'Pierson-Moskowitz' sea surface,'' J. Acoust. Soc. Am. **88**, 335–349.

Thorsos, E. I. (**1996**). ''The accuracy of perturbation theory for acoustic penetration of sediment due to interface roughness,'' J. Acoust. Soc. Am. **99**, 2475.

Thorsos, E. I., and Jackson, D. R. (**1989**). ''The validity of the perturbation approximation for rough surface scattering using a Gaussian roughness spectrum,'' J. Acoust. Soc. Am. **86**, 261–277.

Thorsos, E. I., Jackson, D. R., Moe, J. E., and Wiliams, K. W. (**1997**). ''Modeling of subcritical penetration into sediments due to interface roughness,'' NATO-Saclant Undersea Research Centre Conference on High Frequency Acoustics in Shallow Water, Lerici, Italy.

Voronovich, A. G. (**1994**). *Wave Scattering from Rough Surfaces* (Springer-Verlag, Berlin), pp. 33–36.

Westwood, E. K. (**1989**). ''Complex ray methods for acoustic interaction at a fluid-fluid interface,'' J. Acoust. Soc. Am. **85**, 1872–1884.

Winebrenner, D., and Ishimaru, A. (**1986**). ''On the far-field approximation for scattering from randomly rough surfaces,'' IEEE Trans. Antennas Propag. **AP-34**, 847–849.

Wingham, D. J. (**1985**). ''The dispersion of sound in sediment,'' J. Acoust. Soc. Am. **78**, 1757–1760.

Ziomek, L. J. (**1982a**). ''Generalized Kirchhoff approach to the ocean surface scatter communications channel. Part I. Transfer function of the ocean surface,'' J. Acoust. Soc. Am. **71**, 116–126.

Ziomek, L. J. (**1982b**). ''Generalized Kirchhoff approach to the ocean surface scatter communications channel. Part II. Second-order functions,'' J. Acoust. Soc. Am. **71**, 1487–1495.

Theory of compressional and shear waves in fluidlike marine sediments

Michael J. Buckingham[a]

Marine Physical Laboratory, Scripps Institution of Oceanography, University of California, San Diego, 9500 Gilman Drive, La Jolla, California 92093-0213

An unconsolidated, saturated marine sediment consists of a more or less loose assemblage of mineral grains in contact, with seawater in the interstices. It is postulated that the two-phase medium possesses no skeletal frame, implying that the elastic rigidity modulus of the material is zero. A theory of wave propagation in such a sediment is developed, in which the medium is treated as a fluid that supports a specific form of intergranular dissipation. Two important equations emerge from the analysis, one for compressional wave propagation and the second describing transverse disturbances. For the type of dissipation considered, which exhibits hysteresis or memory, the shear equation admits a wavelike solution, and is thus a genuine wave equation, even though the sediment shows no elastic rigidity. In effect, the medium possesses a ''dissipative'' rigidity, which is capable of supporting shear. This behavior is distinct from that of a viscous fluid, for which the shear equation is diffusionlike in character, giving rise to critically damped disturbances rather than propagating waves. The new theory predicts an attenuation coefficient for both compressional and shear waves that scales with the first power of frequency, in accord with published data. The wave theory is combined with a model of the mechanical properties of marine sediments to yield expressions relating the compressional and shear wave speeds to the grain size, the porosity, and the density of the medium. These expressions show compelling agreement with a number of measurements from the literature, representing a variety of sediment types ranging from clay to coarse sand. © *1998 Acoustical Society of America.* [S0001-4966(98)05901-3]

PACS numbers: 43.30.Ma [DLB]

LIST OF SYMBOLS

c_p	compressional wave speed (m/s)
c_s	shear wave speed (m/s)
c_0	compressional wave speed in absence of intergranular friction (m/s)
α_p	compressional attenuation coefficient (nepers/m)
α_s	shear attenuation coefficient (nepers/m)
β_p	compressional loss tangent
β_s	compressional loss tangent
Q	quality factor
χ_f	compressional dissipation coefficient
μ_c	compressional frictional rigidity modulus
μ_s	shear frictional rigidity modulus
ω	angular frequency
k_0	wave number in absence of intergranular friction
t	time
p	pressure fluctuation
$\mathbf{v}$	particle velocity
ρ	density fluctuation
$\psi(t)$	velocity potential
$\mathbf{A}(t)$	vector potential
$\Psi(j\omega)$	Fourier transform of $\psi(t)$
$h(t)$	compressional material memory function
$h_s(t)$	shear material memory function
$H(j\omega)$	Fourier transform of $h(t)$
$H_s(j\omega)$	Fourier transform of $h_s(t)$
n	compressional material memory exponent ($0<n<1$)
m	shear material memory exponent ($0<m<1$)
u_g	mean grain diameter, microns
N	porosity ($0<N<1$)
ρ_0	bulk density of sediment (kg/m^3)
κ	bulk modulus of sediment (Pa)
γ	volume ratio of smaller to larger grains in a bimodal sediment
$\rho_w=1024$ kg/m^3	density of pore water
$\rho_g=2700$ kg/m^3	density of mineral grains
$\kappa_w=2.25\times10^9$ Pa	bulk modulus of pore water
$\kappa_g=1.47\times10^{10}$ Pa	bulk modulus of mineral grains
$\Delta=3$ μm	rms particle roughness
$P=0.63$	packing factor of randomly packed smooth spheres
$u_0=1000$ μm	reference grain diameter
$\mu_0=2\times10^9$ Pa	compressional frictional rigidity constant
$\mu_1=5.1\times10^7$ Pa	shear frictional rigidity constant

---

[a]Also affiliated to: Institute of Sound and Vibration Research, The University, Southampton SO17 1BJ, England.

INTRODUCTION

A theory of the acoustic and mechanical properties of unconsolidated marine sediments was recently introduced and developed in a paper by Buckingham,[1] hereafter referred to as I. Central to the theory is a specific form of intergranular dissipation, which exhibits an unusual form of hysteresis. It is shown in I that this particular type of dissipation gives rise to many of the observed properties of saturated sands and silts. The sediment was treated in I as an equivalent fluid in which shear-wave propagation was neglected.

Actual sediments have long been known to support shear waves,[2–4] although the shear speed is low compared with the compressional speed. For instance, a medium-to-coarse sand with a grain diameter of 500 μm has a compressional wave speed in the region of 1750 m/s, whereas the shear speed is of the order of 100 m/s.[5] In finer sediments the shear speed is even lower. Typically, the ratio of compressional speed to shear speed is somewhat greater than 10 in saturated sediments,[6] but is less than 2 for water-saturated rocks,[7] suggesting that the geoacoustic properties of consolidated rocks and unconsolidated sediments may be governed by different physical mechanisms.

In a series of classic papers, Biot[8–11] developed a theory of acoustic propagation in fluid-saturated porous media. The materials he considered consist of a solid elastic matrix, or skeletal frame, containing a compressible, viscous fluid. An example of such a medium is water-saturated rock. Biot's viscoelastic theory leads to the prediction of three types of body wave, of which two are longitudinal (compressional) and one is transverse (shear). The compressional wave of the first kind, or fast wave, shows relatively little attenuation and corresponds to displacements of the frame and the interstitial fluid which are in phase. Out of phase displacements give rise to the compressional wave of the second kind, the slow wave, which suffers relatively high attenuation.

Observations of fast, slow, and shear waves have been reported in a porous medium consisting of fused glass beads immersed in water.[12,13] Such a material resembles rock in that the fused beads formed a consolidated, elastic skeletal frame. This is the type of medium addressed by the Biot theory, and it was found that all the measured wave speeds (2.81, 0.96, and 1.41 km/s for the fast, slow, and shear waves, respectively) conformed with the predictions of the theory.

In a second experiment by the same researchers,[13] a minor change in the microgeometry lead to a radical change in the acoustic behaviour of the porous medium. Instead of being fused, the beads were left loose, or unconsolidated, much like a sediment consisting of mineral grains and seawater. A fast wave with a speed of 1.79 km/s was observed, comparable with that of the compressional wave in sediments, but neither a slow wave nor a shear wave were detected. The absence of a shear wave was attributed to scattering of the short, ultrasonic shear wavelengths used in the experiment.

As with the compressional-to-shear speed ratio, the fundamentally distinct behavior of the fused and loose glass beads suggests that different physical processes may be at work in consolidated and unconsolidated materials. In this article, we shall identify the terms ''consolidated'' and ''un-

consolidated'' with the presence and absence, respectively, of a skeletal frame. In a consolidated medium like rock, the porous mineral structure constitutes the elastic, skeletal frame, and the Biot theory or an appropriate modification of it is expected to hold. By way of contrast, the mineral grains in an unconsolidated sediment are, on a microscopic scale, mobile with respect to one another, suggesting that the material possesses no skeletal frame. In this case, the mechanism of intergranular friction introduced in I is presumed to govern the acoustic properties of the medium. The absence of a frame eliminates the possibility of a slow wave in an unconsolidated material.

If it is accepted that an unconsolidated marine sediment does not possess a skeletal frame, the medium cannot be regarded as an elastic solid. In fact, in several ways a saturated sediment is fluidlike in character. We postulate here that the sediment acts as a true fluid, in the sense that its dynamic rigidity or elastic shear modulus is identically zero. This would seem to suggest that the sediment is incapable of supporting shear waves, in contradiction with observations in the laboratory and *in situ*, but this is not so.

There is no doubt that a saturated sediment exhibits an ''effective rigidity,'' allowing the medium to support the transmission of transverse waves. It is demonstrated here that the rigidity may arise from a certain type of dissipation at intergrain contacts. In other words, internal dissipation (not elasticity) in the fluid medium is responsible for shear wave propagation. This is a fairly radical statement, since it is easily proved that a conventional fluid, in which the dissipation is due to viscosity, cannot support transverse waves.[14] It turns out, however, that if the internal dissipation exhibits an appropriate form of memory, a degree of stiffness or rigidity is introduced into the medium, which allows shear waves to propagate.

The properties of a particular type of fluid that is capable of supporting shear waves and is also representative of unconsolidated marine sediments, are developed in this article. The basic theoretical ideas in I are extended to include the effects of shear arising from intergranular dissipation. By adapting a standard argument, separated wave equations are established for the compressional and shear waves in a sediment whose rigidity arises, not from frame elasticity, but from the dissipative force between contiguous mineral particles. As in I, the dissipation term in each wave equation is formulated as a temporal convolution between a material memory function and the particle velocity. The inclusion of the shear wave has no effect on the properties of the compressional wave, which remain exactly as described in I. Both the compressional and the shear wave emerging from the new theory show characteristics that are in accord with available experimental data. In particular, the attenuation coefficient of both waves is accurately proportional to the first power of frequency, consistent with the observations of Hamilton,[15,16] Brunson,[17,18] and others.

I. BASIC FORMULATION

To derive the wave equations for compressional and shear waves in an unconsolidated sediment, we assume that the material is macroscopically homogeneous, isotropic, time

invariant, and infinite. In effect, the granular medium is treated as a dissipative (but not viscous), compressible fluid, with an elastic rigidity modulus of zero. The absence of elastic rigidity means that the material is not a Hookean solid, even though it will be shown to support transverse waves.

To begin, consider first the (fictitious) case when dissipation is entirely absent, that is, the medium is simply a lossless, compressible fluid. Then the equation of motion is

$$\rho_0 \frac{\partial \mathbf{v}}{\partial t} + \mathrm{grad}\ p = 0, \tag{1}$$

where $\mathbf{v}$ is particle velocity, ρ_0 is bulk density, and p is the pressure fluctuation. From conservation of mass and the equation of state,

$$\frac{\partial p}{\partial t} + \kappa\ \mathrm{div}\ \mathbf{v} = 0, \tag{2}$$

where κ is the bulk modulus of the medium, and, on combining Eqs. (1) and (2), the familiar wave equation for compressional waves in the medium is obtained:

$$\rho_0 \frac{\partial^2 \mathbf{v}}{\partial t^2} = \kappa\ \mathrm{grad}\ \mathrm{div}\ \mathbf{v}. \tag{3}$$

There is no solution of this equation that corresponds to transverse waves. The speed of sound (i.e., the phase speed of the compressional wave) in the lossless fluid, c_0, follows from Eq. (3):

$$c_0 = \sqrt{\frac{\kappa}{\rho_0}}. \tag{4}$$

An expression for c_0 in terms of the bulk moduli and densities of the two constituents of the lossless sediment, mineral grains and seawater, will be given later.

Now suppose that the medium is allowed to support intergranular dissipation. Following the spirit of I, Eq. (3) must be modified by adding to the right-hand side two dissipation terms [see, for example, the analogous Navier–Stokes equation (2.3.18) for viscous dissipation, p. 162 in Morse and Feshbach[14]]. Thus the equation appropriate to a saturated sediment is proposed as

$$\rho_0 \frac{\partial^2 \mathbf{v}}{\partial t^2} = \kappa\ \mathrm{grad}\ \mathrm{div}\ \mathbf{v} + \left(\frac{4}{3}\ \eta_f + \lambda_f \right) \mathrm{grad}\ \mathrm{div}\ \frac{\partial}{\partial t}\ [h(t)$$

$$\otimes \mathbf{v}(t)] - \eta_f\ \mathrm{curl}\ \mathrm{curl}\ \frac{\partial}{\partial t}\ [h_s(t) \otimes \mathbf{v}(t)], \tag{5}$$

where $h(t)$ and $h_s(t)$ are, respectively, material "memory" functions for compressional and shear disturbances, and the symbol $\otimes$ denotes a temporal convolution. The basis of the dissipation terms in Eq. (5) is that the components of the frictional stress tensor involve the appropriate memory function convoluted with the particle velocity, rather than the velocity itself.

If $h(t)$ and $h_S(t)$ were delta functions, Eq. (5) would reduce identically to the form appropriate to a viscous fluid,[19,20] since $\delta(t) \otimes \mathbf{v}(t) = \mathbf{v}(t)$. Thus viscosity corresponds to the situation where the medium has no memory, that is, previous events have no effect on the current response. How-

ever, with other forms for the memory functions, representing the influence of earlier states on present behaviour, the dissipation may be radically different in character from viscosity. A specific form for $h(t)$ was introduced in I as being representative of dissipation in marine sediments.

Although the dissipation coefficients η_f and λ_f in Eq. (5) are analogous, respectively, to the shear and bulk viscosities of a fluid, the subscript f highlights the fact that these coefficients are actually associated with intergranular friction, not with viscosity. It is important to notice that there is no term in Eq. (5) of the form μ curl curl $\mathbf{v}$, which would necessarily be present to represent the effects of rigidity if the medium were elastic with rigidity modulus μ. The absence of such a term is consistent with our hypothesis that a marine sediment has no elastic rigidity, that is, the rigidity modulus, μ, is strictly zero. If the dissipation mechanism were viscosity, the absence of the rigidity term in Eq. (5) would lead to a diffusion type of equation for the vector potential of the field, implying that the shear disturbance would not be a true wave but would decay in time and space. In other words, a viscous fluid does not support shear waves. However, as shown below, with an appropriate choice of the memory function $h_s(t)$, a wavelike solution of Eq. (5) for transverse disturbances is admissible and shear wave transmission is possible as a direct result of the intergranular dissipation.

The functions $h(t)$ and $h_s(t)$, representing, respectively, the material memory functions for the compressional and shear waves, are assigned the forms

$$h(t) = u(t)\ \frac{t_0^{n-1}}{t^n}, \quad 0 < n \ll 1 \tag{6}$$

and

$$h_s(t) = u(t)\ \frac{t_1^{m-1}}{t^m}, \quad 0 < m \ll 1, \tag{7}$$

where the presence of $u(t)$, the unit step function, ensures that the medium is causal. This type of memory function has been discussed at length in I. It is shown below that the small exponents n and m, respectively, control the attenuation of the compressional and shear wave, but have only a very minor dispersive effect on the wave speeds. The temporal coefficients t_0 and t_1 appear in Eqs. (6) and (7) to maintain the correct units of inverse time for the memory functions, that is, the convolutions have the dimensions of velocity.

Equation (5) in conjunction with Eqs. (6) and (7) is the fundamental equation governing the propagation of compressional and shear waves in the dissipative fluid sediment.

II. WAVE EQUATIONS

According to Helmholtz's theorem,[14] any vector field, $\mathbf{v}$, may be expressed as the sum of the gradient of a scalar potential, ψ, and the curl of a zero-divergence vector potential $\mathbf{A}$:

$$\mathbf{v} = \mathrm{grad}\ \psi + \mathrm{curl}\ \mathbf{A}; \quad \mathrm{div}\ \mathbf{A} = 0. \tag{8}$$

Following a standard form of analysis,[21] the first of the expressions in Eq. (8) is substituted into Eq. (5), which may

then be separated into two equations by equating terms in ψ and $\mathbf{A}$:

$$\nabla^2\psi - \frac{1}{c_0^2}\frac{\partial^2\psi}{\partial t^2} + \frac{(\frac{4}{3}\eta_f + \lambda_f)}{\rho_0 c_0^2}\frac{\partial}{\partial t}\nabla^2[h(t)\otimes\psi(t)] = 0 \quad (9)$$

and

$$\frac{\eta_f}{\rho_0}\frac{\partial}{\partial t}\nabla^2[h_s(t)\otimes\mathbf{A}(t)] - \frac{\partial^2\mathbf{A}}{\partial t^2} = 0, \quad (10)$$

where ∇^2 is the Laplacian. The identities curl grad $\psi=0$, div curl $\mathbf{A}=0$, and curl curl $\mathbf{A} = -\nabla^2\mathbf{A}$ were used in deriving these expressions. The wave equation for compressional waves [Eq. (9)] formed the basis of the discussion in I.

For a shear wave of vertical polarization, the vector potential can be chosen so that only one component differs from zero. Setting

$$\mathbf{A} = -\frac{\partial\psi_s}{\partial r}\,\mathbf{e}_\phi, \quad (11)$$

where r is horizontal range, $\mathbf{e}_\phi$ is the unit vector normal to the plane of propagation and ψ_s is a scalar shear potential, Eq. (10) reduces to

$$\frac{\eta_f}{\rho_0}\nabla^2[h_s(t)\otimes\psi_s(t)] - \frac{\partial\psi_s}{\partial t} = 0. \quad (12)$$

This is a new equation for transverse disturbances, which is discussed below.

Although it may look diffusionlike in character, Eq. (12) together with the expression for $h_s(t)$ in Eq. (7) admits a wavelike solution and hence may be regarded as a genuine wave equation. It is easy to see, however, that if $h_s(t)$ were a delta function, corresponding to viscous dissipation, Eq. (12) would indeed take the form of a diffusion equation, whose only solution is a critically damped disturbance, which is not a true wave. This, of course, is why a viscous fluid cannot support transverse waves. Clearly, Eq. (12) is an important result: while being consistent with the special case of a viscous fluid, it allows for the possibility that certain types of dissipative fluids (i.e., media whose elastic rigidity modulus is zero) are capable of supporting propagating shear waves.

The wave equations in Eqs. (9) and (12) are expressed in the time domain, and the coefficients appearing in them are real constants representing the mechanical properties of the medium. Thus these constants are not permitted to become complex, nor may they show any frequency dependence.

When the compressional and shear-wave equations are Fourier transformed with respect to time they become

$$\nabla^2\Psi + \frac{\omega^2}{c_0^2}\Psi + j\omega\frac{(\frac{4}{3}\eta_f + \lambda_f)}{\rho_0 c_0^2}H(j\omega)\nabla^2\Psi = 0 \quad (13)$$

and

$$\frac{\eta_f}{\rho_0}H_s(j\omega)\nabla^2\Psi_s - j\omega\Psi_s = 0, \quad (14)$$

where ω is angular frequency, (Ψ, Ψ_s) are the Fourier transforms of the compressional and shear waves (ψ, ψ_s), and

similarly (H, H_s) are the transforms of the memory functions (h, h_s). Now the Fourier transform of the memory functions in Eqs. (6) and (7) is a standard form:[22]

$$H(j\omega) = \frac{\Gamma(1-n)}{(j\omega t_0)^{1-n}} \quad (15)$$

and

$$H_s(j\omega) = \frac{\Gamma(1-m)}{(j\omega t_1)^{1-m}}, \quad (16)$$

where $\Gamma(..)$ is the gamma function, which is essentially unity since n and m are very small numbers. On substituting these expressions into Eqs. (13) and (14), we arrive at the following reduced wave equations for the compressional and shear waves:

$$[1 + (j\omega t_0)^n\chi_f]\nabla^2\Psi + \frac{\omega^2}{c_0^2}\Psi = 0 \quad (17)$$

and

$$\frac{\mu_s}{\rho_0}\nabla^2\Psi_s + \frac{\omega^2}{(j\omega t_1)^m}\Psi_s = 0. \quad (18)$$

As in I, the dimensionless dissipation coefficient χ_f appearing in Eq. (17) is simply an amalgamation of several parameters:

$$\chi_f = \frac{(\frac{4}{3}\eta_f + \lambda_f)\Gamma(1-n)}{\rho_0 c_0^2 t_0} = \frac{\mu_c}{\rho_0 c_0^2}, \quad (19)$$

where μ_c may be regarded as the compressional, dissipative rigidity modulus. The coefficient χ_f governs the properties of the compressional wave, that is to say, the wave speed and attenuation. The new coefficient, μ_s, appearing in the reduced shear wave equation [Eq. (18)] is

$$\mu_s = \frac{\eta_f}{t_1}\Gamma(1-m). \quad (20)$$

The importance of this coefficient should be recognized, since it is the transverse "effective rigidity modulus" of the sediment, arising directly from the intergranular dissipation. It is because of the nonzero value of μ_s that shear waves can propagate in the fluidlike sediment. Notice that, like the rigidity modulus of an elastic solid, μ_c and μ_s have the dimensions of pressure, but neither is an elastic modulus: Both scale with the level of the intergranular dissipation, and hence are direct measures of the dissipative rigidity of the medium.

III. WAVE SPEED AND ATTENUATION

Consider one-dimensional, plane-wave propagation in the x direction. For this simple situation, the reduced wave equation for the compressional wave [Eq. (17)] can be written as

$$\frac{\partial^2\Psi}{\partial x^2} + \frac{\omega^2}{c_0^2[1 + (j\omega t_0)^n\chi_f]}\Psi = 0 \quad (21)$$

and similarly for the shear wave [Eq. (18)],

$$\frac{\partial^2 \Psi_s}{\partial x^2} + \frac{\omega^2}{(j\omega t_1)^m (\mu_s/\rho_0)}\, \Psi_s = 0. \tag{22}$$

By inspection, the solutions of these equations are

$$\Psi = \Psi_0\, \exp - j\, \frac{\omega}{c_0\sqrt{1 + (j\omega t_0)^n \chi_f}}\, |x| \tag{23}$$

and

$$\Psi_s = \Psi_{s0}\, \exp - j\, \frac{\omega}{\sqrt{(j\omega t_1)^m (\mu_s/\rho_0)}}\, |x|, \tag{24}$$

where Ψ_0 and Ψ_{s0} are the amplitudes of the compressional and shear wave, respectively. Both of these expressions represent a propagating, exponentially damped wave, that is, the dissipative fluid described by Eqs. (17) and (18) supports not only a compressional wave but also a well-behaved shear wave.

Following I, accurate approximations for the wave speeds and attenuations may be developed on the basis of a straightforward argument. To first order in the small parameter n, the following expressions are valid:

$$[\mathrm{sgn}(\omega)j]^n = \cos(n\pi/2) + j\, \mathrm{sgn}(\omega)\, \sin(n\pi/2)$$

$$\approx 1 + (jn\pi/2)\mathrm{sgn}(\omega), \tag{25}$$

and

$$(|\omega|t_0)^n = \exp[n\, \ln(|\omega|t_0)] = 1 + n\, \ln(|\omega|t_0) + \cdots. \tag{26}$$

Obviously, similar expressions hold for the term raised to the power of m in Eq. (24). The signum function in Eq. (25) has been included to accommodate negative frequencies. Hence, to the same order of approximation, the compressional and shear-wave speeds, c_p and c_s, respectively, can be written as

$$c_p = c_0\, \mathrm{Re}\sqrt{1 + (j\omega t_0)^n \chi_f}$$

$$= c_0 \sqrt{1 + \chi_f}\left[1 + \frac{n\chi_f}{2(1 + \chi_f)}\, \ln(|\omega|t_0) \right] \tag{27}$$

and

$$c_s = \mathrm{Re}\sqrt{(j\omega t_1)^m (\mu_f/\rho_0)}$$

$$= \sqrt{\frac{\mu_s}{\rho_0}}\left[1 + \frac{m}{2}\, \ln(|\omega|t_1) \right]. \tag{28}$$

According to these expressions, both wave speeds show very weak logarithmic dispersion, which in most circumstances is entirely negligible (see I). Thus the wave speeds are essentially given by the frequency-independent expressions

$$c_p = c_0\sqrt{1 + \chi_f} \tag{29}$$

and

$$c_s = \sqrt{\frac{\mu_s}{\rho_0}}. \tag{30}$$

It is interesting that the shear speed takes exactly the same form as it would in an elastic solid, except that the dynamic rigidity modulus, μ, has been replaced by the dissipative rigidity modulus, μ_s. Since μ_s scales with the level of dissipation [Eq. (20)], it is clear that the shear speed goes to

zero as the losses vanish, consistent with observations in actual marine sediments.[3,23,24]

To first order in n and m, the compressional and shear attenuation coefficients, α_p and α_s, respectively, from Eqs. (23)–(26), are

$$\alpha_p = \beta_p\, \frac{|\omega|}{c_p} = \frac{n\pi\chi_f}{4(1 + \chi_f)}\, \frac{|\omega|}{c_p}, \tag{31}$$

and

$$\alpha_s = \beta_s\, \frac{|\omega|}{c_s} = \frac{m\pi}{4}\, \frac{|\omega|}{c_s}. \tag{32}$$

The dimensionless, frequency-independent loss tangents β_p and β_s, representing the imaginary part of the complex wave number relative to the real part, are defined by these expressions. Notice that both attenuation coefficients, α_p and α_s, scale as the first power of frequency. Moreover, the weak dispersion expressed in Eqs. (27) and (28) is exactly as required by the Kronig–Kramers relationships[25,26] for a medium with attenuation of the form given in Eqs. (31) and (32), irrespective of the details of the mechanism responsible for the dissipation.[27] The linear scaling of attenuation with frequency emerges from the new theory quite naturally. It has been discussed at length in I in connection with attenuation of the compressional wave, for which extensive supporting data are available.[15,16] Far fewer measurements have been made on the attenuation of shear waves in unconsolidated marine sediments, but the little evidence that has been published is consistent with Eq. (32).

IV. SHEAR ATTENUATION VERSUS FREQUENCY MEASUREMENTS

Figure 1 shows the attenuation of shear waves as a function of frequency in water-saturated medium sand, as measured in the laboratory by Brunson and Johnson[17] and Brunson.[18] The data points in the figure show the values tabulated by these authors. All three sand samples represented in the figure had approximately the same mean grain diameter, lying between 350 and 380 μm. The solid lines in the figure are least-squares, power-law fits to the data, and the exponent of each is shown in the corresponding panel. These exponents are all very close to unity, consistent with the linear frequency dependence for the attenuation expressed in Eq. (32). No shear speed was reported for the laboratory sediments, but if for the moment it is assumed to be $c_s = 120$ m/s, then from Eq. (32) the value of m is found to be $m \approx 0.049$, which is comparable to the values of n found for compressional waves in I.

In addition to his sand data, Brunson[18] also reported measurements of shear attenuation in a granular medium consisting of loose, spherical, quartz glass beads immersed in water. The beads were sorted, with a mean diameter of 380 μm, that is, much the same as the sands in Fig. 1. Figure 2 shows the results of the measurements, as tabulated by Brunson, and also a power-law, least-squares fit to the data. The linear relationship between attenuation and frequency exhibited by this particular medium is quite striking, and, as with the sand data in Fig. 1, is in excellent agreement with
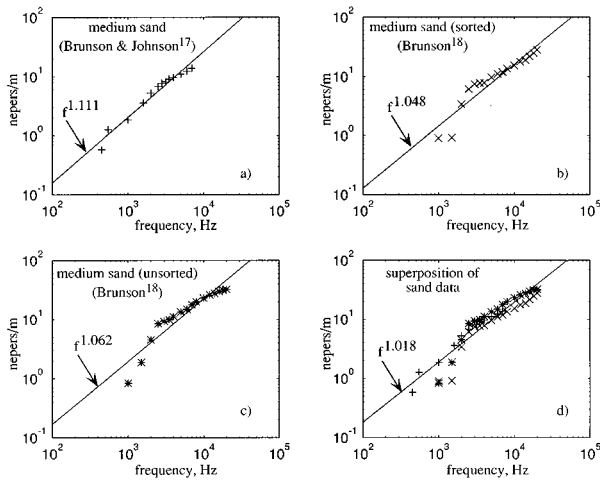
FIG. 1. Shear-wave attenuation, α_s, versus frequency, f, in saturated medium sands with mean grain diameters between 350 and 380 μm. The symbols represent laboratory data as follows: (a) saturated angular sand, from Brunson and Johnson (Ref. 17), Table II; (b) sorted sand, from Brunson (Ref. 18), Table 2; (c) unsorted sand, from Brunson (Ref. 18), Table 2; and (d) superposition of the data in panels (a)–(c). The solid lines are least-squares fits to the data of the power law $\alpha_s = af^b$, where f is frequency and a, b are constants.

Eq. (32). Assuming the same shear speed of 120 m/s, the value of the exponent m for the glass beads is $m \approx 0.025$, which is about half that found for the sand.

Although the data sets in Figs. 1 and 2 represent a very limited sample, the trend that they follow is consistent with the linear frequency dependence expressed by Eq. (32). Curiously, in assessing his own shear-attenuation experiments on sands and glass beads, Brunson[18] made the following statement. ''None of the three sediments exhibited a truly linear frequency dependence across the entire frequency range, although linear regression fits to the data produced reasonable results, particularly for the ''ideal'' spherical beads.'' This conveys the impression that the shear attenuations measured by Brunson do not scale as the first power of frequency. Such an interpretation is difficult to reconcile with the plots shown in Figs. 1 and 2.
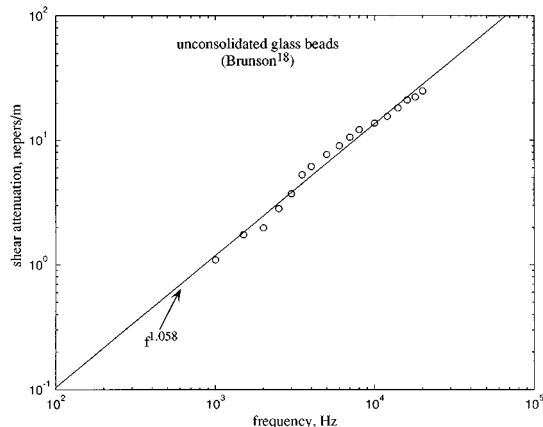
FIG. 2. Shear-wave attenuation, α_s, versus frequency, f, in water-saturated, unconsolidated glass beads. The symbols represent data from Brunson (Ref. 18), Table 2, and the solid line is a least-squares fit to the data of the power law $\alpha_s = af^b$, where a, b are constants.

From a theoretical point of view, the question of whether the attenuation (compressional and shear) in sediments is proportional to frequency is extremely important. Attenuation measurements, especially for shear, are difficult to make and invariably the data points will show some random scatter, especially at lower frequencies, where the wavelength becomes comparable to the dimensions of the experimental set up. There is some evidence of such scatter in Brunson's sand data shown in Fig. 1(a), (b), and (c). However, the only feature common to all three data sets in Fig. 1 is their near-linear dependence on frequency. The detailed excursions of the data points about the regression lines show no obvious systematic behavior, suggesting that the fine structure in the data bears little relation to the primary physical mechanism responsible for the attenuation in these materials. Accordingly, the only reasonable interpretation of Brunson's data[17,18] for sands, and also of course for the glass beads, is that the principal dependence exhibited by the shear attenuation is a near-linear scaling with frequency.

V. WOOD'S EQUATION FOR c_0

The parameter c_0 defined in Eq. (4) is a constant for a given sediment, since it depends only on the bulk modulus and the density of the medium. It is the value that the compressional wave speed would have in the absence of inter-granular losses, that is, if there were no dissipative rigidity. The effect of the rigidity is to increase the stiffness of the medium, which in turn raises the compressional speed, c_p, above the value c_0. This physical interpretation of c_0 and c_p is consistent with Eqs. (3) and (5), and also with the expression for c_p in Eq. (29).

In the absence of inter-granular dissipation, the material would be a simple, lossless, two-phase medium, consisting of mineral grains and seawater. The sound speed, c_0, in such a medium is given by Wood's equation,[28] in terms of weighted means of the bulk moduli and the densities of the constituent materials. An interesting aspect of Wood's equation is that, over the years, it has been discussed by several authors in connection with marine sediments, but always in the context of the observable compressional wave speed, c_p, rather than the nonobservable speed, c_0. Although Wood's equation alone does not yield c_p, since it takes no account of rigidity in the material, it is developed below to provide an expression for c_0, which will be used later when evaluating the actual wave speed, c_p, in Eq. (29).

To express c_0 in terms of the densities and bulk moduli of the mineral grains and seawater, the density of the sediment is written as

$$\rho_0 = N\rho_w + (1-N)\rho_g, \tag{33}$$

where N is the porosity of the material, $\rho_w = 1024$ kg/m^3 is the density of seawater, and $\rho_g = 2700$ kg/m^3 is the density of quartz sand grains. Similarly, the bulk modulus of the medium, κ, is given by

$$\frac{1}{\kappa} = N\frac{1}{\kappa_w} + (1-N)\frac{1}{\kappa_g}, \tag{34}$$

where $\kappa_w = 2.25 \times 10^9$ Pa is the bulk modulus of the interstitial seawater. As in I, the bulk modulus of the mineral grains is taken to be $\kappa_g = 1.47 \times 10^{10}$ Pa, which is the geometric mean of the values reported by Chotiros[29,30] (6×10^9 Pa) and Stoll[31] (3.6×10^{10} Pa). From the definition in Eq. (4), the sound speed in the absence of friction can now be written as

$$c_0 = \sqrt{\frac{\kappa_w \kappa_g}{[N\rho_w + (1-N)\rho_g][N\kappa_g + (1-N)\kappa_w]}}, \qquad (35)$$

which is Wood's equation for c_0.

The porosity, N, in Eq. (35) is related to the mean diameter, u_g, of the mineral grains comprising the sediment. To establish the relationship between N and u_g, a packing argument must be invoked. Such a relationship, in conjunction with Eq. (35), will allow c_0 to be evaluated for various types of sediment, as characterized by the grain size.

VI. COUPLING OF WAVE PROPERTIES AND MECHANICAL PARAMETERS

A simple packing model of a saturated sediment was introduced in I, in which the roughness of the mineral particles plays an important role. The sediment was assumed to consist of randomly packed, rough spheres, which gave rise to the following expression for the porosity as a function of grain size:

$$N = 1 - P\left\{\frac{u_g + 2\Delta}{u_g + 4\Delta}\right\}^3, \qquad (36)$$

where $P = 0.63$ is the packing factor for a random arrangement of smooth spheres.[32] In Eq. (36), the mean particle diameter, u_g, is measured in microns, and Δ is the rms roughness measured about the mean surface of a particle. A value of $\Delta = 3\ \mu$m, independent of particle size, is appropriate for surficial sediments but may need modification for deeper sediments, where the overburden pressure could reduce the porosity by squeezing the particles closer together.

According to Eq. (36), the porosity of a very coarse-grained sediment having a mean grain size much greater than the roughness scale is $N_{min} = 1 - P = 0.37$, whereas the very finest-grained material, in which u_g is vanishingly small, shows a porosity $N_{max} = 1 - (P/8) = 0.92$. In between these two extreme values, the porosity expressed by Eq. (36) decays monotonically with increasing grain size, as shown in Fig. 3. The measured porosity of many marine sediments is in accord with Eq. (36), as can be seen in Fig. 3(a), where the symbols represent data from Hamilton[15,33] and Richardson and Briggs.[24] Note that the data span almost three decades of grain size, corresponding to sediment types ranging from the finest-grained clays to coarse sand. At either end of this range, the data approach the values $N_{min} = 0.37$ and $N_{max} = 0.92$, as predicted by Eq. (36), and elsewhere the measurements fall nicely on the theoretical curve. Similar agreement is found between the theoretical density determined from Eqs. (33) and (36) and Hamilton's[15,33] measurements of density versus grain size, as shown in Fig. 4(a).

However, not all sediments are described by Eq. (36), as illustrated in Fig. 3(b), which is the same as Fig. 3(a) except

FIG. 3. Porosity versus grain size. In (a) and (b) the solid line is the theoretical expression in Eq. (36) and the symbols represent data from the following sources: (a) and (b) open circle ($\bigcirc$), Hamilton (Refs. 15, 33); (a) and (b) circle with cross ($\otimes$), Richardson and Briggs (Ref. 24); (b) cross ($\times$), Richardson et al. (Refs. 23, 34–38). The key to the sediment types is: cs=coarse sand; ms=medium sand; fs=fine sand; vfs=very fine sand.

that it includes several additional data sets from Richardson and colleagues.[23,34–38] It is evident that the porosity exhibited by some of the finer sediments, the silts and clays, is not a single-valued function of the particle size, and that many of the data points for these materials fall below the theoretical curve [Eq. (36)]. The corresponding densities are higher than predicted by Eqs. (33) and (36), as shown in Fig. 4(b), which is the same as Fig. 4(a) but with the addition of data from Richardson et al.[23,36,37] Incidentally, most of Richardson's density data are not determined directly as a mass-to-volume ratio but are computed from the measured porosity using the weighted mean of the two-phase medium in Eq. (33). Thus the data represented by the crosses (x) in Figs. 3(b) and 4(b) are not independent, making it inevitable that low porosities will appear as high densities.

Several factors could be responsible for the reduced porosity in silts and clays. As discussed in I, one possibility is the presence of a secondary, smaller particle species, which in-fills the pores spaces, thus displacing water and reducing the porosity of the medium. To accommodate a bimodal grain-size distribution, the expression in Eq. (36) must be modified as follows:

$$N = 1 - P\left\{\frac{u_g + 2\Delta}{u_g + 4\Delta}\right\}^3 (1+\gamma), \qquad (36')$$

where γ is the volume ratio of the primary particle species to the smaller, in-filling particles. In the case of the coarser
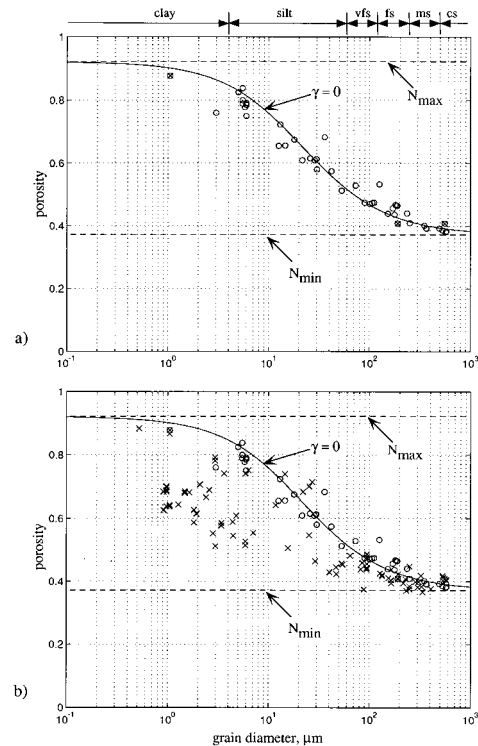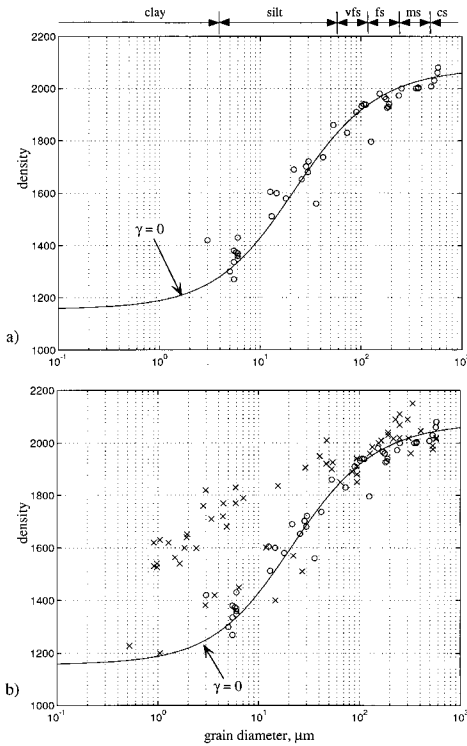
FIG. 4. Density versus grain size. In (a) and (b) the solid line is the theory from Eqs. (33) and (36), and the symbols represent data from the following sources: (a) and (b) open circle (○), Hamilton (Refs. 15, 33); (b) cross (×), Richardson *et al.* (Refs. 23, 36, 37). The key to the sediment types is in the legend to Fig. 3.

sediments, the sands and many of the coarser silts, which tend to show a unimodal grain-size distribution, the value of γ may be safely set to zero, but, for the finer sedimentary materials with an admixture of clay, it is important to identify the appropriate value of γ. Sometimes γ is reported indirectly, for example, as a percentage clay in silt. Otherwise, γ could be evaluated by matching Eq. (36′) to a direct measurement of porosity.

The sound speed, c_0, in the absence of friction varies with the mean grain size, u_g, as given by Eqs. (35) and (36′). In order to go one step further and express the compressional speed c_p [Eq. (29)] and shear-wave speed c_s [Eq. (30)] in terms of the grain size, the compressional and shear dissipation coefficients, μ_c and μ_s, respectively, must be expressed as functions of u_g. To help establish the required relationships, the Hertz theory of deformation of two spherical, elastic bodies in contact[39] is used as a guide.

According to the Hertz theory, when two identical elastic spheres are pressed together by a force F, a circular area of contact forms between them whose radius, a, is given by the cube-root expression

$$a = \sqrt[3]{\frac{3}{4} \frac{F(1-\sigma^2)}{E}} R, \tag{37}$$

where R is the sphere radius and (E, σ) are, respectively, Young's modulus and Poisson's ratio of the material constituting the spheres. The maximum tensile stress occurs around the circumference, $2\pi a$, of the area of contact, and acts in the radial direction. In the present context, the two spheres, of course, are being considered as adjacent mineral particles with diameter $2R = u_g$.

Returning to the problem of specifying the unknown compressional rigidity modulus

$$\mu_c = \frac{(\frac{4}{3}\eta_f + \lambda_f)}{t_0} \Gamma(1-n), \tag{38}$$

it is now assumed that μ_c is proportional to the radius, a, of the area of contact between contiguous mineral grains, as given by Eq. (37). Accordingly, the coefficient of compressional dissipation may be expressed in the form

$$\chi_f = \frac{\mu_c}{\rho_0 c_0^2} = \left(\frac{u_g}{u_0}\right)^{1/3} \frac{\mu_0}{\rho_0 c_0^2}, \tag{38′}$$

where, as in the phi units of grain size, the reference grain diameter is chosen as $u_0 = 1000\ \mu\text{m}$, representing very coarse sand, and $\mu_0 = 2\times10^9$ Pa is a constant of proportionality that has been selected on the basis of a best fit to compressional-wave speed versus grain-size data (see Fig. 8 in I). Although Eq. (38′) apparently contains two scaling parameters, u_0 and μ_0, it should be obvious that they are not independent and that there is in effect only one, namely $\mu_0/(u_0)^{1/3} = 2\times10^8$ Pa/$(\mu\text{m})^{1/3}$. The formulation in Eq. (38) has been chosen to avoid a single scaling constant with the rather awkward units of pressure/(length)$^{1/3}$.

Equation (38′) states that the compressional rigidity modulus, μ_c, is proportional to the length of the line of highest tensile stress between grains. According to Hertz's result in Eq. (37), the length of this line depends on several factors apart from particle size, including the force, F, pressing the two particles together. If it were assumed that this force scales with the overburden pressure, which itself is approximately proportional to the depth of the sediment, D, then Eq. (38′) could easily be extended to give the near-interface depth dependence of μ_c, χ_f and thence of c_p. That is to say, the depth dependence of μ_c, χ_f, and c_p is contained in the coefficient μ_0, and $\mu_0 \propto F^{1/3} \propto D^{1/3}$, which implies that c_p varies rather weakly with depth, consistent with the observations of Hamilton[6] and Richardson and Briggs.[24] Although the depth dependence of c_p is of considerable interest in connection with various applications, it is not pursued here. For our present purpose, we confine our attention to surficial sediments and treat μ_0 as a constant with the value given above. Then, it follows from Eq. (38′) that the functional dependence of the compressional speed on particle size is given by

$$c_p = \sqrt{c_0^2 + \left(\frac{u_g}{u_0}\right)^{1/3} \frac{\mu_0}{\rho_0}}, \tag{39}$$

where c_0 and ρ_0 themselves depend on u_g through Eqs. (33), (35), and (36′).

To establish its dependence on particle size, the dissipative, shear rigidity modulus, μ_s, in Eq. (20) is treated in a similar way to μ_c in the expression for χ_f. In this case, however, we assume that μ_s is proportional to the area, πa^2, of the circle of contact between mineral grains, which gives rise to the expression

$$\mu_s = \left(\frac{u_g}{u_0}\right)^{2/3} \mu_1, \tag{40}$$

where the constant of proportionality is $\mu_1 = 5.1 \times 10^7$ Pa and, as before, $u_0 = 1000\ \mu m$. Again, only one scaling constant is actually present in the formulation in Eq. (40), namely $\mu_1/(u_0)^{2/3} = 5.1 \times 10^5$ Pa/$(\mu m)^{2/3}$. It is implicit in Eqs. (37) and (40) that $\mu_s \propto F^{2/3} \propto D^{2/3}$, that is, μ_s scales as the sediment depth, D, raised to the power of 2/3. From Eq. (30), this corresponds to a shear speed, c_s, that is proportional to $D^{1/3}$, which is very close to the empirical fractional power-law depth dependencies for c_s discussed by Hamilton[40] and Richardson et al.[34] As with c_p, the depth dependence of c_s is not pursued here, but instead only surficial sediments are considered, as described by Eq. (40), with μ_1 taking the value stated above.

It follows from Eqs. (30) and (40) that the dependence of the shear speed on particle size is given by

$$c_s = \left(\frac{u_g}{u_0}\right)^{1/3} \sqrt{\frac{\mu_1}{\rho_0}}, \tag{41}$$

where ρ_0 is a function of u_g through Eqs. (33) and (36′).

The expressions discussed in this and the preceding section allow the wave speeds c_p and c_s, along with the associated attenuation coefficients, to be plotted as functions of any one of the mechanical properties of the sediment (i.e., particle size, density, or porosity). Only four unknown parameters appear in the theory of the mechanical properties of the sediment, three of which (Δ, μ_0, and μ_1) have been assigned non-adjustable values, which are representative of surficial sediments. The fourth parameter, γ, which appears in Eq. (36a) for the porosity, is zero for sands and many of the coarser silts but, for the finer sediments, γ should be determined from a match to porosity data.

VII. COMPARISON WITH DATA

The expressions developed above relating to compressional-wave properties have been compared in I with a number of comprehensive data sets and shown to align accurately with the measurements. The expressions for the shear properties are rather more difficult to verify because published shear data are comparatively rare. This is especially true of direct measurements of shear parameters. Indirect estimates of shear properties, for example, shear speed inferred from the measured speed of an interface wave, are unsuitable for comparison with the predictions of the new theory. However, a few direct measurements of shear parameters can be found in the literature and these are compared below with the theory.

Figures 5 to 7 show the shear speed versus mean grain size, porosity and compressional speed, for a variety of sediments ranging from very fine-grained clays to coarse sand. As identified in the legends to the figures, the data in Figs. 5–7 are from a number of papers that have been published over recent years by Richardson[23,24,34–36,41] and colleagues. For the purpose of the comparisons, the theoretical curves in Figs. 5–7 have been computed with the bimodal size parameter, γ, set to zero.
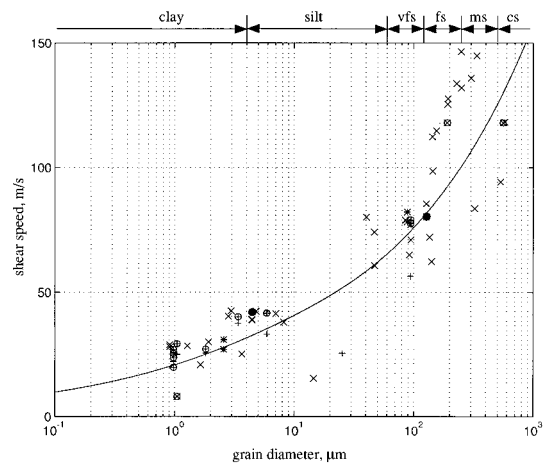
FIG. 5. Shear speed versus grain size. The solid line is the theoretical expression in Eq. (41) and the symbols represent data from the following publications: circle with plus sign (⊕), Richardson et al. (Ref. 23); circle with cross (⊗), Richardson and Briggs (Ref. 24); plus sign (+), Richardson et al. (Ref. 34), asterisk (*), Barbagaleta et al. (Ref. 35); cross (×), Richardson (Ref. 36); solid circle (●), Richardson (Ref. 41). The key to the sediment types is in the legend to Fig. 3.

It can be seen in Fig. 5 that the predicted shear speed follows the trend of the data fairly accurately over some three decades of particle size. Similarly, the theoretical relationship in Fig. 7, between shear speed and compressional speed, aligns quite nicely with the data. The shear speed as a function of porosity in Fig. 6 is also predicted reasonably well by the theory, although in this case the data for the higher porosity, finer sediments fall slightly below the theoretical line. This is perhaps not surprising, since these are the types of sediment that often show a bimodal particle-size distribution and a correspondingly reduced porosity. With γ set to zero, this effect has been excluded from the theoretical curve in Fig. 6, which accordingly is somewhat high.

It is evident in Figs. 3–7 that the experimental points show some spread, part of which may be attributed to experimental error and also to the fact that the various data sets were collected under very different environmental conditions. Factors such as ambient temperature, water depth, measurement depth beneath the bottom interface, sediment

FIG. 6. Shear speed versus porosity. The solid line is the theory from Eqs. (41) and (36a) with $\gamma = 0$, and the symbols represent data, as identified in the legend to Fig. 5.
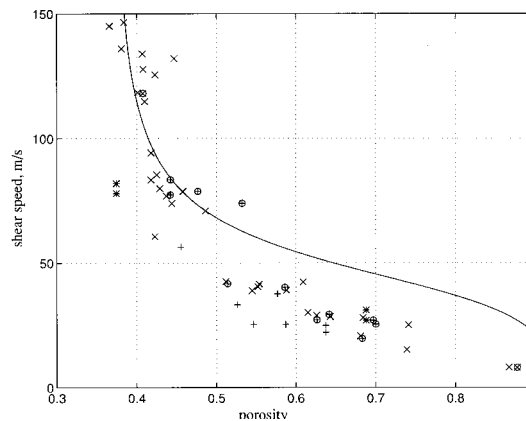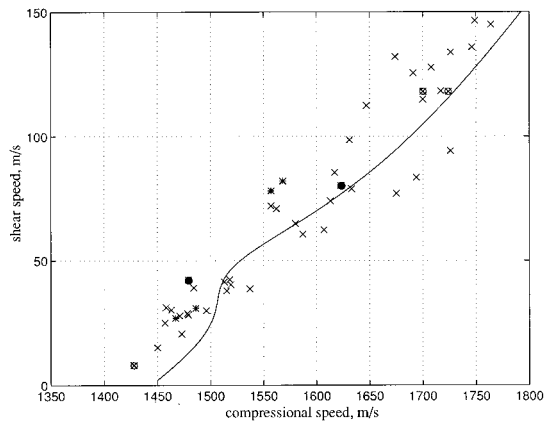
FIG. 7. Shear speed versus compressional speed. The solid line is from the theory in the text and the symbols represent data, as identified in the legend to Fig. 5.

inhomogeneity, bioturbation, and gas-bubble inclusions could all lead to variations in the observed properties of the sediment. Similarly, deviations in the bulk modulus and density of the mineral particles from the values cited above could also introduce some variability into the data. Nevertheless, the theoretical curves plotted in Figs. 5–7, as evaluated from the expressions developed here, with fixed values for all the constants, can be seen to follow the trends of the data very satisfactorily.

In fact, the good agreement between theory and experiment warrants some comment. For instance, the compressional and shear wave speeds, respectively, vary with particle size as shown in Fig. 8 in I and in Fig. 5. In both cases, the agreement between theory and data extends over about three decades of particle size, from coarse sands down to fine clays. Now, the theoretical expressions for the wave speeds have been developed principally on the basis of the Hertz theory of elastic spheres in contact, which is a reasonable model of sand grains. However, the mineral particles in clay are rather more like platelets with a very high aspect ratio, which raises the question as to why the theory should fit the data for clayey materials as well as it does?

With regard to intergranular dissipation, it seems that the mineral particles in clay interact, not individually but on average as an ensemble, as though they were "equivalent spheres" of volume equal to the mean volume of the particles themselves. In this sense, it could be argued, clay particles are little different from sand grains. This interpretation is consistent with the continuity in the data points in Fig. 5, for example, which appear to follow a smooth curve, exhibiting no abrupt change in behavior in the region separating clays from the coarse silts and sands. The physics of particle interactions in clays, especially in the context of wave propagation, is a subject which is still under development, so must be deferred to another time.

Perhaps the most pressing need now is the acquisition of more, directly measured, *in situ* wave properties, particularly attenuations, supplemented by mechanical data from cores. Such measurements are challenging but feasible with the advent of remotely deployed platforms like ISSAMS,[35,42]

which employs bimorph ceramic bender transducers for measuring shear-wave properties directly.

VIII. ATTENUATION AND THE MATERIAL MEMORY FUNCTIONS

The small exponents n and m in the material response functions, Eqs. (6) and (7), characterize the length of the "memory" of the medium. A longer memory corresponds to a smaller exponent and *vice versa*. These exponents, n and m, respectively, also govern the levels of the compressional and shear attenuation in the sediment. This is evident from the expressions in Eqs. (31) and (32) for the loss tangents β_p and β_s:

$$\beta_p = \frac{n\pi}{4} \frac{\chi_f}{(1+\chi_f)} \tag{42}$$

and

$$\beta_s = \frac{m\pi}{4}. \tag{43}$$

According to these expressions, the attenuation in sediments is a direct manifestation of the material memory. With an indefinitely long memory (i.e., n and m vanishingly small), there would be no attenuation. Notice that β_s is independent of the particle size but β_p depends on grain size through the presence of χ_f.

It has been argued in I that the exponent of the memory function is not determined primarily by the bulk mechanical properties of the sediment (grain size, density, or porosity) but by the bonding forces between particles, which depend on the microstructure and physicochemical nature of the sediment grains. Evidence for this conclusion lies in the fact that sediments with essentially identical mechanical properties may show significantly different levels of attenuation. That is to say, there is a lack of correlation between the attenuation and the bulk properties of sediments (see Figs. 11 and 13 in I). This implies that the attenuation and hence the memory are governed by the microstructure of the medium.

Supposing this to be the case, then in a given sediment, which is assumed to be (locally) homogeneous and isotropic, it is reasonable to surmise that the compressional and shear memories are each determined by the same microscopic interactions between particles. According to this hypothesis, the two memories would have exactly the same length, that is, the exponents of the compressional and shear memory functions, n and m, respectively, would be equal.

Assuming that equality does hold between n and m, then the ratio of the compressional and shear attenuation coefficients in Eqs. (42) and (43) is independent of the memory exponents:

$$\frac{\beta_s}{\beta_p} = \frac{(1+\chi_f)}{\chi_f}, \qquad \text{for} \quad m=n. \tag{44}$$

It is evident from this expression that, with $m=n$, the shear attenuation must always be greater than the compressional attenuation. Figure 8 shows the attenuation ratio versus particle size, u_g, as evaluated using the expressions in Eqs. (44) and (38). It can be seen that the ratio in Eq. (44) decreases
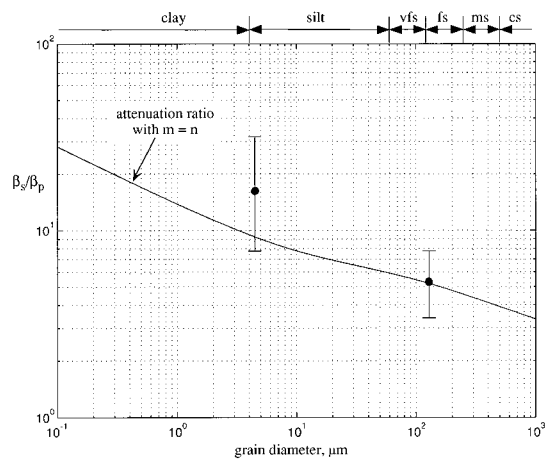
FIG. 8. Ratio of shear to compressional attenuation (loss tangents) as a function of the mean particle size. The solid line is the theory for $n = m$ from Eqs. (44) and (38a). The solid circles (●) represent the two data points from Richardson (Ref. 41), and the key to the sediment types is in the legend to Fig. 3.

monotonically with increasing particle size, from a value of 15 for clay ($u_g \approx 1 \ \mu$m) to 4 for coarse sand ($u_g \approx 500 \ \mu$m). This variation arises entirely from the dependence of β_p on particle size.

To test the hypothesis that $m = n$, measurements of the compressional and shear attenuation in the same sediment are required for comparison with the theoretical prediction in Fig. 8. It is emphasized, however, that these measurements must be performed on the same sediment sample. Otherwise, even with nominally similar sediments, the microscopic intergrain interactions could be quite different, which would compromise the comparison.

Measurements of the compressional and shear attenuation coefficients in the same sediment were reported recently by Richardson.[41] He investigated two types of sedimentary material from the northern California continental shelf, a fine sand, and a clayey silt, with mean particle diameters of 128 and 4.4 μm, respectively. The ratio of the measured attenuations in each of these materials is shown in Fig. 8 as the solid circles, with the error bars representing standard deviations, as reported by Richardson[41] in his Table I.

It is apparent that, within the limits of experimental error, both of Richardson's[41] data points support the hypothesis that $m = n$. For these two sediments, the numerical values of the memory exponents may be determined from Richardson's[41] shear attenuation coefficients: $\beta_s = 0.0875$ (fine sand) and 0.0656 (clayey silt), corresponding to values of $m = 0.11$ and $m = 0.084$, respectively. Although the comparison of data with theory in Fig. 8 is consistent with the idea that the shear and compressional memory exponents are the same, it should be borne in mind that a sample population of two is hardly sufficient to reach a definitive conclusion. Whether equality between m and n is a general property of marine sediments is a question that will be resolved only as more experimental evidence on shear and compressional attenuation becomes available.

IX. CONCLUDING REMARKS

A new analysis of wave propagation in a saturated marine sediment, consisting of mobile mineral grains and seawater, has been presented above. The medium has been treated as a fluid, with an elastic rigidity modulus set identically to zero. Dissipation, associated with intergrain contacts, has been formulated to account for hysteresis in the material by introducing material memory functions with a specific functional form. These memory functions give rise to a wave equation not only for a compressional wave but also for a transverse wave, that is to say, this particular type of dissipative fluid can support the propagation of shear waves. In effect, the intergranular dissipation provides the material with a certain ''dissipative'' rigidity, even though the medium has no elastic rigidity. Such behavior is not possible in say a viscous fluid, where a transverse disturbance is critically damped and does not propagate as a true wave.

One of the interesting predictions of the new theory is an attenuation coefficient for both the compressional and shear wave that is proportional to the first power of frequency. Fairly compelling experimental evidence[15] indicates that this type of frequency dependence is exhibited by the attenuation coefficient of compressional waves in sediments. The data on attenuation of shear waves in sediments are more limited, but a linear dependence on frequency has been observed,[17,18] under laboratory conditions, in water-saturated sands and unconsolidated glass beads.

In I, a model of the mechanical properties of a sediment was introduced, which has been combined here with the wave analysis to obtain expressions relating the compressional and shear-wave speeds to the grain size, porosity, and density of the medium. Comparisons of these expressions with published data, for a variety of sediments ranging from clays to coarse sand, show that the theory follows the trend of the measurements reasonably accurately. Thus by specifying the grain size, for example, the theory yields sensible estimates of the compressional and shear speeds, the density and the porosity.

If certain dissipative, fluidlike (zero elastic rigidity modulus) sediments can support shear, they should also be capable of supporting an interface wave at the water–sediment boundary, the theoretical properties of which have yet to be established. Such a development would be relevant to a number of applications, where interface waves are used as tools for investigating the properties of ocean sediments.[3,43]

[1] M. J. Buckingham, ''Theory of acoustic attenuation, dispersion and pulse propagation in granular materials including marine sediments,'' J. Acoust. Soc. Am. **102**, 2579–2596 (1997).

298   J. Acoust. Soc. Am., Vol. 103, No. 1, January 1998

M. J. Buckingham: Theory of compressional and shear waves   298

[2] J. M. Hovem, M. D. Richardson, and R. D. Stoll (Eds.), *Shear Waves in Marine Sediments* (Kluwer, Dordrecht, 1991).

[3] E. L. Hamilton, H. P. Bucker, D. L. Keir, and J. A. Whitney, ''Velocities of compressional and shear waves in marine sediments determined in situ from a research submersible,'' J. Geophys. Res. **75**, 4039–4049 (1970).

[4] E. L. Hamilton, ''Elastic properties of marine sediments,'' J. Geophys. Res. **76**, 579–604 (1971).

[5] K. B. Briggs, ''Comparison of measured compressional and shear wave velocity values with predictions from Biot theory,'' in *Shear Waves in Marine Sediments*, edited by J. M. Hovem, M. D. Richardson, and R. D. Stoll (Kluwer, Dordrecht, 1991), pp. 121–130.

[6] E. L. Hamilton, ''V_p/V_s and Poisson's ratios in marine sediments and rocks,'' J. Acoust. Soc. Am. **66**, 1093–1101 (1979).

[7] A. R. Gregory, ''Fluid saturation effects on dynamic elastic properties of sedimentary rocks,'' Geophysics **41**, 895–921 (1976).

[8] M. A. Biot, ''Theory of propagation of elastic waves in a fluid-saturated porous solid: I. Low-frequency range,'' J. Acoust. Soc. Am. **28**, 168–178 (1956).

[9] M. A. Biot, ''Theory of propagation of elastic waves in a fluid-saturated porous solid: II. Higher frequency range,'' J. Acoust. Soc. Am. **28**, 179–191 (1956).

[10] M. A. Biot, ''Mechanics of deformation and acoustic propagation in porous media,'' J. Appl. Phys. **33**, 1482–1498 (1962).

[11] M. A. Biot, ''Generalized theory of acoustic propagation in porous dissipative media,'' J. Acoust. Soc. Am. **34**, 1254–1264 (1962).

[12] T. J. Plona, ''Observation of a second bulk compressional wave in a porous medium at ultrasonic frequencies,'' Appl. Phys. Lett. **36**, 259–261 (1980).

[13] D. L. Johnson and T. J. Plona, ''Acoustic slow waves and the consolidation transition,'' J. Acoust. Soc. Am. **72**, 556–565 (1982).

[14] P. M. Morse and H. Feshbach, *Methods of Theoretical Physics: Part I,* International Series in Pure and Applied Physics (McGraw-Hill, New York, 1953).

[15] E. L. Hamilton, ''Compressional-wave attenuation in marine sediments,'' Geophysics **37**, 620–646 (1972).

[16] E. L. Hamilton, ''Acoustic properties of sediments,'' in *Acoustic and the Ocean Bottom*, edited by A. Lara-Saenz, C. Ranz Cuierra, and C. Carbo-Fité (Consejo Superior de Investigacions Cientificas, Madrid, 1987), pp. 3–58.

[17] B. A. Brunson and R. K. Johnson, ''Laboratory measurements of shear wave attenuation in saturated sand,'' J. Acoust. Soc. Am. **68**, 1371–1375 (1980).

[18] B. A. Brunson, ''Shear wave attenuation in unconsolidated laboratory sediments,'' in *Shear Waves in Marine Sediments*, edited by J. M. Hovem, M. D. Richardson, and R. D. Stoll (Kluwer, Dordrecht, 1991), pp. 141–147.

[19] J. W. S. Baron Rayleigh, *The Theory of Sound I* (Dover, New York, 1945).

[20] J. W. S. Baron Rayleigh, *The Theory of Sound II* (Dover, New York, 1945).

[21] K. F. Graff, *Wave Motion in Elastic Solids* (Dover, New York, 1975).

[22] A. Erdélyi (Ed.) *Tables of Integral Transforms, Volume 1*, Bateman Manuscript Project (McGraw-Hill, New York, 1954).

[23] M. D. Richardson, E. Muzi, L. Troiano, and B. Miaschi, '' Sediment shear waves: A comparison of *in situ* and laboratory measurements,'' in *Micro-structure of Fine-Grained Sediments*, edited by R. H. Bennett, W. R. Bryant, and M. H. Hulbert (Springer-Verlag, New York, 1991), pp. 403–415.

[24] M. D. Richardson and K. B. Briggs, ''*In situ* and laboratory geoacoustic measurements in soft mud and hard-packed sand sediments: Implications for high-frequency acoustic propagation and scattering,'' Geo-Marine Lett. **16**, 196–203 (1996).

[25] R. Kronig, ''On the theory of dispersion of x-rays,'' J. Opt. Soc. Am. **12**, 547–557 (1926).

[26] H. A. Kramers, ''La diffusion de la lumiere par les atomes,'' Atti Congr. Intern. Fisica, Como 2, 545–557 (1927).

[27] M. O'Donnell, E. T. Jaynes, and J. G. Miller, ''Kramers-Kronig relationship between ultrasonic attenuation and phase velocity,'' J. Acoust. Soc. Am. **69**, 696–701 (1981).

[28] A. B. Wood, *A Textbook of Sound* (G. Bell, London, 1964).

[29] J. C. Molis and N. P. Chotiros, ''A measurement of the grain bulk modulus of sands,'' J. Acoust. Soc. Am. **91**, 2463(A) (1992).

[30] N. P. Chotiros, ''Biot model of sound propagation in water-saturated sand,'' J. Acoust. Soc. Am. **97**, 199–214 (1995).

[31] R. D. Stoll, *Sediment Acoustics* (Springer-Verlag, Berlin, 1989).

[32] O. K. Rice, ''On the statistical mechanics of liquids, and the gas of hard elastic spheres,'' J. Chem. Phys. **12**, 1–18 (1944).

[33] E. L. Hamilton, ''Sound velocity and related properties of marine sediments, North Pacific,'' J. Geophys. Res. **75**, 4423–4446 (1970).

[34] M. D. Richardson, E. Muzi, B. Miashi, and F. Turgutcan, ''Shear wave velocity gradients in near-surface marine sediment,'' in *Shear Waves in Marine Sediments*, edited by M. Hovem, M. D. Richardson, and R. D. Stoll (Kluwer, Dordrecht, 1991), pp. 295–304.

[35] A. Barbagelata, M. D. Richardson, B. Miashi, E. Muzi, P. Guerrini, L. Troiano, and T. Akal, ''ISSAMS: An *in situ* sediment acoustic measurement system,'' in *Shear Waves in Marine Sediments*, edited by J. M. Hovem, M. D. Richardson, and R. D. Stoll (Kluwer, Dordrecht, 1991), pp. 305–312.

[36] M. D. Richardson, ''*In situ* shallow-water sediment geoacoustic properties,'' in *Shallow Water Acoustics*, edited by J. X. Zhou (Institute of Acoustics, Beijing, 1997).

[37] M. D. Richardson and K. B. Briggs, ''On the use of acoustic impedance values to determine sediment properties,'' Proc. Inst. Acoust. **15**, 15–24 (1993).

[38] M. D. Richardson, ''Spatial variability of surficial shallow water sediment geoacoustic properties,'' in *Ocean-Seismo Acoustics: Low-Frequency Underwater Acoustics,* edited by T. Akal and J. M. Berkson (Plenum, New York, 1986), pp. 527–536.

[39] S. P. Timoshenko and J. N. Goodier, *Theory of Elasticity* (McGraw-Hill, New York, 1951).

[40] E. L. Hamilton, ''Shear-wave velocity versus depth in marine sediments: A review,'' Geophysics **41**, 985–996 (1976).

[41] M. D. Richardson, ''Attenuation of shear waves in near-surface sediments,'' in *High Frequency Acoustics in Shallow Water*, edited by N. G. Pace (NATO SACLANT Undersea Research Centre, La Spezia, 1997), pp. 451–458.

[42] S. R. Griffin, F. B. Grosz, and M. D. Richardson, ''*In situ* sediment geoacoustic measurement system,'' Sea Technol. 19–22 (1996).

[43] G. Nolet and L. M. Dorman, ''Waveform analysis of Scholte modes in ocean sediment layers,'' Geophys. J. Int. **125**, 385–396 (1996).

Sound radiation by various types of laboratory breaking waves in fresh and salt water

Ali R. Kolaini

National Center for Physical Acoustics, University of Mississippi, Coliseum Drive, University, Mississippi 38677

A recent article [A. R. Kolaini and L. A. Crum, J. Acoust. Soc. Am. **96**, 1755–1765 (1994)] reported the measurements of the ambient sound generated by laboratory breaking waves over the range 100–20 000 Hz in fresh water. Those observations from both spilling- and plunging-type breakers have been repeated in the same manner and wavemaker/anechoic tank with water that had 25‰ salt in its content. The observations in salt water, just like those in fresh water, reveal that the sources of sound in laboratory spilling breakers are due primarily to single bubble oscillations that can have frequencies lower than a few hundred Hertz. In the case of weak spilling breakers, the sound spectra level in fresh water was due primarily to single bubble oscillation, while the same breakers in salt water have introduced smaller size bubbles with large density. The relatively high-density populated bubble cloud generated by weak breakers shows the evidence of the onset of collective oscillation that was absent for the same breakers in the fresh water. In the case of moderate spilling and plunging breakers, it appears that both individual bubbles and bubble clouds can contribute to the acoustic emissions in fresh and salt water. The average sound spectra reveal that the peak frequencies of the spectra shift from a few kHz (weak, spilling breaker) to few hundred Hz (plunging breaker), and the high-frequency portions have slopes approximately 5–6 dB/oct, which are the slopes observed from the noise spectra of the ocean. Besides the high bubble density and smaller bubble sizes in salt water, all breakers experienced a significant increase in sound-pressure level in all observed frequency range. The ionic structure of the medium alters the sound radiation from bubbles. In this paper some of the observed acoustic signatures from breaking waves are discussed and a plausible explanation of how salt can effect the sound radiation from bubbles is given. © *1998 Acoustical Society of America.* [S0001-4966(97)04612-2]

PACS numbers: 43.30.Nb, 43.30.Jx, 43.25.Yw [JHM]

INTRODUCTION

Underwater sound from the sea surface was first studied several decades ago. The earliest measurements of ambient-sound spectra levels in the ocean were reported by Knudsen *et al.*[1] In his classical paper Wenz[2] speculated that one possible source of high-frequency, wind-related noise is the bubble oscillations located near the sea surface. Recently, several international conferences have been devoted to the understanding of the source mechanisms for ambient noise production at the sea surface[3–5] and lend further support to the contributions of gas bubbles as the principal source of this noise. However, a detailed description of the specific roles of these bubbles has not yet been given.

Breaking waves are believed to be the main source of wind-generated noise in the ocean. The understanding of the physics of wave breaking and sound generation mechanisms is essential to have an accurate knowledge of the ambient noise from breaking waves. Previous studies have shown a good correlation exists between ambient noise levels and wind speed in a variety of field conditions. Some researchers have used the ambient noise to measure the wind speed.[6] Earlier laboratory work by Loewen and Melville[7] has shown that the acoustic energy radiated by breaking waves is well correlated with the wave energy dissipated due to breaking and significant dissipated energy was consumed in entraining air bubbles. Recently laboratory studies of weak spilling breaking waves were reported, where the absolute pressure level was measured in an anechoic tank. The noise radiated by these weak breakers was attributed to newly created bubbles.[8]

The whitecap coverage and its lifetime studies in a laboratory setting have been reported to have a correlation with salinity.[9] The absence of bubble coalescence in salt water, which leads to significant change in bubble distribution, have been reported by numerous researchers, for example, Scott[10] and Monahan and Zeitlow.[11] The process of the bubble non-coalescence was ascribed by Kitchener[12] to be related to the existence of organic active materials that adsorbed on water–air interfaces which would reduce the surface tension and in turn prevent thin films from rupturing. Another mechanism was suggested by Pounder[13] to be the preferential ion attachment on bubble surface due to sodium chloride present in sea water that contributes an electric repulsion which tends to keep bubbles from coalescing. Recently, the laboratory bubble cloud generated by a tipping bucket by Carey *et al.*[14] and bubble plume generation from transient cylindrical water jet by Kolaini *et al.*[15] have shown a 3–4-dB reduction in sound-pressure level from the cloud in salt water. They attributed the level reduction to the increase in the number of small bubbles in salt water which resulted in enhanced thermal damping coupled with an increase in the air/water interface area as was hypothesized by Prosperetti.[16] Despite re-
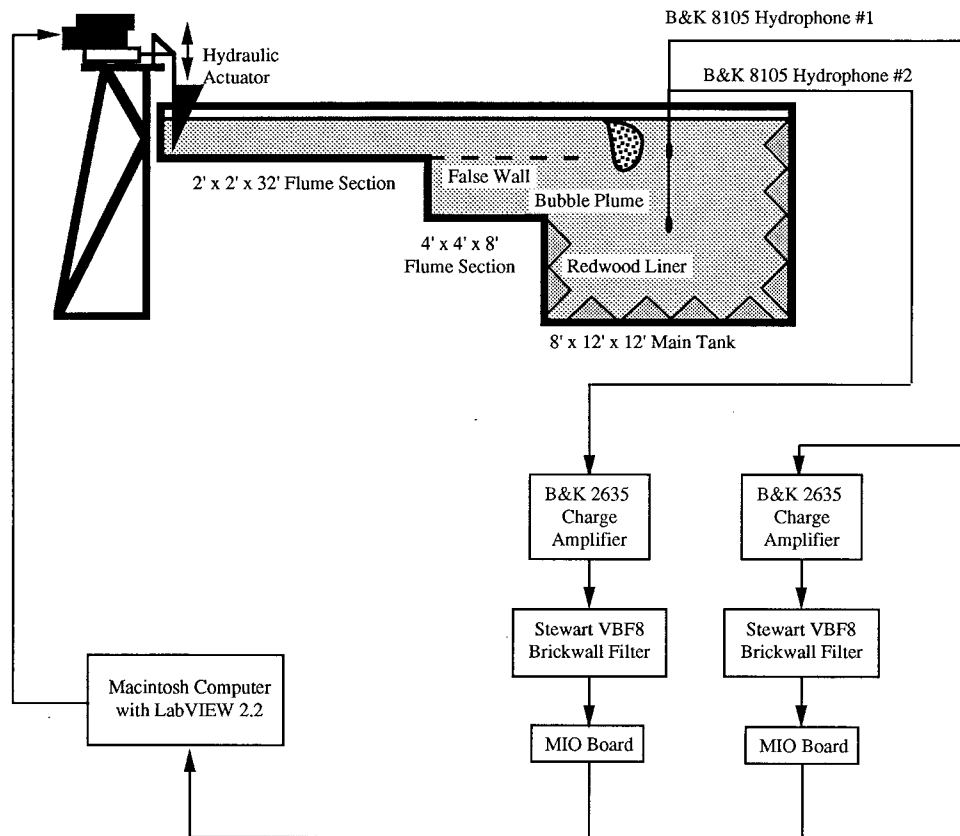
FIG. 1. Schematic drawing of the research wavemaker/anechoic tank facilities and data acquisition system (not drawn to scale).

cent studies of the effect of salt on bubble distribution, an accurate understanding of the effect of salt on the radiated sound pressure from bubbles has not yet been given.

In this paper, which is the continuation of a paper published in the *Journal of Acoustical Society of America*[17] where we reported the absolute sound-pressure levels obtained from various laboratory breaker intensities in fresh water, we report the effect of salt on the acoustic characteristics of breaking waves. We were able to reproduce carefully the conditions for each breaking wave event in salt water (25‰ by volume, Utah mountain salt). We discuss in detail the effect of the salinity on sound generation, bubble distribution, and source mechanisms from these breakers.

I. EXPERIMENTAL PROCEDURES

The experiment was conducted in an anechoic tank/ wavemaking facility. A wedge-shaped wavemaker was mounted at one end of the 0.7 m×0.7 m×12.7 m flume which ultimately connected to a 2.5 m×3.6 m×3.6 m tank with an anechoic linings. This wavemaker was operated by a hydraulic piston actuator which was guided by a Parker state-of-the-art proportional valve and was controlled by an electronic box connected to a personal computer. This system enabled us to produce gravity waves that would break at any user-specific location within the bank (see Fig. 1). The sound emission from bubble clouds generated by breaking waves was measured using a B&K 8105 broadband hydrophone with plane wave sensitivities of -208.5 dB *re:* 1 V/

μPa, which was connected to a MIO board via B&K 2635 charge amplifier, and was high-pass filtered above 100 Hz using an analog filter. The bubble size distribution within the clouds was measured using an Olympus fiberscope lens connected to a high-speed Kodak/Ekta-Pro video camera, typically used at a framing rate of 500 frames/s. The detailed description of the tank/wavemaking facility, data collection, and analysis are given by Kolaini and Crum.[17]

II. RESULTS AND DISCUSSION

Breaking waves in the ocean are now believed to be the main source of wind-generated ambient noise. The determination of the sound pressure level from breaking waves depends on the source mechanisms and the wave-breaking hydrodynamic processes. The salinity change in the medium could also have an adverse effect on the sound mechanisms and sound pressure level. In the following sections we discuss physical parameters that may be important for the understanding of the noise generation from breaking waves. Accurate measurements of these parameters may also be used as an input for the development of a theory predicting noise generation from breaking wave in the ocean.

A. Bubble size distribution

To predict the sound-pressure level accurately in low- and high-frequency ranges from breaking waves an accurate knowledge of bubble size distribution and void fraction distribution in the cloud are necessary. There have been numer-
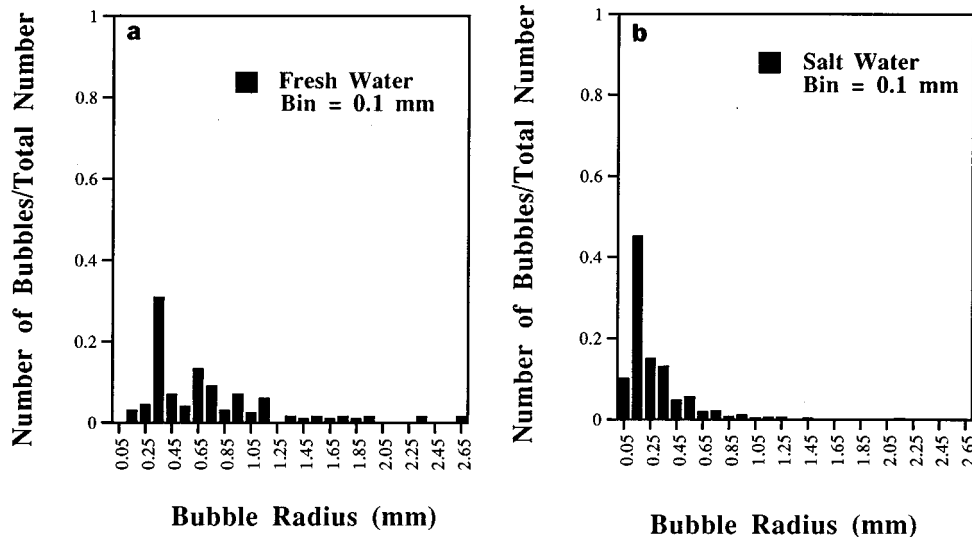
FIG. 2. Histograms of bubble production by weak spilling breakers normalized by total number of bubbles: (a) fresh water (total number of bubbles ≈130) and (b) salt water (total number of bubbles ≈380). Note the existence of large numbers of smaller bubbles in salt water.

ous experimental measurements of bubble population and distribution below the sea surface. Acoustical and optical techniques have commonly been used to infer the bubble size distribution in the upper ocean layer.[18–21] Laboratory measurements of the average bubble size distribution generated by breaking waves in fresh water and salt water in the range of 34–1200 μm in radius were given by Su et al.[22] An order of magnitude increase in the number density over the entire range was observed for salt water (30‰) versus fresh water. Most of these investigators have shown a power law for the size distribution with exponent varying from −1 to −8. The difference in the exponent values are probably attributed to the variation in the environmental parameters and the limitations on the measurement techniques. The stark difference in size distribution between salt water and fresh water has a profound effect on the sound-pressure level in the ocean.

In the present experiment, the size distribution of bubbles generated by laboratory breaking waves in fresh and salt water was measured by utilizing a high-speed video camera with a fiber optic cable, enabling views to be obtained of the individual bubbles entrained by the breaker. Figure 2(a) and (b) shows histograms of the normalized bubble size distributions of the weak spilling breaker in fresh and salt water, respectively. Each point in these figures was averaged over two samples and was measured at the breaker maximum growth with the same cross-sectional area in two media (see Fig. 9 for the breaker growth). As expected, the bubble spectra show shift to lower size and have marked increase in the density in salt water with salinity level of 25‰. Note that there are a few individual bubbles with radii in the range from 1.75–2.5 mm in fresh water that are absent in the salt water spectrum. As the intensity of the spilling breaker increases, the generation of larger bubbles is evident from the bubble size histogram for moderate breakers in fresh water shown in Fig. 3(a), which demonstrates the existence of individual bubbles as large as 8 mm in radius. The same breaker creates a bubble size distribution in salt water

that has large numbers of smaller bubbles with the largest being smaller than 4 mm [Fig. 3(b)]. It has been hypothesized that there are two mechanisms by which the presence of salt may affect the observed bubble size distribution. One is the coalescence retardation effect in salt water. The greater portion of smaller bubbles produced by breaking waves is due to the absence of coalescence. Another mechanism is that salt has the tendency to stabilize the surface of bubbles by contamination of surfactant additives. These mechanisms are probably the prime reasons for extending the whitecap coverage and its life in the ocean.[11]

B. Sound spectra level

Earlier we reported the sound pressure level measurements from laboratory breaking waves in fresh water. We have discussed the possible mechanisms of the sound generation for frequency range 0.1–25 kHz.[17] In this section we report the sound-pressure levels for the same breakers produced in salt water and use the fresh water spectra reported earlier for comparison. Figure 4 shows the power density plots for weak spilling breakers, averaged over 100 events, measured both in fresh and salt water. The comparison of the Minnaert frequencies of the average power spectrum of the weak breakers in fresh water with the size distribution shown in Fig. 2(a) reveals that single bubbles are most probably responsible for sound generation. However, the average sound spectrum of the same beakers in salt water shows a broader peak center at around 2 kHz and another one around 1.2 kHz. It appears from the size distribution that the single bubbles may be responsible for the 2-kHz peak and above, while another mechanism may be responsible for the 1.2-kHz peak which corresponds to a bubble size of about 2.7 mm. This size or larger bubbles have not been observed in the cloud as depicted in size distribution Fig. 2(b). The weak breakers in salt water generate many more smaller size bubbles than fresh water. It has been shown that when a few
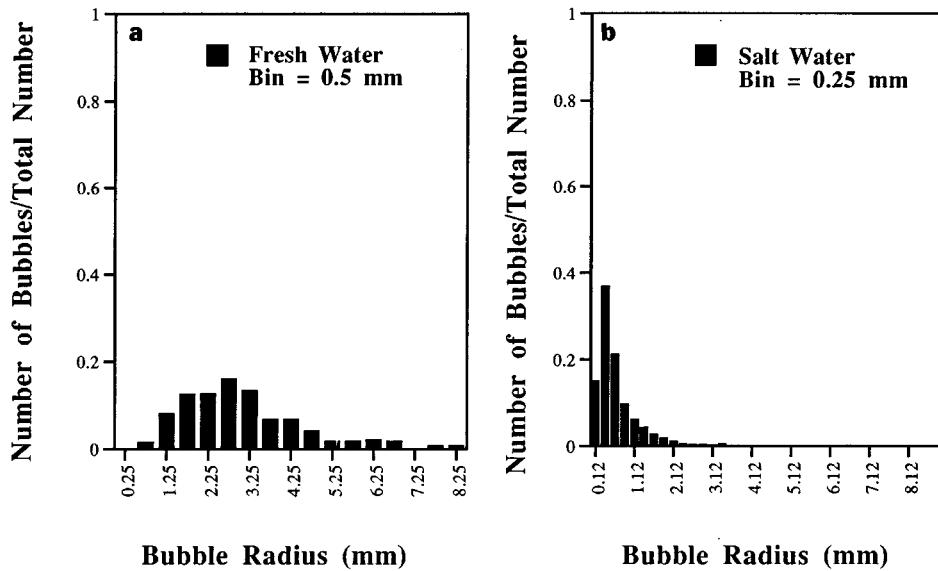
FIG. 3. Histograms of bubble production by moderate spilling breakers: (a) fresh water (total number of bubbles ≈ 300) and (b) salt water (total number of bubbles ≈ 2440). Note the existence of large numbers of smaller bubbles in salt water. The largest bubbles measured in salt water is less than 4 mm whereas fresh water has bubbles as high as 8 mm.

bubbles are placed a few radii away from each other, all the bubbles may couple and resonate at a frequency much smaller than their natural frequency.[23] The peak at around 1.2 kHz shown in the salt water spectrum by weak breakers may be the result of the bubble cloud beginning to oscillate collectively. This effect has not been observed in fresh water spectrum. The spectral slopes of the noise from the weak breakers in fresh and salt water are the same and are roughly 6 dB/oct from 2 to 20 kHz. Another significant difference between these two spectra is the increase in sound pressure level in frequency above 1000 Hz by the breakers in salt water. This effect will be discussed later.

The average power densities of the moderate spilling

breakers in fresh and salt water are shown in Fig. 5. The time series used to compute the power densities throughout this paper are taken to be the periods from the moment first bubbles are entrained until all bubble-related noise has ceased. Increasing breaker severity entrains more air and produces larger bubbles. The power densities of the moderate breakers shown in Fig. 5 clearly indicate a shift to lower frequencies as the intensity of breakers was increased. The first two spectral peaks at around 200 and 500 Hz in the fresh water spectrum correspond to bubble sizes of 1.6 cm and 6.6 mm, respectively. The size distribution function for moderate breakers shown in Fig. 3(a) shows the existence of a few

FIG. 4. Power densities averaged over 100 acoustic signals of the weak spilling breakers in both fresh water and salt water. The salt water power density shows a peak around 1 kHz that may be due to collective oscillations of the cloud that is absent for the same breaker in fresh water. Note the increase in sound-pressure level in all frequency ranges in salt water.

FIG. 5. Power densities averaged over 100 acoustic signals of the moderate spilling breakers in both fresh water and salt water. Spectra in fresh water and salt water show broader peaks below 2 kHz. Both larger bubbles and collective oscillations of bubbles may be responsible for these peaks. The peak near 930 Hz is most likely due to one of the modes in the tank that appear in both of the spectra. Note the increase in sound pressure level in all frequency ranges in salt water.

large bubbles with radii around 8 mm. Larger bubbles, in general, radiate higher energies than the smaller ones and the overall energy of a few larger bubbles may be greater than a large quantity of smaller bubbles. The third peak at around 930 Hz is very close to the tank resonance. The histogram shown in Fig. 3(a) does not indicate the existence of bubbles larger than 8 mm in fresh water. The broadband peaks in the salt water spectral density at about 150 and 400 would correspond to bubble radii of 2.2 cm and 8.5 mm, respectively. The size distribution for salt water indicates the absence of bubbles larger than 4 mm. One of the possible mechanisms responsible for these peaks may be the collective oscillations of bubble cloud. As we will discuss later, single bubbles may still account for these low-frequency peaks. The peak at around 930 Hz that appears in the fresh water spectrum as well is believed to be tank resonance frequency. The acoustic reverberation characteristics of the anechoic tank were determined using the peak response method with an underwater source and broadband excitation. The transfer function between two hydrophones (one close to an acoustic source where it received the source response and the other was placed in grid locations, where the response of the tank and the source could be measured) was used to identify the tank reverberation in fresh water[17] and was assumed to be the same in salt water. Since one of the peaks was identified to be the tank mode, the power spectra were not normalized with respect to the transfer function. The spectral slopes of the power densities shown in Fig. 5 are roughly 5 dB/oct from 500 Hz to 25 kHz in both fresh and salt water. These slopes are close to that observed for wind-dependent ambient noise in the ocean, which follows $f^{-1.5}$ behavior. The surprising increase in the sound pressure level in salt water in the whole frequency range will be discussed below. Hydrodynamically, these bubbles are entrained by a turbulent flow field produced by shear across the interface and a vorticity field at the leading edge of the whitecap. Finally, the shift in the spectral peak to lower frequencies is evident in the power densities shown in Fig. 6 for plunging breakers in fresh and salt water. The plunging breakers are much stronger, hydrodynamically speaking, than the previous spilling breakers. They entrain such a markedly broader range of bubbles sizes that the limitation of the optical technique used in this study prevented us from measuring bubble size spectrum. The video images of the breakers have shown that there were a lot of larger bubbles present in the cloud. These observations demonstrate that collective oscillation of the bubble cloud is possible with breaking waves. However, it is neither the sole mechanism nor is it the dominant one for the observed broadband noise generation below a few hundred Hz (see discussion in the next section). The comparison of the spectral densities for plunging breakers between salt and fresh water also shows higher pressure level in salt water as was the case with the other types of breakers.

C. Single bubble versus the collective oscillations of bubbles

Generally, there are two separate bubble-related mechanisms that lead to acoustic emissions by breaking waves. First, sound may be generated by the entrainment of indi-

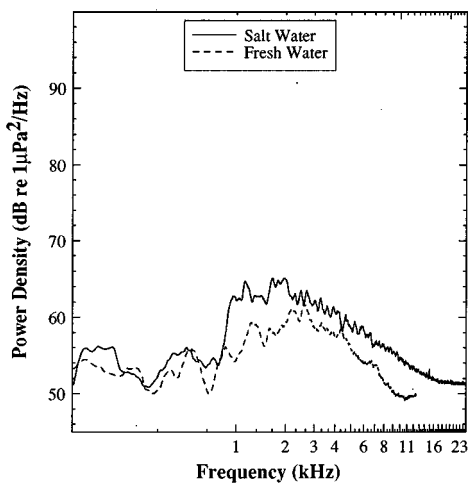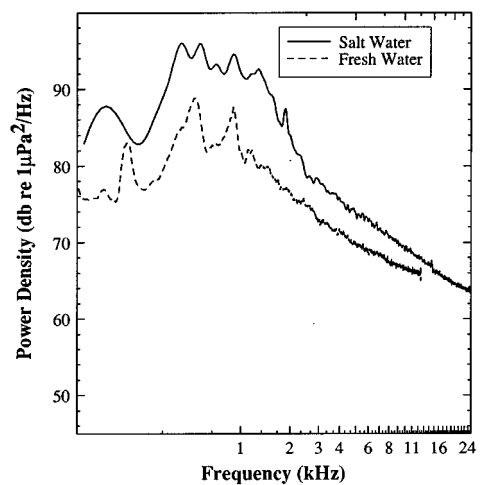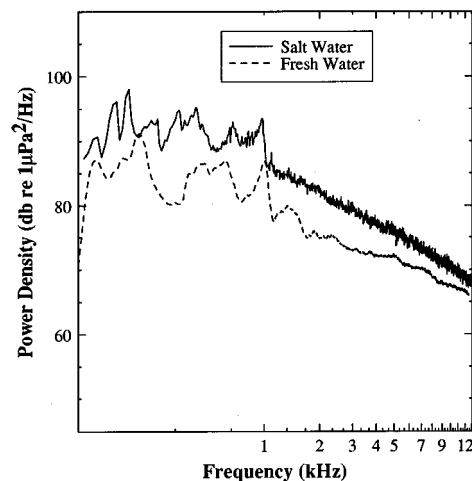

FIG. 6. Power densities averaged over 100 acoustic signals of the plunging breakers in both fresh water and salt water. Spectra in fresh water and salt water show broader peaks below 2 kHz. Both larger bubbles and collective oscillations of bubbles may be responsible for these peaks. The peak near 930 Hz is most likely due to one of the modes in the tank that appear in both of the spectra. Note the increase in sound pressure level in all frequency ranges in salt water.

vidual bubbles, which subsequently radiate at their natural resonance. Second, the individual bubbles within the cloud may oscillate coherently in a collective mode. Typically, the frequency radiated by individual bubbles is much higher than that radiated by the collective oscillations of bubble cloud. The average spectral densities of three different breakers shown earlier demonstrate the sound generation by these mechanisms is possible. The notion that the breakers in the ocean may not be able to generate frequencies lower than a few hundred Hz corresponding to single bubbles with radii larger than several millimeters exists in the underwater community. Observation of the laboratory breaking waves in this study have shown that it is possible to generate larger bubbles with all types of breakers including those generated by spilling breakers in salt water.

To gain insight on the possibility of existence of large bubbles that may contribute to low-frequency oscillations, we show in Fig. 7 sound pressure levels of a typical acoustic event with 1-s duration of a moderate breaker in salt water spectra in terms of an arbitrary scale. A wavelet analysis was applied to the signature and results are shown at each 100-ms interval for clarity. The first curve starts with the onset of breaker (first entrained bubbles) and the last one contains the last emitted sound from the breaker. The sound spectra of the first few 100 ms show a peak at around 170 Hz. The photographic images of the bubble cloud generated by these laboratory breaking waves show that its shape is roughly a finite length cylinder. To determine the approximate collective frequency of the bubble cloud, we assume that this shape can be represented by an effective spherical bubble cloud. The wave number in the liquid–bubble mixture k_m is given by

$$k_m^2 = \frac{\omega^2}{c^2} + 4\pi\omega^2\bar{n}\int_0^\infty \frac{af(a)\,da}{\omega_0^2 - \omega^2 + 2ib\omega}, \quad (1)$$

where $\bar{n}$ is the number of bubbles per unit volume, a is the
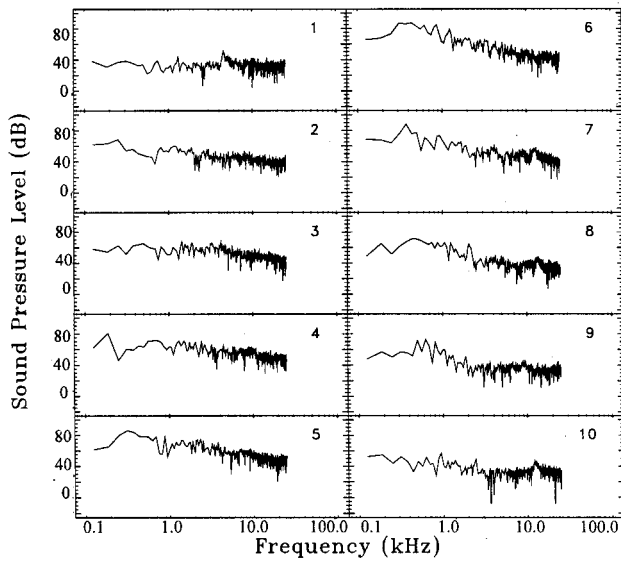
FIG. 7. Power spectra of a typical acoustic signature with 1-s duration of a moderate spilling breaker in salt water. The wavelet analysis was applied and the results are shown at the end of 100-ms intervals. Note the low-frequency noise at early stages of bubble cloud growth that are most probably caused by larger bubbles. The broadband low frequency at later stages (labeled 5–8) is most probably due to the collective oscillations of bubble cloud.

FIG. 8. Power spectra of a typical acoustic signature with 1.5-s duration of a plunging breaker in salt water. The wavelet analysis was applied and the results are shown at the end of 150-ms intervals. Note the low-frequency noise at early stages of bubble cloud growth that are most probably caused by larger bubbles. The broadband low frequency at later stages (labeled 5–8) are most probably due to the collective oscillations of bubble cloud.

radius, c is the sound speed in pure liquid, and ω_0 and b are the natural frequency of the bubble and its damping coefficient, respectively. In this equation $f(a)$ is the bubble size distribution measured experimentally. Below the resonance frequency of the largest bubble in the cloud, Eq. (1) becomes independent of the bubble size distribution and depends only on the void fraction, β. The void fraction, β, in the cloud can be determined by (see Ref. 24)

$$\beta = \frac{4\pi\bar{n}}{3} \int_{a_{\min}}^{a_{\max}} a^3 f(a) \, da, \qquad (2)$$

where $a_{\min}$ and $a_{\max}$ are the radius of the smallest and largest bubble, respectively. The frequencies f_n of the normal modes of the cloud are readily estimated. The lowest one is given by[25]

$$f \approx \frac{1}{2R_c} \sqrt{\frac{P_0}{\rho\beta}}, \qquad (3)$$

where P_0 is the ambient pressure, ρ is the liquid density, and R_c is the effective spherical bubble cloud radius. A cloud with an average void fraction of about 0.1 and first normal mode frequency of about 170 Hz requires a radius of about 9 cm. The collective oscillation of a bubble cloud with frequency as low as 170 Hz requires that bubbles first be formed and then be stimulated into oscillation by the generation of new bubbles and or eddies generated by breakers. This mechanism is unlikely to occur at the very beginning of the breaker growth. The likely mechanism responsible for the 170 Hz shown in Fig. 7, label 2, is the generation of larger bubbles when waves begin to break. We have observed in the laboratory that a smaller jet at the beginning of the spilling breakers forms. It is plausible to assume that this

jet could entrap a ''sausage''-shaped bubble that breaks up into spherical bubbles due to surface instability. These spherical bubbles radiate sound at the instant the ''sausage'' breaks up. Since they are large in size and are created very close to the surface at the initial phase of the breaker growth, they tend to move to the surface very fast, thus making it very difficult to capture them optically or with any other commonly used techniques. Since the size of the large bubbles very close to the surface at early stages of the breakers are difficult to measure, the quantitative estimate of their resonance frequencies and sound pressure levels and checking them against the low-frequency peaks in the spectra shown in Fig. 7 are difficult. These observations are just a plausible explanation of the observed low-frequency sound generated at early stages of the breaker. The spectra labeled 2–6 of Fig. 7 show generation of a broad range of low frequencies that are possibly generated by large bubble. It is interesting to note that the spectra labeled 8–10 show a peak at around 150 Hz that lasts more than 200 ms and a broadband peak at around 350 Hz (spectrum labeled 8) that occurs 800 ms after breaker onset. These peaks would correspond to bubble sizes of 2.2 and 0.95 cm, which are unlikely to be entrained at this stage in the breaker growth. Therefore, it is reasonable to suggest that the bubble cloud was formed by entraining a broad range of bubble sizes including larger bubbles of the order of 1 cm in the first 600 ms. Later it begins to oscillate collectively as is shown by the spectra labeled 8 and 9 in Fig. 7. The bubble cloud was set to oscillate collectively by newly created bubbles and or by vorticity field. Figure 8 is the power spectrum of a typical event with 1.5-s duration generated by a plunging breaker in salt water. The results of the wavelet analysis are shown at the end of 150-ms intervals. In this case too the spectra labeled 1–3 clearly show the generation of low frequency which may
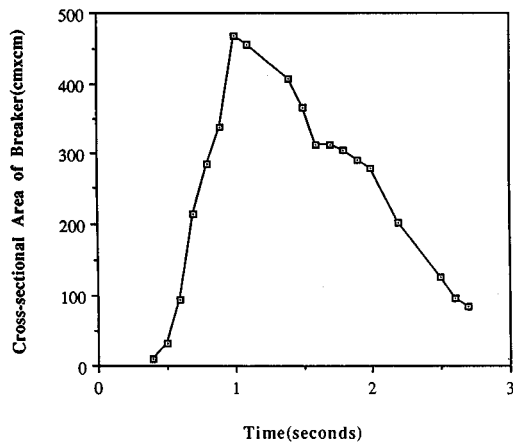
FIG. 9. The breaker cross-sectional (i.e., bubble cloud) area growth for a moderate breaker in fresh water is depicted. The air is being entrained until the breaker reaches its maximum growth. The bubble cloud is acoustically inactive after the breaker has reached its maximum.

have caused by break up of the ''sausage.'' The subsequent spectra show the breaker continues to entrain a broad range of bubble sizes. The low-frequency collective oscillations of the bubble cloud may begin at spectra labeled 6–7. The same processes happen in the fresh water spectra. The type of examples shown in Figs. 7 and 8 demonstrate how generation of single large bubbles at the beginning of the breakers are possible and may be much more important in their contribution to the ambient noise in the ocean in comparison with the collective oscillations of bubbles. Therefore, it is very important to point out that the void fraction measurement in the cloud by itself may not be adequate to use for predicting low-frequency noise generation.

D. Breaker growth

The breaker cross-sectional area (bubble cloud cross section) for a typical moderate spilling breaker as a function of time is plotted in Fig. 9 in fresh water. We assume the same breakers in salt water would hydrodynamically behave like those in fresh water. The bubble cloud generated by the breaker grows approximately linearly from the onset, reaching a maximum at about 1 s, which is close to the breaking wave period, and then declines due to loss of breaker energy. In this period bubbles of various sizes are generated. Once the bubble cloud cross section reaches its maximum, the air entrainment ceases. During the bubble cloud growth, it consists primarily of newly created bubbles (average void fraction of 10%). The bubble cloud is acoustically active only in its growing phase. After reaching its maximum growth, larger bubbles tend to move to the surface due to buoyancy. The air content in the declining region of the cloud, which consists of smaller bubbles, decreases and remains in the water for a longer period (void fraction $\sim 0.1\%$). The volume rate of flow feeding the breaker may be roughly estimated from its rate of area growth.[26] The estimated value of the air entrainment rate (rate of change of the void fraction, β) for the moderate breaker in fresh water is about 0.2/s, which is consistent with the value obtained photographically.
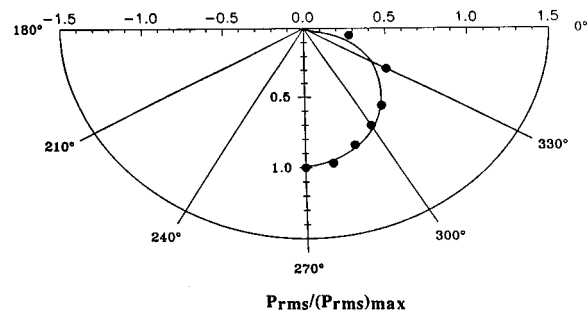
FIG. 10. The normalized rms acoustic pressure as a function of angle for moderate spilling breakers in fresh water measured at a radial distance of 1.0 m which exhibits the predicted $\cos(\theta)$ dependence shown by the solid line.

The estimated air entrainment rate is one of the crucial parameters required to develop a model for the type of breaker under study.

The newly generated bubbles and the bubble cloud from breaking waves possess characteristic dimensions that are much smaller than the acoustic wavelength. Such acoustic sources are well approximated by a monopole, and the contribution for surface reflection can be accounted for by the method of images. The radiated acoustic pressure is therefore a $\cos(\theta)$ dependent, where θ is the angle subtended by r, the distance from the bubble cloud to the field point. The normalized rms radiation pressure pattern measured at a radial distance of 1.0 m from moderate breaking waves in fresh water is given in Fig. 10 which exhibits the $\cos(\theta)$ dependence and is shown with a solid line.

E. Salinity effects on sound-pressure level

All the sound spectral densities shown in Figs. 4–6 for various breaker intensities show a significant increase in sound pressure level in all frequency bands in salt water compared to fresh water. It has been shown that the effect of salt reduces bubble coalescence in aqueous solutions[27] (see Figs 2 and 3). The observations of foam as a whitecap produced by breaking waves in the surf zone is related to salinity of the ocean waters.[11] The efficiency of the whitecap in the ocean is related to drastic reduction in the bubble sizes generated by breaking waves as the salinity of the water is raised.[28] The transient nature of the effect of salt on bubble cloud persistence has been observed in the ocean. All the available literature on this subject, including this study, shows significant change in the bubble size spectrum generated by breaking waves. The generation of the large numbers of smaller bubbles is attributed to the absence of coalescence in salt water. However, the reasons for the more rapid coalescence of bubbles in fresh water than in sea water has not been fully understood. Even though the change in bubble spectrum will affect the sound-pressure level, the effect is not sufficient to account for the observed increase in sound-pressure level in all frequencies. The surprising increase in sound-pressure level has persuaded us to look at the effect of salt on single bubbles detaching from submerged needles. Figures 11 and 12 depict the acoustic pressure of 2.4- and 1.1-mm bubbles in fresh water and water with 25‰ sodium chloride. For details of the experimental procedures on
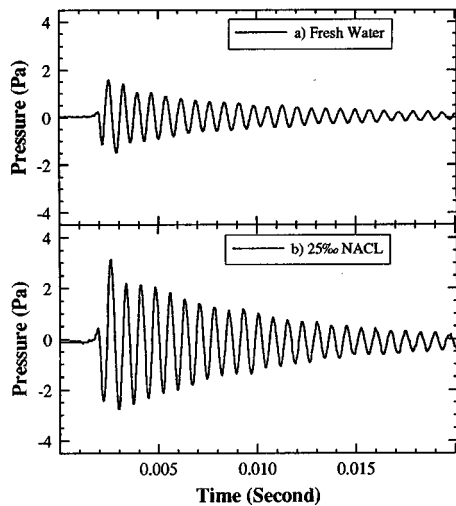
FIG. 11. Pressure traces of acoustic emissions from a bubble with radius of 2.4 mm released from a submerged needle in fresh water and in water with 25‰ sodium chloride. The quality factor in fresh water is 36, which reduces to 24 in salt water. Also note the increase in acoustic pressure in salt water.

bubble dynamics in salt water refer to an article by Kolaini.[29] The quality factors of the acoustic signatures decreased from 35 to 24, and 25 to 15 for bubble sizes 2.4 and 1.1 mm, respectively. The bubble sizes remained the same in the two different media. These stark changes in the acoustic characteristics of bubbles in salt water may account for the sound-pressure level increase observed with the laboratory breaking waves under study. The preliminary studies of the effects of salt on bubble sounds show that the change in sound-pressure level and the quality factor of bubbles depend upon the size of bubbles and are very sensitive to the host liquid. It is clear that the acoustical characteristics of bubbles can be altered significantly in salt water. The reason why the salinity could significantly alter the acoustic signature is not yet known and is the subject of current investigation.
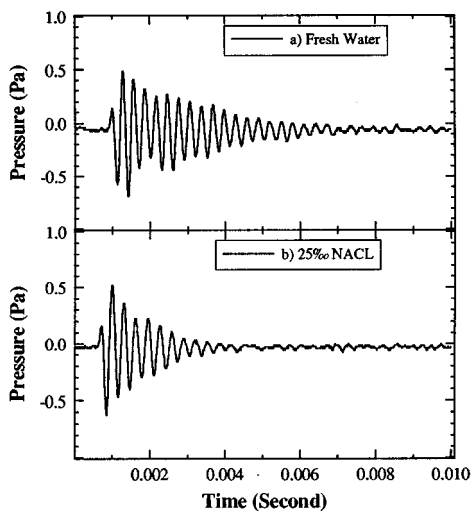
FIG. 12. Pressure traces of acoustic emissions from a bubble with radius of 1.1 mm released from a submerged needle in fresh water and in water with 25‰ sodium chloride. The quality factor in fresh water is 25, which reduces to 15 in salt water.

III. CONCLUSIONS

An experiment has been performed under controlled conditions to measure the acoustic radiation from various breaker intensities in fresh and salt water. We observe a gradual transition from relatively low-intensity, high-frequency acoustic emissions from gently spilling breakers to relatively high-intensity, low-frequency emissions from plunging breakers. For the gentle breakers, small numbers of individual bubbles of relatively small size are produced. It appears that the majority of sound is produced by these individual bubbles resonating at their natural frequencies. However, as the intensity of the breaker increases, more bubbles are produced. Almost all breakers, spilling and plunging types, exhibit a small jet at the onset of breaking. Once the speed of the jet exceeds the phase velocity of the waves, the jet overturns and may encapsulate ''sausage''-shaped bubbles. The surface instability may cause the sausage-shaped bubble to break. This happens in the very early stages of the breaker growth. The analysis of the acoustic signature from moderate spilling and plunging breakers demonstrates that the sausage-shaped bubble may break into larger bubbles and emit a significant acoustic energy that may account for frequencies as low as a few hundred Hz. Collective oscillations of the bubble cloud that leads to low frequency may occur at later stages of the breaker growth (i.e., bubble cloud growth). For a bubble cloud to oscillate collectively, a broad range of bubble sizes are to be generated first. Once bubbles are influenced by the neighboring bubbles, the cloud may begin to oscillate collectively. This has been demonstrated by a weak spilling breaker sound spectra in salt water. The less dense and relatively larger bubbles for the same breakers were responsible for the spectrum in fresh water while the more dense and smaller bubbles in the salt water spectrum have shown evidence of the collective oscillations that were absent in fresh water. The large numbers of smaller bubbles may be influenced by neighboring bubbles that ultimately lead to collective oscillations. As the breaking wave tends more and more towards a plunging breaker, the concentration of bubbles and the associated void fraction becomes relatively large. The hydrodynamics of the breaking process leads to the production of eddies that may induce collective oscillations of bubble clouds. The resulting acoustic emissions of bubble clouds, radiating as a collective unit, extend to very low frequencies ($\leqslant 200$ Hz). The spectral slope resembles the Knudsen wind wave spectra at sea with 5–6-dB/oct falloff in the frequency range 0.5–20 kHz both in fresh and salt water. As the intensity of the breaking wave increases or, in the open ocean case, as the wind speed increases, there is an associated increase in the magnitude of the acoustic radiation and a gradual shift to lower frequencies.

The nearly linear growth of the moderate breaker area could be used to estimate the air entrainment rate. The estimated value of the air entrainment rate for the moderate breaker of about 0.2/s, which is consistent with the value obtained photographically, is one of the crucial parameters that is required in development of theory. The knowledge of another parameter in the theoretical development is the radiation pattern of the acoustic pressure. It has been shown

the pressure radiation patterns behave very close to $\cos(\theta)$.

It has been clearly shown that the bubble size spectrum increases in numbers and shifts to smaller bubbles in salt water. This will indeed change the sound-pressure spectra level. However, the significant increase in sound-pressure levels at all frequencies and for all the breaker types investigated in this report is not due to the change in size spectrum only. The analysis of sound radiation from bubbles pinching off from the hypodermic needle as a function of salinity level shows that the ionic structure of the water does have a profound effect on the acoustic signature. The pressure amplitude increases in certain frequency ranges and the quality factor of the bubble drops from 30 to as low as 15 for water with 25‰ sodium chloride. The reason behind this has not yet been determined.

Our laboratory results produce a rational explanation for the origin of wind-dependent ambient noise in the ocean, for frequencies that range from more than several tens of kHz to a few tens of Hz. The existence of larger bubbles, which may weigh more in their contribution to the ambient noise in the ocean than collective oscillations of bubble clouds, is fully explored in this experiment. Measurements of some of the parameters such as the air entrainment rate and the radiation pattern of the noise generated by breaking waves which are otherwise inaccessible in the ocean may provide tools to better develop an analytical model to predict the ocean ambient noise spectra.

ACKNOWLEDGMENTS

[1] V. W. Knudsen, R. S. Alford, and J. W. Emiling, ''Underwater ambient noise,'' J. Mar. Res. **7**, 410–429 (1948).

[2] G. M. Wenz, ''Acoustic ambient noise in the ocean: spectra and sources,'' J. Acoust. Soc. Am. **34**, 1936–1956 (1962).

[3] B. R. Kerman (Ed.), ''Natural mechanisms of surface-generated noise in the ocean,'' in *Sea Surface Sound* (Kluwer, Dordrecht, The Netherlands, 1988).

[4] B. R. Kerman (Ed.), ''Natural mechanisms of surface-generated noise in the ocean,'' in *Natural Physical Sources of Underwater Sound* (Kluwer, Dordrecht, The Netherlands, 1993).

[5] M. J. Buckingham and J. R. Potter, *Sea Surface Sound '94*, Proceedings of the Third International Meeting on Natural Physical Processes Related to Sea Surface Sound (World Scientific, Singapore, 1995).

[6] S. Vagle, W. Large, and D. M. Farmer, ''An evaluation of the WOTAN techniques of inferring oceanic winds from underwater ambient sounds,'' J. Atmos. Ocean Technol. **7**, 576–595 (1990).

[7] M. R. Lowen and W. K. Melville, ''Microwave backscatter and acoustic radiation from breaking waves,'' J. Fluid Mech. **224**, 601–623 (1991).

[8] H. Medwin and A. C. Daniel, ''Acoustical measurements of bubble production by spilling breakers,'' J. Acoust. Soc. Am. **88**, 408–412 (1990).

[9] E. C. Monahan and C. R. Zeitlow, ''Laboratory comparisons of fresh and salt water whitecap,'' J. Geophys. Res. **74**, 6961–6966 (1969).

[10] J. C. Scott, ''The role of salt in whitecap persistence,'' Deep-Sea Res. Oceanogr. Abstr. **22**, 653–657 (1975).

[11] E. C. Monahan and C. R. Zeitlow, ''Laboratory comparisons of fresh-water and salt-water whitecap,'' J. Geophys. Res. **74**, 6961–6966 (1969).

[12] J. A. Kitchener, ''Foams and free liquid film,'' in *Recent Progress in Surface Science, Vol. 1* (Academic, New York, 1964), pp. 51–93.

[13] C. Pounder, ''Sodium chloride and water temperature effects on bubbles,'' in *Oceanic Whitecap and Their Role in Air-Sea Exchange Processes*, edited by E. C. Monahan and G. Mac Niocaill (Reidel, Dordrecht, 1986).

[14] W. M. Carey and D. G. Browning, ''Low-frequency ocean surface noise sources: measurements and theory,'' in *Sea Surface Sound*, edited by B. R. Kerman (Kluwer, Dordrecht, The Netherlands, 1988), pp. 361–376.

[15] A. R. Kolaini, R. A. Roy, and D. L. Gardner, ''Low-frequency acoustic emissions in fresh and salt water,'' J. Acoust. Soc. Am. **96**, 1966–1772 (1994).

[16] A. Prosperetti, ''Bubble-related ambient noise in the ocean,'' J. Acoust. Soc. Am. **84**, 1042–1054 (1988).

[17] A. R. Kolaini and L. A. Crum, ''Observations of underwater sound from laboratory breaking waves and the implications concerning ambient noise in the ocean,'' J. Acoust. Soc. Am. **96**, 1755–1765 (1994).

[18] H. Medwin and N. D. Breitz, ''Ambient and transient bubble spectral densities in quiescent areas and under spilling breakers,'' J. Geophys. Res. **84**, 12 751–12 759 (1989).

[19] P. A. Kolovayev, ''Investigation of the concentration and statistical size distribution of wind-produced bubbles in the near-surface ocean layer,'' Oceanologia **15**, 1013–1017 (1975).

[20] B. D. Johnson and R. C. Cooke, ''Bubble populations and spectra in coastal waters: A photographic approach,'' J. Geophys. Res. **84**, 3761–3766 (1979).

[21] J. Wu, ''Bubbles in the near-surface ocean: a general description,'' J. Geophys. Res. **93**, 587–590 (1987).

[22] M. Y. Su, D. Todoroff, and J. Cartmill, ''Laboratory comparisons of acoustic and optical sensors for microbubble measurement,'' J. Atomos., Ocean. Technol. **11**(1), 170–181 (1994).

[23] A. Prosperetti, ''Bubble dynamics: some things we did not know 10 years ago,'' in *Bubble Dynamics*, edited by J. Blake (Kluwer, Dordrecht, 1994).

[24] H. Oguz, ''A theoretical study of low frequency oceanic ambient noise,'' J. Acoust. Soc. Am. **95**, 1895–1912 (1994).

[25] W. M. Carey, J. W. Fitzgerald, E. C. Monahan, and Q. Wang, ''Measurements of the sound produced by a tipping trough with fresh and salt water,'' J. Acoust. Soc. Am. **93**, 3178–3192 (1993).

[26] A. R. Kolaini and M. P. Tulin, ''Laboratory measurements of breaking inception and post-breaking dynamics of steep short-crested waves,'' Int. J. Offshore Polar Eng. **5**(3), 212–218 (1995).

[27] V. S. Craig, B. W. Ninham, and R. M. Pashley, ''The effect of electrolytes on bubble coalescence in water,'' J. Phys. C **97**, 10 192–10 197 (1993).

[28] E. C. Monahan, Q. Wang, W. Wang, and M. B. Wilson, ''The role of oceanic whitecaps and the associated sub-surface bubble plumes in various air-sea interface phenomena,'' Tech. Report, Whitecap Report No. 11, University of Connecticut at Avery Point (1991).

[29] A. R. Kolaini, ''Effect of salt on bubble acoustic radiation,'' Sea Surface Sound '97, University of Southampton, England (1997).

From geology to geoacoustics—Evaluation of Biot–Stoll sound speed and attenuation for shallow water acoustics

Mohsen Badiey
Ocean Acoustics Laboratory, Graduate College of Marine Studies, University of Delaware, Newark, Delaware 19716

Alexander H-D. Cheng and Yongke Mu
Department of Civil and Environmental Engineering, University of Delaware, Newark, Delaware 19716

A procedure for estimating acoustic wave velocity and attenuation in ocean sediment using a minimum amount of geological and geotechnical data is demonstrated. First, the Biot–Stoll theory is presented. Next, various asymptotic formulae for the attenuation coefficient are derived for high, low, and intermediate frequencies. These expressions clearly isolate the effects of intergranular Coulomb friction and fluid viscous dissipation on the attenuation of shear and compressional waves. Under the constraint of a minimum amount of geological and geotechnical information, a sequence of empirical equations is compiled to convert basic data, such as blow count number from a Standard Penetration Test or shipboard density, into sediment geoacoustic properties. As a demonstration, two well-known field cases, the Atlantic Generating Station (AGS) site and the Atlantic Margin Coring (AMCOR 6010) site, are examined. By incorporating the uncertainty involved in the data collection, the estimated geoacoustical parameters are provided with a standard deviation. © *1998 Acoustical Society of America.* [S0001-4966(98)02701-5]

PACS numbers: 43.30.Pc, 43.30.Ma, 43.20.Gp [JHM]

INTRODUCTION

The problem of describing acoustic waves propagating in the ocean over a porous seabed is of interest in many ocean related applications. Usually the sediment is considered either as a fluid, or as an elastic or viscoelastic solid. More realistically, sediment is composed of granular solid forming a porous skeleton which is filled with a fluid. Modeling the seabed as a poroelastic material using Biot's theory[1,2] was pioneered by Stoll.[3] It has been found that poroelastic material parameters, such as porosity and permeability, play an important role in the reflection, scattering and attenuation of ocean acoustic waves.

Although poroelasticity theory provides a more correct account of acoustic wave propagation in sediments, its application requires the knowledge of additional physical parameters. The difficulties involved in gathering ocean sediment samples and testing for their properties have hampered the application of Biot–Stoll theory.[4]

With or without ocean acoustics in mind, during the last two decades there have been a number of efforts in applying geotechnical techniques to gather sediment properties. Empirical relations have been constructed which connect properties such as shear modulus and porosity to data collected by geotechnical techniques, such as the Vane Shear Test, Standard Penetration Test, etc. This accumulated knowledge which allows the conversion of geological to geoacoustic data, creates an opportunity for the application of Biot–Stoll theory.

In any large scale engineering project, a site survey of geology always precedes the construction activity. There exist several offshore, shallow water sites where a reasonably dense network of coring has been conducted.[5–7] If the complete set of Biot–Stoll acoustic model parameters can be inferred from these testing results, these sites can serve as shallow water acoustic testing laboratories.

In this paper, we combine some earlier results with our own investigations into a step-by-step procedure for constructing geoacoustic parameters from geological data using empirical means. Although many of these results are already available in the literature, it is hoped that a clearer synthesis could be useful to the acoustics community.

We also investigate the attenuation of compressional and shear waves. A number of asymptotic formulae are derived for high, low, and intermediate frequencies. The dependence of attenuation coefficient on intergranular Coulomb friction and fluid viscous dissipation are explicitly established. These simple relations can be useful for designing inverse procedures for parameter determination, although no such effort is attempted here.

As demonstrations, we process data from two well-known sites: the Atlantic Generating Station (AGS) site and the Atlantic Margin Coring (AMCOR 6010) site. In particular, we demonstrate that the attenuation coefficient can either be constant with depth, or vary strongly with depth, depending on the frequency range of the acoustic waves. Also, by accounting for the uncertainty involved in the data collection, the estimated geoacoustical data are assigned standard deviations.

I. SOUND SPEED

A. Biot–Stoll model

The derivation of Biot–Stoll sound speed can be found in several places,[1–3,8] hence only the final result is provided. Due to the large numbers of variables involved, we present a

"Table of Nomenclature" in Appendix A. The fast (V_{p1}) and slow (V_{p2}) compressional wave velocities, and the shear wave velocity (V_s) are expressed in the following form:[9]

$$\begin{pmatrix} V_{p1} \\ V_{p2} \end{pmatrix} = \left[\frac{2(HM - C^2)}{(\rho M + m'H - 2\rho_f C) \mp A^{1/2}} \right]^{1/2}, \tag{1}$$

$$V_s = \left(\frac{Gm'}{\rho m' - \rho_f^2} \right)^{1/2}, \tag{2}$$

where

$$\rho = (1 - \phi)\rho_s + \phi\rho_f \tag{3}$$

is the bulk density, with ρ_f the fluid density, ρ_s the solid grain density, and ϕ the porosity. The material coefficients are

$$A = (m'H - \rho M)^2 + 4(\rho_f H - \rho C)(\rho_f M - m'C), \tag{4}$$

$$H = \frac{(K_s - K)^2}{D - K} + K + \frac{4}{3}G, \tag{5}$$

$$M = \frac{K_s^2}{D - K}, \tag{6}$$

$$C = \frac{K_s(K_s - K)}{D - K}, \tag{7}$$

$$D = K_s \left[1 + \phi \left(\frac{K_s}{K_f} - 1 \right) \right]. \tag{8}$$

We note that K is the bulk modulus of the porous frame, G is the shear modulus of the frame, K_f is the bulk modulus of the pore water, and K_s is the bulk modulus of the solid grains.

The intergranular Coulomb friction is modeled by introducing the complex moduli G and K as

$$G = G_0(1 + i\delta'), \tag{9}$$

$$K = K_0(1 + i\delta''), \tag{10}$$

where $i = \sqrt{-1}$, G_0 and K_0 are, respectively, shear and bulk moduli of the frame, δ' and δ'' are respectively specific losses associated with shear and volumetric deformation of the frame. In Eqs. (1), (2), and (4), m' is given by

$$m' = (1 + c)\frac{\rho_f}{\phi} - i\frac{\mu_f F}{k\omega}, \tag{11}$$

in which c is the added mass coefficient, μ_f is fluid dynamic viscosity, k is the intrinsic permeability (with dimension of length squared), and ω is the angular frequency. We also note that F is a viscosity correction factor:

$$F = \frac{\kappa T}{4[1 + 2iT/\kappa]}, \tag{12}$$

in which

$$T = \frac{\mathrm{ber}'(\kappa) + i\,\mathrm{bei}'(\kappa)}{\mathrm{ber}(\kappa) + i\,\mathrm{bei}(\kappa)}, \tag{13}$$

where ber and bei are, respectively, the real and imaginary parts of the Kelvin function of the first kind of order zero,

TABLE I. Input sediment parameters (Ref. 3).

Parameter	Symbol	Unit	Sediment Hard	Sediment Soft
Grain density	ρ_s	kg/m^3	2650	2650
Fluid density	ρ_f	kg/m^3	1000	1000
Grain bulk modulus	K_s	Pa	3.6×10^{10}	3.6×10^{10}
Fluid bulk modulus	K_f	Pa	2.25×10^9	2.25×10^9
Frame bulk modulus	K_0	Pa	4.36×10^7	3.69×10^7
Frame shear modulus	G_0	Pa	2.61×10^7	2.21×10^7
Fluid viscosity	μ_f	kg/m s	1.0×10^{-3}	1.0×10^{-3}
Permeability	k	m^2	1.0×10^{-10}	1.0×10^{-11}
Porosity	ϕ	$\cdots$	0.47	0.76
Degree of saturation	S	$\cdots$	1.0	1.0
Shear specific loss	δ'	$\cdots$	0.01	0.03
Volumetric specific loss	δ''	$\cdots$	0.0075	0.0225
Added mass coefficient	c	$\cdots$	0.25	0.25

and ber$'$ and bei$'$ are their derivatives.[10] The argument κ is defined as

$$\kappa = a\sqrt{\frac{\omega\rho_f}{\mu_f}}, \tag{14}$$

where a is a pore size factor. Based on models of slits and circular tubes, Biot[2] argued that

$$a = \eta\sqrt{\frac{k}{\phi}}, \tag{15}$$

where $\eta = \sqrt{16/3} \approx 2.3$ and $\sqrt{8} \approx 2.8$, respectively, for slitlike and capillary tube geometries. Stoll[11] on the other hand suggested that

$$a = \frac{1}{7}d_{\mathrm{mean}}, \tag{16}$$

where d_{mean} is the mean grain size. We shall follow Eq. (15) in the following. As indicated by Biot,[2] the η value needs to be multiplied by a tortuosity factor. Experiments conducted on assemblies of spheres[12] show that $\eta = 3.2$. Although some recent studies have explored the variability of the pore size parameter on the Biot theory,[13,14] without the availability of further evidence, $\eta = 3.2$ will be adopted herein for the computation of sound speed.

B. Frequency-dependent sound speed

To gain insight into the attenuation of acoustic waves in sediments, the real and imaginary parts of the three complex velocities are plotted in Fig. 1(a) and (b), together with the viscosity correction factor F, versus frequency f. The velocity values are normalized using sound speed in seawater $C_w \approx 1500$ m/s. The sediment properties follow that of a "hard" and a "soft" sediment cases in Stoll and Kan[3,9] (Table I). This type of velocity plot has been presented by Yamamoto,[8,15] hence only a brief discussion relevant to the present study is provided.

The curves in Fig. 1(a) and (b) have similar characteristics. However, we observe a large shift of curve positions with respect to frequency between the two sediments. In particular, the imaginary parts of the velocities peak around $f \approx 100$–1000 Hz for the hard sediment, and around f
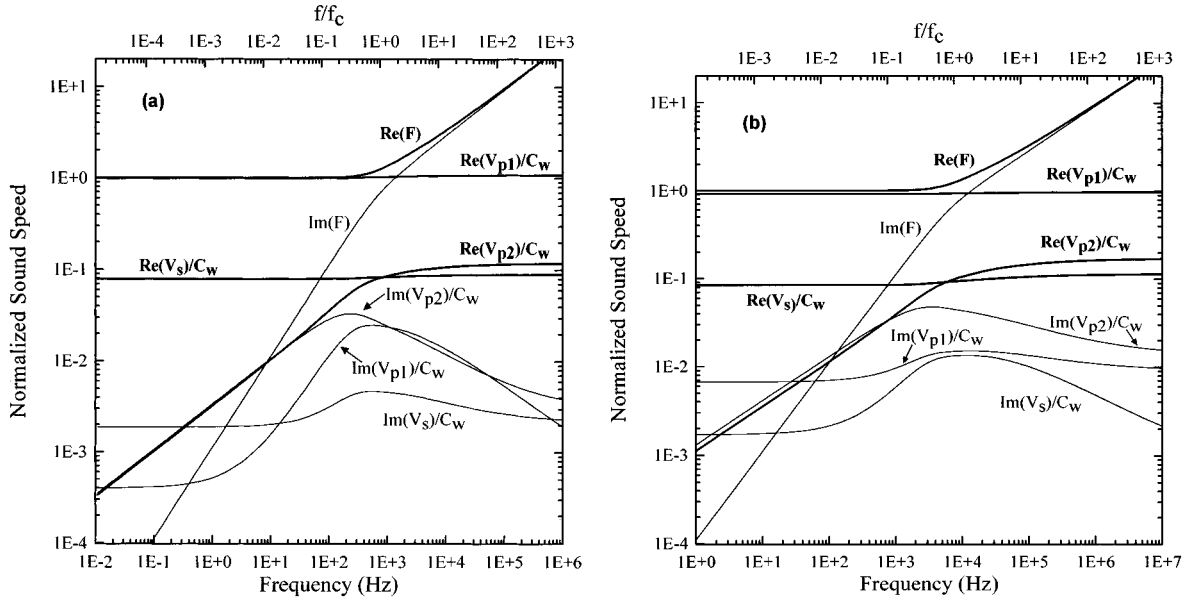
FIG. 1. Real and imaginary parts of normalized compressional waves V_{p1} and V_{p2}, and shear wave V_s, and viscosity correction factor F, versus frequency f (bottom axis) and dimensionless frequency f/f_c (top axis) for (a) hard sediment case, (b) soft sediment case (see Table I).

$\approx 1–10$ kHz for the soft sediment. These frequency ranges seem to coincide with the characteristic frequency f_c introduced by Biot:[1,2]

$$f_c = \frac{\phi \mu_f}{2 \pi \rho_f k}. \tag{17}$$

For the present cases, we calculate $f_c = 748$ Hz for the hard sediment, and $f_c = 7.56$ kHz for the soft sediment. By observing the expression in Eq. (17), we suggest that the relative shift of curves for the two sediments with respect to frequency is largely caused by the permeability difference (Table I). In Fig. 1(a) and (b), we present the dimensionless frequency f/f_c as the upper axes. The peaks occur around $f/f_c \approx 1$. Similar argument was made in Yamamoto,[8,15] in which a poroviscous frequency number

$$N_f = \frac{\rho_f k f}{\phi \mu_f} = \frac{1}{2 \pi} \frac{f}{f_c} \tag{18}$$

was introduced. Apparently N_f differs from f/f_c only by a constant factor $1/2\pi$. $N_f = 0.1$ was chosen by Yamamoto[8] to identify the peak.

II. ATTENUATION

A. Biot–Stoll model

The most commonly used measure of acoustic energy dissipation is the attenuation coefficient α which is the exponential decay constant of the amplitude of a propagating wave in a homogeneous medium. We note that $\alpha = l_i$, where l_i is the imaginary part of the complex wave number l. It is related to the inverse of quality factor Q^{-1} and the logarithmic decrement δ as

$$Q^{-1} = \frac{\alpha v}{\pi f} = \frac{\delta}{\pi}, \tag{19}$$

in which v is the phase velocity given by

$$v = \frac{2 \pi f}{|l_r|} \tag{20}$$

and l_r is the real part of l. The quantity Q^{-1} is also known as the attenuation coefficient per wave cycle. Given the complex wave speed V, these quantities are evaluated as

$$Q^{-1} = 2 \left| \frac{V_i}{V_r} \right| \tag{21}$$

and

$$\alpha = 2 \pi f \frac{|V_i|}{|V|^2}, \tag{22}$$

where V_r and V_i are respectively the real and the imaginary part of V. We note that α in Eq. (22) has the unit of inverse length. In acoustic literature, α is sometimes given in dB/λ unit, hence

$$\alpha(\text{dB}/\lambda) = 8.686 \pi \frac{2 |V_i|}{|V_r|}. \tag{23}$$

In marine sediments, α, Q, and δ are frequency dependent.

B. Frequency-dependent attenuation

In Fig. 2(a) and (b) we present the inverse of quality factor as a function of normalized frequency f/f_c in solid lines for a hard and a soft sediment (Table I). We observe that curves for the first compressional wave and the shear wave have similar characteristic as those shown in Fig. 1(a) and (b). In particular, they peak around $f/f_c \approx 1$, which is marked by a vertical dashed line. We also notice that shear wave attenuates much faster than the first compressional wave. For the second compressional wave, even larger attenuation is observed. It decreases monotonically toward higher frequency.

311   J. Acoust. Soc. Am., Vol. 103, No. 1, January 1998

Badiey *et al.*: Geology to geoacoustics   311
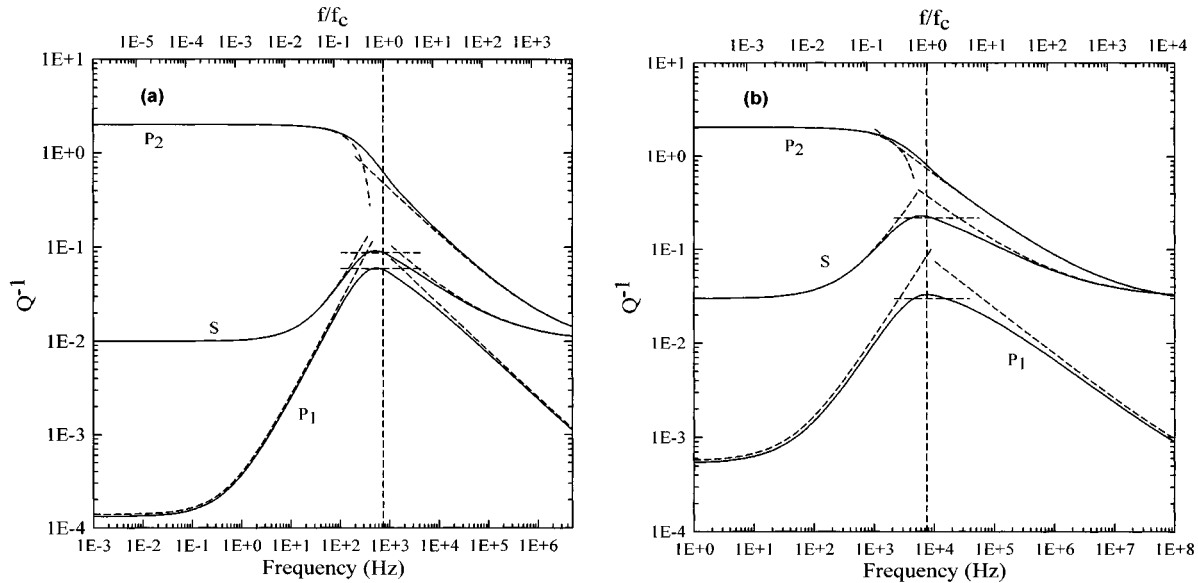
FIG. 2. Inverse of quality factor versus frequency for three waves (exact and asymptotic solution). (a) Hard sediment. (b) Soft sediment.

C. Asymptotic formulae

For the purpose of developing a keener physical insight into the parameter dependence, and also attaining simpler mathematical expressions for use in inverse procedures, asymptotic expressions at low, high, and critical frequency ranges are desirable. While some earlier attempts[2,16] have achieved partial success in providing asymptotic expressions, a complete exposition is presented below.

To obtain simpler mathematical expressions, we assume that for ocean sediments the solid grain bulk modulus K_s ($\sim 10^{10}$ Pa) is much greater than the fluid bulk modulus K_f ($\sim 10^9$ Pa), which in turn is much greater than the frame bulk modulus K ($\sim 10^7$ Pa). The first assumption can introduce a small error in the computation of sound speed and attenuation, while the second one is excellent for the case of saturated sediment. However, in the case of unsaturated sediment, a small amount of entrapped air can reduce the bulk modulus of pore water drastically, leading to a breakdown of the second assumption. In the present work, the sediment is assumed to be fully saturated.

1. Shear wave

For the attenuation of shear waves, formulae were provided by Biot,[2] which however did not take into account Coulomb friction. Repeating the analysis (see Appendix B), we obtain the modified version of this result. For low frequencies, we obtain

$$Q_s^{-1} \approx \delta' + \frac{\phi\rho_f}{\rho}\frac{f}{f_c} = \delta' + \frac{2\pi\rho_f^2 kf}{\rho\mu_f} \quad (24)$$

and for high frequencies,

$$Q_s^{-1} \approx \delta' + \frac{\sqrt{2}\,\eta\phi\rho_f}{8\rho_A}\left(\frac{f_c}{f}\right)^{1/2}$$

$$= \delta' + \frac{\eta\phi}{8\sqrt{\pi}\rho_A}\left(\frac{\phi\rho_f\mu_f}{kf}\right)^{1/2}, \quad (25)$$

where

$$\rho_A = (1+c)[(1+c)\rho - \phi\rho_f]. \quad (26)$$

We notice the behavior of $Q_s^{-1} \sim f$ and $Q_s^{-1} \sim f^{-1/2}$ respectively at low and high frequencies, as pointed out by Biot,[2] and also by Stoll.[11] These two asymptotic formulae are plotted against Q_s^{-1} evaluated using Eq. (21) for both soft and hard sediment cases in Fig. 2(a) and (b) in dashed lines. We observe that the agreement is excellent for most part of the frequencies. The only deviation is found around the relaxation frequency, $f/f_c \approx 1$.

To predict the peak near the characteristic frequency f_c, an approximate formula can be derived based on $f/f_c \approx 1$. First, we notice that the argument κ defined in Eq. (14), with an estimate of a given by Eq. (15) and $\eta = 3.2$, takes the following value:

$$\kappa = \eta\left(\frac{f}{f_c}\right)^{1/2} = \eta = 3.2. \quad (27)$$

The viscosity correction function then takes the value $F(3.2) = 1.089 + 0.399i$. By assuming an added mass coefficient $c = 0.25$, we are able to approximate

$$Q_s^{-1} \approx \delta' + 0.28\frac{\phi\rho_f}{\rho} + 0.12\left(\frac{\phi\rho_f}{\rho}\right)^2$$

$$\approx 0.28\frac{\phi\rho_f}{\rho} + 0.12\left(\frac{\phi\rho_f}{\rho}\right)^2. \quad (28)$$

This new result is shown in Fig. 2(a) and (b) as horizontal dashed lines. The agreement with the exact peak is excellent. In fact, we observe that for shear waves these three asymptotic formulae alone are able to approximate the entire curve quite reasonably.

2. First compressional wave

Biot[2] also investigated the asymptotic behavior of the first compressional wave. However, those formulae were not resolved into explicit forms, hence it is difficult to gain in-

sight. Using the realistic assumption $K_s \gg K_f \gg K$, the following results can be obtained: for low frequencies

$$Q_{p1}^{-1} \approx \delta_H + \frac{\phi(\rho - \rho_f)^2}{\rho \rho_f} \frac{f}{f_c},$$ (29)

for high frequencies,

$$Q_{p1}^{-1} \approx \frac{(1 + c - \phi)^2 \rho_f^2}{\rho_B^2} \delta_H$$

$$+ \frac{\sqrt{2} \eta \phi (1 + c)(\rho - \rho_f)^2}{8 \rho_A \rho_B} \left(\frac{f_c}{f} \right)^{1/2},$$ (30)

and at the relaxation frequency,

$$Q_{p1}^{-1} \approx \delta_H + 0.28 \frac{\phi(\rho - \rho_f)^2}{\rho \rho_f} + 0.12 \frac{\phi^2(\rho - \rho_f)^2}{\rho^2}$$

$$\approx 0.28 \frac{\phi(\rho - \rho_f)^2}{\rho \rho_f} + 0.12 \frac{\phi^2(\rho - \rho_f)^2}{\rho^2},$$ (31)

in which

$$\rho_B = \phi \rho + (1 + c) \rho_f - 2 \phi \rho_f.$$ (32)

Following the pattern of Eqs. (9) and (10), we define

$$H = H_0(1 + i \delta_H),$$ (33)

where

$$H_0 = \frac{K_f}{\phi},$$ (34)

$$\delta_H = \frac{\phi}{K_f} \left[\frac{4}{3} G_0 \delta' + K_0 \delta'' \right].$$ (35)

We note that Yamamoto and Turgut[16] have also obtained Eq. (29) and the equivalent of Eq. (31), but not (30). For Eq. (31), their formula is slightly different:[16]

$$Q_{p1}^{-1} \approx \delta_H + 0.33 \frac{\phi(\rho - \rho_f)^2}{\rho \rho_f}.$$ (36)

The asymptotic formulae (29)–(31) are plotted as dashed lines in Fig. 2(a) and (b) against the first compressional wave curve. We again observe excellent agreement. Equation (36), which is not plotted, is off by a small amount.

3. Second compressional wave

The second compressional wave is highly dissipative and hence is difficult to measure in the field. Nevertheless, we present its asymptotic expressions as follows: for low frequencies,

$$Q_{p2}^{-1} \approx 2(1 + \delta_0) - \left(\frac{2 \rho_B}{\rho_f} + \frac{\eta^2}{12} \right) \frac{f}{f_c},$$ (37)

and for high frequencies,

$$Q_{p2}^{-1} \approx \delta_0 + \frac{\sqrt{2} \eta \rho_f}{8 \rho_B} \left(\frac{f_c}{f} \right)^{1/2},$$ (38)

where

$$\delta_0 = \frac{\frac{4}{3} G_0 \delta' + K_0 \delta''}{\frac{4}{3} G_0 + K_0}.$$ (39)

These results are again plotted in dashed line in Fig. 2(a) and (b) with excellent agreement with the exact result.

4. Discussion

The attenuation coefficient (or log decrement) is among the most difficult of parameters to determine in sediment acoustics. In the past, due to the lack of measurements, constant values were often used.[11,17] The present result demonstrates that at very low and very high frequencies, the log decrement $\delta_s (= \pi Q_s^{-1})$ of shear waves is dominated by the Coulomb friction coefficient δ' only, as per Eqs. (24) and (25). For the second compressional wave, δ_{p2} is either a constant (low frequency) or dependent on a combination of δ' and δ'' weighted by elastic properties (high frequency); see Eqs. (37) and (38). For the first compressional wave, porosity, density, permeability and material elastic properties come into play; see Eqs. (29) and (30). Outside of these low- and high-frequency ranges, attenuation is generally frequency dependent, which is further modulated by porosity, density, permeability, etc. Near the peak frequency, Coulomb friction is overshadowed by the fluid viscous dissipation. From these considerations, we realize that attenuation coefficient must be considered as a function of frequency and sediment properties in modeling sediment acoustics.

III. EMPIRICAL EVALUATION OF SOUND SPEED

The sediment sound speed and attenuation model presented requires the knowledge of the following material parameters: K_f, K_0, G_0, ρ_f, ρ_s, ϕ, δ', δ'', c, μ_f, k, η, and also the frequency f. It is the purpose of this section to demonstrate that based on certain standard geotechnical measurements, combined with a data base and educated guesses, it is possible to acquire the full list of parameter values for the determination of Biot–Stoll sound speed and attenuation.

In the above list, the seawater density ρ_f, viscosity μ_f, and bulk modulus K_f are readily available (they are functions of temperature and salinity). The solid grain density ρ_s has a value between 2.45 and 2.78 g/cm³ for a range of clayey to sandy sediments in shallow and deep oceans.[18] We shall use $\rho_s = 2.65$ g/cm³ in the present study.

Very little is known about the geometric factor η and the added mass coefficient c. Several authors have used different values for the added mass coefficient.[12–14,19] We shall use $\eta = 3.2$ following the discussion in Sec. II A, and adopt c values from 0.25 for sand to 2 for clay, following Stoll.[11] The sound speed is actually sensitive to the variation of added mass coefficient in the high-frequency range (higher than the relaxation frequency). Unfortunately, little is known about its proper selection.

Values of the shear damping coefficient δ' have been reported to range from 0.003 to 0.015 for sand, 0.02 to 0.03 for silt, and 0.003 to 0.006 for sedimentary rocks.[11] It is speculated that δ' should be dependent on porosity, effective overburden stress, and frequency. Unfortunately, there is no

known empirical relation that can correlate geotechnical data to Coulomb specific loss. Before such a study is conducted, we can estimate according to the above suggested ranges. For the volumetric damping coefficient δ'', even less information is available. It can be estimated as $\delta'' = 0.75\delta'$.[20]

The rest of the parameters, K_0, G_0, ϕ, and k, can be determined by empirical relations based on geotechnical measurements. A commonly used geotechnical method for *in situ* measurement of shear modulus is the Standard Penetration Test. In this technique, the number of blows that is required to drive a 2-in. diameter split spoon sampler into the sediment for a distance of 1 ft, by dropping a hammer in air weighing approximately 140 lb from a height of 30 in., is recorded.[21] Shear modulus is then calculated from an empirical formula[22]

$$G_0 = 11.9 \times 10^6 N^{0.8}, \tag{40}$$

where N is the blow count number.

Another typical engineering technique is the Vane Shear Test for measuring the shear strength S_u. In this test, the vane is forced into the sediment and then the torque required to rotate the vane is measured. The shear strength is determined from the torque required to shear the soil along the vertical and horizontal edges of the vane.[21] Geotechnical literature shows that the ratio of G_0/S_u ranges from 500 to 1000 for clay and 1000 to 5000 for sand.[23] Based on our compilation of AGS site[5,24] data, we find

$$G_0 \approx 700 S_u \quad \text{for clay}$$
$$\approx 3800 S_u \quad \text{for sand.} \tag{41}$$

A third technique involves the use of an instrument known as the Bottom Shear Modulus Profiler (BSMP).[25,26] Using gravity (water) waves as excitation, the seabed acceleration is measured. Using an inverse technique, shear modulus can be calculated for down to 200-m sediment depth. This instrument together with its inverse algorithm provides a ''direct'' measurement of shear modulus.

Geotechnical studies have demonstrated that the shear modulus of ocean sediment is related to its void ratio and the overburden pressure.[27] Based on a compilation of experimental data, Yamamoto *et al.*[28] suggest the following formula:

$$G_0 = 1.84 \times 10^5 \cdot \epsilon^{-1.12} \cdot \sigma_0^{0.5}, \tag{42}$$

where $\epsilon = \phi/(1-\phi)$ is the void ratio and σ_0 is the average confining normal stress of sediment (in Pascal) given by

$$\sigma_0 = \frac{1}{3}(1 + 2R_0) \int_0^z g(\rho_s - \rho_f)[1 - \phi(z)]dz, \tag{43}$$

in which R_0 is the coefficient of earth pressure at rest,[25] taken as 0.5, and g is the gravitational acceleration. Equation (42) does not differentiate among sediment types. Our own compilation using data from the AGS site shows that the data tend to separate into two groups, a clay-dominated, and a sand-dominated group; see Fig. 3. Hence three linear regression lines are fitted and shown in solid lines:
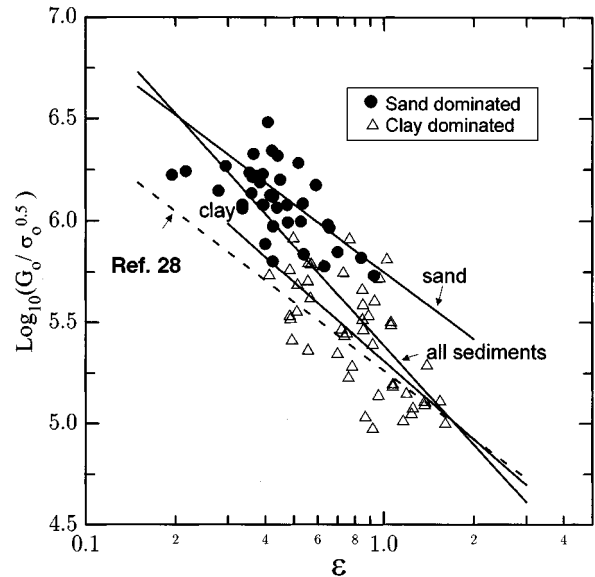
FIG. 3. Empirical relation of shear modulus as a function of void ratio.

$$G_0 = 6.56 \times 10^5 \cdot \epsilon^{-1.10} \cdot \sigma_0^{0.5} \quad \text{for sand dominant sediments}$$

$$= 2.05 \times 10^5 \cdot \epsilon^{-1.29} \cdot \sigma_0^{0.5} \quad \text{for clay dominant sediments}$$

$$= 2.44 \times 10^5 \cdot \epsilon^{-1.628} \cdot \sigma_0^{0.5} \quad \text{all sediments.} \tag{44}$$

In Fig. 3, we also have plotted Eq. (42) in dashed line for comparison. If the sediment can be identified as sandy or clayey based on geological classification, either the first or the second formula in Eq. (44) should be used. Otherwise, the third formula is used as an average. Using Eqs. (43) and (44), the porosity ϕ can be calculated in an iterative procedure.

Intrinsic permeability k is generally a function of porosity and grain size. For certain deep sea sediments it has been demonstrated that permeability is a function of porosity only.[29] However, when applied to shallow-water, unconsolidated sediments, these formulae produce erroneous results. We hence revert to the Carman-Kozeny equation expressed as[30]

$$k = 5.5 \times 10^{-3} d_{\text{mean}}^2 \frac{\phi^3}{(1-\phi)^2}, \tag{45}$$

where d_{mean} is the mean sediment grain size. The deficiency of the above equation is that the additional information of mean grain size is needed. Without a direct measurement, the mean grain size of a sediment can be estimated from Table II, which is complied from AGS[5] and AMCOR[31] data, and Hamilton.[18]

Finally, the bulk modulus needs to be estimated. According to Hamilton,[32] for natural marine sands:

$$\log_{10} K_0 = 2.709\,32 - 4.253\,91\phi, \tag{46}$$

and for natural silty clay:

$$\log_{10} K_0 = 2.735\,80 - 4.250\,75\phi, \tag{47}$$

where K_0 is given in 10^9 dyne/cm^2.

TABLE II. Sediment description and grain diameters reported in Hamilton (Ref. 18), at AGS site (Ref. 5) and AMCOR 6010 (Ref. 3).

Sediment description	Range of d_{mean} (μm)
Brown medium to coarse sand with gravel or sandy gravel	525–695
Coarse sand	528
Gray fine to medium sand with gravel	385–525
Gray fine sand with trace of silt and some shells	175–235
Brown and gray fine sand with trace of silt	185–225
Fine sand	164
Very fine sand	92
Gray very fine sand with rockets or organic silty clay	65–75
Silty sand	68
Gray very fine clayey sand or silty fine sand	49
Sandy silt	31
Silt	21
Dark gray and brown sandy silty clay with trace of fine to coarse sand	17–19
Sand-silt-clay	18
Dark gray silty clay with a little silt to clayey silt	7.7–9
Clayey silt	7.4
Dark gray organic silty clay with trace of silt	2.7–4.5
Silty clay	2.7

TABLE III. Core descriptions for Figs. 4 and 8.

Symbol	Core material
CL	Silty clay
CS	Sandy clay
SS	Silty clay mixed with fine sand
SP	Fine to medium sand
SM	Silty sand

IV. EXAMPLES

As a demonstration, two sets of field data, one referred to as the Atlantic Generating Station (AGS) site and the other as the Atlantic Margin Coring (AMCOR) site, are processed.

A. AGS data

The geology of the AGS site has been the subject of several studies.[24,33] In this area, we have obtained 24 core data from a total of 104 taken about 20 years ago.[5] A geological description of the layering is given for each core. Figure 4 displays that information for core 816. The corresponding core description symbols are denoted in Table III. Standard Penetrating Test was conducted at a large number of boreholes. Blow counts were recorded versus depth as shown in Fig. 4. To take into consideration of the random error in field measurements, we assume that the recorded blow counts are normally distributed. A standard deviation of 33% is arbitrarily imposed and shown as dashed lines that envelop the measured values.

Utilizing Eq. (40), it is possible to determine the real part of shear modulus. Shear strength was recorded at a few depths. These data offer an alternative method for evaluating shear modulus. However, the number of data is too few to be useful. Such information is ignored in the present study. Gamma ray probing was conducted which may be used to interpret the bulk density. This in turn can be used to evaluate porosity. Since the present work is a demonstration of the possibility of using minimum geological information to determine the sediment sound speed, porosity is calculated from Eqs. (43) to (44) by iterative method.

In Fig. 5 we present the calculated shear modulus, porosity, density and permeability of core 816 using the procedure outlined in Sec. III. Based on a technique developed by Badiey et al.,[34] the standard deviations of these quantities are evaluated and shown as dashed lines in Fig. 5. These profiles are used as input data to generate sound speed and attenuation profiles. Since these profiles are frequency dependent,
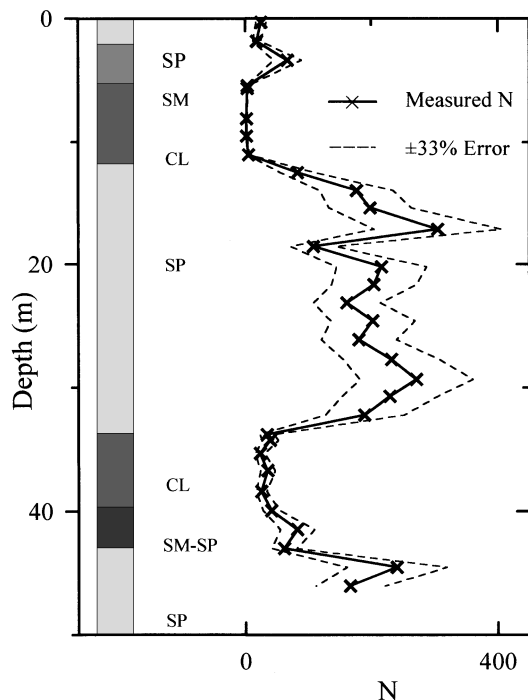

FIG. 4. Profile of core layer description and blow count number for core 816 at AGS site. Blow count is assumed to be normally distributed with an arbitrary standard deviation of 33%.
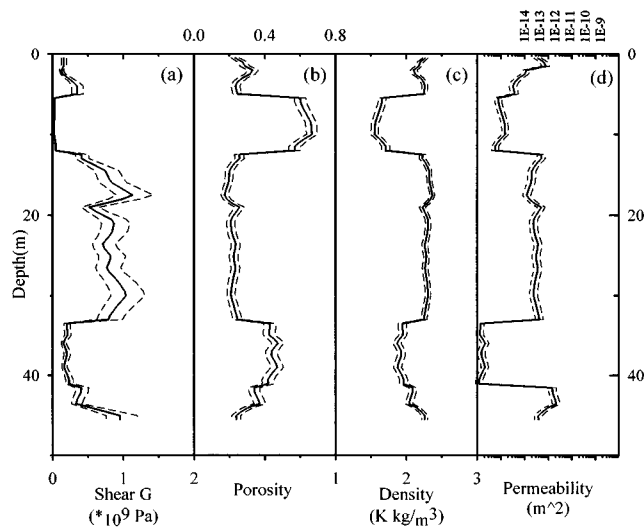
FIG. 5. Calculated profiles of shear modulus, porosity, density and permeability for AGS core 816 using empirical relationships. Solid lines are mean values and dashed lines are $\pm$ one standard deviation.
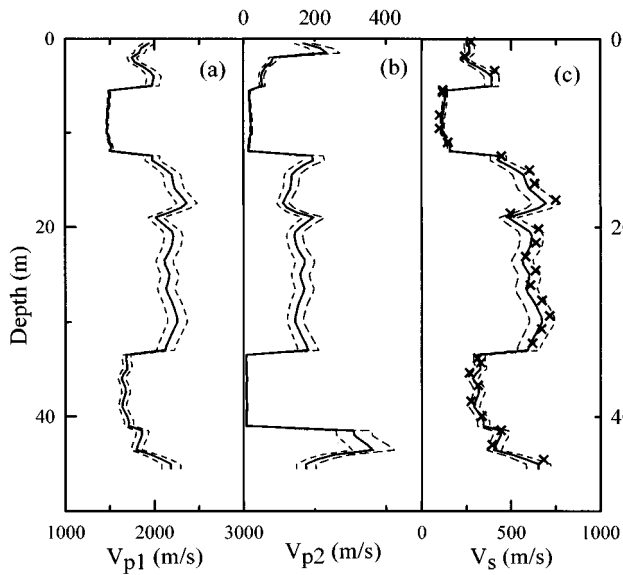
FIG. 6. Predicted sound speed of the (a) first compressional (V_{p1}), (b) second compressional (V_{p2}), and (c) shear (V_s) waves for AGS core 816; (×) shows the calculated shear wave speed using a simplified formula provided in Ref. 33. Solid lines are mean values and dash lines are ± one standard deviation.

FIG. 7. Predicted attenuation at 300 Hz for first compressional (α_{p1}), second compressional (α_{p2}), and shear (α_s) waves for AGS core 816. Solid lines are mean values and dash lines are ± one standard deviation.

$f = 300$ Hz is used in the calculation. Figure 6 gives the profiles of the three sound speeds V_{p1}, V_{p2}, and V_s, together with their standard deviation envelopes. We use a simplified shear velocity formula provided by Ewing[33] and plot the data in Fig. 6(c) for comparison with our prediction. We notice the layered structure of this core corresponding to the geological description shown in Fig. 4. Figure 7 presents attenuation coefficients α_{p1}, α_{p2}, and α_s, and their standard deviation. We note here that the attenuation profiles in Fig. 7 are different from our previously reported data[24,35] due to the improved assumptions of the permeability and specific loss parameters.

B. AMCOR data

Similar to the AGS data, in the AMCOR case, a geological description of the core layering was given.[31] Data from core 6010 are presented in Fig. 8, with the core description given in Table III. We observe that the core is clay dominated. In this case, rather than the blow count number, the shipboard bulk density was reported. The procedure for determining the physical parameters is different from the AGS case, as demonstrated below.

Figure 8 shows the profile of shipboard measurement density shown as a solid line along with several values from laboratory measurements, shown as triangle symbols. An standard deviation of ± 2.5% was arbitrarily assumed for the density profile and shown as dashed lines. Given the shipboard bulk density profile and assume a sediment grain density $\rho_s = 2.65$ g/cm^3, it is possible to calculate the porosity profile based on Eq. (3). Referring to Table II for grain sizes, the permeability can be calculated from Eq. (45). The shear modulus is then inferred from Eqs. (43) and (44). In Fig. 9, these profiles are shown in solid lines with their standard deviation marked in dashed lines. Similarly, the several labo-

ratory measurements of density are processed to obtain values of porosity, permeability and shear modulus. These are shown in triangle symbols in Fig. 9. The core data also provide at a number of points the grain size diameter d_{mean}. In these cases, the data are still processed using shipboard density, but the permeability is calculated using the measured grain size, rather than that inferred from Table II. These permeability values are plotted as solid circles in Fig. 9.
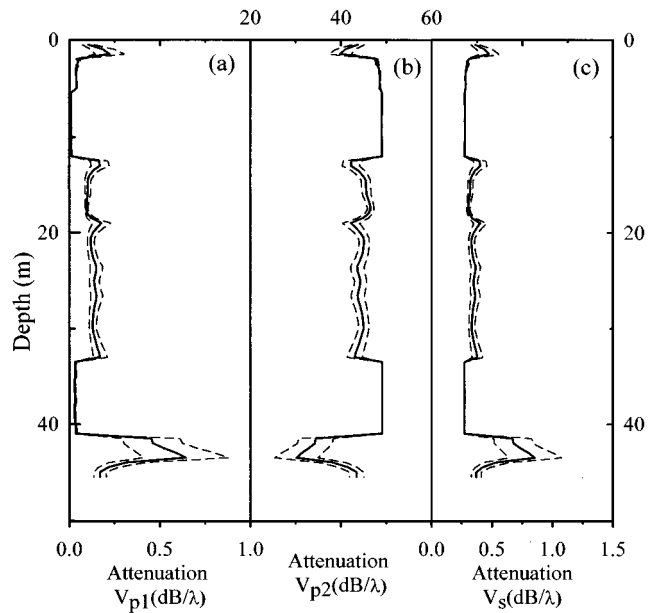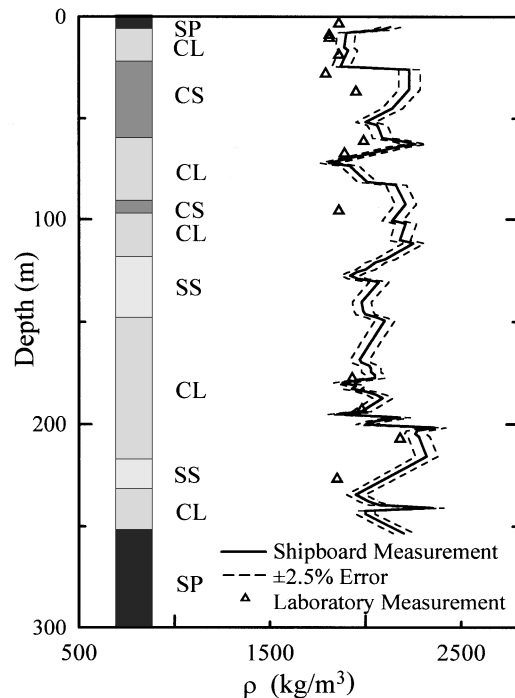
FIG. 8. Profile of core layer description and shipboard density for AMCOR 6010. Density is assumed to be normally distributed with an arbitrary standard deviation of 2.5%.
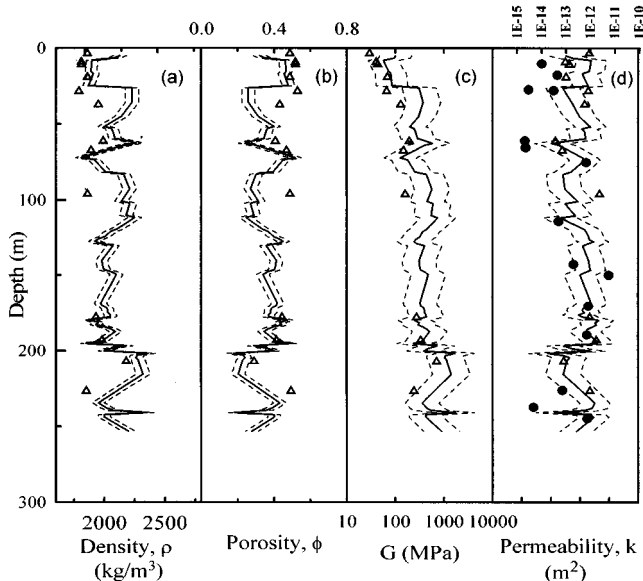
FIG. 9. Measured density profile and calculated profiles of porosity, shear modulus, and permeability for AMCOR 6010. △ corresponding to data based on laboratory measured density, and ● are based on measured grain diameters. Solid lines are mean values and dash lines are ±one standard deviation.

FIG. 10. Predicted sound speed of the first compressional (V_{p1}), second compressional (V_{p2}), and shear (V_s) waves for AMCOR 6010. △ corresponds to data based on laboratory measured density, and ● is based on measured grain diameters. Solid lines are mean values and dash lines are ±one standard deviation.

These profiles and individual data points are used as input for calculating the velocity and attenuation similar to the AGS case. They are respectively shown in Figs. 10 and 11. The attenuation coefficients in Fig. 11 are calculated using $f = 50$ Hz. We observe in Fig. 10 that the calculated V_{p1} and V_s are fairly consistent with each other, despite that different methods are used in their calculation due to different data availability. The consistency of V_{p2} is not as good, but still reasonable.

C. Discussion

In shallow water acoustics very little information about attenuation in bottom sediments is available. The attenuation coefficient is typically provided as a frequency independent parameter and sometimes as a constant throughout the depth. The Biot–Stoll model shows that attenuation is a function of frequency as well as sediment properties such as permeability, porosity, Coulomb friction coefficient, etc. Since very little is known about the depth variation of Coulomb specific loss, in the current calculation constant values, $\delta' = \delta'' = 0.02$ for the AGS site, and $\delta' = \delta'' = 0.025$ for the AMCOR site, have been adopted. Despite the use of constant Coulomb damping coefficients, we find that the calculated attenuation shows a large variation in depth. This is true for α_{p1}, α_{p2}, and α_s in Fig. 7, and α_{p1} in Fig. 11. α_{p2} and α_s in Fig. 11, however, show little variation in depth. These characteristics can be explained by the functional behavior of attenuation coefficient in Fig. 2 and their asymptotic formulae in Sec. III.

As we observe from the asymptotic formulae (24), (25), (28), (30), (37), and (38), attenuation coefficients are generally frequency dependent, except for cases of very low and very high frequencies. When the frequency terms are not negligible, material properties such as density, porosity, and permeability play a large role in the value of attenuation coefficient. A variation in depth of these parameters is then translated into variations in attenuation coefficients. This is the case for the AGS core example, which is a hard sediment, at $f = 300$ Hz. For the AMCOR case, it is a soft sediment. Around $f = 50$ Hz we observe from Fig. 2(b) that Q_s^{-1} and Q_{p2}^{-1} are roughly constant. In fact, the asymptotic formulae (24) and (37) show that $Q_s^{-1} \approx \delta'$ and $Q_{p2}^{-1} \approx 2$. These
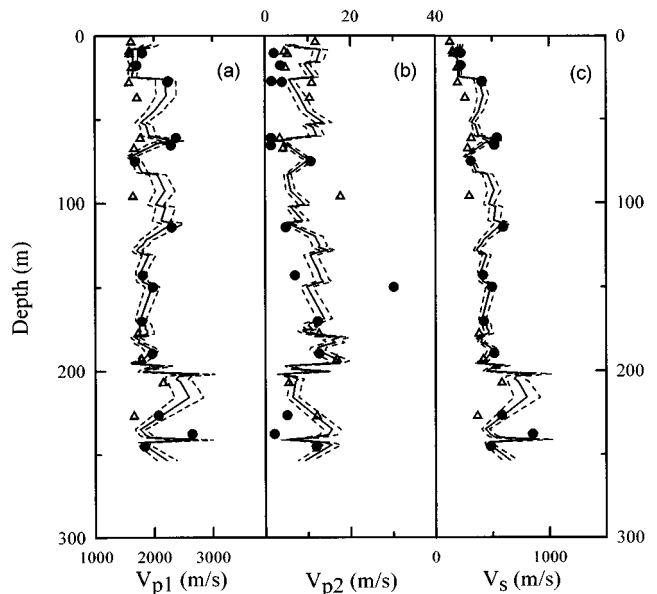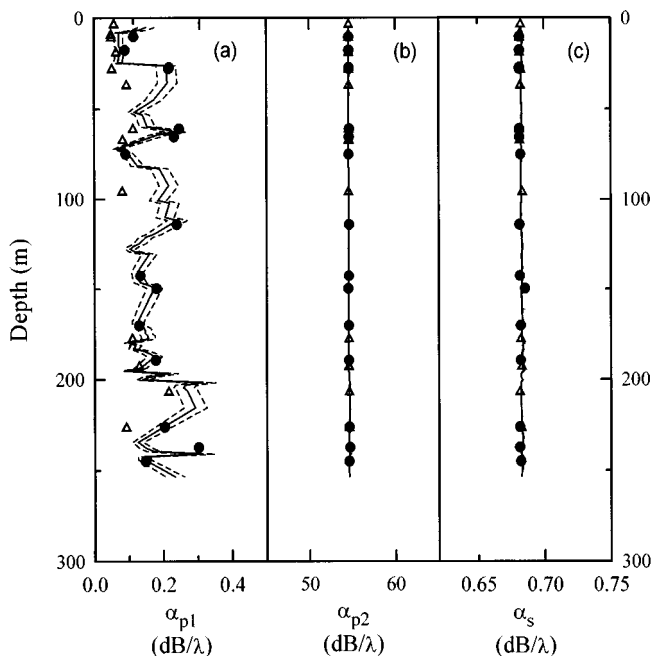
FIG. 11. Predicted attenuation at 50 Hz for first compressional (α_{p1}), second compressional (α_{p2}), and shear (α_s) waves for AMCOR 6010. △ corresponds to data based on laboratory measured density, and ● is based on measured grain diameters. Solid lines are mean values and dash lines are ±one standard deviation.
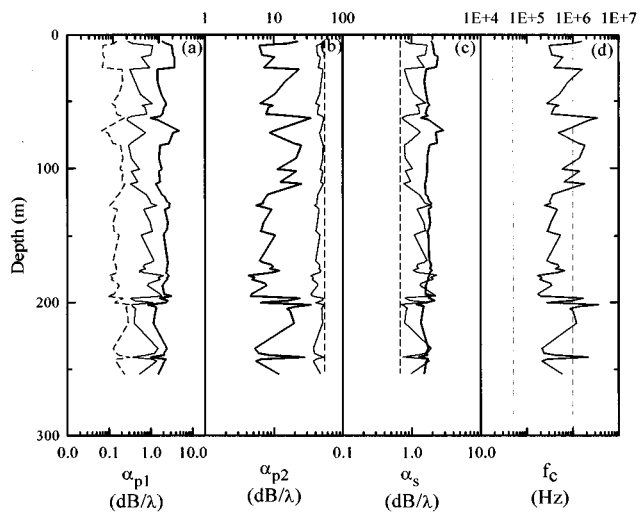
FIG. 12. Effect of frequency on attenuation profiles: (a) α_{p1}, (b) α_{p2}, and (c) α_s for AMCOR 6010. Dash lines are calculated at frequency 50 Hz, thin solid lines are at 10^5 Hz, and thick solid lines are at 5×10^6 Hz. (d) Critical frequency f_c as a function of depth (solid line). The two dashed lines mark $f=10^5$ Hz and 5×10^6 Hz.

attenuation coefficients are otherwise independent of material parameters. Hence we observe that they are constants across the depth. This is however not the case for α_{p1} as shown in Fig. 11.

To bring the frequency effect in attenuation into focus, we examine the AMCOR case further. In Fig. 12(a), (b), and (c) we present the three attenuation profiles α_{p1}, α_{p2}, and α_s, respectively. In each figure, the attenuation coefficient is calculated according to three different frequencies: $f=50$ Hz (dashed lines), 10^5 Hz (thin lines), and 5×10^6 Hz (thick lines). For α_{p1} and α_s we observe that attenuation increases with frequency. In making such an observation, we recall from Fig. 2 that attenuation coefficients for the first compressional and shear waves peak around the critical frequency f_c. From Eq. (17) it is observed that f_c is a function of material properties, hence is a function of depth. In Fig. 12(d) we plot f_c versus depth for this core in solid line. We also mark by dashed lines two frequencies used in the previous computation: $f=10^5$ Hz and 5×10^6 Hz. We find that $f=5\times10^6$ is near critical frequency for most part of the core. Hence we expect α_{p1} and α_s to be largest around $f=5\times10^6$. We also notice that the curves of α_{p1} flip over from low frequencies to higher frequencies (Fig. 12). This can be observed from the asymptotic formulae (29) and (30). Physically this is because at low frequencies the attenuation is mainly caused by the viscous resistance, and at higher frequencies by the inertia resistance. For α_{p2}, Fig. 2 shows that maximum attenuation takes place at the lowest frequency. This is reflected in Fig. 12(b). Finally, we note that at low frequency, both α_{p2} and α_s become constant in depth.

V. SUMMARY

We have examined the acoustic velocity and attenuation in ocean sediments based on the Biot–Stoll theory. Partly due to the complicated mathematical expressions and the large number of physical parameters required to define the model, this theory has not gained a wide usage in the acoustic community.

In this paper the expressions for sound speed and their relation to the various physical parameters are clearly presented. Using a hard and a soft sediment cases presented by Stoll and Kan[3] as examples, the frequency dependence of sound speed is demonstrated. The role of a critical frequency f_c in the sound speed frequency dependence is identified. Next, the frequency dependence of attenuation coefficients is demonstrated. Asymptotic formulae are presented at low, high, and critical frequencies. The asymptotic formulae clearly separate the contribution of attenuation to a Coulomb friction part, which is independent of frequency, and a viscous fluid part, which is a function of frequency, density, porosity, viscosity, etc.

In view of the practical difficulty in applying Biot–Stoll theory due to the lack of measured data, we have proposed empirical procedures in which only a minimum amount of sediment property measurements are necessary. Geotechnical data such as blow count number from Standard Penetration Test, or shipboard bulk density measurements can be used to infer other sediment properties such that wave speed and attenuation can be interpreted. Two different geological cores, one from the AGS site and one from the AMCOR site are used for demonstration. We note that data interpreted from these cores have been used as input to acoustic models elsewhere.[28,36,37] Due to the lack of information, the attenuation coefficients are normally considered as constants. The current analysis, however, shows that the attenuation profiles are generally strong functions of frequency and sediment depth.

In conclusion, by a compilation of existing empirical relations we are able to construct a complete procedure for the evaluation of sediment sound speed and attenuation using a minimum amount of information. We recognize that the accuracy of some of the empirical relations needs improvement. However, given the alternative of making a guess without sound basis, the current practice will allow an estimate within a reasonable range for shallow water acoustic modeling purposes.

ACKNOWLEDGMENTS

APPENDIX A: TABLE OF NOMENCLATURE

a	pore size factor (m)
c	added mass coefficient
f	frequency (Hz)
f_c	critical frequency (Hz)
k	intrinsic permeability (m^2)
l	wave number
F	viscosity correction factor
G	complex shear modulus (Pa)

G_0	shear modulus (Pa)
K	complex bulk modulus of frame (Pa)
K_0	bulk modulus of frame (Pa)
K_f	bulk modulus pore fluid (Pa)
K_s	bulk modulus of sediment grain (Pa)
N	blow count number
Q	quality factor
Q^{-1}	attenuation coefficient per wave cycle
S_u	ultimate shear strength
V_{p1}	fast compressional wave velocity (m/s)
V_{p2}	slow compressional wave velocity (m/s)
V_s	shear wave velocity (m/s)
α	attenuation coefficient (dB/λ)
δ	log decrement
δ'	Coulomb specific loss of shear deformation
δ''	Coulomb specific loss of volumetric deformation
ϵ	void ratio
η	pore geometry factor
λ	wave length
μ_f	fluid dynamic viscosity (kg/m·s)
ρ	bulk density (kg/m^3)
ρ_f	density of pore fluid (kg/m^3)
ρ_s	density of sediment grain (kg/m^3)
σ_0	overburden pressure (Pa)
ϕ	porosity
ω	angular frequency (rad/s)

APPENDIX B: DERIVATION OF ASYMPTOTIC EXPRESSIONS

We present here a derivation of the asymptotic expressions of the inverse of quality factor Q^{-1}. The presentation is aimed at providing a clue than being complete in derivation.

To avoid taking square root of complex variable, we rewrite Eq. (21) as follows:

$$Q^{-1} = 2 \frac{|V|^2}{|\text{Im}(V^2)|} \left[1 \mp \sqrt{1 - \left(\frac{|\text{Im}(V^2)|}{|V^2|} \right)^2} \right]. \qquad (B1)$$

In the above the sign $\mp$ takes the negative value for all cases except for the second compression wave at low frequency. In that particular case, $\text{Im}(V_{p2}^2) > \text{Re}(V_{p2}^2)$ [see Fig. 1(a) and (b)] and the positive sign is taken. For all other cases, we observe that the condition $\text{Re}(V^2) \gg \text{Im}(V^2)$ is satisfied at high and low frequencies. This allows us to approximate

$$Q^{-1} \approx \frac{|\text{Im}(V^2)|}{|V^2|}. \qquad (B2)$$

We notice from the sound speed definitions (1) and (2) that the dependence of frequency is entirely contained in the term m' defined in Eq. (11). The asymptotic behavior of m' is such:

$$m' \approx \frac{1+c}{\phi} \rho_f + \frac{\eta^2 \rho_f}{24\phi} - i \frac{\rho_f}{\phi} \frac{f_c}{f} \quad \text{as } f \to 0 \qquad (B3)$$

$$\approx \frac{1+c}{\phi} \rho_f - i \frac{\sqrt{2}\eta\rho_f}{8\phi} \left(\frac{f_c}{f} \right)^{1/2} \quad \text{as } f \to \infty. \qquad (B4)$$

Since asymptotic results for shear wave is relatively easy to obtain, only the compressional wave cases are discussed here. Under the assumptions of $K_s \gg K_f \gg K$, and $\delta', \delta'' \ll 1$, the following approximations are obtained:

$$H \approx \frac{K_f}{\phi} + i \left(\frac{4}{3} G_0 \delta' + K_0 \delta'' \right), \qquad (B5)$$

$$M \approx \frac{K_f}{\phi}, \qquad (B6)$$

$$C \approx \frac{K_f}{\phi}. \qquad (B7)$$

However, in evaluating the quantity $HM - C^2$ in the numerator of Eq. (1), more terms are kept for H:

$$H \approx \frac{K_f}{\phi} + K_0 + \frac{4}{3} G_0 + i \left(\frac{4}{3} G_0 \delta' + K_0 \delta'' \right), \qquad (B8)$$

such that

$$HM - C^2 \approx \frac{K_f}{\phi} \left[K_0 + \frac{4}{3} G_0 + i \left(K_0 \delta'' + \frac{4}{3} G_0 \delta' \right) \right]. \qquad (B9)$$

Next, we examine the denominator of Eq. (1). We define

$$B = \rho M + m'H - 2\rho_f C \qquad (B10)$$

and

$$\Delta = B^2 - A = 4(HM - C^2)(\rho m' - \rho_f^2). \qquad (B11)$$

It is noticed that $B^2 \approx A$, and Δ/B^2 is a small quantity. Based on Taylor series expansion, we can approximate

$$B + A^{1/2} \approx 2B - \frac{\Delta}{2B}, \qquad (B12)$$

$$B - A^{1/2} \approx \frac{\Delta}{2B} + \frac{\Delta^2}{8B^3}. \qquad (B13)$$

We further approximate B in Eq. (B10) as

$$B \approx \frac{K_f}{\phi} [\rho - 2\rho_f + m'(1 + i\delta_H)]. \qquad (B14)$$

Substituting the above into Eq. (1) and taking Taylor series expansion for small f (low-frequency approximation) or $1/f$ (high-frequency approximation), we can obtain: at low frequency

$$V_{p1}^2 \approx \frac{K_f}{\phi\rho} + i\delta_H \frac{K_f}{\phi\rho} + i \frac{(\rho - \rho_f)^2 K_f}{\rho_f \rho^2} \frac{f}{f_c}, \qquad (B15)$$

and at high frequency

$$V_{p1}^2 \approx \frac{(1+c)\rho_B K_f}{\phi \rho_f \rho_A} + i\delta_H \frac{(1+c)(1+c-\phi)^2 \rho_f K_f \delta_H}{\phi \rho_A \rho_B}$$
$$+ i \frac{\sqrt{2}\eta(1+c)^2 K_f}{8\rho_f \rho_A^2} \left(\frac{f_c}{f} \right)^{1/2}. \qquad (B16)$$

From the above we find

$$\frac{|\mathrm{Im}(V_{p1}^2)|}{|V_{p1}^2|} \approx \delta_H + \frac{\phi(\rho-\rho_f)^2}{\rho\rho_f}\frac{f}{f_c} \quad \text{as} \ f\to 0 \tag{B17}$$

$$\approx \frac{(1+c-\phi)^2\rho_f^2}{\rho_B^2}\,\delta_H$$

$$+ \frac{\sqrt{2}\,\eta\phi(1+c)(\rho-\rho_f)^2}{8\rho_A\rho_B}$$

$$\times\left(\frac{f_c}{f}\right)^{1/2} \quad \text{as} \ f\to\infty. \tag{B18}$$

Without detailed derivation, we also present

$$\frac{|\mathrm{Im}(V_{p2}^2)|}{|V_{p2}^2|} \approx 1 - \frac{1}{2}\,\delta_0^2 + \delta_0\left(\frac{\rho_B}{\rho_f}+\frac{\eta^2}{24}\right)\frac{f}{f_c} \quad \text{as} \ f\to 0 \tag{B19}$$

$$\approx \delta_0 + \frac{\sqrt{2}\,\eta\rho_f}{8\rho_B}\left(\frac{f_c}{f}\right)^{1/2} \quad \text{as} \ f\to\infty, \tag{B20}$$

$$\frac{|\mathrm{Im}(V_s^2)|}{|V_s^2|} \approx \delta' + \frac{\phi\rho_f}{\rho}\frac{f}{f_c} \quad \text{as} \ f\to 0 \tag{B21}$$

$$\approx \delta' + \frac{\sqrt{2}\,\eta\phi\rho_f}{8\rho_A}\left(\frac{f_c}{f}\right)^{1/2} \quad \text{as} \ f\to\infty. \tag{B22}$$

The inverse of quality factor Q^{-1} can then be obtained from either Eq. (B1) or (B2).

[1] M. A. Biot, ''Theory of propagation of elastic waves in a fluid-saturated porous solid, Part I: Low frequency range,'' J. Acoust. Soc. Am. **28**, 168–178 (1956).

[2] M. A. Biot, ''Theory of propagation of elastic waves in a fluid-saturated porous solid, Part II: Higher frequency range,'' J. Acoust. Soc. Am. **28**, 179–191 (1956).

[3] R. D. Stoll and T. K. Kan, ''Reflection of acoustic waves at a water–sediment interface,'' J. Acoust. Soc. Am. **70**, 149–156 (1981).

[4] C. A. Kibblewhite, ''Attenuation of sound in marine sediments: A review with emphasis on new low-frequency data,'' J. Acoust. Soc. Am. **86**, 716–728 (1989).

[5] Dames and Moore, ''Supplementary subsurface investigation: Vibrocore program, Atlantic Generating Station, for the Public Service Electric and Gas Company, Newark, NJ'' (1974).

[6] H. J. Miller and C. Dill, ''Final Report, Geophysical investigation of Atlantic Generating Station site and offshore region, for the Public Service Electric and Gas Company, Newark, NJ'' (1974).

[7] C. J. Hathaway, C. W. Poag, C. P. Valentine, E. R. Miller, M. D. Schultz, T. F. Manheim, A. F. Kohout, H. M. Bothner, and A. D. Sangrey, ''U.S. Geological Survey core drilling on the Atlantic Shelf,'' Science **206**, 515–527 (1979).

[8] T. Yamamoto, ''Acoustic propagation in the ocean with a poro-elastic bottom,'' J. Acoust. Soc. Am. **73**, 1587–1596 (1983).

[9] M. Badiey, A. H-D. Cheng, and I. Jaya, ''Propagator matrix for plane wave reflection from inhomogeneous anisotropic poroelastic seafloor,'' J. Comput. Acoust. **2**, 11–27 (1994).

[10] M. Abramowitz and I. A. Stegun, *Handbook of Mathematical Functions* (Dover, New York, 1972).

[11] R. D. Stoll, *Sediment Acoustics* (Springer-Verlag, New York, 1989).

[12] G. Bonnet and J.-L. Auriault, ''Dynamics of saturated and deformable porous media: Homogenization theory and determination of the solid-liquid coupling coefficients,'' in *Physics of Finely Divided Matter*, edited by N. Boccara and M. Daoud (Springer-Verlag, New York, 1985), pp. 306–316.

[13] N. P. Chotiros, ''Biot model of sound propagation in water-saturated sand,'' J. Acoust. Soc. Am. **97**, 199–214 (1995).

[14] B. Yavari and A. Bedford, ''Comparisons of numerical calculations of two Biot coefficients with analytical solutions,'' J. Acoust. Soc. Am. **90**, 985–990 (1991).

[15] T. Yamamoto, ''Propagator matrix for continuously layered porous sea-beds,'' Bull. Seismol. Soc. Am. **73**, 1599–1620 (1983).

[16] A. Turgut and T. Yamamoto, ''Synthetic seismograms for marine sediments and determination of porosity and permeability,'' Geophysics **53**, 1056–1067 (1988).

[17] T. Yamamoto, ''On the response of a Coulomb-damped poroelastic bed to water waves,'' Mar. Geotechnol. **5**, 93–130 (1983).

[18] E. L. Hamilton, ''Geoacoustic modeling of the seafloor,'' J. Acoust. Soc. Am. **68**, 1313–1340 (1980).

[19] J. I. Dunlop, ''Propagation of acoustic waves in marine sediments, A review,'' Explor. Geophys. **19**, 513–535 (1988).

[20] B. O. Hardin, ''The nature of damping in sands,'' J. Soil Mech. Found. Div., ASCE **91**, 63–97 (1965).

[21] T. W. Lambe and R. V. Whitman, *Soil Mechanics* (Wiley, New York, 1969).

[22] Y. Ohsaki and R. Iwasaki, ''On dynamic shear moduli and Poisson's ratios of soil deposits,'' J. Soils Found., Jpn. Soc. Soil Mech. Found. Eng. **13**, 61–73 (1973).

[23] F. Tatsuoka and S. Shibuya, ''Deformation characteristics of soil and rocks from filed and laboratory tests,'' Report of the Institute of Industrial Science, Univ. Tokyo, **37** (1992).

[24] M. Badiey, I. Jaya, and A. H-D. Cheng, ''A shallow water acoustic/geoacoustic experiment near the New Jersey Atlantic Generating Station site,'' J. Acoust. Soc. Am. **96**, 3593–3604 (1994).

[25] M. V. Trevorrow, T. Yamamoto, M. Badiey, A. Turgut, and C. Conner, ''Experimental verification of seabed shear modulus profile inversions using surface gravity (water) wave-induced seabed motion,'' Geophys. J. Int. **93**, 419–436 (1988).

[26] M. V. Trevorrow and T. Yamamoto, ''Summary of marine sedimentary shear modulus and acoustic speed profile results using a gravity wave inversion technique,'' J. Acoust. Soc. Am. **90**, 441–456 (1991).

[27] G. M. Bryan and R. D. Stoll, ''The dynamic shear modulus of marine sediments,'' J. Acoust. Soc. Am. **83**, 2159–2164 (1988).

[28] T. Yamamoto, M. V. Trevorrow, M. Badiey, and A. Turgut, ''Determination of the seabed porosity and shear modulus profiles using a gravity wave inversion,'' Geophys. J. Int. **98**, 173–182 (1989).

[29] W. R. Brant, W. Hattman, and P. Trabant, ''Permeability of unconsolidated and consolidated marine sediments, Gulf of Mexico,'' Mar. Geotechnol. **1**, 1–14 (1975).

[30] P. C. Carman, *Flow of Gases through Porous Media* (Academic, New York, 1956).

[31] L. J. Poppe, ''The 1976 Atlantic Margin Coring (AMCOR) Project of the U.S. Geological Survey,'' U.S. Geological Survey Open-File Report 81-239 (1981).

[32] E. L. Hamilton, ''Elastic properties of marine sediments,'' J. Geophys. Res. **76**, 579–604 (1971).

[33] J. Ewing, J. A. Carter, G. H. Sutton, and N. Barstow, ''Shallow water sediment properties derived from high frequency shear and interface waves,'' J. Geophys. Res. **92**, 4739–4762 (1992).

[34] M. Badiey, A. H-D. Cheng, and Y. Mu, ''Statistical analyses of acoustical wave velocity in porous seafloor,'' Proc. 11th ASCE Eng. Mech. Conf., edited by Y. K. Lin and T. C. Su, pp. 800–803 (1996).

[35] M. Badiey, A. H-D. Cheng, and I. Jaya, ''Deterministic and stochastic analyses of acoustic plane-wave reflection from inhomogeneous porous seafloor,'' J. Acoust. Soc. Am. **99**, 903–913 (1996).

[36] W. M. Carey, J. Doutt, R. B. Evans, and L. M. Dillman, ''Shallow-water sound transmission measurements on the New Jersey Continental Shelf,'' IEEE J. Ocean Eng. **20**, 321–336 (1995).

[37] M. Badiey, K. P. Bongiovanni, and W. L. Siegmann, ''Analysis and model/data comparison of broadband acoustic propagation at the Atlantic Generating Station (AGS) site,'' J. Acoust. Soc. Am. **101**, 1921–1935 (1997).

Separation of current and sound speed in the effective refractive index for a turbulent environment using reciprocal acoustic transmission

Daniela Di Iorio[a)] and David M. Farmer
Institute of Ocean Sciences, P.O. Box 6000, Sidney, British Columbia V8L 4B2, Canada

Here a high-frequency acoustic experiment through a turbulent flow in Cordova Channel is described which is specifically designed to measure the contribution of scalar and vector fluctuations to the total scattered signal over a 48-h period. The effective refractive index fluctuations are determined by both the random changes in sound speed (scalars) and the random motion of the medium (vectors), and so in this paper it is demonstrated that reciprocal acoustic transmission is a technique which unambiguously separates their effects. The effective refractive index structure parameter, $C_{\eta_{\mathrm{eff}}}^2$ is defined as the sum of scalar $C_{\eta_s}^2$ and vector $C_{\eta_v}^2$ contributions through the equation $C_{\eta_s}^2 + 11/6 C_{\eta_v}^2$. The effective refractive index structure parameter is also measured from the forward propagation acoustical scintillation variances, thus providing an independent check on the interpretation. © *1998 Acoustical Society of America.* [S0001-4966(97)00411-6]

PACS numbers: 43.30.Pc, 43.30.Re [JHM]

INTRODUCTION

The coastal environment of British Columbia is often characterized by enhanced mixing of water properties due to strong tidal currents; an important example is provided by the mixing of fresh water runoff and oceanic water in the tidal passes separating the Straits of Georgia and Juan de Fuca. Some of this mixing takes place in the relatively shallow and narrow channels formed by the coastal islands. In this paper we describe an acoustic experiment carried out in September 1994, in Cordova Channel (see Fig. 1) specifically designed to measure the separate contributions of temperature/salinity and current variability to the total scattered signal and compare those measurements to available theory. The experiment described and the results obtained differ from the 1986 experiment in Cordova Channel in that we also measure reciprocal travel time.

Sound propagation is sensitive to random variations in the effective refractive index which is a function of scalar (temperature/salinity) and vector (medium motion) fluctuations.[1] The variability of sound speed and the resolved component of flow along the acoustic path contribute to the measurement of acoustic fluctuations. Di Iorio and Farmer[2] showed that the velocity fluctuations can be a dominant source of acoustic scattering and in this paper we show that the random variations in temperature and salinity also contribute to the total scattered signal. Without independent measurements of the temperature/salinity or turbulent intensity structure it is impossible to determine from propagation in a single direction which physical parameter contributes to the total scattered signal and in what proportion. Since independent measurements are usually at point locations the comparison to path-averaged acoustic measurements can show significant differences.

Path-averaged measurements of turbulent sound speed

(hence temperature) and current have some unique advantages to traditional measurements at point locations. First, local anomalies in turbulent flow which can be caused by topography are averaged out and hence may be more valuable for input and comparison to transport models. Second, a reciprocal acoustic scintillation system can be easily deployed in coastal waters over a long period of time and used to monitor transport, mixing, and circulation patterns in real time.

In past experiments in Cordova Channel, Di Iorio and Farmer[3] made independent measurements of the sound speed by sampling the temporal variations of temperature and salinity. In this paper we make use of forward and reciprocal acoustic transmission to obtain path-averaged measurements of both the sound speed and current speed along the acoustic path, thus giving the effective refractive index. With these measurements we compute both the structure parameter (C_η^2) and the effective structure parameter ($C_{\eta_{\mathrm{eff}}}^2$) for comparison with the scintillation variances from one way propagation.

In Sec. I of this paper we summarize the theoretical results of Tatarskii[4] and Ostachev[5] so that we can make direct comparison with our acoustic observations. Mathematical results are stated without derivations since more complete discussions are found in the references. In Sec. II we describe the experiment which follows earlier experimental design in Cordova Channel. Oceanographic measurements using the forward-scattered signal and reciprocal acoustic measurements are discussed in Secs. III and IV. Comparison of the forward-scattered signal to the intensity of scalar and vector fluctuations is then carried out in the discussion of Sec. V.

I. THEORETICAL BACKGROUND

A. Sound propagation in a moving random medium

The Helmholtz equation for wave propagation in a moving random medium is

---

[a)]Present affiliation is SACLANT Undersea Research Centre, Viale San Bartolomeo 400, 19138 La Spezia, Italy.
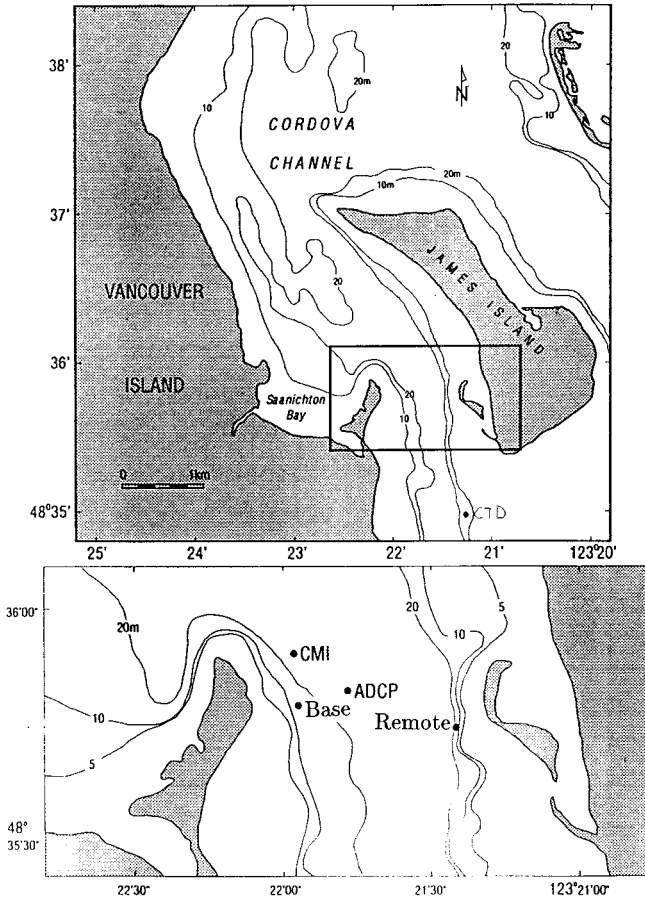
FIG. 1. Cordova Channel showing the location of the acoustic remote and base sites together with moored oceanographic instrumentation. A mooring consisting of one current meter and two CTDs is at CM1 and an acoustic Doppler current profiler is at ADCP.

$$\nabla^2 p(\mathbf{r}) + n^2(\mathbf{r})k^2 p(\mathbf{r}) = -2ikn^2(\mathbf{r})\frac{\mathbf{u}\cdot\nabla p(\mathbf{r})}{c_0}, \qquad (1)$$

where $n(\mathbf{r})$ is the refractive index of the medium due to sound speed changes from temperature and salinity (scalars), k is the acoustic wave number, and c_0 is the mean sound speed. Orders of u^2/c^2 have been neglected. This equation is a simplified form of the full linearized sound pressure equation obtained by Ostachev[5] since we neglect gradients of oceanographic properties.

Following Tatarskii[4] the transformation $\Psi(\mathbf{r}) = \ln p(\mathbf{r})$ and the perturbations

$$n = n_0 + \eta_s \sim 1 + \eta_s, \qquad (2)$$

$$\Psi = \Psi_0 + \Psi_1 \qquad (3)$$

result in zeroth- and first-order equations:

$$\nabla^2 \Psi_0 + \nabla \Psi_0 \cdot \nabla \Psi_0 = -k^2, \qquad (4)$$

$$\nabla^2 \Psi_1 + 2\nabla\Psi_0\cdot\nabla\Psi_1 = -2\eta_s k^2 - 2ik\frac{\mathbf{u}\cdot\nabla\Psi_0}{c_0}. \qquad (5)$$

Here η_s is the refractive index fluctuations from scalar fluctuations (temperature and salinity) and u/c_0 is considered first order.

The solution to the zeroth-order equation is $p_0 = (Q/r)e^{ikr}$ which corresponds to outward spherical wave propagation in a medium with no motion and no refractive index variability. Given the zeroth-order solution, the first-order equation is

$$\nabla^2 \Psi_1 + 2\nabla\Psi_0\cdot\nabla\Psi_1 = -2\eta_{\text{eff}}k^2, \qquad (6)$$

where the effective refractive index is

$$\eta_{\text{eff}} = \eta_s - \frac{\mathbf{u}\cdot\hat{n}}{c_0} - \frac{i}{kr}\frac{\mathbf{u}\cdot\hat{n}}{c_0}, \qquad (7)$$

$$\sim \eta_s - \frac{\mathbf{u}\cdot\hat{n}}{c_0}. \qquad (8)$$

The unit vector directed along the incident acoustic wave number is denoted as $\hat{n}$. The last equality arises since $kr \gg 1$ and hence the imaginary term can be ignored when looking at the statistics of η_{eff}. Thus, the equations reduce to the plane wave perturbations of Tatarskii.[4] The solution to (6) follows the theoretical work of Tatarskii,[4] provided we work with the statistics for the effective refractive index fluctuations (see Ref. 5).

B. Statistics for Kolmogorov turbulence

Following Tatarskii[4] and Ostachev,[5] the structure function for the effective refractive index fluctuations is

$$D_{\text{eff}}(\mathbf{r}) = D_{\eta_s}(\mathbf{r}) + \frac{n_j n_k D_{jk}(\mathbf{r})}{c_0^2}, \qquad (9)$$

and the three-dimensional spectrum is

$$\Phi_{\text{eff}}(\mathbf{K}) = \Phi_{\eta_s}(\mathbf{K}) + \frac{n_j n_k \Phi_{jk}(\mathbf{K})}{c_0^2}. \qquad (10)$$

Inherent in these equations is the assumption that the scalar and vector fluctuations are uncorrelated (i.e., $\langle \eta_s u_j \rangle = 0$).

Assuming isotropic and homogeneous turbulence it follows that the structure function is

$$D_{\eta_s}(r) = C_{\eta_s}^2 r^{2/3}, \qquad (11)$$

and the three-dimensional spectrum is

$$\Phi_{\eta_s}(K) = 0.033 C_{\eta_s}^2 K^{-11/3}, \qquad (12)$$

where $C_{\eta_s}^2$ characterizes the level of the refractive index fluctuations from scalars (temperature, salinity) and the multiplier 0.033 in (12) is an integration constant (see Ref. 6). The structure function tensor is

$$D_{jk}(r) = \tfrac{1}{3}C_v^2 r^{2/3}(4\delta_{jk} - m_j m_k), \qquad (13)$$

where m is the unit vector directed along $\mathbf{r}$, δ_{jk} is the Kronecker function, and C_v^2 is the structure parameter for velocity fluctuations. The three-dimensional energy spectrum tensor is (see Ref. 7)

$$\Phi_{jk}(K) = \frac{E(K)}{4\pi K^2}\left(\delta_{jk} - \frac{K_j K_k}{K^2}\right), \qquad (14)$$

where the energy spectrum $E(K)$ is defined such that the total turbulent kinetic energy per unit mass is

$$\frac{1}{2}\langle u_j u_j\rangle = \int_0^{-\infty} E(K)dK. \tag{15}$$

Also it can be shown that

$$\frac{E(K)}{4\pi K^2} = 0.033\left(\frac{11}{6}\,C_v^2\right)K^{-11/3}. \tag{16}$$

For $E(K) = 1.5\epsilon^{2/3}K^{-5/3}$ within the inertial subrange, the level of the turbulent velocity fluctuations is related to the turbulent kinetic energy dissipation rate by $C_v^2 = 1.97\epsilon^{2/3}$.

If we insert Eqs. (11)–(14) into (9) and (10), then it can be shown that the statistics for the effective refractive index reduce to

$$D_{\mathrm{eff}}(r) = C_{\eta_s}^2 r^{2/3} + \frac{C_v^2}{c_0^2}\left(1 + \frac{\sin^2\alpha}{3}\right)r^{2/3}, \tag{17}$$

$$= (C_{\eta_s}^2 + C_{\eta_v}^2)r^{2/3}, \tag{18}$$

$$= C_\eta^2 r^{2/3}, \tag{19}$$

$$\Phi_{\mathrm{eff}}(K) = 0.033 C_{\eta_s}^2 K^{-11/3} + \frac{E(K)}{4\pi K^2 c_0^2}\cos^2(\theta/2) \tag{20}$$

$$= 0.033\left(C_{\eta_s}^2 + \tfrac{11}{6}C_{\eta_v}^2\right)K^{-11/3} \tag{21}$$

$$= 0.033 C_{\eta_{\mathrm{eff}}}^2 K^{-11/3}, \tag{22}$$

where $C_{\eta_v}^2 = C_v^2/c_0^2$, $\cos\alpha = \hat{n}\cdot\hat{m}$ and represents the angle between the acoustic propagation direction and the vector $\mathbf{r}$, and θ is the acoustic scattering angle which equals zero for forward-scattered waves. If we write $\mathbf{r} = \mathbf{r}_\perp + \mathbf{r}_\parallel$ in terms of vectors perpendicular and parallel to acoustic propagation then $\tan\alpha = r_\perp/r_\parallel \sim 0$ as the propagation path becomes much greater than $r_\perp$.[5] The constant C_η^2 is defined as the structure parameter and $C_{\eta_{\mathrm{eff}}}^2$ is the effective structure parameter both for the effective refractive index fluctuations. Note that $C_\eta^2 \neq C_{\eta_{\mathrm{eff}}}^2$.

In the early work of Tatarskii[4] the structure parameter was used to define the level of the refractive index fluctuations. According to the recent work of Ostachev,[5] the effective structure parameter is the correct form to use and we will test this result with our measurements.

Thus far we have shown the three-dimensional statistics for scalar and vector random variables. However, our measurements are in general limited to one-dimensional spectral statistics. Writing the energy spectrum for velocity fluctuations as $E(K) \propto K^{-p}$, then it can be shown that (see Ref. 8) the one-dimensional spectrum is

$$F_\theta(K_1) = \int_{K_2}\int_{K_3}\Phi_\theta(\mathbf{K})dK_2\,dK_3 \tag{23}$$

$$= 4\pi(0.033)\left(\frac{11}{6}C_v^2\right)K_1^{-p}\frac{\cos^2\theta + p\sin^2\theta + 1}{2p(p+2)}, \tag{24}$$

where the velocity component is measured along the angle θ from the x axis [in the (x,y) plane]. For isotropic turbulence in the inertial subrange $p = \frac{5}{3}$. For scalars the one-dimensional spectrum is

$$F_{\eta_s}(K_1) = \int_{K_2}\int_{K_3}\Phi_{\eta_s}(\mathbf{K})dK_2\,dK_3 \tag{25}$$

$$= 4\pi(0.033)C_{\eta_s}^2 K_1^{-p}\frac{1}{2p}, \tag{26}$$

which has no angular dependence.

C. Path-averaging effects

Our current and sound speed measurements from reciprocal acoustic transmissions are averaged along the path. Thus the path-averaged effective refractive index is

$$\widetilde{\eta}_{\mathrm{eff}} = \widetilde{\eta}_s - \frac{\overline{u}_\theta}{c_0}, \tag{27}$$

where the velocity component is measured along the angle θ from the x axis. Proceeding as before we can write the three- and one-dimensional spectra as

$$\widetilde{\Phi}_{\mathrm{eff}}(\mathbf{K}) = \widetilde{\Phi}_{\eta_s}(\mathbf{K}) + \frac{\widetilde{\Phi}_\theta(\mathbf{K})}{c_0^2}, \tag{28}$$

$$\widetilde{F}_{\mathrm{eff}}(K_1) = \widetilde{F}_{\eta_s}(K_1) + \frac{\widetilde{F}_\theta(K_1)}{c_0^2}. \tag{29}$$

Following the method of Menemenlis,[8] and extending the theory to scalar refractive index fluctuations, the path-averaged one-dimensional spectrum for refractive index fluctuations from scalars is

$$\widetilde{F}_{\eta_s}(K_1) = \frac{4\pi(0.033)C_{\eta_s}^2 K_1^{-p}}{K_1 L}\frac{G(p)}{p}\sin^p\theta, \tag{30}$$

and from vectors it is

$$\widetilde{F}_{\eta_v}(K_1) = \frac{\widetilde{F}_\theta(K_1)}{c_0^2}$$

$$= \frac{4\pi(0.033)(11/6)C_{\eta_v}^2 K_1^{-p}}{K_1 L}\frac{G(p)}{p}\sin^p\theta, \tag{31}$$

where $G(p) = \Gamma(1/2)\Gamma(p/2 + 1/2)/\Gamma(p/2) = 1.4022$ for $p = \frac{5}{3}$. This analytical solution is obtained because the measuring baseline is much longer than the turbulent scales of interest (i.e., $K_1 L\sin\theta \gg 4\pi$).

Since temporal measurements are made instead of spatial ones, we invoke the Taylor hypothesis to transform from wave number to frequency space:

$$\widetilde{F}_{\mathrm{eff}}(f) = \widetilde{F}_{\mathrm{eff}}\left(K_1 = \frac{2\pi f}{U}\right)\frac{2\pi}{U}, \tag{32}$$

where U is the current magnitude. By measuring $\widetilde{F}_{\eta_s}(f)$ and $\widetilde{F}_{\eta_v}(f)$ we can determine $C_{\eta_s}^2$ and $C_{\eta_v}^2$ respectively.

II. EXPERIMENTAL APPROACH

The acoustic instrumentation is divided into two sections: a forward and reciprocal system. In the forward direction the instrumentation is the same as that described by Di

323   J. Acoust. Soc. Am., Vol. 103, No. 1, January 1998

D. Di Iorio and D. M. Farmer: Turbulent environment   323

TABLE I. Transducer configuration for acoustic scintillations in Cordova Channel. The base receivers (BR) and transmitter (BT) are on the west side of the Channel and the remote transmitters (RT) and receiver (RR) are on the east side (see Fig. 1).

Base station (west) Cordova Spit	Remote station (east) James Island
BR4	RT4
$\updownarrow$0.61 m	$\updownarrow$0.61 m
BR3	RT3
$\updownarrow$0.61 m	$\updownarrow$0.61 m
BR2	RT2
$\updownarrow$0.60 m	$\updownarrow$0.60 m
BR1	RT1/RR1
$\updownarrow$0.20 m	
BT1	

TABLE II. Acoustic parameters for forward and reciprocal propagation in Cordova Channel.

Observation period (PDT)	28/09/94 10:00h to 30/09/94 07:00h
Remote site location	N48° 35.729′ W123° 21.425′
Base site location	N48° 35.778′ W123° 21.955′
Transducer array depth (m)	19.5
Mean sound speed (m s^{-1})	1491
Path length L (m)	695
Acoustic frequency (Hz)	67567
Acoustic wave number k (m^{-1})	284.7
Fresnel radius $\sqrt{\lambda L}$ (m)	3.9
Transducer separation (m)	$\rho_x=0.6, 1.2, 1.8$
M-sequence code length [bits (ms)]	63 (8.4)
Bit width [cycles/bit (μs/bit)]	9 (133)
Phase shift for coding (deg)	180
Digitization rate [samples/bit (kHz)]	
—forward transmission	3.0 (22.5)
—two reciprocal paths	2.08125 (15.625)
Mean repetition rate (Hz)	
—forward transmission	6.0
—two reciprocal paths	2.5

Iorio and Farmer:[2,3] four remote transmitters (RT) are set up on the east side of Cordova Channel with four base receivers (BR) on the west side, thus giving 16 different transmitter/receiver combinations all processed by one main computer system. Table I outlines the linear configuration with appropriate spacings between transducers. Since the transducers had 10° beam widths, divers were used to align the arrays. The normal of the transmitter and receiver axis was aligned to 278 °T and 98 °T, respectively. For reciprocal propagation a separate transmitter (BT1) was placed next to BR1 on the west side; on the east side, one of the transmitters was also used as a receiver (RT1/RR1). Transmissions were carried out at a repetition rate of 6.0 Hz in both directions.

In addition to UHF radio communication, a cross-channel cable was used to obtain precise travel time information. The signal from the base transmitter (BT1) was detected by the remote receiver (RR1) and sent via underwater cable to the base together with the remote transmit trigger used to calculate true travel time in the forward direction and also used to trigger the reciprocal transmitter. The two reciprocal paths (RT1/BR1, BT1/RR1) were processed with an independent computer and thus, depending on the processing demands and other factors, the data collection rate was variable with a mean of approximately 2.5 Hz. Table II summarizes the experimental parameters for both systems.

A. Amplitude and phase measurements

Incoming signals were complex demodulated, digitized, and then correlated with a template of the transmitted pseudo-random noise (PRN) code. The correlated in-phase (I) and quadrature (Q) data give amplitude,

$$A(t) = \sqrt{I(t)^2 + Q(t)^2}, \qquad (33)$$

as a function of travel time t for each transmitter/receiver combination. Since the correlation peaks can be modeled according to Menemenlis and Farmer,[9] a maximum likelihood estimation (MLE) algorithm, discussed by Di Iorio and Farmer,[10] is used to calculate the amplitude ($\mathscr{A}$) and arrival time ($\mathscr{T}$) that best fit the signal to the model. This method differs from peak detection and triangular interpolation used in past experiments.[2,3]

Figure 2 shows amplitude as a function of relative travel time for signals from RT1/BR1 processed by the forward propagation system. Both the direct and surface-reflected paths are shown. This figure clearly shows a good signal-to-noise ratio of order 28 dB. Superimposed on the received signal is the theoretical correlation peak that best fits (in a least squares sense) the amplitude and arrival time for the direct path.

The MLE technique has some nice advantages to peak detection algorithms. First, it does not require a threshold nor a window for locating an arrival since it uses previous amplitude and travel time information to find the peak characteristics for the next transmission. This can be very important if the amplitude varies substantially or the travel time changes significantly. The second advantage is that the travel time calculation is less noisy than that calculated from triangular or quadratic interpolation. Since the arrival time may
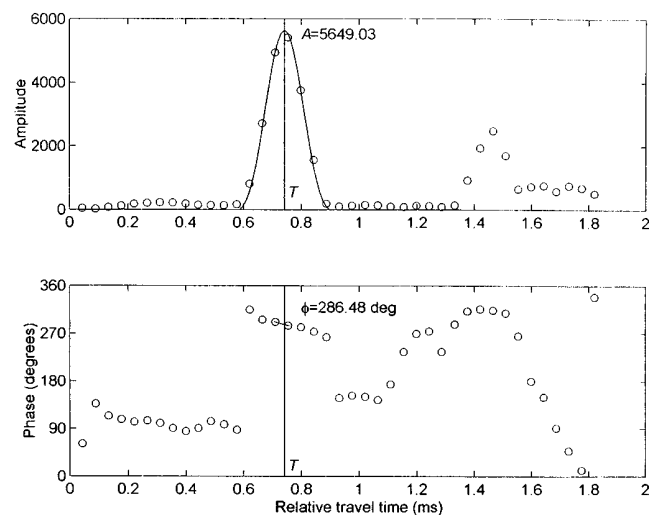

FIG. 2. Amplitude and phase as a function of relative travel time for RT1/BR1 processed by the forward scintillation system. Solid curve on the amplitude is the theoretical least squares fit to the data. Linear interpolation at the arrival time $\mathscr{T}$ gives the phase.
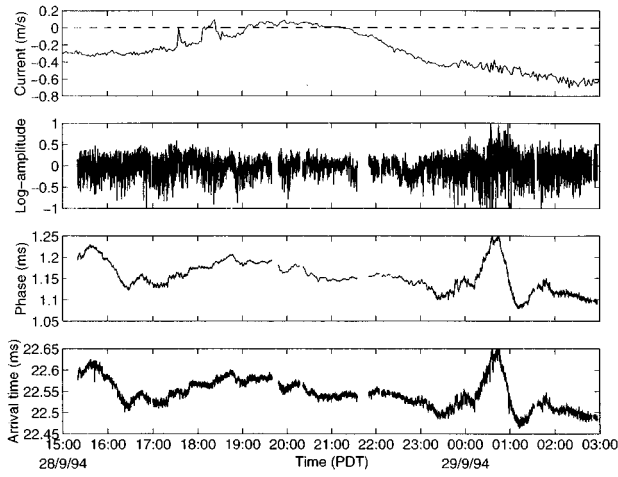
FIG. 3. Log-amplitude (χ), phase (ϕ), and relative arrival time ($\mathscr{T}$) for 12 h of data from the forward propagation system during the tidal cycle shown. Both the phase and relative arrival time are shown with the same scale, expressed in milliseconds.

FIG. 4. Acoustic arrival time in the forward ($\mathscr{T}_+$) and reciprocal ($\mathscr{T}_-$) direction for 48 h.

have to be used to determine 2π phase ambiguities, accuracy to within one cycle is very important.

Linear interpolation of the phase,

$$S(t) = \arctan\left(\frac{Q(t)}{I(t)}\right), \tag{34}$$

at the peak amplitude location gives a more precise measurement for arrival time variability. The computed arrival time ($\mathscr{T}$) is used for resolving 2π phase ambiguities inherent in the arctan function of (34). Figure 2 shows the phase as a function of relative travel time together with a linear fit at the arrival time location so that $\phi = S(\mathscr{T})$.

Figure 3 shows log-amplitude $\chi = \ln(A/\langle A \rangle)$ (where $\langle \ \rangle$ denotes a time average), phase ϕ, and relative arrival time $\mathscr{T}$ for approximately 12 h of data (sampling rate 6.0 Hz) for RT1/BR1 processed by the forward system. The phase is expressed in ms and put to the same scale as the relative arrival time. Both the log-amplitude and phase data show much variability during the changing tidal flow. Since both temperature and current variability contribute to the acoustic scintillation no correlation with the current speed is intended. The high-frequency variability observed in the log-amplitude is due to Fresnel scale ($\sqrt{\lambda L} = 3.9$ m) structures advected past the acoustic paths. The phase, on the other hand, is most sensitive to the advection of larger scale features. Based on a signal-to-noise ratio of 28 dB, the rms noise in the phase measurement is $\pm 2.3°$ (0.09×10^{-6}).

Similar processing on a separate computer was carried out for the two reciprocal paths (RT1/BR1, BT1/RR1). In this processing, however, absolute arrival times are measured in both directions and thus the resulting phase measurement gives the true arrival time variability. The arrival time in the forward ($\mathscr{T}_+$) and reciprocal ($\mathscr{T}_-$) direction for the duration of the experiment (48 h) are shown in Fig. 4 (mean sampling rate 2.5 Hz). It should be mentioned that, for practical reasons, there was a small digitization rate discrepancy between the received signal and the PRN template resulting in a signal-to-noise ratio of 12 dB for data processed by this
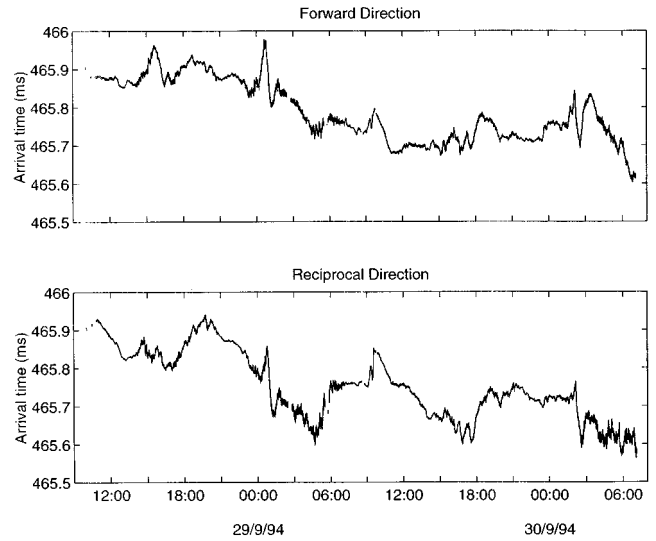
separate computer. As a result, the phase (or arrival time) accuracy for the two reciprocal paths was $\pm 14.4°$ (0.6×10^{-6} s).

It is interesting to note that the reciprocal travel time measurements show simultaneity of some of the perturbations. For example on 29/9/94 00:00, 09:00 and 30/9/94 03:00, the sudden changes in the travel time are associated with advection of imperfectly mixed water through the acoustic path as will be shown.

III. CURRENT VELOCITY AND SOUND SPEED

The mean current speed perpendicular to the measuring baseline ($u_\perp$), which is approximately along channel (9°T), can be determined by the scintillation drift as discussed by Farmer et al.[11] Instead of using diverging acoustic paths (one transmitter, two receivers) we make use of parallel paths (two transmitters, two receivers) and the delay to peak of the cross covariance of log-amplitude. This gives

$$\widetilde{u}_\perp = \frac{\rho_x}{\tau}, \tag{35}$$

where ρ_x is the horizontal separation of the transducers, τ is the time lag, and the tilde ($\sim$) represents a path average. The along channel current result for 5-min averages is shown in Fig. 5.

Since we measure the travel time in two reciprocal directions we can determine the mean and fluctuating components of both the current and sound speed along the measuring baseline. The current speed along the measuring baseline (278 °T), which is approximately cross channel, is

$$\widetilde{u}_\theta = \frac{L(\mathscr{T}_- - \mathscr{T}_+)}{2\mathscr{T}_+\mathscr{T}_-}, \tag{36}$$

and the sound speed is

$$\widetilde{c} = \frac{L(\mathscr{T}_- + \mathscr{T}_+)}{2\mathscr{T}_+\mathscr{T}_-}, \tag{37}$$
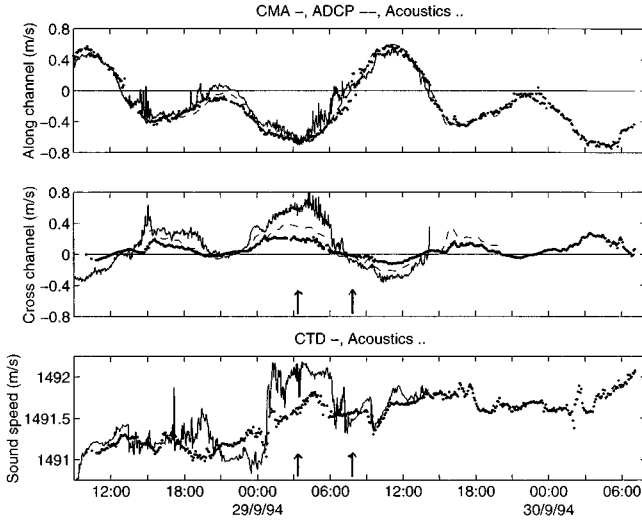
FIG. 5. Current speed perpendicular to the acoustic path (along channel) measured by the scintillation drift. Current speed parallel to the acoustic path (cross channel) measured by the difference in reciprocal travel times. Sound speed measured by the average travel time in two opposite directions. Moored current meter and CTD observations are solid curves, acoustic Doppler is a dashed curve, and acoustic scintillation measurements are dots. Arrows are used to indicate a time of strong and weak flow.

where $L = 695$ m is the acoustic path length. The mean quantities for 5-min averages are also shown in Fig. 5. Arrows indicate a time of strong and weak flow which is discussed subsequently. The combination of scintillation drift (35) and reciprocal transmission (36) make it possible to measure the mean current velocity resolved into components perpendicular and parallel to the measuring baseline.

Also shown in Fig. 5 are *in situ* measurements of the current velocity [resolved into along ($u_\perp$) and cross (u_θ) channel components] from a moored current meter and acoustic Doppler current profiler located somewhat away from the acoustic path as shown in Fig. 1. The sound speed measured from a moored CTD is also shown. The comparison of the current measured by different techniques shows relative consistency considering the placement of the current meter mooring relative to the acoustic path. Better agreement for both current components is with the ADCP which is moored in the center of the channel near the acoustic path. The sound speed from the moored CTD shows much variability compared to the acoustic measurement but the trends are consistent. Discrepancies between the measurements also arise because of the spatial differences between a point location and a path average. The simultaneous structure observed in the reciprocal travel times as mentioned previously can be seen in the sound speed measurement confirming that imperfectly mixed structures create large travel time variations in both directions.

In addition to slowly varying quantities we can observe the short-period random variations in the cross-channel current and sound speed. These are shown in Fig. 6(a) and (b) during strong ebb and weak flow, respectively (as indicated by the arrows in Fig. 5). A rms phase noise of 14.4° (0.6 $\times 10^{-6}$ s) corresponds to a current speed and sound speed sensitivity of ~ 1.5 mm s^{-1}.
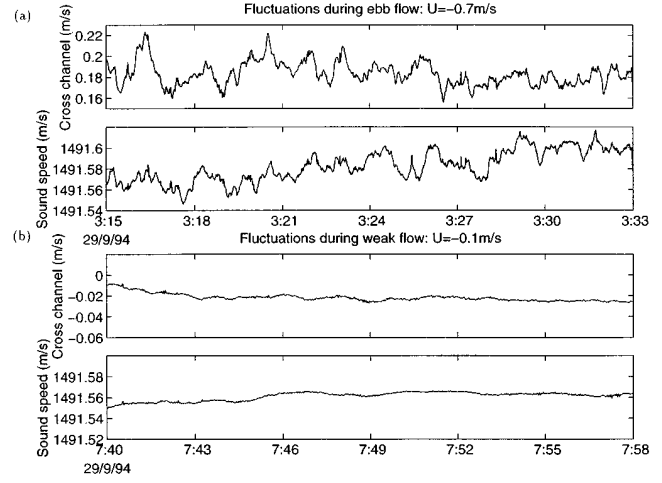
FIG. 6. Cross channel current and sound speed during (a) strong ebb and (b) weak flow for 17 min data. Measurement times are shown as arrows in Fig. 5.

IV. REFRACTIVE INDEX FLUCTUATIONS

A. Total fluctuations

There are two ways in which the level of the total refractive index fluctuations can be determined from the forward-scattered signal depending on scales of interest and path weighting. One is by the log-amplitude variance defined as

$$\sigma_\chi^2 = 4\pi^2 k^2 \int_0^L dy \int_0^\infty dK \, K \Phi_\Sigma(K) \sin^2\left(\frac{K^2 y(L-y)}{2kL}\right) \tag{38}$$

$$= 0.124 C_\Sigma^2 L^{11/6} k^{7/6}, \tag{39}$$

where the greatest sensitivity occurs at the Fresnel scale ($l = \sqrt{\lambda L} = 3.9$ m) and the weighting on C_Σ^2 is in the center of the channel. Here we have arbitrarily defined the level of the total refractive index fluctuations as C_Σ^2 and hence the spectrum as $\Phi_\Sigma(K)$ so that we can compare the measurement to independent measurements of C_η^2 and $C_{\eta_{\text{eff}}}^2$.

The other method for determining the level of the total refractive index fluctuations using the forward-scattered signal is by the wave structure function defined as

$$D(\rho_x, \tau = 0) = 8\pi^2 k^2 \int_0^L dy \int_0^\infty dK \, K \Phi_\Sigma(K)[1 - J_0(K\rho_x)] \tag{40}$$

$$= 2.91 C_\Sigma^2 k^2 L \rho_x^{5/3}. \tag{41}$$

This measurement is dominated by the phase difference variance and is defined for parallel acoustic paths where the receivers are separated by ρ_x. The scale of most sensitivity is $l = 4.5 \rho_x$. We choose parallel paths since the weighting on C_Σ^2 is uniform along the path and is thus expected to compare very well to the reciprocal transmission measurements; diverging paths give a weighting toward the receiver array.

In making both these measurements it is assumed that the scale of sensitivity lies within the dissipating and energy containing scales of the turbulent random medium (i.e., the

FIG. 7. Current speed perpendicular to the measuring baseline ($\widetilde{u}_\perp$) calculated from the scintillation drift. The level of the total refractive index fluctuations measured by the log-amplitude variance and the wave structure function from parallel paths for $\rho_x = 1.22$ m.

inertial subrange $l_0 \ll l \ll L_0$). Thus scaling the acoustic wavelength, path length, and receiver spacing allows measurement of the scales of interest provided that the scintillations remain within the weak scattering regime $\sigma_\chi^2 \ll 0.25$. For example, in Cordova Channel (where the path length is ≈ 700 m) we cannot use acoustic frequencies below 20 kHz and expect to probe isotropic turbulent scales.

Figure 7 shows C_Σ^2 derived from the measured log-amplitude variance using (39) and the measured wave structure function using (41) for $\rho_x = 1.22$ m. Each point represents an average over 5 min. Increased levels in the total refractive index fluctuations occur predominantly during the ebb. During the flood there is no significant increase in the level of the total refractive index fluctuations. This is contrary to the observations in past experiments but consistent with the reciprocal transmission measurements as discussed below. The levels are also approximately a factor of 2 greater than those observed in past experiments (see, for example, Refs. 3 and 11) even though the current speed is less.

B. Scalar and vector contributions

As outlined in the theoretical framework of this paper we can calculate the level of the refractive index fluctuations by both scalars ($C_{\eta_s}^2$) and vectors ($C_{\eta_v}^2$) since we can determine the path-averaged one-dimensional spectra. If we align our coordinate system such that the x-axis is in the direction of current magnitude U then $u_\perp = U \sin \theta$, and $u_\theta = U \cos \theta$ allows us to remove the angular dependence in (30) and (31). The spectra defined by (30) and (31), together with the transformation (32), give the corresponding frequency spectra,

$$\widetilde{F}_{\eta_s}(f) = \frac{4\pi(0.033)(0.84)}{L}\left(\frac{\widetilde{u}_\perp}{2\pi}\right)^{5/3} C_{\eta_s}^2 f^{-8/3}, \quad (42)$$
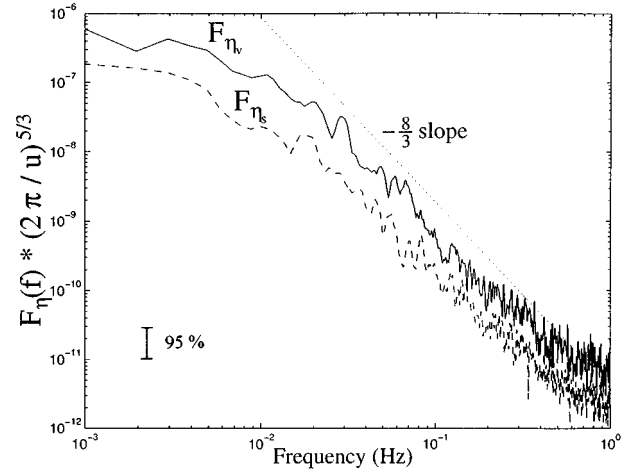
FIG. 8. The path-averaged one-dimensional spectrum for scalar and vector refractive index fluctuations during strong ebb. An $-\frac{8}{3}$ slope is shown for comparison and the 95% confidence interval is displayed.

$$\widetilde{F}_{\eta_v}(f) = \frac{4\pi(0.033)(0.84)}{L}\left(\frac{\widetilde{u}_\perp}{2\pi}\right)^{5/3}\frac{11}{6} C_{\eta_v}^2 f^{-8/3}, \quad (43)$$

where $G(p)/p = 0.84$. In these relations we use the path averaged current perpendicular to the acoustic axis measured from (35).

The refractive index fluctuations from scalars and vectors are defined in terms of fluctuations in sound speed and cross channel current,

$$\eta_s = -\frac{c'}{c_0}, \quad (44)$$

$$\eta_v = -\frac{u'_\theta}{c_0}. \quad (45)$$

Since we measure precise travel time in two reciprocal directions we use (36) and (37) for calculations of $\widetilde{u}_\theta$ and $\widetilde{c}$, respectively. Mean and fluctuating parts are then calculated, thus giving $\widetilde{\eta}_s$ and $\widetilde{\eta}_v$.

The time series of $\widetilde{\eta}_s$ and $\widetilde{\eta}_v$ have a variable sampling rate ranging from 1.0–3.0 Hz with an average rate of 2.5 Hz. In order to obtain an estimate of the power spectral density the time series were resampled. First, the data were averaged to give a constant sampling rate of 2 Hz. Second, where there were occasional gaps because of a sampling rate less than 2 Hz, the data were linearly interpolated. A 34-min time series was then broken up into five overlapping segments (75% overlap) with each segment having 2048 points (~ 18 min of data as shown in Fig. 6). The current speed and power spectrum were determined for each detrended segment and the product $\widetilde{F}_\eta(f)(2\pi/\widetilde{u}_\perp)^{5/3}$ computed. Each of the five segments were then averaged to obtain one result over the 34-min time period. Segments having current speeds less than 0.10 m s^{-1} were eliminated from the average because of the likely breakdown of the Taylor hypothesis. Figure 8 shows the averaged spectrum taken during strong ebb for both the scalar and vector contributions. The one-dimensional path-averaged spectrum from velocity fluctuations is scaled verti-
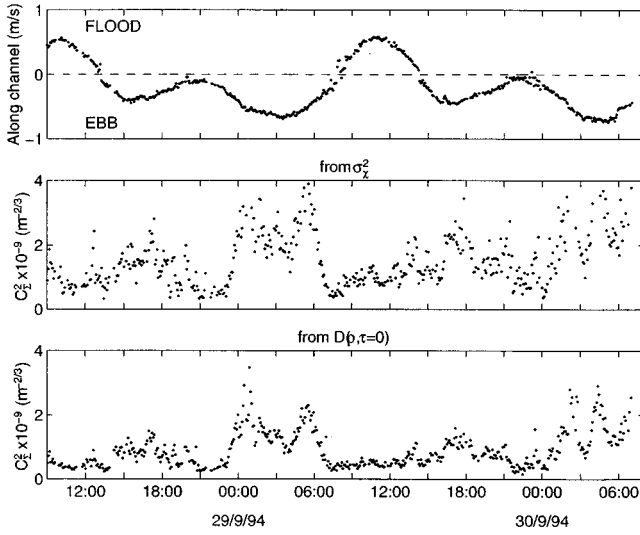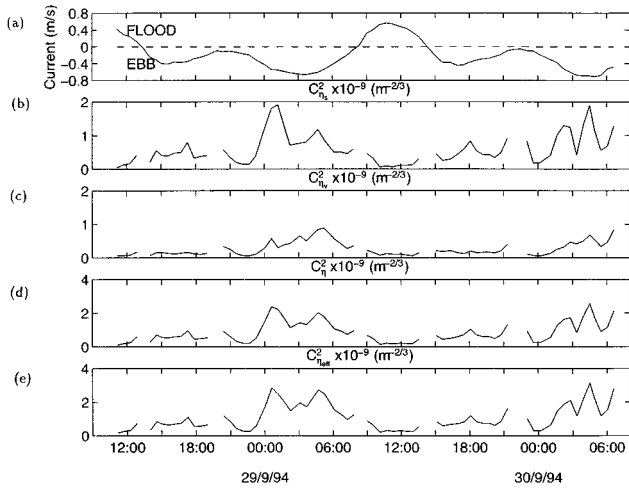
FIG. 9. (a) Current speed perpendicular to the measuring baseline ($\tilde{u}_\perp$) calculated from the scintillation drift. The level of the refractive index fluctuations from (b) scalars and (c) vectors. (d) The structure parameter and (e) effective structure parameter for the effective refractive index fluctuations. Gaps in the data correspond to current speeds less than 0.1 m/s.

FIG. 10. Comparison between the level of the total refractive index fluctuations C_Σ^2 and (a) the structure parameter and (b) the effective structure parameter. Measurements from the log-amplitude variance and wave structure function are denoted by + and *, respectively.

cally by an arbitrary amount so that the details of both spectra are seen. An $-\frac{8}{3}$ slope and the 95% confidence interval are also shown.

Within the frequency band ($0.04\ \text{Hz} \leqslant f \leqslant 0.3\ \text{Hz}$) both spectra have a slope of approximately $-\frac{8}{3}$. This frequency band corresponds to scale sizes ranging from 2–15 m since the mean path-averaged flow during this time is $u_\perp \sim -0.6$ m/s. It is within this range of scales that we compute the level of the spectra so as to obtain $C_{\eta_s}^2$ and $C_{\eta_v}^2$ as a function of time for the tidal cycle shown in Fig. 9(a). Since large scale features are predominantly anisotropic, the low-frequency part of the spectra are due to anisotropic turbulent effects. This can erode the isotropic spectral slope at higher frequencies. However, in the coastal environment where there are strongly stirred flows, we can expect to approach isotropic turbulence over some range of scales and during certain times of the tidal cycle. Anisotropy in Cordova Channel was observed with two-dimensional transmitter and receiver arrays (see Ref. 2), but it was weak at the scales of interest.

The spectral levels are shown in Fig. 9(b) and (c), respectively. During this time the scalar component of the refractive index variability generally exceeds the vector component. Each also have different characteristics. The maximum of $C_{\eta_s}^2$ on 29/9/94 01:00 occurs during a large change in sound speed apparent in Fig. 5. This increase may correspond to passage of a front through the acoustic path. The maximum of $C_{\eta_v}^2$ on 29/9/94 05:00 occurs during maximum ebb when there are large velocity fluctuations (see Fig. 5).

Both the structure parameter,

$$C_\eta^2 = C_{\eta_s}^2 + C_{\eta_v}^2, \tag{46}$$

and the effective structure parameter,

$$C_{\eta_{\text{eff}}}^2 = C_{\eta_s}^2 + \tfrac{11}{6} C_{\eta_v}^2, \tag{47}$$

for the effective refractive index fluctuations can be determined and are shown in Fig. 9(d) and (e). These parameters can be compared to C_Σ^2 in order to define its relation. This is our test of the Ostachev[5] model.

V. DISCUSSION

Reciprocal acoustic transmission allows unambiguous separation of scalar and vector contributions to the refractive index fluctuations yielding path-averaged values with uniform weighting. In Fig. 10(a) and (b) we compare the structure and effective structure parameter, defined by (46) and (47) and evaluated from the separated components $C_{\eta_s}^2$ and $C_{\eta_v}^2$, with C_Σ^2 derived from the scintillation variances for one-way propagation. The + and * measurements for C_Σ^2 are from the log-amplitude variance (39) and the wave structure function (41), respectively, using one-way acoustic propagation. In order to obtain the same time interval, C_Σ^2 from the scintillation variances were obtained over 5 min and then the data were averaged over 35 min corresponding to the time interval of the spectral averages.

While the results show some scatter, the comparison in
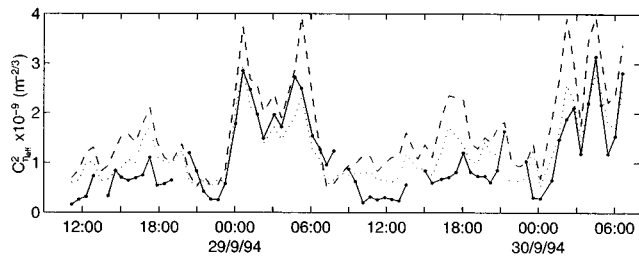
FIG. 11. The effective structure constant $C_{\eta_{\text{eff}}}^2$ determined by the log-amplitude variance (dashed line), the wave structure function (dotted line), and the sum $C_{\eta_s}^2 + 11/6C_{\eta_v}^2$ (solid line).

Fig. 10(b) implies consistency with $C_{\Sigma}^2 = C_{\eta_{\text{eff}}}^2$, thus providing support for the use of Tatarskii's[4] model provided we work with the effective structure parameter as shown by Ostachev.[5] The independent measurements of C_{Σ}^2 and $C_{\eta_{\text{eff}}}^2$ also demonstrate agreement between the measured scintillations and the turbulence and weak scattering models for the random media.

We now have three independent ways of determining the effective refractive index structure parameter. Figure 11 is a time series of $C_{\eta_{\text{eff}}}^2$ determined from the log-amplitude variance, the wave structure function ($\rho_x = 1.22$ m), and the sum $C_{\eta_s}^2 + 11/6C_{\eta_v}^2$.

It should be noted that the effective structure parameter for the effective refractive index fluctuations measured from both the separated components and the wave structure function are path averaged with uniform weighting whereas the parameter measured from the log-amplitude variance is weighted towards the center of the channel. In addition, the scale sizes to which each of the acoustic measurements are sensitive are different but are assumed to lie within the inertial subrange of the turbulence. The log-amplitude variance is most sensitive for refractive variability at scale of 3.9 m whereas the wave structure function is most sensitive at $4.5\rho_x = 5.5$ m. As pointed out by Menemenlis,[8] the line-averaged determination of velocity and sound speed fine structure is based on the assumption that the turbulent scales being probed are much smaller than the acoustic path length ($\ll 695$ m), but larger than the first Fresnel zone (> 3.9 m). Probing scales outside the inertial subrange will cause some differences in the independent measurements of $C_{\eta_{\text{eff}}}^2$.

VI. CONCLUSIONS

We have shown that during the measurement period the acoustical scintillations (amplitude and phase fluctuations) are affected by both the sound speed (hence temperature and salinity) and current speed variability. Since the forward-scatter measurements cannot distinguish between these effects we have used reciprocal transmission to measure path-averaged sound speed and cross-channel current in a turbulent flow. With these novel measurements we demonstrate the separation of scalar versus vector effects on the effective refractive index.

The simultaneous use of both reciprocal transmission and forward-scatter acoustic measurements has made it pos-

sible to verify that the forward scatter scintillations are represented in terms of the effective structure parameter for the effective refractive index fluctuations as predicted by Ostachev.[5] From the two acoustic measurements we are then able to obtain three independent estimates of the effective structure parameter. Our comparison shows that the measurements from the wave structure function and the sum $C_{\eta_s}^2 + 11/6C_{\eta_v}^2$ compare most favorably since they are both uniform path averages. One interesting and consistent feature in all the independent measurements of $C_{\eta_{\text{eff}}}$ is that during high water there is little increase in turbulence levels compared to those observed during low water.

During this experiment we observed dominance of temperature/salinity and velocity on separate occasions. Specifically, the large value of the effective structure parameter at 29/9/94 01:00 in Fig. 9(e) is primarily a result of scalar variability whereas the second peak at 29/9/94 05:00 in Fig. 9(e) is dominated by velocity fluctuations since $11/6C_{\eta_v}^2 > C_{\eta_s}^2$. It is certain that reciprocal transmission provides a greatly enhanced capability for analyzing turbulent flows and their impact on high-frequency propagation.

[1] V. E. Ostashev, ''Propagation and scattering of sound waves in the turbulent media (atmosphere or ocean),'' Atmos. Opt. **4**, 653–656 (1991).
[2] D. Di Iorio and D. M. Farmer, ''Two-dimensional angle of arrival fluctuations,'' J. Acoust. Soc. Am. **100**, 814–824 (1996).
[3] D. Di Iorio and D. M. Farmer, ''Path-averaged turbulent dissipation measurements using high frequency acoustical scintillation analysis,'' J. Acoust. Soc. Am. **96**, 1056–1069 (1994).
[4] V. I. Tatarskii, *The Effects of the Turbulent Atmosphere on Wave Propagation*, translated from Russian by Israel Program for Scientific Translations, Jerusalem, 1971.
[5] V. E. Ostachev, ''Sound propagation and scattering in media with random inhomogeneities of sound speed, density and medium velocity,'' Waves Random Media **4**, 403–428 (1994).
[6] V. I. Tatarskii, *Wave Propagation in a Turbulent Medium*, translated from Russian by R. A. Silverman (McGraw-Hill, New York, 1961).
[7] J. O. Hinze, *Turbulence: An Introduction to its Mechanism and Theory*, McGraw-Hill Series in Mechanical Engineering (McGraw-Hill, New York, 1959).
[8] D. Menemenlis, ''Line-averaged measurement of velocity fine structure in the ocean using acoustical reciprocal transmission,'' Int. J. Remote Sens. **15**(2), 267–281 (1994).
[9] D. Menemenlis and D. M. Farmer, ''Acoustical measurements of current and vorticity beneath ice,'' J. Atmos. Ocean Technol. **9**(6), 827–849 (1992).
[10] D. Di Iorio and D. M. Farmer, ''Observations of acoustical scintillations in Saanich Inlet,'' in Oceans 1993 Proceedings, Engineering in Harmony with the Ocean, Victoria, BC Canada, 18–21 October 1993.
[11] D. M. Farmer, S. F. Clifford, and J. A. Verrall, ''Scintillation structure of a turbulent tidal flow,'' J. Geophys. Res. **92**(C5), 5369–5382 (1985).

Predicted scattering of sound by diffuse hydrothermal vent plumes at mid-ocean ridges

Timothy F. Duda

Applied Ocean Physics and Engineering Department, Woods Hole Oceanographic Institution, Woods Hole, Massachusetts 02543

D. Andrew Trivett

Trivett Technologies, Inc., Mahone Bay, Nova Scotia B0J 2E0, Canada

Amplitude and phase fluctuations of monochromatic acoustic signals traveling through diffuse mid-ocean ridge hydrothermal vent plumes are modeled using existing theory in an attempt to find suitable frequencies and path lengths for plume monitoring. Weak-scattering solutions are evaluated numerically, with model parameters adjusted to match observed plume characteristics. Constraints required for weak-scattering solutions to be valid can be met for transmission ranges of 500–2000 m and frequencies of 20–80 kHz. Therefore, because fluid structure and scattering strength are more closely linked for weak scattering than for stronger scattering, inversion for fluid statistical properties may be possible, enabling diffuse vent monitoring. Such monitoring would be subject to geometric assumptions such as transmission entirely within a statistically homogeneous plume. Performance-limiting phase fluctuations have also been computed for a 13–17 kHz geodetic survey system. © *1998 Acoustical Society of America.* [S0001-4966(98)01801-3]

PACS numbers: 43.30.Pc, 43.30.Re [JHM]

INTRODUCTION

Fluctuations that develop as radiation passes through a randomly inhomogeneous medium can provide a view of the medium characteristics. Since sound propagates freely through water, it has been the wave of choice for this type of remote sensing in the ocean. The usefulness of the view obtained, and the reliability of its interpretation, is dependent on the both the nature of the inhomogeneities and the regime of the acoustic scattering.

Propagation modeling in the Rytov weak-scattering regime (Fante, 1975; Strohbehn, 1978; Tatarskii, 1971) is used here to investigate the potential of a forward-scattered acoustic measurement of mid-ocean ridge hydrothermal venting. This type of measurement would involve transmission from a tethered source to a tethered receiver. The signals would be fluctuations of phase and amplitude, to be associated in an inverse fashion with thermal fluctuation statistics along the propagation path. Details of the modeling technique are described in two previous publications (Duda, 1991; Duda *et al.*, 1988). Parameters of the modeling are adjusted to be appropriate for diffuse vent fluid using data from a field study at the Juan de Fuca Ridge (Trivett and Williams, 1994). Since a forward model is required for inverse estimation of fluid properties, a primary aspect of this work is ascertaining that the Rytov model is applicable to experimentally realistic frequencies and propagation distances. The Rytov model is accurate for situations having acoustic fluctuations below some threshold, but breaks down for increased fluctuation strength.

Diffuse vent effluent is only slightly warmer than the deep ocean water and generally resides in a bottom-hugging plume (Trivett, 1994) rather than in a buoyant plume wafting in the current. An acoustic remote sensing scheme may be possible for these plumes since they are trapped at a known vertical location near the bottom. Remote sensing may be beneficial for diffuse plume monitoring because of the inherent volumetric averaging. For example, a volumetric measure may determine whether point measurements (such as with thermometers) are spatially representative, or may more accurately characterize a larger volume. Also, some success may be achieved at circumventing the so-called ''gopher-hole'' problem of outflow sensing, where the total output of a hydrothermal area may not be measurable with sensors at a few vent openings because of transient vent birth or mortality (Tivey, 1991).

In principle, if the acoustic fluctuations are not too large, weak-scattering theory can be used to relate aspects of the scattered field to the intervening medium. The weak-scattering behavior is an important requirement for fluid characterization because it implies a close link between medium fluctuation statistics and acoustic fluctuation statistics. This close relation is not true for stronger scattering which exhibits ''saturation'' (Ishimaru, 1978), a convergence of statistics. Many underwater propagation regimes exhibit either very weak or very strong scattering, such as vertical propagation away from boundaries (weak) and horizontal propagation through strong turbulence in a mixed layer or a coastal region (strong). The weak-scattering cases may not provide adequate signal for fluid characterization, a problem as severe as saturation from strong scattering. On the other hand, diffuse vent flows in otherwise essentially thermally homogeneous deep-ocean water masses may be a situation of adequate scattering, but not strong scattering, where acoustics can be modeled, understood, and inverted for measurement purposes. Other constraints on fluid characterization exist, such as homogeneity and isotropy of refractive index variations within the water, but these complications of

inverse-based remote sensing can be considered and dealt with only after weak scattering has been verified.

The physics behind this possibility of acoustic remote sensing are easily understood. The development of a sound pulse moving through a strongly heterogeneous medium from a simple to a complex pattern, as range increases, eventually provides multiple arrivals at great range. At short ranges multipath may not exist, but the propagation processes which eventually lead to multipath cause pulse distortions. Properties of these distortions (which can be thought of as incipient multipath) are dependent on properties of the medium. We suppose that these distortions, manifested as phase and amplitude fluctuations, can be measured and used to monitor rms thermal gradients at deep-ocean vent sites.

The obvious analog of the long-range ocean tomographic mapping (Munk *et al.*, 1995), i.e., the use of pulse timing to map an anomalously warm plume, is not feasible near hydrothermal vent areas unless acoustic sources and receivers can be firmly fixed to the bottom. This is because timing signals developed over the short ranges would be very small, and any motions would overwhelm the signals (Trivett, 1991). Because the pressure gradient in the nearly isothermal deep ocean causes sound to refract upward, only instruments on promontories could avoid the shadowing effect. However, the statistics of fluctuations in phase and amplitude which develop can be measured with tethered devices, without consideration of overall timing, and related to the sound-speed (temperature) statistics of the intervening medium. Such statistical remote sensing has been used in the atmosphere and the solar wind (Coles and Kaufman, 1978; Yeh and Liu, 1982).

The goals of this short study are to determine frequencies and path lengths where weak scattering describes the propagation, and to determine the sensitivity of intensity fluctuation statistics to plume turbulence properties. Additionally, phase statistics of 15-kHz weakly scattered signals will be calculated for the purpose of providing signal-processing bounds on deep-ocean ridge acoustic geodetic systems (Spiess and Hildebrand, 1995).

I. WEAK SCATTERING

The Rytov weak-scattering model, also called the method of smooth perturbations, quantifies forward scattering through a random medium. This is a single-scattering approximation, with the field at the receiver expressed as an integral over range of scattered fields. The incident field at each range is composed of the field as it would exist in the absence of medium fluctuations. Statistical properties of fields in planes transverse to the propagation direction can be expressed in terms of statistical properties of the intervening medium. The expressions for spatial spectra of phase and amplitude perturbations can be integrated to give variances, assuming spatial variability can be substituted for ensemble averaging, an assumption consistent with homogeneity and stationarity of environmental fluctuation statistics, and also consistent with the spectral description. A suitable expression from previous work is the double integral (Duda, 1991; Duda *et al.*, 1988)

$$\Theta(m) = 2\pi R q^2 \int_0^1 ds \, \frac{m}{s^2} \int_{-\infty}^{\infty} dl \, F\left(0, k_y = \frac{lm}{s}, k_z = \frac{m}{s}\right)$$

$$\times G\left[\frac{m^2 R_f^2}{4\pi s}(1-s)(l^2+1)\right]. \tag{1}$$

The notation is consistent with the cited publications. Transmission is in the x direction over a range R. $F(\mathbf{k})$ is the vector spectrum of sound-speed fluctuations, so that sound-speed variance $\langle\mu^2\rangle = \int d^3\mathbf{k} F(\mathbf{k})$, with $\mathbf{k} = (k_x, \mathbf{k_T}) = (k_x, k_y, k_z)$ and $k = |\mathbf{k}|$. Θ is the wave number power spectrum of either log amplitude or phase, m is wave number in the z-direction transverse to the propagation path at range R (vertical as written), k_z and k_y are transverse wave numbers of inhomogeneities in the intervening medium, q is a reference acoustic wave number in an isovelocity medium, $s = x/R$ is a normalized range coordinate, and $l = k_y s/m$ is a scaled lateral wave number. The Fresnel radius is $R_f = (2\pi R/q)^{1/2}$. The function G is sine^2 if we consider log amplitude, cosine^2 if phase.

Expression (1) for the acoustic fluctuation spatial spectrum is derived from the expression for the acoustic field under the aforementioned scattering assumption, from which a covariance expression is developed. The spectrum follows directly from the covariance via Fourier transform. Expression (1) is useful for modeling scattering from turbulence because it involves the spatial spectrum of the thermal fluctuations, which are related in a known manner to fundamental properties of the turbulent field such as turbulent energy production rate and thermal variance dissipation rate χ (Batchelor, 1959).

Computations will include integration of log-amplitude spectra Θ over wave number m, giving log-amplitude variance, which is 1/4 times log-intensity variance, since log-intensity $\iota = 2 \ln A = \ln(I/\langle I\rangle)$. Since $\iota + 1 \approx I/\langle I\rangle$ in the region of validity, log-intensity variance is equal to the scintillation index $\sigma_I^2 = (\langle I^2\rangle - \langle I\rangle^2)/\langle I\rangle^2$, a measure of scattering, which is a normalized intensity variance. The limits of applicability of Rytov theory are often quoted to be $\sigma_I^2 < 0.3$ (Fante, 1975), but phase fluctuation calculations may be valid beyond this to $\sigma_I^2 < 0.7$ (Ewart and Reynolds, 1984).

II. SPECTRA OF SOUND-SPEED STRUCTURE

As in the previous work, the medium is modeled as a homogeneous volume of isotropic sound-speed fluctuations. These are modeled with an isotropic inertial-convective scalar subrange spectrum (Batchelor, 1953; Tatarskii, 1971). A high-pass filter with outer scale k_t is used to confine the subrange to $k_t < k$, and a diffusive roll-off R_b from the Batchelor spectrum is included, giving

$$F_m(\mathbf{k}) = \frac{\phi_t}{(k^2 + k_t^2)^{11/6}} \frac{k^2}{k^2 + k_t^2} R_b(k). \tag{2}$$

The scalar quantity ϕ_t is a spectral amplitude parameter. F_m indicates model F. This model is most sensible in a weakly stratified region, such as a surface mixed layer or a bottom boundary layer. It can also be realistic in stratified parts of the ocean, but stratification generally confines the subrange

to scales of 1 m and less (Dillon, 1982). Sound-speed structure at scales smaller than the viscous cutoff scale $l_c = (\nu^3 \epsilon^{-1})^{1/4}$, tens of centimeters or less, is poorly modeled by F_m (ν is the kinematic viscosity and ϵ is the rate of dissipation of kinetic energy), but the precise form in the roll-off region is not relevant since microstructure of scales R_f or larger contribute dominantly to acoustic fluctuations in the weak fluctuation regime. The simulations here have R_f ranging from 12.2 m (20-kHz, 2-km range) to 2.1 m (80-kHz, 250-m range), and most of the scattering is caused by the largest modeled scales, determined by $k_t = 0.1$ rad m^{-1}.

Vector spectra F which are isotropic, as are F_m, can be integrated over spherical shells to give wave number magnitude spectra (also called three-dimensional spectra), $E(k) = 2\pi k^2 F(k)$. One-dimensional spectra $D(k_x)$ for any direction x, which contain aliased contributions from high wave numbers, are related by the expression $E(k) = -k \times (dD(k)/dk)$ (Tennekes and Lumley, 1972). In the next section it is shown that measured $D(k)$ from diffuse plume fluid can be used to find parameters of $F_m(k)$ which are best matched to diffuse plumes.

III. MODEL MEDIUM CONSTRAINTS FROM FIELD MEASUREMENTS

One-dimensional spectra $D(k)$ can be computed from the temperature records of Trivett and Williams. During 1990, two bottom-resting, 5-m tall tripods with vertical arrays of thermistors and three-axis current meters were placed on the Southern Juan de Fuca Ridge during the VENTS'90 field study. Four tethered arrays of thermistors were also deployed. Representative data from one tripod are used here. The 45-m tall tethered arrays exhibited a clear distinction between variable (in plume) and essentially isothermal (out of plume) periods, each of many hours duration, encouraging this study of an averaging acoustic measurement tool. The tripod records were closer to the mixing influences of the rough volcanic terrain and had lower peak variances than the higher thermistors, so we will examine model spectra of magnitude equal to and greater than those consistent with the tripod measurements.

Spectra $D(k_x)$ of sound-speed fluctuations recorded from fluid advecting past tripod BS3 are shown in Fig. 1. These are recorded within 3 m of the bottom. The temporal sampling is once per minute, the mean velocity past the array is 3.5 cm s^{-1}, and anisotropic fluctuations having horizontal scales of up to tens of meters are included. The spatial spectra of Fig. 1 are calculated from temperature time-series assuming Taylor's frozen field hypothesis and the above stated velocity. A loosely fit $k^{-5/3}$ inertial-subrange spectrum is also shown.

Properly scaled acoustic fluctuation predictions would result from models having spectra F_m sharing common spectra E with the measured D of Fig. 1. This is because E can be computed from either D or F using relations of the previous section. Figures 2 and 3 show E computed from the higher-level D of Fig. 1, along with E spectra from the loosely fit inertial-subrange D. The slope of the measured E changes at wavelength of roughly 40 m, possibly indicating a change in dynamics at that scale. Figures 2 and 3 also show
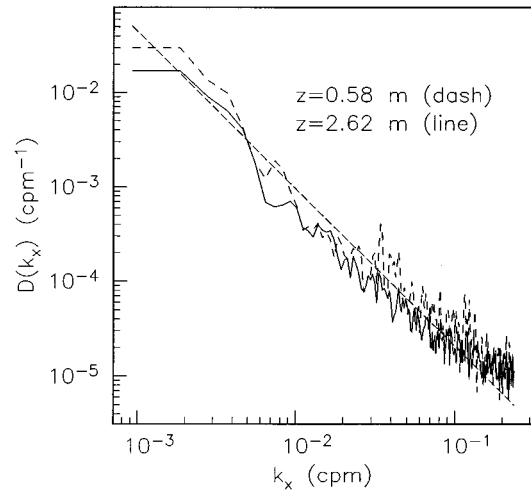
FIG. 1. The one-dimensional spectra $D(k_x)$ of sound speed (c) from temperature (T) records at levels 1 and 4 of the tripod BS3 are shown (Trivett and Williams, 1994). The heights above the bottom are indicated. The sampling rate was 2 Hz, but these data are averaged and recorded at 1-min intervals, so the Nyquist period is 120 s. The conversion to wave number uses the mean speed measured at the same tripod, 0.035 m/s, giving a Nyquist wave number of about 4.2 m. The local dc/dT coefficient is 4.37 m s^{-1} °C^{-1}. The straight dashed line shows a fitted $k^{-5/3}$ inertial subrange spectrum.

three example $E(k)$ derived from $F_m(k)$ used for propagation modeling. An important physical parameter is the thermal dissipation rate χ, which in the absence of salinity variations can be computed from the spectrum in this way:

$$\chi = 2D_t \alpha^2 \int_0^\infty k^2 E(k)\, dk, \tag{3}$$

where D_t is the molecular diffusivity of heat, $\alpha = dT/dc$, T is temperature, and c is sound speed. A more general defini-
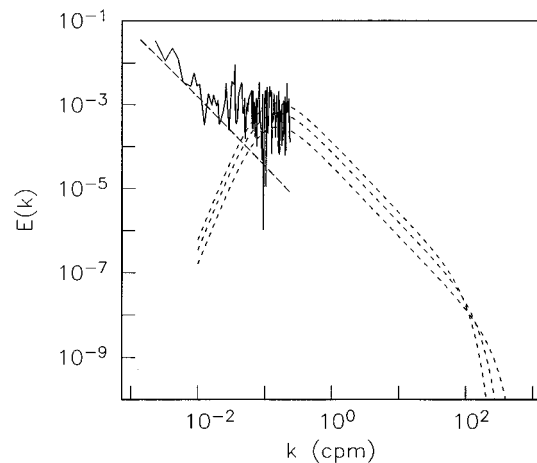
FIG. 2. Spectra E computed from the one-dimensional spectra of Fig. 1 are compared with E computed from three model spectra F_m. The curves at lower wave number are from the $k^{-5/3}$ power-law example D (straight dashed line) and the more elevated of the two measured D (solid line). Each of the three model curves (dashed curves) has thermal dissipation rate $\chi = 10^{-9}$ °K^2 s^{-1}, with energy dissipation equal to 10^{-9}, 10^{-10}, and 2×10^{-11} W kg^{-1}. The model height at the peak is inversely related to ϵ and to bandwidth.
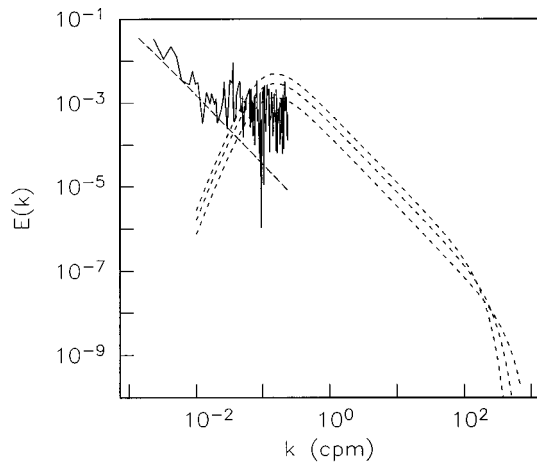
FIG. 3. Similar to Fig. 2, but the model E use $\chi=10^{-8}$ °K^2 s^{-1}, and energy dissipations 10^{-8}, 10^{-9}, and 2×10^{-10} W kg^{-1}. These models spectra have significantly more variance at R_f scales (meters) than those of Fig. 2.

tion of χ is in terms of the temperature gradient variance. The parameter χ is fixed for the family of model curves in each figure; energy dissipation rate ϵ varies.

Some details of $F_m(k)$ are useful to keep in mind. Since F_m are band limited, for a given χ the spectral magnitude at a given scale varies inversely with the turbulence spatial bandwidth, which is governed at high wave number by Batchelor's theory and increases with increasing ϵ (Batchelor, 1959). The ratio $M=\chi/\epsilon$ is a scaled version of mixing efficiency in the steady-state situation, because χ is proportional to thermal variance elimination (mixing) and ϵ is related to source energy in the steady state. Since the outer scale is fixed at $k_t=0.1$ rad m^{-1}, the maximum variance occurs at 5–10 m wavelength. Substantial fluctuations exist to wavelengths as long as 15 m. Fluctuations drop off rapidly away from the peak wavelength. The outer scale is chosen to loosely conform with our best ideas of plume dynamics (Trivett, 1994). It is consistent with a weakly stratified lateral plume many tens of meters in height above the seafloor, entraining fluid, with eddies at all scales up to the plume height.

IV. WEAK SCATTERING MODEL RESULTS

Models F_m [given by Eq. (2)] consistent with measured D are chosen for evaluation of Eq. (1), with subsequent integration of $\Theta(m)$ (spectrum of either log intensity or phase) over all m to give σ_I^2 or the variance of phase. Based on comparisons resembling Figs. 2 and 3, F_m having χ of 4×10^{-8}, 10^{-8}, 4×10^{-9}, and 10^{-9} °K^2 s^{-1} were used. These had variable energy dissipation (or turbulent production), and thus variable spatial bandwidth, plus a variable mixing efficiency M. The resultant sound-speed spectra bracket the experimental spectra in the band from 10 m to 2 m wavelength. These are the smallest measured scales and the largest modeled scales. Their effect will dominate the modeled acoustic fluctuations, which should be compared to acoustic observations after longer period fluctuations (such as from tidal effects) are filtered out.
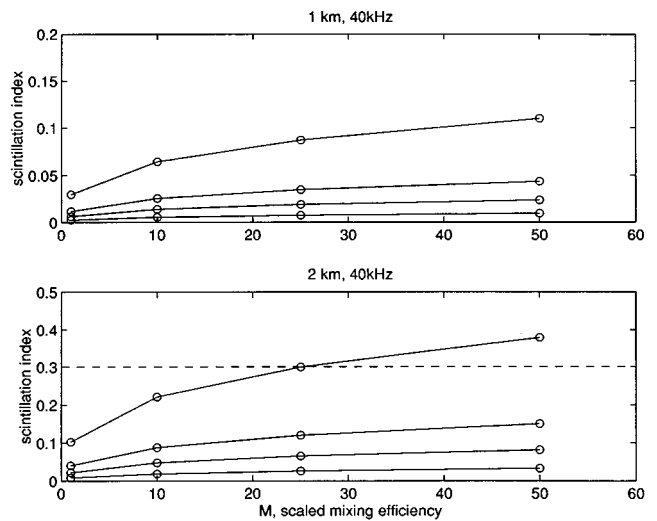
FIG. 4. Scintillation index (σ_I^2) results for the 40-kHz frequency, 1- and 2-km range ($R_f=6.1,8.7$ m) are plotted versus scaled mixing efficiency M. Thermal dissipation χ is fixed for each curve in the family, with $\chi=4\times10^{-8}$ °K^2 s^{-1} for the upper curve, descending to 10^{-8}, 4×10^{-9}, and 10^{-9}. The scaled mixing efficiency is the ratio χ/ϵ, units °K^2 s^{-1} over W kg^{-1}. It can be seen that σ_I^2 is below or near the weak-scattering limit (dashed line) for many situations.

Figures 4 through 6, showing σ_I^2 for 40–80 kHz at 1–2 km range, show σ_I^2 exceeding 0.3 for the highest of the models, but well below it in most cases. This is a promising result for plume monitoring. Figures 7 and 8 show weaker fluctuations for 20-kHz acoustics and short-range 80 kHz.

The figures show that σ_I^2 is a weak function of M, as expected, compared with the sensitivity to χ. Factor of 40 changes of χ at fixed M have about triple the effect of a factor of 50 change in M at fixed χ. This is expected, since M changes vary the turbulent bandwidth only a small percentage, with small changes in spectral height near R_f and thus in scattering.
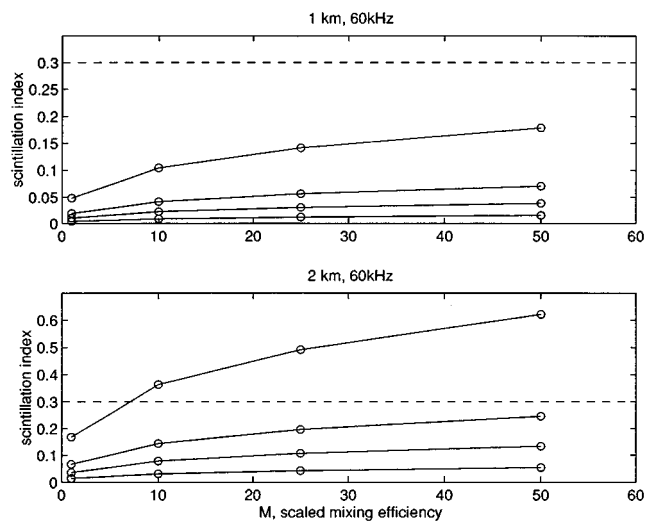
FIG. 5. Scintillation index results for the 60-kHz frequency, 1-and 2-km range ($R_f=5.0,7.1$ m), which are slightly greater than the 40-kHz results of Fig. 4. The parameter χ is fixed for each curve, having the same values as in Fig. 4.
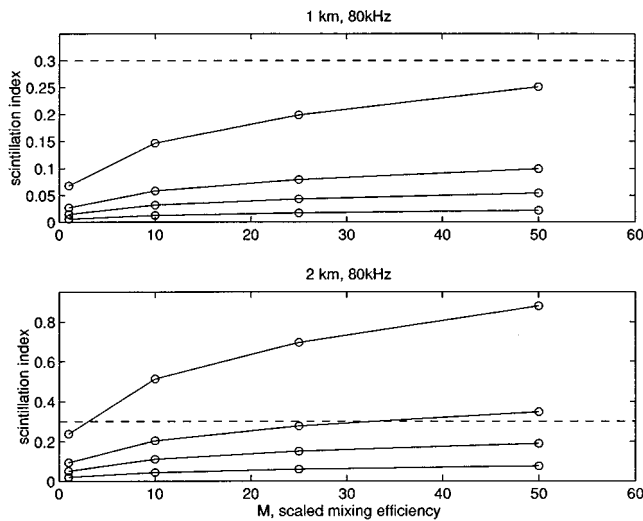
FIG. 6. Scintillation index results for the 80-kHz frequency, 1 and 2 km ($R_f = 4.3, 6.1$ m) are shown. The index greatly exceeds the weak scattering limits of applicability (0.3) for $\chi = 4 \times 10^{-8}$, at most energy dissipations for the 2-km range, but not for the 1-km range. χ for each curve is as in Fig. 4.

The curves in each of the panels show that multiple values of χ and M will give identical σ_I^2 values. This nonuniqueness means that either additional observations, or better constraints on plume structures and physics, may be required for total accuracy of monitoring.

An indirect-path seafloor geodetic system (Spiess and Hildebrand, 1995) using 13–17 kHz frequency-sweep pulse compression has been designed. The indirect-path system measures the acoustic travel time between a deep-towed platform and individual bottom-mounted transceivers in order to infer their positions with respect to one another. To provide estimates of how diffuse venting would degrade the signals, rms phase (travel time) fluctuation is estimated for 15 kHz, and the three ranges 1, 2, and 4 km. Figure 9 shows that the rms phase (arrival time) fluctuations are distributed from a
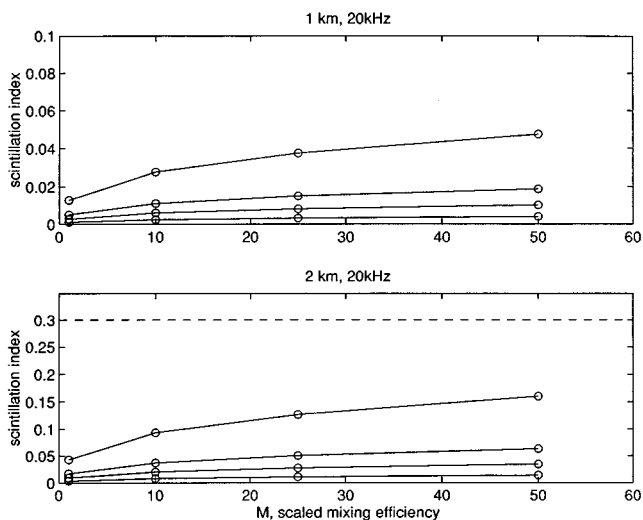
FIG. 7. Scintillation indices for the 20-kHz frequency, 1 and 2 km ($R_f = 8.7, 12.2$ m), are quite weak, especially for 1 km. χ for each curve is as listed in Fig. 4.
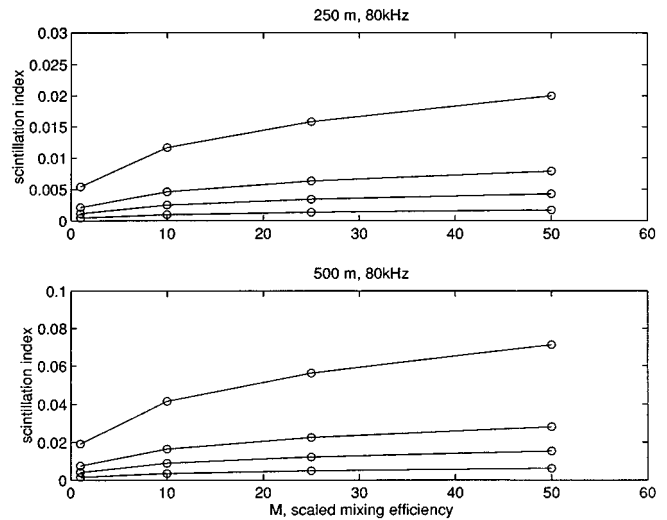
FIG. 8. Scintillation indices for the 80-kHz frequency, 250-m and 500-m range ($R_f = 2.2, 3.1$ m), are smaller than those of Figs. 4–7 for longer ranges. There is less propagation range over which phase interference patterns can develop, resulting in very small fluctuations. χ for each curve is as in Fig. 4.

few degrees, for low mixing efficiency, to maxima near 40 degrees for propagation through 4 km of weak plume heterogeneities, and near 20 degrees for 1-km propagation. Converting to length units, 25 degrees of a 15-kHz wave is equal to 7 mm. This is near the desired performance levels of the systems, which are intended to measure possible variability of seafloor spreading rates which average a few centimeters per year.

V. SUMMARY

Our modeled acoustic propagation through isotropic, homogeneous random sound-speed (temperature) structures show that the weak-scattering criteria can be met for a selection of ranges and frequencies. The structures are consistent with observations taken near an ocean ridge hydrothermal vent. When these criteria are met, changes in intensity variance can be related to changes in the medium with some reliability, assuming some knowledge of the physics of the fluctuation medium.

Strong, measurable scintillations, but not too strong to invalidate the modeling, are predicted for 40–80 kHz signals over ranges of 1–2 km. Many effects are scalable and other ranges and frequencies will give similar results.

The scale length of the inhomogeneities which have the dominant effect is a function of both the acoustic frequency and range. The ranges and frequencies quoted above are most sensitive to structures of 4–9 m wavelength. Temperature variability at such scales is enhanced in vent plumes (Trivett and Williams, 1994) but is typically weak in the deep ocean, implying scattering to be a good diagnostic tool for verification of plume existence.

The solution of the forward problem does not necessarily put the inverse problem within grasp. Nonuniqueness, or multiple possible natural conditions consistent with acoustic observations, is a potential difficulty. More detailed monitoring would be possible when future measurements and better
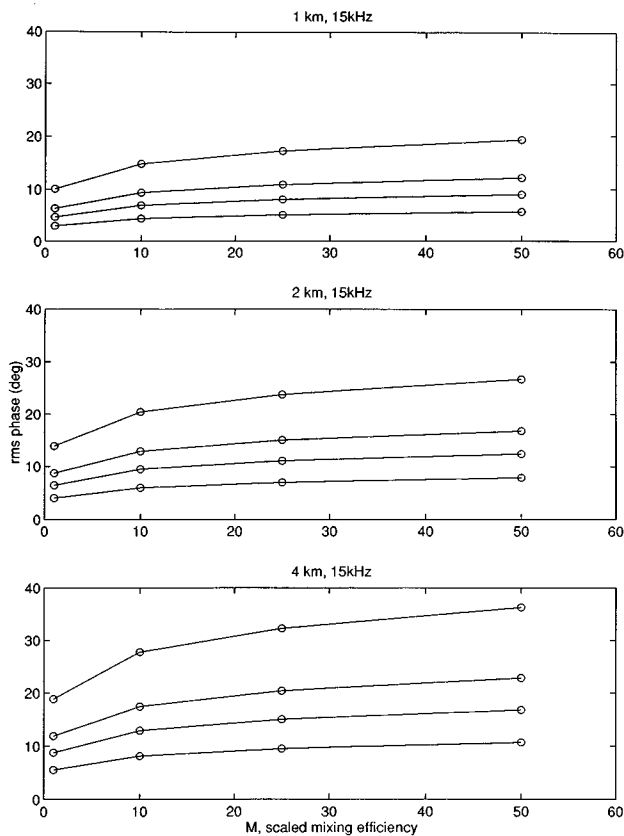
FIG. 9. rms phase fluctuation estimates for 15 kHz at the 1-, 2-, and 4-km range ($R_f = 10$, 14, and 20 m) are shown. These are functions of M and thermal dissipation rate χ, as in Figs. 4–8. The parameter χ is fixed for each curve; the values are as listed in Fig. 4. The acoustic wavelength is 10 cm, so the indicated fluctuations approach travel times equivalent to a centimeter of range.

plume understanding allow more restrictive propagation modeling and unique invertibility. However, plume monitoring should be possible initially, even without full verification of plume dynamics. Signals should exist as long as the plumes are weakly mixing, and not fully mixed, so that the larger meter-scale gradients remain.

Phase fluctuations were estimated for deep-sea acoustic geodetic systems signals, and these show that fluctuations of the same magnitude of the expected signals may exist in the worst case scenario of propagation fully through an effluent plume. In this case, a more elaborate survey with higher redundancy and greater data quantity may be required.

Batchelor, G. K. (**1953**). *The Theory of Homogeneous Turbulence* (Cambridge U.P., New York).

Batchelor, G. K. (**1959**). ''Small-scale variation of convected quantities like temperature in a turbulent fluid,'' J. Fluid Mech. **5**, 113–133.

Coles, W. A., and Kaufman, J. J. (**1978**). ''Solar wind estimation from multi-station IPS,'' Radio Sci. **13**, 591–597.

Dillon, T. M. (**1982**). ''Vertical overturns: A comparison of Thorpe and Ozmidov length scales,'' J. Geophys. Res. **87**, 9601–9613.

Duda, T. F. (**1991**). ''Modeling weak fluctuations of undersea telemetry signals,'' IEEE J. Ocean Eng. **16**, 3–11.

Duda, T. F., Flatté, S. M., and Creamer, D. B. (**1988**). ''Modelling meter-scale acoustic intensity fluctuations from oceanic fine structure and microstructure,'' J. Geophys. Res. **93**, 5130–5142.

Ewart, T. E., and Reynolds, S. A. (**1984**). ''The mid-ocean acoustic transmission experiment: MATE,'' J. Acoust. Soc. Am. **75**, 785–802.

Fante, R. L. (**1975**). ''Electromagnetic beam propagation in turbulent media,'' Proc. IEEE **63**, 1669–1692.

Ishimaru, A. (**1978**). *Wave Propagation and Scattering in Random Media* (Academic, New York), Vol. 2.

Munk, W., Worcester, P., and Wunsch, C. (**1995**). *Ocean Acoustic Tomography* (Cambridge U.P., New York).

Spiess, F. N., and Hildebrand, J. A. (**1995**). ''Employing geodesy to study temporal variability at a mid-ocean ridge,'' EOS Trans. Am. Geophys. Union **76**, 451,455.

Strohbehn, J. W. (**1978**). ''Modern theories in the propagation of optical waves in a turbulent medium,'' in *Laser Beam Propagation in the Atmosphere*, edited by J. W. Strohbehn (Springer-Verlag, New York).

Tatarskii, V. I. (**1971**). The Effects of the Turbulent Atmosphere on Wave Propagation, National Technical Information Service, TT-68-50464, Springfield, VA.

Tennekes, H., and Lumley, J. L. (**1972**). *A First Course in Turbulence* (MIT, Cambridge, MA).

Tivey, M. K. (**1991**). Private communication.

Trivett, D. A. (**1991**). ''Diffuse flow from hydrothermal vents,'' Mass. Inst. Technol./Woods Hole Oceanogr. Inst. Joint Program in Oceanogr. Eng., Sc.D. Dissertation, Woods Hole, MA.

Trivett, D. A. (**1994**). ''Effluent from diffuse hydrothermal venting 1. A simple model of plumes from diffuse hydrothermal sources,'' J. Geophys. Res. **99**, 18 403–18 415.

Trivett, D. A., and Williams III, A. J. (**1994**). ''Effluent from diffuse hydrothermal venting 2. Measurement of plumes from diffuse hydrothermal vents at the southern Juan de Fuca Ridge,'' J. Geophys. Res. **99**, 18 417–18 432.

Yeh, K. C., and Liu, C. H. (**1982**). ''Radio wave scintillations in the ionosphere,'' Proc. IEEE **70**, 324–360.

Scattering from elastic sea beds: First-order theory

Darrell R. Jackson

Applied Physics Laboratory, College of Ocean and Fishery Sciences, 1013 N.E. 40th Street, Seattle, Washington 98105-6698

Anatoliy N. Ivakin

Andreev Acoustics Institute, Shvernika 4, Moscow 117036, Russia

A perturbation model for high-frequency sound scattering from an irregular elastic sea bed is considered. The sea bed is assumed homogeneous on the average and two kinds of irregularities are assumed to cause scattering: roughness of the water–sea bed interface and volume inhomogeneities of the sediment mass density and the speeds of compressional and shear waves. The first-order small perturbation approximation is used to obtain expressions for the scattering amplitude and bistatic scattering strength. The angular dependence of the scattering strength is calculated for sedimentary rock and the influence of shear elasticity is examined by comparison with the case of a fluid bottom. Shear effects are shown to be strong and complicated. © *1998 Acoustical Society of America.* [S0001-4966(98)01901-8]

INTRODUCTION

The Born approximation (first-order perturbation theory) has been applied to sound scattering by rough, elastic sea beds by Lapin,[1,2] Dacol and Berman,[3] and Kuo.[4] Kuperman and Schmidt[5] have used the Born approximation to obtain the coherent field in layered elastic sea beds with rough interfaces. Essen[6] has also used the Born approximation to treat rough sea bed types ranging from very soft sediment to basalt. In addition to this work with the perturbation method, the small-slope[7] and Dashen–Wurmser[8] approximations have also been applied to scattering by rough elastic boundaries. This previous work on interface scattering leaves open the question of the effect of shear on scattering from within the volume of the sea bed. Numerous authors have applied the Born approximation to volume scattering in fluid sediments,[9–19] and these results show that volume scattering can be an important mechanism. Crowther,[20] Ivakin,[21–25] and Kuo[26] have applied the Born approximation to the joint roughness-inhomogeneity problem for fluid sediments. While Ivakin[27] has given a formal Born approximation treatment of the volume scattering problem for elastic sea beds, there has been no joint treatment of roughness and volume scattering for elastic sea beds. The purpose of the present article is to put the rather complicated roughness and volume scattering theoretical results into a common and general format that is straightforward from a numerical point of view and that lends itself to systematic study of these two processes. A subsequent article[28] uses this new formulation in an evaluation of the importance of shear effects in scattering from the sea bed.

I. FORMULATION

Much previous work on acoustic scattering from the sea bed assumes that the sediment can be treated as a lossy fluid, in which case scattering at the interface is controlled by the discontinuities in density and compressional wave speed.

Volume scattering is controlled by inhomogeneities in the same two parameters. We will refer to these controlling factors as *scattering mechanisms*. Note that the choice of compressional wave speed as a bulk parameter is somewhat arbitrary; the bulk modulus or some other independent parameter could be used. When an elastic model is used for the sediment, additional degrees of freedom appear which introduce additional scattering mechanisms. In particular, one must now consider the discontinuities and inhomogeneities in shear wave speed as well as the density and compressional wave speed. Furthermore, the scattering mechanisms may generate shear waves within the sediment. As illustrated by Fig. 1, this leads to a number of scattering mechanisms. For volume scattering, for example, one mechanism is scattering of a compressional wave by a density fluctuation, leading to conversion to a shear wave. This shear wave can be converted to a water-borne compressional wave upon encountering the interface. If the shear wave is polarized such that the particle motion is in a vertical plane, conversion is possible even for the flat interface. As a result, this scattering mechanism is evident in a first-order perturbation treatment. Scattering to the other possible polarization (with particle motion in a horizontal plane) will only be evident at higher order, as such a wave suffers total internal reflection at a horizontal, flat interface.

A. Basic equations

Figure 2 depicts the general physical situation to be considered. A rough interface described by the random function

$$x_3 = \zeta(\mathbf{R}) \qquad (1)$$

separates a lossless, homogeneous fluid from an inhomogeneous elastic medium. In Eq. (1) and following equations, upper-case letters will be used to denote two-dimensional vectors and lower-case letters will denote three-dimensional vectors. Thus the three-dimensional position vector, $\mathbf{r}$, is decomposed into its transverse and vertical components as
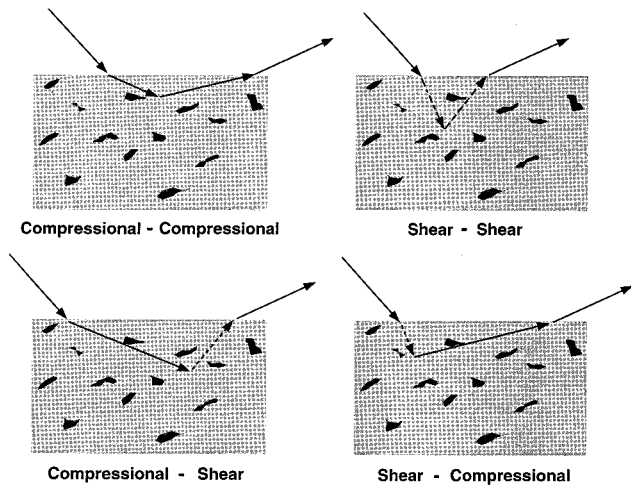
FIG. 1. Volume scattering mechanisms contributing in first order for an inhomogeneous, elastic sea bed. In addition to the four conversion processes indicated, there are three types of inhomogeneities to consider: density, compressional wave speed, and shear wave speed fluctuations.

$$\mathbf{r} = (\mathbf{R}, x_3), \tag{2}$$

where

$$\mathbf{R} = (x_1, x_2). \tag{3}$$

It is convenient to describe wave motion in terms of the particle displacement field, $\mathbf{u}(\mathbf{r})$. This field, in turn, is expressed in terms of scalar and vector potentials[29]

$$\mathbf{u}(\mathbf{r}) = \nabla \phi(\mathbf{r}) + \nabla \times \boldsymbol{\psi}(\mathbf{r}). \tag{4}$$

These potentials describe two different types of waves, compressional and shear, supported by an elastic medium. As the water does not support shear, the vector potential, $\boldsymbol{\psi}(\mathbf{r})$, in the water is taken to be zero.

The general equation obeyed by the displacement field is[30]

$$\omega^2 \rho u_i + \partial_i (\lambda \nabla \cdot \mathbf{u}) + \sum_j \partial_j (\mu(\partial_i u_j + \partial_j u_i)) = 0, \tag{5}$$
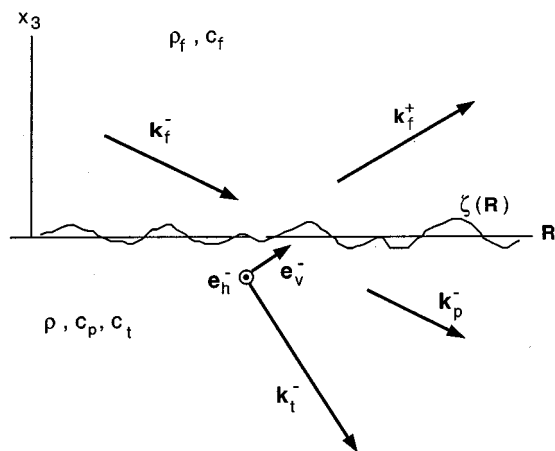
FIG. 2. Geometry relevant to bistatic scattering from a random sea bed. This is a two-dimensional view, but the analysis is three-dimensional. The horizontal polarization vector, $\mathbf{e}_h^-$, is directed out of the page.

where the density, ρ, and the Lamé parameters, λ and μ, can be functions of position, and $\partial_i = \partial/\partial x_i$. In the water, μ is taken to be zero. The time dependence of all field quantities is assumed to be $\exp(-i\omega t)$.

The boundary conditions on the interface $[x_3 = \zeta(\mathbf{R})]$ are continuity of the normal component of displacement

$$\mathbf{u}^{(f)} \cdot \mathbf{N} = \mathbf{u} \cdot \mathbf{N}, \tag{6}$$

and continuity of normal tractions for the stress tensor, σ_{ij},

$$\sigma_{ij} = \lambda \, \delta_{ij} \nabla \cdot \mathbf{u} + \mu(\partial_i u_j + \partial_j u_i), \tag{7}$$

where δ_{ij} is the Kronecker delta function. Continuity of normal tractions can be expressed in the form

$$\sum_j \sigma_{ij}^{(f)} N_j = \sum_j \sigma_{ij} N_j, \tag{8}$$

where the superscript, f, denotes the fluid medium (water) and no superscript is used for the elastic medium (sea bed material). The vector, $\mathbf{N}$, is the (unnormalized) interface normal,

$$\mathbf{N} = -\nabla \zeta(\mathbf{R}) + \mathbf{e}_3, \tag{9}$$

where $\mathbf{e}_3$ is the unit vector in the vertical direction.

As the traction boundary condition, Eq. (8), is actually three equations, there are a total of four equations that must be satisfied. There are also four unknowns: the scattered compressional field in the water and the three scattered fields in the sea bed material (one compressional field and two shear fields having horizontal and vertical polarizations).

B. Sea bed parameters

As mentioned above, other parameters can be used instead of λ and μ. In the present case, compressional and shear wave speeds, c_p and c_t, will be employed rather than the Lamé parameters. The various parameters are related as follows:

$$\lambda = \rho(c_p^2 - 2c_t^2), \quad \mu = \rho c_t^2. \tag{10}$$

Subscripts p and t here and below denote compressional (longitudinal) and transverse (shear) waves, respectively. In the water, c_t and μ are taken to be zero.

The parameters will be divided into two classes: those representing the average, nonfluctuating values of bulk properties such as density and wave speeds, and those describing the random fluctuation of bulk properties and interface relief. In the context of perturbation theory, the zeroth-order solution is that solution corresponding to the average properties with a planar interface. The first-order correction to this solution, for the scattered field, is linear in the fluctuating parameters, including the relief of the interface.

It is convenient to use dimensionless ratios of the average parameters. For simplicity, average wave speeds and density are simply denoted c_p, c_t, and ρ, although these symbols were earlier used for the position-dependent quantities, that is, the average value plus fluctuations. This simplified notation will be employed in the remainder of this article. Thus define

$$a_f = 1, \quad a_p = c_p/c_f, \quad a_t = c_t/c_f, \quad a_\rho = \rho/\rho_f. \tag{11}$$

The trivial ratio a_f is defined for convenience in later expressions. The compressional wave speed ratio, a_p, is the ratio of the average sediment compressional wave speed and the water compressional wave speed. This ratio is complex, with imaginary part determining absorption loss. The shear speed ratio, a_t, is likewise the ratio of the average complex sediment shear speed, and the compressional wave speed in the water and the density ratio, a_ρ, is the ratio of the average sediment mass density to the density of the overlying water.

Interface roughness will be described by the spectral density function, $\mathbf{\Phi}^{(r)}(\mathbf{K})$, where $\mathbf{K}$ is the two-dimensional spectral argument. In the Born approximation, this is a sufficient description of the statistics of the random interface. In other approximations, such as higher-order perturbation theory, additional statistical information must be provided by specifying higher-order statistics or by assuming Gaussian statistics.

A description of the statistics of volume inhomogeneities is given by a matrix of spatial (three-dimensional) cross spectra. These are Fourier transforms of cross-correlation functions for the relative fluctuations $\epsilon_\rho = \Delta\rho/\rho$, $\epsilon_p = \Delta c_p/c_p$, $\epsilon_t = \Delta c_t/c_t$. These relative fluctuations will be collectively designated ϵ_β with $\beta = \rho, p, t$. In this notation, the cross spectra are $\mathbf{\Phi}^{(v)}_{\beta\beta'}(\mathbf{k})$, where $\mathbf{k}$ is a three-dimensional vector. Again, these spectra provide a sufficient description of the inhomogeneities in the Born approximation.

II. THEORETICAL RESULTS

The end result of the formulas to be presented is the scattering coefficient, σ, or scattering cross section per unit area per unit solid angle. The term ''cross section'' will be used for brevity, even though this quantity is dimensionless. The quantity $10 \log \sigma$ is commonly called the scattering strength and is expressed in decibels. The scattering cross section characterizes the frequency-angular distribution of the mean intensity of field fluctuations in the Fraunhofer zone (or far zone, relative to a scattering surface or volume). In the far zone, the scattered acoustic wave can be approximated as a plane wave. Likewise, it is implicit in the definition of scattering strength that the scattering interface is in the far zone of the source, so that the incident field can also be approximated by a plane wave. The scattering cross section is assumed here to be the sum of contributions from interface roughness and volume inhomogeneity. In the first-order approximation used here, this will be the case if the interface relief is uncorrelated with the volume inhomogeneities.[20,21,23,26]

$$\sigma(\mathbf{K}_s, \mathbf{K}_i) = \sigma_r(\mathbf{K}_s, \mathbf{K}_i) + \sigma_v(\mathbf{K}_s, \mathbf{K}_i). \quad (12)$$

Expressions for these two components are given without derivation in the two following subsections. The Appendices give outlines of the derivation of $\sigma_r(\mathbf{K}_s, \mathbf{K}_i)$ and $\sigma_v(\mathbf{K}_s, \mathbf{K}_i)$ using unified notation. In addition, the volume scattering formalism of Ivakin[27] is generalized to include a wider class of scattering mechanisms. The formulas presented in this section are written in a form convenient for coding in higher-level matrix-oriented computational language.

A. Plane waves

It is convenient to present a solution of the first-order scattering problem in terms of solutions of the unperturbed wave equations, in particular, plane waves propagating in the upward and downward directions,

$$\exp(i\mathbf{k}^\pm_\alpha \cdot \mathbf{r}), \quad \alpha = f, p, t,$$

with the subscripts α denoting the wave vectors for compressional waves in the water, compressional waves in the sea bed, and shear waves in the sea bed, respectively. The superscripts $+$ and $-$ denote the direction of the wave propagation, upward and downward, respectively.

It is also appropriate to define the general three-dimensional wave vectors through the transverse components of the incoming and outgoing wave vectors

$$\mathbf{k}^\pm_\alpha(\mathbf{K}) = (\mathbf{K}, \pm k_f \nu_\alpha(\mathbf{K})). \quad (13)$$

The unperturbed wave equations obeyed by the potentials determine the relation between the transverse and vertical components of the wave vectors:

$$\nu_\alpha(\mathbf{K}) = \sqrt{a_\alpha^{-2} - K^2/k_f^2}. \quad (14)$$

The speed ratios, a_α, were defined earlier.

The following unit vectors specifying the directions of propagation are also useful.

$$\mathbf{e}^\pm_\alpha(\mathbf{K}) = \mathbf{k}^\pm_\alpha(\mathbf{K})/k_\alpha, \quad (15)$$

where

$$k_\alpha = \frac{\omega}{c_\alpha}, \quad \alpha = f, p, t, \quad (16)$$

are the wave numbers, respectively, of compressional waves in water, compressional waves in the sea bed, and shear waves in the sea bed. The latter two wave numbers are complex.

There are two plane-wave shear polarizations to consider, both having particle displacement normal to the direction of propagation. The shear wave having particle displacement in the direction

$$\mathbf{e}^\pm_h(\mathbf{K}) = \mathbf{k}^\pm_t \times \mathbf{e}_3/K = (K_2/K, -K_1/K, 0), \quad (17)$$

will be referred to as ''horizontally polarized'' as the particle displacement is in a horizontal plane. In this case, the polarization vector does not depend on whether propagation is upward or downward, but the superscripts $\pm$ are used for consistency with the vertical polarization case. A plane shear wave having transverse wave vector, $\mathbf{K}$, and particle displacement in the direction of the unit vector

$$\mathbf{e}^\pm_v(\mathbf{K}) = \mathbf{e}^\pm_h \times \mathbf{k}^\pm_t(\mathbf{K})/k_t = \mp \mathbf{K} a_t \nu_t(\mathbf{K})/K + \mathbf{e}_3 K/k_t, \quad (18)$$

will be referred to as ''vertically polarized,'' as the displacement is in a vertical plane. In this case, the polarization vector depends on whether the wave is propagating upward or downward. Scattering by interface roughness and inhomogeneities within the sea bed causes conversion between the wave types defined above. For example, while incidence of a plane compressional wave in the water on a flat interface only gives rise to a vertically polarized shear wave, scatter-

ing by interface roughness causes conversion of compressional energy in the water to both the vertical and horizontal shear polarizations. Scattering by inhomogeneities within the sea bed causes conversion between all three wave types.

The expressions above for wave vectors and polarization vectors are written in terms of a general transverse wave vector, $\mathbf{K}$, for later use in the theoretical development. In computing the scattering cross section, however, one must take $\mathbf{K} = \mathbf{K}_{i,s}$. In this case, it is convenient to define the transverse components in terms of the angular coordinates of interest:

$$\mathbf{K}(\theta, \phi) = (k_f \cos \theta \cos \phi, k_f \cos \theta \sin \phi), \quad (19)$$

and

$$\mathbf{K}_{i,s} = \mathbf{K}(\theta_{i,s}, \phi_{i,s}), \quad (20)$$

where θ_i and θ_s, are the grazing angles of the incident and scattered acoustic waves, respectively, and ϕ_i and ϕ_s are the azimuthal angles of the incident and scattered waves, respectively. The unit vectors can then be expressed as follows:

$$\mathbf{e}_\alpha^\pm(\mathbf{K}) = a_\alpha[\cos \theta \cos \phi, \cos \theta \sin \phi, \pm \nu_\alpha(\mathbf{K})], \quad (21)$$

$$\mathbf{e}_h^\pm(\mathbf{K}) = [\sin \phi, -\cos \phi, 0], \quad (22)$$

$$\mathbf{e}_v^\pm(\mathbf{K}) = a_t[\mp \nu_t(\mathbf{K})\cos \phi, \mp \nu_t(\mathbf{K})\sin \phi, \cos \theta], \quad (23)$$

with

$$\nu_\alpha(\mathbf{K}) = \sqrt{a_\alpha^{-2} - \cos^2 \theta}. \quad (24)$$

In Eqs. (21)–(24), subscripts i and s must be added to $\mathbf{K}$ and to the angles θ and ϕ as appropriate.

B. Scattering due to interface roughness

The derivation of the results presented here is given in Appendix B. The scattering cross section for interface roughness is of the form

$$\sigma_r(\mathbf{K}_s, \mathbf{K}_i) = |H_f(\mathbf{K}_s, \mathbf{K}_i)|^2 \Phi^{(r)}(\mathbf{K}_s - \mathbf{K}_i), \quad (25)$$

where $\Phi^{(r)}$ is the roughness spectrum defined in Eq. (55), and $H_f(\mathbf{K}_s, \mathbf{K}_i)$ is the first element of the column matrix

$$H(\mathbf{K}_s, \mathbf{K}_i) = \begin{pmatrix} H_f(\mathbf{K}_s, \mathbf{K}_i) \\ H_p(\mathbf{K}_s, \mathbf{K}_i) \\ H_v(\mathbf{K}_s, \mathbf{K}_i) \\ H_h(\mathbf{K}_s, \mathbf{K}_i) \end{pmatrix}. \quad (26)$$

As explained in Appendix B, the elements of $H(\mathbf{K}_s, \mathbf{K}_i)$ determine the plane-wave spectra of energy scattered into the water, into compressional waves in the sea bed, and into vertically and horizontally polarized shear waves in the sea bed. This matrix, in turn, is computed as follows:

$$H(\mathbf{K}_s, \mathbf{K}_i) = k_f^2 Y_1(\mathbf{K}_s)[P^{(3)}(\mathbf{K}_s)]^{-1} B(\mathbf{K}_s, \mathbf{K}_i) D_0(\mathbf{K}_i). \quad (27)$$

In this equation, $D_0(\mathbf{K}_i)$ is a five-row column vector comprised of the four transformation (reflection-transmission) coefficients contained in the column vector, $S_0(\mathbf{K}_i)$, and supplemented with unity in the last row.

$$D_0(\mathbf{K}_i) = \begin{pmatrix} S_0(\mathbf{K}_i) \\ - - - \\ 1 \end{pmatrix}. \quad (28)$$

An expression for computation of $S_0(\mathbf{K}_i)$ will be given later. Matrix $B(\mathbf{K}_s, \mathbf{K}_i)$ is

$$B(\mathbf{K}_s, \mathbf{K}_i) = k_f^{-1}[(K_{s1} - K_{i1})E^{(1)}(\mathbf{K}_i) + (K_{s2} - K_{i2}) \times E^{(2)}(\mathbf{K}_i)] - E^{(3)}(\mathbf{K}_i) Y_2(\mathbf{K}_i). \quad (29)$$

Note that the terms $k_f^{-1}(K_{sn} - K_{in})$, $n = 1,2$, are dimensionless and can be expressed conveniently in terms of the angles defined in Eq. (19). The matrices Y_1 and Y_2 are

$$Y_1(\mathbf{K}) = \begin{pmatrix} \nu_f(\mathbf{K}) & 0 & 0 & 0 \\ 0 & \nu_p(\mathbf{K}) & 0 & 0 \\ 0 & 0 & \nu_t(\mathbf{K}) & 0 \\ 0 & 0 & 0 & \nu_t(\mathbf{K}) \end{pmatrix}, \quad (30)$$

$$Y_2(\mathbf{K}) = \begin{pmatrix} \nu_f(\mathbf{K}) & 0 & 0 & 0 & 0 \\ 0 & -\nu_p(\mathbf{K}) & 0 & 0 & 0 \\ 0 & 0 & -\nu_t(\mathbf{K}) & 0 & 0 \\ 0 & 0 & 0 & -\nu_t(\mathbf{K}) & 0 \\ 0 & 0 & 0 & 0 & -\nu_f(\mathbf{K}) \end{pmatrix}. \quad (31)$$

There are three matrices, $E^{(n)}(\mathbf{K})$, defined for each of the coordinate indices, $n = 1,2,3$

$$E^{(n)}(\mathbf{K}) = \begin{pmatrix} P_{f1}^{(n)}(\mathbf{K}) & P_{p1}^{(n)}(\mathbf{K}) & P_{v1}^{(n)}(\mathbf{K}) & P_{h1}^{(n)}(\mathbf{K}) & | & Q_1^{(n)}(\mathbf{K}) \\ P_{f2}^{(n)}(\mathbf{K}) & P_{p2}^{(n)}(\mathbf{K}) & P_{v2}^{(n)}(\mathbf{K}) & P_{h2}^{(n)}(\mathbf{K}) & | & Q_2^{(n)}(\mathbf{K}) \\ P_{f3}^{(n)}(\mathbf{K}) & P_{p3}^{(n)}(\mathbf{K}) & P_{v3}^{(n)}(\mathbf{K}) & P_{h3}^{(n)}(\mathbf{K}) & | & Q_3^{(n)}(\mathbf{K}) \\ P_{f4}^{(n)}(\mathbf{K}) & P_{p4}^{(n)}(\mathbf{K}) & P_{v4}^{(n)}(\mathbf{K}) & P_{h4}^{(n)}(\mathbf{K}) & | & Q_4^{(n)}(\mathbf{K}) \end{pmatrix}, \quad (32)$$

where the dashed vertical line in Eq. (32) separates it into the the 4×4 matrices, $P^{(n)}(\mathbf{K})$, and the column matrices, $Q^{(n)}(\mathbf{K})$. Note that $P^{(3)}(\mathbf{K}_s)$ appears in Eq. (27). The elements of $P^{(n)}(\mathbf{K})$ and $Q^{(n)}(\mathbf{K})$ are

$$P_{fm}^{(n)}(\mathbf{K}) = \delta_{mn}, \quad m = 1,2,3, \tag{33}$$

$$P_{f4}^{(n)}(\mathbf{K}) = e_{fn}^{+}(\mathbf{K}), \tag{34}$$

$$P_{pm}^{(n)}(\mathbf{K}) = a_\rho [-\delta_{mn} + 2(a_t/a_p)^2(\delta_{mn} - e_{pm}^{-}e_{pn}^{-})],$$
$$m = 1,2,3, \tag{35}$$

$$P_{p4}^{(n)}(\mathbf{K}) = -a_p^{-1} e_{pn}^{-}(\mathbf{K}), \tag{36}$$

$$P_{(v,h)m}^{(n)}(\mathbf{K}) = -a_\rho [e_{tm}^{-}e_{(v,h)n}^{-} + e_{tn}^{-}e_{(v,h)m}^{-}], \quad m = 1,2,3, \tag{37}$$

$$P_{(v,h)4}^{(n)}(\mathbf{K}) = -a_t^{-1} e_{(v,h)n}^{-}(\mathbf{K}), \tag{38}$$

$$Q_m^{(n)}(\mathbf{K}) = \delta_{mn}, \quad m = 1,2,3, \tag{39}$$

$$Q_4^{(n)}(\mathbf{K}) = e_{fn}^{-}(\mathbf{K}), \tag{40}$$

where δ_{nm} is the Kronecker delta function and the unit vectors defined earlier are employed.

The transformation matrix, $S_0(\mathbf{K}_i)$, is computed as follows:

$$S_0(\mathbf{K}_i) = -[P^{(3)}(\mathbf{K}_i)]^{-1} Q^{(3)}(\mathbf{K}_i). \tag{41}$$

The four elements of this matrix are denoted

$$S_0(\mathbf{K}_i) = \begin{pmatrix} W_f(\mathbf{K}_i) \\ W_p(\mathbf{K}_i) \\ W_v(\mathbf{K}_i) \\ W_h(\mathbf{K}_i) \end{pmatrix}, \tag{42}$$

and are the in-water reflection coefficient for compressional waves, and the transmission coefficients for compressional waves and the two shear waves in the sea bed (see Appendix B). Alternative expressions for these coefficients are given in Brekhovskikh.[29] Note that $W_h(\mathbf{K}_i) = 0$. These coefficients are also required for the volume scattering computation.

C. Scattering due to volume inhomogeneity

The scattering cross section for volume inhomogeneity is of the form

$$\sigma_v(\mathbf{K}_s, \mathbf{K}_i) = -\frac{\pi k_f^4 a_\rho^2}{2} \mathrm{Im}\left(\sum_{\eta,\beta,\eta',\beta'} d_{\eta\beta} d_{\eta'\beta'}^{*} \right.$$
$$\left. \times \frac{\Phi_{\beta\beta'}((\mathbf{q}_\eta + \mathbf{q}_{\eta'}^{*})/2)}{(q_{\eta 3} - q_{\eta'3}^{*})} \right), \tag{43}$$

where $\Phi_{\beta\beta'}$ is the matrix of cross spectra for volume inhomogeneities defined in Eq. (56). Thus the β and β' sums run over the three types of inhomogeneity: density, compressional wave speed, and shear wave speed $(\beta,\beta' = \rho,p,t)$. Generally, these fluctuations are expected to be correlated, thus the $\beta \neq \beta'$ cross terms can be important. Note that the arguments of the cross spectra are complex; the Fourier transform relation between the spectra and the corresponding (real) covariances defines the continuation of the spectra into the complex domain. The sum in Eq. (43) is purely imaginary, so the Im operator is only needed for numerical reasons. The η and η' sums run over the four types of wave conversion caused by volume scattering: compressional to compressional $(\eta = \eta_{pp} = 1)$, shear to compressional $(\eta = \eta_{pt} = 2)$, compressional to shear $(\eta = \eta_{tp} = 3)$, and shear to shear $(\eta = \eta_{tt} = 4)$. Thus, we can put

$$\eta = \eta_{\alpha\alpha'}, \tag{44}$$

where α and α' run over the two types of waves $(\alpha,\alpha' = p,t)$. As noted earlier, volume inhomogeneities cause conversion to both shear polarizations, but upgoing shear waves with horizontal particle motion suffer total reflection at the interface and do not contribute to the scattering cross section in first order. The scattering vectors for the four relevant types of conversion corresponding to different channels of scattering are

$$\mathbf{q}_\eta = \mathbf{k}_\alpha^{+}(\mathbf{K}_s) - \mathbf{k}_{\alpha'}^{-}(\mathbf{K}_i). \tag{45}$$

These vectors give the change in wave vector for the corresponding conversion and appear as arguments in the cross spectra in Eq. (43). All of these vectors have the same transverse components

$$\mathbf{q}_\eta = (\mathbf{K}_s - \mathbf{K}_i, q_{\eta 3}). \tag{46}$$

The vertical components are

$$q_{\eta 3} = k_f [\nu_\alpha(\mathbf{K}_s) + \nu_{\alpha'}(\mathbf{K}_i)]. \tag{47}$$

The coefficients $d_{\eta\beta}$ are

$$d_{\eta\beta} = w_\eta D_{\eta\beta}, \tag{48}$$

where

$$w_\eta = W_\alpha(\mathbf{K}_s) W_{\alpha'}(\mathbf{K}_i) a_\alpha^{-1} a_{\alpha'}^{-1}, \quad \alpha,\alpha' = p,t, \tag{49}$$

with $W_t = W_v$. The coefficients $D_{\eta\beta}$ are elements of the three-column matrix

$$D = (D_\rho | D_p | D_t) \tag{50}$$

where $D_\rho = D_\rho' + D_t/2$ and

$$D_\rho' = \begin{pmatrix} 1 - b_{pp} \\ b_{pv} \\ -b_{vp} \\ b_{vv} \end{pmatrix}, \tag{51}$$

$$D_p = \begin{pmatrix} 2 \\ 0 \\ 0 \\ 0 \end{pmatrix}, \tag{52}$$

$$D_t = 2 \begin{pmatrix} 2g^2 b_{pp}^2 - 2g^2 \\ -2g b_{pt} b_{pv} \\ 2g b_{tp} b_{vp} \\ -b_{vt} b_{tv} - b_{vv} b_{tt} \end{pmatrix}, \tag{53}$$

with $g = a_t/a_p = c_t/c_p$ and

$$b_{\alpha\alpha'} = \mathbf{e}_\alpha^{+}(\mathbf{K}_s) \cdot \mathbf{e}_{\alpha'}^{-}(\mathbf{K}_i), \tag{54}$$

where $\alpha,\alpha' = p,t,v$ and the unit vectors $\mathbf{e}_\alpha^{\pm}(\mathbf{K})$ are defined in Eqs. (21) and (23).

III. CALCULATIONS AND DISCUSSION

A. Model parameters

To illustrate some of the effects of shear elasticity on sea bed scattering, calculations will be presented for a single set of parameters, with average physical parameters appropriate to sedimentary rock.[6] These are density ratio, $a_\rho = 2.5$, compressional speed ratio, $a_p = 2.3 - 0.004i$, and shear speed ratio, $a_t = 1.3 - 0.11i$. The water sound speed is taken to be 1500 m/s and the frequency is taken to be 1 kHz. As noted later, the roughness and volume fluctuation parameters used are such as to yield negligible frequency dependence.

The roughness spectrum is taken to be of the form

$$\mathbf{\Phi}^{(r)}(\mathbf{K}) = \frac{(2/\pi)A^{(r)}}{(K_0^2 + K^2)^2}. \qquad (55)$$

Equation (55) assumes that roughness statistics are stationary and isotropic, with a spectrum that obeys a power law for $K_0^2 \ll K^2$. The parameter K_0 is an inverse correlation scale for roughness in the transverse directions. The roughness spectral parameters were assigned the following values: $K_0 = 10^{-2}$ m^{-1} and $A^{(r)} = 10^{-5}$. The form of the spectrum and parameter K_0 were chosen so that the scattering cross section is essentially independent of frequency except for scattering very close to the specular direction. The parameter $A^{(r)}$ is dimensionless and was chosen arbitrarily to yield scattering strengths that are, except near the specular direction, within the likely region of validity of the Born approximation. The factor $2/\pi$ is included in Eq. (55) for convenience.[28]

For simplicity, the volume inhomogeneity spectra were taken to be of the form

$$\mathbf{\Phi}^{(v)}_{\beta\beta'}(\mathbf{K}, q) = \frac{\delta_{\beta\beta'}A^{(v)}/(2\pi)}{(K^2 + q^2 + q_0^2)^{3/2}}, \qquad (56)$$

with $q_0 = 10^{-2}$ m^{-1}, $A^{(v)} = 10^{-5}$. Because of the Kronecker delta used in Eq. (56), all the nondiagonal elements of the correlation matrix vanish, that is, correlations between the three types of fluctuation are neglected. Also, all three types of fluctuations are assumed to have the same strength, and anisotropy is neglected. In another article,[28] fluctuation strength, correlations, and anisotropy are treated in a more realistic fashion.

The form of the spectra and parameter q_0 in Eq. (56) are chosen so that the scattering cross section is essentially independent of frequency for all scattering directions. The parameter $A^{(v)}$ is dimensionless and was chosen under the same rationale as $A^{(r)}$ with a factor $1/(2\pi)$ included for convenience.[28] In the simple case considered here, the scattering cross section, according to Eq. (43), will be simply the sum of three components

$$\sigma_v = \sum_\beta \sigma_\beta, \qquad (57)$$

where σ_β correspond to contributions of fluctuations of the three different bulk parameters ($\beta = \rho, c_p, c_t$). Calculations are presented below for each of the terms in Eq. (57). For example, σ_ρ is considered for the case in which there are
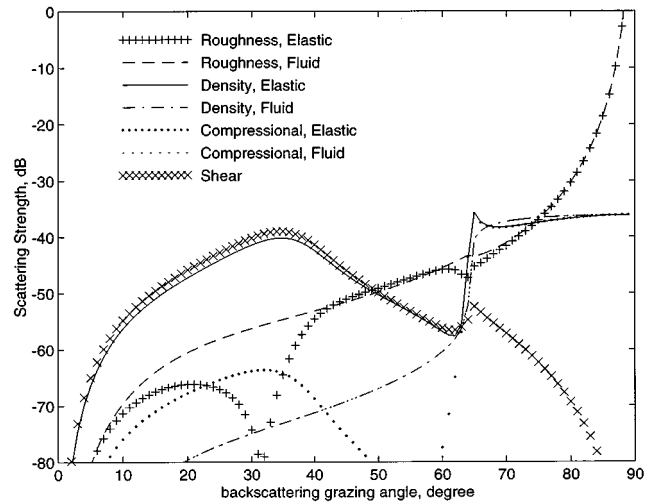
FIG. 3. Backscattering strength as a function of grazing angle for sedimentary rock. The fluid case uses identical parameters, except the complex shear wave speed ratio is set to zero, causing the density and compressional curves to coincide.

density fluctuations but no compressional or shear speed fluctuations.

B. Numerical results

The parameters specified above were used in computing angular dependencies of the backscattering strength. The results of these calculations are shown in Fig. 3 which shows the relative contributions of different types of perturbation for the elastic case and compares them to the fluid case. As three different types of volume fluctuation are considered, this comparison involves a set of seven different curves that includes three pairs comparing the elastic and fluid cases for scattering by roughness, by density fluctuations, and by compressional wave speed fluctuations. The seventh curve is for scattering by shear wave speed fluctuations, which have no fluid counterpart.

The results show that for sedimentary rock the effects of shear elasticity on both roughness and volume scattering are very strong. As the average parameters are taken from Essen,[6] the roughness scattering results are identical to his. Figure 3 shows that roughness backscattering strength exhibits marked dips at grazing angles immediately below the critical angles for shear and compressional waves (39.7° and 64.2°, respectively). The inclusion of lossy elasticity is seen to decrease the roughness scattering strength for certain angles compared to the fluid case in which the shear speed is set to zero. But, at the same time, it somewhat enhances scattering for other angles (in the 40°–60° range). Clearly, treating sedimentary rock as a fluid, albeit a massive and stiff fluid, is a poor approximation.

Figure 3 shows that, in contrast to the case of roughness scattering, elasticity greatly enhances volume backscattering in rock for grazing angles smaller than the shear wave critical angle for all the types of volume fluctuations, but can cause a great reduction in scattering from compressional speed fluctuations for grazing angles in the 40°–60° range. Elasticity effects for volume scattering are much larger than the effects for roughness scattering.

As these results show, the effects of elasticity on roughness and volume backscattering for rock are strong and complicated. A more detailed numerical study of the effects of elasticity for different sea bed types, different sets of statistical parameters, and different types of geometry (both monostatic and bistatic cases) will be given in a subsequent article.[28]

IV. CONCLUSIONS

First-order perturbation theory has been used to develop expressions for the scattering strength of elastic sea beds. Both roughness and volume components of scattering are included. The roughness component of the scattering strength is related to the spatial two-dimensional spectrum of roughness. The volume component is expressed through three-dimensional cross spectra for spatial fluctuations of density, compressional and shear wave speed. Shear effects on both roughness and volume scattering are complicated and strong, at least for the case of backscattering from the sedimentary rock taken as an example for calculations. Generally, an assessment of shear effects for various sea bed types requires more detailed numerical study, using available data on sea bed parameters, including their statistics.

ACKNOWLEDGMENT

APPENDIX A: SCATTERING AMPLITUDES

Regardless of the complexity of the random sea bed, whether scattering is due to roughness or volume inhomogeneity, the scattered field in the water above the highest point on the interface can be expressed as a superposition of plane waves. In the Born approximation, plane-wave superpositions are also used to describe the fields in the sediment. If the incident field is a plane wave of unit amplitude having wave vector with transverse component, $\mathbf{K}_i$, then the scattered potential for particle displacement in the water is

$$\phi_f(\mathbf{r}) = \int \frac{d^2 K}{k_f \nu_f(\mathbf{K})} A_f(\mathbf{K}, \mathbf{K}_i) \exp(i\mathbf{k}_f^+(\mathbf{K}) \cdot \mathbf{r}), \quad (A1)$$

where $A_f(\mathbf{K}, \mathbf{K}_i)$ is the scattering amplitude, taken in the form of Ivakin[27] and related to the transition matrix ("T matrix")[31,32] as follows:

$$A_f(\mathbf{K}, \mathbf{K}_i) = k_f \nu_f(\mathbf{K}) T(\mathbf{K}, \mathbf{K}_i). \quad (A2)$$

The potential, $\phi_f(\mathbf{r})$, does not include the incident field but does include all other portions of the field (coherent and incoherent). The scattering amplitude obeys the reciprocity relation

$$A_f(\mathbf{K}, \mathbf{K}_i) = A_f(-\mathbf{K}_i, -\mathbf{K}). \quad (A3)$$

When the in-water scattering amplitude has been found, all the basic characteristics of the scattered field can be determined. For example, the coherent reflection coefficient is defined by the following equation for the averaged scattering amplitude, or its coherent component

$$\langle A_f(\mathbf{K}, \mathbf{K}_i) \rangle = \delta(\mathbf{K} - \mathbf{K}_i) \overline{W}_f(\mathbf{K}_i) \nu_f(\mathbf{K}_i) k_f. \quad (A4)$$

Generally, the coherent reflection coefficient, $\overline{W}_f(\mathbf{K}_i)$, is not equal to the zeroth-order reflection coefficient, but this distinction is not significant in the present problem.

The scattering amplitude will be used to obtain the scattering cross section through the equation[31–34]

$$\langle A_f'(\mathbf{K}_s, \mathbf{K}_i) A_f'^*(\mathbf{K}_s', \mathbf{K}_i) \rangle = \delta(\mathbf{K}_s - \mathbf{K}_s') \sigma(\mathbf{K}_s, \mathbf{K}_i), \quad (A5)$$

where $A_f'(\mathbf{K}_s, \mathbf{K}_i) = A_f(\mathbf{K}_s, \mathbf{K}_i) - \langle A_f(\mathbf{K}_s, \mathbf{K}_i) \rangle$ is the incoherent component of the scattering amplitude and it is assumed that the statistics of the random sea bed are stationary in the two transverse (horizontal) coordinates. The water column is assumed to be homogeneous, supporting plane waves, and the scattering cross section is assumed to be the sum of contributions from interface roughness and volume inhomogeneity.

APPENDIX B: INTERFACE SCATTERING

The total scalar potential for particle displacement in the sea bed will be expressed in terms of a scattering amplitude, invoking the Rayleigh hypothesis (waves traveling toward the boundary are neglected).

$$\phi_p(\mathbf{r}) = \int \frac{d^2 K}{k_f \nu_p(\mathbf{K})} A_p(\mathbf{K}, \mathbf{K}_i) \exp(i\mathbf{k}_p^-(\mathbf{K}) \cdot \mathbf{r}), \quad (B1)$$

and the vector potential for particle displacement in the sediment will be expressed as

$$\boldsymbol{\psi}(\mathbf{r}) = \int \frac{d^2 K}{k_f \nu_t(\mathbf{K})} \mathbf{A}_t(\mathbf{K}, \mathbf{K}_i) \exp(i\mathbf{k}_t^-(\mathbf{K}) \cdot \mathbf{r}), \quad (B2)$$

where

$$\mathbf{A}_t(\mathbf{K}, \mathbf{K}_i) = \mathbf{e}_h^-(\mathbf{K}) A_v(\mathbf{K}, \mathbf{K}_i) + \mathbf{e}_v^-(\mathbf{K}) A_h(\mathbf{K}, \mathbf{K}_i). \quad (B3)$$

These scattering amplitudes include both the coherent and incoherent parts of the fields. The incoherent roughness scattering amplitudes in the Born approximation have the general form

$$A_\alpha'(\mathbf{K}_s, \mathbf{K}_i) = iH_\alpha(\mathbf{K}_s, \mathbf{K}_i) Z(\mathbf{K}_s - \mathbf{K}_i), \quad \alpha = f, p, v, h, \quad (B4)$$

where $Z(\mathbf{K})$ is the Fourier transform of the interface relief function, Eq. (1). Then Eq. (A5) leads directly to the equation for the roughness scattering cross section, Eq. (25). Thus the purpose of this appendix is to outline the derivation of the roughness scattering amplitude and, particularly, Eq. (27). As discussions of this problem have been given by others,[3,6] this appendix will only give a brief outline that emphasizes the physics and establishes notation convenient for computation and consistent with the volume scattering case.

The scattering amplitude is determined by imposing the boundary conditions, Eqs. (6) and (8), on the fields. The derivative operations that yield the displacement and shear are readily implemented in the plane-wave expansions, where derivatives become multiplication. For example, the displacement due to the upward wave in the water is

$$\mathbf{u}^{(f)}(\mathbf{r}) = i \int \frac{d^2 K}{\nu_f(\mathbf{K})} \mathbf{e}_f^+(\mathbf{K}) A_f(\mathbf{K},\mathbf{K}_i) \exp(i\mathbf{k}_f^+(\mathbf{K}) \cdot \mathbf{r}),$$

(B5)

and the displacement due to shear in the sea bed is

$$\mathbf{u}^{(t)}(\mathbf{r}) = i a_t^{-1} \int \frac{d^2 K}{\nu_t(\mathbf{K})} \left[-\mathbf{e}_v^-(\mathbf{K}) A_v(\mathbf{K},\mathbf{K}_i) \right.$$
$$\left. + \mathbf{e}_h^-(\mathbf{K}) A_h(\mathbf{K},\mathbf{K}_i) \right] \exp(i\mathbf{k}_t^-(\mathbf{K}) \cdot \mathbf{r}).$$

(B6)

The additional derivatives needed to form the stress tensor introduce additional wave vector factors, which are taken as unit vectors multiplied by wave numbers. The derivative factors comprise the matrix given in Eq. (32). The first column of $E^{(n)}(\mathbf{K})$ pertains to the in-water scattering amplitude, while the second, third, and fourth pertain to the p, v, and h fields in the sea bed material. The fifth column pertains to the incident field. The boundary conditions require that the differences in normal displacement and normal tractions vanish across the boundary, accordingly, the matrix $E^{(n)}(\mathbf{K})$ contains appropriate sign reversals. The first three rows ($m = 1,2,3$) of $E^{(n)}(\mathbf{K})$ express the derivatives needed for the stress tensor, σ_{mn}, and the last row expresses the derivatives needed for the nth component of displacement. That is, considering the plane-wave expansion

$$X^{(n)} = \int d^2 K \, E^{(n)}(\mathbf{K}) U,$$

(B7)

with

$$U = \begin{pmatrix} \nu_f^{-1}(\mathbf{K}) A_f(\mathbf{K},\mathbf{K}_i) \exp(i\mathbf{k}_f^+(\mathbf{K}) \cdot \mathbf{r}) \\ \nu_p^{-1}(\mathbf{K}) A_p(\mathbf{K},\mathbf{K}_i) \exp(i\mathbf{k}_p^-(\mathbf{K}) \cdot \mathbf{r}) \\ \nu_t^{-1}(\mathbf{K}) A_v(\mathbf{K},\mathbf{K}_i) \exp(i\mathbf{k}_t^-(\mathbf{K}) \cdot \mathbf{r}) \\ \nu_t^{-1}(\mathbf{K}) A_h(\mathbf{K},\mathbf{K}_i) \exp(i\mathbf{k}_t^-(\mathbf{K}) \cdot \mathbf{r}) \\ k_f \delta(\mathbf{K} - \mathbf{K}_i) \exp(i\mathbf{k}_f^-(\mathbf{K}) \cdot \mathbf{r}) \end{pmatrix},$$

(B8)

the mth row of $X^{(n)}$ ($m = 1,2,3$) is proportional to the water–sea bed difference in the mn component of stress, and the fourth row is proportional to the water–sea bed difference in the nth component of the displacement vector.

The boundary conditions can now be written as

$$X^{(1)} \partial_1 \zeta(\mathbf{R}) + X^{(2)} \partial_2 \zeta(\mathbf{R}) - X^{(3)} = 0,$$

(B9)

with $x_3 = \zeta(\mathbf{R})$. To obtain the zeroth- and first-order solutions, the scattering amplitudes are expressed as a sum of zeroth- and first-order terms, the former being the flat-surface solution and the latter being linear functionals of $\zeta(\mathbf{R})$:

$$A_\alpha(\mathbf{K},\mathbf{K}_i) = A_\alpha^{(0)}(\mathbf{K},\mathbf{K}_i) + A_\alpha'(\mathbf{K},\mathbf{K}_i).$$

(B10)

Also, the exponentials used are expanded to first order in $\zeta(\mathbf{R})$ with $x_3 = \zeta(\mathbf{R})$,

$$\exp(i\mathbf{k}_\alpha^\pm(\mathbf{K}) \cdot \mathbf{r}) = \exp(i\mathbf{K} \cdot \mathbf{R})[1 \pm i k_f \nu_\alpha(\mathbf{K}) \zeta(\mathbf{R}) + \cdots].$$

(B11)

Finally, a Fourier transform of Eq. (B9) with respect to $\mathbf{R}$ is taken, the definition

$$Z(\mathbf{K}) = \frac{1}{(2\pi)^2} \int d^2 R \, \exp(-i\mathbf{K} \cdot \mathbf{R}) \zeta(\mathbf{R})$$

(B12)

is used, and the derivatives of $\zeta(\mathbf{R})$ in Eq. (B9) are treated using

$$i\mathbf{K}Z(\mathbf{K}) = \frac{1}{(2\pi)^2} \int d^2 R \, \exp(-i\mathbf{K} \cdot \mathbf{R}) \nabla \zeta(\mathbf{R}).$$

(B13)

The zeroth-order terms yield

$$P^{(3)}(\mathbf{K}_i) Y_1^{-1}(\mathbf{K}_i) \mathbf{A}^{(0)}(\mathbf{K}_s,\mathbf{K}_i) + k_f \mathbf{Q}^{(3)}(\mathbf{K}_i) \delta(\mathbf{K}_s - \mathbf{K}_i) = 0,$$

(B14)

where the zeroth-order scattering amplitudes are related to the transformation coefficients as follows:

$$A^{(0)}(\mathbf{K}_s,\mathbf{K}_i) = k_f Y_1(\mathbf{K}_i) S_0(\mathbf{K}_i) \delta(\mathbf{K}_s - \mathbf{K}_i).$$

(B15)

Equation (B14) is equivalent to Eq. (41).

The equation for first-order terms is

$$i k_f^2 B(\mathbf{K}_s,\mathbf{K}_i) D_0(\mathbf{K}_i) Z(\mathbf{K}_s - \mathbf{K}_i)$$
$$- P^{(3)}(\mathbf{K}_s) Y_1^{-1} A'(\mathbf{K}_s,\mathbf{K}_i) = 0,$$

(B16)

where $B(\mathbf{K}_s,\mathbf{K}_i)$ is given by Eq. (29) and $A'(\mathbf{K}_s,\mathbf{K}_i)$ is a column matrix comprised of the first-order approximation to the incoherent scattering amplitudes. Equation (B16) is equivalent to Eqs. (27) and (B4).

APPENDIX C: VOLUME SCATTERING

This Appendix outlines first-order perturbation theory (Born approximation) for scattering from an inhomogeneous elastic half space with planar boundary and fluid above. This treatment is the same in principle, but less detailed than that given by Ivakin.[27] This appendix uses different notation than Ivakin,[27] and a more general expression for the bistatic cross section is developed here, in a form convenient for computation.

Consider small fluctuations of elastic medium parameters and corresponding corrections to the displacement field and potentials, making corresponding change in the wave equations

$$\rho, \lambda, \mu, \mathbf{u}, \phi, \boldsymbol{\psi} \to \rho + \rho', \lambda + \lambda', \mu + \mu', \mathbf{u} + \mathbf{u}', \phi + \phi',$$
$$\boldsymbol{\psi} + \boldsymbol{\psi}'.$$

This gives, for the zero-order potentials, the following well-known wave equations for a homogeneous elastic medium

$$(\nabla^2 + k_p^2) \phi = 0,$$

(C1)

$$(\nabla^2 + k_t^2) \boldsymbol{\psi} = 0,$$

(C2)

and the following equation for the first-order field perturbation in the displacement

$$\rho \omega^2 \mathbf{u}' + \rho c_p^2 \nabla(\nabla \cdot \mathbf{u}') - \rho c_t^2 \nabla \times \nabla \times \mathbf{u}' = \mathbf{f},$$

(C3)

where $\mathbf{f}$ is a vector with components

$$f_i = -\rho' \omega^2 u_i - \partial_i(\lambda'(\nabla \cdot \mathbf{u})) - \sum_j \partial_j(\mu'(\partial_i u_j + \partial_j u_i)),$$

$$i, j = 1,2,3.$$

(C4)

This corresponds to the following pair of first-order equations for the perturbed potentials:

$$\rho(\omega^2 + c_p^2 \nabla^2)\nabla^2\phi' = \nabla \cdot \mathbf{f}, \tag{C5}$$

$$\rho(\omega^2 + c_t^2 \nabla^2)\nabla \times \nabla \times \boldsymbol{\psi}' = \nabla \times \mathbf{f}. \tag{C6}$$

A solution of these equations is

$$\phi'(\mathbf{r}) = -\frac{1}{\rho\omega^2}\int G_p(\mathbf{r}-\mathbf{r}')\nabla\cdot\mathbf{f}(\mathbf{r}')d^3r', \tag{C7}$$

$$\boldsymbol{\psi}'(\mathbf{r}) = \frac{1}{\rho\omega^2}\int G_t(\mathbf{r}-\mathbf{r}')\nabla\times\mathbf{f}(\mathbf{r}')d^3r', \tag{C8}$$

where $G_\alpha(\mathbf{r})$, $\alpha = p,t$, are free-space Green's functions, which can be expressed as expansions in plane waves propagating up toward the interface

$$G_\alpha(\mathbf{r}) = -\frac{1}{4\pi r}\exp(ik_\alpha r)$$

$$= -\frac{i}{8\pi^2}\int \frac{d^2K}{k_f\nu_\alpha(\mathbf{K})}\exp(i\mathbf{k}_\alpha^+(\mathbf{K})\cdot\mathbf{r}). \tag{C9}$$

Then the scattered fields which are incident on the interface can be also expressed in terms of plane wave expansions

$$\phi'(\mathbf{r}) = \int \frac{d^2K}{k_f\nu_p(\mathbf{K})}A_p'(\mathbf{K},\mathbf{K}_i)\exp(i\mathbf{k}_p^+(\mathbf{K})\cdot\mathbf{r}), \tag{C10}$$

$$\boldsymbol{\psi}'(\mathbf{r}) = \int \frac{d^2K}{k_f\nu_t(\mathbf{K})}\mathbf{A}_t'(\mathbf{K},\mathbf{K}_i)\exp(i\mathbf{k}_t^+(\mathbf{K})\cdot\mathbf{r}), \tag{C11}$$

where

$$A_p' = \frac{i\pi}{\rho\omega^2}F_{\mathbf{k}_p^+}(\nabla\cdot\mathbf{f}), \tag{C12}$$

$$\mathbf{A}_t' = -\frac{i\pi}{\rho\omega^2}F_{\mathbf{k}_t^+}(\nabla\times\mathbf{f}), \tag{C13}$$

$$F_{\mathbf{k}}(Q) = (2\pi)^{-3}\int Q(\mathbf{r})\exp(-i\mathbf{k}\cdot\mathbf{r})d^3r. \tag{C14}$$

Transmission of these waves through the flat interface is governed by the expression

$$\frac{A_f'(\mathbf{K},\mathbf{K}_i)}{\nu_0(\mathbf{K})} = W_p^+(\mathbf{K})\frac{A_p'(\mathbf{K},\mathbf{K}_i)}{\nu_p(\mathbf{K})}$$

$$+ W_t^+(\mathbf{K})\frac{\mathbf{e}_h(\mathbf{K})\cdot\mathbf{A}_t'(\mathbf{K},\mathbf{K}_i)}{\nu_t(\mathbf{K})}, \tag{C15}$$

where the W_α^+ are the transmission coefficients for the upward direction and are related to downward direction coefficients, W_α, as follows

$$W_p^+/\nu_p = a_\rho W_p/\nu_f, \tag{C16}$$

$$W_t^+/\nu_t = -a_\rho W_t/\nu_f. \tag{C17}$$

Note that $W_t = W_v$, and that our choice of polarization conventions differs from that of Brekhovskikh,[29] thereby introducing a negative sign in the relation between the upward and downward shear wave transmission coefficients.

Then, using the zero-order solution in Eq. (C4), one obtains the following expression for the scattering amplitude

$$A_f'(\mathbf{K},\mathbf{K}_i) = -i\pi k_f^2 a_\rho \sum_{\eta,\beta} d_{\eta\beta}F_{\mathbf{q}_\eta}(\boldsymbol{\epsilon}_\beta), \tag{C18}$$

with $\mathbf{q}_\eta$ as defined by Eqs. (45)–(47) and $d_{\eta\beta}$ as defined by Eqs. (48)–(54). Using Eqs. (C14) and (C18), the expression for the cross section, Eq. (43), can be obtained.

[1] A. D. Lapin, ''Sound scattering at a rough solid surface,'' Sov. Phys. Acoust. **10**, 58–64 (1964).

[2] A. D. Lapin, ''Scattering of sound by a solid layer with rough boundaries,'' Sov. Phys. Acoust. **12**, 46–51 (1966).

[3] D. K. Dacol and D. H. Berman, ''Sound scattering from a randomly rough fluid–solid interface,'' J. Acoust. Soc. Am. **84**, 292–302 (1988).

[4] E. Y. T. Kuo, ''Acoustic wave scattering from two solid boundaries at the ocean bottom,'' IEEE J. Ocean Eng. **17**, 159–170 (1992).

[5] W. A. Kuperman and H. Schmidt, ''Rough surface elastic wave scattering in a horizontally stratified ocean,'' J. Acoust. Soc. Am. **79**, 1767–1777 (1986).

[6] H. H. Essen, ''Scattering from a rough sedimental seafloor containing shear and layering,'' J. Acoust. Soc. Am. **95**, 1299–1310 (1994).

[7] T. Yang and S. L. Broschat, ''Acoustic scattering from a fluid–elastic–solid interface using the small slope approximation,'' J. Acoust. Soc. Am. **96**, 1796–1803 (1994).

[8] D. Wurmser, ''A manifestly reciprocal theory of scattering in the presence of elastic media,'' J. Math. Phys. **37**, 4434–4479 (1996).

[9] A. N. Ivakin, ''On sound scattering by multi-scale bottom inhomogeneities,'' Oceanology **21**, 26–27 (1981).

[10] A. N. Ivakin and Yu. P. Lysanov, ''Theory of underwater sound scattering by random inhomogeneities of the bottom,'' Sov. Phys. Acoust. **27**, 61 (1981).

[11] A. N. Ivakin and Yu. P. Lysanov, ''Underwater sound scattering by volume inhomogeneities of a bottom medium bounded by a rough surface,'' Sov. Phys. Acoust. **27**, 212–215 (1981).

[12] A. N. Ivakin, ''Sound scattering by random inhomogeneities of stratified ocean sediments,'' Sov. Phys. Acoust. **32**, 492–496 (1986).

[13] P. C. Hines, ''Theoretical model of acoustic backscattering from a smooth seabed,'' J. Acoust. Soc. Am. **88**, 325–334 (1990).

[14] D. R. Jackson, ''Models for scattering from the sea bed,'' Proc. Inst. Acoust. **16**, 161–169 (1994).

[15] A. P. Lyons, A. L. Anderson, and F. S. Dwan, ''Acoustic scattering from the seafloor: Modeling and data comparison,'' J. Acoust. Soc. Am. **95**, 2441–2451 (1994).

[16] N. G. Pace, ''Low frequency acoustic backscatter from the sea bed,'' Proc. Inst. Acoust. **16**, 181–188 (1994).

[17] D. Tang, ''Acoustic wave scattering from a random ocean bottom,'' Ph.D. thesis, Massachusetts Institute of Technology and Woods Hole Oceanographic Institution 1991.

[18] D. Tang, ''A note on scattering by a stack of rough interfaces,'' J. Acoust. Soc. Am. **99**, 1414–1418 (1996).

[19] T. Yamamoto, ''Acoustic scattering in the ocean from velocity and density fluctuations in the sediments,'' J. Acoust. Soc. Am. **99**, 866–879 (1996).

[20] P. A. Crowther, ''Some statistics of the sea-bed and acoustic scattering therefrom,'' in *Acoustics and Sea-Bed*, edited by N. G. Pace (Bath University, Bath, England, 1983).

[21] A. N. Ivakin, ''Sound scattering by random volume inhomogeneities and small surface roughness of an underwater ground,'' in Voprosy sudostroenija: Akustika **17**, 20–25 (1983) (in Russian).

[22] A. N. Ivakin, ''Backscattering of sound by the ocean bottom. Theory and experiment,'' in *Acoustics of Ocean Medium*, edited by L. M. Brekhovskikh and I. B. Andreeva (Nauka, Moscow, 1989), pp. 160–169 (in Russian).

[23] A. N. Ivakin, ''Modeling of sound scattering by the sea floor,'' J. Phys. IV, Colloque C5 **4**, 1095–1098 (1994).

[24] A. N. Ivakin, ''Reverberation in a plane randomly inhomogeneous waveguide under narrow-band acoustic probing,'' Acoust. Phys. **40**, 426–427 (1994).

[25] A. N. Ivakin, ''Sound scattering by rough interface and volume inhomogeneities of the sea bottom,'' Acoust. Phys. **40**, 427–428 (1994).

[26] E. Y. T. Kuo, ''Joint perturbation scattering characterization of a littoral

ocean bottom reverberation: Theory, scattering strength predictions, and data comparisons," IEEE J. Ocean. Eng. **20**, 198–210 (1995).

[27] A. N. Ivakin, "Sound scattering by inhomogeneities of an elastic half-space," Sov. Phys. Acoust. **36**, 377–380 (1990).

[28] A. N. Ivakin and D. R. Jackson, "Effects of shear elasticity on sea bed scattering: Numerical examples," J. Acoust. Soc. Am. **103**, 346–354 (1998).

[29] L. M. Brekhovskih, *Waves in Layered Media* (Academic, San Diego, 1980).

[30] L. D. Landau and E. M. Lifshitz, *Theory of Elasticity* (Pergamon, New York, 1970).

[31] G. G. Zipfel, Jr. and J. A. DeSanto, "Scattering of a scalar wave from a random rough surface: a diagrammatic approach," J. Math. Phys. **13**, 1903–1911 (1972).

[32] E. I. Thorsos and D. R. Jackson, "The validity of the perturbation approximation for rough surface scattering using a Gaussian roughness spectrum," J. Acoust. Soc. Am. **86**, 261–277 (1989).

[33] A. G. Voronovich, *Wave Scattering from Rough Surfaces* (Springer-Verlag, Berlin, 1994).

[34] D. H. Berman, "Renormalization of propagation in a waveguide with rough boundaries," J. Acoust. Soc. Am. **92**, 309–314 (1992).

Effects of shear elasticity on sea bed scattering: Numerical examples

Anatoliy N. Ivakin
Andreev Acoustics Institute, Shvernika 4, Moscow 117036, Russia

Darrell R. Jackson
Applied Physics Laboratory, College of Ocean and Fishery Sciences, 1013 N. E. 40th Street, Seattle, Washington 98105-6698

It is known that marine sediments can support both compressional and shear waves. However, published work on scattering from irregular elastic media has not examined the influence of shear on sea bed scattering in detail. A perturbation model previously developed by the authors for joint roughness-volume scattering is used to study the effects of elasticity for three sea bed types: sedimentary rock, sand with high shear speed, and sand with ''normal'' shear wave speed. Both bistatic and monostatic cases are considered. For sedimentary rock it is found that shear elasticity tends to increase the importance of volume scattering and decrease the importance of roughness scattering relative to the fluid case. Shear effects are shown to be small for sands. © *1998 Acoustical Society of America.* [S0001-4966(98)02001-3]

PACS numbers: 43.30.Pc, 43.60.Pt, 43.30.Gv, 43.30.Ma [JHM]

INTRODUCTION

In a previous paper, the Born approximation (first-order perturbation theory) was developed for sound scattering by rough, elastic sea beds.[1] This formalism combines roughness scattering and scattering due to volume inhomogeneities. An example was given showing strong and complicated elasticity effects for roughness and volume scattering for sea bed rock. Essen[2] has used the Born approximation to treat sea bed roughness scattering for types ranging from very soft sediment to basalt. His results indicate that shear effects can be important for sands as well as for consolidated sediments and basalt. Yang and Broschat,[3] however, have applied the Born approximation and small-slope approximation to the interface scattering problem and give an example indicating that shear effects should not be important for rough sands. Ivakin[4] reached a similar conclusion with respect to volume scattering from sands.

One purpose of the present article is to provide an evaluation of the importance of shear effects in both volume and roughness scattering from sea bed types ranging from sand to rock along with a comparison of the volume and roughness components of scattering. Another purpose is to study the dependence of volume scattering on the statistics obeyed by the volume fluctuations, e.g., correlations between volume parameters.

Use of the Born approximation limits the quantitative validity of the results of this article to sea beds having small roughness and relatively low levels of fluctuation in volume parameters. It is expected, however, that our results will have *qualitative* validity more generally. That is, when the Born approximation indicates that shear effects are large, this qualitative statement is likely to be true even when the level of roughness or volume inhomogeneity is sufficient to invalidate the Born approximation.

I. SEA BED STATISTICAL MODEL

It is assumed that a rough interface separates a lossless, homogeneous fluid (representing sea water) from an inhomogeneous elastic sea bed medium. Bulk properties of the sea bed are defined by density, ρ, and compressional and shear wave speeds, c_p and c_t. Subscripts, p and t, here and below denote longitudinal (compressional) and transverse (shear) waves, respectively. In the water, c_t is taken to be zero.

The sea bed parameters will be divided into two classes: those representing the average, nonfluctuating values of bulk properties, such as density and wave speeds, and those describing sea bed random properties. The former are defined by the sea bed type and will be assigned values appropriate to sand and rock. The latter are defined by the statistics of the random fluctuation of bulk parameters and interface relief.

A. Average properties

The average sea bed parameters of interest are as follows. The density ratio, $a_\rho = \rho/\rho_f$, is the ratio of the average sediment mass density to that of the overlying water. The compressional wave speed ratio, $a_p = c_p/c_f$, is likewise the ratio of the average sediment compressional wave speed, c_p, and the water compressional wave speed, c_f. This ratio is complex, with imaginary part determining absorption loss. The shear speed ratio, $a_t = c_t/c_f$, is the ratio of the average complex sediment shear speed, c_t, and the compressional wave speed in the water. The ''loss parameters'' [5,6] can be expressed in terms of the real and imaginary parts of the compressional and shear speed ratios

$$\delta_\alpha = -\frac{\text{Im}[a_\alpha]}{\text{Re}[a_\alpha]}, \tag{1}$$

where the subscript $\alpha = p, t$ denotes the wave type in the seabed.

B. Model for roughness

The roughness two-dimensional (2-D) spectrum is taken to be of the form

$$\Phi_2^{(r)}(\mathbf{K}) = \frac{B^{(r)}}{(K^2 + K_0^2)^{\gamma_r/2}}, \tag{2}$$

where $\mathbf{K} = (K_1, K_2)$, $K = \sqrt{K_1^2 + K_2^2}$. Equation (2) assumes that roughness statistics are stationary and isotropic, with a spectrum that obeys a power law for $K^2 \gg K_0^2$. The parameter K_0 is an inverse correlation scale for roughness in the transverse directions. The roughness spectrum strength, $B^{(r)}$, and the power exponent, γ_r, can be estimated, as shown below, from available one-dimensional (1-D) data.

The integral over all $\mathbf{K}$ (including negative spatial frequencies) of the spectrum yields the mean-square roughness,

$$h^2 = \int \Phi_2^{(r)}(\mathbf{K}) d^2 K. \tag{3}$$

This gives the following expression for the dimensionless spectral strength:

$$B^{(r)} = h^2 K_0^{\gamma_r - 2}(\gamma_r/2 - 1)/\pi. \tag{4}$$

This requires $\gamma_r > 2$, but this is shown below to be usually valid.

Most available data on roughness properties are in the form of one-dimensional spectra, $\Phi_1^{(r)}(K_1)$. Usually they can be well approximated by the power law

$$\Phi_1^{(r)}(K_1) = \frac{A^{(r)} h_0^{3-\xi_r}}{K_1^{\xi_r}}, \quad K_1 \gg K_0. \tag{5}$$

The trivial parameter $h_0 = 1$ m is introduced for convenience to yield a dimensionless roughness spectrum strength, $A^{(r)}$. Typical measured values (see, e.g., Ref. 7) are $A^{(r)} \approx 10^{-6}$ to 10^{-2}, and $\xi_r \approx 1$ to 3.

The relation between 1-D and 2-D spectra is given by the integral

$$\Phi_1^{(r)}(K_1) = \int \Phi_2^{(r)}(\mathbf{K}) dK_2. \tag{6}$$

Then, using Eq. (2), one obtains

$$\Phi_1^{(r)}(K_1) = \frac{2B^{(r)}}{(K_1^2 + K_0^2)^{(\gamma_r - 1)/2}} \int_0^\infty \frac{dx}{(x^2 + 1)^{\gamma_r/2}}. \tag{7}$$

Comparing Eq. (7) to (5), one obtains the relation between parameters $B^{(r)}$ and $A^{(r)}$, γ_r and ξ_r,

$$\gamma_r = \xi_r + 1, \tag{8}$$

$$B^{(r)} = h_0^{3-\xi_r} F(\xi_r) A^{(r)}, \tag{9}$$

where

$$F(\xi_r) = \frac{\Gamma((1+\xi_r)/2)}{\Gamma(1/2)\Gamma(\xi_r/2)}, \tag{10}$$

with Γ being the gamma function. In particular, one obtains $F(1) = 1/\pi$, $F(2) = 1/2$, $F(3) = 2/\pi$, $F(4) = 3/4$. This generalizes the result, given in Jackson and Briggs[5] for the case $K_0 = 0$. Note that $\xi_r \approx 1$ to 3 corresponds to $\gamma_r \approx 2-4$.

C. Model for volume inhomogeneities

A description of the statistics of volume inhomogeneities is given by a matrix of spatial (three-dimensional) cross spectra. These are Fourier transforms of cross-correlation functions for the relative fluctuations $\epsilon_\rho = \Delta\rho/\rho$, $\epsilon_p = \Delta c_p/c_p$, $\epsilon_t = \Delta c_t/c_t$. These relative fluctuations will be collectively designated ϵ_β with $\beta = \rho, p, t$. In this notation, the cross spectra are taken to be of the form

$$\Phi_{\beta\beta'}^{(v)}(\mathbf{K}, q) = \frac{B_{\beta\beta'}}{(q_0^2 + q^2 + K^2 a^2)^{\gamma_v/2}}. \tag{11}$$

This equation assumes that inhomogeneity statistics are stationary and isotropic in transverse directions, with a spectrum that obeys a power law if $q^2 + K^2 a^2 \gg q_0^2$. The parameter q_0 is an inverse correlation scale for inhomogeneities in the vertical direction. The so-called aspect ratio, a, specifies the anisotropy of the inhomogeneities and is the ratio of horizontal to vertical correlation scales.[8-11] For $a = 1$, the inhomogeneities are isotropic on the average and have a spherical form (referring to surfaces of constant correlation in spatial lag space). For $a \gg 1$, the inhomogeneities are strongly anisotropic and constant correlation surfaces are thin oblate ellipsoids. Generally, in the case of transverse anisotropy, one more aspect ratio must be introduced corresponding to the third correlation scale.[12] Angular coordinates for orientation of the inhomogeneity ellipsoids in space can also be introduced.[10,11]

The three-dimensional integrals analogous to Eq. (3) are the elements of the covariance matrix for volume fluctuations

$$\langle \epsilon_\beta \epsilon_{\beta'}^* \rangle = \int \Phi_{\beta\beta'}^{(v)}(\mathbf{K}, q) d^2 K \, dq. \tag{12}$$

These integrals are infinite if $\gamma_v \leq 3$ but can be made finite for all γ_v if a high-frequency cutoff is introduced. Accordingly, it will be assumed that

$$\Phi_{\beta\beta'}^{(v)}(\mathbf{K}, q) = 0 \tag{13}$$

for

$$K^2 a^2 + q^2 > (q_0/\epsilon)^2, \quad \epsilon \ll 1. \tag{14}$$

Introduction of the small dimensionless cutoff parameter, ϵ, provides smooth behavior of the corresponding correlation functions for small spatial lags and also yields finite variance for the inhomogeneity fluctuations for any γ_v. Obviously, this is important as experimental data have finite variance and have finite spatial resolution with respect to both large and small scales. The "small" spatial lags for which the cutoff has effect have scales comparable to, or smaller than the components of the vector $(a, a, 1)\epsilon/q_0$.

The matrix elements $B_{\beta\beta'}$ can be determined from Eq. (12); see the Appendix. Otherwise, available geoacoustic data can be used for the estimation of the spectrum parameters. In the case of strongly correlated or anticorrelated fluctuations one can consider any one of the three fluctuations, say density, as defining the other two. This parameter will be called the "reference" parameter. In this case, put

$$\epsilon_\beta = r_{\beta\rho} \epsilon_\rho, \tag{15}$$

where the corresponding speed fluctuation ratios (with respect to fluctuations of the density) are

$$r_{\beta\rho} = \frac{\rho}{c_\beta}\left(\frac{\partial c_\beta}{\partial \rho}\right), \quad \beta = p, t, \tag{16}$$

where $r_{\beta\rho}$ can be taken from compilations of geoacoustic data, for example, Hamilton's[13–16] and others:[17,18] In this case

$$B_{\beta\beta'} = r_{\beta\rho} r_{\beta'\rho} B_{\rho\rho} \tag{17}$$

for all combinations of β and β', with $r_{\rho\rho} = 1$.

The parameters $B_{\rho\rho}$ and γ_v can be also obtained from available data. Most data on fluctuations of bulk properties provide only one-dimensional (vertical) spectra, $\Phi_1^{(v)}(q)$. Usually they can be well approximated by the power law

$$\Phi_1^{(v)}(q) = \frac{A^{(v)} h_0^{1-\xi_v}}{q^{\xi_v}}, \quad q \gg q_0. \tag{18}$$

Again, the parameter $h_0 = 1$ m is used to obtain a dimensionless spectrum strength, $A^{(v)}$. Typical measured values (see, e.g., Refs. 9, 10, 19–22) are $A^{(v)} \approx 10^{-5} - 10^{-2}$, $\xi_v \approx 0.5 - 2$. Typical estimates obtained from inversions of geoacoustical data[8–10] are $a \approx 1 - 10$.

The relation between 1-D and 3-D spectra, generalized in Yefimov et al.[9] for anisotropic inhomogeneities with aspect ratio a, is given by the expression

$$\Phi_3^{(v)}(q') = -\frac{a^2}{2\pi q'}\frac{d\Phi_1^{(v)}(q')}{dq'}, \tag{19}$$

where

$$q' = \sqrt{q^2 + K^2 a^2}. \tag{20}$$

Then, using Eq. (18), one obtains the relation between parameters $B^{(v)}$ and $A^{(v)}$, γ_v and ξ_v,

$$\gamma_v = \xi_v + 2, \tag{21}$$

$$B^{(v)} = h_0^{1-\xi_v} A^{(v)} a^2 \xi_v / (2\pi). \tag{22}$$

II. NUMERICAL EXAMPLES

To illustrate the effects of shear elasticity, we consider scattering from sea beds of varying composition, ranging from sand to solid rock. Finer-grained silts and clays are not considered, as their low shear speeds[2,22] result in negligible shear effects. The parameters c_p, c_t, and ρ that characterize these examples were chosen primarily to illustrate certain points rather than to provide extensive coverage of a range of realistic sea bed types. Some of the chosen examples are
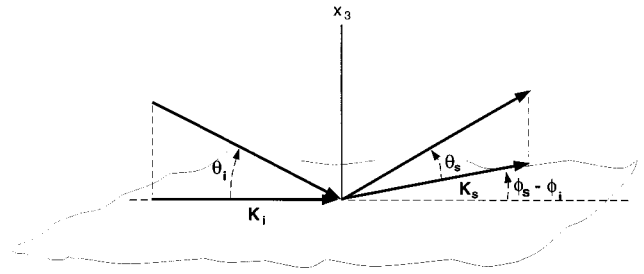
FIG. 1. Geometry relevant to bistatic scattering from a random sea bed.

fairly realistic, others are not. The parameters specified below were used in computing angular dependencies of the scattering strength. With regard to roughness scattering, some of the effects seen in the present examples are visible in other published work.[23,3,2] The intent here is to compare and contrast elasticity effects as they appear in roughness *and* volume scattering.

A. Scattering strength

In this section, the expressions given in Jackson and Ivakin[1] are used for calculation of scattering strength, $10 \log \sigma$, where σ is the scattering cross section per unit area of the sea bed and characterizes the frequency-angular distribution of the mean intensity of field fluctuations in the Fraunhofer zone (or far zone, relative to a scattering surface or volume). The scattering cross section is assumed to be the sum of contributions from interface roughness and volume inhomogeneity in the form

$$\sigma = \sigma_r(\mathbf{K}_s, \mathbf{K}_i) + \sigma_v(\mathbf{K}_s, \mathbf{K}_i), \tag{23}$$

where σ_r and σ_v are components due to roughness and volume scattering, respectively, $\mathbf{K}_s$ and $\mathbf{K}_i$ are horizontal (transverse) components of the scattered and incident wave vectors, correspondingly. Vectors $\mathbf{K}_s$ and $\mathbf{K}_i$ are expressed through the essential angular coordinates of the problem

$$\mathbf{K}_{s,i} = (k_f \cos\theta_{s,i}\cos\phi_{s,i}, \ k_f \cos\theta_{s,i}\sin\phi_{s,i}). \tag{24}$$

These are: grazing angles, θ_i and θ_s, for the incident and scattered acoustic waves, respectively, and the azimuths, ϕ_s and ϕ_i for the incident and scattered waves (see Fig. 1). Frequency enters through the acoustic wave number in the water $k_f = \omega/c_f$. Roughness and volume scattering cross sections, σ_r and σ_v, are expressed in terms of the average parameters of the sea bed, a_ρ, a_p, a_t, and its statistical parameters, the two-dimensional spatial spectrum of roughness, $\Phi^{(r)}(\mathbf{K})$, and the three-dimensional cross-spectra of volume fluctuations, $\Phi_{\beta\beta'}^{(v)}(\mathbf{K},q)$, where $\mathbf{K} = \mathbf{K}_s - \mathbf{K}_i$ and q is the vertical component of the spectral argument.[1]

TABLE I. Parameters defining average, nonfluctuating bulk properties of the illustrative sea bed types.

Descriptive name	Density ratio a_ρ	Compressional speed ratio a_p	Shear speed ratio a_t	Reference
"Normal" stand	2.0	$1.20 - 0.02i$	$0.133 - 0.01i$	Hamilton (1980)
"Shear" sand	2.0	$1.20 - 0.005i$	$0.32 - 0.07i$	Essen (1994)
Sedimentary rock	2.5	$2.30 - 0.004i$	$1.30 - 0.11i$	Essen (1994)

Sea bed type	Volume spectr. strength $A^{(v)}$	Volume spectr. expon. ξ_v	Volume aspect ratio a	Compress. speed fluct. ratio $r_{p\rho}$	Shear speed fluct. ratio $r_{t\rho}$	Rough. spectr. strength $A^{(r)}$	Rough. spectr. expon. ξ_r
Sand	10^{-5}	1	3	0.1	2.0	10^{-5}	3
Rock	10^{-5}	1	3	3.0	4.0	10^{-5}	3

B. Input parameters

Table I lists the average properties of the three sea bed types chosen for illustration of the effects of elasticity on acoustic scattering. These sea bed types include a strongly elastic case (sedimentary rock), a moderately elastic case (sand with unusually high shear speed, ''shear'' sand), and a weakly elastic case (sand with a more typical, ''normal,'' shear speed).

Two different sets of random parameters are used for sands and rock. The roughness and volume parameters are specified below.

The roughness spectral parameters were assigned the values used in Jackson and Ivakin:[1] $\gamma_r = 4$, $K_0 = 10^{-2}$ m^{-1}, and $B^{(r)} = (2/\pi) \times A^{(r)}$ with $A^{(r)} = 10^{-5}$, with the factor $(2/\pi)$ resulting from the relation between 2-D and 1-D roughness spectra.

The reference (density) inhomogeneity spectrum was taken to be of the form given in Eq. (11) with $\gamma_v = 3$, $q_0 = 10^{-2}$ m^{-1}, $B^{(v)}_{\rho\rho} = (2\pi)^{-1} a^2 \times A^{(v)}$ and $A^{(v)} = 10^{-5}$. Again, these parameters were used in Jackson and Ivakin,[1]

FIG. 2. Backscattering strength as a function of grazing angle for the sedimentary rock example. The fluid case uses identical parameters, except the shear wave speed is set to zero. The abscissa is $\theta_s = \theta_i$ with $\phi_s - \phi_i = 180°$. With the parameters used, there is no frequency dependence. Here and below: (a) roughness scattering, total volume perfectly correlated and total volume uncorrelated scattering; (b) scattering from different types of volume inhomogeneities.
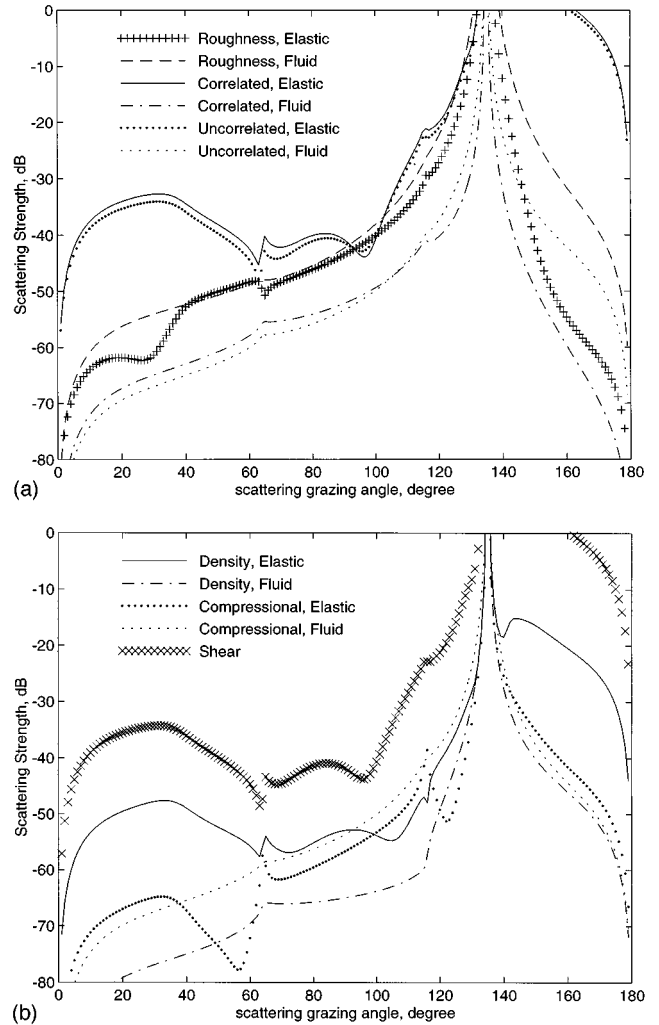
FIG. 3. Bistatic scattering strength as a function of scattered grazing angle for the sedimentary rock example. The grazing angle of the incident wave is 45°. The abscissa is θ_s with $\phi_s - \phi_i = 180°$. All parameters are the same as for Fig. 2.
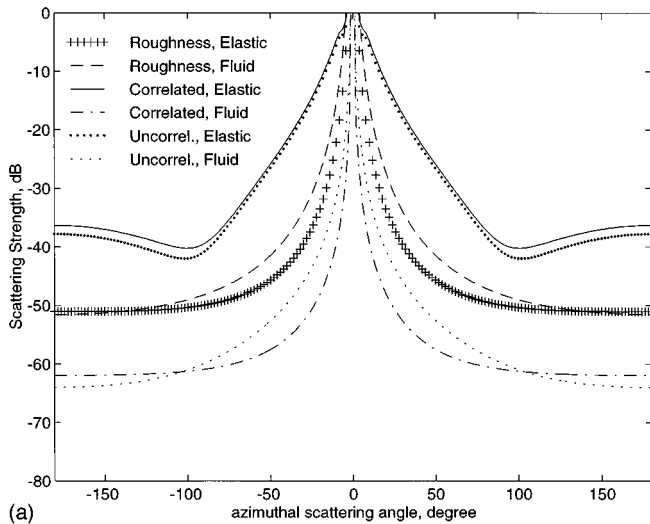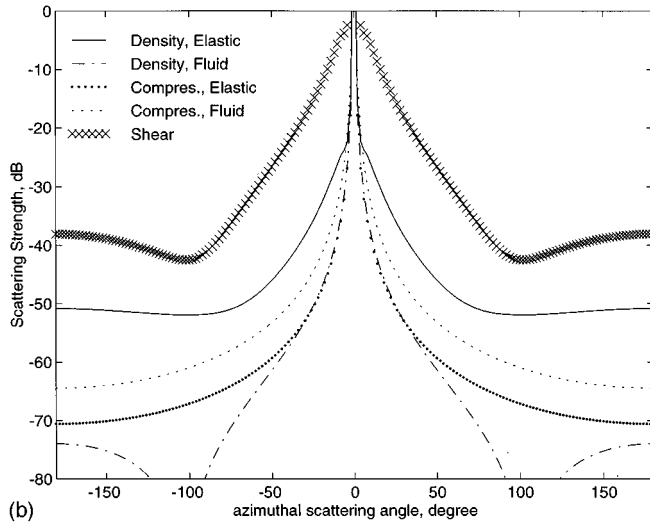
FIG. 4. Bistatic scattering strength as a function of scattered azimuth, $\phi_s - \phi_i$, for the sedimentary rock example. The grazing angles of the incident and scattered waves are $\theta_s = \theta_i = 45°$. All parameters are the same as for Fig. 2.

FIG. 5. Backscattering strength as a function of grazing angle for the ''shear'' sand example. The fluid case uses identical parameters, except the shear wave speed is set to zero. The abscissa is $\theta_s = \theta_i$ with $\phi_s - \phi_i = 180°$. With the parameters used, there is no frequency dependence.

except, here, the aspect ratio is not taken to be unity. The parameter $B^{(v)}_{\rho\rho}$ contains a factor $a^2/(2\pi)$ resulting from the relation between 3-D and 1-D spectra. The corresponding one-dimensional (vertical) spectrum is simply $A^{(v)}/K$, which gives a reasonable fit to the available data.[9]

In the ''correlated'' case, the cross spectrum matrix elements were calculated using Eq. (17) with the ratios $r_{\beta\rho}$ estimated from published relations between geoacoustic parameters[15,17] and listed in Table II for the sea bed types chosen for illustration.

In another case to be considered, the elements of the correlation matrix are taken to be of the form

$$B^{(v)}_{\beta\beta'} = \delta_{\beta\beta'} r^2_{\beta\rho} B^{(v)}_{\rho\rho}.$$ (25)

Because of the Kronecker delta used in Eq. (25), all the nondiagonal elements of the correlation matrix vanish. In this ''uncorrelated'' case, the volume component of the scattering cross section, according to Jackson and Ivakin,[1] will be simply the sum of three components
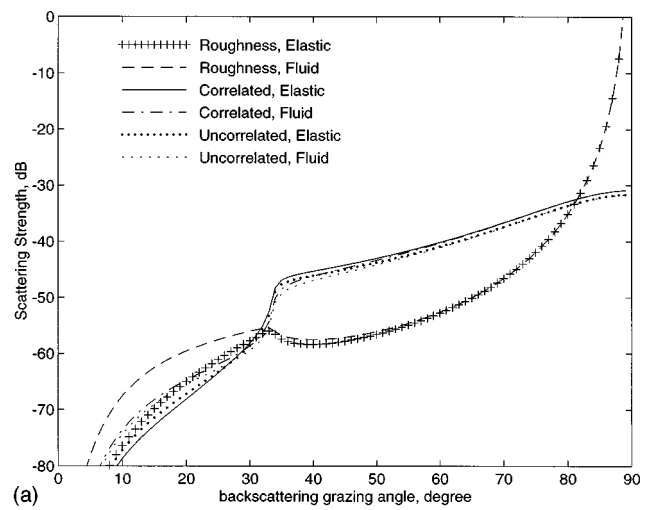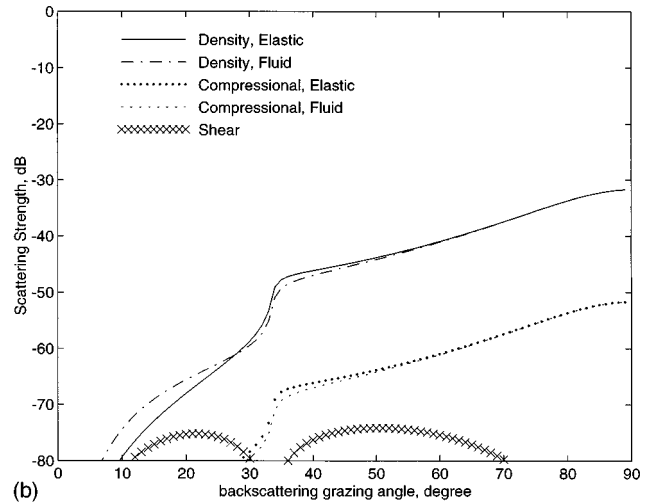
$$\sigma_v = \sum_\beta \sigma^{(v)}_\beta,$$ (26)

where $\sigma^{(v)}_\beta$ correspond to contributions of fluctuations of the three different bulk parameters ($\beta = \rho, c_p, c_t$).

Calculations are presented both for the sum and for each of the terms in Eq. (26). The former permits an evaluation of the role of cross correlations between different volume fluctuations, or nondiagonal elements of the correlation matrix, by comparison of the two extremes: the strongly correlated case and the uncorrelated case. The latter permits a comparison of the role of different types of fluctuation.

III. DISCUSSION

The first example to be considered uses parameters appropriate to sedimentary rock.[2] As the set of figures used in this and following examples is rather involved, an explanation of the arrangement of the figures will be given before discussing the results. Figure 2 shows the monostatic or backscattering case, giving the dependence of scattering strength on backscattering grazing angle. Figure 3 shows the
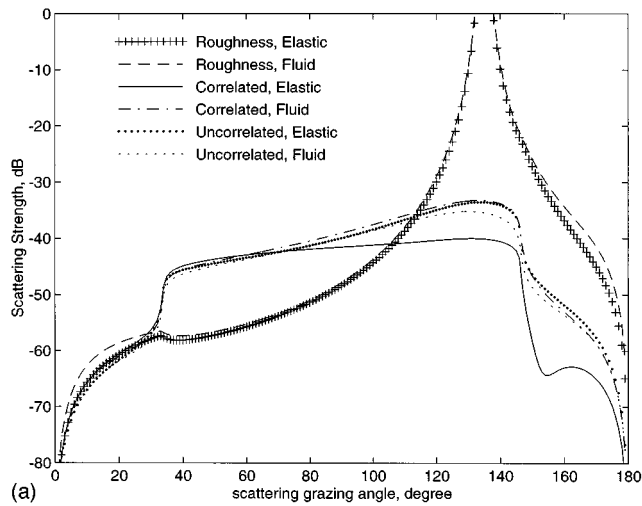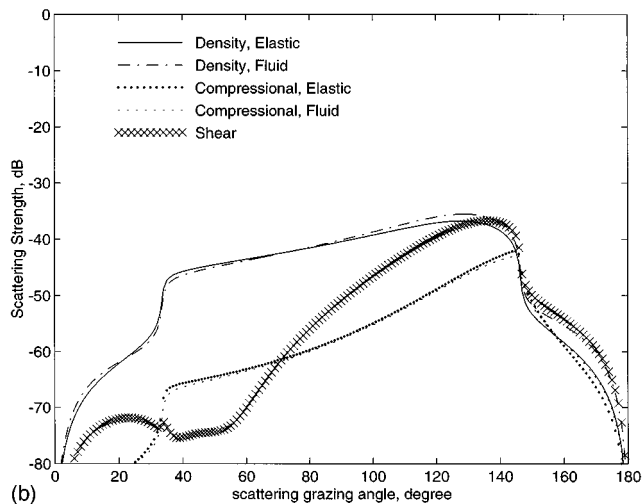
FIG. 6. Bistatic scattering strength as a function of scattered grazing angle for the ''shear'' sand example. The abscissa is θ_s with $\phi_s - \phi_i = 180°$. All parameters are the same as for Fig. 5.

FIG. 7. Bistatic scattering strength as a function of scattered azimuth, $\phi_s - \phi_i$, for the ''shear'' sand example. The grazing angles of the incident and scattered waves are $\theta_s = \theta_i = 45°$. All parameters are the same as for Fig. 5.

dependence of bistatic scattering strength upon scattered grazing angle with the incident grazing angle fixed at 45° and the difference between scattered and incident azimuth fixed at 180°. As the scattered grazing angle varies from 0° to 180°, it passes through the backscatter direction (45°) and the forward, or ''specular,'' direction (135°). Figure 4 shows the dependence of bistatic scattering strength on the difference between scattered and incident azimuthal angles at fixed incidence and scattered grazing angles, both taken to be 45°. All three figures compare the elastic and fluid cases. In the fluid case, the shear wave speed is set to zero and all other parameters are kept the same as in the elastic case. Each of the figures is divided into parts (a) and (b). Part (a) compares three separate cases: roughness scattering, correlated volume scattering and uncorrelated volume scattering. Part (b) compares separate volume scattering mechanisms, fluctuations in density, compressional wave speed, and shear wave speed.

For sedimentary rock, the effects of shear elasticity on both roughness and volume scattering are very strong, as illustrated by Figs. 2–4. Noteworthy effects are:

(i) Figures 2(a) and 3(a) show that roughness scattering strength exhibits dips at grazing angles immediately below the critical angles for shear and compressional waves (39.7° and 64.2°, respectively).

(ii) Shear elasticity decreases roughness scattering strength compared to the fluid case for grazing angles less than the shear critical angle and near the forward direction [Figs. 2(a), 3(a), and 4(a)].

(iii) Elasticity greatly enhances scattering strength for volume scattering in the directions where it decreases roughness scattering (Figs. 2–4). The effects for volume scattering are much larger than the effects for roughness scattering.

(iv) For grazing angles below the compressional critical angle, scattering due to density fluctuations has nearly the same angular dependence as scattering due to shear speed fluctuations [Figs. 2(b) and 3(b)]. For grazing angles above the compressional critical angle, backscattering due to density fluctuations and due to compressional wave fluctuations have nearly the same angular dependence [Fig. 2(b)].

In these examples, the ''correlated'' and ''uncorrelated'' cases are rather similar. This is because the chosen strengths of the three types of fluctuation (density, compressional
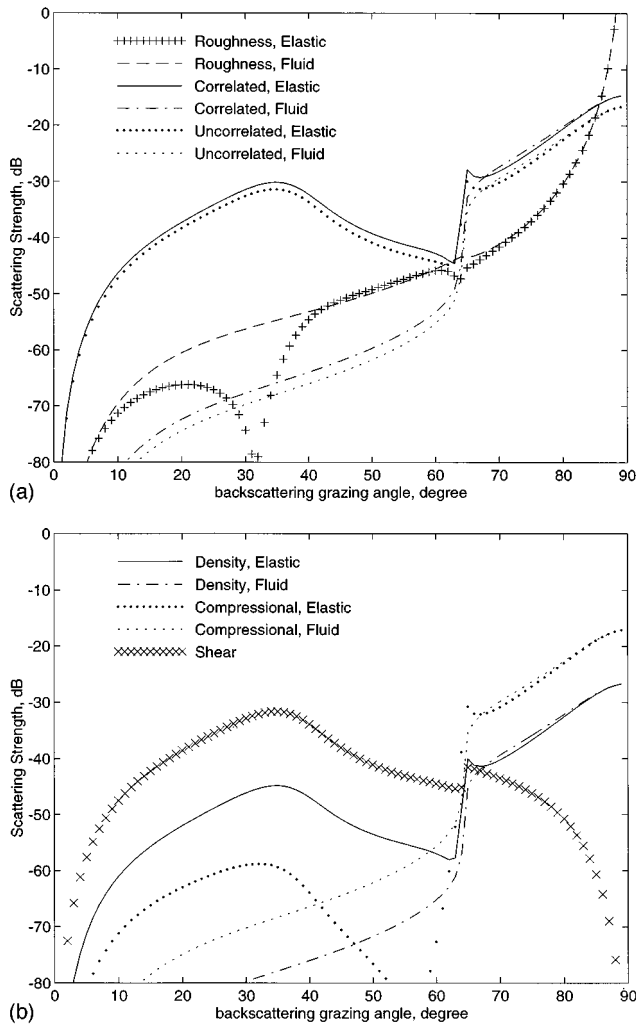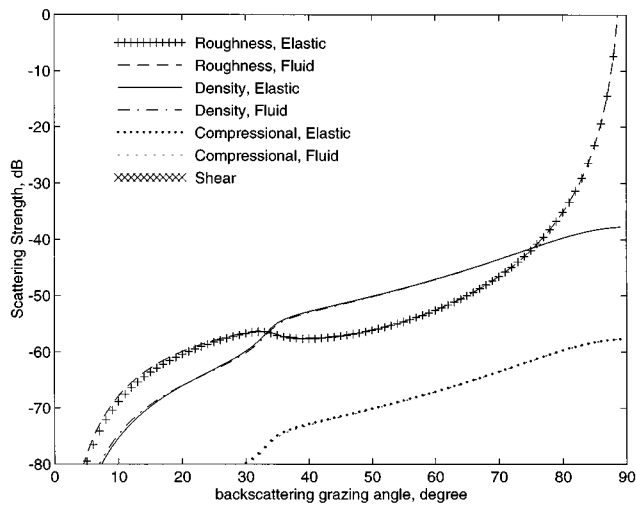
FIG. 8. Backscattering strength as a function of grazing angle for the ''normal'' sand example. The fluid case uses identical parameters, except the shear wave speed is set to zero. The abscissa is $\theta_s = \theta_i$ with $\phi_s - \phi_i = 180°$. With the parameters used, there is no frequency dependence.

wave speed, and shear wave speed) are quite different, with shear fluctuations being the dominant source of scattering. If at least two fluctuation types are dominant, correlations between dominant fluctuations will have an important effect on angular dependence.

The influence of shear elasticity in surficial sands is expected to be rather small as they typically have shear speeds much lower than the water compressional wave speed (see, e.g., Refs. 15, 18). For illustrative purposes, therefore, an example will first be considered in which shear effects are exaggerated. This example is used by Essen[2] and is distinguished by a shear speed of 480 m/s. This case of sand with high shear speed, the ''shear'' sand case, is illustrated in Figs. 5–7. These figures show the following effects:

(v) Both roughness and volume backscattering [Fig. 5(a)] are reduced relative to the fluid case for grazing angles smaller than the compressional critical angle (33.6°). Compared to the sedimentary rock example, this is the same be-
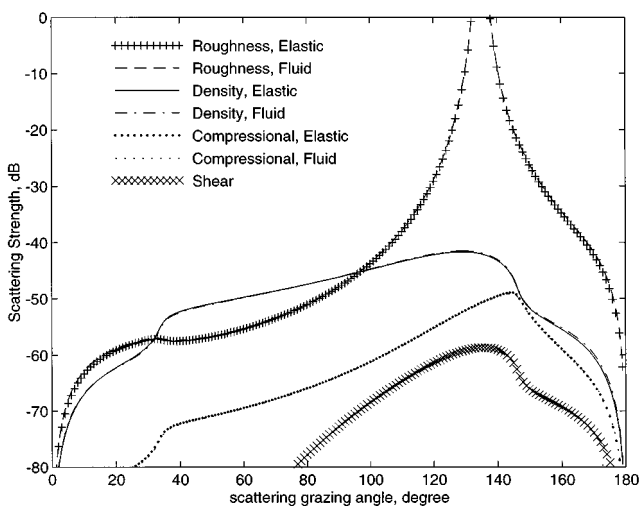
FIG. 9. Bistatic scattering strength as a function of scattered grazing angle for the ''normal'' sand example. Incident grazing angle $\theta_i = 45°$. The abscissa is θ_s with $\phi_s - \phi_i = 180°$. All parameters are the same as for Fig. 8.
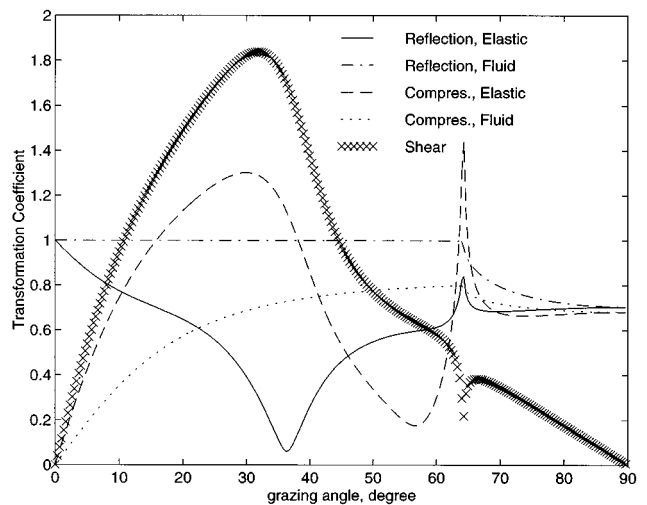
FIG. 10. Transformation (reflection and transmission) coefficients for the sedimentary rock example.

havior regarding roughness but the opposite regarding volume scattering.

(vi) The relative contributions of volume and roughness scattering [Figs. 5(a), 6(a), 7(a)] are very dependent on scattering angle. Roughness scattering is dominant near the specular direction, but volume scattering can be important for incident or scattering angles greater than the compressional critical angle.

(vii) The effect of cross correlation for different perturbations is large, in Fig. 6(a) (in the range 80°–180°) and in Fig. 7(a) ($-100°-100°$). Note that this difference is due to the interference between comparable scattering contributions by density and shear speed fluctuations, hence correlation effects are negligible in the fluid case.

(viii) Volume scattering in backward directions for sands [Figs. 5(b), 6(b), 7(b)] is mostly due to density fluctuations, while both compressional and shear wave speed fluctuations are unimportant. But, at the same time, even weak fluctuations of compressional speed (an order of magnitude smaller than density fluctuations) can be important
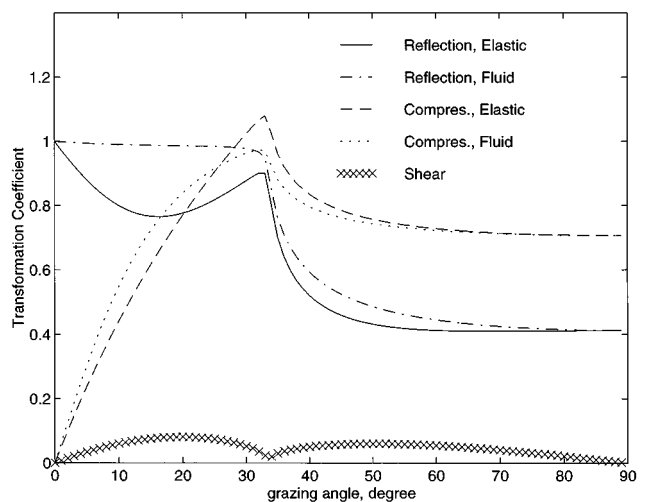
FIG. 11. Transformation (reflection and transmission) coefficients for the ''shear'' sand example.

near the forward direction [Fig. 6(b)]. Shear fluctuations also provide significant scattering near the forward direction [Figs. 6(b), 7(b)].

The last example, with scattering strength shown in Figs. 8 and 9, is a sand with shear speed of about 200 m/s, similar to typical measured values.[15,22] Here again, the relative importance of roughness and volume scattering is dependent on angle. Density fluctuations are generally more important than compressional speed fluctuations in the backscattering case (Fig. 8) with relatively reduced contribution in forward directions (Fig. 9). These effects have little to do with shear elasticity, however. In fact, the effects of shear elasticity are negligible for both roughness and volume scattering. Scattering by shear speed fluctuations in forward and near specular directions is about 10 dB lower than scattering by density and compressional speed fluctuations (Fig. 9) and absolutely negligible in the backscattering case (the shear component is not seen in Fig. 9 as its level is too low). Thus even though surficial sand is definitely a shear-supporting medium in a geotechnical sense, it can be treated by a simple fluid acoustic model.

The effects of elasticity on roughness and volume scattering for rock can be summarized by saying that elasticity ''softens'' the interface, decreasing the acoustic contrast with water with a corresponding decrease in reflection and roughness scattering and a corresponding increase in transmission and volume scattering. This view is substantiated by Fig. 10, which compares the magnitudes of reflection and transmission coefficients for the fluid and elastic cases. In the fluid case, the reflection coefficient is very nearly equal to unity for grazing angles below the compressional critical angle. The inclusion of lossy shear greatly alters this picture, with the energy reflection coefficient dropping to very small values for grazing angles in the vicinity of 35°. This causes the decrease noted in roughness scattering. At the same time, Fig. 10 shows that the transmission coefficient for pressure waves is greatly increased when elastic effects are included. The conversion to shear energy is also efficient, and both effects enhance volume scattering. The opposite effect for scattering in high shear speed sand, mentioned above, is explained analogously by Fig. 11.

For the sedimentary rock example, when the incident and scattered grazing angles are less than the compressional critical angle, only incident and scattered vertically polarized shear waves are important. Thus there is no interference between different scattering channels; only shear-to-shear scattering is important. This causes the similarity observed in the angular dependences of scattering by density and shear speed fluctuations. The scattering levels due to these two mechanisms are different only because different fluctuation levels are assumed (Table II).

IV. CONCLUSIONS

First-order perturbation theory results obtained in Ref. 1 have been used to study the effects of shear elasticity on acoustic scattering by sea beds of different types. While the calculations presented here are quantitatively correct only in a region of small roughness and small volume fluctuations, it is likely that the general conclusions drawn from these examples will be qualitatively valid outside this region.

With respect to scattering by rock, shear elasticity weakens roughness scattering and strengthens volume scattering. Surprisingly, this suggests that volume scattering may sometimes dominate, or at least compete with, roughness scattering, in sharp contrast to the predictions of the fluid model. The other general conclusion resulting from these examples, is that sand can be treated as an acoustic fluid. This reinforces the results presented by Yang and Broschat.[3]

APPENDIX: VOLUME CROSS SPECTRUM MATRIX

The matrix elements, $B_{\beta\beta'}$, can be determined from Eq. (12) which gives

$$B_{\beta\beta'} = \sigma_\beta \sigma_{\beta'} R_{\beta\beta'} a^2 q_0^{\gamma_v - 3} (\gamma_v/2 - 1)/[\pi Q(\gamma_v, \epsilon)], \quad \text{(A1)}$$

where

$$\sigma_\beta = \sqrt{\langle |\epsilon_\beta|^2 \rangle} \quad \text{(A2)}$$

are the standard deviations of the three different fluctuation types, and

$$R_{\beta\beta'} = \frac{\langle \epsilon_\beta \epsilon_{\beta'}^* \rangle}{\sigma_\beta \sigma_{\beta'}} \quad \text{(A3)}$$

are their cross-correlation coefficients. In the case of strongly correlated or anticorrelated fluctuations one can put $R_{\beta\beta'} = \pm 1$ respectively, and in the ''uncorrelated'' case, $R_{\beta\beta'} = \delta_{\beta\beta'}$. The parameter $Q(\gamma_v, \epsilon)$ is a dimensionless normalizing factor

$$Q(\gamma, \epsilon) = 2 \int_0^{1/\epsilon} \frac{1}{(1+x^2)^{\gamma/2 - 1}} \, dx. \quad \text{(A4)}$$

For $\gamma_v = 3$, one obtains

$$Q \approx 2 \ln(1/\epsilon), \quad \text{(A5)}$$

while, for $\gamma_v < 3$,

$$Q \approx 2 \epsilon^{-(3-\gamma_v)}/(3-\gamma_v), \quad \text{(A6)}$$

and, for $\gamma_v > 3$,

$$Q \approx Q(\gamma_v, 0) = \Gamma(1/2)\Gamma(\gamma_v/2 - 3/2)/\Gamma(\gamma_v/2 - 1). \quad \text{(A7)}$$

For $\gamma_v = 4$, in particular, $Q = \pi$. Expression (A7) is exact if $\epsilon = 0$.

[1] D. R. Jackson and A. N. Ivakin, ''Scattering from elastic sea beds: First-order theory,'' J. Acoust. Soc. Am. **103**, 336–345 (1998).
[2] H. H. Essen, ''Scattering from a rough sedimental seafloor containing shear and layering,'' J. Acoust. Soc. Am. **95**, 1299–1310 (1994).
[3] T. Yang and S. L. Broschat, ''Acoustic scattering from a fluid-elastic-solid interface using the small slope approximation,'' J. Acoust. Soc. Am. **96**, 1796–1803 (1994).
[4] A. N. Ivakin, ''Sound scattering by inhomogeneities of an elastic half-space,'' Sov. Phys. Acoust. **36**, 377–380 (1990).
[5] D. R. Jackson and K. B. Briggs, ''High-frequency bottom backscattering:

Roughness versus sediment volume scattering,'' J. Acoust. Soc. Am. **92**, 962–977 (1992).

[6] P. D. Mourad and D. R. Jackson, ''A model/data comparison for low-frequency bottom backscatter,'' J. Acoust. Soc. Am. **94**, 344–358 (1993).

[7] K. B. Briggs, ''Microtopographical roughness of shallow-water continental shelves,'' IEEE J. Ocean Eng. **14**, 360–367 (Oct. 1989).

[8] A. N. Ivakin, ''On sound scattering by multi-scale bottom inhomogeneities,'' Oceanology **21**, 26–27 (1981).

[9] A. V. Yefimov, A. N. Ivakin, and Yu. P. Lysanov, ''A geoacoustic model of sound scattering by the ocean bottom based on deep sea drilling data,'' Oceanology **28**, 290–293 (1988).

[10] T. Yamamoto, ''Velocity variabilities and other physical properties of marine sediments measured by crosswell acoustic tomography,'' J. Acoust. Soc. Am. **98**, 2235–2248 (1995).

[11] T. Yamamoto, ''Acoustic scattering in the ocean from velocity and density fluctuations in the sediments,'' J. Acoust. Soc. Am. **99**, 866–879 (1996).

[12] A. V. Bunchuk and A. N. Ivakin, ''Azimuthal anisotropy of sound backscattering from the ocean bottom in shallow water,'' in *V Seminar on Acoustic and Statistical Models of the Ocean* (1985), pp. 47–51 (in Russian).

[13] E. L. Hamilton, ''Attenuation of shear waves in marine sediments,'' J. Acoust. Soc. Am. **60**, 334–338 (1976).

[14] E. L. Hamilton, ''Sound velocity-density relations in sea-floor sediments and rocks,'' J. Acoust. Soc. Am. **63**, 366–377 (1978).

[15] E. L. Hamilton, ''Geoacoustic modeling of the seafloor,'' J. Acoust. Soc. Am. **68**, 1313–1340 (1980).

[16] E. L. Hamilton and R. T. Bachman, ''Sound velocity and related properties of marine sediments,'' J. Acoust. Soc. Am. **72**, 1891–1904 (1982).

[17] P. Milholland, M. H. Manghnani, S. O. Schlanger, and G. H. Sutton, ''Geoacoustic modelling of deep-sea carbonate sediments,'' J. Acoust. Soc. Am. **68**, 1351–1360 (1980).

[18] M. D. Richardson and K. B. Briggs, ''On the use of acoustic impedance values to determine sediment properties,'' in *Acoustic Classification and Mapping of the Seabed*, edited by N. G. Pace and D. N. Langhorne (Institute of Acoustics, Bath, 1993), pp. 15–25.

[19] T. Akal, ''Acoustical characteristics of the sea floor: Experimental techniques and some examples from the Mediterranean sea,'' in *Physics of Sound in Marine Sediments*, edited by L. Hampton (Plenum, New York, 1974), pp. 447–480.

[20] K. B. Briggs, ''High-frequency acoustic scattering from sediment interface roughness and volume inhomogeneities,'' Naval Research Laboratory, NRL/FR/7431-94-9617, Dec. 1994.

[21] A. P. Lyons, A. L. Anderson, and F. S. Dwan, ''Acoustic scattering from the seafloor: Modeling and data comparison,'' J. Acoust. Soc. Am. **95**, 2441–2451 (1994).

[22] M. D. Richardson, E. Muzi, B. Miaschi, and F. Turgutcan, ''Shear wave velocity gradients in near-surface marine sediment,'' in *Shear Waves in Marine Sediments*, edited by J. M. Hovem *et al.* (Kluwer, Dordrecht, 1991).

[23] D. K. Dacol and D. H. Berman, ''Sound scattering from a randomly rough fluid–solid interface,'' J. Acoust. Soc. Am. **84**, 292–302 (1988).

Wideband optimal *a posteriori* probability source localization in an uncertain shallow ocean environment

J. A. Shorey and L. W. Nolte
Department of Electrical Engineering, Box 90291, Duke University, Durham, North Carolina 27708-0291

A wideband extension of the Optimum Uncertain Field Processor (OUFP) is presented. Combined with Monte Carlo estimation methods, this processor provides a fast, efficient, and robust technique for Matched-Field Processing (MFP). Under a simulated Hudson Canyon environment, a quantitative, probabilistic analysis of the sensitivity of the Optimum Matched-Field Processor (OMFP) to various kinds of environmental mismatch is shown. Similarly, the performance of the OUFP is calculated. Finally, the optimum wideband OUFP is applied to a data set collected from the Hudson Canyon, the results tabulated, and then compared to a standard Bartlett processor. The performance of the optimum wideband OUFP and the suboptimum Bartlett processor are in very good agreement with the performance predicted from simulation results. © *1998 Acoustical Society of America.* [S0001-4966(97)04712-7]

PACS numbers: 43.30.Wi, 43.60.Lq [SAC-B]

INTRODUCTION

Matched-field processing is a method by which full field modeling of multipath propagation is used to localize an acoustic source.[1] Typically this is done only using narrow-band acoustic sources. However, because of the characteristic ambiguities which occur at regular intervals around the true source location, either high SNR or extremely accurate environmental modeling is required to induce correct localization. The proper utilization of wideband acoustic sources is seen as a way to increase localization performance, particularly for weak, undersampled, or complicated shallow water problems. The wideband signal may be from a coherent broadband source,[2–6] but often the exact source signature is not known or is spectrally incoherent. If the implementation of the matched-field processor is optimal, it also provides an upper bound on the performance of any such processor. However, even with the added performance potential of a wideband source, the problem of environmental mismatch must still be properly addressed to provide optimal performance.

In the first section of this paper the optimum uncertain field processor (OUFP), which optimally accounts for environmental uncertainty, is extended to cover the wideband problem. Next, having addressed the issue of environmental uncertainty, the sensitivity of the suboptimum (known ocean) processor to these uncertainties is explored using quantitative techniques. Taking advantage of Monte Carlo techniques which allow the OUFP to handle complex environments in a computationally efficient manner, the performance of the optimum processor is evaluated for varying degrees of uncertainty. Finally, the wideband OUFP is applied to experimental data and the results presented.

I. WIDEBAND PROCESSOR FOR A RANDOM SOURCE SIGNAL

A. Source signal definition

The received data or observation at a given hydrophone for a particular frequency is a deterministic value dependent on various source parameters, environmental parameters, source location parameters, and, of course, frequency. It is a complex acoustic pressure with additive complex Gaussian noise defined as follows:

$$\mathbf{r}_f = \mathbf{s}_f(\mathbf{S}, \boldsymbol{\Psi}, \boldsymbol{\Phi}_f) + \mathbf{w}_f,$$

where f is the frequency index, $\mathbf{r}_f$ is a received data vector at a particular frequency containing data from all the receivers, $\mathbf{S}$ is the source location parameters, $\boldsymbol{\Psi}$ is the uncertain environmental parameters, $\boldsymbol{\Phi}_f$ is the uncertain source parameters at a particular frequency, and $\mathbf{w}_f$ is complex additive Gaussian noise at a particular frequency. Note that $\mathbf{r}_f$ and $\mathbf{w}_f$ are the complex amplitudes of the real valued data time series and noise time series such that $r(t) = |\mathbf{r}_f| \cos(2\pi f t + \theta_{\mathbf{r}_f})$ and $w(t) = |\mathbf{w}_f| \cos(2\pi f t + \theta_{\mathbf{w}_f})$.

B. Derivation of processor

The goal of optimum source localization is to first obtain the *a posteriori* probability of that source location:

$$p(\mathbf{S}|\mathbf{r}) = \frac{p(\mathbf{S})}{p(\mathbf{r})} \int_{\boldsymbol{\Psi}} p(\mathbf{r}|\mathbf{S}, \boldsymbol{\Psi}) p(\boldsymbol{\Psi}|\mathbf{S}) d\boldsymbol{\Psi}. \tag{1}$$

The ensemble of the received data at all the frequencies of interest is denoted $\mathbf{r}$.

If the signal at the source is random in the sense that the different frequency components are statistically independent, the conditional density function can be expanded as

$$p(\mathbf{r}|\mathbf{S}, \boldsymbol{\Psi}) = \prod_f p(\mathbf{r}_f|\mathbf{S}, \boldsymbol{\Psi}). \tag{2}$$

This assumption is justified in that stationary Gaussian signals have statistically independent Fourier components.

Richardson and Nolte[7] have derived an analytical expression for $p(\mathbf{r}_f|\mathbf{S}, \boldsymbol{\Psi})$ when $\boldsymbol{\Phi}$ consists of a uniformly distributed random phase and a Rayleigh distributed magnitude (i.e., complex Gaussian amplitude). Modified for the frequency domain scenario, the expression becomes

$$p(\mathbf{r}_f | \mathbf{S}, \mathbf{\Psi}) = C_f \frac{1}{E(\mathbf{S}, \mathbf{\Psi}, f) + 1} \exp\left(\frac{|R(\mathbf{r}_f, \mathbf{S}, \mathbf{\Psi}, f)|^2}{E(\mathbf{S}, \mathbf{\Psi}, f) + 1} \right),$$
(3)

where

$$E(\mathbf{S}, \mathbf{\Psi}, f) = \sigma_A^2 \mathbf{H}^*(\mathbf{S}, \mathbf{\Psi}, f) \mathbf{Q}^{-1} \mathbf{H}(\mathbf{S}, \mathbf{\Psi}, f),$$

$$R(\mathbf{r}_f, \mathbf{S}, \mathbf{\Psi}, f) = \frac{\sigma_A}{\sqrt{2}} \mathbf{H}^*(\mathbf{S}, \mathbf{\Psi}, f) \mathbf{Q}^{-1} \mathbf{r}_f,$$

σ_A is the transmitted amplitude Rayleigh distribution parameter, $\mathbf{Q}$ is the spatial noise covariance matrix, $\mathbf{H}(\mathbf{S}, \mathbf{\Psi}, f)$ is the acoustic transfer function or replica field, and C_f is a constant term only dependent on $\mathbf{r}_f$. The signal to noise ratio (SNR) is defined as the ratio of σ_A^2 to σ_w^2, the noise variance.

C. Final processor

Substituting equation (3) into equation (1), using equation (2), one obtains the wideband optimum uncertain field processor (wideband OUFP)

$$p(\mathbf{S} | \mathbf{r}) = C(\mathbf{r}) p(\mathbf{S}) \int_{\mathbf{\Psi}} \prod_{f=1}^{N_f} \left[\frac{1}{E(\mathbf{S}, \mathbf{\Psi}, f) + 1} \right.$$
$$\left. \times \exp\left(\frac{|R(\mathbf{r}_f, \mathbf{S}, \mathbf{\Psi}, f)|^2}{E(\mathbf{S}, \mathbf{\Psi}, \mathbf{f}) + 1} \right) \right] p(\mathbf{\Psi} | \mathbf{S}) d\mathbf{\Psi}, \qquad (4)$$

where

$$E(\mathbf{S}, \mathbf{\Psi}, f) = \sigma_A^2 \mathbf{H}^*(\mathbf{S}, \mathbf{\Psi}, f) \mathbf{Q}^{-1} \mathbf{H}(\mathbf{S}, \mathbf{\Psi}, f),$$

$$R(\mathbf{r}_f, \mathbf{S}, \mathbf{\Psi}, f) = \frac{\sigma_A}{\sqrt{2}} \mathbf{H}^*(\mathbf{S}, \mathbf{\Psi}, f) \mathbf{Q}^{-1} \mathbf{r}_f.$$

Here, $p(\mathbf{S} | \mathbf{r})$ is the *a posteriori* probability of the source location, $C(\mathbf{r})$ is a normalization constant, and $p(\mathbf{S})$ is the *a priori* probability density of the source location. The core of the processor is a function of E, which is related to the replica field self-energy, and R, which is related to the correlation of the replica field with the observer field, that is then operated on by a product over frequency, multiplied by the *a priori* density of the environmental parameters, and finally integrated over those parameters.

An ambiguity surface is formed by calculating $p(\mathbf{S} | \mathbf{r})$ over the range of possible source position parameters $\mathbf{S}$. The density over which $\mathbf{S}$ should be sampled to produce a representative ambiguity surface is dependent on the behavior of $p(\mathbf{S} | \mathbf{r})$; it must be sampled sufficiently so as not to skip important features. This is particularly important for larger numbers of frequencies.

As shown by Shorey *et al.*[8] Monte Carlo integration techniques can be used to alleviate the computational intensity of the evaluation of the integral over $\mathbf{\Psi}$. This can be done without loss of localization performance for low and intermediate SNRs. For highly uncertain environments at high SNRs, the Monte Carlo estimation error, although very small, is detectable. The amount of error is dependent on the number of iterations used for the integration.
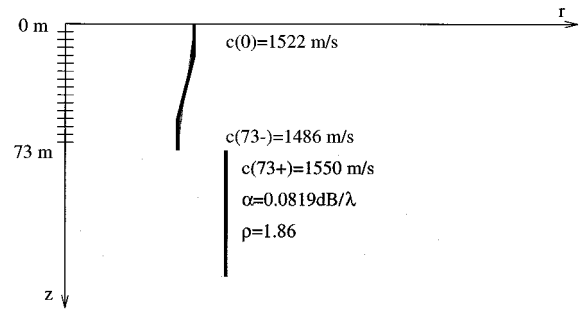
FIG. 1. Hudson Canyon environment.

II. ENVIRONMENT DESCRIPTION

A. Hudson Canyon environment

A 1988 experiment off the New Jersey Continental Shelf was conducted by Carey *et al.*[9] wherein an acoustic source was towed past a 24-element vertical array out to ranges of approximately 5 km in several tracks. These 24 elements are spaced 2.5 m apart starting from about 14 m below the surface. A radar link provided accurate telemetry with which to verify the source track. CTD and SVP measurements were taken along each track to record sound-speed profiles, and an averaged ''basis'' profile calculated. For each track, a combination of four tonals were measured: either 75, 275, 525, and 600 Hz or 50, 175, 375, and 425 Hz. For the simulations which follow, only the first set of four frequencies will be used.

Figure 1 shows the environmental model used to simulate the Hudson Canyon environment. KRAKEN,[10] a normal mode acoustic propagation model, is used to generate the individual frequency components in the replica fields of the processor and the simulated data of the sensitivity and performance simulations. It is a well-documented propagation model and ideally suited for an assumed range-independent environment such as this.

B. Uncertainties

The ship tracks were chosen to lie on isobaths so that the bottom depth would be invariant. It is possible, however, for the bottom parameters (sound speed, density, and attenuation) to vary along the path. Furthermore, the many sound speed measurements indicate a wide variation of values in water column sound speed between the different tracks.

Table I contains the averaged basis sound-speed profile in the water column for the experimental data as well as a range of uncertainty for each sound-speed parameter. These uncertainties are in the form of a uniformly distributed variation on the basis sound speed, each independent of the sound speeds in other ranges. The uncertainties were determined by observing the variation of the various separate sound-speed profiles. Physical causes of these uncertainties are many: time varying environment over the experiment, range dependence in the environment, and measurement inaccuracies.

A simple half-space bottom model was found sufficient to produce accurate source localization results, and thus there is only one parameter to model the bottom: the bottom sound

TABLE I. Hudson Canyon environmental parameters and uncertainties.

Description	Depth	Basis sound speed	Uniform uncertainty
Water column sound speeds	0+ m	1522 m/s	±2 m/s
	15 m	1522 m/s	±2 m/s
	20 m	1503 m/s	±2 m/s
	30 m	1490 m/s	±2 m/s
	40 m	1486 m/s	±2 m/s
	50 m	1484 m/s	±2 m/s
	60 m	1486 m/s	±2 m/s
	73− m	1486 m/s	±2 m/s
Bottom half-space sound speed	73+ m	1550 m/s	±50 m/s

speed. This is indicative of the limited acoustic propagation into the bottom sediment—the interface effects dominate the acoustic interaction between the water column and the bottom.

C. Simulations

Figures 2 and 3 show ambiguity surfaces generated by the wideband OUFP for a simulated environment using the frequencies 75, 275, 525, and 600 Hz at SNRs of 40 and 15 dB, respectively. The integral over Ψ was calculated using 1000 Monte Carlo integrations. A gridding of the possible source locations was done every meter in depth and every 10 m in range. In these particular simulations, the source is correctly localized within 1 grid point (10 m) in range for the 40-dB case, 2 grid points (20 m) for the 15-dB case, and correctly localized in depth in both cases.

III. SENSITIVITY TO MISMATCH

A. PCL curves

Sensitivity to mismatch has traditionally been shown through the use of individual ambiguity surfaces, generally showing an incorrect localization in the presence of environmental mismatch and good localization when the environment is matched to that of the processor. However, it is difficult to draw any conclusions from these demonstrations other than the fact that there is indeed sensitivity for that particular SNR and source location.
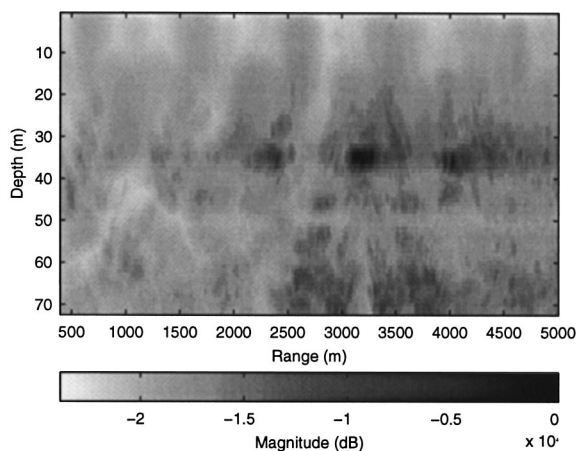
A more complete analysis would show the degree of sensitivity in comparison with SNR and for a variety of source locations. In this manner a quantitative analysis of sensitivity can be produced and an accurate hierarchy of parameter sensitivities constructed. One way to achieve this goal is through the use of probability of correct localization (PCL) curves.

A PCL curve is a plot of probability of correct localization as a function of the average SNR at the array per sensor and per snapshot of received data. It is most useful if it is averaged over the set of possible source positions, as otherwise it may be artificially low or high depending on the location. This is particularly important for the situation where the noise variance is the same regardless of the source position. Because of cylindrical spreading, the SNR at the near source positions will be higher than at the far positions and therefore a bias in the results would more than likely exist if only a single source position were chosen.

It is not the purpose of the PCL curve to measure the ''variance'' of the source position error, particularly since for these shallow water matched field processing scenarios the distribution of the estimated source position is not Gaussian in either depth or range. Rather it provides a more useful statistic in the form of the probability of picking the correct ambiguity region, irrespective of whether the peak of that ambiguity falls exactly on the true source position. For these particular shallow water experiments, this means giving an acceptable allowance in range and depth error for a localization to still be considered correct. This allowance will vary depending upon the environment, but for this case it is a ±200 m error in range and a ±4 m error in depth.

B. Sound-speed mismatch in the water column

Mismatch in this environment comes from two sources: the bottom parameters and the water column parameters. Sensitivity to water column parameters, the sound speed at various depths, is well known and has been repeatedly shown. Quantitative measurements of its effect on source localization as a function of SNR have not been made, however.

Figure 4 presents PCL curves demonstrating the sensitivity of the wideband optimum matched field processor

FIG. 2. Simulated environment localization, 40 dB SNR.
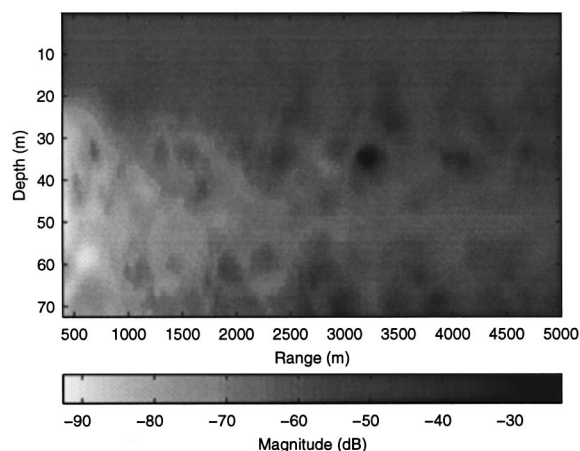
FIG. 3. Simulated environment localization, 15 dB SNR.

357   J. Acoust. Soc. Am., Vol. 103, No. 1, January 1998

J. A. Shorey and L. W. Nolte: Localization: Uncertain media   357
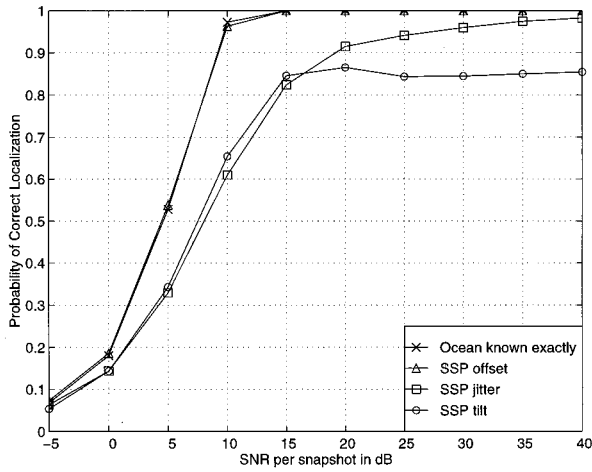
FIG. 4. Water column sound-speed mismatch sensitivity.

FIG. 5. Bottom mismatch sensitivity.

(wideband OMFP) to several kinds of water column sound speed mismatch:

profile jitter: an alternating ± 2 m/s error is added to the sound speed at each depth in Table I, starting with a -2 m/s error at the surface.

profile offset: a depth-independent error of $+2$ m/s is added to each sound speed in the water column.

profile tilt: a linearly depth-dependent error is added to the sound speeds starting with a -2 m/s error at the surface and a $+2$ m/s error at the bottom.

The wideband OMFP is a special case wideband OUFP where Ψ has only one configuration and thus there is no integral over Ψ. In essence the processor assumes the ocean environment is known. For each of these mismatch cases, the error is in the assumed or replica environments—the actual environment is always the basis environment.

Each PCL sensitivity curve is averaged over an ensemble of possible source positions with a depth of 35 m and ranges of 500 m to 5000 m spaced in 100-m increments. There are 20 random noise realizations made at each possible source position. The ambiguity surface gridding is set at every meter in depth from 1 m to 72 m and every 10 m in range from 400 m to 5000 m.

Several conclusions about the nature of water column sound-speed sensitivity can be drawn from this plot. First, an overall offset in the assumed sound-speed profile has little if any effect on the performance of the wideband OMFP. Second, a ''jitter'' on the sound-speed profile causes a significant performance loss as low SNRs, but very little at very high SNRs. Finally, a ''tilt'' in the sound-speed profile has a similar effect to jitter at low SNRs, but also imposes a substantial performance cap at higher SNRs.

C. Sound-speed mismatch in the bottom

Sensitivity of the wideband OMFP to bottom mismatch is not as well known as the effect of water column mismatch, perhaps because bottom effects are not as pronounced and because in most shallow water scenarios propagation into the bottom is severely attenuated. However, most temperate or summer environments have properties such that almost all the energy that reaches the receivers has interacted at least
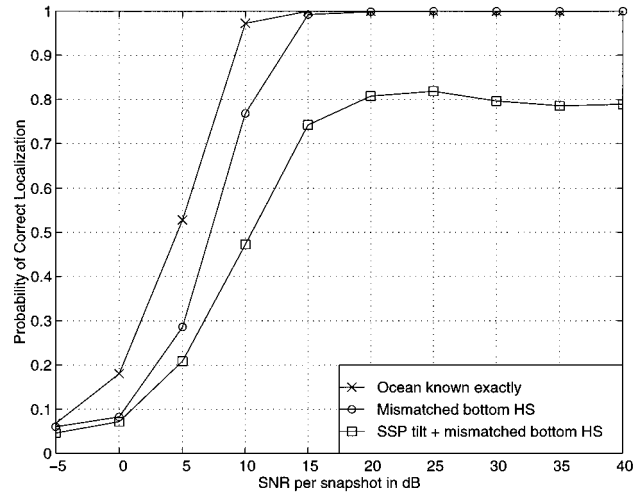
once with the bottom. This causes bottom depth and bottom boundary characteristics to be important considerations in environmental modeling.

Two scenarios involving bottom mismatch can be considered: the case where the sound speed in the bottom sediment half-space is mismatched and the case where both the bottom sediment sound speed and the water column sound speed are mismatched. The bottom sound-speed mismatch of $+100$ m/s is sufficient to demonstrate sensitivity in the wideband processor.

The effects of bottom mismatch on the wideband OMFP are shown in Fig. 5. The performance for the difference situations are shown using PCL curves, each generated in the same manner as those in Fig. 4. The offset of the bottom mismatch PCL curve toward higher SNRs indicates a mild sensitivity of the wideband processor. This curve meets up with the ocean known exactly PCL curve at higher SNRs demonstrating that the wideband OMFP is insensitive to this mismatch at higher SNRs. On the other hand, a SSP tilt in addition to the bottom mismatch induces a much stronger mismatch as shown by its PCL curve falling much lower than the ocean known exactly curve. Also, this curve does not approach the ocean known exactly curve at higher SNRs—it levels out to about 80% probability of correct localization. These curves indicate that bottom mismatch by itself is not terribly important (for this scenario), but when combined with a sound speed mismatch suddenly becomes a major limiting factor in the wideband OMFP processor performance.

IV. OPTIMAL PROCESSOR PERFORMANCE

In the previous section, the sensitivity of the wideband OMFP was quantitatively demonstrated. The optimum way to account for this mismatch is to specify the *a priori* uncertainty explicitly in the processor, which is manifested in the integral over Ψ. In doing so, the processor thus becomes robust to these uncertainties. Furthermore, being an optimal processor, it will demonstrate an upper bound in performance for every processor subjected to that same degree and manner of uncertainty.
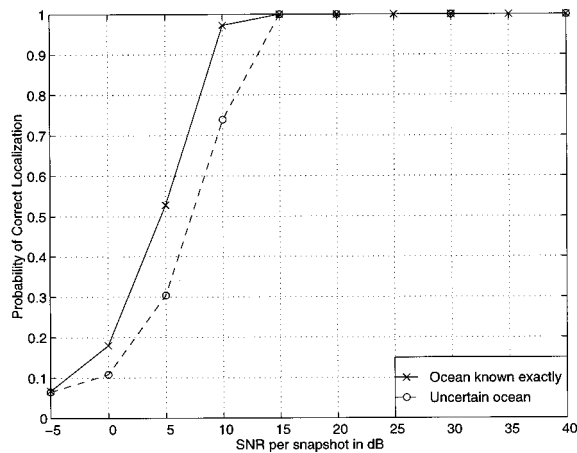
FIG. 6. Optimum processor performances.

FIG. 7. Experimental ambiguity surface for site 4.

Intuitively the performance of the optimum processor will be a function of the source location data it receives. This information comes in the form of *a priori* uncertainties about the signal and environment and the source location data contained in the signal. The amount of contribution from each is uncertainty limited and noise limited, respectively.

In the same manner as the sensitivity PCL curves were used to show sensitivity to various environmental parameters, PCL curves can show the relative performance of the optimum processors for varying degrees of environmental uncertainty.

The wideband OUFP for the simulated Hudson Canyon environment utilized the environmental parameters, median values, and associated uncertainties shown in Table I. The source location gridding is the same as that used for the sensitivity studies in the previous sections. A total of 1000 Monte Carlo iterations is used to estimate the integral over Ψ in Eq. (4). In order to make the PCL results independent of a particular source location, the source location sampling is the same as used for the sensitivity studies. Also, a single noise realization is used for each simulated source location.

Figure 6 shows the performance of the wideband OMFP and the wideband OUFP, under a known environment and an uncertain environment, respectively. The only performance difference between the two processors is noted between the SNRs of −5 and 15, with the largest difference being approximately a 20% performance decrease. This performance decrease of the wideband OUFP can be attributed to the less precise *a priori* knowledge present, i.e., the uncertainty of the environment.

Note that the performance of the wideband OUFP is still substantially better than the wideband OMFP in the presence of mismatch, as shown in the lower curve of Fig. 5. The difference between mismatched and optimum ranges from 15% to 20% for lower SNRs and has a consistent decrease of 10% at higher SNRs. It should be mentioned that the processor that fits the *a priori* knowledge should be used, otherwise performance will be suboptimum and fall below that of the optimum processor. This is true both for an exaggeration of the uncertainty and for an understatement of the uncertainty in the processor's *a priori* knowledge.
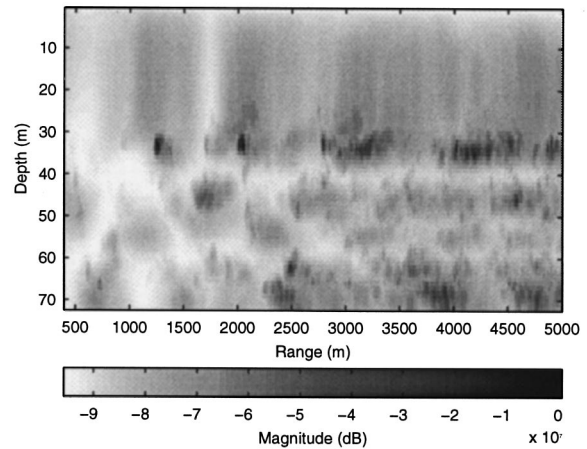
V. EXPERIMENTAL RESULTS

The previous sections have shown the expected performance of the wideband OUFP in a simulated Hudson Canyon environment. The motivation for the use of this environment is the availability of an excellent experimental data set. The SNR of the data set appears to be approximately 10 dB.

This data set consists of 20 source locations split evenly between an incoming ship path and an outgoing ship path. The data from these paths contain different frequency sets: 75, 275, 525, and 600 Hz for the incoming and 50, 175, 375, and 425 Hz for the outgoing. Each source location contains 10 snapshots of data. Although the ship was moving slightly between snapshots, the processor considers the environment to be invariant between those snapshots for a particular source location.

A. Example ambiguity surfaces

The wideband OUFP applied to this data uses the same gridding as used in the earlier simulations. Figures 7 and 8 show ambiguity surfaces from two of the sites from the incoming track. A total of 2500 Monte Carlo iterations were used to generate these surfaces. The uncertainties incorporated into the wideband OUFP are the same as in Table I.

Upon examination of the two ambiguity surfaces, they
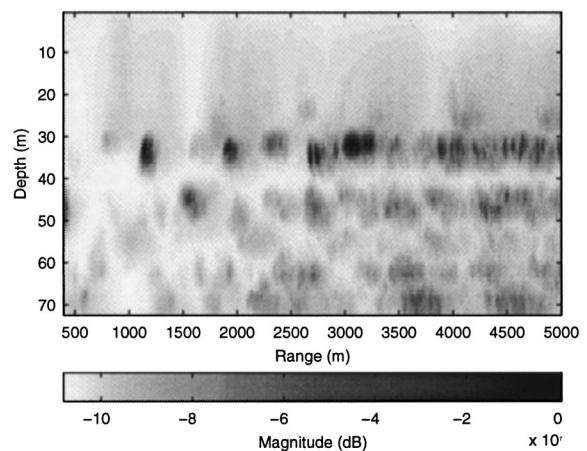
FIG. 8. Experimental ambiguity surface for site 5.
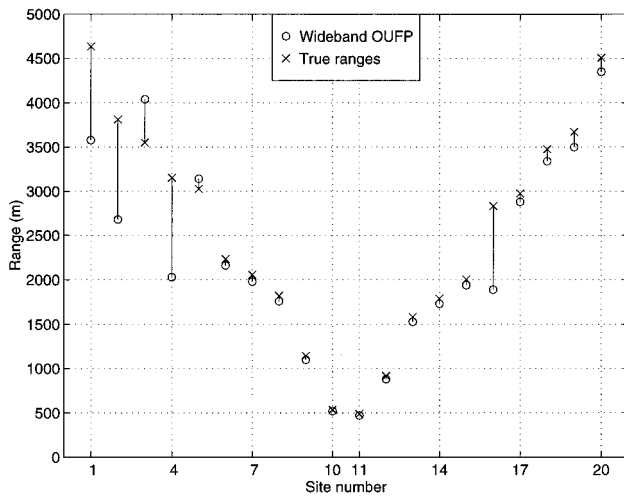
FIG. 9. Experimental source track.

both have similar appearance and ''degree of ambiguity'' in the sense that the number of competing peaks in each is about the same and the nature of the peaks are similar within each surface. However, despite their appearances, the surface in Fig. 7 shows an incorrect localization and Fig. 8 shows a correct one. The correct range locations are 3152 and 3025 m, respectively, and the peaks of the two ambiguity surfaces fall on range values of 2050 and 3070 m, respectively. This kind of effect provides motivation for sensitivity studies as shown in a previous section; the appearance of a single ambiguity surface gives little insight into the sensitivity of a particular processor to a particular environment or for that matter its performance in similar environments.

B. Experimental results summary

As mentioned previously, the actual experimental data consists of 10 source locations each from two ship tracks. These source locations are located at approximately even intervals along the ship track, which in turn lends the data to being analyzed by a source tracking processor. However, for the purposes of this paper each source location will be considered an independent experiment.

Figure 9 graphically shows the results of applying the wideband OUFP to the 20 experimental source locations. Only the range is plotted, as this seems to be the critical parameter. The depth results, which are not shown in a figure, were within the range of 32 m to 35 m in every case except for site 3, where the depth is incorrectly determined to be at 64 m.

The source location gridding in the processor used to generate these localizations is the same as in the previous sensitivity and performance analyses. A total of 3000 Monte Carlo iterations were used to perform the integration over the uncertain ocean parameters. The basis profile and uncertainties used are the same as those shown in Table I.

For this experiment, 15 out of 20 source locations are correctly localized. This corresponds to a PCL of 75%, which is what would be expected from data with a SNR of

approximately 10 dB. Note also that at this particular SNR, if the exact environmental parameters were known, the wideband OMFP could be used and would be expected to give a PCL of around 95%. This can be seen upon examination of the upper curve in Fig. 6 at an abscissa value of 10 dB SNR. In contrast, if the wideband OMFP was used with incorrect environmental parameters, the PCL could fall to about 50%. This can be by found by examining the 10 dB SNR point on the lower curve of Fig. 5.

When the wideband extension of the traditional Bartlett matched-field processor[11] of Eq. (5) is applied to this data set using the median environmental parameters, 11 out of 20 source locations are correctly localized:

$$f(\mathbf{S}) = \sum_{f=1}^{N_f} \frac{|R(\mathbf{r}_f, \mathbf{S}, \boldsymbol{\Psi}, f)|^2}{E(\mathbf{S}, \boldsymbol{\Psi}, \mathbf{f})}. \tag{5}$$

In this extension, the Bartlett ambiguity surfaces for the different pings and frequencies are averaged together to calculate a final ambiguity surface from which the source location is calculated. This coarse performance measure of 55% compares very well with the predicted mismatched performance of 50%. Although the predicted mismatched performance is for the OMFP, the Bartlett processor approximates the OMFP at high SNRs and should give similar performance. Thus a performance gain of 20% (11 out of 20 source locations versus 15 out of 20 source locations) is accrued through the use of the wideband OUFP over the Bartlett processor for this particular data set.

VI. SUMMARY

In the previous sections, the OUFP has been extended to a wideband scenario in an effort to gain an improvement over narrow-band matched-field processing performance. The sensitivity of the suboptimum processor was then quantitatively demonstrated in the presence of various types of environmental mismatch, where it was found that significant performance losses could occur for common mismatches. Using a similar technique, the performance of the optimum processor was gauged against different degrees of environmental uncertainty and it was found that uncertainties in the environment could be accounted for with little loss in overall processor performance. Finally, the optimum processor was applied to experimental data with results that were accurately predicted by the preceding performance analyses. In so doing, the wideband OUFP has proven its ability to produce good localization performance even when hampered by imprecise *a priori* knowledge of the acoustic propagation environment as shown both by simulation and application to a real data set.

[1] H. P. Bucker, ''Use of calculated sound fields and matched-field detection to locate sound sources in shallow water,'' J. Acoust. Soc. Am. **59**, 368–373 (1976).

[2] A. B. Baggeroer, W. A. Kuperman, and H. Schmidt, ''Matched field processing: source localization in correlated noise as an optimum parameter estimation problem,'' J. Acoust. Soc. Am. **83**, 571–587 (1988).

[3] P. C. Mignerey and S. Finette, ''Multichannel deconvolution of an acoustic transient in an ocean waveguide,'' J. Acoust. Soc. Am. **92**, 351–364 (1992).

[4] T. C. Yang, ''Broadband source localization and signature estimation,'' J. Acoust. Soc. Am. **93**, 1797–1806 (1993).

[5] R. Pitre and N. R. Davis, ''Application of probability modeling and Bayesian inversion to passive sonar signal processing. I. Concepts and formulation,'' J. Acoust. Soc. Am. **97**, 978–992 (1995).

[6] N. R. Davis and R. Pitre, ''Application of probability modeling and Bayesian inversion to passive sonar signal processing. II. Application to ocean acoustic source localization,'' J. Acoust. Soc. Am. **97**, 993–1005 (1995).

[7] A. M. Richardson and L. W. Nolte, ''*A posteriori* probability source localization in an uncertain sound speed, deep ocean environment,'' J. Acoust. Soc. Am. **89**, 2280–2284 (1991).

[8] J. A. Shorey, L. W. Nolte, and J. L. Krolik, ''Computationally efficient monte carlo estimation algorithms for matched field processing in uncertain ocean environments,'' J. Comput. Acoust. **2**, 285–314 (1994).

[9] W. Carey, L. M. Dillman, and J. A. Doutt, ''Shallow-water transmission measurements taken on the New Jersey continental shelf,'' Naval Undersea Warfare Center Tech. Doc. 10,025 (1992).

[10] M. B. Porter and E. L. Reiss, ''A numerical method for ocean acoustic normal modes,'' J. Acoust. Soc. Am. **76**, 244–252 (1984).

[11] A. Tolstoy, *Matched Field Processing for Underwater Acoustics* (World Scientific, Singapore, 1993).

Tracking and localizing a moving source in an uncertain shallow water environment

Stacy L. Tantum[a] and Loren W. Nolte[b]

Department of Electrical Engineering, Box 90291, Duke University, Durham, North Carolina 27708-0291

An optimal approach to tracking a moving source in the presence of environmental variability is presented. This tracking algorithm, called the optimum uncertain field tracking algorithm (OUFTA), incorporates a model for the source motion as well as the uncertain ocean environment. The performance of the OUFTA is evaluated over a range of signal-to-noise ratios (SNRs) as a function of the number of observations by examining its ability to correctly estimate both the current source position and the entire source track. The improvement in performance provided by the OUFTA is illustrated by comparison to two suboptimal tracking algorithms. Results show that incorporating *a priori* knowledge of both the source dynamics and the ocean model provides the most accurate estimates of the source track. © *1998 Acoustical Society of America.* [S0001-4966(98)04001-6]

PACS numbers: 43.30.Wi, 43.60.Gk [SAC-B]

INTRODUCTION

Matched-field processing exploits the complicated multipath acoustic pattern created by an acoustic source. Using the full acoustic field provides an effective method for source localization. However, matched-field processing often assumes the source parameters and propagation environment are completely known, rendering this approach highly sensitive to source parameter and environmental mismatches.[1] The optimum uncertain field processor (OUFP), developed by Richardson and Nolte, incorporates parameter estimation theory into standard source localization procedures, resulting in a method of matched-field processing which is robust to uncertainties in the propagation environment and source parameters.[2] The OUFP is the optimal processor for localizing a source in an uncertain ocean environment; however, a series of independent optimal source localizations does not provide the optimal approach to tracking and localizing a moving source in an uncertain environment. The optimal approach is one which considers both the relatively stable state of the ocean over the observation interval and *a priori* knowledge of the source dynamics.

In this paper, a motion based tracking algorithm (MBTA) which incorporates both the stability in the uncertain environment over the observation interval and a model for the source motion, called the optimum uncertain field tracking algorithm (OUFTA), is presented. The performance of this tracking algorithm is compared to the performance attained by the conventional tracking algorithm (CTA) which implements a series of optimal source localizations, termed the OUFP-CTA. It is also compared to a motion based tracking algorithm which utilizes the mean environment processor (MEP), called the MEP-MBTA. This algorithm ignores uncertainty in the parametrization of the environment by assuming that the mean environment is the actual environment. In addition, it is compared to the motion based tracking al-

gorithm which uses the matched-field processor, called the Match-MBTA. This algorithm knows the uncertain environmental parameters and provides an upper bound on the performance which can be expected to be attained when the MBTA is implemented and there is no environmental uncertainty. The performance of these tracking algorithms is evaluated by examining their ability to correctly localize a moving source, as well as their ability to correctly estimate the entire path traversed by the source. The performance measures are computed for a range of signal-to-noise ratios (SNRs) as a function of the number of observations. Of the algorithms dealing with the variability in the environment, the OUFTA has the highest probability of producing correct estimates of both the source path and the current source position, particularly at low SNRs. In addition, the accuracy of both the path and location estimates computed by the motion based tracking algorithms improves as the number of observations increases, while as expected the performance of the conventional tracking algorithm does not improve with additional observations. In addition, it is shown that including a model for the source motion is not sufficient, and in order to achieve the most accurate location estimates the variability in the propagation environment must also be considered.

A general description of the tracking and localization problem, including the physical models employed and the localization processors and tracking algorithms implemented, is presented in Section I. Numerical simulations are included in Section II, and Section III concludes with a discussion of the results.

I. PROBLEM DESCRIPTION

A moving narrow-band source is tracked and localized at short range in a shallow water environment containing an uncertain sound speed profile. The ocean model for this scenario is described in Section I A. The acoustic propagation due to the source is simulated using the normal mode solution to the wave equation, and the resulting acoustic pressure field is sampled by a fully spanning vertical array of receivers. The propagation model is discussed in further detail in
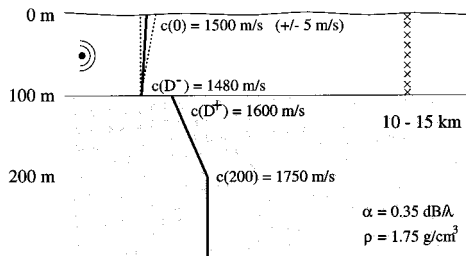
FIG. 1. Range independent shallow water ocean model.

Section I B. The acoustic source emits a continuous sinusoidal wave with a known frequency and a random complex amplitude whose distribution is known *a priori*. The initial position of the source is unknown, however its motion is modeled *a priori* by a Markov model. The models describing the acoustic source and its motion are provided in Section I C.

The optimum uncertain field processor (OUFP), the mean environment processor (MEP), and the matched field processor (MFP) are methods of matched-field processing commonly used for source localization. Each of these processors is implemented in the context of two tracking algorithms, the conventional tracking algorithm (CTA) and the motion based tracking algorithm (MBTA), to track and localize the moving source. The conventional tracking algorithm approaches this problem as a series of independent source localizations. The motion based tracking algorithm differs from this approach by maximizing the probability of the source path given the entire sequence of observations. This maximization problem grows exponentially with the number of observations if the conditional probability is computed for every possible source path. The computational intensity is reduced to linear growth with the number of observations without sacrificing optimality through the use of the Viterbi algorithm, which is discussed in Section I D. The source localization processors are described in further detail in Section I E, and the tracking algorithms are explained in Section I F.

A. Ocean model

The ocean environment, illustrated in Fig. 1, is an idealized range independent shallow water channel which is 100 m in depth, and is similar to an environmental scenario provided for the May 1993 NRL Workshop on Acoustic Models in Signal Processing.[3] The sound speed in the water is modeled as a downward refracting linear profile with uncertainty on the sound speed at the surface. The sound speed at the water surface has a value in the range of 1495 m/s to 1505 m/s, and at the bottom of the channel it is 1480 m/s. The ocean bottom is modeled as two layers which meet at a depth of 200 m. The sound speed in the upper layer increases linearly from 1600 m/s to 1750 m/s between 100 m and 200 m in depth, at which point it becomes constant at 1750 m/s. The bottom attenuation, α, is 0.35 dB/λ, and the bottom density, ρ, is 1.75 g/cm^3.

B. Propagation model

The acoustic pressures at the receivers are calculated using normal mode theory to solve the acoustic wave equa-

tion. This method expresses the pressure field in terms of a normal mode expansion, and then solves for the eigenfunctions and eigenvalues which are solutions to the wave equation and satisfy the boundary conditions.[4] The total acoustic pressure field is then calculated as the weighted sum of the contributions from each mode, where the weighting of the mth mode is proportional to the amplitude of that mode at the source depth. For an isotropic point source with a known frequency f [Hz], the result is a Sturm–Liouville eigenvalue problem with an infinite number of solutions, each characterized by an eigenfunction and eigenvalue. The eigenvalues, or acoustic wavenumbers, k_m, are all distinct and the eigenfunctions, or acoustic modes, $\Phi_m(z)$, form a complete orthonormal set. The normal mode program KRAKEN efficiently and accurately calculates the eigenfunctions and eigenvalues for an ocean acoustic waveguide.[5,6] Once the acoustic wavenumbers and modes are determined by KRAKEN, the complex-valued acoustic pressure field generated by a source located at range r_s and depth z_s in a range independent ocean is calculated from

$$p(z;r_s,z_s) = p_0 \sum_{m=1}^{M} \Phi_m(z_s)\Phi_m(z) \frac{e^{ik_m r_s}}{\sqrt{k_m r_s}}, \qquad (1)$$

where z is the depth of the receiver, p_0 is the pressure generated by the source at $r_s = 1$ m, and M is the number of propagating acoustic modes.

C. Acoustic source model

The acoustic source is modeled as a narrow-band source with a known frequency f [Hz] and a random complex amplitude A. Consequently, the signal emitted by the source is $s(t) = \Re e\{A\sqrt{2}e^{i2\pi ft}\}$. Although the frequency of the source is precisely known, the random amplitude is not. However the amplitude is assumed to follow a known *a priori* distribution.

The source motion is modeled as a finite-state discrete-time Markov process, with each of the possible source locations considered a state of the process. This model fits well into the matched-field processing framework because the range and depth parameters are already discretized. The *a priori* knowledge of the source motion is represented by a state transition matrix:

$$\mathbf{P} = \begin{bmatrix} P_{-1,-1} & P_{0,-1} & P_{1,-1} \\ P_{-1,0} & P_{0,0} & P_{1,0} \\ P_{-1,1} & P_{0,1} & P_{1,1} \end{bmatrix}. \qquad (2)$$

The state transition matrix contains the probabilities of the source moving from its location at the current observation to a neighboring location at the next observation, where $P_{m,n}$ is the probability of the source moving m gridpoints in range and n gridpoints in depth. The state transition matrix is not limited in size to a 3×3 matrix; it may be made as large as is necessary to include all possible transitions.

D. The Viterbi algorithm

The Viterbi algorithm was originally proposed by Andrew J. Viterbi as a method for decoding convolutional

codes.[7] G. David Forney later recognized that this algorithm is also a maximum likelihood algorithm for trellis codes, making it a useful method for finding the maximum *a posteriori* (MAP) estimate of the state sequence of a finite-state discrete-time Markov process observed in memoryless noise.[8,9] It accomplishes this by finding the state sequence which maximizes the conditional *a posteriori* probability of the underlying state sequence given the sequence of noisy observations, $p_{\mathscr{S}_k|\mathscr{X}_k}(\mathscr{S}_k|\mathscr{X}_k)$, where $\mathscr{S}_k = s_1, s_2, \ldots, s_k$ is the state sequence and $\mathscr{X}_k = x_1, x_2, \ldots, x_k$ is the sequence of observations. The received signal at each observation, r_i, is a function of the current state of the system, s_i, and the observations are composed of signal, $\mathscr{R}_k = r_1, r_2, \ldots, r_k$, plus noise, $\mathscr{N}_k = n_1, n_2, \ldots, n_k$; $\mathscr{X}_k = \mathscr{R}_k + \mathscr{N}_k$.

If the conditional *a posteriori* probability is calculated for every possible state sequence, the computational complexity of this problem grows exponentially with the number of observations. However, the Viterbi algorithm reduces the complexity so that it grows linearly with the number of observations by determining the most likely state sequence leading to every possible ending state after each observation. After any observation, the number of remaining state sequences is equal to the number of possible ending states. This remains an optimal solution to the maximization problem because the most likely state sequence leading to any state after observation i must include one of the most likely state sequences determined after observation $i-1$. Thus, the Viterbi algorithm naturally lends itself to a sequential implementation.

Using Bayes' rule, the conditional *a posteriori* probability of the state sequence given the noisy observations can be expressed as

$$p_{\mathscr{S}_k|\mathscr{X}_k}(\mathscr{S}_k|\mathscr{X}_k) = \frac{p_{\mathscr{X}_k|\mathscr{S}_k}(\mathscr{X}_k|\mathscr{S}_k)p_{\mathscr{S}_k}(\mathscr{S}_k)}{p_{\mathscr{X}_k}(\mathscr{X}_k)}. \tag{3}$$

Since the underlying process generating the state sequence is known to be Markovian, the probability of any given state sequence, $p_{\mathscr{S}_k}(\mathscr{S}_k)$, reduces to

$$p_{\mathscr{S}_k}(\mathscr{S}_k) = p_{\mathscr{S}_k}(s_1, s_2, \ldots, s_k)$$

$$= p_{s_1} \prod_{i=2}^{k} p_{s_i|s_{i-1}}(s_i|s_{i-1}), \tag{4}$$

where p_{s_1} represents the probability of starting in the initial state and $p_{s_i|s_{i-1}}(s_i|s_{i-1})$ represents the probability of the process making a transition from the state at observation $i-1$ to the state at observation i. Assuming the observations generated by different states are independent and that different observations generated by the same state are also independent, the conditional density of the observations given the state sequence reduces to

$$p_{\mathscr{X}_k|\mathscr{S}_k}(\mathscr{X}_k|\mathscr{S}_k) = p_{\mathscr{X}_k|\mathscr{S}_k}(x_1, x_2, \ldots, x_k|s_1, s_2, \ldots, s_k)$$

$$= \prod_{i=1}^{k} p_{x|s}(x_i|s_i). \tag{5}$$

Under these two assumptions, the conditional *a posteriori*
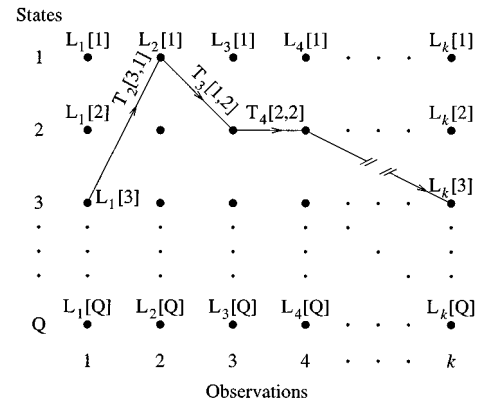
FIG. 2. Calculation of the weight of a path through a trellis using the Viterbi algorithm.

probability of the state sequence given the observations becomes

$$p_{\mathscr{S}_k|\mathscr{X}_k}(\mathscr{S}_k|\mathscr{X}_k)$$

$$= p_{\mathscr{S}_k|\mathscr{X}_k}(s_1, \ldots, s_k|x_1, \ldots, x_k)$$

$$= \frac{\prod_{i=1}^{k} p_{x|s}(x_i|s_i) \times p_{s_1} \prod_{i=2}^{k} p_{s_i|s_{i-1}}(s_i|s_{i-1})}{p_{\mathscr{X}_k}(x_1, \ldots, x_k)}$$

$$= \frac{\prod_{i=1}^{k} p_{x|s}(x_i|s_i) p_{s_i|s_{i-1}}(s_i|s_{i-1})}{p_{\mathscr{X}_k}(x_1, \ldots, x_k)}, \tag{6}$$

where $p_{s_i|s_{i-1}}(s_1|s_0)$ is defined to be p_{s_1}, the probability of starting in the initial state.

The state sequence which maximizes the numerator of the previous expression, $\prod_{i=1}^{k} p_{x|s}(x_i|s_i) p_{s_i|s_{i-1}}(s_i|s_{i-1})$, will also maximize $p_{\mathscr{S}_k|\mathscr{X}_k}(\mathscr{S}_k|\mathscr{X}_k)$. To find the MAP estimate of the state sequence given a sequence of noisy observations, the Viterbi algorithm solves the equivalent problem of maximizing

$$\sum_{i=1}^{k} \{\ln p_{x|s}(x_i|s_i) + \ln p_{s_i|s_{i-1}}(s_i|s_{i-1})\}, \tag{7}$$

where the natural logarithm does not affect the maximization because it is a monotonic increasing function. This procedure can be interpreted as finding the optimum path through a graph, where each path is assigned a weight, given by Equation (7), based on the states through which it passes and the transitions which occur between the states. In the context of the Viterbi algorithm, the graph is known as a trellis; the path is the state sequence; the terms $L_i = \ln p_{x|s}(x_i|s_i)$ are associated with the nodes in the trellis, or the states in the sequence; and the terms $T_i = \ln p_{s_i|s_{i-1}}(s_i|s_{i-1})$ are associated with the branches in the trellis, or the transitions between the states. A graphical depiction of this is illustrated in Fig. 2. It shows the trellis with a typical path extending from the left column of nodes, corresponding to the first observation, to the right column of nodes, corresponding to the final observation, and the calculation of its weight. The state sequence with the maximum weight is the most likely state sequence

given the noisy observations and is the MAP estimate of the state sequence.

E. Source localization processors

For the numerical simulations, the optimum uncertain field processor (OUFP), the mean environment processor (MEP), and the matched field processor (MFP) are implemented in the context of two tracking algorithms to track a moving source and estimate its location. These source localization processors are in a class of algorithms known as matched-field processing. Matched-field source localization typically involves correlating the measured acoustic pressure field at an array of receivers with the fields expected to be observed for all possible source locations. The expected fields, or replicas, are calculated for each hypothesized source position in the assumed propagation environment using a propagation model such as KRAKEN. The measured field is then correlated with each replica field, and the correlation which is maximum identifies the most likely source location.

The mean environment processor assumes the average sound speed profile is the actual sound speed profile. This processor is extremely fast and easy to implement; however, it is also quite sensitive to mismatch between the actual sound speed profile and the assumed sound speed profile. This sensitivity severely limits its performance in an uncertain ocean environment. The OUFP incorporates environmental variability into the processor, making it robust to the uncertainty in the sound speed profile. This processor implements the optimal approach to localizing an acoustic source in an uncertain environment. The matched field processor knows the parameters describing the ocean environment exactly and provides an upper bound on localization performance. These processors are described in further detail in Secs. I E 1 through I E 3.

1. The optimum uncertain field processor

Matched-field source localization is often highly sensitive to mismatches in the assumed source parameters and propagation environment that are used in computing the replica fields, and the actual source parameters and environment which exist when the observation is made.[1] The optimum uncertain field processor (OUFP), developed by Richardson and Nolte, incorporates parameter estimation theory into acoustic source localization, making it a method of matched-field processing which is robust to uncertainties in the propagation environment and the source parameters.[2] Using *a priori* probability density functions for the array and propagation parameters as well as the source location, the OUFP calculates $p_{S|r}(S|r)$, the *a posteriori* probability density function of the source location S given the received signal r. The OUFP is robust to environmental variability because it does not assume a particular propagation environment. Instead, it assumes a range of probable propagation environments and then integrates over the environmental uncertainty to calculate the *a posteriori* probability density function,

$$p_{S|r}(S|r) = \frac{\int_{\Psi} p_{r|S,\Psi}(r|S,\Psi) p_{S|\Psi}(S|\Psi) p_{\Psi}(\Psi) d\Psi}{p_r(r)}, \quad (8)$$

where Ψ is a vector containing the environmental variables describing the acoustic environment, such as parameters describing the sound speed profile and boundary conditions.

The OUFP assumes the ocean is modeled as a deterministic linear system, allowing the replica fields to be calculated. It also assumes the signal emitted by the acoustic source is a narrow-band sinusoid with a known frequency f [Hz]; $s(t) = \Re e\{A\sqrt{2}e^{i2\pi ft}\}$. The signal observed at the array of receivers consists of the source signal with an uncertain complex amplitude plus additive noise,

$$r(t) = As(\hat{S},\hat{\Psi},t) + n(t), \quad (9)$$

where $\hat{S}$ is the actual source position and $\hat{\Psi}$ is the actual environment. The frequency transform of the received signal is of the form

$$P(r) = AH(\hat{S},\hat{\Psi}) + N, \quad (10)$$

where $H(\hat{S},\hat{\Psi})$ is the acoustic transfer function, or replica field in matched-field terminology, for the narrow-band source located at the position $\hat{S}$ in the ocean $\hat{\Psi}$. The elements of $P(r)$ are computed from the discretized time-domain signal received at hydrophone z, $r_z[l]$, by

$$P_z = \frac{1}{L} \sum_{l=1}^{L} r_z[l] e^{-i2\pi fTl}, \quad (11)$$

where L is the number of snapshots in time and T is the sampling period. The observation $P(r)$ is assumed to contain additive zero-mean Gaussian noise N with a known spatial covariance matrix Q. In this work the noise is assumed to be isotropic, consequently $Q = \sigma_N^2 I$. Assuming the uncertain amplitude A of the narrowband source is a zero-mean complex Gaussian random variable with variance σ_A^2, the conditional probability density $p_{S|r}(S|r)$, or ambiguity surface, can be expressed as

$$p_{S|r}(S|r) = C(r) p_S(S) \int_{\Psi} \frac{1}{E(S,\Psi) + 1}$$

$$\times \exp\left(\frac{\frac{1}{2}|R(r,S,\Psi)|^2}{E(S,\Psi) + 1} \right)$$

$$\times p_{\Psi|S}(\Psi|S) d\Psi, \quad (12)$$

where S contains the uncertain source location parameters of range and depth, and $C(r)$ is a normalization constant chosen to make $p_{S|r}(S|r)$ a proper probability density function; $\int_S p_{S|r}(S|r) dS = 1$. The *a priori* knowledge of the source position, $p_S(S)$, is assumed to be uniform over all possible source locations. E and R are defined by

$$E(S,\Psi) = \sigma_A^2 H^\dagger(S,\Psi) Q^{-1} H(S,\Psi)$$

$$= \frac{\sigma_A^2}{\sigma_N^2} H^\dagger(S,\Psi) H(S,\Psi) \quad (13)$$

and

$$R(r,S,\Psi) = \sigma_A^2 H^\dagger(S,\Psi) Q^{-1} P(r) = \frac{\sigma_A^2}{\sigma_N^2} H^\dagger(S,\Psi) P(r). \quad (14)$$

The signal-to-noise ratio (SNR) is defined at the receivers, and is given by

$$\text{SNR} = E(\hat{\mathbf{S}}, \hat{\Psi}) = \sigma_A^2 \mathbf{H}^\dagger(\hat{\mathbf{S}}, \hat{\Psi}) \mathbf{Q}^{-1} \mathbf{H}(\hat{\mathbf{S}}, \hat{\Psi})$$

$$= \frac{\sigma_A^2}{\sigma_N^2} \mathbf{H}^\dagger(\hat{\mathbf{S}}, \hat{\Psi}) \mathbf{H}(\hat{\mathbf{S}}, \hat{\Psi}). \tag{15}$$

When Ψ contains a small number of environmental parameters, a brute force numerical integration is performed to evaluate the integral. However, when Ψ contains many uncertain parameters brute force integration is computationally prohibitive. In this case, the integral can be evaluated efficiently using Monte Carlo integration.[10]

2. The mean environment processor

The mean environment processor (MEP) is similar to the traditional Bartlett processor in that it assumes the actual environment is the mean environment, $\bar{\Psi}$. In addition to using the mean environment, the Bartlett processor also assumes the complex-valued signal amplitude A is known exactly. The mean environment processor differs slightly from this by assuming the signal amplitude follows a complex Gaussian distribution. The probability of the source location given the observation computed by the MEP follows from the probability calculated by the OUFP [Eq. (12)] and is given by

$$p_{\mathbf{S}|\mathbf{r}}(\mathbf{S}|\mathbf{r}) = C(\mathbf{r}) p_{\mathbf{S}}(\mathbf{S}) \frac{1}{E(\mathbf{S}, \bar{\Psi}) + 1}$$

$$\times \exp \left(\frac{\frac{1}{2} |R(\mathbf{r}, \mathbf{S}, \bar{\Psi})|^2}{E(\mathbf{S}, \bar{\Psi}) + 1} \right). \tag{16}$$

3. The matched-field processor

When the acoustic environment $\hat{\Psi}$ is known exactly, the environmental integration performed by the OUFP [Eq. (12)] is not necessary and the conditional probability density calculated by the matched-field processor (MFP) is

$$p_{\mathbf{S}|\mathbf{r}}(\mathbf{S}|\mathbf{r}) = C(\mathbf{r}) p_{\mathbf{S}}(\mathbf{S}) \frac{1}{E(\mathbf{S}, \hat{\Psi}) + 1}$$

$$\times \exp \left(\frac{\frac{1}{2} |R(\mathbf{r}, \mathbf{S}, \hat{\Psi})|^2}{E(\mathbf{S}, \hat{\Psi}) + 1} \right). \tag{17}$$

F. Source tracking algorithms

Two algorithms are implemented to track a moving source and estimate its current location. The first, the conventional tracking algorithm (CTA), is the traditional approach to this problem. This method performs a series of independent source localizations using the chosen localization processor. This algorithm is quite fast; however, it does not incorporate the *a priori* knowledge of the source movement, resulting in source path estimates which are discontinuous and unrealistic. Although the environment is un-

known, it is constant over the total observation time and the CTA ignores the fact that it is possible to learn about the environment by carrying forth information contained in the previous observations when processing the current observation.

The motion based tracking algorithm (MBTA) determines the most likely source path after considering all the observed data. It utilizes the nature of the source motion as well as the assumption of a constant environment when tracking the source. Using all of the observed data and incorporating the assumption of a constant environment enables the MBTA to increase its knowledge of the uncertain parameters as more data is obtained, and improves its performance. These algorithms are described in further detail in Sections I F 1 and I F 2.

1. The conventional tracking algorithm

The conventional tracking algorithm (CTA) implements the traditional approach to the source tracking problem. It performs a series of independent source localizations, ignoring the *a priori* knowledge of the source dynamics and the constant state of the unknown environment during the observation time. For each observation, the ambiguity surface is computed by the chosen localization processor, and the estimated source position for that observation, $\mathbf{S}_i$, is determined by choosing the value of $\mathbf{S}$ which maximizes the ambiguity surface. The estimate of the source track for k observations, $\mathscr{S}_k$, is then formed by concatenating the individual source location estimates:

$$\mathscr{S}_k = \mathbf{S}_1, \mathbf{S}_2, \ldots, \mathbf{S}_k. \tag{18}$$

2. The motion based tracking algorithm

The motion based tracking algorithm (MBTA) implements an optimal approach to the source tracking problem by maximizing the conditional probability of the source path given the sequence of k data observations, $p_{\mathscr{S}_k | \mathscr{R}_k}(\mathscr{S}_k | \mathscr{R}_k)$. It incorporates both the *a priori* knowledge of the source movement and the stability of the unknown environment through which the source is moving.

The most general expression for the conditional probability of the source path given the observed data in an uncertain environment is

$$p_{\mathscr{S}_k | \mathscr{R}_k}(\mathscr{S}_k | \mathscr{R}_k) = \frac{p_{\mathscr{S}_k}(\mathscr{S}_k)}{p_{\mathscr{R}_k}(\mathscr{R}_k)} \int_{\Psi_k} p_{\mathscr{R}_k | \mathscr{S}_k, \Psi_k}(\mathscr{R}_k | \mathscr{S}_k, \Psi_k)$$

$$\times p_{\Psi_k | \mathscr{S}_k}(\Psi_k | \mathscr{S}_k) d\Psi_k. \tag{19}$$

The source path is represented by $\mathscr{S}_k = \mathbf{S}_1, \mathbf{S}_2, \ldots, \mathbf{S}_k$, and the sequence of observed data for the k snapshots is denoted by $\mathscr{R}_k = \mathbf{r}_1, \mathbf{r}_2, \ldots, \mathbf{r}_k$, where $\mathbf{S}_i$ is the source position at the ith snapshot, and $\mathbf{r}_i$ is the corresponding data observation. The sequence of environments which exists for the series of observations is represented by $\Psi_k = \Psi_1, \Psi_2, \ldots, \Psi_k$.

Assuming the observation time is sufficiently small compared to the temporal variability of the ocean, the environment will remain constant over the observations and Ψ_k can be replaced by a single environmental parameter set Ψ. Assuming that the random complex amplitude of the source

is independent across snapshots and that observations generated from different source locations are also independent, the conditional probability of the observed data sequence given the source path and the environment reduces to

$$p_{\mathscr{R}_k|\mathscr{S}_k,\Psi}(\mathscr{R}_k|\mathscr{S}_k,\Psi) = \prod_{i=1}^{k} p_{\mathbf{r}|\mathbf{S},\Psi}(\mathbf{r}_i|\mathbf{S}_i,\Psi). \qquad (20)$$

If the source movement is Markov in nature, the probability of any source path is

$$p_{\mathscr{S}_k}(\mathscr{S}_k) = \prod_{i=1}^{k} p_{\mathbf{S}|\mathbf{S}_{-1}}(\mathbf{S}_i|\mathbf{S}_{i-1}), \qquad (21)$$

where $p_{\mathbf{S}|\mathbf{S}_{-1}}(\mathbf{S}_1|\mathbf{S}_0)$ is defined to be $p_{\mathbf{S}_1}$, the probability of the source starting at the initial location. Under these assumptions, the conditional probability of the source path given the observed data becomes

$$p_{\mathscr{S}_k|\mathscr{R}_k}(\mathscr{S}_k|\mathscr{R}_k) = \frac{\Pi_{i=1}^{k} p_{\mathbf{S}|\mathbf{S}_{-1}}(\mathbf{S}_i|\mathbf{S}_{i-1}) \int_{\Psi} \{\Pi_{i=1}^{k} p_{\mathbf{r}|\mathbf{S},\Psi}(\mathbf{r}_i|\mathbf{S}_i,\Psi)\} p_{\Psi|\mathscr{S}_k}(\Psi|\mathscr{S}_k) d\Psi}{p_{\mathscr{R}_k}(\mathscr{R}_k)}. \qquad (22)$$

The most likely source path can be found by computing $p_{\mathscr{S}_k|\mathscr{R}_k}(\mathscr{S}_k|\mathscr{R}_k)$ for all possible source paths, and subsequently choosing the path with the maximum *a posteriori* probability. However, the computational intensity of this problem grows exponentially with the number of observations. Although this conditional probability cannot be expressed in a form exactly like that required by the Viterbi algorithm, it is in a similar form, thus allowing the idea of the Viterbi algorithm to be used to reduce the computational intensity to linear growth without sacrificing optimality. The source track which maximizes the log of the numerator also maximizes $p_{\mathscr{S}_k|\mathscr{R}_k}(\mathscr{S}_k|\mathscr{R}_k)$. Consequently, the most likely source path given the sequence of observed data can be found by solving the equivalent maximization problem of

$$\mathscr{S}_k = \max_{\mathscr{S}_k} \left\{ \sum_{i=1}^{k} \ln p_{\mathbf{S}|\mathbf{S}_{-1}}(\mathbf{S}_i|\mathbf{S}_{i-1}) \right.$$
$$\left. + \ln \int_{\Psi} \left[\prod_{i=1}^{k} p_{\mathbf{r}|\mathbf{S},\Psi}(\mathbf{r}_i|\mathbf{S}_i,\Psi) \right] p_{\Psi|\mathscr{S}_k}(\Psi|\mathscr{S}_k) d\Psi \right\}. \qquad (23)$$

This implementation of the MBTA in an uncertain environment is termed the optimum uncertain field tracking algorithm (OUFTA). From the definition of the OUFP [Eq. (12)],

$$p_{\mathbf{r}|\mathbf{S},\Psi}(\mathbf{r}|\mathbf{S},\Psi) = \frac{1}{E(\mathbf{S},\Psi)+1} \exp\left(\frac{\frac{1}{2}|R(\mathbf{r},\mathbf{S},\Psi)|^2}{E(\mathbf{S},\Psi)+1} \right), \quad (24)$$

thereby allowing the integral in the second term to be computed. This sum [Eq. (23)] can be related to the path weight calculated by the Viterbi algorithm [Eq. (7)] by recognizing that the first term, $\ln p_{\mathbf{S}|\mathbf{S}_{-1}}(\mathbf{S}_i|\mathbf{S}_{i-1})$, is based on the movement of the source and is analogous to T_i and the second term,

$$\ln \int_{\Psi} \left[\prod_{i=1}^{k} p_{\mathbf{r}|\mathbf{S},\Psi}(\mathbf{r}_i|\mathbf{S}_i,\Psi) \right] p_{\Psi|\mathscr{S}_k}(\Psi|\mathscr{S}_k) d\Psi,$$

is based on the position of the source and is analogous to $\Sigma_{i=1}^{k} L_i$.

The optimum uncertain field tracking algorithm incorporates the *a priori* knowledge of the source movement and the variable ocean environment directly into the processor by combining the concepts of the OUFP and the Viterbi algorithm. In an uncertain environment, it considers all the observed data before performing the environmental integration.

When the chosen localization processor assumes a particular environment, as is the case for both the mean environment processor and the matched field processor, the environmental integration is unnecessary, and the conditional probability of the source path given the observed data can be expressed in a form exactly like that required by the Viterbi algorithm. The maximization problem can then be posed as

$$\mathscr{S}_k = \max_{\mathscr{S}_k} \sum_{i=1}^{k} \{\ln p_{\mathbf{S}|\mathbf{S}_{-1}}(\mathbf{S}_i|\mathbf{S}_{i-1}) + \ln p_{\mathbf{r}|\mathbf{S},\Psi}(\mathbf{r}_i|\mathbf{S}_i,\Psi)\}. \qquad (25)$$

Here, $\ln p_{\mathbf{S}|\mathbf{S}_{-1}}(\mathbf{S}_i|\mathbf{S}_{i-1})$ is analogous to T_i in the Viterbi algorithm, and $\ln p_{\mathbf{r}|\mathbf{S},\Psi}(\mathbf{r}_i|\mathbf{S}_i,\Psi)$ is analogous to L_i in the Viterbi algorithm.

II. NUMERICAL SIMULATIONS AND RESULTS

For the numerical simulations, a 250-Hz source is moving through the ocean at ranges between 10 km and 15 km and at depths between 10 m and 90 m. The ocean in which the source is moving has a stable, but uncertain, linear sound speed profile, with variability on the sound speed at the surface. The uncertain surface sound speed is gridded to 25 equally spaced values over its range for the environmental integration, and is chosen from a uniform probability density function. The observation of the pressure field is made at a fully spanning vertical line array of hydrophones consisting of 101 receivers spaced 1 m apart from the ocean surface to 100 m in depth.

The random amplitude of this narrow-band source is assumed to obey a zero-mean complex Gaussian distribution with variance σ_A^2. The unknown source position parameter of range is gridded to 101 possible values over its range, and the depth parameter is gridded to 41 possible values. These are the locations at which the replica fields are computed.
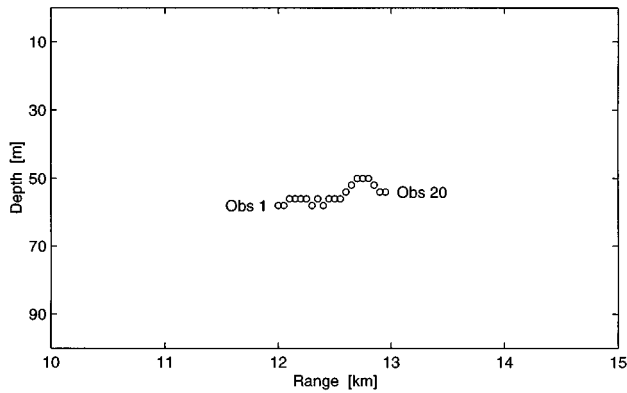
FIG. 3. Typical random realization of a source path.

FIG. 4. Localization processor performance shown as (a) probability of correct localization, (b) rms range error, and (c) rms depth error.

The source dynamics are modeled by a Markov model, and the transition matrix describing the source motion is

$$\mathbf{P} = \begin{bmatrix} P_{-1,-1} & P_{0,-1} & P_{1,-1} \\ P_{-1,0} & P_{0,0} & P_{1,0} \\ P_{-1,1} & P_{0,1} & P_{1,1} \end{bmatrix} = \begin{bmatrix} 0.01 & 0.02 & 0.27 \\ 0.01 & 0.03 & 0.36 \\ 0.01 & 0.02 & 0.27 \end{bmatrix}. \tag{26}$$

This particular transition matrix was chosen in an effort to realistically simulate the movement of a source traveling to its desired destination. For this work, the difference between two gridpoints in range is 50 m and the difference between two gridpoints in depth is 2 m. At the boundaries of the search grid, the probabilities of invalid transitions are set to zero. Although the statistics describing the source motion are assumed to be known, the initial location of the source is unknown and the *a priori* information of the initial source position is uniform over the search grid.

A typical random realization of the path taken by a source obeying this model is illustrated in Fig. 3. The source starts at 12 km in range and 60 m in depth and progressively moves away from the receivers to a range of 12.95 km and a depth of 56 m. This source is most likely to move 50 m away from the receivers in range and -2 m to $+2$ m in depth from observation to observation; however, it is also possible for it to move in other directions.

The OUFP, the mean environment processor, and the matched field processor are implemented in the context of both the conventional tracking algorithm and the motion based tracking algorithm to estimate both the path taken by the source and the most recent source location. The abilities of these algorithms to track and localize a moving source are evaluated independently. The source location is estimated in Section II A, and the source path is estimated in Section II B.

A. Localization performance

The performance of the source localization processors over a range of signal-to-noise ratios (SNRs) is summarized by probability of correct localization (P_{CL}) curves.[10] This measure of performance is generated by repeatedly performing source localization for a set of SNRs and finding the probability that the source location is correctly estimated for
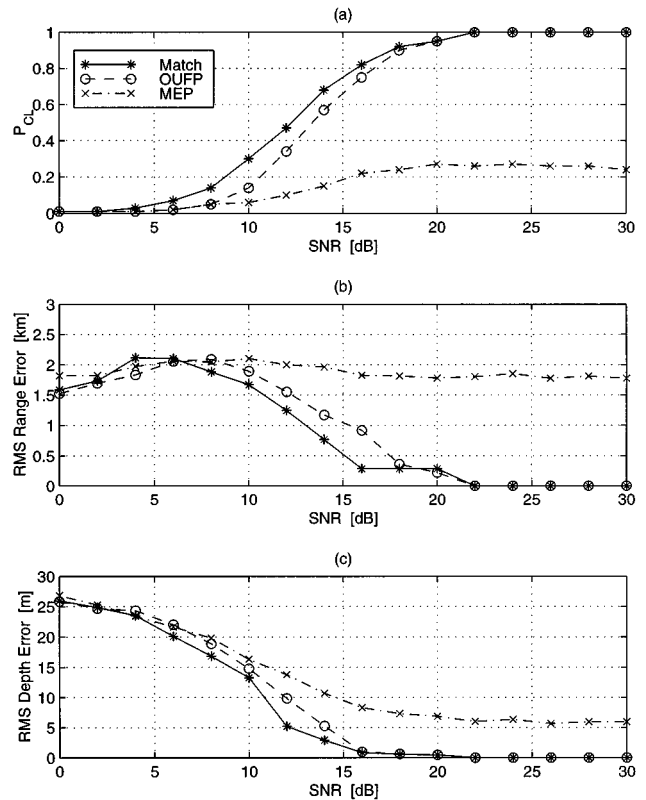
each SNR. The SNR [Eq. (15)] is set to the desired level by fixing the parameter σ_A^2 for the signal amplitude and then adjusting the variance of the noise, σ_N^2.

The P_{CL} curves for the OUFP, the mean environment processor (MEP), and the matched field processor are shown in Fig. 4(a). A localization is considered to be correct when the processor correctly identifies the grid point at which the source actually is located. For these simulations, a grid point covers 50 m in range and 2 m in depth. The matched field processor provides an upper bound on localization performance in this scenario. It knows the propagation environment exactly, so its performance level is limited by the presence of noise. The OUFP attains nearly the same level of performance as the matched field processor. The slight loss in performance is due to the limited amount of uncertainty in the parametrization of the environment. By integrating over this uncertainty, it is robust to the variability in the surface sound speed. The performance of the MEP is very poor in this situation. Its performance levels off at $P_{CL} = 0.2$, and does not improve with increasing SNR due to the environmental variability. This illustrates the degradation in performance which results when the uncertainty in the environmental parameters is not included in the model. The rms errors in the range and depth estimates are presented in Fig. 4(b) and (c). The range and depth errors are examined independently since a true distance measure of the error would be dominated by the error in range due to the large difference in the range and depth scales under consideration here. They too illustrate the effect that incorrect environmental modeling has on the performance, particularly in the range esti-

FIG. 5. Ambiguity surfaces computed by the conventional tracking algorithm using the OUFP (OUFP-CTA) after (a) 1 observation, (b) 2 observations, (c) 3 observations, (d) 5 observations, (e) 7 observations, (f) 10 observations, (g) 15 observations, and (h) 20 observations.

FIG. 6. Ambiguity surfaces computed by the motion based tracking algorithm using the OUFP (OUFTA) after (a) 1 observation, (b) 2 observations, (c) 3 observations, (d) 5 observations, (e) 7 observations, (f) 10 observations, (g) 15 observations, and (h) 20 observations.

mates. It is important to note that rms measures are meaningful only when the errors are local, and these measures are intended to quantify the accuracy of the location estimates when they are close to the actual source position. Local errors occur when the noise in the problem causes the peak in the ambiguity surface to shift slightly. When the noise level increases, the incorrect peaks in the ambiguity surface become more widely scattered, and global errors occur when the source is localized at these ambiguous peaks. At low SNRs, the majority of the localization errors are global, resulting in rms measures of performance which are not as meaningful. The rms errors in the estimates produced by the matched field processor decrease as the SNR increases, and the rms errors in the estimates computed by the OUFP closely follow those of the matched field processor. In contrast, the rms errors resulting from the mean environment processor level off and do not improve with increasing SNR.

For the sake of brevity, the remainder of the results in this paper will be presented for only the conventional tracking algorithm using the OUFP (OUFP-CTA), the motion based tracking algorithm using the mean environment processor (MEP-MBTA), and the motion based tracking algorithm using the OUFP (OUFTA). These results illustrate the effects of including only the environmental uncertainty, only the source motion model, and both the environmental variability and the source motion model, respectively, on processor performance. In addition, the performance of the motion based tracking algorithm using the matched-field processor (Match-MBTA) is presented in order to provide an upper

bound on the performance which can be expected to be achieved by the MBTA. The conventional tracking algorithm using the matched-field processor will perform slightly better than when the OUFP is the chosen localization processor, and the performance of the conventional tracking algorithm using the mean environment processor (MEP-CTA) falls below that of the motion based tracking algorithm using the mean environment processor (MEP-MBTA).

The ambiguity surfaces computed by the OUFP-CTA for a single realization after 1, 2, 3, 5, 7, 10, 15, and 20 observations are shown in Fig. 5. They display the log probability of the source location given the observation as a function of source range and depth [Eq. (12)]. The ambiguity surfaces computed for a single realization by the OUFTA follow in Fig. 6. Here, the path weights of all the surviving paths are displayed as a function of the source range and depth [Eq. (23)]. These path weights are equal to the numerator of the probability expression given by Eq. (22), and can be converted to probabilities by computing the normalization constant for each observation. Recall that using the Viterbi algorithm results in one remaining path leading to each possible source position after every observation. As a result, this subset of probabilities displayed will not integrate to 1 because many possible source tracks have been discarded, along with their associated probabilities. The actual source path corresponding to these ambiguity surfaces is the realization illustrated in Fig. 3, and the SNR is 10 dB per observation. The characteristics of the ambiguity surfaces computed by the OUFP-CTA (Fig. 5) do not change as more

FIG. 7. Tracking algorithm localization performance shown as probability of correct localization after (a) 3 observations, (b) 10 observations, and (c) 20 observations.

FIG. 8. Tracking algorithm localization performance shown as rms range error after (a) 3 observations, (b) 10 observations, (c) 20 observations.

observations are made. Each of the surfaces in the time sequence has many ambiguous peaks, and one cannot visually locate a single moving peak which identifies the source position. In contrast, the ambiguity surfaces computed by the OUFTA (Fig. 6) evolve over time. The errant peaks become less prominent and a single moving peak which identifies the source position emerges. The ambiguity surfaces computed by the OUFTA converge to the actual source location as more observations are made, but the OUFP-CTA does not converge to the correct source location with more observations.

The localization performance of the tracking algorithms is summarized by examining the evolution in the P_{CL} curves with an increasing number of observations. To generate these curves, 100 source localizations were performed, each with an independent realization of the source path and the ocean environment. The current source location is estimated by taking the final source position of the MAP estimate of the source track, and to be counted as correct the location estimate must be exactly correct. The results after 3, 10, and 20 observations are shown in Fig. 7. Neither the OUFP-CTA nor the MEP-MBTA exhibits performance gains with an increasing number observations. However, both the OUFTA and the Match-MBTA show improved performance, particularly at low SNRs. In addition, the performance of the OUFTA approaches the bound provided by the Match-MBTA, indicating that the OUFTA is learning the uncertain environment as more observations become available.

Another gauge of performance is the accuracy of the source position estimate. The rms range and depth errors are examined independently since a distance measure would be dominated by the error in range due to the large difference in the range and depth scales. The range and depth errors are shown in Figs. 8 and 9. (Recall that the rms measures of performance are most meaningful at SNR levels where the errors are local.) Since the OUFP-CTA incorporates only the uncertainty in the environment, not the source motion, the errors in the estimates it computes do not improve with additional observations. Both the MEP-MBTA and the OUFTA produce estimates with lower rms errors as more observations are obtained. However, the environmental mismatch hinders the performance of the MEP-MBTA. The rms errors associated with its estimates level off and do not improve with increasing SNR. The rms errors resulting from the OUFTA decrease as more observations are made, and they also approach zero as the SNR increases. Although the rms errors in both range and depth go to zero for high SNR, this does not indicate that the source position estimate is exactly correct for each realization, only that it is within a gridpoint for each realization. The search grid would have to be refined to capture the smaller errors which are present at high SNR. Of the two source position parameters, range is more difficult to estimate. Consequently, the depth estimates approach their limits of accuracy more quickly. This can be seen by observing that the rms depth errors after 10 and 20 observations are nearly the same, but the rms range errors after 20 observations are significantly lower than those after 10 observations.
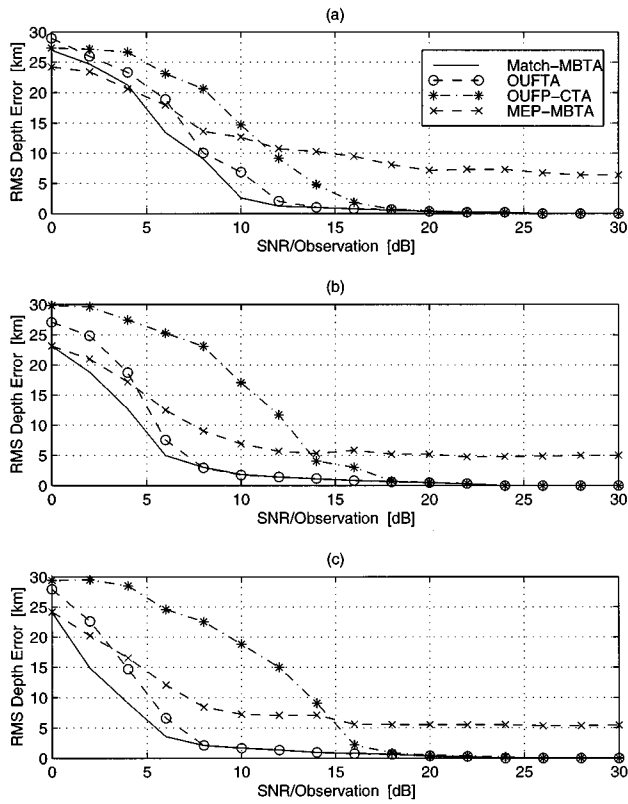
FIG. 9. Tracking algorithm localization performance shown as rms depth error after (a) 3 observations, (b) 10 observations, and (c) 20 observations.
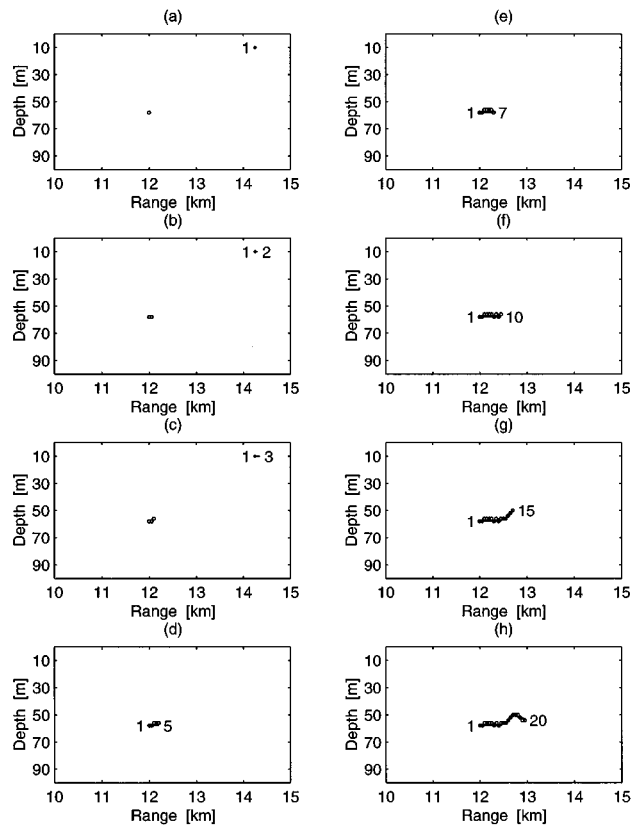
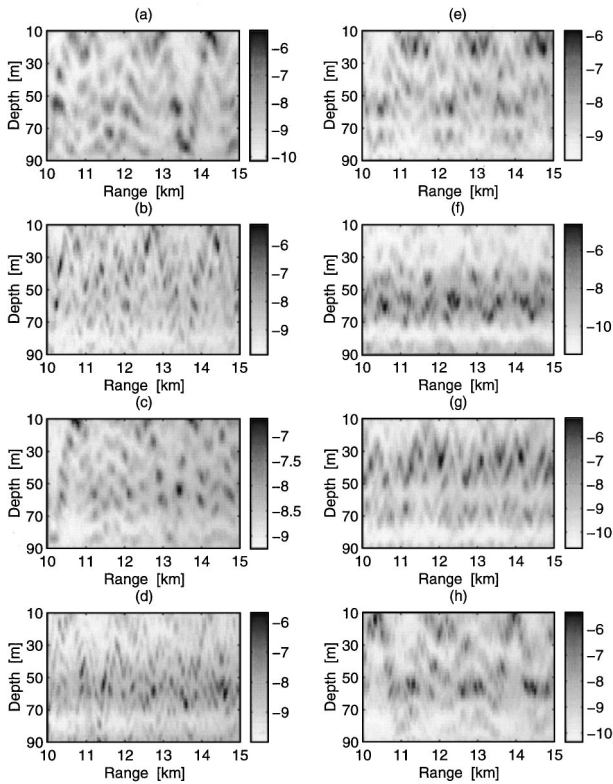FIG. 10. Source path estimates computed by the conventional tracking algorithm using the OUFP (OUFP-CTA) after (a) 1 observation, (b) 2 observations, (c) 3 observations, (d) 5 observations, (e) 7 observations, (f) 10 observations, (g) 15 observations, and (h) 20 observations.
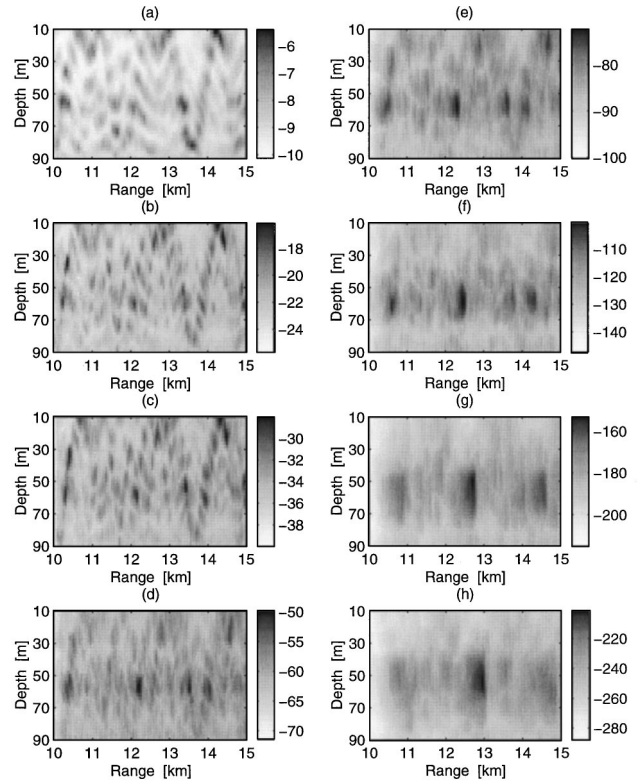

FIG. 11. Source path estimates computed by the motion based tracking algorithm using the OUFP (OUFTA) after (a) 1 observation, (b) 2 observations, (c) 3 observations, (d) 5 observations, (e) 7 observations, (f) 10 observations, (g) 15 observations, and (h) 20 observations.
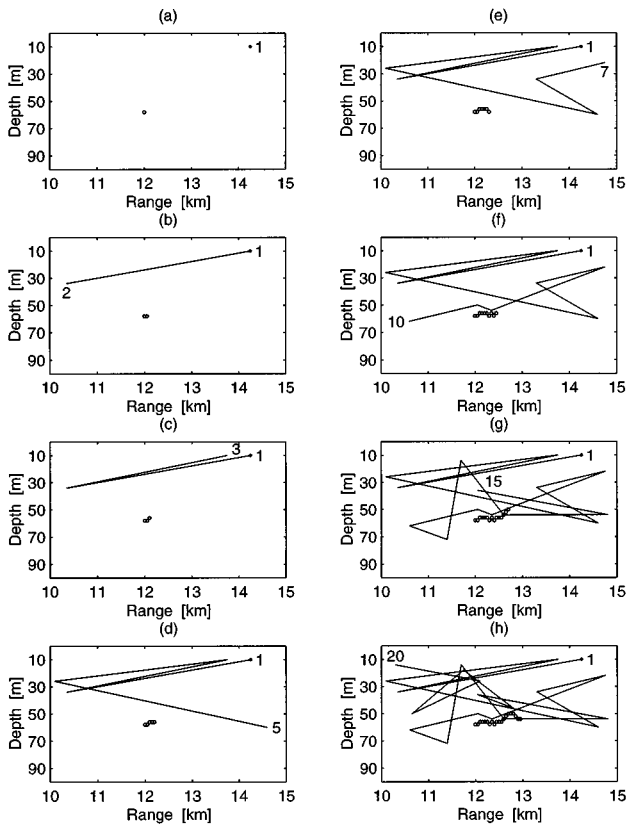
B. Tracking performance

The source tracks estimated by the OUFP-CTA for a single realization after 1, 2, 3, 5, 7, 10, 15, and 20 observations are shown along with the actual path taken by the source in Fig. 10, and the tracks estimated by the OUFTA are shown in Fig. 11. The actual path, denoted by the dots, is the typical path illustrated in Fig. 3, and the SNR is 10 dB per observation. The estimated source track is illustrated by a solid line connecting the source location estimates. The estimate of the starting position is also marked by an asterisk, and the final position estimate is identified by the observation number. The OUFP-CTA estimates the first location to be at 14.25 km in range and 10 m in depth, and the source position after 20 observations to be 10.3 km in range and 14 m in depth. Even though it correctly locates the source at observation 13, it does not continue to do so. The OUFTA also initially estimates the source path incorrectly. After 3 observations, it places the source at 14.35 km in range and 10 m in depth. However, by the fifth observation, it has refined the path estimate so that it follows the actual source path fairly accurately, and it continues to follow the source up to observation 20. The ability of the OUFTA to revise its source track estimates when new observations become available is also illustrated by this example. Because the OUFTA is designed to estimate the entire path, not just the current position, later observations affect the estimates of earlier locations.
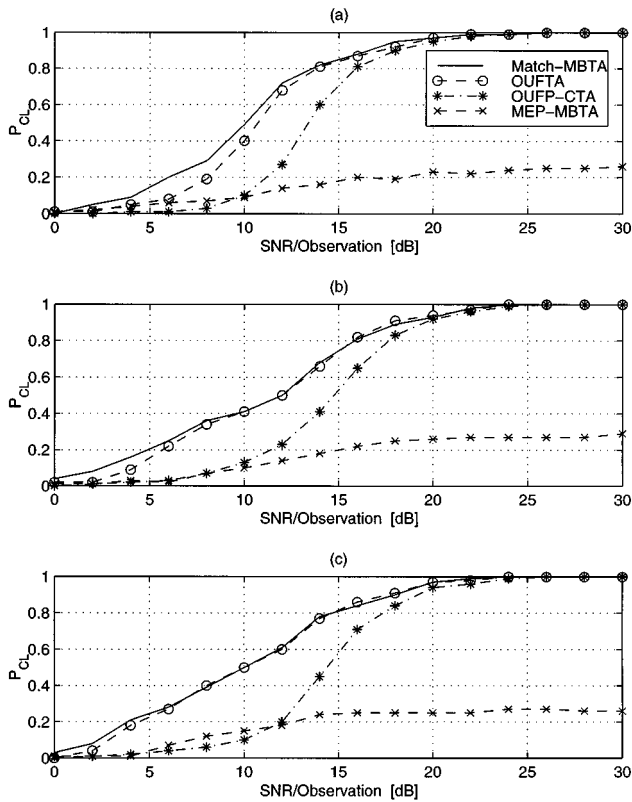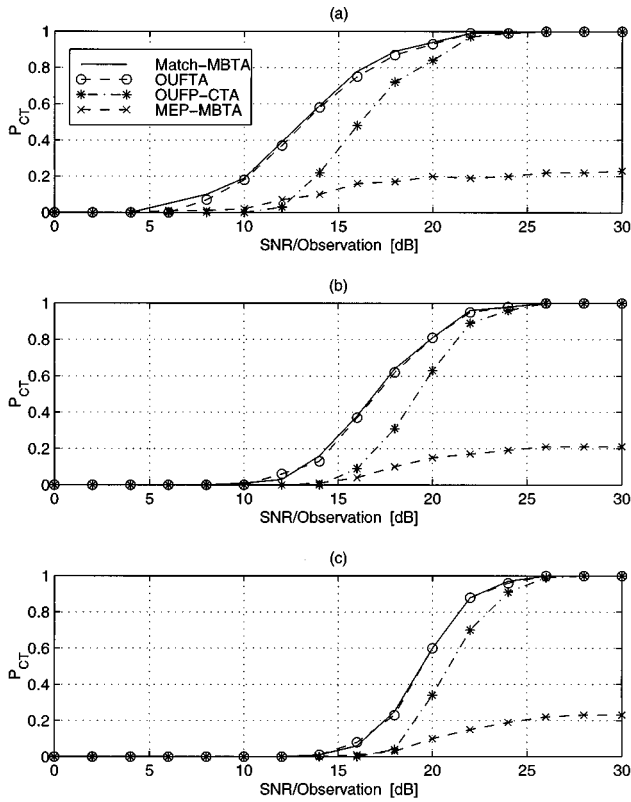
FIG. 12. Tracking algorithm tracking performance shown as probability of correct track after (a) 3 observations, (b) 10 observations, and (c) 20 observations.

FIG. 13. Tracking algorithm tracking performance shown as rms range error per observation after (a) 3 observations, (b) 10 observations, and (c) 20 observations.

Using P_{CL} curves to summarize the ability of these tracking algorithms to estimate the current location of a moving source can be extended to evaluate their tracking performance by determining the probability of correct track (P_{CT}). However, this measure only determines whether the entire estimated path is correct, not the degree of error associated with the estimated path. Consequently, P_{CT} curves may be deceiving because as the number of observations approaches infinity, the probability of exactly determining the correct source location for every observation approaches zero.[8] For this reason, the rms errors per observation in both range and depth are also examined in order to measure how closely the estimated path mimics the actual path.

The summary statistics after 3, 10, and 20 observations are presented in Figs. 12, 13, and 14. These curves are generated by applying the tracking algorithms to 100 independent realizations, each with a different source path and ocean environment. A source track is considered to be correct when each of the position estimates is exactly correct. As expected, the P_{CT} curves (Fig. 12) for all three algorithms fall as the number of observations increases. The P_{CT} curves seem to indicate that these algorithms experience significant performance losses as more observations are made available. However, upon examination of the rms errors per observation in range and depth (Figs. 13 and 14) it can be seen that while the probability of correctly estimating the entire path decreases, the path estimates become more accurate as the number of observations increases. The rms errors per observation computed here exhibit the same characteristics as the
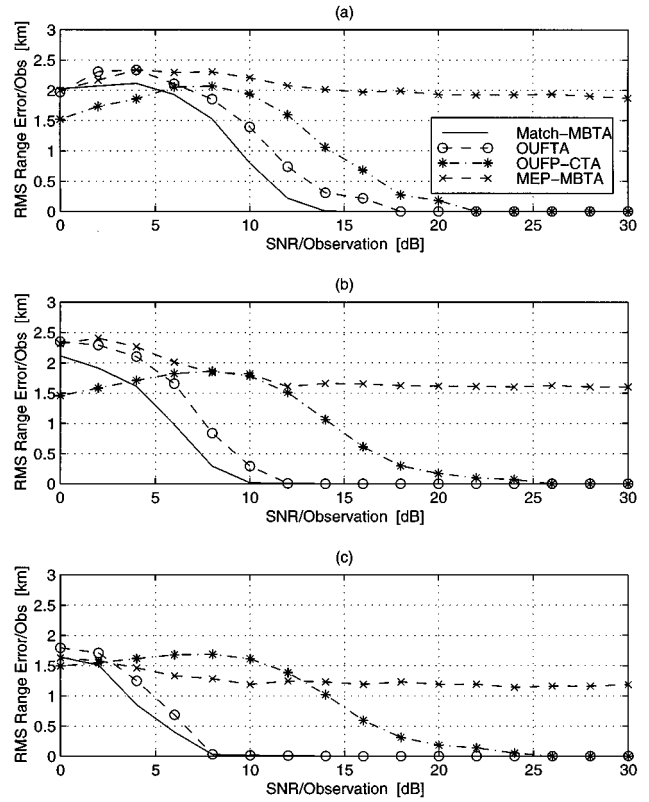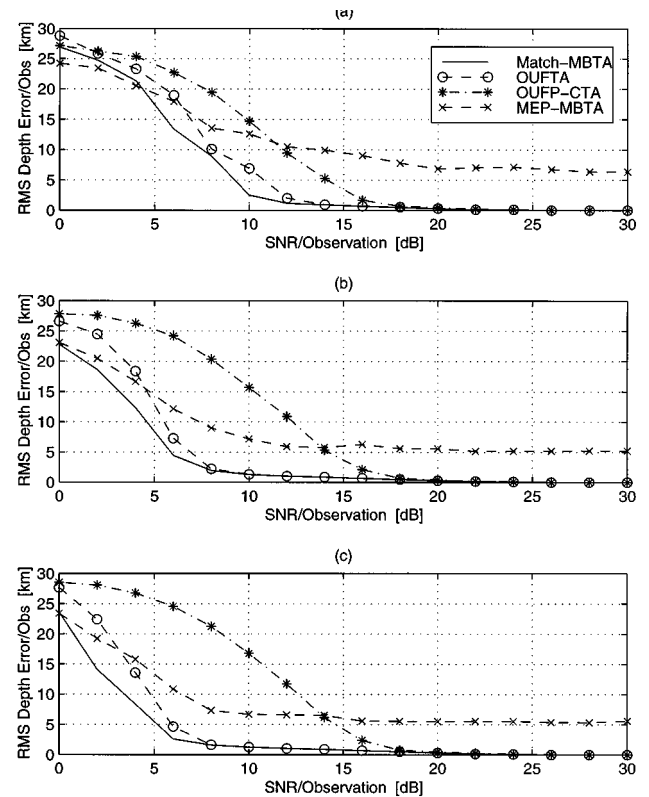
FIG. 14. Tracking algorithm tracking performance shown as rms depth error per observation after (a) 3 observations, (b) 10 observations, and (c) 20 observations.

rms errors calculated in evaluating the localization performance, and once again it is important to note that this performance measure is more meaningful at SNRs where the errors in the estimates are local. The rms errors per observation in the estimates computed by the OUFP-CTA do not decrease as more observations are made. Both the MEP-MBTA and the OUFTA compute estimates with lower rms errors per observation as more observations are made; however, only the OUFTA produces estimates with rms errors per observation approaching zero as the SNR increases. Of the two source position parameters, range is more difficult to estimate for the tracking problem as well. Similar to the results attained for the localization problem, the depth estimates approach their limits of accuracy more quickly.

III. CONCLUSIONS

This paper has presented a tracking algorithm, termed the optimum uncertain field tracking algorithm (OUFTA), which incorporates *a priori* knowledge of both the source motion and the uncertain ocean environment. This algorithm exhibits improved performance in estimating both the current position of the source and entire path taken by the source when compared to implementing a series of optimal source localizations and a suboptimal motion based tracking algorithm. In particular, the rms errors in the range and depth estimates computed by this tracking algorithm decrease as more observations are made and as the SNR increases, but the rms errors in the estimates produced by a series of optimal source localizations do not change as additional observations are made and the rms errors in the estimates computed by the suboptimal motion based tracking algorithm do

not decrease as the SNR increases. The improvements incurred when the SNR increases can be attributed to incorporating environmental uncertainty into the model, and the gains realized when more observations are made can be attributed to including a model describing the source motion.

[1] A. Tolstoy, ''Sensitivity of matched field pocessing to sound-speed profile mismatch for vertical arrays in a deep water Pacific environment,'' J. Acoust. Soc. Am. **85**, 2394–2404 (1989).

[2] A. M. Richardson and L. W. Nolte, ''*A posteriori* probability souce localization in an uncertain sound speed, deep ocean environment,'' J. Acoust. Soc. Am. **89**, 2280–2284 (1991).

[3] M. B. Porter and A. Tolstoy, ''The matched field processing benchmark problems,'' J. Comput. Acoust. **2**, 161–185 (1994).

[4] F. B. Jensen, W. A. Kuperman, M. B. Porter, and H. Schmidt, *Computational Ocean Acoustics* (American Institute of Physics, Woodbury, NY, 1994).

[5] M. B. Porter, *The KRAKEN normal mode program*, Rep. SM-245 (SACLANT Undersea Research Centre, La Spezia, Italy, 1991).

[6] M. B. Porter and E. L. Reiss, ''A numerical method for ocean acoustic normal modes,'' J. Acoust. Soc. Am. **76**, 244–252 (1984).

[7] A. J. Viterbi, ''Error bounds for convolutional codes and an asymptotically optimum decoding algorithm'' IEEE Trans. Inf. Theory **IT-13**, 260–269 (1967).

[8] G. D. Forney, Jr., ''The Viterbi Algorithm,'' Proc. IEEE **61**, 268–278 (1973).

[9] C. W. Therrien, *Discrete Random Signals and Statistical Signal Processing* (Prentice–Hall, Englewood Cliffs, NJ, 1992).

[10] J. A. Shorey, L. W. Nolte, and J. L. Krolik, ''Computationally efficient Monte Carlo estimation algorithms for matched field processing in uncertain ocean environments,'' J. Comput. Acoust. **2**, 285–314 (1994).

Efficient estimation of the probability that a source track is examined in a matched-field processing tracking algorithm

Cedric A. Zala
Barrodale Computing Services Ltd., P.O. Box 3075, Victoria, British Columbia V8W 3W2, Canada

John M. Ozard
Defence Research Establishment Atlantic, Esquimalt Defence Research Detachment, P.O. Box 17000 STN FORCES, Victoria, British Columbia V9A 7N2, Canada

Michael J. Wilmut
Royal Military College of Canada, P.O. Box 17000 STN FORCES, Kingston, Ontario K7K 7B4, Canada

Tracking techniques may be used to reduce the ambiguity of an acoustic source's position in matched-field processing, particularly for low signal-to-noise ratios. An efficient tracking algorithm was recently described, in which the performance would be comparable to that of an exhaustive tracker; that is, the probability that the source track is examined is close to unity for cases of interest. The current paper describes an efficient technique to estimate the probability that the source track is examined. The procedure involves the use of noise-only data to define statistical thresholds for the strongest peaks in the ambiguity surface. Once these thresholds are defined, the required probabilities may be estimated by evaluating the ambiguity function for signal-plus-noise data within a small region surrounding the known source location, and identifying any peaks exceeding the thresholds. Results of simulations obtained for a slanted array indicate that this approach provides an effective way to estimate the probability that the source track is examined. [S0001-4966(97)03512-1]

PACS numbers: 43.30.Wi, 43.60.Gk [SAC-B]

INTRODUCTION

An efficient detect-after-track scheme was recently proposed[1,2] for use in matched-field processing (MFP) of low signal-to-noise ratio (SNR) data. Briefly, in that technique, the strongest peaks in a sequence of ambiguity surfaces are used to define possible source tracks. This is done by considering all pairwise combinations of the strongest peaks, where each element of the pair is taken from a different ambiguity surface. Linear tracks based on the positions of the peaks are then formed and those tracks which are not physically realizable are rejected. The number of tracks formed is many orders of magnitude less than the exhaustive case of all possible linear, constant speed tracks through all grid point pairs on the different ambiguity surfaces. For each physically realizable track, the processor outputs in the ambiguity surfaces for each position predicted by the track are then averaged. Those tracks with the largest such averages (and exceeding a specified threshold) constitute the estimates for the track of a source moving at constant speed and heading.

The detect-after-track procedure requires, as input, estimates of the positions of a specified number of peaks m in each of the ambiguity surfaces, in order to formulate possible tracks to be examined. To characterize the performance of this detect-after-track procedure, it is essential to estimate PTE, the probability that the track is examined. As noted in Ref. 2, this probability may be expressed as

$$\text{PTE} = 1 - \left[\prod_{i=1}^{N_S} (1 - P_i) + \sum_{i=1}^{N_S} P_i \prod_{j \neq i} (1 - P_j) \right], \quad (1)$$

where P_i is the probability of localized detection of the source peak in the ith ambiguity surface, and N_S is the number of consecutive ambiguity surfaces in time. Localized detection is defined here as the occurrence of one of the m strongest peaks in the ambiguity surface within a specified distance tolerance of the true location of the source. For example, if all $P_i = 0.225$ and $N_S = 20$, then PTE=0.96, so that even for fairly small values of P_i and a realistic value for N_S, PTE approaches unity.

The estimation of P_i is a necessary step in estimating the performance of the detect-after-track procedure. However, estimation of P_i is not straightforward because the ambiguity surface statistics are correlated, as pointed out by Sullivan and Middleton.[3,4] This quantity depends on numerous parameters, including the source location, the SNR, the configuration of the array, the conditions for covariance estimation, the spatial extent of the ambiguity surfaces, the number of peaks chosen from the ambiguity surfaces, and the criteria chosen for localized detection. For a particular application, however, many of these parameters are fixed. Then, PTE will depend on a small number of parameters, including the source and noise levels, the source location, and the number of peaks chosen for analysis.

I. DESCRIPTION OF THRESHOLDING APPROACH

In this section, we discuss background signal processing considerations and describe an efficient method for estimating P_i.

A. Background signal processing considerations

We start with the problem of deciding whether a spatially coherent signal is present in the search region. This decision is made for a known source location, using frequency domain data obtained from an array of sensors in the presence of spatially incoherent Gaussian noise. The optimum processor is the Bartlett processor applied to the data covariance matrix $\mathbf{Q}$ for the N-element array, where $\mathbf{Q}$ has been estimated by averaging over K realizations. It is assumed that the signal is incoherent between these realizations, the noise intensity at each sensor is σ^2, and the real and imaginary components of the noise vector $\mathbf{n}$ are independently distributed $N(0,\sigma^2/2)$. (We note here that in situations for which the noise is spatially correlated, prewhitening techniques may be applied to the data to yield uncorrelated noise.[5,6]) It will be assumed that the signal is described by a vector $\mathbf{s}$, consisting of the field values at the sensors which would be observed after propagation from an acoustic source at the known location.

The noise covariance matrix $\mathbf{Q}_n$ is defined as

$$\mathbf{Q}_n = \frac{1}{K} \sum_{k=1}^{K} \mathbf{n}_k \mathbf{n}_k^*, \qquad (2)$$

where $\mathbf{n}_k$ is the kth noise vector realization, and "*" denotes the conjugate transpose. Similarly, the signal-plus-noise covariance matrix $\mathbf{Q}_{s+n}$ is defined as

$$\mathbf{Q}_{s+n} = \frac{1}{K} \sum_{k=1}^{K} (\mathbf{s}_k + \mathbf{n}_k)(\mathbf{s}_k + \mathbf{n}_k)^*, \qquad (3)$$

where $\mathbf{s}_k$ is the kth signal vector realization for the source. It is assumed that the signal is incoherent between realizations, so that $\mathbf{s}_k = \mathbf{s}e^{i\phi_k}$, where $\mathbf{s}$ is the unperturbed signal vector and ϕ_k is a random phase angle.

The normalized Bartlett processor $B(\mathbf{r})$ for a data covariance matrix $\mathbf{Q}$ is defined[6] as

$$B(\mathbf{r}) = \mathbf{r}^*\mathbf{Q}\mathbf{r}, \qquad (4)$$

where $\mathbf{r}$ is a replica vector consisting of the field values which would be observed at the array elements for a source at a particular location, normalized so that $|\mathbf{r}|^2 = 1$. The output of the Bartlett processor for $\mathbf{r} \propto \mathbf{s}$ is distributed noncentral chi-square with $2K$ degrees of freedom.[7] The signal is said to be present (i.e., $\mathbf{Q} = \mathbf{Q}_{s+n}$) if $B(\mathbf{r})$ exceeds a threshold determined for a preassigned false alarm probability.

In MFP, the robust Bartlett processor is commonly applied to the replica vectors covering the search region to produce the Bartlett ambiguity surface. Decisions on whether a signal is present in the search region are based on these Bartlett statistics. This is done despite the fact that the Bartlett processor is only known to be optimum for detection at a single source position. However, our method of estimating PTE could equally well be applied to other processors.

B. Threshold estimation and source detection

The aim of this paper is to outline an efficient approach by which P_i, and consequently PTE, can be estimated for particular tracks. This approach involves two stages. In the
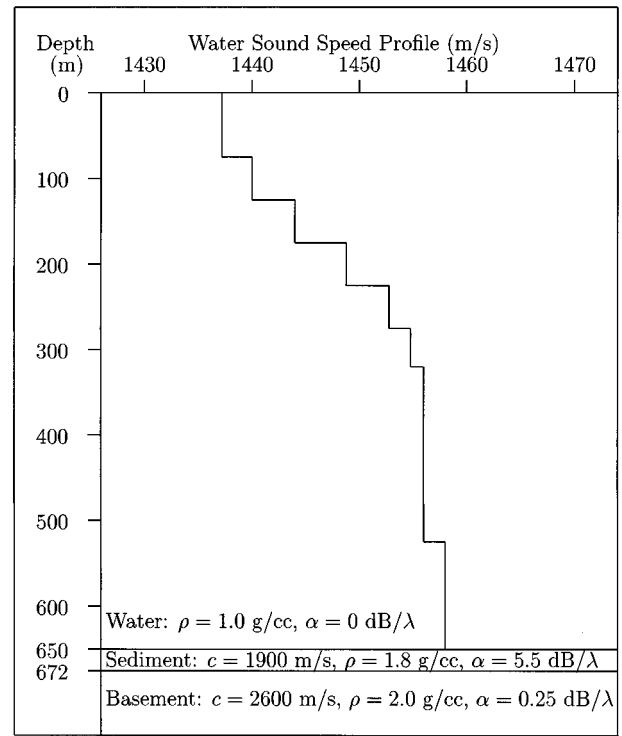
FIG. 1. Geoacoustic model for the Arctic environment used in the simulations. The symbols c, ρ, and α denote sound speed, density, and attenuation, respectively.

first, full ambiguity surfaces are generated by means of simulations with noise-only data, for a specified noise level. These are used to estimate an average threshold value which corresponds to the power of the mth largest peak in the surface. Then, in the second stage, a source of specified source level is modeled, and replicate simulations are performed for each of the positions of that source along a specified track. These simulations provide an estimate for P_i at each source location. This is done very efficiently by generating the ambiguity surface only within a small region defined by a specified distance tolerance (i.e., the radius of a circle centered at the known location of the source). For a particular array and environment, an appropriate value for this tolerance can be determined from the peak widths and separations in representative full ambiguity surfaces (see Sec. III B). When a peak within the region defined by the tolerance exceeds the threshold corresponding to the mth largest peak, a localized detection has occurred. In this scheme, the need to generate the full ambiguity surface is overcome through the use of the precomputed thresholds.

The probabilities of localized detection P_i can be estimated for various thresholds and source levels, at each of the locations along the source track. These probabilities can then be used to estimate PTE using Eq. (1). In this way, the performance of the detect-after-track scheme can be estimated for a particular scenario.

The threshold-based approach described here provides the capability for estimating the PTE for various arrays, environments, tracks, m, and distance tolerances, with much less computing effort than would be required by procedures involving full ambiguity surfaces for all simulations.

II. APPLICATION TO ARCTIC SCENARIO

The scheme for estimating PTE outlined above was applied to the analysis of simulated data generated for a slanted array operating in an Arctic environment, under the conditions described in this section.

A. Geoacoustic and propagation models of Arctic environment

The geoacoustic environment used for the simulations was a range-independent upward-refracting channel with a water depth of 650 m. The sound speed profile for this environment and the bottom layer structure are given in Fig. 1. The bottom was characterized by a 22-m-thick sediment layer with high attenuation. The attenuation coefficient in the sediment and the compressional speeds of the fluid layers were previously selected to achieve agreement between measured propagation losses for this environment and propagation losses computed using a normal mode model. In this upward-refracting environment, a high value of attenuation in the sediment was used to simulate the effects of ice roughness on the propagation loss data (unpublished results). This value exceeds the intrinsic attenuation in the sediment.[8]

Acoustic propagation was modeled by running a normal mode model[9] for the environment described above at a frequency of 25 Hz. Under these conditions, 19 water-borne modes were found to be present. This model did not specifically include an ice layer, as the presence of a uniform ice layer has a minimal impact on the propagation.

B. Array

A slanted 20-element linear equispaced array was used, which spanned the water column. The vertical and horizontal separation between the array elements was 32.5 m and 29.0 m, respectively, giving a slant angle of 41.75° from the vertical. The vertical extent of this array allowed for estimation of range and depth by effectively sampling the strongest modes. The horizontal extent, with elements at half-wavelength spacing, allowed for estimation of bearing without spatial aliasing. The slanted design thus provided the capability of localization of sources in range, bearing and depth. In these simulations, the array was oriented so that its horizontal extent was along the x axis.

C. Source modeling and covariance matrix generation

Simulations were performed in the frequency domain. A 100-m-deep source was modeled at various locations along a linear radial track, with the source at an initial range of 12 km and proceeding along a constant bearing of 0° (i.e., broadside to the array). A total of 20 source positions along the track was used for the analysis. For different values of K, the source speed was adjusted to give 500 m between the successive source positions. The source level was varied between 90 dB and 120 dB re: 1 μPa at 1 m to give a range of SNRs for which PTE spanned most of the range between zero and one.

The source was assumed to be stationary during covariance matrix estimation, which was performed using $K=5$,
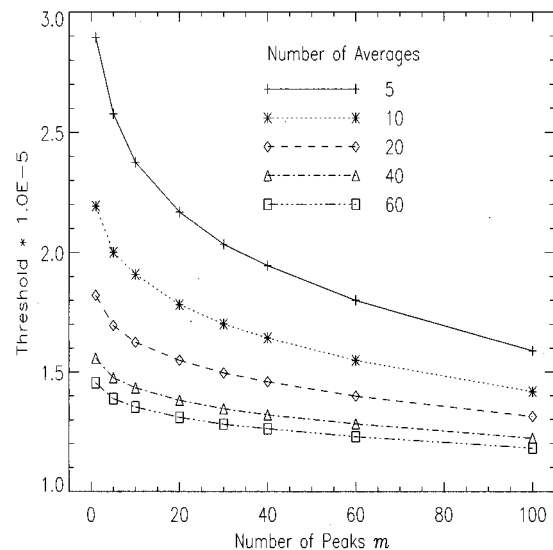
FIG. 2. Estimated thresholds for the peak value corresponding to the mth largest peak in the noise-only ambiguity surface, as a function of m, for the numbers of averages indicated. The noise level used here was 50 dB, for which the mean Bartlett power would be 10^5.

10, 20, 40, or 60 averages. For each source location and level, the normal mode propagation model was used to compute the signal vector $\mathbf{s}$; thus the signal received at the array had a source position-dependent strength.

Noise-only covariance matrices $\mathbf{Q}_n$ were simulated as described above, using a noise level at the sensors of 50 dB re: 1 μPa. Signal-plus-noise covariance matrices $\mathbf{Q}_{s+n}$ were also simulated as above, using phase-randomized signal vectors. Phase randomization was performed by taking $\mathbf{s}_k = \mathbf{s}e^{i\phi_k}$, where $\mathbf{s}$ is the signal vector for the (stationary) source and ϕ_k is a realization from a uniform distribution defined on $[0,2\pi]$.

D. Ambiguity surface generation and analysis

A rectangular search region for evaluation of the discrete ambiguity surface was defined with limits of x between −11 000 and +11 000 m, and y between 11 000 and 27 900 m, and with sampling intervals of 100 m in both x and y. The discretized ambiguity surface (consisting of 3.7 $\times 10^4$ points per depth) for a particular covariance matrix was generated by computing the Bartlett processor output at the points of this 2-D grid, using normalized replica vectors corresponding to the correct source depth (100 m).

Positions and maximum values of the peaks in the ambiguity surfaces were estimated from the grid values by quadratic interpolation of points surrounding local grid maxima.

It should be noted that the current simulations examined only 2-D constant-depth ambiguity surfaces, but the approach can easily be extended to 3-D.

III. RESULTS AND DISCUSSION

A. Threshold estimation

Thresholds corresponding to the number of largest peaks m and numbers of averages K under the conditions described above were estimated by averaging the results of 100 repli-
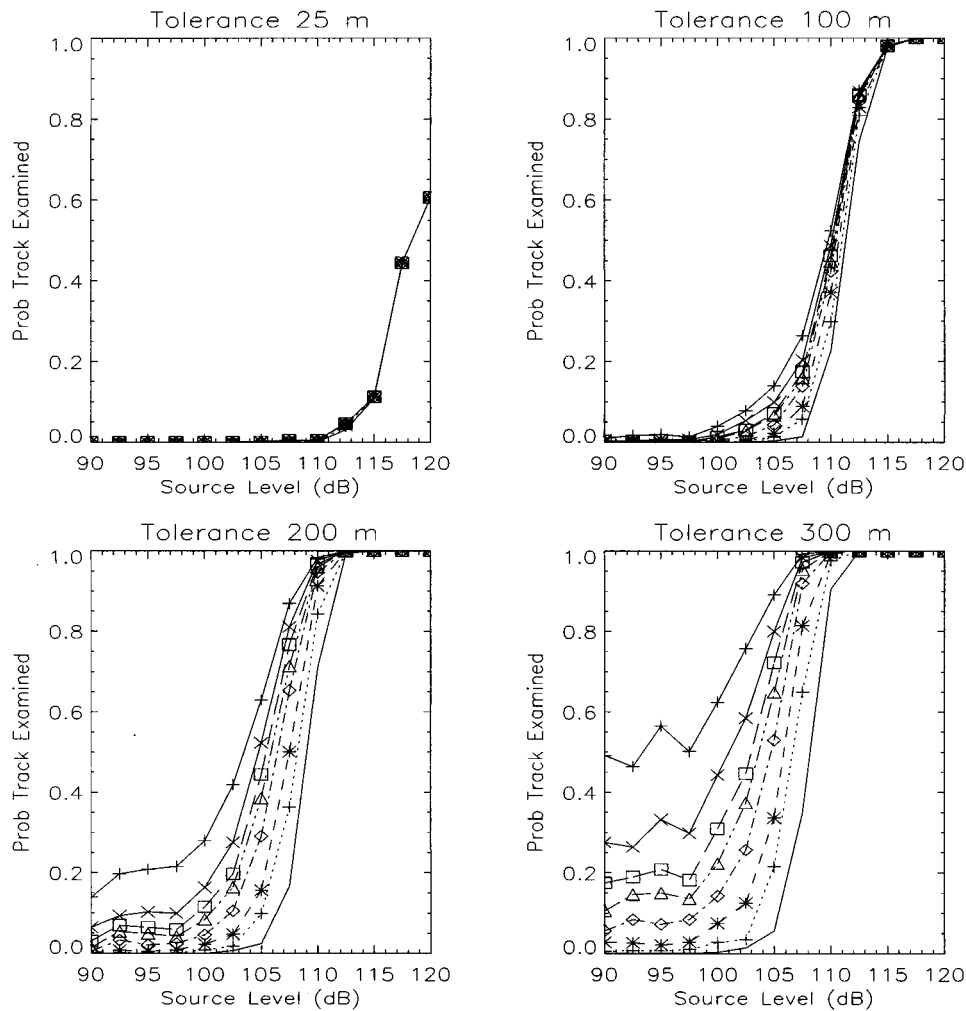
FIG. 3. The probability the track is examined (PTE), using $K=5$ averages. The different line symbol combinations within each plot indicate the results using thresholds corresponding to the mth largest peaks (for $m=1$, 5, 10, 20, 30, 40, 60, and 100, increasing vertically).

cate runs for each value of K. In each run, a noise-only covariance matrix was generated and an ambiguity surface was then calculated for this matrix, using previously computed replicas. The strongest 100 peaks in this surface (out of approximately 360 peaks in the entire surface under these conditions) were ordered, and the peak values corresponding to the mth largest peaks were determined, where $m=1$, 5, 10, 20, 30, 40, 60, and 100. These values were separately averaged over the 100 replicates to provide the thresholds corresponding to each value of m.

Figure 2 shows representative values of thresholds corresponding to various m and K. These values were used in the simulations described in the next section.

B. Probability the source track is examined

Estimation of probabilities of localized detection (P_i) was performed as follows for the m largest peaks, at each of the 20 source locations in the radial track described above. For each location, number of averages K, and source level, 100 replicate runs were performed. In each run a signal-plus-noise matrix was formed and the ambiguity function was generated within a region (defined by a distance tolerance) surrounding the known location of the source. Then, for each

threshold (corresponding to a particular m and K), it was determined whether any peak in this region exceeded that threshold. The results of these replicate runs were combined to yield estimates of the probabilities P_i of localized detection, for each of these values of m. The probabilities estimated for each of the 20 source positions were then combined to predict PTE, using Eq. (1).

We confirmed that the efficient method of estimating P_i agreed with the exhaustive approach for calculating P_i by finding the m largest peaks for the whole ambiguity surface. It should also be noted that the number of ambiguity surface points to be calculated for the efficient method is the square of the number of points surrounding the source position, compared to the overall number of points in the entire surface for the full method. For example, in the Arctic scenario with 5 cells by 5 cells, the speedup for the second stage (i.e., the time-consuming ambiguity surface calculation) is approximately $(221)(170)/25 \approx 1500$.

Some examples of the use of the thresholding procedure for estimating PTE are shown in Figs. 3 (for $K=5$ averages) and 4 (for $K=60$ averages). These figures show PTE as a function of source level, and illustrate the effects of several parameters involved in the estimation, including K, m, and
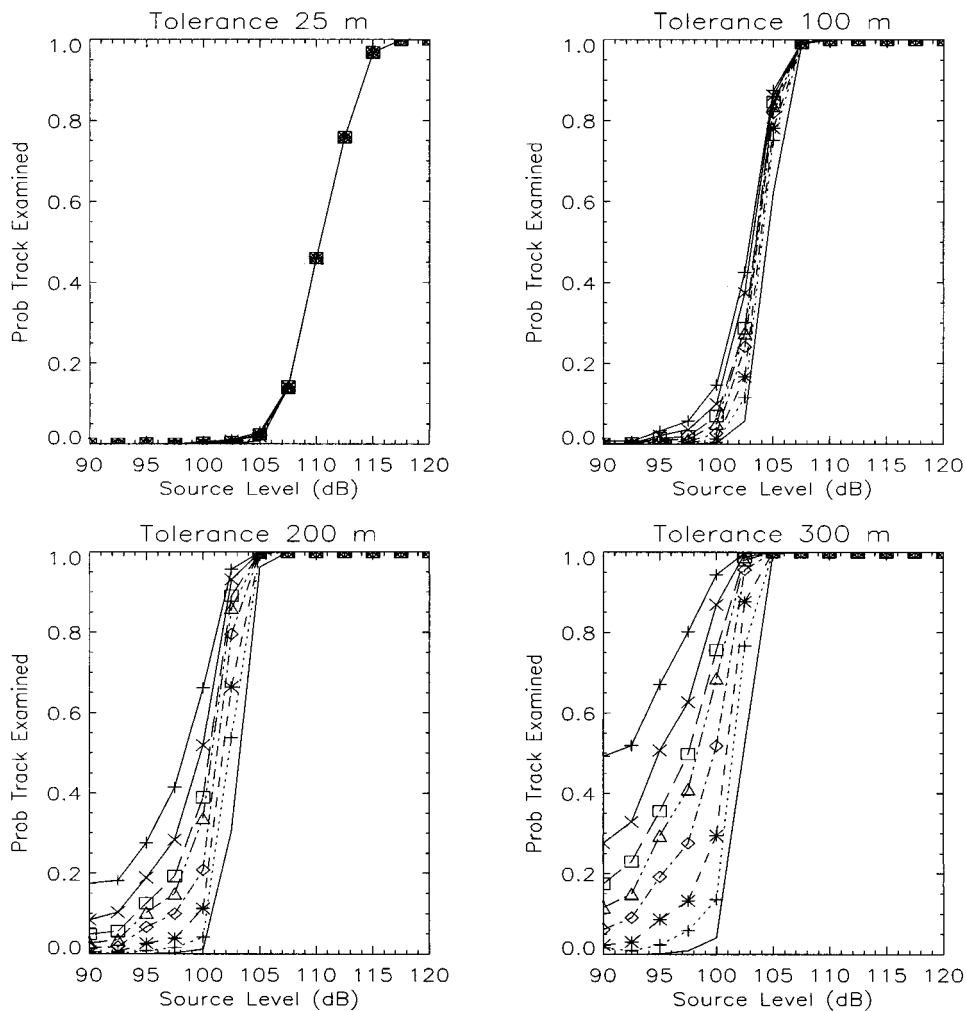
FIG. 4. The probability the track is examined (PTE), using $K = 60$ averages. The different line symbol combinations within each plot indicate the results using thresholds corresponding to the mth largest peaks (for $m = 1$, 5, 10, 20, 30, 40, 60, and 100, increasing vertically).

distance tolerance. Several observations may be made from these results.

First, as expected, the source level required to achieve a particular PTE decreases as K increases. This effect is due to the increasing processing gain, which varies as $\sqrt{K}$.

Second, PTE increases as m increases. However, this increase is at the expense of increasing computational cost at a later stage, since the number of tracks to be examined, approximately $N_s m^2/2$, also increases rapidly with m.

Third, PTE increases as the distance tolerance increases. This is expected since the presence of noise can perturb the positions of the source peaks away from their true locations in a noise-free ambiguity surface. Increasing the distance tolerance would allow a signal present with these perturbations to be considered a localized detection. This would increase the estimates for P_i and hence, for PTE. Figures 3 and 4 illustrate these effects of distance tolerance on PTE. It is evident that if a low value (e.g., 25 m) is chosen for this tolerance, not only is the PTE low, but also the curves for all m coincide. This occurs because the position of the source peak will be estimated to within this small tolerance only when the SNR is high, and in this case the source peak will usually be the largest one. Conversely, if the tolerance is set too high (e.g., 300 m), the estimated probabilities can be

unrealistically high, particularly as the SNR decreases and m increases. This arises from the increasing likelihood, as m and the tolerance increase, that the noise-perturbed source peak or a noise peak exceeding the threshold will occur in the region defined by the tolerance. (Note that the area of this region, and consequently the probability of a noise peak occurring within the region, increases as the square of the distance tolerance.)

The appropriate tolerance is one which is consistent with the localization accuracy requirements for the tracker. We cannot use too high a tolerance because the tracks as defined may not pass sufficiently close to the source positions along the track. This would result in a significant loss in estimated track signal-to-noise ratio. For the present case, a value of about 100 m, which corresponds to 10% of the average minimum peak-to-peak separation (approximately 1000 m), is an appropriate choice for the distance tolerance.

In summary, these results demonstrate that the method described here provides an efficient means of estimating PTE. In addition, this type of analysis can assist in choosing an appropriate number of peaks from which to form tracks, and in determining suitable distance tolerances (which are related to localization accuracy) to use in the simulations.

C. Generalization

The above results for estimating PTE were obtained for simulated data involving spatially uncorrelated Gaussian noise. In this case, it is straightforward to estimate the thresholds for the numbers of peaks. The approach can be extended to the analysis of real data by estimating the required thresholds using ambiguity surfaces for data from nearby nonsignal frequencies.

The PTE analysis technique can be applied to any noise data, and is not restricted to spatially white Gaussian noise. The Gaussian noise model was used here as a first approximation to that encountered in practice.

In practical situations where the noise is not spatially white, it is probably preferable to spatially prewhiten the data prior to analysis.[5,10] For example, recent analysis of Arctic data showed the fields to be strongly spatially correlated; after prewhitening it was demonstrated that the data became effectively spatially white. The PTE analysis can also be applied to such prewhitened data. Prewhitening provides an effective means of enhancing array gain for the pointlike sources representative of ice ridging.

Finally, the tracking algorithm and the performance analysis procedures outlined above can also be extended to tracking using multiple frequencies, with ambiguity surfaces combined incoherently or coherently.[11]

IV. CONCLUSIONS

The probability the source track is examined in an efficient detect-after-track algorithm,[1,2] in which the largest peaks in an ambiguity surface are taken as possible estimates of the source position, can be effectively predicted for particular scenarios using the procedures described in this paper. The results presented here, in conjunction with previous work, provide insight and understanding of an algorithm that has been successfully applied to the analysis of simulated and experimental data.

[1] M. J. Wilmut, J. M. Ozard, and B. Woods, ''An efficient target tracking algorithm for matched-field processing,'' in *Proceedings, IEEE Oceans 93* (IEEE, Victoria, BC, Canada, 1993), Vol. III, pp. 81–85.

[2] M. J. Wilmut, J. M. Ozard, and P. Brouwer, ''Evaluation of two efficient target tracking algorithms for matched-field processing with horizontal arrays,'' J. Comput. Acoust. **3**, 311–326 (1995).

[3] E. J. Sullivan and D. Middleton, ''Estimation and detection issues in matched-field processing,'' IEEE J. Ocean Eng. **18**, 156–167 (1993).

[4] E. J. Sullivan and D. Middleton, ''Estimation and detection in matched-field processing,'' in *Proceedings, IEEE Oceans 93* (IEEE, Victoria, BC, Canada, 1993), Vol. III, pp. 70–74.

[5] C. A. Zala, J. M. Ozard, and M. J. Wilmut, ''Prewhitening for improved detection by matched-field processing in ice-ridging correlated noise,'' J. Acoust. Soc. Am. **98**, 2726–2734 (1995).

[6] A. Tolstoy, *Matched-Field Processing for Underwater Acoustics* (World Scientific, Singapore, 1993).

[7] H. L. van Trees, *Detection, Estimation and Modulation Theory*, Part I (Wiley, New York, 1968).

[8] S. E. Dosso and G. H. Brooke, ''Measurement of seismo-acoustic ocean-bottom properties in the high Arctic,'' J. Acoust. Soc. Am. **98**, 1657–1666 (1995).

[9] G. H. Brooke, ''Normal mode properties in elastic waveguides: Application of of power conservation and reciprocity,'' Defence Research Establishment Pacific Technical Memorandum No. 93–28, 1993.

[10] R. G. Racca, M. J. Wilmut, and J. M. Ozard, ''Prewhitening of Arctic ambient noise and its implications for matched-field processing,'' Navy J. Underwater Acoust., special issue on Arcticacoustics, 1997 (to appear).

[11] Z.-H. Michalopoulou and M. B. Porter, ''Source tracking in the Hudson Canyon experiment,'' J. Comp. Acoust. **4**, 371–383 (1996).

Time-average temperature distribution in a thermoacoustic stack

George Mozurkewich

Ford Motor Company Research Laboratory, Mail Drop 3028, P.O. Box 2053, Dearborn, Michigan 48121-2053

The three-dimensional time-average temperature distribution in a pore of a thermally isolated thermoacoustic stack is calculated. A boundary-value problem is formulated in the acoustic and short-stack approximations from the equation of conservation of energy using literature results for the time-average energy flux. In the central region of the pore, the solution for the time-average temperatures of the wall, T_w, and of the gas along its center line, T_g, share a common profile, linear in the axial coordinate, z. Near the pore ends, where the energy flux approaches zero, the axial gradient of T_g approaches the critical temperature gradient over a distance of order the acoustic displacement amplitude. The axial gradient of T_w approaches zero over a much smaller distance, provided the wall has small thermal conductivity. The transverse heat-flux density, q, is nonzero only near pore ends. Under certain conditions, $q = h_1(T_g - T_w)$, where h_1 is proportional to the thermal conductivity of the gas divided by the thermal penetration depth. The constant of proportionality, of order unity, depends on pore width and Prandtl number. Results agree favorably with recently published numerical calculations. © *1998 Acoustical Society of America.* [S0001-4966(98)01001-7]

INTRODUCTION

Thermoacoustic engines are devices that involve thermodynamic interactions between heat and sound.[1] They include refrigerators, heat pumps, and prime movers. The key physical process is imperfect heat transfer between an acoustic medium and adjacent solid walls, which introduces a phase difference between the oscillatory temperature variation and the acoustic displacement. Thermoacoustic effects are therefore most readily observed in pores or ducts whose transverse dimensions are comparable to the thermal penetration depth, δ_k, i.e., the distance through which heat can diffuse in the acoustic medium during one acoustic period. The collection of pores in which thermoacoustic processes occur is called a stack. The ''standard'' theory of thermoacoustics[1–3] draws out the thermodynamic consequences of phase differences in the pores within the linear acoustic approximation, and while nonlinear effects have been observed,[4–6] the linear theory seems to suffice for quantitative treatment of the heat-pumping processes in actual devices, at least for refrigerators.

The standard theory of thermoacoustics assumes (a) that the time-average temperature of the fluid across any cross section of a pore is equal to the time-average temperature of the adjacent pore walls, and (b) that the acoustic displacement amplitude is negligible compared to the length of the stack. The first assumption precludes treatment of time-average heat transfer between fluid and pore walls. Both assumptions are suitable well within the stack but fail near its ends. This circumstance has been anticipated on physical grounds[4] and has been demonstrated explicitly in a recent numerical computation.[7] In particular, the numerical work found that ''the [transverse] heat exchange is most intense at the extreme edge of each plate, rather than being more uni-

formly distributed across the width of the displacement amplitude,'' a result that was characterized as ''surprising'' and ''a challenge to analytical theory.''

The goal of the present work is to investigate analytically the time-average temperature distribution and associated time-average transverse heat transfer in a thermally isolated thermoacoustic stack. Previously published results for the oscillatory temperature and associated time-average energy-flux density are assumed as starting points. The equation of conservation of energy is used to derive a differential equation for the time-average fluid temperature which holds in the acoustic and short-stack approximations. This equation is coupled to one for the time-average wall temperature, and the pair is solved for thermally isolated boundary conditions. The rate of transverse heat transfer is deduced from the resulting temperature distribution.

This work was motivated as an essential step toward analyzing time-average heat-transfer processes in thermoacoustic heat exchangers, without which no practical thermoacoustic engine can function. The author has developed a one-dimensional model in which the time-average fluid temperature is regarded as a function of axial coordinate only, and the fluid temperature is coupled to the wall temperature through an effective transverse heat-transfer coefficient h_1.[8] The present analysis derives an expression for h_1 and delimits its range of usefulness.

To orient the reader, the essential features of the analysis are sketched here for the case of isothermal walls. The standard theory of thermoacoustics obtains the time-average energy-flux density parallel to a pore axis in the form $h_z = A \nabla T_c - B \, dT/dz$, where $A \nabla T_c$, and B are constant in the short-stack approximation. Nonconstant h_z implies local deposition of heat at rate $-dh_z/dz$, and, in steady state, the
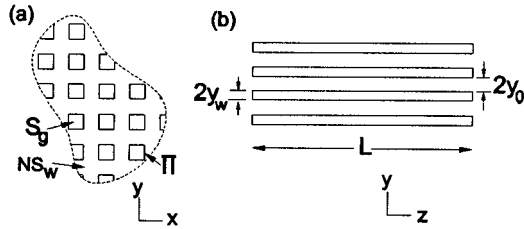
FIG. 1. Geometry for the calculation. (a) Transverse section of a stack containing N square pores. (b) Axial section of a stack of planar pores.

deposited heat must diffuse to the adjacent walls. Assuming that the rate of transverse heat flow is proportional to the temperature difference between fluid and walls, $q = h_1 T$, one finds $B \, d^2 T/dz^2 = h_1 T$, and thus both T and q vary axially according to $\exp(\pm \sqrt{h_1/Bz})$. This central result accounts for the sharp temperature gradient near pore ends, discovered in Ref. 7.

Section I formulates the analysis as a boundary-value problem and presents a formal solution for cylindrical pores of unspecified section in terms of axial and transverse eigensolutions. Section II explicitly treats the transverse eigenproblem for planar pores. Section III examines the results for cases of infinite and finite wall conductivity and contains a comparison to the numerical work. A critical issue considered there is an ambiguity in the boundary condition at pore ends. The transverse heat-transfer coefficient is derived and discussed. Section IV draws conclusions and discusses limitations. Two appendices provide mathematical details.

I. BOUNDARY-VALUE PROBLEM

The calculation is performed in a long, straight pore of constant cross-sectional area S_g, constant perimeter Π, and length L, with the pore axis lying along z (Fig. 1). The cross-sectional area of the wall material is S_w per pore. Transverse dimensions are characterized by hydraulic radii, S_g/Π for the gas, and S_w/Π for the wall. For the special case of planar pores, these are y_0 and y_w, the half-thicknesses of pore and wall, respectively. The vector $\boldsymbol{\rho}$ specifies transverse coordinate within the pore. The working fluid is assumed to be an ideal gas with time-average temperature T_g and density ρ_0, heat capacity c_p, thermal conductivity k_g, Prandtl number σ, and thermal expansion coefficient $\beta = 1/T_g$. (Except in the expression for β, temperatures may be referred to any convenient reference value.) The thermal and viscous penetration depths are defined by $\delta_k = \sqrt{2k_g/\rho_0 c_p \omega}$ and $\delta_v = \delta_k \sqrt{\sigma}$, respectively, where ω is the angular frequency. The thermal conductivity of the wall material is k_w. Swift's parameter ε_s is neglected.

The pores are assumed to be thermally isolated from the external world. This means that no heat may enter or leave through the pore ends. Consequently, the net energy flux through any transverse section must vanish: All heat that is thermoacoustically pumped in one direction must eventually be transferred to the walls and diffuse backward in the other direction.

The sound field is represented by dynamic pressure amplitude p_1 and its derivative, dp_1/dz. The latter is related to the velocity amplitude u_1, and the corresponding displacement amplitude is $z_1 = u_1/\omega$. By restricting attention to the short-stack approximation,[1] p_1 and u_1 are assumed not to vary with axial coordinate z, notwithstanding the proportionality between u_1 and dp_1/dz.

Appendix A shows that the axial energy-flux density (power per unit area), including both hydrodynamic and diffusive heat transport, may be written in the form:

$$h_z(z,\boldsymbol{\rho}) = R\left[w'(\boldsymbol{\rho}) \boldsymbol{\nabla} T_c - w(\boldsymbol{\rho}) \frac{\partial T_g(z,\boldsymbol{\rho})}{\partial z} \right]$$
$$- k_g \frac{\partial T_g(z,\boldsymbol{\rho})}{\partial z}. \qquad (1)$$

Because the hydrodynamic transport is parallel to z, the transverse components contain only the diffusive term: $h_x = -k_g \, \partial T_g/\partial x$, etc. The various quantities are defined in Appendix A. The prefactor R and critical temperature gradient $\boldsymbol{\nabla} T_c$ are independent of transverse coordinates, and w and w' are functions of transverse coordinates only that express, respectively, the transverse variations of acoustic velocity, u_1, and oscillatory temperature, T_1. In principle, R and $\boldsymbol{\nabla} T_c$ are functions of axial position z, because the acoustic field variables vary with location in the standing wave and because the fluid properties vary with temperature. They may be assumed constant, however, if the stack is much shorter than the acoustic wavelength and the temperature difference across the stack is much less than the mean temperature; this is called the short-stack approximation.[1]

The equation of conservation of energy is[9]

$$\frac{\partial}{\partial t}(\rho e) = -\boldsymbol{\nabla} \cdot \mathbf{h}, \qquad (2)$$

where e is energy density. Upon averaging over time, the left-hand side vanishes. Making the short stack approximation, all quantities in Eq. (1) except dT_g/dz are assumed independent of z. Because the displacement amplitude is typically an order of magnitude greater than δ_k, Eq. (A5) implies $k_g \ll R$. Thus

$$R w(\boldsymbol{\rho}) \frac{\partial^2 T_g}{\partial z^2} + k_g \nabla_\tau^2 T_g = 0, \qquad (3)$$

where ∇_τ^2 is the Laplacian in transverse variables only. A boundary-value problem may be formulated by supplementing this partial differential equation with suitable boundary conditions. Let these be $T_g = T_w(z)$ on the pore wall and $\partial T_g/\partial z = \boldsymbol{\nabla} T(\boldsymbol{\rho})$ at the pore ends, where $\boldsymbol{\nabla} T(\boldsymbol{\rho})$ is a prescribed function of transverse coordinates to be discussed in Sec. III A. Also let $dT_w/dz = 0$ at pore ends, on the grounds that no heat may enter the walls except transversely from the gas. Assuming that the wall temperature is constant across any solid section, T_w obeys

$$S_w k_w \frac{d^2 T_w}{dz^2} + \Pi q(z) = 0, \qquad (4)$$

where $q(z)$ is the heat transferred out of the gas, per unit area, to be deduced from the solution for $T_g(z,\boldsymbol{\rho})$.

The solution will be represented as the sum of two parts, one with $T_g=0$ on the wall, and the other satisfying the condition that the gas temperature at the wall must equal the wall temperature. Separating variables according to $T_g(z,\rho)=Z(z)P(\rho)$,

$$\frac{R}{k_g}\frac{Z''}{Z}=-\frac{1}{w}\frac{\nabla_\tau^2 P}{P}.$$

Letting the separation constant be some positive number λ and writing $P=\Theta$, the permitted values of λ are the eigenvalues of

$$\nabla_\tau^2\Theta_m(\rho)+\lambda_m w(\rho)\Theta_m(\rho)=0, \tag{5}$$

satisfying the boundary condition $\Theta=0$ on the wall. The resulting T_g is capable of satisfying the prescribed Neumann condition at the pore ends. Determination of these functions is postponed to Sec. II, but they may be normalized in the usual way:

$$\int_{S_g}\!\!\int \Theta_m(\rho)\Theta_n(\rho)w(\rho)d\rho=S_g\delta_{m,n}. \tag{6}$$

Alternatively, if the separation constant is some negative number $-k^2$, its permissible values are the eigenvalues of

$$\frac{d^2 Z_n}{dz^2}+\frac{k_g}{R}k_n^2 Z_n=0, \tag{7}$$

satisfying the boundary condition of zero derivative at the pore ends at $z=\pm L/2$; i.e.,

$$k_n=\frac{n\pi}{L}\sqrt{\frac{R}{k_g}}. \tag{8}$$

The corresponding transverse equation is ($P=\Psi$)

$$\nabla_\tau^2\Psi(\rho)-k_n^2 w(\rho)\Psi(\rho)=0. \tag{9}$$

Because Ψ does not vanish on the walls, Dirichlet conditions may be satisfied there.

The full solution may be expressed in the form

$$T_g(z,\rho)=\sum_m \frac{\nabla T_m}{s_m}\frac{\sinh(s_m z)}{(s_m L/2)}\Theta_m(\rho)$$

$$+\sum_{n\text{ odd}} B_n \sin\left(n\pi\frac{z}{L}\right)\frac{\Psi_n(\rho)}{\Psi_n(\text{wall})}. \tag{10}$$

The notation Ψ_n designates the solution to Eq. (9) with specified k_n, and, for brevity,

$$s_m^2=\lambda_m\frac{k_g}{R}. \tag{11}$$

The first sum represents a function which vanishes on the pore walls. Its coefficients were evaluated by setting $\partial T_g/\partial z=\nabla T(\rho)$ at the pore ends and using an eigenfunction expansion for the end condition: $\nabla T(\rho)=\Sigma \nabla T_m\Theta_m(\vec{\rho})$, where

$$\nabla T_m=S_g^{-1}\int_{S_g}\!\!\int \nabla T(\rho)\Theta_m(\rho)w(\rho)d\rho. \tag{12}$$

The second sum, containing only odd n, represents a function with period $2L$, odd with respect to $z=0$ (as required to

describe an imposed temperature gradient) and even with respect to $z=\pm L/2$ (to satisfy the thermal isolation condition on the wall, $\partial T_w/\partial z=0$). The form of the second sum ensures that the gas temperature adjacent to the wall equals the wall temperature,

$$T_w(z)=\sum_{n\text{ odd}} B_n \sin\left(n\pi\frac{z}{L}\right). \tag{13}$$

The coefficients B_n, specifying the temperature variation in the wall, can be deduced from Eq. (4) as follows. Heat leaves the gas transversely through the pore walls by thermal conduction. The outward rate per unit wall area is

$$q(z)=-\frac{k_g}{\Pi}\oint \frac{\partial T_g}{\partial n}d\Pi. \tag{14}$$

The normal derivatives can be evaluated by integrating Eq. (5) over S_g and applying Gauss's theorem:

$$\int_{S_g}\!\!\int \nabla_\tau^2\Theta_m(\rho)d\rho=\oint \frac{\partial \Theta_m}{\partial n}d\Pi$$

$$=-\lambda_m\int_{S_g}\!\!\int w(\rho)\Theta_m(\rho)d\rho, \tag{15}$$

and similarly for Ψ, replacing λ_m by $-k_n^2$. Defining the w-weighted cross-sectional average of a variable $P(\rho)$ by

$$\langle P\rangle_w\equiv\frac{1}{S_g}\int_{S_g}\!\!\int w(\rho)P(\rho)d\rho, \tag{16}$$

one obtains from Eq. (10)

$$\frac{\Pi}{k_g S_g}q(z)=\sum_m \nabla T_m s_m\frac{R}{k_g}\frac{\sinh(s_m z)}{\cosh(s_m L/2)}\langle\Theta_m\rangle_w$$

$$-\sum_{n\text{ odd}} B_n k_n^2 \sin\left(n\pi\frac{z}{L}\right)\frac{\langle\Psi_n\rangle_w}{\Psi_n(\text{wall})}. \tag{17}$$

Substituting Eqs. (17) and (13) into (4) yields, with the help of (B2),

$$B_n=\frac{4L}{n^2\pi^2}\sin\left(\frac{n\pi}{2}\right)\left(\frac{R}{k_g}\frac{\langle\Psi_n\rangle_w}{\Psi_n(\text{wall})}+\frac{S_w k_w}{S_g k_g}\right)^{-1}$$

$$\times\sum_m \frac{\nabla T_m\lambda_m\langle\Theta_m\rangle_w}{\lambda_m(k_g/R)+n^2\pi^2/L^2}. \tag{18}$$

Expressions (10), (13), and (18) represent the general solution of the differential equations (3) and (4) in terms of the end condition $\nabla T(\rho)$. Before discussing that condition, the transverse functions will be examined.

II. TRANSVERSE EIGENSOLUTIONS

To obtain explicit expressions, the transverse equations (5) and (9) must be solved for specific pore shape. For planar pores, the weighting function is [see Eq. (A8) and Eq. (66) in Ref. 3]
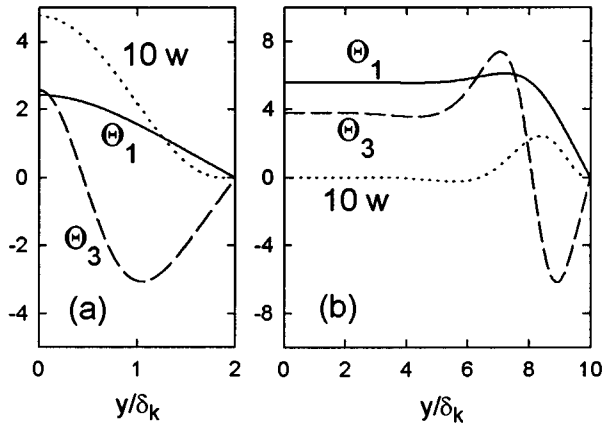
FIG. 2. Representative eigensolutions for planar pores for $\sigma = 0.68$. Solid lines and dashed lines are Θ_m; dotted lines are weighting functions w (multiplied by 10). $y_0/\delta_k = 2$ in (a) and 10 in (b).

$$w(y) = \frac{1}{1-\sigma} \, \mathrm{Im}\left\{ \left(1 - \frac{\cosh((1-i)y/\delta_\nu)}{\cosh((1-i)y_0/\delta_\nu)} \right) \right.$$
$$\left. \times \left(1 - \frac{\cosh((1+i)y/\delta_k)}{\cosh((1+i)y_0/\delta_k)} \right) \right\}. \tag{19}$$

The eigensolutions Θ_m were found numerically by the shooting method.[10] Some representative solutions are shown in Fig. 2. In wide pores, Θ_m is fairly uniform over the central portion of the pore. The transverse heat flux depends only on λ_m (i.e., s_m) and $\langle \Theta_m \rangle_w$, whose typical dependencies on y_0/δ_k are shown in Fig. 3, where the eigenvalues are expressed dimensionlessly as

$$\lambda_m^0 = \lambda_m \delta_k^2. \tag{20}$$

Only odd m are considered for planar pores because they correspond to even functions of y. In accord with asymptotic Sturm–Liouville theory,[11] $\lambda_m \propto m^2$ and $\langle \Theta_m \rangle_w \propto (-1)^{(m-1)/2} m^{-1}$ for large m; these forms already hold approximately for $m > 3$. In the boundary-layer limit, the eigenvalues approach well-defined values, given in Fig. 4 as function of σ.

For Ψ_n, an approximate solution suffices when the second term in Eq. (9) is small. Using Eqs. (8) and (A5), one finds that the relevant parameter is $k_n \delta_k \approx n\pi(|\bar{z}_1|/L)$, and typically $|\bar{z}_1| \ll L$. Therefore, as a first approximation, Ψ_n can be taken to be unity, constant across the section, and a second approximation may be generated by substituting unity for Ψ in the second term in Eq. (9) and integrating twice with the aid of addition formulas for the hyperbolic functions. The result is

$$\Psi_n(y_0) \approx 1 + k_n^2 \delta_k^2 \psi, \tag{21a}$$
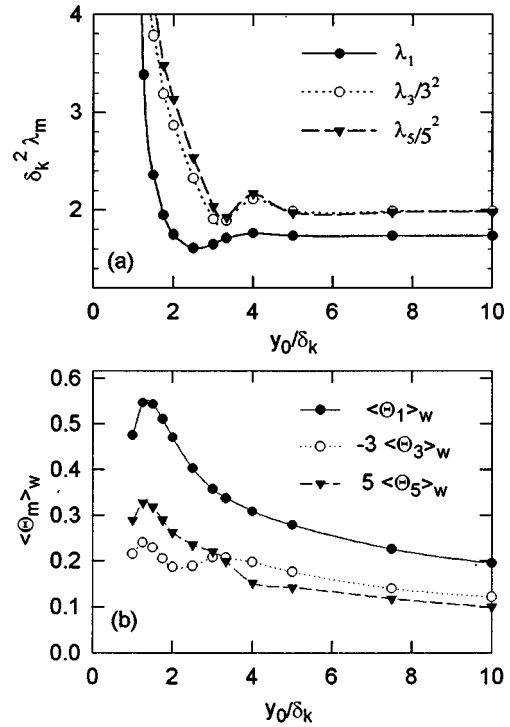
FIG. 3. Dependencies of $\lambda_m^0 = \delta_k^2 \lambda_m$ and $\langle \Theta_m \rangle_w$ on y_0/δ_k. Planar pores, $\sigma = 0.68$.

$$\psi = \frac{1}{1-\sigma} \, \mathrm{Im}\left\{ -i\frac{\sigma}{2}(1-e_\nu) + i\frac{1}{2}(1-e_k^*) \right.$$
$$+ i\frac{\sigma(1-\sigma)}{2(1+\sigma)^2}(1-e_\nu e_k^*) + \frac{\sigma\sqrt{\sigma}}{(1+\sigma)^2}$$
$$\left. \times \tanh\left((1-i)\frac{y_0}{\delta_\nu}\right)\tanh\left((1+i)\frac{y_0}{\delta_k}\right) \right\}, \tag{21b}$$

where
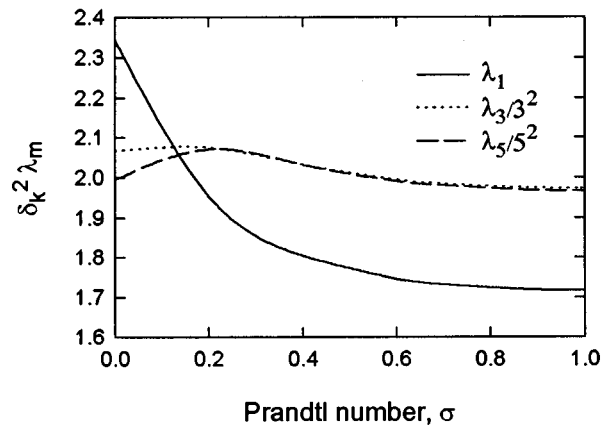
FIG. 4. Prandtl number dependence of the boundary-layer limit of λ_m^0 for planar pores.
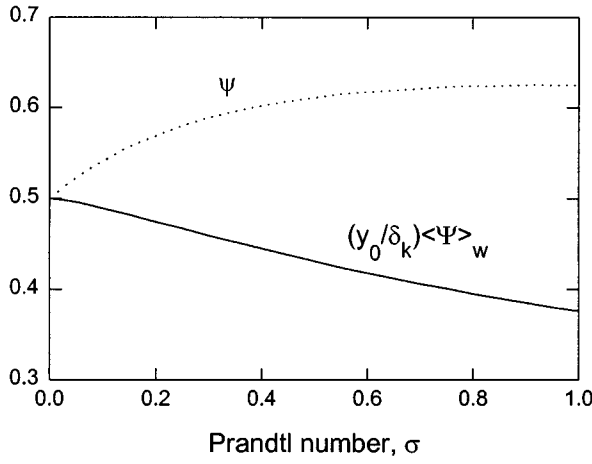
FIG. 5. Prandtl number dependence of $(y_0/\delta_k)\langle\Psi\rangle_w$ and ψ for planar pores in the boundary-layer limit.

$$e_\nu = \frac{1}{\cosh\left((1-i)\dfrac{y_0}{\delta_\nu}\right)}, \tag{21c}$$

and likewise for e_k, substituting δ_k for δ_ν. Only a single integration is necessary for $\langle\Psi_n\rangle_w$, by virtue of the Ψ equivalent of Eq. (15):

$$\langle\Psi_n\rangle_w \approx \frac{\mathrm{Im}(\sigma\bar{F}_V + \bar{F}_T^*)}{1-\sigma^2} = \bar{w}, \tag{22}$$

where

$$\bar{F}_V = 1 - \frac{\tanh((1-i)y_0/\delta_\nu)}{(1-i)y_0/\delta_\nu} \tag{23}$$

and analogously for $\bar{F}_T$, with δ_k substituted for δ_ν. Within this approximation, $\langle\Psi\rangle_w$ is independent of n, and these approximations are in good agreement with numerical results over the appropriate range of $k_n\delta_k$. For large n, however, $\langle\Psi_n\rangle_w/\Psi_n(\text{wall}) \propto n^{-1}$. Figure 5 gives $\langle\Psi\rangle_w$ and ψ vs the Prandtl number; $\Psi_n(y_0)$ can be deduced from the latter. Ψ_n is fairly uniform across the section whenever $k_n\delta_k < 1$, yet despite its near constancy, $\langle\Psi\rangle_w/\Psi_n(\text{wall})$ is small because of the smallness of w.

III. ANALYSIS OF RESULTS

A. The end condition

The problem of the thermally isolated stack is uniquely solved once $\nabla T(\boldsymbol{\rho})$ is specified at the ends of the pores. The solution is given by Eq. (10) for the gas and Eq. (13) for the walls. The first sum in Eq. (10) depends on the coefficients ∇T_m, defined by Eq. (12) in terms of $\nabla T(\boldsymbol{\rho})$. Because nonzero wall temperature in a thermally isolated stack is caused only by heat transfer from the gas, T_w is also determined by ∇T_m. Lastly, the second sum in Eq. (10) roughly follows the temperature in the adjacent wall; recall that Ψ_n is nearly uniform across the pore section, at least for small n.

Unfortunately, $\nabla T(\boldsymbol{\rho})$ is ambiguous. Given an analytical expression for the thermoacoustic behavior beyond the pore ends, one could explicitly determine the required $\nabla T(\boldsymbol{\rho})$ by

matching that expression to Eq. (10). Lacking such expression, there remains only the weaker condition, that the integral of h_z over pore section must vanish to ensure thermal isolation, which is inadequate to specify $\nabla T(\boldsymbol{\rho})$ uniquely. An auxilliary assumption must be made. For simplicity, omit the diffusive term in Eq. (1) on the grounds that $k_g \ll R$. Although one could satisfy the thermal isolation condition by setting the contents of the square brackets in Eq. (1) equal to zero, this requirement seems to be too strong, because processes occurring outside the pores are likely to tend to homogenize the temperature across the section. An alternative that acknowledges this tendency is to take $\nabla T(\boldsymbol{\rho})$ constant across the section, in which case the integral of Eq. (1) implies

$$\nabla T(\boldsymbol{\rho}) = \frac{\overline{w}'}{\overline{w}}\nabla T_c \tag{24}$$

at pore ends. Although absolutely uniform, nonzero $\partial T_g/\partial z$ at pore ends is inconsistent with the condition that $dT_w/dz = 0$, as long as only a finite number of terms is included in the sum on m, $\partial T_g/\partial z$ will approach zero near the walls. For uniform end gradient, the expansion coefficients (12) become

$$\nabla T_m = \nabla T_c\langle\Theta_m\rangle_w\overline{w}'/\overline{w}, \tag{25}$$

which fall off proportional to m^{-1} for large m. The requirement that $\nabla T(\boldsymbol{\rho})$ approaches zero near the walls implies a more rapid decrease at large enough m.

B. Perfectly conducting walls

For perfectly conducting walls, the wall temperature is constant, taken here to be zero. Only the first sum in Eq. (10) is nonzero because of the appearance of k_w in the denominator of Eq. (18). By Eq. (1), the rate of thermoacoustic heat pumping is large when the temperature gradient is zero. In a thermally isolated stack, the entire quantity of pumped heat must be abstracted from one end of the stack (the end nearer the pressure node) and deposited into the other; in a perfectly conducting stack, the heat thus deposited is immediately spread throughout the wall. The first sum in Eq. (10) describes the temperature distribution resulting from these physical processes.

The hyperbolic functions in Eq. (10) represent exponential decays with distance from the pore ends. The argument of the hyperbolic sine is $s_m z$, where, from Eqs. (11) and (A5),

$$s_m = \sqrt{\lambda_m^0}\frac{|\bar{F}_V|}{|\bar{z}_1|}. \tag{26}$$

Thus the characteristic decay distance, s_1^{-1}, is fixed by the acoustic displacement amplitude, in agreement with Ref. 7. Physically, this distance is fixed by the trade-off between the rate of thermoacoustic heat pumping, proportional to R, and the rate of transverse heat transfer, proportional to k_g. Because higher m terms decay over a shorter distance from the ends, the $m = 1$ solution should dominate over most of the length of the pore. Near the ends, the temperature may be fairly represented by a single exponential because both ∇T_m

George Mozurkewich: Time-average temperature distribution
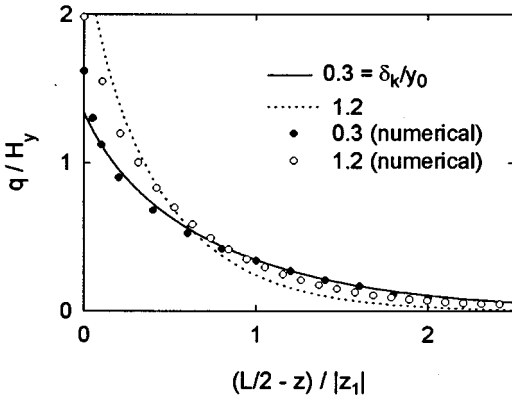
FIG. 6. Normalized transverse heat-flux density versus normalized distance from pore end for $\sigma = 0.68$. Lines are analytical results, points are numerical data from Ref. 7.

and s_m^{-1} decrease with increasing m. A single exponential may be less satisfactory for $q(z)$ because of the extra factor of s_m^2 in the first sum of Eq. (17).

The results are directly applicable to the recent numerical calculation by Cao *et al.*[7] for an isolated, isothermal stack, which found that $|q|$ increases sharply toward the end of a pore, rather than being spread out more uniformly over a distance z_1. That sharp, continuously increasing behavior may now be interpreted. According to boundary condition (24), the temperature gradient in the gas at a thermally isolated end of a pore tends toward a numerical factor times the critical temperature gradient, regardless of its value closer to the center of the pore. Physically, h_z must decrease to zero through some as yet undetermined distance outside the pore, thereby depositing (extracting) heat outside the pore which must flow back into (out of) the pore, and eventually into (out of) the walls. The resulting increase in temperature gradient near the end of the pore forces h_z to decrease according to Eq. (1) and the gradient to approach $(\overline{w}'/\overline{w})\nabla T_c$ self-consistently. Thus the continuously increasing gradient is a consequence of the monotonic variation of h_z.

An explicit comparison can be made by taking $T_w(z) = 0$ (perfectly conducting walls) and normalizing the transverse heat flux as in the numerical work. In the present notation, the normalization factor is

$$H_y = \frac{R\nabla T_c y_0 \overline{w}'}{|\overline{z}_1|}. \qquad (27)$$

If $\nabla T(y)$ is assumed uniform over pore section, Eq. (25) may be used in Eq. (17) to deduce

$$\frac{q(z)}{H_y} = \frac{|\overline{F}_V|}{\overline{w}} \cdot \sum_m \sqrt{\lambda_m^0} \langle \Theta_m \rangle_w^2 \frac{\sinh(s_m z)}{\cosh(s_m L/2)}. \qquad (28)$$

This quantity is plotted vs $(L/2-z)/|\overline{z}_1|$ in Fig. 6 for $\delta_k/y_0 = 0.3$ and 1.2, including four nonzero terms in the sum ($m = 1, 3, 5,$ and 7). Agreement with the numerical data[7] is good for $\delta_k/y_0 = 0.3$, except at the extreme end of the pore, and the trend with increasing δ_k/y_0 is correct. The larger discrepancy for $\delta_k/y_0 = 1.2$ may imply that the present treatment works better in the boundary-layer limit. The analytical

results (not shown here) exhibit little or no dependence on Prandtl number for either value of δ_k/y_0. While the numerical results also show only a mild σ dependence for $\delta_k/y_0 = 0.3$, they vary strongly with σ for $\delta_k/y_0 = 1.2$ (cf. Fig. 8 of Ref. 7).

C. Finite conductivity walls

When heat that has been pumped thermoacoustically in one direction through the gas is conducted back in the other direction through walls of finite conductivity, a temperature gradient is produced in walls and gas. According to Eq. (1), the gradient reduces the rate of thermoacoustic pumping. In steady state in a thermally isolated stack, the reduction is by such an amount that the two heat currents are equal and opposite. Because the gradient in the walls is proportional to the local axial heat current in the walls, it should tend toward zero as the end of the stack is approached. The physics of these processes is contained in Eq. (13) and the second sum of Eq. (10). Results can be plotted from the formulae given, although some effort may be required to evaluate the transverse functions Θ and Ψ to desired accuracy.

Analytical progress being helpful for developing intuition, some rough approximations will now be made. Notwithstanding the caveat in Sec. III A, it will be assumed that the temperature gradient at pore ends is perfectly uniform, in which case Eq. (25) holds for all m. With this assumption, the sum in Eq. (18) can be performed explicitly. With aid of the weighted transverse average of Eq. (B4), (13) becomes

$$T_w(z) = \frac{\overline{w}'}{\overline{w}} \nabla T_c \sum_{n \text{ odd}} \frac{4L}{n^2\pi^2} \sin\left(\frac{n\pi}{2}\right)$$
$$\times \left[1 + \frac{S_w k_w}{S_g R} \frac{\Psi_n(\text{wall})}{\langle \Psi_n \rangle_w}\right]^{-1} \sin\left(n\pi\frac{z}{L}\right). \qquad (29)$$

This vanishes as $k_w \to \infty$, and as $k_w \to 0$ it represents a line with constant slope given by Eq. (24). To the extent that the variation of $\Psi_n(\text{wall})/\langle\Psi\rangle_w$ with n can be neglected, the slope remains constant for intermediate k_w and is reduced by the factor in square brackets. With the more suitable assumption that Eqs. (21a) and (22) hold over a sizeable range of n, which is true for sufficiently small acoustic amplitude, the denominator is proportional to n^2 times a factor linear in n^2. Upon expanding in partial fractions and using Eqs. (B1) and (B2), one finds

$$T_w(z) \approx \frac{\overline{w}'}{\overline{w}} \nabla T_c \frac{1}{1+\alpha}\left[z - \frac{1}{s_w}\frac{\sinh(s_w z)}{\cosh(s_w L/2)}\right], \qquad (30)$$

where

$$\alpha = \frac{S_w k_w}{S_g R \langle \Psi_n \rangle_w} \qquad (31)$$

and the spatial scale in the second term is

$$\frac{1}{s_w} = \delta_k \sqrt{\frac{R}{k_g}} \sqrt{\frac{\alpha}{1+\alpha}}. \qquad (32)$$

Thus T_w has a linear profile with an end correction that ensures $dT_w/dz = 0$ at $z = \pm L/2$, consistent with the thermal isolation boundary condition. The spatial scale of the end

correction approaches zero as $k_w \to 0$ and approaches $|\overline{z}_1|/|\overline{F}_V|$, similar to (26), as $k_w \to \infty$. In particular, $s_w^{-i} \ll s_1^{-1}$ when $\alpha \ll 1$.

T_g can be analyzed under the same approximations. Upon substituting Eq. (B4) for the additional factor in the second sum of Eq. (10), the denominator contains an additional factor linear in n^2. Proceeding as before and assuming $s_w^{-1} \ll s_1^{-1}$, one finds for the second sum

$$T_{g2} \approx \frac{\overline{w}'}{\overline{w}} \nabla T_c \frac{1}{1+\alpha} \left\{ z + \sum_m \langle \Theta_m \rangle_w \Theta_m(\boldsymbol{\rho}) \right.$$
$$\left. \times \left[-\frac{1}{s_m} \frac{\sinh(s_m z)}{\cosh(s_m L/2)} + \frac{s_m^2}{s_w^3} \frac{\sinh(s_w z)}{\cosh(s_w L/2)} \right] \right\}. \quad (33)$$

The second term in square brackets, which is small when $s_w^{-1} \ll s_1^{-1}$, mirrors the end correction in T_w. The first term in square brackets has the same form as the first term in Eq. (10). Combining them, and neglecting the last term in Eq. (33),

$$T_g \approx \frac{\overline{w}'}{\overline{w}} \nabla T_c \left\{ \frac{1}{1+\alpha} z \right.$$
$$\left. + \frac{\alpha}{1+\alpha} \sum_m \frac{\langle \Theta_m \rangle_w \Theta_m(\boldsymbol{\rho})}{s_m} \frac{\sinh(s_m z)}{\cosh(s_m L/2)} \right\}. \quad (34)$$

The linear term has the same slope as that in T_w, and the magnitude of that slope makes the rate of thermoacoustic heat pumping equal and opposite the rate of heat conduction through the walls. Finally, with aid of Eq. (B3), one can see that $\partial T_g / \partial z$ in this approximation obeys the end condition (24). It must be remembered that these results are approximate because of the assumption of perfectly uniform axial temperature gradient across the ends of the pore and the assumption that the initial variation of Ψ with n extends to sufficiently large n, which allow the sums on m and n, respectively, to be performed.

D. Transverse heat-transfer coefficient

Under certain conditions, the transverse heat flux can be simply related to the transverse temperature difference. A transverse heat-transfer coefficient, h_0, defined using the temperature along the center line of the pore by

$$h_0(z) = \frac{q(z)}{T_g(z,0) - T_w(z)}, \quad (35)$$

will in general depend on axial coordinate; the definition is useful if h_0 is substantially constant. (It may alternatively be defined in terms of weighted or unweighted section-averaged gas temperature.) Considering first the case of perfectly conducting walls ($T_w = 0$), the ratio of the first term in the first sum for q, Eq. (17), to the corresponding term in T_g, Eq. (10), is

$$h_1 = k_g \frac{S_g}{\Pi} \lambda_1 \frac{\langle \Theta_1 \rangle_w}{\Theta_1(0)}. \quad (36)$$

Thus whenever the $m=1$ term dominates in q, it follows that $h_0 \to h_1$. This will hold rather generally except when $|L/2 - z| \ll |\overline{z}_1|$.

In order to treat the more general case of finite wall conductivity, $q(z)$ will be analyzed under the approximations of the previous subsection. The second sum in Eq. (17) differs from the second sum in Eq. (10) by the factor $-k_n^2$, which cancels the factor n^{-2} in B_n. Therefore $q(z)$ contains no term linear in z, which is consistent with the absence of a transverse dependence in the linear term in Eq. (34). (In other words, the behavior $T_g(\rho,z) = T_w(z) = z, q(z) = 0$ satisfies the differential equations of Sec. I.) Again assuming $s_w^{-1} \ll s_1^{-1}$, one finds

$$\frac{\Pi}{k_g S_g} q \approx \frac{\overline{w}'}{\overline{w}} \nabla T_c \sum_m \lambda_m \langle \Theta_m \rangle_w^2 \left[\frac{\alpha}{1+\alpha} \frac{1}{s_m} \frac{\sinh(s_m z)}{\cosh(s_m L/2)} \right.$$
$$\left. + \frac{1}{1+\alpha} \frac{1}{s_w} \frac{\sinh(s_w z)}{\cosh(s_w L/2)} \right]. \quad (37)$$

Upon comparing with the $m=1$ term of Eq. (34), one finds that $h_0 \to h_1$ under the same conditions as before.

For any specific pore geometry, h_1 may be simplified. For example, consider planar pores in the boundary-layer limit. The quantity $(\delta_k/y_0)\langle \Theta_1 \rangle_w / \Theta_1(0)$ has a well-defined boundary-layer limit that depends only mildly on Prandtl number; it equals 0.35, 0.38, and 0.39 for $\sigma = 0.68$, 0.40, and 0.25 respectively. Also, from Fig. 4, $\lambda_1 = 1.73/\delta_k^2$ for $\sigma = 0.68$. Thus Eq. (36) becomes

$$h_1 \approx 0.61 \frac{k_g}{\delta_k} \quad (38)$$

for $\sigma = 0.68$; the numerical factor is a mildly decreasing function of Prandtl number. Accordingly, the transverse heat-transfer coefficient, defined in terms of the center-line temperature, has the form previously postulated[4,12–14] with a numerical factor that is derived here for the first time.

The second term in Eq. (37), which mirrors the end correction in T_w, is somewhat problematic. Because $\lambda_m \propto m^2$ and $\langle \Theta_m \rangle_w \propto m^{-1}$, the sum over the second term does not converge. This follows from the assumption of perfectly uniform axial gradient at the pore ends, which causes the transverse gradient to become infinitely steep near the walls as $m \to \infty$. In a physically realizable situation, the sum would converge because ∇T_m would eventually fall off more rapidly than $\langle \Theta_m \rangle_w$, as discussed earlier. Furthermore, the first few partial sums of $\lambda_m^0 \langle \Theta_m \rangle_w^2$ for $y_0/\delta_k = 3.333$ and $\sigma = 0.68$ are 0.195, 0.276, 0.353, and 0.391 for $m = 1$, 3, 5, and 7. Thus many terms must be included before the sum becomes large. If one defines an h_w analogously to Eq. (36) using the $s_w z$ terms in Eqs. (37), (34), and (30), one finds that it equals $k_g y_0 / \delta_k^2$ times the partial sums given. Hence it is of the same form as Eq. (36).

IV. CONCLUSION

The three-dimensional time-average temperature distribution in a pore of a thermally isolated thermoacoustic stack has been calculated. In the central region of the pore, the time-average temperatures of gas and wall share a common profile, linear in the axial coordinate, z, with slope depending on k_w. Near the pore ends, $\partial T_g / \partial z$ approaches a constant, approximately equal to the critical temperature gradi-

ent, over a distance of order the acoustic displacement amplitude, and dT_w/dz approaches zero over a much smaller distance, provided the wall has low thermal conductivity.

The transverse heat-flux density, q, is confined to the vicinity of the pore ends, in agreement with a recent numerical calculation.[7] It increases sharply and continuously toward the end of the pore because the hydrodynamic energy flux smoothly approaches zero near the end of a thermally isolated pore, causing the temperature difference between wall and gas to increase. Quantitative comparison between analytical predictions and the numerical results provides some degree of validation for the suitability of the approximations made herein.

The ratio of transverse heat flux to a suitably defined transverse temperature difference is nearly constant, except very near the pore ends. That ratio, if defined in terms of center-line temperature, is proportional to k_g/δ_k, in agreement with conjecture,[4,12-14] and the value of the proportionality constant has been calculated. One would expect such a form for the oscillating heat flux at frequency ω. The reason it also applies to time-average heat flux is that the energy flux h_z, and therefore also the heat deposition $-\partial h_z/\partial z$, peaks at a distance approximately δ_k from the walls.

Because transverse heat flux may reasonably be approximated by such an effective transverse heat-transfer coefficient, it is possible to devise a one-dimensional model for transverse heat flux. The gas temperature may be described by $\langle T_g(z)\rangle_w$ or $T_w(0, z)$ without regard to its detailed variation across the pore section, the wall temperature by $T_w(z)$, and their coupling by an expression of the form (35). Thermoacoustic heat exchangers may be treated, by extension, by assuming that $h_0 \rightarrow h_1$ even for pores that are not thermally isolated. This approach will be explored in a separate paper.

Accuracy of these results very near the pore ends is limited by several factors. First, the assumed boundary condition, (24), is not strictly correct, as already explained. Second, this analysis depends on previous calculations[1,3] of the oscillating temperature field, T_1, which may be inaccurate near the pore ends. Third, details of the three-dimensional flow patterns near a sudden change of cross-sectional area, including vortex generation,[15] streaming,[6] and jetting effects, become important near the ends. Finally, the thermal effect from acoustic dissipation has been ignored throughout this analysis, and in particular, entrance and exit effects (so-called "minor" losses) may become major contributors there. Further theoretical analysis of thermoacoustics, especially near *and outside* pore ends, would be valuable for correcting these shortcomings.

ACKNOWLEDGMENTS

APPENDIX A

This Appendix outlines the derivation of Eq. (1) from expressions in the literature and defines certain notations.

Following Ref. 3, time development is $e^{-i\omega t}$. (Reference 1 uses the opposite convention.) The total energy flux (power) includes both heat and work flux; this is expressed in Ref. 3 in the form $\bar{H}_2 = \dot{Q}_2 + \dot{W}_2 - \dot{Q}_{\text{loss}}$. The last term, which describes thermal conduction, will be neglected for the moment. Specializing to an ideal gas by taking $\beta T_g = 1$, the energy flux is given by the integral on the right-hand side of Eq. (42) in Ref. 3. Writing ΩS_{res} for the open cross-sectional area of the stack,

$$\bar{H}_2 = \frac{\Omega S_{\text{res}}}{S_g} \int_{S_g} \int h_z \, d\boldsymbol{\rho}. \tag{A1}$$

Using $(\gamma-1)/c^2 \beta = T_g \beta/c_p$ and noticing that $\text{Im}(F_V F_V^*) = 0$, the energy-flux density (power per unit area) is

$$h_z(z, \boldsymbol{\rho}) = \frac{1}{2\omega\rho_0} \text{Im}\left[\frac{dp_1}{dz} p_1^* F_V(\boldsymbol{\rho}) F_T^*(\boldsymbol{\rho})\right]$$
$$- \frac{c_p}{2\rho_0\omega^3} \frac{\partial T_g(z,\boldsymbol{\rho})}{\partial z} \left|\frac{dp_1}{dz}\right|^2 \text{Im}\left[\frac{F_V(\boldsymbol{\rho})F_T^*(\boldsymbol{\rho})}{1-\sigma}\right]. \tag{A2}$$

In the notation of Ref. 3, $F_V(\boldsymbol{\rho}) = F(x,y;\lambda)$ and $F_T(\boldsymbol{\rho}) = F(x,y;\lambda_T)$. These quantities satisfy differential equations in the transverse coordinates only and express the transverse variations of acoustic velocity and oscillating temperature, respectively. An important feature of Eq. (A2) is that it contains the axial derivative of the gas temperature, not the wall temperature.

While the acoustic pressure and its axial derivative do not vary appreciably over pore section, the velocity amplitude does vary. Defining the average over pore section of any transverse function P by an overbar,

$$\bar{P} \equiv S_g^{-1} \int_{S_g} \int P(\boldsymbol{\rho}) d\boldsymbol{\rho}, \tag{A3}$$

one may write [cf. Eq. (31) in Ref. 3, Eq. (73) in Ref. 1],

$$\bar{u}_1 = \frac{-i}{\omega\rho_0} \frac{dp_1}{dz} \bar{F}_V \equiv -i\bar{u}_1^s. \tag{A4}$$

In standing-wave phasing, p_1 and $\bar{u}_1^s$ are in phase and can be chosen real [Ref. 1, p. 1159]. Defining

$$R = \frac{c_p}{2\rho_0\omega^3} \left|\frac{dp_1}{dz}\right|^2 = \frac{k_g}{\delta_k^2} \frac{|\bar{z}_1|^2}{|\bar{F}_V|^2}, \tag{A5}$$

$$\boldsymbol{\nabla} T_c = \frac{\omega p_1}{\rho_0 c_p \bar{u}_1^s}, \tag{A6}$$

the energy-flux density becomes

$$h_z(z, \boldsymbol{\rho}) = R\left[w'(\boldsymbol{\rho})\boldsymbol{\nabla} T_c - w(\boldsymbol{\rho})\frac{\partial T_g(z,\boldsymbol{\rho})}{\partial z}\right], \tag{A7}$$

where

$$w(\boldsymbol{\rho}) = \frac{\text{Im}[F_V(\boldsymbol{\rho})F_T^*(\boldsymbol{\rho})]}{1-\sigma},$$
$$w'(\boldsymbol{\rho}) = \text{Im}[\bar{F}_V^* F_V(\boldsymbol{\rho})F_T^*(\boldsymbol{\rho})]. \tag{A8}$$

(Notice that w remains finite for $\sigma = 1$.) Upon adding the contribution from thermal conduction through the gas, Eq. (1) results.

It is conventional to define the "critical temperature gradient" by Eq. (A6), even though the temperature gradient for which the section average of Eq. (A7) vanishes is $(\overline{w}'/\overline{w})\nabla T_c$, where

$$\overline{w} = \frac{\text{Im}(\sigma \overline{F}_V + \overline{F}_T^*)}{1-\sigma^2}, \quad \overline{w}' = \frac{\text{Im}(\overline{F}_V^* \overline{F}_T^*)}{1+\sigma}. \tag{A9}$$

APPENDIX B

This Appendix presents useful mathematical results. Any function defined on the domain $-L/2 \leq z \leq L/2$ that has period $2L$, is odd with respect to $z=0$, and is even with respect to $z = \pm L/2$ can be represented as a Fourier sine series containing only odd-n terms. Consider the triangle function defined by $f(z)=z$ for $-L/2 \leq z \leq L/2, f(z)=L-z$ for $L/2 \leq z \leq 3L/2, f(z+2L)=f(z)$. On the domain of interest, one finds

$$z = \sum_{n \text{ odd}} \frac{4L}{\pi^2 n^2} \sin(n\pi/2)\sin(n\pi z/L). \tag{B1}$$

Under the same conditions of symmetry and periodicity,

$$\frac{\sinh(sz)}{\cosh(sL/2)} = \frac{4}{L} \sum_{n \text{ odd}} \frac{s}{s^2+(n\pi/L)^2}$$
$$\times \sin(n\pi/2)\sin(n\pi z/L). \tag{B2}$$

By expanding unity in eigenfunctions, one can show that [cf. Eq. (12)]:

$$1 = \sum_m \langle \Theta_m \rangle_w \Theta_m(\boldsymbol{\rho}). \tag{B3}$$

Green's theorem in two dimensions says

$$\int_{S_g}\!\!\int [\Theta_m \nabla^2 \Psi_n - \Psi_n \nabla^2 \Theta_m] d\boldsymbol{\rho}$$

$$= \oint \left[\Theta_m \frac{\partial \Psi_n}{\partial n} - \Psi_n \frac{\partial \Theta_m}{\partial n}\right] d\Pi.$$

Using Eqs. (5) and (9) on the left-hand side, and observing that Θ_m vanishes on the wall,

$$(k_n^2 + \lambda_m) \int\!\!\int w(\boldsymbol{\rho})\Theta_m(\boldsymbol{\rho})\Psi_n(\boldsymbol{\rho}) d\boldsymbol{\rho}$$

$$= -\Psi_n(\text{wall}) \oint \frac{\partial \Theta_m}{\partial n} d\Pi.$$

The integral on the left is just the expansion coefficient of Ψ_n in terms of Θ_m. Thus using Eq. (15),

$$\frac{\Psi_n(\boldsymbol{\rho})}{\Psi_n(\text{wall})} = \sum_m \frac{\lambda_m \langle \Theta_m \rangle_w}{k_n^2 + \lambda_m} \Theta_m(\boldsymbol{\rho}). \tag{B4}$$

[1] G. W. Swift, "Thermoacoustic engines," J. Acoust. Soc. Am. **84**, 1145–1180 (1988).

[2] N. Rott, "Thermoacoustics," Adv. Appl. Mech. **20**, 135–175 (1980), and references therein.

[3] W. P. Arnott, H. E. Bass, and R. Raspet, "General formulation of thermoacoustics for stacks having arbitrarily shaped pore cross sections," J. Acoust. Soc. Am. **90**, 3228–3237 (1991).

[4] G. W. Swift, "Analysis and performance of a large thermoacoustic engine," J. Acoust. Soc. Am. **92**, 1551–1563 (1992).

[5] J. R. Olson and G. W. Swift, "Similitude in thermoacoustics," J. Acoust. Soc. Am. **95**, 1405–1412 (1994).

[6] D. F. Gaitan, A. Gopinath, and A. Atchley, "Experimental study of acoustic turbulence and streaming in a thermoacoustic stack," J. Acoust. Soc. Am. **96**, 3220 (1994).

[7] N. Cao, J. R. Olson, G. W. Swift, and S. Chen, "Energy flux density in a thermoacoustic couple," J. Acoust. Soc. Am. **99**, 3456–3464 (1996).

[8] G. Mozurkewich, "A model for transverse heat transfer in thermoacoustics," J. Acoust. Soc. Am. (submitted).

[9] L. D. Landau and E. M. Lifshitz, *Fluid Mechanics* (Pergamon, Oxford, 1982), Eq. 49.21.

[10] W. H. Press, B. P. Flannery, S. A. Teukolsky, and W. T. Vetterling, *Numerical Recipes* (Cambridge University Press, Cambridge, England, 1986), p. 579.

[11] P. M. Morse and H. Feshbach, *Methods of Theoretical Physics* (McGraw-Hill, New York, 1953), Vol. 1, pp. 739–743.

[12] W. C. Ward and G. W. Swift, "Design environment for low-amplitude thermoacoustic engines," J. Acoust. Soc. Am. **95**, 3671–3672 (1994).

[13] S. L. Garrett, D. K. Perkins, and A. Gopinath, "Thermoacoustic refrigerator heat exchanegrs: design, analysis, and fabrication," in *Heat Transfer 1994*, Proceedings of the Tenth International Heat Transfer Conference, edited by G. F. Hewitt (Inst. of Chem. Engineers, London, 1994), Vol. IV, pp. 375–380.

[14] B. L. Minner, "Design optimization for thermoacoustic cooling systems," Ph.D. thesis, Purdue University (1996).

[15] A. S. Worlikar and O. M. Knio, "Numerical simulation of a thermoacoustic refrigerator. I. Unsteady adiabatic flow around the stack," J. Comput. Phys. **127**, 424–451 (1996).

Microstructured elastomeric electromechanical film transducer

Lorne A. Whitehead

Physics Department, University of British Columbia, 6224 Agricultural Road, Vancouver, British Columbia V6T 1Z1, Canada

Brent J. Bolleman

GMW Speaker Tape Corporation, #201, 2386 East Mall, Vancouver, British Columbia V6T 1Z3, Canada

A new electrostatic film transducer is described. This transducer uses a flexible sheet of elastomeric microstructures to achieve a wide range of internal impedance and driving pressure. A simple single degree of freedom model is used to predict the performance of the device and the predictions have been confirmed by measurements made on a prototype device. © *1998 Acoustical Society of America.* [S0001-4966(97)04412-3]

PACS numbers: 43.38.Bs, 43.28.Py, 43.50.Ki, 43.28.Tc [SLE]

INTRODUCTION

There appear to be a number of applications in acoustics that could benefit from an electromechanical transducer which efficiently radiates acoustic waves into an adjacent medium and comes in the form of a flexible sheet that can be bonded to a surface like tape. In the case where the medium is a gas, such as air, examples of potential applications include active noise control,[1] acoustic flow control,[2] airborne ultrasonic imaging,[3] specialty audio systems, etc. In the case where the medium is a liquid, such as water, examples include sonar, surface marine fouling prevention,[4] membrane filtration enhancement,[5] sonochemistry,[6] ultrasonic cleaning, etc.

There are high-quality electromechanical film transducers, such as polyvinylidene fluoride (PVDF)[7] and PiezoRubber,[8] currently available on the market. However, when coupling to gas media, the efficiency of these actuators in a planar clamped mode is quite low. When coupling to liquid media, their efficiency is improved due to the better acoustic impedance match, but a high cost per unit area limits their use in applications requiring large areas such as marine fouling prevention. Their efficiency is also too low for continuous duty high-power applications such as ultrasonic cleaning.

Experimental film transducers have been proposed which use electrostatic instead of piezoelectric transduction.[9,10] These actuators have lower internal impedance than their piezoelectric counterparts, but their driving efficiency in gases is still quite low. These devices also use relatively high operating voltages which is undesirable in many instances.

In this paper a new type of electrostatic transducer technology is presented, which is based on the use of elastomeric microstructures. We have proposed the term ''Elastomeric Micro Electro Mechanical Systems'' (EMEMS) to describe this general new area of technology, in reference to the rapidly growing field of Micro Electro Mechanical Systems (MEMS),[11,12] which has to date focused on comparatively rigid fabrication materials. As described herein, the microstructural design capability in EMEMS allows one to produce very small interelectrode gaps and exert careful control over mechanical impedance. This enables the construction of electromechanical film transducers with properties which are tailored to specific applications.

While EMEMS technology can be used to construct film transducers for use in a variety of applications, this paper will focus on electroacoustic transducer designs intended for use in gas media. This first application demonstrates many of the key features of the EMEMS concept.

I. PRINCIPLES OF MICROSTRUCTURED ELASTOMERIC TRANSDUCERS

Electrostatic transducers have been in use for over a century. Most designs are based on a rigid planar electrode and a thin flexible membrane electrode which is supported some distance away (Fig. 1). The membrane electrode is typically a thin (e.g., 6 μm thick) vacuum-metalized polymer such as polyester, and the rigid electrode is typically a perforated metal sheet or wire mesh. The gas in the intervening gap is typically air, and the gap thickness ranges from about 1 mm in hifidelity electrostatic loudspeakers to a few micrometers in condenser microphones and electrostatic transducers used for ultrasonic ranging and imaging.

When used as an actuator, a voltage is applied across the two electrodes, and this induces electrostatic attraction between them. This electrostatic force per unit area in turn causes the relatively flexible membrane electrode to deform as illustrated in Fig. 1. If a time-varying voltage is applied, the flexible membrane will experience a time-varying force per unit area, and in response it will vibrate and acoustic waves will be radiated. When used as a sensor, a constant voltage is applied across the electrodes either by permanent charging of the polymer membrane, or by an imposed voltage. When the membrane moves in response to incoming acoustic waves, this motion is detected as current flow through the device. The detailed theory of operation of these conventional electrostatic transducers has been well developed and reviewed by others.[13–18]

A basic problem with conventional electrostatic transducer designs is that the relative motion of the opposing electrodes is provided by the deformation of one of the electrodes. This requires that the membrane electrode be relatively thin, which in turn means that it will be relatively fragile. Although film transducers based on this flexible
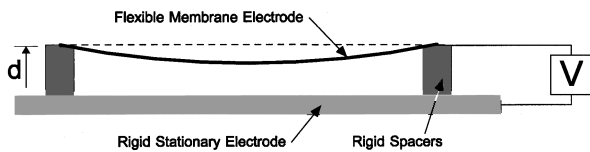
FIG. 1. Conventional electrostatic transducer design using a flexible membrane electrode.

membrane design have been used in the past,[19] design constraints such as fragility render them unsuitable for many important applications.

The problem of fragility can be circumvented by using a deformable dielectric structure between the two rigid planar electrodes to allow variation of their separation distance.[10] Since the mobile electrode need not stretch, it can be thicker and more durable than previous highly flexible membranes. The only constraint on thickness is that the mass per unit area be small enough to permit a good high-frequency response. An example of one such device is shown in the cross section in Fig. 2. Here a combination of air pockets and elastomeric spacers is used to produce a compressible dielectric.

The design shown in Fig. 2 also allows the thickness d of the interelectrode gap to be controlled more easily. This is very important to prevent electrical breakdown in the interelectrode gap. Paschen's law indicates that the breakdown voltage of a gas V_b is a function of pd alone, where p is the gas pressure and d is the gap thickness, i.e., $V_b = f(pd)$. It turns out that for most gases, including air, this voltage decreases with decreasing pd only to a point and then begins increasing as pd is further reduced as shown in Fig. 3.[20] It is important to note that such breakdown voltages should be taken only as an approximate guide, as actual results depend substantially on conditions such as the electrode shape, surface structure, and composition.

For air at standard pressure, this Paschen effect on the maximum electric field $E = V/d$ for a given air gap thickness d is also shown in the graph of Fig. 3. An air gap of a few micrometer can support a large electric field E which in turn generates a large electrostatic pressure P_e according to the following relation:

$$P_e = \tfrac{1}{2}\kappa\varepsilon_0 E^2, \qquad (1)$$

where κ is the dielectric constant ($\kappa \approx 1$ for air), and $\varepsilon_0 = 8.85 \times 10^{-12}$ F/m is the permittivity of free space.[21] It is important to note that since the electrostatic pressure is proportional to the square of the electric field, and since the radiated acoustic power will be proportional to the square of the electrostatic pressure, even a seemingly minor increase in
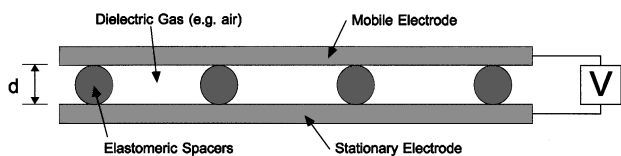
FIG. 2. Compressible dielectric electrostatic transducer design using deformable elastomeric spacers.
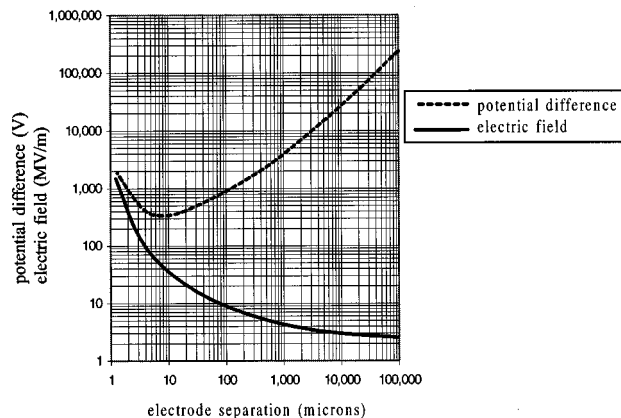
FIG. 3. Breakdown electric potential and field of air at 1 atm versus interelectrode gap spacing (Note: 1 micron≡1 micrometer).

maximum field can substantially improve the transducer's performance.

Since Paschen's law tells us that reducing the gas pressure p has the same effect as reducing the gap spacing d, one might wonder if the electric field, and hence the electrostatic pressure, could be made extremely large by operating under vacuum. In practice, although the gas no longer breaks down, a number of other breakdown mechanisms such as field emission[22] occur and appear to limit the maximum electrostatic pressure to values of the order 5–10 atm.[23,24] While this pressure is much less than that obtainable from piezoelectric crystals, it is sufficient for many applications in liquids.

In addition to allowing higher driving pressures, smaller interelectrode gaps have the added benefit of requiring much lower operating voltages than a typical electrostatic loudspeaker. However, a major disadvantage to small air gaps in compressible dielectric electrostatic transducers is that the air pockets inside the dielectric cannot be vented, and hence the dynamic stiffness of the air becomes very large and the coupling efficiency is reduced. Therefore, while compressible dielectric designs may be useful in certain applications, they are not generally suitable for high efficiency coupling to gaseous media.

The microstructured elastomeric transducer described here, which is based on the EMEMS concept, retains the benefits of small interelectrode gaps, and eliminates the problem of increased gas stiffness by allowing the gas to flow into comparatively large gas reservoirs incorporated in the structure. An example of such a microstructured elastomeric transducer design is shown in Fig. 4.

In this device, microstructured elastomer posts spaced at regular intervals compliantly support the mobile electrode sheet at a fixed spacing d above a series of microelectrodes below. The dielectric gas in the thin regions ($d \approx 15\ \mu$m) between the electrodes is able to flow to the relatively voluminous regions ($h \approx 500\ \mu$m) of the adjacent gas reservoirs, thereby reducing the effective stiffness of the air. This bears similarity to the "grooved" back plate design of some conventional electrostatic transducers used in ultrasonic imaging and in condenser microphones.[25] The distance between
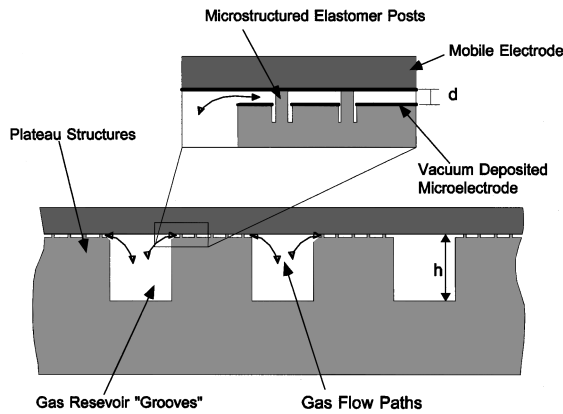
FIG. 4. Example of a microstructured elastomeric transducer design.

grooves and their width is determined by a tradeoff between viscous damping and reduced active driving area.

The elastomeric support ridges or posts serve the key purpose of providing the necessary degree of compliance. This design also allows the overall structure to be durable and flexible, in contrast to conventional MEMS devices based on rigid silicon materials.

II. MODEL OF A MICROSTRUCTURED ELASTOMERIC TRANSDUCER

In the model considered below (see Fig. 5), the microstructured elastomeric transducer is treated as a system with a single degree of freedom. This model works well because the majority of the moving mass is contained in the radiating electrode sheet, and the majority of the compliance is in the elastomeric layer.

The lumped mechanical parameters per unit area and external pressures shown in Fig. 5 are briefly described as follows:

m is the mass per unit area of the radiating sheet

k_a is the dynamic stiffness per unit area due to the compressive stiffness of the trapped gas pockets

k_e is the dynamic stiffness per unit area of the elastomer structure

z_a is the mechanical impedance per unit area of air

c_a is the damping per unit area due to viscous losses in the air

c_e is the damping per unit area due to hysteresis in the elastomeric microstructure

P_e is the average electrostatic pressure applied to the radiating structure

P_a is the average acoustic pressure at the surface of the radiating structure

The best method of determining these parameters will vary from case to case but some general guidelines are provided in Table I.[26–31]
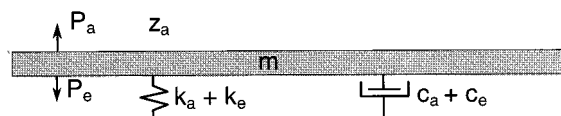
FIG. 5. Microstructured elastomeric transducer model.

In an electrostatic transducer with plane parallel electrodes, the electric field is simply $E = V/d$ and Eq. (1) can be rewritten as Eq. (2) below:

$$P_e = \frac{1}{2} \kappa \varepsilon_0 \left(\frac{V}{d}\right)^2. \tag{2}$$

It is important to note that d itself will be a function of P_e, with the result that (2) is a recursive relationship which cannot be solved exactly. However, in many cases the fractional variations in d are small and it is a reasonable approximation to treat it as a constant. As will be seen, this is a suitable approximation for the work described here.

There are two fairly simple ways to drive such a transducer. In the first, a simple ac voltage is applied. Since P_e is proportional to the square of V, and since the square of a sinusoidal variation is a dc term plus a sinusoid at twice the original frequency, this results in an ac component of P_e at that doubled frequency. A second way to drive the transducer is to apply a dc voltage added to an ac voltage. This results in an ac component of P_e at the same frequency as the applied ac, but a frequency doubled component is generated as well.

Let us consider this quantitatively. For an applied voltage with components V_{dc} and V_{ac}, the electrostatic pressure is given by Eq. (3):

$$P_e = \frac{\kappa \varepsilon_0 (V_{ac} + V_{dc})^2}{2d^2} = \frac{\kappa \varepsilon_0 V_{dc}^2}{2d^2} + \frac{\kappa \varepsilon_0 V_{dc} V_{ac}}{d^2} + \frac{\kappa \varepsilon_0 V_{ac}^2}{2d^2}. \tag{3}$$

The first component is a static pressure, the second is a time-varying pressure which is proportional to V_{ac}, and the third is a time-varying pressure which is proportional to V_{ac}^2. The second term corresponds to an ac response at the drive frequency, whereas the third term yields a response at twice the drive frequency.

For transducers in which it is desired to faithfully reproduce a given signal, it is obviously preferable to maximize the second term relative to the third, which implies that the V_{ac} signal must be much less than the bias voltage. Then, based on the single degree of freedom model presented above, one obtains a simple approximate transfer function between the oscillation amplitude x and the signal voltage V_{ac} as shown in Eq. (4) below, where it is assumed that d does not vary substantially in response to the electrostatic force:

$$\frac{x}{V_{ac}} = \frac{\dfrac{\kappa \varepsilon_0 V_{dc}}{d^2}}{\sqrt{[\omega(z_a + c_e + c_a)]^2 + [(k_a + k_e) - m\omega^2]^2}}. \tag{4}$$

The difficulty with the above approach is that the requirement that V_{ac} be much less than the bias voltage results in a reduced output power. In a situation where it is desirable to have the maximum output power at a specific frequency, it is better to set V_{dc} to zero, so that V_{ac} can be as large as possible without dielectric breakdown, with the result that almost all of the ac component of P_e is at a single frequency equal to twice the applied ac frequency. In this case the displacement will be given by

TABLE I. Microstructured elastomeric transducer model parameter evaluation.

Parameter	Evaluation
m	Readily calculated using the known density and thickness of the radiating sheet materials.
k_a	Assuming the compression of the trapped gas is adiabatic, which is true for most situations of interest here, the dynamic stiffness per unit area can be calculated using the adiabatic bulk modulus $B = \rho c^2$ as follows:[26] $$k_a = \frac{\Delta p A}{\Delta V} = B\frac{A}{V} = \rho c^2 \frac{A}{V} = \frac{\rho c^2}{d_{eq}},$$ where ρ is the density, c is the speed of sound, Δp and ΔV are the change in pressure and volume, respectively, and A and V are the area and gas volume in question. d_{eq} is the volume of gas per unit area which may be thought of as an ''effective'' thickness of trapped gas. d_{eq} is calculated based on the geometry of the device. At very low frequency (i.e., less than a few Hz) the dynamic stiffness of the air will be zero because the gas contained in the transducer is vented to the atmosphere to prevent variations with ambient pressure and temperature.
k_e	The dynamic stiffness of the elastomeric microstructure depends on the shape of the microstructure, the type of elastomer, and the operating frequency and temperature. This stiffness can be predicted to first order using simple structural models and the published material properties for the elastomers. More accurate predictions require specific material testing and finite element modeling.
z_a	The mechanical impedance per unit of air (specific acoustic impedance) is given by $|z_a| = \rho c$, where ρ is the density of air and c is the speed of sound. This simple model is adopted because in most cases the elastomer damping c_e will be nearly an order of magnitude greater than $|z_a|$. However, as c_e is reduced with newer designs, more careful consideration of the calculation of $|z_a|$ will need to be made.
c_a	Damping in the trapped air inside the transducer occurs due to viscous effects. For example, the flow of air between the thin air pockets and the thick air pockets of the microstructured elastomer design shown in Fig. 4 results in viscous losses. These can be estimated by assuming laminar flow and using the resulting wall shear stress relations.[27] In air flow channels which are of a dimension less than two orders of magnitude greater than the mean free path of the air molecules, slip-flow may occur which will reduce the shear predicted by a continuum treatment of the fluid. For air at 1 atm and 25 °C, the mean free path of molecules is 0.09 μm, and so a channel less than 9 μm will experience substantial slip-flow.[28]
c_e	Damping in the elastomer due to internal hysteresis is given by the relation[29] $c_e = \tan \delta k_e / \omega$, where $\tan \delta$ is the loss factor and ω is the radian frequency of oscillation. Like the dynamic stiffness, the loss factor of elastomers varies significantly with frequency and temperature, especially in the region close to the glass transition point of the material.
P_e	The electrostatic driving pressure can be calculated from a model of the electric field distribution using the relation given earlier in Eq. (1). The electric field distribution can be determined with techniques such as finite difference, finite element, charge simulation, etc.[30]
P_a	The acoustic pressure induced on the radiating sheet due to its vibration in the adjacent fluid medium can be calculated using well-known relations.[31] However, for many microstructured elastomeric designs, the acoustic pressure is small compared to those associated with the internal impedances and, therefore, does not substantially affect the motion of the radiating sheet.

$$x = \frac{\dfrac{\kappa \varepsilon_0 V_{ac}^2}{2d^2}}{\sqrt{[\omega(z_a + c_e + c_a)]^2 + [(k_a + k_e) - m\omega^2]^2}}, \qquad (5)$$

where ω is now the doubled angular frequency, and where again it is assumed that d does not vary substantially in response to the applied force. This is the approach which we employed in the work reported here, in order produce fairly intense and pure sinusoidal excitation. It should be noted, however, that this requires twice the ac amplitude than would be needed if an equal combination of ac and dc were to be used. In some cases, where serious losses are primarily associated with the ac component, such an ac/dc combination may be preferred.

III. DISCUSSION

If the electrode oscillation amplitude x is small compared to the interelectrode spacing, and one knows the electric field distribution, the magnitude of P_e can be readily determined for a given voltage. However, in many applications the oscillation amplitude will be a significant fraction of the electrode spacing, and such a simple treatment will be

inaccurate because the electrostatic pressure and dynamic stiffness are a function of displacement. In such a case, an accurate analysis requires solving the coupled problem of the electrostatic forces and the mechanical stiffness of the elastomer microstructure and air pockets. Numerical techniques for solving this coupled problem have recently become available.[32]

In conventional electrostatic transducers operating with a dc polarization, where the deflection stiffness of the membrane electrode is approximately constant with deflection, the forces on the membrane become unstable at deflections greater than one-third of the initial electrode separation.[33] This is because the electrostatic attractive forces increase more rapidly than the mechanical restoring forces for such large displacements. The resultant ''snap-down'' effect in conventional electrostatic transducers limits their maximum amplitude of operation. However, in microstructured elastomeric transducers, the shape of the mechanical support structure can be designed so that its stiffness increases substantially with deflection. The system can remain stable for much larger deflections, and hence produce larger amplitudes of motion for a given interelectrode gap spacing.

Typically, the interelectrode spacing will be less than 15

FIG. 6. Microstructured elastomeric transducer prototype.

FIG. 7. Scanning electron micrograph ($\times$600) of the microstructured elastomer surface used in the prototype.
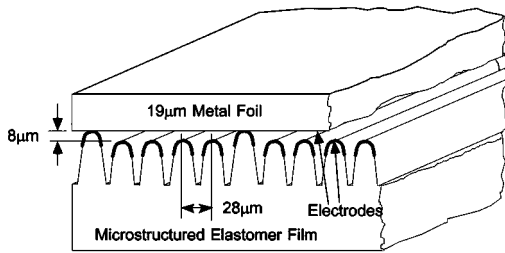
μm in order to maintain high electrostatic pressure capability and low operating voltage. The maximum displacement amplitude will be of the order 1.5 μm rms. While this amplitude represents a substantial acoustic power at high frequency, it may not be sufficient for low-frequency applications. However, at low frequencies for which the mass impedance is not as critical, several transducer layers could be stacked to achieve greater amplitudes (e.g., 15 μm rms with ten layers). In addition, more complex structural designs can be employed to allow greater amplitude without compromising the small interelectrode spacing.

IV. CONSTRUCTION AND TESTING OF A PROTOTYPE TRANSDUCER

A proof-of-principle microstructured elastomeric transducer prototype has been constructed to verify the physical principles described above. The layout of this prototype is shown in Fig. 6 below.

The prototype consists of three components: an elastomeric sheet with a microstructured surface, vacuum-deposited microelectrodes, and a planar sheet of metal foil. The microstructure is formed from a series of linear ridges which are spaced 28 μm apart; every fifth ridge is about 8 μm higher than its neighbors. The metal foil rests on the tops of the taller ridges which compliantly support it at a fixed distance (8 μm) from the tops of the shorter ridges. The tops of the ridges are coated with metal to form an array of linear microelectrodes which are all connected to one terminal of the voltage source, while the metal foil is connected to the other terminal. A short circuit which initially exists between the metal on the tops of the tall ridges and the foil electrode is removed by vaporizing the thin film of metal with a current pulse. The planar dimensions of the prototype are approximately 30 mm$\times$30 mm.

When an excitation voltage is applied, electrostatic force is generated between the microelectrodes and the foil electrode. This force is borne by the taller ridges which deform in response and thus allow relative motion of the electrodes. If the microstructured elastomer sheet is fixed to a foundation, and the foil is in contact with a fluid medium (e.g., air), then most of the relative motion will occur in the foil. This, in turn, generates acoustic waves.

The purpose of the ''valleys'' between the short ridges is to provide an increased gas volume which reduces the dynamic stiffness of the air. The ''valleys'' adjacent to the tall ridges also contribute to the gas volume, but their additional purpose is to create an increased path length along the
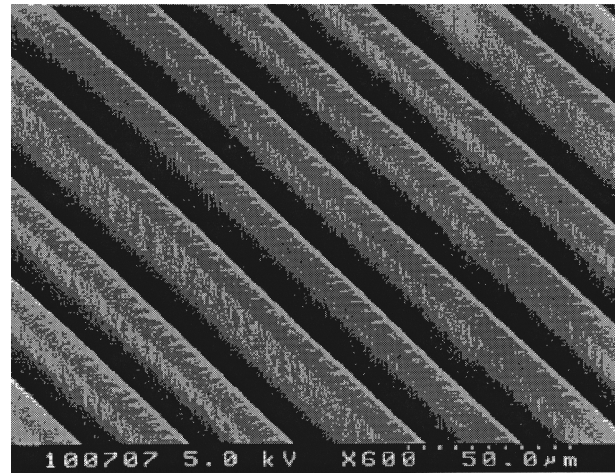
elastomeric material, leading from the micro-electrodes to the top metal foil. This reduces the chance of surface breakdown. The tops of the shorter ridges carrying the electrodes are made round to reduce local amplification of the electric field which could accelerate electrical failure of the gas and/or surface.[34] The linear design shown was selected to simplify fabrication and the electrical connection scheme. A scanning electron micrograph of the microstructured elastomer surface is shown in Fig. 7.

For the tests outlined below, the metal foil radiating electrode was held in place on the tops of the tall ridges by sealing the edges of the prototype sample and reducing the pressure of the air within the transducer by 200 Pa. The microelectrodes on the ridges were all connected together by a strip of conductive ink which in turn was connected to one terminal of the voltage source. The foil electrode was then connected to the other terminal via a thin strip of similar foil bonded to the top surface with conductive ink.

The first set of tests measured the deflection of the foil electrode in response to application of dc voltage, and, as a calibration, in response to applied gas pressure differential. These deflections were measured using a fiber optic microdisplacement meter.[35] Using data from the deflection versus gas pressure test, the electrostatic pressure causing the electrostatically induced deflection was determined over the applied voltage range. The resultant values agree reasonably well with the electrostatic pressure predicted from electric field modeling done using a computer-assisted boundary element solution to Laplace's equation. The geometry of the electrodes in this model was made nearly identical to that observed in the SEM photos of the actual prototypes. Both of these data are presented in Fig. 8. We do not know the cause of the observed discrepancy, but it may be due to variations in the precise shape of the conductive regions of the deposited microelectrodes. A reduction in conductive area would reduce the average electric field and hence reduce the electrostatic pressure.

The next tests were performed with unbiased single-tone ac voltage excitation to obtain the simplest (i.e., no harmonics) output response possible. Since the electrostatic pressure is proportional to the square of the applied voltage, with a
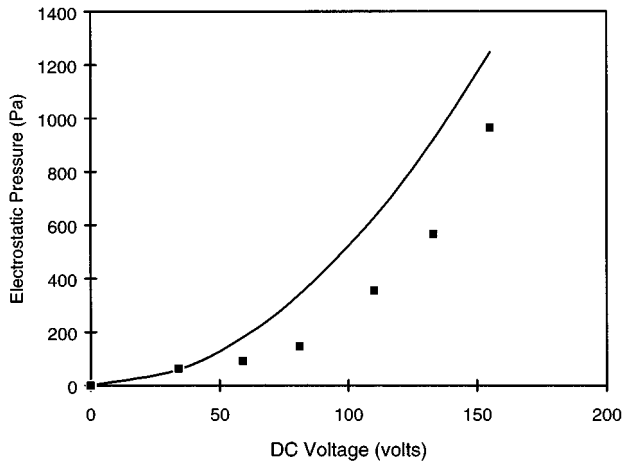
FIG. 8. Electrostatic pressure versus dc voltage in microstructured elastomeric prototype: —: theoretical estimate, ■: value determined from displacement measurements.

FIG. 9. Radiating electrode oscillation amplitude (rms) versus ac voltage (rms): —: predicted by model using parameter values in Table II, ■: measured on sample A.

single pure tone ac voltage excitation the ac electrostatic pressure is also a pure tone, but at double the frequency of the applied voltage. There will also be a dc electrostatic pressure component produced which is equal to the amplitude of the ac electrostatic pressure. However, this does not significantly alter the equilibrium interelectrode spacing in the device because of the high stiffness (k_a+k_e). The ac voltage source consisted of an oscillator connected to an audio power amplifier whose voltage was stepped up with a 20:1 transformer. The ac voltage being applied to the transducer was measured using a high bandwidth voltmeter. Once again, an optical probe was used to nonintrusively sense the oscillation amplitude of the foil electrode. The ac voltage signal generated by the optical probe was observed with a spectrum analyzer.

The ac amplitude response of the transducer was observed to be substantially flat from dc up to 25 kHz. The high-frequency limitations of the driving equipment did not allow for the measurement of the device response through resonance. The low-frequency response is consistent with the single degree of freedom model, which predicts a flat response in the measured range, because the first resonance is predicted to be at about 62 kHz.

The ac amplitude response measured as a function of applied rms voltage at $f=10$ kHz is shown in Fig. 9 together with the response predicted by the transfer function in Eq. (5). This response was calculated using the parameter values shown in Table II. The moderate discrepancy between the measured and predicted response is consistent with the degree of uncertainty of these parameter values. For example, the damping of the elastomer could have been significantly greater than predicted based on a simple rebound test.

The maximum amplitude shown in Fig. 9 is about 30 nm rms, which is small compared to the interelectrode gap of 8 μm, and is consistent with the fairly high internal stiffness of this particular design (i.e., $k_t=k_a+k_e=8$ GPa/m). It should be noted that in this device, the indentations between the electrodes yields an effective air thickness of about 27 μm, significantly greater than the interelectrode spacing of 8 μm. This prototype demonstrates that there are no fundamental
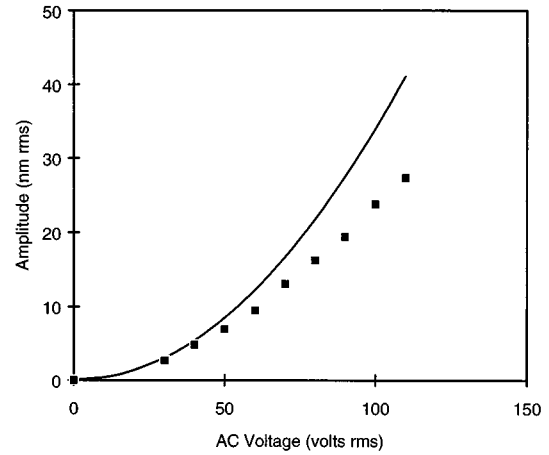
problems with the basic design principles and construction techniques. However, with only a 30-nm displacement, the practical utility of this particular transducer would be quite limited. For this reason, a second generation prototype is currently being developed, which will use the gas reservoir concept described earlier to reduce further the dynamic stiffness of the air. Also, softer elastomers and different support configurations are being used to reduce further the stiffness of the elastomeric supports.

While most of the evaluation experiments were done at relatively low voltage to avoid accidental breakdown, some prototypes were tested to destruction to determine their maximum drive voltage. The results of one of these tests, presented in Fig. 10, indicates two things: (a) the transducer does not fail catastrophically upon the first signs of breakdown; and (b) the loss of performance does not occur until an ac rms amplitude of about 225 V, which is consistent with the predicted gas breakdown threshold for air.[36] This result, together with the absence of any observable output decay after continuous operation for several hours at electric fields greater than 25 MV/m, suggests that the components of this microstructured elastomeric transducer are very resistant to

TABLE II. Parameter values used in modeling prototype

Parameter	Value/Determination
m	density of Al (2800 kg/m3) × foil thickness (19 μm) =0.053 kg/m2
k_a	geometric calculation of trapped air volume $d_{eq}\sim 27$ μm, $\therefore k_a=5$ GPa/m
k_e	slope of measured load deflection curve at mean pressure, $k_e=3$ GPa/m
c_a	viscous damping of air is negligible in this design
c_e	tan $\delta=0.4$, based on rebound test, manufacturer's data
P_e	using measured electrostatic pressures from DC tests
P_a	assuming pressure due to free field specific acoustic impedance $z=408$ Pa·slm, i.e., $P_a=zv$, where v is the instantaneous flow velocity
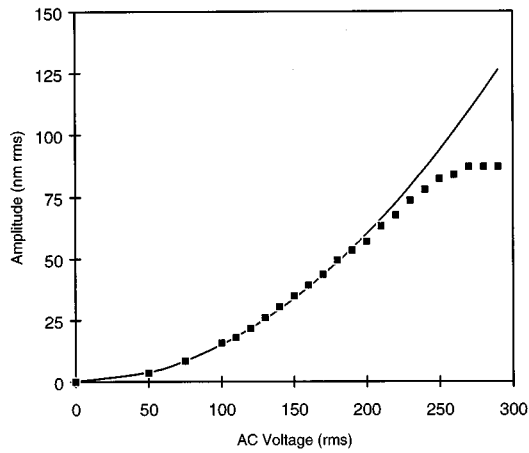
FIG. 10. The breakdown voltage test: —: amplitude $\propto V^2$, ■: measured amplitude (voltage is in volts rms).

lectrical failure modes. Continued work is currently planned to investigate performance over much longer time periods.

In summary, these measurements have shown that there is reasonable agreement between the actual performance of this prototype microstructured elastomeric transducer and that predicted by a single degree of freedom model.

V. CONCLUSION

A new type of electrostatic transducer based on EMEMS technology has been described which exhibits a unique combination of features such as flexible film form, moderate operating voltage, and substantial driving pressure capability. The single degree of freedom model has been presented for predicting the performance of these transducers along with some guidelines for evaluating the individual lumped parameters. A proof-of-principle prototype has been successfully constructed and its experimental performance is in reasonable agreement with that predicted by the model. Future work already underway includes the construction of single and multilayer prototypes with a large gas reservoir to reduce the dynamic stiffness of the air. Better measurements of system parameters will also be used to further refine the model.

[1] W. Gossman and G. Eatwell, ''Active High Transmission Loss Panel,'' U.S. Patent 5,315,661.

[2] S. K. Sinha and F. D. Shields, ''Acoustically active surfaces for boundary layer control,'' PVP/Pressure Vessels and Piping Division/ASME, PVP Series, Vol. 224 (1991), pp. 17–19.

[3] W. Manthey, N. Kroemer, and V. Magor, ''Ultrasonic Transducers with Piezoelectric Polymer Foil,'' Meas. Sci. Technol. **3**, 249–261 (1992).

[4] P. V. Murphy and M. J. Latour, ''Preventing Marine Fouling,'' U.S. Patent 4,170,185.

[5] J. Kost and R. S. Langer, ''Ultrasound Enhancement of Membrane Permeability,'' U.S. Patent 4,780,212.

[6] B. J. Bolleman and A. B. Dunwoody, ''Acoustic Liquid Processing Device,'' U.S. Patent 5,395,592.

[7] AMP Inc., P.O. Box 799, Valley Forge, PA 19482.

[8] NTK Technical Ceramics, NGK Spark Plugs (U.S.A.), Inc., Mt. Prospect, IL 60056.

[9] K. Kirjavainen, ''Electromechanical Film and Procedure For Manufacturing Same,'' U.S. Patent 4,654,546.

[10] L. A. Whitehead, R. L. Clark, and F. L. Curzon, ''Elastomer Membrane Enhanced Electrostatic Transducer,'' U.S. Patent 4,885,783.

[11] J. Bryzek, K. Petersen, and W. McCulley, ''Micromachines on the march,'' IEEE Spectrum, 20–31 (May 1994).

[12] M. Elwenspoek et al., ''Transduction Mechanisms and Their Applications in Micromechanical Systems,'' Micro Electro Mechanical Systems Workshop, 126–132 (1989).

[13] M. J. Anderson, J. A. Hill, C. M. Fortunko, N. S. Dogan, and R. D. Moore, ''Broadband electrostatic transducers: Modeling and experiments,'' J. Acoust. Soc. Am. **97**, 262–272 (1995).

[14] F. V. Hunt, *Electroacoustics: The Analysis of Transduction, and Its Historical Background* (Acoustical Society of America, New York, 1982), p. 168.

[15] J. Merhaut, ''A Contribution to the Theory of Electroacoustic Transducers Based on Electrostatic Principle,'' Acustica **17**, 283–292 (1967).

[16] H. Carr and C. Wykes, ''Diagnostic Measurements in Capacitive Transducers,'' Ultrasonics **31**(1), 13–20 (1993).

[17] A. J. Zuckerwar, ''Theoretical response of condenser microphones,'' J. Acoust. Soc. Am. **64**, 1278–1285 (1978).

[18] J. Hietanen, J. Stor-Pellinen, and M. Luukkala, ''A model for an Electrostatic Ultrasonic Transducer with a Grooved Backplate,'' Meas. Sci. Technol. **3**, 1095–1097 (1992).

[19] S. P. Wilkinson and R. Balasubramanian, ''Turbulence Burst Control Through Phase-Locked Travelling Surface Depressions,'' AIAA Paper No. 85-0536 (1985).

[20] *American Institute of Physics Handbook* (McGraw-Hill, New York, 1963), 2nd ed., Chap. 5.

[21] D. Halliday and R. Resnick, *Fundamentals of Physics* (Wiley, New York, 1986), p. 529.

[22] J. M. Meek and J. D. Craggs, *Electrical Breakdown of Gases* (Wiley, New York, 1978), p. 129.

[23] H. Fujita, ''Studies of Micro Actuators in Japan,'' IEEE Int. Conf. Robotics and Automation 1559–1564 (1989).

[24] E. Kuffel and W. S. Zaengl, *High Voltage Engineering Fundamentals* (Pergamon, Oxford, 1984), p. 359.

[25] F. V. Hunt, *Electroacoustics: The Analysis of Transduction, and Its Historical Background* (Acoustical Society of America, New York, 1982), p. 172.

[26] A. D. Pierce, *Acoustics: An Introduction to Its Physical Principles and Applications* (Acoustical Society of America, New York, 1989), p. 30.

[27] F. M. White, *Fluid Mechanics, Second Edition* (McGraw-Hill, New York, 1986), p. 324.

[28] J. B. Starr, ''Squeeze-Film Damping in Solid-State Accelerometers,'' Solid State Sensors and Actuators, 1990 Workshop, pp. 44–47.

[29] J. C. Snowdown, ''Rubberlike Materials, Their Internal Damping and Role in Vibration Isolation,'' J. Sound Vib. **2**(2), 175–193 (1965).

[30] E. Kuffel and W. S. Zaengl, *High Voltage Engineering Fundamentals* (Pergamon, Oxford, 1984), p. 260.

[31] M. C. Junger and D. Feit, *Sound, Structures, and Their Interaction* (Acoustical Society of America, New York, 1993).

[32] J. Gilbert, P. M. Osterberg, R. M. Harris, D. O. Ouma, X. Cai, A. Pfajfer, J. White, and S. D. Senturia, ''Implementation of a MEMCAD System for Electrostatic and Mechanical Analysis of Complex Structures from Mask Descriptions,'' IEEE Micro Electro Mechanical Systems, 207–212 (1993).

[33] F. V. Hunt, *Electroacoustics: The Analysis of Transduction, and Its Historical Background* (Acoustical Society of America, 1982), p. 183.

[34] E. Kuffel and W. S. Zaengl, *High Voltage Engineering Fundamentals* (Pergamon, Oxford, 1984), p. 210.

[35] Opto-Acoustic Sensors, Inc., 1706A Medfield Rd., Raleigh, NC 27607.

[36] E. Kuffel and W. S. Zaengl, *High Voltage Engineering Fundamentals* (Pergamon, Oxford, 1984), p. 359.

Comparison of two structural sensing approaches for active structural acoustic control

Julien P. Maillard and Chris R. Fuller

Vibration and Acoustics Laboratories, Mechanical Engineering Department, Virginia Polytechnic Institute and State University, Blacksburg, Virginia 24061-0238

A numerical study comparing the use of two structural sensing approaches for sound radiation control is performed on a baffled rectangular plate. The first sensing approach implements an array of accelerometers whose outputs are filtered to construct an estimate of the sound pressure radiated at given angles in the far field. The second method uses the same array of point sensors to estimate the net volume acceleration of the plate. Results show the improved performances of the sensor observing far-field sound radiation over a volume acceleration based on sensor. © *1998 Acoustical Society of America.* [S0001-4966(98)00801-7]

INTRODUCTION

An important issue in the active control of structurally radiated noise remains the design and implementation of error sensors. The early works on active structural acoustic control (ASAC)[1] were concentrated on the design of structural actuators[2] while the error signals to minimize were provided by microphones located in the far field. For the last couple of years, the research in ASAC has made some progress in replacing error microphones by error sensors integrated in the structure.[3] Unlike microphones which directly measure the quantity to be minimized, i.e., acoustic pressure, structural sensors only measure information related to the structural vibrations. The goal is then to design a structural sensor whose output is strongly related to radiated sound pressure so that minimizing the magnitude of the sensor output signal will also minimize the total radiated sound power. In other words, an efficient structural sensing technique should take into consideration the structure–fluid interaction such that only the radiating part of the structural vibrations is observed by the sensor. Indeed, minimizing both radiating and nonradiating components of the vibrations typically requires more control effort below the coincidence frequency.

Spatially distributed structural sensors such as polyvinylidene fluoride (PVDF) materials have shown potential for observing the radiating part of the structural vibrations. In modal sensing, the PVDF film is designed to observe the dominant radiating modes among those found in the structural response.[4–6] The concept of ''radiation modes'' has also been used in designing error sensors.[7,8] In particular, several authors have demonstrated the use of PVDF sensors designed to observe the first radiation mode of a rectangular plate.[8–11] This mode, also referred to as the piston mode, presents the greatest radiation efficiency of all radiation modes. It can be detected by measuring the net volume displacement over the surface of the structure and specially designed PVDF sensors have been constructed for this task.[8–11]

Recently, a sensing technique referred to as discrete structural acoustic sensing (DSAS) was demonstrated both analytically and experimentally on baffled planar radiators.[12–14] The technique implements an array of structural point sensors (usually accelerometers) whose outputs are passed through digital filters to estimate in real time the far-field radiated pressure in a given direction, or equivalently, a given wave-number component, over a broad frequency range. The digital filters are usually finite impulse response (FIR) filters designed to model the appropriate Green's function associated with each point sensor and far-field locations. It was shown that only a low number of point sensors is needed to provide accurate sound radiation estimates over a bandwidth encompassing the first few modes of a rectangular plate. Moreover, the sensor's output can be shifted in time such that the acoustic path delay present in the Green's functions is removed. This allows the use of only a few coefficients in the sensor FIR filter array and makes its implementation on a digital signal processor (DSP) very efficient in terms of computational load.

A simplified version of the above approach that has been suggested consists of replacing the radiation Green's functions by a unity transfer function. The sensor output then simply becomes the sum of the acceleration signals. The resulting error information thus represents an estimate of the net volume acceleration of the structure. It is therefore somewhat equivalent to the PVDF volume velocity sensor referred above except it is implemented in discrete form. This alternative sensing approach will be referred to as discrete structural volume acceleration sensing (DSVAS). For planar radiators, this error information is also equivalent to measuring the far-field pressure in the direction normal to the plane of the radiator.[15]

This paper presents a short numerical study comparing the performance of the two sensing approaches introduced above, i.e., DSAS and DSVAS methods, in active structural acoustic control applied to a rectangular baffled plate. The plate is excited by a normal point force over a bandwidth encompassing its first nine flexural modes. The control is achieved through two single-sided piezoelectric patches. The system modeling is briefly described in the first two sections along with the plate's physical characteristics. The third section then presents the control performance in terms of mean-

square velocity and radiated power attenuation obtained for various sensing configurations.

I. SYSTEM MODELING

The numerical model describing the structural response of the plate excited by point forces and piezoelectric patches is briefly presented. In this model, the mechanical displacements and electrical fields generated in the piezoelectric inclusions are fully coupled. In order to solve for the dynamics of this coupled electromechanical system, a Rayleigh–Ritz formulation is derived based on the generalized form of Hamilton's principle for coupled electromechanical system.[16] This energy-based method also allows modeling of arbitrary boundary conditions applied along the edges of the plate. The plate midplane displacements along the two longitudinal and transverse directions are approximated by a polynomial series where the unknown polynomial amplitudes are the solution of a linear system. After solving this system at each frequency of interest, various structural quantities, such as mean-square velocity, or point acceleration, can be computed. For a complete derivation of this approach applied to rectangular plates, the reader is referred to the work of Berry.[17]

The far-field sound pressure radiated from the plate is obtained from the normal displacement amplitudes by computing the continuous wave-number transform of the acceleration distribution over the frequency bandwidth. The radiated power is estimated from the radiation impedance matrix associated with the polynomial basis used to approximate the structural response. This approach is more efficient than simply integrating the far-field pressure over the hemisphere surrounding the plate. More details can be found in Ref. 18.

The output from the discrete structural acoustic sensor is computed from the structural acceleration evaluated at nine point sensor locations on the plate and multiplied by the appropriate sensor transfer functions as described in Ref. 14. Note that the sensor transfer functions used in this numerical study correspond to the ideal case of perfect filter modeling. It was shown in previous work, however, that these transfer functions are easily modeled to a high level of accuracy with only a few coefficients per FIR filter.[12]

The controlled structural response is obtained by adding to the uncontrolled response due to the point force excitation, the control field response due to the two one-sided piezoelectric patches. The optimal control voltage to each PZT is computed using standard linear quadratic optimal control theory (see, for example, Ref. 19), where the cost function to be minimized is a quadratic function of the control voltage amplitudes. It should be noted that this frequency domain optimal controller does not take into account the causality constraint inherent to a real-time implementation on a DSP. In other words, the optimal controller transfer functions in the frequency domain might be acausal and therefore impossible to reproduce using a digital filter. This results in overestimating the attenuation achieved by the controller, however, it does represent the maximum achievable attenuation if the system is causal. Also, the limitation due to the finite dynamic range of the analog to digital converters is not included in this model.
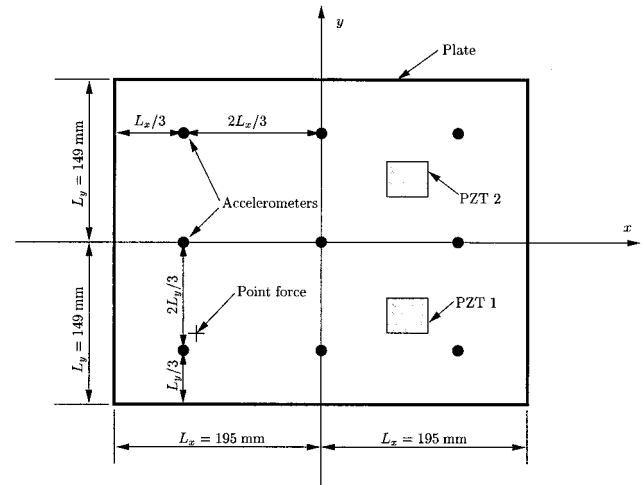
FIG. 1. Plate geometry and transducer locations.

As mentioned above, the plate is excited by a point force while two PZT patches are implemented to achieve control. Preliminary tests showed that a single piezoelectric actuator was not sufficient to achieve global sound radiation attenuation over the entire frequency bandwidth. The sensor based on unit transfer functions, i.e., estimating the structural net volume acceleration, provides one single error signal. To facilitate the comparison with the sensor based on far-field pressure estimates, only one far-field direction is considered. This control layout, i.e., two control outputs and one error input, results in an underdetermined system which is solved by including in the cost function the weighted control effort (sum of the square modulus of each control voltage) as an additional quantity to minimize, effectively constraining the solution. This second variable is scaled down (by varying its weighting) so that the main forces of the control are directing towards minimizing the error information rather than the control voltages.

II. SYSTEM CHARACTERISTICS

The system studied here is a model based on the plate tested experimentally in a previous paper.[14] The translation and rotation stiffness factors along each side of the plate were numerically adjusted in an effort to match the experimental natural frequencies. The resulting modeled boundary conditions were close to the simply supported case. The plate geometry is shown in Fig. 1 along with the location of the normal point force disturbance, the two PZT control inputs, and the nine accelerometers implemented in the discrete structural acoustic sensor. The physical parameters and dimensions for the plate and piezoelectric patches are shown in Table I. The point force and PZT center locations are presented in Table II. As mentioned earlier, the PZT patches are single-sided. The impact of the resulting asymmetry will be discussed later in the paper. The control actuator locations in Table II were optimally chosen for minimizing the (3,1) and (1,3) flexural modes, while the disturbance force location ensures all nine modes present in the bandwidth of interest are excited. Finally, the model's natural frequencies are shown in Table III.

TABLE I. Plate and PZT's dimensions and material properties.

Parameter	Plate	PZT
Length in x axis (mm)	380	38
Length in y axis (mm)	298	32
Thickness, h (mm)	1.93	0.1905
Young's modulus (N/m^2)	2.04×10^{11}	6.1×10^{10}
Poisson ratio	0.28	0.33
Mass density (kg/m^3)	7700	7750
Hysteretic damping factor	0.0005	0
d_{31} constant (m/V)	...	171×10^{-12}

TABLE III. Plate natural frequencies.

Mode (m,n)	Natural frequency (Hz)
(1,1)	86.0
(2,1)	181.2
(1,2)	241.4
(2,2)	332.7
(3,1)	339.1
(3,2)	484.6
(1,3)	494.5
(4,1)	557.7
(2,3)	580.7
(4,2)	695.5

The structure's response is computed over the frequency bandwidth, 50–650 Hz, with a 1-Hz increment. Note that the peak levels of the response at those frequencies is likely to be significantly below the actual resonance level reached at the resonance frequency: The small level of damping included in the system (see Table I) results in sharp resonance peaks relative to the above frequency resolution.

III. CONTROL PERFORMANCES

Figure 2 shows the sound radiated power plotted versus frequency for the uncontrolled plate (solid line) and the controlled plate using the two sensing approaches described earlier. The dashed line corresponds to the DSAS approach (pressure estimate based sensor) and the dotted line to the DSVAS approach (net volume acceleration based sensor). The direction of minimization for the DSAS approach is set to ($\theta = 36°$, $\phi = 30°$). This direction was chosen so that it does not coincide with any of the nodal lines of the radiation directivity of the modes present in the bandwidth. In other words, the sensor based on the far-field pressure estimate observes the radiation of all the flexural modes of the plate.

The first sensing approach of DSAS achieves good control over the entire bandwidth with a very small amount of spillover. The largest level of attenuation is obtained for mode (1,1) around 86 Hz. Very good attenuation is also seen for the other modes present in the frequency bandwidth except for the resonance at 333 Hz corresponding to the (2,2) mode of the plate. Around this frequency, the control system only reduces the radiated power level by about 10 dB. Looking at the pressure spatial directivity of the uncontrolled and controlled plate at this frequency reveals that the pressure distribution is slightly shifted along the ϕ direction so that the (2,2) mode radiation nodal lines go through the direction of minimization ($\theta = 36°$, $\phi = 30°$). In other words, the amplitude of this mode is not reduced. Indeed, the structural velocity distribution at this frequency shows hardly any changes between the uncontrolled and controlled responses. This phenomenon is commonly referred to as modal restructuring. This is a direct consequence of minimizing the sound

TABLE II. Transducer location.

Transducer type	Center coordinate, x/L_x	Center coordinate, y/L_y
Disturbance point force	−0.60526	−0.56376
Control PZT 1	0.41579	−0.45302
Control PZT 2	0.41579	0.38926

pressure field in a single direction. To obtain a larger level of sound power reduction, additional far-field pressure error estimates in other directions could be included in the control system. Or alternatively, a single error signal directly related to the radiated power would also provide better overall sound attenuation.

The latter solution motivates the use of a sensor based on net structural volume acceleration. The resulting error information directly relates to the volumetric modes of the radiators, i.e., the odd–odd modes for a plate. These modes are the most efficient radiators, and the sensor output is therefore directly related to sound radiated power. This approach corresponds to the dotted line where the sensor output is the sum of the nine acceleration signals (unit transfer function). As seen in Fig. 2, this second sensing approach performs well near the resonance frequencies of the odd–odd modes of the plate. On the other hand, the radiated power around the resonances of odd–even or even–even modes is not significantly reduced. The global radiation level of the (2,1) mode, for example, even increases after control. By definition, the net volume acceleration-based sensor does not observe any of the odd–even or even–even modes of the plate. Therefore the system is unable to effectively control these modes. However, they still contribute to the total radiated power, despite their lower radiation efficiency compared to the odd–odd modes. In fact for some frequencies they can radiate more power than volumetric modes.[3]
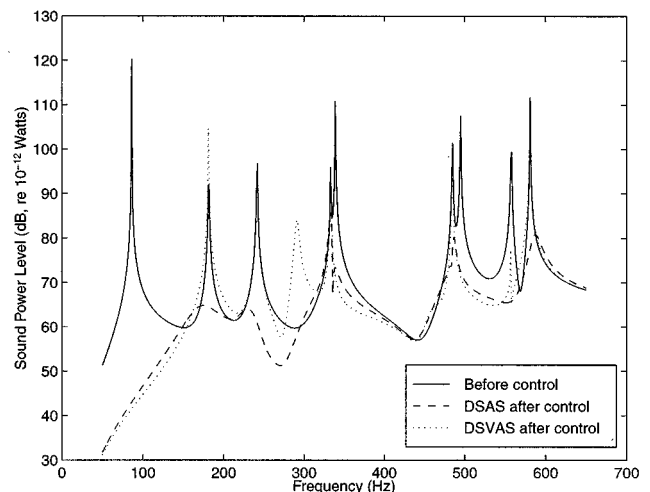
FIG. 2. Radiated power.

FIG. 3. Radiated power.

Attenuation (dB)	Mean-square velocity	Radiated power
Error mic.	17.7	23.8
DSAS	17.1	23.8
DSVAS (3×3)	5.5	10.1
DSVAS (20×20)	3.9	8.2
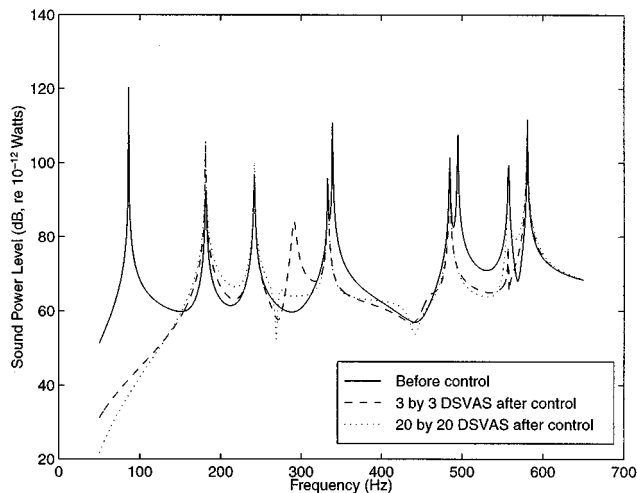
Another interesting feature of the control performance of the volume acceleration based sensor is the large control spillover occurring around 290 Hz. In this frequency range, the controlled structural response exhibits a velocity distribution which perfectly cancels the summation of the nine acceleration amplitudes. However, this velocity distribution radiates significantly in the far field which explains the control spillover. Examining the radiated power level at the resonance frequency of mode (4,1), significant reduction can be observed (dotted line) even though the symmetry of the velocity distribution associated with the (4,1) mode should cancel the sensor output. This phenomenon is explained by the presence of the two PZT patches in the model resulting in slightly asymmetric modes. These slight differences in magnitude and phase of the acceleration amplitudes measured at the nine locations shown in Fig. 1 result in a nonzero error signal amplitude. Note that these differences are averaged out when using a higher level of discretization. To illustrate this point, another simulation was performed where the sensor uses a 20×20 grid of acceleration point measurements to estimate the net volume acceleration. This level of discretization ensures an almost perfect estimate of the net volume acceleration in the frequency bandwidth of interest. Figure 3 shows the radiated power before (solid line) and after control using the previous 3×3 sensor (dashed line) and the 20×20 sensor (dotted line). The 20×20 sensor yields a much more accurate estimate of the net volume displacement. This is apparent around 558 Hz where the (4,1) mode is not observed by the sensor and results in no radiated power attenuation. Also, the system's behavior noticed in the case of the 3×3 sensor around 290 Hz no longer appears with the 20×20 sensor. In conclusion, even though the 3×3 sensor might yield larger global attenuation in some cases such as at a frequency around 558 Hz, a higher level of discretization ensures a better estimate of the net volume acceleration and thus enables the controller to observe all volumetric velocity distributions. Note that a PVDF continuous sensor designed to observe the same information is therefore likely to perform better compared to a 3×3 sensor. However, several authors have shown the difficulties of designing such a sensor with the required accuracy, especially for two-dimensional radiators.[9,11]

To summarize the above results, the reduction levels for the total mean-square velocity and sound radiated power computed over the frequencies of interest are shown in Table IV. The first line corresponds to an additional simulation case where the far-field pressure error estimate (sensor output) is replaced by the actual far-field pressure evaluated in the same direction. Note that this configuration nearly yields the same level of reductions as the pressure estimate structural sensor (DSAS). This demonstrates the ability of the sensor to replace far-field measurements as it was shown in previous work. On the other hand, the sensors based on the net volume acceleration (DSVAS) yield a small level of overall reduction (10 dB for the 3×3 sensor and 8 dB for the 20×20 sensor) when compared to the performance of the DSAS sensor. The higher levels of attenuation achieved by the 3×3 sensor are consistent with the curves of Fig. 3 discussed earlier. Despite strong attenuation levels at the resonance frequencies of the odd–odd modes, the overall reduction level remains small due to the remaining peaks in the controlled response of the odd–even and even–even modes.

IV. CONCLUSIONS

The discrete structural volume acceleration sensing (DSVAS) approach, i.e., based on unit transfer functions, performs well in the low-frequency range below the resonance of the first nonvolumetric mode of the plate. Due to its simplicity, it is the recommended method in this frequency range. At higher frequencies, the discrete structural acoustic sensing (DSAS) approach, i.e., based on radiation transfer functions, provides much increased performance due to the fact that it observes radiation from all modes. Thus near and above the resonance frequency of the first nonvolumetric mode, DSAS is the recommended sensing approach for ASAC.

ACKNOWLEDGMENTS

[1] C. R. Fuller, "Active control of sound transmission/radiation from elastic plates by vibration inputs. I. Analysis," J. Sound Vib. **136**, 1–15 (1990).
[2] C. R. Fuller, C. H. Hansen, and S. D. Snyder, "Active control of structurally radiated noise using piezoceramic actuators," in *Proceedings of Inter-Noise 89*, Newport Beach, CA, edited by G. C. Maling (Noise Control Foundation, Poughkeepsie, NY, 1989), pp. 509–511.
[3] C. R. Fuller, S. J. Elliott, and P. A. Nelson, *Active Control of Vibration* (Academic, London, 1996).
[4] C. K. Lee and F. C. Moon, "Modal sensors/actuators," Trans. ASME, J. Appl. Mech. **57**, 434–441 (1990).

[5] Yi Gu, R. L. Clark, C. R. Fuller, and A. C. Zander, ''Experiments on active control of plate vibration using piezoelectric actuators and polyvinylidene (PVDF) modal sensors,'' ASME J. Vib. Acoust. **116**, 303–308 (1994).

[6] R. L. Clark and C. R. Fuller, ''Modal sensing of efficient radiators with PVDF distributed sensors in active structural acoustic approaches,'' J. Acoust. Soc. Am. **91**, 3321–3329 (1992).

[7] G. V. Borgiotti, ''The power radiated by a vibrating body in an acoustic fluid and its determination from boundary measurements,'' J. Acoust. Soc. Am. **88**, 1884–1893 (1990).

[8] M. E. Johnson and S. J. Elliott, ''Volume velocity sensors for active control,'' Proc. Inst. Acoust. **15**, 411–420 (1993).

[9] J. Rex and S. J. Elliott, ''The QWSIS, a new sensor for structural radiation control,'' in *First International Conference on Motion and Vibration Control*, Yokohama (1992), pp. 339–343.

[10] C. Guigou, F. Charette, and A. Berry, ''Active control of sound by minimization of volume velocity on finite beam,'' in *Proceedings of the Third International Congress on Air- and Structure-Borne Sound and Vibration*, Montreal, edited by M. J. Crocker (ME Dept. Auburn University, Auburn, AL, 1994), pp. 1507–1514.

[11] C. Guigou, A. Berry, and F. Charette, ''Active control of plate volume velocity using shaped PVDF sensor,'' Adaptive Structures and Composite Materials: Analysis and Application ASME **45**, 247–255 (1994).

[12] J. P. Maillard and C. R. Fuller, ''Advanced time domain wave-number sensing for structural acoustic systems. I. Theory and design,'' J. Acoust. Soc. Am. **95**, 3252–3261 (1994).

[13] J. P. Maillard and C. R. Fuller, ''Advanced time domain wave-number sensing for structural acoustic systems. II. Active radiation control of a simply-supported beam,'' J. Acoust. Soc. Am. **95**, 3262–3272 (1994).

[14] J. P. Maillard and C. R. Fuller, ''Advanced time domain wave-number sensing for structural acoustic systems. III. Experiments on active broad-band radiation control of a simply-supported plate,'' J. Acoust. Soc. Am. **98**, 2613–2621 (1995).

[15] C. Guigou, Z. Li, and C. R. Fuller, ''The relationship between volume velocity and far-field radiated pressure of a planar structure,'' J. Sound Vib. **197**, 252–254 (1996).

[16] N. W. Hagood, W. H. Chung, and A. Von Flotow, ''Modeling of piezoelectric actuator dynamics for active structural control,'' AIAA J. **90(1087-CP)**, 2242–2256 (1990).

[17] A. Berry, J.-L. Guyader, and J. Nicolas, ''A general formulation for the sound radiation from rectangular, baffled plates with arbitrary boundary conditions,'' J. Acoust. Soc. Am. **88**, 2792–2802 (1990).

[18] A. Berry, ''Vibrations et rayonnement acoustique de structures planes complexes immergées dans un fluide léger ou dans un fluide lourd,'' Ph.D. thesis, Université de Sherbrooke, Sherbrooke, Canada, 1991.

[19] P. A. Nelson and S. J. Elliott, *Active Control of Sound* (Academic, London, 1992), pp. 416–420.

The measurement of coupling loss factors using the structural intensity technique

Ruisen Ming

Department of Mechanical and Materials Engineering, The University of Western Australia,
Nedlands 6907, Western Australia, Australia

The structural intensity technique can directly measure and distinguish power transmissions between different structural wavetypes across a joint, and its applications are numerous in practical engineering. In this paper, a new method is proposed for the measurement of coupling loss factors (CLFs) using the structural intensity technique. An outline of the method's theory is also given. Theoretically the proposed method gives an approximate estimation of CLFs. The approximate error depends on the ratios of the effective modal overlap factor of the receiving subsystem to the modal overlap factors of the subsystems coupled through the joint of interest. If the effective modal overlap factor of the receiving subsystem is large compared with the modal overlap factors of the coupled subsystems, the approximate error is small and negligible. A series of measurements were carried out to verify the outlined theory. The results measured on the joints with two subsystems showed that this proposed method can be used to accurately measure CLFs when the modal overlap factor of the receiving subsystem is larger than that of the source subsystem. The approximate error decreases with increasing frequency and the modal overlap factor ratio of the receiving subsystem to the source subsystem. © *1998 Acoustical Society of America.* [S0001-4966(98)02601-0]

PACS numbers: 43.40.At [CBB]

INTRODUCTION

Statistical energy analysis (SEA) is a powerful tool suitable for studying power transmission and energy distribution in large and complex structures. It has been used with considerable success in many areas such as spacecraft structures, ship structures, and building structures. In SEA a complex structure is divided into several subsystems.[1] One wavetype in a structural element is usually modeled as one subsystem. Therefore there could be more than one SEA subsystem in a structural element if there is more than one type of structural wave, which carries a similar level of energy. The coupling loss factor (CLF) is used for characterizing the power transmission between subsystems in SEA.[1,2] Several methods are available to measure CLFs, such as the direct method (where the power flow is directly measured using an impedance head or a force transducer and an accelerometer pair), the power injection method,[3] the energy level difference method,[4] and the mobility method.[1,5] The power injection method is widely used in both laboratory and field measurements. In this method, the dissipation and coupling loss factors of the system of interest are obtained by solving the energy balance equations where the elements of the coefficient matrix are the mean values of the measured energies. However, this method has two main disadvantages if the number of SEA subsystems is large. The first disadvantage is that it is very time consuming, especially in the cases where only a few of the CLFs need to be determined. The second disadvantage is that the energy coefficient matrix may be ill-conditioned since most of the elements in the coefficient matrix are zero.

By definition, the estimation of the CLF involves the measurement of the power flow across the joint and the energy stored at the source subsystem.[1] The net power flow can be measured using the structural intensity technique. Therefore it is of practical interest to employ the structural intensity technique to measure CLFs. In comparison with other power flow measurement techniques, the structural intensity technique offers two advantages. The first is that the net power flows associated with different structural wavetypes can be distinguished. This can result in an easy and quick measurement of the CLF between different wavetypes. The second is that the net power flow across a structural joint can be directly measured on the receiving structure. This will save time if only a few of the CLFs are required in a complex structure.

There are several structural intensity techniques. By comparison, the biaxial accelerometer technique[6] and the two-accelerometer array technique[7] are easy to implement in practice. Although these two techniques are established on the assumption that only traveling waves are present, the measurements on one-dimensional beams[8] and two-dimensional plates and walls[9] show that they can give reasonably accurate results even in the near-field where decaying waves are present. The bias error due to the presence of decaying waves is negligible if the intensity probe is located within half a wavelength from sources or coupling boundaries.[9]

In this paper, the measurement of CLFs using the structural intensity technique is studied. The theory is outlined and also verified experimentally.

I. MEASUREMENT OF POWER TRANSMISSION

In two-dimensional structures, the structural wave intensity vector may be determined from the intensity components measured in two orthogonal directions. In the far field, the expression for the x (or y) component of the spectral density

two-accelerometer array
technique probe

biaxial accelerometer
technique probe
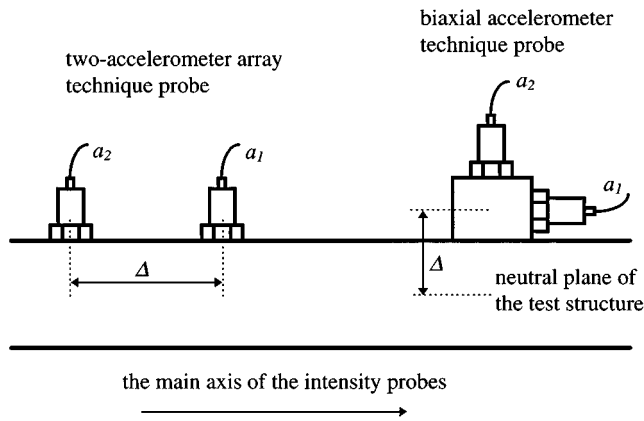
FIG. 1. Block diagram of two intensity probes.

FIG. 2. Block diagram of the test structures: (a) point coupling; (b) line coupling.

of the bending wave intensity in a two-dimensional plate is the same as that in a one-dimensional beam. That is[6,7]

$$I_x = \frac{2\sqrt{Bm_s}}{\omega^2} \, \mathrm{Im}\left\{ G\left(\frac{\partial a}{\partial x}, a\right) \right\}, \tag{1}$$

where B is the bending stiffness for a beam or the bending stiffness per unit width for a plate; m_s is the mass per unit length for a beam or the surface density for a plate; $\omega = 2\pi f$ is the radian frequency; $\mathrm{Im}\{G(\partial a/\partial x, a)\}$ is the imaginary part of the cross spectral density $G(\partial a/\partial x, a)$ between translational acceleration a and its first spatial derivative. A translational acceleration can be measured directly using an accelerometer, but the measurement of its first spatial derivative is not a straightforward procedure. For the biaxial accelerometer technique,[6] the first spatial derivative of a translational acceleration is indirectly measured using a rotational accelerometer, and the intensity probe is a biaxial (or triaxial) accelerometer, as shown in Fig. 1. For the two-accelerometer array technique,[7] the first spatial derivative of the translation acceleration is approximated from the translational accelerations measured at two neighboring positions close to the point of interest, and the intensity probe is a two-accelerometer array, as shown in Fig. 1. For each of these two intensity techniques, the intensity probe consists of two accelerometers. Equation (1) can be approximated by

$$I_x = \frac{2\sqrt{Bm_s}}{\omega^2 \Delta} \, \mathrm{Im}\{G(a_1, a_2)\}, \tag{2}$$

where a_1 and a_2 are the outputs of the accelerometers in the intensity probe and Δ is the accelerometer separation for the two-accelerometer array technique or the distance from the center axis of the rotational accelerometer to the neutral plane of the test structure for the biaxial accelerometer technique, as shown in Fig. 1.

The intensity probes of both the biaxial accelerometer technique and the two-accelerometer array technique have the same directivity function, i.e., $\cos\theta$ where θ is the angle from the main axis of the intensity probes. If the main axis of the intensity probes departs from the intensity vector direction in an angle of θ, the normalized measurement error is equal to $1-\cos\theta$ which is smaller than 10% (the bias error is less than 0.5 dB) if θ is less than 26°. The intensity probes
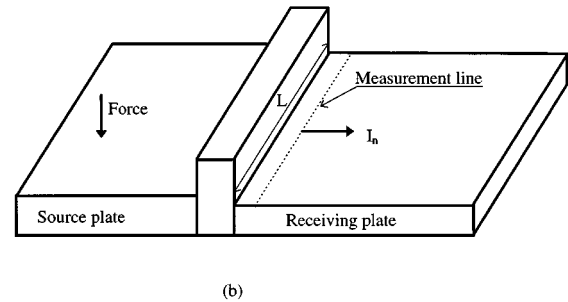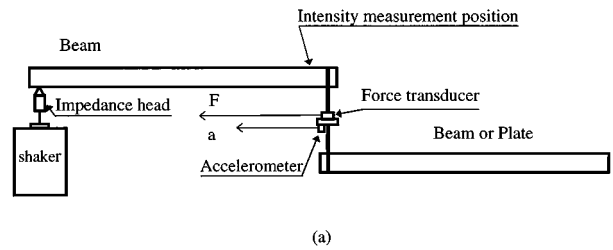
are insensitive to a small departure angle error. In practice, the departure angle is unlikely greater than 26°. Therefore this kind of error can be negligible in practical measurements.

The structural wave intensity represents the total power flow in a one-dimensional beam or the power flow per unit width in a two-dimensional plate. When beams are coupled at a point connection, the net power flow P can be measured at a position close to the connection point. When plates are connected along a line, the net power flow into a plate across the joint can be estimated from the averaged normal intensity component I_n, measured at positions along and close to the connection line on the plate of interest, as shown in Fig. 2(b),

$$P = I_n L, \tag{3}$$

where L is the coupling length at the joint. If the intensity probe departs from the normal direction at an angle θ, the mean value of the measured net power flow will be equal to $I_n L \cos\theta$ because the mean value of the intensity component in the direction parallel to the connection line is zero. For a small angle θ, the resulting error can be negligible.

II. MEASUREMENT OF COUPLING LOSS FACTOR

If N subsystems are coupled through a structural joint, the net power flow into the jth subsystem across the joint can be expressed as[1]

$$P = \sum_{\substack{k=1 \\ k \neq j}}^{N} \omega(\eta_{kj} E_k - \eta_{jk} E_j), \tag{4}$$

where η_{kj} is the CLF from the kth to jth subsystem and E_k is the energy stored in the kth subsystem. Combining Eqs. (3) and (4) gives

$$\eta_{ij} = \frac{I_n L}{\omega E_i} + \eta_{ji} \frac{E_j}{E_i} + \sum_{\substack{k=1 \\ k \neq i,j}}^{N} \left(\eta_{jk} \frac{E_j}{E_i} - \eta_{kj} \frac{E_k}{E_i} \right), \qquad (5)$$

where L is equal to 1 for a one-dimensional beam if the width of the beam is taken into account in the calculation of the intensity component I_n. In the above equation the first term characterizes the net power flow into the jth subsystem across the joint, the second term characterizes the power flow from the jth to ith subsystem and the third term characterizes the net power flow from the jth subsystem to other subsystems. It can be seen from the above equation that the determination of η_{ij} requires the simultaneous measurement of the intensity components and the energies stored in all the subsystems coupled through this joint. In addition it is necessary to know η_{jk} emanating from the jth subsystem and $\eta_{kj}(k \neq i)$ emanating from other subsystems to the jth subsystem through this joint. It is rarely possible, in practice, to obtain η_{ij} using the above equation.

If the ith subsystem is the only source subsystem, the third term in Eq. (5) relates to the net power flow between nonsource subsystems. If the modal overlap factor of the receiving subsystem is comparable with or greater than those of other subsystems which are coupled through this joint, the power flow from the source (ith) subsystem to the receiving (jth) subsystem will dominate the total net power flow into the receiving subsystem. By comparison, the power returning from the receiving (jth) subsystem to the source (ith) subsystem and the net power flow from the receiving subsystem to other nonsource subsystems should be small and their summation can be negligible. In this case, Eq. (5) can be approximated by

$$\eta_{ij} = \frac{I_n L}{\omega E_i}. \qquad (6)$$

It has been shown[1,2,10] that the damping in the receiving subsystem has a little (or strong) influence on the CLF when the modal overlap factor of the receiving subsystem is large (or less than 1). Therefore in the case where the modal overlap factors of all coupled subsystems are small, the increase of damping in the receiving subsystem will increase the power flow from the source subsystem to the receiving subsystem. This leads to the increase in the ratio of the first term to the sum of the second and third terms in Eq. (5), and then to the decrease in the approximate error of Eq. (6).

The approximate error for the estimation of the CLF using Eq. (6) depends on the modal overlap factor ratios of the receiving subsystem to the subsystems coupled via the joint of interest. If the modal overlap factor of the receiving subsystem is very large compared with those of the coupled subsystems, the power flow from the source subsystem to the receiving subsystem should be mainly dissipated in the receiving subsystem. The approximate error of Eq. (6) will be negligible. If the modal overlap factor of the receiving subsystem is relatively small compared with those of the coupled subsystems and the joint of interest is only the coupling boundary of the receiving subsystem, most of the power flow from the source subsystem into the receiving subsystem will be returned to the source subsystem or trans-

mitted to other coupled subsystems through the joint of interest. Only a small part of the power flow can be dissipated in the receiving subsystem. In this case, the neglect of the second and third terms in Eq. (5) may result in a large approximate error. However, if the receiving subsystem has a small modal overlap factor compared to the coupled subsystems and it is coupled with other nonsource subsystems with large modal overlap factors through other joints rather than the joint of interest, then the measured net power at the joint of interest will be dominated by the power flow from the source subsystem to the receiving subsystem. This means that the receiving subsystem has a large ''effective'' modal overlap factor and will ''absorb'' most of the power flow from the source subsystem through the joint of interest. The effective modal overlap factor is obtained by considering that the ''effective'' dissipation loss factor of the receiving subsystem is the sum of the dissipation loss factor of the receiving subsystem and the coupling loss factors from the receiving subsystem to the subsystems coupled through other joints rather than the joint of interest. In this case, the neglect of the second and third terms in Eq. (5) will result in a negligible approximate error.

Apart from the approximate error, other error sources for the measurement of CLFs using Eq. (6) are the intensity measurement errors[8,9,11] and the uncertainty in effective subsystem mass for nonideal structures. To improve the accuracy of this proposed method, these three factors must be considered simultaneously.

III. PREDICTION OF COUPLING LOSS FACTOR

In practice, the coupling loss factor is usually predicted using the ''traveling wave'' method where the subsystems are assumed to be semi-infinite.[1,2] Coupling loss factor η_{12} can be expressed in terms of the transmission coefficient τ as[1,2]

$$\eta_{12} = \alpha \tau, \qquad (7)$$

where α depends on the type of source structure. When the source structure is a one-dimensional beam, $\alpha = c_1/\omega L_1$, where c_1 and L_1 are the bending wave speed and the length of the beam, respectively.[12] When the source structure is a two-dimensional plate, $\alpha = c_1 L / \pi \omega S_1$ where S_1 is the surface area of the plate.[1,2]

If two semi-infinite uniform beams are lying in the same direction (along the X axis) and their ends are connected through a single bridge (a point joint), as shown in Fig. 2(a), where the bridge length is much smaller than the longitudinal wavelengths at the frequencies of interest, the moment-induced power transmission can be considered negligible in comparison with the force-induced power transmission.[2] The transmission coefficient τ can be derived by using the ''traveling wave'' method,

$$\tau = \frac{2(m_2 c_2 / m_1 c_1)}{[1 + (m_2 c_2 / m_1 c_1)]^2}, \qquad (8)$$

where m_i is the mass per unit length of beam i ($i = 1,2$). This equation shows that the transmission coefficient τ is independent of frequency. When two beams are made of the same

TABLE I. Physical and material properties of the test structures.

Coupling type	Subsystems	Length (m)	Width (mm)	Thickness (mm)	Density (kg/m^3)	Longitudinal wave speed (m/s)
Point coupling	beam 1	2.5	50	6	7800	5400
	beam 2	3.0	50	6	7800	5400
Point coupling	beam	2.5	50	6	7800	5400
	plate	2.0	1200	6	7800	5400
Line coupling	plate 1	0.9	800	2	7800	5400
	plate 2	1.1	800	2	7800	5400
	coupling beam	0.8	20	10	7800	5400

material, the transmission coefficient τ depends only on the ratio of the beam thicknesses. If two beams have the same thickness, τ becomes 0.5.

If the end of a semi-infinite uniform beam is coupled with an infinite uniform plate through a single bridge (a point joint) where the bridge length is much smaller than the longitudinal wavelengths at the frequencies of interest, the transmission coefficient τ from the beam to the plate can be derived by using the ''traveling wave'' method,

$$\tau = \frac{16}{21} \frac{16\sqrt{Bm_p}}{m_b c_1} \left[1 + \left(1 + \frac{16\sqrt{Bm_p}}{m_b c_1} \right)^2 \right]^{-1}, \qquad (9)$$

where m_b is the mass per unit length of the beam and m_p is the mass per unit area of the plate. When the beam and the plate are made of the same material and are of the same thickness, the CLF depends only on the thickness to length ratio of the beam. The above equation can be simplified as

$$\eta_{12} \approx \frac{b}{21L}, \qquad (10)$$

where b is the width of the beam. This equation shows that the coupling between beam and plate through a single bridge is much weaker than that through a clamped joint.[13]

If two semi-infinite uniform plates, which are made of the same material and are of the same thickness, are coupled through a uniform beam, as shown in Fig. 2(b), the transmission coefficient τ can be expressed as[2]

$$\tau = \frac{m_2 c_2}{m_1 c_1} \int_0^1 \frac{\beta_1^2 (4 + \beta_3 - \beta_2)^2}{\beta_1^2 (4 + \beta_3 - \beta_2 - \beta_2 \beta_3/2)^2 + (\beta_3 + \beta_1^2 \beta_2 - \beta_2 \beta_3 (1 - \beta_1^2)/4)^2} \, d(\sin \theta), \qquad (11)$$

where θ is the incident angle;

$$\beta_1 = \frac{\cos \theta}{\sqrt{1 + \sin^2 \theta}},$$

$$\beta_2 = \frac{k\sqrt{1 + \sin^2 \theta}}{\sqrt{Bm_p}} \left(\omega\Theta - \frac{Tk^2 \sin^2 \theta}{\omega} \right),$$

$$\beta_3 = \frac{\omega m_b - Bk^4 \sin^4 \theta / \omega}{k\sqrt{Bm_p}\sqrt{1 + \sin^2 \theta}},$$

k is the bending wave number; T and Θ are the torsional stiffness and the mass moment of inertia per unit length of the coupling beam, respectively.

IV. EXPERIMENTAL RESULTS

In order to justify the feasibility of the proposed method, i.e., the intensity method, a series of measurements were carried out under laboratory conditions. The predictions were made from the equations given in the above section. The CLF measured using the intensity method was compared with that measured using the direct method or the power injection method. The standard deviation of the CLF measured using the intensity method is the combined standard deviation[14] of the measured intensity level and the measured energy level. For the case where the power injection method is used as a reference method, the accuracy of the intensity method is assessed on the basis of the combined 95% confidence interval.

A. Test structures and instrumentation

Three types of coupled structures were tested, as shown in Fig. 2. The physical and material properties of the test structures are given in Table I. The beams and the plates were damped on one side using a free viscoelastic layer. In Fig. 2(a), the structures were coupled through a steel rod (5.1 mm in diameter) where a force transducer and an accelerometer were installed to measure the power flow. The length of the steel rod is much smaller than the longitudinal wavelengths in the frequency range of interest. During the measurements, only one beam was excited at its free end by a shaker fed with pseudo-random noise signals. For the line

Ruisen Ming: Measurement of coupling loss factors   404
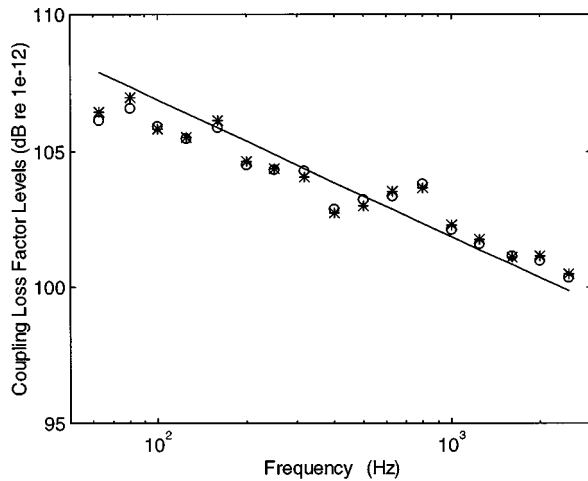
FIG. 3. Measured (*: direct method; ○: intensity method) and predicted (———) coupling loss factors between bending waves in two steel beams which are coupled through a steel rod at their ends.

FIG. 4. Measured and predicted coupling loss factors between bending waves from a steel beam to a steel plate which are coupled through a steel rod. *: measured using the direct method; ○: measured using the intensity method; ———: predicted using Eqs. (7) and (9); -----: predicted using Eq. (10).

coupling shown in Fig. 2(b), each plate was excited at three positions in turn by a shaker. For each excitation, the mean values of the structural intensity component in the direction normal to the coupling line and the energies stored in the plates were obtained respectively from 25 individual data.

The biaxial accelerometer technique[6] was used to measure the structural wave intensity. The phase difference in the intensity probe was smaller than $0.5°$ within the frequency range of interest ($f < 3$ kHz). This should result in a negligible phase-mismatching error. Before commencing every measurement, the accelerometers were calibrated using the B&K4294 calibration exciter. All the analyses were made in one-third octave frequency bands from 63 Hz to 2.5 kHz. To eliminate the effect of decaying waves, the distance between the intensity probe and the coupling boundary should be larger than half the wavelength of interest. For the measurement of power flow across a joint, however, the intensity probe should be located close to the coupling boundary. By considering these two factors, the distance was kept as a constant (0.2 m) in all intensity measurements. The effect of decaying waves can be neglected at frequencies above 364 Hz for the intensity measurement on the beams ($h = 6$ mm) and 121 Hz on the plate ($h = 2$ mm).

B. Measured results

Figure 3 shows the measured and predicted CLFs between bending waves in two uniform beams coupled through a steel rod (5.1 mm in diameter), as shown in Fig. 2(a). The modal overlap factor is larger than 0.21 for the source beam and 0.26 for the receiving beam at frequencies above 63 Hz. The prediction is made from Eqs. (7) and (8). Both the predicted and measured CLFs decrease with increasing frequency. Two measured CLF curves agree very well at all frequencies of interest. At 63 and 80 Hz, the direct method gives a slightly higher value than the intensity method. This could mainly result from the presence of decaying waves because the distance (0.2 m) between the coupling point and the intensity measurement position was smaller than one-

quarter of the wavelength. It was shown during the measurements that the narrow-band structural intensity curves measured at the connection ends of both source and receiving beams agree well with the power flow curve directly measured using the force transducer and the accelerometer in the frequency range of interest.
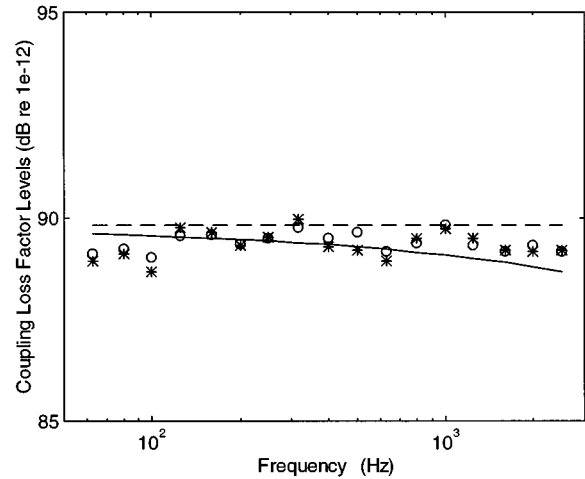
Figure 4 shows the comparison of the measured and predicted CLFs between bending waves from a steel beam to a steel plate. The beam and the plate were coupled through a steel rod (5.1 mm in diameter), as shown in Fig. 2(a). The modal overlap factor is larger than 0.21 for the beam and 0.73 for the plate at frequencies above 63 Hz. The CLF is predicted approximately using Eq. (10) and exactly using Eqs. (7) and (9). The approximate error of the prediction using Eq. (10) increases with increasing frequency but it is small at the frequencies of interest. The structural wave intensity was measured on the beam. Similarly to Fig. 3, the CLF measured using the intensity method agrees very well with the CLF measured using the direct method in all frequency bands of interest.

Figure 5 shows the comparison of the measured and predicted CLFs between bending waves in two uniform plates which were coupled through a uniform beam, as shown in Fig. 2(b). The modal overlap factor is larger than 0.51 for the source plate and 0.65 for the receiving plate at frequencies above 63 Hz. The power injection method[3] was chosen as a reference method in this case because the transmitted power between the plates cannot be directly measured. The level difference between two measured CLFs fluctuates around zero and most of them fall inside the combined 95% confidence interval, as shown in Fig. 6. At 100 and 500 Hz, the level differences fall outside the combined 95% confidence interval but they are very close to the upper limit. At 100 Hz, the large level difference could result from the error due to the effect of decaying waves. But the reason for the large level difference at 500 Hz is not clear. However, the level differences in all frequency bands of interest are
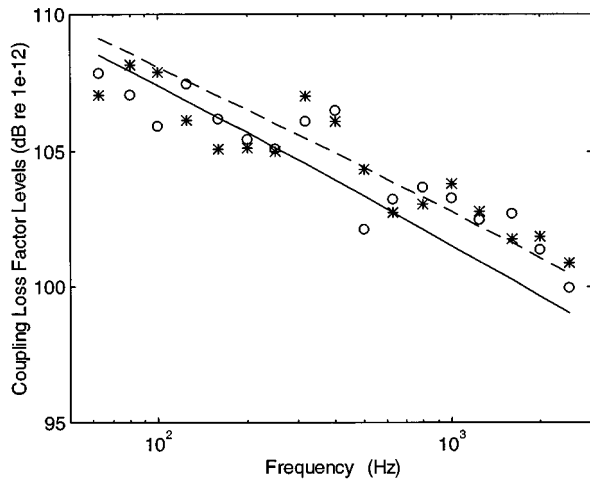
FIG. 5. Measured and predicted coupling loss factors between bending waves in two steel plates which are coupled through a steel beam. ∗: measured using the power injection method; ○: measured using the intensity method; -----: predicted by assuming that the incident angle is 90°; ———: predicted by assuming that the incident angle is from 0° to 90°.

smaller than 3 dB. From a practical point of view, the CLF measured using the intensity method is ''equal'' to the CLF measured using the power injection method. The prediction is made from Eqs. (7) and (11). At low frequencies the measured results agree with the predicted value where the incident angle θ is assumed to vary from 0° to 90° (solid line). At high frequencies the measured results agree with the predicted CLF where the incident angle θ is assumed to be 90° (broken line).

Figure 7 shows the approximate errors of the CLFs measured using the intensity method. They were calculated from Eqs. (5) and (6) by using the measured energies and the CLF η_{21} obtained from the consistency relationship[1] and the predicted modal densities in curves (○) and (×) or the CLF η_{21} measured using the power injection method in curve (∗). For all the cases, the modal overlap factors of the subsystems are less than 1 at low frequencies, but they increase with increas-
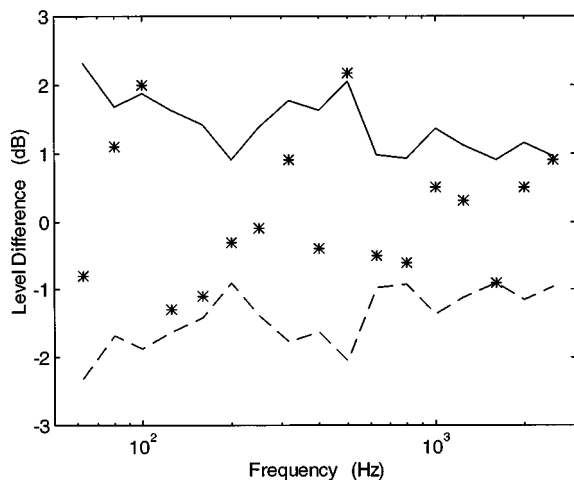
FIG. 6. The level difference (∗) between the CLFs measured using the power injection method and the intensity method and its combined 95% confidence interval (———: upper limit; ----: lower limit).
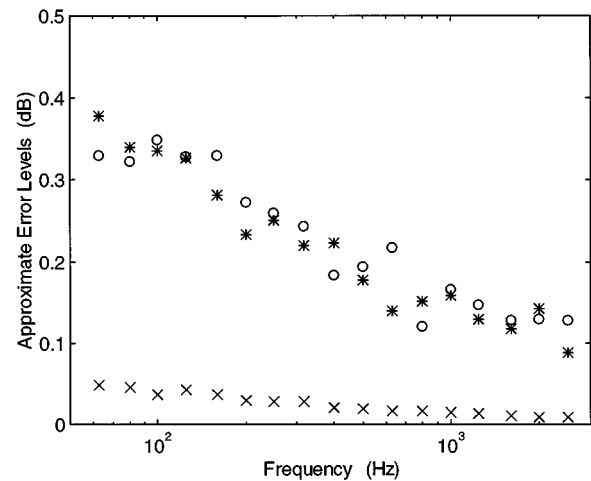
FIG. 7. The approximate errors of the CLFs measured using the intensity method. ○: beam to beam (point coupling); ×: beam to plate (point coupling); ∗: plate to plate (line coupling).

ing frequency and become greater than 1 at high frequencies. The modal overlap factor of the receiving subsystem is greater than that of the source subsystem. It can be seen that the approximate error decreases with increasing frequency and the modal overlap factor ratio of the receiving subsystem to the source subsystem. All the approximate errors are very small and negligible in the frequency bands of interest. This indicates that the approximate error depends on the modal overlap factor ratio of the receiving subsystem to the source subsystem rather than the modal overlap factor magnitude of the receiving subsystem. Equation (6) can give a very accurate estimation of CLFs as long as the modal overlap factor of the receiving subsystem is larger than that of the source subsystem.

V. CONCLUSIONS

A new method is proposed in this paper for the measurement of CLFs using the structural intensity technique. The outlined theory is experimentally verified in three cases. This proposed method gives an approximate estimation of CLFs. The approximate error depends on the ratios of the effective modal overlap factor of the receiving subsystem to the modal overlap factors of the subsystems coupled through the joint of interest. If the effective modal overlap factor of the receiving subsystem is large compared with the modal overlap factors of the coupled subsystems, the approximate error is small and negligible. For the joints with two coupled subsystems, the measured results show that CLFs can be accurately measured using this proposed method when the modal overlap factor of the receiving subsystem is larger than that of the source subsystem. The approximate error decreases with increasing frequency and the modal overlap factor ratio of the receiving subsystem to the source subsystem.

The structural intensity technique has the ability to distinguish different types of structural wave power flows. Therefore this proposed method has an advantage over other methods in the measurement of CLFs between different

wavetypes at a structural joint. However, this paper only studies the feasibility for applying this proposed method to measure the CLF between bending waves.

ACKNOWLEDGMENTS

[1] R. H. Lyon and R. DeJong, *Theory and Application of Statistical Energy Analysis* (Butterworth-Heinemann, Boston, 1995), 2nd ed.

[2] L. Cremer, M. Heckl, and E. E. Ungar, *Structure-borne Sound* (Springer-Verlag, Berlin, 1988).

[3] D. A. Bies and S. Hamid, ''In situ determination of loss and coupling loss factors by the power injection method,'' J. Sound Vib. **70**, 187–204 (1980).

[4] R. J. M. Craik, ''A study of sound transmission through buildings using statistical energy analysis,'' Ph.D. thesis, Heriot-Watt University, U.K. (1980).

[5] C. Cacciolati and J. L. Guyader, ''Measurement of SEA coupling loss factors using point mobilities,'' *Statistical Energy Analysis*, edited by A. J. Keane and W. G. Price (Cambridge U.P., Cambridge, England, 1997), pp. 35–45.

[6] D. U. Noiseux, ''Measurement of power flow in uniform beams and plates,'' J. Acoust. Soc. Am. **47**, 238–247 (1970).

[7] G. Pavic, ''Measurement of structure-borne wave intensity, part I: formulation of the methods,'' J. Sound Vib. **49**, 221–230 (1976).

[8] P. D. Bauman, ''Measurement of structural intensity: analytic and experimental evaluation of various techniques for the case of flexural waves in one-dimensional structures,'' J. Sound Vib. **174**, 677–694 (1994).

[9] R. S. Ming, ''The measurement of structural wave intensity applied to buildings,'' Ph.D. thesis, Heriot-Watt University, U.K. (1993).

[10] M. Heckl and M. Lewit, ''Statistical energy analysis as a tool for quantifying sound and vibration transmission paths,'' *Statistical Energy Analysis*, edited by A. J. Keane and W. G. Price (Cambridge U.P., Cambridge, England, 1997), pp. 19–34.

[11] R. S. Ming and R. J. M. Craik, ''Errors in the measurement of structure-borne power flow using two-accelerometer techniques,'' J. Sound Vib. **204**, 59–71 (1997).

[12] F. J. Fahy and A. D. Mohammed, ''A study of uncertainty in applications of SEA to coupled beam and plate systems, part I: computational experiments,'' J. Sound Vib. **158**, 45–67 (1992).

[13] R. H. Lyon and E. Eichler, ''Random vibration of connected structures,'' J. Acoust. Soc. Am. **36**, 1344–1354 (1964).

[14] J. R. Green and D. Margerison, *Statistical Treatment of Experimental Data* (Elsevier, New York, 1987).

Free and forced in-plane vibration of rectangular plates

N. H. Farag and J. Pan

Department of Mechanical and Materials Engineering, University of Western Australia, Nedlands, Western Australia 6907, Australia

A mathematical model is developed for the prediction of the forced response of finite plates to in-plane point force excitations. The model illustrates the nature of the coupling between in-plane longitudinal and in-plane shear waves and the resonant characteristics of the in-plane vibrational behavior of finite flat plates. The predicted resonance frequencies and mode shapes are compared against the finite element results and good agreement is found. The mode shapes of the in-plane vibration are depicted for frequencies below and above the first resonance frequency. It is illustrated by example that the input power due to in-plane force excitation at the in-plane resonance frequencies is at the same level as that due to out-of-plane force excitations at the flexural resonances in the same frequency band. The participation of the longitudinal and in-plane shear waves in transmitting the vibrational power and the resulting circulatory pattern of structural intensity is also presented. © *1998 Acoustical Society of America.* [S0001-4966(97)02112-7]

PACS numbers: 43.40.Dx [CBB]

LIST OF SYMBOLS

a,b,h	plate dimensions along the X, Y, Z directions, respectively
ρ	mass density
ν	Poisson's ratio
η	structural (hysteretic) damping coefficient
$\bar{E} = E(1 - i\eta)$	complex modulus of elasticity
$[X_e, Y_e]^T$	excitation force vector; the components are, respectively, the linear forces in X and Y directions
N_{xx}, N_{yy}, N_{xy}	in-plane force components (force per unit length) in the directions shown in Fig. 1
(x_e, y_e)	excitation position on the middle plane of the plate
u, v	components of the in-plane displacement in X and Y directions
ω	angular frequency (radian per second)
p,s (or q,r)	mode numbers
$D = Eh^3/12(1-\nu^2)$	flexural stiffness of the panel
$C_1^2 = E/\rho(1-\nu^2)$	square of the longitudinal wave speed in the panel
$C_s^2 = E/2\rho(1+\nu)$	square of the transverse (in-plane) shear wave speed in the panel

INTRODUCTION

The resonant response and power flow characteristics of the in-plane vibrations of finite flat panels is the concern of this paper. The boundary conditions considered here represent the practical case of flat plate panels fixed to frames from two parallel edges and to stiffening beams along the other two sides so that linear displacements along the boundaries can be considered negligible while rotational displacements are permissible. These correspond to the simply supported conditions for flexural vibration and the clamped conditions for the in-plane vibration.

The prediction of the in-plane dynamic response at in-plane resonances is of practical importance. This is because in most applications the forces transmitted to platelike structures, even if they are designed to be perpendicular to the middle plane of the plate panel, are practically inclined and have in-plane components due to imperfections in the manufacturing, assembly, or alignment of the supporting mounts.

Much effort has been devoted to the forced response of flexural vibrations in platelike structures. For example, the flexural response to point force and point moment excitations has been investigated for infinite plates in Ref. 1 and for finite plates in Ref. 2. In recent years, the in-plane vibrational response of single and coupled plates has attracted the attention of the researchers. While the forced response of the in-plane vibration of infinite plates can be found in many references (see, for example, Refs. 3 and 4), much less work is reported about the in-plane response of finite plates. References 5–9 report some of the present efforts to include the in-plane response into the predictions and measurements of the response to simultaneous flexural and in-plane excitations. They emphasize the importance of the in-plane response at high frequencies and in large coupled platelike structures.

While the resonance frequencies and mode shapes for flexural vibration are well documented,[10] similar information for the in-plane vibration, to the knowledge of the authors, is lacking.

In this paper, the equations of motion based on the assumptions of the thin plate theory and a hysterical damping model, which is important for the forced vibrational response

predictions, are presented. A solution to the two coupled equations of motion for forced in-plane vibration is developed taking into consideration the coupling between the longitudinal and in-plane shear waves. Power flow and structural intensity relations are derived. The resonance frequencies and mode shapes of in-plane vibration obtained from the present method are compared against the finite element predictions. Mode shapes are depicted for frequencies below and slightly above the first resonance frequency. The inplane frequency response, input power spectrums, and structural intensity characteristics are also presented and discussed. The input power to the same panel due to in-plane excitation is compared to that due to flexural excitation.

I. IN-PLANE VIBRATION OF THIN PLATE PANELS

In this section, the equations governing the in-plane forced vibration are presented. The assumptions leading to these equations will be briefly discussed together with the introduction of damping and the Dirac delta function representation of the concentrated excitation forces. A new method for the solution of the equations for the prediction of the free and forced in-plane response will be developed. The basic relations for input and transmitted power will be derived.

A. Equations of motion for forced in-plane vibration

The equations governing the forced vibration of thin plates excited by an in-plane excitation force vector $[X_e, Y_e]^T$ at a point (x_e, y_e) in the middle plane of the plate may be written in the form (see Refs. 7 and 10):

$$C_l^2 \frac{\partial^2 u}{\partial x^2} + C_s^2 \frac{\partial^2 u}{\partial y^2} + (\nu C_l^2 + C_s^2) \frac{\partial^2 v}{\partial x\, \partial y} - \ddot{u}$$

$$= -\frac{X_e}{\rho h} \delta(x - x_e) \delta(y - y_e), \qquad (1)$$

$$C_l^2 \frac{\partial^2 v}{\partial y^2} + C_s^2 \frac{\partial^2 v}{\partial x^2} + (\nu C_l^2 + C_s^2) \frac{\partial^2 u}{\partial x\, \partial y} - \ddot{v}$$

$$= -\frac{Y_e}{\rho h} \delta(x - x_e) \delta(y - y_e). \qquad (2)$$

The terms in the right-hand sides of Eqs. (1) and (2) are the equivalent distributed forces to the corresponding concentrated force components using Dirac delta functions. The positive directions of force and displacement components are illustrated in Fig. 1. They are defined such that positive force components when combined with the corresponding velocity components in the positive directions will produce power flowing in the positive directions of the coordinate axes.

The above equations are based on the assumptions of the thin plate theory for isotropic materials which are discussed in detail in Ref. 10. The basic assumption of small deflections and small slopes of the deformed shape leads to one equation representing the flexural vibration uncoupled from Eqs. (1) and (2) which together represent the in-plane vibration. The thin plate assumption also implies neglecting of shear deformation and rotary inertia and consequently puts a high-frequency limit to the solution.
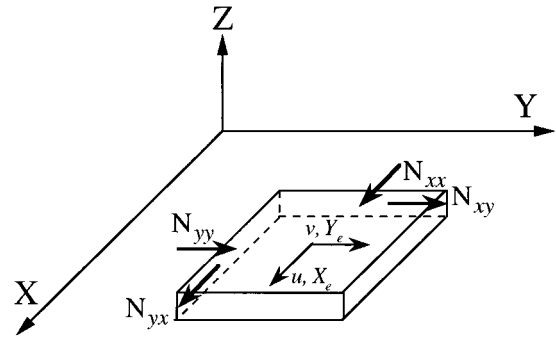
FIG. 1. Positive directions of in-plane force and displacement components on a plate element.

In the prediction of the forced response of structures, damping has to be introduced to the model to represent the practical damping in the structure and to prevent numerical instability at resonances. The structural (hysteretic) damping model is employed in this work via using the complex modulus $\bar{E}$.[2] The case of steady-state harmonic vibration and time dependence of the form $e^{-i\omega t}$ is considered in the present work. Consequently, $\ddot{u}$ and $\ddot{v}$ in the above equations may be replaced by $-\omega^2 u$ and $-\omega^2 v$, respectively, and the components of the excitation and response are represented by their complex amplitudes.

B. Forced response to in-plane excitation

To satisfy the clamped boundary conditions, a steady-state solution for harmonic time variation is assumed in the form:

$$u(x,y,t) = \sum_{p=1}^{\infty} \sum_{s=1}^{\infty} A_{ps} \sin \frac{p\pi x}{a} \sin \frac{s\pi y}{b} e^{-i\omega t}, \qquad (3)$$

$$v(x,y,t) = \sum_{p=1}^{\infty} \sum_{s=1}^{\infty} B_{ps} \sin \frac{p\pi x}{a} \sin \frac{s\pi y}{b} e^{-i\omega t}. \qquad (4)$$

Substitution into Eqs. (1) and (2) and using the orthogonality properties of the assumed mode shapes and the selective properties of the delta functions lead to the following equations for the modal amplitudes A_{ps} and B_{ps}:

$$\left[\left(\frac{p\pi C_l}{a} \right)^2 + \left(\frac{s\pi C_s}{b} \right)^2 - \omega^2 \right] A_{ps} + (\nu C_l^2 + C_s^2) \frac{4\pi^2}{ab} I_{B_{ps}}$$

$$= \frac{4X_e}{\rho h ab} \sin \frac{p\pi x_e}{a} \sin \frac{s\pi y_e}{b}, \qquad (5)$$

$$\left[\left(\frac{s\pi C_l}{b} \right)^2 + \left(\frac{p\pi C_s}{a} \right)^2 - \omega^2 \right] B_{ps} + (\nu C_l^2 + C_s^2) \frac{4\pi^2}{ab} I_{A_{ps}}$$

$$= \frac{4Y_e}{\rho h ab} \sin \frac{p\pi x_e}{a} \sin \frac{s\pi y_e}{b}, \qquad (6)$$

where

$$I_{A_{ps}} = \sum_{q=1}^{\infty} \sum_{r=1}^{\infty} \alpha_{ps,qr} A_{qr}, \qquad (7)$$
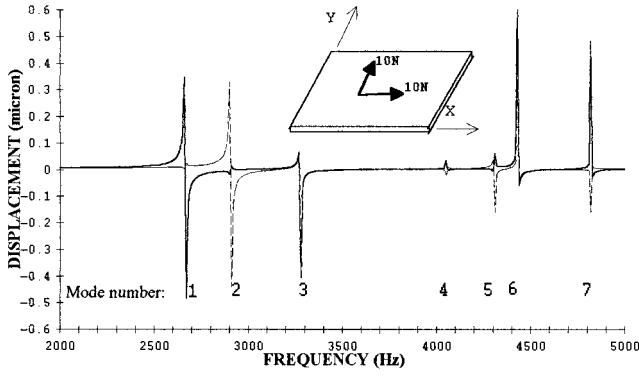
FIG. 2. In-plane displacement response to harmonic in-plane force excitation vector $[10,10]$ N; u: ——, v: -----.

$$I_{B_{ps}} = \sum_{q=1}^{\infty} \sum_{r=1}^{\infty} \alpha_{ps,qr} B_{qr}, \tag{8}$$

$$\alpha_{ps,qr} = -\frac{qr}{ab} \int_{x=0}^{a} \sin \frac{p\pi x}{a} \cos \frac{q\pi x}{a} \, dx$$

$$\times \int_{y=0}^{b} \sin \frac{s\pi y}{b} \cos \frac{r\pi y}{b} \, dy. \tag{9}$$

Evaluation of the integrals in (9) gives

$$\alpha_{ps,qr} = \frac{4}{\pi^2} \frac{(qr-ps)}{(p^2-q^2)(s^2-r^2)},$$

when both $(p+q)$ and $(s+r)$ are odd integers

$$= 0, \quad \text{otherwise.} \tag{10}$$

The coupling terms in Eqs. (5) and (6) highlight the nature of coupling to be due to two reasons: first, Poisson's effect as expressed by the term νC_l^2 and second, due to in-plane shear accompanying the in-plane longitudinal waves as indicated by the C_s^2 in the coupling term. Equation (10) describes the selection rule and coupling strength between modes.

While Eqs. (3), (4), (7), and (8) assume an infinite number of modes participating in the dynamic response, in the practical computations a limited number k is used. Equations (5) and (6) may be written in a more compact form as

$$K_{ps}^x A_{ps} + \sum_{q=1}^{k} \sum_{r=1}^{k} \alpha_{ps,qr} B_{qr} = F_{ps}^x, \tag{11}$$

$$K_{ps}^y B_{ps} + \sum_{q=1}^{k} \sum_{r=1}^{k} \alpha_{ps,qr} A_{qr} = F_{ps}^y. \tag{12}$$

Equations (11) and (12) have to be written for each pair of modes leading to $2 \times k \times k$ equations when k modes are used for both u and v. By matrix inversion, $k \times k$ complex amplitudes A_{ps} and the same number for B_{ps} are computed. These amplitudes are then used in Eqs. (3) and (4) to find the total response at any point (x,y) at any frequency. A convergence check has to be performed in the choice of the number of terms k in the series solution [Eqs. (11) and (12)]. Computational examples indicate that about ten terms may produce reasonable accuracy in the prediction of resonance frequencies and dynamic response (as compared to finite element predictions) in the frequency range covering approximately the first ten resonance modes. This means an inversion of a matrix of the order 200. The computational time and storage is still small as compared to the finite element requirement.

C. Input power due to in-plane excitation

The solution of Eqs. (11) and (12) gives the displacement vector at any point (x,y):

$$\mathbf{S}(x,y) = [u,v]^T. \tag{13}$$

For harmonic vibration and time variation of the form $e^{-i\omega t}$, the velocity vector is given by the relation

$$\dot{\mathbf{S}}(x,y) = -i\omega \mathbf{S}(x,y). \tag{14}$$

A diagonal matrix for the in-plane excitation force components

$$\mathbf{F}_{ed} = \begin{bmatrix} X_e & 0 \\ 0 & Y_e \end{bmatrix}$$

may be used to compute the input power by the components of the excitation force employing the relation

$$\mathbf{P}_e = \begin{bmatrix} P_{X_e} \\ P_{Y_e} \end{bmatrix} = \frac{1}{2} \operatorname{Re}\{\mathbf{F}_{ed}\dot{\mathbf{S}}^*(x_e, y_e)\}, \tag{15}$$

where the asterisk denotes the complex conjugate.

D. In-plane structural intensity

The internal forces (per unit width) on an infinitesimal plate element are shown in Fig. 1. According to the thin plate theory, these internal forces are related to the displacement components by the following relations:

$$N_{xx} = \frac{-Eh}{1-\nu^2} [u_{,x} + \nu v_{,y}], \tag{16a}$$

TABLE I. Resonance frequencies and mode shapes for in-plane vibration of a clamped panel.

Mode number (refer to Fig. 2)	1	2	3	4	5	6	7
Frequency Hz (present model)	2666	2906	3279	4052	4308	4431	4820
Frequency Hz (finite element)	2658	2898	3260	4024	4268	4404	4769
Percentage difference	0.3	0.3	0.6	0.7	1.0	0.6	1.1
Mode shape of u displacement	1,1	2,2	1,2	1,2	2,2	2,1	1,3
Mode shape of v displacement	2,2	1,1	2,1	2,1	3,1	3,2	2,2
Peak value of u (micron)	0.377	0.056	0.598	0.046	0.152	1.271	0.882
Peak value of v (micron)	0.041	0.495	0.680	0.044	0.312	0.680	0.471
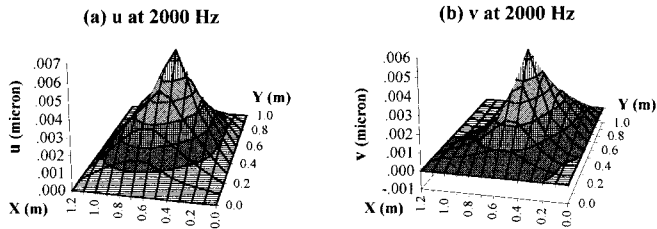
FIG. 3. Response to in-plane harmonic force vector [10,10] N below the first resonance frequency; (a) displacement in X direction, (b) displacement in Y direction.

$$N_{yy} = \frac{-Eh}{1-\nu^2}[v_{,y} + \nu u_{,x}],\qquad (16b)$$

$$N_{xy} = \frac{-Eh}{2(1+\nu)}[v_{,x} + u_{,y}].\qquad (16c)$$

The spatial derivatives $u_{,x}$, $u_{,y}$, $v_{,x}$, and $v_{,y}$ are obtained by direct differentiation of Eqs. (3) and (4) after substitution for the complex values of the modal amplitudes A_{ps} and B_{ps}.

For in-plane vibration in rectangular coordinates, the structural intensity vector $\mathbf{I}(x,y)$ has two components:

$$I_x(x,y) = \tfrac{1}{2}\,\mathrm{Re}\{N_{xx}(x,y)u^*(x,y) + N_{xy}(x,y)v^*(x,y)\},$$
$$(17a)$$

$$I_y(x,y) = \tfrac{1}{2}\,\mathrm{Re}\{N_{yy}(x,y)v^*(x,y) + N_{xy}(x,y)u^*(x,y)\}.$$
$$(17b)$$

In the right-hand side of each of the above two equations, the first term is the part of the power transmitted by the longitudinal wave (per unit width) and the second term is that part transmitted by the shear wave (per unit width).

II. COMPUTATIONAL EXAMPLES

A. In-plane vibration of a clamped plate panel

The modal coupling model described in the previous section is used to predict the in-plane dynamic response of a $1.2 \times 1.0 \times 0.025$-m^3 aluminum panel clamped at all edges. A Young's modulus of 70×10^9 N/m^2, density of 2700 kg/m^3, Poisson's ratio of 0.33, and a structural loss factor of 0.001 are assumed. The panel is excited at point (0.5,0.4) m by an in-plane force vector [10,10] N in the x and y directions, respectively, as shown schematically in the upper part of Fig. 2. The in-plane response spectrums for the displacement components u and v at the excitation point are shown in Fig.
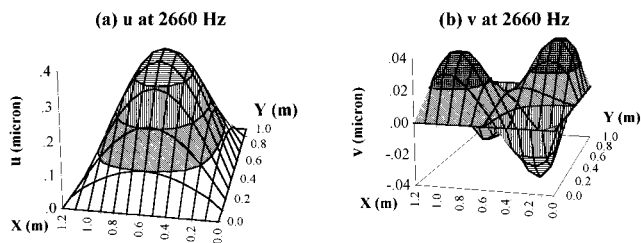
FIG. 4. Response to in-plane harmonic force vector [10,10] N at the first resonance mode: (a) displacement in X direction, (b) displacement in Y direction.

2 for the frequency range 2000–5000 Hz. The peak response corresponds to the resonance frequencies. The mode shapes may be viewed from the distributed response predicted at a grid of points at each resonance frequency. The frequency band 0–5000 Hz includes the first seven resonance frequencies for the in-plane vibration of the panel. To examine the accuracy of the present method, the resonance frequencies and mode shapes were also computed using the finite element method. The plate was modeled, using MSC NASTRAN, by 480 plate elements ($0.05 \times 0.05 \times 0.025$ m each) of the 4-node type. Table I presents a comparison between the present method and the finite element predictions of the resonance frequencies, the difference being within 1.1% in the frequency range investigated. In general, the finite element predictions become less accurate as the number of half-wavelengths of the mode shape increases due to the decreased number of elements representing a half-wavelength. The mode shapes predicted by both methods are very close. Below the resonant band of the first resonance frequency, the response is fully attenuated and the spatial distribution of the response takes the shape depicted in Fig. 3 with the u and v response being of the same order of magnitude, though about three orders of magnitude below the response values at the first resonance. The mode shapes of u and v are listed in Table I for the first seven resonance modes in terms of half-wavelengths in the X and Y directions, respectively. The mode shapes at the first resonance frequency are depicted in Fig. 4. The v displacement is about an order of magnitude below the u displacement for the first resonance. The situation is reversed in the second resonance. At the third resonance the two displacements are of the same order of magnitude (see Table I). In general the pattern of in-plane vibration is different for the different resonances.

It can be seen from Table I that modes 3 and 4 have the same mode shapes [(1,2) for u and (2,1) for v]. This is true because the plate response at the frequencies of examination is mainly represented by the coupling of (1,2) mode for u and (2,1) mode for v. The effect of coupling results in two resonance frequencies for each pair of coupled modes for u and v. The response at the higher-resonance frequency is much smaller than that of the lower-resonance frequency as shown in Fig. 2 for modes 3 and 4. The accuracy of the predictions of the present method depends upon the number of coefficients used in the series solution of Eqs. (11) and
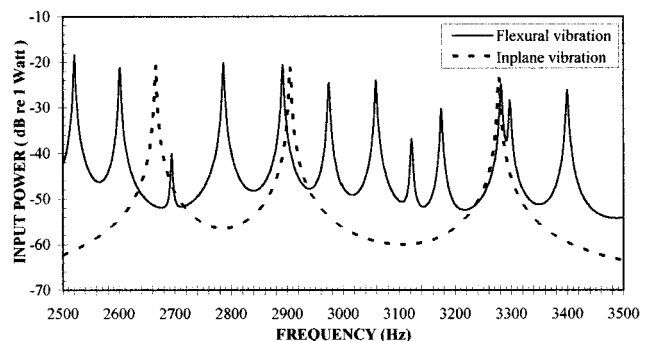
FIG. 5. Input power spectrums due to unit force excitations; (a) ———: out-of-plane force, (b) -----: in-plane force.
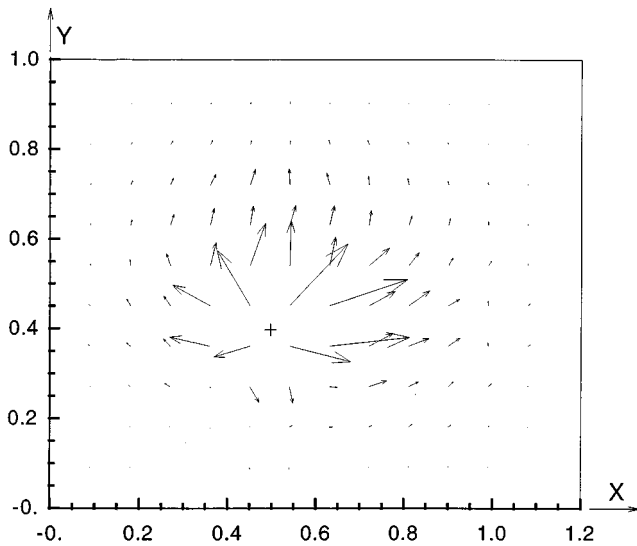
FIG. 6. In-plane structural intensity distribution in the panel at the first resonance frequency due to excitation $N_x = 10N$ at (0.5,0.4) m.

(12). In the present example ten coefficients are used for both u and v to obtain a solution correct to two significant digits.

B. In-plane versus flexural input power

The input power spectrum due to an in-plane harmonic force of magnitude 1.0 N at an angle of 45° to the X direction is calculated employing Eq. (15). The input power spectrum due to an out-of-plane excitation force of 1.0 N is also computed for the same plate and the same excitation position as in the previous example. Simply supported boundary conditions are used for the computation of the flexural response for the reasons discussed in the Introduction. The two spectrums of input power, due to in-plane and flexural excitation, are plotted in Fig. 5 for the frequency range 2500–3500 Hz. While the flexural input power includes 12 peaks corresponding to the dominant flexural modes (15 resonant flexural modes exist in this frequency band), the in-plane input power exhibits only three peaks due to the three resonances in this frequency band. The peak values of the input power are of the same level for both flexural and in-plane vibration but the nonresonance power due to in-plane vibration is more
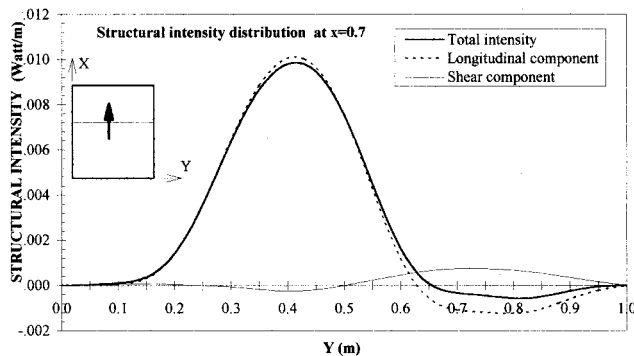
FIG. 7. Structural intensity distribution at cross section $x = 0.7$ m in the panel at the first resonance frequency due to excitation $N_x = 10N$ at (0.5,0.4) m.
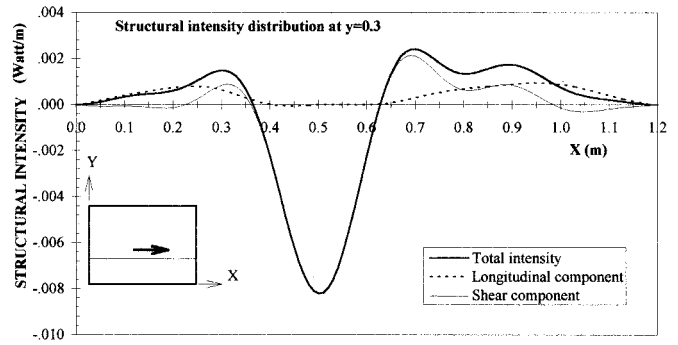
FIG. 8. Structural intensity distribution at cross section $y = 0.3$ m in the panel at the first resonance frequency due to excitation $N_x = 10N$ at (0.5,0.4) m.

than 10 dB lower than that of the flexural vibration. This suggests that the in-plane excitation is as important as the out-of-plane excitation as far as the resonance input power is concerned. It is important to identify the resonance frequencies for in-plane vibration and to be aware that, at these resonances, the power injected into the structure by the in-plane excitations is at the same level as the power injected by out-of-plane excitations of the same magnitude.

C. Structural intensity pattern of in-plane vibration

Figure 6 presents the structural intensity field in the flat panel of the previous example under in-plane force vector $[10,0]$ N near the first resonance frequency of the inplane response (2600 Hz). The qualitative picture of energy flow from the external excitation force into the panel is shown. The contribution of longitudinal and shear in transmitting the vibrational power is plotted in Fig. 7 at a cross section $x = 0.7$ m (I_x) and in Fig. 8 at a cross section $y = 0.3$ m (I_y). These two figures clearly illustrate the participation of both the longitudinal and in-plane shear waves in transmitting the vibrational power across the cross sections. The reason for the power flow towards the excitation point in some limited areas of the panel becomes evident. For example, Fig. 7 shows that the power flowing through the cross section $x = 0.7$ m is in the same direction as the excitation force (the positive X direction) between $y = 0.0$ m and $y = 0.651$ m. The vibrational power flows in a direction opposite to the excitation force between $y = 0.651$ m and $y = 1.0$ m. The net power flow across the whole cross section is in the positive X direction as to be expected.

III. CONCLUSIONS

The equations governing the in-plane vibrational response to a general in-plane force excitation vector are presented for thin plates of isotropic materials. Considering the coupling between the in-plane longitudinal and in-plane shear waves, a new method is developed for the prediction of the forced in-plane response, input power spectrums, and structural intensity distributions. The resonance frequencies and mode shapes of in-plane vibration obtained from the present method compare well with the finite element predictions at least in the frequency range examined. The nature of

the coupling between the in-plane longitudinal and in-plane shear waves in finite plate panels, their participation in the transmission of vibrational power, and the circulatory pattern of structural intensity are illustrated. It is shown by example that the input power due to in-plane force excitation at the in-plane resonance frequencies is at the same level as that due to out-of-plane force excitations at the flexural resonances in the same frequency band.

ACKNOWLEDGMENT

[1] H. G. D Goyder and R. G. White, ''Vibrational power flow from machines into built-up structures, Part 1: Introduction and approximate analyses of beam and plate-like foundations,'' J. Sound Vib. **86**, 59–75 (1980).

[2] W. Soedel, *Vibrations of Shells and Plates* (Marcel Dekker, New York, 1981).

[3] L. Cremer, M. Heckl, and E. E. Ungar, *Structure-Borne Sound* (Springer-Verlag, Berlin, 1988).

[4] K. F. Graff, *Wave Motion in Elastic Solids* (Clarendon, Oxford, 1975).

[5] J. L. Guyader, C. Boisson, and C. Lesueur, ''Energy transmission in finite coupled plates, Part 1: Theory,'' J. Sound Vib. **81**, 81–92 (1982).

[6] R. H. Lyon, ''Inplane contribution to structural noise transmission,'' Noise Control Eng. J. **26**, 22–27 (1986).

[7] B. A. Ovunc, ''Inplane vibration of plates under external disturbances applied at singular points,'' J. Thin-Walled Structures **18**, 83–95 (1994).

[8] J. S. Kim, H. S. Kim, H. J. Kang, and S. R. Kim, ''Effect of inplane modes in SEA on structure-borne noise transmission in ship structures,'' in *4th International Congress on Sound and Vibration* (The International Institute of Acoustics and Vibration, St. Petersburg, Russia, 1996), pp. 217–222.

[9] K. M. Liew, K. C. Hung, and M. K. Lim, ''Three-dimensional vibration of rectangular plates: variance of simple support conditions and influence of in-plane inertia,'' Int. J. Solids Struct. **31**, 3233–3247 (1994).

[10] A. Leissa, *Vibration of Plates* (Acoustical Society of America, Woodbury, NY, 1993).

Mean-square responses in a plate with sprung masses, energy flow and diffusion

Richard L. Weaver

Department of Theoretical and Applied Mechanics, University of Illinois, 104 South Wright Street, Urbana, Illinois 61801-2935

Diagrammatic multiple-scattering theory is applied to the calculation of ensemble average square responses in an infinite homogeneous plate in flexure attached to a random distribution of undamped sprung masses. This system is a prototypical example of a wave-bearing master structure with a locally reacting ''fuzzy'' substructure. Results for mean fields were obtained in an earlier work. Here it is found that fluctuations away from the mean are weak if the spectral and areal number density of sprung masses is great. A radiative transfer equation is found to govern the flow of energy on time scales greater than the inverse of the frequency, and a diffusion equation is found to govern the flow of energy at times greater than the dwell time of energy in the substructure. The diffusion rate is very slow if the dwell time in the substructure is long. The effect of true damping on these results is discussed. © *1998 Acoustical Society of America.* [S0001-4966(98)03601-7]

INTRODUCTION

The mean response of a random system, such as that of a previous study,[1] exhibits an apparent damping that is unrelated to true losses. This damping may be attributed to two distinguishable mechanisms. Random phase variations between responses in different realizations of an ensemble of random structures can result, when the ensemble average is taken, in destructive interference. The amplitude of the resulting average can thereby be unrepresentative of any single sample from the ensemble. Such apparent losses do not manifest in a single realization and are arguably of no practical relevance. Another mechanism is loss of energy as it flows from the master structure into dynamic degrees of freedom in the substructure. This latter mechanism is relevant to understanding the response of a single sample from the ensemble and is of great practical importance. On sufficiently long time scales, however, and as emphasized recently,[2–4] that energy can return to the master structure. In this sense the loss mechanism which was just termed the relevant one, is perhaps less effective than might otherwise have been thought.

While the ensemble average response $\langle G \rangle$ discussed in Ref. 1 does not allow one to distinguish between these mechanisms, or to describe the return of energy from the substructure to the master, the mean square $\langle G^2 \rangle$, which is essentially equivalent to energy density, does. Phase incoherence across an ensemble will not affect an average square, and so the less relevant part of apparent losses will not manifest in the evolution of $\langle G^2 \rangle$. The flow of energy into the substructure, however, will manifest as a diminishment of $\langle G^2 \rangle$ with time. The energy which was absorbed by the substructure will generally return in an incoherent fashion. It can therefore only be predicted by a calculation of mean energy, not by one of mean field.

Calculations of $\langle G^2 \rangle$ also allow evaluation of field variances $\langle G^2 \rangle - \langle G \rangle^2$ thereby measuring the fluctuations away from the mean and illuminating the extent to which the mean

Green's function $\langle G \rangle$ obtained in Ref. 1 represents actual responses in single samples from the ensemble.

It is the intent of the present paper to calculate mean-square responses in order to (a) evaluate variances thereby ascertaining the degree to which the results[1] for $\langle G \rangle$ represent actual responses and to (b) distinguish between the apparent loss mechanisms and to (c) study the flow of energy into and out of the substructure.

In the next section we define the chief quantity of present interest, the ensemble average of the square of the Green's function, Fourier transformed as appropriate. This quantity is loosely termed energy density. A diagrammatic multiple-scattering theory similar to that used elsewhere for calculations of electronic conductivity[5] and ultrasonic diffusion[6] is then presented for its evaluation, and a Bethe–Salpeter equation is derived which governs the evolution of energy density in the plate. A ladder approximation is introduced using the Foldy description[1] of the scattering from a single oscillator. A solution for the temporal and spatial Fourier transform of the mean-energy density is then obtained in closed form.

In Sec. II this solution is analyzed for the case of the area-integral of the energy density. The governing ordinary differential equations for this total energy are shown to describe, in the time domain, simple flow of energy into and out of the substructure. The solution is found to describe an asymptotic approach to equipartition between plate and substructure.

In Sec. III the full solution, without the area-integration, is shown to reduce to governing equations describing the propagation, scattering, absorption, and reemission of energy in the plate. An equation of radiative transfer, describing the evolution of specific intensity, is obtained on time scales comparable to or longer than the scattering time. This reduces to a diffusion equation for the energy density on time scales long compared to typical dwell times within the sub-

structure. Section IV briefly discusses the effect that true losses may have on this picture.

I. DIAGRAMMATIC MULTIPLE-SCATTERING THEORY FOR THE MEAN-SQUARE GREEN'S FUNCTION

This section is structured in a fashion parallel to Ref. 6. It begins by motivating the study of the triple Fourier transform of $\langle G^2 \rangle$, in time and space. It then derives, using diagrammatic multiple-scattering theory, a Bethe–Salpeter equation for that quantity. A closed-form solution to this equation for the triply Fourier transformed mean-square Green's function is then obtained.

A. Energy density

We begin by defining the areal energy density in the plate at position $\mathbf{x}$ due to an impulse applied at position $\mathbf{x}'$. The energy in the substructure is not included in the definition.

$$e(\mathbf{x},\mathbf{x}',t) = \tfrac{1}{2} m \dot{G}(t,\mathbf{x},\mathbf{x}')^2 + \text{strain energy density.} \quad (1)$$

The total energy density is equal, on suitable short-range spatial and temporal averaging, to twice the kinetic energy density. Thus we are led to define a quantity which is a temporal Fourier transform (on a time scale $\Omega^{-1} \gg \omega^{-1}$) associated with a bandpassed process:

$$e(\mathbf{x},\mathbf{x}',\Omega) = m \int_0^{\infty} \exp\{-i\Omega t\} |B * \dot{G}(t,\mathbf{x},\mathbf{x}')|^2 \, dt, \quad (2)$$

where B represents a moderately narrow (width $\Delta\omega$) and moderately well-damped bandpass process, centered at the frequency, ω, of interest. Ω is of the order of the inverse of the time scale on which the relatively slow evolution of the diffuse field is to be studied: $\Omega \ll \Delta\omega \ll \omega$. Ω may be termed the ''outer frequency,'' while ω is the ''inner'' frequency. The lower asterisk represents a temporal convolution. We also note that all poles of e must be in the upper half Ω plane.

By employing the Fourier representation of G, which is the inverse transform of Eq. (2) of Ref. 1, e may also be written as

$$e(\mathbf{x},\mathbf{x}',\Omega) = m \int_{-\infty}^{\infty} \int_{-\infty}^{\infty} \int_0^{\infty} \exp\{-i\Omega t + i\omega t - i\omega' t\} B(\omega)$$

$$\times B^*(\omega') G(\omega,\mathbf{x},\mathbf{x}') G^*(\omega',\mathbf{x},\mathbf{x}') \, \frac{dt \, d\omega \, d\omega'}{4\pi^2}, \quad (3)$$

where the raised asterisk indicates complex conjugation. The time integration may be extended to $-\infty$ [because $G(t)$ vanishes at negative times anyway] and performed, yielding a delta function; the ω' integration is then simple and one obtains:

$$e(\mathbf{x},\mathbf{x}',\Omega) = m \int_{-\infty}^{\infty} B\left(\omega + \frac{\Omega}{2}\right) B^*\left(\omega - \frac{\Omega}{2}\right) \left(\omega + \frac{\Omega}{2}\right)$$

$$\times \left(\omega - \frac{\Omega}{2}\right) G\left(\omega + \frac{\Omega}{2}, \mathbf{x}, \mathbf{x}'\right)$$

$$\times G^*\left(\omega - \frac{\Omega}{2}, \mathbf{x}, \mathbf{x}'\right) \frac{d\omega}{2\pi}. \quad (4)$$

As B is a smooth function with width $\Delta\omega \ll \omega$, and as $\Omega \ll \omega$,

$$e(\mathbf{x},\mathbf{x}',\Omega) \approx m \int_{-\infty}^{\infty} |\omega B(\omega)|^2 G\left(\omega + \frac{\Omega}{2}, \mathbf{x}, \mathbf{x}'\right)$$

$$\times G^*\left(\omega - \frac{\Omega}{2}, \mathbf{x}, \mathbf{x}'\right) \frac{d\omega}{2\pi}. \quad (5)$$

The substitution $\omega \pm \Omega/2 \sim \omega$ cannot be made in the factors G and G^* because they are not expected to be smooth functions of frequency, especially at large source–receiver separations $|\mathbf{x} - \mathbf{x}'|$. Equation (5) indicates that e is a frequency-weighted average of the product of two Green's functions at slightly different frequencies. By an ergodic hypothesis this frequency average is equivalent to an ensemble average and we may conclude

$$e(\mathbf{x},\mathbf{x}',\Omega) \approx 2m \frac{|\omega B(\omega)|^2 \Delta\omega}{2\pi} \left\langle G\left(\omega + \frac{\Omega}{2}, \mathbf{x}, \mathbf{x}'\right) \right.$$

$$\left. \times G^*\left(\omega - \frac{\Omega}{2}, \mathbf{x}, \mathbf{x}'\right) \right\rangle. \quad (6)$$

The extra factor of 2 is inserted to account for the, equal, contribution in the above integral from negative frequencies. It is most convenient to think of B as being unity across a band of width $\Delta\omega$ and to vanish outside this band. Then e is precisely areal energy density in that frequency band. We now drop the uninteresting prefactors and recognize that this quantity can depend only on $\mathbf{x} - \mathbf{x}'$, not on $\mathbf{x}$ and $\mathbf{x}'$ separately. Thus we are led to define a quantity which shall play the role of the spectral and areal energy density at position $\mathbf{r}$ due to a source at position 0.

$$E(\Omega,\mathbf{r}) \equiv \left\langle G\left(\omega + \frac{\Omega}{2}, \mathbf{r}, \mathbf{0}\right) G^*\left(\omega - \frac{\Omega}{2}, \mathbf{r}, \mathbf{0}\right) \right\rangle. \quad (7)$$

The structure is statistically homogeneous. It is therefore anticipated that the equations governing the evolution of E will decouple after a spatial Fourier transforming. The spatial Fourier transform is defined by:

$$E(\Omega,Q) \equiv \int d\mathbf{r} \exp\{iQ \cdot \mathbf{r}\} \left\langle G\left(\omega + \frac{\Omega}{2}, \mathbf{r}, \mathbf{0}\right) \right.$$

$$\left. \times G^*\left(\omega - \frac{\Omega}{2}, \mathbf{r}, \mathbf{0}\right) \right\rangle. \quad (8)$$

On sufficiently long length and time scales (Ω and $\mathbf{Q}$ small) this should reduce to

$$E = \frac{\text{constant}}{i\Omega + \mathscr{D}Q^2} \quad (9)$$

characteristic of the Fourier-domain solution of a diffusion equation; $\mathscr{D}$ is the diffusivity.

We now seek a multiple-scattering theory for E.

B. Diagrammatic multiple-scattering theory for energy density

The literature on multiple-scattering theory for waves in a random medium is extensive and the techniques used, especially the diagrammatic ones, are specialized. It is outside the scope of this paper to provide a review sufficient for all readers. Those unfamiliar with multiple-scattering theory or diagrammatic techniques may wish to refer to the recent paper by Photiades,[7] or to the tutorial by Frisch.[8] Alternatively a reader may wish to skip the remainder of this section and proceed directly to the later more physically based discussions.

We begin by defining a fourth rank spatial convolution operator

$$
{}_y^x H_{y'}^{x'}(\omega,\Omega) \equiv \left\langle G\left(\omega+\frac{\Omega}{2},\mathbf{x},\mathbf{x}'\right) G^*\left(\omega-\frac{\Omega}{2},\mathbf{x},\mathbf{x}'\right)\right\rangle
$$

$$
= \;\rule[0.5ex]{2.5em}{0.4pt} \tag{10}
$$

The spatial dependence has been written in this peculiar form, with superscripts, subscripts, prescripts, and postscripts in order to be consistent with the convention that adjacent indices are contracted and summed (integrated) over in analogy with matrix multiplication.

The outer product of G and G^* is written, in diagrammatic form, by making two copies of Ref. 1's expanded equations (27) and (39). For example, to second order in u,

$$\tag{11}$$

where it is understood that the operators in the lower parts of the diagrams are complex conjugates of the operators in the upper parts, and that they are evaluated at $\omega-\Omega/2$, while the upper parts are evaluated at $\omega+\Omega/2$. Except for the diagrams with links connecting upper and lower parts (like the fifth term on the right-hand side above), all other double diagrams are merely outer products of the single diagrams appearing earlier and their complex conjugates.

The notation may be illustrated by writing out a representative term. The fifth diagram on the right side is

$$
\sum_g \int\int\int d\mathbf{x}''\, d\mathbf{y}''\, d\mathbf{x}'''\, d\mathbf{y}'''\; G^0(\mathbf{x},\mathbf{x}'',\omega+\Omega/2) G^{0*}(\mathbf{y},\mathbf{y}'',\omega-\Omega/2)
$$

$$
\times u_g(\mathbf{x}'',\mathbf{x}''',\omega+\Omega/2) u_g^*(\mathbf{y}'',\mathbf{y}''',\omega-\Omega/2) G^0(\mathbf{x}''',\mathbf{x}',\omega+\Omega/2) G^{0*}(\mathbf{y}''',\mathbf{y}',\omega-\Omega/2). \tag{12}
$$

We define an ''intensity operator'' K as the sum of all uncuttable double diagrams. If the expansions are being done in terms of the scattering potentials u and not the scattering operators t, then K is expressed in terms of the u. To order u^4 it is:

$$
{}_y^x K_{y'}^{x'} = \blacksquare = \cdots \tag{13}
$$

K may also be written as a similar series, but with bold horizontal lines $\langle G \rangle$ instead of the thin line used in (13) representing G^0; in this case a few of the higher terms would drop out. K may also be expressed in terms of the scattering operators t. To order t^4 it is

$$\qquad\qquad\qquad\qquad\qquad\qquad\qquad\qquad\qquad (14)$$

where again the infinite series would be a little bit simpler if one used bold $\langle G \rangle$ instead of G^0.

On averaging, the resulting infinite series for H may be summed by writing a Bethe–Salpeter equation[3,7,8] for the mean double Green's function

$$\qquad\qquad\qquad\qquad\qquad\qquad\qquad\qquad\qquad (15)$$

or, in explicit form,

$$_y^x H_{y'}^{x'}(\omega,\Omega) = \langle G(\mathbf{x},\mathbf{x}',\omega+\Omega/2) G^*(\mathbf{y},\mathbf{y}',\omega-\Omega/2) \rangle = \langle G(\mathbf{x},\mathbf{x}',\omega+\Omega/2) \rangle \langle G^*(\mathbf{y},\mathbf{y}',\omega-\Omega/2) \rangle$$

$$+ \int \int \int \int d\mathbf{x}''\, d\mathbf{x}'''\, d\mathbf{y}''\, d\mathbf{y}''' \langle G(\mathbf{x},\mathbf{x}'',\omega+\Omega/2) \rangle \langle G^*(\mathbf{y},\mathbf{y}'',\omega-\Omega/2) \rangle _{y''}^{x''} K_{y'''}^{x'''}\, _{y'''}^{x'''} H_{y'}^{x'}(\omega,\Omega). \qquad (16)$$

Equation (15) may be proven by iterating it in powers of K and comparing the result with (11).

1. The Ladder approximations

The leading-order approximation for the intensity operator is, using the scattering potentials u:

$$\qquad\qquad\qquad\qquad\qquad\qquad\qquad\qquad\qquad (17)$$

or

$$_y^x K_{y'}^{x'} \approx \sum_g \langle u_g(\mathbf{x},\mathbf{x}';\omega+\Omega/2) u_g^*(\mathbf{y},\mathbf{y}';\omega-\Omega/2) \rangle = \rho \int_{-\infty}^{\infty} p(\varpi) d\varpi\, \phi(\varpi) \phi^*(\varpi) \delta^2(\mathbf{x}-\mathbf{y}) \delta^2(\mathbf{x}'-\mathbf{y}') \delta^2(\mathbf{x}-\mathbf{x}'). \qquad (18)$$
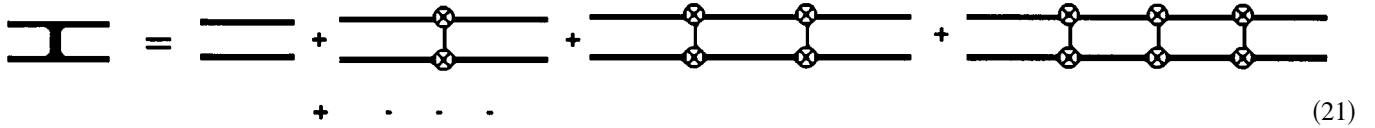
ϕ depends on ω; correspondingly one must understand that complex conjugation (asterisk) implies evaluation at $\omega-\Omega/2$, and unasterisked frequency-dependent quantities are evaluated at $\omega+\Omega/2$. Similarly, the leading-order approximation to K using the scattering operators is

$$\qquad\qquad\qquad\qquad\qquad\qquad\qquad\qquad\qquad (19)$$

or

$$_y^x K_{y'}^{x'} \approx \sum_g \langle t_g(\mathbf{x},\mathbf{x}';\omega+\Omega/2) t_g^*(\mathbf{y},\mathbf{y}';\omega-\Omega/2) \rangle = \rho \int_{-\infty}^{\infty} p(\varpi) d\varpi\, \tau(\varpi) \tau^*(\varpi) \delta^2(\mathbf{x}-\mathbf{y}) \delta^2(\mathbf{x}'-\mathbf{y}') \delta^2(\mathbf{x}-\mathbf{x}'). \qquad (20)$$

Both of these approximations are termed ''ladder'' approximations, because of the shapes of the diagrams obtained by expanding the Bethe–Salpeter equation for H in powers of K. For example, using the latter version:

$$\mathbf{I} \;=\; = \;+\; \text{(ladder diagrams)} \;+\; \text{(ladder diagrams)} \;+\; \text{(ladder diagrams)}$$
$$+\;\cdots \tag{21}$$

For each of these ladder approximations, and for the present case in which the scatterers are point scatterers, the intensity operator takes the form

$$\,^{x}_{y}K^{x'}_{y'} = \kappa(\omega,\Omega)\,\delta^2(\mathbf{x}-\mathbf{x}')\,\delta^2(\mathbf{y}-\mathbf{y}')\,\delta^2(\mathbf{x}-\mathbf{y}). \tag{22}$$

In the first-order smoothing approximation (FOSA) defined by Frisch,[8] and equivalent to (17), κ is given by

$$\kappa(\Omega)=\rho\int_{-\infty}^{\infty}p(\varpi)\phi(\varpi)\phi^{*}(\varpi)\,d\varpi=\rho\int_{-\infty}^{\infty}\frac{\omega_0/\pi}{\omega_0^2+\varpi^2}\frac{\omega^4 k^2}{[\varpi^2-(\omega-i\epsilon+\Omega/2)^2][\varpi^2-(\omega+i\varpi-\Omega/2)^2]}\,d\varpi. \tag{23}$$

The integrand has poles in the lower half plane at $\varpi=-i\omega_0$, $\varpi=\omega-\iota\epsilon+\Omega/2$, and $\varpi=-\omega-\iota\epsilon+\Omega/2$. Upon closing the contour and evaluating the residues one finds

$$\kappa=\frac{-2i\pi\rho\omega_0\omega^4 k^2}{\pi}\left[\left.\frac{1}{2\varpi(\varpi^2-(\omega-i\epsilon+\Omega/2)^2)(\varpi^2-(\omega+i\epsilon-\Omega/2)^2)}\right|_{\varpi=-i\omega_0}\right.$$
$$\left.+\frac{1}{\varpi^2+\omega_0^2}\frac{1}{2\varpi}\left.\frac{1}{(\varpi^2-(\omega+i\epsilon-\Omega/2)^2)}\right|_{\varpi=\omega-i\epsilon+\Omega/2}+\frac{1}{\varpi^2+\omega_0^2}\frac{1}{2\varpi}\left.\frac{1}{(\varpi^2-(\omega-i\epsilon+\Omega/2)^2)}\right|_{\varpi=-\omega-i\epsilon+\Omega/2}\right]. \tag{24}$$

Neglecting Ω compared to ω, this is

$$\kappa(\Omega)=-2i\rho\omega_0\omega^4 k^2\left[\frac{1}{(-2i\omega_0)(\omega_0^2+\omega^2)^2}+2\frac{1}{2\omega}\frac{1}{\omega^2+\omega_0^2}\frac{1}{2\omega\Omega}\right]=\rho k^2\frac{\omega^4}{(\omega_0^2+\omega^2)^2}+\rho k^2\frac{\omega_0\omega^2}{(\omega_0^2+\omega^2)i\Omega}. \tag{25}$$

In the Foldy approximation, equivalent to (19) and defined in Ref. 1, κ is

$$\kappa(\Omega)=\rho\int_{-\infty}^{\infty}p(\varpi)\tau(\varpi)\tau^{*}(\varpi)\,d\varpi=\rho\int_{-\infty}^{\infty}d\varpi\,\frac{\omega_0/\pi}{\omega_0^2+\varpi^2}\frac{\omega^2 k}{\varpi^2-(\omega+\Omega/2)^2-\omega^2 kG^0(\mathbf{0})}\frac{\omega^2 k}{\varpi^2-(\omega-\Omega/2)^2-\omega^2 kG^{0*}(\mathbf{0})}$$

$$=-2i\rho\omega_0\omega^4 k^2\left[\frac{1}{(-2i\omega)(\omega_0^2+\omega^2)^2}+2\frac{1}{2\omega}\frac{1}{\omega^2+\omega_0^2}\frac{1}{2\omega\Omega+2i\,\mathrm{Im}\{\omega^2 kG^0(\mathbf{0})\}}\right]$$

$$=\left[\frac{\rho\omega^4 k^2}{(\omega_0^2+\omega^2)^2}+\frac{\rho\omega_0\omega^2 k^2}{\omega^2+\omega_0^2}\frac{1}{i\Omega+k/8\sqrt{D}}\right] \tag{26}$$

again neglecting Ω and $\omega kG^0(\mathbf{0})$ in comparison with ω. In this analysis the infinitesimal ε has been neglected compared to the finite imaginary part of ωkG^0. If ε were finite, as it might be if it represented true viscous losses, it might not be neglectable. The first term of the above may be identified with the source of the energy which is promptly scattered from the substructure without entering the substructure. Similarly, the second term is identified with the source of the energy which sojourns in the substructure and leaks back on a time scale (a ''dwell time'') $t_{\mathrm{dwell}}=8\sqrt{D}/k$.

The ratio of the first term to the second term evaluated at $\Omega=0$, i.e., the total energy returned over all time, is

$$\frac{\text{promptly scattered energy}}{\text{absorbed and reradiated energy}}=\frac{\omega^2 k}{(\omega_0^2+\omega^2)\omega_0 8\sqrt{D}}=\frac{1}{\omega t_{\mathrm{dwell}}}\frac{\omega^3}{(\omega_0^2+\omega^2)\omega_0}. \tag{27}$$

If ω is of the order of ω_0 this is of the order of $\xi_{\mathrm{ism}}=\sigma_{\mathrm{ism}}/\omega=(\omega t_{\mathrm{dwell}})^{-1}$ and is, in those applications which consist of a high density of weak springs, very small. Thus most energy which scatters from the substructure does so with a long sojourn in the substructure, rather than scattering promptly without entering the substructure.

2. Equation for energy density

The form (22) for the intensity operator leads to a simple equation for the energy density. In either the Foldy or FOSA cases the Bethe–Salpeter equation becomes

$$
{}_y^x H_{y'}^{x'}(\omega,\Omega) = \langle G(\mathbf{x},\mathbf{x}',\omega+\Omega/2)\rangle\langle G^*(\mathbf{y},\mathbf{y}',\omega-\Omega/2)\rangle
$$
$$
+ \kappa(\omega,\Omega)\int d\mathbf{x}''\langle G(\mathbf{x},\mathbf{x}'',\omega+\Omega/2)\rangle
$$
$$
\times\langle G^*(\mathbf{y},\mathbf{x}'',\omega-\Omega/2)\rangle_{x''}^{x''}H_{y'}^{x'}(\omega,\Omega). \quad (28)
$$

The $\mathbf{x}=\mathbf{y}$ and $\mathbf{x}'=\mathbf{y}'$ components of H decouple from the others. The Bethe–Salpeter equation for these components is

$$
{}_x^x H_y^y(\omega,\Omega) = \langle G(\mathbf{x},\mathbf{y},\omega+\Omega/2)\rangle\langle G^*(\mathbf{x},\mathbf{y},\omega-\Omega/2)\rangle
$$
$$
+ \kappa(\omega,\Omega)\int d\mathbf{x}'\langle G(\mathbf{x},\mathbf{x}',\omega+\Omega/2)\rangle
$$
$$
\times\langle G^*(\mathbf{x},\mathbf{x}',\omega-\Omega/2)\rangle_{x'}^{x'}H_y^y(\omega,\Omega) \quad (29)
$$

or,

$$
E(\Omega,\mathbf{r}) = \langle G(\mathbf{r})\rangle\langle G^*(\mathbf{r})\rangle + \kappa(\Omega)\int d\mathbf{r}'\langle G(\mathbf{r}-\mathbf{r}')\rangle
$$
$$
\times\langle G^*(\mathbf{r}-\mathbf{r}')\rangle E(\Omega,\mathbf{r}'), \quad (30)
$$

which is a Bethe–Salpeter equation for the energy density. The dependence on inner frequency ω is now suppressed. That the Bethe–Salpeter equation reduces to an equation for energy density is not usual. It more commonly (e.g., Refs. 6 and 9) reduces to a radiative transfer equation governing the specific intensity. An equation governing just energy density is usually only derived in a long length scale diffusion limit.[6] That an equation for energy density is obtained directly in the present case may be traced to the special present circumstances in which the intensity operator K has the triple delta-function character seen in Eq. (22).

3. Solution of the Bethe–Salpeter equation

The Bethe–Salpeter equation (30) may be solved in the spatial Fourier transform domain. Upon substituting for $\langle G\rangle$ in terms of its spatial Fourier transform [Eq. (32) of Ref. 1], one obtains

$$
E(\Omega,\mathbf{r}) = \int\int\int\int \frac{\exp\{-i\mathbf{q}\cdot\mathbf{r}+i\mathbf{q}'\cdot\mathbf{r}\}d^2\mathbf{q}\,d^2\mathbf{q}'/16\pi^4}{[D\mathbf{q}^4-(\omega+\Omega/2)^2-\mathfrak{m}(\omega+\Omega/2)][D\mathbf{q}'^4-(\omega-\Omega/2)^2-\mathfrak{m}^*(\omega-\Omega/2)]}
$$
$$
+\int\int\int\int\int \frac{\kappa(\Omega)E(\Omega,\mathbf{r}')\exp\{-i\mathbf{q}\cdot(\mathbf{r}-\mathbf{r}')+i\mathbf{q}'\cdot(\mathbf{r}-\mathbf{r}')\}d^2\mathbf{q}\,d^2\mathbf{q}'\,d\mathbf{r}'/16\pi^4}{[D\mathbf{q}^4-(\omega+\Omega/2)^2-\mathfrak{m}(\omega+\Omega/2)][D\mathbf{q}'^4-(\omega-\Omega/2)^2-\mathfrak{m}^*(\omega-\Omega/2)]} \quad (31)
$$

$\mathfrak{m}$ is the mean field's self-energy[8] and was defined in Ref. 1. The integration over $\mathbf{r}'$ may be recognized to be a spatial Fourier transform of E. We also take a spatial Fourier transform of the entire equation to obtain:

$$
E(\Omega,\mathbf{Q}) = \int\int\int\int \frac{\delta^2(\mathbf{Q}+\mathbf{q}'-\mathbf{q})d^2\mathbf{q}\,d^2\mathbf{q}'/4\pi^2}{[D\mathbf{q}^4-(\omega+\Omega/2)^2-\mathfrak{m}(\omega+\Omega/2)][D\mathbf{q}'^4-(\omega-\Omega/2)^2-\mathfrak{m}^*(\omega-\Omega/2)]}
$$
$$
+\int\int\int\int \frac{\kappa(\Omega)\delta^2(\mathbf{Q}+\mathbf{q}'-\mathbf{q})E(\Omega,\mathbf{q}-\mathbf{q}')d^2\mathbf{q}\,d^2\mathbf{q}'/4\pi^2}{[D\mathbf{q}^4-(\omega+\Omega/2)^2-\mathfrak{m}(\omega+\Omega/2)][D\mathbf{q}'^4-(\omega-\Omega/2)^2-\mathfrak{m}^*(\omega-\Omega/2)]} \quad (32)
$$

or,

$$
E(\Omega,\mathbf{Q}) = \frac{1}{4\pi^2}\int\int \frac{d^2\mathbf{q}}{[D(\mathbf{q}+\mathbf{Q}/2)^4-(\omega+\Omega/2)^2-\mathfrak{m}(\omega+\Omega/2)][D(\mathbf{q}-\mathbf{Q}/2)^4-(\omega-\Omega/2)^2-\mathfrak{m}^*(\omega-\Omega/2)]}
$$
$$
+\frac{\kappa(\Omega)}{4\pi^2}\int\int \frac{d^2\mathbf{q}}{[D(\mathbf{q}+\mathbf{Q}/2)^4-(\omega+\Omega/2)^2-\mathfrak{m}(\omega+\Omega/2)][D(\mathbf{q}-\mathbf{Q}/2)^4-(\omega-\Omega/2)^2-\mathfrak{m}^*(\omega-\Omega/2)]}
$$
$$
\times E(\Omega,\mathbf{\Omega}). \quad (33)
$$

The above is a simple algebraic relation for E. If $C(\Omega,\mathbf{Q})$ is defined as the first term in the above:

$$
C(\Omega,\mathbf{Q}) \equiv \frac{1}{4\pi^2}\int\int \frac{d^2\mathbf{q}}{[D(\mathbf{q}+\mathbf{Q}/2)^4-(\omega+\Omega/2)^2-\mathfrak{m}(\omega+\Omega/2)][D(\mathbf{q}-\mathbf{Q}/2)^4-(\omega-\Omega/2)^2-\mathfrak{m}^*(\omega-\Omega/2)]} \quad (34)
$$

then it is concluded that E is

$$
E(\Omega,\mathbf{Q}) = \frac{1}{C(\Omega,\mathbf{Q})^{-1}-\kappa(\Omega)}. \quad (35)
$$

which solves the Bethe–Salpeter equation.

II. ANALYSIS OF THE SOLUTIONS AT $Q=0$

The above expression is a closed-form solution for the triple-Fourier transform of the mean-energy density. It is best understood by transforming back to the time and space domains. In this section we do so for the case $\mathbf{Q}=0$, that is, for the case

of area-integrated or total energy in the plate. The area integral of $\langle G \rangle^2$ is then compared to that of $\langle G^2 \rangle$. The difference is ascribed to fluctuations away from the mean and the conditions under which the difference is small are obtained.

At $\mathbf{Q}=0$, $E(\Omega,\mathbf{Q})$ represents the temporal Fourier transform of the area integral of the energy density in the plate. $C(\Omega,\mathbf{Q}=0)$ represents the temporal Fourier transform of the area integral of the energy density in the mean field $\langle G \rangle$. C is, for $\mathbf{Q}=0$,

$$C(\Omega,\mathbf{0}) = \frac{1}{4\pi^2} \int \int \frac{d^2\mathbf{q}}{[D\mathbf{q}^4 - (\omega+\Omega/2)^2 - \mathfrak{m}][D\mathbf{q}^4 - (\omega-\Omega/2)^2 - \mathfrak{m}^*]}, \tag{36}$$

where we have recognized that the ω dependence of $\mathfrak{m}$ is slow enough that $\mathfrak{m}(\omega\pm\Omega/2) \sim \mathfrak{m}(\omega)$. This integral may be performed exactly by (i) replacing the angular integration over the direction of $\mathbf{q}$ by a factor 2π, (ii) changing variables by defining $s=q^2$, and (iii) extending the integration range.

$$C(\Omega,\mathbf{0}) \equiv \frac{1}{8\pi} \int_{-\infty}^{\infty} \frac{ds}{[Ds^2 - (\omega+\Omega/2)^2 - \mathfrak{m}][Ds^2 - (\omega-\Omega/2)^2 - \mathfrak{m}^*]}. \tag{37}$$

This integrand has poles at $s=\pm[(\omega+\Omega/2)^2+\mathfrak{m}]^{1/2}/\sqrt{D}$ and at $s=\pm[(\omega-\Omega/2)^2+\mathfrak{m}^*]^{1/2}/\sqrt{D}$. We recall that $\mathfrak{m}$ has a negative imaginary part and close the contour in the lower half-plane:

$$C(\Omega,\mathbf{0}) \equiv -\frac{2i\pi}{8\pi} \left[\frac{1}{[Ds^2-(\omega+\Omega/2)^2-\mathfrak{m}][2Ds]} \right|_{s=-[(\omega-\Omega/2)^2+m^*]^{1/2}/\sqrt{D}}$$

$$\times \frac{1}{[2Ds][Ds^2-(\omega-\Omega/2)^2-\mathfrak{m}^*]} \Bigg|_{s=[(\omega+\Omega/2)^2+m]^{1/2}/\sqrt{D}} \Bigg]. \tag{38}$$

If Ω and Im $\mathfrak{m}/\omega$ are neglected compared to ω then

$$C(\Omega,\mathbf{0}) \equiv -\frac{i}{8\sqrt{D}\omega} \left[\frac{1}{\omega\Omega + i \text{ Im } \mathfrak{m}} \right]. \tag{39}$$

$C(\mathbf{Q}=0)$ represents the spatially integrated, or total, energy of the mean field in the plate $\int d\mathbf{x}\langle G \rangle^2$. It has a simple pole in the upper half-plane at $\Omega = -i$ Im $\mathfrak{m}/\omega$. Thus this energy decays in time like a simple exponential

$$E_{\langle G \rangle}(t) = \frac{1}{8\omega^2\sqrt{D}} \exp\{\text{Im } \mathfrak{m}t/\omega\}. \tag{40}$$

The decay is due to loss of energy into the substructure, and loss of phase coherence of the waves that scatter promptly from the sprung masses without entering the substructure.

Upon substituting this expression for C into (35) an expression for the mean total energy in the plate $\int d\mathbf{x}\langle G^2 \rangle$ is recovered:

$$E(\Omega,\mathbf{0}) = \frac{1}{C(\Omega,\mathbf{0})^{-1} - \kappa(\Omega)}$$

$$= \frac{1/8\omega\sqrt{D}}{i\omega\Omega - \text{Im } \mathfrak{m} - \kappa(\Omega)/8\omega\sqrt{D}}. \tag{41}$$

Various predictions for the evolution of the total energy density in the plate are obtained by substituting different approximations for $\mathfrak{m}$ and κ.

A. Total energy in an uncoupled plate

If $\mathfrak{m}$ and κ vanish (which occurs if ρ or k vanish, corresponding to a plate without a substructure) then $E(\Omega)$ scales inversely with Ω. In the time domain E is a step function

with a constant value for $t>0$ of $E(t)=1/8\omega^2\sqrt{D}$. Upon reinserting the "uninteresting pre-factors" that were removed following Eq. (6) this becomes

$$\int e(\mathbf{x},\mathbf{x}',t>0)d\mathbf{x} = 2m \frac{|\omega B(\omega)|^2 \Delta\omega}{2\pi} \frac{1}{8\omega^2\sqrt{D}}$$

$$= \frac{m|B(\omega)|^2\Delta\omega}{8\pi\sqrt{D_B/m}}. \tag{42}$$

$|B|$ must be set to unity if this is to represent actual energy.

This may be compared to a well-known result for the energy deposition from a concentrated impulse. A unit concentrated impulse generates, in an elastic body, an average amount of energy per mode of one over twice the mass of the body $M_{\text{body}}=Am$. If the impulse has magnitude m, then the energy deposited in a band is

$$\int e(\mathbf{x},\mathbf{x}',t>0)d^2\mathbf{x} = \frac{m^2}{2M_{\text{body}}} A\mathcal{N}\Delta\omega$$

$$= \frac{m}{2} \mathcal{N}\Delta\omega = \frac{m}{8\pi} \sqrt{\frac{m}{D_B}}\Delta\omega, \tag{43}$$

where $A\mathcal{N}\Delta\omega$ is the number of modes in the band spanned by $\Delta\omega$. This agrees with the above expression if $|B|=1$. Thus our complicated analysis has correctly predicted the behavior of the total plate energy in the absence of a substructure.

420   J. Acoust. Soc. Am., Vol. 103, No. 1, January 1998

Richard L. Weaver: Plate with sprung masses   420

B. Total energy in a coupled plate. FOSA

If $\mathfrak{m}$ and κ do not vanish, then E has a richer time dependence. The details depend on which approximation one invokes for the self energy and for the intensity operator. If one uses the FOSA, one finds that

$$\text{Im } \mathfrak{m}_{\text{FOSA}} = \text{Im } \mathfrak{m}_{\text{FOSA}-1} + \text{Im } \mathfrak{m}_{\text{FOSA}-2}$$

$$= -\frac{\rho k \omega \omega_0}{\omega_0^2 + \omega^2} - \frac{k^2 \rho \omega^4}{8\omega\sqrt{D}(\omega_0^2 + \omega^2)^2}, \tag{44}$$

while $\kappa(\Omega)$ is given by (25). $E(\Omega,0)$ is then,

$$E(\Omega,0) = \cfrac{1/8\omega\sqrt{D}}{i\omega\Omega + \cfrac{\omega\omega_0\rho k}{\omega^2 + \omega_0^2} + \cfrac{\omega^2\rho k^2}{(\omega^2 + \omega_0^2)^2 8\sqrt{D}} - \cfrac{1}{8\omega\sqrt{D}}\left[\cfrac{\omega^4\rho k^2\omega_0}{\omega_0(\omega^2 + \omega_0^2)^2} - \cfrac{i\omega^2\rho k^2\omega_0}{(\omega^2 + \omega_0^2)\Omega}\right]}$$

$$= \cfrac{1/8\omega\sqrt{D}}{i\omega\Omega + \cfrac{\omega\omega_0\rho k}{\omega^2 + \omega_0^2} + \cfrac{1}{8\sqrt{D}}\left[\cfrac{i\omega\rho k^2\omega_0}{(\omega^2 + \omega_0^2)\Omega}\right]} = \cfrac{1/8\omega^2\sqrt{D}}{i\Omega + \sigma_{\text{PSR}} - \sigma_{\text{PSR}}\sigma_{\text{ism}}/i\Omega}. \tag{45}$$

In the limit that ρk^2 is small, but ρk is not, the third term in the denominator is negligible, and E is seen to reduce to C and evolve like a decaying exponential. If one is interested, however, in arbitrarily late times (small Ω) then that term is not neglectable. An inverse temporal Fourier transform of the above will, if the term is not neglected, have contributions from two poles. One corresponds to the early time decay discussed above (the pole is at, approximately, $\Omega = i\omega_0\rho k/(\omega^2 + \omega_0^2) = i\sigma_{\text{PSR}}$); the other results in an exponentially slowly growing term (from a pole at, approximately, $\Omega = -ik/8\sqrt{D} = -i\sigma_{\text{ism}}$). The terms PSR (Pierce–Sparrow–Russell) and ISM (independent sprung mass) were defined in Ref. 1. Exponential growth is, at sufficiently late times, unacceptable. One of course expects that E should decay at early times as the energy leaks into the substructure, but eventually cease decaying as a dynamic equipartition is set up between the plate and the substructure, much as was observed in Refs. 2 and 3. Thus the FOSA has correctly indicated that the decay must cease, but it has not managed to describe a final steady-state equipartition. Its chief value is perhaps that it gives hints that the simple decay must be supplemented with something else at late times, and that the time scale for this supplementing is of the order of $(8\sqrt{D})/k$.

Some insight into the FOSA failure can be obtained by rewriting the above closed-form expression for $E(\Omega,0)$ as a time domain integro-differential equation for $E(t)$. This is done by replacing factors of $i\Omega$ with d/dt:

$$\frac{d}{dt}E(t) + \frac{\omega_0\rho k}{\omega^2 + \omega_0^2}E(t)$$

$$= \frac{\delta(t)}{8\omega^2\sqrt{D}} + \frac{k}{8\sqrt{D}}\int_0^t\left[\frac{\rho k\omega_0}{\omega^2 + \omega_0^2}\right]E(t')dt'. \tag{46}$$

In this form we see that E decays at the PSR decay rate due to the second term on the left side, but is augmented by a secondary source represented by the last term on the right corresponding to energy leaking from the substructure back into the plate. The integral in the last term is the total amount of energy which has leaked from the plate into the substructure. The factor $k/8\sqrt{D}$ represents a rate (inverse time) at which this energy leaks back. The failure of the FOSA can now be seen to be due to its failure to account, in this integrand, for the energy that has been reradiated out of the substructure. The integrand lacks a factor which diminishes the contribution, at time t, from energy deposited at times t' long before t.

This feature of the FOSA is related to the simple form that its intensity operator takes, in which $\kappa(\Omega)$ has a simple constant/$i\Omega$ dependence at small Ω. It says, therefore, that the energy in a single oscillator after being excited by an impulse achieves a constant value at late times. FOSA gives no indication that the oscillator must lose energy as it reradiates to the plate.

C. Total energy in a coupled plate. Foldy

The Foldy approximation intensity operator, however, does have the property of describing the loss of energy from the substructural oscillators as they reradiate to the plate. This is seen most readily in the form (26) for the Foldy $\kappa(\Omega)$ which has an inverse Fourier transform with a decay in time like $\sim\exp\{-kt/8\sqrt{D}\} = \exp\{-\sigma_{\text{ism}}t\}$. The FOSA expression (46) for $E(t)$ did not approach a constant at late times. E can do so only if its Fourier transform scales inversely with Ω at low Ω. If Foldy's $E(t)$ is to scale at low Ω like $\alpha/i\Omega$, where α is the late time steady-state energy density remaining in the plate, then its κ must approach, as Ω vanishes, a value $-8\omega\sqrt{D}$ Im$\{\mathfrak{m}\}$.

$$\lim_{\Omega\to 0}\kappa(\Omega) = -\text{Im}\{\mathfrak{m}\}8\omega\sqrt{D}. \tag{47}$$

A comparison of Eq. (26) and Eq. (57) of Ref. 1 does not readily show this to be the case. The identity is, however, a version of the optical theorem (38) of Ref. 1 relating Im$\{\tau\}$ and $|\tau|^2$. From that theorem, and the recognition that $\mathfrak{m}$ and κ are weighted averages of τ and $|\tau|^2$, respectively.

$$\mathfrak{m}_{\text{Foldy}} = \rho \int_{-\infty}^{\infty} d\varpi \, \frac{\omega_0/\pi}{\omega_0^2 + \varpi^2} \, \tau(\varpi)$$

and   (48)

$$\kappa(\Omega=0) = \rho \int_{-\infty}^{\infty} d\varpi \, \frac{\omega_0/\pi}{\omega_0^2 + \varpi^2} \, |\tau(\varpi)|^2$$

one deduces the above identity. In particular one deduces an expression for the imaginary part of $\mathfrak{m}_{\text{Foldy}}$.

$$-\operatorname{Im} \mathfrak{m}_{\text{Foldy}} = \frac{\rho \omega^3 k^2}{8\sqrt{D}(\omega^2 + \omega_0^2)^2} + \frac{\rho \omega \omega_0 k}{\omega^2 + \omega_0^2}$$

$$= \sigma_{\text{ism}} \sigma_{\text{PSR}} \frac{\omega^3}{(\omega^2 + \omega_0^2)\omega_0} + \omega \sigma_{\text{PSR}}$$

$$= \omega \sigma_{\text{PSR}} \left[1 + \frac{\sigma_{\text{ism}}}{\omega} \frac{\omega^3}{(\omega^2 + \omega_0^2)\omega_0} \right].$$ (49)

We therefore now substitute the Foldy $\kappa(\Omega)$ and Foldy $\mathfrak{m}$ into (41) to obtain:

$$E(\Omega, \mathbf{0}) = \frac{1/8\omega\sqrt{D}}{i\omega\Omega - \operatorname{Im} \mathfrak{m} - \kappa(\Omega)/8\omega\sqrt{D}}$$

$$= \frac{1}{8i\omega^2\sqrt{D}\Omega - [\kappa(\Omega) - \kappa(0)]}$$

$$= \frac{1}{8\omega^2\sqrt{D}i\Omega} \frac{1}{1 + \omega_0\rho k/[(\omega^2 + \omega_0^2)(i\Omega + k/8\sqrt{D})]}$$

$$= \frac{1}{8\omega^2\sqrt{D}i\Omega} \frac{1}{[1 + \sigma_{\text{PSR}}/(i\Omega + \sigma_{\text{ism}})]}.$$ (50)

By defining

$$F(\Omega) = \frac{\omega_0\rho k}{\omega^2 + \omega_0^2} \frac{1}{i\Omega + k/8\sqrt{D}} E(\Omega)$$

$$= \sigma_{\text{PSR}} [i\Omega + \sigma_{\text{ism}}]^{-1} E(\Omega)$$ (51)

and transforming Eqs. (51) and (50) to the time domain by means of the substitution $i\Omega \to d/dt$, one finds

$$\left(\frac{d}{dt} + \frac{k}{8\sqrt{D}} \right) F(t) = \frac{\omega_0\rho k}{\omega^2 + \omega_0^2} E(t),$$ (52a)

$$\left(\frac{d}{dt} + \frac{\omega_0\rho k}{(\omega^2 + \omega_0^2)} \right) E(t) = \frac{\delta(t)}{8\omega^2\sqrt{D}} + \frac{k}{8\sqrt{D}} F(t).$$ (52b)

It is seen that F represents the energy in the substructure. Equation (52a) indicates that F decays at a rate (inverse time) of $\sigma_{\text{ism}} = k/8\sqrt{D}$, and is augmented by the leaking from the plate into the substructure at a rate proportional to the energy in the plate E. Equation (52b) indicates that the energy in the plate decays due to leaking into the substructure at a rate (inverse time) of $\sigma_{\text{PSR}} = \omega_0\rho k/(\omega^2 + \omega_0^2)$ but is augmented by reradiation from the substructure. These equations can also be interpreted as time-domain SEA equations. The coupling factors, the coefficients of E and F in these equations, are σ_{ism} and σ_{PSR} and, in accordance with the

usual SEA prescriptions, are in a ratio [see Eqs. (12) and (13) of Ref. 1] of the modal densities.

Equation (52a) for F may be solved in terms of E and substituted into (52b). The result is an integro-differential equation for E:

$$\left(\frac{d}{dt} + \frac{\omega_0\rho k}{(\omega^2 + \omega_0^2)} \right) E(t) = \frac{\delta(t)}{8\omega^2\sqrt{D}} + \frac{k}{8\sqrt{D}} \int_0^t \frac{\omega_0\rho k}{(\omega^2 + \omega_0^2)}$$

$$\times E(t') \exp\left\{ -\frac{k(t-t')}{8\sqrt{D}} \right\} dt', \quad (53)$$

which has the character anticipated in the discussion following Eq. (46).

These differential-integral equations may also be solved in closed form by doing the inverse Fourier transform with respect to the outer frequency Ω. There are poles at $\Omega = 0$ and at $\Omega = i(\sigma_{\text{ism}} + \sigma_{\text{PSR}})$. The result is

$$E(t) = \frac{1}{8\omega^2\sqrt{D}} \frac{\sigma_{\text{ism}} + \sigma_{\text{PSR}} \exp\{-(\sigma_{\text{ism}} + \sigma_{\text{PSR}})t\}}{\sigma_{\text{ism}} + \sigma_{\text{PSR}}},$$ (54)

which is the multiple-scattering theory prediction for the time dependence of the total energy in the plate. This may be compared with the energy in the PSR response

$$E_{\text{PSR}}(t) = \frac{1}{8\omega^2\sqrt{D}} \exp\{-\sigma_{\text{PSR}}t\}$$ (55)

and with the energy in the mean field as predicted by the Foldy multiple-scattering theory

$$E_{\langle G \rangle}(t) = C(t) = \frac{1}{8\omega^2\sqrt{D}} \exp\{\operatorname{Im} \mathfrak{m}_{\text{Foldy}}t/\omega\}$$ (56)

both of which decay indefinitely. The actual energy (54) asymptotes at a level which is less than the amount of the original deposition. At late times a fraction

$$\frac{\sigma_{\text{ism}}}{\sigma_{\text{ism}} + \sigma_{\text{PSR}}} = \frac{\eta}{1 + \eta} = \frac{\mathcal{N}_{\text{plate}}}{\mathcal{N}_{\text{plate}} + \mathcal{N}_{\text{substructure}}}$$

remains, in accord with equipartition.

A comparison of $E_{\langle G \rangle}$ with E itself can reveal the degree of fluctuation away from $\langle G \rangle$. One quantity of interest for that comparison is a normalized variance, the ratio of the area average of the difference to the area average of E itself.

$$\text{nvar} \equiv \frac{E - E_{\langle G \rangle}}{E}$$

$$= \frac{\dfrac{\exp\{-(1+\eta)T\} + \eta}{1+\eta} - \exp\{-(1+\eta\xi)T\}}{\dfrac{\exp\{-(1+\eta)T\} + \eta}{1+\eta}}, \quad (57)$$

where T is a dimensionless time, $T = t\sigma_{\text{PSR}}$ and ξ is approximately the PSR loss tangent: $\xi = \sigma_{\text{PSR}}\omega^2/\omega_0(\omega^2 + \omega_0^2)$. At

short times $T \ll 1$ this vanishes; the variance is small; the mean field well describes actual responses. If η is small, in accord with the PSR limit, and if ξ is small, in accord with the applications envisioned here, then nvar does not approach unity until a time $T \sim -\log_e \eta$ at which time equipartition is nearly established. If η is not small, but only of order unity, however, corresponding to a substructure with a modal density comparable to the modal density of the plate, then nvar approaches unity at a time T of order one; that is, the mean field is a good description of an actual field only over a single PSR decay time, that is until time $t \sim 1/\sigma_{\text{PSR}}$. In either case one can state that the mean field is a good description of an actual field only until a time comparable to the time at which the energies equilibrate. This was a major goal of the present work, the assessment of the limits of applicability of the PSR theory. As expected, in the limit that the areal number density of sprung masses is infinite (and the spring stiffnesses are proportionally infinitesimal) the PSR theory becomes exact. It is found, however, that the time period over which the theory is good scales only with the logarithm of the number density of sprung masses. Therefore it is necessary to have an exponentially large number density of sprung masses if one is to have a merely algebraically long domain in which the PSR theory is accurate.

Another quantity of interest for comparison might be the absolute deviation from the PSR theory, rather than the fractional deviation. One then notes that $E - E_{\langle G \rangle}$ peaks at a time T of order log η and takes a value there of order η. Thus small η corresponds to small absolute differences of order η; one need have only an algebraically large number of sprung masses to have algebraically weak fluctuations away from the mean.

III. SOLUTION AT $Q \neq 0$

If $\mathbf{Q} \neq 0$ it becomes necessary to evaluate the integral (34). That integral may be rewritten using partial fractions:

$$C(\Omega, \mathbf{Q}) = \int \int d^2\mathbf{q} \left[\frac{J/4\pi^2}{[D(\mathbf{q}+\mathbf{Q}/2)^4 - (\omega+\Omega/2)^2 - \mathfrak{m}(\omega+\Omega/2)]} - \frac{J/4\pi^2}{[D(\mathbf{q}-\mathbf{Q}/2)^4 - (\omega-\Omega/2)^2 - \mathfrak{m}^*(\omega-\Omega/2)]} \right], \quad (58)$$

where J is defined by

$$J^{-1} \equiv D[(\mathbf{q}-\mathbf{Q}/2)^4 - (\mathbf{q}+\mathbf{Q}/2)^4] - [(\omega-\Omega/2)^2 - (\omega+\Omega/2)^2] - [\mathfrak{m}^* - \mathfrak{m}]. \quad (59)$$

As $\omega \ll \Omega$, and similarly $Q \ll q$ (corresponding to length scales for the analysis of the diffuse field that are greater than wavelengths,) J^{-1} may be approximated by neglecting terms of order DQ^3q in comparison to DQq^3:

$$J^{-1} = D[-4\mathbf{q}^2\mathbf{q}\cdot\mathbf{Q}] + 2\omega\Omega + 2i \text{ Im}\{\mathfrak{m}\}. \quad (60)$$

Thus C becomes

$$C(\Omega, \mathbf{Q}) = \int \int \frac{d^2\mathbf{q}}{4\pi^2} \left[\frac{1}{[D(\mathbf{q}+\mathbf{Q}/2)^4 - (\omega+\Omega/2)^2 - \mathfrak{m}(\omega+\Omega/2)]} \right] \left[\frac{1}{D[-4\mathbf{q}^2\mathbf{q}\cdot\mathbf{Q}] + 2\omega\Omega + 2i \text{ Im}\{\mathfrak{m}\}} \right]$$

$$- \int \int \frac{d^2\mathbf{q}}{4\pi^2} \left[\frac{1}{[D(\mathbf{q}-\mathbf{Q}/2)^4 - (\omega-\Omega/2)^2 - \mathfrak{m}^*(\omega-\Omega/2)]} \right] \left[\frac{1}{D[-4\mathbf{q}^2\mathbf{q}\cdot\mathbf{Q}] + 2\omega\Omega + 2i \text{ Im}\{\mathfrak{m}\}} \right]. \quad (61)$$

We may, in the first integral, change variables by letting $\mathbf{q}' = \mathbf{q} + \mathbf{Q}/2$, and in the second integral by letting $\mathbf{q}' = \mathbf{q} - \mathbf{Q}/2$. Invoking once more the approximation $Q \ll q$, one finds

$$C(\Omega, \mathbf{Q}) = \int \frac{q' \, dq'}{4\pi^2} \int d\theta \left[\frac{1}{[Dq'^4 - (\omega+\Omega/2)^2 - \mathfrak{m}(\omega+\Omega/2)]} \right] \left[\frac{1}{D[-4q'^3 Q \cos \theta] + 2\omega\Omega + 2i \text{ Im}\{\mathfrak{m}\}} \right]$$

$$- \int \frac{q' \, dq'}{4\pi^2} \int d\theta \left[\frac{1}{[Dq'^4 - (\omega-\Omega/2)^2 - \mathfrak{m}^*(\omega-\Omega/2)]} \right] \left[\frac{1}{D[-4q'^3 Q \cos \theta] + 2\omega\Omega + 2i \text{ Im}\{\mathfrak{m}\}} \right], \quad (62)$$

where θ is the angle between $\mathbf{Q}$ and $\mathbf{q}$. As the first factors are singular near $q' = (\omega^2/D)^{1/4}$, q' may be approximated in the second factor by $q' = (\omega^2/D)^{1/4}$. Thus the angular and magnitude integrations above decouple:

$$C(\Omega, \mathbf{Q}) = \frac{1}{2\pi} \int_0^\infty q' \, dq' \left[\frac{1}{[Dq'^4 - \omega^2 - \mathfrak{m}]} - \frac{1}{[Dq'^4 - \omega^2 - \mathfrak{m}^*]} \right] \frac{1}{2\pi} \int_0^{2\pi} d\theta$$

$$\times \frac{1}{D[-4(\omega^2/D)^{3/4} Q \cos \theta] + 2\omega\Omega + 2i \text{ Im}\{\mathfrak{m}\}}. \quad (63)$$

The integrals over q' have been done previously. Neglecting corrections of order $\mathfrak{m}/\omega^2$, one obtains

$$C(\Omega, \mathbf{Q}) = \frac{-i}{8\omega\sqrt{D}} \frac{1}{2\pi} \int_0^{2\pi} d\theta \frac{1}{D[-2(\omega^2/D)^{3/4} Q \cos \theta] + \omega\Omega + i \text{ Im}\{\mathfrak{m}\}}, \quad (64)$$

which may be seen to reduce correctly to (39) for $Q=0$.

The above integral may be done exactly:

$$C(\Omega,\mathbf{Q}) = \frac{i}{8\omega D^{3/4}\omega^{3/2}Q} \frac{1}{2\pi} \int_0^{2\pi} d\theta \frac{1}{2\cos\theta - \beta}, \quad (65)$$

where

$$\beta \equiv \frac{\omega\Omega + i \text{ Im}\{\mathfrak{m}\}}{D^{1/4}\omega^{3/2}Q}. \quad (66)$$

Changing variables by $z = \exp(i\theta)$ one finds

$$C(\Omega,\mathbf{Q}) = \frac{i}{8\omega D^{3/4}\omega^{3/2}} \frac{1}{Q2i\pi} \oint_{|z|=1} dz \frac{1}{z^2 - \beta z + 1}, \quad (67)$$

where the integration is counterclockwise. By means of the Cauchy residue theorem one finds that

$$C(\Omega,\mathbf{Q}) = -\frac{i}{8\omega D^{3/4}\omega^{3/2}Q} \frac{1}{\sqrt{\beta^2 - 4}}. \quad (68)$$

Substituting for β, one recovers

$$C(\Omega,\mathbf{Q})^{-1} = 8i\omega\sqrt{D}\sqrt{(\omega\Omega + i \text{ Im}\{\mathfrak{m}\})^2 - 4Q^2\sqrt{D}\omega^3}. \quad (69)$$

This is the propagator for bandlimited coherent energy density. It may be triply inverse Fourier transformed. After a small amount of analysis one concludes, exactly,

$$C(t,\mathbf{x}) = \frac{1}{16\pi\omega^2\sqrt{D}} \exp\left\{\frac{\text{Im } \mathfrak{m}t}{\omega}\right\} \frac{\delta(c_g t - |\mathbf{x}|)}{|\mathbf{x}|}, \quad (70)$$

where c_g is the group velocity at frequency ω, $c_g = 2\omega^{1/2}D^{1/4}$. Thus the average field has an energy density which propagates at the group velocity, attenuates geometrically like $1/r$, and attenuates exponentially in time at a rate $\sigma_{\text{Foldy}} = -\text{Im } \mathfrak{m}/\omega$. One recalls that σ_{Foldy} exceeds σ_{PSR} by an amount corresponding to the prompt scattering; thus C dissipates due to absorption by the substructure, and due to prompt scattering out of the coherent field.

After substituting the above form for the propagator C into (35) one concludes with an expression for the solution to the Bethe–Salpeter equation:

$$E(\Omega,\mathbf{Q})$$
$$= \frac{1}{8i\omega\sqrt{D}[(\omega\Omega + i \text{ Im}\{\mathfrak{m}\})^2 - 4Q^2\sqrt{D}\omega^3]^{1/2} - \kappa(\Omega)}. \quad (71)$$

This expression for $E(\Omega)$ is exact within the limits set by the approximations so far. These include the Foldy approximation for the self-energy and the Foldy–Ladder approximation for the intensity operator. These are considered accurate[6,8] if $\text{Im}\{\mathfrak{m}\} \ll \omega^2$, or, alternatively and equivalently, for weak attenuation per wavelength: $\text{Im}\{q^*\}/\text{Re}\{q^*\} \ll 1$; $\xi_{\text{PSR}} \ll 1$. Further approximations invoked in this section include the assumption $Q \ll q$, and $\Omega \ll \omega$, that is, that interest is confined to energy density smoothed over length and time scales long compared to wavelengths and (inner) periods.

E is an irrational function of $\mathbf{Q}$ and Ω. As such it is not easily transformed into the time and frequency domains.

There are, however, at least two ways this can be done. One is to write it as an equation of radiative transfer; the other to take a long length scale, or diffusion, limit.

A. Radiative transfer

The approximations used to derive (71) are common elsewhere[6,8] in the derivation of radiative transfer equations. Thus Eq. (71) may be considered equivalent to such equations. Unlike a radiative transfer equation, however, the dependent variable here is energy density, not specific intensity. It can nevertheless be made to look like radiative transfer by an analysis that entails a new independent variable θ, that represents the direction of propagation $\mathbf{q}/q$ of the waves constituting the energy E. This angle is not the direction of the Fourier transform variable $\mathbf{Q}$, but rather the direction of $\mathbf{q}$ relative to $\mathbf{Q}$. $\mathbf{Q}$ and θ are distinct independent variables.

We define a quantity $\mathscr{T}$, the specific intensity associated with the mean field,

$$\mathscr{T}(\theta,\mathbf{Q},\Omega) \equiv \frac{1}{i\Omega + \sigma_{\text{Foldy}} - i|\mathbf{Q}|c_g \cos\theta}. \quad (72)$$

The angle integral of $\mathscr{T}$ is related to C:

$$C(\Omega,\mathbf{Q}) = \frac{1}{8\omega^2\sqrt{D}} \frac{1}{2\pi} \int d\theta \, \mathscr{T}(\theta,\mathbf{Q},\Omega) \quad (73)$$

as may be seen by reference to Eq. (64). We also define a quantity $I(\theta,\mathbf{Q},\Omega)$, which will be seen to be the specific intensity of the total field. I is the solution to

$$\mathscr{T}^{-1}(\theta,\mathbf{Q},\Omega)I(\theta,\mathbf{Q},\Omega) = 1 + \kappa(\Omega)E(\Omega,\mathbf{Q}) \quad (74)$$

or

$$I(\theta,\mathbf{Q},\Omega) = [1 + \kappa(\Omega)E(\Omega,\mathbf{Q})]\mathscr{T}(\theta,\mathbf{Q},\Omega) \quad (75)$$

whose angle integral is

$$\frac{1}{16\pi\omega^2\sqrt{D}} \int d\theta \, I(\theta,Q,\Omega)$$
$$= C(\Omega,Q)[1 + \kappa(\Omega)E(\Omega,\mathbf{Q})]. \quad (76)$$

By comparing with (35) it is seen that the left side may be identified with E itself. We conclude that the radiative transfer equation (74) is equivalent to (35). On substituting for $\mathscr{T}$ and E (74) takes the form

$$[i\Omega + \sigma_{\text{Foldy}} - ic_g|\mathbf{Q}|\cos\theta]I(\theta,\mathbf{Q},\Omega)$$
$$= 1 + \kappa(\Omega) \frac{\int d\theta \, I(\theta,\mathbf{Q},\Omega)}{16\pi\omega^2\sqrt{D}}, \quad (77)$$

which may be transformed to the time and space domains

$$\left[\frac{\partial}{\partial t} + \sigma_{\text{Foldy}} + c_g\hat{\mathbf{e}}_\theta \cdot \nabla\right]I(\theta,\mathbf{x},t)$$
$$= \delta(t)\delta^2(\mathbf{x} - \mathbf{x}') + \kappa * \frac{\int d\theta \, I(\theta,\mathbf{x},t)}{16\pi\omega^2\sqrt{D}}, \quad (78)$$

where $\mathbf{e}_\theta$ is a unit vector in direction θ. The asterisk repre-

sents a temporal convolution between κ and the time-dependent quantity following it. This equation is a radiative transfer equation. It is written in a rational form amenable to direct solution but is also exactly equivalent to (35). The left side of (78) describes propagation in direction $\mathbf{e}_\theta$ at a speed c_g, and dissipation at a rate σ_{Foldy}. The right side consists of a primary source and a secondary source. The secondary source has a contribution corresponding to the reemission of energy originally absorbed, corresponding to the

second term in κ as given by Eq. (26), and another contribution corresponding to the first term in (26) that represents the promptly scattered energy.

B. Diffusion limit

E may also be given a rational dependence on Q and Ω by confining attention to large enough length and time scales. Equation (35) is first rewritten by use of the optical theorem, Eq. (38) of Ref. 1.

$$E(\Omega,\mathbf{Q}) = \frac{1/8\omega^2\sqrt{D}}{\sqrt{(i\Omega-\text{Im}\{\mathfrak{m}\}/\omega)^2+4Q^2\sqrt{D}\omega}-\dfrac{[\kappa(\Omega)-\kappa(0)]}{8\omega^4\sqrt{D}}+\text{Im}\{\mathfrak{m}\}/\omega}. \tag{79}$$

On substituting for κ (26), one then obtains

$$\begin{aligned}E(\Omega,\mathbf{Q}) &= \frac{(1/8\omega^2\sqrt{D})}{[(i\Omega-\text{Im}\{\mathfrak{m}\}/\omega)^2+4Q^2\sqrt{D}\omega]^{1/2}+\text{Im}\{\mathfrak{m}\}/\omega+[i\Omega/(i\Omega+k/8\sqrt{D})](k\rho\omega_0/\omega^2+\omega_0^2)} \\[6pt] &= \frac{1/8\omega^2\sqrt{D}}{\sqrt{(i\Omega+\sigma_{\text{Foldy}})^2+4Q^2\sqrt{D}\omega}-\sigma_{\text{Foldy}}+[i\Omega/(i\Omega+\sigma_{\text{ism}})]\sigma_{\text{PSR}}}.\end{aligned} \tag{80}$$

We now confine attention to long time scales, $\Omega\ll\sigma_{\text{Foldy}}$, i.e., long compared to the time over which the coherent field is dissipated. We also confine attention to an E which is spatially smoothed over length scales long compared to the distance the coherent field has propagated in that time, $Q\ll\sigma_{\text{Foldy}}/2\omega^{1/2}D^{1/4}=\sigma_{\text{Foldy}}/c_g$. The square root in the above expression for E can then be expanded in powers of Ω and Q^2 and the two terms σ_{Foldy} allowed to cancel:

$$E(\Omega,\mathbf{Q}) \approx \frac{1/8\omega^2\sqrt{D}}{i\Omega+Q^2(c_g^2/2\sigma_{\text{Foldy}})+[i\Omega/(i\Omega+\sigma_{\text{ism}})]\sigma_{\text{PSR}}}. \tag{81}$$

This has some of the appearance of a diffusion propagator (9) and is in any case a rational function of Ω and Q and could therefore be transformed into the time and space domains as an integro-partial differential equation. The result would have the attractive property of seeming to describe energy flow on time scales long compared to the absorption time, but not necessarily long compared to the dwell time. Such an application would, however, be in error. At times short compared to the dwell time, such that $\Omega<\sigma_{\text{ism}}$ the last term in the denominator is $\sim\sigma_{\text{Foldy}}$ and must, if the inverse of the above propagator is evaluated by residues, be balanced by the terms in Ω and Q^2. But this contradicts the approximations invoked in the discussion following Eq. (80). Thus at times less than the dwell time a rational time- and space-domain governing equation appears to be available only by means of radiative transfer (78).

A diffusion equation can, however, be obtained in the limit that the times scales of interest exceed $1/\sigma_{\text{ism}}$. Expanding the expression (81) for long times, $\Omega\ll\sigma_{\text{ism}}$, one finds

$$\begin{aligned}E(\Omega,\mathbf{Q}) &\approx \frac{1/8\omega^2\sqrt{D}}{i\Omega(1+1/\eta)+Q^2(c_g^2/2\sigma_{\text{Foldy}})} \\[6pt] &= \frac{\eta}{(1+\eta)8\omega^2\sqrt{D}}\frac{1}{i\Omega+\mathscr{D}Q^2}.\end{aligned} \tag{82}$$

The diffusivity is the ratio of the coefficients of Ω and Q^2:

$$\mathscr{D}=\frac{c_g^2}{2\sigma_{\text{Foldy}}}\frac{\eta}{1+\eta}. \tag{83}$$

Diffusion is very slow if η is small, corresponding to a high number density of sprung masses.

This is one of the chief results of the present calculation. On time scales greater than the greater of $1/\sigma_{\text{Foldy}}$ and $1/\sigma_{\text{ism}}$ the energy in the plate has an apparent diffusion rate which is, if the modal density in the substructure is much greater than the modal density in the plate, much slower than would be anticipated by a naive application of the classical argument that the diffusivity is essentially a wave speed times a mean free path. The result is similar to that of Albada et al.[10] in which optical diffusivities in certain turbid media were found to be much slower than predicted by the classical argument. The result was explained by Kogan and Kaveh[11] and discussed at great length by Tiggelen[12] as related to long dwell times in resonant scatterers.

The regime in which the PSR theory is accurate may be more restricted than was indicated in Sec. II C. The estimate there was based on a comparison of energy densities at $Q = 0$, that is, as smoothed over very long length scales. It was found that, at short times $T < \ln \eta$, these infinite area integrations do not differ by a high fraction. It was not, however, established that $G \sim \langle G \rangle$ at all positions. Regions in which $\langle G \rangle$ is small do not contribute significantly to the area integrations, and large fractional discrepancies could occur that would not be reflected in (57). For example, the mean field, and the PSR theory, both predict propagation with dissipation but without diffusion. In the wake of a PSR or mean field wavefront there is zero disturbance. Yet the actual field will, in this region, be nonzero, having contributions from the diffusely reradiated field that is leaking back from the substructure and from the promptly scattered parts. At early times this field is much weaker than the main pulse, but the main pulse is elsewhere. In this region therefore the normalized variance is unity and the PSR theory qualitatively misdescribes the actual fields. Thus the question of the range of validity of the predictions of the PSR theory has an answer that depends on what one wishes to predict.

IV. INTERNAL FRICTION

The present work has been directed towards the case of systems with no internal friction, i.e., no true loss mechanisms. The assumption of no damping, however, is not required for application of the methods used. Indeed, damping may be incorporated by the simple expedient of letting the plate modulus D and the sprung mass stiffnesses k become complex.

The effect of an introduction of moderate amounts of true internal friction may also be understood by the following discussion. If the plate and the substructure have equal true internal friction σ_{if}, the effect is simply one of multiplying all responses G by $\exp\{-\sigma_{if}t/2\}$ and all energy responses G^2 by $\exp\{-\sigma_{if}t\}$. If the substructure has an internal friction σ_{ssif} that exceeds that of the plate σ_{pif} by an amount $\sigma_{dif} = \sigma_{ssif} - \sigma_{pif}$, then the effect is approximately one of (a) repeating the analysis of this paper but with an assumption of no internal friction in the plate and an assumption of an internal friction σ_{dif} in the substructure. This leads to changes in the effective $\mathfrak{m}$ and κ. One must also then (b) multiply all responses G by $\exp\{-\sigma_{pif}t/2\}$ and all responses G^2 by $\exp\{-\sigma_{pif}t\}$.

The change induced in $\mathfrak{m}$ by sprung mass internal friction is, though, expected to be negligible. This is seen most easily in the form (53) of Ref. 1 for $\mathfrak{m}$ in the Foldy-1, or PSR, theory where k gaining an imaginary part of order 10% has little effect on the imaginary part of $\mathfrak{m}$, at least for values of ω of the order of ω_0.

The change induced in κ can be more significant. It may be described most easily by letting ϵ, in the expressions for κ, be finite; $\epsilon = \sigma_{dif}/2$. The result is identical to the original expression for κ (26), except that k^2 must be understood as $|k|^2$ and the denominator of the second term, which was $i\Omega + k/8\sqrt{D}$, becomes $i\Omega + k/8\sqrt{D} + \sigma_{dif}$. Thus the energy which sojourns in the substructure now decays at a new rate

$\exp\{-(\sigma_{ism} + \sigma_{dif})t\}$. If σ_{dif} exceeds σ_{ism} then the new behavior of κ is very different from the original behavior. The impact is most easily appreciated by considering the radiative transfer equations (78) where the more rapid decay of $\kappa(t)$ would lead to less energy returned to the plate, and, if σ_{dif} significantly exceeds the return rate σ_{ism}, to a negligible term in κ. The resulting radiative transfer equation would then describe propagation and absorption, with negligible reemission. If the prompt scattering is weak, the variance would then vanish and the mean field would be a good approximation to actual responses at all times. One concludes that substructural damping which exceeds the reradiation rate $\sigma_{ism} = k/8\sqrt{D}$ would result in a PSR Green's function that well represents typical actual responses.

Much previous work[2,3,13] on master structures of a small number of degrees of freedom have called for damping greater than the inverse of the modal density in order for the simple arguments to be correct. It appears that a wave-carrying master structure requires damping strong compared to the reemission rate, not strong compared to a modal density.

V. CONCLUSIONS

Agreement between mean responses and PSR responses is a necessary requirement for the PSR result to be representative of actual responses, but it is not sufficient. A further requirement is that the variances, representative of fluctuations away from the mean, be small. Variances were found to be of order η and to approach that level at times of order $-\log_e \eta/\sigma_{PSR}$ at which time the energy distribution is approaching an equipartition between the modes of the plate and those of the substructure. For times in excess of this the mean field approaches zero, while the actual energy in the plate has reached a steady state. Normalized variances, or fractional fluctuations, when averaged over smaller areas, can be significant even before this time. Thus the PSR[14] and Belyaev and Palmov[15–17] conjecture that their theories become exact in the limit of a high density of internal degrees of freedom, corresponding to small η, is corroborated. It was argued that true loss mechanisms in the substructure, with loss rates that exceed σ_{ism} can also lead to small variances.

On time scales long compared to the inverse of the inner frequency ω^{-1} and length scales long compared to wavelengths, it was found that an equation of radiative transfer governs the flow, scattering, absorption, and reemission of intensity. On time scales longer yet, greater than the equipartition time σ_{ism}^{-1} and greater than the mean free time against absorption or scattering, the governing equation becomes a diffusion equation. In the limit that the modal density in the substructure greatly exceeds that of the plate ($\eta \ll 1$), the diffusion is very slow.

[1] R. L. Weaver, ''Multiple scattering theory for mean responses in a plate with sprung masses,'' J. Acoust. Soc. Am. **101**, 3466–3474 (1997).

[2] R. Weaver, ''The effect of an undamped finite degree of freedom ''fuzzy'' substructure: numerical solutions and theoretical discussion,'' J. Acoust. Soc. Am. **100**, 3159–3164 (1996).

[3] R. L. Weaver, ''Mean and mean square responses of a prototypical master/fuzzy system,'' J. Acoust. Soc. Am. **101**, 1441–1449 (1997).

[4] G. Maidanik, ''Loss factor of a complex composed of coupled harmonic oscillators,'' J. Acoust. Soc. Am. **101**, 3024 (1997).

[5] P. A. Lee and T. V. Ramakrishnan, ''Disordered electronic systems,'' Rev. Mod. Phys. **57**, 287–337 (1985).

[6] R. Weaver, ''Diffusivity of ultrasound in polycrystals,'' J. Mech. Phys. Solids **38**, 55–86 (1990).

[7] D. Photiades, ''Acoustics of a fluid loaded plate with attached oscillators: Part I. Feynman rules,'' J. Acoust. Soc. Am. **102**, 348–357 (1997).

[8] U. Frisch, ''Wave propagation in random media,'' in *Probabilistic Methods in Applied Mathematics*, edited by Bharucha-Reid (Academic, New York, 1968), Vol. 1, pp. 75–197.

[9] J. A. Turner and R. L. Weaver, ''Radiative transfer of ultrasound in a polycrystal, '' J. Acoust. Soc. Am. **96**, 3675–83 (1994).

[10] M. P. Albada, B. A. Tiggelen, A. Lagendijk, and A. Tip, ''Speed of propagation of classical waves in strongly scattering media,'' Phys. Rev. Lett. **66**, 3132–3125 (1991).

[11] E. Kogan and M. Kaveh, ''Diffusion constant in a random system near resonance,'' Phys. Rev. B **46**, 10636–10646 (1992).

[12] B. A. van Tiggelen, ''Multiple scattering and localization of light,'' Ph.D. thesis, FOM-Institute for Atomic and Molecular Physics, Amsterdam, Netherlands, 1992.

[13] M. Strasberg and D. Feit, ''Vibration damping of large structures induced by attached small resonant structures,'' J. Acoust. Soc. Am. **99**, 335–344 (1996).

[14] A. D. Pierce, V. W. Sparrow, and D. A. Russell, ''Fundamental structural-acoustic idealizations for structures with fuzzy internals,'' J. Vib. Acoust. **117**, 339–348 (1995).

[15] A. K. Belyaev and V. A. Palmov, ''Integral theories of random vibration of complex structures,'' in *Random Vibration—Status and Recent Developments*, edited by R. H. Lyon and I. Elishakoff (Elsevier, Amsterdam, 1986), pp. 19–38.

[16] A. K. Belyaev, ''Vibrational state of complex mechanical structures under broad-band excitation,'' Int. J. Solids Struct. **27**, 811–823 (1991).

[17] A. K. Belyaev, ''High-frequency vibration of extended complex structures,'' Prob. Eng. Mech. **8**, 15–24 (1993).

A theoretical formulation of active control eardefenders

Jiaqiang Pan
Department of Mechanical Engineering, Zhejiang University, Hangzhou 310027, People's Republic of China

Yingshu Liu
Department of Mechanical Engineering, Tianjing University, Tianjing 300072, People's Republic of China

Jie Pan
Department of Mechanical and Materials Engineering, University of Western Australia, Nedlands, WA6009, Australia

This paper is concerned with the analysis and design of a feedback control active eardefender. By using classical control theory, the authors investigated the system stability and robustness of stability, the noise reduction level and its parameter sensitivity, and the working frequency range of the active eardefender. A general method for designing a stable feedback control eardefender is developed. In this theory, a special type of second-order compensator is used to improve the robustness of stability, the noise reduction level and its robustness, and the working area of the active eardefender, particularly at the low-frequency range of interest. © *1998 Acoustical Society of America.* [S0001-4966(97)06012-8]

INTRODUCTION

Since the 1980s, the concept of active noise control has been used to investigate the possibility of making active control eardefenders which more efficiently suppress noise entering the human ear than the passive control eardefenders do. Dorey *et al.*, Wheeler *et al.*, Jones *et al.*, Lee, Veit, McKinley, and Shen *et al.* have presented experimental results from the investigation of feedback active eardefenders.[1–7] Their work demonstrated the possibility and feasibility for the use of active eardefenders. Using numerical simulation, Carmer[8] has proposed a design method for a filter to be inserted into a feedback control loop. The active eardefender based on the self-adaptive control or feedforward principle has also been investigated by Brammer *et al.*,[9] Ryan *et al.*,[10] and Sha and Tian.[11,12]

Previous work has clearly shown that, by superimposing a controlled secondary sound to the original sound field, both feedforward and feedback control structures may be used to obtain further noise reduction over the passive control. The problem addressed in this paper is how to design a control system such as an active eardefender, so that the given demand on the stability, robustness of stability, noise reduction, and parameter sensitivity over a range of frequencies of interest are satisfied. Resolving this problem is a key step toward designing an active control eardefender for practical applications.

In this paper only the feedback active eardefender shown in Fig. 1 is considered. In Sec. I we present an analysis of the feedback control active eardefender, focusing on the system stability and its robustness, noise reduction level and its parameter sensitivity, and the working frequency range of the active eardefender. In Sec. I we also describe how to design a constant gain amplifier that can make the system satisfy the demands on the stability and robustness of

stability, noise reduction, and its parameter sensitivity over a given frequency range. The effect of the design parameters on the specifications of the active eardefender is also discussed. In Sec. II we focus on the use of the control compensation technology. It is shown that using a special type of second-order cascade compensators can effectively improve the specifications of the active eardefender.

I. ANALYSIS AND DESIGN OF FEEDBACK ACTIVE EARDEFENDER

Figure 2 shows the block diagram of a feedback control eardefender, where H_m and H_l are, respectively, the transfer functions of the microphone and the loudspeaker. The gain K of the feedback amplifier is regarded as a real constant. The positive (negative) K value corresponds to the negative (positive) feedback. It can be seen from the figure that the transfer function of the forward path of the system is one, and the feedback path includes a microphone, a loudspeaker, and a feedback amplifier to be designed. The characteristic equation of the system is

$$|1 + KH_m(s)H_l(s)| = 0, \qquad (1)$$

where s is Laplace's variable (i.e., complex frequencies). As we know, over the low sound frequency range, the transfer function H_m of the microphone (for example, the condenser microphone) can be considered as a positive constant and the transfer function H_l of the loudspeaker (for example, the piezoelectric or electrodynamic loudspeaker) can be modeled as a second-order rational function as follows:

$$H_m(s) = g_m, \qquad (2)$$

$$H_l(s) = \frac{g_l s^2}{s^2 + 2\zeta\omega_n s + \omega_n^2}, \qquad (3)$$

FIG. 1. Feedback control active eardefender.
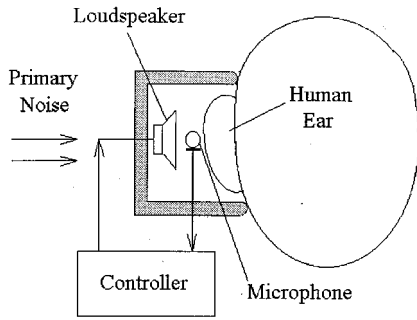
FIG. 3. Working area of a feedback control eardefender.

where g_m is the gain of the microphone and g_l, ζ, and ω_n represent the gain, the loss factor, and the resonance radian frequency of the loudspeaker. They can be either calculated by physical parameters of the microphone and loudspeaker or numerically fitted from the experimental data (see the Appendix). It is assumed that g_m, g_l, $\omega_n > 0$, and usually $0.7 > \zeta > 0$. Substituting Eqs. (2) and (3) into Eq. (1), the characteristic equation becomes

$$(1+k)s^2 + 2\zeta\omega_n s + \omega_n^2 = 0, \tag{4}$$

where the dimensionless open-loop gain k is defined as $k = Kg_m g_l$. Two roots of the characteristic equation both have negative real parts, if and only if

$$k \geqslant -1. \tag{5}$$

This is the condition under which the feedback eardefender is a stable system.

The noise reduction ratio of the feedback eardefender is defined as

$$\mu(\omega) = \left| \frac{P_1(j\omega)}{P_2(j\omega)} \right|, \tag{6}$$

where $P_1(j\omega)$ and $P_2(j\omega)$ are, respectively, the sound pressures of the noise into the human ear before and after the closed-loop control signal introduced. From Fig. 2 it can be obtained that

$$\mu(\omega) = \left| 1 + K H_m(j\omega) H_l(j\omega) \right|. \tag{7}$$

To effectively suppress the noise, it must be satisfied that $\mu(\omega) > 1$. Thus

$$\left| 1 - \frac{k\omega^2}{\omega_n^2 - \omega^2 + j2\zeta\omega_n\omega} \right| > 1. \tag{8}$$

FIG. 2. Block diagram of a feedback control eardefender.

Synthesizing the solutions of the inequality and Eq. (5) gives the working area of the feedback eardefender as follows:

(i) The negative feedback eardefenders

$$k > 2(\lambda^{-1} - 1), \quad \text{when } \lambda \leqslant 1, \tag{9a}$$

$$k > 0, \quad \text{when } \lambda \geqslant 1. \tag{9b}$$

(ii) The positive feedback eardefenders:

$$k < 0, \quad \text{when } \lambda \leqslant 1, \tag{10a}$$

$$k < 2(\lambda^{-1} - 1), \quad \text{when } \lambda \geqslant 1, \tag{10b}$$

where the dimensionless frequency ratio λ is defined as $\lambda = \omega^2 / \omega_n^2$. A stable, noise-attenuated feedback eardefender must work in the area as shown in Eq. (9) or (10). The shadow area shown in Fig. 3 is a figured expression of the working area. From Fig. 3, it can be seen that the positive feedback eardefender has a rather narrow working area, so that the positive feedback control strategy is impractical. Therefore, only the negative feedback eardefender is further discussed.

Define the noise reduction level as

$$\varepsilon = 20 \log \mu. \tag{11}$$

For the case that a feedback amplifier with constant gain k is used in control over a whole frequency range of interest, the noise reduction level will depend upon the noise frequency, as follows:

$$\varepsilon(\lambda) = 10 \log \left\{ \frac{k[k - 2(\lambda^{-1} - 1)]}{(\lambda^{-1} - 1)^2 + 4\zeta^2\lambda^{-1}} + 1 \right\}. \tag{12}$$

The noise reduction level curves corresponding to various loudspeaker loss factors and two different gain factors ($k = 0.5$ and 10) are shown in Fig. 4(a) and (b), respectively. From the two figures, some features can be observed:

(1) There is a low limit of frequency λ_c which corresponds to $\varepsilon = 0$. This so-called cross-over frequency ratio λ_c can be found from Eq. (12) as

$$\lambda_c = \frac{\omega_c^2}{\omega_n^2} = \frac{1}{0.5k + 1}. \tag{13}$$
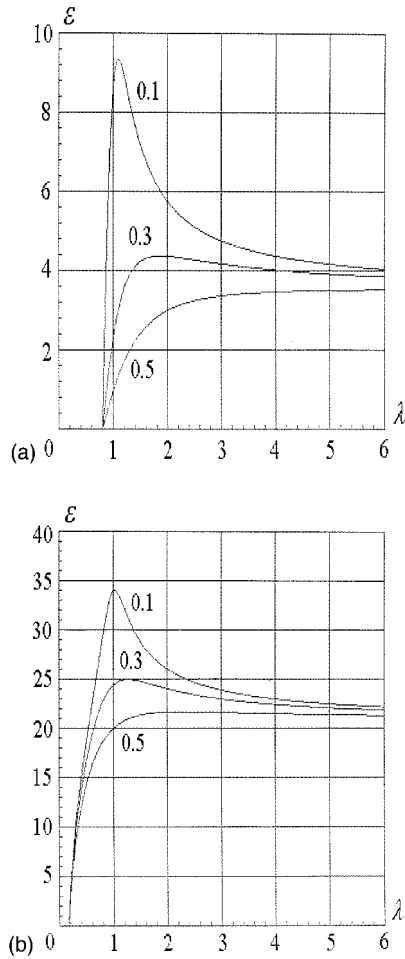
FIG. 4. (a) ϵ curves corresponding to $k=0.5$. (b) ϵ curves corresponding to $k=10$.

(2) The loss factor ζ of the loudspeaker has a significant effect on the noise reduction level. The smaller the loss factor is, the higher the noise reduction level is.

(3) It also can be seen from Eq. (12) that increase of feedback gain k will raise the noise reduction level and decrease the cross-over frequency, namely, improve the performance of the eardefender, particularly at low-frequency range.

The feedback system has two complex characteristic roots in the dimensionless complex frequency plane—(s/ω_n) plane. With considering $k>0$ and $0.7>\zeta>0$, they can be expressed as

$$\frac{\bar{s}}{\omega_n}=\frac{\bar{\sigma}}{\omega_n}\pm j\frac{\bar{\omega}}{\omega_n}=-\frac{\zeta}{k+1}\pm j\frac{\sqrt{k+1-\zeta^2}}{k+1}, \tag{14}$$

where $j=\sqrt{-1}$. As the two complex characteristic roots are always at the negative half-plane, the feedback eardefender system is stable. However, as it can be seen from Eq. (14), when $k>1$, the argumental angles of the complex roots will be beyond the phase margin (60°) required by classical design criterion of stability robustness. It means a proper compensator is needed for the closed-loop system to satisfy the requirement on the robustness of stability.

The robustness of performance also needs to be investigated. This property can be described by the parameter sen-

sitivity of the noise reduction ratio when the design parameters k, ζ, and ω_n vary. The parameter sensitivity S can be defined as the ratio of the relative variation of the noise reduction ratio to the relative variation of the open-loop transfer function $H(j\omega)=KH_m(j\omega)H_l(j\omega)$ when the design parameters vary (the latter synthesizes the system variation caused by the variations of the design parameters), as follows:

$$S=\frac{|\Delta\mu/\mu|}{|\Delta H/H|}. \tag{15}$$

From Eq. (7), S can be obtained as

$$S=\frac{|\mu-1|}{\mu}=\frac{k}{\sqrt{[\lambda^{-1}-(k+1)]^2+4\zeta^2\lambda^{-1}}}. \tag{16}$$

Figure 5 shows the parameter sensitivity S of the negative feedback active eardefenders with the loss factor $\zeta=0.1$, where different curves correspond to different gain factors $k=1$, 4, 7, and 10, and each of the curves starts from the corresponding cross-over frequency ratio λ_c. It can be seen that $S<1$ if and only if $\lambda>1$. When $\lambda\rightarrow\infty$, $S\rightarrow k/(k+1)$. Equation (16) also shows that the parameter sensitivity S will reduce with the loss factor ζ increasing.

For the above analysis, the effect of the system parameters on the performance, stability, and robustness of the active eardefender can be summarized as follows:

(1) ω_n: Changing the loudspeaker resonance frequency ω_n gives no effect on the stability and robustness of stability. However, smaller ω_n is helpful to expand the robust working frequency range where the parameter sensitivity of the noise reduction ratio $S>1$.

(2) ζ: Smaller loudspeaker loss factor ζ will be helpful to raise the noise reduction level but unfavorable to the system robustness of both stability and performance.

(3) k: Higher feedback gain factor k will be helpful to raise the noise reduction level and widen the working frequency range. However, the robustness of both the stability and performance worsens.
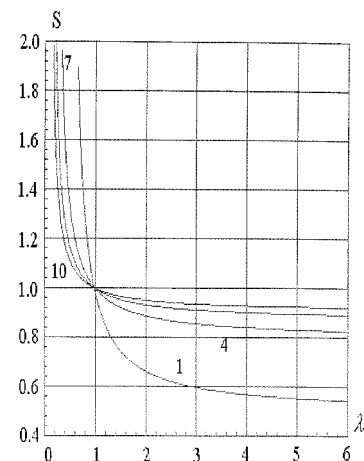
FIG. 5. Parameter sensitivity of the noise reduction ($\zeta=0.1$).
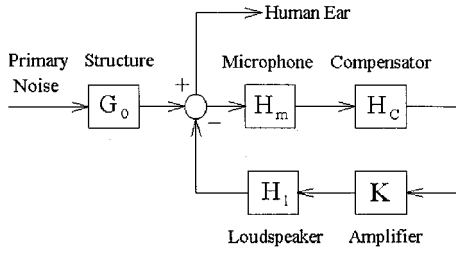
FIG. 6. Cascade compensation.

II. COMPENSATION DESIGN

Due to the rather small size of an eardefender, the control loudspeaker must be small enough to fit into the hull of the eardefender. A loudspeaker with a small diameter has high basic resonance frequency ω_n which could exceed the upper limit of the frequency range of interest. This means that the eardefender has to work in a frequency range $\lambda < 1$. Thus, the system will work at an area where the robustness of stability is questionable, and the feedback gain factor must be quite high for having an even low noise reduction so that a multistage amplifier, which is costly and has a large volume, has to be employed. Therefore, the compensation technology will be used to solve this problem. To reach this end, a special type of second-order cascade compensator is designed. Its block diagram is shown in Fig. 6.

This special type of second-order cascade compensator has a transfer function as follows:

$$H_c(s) = \frac{s^2 + 2\beta\omega_n s + \gamma\omega_n^2}{s^2}, \tag{17}$$

where compensator parameters β and γ are both positive constants. Obviously, $\beta = \gamma = 0$ is corresponding to the system without the compensation.

Two characteristic roots of the closed-loop system after the compensation are

$$\frac{\bar{s}}{\omega_n} = \frac{\bar{\sigma}}{\omega_n} \pm j \frac{\bar{\omega}}{\omega_n}$$

$$= -\frac{\zeta + k\beta}{k+1} \pm j \frac{\sqrt{(k+1)(k\gamma+1) - (\zeta + k\beta)^2}}{k+1}. \tag{18}$$

It can be seen from Eq. (18) that the compensation significantly improves the stability robustness of the closed-loop system. Particularly, when β and γ are properly selected, the robustness design requirement (maximum phase margin 60°) can be certainly satisfied.

The working area of the feedback eardefender after the compensation is found as

$$k > \max\{\kappa(\lambda), 0\}, \tag{19}$$

where

$$\kappa(\lambda) = \frac{2[(\gamma\lambda^{-1} - 1)(1 - \lambda^{-1}) + 4\beta\zeta\lambda^{-1}]}{(\gamma\lambda^{-1} - 1)^2 + 4\beta^2\lambda}. \tag{20}$$

We only discuss a special case that $\gamma = 2\beta^2$ in detail. For this case, the analysis based on Eq. (20) shows that always $\kappa(\lambda) < 0$ and thus the feedback eardefender is always stable

TABLE I. β_1 and β_2.

ζ	β_1	β_2
0.1	1.187	0.417
0.2	1.475	0.339
0.3	1.724	0.290
0.4	1.959	0.227
0.5	2.187	0.225

and noise reduced, if β is selected between two positive numbers β_1 and β_2, which can be calculated as follows:

$$\beta_{1,2} = \left(\frac{\sqrt{2}}{2} + \zeta\right) \pm \sqrt{\left(\frac{\sqrt{2}}{2} + \zeta\right)^2 - \frac{1}{2}}. \tag{21}$$

Table I gives the values of β_1 and β_2 corresponding to $\zeta = 0.1 - 0.5$. Also, the analysis based on the root locus method shows that the robustness phase margin (60°) has been satisfied for any $k > 0$.

The noise reduction lever after the compensation is

$$\varepsilon = 10 \log\left\{\frac{k[k + 2A(\lambda)B(\lambda)]}{A(\lambda)} + 1\right\}, \tag{22}$$

where $A(\lambda)$ and $B(\lambda)$ represent, respectively,

$$A(\lambda) = \frac{(\lambda^{-1} - 1)^2 + 4\zeta^2\lambda^{-1}}{(2\beta^2\lambda^{-1} - 1)^2 + 4\beta^2\lambda^{-1}},$$

$$B(\lambda) = \frac{(2\beta^2\lambda^{-1} - 1)(\lambda^{-1} - 1) + 4\beta\zeta\lambda^{-1}}{(\lambda^{-1} - 1)^2 + 4\zeta^2\lambda^{-1}}. \tag{23}$$

Figure 7 shows the ε curves before and after the compensation, where $\beta = 1.1$, $\gamma = 2.42$, $\zeta = 0.1$, and $k = 20$. Curve I and curve II are respectively correspond to the system before and after the compensation. It can be seen from Fig. 7 that the cascade compensation significantly raises the noise reduction level, particularly at the low-frequency range ($\approx 10 - 30$ dB).

The parameter sensitivity S of noise reduction after the compensation can be obtained as
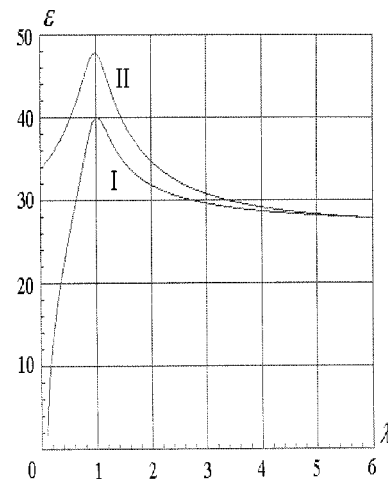
FIG. 7. ϵ-curves for a feedback eardefender with or without the compensation (curve II and curve I, respectively). $\beta = 1.1$, $\gamma = 2.42$, $\zeta = 0.1$, and $k = 20$.
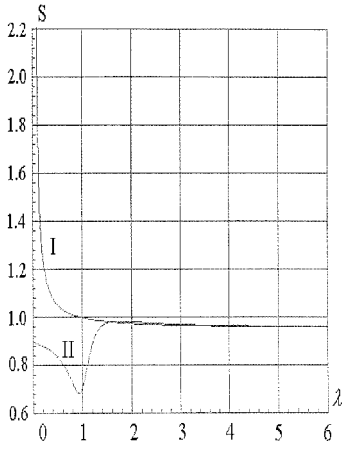
FIG. 8. S-curves for a feedback eardefender with or without the compensation (curve II and curve I, respectively). $\beta=1.1$, $\gamma=2.42$, $\zeta=0.1$, and $k=20$.

$$S = \frac{k}{\sqrt{A(\lambda) + 2kB(\lambda) + k^2}}. \quad (24)$$

Figure 8 shows the S-curves before and after the compensation, where still $\beta=1.1$, $\gamma=2.42$, $\zeta=0.1$, and $k=20$. Curve I and curve II respectively correspond to the system before and after the compensation. It can be seen that over the whole frequency range (including the range $\lambda<1$) there is $S<1$ now. This means that the system with a properly designed compensator can be robust in performance at any frequency of interest.

In brief, the merits of the cascade compensation for improving the specifications of the designed eardefender can be summarized as follows:

(1) The system stability and the robustness of stability: With use of a properly designed cascade compensator described by Eq. (17), the requirements on the system stability and its robustness can certainly be satisfied over the whole frequency range.
(2) The noise reduction level: When open-loop gain k remains constant, using a properly designed compensator can raise the noise reduction level over the whole frequency range, particularly at the low-frequency range.
(3) The parameter sensitivity of noise reduction: Use of a properly designed compensator can ensure $S<1$ over the whole frequency range.
(4) Simply stated, use of a properly designed compensator makes the system practically work at any frequency of interest.

III. CONCLUSIONS

This paper provides a theoretical method that can be used for the design of a feedback control active eardefender. By using the results from the paper, the main performance specifications, such as the system stability and its robustness, the noise reduction level and its parameter sensitivity, the working frequency range, and the parameters of the cascade

compensator used in the feedback control system can be explicitly calculated and the design parameters k, ζ, and ω_n can be properly selected.

ACKNOWLEDGMENTS

APPENDIX: CALCULATIONS OF g_m, g_l, ζ, and ω_n

The parameters in the transfer functions of microphone and loudspeaker, g_m, g_l, ζ, and ω_n, can be calculated by using their electrical and mechanical parameters.[13,14]

For the condenser microphone,

$$g_m = \frac{\pi e_g a^2}{x_0 k_0}, \quad (A1)$$

where e_g is the polarizing voltage of the microphone, a is the radius of the microphone diaphragm, x_0 is the distance between the diaphragm and the rigid plate in the microphone, and k_0 is the mechanical stiffness of the diaphragm

For the piezoelectric loudspeaker,

$$g_l = \frac{\alpha a \rho_0}{2 r_0 M}, \quad \omega_n^2 = \frac{1}{MC}, \quad \zeta = \frac{R}{2} \sqrt{\frac{C}{M}}, \quad (A2)$$

where α is the electromechanical transformation factor of the loudspeaker, a is the radius of the loudspeaker diaphragm, ρ_0 is the density of air, and r_0 is the distance between the centers of the loudspeaker and the microphone head. $M = M_0 + M_v + M_r$, where M_0, M_v, and M_r are respectively the diaphragm mass, the mass of the piezoelectric vibrator, and the radiation mass (reactance). $R = R_0 + R_v + R_r$, where R_0, R_v, and R_r are respectively the mechanical resistance of the diaphgram and the piezoelectric vibrator, and the radiation resistance. $C = C_0 C_v / (C_0 + C_v)$, where C_0 is the mechanical flexibility of the diaphragm and C_v is the mechanical flexibility of the piezoelectric vibrator.

For the electrodynamic loudspeaker,

$$g_l = \frac{\alpha a \rho_0 BL}{2 r_0 RM}, \quad \omega_n^2 = \frac{1}{MC},$$

$$\zeta = \frac{1}{2} \left(2R_r + \frac{B^2 L^2}{R} \right) \sqrt{\frac{C}{M}}, \quad (A3)$$

where α is the electromechanical transformation factor, a is the radius of the diaphragm, ρ_0 is the density of air, B is the intensity of the magnetic field, L is the length of wire in voice coil, and r_0 is the distance between the centers of the loudspeaker and microphone head. $M = M_d + 2M_r$, where M_d is the mass of the diaphragm (including the voice coil) and M_r is the radiation mass (reactance). R_r is the radiation resistance. C is the mechanical flexibility of the loudspeaker diaphragm. $R = R_g + R_e$, where R_g is the inner resistance of the signal source to the loudspeaker and R_e is the resistance of voice coil.

These parameters can also be identified by using the curve fitting to the experimental data.[15]

[1] A. P. Dorey, S. Pelc, and P. Watson, ''An active noise reduction system for use with ear defender,'' The Proceedings of 8th International Aerospace Symposium, Cranfield, 1975, pp. 24–27.

[2] P. D. Wheeler, R. D. Rawlinson, S. F. Pelc, and A. P. Dorey, ''The development and testing of an active noise reduction system for use in ear defenders,'' Inter-Noise '78 (1978), pp. 977–982.

[3] O. Jones and R. Smith, ''The selective anti-noise ear defender,'' Inter-Noise '83 (1983), pp. 375–378.

[4] C. Lee, ''Active noise reducing earmuffs,'' Inter-Noise '87 (1987), pp. 521–524.

[5] I. Veit, ''A lightweight headset with an active compensation,'' Inter-Noise '88 (1988), pp. 1087–1090.

[6] R. L. Mckinley, ''Active noise reduction headset,'' in The Proceedings of 6th International Conference on Noise As a Public Health Hazard (Nice), 1993, Vol. 2, pp. 83–86.

[7] H. Shen, ''Active noise reduction earmuff,'' Technol. Electr. Sound **7**, 2–6 (1993) (in Chinese).

[8] C. Carme, ''A new filtering method by feedback for ANC at the ear.'' Inter-Noise '88 (1988), pp. 1083–1086.

[9] A. J. Brammer et al., ''Attenuation of noise reducing headset at high sound pressure levels,'' in The Proceedings of Vth International Symposium on the Effects of Noise on Hearing, Gofhenburg, 1994.

[10] J. G. Ryan et al., ''Enclosure for low-frequency assessment of active noise reducing circumaural headset and hearing protectors,'' Can. Acoust. **21**(4), 19–20 (1993).

[11] J. Sha, J. Tian, and N. Li, ''A new active ear defender,'' Inter-Noise '91 (1991), pp. 241–244.

[12] J. Tian et al., ''Active eardefender design and principles,'' Acta Acoust. **16**(2), 122–127 (1991).

[13] L. E. Kinsler et al., Fundamentals of Acoustics (Wiley, New York, 1982).

[14] Acoustical Institute of Nangjing, University, ''Electro-acoustic Transducers—Course Notes'' (in Chinese) (1980).

[15] Y. Liu, ''Research on active noise control cardefenders,'' Master degree thesis (in Chinese), Zhejiang University, PRC, 1995.

Spatial aspects of reproduced sound in small rooms

Søren Bech[a)]

Department of Acoustic Technology, Technical University of Denmark, DK-2800 Lyngby, Denmark

This paper reports on the influence of individual reflections on the auditory spatial aspects of reproduced sound. The sound field produced by a single loudspeaker positioned in a normal listening room has been simulated using an electroacoustical synthesis of the direct sound, 17 individual reflections and the reverberant field. The threshold of detection was measured using the method of adjustment for five reflections using three subjects for noise and speech. The thresholds have been measured for two simulated situations (1) a loudspeaker with a frequency independent directivity characteristics and frequency independent absorption coefficients of the room surfaces and (2) a loudspeaker with directivity similar to a standard two-way system and absorption coefficients according to measurements of real materials. The results have shown that subjects can reliably distinguish between timbre and spatial aspect of the sound field, that the spectral energy above 2 kHz of the individual reflection determines the importance of the reflection for the spatial aspects, and that only the first order floor reflection will contribute to the spatial aspects. © *1998 Acoustical Society of America.* [S0001-4966(98)05701-4]

PACS numbers: 43.55.Hy, 43.55.Jz, 43.55.Lb, 43.66.Qp [JDQ]

INTRODUCTION

This is a report on the third experimental investigation of perception of reproduced sound in small rooms. The first two investigations (Bech[1] referenced below as Paper I and Bech[2] referenced as Paper II) were concerned with the influence of individual reflections on the timbre of the sound field produced by a single loudspeaker positioned in a room the size of a normal living room. This report is concerned with the influence of individual reflections on the spatial aspects of reproduced sound.

The overall purpose of the experiments reported in Papers I and II and the present is to examine the importance of individual early reflections on the perceived sound quality. The results might form the basis for development of new loudspeaker systems which in some way can accommodate the acoustics of the room in which they are placed. Therefore, the experiments have been designed to illuminate questions of relevance for the design of such new loudspeaker systems. In this report the following question has been addressed:

Which of the early reflections are sufficiently strong to contribute individually to the auditory spatial aspects of reproduced sound, and which only contribute collectively?

This question is primarily related to the design of the directivity characteristics of the loudspeaker.

To facilitate the investigations, the sound field from a single loudspeaker in a listening room has been simulated using an electroacoustic setup. Two situations have been simulated using the same room dimensions and positions of the listener and loudspeaker.

One simulates the sound field from an idealized loudspeaker with a frequency-independent cardioid directivity, positioned in a room where the surfaces have idealized frequency-independent absorption characteristics. This situation is termed ''unfiltered'' in the following.

The other, termed filtered, simulates the sound field from a loudspeaker with directivity characteristics like a standard two-way loudspeaker system, positioned in a room where the surfaces have realistic absorption characteristics.

The results from the unfiltered situation provide a link with previous research in this area, which almost exclusively has been based on conditions similar to the unfiltered situation. Furthermore, the unfiltered situation is better suited to examine the importance of different regions in the spectrum of the reflections.

The filtered situation is expected to provide results which are more in agreement with the conditions in a real room. By comparing results from the unfiltered and filtered situations it is expected to provide further information on the relative importance of different frequency regions.

I. EXPERIMENTAL SETUP

The sound field produced by the right hand loudspeaker of a stereophonic setup positioned in a domestic listening room was electroacoustically simulated. The listening room which has formed the basis for the simulation was built in accordance with the IEC 268-13[3] recommendation, whereby the room should be representative of a domestic listening room.

Two different versions of the sound field have been used for the investigations. The first, the ''unfiltered'' version modeled the directivity characteristics of the loudspeaker as a cardioid, independent of frequency. The absorption coefficients of the room surfaces were also modeled as being independent of frequency.

The ''filtered'' version was modeled as a two-way loudspeaker system with directivity characteristics according to the measurements of a selected loudspeaker (KEF 103.2).

[a)]Present address: Bang and Olufsen A/S, Peter Bangs Vej 15, DK-7600 Struer, Denmark.

TABLE I. Positions of loudspeakers and delay and attenuation of the signals to the loudspeakers for primary loudspeaker, images and reverberation channels included in the setup. The attenuation values are given for the unfiltered situation (Att. I) and the filtered situation (Att. II). The last wall of the reflection path is also given. All angles and wall references are relative to the listening position and the left-hand side of the subject defines positive angles.

Delay [ms]	Att. I [dB]	Att. II [dB]	Azimuth [degrees]	Elevation [degrees]	Reflection number	Last surface of reflection
0	0	0	−22	0	⋯	primary lsp
1.64	3.6	1.36	−25	−28	1	floor
4.16	9.2	3.1	−50	−2	2	right wall
4.48	5	3.28	−25	48.2	3	ceiling
5.36	11.6	3.81	−53	−28	4	floor
7.6	11.8	5.01	−50	48	5	ceiling
9.2	10	5.78	−25	48.2	6	ceiling
9.2	10	5.78	−25	−56	7	floor
9.94	9.7	6.11	65	0	8	left wall
10.8	11.8	6.48	65	−14	9	left wall
11.64	15.5	6.83	−53	−56	10	floor
11.64	15.5	6.83	−50	48	11	ceiling
12.5	11.5	7.17	65	30	12	left wall
12.7	9.9	7.25	−170	0	13	backwall
13.46	11.9	7.54	−170	−15	14	back wall
14.42	14.3	7.9	−25	−56	15	floor
14.8	14.6	8.03	−154	0	16	back wall
14.98	11.3	8.09	−170	33	17	back wall
22	0.5	6	71	0	⋯	rev. syst.
22	0.5	6	−71	0	⋯	rev. syst.
22	7.5	6	127	0	⋯	rev. syst.
22	7.5	6	−127	0	⋯	rev. syst.
22	8.5	6	180	0	⋯	rev. syst.
22	0.5	6	0	0	⋯	rev. syst.

The absorption coefficients of the room surfaces were modeled as a function of frequency.

The electroacoustic setup models the direct sound, 17 individual reflections arriving less than 22 ms after the arrival of the direct sound, and the reverberant part of the sound field or reflections arriving more than 22 ms after the arrival of the direct sound. The setup was positioned in the large (1000 m^3) anechoic chamber of the Department of Acoustic Technology, and all loudspeakers were located, with correct azimuth and elevation, on the surface of an imaginary sphere of 3-m radius centered at the listening position. The positions of all the loudspeakers, and the delay and attenuation of all signals representing individual images and reverberation channels, are given in Table I. In the following, individual reflections will be identified either by the delay relative to the direct sound, or by the number given in Table I. General considerations on electroacoustical simulation of sound fields are given in Paper I and a detailed discussion of the setup used for the present experiments is given in Paper II.

A. Implementation of the direct sound and individual reflections for the unfiltered situation

The directivity characteristics of the loudspeaker were modeled as a cardioid, independent of frequency. The absorption coefficients of the room surfaces were modeled independent of frequency with the following values: ceiling =0.05, floor=0.3, and walls=0.44. These values resulted in a calculated reverberation time of 0.4 s, independent of frequency.

Delay and attenuation due to path lengths of the direct sound and individual reflections were calculated using the image source theory, implemented as a computer program by KEF Audio Ltd. The calculated levels of the individual reflections are hereafter referred to as the natural levels, as they represent the levels that the reflections would have in a real room with the specified properties.

For a general discussion of the image source principle, see, e.g., Cremer and Müller[4] and Berman[5] for use in a rectangular room.

B. Implementation of the direct sound and individual reflections for the filtered situation

The modeled loudspeaker was a two-way system (KEF 103.2) with an 8-in. woofer and a 1-in. tweeter, and a crossover frequency of 2.5 kHz. They were mounted in a closed box of dimensions (w*h*d*) 264*501*240 mm. The free-field frequency response of the loudspeaker was measured in directions corresponding to the position of the images given in Table I at a distance of 3 m, with the fabric grille removed. The geometrical center of the baffle was defined as the center of the loudspeaker.

The frequency-dependent absorption of the room surfaces was modeled according to measurements of the diffuse field absorption coefficient and the cosine law (see, e.g., Cremer & Müller[4]) in the following way:

The absorption material used on the walls in the modeled listening room was distributed in such a way that the same mean absorption coefficient could be used for all four

TABLE II. Diffuse field absorption coefficients for the various room surfaces as a function of one-third octave frequencies.

One-third oct. frequency [Hz]	Absorption coefficient for walls	Absorption coefficient for floor	Absorption coefficient for ceiling
50	0.05	0.05	0.15
63	0.17	0.06	0.13
80	0.28	0.07	0.11
100	0.45	0.08	0.1
125	0.46	0.09	0.09
160	0.35	0.1	0.08
200	0.34	0.12	0.08
250	0.41	0.14	0.07
315	0.37	0.16	0.07
400	0.4	0.19	0.07
500	0.41	0.24	0.06
630	0.33	0.28	0.06
800	0.25	0.33	0.06
1,000	0.24	0.35	0.05
1,250	0.31	0.33	0.05
1,600	0.15	0.31	0.05
2,000	0.16	0.28	0.04
2,500	0.18	0.25	0.04
3,150	0.16	0.22	0.04
4,000	0.14	0.2	0.03
5,000	0.18	0.18	0.03
6,300	0.18	0.16	0.03
8,000	0.19	0.14	0.02

walls, and was estimated using diffuse field measurements of the individual components. The absorption coefficients for the floor and the ceiling were also based on diffuse field measurements.

The absorption coefficients for the walls, the floor, and the ceiling are given in Table II. The absorption coefficient as a function of angle was found by setting the diffuse field coefficient equal to the absorption at an angle-of-incidence of 45 degrees, and then applying the cosine law for other angles. Rindel[6] discusses the derivation of an angle-dependent absorption coefficient based on diffuse field measurements[7]

The frequency responses of the signal paths for individual loudspeakers in the simulation setup were calculated taking into account the directivity characteristics and absorption coefficients as discussed above, and were implemented as digital filters. The digital signal processing system has been described by Fincham and Small,[8] Brookes et al.[9] and Christensen.[10]

The implemented transfer function for selected reflections are shown in Fig. 1. Note that the transfer functions have been adjusted to include the attenuation due to distance, as given in Table I.

C. Implementation of the reverberant field

The reverberant field was created by six loudspeakers positioned in the equatorial plane of the imaginary sphere described above. Signals for the six loudspeakers were based on the outputs from three commercially available reverberation units (Lexicon PCM 70). Each unit produces two uncorrelated outputs and the settings of the units were slightly different, so that a total of six uncorrelated signals were produced. A block diagram of the complete setup is shown in Fig. 2.

The level of the reverberant field, relative to the level of the direct sound and individual early reflections was calculated for the unfiltered situation, assuming a reverberation time of 0.4 s at 1 kHz, and an exponential decay.

For the filtered situation, the ratio was adjusted to be equal to the ratio measured in the real room at 1 kHz. The ratio as a function of frequency is shown in Table III for the setup and the real room.

D. Subject positioning and calibration procedures

The listener's ears were moved to the specified listening position using a motorized adjustment mechanism built into the chair supporting the subject, and a fixed video camera. A curtain prevented the listener from seeing the simulation setup, while a single LED was used to define the front angular reference. Listeners were free to move their heads, but were instructed to focus their attention on the LED. The performance and calibration of the entire setup was checked on a daily basis using a PC-controlled measuring system. For further details see Paper I.

II. STIMULI

The signals used were continuous broadband (20 Hz–20 kHz) pink noise, and a repeated 1.45-min segment of continuous male speech. The spoken text was a recording of an excerpt of the text used for the standardized Danish speech material for audiometric purposes, made in the large anechoic chamber of the Department of Acoustic Technology. The time structure and spectrum of the chosen speech sample are representative of average Danish speech. High and low pass filtered (24 dB/octave) pink noise, with crossover frequencies at 500 Hz and 2 kHz, respectively, were used for the experiments reported in Sec. V A 3.

For a further description of the speech recordings see Hansen and Munch[11] or the CD cover (Bang and Olufsen CD 101, track 9). The signals were turned off and on using 1.5 s cosine-squared ramps.

The reproduction level was 60 dB SPL for the noise stimuli and approximately 50 dB SPL (time weighting Fast) for the speech. The level of the speech stimulus was set to correspond to normal conversational level at 3-m distance in a living room. The background noise level with the simulation system switched on was 27 dB SPL (time weighting Fast). The one-third octave band level of the background noise is constant ±2 dB for the frequency range 20 Hz–20 kHz.

III. SUBJECTS

Three subjects participated in the experiments. They had all participated in the experiments reported in Papers I and II and must therefore be considered highly trained subjects. They furthermore participated in training experiments before the main experiments. The subjects were paid an hourly rate for their services.
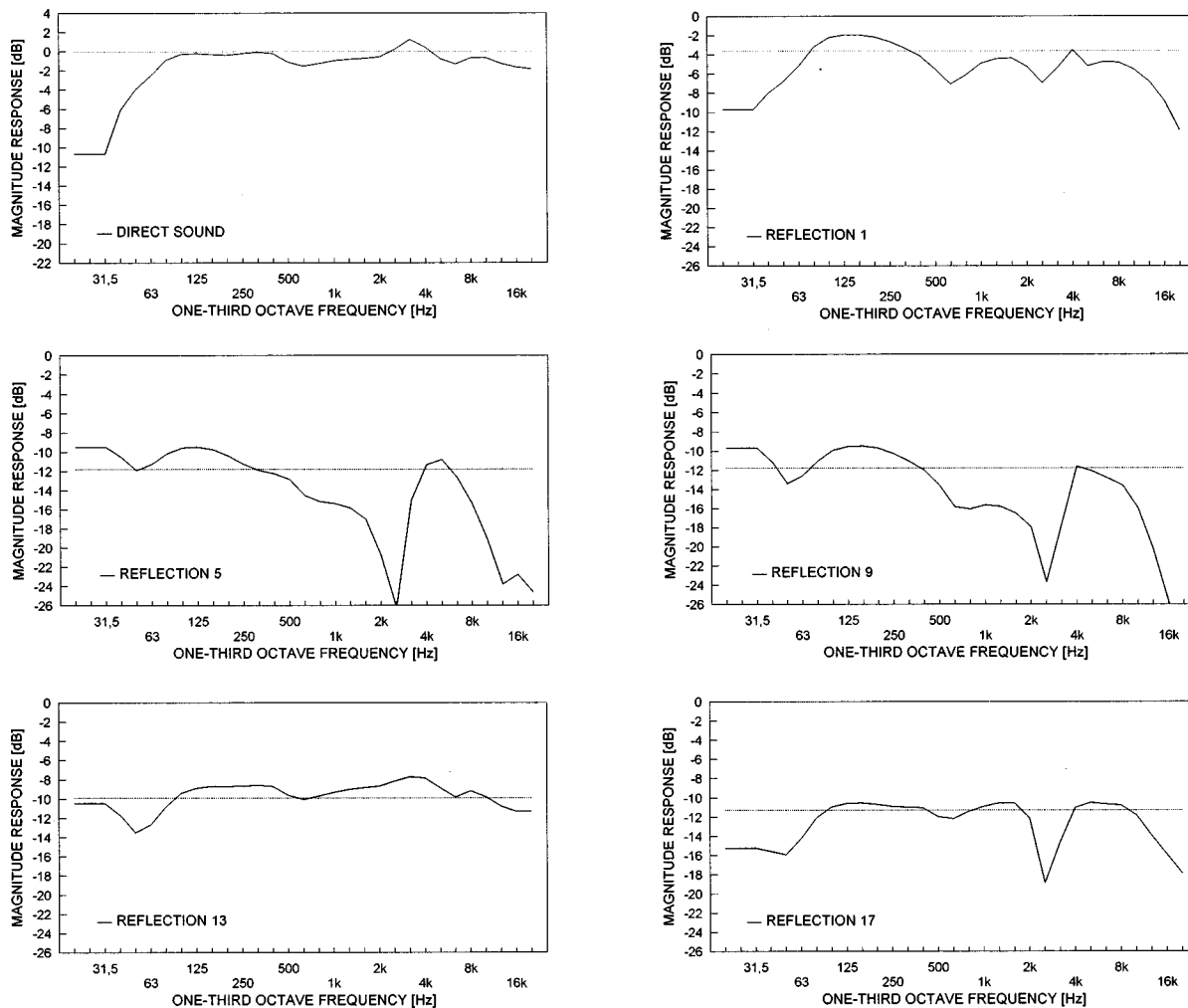
FIG. 1. Magnitude response of the filter functions implemented for the direct sound and individual reflections for the filtered situation. The dashed line represents the frequency-independent attenuation used for the unfiltered situation. Note that transfer functions are only given for the investigated reflections. The reflection number refers to Table I.

IV. GENERAL PROCEDURE

A. Subject's task

The purpose of the experiments was to establish threshold values for changes in the auditory spatial aspects of reproduced sound. In contrast to the timbral thresholds discussed in Papers I and II, the spatial aspects could include a number of different attributes that all could be potential candidates for a definition of a threshold.

Haas,[12] Meyer and Schodder,[13] Lochner and Burger,[14] and Olive and Toole[15] have all investigated the spatial effects of combining a direct sound with a single reflection. They have reported a number of spatial attributes, depending on the signal, the time delay, and level of the reflection, that are all potential cues for a threshold definition.

Haas,[12] for the same level of the direct sound and the reflection, noted changes in the position of the virtual sound source (0–1 ms delay of the reflection), an increase in ''liveliness,'' ''body,'' spaciousness (''pseudostereophonic'' effect) of the sound, and an increase in the overall loudness (0–30 ms).

Meyer and Schodder[13] found an increase in the apparent size of the direct sound source and the spaciousness of the overall sound for a situation where the direct sound and the reflections were equally loud.

Lochner and Burger[14] note that the effects of the reflection was distinctly noticeable long before it was perceived as a separate sound source (0–10 ms delay).

Olive and Toole[15] note an image shift or spreading (delay less than 10 ms), spaciousness and image spreading (10–40 ms) for levels of the reflection well above the absolute threshold which corresponds to a detection of any audible changes.

Toole[16] has an excellent review of the different spatial effects discussed above. The experience thus indicates that great care should be taken in defining the auditory cue when measuring spatial aspects of reproduced sound. The literature reviewed above suggests three distinctly different thresholds based on (1) equal loudness of the direct sound and the reflection as used by Haas,[12] Meyer and Schodder,[13] and Lochner and Burger,[14] (2) the reflection can be identified as a separate sound source as used by Meyer and Schodder[13] and Lochner and Burger,[14] and (3) a just discernible shift in the
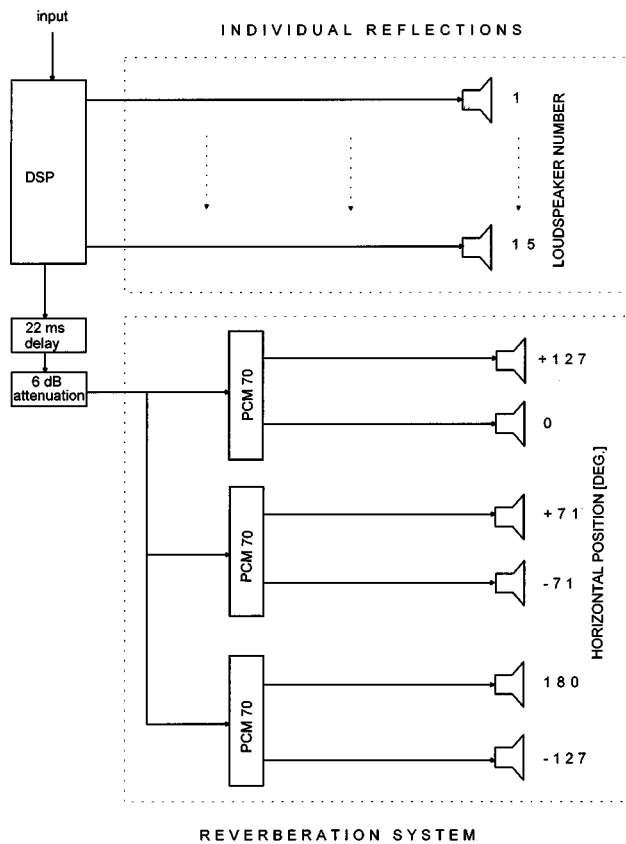
FIG. 2. Block diagram of the complete experimental setup. The DSP unit implemented the transfer functions shown in Fig. 1 and the delay and attenuation due to distance, here shown separately for sake of clarity. Note that the reflection loudspeakers can represent more than one image, cf. Table I and that 0 degrees corresponds to the front angular reference for the subject and positive angles are to the left-hand side.

location or size of the principal auditory image as used by Olive and Toole.[15]

The threshold values corresponding to the definitions (1)–(3) are each separated by approximately 10 dB in level of the reflection and definition 3 leads, according to Olive and Toole,[15] to the lowest threshold approximately 7 dB above the absolute threshold based on timbre. The threshold definitions according to (2) and (3) were thus judged to be the most relevant for the present series of experiments and the subjects were instructed to base their detection on either the appearance of a second and separate sound source or a change in perceived size or position of the principal sound

TABLE III. The level of the direct sound and the early reflections relative to the level of the diffuse part of the sound field as measured in the real room and in the simulation setup.

One octave frequency [Hz]	Ratio for real room [dB]	Ration for simulation [dB]
125	−0.8	2.2
250	0.4	5
500	4.6	5.2
1000	5.3	5.3
2000	6.4	5.4
4000	4.4	9.1
8000	6.5	11.7

source. A pilot experiment was conducted to gain more experience and the results showed quite clearly that the only well defined spatial cue was based on the appearance of a second sound source. By a secondary sound source it is meant that, in addition to the principal sound source, a second source with a distinct spatial position different from the principal source appeared in the sound field. The subjects all agreed on the existence of this cue and its definition. The subjects were thus instructed to use this cue for the main experiments.

Note that in the following part of the paper the threshold related to the appearance of a second sound source will be referred to as the threshold for spatial aspects of the sound field. This is justified by the existence of only three distinctly different thresholds in the simulated sound field: timbre, appearance of a second sound source, and loudness. Of these only one was related to changes in the spatial aspects of the sound field.

B. Method

The threshold of detection of the reflection under investigation was determined using the method of adjustment procedure. The subject could switch between the standard and a comparison sound field by means of two push buttons at any time during the experiment.

The standard and the comparison stimuli are defined as follows:

The *standard* is the complete sound field simulating a single loudspeaker in the listening room, except that the reflection under investigation is missing (−50 dB *re:* direct sound). The *comparison* stimulus is formed by adding, at a variable level, the reflection under investigation to the standard sound field.

The level of the reflection was controlled by the subject by two other push buttons; one would increase the level and the other decrease the level in steps of 0.5 dB. A fifth push button allowed the subject at any time to switch to the initial comparison field with the reflection at it's initial level. This feature allowed the subject to ''refresh'' the initial character of the change in the sound field. Note that the sound was switched on and allowed to reach the maximum reproduction level before the subject could start to adjust the level of the reflection.

The subjects were instructed to stop the experiment with the reflection at a level where they could just discriminate between the standard and the comparison stimulus, and such that a 1 step reduction in level (equal to 0.5 dB) caused the difference to disappear.

The chosen step size was a compromise between resolution of the procedure and ease of use, as a smaller step size caused difficulties for the subjects at the threshold. They found it difficult to adjust the level such that one step down caused the difference to disappear.

The initial level of the reflection was set to either 0 dB or +5 dB re the direct sound, depending on the experiment. This ensured that there was a definite difference between the standard and the comparison stimulus.

Each subject participated in eight experiments as shown in Table IV and in each experiment threshold values were

Exp. number	Attribute	Stimulus	Filtering	Results in Fig.
1	spatial aspects	noise	no	3, 4, 5
2	spatial aspects	noise HP, 500 Hz	no	4
3	spatial aspects	noise LP, 500 Hz	no	4
4	spatial aspects	noise HP, 2 kHz	no	4
5	spatial aspects	noise LP, 2 kHz	no	4
6	timbre	noise	no	3, 8
7	spatial aspects	noise	yes	5, 6
8	spatial aspects	speech	yes	6, 7

measured for five reflections (nos. 1, 5, 9, 13, and 17). The individual thresholds are defined as the mean of four repetitions and the reported threshold is the mean across subjects. The mean threshold is reported relative to the level of the direct sound.

The subject's participation was organized so that two subjects participated at the same time. While one subject was running one block of four repetitions, that is measuring the threshold for one reflection, the other subject was resting. The four repetitions were separated by small breaks of 2–5 min. while the subject remained in the setup and rested. One block lasted approximately 15 min. After completing one block the two subjects interchanged and the other subject ran a block. A pair of subjects would work for approximately two hours equal to running five blocks each, before they had a break of 2–4 h. No subject would participate in more than two such 2 h sessions per day.

Threshold values have only been measured for reflections 1, 5, 9, 13, and 17 in the experiments. The limitations in number of reflections was caused by time constraints, and the selection of reflections was based on a wish to be able to compare results with those of timbre, reported in Paper II.

C. Discussion of experimental method

When the level of the reflection was set to its initial level there was a definite perceived difference between the standard and the comparison stimulus. The difference consisted of a loudness difference, the appearance of a second sound source, and a timbral difference. A decrease in the reflection level caused the loudness difference to disappear, and a further decrease caused the differences related to the second source to disappear. The difference in timbre was the last to disappear, which means that the threshold of interest in the present series of experiments was reached while the timbral differences still existed. This means that the chosen experimental method should allow the subjects to discriminate between two coexisting cues. This proved difficult when the adaptive two alternative forced choice method as employed in Papers I and II was used. Another method was thus needed and as other researchers in this area (Haas,[12] Seraphim,[17] and Olive and Toole[15]) had used the method of adjustment (MOA) it was decided to examine this method further.

Cardozo[18] noted that one of the principal applications of the MOA is in cases where the stimuli differ for one or more attributes at the same time. It is well known (Cardozo,[18] Wier et al.,[19] and Hesse[20]), however, that results obtained with adjustment procedures, where the subject actively changes the stimuli under test, are different from those obtained with forced choice procedures, where the subjects have to choose one of two or more alternative presentations. The main criticism of the MOA is caused by the fact that the influence of variables like the step size, the number of stimuli presentations used for the evaluation, and the subjects' strategy for termination cannot be quantified like they can for the forced choice procedures. The MOA procedure, however, has been shown (Cardozo,[18] Hesse[20]) to possess a number of advantages compared to forced choice procedures. These include the ability to focus on a specific attribute of several possibilities, that the subject can optimize the stimulus presentation to suit his needs, that it has a significantly higher efficiency, and that the intra-individual reproducibility is higher.

The advantages of the MOA procedure, as discussed above, were found to outweigh the disadvantages in the present situation and it was decided to test the method in a series of training experiments. The results showed that the subjects were quite comfortable with the method and that they had no problems in separating the two auditory cues. It was thus decided to use the method in the main experiments.

However, to be able to link the current set of results to those reported in Papers I and II it was decided to measure the differences between timbral thresholds obtained with the MOA and 2AFC procedures. It was thus implicitly assumed that similar differences would be found for spatial aspects. The results are further discussed in Sec. VI C.

V. RESULTS

A. Results for the unfiltered situation

The purpose of these experiments (Nos. 1–6 in Table IV) was to measure the threshold of detection (TD) for individual reflections for different conditions, and to compare the TD values with the natural level of the reflection as calculated by an image model. However, the basic assumption that the subject can discriminate between a change in the spatial aspects of the reproduced sound and a timbral change, will first be examined.

1. Discrimination between thresholds for timbre and spatial aspects

The experiments are based on the assumption that subjects can discriminate between a change in spatial aspects and timbre of the sound field. The timbral threshold is assumed to represent the lowest threshold and changes in spatial aspects are found for higher levels of the reflection. Below the lowest threshold there are no subjective differences at all between the two sound fields.

The threshold of detection for the two tasks were measured and are shown in Fig. 3. The results show that the TD values for timbre are always lower than the TD's for spatial

FIG. 3. Mean threshold values for a change in spatial aspects and in timbre for the unfiltered situation and the noise signal. The mean values are based on three subjects and four repetitions for each subject. Confidence intervals (95%) based on the within-subject variance are ±1.2 dB (spatial) and ±1.8 dB (timbre). The natural levels of the individual reflections based on an image model are also shown as are the individual reflection numbers according to Table I.

FIG. 4. Mean threshold values for a change in spatial aspects for the unfiltered situation as a function of band width of the noise signal. The mean values are based on three subjects and four repetitions for each subject. Confidence intervals (95%) based on the within-subject variance are ±1.2 dB (broadband), ±1.1 dB (LP500 Hz), ±1.8 dB (HP500), ±1.1 dB (LP2K) and ±1.8 dB (HP2K). The individual reflection numbers are shown according to Table I.

aspects. This is in agreement with the reports of the subjects, who claimed that they always could hear a timbre difference when they reached the spatial threshold.

The differences observed in Fig. 3 between the timbral and spatial thresholds are approximately 3 dB for reflections 1, 5, 9, and 17 and 1.5 dB for reflection 13. Olive and Toole[15] found that their "image shift" thresholds were approximately 7 dB higher than the timbral thresholds. According to the discussion in Sec. IV A it was, however, expected that the "image shift" threshold would be some where between the timbre thresholds and the threshold based on the present "separate sound source" definition. It should, however, be remembered that it was not possible to detect any changes in the simulated sound field corresponding to the Olive and Toole[15] definition. Thus care should be taken when relating the threshold values based on the two definitions.

It should be noted that the TD's for spatial aspect and timbre are only significantly different for reflections 1, 5 and 9 and that the 95% confidence interval of the timbre threshold is nearly twice the value of the interval for the spatial threshold. This suggests that the psychometric functions for spatial aspects are apparently steeper than those for timbre.

The results thus indicate that subjects are able to reliably discriminate between the two types of changes in the auditory impression.

The use of loudness differences as cues were also examined. Papers I and II reported on measurements of SPL differences between the standard and the comparison stimulus with the reflection at TD values similar or higher than those reported in this paper. As all the SPL differences corresponding to those TD's were lower than those required for discrimination based on loudness differences, it is concluded that loudness could not have been a cue in any of the present situations.

2. Comparison of natural levels and measured thresholds of individual reflections

The TD's for spatial aspects are shown in Fig. 3 for the noise signal, together with the natural levels. The TD's for reflections 1 (floor), 5 (ceiling), and 9 (left wall) are either lower or not significantly different from the natural levels. This suggests that the first order reflection from the floor and second order reflections from the ceiling and left-hand wall contribute on an individual basis to the auditory spatial aspects of the sound field.

The TD's for timbre for reflections 1, 5, and 9 are all seen to be significantly lower than the natural levels and thereby contributing individually to the timbre of the sound field. This confirms the findings of Paper II for reflections 1 and 9, although the present TD's are lower than those found in Paper II. The discussion in Sec. VI C shows that the differences in the TD's are the result of using two different experimental procedures.

The results of Papers I and II, and the present thus indicate that the first order reflection from the floor and the second order reflections from the left hand wall will individually influence both timbral and spatial aspects of the sound field.

3. Threshold of detection for individual reflections for high- and low-pass filtered noise signals

The frequency bandwidth of the signal is known to have an influence on the ability to localize a sound source (see Blauert[21] for a review). Further, it would be of great interest for the designers of loudspeakers to know how the different frequency ranges influence the spatial aspects, as this would help in the definition of how loudspeaker directivity characteristics should be designed as a function of frequency.

Thus, it was decided to conduct a series of experiments with the purpose of examining the influence of frequency range of the signal. Threshold values were measured using high- and low-pass filtered pink noise. The crossover points for the high- and low-pass filters were chosen to be representative of the crossover frequencies used in standard two or three-way loudspeaker systems.

The TD's for high- and low-pass filtered noise signals are shown in Fig. 4, together with the TD's for a broadband noise signal from Fig. 3. The results show that the TD's increase significantly for reflections 1, 5, 9, and 13 when the signal is low-pass filtered at 500 Hz and for reflections 1, 5, and 9 when the signal is low-pass filtered at 2 kHz. The threshold values for the high-pass filtered signal are not sig-

nificantly different from the broadband based thresholds. Here, it is interesting to note that the results reported in paper II suggested that the spectral changes in the frequency range 500 Hz–2 kHz are most important for the threshold detection of timbral differences.

A comparison between the natural levels (see Fig. 3) and the TD's shown in Fig. 4 shows that the TD's for both high- and low-pass filtered signals for reflection 1 are lower than the natural levels. For reflections 5 and 9 only the high-pass filtered TD's are lower than the natural levels. For reflections 13 and 17 all the filtered TD's are higher than the naturals levels.

The results thus suggest that the spectral energy above 2 kHz, for some of the individual reflections, determines the degree of influence the reflection will have on the spatial aspects of the reproduced sound. The results show that reflections 1 (floor), 5 (ceiling), and 9 (left wall) are so strong that they will contribute separately to the spatial aspects, if their spectra contain sufficient energy in the frequency range above 2 kHz. If the reflections only contain energy below 500 Hz, only the first-order floor reflection will contribute to spatial aspects.

B. Results for the filtered situation

The purpose of these experiments (nos. 7 and 8 in Table IV) was to measure the threshold of detection for individual reflections, with transfer functions modified according to measured directivity characteristics of a real loudspeaker, and absorption as a function of frequency for the room surfaces. The measured thresholds will be compared with those for the unfiltered situation to assess the effect of the filtering, and also compared with the "natural" level of the reflection as calculated by an image model. Note that the use of the natural levels is a compromise to describe the transfer functions shown in Fig. 1 by a single number. It is seen to be a reasonable approximation for reflections 1, 13, and 17. The threshold values for the filtered situation are assumed to be more in accordance with the conditions of a real room. The thresholds have also been measured using speech in order to assess the importance of signal type.

1. The influence of filtering

The measured threshold values for the filtered situation are compared to those of the unfiltered situation and the natural levels, in Fig. 5.

The thresholds for the filtered situation are significantly higher for all reflections except reflection 17, and especially large changes are seen for reflections 5 and 9. A visual inspection of the transfer functions for the individual reflections shown in Fig. 1 shows that the filtering mainly attenuates energy in the middle and high frequency regions. This is especially the case for reflections 5 and 9. These two reflections also have the largest changes in their TD's. The changes in threshold level caused by the introduced filtering are thus in agreement with the results based on the high- and low-pass filtered signals, shown in Fig. 4.

The effect of the filtering is also that all thresholds except that for reflection 1 are now significantly above the natural levels. This means that only the first-order floor re-
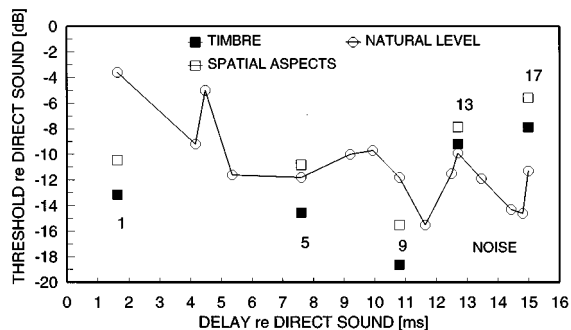

FIG. 5. Mean threshold values for a change in spatial aspects for the filtered and unfiltered situations for the noise signal. The mean values are based on three subjects and four repetitions for each subject. Confidence intervals (95%) based on the within-subject variance are ±1.1 dB (filtered) and ±1.2 dB (unfiltered). The natural levels of the individual reflections based on an image model are also shown as are the individual reflection numbers according to Table I.

flection is likely to be individually audible and so be able to influence the spatial aspects of the sound field.

2. The influence of signal type

Previous results (Olive and Toole,[15] Papers I and II) have shown that the signal type can have an influence on TD values for timbre so it was decided to test this for the spatial aspects as well. Two classes were identified: continuous and discontinuous sounds represented in this experiments by noise and speech, respectively.

The thresholds of detection for the noise and speech signals are shown in Fig. 6. The threshold values for the speech signal are seen to be significantly higher than those for the noise signal for all reflections. This has the consequence that the thresholds for the speech signal are all higher than the natural levels (see Fig. 5) except for reflection 1. This suggests that only reflection 1 will individually influence the spatial aspects for signals like speech.

A comparison between threshold values based on noise, low-pass filtered at 500 Hz and the speech signal, respectively shows that the thresholds are not significantly different except for reflections 5 and 9. The similarity between the

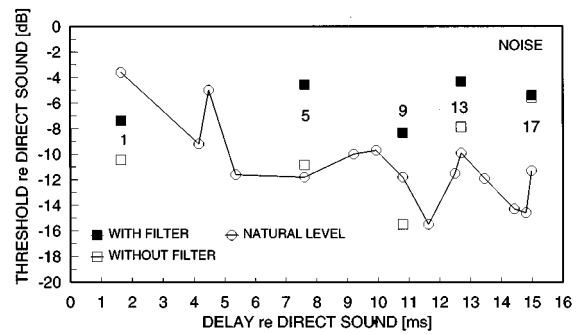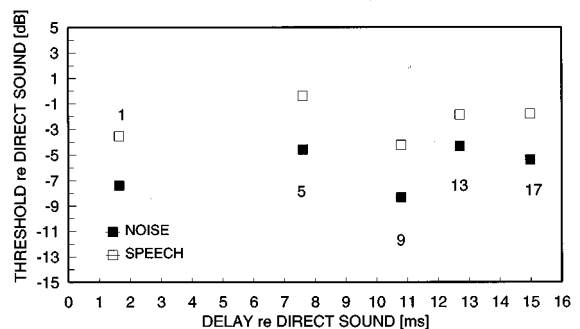

FIG. 6. Mean threshold values for a change in spatial aspects for the filtered situation and speech and noise. The mean values are based on three subjects and four repetitions for each subject. Confidence intervals (95%) based on the within-subject variance are ±1.1 dB (noise) and ±0.8 dB (speech). The individual reflection numbers are shown according to Table I.
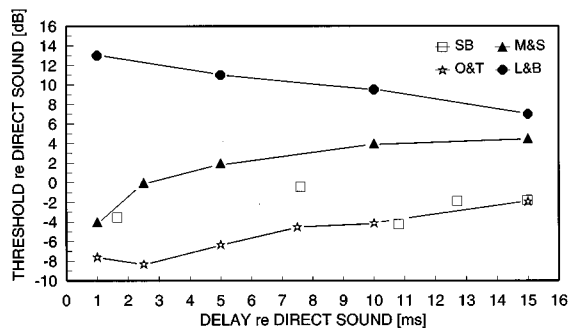
FIG. 7. Results from Meyer and Schodder[13] (M&S) (anechoic), Lochner and Burger[14] (L&B) (anechoic), Olive and Toole[15] (O&T) (IEC room), and the TD's from Fig. 6 (SB) plotted for comparative reasons. The signal was speech for all cases and the note in brackets indicate in which environment the data were obtained.

thresholds could be explained by the fact that the spectrum of the speech signal has its main part of the energy in the frequency range 70–500 Hz.

VI. DISCUSSION

A. Comparison with the literature

This investigation is, to the knowledge of the author, the first to measure the threshold of detection of several individual reflections for a change in the spatial aspects of a reproduced sound field. No other results are therefore available to directly compare with, however, a number of results have been published for situations that are closely related so these will be examined in the following.

Olive and Toole[15] measured the "image shift" threshold for a single controlled reflection using speech in an anechoic chamber, a semianechoic room and a standard listening room. Their "image shift" threshold criterion was, as discussed in Sec. IV A, however, different from the present. Meyer and Schodder[13] and Lochner and Burger[14] measured the threshold for a single reflection in an anechoic chamber using speech for a number of threshold definitions including one similar to the present. For comparisons, the results of Olive and Toole,[15] Meyer and Schodder,[13] Lochner and Burger,[14] and the TD's for speech from Fig. 6 are shown in Fig. 7.

The difference between the Meyer and Schodder[13] and Lochner and Burger's[14] results are at least partly due to the difference between the threshold definition "echo barely inaudible" as defined by Meyer and Schodder[13] and "echo clearly audible" as used by Lochner and Burger.[14] The present TD's are based on a threshold definition that is most similar to that used by Lochner and Burger[14] so the difference between their results and the present suggest that the presence of other individual reflections and a reverberant field increases the audibility of individual reflection quite significantly. This would be supported by results of Leakey and Cherry[22] and Chiang and Freyman[23] who showed that addition of noise uncorrelated both spatially and electrically with the main signal increased the audibility of a delayed signal significantly. Cremer and Müller[4] has shown that the reverberant field is uncorrelated with the individual reflec-

tions and it is argued in Paper I that this also applies to the simulated sound field.

Olive and Toole's[15] results, obtained in a listening room similar to the present, are shown in Fig. 7. They are seen to be significantly lower than the present TD's for short delay times (<10 ms) and similar for longer delays. The lower thresholds could be explained by the difference between the "image shift" and "separate sound source" definitions as discussed in Sec. IV A. However, as discussed in Sec. V A 1, it might not be possible to compare the two situations as the Olive and Toole[15] defined threshold did not exist in the simulated sound field.

The hypothesis that the reverberant field increases the audibility of individual reflections is not completely supported by the results of Olive and Toole.[15] They found insignificant differences between threshold values for short delays (<8 ms) in the three tested environments. For longer delays (10–20 ms) they found larger differences (up to 6 dB), but only partly supporting the hypothesis. Two factors should be considered in this context. The first is that the loudspeaker used to simulate the investigated reflection, had the same full bandwidth as the loudspeaker producing the direct sound. This means that there must have been a spectral difference between the natural reflection, present when the test reflection was switched off, and the test reflection. Freyman et al.[24] and Clifton et al.[25] have shown that sudden changes in the spectral content of the reflection causes the precedence effect to break down. The second factor is the "plausibility effect" suggested by Rakerd and Hartmann.[26] They showed that if the delay, the spectrum or the angle of incidence of the reflection are not "plausible" in relation to the test environment it will cause the precedence effect to break down. Both of these factors could have had an influence on the thresholds obtained by Olive and Toole.

B. Comparison with results on the precedence effect

The precedence effect is the effect that the auditory event appears in a single direction determined by the direction of the first arriving wavefront. Later arriving wavefronts, for example reflections from walls close to the sound source emitting the first wavefront, does not influence the directional impression.

Experiments on this phenomena requires a definition of the threshold and as the discussion in Sec. IV A indicated, several definition have been used by the researchers in this field. The reader is referred to Blauert[21] (sections 3.1.2, 4.4.2, and 5.4) for further discussions of threshold definitions.

The definition used by Blauert[21] is the so-called "echo" threshold where "echo" refers to the impression of a second auditory event in addition to the primary event generated by the first wave front. Note that "echo" includes more than the traditional definition of an echo, that is a replication of an auditory event, separated in time from the first. Blauerts "echo" threshold definition is that introduced by Lochner and Burger[14] where the "echo is clearly audible." This definition is quite close to the definition used by the author for the present series of experiments as the subjects were instructed to stop the experiment when they could just dis-

criminate between the standard and the comparison stimulus. It was therefore found worthwhile to compare the obtained results to some of those reported in the literature on the precedence effect. Blauert[21] has an excellent review of the results on the precedence effect, so only results in direct relation to the present investigation will be examined.

1. The effect of angle of incidence of the reflection

Rakerd and Hartmann[26] found that vertical reflections have a smaller influence on the precedence effect compared to horizontal reflections. This applies to delay times in the range 0.6 to 2.3 ms. However, Guski[27] found that adding reflective surfaces on the floor and ceiling in an otherwise anechoic environment had a larger influence on localization accuracy compared to adding surfaces in the horizontal plane (walls). The reported results are in agreements with the results of Guski,[27] as only the floor reflection is likely to have a significant influence on the spatial aspects of the sound field.

2. The effect of signal bandwidth

The influence of signal bandwidth on the effectiveness of the precedence effect has been examined by Blauert and Cobben[28] using a standard stereophonic arrangement and narrow-band (one-third octave) pulses with center frequencies 0.5, 1, and 2 kHz. They found that the horizontal angle of the sound image as a function of delay of the right loudspeaker signal was similar for the broadband signal and the 2 kHz signal. The mean values for the 1 and 0.5 kHz signals deviated from the broadband results, and varied strongly as a function of the delay of the signal. This leads to the conclusion that the precedence effect shows anomalies for low frequency narrow-band signals. The results in Fig. 4 also suggest that the localization mechanism works differently for high- and low-pass filtered signals. The broadband noise thresholds are similar to those for the 0.5 and 2 kHz high-pass filtered noise, and significantly different from those based on low-pass filtered noise at 0.5 and 2 kHz. These results are further supported by Blauert and Col[29] who found that the echo thresholds in a precedence effect paradigm were similar for broadband impulses, 2.5 kHz bandpass, and 2.7–3.4 kHz bandpass impulses. Low-pass filtered impulses at 1 kHz, 1.5 kHz, and 270 Hz–340 Hz bandpass filtered impulses had significantly higher echo threshold values. Freyman *et al.*[24] also found evidence that the echo suppression is influenced differently for high- and low-pass filtered signals.

Blauert and Cobben[28] attributed the anomalies in the precedence effect at lower frequencies to the fluctuation in position of the absolute maximum of the interaural cross correlation function (IACCF). They speculate that the position of the maximum corresponding to the first sound will fluctuate for several milliseconds and this will interact with the maximum corresponding to the delayed sound. If this assumption is correct it follows that (1) the precedence effect should return to normal for delays longer than the time of fluctuation and (2) that the use of a stationary signal would enable the subject to delay the decision on the position of the sound source until the IACCF had stabilized. This suggests that the anomalies observed at low frequencies using click stimuli would not be present if a continuous signal was used. However, the results in Fig. 4 shows that the TD's also depends on the frequency content for a stationary signal, for reflections with delays similar to the length (1–2 ms) of the fluctuations in the IACCF, and for reflections with delays so long that the IACCF should have stabilized. This suggests that the difference in threshold values for the high- and low-pass filtered signal, as shown in Fig. 4, cannot be explained by fluctuations in the IACCF for the low-pass filtered signals.

Another factor should be considered for an explanation of the dependency of frequency range for the precedence effect. This is a subject's ability to localize low-pass filtered signals. Hartmann[30] noted that it is very difficult to localize low frequency pure tones in a room. He noted that subjects in that case adopt a strategy with a high consistency, but that the strategy depends strongly on the subject. The same tendency has been observed in the present experiments. The between-subject variance was four to ten times higher for the low-pass filtered signals compared to the broadband and high-pass filtered signals. However, the within-subject variance (consistency) was similar for all the signal types. Subjects also reported that they had difficulty in finding a cue for the low-pass filtered signals.

C. Influence of experimental procedure

The method of adjustment (MOA) has been used for the experiments reported in this paper for reasons discussed in Sec. IV C. However, the results presented in Papers I and II on the detection of timbral differences are based on an adaptive two alternative forced choice (2 AFC) procedure, and in order to be able to compare the two sets of results, the threshold of detection for timbre is shown for the two procedures in Fig. 8. The thresholds of detection, based on the MOA procedure, are seen to between 3–5 dB lower than those based on the 2 AFC procedure. This range of differences is in agreement with that observed by Bech[31] for experiments on a single reflection in combination with the direct sound.

VII. SUMMARY OF FINDINGS

This section contains a summary of the major findings. The validity and generality of these depend among other things on the accuracy of the electroacoustic simulation of the sound field. This subject has been discussed in some detail in Papers I and II and readers are referred to those papers. The validity of the findings also depends on the generality of the characteristics of the modeled loudspeaker and the room.

The loudspeaker was a standard two-way system both in terms of size, electrical, and acoustic characteristics. It is still believed to be representative of a large portion of today's available loudspeaker systems.

The dimensions of the modeled room and its reverberation time are within the requirements of the IEC 268-13 recommendation, whereby the room should be representative of a domestic listening room. The modeled absorption charac-
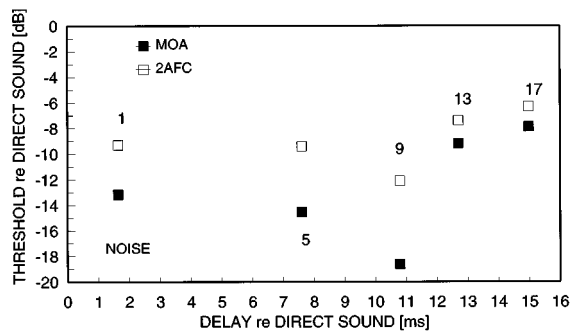
FIG. 8. Mean threshold values for a change in timbre for the unfiltered situation and the noise signal obtained by Method of Adjustment (MOA) and an adaptive (two down-one up) two-alternative forced choice procedure (2AFC). Mean values are based on three subjects and four repetitions per subject (MOA) and eight subjects and 400 trials per subject (2AFC). Confidence intervals (95%) based on the within-subjects variance are ±1.2 dB (MOA) and ±1 dB (2AFC). The individual reflection numbers are shown according to Table I.

teristics are based on the actual materials used in the room. The carpet is typical of a Danish domestic carpet used in living rooms, etc., and it is difficult to estimate how representative this would on a world wide basis. The absorption characteristics of the walls are determined by a specially constructed panel system that includes both membrane (low-frequency) and porous (high-frequency) absorbers. The same panel was used on all walls so the same absorption characteristics could be used for all walls. This would not be seen as representative of a standard domestic room and the same apply for the use of membrane absorbers on the walls. The ceiling consists of a flat and highly reflective metal surface that functions as a cooling panel. The absorption characteristics are only slightly higher than those of a painted hard surface like concrete. Such surfaces are fairly common in Denmark and are also believed to be representative of many modern buildings in Europe.

The results have indicated that the spectral energy above 2 kHz of the individual reflection determines the importance of the reflection for the spatial aspects. The discussion above thus indicates, that the influence of the wall reflections would be underestimated in the modeled situation, because of the nontypical porous absorbers on the wall surfaces. The influence of the floor reflection would tend to be overestimated, especially in rooms where a carpet with more high frequency absorption was used. However, although such carpets are fairly common in certain countries, they are not in the northern part of Europe. Thus to conclude on the generality of the results: they are strictly speaking only applicable to rooms that are acoustically fairly similar to that modeled.

It should also be emphasized that the findings of this paper are based on the threshold of detection values. This means that one should be careful when discussing the qualitative effects of reflections that have levels above the measured threshold values. This is especially important if the results are used as basis for, for example, the design of the directivity characteristics of loudspeaker systems.

The major findings are:

(1) Subjects can reliably discriminate between spatial and timbre cues.
(2) The spectral energy above 2 kHz of individual reflections determines the degree of influence the reflection will have on the spatial aspects of the reproduced sound field.
(3) Under conditions as in the simulated room, with a standard two-way loudspeaker system reproducing broadband noise or speech, only the first order floor reflection is so strong that it will contribute separately to the spatial aspects of the sound field.

ACKNOWLEDGMENTS

[1] S. Bech, ''Timbral aspects of reproduced sound in small rooms. I,'' J. Acoust. Soc. Am. **97**, 1717–1726 (1995).
[2] S. Bech, ''Timbral aspects of reproduced sound in small rooms. II,'' J. Acoust. Soc. Am. **99**, 3539–3549 (1996).
[3] IEC Recommendation 268-13. ''Sound System Equipment, Part 13: Listening Tests on Loudspeakers.'' International Electrotechnical Commission, Publication 268-13, 1985.
[4] L. Cremer and H. A. Müller (translated by T. J. Schultz), *Principles and Applications of Room Acoustics* (Applied Science Publishers, New York, 1982), Vol. 1, pp. 17–19.
[5] J. M. Berman, ''Behaviour of sound in a bounded space,'' J. Acoust. Soc. Am. **57**, 1275–1291 (1975).
[6] J. H. Rindel, ''Modeling the angle-dependent pressure reflection factor,'' Appl. Acoust. **38**, 223–234 (1993).
[7] Note that Rindel[6] concludes that the diffuse field coefficient should be set equal to the absorption at 55 degrees angle of incidence. The 55 degrees was found in experiments conducted after the present. The maximum error is 0.9 dB for 100 and 125 Hz for reflection No. 5. For all other situations the error is smaller than 0.5 dB.
[8] L. R. Fincham and R. H. Small, ''The application of digital signal processing to large scale simulation of room acoustics. Part I-Signal processing requirements in the Archimedes project,'' 90th Convention of The Audio Engineering Society, Paris, France, 19–22 February (1991), Preprint 3055.
[9] D. M. Brookes, R. I. Harris, and R. J. Wilson, ''The application of digital signal processing to large scale simulation of room acoustics. Part III-DSP engine hardware topology and control software for multichannel simulation,'' 90th Convention of The Audio Engineering Society, Paris, France, 19–22 February (1991), Preprint 3057.
[10] K. B. Christensen, ''The application of digital signal processing to large scale simulation of room acoustics. Part II—Frequency response modeling and optimization software for a multichannel DSP engine,'' J. Audio Eng. Soc. **40**, 260–276 (1992).
[11] V. Hansen and G. Munch, ''Making recordings for simulation tests in the Archimedes Project,'' J. Audio Eng. Soc. **39**, 768–774 (1991).
[12] H. Haas, ''Über den Einfluss eines Einfachechos auf die Hörsamkeit von Sprache,'' Acustica **1**, 49–58 (1951) [''The influence of a single echo on the audibility of speech,'' J. Audio Eng. Soc. **20**, 147–159 (1972)].
[13] E. Meyer and G. R. Schodder, ''Über den Einfluss von Schallrückwürfen auf Richtungslokalisation und Lautstärke bei Sprache,'' Nach. Akad. Wiss. Göttingen, Math. Phys., Klasse IIa **6**, 31–42 (1952).
[14] J. P. A. Lochner and J. F. Burger, ''The subjective masking of short time delayed echoes by their primary sounds and their contribution to the intelligibility of speech,'' Acustica **8**, 1–10 (1958).
[15] S. E. Olive and F. E. Toole, ''The detection of reflections in typical rooms,'' J. Audio Eng. Soc. **37**, 539–553 (1989).
[16] F. E. Toole, ''Loudspeakers and rooms for sterephonic sound reproduction,'' Proceedings of 8th International Conference of the Audio Engineering Society, 3–6 May, Washington, DC, 71–91 (1990).

[17] H. P. Seraphim, ''Über die Wahrnehmbarkeit mehrerer Rückwürfe von Sprachschall,'' Acustica **11**, 80–91 (1961).

[18] B. L. Cardozo, ''Adjusting the method of adjustment: SD vs DL,'' J. Acoust. Soc. Am. **37**, 786–792 (1965).

[19] C. C. Wier, W. Jesteadt, and D. M. Green, ''A comparison of method-of-adjustment and forced-choice procedures in frequency discrimination,'' Percept. Psychophys. **19**, 75–79 (1976).

[20] A. Hesse, ''Comparison of several psychophysical procedures with respect to threshold estimates, reproducibility and efficiency,'' Acustica **59**, 263–273 (1986).

[21] J. Blauert, *Spatial Hearing. The Psychophysics of Human Sound Localization* (MIT, London, 1997).

[22] D. M. Leakey and E. C. Cherry, ''Influence of noise upon the equivalence of intensity differences and small time delays in two loudspeaker systems,'' J. Acoust. Soc. Am. **29**, 284–286 (1957).

[23] Y. Chiang and R. L. Freyman, ''The effect of background noise on the precedence effect,'' J. Acoust. Soc. Am. **97**, 3280 (A) (1995).

[24] R. L. Freyman, R. K. Clifton, and D. D. McCall, ''Sudden changes in simulated room acoustics influence echo suppression,'' J. Acoust. Soc. Am. **95**, 2898 (A) (1994).

[25] R. K. Clifton, R. L. Freyman, R. Y. Litocski, and D. D. McCall, ''Listeners' expectations about echoes can raise and lower echo threshold,'' J. Acoust. Soc. Am. **95**, 1525–1533 (1994).

[26] B. Rakerd and W. M. Hartmann, ''Localization of sound in rooms. II: The effects of a single reflecting surface,'' J. Acoust. Soc. Am. **78**, 524–533 (1985).

[27] R. Guski, ''Auditory localization: effects of reflecting surfaces,'' Perception **19**, 819–830 (1990).

[28] J. Blauert and W. Cobben, ''Some consideration of binaural cross correlation analysis,'' Acustica **39**, 96–104 (1978).

[29] J. Blauert and J. Col, ''Irregularities in the precedence effect,'' Adv. Biosci. **83**, 531–539 (1992).

[30] W. M. Hartmann, ''Localization of sound in rooms,'' J. Acoust. Soc. Am. **74**, 1380–1391 (1983).

[31] S. Bech, ''Audibility of a single reflection with short delay times,'' 13th International Congress on Acoustics, Yugoslavia **1**, 447–450 (1989).

Use of reciprocity to characterize ultrasonic transducers in air above 100 kHz

Michael J. Anderson and Xu Liu

Department of Mechanical Engineering, University of Idaho, Moscow, Idaho 83844-0902

The three-transducer free-field reciprocity calibration technique has been extended to apply to ultrasonic transducers operating in air at frequencies above 100 kHz. The reciprocity method was extended to apply to this frequency range by correcting for attenuation, which is severe in air, and for diffraction. Validation of the extended reciprocity calibration technique was performed by comparing experimental determinations of receive and transmit sensitivity with predictions obtained from a mathematical model for the test transducers and calibration system. It is believed that these are the first comprehensive, broadband experimental determinations of absolute transmit and receive sensitivity to appear in the technical literature for transducers operating in air over the frequency range 100–500 kHz. Receive and transmit sensitivity measurements obtained with the extended reciprocity calibration technique agreed to within 2.5 dB of model predictions. The location of the resonance peaks in the sensitivity measurements had a maximum difference of 7% from those inferred from measurements of transducer admittance and those predicted by the transducer model. It was concluded that both the extended reciprocity calibration technique and the transducer model were accurate to within this level of discrepancy. © *1998 Acoustical Society of America.* [S0001-4966(98)05601-X]

PACS numbers: 43.58.Vb, 43.35.Yb [SLE]

INTRODUCTION

The availability of a mathematical model to describe the performance of a transducer is of prime importance in its development and application. Several new models[1–5] have been proposed to predict the performance of ultrasonic transducers intended for generation and detection of ultrasound in air in the frequency range 50 kHz–2 MHz. The utility of a model is only as good as it is able to accurately predict the actual transducer performance. Consequently, an experimental technique must be used to characterize the transducer and determine the accuracy of the transducer model.

Several factors contribute to the difficulty in characterizing the performance of ultrasonic transducers operating in air over the frequency range 100 kHz–1 MHz. Diffraction is important at frequencies in the lower end of this bandwidth for transducers of normal size, between 3.12 mm (1/8 in.) and 50.8 mm (2 in.) in diameter. Attenuation of acoustic waves in air increases steadily, affecting measurements near 100 kHz and becoming very significant as frequencies approach 500 kHz. At 100 kHz, 500 kHz and 1 MHz, attenuation rates in air are approximately 0.0297, 0.45, and 1.70 dB/cm, respectively. The current standard[6] for prediction of attenuation in air only guarantees 10% accuracy at ultrasonic frequencies. Methods used for calibrating transducers that operate in the audio and lower ultrasonic frequency range, 1 Hz–100 kHz, are not easily extended to ultrasonic frequencies. Apparatus designed for calibration in the audio frequency range, the pistonphone, electrostatic actuator, laboratory standard microphone or reciprocity calibrators are not appropriate for frequencies exceeding 100 kHz. In all cases, the characterization procedure must be validated by an independent mechanism. Preferably, an independent physical mechanism is used to validate the characterization technique,

such as with optical techniques, in which the wavelength of light can be measured by several independent ways. An alternate way to validate the characterization technique is to show that the measurements converge to an accurate model of the transducers and calibration system.

Experimental techniques that have been used to characterize ultrasonic transducers intended for use in air include seven types; measurement of electrical impedance (or admittance),[1,7] use of calibrated reference microphones,[3–5,8–11] laser interferometry,[2,10,12] measurement of insertion loss,[2] impulse response with a transmitter–receiver pair and use of calibrated airborne waves generated by laser excitation of solid plates,[13] and optical tomography synthesized from Raman–Nath diffraction of laser light in an airborne sound beam.[14] In a recently published article,[15] a PVDF membrane hydrophone was used as a reference to calibrate ultrasonic transducers operating in air over the frequency range 0.25–20 MHz. This reference microphone calibration method relied upon a linear systems model to relate the calibrated performance of the hydrophone as it operates in water to its performance in air.

As reported, all of these techniques, with the exception of the impulse measurement of frequency response, gave an absolute measure of transducer behavior. Measurement of electrical impedance is capable of verifying internal lumped impedances of the transducer model, including the radiation impedance, but does not directly determine the acoustic performance of the transducer. Calibrated microphones are limited to frequencies below 140 kHz, and diffraction corrections must be made because the diameter of the microphone is ≈1.3 wavelengths at 140 kHz. Laser interferometric methods have a wide frequency response, 10 kHz to 10 MHz, and give an absolute measure of the motion of the active trans-

ducer surface. Laser interferometry is, however, sensitive to spatial phase variations in the motion of the transducer active area, and a measure of the spatial resolution of this technique was not reported in Ref. 12. This is a problem in the application of interferometry to the calibration of transducers that use a flexible diaphragm to generate and detect airborne ultrasound. Validation of the insertion loss characterization technique relies upon the convergence of the experimental measurements to the predictions of an accurate physical model for the transducer. Measurements contained in Ref. 2 show an impressive correspondance between measured and predicted insertion loss for a capacitive transducer over the frequency range 1–2.5 MHz. Like measurement of transducer impedance, measurement of insertion loss does not give a direct measure of the acoustic performance of the transducer. Use of waves generated by laser interaction with a solid plate is a promising technique, but further work is required to quantify the geometry of the airborne acoustic field, and its interaction with the receiving transducer. Measurement of transmit sensitivity is not practical with this method due to the severe impedance mismatch between the solid material and the surrounding air medium. Absolute measurements of ultrasonic airborne sound beams using Raman–Nath diffraction suffers from incomplete knowledge of the optoelastic coefficient for air.

In this paper, the three-transducer free field reciprocity calibration technique[16–18] is extended to apply to ultrasonic transducers that operate in air at frequencies greater than 100 kHz. This procedure has the advantage that the acoustic performance of the transducer is directly determined, and no specialized calibration apparatus is required other than three transducers and commonly available laboratory instrumentation. In this paper, the validity of this technique is judged by the correspondence of experimental measurements with a mathematical model of the transducers and calibration system. We believe that the experimental determinations of transducer transmit and receive sensitivities contained in this paper are the most comprehensive to appear in the technical literature for the frequency range 100–500 kHz.

Application of the reciprocity technique to the calibration of transducers at ultrasonic frequencies in air has not been common. To our knowledge, the first mention of the use of reciprocity to calibrate ultrasonic transducers in air was by Rudnick and Stein.[19] The method described in this reference corrected for attenuation in air, but retained the restriction of limiting the calibration to wavelengths that were greater than the characteristic dimension of the transducers. Other works,[20–22] apparently directed to the calibration of hydrophones in water, recommended corrections due to diffraction for various geometries and frequency ranges. A description of a reciprocity technique that used an approximate correction for diffraction in the frequency range 0.5–15 MHz in water was reported by Beissner.[23] Since the transducer separation distance was selected such that the measurements were taken at the boundary between near and far fields, an approximate compensation for the effect of diffraction was performed. Later, an exact correction for diffraction was reported by Beissner.[24] In these investigations, no measurements accompanied the analysis to support the validity of the calibration procedures.

I. EXTENSION OF THE RECIPROCITY CALIBRATION PROCEDURE TO ACCOUNT FOR DIFFRACTION

The relation between the performance of a reciprocal transducer when used as a transmitter to the performance when used as a receiver is[25]

$$\frac{U}{I} = \frac{V}{\langle P_i + P_s \rangle_A}. \tag{1}$$

The ratio U/I is the performance of the transducer when used as a transmitter; U is the complex amplitude of the volume velocity output given a driving current of complex amplitude I. The ratio $V/\langle P_i + P_s \rangle_A$ is the pressure response MP (as defined in ANSI S1.10[26]) of the transducer used as a receiver; V is the complex amplitude of the open circuit voltage caused by a pressure $P_i + P_s$ due to an external source. The symbol $\langle \bullet \rangle_A$ indicates a spatial average over a diaphragm of area A. The pressure field P_i is the acoustic field due to an external source that exists in the absence of the receiver, P_s is the field scattered by the receiver. Because the performance as a transmitter is specified in terms of the volume velocity output, while the performance as a receiver is specified in terms of the spatially averaged pressure over the diaphragm, account for diffraction in the use of (1) for reciprocity calibration must be made when wavelengths are on the order of, or smaller than the characteristic dimension of the transducer.

In general, there are three pressures that act on an acoustic transducer. They are P_i, the incident field due to an external source, P_s, the portion of the incident field scattered by the microphone body, and P_r, the pressure on the diaphragm due to its motion. The acoustic pressure P_r is incorporated into the lumped impedances of the transducer model using the radiation impedance.[25] Due to the structure of the radiation impedance, the acoustic velocity associated with this pressure vanishes on the remaining surface of the transducer. The scattered field P_s is calculated by requiring the acoustic velocity normal to the transducer body associated with the sum $P_i + P_s$ to vanish everywhere. In this way, the acoustic velocities caused by the sum $P_i + P_s$ do not make a contribution on the surface of the diaphragm.

We describe the three transducer method for reciprocity calibration while retaining terms that will be used for the extension to arbitrary wavelengths. Consider the three measurements (i), (ii), and (iii) shown in Fig. 1, in which the notation of Ref. 16 is adopted. Transducer T is a transmitter, R is a reversible transducer, and X is an unknown transducer that is being calibrated. The reversible transducer R is assumed to be reciprocal. The diaphragm areas of the transducers are plane, circular in shape and of radius a, and the transmitter and receiver are aligned coaxially a distance d apart as shown. In the first two measurements (i) and (ii), a known harmonic voltage of amplitude V_T is applied to transducer T, and the open circuit voltage amplitudes V_{TR} and V_{TX} are measured. These voltages are related to the pressure sensitivities MP_R and MP_X of transducers R and X by

i) $V_T \uparrow \quad \xrightarrow{I_T} \quad \boxed{T} \quad P_i \quad) \,) \,) \,) \,) \quad \boxed{R} \quad I_{TR}=0 \; \uparrow V_{TR}$

ii) $V_T \uparrow \quad \xrightarrow{I_T} \quad \boxed{T} \quad P_i \quad) \,) \,) \,) \quad \boxed{X} \quad I_{TX}=0 \; \uparrow V_{TX}$

iii) $V_R \uparrow \quad \xrightarrow{I_R} \quad \boxed{R} \quad P_i' \quad) \,) \,) \,) \quad \boxed{X} \quad I_{RX}=0 \; \uparrow V_{RX}$
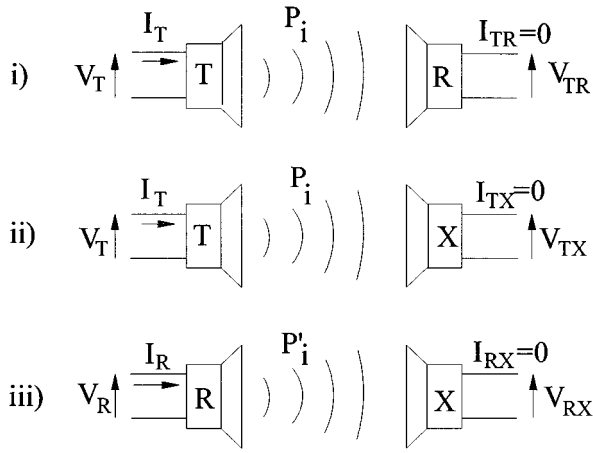
FIG. 1. Sequence for three transducer reciprocity calibration.

$$MP_R = \frac{V_{TR}}{\langle P_i + P_s \rangle_R}, \tag{2}$$

$$MP_X = \frac{V_{TX}}{\langle P_i + P_s \rangle_X}. \tag{3}$$

In the third measurement (iii), the current I_R supplied to transducer R and the open circuit voltage V_{RX} are measured. The pressure sensitivity MP_X is related to the measurement of V_{RX} by

$$MP_X = \frac{V_{RX}}{\langle P_i' + P_s' \rangle_X}, \tag{4}$$

where a prime superscript has been added to the incident and scattered pressure fields to denote that they originate from the reversible transducer R in measurement (iii). The reciprocal property for transducer R in experiments (i) and (iii) is

$$MP_R = \frac{V_{TR}}{\langle P_i + P_s \rangle_R} = \frac{1}{\Gamma e^{-\alpha r}} \frac{P_i'}{I_R}, \tag{5}$$

where Γ is the on-axis field such that $P_i = \Gamma e^{-\alpha r} U$, i.e.,

$$\Gamma = \begin{cases} \dfrac{2\rho c}{A} \left| \sin\left\{ \dfrac{1}{2} kr \left[\sqrt{1 + \left(\dfrac{a}{r}\right)^2} \, ^2 - 1 \right] \right\} \right| & (6a) \\[2ex] \dfrac{\omega \rho}{4\pi r}. & (6b) \end{cases}$$

Equation (6a) assumes that the source is a baffled rigid circular piston at arbitrary wavelengths, while (6b) assumes that the source is an unbaffled monopole; $r=d$ is the axial distance from the transmitter, ρ is the ambient fluid density, c is the ambient sound speed, $k=\omega/c$ is the wave number, ω is the circular frequency in rad/s, a is the piston radius, and $A=\pi a^2$ is the area of the piston. The symbol α is the coefficient of attenuation for air, which can be estimated from ANSI S1.26.[6]

If transducers R and X are of the same dimensions, the voltage ratio V_{TX}/V_{TR} from (2), (3) can be used to find the ratio MP_X/MP_R. This ratio can be combined with (4) and (5) to eliminate MP_R and obtain the following expression for MP_X:

$$MP_X = \sqrt{\frac{V_{TX}}{V_{TR}} \frac{V_{RX}}{I_R} \cdot \frac{P_i'}{\Gamma \langle P_i' + P_s' \rangle_X}} \, e^{\alpha d}. \tag{7}$$

The ratio $P_i'/\Gamma \langle P_i' + P_s' \rangle_X$ is known as the general reciprocity parameter.[27]

If the frequency is low, or the transducers are small, then $\lambda/a \gg 1$, and $\langle P_i' + P_s' \rangle_X \rightarrow P_i'$, $\Gamma \rightarrow (6b)$; and MP_X becomes

$$MP_X = \sqrt{\frac{V_{TX}}{V_{TR}} \frac{V_{RX}}{I_R} \cdot \frac{4\pi d}{\rho \omega}} \, e^{\alpha d}. \tag{8}$$

Since $\lambda/a \gg 1$, the free field sensitivity MF_X is the same as the pressure response, and the above expression gives MF_X as well.

If $\lambda \sim a$, or $\lambda < a$, then the calibration expression (8) must be modified. We first make the assumption that the scattered field is determined by pressure doubling of each plane wave in the angular spectrum of the beam at the blocked receiver diaphragm. If the transducer behaves geometrically as a semi-infinite rod, this assumption appears to be accurate within 1% for $ka > 10$.[28] Under this assumption, $\langle P_i' + P_s' \rangle_X \approx 2\langle P_i' \rangle_X$. Then the general reciprocity parameter $P_i'/\Gamma \langle P_i' + P_s' \rangle_X$ can be calculated as

$$\frac{P_i'}{\Gamma \langle P_i' + P_s' \rangle_X} \approx \frac{P_i'}{2\Gamma \langle P_i' \rangle_X} = \frac{A_X}{2\rho c D}, \tag{9}$$

where A_X is the diaphragm area of transducer X, and D is the exact correction for diffraction[24]

$$D = 1 - \frac{2}{\pi} \int_0^2 \sqrt{1 - \left(\frac{\tau}{2}\right)^2} \, \exp[-jka(\sqrt{\tau^2 + (\eta s)^2} - \eta s)] d\tau.$$

The symbols η and s are $\eta = af/c = a/\lambda$, $s = dc/fa^2 = \lambda d/a^2$, $1/s$ is the nondimensional Fresnel parameter.[29] The above expression for D assumes that the transmitter and receiver behave as baffled, circular, rigid pistons, and are of equal size. Upon placing the calculation (9) for the general reciprocity parameter into the general calibration equation (8), we obtain

$$MP_X = \sqrt{\frac{V_{TX}}{V_{TR}} \frac{V_{RX}}{I_R} \cdot \frac{A_X e^{\alpha d}}{2\rho c D}}. \tag{10}$$

The free field sensitivity MF_X of the receiver is related to the pressure sensitivity MP_X by the diffraction factor D.

Diffraction and attenuation effects on reciprocity calibration have influences in different frequency ranges, due to the properties of air at frequencies exceeding 100 kHz. Consider the plot of $1/\sqrt{D}$ and $\sqrt{e^{\alpha d}}$ versus frequency $f = 2\pi\omega$ shown in Fig. 2. The variables used in this plot are $a = 2.54$ cm, $d = 13.34$ cm, and the frequency is varied from 100–500 kHz. This plot shows the relative magnitudes of the corrections in the extended reciprocity calibration expression (10) as they depend upon the transducer size, separation, and frequency range. The two corrections to the basic reciprocity calibration equation are on the order of 10%, except in the case for frequencies that exceed 500 kHz, where attenuation becomes an exceedingly large factor. There is a certain frequency, in this case ≈ 200 kHz, below which diffraction is the dominant correction, above which attenuation is the
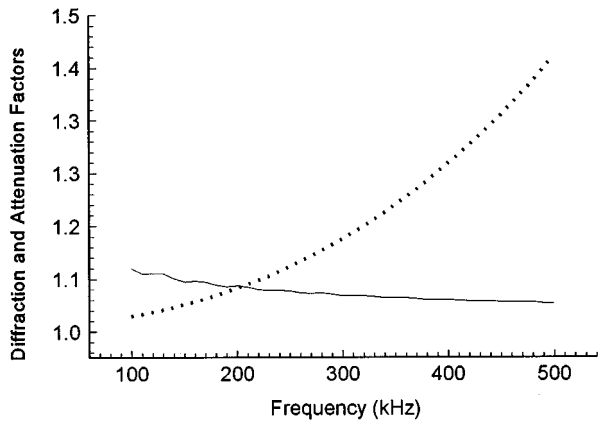
FIG. 2. Effect of diffraction and attenuation on calibration in air. $1/\sqrt{D}$ is solid line, $\sqrt{e^{\alpha d}}$ is the broken line.

dominant correction. For fixed ambient conditions in air, this tradeoff frequency will be determined from the equality

$$e^{\alpha(f)d}D(d,a,f)=1.$$

Whether or not the tradeoff frequency will be included in a particular calibration depends upon the transducer dimension a, and the separation distance d.

Once the pressure sensitivity MP_X of transducer X is known, it can then be used to determine the transmit sensitivities of transducers R and T from experiments (ii) and (iii), respectively. Since the pressure response of transducer X is used to determine the acoustic field P_i and P_i' from transducers R and T, the correction for diffraction and attenuation discussed previously must be used. This determination relies upon the knowledge of the corrections for diffraction and attenuation discussed previously.

Most definitions of transmit sensitivity are based upon the ratio of on-axis pressure amplitude at a distance of 1 m from the source.[16] However, this is not suggested for the definition of transmit sensitivity for transducers designed to operate in air, because attenuation in air precludes operation in the far field for frequencies that exceed 200 kHz. Most applications of transducers in air above 200 kHz will occur in the near field, and will rely on the approximately plane nature of the wavefield in front of the transducer as frequencies are increased. For example, a transducer with radius a of 2 cm will have farfield distances of 11.5 and 58.3 cm at 100 and 500 kHz, respectively. Smaller transducers that operate at higher frequencies will have similar farfield distances. Some researchers[2] state the performance of their transducers in terms of the displacement amplitude per input volt amplitude. In this paper, we suggest a similar definition, based upon the amplitude of the approximately plane waves in the near field. Accordingly, we define the transmit sensitivity of an ultrasonic transducer designed to operate in air as

$$TS=\frac{2\rho c}{V}\cdot\frac{U}{A},\qquad(11)$$

where U is the volume velocity amplitude of the transmitter, and V is the input voltage amplitude. If the velocity of the diaphragm is free from spatial phase variation, then the ratio

U/A is the velocity amplitude of the diaphragm, and $2\rho c(U/A)$ is the pressure amplitude of the approximately plane waves in the near field of the transducer.

Calculation of the transmit sensitivity TS_R and TS_T of transducers R and T from the measured pressure sensitivity MP_X of transducer X and the voltage amplitudes V_R and V_T from experiments (ii) and (iii) gives

$$TS_R=\frac{V_{RX}}{V_R MP_X D}\,e^{\alpha d},\qquad(12)$$

$$TS_T=\frac{V_{TX}}{V_T MP_X D}\,e^{\alpha d}.\qquad(13)$$

II. MODEL USED FOR PREDICTION OF TRANSDUCER PERFORMANCE

To assess the validity of the high frequency reciprocity calibration procedure, experimental measurements were compared with theoretical predictions of transducer performance. This comparison gives a measure of the validity of both the transducer model and the calibration procedure.

The model used to predict transducer performance is described by Anderson et al.[1] This model can be used to predict the performance of capacitive transducers that use a diaphragm whose bending stiffness is a significant contributor to the total internal mechanical impedance. In this paper, the model was slightly modified to include the effect of the gold layer on the area-specific mass density ρ_d and bending stiffness D_b of the diaphragm. The diaphragm was made from 5-μm-thick polyethylene terephthalate coated with a 75-nm-thick gold layer.

The mass density of the diaphragm was corrected by directly adding the mass of the gold layer to the polymer substrate. The densities of polyethylene terephthalate and gold are 1 395 and 19 700 kg/m^3, respectively. Although the thickness of the gold layer was very small, 75 nm, it caused the mass per unit area of the diaphragm to increase from 6.9 g/m^2 without accounting for the gold layer to 8.5 g/m^2.

The bending stiffness of the two layer diaphragm structure can be derived from layered plate theory[30]

$$D_b=\frac{E_g t^3}{12(1-\nu_g^2)}\left[1+3\left(\frac{h}{t}\right)^2\right]$$
$$+\frac{E_m t^3}{12(1-\nu_m^2)}\left[1+3\left(\frac{t}{h}\right)^2\right],$$

where E_g, ν_g, t and E_m, ν_m, h are the Young's modulus, Poisson's ratio, and thickness for the gold and polyethylene terephthalate layers, respectively. Values used for these parameters in subsequent model predictions were $E_g=80.6$ GPa, $\nu_g=0.4$, $t=75$ nm$=0.075$ μm, $E_m=4.48$ GPa, $\nu_m=0.4$, and $h=5$ μm. It should be noted that the equations of motion for bending of a layered plate that is asymmetrical about the neutral axis will couple with extensional deflections of the plate, however, this effect is minimized for the case of one thin layer placed on a much thicker substrate. In this investigation, it was assumed that coupling between bending and extensional vibrations were negligible.
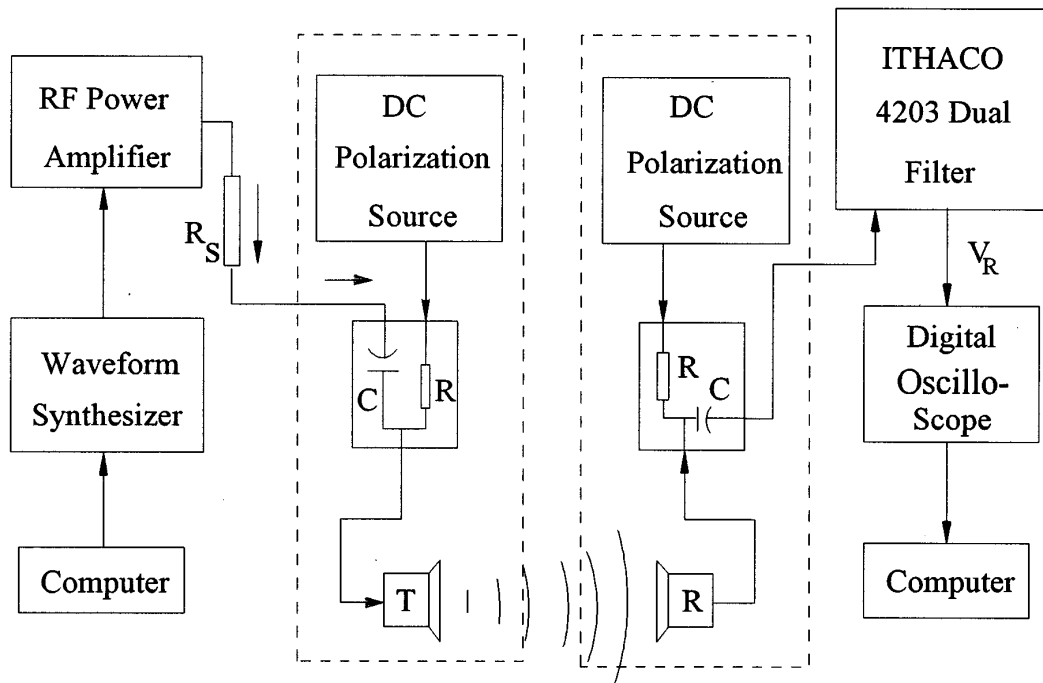
FIG. 3. Apparatus used for reciprocity calibration of transducers in air.

III. APPARATUS AND PROCEDURES USED FOR RECIPROCITY CALIBRATION MEASUREMENTS

The apparatus used to take reciprocity measurements is shown in Fig. 3. In this figure, transducer T is the transmitter, and transducer R is the receiver. Air was the coupling fluid, and the measurements were taken in a free field configuration. The path separation for the reciprocity measurements was $d = 13.97 \pm 0.1$ cm. N-cycle ($N = 20$) tone bursts were used for the waveform to eliminate multiple reflections from the transducers or extraneous hardware in the laboratory.

Three transducers, each identified by a letter A, B, and C, were used for the reciprocity measurements. The transducers were of electrostatic type, and are described by Anderson et al.,[1] They had active diaphragm areas that were plane, circular in shape, and 5.08 cm in diameter. In this type of transducer, the diaphragm was separated from the backplate by ridges micromachined on the backplate. The spacing between ridges and ridge heights for the three transducers are shown in Table I. The diaphragm was made from 5-μm-thick polyethylene terephthalate sputtered with a approximately 75-nm-thick layer of gold on one side. The transducers are nominally capable of receiving and detecting airborne ultrasound in the frequency range 50–500 kHz.

TABLE I. Ridge dimensions for transducers; comparison of selected experimental measurements and theoretical predictions. Each transducer is identified by a letter A, B, C.

	Transducer		
Dimension	A	B	C
Groove depth, μm	4.48	3.89	2.64
Groove width, μm	200	200	200
Res freq, predicted, kHz	366	373	400
Peak freq, measured, kHz	340	370	390

Each transducer was coupled to the drive signal with a blocking capacitor $C = 0.1$ μF, and was polarized by a dc source through a blocking resistor $R = 0.989$ MΩ. A N-cycle tone burst of 1-V amplitude and frequency selected by the computer was generated by a waveform synthesizer. This signal was amplified to approximately 40 V in amplitude by the rf amplifier. The transmit transducer converted the waveform into an acoustic signal, which propagated to the receive transducer R. The receive transducer R converted the acoustic signal into a voltage waveform, which was filtered as shown. The signal was then recorded with the digital oscilloscope. Amplitude measurements were taken as early as possible on the waveform, as soon as steady state had been reached. The amplitude measurements were then corrected for the filter transfer function. For measurement of the current I_T supplied to the transmit transducer T, another digital oscilloscope was used to measure the voltage amplitudes V_1 and V_2 across the series resistor $R_s = 1\,946 \pm 5$ Ω, as well as the relative phase ϕ between these voltages.

The instrumentation system was designed such that parasitic current losses were less than 0.2% from the ideal open circuit conditions. A 10$\times$ probe was used with the digital oscilloscope, its input impedance was 10 MΩ and 13 pF in parallel. The input impedance of the filter was 20 MΩ and 30 pF in parallel.

Because the calibration equations (10), (12), (13) for transducer sensitivity contain the density, sound speed, and attenuation of the medium; ambient conditions were recorded during a calibration measurement. The recorded ambient humidity, barometric pressure, and temperature were used in the calculation of density, sound speed and attenuation, and ultimately, the experimental determination of sensitivity.

A similar apparatus was used to verify the reciprocal

behavior of the transducer-fluid coupling-receiver network as described by Rudnick and Stein.[19] For this experimental verification, two transducers were coupled by the fluid to form a two port network. Measurements of driving current I_a to the transmitter and open circuit receiving voltage V_a were taken. The function of the transducer as transmitter and receiver were then exchanged. Measurements of the driving current I_b and receiving voltage amplitude V_b were then taken. If the network was reciprocal, then the ratio $y = I_a V_b / I_b V_a$ would be unity. It was assumed that a necessary condition for the network to be reciprocal is that the two transducers are likewise reciprocal.

The procedure for one reciprocity measurement follows the sequence outlined in the previous section. From one sequence (i) through (iii), the pressure response of receiver X is determined from measured voltages and current using (10). Then the transmit sensitivities of transducers R and T were calculated using (12) and (13). The procedure was repeated two times, each time the positions of the transducers A, B, and C being rotated through positions R, T, and X to obtain an interlocking set of measurements.

IV. RESULTS AND DISCUSSION

Measurements taken to verify the reciprocal behavior of transducers A, B, and C when coupled in a two port network as described in the previous section showed that the network was reciprocal to within the errors propagated to y from measurements of I_a, V_b, I_b, and V_a. Our estimation of the uncertainties on the measurements of I_a and I_b were 0.5% of the nominal value, while V_a and V_b had an uncertainty of 2.5% of the nominal value. In general, the measurements of voltage signals at the receiver had a lower signal to noise ratio than the voltage signals supplied to the transmitter, and as a consequence, a larger uncertainty had to be assigned to the measurement of receiver voltage amplitude.

The experimental determinations and model predictions of pressure sensitivity MP and transmit sensitivity TS for transducers A, B, and C are shown in Figs. 4, 5, and 6. The figures contain multiple experimental determinations of transmit sensitivity and pressure sensitivity, each being coded to identify with the repetitions of the reciprocity calibration procedure described in Table II. Part a of each figure is the determination of pressure sensitivity MP, and part b contains the determination of transmit sensitivity TS. Each figure shows a determination of MP from one test, and two determinations of TS from the remaining two tests. The experimentally determined sensitivities are indicated by solid circles and squares, and error bars are included to indicate the propagation of uncertainty from the individual measurements to the determination of sensitivity. In general, a one standard deviation uncertainty of 0.75% was assigned to the measurements of I_R, ρ, c, and d; 2.5% to V_{TX}, V_{RX}, V_{TR}, A, and D; while 5% was assigned to α. A theoretical prediction of the pressure sensitivity using the model described by Anderson et al.[1] slightly modified as described in Sec. II, is shown on each figure with a solid line. The mechanical damping in the model was adjusted to make the model predictions of transducer performance to agree with the experi-
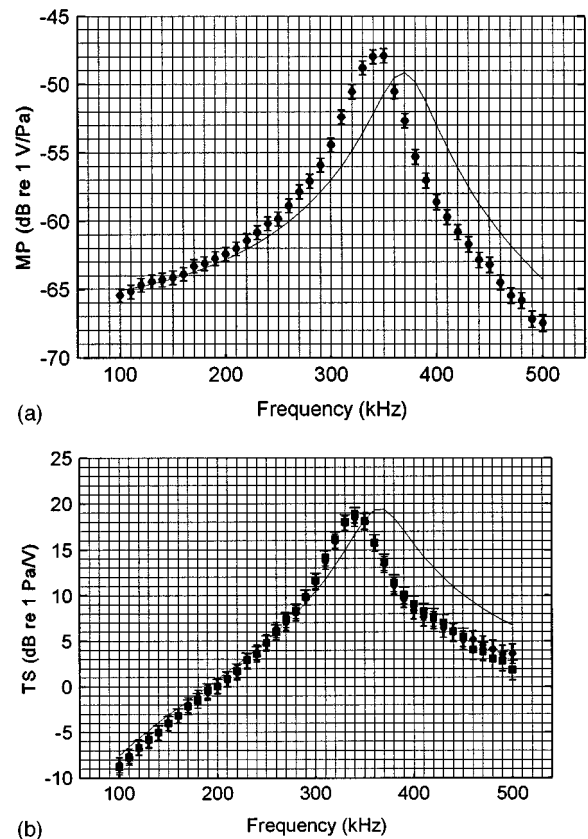
FIG. 4. Receive pressure sensitivity MP and transmit sensitivity TS for transducer A. ■ TS determined from expression (12), ● TS determined from expression (13), solid line is the model prediction.

mental measurements near the resonance frequency. Mechanical damping will have little effect in the stiffness and inertial controlled frequency ranges.

The experimentally determined sensitivities compared closely with theoretical predictions. In the stiffness controlled frequency range the experimental measurements and model predictions were the same for the pressure response MP_A of transducer A. For transducers B and C, the experimentally determined values of MP_B and MP_C were statistically different than the theoretical prediction, but the nominal values were only 2–2.5 dB lower. On a percentage basis, this is a difference of approximately 25%–30% from the nominal value, but the uncertainty on the measurement indicates that this difference could be smaller by a third.

The three sequential reciprocity tests, labeled Tests #1, #2, and #3 in Table II, allowed an independent check on the experimentally determined transmit sensitivity using the reciprocity technique. As is evident from Figs. 4(b)–6(b), the separate experimental determinations of transmit sensitivity for each transducer are statistically the same, thus giving evidence for the ''repeatability'' of the calibration procedure when the transducers are changed.

It should be noted that the experimentally determined transducer sensitivities contain voltage and current measurements, as well as the particular corrections for diffraction and attenuation described in Sec. I. Other models for diffraction and attenuation may by used to recalculate the sensitivities contained in Figs. 4–6, since the corrections for diffraction
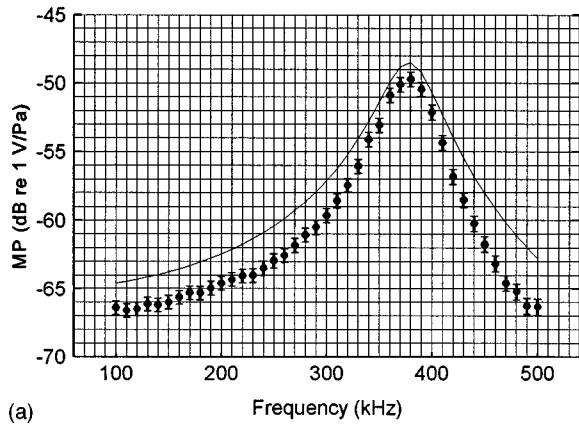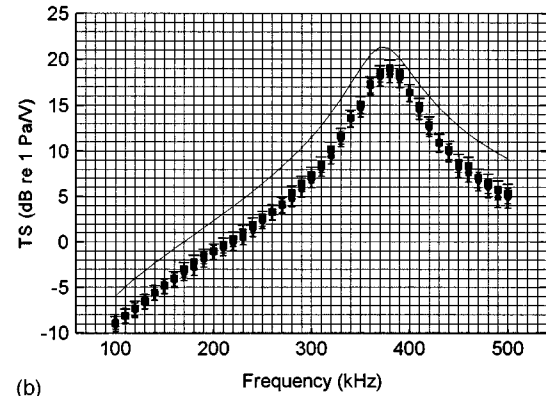
FIG. 5. Receive pressure sensitivity MP and transmit sensitivity TS for transducer B. ■ TS determined from expression (12), ● TS determined from expression (13), solid line is the model prediction.

FIG. 6. Receive pressure sensitivity MP and transmit sensitivity TS for transducer C. ■ TS determined from expression (12), ● TS determined from expression (13), solid line is the model prediction.

and attenuation in expression (10) are isolated from the voltage and current measurements.

Admittance measurements were taken to determine the resonance frequency of the three transducers, these resonance frequencies are shown in Table I next to the values predicted by the model. Measurement of admittance, conductance and susceptance, gives an especially sensitive measure of resonance frequency. These determinations of resonance frequency can be used to compare with the location of resonance peaks in the measurements of transmit and receive sensitivity, and with model predictions. The exact location of the transducer resonance is not always easy to locate from plots of sensitivity, because they contain amplitude data only.

Admittance and pressure sensitivity measurements show close agreement to the model predictions for each transducer. Resonance frequencies inferred from admittance measurements differ by a maximum of 7% from the values predicted by the model. The resonance peaks contained in the reciprocity determinations of transmit and receive sensitivity occured at frequencies that agreed with the admittance measurements. For transducer A, the measurements indicated that the actual resonance frequence was 7% lower than the model prediction. This discrepancy is consistent with the 3 dB difference in sensitivity in the high frequency limit, indicating a model underestimate of the mechanical inertia of the transducer.

One important factor not considered in the present paper

was the effect of transducer misalignment on the calibration measurements. The apparatus used in the measurements consisted of precisely machined fixtures, but no quantitative measure of the transducer alignment was available. Further studies of the effect of this factor on the quality of calibration measurements would be desirable.

V. CONCLUSIONS

The three transducer reciprocity calibration procedure has been extended to apply to geometrically similar ultrasonic transducers operating in air at frequencies that exceed 100 kHz. In this technique, correction for diffraction is important at lower frequencies, while correction for attenuation becomes more important at higher frequencies. Experimental determinations of sensitivity were within 2.5 dB of the

TABLE II. Assignment of the transducers A, B, and C to T, R, and X for the three tests.

	Test		
Test transducer	Test #1	Test #2	Test #3
Transmitter T	C	A	B
Receiver R	B	C	A
Transducer X	A	B	C
Sensitivity obtained in test, (Equation)	MP_A, (10)	MP_B, (10)	MP_C, (10)
	TS_B, (12)	TS_C, (12)	TS_A, (12)
	TS_C, (13)	TS_A, (13)	TS_B, (13)

model predictions, and the location of resonance peak in the experimentally determined sensitivities was within 7% of those inferred from transducer admittance measurements and model predictions. It was concluded that both the transducer model and the extended reciprocity calibration procedure were accurate to within the maximum discrepancies observed in the comparison between the these two performance indicators.

[1] M. J. Anderson, J. A. Hill, C. M. Fortunko, N. S. Dogan, and R. D. Moore, ''Broadband electrostatic transducers: Modeling and experiments,'' J. Acoust. Soc. Am. **97**, 262–272 (1995).

[2] M. I. Haller and B. T. Khuri-Yakub, ''A surface micromachined electrostatic ultrasonic transducer,'' Proceedings of the 1994 IEEE Ultrasonics Symposium, pp. 1241–1244.

[3] M. Rafiq and C. Wykes, ''The performance of capacitive ultrasonic transducers using V-grooved backplates,'' Meas. Sci. Technol. **2**, 168–174 (1991).

[4] P. Mattila, F. Tsuzuki, H. Vaataja, and K. Sasaki, ''Electoacoustic model for electrostatic ultrasonic transducers with V-grooved backplates,'' IEEE Trans. Ultrason. Ferroelectr. Freq. Control **42**, 1–7 (1995).

[5] O. Krauss, R. Gerlach, and J. Fricke, ''Experimental and theoretical investigations of SiO_2-aerogel matched piezo-transducers,'' Ultrasonics **32**(3), 217–222 (1994).

[6] ANSI S1.26-1995, ''Method for the calculation of the absorption of sound by the atmosphere'' (American National Standards Institute, New York, 1995).

[7] F. V. Hunt, *Electroacoustics: The Analysis of Transduction, and its Historical Background* (Harvard Univ., Cambridge, MA, 1954).

[8] W. S. H. Munro and C. Wykes, ''Arrays for airborne 100 kHz ultrasound,'' Ultrasonics **32**(1), 57–64 (1994).

[9] P. Mattila and J. Heitanen, ''Bandwidth control of an electrostatic ultrasonic transducer,'' Sens. Actuators A **45**, 203–208 (1994).

[10] H. Carr and C. Wykes, ''Diagnostic measurements in capacitive transducers,'' Ultrasonics **31**(1), 13–20 (1993).

[11] K. Suzuki, K. Higuchi, and H. Tanigawa, ''A silicon electrostatic ultrasonic transducer,'' IEEE Trans. Ultrason. Ferroelectr. Freq. Control **36**, 620–627 (1989).

[12] H. Carr, M. Rafiq, and C. Wykes, ''The use of interferometery in the investigation of ultrasound transducers,'' J. Phys. D **22**, 495–499 (1989).

[13] D. W. Schindel, D. A. Hutchins, L. Zou, and M. Sayer, ''The design and characterization of micromachined air-coupled capacitance transducers,'' IEEE Trans. Ultrason. Ferroelectr. Freq. Control **42**(1), 42–50 (1995).

[14] A. Holm and H. W. Persson, ''Optical diffraction tomography applied to airborne ultrasound,'' Ultrasonics **31**(4), 259–265 (19xx).

[15] A. Gachagan, G. Hayward, S. P. Kelly, and W. Galbraith, ''Characterization of air-coupled transducers,'' IEEE Trans. Ultrason. Ferroelectr. Freq. Control **43**(4), 678–689 (1996).

[16] L. E. Kinsler, A. R. Frey, A. B. Coppens, and J. V. Sanders, *Fundamentals of Acoustics* (Wiley, New York, 1982), 3rd ed.

[17] *AIP Handbook of Condenser Microphones, Tehory, Calibration, and Measurements*, edited by G. S. K. Wong and T. F. W. Embleton (American Institute of Physics, New York, 1995).

[18] E. D. Burnett and V. Nedzelnitsky, ''Free-field reciprocity calibration of microphones,'' J. Res. Natl. Bur. Stand. **92**(2), 129–151 (187).

[19] I. Rudnik and M. N. Stein, ''Reciprocity free filed calibration of microphones to 100 Kc in air,'' J. Acoust. Soc. Am. **20**(6), 818–825 (1948).

[20] B. D. Simmons and R. J. Urick, ''The plane wave reciprocity parameter and its application to the calibration of electroacoustic transducers at close distances,'' J. Acoust. Soc. Am. **21**(6), 633–635 (1949).

[21] T. A. Henriques, ''Diffraction constants of acoustic transducer,'' J. Acoust. Soc. Am. **36**(2), 267–269 (1964).

[22] R. J. Bobber, ''Diffraction constants of transducers,'' J. Acoust. Soc. Am. **37**(4), 591–595 (1965).

[23] K. Beissner, ''Free-field reciprocity calibration in the transition range between near field and far field,'' Acustica **36**, 167–203 (1980).

[24] K. Beissner, ''Exact integral expression for the diffraction loss of a circular piston source,'' Acustica **49**, 212–217 (1981).

[25] A. D. Pierce, *Acoustics, An Introduction to its Physical Principles and Applications* (McGraw-Hill, New York, 1981).

[26] ANSI S1.10-1966, ''American National Standard Method for the Calibration of Microphones'' (American National Standards Institute, Bethesda, 1966), reaffirmed 1976.

[27] R. J. Bobber, ''General reciprocity parameter,'' J. Acoust. Soc. Am. **39**(4), 680–687 (1966).

[28] D. S. Jones, ''The scattering of a scalar wave by a semi-infinite rod of circular cross section,'' Proc. R. Soc. London, Ser. A **247**, 499–528 (1955).

[29] G. Kino, *Acoustic Waves: Devices, Imaging, & Analog Signal Processing* (Prentice-Hall, Englewood Cliffs, NJ, 1987).

[30] R. M. Jones, *Mechanics of Composite Materials* (Hemisphere, Boston, 1975).

Ear canal reflectance in the presence of spontaneous otoacoustic emissions. I. Limit-cycle oscillator model

Arnold Tubis and Carrick L. Talmadge

Department of Physics, Purdue University, West Lafayette, Indiana 47907

Allen *et al.* [Abstract in *Eighteenth Midwinter Research Meeting of the Association for Research in Otolaryngology*, Des Moines, IA (1995)] have found that the ear canal reflectance passes through a minimum around the frequency of a spontaneous otoacoustic emission (SOAE). They considered this result to constitute evidence against active nonlinear cochlear function as the basis for SOAEs. In order to investigate theoretically the expected behavior of ear canal reflectance in the neighborhood of a SOAE associated with an active-nonlinear cochlea, we use a simplified model in which the ear drum end of the ear canal is effectively terminated by a nonlinear-active element. Under the influence of a sinusoidal driver at the entrance of the ear canal, this element will, to a good approximation, either (1) oscillate at both the frequency of the driver (at which the reflectance is determined) and the SOAE (at a suppressed level, corresponding to nonentrainment), or (2) be entrained and only oscillate at the driving frequency. The magnitude of the nonlinear ear canal reflectance is found to exceed unity only at sufficiently low stimulus levels, and occurs under conditions of entrainment and nonentrainment of the spontaneous emission. Otherwise, the reflectance is less than unity and, as a function of frequency, has a minimum around the SOAE frequency. © *1998 Acoustical Society of America.* [S0001-4966(97)06812-4]

PACS numbers: 43.64.Bt, 43.64.Ha, 43.64.Jb [BLM]

LIST OF SYMBOLS

a_0	unsuppressed oscillator amplitude
$\bar{a}_0$	suppressed oscillator amplitude
c	wave velocity of sound in the ear canal
E	$S_0 P_{dr}/m_0$
k_0	$m_0 \omega_0^2 =$ spring constant of ear canal termination
m_0	effective mass of ear canal termination
ω_0	$\sqrt{k_0/m_0} =$ natural frequency of SOAE in the absence of acoustic loading
ω_{cav}^2	$\rho_0 c^2 S_0^2/m V_e$
$\tilde{\omega}_0$	natural frequency of SOAE when coupled to ear canal
$\mathscr{P}$	$(S_0/2)\text{real}(P_e \dot{\xi}_0^*)$
$P_e(t)$	ear canal incremental pressure (assumed constant throughout the ear canal)
P_e	amplitude of ear canal incremental pressure
P_{SOAE}	ear canal pressure amplitude of SOAE in the absence of external driving
$P_{dr}(t)$	$(\rho_0 c^2/V_e)S_{dr}\xi_{dr}(t) =$ calibrated ear canal driving pressure
P_{dr}	amplitude of calibrated ear canal driving pressure
$r(\xi_0(t))$	$-r_0 + r_2 \xi_0(t)^2 =$ effective nonlinear-active damping of ear canal termination
ρ_0	density of air in ear canal
R_e	ear canal reflectance
S_0	effective area of ear canal termination
S_{dr}	area of ear canal driver
V_e	ear canal volume
$\xi_{dr}(t)$	displacement of ear canal driver
$\xi_0(t)$	displacement of ear canal termination
$\dot{\xi}_0(t)$	$d\xi_0(t)/dt$, etc., $t =$ time

INTRODUCTION

There is now a large body of experimental evidence in support of spontaneous otoacoustic emissions (SOAEs) being rooted in noise-perturbed limit-cycle oscillations in a nonlinear-active cochlea. This evidence is related to the statistical properties of SOAEs (reviewed in Talmadge *et al.*, 1991), and static and dynamic aspects of SOAE suppression and frequency locking by external tones (reviewed in Murphy *et al.*, 1995a, 1995b).

However, Allen *et al.* (1995) have raised the very interesting and fundamental question of how the reflectance in the ear canal behaves in the neighborhood of an SOAE, and the implications of this behavior for the intrinsic nature of SOAEs (noise-perturbed limit-cycle oscillations in a nonlinear-active cochlea versus narrow-band filtering of cochlear noise in a passive cochlea). In particular, they found that the magnitude of the reflectance passes through a minimum around the SOAE frequency (instead of increasing above one, as might be naively expected for a nonlinear active cochlea). They thereby inferred that SOAEs could not be interpreted in terms of active mechanisms.

In order to address the question of the ear canal reflectance in the neighborhood of a SOAE, the implications of the simple model of a SOAE illustrated in Fig. 1 are considered. The model is based on the assumption that in the neighborhood of an SOAE, the nonlinear active cochlear function results in a corresponding effective nonlinear active element at the interface of the ear canal and the middle ear. The limit
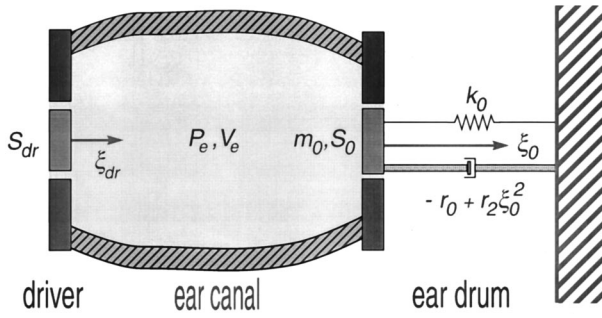
FIG. 1. Simple model of nonlinear-active ear canal termination which gives rise to an SOAE. See the Table of Symbols for definitions.

cycle motion of this element (with the neglect of higher harmonics) gives rise to a sinusoidal ear-canal incremental pressure (SOAE) in the absence of external driving $[\xi_{\mathrm{dr}}(t)=0]$.

The specific dynamical form of the interface element incorporates in a very transparent manner, the balance between active and passive elements which are necessary for self-sustained oscillations. It has been previously shown that this model provides a good description of a number of characteristic properties of SOAEs. These include statistical properties (Bialek and Wit, 1984; Wit, 1986; Talmadge et al., 1991), suppression by external tones (Long et al., 1991; Murphy et al., 1995a, 1995b, 1996), synchronization (phase locking) by external tones (e.g., van Dijk and Wit, 1988, 1990a; Long et al., 1991), amplitude and frequency fluctuations (van Dijk and Wit, 1990b, 1994), and the reduction of level by aspirin administration (e.g., Long and Tubis, 1988; Long et al., 1988; Tubis et al., 1988). In light of this, it is reasonable to use the model in a first attempt to predict theoretically the behavior of ear canal reflectance near a SOAE.

The validity of the model is limited to the neighborhood of a single SOAE. A distributed cochlear model must be used in order to account for features such as the 0.4 bark spectral spacing which characterizes the various types of otoacoustic emissions as well as the microstructure of the hearing threshold (Talmadge and Tubis, 1993; Talmadge et al., 1997). However, it will be shown in a future study that the implications of the model used in this paper are in many respects very similar to those obtained with a distributed cochlear model.

On the basis of this model, it will be demonstrated that the results of Allen et al. (1995) do not constitute evidence against nonlinear active signal processing in the cochlea, and that in fact their results are expected in the case of such processing. For sinusoidal driving at the entrance of the ear canal, the nonlinear-active termination will, to a good approximation, either (1) oscillate at both the frequency of the driver (the frequency at which the reflectance is determined) and the SOAE (at a suppressed level), or (2) be entrained and only oscillate at the driver frequency (e.g., Hangii and Riseborough, 1983; van Dijk and Wit, 1990b; Long et al., 1991). As we shall see in Sec. III of this paper, our model implies a dip in the magnitude of the reflectance around an SOAE frequency for driving levels (presumably those used by Allen

et al., 1995) that are large enough to entrain the emission. However, we also show that the model predicts ear canal reflectance magnitudes greater than one, but only for low-level stimulation.

In Sec. I, the model is described and the model parameters are related to the physical features of the SOAE. The effects of an external tonal stimulus are described in Sec. II for the conditions of a suppressed, but not entrained, SOAE, and also for an entrained SOAE. Approximate analytic results are given for the model ear canal reflectance in Sec. III, and are compared with computer simulations of the model in Sec. IV. Section V contains a discussion of results.

I. A LIMIT-CYCLE OSCILLATOR MODEL OF SOAEs

In the model of an SOAE shown in Fig. 1, the ear canal is assumed to be a chamber of constant cross section. Also, for simplicity, the sound wavelength in the ear canal is assumed to be much longer than the length of the canal, so that the pressure is the same throughout the ear canal. The ear canal is terminated by a nonlinear-active element whose limit-cycle motion gives rise to a sinusoidal ear-canal incremental pressure.

The behavior of the limit-cycle oscillator in the absence of external driving is considered first. For this case, the incremental pressure P_e in the ear canal is given by (see the List of Symbols),

$$P_e(t) = -\frac{\rho_0 c^2}{V_e} S_0 \xi_0(t), \qquad (1)$$

where ρ_0 is the ambient air density, c is the sound velocity in the ear canal, and $\xi_0(t)$ is the displacement of the terminating element (e.g., Kinsler et al., 1982, pp. 98–107). Equation (1) was obtained under the assumption that the incremental pressure is much smaller than the ambient air pressure. It is also assumed that air compression/expansion occurs under adiabatic conditions. With Van der Pol type nonlinear-active damping (e.g., Hangii and Riseborough, 1983) assumed for the terminating element at the ear drum end, the application of Newton's second law to the element gives

$$m_0 \ddot{\xi}_0(t) + m_0[-r_0 + r_2 \xi_0^2(t)]\dot{\xi}_0(t) + k_0 \xi_0(t) = S_0 P_e(t), \qquad (2)$$

where

$$k_0 = m_0 \omega_0^2. \qquad (3)$$

Equation (2) can be rewritten as

$$m_0 \ddot{\xi}_0(t) + m_0[-r_0 + r_2 \xi_0^2(t)]\dot{\xi}_0(t)$$
$$+ m_0\left[\omega_0^2 + \frac{\rho_0 c^2 S_0^2}{m_0 V_e}\right]\xi_0(t) = 0. \qquad (4)$$

With the definitions,

$$\omega_{\mathrm{cav}}^2 \equiv \frac{\rho_0 c^2 S_0^2}{m_0 V_e}, \qquad (5)$$

$$\widetilde{\omega}_0^2 \equiv \omega_0^2 + \omega_{\mathrm{cav}}^2, \qquad (6)$$

Eq. (4) becomes

$$\ddot{\xi}_0(t) + [-r_0 + r_2 \xi_0^2(t)] \dot{\xi}_0(t) + \widetilde{\omega}_0^2 \xi_0(t) = 0. \quad (7)$$

Using the Krylov–Bogoliubov averaging method (see, e.g., Hangii and Riseborough, 1983; Jackson, 1989), it is found that

$$\xi_0(t) \approx a_0 \cos(\widetilde{\omega}_0 t + \varphi), \quad (8)$$

$$a_0 \approx 2 \sqrt{\frac{r_0}{r_2}}. \quad (9)$$

These equations predict that in the absence of external stimulation, the ear canal termination, and consequently the incremental pressure, will sinusoidally oscillate at a limit-cycle angular frequency of $\widetilde{\omega}_0$ with a stationary amplitude a_0. This behavior constitutes the model SOAE. In obtaining these results, the effects of noise as well as of higher-order nonlinear contributions (which give rise to, e.g., $3\widetilde{\omega}_0$ frequency components) have been neglected.

The response of the model ear canal to sinusoidal stimulation and the associated reflectance for frequencies around that of the SOAE will now be investigated.

II. THE EFFECT OF AN EXTERNAL STIMULUS ON THE MODEL SOAE

A sinusoidal stimulus presented to the ear canal is assumed. For simplicity, the ear canal entrance is modeled as a piston with surface area S_{dr} and instantaneous displacement $\xi_{dr}(t)$, so that,

$$P_e(t) = -\frac{\rho_0 c^2}{V_e} [S_0 \xi_0(t) - S_{dr} \xi_{dr}(t)], \quad (10)$$

$$\ddot{\xi}_0(t) + [-r_0 + r_2 \xi_0^2(t)] \dot{\xi}_0(t) + \widetilde{\omega}_0^2 \xi_0(t)$$
$$= \frac{\rho_0 c^2}{m_0 V_e} S_{dr} S_0 \xi_{dr}(t). \quad (11)$$

Equation (10) gives the incremental ear canal pressure in the presence of both the model SOAE and an external driving tone, and Eq. (11) characterizes the effect of the external tone on the terminating element. Note that, other than the addition of a forcing term, Eq. (11) is identical to Eq. (7). Equation (10) can be related to experimentally measurable values by noting that for a ''hard'' termination, $\xi_0(t) = 0$, and

$$P_e(t)|_{\substack{\text{hard} \\ \text{term.}}} = \frac{\rho_0 c^2}{V_e} S_{dr} \xi_{dr}(t) \equiv P_{dr}(t). \quad (12)$$

The quantity $P_{dr}(t)$ is referred to in this study as the ''calibrated ear canal driving pressure.'' Using Eqs. (5) and (12), Eq. (10) becomes

$$P_e(t) = P_{dr}(t) - \frac{m_0}{S_0} \omega_{cav}^2 \xi_0(t), \quad (13)$$

and

$$P_e(t) = \frac{m_0}{S_0} [E \cos \omega_{dr} t - \omega_{cav}^2 \xi_0(t)], \quad (14)$$

where a sinusoidal driving of the form

$$P_{dr}(t) = \frac{E m_0}{S_0} \cos \omega_{dr} t, \quad (15)$$

has been assumed. Using Eq. (15), Eq. (11) can be rewritten as

$$\ddot{\xi}_0(t) + [-r_0 + r_2 \xi_0^2(t)] \dot{\xi}_0(t) + \widetilde{\omega}_0^2 \xi_0(t) = E \cos \omega_{dr} t. \quad (16)$$

Equation (16) describes the effects of the external driver on the oscillator, and Eq. (14) relates the model SOAE response and the ear canal driving pressure to the incremental pressure in the ear canal. It should be noted that the expression, Eq. (14), for $P_e(t)$ is entirely algebraic (there are no derivatives of quantities in the expression). This is a result of the long-wavelength assumption used in obtaining Eq. (1).

In solving Eq. (16), the two cases where the SOAE is suppressed but not entrained, and where the external tone entrains the SOAE will be considered.

A. Nonentrained SOAE

The case where the SOAE is not entrained is first considered. In this case, nonzero amplitude components of the oscillator at both its natural limit-cycle frequency, $\widetilde{\omega}_0$, as well as at the driving frequency, ω_{dr}, will be present. Higher-order nonlinear contributions to the SOAE response will gives rise to nonzero amplitude components at, e.g., $3\widetilde{\omega}_0$, $2\widetilde{\omega}_0 - \omega_{dr}$, $-\widetilde{\omega}_0 + 2\omega_{dr}$, $3\widetilde{\omega}_0$. These higher-order contributions do not have a significant effect on the results presented here and will be neglected. Under this assumption, the ear drum displacement $\xi_0(t)$ can be expressed as

$$\xi_0(t) = a(t) \cos[\widetilde{\omega}_0 t + \varphi(t)] + a_{dr} \cos[\omega_{dr} t + \varphi_{dr}], \quad (17)$$

where $a_0(t)$ gives the instantaneous amplitude of the oscillator at $\widetilde{\omega}_0$ and a_{dr} is the instantaneous amplitude of the response of the oscillator to the external driver at ω_{dr}. After substituting Eq. (17) into Eq. (16), and applying the standard Krylov–Bogoliubov formalism, it is found that

$$\dot{a}(t) = \frac{1}{2} r_0 a(t) \left[1 - \frac{r_2}{2r_0} a_{dr}^2 - \frac{r_2}{4r_0} a(t)^2 \right], \quad (18)$$

$$\dot{\varphi}(t) = 0. \quad (19)$$

Equation (18) describes the time evolution of the model SOAE amplitude in the presence of an external tone. Also, the fact that $\dot{\varphi}(t) = 0$ in Eq. (19) signifies that to first order the frequency of the oscillator is unaffected by the external tone. From Eq. (18), the steady-state suppressed amplitude [$\dot{a}(t) \equiv 0$] of the SOAE is

$$\bar{a}_0^2 = a_0^2 - 2a_{dr}^2, \quad (20)$$

$$a_0^2 = \frac{4r_0}{r_2}. \quad (21)$$

For the component of $\xi_0(t)$ at the driving frequency, it is found that

$$-a_{dr} \sin \varphi_{dr} r_0 \omega_{dr} \left(1 - 3 \frac{a_{dr}^2}{a_0^2} \right) + a_{dr} \cos \varphi_{dr} (\widetilde{\omega}_0^2 - \omega_{dr}^2) = E, \quad (22)$$

$$a_{dr} \cos \varphi_{dr} r_0 \omega_{dr} \left(1 - 3\frac{a_{dr}^2}{a_0^2}\right) + a_{dr} \sin \varphi_{dr} (\widetilde{\omega}_0^2 - \omega_{dr}^2) = 0. \quad (23)$$

Solving these equations for a_{dr}, $\sin \varphi_{dr}$, and $\cos \varphi_{dr}$ gives

$$\sin \varphi_{dr} = -\frac{a_{dr}}{E} r_0 \omega_{dr} \left(1 - 3\frac{a_{dr}^2}{a_0^2}\right), \quad (24)$$

$$\cos \varphi_{dr} = \frac{a_{dr}}{E} (\widetilde{\omega}_0^2 - \omega_{dr}^2), \quad (25)$$

$$\frac{a_{dr}^2}{a_0^2} \left[r_0^2 \omega_{dr}^2 \left(1 - 3\frac{a_{dr}^2}{a_0^2}\right)^2 + (\widetilde{\omega}_0^2 - \omega_{dr}^2)^2 \right] = \frac{E^2}{a_0^2}. \quad (26)$$

Equations (24)–(26) relate the amplitude and phase of the oscillator response at ω_{dr} to the level of the external driver. In these equations, $\sin \varphi_{dr}$ and $\cos \varphi_{dr}$ are given separately instead of their ratio, $\tan \varphi_{dr}$, in order to unambiguously define the quadrant of the phase φ_{dr}. Equation (26) has the approximate solution

$$a_{dr} \approx \frac{E}{|\omega_{dr}^2 - \widetilde{\omega}_0^2|}, \quad (27)$$

if $r_0 \ll \widetilde{\omega}_0$, which predicts a proportionality between a_{dr} and E in the case of nonentrained SOAEs.

B. Entrained SOAE

The case of an entrained SOAE is considered next. By definition there will be no nonzero amplitude component at $\widetilde{\omega}_0$ in the oscillator response. Again neglecting higher-order nonlinear contributions, the response of the oscillator is taken to be

$$\xi_0(t) = a_{dr} \cos[\omega_{dr}t + \varphi_{dr}]. \quad (28)$$

It is found that

$$-a_{dr} \sin \varphi_{dr} r_0 \omega_{dr} \left(1 - \frac{a_{dr}^2}{a_0^2}\right) + a_{dr} \cos \varphi_{dr} (\widetilde{\omega}_0^2 - \omega_{dr}^2) = E, \quad (29)$$

$$a_{dr} \cos \varphi_{dr} r_0 \omega_{dr} \left(1 - \frac{a_{dr}^2}{a_0^2}\right) + a_{dr} \sin \varphi_{dr} (\widetilde{\omega}_0^2 - \omega_{dr}^2) = 0. \quad (30)$$

Solving for a_{dr}, $\sin \varphi_{dr}$, and $\cos \varphi_{dr}$ gives

$$\sin \phi_{dr} = \frac{a_{dr}}{E} r_0 \omega_{dr} \left(1 - \frac{a_{dr}^2}{a_0^2}\right), \quad (31)$$

$$\cos \phi_{dr} = \frac{a_{dr}}{E} (\widetilde{\omega}_0^2 - \omega_{dr}^2), \quad (32)$$

$$\frac{a_{dr}^2}{a_0^2} \left[r_0^2 \omega_{dr}^2 \left(1 - \frac{a_{dr}^2}{a_0^2}\right)^2 + (\widetilde{\omega}_0^2 - \omega_{dr}^2)^2 \right] = \frac{E^2}{a_0^2}. \quad (33)$$

Equations (31)–(33) give the analogs to Eqs. (24)–(26) for the case of entrainment. As before, Eq. (33) has the approximate solution

$$a_{dr} \approx \frac{E}{|\omega_{dr}^2 - \widetilde{\omega}_0^2|}, \quad (34)$$

which is valid for $a_{dr} \lesssim a_0$ and $r_0 \ll \widetilde{\omega}_0$, and again predicts a proportionality between a_{dr} and E under these conditions. For $a_{dr} \gg a_0$, Eq. (33) gives

$$a_{dr} = \left(\frac{Ea_0^2}{r_0 \omega_{dr}}\right)^{1/3}, \quad (35)$$

which predicts a proportionality between a_{dr} and $E^{1/3}$.

C. Entrainment conditions

It can be shown (e.g., Hangii and Riseborough, 1983), that the criteria for the stability of entrainment are

$$\left(\frac{a_{dr}}{a_0}\right)^2 > \frac{1}{2}, \quad (36)$$

$$3\left(\frac{a_{dr}}{a_0}\right)^4 - 4\left(\frac{a_{dr}}{a_0}\right)^2 + 1 + \frac{4}{r_0^2}(\omega_{dr} - \omega_0)^2 > 0. \quad (37)$$

The minimum of the left-hand side of Eq. (37) as a function of $(a_{dr}/a_0)^2$ is

$$-\frac{1}{3} + \frac{4}{r_0^2}(\omega_{dr} - \omega_0)^2. \quad (38)$$

Thus if

$$\frac{|\omega_{dr} - \omega_0|}{r_0} > \frac{1}{2\sqrt{3}} \quad (39)$$

the inequality of Eq. (37) will be satisfied for all values of $(a_{dr}/a_0)^2$ which satisfy the inequality of Eq. (36).

For values of ω_{dr} and ω_0 that violate Eq. (39) the conditions for stability are more complex, and for simplicity will not be considered here. Using the values for the SOAE parameters in Sec. IV, the ''near frequency'' region, for which both Eqs. (36) and (37) must be considered, is quite narrow for the SOAEs under consideration (corresponding to about 9 Hz).

For purposes of this analysis, only driving frequencies that satisfy Eq. (39) will therefore be considered. Consequently, the simpler entrainment condition of Eq. (36) has been used in this study to determine whether or not the SOAE is entrained.

III. COMPUTING THE EAR CANAL REFLECTANCE

To calculate $R_e(\omega_{dr})$, the nonlinear reflectance associated with the ear canal termination, the ω_{dr} components of $\xi_0(t)$, $\dot{\xi}_0(t)$, and $P_e(t)$ as the real parts of the complex representations, are expressed as

$$\xi_0(t) = a_{dr} e^{i(\omega_{dr}t + \varphi_{dr})}, \quad \dot{\xi}_0(t) = i\omega_{dr}\xi_0(t), \quad (40)$$

$$P_e(t) = \widetilde{P}_e e^{i\omega_{dr}t} = \frac{m_0}{S_0}(E - \omega_{cav}^2 a_{dr} e^{i\varphi_{dr}}) e^{i\omega_{dr}t}, \quad (41)$$

respectively. Then

$$\frac{P_e(t)}{\dot{\xi}_0(t)} = \rho_0 c \frac{1 + R_e}{1 - R_e}, \quad (42)$$

where it is understood that only the ω_{dr} Fourier component of $\xi_0(t)$ is considered. Using Eqs. (5), (6), (16), (17), and (20)–(26), under the conditions of suppression (but not entrainment),

$$\frac{P_e(t)}{\dot{\xi}_0(t)} = \frac{m_0}{i\omega_{dr}S_0}\left(\frac{E}{a_{dr}e^{i\varphi_{dr}}} - \omega_{cav}^2\right)$$

$$= \frac{m_0}{i\omega_{dr}S_0}\left[\tilde{\omega}_0^2 - \omega_{dr}^2 + i\omega_{dr}r_0\left(1 - \frac{3a_{dr}^2}{a_0^2}\right) - \omega_{cav}^2\right]$$

$$= \frac{m_0}{S_0}\left[\frac{\omega_0^2 - \omega_{dr}^2}{i\omega_{dr}} + r_0\left(1 - \frac{3a_{dr}^2}{a_0^2}\right)\right]. \tag{43}$$

Similarly, for conditions of entrainment, Eqs. (5), (6), (14), (16), and (28)–(33), give

$$\frac{P_e(t)}{\dot{\xi}_0(t)} = \frac{m_0}{i\omega_{dr}S_0}\left[\tilde{\omega}_0^2 - \omega_{dr}^2 - i\omega_{dr}r_0\left(1 - \frac{a_{dr}^2}{a_0^2}\right) - \omega_{cav}^2\right]$$

$$= \frac{m_0}{S_0}\left[\frac{\omega_0^2 - \omega_{dr}^2}{i\omega_{dr}} + r_0\left(\frac{a_{dr}^2}{a_0^2} - 1\right)\right]. \tag{44}$$

Equations (42) and (43) give, for conditions of nonentrainment,

$$|R_e(\omega_{dr})|^2$$

$$= \frac{(\omega_0^2 - \omega_{dr}^2)^2 + \omega_{dr}^2[r_0(1 - 3a_{dr}^2/a_0^2) - \rho_0cS_0/m_0]^2}{(\omega_0^2 - \omega_{dr}^2)^2 + \omega_{dr}^2[r_0(1 - 3a_{dr}^2/a_0^2) + \rho_0cS_0/m_0]^2}, \tag{45}$$

and Eqs. (42) and (44) give, for conditions of entrainment,

$$|R_e(\omega_{dr})|^2$$

$$= \frac{(\omega_0^2 - \omega_{dr}^2)^2 + \omega_{dr}^2[r_0(a_{dr}^2/a_0^2 - 1) - \rho_0cS_0/m_0]^2}{(\omega_0^2 - \omega_{dr}^2)^2 + \omega_{dr}^2[r_0(a_{dr}^2/a_0^2 - 1) + \rho_0cS_0/m_0]^2}. \tag{46}$$

For the case of nonentrainment, $|R_e(\omega_{dr})|$ will be greater than 1 if

$$a_{dr} \approx \frac{E}{|\omega_{dr}^2 - \omega_0^2|} > \frac{a_0}{\sqrt{3}}, \tag{47}$$

and less than 1 if

$$a_{dr} < \frac{a_0}{\sqrt{3}}. \tag{48}$$

In the case of entrainment, Eqs. (36) and (46) imply that $|R_e(\omega_{dr})|$ will be greater than 1 if

$$\frac{a_0}{\sqrt{2}} < a_{dr} < a_0, \tag{49}$$

and less than 1 if

$$a_{dr} > a_0. \tag{50}$$

In the latter case, $|R_e(\omega_{dr})|$ has a minimum around the SOAE frequency ω_0.

From a physical point of view, it is instructive to note the connection between $\mathscr{P}$, the power transfer to the middle ear, and the complex ratio $P_e/\dot{\xi}_0$,

$$\mathscr{P} = \frac{S_0}{2}\,\text{real}(P_e\dot{\xi}_0^*)$$

$$= \frac{S_0}{2}\,|\dot{\xi}_0|^2\,\text{real}\left(\frac{P_e}{\dot{\xi}_0}\right)$$

$$= \frac{S_0}{2}\,|\dot{\xi}_0|^2\rho_0c\,\frac{1 - |R_e|^2}{|1 - R_e|^2}. \tag{51}$$

Thus power will flow in (out) of the middle ear depending on whether the sign of $P_e/\dot{\xi}_0$ is positive (negative). This connection does not, of course, depend on the intermediary use of the reflectance R_e. Note, however, as expected, $|R_e| > 1$ corresponds to $\mathscr{P} < 0$.

IV. SIMULATION RESULTS

A. Parameter values used

In this section, results from numerical simulations of Eq. (2) are presented and compared to the analytic results of the previous section. In doing so, values for the oscillator parameters are chosen that are typical of large SOAEs:

$$f_0 = \frac{\omega_0}{2\pi} = 4000\;\text{Hz}, \tag{52}$$

$$r_0 = 100\;\text{Hz}, \tag{53}$$

$$\omega_{cav} = (240 - 480)\text{rad s}^{-1}, \tag{54}$$

$$P_{SOAE} \cong 10\;\text{dB SPL}. \tag{55}$$

The value for r_0 is taken from typical estimates of r_0 obtained for large SOAEs from the studies of Talmadge et al. (1990) and of Murphy et al. (1995a, 1995b, 1996) on the pulsed suppression and release from suppression of SOAEs by external tones.

The value for ω_{cav} was obtained from SOAE synchronization tuning curve measurements. These involve determining for each frequency ω_{dr} the pressure level P_{dr} necessary to just entrain the SOAE. For a review of how this procedure is performed experimentally, see for example, Long and Tubis (1988). An approximation of the tuning curve can be obtained from Eq. (36) using an appropriate change of variables. The ambient pressure amplitude P_{SOAE} in the ear canal in the absence of driving can be related to the ambient limit-cycle oscillator level. From Eq. (1),

$$P_{SOAE} = \frac{\rho_0c^2}{V_e}S_0a_0. \tag{56}$$

Then, using Eqs. (15) and (34), a_{dr} can be related to P_{dr} [the amplitude of $P_{dr}(t)$]:

$$a_{dr} = \frac{S_0}{m_0}\frac{P_{dr}}{|\omega_{dr}^2 - \tilde{\omega}_0^2|}. \tag{57}$$

Combining Eqs. (6), (56), and (57), together with Eq. (36), it is found that
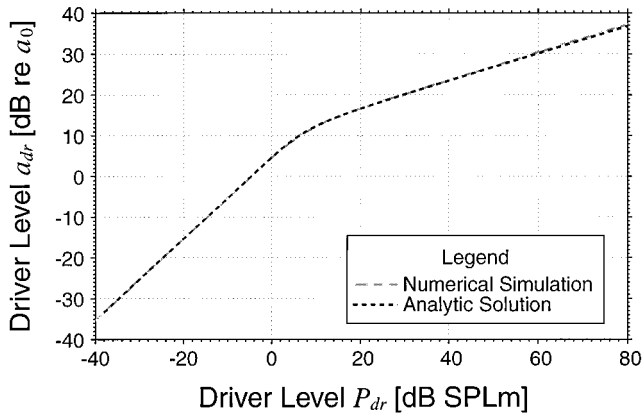
FIG. 2. Input/output curves for driver response a_{dr} versus pressure level in the ear canal P_{dr} for the driver frequency $f_{dr}=3850$ Hz and oscillator limit-cycle frequency at 4000 Hz. The solid line signifies the results of the numerical integration of Eq. (2), and the dashed line is from Eqs. (26) and (33). Note that the numerical and analytic solutions nearly overlay each other, except at very high driver levels, for which a small deviation between the two solutions is visible.

$$P_{dr}(\omega_{dr}) = \frac{P_{SOAE}}{\sqrt{2}} \frac{|\omega_{dr}^2 - \widetilde{\omega}_0^2|}{\omega_{cav}^2}. \tag{58}$$

Equation (58) was fit to the tuning curve data of Long and Tubis (1988) to obtain the estimate for ω_{cav} given in Eq. (54). For a 4000-Hz SOAE, a shift of less than 1.0 Hz is expected between $\omega_0/2\pi$ and $\widetilde{\omega}_0/2\pi$.

The purpose of the simulations presented in this section is to verify the approximate analytic results presented in the previous sections. In this verification procedure, more than 5000 simulations were performed in equal frequency intervals of $f_{dr}=\omega_{dr}/2\pi$ between 3750 and 4250 Hz.

B. Input/output curves

A comparison of the simulated input/output curve for the oscillator response a_{dr} versus the driver level P_{dr} and the corresponding analytic result obtained using Eqs. (26) ($a_{dr}<a_0/2$) and (33) ($a_{dr}>a_0/2$) is given in Fig. 2. The driving frequency f_{dr} is 3850 Hz. The simulated and analytical results are in excellent agreement.

Figure 2 also gives insight into the response of the ear drum to an external tone at the driver frequency ω_{dr}. In accordance with the approximate solutions to Eqs. (26) and (33), the input/output curve has an approximate slope of 1 for $a_{dr}<a_0$ and a slope of 1/3 for $a_{dr}\gg a_0$. As expected, in the region near $a_{dr}\approx a_0/2$, the input/output curve has a slope which varies between 1/3 and 1.

A more stringent comparison of the predicted input/output curve comes from comparing simulation and analytic results for $\sin \varphi_{dr}$ and $\cos \varphi_{dr}$ vs a_{dr}, as is done in Fig. 3. This comparison is particularly useful because the relative sign of the $\sin \varphi_{dr}$ and $\cos \varphi_{dr}$ components governs whether or not $|R_e(\omega_{dr})|>1$. Over most of the range of a_{dr}, the simulation and analytic results are in excellent agreement. However, for $a_{dr}\gg a_0$, the simulation results diverge from the analytic ones for $\cos \varphi_{dr}$. This deviation is very likely the result of the neglect of the harmonic distortion products such as the ones at $3\omega_{dr}$, $5\omega_{dr}$, etc.
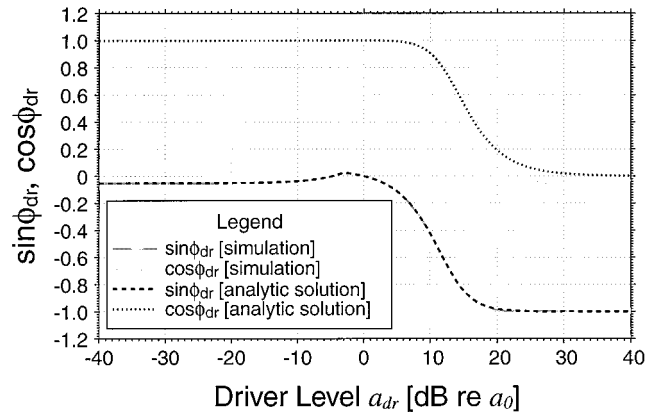
FIG. 3. Input/output curves for $\cos \varphi_{dr}$ and $\sin \varphi_{dr}$ as functions of the driver response a_{dr}, for the driver frequency at 3850 Hz and oscillator frequency at 4000 Hz. The solid lines signify the results of the numerical integration of Eq. (2). The dashed line ($\sin \varphi_{dr}$) is from Eqs. (24) and (31), and the dotted line ($\cos \varphi_{dr}$) is from Eqs. (25) and (32). Note that the analytic results are in excellent agreement with the simulation results, except for $a_{dr}\gg a_0$, for which a significant deviation in $\cos \varphi_{dr}$ is observed. This deviation probably stems from the influence of the neglected higher-order harmonic signal components ($\omega=3\omega_{dr}, 5\omega_{dr},...$).

C. Reflectance

The comparison of simulations and analytic results for $|R_e(\omega_{dr})|$ vs a_{dr} are given in Fig. 4 for $f_{dr}=3850$ Hz, with Eq. (45) used for $a_{dr}<a_0/2$ and Eq. (46) used for $a_{dr}>a_0/2$. Again, excellent agreement is obtained.

The value of $|R_e(\omega_{dr})|$ calculated from the simulations is plotted in Fig. 5 versus the driver frequency f_{dr} and a_{dr}. As predicted from the formalism of Sec. IV, $|R_e(\omega_{dr})|>1$ only in the narrow region $a_0/\sqrt{3}\leqslant a_{dr}\leqslant a_0$ (the band running across the figure). Outside of this band of levels of a_{dr}, this simulation predicts a dip in $|R_e(\omega_{dr})|$ around $f_{dr}=f_0$.

$|R_e(\omega_{dr})|$ is also plotted as a function of f_{dr} for various choices of fixed a_{dr} in Fig. 6. For $a_{dr}<a_0/\sqrt{3}[-4.77$ dB $re:a_0]$, a shallow minima occurs as f_{dr} is swept through the SOAE frequency region. At $a_{dr}=a_0/\sqrt{3}$, $|R_e|=1$ for all f_{dr}. At $a_{dr}=10^{-1/10}a_0[-2$ dB $re:a_0]$, a maximum in $|R_e|$ with
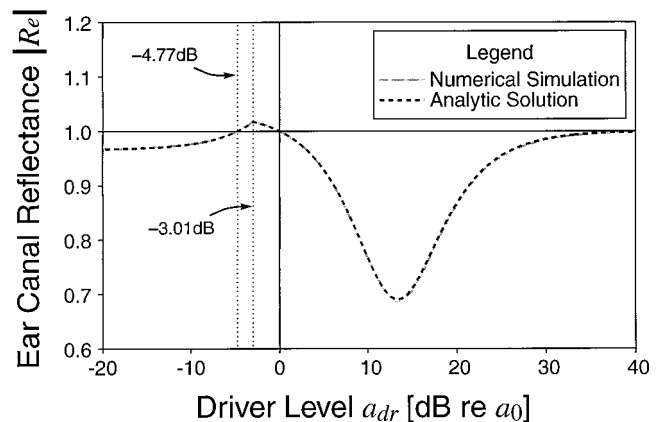
FIG. 4. Ear canal reflectance $|R_e|$ as a function of the driver response a_{dr} for the driver frequency $f_{dr}=3850$ Hz and oscillator frequency at 4000 Hz. The solid line signifies the numerical simulation results, and the dashed line signifies the analytic results, as described in the text. The vertical dotted line denoted -4.77 dB corresponds to $a_{dr}=a_0/\sqrt{3}$ and the line denoted -3.01 dB corresponds to $a_{dr}=a_0/\sqrt{2}$.
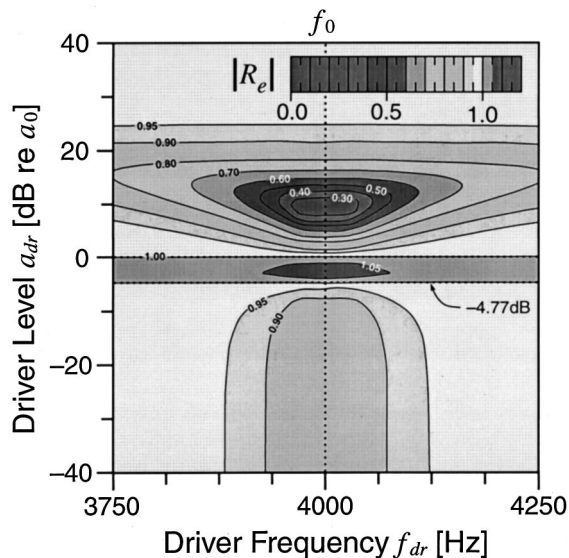
FIG. 5. Density plot of the magnitude of ear canal reflectance $|R_e|$ versus driver frequency f_{dr} and driver response a_{dr} from the numerical simulation results with an oscillator frequency of 4000 Hz. Notice that $|R_e|>1$ only in the horizontal band denoted by the dashed lines. Since -4.77 dB corresponds to $a_{dr}/a_0 = 1/\sqrt{3}$, then $|R_e|>1$ for $a_0/\sqrt{3} \lesssim a_{dr} \lesssim a_0$.

$|R_e|>1$ is observed at $f_{dr}=f_0$. For $a_{dr}>a_0$, $|R_e|<1$ for all values of f_{dr}, with a minimum again occurring at $f_{dr}=f_0$. However, for $a_{dr} \gg a_0$, $|R_e|$ becomes nearly independent of f_{dr}.

$|R_e(\omega_{dr})|$ is also plotted as a function of P_{dr} and f_{dr} in Fig. 7. This is useful since P_{dr} and f_{dr} are the variables that are normally used in presenting the experimental data. The significance of the results shown in Fig. 7 can be illuminated by plotting $|R_e(\omega_{dr})|$ as a function of f_{dr} for various choices of P_{dr}, as is done in Fig. 8. In this figure, for no choice of P_{dr} was a peak in $|R_e|$ seen exactly at $f_{dr}=f_0$. Instead, for a few choices of P_{dr}, maxima in $|R_e|$ occurred at frequencies close to f_0, while minima occurred at $f_{dr}=f_0$. For most of the choices of P_{dr}, however, $|R_e|$ was never greater than 1, and a broad minimum was present at $f_{dr}=f_0$.

V. DISCUSSION AND CONCLUSIONS

The behavior of the ear canal reflectance in the neighborhood of a SOAE has been studied on the basis of a simple

FIG. 7. Density plot of the magnitude of ear canal reflectance $|R_e|$ versus driver frequency f_{dr} and ear canal driving pressure P_{dr} for an oscillator frequency of 4000 Hz.

limit-cycle oscillator model of the emission. This model has been shown to give a good accounting for the statistical properties of SOAEs and their interactions with external tones (see the Introduction), and it seems reasonable to use it in a first theoretical study of the reflection problem. (Follow-up studies of this problem, which will be described in subsequent papers in this series, will incorporate the effect of cochlear noise and a distributed nonlinear-active cochlear model.)

The limit-cycle oscillator model shows that the behavior of the reflectance depends on the level of the external stimulus, and may exceed 1 in magnitude under conditions of the SOAE being entrained, or not entrained but suppressed. Let a_0 be the SOAE amplitude of the ear canal termination in the absence of external driving, and $a_{dr}(\omega_{dr})$ be the amplitude of the ω_{dr} component of the termination in the presence of driving. Then, as discussed in Sec. IV, it is found that

FIG. 6. Magnitude of ear canal reflectance $|R_e|$ versus driver frequency f_{dr} for various choices of the fixed driver response level a_{dr} for an oscillator frequency of 4000 Hz. Each curve is labeled by the level of a_{dr} in dB relative to the unsuppressed oscillator amplitude a_0.
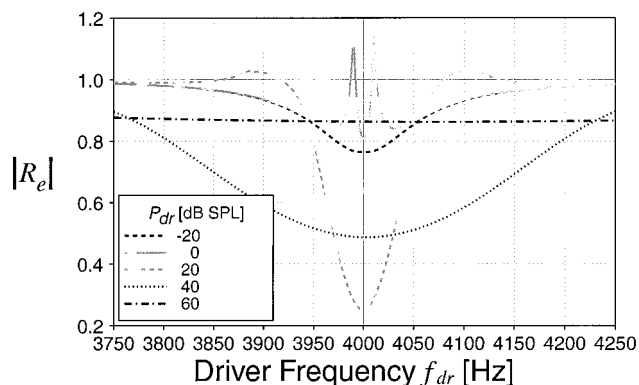
FIG. 8. Magnitude of ear canal reflectance $|R_e|$ versus driver frequency f_{dr} for various choices of fixed ear canal driving pressure P_{dr} for an oscillator frequency of 4000 Hz.

$$\frac{a_{\mathrm{dr}}(\omega_{\mathrm{dr}})}{a_0} < \frac{1}{\sqrt{3}}; \quad \text{SOAE suppressed but not entrained;}$$

$$|R_e(\omega_{\mathrm{dr}})| < 1, \tag{59}$$

$$\frac{a_0}{\sqrt{3}} < a_{\mathrm{dr}}(\omega_{\mathrm{dr}}) < \frac{a_0}{\sqrt{2}}; \quad \text{SOAE suppressed but not entrained;}$$

$$|R_e(\omega_{\mathrm{dr}})| > 1, \tag{60}$$

$$\frac{a_0}{\sqrt{2}} < a_{\mathrm{dr}}(\omega_{\mathrm{dr}}) < a_0; \quad \text{SOAE entrained;} \quad |R_e(\omega_{\mathrm{dr}})| > 1, \tag{61}$$

$$a_0 < a_{\mathrm{dr}}(\omega_{\mathrm{dr}}); \quad \text{SOAE entrained;} \quad |R_e(\omega_{\mathrm{dr}})| < 1. \tag{62}$$

In cases where $|R_e(\omega_{\mathrm{dr}})| < 1$, $|R_e(\omega_{\mathrm{dr}})|$ has a minimum around the SOAE frequency, and when $|R_e(\omega_{\mathrm{dr}})| > 1$, $|R_e(\omega_{\mathrm{dr}})|$ has a maximum around the SOAE frequency.

The results of Allen *et al.* (1995), which indicate $|R_e(\omega_{\mathrm{dr}})| < 1$ and have $|R_e(\omega_{\mathrm{dr}})|$ passing through a minimum around the SOAE frequency, presumably correspond to the conditions of Eq. (62). More recently Burns and Keefe (1997) have obtained reflectance magnitudes around SOAEs that do appear to exceed 1. According to the model used in this study, these should correspond to the conditions of Eqs. (60) or (61).

One of the main conclusions of the analysis presented in this study is that not finding $|R_e(\omega_{\mathrm{dr}})| > 1$ around an SOAE under some driving level conditions does not constitute evidence against the interpretation of SOAEs in terms of nonlinear active signal processing in the cochlea. On the other hand, a demonstration that $|R_e(\omega_{\mathrm{dr}})| > 1$ would indeed constitute strong evidence for such signal processing.

More theoretical and experimental work is needed to provide definitive confirmation of reflectance magnitudes which exceed 1. However, in light of the success of nonlinear active models in describing many other features of SOAEs, this confirmation seems very plausible.

ACKNOWLEDGMENTS

Allen, J. B., Shaw, G., and Kimberley, B. P. (**1995**). ''Characterization of the nonlinear ear canal impedance at low sound levels,'' in *Abstracts of the Eighteenth Midwinter Research Meeting of the Association for Research in Otolaryngology*, edited by G. R. Popelka (Association for Research in Otolaryngology, Des Moines), p. 190.

Bialek, J. S., and Wit, H. P. (**1984**). ''Quantum limits to oscillator stability: theory and experiments on acoustic emissions from the human ear,'' Phys. Lett. A **104**, 173–184.

Burns, E. M., and Keefe, D. H. (**1997**). ''SOAEs and power transfer in the middle and external ears of children and adults,'' in *Abstracts of the Twentieth Midwinter Research Meeting of the Association for Research in Otolaryngology*, edited by G. R. Popelka (Association for Research in Otolaryngology, Des Moines), p. 168.

Hangii, P., and Riseborough, P. (**1983**). ''Dynamics of nonlinear dissipative oscillators,'' Am. J. Phys. **84**, 347–351.

Jackson, E. A. (**1989**). *Perspectives of Nonlinear Dynamics* (Cambridge U.P., Cambridge, England).

Kinsler, L. E., Frey, A. R., Coppens, A. B., and Sanders, J. V. (**1982**). *Fundamentals of Acoustics* (Wiley, New York), 3rd ed.

Long, G. R., and Tubis, A. (**1988**). ''Investigations into the nature of the association between threshold microstructure and otoacoustic emissions,'' Hearing Res. **36**, 125–138.

Long, G. R., Tubis, A., and Jones, K. L. (**1991**). ''Modelling the synchronization and suppression of spontaneous otoacoustic emissions using Van der Pol oscillators: Effects of aspirin administration,'' J. Acoust. Soc. Am. **89**, 1201–1212.
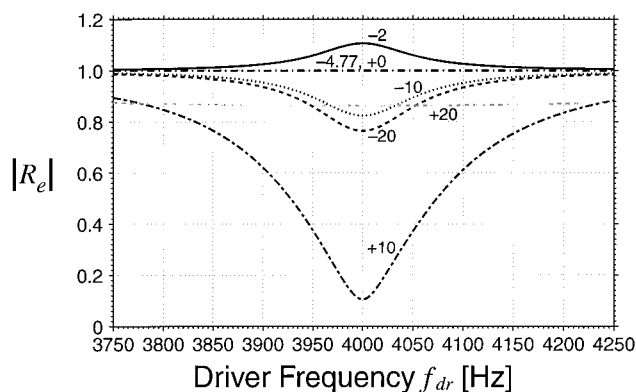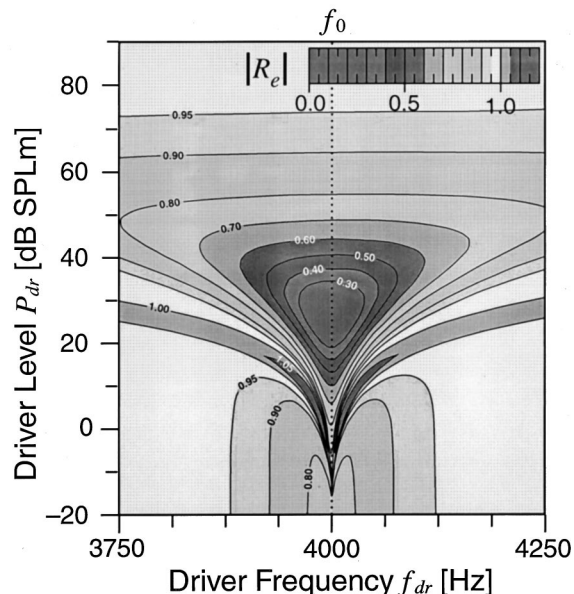
Long, G. R., Tubis, A., Jones, K. L., and Sivaramakrishnan, S. (**1988**). ''Modifications of the external-tone synchronization and statistical properties of spontaneous otoacoustic emissions by aspirin consumption,'' in *Basic Issues of Hearing*, edited by H. Duifhuis, J. W. Horst, and H. P. Wit (Academic, London), pp. 93–100.

Murphy, W. J., Talmadge, C. L., Tubis, A., and Long, G. R. (**1995a**). ''Relaxation dynamics of spontaneous otoacoustic emissions perturbed by external tones: I. Response to pulsed single-tone suppressors,'' J. Acoust. Soc. Am. **97**, 3702–3710.

Murphy, W. J., Talmadge, C. L., Tubis, A., and Long, G. R. (**1995b**). ''Relaxation dynamics of spontaneous otoacoustic emissions perturbed by external tones: II. Suppression of interacting tones,'' J. Acoust. Soc. Am. **97**, 3711–3721.

Murphy, W. J., Talmadge, C. L., Tubis, A., Long, G. R., and Krieg, E. F. (**1996**). ''Relaxation dynamics of spontaneous otoacoustic emissions perturbed by external tones: III. Response to a single tone at multiple suppression levels,'' J. Acoust. Soc. Am. **100**, 3979–3982.

Talmadge, C., and Tubis, A. (**1993**). ''On modeling the connection between spontaneous and evoked otoacoustic emissions,'' in *Biophysics of Hair Cell Sensory Systems*, edited by H. Duifhuis, J. W. Hosrt, P. van Dijk, and S. M. van Netten (World Scientific, Singapore), pp. 25–32.

Talmadge, C., Tubis, A., Long, G. R., and Piskorski, P. (**1997**). ''Modeling otoacoustic emission fine structure,'' in *Diversity in Auditory Mechanics*, edited by E. Lewis, G. Long, R. Lyon, P. Narins, and C. Steele (World Scientific, Singapore), pp. 462–471.

Talmadge, C. L., Long, G. R., Murphy, W. J., and Tubis, A. (**1990**). ''Quantitative evaluation of limit-cycle oscillator models of spontaneous otoacoustic emissions,'' in The Mechanics and *Biophysics of Hearing*, edited by P. Dallos, C. D. Geisler, J. W. Matthews, M. A. Ruggero, and C. R. Steele (Springer-Verlag, Berlin), pp. 235–242.

Talmadge, C. L., Tubis, A., Wit, H. P., and Long, G. R. (**1991**). ''Are spontaneous otoacoustic emissions generated by self-sustained cochlear oscillators?,'' J. Acoust. Soc. Am. **89**, 2391–2399.

Tubis, A., Long, G. R., Sivaramakrishnan, S., and Jones, K. L. (**1988**). ''Tracking and interpretive models of the active-nonlinear cochlear response during reversible changes induced by aspirin consumption,'' in *Cochlear Mechanisms, Structure, Function, and Models*, edited by J. P. Wilson and D. T. Kemp (Plenum, New York), pp. 323–330.

van Dijk, P., and Wit, H. P. (**1988**). ''Phase-lock of spontaneous otoacoustic emissions to a cubic difference tone,'' in *Basic Issues of Hearing*, edited by H. Duifhuis, J. W. Horst, and H. P. Wit (Academic, London), pp. 323–330.

van Dijk, P., and Wit, H. P. (**1990a**). ''Synchronization of spontaneous otoacoustic emissions to a $2f_1 - f_2$ distortion product,'' J. Acoust. Soc. Am. **88**, 850–856.

van Dijk, P., and Wit, H. P. (**1990b**). ''Amplitude and frequency fluctuations of spontaneous otoacoustic emissions,'' J. Acoust. Soc. Am. **88**, 1779–1793.

van Dijk, P., Wit, H. P., Tubis, A., Talmadge, C. L., and Long, G. R. (**1994**). ''Correlation between amplitude and frequency fluctuations of spontaneous emissions,'' J. Acoust. Soc. Am. **96**, 163–169.

Wit, H. P. (**1986**). ''Statistical properties of a strong spontaneous otoacoustic emission,'' in *Peripherial Auditory Mechanims*, edited by J. B. Allen, A. Hubbard, S. T. Neely, and A. Tubis (Springer-Verlag, Berlin), pp. 221–228.

Energy reflectance in the ear canal can exceed unity near spontaneous otoacoustic emission frequencies

Edward M. Burns
University of Washington, 1417 NE 42nd Street, Seattle, Washington 98105

Douglas H. Keefe
Boys Town National Research Hospital, 555 North 30th Street, Omaha, Nebraska 68131

Robert Ling
Department of Speech and Hearing Sciences, University of Washington, Seattle, Washington 98195

There is some controversy in the literature over whether the so-called ''active mechanism'' or ''cochlear amplifier'' is actually a power amplifier that can produce an output signal with more power than its input, or whether it simply minimizes dissipative losses within the cochlea without providing an actual power gain greater than unity. A corollary of this controversy is whether spontaneous otoacoustic emissions (SOAEs) represent the output of a nonlinear oscillator mechanism, i.e., a power amplifier which can produce an oscillatory output signal in the absence of an input oscillatory signal, or whether they represent the output of a noise-driven, passive, nonlinear system. This paper describes measurements of energy reflectance and acoustic impedance in the ear canals of human subjects with strong SOAEs. The reflectance, and the resistive and reactive parts of the acoustic impedance, all show a frequency fine structure which correlates with SOAE frequencies, and which becomes more pronounced at low stimulus levels. In some ears at some SOAE frequencies, energy reflectance exceeds unity, and correspondingly, acoustic resistance is negative. This result demonstrates that there is a power gain at these frequencies: The power reflected from the cochlea to the ear canal exceeds the power incident. It is also consistent with the theory that these SOAEs are produced by a nonlinear oscillator mechanism in the cochlea. © *1998 Acoustical Society of America.* [S0001-4966(97)05312-5]

PACS numbers: 43.64.Jb, 43.64.Kc [BLM]

INTRODUCTION

It is generally accepted that the mammalian cochlea has an ''active'' mechanism (the ''cochlear amplifier'') that uses metabolic energy to overcome the high dissipative losses in the passive cochlea in order to obtain high sensitivity and sharp frequency selectivity (e.g., Dallos, 1992; de Boer, 1993). However, there has been some controversy over exactly what constitutes an active mechanism, and whether the cochlear amplifier is indeed active, and is indeed an amplifier. To clarify the issues discussed below, we first summarize precise definitions. Except for the concept of the cochlear amplifier, the remaining concepts have existed in the literature for at least half a century.

An active system is one with an internally accessible source of power; a live cochlea is, therefore, an active system due to the electrical potential differences that exist within it. A system that is not active is passive. An active system may, and does, contain passive elements. A power amplifier is an active system that can produce an output oscillatory signal with more power than its input oscillatory signal. The power gain is the ratio of the output to the input power. A cochlear amplifier represents a power amplification structure and mechanism within the cochlea. A nonlinear oscillator is a particular form of power amplifier that can produce an output oscillatory signal (a limit cycle) in the absence of an input oscillatory signal.

Rayleigh (Strutt, 1883) was the first to state explicitly that because the losses in a dissipative vibrating system tend to attenuate the vibration, a source of power is necessary to maintain a vibration. His quantitative theory of a limit cycle oscillator is equivalent to the experimental systems later studied by van der Pol. A passive system has no additional source of power and conservation of energy requires that the output power cannot exceed its input power. Hence total power gain of a passive system across all frequencies can never exceed one and is equal to one only if there are no internal losses in the system. However, a nonlinear passive system can generate distortion components at frequencies not contained in the input signal; thus the apparent power gain at the frequencies of such distortion does exceed unity, but at the cost of a power loss at other frequencies. A nonlinear passive system with dissipation cannot function as a nonlinear oscillator.

A power amplifier and nonlinear oscillator must contain an element that incorporates negative resistance so that the total power gain within the element exceeds one. It follows that neither a power amplifier nor a nonlinear oscillator can be constructed as a passive device for a system with internal losses. Familiar active devices capable of power gain and limit-cycle behavior include the vacuum tube and the transistor among electronic devices, and the bowed violin string and the organ pipe among acoustic devices.

Many of these definitions were implicit in the pioneering theoretical research by Gold (1948) on the physical basis of

the action of the cochlea. For example, Gold states that we should ''regard the cochlea no longer as a passive instrument where nerve endings merely record the displacement due to an applied force, but as an active mechanism where an applied signal releases a chain of events involving an additional supply of energy.''

In the original report on transient-evoked otoacoustic emissions (TEOAEs), Kemp (1978) estimated power flow using a middle ear model and suggested that the emission power at low intensities was of the same order as stimulus power, but he did not measure injected and emitted power. He concluded that TEOAEs have a cochlear origin as a wave amplifying mechanism, and suggested that outer hair cell functioning might play a central role. The term, cochlear amplifier, was introduced by Davis (1983) to propose an essential role for the outer hair cells in accounting for a variety of measurements in auditory neurophysiology, and by Neely (1983) in a report on a computational model of a cochlear amplifier. Power relationships in cochlear mechanics have recently been reviewed by Allen (1996).

Kemp (1979a) reported the existence of spontaneous otoacoustic emissions (SOAEs) and compared the fine structure in the acoustic impedance magnitude, measured at a location in the ear canal, at three stimulus levels in the vicinity of a SOAE near 1750 Hz. The frequency of the SOAE was higher than the zero-crossing frequency associated with the fine structure of the impedance, and was approximately aligned with the minimum in the impedance level. How the impedance magnitude was measured in the vicinity of 1750 Hz was not described.

A pressure reflectance is the ratio of the reflected pressure signal to the incident pressure signal. Kemp (1979a) proposed a reflectance model for the evoked OAE in terms of two pressure reflectances R_p and R_b. R_p is associated with a wave discontinuity on the cochlea describing the reflection of an apically incident signal back towards the basal end of the cochlea. R_b describes the reflection of this retrograde cochlear wave from the basal end of the cochlea due to the impedance discontinuity at the oval window. This model functions as a nonlinear mechanical filter capable of generating the observed emissions, but stability is possible only if the net damping remains positive. The evoked OAE increases damping in the form of a radiation loss from the cochlea. A more robust, and nonlinear, stabilizing mechanism was subsequently posited such that if $R_p R_b$ ever did exceed unity then self-sustained standing wave oscillations on the basilar membrane could occur, but, as their intensity grew, the cochlear reflectance R_p would decrease (Kemp, 1979b). This results in stable SOAEs.

Some studies have addressed whether SOAEs are produced by a deterministic limit cycle as a nonlinear oscillator or as a consequence of filtered bandpass noise. Bialek and Wit (1984) measured the statistical properties of SOAEs. They concluded that the measured distributions were consistent with the behavior of a limit-cycle model, and inconsistent with a SOAE model based upon narrow-band filtered noise. The existence of dynamically linked SOAEs was explained as further evidence for a nonlinear oscillator theory of SOAEs involving multiple cochlear sites with feedback

(Burns *et al.*, 1984). Some linked SOAEs have a quasiperiodic, phase-locked, spectrum (Keefe *et al.*, 1990), which is most simply explained by a dynamical feedback between multiple sites. Such an oscillation is structurally stable.

An alternative test of whether SOAEs are nonlinear oscillators or nonlinearly filtered noise is to measure the correlation dimension of the waveforms by reconstructing the phase space of the system in a higher-dimensional embedding space. If the system is noise, which has an infinite number of dynamical degrees of freedom, then the measured correlation dimension increases with the embedding dimension for arbitrarily large embedding dimensions. If the system is deterministic and of low dimensionality, then the correlation dimension converges to a small value. The measured correlation dimension of SOAEs was less than four, indicating that the dynamical system was deterministic, and of low dimensionality, rather than stochastic (Keefe *et al.*, 1990).

Long *et al.* (1991) demonstrated that a van der Pol model accounts for many of the effects seen in interactions of SOAEs with external stimuli including: suppression-tuning-curve effects measured on SOAEs in the presence of an external sinusoidal tone, the entrainment of the SOAE frequency by an external sinusoidal tone, and the broadening of the tuning curve of entrained SOAEs lower in level compared to those higher in level. The evidence supporting the theory that SOAE are nonlinear oscillators driven by weak random noise forces was reviewed by Talmadge *et al.* (1991). They also replicated the observations of Bialek and Wit (1984) and extended their results to a more general class of nonlinear oscillators.

Allen and Fahey (1992) proposed and applied a model to experimental data from which they inferred the power gain of the cochlear amplifier. They concluded that the gain of the cochlear amplifier must be close to one, and that the simplest interpretation of their experimental results does not require the concept of a cochlear amplifier. A power gain greater than, or equal to, unity was their criterion for the presence of power amplification. The two conclusions are not equivalent, because the first leaves open the possibility that the gain may exceed one but the second discards this possibility. The authors proposed an alternative hypothesis to account for the measurement of Bialek and Wit, namely, that SOAEs are produced with Gaussian noise as an input, and that a nonlinear reflectance, which might arise from a passive nonlinearity, produces an output whose amplitudes are distributed in a non-Gaussian distribution. No detailed mechanism was proposed to explain how the nonlinear reflectance accomplishes this effect. In contrast, Talmadge *et al.* (1991) considered this same issue by constructing a computational model, and concluded that a saturating nonlinearity driven by noise could not satisfactorily account for the behavior of SOAEs.

In a recent presentation, Allen *et al.* (1995) measured the energy reflectance in the ear canal. The energy reflectance (sometimes called power reflectance, or power transfer function), is defined as the squared magnitude $|R(f)|^2$ of the corresponding pressure reflectance $R(f)$ and measures the ratio of reflected energy to incident energy injected into the ear canal at frequency f. They reported that ''the power reflectance...we find is always less than one, even near spon-

taneous emissions.'' They further stated: ''We have found that near an SOAE frequency...the power reflectance decreases.''

The results of Allen *et al.* (1995) appear to be the only evidence that might support the theory that SOAEs are produced by a noise-driven, passive, nonlinear system. The alternative theory of SOAEs as nonlinear oscillators necessarily requires the existence of an internal source of power to make up for the existence of internal power dissipation. That theory implies a device whose power gain exceeds unity for at least part of an oscillatory cycle to make up for the power losses in other parts of the oscillatory cycle. Some component of the nonlinear oscillator should exist whose energy reflectance exceeds unity. Allen *et al.* (1995) appear to imply that this component of the nonlinear oscillator must be observable in the ear canal as an energy reflectance exceeding unity, but this need not be the case if dissipation exists in the middle ear, eardrum, and ear canal. On the other hand, if an energy reflectance were demonstrated to exceed unity in the ear canal, this would support the nonlinear oscillator theory.

In this report we describe new measurements of input impedance and reflectance at various stimulus levels in three subjects with a documented history of high-level SOAEs. We show that: (1) there are numerous frequencies where the energy reflectance at fairly low stimulus levels exceeds unity (in some cases by almost an order of magnitude); (2) the relationships among SOAE frequencies, local minima and maxima in energy reflectance, and the real and imaginary parts of the input impedance, are complicated and varied. In particular, the SOAE frequency does not always correspond to a local minimum in energy reflectance, as Allen *et al.* (1995) observed.

I. METHODS

The methodology for measuring input impedance and energy reflectance has been described (Keefe *et al.*, 1992). Briefly, the Thevenin pressure and impedance of the Etymotic ER-10C probe assembly are determined using a calibration procedure during which a wideband chirp stimulus is used to create a sound field in six equal-diameter closed tubes of differing lengths. The chirp stimulus is constructed using as input a short-duration clicklike stimulus that is all-pass filtered with a group delay proportional to frequency over a frequency range from 200 to 10 000 Hz during a period of about 50 ms. The output chirp is akin to a rapidly swept sine wave with frequency-dependent amplitude. The spectral envelope is shaped to give approximately equal energy across frequency in the calibration tubes. The chirps are presented at a rate of 12 per s. A response is discarded if any sample of the response differs from the corresponding sample of the previous response by more than a user-set threshold (Keefe and Ling, 1997). This threshold is typically 1%–2% of the peak amplitude of the response. Calibration measurements are usually based on the time-averaged responses to 64 chirps but, for calibrations at low stimulus levels (see below), may be based on as many as 256 averages. The Thevenin parameters are determined by fitting the measured pressure responses to models of closed tubes, including viscothermal losses. Once the Thevenin parameters

have been determined from the calibration procedure, the impedance at the tip of the probe assembly, after leak-free insertion in the ear canal, is calculated from the measured pressure response.

The pressure and energy reflectances are calculated in terms of the measured impedance and the cross-sectional area of the ear canal. The measurement method also provides an acoustical estimate of ear canal cross-sectional area. Since this estimate is most accurate when the estimated area is within 20% of the calibration tube area, and since impedance measurements were made in both adults and 7-year-olds, two sets of calibration tubes were employed: an 8.02-mm-diam set for use with the Etymotic ER-10C adult (ER10C-14A) foam tips; and a 5.64-mm-diam set for use with the child (ER10C-14B) foam tips. Because differences between individual foam tips can lead to significant differences in Thevenin parameters, calibrations were obtained for each tip used. Finally, since linear-systems techniques are being used to measure an inherently nonlinear system, calibrations were obtained at each stimulus level. An example of the Thevenin parameters from the calibration of a child tip is shown in Fig. 1. As the stimulus level is varied, the Thevenin pressure level approximately varies with stimulus level, whereas the Thevenin impedance is nearly constant.

The subjects were two adults and one 7-year-old child, all of whom are participants in a study of longitudinal measurements of SOAEs, and all of whom have a history of multiple high-level (>10 dB SPL) SOAEs. Impedance/reflectance measurements were obtained at the moderate stimulus levels at which adult and child subjects are normally run in our laboratory, and at successively lower levels, in steps of 10 (or 5) dB, down to the lowest level for which a valid calibration could be obtained. The ear-canal sound-pressure levels at various attenuation values shown in Fig. 3(d) for an adult subject are repesentative of levels both for adults and for children who were run with 6 dB greater overall attenuation. After fitting the probe in the ear, and determining from the stimulus waveform in the ear canal that a leak-free fit had been obtained, the chirp stimulus was presented repeatedly and data were collected. A minimum of eight responses from the stimulus were discarded before data was collected and averaged. Responses that were judged to be too noisy, or that contained artifacts, were discarded using the noise-rejection procedure described above. In this study measurements were based on an average of at least eight responses, but at the lowest stimulus levels as many as 64 responses were averaged.

Two types of SOAE measurements were also performed using the same probe fitting that was used to measure impedance: (a) a 15-s sample of the microphone signal from the unstimulated ear canal was digitally recorded and analyzed off line via a discrete Fourier transform (DFT) with spectral averaging of 350 spectra obtained by applying a 4096-sample Hanning window (normalized to unity energy) with a 2:1 overlap factor across the entire recording; (b) synchronous SOAEs (SSOAEs) were measured by presenting 80-μs duration clicks at a peak level of approximately 80 dB SPL, and at a rate of 11.8 clicks per second, time-averaging 256 of the responses in the 85-ms time window between clicks, and
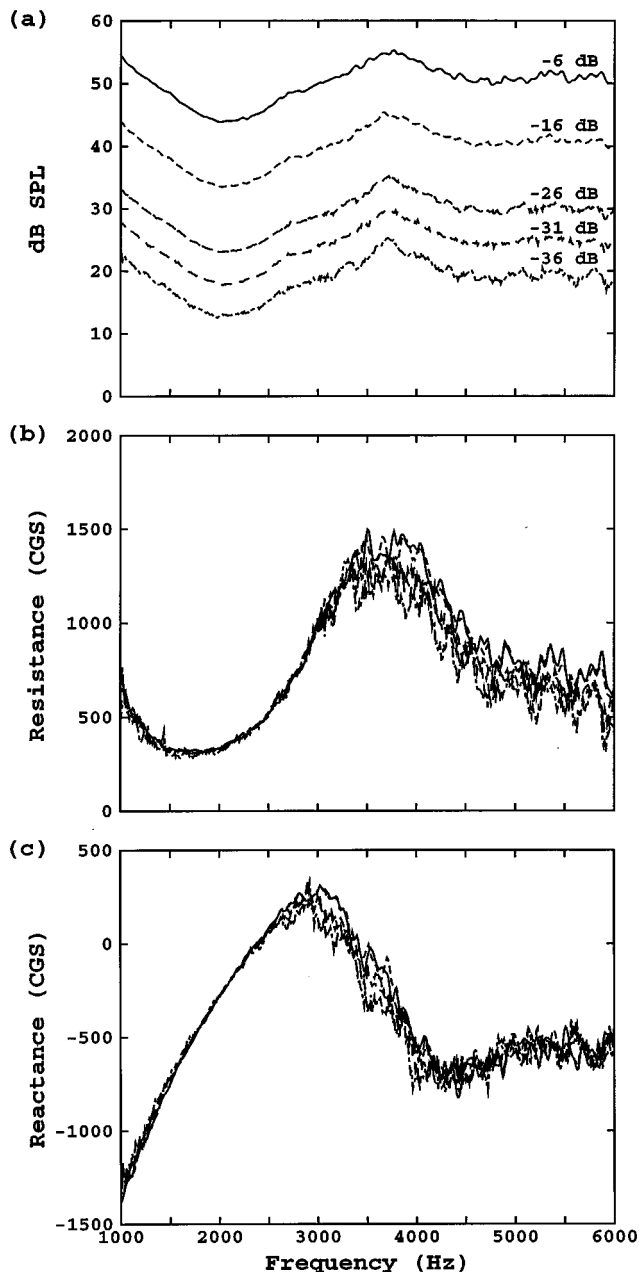
FIG. 1. The Thevenin pressure level, expressed as a SPL in dB, is displayed in plot (a). The resistive and reactive parts of the Thevenin impedance of the probe assembly with a child ear tip are displayed in plots (b) and (c), respectively. Impedance values are expressed in CGS units, sometimes called CGS Ohms, such that 1 CGS ohm is 1 dyn-s/cm^5.

FIG. 2. Recordings from the left ear of subject A-3 showing: (a) SOAE spectrum; (b) click-evoked SSOAE spectrum; (c) time-averaged SOAE spectrum. Frequency resolution and total averaging time are comparable for these spectra. See text for measurement details.

performing a DFT on this average after deleting the click artifact in the first 5 ms. Although the clicks will also evoke TEOAEs, these decay within about 20 ms, and the response is dominated by SSOAEs which are entrained by the clicks and persist over the entire 85 ms (e.g., Wilson, 1980; Ruggero *et al.*, 1983). This is essentially the same method that is used by a commercial device (Otodynamics ILO-92) for measuring SSOAEs.

II. RESULTS

The spectra from the two types of SOAE measurements are shown in Fig. 2. Figure 2(a) (top) is an average of 350

DFTs, each of length 4k samples (corresponding to a window duration of 85 ms), from the unstimulated-ear recording and shows the SOAEs for the right ear of female-adult subject A-3. The recordings were also analyzed with DFTs based on a length of 256k samples, (not shown) for more precise determination (0.2-Hz resolution) of SOAE frequencies. Figure 2(b) (middle) shows the SSOAE measurement for the same ear: a 4k sample DFT of 256 time-averaged responses. The differences between the SOAE and SSOAE measurements for A-3 are typical of the differences seen in general between SOAEs and SSOAEs: The higher-level

SOAEs are about the same level for the two measurements, whereas the lower-level SOAEs are relatively lower in the SSOAE measure. In addition, there are sometimes strong SSOAEs at frequencies where either no, or only very low-level, SOAEs are evident. For example, the SSOAE at about 1420 kHz in subject A-3 is not apparent in the SOAE measurements.

It is of interest to examine the SSOAE spectrum in the limit that the click-stimulus amplitude, which synchronizes the SOAE, is equal to zero. This is obtained by averaging the 15-s, unstimulated-ear-canal recording in the time domain. Figure 2(c) (bottom) shows the resulting time-averaged SOAE spectrum, based upon an average of 175 windows, calculated using a 4k-sample Hanning window. The time-averaged SOAE spectrum has markedly lower signal amplitudes as compared to Fig. 2(a), and a much lower noise floor. Figure 2(c) shows one peak near 2.3 kHz that is 10 dB lower than the corresponding peak in Fig. 2(a), and another peak near 4.1 kHz that is 29 dB lower. Most of the remaining peaks apparent in the SOAE spectrum vanish in the time-averaged SOAE spectrum. The lower-amplitude SOAE peaks result from the lack of a synchronizing stimulus, whether it be a click or some other waveform. If a greater number of averages were taken, these peak amplitudes in Fig. 2(c) would be reduced even further. The lower noise floor in Fig. 2(c) relative to Fig. 2(a) is due to the difference between a coherent and incoherent averager. The SOAE spectrum [Fig. 2(a)] is calculated by averaging the magnitude of the DFT, whereas the SSOAE and time-domain SOAE spectra [Fig. 2(b) and (c)] are calculated in a manner that is equivalent to averaging both the magnitude and phase of the DFT.

It is also interesting to directly compare the SSOAE and the time-averaged SOAE, because both are calculated by a similar coherent averaging process. The presence of the click has a significant effect in evoking a synchronous cochlear response, which largely disappears when the click stimulus is not present.

Figure 3 shows the ear-canal sound-pressure level (SPL), the real (resistance) and imaginary (reactance) parts of the impedance at the probe tip, and the energy reflectance ($|R|^2$), in the left ear of subject A-3 for four stimulus levels; denoted by attenuation settings of 0, 10, 20, and 25 dB. In all of the functions there is fine structure associated with many of the SOAE frequencies which is apparent even at the highest stimulus level, and which becomes progressively more pronounced at lower stimulus levels. The main point is that, at the lowest stimulus level, for two frequencies $|R|^2 \geq 1$ and, correspondingly, the resistance is zero or negative. Thus at these frequencies the ear is emitting as much or more power as it is absorbing.

Figures 4, 5, and 6 show, respectively, the SSOAE spectrum and the reflectance functions at different stimulus levels for the right ear of subject A-3; the right ear of a male adult, A-1; and the right ear of a 7-year-old female, K-1. For these ears also there are frequencies that correspond to the frequencies of high-level SSOAEs, such that $|R|^2 > 1$ at the lower stimulus levels. Note that, because of her high reflectance levels, reflectance is plotted on a logarithmic scale for

A-3 (Figs. 3 and 4), whereas for subjects A-1 and K-1 it is plotted on a linear scale.

Figures 7–11 show plots of SPL, resistance, reactance, and $|R|^2$ for frequency regions in the above ears where $|R|^2$ is close to, or greater than, one. Short-dashed vertical lines on all these figures denote frequencies corresponding to strong SOAEs (resolution, 0.2 Hz), and long-dashed vertical lines denote either frequencies corresponding to SSOAEs, and where either no, or only very low-level SOAEs are observed (resolution, 12 Hz). The region between 1 and 2 kHz in subject A-3's left ear (Fig. 7) shows the reflectance function which most closely resembles those measured by Allen et al. (1995). With one exception, the reflectance shows either only a local minimum (dip) near the SOAE frequency, or a local maximum (peak) and a dip, with the dip closest to the SOAE frequency, and with $|R|^2 < 1$ in all cases. The exception occurs near the SOAE frequency at 1266 Hz where there is a reflectance peak which is close to one, and a corresponding dip in the resistance which is close to zero. However, for the reflectance peak of 7.8 in the vicinity of 4 kHz in the same ear, shown in Fig. 8, the frequency of the SOAE coincides with the peak. At this frequency, the corresponding SPL is midway between a peak and dip, and the reactance has a peak. Although there are several other cases in Figs. 8–11 where the SOAE frequency is closest to a local reflectance minimum, for all five cases where $|R|^2 > 1$ the SOAE frequency corresponds to a peak in $|R|^2$ and a negative dip in the resistance.

The relationship between the fine structure of $|R|^2$ and reactance is variable. Peaks in $|R|^2$ can correspond to either peaks or dips in reactance, or to a frequency intermediate between a peak and dip. The fine structure of the SPL is similarly variable.

As a check on the reliability of the impedance/reflectance measures, repeat measurements were made on some of the subjects. Figure 12 shows the reflectance function for the right ear of subject A-1, at an attenuation of -25 dB, measured in two different sessions, about five months apart. Both the macrostructure and the microstructure of the reflectance function are very similar in the two measurements. The standard deviation of the reflectance peak near 2250 Hz was 0.28 over three within-session measurements. The shift in frequency of this reflectance peak from 2250 to 2262 Hz between the two across-session measurements correlates with a shift in the SOAE frequency from 2249 to 2263 Hz over the same time period.

III. DISCUSSION

The reflectance measurements on these subjects clearly show that, at low stimulus levels, emitted power is greater than injected power at certain frequencies. These frequencies always correspond to frequencies where strong SOAEs are present. The largest energy reflectance measured was 7.8, which means that, at that frequency, almost an order of magnitude more power was being reflected from the ear than being injected into the ear.

The differences between our results and those of Allen et al. (1995) are probably due to two factors. The first is intersubject variability. Not all, or even most, strong SOAEs
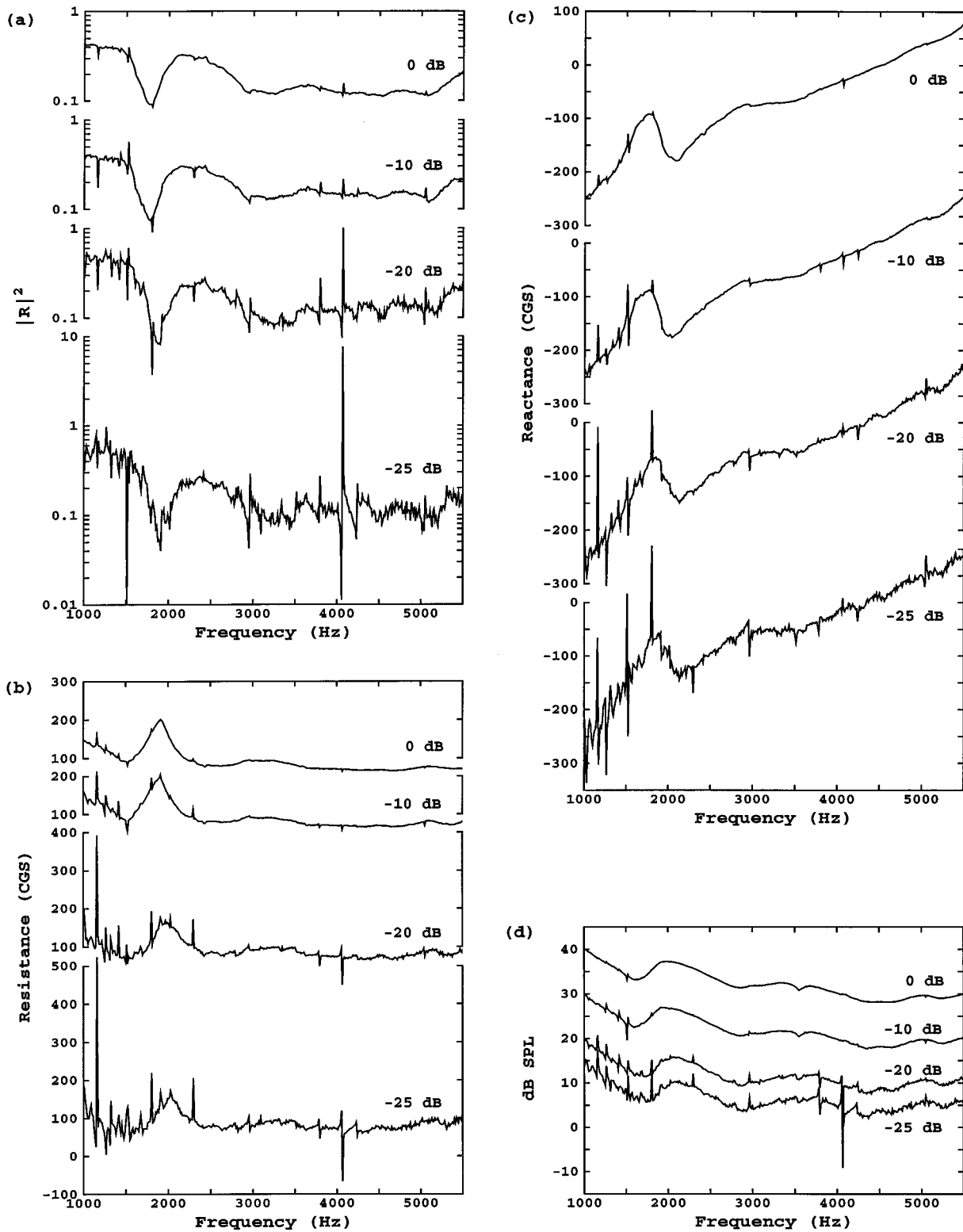
FIG. 3. The reflectance (a), the resistive (b), and reactive (c) parts of the impedance, and the ear-canal sound-pressure level (d), measured at the probe tip in the left ear of subject A-3. Measurements for different stimulus levels are denoted by attenuation values in dB.

result in $|R|^2 > 1$, so obviously many subjects with strong SOAEs will not show any frequencies with $|R|^2 > 1$ at the lowest stimulus level at which we are able to measure. Whether or not $|R|^2 > 1$ at a particular SOAE frequency seems to be only weakly correlated with the level or power of the SOAE.[1]

The other difference lies in the details of the measurement methods. The range of the acoustical power spectral density of our chirp stimuli [see Fig. 3(d) in the region of 1500 Hz] were similar to the range used by Allen *et al.* (1995) in the frequency bin at which the reflectance attained high values. However, our chirp stimulus produced signifi-
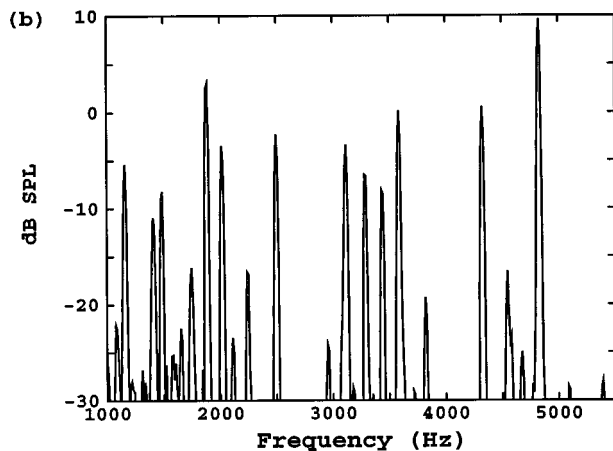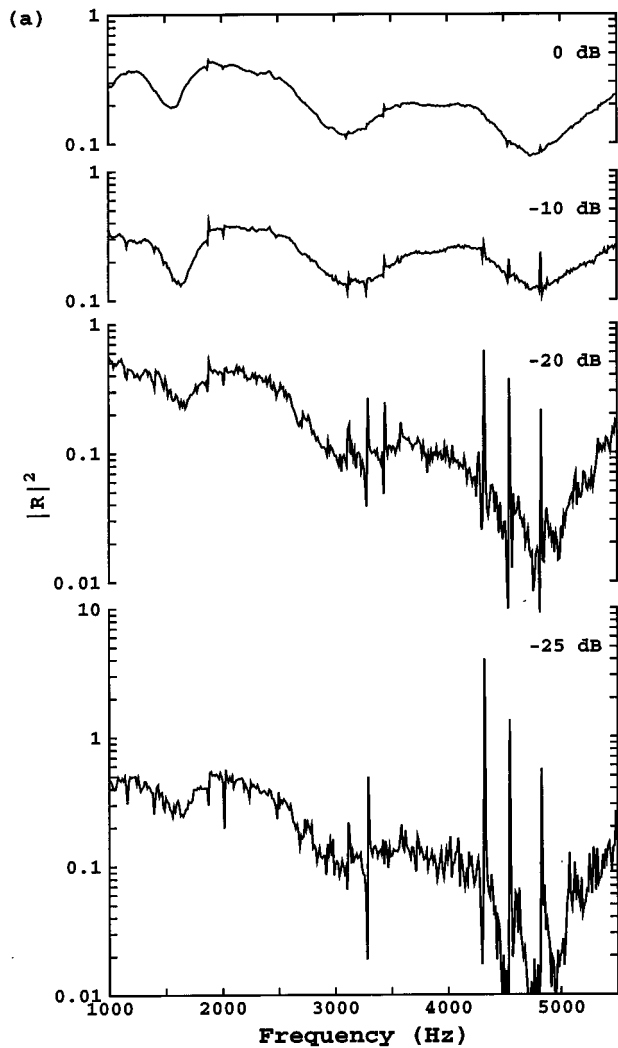
FIG. 4. The reflectance at four stimulus levels, denoted by attenuation values in dB (a), and the SSOAE spectrum (b) for the right ear of subject A-3.

FIG. 5. Same as Fig. 4, for the right ear of subject A-1.

cant stimulus power in neighboring frequency bins whereas the pure-tone stimulus used by (Allen *et al.*, 1995) had very small levels of stimulus power in neighboring bins. Their pure tone was stepped in frequency, and was fixed at a given frequency for a (unspecified) period of time.

Numerous studies (e.g., Wilson and Sutton, 1981; Long *et al.*, 1991; Talmadge *et al.*, 1991) have described the phase-locking of an SOAE by an external sinusoidal tone in terms of ear-canal pressure measurements, subjective correlates, and the response of limit-cycle oscillator models of SOAEs. In particular, Tubis *et al.* (1997) have shown that the response of both a simple limit-cycle oscillator model of a single SOAE, as well as the response of a full cochlear model which produces a series of SOAEs, gives reflectance functions in the vicinity of SOAEs which are consistent with
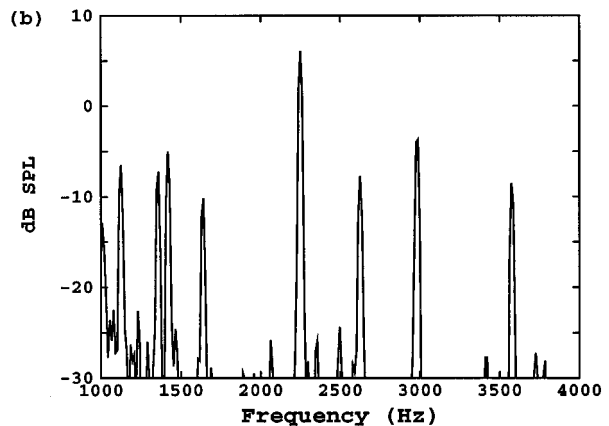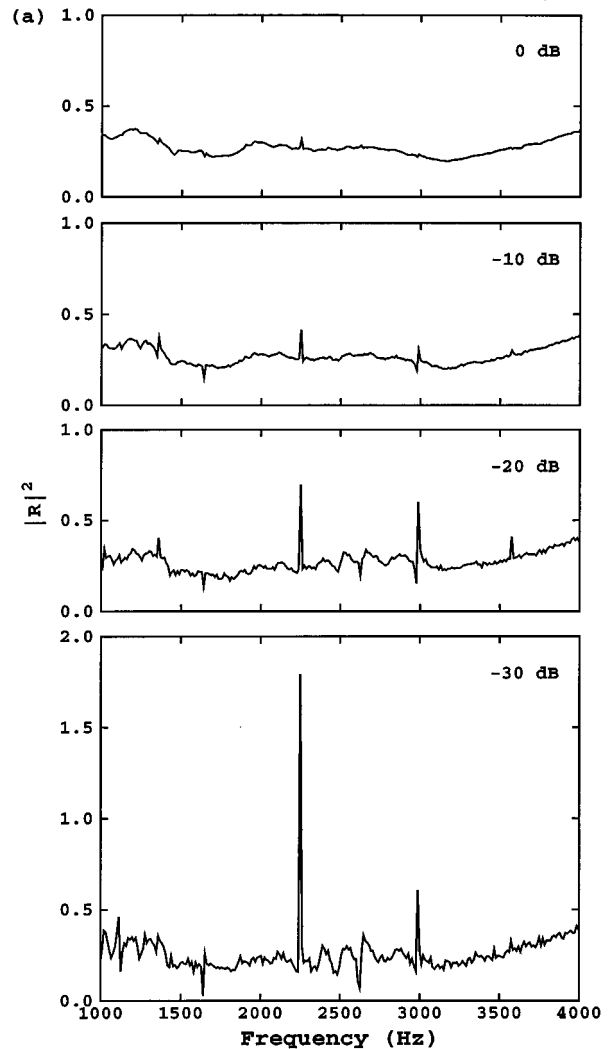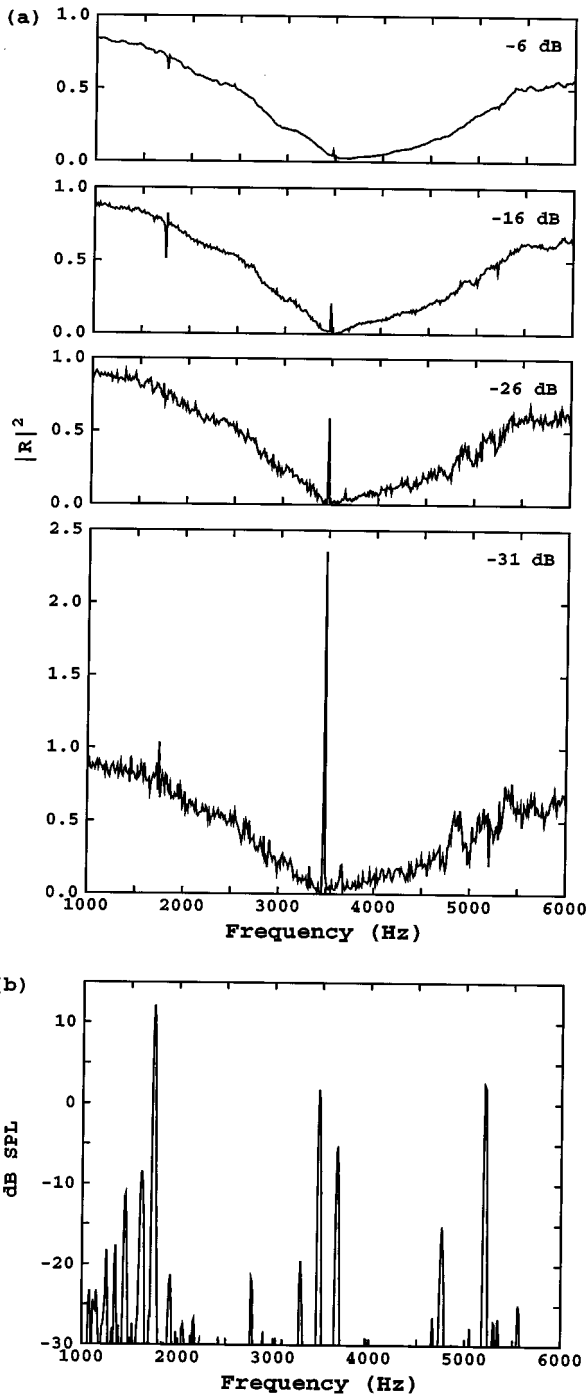
FIG. 6. Same as Fig. 4, for the right ear of subject K-1.

FIG. 7. Ear-canal SPL (top plot), resistive and reactive parts of impedance (middle plots), and reflectance (bottom plot) in the frequency region from 1 to 2 kHz in the left ear of subject A-3, measured at the lowest stimulus level. Short-dashed vertical lines denote frequencies corresponding to strong SOAEs (resolution, 0.2 Hz), long-dashed verticle lines denote frequencies corresponding to SSOAEs, and where either no, or only very low-level, SOAEs are observed (resolution, 12 Hz)

the functions measured by Allen *et al.* (1995). That is, there is a minimum in the energy reflectance in the neighborhood of a SOAE, and the predicted reflectance does not exceed unity therein. The Tubis *et al.* (1997) model is based upon the assumption that there exists phase locking of the SOAE to the external sinusoidal tone used to measure the reflectance. The phase locking results in a more efficient transfer of power to the ear at those frequencies, which presumably explains the strong correlation between SOAE frequencies, and dips (regions of high sensitivity) in behavioral thresholds (Zwicker and Schloth, 1984; Long and Tubis, 1988). It is possible that the rapid frequency sweep of the chirp stimulus

influences the phase-locking mechanism for individual frequency components in the SOAE spectrum. This might also explain the run-to-run variability in the reflectance values at peaks and dips. As subsequent discussion shows, it is more
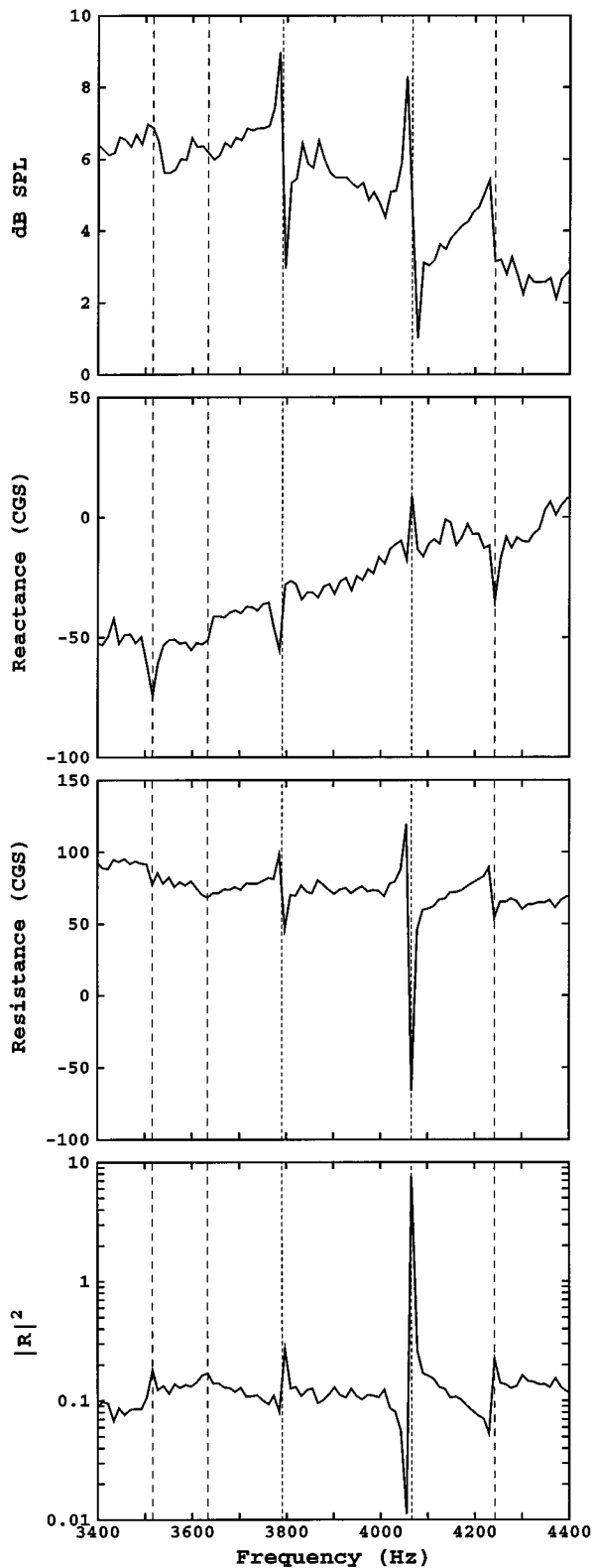
FIG. 8. Same as Fig. 7, for the frequency region from 3.4 to 4.4 kHz.

FIG. 9. Same as Fig. 7, for the frequency region from 4.2 to 5.0 kHz in subject A-3's right ear.

likely that the chirp stimulus succeeded in phase locking the SOAE.

The fact that the energy reflectance exceeds one at a given frequency means that there is a net gain in power at that frequency. In terms of the linear-dynamics description, one would predict that the reflected power would become increasingly large when the reflectance exceeds one, but it must be the case that nonlinear effects act to limit the rate of growth of the reflected amplitude. The linear dynamics provide for power gain greater than one at selected frequencies, and the nonlinear dynamics provide structural stability by

470   J. Acoust. Soc. Am., Vol. 103, No. 1, January 1998

Burns *et al.*: Reflectance SOAEs   470
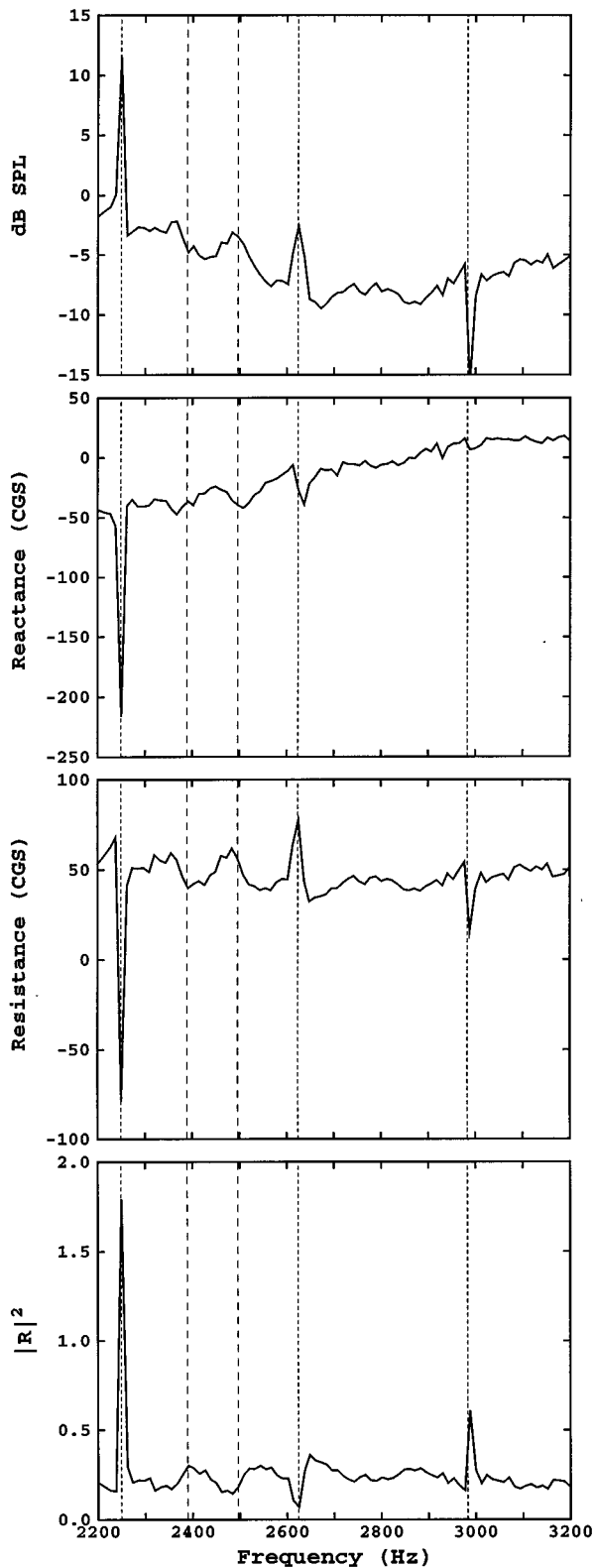
FIG. 10. Same as Fig. 7, for the frequency region from 2.2 to 3.2 kHz in subject A-1's right ear.

FIG. 11. Same as Fig. 7, for the frequency region from 3.2 to 3.8 kHz in subject K-1's right ear.

distributing that energy across frequencies where the power gain is less than one.

Other reports of energy reflectance exceeding unity are found in the literature. For example, the acoustic energy reflectance has been measured at the first and second harmon-

ics of a complex tone for a pipe ending with a flaring horn. In the absence of mean flow through the pipe, the energy reflectance is less than one, but in the presence of mean flow, the energy reflectance of the second harmonic can exceed 2.0 (Hirschberg *et al.*, 1991). The acoustic propagation in the
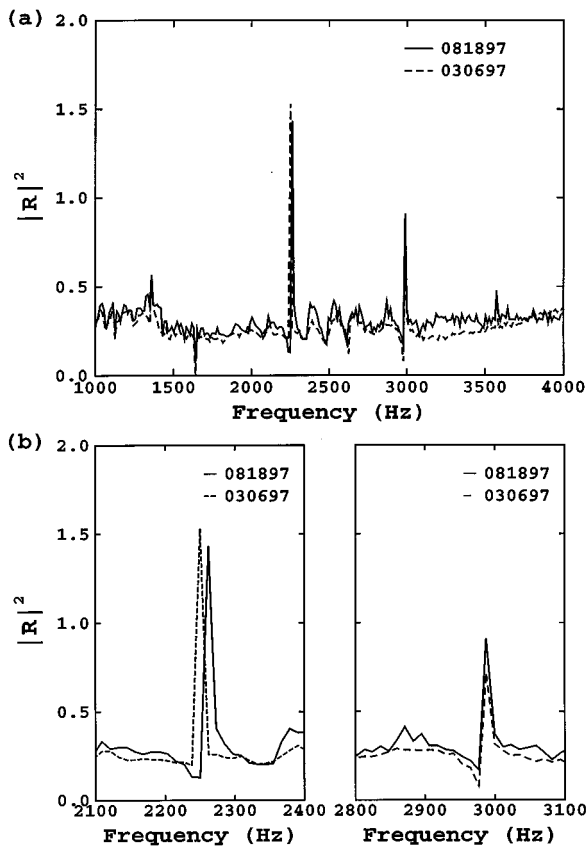
FIG. 12. Reflectance measurements from the right ear of subject A-1, at an attenuation level of −25 dB, taken in two different sessions approximately five months apart.

FIG. 13. Comparison of time-averaged SPL spectra for the left ear of subject A-3: (a) chirp stimulus at −25 attenuation level replotted from Fig. 4(b); (b) click stimulus response similar to the SSOAE response in Fig. 2(b), except that Fig. 2(b) was a spectrum of the response after zeroing the initial 5 ms whereas this spectrum is the DFT of the complete response including the click.

horn is a passive nonlinear process in the absence of mean flow, but becomes active in the presence of mean flow. Power can be converted into reflected acoustic power at the second harmonic, in this case, by an interaction between mean flow, vortex shedding, and the acoustic field at both the first and second harmonics. There is a sound and ''flow resonance'' effect (not to be confused with the ordinary resonance behavior of a linear system) that produces very large reflectance magnitudes in a particular range of mean flow velocities. Thus the phenomenon we have measured is consistent with the behavior of other active nonlinear systems.

Measurements of chirp-evoked reflectance in adults and children in the normal frequency range of SOAEs have been reported using stimuli of moderate sound pressure (Keefe et al., 1993; Voss and Allen, 1994; Keefe et al., 1995) but no measurement of energy reflectance exceeded unity, except at frequencies where the reflectance calibration was inaccurate. Such cases are artifacts. However, the reflectance responses were reported as averages of reflectance across frequency in bin widths ranging from 1/12 to 1/3 oct. Thus even if the reflectance were greater than unity in a narrow range of frequency it would not have been seen in these measurements.

A simple, but flawed, explanation may be proposed to account for some of our experimental results, which proceeds as follows. The energy reflectance is the ratio of the reflected to the incident power at some frequency. Our results show that this reflectance increases to values exceeding unity near SOAE frequencies as the incident power de-

creases. A simple model to account for our results is that the chirp stimulus used in the reflectance measurements is so small at the higher attenuation settings used on the DAC that the incident energy does not influence the SOAE at all. Were the incident power to approach zero, it seems obvious that the reflectance would grow to arbitrarily large values at SOAE frequencies. Thus the reflectance from a SOAE site should exceed unity at sufficiently small stimulation levels.

The flaw in this explanation is that the ear-canal pressure response measured in the reflectance experiment was strongly synchronized to the presentation rate of the chirp stimulus evoking the response. That is inferred from Fig. 13, which replots the SPL spectrum from Fig. 3(d) corresponding to an attenuation level of −25 dB on the same set of axes as the click-evoked SPL that was used to calculate the SSOAEs in Fig. 2(b). The two resulting spectra are time-averaged spectra, synchronous with the 85-ms periodicity of the repetitive chirp and click stimuli, respectively. The click-evoked SPL in Fig. 13(b) differs from the SSOAE in Fig. 2(b) only in that the click-dominated response in the initial 5 ms of the waveform is included in the spectrum in Fig. 13(b). The chirp response contributes a broad hump in the spectrum near 3.6 kHz, which tends to obscure SSOAE frequencies in the 3.0–3.8-kHz range, but the spectra are otherwise similar.

In terms of the experimental protocol during the ear-canal measurements, the only difference between the reflectance and the SSOAE measurements is the substitution of a

472   J. Acoust. Soc. Am., Vol. 103, No. 1, January 1998

Burns et al.: Reflectance SOAEs   472

chirp for a click stimulus. The chirp-evoked spectrum in Fig. 13(a) has peaks at similar SSOAE frequencies as the strong peaks in Fig. 13(b), but many of the SSOAE peaks are obscured by the direct chirp response, which contributes the broadband component to the spectrum always exceeding 0 dB SPL. Comparison of the broadband components in the two plots in Fig. 13 shows that the spectral level of the chirp was much higher (typically 20 dB higher) than that of the click, yet the click was successful in synchronizing the SSOAE. The degree of success is evident in comparing the click-evoked SSOAE in Fig. 2(b) with the time-averaged SOAE in Fig. 2(c) in the absence of a click. There is a qualitative difference in this latter pair of spectra, which indicates qualitatively different dynamics. Such a qualitative change in the dynamics as a function of some control parameter is termed a *bifurcation* (Thompson and Stewart, 1986).

The incident sound power associated with even the lowest-level chirp used was sufficient to synchronize the cochlear reflected signal. Whereas the simple explanation outlined above may be relevant to the limit of vanishingly small chirp (or click) amplitude, it is not applicable to the click-evoked SSOAE, and thus not applicable to the chirp-evoked response, because the chirps used contained more incident power than the click. One possibility is that there exists a bifurcation in the cochlear response as the incident power is slowly decreased from moderate amplitudes down to zero amplitudes. Consider the case where one or more frequency components are present in a SSOAE evoked by a repetitive sequence of clicks, but not in the corresponding SOAE spectrum. The periodic click stimulus is responsible for evoking this qualitative change in the signal. Thus the fact that the energy reflectance exceeds unity is associated with the dynamics of the periodically forced cochlear amplifier sites, rather than a trivial artifact associated with small levels of incident power. In particular, strong SSOAE components were observed both with and without corresponding SOAE components. Both cases are consistent with this qualitative bifurcation theory, although its theoretical implementation in a time-domain cochlear model is outside the scope of the present experimental study.

In some subjects with linked SOAEs (Burns *et al.*, 1984), some frequency components are present in the SOAE at one time, but not at another, i.e., there appears to be more than one dynamical state, each of which is structurally stable. Transitions between a pair of structurally stable SOAEs are sometimes associated with intermittent tinnitus (Burns and Keefe, 1992), which can be regarded as another type of bifurcation. We have observed in some subjects that when the corresponding SSOAEs are measured with a conventional click-evoking stimulus, the frequency components in both of the linked SOAEs can be present in the SSOAE. This suggests that the cochlear mechanisms underlying linked SOAEs and SSOAEs are similar, and that one frequency component in a linked SOAE can stabilize other components. In fact, the frequency components in some linked SOAEs form a phase-locked biperiodic spectrum (Keefe *et al.*, 1990).

We remarked earlier that the Tubis *et al.* (1997) model of a sinusoidally phase-locked SOAE predicted an energy reflectance less than unity.[2] We have strong evidence that there is a synchronous phase locking of the SSOAE spectrum to the chirp, which suggests that reflectance exceeds unity in the presence of phase locking. It would be interesting to model these SOAE/stimulus interactions in the time domain. We have not investigated the influence of changes in the temporal structure of the chirp stimulus on the microstructures of the reflectance and other variables, which may vary according to the use of a pure tone, click, or other chirp. But while the wide variability in the relationships among the peaks and dips in energy reflectance, resistance, reactance, and SPL remains poorly understood, it is nonetheless clear that there is a net power gain at some frequencies, which is the central result of our investigations. Our results support the theory that SOAE generation and SOAE interactions with external periodic stimuli are the result of an underlying nonlinear oscillator mechanism.

IV. CONCLUSIONS

The energy reflectance, acoustic resistance, and acoustic reactance have been measured in the ear canals of adult subjects with strong SOAE and SSOAE sites, and all show rapidly changing amplitudes at frequencies near SOAE frequencies. At such frequencies, the energy reflectance can exceed unity in some ears, and the acoustic resistance is correspondingly negative. These effects are most pronounced at low-amplitude levels of stimulation. This demonstrates that there is power gain at such frequencies: The power reflected from the cochlea through the middle ear to the ear-canal microphone can exceed the power incident. This is consistent with the theory that SOAEs and SSOAEs are produced by a nonlinear oscillator mechanism within the cochlea.

[1]In a separate paper (Keefe and Burns, 1997; Burns and Keefe, 1997) we describe measurements of SOAEs in terms of power absorbed by the probe at SOAE frequencies, and compare power measurements with ear-canal SPL measurements. Although only strong SOAEs, in terms of both power and level, show reflectances greater than one at low stimulus levels, whether or not a particular SOAE shows a reflectance greater than one does not appear to be predictable from either its relative power or its relative level.

[2]Tubis and Talmadge (1997) report that further analyses of the model of Tubis *et al.* (1997) show that the predicted energy reflectance can exceed unity.

Allen, J. (**1996**). ''A review of active and passive basilar membrane cochlear mechanics,'' J. Acoust. Soc. Am. **99**, 2582(A).

Allen, J. B., and Fahey, P. (**1992**). ''Using acoustic distortion products to measure the cochlear amplifier gain on the basilar membrane,'' J. Acoust. Soc. Am. **92**, 178–188.

Allen, J. B., Shaw, G., and Kimberley, B. P. (**1995**). ''Characterization of the nonlinear ear canal impedance at low sound levels,'' in *Abstracts of the 18th Midwinter Research Meeting of the ARO*, edited by R. Popelka (Association for Research in Otolaryngology, Des Moines), pp. 190.

Bialek, W., and Wit, H. P. (**1984**). ''Quantum limits to oscillator stability: Theory and experiments on acoustic emissions from the human ear,'' Phys. Lett. **104A**, 173–178.

Burns, E. M., and Keefe, D. H. (**1992**). ''Intermittent tinnitus resulting from unstable otoacoustic emissions,'' in *Proceedings of the IV International Tinnitus Seminar*, edited by J. Aran and R. Dauman (Kugler, Amsterdam).

Burns, E. M., and Keefe, D. H. (**1997**). ''SOAEs and power transfer in the middle and external ears of children and adults,'' in *Abstracts of the 20th Midwinter Research Meeting of the ARO*, edited R. Popelka (Association for Research in Otolaryngology, Des Moines), pp. 168.

Burns, E. M., Strickland, E. A., Tubis, A., and Jones, K. L. (**1984**). ''Interactions among spontaneous otoacoustic emissions. I. Distortion products and linked emissions,'' Hearing Res. **16**, 271–278.

Dallos, P. (**1992**). ''The active cochlea,'' J. Neurosci. **12**, 4575–4585.

Davis, H. (**1983**). ''An active process in cochlear mechanics,'' Hearing Res. **9**, 79–90.

de Boer, E. (**1993**). ''Some like it active,'' in *Biophysics of Hair Cell Sensory Systems*, edited by H. Duifhuis, J. Horst, P. van Dijk, and S. van Netten (World Scientific, Singapore), pp. 3–22.

Gold (**1948**). ''Hearing II. The physical basis of the action of the cochlea,'' Proc. R. Soc. Sec. B. **135**, 492–498.

Hirschberg, A., Gilbert, J., Wijnands, A. P. J., and Houtsma, A. J. M. (**1991**). ''Non-linear behavior of single-reed woodwind musical instruments,'' Ned. Akoestisch Genootschap J. **107**, 31–43.

Keefe, D. H., Bulen, J. C., Arehart, K. H., and Burns, E. M. (**1993**). ''Earcanal impedance and reflection coefficient in human infants and adults,'' J. Acoust. Soc. Am. **94**, 2617–2638.

Keefe, D. H., Bulen, J. C., Harrison, W., Dunnell, J., and Norton, S. (**1995**). ''Impedance and reflectance in the middle ears of children,'' in *Abstracts of the 18th Midwinter Research Meeting of the ARO*, edited R. Popelka (Association for Research in Otolaryngology, Des Moines), pp.5.

Keefe, D. H., and Burns, E. M. (**1997**). ''Power transfer in the middle and external ears of children and adults,'' (in preparation).

Keefe, D. H., Burns, E. M., Ling, R., and Laden, B. (**1990**). ''Chaotic dynamics of otoacoustic emissions,'' in *Mechanics and Biophysics of Hearing*, edited by P. Dallos, C. Geisler, J. Matthews, M. Ruggero, and C. Steele (Springer-Verlag, Berlin), pp. 194–201.

Keefe, D. H., and Ling, R. (**1997**). ''Double-evoked otoacoustic emissions: II, Intermittent noise rejection, calibration and ear-canal measurements,'' J. Acoust. Soc. Am. (submitted).

Keefe, D. H., Ling, R., and Bulen, J. C. (**1992**). ''Method to measure acoustic impedance and reflection coefficient,'' J. Acoust. Soc. Am. **91**, 470–485.

Kemp, D. T. (**1978**). ''Stimulated acoustic emissions from within the human auditory system,'' J. Acoust. Soc. Am. **64**, 1386–1391.

Kemp, D. T. (**1979a**). ''Evidence of mechanical nonlinearity and frequency selective wave amplification in the cochlea,'' Arch. Otol. Rhinol. Laryngol. **224**, 37–45.

Kemp, D. T. (**1979b**). ''The evoked cochlear mechanical response and the auditory microstructure-Evidence for a new element in cochlear mechanics,'' in *Models of the Auditory System and Related Signal Processing Techniques*, edited by M. Hoke and E. de Boer (Scandanavian Audiology Supplements, Stockholm), Vol. 9, pp. 35–47.

Long, G., and Tubis, A. (**1988**). ''Investigations into the relationship between threshold microstructure and otoacoustic emissions,'' Hearing Res. **36**, 125–138.

Long, G., Tubis, A., and Jones, K. (**1991**). ''Modeling synchronization and suppression of spontaneous otoacoustic emissions using Van der Pol oscillators: Effects of aspirin administration,'' J. Acoust. Soc. Am. **89**, 1201–1212.

Neely, S. T. (**1983**). ''The cochlear amplifier,'' in *Mechanics of Hearing*, edited by E. de Boer and M. A. Viergever (Martinus Nijhoff, The Hague), pp. 111–118.

Ruggero, M. A., Rich, N. C., and Freyman, R. (**1983**). ''Spontaneous and impulsively evoked otoacoustic emissions: Indicators of cochlear pathology?,'' Hearing Res. **10**, 283–300.

Strutt, J. W. (**1883**). ''On maintained vibrations,'' Philos. Mag. **XV**, 229–235.

Talmadge, C., Tubis, A., Wit, H. P., and Long, G. (**1991**). ''Are spontaneous otoacoustic emissions generated by self-sustained cochlear oscillators?'' J. Acoust. Soc. Am. **89**, 2391–2399.

Thompson, J. M. T., and Stewart, H. B. (**1986**). *Nonlinear Dynamics and Chaos* (Wiley, New York).

Tubis, A., and Talmadge, C. L. (**1997**). ''Ear canal reflectances in the presence of spontaneous otoacoustic emissions: I. Limit-cycle oscillator model,'' J. Acoust. Soc. Am. **103**, 454–461.

Tubis, A., Talmadge, C., and Long, G. R. (**1997**). ''Ear canal reflectance in the presence of spontaneous otoacoustic emissions,'' in Abstracts of the 20th Midwinter Research Meeting of the ARO, *Des Moines* (Association for Research in Otolaryngology), pp. 169.

Voss, S. E., and Allen, J. B. (**1994**). ''Measurement of acoustic impedance and reflectance in the human ear canal,'' J. Acoust. Soc. Am. **95**, 372–384.

Wilson, J. P. (**1980**). ''Evidence for cochlear origin for acoustic reemissions, threshold fine structure, and tonal tinnitus,'' Hearing Res. **2**, 233–252.

Wilson, J. P., and Sutton, G. J. (**1981**). ''Acoustic correlates of tonal tinnitus,'' in *Tinnitus*, edited by D. Evered and G. Lawrenson (Pitman Medical, London).

Zwicker, E., and Schloth, E. (**1984**). ''Interrelation of different oto-acoustic emissions,'' J. Acoust. Soc. Am. **75**, 1148–1154.

A model for binaural response properties of inferior colliculus neurons. I. A model with interaural time difference-sensitive excitatory and inhibitory inputs

Hongmei Cai, Laurel H. Carney, and H. Steven Colburn

Department of Biomedical Engineering, Boston University, 44 Cummington Street, Boston, Massachusetts 02215

A model was developed that simulates the binaural response properties of low-frequency inferior colliculus (IC) neurons in response to several types of stimuli. The model incorporates existing models for auditory-nerve fibers, bushy cells in the cochlear nucleus, and cells in medial superior olive (MSO). The IC model neuron receives two inputs, one excitatory from an ipsilateral MSO model cell and one inhibitory from a contralateral MSO model cell. The membrane potential of the IC model neuron (and the other model neurons) is described by Hodgkin–Huxley type equations. Responses of IC neurons are simulated for pure-tone stimuli, binaural beat stimuli, interaural phase-modulated tones, single binaural clicks, and pairs of binaural clicks. The simulation results show most of the observed properties of IC discharge patterns, including the bimodal and unimodal interaural time difference (ITD) functions, sensitivities to direction and rate of change of ITD, ITD-dependent echo suppression, and early and late inhibitions in response to clicks. This study demonstrates that these response properties can be generated by a simple model incorporating ITD-dependent excitation and inhibition from binaural neurons. © *1998 Acoustical Society of America.* [S0001-4966(98)00501-3]

PACS numbers: 43.64.Bt, 43.66.Pn [RDF]

INTRODUCTION

The inferior colliculus (IC) is a critical structure for the integration of ascending monaural and binaural pathways. It is an obligatory station for all major pathways from the lower auditory brain stem (see review by Oliver and Huerta, 1992). However, it is still not clear how these afferents interact with each other and what processing is conducted within the IC. Neural modeling of the auditory pathway is useful in providing a better understanding of the neuronal mechanisms. This study focused on the interaction of excitation and inhibition in the low-frequency region of the IC.

There have been many studies of the monaural and binaural responses of the central nucleus of the IC (Kuwada and Yin, 1983; Yin and Kuwada, 1983a, b; Kuwada *et al.*, 1984, 1987, 1989; Yin *et al.*, 1986, 1987; Carney and Yin, 1989; Spitzer and Semple, 1991, 1993; Litovsky and Yin, 1993, 1994; Yin, 1994; Fitzpatrick *et al.*, 1995). However, little modeling has been done so far with the goal of describing all available data, even though there are a few models simulating specific aspects of the data (Sujaku *et al.*, 1981; Colburn and Ibrahim, 1993; Brughera *et al.*, 1996). The lack of an inclusive model is partly due to the fact that the responses of the IC neurons show considerable variety and it is hard to describe all the data with a single model. The models of Sujaku *et al.* (1981) and Colburn and Ibrahim (1993) derive their input discharge patterns from mathematically generated patterns of action potentials simulating the discharges of monaural nuclei from each side. Another, more physiological model, such as the model of the medial superior olive (MSO) by Brughera *et al.* (1996) which simulates click responses of MSO and IC neurons, derives the input discharge patterns from bushy cell models which are in turn driven by the auditory-nerve fiber model of Carney (1993). All of these IC models restrict binaural interaction to a single neural level; hence they are unable to describe some of the data that require a hierarchy of binaural neurons to interpret.

The objective of this study was to build an explicit computational model that simulates diverse responses of cells in the IC. The modeling approach in this study has emphasized the physiological basis of the model and its components. Since an abstract model which functionally simulates the responses of neurons would constrain its physiological realism, such a generic model was not employed in this study. The IC model presented in this paper incorporates a model of auditory-nerve fibers (Carney, 1993), models of globular and spherical bushy cells (Rothman *et al.*, 1993; Joris *et al.*, 1994), and a model of MSO cells (Brughera *et al.*, 1996). The discharge patterns of each component model neuron are compatible with available physiological data. The IC neuron model is similar to the models of bushy cells and MSO cells. Specifically, it is a single-compartment neuron with a membrane specified by capacitance and conductances for several channels including voltage-sensitive (Hodgkin and Huxley, 1952) and ligand-gated excitatory and inhibitory channels (Eccles, 1964). The IC model neuron is excited by a binaural (MSO) model neuron which is sensitive to interaural time differences (ITDs) and is inhibited by another (MSO) model neuron with similar discharge properties as the excitatory binaural neuron.

The responses of IC neurons that are simulated include the responses to tone stimuli (Yin and Kuwada, 1983a), binaural beat stimuli (Yin and Kuwada, 1983a), interaural
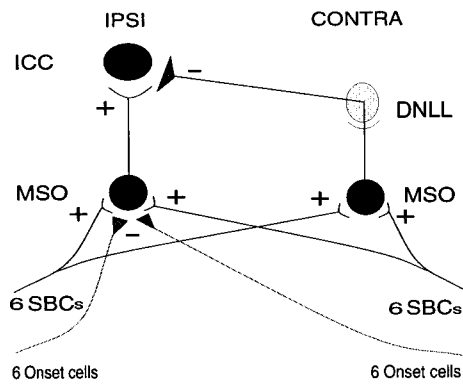
FIG. 1. Structure of the IC model, which incorporated models of peripheral structures, e.g., MSO, SBC, and AN fiber (not shown). The outlined structure of the DNLL neuron did not exist in the model but does exist anatomically. In other words, it was modeled as a relay of its input with a 1-ms delay. The SBC and onset model cells were driven by auditory-nerve fiber models. Excitatory synapses are marked by ''+'' and inhibitory synapses by ''−''.

phase-modulated stimuli (Spitzer and Semple, 1993), binaural clicks (Carney and Yin, 1989), and pairs of binaural clicks (Litovsky and Yin, 1993, 1994; Fitzpatrick *et al.*, 1995). A detailed description of these data is given where the physiological data are compared with simulation results. It will be seen that the sensitivity of IC neurons to dynamically changing ITDs cannot be described by this model. A modified IC model which has a different membrane equation and which can describe these data is presented in the accompanying paper (Cai *et al.*, 1998). In the present paper, the abilities of the simpler IC model to describe the physiological data are demonstrated.

I. METHODS

A. Description of the model

The structure of the model is based on anatomical and physiological evidence but with some simplifications. The IC model neuron is driven by an ipsilateral MSO model neuron and inhibited by a contralateral MSO model neuron via an inhibitory interneuron, presumed to be within the dorsal nucleus of the lateral lemniscus (DNLL) (Fig. 1). This structure is based on the facts that the MSO provides tonotopical projections ipsilaterally to the IC (Henkel and Spangler, 1983) and that the DNLL provides tonotopical GABAergic projections contralaterally to the IC that are presumed to be inhibitory (Adams and Mugnaini, 1984; Shneiderman *et al.*, 1988, 1993). Since the MSO projects to the DNLL ipsilaterally and tonotopically with synaptic endings associated with excitatory transmitters (Glendenning *et al.*, 1981; Henkel and Spangler, 1983), the model can be further simplified by having the contralateral MSO send inhibitory inputs directly to the IC. Although the DNLL receives many of the same inputs as the IC, to simplify the model we made the assumption that the DNLL mirrored the activity of the MSO on its ipsilateral side. Therefore the input to the IC model neuron in this study consists of two binaural neurons, one from the ipsilateral MSO and the other from the contralateral MSO. The two MSO model neurons in turn receive binaural exci-

tatory inputs from model spherical bushy cells (SBC), which have convergent inputs from model auditory-nerve fibers.

For some simulations, the MSO model neurons also receive inhibitory inputs from onset cells, which are presumably relayed from globular bushy cells (GBCs) in the anteroventral cochlear nucleus (AVCN) via the medial nucleus of the trapezoid body (MNTB) and the lateral nucleus of the trapezoid body (LNTB) (Smith *et al.*, 1991; Cant and Hyson, 1992). The discharge patterns at each stage of the model above the auditory-nerve level are derived from the discharge times of the previous stage. Note that the inhibitory inputs from onset cells to the MSO model neuron are only relevant for the simulation of the responses to transient stimuli. Since these inhibitory inputs are assumed to be onset cells (Brughera *et al.*, 1996), the inhibition from these neurons only lasts a few milliseconds after the onset of stimulation and the presence of these cells has little influence on the responses of the model neurons one second after the onset of the stimulus, which is the beginning of the window for sustained responses to long-duration stimuli.

The bushy cells, MSO cells, and IC cells are modeled with single-compartment Hodgkin–Huxley–Eccles models (Hodgkin and Huxley, 1952; Eccles, 1964) similar to the bushy cell model in Rothman *et al.* (1993). This membrane model incorporates a nonlinear conductance as observed in bushy cells of the AVCN (Manis and Marx, 1991) and principal cells of the MSO (Smith, 1995). The primary reason for also using it for the IC cells in this study is the availability of the Rothman *et al.* (1993) model in the literature. This model accurately reproduced bushy cell membrane characteristics observed in real bushy cells by Manis and Marx (1991), Oertel (1983, 1985), and Wu and Oertel (1984). Although there is no conclusive evidence for the existence of the low-threshold potassium channels in IC neurons, nonlinear membrane characteristics associated with this channel have been observed in some IC cells (Peruzzi and Oliver, 1995). We believe that other simpler membrane models would generate essentially the same results as the Rothman *et al.* (1993) model used for the IC model neuron.

B. Auditory nerve model

The auditory nerve (AN) model of Carney (1993) was used to generate the discharge patterns of AN fibers in response to both transient and long-duration stimuli. Model parameters were the same as those used by Carney (1993). The rate function, which described the average arrival rate of the nonhomogeneous Poisson process, was slightly modified so that it closely matched the one used by Rothman *et al.* (1993). The rate function is expressed as:

$$R(t) = S(t)[1 - c_0 e^{-(t-t_l-R_A)/s_0} - c_1 e^{-(t-t_l-R_A)/s_1}]$$
$$\times u(t-t_l-R_A), \qquad (1)$$

where $S(t)$ is the synapse output, t_l is the time of the most recent discharge, and R_A is the absolute refractoriness of 0.75 ms. The function $u(t)$ represents the unit step function. An initial settling time of 15 ms was added to the AN model to reduce the effects of parameter initialization. Also, the time of the first action potential was set at the beginning of

the settling period rather than at the beginning of the stimulus.

C. Bushy cell model

The responses of bushy cells, including the SBCs and the GBCs, were simulated using the Rothman *et al.* (1993) model, which is based on the assumption that the soma of the bushy cell is uniform and adendritic. The model membrane contained three voltage-dependent ion channels (a fast sodium channel, a delayed-rectifierlike potassium channel, and a low-threshold potassium channel) and a voltage-independent leakage channel. The membrane potential was determined by the currents of these channels as well as those of the excitatory and inhibitory synaptic inputs. The differential equation describing the change in membrane potential V is

$$C \frac{dV}{dt} + G_B(V - E_K) + G_K(V - E_K) + G_{Na}(V - E_{Na})$$
$$+ G_L(V - E_L) + G_I(V - E_I) + G_E(V - E_E) = I_{ext}, \qquad (2)$$

where C is membrane capacitance. The conductances of the low-threshold slow potassium channel (G_B), sodium channel (G_{Na}) and delayed-rectifierlike potassium channel (G_K) were described by Hodgkin–Huxley-type equations as in Rothman *et al.* (1993).

The time course of the excitatory synaptic conductance was described by the following alpha function with a time constant τ_{ex} of 0.1 ms:

$$G_E(t - t_0) = G_{E_{max}} \frac{t - t_0}{\tau_{ex}} \exp\left[1 - \frac{t - t_0}{\tau_{ex}}\right] u(t - t_0). \qquad (3)$$

The conductance starts to increase when an input action potential arrives at time t_0 and reaches its maximum value $G_{E_{max}}$ at time $t_0 + \tau_{ex}$.

The model SBCs had 25 inputs from model AN fibers with characteristic frequencies (CFs) of approximately 500 Hz. The maximum conductance of each input was 7 nS, which gave the bushy cells a primarylike peristimulus time (PST) histogram with high synchronization index to tone burst stimuli at CF (Joris *et al.*, 1994). None of the model bushy cells received inhibitory inputs.

The ''onset'' cells received inputs from 16 AN fibers with CFs evenly distributed between 350 and 650 Hz. Each input had a (subthreshold) synaptic strength of 4.0 nS. These cells showed both an onset response and a low sustained response to a tone burst. Since they were included in the model only in the simulations of the responses to transient stimuli, in which case the low sustained part of the response did not play an important role, the model was equivalent to having inhibition from onset cells when it was considered for the responses to both transient and sustained stimuli. Responses of model SBCs and onset cells are illustrated in Brughera *et al.* (1996).

D. MSO model

The MSO model neurons in this study had the same structure as the MSO model developed by Brughera *et al.*

(1996), in which the differential equation for the MSO membrane potential was the same as that in the bushy cell model of Rothman *et al.* (1993) [shown in Eq. (2)]. The MSO model neurons received excitatory inputs from SBCs on both sides unless otherwise indicated. For simulations of transient stimuli, they also received inhibitory inputs from onset cells on one or both sides. The onset inhibition is presumably from GBCs in the AVCN via the nuclei of the trapezoid body; GBCs are characterized by primarylike-with-notch or onset-L responses (Smith and Rhode, 1987); both types are onset dominated. The effects of the sustained response are not explored in this study. Based on the assumption that the ventral part of the medial nucleus of the trapezoid body (MNTB) is a faithful relay of the GBCs in the AVCN, the input patterns of the MSO were taken directly from the discharge times of model SBCs and GBCs. There were four possible input types to each MSO model neuron. They were ipsilateral SBC, ipsilateral GBC, contralateral SBC, and contralateral GBC. The parameters of each input type included the number of projecting neurons, the synaptic strength, the time constant, and the delay of arrival of the input. For each of the four input types, the number of projecting neurons was six, unless otherwise indicated. The synaptic strength of the excitation was 2.5 nS, except in the simulation of responses to pairs of binaural clicks, for which the synaptic strength was 2.0 nS (which gave a sharper click ITD function). The time constant for excitation was the same as used for model bushy cells, i.e., 0.1 ms. The difference in the delay of arrival between two excitatory inputs determined the characteristic delay (CD) of the model neuron. A positive CD indicated that the excitatory inputs from the SBCs on the contralateral side of that neuron were delayed. The parameters of the inhibitory inputs were adjusted to fit different data and will be described later.

The CD of the ipsilateral MSO model neuron in our simulation was either 100 μs or zero, indicating that the model neuron was most sensitive to sounds coming from the contralateral side (when 100 μs) or the midline (when zero). The CDs of the contralateral MSO model neuron were varied for two purposes: first, to systematically study their effects on the ITD functions of the IC model neurons (in the simulation of the responses to tone stimuli) and second, to fit different properties of the physiological data (in the simulation of the responses to pairs of binaural clicks). Direct comparisons between the responses of MSO model neurons and physiological data are provided in Brughera *et al.* (1996).

E. IC model

Both linear and nonlinear current-voltage relationships have been observed in IC neurons (Peruzzi and Oliver, 1995). Due to the small number of samples, no correlation can be made between the morphology of the neurons and their current-voltage functions. There was no compelling reason as to what type of membrane equation should be used in the IC model. For simplicity, the Rothman *et al.* (1993) model was used for the IC model neuron. The differential equation describing the membrane potential was the same as that for the MSO model neurons and model bushy cells [Eq. (2)]. The excitatory synaptic conductance function was al-

477   J. Acoust. Soc. Am., Vol. 103, No. 1, January 1998

Cai *et al.*: IC binaural model with inhibitory inputs   477

ways an alpha function as described in Eq. (3), whereas the inhibitory conductance function was a linear summation of an alpha function and an exponential function, i.e.,

$$G_I(t-t_0) = \left(G_{I_{\text{input}}} \frac{t-t_0}{\tau_{\text{inh}}} \exp\left[1 - \frac{t-t_0}{\tau_{\text{inh}}}\right] \right.$$
$$\left. + 1.5 G_{I_{\text{input}}} \exp\left[-\frac{t-t_0}{\tau_{\text{inh}}}\right] \right) u(t-t_0), \qquad (4)$$

where $G_{I_{\text{input}}}$ is the synaptic strength of the inhibitory input. The function described in Eq. (4) ensures that the inhibition increases rapidly at onset and decays slowly, unlike the alpha function alone which builds up slowly before it reaches the peak. The rapid onset and slow decay of inhibitory postsynaptic potential have been observed in MSO cells (Smith, 1995).

The inhibitory input to the IC was always delayed by 1 ms because of the longer pathway to the IC and the extra synapse (omitted here) at the DNLL. This delay would not change the model results in any significant way (Cai, unpublished observation). The inhibitory synaptic strength and time constant of the IC were either systematically studied (in the simulations of the responses to sustained stimuli) or varied to fit the physiological data (in the simulations of the responses to transient stimuli). Detailed parameter specifications are provided in later sections.

F. Stimulus generation and simulation data analysis

Five kinds of stimuli were generated: long-duration tone stimuli, binaural beat stimuli, interaural phase-modulated stimuli, single binaural clicks, and pairs of binaural clicks. These stimuli are described in detail in later sections where the physiological data and simulation results are compared. The analyses of simulation results replicated those used in physiological experiments. All simulations were run on Silicon Graphics workstations using C under the IRIX operating system.

II. RESULTS

A. Responses to pure-tone stimuli

Responses of IC neurons to both binaural and monaural tone stimuli have been reported for physiological studies. Binaural tone stimuli are used to study the ITD functions at various stimulus frequencies, including tones at CF and off CF (Yin and Kuwada, 1983b). Monaural tone stimuli are used to study the phase locking of neurons (Kuwada *et al.*, 1984). In this section, simulations of these binaural and monaural response properties related to tone stimuli are presented.

1. Tone ITD functions

The ITD function describes the relationship between response rate and interaural time difference. The ITD functions from MSO neurons obtained from tone stimulus are usually approximately sinusoidal with a frequency equal to stimulus frequency (Yin and Chan, 1990; Goldberg and Brown, 1969). The tone ITD functions from IC neurons, however, show wide variations in shape. Yin and Kuwada (1983a)

gave some examples of the interaural phase difference (IPD) functions of IC neurons in response to tone stimuli (their Fig. 3). Some of the IPD functions have a single peak in one cycle, while some others show a bimodal shape. Bimodal IPD functions have not been observed in MSO neurons.

Figure 2 shows the IPD function of some IC model neurons. The tone stimuli in our simulations were 65-dB sine waves with a duration of three seconds. The frequency of the tone was 500 Hz. For each ITD, only one sweep of the stimulus was presented and the response rate was calculated from the number of discharges during the last two seconds of the stimulus. The range of ITDs, from -2 to $+2$ ms with steps of 0.1 ms, represented two cycles of the ITD function for a tone frequency of 500 Hz. The IPD function was obtained by averaging the ITD functions over both cycles and converting the horizontal axis from time to phase.

The model parameters for tone stimuli, including ipsilateral and contralateral MSO and IC model neurons, are listed in Table I. The synaptic strength and time constant of the inhibitory input to the IC were systematically varied. Three combinations of these two parameters representing weak, moderate, and strong inhibition are listed in Table II. The excitatory synaptic strength from the ipsilateral MSO model neuron to the IC model neuron was chosen such that an input discharge from the ipsilateral MSO would generate an output discharge in the IC over the full range of its discharge rates in the ITD function, when inhibition was absent. The CD of the ipsilateral MSO neuron was 100 μs, and the CD of the contralateral MSO neuron was set at four different values: -60, 50, 150, and 400 μs. These values were chosen based on the fact that most (93%) of the CDs of MSO neurons in a cat are distributed between 0 and $+400$ μs, corresponding to stimuli in the contralateral sound field (Yin and Chan, 1990). Very few MSO neurons respond preferentially to sound coming from the ipsilateral side, corresponding to a negative CD.

The four panels of Fig. 2 correspond to four different CDs of the contralateral MSO model neuron. For each CD, in the case of weak inhibition (solid curve), the IPD function of the IC model neuron was almost the same as that of the ipsilateral MSO. The inhibition from the contralateral MSO was not strong enough to affect the ITD sensitivity of the IC. When the inhibition became stronger, however, the contralateral inhibition reshaped the IPD function of the IC. The response rate of the IC model neuron at a certain ITD depended on the interaction of the excitation and the inhibition. Note that the relation between the output response rate and the excitatory and inhibitory input rates of the IC was nonlinear. The peak of the ITD function was more likely to be affected by inhibition than the trough, because at a high response rate the interspike interval of the input firing was short. An inhibitory conductance change during a short period of time might be sufficiently long to inhibit the neuronal discharge at the time of the next excitatory input firing. The lower the excitatory input discharge rate, the less it would be affected by the inhibition.

The CD of the contralateral MSO affected the ITD-tuning of the IC such that excitations interacted with different levels of inhibition over the IPD range, and therefore
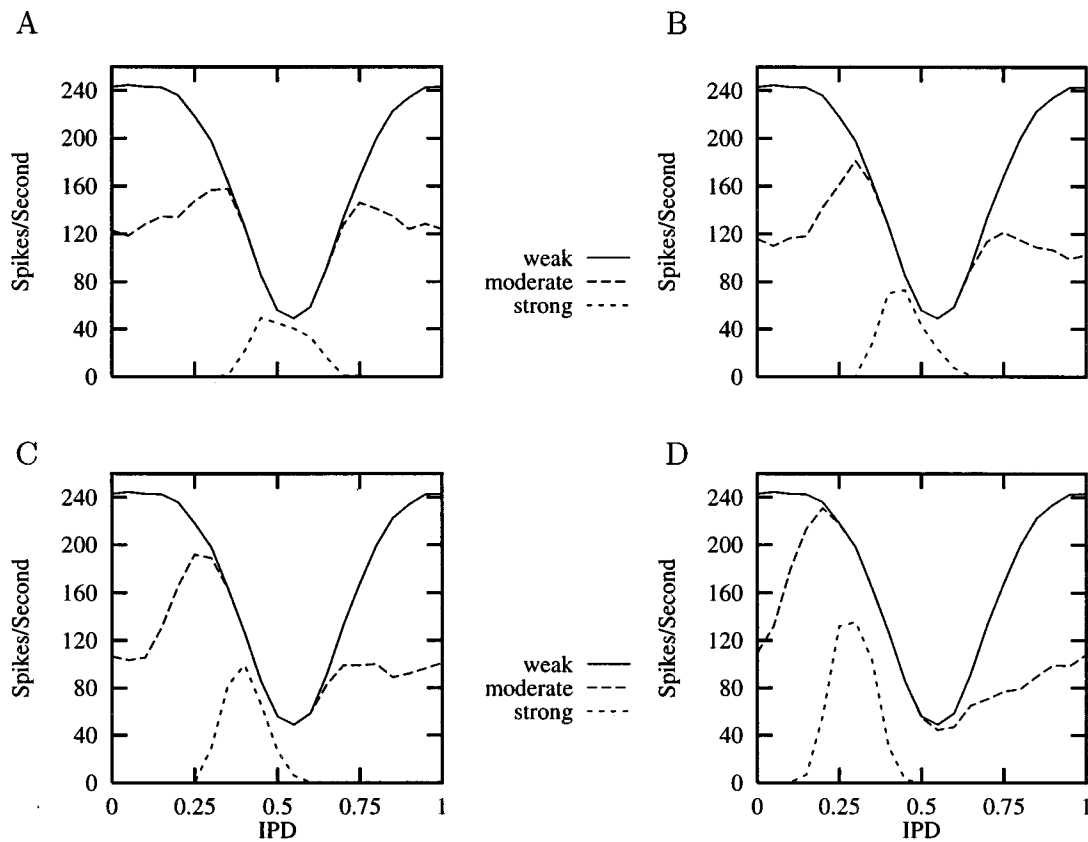
FIG. 2. IPD functions of IC model neurons when the inhibitions to the IC were ''weak,'' ''moderate,'' and ''strong.'' The three IPD functions in each panel from top to bottom represent ''weak'' (solid), ''moderate'' (long dashes), and ''strong'' (short dashes) inhibition. The CDs of the contralateral MSO model neuron were: $-60\ \mu s$ (A), $50\ \mu s$ (B), $150\ \mu s$ (C), and $400\ \mu s$ (D). Input parameters of the IC model neurons are given in Tables I and II.

influenced the shape of the IPD function of IC. A given set of parameters, e.g., those for moderate inhibition, may result in either single-peaked [contralateral CD of 150 and 400 μs, Fig. 2(C) and (D)] or double-peaked [contralateral CD of -60 and 50 μs, Fig. 2(A) and (B)] IPD functions.

2. Changing stimulus frequency

The effects of stimulus frequency on the ITD functions of IC neurons have been studied physiologically by Yin and Kuwada (1983b). They plotted the ITD functions at different frequencies on a common axis and found that for some cells the ITD functions showed peaks or troughs at a common CD. The ITD functions of the IC model neurons at three frequen-

cies, i.e., 400, 500, and 600 Hz, were simulated with stimulus intensity and duration the same as those in previous simulations. Figure 3 shows the ITD functions of the ipsilateral MSO and IC model neurons at the three frequencies. The CD of the ipsilateral MSO was 100 μs, whereas that of the contralateral MSO was 50 μs. Each ITD function of the ipsilateral MSO model neuron [Fig. 3(A)] was a sinusoidlike function with a frequency equal to stimulus frequency. By visual inspection, these curves showed a common peak at the CD of the model neuron, which was 100 μs. The relationship between the mean interaural phase of the response and the stimulus frequency was linear. The ITD functions of the IC model neuron with weak inhibition showed a similar prop-

TABLE I. Model parameters for tone stimuli. The two MSO model neurons receive only excitatory inputs. The ''C'' or ''I'' indicates that the inputs come from the contralateral side (''C'') or the ipsilateral side (''I'') with respect to the neuron that receives the inputs. The dash, —, represents ''not applicable.''

Parameters	Ipsilateral MSO exc	Contralateral MSO exc	IC exc	IC inh
Number of projecting neurons	6(C,I)	6(C,I)	1(I)	1 (C)
Synaptic strength (nS)	2.5	2.5	25	varied[a]
Time constant (ms)	0.1	0.1	0.1	varied[a]
CD of MSO (μs)	100	50[b]	—	—
Delay of arrival (ms)	0	0	0	1

[a]The parameter values are given in Table II.
[b]Note that the CD of the contralateral MSO cell was systematically varied in the simulation of the responses to 500-Hz tone stimuli.

TABLE II. Inhibitory input parameters to the IC in the cases of ''weak,'' ''moderate,'' and ''strong'' inhibition.

	Weak	Moderate	Strong
Synaptic strength	6 nS	8 nS	10 nS
Time constant	2 ms	3.5 ms	10 ms

FIG. 4. Synchronization index of ipsilateral MSO and IC model neurons with different inhibitions. The excitatory synaptic strengths were 25 and 16 nS. The IC model neurons with weak, moderate, and strong inhibition are represented by ICw, ICm, and ICs, respectively. The CD of the ipsilateral MSO was 100 μs, whereas that of the contralateral MSO was 50 μs. Parameters of the IC model neurons are given in Tables I and II. The synchronization index was the average of those obtained from monaural stimuli to each side. The stimulus was a 500-Hz monaural tone with a duration of 3 s.

erty, although the peak of the ITD function at 400 Hz was affected. The ITD functions of the IC model neurons with moderate and strong inhibition, however, did not have a peak at a common ITD. In fact, with strong inhibition, the ITD functions have a common minimum and appear similar to the response of excitatory-inhibitory cells in the LSO (Kuwada *et al.*, 1997). It was also found that an ITD function with a single peak for some frequencies may be bimodal for some other frequencies, such as the IC model neuron with moderate inhibition. The ITD function of this model neuron was unimodal at 600 Hz, whereas the ITD functions were bimodal at 500 and 400 Hz.

3. Phase locking to monaural stimuli

The phase locking of IC model neurons in response to 500-Hz monaural tone stimuli was characterized by the synchronization index (Johnson, 1980). The period histogram of the responses during the last 2 s of the 3-s stimulus duration was used for these calculations. The significance of the synchronization index was evaluated by the Rayleigh criterion (Mardia, 1972), which tests whether the histogram was a sample of a uniform distribution. If for a histogram, $2nR^2 > 13.8$, where n is the number of discharges and R is the synchronization index, the probability that the histogram is a sample of a uniform distribution is 0.001.

The synchronization indices obtained from monaural stimulation of each side were averaged. Figure 4 shows the mean synchronization index for the ipsilateral MSO model neuron and for IC model neurons with weak, moderate, and strong inhibition. For these model neurons, the CD of the
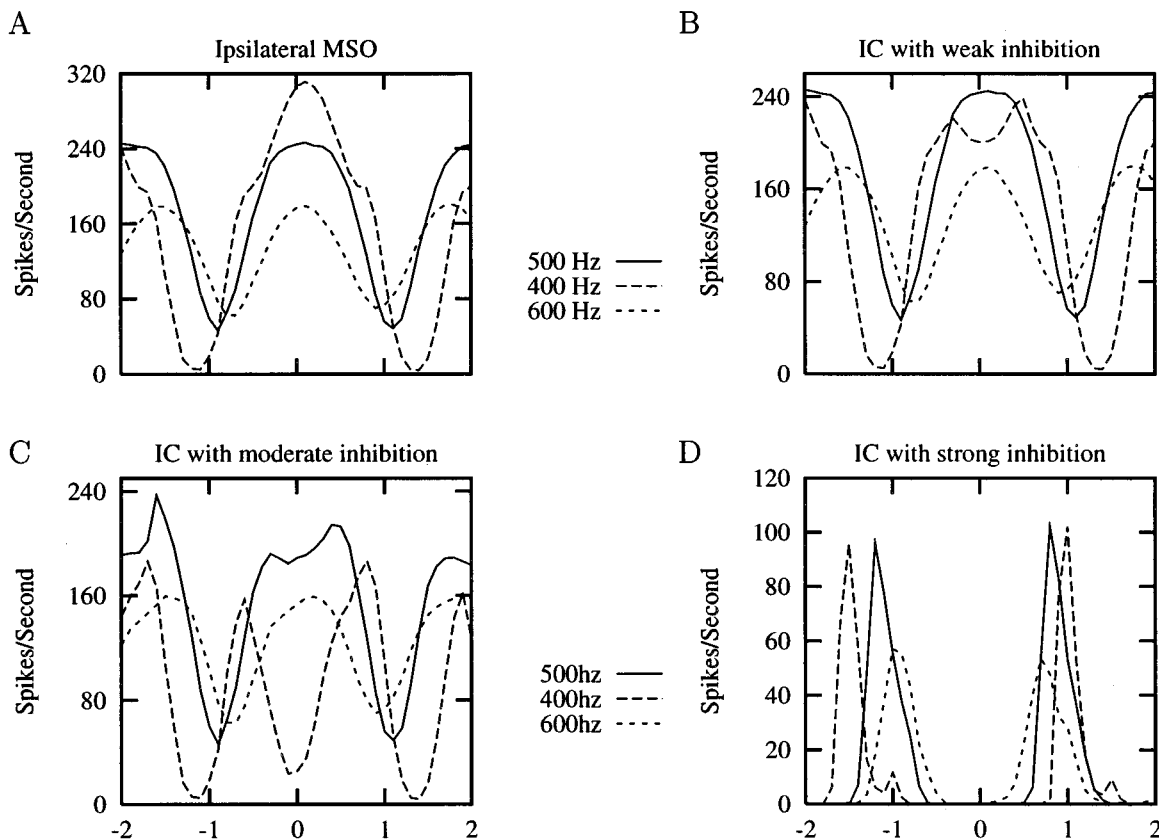
FIG. 3. Frequency dependence of ITD functions of ipsilateral MSO and IC model neurons with different strengths of inhibition. The CD of the ipsilateral MSO was 100 μs, whereas that of the contralateral MSO was 50 μs. Input parameters of the IC model neurons are given in Tables I and II.

ipsilateral MSO was 100 μs and that of the contralateral MSO was 50 μs. Two values of the excitatory synaptic strength were studied, i.e., 25 and 16 nS. The synchronization index of the IC model neuron was slightly lower than that of the ipsilateral MSO model neuron in each case. Weaker excitation (16 nS) resulted in a larger decrease in synchronization index. Physiological data show that most, if not all, MSO neurons show phase locking (Yin and Chan, 1990); however, only a small number of low-frequency IC neurons phase lock to monaural stimuli (18% in Kuwada *et al.*, 1984). For those which do phase lock, the synchronization index is low. The model failed in simulating these physiological responses.

B. Responses to binaural beat stimuli

For the tonal stimuli described above, the IPD is constant over the duration of the stimulus. The IPD function obtained from the tone responses is thus referred to as the static IPD function. For other types of tonal stimuli, such as the binaural beat stimuli, the IPD dynamically changes over the time course of the stimuli. The IPD function converted from the PST histograms in response to such stimuli is referred to as the dynamic IPD function. In this section, the responses of IC model neurons to binaural beat stimuli are reported.

The binaural beat stimulus involves two tones with slightly different frequencies presented simultaneously and separately to the two ears. The larger the difference, or beat frequency, the faster the IPD changes over time. The sign of the beat frequency determines the direction of motion of the perceived sound. Our convention is that a positive beat frequency indicates that the higher-frequency tone is delivered to the contralateral ear. A comparison between dynamic and static IPD functions has been provided by Yin and Kuwada (1983a); the dynamic functions are sharper than the static ones (their Fig. 3). Note that the dynamic functions go to zero at some troughs while the static ones do not. Even though these functions are normalized to their maximum response rates, normalization does not affect zero rate.

In our simulations, the frequencies of the tones delivered to the two sides were 500 and 501 Hz (beat frequency=± 1 Hz), unless otherwise indicated. The duration of the stimulus was 8 s, repeated every 8.5 s for five presentations. The PST histograms during the last 7 s of the stimulus were averaged to get the dynamic IPD functions. The parameters of the IC model were identical to those used in the simulation of the responses to tone stimuli (Table I) with the CD of the contralateral MSO model neuron fixed at 50 μs.

Binaural beat stimuli were presented in both directions for each simulation. Figure 5 shows the result of the same three model neurons as in Fig. 2(B). The dynamic IPD functions obtained from the binaural beat stimulus (shown as bars) are plotted along with the static IPD functions from tones (solid curves). The left column shows the responses in one direction (positive beat frequency) and the right column shows those in the opposite direction (negative beat frequency). For these three inhibitory levels, no matter what the shapes of IPD functions were [unimodal as in Fig. 5(A), (B),

(E), and (F), or bimodal as in Fig. 5(C) and (D)], the dynamic and static IPD functions were always consistent or overlapping.

Most IC neurons have approximately the same response to the two directions of dynamic phase change (like the above model neurons). However, a small number of cells in the IC exhibited sensitivity to the sign of the beat frequency (Yin and Kuwada, 1983a). In addition, there were some other cells sensitive to the absolute value of the beat frequency or the rate of interaural phase change (Yin and Kuwada, 1983a). The IC model with a long inhibitory time constant was capable of describing this phenomenon. A long time constant for the inhibition had an effect similar to a low-pass filter, which made it possible for excitatory input at one moment to interact with inhibitory input at a previous time. The long-lasting inhibition resulted in a shift of the maximum inhibition in the PST histogram. Therefore the maximum inhibition occurred at different IPDs for different directions or rates of the binaural beat stimuli. For a dynamic phase change in one direction, if the strong inhibition coincided with strong excitation, the response of the IC neuron was weak at some IPDs. If in the other direction, strong inhibition happened to coincide with weak excitation, the IC cell still received strong excitation during part of the cycle and responded vigorously at the same IPDs. Therefore the model IC neuron responded differently to different directions of the binaural beat stimuli at a given interaural phase.

A model neuron was simulated with a long inhibitory time constant, relative to that of the model neurons in Fig. 5. The detailed parameters are listed in Table III. The inhibitory synaptic strength was kept at 6 nS, as in the "weak inhibition" case. The time constant of inhibition was 30 ms. The excitatory synaptic strength to the IC was increased from 25 to 40 nS to obtain a reasonable response rate at a favorable beat frequency.

Figure 6 shows the responses of this model neuron to a 1-Hz binaural beat stimulus and to a 5-Hz beat stimulus in both directions. The neuron showed a stronger response to the 1-Hz beat than to the 5-Hz beat. When the binaural beat frequency was 5 Hz, both excitatory and inhibitory input firings were repeated every 200 ms. Since the inhibition had a long time constant, inhibition built up from cycle to cycle but excitation did not. The neuron did not catch up with the dynamic IPD change and consequently responded very weakly. If the inhibition were not so strong, a stronger response to the 5-Hz binaural-beat stimulus would have been seen. In response to the 1-Hz beat frequency, the model neuron responded better to the motion of sound in the direction toward the ipsilateral ear (negative beat frequency).

The current model could only simulate neurons that respond more vigorously to slower binaural beats than to faster beats. However, some IC cells show the opposite property (Yin and Kuwada, 1983a). Other processes must be involved in those neurons.

C. Response to interaural phase-modulated stimuli

The interaural phase-modulated (IPM) stimulus is another type of tonal stimuli in which the IPD is varying over the duration of stimuli. It is different from the binaural beat
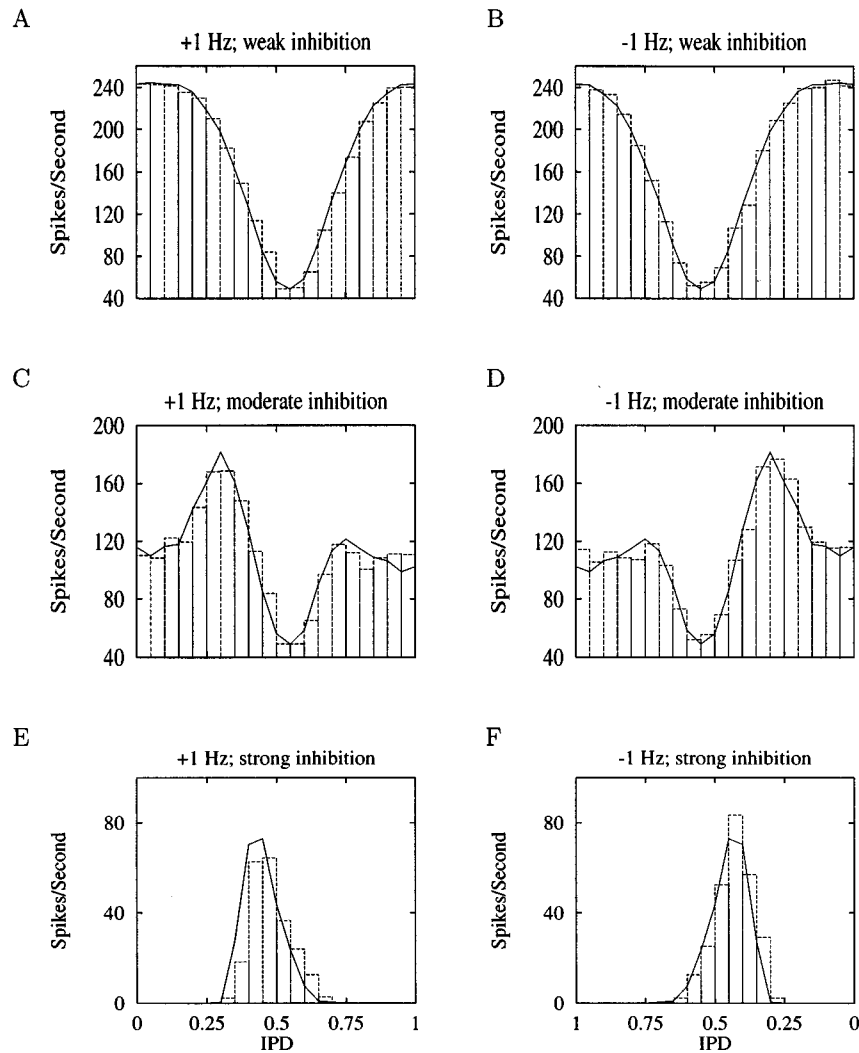
FIG. 5. Dynamic IPD functions (bars) of IC model neurons obtained from binaural beat stimuli along with the static IPD functions (solid curves) obtained from tone stimuli. The beat frequency and the inhibition level to the IC are shown at the top of each panel. Parameters of the IC model neurons are given in Tables I and II.

stimulus in that two tones of the same average frequency are delivered to the two ears. However, the phase of one of the sine waves is modulated by a triangular wave. When a constant phase offset is included in one of the tone waveforms, the direction, the range, and the center position of the apparent sound movement can be manipulated.

Spitzer and Semple (1993) used triangular interaural phase-modulated tones in studies of IC cells in anesthetized cats and gerbils. The static IPD functions of IC neurons were compared with the IPD arcs obtained from IPM stimuli over partially overlapping IPD ranges. The majority of units (about 94%) showed a systematic relationship between the

TABLE III. Parameters of the IC model neuron simulating directional sensitive neurons for binaural beat stimuli. The two MSO model neurons receive only excitatory inputs. The "C" or "I" represents that the inputs come from contralateral side ("C") or ipsilateral side ("I") with respect to the neuron that receives the inputs. The dash, —, represents "not applicable." Parameter values chosen specifically for this simulation are shown in italics.

Parameters	Ipsilateral MSO exc	Contralateral MSO exc	IC exc	IC inh
Number of projecting neurons	6(C,I)	6(C,I)	1(I)	1(C)
Synaptic strength (nS)	2.5	2.5	*40*	*6*
Time constant (ms)	0.1	0.1	0.1	*30*
CD of MSO (μs)	100	50	—	—
Delay of arrival (ms)	0	0	0	1
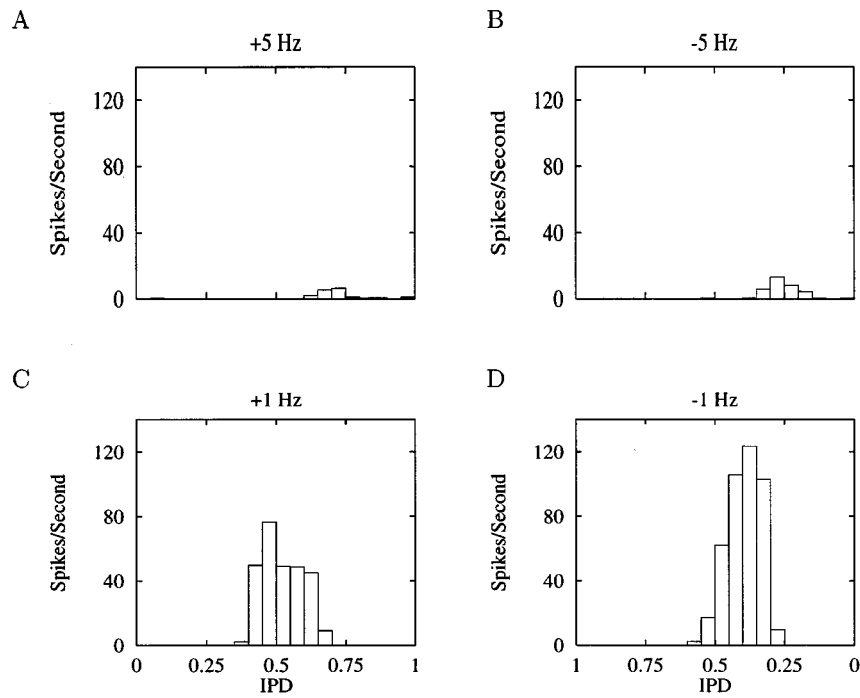
FIG. 6. IPD functions of a direction- and rate-sensitive IC model neuron. The model neuron responded more vigorously when the rate of binaural beat was slow and/or when the direction of the beat was towards the ipsilateral ear (negative beat frequencies). Parameters of the IC model neurons are given in Table III.

IPD function obtained from IPM and that from pure tones. Motion of IPD toward the peak of the function is associated with increased discharge probability and motion toward the trough is associated with decreased discharge probability. Within each IPD range, the IPD function is consistently sharpened by the dynamics of IPD (cf. their Fig. 8).

Binaural tones of 65 dB SPL with triangular modulated interaural phase were applied in the simulation. The carrier frequency of both tones was set to the CF of the model neuron, i.e., 500 Hz. The modulation frequency was 2 Hz and the modulation depth was 90° such that the phase changed at the same rate as for a binaural beat stimulus with a beat frequency of 1 Hz. The duration of the stimulus was 10 s, and it was repeated four times. The PST histograms of the last 9 s were averaged and converted to an IPD function.

Figure 7 shows the IPD functions of three model neurons, with ''weak,'' ''moderate,'' and ''strong'' inhibition, in response to IPM stimuli (dashed curves) and constant-phase tones (solid curves). The parameters of the model neurons are given in Table I. Arrows on the top of each curve indicate the range and direction of the IPD change. Each panel shows the profiles for half the cycle of IPD, i.e., the IPD change in one direction. Curves on the left column correspond to increasing IPD, while those on the right correspond to decreasing IPD. In contrast to the physiological data obtained by Spitzer and Semple (1993), the response profiles for overlapping IPDs were continuous in both directions. The IPD arcs could be superimposed to form a continuous IPD function, which resembled the static function. A very small shift of the dynamic IPD functions toward the direction of IPD variation was associated with the latency of the responses of IC neurons. The shift observed in the bot-

tom panels was also contributed by the long time constant of inhibitory input in addition to the latency. Except for the shift, the response profiles of IPM stimuli and the static-phase tones were identical. Although the IPD profiles for both directions were not plotted on a common axis, they were still comparable since they all followed the static function, which was the same for both directions. When these IPD profiles were plotted with the IPD functions obtained from the binaural beat stimuli at a beat frequency of 1 Hz (not shown), it was clear that these functions were perfectly overlapping.

In the above sections, the simulation results of the responses of IC model neurons to long-duration tonal stimuli were demonstrated. In the following sections, the responses of IC model neurons to transient stimuli will be described, including single binaural clicks and pairs of binaural clicks.

D. Responses to single binaural clicks

The responses of IC neurons to clicks with interaural delays were studied by Carney and Yin (1989). Simulations are presented below for comparison to the neuron of which the responses are shown in Fig. 8. Although ipsilaterally driven neurons such as this one are not the major types of neurons in the IC, this neuron possesses some features common to the click responses of many IC neurons: sensitivity to short ITDs; late, long-lasting inhibitions; and early, short-lasting inhibitions (Carney and Yin, 1989).

To model this particular neuron, the structure of IC models in this study (Fig. 1) was simplified in two ways. First, the ipsilateral MSO neuron received inhibitory input only from the contralateral onset cells. This unbalanced in-
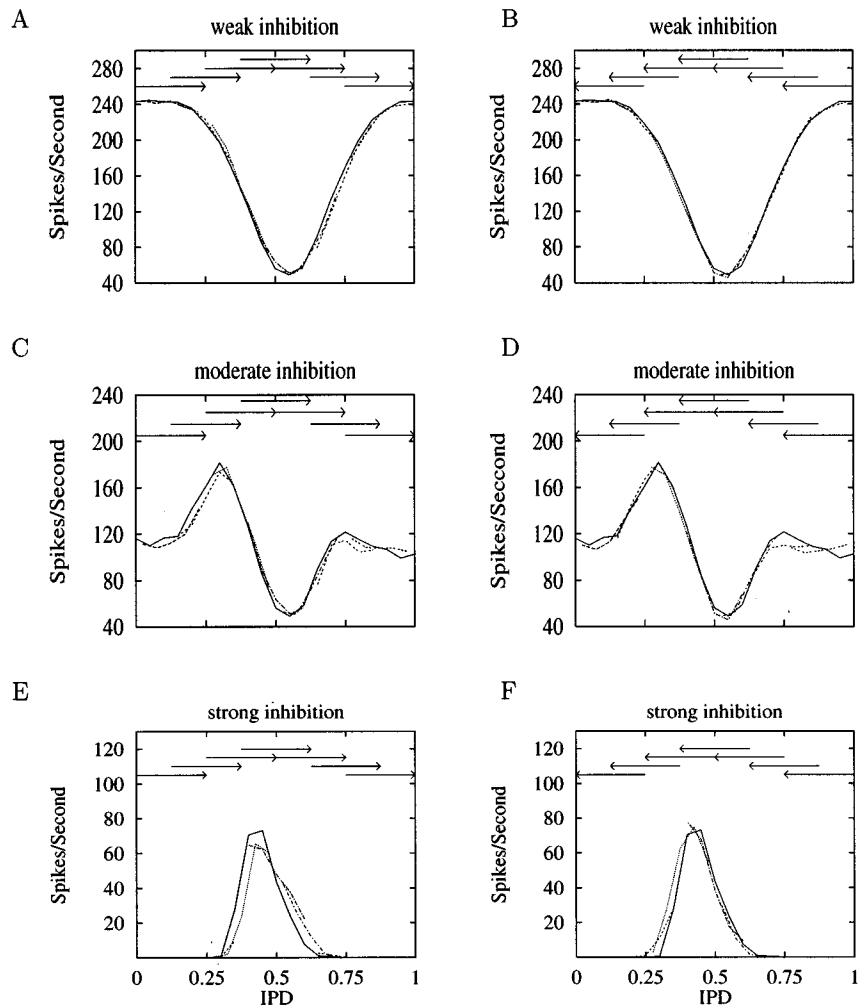
FIG. 7. Comparison of the IPD functions of three model neurons with "weak inhibition" [(A) and (B)], "moderate inhibition" [(C) and (D)], and "strong inhibition" [(E) and (F)], obtained from IPM stimuli (dashed curves). The solid curves are the static IPD functions obtained from 3-s tone stimuli. Arrows on the top show the range and direction of IPD change in IPM stimuli. The rate of IPD change was 360°/s. Parameters of the IC model neurons are given in Tables I and II.

hibition resulted in the asymmetric monaural responses of the MSO model neuron itself and hence the IC model neuron. Second, the contralateral MSO model neuron received excitation only from the SBCs on its ipsilateral side. In this case, only the contralateral stimulus (with respect to the IC model neuron) could trigger the contralateral MSO and hence caused the long-lasting inhibition to the IC. Empirically, about 18% of MSO neurons have been observed as monaural cells (Yin and Chan, 1990). Note that the asymmetry in model structure was required for some cells such as the one in Fig. 8. For other cells which showed approximately symmetric responses, a symmetric structure, which includes all pathways in Fig. 1, could be used. A model neuron with no inputs from one side is an extreme case of weak inputs from that side.

The parameters used for this model neuron are listed in Table IV. The excitatory input parameters to the two MSO model neurons were identical to those of the previous simulation, except that the contralateral MSO model neuron received excitatory inputs only from its ipsilateral side. It was assumed that the inhibitory inputs are relayed from GBCs in the AVCN via the nuclei of the trapezoid body (Smith *et al.*, 1991; Cant and Hyson, 1992). GBCs have thicker axons than SBCs and the synaptic connections between GBCs and cells in MNTB are secure (Finlayson and Caspary, 1989). Therefore it is possible that the contralateral inhibitory inputs arrive earlier than those from the SBCs. For the ipsilateral MSO model neuron, inhibitory inputs arrived 3 ms earlier than the excitatory inputs from both sides. The value of 3 ms was chosen based on the observation (Carney and Yin, 1989) that at small negative ITDs, the response to the leading (ipsilateral monaural) click is suppressed by the lagging (contralateral monaural) click when the ITD is as large as -2.8 ms (Fig. 8). The synaptic strength and time constant of the inhibition to the IC were 40 nS and 5 ms, respectively.

The click stimulus used in this study was a 100-μs pulse. The intensity of the binaural clicks was 55 dB peak-equivalent SPL, unless otherwise indicated. Fifty repetitions of single binaural click stimuli were presented every 150 ms. The range of interaural time differences, or the delay between the two monaural clicks, was extended from -10 ms to 30 ms.
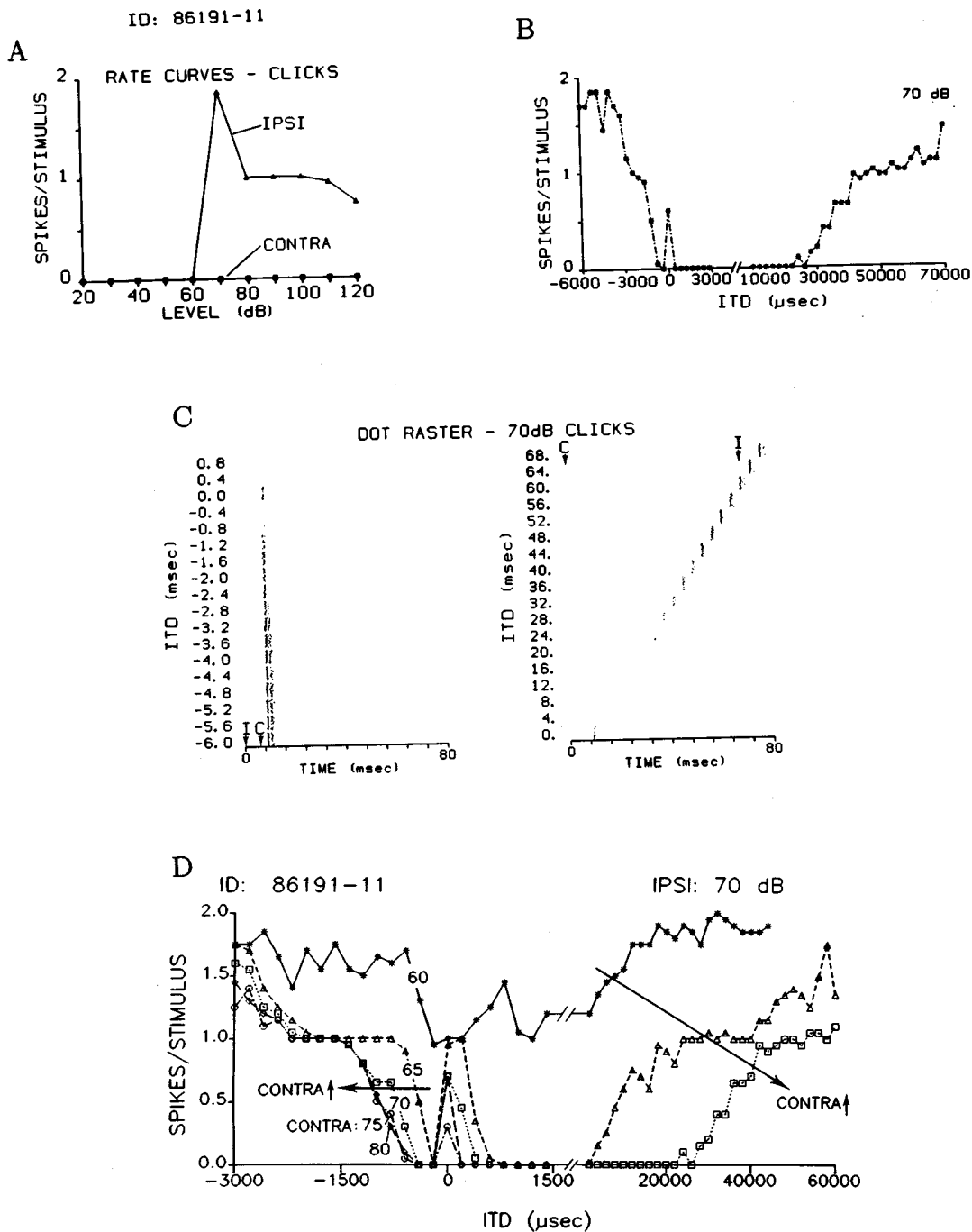
FIG. 8. Response of an IC neuron with early and late inhibition. Estimated best frequency was 2.8 kHz. (A) Rate-level curves of monaural clicks. (B) Click ITD function at 70 dB. (C) Dot rasters for responses to 70-dB clicks with varied ITDs. (D) Click ITD functions at various contralateral intensities when ipsilateral intensity was fixed at 70 dB. [From Carney and Yin (1989), their Figs. 6C, D, E and Fig. 8C. Reprinted with permission.]

1. Rate-level curves

The rate-level curves of the model neuron for monaural click stimuli are plotted in Fig. 9(A). The IC model neuron did not respond to contralateral stimuli except at low levels. At a high level, since the inhibition from the contralateral onset cells arrived earlier at the ipsilateral MSO model neuron than the excitation from the SBCs, the ipsilateral MSO model neuron and hence the IC model neuron did not respond to the stimulus. At levels lower than 45 dB, the inhibition to the ipsilateral MSO model neuron from the contralateral onset cells was not strong enough to suppress the excitation driven by both the spontaneous response of ipsilateral SBCs and the stimulus-evoked response of the contralateral SBCs. For ipsilateral monaural stimuli, the response rate increased monotonically when the intensity of the stimulus was increased up to 75 dB. The model IC neuron responded to ipsilateral stimuli because the inhibition from the onset cells was too weak to suppress the response of the ipsilateral MSO model neuron. The slight decrease of response rate at 90 and 105 dB was due to the ringing of model auditory-nerve fibers, which reduced the synchronization of the first spike in the response (Cai, 1997).

TABLE IV. Parameters of the IC model neuron simulating click response of neuron ID 86191-11 in Carney and Yin (1989) (also shown in Fig. 8). The parameters that are different from Table I are represented in italics. "C" represents input from the contralateral side of a certain neuron, and "I" represents input from the ipsilateral side of a neuron.

Parameters	Ipsilateral MSO		Contralateral MSO	IC	
	exc	inh	exc	exc	inh
Number of projecting neurons	6(C,I)	6(C)	6(I)	1(I)	1(C)
Synaptic strength (nS)	2.5	*3.0*	2.5	25	*40*
Time constant (ms)	0.1	2	0.1	0.1	5
CD of MSO (μs)	0		—	—	—
Delay of arrival (ms)	0	*−3*	0	0	1

2. ITD functions

The ITD function of this model neuron for ipsilateral and contralateral clicks at 55 dB SPL is shown in Fig. 9(B) (solid curve). When the clicks from the two sides were presented simultaneously (zero ITD), the model neuron responded with 1 spike/stimulus. The model neuron demonstrated ITD sensitivity at small ITDs. When the stimulus to the contralateral side was delivered shortly after the stimulus to the ipsilateral side (ITDs around −2 ms), the response of the model neuron to the ipsilateral stimulus was suppressed due to the early inhibition to the ipsilateral MSO model neuron. For large ITDs in either direction, the neuron responded to each click separately. Since the model neuron did not

respond to the contralateral monaural click at 55 dB, the discharge probability at large ITDs was the same as that to the ipsilateral click alone, which was about 0.9.

A comparison of the ITD function of the IC model neuron with that of the ipsilateral MSO cell (Cai, 1997) indicated that the low discharge rates of the IC model neuron at ITDs between 2 and 11 ms were caused by the inhibition from the contralateral MSO neuron. At these ITDs, the response of the IC model was remarkably suppressed. The MSO model cell, however, showed a clear cyclic dependence of response rate on ITD with a frequency equal to the CF (500 Hz) and the peak response probabilities between 1 and 0.8. The trough rates increased with ITD until they reached
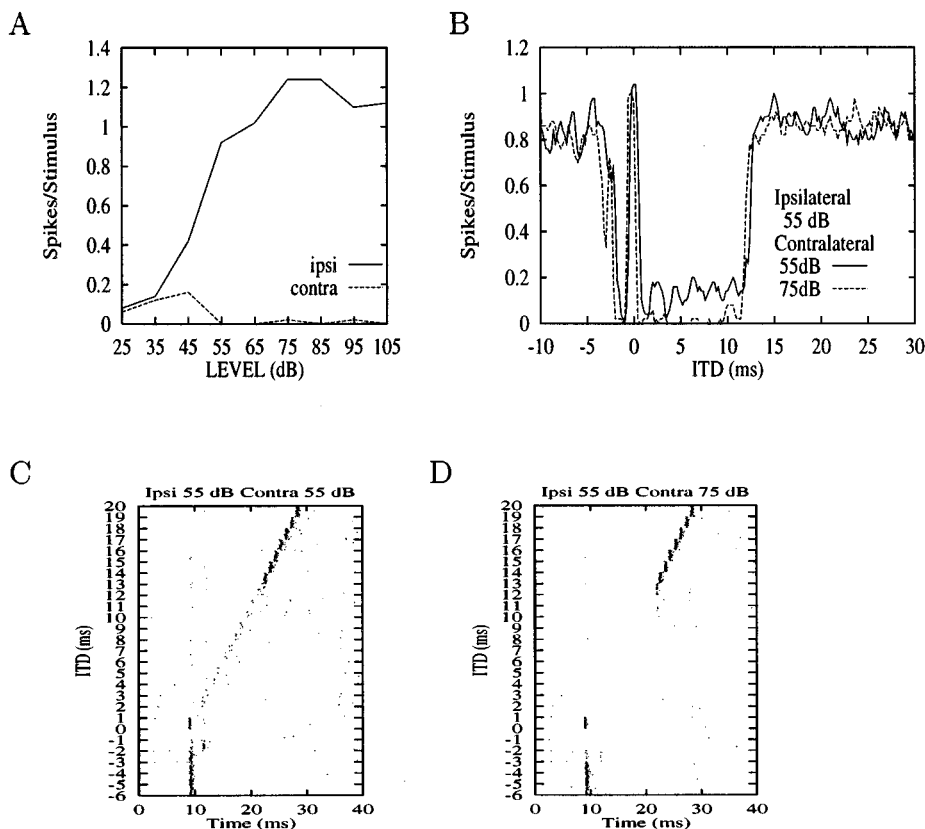
FIG. 9. Response of the IC model neuron simulating click responses of neuron ID 86191-11 (Carney and Yin, 1989) shown in Fig. 8. (A) Rate-level curves of monaural responses. (B) Click ITD functions of IC model neuron for two contralateral stimulus levels. Solid curve: ipsilateral 55 dB SPL and contralateral 55 dB SPL. Dashed curve: ipsilateral 55 dB SPL and contralateral 75 dB SPL. (C) and (D) dot-raster plots of the responses for ITDs between −6 and 19 ms with 1-ms steps. Ipsilateral stimulus intensity was 55 dB in both plots. Contralateral stimulus intensity was 55 dB in (C) and 75 dB in (D). Parameters of the IC model neuron are given in Table IV.

Parameters	Ipsilateral MSO		Contralateral MSO		IC	
	exc	inh	exc	inh	exc	inh
Number of projecting neurons	6(C,I)	6(C,I)	6(C,I)	6(C,I)	1(I)	1(C)
Synaptic strength (nS)	2.0	7.0	2.0	4	25	*30*
Time constant (ms)	0.1	4	0.1	2	0.1	*20*
CD of MSO (μs)	0		*0*		—	—
Delay of arrival (ms)	0	0	0	0	0	1

around 0.9. The peaks of the MSO response rate were seen in the response of the IC model cell, since the inhibition at this stimulus intensity was not strong enough to overcome the excitation from the ipsilateral MSO.

The dot-raster plot of the responses of the IC model neuron [shown in Fig. 9(C)] shows the discharge times at ITDs between −6 and 19 ms for an integer step of 1 ms. This plot basically indicates the same things as the ITD function shown in Fig. 9(B). The early inhibition was indicated by the absence of responses at an ITD of −1 ms. The late inhibition was indicated by the weak response (fewer dots) at ITDs between 1 and 12 ms.

3. Changing contralateral stimulus level

The effects of stimulus intensity on the ITD function of IC neurons were studied both in physiological data (Carney and Yin, 1989) [reprinted in Fig. 8(D)] and in simulation [Fig. 9(B), dashed curve]. In the simulation, the ipsilateral level was fixed at 55 dB SPL while the contralateral level was either 55 dB or 75 dB SPL.

Note that the dashed ITD function was shifted to the left of the solid curve and its peak near zero ITD was narrower. When the stimulus intensity was higher, the first action potentials of the SBCs were evoked with a shorter latency. The effect was similar to having a more positive ITD. The narrowness of the peak near zero ITD was caused by the higher synchronization of the first action potentials at 75 dB SPL. Since the probability of discharge of the contralateral MSO model neuron was larger when the stimulus intensity was higher, a stronger suppression was observed at large ITDs in the 75-dB case. However, it was interesting to note that the duration of the suppression was not so prolonged as was observed in the physiological data (cf. Fig. 8). Also, the recovery of the lagging response was not gradual as in the physiological data. Two factors contributed to these observations. First, there was only *one* inhibitory input to the model IC neuron and the maximum number of inhibitory spikes triggered by each click was *one*, so the time of arrival and the strength of the inhibition was approximately the same in both levels, except for a small latency shift caused by the difference in intensity. Second, the inhibitory conductance function was a deterministic function driven by each inhibitory input action potential. The dot raster of the response in the 75-dB case is shown in Fig. 9(D). A comparison between the dot raster plots in Fig. 9(C) and (D) indicated that the late inhibition was stronger in the 75-dB case because of the complete lack of responses at ITDs between 1 and 10 ms.

E. Responses to pairs of binaural clicks

The responses of IC cells to pairs of dichotic clicks that mimic the stimulus used to observe the precedence effect have been studied in physiological experiments. The precedence effect, sometimes called the law of the first wavefront, refers to the psychophysical observation that the first stimulus in a pair of stimuli dominates the perceived location of the pair, when the pair is closely spaced in time (Blauert, 1983). Recent physiological studies have explored this phenomenon by using pairs of binaural click stimuli (Litovsky and Yin, 1993, 1994; Fitzpatrick *et al.*, 1995). When a pair of binaural clicks is presented to the two ears with a short interclick delay (ICD), the response of an IC neuron to the lagging stimulus is suppressed. When the ICD is increased, the response to the lagging stimulus recovers (Litovsky and Yin, 1993, 1994; Fitzpatrick *et al.*, 1995). The amount of suppression depends on the ITD of the leading stimulus. In some neurons, a leading stimulus with an ITD that evokes a strong response (referred to as strong ITD) has stronger suppressive effect than that with an ITD that evokes a weak response (referred to as weak ITD); in other neurons, a leading stimulus with a weak ITD has a stronger suppressive effect than a leading stimulus with a strong ITD (Litovsky and Yin, 1993, 1994; Fitzpatrick *et al.*, 1995).

Responses to 20 repetitions of pairs of binaural clicks were simulated with 150 ms between each pair. The range of ICDs was between 1 and 70 ms. The technique used to count the number of discharges in response to the leading and lagging clicks was the same as that used in the physiological studies (Litovsky and Yin, 1993, 1994; Fitzpatrick *et al.*, 1995). Specifically, the number of spikes in response to each click was counted in a window with a fixed duration, which was determined by the observation of the PST histogram or dot-raster plot. (If the windows for the leading and lagging stimuli overlapped, the number of spikes in response to the leading stimulus was set to the average number of spikes when the stimulus was given alone. Then, the number of spikes in response to the lagging click was calculated by subtracting this average number from the total number of spikes in the overlapping window.)

1. Leading stimulus with strong ITD more suppressive

The model IC neuron received inputs from the ipsilateral and contralateral MSO model neurons with both CDs equal to zero. Detailed parameters of the IC and MSO model neurons in this case are listed in Table V. The excitatory input parameters of the IC model were identical to those described

A

Click ITD Function

B

Recovery Curve

C

Click ITD Function

D

Recovery Curve
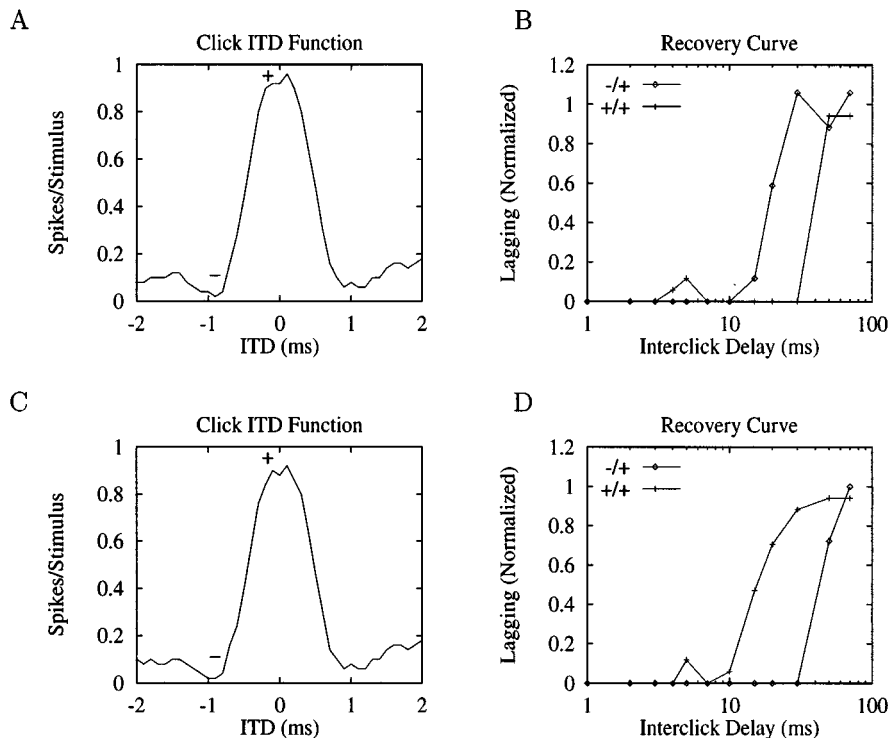
FIG. 10. Response of two model IC neurons to pairs of binaural clicks. For the model neuron with responses shown in upper panels (parameters are given in Table V), a leading stimulus with an ITD that elicited a strong response (a strong ITD) was more suppressive. For the model neuron with responses shown in lower panels (parameters are given in Table VI), a leading stimulus with an ITD that elicited a weak response (a weak ITD) was more suppressive. (A) and (C) click ITD functions. The plus sign ("+") indicates the strong ITD (0 μs) and the minus sign ("−") indicates the weak ITD (−900 μs). Using these notations, conditions for paired binaural clicks are indicated in panels (B) and (D) as follows: "+/+" indicates that the strong ITD value (0 μs) was used for both the leading and the lagging clicks, and "−/+" indicates that the weak ITD (−900 μs) was used for the leading click and the strong ITD (0 μs) was used for the lagging click.

in Table I. The input parameters of the ipsilateral MSO neuron were chosen such that its ITD function showed a maximal response of approximately 1 spike/stimulus (at around zero ITD) and a minimal response of approximately no discharges (at an ITD of −900 μs). The parameters of the contralateral MSO neuron were chosen so that the response rates at 0 and 900 μs differed by at least 50%. Other choices of the parameters did not change the essential properties of the simulation results as long as the ITD sensitivities of the two MSO neurons were preserved.

The click ITD function of the IC model neuron in Fig. 10(A) shows a peak around zero ITD and troughs around +1 and −1 ms. The absence of peaks at ±2 ms was due to the inhibitions from onset cells to the ipsilateral MSO model neuron. Based on this ITD function, the strong ITD was chosen at zero and the weak ITD at −900 μs. As in physiological studies, in order to study the effects of the leading stimulus on the suppression of the response to the lagging stimulus, the lagging stimulus was always at the strong ITD of the cell whereas the leading ITD could be at either the strong or the weak ITD. The former case was represented by "+/+" and the latter case by "−/+" in Fig. 10.

The recovery curves in Fig. 10(B) illustrate the responses of the model neuron to lagging stimuli at various interclick delays for both "+/+" and "−/+" cases. The responses to lagging stimuli were normalized by dividing the number of discharges by the average number of discharges

when the stimulus was delivered alone (Fitzpatrick *et al.*, 1995). In the "+/+" case, the response of the model neuron to the lagging click was suppressed for as long as 40 ms. In the "−/+" case, on the other hand, the response to the lagging click was recovered 15 ms after the leading click.

A comparison between the recovery curves of the model neuron [Fig. 10(B)] and real IC neurons indicated that the recovery of real neurons was more gradual. This difference may be due to the facts that the IC model neuron received only one inhibitory input and that this inhibition had a fixed synaptic strength and time constant. It is suggested that IC neurons may receive multiple inputs and/or that the amount of inhibitory neurotransmitter released varies from trial to trial.

2. Leading stimulus with a weak ITD more suppressive

To simulate the IC neurons for which a leading stimulus with a weak ITD was more suppressive, a different CD of the contralateral MSO model neuron was chosen. Detailed information on model parameters is given in Table VI. Note that the parameters for the ipsilateral MSO and IC model neurons were the same as in above simulation. The contralateral MSO neuron had a CD of 900 μs. Although this CD was out of the physiologically related ITD range for cats, this value was used simply to illustrate the possibility for prominent

TABLE VI. Parameters of an IC model neuron simulating ITD-dependent echo suppression. This neuron showed stronger suppression when the leading click had an ITD that elicited a weak response. Parameters shown in italics are those critical for the simulation of data. The dashes, —, represent ''not applicable.''

Parameters	Ipsilateral MSO exc	Ipsilateral MSO inh	Contralateral MSO exc	Contralateral MSO inh	IC exc	IC inh
Number of projecting neurons	6(C,I)	6(C,I)	6(C,I)	6(C,I)	1(I)	1(C)
Synaptic strength (nS)	2.0	7.0	2.0	1	25	*30*
Time constant (ms)	0.1	4	0.1	2	0.1	*20*
CD of MSO (μs)	0		900		—	—
Delay of arrival (ms)	0	0	0	0	0	1

effects with parameters similar to those used for other simulations here. A MSO model neuron of CF of 1000 Hz with CD at 400 μs would have given a similar result.

Figure 10(C) shows the click ITD function of the model neuron. Since the inhibitory input to the IC was delayed by 1 ms, the inhibitory MSO model neuron did not affect the click ITD function of the IC at small interaural delays. Therefore the ITD function in Fig. 10(C) is identical to that in Fig. 10(A). As noted above, the strong ITD was chosen at zero and the weak ITD at −900 μs. The same stimuli were presented and the same methods were employed to generate and analyze the simulation results. The recovery curves are shown in Fig. 10(D). It is clear that this neuron showed the opposite result to that in Fig. 10(B). For this model neuron, the responses to the lagging stimulus in the ''−/+'' case were more strongly suppressed than those in ''+/+'' case. The suppression lasted tens of milliseconds even when the neuron did not respond to the leading stimulus. Like the model neuron with responses shown in the upper panels of Fig. 10, this model neuron recovered from the suppression more abruptly than real IC neurons.

III. DISCUSSION

The Hodgkin–Huxley type model for the IC neurons in this paper received an excitatory and an inhibitory input from MSO model neurons. This simple structure is not necessarily a realistic description of the anatomy; however, it has the ability to describe a variety of physiological data from the IC, including the responses to pure tones, binaural beat stimuli, interaural phase-modulated stimuli, single binaural clicks, and pairs of binaural clicks. An abstract model, which functionally simulates the excitatory and inhibitory effects of the inputs, would be able to give similar results. Physiological models seem to be more appropriate in this study based on the rationale for the modeling approach stated in the Introduction.

A. Responses to sustained stimuli

1. ITD sensitivities

The ITD sensitivity of IC neurons has been studied extensively. It was found that more than 80% of low-frequency IC neurons were sensitive to interaural delay (Yin and Kuwada, 1984). These neurons show cyclic responses at the stimulating frequency. Two types of ITD functions were generated in our simulations. One had only one maximum in a cycle and the other, more unusual, had two peaks in one

cycle. The double-peaked ITD functions have been observed from IC neurons but have not been observed in MSO neurons (Yin, personal communication). These observations suggest that the bimodal function is associated with the convergence of auditory pathways on the IC.

Based on the simulation results, the shape of ITD functions depends on the interaction between the excitation and inhibition to the IC at given ITDs. Therefore the stimulus frequency or the CD of either of the MSO model neurons could affect the ITD sensitivity of the IC model neuron. The simulation of the ITD functions of IC model neurons at three different stimulus frequencies showed that an ITD function which was unimodal at some frequencies could be bimodal at other frequencies. Consistent with the model prediction, a neuron showing this property is illustrated in Yin and Kuwada (1983a, their Fig. 3, neuron 78145-3).

2. Characteristic delay and phase-frequency function

The concept of ''characteristic delay'' was introduced by Rose *et al.* (1966). They found that the ITD functions at different frequencies appeared to have a peak or trough at a common delay, which is referred to as the characteristic delay. In our simulations, ITD functions with a single peak could be obtained with either weak inhibition or strong inhibition from the contralateral MSO model neuron. In the case of weak or absent inhibition, the peak in the ITD function corresponds to the characteristic delay of the neuron, as in the MSO model neuron. In these cells, a common peak can be observed for different stimulus frequencies. In the case of strong inhibition, however, the peak in the ITD function may not correspond to a CD in this sense because the peak response may not happen at the same ITD for different stimulation frequencies. In this case, the minima occur at a common ITD. A response of this type in the IC might be interpreted as the result of excitatory-inhibitory inputs from the LSO; however, these modeling results indicate that the same response pattern can occur due to inhibition from the contralateral MSO.

A quantitative measurement of the CD was introduced by Yin and Kuwada (1983b). They explored the concept of characteristic delay in great detail both with physiological experiments and with computer simulations. They plotted the mean interaural phase of the response against the stimulating frequency and found that for the 201 runs on 82 phase-sensitive IC neurons, about 60% were identified as having a

CD at an acceptable significance level, meaning that the relationship of phase and frequency is linear.

If phase-frequency functions of IC model neurons in this study were plotted with a denser sampling frequency, we believe that both linear and nonlinear functions would result. When the inhibition from the contralateral MSO model neuron was weak or absent, the response of the IC model neuron basically followed that of the ipsilateral MSO model neuron and showed a linear phase-frequency plot for the frequencies near its CF. When the inhibition from the contralateral MSO was strong enough to affect the ITD-tuning of the IC, the phase-frequency function was not generally linear, since there was no common peak for these ITD functions. The peak of the ITD function of the IC model neuron depended not only on the stimulus frequency but also on the interaction between two MSO model neurons. Consistent with this prediction, neuron 79151-6 in Fig. 6 of Yin and Kuwada (1983b) showed bimodal ITD functions at several stimulus frequencies and its phase-frequency function was nonlinear.

3. Phase locking

Phase locking is an important feature for neurons responsible for ITD encoding. Although many low-frequency IC neurons are sensitive to interaural delay, only a small percent of them phase lock to monaural stimuli [about 18% in 82 neurons in Yin and Kuwada (1984)]. For those which do phase lock, the synchronization index is low. The synchronization index of the IC model neuron to monaural stimuli showed a slight decrease relative to that of the MSO model neurons. The slight decrease in the degree of phase locking resulted partly from the inhibitory input to the IC model neurons. The decrease of the synchronization index was proportional to the strength of inhibition. Since the inhibition to the IC was not perfectly phase locked, it made the membrane potential more random. Hence the inhibition not only changed the probability of firing at a certain time, but also changed the exact time of firing of the neuron.

A possible mechanism for the decrease of phase locking in actual IC neurons is that IC neurons receive multiple inputs. A cell that is driven by several inputs which are phase locked to different phases will be phase locked at a lower degree than each of its inputs. In addition, the phase locking of the model cell is also influenced by its membrane properties. In any case, it is clear that the current model with only one excitatory and one inhibitory input cannot describe the dramatic decrease in phase locking of the IC.

4. Sensitivity to dynamic temporal features

In binaural beat stimuli and interaural phase-modulated tones, the interaural time differences change as a function of time. The sensitivity of IC neurons to these dynamic temporal features was first systematically studied by Spitzer and Semple (1993). The nonoverlapping IPD arcs in response to IPM stimuli are consistent with the binaural beat data of the IC (Yin and Kuwada, 1983a; Spitzer and Semple, 1991), which showed the sharpening effect of a dynamically elicited response. Spitzer and Semple used the same time-varying IPD stimuli on gerbil SOC neurons and found that for most

units the responses to IPM stimuli were overlapping for overlapping IPD ranges (Spitzer and Semple, 1992). Their results suggest that the SOC initially encodes instantaneous IPD, while further processing in the IC provides the dependence on the time course of IPD.

In the IC model presented in this paper, there was no mechanism incorporated that was influenced by the history of the response. It is not surprising that the current model does not describe the nonoverlapping IPD arcs in response to IPM stimuli. An extension of this model with an adaptation mechanism, presented in the accompanying paper, is able to describe the effects of dynamic phase (Cai et al., 1997).

B. Responses to transient stimuli

1. Gradualness of recovery

When pairs of binaural clicks are presented at short interstimulus delays, the number of discharges of IC neurons evoked by the lagging stimulus is smaller than that evoked by the lagging stimulus alone. As the interclick delay gets longer, the response to the lagging stimulus recovers (Litovsky and Yin, 1993, 1994; Fitzpatrick et al., 1995). The recovery can be also observed in the responses to single binaural clicks at a large ITD (Carney and Yin, 1989). The comparison of the recovery of IC neurons with that of the model neuron indicated that the recovery of real neurons is more gradual than that of the model neuron. This observation suggests that a single IC neuron receives inhibition from multiple sources. Since the stellate cells in the IC have dendrites extended across the fibrodendritic laminae, each of them may receive inputs from more than one population of synaptic endings (Oliver and Morest, 1984). Even though the dendritic field of disk-shaped cells is confined in a very narrow range (about 50 μm), these cells also receive large numbers of synaptic inputs on both dendrites and, in some cases, cell bodies (Oliver and Morest, 1984; Oliver, 1987; Shneiderman and Oliver, 1989). In addition, most, if not all, IC neurons send collaterals to nearby neurons (Oliver and Huerta, 1992). The effects of these synaptic inputs are not clear; however, they may affect the response of IC neurons, including the recovery to the lagging stimulus.

2. Onset inhibition to the IC

We found that the inhibitory inputs to the IC model in the simulation of the responses to sustained stimuli had to be much weaker to describe the data than those in the simulation of the responses to transient stimuli. If the parameters of the inhibition from the contralateral MSO were made strong enough to cause tens of milliseconds of silence of the model neuron at stimulus onset, the sustained response of the model neuron to a long-duration tone would be eliminated. The same issue has been discussed in Brughera et al. (1996). The coexistence of strong inhibition at stimulus onset and sustained response to an ongoing stimulus (Carney and Yin, 1989) indicates that IC neurons may receive strong onset inhibition in addition to the sustained inhibition. Many IC neurons with onset inhibition were reported in Kuwada et al. (1989).

There are several possible causes for this phenomenon. First, IC neurons may receive onset inhibition in addition to the inhibition from DNLL. This inhibition may come from monaural nuclei or interneurons inside the IC. The projections from the VNLL to the IC are apparently glycinergic, suggesting that cells in the VNLL act as inhibitory interneurons between the octopus cells in the cochlear nucleus and the IC (Adams and Wenthold, 1987). It is possible that IC neurons receive onset inhibition from octopus cells directly via VNLL (Adams and Wenthold, 1987). Second, the DNLL may not be a faithful relay of the MSO on its ipsilateral side. Some neurons in the DNLL responded to binaural tones with only onset responses or onset responses followed by weak sustained responses (Brugge *et al.*, 1970) depending on interaural disparities. Third, some neurons in the contralateral MSO might be onset cells. The lack of any report of onset cells in the MSO might be related to the lack of recording of the responses of MSO neurons to transient stimuli, which is due to the strong field potential within the MSO (Guinan *et al.*, 1972). Further physiological experiments are needed to clarify these possibilities.

C. Comparisons with other models

1. Comparison with the MSO model

Since the IC model in this study incorporated MSO models to provide inputs, the responses of the MSO model neurons to each stimulus were obtained. Therefore it was convenient to compare the MSO model and the IC model in this study.

The MSO model showed a cyclic ITD function when a pure-tone stimulus was presented. In response to binaural click stimuli, the MSO model cell with inhibitory inputs also showed early and/or late inhibition. The asymmetry of responses with positive and negative interaural delay depended on the asymmetry of the inhibitory inputs to the neuron. The single MSO cell model did not show bimodal ITD functions, direction and rate sensitivities, ITD-dependent echo suppression, and sharpened dynamic IPD functions. Therefore it was not adequate as a model for cells in the IC.

The IC model presented in this paper was consistent with a larger set of observed IC behavior. In addition to properties demonstrated by the MSO model, it showed bimodal IPD functions with some choices of the inhibitory parameters from the contralateral MSO. It also showed sensitivity to the direction and the speed of the binaural beat stimulus, when the contralateral inhibition lasted for a long time (tens of milliseconds). In response to pairs of binaural clicks, the model neuron showed ITD-dependent echo suppression. This ITD-dependence was determined by the characteristic delay of the inhibitory MSO model neuron.

Neither of these models described the gradual recovery of the response to a lagging transient stimulus when two stimuli are applied one after another with a short delay. It was suggested that this gradual recovery may reflect the fact that IC neurons may receive multiple inhibitory and excitatory inputs. The variability of the synaptic characteristics and the response probability of these sources might also contribute to the gradual recovery. The model did not show the coexistence of strong onset inhibition and sustained responses to long-duration stimuli, unless inhibitory inputs were provided to the IC by onset neurons. [See the related discussion by Brughera *et al.* (1996).] Finally, this IC model did not show sharpened dynamic IPD functions.

2. Comparison with a functional model with lateral inhibition

Besides the physiological models developed for the IC, functional models for psychophysics (such as cross-correlation models) have been developed for several decades (see the review by Colburn, 1996). Among those models, the Lindemann (1986a, b) model incorporated a dynamic lateral inhibition mechanism and monaural channels that provided inputs to the interaural cross-correlation function. These extensions allow the model to provide a basis for the precedence effect. When there are coincidences at one value of ITD, the model generates inhibitions to the coincidences at other values of ITD. Hence the Lindemann model predicts that minimum echo suppression happens when the leading stimulus and lagging stimulus come from the same location and maximum suppression happens when the leading stimulus and lagging stimulus are lateral to each other in space. Psychophysical evidence also suggests (on the basis of very little data) (Boerger, 1965) that echo suppression is stronger when sources are widely separated. This relationship only partially describes the data observed in physiology (Litovsky and Yin, 1993, 1994; Fitzpatrick *et al.*, 1995). The Lindemann model cannot predict the data in which suppression can be strongest when both the leading and lagging stimuli come from the same source. The physiological model described in this paper with excitation and inhibition coming from independent sources described both psychophysical and physiological data.

IV. CONCLUSIONS

Simulation results revealed that the IC model with ipsilateral excitation and contralateral inhibition from ITD-sensitive neurons showed unimodal and bimodal ITD functions, rate and direction sensitivities to binaural beat stimuli, early and late inhibition in response to binaural clicks, and ITD-dependent echo suppression in response to pairs of binaural clicks. With the current model structure and membrane function, the model did not show sensitivity to dynamic temporal features or sharpened dynamic IPD functions in response to binaural beat stimuli and interaural phase-modulated stimuli. It also did not show gradual recovery curves in response to transient stimuli and the dramatic decrease of phase locking to monaural tone stimuli. In order to show some of these features, mechanisms such as adaptation (Cai *et al.*, 1997) and a more complex model structure were needed.

ACKNOWLEDGMENTS

Adams, J. C., and Mugnaini, E. (**1984**). ''Dorsal neucleus of lateral lemniscus: A nucleus of GABAergic projection neurons,'' Brain Res. Bull. **13**, 585–590.

Adams, J. C., and Wenthold, R. J. (**1987**). ''Immunostaining of ascending auditory pathways with glycine antiserum,'' Assoc. Res. Otolaryngol. **10**, 63.

Blauert, J. (**1983**). ''The psychophysics of human sound localization,'' in *Spatical Hearing* (MIT, Cambridge, MA), pp. 1–408.

Boerger, G. (**1965**). ''Über die Trägheit des Gehörs bei der Richtungsempfindung [On the persistence of the directional sensation in hearing],'' *Proceedings of the 5th International Congress on Acoustics*, liége, B 27.

Brugge, J. F., Anderson, D. J., and Aitkin, L. M. (**1970**). ''Responses of neurons in the dorsal nucleus of lateral lemniscus of cat to binaural tonal stimulation,'' J. Neurophysiol. **33**, 441–458.

Brughera, A. R., Stutman, E. R., Carney, L. H., and Colburn, H. S. (**1996**). ''A model with excitation and inhibition for cells in the medial superior olive,'' Aud. Neurosci. **2**, 219–233.

Cai, H. (unpublished).

Cai, H. (**1997**). ''Models for the binaural response properties of inferior colliculus neurons,'' dissertation, Boston University.

Cai, H., Carney, L. H., and Colburn, H. S. (**1998**). ''A model for binaural response properties of inferior colliculus neurons: II. A model with interaural time difference sensitive excitatory and inhibitory inputs and an adaptation mechanism,'' J. Acoust. Soc. Am. **103**, 494–506.

Cant, N. B., and Hyson, R. L. (**1992**). ''Projections from the lateral nucleus of the trapezoid body to the medial superior olivary nucleus in the gerbil,'' Hearing Res. **49**, 281–298.

Carney, L. H. (**1993**). ''A model for the responses of low-frequency auditory-nerve fibers in cat,'' J. Acoust. Soc. Am. **93**, 401–417.

Carney, L. H., and Yin, T. C. T. (**1989**). ''Responses of low-frequency cells in the inferior colliculus to interaural time differences of clicks: Excitatory and inhibitory components,'' J. Neurophysiol. **62**, 144–161.

Colburn, H. S. (**1996**). ''Computational models of binaural processing,'' in *Auditory Computation*, edited by H. Hawkins and T. McMullen (Springer-Verlag, Berlin), pp. 332–400.

Colburn, H. S., and Ibrahim, H. (**1993**). ''Modeling of precedence effect behavior in single neurons and in human listeners,'' J. Acoust. Soc. Am. **93**, 2293(A).

Eccles, J. C. (**1964**). *The Physiology of Synapses* (Academic, New York).

Finlayson, P. G., and Caspary, D. M. (**1989**). ''Synaptic potentials of chinchilla lateral superior olivary neurons,'' Hearing Res. **38**, 221–228.

Fitzpatrick, D. C., Kuwada, S., Batra, R., and Trahiotis, C. (**1995**). ''Neural responses to simple simulated echoes in the auditory brain stem of the unanesthetized rabbit,'' J. Neurophysiol. **74**, 2469–2486.

Glendenning, K. K., Brunso-Bechtold, J. K., Thompson, G. C., and Masterton, R. B. (**1981**). ''Ascending auditory afferents to the nuclei of the lateral lemniscus,'' J. Comp. Neurol. **197**, 673–703.

Goldberg, J. M., and Brown, P. B. (**1969**). ''Response of binaural neurons of dog superior olivary complex to dichotic tonal stimuli: some physiological mechanisms for sound localization,'' J. Neurophysiol. **32**, 613–636.

Guinan, Jr., J. J., Norris, B. E., and Guinan, S. S. (**1972**). ''Single auditory units in the superior olivary complex. II. Locations of unit categories and tonotopic organization,'' Int. J. Neurosci. **4**, 147–166.

Henkel, C. K., and Spangler, K. M. (**1983**). ''Organization of the efferent projections of the MSO nucleus in the cat as revealed by HRP and autoradiographic tracing methods,'' J. Comp. Neurol. **221**, 416–428.

Hodgkin, A. L., and Huxley, A. F. (**1952**). ''A quantitative description of membrane current and its application to conduction and excitation in the nerve,'' J. Physiol. (London) **117**, 500–544.

Johnson, D. H. (**1980**). ''The relationship between spike rate and synchrony in responses of auditory-nerve fibers to single tones,'' J. Acoust. Soc. Am. **68**, 1115–1122.

Joris, P. X., Carney, L. H., Smith, P. H., and Yin, T. C. T. (**1994**). ''Enhancement of neural synchronization in the anteroventral cochlear nucleus. I. Responses to tones at the characteristic frequency,'' J. Neurophysiol. **71**, 1022–1036.

Kuwada, S., Batra, R., and Fitzpatrick, D. C. (**1997**). ''Neural processing of binaural temporal cues,'' in *Binaural and Spatial Hearing in Real and Virtual Environments*, edited by R. H. Gilkey and T. R. Anderson (Erlbaum, Mahwah, NJ), pp. 399–426.

Kuwada, S., Batra, R., and Stanford, T. R. (**1989**). ''Monaural and binaural response properties of neurons in the inferior colliculus of the rabbit: Effects of sodium pentobarbital,'' J. Neurophysiol. **61**, 269–282.

Kuwada, S., Stanford, T. R., and Batra, R. (**1987**). ''Interaural phase-

sensitive units in the inferior colliculus of the unanesthetized rabbit: Effects of changing frequency,'' J. Neurophysiol. **57**, 1338–1360.

Kuwada, S., and Yin, T. C. T. (**1983**). ''Binaural interaction in low-frequency neurons in inferior colliculus of the cat. I. Effects of long interaural delays, intensity, and repetition rate on interaural delay function,'' J. Neurophysiol. **50**, 981–999.

Kuwada, S., Yin, T. C. T., Syka, J., Buunen, T. J. F., and Wickesberg, R. E. (**1984**). ''Binaural interaction in low-frequency neurons in inferior colliculus of the cat. IV. Comparison of monaural and binaural response properties,'' J. Neurophysiol. **51**, 1306–1325.

Lindemann, W. (**1986a**). ''Extension of a binaural cross-correlation model by contralateral inhibition. I. Simulation of lateralization for stationary signals,'' J. Acoust. Soc. Am. **80**, 1608–1622.

Lindemann, W. (**1986b**). ''Extension of a binaural cross-correlation model by contralateral inhibition. II. The law of the first wave front,'' J. Acoust. Soc. Am. **80**, 1623–1630.

Litovsky R., and Yin, T. C. T. (**1993**). ''Single-unit responses to stimuli that mimic the precedence effect in the inferior colliculus of the cat.'' Assoc. Res. Otolaryngol. Abstr. **16**, 128.

Litovsky, R., and Yin, T. C. T. (**1994**). ''Physiological correlates of the precedence effect: Free field recordings in the inferior colliculus of the cat,'' Assoc. Res. Otolaryngol. Abstr. **17**, 337.

Manis, P. B., and Marx, S. O. (**1991**). ''Outward currents in isolated ventral cochlear nucleus neurons,'' J. Neurosci. **11**, 2865–2880.

Mardia, K. V. (**1972**). *Statistics of Directional Data* (Academic, London).

Oertel, D. (**1983**). ''Synaptic responses and electrical properties of cells in brain slices of the mouse anteroventral cochlear nucleus,'' J. Neurosci. **3**, 2043–2053.

Oertel, D. (**1985**). ''Use of brain slices in the study of the auditory system: spatial and temporal summation of synaptic inputs in cells in the anteroventral cochlear nucleus of the mouse,'' J. Acoust. Soc. Am. **78**, 328–333.

Oliver, D. L. (**1987**). ''Projections to the inferior colliculus from the anteroventral cochlear nucleus in the cat: possible substrates for binaural interaction,'' J. Comp. Neurol. **264**, 24–46.

Oliver, D. L., and Huerta, M. F. (**1992**). ''Inferior and superior colliculus,'' in *The Mammalian Auditory Pathway: Neuroanatomy*, edited by D. B. Webster, A. N. Popper, and R. R. Fay (Springer-Verlag, Berlin), pp. 168–221.

Oliver, D. L., and Morest, D. K. (**1984**). ''The central nucleus of the inferior colliculus in the cat,'' J. Comp. Neurol. **222**, 237–264.

Peruzzi, D., and Oliver, D. L. (**1995**). ''Intrinsic membrane properties and morphology of neurons in the rat inferior colliculus,'' Assoc. Res. Otolaryngol. Abstr. **18**, 515.

Rose, J. E., Gross, N. B., Geisler, C. D., and Hind, J. E. (**1966**). ''Some neural mechanisms in the inferior colliculus of the cat which may be relevant to localization of a sound source,'' J. Neurophysiol. **29**, 288–314.

Rothman, S. R., Young, E. D., and Manis, P. B. (**1993**). ''Convergence of auditory nerve fibers onto bushy cells in the ventral cochlear nucleus: implications of a computational model,'' J. Neurophysiol. **70**, 2562–2583.

Shneiderman, A., Chase, M. B., Rockwood, J. M., Benson, C. G., and Potashner, S. J. (**1993**). ''Evidence for a GABAergic projection from the dorsal nucleus of the lateral lemniscus to the inferior colliculus,'' J. Neurochem. **60**, 72–82.

Shneiderman, A., and Oliver, D. L. (**1989**). ''EM autoradiographic study of the projections from the dorsal nucleus of the lateral lemniscus: A possible source of inhibitory inputs to the inferior colliculus,'' J. Comp. Neurol. **286**, 28–47.

Shneiderman, A., Oliver, D. L., and Henkel, C. K. (**1988**). ''Connections of the dorsal nucleus of the lateral lemniscus: An inhibitory parallel pathway in the ascending auditory system?,'' J. Comp. Neurol. **276**, 188–208.

Smith, P. H. (**1995**). ''Structural and functional differences distinguish principal from non-principal cells in the guinea pig MSO slice,'' J. Neurophysiol. **73**, 1653–1667.

Smith, P. H., Joris, P. X., and Carney, L. H. (**1991**). ''Projections of physiologically characterized globular bushy cell axons from the cochlear nucleus of cat,'' J. Comp. Neurol. **304**, 387–401.

Smith, P. H., and Rhode, W. S. (**1987**). ''Characterization of HRP-labeled globular bushy cells in the cat anteroventral cochlear nucleus,'' J. Comp. Neurol. **266**, 360–375.

Spitzer, M. W., and Semple, M. N. (**1991**). ''Interaural phase coding in auditory midbrain: influence of dynamic stimulus features,'' Science **254**, 721–724.

Spitzer, M. W., and Semple, M. N. (**1992**). ''Responses to time-varying

phase disparity in gerbil superior olive: evidence for hierarchical processing,'' Soc. Neurosci. Abstr. **18**, 149.

Spitzer, M. W., and Semple, M. N. (**1993**). ''Responses of inferior colliculus neurons to time-varying interaural phase disparity: effects of shifting the locus of virtual motion,'' J. Neurophysiol. **69**, 1245–1263.

Sujaku, Y., Kuwada, S., and Yin, T. C. T. (**1981**). ''Binaural interaction in the cat inferior colliculus: comparison of the physiological data with a computer simulated model,'' in *Neuronal Mechanisms of Hearing*, edited by J. Syka and L. Aitkin (Plenum, New York), pp. 233–238.

Wu, S. H., and Oertel, D. (**1984**). ''Intracellular injection with horseradish peroxidase of physiologically characterized stellate and bushy cells in slices of mouse anteroventral cochlear nucleus,'' J. Neurosci. **4**, 1577–1588.

Yin, T. C. T. (personal communication).

Yin, T. C. T. (**1994**). ''Physiological correlates of the precedence effect and summing localization in the inferior colliculus of the cat,'' J. Neurosci. **14**, 5170–5186.

Yin, T. C. T., and Chan, J. C. K. (**1990**). ''Interaural time sensitivity in medial superior olive of cat,'' J. Neurophysiol. **64**, 465–488.

Yin, T. C. T., Chan, J. C. K., and Carney, L. H. (**1987**). ''Effects of interaural time delays of noise stimuli on low-frequency cells in the cat's inferior colliculus. III. Evidence for cross-correlation,'' J. Neurophysiol. **58**, 562–583.

Yin, T. C. T., Chan, J. C. K., and Irvine, D. R. F. (**1986**). ''Effects of interaural time delays of noise stimuli on low-frequency cells in the cat's inferior colliculus. I. Responses to wideband noise,'' J. Neurophysiol. **55**, 280–300.

Yin, T. C. T., and Kuwada, S. (**1983a**). ''Binaural interaction in low-frequency neurons in inferior colliculus of the cat. II. Effects of changing rate and direction of interaural phase,'' J. Neurophysiol. **50**, 1000–1019.

Yin, T. C. T., and Kuwada, S. (**1983b**). ''Binaural interaction in low-frequency neurons in inferior colliculus of the cat. III. Effects of changing frequency,'' J. Neurophysiol. **50**, 1020–1042.

Yin, T. C. T., and Kuwada, S. (**1984**). ''Neuronal Mechanisms of Binaural Interaction,'' in *Dynamic Aspects of Neocortical Function*, edited by G. M. Edelman, W. E. Gall, and W. M. Cowan (Wiley, New York), pp. 263–313.

A model for binaural response properties of inferior colliculus neurons. II. A model with interaural time difference-sensitive excitatory and inhibitory inputs and an adaptation mechanism

Hongmei Cai, Laurel H. Carney, and H. Steven Colburn
Department of Biomedical Engineering, Boston University, 44 Cummington Street, Boston, Massachusetts 02215

The inferior colliculus (IC) model of Cai *et al.* [J. Acoust. Soc. Am. **103**, 475–493 (1998)] simulated the binaural response properties of low-frequency IC neurons in response to various acoustic stimuli. This model, however, failed to simulate the sensitivities of IC neurons to dynamically changing temporal features, such as the sharpened dynamic interaural phase difference (IPD) functions. In this paper, the Cai *et al.* (1998) model is modified such that an adaptation mechanism, viz., an additional channel simulating a calcium-activated, voltage-independent potassium channel which is responsible for afterhyperpolarization, is incorporated in the IC membrane model. Simulations were repeated with this modified model, including the responses to pure tones, binaural beat stimuli, interaural phase-modulated stimuli, binaural clicks, and pairs of binaural clicks. The discharge patterns of the model in response to current injection were also studied and compared with physiological data. It was demonstrated that this model showed all the properties that were simulated by the Cai *et al.* (1998) model. In addition, it showed some properties that were not simulated by that model, such as the sharpened dynamic IPD functions and adapting discharge patterns in response to current injection. © *1998 Acoustical Society of America.* [S0001-4966(98)00601-8]

PACS numbers: 43.64.Bt, 43.66.Pn [RDF]

INTRODUCTION

The inferior colliculus (IC) is a critical structure in the midbrain because it is the target of almost all ascending fibers from the lower auditory brain stem. In recent years, there have been diverse studies of the IC, regarding its morphology and physiology. The physiological responses of low-frequency IC neurons reported in the literature include responses to pure tones (Kuwada and Yin, 1983; Yin and Kuwada, 1983a, b; Kuwada *et al.*, 1984), responses to binaural beat stimuli (Yin and Kuwada, 1983a; Spitzer and Semple, 1991), and responses to interaural phase-modulated tones (Spitzer and Semple, 1993). In addition to the responses to sustained stimuli, the responses of IC neurons to transient stimuli have also been studied, including responses to binaural click stimuli (Carney and Yin, 1989) and to pairs of binaural clicks (Litovsky and Yin, 1993, 1994; Fitzpatrick *et al.*, 1995). All of these studies revealed interesting binaural response properties of the IC. Recently, membrane properties of the IC have been explored by Peruzzi and Oliver (1995) with voltage and current clamping and intracellular recording techniques on slices of the IC from rats. One way to understand these separate data is to build a simple but adequate model which simulates all of the above responses.

There have been several models that simulated the data from the IC, including those of Sujaku *et al.* (1981), Colburn and Ibrahim (1993), Brughera *et al.* (1996), and Cai *et al.* (1998). Among these models, the Cai *et al.* (1998) model was designed to simulate a wide variety of the properties of IC neurons. This model, however, with its membrane equa-

tions identical to those of the bushy cell model of Rothman *et al.* (1993), did not describe the sensitivities of IC neurons to dynamically changing temporal features, as represented by nonoverlapping interaural phase difference (IPD) functions in response to interaural phase-modulated (IPM) tones (Spitzer and Semple, 1993) and by sharpened dynamic IPD functions obtained from binaural beat stimuli (Yin and Kuwada, 1983a; Spitzer and Semple, 1991). The mechanism responsible for these phenomena is still not clear; however, it is consistent with an adaptation mechanism. Intracellular recordings from some IC neurons in a slice preparation of the rat midbrain also demonstrated adapting discharge patterns in response to depolarizing current injection (Peruzzi and Oliver, 1995). In this paper, the Cai *et al.* (1998) model is modified by incorporating an adaptation mechanism in the IC model neurons.

The simulation results of this model in response to a variety of stimuli are presented. These stimuli include depolarizing current injection and sustained acoustic stimuli, such as pure tones, binaural beat stimuli, and interaural phase-modulated tones. Although the IC model in Cai *et al.* (1998) successfully described some of these responses, those simulations were repeated with the modified model so that the effects of the adaptation mechanism on these basic responses could be studied. The responses of the model to transient stimuli, including single binaural clicks and pairs of binaural clicks, were also repeated but are not presented in this paper, since the adaptation mechanism did not affect these responses in any obvious way. The responses to transient
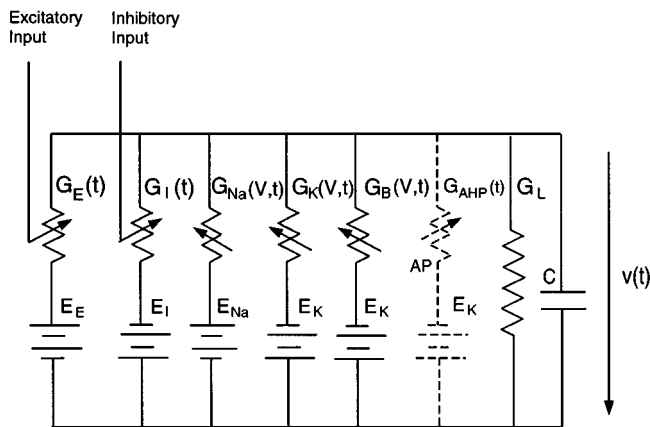
FIG. 1. Circuit diagram of the IC model which was based on the Rothman *et al.* (1993) model but modified with an additional channel simulating a calcium-activated, voltage-independent potassium channel (dashed structure). This channel was triggered by action potentials (APs) in the model.

stimuli were very similar to those obtained with the Cai *et al.* (1998) model (Cai, 1997).

I. METHODS

The structure of the model was identical to the model described in Cai *et al.* (1998). A detailed description of the model structure and each model component is given by Cai *et al.* (1998). The IC model neuron was driven by an ipsilateral medial superior olive (MSO) neuron and inhibited by a contralateral MSO neuron via an inhibitory interneuron, presumed to be within the dorsal nucleus of the lateral lemniscus (DNLL). The MSO model neurons received convergent inputs from model spherical bushy cells (Rothman *et al.*, 1993) which in turn were driven by models of auditory-nerve fibers (Carney, 1993). The model MSO cells might also receive inhibition from onset cells, presumably from globular bushy cells in the anteroventral cochlear nucleus (AVCN). In the following paragraphs, we focus on the difference between the current and the previous model.

The membrane equations for the model IC cell were similar to those of the Rothman *et al.* (1993) model with one modification. An additional potassium channel was added, simulating a calcium-activated, voltage-independent potassium channel which resulted in afterhyperpolarization (AHP) and therefore modulated the discharge frequency. The circuit diagram of the IC model membrane is shown in Fig. 1. The differential equation describing the membrane potential change is

$$C \frac{dV}{dt} + G_B(V - E_K) + G_K(V - E_K) + G_{Na}(V - E_{Na})$$

$$+ G_L(V - E_L) + G_I(V - E_I) + G_E(V - E_E)$$

$$+ G_{AHP}(V - E_K) = I_{ext}, \tag{1}$$

where C is membrane capacitance. The conductances of the low-threshold, slow potassium channel (G_B), sodium channel (G_{Na}), and delayed-rectifierlike potassium channel (G_K) were described by Hodgkin–Huxley-type equations, as given in Rothman *et al.* (1993). The conductance, G_{AHP}, of the

channel which leads to the adaptation effects is described in detail below.

Although there is no direct evidence that the calcium-activated, voltage-independent potassium channel exists in the IC, action potentials with a long tail of hyperpolarization have been observed in the intracellular recordings from the IC (Nelson and Erulkar, 1963). In addition, current clamp responses of IC neurons show both regular and adapting discharge patterns (Peruzzi and Oliver, 1995). The adapting pattern could be caused by an AHP mechanism, but other equivalent mechanisms would give similar results.

The conductance of the calcium-activated, voltage-independent potassium channel was modeled in a simplified way. Since the IC model membrane did not have a calcium channel, changes in the conductance of the calcium-activated, voltage-independent potassium channel in the model were triggered by action potentials rather than by an associated calcium influx. The conductance of this channel was increased by a fixed amount half a millisecond after the rising edge of an action potential was detected. Then the conductance decreased exponentially with a long time constant τ_{AHP} (500 ms):

$$G_{AHP}(t - t_{AP} - 0.5) = G_{AHP_{max}} \exp\left(-\frac{t - t_{AP} - 0.5}{\tau_{AHP}}\right)$$

$$\times u(t - t_{AP} - 0.5), \tag{2}$$

where t_{AP} is the time when an action potential is detected and the time is measured in milliseconds.

This model was based on the observation that the slow calcium-dependent potassium current followed an exponential function with a time constant of several hundreds of milliseconds in bullfrog sympathetic ganglion cells (Pennefather *et al.*, 1985); however, the exact time course of this current during an action potential is uncertain. In this model, the rapid buildup of internal calcium concentration was simplified by delaying the increment of the AHP conductance by 0.5 ms in our model. This simplification had little effect on the membrane potential both during and after an action potential (Cai, 1997).

Model parameters other than those related to AHP were identical to those used in the IC model of Cai *et al.* (1998).

II. RESULTS

A. Single action potentials

Since the presence of the AHP mechanism changed the differential equation of membrane potentials defined in Rothman *et al.* (1993), it was important to examine the membrane dynamics of the model before the model was used to simulate the responses of IC neurons.

A very short current pulse (1 ms in duration) with sufficient level (200 pA) to trigger an action potential was applied to the model neuron. The current associated with afterhyperpolarization, I_{AHP}, and the membrane potential with and without this current are depicted in Fig. 2(A) and (B), respectively. The amplitude of this current was very small,

A
AHP current

B
Membrane potential
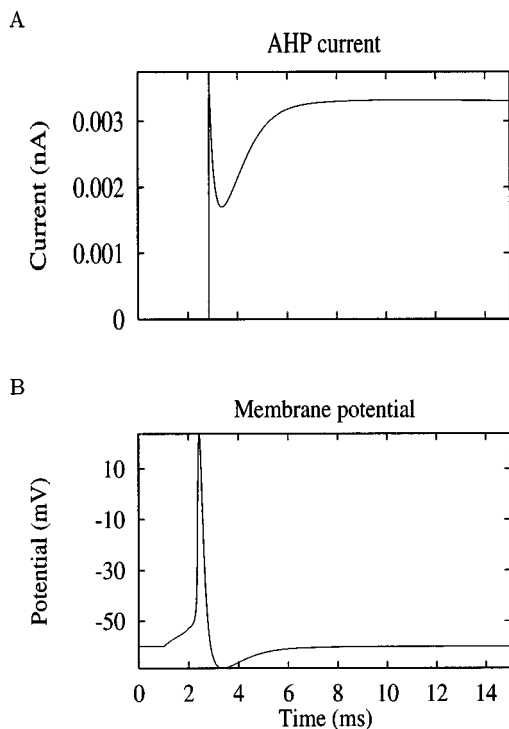
FIG. 2. (A) Current associated with the AHP (I_{AHP}) following the injection of a 1-ms depolarizing current of 200 pA starting at a time of 1 ms. (B) Membrane potentials of the IC models.

thousands of times smaller than those of the sodium current and other potassium currents during an action potential. The extended tail of I_{AHP} (only the initial part is shown) was caused by the slow decay of G_{AHP}, which had a time constant of 500 ms in the model. The model prediction of the current could be compared with the simulation result of another study conducted by Yamada *et al.* (1989). Their model, which was built for bullfrog sympathetic ganglion cells, incorporated sodium and calcium channels, along with three types of potassium channels, including a calcium-activated, voltage-independent potassium channel. In their model, the calculated time constant of I_{AHP} at the peak of internal calcium concentration was 0.5 ms, which was comparable to the 0.5-ms delay followed by the abrupt onset of G_{AHP} in our model. The shape of I_{AHP} in our model resembled Yamada *et al.*'s (1989) model. The dip of I_{AHP} a few milliseconds after the onset in both studies was caused by the hyperpolarization of membrane potential [cf. Fig. 2(B)]. The current increased as the membrane potential returned to its resting potential before a very slow decrease to zero. The time course of membrane activity was slower in the Yamada *et al.* (1989) model, due to its overall different membrane dynamics. Also the rate constants in their model for the bullfrog were normalized for 22 °C, rather than 38 °C as in this study for mammalian neurons.

The action potential generated by the models with AHP is shown in Fig. 2(B). This curve completely overlaps with the action potential generated with the model without AHP. Although I_{AHP} became dominant when other currents returned to zero after an action potential, it was still too small to make any noticeable difference (with current values of

model parameters) in the membrane potential compared with that of the model without AHP. Note, however, that a series of action potentials would result in accumulation of calcium (a superposition of I_{AHP} components in our model) so that the membrane potential would eventually be affected by this current.

B. Responses to long-duration current injection

To study the discharge patterns in response to long-duration currents, depolarizing currents with a duration of 250 ms and current levels of 250, 350, and 450 pA were applied to the model. The discharge patterns of the model are shown in the left column panels of Fig. 3. At a low current level (e.g., 200 pA), only one action potential was generated at the onset of current injection (not shown). When the current was 250 pA [Fig. 3(A)], five action potentials were elicited. As the current level was increased, a continuous stream of discharges was generated. Note particularly that the interspike interval of the discharges increased during the current pulse. In the simulation of current injection of 350 pA [Fig. 3(C)], the discharge rate dropped dramatically after 170 ms so that the interspike interval (ISI) did not linearly change with time. At a current level of 450 pA [Fig. 3(E)], the ISI was a linear function of time. The conductance of AHP increased by a certain amount after each action potential. Since the time constant of G_{AHP} was very slow, the conductance accumulated and the threshold of action potentials became larger as a function of time. This increase in threshold in turn meant that a greater depolarization was required to generate an action potential. Therefore the response rate varied with the history of response. This kind of response pattern was referred to as an adapting discharge pattern.

A comparison between the responses of our earlier IC model (Cai *et al.*, 1998) (right column, Fig. 3) and the responses of the current IC model (left column, Fig. 3) showed the effects of AHP mechanism on discharge patterns. A train of equally spaced action potentials was produced for the duration of the current at each current level in the earlier model. At a high current level, the model neuron was depolarized quickly so the response rate was also high. Since the currents associated with each action potential lasted only a few milliseconds, previous action potentials did not affect successive responses. Hence a constant response rate was produced. This kind of response pattern was referred to as a regular discharge pattern.

Notice that the model cell produces multiple action potentials in response to high-level current injection; this result is not consistent with recordings from bushy cells, which respond with action potentials only at the onset of current pulses (Oertel, 1983; Wu and Oertel, 1984), and thus represents a limitation of the model of Rothman *et al.* (1993). However, this sustained response to current injections is not a limitation for modeling many IC neurons. Peruzzi and Oliver (1995) described three response patterns for IC cells: regular and adapting cells had sustained responses to current injection similar to those shown for the model cell (Fig. 3). They also described cells with onset responses to current injection for which the limitations of the Rothman bushy cell

496   J. Acoust. Soc. Am., Vol. 103, No. 1, January 1998

Cai *et al.*: IC binaural model with adaptation   496
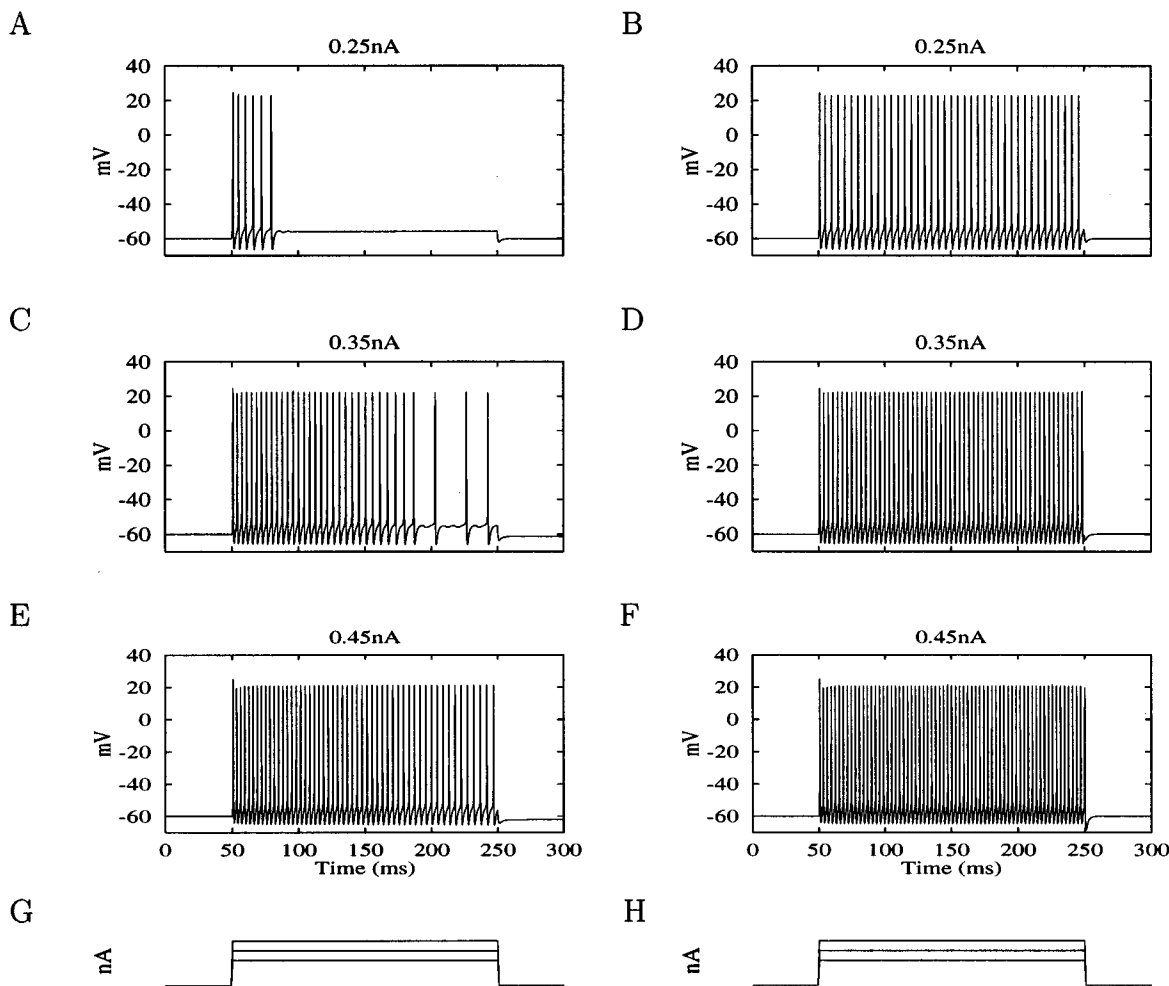
FIG. 3. Discharge patterns of IC models in response to three levels of external depolarizing current. Left column: current IC model. Right column: earlier IC model (Cai *et al.*, 1998). The levels of current are shown on the top of each figure. The current was presented between 50 and 250 ms, as shown in the bottom panels.

model would be a factor; cells with onset responses to current injection were not considered further in this study.

All three types of discharge patterns have been observed in disk-shaped cells and stellate cells of the IC neurons of the rat (Peruzzi and Oliver, 1995). No correlation, however, has been found between the morphology of the neurons and their response types. For the adapting and regular discharge patterns, the interspike interval as a function of time during the current injection could be described as either a linear function or two linear functions crossing each other, depending on the current level (Peruzzi, personal communication). These observations are consistent with the simulation results.

In the following sections, the simulation results of the IC model neuron to acoustic stimuli are presented, including the responses to pure-tone stimuli, binaural beat stimuli, and interaural-phase-modulated stimuli.

C. Responses to pure-tone stimuli

The responses of IC neurons to pure-tone stimuli have been studied extensively by presenting tone stimuli with a delay between the signals to the ipsilateral and contralateral sides. The IPD functions obtained from IC neurons vary in shape [Fig. 3 of Yin and Kuwada (1983a)]. Some of them have a single prominent peak in one phase cycle, while others have more than one peak in a cycle. When the stimulus frequency is changed, the shape of the IPD functions may change (Yin and Kuwada, 1983b). Besides the binaural properties, monaural tone stimuli have also been applied to study the phase locking of the IC neurons (Kuwada *et al.*, 1984). In this section, the ITD sensitivities of IC neurons to tone stimuli at various frequencies and their phase-locking properties were simulated.

1. ITD functions

The pure-tone stimuli in the simulation were 65-dB sine waves with a duration of 3 s. The frequency of the tone was at the characteristic frequency (CF) of the model neuron, which was 500 Hz, unless otherwise indicated. Only one sweep of the stimulus was presented. The response rate for each ITD was calculated from the number of action potentials during the last 2 s of the stimulus. The parameters of the MSO and IC model neurons were identical to those used in the Cai *et al.* (1998) model for corresponding stimuli. The
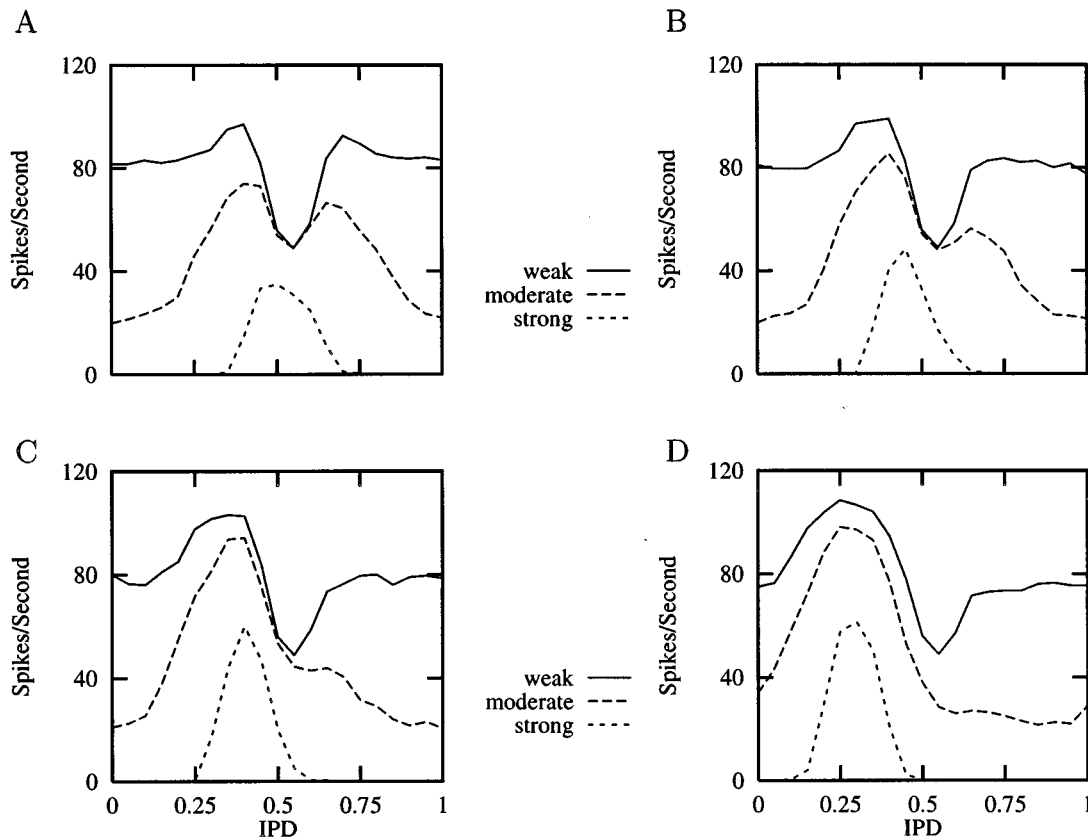
FIG. 4. IPD functions of the IC model neurons when the inhibition to the IC was varied. The CDs of the contralateral MSO model neurons were -60 μs (A), 50 μs (B), 150 μs (C), and 400 μs (D).

inhibitory input parameters to the IC were systematically varied so that three levels of inhibition were obtained: weak, moderate, and strong, as in Cai et al. (1998).

The IPD functions of the IC model neurons with four different characteristic delays (CDs) of the contralateral MSO model neuron are shown in Fig. 4. At a high excitatory input rate, the response of the IC saturated at a low rate. Therefore none of the IPD functions followed that of the ipsilateral MSO model neuron, which had a maximum response rate of about 230 spikes/s, even when the inhibition was weak or nonexistent. Both unimodal and bimodal ITD functions were generated with different inhibition levels. Compared with the results from the earlier model (Cai et al., 1998), the overall response rate of these neurons decreased dramatically when the AHP mechanism was incorporated, especially the response rates near the peaks of the IPD function of the ipsilateral MSO model neuron. The basic properties of the IPD functions are consistent with physiological data for both models.

2. Changing stimulus frequency

The ITD functions of the IC model neurons at three frequencies, 400, 500, and 600 Hz, were generated. The stimulus intensity and duration were the same as those in previous simulations. Figure 5 shows the ITD functions of the ipsilateral MSO and IC model neurons (with the CD of the contralateral MSO model neuron at 50 μs) at the three frequencies. These IC model neurons are the same as those

of which the responses are shown in Fig. 4(B). The ITD functions of the ipsilateral MSO model neuron [Fig. 5(A)] were sinusoidlike functions with a frequency equal to the stimulus frequency. By visual inspection, these functions showed a common peak at the CD of the model neuron, which was 100 μs, and the relationship between the mean interaural phase of the response and the stimulus frequency is linear. The ITD functions of the IC model neurons, however, did not show a common peak at a certain ITD [Fig. 5(B), (C), and (D)]. None of the ITD functions of these IC model neurons followed that of the ipsilateral MSO model neuron because of both the adaptation mechanism and the inhibition from the contralateral MSO model neuron. For an IC model neuron with only excitation from an ipsilateral MSO model neuron with a low response rate, such that the response of the IC model neuron was not saturated, the peaks of ITD functions at different frequencies would be at the same ITD, as in the MSO model neurons.

3. Phase locking to monaural stimuli

The phase locking of the IC model neurons was studied in the same way as the earlier model (Cai et al., 1998). A monoaural tone of 500 Hz was used in the simulation. Figure 6 shows the mean synchronization index of the ipsilateral MSO model neuron and IC model neurons with weak, moderate, and strong inhibition. The CD of the ipsilateral MSO was 100 μs and that of the contralateral MSO was 50 μs. Two values of the excitatory synaptic strength were studied, i.e., 25 and 16 nS. The synchronization index of the IC
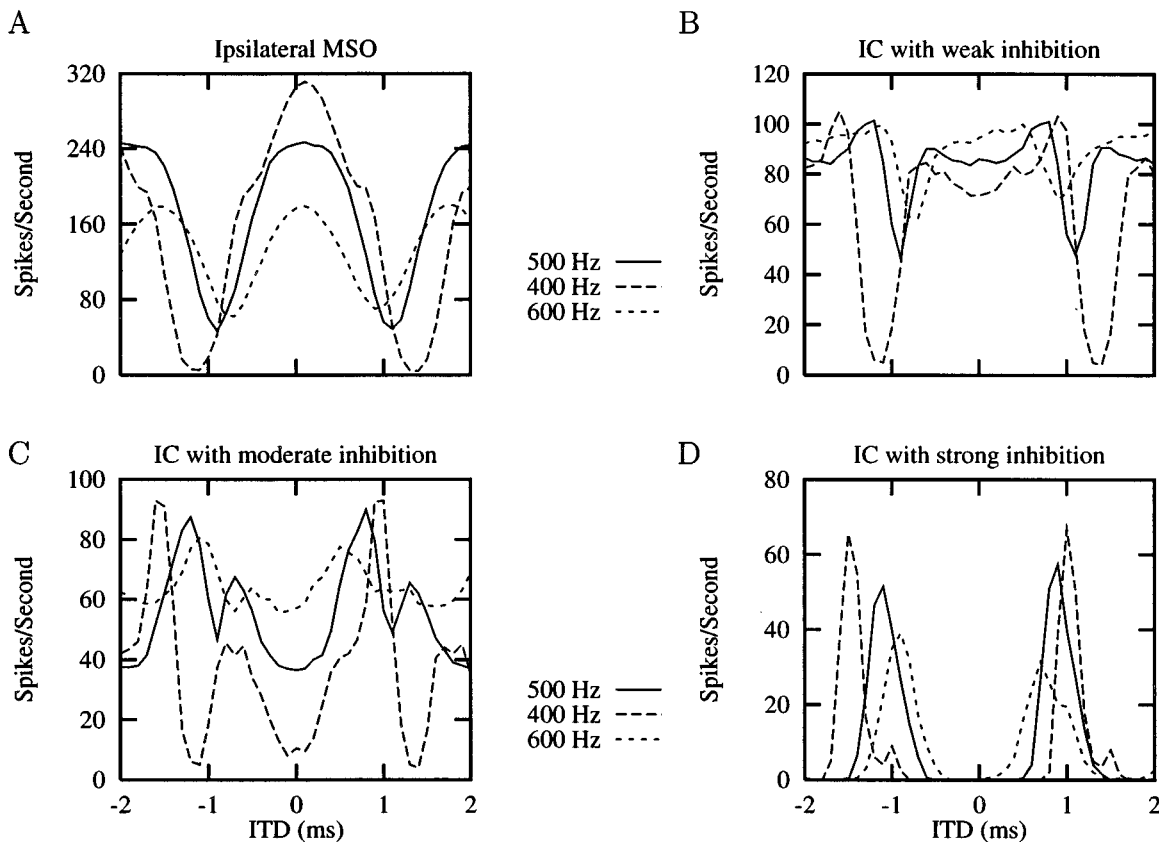
FIG. 5. ITD functions of ipsilateral MSO and IC model neurons at different frequencies.

model neuron with strong inhibition and excitatory synaptic strength of 16 nS was not plotted, because the calculated index did not pass the Rayleigh test (Cai *et al.*, 1998; Mardia, 1972). It can be seen that in both cases, the synchronization indices of the IC model neurons were slightly lower than those of the ipsilateral MSO model neuron. The synchronization index decreased as the inhibition became stronger. The decrease of phase locking was greater in the case of 16 nS, when the relative inhibition was stronger.

The membrane potential was also influenced by the his-
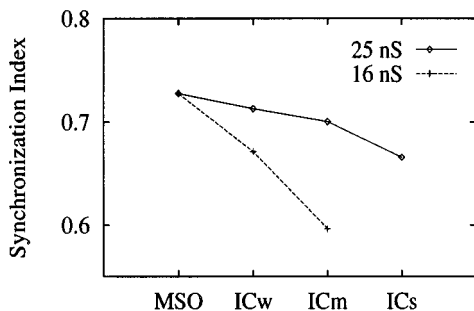
FIG. 6. Synchronization index of ipsilateral MSO and IC model neurons. The excitatory synaptic strengths were 25 and 16 nS. The IC model neurons with weak, moderate, and strong inhibition are represented by ICw, ICm, and ICs, respectively. The synchronization index of ICs at 16 nS is not shown due to the failure of the Rayleigh test (Cai *et al.*, 1998; Mardia, 1972). The CD of the ipsilateral MSO was 100 μs, whereas that of the contralateral MSO was 50 μs. The synchronization index was the average of those obtained from monaural stimuli of the two sides. Stimulus was a 500-Hz monaural tone with a duration of 3 s.

tory of the response of the neuron. The variation in membrane potential affected the time of firing and thus the phase locking. In this case, both inhibition to the IC and the adaptation mechanism contributed to the decrease of phase locking. Therefore the synchronization index was lower in the model with AHP than in the model without AHP (Cai *et al.*, 1998). In neither case, however, was the decrease of phase locking in the IC model neurons with respect to MSO model neurons comparable with that observed in physiological data.

D. Responses to binaural beat stimuli

The binaural beat stimulus in this study consisted of two tones presented to the two sides of the model, one at 500 Hz and the other at 501 Hz, unless otherwise indicated. The IPD functions obtained from binaural beat stimuli were referred to as dynamic IPD functions, whereas those obtained from pure tones were referred to as static IPD functions.

1. Comparison of dynamic and static IPD functions

The comparisons of dynamic and static IPD functions of IC neurons can be found directly or indirectly in the literature. Normalized dynamic and static IPD functions were given in Yin and Kuwada (1983a, their Fig. 3). The dynamic functions appear sharper than the static ones in that the amplitude differences between peaks and troughs are usually larger in the dynamic functions. For one neuron, both the peristimulus time (PST) histogram of responses to binaural beat stimulus and the ITD function of tone responses are given [Fig. 2 of Yin and Kuwada, (1983a)], the absolute (not normalized) response
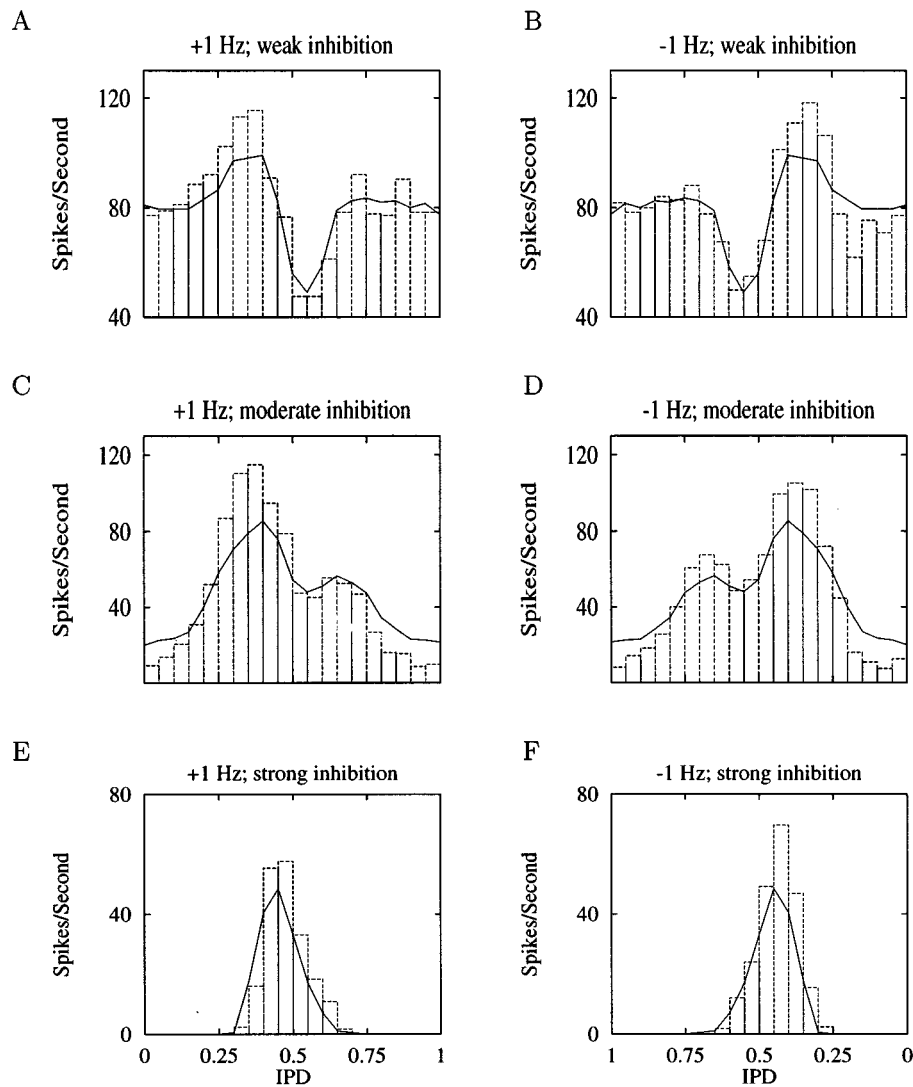
FIG. 7. Dynamic IPD functions (bars) of IC model neurons obtained from binaural beat stimulus along with the static IPD functions (solid curves) obtained from tone stimulus. The beat frequency and the inhibition level to the IC are indicated on the top of each panel.

rates of the dynamic IPD function could be calculated and compared with the static function. Results show that the peak response rate obtained from the binaural beat stimulus (about 96 spikes/s) is much larger than that obtained from the tone stimulus (about 75 spikes/s). A more direct comparison of the dynamic and static IPD functions was provided by Spitzer and Semple (1991), who showed results in an IC cell for which the peak of the dynamic function was twice as high as that of the static function.

The dynamic IPD functions of the IC model neurons with weak, moderate, and strong inhibitions are shown in Fig. 7. Consistent with physiological data, the dynamic IPD functions had the same general shape as the static ones; however, the exact response rates were different between the two functions. The dynamic functions were sharper than the static functions, as observed in real IC neurons (Yin and Kuwada, 1983a; Spitzer and Semple, 1991). At the peak of the IPD function, the response to the dynamic-IPD stimulus was higher than that to the static one. At the trough of the function, the opposite was true. For a given IPD, the difference in the stimuli was the history of temporal features. For

tone stimuli, the IPD was kept constant during the entire stimulus duration, while for binaural beat stimuli, the IPD changed with time. The model neuron tended to respond less strongly if it had responded strongly in its recent history (which could be hundreds of milliseconds or even seconds). The adaptation mechanism enabled the model neuron to "remember" the history or context of its responses.

2. Rate and direction sensitivities

Some IC neurons are sensitive to the direction and/or the speed of binaural beat stimuli (Yin and Kuwada, 1983a). The responses of such neurons were modeled by choosing different input parameters for the IC model neuron. Figure 8 shows the responses of the model neuron, which had the same parameters as the one in Cai *et al.* (1998) which showed rate and direction sensitivities. This model neuron responded strongly at a lower beat rate and negative beat frequency. In this model, the long-lasting inhibitory effect was still the key for direction and rate sensitivities. The adaptation mechanism did not have much effect on these sen-
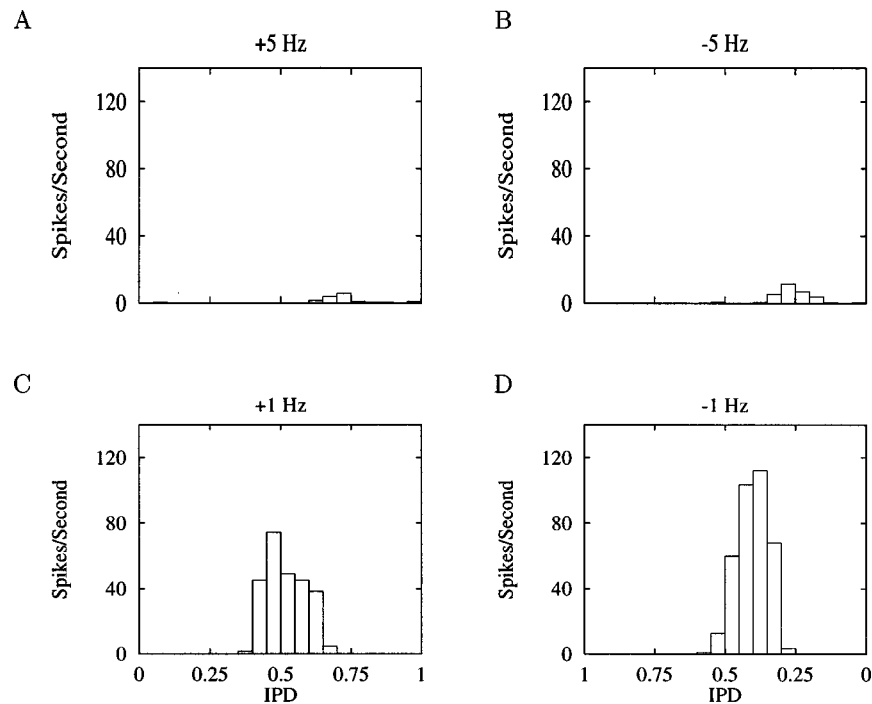
FIG. 8. IPD functions of a direction- and rate-sensitive IC model neuron. The neuron responded more vigorously when the rate of the binaural beat was slow and when the direction of the beat was towards the ipsilateral ear (-1-Hz beat frequency).

sitivities of the IC model, except for small effects on the overall response rate at a beat frequency of ± 1 Hz. This model shows some of the properties observed in the physiological data, but not all (cf. Cai *et al.*, 1998).

E. Responses to interaural phase-modulated (IPM) stimuli

The IPM stimulus is different from the binaural beat stimulus in the extent of the phase variation. For the binaural beat stimulus, the IPD in each beat cycle spans a fixed range of 360°, while in the IPM stimulus, both the range and the mean of the IPD could be varied.

The effect of context or history on IPD-tuning properties was examined by comparing the responses over equivalent ranges of IPD presented within the context of different dynamic stimuli (Spitzer and Semple, 1993, reprinted in Fig. 9). It was found that the IPD functions in each partially overlapping IPD range were nonoverlapping. When compared with the static IPD function obtained from tone stimuli, these functions often showed an ''overshoot'' (at the rising edge) or ''undershoot'' (at the falling edge). These data could not be described by our earlier model (Cai *et al.*, 1998).

In the simulation, the interaural phase disparity was a triangular waveform with a constant offset, as it was in Spitzer and Semple (1993). The carrier frequency of both tones was set at the CF of the model neuron (500 Hz). The modulation frequency was 2 Hz with a modulation depth of 90° at various phase offsets. These parameters were chosen such that the IPD changed at the same speed as in the simulations of binaural beat stimuli and as that used in physiological experiments (Spitzer and Semple, 1993), which was 360°/s. A sequence of stimuli was presented with phase off-

set from 45° to 315°, with a step of 45°. Since the step of phase offset equals one-half of the modulation depth (90°), the IPD ranges shared one-half of the entire modulation depth with adjacent stimuli.

The duration of the stimulus was 10 s, and it was repeated four times. The PST histograms of the last 9 s were averaged and converted to an IPD function. The IC model input parameters were identical to those used in the simulation of responses to binaural beat stimuli and to those used in Cai *et al.* (1998) for the simulation of the same responses, except for the addition of the AHP-related conductance.

To compare the responses to overlapping IPD regions, profiles of the individual period histograms are plotted on a common IPD axis. Figure 10 shows the IPD sensitivities of three model neurons, with ''weak,'' ''moderate,'' and
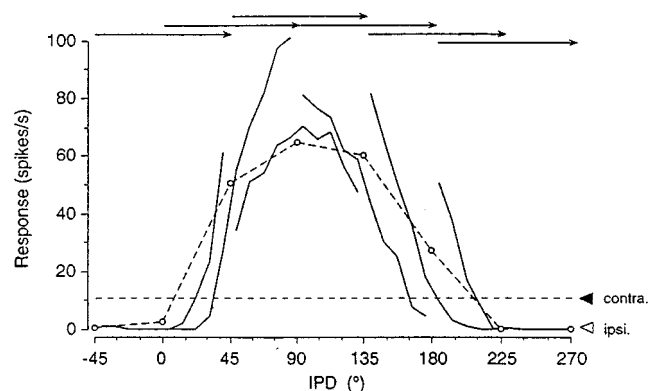
FIG. 9. IPD functions (solid curves) of an IC neuron in response to IPM stimuli, along with the static IPD function (dashed curve). [From Fig. 7 of Spitzer and Semple (1993) reprinted with permission.]
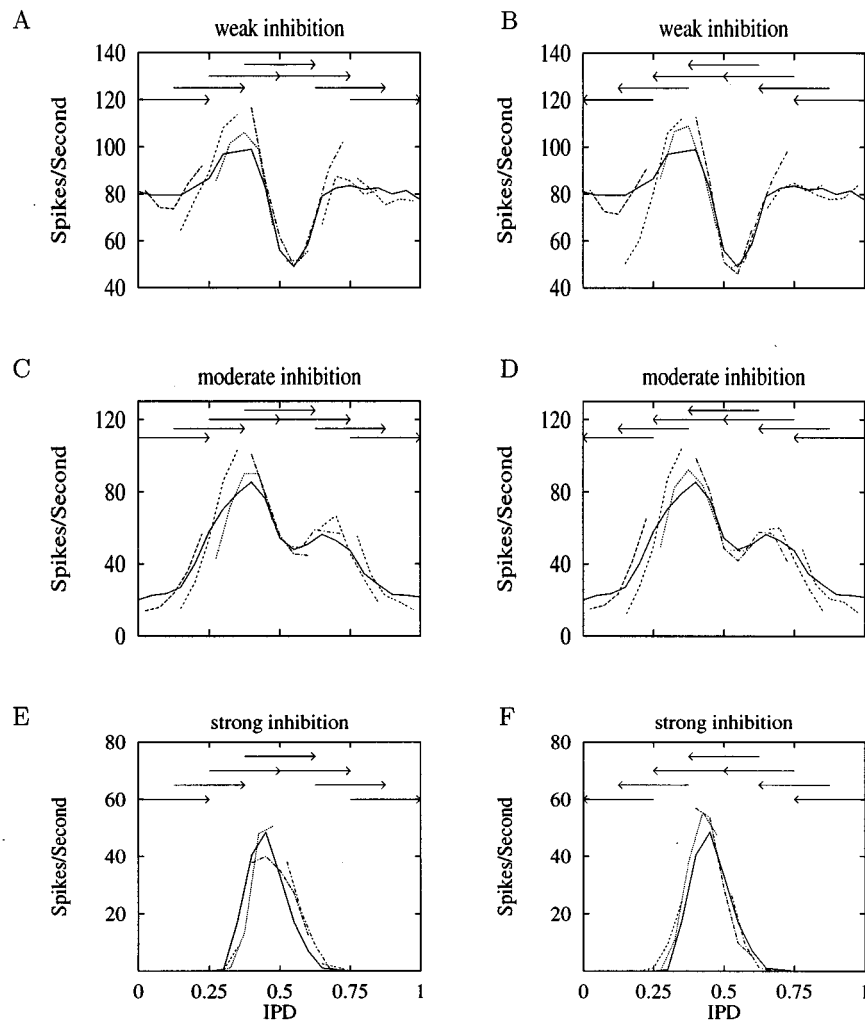
FIG. 10. IPD functions of three model neurons with ''weak inhibition'' [(A) and (B)], ''moderate inhibition'' [(C) and (D)], and ''strong inhibition'' [(E) and (F)], obtained from IPM stimuli (dashed curves). The solid curves are the static IPD functions obtained from a 3-s tone. Arrows on the top show the range and direction of IPD change in IPM stimuli. The rate of IPD change was 360°/s.

''strong'' inhibition, in response to IPM stimuli (dashed curves), along with their static IPD functions (solid curves). Curves on the left column correspond to increasing IPD, while those on the right correspond to decreasing IPD. It can be seen that the profiles of IPD in response to IPM stimuli did not overlap with each other, although the trend of the group of profiles followed the general shape of the static IPD function. The discharge rate at any given IPD depended on the recent history of the stimulus. A systematic relation between the discharge rate in IPM and in static IPD exists such that the dynamic IPD arcs were always steeper than the static IPD function, no matter which direction the IPD changed. If the profiles for the two directions (left-hand panel and right-hand panel) of a neuron were plotted together, they would not be identical. This result is not surprising since the recent history was different for IPD changes in opposite directions. The same phenomenon has been observed in physiological data (Spitzer and Semple, 1993, Fig. 9).

The degree of discontinuity between the static IPD function and dynamic IPD profiles varied over the IPD range (from zero to unity). For example, from panels (A) and (B)

of Fig. 10, it seems that the difference between dynamic IPD profiles and the static IPD function near an IPD of 0.55 (the trough of the curve) was not so apparent as those elsewhere. Since the slope near the trough of the static IPD function was sharper than anywhere else on the curve, the impact of changing IPD was not as obvious. Thus there was a limit of maximum response-rate change for a given set of parameters of the IC model. When the rate change or slope approached this limit, the effect of dynamic temporal features was not apparent.

Although the majority of neurons (more than 90%) is sensitive to dynamic stimulus features, the sensitivity varied among these units (Spitzer and Semple, 1993). The three model neurons in Fig. 10 also showed different sensitivity to temporal stimulus features. The one with ''strong inhibition'' [Fig. 10(E) and (F)] was the most insensitive neuron of the three. The low overall response rate and sharp IPD tuning were the causes of the relative insensitivity. Different AHP parameters, e.g., the time constant and conductance increment, might also result in different sensitivities for dynamic

IPD variation. Variations in these parameter values were not explored.

III. DISCUSSION

Simulation results demonstrated that the IC model with an adaptation mechanism was able to simulate diverse physiological data of the IC, including the responses of IC neurons to depolarizing current injection, pure tones, binaural beat stimuli, and interaural phase-modulated tones. In particular, this model was able to simulate response properties that were not described by the IC model without the adaptation mechanism (Cai et al., 1998), including the adapting discharge patterns in response to current injection and the sensitivities to dynamic temporal features.

Based on the physiological model in Cai et al. (1998), a single channel added to the membrane equation is adequate in describing these features of the IC. If a generic model were used, the modification might be more complicated and less physiologically interpretable.

A. Adaptation in the IC

Although the sensitivity of IC neurons to interaural delay has been studied in detail, both with tone stimuli and binaural beat stimuli, the difference between the static and dynamic IPD functions has received little attention. The adaptation of IC neurons as reflected in the response rate has been observed not only in the binaural responses, but also in monaural responses. For example, neuron 78197-5 in Kuwada et al. (1984) showed a slow adaptation in response to a 1-s tone applied to the contralateral ear.

A model for an IC neuron that included an afterhyperpolarization current (I_{AHP}), simulating a calcium-activated, voltage-independent potassium current, was able to show the adaptation observed in physiological data. The I_{AHP} has been found in many sites of the nervous system in different species, e.g., bullfrog sympathetic neurons (Pennefather et al., 1985), hippocampal pyramidal neurons (Sah and Isaacson, 1995), rat skeletal muscle (Romey and Lazdunski, 1984; Blatz and Magleby, 1986), neuroblasma cells (Hugues et al., 1982) and vagal motoneurons in the guinea pig (Sah, 1995). However, it is not known whether a calcium-activated, voltage-independent potassium channel exists in the IC. The afterhyperpolarization, which has been observed in the intracellular recordings of the IC (Nelson and Erulkar, 1963), could also be explained by a slow inhibitory postsynaptic potential. If this were true, then there would be three candidates for the inhibitory inputs to the IC.

First, intrinsic inhibitory circuitry might exist within the IC. Immunocytochemistry studies demonstrated that up to 20% of the neurons in the central nucleus of the IC are GAD- or GABA-positive (Oliver et al., 1994). Since most, if not all, of the neurons in the IC contribute local axonal collaterals (Oliver and Morest, 1984; Oliver et al., 1994), the GABAergic neurons in the IC are expected to contribute to local inhibitory synapses. Many GABA-positive neurons are large or medium sized. Some of them have processes oriented in parallel with the fibrodendritic laminae; therefore, these neurons may be disk-shaped cells with axons confined to the lamina of origin. Hence it is possible that they provide a delayed suppression to other neurons with similar CF.

Second, the input might come from the corticofugal pathway. Anatomical studies have demonstrated cortico-thalamic, cortico-collicular, and colliculo-olivary efferent pathways. Recent tract-tracing studies in the cat have demonstrated descending projections from the auditory cortex to all subdivisions of the IC, including the central nucleus (Feliciano and Thompson, 1995). It was shown that electrical stimulation of the primary auditory cortex (AI) inhibited the acoustically evoked responses of neurons in the inferior colliculus in bats (Sun et al., 1989). Electrical stimulation of the AI of the cat also generated excitatory postsynaptic potentials (EPSPs), inhibitory postsynaptic potentials (IPSPs), or EPSP-IPSP sequences in IC neurons (Mitani et al., 1983).

Third, the inhibitory input from the ascending pathway, e.g., from DNLL, is a possible source. The GABAergic synapse from the DNLL contributes to one third of the GABAergic synapses in the IC (Shneiderman et al., 1988).

The responses of the inhibitory input to the IC must be highly correlated with those of the neuron to which it is projecting. Otherwise, the dynamic responses may not follow a consistent rule when compared with the static IPD sensitivity. If the two neurons are highly correlated, a simple neural circuit to implement this function would have the IC neuron send inhibition to itself with a short delay simulating the neural transmission time. This recurrent inhibition can be modeled in exactly the same way as the AHP in the simulation presented in this study, except that the reversal potential of the channel associated with the AHP may not be the potassium equilibrium potential. The simulation result should be similar to that obtained in this study.

It is important to note that this inhibition cannot replace the inhibition from the contralateral MSO in the model. This inhibition cannot explain the ITD-dependent echo suppression observed in the IC, since internal inhibition linked to the cell would allow only the leading stimulus with an ITD that evokes a strong response to be more suppressive. Although no data are available on both the ITD dependence of echo suppression and IPM response from a single IC neuron, it is unlikely that the adaptation and echo suppression originate from the same source. The former is much weaker than the latter. The neural mechanism that causes dynamic sensitivity requires further study.

There are several other ways of creating neural modulation, including changes in the amount of neurotransmitters released at presynaptic sites; changes in the synthesis, transport, and processing of neurotransmitters; and changes in the conductances of ion channels of the membrane. It is unlikely that the neural modulation (or adaptation) in the IC is completely caused by these factors, since adaptation was observed with the injection of depolarizing currents (Peruzzi and Oliver, 1995), which were not related to neurotransmitters. The postsynaptic adaptation mechanisms include prespike (e.g., M current) and postspike (e.g., AHP current) mechanisms. The M current is activated at a membrane potential between the resting potential and the threshold of action potential, whereas the AHP current is activated by calcium influx during an action potential. These two

TABLE I. Summary of the abilities of MSO (Brughera *et al.*, 1996), IC model without adaptation (Cai *et al.*, 1998), and IC model with adaptation as described in this paper. "√" indicates that the model can describe the property of data. "×" indicates that it cannot.

Properties	MSO	IC without adaptation	IC with adaptation
Unimodal ITD functions	√	√	√
Early or late inhibitions	√	√	√
Bimodal ITD functions	×	√	√
Direction and rate sensitivity	×	√	√
ITD-dependent echo suppression	×	√	√
Sharpened dynamic IPD functions	×	×	√
Adapting discharge pattern	×	×	√

mechanisms can be differentiated by measuring the potassium current before and after an action potential and measuring the potassium current at different voltage clamp levels. They can also be separated by applying different antagonists. Experiments such as these have not been reported.

B. Adaptation and binaural sluggishness

The adaptation mechanism included in this model might be hypothesized to affect sound localization ability, especially the localization of a moving sound source, to emphasize changes in the acoustic environment. It has been shown both empirically and in simulation that the dynamic IPD functions are sharper than the static functions. Provided that the response rate of an ensemble of IC neurons is an indication of a sound source in the azimuthal plane (Yin, 1994), the localization of a sound source moving within a given range in azimuth should be perceived moving in a wider range, if the rate of movement is high enough. It was found in psychophysics that when a sound motion was too fast to be followed, a ''wider'' or ''more diffused'' image was perceived (Grantham and Wightman, 1978). This finding is consistent with expectations from this model.

Psychophysical studies show that the auditory system responds sluggishly to changes in the interaural differences (Grantham and Wightman, 1978) and to the motion of a sound source (Blauert, 1972). Specifically, when a sound source moves rapidly, the motion can not be followed ''in detail.'' It is not clear whether the adaptation in the IC is related to the mechanism of binaural sluggishness. Psychoacoustic experiments (Grantham and Wightman, 1978) lead to estimates of frequency cutoff of the binaural system of about 10 Hz, corresponding to a time constant of about 16 ms, which is much shorter than the time constant of adaptation (500 ms) in the model. Thus the adaptation in the IC seems to be too slow to be responsible for binaural sluggishness.

A recent study by Joris (1996) explored the possible correlation between physiology and psychoacoustics related to binaural sluggishness. Interaural-correlation-modulated stimuli, similar to those used by Grantham (1982), were presented to anesthetized cats. Single-cell recordings were made from IC neurons. The function relating sensitivity to modulation, represented by the synchronization index versus the modulation frequency, shows a cut-off frequency near 50 Hz on average. The cutoff frequency is much higher than that measured psychophysically by Grantham and Wightman

(1978), and indicates that sluggishness is probably due to mechanisms at higher levels in the auditory pathway.

C. Comparison with previous models

A trend in neural modeling is to include more physiological details in the models. The physiologically based models available so far that are most relevant to the model presented in this paper are the MSO model by Brughera *et al.* (1996) and the IC model by Cai *et al.* (1998). The difference between the IC model of Cai *et al.* (1998) and the IC model in this paper is that the current IC model incorporated an adaptation mechanism. The abilities of these three models are summarized in Table I.

The MSO model (Brughera *et al.*, 1996) can show unimodal ITD sensitivities in response to binaural tone stimuli and binaural beat stimuli. It can also show early or late inhibitions in response to binaural clicks.

In addition to properties demonstrated by the MSO model, the IC model without the adaptation mechanism (Cai *et al.*, 1998) shows bimodal IPD functions with some choices of the inhibitory parameters from the contralateral MSO. It may also show sensitivity to the direction and the speed of the binaural beat stimulus, when the contralateral inhibition lasts for a long time (tens of milliseconds). In response to pairs of binaural clicks, the model neuron showed ITD-dependent echo suppression. The responses of this model to depolarizing current injections show regular discharge patterns.

The IC model with the adaptation mechanism demonstrated sensitivities to dynamic temporal features not shown by the IC model without the AHP mechanism. These sensitivities are represented by the nonoverlapping IPD profiles in response to interaural phase-modulated stimuli, by a sharpened IPD function obtained from binaural beat stimulus, and by the changing response rate in the course of current injection. All of these features have been observed in physiological studies of the IC. The responses of the model to transient stimuli were not changed as compared with the Cai *et al.* (1998) model, since the adaptation mechanism had little effect if it was triggered infrequently.

Both of the IC models showed a decrease in phase locking to monaural stimuli as compared with the MSO model. In the current IC model, further decrease of phase locking was contributed by the adaptation mechanism; therefore the decrease in the synchronization index was more obvious.

However, the degree of phase locking was still high compared with physiological data.

In the current IC model, the excitatory inputs to the IC from ITD-sensitive neurons were responsible for the unimodal or sinusoid-like ITD functions of the IC. The inhibition to the MSO from onset cells was the cause of early inhibition observed in the IC model neuron. The inhibition to the IC from ITD-sensitive neurons was important for the behavior of the model that distinguished the IC from MSO, such as the bimodal ITD functions, ITD-dependent echo suppression, and direction and/or rate sensitivities. This inhibition was also the source of late inhibition in the simulation of the responses to binaural clicks. The adaptation mechanism was important for producing adaptive discharge patterns and sharpened dynamic IPD functions.

Alternative structures of models for the IC exist and could be evaluated. For example, an IC model which receives excitatory input from an ITD-sensitive neuron and inhibitory input from a monaural neuron should be able to describe unimodal ITD functions, early inhibition and late inhibition. If it has an adaptation mechanism, it will also describe adaptive discharge patterns and sharpened ITD functions. It will not explain the ITD-dependent echo suppression, the direction/rate sensitivities, and bimodal IPD functions. A MSO model with inhibition and an adaptation mechanism would show the same properties as this alternative IC model, including unimodal ITD function, early and/or late inhibition, adapting discharge patterns, and sharpened ITD functions.

D. Tests of the model and model predictions

The current model can be modified to address the simplifying assumption of the relay at DNLL. With a better understanding of the responses of the DNLL neuron, a model of the DNLL could be built and incorporated as an input to the IC model. It is expected that such a model would simulate more properties of the IC, such as the strong onset inhibition.

The mechanisms of the model could be tested with several types of physiological experiments. The hypothetical mechanism for the adapting behavior following discharge of the IC neuron is afterhyperpolarization caused by a calcium-activated, voltage-independent potassium channel. It would be of interest to test this hypothesis by blocking the calcium influx. If the adaptation is not calcium dependent, other channels or mechanisms might be responsible.

In the current models, it is assumed that the early inhibition comes from monaural neurons. This assumption can be tested by applying a binaural click following a monaural click. The bimodal ITD functions and direction and/or rate sensitivities in the responses of the model are caused by the interaction of excitatory and inhibitory ITD-sensitive neurons. This mechanism can be tested by blocking the inhibitory inputs to the IC.

The model can be used to predict the results of physiological experiments. First, since the ITD-dependent echo suppression is presumably caused by the inhibition from binaural neurons, the recovery curve with a monaural leading click should fall between those of the strongest and weakest suppressions obtained with binaural leading clicks with varied ITDs, based on the fact that the monaural response rate of a binaural neuron falls within the range of the responses to its bad ITD and good ITD. Second, short binaural noise bursts with various durations on the order of a few milliseconds followed by binaural clicks at good ITDs could be presented at varied interstimulus delay. If these stimuli were presented to the neurons which show long-lasting ITD-dependent echo suppression and sustained responses to long-lasting stimuli, it is predicted that the recovery function for different noise burst durations would not differ, since the inhibition to the IC is presumed to be driven by the stimulus onset. Third, if long-duration binaural tone bursts (e.g., 50 ms in duration) followed by short binaural tone bursts (e.g., 5 ms) were presented to direction or rate-sensitive neurons, keeping the ITD of the lagging tone at a good ITD and varying the ITD of the leading tone, it is predicted that the responses to the lagging tone would depend on the ITD of the leading tone, due to the rate-dependent nature of the afterhyperpolarization adaptation mechanism.

IV. CONCLUSION

The incorporation of an adaptation mechanism made it possible for the model to simulate the sensitivity of IC neurons to dynamic temporal features such as modulation of interaural phase and the adapting discharge patterns in response to current injection. At the same time, this mechanism did not deteriorate the abilities of our previous IC model (Cai *et al.*, 1998) which does not include an adaptation mechanism.

In conclusion, models for IC neurons with simple structures are consistent with a large amount of physiological data. These models contribute to our understanding of several mechanisms involved in binaural processing. In order to show essentially all the observed properties of IC discharge patterns, a model requires ITD-sensitive excitatory input, ITD-sensitive inhibitory input, and an adaptation mechanism such as afterhyperpolarization.

Blatz, L. A., and Magleby, K. L. (**1986**). ''Single apamin-clocked Ca-activated K+ channels of small conductance in cultured rat skeletal muscle,'' Nature (London) **323**, 718–720.

Blauert, J. (**1972**). ''On the lag of lateralization caused by interaural time and intensity differences,'' Audiology **11**, 265–270.

Brughera, A. R., Stutman, E. R., Carney, L. H., and Colburn, H. S. (**1996**). ''A model with excitation and inhibition for cells in the medial superior olive,'' Aud. Neurosci. **2**, 219–233.

Cai, H. (**1997**). ''Models for the binaural response properties of inferior colliculus neurons,'' dissertation, Boston University.

Cai, H., Carney, L. H., and Colburn, H. S. (**1998**). ''A model for binaural response properties of inferior colliculus neurons: I. A model with interaural time difference sensitive excitatory and inhibitory inputs,'' J. Acoust. Soc. Am. **103**, 475–493.

Carney, L. H. (**1993**). ''A model for the responses of low-frequency auditory-nerve fibers in cat,'' J. Acoust. Soc. Am. **93**, 401–417.

Carney, L. H., and Yin, T. C. T. (**1989**). ''Responses of low-frequency cells in the inferior colliculus to interaural time differences of clicks: Excitatory and inhibitory components,'' J. Neurophysiol. **62**, 144–161.

Colburn, H. S., and Ibrahim, H. (**1993**). ''Modeling of precedence effect behavior in single neurons and in human listeners,'' J. Acoust. Soc. Am. **93**, 2293(A).

Feliciano, M., and Thompson, A. M. (**1995**). ''Descending auditory cortical projections to midbrain and brainstem auditory structures in the cat,'' Assoc. Res. Otolaryngol. Abstr. **18**, 163.

Fitzpatrick, D. C., Kuwada, S., Batra, R., and Trahiotis, C. (**1995**). ''Neural responses to simple simulated echoes in the auditory brain stem of the unanesthetized rabbit,'' J. Neurophysiol. **74**, 2469–2486.

Grantham, D. W. (**1982**). ''Detectability of time-varying interaural correlation in narrow-band noise stimuli,'' J. Acoust. Soc. Am. **72**, 1178–1184.

Grantham, D. W., and Wightman, F. L. (**1978**). ''Detectability of varying interaural temporal differences,'' J. Acoust. Soc. Am. **63**, 511–523.

Hugues, M., Romey, G., Duval, D., Vincent, J. P., Lazdunski, M. (**1982**). ''Apamin as a selective blocker of the Ca-dependent K channel in neuroblastoma cells. Voltage-clamp and biochemical characterization,'' Proc. Natl. Acad. Sci. USA **79**, 1308–1312.

Joris, P. X. (**1996**). ''Brainstem responses to modulated interaural cues,'' Acustica **82**, Suppl.1, S97.

Kuwada, S., and Yin, T. C. T. (**1983**). ''Binaural interaction in low-frequency neurons in inferior colliculus of the cat. I. Effects of long interaural delays, intensity, and repetition rate on interaural delay function,'' J. Neurophysiol. **50**, 981–999.

Kuwada, S., Yin, T. C. T., Syka, J., Buunen, T. J. F., and Wickesberg, R. E. (**1984**). ''Binaural interaction in low-frequency neurons in inferior colliculus of the cat. IV. Comparison of monaural and binaural response properties,'' J. Neurophysiol. **51**, 1306–1325.

Litovsky R., and Yin, T. C. T. (**1993**). ''Single-unit responses to stimuli that mimic the precedence effect in the inferior colliculus of the cat,'' Assoc. Res. Otolaryngol. Abstr. **16**, 128.

Litovsky R., and Yin, T. C. T. (**1994**). ''Physiological correlates of the precedence effect: Free field recordings in the inferior colliculus of the cat,'' Assoc. Res. Otolaryngol. Abstr. **17**, 337.

Mardia, K. V. (**1972**). *Statistics of Directional Data* (Academic, London).

Mitani, A., Shimokouch, M., and Nomura, S. (**1983**). ''Effects of stimulation of the primary auditory cortex upon colliculogeniculate neurons in the inferior colliculus of the cat,'' Neurosci. Lett. **42**, 185–189.

Nelson, P. G., and Erulkar, S. D. (**1963**). ''Synaptic mechanisms of excitation and inhibition in the central auditory pathway,'' J. Neurophysiol. **26**, 908–923.

Oertel, D. (**1983**). ''Synaptic responses and electrical properties of cells in brain slices of the mouse anteroventral cochlear nucleus,'' J. Neurosci. **3**, 2043–2053.

Oliver, D. L., and Morest, D. K. (**1984**). ''The central nucleus of the inferior colliculus in the cat,'' J. Comp. Neurol. **222**, 237–264.

Oliver, D. L., Winer, J. A., Bechius, G. E., and Marie, R. L. S. (**1994**). ''Morphology of GABAergic neurons in the inferior colliculus of the cat,'' J. Comp. Neurol. **340**, 27–42.

Pennefather, P., Lancaster, B., Adams, P. R., and Nicoll, R. A. (**1985**). ''Two distinct Ca-dependent K currents in bullfrog sympthetic ganglion cells'' Proc. Natl. Acad. Sci. USA **83**, 3040–3044.

Peruzzi, D. (personal communication).

Peruzzi, D., and Oliver, D. L. (**1995**). ''Intrinsic membrane properties and morphology of neurons in the rat inferior colliculus,'' ARO, **18**, 515.

Romey, G., and Lazdunski, M. (**1984**). ''The coexistence in rat muscle cells of two distinct classes of Ca^{2+}-dependent K^+ channels with different pharmacological properties and different physiological functions,'' Biochem. Biophys. Res. Commun. **118**, 669–674.

Rothman, S. R., Young, E. D., and Manis, P. B. (**1993**). ''Convergence of auditory nerve fibers onto bushy cells in the ventral cochlear nucleus: implications of a computational model,'' J. Neurophysiol. **70**, 2562–2583.

Sah, P. (**1995**). ''Properties of channels mediating the apamin-insensitive afterhyperpolarization in vagal motoneurons,'' J. Neurophysiol. **74**, 1772–1776.

Sah, P., and Isaacson, J. S. (**1995**). ''Channels underlying the slow afterhyperpolarization in hippocampal pyramidal neurons: Neurotransmitters modulate the open probability,'' Neuron **15**, 435–441.

Shneiderman, A., Oliver, D. L., and Henkel, C. K. (**1988**). ''Connections of the dorsal nucleus of the lateral lemniscus: An inhibitory parallel pathway in the ascending auditory system?,'' J. Comp. Neurol. **276**, 188–208.

Spitzer, M. W., and Semple, M. N. (**1991**). ''Interaural phase coding in auditory midbrain: influence of dynamic stimulus features,'' Science **254**, 721–724.

Spitzer, M. W., and Semple, M. N. (**1993**). ''Responses of inferior colliculus neurons to time-varying interaural phase disparity: effects of shifting the locus of virtual motion,'' J. Neurophysiol. **69**, 1245–1263.

Sujaku, Y., Kuwada, S., and Yin, T. C. T. (**1981**). ''Binaural interaction in the cat inferior colliculus: comparison of the physiological data with a computer simulated model,'' in *Neuronal Mechanisms of Hearing*, edited by J. Syka and L. Aitkin (Plenum, New York), pp. 233–238.

Sun, X., Jen, P. H. S., Sun, D., and Zhang, S. (**1989**). ''Corticofugal influences on the responses of bat inferior collicular neurons to sound stimulation,'' Brain Res. **495**, 1–8.

Wu, S. H., and Oertel, D. (**1984**). ''Intracellular injection with horseradish peroxidase of physiologically characterized stellate and bushy cells in slices of mouse anteroventral cochlear nucleus,'' J. Neurosci. **4**, 1577–1588.

Yamada, W. M., Koch, C., and Adams, P. R. (**1989**). ''Multiple channels and calcium dynamics,'' in *Methods in Neuronal Modeling—From Synapese to Networks*, edited by Christof Koch and Idan Segev (MIT, Cambridge), pp. 97–133.

Yin, T. C. T. (**1994**). ''Physiological correlates of the precedence effect and summing localization in the inferior colliculus of the cat,'' J. Neurosci. **14**, 5170–5186.

Yin, T. C. T., and Kuwada, S. (**1983a**). ''Binaural interaction in low-frequency neurons in inferior colliculus of the cat. II. Effects of changing rate and direction of interaural phase,'' J. Neurophysiol. **50**, 1000–1019.

Yin, T. C. T., and Kuwada, S. (**1983b**). ''Binaural interaction in low-frequency neurons in inferior colliculus of the cat. III. Effects of changing frequency,'' J. Neurophysiol. **50**, 1020–1042.

Interpretation of distortion product otoacoustic emission measurements. II. Estimating tuning characteristics using three stimulus tones

David M. Mills[a)]

Department of Otolaryngology, Head & Neck Surgery, Virginia Merrill Bloedel Hearing Research Center, University of Washington, Box 359723, Seattle, Washington 98195-7923

The simple model introduced in Part I [J. Acoust. Soc. Am. **102**, 413–429 (1997)] is used to simulate the response of the cochlea to three stimulus tones. The focus is on ''emission suppression tuning curves'' constructed using a third tone to suppress the cubic distortion tone emission (CDT, $2f_1 - f_2$) generated by two primary tones at frequencies f_1 and f_2 (intensities L_1 and L_2). A criterion decrease (here, 5 dB) of the CDT emission amplitude defines the $2f_1 - f_2$ emission suppression tuning curve. Applying traditional tuning curve measures to emission suppression tuning curves appears ineffective in determining the underlying cochlear amplifier characteristics. However, it is shown that there are three characteristics of emission suppression tuning curves which are particularly useful: (1) the ''f_2 threshold'' which is the level of the third tone, L_3, required for the criterion CDT amplitude decrease, under the condition that the third tone frequency, f_3, is approximately equal to f_2; (2) the ''shoulder threshold'' similarly defined for $f_3 \ll f_2$; and (3) the ''tuning width,'' w_{40}. The tuning width is defined to be the distance (in octaves) from the frequency f_2 to the upper f_3 frequency for which there is a criterion CDT decrease, in this case using the L_3 level which is 40 dB above the f_2 threshold. Model calculations appropriate to gerbils show that these measures are most accurately related to the underlying cochlear amplifier characteristics for parameters where the primary stimulus amplitudes satisfy $L_1/L_2 > 20$ dB and for which L_1 is 25 dB or more below the sharp ''notch'' seen in the two tone input–output function. In this parameter region, the cochlear amplifier characteristics are related to measured quantities by the relationships $w_r \cong w_{40}$ and $G_a \cong T_E + w_{40}g_p$. Here, G_a is the gain (dB) of the cochlear amplifier, defined as the total increase in cochlear response over the passive response, w_r is the distance (octaves) over which the active cochlear response rises to a maximum, and g_p is the passive increase (dB/octave) of the traveling wave along the basilar membrane. The measured quantities are T_E, the difference (dB) between the shoulder threshold and the f_2 threshold, and the tuning width, w_{40} (octaves), defined above. Model predictions are confirmed by measurements in adult gerbils. © *1998 Acoustical Society of America.* [S0001-4966(98)01401-5]

INTRODUCTION

From their discovery, otoacoustic emissions have held the promise of elucidating some of the basic mysteries of mammalian hearing (Kemp, 1978). It is now well established that the presence of emissions at low stimulus levels in mammals is generally indicative of good cochlear function (e.g., Brown *et al.*, 1989; Rübsamen *et al.*, 1995). However, the goal of using emission measurements to determine the basic characteristics of cochlear amplifier function remains largely unmet (Davis, 1983).

These basic characteristics include the determination of the overall gain of the cochlear amplifier, which can be defined as the net improvement in hearing threshold over the passive cochlear response (Nuttall and Dolan, 1996; Ruggero and Rich, 1991). It is true that distortion product emissions using two stimulus tones can provide an estimate of the cochlear amplifier gain at any given frequency (Mills, 1997). However, the precise determination requires the invasive use

of an ototoxic agent such as furosemide, to temporarily interrupt the cochlear amplifier function. This limits its usefulness to laboratory animals. Further, two tone emission measurements cannot in general adequately distinguish moderate from severe cochlear amplifier dysfunction (Mills, 1997).

It now appears that two tone emission measurements also cannot provide accurate information on the other fundamental characteristic of the cochlear amplifier, the effective ''tuning width'' or equivalent measure of the sharpness of the peak response. It had been hoped that this information could be provided by measurements of the emission amplitude as a function of the stimulus frequency ratio, which appears to be in the form of a bandpass ''filter'' (Allen and Fahey, 1993; Brown and Gaskill, 1990; Brown *et al.*, 1993; Brown and Kemp, 1985). That is, the emission amplitude would be expected to decrease as the stimulus frequency ratio increased, because of the decrease in the amount of ''overlap'' between the two traveling wave patterns associated with each stimulus frequency.

While this decrease generally does occur, the interpretation in terms of intrinsic peak sharpness is confounded by a

---

[a)]Electronic mail: dmmills@u.washington.edu

number of factors. Perhaps most troubling is that, at least in some mammals, it is very difficult to determine the overall shape of the response as a function of stimulus frequency ratio because of the presence of a number of very sharp peaks in the response (Kössl *et al.*, 1996; Mills and Rubel, 1997). Also, the emission response seen in the ear canal decreases as the two stimulus frequencies become close together, but *not* the same distortion frequency measured psychoacoustically (e.g., Allen and Fahey, 1993). This is incompatible with a simple overlap model. The decrease in the ear canal may be related to the fact that, in addition to the main source located near the maxima of the primary stimuli, there is another apparent ''source'' of emission (Gaskill and Brown, 1996; Moulin and Kemp, 1996a, b; Stover *et al.*, 1996). This source is most prominent when the stimulus frequency ratio is near one.

The sharpness of tuning *can* be determined more centrally using neural frequency tuning curves or equivalent psychoacoustic measures of tuning (e.g., Moore *et al.*, 1984). However, the exact relationship between these measures and cochlear amplifier characteristics remains unclear (e.g., Abdala *et al.*, 1996). Further, central measures are dependent on neural function and cannot differentiate between cochlear amplifier dysfunction and subsequent neural dysfunction.

This situation has led to investigating the use of emissions with three stimulus tones to provide tuning information. Because of the noninvasive nature of the measurement, these measures are particularly useful in human studies (Abdala and Sininger, 1996; Abdala *et al.*, 1996; Brown and Kemp, 1984; Cianfrone *et al.*, 1994; Gaskill and Brown, 1996; Harris *et al.*, 1992; Kummer *et al.*, 1995; Williams and Brown, 1995). There have also been three tone measurements in rabbits (Martin *et al.*, 1987), rodents (Brown and Kemp, 1984; Kössl *et al.*, 1996), marsupials (Faulstich *et al.*, 1996), and bats (Frank and Kössl, 1995). In most of these studies, the paradigm has been to fix the two ''primary'' stimulus tones, and to monitor the emission amplitude from these tones. A third, ''suppressor'' tone is introduced, and stepped through a wide range in frequency and intensity. For some combinations of suppressor frequency and intensity, the measured emission amplitude decreases. Connecting those suppressor tone values which have the same criterion decrease in emission amplitude results in what has been termed a ''suppression tuning curve'' (e.g., Abdala and Sininger, 1996; Abdala *et al.*, 1996). To avoid possible confusion with tuning curves obtained from neural measurements, in this report tuning curves obtained using emissions will be termed ''emission suppression tuning curves'' or ''$2f_1-f_2$ suppression tuning curves'' (Frank and Kossl, 1995).

Emission suppression tuning curves often have a similar appearance to neural tuning curves. There is a minimum threshold, usually near the frequencies of the primaries, and the high-frequency slope is usually steeper than the low-frequency slope. However, these similarities can be misleading. There are several indications that these responses are *essentially* different.

The best frequency threshold of a neural tuning curve gives an indication of the sensitivity of the auditory system to low level signals. The threshold of an emission suppres-

sion tuning curve, on the other hand, depends almost entirely on the amplitude of the primary stimuli. Usually, the threshold is comparable to the weaker of the two primary stimuli (e.g., see Kössl *et al.*, 1996, Fig. 7-8). That is, the amplitude of the third tone required to suppress, by a criterion amount, the emission resulting from the primary tones for a third tone frequency near the primary stimulus frequencies is approximately equal to the weaker of the two primary stimuli. Further, the intrinsic scale of the emission response is set by saturation (Mills, 1997). It seems reasonable to associate saturation more with the high level response of the system than with the sensitive, low level response. [However, it should be noted that the effects of saturation *are* apparently evident even at very low levels, as linear responses of the basilar membrane are found only at levels *below* the neural threshold of hearing (Nuttal and Dolan, 1996).]

The width of the emission suppression tuning curve depends strongly on the ratio of the primary stimulus frequencies (Brown and Kemp, 1984). Presumably, the width and other aspects of the tuning curve also depend on the ratio of the stimulus intensities, but this possibility has not been investigated systematically in published studies.

Neither the width nor the threshold of an emission suppression tuning curve then have the same meaning as for a neural tuning curve. There is therefore no well established relationship between emission tuning curves and basic cochlear amplifier characteristics. Further, distortion product emission suppression tuning curves have a serious additional problem not faced by neural tuning curves. One must choose two particular primary stimulus tones from a possible four-dimensional space, i.e., the frequencies and intensities of both primary tones. There is no established, well-justified way of doing this. Sometimes, the primary stimulus frequency ratio is held constant and the stimulus amplitude ratio varied to find the maximum emission amplitude (e.g., Harris *et al.*, 1992). More often, fixed ratios for the primary frequencies and intensities are used, with the frequency ratio in the mid-range and the lower-frequency stimulus 10–15 dB more intense than that at the higher frequency. Neither approach has been justified in terms of the characteristics of the tuning curves obtained by these methods.

The remainder of this report is largely devoted to describing a procedure for the choice of primary stimulus parameters that is derived from basic considerations. To reasonably limit the complexity, a fixed, mid-range primary frequency ratio is assumed. However, the primary stimulus amplitude levels and ratios are allowed to vary widely. The analysis includes a determination of the characteristics of suppression tuning curves which should be measured, the relationship of these measures to the underlying fundamental cochlear amplifier response, and the expected accuracy of such measures.

In Part I (Mills, 1997), a simple model for emission generation was introduced and employed to assist in the interpretation of emission measurements using two stimulus tones. In Part II, the model is used to assist in the interpretation of three tone responses. Typical model results are compared with three tone measurements in several adult gerbils.

I. METHODS

Adult gerbils were anesthetized and prepared for emission measurements as described previously (Mills and Rubel, 1996). The high-frequency emission system used previously was modified for the addition of a third tone. As before, the two primary tones (f_1 and f_2) were synthesized by a computer so that the combined signal was exactly repeated once every 0.16 s. The microphone response was sampled at the rate of 100 kHz during a time segment of the same length, and sequential time segments summed in a 16k buffer. In this manner, the primary signals and all their distortion products were synchronously time averaged, for a total time of 2–4 s. In contrast, the third, or ''suppressor'' signal, while under computer control, was synthesized nonsynchronously by an external signal generator (HP 8409A, Hewlett Packard). Distortion products caused by the interaction of the suppressor tone with either of the primary tones were not generally detected in the FFT of the synchronously averaged signal. Further, the suppressor, or f_3, frequencies were carefully chosen so that there would be no direct interference with the cubic distortion tone detection at $2f_1 - f_2$. That is, spurious loading of the ($2f_1 - f_2$) bin of the FFT was avoided by consistently choosing suppressor frequencies, f_3, that were not too close to f_1 or f_2, and so that potentially strong emission frequencies such as ($2f_2 - f_3$) would not be too close to ($2f_1 - f_2$), etc.

After generation, all three signals were separately amplified by low-noise power amplifiers and led to separate tweeters in custom enclosures. The acoustic signals generated were separately led by tubes to a coupler described previously (Mills and Rubel, 1996). This coupler included a low-noise microphone (ER-10B, Etymotic) and a custom probe tube microphone (2541, Larson Davis). After sealing the coupler to the ear canal, a wide-band noise signal was introduced into the ear canal by one of the speakers, and the low-noise microphone response calibrated with reference to the probe tube microphone (Mills and Rubel, 1996). Distortion product measurements with both two and three tone stimuli were carried out under computer control, with sequences of tones presented automatically.

II. MODEL CALCULATIONS

A. Emission suppression tuning curves

In this section, the model described in Part I (Mills, 1997) is applied to cases with three stimulus tones. Briefly, this model allows the simulation of any number of stimulus frequencies, and the response at each frequency is assumed linear except in the region where the traveling wave is amplified by the cochlear amplifier. In this ''active'' region, the rate of gain of the wave traveling down the basilar membrane is limited by a physiologically reasonable saturation as its response amplitude increases. The only interaction assumed between the waves is due to this saturation. That is, the total amplitude of all waves present at any given point on the basilar membrane is assumed to determine the degree of saturation for a wave being amplified at that point. Distortion product emissions are assumed to be generated by the same nonlinearity that causes the saturation. Note that the cochlear

response given by the model is not necessarily equal to the basilar membrane response alone, but is assumed to reflect that dynamical variable which best measures the ability of the cochlear amplifier to improve hearing function. For example, this variable might be the deflection angle of the inner hair cell stereocilia relative to the cuticular plate. Note also that, for simplicity, the model does not include effects due to ''reflection'' or re-emission of the $2f_1 - f_2$ emission at its place. As this effect is only important at primary stimulus frequency ratios near unity (Stover et al., 1996), the ratio of the primary stimulus frequencies must satisfy $f_2/f_1 > 1.1$ for the model to be valid. For this report, $f_2/f_1 = 1.25$.

The model provides two natural scales, one for the amplitude of the cochlear response, and the other for the frequency. The saturation level defines the scale for the cochlear response amplitude. By definition, when the cochlear response is equal to the saturation level, y_{sat}, the cochlear amplifier rate of gain along the basilar membrane is reduced to 76% of the normal low-level rate of gain (Fig. 1C, Mills, 1997). By assuming a transparent middle ear, the stimulus amplitude can be directly related to this characteristic saturation level. For convenience in the present report, the level y_{sat} will be set equal to 100 dB, and all stimulus levels in model calculations will be in relationship to this level, with the reference level understood. That is, a stimulus level equal to ''100 dB'' will correspond to a stimulus which would cause at the base of the cochlea a cochlear response equal to the characteristic saturation level, y_{sat}. (Note that in Part I, the corresponding level was taken to be 0 dB.)

The other natural scale in the model is the frequency scale set by the base cutoff frequency, f_b, above which waves do not propagate down the basilar membrane. However, for results presented here, all stimulus frequencies are low enough that base cutoff effects are not encountered. The primary stimulus frequencies then effectively set the frequency scale. For model calculations, distances along the basilar membrane from the base are measured in octaves of the characteristic frequency, with increasing distance denoting a decrease in characteristic frequency. Note that the ratio of characteristic frequency in octaves to location along the basilar membrane is approximately constant (e.g., see Tarnowski et al., 1991, for gerbil). The octave distance scale can then be converted to an actual distance scale if the ratio, octaves/mm, can be estimated for a given cochlea.

Results for a typical model cochlea are shown in Fig. 1. Figure 1(A) presents the cochlear response along the basilar membrane for a single tone stimulus. Very low stimulus levels are assumed, so that a linear response is obtained. The passive response is assumed to provide an increase in the cochlear response at the rate, g_p, in dB/octave. For simplicity, this slope is assumed to be independent of frequency, as are all other model parameters. When the stimulus reaches the active amplification zone associated with the stimulus frequency, the growth rate increases to g_a, the active amplification rate (dB/octave). As the end of the active amplification zone is reached, resistive losses dominate, and the wave rapidly decays. The difference between the peak response with normal cochlear amplifier operation and that with zero gain ($g_a = 0$) is defined as the gain of the cochlear amplifier,
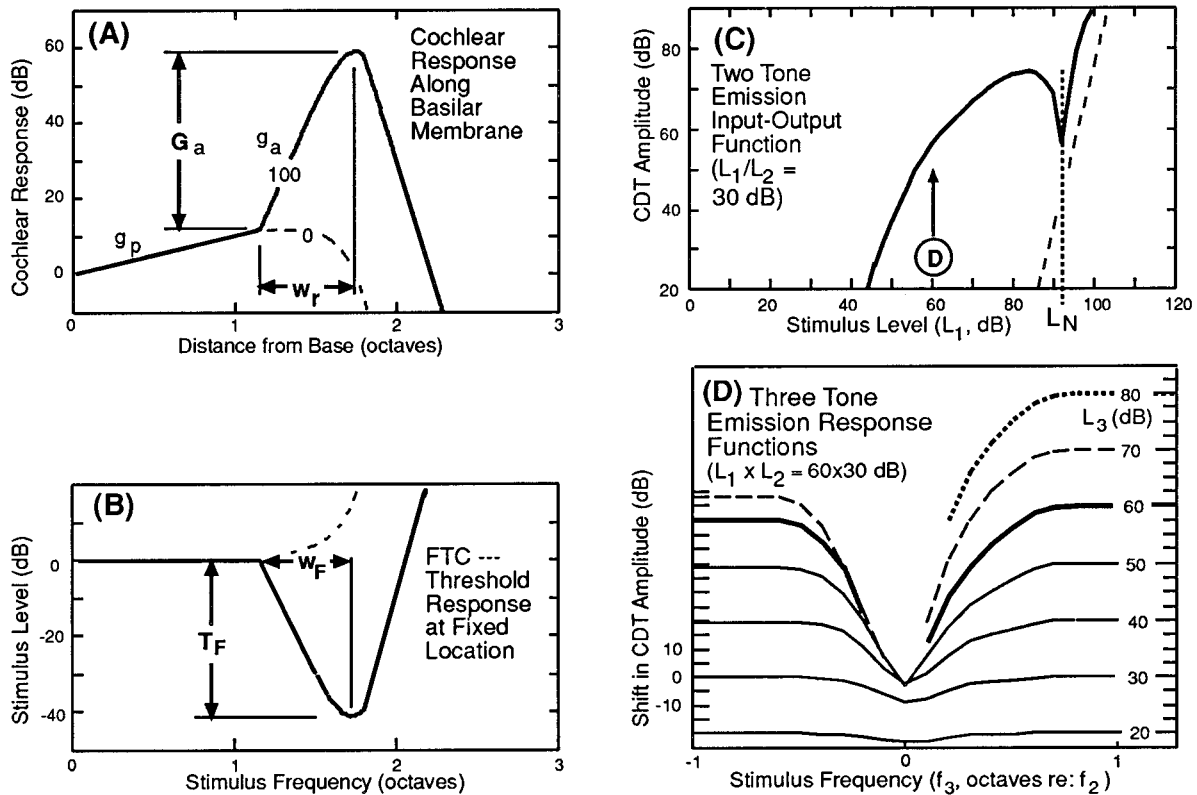
FIG. 1. Response of a particular model cochlea. (A) Cochlear response is plotted versus distance along basilar membrane, measured in octaves from the base, for a single tone stimulus of small amplitude. Response shown is for the passive growth rate, g_p, equal to 10 dB/octave and the intrinsic cochlear amplifier growth rate, g_a, equal to 100 dB/octave. The active response is indicated by the solid line. For comparison, the cochlear response in the passive case, that is, for a cochlear amplifier gain, g_a, of zero, is indicated by the dashed line. The net cochlear amplifier gain, denoted G_a, is defined to be the improvement the peak response in the active case gives over the passive peak response, and equals 46 dB in this case. The cochlear amplifier response reaches its maximum in a distance, w_r, as illustrated, here equal to 0.58 octaves. (B) The threshold frequency tuning curve (FTC) is defined to be the stimulus level to reach a criterion cochlear response at a fixed location, as the stimulus frequency is varied, at low stimulus levels. The threshold shift from the low frequency shoulder to the tip of the tuning curve is defined to be T_F, and is 41 dB for this case. The width of the low-frequency side of the tuning curve is denoted w_F. (C) The amplitude of the cubic distortion tone (CDT, $2f_1 - f_2$) emission versus stimulus level, L_1. The emission amplitude is given in dB, with an arbitrary reference level. For this emission growth function, the stimulus level, L_2, is always 30 dB below L_1. The stimulus frequency ratio is $f_2/f_1 = 1.25$ in all figures. For later use, the stimulus level, L_N, required to reach the notch is defined as shown. The vertical arrow indicates the stimulus level employed in the panel below. (D) Emission response functions for a primary stimulus level of $L_1 \times L_2 = 60 \times 30$ dB. For each curve, the suppressor stimulus level, L_3, is held constant while the suppressor frequency, f_3, is varied from one octave below f_2 to one octave above, in 0.1-octave steps. The suppressor stimulus level, L_3, then is stepped up 10 dB. Cochlear response functions are offset 20 dB in the presentation. The low-frequency CDT response for $L_3 = 80$ dB was more than a 30-dB decrease and is omitted for clarity.

denoted G_a [dB; Fig. 1(A)]. The distance from the start of the active amplification zone to the peak of the response is denoted the "active width," w_r, associated with the active cochlear response [octaves; Fig. 1(A)].

Figure 1(B) displays the frequency tuning curve (FTC), defined to be the set of stimulus levels and frequencies required to obtain a criterion cochlear response at a fixed point along the basilar membrane, at low stimulus levels. Note that the FTC is similar to an inversion of the single tone basilar membrane response, but it is *not* identical to it. For example, the shift T_F is smaller than the actual gain, G_a, and w_F is smaller than the actual width w_r. Note also that, at low frequencies, there is a prominent "shoulder" in the FTC. Because the frequency tuning curve is taken at a fixed location, and the passive increase [in Fig. 1(A)] is assumed independent of frequency, the FTC shoulder is flat, not sloped at 10 dB/octave as is the cochlear response along the basilar membrane. The frequency tuning curve will be identical to an inversion of the response function *only* in the case that

there is exactly zero passive increase along the basilar membrane at all frequencies ($g_p = 0$) and the cochlear amplifier parameters are completely independent of stimulus frequency. The relationship between the *emission suppression tuning curve*, to be defined next, and the cochlear response is more complex. This relationship is the subject of the remainder of this section.

A two tone emission input–output function for the model cochlea of Fig. 1(A) is shown in Fig. 1(C). For this "growth function," it is assumed that $f_2/f_1 = 1.25$ and $L_1/L_2 = +30$ dB. The reasons for assuming a relatively large difference between L_1 and L_2 will be discussed later. Note that there is a relative maximum in the CDT emission amplitude followed by a sharp dip at the "notch level" L_N.

To obtain the data required to construct emission suppression tuning curves, the primary stimuli (at frequencies f_1 and f_2) are fixed, and the CDT at $2f_1 - f_2$ is monitored. A third tone is introduced at the frequency, f_3, and intensity, L_3. For the results here, usually it will be assumed that the

intensity, L_3, is held constant while the frequency, f_3, is varied. The resulting curve, giving the change in CDT amplitude with the suppressor frequency, f_3, will be termed an "emission response function." The intensity L_3 is then incremented and the procedure repeated.

Figure 1(D) shows emission response functions for a primary stimulus of $L_1 \times L_2 = 60 \times 30$ dB [indicated by the point "D" in Fig. 1(C)]. Tick intervals are 5 dB for the CDT amplitude, and the zeros of the emission response functions are offset at 20-dB intervals. The levels, L_3, increase 10 dB between each function, as noted on the right side of Fig. 1(D). These emission response functions are used to establish the "emission suppression tuning curve," by connecting the points where the emission response functions have decreased by the criterion amount (Fig. 2).

The cochlear responses in Fig. 1 are shown in Fig. 2 in more detail. Here the L_3 intervals are 5 dB, and the emission response functions are offset by 10 dB. An emission suppression tuning curve is delineated by marking all of the points on the emission response functions for which the CDT amplitude has decreased 5 dB. These points are indicated by the filled-in circles. The emission suppression tuning curve for the 5-dB criterion is emphasized by the wide shaded lines. The L_3 stimulus level scale for this tuning curve is indicated on the right side (outside) of the vertical axis.

For this emission suppression tuning curve, the 5-dB reduction for the case where the suppressor frequency is approximately equal to f_2 (i.e., for $f_3 \cong f_2$) occurs for $L_3 = 25$ dB. This point is identified by the circled letter "A" in Fig. 2. The L_3 level which causes the criterion decrease to occur for $f_3 \cong f_2$ is defined as the "f_2 threshold."

The "shoulder" threshold of the tuning curve is determined by the responses for $f_3 \ll f_2$, in this case for $f_3 = f_2/2$. For the stimulus parameters and model cochlea used, the suppression of emission by the suppressor tone at this f_3 frequency is entirely due to the passive part of the f_3 response [demonstrated in Fig. 3(B) below]. For the model calculations, any f_3 frequency in the passive regime (near or below $f_2/2$) will give the same shoulder threshold, because the passive increase, g_p, is assumed to be independent of frequency. For the example shown, the shoulder is determined to be located at $L_3 = 61$ dB by interpolating between the emission response function values. The difference between the shoulder and f_2 threshold is defined to be the shift in emission threshold, T_E. In this case, T_E is 36 dB, in comparison to the actual cochlear amplifier gain in the model which is $G_a = 46$ dB [Fig. 1(A)]. Reasons for this difference, as well as choices of stimulus parameters to minimize the difference, are discussed below.

Also defined in Fig. 2 is the "tuning width," w_{40}. Precisely, this is defined to be the distance from the f_2 frequency to the f_3 frequency above f_2 denoted by f_c, measured at a stimulus level, L_3, exactly 40 dB above the f_2 threshold level. The frequency f_c is that which causes a criterion reduction in the CDT amplitude at this L_3 level. For the cochlear model in Figs. 1 and 2, the measured w_{40} is 0.56 octave, compared to the model $w_r = 0.58$ octave.

To some extent, the distance 40 dB is arbitrary. However, it can be seen from Fig. 2 that the measurement is
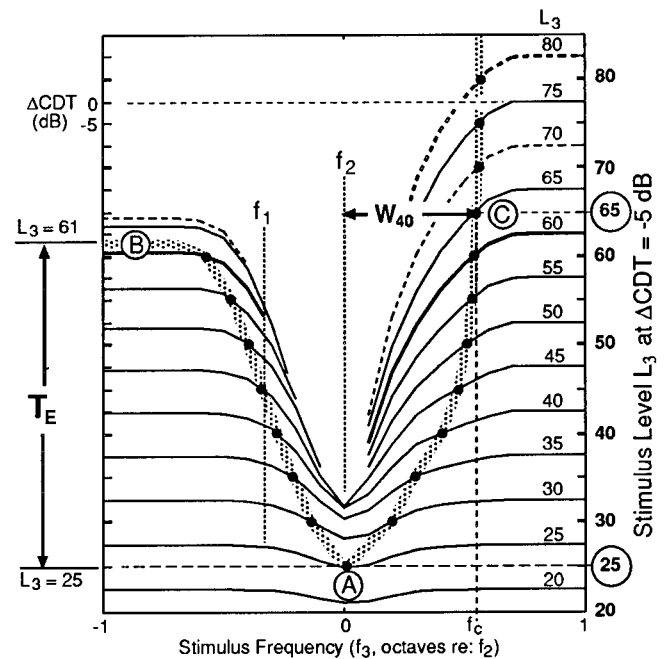
FIG. 2. Emission response functions calculated for $L_1 \times L_2 = 60 \times 30$ dB, and the same model parameters as Fig. 1. Stimulus levels, L_3, have been stepped in 5-dB increments, and the points where the CDT amplitude has been depressed by 5 dB are indicated by filled circles. A typical CDT $(2f_1 - f_2)$ amplitude scale is indicated on the left axis; emission response curves are displaced at 10-dB intervals. The filled-in points define a $2f_1 - f_2$ emission suppression tuning curve as also indicated by the wide shaded lines. The stimulus levels, L_3, corresponding to the 5-dB points are indicated on the right axis. The stimulus level corresponding to the f_2 threshold and the level at the shoulder of the tuning curve are determined by interpolation when necessary. In this case, the criterion threshold decrease of 5 dB is found when L_3 is exactly 25 dB; this is then the f_2 threshold. Interpolation gives the shoulder level for the criterion decrease of the CDT amplitude to be $L_3 = 61$ dB. The change in L_3 between f_2 and shoulder thresholds determines a threshold shift T_E as indicated. This is 36 dB for this case. Also defined is the tuning width, w_{40}, as indicated. This distance is defined as the difference between f_2 and the f_3 frequency for which the CDT emission is depressed by 5 dB measured at a L_3 stimulus level 40 dB above the f_2 threshold. For the case shown, the tuning width, w_{40}, is 0.56 octaves at the stimulus level $L_3 = 65$ dB. For clarity, only the emission responses for $f_3 > f_2$ are shown for the top two curves, for $L_3 = 75$ and 80 dB. Circled letters indicate stimulus conditions which will be examined in detail in the next figure.

insensitive to the exact distance or the precise determination of the f_2 threshold because the emission suppression tuning curve is so steep in this region. Further reasons for the choice of w_{40} will be covered in Sec. V. Also, as shown below, there are a number of conditions for the primary stimulus parameters which must hold so that the tuning width, w_{40}, is a good estimate of the actual width, w_r.

The locations of three sets of stimulus conditions of particular interest are indicated in Fig. 2 by the circled letters, which refer to the corresponding panels in Fig. 3. These panels show the cochlear responses along the basilar membrane for the stimuli defined by these locations. In each panel of Fig. 3, the primary frequencies f_1 and f_2 are shown by light dashed lines, and the f_3 stimulus required for a CDT reduction of 5 dB is shown by a heavy solid line. Note that while the stimulus levels L_1 and L_2 and the frequencies f_1 and f_2 are the same in each panel, the cochlear *responses* at these

frequencies vary slightly from panel to panel due to the effects of the suppressor stimulus, which varies in both frequency and intensity from panel to panel.

Figure 3(A) displays the responses for the three stimulus frequencies at the "f_2 threshold," i.e., at the level L_3 required to achieve the criterion decrease in emission amplitude when the f_3 stimulus frequency is approximately (not exactly) equal to f_2. The 5-dB criterion threshold response occurs for $L_3 = 25$ dB. For comparison, the low intensity cochlear amplifier gain G_a is shown. Note that the actual gain for the f_3 stimulus is slightly less than G_a, due to the partial saturation of the gain at the f_3 frequency by the more intense f_1 stimulus.

Figure 3(B) displays, for contrast, the situation at the shoulder of the tuning curve, where $f_3 = f_2/2$, and $L_3 = 61$ dB for the criterion decrease. Note that the decrease in the emission near the f_2 place must be due entirely to the *passive* part of the f_3 cochlear response, i.e., to the solid straight line segment. The increase in L_3 required to obtain a criterion reduction in CDT amplitude at the shoulder frequency compared to the f_2 threshold is the threshold shift, T_E, as defined in Fig. 2. Comparison of Fig. 3(A) and 3(B) shows that the value of T_E is plausibly related to the gain, G_a. The precise relationship in the "ideal" case will be illustrated later (in Fig. 9).

Figure 3(C) illustrates the model responses with the suppressor at the level L_3 which is 40 dB above the f_2 threshold and with f_3 at the frequency denoted f_c (Fig. 2). The frequency f_c is by definition w_{40} octaves above f_2. At this frequency, the distance between the passive–active transition of f_3 and the same transition in the f_2 response is exactly w_{40} octaves, as noted in Fig. 3(C). For this frequency interval, it can be seen that the peak of the f_3 response is situated so that it affects the gain of the f_2 response just at the beginning of the active zone, producing the 5-dB decrease in CDT amplitude. Note, that, because of the high stimulus level at the frequency f_3, this traveling wave is substantially saturated, and the peak at this frequency is shifted basally. For comparison, the active width, w_r, as defined in Fig. 1 is also shown. It can be seen that w_{40} is a reasonable estimate of the width w_r.

B. Choice of primary stimulus parameters

As mentioned in the Introduction, the use of three tones increases considerably the number of free parameters for emission measurements. In this section, model results with three tones will be employed to make a preliminary determination of a preferred parameter space. The preferred space refers to that range of primary stimulus parameters which is expected to give the most consistent and most accurate results for determining cochlear amplifier tuning characteristics. For the typical construction of emission suppression tuning curves, the third stimulus tone is varied throughout its complete parameter space, f_3 and L_3, while the primary stimulus tone parameters, frequencies f_1 and f_2 and levels L_1 and L_2, are fixed. For this report, the primary frequency ratio is fixed at $f_2/f_1 = 1.25$, and sets of emission suppression tuning curves are determined for a number of different primary stimulus intensities, L_1 and L_2. The end result is the
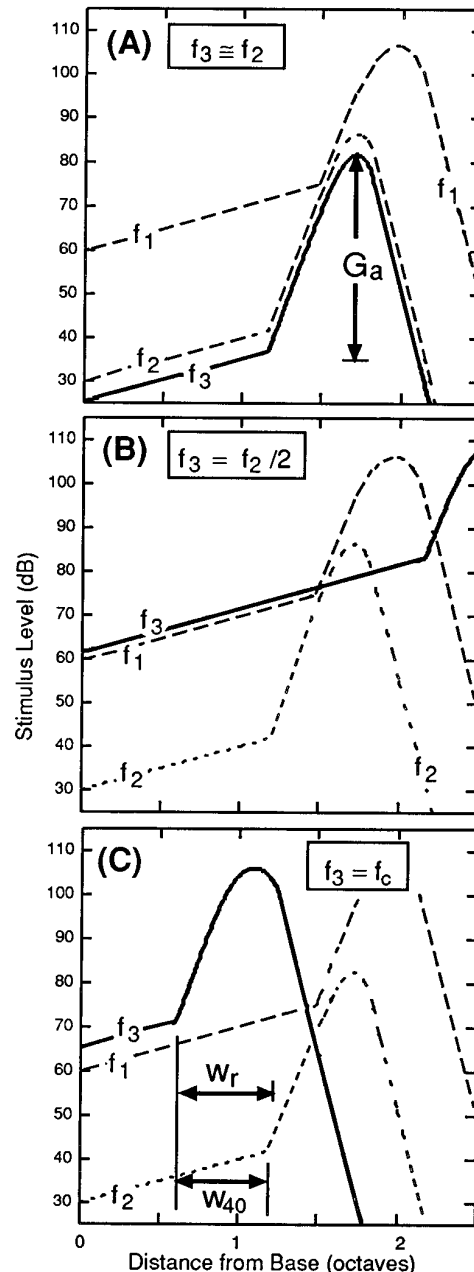
FIG. 3. Detailed cochlear responses along the basilar membrane for three different stimulus conditions, as indicated by the circled letters in Fig. 2. For all panels, the primary stimulus levels are $L_1 \times L_2 = 60 \times 30$ dB, and $f_2/f_1 = 1.25$. The cochlear responses at the primary frequencies, f_1 and f_2, are indicated by the light dashed lines. The f_3 response is shown by a heavy solid line, and in each case is that stimulus which causes the amplitude of the CDT at $2f_1 - f_2$ to be reduced by 5 dB. (A) The response at the "f_2 threshold," where the stimulus frequency f_3 is approximately equal to f_2 and the stimulus level for the 5-dB CDT reduction is $L_3 = 25$ dB. The gain of the cochlear amplifier, G_a, at low stimulus levels is shown for reference. (B) The response at the shoulder of the tuning curve, where the stimulus frequency, f_3, is $f_2/2$ and the level for a 5-dB decrease is $L_3 = 61$ dB. (C) The response which determines the tuning width, w_{40}. The suppressor frequency f_3 is w_{40} octaves above the frequency f_2 in this case, and the stimulus level is 40 dB above the f_2 threshold level of 25 dB.

derived relationships, as a function of the primary stimulus intensities, between "measured" quantities in the emission suppression tuning curves, primarily the threshold shift, T_E, and the width, w_{40}, and the corresponding quantities in the model cochleas, the gain, G_a, and the width, w_r.
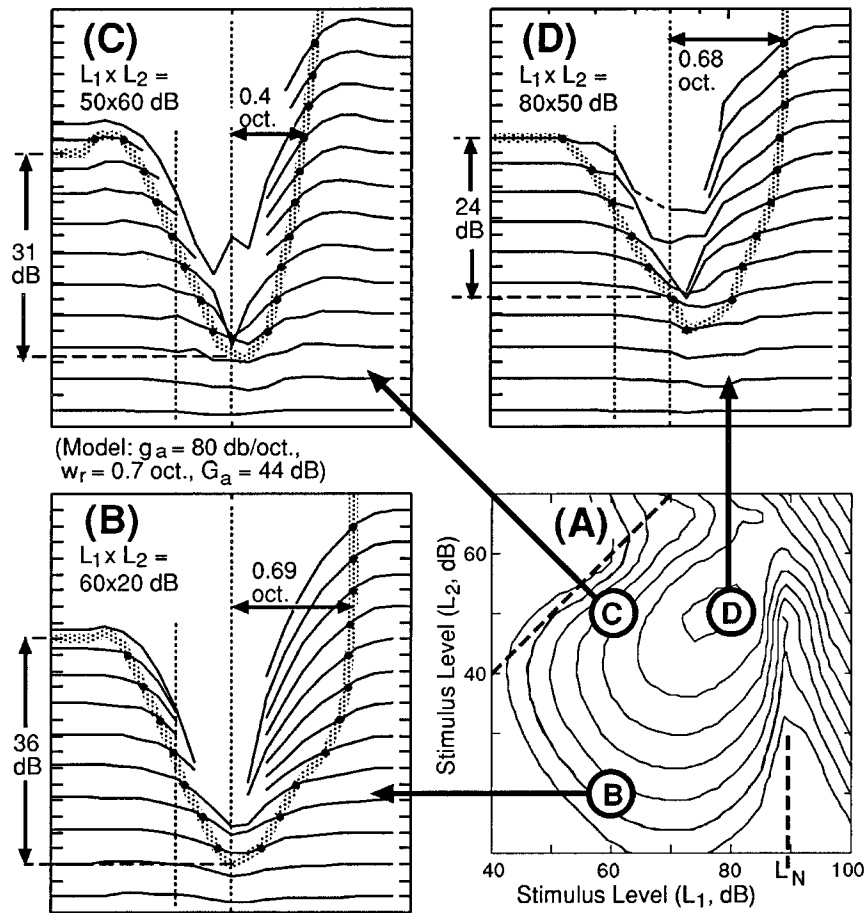
FIG. 4. Responses for one cochlear model for three different primary stimulus conditions. *Clockwise from lower right.* (A) Contour map showing the undisturbed CDT emission resulting from the variation of the stimulus levels, L_1 and L_2, independently over the whole normal range. Contours of constant CDT amplitude are shown at 5-dB intervals. Contours are omitted below a certain level to simulate a typical noise floor. Note the strong notch at $L_1 = L_N = 90$ dB, i.e., 10 dB below the characteristic saturation level. For reference, the 45° dashed line indicates the location of equal-level primaries, $L_1 = L_2$. The circled letters locate stimulus levels, $L_1 \times L_2$, for which emission response functions are plotted in the corresponding panels. (B)–(D) Emission response functions and emission suppression tuning curves, as defined in Fig. 2. The threshold shift, T_E, is noted on the left side of each panel, and the tuning width, w_{40}, by the heavy solid line with arrowheads located at the appropriate L_3 level. The frequencies, f_1 and f_2, are indicated by the vertical dashed lines.

Figure 4 presents an overview, with the emission response functions illustrated for three different primary stimulus level pairs, for one model cochlea. This model, with parameters $g_a = 80$ dB/octave and $w_r = 0.7$ octave, is considered in detail in Figs. 4 and 5 because these parameters appear to be approximately correct for the adult gerbil measurements to be presented later. For the model, Fig. 4(A) (lower right panel) presents the undisturbed emission amplitude distribution resulting from varying the primary stimulus levels, L_1 and L_2, independently. Lines of equal-level CDT emission amplitude are shown at 5-dB intervals. Lines are omitted below a certain level to represent the typical noise floor. The circled letters denote primary stimulus intensities for which emission response functions are shown [Fig. 4, panels (B)–(D)]. Figure 4(B) illustrates typical results obtained for large L_1/L_2, but for L_1 much smaller than the notch level, L_N. A threshold shift of 36 dB is obtained, compared to the actual gain of $G_a = 45$ dB. No larger threshold shifts were found across the stimulus parameter space for this model cochlea. In Fig. 4(B), the tuning width, w_{40} equals 0.69 octaves, compared to the actual $w_r = 0.70$ octaves.

Figure 4(C) shows emission response functions for pri-mary stimulus levels that are nearly equal. In this case, the suppressor tone, f_3, causes modest *enhancements* of the emission amplitude for a small range of f_3 frequencies above f_2. This behavior is to be expected from a saturating nonlinearity when y_1 and y_2 are approximately equal and y_2 is suppressed. This enhancement effectively moves the 5-dB criterion point to the left, causing a significant decrease for the measured tuning width, w_{40}.

There is also some enhancement seen on the low-frequency side in Fig. 4(C). However, this does not interfere with the measurement of the shoulder level, as this measurement by definition must be done at an f_3 frequency which is low enough to avoid such effects. The threshold shift, T_E, measured in case (C) is 5 dB below the best value as determined in Fig. 4(B).

Figure 4(D) shows emission response functions for stimulus levels nearer the notch, while still having relatively large L_1/L_2. In this case, the tuning width is near the best value, but the threshold is significantly decreased. Note that for these primary stimulus parameters, the most sensitive part of the tuning curve, or the "tip," is not at f_2, but actually at a higher frequency. Nonetheless, the threshold shift is

measured at f_2 for comparison with the gain. Reasons for this choice are summarized in the discussion.

Determinations of T_E and w_{40} were made as illustrated above (Fig. 2) for the model cochlea in Fig. 4(A) for points at 5-dB intervals in L_1 and L_2, varied independently. The results are presented in Fig. 5. The lowest CDT contour shown in Fig. 4(A) is repeated in Fig. 5(A) and (B) for reference. Note that the values of T_E and w_{40} are only well defined for stimulus levels, $L_1 < L_N$, for this model cochlea.

For this model, the gain, $G_a = 45$ dB, and the actual width is $w_r = 0.7$ octaves. The region where the ''measured'' values of threshold shift, T_E and tuning width, w_{40}, are closest to these values is defined by $L_1/L_2 \geqslant 20$ dB. In addition, the results in Fig. 5 confirm the importance of choosing stimulus levels for $L_1 \ll L_N$, particularly with regard to accurate threshold shifts.

For some of the areas in Fig. 5, the fact that the derived values appear close to the actual model parameters is fortuitous. This includes the area near $L_1 = L_2 = 40$ dB in Fig. 5(A) and the area for $L_1 \cong 80$ dB in Fig. 5(B) [including the example in Fig. 4(D)]. A slight change in model parameters can lead to the disappearance of such apparent agreement, as is shown below. It is extremely important that the estimates of cochlear amplifier characteristics be derived for stimulus areas where the results are consistent and *not* strongly dependent on specific model parameters or primary stimulus parameter choices.

To avoid conclusions based on such fortuitous agreement, Fig. 6 presents calculations for the variation in the derived values as a function of the stimulus level ratio, L_1/L_2, using three different model cochleas. For these calculations, the stimulus levels $L_1 \times L_2$ which give equal CDT amplitudes are determined from the contour maps, and a particular contour line is followed as the stimulus levels move from those with equal level primaries, $L_1 = L_2$, to those with larger L_1/L_2. Note that moving in the direction of increasing L_1/L_2 involves a counterclockwise rotation along the lower contours in Fig. 4(A). Stimulus levels which give a CDT amplitude about 40 dB below the relative maximum are chosen in all cases for Fig. 6. The three different model cochleas are illustrated in Fig. 6(A). Between these models, the active gain, g_a, is varied in 20 dB/octave steps, but the distance w_r is also varied so that the total gain, G_a, is approximately constant. (The constancy of gain, G_a, is not essential. This requirement, however, makes the growth functions approximately the same total height between the different models and simplifies the comparison.)

The calculations also include the results for zero passive increase ($g_p = 0$) for the model with $g_a = 100$ dB/octave. The horizontal axes in Fig. 6(B) and (C) are the same, and equal to the ratio of the stimulus levels, L_1/L_2, in dB. The vertical axis in Fig. 6(B) is the value of T_E determined from the model calculations *relative* to the true gain, G_a. For stimulus levels where L_1 and L_2 are approximately equal [i.e., near the left axis in Figs. 6(B) and 4(C)], the four model calculations give wildly different values of T_E relative to the true gain, G_a. However, as L_1 becomes much larger than L_2, the model results converge. Similar behavior is noted for the tuning width, w_{40}, in Fig. 6(C).
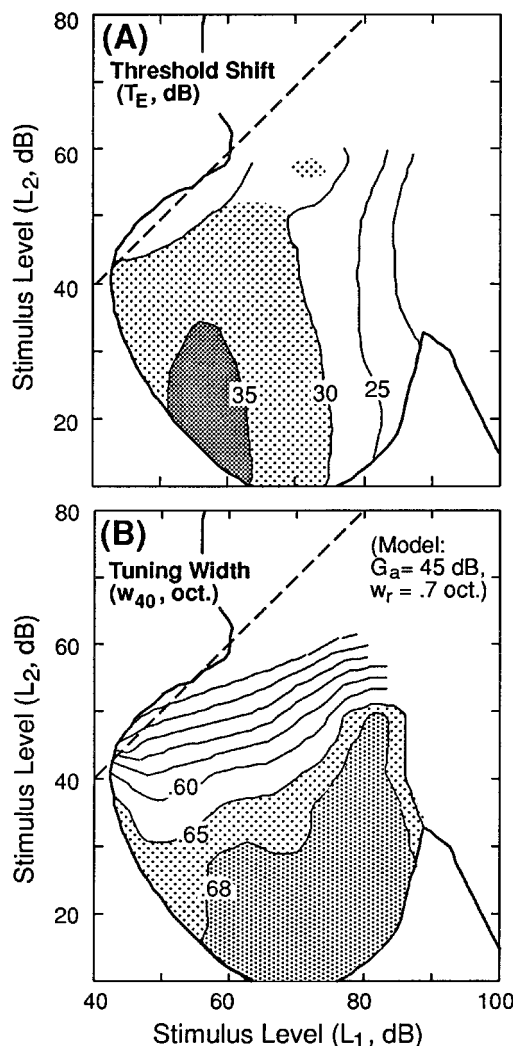
FIG. 5. Detailed response for the cochlear model in Fig. 4 for primary stimulus levels in the lower left region, i.e., to the left of the notch and below the line $L_1 = L_2$ (shown by the heavy dashed line in each panel). The lowest contour in (A) is repeated here, and values only determined within its boundaries. (A) Values of the threshold shift, T_E, as defined in Fig. 2, as a function of the primary stimulus levels. The most heavily shaded region has a threshold shift $T_E \geqslant 35$ dB. A typical emission suppression tuning curve in this region was shown in Fig. 4(B). (B) Values of the tuning width, w_{40}, as defined in Fig. 2, as a function of the primary stimulus levels. The contour interval is 0.05 octave except as noted.

In summary, the most consistent and accurate results are found for L_1/L_2 ratios equal to 20 dB and up. This measurement region where results are relatively insensitive to model and stimulus parameters is indicated by the bold arrow. In the region $L_1/L_2 > 20$ dB, the threshold measure T_E typically underestimates the true gain, G_a, for the model by 5–10 dB. Since the gain for these models is $G_a = 45$–46 dB, this is an accuracy of 10 to 20%. The tuning width w_{40} is a better estimate of w_r. The error is less than 0.05 octaves for stimulus intensity ratios satisfying $L_1/L_2 \geqslant 20$ dB [Fig. 6(C)]. Since w_r ranges from 0.5 to 0.7 for these models, the accuracy in the estimate of w_r by w_{40} is 10% or better.

The recommendation resulting from the above considerations is that, for the most accurate estimates, the stimulus level ratio, L_1/L_2, should be $+20$ dB or more. This result
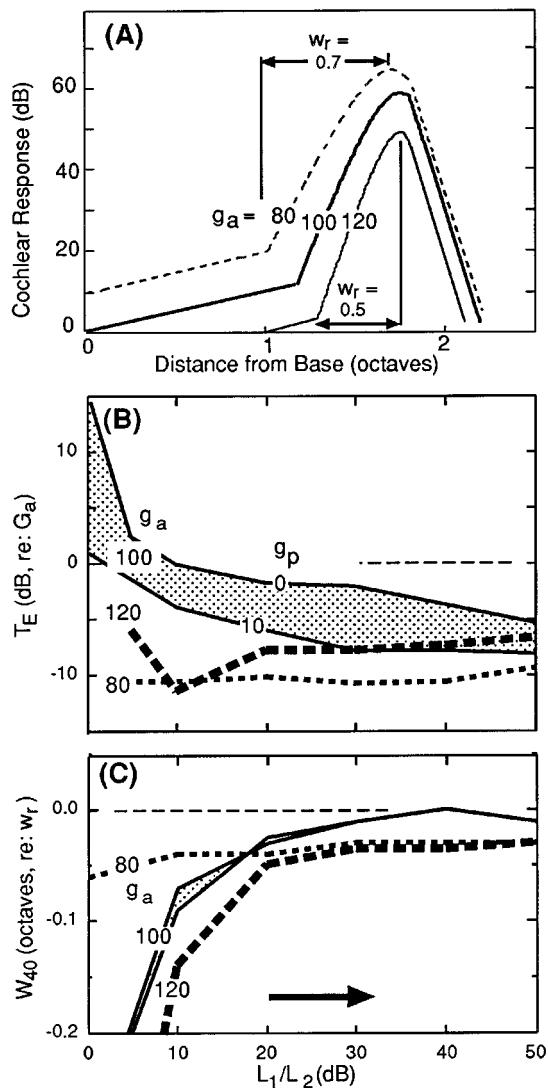
FIG. 6. (A) The cochlear responses in the linear regime illustrated for three different sets of model parameters, chosen so that the total gain, G_a, is approximately constant while giving a range in the width, w_r, from about 0.5 to 0.7 octaves. The cochlear amplifier gain, G_a, is 45–46 dB for all three models. The three curves are displaced vertically at 10-dB intervals for clarity. (B) The variation of the threshold shift, T_E, with stimulus intensity ratio, L_1/L_2. The values of T_E are given relative to the cochlear amplifier gain for each model. For all three models, the same undisturbed CDT amplitude was maintained as the ratio, L_1/L_2, was changed. The passive growth rate, g_p, was 10 dB/octave for all three models. For comparison, results are also shown for $g_p = 0$, for the model case $g_a = 100$ dB/octave. (C) The variation of the tuning width, w_{40}, with stimulus intensity ratio under the same conditions. The widths are given relative to the model width, w_r, for each case. The bold arrow indicates the direction for optimum measurements.

for three tone measurements contrasts with previous results for determination of the gain, G_a, using two tone emission measurements combined with furosemide injection (Mills, 1997, Fig. 3C). In that case, a range of L_1/L_2 from -10 to $+20$ was found to give reasonable results. This is not true here. A ratio of $L_1/L_2 \lesssim 10$ dB would give very poor results for these quantities, especially for higher gain models (100–120 dB/octave). The error is larger for the tuning curve width, w_{40}, a result of the appearance of the ''enhancements'' seen in Fig. 4(C).

Note that there is nothing lost, in terms of signal-to-noise, in taking a larger stimulus level ratio, L_1/L_2, at least not the way that this was done for these simulated measurements. As the ratio was changed, the stimulus levels were both varied so that the CDT amplitude was held constant.

By considering the results for both measures, T_E and w_{40}, the optimal region for measurements is determined to be

$$L_1/L_2 > 20 \text{ dB}, \quad L_N/L_1 > 25 \text{ dB}. \qquad (1)$$

That is, L_2 should be 20 dB or more lower than L_1, which in turn should be 25 dB below the notch level, L_N. This implies that $L_2 \ll L_1 \ll L_N$, and numerically that L_2 should be 45 dB or more below the notch level. With typical notch levels of 70–90 dB SPL in the gerbil, this restricts L_2 levels to be below 25–45 dB SPL. This can be a serious restriction in situations where the emission amplitudes are intrinsically low. One cannot measure an emission suppression tuning curve like that in Fig. 2 when an emission cannot be detected. In practice, the unsuppressed emission amplitude must be at least 10 dB above the noise floor. The relationships in Eq. (1), in any case, indicate the optimal region for such measurements, even if that area cannot be actually reached.

Note that the notch level, L_N, both from observation and model, is essentially independent of L_2 level, that is, it occurs for the same L_1 level as long as the L_2 levels are 20 dB or more below L_1 [e.g., Fig. 4(A)]. Reasons for this have been discussed in Part I (Mills, 1997). Briefly, the notch occurs at the same value of L_1 for low L_2 because only the relative degree of saturation of the L_1 signal itself determines the relative amounts of peak and basal emission components. This occurs because the L_2 signal is much weaker than the L_1 in this region, and the saturation of the response at f_2 is relatively unimportant for the determination of the emission distribution.

The contour lines of constant threshold shift, T_E, are also nearly vertical in Fig. 5(A) in the region near the notch. That is, the derived threshold shifts depend only weakly on the L_2 stimulus level. Reasons for this appear to be related to the reasons given above for the location of the notch itself.

C. Variation of emission suppression tuning curves with cochlear amplifier gain

To this point, only models with moderately high gains ($G_a \cong 45$ dB) have been considered, characteristic of normal cochlear function. It is also important to estimate how well the threshold shift, T_E, might measure lower gain values which are more typical of cochlear amplifier dysfunction. For this determination, a series of model calculations with decreasing gains, g_a, are made [Fig. 7(A)]. Only the active gain is varied, the width of the active zone and the loss rates are kept constant. In consequence, the peak of the response then moves toward the base as the gain is decreased, so that w_r decreases from 0.6 to 0.4 octave as the gain decreases from 120 to 20 dB/octave [Fig. 7(A)]. Note that the same assumptions were used in Part I (Mills, 1997) for model calculations which successfully simulated the observed effects of acute furosemide intoxication in gerbils.

(A) Model: g_a (dB/oct.)

Cochlear Response (dB)

120
100
80
60
40
20

Distance from Base (octaves)

(B) $L_1/L_2 = 30$

CDT Amplitude (dB)

g_a
120 100 80 60 40 20

L_1 (dB)

Vary Active Gain, g_a

(A)

Actual Gain, G_a (dB)

g_p 10 0

10
0 g_p (dB/oct.)

- - - - $G_a = T_E + g_p w_{40}$

Threshold Shift, T_E (dB)

(B)

w_r (octaves, re: w_{40})

.05
0
-.05

0.5 W_{40} (octaves) 0.6
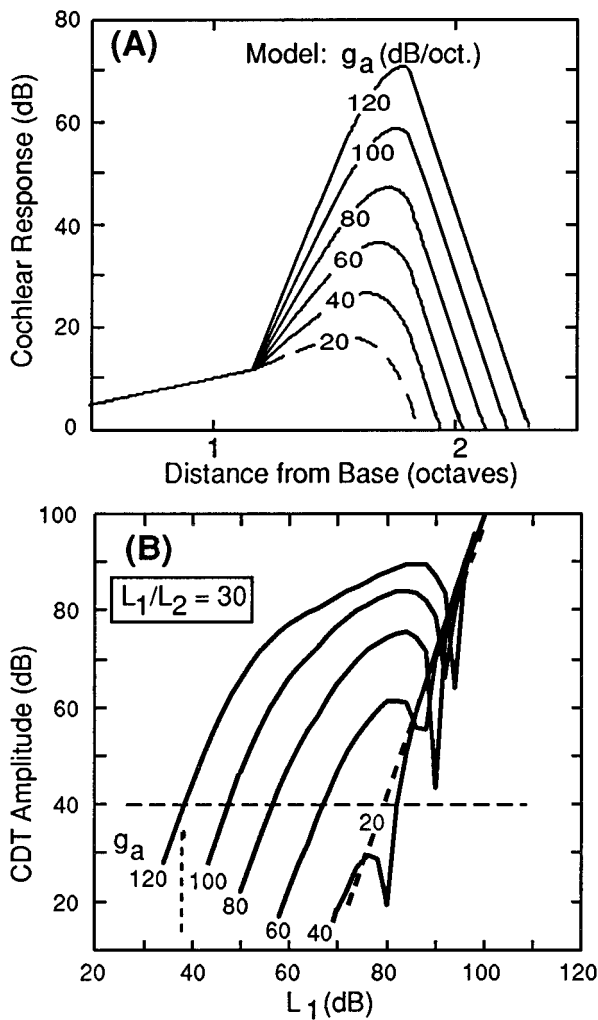
FIG. 7. (A) Cochlear responses as a function of distance from the base with the parameter the cochlear amplifier gain, g_a. Low stimulus levels are assumed. Other model parameters are constant, and are for the same basic model as Figs. 1–3. (B) Emission growth functions for $L_1/L_2 = +30$ dB and passive increase, g_p, equal to 10 dB/octave. Emission suppression tuning curves are simulated for stimulus levels chosen to give a constant CDT amplitude, as indicated by the dashed horizontal line. For example, the dashed vertical line indicates that the appropriate stimulus level for the model with $g_a = 120$ dB/octave is $L_1 \times L_2 = 38 \times 8$ dB.

FIG. 8. Variation of the derived measures T_E and w_{40} as a function of the cochlear amplifier gain for the model in Fig. 7. These results have been inverted, so that from the observed measures T_E and w_{40} one may obtain the correction necessary to estimate the values of G_a and w_r. Results for passive increase, g_p, equal to zero and to 10 dB/octave are shown for comparison, and the shaded area indicates the region between these two values. Model parameters are otherwise the same as in Figs. 1–3. The dashed lines show the curves for the equation $G_a = T_E + g_p w_{40}$, the derivation of which is illustrated in Fig. 9.

The emission growth functions found for these model cochleas are shown in Fig. 7(B). In all cases, the stimulus level ratio, L_1/L_2, is 30 dB. To simulate the effect of a realistic noise floor, the stimulus level L_1 for each emission suppression tuning curve is chosen to give a constant CDT amplitude, as indicated by the dashed horizontal line. For example, in the case with a gain of 120 dB SPL, the stimulus level L_1 was chosen to be 38 dB, indicated by the vertical dashed line in Fig. 7(B), with the corresponding $L_2 = 8$ dB.

The results are summarized in Fig. 8. In both panels, the results have been inverted, so that the correct values, G_a and w_r, on the vertical axes can be estimated from the corresponding measured values on the horizontal axis. Note that the corrections for measured values of the width are so small that it can simply be taken that $w_r \cong w_{40}$. Generally, it appears that, as long as the actual gain is 15 dB or more, the actual gain could be estimated by adding about 5 dB to the measured threshold shift. For comparison, the dashed lines summarize estimates derived from a consideration of the "ideal" case, discussed next.

Consideration of cochlear response functions for three tones, i.e., comparing those shown in Fig. 3(A) with (B), suggest a simple geometric derivation of the relationship between T_E and G_a. This is indicated in Fig. 9. Consider the "ideal" case where L_1/L_2 is large but L_1 is small compared to the notch level, L_N (so that L_2 is *very* small). The region where these assumptions are satisfied lies in the lower left of Fig. 5(A), far from the notch region and well below the line $L_1 = L_2$. Under these stimulus conditions, it appears that the reduction of the CDT by a criterion amount is accomplished whenever the f_3 stimulus reaches approximately the *same level* in the region of the peak of the f_2 cochlear response. This results from the fact that, under these "ideal" conditions, the f_2 response, being much weaker than the f_1 re-

sponse, is more affected by these low levels of f_3 than the f_1 response.

Now compare the responses to an f_3 stimulus for two frequencies, $f_3 = f_2$ and $f_3 \lesssim f_2/2$. The L_3 levels associated with the two frequencies are adjusted so that the f_3 cochlear responses are equal at the f_2 place, as shown.

By the equilevel assumption above, these two f_3 stimuli will both cause a criterion reduction in the CDT amplitude. That is, the difference between these L_3 levels is equal to the measured threshold shift, T_E. By geometry,[1]

$$T_E = G_a - g_p w_r. \tag{2}$$

Under ''ideal'' measurement conditions, $w_r = w_{40}$, so that this equation can be inverted to give an estimate for G_a in terms of two measured quantities:

$$G_a = T_E + g_p w_{40}. \tag{3}$$

This expression still contains an unknown, the rate of passive growth, g_p. However, this quantity is determined by the *passive* response of the cochlea and does not depend on cochlear amplifier function at all. If an appropriate value can be estimated for a given frequency range in a particular species, the value could be employed in Eq. (3) to provide a useful correction to measured T_E values for a variety of manipulations or conditions affecting the cochlear amplifier response. Further, as noted earlier (Mills, 1997), the value of g_p is estimated from passive cochlear response measurements and modeling to be about 5–7 dB/octave, and is almost certainly within the range 0–10 dB/octave. The use of such a correction factor for the two extreme values was illustrated in Fig. 8 by the dashed lines. Note that Eq. (3) also implies that the threshold shift, T_E, is a better approximation to the actual cochlear amplifier gain the sharper the peak of the amplifier response (i.e., for smaller w_r).

III. EXPERIMENTAL RESULTS

The results predicted by the model were generally confirmed by emission measurements in adult gerbils. Figure 10 illustrates the typical variation of measured emission suppression tuning curves with the primary stimulus amplitudes, $L_1 \times L_2$, sampled over the entire normal range. The undisturbed CDT emission amplitude distribution is shown by the contour map [Fig. 10(A), lower center panel]. The primary stimulus frequency was $f_2 = 18$ kHz, and the notch was found at $L_1 = L_N = 75$ dB SPL. The location for $L_1 = L_2$ is shown by the dashed 45° line.

Emission response functions were taken at the locations in $L_1 \times L_2$ noted by the circled letters, which indicate the corresponding panels in Fig. 10. For example, panel (B) displays the response of the CDT amplitude to a suppressor tone for the primary stimulus $L_1 \times L_2 = 60 \times 37$ dB SPL. In each panel [(B)–(F)], the stimulus level, L_3, was stepped in 5-dB increments while the frequency, f_3, was varied in approximately 0.1 octave intervals from 5.5 to 37 kHz. The points at which the CDT emission was decreased by 5 dB are indicated by the filled circles. Tuning curves consistent with these points are indicated by the wide shaded lines. Note that for all curves the stimulus frequency ratio was $f_2/f_1 = 1.25$, or about 1/3 of an octave.
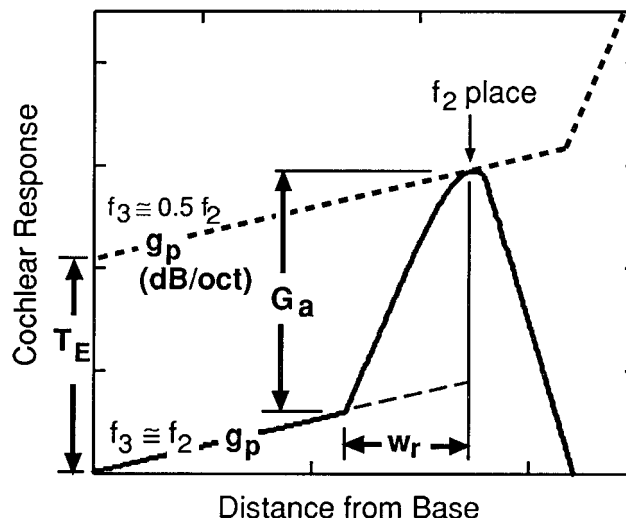
FIG. 9. The relationship between the gain, G_a, and the threshold shift, T_E, for the ''ideal'' case. The ''ideal'' occurs for low stimulus levels, for $L_1 \ll L_N$ and for $L_1/L_2 \gg 0$. In this case, a given reduction of the CDT ($2f_1 - f_2$) occurs whenever the stimulus at frequency f_3 is about the same amplitude *near the f_2 place*. This occurs because only the response at frequency f_2 is significantly suppressible by small levels of the f_3 stimulus under these conditions, and the magnitude of f_3 near the f_2 place is the main determinant of the amount of suppression. The two important f_3 conditions are illustrated. One condition is with the f_3 frequency approximately equal to f_2. This f_3 stimulus determines the ''f_2 threshold'' and is indicated by the solid line. The other, with $f_3 = f_2/2$, determines the ''shoulder'' threshold and is indicated by the dashed line. The difference between these two responses at the base is the measured threshold shift, T_E. For reference, the cochlear amplifier gain is indicated by G_a, the passive growth by g_p, and the width by w_r.

Figure 10(B), (C), and (D) indicates the effect on the observed emission suppression tuning curves of progressively increasing L_2, with L_1 held constant at 60 dB SPL. For panel (B), with $L_2 \ll L_1$, the tuning curve has a very sensitive tip located at or very near to the f_2 frequency. As L_2 increases, the tuning curves become progressively less sensitive, and the tip of the tuning curve moves to slightly lower frequencies. Panel (C) shows the response for $L_1 = L_2$, and panel (D) for $L_2 > L_1$. For $L_2 > L_1$, the tip of the tuning curve is located near f_1, rather than f_2.

Figure 10(E) and (F) shows the responses for primary levels with L_1 above the notch, panel (E) for $L_1 = L_2$, and panel (F) for $L_1 > L_2$. It is clear that measurements using primary stimulus levels located above the notch do not produce useful tuning curves.

Overall, observed emission suppression tuning curves such as those in Fig. 10 illustrate the same general character as those resulting from model calculations. It appears that only the primary stimulus area at and below the line $L_1 = L_2$ and to the left of the notch level, L_N, is of general interest in determining the tuning characteristics of the cochlea. This is the region $L_N > L_1 > L_2$.

For precise determinations of T_E and w_{40}, complete emission response functions, such as those in Fig. 10, contain both too much and too little data. Too little, because these curves do not accurately locate the f_2 and shoulder thresholds, or the points required to determine w_{40}. The
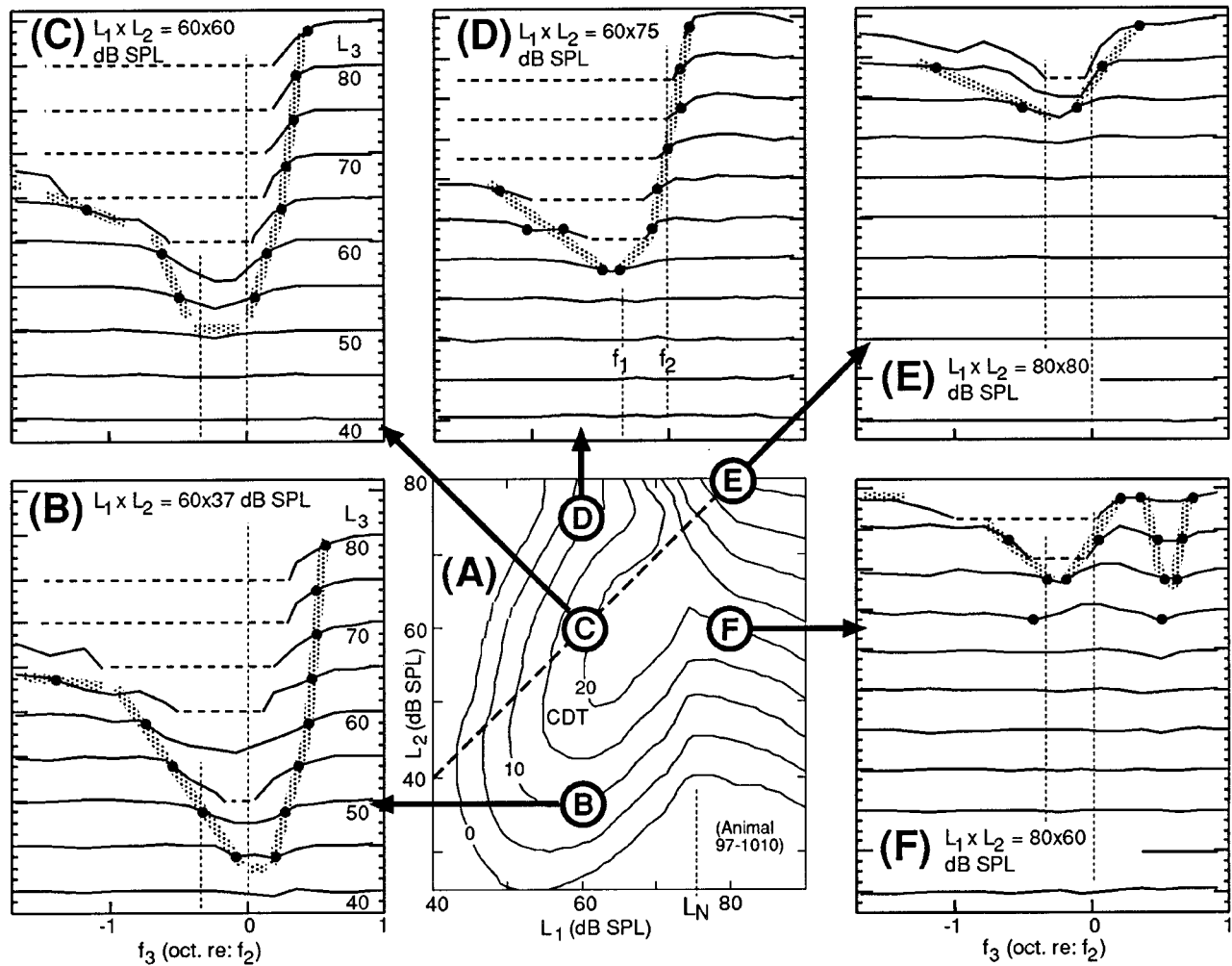
FIG. 10. Data from an individual adult gerbil, showing typical complete cochlear response functions for five different primary stimulus levels, $L_1 \times L_2$. For all panels, the primary stimulus frequencies were $f_1 = 14.4$ kHz and $f_2 = 18$ kHz ($f_2/f_1 = 1.25$). *Clockwise from lower center panel.* (A) Contour map showing emission amplitude responses to the primary tones only, with L_1 and L_2 varied independently. Lines show locations in $L_1 \times L_2$ coordinates of the amplitude of the CDT ($2f_1-f_2$) emission, starting at 0 dB SPL and increasing in 5-dB steps. The circled letters locate the $L_1 \times L_2$ values for which the CDT response was measured as a function of a third tone varied in both frequency (f_3) and level (L_3). The dashed, 45° line indicates the points for which $L_1 = L_2$. (B)–(F). Responses of the CDT amplitude to the third tone for the primary stimulus levels $L_1 \times L_2$ noted. The change in CDT amplitude is given on the vertical axis with the corresponding L_3 level indicated on the right (in dB SPL). The suppressor levels, L_3, were stepped at 5-dB intervals, and have the same distribution in all panels. The horizontal axis is the f_3 frequency in octaves *re*: f_2; the locations of the f_1 and f_2 frequencies are also indicated by the vertical dashed lines in each panel. The vertical tick interval for the CDT amplitude scale is 5 dB, and CDT response functions are displaced vertically by 20 dB for clarity. In each panel, measured emission levels which were near or below the measured noise floor have been omitted, and replaced with a horizontal dashed line. Note that the noise floor and the absolute signal levels vary between panels. Filled circles indicate locations where the CDT amplitude has been decreased by 5 dB by the third tone. The emission suppression tuning curves for the 5-dB suppression consistent with these points are indicated by the wide shaded lines. These tuning curves are only suggestive of the main features of the tuning curves at different $L_1 \times L_2$. For quantitative results, additional data points are required for accurate estimates, as illustrated in Figs. 11 and 12.

complete functions would work if the L_3 level increments were halved, which would double the required number of emission response functions. However, the set of response functions in Fig. 10 already typically requires 15 min for each primary stimulus level. For clinical usefulness, a shorter time would be more desirable. Shorter times are possible, because much of the time taking a complete set of emission response functions is wasted because most of these data are not actually needed to accurately determine T_E and w_{40}.

To accurately and efficiently obtain the most relevant tuning characteristics, the minimum data set illustrated in Fig. 11 was obtained for each primary stimulus point ($L_1 \times L_2$) for another adult gerbil. This algorithm is illustrated for

a primary f_2 frequency of 8 kHz. First, the level of a suppressor tone at the shoulder frequency of $f_3 = 2.02$ kHz was increased in 3-dB increments until a decrease of at least 10 dB was observed in the CDT amplitude [Fig. 11(A), right most curve]. Note that this lower f_3 frequency (rather than $f3 \cong f_2/2 \cong 4$ kHz, say) was employed for the particular case $f_2 = 8$ kHz in the gerbil. The reason is that there is apparently a middle ear resonance around 4 kHz in this species, similar to that in other gerbil species (Plassmann and Kadel, 1992). This resonance appears to significantly decrease the threshold for f_3 frequencies between 2.5 and 5.5 kHz. In any case, whatever the f_3 frequency chosen for the shoulder threshold, the absolute threshold shift will be affected by the difference

in passive conduction between this frequency and the frequency f_2. However, the *relative* shifts as a function of L_1/L_2, such as those shown in Figs. 11 and 12, will not depend on such passive differences.

The frequency f_3 is then set near to f_2 (in this case to 7.95 kHz) and the f_2 threshold is determined by stepping L_3 in 3-dB steps [left curve in Fig. 11(A)]. As discussed, it is the f_2 threshold, rather than the most sensitive tip of the tuning curve, that is determined for both model and observation.

After the f_2 threshold is found, the tuning width w_{40} is determined for a stimulus level L_3 which is 40 dB above the f_2 threshold. In principle, only one emission response function is required, holding L_3 constant and stepping f_3 down from a frequency of about $2f_2$ in 0.1 octave steps, until a decrease in the CDT amplitude exceeding 5 dB is observed. In practice, three or more such curves were taken as shown in Fig. 11(B), with L_3 levels at 3-dB intervals so that the desired L_3 level was securely bracketed.

The undisturbed CDT amplitude distribution for $f_2 = 8$ kHz for an adult gerbil is shown in Fig. 12(A). Dots indicate the location of stimulus level parameters, $L_1 \times L_2$, for which the minimum data set was taken as illustrated in Fig. 11. Note that only values for $L_1 < L_N$ were taken, in accordance with the results of Fig. 10. The derived values for the threshold shift, T_E, are shown in Fig. 12(B), and the tuning width, w_{40}, in Fig. 12(C). These results are in excellent agreement with the model predictions of Figs. 4 and 5.

Because of the agreement between model and observation, it is suggested that the most accurate observational estimates should be found in the most heavily shaded areas in Fig. 12(B) and (C), for which the primary stimulus levels obey the relationships:

$$L_1/L_2 > 15 \text{ dB}, \quad L_N/L_1 > 25 \text{ dB}. \quad (4)$$

These requirements are very similar to those based on model calculations, expressed by Eq. (1). Model calculations and observations in gerbils therefore converge to the conclusion that in this region [Eqs. (1) or (4)] the calculated tuning curves are not strongly dependent on model or stimulus parameters, and observed tuning curves are not strongly dependent on stimulus parameters.

Also note in Fig. 12(B), similar to model results in Fig. 5(A), that the contour lines for the measured threshold shift, T_E, near the notch are parallel to it. That is, they do not depend strongly on the L_2 value in this region, for which $L_1/L_2 > 10$ dB.

For this animal, at this f_2 frequency, the threshold shift is then $T_E \cong 37$ dB and the tuning width $w_{40} \cong 0.74$ octave, as estimated from the actual maximum values measured in the heavily shaded regions of Fig. 12(A) and (B). These values are in excellent agreement with those obtained psychoacoustically in adult gerbils (Burkey and Glans, 1991). From the previous model calculations, it can be concluded that the actual width w_r is probably very close to three quarters of an octave. From Eq. (3), the actual gain can be estimated from

$$G_a = 37 + 0.74 g_p, \quad (5)$$
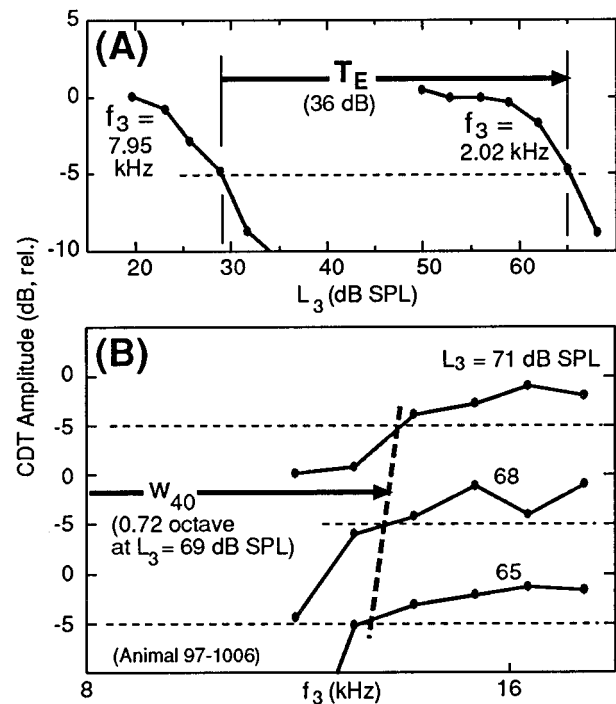
FIG. 11. Typical experimental data for the minimum number of measurements needed to accurately determine the threshold shift, T_E, and the tuning width, w_{40}. (A) First, the threshold for the low-frequency shoulder was found by setting the frequency f_3 to a constant value, and increasing the level L_3 in small steps until a 10-dB decrease in the CDT amplitude was exceeded (right hand curve in this panel). The case shown is for a primary frequency $f_2 = 8$ kHz, with $f_2/f_1 = 1.25$ and $L_1 \times L_2 = 40 \times 20$ dB SPL. The f_3 frequency was equal to 2.02 kHz, two octaves below f_2, and L_3 was incremented in 3-dB steps. The undisturbed CDT amplitude was 1 dB SPL, and the values shown are relative to this value. Next, the suppressor frequency, f_3, was set approximately equal to f_2 (but *not* exactly equal to it) and the level, L_3, increased in small steps until the CDT decreased below its undisturbed value by more than 10 dB [left hand curve in panel A]. The criterion decrease (dashed line) determines the ''f_2 threshold.'' For the animal shown, the f_3 frequency used was 7.95 kHz, and the f_2 threshold was determined to be 29 dB SPL as shown. The difference between the threshold at 2.02 and that at 7.95 kHz is the threshold shift, T_E, equal to 36 dB in this case. (B) The f_2 threshold establishes the desired level L_3 for the subsequent determination of w_{40}, since the desired L_3 level is equal to the f_2 threshold plus 40 dB, equal to 69 dB SPL in this example. For the estimate of w_{40}, three or more high-frequency response functions were obtained, at short intervals in L_3 and bracketing the desired L_3 level. For each function, the level, L_3, was held constant while the frequency, f_3, was decreased until the CDT amplitude dropped 10 dB or more below its undisturbed value. Three different L_3 values, 65, 68, and 71 dB SPL are illustrated. The responses are separated 10 dB vertically for clarity. For each function, the f_3 frequency was started at 18 kHz and decreased in approximately 0.1-octave steps. The estimate of the w_{40} value, at an L_3 level of 69 dB SPL, was 0.72 octaves as illustrated.

which gives an estimate of $G_a = 37-44$ dB for g_p from 0 to 10 dB/octave, with the most likely value being about 41 dB. This estimate of G_a is higher than the value of about 25 dB determined for adult gerbils by two tone stimuli alone using furosemide injection (Mills and Rubel, 1996). Probable reasons for the lower value using the two tone stimuli have been discussed in Part I (Mills, 1997).

IV. SUMMARY

The agreement between model and data suggest strongly that three tone measurements can indeed provide adequate
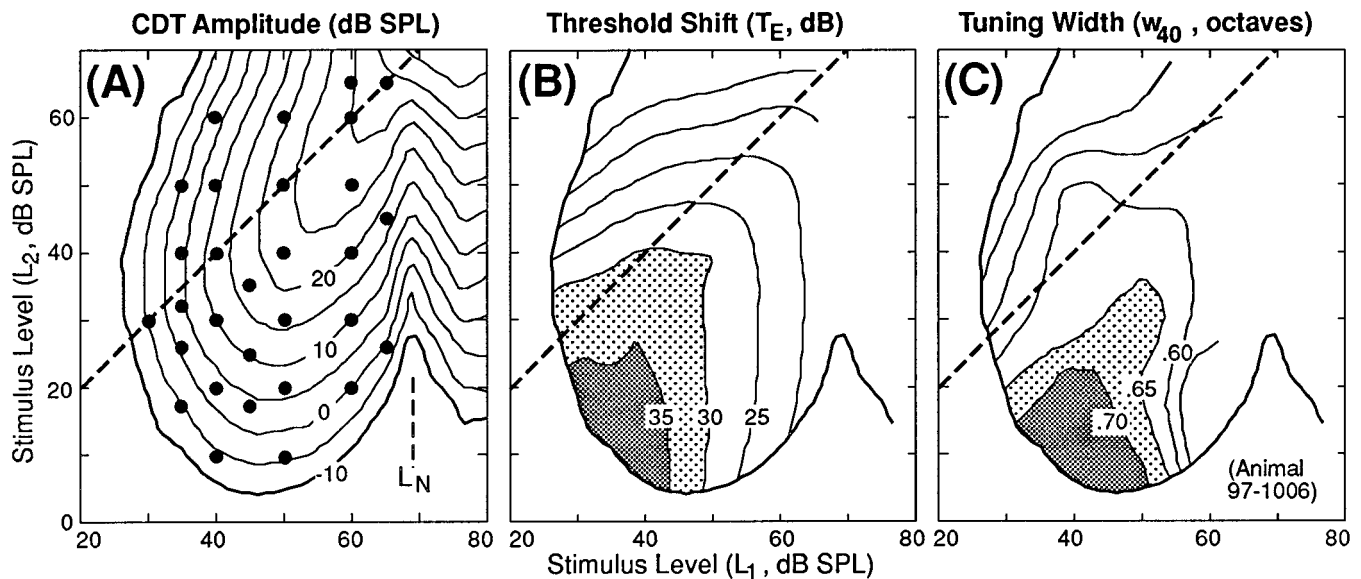
FIG. 12. For an adult gerbil, determination of the threshold shift, T_E, and the tuning width, w_{40}, as a function of the primary stimulus levels, $L_1 \times L_2$. Determinations were made, as outlined in Fig. 11, for 30 different values of $L_1 \times L_2$. The primary stimulus frequencies were $f_2 = 8$ kHz and $f_1 = 6.4$ kHz ($f_2/f_1 = 1.25$). (A) A contour map of the undisturbed CDT ($2f_1 - f_2$) emission for the stimulus amplitudes $L_1 \times L_2$ varied independently. This map is similar to that in Fig. 10(A), except that the CDT amplitudes here begin at -10 dB SPL. This lower value is possible because of the lower noise floor at this CDT frequency (4.8 kHz). Determinations were made only for stimulus levels, L_1, to the left of the notch at $L_1 = 70$ dB SPL and above the -10 dB SPL CDT level. Filled circles denote the locations (values of $L_1 \times L_2$) for which determinations were made. The dashed line at 45° indicates the location of primary stimulus values where $L_1 = L_2$. (B) The lowest contour of (A) is reproduced here, and the measured threshold shifts within this contour indicated. For example, the darkest shaded region indicates that the maximum threshold shifts, equaling 35 dB or more, occurred in the region $L_1 \le 40$ dB SPL and $L_2 \le 20$ dB SPL. (C) Values of the tuning width, w_{40}, as defined in Fig. 2, are plotted versus $L_1 \times L_2$. The most heavily shaded area indicates that the tuning width, w_{40}, was greater than or equal to 0.70 octaves in the region $L_1 \le 50$ dB SPL and $L_1/L_2 \le 15$ dB.

estimates of the two most important quantities characterizing the cochlear amplifier. These are the total gain provided by the amplifier, G_a, and the distance from the start of the amplification region to the peak of the cochlear response, denoted w_r. This "active width," w_r, is related to the effective frequency specificity provided by the amplifier.

The model and data summarized in this report converge on the following recommendations for determining the gain and width of the cochlear amplifier response at any frequency, f_2. Using moderate primary stimulus frequency ratios (in this case, $f_2/f_1 = 1.25$) the best estimates for gerbils will be obtained if the stimulus intensities lie in the region delineated by Eqs. (1) and (4). This region is conservatively outlined in Fig. 13, laid over a contour map of emission amplitudes from Fig. 12. To simulate the more typical signal to noise ratios found, the lowest two contours on the map in Fig. 12 have been removed, so that the lowest contour in the map in Fig. 13 is for the CDT amplitude equal to 0 dB SPL.

At a given f_2 frequency, the recommended procedure would be to first obtain a two tone input–output function using $L_1/L_2 = 20$ dB. This normally is sufficient to establish the location of the notch in terms of the L_1 stimulus. If not, a growth function with larger L_1/L_2 ratio may be required. With L_N determined, three tone measurements may begin at the location suggested by the filled circle in Fig. 13, for which $L_1/L_2 = 20$ dB and $L_N/L_1 = 25$ dB. If there is sufficient signal to noise, additional measurements could be made in the direction of the dashed arrow.

Note, however, that both calculations and observations (Figs. 5 and 12) do not indicate any really large advantage in going to weaker emissions once one is *within* the region indicated in Fig. 13. Confronted by low signal-to-noise, one may as well take measurements at the upper part of the region, at the location of the filled circle. At this point, the undisturbed emission amplitudes are as strong as possible while staying within the optimal primary stimulus region. If the emission amplitudes are too small even at this point, the current results suggest that the measurement should move back up the arrow direction suggested in Fig. 13.

Overall, the model results imply that the maximum values found for the threshold shift, T_E, and tuning width, w_{40}, within the preferred area normally give the closest estimates of G_a and w_r. The maximum measured w_{40} then gives w_r directly. Knowing w_r and T_E, the gain can be estimated from Eq. (5) if g_p can be estimated, or alternately from the relationship between G_a and T_E suggested by the shaded region in Fig. 8. Note, however, that while the general procedures recommended here are expected to be robust, the specific recommended parameters [e.g., Eq. (4)] will generally need to be determined anew for each species. Even for gerbils, the precise parameter recommendations may change with frequency and/or frequency ratio (Mills and Rubel, 1994). The model and general approach presented here, however, are expected to be valid for all relatively nonspecialized mammalian cochleas and frequency ratios $f_2/f_1 > 1.1$.
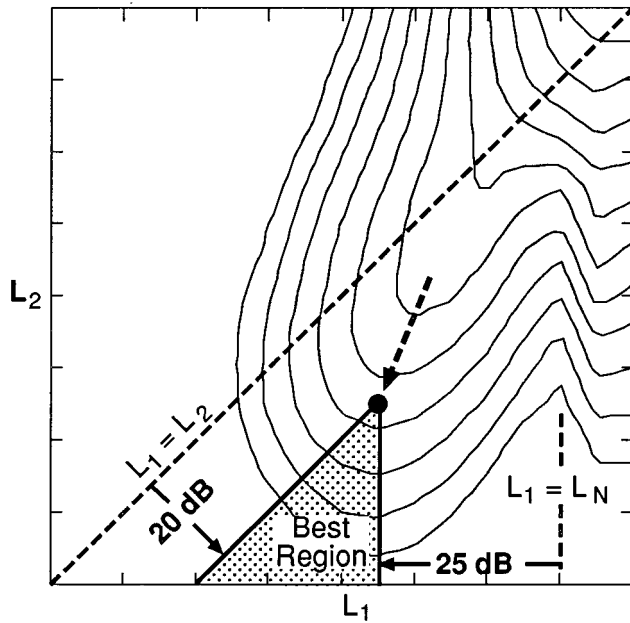
FIG. 13. The best region in the primary stimulus levels, $L_1 \times L_2$, for estimating tuning characteristics as determined by model calculations and experiments is indicated by the solid triangle. A typical undisturbed CDT emission is indicated by the contour lines. This is the same map as in Fig. 12 (A), but with the lowest contour at a CDT amplitude of 0 dB SPL.

V. DISCUSSION

A. The choice of observables in the emission suppression tuning curves

With three stimulus tones providing a total of six independent variables, there is a very large space of possible results. To limit this space, the primary stimuli were temporarily fixed, and the entire space of the third tone investigated. This led to an ''emission suppression tuning curve.'' Choosing the values to abstract from this tuning curve was based on one main principle: *The values found from the tuning curve should depend as little as possible on the precise parameters of the primary stimuli*. The intent of the tuning curve is to measure the underlying, fundamental characteristics of the cochlea and the cochlear amplifier, not the particular qualities associated with the two tone distortion product response. Hundreds of model calculations and many observations confirm (in retrospect) the obvious: In order to measure quantities which have as little as possible to do with the primary stimuli at f_1 and f_2, one should measure as far as possible from either of these two frequencies. At the least, one should avoid the region between them. For example, the shape of the emission suppression tuning curve near and between f_1 and f_2 is a very sensitive function of the stimulus intensity ratios (Fig. 10). It appears to give no useful information on the shape of the actual single frequency cochlear response, i.e., the frequency tuning curve (FTC). If a measurement must be taken close to one of the frequencies, f_1 or f_2 (as one measurement must) the primary stimuli should be arranged so that only that particular traveling wave is substantially affected by the third tone. It is the choice to measure the f_2 threshold that leads to the recommendation that the primary stimulus levels satisfy $L_1 \gg L_2$. Other consider-

ations for the measures which were adopted, and for some which were not adopted, are discussed below.

Note that the main purpose of the model calculations presented here was not to provide a detailed examination of the variation in emission suppression tuning curves with stimulus parameters. Rather, it was to establish a region in stimulus parameter space where the resulting estimates were relatively *insensitive* to small variations in the model parameters. For example, for cochlear amplifier parameters appropriate to the gerbil, the model results generally suggest that the desired relatively insensitive region is bounded by $L_1/L_2 > 20$ dB (Fig. 6). In contrast, model calculations for which $L_1 \cong L_2$ show that the resulting emission suppression tuning curves are very sensitive to precise model parameters (e.g., Fig. 6). These results indicate that observed emission suppression tuning curves may vary considerably with frequency and between species in similar circumstances, i.e., using approximately equal level primaries. For that reason, the emission suppression tuning curves presented here are not intended to be the correct predictions of emission suppression tuning curves for $L_1 \cong L_2$, or even of the variation with L_1/L_2, but simply to be illustrative of the general conclusion. In other words, with slightly different model characteristics, a large number of very different emission suppression tuning curves can be calculated with $L_1 \lesssim L_2$. However, as L_1/L_2 becomes large, for both model and observation the generated tuning curves begin to look much more similar. The focus of this paper is the determination of the region of similarity, over which small variations cause little change in the estimates of the basic characteristics of the cochlear amplifier, for both model and observation.

B. Response criterion

In both model calculations and observation, a criterion response equal to a 5-dB decrease in CDT amplitude was adopted for this report. This value was chosen as a compromise for the observational data, since a higher value requires a higher minimum signal-to-noise ratio, and a lower value is sensitive to small changes in the primary stimulus amplitudes and to noise. Lower criterion thresholds have been avoided in this report for an additional reason. This is because criterion thresholds under 5 dB often show dips for f_3 values near the $2f_1 - f_2$ frequency (Gaskill and Brown, 1996; Kummer *et al.*, 1995). The present model does not attempt to include this behavior.

C. The tuning width, w_{40}

It may be a reasonable approach to characterize neural or psychoacoustic tuning curves by the full width of the response at a given level, e.g., at 10 dB above threshold. This is not a useful approach with emission suppression tuning curves. The *full width* of the emission suppression tuning curve at any level above threshold depends strongly on the stimulus frequency ratio, f_2/f_1 (Figs. 4 and 10; Brown and Kemp, 1984). Any effects due to the fundamental width, w_r, are masked by this very strong dependence. The higher frequency ''half-width,'' that is, the distance from f_2 to the emission suppression tuning curve is a reasonable alterna-

tive. However, even this distance is quite sensitive to stimulus parameters at small distances (in L_3) above the f_2 threshold. Observations and model calculations both indicate, however, that the emission suppression tuning curve typically becomes quite steep at a location about 30 dB above the tip threshold [Figs. 2 and 10(B)]. These calculations suggest that measuring the response 40 dB above the f_2 threshold is a good compromise. This level gives a consistent, accurate approximation of the active width, w_r, while it is still low enough in intensity that it usually does not require extreme sound levels in the ear canal. The choice of the reference frequency, f_2, for the calculation of w_{40} rather than the actual most sensitive f_3 frequency, when different, is justified by the same arguments (summarized below) in favor of using the f_2 threshold itself rather than the actual tip of the emission suppression tuning curve.

D. The shoulder threshold

At all f_3 frequencies well below f_1 and f_2, the effect of the suppressor tone on the CDT amplitude is due entirely to the passive part of the f_3 traveling wave [Fig. 3(B)]. In the model, it is assumed that the passive increase does not depend on frequency, and the middle ear is assumed transparent. With these assumptions, the emission suppression tuning curve is flat in this region (Fig. 2). In real mammals, middle ear and passive cochlear effects will cause deviations from this ideal case. However, the shoulder region can usually be recognized, if not obvious from the emission suppression tuning curve, then from a close examination of the emission response functions themselves [e.g., Fig. 10(B)]. Unfortunately, many published reports do not use low enough suppressor frequencies and/or high enough suppressor stimulus levels to establish the existence of a shoulder.

In the present report, frequencies for the shoulder determination were chosen based on the shapes of the tuning curves. The shoulder frequency was chosen to be 1 octave below f_2 for the model results and between 1.5 and 2 octaves below f_2 for the animal data. At whatever frequency the shoulder threshold determination is made, it must be recognized that in the real case the difference in threshold between the response at f_2 and the shoulder frequency *includes* whatever differences in passive transmission there are between these two frequencies. The relevant passive transmission path includes the entire passive input transmission path, from the outer ear to the place on the cochlea where active amplification begins (Mills, 1997; Mills and Rubel, 1996).

E. The f_2 threshold

It is certainly necessary to find the most sensitive frequency, the "tip" frequency, in constructing neural tuning curves. The most sensitive frequency defines the characteristic frequency for the neuron, and its sensitivity. However, *neither* of these quantities is determined by the tip of the emission suppression tuning curve. The frequencies characteristic of the emission suppression tuning curve are defined by the primary stimulus frequencies, f_1 and f_2, themselves. The actual location of the tip depends strongly on the stimulus intensity ratio, L_1/L_2 (e.g., Figs. 4 and 10). It also de-

pends on the stimulus frequency ratio, f_2/f_1 (Brown and Kemp, 1984). The absolute threshold of the emission suppression tuning curves does not reflect the sensitivity of the cochlea, i.e., its low level performance. Rather, the emission threshold depends essentially on the saturation of the cochlea. That is, emission scales depend on the cochlear signal compression characteristics and therefore its high level responses. This is apparent from the model, since the only scale in the emission amplitude response is the saturation level (Mills, 1997).

It is concluded that in both model calculations and observations, *it is not at all necessary to search for the absolute lowest threshold for the emission suppression tuning curve*. This search is to be avoided, in fact, because it adds an unnecessary dimension to the observations that would be required. For example, such a search would require the left hand curve seen in Fig. 1(A) to be repeated for a wide range of nearby frequencies in f_3, from above f_2 to below f_1. In any case, it has been already established for both model and observation that in the region where the most sensitive emission suppression tuning curves are obtained, i.e., where $L_N \gg L_1 \gg L_2$, the tip is generally located at or near to the f_2 frequency. The process of determining the actual tuning characteristics is simplified considerably by focusing both model calculations and observation on the determination of the f_2 frequency threshold. That is, the relationships between model parameters and observation are derived using the f_2 frequency threshold for both, even in cases where this is not necessarily the lowest absolute threshold for the emission suppression tuning curve.

F. Application to other species

The following procedure is suggested for applying the results presented here to estimating cochlear amplifier characteristics in species other than gerbils. For each species, an initial survey such as illustrated in Fig. 12 would be required. The purpose of the survey is to establish the parameter values (as shown in Fig. 13 for gerbil) which are needed for adequate estimates of the cochlear amplifier characteristics. For most mammals, considering the parameter space for $L_1 \gg L_2$ (at and below the dashed lines in Figs. 12 and 13) should be sufficient. Note that the time required to obtain such data is not inordinate, as long as the minimum data set illustrated in Fig. 11 is used. The hope is that, as in the gerbil, one will obtain a region where the derived values are approximately constant (as in the heaviest shaded regions in Figs. 12 and 13). If so, these areas define a region in which subsequent data collection can usefully be concentrated. Following such measurements, detailed model calculations can provide additional accuracy for the estimation of basic cochlear amplifier characteristics from the observed tuning characteristics.

Values for the total cochlear amplifier gain of about 40 dB with a width of 0.7 octave have been estimated here for the gerbil. This implies a cochlear amplifier growth rate of about 60 dB/octave. Preliminary indications are that these values may vary considerably between species. For example, in humans indications are that the width may be smaller, near 0.4 octave, with a total gain of about the same magnitude as

gerbil (Abdala and Sininger, 1996). If substantiated, this would imply a typical gain rate of about 100 dB/octave in humans.[1] The simple model presented here can easily be extended to include such values and can give emission suppression tuning curves similar to those reported (e.g., Abdala and Sininger, 1996; Kummer *et al.*, 1995).

ACKNOWLEDGMENTS

[1]The same relation holds (exactly) for the threshold shift, T_F, defined in Fig. 1(B).

[2]A potential complication to obtaining accurate emission tuning curves in humans arises from the presence of ''fine structure'' in the emissions (He and Schmiedt, 1993, 1997). The fine structure can cause rapid emission amplitude variations with small changes in the primary (two tone) stimulus levels; the specific effect on emission suppression tuning curves has not been studied.

Abdala, C., and Sininger, Y. S. (**1996**). ''The development of cochlear frequency resolution in the human auditory system,'' Ear Hear. **17**, 374–385.

Abdala, C., Sininger, Y. S., Ekelid, M., and Zeng, F.-G. (**1996**). ''Distortion product otoacoustic emission suppression tuning curves in human adults and neonates,'' Hearing Res. **98**, 38–53.

Allen, J. B., and Fahey, P. F. (**1993**). ''A second cochlear-frequency map that correlates distortion product and neural tuning measurements,'' J. Acoust. Soc. Am. **94**, 809–816.

Brown, A. M., and Gaskill, S. A. (**1990**). ''Measurement of acoustic distortion reveals underlying similarities between human and rodent mechanical responses,'' J. Acoust. Soc. Am. **88**, 840–849.

Brown, A. M., and Kemp, D. T. (**1984**). ''Suppressibility of the $2f_1-f_2$ stimulated acoustic emissions in gerbil and man,'' Hearing Res. **13**, 29–37.

Brown, A. M., and Kemp, D. T. (**1985**). ''Intermodulation distortion in the cochlea: could basal vibration be the major cause of round window CM distortion?'' Hearing Res. **19**, 191–198.

Brown, A. M., McDowell, B., and Forge, A. (**1989**). ''Acoustic distortion products can be used to monitor the effects of chronic gentamicin treatment,'' Hearing Res. **42**, 143–156.

Brown, A. M., Gaskill, S. A., Carlyon, R. P., and Williams, D. M. (**1993**). ''Acoustic distortion as a measure of frequency selectivity: Relation to psychophysical equivalent rectangular bandwidth,'' J. Acoust. Soc. Am. **93**, 3291–3297.

Burkey, J., and Glans, D. (**1991**). ''Psychophysical tuning curves in gerbils,'' J. Acoust. Soc. Am. **89**, 1822–1823.

Cianfrone, G., Altissimi, G., Cervellini, M., Musacchio, A., and Turchetta, R. (**1994**). ''Suppression tuning characteristics of $2f_1-f_2$ distortion product otoacoustic emissions,'' Br. J. Audiol. **28**, 205–212.

Davis, H. (**1983**). ''An active process in cochlear mechanics,'' Hearing Res. **9**, 79–90.

Faulstich, M., Kössl, M., and Reimer, K. (**1996**). ''Analysis of non-linear cochlear mechanics in the marsupial *Monodelphis domestica*: Ancestral and modern mammalian features,'' Hearing Res. **94**, 47–53.

Frank, G., and Kossl, M. (**1995**). ''The shape of $2f_1-f_2$ suppression tuning curves reflects basilar membrane specializations in the mustached bat, *Pteronotus parnelli*,'' Hearing Res. **83**, 151–160.

Gaskill, S. A., and Brown, A. M. (**1996**). ''Suppression of human acoustic distortion product: Dual origin of $2f_1-f_2$,'' J. Acoust. Soc. Am. **100**, 3268–3274.

Harris, F. P., Probst, R., and Xu, L. (**1992**). ''Suppression of the $2f_1-f_2$ otoacoustic emission in humans,'' Hearing Res. **64**, 133–141.

He, N.-j., and Schmiedt, R. A. (**1993**). ''Fine structure of the $2f_1-f_2$ acoustic distortion product: Changes with primary level,'' J. Acoust. Soc. Am. **94**, 2659–2669.

He, N.-j., and Schmiedt, R. A. (**1997**). ''Fine structure of the $2f_1-f_2$ acoustic distortion product: Effect of primary level and frequency ratios,'' J. Acoust. Soc. Am. **101**, 3554–3565.

Kemp, D. T. (**1978**). ''Stimulated acoustic emissions from within the human auditory system,'' J. Acoust. Soc. Am. **64**, 1386–1391.

Kössl, M., Frank, G., Burda, H., and Müller, M. (**1996**). ''Acoustic distortion products from the cochlea of the blind African mole rat, *Cryptomys spec.*,'' J. Comp. Physiol. A **178**, 427–434.

Kummer, P., Janssen, T., and Arnold, W. (**1995**). ''Suppression turning characteristics of the $2f_1-f_2$ distortion-product otoacoustic emission in humans,'' J. Acoust. Soc. Am. **98**, 197–210.

Martin, G. K., Lonsbury-Martin, B. L., Probst, R., Scheinin, S. A., and Coats, A. C. (**1987**). ''Acoustic distortion products in rabbit ear canal. II. Sites of origin revealed by suppression contours and pure-tone exposures,'' Hearing Res. **28**, 191–208.

Mills, D. M. (**1997**). ''Interpretation of distortion product otoacoustic emission measurements. I. Two stimulus tones,'' J. Acoust. Soc. Am. **102**, 413–429.

Mills, D. M., and Rubel, E. W. (**1994**). ''Variation of distortion product otoacoustic emissions with furosemide injection,'' Hearing Res. **77**, 183–199.

Mills, D. M., and Rubel, E. W. (**1996**). ''Development of the cochlear amplifier,'' J. Acoust. Soc. Am. **100**, 428–441.

Mills, D. M., and Rubel, E. W. (**1997**). ''Development of distortion product emission in the gerbil: Filter response and signal delay,'' J. Acoust. Soc. Am. **101**, 395–411.

Moore, B. C. J., Glasberg, B. R., and Roberts, B. (**1984**). ''Refining the measurement of psychophysical tuning curves,'' J. Acoust. Soc. Am. **76**, 1057–1066.

Moulin, A., and Kemp, D. T. (**1996a**). ''Multicomponent acoustic distortion product otoacoustic phase in humans. I. General characteristics,'' J. Acoust. Soc. Am. **100**, 1617–1639.

Moulin, A., and Kemp, D. T. (**1996b**). ''Multicomponent acoustic distortion product otoacoustic phase in humans. II. Implications for distortion product otoacoustic emissions generation,'' J. Acoust. Soc. Am. **100**, 1640–1662.

Nuttall, A. L., and Dolan, D. F. (**1996**). ''Steady-state sinusoidal velocity responses of the basilar membrane in guinea pig,'' J. Acoust. Soc. Am. **99**, 1556–1565.

Plassmann, W., and Kadel, M. (**1991**). ''Low-frequency sensitivity in a gerbiline rodent, Pachyuromys duprasi,'' Brain Behav. Evol. **38**, 115–126.

Rübsamen, R., Mills, D. M., and Rubel, E. W. (**1995**). ''Effects of furosemide on distortion product otoacoustic emissions and on neuronal responses in the anteroventral cochlear nucleus,'' J. Neurophysiol. **74**, 1628–1638.

Ruggero, M. A., and Rich, N. C. (**1991**). ''Furosemide alters organ of Corti mechanics: Evidence for feedback of outer hair cells upon the basilar membrane,'' J. Neurosci. **11**, 1057–1067.

Stover, L. J., Neely, S. T., and Gorga, M. P. (**1996**). ''Latency and multiple sources of distortion product otoacoustic emissions,'' J. Acoust. Soc. Am. **99**, 1016–1024.

Tarnowski, B. I., Schmiedt, R. A., Hellstrom, L. I., Lee, F. S., and Adams, J. C. (**1991**). ''Age-related changes in cochleas of mongolian gerbils,'' Hearing Res. **54**, 123–134.

Williams, D. M., and Brown, A. M. (**1995**). ''Contralateral and ipsilateral suppression of the $2f_1-f_2$ distortion product in human subjects,'' J. Acoust. Soc. Am. **97**, 1130–1140.

A dynamic model of outer hair cell motility including intracellular and extracellular fluid viscosity

J. A. Tolomeo
Department of Physiology, University of Bristol, Bristol BS8 1TD, United Kingdom

C. R. Steele
Division of Applied Mechanics, Stanford University, Stanford, California 94305

The deformation response of a guinea pig outer hair cell is modeled for mechanical and electrical stimulation up to 25 kHz. The analysis uses a Fourier series technique for a finite length cell surrounded internally and externally by a much larger continuum of viscous fluid. The analytical solution predicts that outer hair cell length changes occur due to applied mechanical or electrical stimulation without significant resonance, characteristic of a highly damped system. The deformation is found to have little attenuation up to a corner frequency of about 2 kHz for long cells and 10 kHz for short cells, in agreement with published experimental results. For electrical loading of 1 mV across the lateral cell wall, deformation for short cells is calculated to be greater than 1 nm for frequencies up to 20 kHz. These results support the proposition that *in vivo* the outer hair cell modifies the character of basilar membrane deformation on a cycle-by-cycle basis. An estimate of the capability of the cell to supply energy to the basilar membrane is given based on published values of outer hair cell material properties. © *1998 Acoustical Society of America.*
[S0001-4966(98)00201-X]

PACS numbers: 43.64.Kc, 43.40.Rj, 43.64.Ld, 43.80.Gx [RDF]

LIST OF SYMBOLS

a	half the length of the cell domain
A_m	applied shear stress Fourier coefficient
B_m	applied normal stress Fourier coefficient
C	resultant stiffness coefficient
$\mathbf{D}$	matrix that converts Fourier coefficients from fluid to cell harmonics
e	piezoelectric constant
E_{avg}	average strain energy
F	unknown coefficient for rotational and irrotational fluid velocity solutions
$I(r)$	modified Bessel function of the first kind
$\mathbf{k}_m$	(2×2) stiffness matrix for the mth Fourier coefficients of cell stress to displacement
$\mathbf{k}$	$(2*mmax\times2*mmax)$ stiffness matrix containing $\mathbf{k}_m$ for all cell harmonics
$\mathbf{K}_n$	(2×2) stiffness matrix for the nth Fourier coefficients for the fluid
$\mathbf{K}$	stiffness matrix containing $\mathbf{K}_n$ for all fluid harmonics
$K(r)$	modified Bessel function of the second kind
L	half the length of the fluid domain
m	Fourier harmonic number in cell domain
$mmax$	maximum number of Fourier coefficients used for cell description
n	fluid domain Fourier harmonic number
N	resultant load in the lateral wall (stress times thickness)
p	fluid pressure
r	radial coordinate measured from cell axis
r_c	radius of the cell wall
t	time
u_r	displacement deformation in the r direction
u_x	displacement deformation in the x direction
u_{mr}	the mth Fourier coefficient of radial displacement
u_{mx}	the mth Fourier coefficient of axial displacement
$\mathbf{u}_m$	(2×1) vector of the mth radial and axial displacement Fourier coefficients
$\mathbf{u}$	$(2*mmax\times1)$ vector containing all the paired displacement coefficients
$U_n(r)$	displacement coefficient in fluid domain harmonics, analogous to u_m
ν	fluid velocity
$\mathbf{v}$	total fluid velocity vector
V	voltage
x	axial coordinate measured from cell center
α	fluid domain Fourier harmonic $=n\pi/2L$
β	Fourier harmonic in cell domain $=m\pi/2a$
θ	circumferential direction
λ	coefficient that governs the radial dependence of the Bessel functions
μ	fluid viscosity
ρ	fluid density
σ_r	total normal stress in the r direction
σ_{rx}	total shear stress in the r,x direction
σ_{mr}	the mth Fourier coefficient of normal stress
σ_{mrx}	the mth Fourier coefficient of shear stress
σ_{applied}	applied stress at the cell wall
$\delta\boldsymbol{\sigma}$	stress jump in fluid across the cell wall (fluid stress interior−stress exterior)
$\boldsymbol{\sigma}_m$	(2×1) vector of the mth paired stress Fourier coefficients
$\boldsymbol{\sigma}$	$(2*mmax\times1)$ vector containing all the paired stress Fourier coefficients

$\Sigma(r)$ stress coefficient in the fluid domain Fourier harmonics, analogous to σ

Φ irrotational fluid solution

Ψ rotational fluid solution

ω radial frequency

INTRODUCTION

Mammalian outer hair cells are believed to enhance frequency discrimination within the cochlea. They accomplish this through a motile mechanism which allows them to undergo high-frequency length changes in response to intracellular voltage (Brownell *et al.*, 1985; Kachar *et al.*, 1986; Ashmore, 1987). Because of this, outer hair cell motility has been proposed to affect basilar membrane motion on a cycle-by-cycle basis, effectively enhancing the membrane motion in some manner which increases frequency tuning.

The molecular mechanism underlying outer hair cell motility has not been discovered. However, numerous investigations have studied the speed and quantitative character of the mechanism. Cell motility is generally viewed as the result of motor proteins which undergo a conformal change within the plasma membrane layer in response to transmembrane potential (Kalinec *et al.*, 1992; Iwasa, 1994). Conversely, an imposed strain rate on the cell wall generates a transmembrane current (Iwasa, 1993; Gale and Ashmore, 1994). This coupled electro-mechanical behavior is the definition of a piezoelectric material. The electrical and mechanical properties are fully coupled so that energy within the cell wall is shared between mechanical and electrical forms in a conservative manner, at least in the static case (Tolomeo and Steele, 1995). Further evidence of the reciprocity of coupling between mechanical and electrical properties is given by the similar time constants for the onset of outer hair cell motility and ''nonlinear'' charge movement (Santos-Sacchi, 1992).

Experiments on the time dependence of outer hair cell motion have generally considered only the effects of electrical properties. The cell is modeled as a simple combination of resistance and capacitance and these parameters are subsequently chosen to fit the observed electrical behavior. The time response of these discrete parameter models is then extrapolated to the high-frequency domain. These analyses show that outer hair cell motility may be greatly attenuated at high frequencies due to electrical damping and thus raise doubt concerning the hypothesized physiological role (Santos-Sacchi, 1992; Dallos and Evans, 1995). However, interpretation of these models is difficult due to the requirement of separating the electrical properties of the cell from the electrical properties and frequency-limiting behavior of the patch clamp-cell system (Santos-Sacchi, 1992). The electrical model assumes that attenuation of cell motility at high frequencies is due to electrical damping and the effect of mechanical damping is neglected. The cells are surrounded internally and externally by a viscous and massive fluid which limits the deformation velocity the cell can generate and this should not be attributed to the electrical properties.

Previous analyses of the fluid coupling effects have focused on the electrokinetics of an ionized fluid. Jen and Steele (1987) developed an asymptotic series technique to reduce the coupled partial differential fluid equations to coupled linear ordinary differential equations. They concluded that the charge distribution on the cell wall required to drive cell motility is within the physiological range. Jerry *et al.* (1995) further simplified the fluid equations by neglecting the radial component of fluid velocity thereby reducing the system to a one-dimensional flow system described by a single ordinary differential equation. They replaced the no-slip constraint at the cell–fluid interface with a velocity boundary condition on the fluid in order to approximate the effect of cell permeability and concluded that electro-osmotic effects can be discounted as a mechanism for fast motility. Ratnanather *et al.* (1996) used a solution technique similar to Jen and Steele in order to perform a parameter study on the viscoelastic properties of the cell wall. They found that better agreement with experimental results can be achieved if some viscoelasticity is included. However, these models consider only isotropic properties of the lateral cell wall. Further, the asymptotic analysis that is used to justify the mathematical simplifications is valid for long slender cells. In the physiologically important high-frequency region of cochlea, the cells are quite short and this large aspect ratio approximation may not be valid. The asymptotic solution has no mechanism for modeling the effects of the fluid beyond the end of the cell. Experiments on isolated cells *in vitro* take place in an environment where a large fluid domain surrounds the cells both radially and longitudinally.

In this study the deformation of the cell is predicted from a model of the cell with a much larger domain of surrounding fluid. The internal and external fluid are each described by the linearized Navier–Stokes equation and the cell is described as an anisotropic membrane. The no slip boundary condition at the cell–fluid interface is rigorously maintained so that this is a fully coupled viscous fluid–structure solution. The driving force is the piezoelectric stress generated due to a prescribed transmembrane electrical potential, similar to a whole cell manipulation of the cell voltage. The model is used to calculate cell deformation as a function of driving frequency given that the prescribed peak-to-peak voltage is held constant. This approach isolates the mechanical damping from electrical damping, since transcellular voltage level is prescribed independent of frequency. Thus the results can be used to estimate the importance of fluid viscosity in relation to experimentally measured motility attenuation. The effects of fluid viscosity represent a physical limitation of the hypothesized active role of the outer hair cell (Hudspeth, 1989) and this issue is directly addressed. This viscoelastic behavior of the fluid–structure system is a prerequisite to understanding the character of outer hair cell motion in relation to basilar membrane motion *in vivo*.
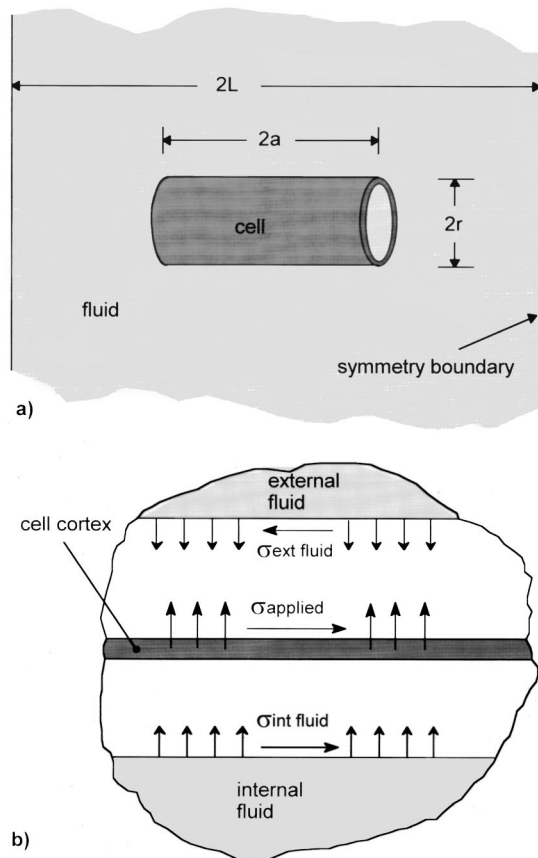
FIG. 1. (a) Model of the outer hair cell and fluid. The cell is surrounded with intracellular and extracellular viscous and massive fluid. (b) Load conditions at the cell–fluid interface. The fluid contributes viscous and mass loads to the internal and external sides of the cell wall. The applied load is prescribed similar to experimental load conditions. The figure shows the fluid artificially separated from the cell wall for the purpose of visualizing the loads.

I. MODEL

A. Geometry

The outer hair cell is modeled as a thin-walled circular cylinder with open ends as shown in Fig. 1(a). The open ends represent an extreme case of the physical system which has compliant ends. The justification for this approximation is that the cell has been shown to deform due to electrical loading without the generation of significant internal pressure changes (Tolomeo and Steele, 1995). This can been seen qualitatively by comparing the similar motility results of experiments where internal pressure is and is not controlled (Dallos *et al.*, 1993; Santos-Sacchi, 1989). This implies that little fluid flow occurs through the model ends so that the mechanical contribution of closed ends may be neglected. This model assumption has been previously verified (Tolomeo, 1995). The cell has length $2a$ and radius r_c and is located at the center of a fluid domain of length $2L$, while the fluid domain is infinite in the radial direction. The fluid is modeled as Newtonian with the viscosity and density of water at 25 °C. Mechanical or electrical loads applied to the lateral cell wall are prescribed to be time harmonic.

B. Cell–fluid interface

The general outline of the analysis is to develop an expression that relates the prescribed traction on the lateral cell wall with the deformation of the cell. A Fourier series technique is to describe the fluid and cell domains using separate Fourier harmonics. At the cell wall, the stress has contributions from the internal fluid, external fluid, and the applied stress as shown in Fig. 1(b). Both the applied radial normal stress (σ_r) and shear stress (σ_{rx}) on the wall surface may be prescribed. Throughout the analysis bold face quantities will be used to denote vector or matrix quantities.

By modeling the cell wall as a thin membrane, the equilibrium equations for the cell can be written in terms of stress Fourier coefficients as Eq. (1). The exact form of the stress vectors ($\boldsymbol{\sigma}$) and the form of the Fourier coefficients they contain will be detailed in subsequent sections:

$$\boldsymbol{\sigma}_{\text{cell}} = \boldsymbol{\sigma}_{\text{applied}} + \delta\boldsymbol{\sigma}_{\text{fluid}}. \tag{1}$$

The subscripts indicate the location of the stress as internal to the cell, due to the difference in fluid tractions across the cell wall ($\delta\boldsymbol{\sigma}$), or due to the applied traction. The no-slip boundary condition for the viscous fluid at the cell requires that at the cell wall the displacement of the internal fluid, external fluid, and cell are all equal:

$$\mathbf{u}_{\text{fluid}} = \mathbf{u}_{\text{cell}}. \tag{2}$$

Again, the exact form of the displacement vectors ($\mathbf{u}$) will be detailed in subsequent sections. At this point is suffices to describe them as containing Fourier coefficients of the unknown displacement which are to be determined.

The following analysis focuses on determining the form of the stiffness matrices relating stress to deformation for the fluid and cell materials based on classical continuum theory so that Eqs. (1) and (2) may be combined. The term ''stiffness matrix'' is used very generally here, and includes the effects of mass, viscosity, and elasticity. It contains complex-valued components that can be directly related to the system impedance through the driving frequency. The stiffness matrices are developed in the subsequent sections using a Fourier series approach.

II. ANALYSIS

A. Fourier series

The total stiffness matrices for general load and deformation conditions are built from Fourier series taken over the cell and fluid domains. The loading is restricted to be axisymmetric in the circumferential direction. Fourier harmonics are defined based on the cell and fluid lengths. The harmonics used for the cell description are different from the harmonics used for the fluid because of the different respective lengths. However, a transformation expression will be developed to equate the two series.

An arbitrary applied stress along the length of the lateral wall is expressed as a Fourier series on the cell domain. A Fourier series can be interpreted in terms of symmetric and antisymmetric forms in the longitudinal direction when the coordinate system is taken about the cell center. The symmetric component of an arbitrary function is described by the

odd harmonics while the antisymmetric component is described by the even harmonics. In the following analysis only symmetric functions corresponding to symmetric loading and boundary conditions will be developed in detail since this will illustrate the form of the solution technique. General load and boundary conditions can be analyzed with the inclusion of the antisymmetric harmonics (Tolomeo, 1995) without any additional conceptual difficulties, however this will not be pursued in the present work.

The coefficients for the symmetric load condition are fully prescribed by the known applied load. Each harmonic is based on the inverse cell length with symmetric forms for the stress in the form $\beta_m = m\pi/2a$, where m is an odd integer and $2a$ is the cell length. This corresponds to positive odd multiples of a half-cosine mode of radial stress and multiples of a half-sine wave of shear stress applied to the cell wall. For computational considerations the series is truncated at the mmax term where mmax is chosen to provide sufficient accuracy:

$$\sigma_{rx_{\text{applied}}} = \text{Re}\left[\sum_{m=\text{odd}}^{mmax} A_m \sin \beta_m x e^{i\omega t}\right], \quad -a \leq x \leq a,$$

(3)

$$\sigma_{r_{\text{applied}}} = \text{Re}\left[\sum_{m=\text{odd}}^{mmax} B_m \cos \beta_m x e^{i\omega t}\right], \quad -a \leq x \leq a. \quad (4)$$

In Eqs. (3) and (4), A_m and B_m are the Fourier coefficients of the mth harmonic of the applied load, ω is the frequency of motion, and t is time. Similarly, the displacement of the lateral wall is assumed in a compatible form:

$$u_x = \text{Re}\left[\sum_{m=\text{odd}}^{mmax} u_{m_x} \sin \beta_m x e^{i\omega t}\right], \quad -a \leq x \leq a, \quad (5)$$

$$u_r = \text{Re}\left[\sum_{m=\text{odd}}^{mmax} u_{m_r} \cos \beta_m x e^{i\omega t}\right], \quad -a \leq x \leq a. \quad (6)$$

The mth stress and displacement vectors are defined for convenience:

$$\sigma_{m_{\text{applied}}} \equiv \begin{bmatrix} A_m \\ B_m \end{bmatrix}, \quad \mathbf{u}_m \equiv \begin{bmatrix} u_{m_x} \\ u_{m_r} \end{bmatrix}. \quad (7)$$

The total stress and displacement is written as vectors of these Fourier coefficients:

$$\sigma_{\text{applied}} \equiv \begin{bmatrix} \sigma_{1_{\text{applied}}} \\ \sigma_{2_{\text{applied}}} \\ \cdots \\ \sigma_{mmax_{\text{applied}}} \end{bmatrix}, \quad \mathbf{u} \equiv \begin{bmatrix} \mathbf{u}_1 \\ \mathbf{u}_2 \\ \cdots \\ \mathbf{u}_{mmax} \end{bmatrix}. \quad (8)$$

B. Stiffness of the cell wall

The cell wall is very thin with large radius-to-thickness ratio (~ 200) and density similar to water. The mass of the cell wall is therefore considered negligible compared to the effective fluid mass. The bending stiffness of the lateral wall can also be shown to be negligible for the smooth modes of

loading and deformation used in this analysis. The equilibrium equations therefore describe the axisymmetric deformation of a thin cylindrical membrane,

$$N_\theta = \sigma_r r_c, \quad (9)$$

$$\frac{\partial N_x}{\partial x} = -\sigma_{rx}, \quad (10)$$

where N is the stress resultant defined as the product of the stress and cell wall thickness, the subscripts θ and x indicate the circumferential and axial directions, respectively, and r_c is the radius at the cell wall. A general Hookean orthotropic constitutive law is used based on the observed behavior and morphology of the cell (Holley and Ashmore, 1990; Tolomeo et al., 1996):

$$\begin{bmatrix} N_x \\ N_\theta \end{bmatrix} = \begin{bmatrix} C_{11} & C_{12} \\ C_{12} & C_{22} \end{bmatrix} \begin{bmatrix} \dfrac{\partial u_x}{\partial x} \\ \dfrac{u_r}{r_c} \end{bmatrix}. \quad (11)$$

In Eq. (11), the Cs are the resultant stiffness coefficients relating stress to strain. Substituting the constitutive law and assumed displacement functions into the membrane equations gives the stiffness matrix in an appropriate form for the mth harmonic:

$$\sigma_{m_{\text{cell}}} = \mathbf{k}_{m_{\text{cell}}} \mathbf{u}_m = \begin{bmatrix} C_{11}\beta_m^2 & C_{12}\dfrac{\beta_m}{r_c} \\ C_{12}\dfrac{\beta_m}{r_c} & C_{22}\dfrac{1}{r_c^2} \end{bmatrix} \mathbf{u}_m. \quad (12)$$

The total cell stiffness matrix is built using the fundamental 2×2 uncoupled harmonic stiffness matrices of Eq. (12). The vector of total Fourier stress coefficients in the cell is

$$\sigma_{\text{cel}} = \mathbf{k}_{\text{cell}} \mathbf{u} = \begin{bmatrix} \mathbf{k}_{1_{\text{cell}}} & & & \text{zeros} \\ & \mathbf{k}_{2_{\text{cell}}} & & \\ & & \cdots & \\ \text{zeros} & & & \mathbf{k}_{mmax_{\text{cell}}} \end{bmatrix} \mathbf{u}. \quad (13)$$

C. Fluid equations

The finite cell was treated by a Fourier series rather than a Fourier integral since it is defined only over a given length. The fluid domain is therefore truncated at some length which is large enough to ensure that significant deformation about the cell appears as a localized phenomenon within the viscous fluid domain, but not so large that it cannot be well represented with a reasonable number of Fourier harmonics. The fluid has length $2L$ where $L \geq a$ and a set of Fourier harmonics are used based on multiples of the inverse fluid length $\alpha_n = n\pi/2L$ where n is odd for symmetric modes. In the radial direction, the exterior fluid is infinite. In terms of the fluid harmonics the fluid stress is

$$\sigma_{rx} = \text{Re}\left[\sum_{n=\text{odd}}^{n\ \text{max}} \Sigma(r)_{n_{rx}} \sin \alpha_n x e^{i\omega t}\right], \quad -L \leq x \leq L,$$

(14)

$$\sigma_r = \text{Re}\left[\sum_{n=\text{odd}}^{n\ \text{max}} \Sigma(r)_{n_r} \cos \alpha_n x e^{i\omega t}\right], \quad -L \leq x \leq L. \quad (15)$$

Similarly, the fluid displacement is written in terms of fluid harmonics.

$$u_{rx} = \text{Re}\left[\sum_{n=\text{odd}}^{n\ \text{max}} U(r)_{n_x} \sin \alpha_n x e^{i\omega t}\right], \quad -L \le x \le L, \tag{16}$$

$$u_r = \text{Re}\left[\sum_{n=\text{odd}}^{n\ \text{max}} U(r)_{n_r} \cos \alpha_n x e^{i\omega t}\right], \quad -L \le x \le L. \tag{17}$$

In Eqs. (14)–(17) the stress and displacement coefficients are given by the symbols Σ and U and include a radial coordinate dependence within the fluid.

The governing equation for the fluid analysis is the Navier–Stokes equation for an incompressible medium. This is an expression of the rate of momentum balance for the Newtonian fluid and includes the effects of viscosity, pressure, and mass. It is straightforward to show through nondimensional analysis that the nonlinear convective terms in the Navier–Stokes equation are negligible for physiological deformation (Tolomeo, 1995); however, the effects of viscosity, mass, and pressure gradient all can be expected to dominate the fluid deformation behavior at different points within the frequency spectrum and therefore these terms must be included in the analysis. The linearized Navier–Stokes equation takes the vector form

$$-\nabla p + \mu \nabla^2 \mathbf{v} = \rho \frac{\partial \mathbf{v}}{\partial t}, \tag{18}$$

where p is the pressure, μ is the viscosity, and $\mathbf{v}$ is the fluid velocity vector. Decomposing the velocity vector into a gradient of a potential term and a curl term gives

$$\mathbf{v} = \nabla \Phi + \nabla \times \mathbf{\Psi}. \tag{19}$$

Substituting this definition into Eq. (18) gives

$$\nabla\left(-p + \mu \nabla^2 \Phi - \rho \frac{\partial \Phi}{\partial t}\right) = \nabla \times \left(\rho \frac{\partial \mathbf{\Psi}}{\partial t} - \mu \nabla^2 \mathbf{\Psi}\right). \tag{20}$$

A solution is sought in which each side of the above equations vanishes separately in the following manner:

$$-p + \mu \nabla^2 \Phi = \rho \frac{\partial \Phi}{\partial t}, \tag{21}$$

$$\rho \frac{\partial(\nabla \times \mathbf{\Psi})}{\partial t} = \mu \nabla^2 (\nabla \times \mathbf{\Psi}). \tag{22}$$

Equation (21) governs the irrotational component of velocity while Eq. (22) governs the rotational component. These are solved separately for both the internal and external fluid domains. The total fluid velocity, displacement, and stress fields are then reconstructed from Eq. (19).

The final equations needed for the fluid analysis are found from the material properties and continuity. The constitutive relation for the Newtonian fluid is

$$\sigma_{rx} = \mu\left(\frac{\partial v_r}{\partial x} + \frac{\partial v_x}{\partial r}\right), \tag{23}$$

$$\sigma_r = -p + 2\mu \frac{\partial v_r}{\partial r}. \tag{24}$$

Continuity for the incompressible fluid places a constraint on the velocity components:

$$\frac{\partial v_x}{\partial x} + \frac{\partial v_r}{\partial r} + \frac{v_r}{r} = 0. \tag{25}$$

D. Irrotational fluid solution

For the incompressible case, the potential is governed by continuity in the form of the Laplace equation. In polar coordinates for the axisymmetric case this gives

$$\frac{\partial^2 \Phi}{\partial r^2} + \frac{\partial \Phi}{r \partial r} + \frac{\partial^2 \Phi}{\partial x^2} = 0. \tag{26}$$

The fluid pressure can be found from the potential solution, independent of viscosity:

$$-p = \rho \frac{\partial \Phi}{\partial t}. \tag{27}$$

A solution is assumed of a form which will satisfy the assumed sinusoidal displacement mode given in Eqs. (16) and (17) and which will facilitate using separation of variables on the radial and axial dependence. Time harmonic motion is prescribed where ω is the frequency of motion. For the internal fluid the velocities must be bounded as $r \to 0$, which gives the solution of the radial dependence as the modified Bessel function of the first kind with order zero. For the external fluid the velocities must be bounded as $r \to \infty$, which gives the radial dependence as the modified Bessel function of the second kind with order zero. The potential solution is given by

$$\Phi = \begin{cases} -F_{p_{\text{int}}} I_0(\alpha_n r)\cos \alpha_n x e^{i\omega t}, & \text{internal,} \\ -F_{p_{\text{ext}}} K_0(\alpha_n r)\cos \alpha_n x e^{i\omega t}, & \text{external.} \end{cases} \tag{28}$$

In Eq. (28), F_p is an unknown constant and the subscripts int and ext denote the interior and exterior solutions, respectively. The irrotational contribution to the velocity and pressure are given by Eqs. (19) and (21). The contribution to the velocity is

$$v_{\Phi_x} = \begin{cases} -\alpha_n F_{p_{\text{int}}} I_0(\alpha_n r)\sin \alpha_n x e^{i\omega t}, & \text{internal,} \\ -\alpha_n F_{p_{\text{ext}}} K_0(\alpha_n r)\sin \alpha_n x e^{i\omega t}, & \text{external,} \end{cases} \tag{29}$$

$$v_{\Phi_r} = \begin{cases} \alpha_n F_{p_{\text{int}}} I_1(\alpha_n r)\cos \alpha_n x e^{i\omega t}, & \text{internal,} \\ -\alpha_n F_{p_{\text{ext}}} K_1(\alpha_n r)\cos \alpha_n x e^{i\omega t}, & \text{external.} \end{cases} \tag{30}$$

E. Rotational fluid solution

Based on the definition of Eq. (19), the rotational contribution is defined as the curl of a vector function

$$\mathbf{v}_\Psi = \nabla \times \mathbf{\Psi}. \tag{31}$$

The rotational contribution to the velocity for the axial component is governed by

$$\frac{d^2 v_{\Psi_x}}{dr^2} + \frac{1}{r}\frac{d v_{\Psi_x}}{dr} - \alpha_n^2 v_{\Psi_x} - \frac{i\omega\rho}{\mu} v_{\Psi_x} = 0. \tag{32}$$

The radial component of rotational velocity is governed by

$$\frac{d^2 \nu_{\Psi_r}}{dr^2} + \frac{1}{r} \frac{d\nu_{\Psi_r}}{dr} - \alpha_n^2 \nu_{\Psi_r} - \frac{i\omega\rho}{\mu} \nu_{\Psi_r} - \frac{1}{r^2} \nu_{\Psi_r} = 0, \quad (33)$$

where the velocity components must also satisfy continuity given by Eq. (25).

For the internal fluid the condition for bounded values of velocity as $r \to 0$ gives the form of the Bessel functions to be used in the radial dependence of the velocity field, while for the external fluid the condition for bounded values of velocity as $r \to \infty$ gives the form of the Bessel functions. Solutions for the axial dependence correspond to the assumed displacement function at the cell wall:

$$\nu_{\Psi_x} = \begin{cases} F_{\nu_{\text{int}}} \dfrac{\lambda_n}{\alpha_n} I_0(\lambda_n r) \sin \alpha_n x e^{i\omega t}, & \text{internal,} \\[2ex] -F_{\nu_{\text{ext}}} \dfrac{\lambda_n}{\alpha_n} K_0(\lambda_n r) \sin \alpha_n x e^{i\omega t}, & \text{external,} \end{cases} \quad (34)$$

$$\nu_{\Psi_r} = \begin{cases} F_{\nu_{\text{int}}} I_1(\lambda_n r) \cos \alpha_n x e^{i\omega t}, & \text{internal,} \\[2ex] F_{\nu_{\text{ext}}} K_1(\lambda_n r) \cos \alpha_n x e^{i\omega t}, & \text{external,} \end{cases} \quad (35)$$

where

$$\lambda_n \equiv \sqrt{\alpha_n^2 + \frac{i\omega\rho}{\mu}}. \quad (36)$$

The unknown constant F_ν uses the subscripts int and ext to denote the interior and exterior fluid solutions. The viscous contribution to stress is found from the constitutive law [Eqs. (23) and (24)].

F. Total contribution of the internal fluid

Adding the contributions from the irrotational and rotational solutions gives the total internal fluid solution. The displacement and stress coefficients are related through the unknown coefficients of the assumed solution, F_p and F_ν. The stiffness matrix is formed by equating the unknown coefficients in the stress and velocity equations:

$$\mathbf{K}_{n_{\text{int}}} \equiv \begin{bmatrix} -\mu\left(\alpha_n + \dfrac{\lambda_n^2}{\alpha_n}\right) I_1(\lambda_n r) & -2\mu\alpha_n^2 I_1(\alpha_n r) \\[2ex] 2\mu\lambda_n I_1'(\lambda_n r) & 2\mu\alpha_n^2 I_1'(\alpha_n r) + i\omega\rho I_0(\alpha_n r) \end{bmatrix} \begin{bmatrix} \dfrac{i\lambda_n}{\omega\alpha_n} I_0(\lambda_n r) & \dfrac{i\alpha_n}{\omega} I_0(\alpha_n r) \\[2ex] \dfrac{-i}{\omega} I_1(\lambda_n r) & \dfrac{-i\alpha_n}{\omega} I_1(\alpha_n r) \end{bmatrix}^{-1}, \quad (37)$$

$$\boldsymbol{\sigma}_{n_{\text{int}}} = \mathbf{K}_{n_{\text{int}}} \mathbf{u}_n. \quad (38)$$

The derivative of the Bessel function used in Eq. (37) is denoted by the superscript apostrophe and is taken with respect to the argument. These are the nth coefficients for the stiffness matrix when displacement and stress vectors are evaluated at the cell wall radius.

G. Total contribution of the external fluid

Adding the contributions from the irrotational and rotational solutions gives the total external fluid solution. The external stiffness matrix is

$$\mathbf{K}_{r_{\text{ext}}} \equiv \begin{bmatrix} -\mu\left(\alpha_n + \dfrac{\lambda_n^2}{\alpha_n}\right) K_1(\lambda_n r) & 2\mu\alpha_n^2 K_1(\alpha_n r) \\[2ex] 2\mu\lambda_n K_1'(\lambda_n r) & -2\mu\alpha_n^2 K_1'(\alpha_n r) + i\omega\rho K_0(\alpha_n r) \end{bmatrix} \begin{bmatrix} \dfrac{-i\lambda_n}{\omega\alpha_n} K_0(\lambda_n r) & \dfrac{i\alpha_n}{\omega} K_0(\alpha_n r) \\[2ex] \dfrac{-i}{\omega} K_1(\lambda_n r) & \dfrac{i\alpha_n}{\omega} K_1(\alpha_n r) \end{bmatrix}^{-1}. \quad (39)$$

The total fluid stress acting on the cell wall is the difference between the internal and external fluid stress. The nth harmonic of coefficients of the fluid stress jump is defined as

$$\mathbf{K}_{n_{\text{fluid}}} \equiv (\mathbf{K}_{n_{\text{int}}} - \mathbf{K}_{n_{\text{ext}}}), \quad (40)$$

$$\Delta\boldsymbol{\Sigma}_{n_{\text{fluid}}} \equiv \boldsymbol{\Sigma}_{n_{\text{int}}} - \boldsymbol{\Sigma}_{n_{\text{ext}}} = \mathbf{K}_{n_{\text{fluid}}} \mathbf{U}_n. \quad (41)$$

This is the discontinuity in the nth harmonic of fluid stress and therefore is the fluid stress that acts on the cell wall. From continuity and the no-slip boundary condition at the cell wall the internal fluid displacement is equal to the external fluid displacement at the cell boundary. The total fluid stiffness at the cell wall can then be written using the 2×2

matrices for each harmonic from Eq. (41) into the form of a diagonal matrix similar to Eq. (13). The total matrix expression containing all the Fourier harmonics for the fluid is then used to relate the total fluid stress jump and fluid displacement at the cell wall.

$$\delta\boldsymbol{\Sigma} = \mathbf{K}_{\text{fluid}} \mathbf{U}. \quad (42)$$

It is necessary to restate this system of uncoupled fluid domain equations as a system of equations in terms of the cell domain harmonics. A matrix of transformation factors can be built that effectively converts the vector of cell domain coefficients into a vector of fluid domain coefficients and similarly fluid coefficients into cell coefficients. This is not generally a square matrix since more harmonics are needed in the fluid domain than in the cell domain to achieve

a given resolution. The minimum wavelength of the fluid harmonic and cell harmonic series should be kept the same to ensure compatible resolution.

H. Transformation of Fourier series

A series expansion is assumed for the change in stress between the internal fluid and the external fluid across the cell wall. In the region of the cell for $-a \leq x \leq a$ the stress jump is expressed as a series using cell harmonics, $\beta_m = m\pi/2a$. In the region beyond the cell where the fluid is not interrupted by the cell wall, the stress jump is identically zero.

The relationship between the coefficients of the series expression in the fluid harmonics and the coefficients in the cell harmonics is found using the orthogonality of the trigonometric functions, that is, expanding the series in the cell harmonics term by term into a series in the fluid harmonics. The geometric quantities are then necessarily defined such that

$$Dc(m,n)$$

$$\equiv \begin{cases} \dfrac{\sin((\beta_m - \alpha_n)a)}{(\beta_m - \alpha_n)} + \dfrac{\sin((\beta_m + \alpha_n)a)}{(\beta_m + \alpha_n)}, & \beta_m \neq \alpha_n, \\ a, & \beta_m = \alpha_n, \end{cases}$$
(43)

$$Ds(m,n)$$

$$\equiv \begin{cases} \dfrac{\sin((\beta_m - \alpha_n)a)}{(\beta_m - \alpha_n)} - \dfrac{\sin((\beta_m + \alpha_n)a)}{(\beta_m + \alpha_n)}, & \beta_m \neq \alpha_n, \\ a, & \beta_m = \alpha_n, \end{cases}$$
(44)

$$D_{ij} \equiv \begin{cases} Ds(m,n), & i = 2m-1, j = 2n-1, \\ Dc(m,n), & i = 2m, j = 2n, \\ 0, & \text{otherwise}, \end{cases}$$
(45)

where the subscripts i and j represent the components of the matrix $\mathbf{D}$. The expansion process for the stress jump can be written in matrix form relating the cell coefficients with the fluid coefficients.

$$\delta\mathbf{\Sigma} = \frac{1}{L} \mathbf{D}^T \delta\boldsymbol{\sigma}.$$
(46)

A similar contraction process for the displacement is used relating the fluid domain coefficients with the cell domain coefficients:

$$\mathbf{u} = \frac{1}{a} \mathbf{D}\mathbf{U}.$$
(47)

Substituting these into Eq. (42) gives the stress-deformation relation for the fluid in terms of cell harmonics

$$\mathbf{u} = \frac{1}{aL} \mathbf{D}\mathbf{K}_{n_{\text{fluid}}}^{-1} \mathbf{D}^T \delta\boldsymbol{\sigma}.$$
(48)

It follows that the fluid stiffness matrix written in terms of cell harmonics is

$$\mathbf{k}_{\text{fluid}} = aL[\mathbf{D}\mathbf{K}_{n_{\text{fluid}}}^{-1} \mathbf{D}^T]^{-1}.$$
(49)

In general the fluid stiffness matrix is a full $mmax \times mmax$ matrix once it has been transformed to cell harmonics. The stiffness matrices for the cell and fluid are then substituted into the equilibrium expression of Eq. (1) and the no-slip constraint at the cell wall in Eq. (2) is used to give the required displacement-stiffness relation:

$$\mathbf{u} = [\mathbf{k}_{\text{cel}} + \mathbf{k}_{\text{fluid}}]^{-1} \boldsymbol{\sigma}_{\text{applied}}.$$
(50)

These are the coefficients of the cell wall displacement. The process described by Eqs. (46)–(50) is to initially express the stress jump in terms of cell harmonics. The stress jump is then expanded into the fluid where the fluid equations are solved in terms of displacement coefficients. The displacement is contracted back to the cell where the cell membrane equations are solved and compatibility is satisfied in order to determine the displacement at the cell wall.

The fluid displacement can be reconstructed throughout the entire fluid domain by strictly following the expansion-contraction process and including the Bessel function radial dependence:

$$\mathbf{U} = \frac{1}{L} \mathbf{K}_{\text{fluid}}^{-1} \mathbf{D}^T \mathbf{k}_{\text{fluid}} \mathbf{u}.$$
(51)

III. RESULTS

The theoretical development of the previous sections is used to analyze two important experimental load cases. These cases are intended to approximate different physiological conditions. Values for cell material properties from a previous static analysis (Tolomeo and Steele, 1995) will be used for numerical computation with stiffness coefficients $C_{11} = 0.02$ N/m, $C_{12} = 0.031$ N/m, and $C_{22} = 0.06$ N/m, and piezoelectric coefficients $e_x = e_\theta = 0.0016$ N/Vm. These values have been modified slightly to reflect recently reported values of axial stiffness (Hallworth, 1995; Tolomeo et al., 1996).

A. Mechanical stimulation

The first load case simulates the experimental conditions of Brundin and Russell (1994). A fluid jet was applied perpendicular to the cell wall and the cell end displacement measured as a function of frequency. This load condition is simulated using an external radial pressure of the first sinusoidal harmonic:

$$\boldsymbol{\sigma}_{\text{applied}} = \begin{bmatrix} 1 \\ 0 \\ 0 \\ \dots \end{bmatrix}.$$
(52)

The effect of fluid length is first identified in order to establish the conditions for the fluid domain length and shown in Fig. 2. It is found that a fluid length of about twice the cell length is needed to ensure that the fluid deformation appears as a localized phenomenon about the cell. This then converges to the infinite fluid domain condition and is used in all the results that follow. The viscosity of the surrounding fluid has a large effect on the deformation response. However, in the absence of experimental values of fluid viscosity, the viscosity of water is used in all calculations. Figure 3
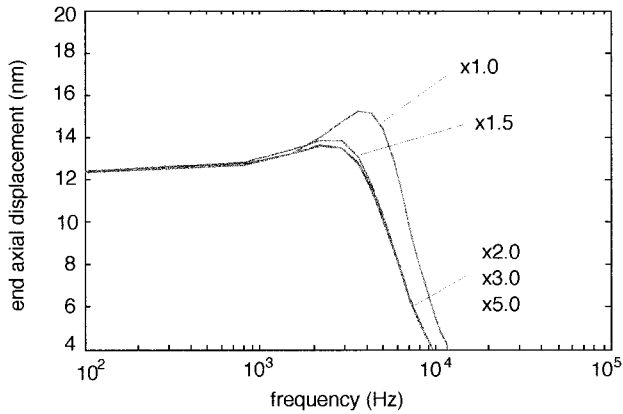
FIG. 2. The effect of fluid length on the deformation response. For lengths greater than twice the cell length, the response converges to the infinite fluid conditions. Cell length shown is 60 μm.

FIG. 4. Fluid and cell deformation pattern for mechanical loading on the lateral wall of the cell. All lines were initially straight and the deformed shape is a measure of the displacement pattern. The cell is outlined in the center of the image. The surrounding fluid shows significant deformation for a distance about the cell equal to about one cell radius. This example deformation is harmonic in time at a prescribed frequency of 1000 Hz. The calculation uses 10 cell harmonics and 20 fluid harmonics. The displacement is magnified 200$\times$ to appear at this scale. Cell length is 60 μm.

shows the frequency-dependent deformation magnitude and phase as a function of cell lengths occurring along the cochlear duct. Short cells corresponding to high-frequency locations have a corner frequency around 10 kHz while long cells of the type usually used in experimental studies have a corner frequency at about 2 kHz. Figure 4 shows a typical deformation pattern characteristic of the first harmonic mode for deformation similar to that described by Brundin and

Russell. The region of fluid participating in the motion is generally within one cell radius about the cell.

B. Electrical stimulation

The second load case considered is the effect of intracellular potential change on the cell wall. This is motivated by the electrical potential changes which result from stereocilia deflection during cochlear function. The unconstrained end conditions approximate the fact that the cell is only partially constrained above by the reticular lamina, and below by the Deiter's cell and basilar membrane. This configuration is also an approximation of the whole cell patch clamp technique used *in vitro* on isolated cell. Using piezoelectric analysis, the electrically generated stress within the cell wall can be related to the transmembrane potential

$$\begin{bmatrix} N_x \\ N_\theta \end{bmatrix} = V \begin{bmatrix} e_x \\ e_\theta \end{bmatrix}, \tag{53}$$

where V_3 is the transmembrane potential change and e_x and e_θ are the piezoelectric stress coefficients in the longitudinal and circumferential directions, respectively. For the thin membrane this can be equated to an applied traction on the cell wall using the Fourier series expansions and Eqs. (9) and (10). Figure 5 shows the deformation frequency response while Fig. 6 shows the calculated fluid deformation field about the cell at 1 kHz.

C. Strain energy

The above solutions can be used to calculate the average energy associated with the deformation where E is the strain energy. The piezoelectric stress was modeled as an applied load on the cell wall. The strain energy stored in the cell is the product of the stress resultant and the strain in the cell wall averaged over one deformation cycle:

FIG. 3. (a) End displacement magnitude and (b) phase for cells of various lengths. The applied load is 1 Pa external pressure in the form of the first harmonic of radial stress. The analysis uses ten harmonics in the cell domain with a fluid length of twice the cell length. The response has the character of a low-pass filter.

$$E_{\mathrm{avg}} = \frac{\omega}{2\pi} \int_0^{2\pi/\omega} \int_{-a}^{a} \pi r \left(N_x \frac{\partial u_x}{\partial x} + N_\theta \frac{u_r}{r} \right) dx \ dt. \tag{54}$$
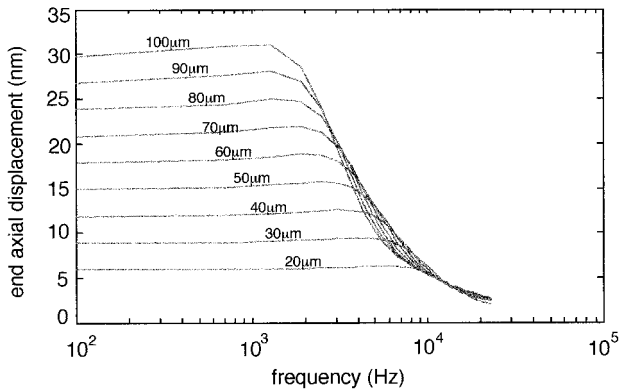
FIG. 5. Deformation response for piezoelectric stimulation of 1-mV transmembrane potential change. The calculation uses 10 cell harmonics and 20 fluid harmonics with a fluid length of twice the cell length.

The energy is summed for each harmonic using the results of Eq. (50) and the orthotropic coefficients of Eq. (11). The average strain energy stored in the cell wall for these unconstrained end conditions is an estimate of the available energy which is converted from electrical to mechanical form and is shown in Fig. 7 as a function of the driving frequency. The actual amount of energy delivered to the organ of Corti depends on the relative impedance of the surrounding structures. The average power is the product of this energy and the driving frequency. For electrical loading of 1 mV the estimated maximum mechanical power output of the cell is on the order of 0.1 pW.

IV. VALIDATION

The predicted frequency response from these calculations is compared with recently reported experimental results from Santos-Sacchi (1992) and Brundin and Russell (1994). The boundary conditions for experimental setup is generally one end fixed, while the boundary conditions in our calculations were unconstrained ends. However, the present results can be used as a good approximation for a fixed end condition by using a cell of twice the length of a fixed end cell. This is because the unconstrained cell has a zero displace-
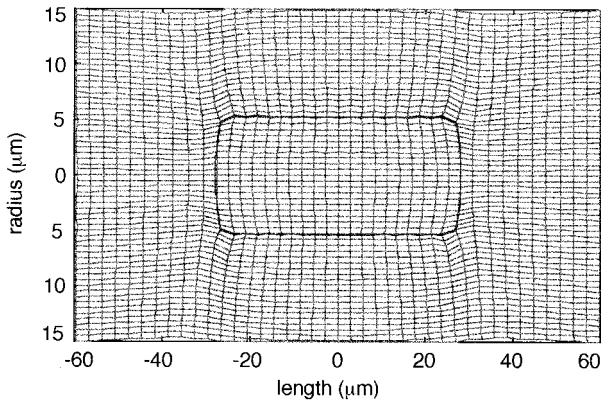
FIG. 6. Fluid deformation pattern for electrical loading on the cell wall. The deformed cell is outlined in the center of the image. Cell length is 60 μm and the calculation uses ten cell harmonics at a prescribed 1000-Hz driving frequency. The displacement is magnified 200$\times$ to appear at this scale.
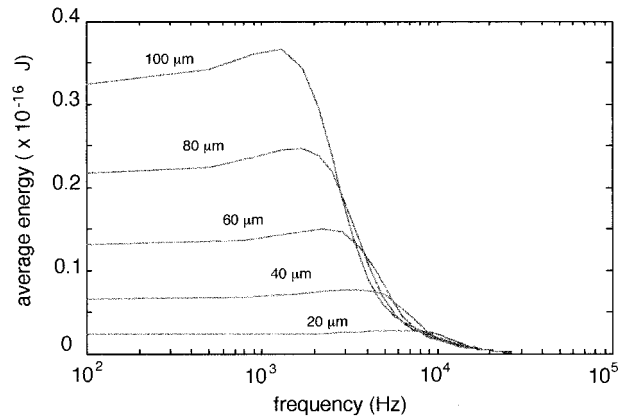
FIG. 7. Average strain energy stored in the unconstrained outer hair cell per of milliVolt transmembrane potential across the lateral cell wall. This represents an estimate of the available energy converted from electrical to mechanical form.

ment condition due to symmetry at the cell center, similar to the fixed condition. When this is done the analytical results presented here are in good agreement with the experime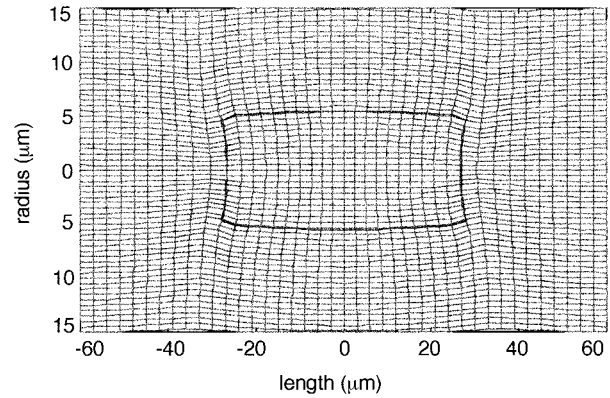ntal results for both electrical and mechanical stimulation as shown in Fig. 8. Corner frequency behavior also agrees reasonable well with data from Gitter and Zenner (1995), although the longitudinal electrical load gradient in their report is not directly analogous to the load cases considered here.

V. DISCUSSION

The calculated outer hair cell deformation under electrical stimulation is greater than 1 nm for frequencies beyond 20 kHz for the shortest cells studied. Thus viscous fluid effects do not discount the hypothesized role of the outer hair cells as a cycle-by-cycle feedback mechanism. The deformation response has the rough character of a low-pass filter
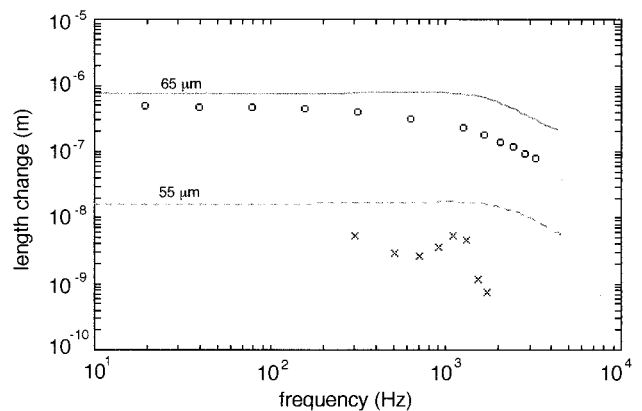
FIG. 8. Comparison of predicted cell deformation with recently reported experimental results. The **o** represent cell motility due to transmembrane voltage loading from the data reported in Santos-Sacchi (1992), Figs. 2, 5, and 6. The solid line is the predicted response from the viscous fluid model from a piezoelectric loading of 25 mV. The actual experimental load was not reported but given as ~20 nm/mV and 500 nm total. Therefore 25 mV was used in the calculations. The **x** represent data from Brundin and Russell (1994), Fig. 6, for a fluid pressure load of approximately 1.45 Pa applied to one side of the cell only. The dotted line is the predicted response for an equivalent average symmetric pressure load of 0.73 Pa external to the cell.

similar to the calculations of Jen and Steele (1987) although here the corner frequency occurs at a much lower frequency due to the overly stiff cell material properties used in the Jen and Steele analysis. The electrical loading conditions used in the analysis was 1 mV of transmembrane electrical loading which corresponds to the order of 10-nm deflection of the stereocilia bundle (Russell *et al.*, 1986).

The fluid deformation field solutions given in Figs. 4 and 6 indicate the region of fluid affected and participating in the cell deformation. At the frequencies plotted this indicates a radial distance of about a cell radius. The figures also show that the region of fluid beyond the cell length that participates can be significant. The open end condition on the cell is not a serious geometric limitation on the model since the fluid deformation pattern is nearly constant across the internal cell radius. This is a direct consequence of the previously recorded result that little fluid pressure is developed during electrically driven motility (Tolomeo and Steele, 1995). It should be noted that the mesh used in these fluid deformation graphs is for visualization of the fluid flow field only and is not a relic of a discretization process such as used in finite element or finite difference techniques.

The exact boundary conditions on the outer hair cell ends *in vivo* are unknown. The relative mechanical impedance of the reticular lamina, Deiter's cells, and basilar membrane are needed to interpret how the cell deforms relative to the isolated condition. However, if the cell is to influence the deformation of the basilar membrane, then it must have at least similar stiffness in relation to these structures and this supports the use of unconstrained end boundary conditions in the predictive calculations. The calculations made here to validate the model were directly compared to the isolated *in vitro* condition. The *in vivo* condition may represent a slightly less viscous environment externally due to the near proximity of other outer hair cells undergoing similar deformation. This could extend the quasi-static part of the deformation response curves and move the corner frequencies towards the higher end of the acoustic range.

The piezoelectric fluid–structure analysis is in general agreement with experiments which use both electrical and mechanical loading and therefore represents a unified model for the prediction of outer hair cell electro-mechanical behavior. The general frequency response is that of a highly damped system where corner frequencies occur in the range of 2 to 10 kHz for the lengths of outer hair cells studied. This range of corner frequencies is similar to measured tonic deformation best frequencies which range from about 0.4 to 10 kHz (Brundin *et al.*, 1989). There is very little resonant behavior indicated by our model and this contradicts experimental results which have shown a tuned peak of about a factor of 2 in phasic deformation (Brudin *et al.*, 1994) for mechanical loading. Such a resonant peak is found in the model results if the fluid viscosity is reduced by a factor of 2; however, such a low value of viscosity is difficult to justify. The resonant behavior does not occur in electrical load conditions where the model is in good agreement with experimental results and this argues against adjusting fluid viscosity. The model does not reconcile why a resonance may occur for mechanical loading but not electrical loading. Our

isolated outer hair cell model results are evidence of a highly damped system with no tuned resonance.

Most models of outer hair cell feedback hypothesize a force generation or energy input onto the basilar membrane due to the outer hair cell. The hypothesis of energy input is addressed with the calculation of the average strain energy in the cell. This represents an estimate of the available work energy to the basilar membrane. The actual amount of energy transferred through the Deiter's cells to the basilar membrane is dependent on the relative impedance of the structures within the organ of Corti. Models of cochlear tuning which assume outer hair cell feedback must be realistically constrained by the energy output capabilities of the outer hair cell. Here it is shown that the peak available energy from the outer hair cell does approximately occur at acoustic frequencies consistent with the characteristic frequency of a given cell length and place.

VI. SUMMARY

This analysis has identified the effects of viscous fluid mass and drag on outer hair cell motility. The frequency response was shown to have distinct corner frequencies between 2 and 10 kHz, depending on the cell length, with significant deformation of 1 nm occurring beyond 20 kHz. Results from the analysis utilized no adjustable parameters and were in good agreement with both electrical and mechanical stimulation experiments. Motility attenuation was fully consistent with the viscous and mass effects of the fluid surrounding the cell, while no significant resonance was predicted. If significant, electrical attenuation could be superimposed on this analysis to develop a more complete model of hair cell motility.

ACKNOWLEDGMENTS

Ashmore, J. F. (**1987**). ''A fast motile response in guinea pig outer hair cells: the cellular basis of the cochlear amplifier,'' J. Physiol. (London) **388**, 323–347.

Brownell, W. E., Bader, C. R., Bertrand, D., and de Ribaupierre, Y. (**1985**). ''Evoked mechanical responses of isolated cochlear hair cells,'' Science **227**, 194–196.

Brundin, L., Flock, A., and Canlon, B. (**1989**). ''Sound-induced motility of isolated cochlear outer hair cells is frequency-specific,'' Nature (London) **342**, 814–816.

Brundin, L., and Russel, I. (**1994**). ''Tuned phasic and tonic motile responses of isolated outer hair cells to direct mechanical stimulation of the cell body,'' Hearing Res. **73**, 35–45.

Dallos, P., Hallworth, R., and Evans, B. N. (**1993**). ''Theory of electrically-driven shape changes of cochlear outer hair cells,'' J. Neurophysiol. **70**, 299–323.

Dallos, P., and Evans, B. N. (**1995**). ''High-frequency motility of outer hair cells and the cochlear amplifier,'' Science **267**, 2006–2009.

Gale, J. E., and Ashmore, J. F. (**1994**). ''Charge displacement induced by rapid stretch in the basolateral membrane of the guinea pig outer hair cell,'' Proc. R. Soc. London, Ser. B **255**, 243–249.

Gitter, A. H., and Zenner, H. P. (**1995**). ''Electomotile responses and frequency tuning of isolated outer hair cells of the guinea pig cochlea,'' Eur. Arch. Otorhino. **252**, 15–19.

Hallworth, R. (**1995**). ''Passive compliance and active force generation in the guinea pig outer hair cell,'' J. Neurophysiol. **74**, 2319–2328.

Holley, M. C., and Ashmore, J. F. (**1990**). ''Spectrin, actin and the structure of the cortical lattice in mammalian cochlear outer hair cells,'' J. Cell. Sci. **96**, 283–291.

Hudspeth, J. (**1989**). ''How the ears works work,'' Nature (London) **341**, 397–404.

Iwasa, K. H. (**1993**). ''Effect of stress on the membrane capacitance of the auditory outer hair cell,'' Biophys. J. **65**(1), 492–498.

Iwasa, K. H. (**1994**). ''A membrane motor model for the fast motility of the outer hair cell,'' J. Acoust. Soc. Am. **96**, 2216–2224.

Jen, D. H., and Steele, C. R. (**1987**). ''Electro-kinetic model of outer hair cell motility,'' J. Acoust. Soc. Am. **82**, 1667–1678.

Jerry, R. A., Popel, A. S., and Brownell, W. E. (**1995**). ''Outer hair cell length changes in an external electric field. I. The role of intracellular electro-osmotically generated pressure gradients,'' J. Acoust. Soc. Am. **98**, 2000–2017.

Kachar, B., Brownell, W. E., Altschuler, R., and Fex, J. (**1986**). ''Electro-kinetic shape changes of cochlear outer hair cells,'' Nature (London) **322**, 365–368.

Kalinec, F., Holley, M. C., Iwasa, K., Lim, D. J., and Kachar, B. (**1992**). ''A membrane-based force generation mechanism in auditory sensory cells,'' Proc. Natl. Acad. Sci. USA **89**, 8671–8675.

Ratnanather, J. T., Spector, A. A., Popel, A. S., and Brownell, W. E. (**1996**). ''Is the outer hair cell wall viscoelastic?,'' in *Proceedings of the Congress in Diversity in Auditory Mechanics*, edited by T. Lewis (Berkeley, to be published).

Russell, I. J., Cody, A. R., and Richardson, G. P. (**1986**). ''The responses of inner and outer hair cells in the basal turn of the guinea-pig cochlea and in the mouse cochlea grown *in vitro*,'' Hearing Res. **22**, 199–216.

Santos-Sacchi, J. (**1989**). ''Asymmetry in voltage-dependent movements of isolated outer hair cells from the organ of Cortie,'' J. Neurosci. **9**, 2954–2962.

Santos-Sacchi, J. (**1992**). ''On the frequency limit and phase of outer hair cell motility: effects of the membrane filter,'' J. Neurosci. **12**, 1906–1916.

Tolomeo, I. A. (**1995**). ''Models of the structure and motility of the auditory outer hair cell,'' Ph.D. thesis, Stanford University.

Tolomeo, J. A., and Steele, C. R. (**1995**). ''Orthotropic piezoelectric properties of the cochlear outer hair cell wall,'' J. Acoust. Soc. Am. **97**, 3024–3029.

Tolomeo, J. A., Steele, C. R., and Holley, M. C. (**1996**). ''Mechanical properties of the lateral cortex of the mammalian outer hair cell,'' Biophys. J. **71**(1), 421–429.

The effects of amplitude perturbation and increasing numbers of components in profile analysis

Jennifer J. Lentz
Department of Bioengineering, 120 Hayden Hall, University of Pennsylvania, Philadelphia, Pennsylvania 19104

Virginia M. Richards
Department of Psychology, 3815 Walnut St., University of Pennsylvania, Philadelphia, Pennsylvania 19104

In a profile-analysis task, the effect of randomly perturbing the amplitudes of the components of multi-tone stimuli was studied in two experiments. In the first experiment, thresholds for a signal added in-phase to the central component of a standard were measured for different numbers of components in two conditions. In one condition thresholds were measured in blocks for six different ''jagged'' standards, and in another, thresholds were measured when one of the six standards was chosen randomly on a presentation-by-presentation basis. Regardless of condition, thresholds did not depend on the numbers of components and increased magnitude of perturbation increased thresholds. Moreover, the slope relating thresholds to number of components did not increase with increasing magnitude of perturbation. In the second experiment, the signal consisted of an increase in amplitude of the central components and a decrease in amplitude of the outer components of the standard (a stimulus type which has been shown to maximize the change in threshold with increasing number of components). The amplitudes of component tones were selected randomly on a presentation-by-presentation basis. Thresholds fell with increases in the number of components, but the slope relating thresholds to numbers of components did not change as the magnitude of perturbation increased. The latter result contrasts with that reported by Kidd *et al.* [J. Acoust. Soc. Am. **90**, 1340–1354 (1991)]. © *1998 Acoustical Society of America.* [S0001-4966(98)06401-7]

PACS numbers: 43.66.Fe, 43.66.Jh [WJ]

INTRODUCTION

Profile-analysis experiments examine the ability of observers to compare levels of a complex stimulus at different frequencies (see Green, 1988b for a history of experiments). In a typical profile-analysis task, observers discriminate between a standard stimulus consisting of the sum of equal-amplitude tones and a stimulus in which a signal tone has been added in-phase to one of the components of the standard. The overall level of the stimuli is altered on every presentation to prevent increases in energy at the signal frequency from serving as a reliable cue. For profile-analysis tasks, both Green *et al.* (1984) and Kidd *et al.* (1991) found that increasing the number of components in the standard while maintaining a constant frequency ratio between tones led to reductions in the observed threshold. A reduction in threshold with increases in the number of components was also observed by Bernstein and Green (1987) for stimuli spanning a fixed frequency range. Such improvements are believed to result from the additional independent estimates of the level of the nonsignal components but also may be due to differences in the rate of learning (e.g., Green, 1992). Individual differences also have the potential to undermine conclusions drawn by different studies as some observers show little improvement in sensitivity with increasing numbers of components (Henn and Turner, 1990; Kidd, 1993).

Using more complex stimuli than those described above, Kidd *et al.* (1991) perturbed the levels of the nonsignal components and measured detection thresholds as a function of the magnitude of perturbation and the number of components in the stimulus. They found that as the variance of the per-turbations increased, the rate at which thresholds fell with increasing numbers of components decreased (i.e., the slope of threshold versus number of components function became shallower). Whatever the underlying mechanism for the reduction in slope with increasing magnitude of perturbation, there are two factors which may contribute to this result: (1) increasing the magnitude of the presentation-by-presentation amplitude perturbation of the nonsignal components may lead to decreases in the stability of the reference points for making comparisons of level across frequency, and (2) the ''jagged'' nature of the spectrum, not the variability in the spectrum, somehow may contribute to the change in slope. The objective of experiment I was to determine the relative contribution of these two factors on the observed reduction in slope with increasing magnitude of perturbation. The stimuli were derived from six precomputed ''jagged'' spectra. In the *fixed* condition, thresholds were measured separately for each of the six ''jagged'' spectra, while in the *random* condition the standard was chosen randomly from the six ''jagged'' spectra on each presentation.

I. EXPERIMENT I

A. Methods

1. Stimuli

The standard was the sum of 3, 5, or 21 tones. The central component of the stimulus was a 1000-Hz tone, and the component tones, rounded to the nearest 10 Hz, were separated by a frequency ratio of 1.175. The 3-component stimulus, for example, was the sum of 850-, 1000-, and

1170-Hz tones, whereas the 21-component stimulus ranged in frequency from 200 to 5000 Hz. On each presentation, the phase of each component was randomly chosen from a uniform distribution ranging from 0 to 2π rad. The signal to be detected was a tone added in phase to the 1000-Hz component of the standard.

The average level of the 1000-Hz component was 55 dB SPL. When there was no variability in the standard stimulus, the standard was comprised of equal-amplitude components. For the ''jagged'' standard stimuli, the average levels of the nonsignal components were initially 55 dB SPL, but by adding an independent zero-mean deviate to each component, a new standard profile was formed. The deviates were drawn from a Gaussian distribution having a mean of 0 dB, and a standard deviation (σ) of either 5 or 10 dB which are referred to as the $\sigma=5$ and $\sigma=10$ levels of perturbation, respectively. For convenience, the flat standard is referred to as the $\sigma=0$ level of perturbation. The 1000-Hz component was not randomly perturbed. The levels of perturbation here were larger than used by Kidd *et al.* (1991). The intent was to obtain a larger change in slope than they observed.

First, the $\sigma=5$ standards were computed. Starting with the 21-component stimulus, six standards were formed by independently drawing deviates for each component. (These spectra are presented in Fig. A1 of the Appendix.) Then, the 5-component standards were formed by removing the outer 16 components of the 21-component standards. Removing two more outer components formed the 3-component standard. After the $\sigma=5$ standards were formed, the $\sigma=10$ standards were generated. For the $\sigma=10$ standards, the general pattern of the levels of the nonsignal components was preserved, but the magnitudes of the added deviates were doubled.

The overall levels of the stimuli were varied on each presentation. The randomization was based on draws from a uniform distribution with a 30-dB range and a 0.1-dB gradation.

2. Procedure

The digitally generated stimuli described above were played via 2 channels of a 16 bit digital-to-analog converter (DAO;TDT DA1) at a sampling rate of 20 kHz, and the DAC output was low-pass filtered (Kemo VBF 8M; approximately 85 dB/octave drop-off) at 6 kHz. Stimuli were presented diotically through Sennheiser HD 410SL earphones, and observers were seated in a double-walled sound-attenuated room. The total duration of each stimulus was 100 ms, including 8-ms cosine-squared rise/decay ramps. The inter-stimulus interval duration was approximately 300 ms.

A two-alternative forced choice paradigm was employed, and a 2-down, 1-up staircase procedure (Levitt, 1971) was used to estimate the signal strength needed to achieve 71% correct responses. The signal was as likely to be in the first as in the second interval, and observers responded via keyboard and were given feedback after each trial. The strength of the signal is described as the amplitude of the signal relative to the amplitude of the component to which it was added, signal *re*: component in dB. The initial signal level for the staircase procedure was set approximately

10 dB above the ultimate threshold and was initially altered by 4-dB steps. The step size was reduced to 2 dB after the third reversal of the staircase. Threshold estimates were measured in 50-trial sets, and the last even number of reversals, excluding at least the first three, were averaged to generate a threshold estimate.

In the *fixed* condition, thresholds were collected using an individual ''jagged'' standard. In the *random* condition, one of the six standards was randomly chosen on each interval.

3. Observers and order of data collection

Four observers, ranging in age from 19 to 32 participated. All observers had pure tone hearing thresholds within 15 dB of normal between 250 and 8000 Hz, and two observers had previous experience in psychoacoustical experiments. Observers 2, 3, and 4 were paid for participation, and observer 1 is the first author.

All observers first finished the $\sigma=0$ level of perturbation, blocked by number of components (N) in the stimulus—either 5 or 21. Data at $N=3$, $\sigma=0$ were collected after the other two were finished. Data acquisition began after thresholds appeared to asymptote, which required approximately 2–8 h of practice, depending on the observer. After the $\sigma=0$ level of perturbation was tested, thresholds were measured for the ''jagged'' standards at $\sigma=5$ and $\sigma=10$ (the *fixed* condition). Two observers were tested first at $\sigma=5$ and the other two observers were tested first at $\sigma=10$. The order of testing the different number of components was selected randomly within each condition. Whenever a new number of components was to be tested, observers practiced for 24 threshold estimates. After finishing the *fixed* condition, observers were tested in the *random* condition. Again, thresholds were measured in $\sigma=5$ and $\sigma=10$ blocks, with the order of testing the different number of components randomly selected within those blocks.

For each standard, at least 12 threshold estimates were obtained. Even though all observers were tested first at different numbers of components and $\sigma=0$, tests of practice were completed for $\sigma=0$ and a large subset of the data points within the *fixed* and *random* conditions. If an effect of practice was evident (by a one-tailed t test), an additional six threshold estimates were obtained. The thresholds reported here are based on the final eight threshold estimates measured.

B. Results and discussion

Figure 1 shows thresholds (signal re component in dB) plotted as a function of number of components for four observers. The solid symbols denote the *fixed* condition, and the open symbols denote the *random* condition, with asterisks, circles, and triangles indicating the $\sigma=0$, $\sigma=5$, and the $\sigma=10$ levels of perturbation, respectively. For the *fixed* condition and for each σ, thresholds are averaged across the different standard stimuli, and error bars indicate standard errors of the mean across the thresholds for the six different standards. For both the *random* condition and the $\sigma=0$ level of perturbation, error bars indicate standard errors of the mean across eight replicate threshold estimates. Note that the abscissa range for Observer 4 is different than for Observers

1–3. Data and corresponding spectra for the individual *fixed* standards are presented in the Appendix. Figure 1 shows only the standard profiles when $\sigma=5$ and $N=21$.

These results show that the number of components in the stimulus does not have any consistent effect on thresholds regardless of the perturbation. An analysis of variance (ANOVA), which treated observers as a random variable and number of components, magnitude of perturbation, and standard profile as fixed variables, indicated significant main effects of magnitude of perturbation [$F(1,3)=21.6$, $p<0.025$] and standard profile [$F(5,15)=12.7$, $p<0.01$]. Recall that the intent of this experiment was to evaluate the contribution of two factors to the decrease in the slope of the function relating thresholds to numbers of components with increasing magnitude of perturbation. These factors were: (1) the magnitude of presentation-by-presentation amplitude perturbation of the nonsignal components and (2) the ''jagged'' nature of the spectrum. Because thresholds did not fall with number of components, we were unable to examine the relative contribution of these two factors to the change in slope.

Unlike the current results, Kidd *et al.* (1991) and Green *et al.* (1984) found that for $\sigma=0$, thresholds fell with increasing numbers of components by approximately 3–7 dB per doubling of number of components. The most likely contributing factor to discrepancy in data sets is individual differences among observers. For example, Kidd (1993) and Henn and Turner (1990) used equal-amplitude standards and found that thresholds did not improve significantly with numbers of components for some observers. Kidd (1993) showed that in general, the higher the threshold for the 3-component complex, the greater the rate of change in threshold as a function of number of components. For all the observers here, sensitivity for a 3-component stimulus (for the *fixed* and $\sigma=0$ conditions) is quite good. A second possible contributing factor is that the rate at which thresholds fall with increasing numbers of components decreases with practice (Green, 1992), but it is unlikely that our observers were more practiced than those of Kidd *et al.*'s (1991). Overall, these data conform to the nongenerality of threshold patterns when observers are detecting a single tone added in-phase to a component tone of a standard.

For the *fixed* condition, thresholds for the $\sigma=10$ level of perturbation are on average 4.5 dB higher than thresholds obtained when $\sigma=0$ and $\sigma=5$. Observers 2 and 4 both show large differences between $\sigma=0$ and $\sigma=5$ (at $N=5$), while Observers 1 and 3 have similar thresholds at the $\sigma=0$ and $\sigma=5$ levels of perturbation. There are large ranges of thresholds depending on the standard tested, but the pattern of thresholds for different standards is inconsistent both within and across observers. The only consistent trend within and across observers is that thresholds for standards 4, 5, and 6 appear to be lower than standards 1, 2, and 3 for all numbers of components (see Fig. A1 of the Appendix).

Because the amplitudes of the middle three components were conserved for each standard across increasing numbers of components, a possible explanation for the present data is that the three components near the signal frequency are the important components in detection of the signal. First, exam-
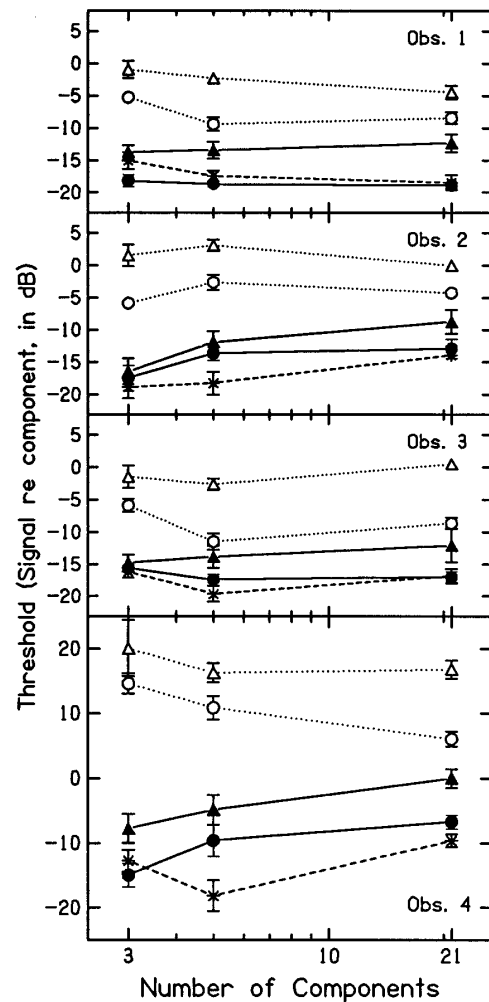
FIG. 1. Thresholds versus number of components are plotted for four observers. Filled symbols denote the *fixed* conditions, and open symbols denote the *random* conditions. Asterisks, circles, and triangles indicate $\sigma=0$, $\sigma=5$, and $\sigma=10$, respectively. For the *fixed* conditions, thresholds are averaged across the different standard profiles for each σ, and error bars indicate standard errors of the mean across the average thresholds for the 6 different standards. For both the *random* conditions and the $\sigma=0$ condition, thresholds are averaged across eight replicate estimates, and error bars indicate standard errors of the mean across the eight threshold estimates.

ining the physical differences between standards 1, 2, and 3 and standards 4, 5, and 6 reveals that those which led to higher thresholds all contain a large-magnitude component adjacent to the signal component. Such an observation suggests that either (1) across-frequency comparisons are more difficult when a large-magnitude component is adjacent to the signal component, or (2) possibly the components are not spaced far enough apart to ensure that nearby components are not masking the signal component. Because the amplitude of the signal component is not randomly drawn, when the magnitude of perturbation is increased, even more masking would be expected. As a result, the difference in thresholds between standards 1, 2, and 3 and standards 4, 5, and 6 would be expected to increase as the magnitude of perturbation is increased. The data are in accord with this expectation. Another possibility aside from masking is that observers are weighing the three central components more heavily than the outer components. Whatever the reason, thresholds

for the 3-component stimuli tend to predict thresholds for the other Ns.

Thresholds obtained in the *random* condition are on average 10 dB higher than thresholds measured in the *fixed* condition. This agrees with data reported by Kidd *et al.* (1986). For the *random* condition, thresholds for $\sigma = 10$ are on average 6 dB larger than when $\sigma = 5$, a value somewhat larger than the corresponding difference in the *fixed* condition. The magnitude of the effect of uncertainty varies for each observer—Observer 4 shows a large decrease in sensitivity in the *random* condition over the *fixed* condition, whereas the magnitude of the effect is much less severe for Observers 1–3. Because the overall level randomization was over a 30-dB range, when thresholds exceed 2 dB (Green, 1988b; a conservative estimate when perturbations are used), it is possible that observers are depending on across-interval changes in level rather than the pattern of levels across frequency. This limit was reached by observer 4 for the *random* condition and by observer 2 in the *random* condition, at $\sigma = 10$ and $N = 5$.

It should be noted that randomization degrades the performance of all observers, and the extent of this degradation cannot be accounted for by a simple mixturelike model. Such a model predicts that the thresholds in the *random* condition would be the average of thresholds obtained for each individual "jagged" standard in the *fixed* condition. Because the same standards used in the *fixed* condition were used for the *random* condition, it is possible that observers were able to recognize the "jagged" standards even in the random condition. If observers were able to learn the standards, the magnitude of the increase in thresholds due to the randomization may be underrepresented in these data. Because the condition tested here did not randomly choose each stimulus on every presentation as in Kidd *et al.* (1991), our observers may be using a different decision strategy than their observers.

In an effort to obtain changes in thresholds with numbers of components, a second experiment was performed using a complex signal which resulted in a balanced change in the spectral profile. According to the channel model of Durlach *et al.* (1986; see also Green, 1992) such a signal maximizes the change in threshold as a function of the number of components. In an experimental test of that theory, Green (1992) found that for such a balanced signal, thresholds fell as $1/\sqrt{N}$, as predicted by the channel model. The present experiment uses a balanced signal to investigate whether the slope of the function relating threshold to number of components decreases with increasing magnitude of perturbation as suggested by the data of Kidd *et al.* (1991). In order to eliminate some of the issues concerning learning as described above, Experiment II uses a procedure in which the component amplitudes of the stimulus are randomly chosen on every presentation

II. EXPERIMENT II

A. Methods

1. Stimuli

The standard was the sum of 4, 8, or 16 tones equally spaced on a logarithmic frequency scale ranging from 200 to 5000 Hz. Note that this frequency spacing differs from that of Experiment I which used a fixed frequency ratio between component tones. On each presentation, the phase of each component was randomly chosen from a uniform distribution ranging from 0 to 2π rad. The signal to be detected was produced by increasing the central components of an equal-amplitude standard by Δ dB and decreasing the outer components of the standard by Δ dB. To be consistent with Experiment I, threshold estimates are reported as signal *re*: component in dB.[1] Because half the components were incremented and half the components were decremented, the resultant change is a balanced change, as defined by Durlach *et al.* (1986).

The average level of each component was 60 dB SPL. When there was no variability in the standard stimulus, the standard was comprised of equal-amplitude components. For the randomly perturbed standard stimuli, the average levels of the components were initially 60 dB SPL, but on each presentation of the stimulus, an independent zero-mean deviate was added to each component. The deviates were drawn from a Gaussian distribution having a mean of 0 dB, and a standard deviation (σ) of either 0, 3, or 6 dB. These levels of perturbation are referred to as $\sigma = 0$, $\sigma = 3$, and $\sigma = 6$, respectively.

The overall levels of the stimuli were varied on each interval. The randomization was based on draws from a uniform distribution with a 30-dB range and a 0.1-dB gradation, the same as in Experiment I.

2. Procedures

The procedures are the same as in Experiment I except that tracking on Δ necessitated the following changes. The initial signal level for the staircase procedure was set at approximately three large step sizes above the final threshold. Depending on the condition tested, the signal level was initially altered by 0.8–0.2 dB steps, and the step size was reduced to approximately half the initial step size upon the third reversal of the staircase.

3. Observers and order of data collection

Four observers, different from those tested in Experiment I, and ranging in age from 19 to 21, participated. All had detection thresholds within 15 dB of normal for pure tones ranging from 200 to 8000 Hz, and all had previous experience in profile analysis tasks. After 4–6 h of practice, all observers were tested on the $\sigma = 0$ level of perturbation. After finishing $\sigma = 0$, $\sigma = 3$ and $\sigma = 6$ were tested, with two observers first finishing the $\sigma = 3$ level of perturbation. For each number of components and level of perturbation, at least 15 threshold estimates were obtained. The thresholds reported here are based on the final ten threshold estimates measured.

B. Results and discussion

Figure 2 shows thresholds, in terms of signal re component in dB, for four observers as a function of number of components. Asterisks, circles, and triangles show thresholds for the $\sigma = 0$, $\sigma = 3$, and $\sigma = 6$ levels of perturbation, respec-
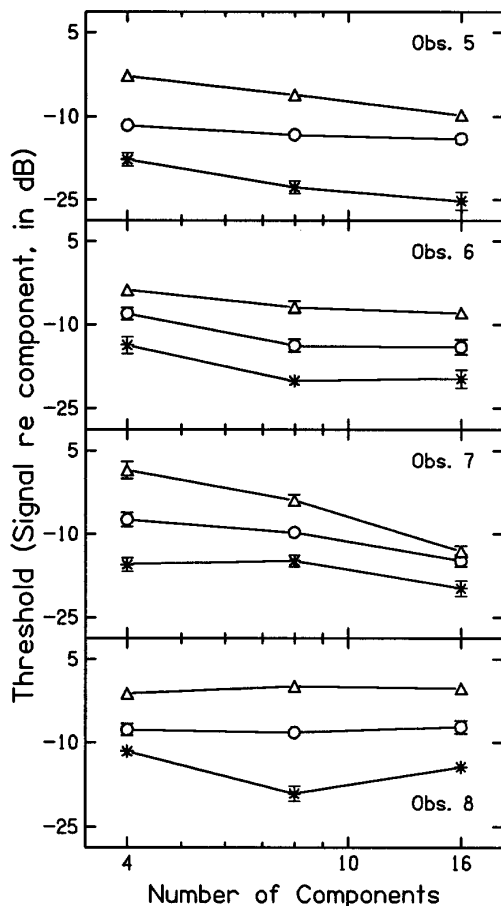
FIG. 2. Thresholds are plotted for four observers as a function of numbers of components. Asterisks, circles, and triangles show thresholds for the $\sigma = 0$, $\sigma = 3$, and $\sigma = 6$ conditions, respectively. Error bars indicate standard errors of the mean across ten threshold estimates.

tively. Error bars indicate standard errors of the mean across ten threshold estimates. At threshold levels above 2 dB, detection may be based on the change in level across intervals, rather than a comparison of levels across-frequency (Green, 1988b; for $\sigma = 0$). All reported thresholds fall below this limit. For all observers, thresholds at $\sigma = 6$ are the highest, and thresholds at $\sigma = 0$ are the lowest. For observers 5–7, thresholds tend to fall with increasing numbers of components, but the rate at which thresholds fall varies for each observer and condition. For Observer 8, thresholds do not appear to depend on numbers of components. Averaging data reveals that thresholds generally fall as $1/\sqrt{N}$, as predicted by the Durlach *et al.* (1986) channel model. However, thresholds at $N = 16$ are slightly elevated from the prediction. Removing Observer 8 (the observer who did not show an effect of N) from the averages brings thresholds in accord with $1/\sqrt{N}$. These results are also in accord with data reported by Green (1992) who tested observers in a condition similar to the current experiment at the $\sigma = 0$ level of perturbation.

In this experiment thresholds did fall with numbers of components for three of the four observers. However, unlike the results of Kidd *et al.* (1991), the slope relating thresholds to numbers of components did not flatten with increases in the magnitude of perturbations. Plotting these results on a

different scale (e.g., thresholds expressed as Δ dB) also yields a similar pattern of thresholds. In the current experiment the component tones were spaced using a fixed frequency range while Experiment I and the experiment of Kidd *et al.* (1991) used a fixed spacing between component tones. This difference in frequency spacing is unlikely to have contributed in the failure to replicate Kidd *et al.* (1991); Green (1988a) showed that sensitivity is largely independent of the distance between components but depends on the number of components in the stimulus for sparse stimuli such as the ones used here. As discussed in Experiment I, the difference in results between the current experiment and that of Kidd *et al.* (1991) might be explained by the relatively large individual differences that are found when observers detect a *single* tone added to a multi-tone complex (Kidd, 1993).

III. SUMMARY AND CONCLUSIONS

For the detection of a signal added in-phase to the middle component of a standard, thresholds measured in Experiment I did not depend on the number of components that comprised the standard. In general, thresholds for the equal-amplitude standards were the lowest, thresholds for *fixed* ''jagged'' standards were intermediate, and thresholds in the *random* condition were the highest. Moreover, thresholds grew as the magnitude of perturbations increased. Because a change in threshold with increasing number of components was not observed, we failed to replicate Kidd *et al.* (1991), and the question this experiment was intended to address (what contributes to the reported finding of a change in slope with increasing level of perturbation; Kidd, 1991) could not be answered. The data, however, do confirm the finding that when observers are detecting a *single* tone added to a multi-tone complex, earlier results cannot be generalized for all observers. This is true both when the standard is composed of equal-amplitude tones and when the component tones of the standard are perturbed.

Because of the large individual differences present for these tasks, a second experiment was performed. The second experiment used a complex, balanced signal, and the component tones were randomly perturbed. The intent was to examine whether the finding of a decrease in slope with increased level of perturbation could be observed using a stimulus construction which maximized the change in threshold with increasing number of components. Thresholds did depend on the magnitude of the perturbation, and thresholds fell with increasing numbers of components for three of the four observers. The data in the current study differ from those obtained by Kidd *et al.* (1991) in that the slope of the function relating threshold to numbers of components did not decrease as the magnitude of the perturbation increased.

APPENDIX

TABLE AI: Thresholds for each observer are indicated as signal re: component, in dB.

	Obs. 1	Obs. 2	Obs. 3	Obs. 4		Obs. 1	Obs. 2	Obs. 3	Obs. 4
Fixed									
$\sigma=5$					$\sigma=10$				
$N=3$					$N=3$				
Standard 1	−17.2 (0.9)	−16.7 (1.7)	−14.6 (0.5)	−18.8 (1.0)		−13.6 (0.6)	−18.6 (1.7)	−13.8 (1.0)	−9.1 (0.7)
Standard 2	−20.2 (1.1)	−15.8 (1.0)	−16.1 (1.4)	−11.6 (1.4)		−10.6 (0.6)	−11.1 (1.4)	−11.4 (2.5)	−3.1 (0.9)
Standard 3	−16.9 (0.8)	−10.9 (1.0)	−13.5 (1.7)	−11.6 (0.9)		−13.8 (1.7)	−9.4 (0.6)	−11.4 (1.4)	−0.1 (0.6)
Standard 4	−21.6 (0.8)	−18.3 (1.7)	−14.6 (0.8)	−18.1 (1.9)		−15.4 (0.7)	−19.7 (1.1)	−15.9 (1.2)	−7.4 (1.2)
Standard 5	−18.0 (2.1)	−17.5 (1.0)	−16.6 (0.7)	−9.9 (1.7)		−17.7 (3.0)	−21.0 (2.5)	−18.2 (1.2)	−15.2 (1.0)
Standard 6	−15.6 (0.5)	−25.8 (2.2)	−18.3 (1.4)	−19.8 (1.1)		−11.4 (1.6)	−19.0 (2.6)	−18.4 (1.0)	−11.8 (3.4)
$\sigma=5$					$\sigma=10$				
$N=5$					$N=5$				
Standard 1	−20.6 (1.4)	−9.6 (1.2)	−17.9 (0.9)	−1.2 (1.2)		−12.6 (1.1)	−7.8 (0.9)	−7.9 (1.0)	−3.0 (0.7)
Standard 2	−16.7 (1.1)	−15.6 (0.8)	−15.0 (1.0)	−11.2 (2.3)		−9.3 (0.5)	−9.8 (0.6)	−14.0 (0.8)	−5.8 (1.1)
Standard 3	−18.0 (1.2)	−13.0 (1.2)	−14.6 (0.9)	−5.2 (0.7)		−10.7 (1.4)	−7.8 (0.5)	−9.8 (0.7)	−2.5 (1.4)
Standard 4	−19.2 (0.6)	−12.2 (0.9)	−19.2 (2.1)	−8.6 (1.4)		−15.7 (1.7)	−12.5 (0.7)	−15.5 (0.6)	−1.6 (1.1)
Standard 5	−19.3 (0.9)	−15.7 (0.6)	−19.2 (1.2)	−17.9 (1.8)		−14.8 (0.9)	−18.2 (1.1)	−18.2 (0.9)	−9.8 (1.6)
Standard 6	−18.3 (1.2)	−16.3 (2.3)	−19.2 (1.1)	−13.9 (1.5)		−17.7 (1.0)	−15.9 (0.7)	−17.8 (0.9)	−12.6 (0.8)
$\sigma=5$					$\sigma=10$				
$N=21$					$N=21$				
Standard 1	−18.4 (1.1)	−12.2 (1.0)	−18.2 (1.8)	−2.4 (0.9)		−13.4 (0.9)	−5.4 (0.9)	−3.3 (0.9)	6.6 (1.0)
Standard 2	−16.5 (1.1)	−9.8 (0.4)	−14.6 (1.2)	−8.0 (1.0)		−6.1 (0.6)	−6.2 (0.7)	−12.9 (0.6)	−1.0 (0.6)
Standard 3	−17.7 (1.4)	−9.5 (1.2)	−15.3 (0.8)	−9.8 (1.0)		−12.7 (1.2)	−2.9 (0.5)	−5.5 (0.7)	−2.6 (1.4)
Standard 4	−19.3 (0.9)	−11.1 (1.1)	−16.0 (0.7)	−8.4 (0.8)		−13.6 (1.5)	−13.5 (2.4)	−17.0 (0.8)	−0.7 (0.5)
Standard 5	−21.1 (1.7)	−17.8 (1.0)	−17.7 (1.5)	−5.7 (0.6)		−11.7 (0.8)	−11.9 (0.8)	−18.5 (1.3)	−0.5 (0.8)
Standard 6	−20.7 (1.4)	−17.3 (1.3)	−21.0 (1.7)	−6.0 (0.8)		−16.5 (1.6)	−12.9 (0.7)	−15.6 (1.0)	−3.4 (0.4)
Flat ($\sigma=0$)									
$N=3$	−15.1 (1.3)	−18.9 (1.7)	−16.2 (1.0)	−12.8 (1.7)					
$N=5$	−17.5 (0.8)	−18.3 (1.8)	−19.7 (1.2)	−18.2 (2.4)					
$N=21$	−18.5 (1.1)	−14 (0.8)	−16.9 (1.1)	−9.7 (1.0)					
Random									
$\sigma=5$					$\sigma=10$				
$N=3$	−5.3 (0.8)	−5.9 (0.7)	−5.9 (1.0)	14.5 (1.6)		−1.0 (1.4)	1.5 (1.6)	−1.5 (1.7)	20.0 (4.3)
$N=5$	−9.5 (1.0)	−2.7 (1.2)	−11.5 (1.3)	10.8 (1.8)		−2.4 (0.7)	3.0 (0.9)	−2.7 (0.9)	16.2 (1.5)
$N=21$	−8.5 (0.9)	−4.3 (0.8)	−8.7 (0.9)	6.0 (1.1)		−4.5 (1.0)	−0.1 (0.8)	0.4 (0.7)	16.7 (1.4)
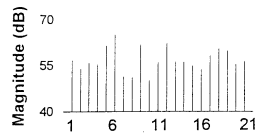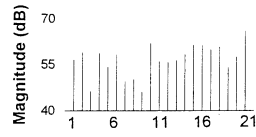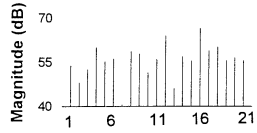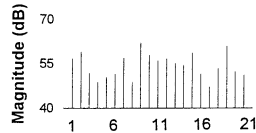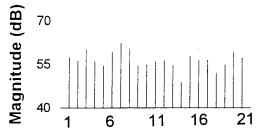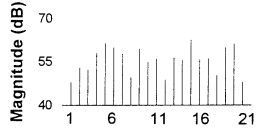
FIG. A1. Magnitude spectra for each of the standards (for $\sigma=5$) in Experiment I are shown.

[1] Because the addition of the signal was either $\pm\Delta$ dB, the amplitudes of the signal components are different, depending on whether the signal was added or subtracted from the mean signal level. Therefore, to compute the signal to standard ratio [signal *re*: component, in dB; $20\log(\Delta A/A)$] for these stimuli, the amplitude of the signal component was defined using $+\Delta$ dB where $\Delta=10\log(I+\Delta I/I)$.

Bernstein, L. R., and Green, D. M. (**1987**). ''The profile-analysis bandwidth,'' J. Acoust. Soc. Am. **81**, 1888–1895.

Durlach, N. I., Braida, L. D., and Ito, Y. (**1986**). ''Towards a model for discrimination of broadband signals,'' J. Acoust. Soc. Am. **80**, 63–72.

Green, D. M. (**1988a**). ''Auditory Profile Analysis: Some Experiments on Spectral Shape Discrimination,'' in *Auditory Function: Neurobiological Bases of Hearing*, edited by G. M. Edelman, W. E. Gall, and W. M. Cowen (Wiley, New York), pp. 609–622.

Green, D. M. (**1988b**). *Profile Analysis: Auditory Intensity Discrimination* (Oxford U.P., New York).

Green, D. M. (**1992**). ''The number of components in profile analysis tasks,'' J. Acoust. Soc. Am. **91**, 1616–1623.

Green, D. M., Mason, C. R., and Kidd, G., Jr. (**1984**). ''Profile analysis: Critical bands and duration,'' J. Acoust. Soc. Am. **75**, 1163–1167.

Henn, C. C., and Turner, C. W. (**1990**). ''Pure-tone increment detection in harmonic and inharmonic backgrounds,'' J. Acoust. Soc. Am. **88**, 126–131.

Kidd, G., Jr. (**1993**). ''Individual differences in the improvement in spectral shape discrimination due to increasing number of nonsignal tones,'' J. Acoust. Soc. Am. **93**, 992–996.

Kidd, G., Jr. Mason, C. R., and Green, D. M. (**1986**). ''Auditory profile analysis of irregular sound spectra,'' J. Acoust. Soc. Am. **79**, 1045–1053.

Kidd, G., Jr., Mason, C. R., Uchanski R. M., Brantley, M. A., and Shah, P. (**1991**). ''Evaluation of simple models of auditory profile analysis using random reference spectra,'' J. Acoust. Soc. Am. **90**, 1340–1354.

Levitt, H. (**1971**). ''Transformed up-down methods in psychoacoustics,'' J. Acoust. Soc. Am. **49**, 467–477.

On possible cues in profile analysis: Identification of the incremented component

Hedwig Gockel[a)]

Graduate Programme "Psychoacoustics," FB 5, Department of Cognitive Psychology, Carl von Ossietzky University of Oldenburg, D-26111 Oldenburg, Germany

The ability to identify the frequency of the incremented component in a multitone complex was assessed in two conditions, both using the same 11-tone complexes (fixed frequency, equilog spaced, random phases). In the standard-plus-signal complex all components had equal level, except one of the inner nine, which was incremented in level by an in-phase addition of a sinusoid of the same frequency (the signal). The overall level and signal position were randomly varied on each presentation. In the "Standard-absent" condition the standard-plus-signal complex was presented first, and it was followed by a single sinusoid either at the signal frequency or at that of an adjacent component (below or above). In the "Standard-present" condition, a complex with equal-level components (the standard complex) was also presented on each trial, either before or after the standard-plus-signal complex (in random order). These two complexes were followed by the single sinusoid. In both conditions, the subjects had to indicate whether the signal frequency was the same as or different from the frequency of the single sinusoid. In a third condition, the ability to discriminate between the standard complex and the standard-plus-signal complex (with signal frequency uncertainty) was investigated. In all three conditions, thresholds for the increment in level for each signal frequency were estimated by the use of nine independent interleaved adaptive procedures. Results showed that the ability to identify the signal frequency was at least as good as the ability to discriminate between the two complexes. The results suggest that an increase in pitch strength of the incremented component is a possible cue in profile analysis tasks. © *1998 Acoustical Society of America.* [S0001-4966(98)03701-1]

PACS numbers: 43.66.Hg, 43.66.Jh, 43.66.Fe, 43.66.Ba [WJ]

INTRODUCTION

Since the early eighties, "profile analysis," as a new approach to studying spectral shape discrimination, has triggered a vast amount of research. In profile analysis experiments the observer has to discriminate between a standard complex spectrum and a signal-plus-standard spectrum. The standard stimulus typically consists of *n* components of equal level, equally spaced on a logarithmic frequency scale. In the signal-plus-standard spectrum, one component is incremented in level. The overall level of the stimulus is varied randomly for each presentation to prevent subjects from basing their judgement on sequential level differences. For stimuli whose individual components are all separated by at least one critical band, an explanation in terms of a simultaneous comparison of output levels measured in different frequency channels (multi-channel model) is still the most favored one (see, e.g., Green, 1992).

In several studies, the role of a possible pitch cue has been investigated (e.g., Richards *et al.*, 1989; Kidd *et al.*, 1991). In these studies, the phrase "pitch cue" was taken to mean a difference in overall pitch between standard and standard-plus-signal stimuli, and it was calculated using the EWAIF or related models (Feth, 1974; Feth and Stover, 1987; Anantharaman and Krishnamurthy, 1993). However,

at least for the case of stimuli with widely spaced components, the pitch calculated in this way does not provide an adequate explanation of the data, although subjects report using a kind of pitch cue. In contrast to this overall pitch (mean frequency) cue, in the present paper, an increase in pitch strength of the incremented component is suggested as a possible cue for stimuli with widely spaced components. The use of this cue is supported by the finding that subjects are able to identify the frequency of the incremented component. Such a pitch-strength cue could be more efficient than an overall pitch cue. For example, Richards *et al.* (1989) randomly varied (roved) the center frequencies of the stimuli over a one-octave range between every presentation. They found that discrimination between a flat standard spectrum and a spectrum where the center component was incremented in level was still above chance level. In their study, the rove range was chosen so as to make overall pitch (difference of EWAIF values between standard and standard-plus-signal stimuli) an unreliable cue. However, the pitch-strength cue proposed in the present study might not have been rendered unreliable by a one-octave rove range. If, for example, subjects listened for an increase in pitch strength within a frequency range of plus/minus one critical bandwidth around the average frequency of the incremented component (750 Hz) then a pitch cue would have been available on a substantial proportion of trials. This is discussed in more detail in a paper by Gockel and Colonius (1997).

The present experiment investigated the ability to decide

---

which one of the spectral components in auditory profile stimuli was incremented in level. The ability to identify each incremented component was assessed in two different conditions and compared with the ability to discriminate between flat and incremented profiles. The difference between the discrimination and the identification tasks in terms of signal detection theory was accounted for and will be described in more detail later (see beginning of Sec. II and the Appendix). The same 11-tone complex (equal level of all components but randomly varied overall level, fixed frequencies, equilog spaced, random phases) was used in all conditions as the standard stimulus. The signal was always an increment in the level of one of the inner nine components. The signal position was randomly varied. In the first identification condition (''Standard-absent''), the standard-plus-signal complex was followed by a sinusoid either at the signal frequency or at that of an adjacent component (below or above). In the second identification condition (''Standard-present''), a complex with equal-level components was also presented on each trial. The flat and incremented stimuli were presented in random order in the first two observation intervals, and were followed by the sinusoid. The subjects had to indicate whether the frequency of the incremented component was the same as or different from the frequency of the sinusoid. In a third condition (''Discrimination''), the ability to discriminate between the flat and the incremented stimuli (with signal frequency uncertainty) was investigated. The ''Standard-present'' condition was used to assess the ability to identify the signal frequency under circumstances which were as similar as possible to those for the ''Discrimination'' condition, i.e., two complex stimuli (the incremented and the flat profile stimulus) were presented in random order. Since one might expect that it is easier to identify the incremented component if the flat profile is presented too (because the ''difference'' between the standard and incremented stimuli defines the signal frequency), the ''Standard-absent'' condition was introduced. A comparison between performance in the ''Standard-absent'' condition and the ''Standard-present'' condition should reveal whether the presence of the flat profile facilitates the identification of the incremented component. If thresholds in one or both identification conditions were lower than or comparable to thresholds in the ''Discrimination'' condition, then one might think of the pitch strength of the incremented component as a possible cue in certain profile analysis experiments. If, on the other hand, thresholds in the identification conditions were higher than in the ''Discrimination'' condition, then this would exclude the possibility that subjects use such a pitch strength cue in the discrimination task. Existing models of profile analysis (see, e.g., Feth and Stover, 1987; Berg and Green, 1990; Kidd et al., 1991; Green, 1992) do not make any predictions of the ability to identify the incremented component.

I. GENERAL METHOD

A. Tasks

Three conditions were employed in this study: one discrimination and two identification conditions. In all three conditions, the same 11-tone complex standards were used. Feedback was provided after each response, indicating a correct or wrong answer.

(1) Discrimination condition: Two successive stimuli were presented to the subject, one being the flat standard spectrum and the other being the standard-plus-signal. The signal was an increment in amplitude of one of the inner nine components, where each signal position was equally probable. The order of the standard and the standard-plus-signal stimulus was randomized and the subject had to indicate the interval containing the signal.

(2) Standard-absent condition: Two successive stimuli were presented to the subject. The first stimulus was always the standard-plus-signal, with the signal position again randomized over the inner nine components. In the second interval, a sinusoid either at the signal frequency or at that of an adjacent component (below or above) was presented. The subject first had to indicate whether the signal frequency was the same as or different from that of the sinusoid. Following the feedback, there were two possibilities: (a) the trial was finished when the subject correctly responded ''SAME''; (b) when the subject responded ''DIFFERENT'' (s)he then had to indicate whether (s)he believed the signal frequency was lower or higher than the frequency of the sinusoid (even if, in fact, the signal frequency was the same as that of the sinusoid). Feedback was also provided at this stage.

(3) Standard-present condition: Three successive stimuli were presented to the subject. The first two were the standard and standard-plus-signal in random order. The third stimulus was a sinusoid either at the signal frequency or at that of an adjacent component. Again, the subject first had to indicate whether the signal frequency was the same as or different from that of the sinusoid. Then, (s)he indicated in which of the first two intervals (s)he heard the signal. Analysis of the results of the second question for condition (2) and (3) are not presented in this paper, but can be found in Gockel (1996).

B. Stimuli and equipment

Table I shows component frequencies, corresponding ERB values (Glasberg and Moore, 1990), and the resulting ERB spacing between adjacent components of the 11-tone complexes that were used for all three conditions. All spectral components were equally spaced on a logarithmic frequency scale. The central component was located at 1000 Hz. Two slightly different tone complexes were used, two subjects being tested with each complex. For the first two subjects (group 1), the lowest/highest component had a frequency of 313 Hz/3200 Hz, yielding a frequency ratio of 1.26 between adjacent components. These component frequencies were chosen initially to be identical with the ones used by Kirschweng (1993) in a profile analysis experiment with signal frequency uncertainty, to allow for a direct comparison of the results. However, as it turned out, one subject had some problems with this specific frequency ratio in the identification condition; these will be discussed later in more detail. Therefore, the frequency ratio was chosen to be different for the second two subjects (group 2). For them, the component frequencies ranged from 269 Hz to 3713 Hz,

TABLE I. Frequencies of the components used in the 11-tone complexes for the two groups of subjects. The number of ERBs corresponding to each frequency and the difference between the number of ERBs corresponding to adjacent frequencies are given below that frequency.

	Group 1 (Subjects: 01, 02)									$f_{i+1}/f_i=1.26$	
Component	1	2	3	4	5	6	7	8	9	10	11
f [Hz]	313	395	498	629	793	1000	1263	1593	2010	2536	3200
E [ERB]	7.99	9.29	10.71	12.24	13.86	15.57	17.37	19.22	21.13	23.08	25.08
Delta E		1.31	1.42	1.54	1.62	1.71	1.80	1.85	1.91	1.96	1.99
	Group 2 (Subjects: 03, 04)									$f_{i+1}/f_i=1.3$	
Component	1	2	3	4	5	6	7	8	9	10	11
f [Hz]	269	350	455	592	769	1000	1300	1690	2197	2856	3713
E [ERB]	7.20	8.60	10.14	11.83	13.64	15.57	17.60	19.70	21.87	24.10	26.37
Delta E		1.40	1.54	1.69	1.81	1.93	2.02	2.11	2.17	2.23	2.27

yielding a factor of 1.3 between the frequencies of adjacent components. The corresponding ERB spacing ranged from about 1.3 between the lowest components to about 2 between the highest components for the first group. The ERB spacing was somewhat larger for the second group of subjects. The stimuli were chosen so, as to satisfy two constraints: (1) they should be comparable to those of other profile analysis experiments (equilog spaced), and (2) all components were separated by more than 1.25 ERBs which should result in better than 70% accuracy in identifying the pitch of individual components (Moore and Ohgushi, 1993).

At the start of each session, nine random phase relationships were determined, and one of these was selected at random for each presentation. The overall level of the tone complexes and sinusoid varied randomly and independently over a range of 20 dB, with a median level of 50 dB SPL. Electrical component levels were adjusted so as to compensate for the frequency characteristic of the headphones used (measured with a B&K Artificial Ear, type 4153) in order to produce roughly an equal amplitude for each component of the standard stimulus at the eardrum. The duration of all stimuli was 500 ms including 20-ms rise/fall times shaped by a hanning window (see, e.g., Oppenheim and Schafer, 1975). All stimuli were generated digitally (Sun ELC), played by a 16-bit digital-to-analog converter (D/A) at a sampling rate of 44 100 Hz and low-pass filtered at 20 KHz (ninth-order elliptic filter; 0.3-dB pass band ripple; −80-dB stop band attenuation). Overall variation of stimulus level was achieved using a computer-controlled audiometer amplifier. The stimuli were presented monaurally over the left ear piece of a Beyer DT 990 Pro headphone. Subjects were individually seated in a double-walled (IAC) sound insulated chamber, and responded via a PC keyboard. Brief instructions (in addition to a more detailed paper version) and feedback were presented using a PC monitor which was located outside the booth in front of its window. The PC, which was connected to the Sun, served only as an input–output terminal. Light emitting diodes (LEDs), fixed at the bottom front of the monitor's frame, indicated the beginning of a new trial and indicated observation intervals. The LEDs were controlled by a signal generated on the Sun and played by the second channel of the D/A converter to ensure precise timing.

C. Procedure

Each trial started with a visual warning signal (LED) presented 700 ms before the first stimulus was presented. Observation intervals were separated by a 500-ms silent interval. In both identification conditions the probability of the event ''the signal frequency is the same as the frequency of the sinusoid'' equalled 0.5 and the probability of ''lower'' or ''higher'' equalled 0.25. In each condition, nine independent interleaved adaptive procedures were used to estimate thresholds, corresponding to 71 percent correct responses, for each of the nine possible signal frequencies. In both identification conditions, only the first response (''SAME''/ ''DIFFERENT'') was used by the adaptive procedure for estimating thresholds. The size of the increments varied according to a 1-up 2-down method, tracking the 70.7% point of the psychometric functions (Levitt, 1971). The initial step size was 4 dB (expressed as the signal-to-standard ratio in decibels). Following two reversals, the step size was decreased to 2 dB. The threshold was defined as the median of at least six reversal points at the minimum step size of 2 dB. All adaptive procedures continued until at least six reversal points were collected for each of them. The total duration of a single session varied between about 75 and 120 min (in the three-interval task), including rest times, and corresponded to about 400–500 trials. All subjects participated in all conditions. Subjects got extensive training in each task. They ran for about 10–20 sessions in each condition, until performance seemed stable (in all conditions strong improvements of 3–10 dB across sessions were observed). Two subjects, 01 and 04, started with the ''Discrimination'' condition, ran for about 10–16 sessions and then changed to the ''Standard-absent'' condition. For the other two subjects, 02 and 03, the order was reversed. The condition ''Standard-present'' was the third in the sequence. Following this, subjects repeated once more the two two-interval tasks for at least four sessions, to control for training effects. In general, only the later sessions with stable performance (at least four sessions) were used for further comparison of data. Response biases were evaluated for increment sizes within 4 dB of the individual thresholds. The subjects showed no significant response bias in the same/different judgements. This is important because $P(c)$ as a measure of sensitivity, as used in the adaptive

procedure in the identification (and in the discrimination) task, is only defensible for unbiased observers and for equal a priori probabilities of the two stimuli.

D. Subjects

Four subjects ranging in age from 21 to 29 years participated in this study. Each of the subjects had some degree of musical training and had normal hearing as measured by conventional audiometry. Stimuli were delivered monaurally to the right ear (in each case the better ear) of each subject.

II. RESULTS

In this section, thresholds measured in the different conditions/tasks will be compared. Of course, comparison of thresholds between various conditions makes sense only if these thresholds correspond to equivalent performance levels in the sense of "true sensitivity" scores. The emphasis lies on true sensitivity scores, since a fixed value of $P(c)$, equal to 0.71 in all conditions, does not necessarily result from equal true sensitivities. In the "Discrimination" condition a classical 2I-2AFC procedure was used to estimate the threshold corresponding to a value of 0.71 for $P(c)$. This corresponds to a value of $d'=0.78$ (see, e.g., Macmillan and Creelman, 1991). For the identification conditions, it would also be appropriate to apply signal detection theory and to convert the scores to an estimate of d'. In the identification conditions, the first response "SAME"/"DIFFERENT" was used to estimate thresholds. Thus one might think of the task as a same–different task. However, this would not be correct, since the stimuli presented in a single trial were never really identical (11-tone complex with an incremented component versus single sinusoid). If one had ignored this fact, one would have concluded that for a certain value of $P(c)$, produced by an unbiased observer, the d' score resulting from a same–different task exceeds the d' score resulting from a 2AFC task. If, instead, one had evaluated the identification conditions as a yes–no task [like Moore and Bacon (1993) did in a comparable experiment] then, for a fixed value of $P(c)$ produced by an unbiased observer, the d' value resulting from the identification conditions would exceed the d' value resulting from the "Discrimination" condition by a factor of $\sqrt{2}$. If one evaluated both tasks (the identification and the discrimination task) by using a double high-threshold model, then, for a fixed value of $P(c)$ produced by an unbiased observer, this would result in equal true sensitivity for both tasks. The double high-threshold model [described and compared to d' measures in Macmillan and Creelman (1991), pp. 95–106] uses proportion correct as the sensitivity measure and behaves in accordance with the d' measure under certain conditions (equal presentation probabilities and unbiased observer) which are met in the present tasks. Thus no matter which model is assumed, for an unbiased observer the same thresholds measured in the identification conditions and in the "Discrimination" condition correspond to either equal sensitivity in the two conditions or *higher* sensitivity in the identification condition. The same conclusion is drawn in the Appendix where optimal
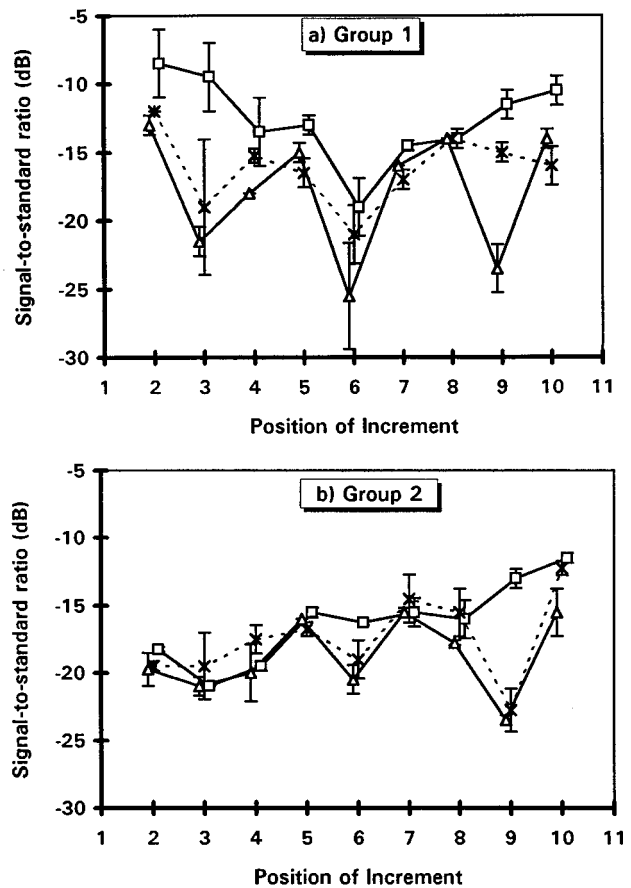
FIG. 1. Group means of thresholds and corresponding standard errors of the mean as a function of the incremented component position. Squares correspond to the "Discrimination," triangles to the "Standard-absent" and crosses to the "Standard-present" condition. (a) Group 1. (b) Group 2.

weights and an estimate of d' are derived for the specific identification condition employed in this experiment.

Figure 1 shows group means and corresponding standard errors of the mean for the three conditions. Squares correspond to the "Discrimination," triangles to the "Standard-absent" and crosses to the "Standard-present" condition. Since the results for the two groups of subjects differ, they will initially be discussed separately. For the first group [shown in Fig. 1(a)], discrimination thresholds (squares) as a function of signal frequency appear to be approximately "bowl shaped," as was reported, e.g., by Bernstein and Green (1988) for conditions with a fixed signal frequency. The component frequencies employed (see Table I) are identical to the ones used by Kirschweng (1993). As in the present experiment, Kirschweng measured discrimination thresholds in a signal-uncertain condition using independent interleaved adaptive procedures. There is quite good correspondence between his data and the present discrimination thresholds as a function of signal frequency. Thresholds in the "Standard-absent" condition (triangles) were in general as low as, or even lower than those for discrimination. This supports the idea of the pitch strength of the incremented component as a possible cue in the "Discrimination" condition. Performance was especially good when the third, sixth, or ninth component was incremented in amplitude. Possible
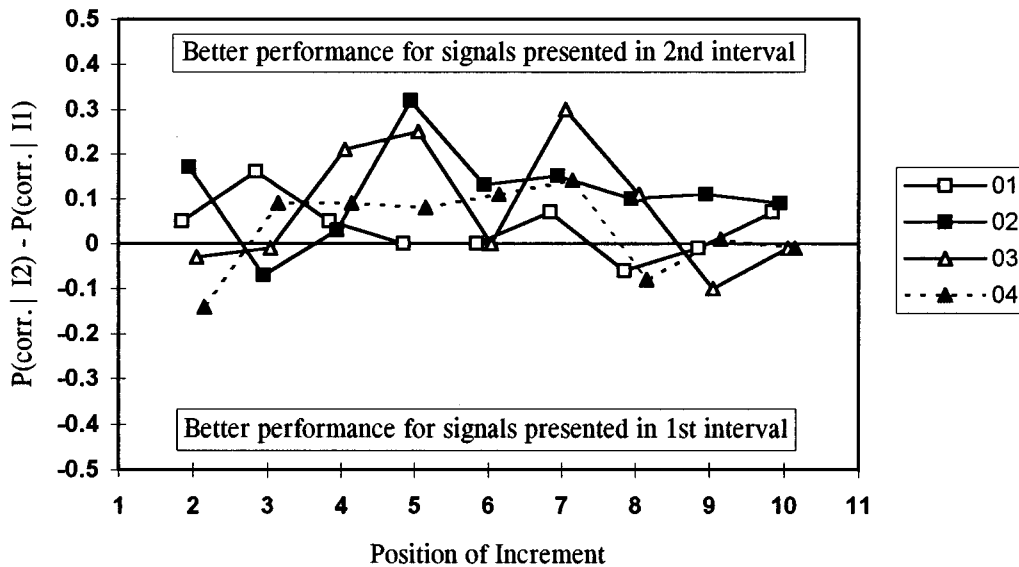
FIG. 2. Dependence of performance in the ''Standard-present'' condition on the sequence of stimuli as a function of the incremented component position. The ordinate shows the difference between the probability of the event ''same/different response was correct'' conditional on the event ''incremented profile has been presented in the second interval'' and the probability of the event ''same/different response was correct'' conditional on the event ''incremented profile has been presented in the first interval.'' A value of +0.5 would mean: all responses were correct when the increment was presented in the second interval and $P(c)$ was about guessing rate when the increment was presented in the first interval. A value of zero would mean: correct responses were given with equal percentages in trials where the increment was presented in the first/second observation interval. Each curve corresponds to one subject.

reasons for this ''dip pattern'' will be discussed later. In the ''Standard-present'' condition (crosses), thresholds were mostly between those of the other two conditions. This implies that the presence of the standard did not help in identifying the incremented component. For the second group [shown in Fig. 1(b)], discrimination thresholds showed a trend to increase with increasing signal frequency. Again, thresholds in the ''Standard-absent'' condition were in general as low as, or even lower than in the ''Discrimination'' condition. Again, especially good performance was observed when the sixth or ninth component was incremented in amplitude. For the low-frequency region there was no difference between performance in the ''Discrimination'' and the ''Standard-absent'' conditions. In the ''Standard-present'' condition, thresholds were higher than or the same as in the ''Standard-absent'' condition.

For the second group of subjects, the frequency ratio between adjacent components was larger than for the first group. The reason for this was as follows: In the ''Standard-absent'' condition one subject of the first group reported that he often made mistakes in the ''same''/''different'' task because he wrongly assumed the signal frequency to be one octave lower or higher than the frequency of the following sinusoid. Thus the nearly one-octave frequency relationship between every third component seemed to be a problem for this subject. The second subject in group one did not report any such problems, even if asked. To reduce such octave effects, the frequency ratio between adjacent components was selected to be larger for the second group. For the three lowest signal frequencies, discrimination thresholds for the second group were about 7–10 dB lower than for the first group. For the higher frequencies, performance was nearly identical. It is likely that an increase of frequency spacing or

ERB spacing is more helpful for such a task when the ERB spacing is rather small (below 1.5) than when it is already large (see Moore and Ohgushi, 1993). The same argument may apply to performance in the identification conditions.

The difference between thresholds measured in the ''Discrimination'' and in the ''Standard-absent'' conditions (calculated over all subjects and increment positions) was significant, based on a two-sided sign test ($p<0.01$). The difference between thresholds measured in the ''Discrimination'' and in the ''Standard-present'' conditions was also significant, based on a two-sided sign test ($p<0.01$). Both of these findings support the idea of the pitch strength of the incremented component as a possible cue in the discrimination task. However, the difference between thresholds measured in the ''Standard-absent'' and in the ''Standard-present'' conditions was not significant based on a two-sided sign test ($p>0.2$). This indicates that the presence of a flat profile did not facilitate identification of the incremented component, at least when the two stimuli (flat profile and incremented profile) were presented in random order.

To investigate this point more closely, trials from the ''Standard-present'' condition in which the standard-plus-signal complex was presented in the first interval were analyzed separately from trials in which the standard-plus-signal complex was presented in the second interval. Figure 2 shows the difference between performance scores for these two categories of trials as a function of the increment position. The calculation includes only those trials for which the size of the increment was within 4 dB of the individual thresholds. Each curve shows data for one subject. A tendency for better performance if the incremented component was presented in the second interval can be seen. The difference between conditional probabilities (calculated over all

subjects and increment positions) was significant based on a two-sided sign test ($p < 0.05$). This finding may reflect decay of a memory trace with time and/or an interfering effect of the flat profile presented after the incremented profile within the identification task. Future experiments with prolonged ISIs may clarify which of the two explanations is more appropriate. Another possible reason for the observed asymmetry in performance levels for the two stimulus sequences is that it might be easier to hear an increase in relative level (when the standard-plus-signal stimulus was presented in the second interval) than to hear a decrease in relative level. However, this seems to be an implausible explanation of the effect, since performance in the ''Standard-absent'' condition was not worse but showed a trend to be better than in the ''Standard-present'' condition for all subjects.

III. DISCUSSION

The data show that the ability to identify which one of the spectral components in profile stimuli is incremented is equal to or better than the ability to discriminate between flat and incremented profile stimuli. This finding may sound rather surprising at a first sight. However, since subjects seem to compare a memory representation of the incremented profile stimulus with the single sinusoid, one might argue that the sinusoid may act as post-cue, which reduces the number of possible increment positions which have to be monitored to three. The Appendix presents details of this argument and derives optimal weights in the identification task.

The finding that identification is at least as good as discrimination does not contradict the mathematical predictions of the multi-channel model which is widely applied in profile analysis (see Durlach *et al.*, 1986; Berg and Green, 1990; Kidd *et al.*, 1991; Green, 1992; Dai, 1994), since, in this model, it has never been made explicit whether listeners hear out the incremented component.

In several studies, where the subjects' task was to discriminate between flat and incremented profile stimuli, the observers' empirical weighting patterns for the frequency components involved were investigated (see, e.g., Berg and Green, 1990; Green and Berg, 1991). This weighting pattern reflects the relative contribution of the different frequency channels in the across-channel level comparison process which the listener is assumed to perform. In these studies, the frequency of the incremented component was fixed and observers were assumed to be able to develop nearly optimal weighting patterns because each measurement started with a suprathreshold size of the increment which enabled ''identification'' of the signal frequency. However, in the case of signal uncertainty this *a priori* weighting function cannot develop. Nevertheless, discrimination thresholds were only slightly elevated in the signal-uncertain condition (Raney *et al.*, 1989; Kirschweng, 1993; Dai, 1994). Dai (1994) measured psychometric functions for spectral-shape discrimination with and without signal-frequency uncertainty and found no significant difference between the slopes of the psychometric functions in the two conditions. In the framework of the multi-channel model, he derived the optimum decision rule for the signal-unknown condition. He then ran simula-

tions according to the optimum decision rules for the signal-known and for the the signal-unknown conditions. Assuming that the subjects were using optimum decision rules in both conditions, the small effect of signal uncertainty could be accounted for if the independent Gaussian noise which is inherent in each channel was assumed to be small compared with other noise components (e.g., the central noise). A second explanation for the small effect of signal uncertainty was that the observers did not really adopt the optimal weighting pattern in the signal-certain condition, thus leading to similar decision rules for both conditions. He noted that further experiments are needed to determine which explanation is more reasonable.

The present study cannot allow a decision between the two alternatives, but suggests a possible cue in profile analysis tasks, available in both signal-certain and signal-uncertain conditions. This cue may be described as a perceived heightening of pitch strength of a single spectral component [for the concept of pitch strength see, e.g., Fastl and Stoll (1979), Zwicker and Fastl (1990)]. This seems to correspond more closely to the subjective reports of subjects than a global change in timbre.

Ellermeier (1996) compared the detectability of an increment and a decrement in the level of the central component of a complex tone. For wide component spacings (a frequency ratio between adjacent components equal to or larger than a value of 1.49) he found no significant difference between the thresholds for discriminating between flat and incremented profiles and the thresholds for discriminating between flat and decremented profiles. For narrower spacings, increment detection was easier than decrement detection. Ellermeier argued that these results contradict a ''simple pitch salience explanation'' (the use of a local pitch strength cue) of spectral shape discrimination ability. According to Ellermeier, the pitch salience cue would only be available for increments and not for decrements in level. If this were true, the equal detectability of increments and decrements for wide component spacings would contradict the pitch salience explanation. However, one might question the assumption that there is no pitch salience cue available in decrement detection. A decrease in level also produces a change in relative pitch strength which may be used as a cue when comparing the standard with the standard-plus-signal.

The multi-channel model may be extended to account for the finding of high ability to identify the incremented component by making the assumption that comparing the output levels of various auditory filters is exactly the underlying mechanism in determining the pitch strength of individual components.

The observed ''dip pattern'' in identification thresholds (especially good performance for signal positions 3, 6, and 9), does not seem to be caused by the nearly octave relationship between every third component for group 1, since it was observed for both groups (although for the second group it is less obvious at position 3, presumably because of the strongly improved performance in the lower frequency region). Moore and Ohgushi (1993) who investigated the audibility of partials in inharmonic complex tones, also reported distinct peaks and dips in their perfomance measures,

at least for component spacings less than 1.5 ERB. They offered an explanation in terms of irregularities in the transmission characteristic of the middle ear (Rosowski, 1991) that would result in different effective levels of the partials. However, this explanation seems unlikely to account for the present results. Firstly, there would have to be a high degree of similarity in the irregularities in the transmission characteristic between subjects to produce the similarity between patterns observed in the present study. Secondly, the component spacing in the present study was mainly between about 1.5 and 2 ERB, a width for which the performance patterns observed in the study of Moore and Ohgushi were much smoother. An alternative explanation is that the third, sixth, and ninth components were especially salient in perception, due to their relative position in the 11-tone complex. While such an assumption may sound rather ad hoc, there are some findings supporting a similar idea in the area of shape perception in vision research. Psotka (1978) investigated the pattern of dot placements created when people individually placed a single dot inside empty outline figures. The superimposed results indicated especially salient loci, which he found to be predicted fairly well by a model proposed by Blum (1973) which is based on local symmetry calculations. Similar local symmetries may explain the present results; for example, the sixth component was the central component in the complex.

Future experiments with different center frequencies of the stimulus complexes may shed some light on the underlying processes. If irregularities in the middle ear transfer functions cause particular salience of certain frequencies, then performance should depend on the frequency of the incremented component rather than on its relative position in the complex. Conversely, if the data reveal fundamental aspects of auditory pattern analysis, then the lower thresholds should not depend on the absolute frequency of the signal component.

IV. SUMMARY AND CONCLUSIONS

An investigation of the ability to identify which one of the spectral components in a profile stimulus was incremented in level, has been presented. Results showed that:

(1) The ability to determine which one of the spectral components was incremented was at least as good as the ability to discriminate between flat and incremented stimuli. This was true for both the ''Standard-present'' and the ''Standard-absent'' condition.
(2) Thresholds in the ''Standard-present'' condition (with randomized order of the standard and standard-plus-signal complexes) were somewhat higher than in the ''Standard-absent'' condition.
(3) In the ''Standard-present'' condition, performance was better when the standard preceeded the incremented stimulus than when the standard followed the incremented stimulus.

The data do not contradict the mathematical predictions of the multi-channel model used in profile analysis, since that model does not specify whether listeners hear out the incremented component. The results suggest a possible cue used in profile analysis tasks which might be described as a perceived heightening of pitch strength of a single spectral component.

APPENDIX: OPTIMAL DECISION STATISTIC FOR THE IDENTIFICATION OF THE INCREMENTED COMPONENT

In this Appendix the idea of the sinusoid acting as a postcue in the identification task is described in more detail. Furthermore, optimal weights in the ''Standard-absent'' condition are derived based on some simplifying assumptions for this task. Derivations are calculated in accordance with the assumptions of the multi-channel model (see, e.g., Green, 1992). Specifically this means: (1) The input signal is resolved into n frequency bands each of which leads to an initially independent level estimate. (2) Inherent in each channel an independent Gaussian noise (with variance s_k^2) adds to the level estimate. (3) A common Gaussian noise variable, W (with variance s_W^2), is added to all channel estimates. Three additional assumptions are made: (1) Since both stimuli (the incremented tone complex and the sinusoid) were randomly roved in level, no reliable successive within-channel level cue was provided. Therefore, it is assumed that decisions were based on simultanous comparisons of component levels in the tone complex. (2) For derivation of optimal weights a perfect memory representation of the stimuli is assumed. (3) Subjects used the fact that there were only three possible signal frequencies in each trial. The identity of these possible signal frequencies was defined by the sinusoid presented.

Now the optimal weights for individual component levels in such a situation will be derived. The ''internal spectrum'' of the stimulus is represented by an n-dimensional vector $\mathbf{X} = [X_1, \ldots, X_n]$, where the X_k are correlated Gaussian random variables with means $M(X_k|S_i) = M_{ik}$, variances $s_W^2 + s_k^2$, covariances s_W^2, and where in this experiment n equals 11. S_i indicates that the ith component of the complex is incremented, where $1 < i < 11$. For each trial, where a single sinusoid of a certain frequency f_s (where the index s indicates the position of the component with the same frequency in the complex) was presented, the probability that the incremented component had the same frequency was 0.5, while the probability that the incremented component had a frequency corresponding to index $s-1$ or $s+1$ was 0.25 each, for $2 < s < 10$. For $s = 2$ or $s = 10$ the probabilities that the incremented component had a frequency corresponding to index $s-1$ or $s+1$ were not equal to each other, but $P(S_2|f_1) = P(S_{10}|f_{11}) = 1$, $P(S_2|f_2) = P(S_{10}|f_{10}) = 2/3$, $P(S_3|f_2) = P(S_9|f_{10}) = 1/3$ and $P(S_1) = P(S_{11}) = 0$, where $P(S_i|f_s)$ represents the conditional probability that the ith

component of the complex was incremented, given that a sinusoid of frequency f_s was presented. The following derivation is restricted to cases where $2<s<10$. For this case, the optimal decision statistic for deciding between the two alternative responses ''Frequency of the incremented component was the SAME as the frequency of the following sinusoid'' and ''Frequency was DIFFERENT'' is based on the likelihood ratio as follows:

If

$$l(\mathbf{X}) = \frac{f(\mathbf{X}|S_s)}{\frac{1}{2}\Sigma_{j=s-1,s+1}f(\mathbf{X}|S_j)} > 1$$

then respond ''SAME,'' otherwise respond ''DIFFERENT'';[1]

where s corresponds to the index of the single sinusoid presented and $f(\mathbf{X}|S_s)$ represents the conditional multivariate probability density function of $\mathbf{X}$, given that the sth component is incremented.

This can be witten as: If

$$l^*(\mathbf{X}) = \frac{1}{l(\mathbf{X})} = \frac{\frac{1}{2}\Sigma_{j=s-1,s+1}f(\mathbf{X}|S_j)}{f(\mathbf{X}|S_s)} > 1$$

then respond ''DIFFERENT,'' otherwise respond ''SAME.'' Thus for the multivariate Gaussian case,

$$l^*(\mathbf{X}) = \frac{1}{2}\sum_{j=s-1,s+1} l_j^*$$

$$= \frac{1}{2}\left(\frac{\exp[-\frac{1}{2}(\mathbf{X}-\mathbf{M}_{s-1})'\mathbf{Q}^{-1}(\mathbf{X}-\mathbf{M}_{s-1})]}{\exp[-\frac{1}{2}(\mathbf{X}-\mathbf{M}_s)'\mathbf{Q}^{-1}(\mathbf{X}-\mathbf{M}_s)]} \right.$$

$$\left. + \frac{\exp[-\frac{1}{2}(\mathbf{X}-\mathbf{M}_{s+1})'\mathbf{Q}^{-1}(\mathbf{X}-\mathbf{M}_{s+1})]}{\exp[-\frac{1}{2}(\mathbf{X}-\mathbf{M}_s)'\mathbf{Q}^{-1}(\mathbf{X}-\mathbf{M}_s)]} \right),$$

(A1)

where l_j^* corresponds to the individual likelihood ratio for realizing the actual value of $\mathbf{X}$ given that the jth component was incremented versus realizing $\mathbf{X}$ given that the sth component was incremented, and $\mathbf{Q}^{-1}$ corresponds to the inverse covariance matrix. Defining r to correspond to the covariance s_W^2, and p to correspond to the individual variance s_k^2 (which is assumed to be equal for all channels), then the covariance matrix $\mathbf{Q}$ has the following form:

$$\mathbf{Q} = \begin{bmatrix} r+p & r & \cdots & \cdots & r \\ r & r+p & r & \cdots & r \\ \vdots & r & \ddots & r & \vdots \\ \vdots & \vdots & r & r+p & r \\ r & \cdots & \cdots & r & r+p \end{bmatrix}. \quad (A2)$$

The inverse of $\mathbf{Q}$ then corresponds to

$$\mathbf{Q}^{-1} = \frac{1}{p(p+nr)} \begin{bmatrix} p+(n-1)r & -r & \cdots & \cdots & -r \\ -r & p+(n-1)r & -r & \cdots & -r \\ \vdots & -r & \ddots & -r & \vdots \\ \vdots & \vdots & -r & p+(n-1)r & -r \\ -r & \cdots & \cdots & -r & p+(n-1)r \end{bmatrix}. \quad (A3)$$

From the individual likelihood ratio l_j^* the optimum decision statistic Z_j^* for the case $j=s-1$ will now be derived. This means that we restrict the derivation of the optimum decision statistic to a case where only one different increment position $(s-1)$ is possible. Later, this derivation will be generalized to the case of two possible different increment positions which corresponds to the actual experimental condition.

For the multivariate Gaussian case, the natural logarithm of

$$l_j^* = \frac{\exp[-\frac{1}{2}(\mathbf{X}-\mathbf{M}_{s-1})'\mathbf{Q}^{-1}(\mathbf{X}-\mathbf{M}_{s-1})]}{\exp[-\frac{1}{2}(\mathbf{X}-\mathbf{M}_s)'\mathbf{Q}^{-1}(\mathbf{X}-\mathbf{M}_s)]} \quad (A4)$$

is equal to (see, e.g., Van Trees, 1968):

$$\ln(l_j^*) = \frac{1}{2}(\mathbf{X}-\mathbf{M}_s)'\mathbf{Q}^{-1}(\mathbf{X}-\mathbf{M}_s) - \frac{1}{2}(\mathbf{X}-\mathbf{M}_{s-1})'$$

$$\times \mathbf{Q}^{-1}(\mathbf{X}-\mathbf{M}_{s-1})$$

$$= (\mathbf{M}_{s-1}-\mathbf{M}_s)'\mathbf{Q}^{-1}\mathbf{X} - \frac{1}{2}(\mathbf{M}_{s-1}'\mathbf{Q}^{-1}\mathbf{M}_{s-1}$$

$$- \mathbf{M}_s'\mathbf{Q}^{-1}\mathbf{M}_s). \quad (A5)$$

The second half of the right-hand side of Eq. (A5),

$$a = -\frac{1}{2}(\mathbf{M}_{s-1}'\mathbf{Q}^{-1}\mathbf{M}_{s-1} - \mathbf{M}_s'\mathbf{Q}^{-1}\mathbf{M}_s), \quad (A6)$$

is a constant and does not influence the optimal weights (the factors by which the random vector has to be multiplied). Therefore, this constant a can be neglected in the following derivation of optimal weights. Defining $\mathbf{D}=\mathbf{M}_{s-1}-\mathbf{M}_s$ one gets the following expression which is monotonic with $\ln(l_j^*)$:

$$Z_j^* = [\Delta_l \quad \cdots \quad \Delta_n]$$

$$\cdot \frac{1}{p(p+nr)} \begin{bmatrix} p+r(n-1) & -r & \cdots & & -r \\ -r & \ddots & & & \vdots \\ \vdots & & \ddots & & -r \\ -r & \cdots & -r & & p+r(n-1) \end{bmatrix}$$

$$\cdot \begin{bmatrix} X_1 \\ \vdots \\ \vdots \\ X_n \end{bmatrix}$$

$$= \frac{1}{p(p+nr)} \sum_{k=1}^{n} \left(\Delta_k(p+r(n-1)) - r \sum_{\substack{u=1 \\ u \neq k}}^{n} \Delta_u \right) X_k$$

$$= \frac{p+r(n-1)}{p(p+nr)} \sum_{k=1}^{n} \left(\Delta_k - \frac{r}{p+r(n-1)} \sum_{\substack{u=1 \\ u \neq k}}^{n} \Delta_u \right) X_k$$

$$= \frac{p/r+n-1}{p(p/r+n)} \sum_{k=1}^{n} \left(\Delta_k - \frac{1}{n-1+p/r} \sum_{\substack{u=1 \\ u \neq k}}^{n} \Delta_u \right) X_k. \quad (A7)$$

Equation (A7) corresponds to the optimum decision variable with weights for the general case of discriminating between two stimuli given by Green (1992):

$$Z_j^* = c_1 \sum_{k=1}^{n} w_k X_k, \quad (A8)$$

where

$$c_1 = \frac{p/r+n-1}{p(p/r+n)} \quad (A9)$$

is a proportionality constant and

$$w_k = \Delta_k - \frac{1}{n-1+p/r} \sum_{\substack{u=1 \\ u \neq k}}^{n} \Delta_u \quad (A10)$$

specifies the optimal weights.

In the present experiment the expected difference in level for each component $\Delta_k = M_{s-1,k} - M_{s,k}$ takes the following values:

$$\Delta_k = +dI_{s-1}, \quad k = s-1,$$

$$\Delta_k = -dI_s, \quad k = s,$$

$$\Delta_k = 0, \quad k = 1,...,n, \quad k \neq s-1,s,$$

where dI_i is the size of the increment at threshold, measured as the level difference in decibels, in adaptive procedure i (remember that there were nine interleaved adaptive procedures, one for each increment position). Therefore,

$$Z_j^* = c_1 \cdot \left[\left(\Delta_{s-1} - \frac{1}{n-1+p/r} \cdot \Delta_s \right) X_{s-1} \right.$$

$$+ \left(\Delta_s - \frac{1}{n-1+p/r} \cdot \Delta_{s-1} \right) X_s$$

$$\left. - \frac{1}{n-1+p/r} \sum_{\substack{k=1 \\ k \neq s-1,s}}^{n} (\Delta_{s-1} + \Delta_s) X_k \right]$$

$$= c_1 \left[\left(dI_{s-1} + \frac{dI_s}{n-1+p/r} \right) X_{s-1} \right.$$

$$- \left(dI_s + \frac{dI_{s-1}}{n-1+p/r} \right) X_s - \frac{1}{n-1+p/r}$$

$$\left. \times \sum_{\substack{k=1 \\ k \neq s-1,s}}^{n} (dI_{s-1} - dI_s) X_k \right]. \quad (A11)$$

For $p/r \ll 1$ the constant c_1 approximately corresponds to

$$c_1 \approx \frac{n-1}{n\sigma_k^2} = c_2 \quad (A12)$$

and Eq. (A11) approximately corresponds to

$$Z_j^* = c_2 \left[\left(dI_{s-1} + \frac{dI_s}{n-1} \right) X_{s-1} - \left(dI_s + \frac{dI_{s-1}}{n-1} \right) X_s \right.$$

$$\left. - \frac{1}{n-1} \sum_{\substack{k=1 \\ k \neq s-1,s}}^{n} (dI_{s-1} - dI_s) X_k \right]. \quad (A13)$$

Scaling the maximum optimal weight to the value one, several cases can be distinguished.

(1) If dI_s and dI_{s-1} are of equal size, then

$$w_k = +1, \quad k = s-1,$$

$$w_k = -1, \quad k = s,$$

$$w_k = 0, \quad k = 1,...,n \quad k \neq s-1,s,$$

and

$$Z_j^* = c_2(X_{j-1} - X_j). \quad (A14)$$

In this case, the optimum decision rule is equivalent to determining the difference in level between the two components that may have been incremented. Components which are never incremented in level (for a given frequency of the sinusoid) are not at all involved in the optimal comparison process.

(2) If dI_s and dI_{s-1} are of different size, and
(a) $dI_s > dI_{s-1}$ then

$$\tfrac{1}{10} < w_k < 1, \quad k = s-1,$$

$$w_k = -1, \quad k = s,$$

$$0 < w_k < \tfrac{1}{10}, \quad k = 1,...,n \quad k \neq s-1,s,$$

or (b) $dI_s < dI_{s-1}$ then

$$w_k = +1, \quad k = s-1,$$

550   J. Acoust. Soc. Am., Vol. 103, No. 1, January 1998

Hedwig Gockel: Identification of the incremented component   550

$$-1 < w_k < -\tfrac{1}{10}, \quad k = s,$$

$$-\tfrac{1}{10} < w_k < 0, \quad k = 1,...,n \quad k \neq s-1, s.$$

Thus the absolute sizes of the weights for the two possible signal components vary depending on the amount of difference between dI_s and dI_{s-1}. The largest (absolute) weight is given to the component with the largest increment size (at threshold). Components which are never incremented in level (given a fixed frequency of the sinusoid) are involved in the optimal comparison process too, but, to a smaller degree.

(3) For extremely large absolute differences between dI_s and dI_{s-1} the weights approximate the extreme case of
(a) $dI_{s-1} = 0$ then

$$w_k = -1, \quad k = s,$$

$$w_k = \tfrac{1}{10}, \quad k = 1,...,n \quad k \neq s,$$

or (b) $dI_s = 0$ then

$$w_k = 1, \quad k = s-1,$$

$$w_k = -\tfrac{1}{10}, \quad k = 1,...,n \quad k \neq s-1.$$

In this case, the optimum decision rule is equivalent to determining the difference in level between the incremented component and the mean of the nonsignal components.

Now, we generalize to the case of two possible different increment positions ($s-1$ and $s+1$). After substituting $\exp(Z_j^* + a)$ for the individual likelihood ratio l_j^* in Eq. (A1), we get the general optimum decision statistic Z (for each trial, after presentation of a sinusoid with index s):

$$Z = \ln l^*(\mathbf{X}) = \ln\left(\frac{1}{2} \sum_{j=s-,s+1} e^{Z_j^* + a}\right)$$

$$= \ln\left(\frac{1}{2} e^a \sum_{j=s-1,s+1} e^{Z_j^*}\right)$$

$$= \ln\left(\sum_{j=s-1,s+1} e^{Z_j^*}\right) + a - \ln 2. \quad \text{(A15)}$$

The last two terms are constants and can be neglected without affecting the optimum decision rule.

The general form of Eq. (A15) resembles the optimum decision statistic Z for the condition of signal-frequency uncertainty in discriminating between flat and incremented profile stimuli, as derived by Dai (1994). The reason for this is that both derivations involve a mixture of several signal-distribution functions. The optimal weights are different for his task and the present task. Note, however, that there are two typing errors in his derivation. Firstly, the constant a is missing and, secondly, the constant factor by which Z_j is multiplied should be $c_3 := (n-1)\Delta/n\sigma_I^2$ [note that in Dai (1994), the constant c_3 is not incorporated in Z_j while, in this Appendix, the constant c_2 is incorporated in Z_j^*, as is done in Green (1992)].

For the present identification task, Eq. (A14) may give some insight into how to evaluate this task in the context of signal detection theory and how to determine the correspond-

ing value of d'. Assume that a sinusoid of frequency f_s was presented on a specific trial. Assume further that there were only two possible positions of the incremented component, one "different component," e.g., with index $s-1$ and the "same component" with index s. Then, for the two channels $s-1$ and s the task might be regarded as identifying in which of the two channels the signal (of size dI_{s-1} or dI_s) was presented. In such a two-dimensional task, d' is higher than d' in a Yes/No task by a factor of $\sqrt{2}$ at most (see Macmillan and Creelman, 1991). This would be the case if dI_{s-1} and dI_s were of equal size. For different sizes of dI_{s-1} and dI_s, d' is still higher than d' in a Yes/No task, but by a factor less than $\sqrt{2}$. Actually, in each trial of the experiment there were two possible 'different components' (with index $s-1$ and index $s+1$). That means there was additional uncertainty about the frequency of the signal which made the task even harder. To summarize, the conclusion is that the identification task is easier than a Yes/No task by not more than the amount a 2AFC task (used in the discrimination condition) is easier than a Yes/No task. Therefore, a threshold of a certain value measured in the identification condition indicates equal or better performance than the same threshold measured in the discrimination condition.

[1]In the "Standard-present" condition the subjects' strategy could be very similar to the one used in the "Standard-absent" condition. After presentation of the single sinusoid they could decide whether it was likely that the signal frequency in either the first or second interval was the same as the frequency of the single sinusoid. It would not have been necessary for them first to decide in which interval the signal was presented.

Anantharaman, J. N., and Krishnamurthy, A. K. (**1993**). "Intensity-weighted average of instantaneous frequency as a model for frequency discrimination," J. Acoust. Soc. Am. **94**, 723–729.

Berg, B. G., and Green, D. M. (**1990**). "Spectral weights in profile listening," J. Acoust. Soc. Am. **88**, 758–766.

Bernstein, L. R., and Green, D. M. (**1988**). "Detection of changes in spectral shape: Uniform vs nonuniform background spectra," Hearing Res. **32**, 157–166.

Blum, H. (**1973**). "Biological shape and visual science (Part I)," J. Theor. Biol. **38**, 205–287.

Dai, H. (**1994**). "Signal-frequency uncertainty in spectral-shape discrimination: Psychometric functions," J. Acoust. Soc. Am. **96**, 1388–1396.

Durlach, N. I., Braida, L. D., and Ito, Y. (**1986**). "Towards a model for discrimination of broadband signals," J. Acoust. Soc. Am. **80**, 63–72.

Ellermeier, W. (**1996**). "Detectability of increments and decrements in spectral profiles," J. Acoust. Soc. Am. **99**, 3119–3125.

Fastl, H., and Stoll, G. (**1979**). "Scaling of pitch strength," Hearing Res. **1**, 293–301.

Feth, L. L. (**1974**). "Frequency discrimination of complex periodic tones," Percept. Psychophys. **15**, 375–378.

Feth, L. L., and Stover, L. J. (**1987**). "Demodulation processes in auditory perception," in *Auditory Processing of Complex Sounds*, edited by W. A. Yost and C. S. Watson (Erlbaum, Hillsdale, NJ), pp. 76–86.

Glasberg, B. R., and Moore, B. C. J. (**1990**). "Derivation of auditory filter shapes from notched-noise data," Hearing Res. **47**, 103–138.

Gockel, H. (**1996**). "Auditory discrimination of spectral shape—Cues and limits in perception" Ph. D. thesis, Universität Oldenburg.

Gockel, H., and Colonius, H. (**1997**). "Auditory profile analysis: Is there perceptual constancy for spectral shape for stimuli roved in frequency?" J. Acoust. Soc. Am. **102**, 2311–2315.

Green, D. M. (**1992**). "The number of components in profile analysis tasks," J. Acoust. Soc. Am. **91**, 1616–1623.

Green, D. M., and Berg, B. G. (**1991**). "Spectral weights and the profile bowl," Q. J. Exp. Psychol. **43A**, 449–458.

Kidd, Jr., G., Mason, C. R., Uchanski, R. M., Brantley, M. A., and Shah, P. (**1991**). "Evaluation of simple models of auditory profile analysis using random reference spectra," J. Acoust. Soc. Am. **90**, 1340–1354.

Kirschweng, S. (**1993**). ''Experimentelle Untersuchung der Aufmerksamkeit beim Hören zusammengesetzter Spektren,'' Diplomarbeit, Universität Regensburg.

Levitt, H. (**1971**). ''Transformed up-down methods in psychoacoustics,'' J. Acoust. Soc. Am. **49**, 467–477.

Macmillan, N. A., and Creelman, C. D. (**1991**). *Detection Theory: A User's Guide* (Cambridge U.P., Cambridge).

Moore, B. C. J., and Bacon, S. P. (**1993**). ''Detection and identification of a single modulated carrier in a complex sound,'' J. Acoust. Soc. Am. **94**, 759–768.

Moore, B. C. J., and Ohgushi, K. (**1993**). ''Audibility of partials in inharmonic complex tones,'' J. Acoust. Soc. Am. **93**, 452–461.

Oppenheim, A. V., and Schafer, R. W. (**1975**). *Digital Signal Processing* (Prentice-Hall, Englewood Cliffs, NJ).

Psotka, J. (**1978**). ''Perceptual processes that may create stick figures and balance,'' J. Exp. Psychol.: Hum. Percept. Perf. **4**, 101–111.

Raney, J. J., Richards, V. M., Onsan, Z. A., and Green, D. M. (**1989**). ''Signal uncertainty and psychometric functions in profile analysis,'' J. Acoust. Soc. Am. **86**, 954–960.

Richards, V. M., Onsan, Z. A., and Green, D. M. (**1989**). ''Auditory profile analysis: Potential pitch cues,'' Hearing Res. **39**, 27–36.

Rosowski, J. J. (**1991**). ''The effects of external- and middle-ear filtering on auditory threshold and noise-induced hearing loss,'' J. Acoust. Soc. Am. **90**, 124–135.

Van Trees, H. L. (**1968**). *Detection, Estimation, and Modulation Theory, Pt. I* (Wiley, New York).

Zwicker, E., and Fastl, H. (**1990**). *Psychoacoustics, Facts and Models* (Springer, Berlin).

Frequency and intensity discrimination measured in a maximum-likelihood procedure from young and aged normal-hearing subjects

Ning-ji He, Judy R. Dubno, and John H. Mills

Department of Otolaryngology and Communicative Sciences, Medical University of South Carolina, Charleston, South Carolina 29425-2242

A maximum-likelihood method was applied in measurements of frequency and intensity discrimination for aged and young normal-hearing subjects with closely matched audiograms. This method was preferred over other psychophysical procedures because it is efficient and controls experimental variance, features that are highly desirable for testing aged subjects. In order to implement the method, psychometric functions for each task were also measured from young subjects using a constant-stimuli procedure. For the young subjects, the differential thresholds obtained from these two procedures were generally comparable. Further, both sets of data were consistent with previous literature, indicating that the maximum-likelihood method was successfully applied for frequency and intensity discrimination. A frequency-dependent difference between young and aged subjects in both frequency and intensity discrimination was observed. Even with closely matched audiograms, aged subjects demonstrated poorer discrimination abilities than young subjects. The age-related difference was always largest at 500 Hz and decreased as frequency increased. © *1998 Acoustical Society of America.* [S0001-4966(98)04901-7]

PACS numbers: 43.66.Sr, 43.66.Fe [JWH]

INTRODUCTION

As part of an ongoing study of age-related changes in auditory function, frequency and intensity discrimination $(\Delta f, \Delta L)$ were measured in aged and young subjects with normal hearing. Numerous studies have shown that sensorineural hearing loss can cause deficits in these discrimination abilities (e.g., Turner and Nelson, 1982; Freyman and Nelson, 1991; Simon and Yund, 1993). Little is known, however, about the effects of age. König (1957) measured Δf in seven age groups from 20–89 years, and reported that Δf (or $\Delta f / f$) increased with each decade increase in age. However, given that there was a concomitant age-related increase in the absolute thresholds for these subjects, it was difficult to determine whether the observed deficit in Δf was due to hearing loss or aging. In a summary of a series of tests of basic auditory capabilities, Humes (1996) reported that aged subjects performed significantly poorer in frequency and intensity discrimination (in percent correct) than young normal-hearing subjects with or without simulated hearing loss to match the audiogram of the aged subjects. The results showed that the deterioration in intensity discrimination for aged subjects was mainly attributed to their hearing loss, whereas differences in frequency discrimination suggested some age-related deficit in performance.

It has long been known that absolute hearing sensitivity generally declines with age (e.g., Zwaardemaker, 1899). However, hearing loss associated with age differs substantially among reports, depending on the sampling of the test populations. Furthermore, even within the same population, the individual history of noise exposure and the tolerance to such factors differs from person to person, resulting in a wide range of hearing sensitivities. Nevertheless, individuals in their sixties and seventies whose auditory thresholds are equivalent to those of young subjects are ideal subjects for studies of age-related effects on auditory function. In order to differentiate the effects of aging and hearing loss, this study measured differential thresholds for both frequency and intensity in aged and young subjects with closely matched normal audiograms.

Large variances in the thresholds of both frequency and intensity discrimination have been reported in the literature, even for young normal-hearing subjects. Rabinowitz *et al.* (1976) summarized data from 15 studies and found the average minimal noticeable level difference (ΔL) ranged from 0.83–6.25 dB for the standard level of 40 dB SPL. An even larger variance was observed in Δf literature, such that differences in Δf thresholds across studies were up to a factor of 10 (Green, 1976). Although some of these differences across studies may be attributed to differences in procedures, large intra- and intersubject variances were also observed within a single study (e.g., Moore, 1973; Nelson *et al.*, 1983). Thus, Green (1988) suggested that "the differences among listeners were the most probable sources of the discrepancies."

A subject's proficiency at a particular task is a nonnegligible source of experimental variance. For a naive subject with no pretest practice, differential thresholds pose more difficulties compared to absolute thresholds. Turner and Nelson (1982) observed sizable practice effects on the shape of the psychometric function for Δf, and test/retest differences in Δf thresholds were as large as a factor of 2. Similarly, for aged subjects, possible age-related differences in learning abilities also should be considered. In order to minimize differences caused by practice effects, none of the subjects here had previous experience with discrimination

tasks. All subjects were given a certain amount of practice prior to the final data collection. In addition, all measurements were repeated four times so that changes in subjects' proficiency for the tasks could be further assessed.

There are other well-known nonsensory sources of experimental variance, such as a subject's bias and inattention. This is especially relevant for time-consuming tasks, such as discrimination tests. The time required for presenting two stimuli in a discrimination test is longer than that for one stimulus in a detection test. To control these factors, more efficient psychophysical methods are required. Recently, a maximum-likelihood yes/no procedure (Green, 1993) has been introduced, a procedure that is known to be efficient and relatively robust to nonsensory factors (Gu and Green, 1994; Green, 1995). The method starts with an array of hypothetical psychometric functions, each of which can be described by a logistic function (Green, 1993):

$$P(\text{yes}) = \alpha + (1-\alpha)(1/(1+e^{-k(X-m)})), \qquad (1)$$

where $P(\text{yes})$ is the probability of a ''Yes'' response in a yes/no task; α is the false alarm rate, which is the probability of a ''Yes'' response to the smallest stimulus magnitude; k is the slope parameter for the function; X is the stimulus magnitude; and m is the mean of the logistic (according to Green, both X and m must be in a logarithmic unit). These psychometric functions differ from each other by the three parameters: m, k, and α. Usually, a constant slope parameter (k) is used in the maximum-likelihood procedure (this will be discussed further in Sec. I). The number of hypothetical psychometric functions and the step size of m determine the variable magnitude range for the test. With each X presented and the subject's response given to that value, the procedure searches among the psychometric functions to find the one that gives the maximum $P(\text{yes})$ over trials.

Another important feature of this method is the ''sweet point'' (Green, 1990, 1993), which refers to the stimulus magnitude that gives the largest slope of a psychometric function. Taking the sweet point as the stimulus magnitude in the next trial can minimize the variance of the threshold estimates, hence increasing the efficiency of the test. The estimates are divergent for the first few trials, but as the number of trials increases and the probabilities are upgraded with each trial, the estimates converge. In our experience, estimates generally asymptote after 20 trials for both young and aged subjects.

The effects of subject bias and inattention on the procedure have been investigated by Green and his colleagues using both human subjects and computer simulations (Green, 1993, 1995; Gu and Green, 1994). The false alarm rate was found to influence the threshold estimates (Gu and Green, 1994). Hence, the addition of catch trials was suggested so that the subject's false alarm rate could be more accurately estimated. The yes/no task is preferable to the forced-choice procedure; it has been found that even for a subject who was inattentive 40% of the time, the procedure can still estimate the threshold with little bias as long as the false alarm rate is moderate (Green, 1995).

Considering the difficulty of the discrimination task, especially for aged subjects, a ''reminder'' design of the same/different procedure (Macmillan and Creelman, 1991) was used in this study. This procedure is also similar to the ''SDH'' paradigm of Jesteadt and Bilger (1974). Each presentation trial contained two intervals, the first of which always contained the standard. The second interval contained the variable stimulus which was either the same as or greater than the standard in magnitude. According to Jesteadt and Bilger (1974), performance was basically equivalent for the single-direction variables, either higher or lower than the standard.

To apply the maximum-likelihood method in studies of frequency and intensity discrimination, a working psychometric function for each task has to be constructed. Unfortunately, no data in the literature are directly applicable here. Accordingly, psychometric functions for Δf and ΔL in a ''same/different'' task were also measured in this study using a constant-stimuli paradigm.

In summary, the main objective of this study was to assess age-related changes in auditory discrimination using an efficient psychometric procedure, while minimizing confounding factors, such as subjects' absolute thresholds and experience.

I. METHODS

Two different experiments, frequency and intensity discrimination, were conducted sequentially. The experimental setup was basically the same for the two experiments, with the exception of the experimental variable. For frequency discrimination, frequency increment (Δf) in Hz was the variable, whereas for intensity discrimination the variable was level difference (ΔL) in dB. For each experiment, psychometric functions were first obtained from four normal-hearing subjects using a constant-stimuli method. The data were then used to construct a working psychometric function for the maximum-likelihood method to measure differential thresholds from another four young subjects and four aged subjects with matched audiograms (ANSI, 1989). The frequencies tested were 500, 1000, 2000, and 4000 Hz.

A. Stimuli and paradigm

A 16-bit waveform synthesizer (Pragmatic, 2210A) was used for signal generation. With a 60-dB output range (0.01–10 V), a 0.001-dB level of accuracy can be obtained. The maximal clock frequency was 2 MHz. Because all frequencies tested in this study were less than 5000 Hz, signals could be synthesized with 400 points per cycle, which provided a frequency resolution of 0.0025 Hz. The signals were continuous pure tones gated by an electronic switch (Coulbourn) with a total duration of 300 ms and a rise/fall time of 25 ms. The tone bursts were then attenuated, fed to a power amplifier, and delivered to the subject's ear canal through an insert earphone (Etymotic Research, ER2). The earphone was coupled to the ear canal by a foam ear tip. The frequency response of the system measured in an ear simulator (Bruel & Kjaer, 4157) was essentially flat up to 6000 Hz

with a level variance less than 2 dB. The system harmonics were at least 52 dB lower than the signals. The experiments were controlled by a PC.

During each presentation trial, two signals were gated on sequentially. The first always served as the standard and the second as the variable stimulus. The two tone bursts were separated by a silence of 300 ms. Subjects were informed that the variable magnitude (in frequency or level) was either higher than or the same as the standard magnitude and their task was to determine whether the variable stimulus matched the standard. Their response should be ''different'' when the variable was judged greater than the standard or ''same'' when not greater.

B. Stimulus scales

A relevant issue is the stimulus scale, which also determines the shape of a psychometric function and its parameters. There is no common consensus in the literature as to which scale is most appropriate for frequency and intensity discrimination. For the maximum-likelihood procedure, it is important to use a scale that produces a uniform slope of the psychometric function across experimental conditions.

Nelson and Freyman (1986) measured psychometric functions of frequency discrimination from subjects with and without sensorineural hearing loss. They found that only when data were plotted in a log–log coordinate of d' and $\Delta f / \Delta f_0$ could the psychometric functions be fitted by straight lines with a slope of one, which is independent of frequency and hearing status. In other words, differences introduced by hearing loss or stimulus frequency were exhibited by a horizontal shift of the psychometric function but not a change in slope. The Δf_0 was a normal Δf threshold estimated by these authors from the literature. In a preliminary study (He *et al.*, 1995), data from the previous study were replotted in percent correct against Δf in logarithmic units. Once transformed into a logarithmic unit, the normalization factor does not affect the slope of the psychometric function. These results confirmed that such data can be fit by a logistic function with a constant slope.

Intensity discrimination thresholds are usually plotted in ratios, such as pressure ratio ($\Delta p/p$), intensity ratio $\Delta I/I$, or ΔL, the level difference. Although these units are interchangeable, ΔL is the most appropriate scale for the maximum-likelihood procedure. Buus and Florentine (1991) examined the form of psychometric functions for intensity discrimination and found that the slope of the psychometric function differs with pedestal level and duration if the data are plotted as a function of $\Delta p/p$ or $\Delta I/I$, but not ΔL. As will be shown below, the present study further found that the slope of the psychometric function for ΔL is also independent of frequency. Furthermore, compared to other scales, ΔL is more convenient for experimental implementation when stimuli are varied by attenuation level. Conventionally, the experimental variable is the sound pressure level of an increment signal (Δp) that is added in phase to the standard signal. The Δp value changes substantially as a function of the pedestal level, as does the number of hypotheses or the step size required by the maximum-likelihood procedure. In

this study, the step size of ΔL was 0.25 dB. For ΔL range from 0.5–6 dB, the 0.25 dB step size corresponds to a 1–3-dB increment in a $\Delta p/p$ scale, which is comparable to those used in other studies.

C. Procedure

1. Orientation trials

All measurements started with an orientation to the stimuli. A pair of stimuli was repeatedly presented every 2 s, with the variable set at the largest difference value predetermined for the specific measurement. Subjects were asked whether the signals sounded clearly different to them in frequency or in level. If the difference was not clearly detectable, the experimenter would adjust the range of the variable until the range was sufficient for the individual subject. The measurement was then initiated by the subject by pressing any button on a votebox.

2. Psychometric functions

As a first step to apply the maximum-likelihood method to discrimination tasks, parameters of the psychometric functions, especially the slope (k), were estimated experimentally for both Δf and ΔL, each from data of four normal-hearing subjects aged 25–42 years. A total of five subjects (Y1–Y5) were tested, with three of them (Y2–Y4) participating in both Δf and ΔL measurements. A constant-stimuli method was used and the standard stimulus level was 60 dB SPL. The range of the variable magnitude was predetermined by the experimenter based on data in the literature with some adjustments for individual subjects. The smallest difference was always zero. The largest Δf in Hz was 0.7% to 1.25% of the standard frequency. The upper end of the ΔL range was 8–10 dB. The range was evenly divided into ten intervals resulting in eleven variable values, each presented 50 times in random order. The measured psychometric functions were then applied to Eq. (1), with P(yes) replaced by P(different), the probability of ''different'' responses, and with both X and m in either Δf or ΔL scale. Slope (k) was estimated for each psychometric function from the data using a best-fit method.

The averaged k value obtained from four young normal-hearing subjects was used in the following maximum-likelihood procedure to measure Δf and ΔL thresholds for both young and aged subjects, assuming that the slope of a psychometric function with a logarithmic scale is independent of age-related difference in discrimination, as is the case for other agents such as hearing loss (Nelson and Turner, 1986). According to Green (1993), a mismatch in slope between a true psychometric function of the subject and the working function only affects the efficiency of the procedure. Further, a mismatch of less than a factor of 5 has very little effect. However, it is still desirable in the maximum-likelihood procedure to use a constant k value which is as close to the true slope as possible.

3. Differential thresholds

Thresholds for Δf and/or ΔL were measured in 13 subjects using the maximum-likelihood method. All subjects
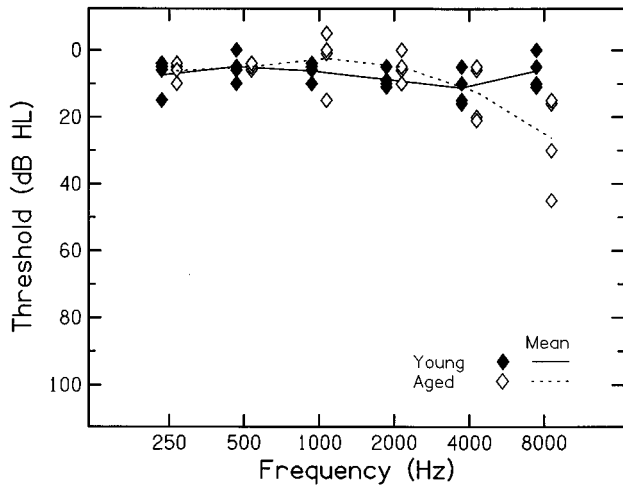
FIG. 1. Pure-tone thresholds measured from four young subjects (filled symbols) and four aged subjects (open symbols) for the Δf experiment. The solid and dashed lines indicate the means for the young and aged groups, respectively.

had normal hearing (i.e., $\leqslant 20$ dB HL) at least at 500, 1000, 2000, and 4000 Hz. Six subjects (A1–A6) were selected from among aged subjects enrolled in our ongoing, longitudinal study of presbyacusis. The remaining seven subjects (Y6–Y12) were young (18–33 years old). All subjects were naive to the discrimination tasks prior this study. Two aged subjects (A1 and A2) and one young subject (Y9) participated in both Δf and ΔL experiments.

The two age groups had essentially matched audiograms at the four test frequencies. Figures 1 and 2 present absolute pure-tone thresholds in dB HL for the subjects who participated in the measurements of Δf and ΔL thresholds, respectively. The solid symbols and line represent individual and group mean thresholds for young subjects; the open symbols and dashed line represent those for aged subjects. As shown in the figures, the mean differences between the two groups were less than 5 dB from 500 to 4000 Hz. At 8000 Hz, however, the difference was larger, because some aged subjects had thresholds >20 dB HL.
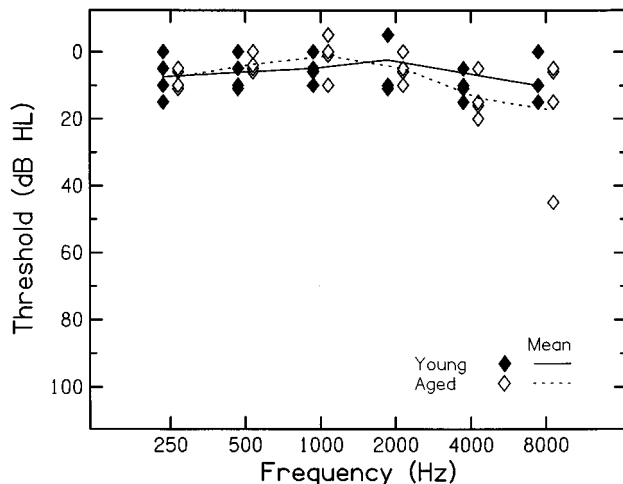
FIG. 2. Similar data as Fig. 1, but for subjects in the ΔL experiment.

For each experiment, data were collected in five sessions. The first session was practice. The standard level used in this session was always 60 dB SPL, a moderate level well audible to all subjects. Discrimination was first tested using a short constant-stimuli paradigm; 11 equally spaced variable magnitudes were presented, each repeated five times in random order. This allowed subjects to become familiar with the entire range of differences and also helped to determine appropriate variable ranges for the maximum-likelihood procedure. The practice was repeated until the subject derived a psychometric function with a reasonably logistic shape. This first training lasted approximately 30 min for the young subjects. The aged subjects required at least twice as much practice time as the young subjects to reach stable performance. After that, differential thresholds were then measured using the maximum-likelihood method, allowing subjects to get familiar with that procedure.

After practice, differential thresholds were repeatedly measured in four sessions using the maximum-likelihood method. Within each session, threshold was first measured using a standard level of 40 dB SPL followed by a standard level of 80 dB SPL. The order for testing frequencies was random. Fifty trials including three catch trials were used in each test. During each catch trial the variable was set to zero difference so that the false alarm rate could be more accurately estimated. The number of hypotheses for the maximum-likelihood procedure varied from experiment to experiment, and was determined by the range and the increment of the variables and then multiplied by four α values: 0, 0.1, 0.2, and 0.3. The ranges and increments for all subjects are given in the Appendix for readers interested in more details.

Each of these four runs lasted less than an hour, including preparation for earphone fitting, etc. The interval between two consecutive sessions ranged from 15 min to several weeks. These repeated data provided a way to assess the stability of each subject's performance.

4. Threshold at $d' = 1$

The outcome of both the constant-stimuli paradigm and the maximum-likelihood procedure is a psychometric function with a specific false alarm rate, α. The data can be used to calculate thresholds corresponding to $d' = 1$, so that the thresholds can be normalized over different false alarm rates. For the constant-stimuli procedure, the thresholds were determined as the intercept of the psychometric function and $d' = 1$ (Swets, 1964, Appendix Table I). For the results from the maximum-likelihood method, psychometric functions were reconstructed from Eq. (1) with specified m, k, and α. Then the threshold values at $d' = 1$ were calculated in the same way as the measured psychometric functions. The d' threshold is highly dependent on the false alarm rate, α. For a constant m value, a higher α will result in a higher percentage of the responses corresponding to $d' = 1$, hence a higher estimated threshold. Note that the smallest α value in the d' table (Swets, 1964) is 0.01; any measured α smaller than this value will be set to 0.01. For the results reported here, $d' = 1$, instead of m values, were used as thresholds, so that the

TABLE I. Summary of parameters for Δf psychometric functions.

Subjects	m	α	k	Δf thresholds ($d'=1$) in Δf (Hz)	in $\Delta f/f$ (%)	Curve fitting r	rms
(500 Hz)							
Y1	1.55	0.18	3.4	1.33	0.266	0.975	0.061
Y2	2.26	0.38	1.7	2.96	0.592	0.795	0.107
Y3	1.57	0.26	2.5	1.40	0.280	0.978	0.061
Y4	1.74	0.38	4.5	1.93	0.386	0.991	0.038
Mean	1.78		3.03	1.91	0.38	0.936	0.067
STD	0.33		1.20	0.75	0.15	0.091	0.029
(1000 Hz)							
Y1	3.43	0.10	2.9	2.66	0.266	0.977	0.051
Y2	4.07	0.40	2.6	5.09	0.509	0.937	0.078
Y3	3.00	0.28	2.8	3.05	0.305	0.980	0.051
Y4	3.94	0.44	2.9	4.84	0.484	0.974	0.047
Mean	3.61		2.80	3.91	0.39	0.967	0.057
STD	0.49		0.14	1.23	0.12	0.020	0.014
(2000 Hz)							
Y1	6.10	0.16	2.1	4.39	0.220	0.984	0.048
Y2	6.18	0.48	3.9	7.50	0.375	0.961	0.062
Y3	5.75	0.26	3.3	5.84	0.292	0.968	0.070
Y4	6.69	0.10	3.4	5.56	0.278	0.991	0.046
Mean	6.18		3.18	5.82	0.29	0.976	0.057
STD	0.39		0.77	1.28	0.06	0.014	0.011
(4000 Hz)							
Y1	21.18	0.04	2.8	7.55	0.189	0.987	0.060
Y2	21.25	0.24	3.6	21.14	0.529	0.968	0.086
Y3	27.00	0.38	2.7	30.00	0.750	0.971	0.048
Y4	17.90	0.10	2.6	13.67	0.342	0.986	0.057
Mean	21.83		2.93	18.09	0.45	0.985	0.063
STD	3.78		0.46	9.69	0.24	0.010	0.016
Grand mean			2.99		0.38		

data can be compared with those from the literature measured using different methods, such as forced choice.

II. RESULTS

A. Experiment I: Frequency discrimination (Δf)

1. Psychometric functions

Figure 3 is an example of the curve fitting of Δf psychometric functions for one subject (Y1). Each panel presents data for a different standard frequency. Filled circles represent the experimental data while the lines show the fitted logistic functions [Eq. (1)] with both X and m in Δf scale. For curve fitting, all Δf's in Hz were transformed into natural logarithmic units [Ln(Δf)] and the zero Hz difference was replaced by 0.001 Hz to avoid the negative infinity. Note that other logarithmic units could also be used but the estimated k value would be changed accordingly.

The estimated parameters of the psychometric functions (m, α, and k), as well as Δf ($d'=1$), for individual subjects across frequency are summarized in Table I. Correlation coefficients (r) and rms differences between the experimental and fitted data are also given (in the last two columns). The high r and low rms values indicate a generally good fit of the

logistic function to the Ln(Δf) data. The average Δf thresholds ranged from 0.29% to 0.45% of the standard frequency, with the minimum $\Delta f/f$ at 2000 Hz and the maximum at 4000 Hz. The k is generally constant across frequency with a grand mean of 2.99. A rounded k value of 3 was used in the following test of Δf thresholds using the maximum-likelihood procedure. Note that the slope was also highly consistent among subjects, especially at 1000 Hz. As can be seen in Table I, all the individual slopes in this experiment were within a factor of 2 of the k value (i.e., 3) used in the subsequent maximum-likelihood procedure.

2. Δf thresholds

Figure 4 illustrates group means and standard deviations of Δf ($d'=1$), which are presented in % of $\Delta f/f$. The filled bars represent data of the young group and the open bars, the aged group. The order of the bars at each frequency represents the order of the four repeated measurements. No consistent improvement in Δf thresholds across repeated sessions was evident for either group; therefore, the pretest training was likely sufficient to allow subjects' performance
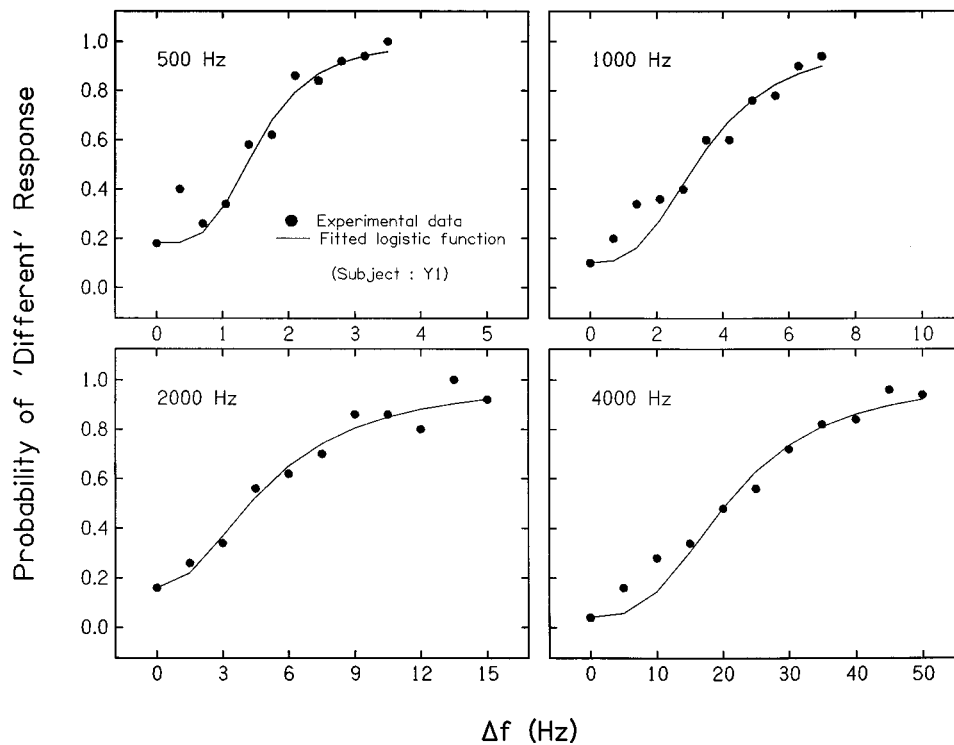
FIG. 3. An example of the curve fitting of the Δf psychometric functions.

to reach the upper asymptote of the training function, largely eliminating any practice effects from the data.

As clearly shown in Fig. 4, there is a substantial age-related difference in $\Delta f/f$ thresholds. The aged subjects have significantly larger thresholds and variances than the young subjects, even though their audiograms were closely matched (see Fig. 1). In addition, the age effect is frequency dependent. For the young subjects the Δf thresholds were between 0.2% to 0.75% of the standard frequencies, with a slight decrease with increasing frequency. On the other hand, a much stronger frequency effect on Δf is observed for the aged group. Means and standard deviations averaged over all sessions for both groups are presented in Table II (columns 2 and 3). For the aged group, the mean $\Delta f/f$ was as large as 1.33% at 500 Hz and decreased with increasing frequency. As shown in column 4 of Table II, the difference between the aged and young groups was largest at 500 Hz and decreased with increasing frequency. Standard level (40 vs 80 dB SPL) had no consistent effect on Δf threshold for either group.

To further assess the variance of the measurements, standard deviations were calculated within each subject across four sessions (intrasubject) and within each session across all subjects (intersubject) for both age groups. The means of these standard deviations for each standard frequency and level are given in pairs (intrasubject/intersubject) in the last two columns of Table II. The intersubject variances are comparable to the overall standard deviations presented in parentheses attached to the averaged Δf thresholds (columns 2 and 3). For the young subjects, there is essentially no difference between intrasubject and intersubject variances. For the aged subjects, however, the intrasubject variances are generally smaller than their counterpart, except

at 4000 Hz. Thus, the larger variability seen in Fig. 4 for the aged subjects is more likely due to differences among subjects than to trial-to-trial differences within individual subjects.
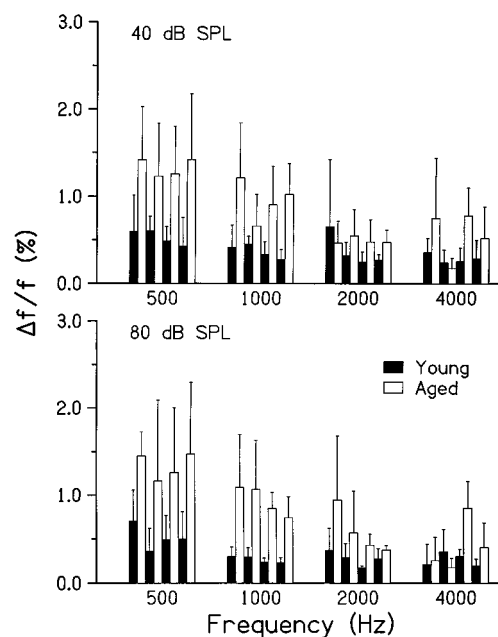
FIG. 4. Group means and standard deviations of Δf thresholds (in % of the center frequency) for the young (filled bars) and aged (open bars) subjects. The order of the bars at each frequency represents the order of the four repeated measures.

TABLE II. Mean $\Delta f/f$ ($d'=1$) averaged over four repeated sessions for the aged and young groups and the difference between the two groups. The standard deviations of the means are given in ( ). The last two columns show means of standard deviations. Each pair of values was calculated within each subject across sessions (intrasubject) and within each session across subjects (intersubject), respectively.

Frequency (Hz)	$\Delta f/f$ thresholds (%)		Difference (Aged−Young)	Means of STD	
	Aged	Young		Aged	Young
(40 dB SPL)					
500	1.33 (0.57)	0.53 (0.27)	0.80	0.32/0.63	0.21/0.27
1000	0.95 (0.46)	0.37 (0.16)	0.58	0.29/0.45	0.14/0.15
2000	0.49 (0.22)	0.36 (0.39)	0.13	0.10/0.24	0.24/0.27
4000	0.46 (0.48)	0.28 (0.16)	0.18	0.41/0.37	0.13/0.17
(80 dB SPL)					
500	1.34 (0.67)	0.51 (0.30)	0.83	0.39/0.69	0.27/0.34
1000	0.93 (0.42)	0.26 (0.08)	0.67	0.26/0.40	0.07/0.08
2000	0.58 (0.46)	0.27 (0.16)	0.31	0.34/0.35	0.15/0.14
4000	0.41 (0.36)	0.26 (0.18)	0.15	0.36/0.24	0.14/0.16

B. Experiment II: Level discrimination (ΔL)

1. Psychometric functions

Figure 5 is an example of the curve fitting of ΔL psychometric functions for one subject (Y2). The filled circles represent the experimental data whereas the lines show the fitted logistic functions [Eq. (1)]. Now both the X and m of Eq. (1) are in dB scale. Each panel presents data for a different frequency. Table III summarizes the estimated middle points (m), false alarm rates (α), slopes (k), and ΔL thresholds ($d'=1$) for four subjects. Similar to Table I, the last two columns present r and rms differences between the experimental and fitted data; the even higher r values (all >0.980) indicate a better fit of the ΔL data than the Δf data.

The false alarm rates (α) were also much smaller than those for Δf data, suggesting that the level discrimination task is relatively easier than the frequency discrimination task.

It is of particular interest that both the slope (k) and thresholds of the ΔL data were generally uniform across subject and frequency. This frequency independency further supports the argument by Buus and Florentine (1991) that ΔL is an appropriate physical unit to describe the psychometric function for intensity discrimination.

The overall mean ΔL threshold was 2.98 dB and the overall mean slope was 1.31. In the subsequent test of ΔL thresholds using the maximum-likelihood method, the slope was set to 1.4.

FIG. 5. An example of the curve fitting for the ΔL psychometric functions.

TABLE III. Summary of parameters for ΔL psychometric functions.

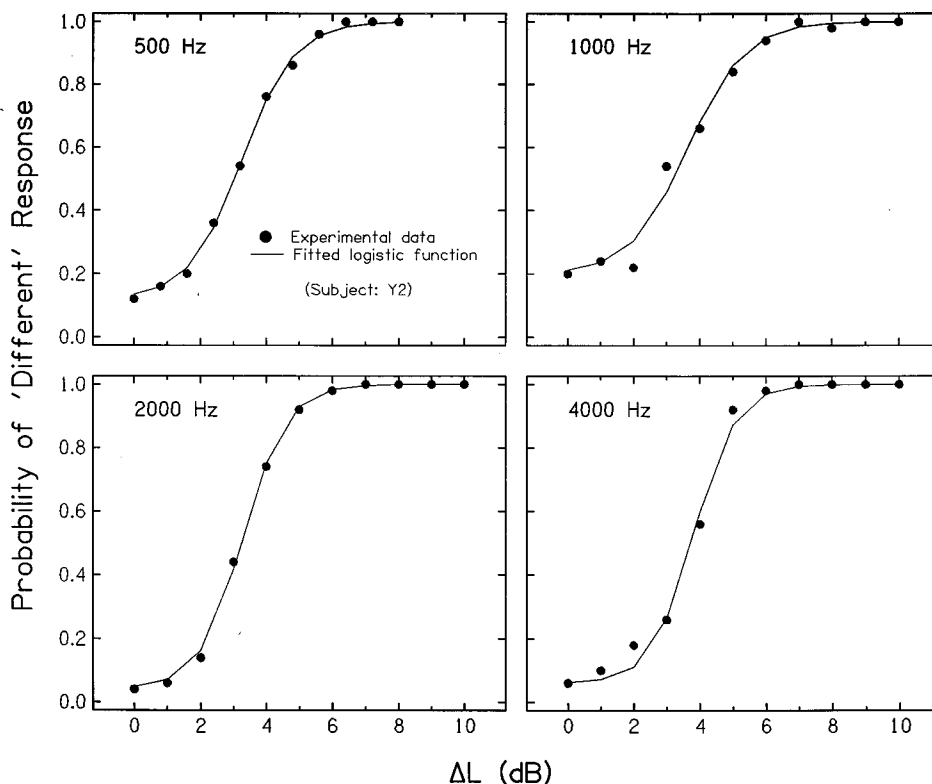| Subjects	m	α	k	ΔL thresholds ($d'=1$)	Curve fitting r	rms
(500 Hz)						
Y2	3.22	0.12	1.20	2.54	0.9993	0.013
Y3	3.55	0.10	1.46	3.03	0.9986	0.020
Y4	4.28	0.12	1.50	3.50	0.9970	0.034
Y5	5.48	0.00	1.08	2.96	0.9953	0.034
Mean	4.13		1.31	3.01	0.9976	0.025
STD	1.00		0.20	0.39	0.0018	0.011
(1000 Hz)						
Y2	3.54	0.20	1.06	3.28	0.9938	0.038
Y3	3.45	0.18	0.88	3.00	0.9961	0.027
Y4	3.13	0.12	1.51	2.45	0.9975	0.028
Y5	5.14	0.00	1.40	3.31	0.9972	0.030
Mean	3.82		1.21	3.01	0.9962	0.031
STD	0.90		0.29	0.40	0.0017	0.005
(2000 Hz)						
Y2	3.29	0.04	1.48	2.35	0.9996	0.011
Y3	3.32	0.14	0.92	2.51	0.9976	0.024
Y4	4.21	0.08	1.85	3.53	0.9964	0.042
Y5	4.94	0.00	1.57	3.49	0.9989	0.021
Mean	3.94		1.46	2.97	0.9981	0.025
STD	0.79		0.39	0.63	0.0014	0.013
(4000 Hz)						
Y2	3.82	0.06	1.57	3.11	0.9978	0.029
Y3	3.17	0.22	1.28	2.90	0.9952	0.030
Y4	4.51	0.04	0.93	2.76	0.9880	0.068
Y5	4.68	0.04	1.32	2.90	0.9823	0.080
Mean	4.05		1.28	2.92	0.9883	0.052
STD	0.69		0.26	0.14	0.0053	0.026
Grand mean	3.98		1.31	2.98		

FIG. 6. Group means and standard deviations of ΔL thresholds for the young and aged subjects. The bars are arranged in the same way as in Fig. 4.

2. ΔL thresholds

The ΔL thresholds are plotted in Fig. 6 in the same manner as Fig. 4. The change in thresholds over four repetitions is not consistent for the young subjects, indicating little practice effect in the data. However, for the aged subjects, a significant trend of improvement is observed in thresholds measured for the 40-dB standard level, where thresholds obtained in the first session were consistently larger than those in later sessions.

Table IV presents ΔL thresholds averaged over the last three sessions and threshold differences between aged and young groups. As in Table II, standard deviations calculated for the pooled data are presented in parentheses attached to the averaged thresholds (columns 2 and 3). In addition, means of intrasubject and intersubject standard deviations are given in the last two columns. Again, the aged subjects showed significantly larger means and standard deviations than those of the young subjects at both standard levels. Similar to the Δf data, these variances were likely due to differences among subjects, because the values were numerically close to the overall standard deviations and were consistently greater than intrasubject standard deviations. The smaller intrasubject variances indicate stable performance of

the subjects from trial to trial. At the 80-dB standard level, the intrasubject standard deviations of the aged group were not significantly different from those of the young subjects.

As shown in both Fig. 6 and Table IV, thresholds were higher for the standard level of 40 dB than for 80 dB SPL, with an average difference of approximately 2 dB for the young subjects and 3 dB for the aged subjects. For the young group, thresholds were generally uniform across frequency, similar to what was observed in measuring the psychometric function. At 40 dB SPL, thresholds were close to 3 dB, while at 80 dB SPL, thresholds decreased to around 1.2 dB. Slightly better performance was obtained at the middle frequencies (1000 and 2000 Hz) at the lower level, but not at the higher level. This uniformity of ΔL thresholds across frequency was not observed in the data of the aged subjects. Instead, the thresholds of the aged group changed with frequency at both standard levels, with the largest ΔL at 500 Hz and the smallest at 4000 Hz. This resulted in a frequency-dependent difference between the two age groups. As shown in the fourth column of Table IV, the difference was greater than 3 dB at 500 Hz and decreased to less than 1 dB at 4000 Hz, a tendency similar to the Δf data as shown in Fig. 3 and Table II.

III. DISCUSSION

A. Psychometric functions for Δf and ΔL

One of the objectives of this study was to apply the maximum-likelihood method to measurements of Δf and ΔL. As discussed in the Introduction, the implementation of the method is based on a psychometric function for a specific task. Therefore, as the first step, a working psychometric function for each test had to be constructed with a specified slope (k).

The psychometric functions for Δf and ΔL were described as a logistic function as shown in Eq. (1) (Green, 1993), which provided a satisfactory description of the experimental data (Figs. 3 and 5). Generally, the percentage of ''different'' responses increases monotonically as a function of the ΔL or $\ln(\Delta f)$. Only one subject (Y4) showed slightly higher P (different) scores at the zero difference than the adjacent Δf or ΔL values at some frequencies. However, this error was too small (<0.10) for the functions to be considered nonmonotonic.

It is convenient for the maximum-likelihood procedure to use a constant slope (k) across experimental conditions. For Δf, a uniform k across frequency was obtained with Δf in Hz transformed into a natural logarithmic unit (Table I). This is consistent with observations by Nelson and Freyman (1986), in which a logarithmic scale for Δf resulted in a uniform slope of the psychometric functions over a wide range of Δf thresholds in both normal-hearing and hearing-impaired subjects.

Special consideration was given to intensity discrimination regarding the choice of an appropriate physical unit to describe the data. Studies of psychometric functions for intensity discrimination in both normal-hearing and hearing-impaired subjects (Buus and Florentine, 1991; Buus et al., 1995) have shown that the slope relating d' to ΔL clustered around 1.0 across standard level and stimulus duration. When data were plotted in $\Delta p/p$ or $\Delta I/I$ scales, however, the slope tended to decrease with increasing standard level. Our results from four normal-hearing subjects further demonstrated that the slope is uniform across frequency with the ΔL unit (Table III). Taken together, this evidence supports the choice of ΔL as an appropriate variable to be used in expressing the psychometric function for intensity discrimination, at least for the maximum-likelihood procedure.

B. Comparison with literature (Young subjects' data)

The success of the application of the maximum-likelihood procedure in discrimination tests can be assessed by comparing current results with those obtained using other procedures. In this study, differential thresholds were measured from young subjects in both the constant-stimuli and
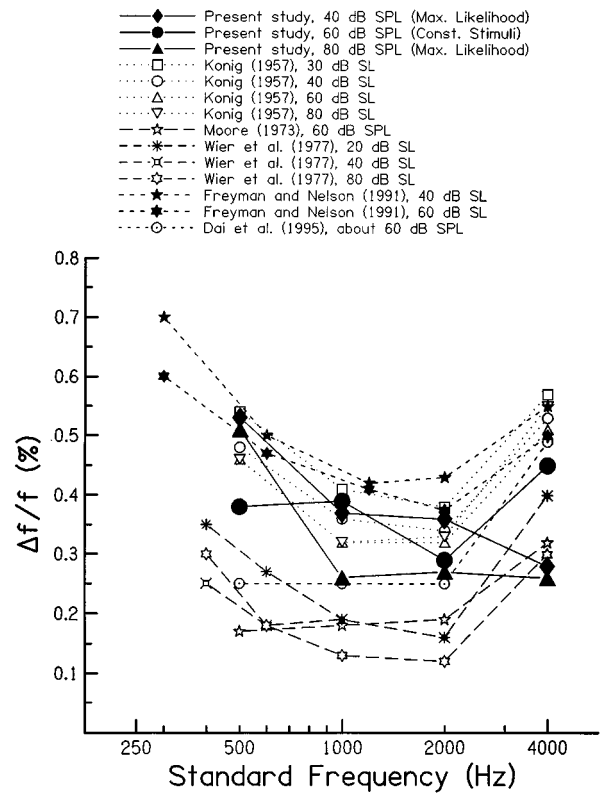
FIG. 7. Comparison of the Δf thresholds (in % of the center frequency) of our young subjects with the data from previous literature.

maximum-likelihood paradigms. Differential thresholds obtained from these two procedures, although at different stimulus levels, were generally consistent. In addition, both sets of data were generally comparable to data in previous literature.

Figure 7 shows $\Delta f/f$ thresholds from this study along with data from other studies (König, 1957; Moore, 1973; Wier et al., 1977; Freyman and Nelson, 1991; Dai et al., 1995). Data from this study fell within the range of previous data. There was a slight tendency for Δf thresholds to improve with increasing stimulus level. However, the improvement was small and inconsistent across frequency. A similar

TABLE IV. The ΔL thresholds ($d'=1$) averaged over the last three repeated sessions for the aged and young groups and differences between the two groups (in dB). The standard deviations of the average are given in ( ). The last two columns show means of standard deviations. Each pair of values was calculated within each subject across sessions (intrasubject) and within each session across subjects (intersubject), respectively.

Frequency (Hz)	ΔL thresholds (dB)		Difference (dB) (Aged−Young)	Means of STD	
	Aged	Young		Aged	Young
(40 dB SPL)					
500	6.86 (2.51)	3.23 (0.99)	3.63	1.33/2.37	0.84/1.00
1000	6.75 (2.04)	2.72 (1.39)	4.03	2.04/2.10	0.97/1.38
2000	6.48 (1.84)	2.63 (1.42)	3.75	1.42/1.97	1.45/0.77
4000	4.49 (2.58)	3.80 (1.81)	0.69	1.54/2.61	1.48/1.78
(80 dB SPL)					
500	4.54 (1.43)	1.30 (0.93)	3.24	0.97/1.51	0.78/0.99
1000	3.81 (1.99)	1.07 (0.66)	2.74	1.01/2.12	0.52/0.58
2000	2.63 (1.20)	1.26 (1.08)	1.40	0.76/1.09	0.87/1.11
4000	1.86 (1.06)	1.17 (1.16)	0.69	0.36/1.14	0.81/0.98

tendency can also be observed in other studies (König, 1957; Wier *et al.*, 1977; Freyman and Nelson, 1991) at similar frequencies and intensities.

In general, $\Delta f/f$ data from the two procedures in this study were in good agreement. At 1000 and 2000 Hz, thresholds obtained from the constant stimuli procedure (at 60 dB SPL) fell in between 40- and 80-dB data from the maximum-likelihood method. However, there is some discrepancy between the two sets of data regarding a frequency effect.

As shown in Fig. 7, the majority of the previous data showed elevated $\Delta f/f$ thresholds at 4000 Hz and some had higher thresholds at 500 Hz and below. Such a bowl-shaped frequency effect was only observable in our constant-stimuli data (60 dB SPL), but not in the data from the maximum-likelihood procedure (40 and 80 dB SPL). Using the latter procedure, $\Delta f/f$ thresholds were largest at 500 Hz and then decreased with increasing frequency. The failure to show elevated thresholds at 4000 Hz in the maximum-likelihood data may be partly attributed to the large intersubject variance at this frequency. As shown in Table I, the individual Δf thresholds at this frequency ranged from 0.19 to 0.75%. Similar variance (0.3 to 0.9%) can also be observed from the young subjects' data from König's report (1957). Another reason for this discrepancy may be related to practice which has been found to have a significant effect on the Δf threshold (Turner and Nelson, 1982). The constant-stimuli paradigm was used in this study to measure psychometric functions and to see if a uniform slope could describe the psychometric functions obtained from heterogenous data (such as would be obtained when practice effects are included). Therefore, subjects who participated in this procedure did not receive pretrial practice.

The measurement of ΔL seemed to be a relatively easier task than measurement of Δf, as indicated by lower false alarm rates and less variance in slopes for the psychometric functions (Table III). Furthermore, mean ΔL thresholds from our young subjects were in good agreement with previous studies regarding the effects of standard level and stimulus frequency, as shown in Fig. 8. Data from this study were near the higher edge of the general range from other studies (Riesz, 1928; Harris, 1963; McGill and Goldberg, 1968; Campbell and Lasky, 1967; Luce and Green, 1974; Green *et al.*, 1979; Florentine, 1983; Turner *et al.*, 1994; Schroder *et al.*, 1994). Note that the majority of data from previous experiments were obtained at 1000 and 2000 Hz. If comparisons were restricted to the data at these two frequencies, the consistency would be even better. Our data followed the general tendency of previous data in that ΔL thresholds decreased with increasing standard level, the so-called ''near miss to Weber's law.'' Also, stimulus frequency had little effect on ΔL, especially at standard levels of 60 (constant stimuli) and 80 dB SPL (maximum likelihood). This agreed with the report from Jesteadt *et al.* (1977), where signal frequency produced no statistically significant difference. Only at 40 dB SPL were somewhat poorer ΔL thresholds observable at 500 and 4000 Hz than at 1000 and 2000 Hz.

Note that this study was one of the few using ER-2 insert earphones to measure frequency and intensity discrimination. A significant difference between this insert ear-
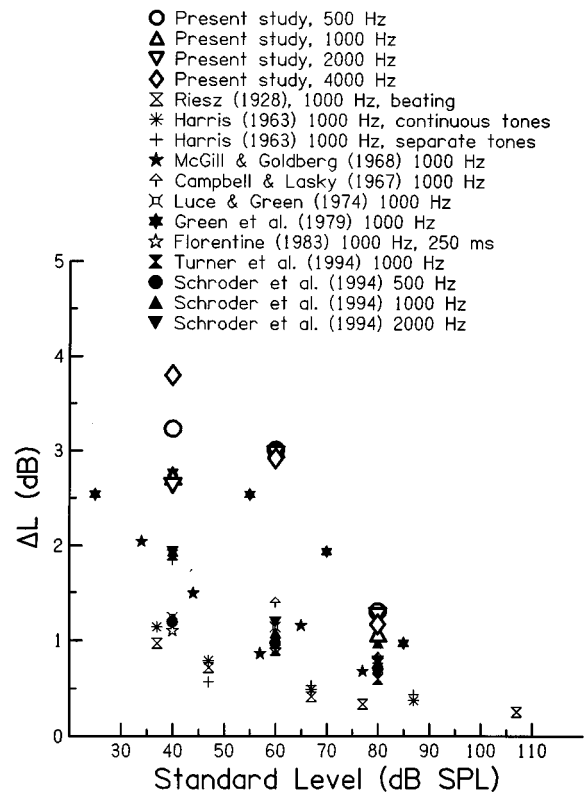
FIG. 8. Comparison of the ΔL thresholds of the young subjects in this study (thick open symbols) with the data from previous studies.

phone and other earphones in common use (e.g., TDH-39) is that the ER-2 was designed to provide a flat SPL frequency response at the eardrum, whereas other earphones target a flat coupler response. This difference may result in level differences across frequency between this study and other studies. Nevertheless, as shown in Figs. 7 and 8, the data from this study were consistent with previous literature regarding a frequency effect on Δf and ΔL.

C. Aging effect on Δf and ΔL

In this study, the aged subjects showed larger intersubject variability in both Δf and ΔL measurements than the young subjects, in addition to elevated differential thresholds. A similar trend is observable in previous studies of frequency discrimination (König, 1957; Moore and Peters, 1992; Humes, 1996). The repeated measurements used in this study allowed a direct comparison of intrasubject and intersubject variability, which showed that the intersubject standard deviations were comparable to overall standard deviations for the averaged thresholds (Tables II and IV). Furthermore, intrasubject standard deviations were generally smaller than intersubject standard deviations for the aged subjects, especially at lower frequencies, whereas for the young subjects the two standard deviations were essentially the same. The comparison suggested that the large variances in the aged subjects' data were mainly due to differences among subjects. This heterogeneity in discrimination abilities is a characteristic of the elderly population and cannot be explained by their quiet thresholds.

FIG. 9. Comparison of the Δf thresholds (in % of the center frequency) of the aged subjects in this study (symbols and lines) with data of young subjects from this study and previous literature from Fig. 7 (shaded area).

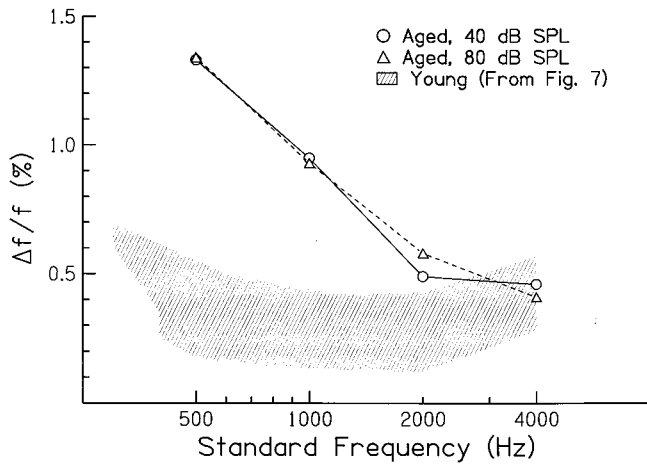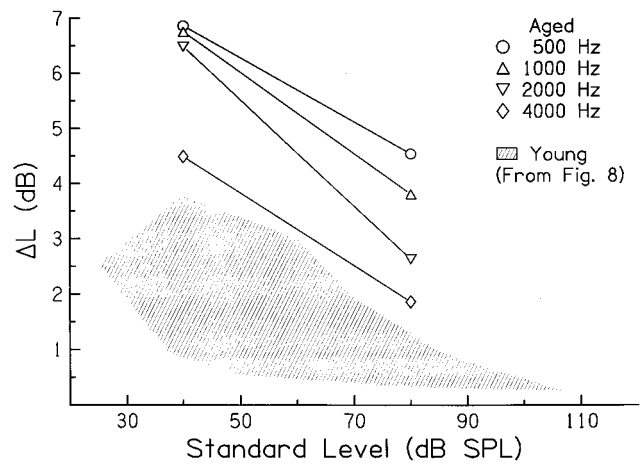FIG. 10. Comparison of ΔL thresholds of our aged subjects (symbols) with the data of the young subjects from this study and previous literature from Fig. 8 (shaded area).

The most interesting finding of this study was a frequency-dependent aging effect for both Δf and ΔL (Figs. 4 and 6). Even with closely matched audiograms, the aged subjects demonstrated poorer discrimination abilities than the young subjects. The difference between young and aged subjects was always largest at 500 Hz and decreased as frequency increased.

For frequency discrimination, aged subjects showed a stronger frequency effect and essentially no level dependency as compared to the young subjects. As shown in Table II, the mean $\Delta f/f$ thresholds for the aged subjects measured at 40 and 80 dB SPL were essentially identical, suggesting that frequency discrimination was independent of stimulus level. On the other hand, there was an orderly improvement in threshold with increasing standard frequency. The difference between the two age groups was larger at lower frequencies than at higher frequencies. Figure 9 plots the data of our aged group with the shaded area representing the range of the data from Fig. 7 (i.e., those of young subjects from present and previous experiments). The largest difference between these two sets of data was observed at 500 Hz, with thresholds for our aged subjects being three times greater than those for the young population. The difference decreased with increasing standard frequency, and at 4000 Hz, the mean $\Delta f/f$ thresholds of our aged subjects fell into the range of the young subjects.

Similar aging effects can also be detected from König's (1957) data. Although the aged subjects (60–69 years) in König's study had substantial hearing loss at higher frequencies, their pure-tone thresholds at 500 and 1000 Hz were only 6–10 dB higher than those of the young group. Their $\Delta f/f$ thresholds at these two frequencies were comparable to those of our aged subjects (i.e., 1.4% at 500 Hz and 1.0% at 1000 Hz). Their data also showed that as frequency decreased from 1000 Hz, the difference in the $\Delta f/f$ thresholds between the aged and young groups increased in an orderly manner. In a study of effects of age and hearing loss, Abel et al. (1990) compared Δf's between aged and young subjects and found that elderly subjects showed poor frequency

discrimination, regardless of hearing sensitivity. However, compared to the aged subjects with hearing loss, the aged normal-hearing subjects showed relatively less deficit at 4000 Hz than at 500 Hz. Moore and Peters (1992) reported that some aged subjects had very large Δf's at low frequencies even with normal hearing and near-normal auditory filters.

For ΔL, the thresholds for the aged subjects changed with both standard level and stimulus frequency. Figure 10 compares ΔL thresholds of our aged group (symbols) with those of the young population from previous experiments (shaded area, from the data in Fig. 8). The thresholds of the aged group improved with increasing standard level, following the same general trend as the young subjects, except that the thresholds were all above the data range of the young subjects. Unlike the young population, the aged subjects showed an orderly frequency effect at both 40 and 80 dB standard levels. Florentine et al. (1993) also found poorer ΔL thresholds in two normal-hearing, aged subjects (55–58 years old) compared to those of young subjects with similar hearing.

This consistent frequency-dependent aging effect on both $\Delta f/f$ and ΔL thresholds could suggest a common component underlying the mechanism for both discrimination tasks, at least in terms of their aging process. Jesteadt and Bilger (1974) found an overall similarity between frequency and intensity discrimination for different psychoacoustic paradigms, suggesting that the two discrimination tasks may involve similar decision-making processes. Zwicker (1956, 1970) generalized the mechanisms for both frequency and intensity discrimination in an excitation pattern model, in which differences in frequency or intensity can be perceived by changes in the output of any single auditory filter. This place theory has been extended to a multiple-filter version for frequency discrimination (Dai et al., 1995) and for intensity discrimination (Florentine and Buus, 1981; Florentine et al., 1987). The latter models can account for other experimental data, including the independence of Δf on the randomized stimulus level (Dai et al., 1995) and the near-miss

to Weber's law at low and middle frequencies but not at high frequencies (Florentine *et al.*, 1987).

The mechanisms for both frequency and intensity discrimination are still uncertain. For example, the poor $\Delta f/f$ performance at the high standard frequency and the lack of dependence on stimulus level are not consistent with the fact that the auditory filter is relatively narrow at high frequencies and broader at higher levels. Therefore, temporal cues based on phase-locking properties of the neural fiber response are also needed to explain these data (Moore, 1973; Sek and Moore, 1995). For intensity discrimination, the excitation model was limited by a ''dynamic range problem'' (Evans, 1981), i.e., a 100-dB range of psychoacoustically perceivable intensity represented by auditory fibers whose typical dynamic range is only 40 dB. The peripheral model also failed to predict the mid-level hump of ΔL threshold at 8 and 10 kHz (Florentine *et al.*, 1987). Viemeister (1988) reviewed the possible cues for intensity coding and found that the only plausible candidates were the cues based on the firing rates of the localized auditory nerve fibers which have different thresholds. Although this explanation is plausible for the middle-level hump (Florentine *et al.*, 1987; Zeng *et al.*, 1991; Zeng and Turner, 1992), there is still a discrepancy between the psychoacoustic data on the dependence of discrimination on level and predicted discrimination behaviors of a representative auditory nerve fiber population (Viemeister, 1988). As the bottom line, Viemeister (1988) concluded that intensity discrimination does not result solely from peripheral processes.

Florentine (1983) suggested that ΔL at high levels is related to high-frequency thresholds as indicated by a significant relation between ΔL thresholds and the lowest frequency at which thresholds exceeded 80 dB SPL. Thresholds at frequencies higher than 8000 Hz were obtained for a majority of our aged subjects in another study (Matthews *et al.*, 1997), and were found to be elevated as compared to the young subjects. However, our data do not support a significant relationship between ΔL and thresholds at extended high frequencies because largest age-related differences were observed at lower frequencies. Rather, the spectrotemporal model (Moore, 1973) may provide a better explanation of our data. This model suggests that discrimination is based on temporal information at low frequencies whereas spectral cues dominate performance at high frequencies. Thus, the pattern of results presented here suggests that age-related effects may be more apparent for auditory processing in the temporal rather than the spectral domain.

IV. SUMMARY

The results from this study can be summarized as follows:

(1) The maximum-likelihood method was successfully applied in experiments of frequency and intensity discrimination, as evidenced by good agreement of the data with other data obtained using different psychophysical procedures. The efficiency of the method allows repeated measurements so that stability of subjects' performance can be assessed.

(2) Frequency and intensity discrimination is poorer in aged subjects and is characterized by increased variability, as compared to young normal-hearing subjects with closely matched audiograms.

(3) Comparison of intra- and intersubject variances reveal that the large variability in aged subjects' data is mainly due to differences among subjects, which is probably related to the increased heterogeneity of the aged population.

(4) The age-related difference in discrimination abilities is greater at low than at high frequencies for both frequency and intensity discrimination. The frequency-dependent aging effect suggests a common component underlying the aging process for both tasks.

ACKNOWLEDGMENTS

APPENDIX

TABLE AI. Frequency ranges in Hz for Δf threshold measurement. The figure inside the parentheses is the increment.

Subject	Sex	Age	Ear	Standard frequency (Hz)			
				500	1000	2000	4000
A1	M	77	R	0–40 (0.50)	0–40 (0.5)	0–60 (1)	0–200 (2)
A2	M	76	L	0–40 (0.50)	0–100 (1.0)	0–100 (1)	0–200 (2)
A3	F	65	R	0–30 (0.50)	0–50 (0.5)	0–100 (1)	0–100 (2)
A4	F	69	R	0–50 (0.50)	0–60 (0.05)	0–120 (2)	0–200 (2)
Y6	F	25	L	0–10 (0.25)	0–20 (0.5)	0–40 (1)	0–80 (2)
Y7	M	18	L	0–10 (0.25)	0–20 (0.5)	0–40 (1)	0–80 (2)
Y8	F	29	R	0–10 (0.25)	0–20 (0.5)	0–40 (1)	0–80 (2)
Y9	M	33	L	0–10 (0.25)	0–20 (0.5)	0–40 (1)	0–80 (2)

TABLE AII. The largest level difference in dB used for each subject in ΔL threshold measurement. The increment was fixed at 0.25 dB.

Subject	Sex	Age	Ear	Standard level (dB SPL)	
				40	80
A1	M	77	R	15	15
A2	M	76	L	15	10
A5	F	72	L	15	10
A6	F	68	R	18–20	12
Y9	M	33	L	10	10
Y10	F	20	L	10–15	10
Y11	F	21	R	10	10
Y12	M	22	R	10	10

Abel, S. M., Krever, E. M., and Alberti, P. W. (**1990**). ''Auditory detection, discrimination and speech processing in aging, noise-sensitive and hearing-impaired listeners,'' Scand. Audiol. **19**, 43–54.

ANSI (**1989**). ANSI S3.6-1989, ''Specifications for audiometers'' (American National Standards Institute, New York).

Buus, S., and Florentine, M. (**1991**). ''Psychometric functions for level discrimination,'' J. Acoust. Soc. Am. **90**, 1371–1380.

Buus, S., Florentine, M., and Zwicker, T. (**1995**). ''Psychometric functions for level discrimination in cochlearly impaired and normal listeners with equivalent-threshold masking,'' J. Acoust. Soc. Am. **98**, 853–861.

Campbell, R. A., and Lasky, E. Z. (**1967**). ''Masker level and sinusoidal signal detection,'' J. Acoust. Soc. Am. **42**, 972–976.

Dai, H., Nguyen, Q. T., and Green, D. M. (**1995**). ''A two-filter model for frequency discrimination,'' Hearing Res. **85**, 109–114.

Evans, E. F. (**1981**). ''The dynamic range problem: Place and time coding at the level of cochlear nerve and nucleus,'' in *Neuronal Mechanisms in Hearing*, edited by J. Syka and L. Aitkin (Plenum, New York), pp. 69–85.

Florentine, M. (**1983**). ''Intensity discrimination as a function of level and frequency and its relation to high-frequency hearing,'' J. Acoust. Soc. Am. **74**, 1375–1379.

Florentine, M., and Buus, S. (**1981**). ''An excitation-pattern model for intensity discrimination,'' J. Acoust. Soc. Am. **70**, 1646–1654.

Florentine, M., Buus, S., and Mason, C. R. (**1987**). ''Level discrimination as a function of level for tones from 0.25 to 16 kHz,'' J. Acoust. Soc. Am. **81**, 1528–1541.

Florentine, M., Reed, C. M., Rabinowitz, W. M., Braida, L. D., Durlach, N. I., and Buus, S. (**1993**). ''Intensity perception. XIV. Intensity discrimination in listeners with sensorineural hearing loss,'' J. Acoust. Soc. Am. **94**, 2575–2586.

Freyman, R. L., and Nelson, D. A. (**1991**). ''Frequency discrimination as a function of signal frequency and level in normal-hearing and hearing-impaired listeners,'' J. Speech Hear. Res. **34**, 1371–1386.

Green, D. M. (**1976**). *An Introduction to Hearing* (Erlbaum, Hillsdale, NJ).

Green, D. M. (**1988**). ''Auditory intensity discrimination,'' in *Human Psychophysics*, edited by W. A. Yost, A. N. Popper, and R. R. Fay (Springer-Verlag, New York), pp. 13–55.

Green, D. M. (**1990**). ''Stimulus selection in adaptive psychophysical procedures,'' J. Acoust. Soc. Am. **87**, 2662–2674.

Green, D. M. (**1993**). ''A maximum-likelihood method for estimating thresholds in a yes–no task,'' J. Acoust. Soc. Am. **93**, 2096–2105.

Green, D. M. (**1995**). ''Maximum-likelihood procedures and the inattentive observer,'' J. Acoust. Soc. Am. **97**, 3749–3760.

Green, D. M., Nachmias, J., Kearney, J. K., and Jeffress, L. A. (**1979**). ''Intensity discrimination with gated and continuous sinusoid,'' J. Acoust. Soc. Am. **66**, 1051–1056.

Gu, X., and Green, D. M. (**1994**). ''Further studies of a maximum-likelihood yes–no procedure,'' J. Acoust. Soc. Am. **96**, 93–101.

He, N., Dubno, J. R., and Mills, J. H. (**1995**). ''Application of the maximum-likelihood method to psychophysical experiments with aged subjects,'' Abstr. Assoc. Res. Otolaryngol. **18**, 61.

Harris, J. D. (**1963**). ''Loudness discrimination,'' J. Speech Hear. Disord. Mon. Suppl. **11**, 1–63.

Humes, L. E. (**1996**). ''Speech understanding in the elderly,'' J. Am. Acad. Audiol. **7**, 161–167.

Jesteadt, W., and Bilger, R. C. (**1974**). ''Intensity and frequency discrimination in one- and two-interval paradigms,'' J. Acoust. Soc. Am. **55**, 1266–1276.

Jesteadt, W., Wier, C. C., and Green, D. M. (**1977**). ''Intensity discrimination as a function of frequency and sensation level,'' J. Acoust. Soc. Am. **61**, 169–175.

König, E. (**1957**). ''Pitch discrimination and age,'' Acta Oto-Laryngol. **48**, 475–489.

Luce, R. D., and Green, D. M. (**1974**). ''Neural coding and psychophysical discrimination data,'' J. Acoust. Soc. Am. **56**, 1554–1564.

Macmillan, N. A., and Creelman, D. C. (**1991**). *Detection Theory: A User's Guide* (Cambridge U.P., Cambridge).

Matthews, L. J., Lee, F. S., Mills, J. H., and Dubno, J. R. (**1997**). ''Extended high-frequency thresholds in older adults,'' J. Speech Hear. Res. **40**, 208–214.

McGill, W. J., and Goldberg, J. P. (**1968**). ''Pure-tone intensity discrimination and energy detection,'' J. Acoust. Soc. Am. **44**, 476–581.

Moore, B. C. J. (**1973**). ''Frequency difference limens for short-duration tones,'' J. Acoust. Soc. Am. **54**, 610–619.

Moore, B. C. J., and Peters, R. W. (**1992**). ''Pitch discrimination and phase sensitivity in young and elderly subjects and its relationships to frequency selectivity,'' J. Acoust. Soc. Am. **91**, 2881–2893.

Nelson, D. A., and Freyman, R. L. (**1986**). ''Psychometric functions for frequency discrimination from listeners with sensorineural hearing loss,'' J. Acoust. Soc. Am. **79**, 799–805.

Nelson, D. A., Stanton, M. E., and Freyman, R. L. (**1983**). ''A general equation describing frequency discrimination as a function of frequency and sensation level,'' J. Acoust. Soc. Am. **73**, 2117–2123.

Rabinowitz, W. M., Lim, J. S., Braida, L. D., and Durlach, N. I. (**1976**). ''Intensity perception. VI. Summary of recent data on deviations from Weber's law for 1000-Hz tone pulses,'' J. Acoust. Soc. Am. **59**, 1506–1509.

Riesz, R. R. (**1928**). ''Differential sensitivity of the ear for pure tones,'' Phys. Rev. **31**, 867–875.

Schroder, A. C., Viemeister, N. F., and Nelson, D. A. (**1994**). ''Intensity discrimination in normal-hearing and hearing-impaired listeners,'' J. Acoust. Soc. Am. **96**, 2683–2693.

Sek, A., and Moore, B. C. J. (**1995**). ''Frequency discrimination as a function of frequency, measured in several ways,'' J. Acoust. Soc. Am. **97**, 2479–2486.

Simon, H. J., and Yund, E. W. (**1993**). ''Frequency discrimination in listeners with sensorineural hearing loss,'' Ear Hear. **14**, 190–201.

Swets, J. A. (**1964**). *Signal Detection and Recognition by Human Observers* (Wiley, New York).

Turner, C. W., and Nelson, D. A. (**1982**). ''Frequency discrimination in regions of normal and impaired sensitivity,'' J. Speech Hear. Res. **25**, 34–41.

Turner, C. W., Horwitz, A. R., and Souza, P. E. (**1994**). ''Forward- and backward-masked intensity discrimination measured using forced-choice and adjustment procedures,'' J. Acoust. Soc. Am. **96**, 2121–2126.

Viemeister, N. F. (**1988**). ''Intensity coding and the dynamic range problem,'' Hearing Res. **34**, 267–274.

Wier, C. C., Jesteadt, W., and Green, D. M. (**1977**). ''Frequency discrimination as a function of frequency and sensation level,'' J. Acoust. Soc. Am. **61**, 178–184.

Zeng, F.-G., and Turner, C. W. (**1992**). ''Intensity discrimination in forward masking,'' J. Acoust. Soc. Am. **92**, 782–787.

Zeng, F.-G., Turner, C. W., and Relkin, E. M. (**1991**). ''Recovery from prior stimulation II: Effects upon intensity discrimination,'' Hearing Res. **55**, 223–230.

Zwaardemaker, H. (**1899**). ''The loss of high tones with increasing age; a new law,'' Arch. Ohreh. 47.

Zwicker, E. (**1956**). ''Die ilementaren Grundlagen zur Bestimmung der Informationkapazitat des Gehors,'' Acustica **5**, 365–381.

Zwicker, E. (**1970**). ''Masking and psychological excitation as consequences of the ear's frequency analysis,'' in *Frequency Analysis and Periodicity Detection in Hearing*, edited by R. Plomp and G. F. Smoorenburg (Sijthoff, Leiden, The Netherlands), pp. 376–396.

A computationally efficient alternative for the Liljencrants–Fant model and its perceptual evaluation

Raymond Veldhuis[a)]

IPO—Centre for Research on User-System Interaction, P.O. Box 513, 5600 MB Eindhoven, The Netherlands

An alternative for the Liljencrants–Fant (LF) glottal-pulse model is presented. This alternative is derived from the Rosenberg model. Therefore, it is called the Rosenberg++ model. In the derivation a general framework is used for glottal-pulse models. The Rosenberg++ model is described by the same set of T or R parameters as the LF model but it has the advantage over the LF model that it is computationally more efficient. It is compared with the LF model in a psychoacoustic experiment, from which it is concluded that in a practical situation it is capable of producing synthetic speech which is perceptually equivalent to speech generated with the LF model. © *1998 Acoustical Society of America.* [S0001-4966(98)00701-2]

PACS numbers: 43.70.Gr, 43.72.Ja, 43.71.Bp [AL]

INTRODUCTION

For analysis and synthesis purposes, speech production is often modeled by a source-filter model. Figure 1 shows two versions of such a source-filter model. On the left we see a model consisting of a source producing a signal $g(t)$, which models the airflow passing the vocal cords, a filter with a transfer function $H(j\omega)$, which models the spectral shaping by the vocal tract, and an operator R, which models the conversion of the airflow to a pressure wave $s(t)$ at the lips and which is called lip radiation. The operator R is essentially a differentiation operator. On the right we see an equivalent model, in which the differentiation operator has been combined with the source, which now produces the time derivative $\dot{g}(t)$ of the airflow passing the vocal cords. The opening between the vocal cords is called the glottis, therefore the source is referred to as the glottal source. In voiced speech the signal $g(t)$ is periodic and one period of $g(t)$ is called a glottal pulse. The glottal pulse or, more often, its time derivative has been the topic of many studies because it is expected to determine the voice quality and to be related to the production of prosody (e.g., Childers and Lee, 1991; Cummings and Clements, 1993; Gobl, 1989; Klatt and Klatt, 1990; Pierrehumbert, 1989; Rosenberg, 1971; Strik, 1994). The time derivative of the glottal pulse is studied rather than the glottal pulse because it is more easily obtained from the speech signal and some of the glottal-source parameters can be more easily derived from it.

The Liljencrants–Fant (LF) model (Fant *et al.*, 1985) has become a reference model for glottal-pulse analysis. Unfortunately, its use in speech synthesizers is limited because of its computational complexity. This computational complexity is mostly due to the difference between the specification parameters and the generation parameters of the LF model. The computation of the generation parameters from the specification parameters is computationally complex, because it involves solving a nonlinear equation. This is ex-

plained in Sec. I. This section presents a general framework for glottal-pulse models and also introduces the LF model. In Sec. II we introduce the Rosenberg++ (R++) model, which has the same features as the LF model but has the advantage that it can be computed directly and simply from the specification parameters. Section III describes an experiment which shows to what extent the R++ model is capable of generating synthetic speech that is perceptually equivalent to speech generated with the LF model. The computational complexities of the R++ and the LF model are compared in Sec. IV. Finally, Sec. V presents conclusions.

I. GLOTTAL-PULSE MODELS

Figure 2 shows typical examples of the glottal waveform $g(t)$ and its time derivative $\dot{g}(t)$ and it introduces the specification parameters t_0, t_p, t_e, t_a and U_o or E_e (Fant *et al.*, 1985). The length of a glottal cycle is t_0. The maximum airflow U_o occurs at t_p and the maximum excitation with amplitude E_e occurs at t_e, which corresponds to the instant when the vocal cords collide. The interval before t_e is called the open phase. The interval with approximate length $t_a = E_e/\ddot{g}(t_e)$ just after the instant of maximum excitation is called the return phase. The interval between t_e, or better $t_e + t_a$, and the end of the glottal cycle is called the closed phase. During this phase the vocal folds have reached maximum closure and the airflow has reduced to its minimum. A minimum airflow greater than 0 is often referred to as leakage (Holmberg *et al.*, 1988). The presence of leakage influences the speech in two ways. First, by introducing a permanent acoustic coupling between vocal tract and trachea it influences the formant resonances and thus the speech spec-
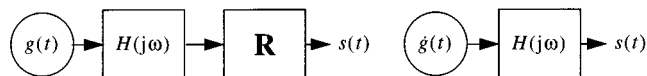

FIG. 1. Left: Source-filter model with glottal source, vocal-tract filter, and lip radiation. Right: Equivalent source-filter model with lip radiation and glottal source combined.

[a)]Electronic mail:veldhuis@ipo.tue.nl

trum. Second, it may affect the glottal excitation by introducing turbulence noise. Due to the differentiating effect of the lip radiation, the constant additional airflow has no effect on the pressure wave at the lips. In a speech synthesizer based on a simple source-filter model, the effects of leakage can be accounted for by adding a noise term to the source and by adapting the transfer function of the filter. Therefore, we assume that there is no leakage and that $g(0) = g(t_0) = 0$. The airflow in the return phase is generally considered to be of perceptual importance, because it determines the spectral slope. The parameters t_0, t_p, t_e, and t_a are called the T parameters. Instead of the T parameters, sometimes the R parameters (Fant *et al.*, 1985) are used, which are defined as follows:

$$r_o = t_e/t_0, \quad r_a = t_a/t_0, \quad r_k = (t_e - t_p)/t_p. \quad (1)$$

The parameters r_o and r_a denote the relative duration of the open phase and the return phase, respectively. The parameter r_k quantifies the symmetry of the glottal pulse.

The following expression is a general description of the glottal-pulse time derivative $\dot{g}(t)$ with an exponential decay modeling the return phase:

$$\dot{g}(t) = \begin{cases} f(t), & \text{for } 0 \leq t < t_e, \\ f(t_e) \dfrac{\exp(-(t-t_e)/t_a) - \exp(-(t_0-t_e)/t_a)}{1 - \exp(-(t_0-t_e)/t_a)} \\ \qquad \text{for } t_e \leq t < t_0. \end{cases} \quad (2)$$

The function $f(t)$ on the first line of (2) describes the glottal-pulse time derivative until the instant of excitation. The second line models the return phase. Integration leads to the following expression for the glottal airflow:

$$g(t) = \begin{cases} \displaystyle\int_0^t f(\tau)\, d\tau, & \text{for } 0 \leq t < t_e, \\ \displaystyle\int_0^{t_e} f(\tau)\, d\tau + t_a f(t_e) \dfrac{1 - \exp(-(t-t_e)/t_a) - [(t-t_e)/t_a]\exp(-(t_0-t_e)/t_a)}{1 - \exp(-(t_0-t_e)/t_a)} & \text{for } t_e \leq t < t_0. \end{cases} \quad (3)$$

Since there is no leakage we require $g(t) \geq 0$ and $g(0) = g(t_0) = 0$, from which one can derive the following continuity condition:

$$\int_0^{t_e} f(\tau)\, d\tau + t_a f(t_e) D(t_0, t_e, t_a) = 0, \quad (4)$$

with

$$D(t_0, t_e, t_a) = 1 - \frac{(t_0 - t_e)/t_a}{\exp((t_0 - t_e)/t_a) - 1}. \quad (5)$$
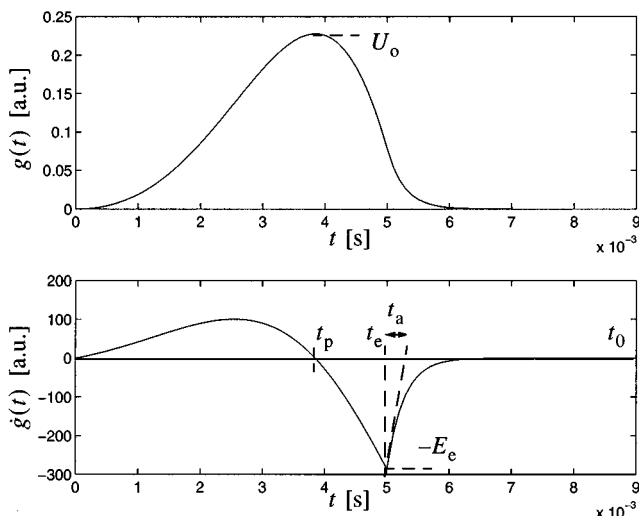

FIG. 2. Glottal pulse (top) and its time derivative (bottom). Arbitrary units.

Any parameters of $f(t)$ must be chosen such that condition (4) is satisfied.

The parameter t_a in the above definitions for the glottal airflow $g(t)$ and its time derivative $\dot{g}(t)$ is the time constant of the exponential decay in the return phase. This is slightly different from the situation in Fig. 2 and the original definition of the LF model (Fant *et al.*, 1985), in which t_a specifies the initial slope of the return phase. In Fant *et al.* (1985) the factor $1/t_a$ in the exponential functions is replaced by another generation parameter ε, determining the time constant of the decay. For $t_a \ll t_0 - t_e$, which is usually the case, we have $\varepsilon = 1/t_a$. Otherwise there exists a simple relation between t_a and ε (Fant *et al.*, 1985), which makes the two definitions equivalent.

The above set of expressions (2)–(5) forms a general framework for glottal-pulse models with an exponential return phase. The LF model follows from this framework for a specific choice of $f(t)$ and so does the Rosenberg model. Other models can be constructed by choosing other functions $f(t)$. Even other choices for the return phase are possible, but will not be discussed here.

The LF model presented in Fant *et al.* (1985), but with the modified definition of t_a, follows from (2) and the choice

$$f(t) = B \sin\left(\pi \frac{t}{t_p}\right) \exp(\alpha t), \quad (6)$$

with B the amplitude of the glottal-pulse time derivative. The generation parameter α can only be solved numerically from the continuity equation (4), which in this case reads

$$\frac{\pi - \exp(\alpha t_e)(\pi \, \cos(\pi(t_e/t_p)) - \alpha t_p \, \sin(\pi(t_e/t_p)))}{\pi^2 + (\alpha t_p)^2}$$

$$+ \frac{t_a}{t_p} \exp(\alpha t_e) \sin\left(\pi \, \frac{t_e}{t_p}\right) D(t_0, t_e, t_a) = 0. \qquad (7)$$

Solving (7) for α is a heavy computational load in a speech synthesizer, where the T parameters may vary typically every 10 ms.

Qi and Bi (1994) propose an approximation in which t_0, t_p, t_e, and E_e are specified rather than t_0, t_p, t_e, and t_a. In this manner (7) needs not to be solved, but it has the disadvantage that the control over the return phase is lost. The R++ model, which is introduced in the next section, allows specification of t_0, t_p, t_e, and t_a and it does not require the solution of (7). One can ask whether the control over the return phase can be maintained without having to solve (7) with the other LF parameters, e.g., $F_a = 1/(2\pi t_a)$, $F_g = 1/(2t_p)$, and $r_g = t_0/(2t_p)$ (Fant et al., 1985; Fant, 1995). Unfortunately, these parameters have simple relations to the T or the R parameters and, therefore, their use still requires the solution of an equation very similar to (7).

II. THE ROSENBERG++ MODEL

The R++ model is an extension of the Rosenberg model (Rosenberg, 1971):

$$g(t) = \begin{cases} At^2(t_e - t) & \text{for } 0 \leq t < t_e, \\ 0 & \text{for } t_e \leq t < t_0, \end{cases}$$

$$\dot{g}(t) = \begin{cases} 3At(\tfrac{2}{3}t_e - t) & \text{for } 0 \leq t < t_e, \\ 0 & \text{for } t_e \leq t < t_0, \end{cases} \qquad (8)$$

with A the amplitude of the glottal pulse. The Rosenberg model does not have a return phase and always has $t_p = 2t_e/3$, or $r_k = 1/2$. This limits its flexibility. Sometimes a pseudo return phase is introduced by applying a first- or second-order recursive low-pass filter to the glottal-pulse time derivative (e.g., Klatt and Klatt, 1990), but this undesirably changes t_p. We propose two extensions to the Rosenberg model, each explaining a "+" in "R++." The first is a return phase as in (2). The second is an extra factor in $f(t)$, which allows us to specify a t_p. The latter extension results in

$$f(t) = 4At(t_p - t)(t_x - t),$$

$$\int_0^t f(\tau)\, d\tau = At^2\left(t^2 - \frac{4}{3}t(t_p + t_x) + 2t_p t_x\right). \qquad (9)$$

The following expression for t_x follows on solving the continuity equation (4):

$$t_x = t_e\left(1 - \frac{\tfrac{1}{2}t_e^2 - t_e t_p}{2t_e^2 - 3t_e t_p + 6t_a(t_e - t_p)D(t_0, t_e, t_a)}\right). \qquad (10)$$

The denominator of (10) vanishes when

$$t_p = \frac{2}{3} t_e \frac{t_e + 3t_a D(t_0, t_e, t_a)}{t_e + 2t_a D(t_0, t_e, t_a)}. \qquad (11)$$

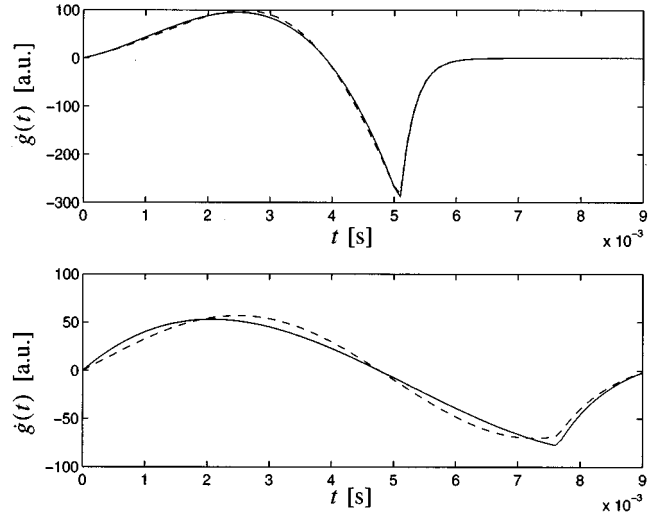In that case, the R++ model reduces to an R+ model:

FIG. 3. The LF (dashed lines) and R++ (solid lines) glottal-pulse time derivatives. Top panel: $f_0 = 1/t_0 = 110$ Hz, $r_0 \neq 0.56$, $r_k = 0.31$, and $r_a = 0.025$. Bottom panel: $f_0 = 110$ Hz, $r_0 = 0.84$, $r_k = 0.60$, and $r_a = 0.10$. Arbitrary units.

$$f(t) = 3At(t_p - t), \quad \int_0^t f(\tau)\, d\tau = At^2\left(\frac{3}{2}t_p - t\right), \qquad (12)$$

which is the Rosenberg model extended with a return phase. The influence of the factor $t_x - t$ on the shape of the glottal-pulse time derivative decreases with increasing $|t_x|$. For $|t_x|$ large enough, therefore, the R++ model can be replaced by the R+ model (12). The following condition guarantees that either $t_x \geq t_e$ or $t_x \leq 0$:

$$\frac{1}{2}t_e \leq t_p \leq \frac{3}{4}t_e\left(\frac{t_e + 4t_a D(t_0, t_e, t_a)}{t_e + 3t_a D(t_0, t_e, t_a)}\right). \qquad (13)$$

It ensures that $g(t)$ is non-negative. The left-hand inequality of (13) gives a lower limit to the skewness of the glottal pulse, which makes it symmetrical when we ignore the return phase. This limit is also known in the LF model. The right-hand inequality of (13) is an upper limit to the glottal-pulse skewness which is not present in the LF model, but so far has not turned out to be a limitation.

Figure 3 shows LF (dashed lines) and R++ (solid lines) glottal-pulse time derivatives for two sets of R parameters. The top panel shows glottal-pulse time derivatives for a modal voice with a distinct closed phase and the bottom panel for an abducted voice without a distinct closed phase. All waveforms have been power normalized to the same value. In general, the R++ waveform approximates the LF waveform closely if $r_k < 0.5$. For higher r_k, the approximation is slightly worse. In any case, the differences between the models are small compared with the differences between the LF model and estimated waveforms (e.g., Childers and Lee, 1991; Strik, 1994). Therefore, we can already assume that both models are equally useful. However, because we want to present the R++ model as a computationally efficient alternative to the LF model with the same specification parameters, we believe it relevant that both models are also perceptually equivalent. This is investigated in Sec. III. The computational complexity is then addressed in Sec. IV.
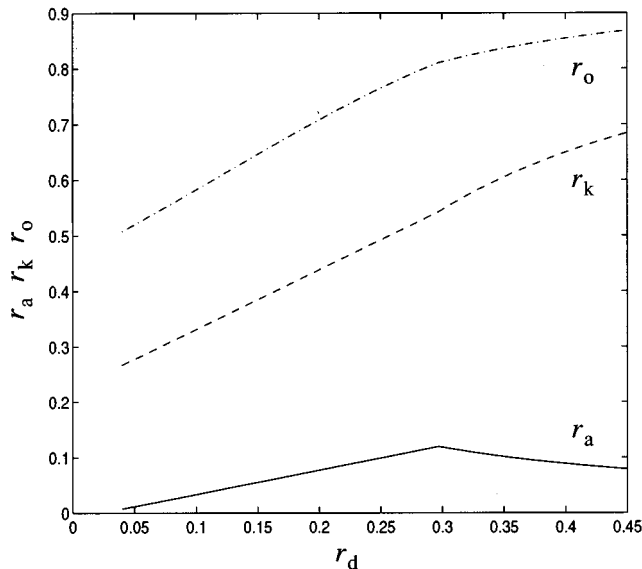
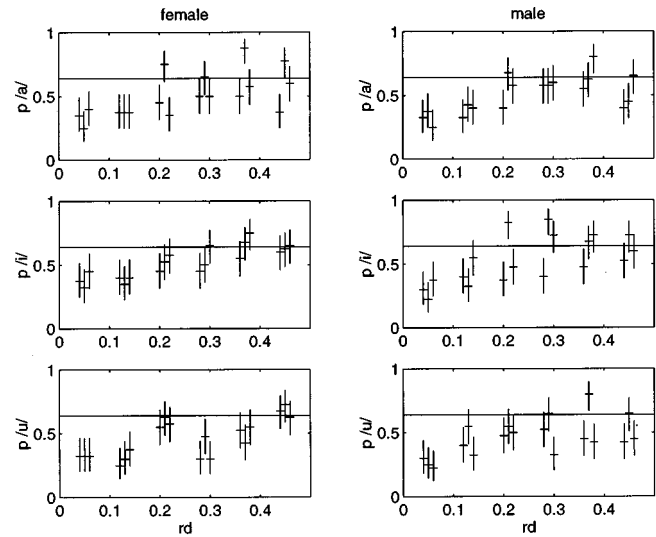FIG. 4. Statistical dependencies of r_a, r_k, and r_o on r_d.

FIG. 5. Fractions correct and 90% confidence intervals, presented in triples for all subjects. Left: EK, middle; RK, right: SP. The values of subject RK are positioned at the correct r_d values. The horizontal line at $p=0.64$ corresponds to $d'=1$.

III. A PERCEPTUAL COMPARISON

By means of a psycho-acoustic experiment we investigated whether synthetic vowels generated with the R++ and the LF model at various choices of the R parameters can be perceptually discriminated. We chose this approach because a psycho-acoustical comparison of isolated vowels is more critical with respect to discrimination than the comparison of synthetic speech in which other synthesis artifacts and the context may mask the perceptual differences.

In order to choose R parameters corresponding to those of natural voices, we used the so-called shape parameter

$$r_d = \frac{U_0}{E_e t_0}, \qquad (14)$$

which has been defined in Fant *et al.* (1994) and has been discussed extensively in Fant (1995). The definition above differs from the one in Fant *et al.* (1994) by a normalization factor. In Fant *et al.* (1994) and Fant (1995) it is observed that there exist simple statistical relations between r_d and the other R parameters, such that each of the R parameters can be predicted from a measured value of r_d. These relations are shown in Fig. 4. We chose the set {0.05, 0.13, 0.21, 0.29, 0.37, 0.45} as the values for r_d and used Fig. 4 to determine the R parameters.

From recordings of one male and one female voice we derived formant filters and fundamental frequencies $f_0 = 1/t_0$ for the vowels /a/, /i/, and /u/. Segments of 0.3 s of these vowels were synthesized for the six values of r_d with the simplified source-filter model of Fig. 1. The glottal-pulse time derivatives were according to the LF and the R++ models, respectively. The fundamental frequencies and formant filters were kept identical to those obtained from the recordings. The fundamental frequencies of the male and female vowels were approximately 110 and 200 Hz, respectively. The sampling frequency was 8 kHz. This resulted in 36 pairs of stimuli.

Three subjects (EK, RK, and SP), two of whom (RK and SP) had experience with psycho-acoustic experiments, were asked to discriminate between the segments generated with the LF and the R++ models in a three-interval three-alternative forced-choice paradigm. Each triple of stimuli was presented 40 times in a random order. In half of the trials the two reference segments were generated with the LF model and the subject's task was to indicate the segment generated with the R++ model. In the other half of the trials the two reference segments were generated with the R++ model and the subject's task was to indicate the segment generated with the LF model. The numbers of correct answers were registered. The experiment was split up into two sessions of equally many trials. The subjects were seated in a sound-proof booth. The stimuli were presented over Beyer DT990 headphones at an overall level of 70 dB SPL with a roving of 1 dB. The subjects received immediate feedback after every trial.

There was no significant difference between the results of the trials with the LF model and those with the R++ model in the reference intervals. Only subject RK showed a small learning effect in the second session, which has been ignored in the presentation of the results. Figure 5 shows a graphical presentation of the fractions correct p with 90% confidence intervals for all the subjects and all the pairs of stimuli as a function of r_d. The fractions correct are plotted in triples, the left, middle, and right one corresponding to subjects EK, RK, and SP, respectively. The values of subject RK are positioned at the correct r_d values. The horizontal line at $p=0.64$ corresponds to $d'=1$. This is the value at which the subjects are assumed to be able to just detect the differences (Green and Swets, 1966).

The results in Fig. 5 show that subject RK sometimes, and the other subjects only very occasionally, detected a difference. These detections occur at the higher values of r_d, where, because of the higher r_k, the waveform approxima-

tion is less good. In general, the fractions correct seem to increase somewhat with increasing r_d.

An interpretation of the 90% confidence interval is the following. If we assume that a subject has a detection probability p, then a hypothesis test based on the data would accept all values of p in the 90% confidence interval with a Type I error of 5%. This implies that when a confidence interval is entirely below the line $d'=1$, the data confirms that there is no discrimination. When a confidence interval is entirely above the line $d'=1$, the data confirms that there is certain discrimination. Finally, when a confidence interval crosses the line $d'=1$, discrimination is undetermined. In this view, certain discrimination is rare. In most cases, especially for lower r_d values below 0.2, there is no discrimination and for the higher r_d values discrimination is either absent or undetermined. On the basis of these observations and the fact that a psycho-acoustical experiment is more critical with respect to discrimination than a comparison of synthetic speech, we believe that, although the results show that the models are not completely perceptually equivalent, it is unlikely that there will be audible differences between synthetic speech generated with the R++ and with the LF model.

IV. COMPUTATIONAL EFFICIENCY

A general comparison of the computational efficiency of the LF and the R++ model is difficult, because its result depends on the specific implementations and on the speech-synthesis hardware. Therefore, we will focus on one aspect of the computational efficiency which is more or less hardware independent: the computational load in terms of numbers of the basic operations addition $(+/-)$, multiplication $(\times)$, division $(/)$ and function evaluation (sin, cos, exp). In addition, processing times of implementations of the two models in C on a RISC-4000 processor with a floating-point unit will be presented as an example.

The computational load of a glottal-pulse model breaks down into the computational load of calculating the samples of the glottal-pulse derivative and that of updating the parameters α for the LF model and t_x for the R++ model. Fant *et al.* (1985) and Lin (1990) propose the second-order recursive expression

$$s_n = 2e^{\alpha T_s} \cos\left(\pi \frac{T_s}{t_p}\right) s_{n-1} - (e^{\alpha T_s})^2 s_{n-2}$$

$$= a_1 s_{n-1} + a_2 s_{n-2}. \qquad (15)$$

for the calculation of the samples before t_e and the first-order recursive expression

$$s_m = e^{-T_s/t_a} s_{m-1} - \frac{(1-e^{-T_s/t_a})e^{-(t_0-t_e)/t_a}}{1-e^{-(t_0-t_e)/t_a}} = \rho s_{m-1} + c \qquad (16)$$

for the samples after t_e. Here T_s is the sampling period. The evaluation of (15) requires two multiplications and one addition. The initial values s_0 and s_1 have to be reset at the beginning of a glottal cycle. The evaluation of (16) requires one multiplication and one addition. The R++ glottal-pulse derivative before t_e, written as $t(t-t_p)(t-t_x)$, requires two multiplications and three additions per sample. The number

TABLE I. Computational load of glottal-pulse models in numbers of basic operations $+$, $\times$, $/$, function evaluation $f(.)$, and measured average processing times. The number of iterations to compute α is denoted by N_{it}.

	$+$	$\times$	$/$	$f(.)$	Processing times (μs)
LF sample	1	r_0+1	0	0	9.4
R++ sample	$2r_0+1$	r_0+1	0	0	13.6
LF update	$5+4N_{it}$	$10+4N_{it}$	7	$8+N_{it}$	57.8
R++ update	8	8	3	1	10.7

of additions is three because each factor is incremented by T_s. The R++ glottal-pulse derivative after t_e is computed recursively by using (16).

In an LF update, $D(t_0,t_e,t_a)$ defined in (5) is computed and α is solved from (7). When α is known, the coefficients and the initial values of (15) and (16) are computed. The computation of $D(t_0,t_e,t_a)$ requires three additions, two divisions, and one function evaluation. Equation (7) is rewritten as

$$Q(u) = 1 + e^{\varphi u}\left(\left(\frac{t_a}{t_e}\varphi D(t_0,t_e,t_a)(1+u^2)+u\right)\right.$$

$$\left.\times \sin(\varphi) - \cos(\varphi)\right), \qquad (17)$$

with $\varphi = \pi t_e/t_p$, and solved for u. The parameter α is then found as $\alpha = u\pi/t_p$. The computation of φ, the parts of (17) independent on u, and α from u require four multiplications, two divisions, and two function evaluations. We propose the following iterative procedure for the finding the zero of (17). The function $Q(u)$ decreases with increasing u. First, if $Q(0)>0$, starting from $u=1$, u is doubled until $Q(u)<0$, or, if $Q(0)\leq 0$, starting from $u=-1$, u is doubled until $Q(u)>0$. Second, the interval in which the sign change occurs is searched for the zero by a binary-search algorithm. This requires a total number of N_{it} iterations, depending on the specification parameters and the required accuracy. Each iteration requires four additions, four multiplications, and one function evaluation. Computing coefficients and the initial values of (15) and (16) requires two additions, six multiplications, three divisions, and five function evaluations. In an R++ update $D(t_0,t_e,t_a)$ is computed and then t_x, which requires five additions, eight multiplications, and one division.

The results are summarized in the first four columns of Table I. In a formant synthesizer the computational loads of the LF and the R++ model for computing the samples are both small compared with that of the formant filters. With respect to computing the samples, the LF model is somewhat more efficient than the R++ model because of the smaller number of additions. The advantage of the R++ model is that the computational load for the parameter updates is smaller for any value of $N_{it}\geq 1$ and much smaller for realistic values of N_{it}, which are around 16 for a maximum relative error in α of 10^{-4}.

As an example, we measured the processing times of C-language implementations for the computation of the updates and one glottal cycle on a 133-MHz RISC-4000 processor with a floating-point unit. In a speech synthesizer run-

ning on a desk-top computer this determines the overall computational complexity, because the glottal cycle can be stored and played out repeatedly until the next parameter update. The sampling frequency was 10 000 Hz, the length of a glottal cycle was 9 ms, and the maximum relative error in α was 10^{-4}. The results were calculated for the r_d values of Sec. IV. The averages are presented in the last column of Table I. The processing times for the samples increased by about 4% for the LF model and 15% for the R++ model with increasing r_d, and, consequently, r_o. These increases and their differences were to be expected on account of the r_o dependence shown in Table I. The average processing time for the samples of the LF model is about 30% less than that of the R++ model, which is due to the larger numbers of additions before t_e of the R++ model. Considering the average processing times for the updates, we see that the R++ model is 5.4 times faster than the LF model. In this example the number of iterations N_{it} was equal to 16 for all values of r_d. The R++ model was overall about 2.8 times faster than the LF model. This number will be higher for voices with shorter glottal cycles.

In addition to the smaller overall computational load, the R++ model has two other advantages over the LF model, which are relevant for an implementation in dedicated hardware. The first is that the computation of t_x is data independent and straightforward, whereas the computation of α is data dependent and involves an iterative search for a zero, requiring additional decision and control logic. The second additional advantage of the R++ model is that, because of the shorter time spent on updates, the samples can be put out more regularly, which reduces the minimum size of a sample output buffer.

V. CONCLUSIONS

We have introduced the R++ model as an alternative for the LF model of the glottal pulse. It is derived from a general framework for glottal-pulse models with an exponential return phase, from which other, yet nonexisting, glottal-pulse models can be derived as well.

A psycho-acoustical comparison of stimuli generated with the R++ and the LF models showed that in some cases discrimination is possible, but that it is very unlikely that this will occur in the practical situation of speech synthesis. Even if there would be small audible differences this would not mean that one of the models would actually yield a percep-

tually better approximation of real speech, since both are simple models of a complex waveform and the differences between models and waveforms are much larger than the differences between the models.

We have compared the computational efficiency of the LF and the R++ model and we found that the parameter-update mechanism of R++ model is computationally more efficient and that an implementation in C of the R++ model requires less processing time. We believe, therefore, that the R++ model can serve as a useful source model in speech synthesizers.

Childers, D. G., and Lee, C. K. 1991. ''Voice quality factors: Analysis synthesis and perception,'' J. Acoust. Soc. Am. **90**, 2394–2410.

Cummings, K. E., and Clements, M. A. (**1993**). ''Application of the analysis of glottal excitation of stressed speech to speaking style modification,'' Proceedings ICASSP-93, Minneapolis, pp. 207–210.

Fant, G. (**1995**). ''The LF model revisited. Transformations and frequency domain analysis,'' Speech Transmission Laboratory Quarterly Progress Report 2-3/95, KTH, pp. 119–156.

Fant, G., Liljencrants, J., and Lin, Q. (**1985**). ''A four-parameter model of glottal flow,'' Speech Transmission Laboratory Quarterly Progress Report 4/85, KTH, pp. 1–3.

Fant, G., Kruckenberg, A., Liljencrants, J., and Båvegård, M. (**1994**). ''Voice source parameters in continuous speech. Transformation of LF parameters,'' in Proceedings of the ICSLP-94, Yokohama, pp. 1451–1454.

Gobl, C. (**1989**). ''A preliminary study of acoustic voice quality correlates,'' Speech Transmission Laboratory Quarterly Progress Report 4/89, KTH, pp. 9–22.

Green, D. A., and Swets, J. A. (**1966**). *Signal Detection Theory and Psychophysics* (Wiley, New York).

Holmberg, E. B., Hillman, R. E., and Perkell, J. S. 1988. ''Glottal airflow and pressure measurements for soft, normal and loud voice by male and female speakers,'' J. Acoust. Soc. Am. **84**, 511–529.

Klatt, D. H., and Klatt, L. C. 1990. ''Analysis synthesis, and perception of voice quality variations among female and male talkers,'' J. Acoust. Soc. Am. **87**, 820–856.

Lin, Q. (**1990**). ''Speech Production Theory and Articulatory Speech Synthesis,'' Ph.D. thesis, Royal Institute of Technology, Stockholm.

Pierrehumbert, J. B. (**1989**). ''A preliminary study of the consequences of intonation for the voice source,'' Speech Transmission Laboratory Quarterly Progress Report 4/89, KTH.

Qi, Y., and Bi, N. 1994. ''A simplified approximation of the four-parameter LF model of voice source,'' J. Acoust. Soc. Am. **96**, 1182–1185.

Rosenberg, A., 1971. ''Effect of glottal pulse shape on the quality of natural vowels,'' J. Acoust. Soc. Am. **49**, 583–590.

Strik, H. (**1994**). ''Physiological Control and Behaviour of the Voice Source in the Production of Prosody,'' Ph.D. thesis, University of Nijmegen.

Evaluation of the effect of speech-rate slowing on speech intelligibility in noise using a simulation of cochlear hearing loss

Yoshito Nejime[a] and Brian C. J. Moore

Department of Experimental Psychology, University of Cambridge, Downing Street, Cambridge CB2 3EB, England

The effect of digital processing, which slows the speed of speech (speech-rate) without changing its pitch, has been examined. The processing is intended to make speech communication easier by allowing more time for cognitive processing when the listening situation is difficult, for example, when listening to a foreign language, or when the user has a hearing loss. The speech-rate slowing makes use of a pitch-synchronous partial expansion of the waveform in the time domain. The processing was evaluated using a simulation of hearing loss which has been shown to lead to reduced intelligibility for normally hearing subjects. The simulation included the major consequences of cochlear hearing loss; loudness recruitment, threshold elevation, and reduced frequency selectivity. Two simulations were used: a moderate flat hearing loss with auditory filters broadened by a constant factor of three (B3R2); and the same loss with linear amplification applied prior to the simulation processing (B3R2+). Two expansion rates were used for the speech-rate slowing, 1.25 and 1.50. The intelligibility of sentences in speech-shaped noise was measured. For both simulation conditions, the speech-rate slowing did not give any improvement in intelligibility. Rather, in condition B3R2+ the slowing produced statistically significant deleterious effects on intelligibility. The results suggest that artificial speech-rate slowing will not improve the intelligibility of speech in noise for hearing-impaired people who have the type of cochlear damage simulated in this test. © *1998 Acoustical Society of America.* [S0001-4966(97)02412-0]

PACS numbers: 43.71.Gv, 43.71.Ky [WS]

INTRODUCTION

Hearing-impaired listeners, especially elderly people, often have difficulty in comprehending fast speech. In everyday situations, speaking more slowly is a common technique for helping such people comprehend more easily. In principle, reduction of the speed of speech could also be achieved in a signal-processing hearing aid, and lead to benefits comparable to those achieved by speaking more slowly.

Several digital signal processing methods have been proposed to modify the time scale of speech signals (Griffin and Lim, 1984; Roucos and Wilgus, 1985; Suzuki and Misaki, 1992). A well-established method is based on an algorithm proposed by Malah (1979), that changes the speed of speech without changing the fundamental frequency. Picheny *et al.* (1985, 1986, 1989) investigated the efficacy of speech-rate reduction for hearing-impaired people using Malah's algorithm. They were not able to demonstrate any benefit of the speed-reducing processing; usually the processing led to poorer intelligibility. This may have been due to the fact that uniform time expansion was applied to the entire speech signal; this makes the speech sound unnatural, since when speech is spoken naturally at a slow rate, some segments are expanded more than others relative to rapidly spoken speech. Later, Uchanski *et al.* (1996) evaluated the efficacy of speech-rate reduction using nonuniform processing. The

speech stimuli were converted into a sequence of power spectrum segments using fast Fourier transforms (FFTs), and the time scale of the sequence of spectral segments was modified by interpolation and deletion of spectral segments. The manipulation was applied to make the local duration of segments of the processed speech similar to those of natural slow speech for the same utterance. The time-scaled spectrum sequence was then converted back into a waveform, using a random phase, following the Griffin–Lim algorithm (Griffin and Lim, 1984). The efficacy of the processing was tested using conversationally (fast) spoken sentences. Four hearing-impaired subjects were tested in quiet. Although the nonuniform time scaling was less deleterious to intelligibility than the uniform time scaling used in earlier studies (Picheny *et al.*, 1985, 1986, 1989), the intelligibility of the slowed speech was less than that of the original speech for all subjects.

A problem with this approach is the use of random phase for the conversion from the frequency domain to the time domain. This causes loss of information (for example, it can disrupt the periodicity of voiced portions of speech) and can introduce artifacts into the output waveform. Hence the results should not be used to reject the efficacy of speech-rate reduction entirely; a more appropriate method of slowing the speed of speech, introducing fewer artifacts, and preserving periodicity, might give better results.

Nejime *et al.* (1996) described a real-time hand-sized portable device that slows the speed of speech without changing the pitch. In this device, a simplified pitch-

---

synchronous time-scale-modification algorithm is used to minimize the complexity of the signal-processing operation. Unlike the traditional algorithm, this dynamic-processing algorithm expands the duration of speech segments whose power exceeds a certain threshold, but does not manipulate segments whose power is below the threshold; typically, these low-power segments are consonants. To evaluate the efficacy of the speech-rate slowing, two experiments using Japanese hearing-impaired subjects were conducted: a word recognition test and a sentence recognition test. Two out of ten subjects showed a clear monotonic improvement with increasing expansion ratio in the sentence recognition test. In the same test, another five subjects showed some improvement when using the largest expansion ratio, but the performance of these subjects at the original speed was too good to allow much improvement to be produced by the speech-rate slowing. No improvement was observed in a word recognition test which did not require long portions of speech to be held in memory. Nejime *et al.* concluded that speech-rate slowing can alleviate hearing difficulty for connected speech, perhaps by making it easier to process stimuli held in auditory memory, i.e., the slowing may allow for more effective cognitive processing.

It is not clear why speech-rate showing has the effect of improving speech comprehension in some hearing-impaired subjects but not in others. One explanation is that the subjects who benefited used the extra time to employ context or knowledge at the language processing level of speech comprehension to compensate for the impoverished information provided by (impaired) peripheral processing. If this is correct, many hearing-impaired people might benefit from speech-rate slowing, since the improved use of context should occur regardless of the type of hearing loss. Another interpretation is that the two subjects who showed large improvements had reduced speed of language processing in addition to their hearing disability, and the speech-rate slowing compensated for this slow processing. The other subjects may have been able to perform linguistic processing sufficiently fast even without the speech-rate slowing; in their case, the main limitation to performance would have been the impaired peripheral processing. If this argument is correct, then only hearing-impaired people who have a deficit in language processing in addition to their hearing loss can expect benefits from speech-rate slowing. The majority of people with hearing loss would not be expected to benefit, since, in general, cochlear hearing loss is not associated with marked reduction of language processing speed [although this can happen in the elderly; see van Rooij and Plomp (1992)].

In this study, we approached this problem in a different way, by using a simulation of cochlear hearing loss with young normally hearing subjects. This makes it possible to study the effects of different types of perceptual abnormalities under well-defined and reproducible conditions that are consistent across subjects. In addition, it seems reasonable to assume that young normally hearing subjects with no reported difficulty in understanding speech stimuli have normal language processing skills. Thus if benefits of the speech-rate slowing are observed, this means that the pro-

TABLE I. The values of the gain in decibels for the linear amplification recommended by the NAL procedure for the simulated flat loss, at each audiometric frequency.

Frequency (kHz)	0.25	0.5	0.75	1.0	1.5	2.0	3.0	4.0	5.0
Gain (dB)	6	15	20	24	24	22	21	21	21

cessing might be of general benefit, rather than being restricted to those with reduced speed of cognitive processing.

The simulation included two major changes in auditory processing associated with cochlear hearing loss: loudness recruitment with absolute threshold elevation and reduced frequency selectivity. The specific question addressed in this study is: How much is the intelligibility of speech in the simulation of hearing loss affected by speech-rate slowing using the algorithm of Nejime *et al.* (1996)?

I. SIGNAL-PROCESSING METHODS

A. Speech-rate slowing

The method for producing speech-rate slowing has been described previously (Nejime *et al.*, 1996) and the reader is referred to that study for details. The algorithm uses expansion in the time domain, and is a modification of Malah's (1979) algorithm. The process uses pitch-synchronous waveform expansion. To reduce distortion of the output signal, the waveform expansion is applied only to segments of the signal whose power exceeded a certain threshold. Segments whose power is below the threshold are passed without any manipulation, resulting in nonuniform time expansion.

B. Method of simulating cochlear hearing loss

Our method of simulating the effect of cochlear hearing loss is described in detail in our previous study (Nejime and Moore, 1997). The effect of reduced frequency selectivity is simulated by smearing the short-term power spectra of the stimuli in such a way that the excitation pattern produced in a normal ear, calculated over a short period of time, will resemble that found with unprocessed stimuli in an impaired ear. The effect of threshold elevation with loudness recruitment is simulated by filtering the stimuli into a number of frequency bands, and applying an expansive nonlinearity in each band independently. For details, see the earlier studies of Baer and Moore (1993, 1994), Moore and Glasberg (1993), Moore *et al.* (1995), and Nejime and Moore (1997).

In the present study, we simulated a flat cochlear hearing loss of 50 dB, assuming that all auditory filters were three times broader than normal. We refer to this as condition B3R2. We also simulated the effect of applying frequency-dependent linear amplification according to the NAL procedure (Byrne and Dillon, 1986) prior to the simulation of hearing loss; this is called condition B3R2+. The values for the NAL gain at each audiometric frequency are given in Table I.

II. EXPERIMENT

A. Processing conditions

Three expansion ratios (1.00, 1.25, 1.50) were tested. For the original speed (1.00), no processing was used for the speech-rate slowing. The stimuli were processed through the speech-rate slowing algorithm prior to processing in the simulation of hearing impairment.

B. Stimuli

The speech materials used were the 18 ASL sentence lists (MacLeod and Summerfield, 1990). Each list consists of 15 sentences, each of which contains three key words, spoken by a male talker of standard British English. The score for each list was always the percent of key words correct out of 45. The speech was presented, at the input of the speech-rate slowing process, at a root-mean-square (rms) level of 65 dB SPL. The speech-shaped noise was presented at levels of 65, 68, 71, and 74 dB for condition B3R2. For condition B3R2+, the levels used were 65, 68, and 71 dB. The sentences and noise were mixed prior to the speech-rate slowing processing. The noise began approximately 0.5 s before each sentence and ended just after the sentence. The output of the simulation was recorded with a 7-s interval between sentences, to allow for subject responses. A band of noise was recorded at the start of each tape for calibration of absolute levels.

The original speech was low-pass filtered at 7 kHz (Kemo VBF8/04, 90 dB/oct slope) and sampled with 12-bit resolution (Masscomp EF12M) at a 16-kHz rate. After processing through the speech-rate slowing and the hearing loss simulation on a UNIX workstation (Silicon Graphics Indy), the output had 16-bit resolution and was converted to a 48-kHz sampling rate, using a standard UNIX program for sampling frequency conversion, and recorded digitally on digital audio tape (DAT). The output of the DAT player was fed to a Quad model 34 preamplifier, whose volume control has discrete setting for precise reproducibility. The output of the preamplifier was fed to a Quad 306 power amplifier and a Monitor Audio MA4 loudspeaker. Subjects were tested in a double-walled sound-attenuating chamber. They sat facing the loudspeaker, at a distance of about 1 m. The walls of the chamber were lined with 100-mm-thick foam to reduce reflected sound. Sound levels were calibrated using a CEL 414/3 precision sound level meter (C-weighting), placed at the center of the position where the subject's head would be.

C. Subjects, design, and procedure

All subjects were self-assessed as having normal hearing and were native English speakers under 30 years old. They were paid for their services.

For condition B3R2, each of the three expansion ratios was tested using four complete ASL lists (one for each speech-to-noise ratio). The order of the lists was the same for each subject, but the order of the expansion ratios was counterbalanced across subjects using a Latin Square design. Prior to formal testing of a given condition, one complete list processed for that condition was given without noise, for
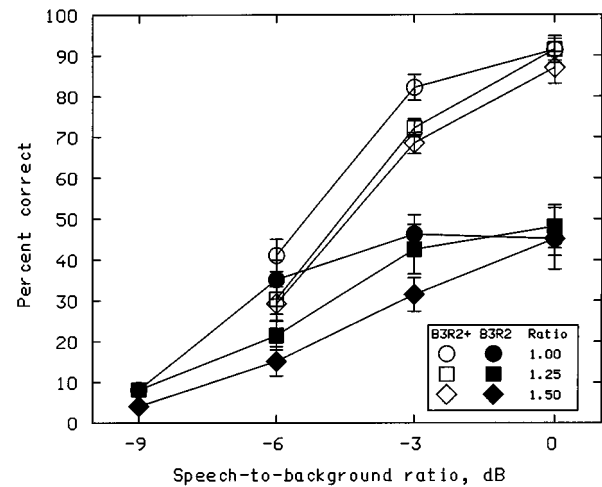

FIG. 1. Mean psychometric functions across the six subjects showing the percent correct as a function of speech-to-noise ratio for each condition and for each expansion rate. Error bars shows ± one standard error across subjects.

practice. Testing for that condition then began, starting with the highest speech-to-noise (S/N) ratio and ending with the lowest. Six subjects were tested using two 3×3 Latin Squares.

For condition B3R2+, where the stimuli were clearly audible, a preliminary test showed strong effects of the test order. Presumably, these reflect practice effects, as subjects became accustomed to the sound of the slowed speech. To reduce practice effects, each of the three expansion ratios was tested using six complete ASL lists (two for each speech-to-noise ratio), and only scores for the second list at each S/N ratio were taken. The order of the lists was the same for each subject, but the order of the expansion ratios was counterbalanced across subjects using a Latin Square design. Six subjects, who were not used for condition B3R2, were tested using two 3×3 Latin Squares. The procedure was the same as described in Nejime and Moore (1997).

D. Results

Figure 1 shows mean psychometric functions (percent correct as a function of speech-to-noise ratio) for each simulation condition and for all expansion ratios. Amplification according to the NAL formula produced marked improvements in performance for speech-to-noise ratios of −3 and 0 dB; compare the open and filled symbols. This is consistent with earlier results using the combined simulation (Nejime and Moore, 1997).

For both simulation conditions, speech-rate slowing did not produce any improvement in performance. Rather, performance for the slowed speech (expansion ratios of 1.25 and 1.50) tended to be worse than that for the original speech-rate (1.00). For condition B3R2 (without NAL amplification), the score for the original speech-rate (1.00) at the highest S/N ratio was not better than that for the expansion ratio of 1.25. However, this is largely due to the extremely low score of one subject at the original speech-rate. Overall, it seems that slowing the speech impaired performance, rather than improving it.

TABLE II. Fifty percent correct points and slopes of the probit functions for each subject and each expansion ratio in each simulation condition

	(a) Simulation condition=B3R2					
Expansion	1.00		1.25		1.50	
ratio Subject	50% point	slope	50% point	slope	50% point	slope
JM	0.64	0.082	1.68	0.118	−0.46	0.141
ET	−0.49	0.121	−0.48	0.152	−1.25	0.182
SM	−4.63	0.202	−3.62	0.208	−0.44	0.206
AJ	2.30	0.100	−1.52	0.147	2.99	0.158
RH	0.00	0.110	1.95	0.119	−0.36	0.218
AO	1.18	0.127	0.84	0.161	2.38	0.147
Mean	−0.17	0.124	−0.19	0.151	0.48	0.175
s.d.	2.39	0.042	2.13	0.033	1.75	0.032

	(b) Simulation condition=B3R2+					
Expansion	1.00		1.25		1.50	
ratio Subject	50% point	slope	50% point	slope	50% point	slope
GK	−4.23	0.267	−4.19	0.200	−4.00	0.338
IR	−6.12	0.208	−4.71	0.350	−3.80	0.408
DH	−6.69	0.282	−4.04	0.381	−4.24	0.299
MS	−5.26	0.354	−4.55	0.463	−4.46	0.156
CL	−4.86	0.288	−5.45	0.252	−3.86	0.289
SD	−5.78	0.462	−4.53	0.390	−5.68	0.294
Mean	−5.49	0.310	−4.58	0.339	−4.34	0.297
s.d.	0.89	0.088	0.49	0.097	0.70	0.082

For further analysis and comparison, the psychometric functions for each subject were fitted using probit analysis (Finney, 1971). This procedure gives estimates of the 50% correct points and of the slopes of the psychometric functions (in probit units). Table II(a) gives the 50% correct points and the slopes for each subject for each expansion ratio in condition B3R2, and Table II(b) gives them in condition B3R2+.

An analysis of variance (ANOVA) was conducted on the 50% points with factors subject and expansion ratio. The variance associated with the two-way interaction was used to estimate the residual variance. The GENSTAT package used gave an estimate of the standard error of the differences between means for the different conditions. This standard error was used to assess the significance of the differences between means using t tests and the degrees of freedom associated with the residual term in the analysis of variance (Lane *et al.*, 1987, p. 110).

For condition B3R2, the effect of subjects was not significant at the 0.05 level $[F(5,10)=2.99, p=0.066]$. The effect of expansion ratio was also not significant $[F(2,10)=0.32, p=0.732]$. A similar ANOVA was conducted on the slope values shown in Table II(a). The effect of subjects was significant $[F(5,10)=5.25, p=0.013]$, indicating that some subjects had shallower slopes overall than other subjects. The effect of expansion ratio was also significant $[F(2,10)=7.57, p=0.010]$. The slopes increased slightly with increasing expansion ratio, an effect which can be seen in Fig. 1. The deleterious effect of the expansion was more marked at speech-to-background ratios of −3 and −6 dB than at 0 dB.

For condition B3R2+, the effect of subjects on the 50% points was not significant $[F(5,10)=0.86, p=0.539]$. The effect of expansion ratio was just significant $[F(2,10)=4.14, p=0.049]$. The 50% point for the expansion ratio of 1.25 was significantly higher than that for the original speed ($p<0.05$), and the 50% point for the expansion ratio of 1.50 was also significantly higher than that for the original speed ($p<0.025$). This indicates that the speech-rate slowing had a significant deleterious effect. An ANOVA conducted on the slope values in Table II(b) showed that the effect of subjects was not significant $[F(5,10)=0.53, p=0.749]$. The effect of condition was also not significant $[F(2,10)=0.29, p=0.751]$.

III. DISCUSSION

The present experiment failed to show any benefit of speech-rate slowing on the simulated hearing loss. Although everyday experience suggests that slow speech is easier to understand, the artificial slowing produced by the algorithm was not effective in improving the intelligibility of speech. In our experiment, the intelligibility of the speech was reduced (relative to unprocessed speech in quiet) by the simulated hearing loss and by the speech-shaped background noise. These would both be expected to result in impoverished information about the speech. We hoped that the loss of information would be partly compensated by the use of context, and that this would be done more effectively with the slowed speech. However, the results suggest that subjects could not take advantage of the slower speech-rate to make more effective use of context.

It may be the case that clear benefits only occur for people with slower than normal cognitive processing abilities. However, we should remember that the speech materials used consisted of short sentences that were spoken rather slowly, and there were long gaps after each sentence for the subject to respond. Such a situation may not place a very heavy load on cognitive processing abilities. It is possible that benefits of speech-rate slowing might be found under more realistic conditions using longer sentences spoken more rapidly and with shorter times allowed for responses; this is more typical of what occurs in everyday life.

The reduction of performance produced by the speech-rate slowing suggests that there were some undesirable side effects of the processing. One possibility is that the processing introduced significant distortion and/or artifacts. Another is that the slowed speech sounded unnatural. Recall that time expansion was only applied to segments of the speech that were above a certain threshold. While this reduced distortion of the consonant portions of speech, its effects were different from those produced when a person actually speaks more slowly. Subjects may need prolonged listening experience to become used to the characteristics of the slowed speech. This idea is supported by the strong practice and order effects that were observed in the experiment.

IV. CONCLUSIONS

The effect of an algorithm for speech-rate slowing was examined. Three expansion ratios were tested: 1.00 (original

575   J. Acoust. Soc. Am., Vol. 103, No. 1, January 1998

Y. Nejime and B. C. J. Moore: Letters to the Editor   575

speed), 1.25, and 1.50. The intelligibility of speech in noise was measured using sounds processed to simulate cochlear hearing impairment. Linear amplification according to the NAL procedure was also implemented. The speech-rate slowing did not give any improvement in intelligibility of speech in noise. Rather, the slowing process had a deleterious effect on intelligibility. The results suggest that speech-rate slowing will not improve the intelligibility of speech in noise for hearing-impaired people who have the type of cochlear damage simulated in this test. However, the possibility remains that the slowing might be beneficial under conditions where there is less time for cognitive processing, for example, when sentences are longer. Also, the processing may prove beneficial for people with reduced speed of cognitive processing or reduced efficiency of cognitive processing, as can occur in the elderly.

ACKNOWLEDGMENTS

Baer, T., and Moore, B. C. J. (**1993**). ''Effects of spectral smearing on the intelligibility of sentences in the presence of noise,'' J. Acoust. Soc. Am. **94**, 1229–1241.

Baer, T., and Moore, B. C. J. (**1994**). ''Effects of spectral smearing on the intelligibility of sentences in the presence of interfering speech,'' J. Acoust. Soc. Am. **95**, 2277–2280.

Byrne, D., and Dillon, H. (**1986**). ''The National Acoustic Laboratories' (NAL) new procedure for selecting the gain and frequency response of a hearing aid,'' Ear Hear. **7**, 257–265.

Finney, D. J. (**1971**). *Probit Analysis* (Cambridge U.P., Cambridge, England).

Griffin, D. W., and Lim, J. S. (**1984**). ''Signal estimation from modified short-term Fourier transform,'' IEEE Trans. Acoust. Speech Signal Process. **ASSP-32**, 236–243.

Lane, P., Galwey, N., and Alvey, N. (**1987**). *Genstat 5. An Introduction* (Clarendon, Oxford).

MacLeod, A., and Summerfield, Q. (**1990**). ''A procedure for measuring auditory and audio-visual speech-reception thresholds for sentences in noise: rationale, evaluation, and recommendations for use,'' Br. J. Audiol. **24**, 29–43.

Malah, D. (**1979**). ''Time-domain algorithms for harmonic bandwidth reduction and time scaling of speech signal,'' IEEE Trans. Acoust. Speech Signal Process. **27**, 121–133.

Moore, B. C. J., and Glasberg, B. R. (**1993**). ''Simulation of the effects of loudness recruitment and threshold elevation on the intelligibility of speech in quiet and in a background of speech,'' J. Acoust. Soc. Am. **94**, 2050–2062.

Moore, B. C. J., Glasberg, B. R., and Vickers, D. A. (**1995**). ''Simulation of the effects of loudness recruitment on the intelligibility of speech in noise,'' Br. J. Audiol. **29**, 131–143.

Nejime, Y., Aritsuka, T., Imamura, T., Ifukube, T., and Matsushima, J. (**1996**). ''A portable digital speech-rate converter for hearing impairment,'' IEEE Trans. Rehab. Eng. **4**, 73–83.

Nejime, Y., and Moore, B. C. J. (**1997**). ''Simulation of the effect of threshold elevation and loudness recruitment combined with reduced frequency selectivity on the intelligibility of speech in noise,'' J. Acoust. Soc. Am. **102**, 603–615.

Picheny, M. A., Durlach, N. I., and Braida, L. D. (**1985**). ''Speaking clearly for the hard of hearing I: Intelligibility differences between clear and conversational speech,'' J. Speech Hear. Res. **28**, 96–103.

Picheny, M. A., Durlach, N. I., and Braida, L. D. (**1986**). ''Speaking clearly for the hard of hearing II: Acoustic characteristics of clear and conversational speech,'' J. Speech Hear. Res. **29**, 434–446.

Picheny, M. A., Durlach, N. I., and Braida, L. D. (**1989**). ''Speaking clearly for the hard of hearing III: An attempt to determine the contribution of speaking rate to differences in intelligibility between clear and conversational speech,'' J. Speech Hear. Res. **32**, 600–603.

Roucos, S., and Wilgus, A. M. (**1985**). ''High quality time-scale modification for speech,'' in *Proceedings of the IEEE International Conference on Acoustics, Speech and Signal Processing (ICASSP), Tampa, FL* (IEEE, New York), pp. 493–496.

Suzuki, R., and Misaki, M. (**1992**). ''Time-scale modification of speech signals using cross-correlation functions,'' IEEE Trans. Consumer Electronics **38**, 357–363.

Uchanski, R. M., Choi, S. S., Braida, L. D., Reed, C. M., and Durlach, N. I. (**1996**). ''Speaking clearly for the hard of hearing IV: Further studies of the role of speaking rate,'' J. Speech Hear. Res. **39**, 494–509.

van Rooij, J. C. G. M., and Plomp, R. (**1992**). ''Auditive and cognitive factors in speech perception by elderly listeners. III. Additional data and final discussion,'' J. Acoust. Soc. Am. **91**, 1028–1033.

Speech reception thresholds in noise with and without spectral and temporal dips for hearing-impaired and normally hearing people

Robert W. Peters
Division of Speech and Hearing Sciences, Department of Medical Allied Health Professions,
The School of Medicine and Department of Psychology, The University of North Carolina at Chapel Hill,
Chapel Hill, North Carolina 27599-7190

Brian C. J. Moore and Thomas Baer
Department of Experimental Psychology, University of Cambridge, Downing Street, Cambridge CB2 3EB,
England

People with cochlear hearing loss often have considerable difficulty in understanding speech in the presence of background sounds. In this paper the relative importance of spectral and temporal dips in the background sounds is quantified by varying the degree to which they contain such dips. Speech reception thresholds in a 65-dB SPL noise were measured for four groups of subjects: (a) young with normal hearing; (b) elderly with near-normal hearing; (c) young with moderate to severe cochlear hearing loss; and (d) elderly with moderate to severe cochlear hearing loss. The results indicate that both spectral and temporal dips are important. In a background that contained both spectral and temporal dips, groups (c) and (d) performed much more poorly than group (a). The signal-to-background ratio required for 50% intelligibility was about 19 dB higher for group (d) than for group (a). Young hearing-impaired subjects showed a slightly smaller deficit, but still a substantial one. Linear amplification combined with appropriate frequency-response shaping (NAL amplification), as would be provided by a well-fitted ''conventional'' hearing aid, only partially compensated for these deficits. For example, group (d) still required a speech-to-background ratio that was 15 dB higher than for group (a). Calculations of the articulation index indicated that NAL amplification did not restore audibility of the whole of the speech spectrum when the speech-to-background ratio was low. For unamplified stimuli, the SRTs in background sounds were highly correlated with absolute thresholds, but not with age. For stimuli with NAL amplification, the correlations of SRTs with absolute thresholds were lower, but SRTs in backgrounds with spectral and/or temporal dips were significantly correlated with age. It is proposed that noise with spectral and temporal dips may be especially useful in evaluating possible benefits of multi-channel compression. © *1998 Acoustical Society of America.* [S0001-4966(97)04812-1]

INTRODUCTION

People with cochlear hearing impairment often complain that their greatest problem is understanding speech when background noise is present. This problem is often quantified in the laboratory by estimating the speech-to-noise ratio required to achieve a given level of intelligibility, such as 50%. We will refer to this ratio as the Speech Reception Threshold (SRT), and will express it in decibels (dB).

For people with moderate to severe cochlear losses, the SRT typically is higher than for normally hearing people. In other words, the hearing impaired need a higher signal-to-noise ratio to achieve the same level of performance. However, the difference in SRT for normal and hearing-impaired people varies greatly depending on the nature of the background sound. When the background sound is a steady noise with the same long-term average spectrum as the speech (called speech-shaped noise), the difference is typically in the range 2–5 dB (Glasberg and Moore, 1989; Plomp, 1994). This represents a substantial deficit, since intelligibility in this situation worsens by 11% to 19% for each 1-dB decrease

in speech-to-noise ratio (Plomp and Mimpen, 1979; Laurence *et al.*, 1983; Moore *et al.*, 1992; Nilsson *et al.*, 1994). When the background is a single competing talker (Carhart and Tillman, 1970; Duquesnoy, 1983; Hygge *et al.*, 1992; Moore *et al.*, 1995), a time-reversed talker (Duquesnoy, 1983), or an amplitude-modulated noise (Duquesnoy, 1983; Takahashi and Bacon, 1992; Eisenberg *et al.*, 1995), the difference in SRT between normal and hearing-impaired people can be much larger, ranging from about 7 dB up to about 15 dB. This represents a very large deficit indeed. At signal-to-background ratios where normally hearing people would achieve almost 100% intelligibility, hearing-impaired people may be understanding almost nothing. Thus, the problems faced by hearing-impaired people, in comparison to normally hearing people, are much greater when the background sound is a single talker than when it is a steady speech-shaped noise.

Normally hearing people achieve markedly lower SRTs in a background of a single talker than in a background of speech-shaped noise, whereas hearing-impaired people do

not (Duquesnoy, 1983; Festen, 1987a, b; Festen and Plomp, 1990; Hygge *et al.*, 1992; Moore *et al.*, 1995). The relatively poor performance of hearing-impaired people when listening in a background of a single talker appears to arise from a failure to take advantage of ''dips'' in the competing voice. These dips may be of two types: temporal and spectral. The temporal dips arise because there are moments when the overall level of the competing speech is low, for example during brief pauses in the speech or during production of low-energy sounds such as m, n, k, or p. During these temporal dips the signal-to-background ratio is high, and this allows brief ''glimpses'' to be obtained of the target speech. The spectral dips arise because the spectrum of the target speech is usually different from that of the background speech measured over any short interval. Although parts of the target spectrum may be completely masked by the background, other parts may be hardly masked at all; the signal-to-background ratio may often exceed 20 dB. Thus, parts of the spectrum of the target speech may be ''glimpsed'' and used to infer the structure of the complete speech sound.

The reasons why hearing-impaired people fail to take advantage of the dips in the background noise are not clearly understood. Specifically, it is not clear whether the problem arises mainly from a failure to take advantage of temporal dips or from a failure to take advantage of spectral dips. People with cochlear hearing loss generally show impaired temporal resolution for stimuli with slowly fluctuating envelopes which would lead to a reduced ability to take advantage of temporal dips (Festen, 1987a, b; Glasberg *et al.*, 1987; Moore and Glasberg, 1988b; Festen and Plomp, 1990; Glasberg and Moore, 1992; Festen, 1993; Moore, 1995). They also show reduced frequency selectivity, which would lead to a reduced ability to take advantage of spectral dips (Glasberg and Moore, 1986; Tyler, 1986; Moore, 1995).

The main goal of this paper is to clarify and quantify the relative importance of spectral and temporal processing for the ability to understand speech in background sounds with temporal and spectral dips, such as a single competing talker. This was done by measuring SRTs in several background sounds, which varied in the extent to which they contained temporal dips, spectral dips, or a combination of the two. Both normally hearing and hearing-impaired subjects were used. In experiment 1, the stimuli were presented without any frequency response shaping. In experiment 2, the hearing-impaired subjects were tested with a frequency-gain characteristic corresponding to the National Acoustics Laboratories' recommendation (Byrne and Dillon, 1986).

I. EXPERIMENT 1

A. Method

1. Subjects

Four groups of subjects were tested:

(a) Ten young subjects (mean age 25.1 years, s.d. 3.3 years) with normal hearing. The absolute thresholds of all subjects were better than 20 dB HL at all of the standard audiometric frequencies (125, 250, 500, 1000, 2000, 4000, 6000, and 8000 Hz) and average thresholds were close to 0 dB HL.

(b) Eleven elderly subjects (mean age 74.1 years, s.d. 3.2 years) with near-normal hearing for frequencies up to 4 kHz. The mean absolute thresholds for this group were 9.5, 9.1, 11.4, and 21.0 dB HL for the frequencies 500, 1000, 2000, and 4000 Hz, respectively. Two of these subjects had hearing losses greater than 30 dB at 4 kHz. Excluding these two subjects, the mean absolute threshold at 4 kHz was 17.4 dB HL. The data for this group were analyzed both including and excluding these two subjects. Most of the 11 subjects had mild losses (10–45 dB) at frequencies above 4000 Hz.

(c) Six young hearing-impaired subjects (mean age 29.2 years, s.d. 9.4 years). Five had moderate to severe cochlear hearing loss and one (S4) had only a mild loss. The data for this group were analyzed both including and excluding the subject with a mild loss.

(d) Ten elderly subjects (mean age 76.5 years, s.d. 4.2 years) with moderate to severe cochlear hearing loss.

The elderly subjects were all alert, able to follow instructions, and able to concentrate. The audiograms of the subjects in groups (c) and (d) are shown in Fig. 1.

2. Stimuli

The speech materials used were the sentence lists recorded at the House Ear Institute in Los Angeles (the Hearing in Noise Test—HINT) (Nilsson *et al.*, 1994). The following background sounds were used:

(1) A steady speech-shaped noise with the same long-term average spectrum as the target speech (referred to as HINT noise). This provided a reference condition against which SRTs in other types of noise can be compared. The spectrum of this noise is shown by the dashed line in Fig. 2.

(2) A single competing female talker. This sound was taken from a compact disc (CD) of test sounds recorded by ReSound Corporation. The passage lasts approximately 1 min. For our tests, the sample was recycled, to give a continuous sample about 7 min in length. This background has both spectral and temporal dips, as described earlier. The speech was digitally filtered so that its long-term average spectrum matched that of the HINT noise. The result is shown as the solid line in Fig. 2.

(3) A noise with the same spectrum as the HINT noise, but with the overall temporal fluctuations of the single talker. This was achieved by extracting the envelope of the speech of the single female talker, and imposing that envelope on the HINT noise. The envelope was extracted by calculating the root-mean-square amplitude of the speech in a 10-ms-long sliding temporal window. We refer to this noise as ''noise modulated by speech.''

(4) Steady HINT noise filtered so as to have spectral dips in several frequency regions. The filtering was based on the equivalent-rectangular-bandwidth (ERB) scale derived from the auditory filter bandwidths for normally hearing subjects (Glasberg and Moore, 1990). Each ERB represents one auditory filter bandwidth. The relationship between number of ERBs and frequency is

$$\text{ERB number} = 21.4 \log_{10}(4.37F + 1), \qquad (1)$$

where F is frequency in kHz.

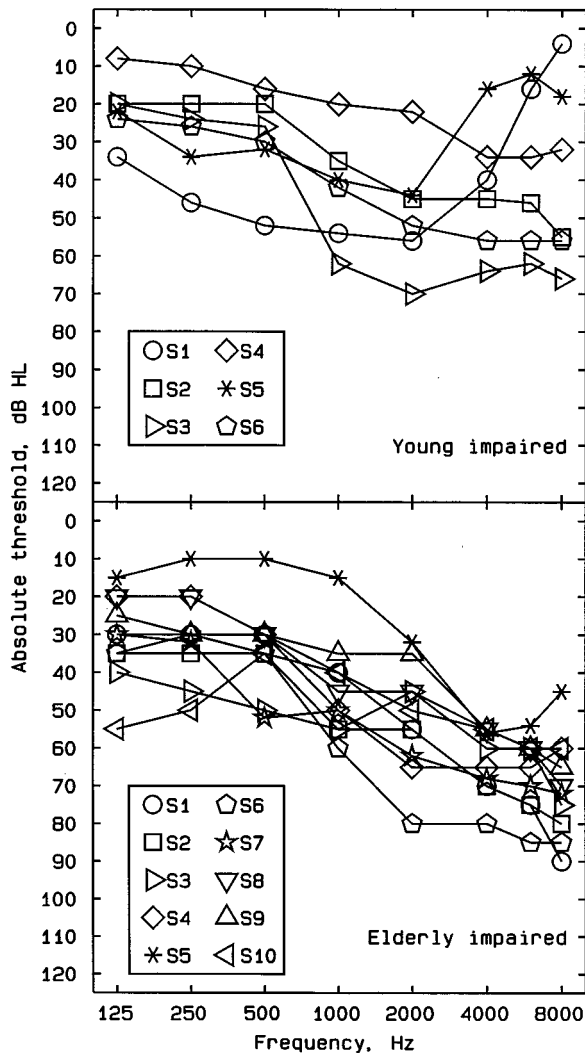The noise was filtered in a number of ways:

FIG. 1. Audiograms for each subject in the young hearing-impaired group (top) and the elderly hearing-impaired group (bottom).
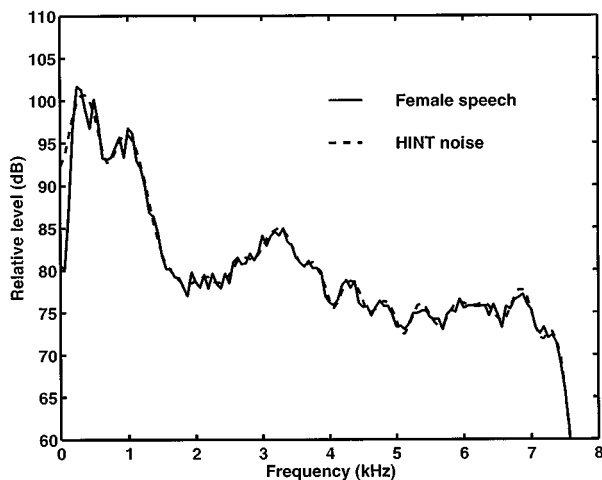

FIG. 2. The dashed line shows the long-term average spectrum of the HINT noise. The solid line shows the long-term average spectrum of the female talker after filtering to match the spectrum to that of the HINT noise.
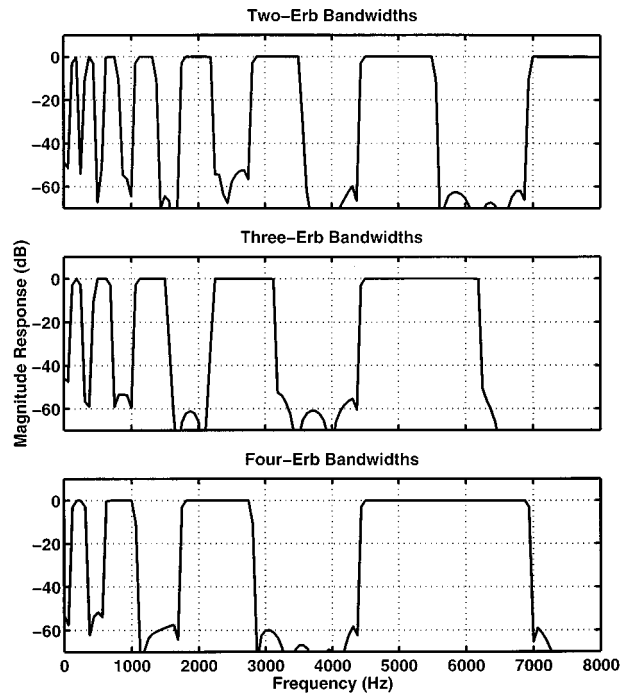

FIG. 3. Characteristics of the digital filters used to produce the noises with multiple spectral notches.

(a) with an alternating pattern of two ERBs present and two ERBs removed,

(b) with an alternating pattern of three ERBs present and three ERBs removed, and

(c) with an alternating pattern of four ERBs present and four ERBs removed.

The characteristics of the digital filters used are illustrated in Fig. 3. The filters were designed using the function fir2 in MATLAB (Krauss *et al.*, 1994) with an *n* of 800. Prior to filtering, the last 400 samples of the source file were appended to its beginning, and the first 400 samples were appended to its end. After filtering, the first 800 samples were discarded, eliminating both filtering onset transients and delays. We anticipated that normally hearing subjects should be able to take advantage of the relatively narrow spectral dips in the noise with 2-ERB spectral gaps. However, hearing-impaired subjects generally have reduced frequency selectivity and so we thought that they might not be able to take advantage of the spectral dips until they became relatively wide (spectral gaps of three and four ERBs).

(5) A noise with both spectral and temporal dips obtained by applying the temporal envelope of a single talker to a speech shaped noise [as in (3)] and then filtering that noise [as in (4)].

The overall level of backgrounds (1)–(3) was always the same for a given subject (usually 65 dB SPL). For backgrounds (4) and (5), the spectrum level of the noise in the passbands of the digital filters was left the same as for the original HINT noise. Thus, the overall level of the noise was slightly reduced by the filtering (by about 3 dB). This was done so that we could examine benefits of removing part of the background spectrum without the confounding effect of increases in level of the remaining part of the spectrum.

Peters *et al.*: Intelligibility in noise   579

TABLE I. Mean SRTs in quiet and in various masking conditions for the four groups of listeners. The SRTs in quiet are expressed as level in dB SPL. The SRTs for the masking conditions are expressed as speech-to-background ratios in dB. A smaller number indicates better performance. Numbers in parentheses are standard deviations across subjects. For the older subjects with near-normal hearing, the upper numbers refer to results for the whole group and the lower numbers refer to results excluding two subjects whose absolute thresholds at 4 kHz exceeded 30 dB HL. For the young hearing-impaired subjects, the upper numbers refer to results for the whole group and the lower numbers refer to results excluding one subject with a mild loss.

	Young normal hearing $N=10$	Older normal hearing $N=11$ $(N=9)$	Young hearing impaired $N=6$ $(N=5)$	Older hearing impaired $N=10$
Speech in quiet	19.7 (2.2)	29.9 (3.8) 29.8 (3.5)	51.8 (10.3) 55.0 (8.0)	57.5 (5.9)
Steady noise masker	−3.8 (2.0)	−2.0 (1.9) −2.2 (2.1)	−1.4 (3.0) −0.6 (2.5)	2.5 (2.2)
Single voice masker	−11.9 (2.8)	−7.7 (2.9) −8.2 (2.9)	−6.1 (3.7) −4.7 (0.9)	0.8 (2.8)
Noise modulated by speech	−10.0 (2.5)	−6.3 (2.2) −6.9 (1.9)	−4.1 (3.3) −2.8 (1.2)	1.5 (1.9)
Noise with two-ERB gaps	−12.5 (1.9)	−8.9 (2.1) −9.4 (2.1)	−6.1 (3.2) −5.1 (2.1)	−0.4 (1.5)
Noise with three-ERB gaps	−16.1 (1.9)	−10.9 (3.1) −11.6 (3.0)	−6.6 (2.8) −5.7 (1.9)	−1.1 (1.4)
Noise with four-ERB gaps	−18.7 (1.7)	−12.6 (2.1) −13.0 (2.1)	−7.1 (2.7) −6.2 (1.8)	−2.1 (1.7)
Modulated noise with two-ERB gaps	−16.5 (1.8)	−12.3 (4.2) −13.5 (3.6)	−7.1 (2.7) −6.0 (0.7)	−1.8 (2.4)
Modulated noise with three-ERB gaps	−17.9 (2.9)	−13.7 (3.2) −14.5 (2.7)	−6.4 (4.6) −5.0 (3.2)	−2.0 (1.8)
Modulated noise with four-ERB gaps	−22.6 (2.6)	−15.7 (2.9) −16.5 (2.5)	−8.5 (3.7) −7.2 (2.3)	−3.1 (2.5)

tBackground sounds (2)–(5) were produced by digital processing using a Silicon Graphics Indy computer. All processing was done using a 16-kHz sampling rate and floating point arithmetic. When processing was complete, samples were converted to 16-bit integers and up-sampled to a 44.1-kHz rate. They were transferred digitally to recordable compact disc (CDR) for use in the experiment. The speech was played back from digital audio tape (DAT). The target speech and background sounds were independently amplified and their levels were controlled by independent manual attenuators. The outputs of the attenuators were mixed using an active mixer. The stimuli were presented to the better hearing ear, or to the left ear if the audiograms were very similar for the two ears, using Sennheiser HD 424 earphones, which have a ''diffuse field'' response.

For the young normally hearing subjects and the elderly subjects with near-normal hearing, backgrounds (1)–(3) were presented at an overall level of 65 dB SPL, which is close to the level of normal conversational speech [as described above, backgrounds (4) and (5) had slightly lower overall levels]. For the hearing-impaired subjects the level of presentation depended on the SRT in quiet. If the SRT in quiet was 55 dB SPL or less, then the presentation level was 65 dB SPL. If the SRT in quiet was greater than 55 dB SPL, the presentation level was the SRT in quiet plus 10 dB.

3. Procedure

An adaptive procedure was used to estimate the SRT in each background noise. The SRTs for speech in quiet were also measured. The adaptive procedure was as recommended for use with the HINT materials (Nilsson *et al.*, 1994). Each SRT reported is based on the use of two complete lists. Prior

to testing, practice was given with the steady noise background, the background with four-ERB spectral dips, and the background with four-ERB spectral dips and temporal dips, using lists 26–28. Testing started with measurement of SRTs in quiet. Then the conditions with background noise were tested, using a different randomized order for each subject. Subjects were seated in a single-walled sound-attenuating booth situated within the testing room. Subjects communicated with the tester via a microphone located in the sound-attenuating chamber.

B. Results

The results obtained are summarized in Table I. The SRTs in quiet are expressed as level in dB SPL. The SRTs in background sounds are expressed as signal-to-background ratios in dB. Lower numbers indicate better performance. For group (b) (elderly subjects with near normal hearing), the upper figure in each row shows results for the whole group, and the lower figure shows results excluding the two subjects whose absolute thresholds at 4 kHz exceeded 30 dB HL. For group (c) (young hearing-impaired subjects), the upper figure in each row shows results for the whole group, and the lower figure shows results excluding the subject with a mild loss.

Consider first the results for the young normally hearing subjects. The mean SRT in quiet is similar to what has been observed in previous studies (Moore and Glasberg, 1993; Nilsson *et al.*, 1994). The highest (poorest) mean SRT with background noise occurs for the steady noise masker (HINT noise). The mean SRT decreases by about 8 dB for the background of a single talker, which is consistent with earlier

work, as reviewed in the introduction. The mean SRT for the noise modulated by speech is 6.2 dB lower than for the steady noise but 1.9 dB higher than for the single talker. This indicates that the temporal dips in the single talker are of major importance, but that spectral dips also play some role. The difference in SRT between the single talker and the modulated noise is unlikely to be due to the fact that the background speech was meaningful; Duquesnoy (1983) showed that SRTs were similar for a background of speech and time-reversed speech. Introducing spectral dips in the steady noise leads to improved performance, and the improvement increases as the width of the spectral dips increases. This confirms that normally hearing subjects are able to take advantage of spectral dips in background sounds. Finally, introducing spectral dips into the noise modulated by speech results in yet further decreases in the SRTs. For the modulated noise with four-ERB gaps, the mean SRT is about 19 dB lower than for the steady HINT noise. This illustrates the very large advantage of listening in spectral and temporal dips that can be obtained by normally hearing subjects.

Consider next the results for the elderly subjects with near-normal hearing. Generally, the pattern of results is similar to that obtained for the young normally hearing subjects. However, the elderly subjects appear to take slightly less advantage of spectral and temporal dips. This may partly reflect the fact that their absolute thresholds were *slightly* higher than for the young subjects, especially at high frequencies. The reduced absolute sensitivity is reflected in the SRT in quiet, which is, on average, about 10 dB higher for the elderly subjects than for the young subjects. Mean SRTs for the speech in background sounds are slightly but consistently lower when the results for the two subjects with a slight hearing loss at high frequencies are excluded. Thus, even this mild hearing loss was sufficient to produce some elevation of the SRTs. Although ''dip listening'' is somewhat reduced in the elderly subjects, its effects are still substantial. For the modulated noise with four-ERB gaps, the mean SRTs are about 14 dB lower than for the steady HINT noise.

We consider the results for the two groups of hearing-impaired subjects together, as the pattern of results was similar. Overall, the elderly subjects performed somewhat more poorly than the young subjects, which may reflect the fact that the elderly subjects had slightly greater hearing losses, on average. This is consistent with the average SRTs in quiet, which were 51.8 dB for the young subjects and 57.5 dB for the elderly subjects. The young subject with the mild hearing loss performed consistently better than the remaining young hearing-impaired subjects. Hence, the mean SRTs for the young hearing-impaired group were consistently higher (and the s.d.s were smaller) when the data for the subject with the mild loss were excluded, although the SRTs remained below those for the elderly group. The SRTs were somewhat lower for the background of a single talker than for the steady HINT noise, but the difference was less than for the normally hearing subjects, indicating a reduced ability to take advantage of spectral and/or temporal dips. The SRTs in the noise modulated by speech were only 1–3 dB lower than for the steady noise, indicating a limited ability to

take advantage of temporal dips. Thresholds in the steady noise with two-ERB gaps were only 3–5 dB lower than in the steady HINT noise with no spectral gaps, which is close to what would be expected from the slightly lower overall level of the noise with spectral gaps. Thus, for this noise, there was very little advantage of the spectral gaps. The SRTs decreased by only 1–2 dB when the width of the spectral gaps was increased from two to four ERBs, indicating a very limited ability to take advantage of spectral dips. The SRTs for the noises with both spectral and temporal dips were much higher than normal. For example, for the modulated noise with four-ERB gaps, the SRTs for the young hearing-impaired subjects were 14–16 dB higher than for the young normally hearing subjects (depending on whether the subject with the mild loss was included), while the SRTs for the elderly hearing-impaired subjects were 12–13 dB higher than for the elderly subjects with near-normal hearing.

To assess the statistical significance of the effects described above, an analysis of variance (ANOVA) was conducted with group as a between-subjects factor and type of background as a within-subjects factor. The main effect of group was highly significant [$F(3,33) = 79.9$, $p < 0.001$]. The main effect of type of background was also significant [$F(8,264) = 149.6$, $p < 0.001$]. Finally, the interaction of group and type of background was highly significant [$F(24,264) = 11.9$, $p < 0.001$]. This confirms that the decrease in SRT produced by the spectral and temporal dips varied across groups; the decrease was greatest for the young normally hearing group and smallest for the elderly hearing-impaired group.

To examine possible interrelationships between audiometric thresholds, age, and the SRTs, correlations between these variables were determined for each group separately and for the combined results of groups (b)–(d), i.e., for all subjects with some degree of hearing loss. The audiometric thresholds were quantified by taking various averages, either weighting low and high frequencies equally, or giving more emphasis to high frequencies. The averages used were: 0.5, 1, and 2 kHz; 1, 2, and 4 kHz; and 2 and 4 kHz. The only case in which age was correlated with the SRTs in quiet or in noise was for the elderly group with near-normal hearing, where correlations ranged from 0.27 to 0.67. These correlations decreased, and were nonsignificant for all backgrounds except one (the steady noise with four-ERB gaps) when the mean absolute threshold at 2 and 4 kHz was partialled out. For groups (b)–(d) taken together, age was not significantly correlated with the SRTs in quiet or in any of the background noises; the maximum correlation was 0.25. It appears then, that age *per se* is only weakly related to SRTs in the various background noises. This is consistent with the finding of van Rooij and Plomp (1992) that almost all of the systematic variance in SRTs in noise for elderly subjects can be accounted for by the audiogram alone. They concluded that age differences in speech perception are probably mainly due to differences in auditory rather than cognitive factors.

In what follows, we will concentrate on the correlations for groups (b)–(d) taken together ($n = 27$). Table II shows the correlation of the SRTs with the audiometric measures. All of the correlations were significant at $p < 0.01$. The SRTs

TABLE II. Correlation of the SRTs with various averages of the audiometric thresholds for the combined results of groups (b)–(d).

| | Average | | |
	0.5, 1, and 2 kHz	1, 2, and 4 kHz	2 and 4 kHz
Speech in quiet	0.95	0.94	0.93
Steady noise masker	0.52	0.58	0.61
Single voice masker	0.67	0.67	0.69
Noise modulated by speech	0.70	0.75	0.77
Noise with two-ERB gaps	0.71	0.76	0.79
Noise with three-ERB gaps	0.71	0.78	0.82
Noise with four-ERB gaps	0.79	0.84	0.87
Modulated noise with two-ERB gaps	0.73	0.74	0.75
Modulated noise with three-ERB gaps	0.76	0.82	0.84
Modulated noise with four-ERB gaps	0.79	0.83	0.85

TABLE III. As Table I except that NAL amplification was applied to all stimuli and results are presented only for the young hearing-impaired and older hearing-impaired groups.

	Young hearing impaired $N=6$ ($N=5$)	Older hearing impaired $N=10$
Speech in quiet	39.1 (7.4) 40.1 (8.0)	42.6 (6.5)
Steady noise masker	−1.2 (1.4) −0.6 (0.6)	1.0 (2.7)
Single voice masker	−8.4 (3.7) −7.9 (3.8)	−1.9 (2.5)
Noise modulated by speech	−5.4 (2.1) −4.9 (1.9)	−1.4 (1.7)
Noise with two-ERB gaps	−6.1 (3.5) −4.8 (1.7)	−3.7 (2.1)
Noise with three-ERB gaps	−7.7 (2.4) −4.8 (2.1)	−3.9 (1.9)
Noise with four-ERB gaps	−10.0 (3.1) −7.1 (2.8)	−4.9 (2.0)
Modulated noise with two-ERB gaps	−9.2 (3.6) −8.4 (3.3)	−5.6 (2.8)
Modulated noise with three-ERB gaps	−10.6 (3.5) −9.7 (3.1)	−5.8 (2.9)
Modulated noise with four-ERB gaps	−11.4 (4.9) −10.1 (4.1)	−7.2 (2.4)

in quiet were highly correlated with all of the audiometric measures, consistent with the idea that the audibility of the speech was the primary factor limiting performance. The SRTs in the steady HINT noise were only modestly correlated with the audiometric measures. This is consistent with the idea that audibility was less important for SRTs in steady noise, since performance was determined mainly by the higher-level portions of the speech which were generally well above absolute threshold. The correlations of the SRTs in quiet and in steady noise with the absolute thresholds are similar to those that have been reported in other studies (Dreschler and Plomp, 1980; Dreschler and Plomp, 1985; Glasberg and Moore, 1989).

For the noises where listening in temporal or spectral dips was assumed to be important, the SRTs were rather highly correlated with the absolute thresholds, and especially with the absolute thresholds at high frequencies (average of 2 and 4 kHz). This could be taken as indicating that the audibility of information in the spectral and temporal dips was of major importance. However, it could also have occurred partly because other factors, such as frequency selectivity, are correlated with the absolute threshold (Pick et al., 1977; Glasberg and Moore, 1986; Moore, 1995). The role of audibility will be examined in more detail later.

To summarize: hearing-impaired subjects gained much less advantage than normally hearing subjects from spectral and temporal dips in background sounds. The noise containing both spectral and temporal dips revealed very considerable differences between normally hearing and hearing-impaired subjects. Thus, this noise provides a potentially very sensitive way of evaluating the effects of signal processing such as frequency-selective amplification and compression.

II. EXPERIMENT 2

A. Method

In this experiment, we examined the extent to which the reduced dip-listening abilities of the hearing-impaired subjects could be restored by improving audibility via linear amplification. In experiment 1, the portions of the target speech in spectral and temporal dips may have had levels so low that the hearing-impaired subjects were not able to make use of them. To compensate for the loss of audibility in the hearing-impaired subjects, the stimuli were subjected to the frequency-gain characteristic prescribed by the NAL (revised) procedure (Byrne and Dillon, 1986). For brevity, we will refer to this as NAL amplification. Subjects were subdivided into five groups on the basis of the pattern and severity of their hearing loss, and the NAL characteristic for each group was calculated on the basis of the average audiometric thresholds for each subgroup. The gain recommended by the NAL procedure ranged from −1–12 dB at 500 Hz and from 14–29 dB at 4 kHz. The required frequency-selective amplification was implemented by digital filtering in real time using a Tucker-Davis AP2 array processor. Speech and background noise stimuli were filtered separately and recorded on DAT. The background noises were presented with a nominal ''input'' level (before NAL amplification) of 65 dB SPL.

Other aspects of the stimuli and procedure were the same as for experiment 1. Only subject groups (c) young hearing-impaired and (d) elderly hearing-impaired were tested. The subjects in each group were the same as for experiment 1.

B. Results

The results are given in Table III. Consider first the SRTs in quiet. The NAL amplification reduced the mean SRT by 13–15 dB for the young subjects (depending on whether the subject with the milder loss was included) and by 14.9 dB for the elderly subjects. The mean SRT for both groups remained above that for the young subjects with normal hearing (Table I), which is not surprising since the frequency-gain characteristics prescribed by the NAL procedure provided only partial compensation for the hearing loss (see the Discussion section). Nevertheless, the ''aided''

SRTs are well below the level of normal conversational speech, which is about 65 dB SPL (Pearsons *et al.*, 1976).

Consider now the SRTs in the presence of background sounds. The NAL amplification had very little effect for the steady HINT noise, reducing the mean SRT (relative to that measured in experiment 1) by 0 to -0.2 dB for the young group and by 1.5 dB for the elderly group. This seems reasonable, since in this noise the low-level portions of the speech would be masked even when linear amplification was applied; only the higher level portions of the speech would have contributed to intelligibility and these were mostly above absolute threshold even without amplification (as in experiment 1).

The NAL amplification improved the mean SRT in modulated noise by about 1–3 dB for both groups, indicating that it partially restored the ability to make use of temporal dips. However, performance with this noise remained well below that for the young normally hearing group (Table I). The NAL amplification produced an improvement in the mean SRT of about 2–3 dB for the single talker background. The fact that the improvement was similar for these two backgrounds suggests that the NAL amplification did not markedly improve the ability to listen in the spectral dips of the single talker.

For the steady noises with spectral gaps, NAL amplification led to modest decreases in mean SRT ranging up to 3 dB. For the modulated noises with spectral gaps, the improvement was somewhat larger, ranging from 2–5 dB. However, the SRTs remained well above the values for the young normally hearing subjects. For example, the mean SRT in the modulated noise with four-ERB spectral gaps was 11.2 dB higher for the young hearing-impaired group with NAL amplification than for the young normally hearing group (12.5 dB higher excluding the subject with the mild loss). For the same noise, the mean SRT for the elderly hearing-impaired group was 15.4 dB higher than for the young normally hearing group and 8.5 dB higher than for the elderly group with near-normal hearing.

To assess the statistical significance of the effects described above, an analysis of variance (ANOVA) was conducted with group as a between-subjects factor and type of background as a within-subjects factor. The main effect of group was significant [$F(1,14)=12.95$, $p=0.003$], the elderly impaired group having higher SRTS than the young impaired group. The main effect of type of background was also significant [$F(8,112)=39.5$, $p<0.001$]. Finally, the interaction of group and type of background was just significant [$F(8,112)=2.25$, $p=0.03$]. This reflects the finding that the decrease in SRT produced by the spectral and temporal dips was greater for the young group than for the elderly group.

As in experiment 1, correlations were determined between the audiometric thresholds, ages, and the SRTs. Within each group, age did not correlate significantly with the SRTs in background sounds. However, for both groups combined, some significant correlations with age did occur. Age was not significantly correlated with the SRT in quiet ($r=0.27$) or in steady HINT noise ($r=0.39$). However, age was moderately correlated with the SRTs in backgrounds

TABLE IV. Correlation of the SRTs with various averages of the audiometric thresholds for the combined results of groups (c) and (d) using stimuli with NAL amplification.

	Average		
	0.5, 1, and 2 kHz	1, 2, and 4 kHz	2 and 4 kHz
Speech in quiet	0.62	0.43	0.39
Steady noise masker	0.33	0.26	0.23
Single voice masker	0.50	0.35	0.32
Noise modulated by speech	0.43	0.33	0.33
Noise with two-ERB gaps	0.59	0.40	0.32
Noise with three-ERB gaps	0.44	0.34	0.35
Noise with four-ERB gaps	0.39	0.23	0.21
Modulated noise with two-ERB gaps	0.58	0.37	0.34
Modulated noise with three-ERB gaps	0.61	0.47	0.48
Modulated noise with four-ERB gaps	0.53	0.32	0.30

with spectral and/or temporal dips. Furthermore, several of these correlations remained significant when the effects of absolute threshold were partialled out. Considering the case where the mean absolute threshold at 0.5, 1, and 2 kHz was partialled out, significant partial correlations were obtained between age and the SRT in a single talker background ($r=0.83$, $p<0.001$), in noise modulated by speech ($r=0.74$, $p<0.001$), in unmodulated noise with three- and four-ERB gaps ($r=0.65$, $p<0.01$ and $r=0.78$, $p<0.001$), and in modulated noise with two-, three- and four-ERB gaps ($r=0.54$, $p<0.05$; $r=0.70$ $p<0.01$; and $r=0.53$, $p<0.05$, respectively). It appears that when reduced audibility is partially compensated for by NAL amplification, age may play a significant role when the background contains spectral and/or temporal dips.

The correlations of the SRTs with the audiometric thresholds are shown in Table IV for the combined results of both groups. The correlations were markedly lower than for stimuli without NAL amplification (Table II), consistent with the idea that NAL amplification partially compensates for loss of audibility. When the contribution of audibility is reduced, other suprathreshold factors, such as reduced frequency selectivity, and individual differences in cognitive factors, may play a greater role.

In summary, NAL amplification only partially compensated for the relatively poor performance of the hearing-impaired subjects when listening to speech in noises with spectral and temporal dips. The SRTs in noises with temporal modulation and spectral dips were improved by 2–5 dB by the NAL amplification, but remained 7–15 dB higher than for young normally hearing subjects. The SRTs for speech in background noise with spectral and/or temporal dips were correlated with age, suggesting a possible role for cognitive factors that decline with age.

III. ASSESSING THE ROLE OF AUDIBILITY

It remains unclear whether the failure of NAL amplification to restore performance to normal reflects deficits in suprathreshold processing, perhaps related to reduced fre-

quency selectivity and/or temporal resolution, or whether the failure occurred because NAL amplification was not sufficient to restore audibility to normal. Even with NAL amplification, part of the speech spectrum may have been below absolute threshold. To clarify this issue we calculated the articulation index (AI) for stimuli at the measured SRTs, taking into account the absolute thresholds of the subjects, the speech spectrum, and the amount of NAL amplification (if any). Our main concern was to determine the proportion of the speech spectrum that was above the *absolute* threshold. Hence, the calculations did not take into account the presence of the background noises. If all of the speech spectrum is above the absolute threshold, then deficits in performance in the presence of background noise must be due to masking effects of that noise.

To calculate the AI, the speech was analyzed in $\frac{1}{3}$-octave bands and the root-mean-square (rms) level in each band was expressed in dB HL, i.e., relative to the normal absolute threshold for that band. The absolute thresholds of each subject at the $\frac{1}{3}$-octave center frequencies, and the amounts of NAL amplification, were estimated by interpolation from the audiometric frequencies. It was then possible to calculate the rms level of the speech relative to the absolute threshold in each $\frac{1}{3}$-octave band. It was assumed that the dynamic range of the speech in each band extended from 12 dB above to 18 dB below the rms level. The proportion of the 30-dB dynamic range that was above the absolute threshold in each band was multiplied by the importance value for that band, and the products were summed to give the AI. Values for the importance function were those for ''average speech'' as specified in Pavlovic (1987). According to ANSI (1969), AI values over approximately 0.7 lead to essentially perfect performance for sentence material. This should be borne in mind when considering the AI values.

Consider first the AIs for speech at the SRTs in quiet without any amplification. The mean AIs for groups (a), (b), (c), and (d) (with standard deviations in parentheses) were 0.26, 0.23 (0.09), 0.16 (0.03), and 0.16 (0.10), respectively. The slightly lower AIs for the impaired groups may have occurred because the hearing-impaired subjects had learned to make more effective use of low-frequency information falling in the range where their hearing was relatively good. When NAL amplification was applied, the SRTs in quiet (expressed as the input level prior to NAL amplification) decreased, but the mean AIs for groups (c) and (d) for speech at the SRT in quiet increased to 0.21 (0.09) and 0.22 (0.16), respectively. Thus, to achieve the same level of intelligibility, these groups required slightly higher AIs when NAL amplification was applied than when it was not. A higher AI with NAL amplification was found for five out of six subjects in group (c) and for seven out of ten subjects in group (d). The higher AIs may have occurred because the NAL amplification partially restored the audibility of higher frequencies, but these subjects did not make very effective use of that information, possibly because of a lack of opportunity for acclimatization (Gatehouse, 1992).

Table V shows the mean AI for each group for speech at a level corresponding to the mean SRT in steady noise, and the mean SRT in modulated noise with four-ERB gaps; these

TABLE V. Mean AIs for speech at levels corresponding to the SRTs in steady noise, and in modulated noise with four-ERB gaps. The calculated AIs do not take into account the effect of the background noise; they indicate the proportion of the speech spectrum that was above the absolute threshold. Numbers in parentheses are standard deviations across subjects. For the older subjects with near-normal hearing, the upper numbers refer to results for the whole group and the lower numbers refer to results excluding two subjects whose absolute thresholds at 4 kHz exceeded 30 dB HL. For the young hearing-impaired subjects, the upper numbers refer to results for the whole group and the lower numbers refer to results excluding one subject with a mild loss.

	Speech level at SRT in	
Group	steady noise	modulated noise, 4-ERB gaps
(a) Young normal	1.0	0.92
(b) Older normal	0.92 (0.04)	0.75 (0.06)
	0.94 (0.02)	0.75 (0.07)
(c) Young impaired	0.47 (0.18)	0.31 (0.13)
	0.41 (0.12)	0.27 (0.07)
(c) With NAL amplification	0.82 (0.14)	0.60 (0.18)
	0.80 (0.14)	0.59 (0.19)
(d) Older impaired	0.43 (0.15)	0.32 (0.16)
(d) With NAL amplification	0.72 (0.15)	0.55 (0.18)

represent the highest and lowest SRTs, respectively, when background sounds were present. Except for group (a), AIs were calculated individually for each subject and then averaged within groups.

For group (a), the AIs for the two cases were 1.0 and 0.92, i.e., almost all of the speech spectrum was above absolute threshold. Thus, for this group, the SRTs in noise must have been determined by the masking effects of the noise rather than by part of the speech spectrum being below absolute threshold. For group (b), the AIs were somewhat smaller, but still at or above 0.75. In particular, the mean AI at the SRT in steady noise, excluding the two subjects with mild-high frequency loss, was 0.94. The SRT for this group was 1.6 dB higher than for the normal subjects. For speech presented at the SRT for the normal subjects (i.e., 1.6 dB lower, on average), the mean AI for this group is 0.93. It seems unlikely that the very small reduction in audibility associated with an AI of 0.93 would be sufficient to account for the difference in SRT between groups (a) and (b). For the modulated noise with four-ERB gaps, the AI was reduced to 0.75, which is still above the value required for near-perfect intelligibility of sentences. Thus performance was probably determined mainly by the masking effects of the background noise. The SRT for group (b) with this noise was 6.9 dB higher than for group (a). For speech presented at the SRT for normal subjects, the AI was reduced to 0.58. This is sufficiently low that performance probably would have been limited partly by some of the speech spectrum being below absolute threshold.

For group (c), the AIs without NAL amplification were markedly lower than 1. It seems likely that performance in this case was partly limited by some of the speech spectrum being below absolute threshold. With NAL amplification the AIs increased markedly, to 0.82 ($N=6$) or 0.80 ($N=5$) for speech at a level corresponding to the SRT in steady noise. For speech presented at the SRT for the normal subjects with

steady noise (i.e., 2.6 dB lower, on average) the mean AI was 0.77 ($N=6$) or 0.74 ($N=5$), high enough to give near-perfect intelligibility. It seems likely that performance with NAL amplification was determined mainly by the masking effect of the background noise, although reduced audibility may have played some role. For speech at the SRT in modulated noise with four-ERB gaps, the AI was increased markedly when NAL amplification was applied, but it remained at or below 0.6. Thus, in this case, performance was probably partly limited by part of the speech spectrum being below absolute threshold. For speech presented at the SRT for the normal subjects with this noise (i.e., 11.2 dB lower, on average) the mean AI was 0.31 ($N=6$) or 0.27 ($N=5$). These values are small enough to indicate that reduced audibility would have played a substantial role.

For group (d), the AIs without NAL amplification were lower still. It seems certain that performance in this case was partly limited by some of the speech spectrum being below absolute threshold. With NAL amplification the mean AI increased markedly, to 0.72 for speech at a level corresponding to the SRT in steady noise. For speech presented at the SRT for the normal subjects with steady noise, the mean AI was 0.61. It seems likely that performance with NAL amplification was determined mainly by the masking effect of the background noise, although reduced audibility may have played some role. For speech at the SRT in modulated noise with four-ERB gaps, the AI was increased to 0.55 when NAL amplification was applied. Thus, in this case, performance was probably partly limited by part of the speech spectrum being below absolute threshold. For speech presented at the SRT for the normal subjects with this noise, the mean AI was 0.21. This value is small enough to indicate that reduced audibility would have played a substantial role.

IV. DISCUSSION

Linear amplification according to the NAL prescription is generally regarded as one of the better formulas for fitting linear hearing aids. Also, our implementation of the NAL prescription, using digital filtering, was more accurate than would normally be achieved in a conventional, wearable, linear hearing aid; even though NAL targets were based on groups, the gains used for each individual were always within 3 dB of the target gains for that individual. In particular, the target gains at higher frequencies were achieved, which is often not the case in wearable aids. Our results showed that, even with NAL amplification, the performance of the hearing-impaired subjects remained worse than that of the normally hearing subjects. Furthermore, the AI calculations indicated that, for the noise giving the lowest SRTs (modulated noise with four-ERB gaps), performance was partly limited by some of the speech spectrum being below absolute threshold. In other words, the NAL amplification did not provide sufficient gain to restore audibility of the low-level parts of the target speech.

While it is possible to increase the amount of linear gain applied, this can only be done to a limited extent because of loudness recruitment, which nearly always is associated with cochlear hearing loss. The threshold for detecting sounds is higher than normal, but once the sound level is increased

above the absolute threshold, the rate of growth of loudness level with increasing level is greater than normal. At a sound level of 90–100 dB SPL, the loudness in an impaired ear often ''catches up'' with that in a normal ear (Fowler, 1936; Steinberg and Gardner, 1937; Moore *et al.*, 1996). As a consequence, the range of sound levels over which sounds are both audible and comfortable (the dynamic range) is much smaller for hearing-impaired than for normally hearing people.

Most rules for prescribing the insertion gain of a linear aid are appropriate for speech inputs with a moderate level. However, in conditions where a wide dynamic range is required, for example, when listening to speech in noise with spectral and temporal dips, it may be impossible to apply sufficient linear gain to ensure that all of the speech spectrum is above absolute threshold while preventing the noise from becoming unpleasantly loud.

One way of dealing with loudness recruitment is to use hearing aids with fast-acting compression or automatic gain control (AGC). Such aids can increase the available dynamic range and can make it possible for the hearing-impaired person to deal with sounds covering a wide range of levels without needing to adjust the volume control on the aid (Villchur, 1973; Lippmann *et al.*, 1981; Moore *et al.*, 1992). In principle, they can also improve the ability to listen in dips of a competing sound by increasing the gain for signals in the dips, thus improving the intelligibility of the speech. However, laboratory studies of systems using fast-acting compression have given mixed results, with some studies showing no benefit or even a worsening in comparison to linear amplification and others showing moderate benefits (Villchur, 1973; Lippmann *et al.*, 1981; Villchur, 1982; Moore and Glasberg, 1988a; Moore *et al.*, 1992; Hickson, 1994; Moore, 1995).

The laboratory studies have generally used test materials covering a much smaller range of sound levels than would be encountered in everyday life. Also, when background sounds have been used, the most common sound has been steady speech-shaped noise. Our results suggest that this is not the most effective noise for revealing benefits of compression; noises with spectral and temporal dips might be much more sensitive; preliminary results obtained in our laboratories indicate that this is, indeed, the case.

Although our results suggest that the relatively poor performance of the hearing-impaired subjects when listening to speech in background noise with spectral and/or temporal dips was at least partly due to part of the target speech spectrum being below absolute threshold, it is likely that other supra-threshold factors also contributed to their poor performance, especially when NAL amplification was applied. In particular, it seems likely that reduced frequency selectivity contributed to the relatively poor performance when the background noise had spectral dips (Patterson *et al.*, 1982; Moore, 1995). Consider, for example, the AI values shown in Table V for the young impaired group and the modulated noise with four-ERB gaps. The mean AI value without NAL amplification was only 0.31, suggesting that a major factor limiting performance was the proportion of the target speech spectrum that was above absolute threshold. However, when

NAL amplification was applied, the AI at the SRT increased to 0.6. Since much more of the speech spectrum was above absolute threshold in this condition, but the same performance level was obtained (50% correct), it seems reasonable to infer that the masking effect of the background noise played a substantial role in limiting performance. The mean SRT for this group with NAL amplification was 11.2 dB higher than for the young normally hearing group, which is a very large difference, probably too large to be explained by the small difference in AI (0.6 for the impaired group with NAL amplification and 0.75 for the normal group without amplification). However, it is very difficult to infer from our results the relative importance of reduced audibility and reduced frequency selectivity.

For stimuli without NAL amplification, age was not correlated with the SRTs in any of the background noises, once the effect of absolute threshold was partialled out. This finding is similar to that of Takahashi and Bacon (1992). They measured speech intelligibility in both unmodulated noise and noise that was sinusoidally amplitude modulated at an 8-Hz rate with 100% modulation depth, using young normally hearing subjects, and three groups of older subjects (mean age 54.3, 64.8 and 72.2 years). They found that even mild hearing impairment had a large effect on the ability to understand speech in modulated noise. However, there was no significant effect of age once the effect of absolute threshold had been partialled out. In contrast, our results for stimuli with NAL amplification showed that SRTs in backgrounds with spectral and/or temporal dips were significantly correlated with age. Several of these correlations remained significant when the effects of the mean absolute threshold at 0.5, 1, and 2 kHz were partialled out. Thus, when reduced audibility is partially compensated for by NAL amplification, age may play a significant role when the background contains spectral and/or temporal dips. It is possible that the ability to reconstruct the speech from incomplete information (glimpses obtained in spectral or temporal valleys) plays a strong role in this situation, and that this cognitive ability declines with age.

In conclusion, people with cochlear hearing loss have a reduced ability to make use of both spectral and temporal dips in background sounds. This reduced ability may occur partly because of supra-threshold deficits such as reduced frequency selectivity. However, inaudibility of part of the speech spectrum may also play an important role. Linear amplification only partially compensates for the deficits. When linear amplification was applied, the SRTs in backgrounds with spectral and/or temporal dips were significantly correlated with age.

ACKNOWLEDGMENTS

ANSI (**1969**). ANSI S3.5-1969, ''American National Standard Methods for the Calculation of the Articulation Index'' (American National Standards Institute, New York).

Byrne, D., and Dillon, H. (**1986**). ''The National Acoustic Laboratories' (NAL) new procedure for selecting the gain and frequency response of a hearing aid,'' Ear Hear. **7**, 257–265.

Carhart, R. C., and Tillman, T. W. (**1970**). ''Interaction of competing speech signals with hearing losses,'' Arch. Otolaryngol. **91**, 273–279.

Dreschler, W. A., and Plomp, R. (**1980**). ''Relations between psychophysical data and speech perception for hearing-impaired subjects. I,'' J. Acoust. Soc. Am. **68**, 1608–1615.

Dreschler, W. A., and Plomp, R. (**1985**). ''Relations between psychophysical data and speech perception for hearing-impaired subjects. II,'' J. Acoust. Soc. Am. **78**, 1261–1270.

Duquesnoy, A. J. (**1983**). ''Effect of a single interfering noise or speech source on the binaural sentence intelligibility of aged persons,'' J. Acoust. Soc. Am. **74**, 739–743.

Eisenberg, L. S., Dirks, D. D., and Bell, T. S. (**1995**). ''Speech recognition in amplitude-modulated noise of listeners with normal and listeners with impaired hearing,'' J. Speech Hear. Res. **38**, 222–233.

Festen, J. (**1987a**). ''Explorations on the difference in SRT between a stationary noise masker and an interfering speaker,'' J. Acoust. Soc. Am. **82**, S4.

Festen, J. M. (**1987b**). ''Speech-reception threshold in fluctuating background sound and its possible relation to temporal auditory resolution,'' in *The Psychophysics of Speech Perception*, edited by M. E. H. Schouten (Nijhoff, Dordrecht, The Netherlands).

Festen, J. M. (**1993**). ''Contributions of comodulation masking release and temporal resolution to the speech-reception threshold masked by an interfering voice,'' J. Acoust. Soc. Am. **94**, 1295–1300.

Festen, J. M., and Plomp, R. (**1990**). ''Effects of fluctuating noise and interfering speech on the speech-reception threshold for impaired and normal hearing,'' J. Acoust. Soc. Am. **88**, 1725–1736.

Fowler, E. P. (**1936**). ''A method for the early detection of otosclerosis,'' Arch. Otolaryngol. **24**, 731–741.

Gatehouse, S. (**1992**). ''The time course and magnitude of perceptual acclimatization to frequency responses: Evidence from monaural fitting of hearing aids,'' J. Acoust. Soc. Am. **92**, 1258–1268.

Glasberg, B. R., and Moore, B. C. J. (**1986**). ''Auditory filter shapes in subjects with unilateral and bilateral cochlear impairments,'' J. Acoust. Soc. Am. **79**, 1020–1033.

Glasberg, B. R., and Moore, B. C. J. (**1989**). ''Psychoacoustic abilities of subjects with unilateral and bilateral cochlear impairments and their relationship to the ability to understand speech,'' Scand. Audiol. Suppl. **32**, 1–25.

Glasberg, B. R., and Moore, B. C. J. (**1990**). ''Derivation of auditory filter shapes from notched-noise data,'' Hearing Res. **47**, 103–138.

Glasberg, B. R., and Moore, B. C. J. (**1992**). ''Effects of envelope fluctuations on gap detection,'' Hearing Res. **64**, 81–92.

Glasberg, B. R., Moore, B. C. J., and Bacon, S. P. (**1987**). ''Gap detection and masking in hearing-impaired and normal-hearing subjects,'' J. Acoust. Soc. Am. **81**, 1546–1556.

Hickson, L. M. H. (**1994**). ''Compression amplification in hearing aids,'' Am. J. Audiol. **3**, 51–65.

Hygge, S., Rönnberg, J., Larsby, B., and Arlinger, S. (**1992**). ''Normal-hearing and hearing-impaired subjects' ability to just follow conversation in competing speech, reversed speech, and noise backgrounds,'' J. Speech Hear. Res. **35**, 208–215.

Krauss, T. P., Shure, L., and Little, J. N. (**1994**). *Signal Processing Toolbox* (The Math Works, Natick, MA).

Laurence, R. F., Moore, B. C. J., and Glasberg, B. R. (**1983**). ''A comparison of behind-the-ear high-fidelity linear aids and two-channel compression hearing aids in the laboratory and in everyday life,'' Br. J. Audiol. **17**, 31–48.

Lippmann, R. P., Braida, L. D., and Durlach, N. I. (**1981**). ''Study of multichannel amplitude compression and linear amplification for persons with sensorineural hearing loss,'' J. Acoust. Soc. Am. **69**, 524–534.

586   J. Acoust. Soc. Am., Vol. 103, No. 1, January 1998

Peters *et al.*: Intelligibility in noise   586

Moore, B. C. J. (**1995**). *Perceptual Consequences of Cochlear Damage* (Oxford U.P., Oxford).

Moore, B. C. J., and Glasberg, B. R. (**1988a**). ''A comparison of four methods of implementing automatic gain control (AGC) in hearing aids,'' Br. J. Audiol. **22**, 93–104.

Moore, B. C. J., and Glasberg, B. R. (**1988b**). ''Gap detection with sinusoids and noise in normal, impaired and electrically stimulated ears,'' J. Acoust. Soc. Am. **83**, 1093–1101.

Moore, B. C. J., and Glasberg, B. R. (**1993**). ''Simulation of the effects of loudness recruitment and threshold elevation on the intelligibility of speech in quiet and in a background of speech,'' J. Acoust. Soc. Am. **94**, 2050–2062.

Moore, B. C. J., Glasberg, B. R., and Vickers, D. A. (**1995**). ''Simulation of the effects of loudness recruitment on the intelligibility of speech in noise,'' Br. J. Audiol. **29**, 131–143.

Moore, B. C. J., Wojtczak, M., and Vickers, D. A. (**1996**). ''Effect of loudness recruitment on the perception of amplitude modulation,'' J. Acoust. Soc. Am. **100**, 481–489.

Moore, B. C. J., Johnson, J. S., Clark, T. M., and Pluvinage, V. (**1992**). ''Evaluation of a dual-channel full dynamic range compression system for people with sensorineural hearing loss,'' Ear Hear. **13**, 349–370.

Nilsson, M., Soli, S. D., and Sullivan, J. A. (**1994**). ''Development of the Hearing in Noise Test for the measurement of speech reception thresholds in quiet and in noise,'' J. Acoust. Soc. Am. **95**, 1085–1099.

Patterson, R. D., Nimmo-Smith, I., Weber, D. L., and Milroy, R. (**1982**). ''The deterioration of hearing with age: frequency selectivity, the critical ratio, the audiogram, and speech threshold,'' J. Acoust. Soc. Am. **72**, 1788–1803.

Pavlovic, C. (**1987**). ''Derivation of primary parameters and procedures for use in speech intelligibility predictions,'' J. Acoust. Soc. Am. **82**, 413–422.

Pearsons, K. S., Bennett, R. L., and Fidell, S. (**1976**). *Speech Levels in Various Environments, Report No. 3281* (Bolt Beranek and Newman, Cambridge, MA).

Pick, G., Evans, E. F., and Wilson, J. P. (**1977**). ''Frequency resolution in patients with hearing loss of cochlear origin,'' in *Psychophysics and Physiology of Hearing*, edited by E. F. Evans and J. P. Wilson (Academic, London).

Plomp, R. (**1994**). ''Noise, amplification, and compression: Considerations of three main issues in hearing aid design,'' Ear Hear. **15**, 2–12.

Plomp, R., and Mimpen, A. M. (**1979**). ''Improving the reliability of testing the speech reception threshold for sentences,'' Audiology **18**, 43–53.

Steinberg, J. C., and Gardner, M. B. (**1937**). ''The dependency of hearing impairment on sound intensity,'' J. Acoust. Soc. Am. **9**, 11–23.

Takahashi, G. A., and Bacon, S. P. (**1992**). ''Modulation detection, modulation masking, and speech understanding in noise in the elderly,'' J. Speech Hear. Res. **35**, 1410–1421.

Tyler, R. S. (**1986**). ''Frequency resolution in hearing-impaired listeners,'' in *Frequency Selectivity in Hearing*, edited by B. C. J. Moore (Academic, London).

van Rooij, J. C. G. M., and Plomp, R. (**1992**). ''Auditive and cognitive factors in speech perception by elderly listeners. III. Additional data and final discussion,'' J. Acoust. Soc. Am. **91**, 1028–1033.

Villchur, E. (**1973**). ''Signal processing to improve speech intelligibility in perceptive deafness,'' J. Acoust. Soc. Am. **53**, 1646–1657.

Villchur, E. (**1982**). ''The evaluation of amplitude-compression processing for hearing aids,'' in *The Vanderbilt Hearing-Aid Report*, edited by G. A. Studebaker and F. H. Bess (Monographs in Contemporary Audiology, Upper Darby, PA).

Tempo and beat analysis of acoustic musical signals

Eric D. Scheirer[a)]

Machine Listening Group, E15-401D MIT Media Laboratory, Cambridge, Massachusetts 02139

A method is presented for using a small number of bandpass filters and banks of parallel comb filters to analyze the tempo of, and extract the beat from, musical signals of arbitrary polyphonic complexity and containing arbitrary timbres. This analysis is performed causally, and can be used predictively to guess when beats will occur in the future. Results in a short validation experiment demonstrate that the performance of the algorithm is similar to the performance of human listeners in a variety of musical situations. Aspects of the algorithm are discussed in relation to previous high-level cognitive models of beat tracking.   © *1998 Acoustical Society of America.* [S0001-4966(98)02801-X]

PACS numbers: 43.75.Yy, 43.75.St [WJS]

INTRODUCTION

Automatic extraction of rhythmic pulse from musical excerpts has been a topic of active research in recent years. Also called *beat-tracking* and *foot-tapping*, the goal is to construct a computational algorithm capable of extracting a symbolic representation which corresponds to the phenomenal experience of ''beat'' or ''pulse'' in a human listener.

''Rhythm'' as a musical concept is intuitive to understand, but somewhat difficult to define. Handel writes ''The experience of rhythm involves movement, regularity, grouping, and yet accentuation and differentiation'' (Handel, 1989, p. 384) and also stresses the importance of the phenomenalist point of view—there is no ''ground truth'' for rhythm to be found in simple measurements of an acoustic signal. The only ground truth is what human listeners agree to be the rhythmic aspects of the musical content of that signal.

As contrasted with ''rhythm'' in general, ''beat'' and ''pulse'' correspond only to ''the sense of equally spaced temporal units'' (Handel, 1989). Where ''meter'' and ''rhythm'' associate with qualities of grouping, hierarchy, and a strong/weak dichotomy, ''pulses'' in a piece of music are only periodic at a simple level. For our purposes, the *beat* of a piece of music is the sequence of equally spaced phenomenal impulses which define a tempo for the music. This paper is only concerned with beat and tempo. The grouping and strong/weak relationships which define rhythm and meter are not considered.

It is important to note that there is no simple relationship between polyphonic complexity—the number and timbres of notes played at a single time—in a piece of music, and its rhythmic complexity or pulse complexity. There are pieces and styles of music which are texturally and timbrally complex, but have straightforward, perceptually simple rhythms; and there also exist musics which deal in less complex textures but are more difficult to rhythmically understand and describe.

The former sorts of musical pieces, as contrasted with the latter sorts, have a ''strong beat,'' and it is with them that this paper is predominantly concerned. For these kinds of music, the rhythmic response of listeners is simple, immediate, and unambiguous, and every listener will agree on the rhythmic content. Rhythmically complex music is discussed toward the end of the paper.

Previous approaches

There is a large body of work originating in the music-psychology community which attempts to group musical *onsets* together into a rhythmic context; that is to say, to construct a model which subsumes multiple onsets separated in time into a rhythmic clock, ''hierarchy,'' grouping, or oscillatory model.

Povel and Essens presented research (Povel and Essens, 1985) on the association of ''internal clocks'' with temporal onset signals. They described an algorithm which could, given a set of inter-onset intervals as input, identify the clock which a listener would associate with such a sequence of intervals. Their research was particularly interested in the way that perceived accents lead to the internal clock. Although obviously related to music, their research purports to examine time intervals in general rather than being restricted to musical stimuli. Parncutt's recent work (Parncutt, 1994) extends this type of model to include a great deal of structural information about duration and phenomenal accent.

Desain and Honing have contributed many results to the computational modeling of beat-tracking. Their models (Desain and Honing, 1992; Desain, 1995) typically also begin with inter-onset intervals and associate a rhythmic pulse with the interval stream. However, unlike the Povel/Essens and Parncutt models, these models are *process models*—they process the input sequentially rather than all-at-once—a necessary aspect of a model of human rhythmic perception. Desain's ''(de)composable'' model calculates rhythmic expectations due to each of the possible inter-onset times in a rhythmic stream, and sums them to create an overall rhythmic expectation.

Large and Kolen have described a beat-tracking model (Large and Kolen, 1994) based on nonlinear oscillators. The model takes a stream of onsets as input, and uses a gradient-descent method to continually update the period and phase of an oscillator. In this manner, the oscillator is matched with

[a)]Electronic mail; eds@media.mit.edu

the input stream, and the resulting oscillation process seems to be a good match for the human perception of beat.

Longuet-Higgens and Lee have written many papers (for example, Longuet-Higgens and Lee, 1984) on the induction of rhythmic hierarchies from monophonic time sequences. They are more interested in the development of theories which describe the relationship of rhythm, meter, and phrasing than on the boot-strapping process which creates a tempo and beat percept. Tempo perception may be viewed as ''underlying'' their models.

These approaches, and others such as Rosenthal (1993) and Brown (1993), require that robust onset detection precede beat analysis, which entails an important restriction to their applicability. The models do not operate on acoustic signals, but on symbolic data such as event lists or MIDI. As the extraction of onsets from multitimbral, polyphonic music is itself a difficult problem, this is a serious restriction of any model which claims to treat human rhythm perception. There has been little attempt to merge these sorts of models with real-time acoustic pattern recognition to allow them to work with acoustic data.

More recently, there has been some research attempting to extract rhythm and/or pulse information directly from acoustic signals. Goto has demonstrated a system which combines both low-level ''bottom-up'' signal processing and high-level pattern matching and ''agent-based'' representations to beat-track and do simple rhythmic grouping for popular music (Goto, in press). His method extracts drum patterns from a signal and uses a template-matching model to determine the beat from the drum track. This system runs in real time on a parallel-processing computer and has been used to control interactive-graphics displays from ecological music signals. His description does not directly address the equivalent processing of signals without drums, but it seems that the required musical knowledge base would be much more difficult to acquire.

N. P. Todd's work (Todd, 1994) has described algorithms which detect onsets in monophonic music under certain timbral constraints, and then group these onsets in a rhythmic framework using a multi-scale smoothing model. The onset model used is a simple one based on leaky integration. The resulting ''rhythmogram'' representation conceives of pulse, and in some cases, meter and phrase, perception as a very low-level process arising directly from the time- and loudness-integration properties of the auditory periphery. The model as presented can be implemented in an incremental manner, but was only tested using toy examples (although, interestingly, a speech example was included).

All of the abovementioned research uses what has been described as a *transcriptive* metaphor for analysis (Scheirer, 1996). That is, the music is first segmented, or assumed to already be segmented, into notes, onsets, timbres, and so forth. Post-processing algorithms are then used to group rhythms and track beats. As high-quality polyphonic music transcription algorithms are still years in the future—the state-of-the-art systems cannot transcribe pieces more complex than four-voice piano music (Martin, 1996)—it seems logical for practical reasons to attempt to construct systems which can arrive at a musical understanding of a piece of
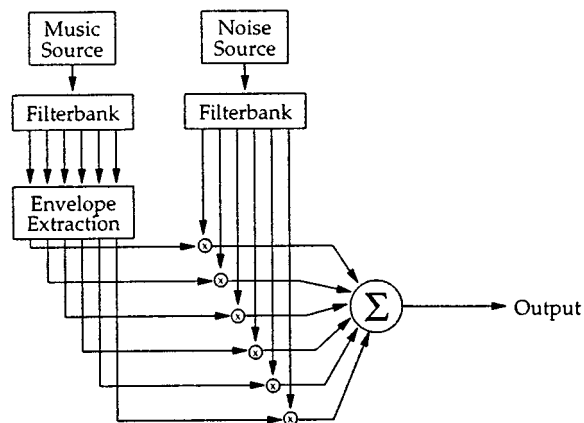

FIG. 1. Creating a ''modulated noise'' signal from a music signal. The output signal, for many sorts of frequency filterbanks, will have the same rhythmic percept as the input music signal, indicating that the amplitude envelopes of the bands are a sufficient representation for rhythmic analysis.

music without going through a transcription step. Further, as the validity of the transcriptive metaphor as a framework for music perception has been challenged (Scheirer, 1996), it is scientifically appropriate as well.

In the body of this paper, the following topics are discussed: psychoacoustic demonstrations which lead to processing simplifications for beat-tracking, the construction of the algorithms themselves, example results from test signals and ecological signals, a validation experiment which compares the behavior of the algorithm to that of human subjects, the relationship of this model to previous models of rhythm perception, and finally, conclusions about beat-tracking and rhythmic grouping and a description of future work to be pursued in these directions.

I. PSYCHOACOUSTIC SIMPLIFICATION

One of the key difficulties with the transcriptive models of rhythmic perception described above is the complexity of grouping harmonic partials together to form notes, and determining the onset times of those notes. Even if simplifying assumptions about the pitch and timbral content are made, identifying attack and release times is no easy task (Scheirer, in press).

However, it seems from a psychoacoustic demonstration on beat perception that certain kinds of signal manipulations and simplifications can be performed without affecting the perceived pulse content of a musical signal. Consider the signal flow network shown in Fig. 1.

An ''amplitude-modulated noise'' is constructed by signal by vocoding a white noise signal with the subband envelopes of a musical signal. This is accomplished by performing a frequency analysis of the music (processing through a filterbank of bandpass filters, perhaps, or grouping output from FFT bins together), and also of a white-noise signal from a pseudo-random generator. The amplitude of each band of the noise signal is modulated with the amplitude envelope of the corresponding band of the musical filterbank output, and the resulting noise signals are summed together to form an output signal.
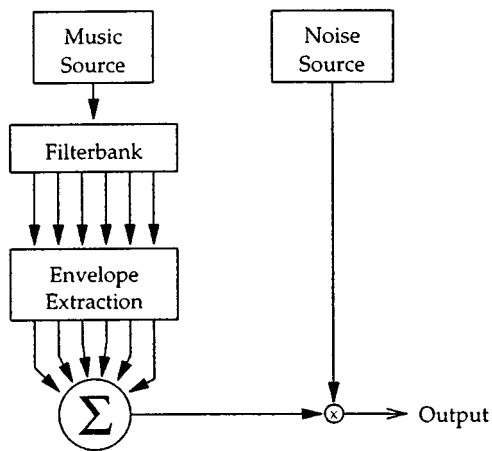
FIG. 2. A noise signal which does not have the same rhythmic characteristics as the musical input, indicating that the sum of the amplitude envelopes is not a sufficient representation for rhythm analysis. Certain types of nonlinear combination by frequency channel are evidently present in the beat perception facility.

For many kinds of frequency filterbanks, the resulting noise signal has a rhythmic percept which is significantly the same as that of the original music signal. Even if there are very few, very broad bands (for example, four three-octave bands covering the audible spectrum), the pulse and meter characteristics of the original signal are instantly recognizable (sound example #1a) [Audio examples for this paper can be found on the author's WWW site at http://sound.media.mit.edu/eds/beat/].

Since the only thing preserved in this transformation is the amplitude envelopes of the filterbank outputs, it stands to reason that only this much information is necessary to extract pulse and meter from a musical signal; that is, algorithms for pulse extraction can be created which operate only on this much input data, and ''notes'' are not a necessary component for hearing rhythm. This is a vast reduction of input data size from the original signal. Shannon has reported a similar effect for the perception of speech (Shannon, 1995).

Certain other kinds of simplifications are not possible. For example, if only one band is used, or equivalently, the subband envelopes are linearly combined before modulating the noise (Fig. 2) (Vercoe, 1994) a listener can no longer perceive the rhythmic content of many signals (sound example #1b). Thus it seems that separating the signal into subbands and maintaining the subband envelopes separately is necessary to do accurate rhythmic processing.

Stated another way, the algorithm in Fig. 2 is a method for generating new signals whose representation under a filterbank-envelope-and-sum process is the same as a given piece of music. However, since these new signals often do not bear a perceptual equivalency with the originals, the filter-envelope-sum framework must be *inadequate* to represent data in the musical signal which is important for rhythmic understanding. This fact immediately leads to a psychoacoustic hypothesis regarding rhythmic perception: some sort of cross-band rhythmic integration, not simply summation across frequency bands, is performed by the auditory system.

A psychoacoustic experiment to examine the exact prop-

erties of filterbank-and-envelope manipulations which do not disturb rhythm perception is underway; in the meantime, it seems important that a rhythmic processing algorithm should treat frequency bands separately, combining results at the end, rather than attempting to perform beat-tracking on the sum of filterbank outputs.

II. DESCRIPTION OF ALGORITHM

The beat-tracking algorithm to be presented here bears most resemblance to the method of Large and Kolen (Large and Kolen, 1994) in that it uses a network of resonators to phase-lock with the beat of the signal and determine the frequency of the pulse. However, the particular method used here is somewhat different; the resonators are analytically much simpler than theirs, a bank of resonators is used rather than gradient descent, and more pre- and post-processing of the signal is necessary in order to accurately extract the desired information, as the present model operates on acoustic data rather than an event stream.

A rhythmic pulse is described in terms of a frequency and phase component, just as for a periodic sound waveform; the frequency of the pulse in a rhythmic musical signal is the tempo or rate of the rhythm, and the phase of the pulse indicates where the ''downbeat'' of the rhythm occurs. That is, the times at which a pulse occurs can be defined to have zero phase, and thus the points in time exactly in-between pulses have phase of π radians, etc. It is important to note that while human pitch recognition is only sensitive to signal phase under certain unusual conditions, rhythmic response is crucially a phased phenomenon—tapping on the beat is not at all the same as tapping against the beat, or slightly ahead of or behind the beat, even if the frequency of tapping is accurate.

Figure 3 shows an overall view of the tempo-analysis algorithm as a signal flow network. The functionality will be briefly described, and then more details given piece-by-piece in the following sections. The algorithms here were developed empirically; however, in Sec. V their relationship to existing models of rhythm perception is discussed.

As the signal comes in, a filterbank is used to divide it into six bands. For each of these subbands, the amplitude envelope is calculated and the derivative taken. Each of the envelope derivatives is passed on to another filterbank of *tuned resonators*; in each resonator filterbank, one of the resonators will phase-lock, the one for which the resonant frequency matches the rate of periodic modulation of the envelope derivative.

The outputs of the resonators are examined to see which ones are exhibiting phase-locked behavior, and this information is tabulated for each of the bandpass channels. These tabulations are summed across the frequency filterbank to arrive at the frequency (tempo) estimate for the signal, and reference back to the peak phase points in the phase-locked resonators determines the phase of the signal.

A. Frequency analysis and envelope extraction

As discussed in Sec. I, envelopes extracted from a small number of broad frequency channels are sufficient information to rhythmically analyze a musical signal, at least for
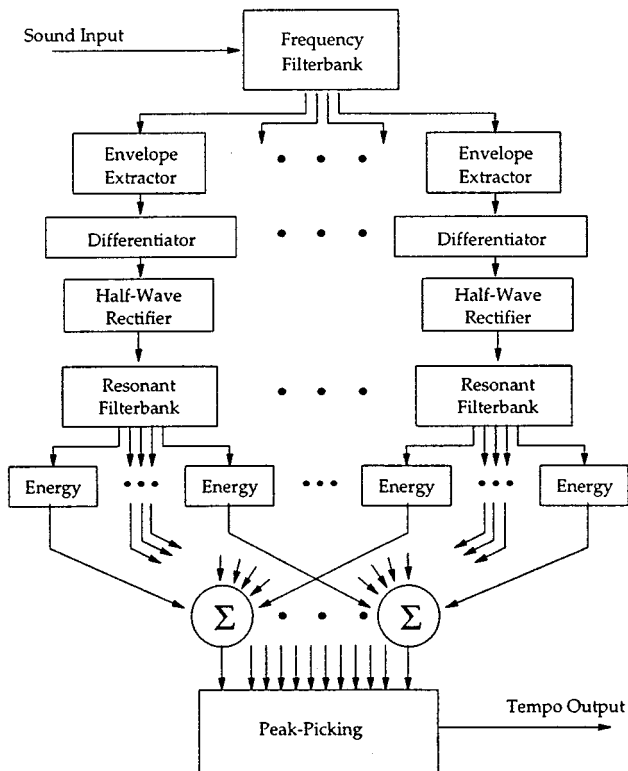
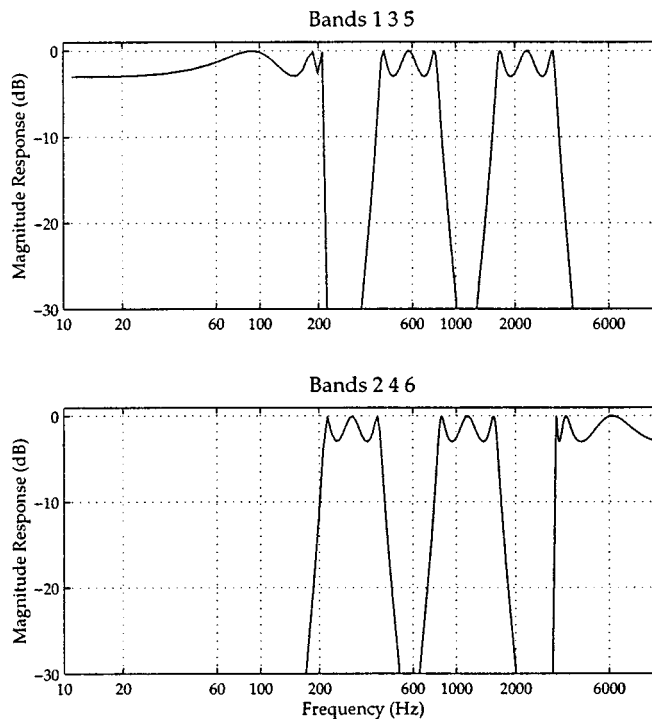FIG. 3. Schematic view of the processing algorithm. See text for details.

FIG. 4. Magnitude response of the frequency filterbank used in the system, plotted in two pieces for clarity. The upper plot shows the first, third, and fifth bands; the lower, the second, fourth, and sixth. Each filter is a sixth-order elliptic filter, with 3 dB of passband ripple and 40 dB of stopband rejection.

human listeners. Further, empirical studies of the use of various filterbanks with this algorithm have demonstrated that the algorithm is not particularly sensitive to the particular bands or implementations used; it is expected that psychoacoustic investigation into rhythmic perception of amplitude-modulated noise signals created with the various vocoder filterbanks would confirm that the same is true of human rhythmic perception.

The filterbank implementation in the algorithm has six bands; each band has sharp cutoffs and covers roughly a one-octave range. The lowest band is a low-pass filter with cutoff at 200 Hz; the next four bands are bandpass, with cutoffs at 200 and 400 Hz, 400 and 800 Hz, 800 and 1600 Hz, and 1600 and 3200 Hz. The highest band is high pass, with cutoff frequency at 3200 Hz. Each filter is implemented using a sixth-order elliptic filter, with 3 dB of ripple in the passband and 40 dB of rejection in the stopband. Figure 4 shows the magnitude responses of these filters.

The envelope is extracted from each band of the filtered signal through a rectify-and-smooth method. The rectified filterbank outputs are convolved with a 200-ms half-Hanning (raised cosine) window. This window has a discontinuity at time $t=0$, then slopes smoothly away to 0 at 200 ms. It has a low-pass characteristic, with a cutoff frequency at about 10 Hz ("frequency" in this case referring to envelope spectra, not waveform spectra), where it has a -15 dB response, and 6-dB/octave smooth rolloff thereafter.

The window's discontinuity in time means that it has nonlinear phase response; it passes slow envelope frequencies with much more delay than rapid ones. High frequencies, above 20 Hz, are passed with approximately zero delay;

0 Hz is delayed about 59 ms and 7 Hz advanced about 14 ms. Thus there is a maximum blur of about 73 ms between these envelope frequencies.

This window performs energy integration in a way similar to that in the auditory system, emphasizing the most recent inputs but masking rapid modulation; Todd (1992) examines the use of temporal integration filters which are directly constructed from known psychoacoustic properties. After this smoothing, the envelope can be decimated for further analysis; the next stages of processing operate on the decimated band envelopes sampled at 200 Hz. There is little energy left in the envelope spectra at this frequency, but it aids the phase-estimation process (see below) to maintain a certain precision of oversampled envelope resolution.

After calculating the envelope, the first-order difference function is calculated and half-wave rectified; this rectified difference signal will be examined for periodic modulation. The derivative-of-envelope function performs a type of onset filtering process (see, for example, Smith's work on difference-of-Gaussian functions for onset segmentations Smith, 1994) but the explicit segmentation, thresholding, or peak-peaking of the differenced envelope is not attempted. The subsequent modulation detectors in the algorithm are sensitive, similar to the sensitivity of autocorrelation, to "imperfections" in an onset track. The half-wave rectified envelope difference avoids this pitfall by having broader (in time) response to perceptual attacks in the input signal. This process might be considered similar to detecting onset points in the signal bands, and then broadening them via low-pass filtering.
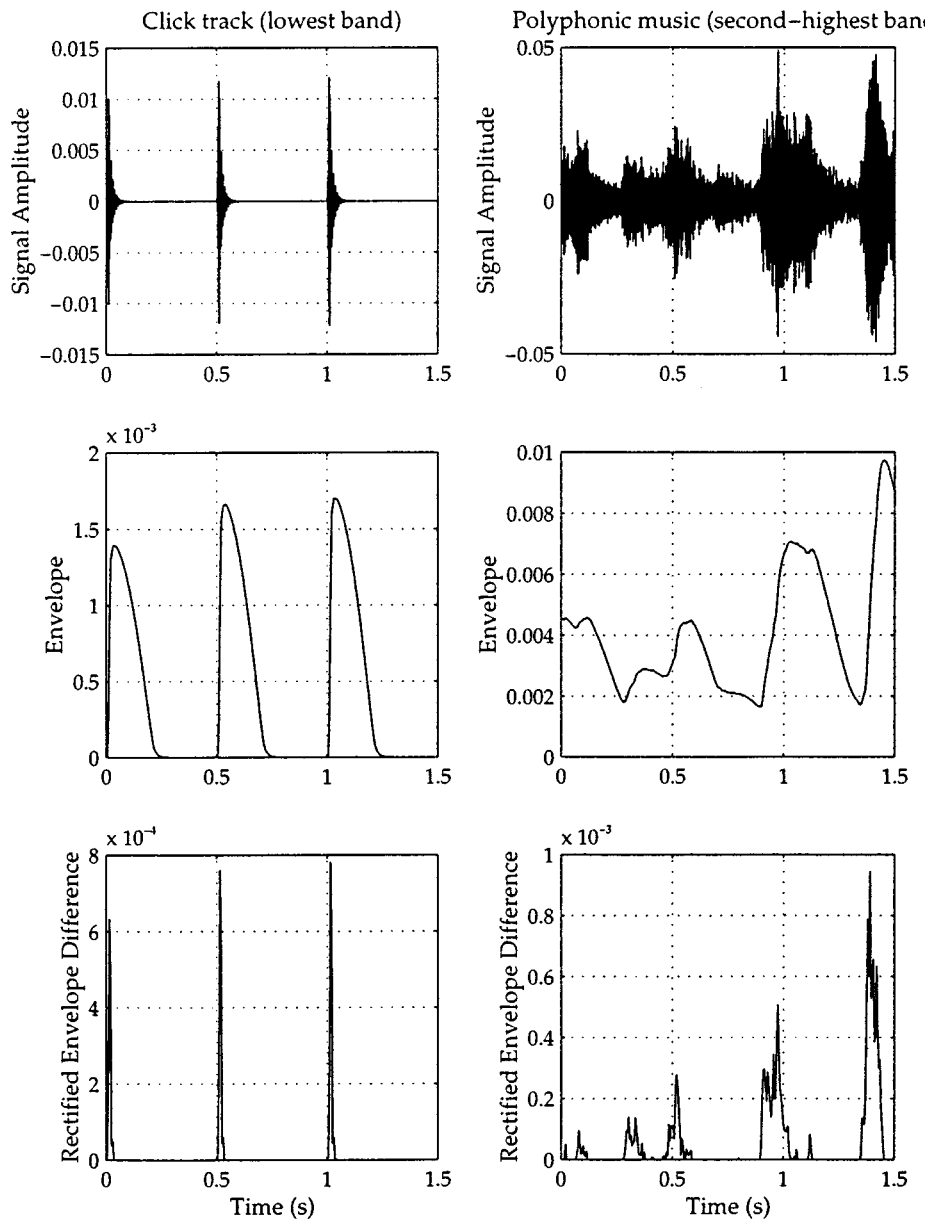
FIG. 5. Envelope extraction process, for a 2-Hz click track (left) and a polyphonic music example (right). The top panels show the audio waveforms; the middle panels, the envelopes; and the bottom, the half-wave rectified difference of envelopes. The lowest filterbank band is shown for the click track, the second-highest for the music. See text for details on algorithms.

Figure 5 shows the envelope extraction process for one frequency band in each of two signals, a 2-Hz click track and a polyphonic music example. The lowest band is shown for the click track, and the second highest for the music track.

B. Resonators and tempo analysis

After the envelope has been extracted and processed for each channel, a filterbank of comb filter resonators is used to determine the tempo of the signal. While comb filters are often used in reverberators and other sorts of audio signal processing, they also have properties which make them suitable for acting as resonators in the phase-locking pulse extraction process.

In particular, if we stimulate a comb filter with delay T and gain α with a right-sided pulse train of height A and

period κ, we get reinforcement (resonance) if $T = \kappa$. Let x_t and y_t be the input and output signals at time t; the equation of the filter is then $y_t = \alpha y_{t-T} + (1-\alpha)x_t$, and

$$y_0 = (1-\alpha)A$$

$$y_\kappa = \alpha(1-\alpha)A + (1-\alpha)A = (1-\alpha)A(1+\alpha)$$

$$y_{2\kappa} = (1-\alpha)A(\alpha^2 + \alpha + 1)$$

$$\vdots$$

$$y_{n\kappa} = (1-\alpha)A\left(\sum_{i=0}^{n} \alpha^i\right).$$

And so $\lim_{n\to\infty} y_{n\kappa} = [(1-\alpha)A]/(1-\alpha) = A$.

On the other hand, if $T \neq \kappa$, the convergence is to a smaller value. Let λ be the least common multiple (common

period) of T and κ; there is only reinforcement every T/λ periods, and by a similar logic as the above,

$$\lim_{n\to\infty} y_{n\lambda} = \frac{(1-\alpha)A}{1-\alpha^{T/\lambda}},$$

and since $|\alpha| < 1$ if the filter is to be stable, and $T/\lambda \geqslant 1$,

$$1 - \alpha^{T/\lambda} \geqslant 1 - \alpha.$$

So a filter with delay matching (or evenly dividing) the period of a pulse train will have larger (more energetic) output than a filter with mismatched delay.

We can see that this is true for any periodic signal by doing the analysis in the frequency domain. The comb filter with delay T and gain α has magnitude response

$$|H(e^{j\omega})| = \left| \frac{1-\alpha}{1-\alpha e^{-j\omega T}} \right|,$$

which has local maxima wherever $\alpha e^{-j\omega T}$ gets close to 1, i.e., at the Tth roots of unity, which can be expressed as

$$e^{-j2\pi n/T}, \quad 0 \leqslant n < T.$$

Using Fourier's theorem we know that these frequency-domain points are exactly those at which a periodic signal of period T has energy. Thus the comb filter with delay T will respond more strongly to a signal with period T than any other, since the response peaks in the filter line up with the frequency distribution of energy in the signal.

For each envelope channel of the frequency filterbank, a filterbank of comb filters is implemented, in which the delays vary by channel and cover the range of possible pulse frequencies to track. The output of these resonator filterbanks is summed across frequency subbands. By examining the energy output from each resonance channel of the summed resonator filterbanks, the strongest periodic component of the signal may be determined. The frequency of the resonator with the maximum energy output is selected as the tempo of the signal.

The α parameter for each comb filter is set differently, so that each filter has equivalent half-energy time. That is, a comb filter of period T has an exponential curve shaping its impulse response. This curve reaches half-energy output at the time t when $\alpha^{T/t} = 0.5$. Thus α is set separately for each resonator, at $\alpha = 0.5^{t/T}$. A half-energy time of 1500–2000 ms seems to give results most like human perception.

Figure 6 shows the summed filterbank output for a 2-Hz pulse train and for a polyphonic music example. The horizontal axis is labeled with ''metronome marking'' in beats per minute; this is a direct mapping of the delay of the corresponding comb filter. That is, for the 2-Hz power envelope signal, a feedback delay of 100 samples corresponds to a 500-ms resonance period, or a tempo of 120 bpm.

In the pulse train plot in Fig. 6, a clear, large peak occurs at 120 bpm, and additional smaller peaks at tempi which bear a simple harmonic relationship (3::2 or 4::5, for example) to the main peak. In the music plot, there are two peaks, which correspond to the tempi of the quarter note and half note in this piece. If the width of the upper plot were extended, a similar peak at 60 bpm would be visible.
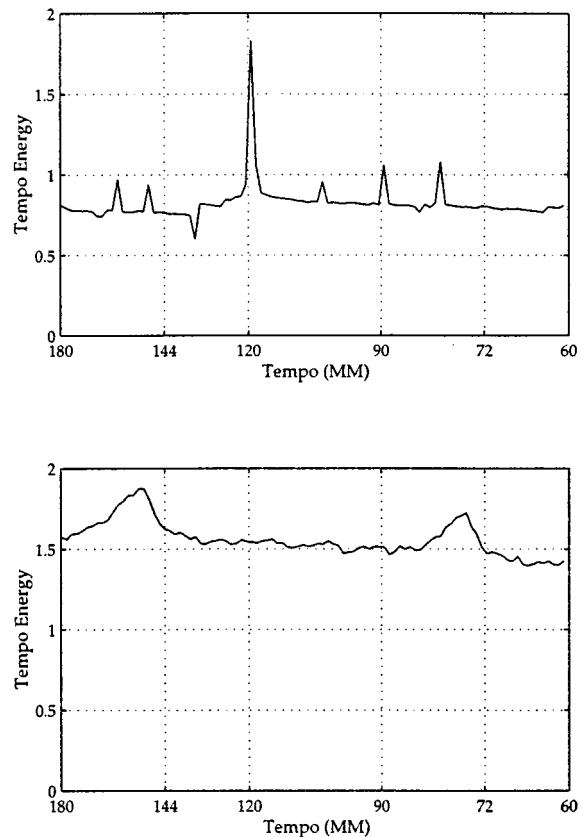

FIG. 6. Tempo estimates, after tracking 5 s of a 2-Hz click track (top) and of a polyphonic music example (bottom). The x-axes are labeled in beats per minute, that is, 120 MM=2 Hz. The polyphonic music shows more overall energy, but the tempo is still seen clearly as peaks in the curve.

C. Phase determination

It is relatively simple to extract the phase of the signal once its tempo is known, by examining the output of the resonators directly, or even better, by examining the internal state of the delays of these filters. The implementations of the comb filters for the resonator filterbank have lattices of delay-and-hold stages. The vector w of delays can be interpreted at a particular point in time as the ''predicted output'' of that resonator; that is, the next n samples of envelope output which the filter would generate in response to zero input.

The sum of the delay vectors over the frequency channels for the resonators corresponding to the tempo determined in the frequency extraction process are examined. The peak of this prediction vector is the estimate of when the next beat will arrive in the input, and the ratio $\omega = 2\pi(t_n - t)/T$, where t_n is the time of the next predicted beat, t the current time, and T the period of the resonator, is the phase ω of the tempo being tracked. The phase and period may thus be used to estimate beat times as far into the future as desired.

The implementation of the model performs the phase analysis every 25 ms and integrates evidence between frames in order to predict beats. Since re-estimation occurs multiple times between beats, the results from each phase analysis can be used to confirm the current prediction and adjust it as
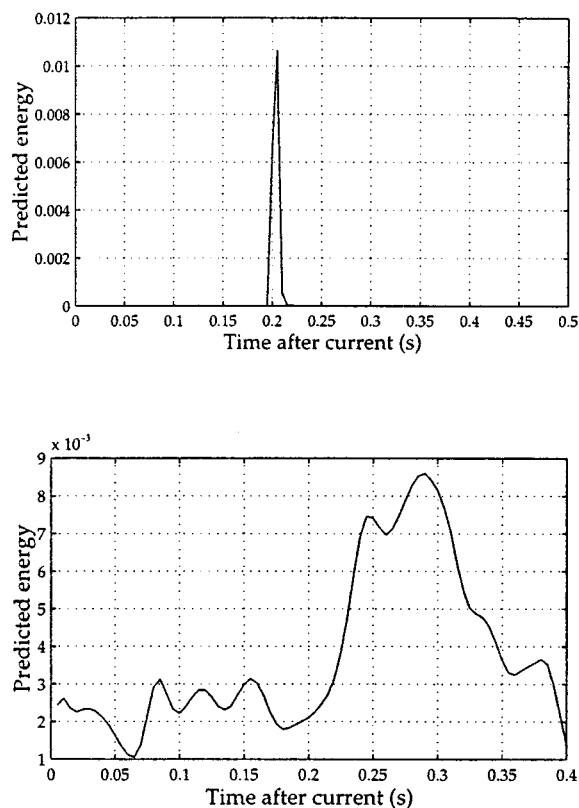
FIG. 7. Phase estimates, after tracking 5 s of a 2-Hz click track (top) and a polyphonic music example (bottom). The *x*-axis in each case covers the next full period of the resonator tracking the tempo, and the peak of the curve shows where the next beat is predicted to occur: about 210 ms in the future for the upper case, and 290 ms for the lower.

needed. Currently, this prediction/adjustment is done in an *ad hoc* manner, requiring only that several successive frames make the same beat prediction within a certain tolerance, and average all of these estimates to arrive at the final prediction. This stage is the appropriate one for the inclusion of high-level information, nondeterministic elements, or more sophisticated rhythmic modeling; see Sec. VI.

Figure 7 shows the phase peaks for a 2-Hz pulse train, and for a polyphonic music example. In the upper plot, as the tempo is 120 bpm, the *x*-axis covers the next half-second of time; and for the lower plot, the estimated tempo is 149 bpm (see Fig. 6), so one period is approximately 400 ms.

D. Comparison with autocorrelation methods

There is a certain analytical similarity between this bank-of-comb-filters approach and previous autocorrelation methods for finding tempo. Insofar as both are ways of detecting periodic energy modulations in a signal, they are performing similar calculations. However, there are several advantages to expressing these operations as multiple comb filters over expressing them as autocorrelation.

Predominantly, comb filtering implicitly encodes aspects of rhythmic hierarchy, where autocorrelation does not. That is, a comb filter tuned to a certain tempo τ has peak response to stimuli at tempo τ, but also lesser response to stimuli with tempi at multiples ($2\tau, 3\tau$), fractions ($\tau/2, \tau/3$), and simple rational relationships ($3/2\tau, 3/4\tau$, etc). The autocorrelation only has this shared response for fractional tempi, not multiples or rationally related tempi. An autocorrelation model asserts that a click track at 60 bpm gives no sense of tempo at 120 bpm, which seems intuitively wrong. The comb filter model asserts instead, that there is such a sense, but a reduced one when compared to a click track to 120 bpm.

These responses can be understood if we imagine building an autocorrelation filter at some lag, versus a comb filter at that same delay, in an FIR manner (that is, to unroll the usual IIR expression of the comb filter into an infinitely long ''FIR'' filter). The autocorrelation requires only a single tap on a delay line, since it only compares ''one cycle back'' in time. The comb filter requires an infinite number of taps, since it compares (with less and less weight) infinitely far back in time.

Autocorrelation methods are zero phase, which means that some other method of determining signal phase must be used. The comb filtering method shown here is phase preserving, and so provides a way of simultaneously extracting tempo and phase, as discussed in the previous section. The fact that the tempo and phase representations arise together gives us additional advantages in constructing higher-level processing algorithms treating the output of the beat-tracker.

One advantage of autocorrelation schemes is that they are more efficient in memory usage than banks of comb filters, as the various lags can all access the same delay line—which is why the autocorrelation is zero phase—whereas each comb filter must maintain a delay line of its own. In return for the extra memory usage, the comb filters provide estimates of output energy at each phase angle of each lag, where the autocorrelation accumulates it and only presents the summary.

Ultimately, it is representationally satisfying to have the frequency and phase of the signal explicitly encoded in the processing units of the algorithm. In an autocorrelation methodology, the rhythmic oscillations of the signal are only represented as post-processed summary results; whereas in the comb filtering method, the filter states themselves explicitly represent the rhythmic content—that is, there is an element of the processing network which phase-locks to and oscillates in synchrony with the signal.

III. IMPLEMENTATION AND COMPLEXITY

The algorithms described above have been implemented in $C++$ code; the resulting program causally processes audio files captured from compact disks or other audio recordings, or coming in via a live microphone input. In this section, the parameters available for controlling the speed and accuracy of the program are described.

A. Program parameters

The current implementation of the system has a number of parameters which can be used to control the accuracy/speed relationship of the algorithms. The program will run in real time on a very fast desktop workstation such as a DEC Alpha, depending on the settings of these parameters and the sampling rate of the incoming audio stream. It is also clear, due to the highly parallel structure of Fig. 3, that the algo-

rithm could efficiently make use of a multiple-processor architecture. This has not yet been accomplished, however.

There are four major areas where the performance and accuracy of the system can be tuned, and control over three of them has been implemented. The algorithm has been tested for audio at sampling rates from 8 KHz to 44.1 KHz and gives roughly equivalent qualitative performance in all of these.

1. Frequency filterbank

As discussed in Sec. II, there is a fair amount of latitude in choosing a frequency filterbank for decomposing the incoming audio stream without affecting human rhythmic perception, and the speed of the system will vary a great deal with the complexity of these filters (since there is a fair CPU load for implementing high-order filters in real time on high-bandwidth audio), and their number (since for each of the frequency channels, a full resonator filterbank structure is implemented).

The performance of the beat-tracking program using filterbanks other than the six-channel sixth-order IIR filterbank described above has not been tested.

2. Envelope sampling rate

The decimation rate of the channel envelopes affects the speed and performance of the system. There are two major implications for using a slow envelope sampling rate: (1) there are many resonator frequencies which cannot be represented accurately with integer delays in the comb filters; and (2) the phase extraction can only be performed with accuracy equal to the envelope sampling rate, since the vector of delays has the same sampling rate.

In tradeoff to this, using a fast sampling rate for the envelopes entails a lot of work in the comb filtering, since the number of multiplies in each comb filter varies proportionately to this rate. Empirical testing over a variety of musical examples suggests that the envelopes should be sampled at least 100 Hz or so for best performance.

3. Number of resonators per frequency channel

The amount of computing incorporated in tracking and analysis of the comb filter resonators varies directly with their number. If too few resonators are used, however, a problem develops with sampling the tempo spectrum too sparsely. That is, since each resonator is attempting to phase-lock to one particular frequency (not to a range of frequencies), if there is no resonator tuned close to the tempo of a particular signal, that signal cannot be accurately tracked.

Also affecting this sparsity consideration is the range of resonator frequencies to be tracked. The wider the range of tempi to track, the sparser a fixed number of resonators will spread over that range.

Good results have been generated using a bank of 150 resonators for each channel, covering a logarithmically spaced range of frequencies from 60 bpm (1 Hz) to 240 bpm (3 Hz).

4. Analysis frame rate

In this particular implementation, a higher-level averaging scheme is used to decide where (at what times) to deduce beats in the input signal. That is, for each analysis frame, the phases of the resonators are examined; the evidence here suggests future beat locations. These suggestions are combined over multiple analysis frames; when several frames in a row point to the same future beat location, evidence accumulates for that time, and a beat is actually assigned there.

Thus the frequency with which the procedure of examining and summing the outputs and internal states of the resonators is executed has a strong effect upon the performance and speed of the program. Good results can be obtained if the analysis frame rate is at least 15 Hz.

Real-time performance cannot be obtained with the parameter values shown above; on an Alpha 3000 using highly optimized filtering and analysis code, with the envelope rate set to 75 Hz, 50 resonators per subband, and frames of beat predictions analyzed every 10 Hz, the required performance for real-time operation on 22-KHz input is reached. This real-time performance includes reading the sound file from disk and playing it back with short noise bursts added to highlight the beats. At this level of accuracy, the algorithm still performs acceptably well on some, but not all, musical examples.

B. Behavior tuning

In addition to controlling the tradeoff between program speed and accuracy, the behavior of the algorithm can be tuned with the α parameters in the comb filters. These parameters can be viewed as controlling whether to value old information (the beat signal extracted so far) or new information (the incoming envelopes) more highly. Thus if α is large (close to unity), the algorithm tends to ''lock on'' to a beat, and follow that tempo regardless of the new envelope information. On the other hand, if α is small, the beat-track can be easily perturbed by changes in the periodicity of the incoming signal. Manipulating these parameters for the comb filter structure is computationally similar to manipulating the windowing function of a narrowed autocorrelation.

Higher-level or domain-specific knowledge could be used to set this parameter based on previous information. For example, in rock or pop music, the beat is usually quite steady, so a high value for α would be appropriate; while for classical music, particularly styles including many tempo changes, a smaller value would be more optimal.

IV. VALIDATION

It is somewhat of a difficult proposition to evaluate the construction of an ecological beat-tracking model, for there are few results in the literature dealing with listeners' tempo responses to actual musical excerpts. Most psychophysical research has dealt primarily with special cases consisting of simple tones in unusual temporal relationships, which will typically be more difficult to track than ''real music'' for a listener. Conversely, most beat-tracking systems have been

TABLE I. Performance of the beat-tracking algorithm, summarized by musical genre. Results were auditioned and classified into groups by qualitative success level. ''Urban'' styles include rap, funk, and R & B music; ''Quiet'' includes muzak and an ''easy-listening'' example. All sounds are available via the WWW.

Genre	No. of cases	Correct	Partial	Wrong
Rock	17	13	3	1
Country	3	3	0	0
Urban	9	7	1	1
Latin	5	3	2	0
Classical	9	4	4	1
Jazz	8	3	1	4
Quiet	3	2	0	1
Reggae	2	2	0	0
Non-Western	4	4	0	0
Total	60	41	11	8

evaluated intuitively, by using a small number of test cases (whether acoustic or MIDI-based) and checking that the algorithm ''works right.''

In this section, the performance of the algorithm is evaluated in both qualitative and quantitative manners. Results are provided on the qualitative performance for 60 ecological music excerpts, with sound examples publicly available for listening. Results are also provided from a short validation pilot experiment which was conducted to confirm that the performance of the algorithm is like the performance of human listeners.

A. Qualitative performance

Examples of many different types of music have been tested with the implemented algorithm, using a short application which reads a sound sample off of disk, causally beat-tracks it, and writes a new sound file with clicks (short noise bursts) added to the signal where beats are predicted to occur. A selection of these sound files is available for listening via the World Wide Web (''results'' page), and the results are summarized below. The wide set of input data contains 60 examples, each 15 s long, of a number of different musical genres. Rock, jazz, funk, reggae, classical, ''easy-listening,'' dance, and various non-Western music are represented in the data set and can be tracked properly. Some of the examples have drums, some do not; some have vocals, some do not. Five of the examples would be judged by human listeners to have no ''beat.'' Table I summarizes the results by musical genre, and some qualitative descriptions of typical results are provided below.

Forty-one of 60 samples (68%) have been qualitatively classified as being tracked accurately, and another 11 (18%) as being tracked somewhat accurately. This accuracy percentage is not directly comparable to that reported for other systems, because the data set used here is more difficult. All of the ''easy'' cases of rock-and-roll with drums keeping a straightforward beat were tracked correctly; and five of the

eight examples not tracked accurately are said by human listeners to have no ''beat'' to begin with. It is premature to interpret these results as indicative of consistent genre-to-genre differences in accuracy; there are too few examples and the within-genre differences in accuracy too great.

For the cases which track correctly, there is a startup period between 2 and 8 s long during which the resonant filters have not yet built up an accurate picture of the signal. After this period, for most signals, the algorithm has settled down and begun to track the signal accurately, placing the clicks in the same locations a human listener would. Examining some of the other, incorrectly tracked examples, is instructive and highlights some of the deficiencies of this method.

Examples #1, #2, and #57 are all up-tempo jazz cases in which human listeners do perceive a strong beat, but no beat is ever extracted by the system. In these three cases, the beat is described by syncopated instrumental lines and complex drum patterns. That is, there is not actually very much energy modulating at the frequency which is the perceptual beat tempo for humans. Human listeners have a great ability to induce ''apparent'' frequencies from complicated modulation sequences. For these examples, the algorithm is not able to find a pulse frequency, and so the beat output is more-or-less random.

The same is apparent in example #37, which is a pop tune that has a ''mixed'' or ''clave'' beat—the beat is not even, but subdivided into oddly spaced groups. Each two measures, containing 16 eighth notes between them, are divided into a 3-3-3-3-2-2 pattern. A human listener has no trouble understanding the relationship between this pattern and a more common 4-4-4-4 pattern, but the algorithm seems to assume that the groups of three are the basic beat, and then get confused when the pattern doesn't come out right.

Among the examples judged as being tracked with some accuracy, but not entirely correctly, the most common problem is phase shifting. For example, in example #16, a jazz piano trio, the beat estimate is correct on the frequency, but switches back and forth between assigning beats to the ''upbeat'' or the ''downbeat.'' Although this behavior is not unlike some human jazz listeners, a human would likely be more consistent in deciding where to place the beat. This behavior could be easily corrected by adding a small amount of high-level knowledge to the beat-tracking system.

Similar to this, in example #7, a rhythm and blues tune, the algorithm is uncertain about assigning the beat to the quarter-note pulse or to the eighth-note pulse, and so switches back and forth between them. A human listener might also suffer from similar confusion, but would likely make an arbitrary decision and then stay with it unless the music changed radically.

Other than these two sorts of confusions for certain rhythmically complex musics, the algorithm seems to perform quite successfully at tracking the musical beats.

1. Tempo modulation

As Todd correctly points out (Todd, 1994), to be an accurate model of human rhythm perception (and, of course, to be maximally useful as a music analysis tool), a beat-
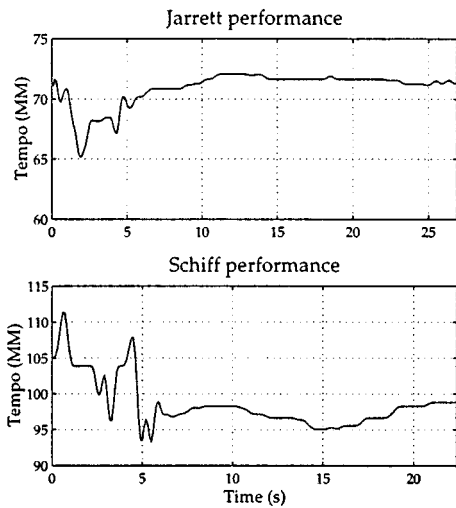
FIG. 8. ''Tempo curve'' for two performances of the same piece of music. Each tempo track has a short startup period during which the tempo estimation is unstable; after that there are clear differences in the two performances. The timescales are slightly different to make the performance scales align (the same musical excerpt is used in both cases).

tracking system must be robust under expressive tempo modulation. The algorithm described here is able to follow many types of tempo modulations; this is effected in the signal processing network by simply examining, over time, the resonator producing the most energetic output. That is, when the tempo of a signal modulates, the response of the resonator corresponding to the old tempo will die away, and that of the resonator corresponding to the new tempo will gain.

Figure 8 shows ''tempo curves'' (Desain and Honing, 1992) for two expressively modulated performances of a piece of music (Keith Jarrett and Andras Schiff performances, of the beginning of the G-minor fugue from book I of Bach's Bach's *Well-Tempered Clavier* [sound example 3]). The algorithm is quite sensitive to the variations in tempo over time.

B. Validation experiment

A short validation experiment has been conducted to confirm the qualitative results given in the previous section. This experiment was not intended to highlight important psychoacoustic effects in beat perception, but only to test whether the beat-tracking algorithm performs generally like a human listener.

1. Subjects

Five adult listeners, all graduate students and staff members at the MIT Media Laboratory, participated in the experiment. All were experienced musicians with normal hearing.

2. Overview of procedure

Subjects listened to seven musical examples, drawn from different musical genres, through headphones. They indicated their understanding of the beat in the music by tapping along with the music on a computer keyboard.

3. Materials

Seven musical excerpts from the above set were used. Each was digitally sampled from an FM radio tuner to produce a monophonic 22-KHz sound file, 15 s long. A computer interface was created on a DEC Alpha workstation with which the musical excerpts were presented to subjects at a comfortable listening level over AKG-K240M headphones.

The musical excerpts were as follows: a Latin-pop song at moderately fast tempo (#10), a jazz piano trio at fast tempo (#17), a ''classic rock'' song at moderately slow tempo (#20), an excerpt from a Mozart symphony at moderate tempo (#40), an ''alternative rock'' song at moderately slow tempo (#45), and a piano etude with varying tempo (#56).

A click track ''step function'' was also created for the experiment, in which 10-ms white noise bursts were presented at a tempo of 120 bpm (interonset time of 500 ms) for 6 s, then at a tempo of 144 bpm (interonset time of 417 ms) for 4.6 s, then again at 120 bpm for 6 more s. This stimulus is used to evaluate the response of human listeners and the beat-tracking algorithm to sudden changes in tempo.

A musical expert (the author) assigned exact beat times to each excerpt by listening repeatedly and placing ''click'' sounds in the perceptually appropriate positions. This task was different than the tapping task in which the subjects participated; the expert listened repeatedly to each stimulus, placing beats, listening to results, and adjusting the beat position if necessary. It is considered to be more accurate and robust than the real-time tapping task, although there is little literature on humans performing either of these sorts of judgments [see Drake *et al.* (1997) and Parncutt (1994) for two other ''tapping tasks'']. The expert labeling was conducted separately from the tapping experiment, the expert did not know the results of the experiment or the algorithm execution, and the subjects were not presented with the expert data. The resulting ''ground truth'' beat times are used for the evaluation of results, below.

4. Detailed procedure

Subjects were seated in front of the computer terminal and instructed in the task: they were to listen to short musical examples and tap along with them using the space bar on the keyboard. They were instructed to tap at whatever tempo felt appropriate to the musical excerpt, but to attempt to tap in equal intervals (a pilot experiment revealed that some subjects like to ''drum along'' in rhythmic or even syncopated patterns with the music if they are not instructed otherwise). They listened to a 120-bpm click-track as a training sample to indicate they understood the procedure, and then proceeded with each of the seven experimental trials.

All seven trials were run in the same sequence for each listener, in a single block. The experiment was not counterbalanced based on an assumption that there is little training effect in this task. After each trial, the subject was instructed by the interface to press a key different than the space bar to continue to the next trial. The entire experiment took approximately 5 min per subject. The computer interface re-

corded the time of each tap, accurate to approximately 10 ms, and saved the times to a disk file for analysis.

Finally, the beat-tracking algorithm was executed on each of these seven stimuli to produce beat times as estimated by the model described in the previous sections. These beat times were saved to a disk file and analyzed for comparison with the human beat times. The algorithm parameters were adjusted to give optimum performance for this set of trials, but not changed from trial-to-trial.

5. Dependent measures

The human and algorithmic beat-tracks were analyzed in two ways. First, the beat placements were compared to the ideal placements as judged by the expert listener; then, the regularity of tapping was assessed by examining the variance of interonset times.

To compare the beat placements, a matching comparison was conducted. Each beat placed by a human subject or by the beat-tracking model was matched with the closest (in time) comparison beat in the expert beat-track. Initially, only the beats actually placed by the expert were used, but since some subjects and the algorithm tapped twice as fast as the expert on some examples, beats were allowed to be matched to the midpoint between expert beats. The root-mean-square deviations of the subject's taps from the expert's taps were collected for each subject and trial, averaging across taps within a trial.

This rms deviation is a measure of how close the tapper came to the "ideal" beat locations. If it is very low, all of the tapper's placements were very close to expert judgments; if high, the tapper's placements were randomly distributed compared to the expert judgments.

This measure leaves open an important aspect of beat-tracking, which is regularity. As described in the qualitative results, the algorithm sometimes demonstrates unusual behavior by switching from one tempo to another, or from off-the-beat to on-the-beat, in the middle of a trial. To evaluate the regularity of tapping, the variance of interonset interval was calculated for each trial-by-subject, each trial by the model, and each trial by the expert. Note that, as described above, the human subjects were explicitly encouraged to tap regularly.

Again, the expert's behavior is taken as ideal; if the variance is larger for some tapper than for the expert, it indicates that the tapping was irregular relative to the expert. If the variance is smaller, it indicates that the tapping was more regular than the expert (not necessarily a positive aspect in the case of changing tempi). Irregularity generally arises in this data from leaving out beats, each occurrence of which adds an inter-onset interval twice as large as the rest, increasing the variance.

6. Results and discussion

The beat-placement comparison is shown in Fig. 9. Results indicate that the performance of the algorithm in placing beats in logical locations was at least comparable to the human subjects tested for all the musical cases; in four of the seven cases, the model was the most or second-most accurate
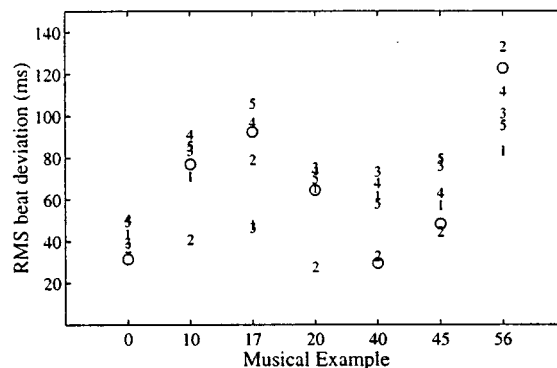

FIG. 9. Scatter plot of human (subj. number) and model (O) beat position accuracy for each of the seven experimental trials. Trial '0' corresponds to the click-track step function. Each point measures how accurate that subject was, relative to the expert, in placing beats in time. The expert judgments are at zero variance for each column. For each trial, the algorithm beat position was at least comparable to the performance of the human subjects. Overall, the algorithm performance showed a highly significant positive correlation with the human subject performance [$r=0.814$; $p(\mathrm{df}=5)$ <0.015].

tapper. This indicates that whenever a beat position was chosen by the algorithm, the position was very close to the ideal beat position as determined by the expert judgment.

The regularity comparison is shown in Fig. 10. Results here indicate that the algorithm was as regular as a human listener for five of the seven trials, and less consistent for two of the trials. In one case, it and several of the human subjects were more consistent than the expert. More *post hoc* analysis is necessary to understand why the algorithm performance is irregular in these trials; preliminary results suggest that these two stimuli have relatively slow onsets carrying the beat (violins in one case, electronically gated drum sounds in the other).

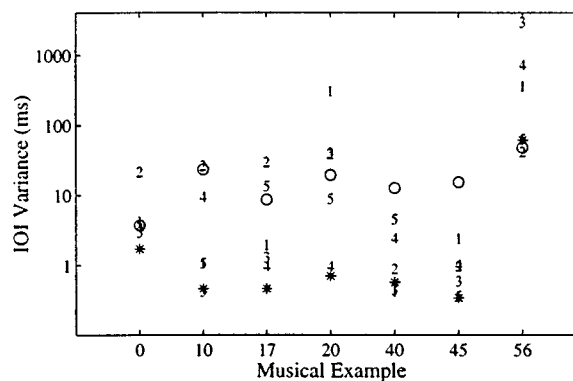These two results are consistent with the qualitative re-

FIG. 10. Scatter plot of human (subj. number), model (O), and expert (*) IOI variances for each of the seven experimental trials. Trial "0" corresponds to the click-track step function. Each point shows the regularity of tapping of a subject for one trial; large values represent less regular tapping. For trials #40 and #45, the algorithm was not as consistent in tapping as a human listener. Overall, the algorithm performance showed a highly significant positive correlation with the human subject performance, and both the algorithm and the human subjects showed highly significant positive correlations with the expert judgement [$r=0.889$, $r=0.863$, $r=0.995$, respectively; $p(\mathrm{df}=5)<0.01$ in each case].

sults described above. When the algorithm chooses to place a beat, it does so with great accuracy and musical relevance; however, for certain musical excerpts, it is somewhat inconsistent in its tapping regularity. That is, for these examples, it drops beats or shifts phase more often than a human listener. This is not a bad result, because it is exactly this inconsistency which could best be addressed by including high-level information in the model (such as simply including instructions to ''try to tap regularly'').

V. DISCUSSION

In previous sections, the construction of a beat-tracking system has been approached from a largely empirical perspective. However, it is also valuable to compare the resulting algorithm to previous work on pulse perception in humans.

A. Processing level

Perhaps the most obvious difference between the method presented here and much of the previous work on beat-tracking is that this algorithm knows almost nothing about musical timbre, genres, or even notes or onsets. This approach to tempo analysis might be called a ''perceptual model'' of tempo, to contrast it with cognitive structuralist models.

That is to say, in models such as Povel and Essens (1985), Desain (1995), or Goto (in press), there are two stages of processing represented (the first is implicit in the Povel/Essen and Desain models). The first stage processes the acoustic stream, classifying the various pieces of sound into onsets and time intervals, separating the streams of sound, and understanding the accent structure and timbre of various components. Then, the second stage places these events in relationship to each other in order to determine the tempo and phase of the signal.

In contrast to this, the model presented here agrees with the viewpoint of Todd (1994), in which tempo and rhythm are low-level ''perceptual judgments'' about sound, with little cognition or memory required for processing. This viewpoint is intuitively appealing for at least one major reason, which is that certain features of tempo and beat are processed in non-attended auditory streams. Music listeners, even nonmusicians, often have the experience of conducting a conversation and suddenly realizing that they have been tapping their foot to background music. If the foot-tapping process requires cognitive structuring of the input data, it seems likely that other cognitive hearing tasks such as speech-understanding would interfere.

The finding of Levitin and Cook (1996) that there is a great ability for listeners to learn and remember absolute musical tempo implies that tempo is a simple, low-level perceptual quality. The body of initial work on rhythm perception in non-human animals (for example, Hulse *et al.*, 1984) would seem to imply similar conclusions.

The resemblance between the algorithm as drawn in Fig. 3 and modern models of pitch hearing is striking. Both models contain frequency-decomposition front ends followed by temporal integration. This comparison is explored in depth in Scheirer (1997) and leads to the question of whether pitch and tempo perception might be related auditory phenomena.

Studies such as that of Povel and Essens (1985) have demonstrated convincingly that beat perception may be explained with a model in which a perceptual clock is aligned with the accent structure of the input. A clock model is fully compatible with the method proposed here; it seems natural and intuitive to posit such an internal clock. However, the Povel and Essens model of clock induction, and similarly the Parncutt model, relies heavily on structural qualities of the input, such as a sophisticated model of temporal accent, to function.

Todd has argued that such phenomena do not need to be modeled cognitively, but rather can be explained as natural emergent qualities of known psychoacoustic properties of masking and temporal integration. This model agrees here as well, for it has demonstrated empirically that musical signals can be accurately beat-tracked without any such factors explicitly taken into account. However, a more thorough evaluation of this model would include testing it on the unusual and difficult sequences tested in the course of developing accent models, to determine if changes to weighting factors or integration constants need to be made in order to replicate these psychophysical effects.

B. Prediction and retrospection

Desain's recent work on beat-tracking has included valuable discussion of the role of prediction and retrospection in rhythmic understanding. Clearly, prediction is a crucial factor in an accurate model of human rhythm perception, as simply to synchronize motor motion (like foot-tapping) with an auditory stream requires prediction. There is a pleasing symmetry between Desain's ''complex expectancy'' curves and the phase-prediction vectors extracted here from the comb filter delay lines (as in Fig. 7).

Desain, citing Jones and Boltz (1989), draws attention to the utility of considering prediction and retrospection to be similar aspects of a single process. ''Retrospection'' refers to the manner in which new stimulus material affects the memory of previous events. Although there is no retrospection included in the model—remembrance would seem to be an inherently cognitive process—the phase-prediction curves could be used as input for this process as well.

When evaluating this model, it is important to keep in mind the complexity of introspection on musical phenomena. Although after-the-fact, listeners have made a rhythmic model of the very beginning of a musical phrase, it is clear that this model must have arisen via retrospection, for there is not enough information in the signal alone to form it progressively. Simply because a listener feels that he ''understands'' the rhythm of the beginning of a musical segment does not mean that the beginning itself contains sufficient information to allow such understanding.

C. Tempo versus rhythm

The effects which are not explained with this model are those related to grouping of stimuli into a rhythmic hierarchy. There are many known effects in this area, ranging from

the low-level, such as Povel and Okkerman's work on perceived accents in nonaccented sequences (Povel and Okkerman, 1981) to very broad theories of generative rhythmic modeling such as the well-known Lerdahl and Jackendoff work (Lerdahl and Jackendoff, 1983).

This model is compatible with and complementary to the bulk of this research, since most of the theories assume that a temporal framework has already been created. Synthesis of a model which operates from an acoustic source and one which includes musical assumptions and explanation should be possible, and would then represent a very robust theory of rhythmic understanding.

However, the model presented here should not be taken as attempting to explain rhythm perception as well as tempo; the viewpoint is rather that these processes are to some extent separable and may be addressed and modeled independently.

VI. CONCLUSION AND FUTURE WORK

An algorithm has been described which can successfully beat-track digital audio representing music of many different types. The music does not have to contain drums or any other specific timbres, and it does not have to conform to any predetermined set of musical templates. The beat-tracking procedure can be run in real-time on an advanced desktop workstation.

There are still aspects of the algorithm which are inadequately tested and understood. For example, would it be equally accurate but more efficient with a different filterbank, or could it be made more accurate in this way? What would be the implications of using a different temporal integration function, with different or more psychoacoustically accurate properties? What about using an entirely perceptually motived front end? These questions are unfortunately still unaddressed.

Errors still made by the algorithm are typically due to the inability to understand beat relationships at various tempi; that is, a human listener intuitively understands the way eighth-note patterns group to form quarter-note and half-note patterns, and while some processing of this sort is done implicitly in the resonators due to phase-locking at harmonic ratios, it would clearly make the algorithm more robust to have an explicit model of this sort of rhythmic grouping.

Perhaps the way to build a system that can track complicated beat patterns is to construct it in two layers. The lower layer would be a simple perceptual beat extraction system as described here, which finds the level at which the pulse is evenly divided in time. Then, a higher-level grouping model selects and processes the beats to form an model of the rhythmic hierarchy present in the signal, based on pattern-recognition detection of accent structures and instrumental beat patterns. Building a system in this manner would allow us to leverage much of the existing work in cognitive rhythm models to apply to the analysis of digital audio as well as symbolically represented music.

Brown, J. C. (**1993**). "Determination of the meter of musical scores by autocorrelation," J. Acoust. Soc. Am. **94**, 1953–1957.

Desain, P. (**1995**). "A (de)composable theory of rhythm perception," Music Perception **9**, 439–454.

Desain, P., and Honing, H. (**1992**). *Music, Mind, and Machine: Studies in Computer Music, Music Cognition, and Artificial Intelligence* (Thesis Publishers, Amsterdam).

Drake, C., Penel, A., Bigand, E., and Stefan, L. (**1997**). "Tapping in time with musical and mechanical sequences," in *Proceedings of the 1997 European Society for Cognition of Music*.

Goto, M., and Muraoka, Y. (**in press**). "Music understanding at the beat level: Real-time beat tracking for audio signals," in *Readings in Computational Auditory Scene Analysis*, edited by D. Rosenthal and H. Okuno (Erlbaum, Mahwah, NJ).

Handel, S. (**1989**). *Listening* (MIT, Cambridge, MA).

Hulse, S. H., Humpal, J., and Cynx, J. (**1984**). "Discrimination and generalization of rhythmic and arrhythmic sound patterns by European starlings (*Sturnus vulgaris*)," Music Perception **1**, 442–464.

Jones, M. R., and Boltz, M. (**1989**). "Dynamic attending and responses to time," Psychol. Rev. **96**, 459–491.

Large, E., and Kolen, J. F. (**1994**). "Resonance and the perception of musical meter," Connection Science **6**, 177–208.

Lerdahl, F., and Jackendoff, R. (**1983**). *A Generative Theory of Tonal Music* (MIT, Cambridge, MA).

Levitin, D. J., and Cook, P. R. (**1996**). "Memory for musical tempo: Additional evidence that auditory memory is absolute," Percept. Psychophys. **58**, 927–935.

Longuet-Higgins, H. C., and Lee, C. S. (**1984**). "The rhythmic interpretation of monophonic music," Music Perception **1**, 424–441.

Martin, K. (**1996**). "Automatic transcription of simple polyphonic music," J. Acoust. Soc. Am. **100**, 2813A.

Parncutt, R. (**1994**). "A perceptual model of pulse salience and metrical accent in musical rhythms," Music Perception **11**, 409–464.

Povel, D.-J., and Essens, P. (**1985**). "Perception of temporal patterns," Music Perception **2**, 411–440.

Povel, D.-J., and Okkenman, H. (**1981**). "Accents in equitone sequences," Percept. Psychophys. **30**, 565–572.

Rosenthal, D. (**1992**). "Machine rhythm: Computer emulation of human rhythm perception," Ph.D. thesis, MIT Media Laboratory.

Scheirer, E. (**1996**). "Bregman's chimerae: Music perception as auditory scene analysis," in *Proceedings of the 1996 International Conference on Music Perception and Cognition*, Montreal.

Scheirer, E. (**1997**). "Pulse tracking with a pitch tracker," in *Proceedings of the 1997 IEEE Workshop on Applications of Signal Processing to Audio and Acoustics*, Mohonk, NY.

Scheirer, E. (**in press**). "Using musical knowledge to extract expressive performance from audio recordings," in *Readings in Computational Auditory Scene Analysis*, edited by H. Okuno and D. Rosenthal (Erlbaum, Mahwah, NJ).

Shannon, R. V., Zeng, F.-G., Wyngoski, J., Kamath, V., and Ekelid, M. (**1995**). ''Speech recognition with primarily temporal cues,'' Science **270**, 303–304.

Smith, L. S. (**1994**). ''Sound segmentation using onsets and offsets,'' J. New Music Res. **23**, 11–23.

Todd, N. P. McA. (**1994**), ''The auditory 'primal sketch': A multiscale model of rhythmic grouping,'' J. New Music Res. **23**, 25–70.

Vercoe, B. L. (**1994**). ''Perceptually-based music pattern recognition and response,'' in *Proceedings of the 1994 International Conference on Music Perception and Cognition*.

The role of vocal tract filtering in identity cueing in rhesus monkey (*Macaca mulatta*) vocalizations

Drew Rendall
Department of Anthropology, University of California at Davis, Davis, California 95616

Michael J. Owren
Department of Psychology, Reed College, Portland, Oregon 97202

Peter S. Rodman
Department of Anthropology, University of California at Davis, Davis, California 95616

The importance of individual identity and kinship has been demonstrated in the social behavior of many nonhuman primates, with some evidence suggesting that individually distinctive acoustic features are present in their vocalizations as well. In order to systematically test whether acoustic cues to identity are reliably present across the vocal repertoire of rhesus monkeys (*Macaca mulatta*), we examined *coos*, *grunts*, and *noisy screams* produced by adult females of two free-ranging groups. First, acoustic analyses were used to characterize spectral patterning, the fundamental frequency, and temporal characteristics of these three distinct call types. Vocalizations were then classified by caller identity, based on discriminant function analyses. Results showed that coos (rich, harmonically structured sounds) were markedly more distinctive by caller than were either grunts or noisy screams, and that spectral-patterning measures related to vocal tract filtering effects were the most reliable markers of individual identity. Grunts (pulsed, noisy calls) were classified at lower, but above-chance rates and spectral patterning cues were again critical in this sorting. Noisy screams (continuous, broadband noise bursts that could include a high-frequency, periodic component) could not be reliably sorted by caller. Playback experiments conducted with the screams showed no response differences when listening animals heard vocalizations produced by kin or nonkin individuals. This result was strikingly different from the corresponding outcome of a previous test with coo calls, but consistent with the acoustic analysis. Implications of these findings for vocal production mechanisms in nonhuman primates and previous studies of rhesus monkey vocalizations are discussed. © *1998 Acoustical Society of America.* [S0001-4966(98)00901-1]

PACS numbers: 43.80.Ka [FD]

INTRODUCTION

A prominent theme of recent work in primatology has been the importance of kinship and inter-individual relationships in shaping the social behavior of monkeys and apes (reviewed in Cheney *et al.*, 1986; Cheney and Seyfarth, 1990; Smuts *et al.*, 1987), which can be described as being both individualistic and nepotistic. Many species are marked by stable dominance relationships among group members, with numerous components of social behavior (e.g., approaching, maintaining proximity during foraging or resting, grooming, and alliance formation during conflict) being strongly influenced by both the identities of the animals involved and their kin relationships. Such complex interaction patterns ultimately require that social primates be able to discriminate among other group members, or more likely, to explicitly recognize one another.

Consistent with such needs, recent studies of nonhuman primate vocal communication have identified a variety of calls whose acoustic structures are individually distinctive (reviewed in Snowdon, 1986). However, little has been done to investigate the degree to which inclusion of identity cues has specifically shaped the repertoire of any particular species, or whether potentially distinctive cues identified through acoustic analysis of calls are perceptually salient to the animals (see Cheney and Seyfarth, 1980, 1982, 1988; Seyfarth and Cheney, 1984; Cheney *et al.*, 1995; Rendall *et al.*, 1996). Thus while evidence from social behavior argues strongly that individual discrimination or explicit recognition occurs among nonhuman primates, it is not clear whether all calls in a given repertoire provide the requisite cues, or whether such cues take a consistent form.

Most studies of individual differentiation in primate vocalizations have emphasized specialized signal functions, such as inter- and intra-group spacing (e.g., Marler and Hobbett, 1975; Waser, 1977; Snowdon *et al.*, 1983). However, commonly occurring, acoustically unspecialized vocalizations used in a variety of contexts can also carry cues to identity or kinship (reviewed by Snowdon, 1986; Rendall *et al.*, 1996). In recent work, Owren *et al.* (1997) found that in wild chacma baboon (*Papio cynocephalus ursinus*) *grunt* calls, spectral energy-peak patterning varied according to caller identity. Discriminant-function analyses based on acoustic measurements revealed that these features were more important than were other aspects in sorting the grunts by caller. In a more direct approach, Rendall *et al.* (1996) used a hidden speaker to play back examples of species-typical *coo* calls to rhesus monkeys (*Macaca mulatta*). In this study, conducted under naturalistic circumstances with free-ranging animals, target monkeys were much more responsive to vocalizations produced by a kin individual rather

than an unrelated animal. Such findings do indeed suggest that individuality is a prominent component of many calls, and underscores the importance of investigating the cues involved in understanding the structure, function, and origin of various sound types. This issue is particularly important in that while nonhuman primates typically use calls exhibiting a variety of acoustic features and concomitant production processes, the extent to which cues to individual identity are either distinctive to particular call types (and associated production characteristics) or show carry over among differentiated call types is unknown. One approach to this general problem is to explicitly examine the acoustic features of calls, as well as the potential for variation in those features, in the context of known vocal production processes.

In the current work, the *source-filter model* of vocal production is used as a basis for investigating important characteristics of rhesus monkey calls. This model was developed in the context of human speech (e.g., Chiba and Kajiyama, 1941; Stevens and House, 1955; Fant, 1960), but has since been applied to the vocalizations of a number of animal species, including nonhuman primates (reviewed by Fitch and Hauser, 1995; Owren and Linker, 1995) and birds (reviewed by Gaunt and Nowicki, in press). While a number of aspects of call production in nonhuman primates differ from sound generation in humans (e.g., Schön Ybarra, 1995), several key features are similar. Most importantly, many vocalizations produced by monkeys and apes combine source energy due to vocal fold movement with filtering effects due to the resonance properties (frequency-specific amplification and attenuation effects) of the supra-laryngeal cavities.

Adopting this perspective, cues to individuality can be seen as arising in three general ways. First, individual distinctiveness may be related to variation in the size, shape, movement, and tissue properties of each animal's vocal folds—structures acting as the sound-generating mechanism. If production of differentiated call types relies on similar vocal-fold action, cues directly related to vibration in these tissues may carry over in the voice of a given animal. Second, variation in the size, shape, movement, and tissue properties of each animal's supra-laryngeal vocal tract may impose distinctive filtering effects on the source energy as it passes through the oral and nasal cavities. Typically, the most discernible effects are prominent peaks in the frequency spectrum of the call, produced by vocal tract resonances (*formants*). To the extent that filtering characteristics remain stable as a given animal uses various calls, the associated cues can also be expected to carry over among call types. Finally, the temporal patterning of sound energy within a call, or across a set of calls, may also provide differentiated cues to caller identity. In this case there is arguably less opportunity for an individual's distinctive patterning cues to carry over among call types, as nonhuman primates typically produce a variety of sounds with widely differentiated temporal organizations. However, a caller could distinguish itself from others by exhibiting distinctive, temporally based patterning for each call type used.

Exactly the same considerations apply to human vocal production, whether of speech or other sounds. However, while theorists have long proposed that human vocalizations
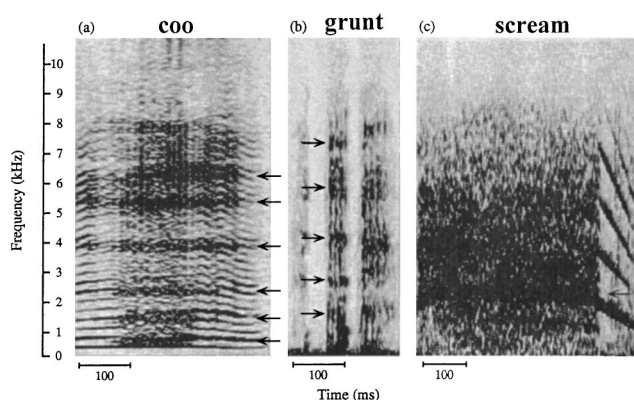

FIG. 1. Narrow-band digital spectrograms of a representative (a) coo, (b) grunt, and (c) noisy scream, each produced by an adult female rhesus monkey. Arrows indicate the approximate locations of resonance peaks, or the ''dominant frequency'' in the case of the scream. (Note that the time scale marker is slightly shorter for the scream, which is therefore proportionately slightly longer than either the coo or grunt.)

routinely include perceptible acoustic features that provide information concerning talker characteristics, such *indexical* cues (e.g., Abercrombie, 1967) have received surprisingly little systematic attention (e.g., Goldinger *et al.*, 1996; Johnson and Mullenix, 1997; Pisoni and Lively, 1995). Available studies of such features (reviewed by Kreiman, 1997) have shown that both source energy and vocal tract transfer function characteristics contribute to the identifiability of a given voice, indicating that individual variation in the anatomy and action of both vocal folds and supralaryngeal vocal tract structures are important (see for instance Carrell, 1984; Fant, 1973; Joos, 1948; Titze, 1994).

In this study, we examined individual differentiation in the acoustic features of *coos*, *grunts*, and *noisy screams*, three calls used by rhesus monkeys. Rhesus monkeys live in large, cohesive groups that exhibit nepotistic relations among female kin, competitive relations among nonkin, and strong indirect evidence of individual recognition (e.g., Kaplan, 1977, 1978). This species is therefore well-suited to examining individual identity cueing occurring in widely used, intra-group acoustic signals. The vocal repertoire of rhesus monkeys is rich and varied (e.g., Peters, 1983; Hauser and Marler, 1993a), and each of the three sounds tested comprises a prominent component of the calling system; representative examples are shown in Fig. 1. As is apparent, coos, grunts, and noisy screams are quite divergent, both in spectral and temporal characteristics. Coos are conspicuous and harmonically rich calls given during moving and foraging. They appear to function in maintaining contact among spatially dispersed group members, particularly female kin (e.g., Rowell and Hinde, 1962; Hauser, 1991; Rendall *et al.*, 1996). Grunts are low-amplitude, atonal, pulsed calls given most frequently in the context of relaxed, face-to-face social interactions, apparently promoting affiliation (Hauser and Marler, 1993a). Screams are very loud, harsh calls given during fights and have been proposed to help in recruiting aid from kin and other social allies. Several scream types have been delineated, based on correlations among acoustic features and the relative dominance rank of the opponent, genetic relatedness of the vocalizer and its opponent, and the

severity of the aggression that has occurred (Gouzoules *et al.*, 1984). Noisy screams, so-called because of their especially harsh, broadband spectral structure, are the type given in circumstances that represent the greatest threat to the caller.

Based on playback experiments that tested kinship-based discrimination using screams (Gouzoules *et al.*, 1986) and coos (Rendall *et al.*, 1996), we expected that both of these two call types would exhibit individual variation in their acoustic features. For grunts, in contrast, no clear outcome could be predicted. On the one hand, these calls resemble coos in being used by rhesus monkeys in a variety of situations, including many circumstances in which coos occur (e.g., Owren *et al.*, 1992). Grunts could therefore also be expected to show individually distinctive acoustic variation. However, as these quiet calls are used in situations in which visual information concerning the identity of the caller is typically available to the receiver, there appears to be little need to include individualized acoustic cues for identification purposes.

Taken as a set, then, coos, grunts, and screams were well-suited to our goal of examining individual differentiation of acoustic structure of divergent calls used by rhesus monkeys. Based on the sound-production principles outlined above, we expected that commonalities in spectral patterning due to vocal tract resonances would be the most likely to carry over among different call types produced by a given individual. In nonhuman primates, such cueing might be particularly robust in that articulation-based modification of supra-laryngeal vocal tract cavities appears to play a relatively small role in call production (e.g., Liebermann, 1984; although see Fitch and Hauser, 1995, and Owren *et al.*, 1997). Coos, grunts, and noisy screams were deemed to involve quite different vocal-fold vibration modes, and source-related variables were therefore predicted to be more individually distinctive within each sound type than among the various calls. Similarly, significant potential for identity cueing based on temporal features was expected within call types, but with few carry over effects. However, while both coos and grunts are frequently given singly, screams are typically produced as a concatenated series of rapidly occurring, but separable calls. To facilitate a uniform comparison of the characteristics of each of the three call types, analyses were therefore restricted to single vocalizations.

This paper reports results of acoustic analyses of coos, grunts, and noisy screams recorded from two groups of free-ranging rhesus monkeys living in a naturalistic setting. The degree to which the features of each call type varied by individual were examined using discriminant function analyses to test the relative role of particular cues in statistical sorting of calls based on caller identity. The outcome of a playback experiment testing noisy screams is also described, following up similar evidence for coos (Rendall *et al.*, 1996) and using the same methodology to test the ability of selected target animals to discriminate between the calls of related and unrelated animals. As screams are very loud and have been proposed to convey to listening animals that the caller is under dire attack (Gouzoules *et al.*, 1984), we expected these sounds to readily elicit responses. Grunts, in contrast, are

quiet, close-range calls that could not be readily tested in this way given that the absence of an actual caller would be readily apparent to any target monkey.

I. METHOD

A. Study site and subjects

Research was conducted with free-ranging rhesus macaques (*Macaca mulatta*) on Cayo Santiago, a 15.2-ha. island off the southeast coast of Puerto Rico. This population has been continuously studied since being established in 1938, and long-term data on both demography and genealogy are therefore available (Rawlins and Kessler, 1986). Each monkey is uniquely marked and matrilineal relatedness is known in every case. Animals receive daily provisions of commercial chow, with the remainder of their diet being natural forage. During the study (conducted from August 1993 to September 1994) there were approximately 1050 animals, comprising seven groups. Work focused on adult females (i.e., more than 4 years old) in two of these groups.

B. Apparatus and procedure

1. Audio recording

Vocalizations were recorded on an ad libitum basis throughout the day (0715–1745 h). Recordings were made using a Sony TC-D5M cassette tape-recorder, a Sennheiser ME88 directional microphone with K3U powering module, and Type-IV Sony ''metal'' cassette tapes. As the monkeys had been observed for decades and had been tape recorded by other investigators (e.g., Gouzoules *et al.*, 1984, 1986; Hauser, 1991, 1992; Hauser and Fowler, 1992; Hauser and Marler, 1993a, 1993b), they were habituated both to humans on foot and to recording equipment. Recordings could therefore be made at very close range, typically 0.5–1.5 m. The vocalization sample used here consisted of 1030 calls from 21 different adult females, including 507 coos from 17 females, 408 grunts from 11 females, and 115 noisy screams from 9 females (see Table I).

2. Acoustic analysis

Recordings were digitized at 22.05 kHz with 16-bit accuracy and low-pass filtered at 10.0 kHz. Four analysis approaches were used. The first was to measure temporal features from waveform displays created with CANARY version 1.1 (CANARY, 1993). The duration of each call (DUR) and the relative temporal position of its peak amplitude (PEAK%) could be measured in all three call types. The pulsatile nature of grunts also permitted measurement of the duration of each component pulse ($DUR\ P_{\#}$) and intervals between successive pulses ($IPI_{\#}$). Grunts varied in consisting of from 2 to 5 pulses, and this number was therefore included as a variable (# $PULSES$). As the first pulse of a grunt was often soft and difficult to measure reliably, its duration was not included. Further, because relatively few grunts contained more than a total of three pulses, the durations of any additional pulses and corresponding inter-pulse intervals were also excluded.

TABLE I. An overview of the call samples used in acoustic analysis.

Female ID	Coos (n = 17)	Grunts (n = 11)	Noisy screams (n = 9)
408	23	60	
693	25	24	11
845	35	67	14
987	44	33	20
E76	19		
E78	31		
F23	16	30	
F82	14	48	
I69	54	23	
J79	45		
J96	22	25	
K08	16	27	6
K17	20		
L41	34		
L81	31	33	
N99			16
O21			14
O24		38	
R62	44		8
S44			13
V66	34		13
	n = 507	n = 408	n = 115

The second approach involved measurements of the fundamental frequency (F_0) of coos, whose tonal qualities and harmonically structured frequency spectra were consistently indicative of periodic underlying source functions—in contrast to the noisy, broadband nature of both grunts and screams. These measurements were taken from spectrogram displays generated in CANARY using a Hamming window and 1024-point fast Fourier transforms (FFTs) with a frequency resolution of 87.42 Hz. Measurements included maximum and minimum F_0 values ($MAX\ F_0$ and $MIN\ F_0$, respectively), and F_0 frequency at the beginning, middle, and end of each call ($BEG\ F_0$, $MID\ F_0$, and $END\ F_0$, respectively). Several composite variables characterizing relational F_0 features were then derived from these values. Variables $END/BEG\ F_0$, $END/MID\ F_0$, $MID/BEG\ F_0$, $MAX/MIN\ F_0$, and $MID/MAX\ F_0$ were simple ratios, while $SLOPE\ F_0$ was computed as the arithmetic difference between $END\ F_0$ and $BEG\ F_0$, divided by DUR.

In the third analysis approach, linear predictive coding (LPC) was used to identify major energy peaks in the frequency spectrum of each call [see Owren and Bernacki (in press) for a conceptual and methodological review]. Autocorrelation-based LPC spectra were computed using the Interactive Laboratory System version 6.0 (ILS, 1986), a generic technique that automatically provides frequency and amplitude values of major spectral energy peaks while avoiding any assumptions about underlying production processes. Analysis parameters were established by first testing 50 vocalizations of each call type recorded from a number of different females by overlaying 512-point (approximately 23 ms) LPC-based spectra on corresponding but independent FFTs (see Owren and Bernacki, in press), using a Hamming window and "full" pre-emphasis (pre-emphasis increases the amplitude of higher frequencies, thereby improving resolution in this range).

Due to the differences in spectral structure between the coos and the noisier grunts and screams, one LPC analysis used different numbers of analysis coefficients for the three call types. With coos, 18 coefficients provided the best fit to the FFT spectrum, usually yielding a set of 8 peaks ($F1$ through $F8$). However, only $F3$ and $F4$ were found to be consistently present for all subjects and none of the subjects displayed all eight peaks in every call. Sometimes one or two peaks were missing in a particular call, but more typically the same one or two peaks were missing from all of an individual's coos, with the specific missing peaks varying by female. The presence or absence of each of the remaining six peaks was therefore recoded in accordance with the recommendations of Tabachnick and Fidell (1989) using six binary, "dummy" variables (see Rendall, 1996, for details of this procedure). As coos also sometimes contained noisy energy, two other binary variables were also used to score the presence or absence of inter-harmonic energy bands (IH) and a noisy overlay ($NOISE$) in each call. Characterizing coo-call frequency spectra thus required a total of 16 variables.

Twelve coefficients provided the best fit to the FFT spectra of grunts, yielding a set of five peaks ($F1$ to $F5$). For screams, the number of coefficients did not significantly affect the number of peaks identified, the resulting LPC spectra invariably contained only one or two peaks. For consistency, we used the same number of coefficients for both grunts and screams, but retained only the strongest, or "dominant" peak for the latter ($DOM\ FREQ$). For coos and screams, LPC peaks were derived by centering the analysis window on the call's midpoint. Both the second and third pulses were analyzed in this way for each grunt, yielding two sets of peaks. This approach maximized the spectrally related data associated with these soft calls, which were difficult to both record and analyze. Nonetheless, sensible results could not be obtained for many pulses and the grunt samples used in various comparisons therefore varied in number and composition.

The last analysis conducted was designed to facilitate direct comparisons of the spectral characteristics of the three call types. Here, a standard set of 18 LPC coefficients was used in each case, providing both a good fit to the spectral structure of coos and easily accommodating grunts and screams ("over-fitting" the spectra of grunts and screams was preferred to "under-fitting" the coos). Other LPC parameters were as before, except that pre-emphasis was eliminated in order to be able to use the first reflection coefficient of each LPC function as a measure of overall spectral slope (see Owren and Bernacki, 1988, in press). Spectral measures were again calculated at the midpoint of coos and screams, and from the second and third pulses of grunts.

3. Statistical analysis

Statistical analyses were conducted using NCSS version 5.1 (Hintze, 1989). Individual variation in the acoustic structure of coos, grunts, and screams were examined with both univariate analysis of variance (ANOVA) and multivariate

discriminant analysis. The latter was used to sort vocalizations by caller based on the acoustic measurements, thereby simulating the recognition problem faced by animals under natural circumstances and characterizing the degree of individual differentiation present in the sounds. Following the conservative, split-sample approach recommended by Klecka (1980), each call-type sample was randomly divided into halves. One set, the reference sample, was used to generate discriminant functions. The functions were then applied to the other set, the test sample, providing independent evaluation of classification performance. As classification results in discriminant analysis are sensitive to the number of variables involved, principle components analysis (PCA) was used to reduce the number of acoustic variables entered for coos. Here, univariate ANOVA analyses of PCA scores were conducted as a basis for retaining only the most important measures, thereby preserving most of the variance in this dataset while making the number of variables used comparable across call types.

Two new samples were also constructed in order to test for intra-individual similarity in the spectra of coos, grunts, and screams. The first sample consisted of coos and grunts from females for which recordings of both call types were available ($n=9$), and the second was similarly constituted of coos and screams ($n=6$). Univariate ANOVA and discriminant analysis were then used in each sample to test for differentiation among females when each subject's coos and grunts (or coos and screams) were considered simultaneously, as though they represented a single call type. This approach was designed to determine whether a female's coos and grunts (or coos and screams), considered as a set, were consistently different from the coos and grunts (or coos and screams) of other females. Discriminant analyses were again performed, with half of each female's calls of a given type assigned to the reference sample and the other half assigned to the test sample.

4. Playback experiments with noisy screams

Playback trials were used to test for perceived differences in the acoustic structure of screams, using the same experimental design as in an earlier study of coos (Rendall *et al.*, 1996). These trials were designed to examine each subject's ability to discriminate between the calls of genetically related adult females (kin) and unrelated, but familiar, adult females (nonkin). The rationale was that if females recognize the screams of other individual group members, a test subject should respond more quickly and for a longer period of time when hearing the screams of kin (*kin trials*) as opposed to nonkin (*nonkin trials*). Kinship was defined with respect to matrilineal genetic relatedness, calculated based on the conservative assumption that sisters were half-siblings (i.e., had different fathers). Animals with coefficients of relatedness greater than or equal to 1/16 were considered kin, while individuals whose relatedness was less than 1/16 were designated as nonkin. The order of trial types was balanced across subjects and across the study.

In each trial, a single scream was presented from a laptop computer connected by a 20-m cable to a Nagra DSM monitor that was concealed in dense vegetation an average of 13.8 m from the subject. Prior to conducting a trial, two observers identified and followed a potential subject (the *target female*), thereby establishing baseline behavior levels and ensuring that the female whose call was to be presented (the *stimulus female*) was out of sight. When these conditions were met and the target female was not looking towards the hidden speaker, one observer videotaped the subject (30 frames per s) while the other operated the laptop computer. Taping began at least 10 s prior to stimulus presentation and continued for at least 10 s afterward. Responses to playback stimuli were scored later, based on frame-by-frame analysis of the videotape record. The measures used were the latency and duration of orientation and subsequent gaze toward the speaker. Latency timing began at the earliest detectable onset of the playback stimulus on the videotape sound track and ended with the first frame in which a change in gaze direction toward the speaker was detected. The duration measure was the length of orientation toward the speaker in the 10 s immediately following stimulus presentation minus the corresponding gaze duration in the 10 s immediately preceding stimulus presentation (see Cheney and Seyfarth, 1980).

To prevent animals from habituating to the experimental protocol, only 1.48 experiments were conducted per day (ranging from 0 to 5) and consecutive experiments were separated by at least 1 h. Further, no given individual could serve either as a target female or as a stimulus female more than once per day. A total of 65 playback experiments were conducted, of which 32 were kin trials and 33 were nonkin trials. In kin trials, 24 different target females were used, while 30 different target females served as subjects in nonkin trials and 16 animals were target females in both. The stimulus set consisted of 25 calls recorded from 18 different females. In cases where a given female was tested twice within either the kin or nonkin conditions, calls from different stimulus animals were used and the subject's responses were averaged over those two trials.

II. RESULTS

A. Acoustic features

As illustrated in Fig. 1, coos, grunts, and noisy screams are quite different, and the acoustic measures shown in Table II bear out the obvious discrepancies in both source energy periodicity and spectral organization of these sounds. As expected, F_0 values could be readily extracted from coos, and LPC-based spectral envelopes revealed prominent and stable patterns of energy variation in each call. Grunts differed from coos in being pulsed rather than continuous and showed broadband spectral energy distribution. Again, peak patterning was evident in the spectral characteristics of these calls, with 5 peaks resulting when 12 coefficients were used. Noisy screams were also characterized by broadband, continuous noise, but typically showed only a single high-amplitude spectral peak unless a fundamental was also present.

B. Variability and split-sample discriminant classification

In order to gauge the acoustic stability of a given female's calls, a coefficient of variation (CV) was calculated

TABLE II. Acoustic features of coos, grunts and noisy screams.

Call type	Variable type	Variable	M^a	CV^b	F value
Coos	temporal (ms)	DUR	349	24.4	45.5**c
		$PEAK\%$	0.33	44.6	8.1**
		$MAX\ F_0$	512	10.9	99.9**
		$MIN\ F_0$	431	10.0	119.1**
		$BEG\ F_0$	444	9.4	128.5**
		$MID\ F_0$	486	10.7	89.7**
		$END\ F_0$	476	11.3	105.5**
		$END/BEG\ F_0$	1.12	12.9	21.7**
		$END/MID\ F_0$	1.00	12.6	10.7**
		$MID/BEG\ F_0$	1.12	10.5	7.3**
		$MAX/MIN\ F_0$	1.24	11.5	18.9**
		$MID/MAX\ F_0$	0.96	7.3	7.7**
		$SLOPE\ F_0$	0.14	35.1	21.8**
	spectral (Hz)	$F1$	635	17.9	21.4**
		$F2$	1400	15.2	18.3**
		$F3$	2627	7.3	54.0**
		$F4$	4142	4.8	56.6**
		$F5$	5569	4.2	10.7**
		$F6$	6459	3.8	46.6**
		$F7$	7532	3.4	49.6**
		$F8$	9020	3.8	60.7**
	(discrete variables)	$DF1$			50.5**
		$DF2$			304.1**
		$DF5$			90.4**
		$DF6$			123.8**
		$DF7$			47.3**
		$DF8$			45.3**
		IH			18.3**
		$NOISE$			12.1**
Grunts	temporal (ms)	DUR	191	15.3	7.7**
		$PEAK\%$	0.45	26.3	1.8
		$DUR\ P_2$	42.1	37.8	4.5**
		$DUR\ P_3$	56.6	34.1	3.8**
		IPI_1	18.1	32.6	4.1*d
		IPI_2	13.6	33.9	9.2**
		$\#PULSES$	3.4		3.8*
	spectral (Hz)	$F1$	819	19.4	15.9**
		$F2$	2569	9.5	15.4**
		$F3$	4087	6.9	11.6**
		$F4$	5755	5.4	21.4**
		$F5$	7220	3.5	32.0**
Screams	temporal (ms)	DUR	483	53.9	0.8
		$PEAK\%$	0.41	48.4	0.6
	spectral (Hz)	$DOM\ FREQ$	2641	21.6	1.5

[a]Mean of the individual means.
[b]Mean coefficient of variation across individuals.
[c]$p < 0.0001$.
[d]$p < 0.001$.

separately by individual for each measure. Grand means for these CV's are shown in Table II. CV's for spectral-peak variables were consistently lower than those for other measures for all three call types, providing preliminary evidence that spectral-peak variables are more consistent within a given individual than are other acoustic features.

Testing coos, univariate ANOVA identified significant heterogeneity among individuals on every measure (Table II). As shown in Table IIIa, discriminant analysis correctly classified 79.4% of coos based on spectral-peak variables and 63.6% based on other measures, 78.0% and 61.0% reductions relative to chance error levels, respectively. When all variables were included, stepwise discriminant analysis strongly favored spectral variables, entering all 14 by step 18 of the process. Here, overall classification performance by caller was 90.9%, an error reduction of 90.3%. Applying PCA to the coo-related variables produced a set of 29 possible components, all but 5 of which showed significant heterogeneity among individuals based on ANOVA results. Retaining only components with the largest F-values and eigenvalues greater than 1.0 yielded a set of 9 variables for discriminant analysis. Resulting discriminant functions successfully classified 84.8% of the calls and stepwise analysis again favored components associated with spectral-peak measures.

For grunts, univariate ANOVA identified significant heterogeneity among individuals on all spectral-peak variables and all temporal variables except PEAK% (Table II). However, the rate of successful classification of calls from discriminant analysis was modest in both cases (see Table IIIa). Spectral-peak variables allowed a correct classification rate of 41.4%, or 34.7% error reduction. The corresponding values for all other variables combined were somewhat lower, with a success rate of 31.6%, corresponding to 23.7% error reduction. For noisy screams, univariate ANOVA did not reveal significant heterogeneity among individuals on any variables, and only 29.8% of the calls were correctly classified in discriminant analysis, an error reduction of 20.1%.

C. Split-sample discriminant classification based on 19 LPC coefficients

When individuality in the frequency spectra of coos, grunts, and screams was compared directly using a standard set of 19 LPC coefficients, univariate ANOVA indicated significant heterogeneity in 18 coefficients for coos, but only 10 and 9 coefficients for grunts and screams, respectively. Classification based on discriminant analysis was markedly better for coos (65.2%) than for either grunts (40.3%) or screams (40.4%), corresponding to nearly twice as much error reduction for coo classification than with the other call types (see Table IIIb).

In order to evaluate intra-individual stability in spectral structure across call types, samples were created that combined coos with grunts, and coos with screams (in cases when both kinds of calls were available from the same individual; see Table I). Here, however, ANOVA comparisons revealed many fewer significant differences among individuals, and thus relatively little intra-individual similarity in spectral peak patterning across call types. Testing the coo–grunt sample revealed significant heterogeneity among individuals for 3 of the 19 coefficients, while similar comparisons using the coo–scream sample produced significant results for 8 coefficients. Classification rates from discriminant analysis were similar in the two cases. For the coo–grunt sample, 50.9% of the calls were correctly assigned, while 59.2% of the calls were correctly assigned in the coo–scream dataset (Table IIIc). Successful classification was largely attributable to accurate sorting of the coos (65.7% and 72.7%, respectively, for the two samples). Grunts and screams were correctly classified at comparatively low levels

Analysis	Call type	Variables	# of females	# of cases[b]	# correct by chance[c]	# correct actual	% correct by chance	% correct actual	% error reduction[d]
(a)	Coos	Formant	17	253	17	201	6.7	79.4	78.0
		All others	17	253	17	161	6.7	63.6	61.0
	Grunts	Formant	11	391	41	162	10.4	41.4	34.7
		All others	11	177	19	56	10.5	31.6	23.7
	Screams	All	9	57	7	17	12.1	29.8	20.1
(b)	Coos		17	253	17	165	6.8	65.2	62.7
	Grunts		11	372	38	150	10.3	40.3	33.5
	Screams		9	57	7	23	12.1	40.4	32.1
(c)	Coos and grunts		9	283	31	144	11.7	50.9	45.1
	coos		9	140	17	92	11.8	65.7	61.1
	grunts		9	143	16	52	11.5	36.4	28.1
	Coos and screams		6	135	24	80	18.6	59.2	46.6
	coos		6	99	18	72	18.2	72.7	66.6
	screams		6	36	7	8	19.0	22.2	4.0

[a]Values in the table are rounded for purposes of presentation.
[b]Sample size used for classification (grunt samples were usually based on two pulses per call, but varied complexly due to deleted cases—see Sec. I).
[c]Values have been modified to correct for unequal numbers of cases per individual.
[d]Calculated as (# correct actual–# correct by chance)/(# of cases–# correct by chance).

in these tests (36.4% and 22.2%, respectively), and classification of the latter did not differ from chance-level performance.

D. Playback experiments with noisy screams

Playbacks elicited immediate attention and orientation in 59 of 65 cases (90.8%); target females failed to respond in only two kin trials and four nonkin trials. However, subjects never responded by calling or approaching the speaker. Means and standard errors for latencies and durations of responses in each trial type are shown in Fig. 2(a). Mann-Whitney U tests based on the entire set showed no differences in response latencies on kin ($M = 1.16$ s, $SE = 0.44$) and nonkin ($M = 1.58$ s, $SE = 0.52$) trials, $U = 362.5$, $p = 0.81$, nor in the duration of responses to screams from kin ($M = 4.14$ s, $SE = 0.49$) and nonkin ($M = 3.99$ s, $SE = 0.55$), $U = 419.5$, $p = 0.63$, $N = 54$. The results of paired comparisons of responses were similar for females who were subjects in both a kin and nonkin trial. Wilcoxon Signed-Ranks tests showed that, again, neither response latencies ($T = 8$, $p = 0.68$) nor durations ($T = 7$, $p = 0.41$, $N = 16$) were significantly different between trial types.

Latencies and durations of response were also examined as a function of degree of relatedness between the stimulus and target females. After a natural-log transformation of coefficient values had first been used to create a continuous variable, regression analysis revealed no significant associations either between relatedness and response latency, $F(1,57) = 0.099$, $p = 0.75$, or between relatedness and response duration, $F(1,63) = 0.002$, $p = 0.97$. The proportion of variance accounted for by least-squares regression was calculated as R^2, which ranges from 0 to 1. R^2 values were 0.002 and 0.00002, for latency and duration of response, respectively.

III. DISCUSSION

A. Rhesus monkey vocal-production mechanisms

1. Coos and grunts

Overall, acoustic analysis results were consistent with proposals by Schön Ybarra (1995) and others that both the vocal folds and supra-laryngeal cavities play important roles in shaping the calls of rhesus monkeys. Coos exhibited a prominent, stable F_0 of 400–500 Hz, comparable to previously reported adult female values in both rhesus monkeys (e.g., Hauser, 1991; Hauser and Marler, 1993a; Hauser et al., 1993; Owren et al., 1992) and other macaques (cf. Hohmann and Herzog, 1985; Bauers and de Waal, 1991; Owren et al., 1992; Palombit, 1992). The broadband nature of energy distribution in grunts indicated an aperiodic energy source—most likely an irregular vibration of the vocal folds (see Schön Ybarra, 1995). Despite this difference, however, broad spectral energy peaks were clearly evident in both call types.

For coos, these peaks were imposed on a rich, harmonically structured frequency spectrum. While acoustic analyses were designed to locate up to eight peaks in the 10.0-kHz range examined, most calls revealed six or seven peaks, depending both on the caller and vocalization involved. Grunt analyses produced five peaks which were generally matched in frequency to values derived for the coos. Following the source-filter approach to call production, these peaks can be interpreted as reflecting vocal tract resonances occurring in the same spectral locations. The length of the rhesus monkey vocal tract can be then be estimated, for instance by modeling this structure as a straight tube closed at one end. Expected length (l) in cm is $l = (2k+1)c/4F$, where F is formant frequency, k is formant number minus 1, and c is 34 400 cm/s, the speed of sound (see Lieberman and Blumstein, 1988; Fitch and Hauser, 1995). Based on using $F1$
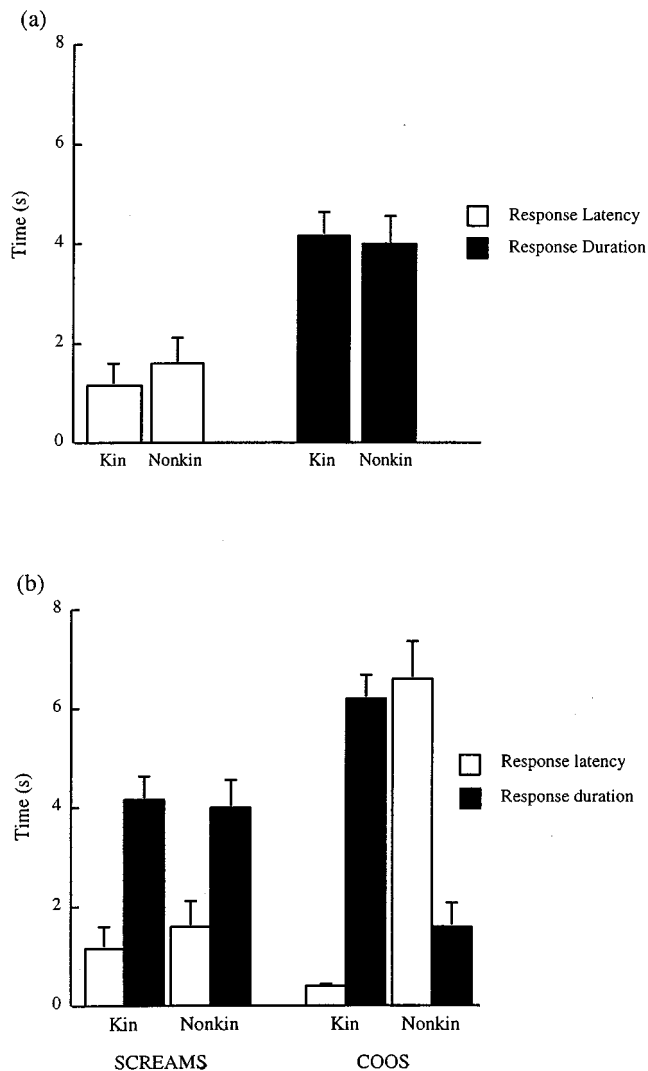
FIG. 2. (a) Means (±SEM) for latencies and durations of looking responses by adult rhesus monkeys on hearing a noisy scream playback. Calls played to adult female subjects were produced either by kin (24 different individuals were tested in 32 trials) or nonkin (30 different individuals were tested in 33 trials). Responses by females to the screams of kin and nonkin were not significantly different on either measure. (b) Means (±SEM) are shown for the latencies and durations of looking responses by adult female rhesus monkeys on hearing either a scream playback [left; redrawn from (a) above] or a coo playback (right; redrawn from Rendall et al., 1996). The number of individual animals and calls tested in the scream trials is described in (a). In the coo trials, calls produced by kin were played back to 27 different individuals in 34 trials, while nonkin calls were presented to 28 different individuals in 29 trials.

through $F8$ values from coos, the resulting mean estimate of vocal tract length was 8.5 cm (see Table II). The comparable value for grunts was 8.9 cm, using $F1$ through $F5$ and considering these peaks to correspond to $F1$, $F3$, $F4$, $F5$, and $F7$ in coos. Restricting the calculation to the peaks that occurred in every female's coos (i.e., $F3$ at 2627 Hz, and $F4$ at 4142 Hz), mean vocal tract length was 9.1 cm. Using the corresponding peaks in grunts (2569 and 4087 Hz, respectively), the estimate was 9.2 cm.

Overall, these results are consistent with the view that the vocal tract can be approximately modeled as a uniform, straight tube, but also suggest that the actual shapes of rhesus monkey vocal tracts deviate from this idealized form. Articu-

lation effects are known to occur in rhesus monkey calls (e.g., Hauser et al., 1993), and Hauser and Schön Ybarra (1994) have specifically found that rhesus monkeys often produce coos with rounded lips, thereby increasing effective vocal tract length and decreasing associated formant locations. Thus observed discrepancies in proposed formant values for coos and grunts may reflect articulatory differences in these two call types. The effects of articulation might also explain the greater variability in frequency values for $F1$ in both coos and grunts, as well as $F2$ in coos, compared to higher formants (as evidenced by their larger CVs). In a fashion analogous to human speech, articulation effects might be expected to impact disproportionately the locations of the first two formants. At the same time, higher formants may be less variable if they reflect the resonance effects of comparatively stable (rigid) components of the supralaryngeal vocal tract (e.g., nasal cavities). However, both the discrepancies in formant values between coos and grunts and the greater variability in $F1$ and $F2$ could equally be due, respectively, to characteristic differences between, and differential variation within, the underlying source energy spectra of the two call types. As the source energy spectrum is not known in detail for either coos or grunts, these alternatives cannot be conclusively distinguished.

Fitch (1997) examined vocal tract length in rhesus monkeys, finding through x-ray imaging that mean oral vocal tract length was 7.9 cm, while nasal vocal tract length was 9.0 cm (see also Lieberman, 1968). His sample of 23 animals included both immature and adult animals with a mean age of 4.5 years, thus being more variable than the present sample of fully grown adult females with a minimum age of 4 years. Taken together, results of the two studies indicate that the vocal tract length is approximately 8–9 cm long in adult female rhesus monkeys. Primary airflow during call production may either be through the oral cavity or the longer nasal cavity. The latter possibility is consistent with observations that coos can in fact be produced with the mouth closed. Fitch also reported that 3–5 prominent formants occur below 10.0 kHz in noisy, pulsed pant-threats, much the same outcome obtained here for the acoustically similar grunts.

2. Noisy screams

Acoustic analysis of screams failed to indicate a well-defined spectral energy pattern that was clearly consistent with vocal tract filtering effects. The occurrence of a single, broad, low-amplitude peak at 2641 Hz (and occasional observation of a second, similar peak at a higher frequency) could result either from resonance effects or periodicity in the source energy. This peak closely matched the peak designated $F3$ in coo calls and $F2$ in grunts. A second version of the noisy scream showed a narrow, high-amplitude peak

in the same location, with higher-frequency harmonics also being present (illustrated by the final one-third of the scream in Fig. 1). As shown by Schön Ybarra (1995), the occurrence of a ''vocal lip'' on the medial aspect of each vocal fold in rhesus monkeys provides a mechanism through which these animals can simultaneously produce both periodic and aperiodic vocal fold vibrations (a phenomenon also reported in Syke's monkeys, *Cercopithecus albogularis*, by Brown and Cannito, 1995). This apparent match between the fundamental of a periodic component and a broad spectral peak in an otherwise noise-based sound may be due either to explicit regulation of vocal-fold vibration rate or to an acoustic *coupling* effect between the source and subsequent filter (Brown and Cannito, 1995). In either case, a resonance in this frequency region would act to amplify the energy of the coincident harmonic partial. Although inconclusive, the evidence of an energy peak at approximately 2600 Hz in coos (i.e., $F3$), grunts (i.e., $F2$), and completely aperiodic versions of noisy screams is indicative of a common vocal tract resonance in these three call types.

B. Statistical discrimination of callers based on acoustic features

1. Coos

Discriminant analysis classification of coos by individual caller indicated that rhesus vocalizations can be acoustically distinct even for a relatively large sample of individuals. This outcome is important in that the sample size of 17 adult females provided a reasonable simulation of typical group size for these monkeys and the corresponding intra-group vocal recognition problem actually faced. Although both formant-related and other acoustic features allowed correct sorting of calls at levels well above chance performance, the former provided better classification (i.e., 79.4%) than did the latter (i.e., 63.6%). When analyzed in stepwise fashion, these formant-related variables accordingly entered the classification functions before other measures. Note that this dominant role of spectral features could not be attributed to the recording procedure in which dummy variables were used to represent the presence or absence of peaks. While sorting accuracy using the 8 peak frequencies and 6 dummy variables was greater than it was using the standard set of 19 coefficients, the difference was approximately 14%; classification of coos continued to occur at a rate far higher than chance performance. Further, as shown in Table II, formant variables showed lower coefficients of variation than did other measures.

Overall then, results indicate that the characteristic spectral peak pattern found in a given female's coos was the most stable and distinctive acoustic attribute of her calls. This outcome is virtually identical to the results of recent work on harmonically rich, tonal grunt vocalizations in adult female baboons (Owren *et al.*, 1997) and a short vowel segment excised from running speech produced by both male and female human subjects (Bachorowski and Owren, in review). In accordance with the source-filter perspective outlined earlier, variation in spectral peak patterning found among individuals in each of these studies was most likely due to minor differences in the sizes and shapes of their supra-laryngeal

vocal tract cavities, one effect of which is to provide reliable acoustic cues to identity. In each of these three cases, other measures also contributed significantly to discrimination classification success, but to a lesser extent. Nonetheless, it is important to note that features related to fundamental frequency and temporal patterning are also likely to be salient to both nonhuman primates like rhesus monkeys and baboons, as well as humans. In addition, some other source-related cues that could potentially contribute to vocal distinctiveness (like jitter and shimmer; see Owren and Linker, 1995) were not investigated either here or by Owren *et al.* (1997). Finally, detailed aspects of the frequency spectrum of periodic sounds like these coos are also affected by vocal-fold characteristics, as noted in the introduction. Therefore, while spectral peak patterning appears to play the greatest role in individual vocal distinctiveness in coos, a variety of factors related to both source energy and vocal tract filter are likely to be involved.

2. Grunts and noisy screams

Univariate statistical analyses indicated a limited, but significant degree of individual differentiation in the acoustic structure of grunts, while showing no appreciable differentiation among noisy screams. The results of multivariate discriminant analyses were equivocal for both call types, however. Discriminant analysis, which provides a more rigorous test of differentiation among individuals than does univariate ANOVA, permitted successful assignment of grunts to individuals with approximately 37% accuracy. Noisy screams were successfully assigned to individuals with only 30% accuracy. Although these outcomes exceed chance performance and thus may indicate some degree of acoustic consistency within each individual's grunts and screams, they are modest when compared to results from coos. Classification for the latter was approximately 9–12 times higher than chance performance, compared to only 3–4 times and 2.5 times higher for grunts and screams, respectively. However, to the degree that correct statistical sorting was possible for grunts and screams, spectral variables again played the greatest role in distinguishing among individuals.

3. Direct comparisons among call-type spectra

Similar disparities in classification success were obtained when the spectral structure of each call type was analyzed using a standard set of LPC coefficients, thereby controlling for differences in the number of variables used to evaluate differentiation. Discriminant analysis correctly assigned 65.2% of coos, compared to only 40.3% of grunts and 40.4% of screams. Superior classification of coos was again achieved despite the inclusion of a much larger number of females than for either grunts or screams, and error reduction was nearly twice as high for coos than the other call types.

C. Playback experiment outcomes

The conclusion that the acoustic features of noisy screams are not individually distinctive was borne out in playback experiments, which provided no evidence that females could discriminate the screams of kin from those of

nonkin. In contrast, earlier experiments in which coos were presented to these same study groups had shown not only that adult females discriminated the coos of kin from those of nonkin, but also that they could distinguish among the coos of various individuals that were all close kin (Rendall *et al.*, 1996). As illustrated in Fig. 2(b), responses to the coos of nonkin in the previous study were both considerably slower and much briefer than were responses to the screams in the current work, while responses to the coos of kin were faster and longer lasting than were responses to screams. These discrepancies cannot readily be attributed to differences in subject motivation in the two experiments, as the animals were clearly interested in and responsive to the test stimuli in both cases. As noted earlier, target females looked in the direction of the speaker on almost every trial.

It is also unlikely that the differences were due to problems in assigning kinship. While assigning individuals to kin and nonkin categories can be problematic, the same criteria were used in both experiments and regression analysis in the present work revealed no significant association between the responses to screams and matrilineal relatedness when the latter was tested as a continuous variable. Overall, the most parsimonious explanation for the failure of subjects to differentiate between the screams of kin and nonkin in the current work—while very clearly doing so for coos in the previous study—is that the generally unpatterned spectral structure and undifferentiated temporal attributes of single noisy screams does not provide sufficient information for this discrimination to occur.

D. Individual differentiation in coos, grunts, and noisy screams

Taken together, acoustic analysis results indicated that the extent of individual variation is much greater in coos than it is in either grunts or noisy screams, and that grunts are somewhat more distinctive than screams. The hypothesized functional difference between coos and screams was then confirmed by the playback experiment results, comparing responses to calls of kin versus nonkin for coos studied earlier and noisy screams tested in the current work. These general outcomes will be considered in turn.

1. Grunts and coos

One possible explanation for the equivocal results obtained with grunts is that the acoustic analysis methods were inadequate for characterizing individual variation that was in fact present. In the absence of explicit testing, for instance involving either playback trials of natural grunts or laboratory-based testing of the perception of artificial, synthetic grunts, this possibility cannot be definitively evaluated. As grunts are much quieter than either of the other call types, strong conclusions about these sounds requires further evidence. Nonetheless, the current results may indicate that there are fewer reliable cues to individual identity in grunts than in coos. One explanation for this apparent difference may be that there is little need to include individually distinctive acoustic features in grunts because they are typically used in close-range, ''face-to-face'' encounters. Whether

sharply distinctive or not, however, the identity cues found in grunts were most clearly related to spectral peak patterning.

2. Noisy screams and coos

Both acoustic analysis and playback experiment results indicated a virtual absence of individual distinctiveness in noisy screams. This outcome was surprising in that screams are given in agonistic encounters and have been widely accepted as playing an important role in recruiting aid from kin, who may be out of sight. Screams are therefore frequently presumed to have been under strong selective pressure to signal caller identity. Indeed, Gouzoules and Gouzoules (1990) reported that distinctive acoustic ''signatures'' occurred in the screams of two matrilines of pigtail macaques (a congener of rhesus monkeys), a result that complements observed patterns of nepotistic aiding among female kin in these and other nonhuman primates. Cheney and Seyfarth (1980) found that vervet monkey mothers (a similar monkey species) can discriminate screams of their own offspring from those of ''other'' offspring, and may even recognize unrelated animals based on these calls. Finally, Gouzoules *et al.* (1986) reported that female rhesus macaques can discriminate not only between the noisy screams of their own and others' offspring, but also among screams produced by closely related versus distantly related immature kin.

One potentially important difference between the present study and this previous work is that here, acoustic analysis of screams emphasized individual rather than kin-related differences. Gouzoules and Gouzoules (1990), in contrast, focused on kin relationships among their pigtail macaque subjects and did not explicitly describe individual differences. It is therefore possible that kin differences are in fact present in the screams of rhesus macaques and that individual differences in screams are obviated by a system of kin signatures. However, this explanation is contradicted by the results of the playback experiments, which showed no evidence of discrimination of screams based on kinship. Further, in an ancillary test of the coo acoustics reported by Rendall *et al.* (1996), Rendall (1996) found kin-based sorting to be much less accurate than classification by individual.

A second, possibly important factor is that, while previous studies have focused on mother–infant recognition (e.g., Cheney and Seyfarth, 1980; Gouzoules *et al.*, 1986; Pereira, 1986), the playback experiments reported here were designed to test recognition of calls produced by adult rather than immature animals. Indeed, the acoustic structure of screams might be more individually distinctive in younger animals, for whom support from kin may be both more critical and more frequent than for adults. Nonetheless, adult females are observed to intervene in fights involving mature kin (Kaplan, 1977; reviewed in Smuts *et al.*, 1987), indicating that the selective advantage potentially gained from using individually distinctive screams does not expire at adulthood. In addition, evidence from both rhesus and Japanese macaques suggests that just the opposite developmental trend occurs in these species—at least in coo calls. Owren *et al.* (1992) analyzed a limited set of acoustic features in food-related coos of captive, socially housed animals and found

that the vocalizations of younger animals were significantly less distinctive by individual than were the calls of adult females.

Acoustically, it is more plausible to suppose that cues to individual identity in noisy screams are carried in the temporal patterning of successive calls rather than in the features of single vocalizations. Although Gouzoules *et al.* (1984) have reported that in playback trials involving individual noisy screams, adult female rhesus monkeys responded more quickly and for a longer duration when hearing calls from their own offspring than from unrelated juveniles, the results both in this study and later work (Gouzoules *et al.*, 1986) actually reflect longer mean response latencies and shorter mean response durations for target females hearing calls from their own offspring than were found in the playback experiment reported here. Thus, in each of three investigations of noisy screams in which target females have heard single screams from kin, results have been different from those obtained with single coo calls by Rendall *et al.* (1996).

At the very least, this outcome pattern shows that single screams are more difficult to discriminate by caller than are coos. However, a stronger conclusion appears warranted. Pilot work described by Gouzoules *et al.* (1984) suggests that a different outcome would have occurred had entire bouts rather than single screams been used in the various experiments (cf. Cheney and Seyfarth, 1980). In these preliminary tests, animals were reported to approach or even charge the speaker when hearing multiple screams. The playback stimuli were therefore deliberately restricted to single calls, with the result that no subjects were reported to approach the speaker during the experiment—the same outcome as in the playback trials described here. It follows that limiting a noisy-scream playback stimulus to a single call actually removes most or all individually distinctive acoustic cues. Clearly, there is a need for direct experimental comparison of the discriminability of noisy screams presented individually and in naturally occurring bouts.

E. The role of the vocal tract filter in individual distinctiveness

Guided by theoretical considerations, we hypothesized that the effects of vocal tract filtering were the most plausible source for common cues to identity across the various calls in the repertoire, should such cues exist. Consistent with this proposal, spectral peak characteristics of coos and grunts were less variable within individuals than were other aspects, as was dominant frequency in the case of screams (shown in Table II). Further, spectral-peak variables permitted better classification of coos and grunts by individual caller than did other aspects of the calls (see Table III). However, when the frequency spectra associated with each of the three call types were modeled using the same number of coefficients, evidence of individual differentiation in the vocal tract filter was more compelling for coos than for either grunts or screams.

Nonetheless, there was some evidence of an effect of the vocal tract filter in grunts. In addition to classifying coos satisfactorily, discriminant analysis based on the combined coo–grunt sample sorted grunts at an overall rate that was both significantly above chance performance (i.e., 36.4%,

see Table III) and close to the level achieved in independent classification of grunts alone (i.e., 40.3%). In other words, when only variables related to spectral structure were used in discriminant analysis, grunts were classified at approximately the same rate whether or not coos were included. In conjunction with the finding that formant-related variables provided the strongest and most stable cues to caller identity in the coos, this outcome indicates that to the extent that grunts could be sorted by individual caller, classification was guided by vocal tract filtering cues. However, evidence concerning whether this filtering was similar to that occurring in coo production was simply inconsistent. Although heterogeneity among callers decreased when coos and grunts were combined rather than being tested separately, 4 of 5 mean peak frequencies derived from grunts could nevertheless arguably be matched to corresponding values from coos.

This apparent match was corroborated by the similarity in estimates of overall vocal tract length that could be derived from the two sets of peaks. The first peak in coos was found to be somewhat lower in frequency than the comparable peak in grunts, but this effect may have been due to differences in characteristic articulation of these two call types. Although coos also exhibited a low-amplitude, low-frequency spectral peak that was not noted in grunts, this discrepancy might also result from differences in articulation. Furthermore, this peak might be absent due simply to a lack of source energy in this frequency range in grunts rather vocal tract filter effects.

Comparable outcomes were not observed in analysis of noisy screams. In this case, no compelling evidence of multiple, formant-based spectral peaks was apparent and the coefficient of variation for the one spectral peak that was observed was higher than for any of the formant peaks hypothesized for coos and grunts. While discriminant functions based on the 19 coefficient analysis of screams allowed sorting at a rate that was significantly above chance performance (i.e., 40.4%), classification of screams based on the combined coo-scream sample was essentially random (i.e., 22.2%). Thus while the acoustic structure of grunts was found to be modestly distinctive among individuals, no such distinctiveness occurred in the noisy screams. Whereas the individual differentiation found in the grunts was evidently related to vocal tract filter characteristics that were at least similar to those apparent in coos, analogous commonality did not occur in the overall spectral patterning of screams and coos.

This apparent difference in signaling individual distinctiveness among the three call types may be partially due to constraints imposed by concomitant facial expressions. As noted above, coos are sometimes given with varying degrees of lip protrusion and rounding (see Hauser *et al.*, 1993, Fig. 1), although at other times the mouth is completely relaxed or even closed. Similarly, grunts occasionally involve lip protrusion (although not to the extent observed in coos), but are usually associated with a closed, or nearly closed, relaxed mouth. In neither case is an obligatory facial display involved and variation in facial expression does not appear to have signaling value. In contrast, screams are given conjointly with the fear grimace, a dramatic facial display that

includes strongly retracted lips. This grimace is one component of a larger suite of facial gestures and body postures that occurs in many nonhuman primate species and is evidently indicative of submission to opponents during agonism. Thus while screams may help in recruiting aid from allies (Gouzoules *et al.*, 1984, 1986), they are also likely to function to alleviate aggression more directly.

The acoustic structure of screams may therefore be subject to constraints that do not affect coos and grunts. One possibility is that there is a causal relationship between exaggerated lip retraction (as well as other elements of submissive facial displays) and characteristic acoustic features of screams. This proposal is consistent with Bauer's (1987) report of a positive correlation between F_0 and lip retraction during chimpanzee (*Pan troglodytes*) screams. Another constraint may be indicated by Morton's (1977, 1982) hypothesis that high-frequency sounds are used during submission in a wide variety of animals (tested in nonhuman primates by Hauser, 1993).

IV. CONCLUSIONS

Overall, the data indicate that the source-filter approach can be a valuable tool in understanding rhesus monkey calls, and provide evidence of individual distinctiveness in some, but not all vocalizations in these animals. Seen in conjunction with previous analyses of call acoustics and production mechanisms in nonhuman primates, the sounds examined here are proposed to involve source energy components that are periodic, aperiodic, or a combination of the two. Coos and grunts, which are periodic and aperiodic, respectively, showed spectral peak patterns that were consistent with the occurrence of stable vocal tract filtering during call production. In addition, detailed aspects of evident formant patterning were found to carry cues to the identity of the particular animal producing a given call. This effect was far more evident in coos, while some formant-related cueing occurred in grunts. Other aspects of these sounds also showed some individual distinctiveness, but were secondary. No compelling evidence of formants or other individually distinctive acoustic cueing was found in noisy screams. Playback trials of single screams confirmed that adult female rhesus monkeys did not discriminate between the calls of kin and nonkin individuals, a markedly different outcome than had been previously obtained with coos.

An implication of these results is that, although communicating identity to kin and other social allies is evidently a critical aspect of some vocalizations used by rhesus monkeys (and other animals), neither the form nor the relative salience of such cueing can be taken for granted. While rhesus monkey coos show evidence of specialized design related to individual distinctiveness due to formant cues, the acoustic structure of screams may be constrained by an additional function of signaling submission. If it is important for rhesus monkeys to produce screams that are differentiated by individual, they may not be doing so in the simplest, most efficient manner. Instead, the available data indicate that reliable cues to identity in noisy screams are available only in bouts of calls rather than in a single call, as for coos. In accordance with the variety of production processes and functions that

may be associated with the acoustic features of any particular call type used by these and other monkeys, a conservative, empirically based approach should therefore be routinely adopted for studies in which individual vocal distinctiveness may be an issue.

Abercrombie, D. (**1967**). *Elements of General Phonetics* (University of Chicago, Chicago).

Bachorowski, J.-A., and Owren, M. J. (**in review**). ''Acoustic cues to gender and talker identity are present in a short vowel segment produced in running speech,'' Psych. Sci.

Bauer, H. (**1987**). ''Frequency code: Orofacial correlates of fundamental frequency,'' Phonetics **44**, 173–191.

Bauers, K. A., and de Waal, F. B. M. (**1991**). ''Coo' vocalizations in stump-tailed macaques: A controlled functional analysis,'' Behavior **119**, 143–160.

Brown, C. H., and Cannito, M. P. (**1995**). ''Modes of vocal variation in Syke's monkey (*Cercopithecus albogularis*) squeals,'' J. Comp. Psych. **109**, 398–415.

CANARY. (**1993**). *Canary: The Cornell Bioacoustics Workstation, Version 1.1* (Cornell Laboratory of Ornithology, Ithaca, NY).

Carrell, T. D. (**1984**). ''Contributions of fundamental frequency, formant spacing, and glottal waveform to talker identification,'' Unpublished doctoral dissertation, Indiana University.

Cheney, D. L., and Seyfarth, R. M. (**1980**). ''Vocal recognition in free-ranging vervet monkeys,'' Animal Beh. **28**, 362–367.

Cheney, D. L., and Seyfarth, R. M. (**1982**). ''Recognition of individuals within and between groups of free-ranging vervet monkeys,'' Am. Zool. **22**, 519–529.

Cheney, D. L., and Seyfarth, R. M. (**1988**). ''Assessment of meaning and the detection of unreliable signals by vervet monkeys,'' Animal Beh. **36**, 477–486.

Cheney, D. L., and Seyfarth, R. M. (**1990**). *How Monkeys See the World* (University of Chicago, Chicago).

Cheney, D. L., Seyfarth, R. M., and Silk, J. B. (**1995**). ''The role of grunts in reconciling opponents and facilitating interactions among adult female baboons,'' Animal Beh. **50**, 249–257.

Cheney, D. L., Seyfarth, R. M., and Smuts, B. (**1986**). ''Social relationships and social cognition in nonhuman primates,'' Science **234**, 1361–1366.

Chiba, T., and Kajiyama, J. (**1941**). *The Vowel: Its Nature and Structure* (Tokyo-Kaiseikan, Tokyo).

Cords, M. (**1992**). ''Post-conflict reunions and reconciliation in long-tailed macaques,'' Animal Beh. **44**, 57–61.

Fant, G. (**1960**). *The Acoustic Theory of Speech Production* (Mouton, The Hague).

Fant, G. (**1973**). *Speech Sounds and Features* (MIT, Cambridge).

Fitch, W. T. (**1997**). ''Vocal tract length and formant frequency dispersion correlate with body size in rhesus macaques.'' J. Acoust. Soc. Am. **102**, 1213–1222.

Fitch, W. T., and Hauser, M. D. (**1995**). ''Vocal production in nonhuman primates: Acoustics, physiology, and functional constraints on 'honest' advertisement,'' Am. J. Prim. **37**, 191–219.

Gaunt, A., and Nowicki, S. (**in press**). ''Vocal production in birds,'' in *Animal Acoustic Communication: Sound Analysis and Research Methods*, edited by S. L. Hopp, M. J. Owren, and C. S. Evans (Springer-Verlag, Berlin).

Goldinger, S. D., Pisoni, D. B., and Luce, P. A. (**1996**). ''Speech perception and spoken word recognition: Research and theory,'' in *Principles of Experimental Phonetics*, edited by N. Lass (Mosby, St. Louis), pp. 277–327.

Gouzoules, H., and Gouzoules, S. (**1990**). ''Matrilineal signatures in the recruitment screams of pigtail macaques, *Macaca nemestrina*,'' Behavior **115**, 327–347.

Gouzoules, H., Gouzoules, S., and Marler, P. (**1984**). ''Rhesus monkey (*Macaca mulatta*) screams: Representational signalling in the recruitment of agonistic aid,'' Animal Beh. **32**, 182–193.

Gouzoules, H., Gouzoules, S., and Marler, P. (**1986**). ''Vocal communication: A vehicle for studying social relationships,'' in *The Cayo Santiago Macaques: History, Behavior, and Biology*, edited by R. G. Rawlins and M. J. Kessler (State University of New York, Albany), pp. 111–129.

Hauser, M. D. (**1991**). ''Sources of acoustic variation in rhesus macaque (*Macaca mulatta*) vocalizations,'' Ethol. **89** 29–46.

Hauser, M. D. (**1992**). ''Articulatory and social factors influence the acoustic structure of rhesus monkey vocalizations: A learned mode of production?'' J. Acoust. Soc. Am. **91**, 2175–2179.

Hauser, M. D. (**1993**). ''The evolution of nonhuman primate vocalizations: Effects of phylogeny, body weight, and social context,'' Am. Nat. **142**, 528–542.

Hauser, M. D., and Fowler, C. A. (**1992**). ''Declination in fundamental frequency is not unique to human speech: Evidence from nonhuman primates,'' J. Acoust. Soc. Am. **91**, 363–369.

Hauser, M. D., and Marler, P. (**1993a**). ''Food-associated calls in rhesus macaques (*Macaca mulatta*): I. Socioecological factors,'' Behav. Ecol. **4**, 194–205.

Hauser, M. D., and Marler, P. (**1993b**). ''Food-associated calls in rhesus macaques (*Macaca mulatta*): II. Costs and benefits of call production and suppression,'' Behav. Ecol. **4**, 206–212.

Hauser, M. D., Evans, C. S., and Marler, P. (**1993**). ''The role of articulation in the production of rhesus monkey, *Macaca mulatta*, vocalizations,'' Animal Beh. **45**, 423–433.

Hauser, M. D., and Schön Ybarra, M. (**1994**). ''The role of lip configuration in monkey vocalizations: Experiments using xylocaine as a nerve block,'' Brain Lang. **46**, 232–244.

Hintze, J. L. (**1989**). *Number cruncher statistical system, NCSS Version 5.1, reference manual* (Number Cruncher Statistical System, Kayesville, UT).

Hohmann, G. M., and Herzog, M. O. (**1985**). ''Vocal communication in lion-tailed macaques (*Macaca silenus*),'' Folia Primatol. **45**, 148–178.

ILS. (**1986**). *Interactive laboratory system, version 6.0* (Signal Technology, Goleta, CA).

Johnson, K., and Mullenix, J. W. (**1997**). *Talker Variability in Speech Processing* (Academic, San Diego).

Joos, M. A. (**1948**). ''Acoustic phonetics,'' Language **24** (Suppl. 2), 1–136.

Kaplan, J. R. (**1977**). ''Patterns of fight interference in free-ranging rhesus monkeys,'' Am. J. Phys. Anthro. **47**, 279–288.

Kaplan, J. R. (**1978**). ''Fight interference and altruism in rhesus monkeys,'' Am. J. Phys. Anthro. **49**, 241–250.

Klecka, W. R. (**1980**). *Discriminant Analysis Series: Quantitative Applications in the Social Sciences* (Sage, London).

Kreiman, J. (**1997**). ''Listening to voices: Theory and practice in voice perception research,'' in *Talker Variability in Speech Processing*, edited by K. Johnson and J. W. Mullenix (Academic, San Diego), pp. 85–108.

Lieberman, P. (**1968**). ''Primate vocalizations and human linguistic ability,'' J. Acoust. Soc. Am. **44**, 1574–1584.

Lieberman, P. (**1984**). *The Biology and Evolution of Language* (Harvard University, Cambridge, MA).

Lieberman, P., and Blumstein, S. E. (**1988**). *Speech Physiology, Speech Perception, and Acoustic Phonetics* (Cambridge University, Cambridge, MA).

Marler, P., and Hobbett, L. (**1975**). ''Individuality in a long-range vocalization of wild chimpanzees,'' Zeitschr. Tierpsychol. **38**, 97–109.

Morton, E. S. (**1977**). ''On the occurrence and significance of motivation-structural rules in some bird and mammal sounds,'' Am. Nat. **111**, 855–869.

Morton, E. S. (**1982**). ''Grading, discreteness, redundancy, and motivation-structural rules,'' in *Acoustic Communication in Birds*, edited by D. E. Kroodsma and E. H. Miller (Academic, New York), Vol. 1, pp. 183–212.

Owren, M. J., and Bernacki, R. H. (**1988**). ''The acoustic features of vervet monkey alarm calls,'' J. Acoust. Soc. Am. **83**, 1927–1935.

Owren, M. J., and Bernacki, R. H. (**in press**). ''Applying linear predictive coding (LPC) to frequency spectrum analysis of animal acoustic signals,'' in *Animal Acoustic Communication: Sound Analysis and Research Methods*, edited by S. L. Hopp, M. J. Owren, and C. S. Evans (Springer-Verlag, Berlin).

Owren, M. J., Dieter, J. A., Seyfarth, R. M., and Cheney, D. L. (**1992**). ''Food' calls produced by adult female rhesus (*Macaca mulatta*) and Japanese (*M. fuscata*) macaques, their normally-raised offspring, and offspring cross-fostered between species,'' Behavior **120**, 218–231.

Owren, M. J., and Linker, C. D. (**1995**). ''Some analysis methods that may be useful to acoustic primatologists,'' in *Current Topics in Primate Vocal Communication*, edited by E. Zimmermann, J. D. Newman, and U. Jürgens (Plenum, New York), pp. 1–27.

Owren, M. J., Seyfarth, R. M., and Cheney, D. L. (**1997**). ''The acoustic features of vowel-like *grunt* calls in chacma baboons (*Papio cynocephalus ursinus*): Implications for production processes and functions.,'' J. Acoust. Soc. Am. **101**, 2951–2963.

Palombit, R. A. (**1992**). ''A preliminary study of vocal communication in wild long-tailed macaques (*Macaca fascicularis*). I. Vocal repertoire and call emission,'' Int. J. Primatol. **13**, 143–182.

Pereira, M. E. (**1986**). ''Maternal recognition of juvenile offspring coo vocalizations in Japanese macaques,'' Animal Beh. **34**, 935–937.

Peters, E. H. (**1983**). ''Vocal communication in an introduced colony of feral rhesus monkey (*Macaca mulatta*),'' Unpublished doctoral dissertation, University of Florida, Gainesville.

Pisoni, D. R., and Lively, S. E. (**1995**). ''Variability and invariance in speech perception: A new look at some old problems in perceptual learning,'' in *Speech Perception and Linguistic Experience*, edited by W. Strange (York, New York), pp. 433–459.

Rawlins, R. G., and Kessler, M. J. (**1986**). *The Cayo Santiago Macaques: History, Behavior and Biology* (State University of New York, Albany, NY).

Rendall, D. (**1996**). ''Social communication and vocal recognition in free-ranging rhesus monkeys (*Macaca mulatta*),'' Unpublished doctoral dissertation, University of California, Davis.

Rendall, D., Rodman, P. S., and Emond, R. E. (**1996**). ''Vocal recognition of individuals and kin in free-ranging rhesus monkeys,'' Animal Beh. **51**, 1007–1015.

Rowell, T. E., and Hinde, R. A. (**1962**). ''Vocal communication by the rhesus monkey (*Macaca mulatta*),'' Proc. Zool. Soc. Lon. **138**, 279–294.

Schön Ybarra, M. (**1995**). ''A comparative approach to the nonhuman primate vocal tract: Implications for sound production,'' in *Current Topics in Primate Vocal Communication*, edited by E. Zimmermann, J. D. Newman, and U. Jürgens (Plenum, New York), pp. 185–198.

Seyfarth, R. M., and Cheney, D. L. (**1984**). ''Grooming, alliances, and reciprocal altruism in vervet monkeys,'' Nature (London) **305**, 541–543.

Smuts, B. B., Cheney D. L., Seyfarth R. M., Wrangham, R. W., and Struhsaker, T. T. (**1987**). *Primate Societies* (University of Chicago Press, Chicago).

Snowdon, C. T. (**1986**). ''Vocal communication,'' in *Comparative Primate Biology, Volume 2A: Behavior, Conservation, and Ecology*, edited by G. Mitchell and J. Erwin (Liss, New York), pp. 495–530.

Snowdon, C. T., Cleveland, J., and French, J. A. (**1983**). ''Responses to context- and individual-specific cues in cotton-top tamarin long calls,'' Animal Beh. **31**, 92–101.

Stevens, K. N., and House, A. S. (**1955**). ''Development of a quantitative description of vowel articulation,'' J. Acoust. Soc. Am. **27**, 484–493.

Tabachnik, B. G., and Fidell, L. S. (**1989**). *Using Multivariate Statistics* (Harper Collins, New York), 2nd ed.

Titze, I. R. (**1994**). *Principles of Voice Production* (Prentice-Hall, Englewood Cliffs, NJ).

Waser, P. M. (**1977**). ''Individual recognition, intragroup cohesion and intergroup spacing: Evidence from sound playback to forest monkeys,'' Behavior **60**, 28–74.

LETTERS TO THE EDITOR

A correction and explanation on: "Acoustic wave propagation through porous media revisited" [J. Acoust. Soc. Am. 100, 2949–2959 (1996)]

Tim W. Geerits

Western Atlas International, 10201 Westheimer, Houston, Texas 77042

The author clarifies and corrects his recent article. © *1998 Acoustical Society of America.*

INTRODUCTION

In this special letter I would like to comment on an extract from an article of mine recently published in JASA (Geerits, 1996). The article contains one typo and a few lines that need to be rephrased in order to prevent from misinterpreting them. In this Letter I will show that these minor changes do not affect the message and conclusions of my article.

I. A CLARIFICATION AND CORRECTION

As mentioned in the article (p. 2950, third paragraph, first line), the physical explanation for the existence of a slow compressional wave in fluid-saturated porous media is out phase motion between the fluid and solid phase. Although not explicitly mentioned in the article, the mathematical equivalent of this statement is: $\langle \nu_i^f \rangle = \langle \nu_i^s \rangle$. However, considering the typo $v_j \langle \tau_{ij}^f \rangle = v_j \langle \tau_{ij}^s \rangle$, $\langle \nu_i^f \rangle = \langle \nu_i^s \rangle$ on p. 2954, first column, 14th line from below (which should be $v_j \langle \tau_{ij}^{f/s} \rangle = v_j \langle \tau_{ij}^{f/s} \rangle$ and $\langle \nu_i^{f/s} \rangle = \langle \nu_i^{f/s} \rangle$), meaning the volume-averaged fluid tractions are equal at either side of the interface, the volume-averaged solid tractions are equal at either side of the interface, the volume-averaged fluid particle velocities are equal at either side of the interface, and the volume-averaged solid particle velocities are equal at either side of the interface), the statement: "So even on the macroscopic level it must be concluded there is no out phase motion between the fluid and the solid phase" is very misleading and consequently results in the wrong conclusion namely that I suggest that Eqs. (22)–(25) imply that $\langle \nu_i^f \rangle = \langle \nu_i^s \rangle$. Of course, this is not true. The wording "out phase motion" is not appropriate at this point. What I've tried to point out here is that Eqs. (22)–(25) show that also on the macroscopic scale this kind of porous medium (a perfectly elastic solid porous skeleton saturated with a linear viscous fluid) is fully continuous, meaning $v_j \langle \tau_{ij}^{f/s} \rangle = v_j \langle \tau_{ij}^{f/s} \rangle$ and $\langle \nu_i^{f/s} \rangle = \langle \nu_i^{f/s} \rangle$. This means that on the macroscopic level differences between $\langle \nu_i^f \rangle$ and $\langle \nu_i^s \rangle$ cannot be resolved by this kind of theory. This is shown in Eqs. (26) and (27), where

the bulk motion and bulk deformation is described. Consequently, the theory shows no out phase motion (only bulk motion $\langle \nu_i \rangle$) although this does not mean that $\langle \nu_i^f \rangle = \langle \nu_i^s \rangle$. If one wants to establish a theory in which the microscopic fluid phase can be modeled as a linear viscous fluid, one needs a different mathematical framework, like the *two-space method of homogenization* (Keller, 1977; Bensoussan *et al.*, 1978). This method was successfully applied to poroelastic media by Burridge and Keller (1981). However my article shows that such a complicated theory is not necessary if the loss mechanism is introduced on a purely phenomenological level by making a physically plausible assumption [i.e., linearization of surface integrals, Eqs. (38), (39), (42), and (43)]. Furthermore, the proposed theory employs volume-averaged field quantities in a consistent manner, whereas all other compatible theories use a mixture of total volume averages [Eq. (18)] and intrinsic volume averages [Eq. (17)]. Such an inconsistent approach serves only one goal, i.e., to arrive at the original Biot equations (Biot, 1956a).

II. CONCLUSION

In order to explain the occurrence of a slow compressional wave in fluid-saturated porous media by means of the method of spatial volume-averaging, it is mathematically inconsistent to model the microscopic fluid phase by a linear viscous fluid.

Benoussan, A., Lions, J. L., and Papanicolaou, G. C. (**1978**). "Asymptotic analyses for periodic structures," in *Studies in Mathematics and Its Applications* (North-Holland, Amsterdam), Vol. 5.

Biot, M. A. (**1956a**). "Theory of propagation of elastic waves in a fluid-saturated porous solid: I. Low-frequency range," J. Acoust. Soc. Am. **28**, 168–178.

Burridge, R., and Keller, J. B. (**1981**). "Poroelasticity equations derived from microstructure," J. Acoust. Soc. Am. **70**, 1140–1146.

Geerits, T. W. (**1996**). "Acoustic wave propagation through porous media revisited," J. Acoust. Soc. Am. **100**, 2949–2959.

Keller, J. B. (**1977**). "Effective behaviour of heterogeneous media," in *Statistical Mechanics and Statistical Methods in Theory and Applications*, edited by U. Landman (Plenum, New York), pp. 631–644.

On the effect of a residual stress field on the dispersion of a Rayleigh wave propagating on a cracked surface

Claudio Pecorari

Institute for Advanced Materials, SCI Unit, P.O. Box 2, 1755-2G Petten, The Netherlands

A heuristic model is presented which quantifies the effect of a compressive residual stress of the dispersion on a Rayleigh wave propagating over a cracked surface. The model shows that a residual stress acting on the outermost part of a surface, and extending for about 20% of the crack depth within the sample, reduces the dispersion of the Rayleigh wave by about 70%. © *1998 Acoustical Society of America.* [S0001-4966(98)01101-1]

INTRODUCTION

The surface mechanical and topographical properties play a critical role in determining the life span and level of performance of ceramic engineering components. These properties may be degraded considerably by the damage introduced in the near-surface region by the processes used to finish such surfaces. Surface damage usually appears in the form of surface roughness, microcrack distributions, and residual stresses. Surface roughness strongly affects the tribological properties of the surface, whereas microcracking controls the strength of the material. The role played by residual stresses is perhaps less dramatic. Marshall *et al.*[1] and Khuri-Yakub and Clarke[2] found that grinding plastically deforms the surface of a ceramic component within a depth approximately equal to 20% of that of cracks generated by the same process. Associated with the plastic deformation, there is a residual stress field that is compressive within the plastic layer and becomes tensile at greater depths. The compressive part of the residual stress is responsible for an effective increase of the material's strength, while the residual stress as a whole causes stable growth of the crack prior to catastrophic failure.[1]

The use of ultrasonic surface waves for the characterization of surface damage has been explored by several authors. The aim of this work is to be present a model which quantifies the effect of the residual compressive field on the phase velocity of a Rayleigh wave propagating over a cracked surface. Of relevance to this problem are the investigations of Pecorari,[3,4] Hirao *et al.*,[5] and Lee *et al.*[6] Pecorari[3,4] presented a model which estimates the dispersion of a Rayleigh wave in terms of parameters characteristics of a distribution of surface-breaking cracks. The model predicts velocity variations of the order of a few percent even for distributions of rather shallow cracks. Hirao *et al.*[5] and Lee *et al.*,[6] on the other hand, reported phase velocity changes of the order of 0.1% or less for a Rayleigh wave propagating over an uncracked surface subjected to an applied or residual stress field.

Although residual stresses cause Rayleigh wave velocity changes much smaller than those due to distributions of surface-breaking cracks, their effect cannot be neglected when the surface contains a crack distribution. In fact, since the strength of a residual stress field is generally much greater than that of the stress field carried by an ultrasonic wave, surface-breaking cracks are expected to behave like subsurface cracks as a result of the compressive residual stress introduced by grinding. In what follows, therefore, the surface-breaking cracks subjected to a compressive residual stress at their mouth's are treated as subsurface cracks, and the region between the upper tip of the crack and the free surface of the system as the host material.

I. MODELING AND NUMERICAL RESULTS

Following the same line of reasoning presented in previous articles,[3,4] to which the reader is referred for details about the approach used here, a cracked surface subjected to a compressive residual stress in its outermost part can be modeled as a layered system consisting of two layers on a substrate Fig. 1. In this work, only one-dimensional, subsurface cracks are considered. The external layer and the substrate have the same elastic properties of the host material, whereas the intermediate layer's constants account for the extra-compliance of the subsurface region of the original system due to the crack distribution. The method used to evaluate the extra-compliance tensor of the intermediate layer utilizes the crack opening displacement (COD) of a subsurface crack as a fundamental quantity. The COD of a subsurface crack insonified by an incident Rayleigh wave can be evaluated by following the treatment presented by Achenbach and Brind.[7] For a distribution of identical subsurface cracks, parallel to each other, and normal to the direction of propagation of the Rayleigh wave, the extra-compliance matrix is found to be diagonal with only three nonzero elements. They are $\Delta S_{11} = 2v(h-d)B_1$, $\Delta S_{55} = v(h-d)B_3/2$, and ΔS_{66}
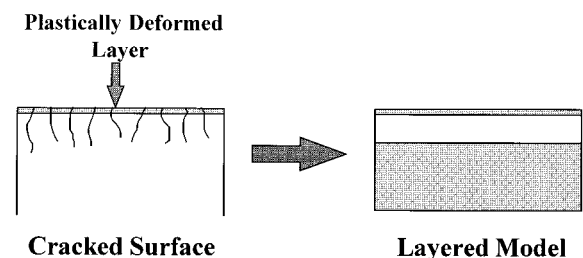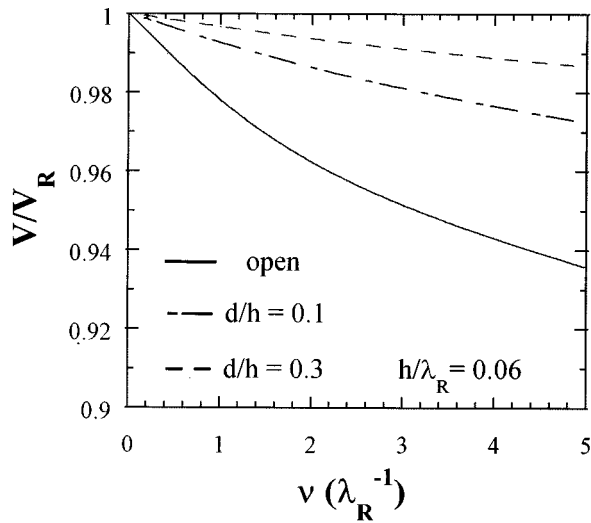

FIG. 1. Cracked surface and layered model.

FIG. 2. Normalized phase velocity versus crack density for two values of the residual stress field's depth extension. The crack is $h/\lambda_R = 0.06$. The case of a distribution of surface-breaking cracks is reported for reference.

FIG. 3. Effect of the residual field depth extension, d/h, on the SAW phase velocity for three values of the crack density. The crack depth is $h/\lambda_R = 0.06$.

$= v(h-d)B_2/2$, where v is the crack density, h is the crack depth, and d is the depth of the layer affected by the compressive residual stress. Here, Voigt's notation has been used.

Figure 2 illustrates the normalized phase velocity change of a surface acoustic wave (SAW) as a function of the crack density v. The SAW is assumed to propagate on a surface with a distribution of cracks having a depth $h/\lambda_R = 0.06$. The symbol λ_R represents the wavelength of the Rayleigh wave propagating over an undamaged surface. Two cases are considered here where the residual compressive stress field extends within the sample by a distance $d/h = 0.1$ and 0.3, respectively. The case of a surface with surface-breaking cracks of the same depth is reported for comparison.

Figure 3 shows the effect of increasing the residual stress extension within the sample on the phase velocity of the SAW. On the vertical axis of Fig. 3, $\Delta V/\Delta V^0$ represents the ratio of the difference between the phase velocities of SAWs propagating over cracked surfaces with and without a residual stress field acting on them, ΔV, and the difference between the phase velocities of SAWs propagating over surfaces with and without the same distribution of surface-breaking cracks, ΔV^0. Three crack distributions with densities $v = 1/\lambda_R$, $3/\lambda_R$, and $5/\lambda_R$ are considered here. The crack depth is $h/\lambda_R = 0.06$. Figure 3 shows that the closure of the cracks along 20% of their depth[1] caused by a compressive residual stress results in a reduction of the SAW dispersion of about 70%. Results very similar to those presented here were obtained for distributions of cracks of smaller depth.
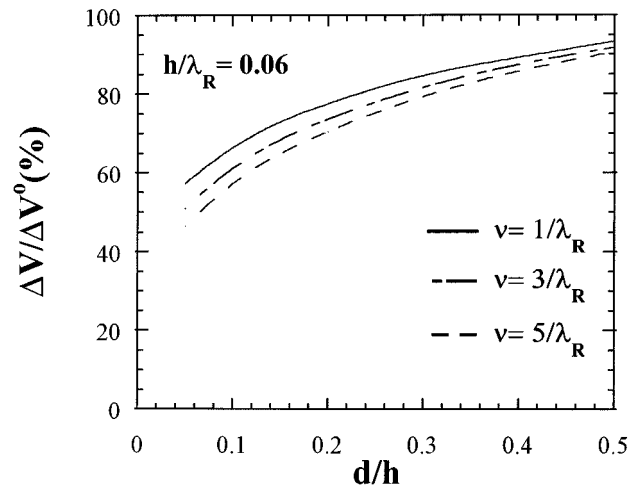
II. CONCLUDING REMARKS

A heuristic model which quantifies the effect of a compressive residual stress on the phase velocity of SAWs propagating over a cracked surface has been presented. Numerical results show that the crack closure caused by a residual stress field may reduce the dispersive effect of the crack distribution of a SAW, and therefore, lead to a considerable underestimation of the surface damage.

[1] D. B. Marshall, A. G. Evans, B. T. Khuri-Yakub, J. W. Tien, and G. S. Kino, Proc. R. Soc. London, Ser. A **385**, 461–475 (1983).
[2] B. T. Khuri-Yakub and L. R. Clarke, "Effect of surface residual stress on crack behavior and fracture stress in ceramics," in *Review of Progess in QNDE,* edited by D. O. Thompson and D. E. Chimenti (Plenum, New York, 1984), Vol. 4B, pp. 1133–1140.
[3] C. Pecorari, "Modeling variation of Rayleigh wave velocity due to distributions of one-dimensional surface-breaking cracks," J. Acoust. Soc. Am. **100**, 1542–1550 (1996).
[4] C. Pecorari, "Rayleigh wave dispersion due to distributions of semielliptical surface-breaking cracks," J. Acoust. Soc. Am. (accepted for publication).
[5] M. Hirao, H. Fukuoka, and K. Hori, "Acoustoelastic effect of Rayleigh surface wave in isotropic materials," J. Appl. Mech. **48**, 119–124 (1981).
[6] Y. C. Lee, J. O. Kim, and J. D. Achenbach, "Measurement of stresses by line-focus acoustic microscopy," Ultrasonics **32**, 359–365 (1994).
[7] J. D. Achenbach and R. J. Brind, "Scattering of surface waves by a sub-surface crack," J. Sound Vib. **76**, 43–56 (1981).

All-optical investigation of the lowest-order antisymmetrical acoustic modes in liquid-loaded membranes

C. Desmet, V. Gusev,[a)] C. Glorieux,[b)] W. Lauriks, and J. Thoen

Laboratorium voor Akoestiek en Thermische Fysica, Departement Natuurkunde, Katholieke Universiteit Leuven, Celestijnenlaan 200 D, B-3001 Leuven, Belgium

The antisymmetrical Scholte–Stoneley wave in liquid-loaded metal and polymer membranes were excited via the laser-induced thermoelastic effect and were detected with a laser beam deflection technique. The experimentally determined dispersion relation for this wave is in accordance with theory in a wide frequency range. However, no evidence of the propagating subsonic lowest-order antisymmetrical pseudo-Lamb wave was found. © *1998 Acoustical Society of America.* [S0001-4966(98)01201-6]

It has been widely confirmed experimentally[1-7] that all-optical excitation and detection of acoustic waves is an extremely useful method for the evaluation of Lamb modes in plates and membranes over a wide frequency range. Recently we demonstrated the possibilities of the all-optical technique for the monitoring of the Scholte and leaky Rayleigh wave propagation on solid–liquid interfaces.[8,9] This Letter presents the experimental results on the evaluation of the dispersion of the antisymmetric Scholte–Stoneley wave in liquid-loaded films. These waves were generated due to the laser-induced thermoelastic effect and were detected by a laser beam deflection method. The most widely used of the traditional methods for the investigation of the waveguide modes in the immersed plates and shells involve the monitoring of the bulk acoustic wave reflection from these objects (see, for example, a very recent report[10] and references therein). We also are aware of experiments[11] on laser visualization of that part of the antisymmetric wave which is localized in the liquid. However, to the best of our knowledge, our experiments are the first all-optical wide-frequency-band experiments with these acoustic modes.

Our experiments were significantly stimulated by the new interesting theoretical results[12-14] concerning propagating modes in liquid-loaded plates. For nearly 50 years after the publication by Osborne and Hart[15] it was widely believed that loading a plate by a liquid can cause the appearance of new propagating modes while the Lamb waves become leaky. Following the terminology of Ref. 10 we will call the antisymmetrical Scholte–Stoneley wave (or A wave) the mode propagating with the velocity v_A, which belongs to the interval $0 \leqslant v_A \leqslant v_S$. Here, v_S denotes the velocity of the Scholte wave propagating on the interface of a semi-infinite solid and liquid. The A wave is subsonic relative to the velocity of sound v_{L2} in the liquid, as $v_S < v_{L2}$. For the lowest-order antisymmetric pseudo-Lamb mode we use the notation A_0 wave.[10] It was assumed for a long time[15] that the velocity of this wave can vary over the range $0 \leqslant v_{A0} \leqslant v_{LR}$, where

v_{LR} is the velocity of the leaky Rayleigh wave on the liquid–solid interface. However, the wave number of this mode was considered to be complex.[15] We do not know any experimental observations of this wave in the subsonic region[10,16] except in the case of loading with air.[6,7] The absence of this wave manifestation is usually explained by its strong damping (i.e., large width of the A_0 resonances in the subsonic region[10,17]). However, it should be pointed out that the experiments were mainly conducted in water and with a rather limited choice of plate materials.

Recently the applications of advanced computer routines provided the opportunity to predict[12-14] the anomalous behavior of the A_0 wave for some combinations of the solid and liquid parameters. This anomalous behavior consists of splitting the modal locus in the subsonic region to form a loop along which the A_0 mode wave number is real. At points on the A_0 locus in the subsonic region which are not on a loop, the A_0 wave is still highly damped, whereas at points on the loop the A_0 wave propagates without loss along the plate.

Clearly, to detect these newly predicted propagating subsonic modes is a challenging experimental problem. We attempted to do it with our all-optical setup[8,9] and present in this Letter preliminary results of the experiments. Though we were able to verify most of the theoretical predictions concerning the antisymmetric Scholte–Stoneley wave (A wave), no evidence for the propagating A_0 wave was found.

A diagram of the measuring cell configuration is presented in Fig. 1. In the case of one-side fluid loading (the other side is in contact with air) the membranes are clamped with a PVC ring on top of a hollow PVC cylinder. In order to obtain a flat surface when the mounted membrane is put vertically, the surface of the film was kept rather small (i.e., a disk with a diameter of about 15 mm). For the membranes two different materials were used: a metal (copper) and a polymer (PET: poly-ethylenetherephtalate). The thicknesses of the membranes were 12 and 100 μm for the PET and 300 μm for the copper. The pump radiation was focused onto the surface of the membrane with a cylindrical lens (beam size $\approx 0.1 \times 10$ mm). The laser-generated waves are detected at a variable distance from the source by a probe He–Ne laser.
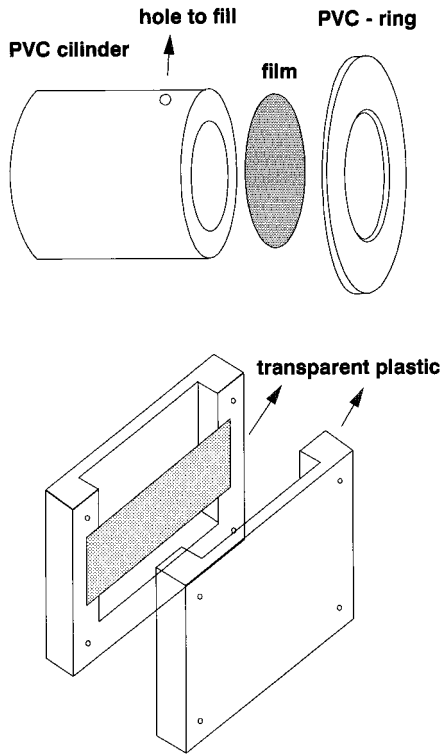
FIG. 1. Diagram of the measuring cell configuration in the cases of one-side loading and two-side loading.

The changes in deflection angle are monitored. A more detailed description of the experimental setup was published elsewhere.[9] In order to obtain a good reflection for the detection beam the front surface of the copper film was polished. For the same reason the PET film was coated with a very thin (30-nm) aluminum layer. The coated surface was the front surface (always in contact with air). After the measurements on the membrane in contact with air, the PVC cylinder was filled with the liquid via a little hole (see Fig. 1). Two different liquids were used: mercury and distilled water. The physical parameters of both the liquids and the solids were published elsewhere.[7–9] In the case of the two-sided loading the membrane is clamped between two optically transparent plastic plates (Fig. 1). The pump radiation and the probe laser beam are focused through the optically transparent cell walls and through the optically transparent liquid (of course only distilled water was used) on the surface of the membrane (only the copper film was used). By calculating the Fourier transform of two signals at two different source–detector distances the dispersion curve of the detected waves can be calculated experimentally. In Fig. 2 the phase velocity dispersion curves of the A wave on a 100-μm-thick PET film are presented in the case of two-side loading with air (solid line), and one-side loading with air and the other side with distilled water (dot-dashed line) and mercury (dashed line). Figure 3 shows the dispersion curves of the A wave for a 12-μm-thick PET film loaded on both sides with air (solid line) and one side with air and the other side with water (dot-dashed line). In Fig. 4 the experimentally determined dispersion curves for the A wave on a 300-μm-thick copper film, one-side loaded with the same liquids
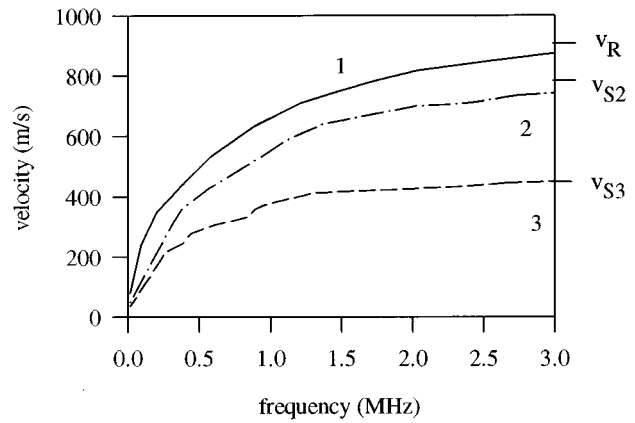

FIG. 2. Experimentally determined phase velocity as a function of frequency for the A wave on a 100-μm-thick PET film two-side loaded with air (curve 1, solid line), and one-side loaded with air and the other side with water (curve 2, dot-dashed line) and mercury (curve 3, dashed line). v_R, v_{S2}, and v_{S3} are the asymptotic values for Rayleigh wave velocity, the Scholte wave velocity for the water–PET interface, and the Scholte wave velocity for the mercury–PET interface, respectively.

as in Fig. 2, are shown. Similar results were obtained in the case of one-side loading of the copper film with acetone and machine oil but are not presented here. We did not present in the figures the uncertainty on the experimental data. It is the same as we reported earlier[9] as the setup was not changed.

It should be mentioned that our membranes and plates were thermally thick at the characteristic time scale of acoustic generation and, consequently, laser-induced thermoelastic stresses were more efficient in the excitation of the antisymmetric modes than of the symmetric ones. Though the signals corresponding to symmetric modes were in fact observed, we do not include these results and their discussion in the present Letter.

The theoretical description (and fitting) of the experimentally determined dispersion curves is based on the evaluation of the roots of the characteristic determinant Δ for the acoustic modes in liquid-loaded plates. In the case of one-side loading (i.e., when only one side of the plate is in con-
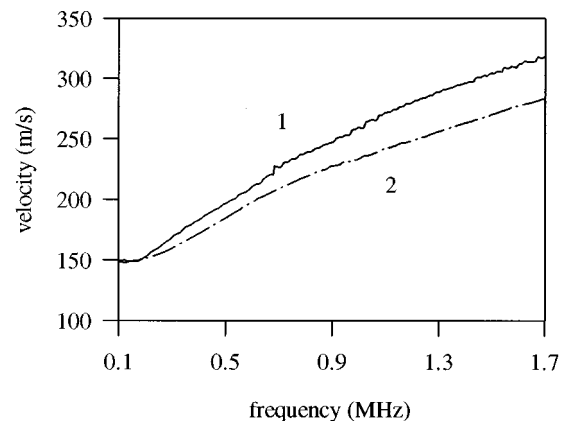

FIG. 3. Experimentally determined dispersion curves of the A wave propagating on a 12-μm-thick PET film two-side loaded with air (curve 1, solid line) and one-side loaded with air and the other side with water (curve 2, dot-dashed line).
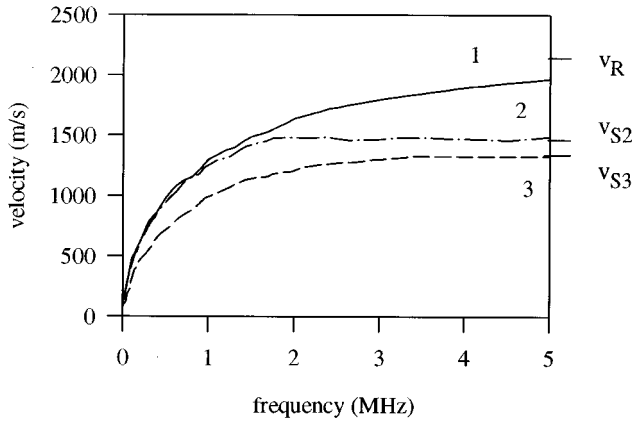
FIG. 4. Experimentally determined phase velocity as a function of frequency for the A wave propagating on a 300-μm-thick copper film two-side loaded with air (curve 1, solid line), and one-side loaded with air and the other side with water (curve 2, dot-dashed line) and mercury (curve 3, dashed line). v_R, v_{S2}, and v_{S3} are the asymptotic values for Rayleigh wave velocity, the Scholte wave velocity for the water–copper interface, and the Scholte wave velocity for the mercury–copper interface, respectively.

tact with liquid while the other is kept mechanically free) this determinant[18,19] can be presented in the form:

$$\Delta = \Delta_A \Delta_S + \frac{K}{2}(\Delta_A + \Delta_S), \tag{1}$$

where Δ_A and Δ_S denote correspondingly the determinants of the antisymmetrical and the symmetrical Lamb modes (in vacuum):

$$\Delta_A \equiv (q^2 + p_{T1}^2)^2 \tanh(p_{L1}H/2)$$
$$\quad -4q^2 p_{T1} p_{L1} \tanh(p_{T1}H/2),$$

$$\Delta_S \equiv (q^2 + p_{T1}^2)^2 \coth(p_{L1}H/2)$$
$$\quad -4q^2 p_{T1} p_{L1} \coth(p_{T1}H/2),$$

$$K \equiv (\rho_2/\rho_1)(p_{L1}/p_{L2})q_{T1}^4, \quad p_{L1} \equiv \sqrt{q^2 - q_{L1}^2},$$

$$p_{T1} \equiv \sqrt{q^2 - q_{T1}^2}, \quad p_{L2} \equiv \sqrt{q^2 - q_{L2}^2},$$

$$q \equiv \omega/v, \quad q_{L1} \equiv \omega/v_{L1}, \quad q_{T1} \equiv \omega/v_{T1},$$

and

$$q_{L2} \equiv \omega/v_{L2}.$$

Here indexes "1" and "2" are introduced for the parameters of solid and liquid correspondingly, indexes "L" and "T" for the longitudinal and the transverse acoustic waves, ρ is the density, ω is the angular frequency, v is the propagation velocity (without indices v corresponds to all possible modes in the liquid loaded plate), and H is the plate thickness. In the case of two-side loading with the same liquid the characteristic determinant can be presented[15,20] in the form:

$$\Delta = (\Delta_A + K)(\Delta_S + K). \tag{2}$$

In the high-frequency limit (formally, when $p_{L2}H \to \infty$ and $p_{T1}H \to \infty$) the determinant in Eq. (1) reduces to $\Delta = \Delta_R \cdot \Delta_{\text{SCH}}$, where Δ_R denotes the Rayleigh determinant and $\Delta_{\text{SCH}} \equiv \Delta_R + K$ denotes the Scholte determinant. Conse-

quently in this case the Rayleigh wave propagates on the mechanically free surface of the plate, while on the loaded liquid surface both Scholte wave (Scholte–Stoneley wave) and leaky Rayleigh wave propagate. In practice the dispersion curve for the antisymmetrical Scholte–Stoneley wave (A wave) starts to approach the constant value v_s exponentially fast already when $(\rho_{T1}H/2) \geqslant 3$, i.e., $\lambda_A \leqslant \sqrt{1 - (v_S/v_{T1})^2}H$ (here λ denotes the acoustical wavelength). This statement is strongly supported by our experiments (see curve 3 in Fig. 2 and curves 2 and 3 in Fig. 4) where fast saturation of the dispersion curve is clearly seen. It should also be pointed out that the observed saturation level is in very good agreement with the magnitude of the Scholte wave velocity which follows from the characteristic equation $\Delta_{\text{SCH}} = 0$.

In the low-frequency limit (formally, when $qH \ll 1$) the characteristic equation $\Delta = 0$ in the case of one-side loading reduces to

$$q^4 = \frac{3q_{T1}^4}{(q_{T1}^2 - q_{L1}^2)H^2}\left[1 + \frac{\rho_2/\rho_1}{qH}\right]. \tag{3}$$

In accordance with Eq. (3) two different regimes for acoustically thin plates are possible. If the density of the loading fluid is so small that the inequality $(\rho_2/\rho_1) \ll qH \ll 1$ holds, then the influence of loading on the phase velocity is negligible and Eq. (3) describes the well-known dispersion of the lowest-order antisymmetric Lamb mode in vacuum:

$$v_{A_0} \cong \left(\frac{v_{S_0}H\omega}{2\sqrt{3}}\right)^{1/2} \propto \omega^{1/2}. \tag{4}$$

In Eq. (4) we used the notation $v_{S_0} \equiv 2v_{T1}\sqrt{1 - (v_{T1}/v_{L1})^2}$ for the low-frequency value of the lowest-order symmetrical Lamb mode in vacuum. The dispersion prescribed by Eq. (4) was observed in our experiments in the absence of liquid loading (i.e., when the experiments were conducted in air, see curve 1 in Figs. 2 and 4).

If the inequality $(qH) \ll \min\{1, (\rho_2/\rho_1)\}$ holds, then evaluation of Eq. (3) leads to the velocity dispersion which importantly differs from $v \propto \omega^{1/2}$:

$$v_A \cong \left[\left(\frac{\rho_1}{\rho_2}\right)\frac{v_{S_0}^2(H\omega)^3}{12}\right]^{1/5} \propto \omega^{3/5}. \tag{5}$$

The formula in Eq. (5) reduces to that derived in Ref. 15 if we first change in it $\rho_2 \to 2\rho_2$. This substitution precisely accounts, in the considered low-frequency regime, for the transition from one-side loading described by the determinant in Eq. (1) to the two-side loading described by the determinant in Eq. (2). In our experiments the dispersion law prescribed by Eq. (5) was clearly observed for the low-frequency part of the spectrum in the case of loading with mercury at frequencies below 0.4 MHz ($qH \leqslant 1$) for the 100-μm-thick polymer membrane (Fig. 2, curve 3) and below 0.15 MHz ($qH \leqslant 1$) for the copper foil (Fig. 4, curve 3). We note that the regime described by Eq. (5) was easily realized due to the high density of mercury ($\rho_2/\rho_1 > 1$). We note, however, that we were also able to realize this regime in the case of water loading in the frequency range $0.7 \leqslant \nu \equiv \omega/2\pi$
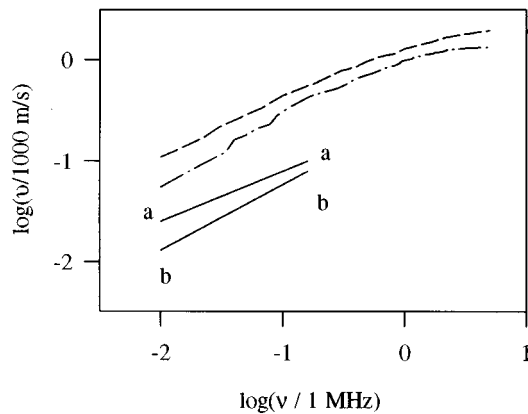
FIG. 5. Log-log plot of the dispersion curves presented by curves 1 and 3 from Fig. 4, together with lines a-a and b-b which reflect the theoretically calculated slopes at low frequencies.

≤ 1.7 MHz for the 12-μm-thick polymer membrane (curve 2 in Fig. 3). For the appreciation of the reader we present the low-frequency parts of curves 1 and 3 from Fig. 4 on a log-log scale in Fig. 5 together with the lines (a-a and b-b) which reflect the slopes predicted by Eqs. (4) and (5). Thus the asymptotic dispersion relations for 300-μm copper foil are well satisfied at frequencies below 0.15 MHz.

We have also checked that the dispersion curves presented in Figs. 2 and 4 can be successfully fitted in the whole examined frequency range by solving the characteristic equation $\Delta = 0$ by currently widely available mathematical programs (for example by FINDROOT in MATHEMATICA). In the case of the thin polymer membrane (Fig. 2) it is additionally necessary to take into account in-plane stresses caused by the film stretching[6,7] in order to explain the weak dependence of the velocity on frequency in the range below 0.2 MHz. All our fittings confirmed that the wave monitored in our experiments is the antisymmetric Scholte–Stoneley wave (i.e., A wave).

Though the employed method favors the excitation of antisymmetrical modes no evidence of the A_0 mode was found experimentally. It should be noted here that for brass two-side loaded with water the looping of the A_0 mode (and thus propagation of the A_0 wave) was predicted[13] in the range $0.025 \leq H/\lambda_{T1} \leq 0.14$. We conducted experiments with copper foil with characteristics which are sufficiently close to those of brass. In Ref. 13 it was formulated that ''the value v_{L2}/v_{T1} is the dominant factor in the creation of anomalous behavior'' and that ''the splitting occurs if v_{L2}/v_{T1} is greater than some value between 0.5 and 0.6.'' In our experiments $v_{L2}/v_{T1} \cong 0.656$ and thus exceeds the critical value. However, we failed to register any manifestation of propagating other slow modes, except the A wave in the range $0.013 \leq H/\lambda_{T1} \leq 0.68$. It should be noted here that in accordance with the predictions[13] the velocity of the propagating A_0 mode can be nearly two times smaller than v_{L2} in the low-frequency part of the loop and always differs from v_{L2} by more than 5%. We made experiments both with one- and two-side loading. Although the dispersion curves differ in these two cases the difference was less than the experimental

uncertainty and because of that we did not present these curves separately in Fig. 4. No signs of any additional A-wave slow signals were found in both cases. We also failed to localize additional to $v = v_A$ real roots of the characteristic equation $\Delta = 0$ by evaluating Δ for some fixed values of the parameter H/λ_{T1} and varying v with steps $\delta v/v_{T1} = 10^{-5}$. Both for copper and for the parameters of brass listed in Ref. 13 our calculations predict a monotonic increase of Δ with increasing $v > v_A$ in the regions of interest.

In conclusion, the results of our experiments confirmed the possibility of all-optical monitoring of the antisymmetrical Scholte–Stoneley wave in fluid-loaded membranes in a wide frequency range. In combination with the earlier demonstrated[21,22] opportunities of using a Lamb-wave oscillator as a multisensor, further advances in this research could lead to the development of noncontact methods for the diagnostics of liquids.

Concerning our unsuccessful attempt to excite and detect the nondamped A_0 wave in the case of liquid loading, it is clear that detailed theoretical investigation of the features of looping (if the latter exists) is necessary in order to get a better understanding of the nature of the A_0 wave in the subsonic regime. Then, perhaps, it will be possible to understand why it was not excited (or was excited significantly less efficiently in comparison with the A wave) by laser-induced thermoelastic stresses in the experiments reported here.

[1] H. Sontag and A. C. Tam, Appl. Phys. Lett. **46**, 725–727 (1985).
[2] R. J. Dewhurst, C. Edwards, A. D. W. McKie, and S. B. Palmer, Appl. Phys. Lett. **51**, 1066–1068 (1987).
[3] D. A. Hutchins, K. Lundgren, and S. B. Palmer, J. Acoust. Soc. Am. **85**, 1441–1448 (1989).
[4] J. S. Meth, C. D. Marshall, and M. D. Fayer, J. Appl. Phys. **67**, 3362–3376 (1990).
[5] J.-D. Aussel and J. P. Monchalin, in *Review of Progress in Quantitative Non-Destructive Evaluation*, edited by D. O. Thompson and D. E. Chimenti (Plenum, New York, 1989), Vol. 8A, pp. 535–542.
[6] J. A. Rogers and K. A. Nelson, IEEE Trans. Ultrason. Ferroelectr. Freq. Control **UFFC-42**, 555–566 (1995).
[7] C. Desmet, U. Kawald, A. Mourad, W. Lauriks, and J. Thoen, J. Acoust. Soc. Am. **100**, 1509–1513 (1996).
[8] C. Desmet, V. Gusev, W. Lauriks, C. Glorieux, and J. Thoen, Appl. Phys. Lett. **68**, 2939–2941 (1996).
[9] C. Desmet, V. Gusev, W. Lauriks, C. Glorieux, and J. Thoen, Opt. Lett. **22**, 69–71 (1997).
[10] J.-P. Sessarego, J. Sagéloli, G. Gazanhes, and H. Überall, J. Acoust. Soc. Am. **101**, 135–142 (1997).
[11] J. A. Clark, J. Sound Vib. **70**, 267–273 (1980).
[12] H. Dabirikhah and C. W. Turner, IEEE Ultrason. Symp. Proc. **1**, 313–317 (1992).
[13] A. Freedman, J. Sound Vib. **183**, 719–737 (1995).
[14] H. Dabirikhah and C. W. Turner, J. Acoust. Soc. Am. **100**, 3442–3445 (1996).
[15] H. F. M. Osborne and S. D. Hart, J. Acoust. Soc. Am. **17**, 1–18 (1945).
[16] R. D. Watkins, W. H. B. Cooper, A. B. Gillespie, and R. B. Pike, Ultrasonics **20**, 257–269 (1992).
[17] A. Freedman, J. Sound Vib. **82**, 197–213 (1982).
[18] A. Grabowska, Arch. Acoust. **4**, 57–64 (1979).
[19] D. E. Chimenti and A. H. Nayfeh, J. Acoust. Soc. Am. **85**, 555–560 (1989).
[20] D. E. Chimenti and S. I. Rokhlin, J. Acoust. Soc. Am. **88**, 1603–1611 (1990).
[21] R. M. White and S. W. Wenzel, Appl. Phys. Lett. **52**, 1653–1655 (1988).
[22] S. W. Wentzel and R. M. White, IEEE Trans. Electron Devices **35**, 735–742 (1988).

Speech articulator measurements using low power EM-wave sensors

J. F. Holzrichter,[a] G. C. Burnett, and L. C. Ng
Lawrence Livermore National Laboratory, P.O. Box 808, Livermore, California 94551

W. A. Lea
Speech Science Institute, P.O. Box 240428, Apple Valley, Minnesota 55124

Very low power electromagnetic (EM) wave sensors are being used to measure speech articulator motions as speech is produced. Glottal tissue oscillations, jaw, tongue, soft palate, and other organs have been measured. Previously, microwave imaging (e.g., using radar sensors) appears not to have been considered for such monitoring. Glottal tissue movements detected by radar sensors correlate well with those obtained by established laboratory techniques, and have been used to estimate a voiced excitation function for speech processing applications. The noninvasive access, coupled with the small size, low power, and high resolution of these new sensors, permit promising research and development applications in speech production, communication disorders, speech recognition and related topics. © *1998 Acoustical Society of America.* [S0001-4966(98)05501-5]

PACS numbers: 43.70.Jt, 43.40.Aj [AL]

INTRODUCTION

Newly developed electromagnetic (EM) radar sensors (McEwan, 1994, 1996) provide a capability for measuring EM wave reflections from speech organ interfaces in a noninvasive, safe, fast, portable, and low cost fashion (Holzrichter *et al.*, 1996). In addition, many other types of EM sensors can be used to make similar measurements of the positions and motions of the human vocal articulators during speech production. (See Fig. 1.) Many problems with microwave imaging (Larsen and Jacobi, 1986; Bolomey and Pichot, 1990) are overcome by their use in modalities described below. The measurements to date include the motions of the glottal tissues (e.g., vocal folds), lips, tongue, jaw, and velum. Examples of useful vocal fold measurements are the pitch, glottal cycle timing for pitch synchronous estimation of the speech transfer functions, and the qualities of the fold contact for speech disorder studies. Similarly, EM sensor measurements of jaw motion with acoustic speech provide constraints on the sound being articulated for speech recognition, and can be used for ''talking head'' and video image synchronization. Many other applications are possible.

PRESENTLY USED EM WAVE SENSORS

The EM radar sensors (see Fig. 2) were used in a survey mode to measure gross features associated with an organ's motion during acoustic speech. They operated with radiated power levels of fractions of milliWatts, at frequencies centered at 2.3 GHz, and in a repetitive pulsed mode with pulse rate frequencies of 2 MHz. The antenna used for this survey work is a monopole which radiates an *E* field (and corresponding *M* field) caused by charge oscillation back and forth along a short 1.5-cm-long conductor. The *E* field is polarized along the field lines defined by the long axis of the

conductor. The EM waves are radiated at intensities far below allowed operational standards for human exposures in continuous use (Polk and Rostow, 1996). The articulator motion information is obtained by measuring the reflection change of the EM waves from a weighted average of dielectric interfaces and conductive discontinuities (i.e., usually air/tissue) that are in the path of the radiated EM field. For the sample data in this report, the radar sensors launched a short pulse train of EM waves into the head and neck at two locations—horizontally into the front of the neck at the laryngeal prominence for glottal tissue measurements, and upward from under the jaw for jaw, tongue, and both soft and hard palate measurements. The EM waves in the transmit cycle have a wavelength of 12 cm in air, which is shortened to about 1.5 cm in tissues because the relative dielectric constant of human tissue is about 64 (Haddad *et al.*, 1997). The reflected EM waves can be used to obtain absolute positional accuracy to about 1/10 wave length, and relative measurements to less than 1/100 wave, in the local dielectric medium.

The sensor detection mode for these experiments uses the general concept of the ''frozen wave'' field disturbance approach (Skolnik, 1990). A short pulse train of four to six cycles, lasting a few nanoseconds, is transmitted. A range gate is delayed, relative to the start of the transmitted pulse, by a fixed time of up to 3 ns. It ''drives'' a diode sample gate that detects the reflected EM waves received by a separate antenna (located next to the transmitter antenna in these experiments). This sampling system samples all reflected energy from all wave-tissue reflections that meet the round-trip time delay conditions determined by the range gate (i.e., about 4 cm into the neck for the leading edge of the pulse). The transmitter generator rate of 2×10^6 pulses per second means that in each 0.14-ms period, 100 pulses are transmitted, received, and integrated into a high S/N analog signal. This signal is electronically filtered to remove information that falls outside the frequency bands of interest for the ap-

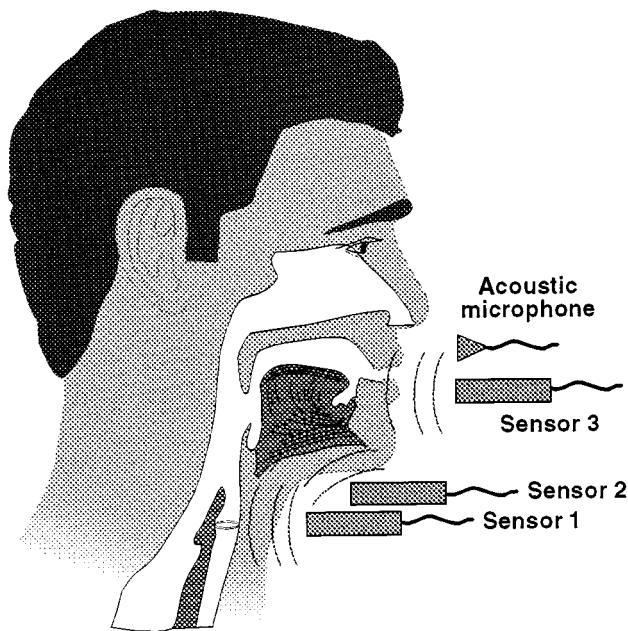[a]Inquiries should be directed to J. F. Holzrichter at Mail stop: L-3 or e-mail: holzrichter1@llnl.gov

FIG. 1. Illustration showing locations of EM sensors along mid sagittal plane of human head for experiments.

plication. The high frequency limit is presently about 7 kHz, and the lower limit varies. For glottal measurements in particular, the low frequency ''clutter'' from the skin/air interface and other stationary, or slowly moving tissue interfaces are removed using low frequency cut-off filtering below 80 Hz. For the jaw and tongue sensor approximately 0.5 Hz
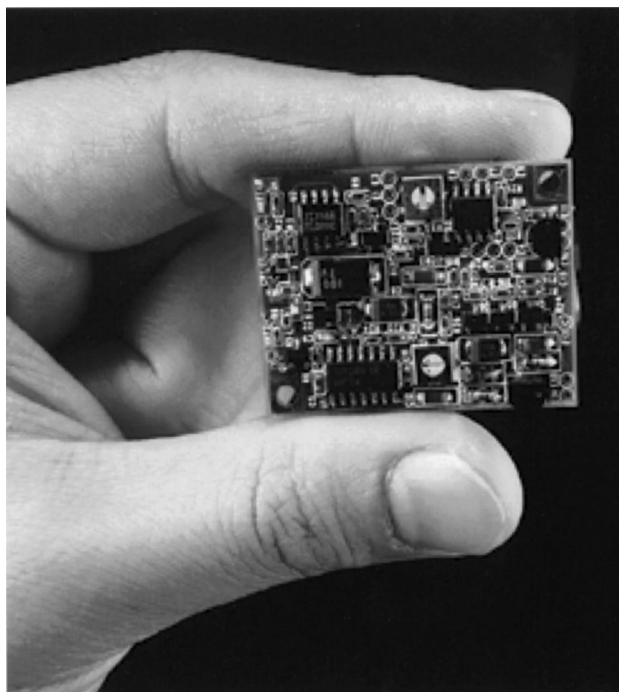

FIG. 2. Photograph of a very low power EM radar sensor of the type used for the experiments in this letter. The separate transmitter and receiver modules are placed side by side on the circuit board, each connected to a separate monopole antenna.
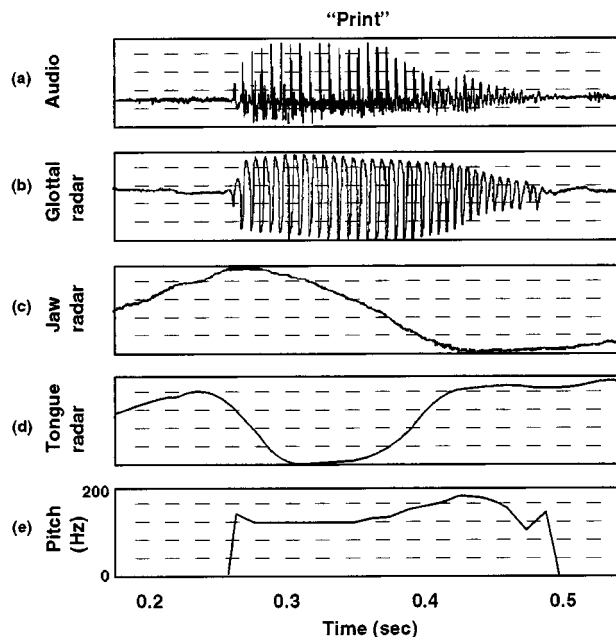

FIG. 3. Typical data obtained as a young adult male speaks the word ''print.'' in isolation. An acoustic microphone's waveform is shown in plot (a). Data from the EM sensor measuring glottal motions is shown in plot (b). Data from a second EM sensor, measuring jaw motions over a range of about 2 mm, is shown in plot (c). A third EM sensor replaced the jaw sensor on a second data set. It was placed under the jaw and was used to detect a signal from the oral cavity, plot (d), including tongue and jaw/palate distance. The data in (c) and (d) are not corrected for low frequency sensor rolloff below 0.5 Hz. An example of data processing is to use the glottal sensor signal to obtain the instant pitch values, presented in plot (e) where the vertical scale is zero to 200 Hz.

filtering is used for data herein. This enables >60 dB signal to background measurements.

Specialized sensors and antennas optimized for other detection modes can be employed as needed for the user's specific application. The *Radar Handbook* by Skolnik (1990) describes many. For example, a focusing antenna or lens can be employed to focus the EM waves onto detailed organ-positions, or multiple view EM sensors can be used for tomographic-like imaging modes. Another more traditional radar mode, used in related experiments and in ultrasonic work, is the ''scanned'' range gate mode. For each range gate time setting (i.e., a specific distance), an organ interface reflection can be measured, if it is present at the defined location. Depending upon the application, it may be necessary to calibrate each EM sensor system on phantoms and on subjects outfitted with auxiliary calibration sensors.

TYPICAL DATA

Examples of acoustic and EM sensor data, simultaneously collected during the articulation of the word ''print,'' are shown in Fig. 3. The individual plots in Fig. 3 show the acoustic signal 3(a), a simultaneously recorded EM glottal sensor signal 3(b), and a separate EM jaw sensor signal showing up/down jaw movements 3(c). Figure 3(d) shows EM sensor data from the oral cavity showing general tongue motion. An example of processed data for each glottal cycle is the instantaneous pitch value versus time in 3(e).
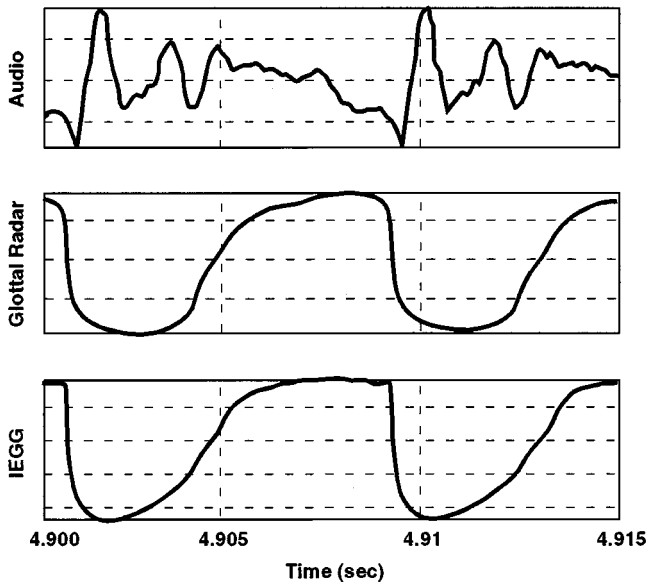
FIG. 4. An acoustic signal, glottal function, and EGG signal measured simultaneously for the sound /a/ in ''father.'' The upper trace acoustic signal is measured with a conventional, low-cost microphone. The glottal signal (middle trace) is measured using a low power EM sensor as shown in the photograph in Fig. 1. The lower trace is plotted as the negative of a conventional electroglottograph signal, showing a signal increase (increased resistance) as the vocal folds part. The horizontal time trace shows time measured in seconds, with 5 ms timing marks.

These data indicate the quality and variety of information presently obtainable. For example, the jaw in Fig. 3(c) and the tongue positions versus time in Fig. 3(d) detected sub-millimeter relative positional changes, showing the upward motion of the organs in preparation for the plosive /p/, where upon the jaw starts to drop, then the tongue lifts for the sequence /i/, /n/, and /t/. Such positional or motional articulator information, when calibrated and statistically validated, may be used in speech recognition by testing measured sequences of positional or motion patterns against those for a trial sequence of phonemes (e.g., jaw motions for /silence/–/p/–/r/, and tongue for /r/–/i/–/n/), then generating a ''closeness score'' using a recognition algorithm. Other uses of these data include determining the type of excitation function used for the speech unit (e.g., voiced or unvoiced), the onset of speech, the presence of noise, as well as estimates of the volume air flow excitation estimation and consequent transfer function.

GLOTTAL TISSUE POSITIONS AND VOICED EXCITATIONS VERSUS TIME

Figure 4 shows an acoustic signal, a glottal EM sensor signal (with filter response removed), and an electroglottograph signal as the speaker pronounced the vowel /a/ as in ''father.'' The data was recorded over two glottal cycles. The lower trace in Fig. 4 shows the corresponding electroglottograph signal plotted as the inverse (IEGG) of the conductivity of the glottal region. It is related to the vocal fold contact area (Childers *et al.*, 1986; Titze, 1984). The EM sensor measurements, middle trace Fig. 4, show EM wave reflections from glottal tissue dielectric interfaces, whose

relative positions change rapidly in time, especially at vocal fold contact when two interfaces disappear. The motions of vocal fold tissues, measured with an EM sensor, are consistent with both EGG and video laryngoscope data (Leonard, 1997; Holzrichter *et al.*, 1996). Related EM sensor measurements of pressed and falsetto voicing show noncontacting vocal fold signals, essentially zero EGG signals, and expected acoustic signals. These and similar data, e.g., Fig. 3(c) and (d), show that EM waves reflect from dielectric interfaces, which for speech can be quite complex in shape and can be associated with other related tissue structure motions. Nevertheless, important time (i.e., spectral) information for speech applications such as instant pitch and vocal fold opening and closure times are easily measurable with the example EM sensors and are consistent among the data sets.

Previously, the authors (Holzrichter *et al.*, 1996) have constructed a simple model of glottal air flow being proportional to the EM sensor signal versus time. They associated the EM reflections with the distance between the folds and used a model of air flow proportional to glottal area (Flanagan, 1965). However, Rothenberg (1981), Titze (1984), and others have analyzed glottal contact data and have shown that such limited tissue structure data is not sufficient to determine ''accurate'' glottal air flow. Nevertheless, the simple model is proving useful (see below) because it appears to capture important excitation spectral information derived from the pitch period, the rate of maximum closure, and the glottal opening shape of the vocal tract excitation. Improved EM reflection models of the glottal structure, and associated air-flow, are available to obtain increasingly accurate, real time excitation information for signal processing and other applications.

VOCAL TRACT TRANSFER FUNCTION ESTIMATION

Using linear source-filter theory, several of the voiced transfer functions have been estimated by Fourier transforming both the acoustic speech and approximated excitation signal (as estimated above), then deconvolving. Data were processed ''pitch synchronously,'' two glottal periods at a time, for four isolated vowel sounds. An autoregressive, moving average (i.e., ARMA) approximation procedure was used (Oppenheim and Schafer, 1984), with 15 poles and 15 zeros, to fit a smooth analytic function to the numerical data. Figure 5 shows the results for the American English vowels, /ɛ/, /i/, /a/, and /u/, as spoken by a young adult male. These data have low noise levels, and appear to approximate formants that match well the locations shown in previous publications (Peterson and Barney, 1952; Olive *et al.*, 1993), but with enhanced low intensity structure as expected by using ''zeros,'' in addition to ''poles.'' Reversing this procedure leads to synthesized acoustic speech signals which match the original speech signals well.

SUMMARY

When these new techniques are more completely explored, with improved sensor calibrations and validated on statistically significant groups of speakers, they should add value to many speech research, diagnostic, and technology
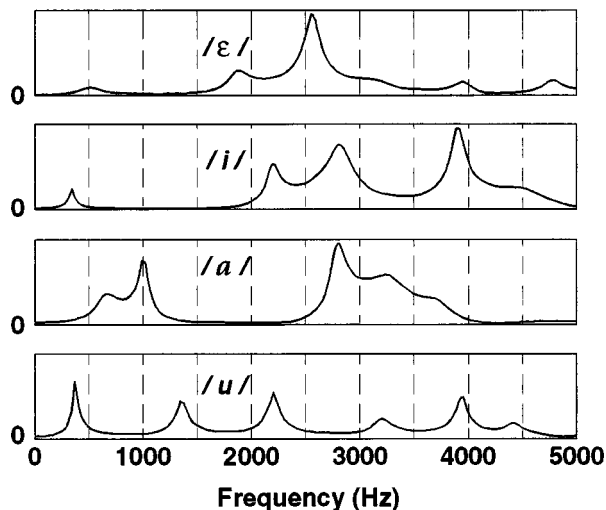
FIG. 5. Transfer functions versus frequency for several American English vowels—/ε/, /i/, /a/, and /u/, on a linear scale. Estimated by deconvolving the excitation function from the acoustic signal, both measured simultaneously and pitch synchronously during two glottal cycles, and approximated by an ARMA procedure using 15 poles and 15 zeros.

applications. Similar EM sensors can be optimized for research, for medical diagnostics, or miniaturized for technology applications such as insertion into microphone housings, telephone headsets, and other devices. The noninvasive aspects appear potentially useful for routinely diagnosing articulator problems and may prove to be a useful source of feedback to speakers, singers, language learners, and the speech disabled. Other promising applications are to use the estimated excitation functions and calculated transfer functions for speech coding as used in telephony transmission, for storage and subsequent synthesis as ''personalized'' speech, and for speech recognition and speaker verification.

ACKNOWLEDGMENTS

Bolomey, J.-Ch., and Pichot, Ch. (**1990**). ''Microwave tomography: From theory to practical imaging systems,'' Int. J. Imaging Systems Tech. **2**, 144–156.

Childers, D. G., Hicks, D. M., Moore, G. P., and Alsaka, Y. A. (**1986**). ''A model for vocal fold vibratory motion, contact area, and the electroglottogram,'' J. Acoust. Soc. Am. **80**, 1309–1320.

Flanagan, J. L. (**1965**). *Speech Analysis, Synthesis, and Perception* (Academic, New York), See pp. 40–41. Also in the 2nd edition in 1972.

Holzrichter, J. F., Lea, W. A., McEwan, T. E., Ng, L. C., and Burnett, G. C. (**1996**). *Speech Coding, Recognition, and Synthesis using Radar and Acoustic Sensors*, University of California Report UCRL-ID-123687 (reprints available from the Office of Scientific and Technical Information, P.O. Box 62, Oak Ridge, TN 37831).

Haddad, W. S., Rosenbury, E. T., Johnson, K. B., and Pearce, F. J. (**1997**). *Measurements of the Dielectric Properties of Body Tissues and Fluids at Microwave Frequencies* (Lawrence Livermore National Laboratory, to be published).

Larsen, L. E., and Jacobi, J. H., editors (**1986**). *Medical Applications of Microwave Imaging* (IEEE, New York).

Leonard, R. J. (**1997**). ''A comparison of laryngoscopic and EM glottal sensor data'' (to be published).

McEwan, T. E. (**1994**). U.S. Patent No. 5,345,471 (1994), U.S. Patent No. 5,361,070 (1994).

McEwan, T. E. (**1996**). U.S. Patent No. 5,573,012 (1996).

Olive, J. P., Greenwood, A., and Coleman, J. (**1993**). *Acoustics of American English Speech* (Springer-Verlag, New York).

Oppenheim, A. B., and Schafer, R. W. (**1984**). *Discrete-Time Digital Processing* (Prentice-Hall, Engleword Cliffs, NJ).

Peterson, G. E., and Barney, H. L. (**1952**). ''Control methods used in a study of the vowels,'' J. Acoust. Soc. Am. **24**, 175–184.

Polk, C., and Rostow, E., editors (**1996**). ''Appendix 2: Safety Standards,'' in *Handbook of Biological Effects of Electromagnetic Fields* (CRC, Boca Raton, FL).

Rothenberg, M. (**1981**). ''Some relations between glottal flow and vocal fold contact area,'' ASHA Rep. **11**, 88–96.

Skolnik, M. (**1990**). *Radar Handbook* (McGraw-Hill, New York), 2nd ed.

Titze, I. R. (**1984**). ''Parameterization of the glottal area, glottal flow, and vocal fold area,'' J. Acoust. Soc. Am. **74**, 570–580.

625   J. Acoust. Soc. Am., Vol. 103, No. 1, January 1998

Holzrichter *et al.*: Letters to the Editor   625

Steady-state spectra of diapason class stops of the Newberry Memorial organ, Yale University

J. M. Harrison

Department of Psychology and the Hearing Research Center, Boston University, 64 Cummington Street, Boston, Massachusetts 02215

N. Thompson-Allen

Yale University School of Music, Stoeckel Hall, 96 Wall Street, New Haven, Connecticut 06511

Steady-state line spectra of the C's (C2 to C9) of eight diapasons of the Newberry Memorial organ were investigated using DAT records made in the hall. To better represent what a listener hears, the SPL spectra were transformed to loudness levels (LL's), and adjusted to accommodate masking between the harmonics. The way the LL transformation altered the levels of the harmonics was shown in detail for C2, C4, and C6. The transformed LL spectral envelopes had essentially identical and well-known ''diapason type'' contours from C4 to C6. These envelopes differed from those at C2, C3 and C7, C8, and C9. Hence, no common diapason pattern was found over the entire frequency range. However, the spectral envelopes of the seven diapason at C2, for example, were similar, and constituted the ''typical diapason'' envelope at C2. The advisability of assuming a ''typical diapason envelope'' for all diapason sounds was discussed. The spectral envelopes at C7 and C8 of the diapason and also of chorus reed stops of the organ were similar. Since diapason type pipes were used for C7 and C8 of the reed stops (as is typical) it is not surprising that they sound similar to these notes of diapason stops. © *1998 Acoustical Society of America.*
[S0001-4966(98)03501-2]

PACS numbers: 43.75.Np [WJS]

INTRODUCTION

The present work investigated the steady-state spectra of a sample of diapason class stops of the Newberry Memorial organ in Woolsey Hall, at Yale University. The sound of the organ was described by Flint (1930) as it was when finished in 1928, and the many agreements between recent sound level measurements of the organ (Harrison and Thompson-Allen, 1996) and Flint's descriptions confirmed that the instrument is as it was in 1928 (Kinzey and Lawn, 1992).

One purpose of the work was to examine the spectra of various classes of diapasons in which the harmonics were transformed to loudness levels (LL's) to better represent the response of the listener to the instrument (Pollard, 1978, 1988). The second purpose was to determine the extent to which the well known characteristic ''diapason spectral envelope'' found typically at C4, was present over the full compass of the key board, and to investigate the presence of other characteristic ''diapason spectral envelopes'' at other frequencies.

I. GENERAL METHOD

The apparatus consisted of a 1-in. Bruel & Kjaer condenser microphone (type 4145) mounted on a tripod in front of seat #13 in the front row of the first balcony, 29.7 m from the organ. The microphone output was fed to a bandpass filter (Khrone-Hite 3100-R) and a digital audio tape deck (DAT, Sony DTC-790, 48-kHz sampling rate) located on the stage adjacent to the organ console. The system was calibrated with a Bruel & Kjaer pistonphone (model 4220).

The high-frequency cutoff of the filter was set to 15 kHz. The low-frequency cutoff was set at the point just below that which lowered the level of the note being measured. The noise level in the hall, measured with a sound level meter (Genrad, 1987), was 61 dB (C). The octave band noise level went from 54 dB, SPL at 63 Hz to 18 dB, SPL at 15 kHz.

All the C's of the Great 16 ft, 8 ft #1, 8 ft #4 Diapasons, the Principal and the Fifteenth, the Swell 8 ft Diapason and Geigen Diapason, and the Solo 8 ft Diapason were recorded. For each note, the tape was started and allowed to record about 10 s of hall ambient noise, the note was then played for 10 s. The tape was then allowed to run for a further 12 s to show the reverberation time.

The DAT records were analyzed using Spectraplus4 (Pioneer Hill) and SpectraPro (Sound Technology, Inc.) software. Line, and third octave band spectra were obtained, the latter being used to calculate the overall loudness levels (ISO 522B) of each note using a program (Zwicker *et al.*, 1984) provided by Dr. Fastl.

A loudness level (LL) transformation of the SPL of each harmonic altered the shape of the spectrum in accordance with the sensitivity of the ear, bringing the appearance of the spectrum one step nearer to the way the note is heard. The SPL spectra were transformed to LL's using the Robinson and Dadson (1956) contours. However, the simple LL transformation of the SPL data ignores the simultaneous masking effects between the harmonics.

Churcher (1962), Pollard (1978, 1988), Beranek *et al.* (1951), and Pollard and Jansson (1982) have suggested quite different transformations designed to take into account these

TABLE I. Adjusted LL transformation: #1 Diap, C2 $F = 0.26$. Final column of this table is plotted in Fig. 2, top panel.

Harm.	Freq	SPL (dB)	LL (phons)	Sones	F*sones	Masked LL
1	65.5	79	67	6.5	⋯	67
2	131	49	40	1.0	0.26	21
3	197	46	43	1.23	0.32	24
4	262	38	36	0.76	0.2	17
5	328	39	41	1.07	0.28	22
6	393	36	39	0.93	0.24	19
7	459	31	32	0.57	0.15	12

TABLE III. Adjusted LL transformation: #1 Diap, C6 $F = 0.72$, Final column of this figure is plotted in Fig. 3, middle panel.

Harm.	Freq.	SPL (dB)	LL (phons)	Sones	F*sones	Masked LL
1	1048	53	53	2.38	⋯	53
2	2096	52	54	2.64	1.9	49
3	3144	24	29	0.47	0.34	24
4	4192	37	44	1.32	0.95	39
5	5240	27	30	0.5	0.36	25
6	6288	17	14	0.17	0.12	9
7	7336	17	11	0.13	0.09	5

masking effects. Churcher's (1962) method was used here since it was developed to deal with line spectra. Examples of the transformation of the SPL data using Churcher's method are given Tables I, II, and III. The numbers in the last column were plotted in the figures.

Sound pressure level measurements of the organ have been made on four occasions. Comparisons of the measurements made in August 1995 (Temp. 86.7 F at the console) and August 1996 (Temp. 87.6 F) showed only small differences. For example, the difference between the August 1996 and August 1995 SPL measurements of the six C's of the Great #1 Diapason were −3 dB, −4 dB, 3 dB, −2 dB, −1 dB, and −3 dB.

II. RESULTS

A. Overall SPL's (dBC) and loudness levels (phons)

The overall SPL (dBC) and the loudness levels (phons), calculated from the DAT recordings using Zwicker's ISO 522B method (Zwicker *et al.*, 1984) of the C's of the diapason stops are shown in the upper and lower panels of Fig. 1. These data show the effect of a loudness level (LL) transformation on the dBC SPL data. The transformed data reflect the changes in auditory sensitivity with frequency revealed in LL contours, and more closely represent what the listener hears than SPL data (Pollard's, 1988, ''psycho-physical level''). The recording of the bottom note of the 16 ft Diapason was unsatisfactory, and the datum is not presented here.

TABLE II. Adjusted LL transformation: #1 Diap, C4 $F = 0.42$. Final column of this table is plotted in Fig. 2, bottom panel.

Harm.	Freq	SPL (dB)	LL (phons)	Sones	F*sones	Masked LL
1	262	68	72	9.19	⋯	72
2	524	67	71	8.57	3.6	58.5
3	786	52	53	2.46	1.03	40.4
4	1048	44	44	1.32	0.55	31.4
5	1310	46	46	1.52	0.64	33.6
6	1572	32	34	0.66	0.28	21
7	1834	36	38	0.87	0.37	25.6
8	2096	25	27	0.41	0.17	14.5
9	2358	18	21	0.27	0.11	8.1
10	2620	21	25	0.35	0.15	12.6
11	2882	24	30	0.5	0.21	17.5

B. LL spectral analysis

1. General considerations

Two classes of sound were produced by the pipes. The first consisted of a wide band noise produced by the wind blowing the pipe. The level of this noise varied from pipe to pipe and was 0–15 dBC above the noise level of the hall.

The second class consisted of a fundamental and a series of higher partials comprising the musical output of the pipe. Measurement of the frequency difference between adjacent partials of middle C of the #1 Diapason showed a mean frequency of 264.98 Hz, with a standard deviation of 3.59 Hz. These figures indicate that the partials were harmonics within the frequency resolution of the FFT program. Similar results were obtained for other pipes. Fletcher *et al.* (1963) and Churcher (1962) also found that the partials of diapason pipes were harmonics within the limits of their measurements.

2. LL spectral data

The transformed LL spectra are shown in Figs. 2, 3, and 4. The effect of the Churcher (1962) transformation on the
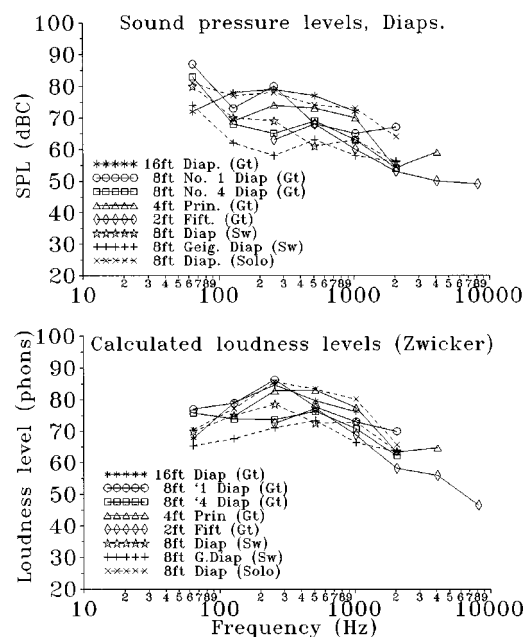

FIG. 1. The top panel shows the dB SPL spectra of the eight diapasons used in the spectral measurements. The bottom panel shows the LL of each stop calculated from the DAT records using the Zwicker *et al.* (1984) ISO 522 B program.
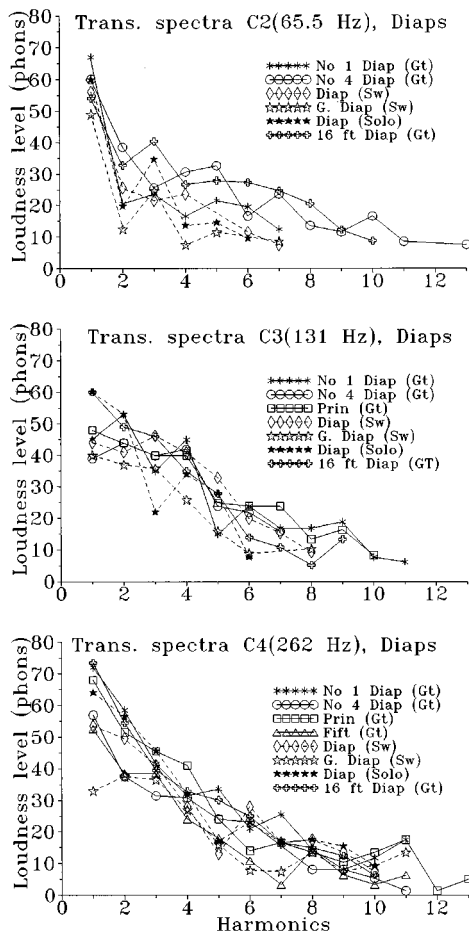
FIG. 2. The LL transformed spectra of C2, C3, and C4. The title of each panel of the figure shows the frequency (Hz) of the first harmonic (fundamental) emitted by all the diapasons shown in that panel.
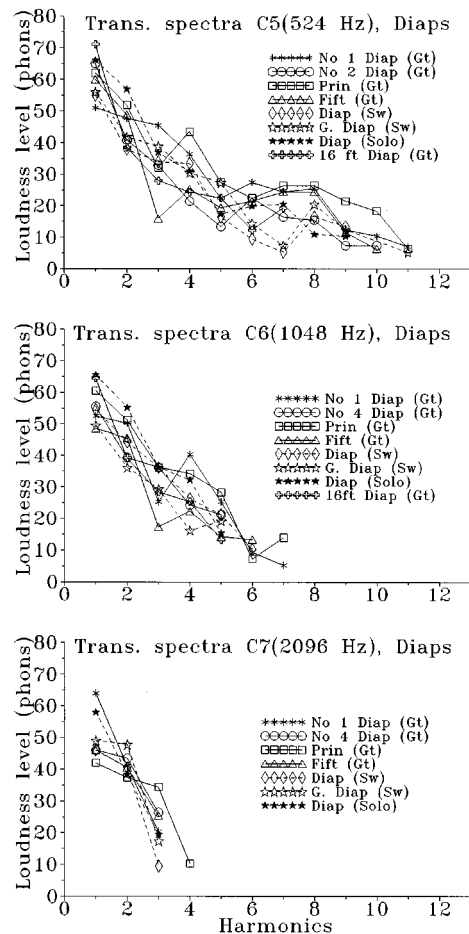

FIG. 3. The LL transformed spectra of C5, C6, and C7. The title of each panel shows the frequency (Hz) of the first harmonic emitted by all the diapasons shown in the figure.

SPL spectra varied with the frequency of the note, and mirrored, to some extent, the changes produced by the LL transformation seen in Fig. 1. Examples of the way the transformation altered the SPL data is illustrated for C2, C4, and C6 of the Great #1 Diapason in Tables I, II, and III. The ''Masked LL'' of the last column is plotted in the figures. The effect of the LL transformation on the first harmonic (fundamental) was as follows. At the bass end (C2 and to a lesser extent, at C3) the absolute level of the fundamental was reduced compared to the SPL data due to the low sensitivity of hearing at these frequencies; an example of this can be seen in Table I. At the middle octave (C4 and C5), the level of the fundamental was raised, due to the increase in LL above the SPL value of the Robinson and Dadson (1956) contours. An example of this is shown in Table II. At C6 the LL level is the same as the dB SPL since LL in phons is defined at 1 kHz; see the example in Table III. At C8 (4192 Hz, the most sensitive region of hearing), the LL of the fundamental was also raised relative to the SPL value. Only the fundamental, which was reduced by the LL transformation from 37.5 dBC, SPL to 30 phons, was present at C9. This reduction was due to the relatively low sensitivity of hearing at 8348 Hz.

The effect of the LL transformation on the higher harmonics is a function of the magnitude of F, which varies

from 0.26 at C2 to 1 and C8 and above, and the interaction between the frequency of the harmonic and the shape of the Robinson and Dadson (1956) LL contours. Examples of the way the higher harmonics were affected can be seen in Tables I, II, and III.

C. Spectral envelopes and pipe classes

Investigations of the envelopes of line spectra of organ pipes are typically limited to studies of the middle octave (C4 to B4) (Harrison and Richards, 1941; Boner, 1938; Strong and Plitnik, 1979). Fletcher *et al.* (1963), studied the
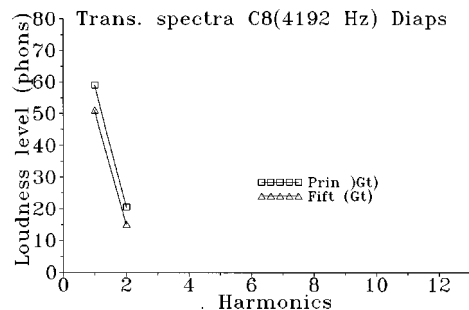

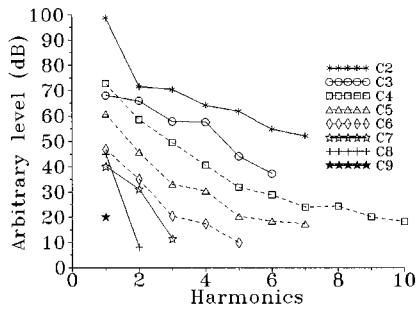FIG. 4. The LL transformed spectra of C8.

FIG. 5. The mean LL transformed spectrum of each C. The number of harmonics varied for the different pipes, so the means were calculated using only up to highest harmonic number present in the all pipes.

TABLE IV. Number of harmonics at C7 and C8 for flue and reed stops.[a]

Flue	C7	C8	Reed	C7	C8
No. 1 Diap (Gt)	3		8 ft Tromb (Gt)	4	
No. 4 Diap (Gt)	3		8 ft Tuba (Solo)	3	
Prin (Gt)	4	2	8 ft Corn (Sw)	3	
Fift (Gt)	3	2	8 ft Trump (Sw)	3	
Diap (Sw)	3		8 ft Trump (Solo)	3	
G. Diap (Sw)	3		4 ft Clar (Gt)	3	2
Diap (Solo)	3		4 ft Clarion (Sw)	3	2

[a]Flue pipes were used at C7 and C8 of the reed stops.

spectra over the range of the keyboard, but their graphs are difficult to read. Data from these studies indicated that in the middle octave, diapasons from several different organs have similar envelopes.

The present data also showed a characteristic ''diapason spectral envelope'' at C4 (Fig. 2, bottom panel). With the exception of the fundamental of the Geigen Diapason, all eight diapason spectral envelopes lie over each other, and, within the variation from harmonic to harmonic, are similar. It also appears that the envelopes of C5 and C6 are similar to C4.

In order to bring out more clearly the shape of the envelopes, the envelopes of C4, C5, and C6 were averaged (see Fig. 3–5) (Boner's, 1938, method). The average contours are similar, and show a typical ''diapason envelope'' (Boner, 1938; Churcher, 1962). The envelopes of C2, C3, C7, C8, and C9 are also plotted in Fig. 5 (solid lines). These clearly differ from the typical middle octave ''diapason envelopes'' of C4, C5, and C6, indicating that the spectral envelopes of diapasons differ over the full keyboard compass.

The fact that the spectral envelopes of C2 and C3 differ from the well-known ''diapason'' type envelopes of C4 to C6 does not mean that they are not also typical diapason envelops. They may be regarded as typical ''diapason spectral envelopes'' at C2 and C3. The envelopes of the seven diapasons at C2, for example, shown in the top panel of Fig. 2, lie over each other and represent a similarity among these seven stops. The mean spectral envelope at C2 (Fig. 5) holds for at least seven different diapasons, and represents the characteristic ''diapason envelope'' at C2 found in this organ. Only measurements in other organs will indicate the further generality of this C2 envelope.

There is a tendency to assume that a diapason sound of any pitch must have the same spectral envelope. However, mere differences in auditory sensitivity across the frequency range of, say, bottom C of a 32-ft open diapason to middle C of an 8-ft diapason, for example, make it unlikely that the shapes of the envelopes at these frequencies will be the same.

The number of harmonics declined above C5 for both diapason stops and in measurements that have been made of chorus reeds of the present organ. At C7 and C8 the number of harmonics, and the spectral envelopes, of the diapasons and the reeds were essentially the same. The number of harmonics for a sample of diapason and chorus reed stops are given in Table IV. Flue pipes (of the diapason class) were used for C7 and C8 of all the reed stops shown in the table, so it is not surprising that similar harmonic envelopes were obtained, and that the pipes sound the same.

ACKNOWLEDGMENTS

Beranek, L. L., Marshall, J. L., Cudworth, A. L., and Petersen, A. P. G. (**1951**). ''Calculation and measurement of the loudness of sounds,'' J. Acoust. Soc. Am. **23**, 261–269.

Boner, C. P. (**1938**). ''Acoustical spectra of organ pipes,'' J. Acoust. Soc. Am. **10**, 32–40.

Churcher, B. G. (**1962**). ''Calculation of loudness levels for musical sounds,'' J. Acoust. Soc. Am. **34**, 1634–1639.

Fletcher, H., Blackham, E. D., and Christensen, D. A. (**1963**). ''Quality of organ tones,'' J. Acoust. Soc. Am. **35**, 314–325.

Flint, E. M. (**1930**). *The Newberry Memorial Organ at Yale University: A study in the history of American organ building* (Yale U.P., New Haven).

Harrison, G. D., and Richards, E. (**1941**). ''Analyses of nine reeds by Dr. Boner,'' Am. Organist. **24**, 235–238.

Harrison, J. M., and Thompson-Allen, N. (**1996**). ''Loudness level survey of the Newberry Memorial organ, Yale University,'' J. Acoust. Soc. Am. **100**, 3909–3916.

Kinzey, A., and Lawn, S. (**1992**). *E. M. Skinner/Aeolian-Skinner Opus List* (The Organ Historical Society, Richmond, VA).

Pollard, H. F. (**1978**). ''Loudness of pipe organ sounds. I. Plenum combinations,'' Acustica **41**, 65–74.

Pollard, H. F. (**1988**). ''Feature analysis of musical sounds,'' Acustica **65**, 232–244.

Pollard, H. F., and Jansson, E. V. (**1982**). ''Analysis and assessment of musical starting transients,'' Acustica **51**, 249–262.

Robinson, D. W., and Dadson, R. S. (**1956**). ''A redetermination of the equal loudness relations for pure tones,'' Br. J. Appl. Phys. **7**, 166–181.

Strong, W. J., and Plitnik, G. R. (**1992**). *Music, Speech and Audio* (Soundprint, Provo, UT).

Zwicker, E., Fastl, H., and Dallmayr, C. (**1984**). ''Basic program for calculating the loudness of sounds from their 1/3-oct band spectra, according to ISO 522B,'' Acustica **55**, 63–67.